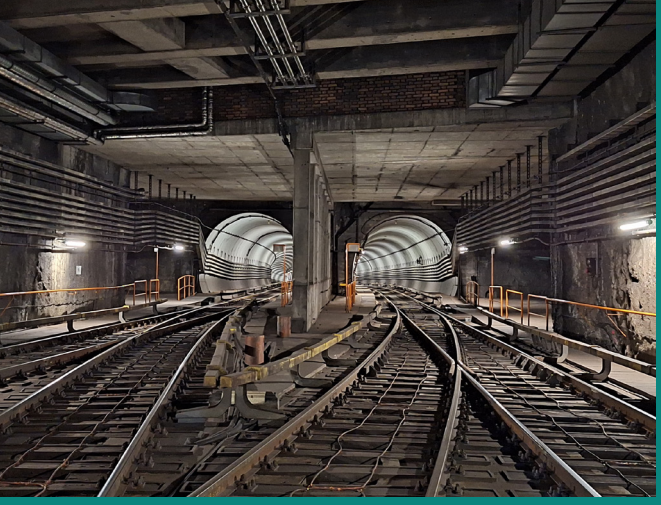






From Research to Structural Reality

Proceedings of the 16th *fib* International PhD Symposium

held in Vienna, Austria
September 9-11, 2026

Editors: A. Strauss and K. Bergmeister

fib
CEB-FIP

Proceedings of the 16th *fib* International PhD Symposium in Civil Engineering

Vienna, Austria
9 - 11 September 2026

Edited by
Alfred Strauss and Konrad Bergmeister

Proceedings of the 16th *fib* PhD Symposium in Civil Engineering, held in Vienna, Austria

Edited by:
Alfred Strauss, University of Natural Resources and Life Sciences, Vienna (BOKU University)
Konrad Bergmeister, University of Natural Resources and Life Sciences, Vienna (BOKU University)

Copyright: Fédération internationale du béton – International Federation for Structural Concrete

Every effort has been made to ensure that all published information has been reviewed by suitable qualified professionals and that all information submitted is original, has not been published previously and is not being considered for publication elsewhere. Further, the *fib* has made every effort to ensure that any and all permissions to quote from other sources has been obtained.

fib Proceedings are not able to, nor intended to, supplant individual training, responsibility or judgement of the user, or the supplier, of the information presented. Although the Scientific Committee did its best to ensure that all the information presented in this publication is accurate, no liability or responsibility of any kind, including liability for negligence, is accepted in this respect by the organization, its members, employees or agents.

All rights reserved. No part of this publication may be reproduced, modified, translated, stored in a retrieval system or transmitted in any form or by any means – electronically, mechanically, through photocopying, recording or otherwise - without prior written permission from the *fib.*

ISSN 2617-4820
ISBN 978-2-940643-32-5

Preface

The *fib International PhD Symposium* renowned held from **9–11 September 2026 in Vienna, Austria,** continues a long-standing tradition of fostering scientific excellence and international collaboration among early-career researchers in structural and civil engineering. Since its inception in 1996, the *fib* PhD Symposium has established itself as a unique international forum dedicated exclusively to doctoral candidates, providing an inspiring environment for presenting innovative research, exchanging ideas, and engaging in constructive scientific discussions.

Unlike conventional scientific conferences, the *fib* PhD Symposium places doctoral researchers at the centre of the scientific programme. All technical presentations are delivered by PhD candidates, creating an atmosphere that encourages scientific exchange, critical reflection, and interdisciplinary dialogue. Each presentation is followed by extensive discussions moderated by internationally recognised experts, allowing participants to receive valuable feedback and strengthen the scientific quality of their research.

The symposium covers a broad spectrum of topics within structural and civil engineering, including concrete structures, innovative construction technologies, structural analysis, reliability and safety assessment, durability, sustainability, life-cycle assessment, digitalisation, structural health monitoring, resilience of infrastructure, and the assessment and rehabilitation of existing structures. The multidisciplinary nature of the programme reflects the rapidly evolving challenges faced by the engineering community and highlights the importance of integrating experimental, numerical, and data-driven approaches for the development of sustainable infrastructure.

Beyond its scientific programme, the symposium provides an outstanding opportunity for international networking and collaboration. Bringing together doctoral candidates, professors, researchers, and industry representatives from around the world, the event promotes the exchange of knowledge across institutions and disciplines while fostering future scientific partnerships within the global *fib* community.

The contributions collected in these Proceedings represent the diversity and high scientific quality of current doctoral research in civil engineering. They demonstrate innovative methodologies, emerging technologies, and practical engineering solutions addressing the challenges of resilient, sustainable, and intelligent infrastructure. Collectively, these papers illustrate the significant role of young researchers in shaping

the future of structural engineering and advancing the objectives of the International Federation for Structural Concrete (*fib*).

The Organising Committee gratefully acknowledges the authors for their valuable scientific contributions, the reviewers for their dedicated efforts in ensuring the high quality of the published papers, the Scientific Committee for its guidance and expertise, and all sponsors and supporting institutions for making this symposium possible. We sincerely hope that the 16th *fib* International PhD Symposium in Vienna will inspire fruitful scientific discussions, foster lasting international collaborations, and contribute to the continued advancement of civil and structural engineering research.

Evolution of the *fib* PhD Symposium Through Its Host Institutions

A defining characteristic of the *fib* International PhD Symposium in Civil Engineering is its rotation among internationally recognised universities and research institutions. Since its establishment in 1996, the symposium has been hosted by leading academic centres across Europe, Asia, and North America, reflecting both the international character of the *fib* community and its commitment to promoting scientific excellence worldwide.

The symposium series was inaugurated in Budapest, Hungary (1996 and 1998) at the Budapest University of Technology and Economics, where the vision of creating an international platform dedicated exclusively to doctoral researchers was first realised.

The event subsequently expanded to major research universities, including the University of Applied Sciences Vienna (2000), the Technical University of Munich and the University of the Federal Armed Forces Munich (2002), Delft University of Technology (2004), ETH Zürich (2006), the University of Stuttgart (2008), the Technical University of Denmark (2010), the Karlsruhe Institute of Technology (2012), Université Laval in Québec City (2014), the University of Tokyo (2016), the Czech Technical University in Prague (2018), Université Gustave Eiffel in Paris (2020), the University of Rome Tor Vergata (2022), and again the Budapest University of Technology and Economics (2024).

The 16th *fib* International PhD Symposium, hosted by BOKU University in Vienna in 2026, marks another milestone in this distinguished series.

Returning to Vienna after more than two decades highlights the city's longstanding tradition in structural and civil engineering research while recognising BOKU University's growing international role in sustainable infrastructure, resilience, digital engineering, natural hazard research, and environmental technologies.

The geographical diversity of the host institutions demonstrates the global reach of the *fib* community and the continuous exchange of scientific knowledge across countries and continents. Each symposium contributes its own scientific profile while maintaining the common objective of supporting doctoral researchers, encouraging interdisciplinary collaboration, and promoting innovative solutions to the challenges of modern structural and civil engineering.

Over the past three decades, the *fib* PhD Symposium has evolved from a European initiative into a truly international scientific forum. Its rotating host institutions not only showcase regional research excellence but also strengthen international cooperation, foster intercultural exchange, and provide young researchers with a unique opportunity to become part of the worldwide *fib* network. This continuing tradition ensures that each edition builds upon the achievements of its predecessors while addressing the emerging challenges and opportunities facing future generations of civil and structural engineers.

Scientific Programme and Main Topics

The scientific programme of the 16th *fib* International PhD Symposium in Civil Engineering reflects the broad spectrum of contemporary research in structural and civil engineering. The selected topics address both established research areas and emerging technologies that are shaping the future of the built environment. Together, they illustrate the interdisciplinary nature of modern engineering, where advances in materials, structural mechanics, computational methods, digital technologies, and sustainability converge to address increasingly complex societal challenges.

The Symposium in Vienna is organised around the following main topics:
Material Performance
Structural Performance
Numerical Modelling and Simulation
Connections and Fastenings
Sustainable Concrete and Circular Construction
Artificial Intelligence and Digital Methods
Structural Monitoring and Assessment
Durability and Reliability
Advanced Reinforcement Systems
Additive Manufacturing in Concrete Construction
Soil–Structure Interaction

These thematic areas demonstrate that the future of construction can only be achieved through the close interaction of multiple scientific disciplines. The design of resilient, safe, sustainable, and resource-efficient infrastructure requires the integration of material science, structural engineering, computational mechanics, digitalisation, sensor technologies, data analytics, environmental assessment, and life-cycle engineering. Increasingly, artificial intelligence and digital engineering methods are

complementing traditional approaches, enabling more efficient design processes, predictive maintenance strategies, and intelligent infrastructure management.

The programme of the 16th *fib* International PhD Symposium therefore reflects not only the current state of scientific research but also the future direction of structural and civil engineering.

Acknowledgements

The successful organisation of the 16th *fib* International PhD Symposium in Civil Engineering, held in Vienna, Austria, from 9–11 September 2026, is the result of the dedication, professionalism, and collaborative spirit of a large international community of researchers, educators, institutions, and volunteers. The Organising Committee is particularly grateful for the continuous encouragement and support received from the International Federation for Structural Concrete (*fib*), especially from the *fib* President and the *fib* Presidium, whose commitment to scientific excellence and doctoral education has played a vital role in the continued success of the symposium series.
On behalf of the Organising Committee, we would like to express our sincere appreciation to all individuals and organisations whose contributions have made this symposium and these Proceedings possible.

Our foremost gratitude is extended to the members of the Scientific Committee, whose expertise, commitment, and scientific judgement ensured the outstanding quality of the symposium. Through the careful peer review of submitted manuscripts, constructive recommendations, and continuous support during the preparation of the technical programme, they have contributed significantly to maintaining the high academic standards that characterise the *fib* PhD Symposium. Their dedication reflects the core values of the International Federation for Structural Concrete (*fib*) and plays a fundamental role in supporting the next generation of researchers.

Honouring Distinguished Contributions

This symposium also provides an opportunity to recognise individuals whose vision and long-standing commitment have shaped the development of the *fib* PhD Symposium and strengthened the international *fib* community.
A special tribute is dedicated to Prof. György L. Balázs, whose vision and leadership led to the establishment of the *fib* International PhD Symposium in 1996. His pioneering initiative created a unique international platform devoted exclusively to doctoral

researchers in structural and civil engineering. For three decades, the symposium has provided generations of young scientists with opportunities to present their research, receive constructive feedback from internationally recognised experts, and establish professional networks that have often developed into long-lasting scientific collaborations. The international reputation and continued success of the *fib* PhD Symposium stand as a lasting testament to his remarkable vision and dedication.
Our sincere appreciation is equally extended to David Fernandes, whose dedicated service within the *fib* Technical Secretariat for more than fifteen years has been essential for the successful organisation and continuity of numerous *fib* scientific events. His professionalism, reliability, and commitment have significantly contributed to maintaining the high standards of the *fib* community.

We gratefully acknowledge all Session Chairpersons, whose scientific expertise, thoughtful moderation, and stimulating discussions transformed every technical session into an inspiring forum for scientific exchange. Their constructive feedback and encouragement provided invaluable guidance for the participating doctoral researchers and substantially enhanced the educational value of the symposium.

Local Organisation

The successful execution of an international scientific event of this scale would not have been possible without the remarkable efforts of the Local Organising Committee and the many colleagues from BOKU University. We would like to thank all researchers, administrative staff, technicians, laboratory personnel, student assistants, and volunteers whose enthusiasm and professionalism ensured the smooth organisation of the symposium.
From the initial planning stages through the scientific sessions, social programme, technical visits, and countless organisational details, their commitment created an inspiring and welcoming environment for participants from all over the world. Their contribution behind the scenes has been indispensable for the success of this symposium.

Above all, this symposium belongs to the PhD candidates. Their enthusiasm, scientific curiosity, creativity, and commitment to advancing knowledge are the driving force behind this event. The exceptional quality of their research demonstrates the outstanding potential of the next generation of structural and civil engineers.
Their work addresses many of today's most significant engineering challenges, including sustainability, resilience, digitalisation, structural health monitoring, advanced materials, and life-cycle engineering. We sincerely hope that the scientific discussions,

constructive feedback, and international collaborations established during the symposium will accompany them throughout their future academic and professional careers.

The Organising Committee also gratefully acknowledges all partner institutions, sponsors, exhibitors, collaborating organisations, and supporting institutions whose generous support has contributed to the success of this symposium. Their commitment demonstrates a shared vision of promoting scientific excellence, engineering education, innovation, and international cooperation.

Final Remarks

The 16th *fib* International PhD Symposium in Civil Engineering, hosted by BOKU University in Vienna, continues a tradition established three decades ago that has evolved into one of the world's foremost scientific forums dedicated exclusively to doctoral researchers in structural and civil engineering.

The Organising Committee expresses its sincere gratitude once again to the *fib* President, the *fib* Presidium, the Scientific Committee, the Session Chairpersons, the Local Organising Committee, all reviewers, sponsors, partners, and especially the PhD candidates, whose enthusiasm and scientific excellence define the spirit of this symposium.
We trust that the contributions presented in these Proceedings will inspire future scientific discoveries, strengthen international cooperation within the *fib* community, and contribute to the development of safer, more resilient, and more sustainable infrastructure for future generations.

Vienna, September 2026
The Organising Committee

Table of Contents

Material Performance

Pullout performance of glass fibre reinforced polymer bars of various diameters in a novel experimental setup **2**
Szinvai, S.; Kovács, T.; Zhang, J.

Differential shrinkage cracking in fully end-restrained fibre reinforced concrete members with conventional reinforcement **10**
Tang, P.; Amin, A.

Strain coupling effects in reinforced concrete membrane elements subjected to in-plane stresses **19**
V G, J.G.; Sengupta, A.K.

Impact of tendon failures: a comparative study on twin post-tensioned box-girder carriageways **26**
Galatà, C.; Messina, D.; De Domenico, D.; Recupero, A.; Proverbio, E.

Mechanical behaviour and coupling effect of hybrid ultra high performance fibre reinforced concrete **34**
Ergin, T.; Colombo, M.; Rampini, M.C.; di Prisco, M.

Cracking behaviour in carbon-reinforced concrete under biaxial tensile loading **40**
Schmidt, J.; Marx, S.; Curbach, M.

Towards a new generation of sustainable precast concrete: the use of limestone calcinded clay cement and reduced binder factors **48**
Rapelli, S.; Coffetti, D.; Salvi, S.; Casali, L.; Coppola, L.

The response of fully cracked solid reinforced concrete subjected to three-dimensional stress states **56**
Schulz, J.M.; Hoang, L.C.; Poulsen, P.N.; Larsen, J.

Microstructural evolution and hardened properties of plain concrete with coal mine overburden sand and ternary binder **66**
Gundala, V.; Kumar, M.V.N.S.; Tezeswi, T.P.

Compression behavior of preloaded carbon fiber-reinforced polymer-confined concrete using digital image correlation **74**
Kian, N.; Tung, N.D.

Key challenges in designing and evaluating lined rock caverns for hydrogen storage **82**
Toosi, A.S.; Della Vecchia, G.; Muciaccia, G.; Ferrara, L.

Drying shrinkage and compressive strength of mortars incorporating low-kaolinitic calcined clay and limestone powder **90**
Pornsiri, N.; Asamoto, S.; Takahashi, K., Tangtermsirikul, S., Saengsoy, W.

A model for restrained shrinkage in rebar-reinforced ultra-high performance fibre-reinforced concrete **98**
Yüksel, S.; Leutbecher, T.

Evolution of stress transfer in the compression zone of reinforced concrete beams under shear-fatigue loading **106**
Linden, C.; Hendricks, J.; Claßen, M.

Finite element analysis of cementitious layer strengthened reinforced concrete beams using different configurations **114**
Nemessányi, C.; Pluzsik, A.

Shrinkage prediction using small concrete specimens **122**
Dohnalová, L.; Havlásek, P.; Šmilauer, V.

Shrinkage and mechanical performance of cement pastes incorporating cellulose nanocrystals **130**
Al-Askary, A.S.J.; Kopecskó, K.

Assessment of corrosion effects on the residual capacity of post-tensioned concrete road bridges **138**
Mezera, A.; Holý, M.; Kněž, P.

Techniques for measuring CO_2 Sequestration in concrete: a review of key methods **146**
Rafique, M.A.; Sidhu, A.S.; Faleschini, F.; Pellegrino, C.

Effects of retrofitting interventions on risk and safety in existing bridges: a case study **155**
Mariolopoulou, E.;Rampini, M.C.; di Prisco, M.

Structural Performance

Bond behaviour of concrete members with fibre-reinforced polymer reinforcement and its influence on cracking behaviour **164**
Lengert, K.; Görtz, S.

Bond performance in horizontally and vertically cast ultra-high-performance fibre-reinforced concrete overlays **172**
Thomassen, M.; Lande, I.

Influence of planted columns on shear resistance of transfer slabs without transverse reinforcement **178**
Long, J.; Vollum, R.; Macorini, L.

Load bearing capacity of hollow core floors subjected to free edge concentrated loads – experimental study **186**
Jeziorski, M.; Derkowski, W.

Efficient implementation of the shear crack propagation theory using algorithmic differentiation **194**
Hendricks, J.; Linden, C.; Claßen, M.

Prediction and measurement of slab construction load and deflection of wall-type residential building **201**
Lee, J.; Hwang, H.; Moon, H.; Park, H.

Experimental investigation on the structural behaviour of reinforced concrete dapped-end beams with bars subjected to mechanically simulated pitting corrosion **209**
Carleschi, E.; Reggia, A.; A. Plizzari, G.

Fibre optic sensing in formed carbon reinforcement: separation of longitudinal strain and transverse pressure **217**
Gündogdu, B.; Beckmann, B.; Marx, S.

Prestressed ultra high-performance concrete-steel composite beams with continuous shear connectors in the tension zone **225**
Harsányi, P.; Randl, N.; Viet Tue, N.

Punching shear strengthening of already shear reinforced structures by use of additionally installed concrete screws **233**
Fröschl, L.; Walkner, R.; Feix, J.

Energy-based evaluation of regular reinforced concrete shear wall building **241**
Issa, M.; Al-Dali, A.

Comparative experimental study of test setups for bond testing of textile reinforcements in concrete **251**
Wachter, J.; Konzilia, J.; Feix, J.; Preinstorfer, P.

Experimental investigation of the shear capacity of reinforced concrete beams with bent-up bars **259**
Jespersen, E.; Jørgensen, H.B.; Autrup, F.

Effect of reinforcement configuration on shear capacity of aged reinforced autoclaved aerated concrete roof panels **267**
Amiri, S.S.; Goodier, C.I.; Blay, K.; Gorse, C.; Waters, K.

Effect of bond of post-tensioned reinforcement on cracking and deflection development of post-tensioned concrete beams **275**
Vízner, T.; Vítek, J.L.

Punching shear in unbonded post-tensioned steel fibre reinforced concrete slabs: the role of fibre distribution **284**
Gaddi, C.; Colombo, M.; di Prisco, M.

Numerical modelling

Development of constitutive models for masonry structures **293**
Fekete, K.; Szép, J.

Modelling of flexural hinge property of equivalent beams for pushover analysis of a building with flat slabs **301**
Akula, P.K.; Sengupta, A.K.

Numerical modelling of hydration heat and shrinkage in gravity dam **309**
Potůčková, S.; Kněž, P.; Holý, M.; Kolísko, J.

Estimation of punching shear strengths of overlay slabs based on dual potential capacity model **317**
Yoon, Y.; Kim, J.M.; Kang, J.; Jeong, H.; Kim, K.S.

Numerical modelling strategies for textile reinforced concrete **324**
Saccomanno, C.; C. Rampini, M.; Zani, G.; Romeo, F.

Numerical investigation of post-installed screw anchors for shear retrofitting of reinforced concrete beams **332**
Alnsour, R.; Muciaccia, G.

Numerical simulation of corrosion-induced rust expansion with crack influence **340**
Noxpanco, G.G.; Marzec, I.

Numerical analysis of pull-out test using a realistic ribbed rebar geometry model **348**
Burdziński, M.; Niedostatkiewicz, M.

Anisotropic nonlinear analysis of timber-concrete composite structures **356**
Gamage, T.; Abbas, A.

Conceptual study on the material-saving potential of prestressed concrete industrial floors **364**
Griniov, E.; Yolcu Sever, R.; Schlicke, D.

Large-scale tests on reinforced concrete shell elements and comparison to multilayer model analyses **372**
Kummer, Y.; Thoma, K.; Kaufmann, W.

Connections and Fastenings

Experimental investigation of uplift in a reversibly dry-jointed timber-concrete composite ceiling system **381**
Müller, R.; Sorg, C.; Ruppert, F.; Glock, C.

Evaluation and prioritisation of sealing elements in contact joints of precast lock chamber walls **389**
Schmied, J.; Lühr, S.; Stephan, C.; Pahn, M.

Dry interlocking joint for CFRP-reinforced modular component: tensile testing with computed tomography and digital image correlation **397**
Ragab, A.; Liebold, F.; Grzesiak, S.; Zierul, L.; de Sousa, C.; Pahn, M.; Beckmann, B.; Adam, V.

Structural Exoskeletons for Sustainable Rehabilitaion of European Cold War Sites **405**
Vazzoler, A.; Plizzari, G.A.; Longo, O.; Marini, A.; Labò, S.

Wood meets minerals: behaviour of timber-to-concrete joints **412**
Özdemir, A.; Mahadik, V.; Hofmann, J.

Numerical investigation of behaviour of connections between bonded laminates and concrete **420**
Burczyk, M.; Mahadik, V.; Hofmann, J.

Validation concept for numerical simulations for the design of fastenings in reinforced concrete **428**
Holder, J.; Lakhani, H.; Hofmann, J.

Connection failure of near surface steel mounts used for flexural strengthening **436**
Upcin, B.D.; Mahadik, V.; Hofmann, J.

Development of a ductile tension anchor in mid-rise timber-hybrid-buildings in context of a circular economy **444**
Gerger, A.; Fadai, A.

Effect of interface morphology on the behaviour of hsc dry joints subjected to concentric loading **452**
Hung, N.D.; Tung, N.D.

Enhanced analytical model for estimating pull-out capacity of power-actuated fasteners **460**
Yousef, A.; Spyridis, P.

3D Printing

Durability assessment of 3D printable concrete under freeze and thaw **468**
Baral, S.; Madsen, G.; Lande, I.; Vysochinskiy, D.

Experimental investigation of interlayer shear behaviour in 3D printed concrete under varying confinement conditions **477**
Giulivo, G.; Mudadu, A.; Menna, C.

Load-bearing behaviour of 3D-printed concrete beams with a rationalised reinforcement approach for automated production **485**
Fritz, F.; Huber, P.; Huber, T.

Influence of variable strand orientation on the strength of 3D-printed concrete **493**
Pfleger, M.; Radl, E.; Huber, P.; Huber, T.

Structural Monitoring

Existing tunnels monitoring, risk evaluation and rehabilitation: an overview of the italian guidelines **502**
Brentana, G.; Trabucchi, I.; Tiberti, G.; Plizzari, G.A..

Rod shape monitoring based on strain measurements from fibre optic sensors **511**
Šplíchal, B.; Grba, D.; Lehký, D.; Strauss, A.

Structural behaviour and crack evolution of full-scale RC dapped-end beams with orthogonal reinforcement **519**
van Ratingen, L.; Vanquaille, A.; Amin, N.; Verstrynge, E.; Mihaylov, B.; Vereecken, E.; Degée, H.

Monitoring crack initiation and propagation in reinforced concrete using two-dimensional distributed fiber optic sensing **527**
Wellmann, T.; Becks, H.; Claßen, M.

Monitoring of reinforced concrete beams with thermoplastic bars using digital image correlation and optical fibers **535**
Mendoza, C.R.; Ortiz, G.; Oller, E.; Murcia-Delso, J.

Thermal imaging–based automated fatigue monitoring for concrete anchorages **543**
Mellios, N.; Ahmad, M.; Rousakis, T.; Spyridis, P.

Reliability assessment of structural health monitoring using model-assisted probability of detection **551**
Jaelani, Y.; Grashorn, J.; Marsili, F.; Keßler, S.

Integrated experimental–numerical study on prestressed concrete girders for structural health monitoring **559**
Shamsaddinlou, A.; De Domenico, D.; Recupero, A.; Rezaie Oshtolagh, M.; Maugeri, N.; Longo, P.; La Mazza, D.; Longo, M.; Mancini, G.

AI and knowledge based modeling

Predicting mechanical response of discrete lattice unit cells using neural networks **568**
Raisinger, J.; Eliáš, J.

Automated characterisation of subsequently cut surfaces of reused RC-elements using optical 3D scans **576**
Pieplow, S.; Sanio, D.; Mark, P.

Automated industry foundation classes modeling of bridge superstructures via knowledge based point cloud slicing **584**
Schellen, M.; Glock, C.

Capturing reality or modeling it? Point clouds vs building information modeling in bridge monitoring **592**
Koehncke, M.; Keßler, S.

Data-driven assessment of urban tunnel alignment options based on resource demands for building strengthening measures **599**
Dengg, F.; Voit, K.

Physical and Mineralogical indicators for the water demand of recycled aggregates and concrete performance **606**
Mešković1, A.,Ali, M.A.,Deiters, M., Platz, C., Bosnjak, J., Ullrich, A., Stemmermann, P., Schack, T., Haist, M.

Experimental study on compressive failure of fibre reinforced polymer reinforced concrete beams with enhanced compression zones **614**
Somlai, B.; Schaul, P.; Solyom, S.

Durability

From potential to corrosion: the role of chloride thresholds in spatial variability of reinforcement corrosion in concrete **623**
Fache, K.; Keßler, S.; Harnisch, J.

Probabilistic modelling of spatial variability in chloride diffusion in the lattice discrete particle model **631**
Billiet, J.; Botte, W.; Wan-Wendner, R.

Mechanical performance and durability of recycled concrete precast elements in infrastructure applications **639**
Pichler, T.; Voit, K.; Bergmeister, K.

Correlation between the splitting crack opening width and the corrosion level in prestressed concrete beams **648**
Merabti, C.; Belletti, B.; Sirico, A.; Palii, O.; Ravasini, S.; Montero, J.S.

Sustainability and Circularity

Innovative arch-based precast ceiling-systems to enable non destructive dismantling and recycling **656**
Dernbach, A.; Glock, C.

Automated strengthening concept for reused concrete members: stress redistribution between metallic and non-metallic reinforcement **664**
Stöhr, B.; Hägle, M.; Hofmann, F.; Stark, A.

A state-of-the-art review of demountable constructions **673**
Schachner, K.; Fadai, A.

Effect of recycled aggregates and portland composite cements on the performance of sprayed concrete **681**
Hlavsa, Z.; Kucharczyková, B.; L. Vítek, J.

Workflow for evaluation of construction kits for element extraction for reuse from cast-in-place concrete structures **689**
Dollendorf, M.; Schürmann, A.; Thewes, M.; Vogel, A.

Economics of a sustainable design – building components as future capital **697**
Valente, M.; Fadai, A.

Stability loss of slender columns with recycled aggregate **705**
Kováčová, A.; Benko, V.

Modular reuse of RC elements: determination of load-bearing capacities and structural design exemplified on a frame structure **711**
Zielonka, H.; Sanio, D.; Mark, P.

Novel Non-Metallic Reinforcement

Textile-reinforced concrete using hemp fibres: flexural behavior and structural implications **720**
Kaliske, M.; Kuhn, S.; Schänzlin, J.; Ricker, M.

Numerical analysis of lightweight textile-reinforced concrete structures **727**
Cengu, S.; Vakaliuk, I.; Scheerer, S.

Experimental and numerical investigation of the bond behavior of FRP quadriaxial anchored fabrics **735**
Ali, H.A.; del Vecchio, C.; di Ludovico, M.; Prota, A.

Investigation of pull-out and beam-end bond behavior of CFRP reinforcing bars in low-clinker concretes **743**
Heber, P.; Sikorski, O.; Schumann, A.; Schütze, E.; Großkopff, P.; Beckmann, B.; Marx, S.

Comparative numerical analysis of the structural performance of steel and basalt-reinforced tunnel segments **751**
Kosta, A.; Mader, T.; Evangelatos, A.; Neuner, M.; Bergmeister, K.

Numerical analysis of cracking behaviour and tension stiffening in GFRP reinforced concrete lap splices **760**
Sandoval, N.; Barris, C.; Baena, M..

Investigation of basalt filaments as mineral reinforcement for filigree sustainable lightweight concrete structures **768**
Miller, O.; Blandini, L..

Structural Assesment

Preservation state assessment of steel tendons in prestressed concrete bridges via direct and indirect inspections **777**
Giglio, M.; Ranedda, L.; Proverbio, E.; Di Vita, C.P.

Calibrating the traffic load model for assessment of existing bridges using short-term weigh-in-motion measurements **785**
Milutinovic, G.; Hajdin, R..

Time-dependent structural safety assessment of corroded prestressed concrete bridges: a defect-to-mechanics framework **793**
Di Criscio, F.; Pedone, L.; Pampanin, S.

Comparative study of empirical and analytical methods for the determination of masonry compressive strength **801**
Al Jabi, M.; Marx, S.

Comparative assessment of beam-to-column connection modelling in multi-storey precast concrete frame structures **809**
Baltrocchi, R.M.A.; Martinelli, P.

Comparative assessment of residual prestress in prestressed concrete bridges through long-term deflection **817**
Zarrella, G.; Losanno, D.; Strauss, A.

Repair strategies for marine reinforced concrete structures: mechanisms, materials and nature-based solutions **825**
Ashokkumar, A.N.; Bastidas-Arteaga, E.; Spyridis, P.

Post-installed basalt fibre reinforced polymer bars **833**
Kendlbacher, M.; Bergmeister, K.

Sustainable Concrete

Comparison of two different activation methods for concrete fines: thermal and carbonation activation **842**
Denu, M.; Höffgen, J. P.; Patel, R. A.; Dehn, F.

Direct shear behaviour of concrete incorporating EAF slag aggregates **850**
Clerici, L.; Piemonti, A.; Plizzari, G.; Conforti, A.

The effect of waste building materials as cement replacement on the properties of sustainable mortars **857**
Filipović, M.; Baloević, G.

Water absorption of crushed sand: measurement and impact on mortars performances **865**
Boudiaf, M.; Amiri, O.; Roziere, E.; Claverie, J.; Rellier, V.; Cussigh, F.; Lafon, R.

Drying shrinkage of blast-furnace slag cement systems under heat-curing: sulfate optimization and cement type effects **871**
Habirun, A.N.; Asamoto, S.; Luan, Y.; Takahashi, K.

Influence of the strand spacing on the material strength of 3D-printed concrete **879**
Radl, E.; Pfleger, M.; Huber, P.; Huber, T.

Mitigating shrinkage effects in thin layers of high performance fiber reinforced concrete for jacketing bridge piers **887**
Beltracchi, I.; Reggia, A.; Sirtoli, D.; Lura, P.; Metelli, G.; Plizzari, G.A.

Experimental investigation of novel precast tunnel segments with hybrid steel–basalt fiber reinforcement **895**
Macha, M.; Evangelatos, A.; Bergmeister, K.; Galler, R.

Soil-Structure interaction

Workflow for consistent soil-structure interaction regarding structural and geotechnical design **904**
Wallner, C.; Tschuchnigg, F.; Schlicke, D.

Concrete edge failure of bonded anchors under shear in recycled aggregate concrete **912**
Mikulić, Z.; Bergmeister, K.

Kinematic measurements of concrete-to-concrete interfaces in full-scale continuous precast girders **920**
Borges, E.A.; Hendriks, M.; Yang, Y.

Reliability Concepts

Reliability quantification of degrading concrete discontinuity regions via strut-and-tie modelling **929**
Luyten, K.; Botte, W.; Caspeele, R.

Comparison between deterministic and probabilistic ground motion estimation methods for performance-based seismic design **939**
Moon, H.; Kim, J.-H.; Park, H.-G.

Reliability of GFRP embedded reinforcement at extreme temperatures **947**
Ježek, J.; Girgle, F.; Vašátko, D.; Čairović, Đ.; Zlámal, M.; Štěpánek, P.

Reliability assessment of conventional versus eco-concrete under overstrength condition **955**
Faghfouri, S.; Strauss, A.

Probabilistic shear strength modelling based on nonlinear fracture mechanics **963**
Večeře, J.; Novák, D.; Lehký, D.; Szczech, D.

Quantification of spatial variability of concrete parameters for the reliability assessment of reused concrete elements **971**
Al-Shboul, O.; Ahmed, R.; Schoen, S.; Schiano, L.; Ringeloth, D.; Fina, M.; Bijeljic, J.; Neu, G. E.; Niederleithinger, E.; Freitag, S.; Curoșu, I.

Safety formats for nonlinear finite element analysis of holistic 3D models **979**
Ober, J.; Schlicke, D.

Numerical modelling and experimental validation of fibre orientation in ultra-high performance concrete flow **987**
Poitevin, L.; Bauer, L.; Massicotte, B.

Organized by:





Patronages:











Sponsors (Gold):









Sponsors (Silver):

















Exhibitors:











Supporter:





Scientific Committee

Alfred Strauss
University of Natural Resources and Life Sciences (BOKU), Vienna, Austria

Konrad Bergmeister
University of Natural Resources and Life Sciences (BOKU), Vienna, Austria

David Fernández-Ordóñez
fib, Lausanne, Switzerland

Jan Hofmann
University Stuttgart, Institue of Construction Materials, Germany

Sylvia Keßler
Helmut-Schmidt-University / University of the Federal Armed Forces Hamburg, Germany

Wit Derkowski
Cracow University of Technology, Poland

Said KENAI
University of Blida 1, Algeria

György L. Balázs
Budapest University of Technology and Economics, Hungary

Joaquim Barros
University of Minho, Portugal

Beatrice Belletti
University of Parma, Italy

Ruben Paul Borg
University of Malta, Malta

Alberto De la Fuente
Universitat Politecnica de Catalunya, Spain

János Lógó
Budapest University of Technology and Economics, Hungary

Giuseppe Mancini
Politecnico di Torino, Italy

Ildiko Merta
Vienna University of Technology, Austria

Cristina Barris Pena
University of Girona, Spain

Jürgen Feix
University of Innsbruck, Austria

Marko Marinković
University of Belgrade, Serbia

Ravindra Gettu
Indian Institute Of Technology Madras, India

Maurizio Guadagnini
University of Sheffield, United Kingdom

Terje Kanstad
Norwegien University of Science and Technology, Norway

Roman Wan-Wender
Magnel Laboratory Of Concrete Structures, Belgium

Patrick Huber
TU Wien, Austria

Martin Claßen
RWTH Aachen, Germany

Bruno Massicotte
Ecole Polytechnique Montreal, Canada

Alessandro Palermo
University of California, San Diego, United States of America

Giovanni Plizzari
University of Brescia, Italy

Fausto Minelli
University of Brescia, Italy

Johan Silfwerbrand
KTH Royal Inst. Of Technology, Sweden

Francesca Ceroni
Parthenope University of Naples, Italy

Sándor Ádány
Budapest University of Technology and Economics, Hungary

Muhammad Imran Rafiq
University of Brighton, United Kingdom

Ivan Markovic
University of Applied Sciences of Eastern Switzerland, Switzerland

Simone Spagnuolo
University of Rome (La tor Vergata), Italy

Robert Vollum
Imperial College London, United Kingdom

Sherif Yehia
American University of Sharjah, United Arab Emirates

Frank Dehn
Karlsruhe Institute of Technology (KIT) – IMB/MPA/CMM, Germany

Akio Kasuga
The University of Tokyo, Japan

Sándor Sólyom
Budapest University of Technology and Economics, Hungary

Billy Boshoff
University of Pretoria, South Africa

Matteo Colombo
Politecnico di Milano, Italy

Abdulkader El-Mir
University of Balamand, Lebanon

Viktor Halvička
Budapest University of Technology and Economics, Hungary

Eva Ollers Ibars
Universtat Politecnica de Catalunya, Spain

Ivan Ignjatović
University of Belgrade, Serbia

Balázs Kövesdi
Budapest University of Technology and Economics, Hungary

Simone Labò
University of Bergamo, Italy

Balázs Nagy
Budapest University of Technology and Economics, Hungary

Salem G. Nehme
Budapest University of Technology and Economics, Hungary

Róbert Németh
Budapest University of Technology and Economics, Hungary

Stijn Matthys
Ghent University, Belgium

Kálmán Koris
Budapest University of Technology and Economics, Hungary

Alexander Stark
Karlsruher Institut für Technologie, Germany

Yahya Kurama
University of Notre Dame, France

Christian Glock
RPTU Kaiserslautern-Landau – Fachgebiet Massivbau und Baukonstruktion, Germany

Tobias Huber
TU Wien, Austria

Duc Tung Nguyen
Helmut-Schmidt-Univ./Univ. der Bundeswehr Hamburg, Germany

François Toutlemonde
University of Gustave Eiffel, France

Danièle Waldmann-Diederich
TU Darmstadt, Germany

Ali Amin
The University of Sydney, Australia

Joseé Bastien
University of Laval, Canada

Eleni Chatzi
ETH Zürich, Switzerland

Numa Joy Bertola
University of Luxembourg, Luxembourg

Theodoros Rousakis
Democritus University of Thrace, Greece

Roberto Torrent
Quali-TI-Mat Ltd., Switzerland

Fabio Biondini
Politecnico di Milano, Italy

Jan Bień
Wrocław University of Science and Technology, Poland

Dieter Pichler
FCP Fritsch, Chiari & Partner ZT GmbH, Austria

Franz Tschuchnigg
Graz University of Technology, Austria

Maria Rosaria Pecce
University of Napoli (Federico II), Italy

Ágoston Restás
Ludovika University of Public Service, Hungary

Samindi Samarakoon
University of Stavanger, Norway

Dirk Schlicke
University of Graz, Austria

Jongsung Sim
Hanyandg University, South Korea

Luc Taerwe
Ghent University, Belgium

Maurizio Taliano
Politecnico di Torino, Italy

Georgia Thermou
University of Nottingham, United Kingdom

Jean-Michel Torrenti
University of Gustave Eiffel, France

Thanasis Triantafillou
University of Patras, Greece

Lukas Vrablik
Czech Technical University Prague, Czech Republic

Giulio Zani
Politecnico di Milano, Italy

Hans Rudolf Ganz
VSL, Switzerland

Max Hendriks
University of Technology Delft, The Netherlands

Alper Ilki
Istanbul University of Technology, Turkey

Tamás Kovács
Budapest University of Technology and Economics, Hungary

Ingrid Lande
University of Adger, Norway

Tamás Nagy-György
Technical University of Timisoara, Romania

Philipp Preinstorfer
TU Wien, Austria

Flora Faleschini
University of Padua, Italy

Jan L. Vítek
Metrostav a.s, Czech Republic

Tomislav Kišiček
University of Zagreb, Croatia

Ivana Štimac Grandić
University of Rijeka, Croatia

Henrik Brøner Jørgensen
University of Southern Denmark, Denmark

Daniele Losanno
Università di Napoli Federico II, Italy

Christoph Adam
University of Innsbruck, Austria

David Lehký
Brno University of Technology, Czech Republic

Rade Hajdin
University of Belgrade, Serbia

Carlo Pellegrino
University of Padova, Italy

Dan Frangopol
Lehigh University, USA

Federico M. Mazzolani
University of Naples “Federico II”, Italy

Irina Stipanovic
University of Twente, Netherlands

Stefano Pampanin
University La Sapienza Rome, Italy

Giovanni Fabbrocino
University of Molise, Italy

Walter Potucek
FH Campus Wien, Austria

Philipp Holzer
Vasko + Partner Ingenieure ZT, Austria

Bruno Briseghella
Fuzhou University, China

Hyunjin Ju
Hankyong National University, Korea

Eduardo Júlio
University of Lisbon, Portugal

Alberto Meda
University of Rome Tor Vergata, Italy

Marco Carlo Rampini
Politecnico di Milano, Italy

Walter Kaufmann
ETH Zürich, Switzerland

Arpad Čeh
University of Novi Sad, Serbia

János Szép
Széchenyi István University, Hungary

Diego Alejandro Talledo
University IUAV of Venice, Italy

John P. Forth
University of Leeds, United Kingdom

László Csetényi
University of Dundee, United Kingdom

Ákos Török
Budapest University of Technology and Economics, Hungary

Marta del Zoppo
University of Napoli (Federico II), Italy

Farid Benboudjema
ENS Paris-Saclay, France

Torsten Leutbecher
Univ. Siegen – Lehrstuhl für Massivbau, Germany

Panagiotis Spyridis
University of Rostock, Germany

Szabolcs Rózsa
Budapest University of Technology and Economics, Hungary

Johann Kollegger
Vienna University of Technology, Austria

Daman K. Panesar
University of Toronto, Canada

István Sajtos
Budapest University of Technology and Economics, Hungary

Michael Fardis
University of Patras, Greece

Marijana Serdar
University of Zagreb, Croatia

Gabriele Bertagnoli
Politecnico di Torino, Italy

Luciana Restuccia
Politecnico di Torino, Italy

Joan Casas
Technical University of Catalonia, Spain

Filippo Ubertini
University of Perugia, Italy

Robert Kowalski
Warsaw University of Technology, Poland

Alois Vorwagner
AIT – Austrian Institute of Technology, Austria

Christian Honeger
ASFINAG BMG, Austria

Giuseppe Andrea Ferro
Politecnico di Torino, Italy

Alireza Fadai
Vienna University of Technology (TU Wien), Austria

Antonio Godoy
Antonio R. Godoy Consulting LLC, Austria

Sangyoung Han
Dong-A University (Busan), Korea

Ivana Carević
University of Zagreb, Croatia

Andrea Dall'Asta
University of Camerino, Italy

Walter Salvatore
University of Pisa, Italy

Wojciech Lorenc
Wrocław University of Science and Technology, Poland

Yiannis Xenidis
Aristotle University of Thessaloniki, Greece

Miroslav Vořechovský
Brno University of Technology, Czech Republic

Vanja Samec
Austria

Jerzy Bobiński
Gdańsk University of Technology, Poland

Avraham Dacygier
Technion – Israel Institute of Technology, Israel

Steffen Marx
Institute of Concrete Structures, Technical **University of Dresden, Germany**

Peter Mark
Ruhr-Universität Bochum – Lehrstuhl für Massivbau, Germany

Hugo Corres
University of Madrid, Spain

Manfred Curbach
Technical University of Dresden, Germany

Agnieszka Bigaj-van Vliet
TNO Delft, The Netherlands

Katalin Kopecskó
Budapest University of Technology and Economics, Hungary

Syed Yasir Alam
Ecole Centrale de Nantes, France

Marco di Prisco
Politecnico di Milano, Italy

Antonio Mari Bernat
Universtat Politecnica de Catalunya, Spain

Thomas Braml
Univ. Bundeswehr München – Prof. für Massivbau, Germany

Hans Rudolf Beushausen
University of Cape Town, South Africa

Silke Scheerer
Institute of Concrete Structures, Technical University of Dresden, Germany

Tor-Ole Olsen
Norway

Viktor Gribniak
Vilnius Gediminas Techn University, Lithuania

Maciej Kożuch
Wrocław University of Science and Technology, Poland

Peter Paulik
University of Bratislava, Slovakia

Elżbieta Szmigiera
Warsaw University of Technology, Poland

Norbert Randl
Carinthia University of Applied Sciences, Austria

Shingo Asamoto
Saitama University – Structural Material Lab, Japan

Drahomír Novák
Brno University of Technology, Czech Republic

Markus Vill
Fachhochschule Campus Wien, Vienna, Austria

Peter Gappmaier
University of Natural Resources and Life Sciences (BOKU), Vienna, Austria

Eva Eichinger-Vill
Vill Ziviltechniker GmbH, Vienna, Austria

Lucio Blandini
Univ. Stuttgart – Inst. für Leichtbau, Entwerfen und Konstruieren, Germany

György Farkas
Budapest University of Technology and Economics, Hungary

Material Performance

Pullout performance of glass fibre reinforced polymer bars of various diameters in a novel experimental setup

Szabolcs Szinvai[1], Tamás Kovács[2], Jiao-Long Zhang[3,4,5,6]

[1,2]Department of Structural Engineering, Faculty of Civil Engineering, Budapest University of Technology and Economics, Műegyetem rkp. 3. H-1111 Budapest, Hungary.

[3]College of Civil Engineering, Tongji University, Shanghai, China

[4]State Key Laboratory of Disaster Reduction in Civil Engineering, Tongji University, Shanghai, China

[5]Belgium-China Joint Laboratory for Industrialized Construction, Tongji University, Shanghai, China

[6]Shanghai Tongji Green Building Prefabrication Construction Engineering Technology Co., Ltd, Shanghai, China

Summary

As durability becomes increasingly critical for concrete structures, glass fibre reinforced polymer (GFRP) bars are gaining popularity as a viable alternative to steel bars. Pullout tests are rarely performed on large diameter bars, even though they are also used in practice. To gain a better understanding of diameter-dependent bond properties, pullout tests were performed on GFRP bars with six nominal diameters: 8, 12, 16, 20, 25, and 32 mm. A novel test setup was applied that can be performed using mobile equipment and requires only electricity. The tested bar product is ribbed, and the relative rib area increases with diameter, then remain the same for 20-, 25-, and 32-mm diameter bars. It was found that the strength of ribs limits bond strength. Lower relative rib areas are needed to optimize the shear strength of the GFRP ribs compared to the shear strength of the concrete keys. As a result, the bond strength of the 25 and 32 mm diameter bars was greatly reduced compared to the smaller diameter bars.

1 INTRODUCTION

Glass fibre reinforced polymer (GFRP) bars have been used as a corrosion-resistant alternative to steel for decades [1]. Concrete structures reinforced with GFRP bars require minimal maintenance compared to traditional steel-reinforced ones, making them more durable and sustainable. However, uncertainties in their bond behaviour embedded inside concrete remain one of the critical challenges limiting widespread adoption.

GFRP products vary significantly, with surface treatments differing from one product to another, resulting in highly variable bond properties [2]. The uncertainty in bond behaviour and performance makes the design of GFRP reinforced concrete structures challenging, as bond affects anchorage length, lap splice length, concrete cover requirements, and the design of bent bars and hooks, parameters that govern structural safety and serviceability performance [3].

The interaction between GFRP bars and concrete is fundamentally different from that of steel bars. The force transfer mechanisms of GFRP bars are more complex and not yet fully represented in design provisions [4]. This complexity manifests in two critical consequences: the governing failure modes are more varied than for steel reinforcement, and average-stress formulations commonly adopted in design codes may give inaccurate crack-width predictions.

Bond failure for steel reinforcement can occur through pullout (shear failure of the concrete keys) or by brittle splitting. However, in the case of GFRP bars, owing to the weaker surface of the bar, pullout failure can happen either by the shear failure of the concrete keys or by the peeling off of the surface of the GFRP bar [5]- [6]. Due to the soft matrix, the surface characteristics of GFRP bars needs optimization, which can mean vast differences between the surface geometry of small and large nominal diameter bars.

Analytical bond stress-slip models are the basis of bond-related design provisions, such as anchorage length or crack width formulas. Early models, developed primarily for steel, were extended to GFRP with varying degrees of success [7]- [8]. For traditional steel bars, the Bertero-Popov-Eligehausen (BPE) model (1983) [9] is prominent and used in the *fib* Model Code (2020) [10]. For GFRP bars, no consensus model exists due to varied surface treatments. The Malvar Model [7] was first proposed in 1994 as a model for FRP bars. Later, the BPE [9] and modified BPE (mBPE) models [8] were tested for GFRP bars. The mBPE model features an exponential ascending branch, a linear decreasing branch, and a constant residual, unlike the BPE model, which has a plateau.

2 PROBLEM STATEMENT AND APPROACH

The composite nature of GFRP bars differs fundamentally from that of traditional homogenous construction materials, such as steel. One key difference is their bond behaviour. The surface treatments of GFRP bars vary significantly and can include helical wrapping, sand coating, ribbing, or a combination of these. Since GFRP bars are unidirectionally reinforced, surface undulations, such as ribs formed, are usually significantly weaker compared to steel ribs. The weaker ribs alter the optimal rib geometry, leading to different bond behaviour and performance, which can change with the diameter.

To assess the bond behaviour of GFRP bars, pullout tests were performed in the laboratory. Six different nominal diameters of ribbed GFRP bars (8, 12, 16, 20, 25, and 32 mm) were tested, totalling 36 specimens. Displacements were measured on both the loaded and unloaded ends of each concrete block by LVDTs. Later bond stress-slip curves were determined for both loaded and unloaded end slips for every diameter and a version of the BPE model was used to create analytical bond stress-slip curves. Finally, conclusions were formed comparing the behaviour of different diameter bars based on the relative rib areas.

3 LABORATORY EXPERIMENTS

Pullout tests of a GFRP bar product were performed for all commercially available nominal diameters: 8, 12, 16, 20, 25, and 32 mm. The ACI 440.3R-12 [11] B3 test gives recommendations about the pullout testing of FRP bars. It recommends at least five successful tests of each bar type. In the experimental program, six specimens were tested for each bar diameter, totalling 36 specimens. A novel test setup was used, which resembles the B5 test setup for bent strength testing as outlined in ACI 440.3R-12 [11]. In the original setup, the two legs of a stirrup connect two separate concrete blocks, and the loading happens by a hydraulic jack placed in the middle. In the modified setup, one straight bar connects two separate concrete blocks, and two hydraulic jacks are used for loading placed symmetrically. The main advantage of the setup is its mobility. The tests can be performed anywhere, without restrictions, and stored when not in use, which was necessary due to the limited laboratory space.

3.1 Specimen preparation

The pullout specimens were made with the help of the industrial partner (Záév-HardConcrete Ltd.). Special formwork was made of steel to cast the specimens. The specimen dimensions are shown in Fig. 1. The aim was to cast the specimens of the same diameter simultaneously.

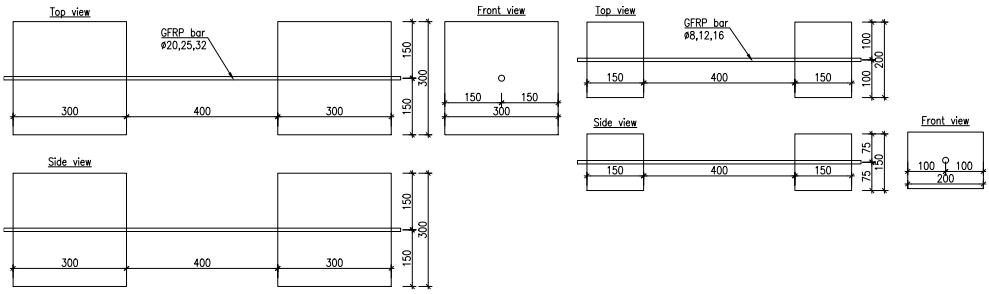


Fig. 1 Dimensions of the pullout specimens: big pullout specimen (left) and small pullout specimen (right)

The same formworks were used for multiple bar diameters. The small pullout specimen was cast with 8-, 12-, and 16-mm bars, and the big pullout specimen was cast with 20-, 25-, and 32-mm bars. The holes in the formworks were made to suit the largest diameter and were fitted using a cork plug. The specimens were transported at one week of age, together with the formwork, to the laboratory. At the laboratory, the formworks were removed, and the specimens were placed on wooden pallets. Five test cubes were placed next to the specimens to test the concrete strength. The front plates on the loaded sides were not removed; they acted together with the loading plate to distribute the loads of the hydraulic jacks. After 4 weeks of casting, the specimens were tested. The testing of one set of specimens took 2 to 3 days. They were tested between 28 and 33 days of age.

The geometry of the specimens is summarised in Table 1. The relative rib area (f_r) is calculated according to Eq. (1), where A_r is the projected rib area, d_b is the nominal diameter, and s_{rib} is the rib spacing. A_b is the bonded area of the given bar.

$$f_r = \frac{A_r}{d_b \pi s_{rib}} \tag{1}$$

Table 1 Summary of the geometrical parameters for the tested specimens

Specimen designation	d_b	l_b	l_{ub}	A_b	Rib height	Rib width	Rib spacing	f_r
	[mm]	[mm]	[mm]	[mm^2]	[mm]	[mm]	[mm]	[-]
2.1A_i	8	40	110	1005	0.5	5.0	9.0	0.052
2.2A_i	12	60	90	2262	0.7	5.0	9.0	0.073
2.3A_i	16	80	70	4021	0.9	5.0	9.0	0.094
3.1A_i	20	100	200	6283	1.0	5.0	9.0	0.106
3.2A_i	25	125	175	9817	0.9	5.0	9.0	0.099
3.3A_i	32	160	140	16085	1.1	5.0	9.0	0.108

The relative rib area was also calculated for typical commercially available B500B steel bars. As visualized in Fig. 2, the relative rib area increases with the increase of the diameter in case of GFRP bars and decreases in case of B500B bars. For the tested GFRP bars, the rib height changes with the diameter; however, all other parameters remain constant. For B500B bars, rib height, rib width, and rib spacing all increase with the diameter. For larger bars, relative rib area is significantly higher for GFRP bars compared to B500B bars.

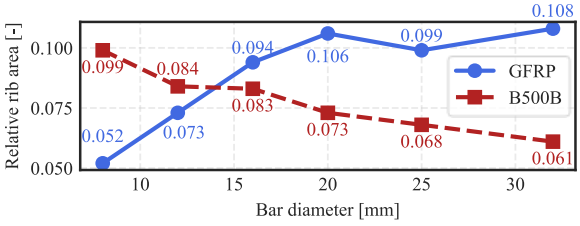


Fig. 2 Relative rib areas of the tested bars

3.2 Test procedure

Fig. 3 illustrates the test setups for the small pullout tests. In Fig. 4, the test setup in the laboratory is shown in action. A mobile testing platform was created using a wooden pallet. During the experiments, two hydraulic jacks provided the loading and were controlled by separate pumps. The simultaneous pumping of the two hydraulic jacks provided the pullout force. The aim was to control the two jacks

separately to keep the two concrete blocks parallel to each other. Thus, the experiment was displacement controlled. The displacements u_1 and u_2, measured between the concrete blocks, were continuously monitored and kept under control. The difference (u_1-u_2) was kept below 0.3 mm in all cases for the ascending branch. For the descending branch, as slippage often occurred suddenly, this difference sometimes reached 0.5 to 1.0 mm. Since larger slips occur at the post-critical stage, this was considered acceptable.

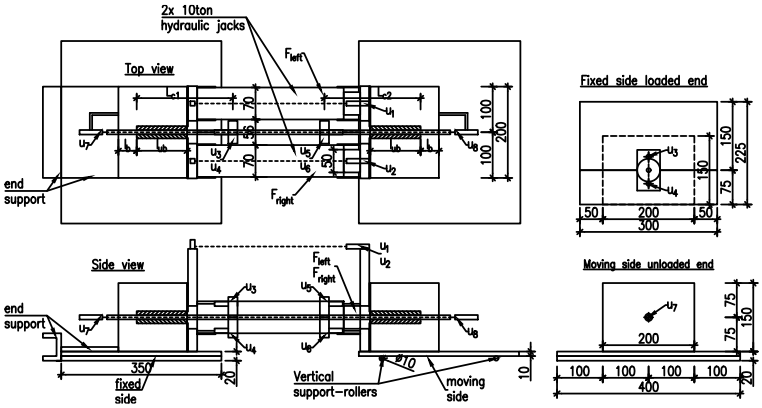


Fig. 3 Overview of the small pullout test setup

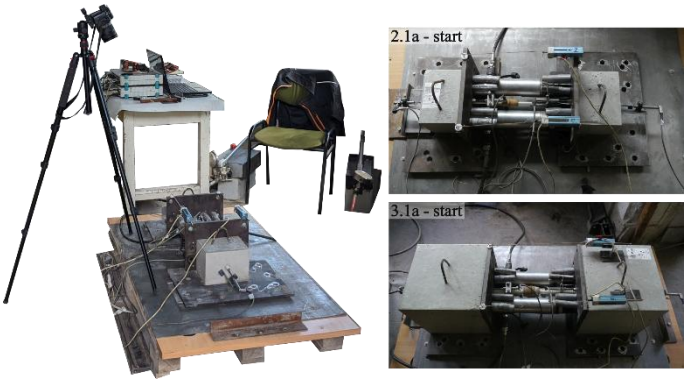


Fig 4 Test setup in the laboratory (left), small pullout specimen (top right), and big pullout specimen (bottom right)

3.3 Evaluation procedure

The test results were gained using the evaluation procedure summarised in this section. The bonded area is calculated according to Eq. (2), where d_b is the nominal diameter and l_b is the bonded length.

$$A_b = \pi d_b l_b \tag{2}$$

The average bond stress is calculated by dividing the pullout force (F, the sum of the forces of the two hydraulic jacks) by the bonded area, according to Eq. (3).

$$\tau = \frac{F}{A_b} \tag{3}$$

The elastic elongations of the bar on the fixed and on the moving side (S_{c1} and S_{c2}, respectively) were calculated according to Eq. (4), where L_{c1} and L_{c2} are the length between the end of the bonded length and the attachment of the measuring devices on the fixed side and on the moving side, respectively.

$$S_{c1,2} = \frac{F L_{c1,2}}{E_f A_f} \tag{4}$$

The unloaded end slip on the fixed side (s_{ul1}) was equal to u_7, and on the moving side (s_{ul2}) was equal to u_8, the displacements measured between the unloaded concrete end and the end of the

embedded bar. The loaded end slip on the fixed side (s_{l1}) and on the moving side (s_{l2}) is given by Eq. (5), where u_3, u_4, u_5, and u_6 were measured between the loading plate and the tested bar. Displacements u_3 and u_4 were measured on the fixed side, while u_5 and u_6 were measured on the moving side.

$$s_{l1,2} = \frac{u_{3,5} + u_{4,6}}{2} - S_{c1,2} \quad (5)$$

4 TEST RESULTS

4.1 Summary of results

The average concrete compressive strength was 67.1, 74.9, 72.1, 66.8, 69.0 and 70.4 MPa for specimens with nominal diameters from 8-32 mm respectively. Five cubes were tested for each set of specimens. The concrete grade, therefore, was approximately C50/60 for all tested specimens.

The pullout test results are summarized in Table 2. The average values, standard deviations (STD), and coefficients of variation (CoV) are provided for the bond strength (τ_b) and both ultimate loaded ($s_{l,u}$) and unloaded slip ($s_{ul,u}$) values upon reaching the bond strength. Specimen 2.3A_6 and 3.3A_2 failed by splitting, while all other specimens failed by pullout.

Table 2 Summary of the average test results for all specimens: ultimate values

Specimen designation	d_b	$\tau_{b,avg}$	$\tau_{b,std}$	$\tau_{b,cov}$	$s_{l,u,avg}$	$s_{l,u,std}$	$s_{ul,u,avg}$	$s_{ul,u,std}$
	[mm]	[MPa]	[MPa]	[-]	[mm]	[mm]	[mm]	[mm]
2.1A	8	21.7	1.1	0.95	0.73	0.14	0.51	0.14
2.2A	12	21.5	1.8	0.92	0.72	0.06	0.39	0.05
2.3A	16	21.4	1.3	0.94	0.75	0.04	0.26	0.03
3.1A	20	21.1	0.5	0.98	0.75	0.10	0.22	0.08
3.2A	25	18.7	0.5	0.97	0.74	0.09	0.14	0.04
3.3A	32	17.2	0.7	0.96	0.77	0.11	0.10	0.05

Fig. 5 presents the measured average bond strength values for each tested bar diameter and material. Using Eq. (6) from the *fib* Model Code 2020 [10], with k=2.5 for 8-20 mm diameter bars, k=2.25 for 25 mm diameter bars, and k=2.00 for 32 mm diameter bars, the results show a good match with the measured bond strength. For the 12- and 16-mm diameter bars, the ratio of the concrete cover to the bar diameter was the same as with the 25- and 32-mm diameter bars, respectively. Therefore, the lower bond strength is not due to confinement issues, but due to the relative rib area not following the linear trend visualized in Fig. 2, for 25-and 32 mm diameter bars. The lower relative rib area can be justified to decrease the tendency of splitting failure.

$$\tau_b = k f_{cm}^{0.5} \quad (6)$$

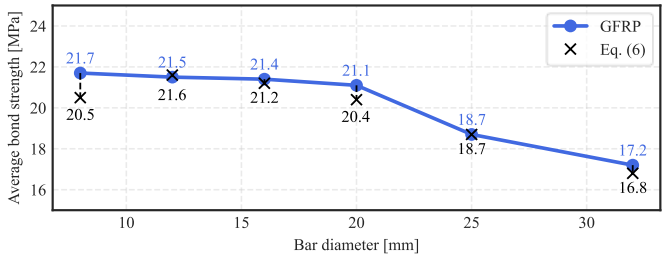


Fig. 5 Bond stress versus diameter

4.2 Failure mode

Fig. 6 shows the bars after pullout failure. The pullout failure occurred through the shearing off of the concrete keys for all specimen types, except for the 8 mm GFRP specimens (2.1A). For the 8 mm GFRP specimens, pullout failure occurred through the combination of the shearing off of the concrete keys and the peeling off of the ribs of the bar. Partially sheared off ribs are apparent. For the other diameter GFRP bars, damage to the ribs is also visible; however, only parallel grooves parallel to the axis of the bar, most likely from the aggregates. It is apparent, that the softer surface of the GFRP bar compared to traditional steel bars can result in new failure types, due to damage to the bar's surface. Furthermore, even if the ribs of the GFRP bar are not sheared off completely, damage due to particles can reduce bond stiffness.

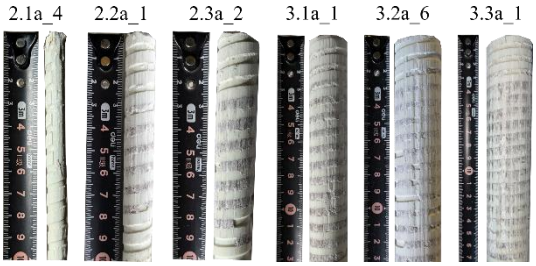


Fig. 6 Typical failed pullout specimens: removed bars

4.3 Bond stress – slip curves

The bond stress- unloaded end slip and bond stress- loaded end slip curves for all specimens are shown in Fig. 7. Only the most important ascending portions of the curves are shown (the first 1.0 mm slip in most cases). The figures also display analytical curves according to the modified BPE model [3] for all specimen types. The bond strength was calculated according to Eq. (6).

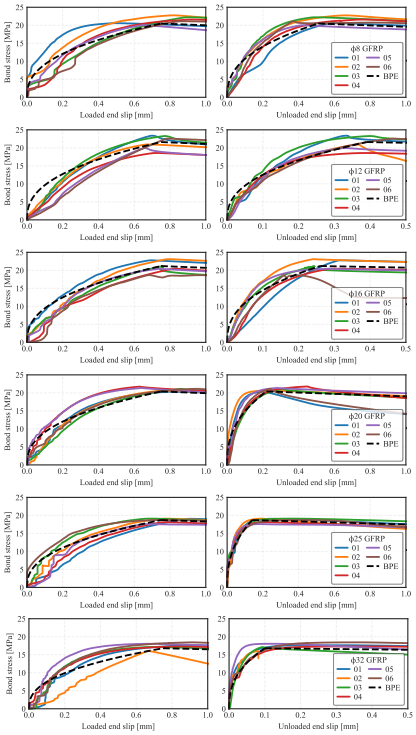


Fig. 7 Bond stress-slip diagrams

The ascending portion of the BPE curves is formulated according to Eq. (7), where α = 0.4 was applied. For the ultimate slip values, the average measured values are used for the unloaded end, and 0.75 mm is applied for the loaded end in all cases.

$$\tau(s) = \tau_{\mathrm{b}} \left(\frac{s}{s_{\mathrm{u}}}\right)^{\alpha} \quad s \leq s_u \tag{7}$$

The BPE curves plotted show good agreement with the measured values regarding the bond stress-unloaded end slip curves. However, the bond stress-loaded end slip BPE curves reach the given maximum values with a different slope. The different slope is problematic, since the most significant discrepancy is at lower slip values, which are used for serviceability limit states. For crack width limits of 0.4-0.7 mm, loaded end slip values of 0.2-0.35 mm correspond. Since the design of GFRP reinforced concrete elements is primarily governed by serviceability criteria, specifically crack width limits, the bond performance at the lower loaded end-slip region will directly influence the design procedure; therefore, it should be investigated with great care and the BPE can not be used for calculating crack widths.

5 CONCLUSIONS

The pullout testing of six different diameter ribbed GFRP bars (8, 12, 16, 20, 25, and 32 mm) was performed in a concrete grade of approximately C50/60. Six GFRP bars were tested per diameter, totalling 36 specimens. The following conclusions can be drawn.

1. Due to the softer surface of GFRP bars compared to B500B bars, higher relative rib area is needed for larger diameter bars to achieve comparable bond performance.
2. Since high relative rib area may cause splitting failure, the relative rib area of the tested GFRP bar product for 25 and 32 mm bars was the same as for the 20 mm bar, instead of increasing linearly as between the 8 and 20 mm diameter bars, causing a significant decrease in bond strength.
3. The fib Model Code 2020 [10] formula was found applicable to calculate the bond strength of the tested GFRP bars as $\tau_b = k{f_{\mathrm{cm}}}^{0.5}$, with k taken as 2.5 for 8-20 mm nominal diameter GFRP specimens, 2.25 for 25 mm nominal diameter, and 2.00 for 32 mm nominal diameter GFRP specimens.
4. The fib Model Code 2020 formula for bond strength however is only applicable for normal strength concrete, as in high strength concrete, the shear failure of the GFRP ribs is also possible, decreasing bond strength.
5. The measured loaded-end slip values were consistent among all tested bar diameters, with a loaded end slip of 0.75 mm upon reaching the bond strength.
6. Unloaded-end slip values decreased with the increase of the embedment length, resulting in inconsistent and unreliable results. To asses diameter dependent effects, a short bond length of 50-100 mm should be used instead of $5d_{\mathrm{b}}$.
7. Using the calculated bond strength values, the BPE model was compared to the measured results, with α = 0.4. At low loaded end slip values, the results showed significant discrepancies with the BPE model. The discrepancy suggests that the BPE model should not be used for calculating the crack width of GFRP bars.

The study demonstrated that the surface characteristics of deformed GFRP bars must be created differently from traditional steel bars, mainly due to the lower strength of the surface undulations. The consequence is lower bond strength for large diameter GFRP bars. In contrast, smaller diameter bars are more prone to the shear failure of the bar's surface due to higher stress concentrations.

Acknowledgements

The authors acknowledge Záév-HardConcrete Ltd. for their assistance with specimen preparation.

References

[1] Bank, Lawrence C. 2006. *Composites for Construction: Structural Design with FRP Materials*. Hoboken, NJ: John Wiley & Sons. https://doi.org/10.1002/9780470121429

[2] Sólyom, Sándor, and Balázs, György L. 2020. "Bond of FRP Bars with Different Surface Characteristics." *Construction and Building Materials* 264:119839. https://doi.org/10.1016/j.conbuildmat.2020.119839

[3] [3] Hosseini, Seyed Arman, Farghaly, Ahmed Sabry, Eslami, Abolfazl, Nanni, Antonio, and Benmokrane, Brahim. 2024. "Bond Behaviour of Lap Spliced GFRP Bars in Concrete Members: A State-of-the-Art Review and Design Recommendations." *Construction and Building Materials* 411:134714. https://doi.org/10.1016/j.conbuildmat.2023.134714

[4] Nepomuceno, Eduarda, Sena-Cruz, José, Correia, Luís, and D'Antino, Tommaso. 2021. "Review on the Bond Behavior and Durability of FRP Bars to Concrete." *Construction and Building Materials* 287:123042. https://doi.org/10.1016/j.conbuildmat.2021.123042

[5] Hao, Qingduo, Wang, Yanlei, He, Zheng, and Ou, Jinping. 2009. "Bond Strength of Glass Fiber Reinforced Polymer Ribbed Rebars in Normal Strength Concrete." *Construction and Building Materials* 23:865–71. https://doi.org/10.1016/j.conbuildmat.2008.04.011

[6] El-Nemr, Amr, Ahmed, Ehab A., Barris, Cristina, Joyklad, Panuwat, Hussain, Qudeer, and Benmokrane, Brahim. 2023. "Bond Performance of Fiber Reinforced Polymer Bars in Normal- and High-Strength Concrete." *Construction and Building Materials* 393:131957. https://doi.org/10.1016/j.conbuildmat.2023.131957

[7] Malvar, Luis Javier. 1994. *Bond Stress-Slip Characteristics of FRP Rebars*. California: Naval Facilities Engineering Service Center.

[8] Cosenza, Edoardo, Manfredi, Gaetano, and Realfonzo, Roberto. 1997. "Behavior and Modeling of Bond of FRP Rebars to Concrete." *Journal of Composites for Construction* 1:40–51. https://doi.org/10.1061/(ASCE)1090-0268(1997)1:2(40)

[9] Eligehausen, Rolf, Popov, Egor P., and Bertero, Vitelmo V. 1983. *Local Bond Stress-Slip Relationships of Deformed Bars under Generalized Excitations*. Report UCB/EERC-83/23. Berkeley, CA: Earthquake Engineering Research Center, University of California, Berkeley.

[10] Fédération internationale du béton (fib). 2023. *fib Model Code for Concrete Structures (2020)*. Version 1. Lausanne: Fédération internationale du béton.

[11] ACI Committee 440. 2012. *Guide Test Methods for Fiber-Reinforced Polymer (FRP) Composites for Reinforcing or Strengthening Concrete and Masonry Structures*. ACI 440.3R-12. Farmington Hills, MI: American Concrete Institute.

Differential shrinkage cracking in fully end-restrained fibre reinforced concrete members with conventional reinforcement

Porsiem Tang, Ali Amin

School of Civil Engineering,
The University of Sydney,
Darlington 2008, Australia

Summary
Fibre reinforcement provides considerable enhancement to concrete's serviceability performance, but its implementation remains limited due to a lack of reliable and comprehensible analytical models that can accurately predict its behaviour. One facet which remains relatively unexplored is the behaviour at early ages when subjected to restrained shrinkage – which can be of significance in sprayed tunnel linings. This paper presents a rational approach to describe the behaviour of a fully restrained fibre reinforced concrete (FRC) member co-reinforced with conventional reinforcement subjected to a non-uniform shrinkage profile through its thickness by building upon the method adopted by Tang et al. [1]. This offers a more realistic representation for members when surfaces are exposed to differing environmental conditions. The results of various FRC specimens are analysed using the proposed model to highlight the influence of fibre reinforcement on post- cracking behaviour.

1 INTRODUCTION

Concrete is widely used in construction with steel reinforcement to mitigate its low tensile strength. The tensile capacity of the steel reinforcement is effectively activated when the concrete cracks, which can lead to serviceability issues such as aesthetic deterioration and lower durability. Cracking may result from externally applied loads or restraints to load-independent deformation such as shrinkage or temperature change. However, the effects of shrinkage are often ignored in design calculations, which can result in wider-than-expected cracks as observed in practice. Shrinkage-induced cracking can be significant particularly at early ages due to high shrinkage rates while the concrete strength is still developing. To address this issue, several models have been developed to quantify the crack width in RC members subjected to uniaxial tension caused by end-restrained uniform shrinkage [2], [3].

Shrinkage in concrete arises from two main processes: chemical reactions (endogenous shrinkage) and drying, causing physical moisture loss (drying shrinkage). Factors affecting drying shrinkage, which is the dominant shrinkage component for thin structural members, include time, environmental conditions and internal moisture content. Many structures – such as slab-on-ground, tunnel linings, steel-composite slabs – are exposed to different environmental conditions at each surface, leading to differential drying shrinkage through the depth of the concrete [4]. Unlike uniform shrinkage, cracks in this case are wider at the surface with higher shrinkage strain, which gradually decrease towards the other surface. Note that the periodic variation in ambient humidity (such as due to seasonal change) can also cause the shrinkage strains to fluctuate over the design life of the structure [5]. As a result, the crack width may also fluctuate (i.e., widen and close) over time.

The incorporation of fibre reinforcement in RC members has been shown to significantly enhance their cracking performance, resulting in a reduction in crack spacing and crack width [6]. This improvement is attributed to the fibres' ability to restrain cracks from further widening as the cracked section can carry residual tensile stress, thereby also reducing the stress in the steel reinforcement [7]. A low post-crack residual tensile stress can provide large improvements with respect to crack control [6]. Tang et al. [1] proposed an analytical model to estimate the average crack width and post-cracking behaviour of fibre reinforced concrete (FRC) members subjected to uniform shrinkage with full and partial end-restraints as a function of time. In the present study, this model is modified to provide a more generalised framework applicable to practical structural members exposed to varying surface environmental conditions. This is done by accounting for the restraining moment induced by the non-uniform shrinkage through the member's depth.

2 ANALYTICAL MODELLING FOR CRACKING IN RESTRAINED FRC MEMBERS WITH DIFFERENTIAL SHRINKAGE

Consider a conventionally reinforced FRC member with infinitely stiff restraints at both ends subjected to differential shrinkage through the depth of the section as shown in Figure 1. The member has length L, width b and depth D. It is assumed that shrinkage strains vary linearly through the depth of the member, and the z-axis is oriented such that the shrinkage at $z = 0$ is smaller in magnitude than at the other surface – it is noted that this convention is easily interchangeable. In this model, the sign convention is positive for tension and negative for compression. The shrinkage gradient induces an axial restraining force $N(t)$ and moment $M(t)$ on the FRC member, which differ with time as shrinkage of the concrete progresses.

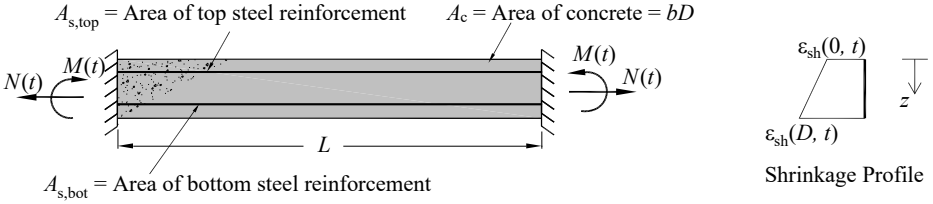


Figure 1. End restrained member subjected to differential shrinkage

The behaviour of an FRC member when uncracked is similar to conventional reinforced concrete (RC) due to the typically low volume percentage of fibre reinforcement used in practice [7]. Hence, the contribution of the fibres prior to cracking is often ignored. At this stage, the total strain in the FRC and steel at every section along the length of the member is equivalent to the ratio of the end restraint movement $\Delta u(z)$ and L. For infinitely stiff restraints, $\Delta u(z)$ is equal to 0 (hence total strain = 0). Since $\varepsilon_{sh}(z, t) < 0$ (compression), the other two components including the elastic strain $\varepsilon_e(z, t)$ and creep strain $\varepsilon_{cc}(z, t)$ are positive. With $\varepsilon_{sh}(z, t) + \varepsilon_e(z, t) + \varepsilon_{cc}(z, t) = 0$, $\varepsilon_e(z, t) = \sigma_c(z, t)/E_c(t)$ and $\varepsilon_{cc}(z, t) = \varphi_c(t)\varepsilon_e(z, t)$, the shrinkage strain component $\varepsilon_{sh}(z, t)$ can be expressed as $-\sigma_c(z, t)/E_e(t)$ where $E_e(t) = E_c(t)/(1+\varphi_c(t))$ is the effective modulus and $\varphi_c(t)$ is the creep coefficient of the FRC.

The first crack occurs once the shrinkage induced concrete tensile stress at the surface that experiences the greatest shrinkage $\sigma_c(z = D, t)$ reaches its tensile capacity $f_{ct}(t)$. Therefore, the shrinkage strain at the bottom surface $\varepsilon_{sh}(D, t) = -f_{ct}(t)/E_e(t)$ and at the top surface $\varepsilon_{sh}(0, t) = -f_{ct}(t)/E_e(t) - \kappa_{sh,cr}D$ where $\kappa_{sh,cr} = (\varepsilon_{sh}(D, t) - \varepsilon_{sh}(0, t))/D$ is the shrinkage gradient when the first crack is initiated. An expression for the elastic stress along the depth of the FRC just before cracking is presented in Equation (1) as derived from $\sigma_c(D, t) = f_{ct}(t)$ and $\sigma_c(0, t) = \kappa_{sh,cr}DE_e(t) + f_{ct}(t)$.

$$\sigma_c(z,t) = \kappa_{sh,cr}E_e(t)(D-z) + f_{ct}(t) \tag{1}$$

Thus, the shrinkage and creep strain of the FRC at any depth along the section just before cracking is

$$\varepsilon_{sh}(z,t) + \varepsilon_{cc}(z,t) = -\left[\kappa_{sh,cr}E_e(t)(D-z) + f_{ct}(t)\right]/E_c(t) \tag{2}$$

2.1 First Cracking

First cracking can occur within the first few days after drying commences [1]. The axial restraining force $N(t)$ and moment $M(t)$ reduces to $N(t_{cr1})$ and $M(t_{cr1})$ respectively as a crack is induced due to the reduced degree of restraint. However, the shrinkage and creep strain components remain the same as just before the onset of cracking since these components vary gradually with time. Thus, the uncracked concrete elastically shortens, opening to a crack width of $w(z, t_{cr1})$, which varies slightly through the depth of the member. At the crack, strain softening FRC is assumed where the residual stress offered by the fibres $\sigma_f(w)$ gradually reduces as the crack continues to widen [7]. Although the crack may not penetrate the entire member depth immediately after the member cracks at $z=D$, the uncracked portion of the section is conservatively ignored, noting that this occurs only over a very short period of time. The stress distribution along the FRC member length at first cracking is presented in Figure 2.

At the crack, the tensile restraining force and moment are shared between the fibres and steel reinforcement as shown in Figure 3(a). The residual stress carried by the fibres $\sigma_f(w)$ is assumed to be constant with depth z due to the relatively small difference in crack width, hence, negligible difference in $\sigma_f(w)$ through the section's depth. The crack causes partial bond breakdown between the steel and

FRC matrix over a distance s_0 before the FRC can resist the full tensile stress $\sigma_{c1}(z, t_{cr1})$. The extent of this stress transition and the crack over the length of the member is classified as Region 2 in Figure 2.

The distance s_0 is dependent on the overall steel-matrix bond, which is impacted by factors such as the steel reinforcement geometry and quantity. Favre et al. [8] proposed using $s_0 = d_b/10\rho$ as an approximation for conventionally reinforced RC where d_b is the reinforcement diameter and ρ is the reinforcement ratio. This was also adopted by Gilbert [2]. To account for two different layers of steel reinforcement, s_0 can be modified to be $s_{0,top} = d_{b,top}/10\rho_{top}$ and $s_{0,bot} = d_{b,bot}/10\rho_{bot}$ for the top and bottom reinforcement respectively, where $\rho_{top} = A_{s,top}/(A_c/2)$, $\rho_{bot} = A_{s,bot}/(A_c/2)$, and $d_{b,top}$ and $d_{b,bot}$ are the steel bars diameter. For $z \leq d_{s,top}$ and $z \geq d_{s,bot}$, $s_{0,top}$ and $s_{0,bot}$ are adopted respectively (where $d_{s,top}$ and $d_{s,bot}$ are defined in Figure 3). Between the two reinforcement layers, s_0 is assumed to vary linearly from $s_{0,top}$ to $s_{0,bot}$. The stress in FRC and steel are assumed to increase parabolically from the crack over this stress transition region due to partial bond breakdowns.

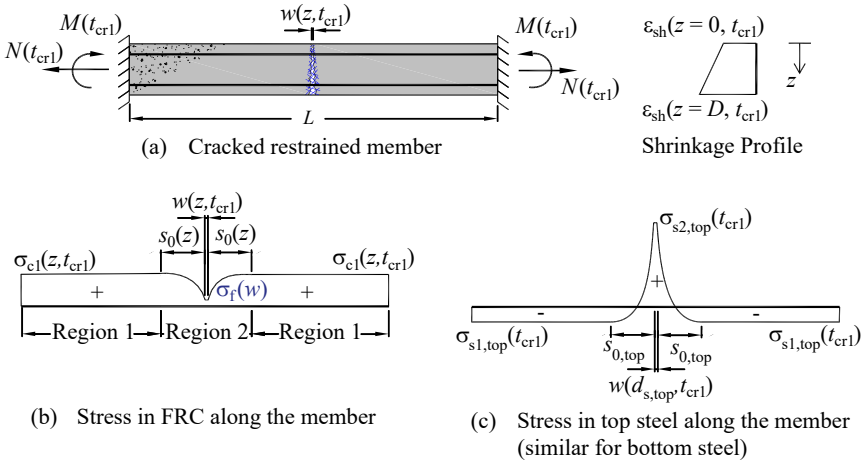


Figure 2. First cracking in end restrained member with shrinkage gradient

In Region 1, the stress in the steel reinforcement and FRC are constant along the member's length but varies with depth as shown in Figure 2 and Figure 3(b). Strain compatibility between the FRC matrix and steel reinforcement is regained in this region. As the total force in the steel reinforcement at the crack is tensile, the steel reinforcement within Region 1 must be in compression (overall) due to the end restraint. Hence, for compatibility, the overall strain in the FRC including creep (> 0) and shrinkage (< 0) within this region is negative noting that the elastic component is positive for equilibrium such that the sum of forces in steel (< 0) and the FRC equates to $N(t_{cr1})$ (> 0).

The deformation of the top steel reinforcement at Region 1 $\Delta_{s1,top}$, at the transition region $\Delta_{st,top}$ and at the crack $\Delta_{sc,top}$ can be quantified using Equations (3)-(5):

$$\Delta_{s1,top} = \left(\sigma_{s1,top}\left(t_{cr1}\right)/E_s\right)\left(L - 2s_{0,top} - w\left(d_{s,top}, t_{cr1}\right)\right) \quad (3)$$

$$\Delta_{st,top} = \left(2s_{0,top}/3E_s\right)\left(\sigma_{s2,top}\left(t_{cr1}\right) + 2\sigma_{s1,top}\left(t_{cr1}\right)\right) \quad (4)$$

$$\Delta_{sc,top} = \left(\sigma_{s2,top}\left(t_{cr1}\right)/E_s\right) w\left(d_{s,top}, t_{cr1}\right) \quad (5)$$

As the restraint is assumed to be infinitely stiff, the overall deformation $\Delta_{s1,top} + \Delta_{st,top} + \Delta_{sc,top} = 0$ and since $s_{0,top} \gg w(d_{s,top}, t_{cr1})$, the stress in the top and bottom steel in Region 1 at cracking can be obtained in Equation (6) and (7) where $C_{1,top} = 2s_{0,top}/(3L - 2s_{0,top})$ & $C_{1,bot} = 2s_{0,bot}/(3L - 2s_{0,bot})$.

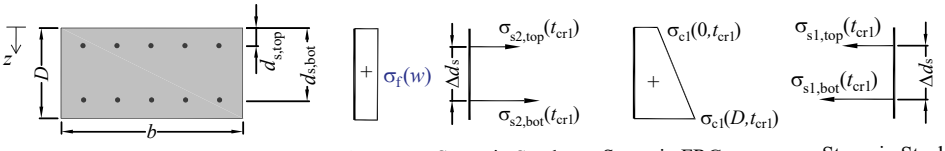
$$\sigma_{s1,top}\left(t_{cr1}\right) = -C_{1,top}\sigma_{s2,top}\left(t_{cr1}\right) \quad (6) \qquad \sigma_{s1,bot}\left(t_{cr1}\right) = -C_{1,bot}\sigma_{s2,bot}\left(t_{cr1}\right) \quad (7)$$

Figure 3(a) shows the cracked section stress distribution as previously described. The sum of the forces in the FRC and steel reinforcement equates to the restraining force $N(t)$ below where $\alpha = A_{s,top}/A_{s,bot}$ and $t = t_{cr1}$:

$$N\left(t\right) = \sigma_f\left(w\right)A_c + \left(\alpha\sigma_{s2,top}\left(t\right) + \sigma_{s2,bot}\left(t\right)\right)A_{s,bot} \quad (8)$$

The axial tensile force in the steel is shared equally between the top and bottom reinforcement, hence, the resulting moment induced force in the bottom steel $F_{M,bot}(t_{cr1}) = (\sigma_{s2,bot}(t_{cr1}) - \alpha\sigma_{s2,top}(t_{cr1}))\, A_{s,bot}/2 = -F_{M,top}(t_{cr1})$ where $F_{M,top}(t_{cr1})$ is the force in the top steel. The resulting restraining moment can then be generally obtained as shown in Equation (9) with $t = t_{cr1}$ where the lever arm $\Delta d_s = d_{s,bot} - d_{s,top}$.

$$M(t) = \left(\sigma_{s2,bot}(t) - \alpha\sigma_{s2,top}(t)\right) A_{s,bot}\Delta d_s / 2 \tag{9}$$



(a) Cracked Section (b) Uncracked Section

Figure 3. Section stress distribution at first cracking

The restraining force $N(t_{cr1})$ and moment $M(t_{cr1})$ are constant at every section along the length of member. Figure 3(b) presents the stress distribution in the FRC and steel reinforcement at Region 1. The stress in the steel reinforcement at this uncracked region $\sigma_{s1,top}(t_{cr1})$ and $\sigma_{s1,bot}(t_{cr1})$ are related to the stress at the cracked region $\sigma_{s2,top}(t_{cr1})$ and $\sigma_{s2,bot}(t_{cr1})$ through Equations (6) and (7). The remaining force and moment are taken by the uncracked concrete with top stress $\sigma_{c1}(0, t_{cr1})$ and bottom stress $\sigma_{c1}(D, t_{cr1})$ where $\sigma_{c1}(0, t_{cr1}) < \sigma_{c1}(D, t_{cr1})$. The restraining force $N(t=t_{cr1})$ in this case can be calculated as:

$$N(t) = \left(\sigma_{c1}(D,\ t) + \sigma_{c1}(0,\ t)\right) A_c/2 + \left(\alpha\sigma_{s1,top}(t) + \sigma_{s1,bot}(t)\right) A_{s,bot} \tag{10}$$

The axial stress in the FRC is $(\sigma_{c1}(0, t_{cr1}) + \sigma_{c1}(D, t_{cr1}))/2$, which is constant along the depth of the member. Thus, the resulting moment stress varies linearly from $(-\sigma_{c1}(D, t_{cr1}) + \sigma_{c1}(0, t_{cr1}))/2$ at the top to $(\sigma_{c1}(D, t_{cr1}) - \sigma_{c1}(0, t_{cr1}))/2$ at the bottom. The moment in the steel reinforcement at Region 1 can be calculated using the same method as Region 2. Equation (11) provides an expression of the restraining moment, which is the sum of the resulting moment in FRC and steel reinforcement where $Z = bD^2/6$ is the elastic section modulus of the uncracked concrete and $t=t_{cr1}$.

$$M(t) = \left(\sigma_{c1}(D,\ t) - \sigma_{c1}(0,\ t)\right) Z/2 + \left(\sigma_{s1,bot}(t) - \alpha\sigma_{s1,top}(t)\right) A_{s,bot}\Delta d_s/2 \tag{11}$$

Due to strain compatibility in Region 1, the FRC total strain is equal to the steel reinforcement strain $\varepsilon_{s1}(z, t_{cr1})$ just after first cracking as shown in Equation (12) whereas the elastic stress with depth z can be defined as a function of $\sigma_{c1}(0, t_{cr1})$ and $\sigma_{c1}(D, t_{cr1})$ (see Equation (13)).

$$\varepsilon_{sh}(z, t_{cr1}) + \varepsilon_{cc}(z, t_{cr1}) + \sigma_{c1}(z, t_{cr1})/E_c = \varepsilon_{s1}(z, t_{cr1}) \tag{12}$$

$$\sigma_{c1}(z, t_{cr1}) = \left(\left(\sigma_{c1}(D, t_{cr1}) - \sigma_{c1}(0, t_{cr1})\right)/D\right) z + \sigma_{c1}(0, t_{cr1}) \tag{13}$$

As the creep and shrinkage strain in the concrete remain the same just before and after cracking, substituting Equation (2) and (13) into Equation (12) gives:

$$\begin{aligned}\varepsilon_{s1}(z, t_{cr1}) = &-\left[\kappa_{sh,cr}E_e(D - z) + f_{ct}\right]/E_c \\ &+\left[\left(\left(\sigma_{c1}(D, t_{cr1}) - \sigma_{c1}(0, t_{cr1})\right)/D\right) z + \sigma_{c1}(0, t_{cr1})\right]/E_c\end{aligned} \tag{14}$$

With $\varepsilon_{s1}(z, t_{cr1}) = \sigma_{s1}(z, t_{cr1})/E_s$, the top reinforcement stress $\sigma_{s1,top}(t_{cr1})$ and bottom reinforcement stress $\sigma_{s1,bot}(t_{cr1})$ can be obtained as a function of $\sigma_{c1}(0, t_{cr1})$ and $\sigma_{c1}(D, t_{cr1})$ by rearranging Equation (14):

$$\sigma_{s1,top}(t_{cr1}) = \kappa_{sh,cr}n_{cr}E_e(d_{s,top} - D) - n_{cr}f_{ct} + \left(\sigma_{c1}(D, t_{cr1}) - \sigma_{c1}(0, t_{cr1})\right) n_{cr}\left(d_{s,top}/D\right) + n_{cr}\sigma_{c1}(0, t_{cr1}) \tag{15}$$

$$\sigma_{s1,bot}(t_{cr1}) = \kappa_{sh,cr}n_{cr}E_e(d_{s,bot} - D) - n_{cr}f_{ct} + \left(\sigma_{c1}(D, t_{cr1}) - \sigma_{c1}(0, t_{cr1})\right) n_{cr}\left(d_{s,bot}/D\right) + n_{cr}\sigma_{c1}(0, t_{cr1}) \tag{16}$$

where $n_{cr} = E_s/E_c$ at first cracking. For simplicity, it is assumed that the top and bottom reinforcement are equal such that $C_{1,top} = C_{1,bot} = C_1$, $A_{s,top} = A_{s,bot} = A_{s,i}$ and $\alpha = 1$. Solving Equations (6), (7), (8), (9), (10), (11), (15) and (16) gives the following expressions for $\sigma_{c1}(0, t_{cr1})$ and $\sigma_{c1}(D, t_{cr1})$. Note that $\sigma_f(w)$ can be simplified by using the residual stress at a crack opening displacement of 0.2mm ($f_{0.2}$), which is close to most practical limits of crack width. In addition, with no shrinkage gradient ($\kappa_{sh,cr} = 0$), the same expressions as the analytical model proposed by Tang et al. [1] can be obtained.

$$\sigma_{c1}\left(D, t_{cr1}\right)=\frac{\left(Z/2+C_{12}\left(C_1+1\right)\right)\left(\sigma_f\left(w\right)A_c-C_2\left(1/C_1+1\right)\right)-C_5\left(A_c/2-C_9\left(C_1+1\right)\right)\left(1/C_1+1\right)}{\left(Z/2+C_{12}\left(C_1+1\right)\right)\left(A_c-\left(C_1+1\right)\left(C_9+C_{10}\right)\right)} \quad (17)$$

$$\sigma_{c1}\left(0, t_{cr1}\right)=\frac{\sigma_f\left(w\right)A_c-C_2\left(1/C_1+1\right)}{A_c/2-C_9\left(C_1+1\right)}-\frac{A_c/2-C_{10}\left(C_1+1\right)}{A_c/2-C_9\left(C_1+1\right)}\sigma_{c1}\left(D, t_{cr1}\right) \quad (18)$$

Where

$$C_2=\kappa_{sh,cr}n_{cr}E_eA_{s,i}\left(d_{s,top}+d_{s,bot}-2D\right)-2n_{cr}f_{ct}A_{s,i} \quad (19)$$

$$C_5=\kappa_{sh,cr}n_{cr}E_eA_{s,i}\Delta d_s^2/2 \quad (20)$$

$$C_{12}=n_{cr}A_{s,i}\Delta d_s^2/\left(2C_1D\right) \quad (21)$$

$$C_9=\frac{n_{cr}A_{s,i}}{C_1}\left(\frac{d_{s,top}+d_{s,bot}}{D}-2\right) \quad (22)$$

$$C_{10}=-\frac{n_{cr}A_{s,i}}{C_1}\left(\frac{d_{s,top}+d_{s,bot}}{D}\right) \quad (23)$$

2.2 Subsequent Cracking

As shrinkage progresses, the concrete stress in Region 1 $\sigma_{c1}(z, t)$ increases. Another crack is formed once it reaches $f_{ct}(t)$. This process continues until the final crack pattern is established (crack stabilisation) where the transfer length between adjacent cracks is insufficient for the bond in the FRC matrix to be developed from $\sigma_f(w)$ to $f_{ct}(t)$. Figure 4 illustrates the average stress in the FRC and the steel reinforcement along the member at time t with $m(t)$ number of cracks and $s(t)$ average spacing. The stress distribution is similar to the case of first cracking where the FRC stress increases parabolically from $\sigma_f(w)$ at the crack to $\sigma_{c1}(z, t)$ within Region 2. The partial bond breakdown distance $s_0(z)$ is assumed to be the same as at first crack, ignoring bond deteriorations, since shrinkage occurs at early age.

At the crack, the tensile restraining force $N(t)$ is shared between the fibres and steel reinforcement where $\sigma_f(w) > 0$, $\sigma_{s2,top}(t) > 0$ and $\sigma_{s2,bot}(t) > 0$. Hence, the steel reinforcement in Region 1 must be in compression due to the overall deformation restraint. The deformation of the top steel reinforcement at Region 1 $\Delta_{s1,top}(t)$, at transition region $\Delta_{st,top}(t)$ and at the crack $\Delta_{sc,top}(t)$ can be quantified using Equations (24)-(26) where there are $m(t)$ number of Regions 1 and 2.

$$\Delta_{s1,top}\left(t\right)=\left(\sigma_{s1,top}\left(t\right)/E_s\right)\left(L-2m\left(t\right)s_{0,top}-m\left(t\right)w\left(d_{s,top}, t\right)\right) \quad (24)$$

$$\Delta_{st,top}\left(t\right)=2s_{0,top}m\left(t\right)\left(\sigma_{s2,top}\left(t\right)+2\sigma_{s1,top}\left(t\right)\right)/\left(3E_s\right) \quad (25)$$

$$\Delta_{sc,top}\left(t\right)=\sigma_{s2,top}\left(t\right)m\left(t\right)w\left(d_{s,top}, t\right)/E_s \quad (26)$$

With infinitely stiff end restraints, $\Delta_{s1,top}(t) + \Delta_{st,top}(t) + \Delta_{sc,top}(t) = 0$ and $s_{0,top} \gg w(d_{s,top}, t)$, Equation (27) can be obtained to describe the relationship between $\sigma_{s2,top}(t)$ and $\sigma_{s1,top}(t)$. Similarly, for the bottom reinforcement, Equation (28) can be used.

$$\sigma_{s1,top}\left(t\right)=-\left(2s_{0,top}m\left(t\right)/\left(3L-2s_{0,top}m\left(t\right)\right)\right)\sigma_{s2,top}\left(t\right) \quad (27)$$

$$\sigma_{s1,bot}\left(t\right)=-\left(2s_{0,bot}m\left(t\right)/\left(3L-2s_{0,bot}m\left(t\right)\right)\right)\sigma_{s2,bot}\left(t\right) \quad (28)$$

Tang et al. [1] presented the concrete stress history in Region 1 with time where there is a gradual stress build up as the concrete starts to shrink. Once the concrete stress reaches $f_{ct}(t_{cr1})$, the first crack is initiated and there is a sudden drop in stress to $\sigma_{c1}(t_{cr1})$. A subsequent crack i is initiated at time t_{cri} and $\sigma_{c1}(t_{cri}) > \sigma_{c1}(t_{cr1})$. As the stress at a certain depth varies between $\sigma_{c1}(z, t_{cri})$ and $f_{ct}(t)$, the average stress in FRC $\sigma_{c1,avg}(z, t)$ may be approximated using Equation (29) where $\sigma_{c1}(0, t_{cri})$ and $\sigma_{c1}(D, t_{cri})$ are obtained from Equations (17) and (18). On the other hand, for compatibility in Region 1, the overall FRC strain must be equal to the steel strain as shown in Equation (30).

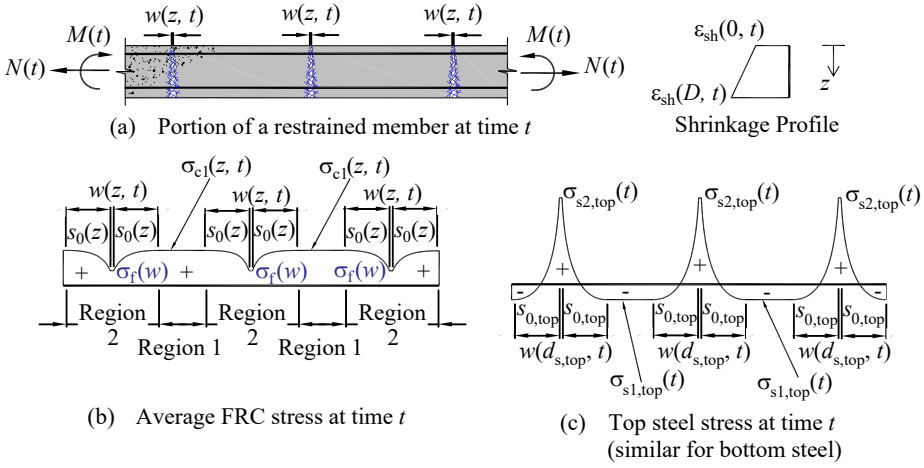
$$\sigma_{c1,avg}\left(z, t\right)=\left(\left(\sigma_{c1}\left(D, t_{cri}\right)-\sigma_{c1}\left(0, t_{cri}\right)\right)/2D\right)z+\left(\sigma_{c1}\left(0, t_{cri}\right)+f_{ct}\left(t\right)\right)/2 \quad (29)$$

$$\varepsilon_{sh}\left(z, t\right)+\varepsilon_{cc}\left(z, t\right)+\sigma_{c1,avg}\left(z, t\right)/E_c\left(t\right)=\varepsilon_{s1}\left(z, t\right) \quad (30)$$

where the shrinkage strain $\varepsilon_{sh}(z, t) = \kappa_{sh}(t)z + \varepsilon_{sh}(0, t)$. The steel reinforcement is assumed to be linearly elastic so $\varepsilon_{s1}(z, t) = \sigma_{s1}(z, t)/E_s$ and the creep strain $\varepsilon_{cc}(z, t) = \varphi_c(t)\sigma_{c1,avg}(z, t)/E_c(t)$. Hence, Equation (30) can be rearranged to get the stress in the top and bottom steel reinforcement at Region 1:

$$\sigma_{s1,top}(t) = n_e(t)\sigma_{c1,avg}(d_{s,top}, t) + n_e(t)E_e(t)\varepsilon_{sh}(d_{s,top}, t) \quad (31)$$

$$\sigma_{s1,bot}(t) = n_e(t)\sigma_{c1,avg}(d_{s,bot}, t) + n_e(t)E_e(t)\varepsilon_{sh}(d_{s,bot}, t) \quad (32)$$



(a) Portion of a restrained member at time t

(b) Average FRC stress at time t

(c) Top steel stress at time t (similar for bottom steel)

Figure 4. Subsequent cracking in end restrained member with shrinkage gradient

The restraining force $N(t)$ and moment $M(t)$ at the crack and at Region 1 can be obtained as per first crack case shown in Equations (8)-(11). At the crack, the residual stress in FRC $\sigma_f(w)$ can be approximated by $f_{0.2}$ while the stress in steel $\sigma_{s2,top}(t)$ and $\sigma_{s2,bot}(t)$ can be calculated from $\sigma_{s1,top}(t)$ and $\sigma_{s1,bot}(t)$ above using Equations (27) and (28). Equations (10) and (11) can be solved to obtain the stress in the FRC at Region 1 assuming symmetrical reinforcement for simplification where $A_{s,top} = A_{s,bot} = A_{s,i}$, $\alpha = 1$ and $\rho_{top} = \rho_{bot} = \rho_i = A_{s,i}/(A_c/2)$:

$$\sigma_{c1}(D, t) = N(t)/A_c + M(t)/Z - \sigma_{s1,top}(t)\left(\rho_i - A_{s,i}\Delta d_s/Z\right)/2 - \sigma_{s1,bot}(t)\left(\rho_i + A_{s,i}\Delta d_s/Z\right)/2 \quad (33)$$

$$\sigma_{c1}(0, t) = 2N(t)/A_c - \sigma_{c1}(D, t) - \rho_i\left(\sigma_{s1,top}(t) + \sigma_{s1,bot}(t)\right) \quad (34)$$

To solve these equations, the number of cracks $m(t)$ is iterated to obtain the smallest number of cracks where $\sigma_{c1}(D, t) < f_{ct}(t)$ as $\sigma_{c1}(D, t) \geq f_{ct}(t)$ means more cracks would have been initiated. However, since $f_{ct}(t)$ is relatively low just after shrinkage commences, this model may show more cracks at earlier ages. Cracks that have already been induced are irreversible, so the larger number of cracks in the previous time step should be used as $m(t)$ instead in this case.

2.3 Average crack width at a specific time, t

The overall concrete deformation at Region 1 Δ_{c1} is the product of the overall strain $\varepsilon_{c1}(z, t)$ and the total length of Region 1. Where $\varepsilon_{c1}(z, t) = \varepsilon_e(z, t) + \varepsilon_{cc}(z, t) + \varepsilon_{sh}(z, t)$ and $\varepsilon_e(z, t) + \varepsilon_{cc}(z, t) = \sigma_{c1}(z,t)/E_e(t)$, the following expression can be obtained:

$$\Delta_{c1} = \left(\sigma_{c1}(z, t)/E_e(t) + \varepsilon_{sh}(z, t)\right)\left(L - 2m(t)s_0(z) - w(z, t)m(t)\right) \quad (35)$$

Assuming that the stress varies parabolically at the transition region from $\sigma_f(w)$ at the crack ($x = 0$) to $\sigma_{c1}(z, t)$ at $x = s_0$ and $d\sigma/dx = 0$ at $x = s_0$, Equation (36) can be used to solve for the stress within the transition region x distance away from the crack:

$$\sigma_{ct}(x, z, t) = \sigma_f(w) - \left[\left(\sigma_{c1}(z, t) - \sigma_f(w)\right)/s_0^2(z)\right]x^2 + \left[2\left(\sigma_{c1}(z, t) - \sigma_f(w)\right)/s_0(z)\right]x \quad (36)$$

Note that the strain within the transition region $\varepsilon_{ct}(x, z, t) = \sigma_{ct}(x, z, t)/E_e(t) + \varepsilon_{sh}(z, t)$. The total FRC deformation within this transition region can then be obtained by integrating the strain $\varepsilon_{ct}(x, z, t)$ over the region (from $x = 0$ to $x = s_0(z)$) and multiplying it by the total number of transition regions $2m(t)$:

$$\Delta_{ct} = 2m(t)s_0(z)\left[\left(2\sigma_{c1}(z, t) + \sigma_f(w)\right)/\left(3E_e(t)\right) + \varepsilon_{sh}(z, t)\right] \tag{37}$$

whereas at the cracks, the total deformation $\Delta_{cr} = m(t)w(z, t)$. Therefore, the overall deformation of the member can be expressed by Equation (38) where $\Delta_{c1} + \Delta_{ct} + \Delta_{cr} = 0$.

$$\begin{aligned}&\left(\sigma_{c1}(z, t)/E_e(t) + \varepsilon_{sh}(z, t)\right)\left(L - 2m(t)s_0(z) - w(z, t)m(t)\right)\\&+2m(t)s_0(z)\left[\left(2\sigma_{c1}(z, t) + \sigma_f(w)\right)/\left(3E_e(t)\right) + \varepsilon_{sh}(z, t)\right] + m(t)w(z, t) = 0\end{aligned} \tag{38}$$

With $s_0(z) \gg w(z, t)$, the crack along the depth at time t can be obtained by rearranging Equation (38) as shown noting that $\sigma_f(w)$ can be simplified by using the residual stress at $f_{0.2}$ without introducing significant error.

$$w(z, t) = -\left[\frac{\sigma_{c1}(z, t)}{E_e(t)}\left(s(t) - \frac{2s_0(z)}{3}\right) + \varepsilon_{sh}(z, t)s(t) + \frac{2\sigma_f(w)s_0(z)}{3E_e(t)}\right] \tag{39}$$

3 SAMPLE ANALYSES

Consider the same restrained FRC slab strip as Tang et al. [1] with 5m length, 1m width and 200mm depth (A_c=200,000 mm^2, Z = 6,666,667 mm^3). The slab is reinforced with 4N16 top and bottom at 30mm clear cover ($d_{s,top}$ = 38 mm, $d_{s,bot}$ = 162 mm, E_s = 200GPa). Table 1 presents the properties of a plain RC specimen and 2 FRC specimens considered where Mix 1 is the same specimen used in Tang et al.'s study [1]. It is assumed that the end restraints are infinitely stiff, and the shrinkage strain varies linearly from $0.2\varepsilon_{sh}$ at the top surface to $1.2\varepsilon_{sh}$ at the bottom as per Australian Steel Composite Code AS2327:2017. In addition, drying commences immediately after casting.

Table 1 Properties of the FRC mixes

Time, t [days]	ε_{sh} ($\times 10^{-6}$) [-]	φ_c [-]	f_c [MPa]	E_c [GPa]	f_{ct} [MPa]	$f_{0.2}$ – Plain RC [MPa]	$f_{0.2}$ – Mix 1 [MPa]	$f_{0.2}$ – Mix 2 [MPa]
1	-200	0.62	7.3	13.7	1.13	0.00	0.43	0.54
3	-300	0.75	19.3	22.2	2.16	0.00	0.60	0.75
7	-380	0.87	28.5	27.0	2.80	0.00	0.68	0.85
14	-440	1.03	37.3	30.9	3.35	0.00	0.73	0.91
28	-500	1.27	44.0	33.5	3.74	0.00	0.78	0.98
90	-610	1.62	57.0	38.2	4.44	0.00	0.80	1.00

Figure 5a illustrates the average crack width at the bottom surface of the 3 specimens over 90 days. The crack widths increase rapidly at early age and slow down with time as the rate of shrinkage decreases for all specimens. The RC specimen has the largest crack, which reduces with more fibre reinforcement (larger residual stress $f_{0.2}$). Note that crack stabilisation has been reached at Day 1 with $m(t)$ = 7, 11 and 13 respectively for the Plain RC, Mix 1 and Mix 2 specimens. Figure 5b presents the crack width results with depth z at Day 1 and Day 90 after commencement of shrinkage. With shrinkage increasing linearly from the top surface to the bottom, the crack width is also larger at the bottom with a linear gradient. At Day 1, both FRC mixes have not been fully cracked with Mix 1 being uncracked to z = 7.5 mm and Mix 2 being uncracked to z = 25 mm.

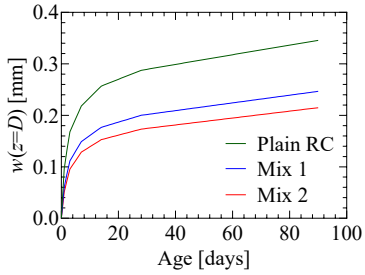


Figure 5a

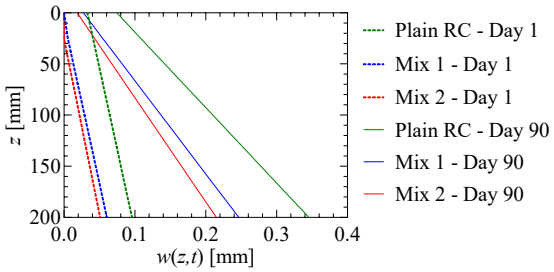


Figure 5b

Figure 5. Crack width results due to restrained non-uniform shrinkage for 3 sample specimens

Figure 6 presents the stresses in the member with time. At the crack, as the force and moment are shared between fibres and steel reinforcement, the presence of fibre reinforcement reduces the stress in steel reinforcement σ_{s2} as depicted in Figure 6a for the bottom steel reinforcement (noting a similar trend for the top reinforcement). On the other hand, as the stress in steel at Region 1 is approximated by using the average concrete stress in Equation (29), the discrepancy in σ_{s1} is less prominent.

Figure 6b presents the top and bottom concrete stress σ_{c1} where $\sigma_{c1}(z = D)$ of the member without fibre reinforcement is the largest. As the plain RC member has the least number of cracks (larger crack spacing) and the largest tensile stress, it is susceptible to larger cracks. However, the top concrete stress $\sigma_{c1}(z = 0)$ of the plain RC is smaller than the FRC members. This is because the FRC members have more cracks, hence, lower restraining moment due to a reduction in the degree of restraint. The larger moment in the plain RC member decreases the tensile stress at the top of the member.

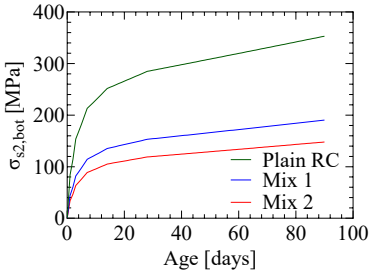


Figure 6a

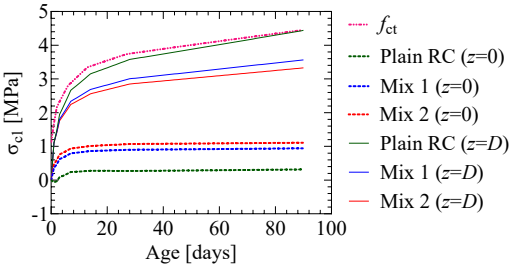


Figure 6b

Figure 6. Post crack stresses due to restrained non-uniform shrinkage for 3 sample specimens

4 CONCLUSIONS

This paper presents an analytical approach to determine the post-cracking behaviour of an infinitely stiff end restrained FRC member co-reinforced with steel reinforcement under differential shrinkage. The proposed model allows for the restraining force, moment and stresses in the individual member components due to shrinkage to be estimated, while accounting for the time dependent effects of the material properties to evaluate the structural response and crack width at each time step. An example with 2 different FRC and a plain RC specimen has been analysed to demonstrate the effectiveness of FRC for crack control. Note that although further work is required to validate the proposed model using experimental/numerical methods (which is currently being undertaken by the authors as part of a broader study), the model shows promise as a practical tool of predicting the extent of shrinkage cracking for serviceability design application such as in shotcrete tunnel linings and large concrete slabs.

References

[1] Tang, Porsiem, Amin, Ali, Gilbert, Raymond Ian, and Kaufmann, Walter. 2023. “Shrinkage cracking in restrained FRC members containing conventional reinforcement.” *Structural Concrete* 25(2):1006–1017.

[2] Gilbert, Raymond Ian. 1992. “Shrinkage Cracking in Fully Restrained Concrete Members.” *ACI Structural Journal* 89(2):141–149.

[3] Burns, Clare. 2012. *Serviceability Analysis of Reinforced Concrete Based on the Tension Chord Model.* Switzerland: Institute of Structural Engineering (IBK).

[4] Kim, Jinkeun, and Lee, C.S. 1998. "Prediction of differential drying shrinkage in concrete." *Cement and Concrete Research* 28(7):985–994.

[5] Podhajecky, Anna-Lena, Oneschkow, Nadja, Kern, Bianca, Lohaus, Ludger, S.Müller, Harald, and Haist, Michael. 2023. "Influence of initial moisture content on creep and shrinkage of concrete at constant and cyclic ambient humidity." *Materials and Structures* 56:170.

[6] Groli, Giancarlo, and Caldentey, Alejandro Pérez. 2017. "Improving cracking behaviour with recycled steel fibres targeting specific applications – analysis according to fib Model Code 2010." *Structural Concrete* 18(1):29–39.

[7] Amin, Ali, and Gilbert, Raymond Ian. 2019. "Steel Fiber-Reinforced Concrete Beams—Part I: Material Characterization and In-Service Behavior," *ACI Structural Journal* 116(2): 101-111.

[8] Favre, Renaud. 1983. *Fissuration et Deformations.* Switzerland: EPFL

Strain Coupling Effects in Reinforced Concrete Membrane Elements subjected to In-Plane Stresses

Jiji Gopan V G and Amlan Kumar Sengupta

Indian Institute of Technology Madras,
Adayar, Chennai 600036, India

Summary

Wall type reinforced concrete structural members, such as shear walls, resist earthquakes primarily through in-plane stiffness and strength. Neglecting the out-of-plane bending, walls can be modelled using membrane elements subjected to in-plane stresses. Accurate prediction of their non-linear behaviour is essential for estimating ductility and for performance-based design. Material nonlinearity can be incorporated by Softened Membrane Model (SMM). This study modifies SMM by incorporating the strain coupling effects of Poisson's effect and shear-extension, generated under in-plane stresses. These effects induce additional strains in an anisotropic membrane element where the principal axes of applied stresses are asymmetrically inclined to the reinforcement grid. A mechanics-based formulation of these additional strains is integrated into the SMM solution algorithm and validated against the experimental shear stress versus strain data of a few panels reported in the literature.

1 INTRODUCTION

Wall-type reinforced concrete (RC) structural members, such as shear walls, are essential for the seismic safety of mid- to high-rise buildings. During earthquakes, these members are subjected to increasing in-plane shear stresses, typically in the presence of constant service-level normal stresses. Conventionally, multi storeyed buildings are analysed for seismic forces using linear elastic finite element methods. But these approaches are inadequate for capturing the non-linear response that governs ductility and energy dissipation, which are key in performance-based design.

Non-linear finite element analysis (FEA) provides an effective method for simulating the seismic behaviour of shear walls. By neglecting the out-of-plane bending resistance, a shear wall can be idealised as an assemblage of two-dimensional (2D) membrane elements subjected to in-plane stresses. These stresses comprise normal stresses due to gravity loads and shear stresses induced by ground motion. Given the smaller thickness of the shear wall compared to its lateral dimensions, the stresses are assumed to be distributed uniformly across its thickness.

The Modified Compression Field Theory (MCFT) and the Softened Membrane Model (SMM) are two approaches to quantify the non-linear shear stress versus strain behaviour of an RC membrane element under increasing in-plane shear demand. The SMM incorporates Poisson's effect into the previously existing fixed-angle softened truss model based on an orthotropic formulation [4]–[6]. Poisson's effect refers to the generation of additional normal strain (in addition to that generated due to the normal stress in the same direction) along a direction due to normal stress along the orthogonal direction. This is an extension-extension strain coupling effect in a membrane element.

When the symmetry of the reinforcement grid about the principal axes of applied stresses, as required in an orthotropic formulation, is violated with increasing shear demand, additional shear strain (even in absence of corresponding shear stress) is generated about the principal axes of stresses. This is referred to as the shear–extension strain coupling effect in an anisotropic membrane element. The present study generalises the formulation of SMM by incorporating this later effect.

In the following sections, an overview of the two strain coupling effects is discussed. Next, a modified SMM algorithm incorporating the strain coupling effects is presented. The proposed algorithm is corroborated with the shear stress versus strain data obtained from testing of a few RC panels as available in the literature.

2 POISSON'S EFFECT IN SOFTENED MEMBRANE MODEL

A general applied in-plane state of stress for an RC membrane element can be expressed in the global reinforcement coordinate system *l*–*t*, as σ_l, σ_t (normal stresses), and τ_{lt} (shear stress). With increasing shear stress, the stresses at cracking can be transformed into principal stresses in the 2–1 coordinate system, where σ_2 and σ_1 represent the applied principal compressive and tensile stresses, respectively, as shown in Fig. 1 (left) and (right). The angle of inclination of the 2–1 axes with respect to the *l*–*t* axes is denoted as α_2. The 2D equilibrium equations, compatibility conditions and constitutive relationships are used in the formulation of SMM for the prediction of the shear stress (τ_{lt}) versus corresponding shear strain (γ_{lt}) behaviour under increasing lateral load and in presence of service level gravity load (constant values of σ_l, σ_t) [2],[3],[6]. The constitutive relationships were developed in terms of the principal stress and strain for each of concrete and steel bars (rebar). Since the relationship for rebar was based on tensile tests of coupons, it can be termed as a uniaxial constitutive model.

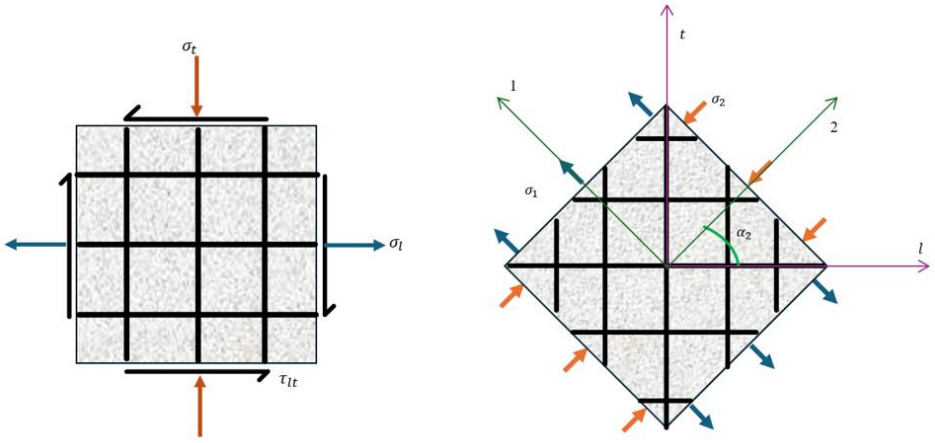


Fig.1 A membrane element with applied stress (left) and equivalent principal stresses at first cracking (right)

Under a state of biaxial stresses, the normal strain in a direction consists of two parts: i) a uniaxial component caused by the stress along that direction, ii) a biaxial component resulting from the stress in the orthogonal direction due to Poisson's effect. Since orthotropy is primarily introduced after the cracking of concrete, the Poisson's effect in SMM is formulated in terms of the 2–1 coordinate system. It is observed that the effect of compressive stress along 2-axis on the orthogonal tensile strain along 1-axis is high. On the contrary, the effect of tensile stress on the orthogonal compressive strain is negligible.

To incorporate the Poisson's effect of compression on tensile strain, the total axial strain in rebar of either the longitudinal (*l*-) or transverse (*t*-) axes (ε_s) is expressed as the sum of the uniaxial strain ε_{su} and the biaxial strain ε_{sb}. The stress in rebar (f_s) should be obtained from ε_{su} using the uniaxial constitutive model. Symbolically, it is shown below as in (1). Else, if f_s is obtained from ε_s using the uniaxial constitutive model, then it is overestimated [9],[10].

$$f_s = F_U(\varepsilon_{su}) \tag{1}$$

To extract the value of ε_{su} along either of *l*- and *t*- axes, the concept of Apparent Poisson's Ratio (APR) is introduced. It is defined as the negative of the ratio of the biaxial strain along the direction of tension (1-axis) to the uniaxial strain in the direction of compression (2-axis) as shown in equation (2):

$$\nu_{12} = -\varepsilon_{1b}/\varepsilon_{2u} \tag{2}$$

Due to the negligible Poisson's effect of the tension on the orthogonal compressive strain, the uniaxial strain along the 2-axis (ε_{2u}) is same as the total strain ε_2. The total tensile strain can be expressed as in equation (3).

$$\varepsilon_1 = \varepsilon_{1u} + \varepsilon_{1b} = \varepsilon_{1u} - \nu_{12}\varepsilon_2 \tag{3}$$

By transposing the terms and based on coordinate transformation, the uniaxial strains along the directions of rebar are given by equations (4) and (5):

$$\varepsilon_{lu} = \varepsilon_l + \nu_{12}\,\varepsilon_2\, sin^2\alpha_2 \tag{4}$$
$$\varepsilon_{tu} = \varepsilon_t + \nu_{12}\,\varepsilon_2 sin^2\alpha_2 \tag{5}$$

In the SMM, ν_{12} is expressed in terms of the strain in rebar. Later, to have an explicit expression, a stress-based formulation was developed. Since ε_2 is considered to be a known variable in the solution algorithm of SMM, ν_{12} is quantified in terms of the generated biaxial tensile strain (ε_{1b}). The later is enhanced by progressive cracking of concrete and subsequent yielding of rebar. Hence, ε_{1b} was expressed as a function of the instantaneous compressive stress in concrete (σ_2^c) and tensile stress in rebar as in equation (6). Here, the variation of ε_{1b} (as a normalised variable $\frac{\varepsilon_{1b}}{\varepsilon_{1b,max}}$) is expressed in terms of σ_2^c. The magnitude of ε_{1b} ($\varepsilon_{1b,max}$) is expressed in terms of f_l.

$$\varepsilon_{1b} = F_1[S(\sigma_2^c)]F_2[R(f_l)] \tag{6}$$

Here $S(\sigma_2^c)$ is the normalised concrete stress and $R(f_l)$ is the normalised rebar stress.

$$S(\sigma_2^c) = {\sigma_2^c}\Big/{\xi f_c'} \tag{7}$$
$$R(f_l) = {f_l}\Big/{f_y} \tag{8}$$

For $S(\sigma_2^c) \leq 1$

$$F_1[S(\sigma_2^c)] = \frac{\varepsilon_{1b}}{\varepsilon_{1b,max}} = \frac{S(\sigma_2^c)}{3.4-2.4\,S(\sigma_2^c)} \tag{9}$$

For $R(f_t) \leq 1$

$$F_2[R(f_l)] = \varepsilon_{1b,max} = 0.00032 + 0.01008\,R(f_l) \tag{10}$$

For $1 < R(f_t) \leq 1.1$

$$F_2[R(f_l)] = \varepsilon_{1b,max} = 0.1158R(f_l) - 0.1054 \tag{11}$$

A modified solution algorithm was proposed to solve the simultaneous equations of SMM, incorporating the stress-based formulation of ε_{1b} [1]. Of course, the above expressions for ε_{1b} need refinement when the requirement of symmetry in an orthotropic formulation is violated.

3 SHEAR—EXTENSION COUPLING EFFECT

With increasing load, if the principal axes of applied stresses (subsequently referred to as principal stress axes) rotate from the 2-1 axes, there will be some shear stress (τ_{21}) and corresponding shear strain (γ_{21}) in that fixed coordinate system. In addition, when the reinforcement grid (principal material directions for an uncracked membrane element) is not symmetric about the principal stress axes (an asymmetric membrane element), the principle of co-axiality is violated. That is, γ_{21} is generated even if $\tau_{21} = 0$. Kosuru and Sengupta (2022) found that SMM overpredicts the shear stress (τ_{lt}) and underestimates the shear strain (γ_{lt}) for panels where the condition of symmetry is violated substantially [7].

In an RC membrane element, asymmetry can occur due to different amounts of reinforcement in longitudinal and transverse directions, or due to the rotation of the principal axes of applied stresses after initial cracking (under increasing lateral load in presence of constant gravity loads), or by a combination of both. A 2D anisotropic formulation was proposed to include shear-extension coupling effect to consider the additional shear strain generated due to the applied normal stresses. An expression for the additional shear strain (γ_{21}) was proposed as a function of the instantaneous tensile stress in rebar (f_i, considering that the transverse bars will have higher stress and hence, yield first), compressive stress in concrete (σ_2^c) and two indices to measure asymmetry as shown in equation (12). The shear-extension coupling effect was incorporated in the solution algorithm of SMM [7]. However, the original formulation of ν_{12} in SMM was retained for the asymmetric elements.

The stress-based formulation of γ_{21} is as follows.

$$\gamma_{21} = \mathcal{F}_1[S(\sigma_2^c)]\,\mathcal{F}_2[R(f_t)]\,(\mathcal{F}_3[H] + \mathcal{F}_4[\alpha_2]) \tag{12}$$

Here, H is the ratio of the amounts (and grades, if any) of reinforcement in the two directions.

For $S(\sigma_2^c) \leq 1$

$$\mathcal{F}_1[S(\sigma_2^c)] = 1 - \sqrt{1 - S(\sigma_2^c)} \tag{13}$$

For $R(f_t) \leq 1$

$$\mathcal{F}_2[R(f_t)] = R(f_t) \tag{14a}$$

For $1 \leq R(f_t) \leq 1.2$

$$\mathcal{F}_2[R(f_t)] = 23.5R(f_t) - 22.5 \tag{14b}$$

Here, the variation of γ_{21} (as a normalised variable $\frac{\gamma_{21}}{\gamma_{21max}}$) is expressed in terms of σ_2^c and f_t. The value of $\gamma_{21,max}$ is governed by the asymmetry indices.

For $H \geq 1$

$$\mathcal{F}_3[H] = -0.0025\sqrt{H - 1} \tag{15}$$

For $0^0 \leq \alpha_2 \leq 45^0$

$$\mathcal{F}_4[\alpha_2] = -0.007\sin(4\alpha_2) \tag{16}$$

4 GENERALISED ALGORITHM

A modified algorithm of Softened Membrane Model (SMM) for developing the shear behaviour curve (τ_{lt}versus γ_{lt}) of a membrane element or a test panel, is proposed by incorporating the two strain coupling effects simultaneously. The algorithm at a certain step of loading is as follows.

1. Read the given variables for concrete and reinforcement, and the applied normal stresses.
2. At a certain step, select an incremental value of compressive strain of concrete (ε_2).
3. Consider the shear strain (γ_{21}) from the previous step of loading.
4. Assume a tensile strain of concrete (ε_1).
5. Calculate the compressive (σ_2^c) and tensile (σ_1^c) stresses in concrete.
6. Calculate the strains in the bars ($\varepsilon_l$and ε_t).
7. Estimate the biaxial strain (ε_{1b}) based on the stress in the governing bars (transverse, if it is higher) in previous step (f_t) and Apparent Poisson's Ratio (ν_{12}).
8. Calculate the uniaxial strains in the bars (ε_{lu} and ε_{tu}).
9. Calculate the stresses in the bars (f_l and f_t).
10. Check the first derived equilibrium condition and iterate ε_1 assumed in Step 4 till convergence.
11. Calculate the shear strain (γ_{21}) and the shear stress in concrete (τ_{21}^c).
12. Check the second derived equilibrium condition and update γ_{21} considered in Step 3 till convergence.
13. Compute the values of τ_{lt} and γ_{lt}.

The steps are repeated till the strain ε_2 reaches the failure value of $\zeta\varepsilon_0$, where the analysis is limited up to the peak value of τ_{lt}. Even if there is no applied shear stress in the 2-1 coordinate system, as in a test panel, shear stress will be generated in concrete (τ_{21}^c) from the generated γ_{21} due to aggregate interlock action at the cracks.

5 EXPERIMENTAL CORROBORATION

To demonstrate the proposed modified algorithm, Panel A3 with symmetric reinforcement grid and Panel B3 with asymmetric reinforcement [8], both tested under increasing biaxial tension–compression ($\sigma_1 = -\sigma_2$, $\tau_{21} = 0$ to simulate the condition of pure shear) with rebar grid inclined at 45° ($\alpha_2 = 45°$), were considered. The strengths of the materials and amounts of reinforcement are provided in Table 1. The predicted and experimental τ_{lt}versus γ_{lt} curves are shown in Figures 2 and 3, respectively. It is observed that the modified algorithm with stress-based formulation of the Poisson's effect predicts the behaviour of Panel A3 accurately at least up to the peak. Since the reinforcement was symmetric, there was no shear-extension coupling effect.

For Panel B3, the original SMM overestimates the shear strength and underestimates the shear strain at a certain level of shear stress. Incorporation of the shear-extension coupling effect in the modified algorithm rectifies this limitation.

Table 1 Strengths of the materials and amounts of reinforcements for the panels

Panels	Concrete		Rebar			
	f_c' (MPa)	ε_0	l- direction		t- direction	
			ρ_l	f_{yl} (MPa)	ρ_t	f_{yt} (MPa)
A3	41.65	0.00194	0.0179	446.45	0.0179	446.45
B3	44.89	0.00215	0.0179	446.45	0.006	444.79

6 CONCLUSIONS

For an RC membrane element, extension–extension (Poisson's effect) and shear–extension strain coupling effects need to be considered for a refined prediction of the shear stress versus strain

behaviour. The orthotropic formulation of Poisson's effect in the existing Softened Membrane Model is precisely valid only for elements that satisfy the condition of symmetry about the axes of loading.

The formulation and solution algorithm are generalised to include both the strain coupling effects based on quantifying the biaxial tensile strain and additional shear strain in terms of the instantaneous stresses in concrete and rebar. Indices for asymmetry of the reinforcement grid with respect to the principal axes of applied stresses are proposed to quantify the additional shear strain. The proposed formulation and algorithm are found to be adequate as a mechanics-based analytical procedure for prediction of the shear stress versus strain behaviour, especially for membrane elements with asymmetric reinforcement. The theoretical formulation can be implemented in numerical simulation.

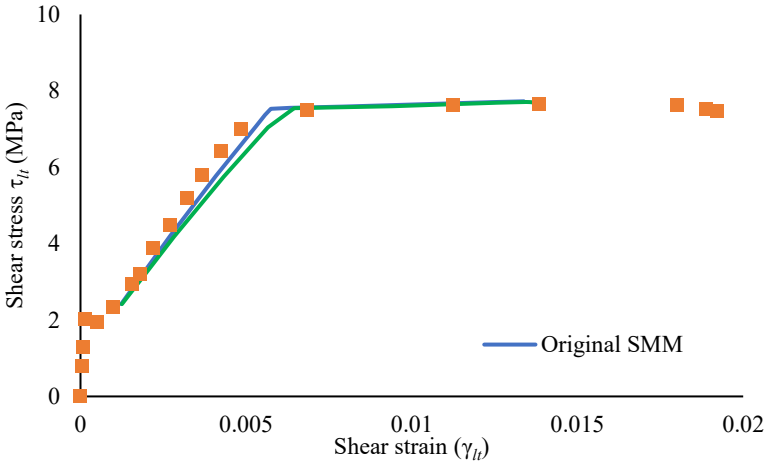


Fig 2. Experimental and predicted shear stress versus strain curves for Panel A3

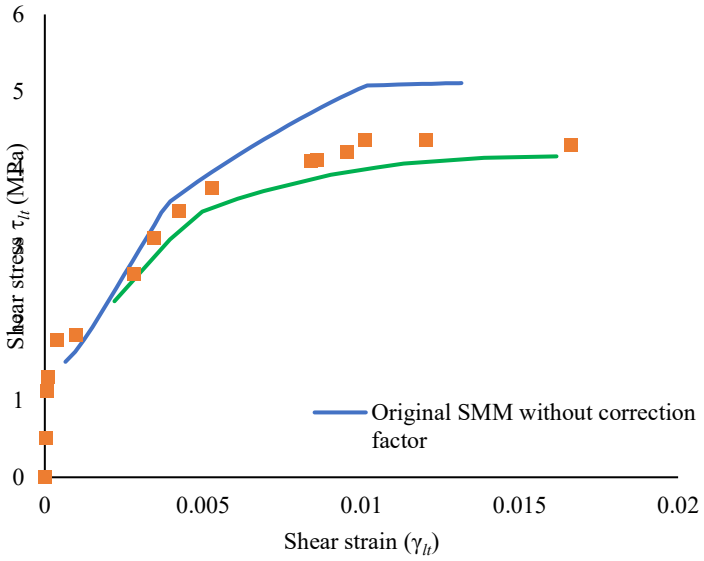


Fig 3. Experimental and predicted shear stress versus strain curves for Panel B3

References

[1] [1] Bavukkatt, Rajeevan. Sengupta, Amlan Kumar. and Belarbi, Abdeldjelil. (2013). "A modified approach to incorporate the Poisson's effect in the softened membrane model". *Journal of Structural Engineering*, CSIR-Structural Engineering Research Centre, 39(6), 632–644.

[2] [2] Belarbi, Abdeldjelil. and Hsu, Thomas.Tseng.Chuang. (1994). "Constitutive laws of concrete in tension and reinforcing bars stiffened by concrete". *Structural Journal*, American Concrete Institute, 91(4), 465–474.

[3] [3] Belarbi, Abdeldjelil. and Hsu, Thomas.Tseng.Chuang. (1995). "Constitutive laws of softened concrete in biaxial tension compression". *Structural Journal*, American Concrete Institute, 92(5), 562–573.

[4] [4] Hsu, Thomas.Tseng.Chuang. (1988), "Softened truss model theory for shear and torsion", *Structural Journal*, American Concrete Institute, 85(6), 624-635.

[5] [5] Hsu, Thomas.Tseng.Chuang. (1993), "Unified theory of reinforced concrete", *First Edition*, John Willey & Sons, West Sussex, U.K.

[6] [6] Hsu, Thomas.Tseng.Chuang. and Zhu, Ronnie.Rong.Hau. (2002), "Softened Membrane Model for Reinforced Concrete Elements in Shear", *Structural Journal*, American Concrete Institute, 99 (4), 460–469.

[7] [7] Kosuru, Ratna. Sai. and Sengupta, Amlan. Kumar. (2022), "Incorporation of shear—extension coupling in Softened Membrane Model", *Journal of Structural Engineering*, CSIR-SERC, 49(3), 181-191.

[8] [8] Pang, X.B., and Hsu, Thomas.Tseng.Chuang. (1995), "Behaviour of Reinforced Concrete Membrane Elements in Shear", *Structural Journal*, American Concrete Institute., 92(6), 665–679.

[9] [9] Sengupta, Amlan. Kumar. and Belarbi, Abdeldjelil. (2001), "Modelling effect of biaxial stresses on average stress–strain relationship of reinforcing bar in reinforced concrete panels", *Structural Journal*, American Concrete Institute, 98(5), 629–637.

[10] [10] Zhu, Ronnie.Rong.Hau. and Hsu, Thomas.Tseng.Chuang. (2002), "Poisson's effect in reinforced concrete membrane elements", *Structural Journal*, American Concrete Institute, Vol. 99(5), 631–640.

Impact of Tendon Failures: A Comparative Study on Twin Post-Tensioned Box-Girder Carriageways

Chiara Galatà, Davide Messina, Dario De Domenico, Antonino Recupero, Edoardo Proverbio

Department of Engineering,
University of Messina,
Contrada Di Dio - Villaggio Sant'Agata, 98166, Messina, Italy

Summary
This study presents a comparative investigation on a twin-carriageway post-tensioned (PT) box-girder viaduct with a mixed tendon system (unbonded and bonded). One carriageway has experienced some tendon failures, whereas the adjacent one remains intact. This configuration allows a direct assessment of how tendon failure influences prestressing losses, and the overall structural response. The study combines semi-destructive stress-release tests on steel wires with dynamic testing, including tendon-vibration-based force estimates. Results are presented in terms of wire-level residual stress, differences in vibration-based tendon force, and comparative vibration-based tendon force estimates between the two carriageways. The combined evidence supports a consistent interpretation of tendon condition in PT box-girder bridges.

1 INTRODUCTION

PT concrete box-girder viaducts are a cornerstone of modern transport networks, their durability and safety hinge on the integrity of the prestressing system and its corrosion protection, in particular the quality of grouting and the details of ducts and anchorages. When defects such as voids, bleeding/sedimentation, or grout segregation occur, tendons become vulnerable to corrosion and stress corrosion cracking, which can cause significant prestress losses or even strand/tendon failure. The specific hazards associated with strand durability and duct injection quality are well documented in industry guidelines [1]-[2]. Historically, the assessment of PT concrete bridges has relied heavily on visual inspections, which are notoriously unreliable for internal defects in grouted ducts. This limitation has driven the engineering community towards Non-Destructive Testing (NDT) and, more recently, towards the integration of vibration-based Structural Health Monitoring (SHM) systems [3],[4]. Ambient-vibration-based dynamic testing, which exploits environmental vibrations, has become a primary solution to overcome the limitations of visual inspections and ensure the long-term safety of infrastructure [5],[6]. The fundamental premise of vibration-based SHM is that a loss of prestressing force results in a reduction of the effective bending stiffness of the girder section, which should translate into measurable changes in natural frequencies. However, interpreting these dynamic data is challenging, mainly because environmental and operational variability (temperature, humidity, traffic) can often mask the relatively small signature of structural damage [7].

This paper leverages a twin-carriageway configuration - one deck with documented tendon failures and the adjacent deck without documented failures - to investigate whether tendon damage produces measurable differences in local residual stress and in the vibration-based force response of the remaining external unbonded tendons. Our approach is based on a cross-validation between: (i) direct measurements of residual stress from semi-destructive detensioning tests, and (ii) indirect force/stress estimates obtained from local tendon-vibration testing on external unbonded tendons.

2 CASE STUDY: TWIN PT BOX-GIRDER CARRIAGEWAYS

2.1 Description of box-girder viaducts

The case under examination concerns a PT concrete motorway viaduct in Southern Italy, completed in the early 2000s. The structure comprises two twin carriageways and adopts a continuous-girder scheme with three main spans of 95.00 m and two terminal counterweights of 24.50 m; the total length is 334.00 m, with a deck width of 11.00 m (Fig. 1). In plan, the viaduct follows a slight horizontal curvature. The

deck is a single-cell box girder of variable depth (approximately 4.75–2.55 m), erected by balanced cantilever using cast-in-situ segments; each span consists of 19 segments, with segment length varying from 5.25 m (maximum) to 3.0 m for the key (closure) segment, with a mixed prestressing system: 32 internal bonded tendons arranged in the deck slab (primarily adopted during the cantilever phase to resist negative moments), and 12 unbonded tendons running along the entire viaduct, with anchorages near the counterweights. The supports consist of two hollow box piers and two U-shaped abutments. Foundations are deep, with 46 and 28 piles for P1 and P2, respectively, common to both carriageways. During an internal inspection, four of twelve unbonded tendons in one carriageway (left) were found failed. As a precaution, the carriageway was closed to traffic, and the other was operated bidirectionally with restrictions for heavy vehicles. Selective openings of tendon ducts and grout sampling revealed heterogeneous grout conditions - whitish, soft segregated material and voids concentrated at high points along inclined tendon paths associated to extended corrosion of steel strands [8].

To quantify the structural implications of the tendon failures, we exploit the twin-deck configuration as a natural control. The strategy targets two complementary sources of evidence: (i) local estimates of residual stress in exposed steel wires via controlled stress-release (detensioning) tests, and (ii) frequency-based force estimates obtained from local vibration testing of external unbonded tendons on both carriageways. The reasonable hypotheses are that (a) the carriageway affected by external prestressing-system damage should exhibit lower wire-level residual stresses relative to the intact twin, and (b) differences in the identified tendon vibration frequencies and in the corresponding force estimates may be observed and could be compatible with different residual force levels in the remaining external tendons; however, this relationship is neither direct nor unique and may be influenced by tendon-specific boundary conditions, effective vibrating length, and environmental or operational variables. The combined outcomes will support an integrated interpretation of the bridge condition by linking semi-destructive stress-release measurements and non-destructive dynamic estimates of tendon force. Detailed test setups, sensor distribution layouts, acquisition parameters, and identification procedures are reported in the next section (Experimental Methodology).

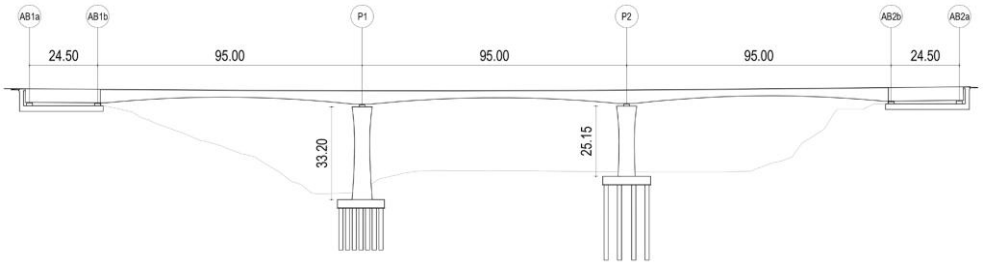


Fig. 1 Longitudinal profile of the generic carriageway.

3 EXPERIMENTAL METHODOLOGY

The experimental investigation relies on two methodologies that are complementary in scale and purpose: (i) local, semi-destructive stress-release tests (detensioning) on the bonded and unbonded prestressing steel to obtain direct indicators of residual stress; and (ii) non-destructive dynamic testing on unbonded tendons (ambient-vibration measurements) to estimate tendon force from identified vibration frequencies. All local investigations (detensioning and tendon-vibration measurements) were concentrated in the first main span. The consistent application of both methodologies on both decks (the damaged and the intact one) serves as a key element for cross-validation.

3.1 Semi-destructive residual prestress assessment (detensioning)

Wire-cutting (detensioning) tests were carried out on selected prestressing tendons - both unbonded and internal bonded - on both carriageways, to obtain a direct, local indicator of the residual tensile stress in the prestressing steel. For the unbonded tendons, the duct has an outer diameter of 140 mm and contains 27 strands, each with a nominal steel area of 139 mm^2. Detensioning was performed at wire level, on a single wire extracted from the strands, for both bonded and unbonded tendons. After local opening of the tendon duct, an individual wire was exposed over a short gauge length, cleaned, and instrumented using strain gauges (see Fig. 2).

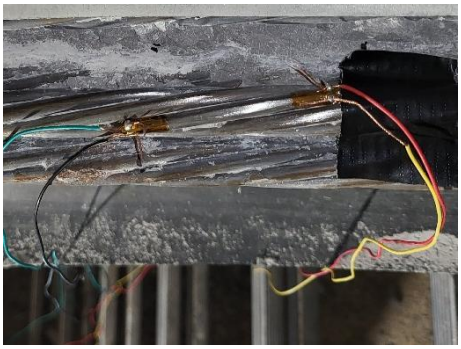


Fig. 2 Detensioning test on an unbonded PT tendon: exposed strand and strain-gauge instrumentation for residual prestress assessment.

Whenever possible, two strain gauges were installed on opposite sides of the wire to minimise the influence of local bending and to provide an average axial strain; in a few locations only one gauge could be used because of limited accessibility or surface condition. Strain readings were stabilised under steady temperature conditions prior to cutting. The wire was then cut using a thin abrasive disc to induce an abrupt stress release. The released strain, Δε, was computed as the difference between the post-cut and pre-cut stable readings and, for double-gauged tests, averaged between the two sensors.

Assuming linear elastic behaviour of the prestressing steel at the measured stress level, the residual tensile stress in the wire was obtained as:

$$\sigma_{\mathrm{det}} = E_s \Delta\varepsilon \tag{1}$$

where E_s is the elastic modulus of the steel and Δε is the released strain measured during cutting. In this campaign, E_s was assumed equal to 206 GPa. The resulting σ_{det} values are intended as 'wire-level' indicators that support a direct comparison between the two decks.

3.2 Vibration tests on unbonded PT tendons (both carriageways)

These tests consisted of local tendon-vibration measurements, not global operational modal testing of the bridge deck. Vibration measurements were carried out on the external unbonded PT tendons of both bridge decks to obtain an independent estimate of the residual prestressing force. Mono-axial IEPE accelerometers were installed on the investigated tendons by means of rigid metallic collars, ensuring that each sensor was integral with the tendon during vibration acquisition (see Fig. 3). Acceleration time histories were acquired mainly under ambient excitation induced by traffic and wind.

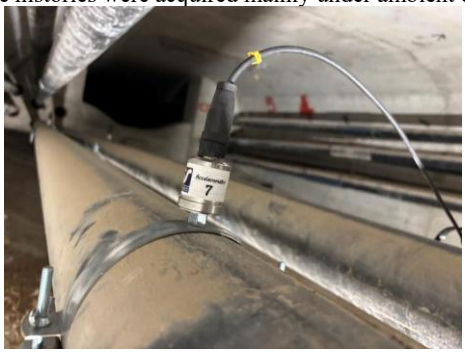


Fig. 3 Accelerometer mounting on unbonded tendon for vibration tests.

Sensor locations were selected according to the tendon layout between consecutive deviators. In general, accelerometers were installed at: (i) the mid-length of the reference segment, Lc/2; (ii) the mid-span of the free vibrating tendon length, L/2, measured between two consecutive deviators; and, for

selected acquisitions, (iii) the quarter-span position, L/4. The quarter-span measurements were mainly used to support mode identification and to check the consistency of the frequency peaks obtained from mid-span measurements.

The geometry and mechanical properties adopted for the back-calculation of the residual force were consistent across all tested tendons. The tests were performed on tendons located in different bridge segments on both the intact (opened to traffic) and the damaged (closed to traffic) carriageways, enabling a comparative assessment. The investigated tendons share common mechanical and geometric properties: the mass per unit length (m) adopted for the dynamic analysis is 46 kg/m. This value was experimentally determined over a short length and includes the mass of the steel strands, the sheath, and the grout, all contributing to the total vibrating mass. The total steel cross-sectional area A_{strands} is 3753 mm^2. It is important to note that the free vibrating length l, measured between deviators, varies for each individual tendon and was recorded during the in-situ testing campaign. For the model incorporating flexural rigidity (Eq. (3)), the moment of inertia I of the tendon was calculated considering the 27 steel strands arranged on three concentric registers and resulting in a value of 1.17E+07 mm^4. The moment of inertia of the grout and of the plastic sheath have been neglected. The elastic modulus E of the strand was assumed equal to 195 GPa. These input parameters, whether fixed or variable, were used in both the simplified taut-string model (Eq. (2)) and the model accounting for flexural rigidity (Eq. (3)) to determine the residual prestressing force T and the tendon stress σ_p in the two distinct bridge decks.

In line with the dynamic identification method, the subsequent methodological step consisted of processing the raw acquired data to isolate the natural vibration frequency of each tendon f_n, which is necessary for the back-calculation formulas.

Signal processing consisted of computing the Fast Fourier Transform (FFT) of the measured acceleration to obtain the amplitude spectrum. The dominant peak associated with the first transverse mode was identified and the corresponding natural frequency was denoted f_1. In the following, f_n indicates the natural frequency of the n-th mode (with $n = 1$ adopted herein).

Two formulations were considered. Eq. (2) reports simplified taut-string model (negligible flexural rigidity) in kN:

$$T_{\text{Taut-string}} = 4\, m\, l^2 \left(\frac{f_n}{n}\right)^2 \tag{2}$$

Eq. (3) reports the model accounting for flexural rigidity (EI) in kN:

$$T_{\text{flexural}} = 4\, m\, l^2 \left(\frac{f_n}{n}\right)^2 - \frac{EI}{l^2}\,(n\pi)^2 \tag{3}$$

Finally, the tendon stress was obtained as $\sigma_p = T/A_{\text{strands}}$. The two formulations were used to bracket the estimated force, acknowledging uncertainty in boundary conditions and in the effective EI of the tendon–sheath system.

4 RESULTS AND DISCUSSION

4.1 Detensioning outcomes: released strains and residual wire stress

Table 1 summarises the detensioning results. The local residual wire stress σ_det was computed as indicated in Eq. (1), where released strain Δε is expressed in microstrain (με).

Since the experimental campaign included both unbonded (UB) and bonded (B) tendons, the results are reported and interpreted separately by tendon type, and no aggregated statistics are computed across the full dataset.

Table 1 Summary of wire detensioning tests on bonded and unbonded tendons.

Tendon	Segment ID	Type	Test ID	σ_{det} (MPa)
T-SX-11-C	1A	B	DT5	490.69
T-SX-15-C	1A	B	DT6	1028.14
T-SX-23-O	3A	UB	DT2	622.12
T-SX-23-O	7A	UB	DT1	1260.20
T-DX-23-C	1A	UB	DT3	1176.26
T-DX-17-O	1A	B	DT8	886.83
T-DX-9-C	4A	B	DT7	949.24
T-DX-23-C	7A	UB	DT4	1259.79
T-DX-10-O	7A	B	DT9	490.07

Note: O = Opened carriageway; C = Closed carriageway; B = bonded tendon; UB = unbonded tendon. Results are not aggregated across tendon types; carriageway comparisons are discussed only within the same type.

For the unbonded specimens (n=4; tendons T-SX-23-O and T-DX-23-C), σ_{det} ranges from 622.12 to 1260.20 MPa. Within this UB subset, the Open carriageway results span 622.12–1260.20 MPa (DT2 and DT1), whereas the Closed carriageway results are consistently high, 1176.26–1259.79 MPa (DT3 and DT4). For the bonded specimens (n=5; tendons T-SX-11-C, T-SX-15-C, T-DX-9-C, T-DX-17-O, T-DX-10-O), σ_{det} ranges from 490.07 to 1028.14 MPa; within this subset, the Open carriageway spans 490.07–886.83 MPa and the Closed carriageway spans 490.69-1028.14 MPa.

The detensioning results show non-zero residual wire stresses in all tested specimens, with values spanning approximately 622-1260 MPa for the unbonded subset and 490-1028 MPa for the bonded subset (Table 1). These values are discussed separately by tendon type, and no quantitative inference on the fraction of original prestress is drawn from the detensioning results alone.

4.1.1 Methodological Reliability and Outliers

Measurement reliability depends on the strain-gauge configuration adopted during detensioning. Whenever two strain-gauges were available on opposite sides of the wire, the released strain was averaged to mitigate local bending sensitivity; conversely, single-gauge measurements are retained but flagged as higher-uncertainty observations.

Importantly, the lowest residual stresses in the dataset (≈490-622 MPa, Table 1) cannot be attributed to gauge configuration alone, as low values also occur in a double-gauged test (e.g., DT5 ≈490 MPa). Therefore, no formal outlier removal is applied to the detensioning results; rather, the lower-band values are reported as part of the observed variability and discussed within each tendon family.

Given the mixed prestressing system, detensioning outcomes are interpreted separately for unbonded (UB) and bonded (B) tendons (Table 1). For the UB subset, σ_{det} ranges from 622 to 1260 MPa; the closed-to-traffic deck shows consistently high values (≈1176-1260 MPa), whereas the open deck spans a wider interval (≈622-1260 MPa). For the internal bonded tendons, σ_{det} ranges from 490 to 1028 MPa. In this case, the variability is expected to be influenced by tendon-specific factors that differ from the external/unbonded system, including stressing conditions and sequence, tendon length/profile and associated friction and anchorage effects, as well as the local demand at the tested segment. Consequently, deck-to-deck comparisons are meaningful only within the same tendon type, and aggregated statistics merging bonded and unbonded results are not reported.

For completeness, sample means specific for each tendon type are: UB-Opened ≈941 MPa (n=2) vs Closed ≈1218 MPa (n=2); B-Opened ≈688 MPa (n=2) vs Closed ≈823 MPa (n=3). These values are provided as descriptive statistics only, given the limited sample size and tendon-specific variability.

4.2 Vibration Test Results: Comparison of Estimation Models

The initial step in analysing the dynamic test results was to quantify the difference in force T calculated using the simplified taut-string model (Eq. (2)) versus the more complete flexural rigidity model (Eq. (3)). This comparison, performed on a representative subset of tested tendons from both carriageways, is summarized in Table 2. The objective was to determine the necessity of incorporating the flexural rigidity component EI in the final analysis. The difference between the force values calculated by the two methods is minimal, not exceeding 4.0% for all analysed cases. Table 2 also reports the corresponding tendon stress values, evaluated as $\sigma_{\mathrm{p}} = T_{\mathrm{flexural}}/A_{\mathrm{strands}}$ and expressed in MPa.

For the subsequent analysis and comparison with the stress-release tests, the results obtained from the flexural rigidity model (Eq. (3)) - being the most theoretically complete - were adopted as the representative prestressing force for the vibration method. The sensor position adopted for frequency identification was generally close to the mid-length of the tested tendon span; additional quarter-span records were used in selected cases to confirm the modal interpretation.

Table 2 Frequency-based force estimates from local vibration tests on unbonded tendons.

Tendon ID	Segment ID	L (m)	Measured f_1 (Hz)	$T_{\mathrm{Taut-string}}$ (kN)	T_{flexural} (kN)	Difference (%)	$\sigma_{\mathrm{p}} = T_{\mathrm{flexural}}/A_{\mathrm{strands}}$ (MPa)
T-SX-23-O	1A	14.22	8.3	4790	4730	1.25%	1260
T-SX-23-O	7A	16.85	9.3	4503	4424	1.75%	1179
T-SX-23-C	1A	14.22	10.8	4325	4214	2.57%	1123
T-SX-23-C	4A	15.96	7	2289	2200	3.89%	586
T-DX-23-C	1A	19.47	11.1	4569	4457	2.45%	1188
T-DX-23-C	4A	10.51	10	4672	4582	1.93%	1221
T-DX-23-C	7A	16.85	9.3	4504	4421	1.84%	1178
T-DX-23-O	1A	14.22	8.3	4790	4730	1.25%	1260
T-DX-23-O	7A	16.85	9.4	4601	4521	1.74%	1205

Note: O = Opened carriageway; C = Closed carriageway. Tendon stress is computed from the flexural rigidity estimate as $\sigma_{\mathrm{p}} = T_{\mathrm{flexural}}/A_{\mathrm{strands}}$ (MPa). L denotes the free vibrating tendon length between consecutive deviators. The reported f_1 values were mainly identified from accelerometers installed close to the mid-length of the reference segment or of the free vibrating tendon length. For selected acquisitions, additional quarter-span measurements were used to support mode identification.

4.3 Validation of Dynamic Prestress Estimation Against Stress-Release Tests

The accuracy of the dynamic testing method was validated by comparing its results with those obtained from the semi-destructive stress-release tests (detensioning) performed on the same bridge segments. This correlation is essential as the stress-release test provides a direct measure of residual stress σ_det within the wire strands. Table 3 presents a direct comparison of the residual stress calculated by the vibration method (σ_vib, using the flexural model) against the measured stress from the detensioning tests.

Table 3 Comparative residual stress assessment: dynamic vs stress-release methods.

Tendon ID	Segment ID	σ_{det} (MPa)	σ_{vib} (MPa)	$\lvert\Delta\sigma\rvert$ (MPa)	Δσ (%)
T-SX-23-O	7A	1260	1179	81	6.89
T-DX-23-C	1A	1176	1188	12	0.98
T-DX-23-C	7A	1260	1178	82	6.96

Note: O = Opened carriageway; C = Closed carriageway.

The results presented in Table 3 provide the crucial validation for the dynamic testing method. The residual stress estimated by the flexural model σ_{vib} shows a strong correlation with the stress directly measured by the semi-destructive detensioning tests σ_{det}.

Quantitatively, the difference Δσ between the two independent methods is consistently low, averaging less than 5% across the sampled tendons used for validation. This high level of agreement supports the reliability of the vibration method as a non-destructive tool for accurately assessing residual prestress in this specific type of PT structure.

Beyond the local validation, the twin-deck comparison is the key expectation of this study: one carriageway lacks four unbonded tendons due to documented ruptures, hence a clearer signature of prestress loss might be anticipated at deck level. In the investigated segments of the first span, however, the measured quantities (wire-level σ_{det}, vibration-based tendon force for the accessible unbonded tendons, and the identified tendon vibration frequencies) do not exhibit a strong, unambiguous contrast between the two carriageways. This suggests that the "rupture effect" may be masked by (i) the intrinsic heterogeneity of a mixed tendon system and tendon-specific loss mechanisms, and/or (ii) the spatial locality of the testing campaign, which was concentrated in the first main span near the anchorage zone. Additionally, tendon-vibration estimates remain sensitive to modelling assumptions (effective vibrating length/boundary conditions), which may reduce sensitivity to subtle force differences in field conditions. An additional aspect concerns the physical meaning of the dynamic measurements. In the present study, vibration tests were performed on the tendons themselves, rather than on the global bridge structure. While the loss of prestressing elements may affect the overall stiffness and dynamic response of the deck, it does not necessarily imply a proportional modification of the dynamic behaviour of the remaining tendons. These are primarily governed by their imposed initial deformation and boundary conditions. Consequently, even in the presence of tendon ruptures at deck level, the vibration-based response of the residual tendons may remain only weakly affected, providing a further explanation for the limited contrast observed between the two carriageways.

5 CONCLUSIONS

This study leveraged a twin-deck PT box-girder configuration (one deck with documented unbonded tendon ruptures and an adjacent deck without documented failures) to examine a combined protocol for residual prestress assessment. Local semi-destructive detensioning tests were performed on both bonded and unbonded tendons, while ambient-vibration measurements were used to estimate the residual force in selected unbonded tendons, enabling a cross-check between complementary approaches. From a methodological standpoint, vibration-based tendon forces were ultimately estimated using the flexural (beam) formulation, i.e., explicitly accounting for tendon flexural rigidity *EI*. A parallel comparison with the simplified taut-string formulation indicates that the contribution of *EI* is minor for the investigated configuration, with typically small differences between the two models; therefore, the taut-string approach may be considered acceptable for preliminary screening, while the flexural model remains the preferred option for the final force/stress estimates. Moreover, in the tendon/segment cases where both methods were available, vibration-based stress estimates were consistent with stress-release results, supporting the potential of tendon vibration as a non-destructive tool for the assessment of residual force in unbonded tendons.

The comparative twin-deck outcome is less distinct than initially expected: despite the documented rupture of four unbonded tendons in one carriageway, the measurements collected in the first main span, close to the anchorage zone, do not reveal a strong and unambiguous deck-level signature of prestress loss. This suggests that, at least in the tested locations, the rupture-related effect may be masked by tendon-to-tendon variability and mixed-system loss mechanisms. In addition, the spatial locality of the campaign and the modelling assumptions inherent to tendon-vibration force estimation

under field boundary conditions may reduce sensitivity to subtle force differences. This outcome is also consistent with the fact that the dynamic tests targeted the tendons rather than the global structure. While tendon ruptures may influence the deck-level response, the vibration characteristics of the remaining tendons are mainly controlled by their initial imposed deformation and local boundary conditions and may therefore exhibit limited sensitivity to the loss of neighbouring prestressing elements.

Regarding the effect of tendon ruptures, the results highlight that detensioning-derived wire-level stresses are local quantities and may exhibit significant tendon-to-tendon scatter. In a mixed prestressing system, tendon family (bonded vs unbonded) and tendon-specific conditions (e.g., stressing procedures, tendon length/profile and friction-related effects in bonded tendons, and distinct long-term loss profiles) can dominate the observed local values. Consequently, deck-to-deck comparisons should be performed only within homogeneous tendon families, and no unique monotonic trend of local residual stress with respect to the presence of ruptures should be assumed a priori. Overall, the combined testing campaign presented herein may support residual-prestress assessment in PT box-girder bridges and may contribute to maintenance-oriented decision making, particularly when a subset of tendons is accessible for dynamic measurements and local stress-release testing.

References

[1] fib Task Group 9.8 Grouting. 2002. "Grouting of Tendons in Prestressed Concrete: Guide to Good Practice." fib Bulletin 20. Lausanne, Switzerland: International Federation for Structural Concrete (fib). doi:10.35789/fib.BULL.0020.

[2] Corven, John, and Moreton, Alan. 2013. "Post-Tensioning Tendon Installation and Grouting Manual." Washington, DC: Federal Highway Administration. FHWA-HIF-13-026.

[3] Peeters, Bart, and De Roeck, Guido. 2001. "One-Year Monitoring of the Z24-Bridge: Environmental Effects versus Damage Events." Earthquake Engineering & Structural Dynamics 30:149-171. doi:10.1002/1096-9845(200102)30:2<149::AID-EQE1>3.0.CO;2-Z.

[4] Salawu, Olusegun S. 1997. "Detection of Structural Damage through Changes in Frequency: A Review." Engineering Structures 19:718-723. doi:10.1016/S0141-0296(96)00149-6.

[5] Xia, Yong, Hao, Hong, Zanardo, Giovanna, and Deeks, Andrew J. 2006. "Long Term Vibration Monitoring of an RC Slab: Temperature and Humidity Effect." Engineering Structures 28:441-452. doi:10.1016/j.engstruct.2005.09.001.

[6] Hasani, Hamed, and Freddi, Francesco. 2023. "Operational Modal Analysis on Bridges: A Comprehensive Review." Infrastructures 8:172. doi:10.3390/infrastructures8120172.

[7] Chillitupa-Palomino, Luis, Renedo, Carlos M. C., García-Palacios, Jaime H., and Díaz, Iván M. 2025. "Long-Term Dynamic Monitoring of Post-Tensioning External Tendons: Temperature Effect Evaluation." Buildings 15:69. doi:10.3390/buildings15010069.

[8] Galatà, Chiara, Messina, Davide, Recupero, Antonino, and Proverbio, Edoardo. 2026. "Failure Assessment of External Bonded Tendon in a Box Girder Post-Tensioned Bridge Deck." Paper presented at Construction Pathology, Rehabilitation Technology and Heritage Management, Bilbao, Spain, May 26-29.

Mechanical Behaviour and Coupling Effect of Hybrid Ultra High Performance Fibre Reinforced Concrete

Tuluhan Ergin, Matteo Colombo, Marco Carlo Rampini, Marco di Prisco

Department. of Civil and Environmental Engineering,
Politecnico di Milano,
Piazza Leonardo da Vinci 32, Milan (20133), Italy

Summary
Developing thin, lightweight, durable precast elements is a key for industrialized construction. This research investigates a hybrid composite, combining non-metallic textiles with a fluid ultra-high performance fibre-reinforced concrete (UHPFRC) matrix. Performance was characterized via four-point bending tests on thin specimens (<30mm) and comparative tests on plain matrices.

Results indicate a coupling effect enabled by the steel fibres leading to increased flexural strength and ductility. The composite demonstrated high load-bearing capacity and thin, distributed cracking prior to failure. This combination makes the hybrid composite promising for resilient, slender precast elements.

1 INTRODUCTION

The construction industry is increasingly moving towards industrialisation and off-site manufacturing to enhance efficiency, quality control, and sustainability. In this context, the development of thin, lightweight, and durable precast concrete elements is important. Reducing the thickness of structural and non-structural elements, such as façade panels, roofing shells, or tunnel linings, minimizes material consumption and transport costs, aligning with the principles of resource-efficient design. However, conventional reinforced concrete (RC) poses limitations due to the substantial cover required for corrosion protection of steel reinforcement, which dictates minimum thickness and adds significant weight.

Textile Reinforced Concrete (TRC), also referred to as Fabric-Reinforced Cementitious Matrix (FRCM), has emerged as a promising solution to these limitations. By replacing steel bars with non-corroding high-strength textiles (e.g., glass, carbon, or basalt), TRC allows for the production of extremely thin and slender elements [1]. Despite these advantages, TRC composites can exhibit a significant drop in stiffness after the first crack where the matrix brittle behaviour is not immediately compensated by the textile reinforcement [1].

To address these challenges, recent research has explored "hybrid" reinforcement systems that combine continuous textile reinforcement with discontinuous short fibres (SF), typically made of steel or polymer, dispersed within the matrix, as the Ultra-High-Performance Fibre-Reinforced Concrete (UHPFRC) SF bridge micro-cracks delaying crack localization [2]. In such hybrid composites, this interaction enhances the stress transfer mechanism to the textile reinforcement providing a synergistic response (coupling effect) [3,4]. This synergy leads to a multiple crack pattern and an improved flexural capacity compared to the individual contributions of the single components [3,4].

Understanding the mechanical performance of these hybrid solutions is essential for the production of new, thin precast elements. The objectives and scope of this investigation are detailed in the following section.

1.1 Objectives and Scope

The paper focuses on the bending behaviour of hybrid cementitious composites specifically optimised for thin, lightweight precast elements. The study investigates the flexural behaviour of two commercial UHPFRC matrices A and B) reinforced with an Alkali-Resistant (AR) glass textile and aims at understanding the specific contribution of each component (matrix, steel micro-fibres, and textile) and their interaction (coupling effect).

A comprehensive experimental programme was conducted, including two levels:

- Matrix Characterisation: Compressive strength and residual flexural tensile strength tests (according to EN 14651) to specify the baseline performance of the fibre reinforced matrices.

- Structural Investigation: Four-point bending tests on thin elements (<30 mm) to investigate the performance of slender precast elements.

In order to deeply analysed the synergistic effect, for the matrix labelled as B, a full breakdown was analysed: plain Ultra-High Performance Concrete (UHPC) (with no fibres/textile), UHPFRC (fibres only), TRC (textile only), and the Hybrid composite (both). Alternatively, for Matrix A only a targeted comparison between the UHPFRC and the Hybrid solution was investigated to validate the influence of the AR fabric addition.

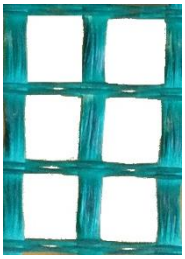
2 EXPERIMENTAL PROGRAM

An experimental campaign was performed to investigate the flexural behaviour of hybrid composites suitable for thin precast elements. This section outlines the materials used and the details of the experimental procedures.

2.1 Material characteristics

The same Alkali-Resistant (AR) glass fabric was adopted in all the investigated solutions in order to ensure a direct comparison between the different matrix systems. It consists of a double-leno weaved fabric, coated with an epoxy-based resin, featuring the same glass cross-section in both orthogonal directions (Table 1).

Table 1 Technical data of the AR-glass fabric (from manufacturer data sheet)

Property	Value (warp/weft)	Photo
Mesh grid (mm)	33 x 33	
Net grid (mm)	26 x 25	
Tensile capacity (kN/m)	165 / 150	
Average axial stiffness in tension (kN/m)	4459 / 4411	
# Roving in 1 m	120 / 30	
Roving fineness (Tex)	2400 / 4 x 2400	
Equivalent thickness (mm/m)	0.108 / 0.108 (±5%)	

Regarding the cement-based matrices, two commercial UHPFRC products specifically designed for flowability were investigated (Matrix A and Matrix B):

- Matrix A is a two-component system with a cement-based premix and high-carbon SF (1.7% by volume).
- Matrix B is a three-component system comprising a premix, a liquid admixture and SF (3.1% by volume).

The physical and mechanical properties of the short SF are listed in Table 2.

Table 2 Physical and mechanical properties of SF

Matrix	Aspect Ratio	Length [mm]	Tensile Strength [MPa]	Elastic Modulus [GPa]	Elongation at Failure (%)
A	62	13	2750	200	1.5-3.0
B	70	14	2600	N.A.	N.A.

Both mixtures can be classified as self-compacting. The selection of a horizontal casting technique, combined with high flowability, was motivated by standard practice for the target application involving large, thin structural elements. The mechanical properties of the matrices were characterized via compressive strength tests on 100 mm cubes (EN 12390-3) and via three-point bending tests on notched prisms (150 x 150 x 600 mm) according to EN 14651. Four nominally identical tests were performed for each material; results are presented in Table 3 and Fig. 1. In the table, $f_{ct,fl}$ represents the limit of

proportionality (LOP), while f_{R1} and f_{R3} denote the residual flexural tensile strengths at 0.5 mm and 2.5 mm crack mouth opening displacement (CMOD), respectively. The results represented in Figure 1 are the average curves of all the nominally identical tests performed for each material.

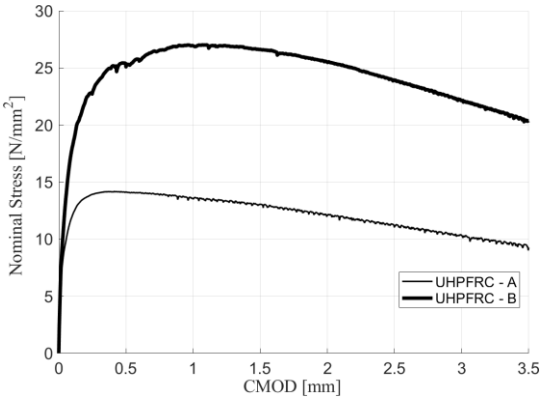


Fig. 1 Nominal stress - CMOD test average results (test performed in according with EN 14651)

Table 3 Mechanical properties of the UHPFRC matrices.

Matrix	Avg. Comp. Strength [MPa] (COV)	$f_{ct,fl}$ [MPa] (COV)	f_{R1} [MPa] (COV)	f_{R3} [MPa] (COV)
A	107.9 (1%)	9.65 (10%)	14.13 (7%)	11.09 (7%)
B	128.4 (8%)	13.26 (9%)	25.06 (10%)	23.92 (12%)

2.2 Specimen Preparation

Four nominally identical specimens were tested for each one of the six alternative solutions analysed, for a total of 24 elements. To assess casting repeatability, for each solution two different production batches were used. (Table 4).

Table 4 Experimental Program Summary

Series ID	Matrix Type	AR Glass Fabric	SF	# Samples	Curing time [days]
B-UHPC	B	–	–	4	42 & 43
B-TRC	B	+	–	4	42 & 43
A-UHPFRC	A	–	+	4	35 & 40
B-UHPFRC	B	–	+	4	35 & 36
A-Hybrid	A	+	+	4	35 & 40
B-Hybrid	B	+	+	4	35 & 36

All matrices were mixed according to the manufacturers' recommendations. The specimens were cast horizontally in ad-hoc moulds aimed at producing thin slabs with nominal dimensions of 500 x 150 x 30 mm³. In cases of AR-glass fabric addition, a two-stage wet-on-wet casting technique was used to ensure proper fabric positioning and good adherence between layers. In these cases, a single layer of AR-glass fabric was placed at a depth of 10 mm from the bottom surface (tension side during the test). This arrangement ensured that the warp direction was aligned with the longitudinal axis of the specimen, five warp bundles (each made of 4 rowing) were placed in each sample providing a 18.00 mm² glass cross-section to effectively resist the flexural tensile stresses. Specimens were demoulded after 24 hours and cured in a humidity chamber (20°C, ~98% RH) until the day of testing.

2.3 Test Setup and Procedure

Four-point bending tests were conducted using a 30 kN capacity electro-mechanical testing machine (Fig. 2). The specimens were simply supported on two steel rollers over a span of 450 mm and with a shear span of 150 mm. Tests were performed under displacement control adopting machine cross-head as a feedback parameter and imposing a displacement rate of 0.003 mm/s.

Although LVDTs were installed to measure crack opening, in several hybrid specimen tests they detached prematurely due to the extensive formation of multiple cracks on the tension side. To ensure a consistent and continuous comparison across all series, the results and discussion presented in this paper are only based on the machine cross-head displacement (CHD) measurements.

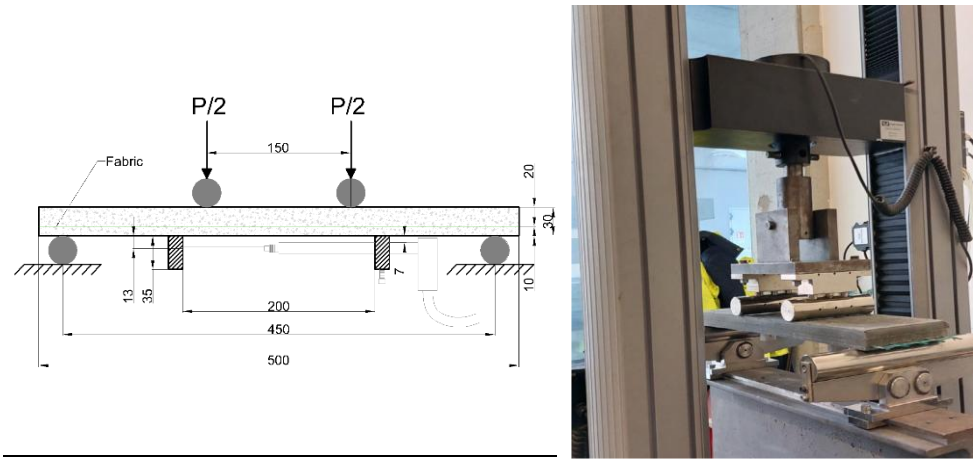


Fig. 2 Test setup scheme (left) and experimental photograph (right).

3 RESULTS AND DISCUSSION

The results of the bending tests for the investigated series are presented in Fig. 3 in terms of nominal flexural stress (computing according to a De Saint Venant formulation for bending assuming an elastic homogeneous cross section) versus CHD. A summary of the key mechanical parameters, including the average peak stress σ_{peak} and the maximum displacement at failure, is provided in Table 5.

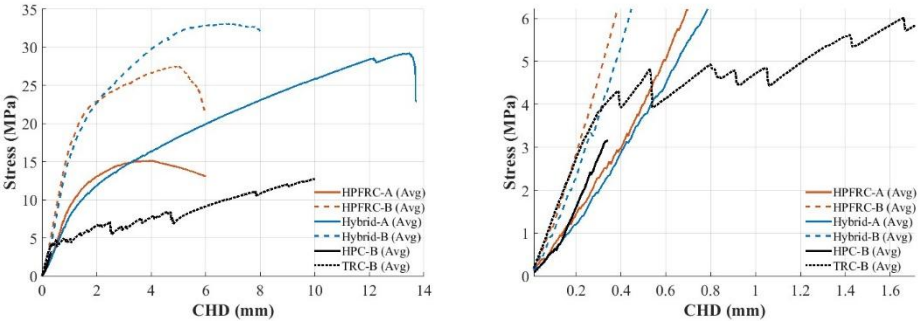


Fig. 3 Nominal flexural stress versus CHD curves: whole graph (left) and zoom of the initial response phase (right).

3.1 Discussion on Matrices Comparison

The comparison between the two plain HPFRC matrices (orange curves in Fig. 3) highlights the superior performance of Matrix B. The HPFRC-B series exhibited a peak stress of approximately 27.50 MPa, significantly higher than the 15.00 MPa recorded for HPFRC-A. This aligns with the residual

tensile strength results (f_{R1}, f_{R3}) obtained from the standard characterization (Table 3) and is also justified by the very different fibre contents.

Table 5 Summary of flexural test results (Avg. Peak Stress, Avg. Max CHD, etc.)

Series ID	Avg. Peak Stress [MPa] / corresponding CHD [mm]	Avg. Max CHD [mm] / corresponding stress [MPa]
B-UHPC	3.16 / 0.34	0.34 / 3.16
B-TRC	12.75 / 9.99	9.99 / 12.75
A-UHPFRC	15.11 / 3.93	6.00 / 13.06
B-UHPFRC	27.50 / 4.95	6.00 / 21.49
A-Hybrid	29.19 / 13.29	13.73 / 22.91
B-Hybrid	33.09 / 6.89	8.00 / 32.15

3.2 Effect of Textile Reinforcement addition

The contribution of the textile reinforcement is evident when comparing the HPC-B (no SF) and TRC-B (textile only) curves. While the plain HPC is brittle, the inclusion of the AR fabric (i.e., TRC system) lead to the typical strain-hardening behaviour of textile-based composites, allowing the element to sustain loads over large deformations, despite its relatively low initial stiffness and cracking stress.

The most remarkable performance is observed in the Hybrid systems (blue curves), where the benefits of the SF and the textile reinforcement are combined:

- Enhanced Load Bearing Capacity: both hybrid series exhibited a “coupling effect”, where the synergy between components resulted in a substantial increase in flexural capacity compared to individual systems. Hybrid-B achieved the highest flexural strength of roughly 33 MPa, while Hybrid-A reached approximately 29 MPa of nominal strength.
- Ductility and Deformability: the presence of steel fibres bridges the micro-cracks in the matrix, delaying the debonding of the textile and allowing it to be engaged more effectively. Hybrid-A demonstrated exceptional deformability, sustaining loads up to a CHD of nearly 14 mm. Hybrid-B, while stiffer and stronger, also showed significant ductility compared to the plain HPFRC.

3.3 Cracking Behaviour

The cracking patterns observed at failure provide further insight into the mechanical response of the different composites. As illustrated in the representative sketches in Fig. 4, the Hybrid specimens exhibited a multiple cracking pattern with thin, distributed cracks along the constant moment region. This contrasts with the localized single crack typical of plain UHPC and UHPFRC or the wider crack spacing observed in TRC systems. This distributed cracking is a direct result of the SFs' ability to transfer stress between the matrix and the textile, preventing premature crack localization.

4 CONCLUSIONS

This study investigated the mechanical performance of hybrid textile-reinforced UHPFRC composites designed for thin precast elements under flexural loads. Based on the experimental results, the following conclusions can be drawn:

- Viability for Precast Applications: the investigated UHPFRC matrices proved suitable for casting thin, reinforced elements using a wet-on-wet casting technique. This approach ensured proper textile bonding without the segregation issues.
- Mechanical Synergy and Coupling Effect: a distinct coupling effect was observed between the SF and the AR-glass textile. The hybrid composites achieved higher flexural strengths than either the HPFRC or TRC counterparts, primarily by optimising crack distribution and delaying the localisation of tensile stresses.

- Deformative Response Improvement: the textile reinforcement transformed the post-cracking behaviour of UHPC and UHPFRC specimens. All the investigated hybrid systems reported a strain-hardening behaviour, ensuring high sustained load under significant deflections.
- Influence of Matrix Quality: the mechanical properties of the matrix hosting the hybrid system are critical. The higher-grade Matrix B leads to a stiffer and stronger composite, than Matrix A one, mainly thanks to the higher SF volume content. This suggests that the composite performance can be tailored to specific design requirements, also changing the different mechanical parameters composing the hybrid solutions.

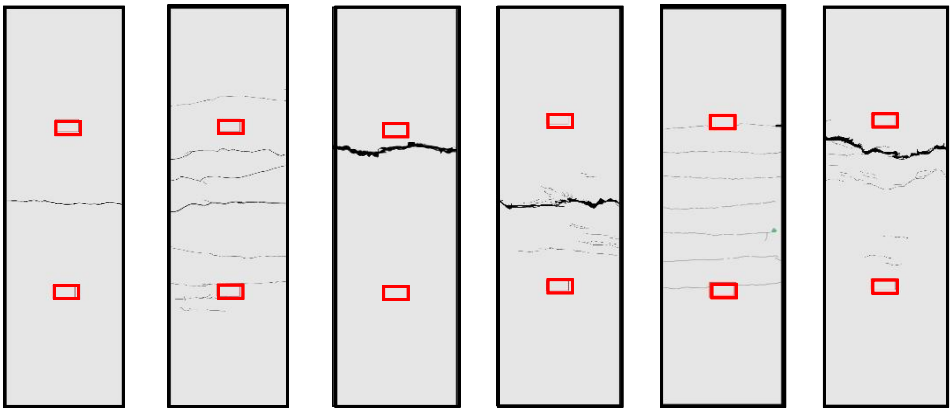


Fig. 4 Representative sketches of crack patterns (I) B-UHPC, (II) B-TRC, (III) A-UHPFRC, (IV) B-UHPFRC, (V) A-Hybrid, (VI) B-Hybrid

Acknowledgements

The authors would like to acknowledge Gavazzi Tessuti Tecnici, Holcim Italia, Lombardi and Mapei for their precious contribution to the research, including discussion and supply of materials. The research was also financially supported by ReLUIS 2024/2026 – WP14.

References

[1] Paul, Sachin, and Ravindra Gettu. 2023. "Engineering the Tensile Response of Glass Textile Reinforced Concrete for Thin Elements" *Sustainability* 15:19. Accessed January 19, 2026. doi: 10.3390/151914502

[2] Gong, Ma, Fu, Hu, Ouyang, Zhang and Wang. 2022. “Utilization of fibers in ultra-high performance concrete: A review.” *Composites Part B: Engineering* 242. Accessed January 19, 2026. doi: 10.1016/109995

[3] Zani, Colombo, di Prisco. 2014. “Flexural behavior of fiber and textile reinforced HPC thin plates.” Paper presented at fib Congress, Mumbai, India, February 10-14

[4] Zhu, Liu, Yao, Li, Du, Shi. 2019. “Effects of short fiber and pre-tension on the tensile behavior of basalt textile reinforced concrete.” *Cement and Concrete Composites* 96:33-45. Accessed January 19, 2026. doi: 10.1016/11015

Cracking behaviour in carbon-reinforced concrete under biaxial tensile loading

Jonathan Schmidt, Steffen Marx and Manfred Curbach

Institute of Conctrete Structures,
TUD Dresden University of Technology,
George-Bähr-Str. 1, 01069 Dresden, Germany

Summary
The service life of concrete pavements is determined by the durability of joint fillers and concrete spalling at the joint flanks. Therefore, the primary objective of this research is to repair damaged concrete pavements with a corrosion-resistant, material-minimised layer of carbon-reinforced concrete (CRC). This layer covers existing joints and enables a continuous pavement which, in addition to traffic loads, is exposed to temperature loads. In winter, low temperatures cause the joints to open and create tensile stresses in the CRC layer. Cracks form, with the carbon grid determining the width and number of cracks. Biaxial stresses occur in the CRC layer above the intersecting joints. These stresses can vary depending on the joint spacing and the deformation limits of the concrete pavement, resulting in variations in the width, spacing, and orientation of the cracks. Therefore, the cracking behaviour of the CRC layer was investigated under various ratios of biaxial tensile loading.

1 INTRODUCTION

Jointed plain concrete pavements (JPCP) cannot be used to their full potential because damage occurs in the joint area after only a short time period. The joints are chemically attacked by pollutants dissolved in water, such as chlorides and alkalis, while at the same time being subjected to mechanical stress from traffic. In addition, joint overpressing due to thermal expansion of the pavement slabs can lead to cracks and spalling. Even a blow-up of the concrete pavement can occur due to overpressure on the joints. The joint fillers and joint flanks are damaged, making repairs necessary every 7 to 10 years [1]. In order to permanently increase the durability of JPCP, a covering layer of CRC can be used as a repair measure.

Carbon-reinforced concrete is not susceptible to corrosion thanks to its non-metallic reinforcement made of carbon fibres, thus enabling a reduction in concrete cover. As a result, CRC offers significant material savings in various applications in new construction and strengthening of existing structures, as shown in [2], [3]. The advantages of CRC can be utilised in the repair of JPCP by applying a 40 to 70 mm thick CRC covering layer over the joints, see Fig. 1. The CRC layer is designed to absorb joint deformations and transfer them into a fine crack pattern. The carbon reinforcement limits the crack widths in the covering layer and, due to the smaller yarn spacing than with conventional steel bars, allows for short distances between the cracks.

Maintenance and repair of existing JPCP with CRC requires first grinding down the damaged concrete and refurbishing the concrete surface. Then, a 400 to 800 mm long separating layer using a bond-interrupting agent is applied on both sides of the joint to allow the CRC layer to deform freely. Cracks appear in the CRC layer above the separation layer when the pavement deforms. These deformations are caused by two factors: concrete shrinkage and temperature-related expansion and contraction of the materials. Since the existing pavement slabs expand under elevated temperatures and contract under low temperatures, the joints will close in summer and open in winter. This leads to compressive stresses under elevated temperatures and to tensile stresses under low temperatures in the CRC layer.

The CRC layer extends beyond the separating layer and is adhesively bonded to the existing concrete pavement. Additional dowels can be used to improve the bond with the existing JPCP. The design of the CRC layer depends on the joint widths and spacing of the existing concrete pavement, but also on the traffic load, thermal deformation, and the creep and shrinkage behaviour of the concrete. Initial investigations into the load-bearing, deformation, crack and bond behaviour of the CRC layer over the joint area of an existing concrete pavement are shown in [4]–[6]. The experimental investigations, shown here, focus on the effects of low temperatures in order to develop initial design limits for a CRC layer.

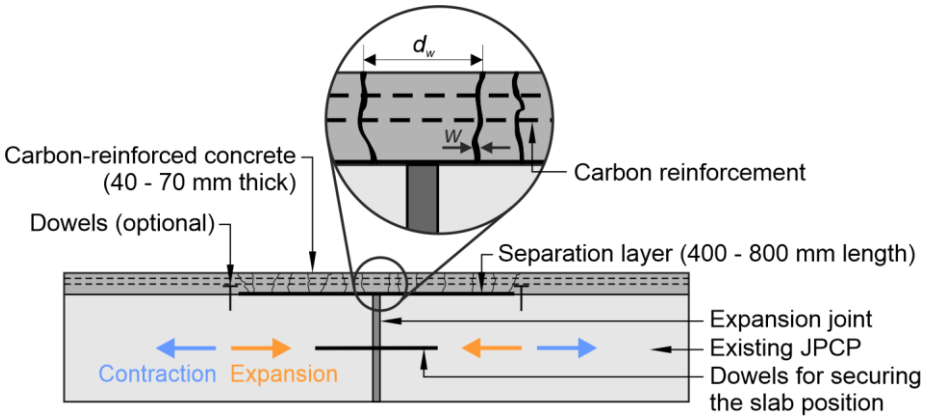


Fig. 1 Covering joints of concrete pavements with CRC: Structure and crack pattern

The cool-down of the ambient and pavement temperatures results in a shortening of the pavement slab length L_0 and a joint opening. Under uniform temperature change ΔT, the concrete pavement slabs change length according to eq. (1) as in [7].

$$\Delta L = L_0 \cdot \alpha_T \cdot \Delta T \quad (1)$$

The length change ΔL of pavement slabs depends on the thermal expansion coefficient α_T of the concrete, which is $10 \cdot 10^{-6}$ 1/K for normal concrete [8]. Friction on the base layer and concrete shrinkage after casting are further factors that affect the length change of pavement slabs. Due to friction c and concrete shrinkage ε_{cs}, the length of a pavement slab changes according to eq. (2) as in [7].

$$\Delta L = c \cdot L_0 \cdot (\alpha_T \cdot \Delta T + \varepsilon_{cs}) \quad (2)$$

The existing pavement slabs have already undergone complete concrete shrinkage by the time the CRC covering layer is applied, making shrinkage negligible. The friction of the pavement slabs on the subbase is 0.65 for a stabilised subbase and 0.80 for a granular base [9].

The expected length change of a concrete pavement slab depends on the zero-stress temperature of the concrete pavement. This zero-stress temperature marks the state at which no stresses or strains occur in the concrete pavement. Accordingly, the zero-stress temperature occurs during the early hardening phase [10]. At a zero-stress temperature of 20 °C for the concrete pavement, a temperature change of −40 K may occur. This can cause the length of a 5 m long concrete pavement slab on granular base to shorten by 1.6 mm. For 20 m concrete pavement slabs on granular base, this would result in a shortening of 6.4 mm. The shortening of the concrete pavement slabs results in a corresponding joint opening. In contrast, the joint between concrete pavement slabs closes when the pavement temperature rises. This leads to compressive stress in the CRC layer and can cause it to buckle.

The layout of the expansion joints in JPCP varies according to the width and length of a roadway. Alongside transverse joints, longitudinal joints can be integrated into JPCP to enable longitudinal and transverse expansion, and to prevent restraint stresses in large concrete surfaces. When the joints open due to low temperatures, biaxial tensile stresses and strains occur in the CRC layer above intersecting joints. Depending on the distance between the longitudinal and transverse joints, the deformation ratio in the CRC layer can range from 0.5/1 at half the longitudinal-to-transverse joint spacing, to 1/1 when the longitudinal and transverse joint spacings are equal. The effect of the deformation ratio on cracking in the CRC layer will therefore be investigated under three different loading ratios, focusing on crack opening and mean crack width under increasing transverse tensile force.

2 EXPERIMENTS

2.1 Materials

The specimens were made from concrete of strength class C30/37 with a mean compressive strength of 45 N/mm². CEM I 42.5 n(sd) cement, sand, and basalt gravel were used for the concrete. The maximum grain size was limited to 8 mm in accordance with the carbon reinforcement, which corresponds to one-third of the mesh size. Due to its air content of over 5.5% by volume, this concrete is frost-thaw resistant and therefore suitable for use as a pavement. The air content and consistency of the concrete were adjusted by adding air-entraining agents and superplasticisers. The slump flow test showed that the

concrete had workability F4 (490 to 550 mm). Selected properties of the concrete in its fresh and hardened state were determined in accompanying tests and are shown in Table 1.

Table 1 Properties of concrete C30/37

Property	Unit	Value
Air content	vol%	8.2
Slump flow	mm	547
Split tensile strength (28 days)	N/mm²	3.9

Two layers of epoxy-coated carbon reinforcement solidian GRID Q95-CCE-38 were used in the specimens [11]. This carbon reinforcement has a yarn spacing of 38 mm and a yarn cross-section of 95 mm²/m in the warp and weft direction. In the yarn tensile test, a mean tensile strength of 4070 N/mm² was determined for the warp yarn and a mean tensile strength of 4230 N/mm² for the weft yarn. The modulus of elasticity of the carbon yarns is 243,000 N/mm².

2.2 Biaxial test setup

The biaxial tensile tests were carried out in a standing steel frame on specimens whose geometry was aligned with the load introduction, as described in [5]. The cross-shaped CRC slabs were clamped with bolts on four sides between profiled clamping plates, see Fig. 2. The tensile force was applied with one hydraulic cylinder in each load direction (x- and y-dir.). On the opposite side to each hydraulic cylinder, the CRC slabs were attached to an abutment. Between the clamping plates and the hydraulic cylinders or abutments, the forces were transmitted via articulated steel plates and threaded rods, allowing the CRC slabs to deform freely in the plane.

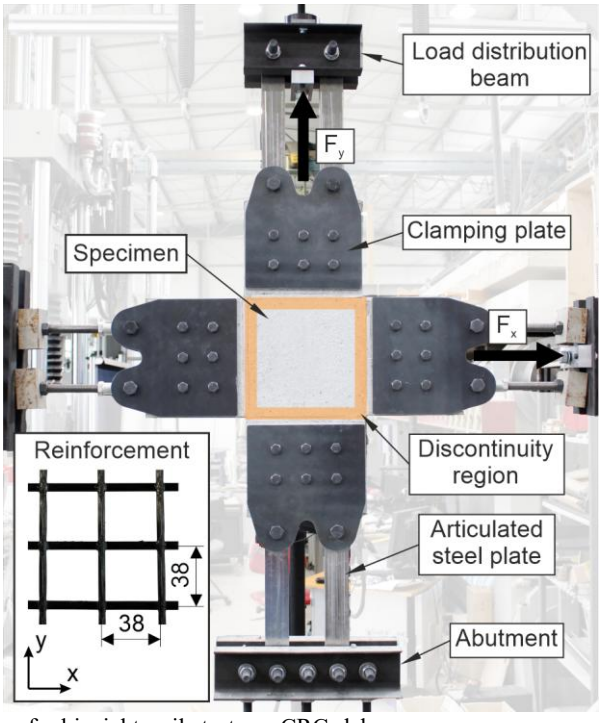


Fig. 2 Test setup for biaxial tensile tests on CRC slabs

The crack behaviour of the CRC covering layer was determined under three different load ratios, with five CRC slabs tested for each ratio. The external dimensions of the 40 mm thick CRC slabs were

800 mm × 800 mm. The CRC slabs contain two layers of Q95-CCE-38 reinforcement, meaning that there are 16 yarns per load direction. A 15 mm concrete cover was used for the carbon reinforcement in the CRC slabs. In the area of the clamping plates, the carbon reinforcement was coated with sand for an increased bond, as shown in [12], and anchored over a length of 250 mm. The test area, which measures 300 mm × 300 mm, is located between the load sides and the abutments. The crack formation of the CRC slabs was investigated in this area. A reduction in cross-section of the CRC slabs between the test and clamping areas using hard foam was used to reduce restraint stresses at the inner corners.

The CRC slabs were loaded force-controlled at 200 to 500 N/s until failure. The horizontal load was adjusted to the vertical load corresponding to the load ratio. The loads were recorded with load cells at a measurement rate of 5 Hz. During loading, deformation and crack formation were measured using digital image correlation (DIC). The ARAMIS 3D measurement system from Zeiss with 12 mega-pixels and a measurement rate of 1 Hz was used.

3 RESULTS AND DISCUSSION

The crack behaviour of CRC slabs was examined in biaxial tensile tests under load ratios F_x/F_y of 0/1, 0.5/1, and 1/1. A representative CRC slab was selected from each series of five specimens in order to demonstrate the differences in crack opening and crack pattern resulting from the three different load ratios. The crack widths were measured in the order in which the cracks occurred. For this purpose, a virtual displacement sensor was placed in the DIC directly above the centre of each crack to avoid the border area with discontinuous strain. When measuring the crack width w, a distinction was made between the respective measurement directions x and y, which were based on the load directions.

The crack width w was evaluated in relation to the concrete stress. In order to calculate the concrete stress according to eq. (3), the cross-sectional area A_c of the CRC slab in the test area was used. The cross-sectional area was 120 cm² in both load directions.

$$\sigma_c = \frac{F}{A_c} \tag{3}$$

The tensile tests on the CRC slab with a load ratio F_x/F_y of 0/1 showed a first crack in the test area at a stress $\sigma_{cr,y}$ of 3.6 N/mm². Two further cracks followed at the same stress level. The fourth crack appeared at a stress $\sigma_{c,y}$ of 5.2 N/mm².

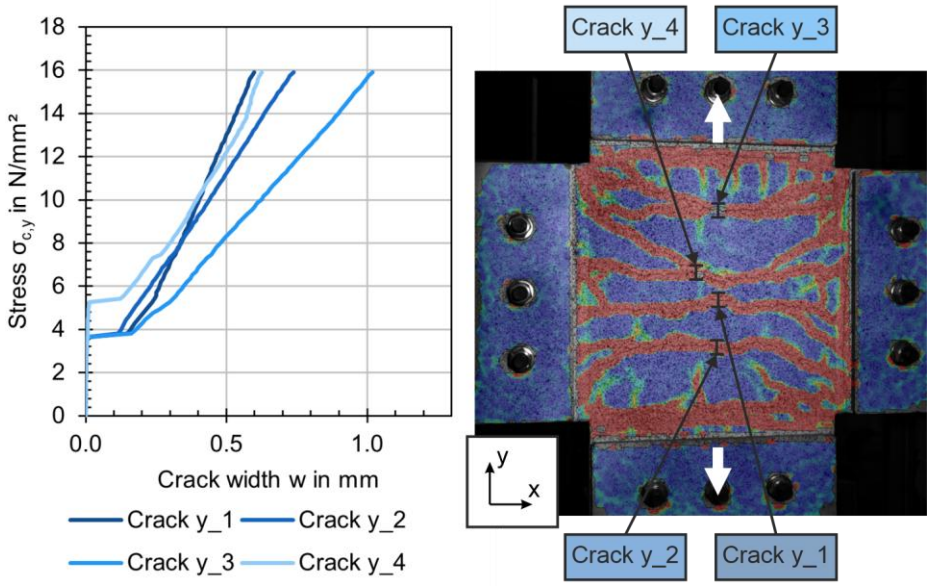


Fig. 3 Crack opening (left) and crack pattern (right) of the CRC slab at a load ratio of 0/1

During crack formation, a crack width of 0.2 mm developed, see Fig. 3 (left). After the cracks have formed, the crack opening curve kinks and the crack widths increase steadily. The crack pattern of the CRC slab under uniaxial tensile loading is shown in Fig. 3 (right). The cracks are perpendicular to the

direction of loading in the centre of the CRC slab. At the edge of the CRC slab, the cracks curve towards the nearest inner corner of the slab. The mean crack width w_{mean} in this CRC slab was 0.75 mm at a maximum stress $\sigma_{c,y,max}$ of 15.9 N/mm².

In the biaxial tensile tests on the CRC slab with a load ratio F_x/F_y of 0.5/1, a first crack perpendicular to the x-direction occurred at a stress $\sigma_{cr,x}$ of 1.6 N/mm² and a first crack perpendicular to the y-direction occurred at a stress $\sigma_{cr,y}$ of 2.7 N/mm², see Fig. 4 (left). The effects of the shear force are reflected in the crack pattern of the CRC slab, see Fig. 4 (right). While five cracks occurred perpendicular to the load F_y, only three cracks formed perpendicular to the load F_x. As a result of biaxial tensile loading, a mesh of cracks forms across the entire test area of the CRC slabs. The cracks intersect, whereby cracks that occur later can end at existing cracks. Furthermore, diagonal cracks appear as a result of the load and deformation in x- and y-direction of the CRC slabs. When the maximum stresses $\sigma_{c,y,max}$ of 16.7 N/mm² and $\sigma_{c,x,max}$ of 8.4 N/mm² are reached, the mean crack width w_{mean} is 0.64 mm for cracks perpendicular to the load F_x and 0.82 mm for cracks perpendicular to the load F_y.

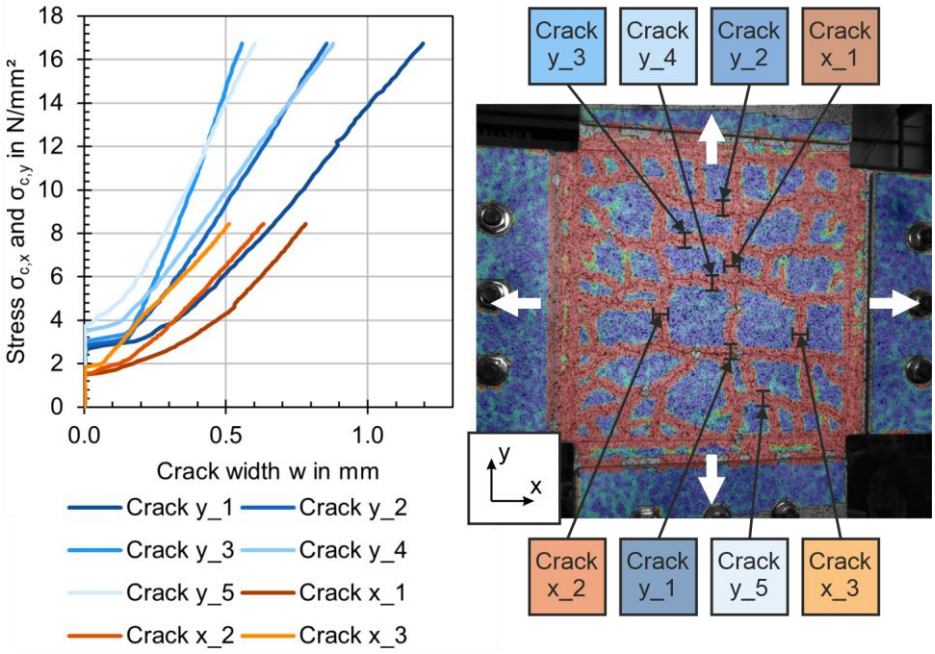


Fig. 4 Crack opening (left) and crack pattern (right) of the CRC slab at a load ratio of 0.5/1

The first cracks in the CRC slabs under biaxial tensile loading with a load ratio F_x/F_y of 1/1 occurred perpendicular to the two load directions at stresses $\sigma_{cr,x}$ and $\sigma_{cr,y}$ of 2.1 N/mm² each, see Fig. 5 (left). Four cracks occurred perpendicular to load F_y and five cracks occurred perpendicular to load F_x, see Fig. 5 (right). At maximum stresses $\sigma_{c,x,max}$ and $\sigma_{c,y,max}$ of 14.6 N/mm² each, the mean crack width w_{mean} is 0.82 mm perpendicular to the load F_x and 1.0 mm perpendicular to the load F_y. The number of cracks perpendicular to load F_y that form at a load ratio of 1/1 is similar to the number of cracks at a load ratio of 0.5/1. The increasing load F_x causes an increase in the number of cracks parallel to the y-direction and a slight increase in the mean crack width.

Compared to uniaxial tensile loading, the crack opening changes continuously under biaxial tensile loading, as shown by the crack width curve. At the end of the formation of new cracks, a curve is obtained under simultaneous longitudinal and transverse tension, see Fig. 4 (left) and Fig. 5 (left). In contrast, the crack opening under uniaxial loading tends to have a kink, see Fig. 3 (left).

In all tensile tests, the CRC slabs show an increasing number of cracks at the transition from the test area to the clamping area, indicating a high concentration of restraint stresses. The reduction of the cross-section and the load transfer through the carbon reinforcement result in a discontinuous stress distribution in this transition area, which is reflected in the crack pattern. The narrow formation of cracks can reduce stress concentrations between the CRC slab and the load introduction.

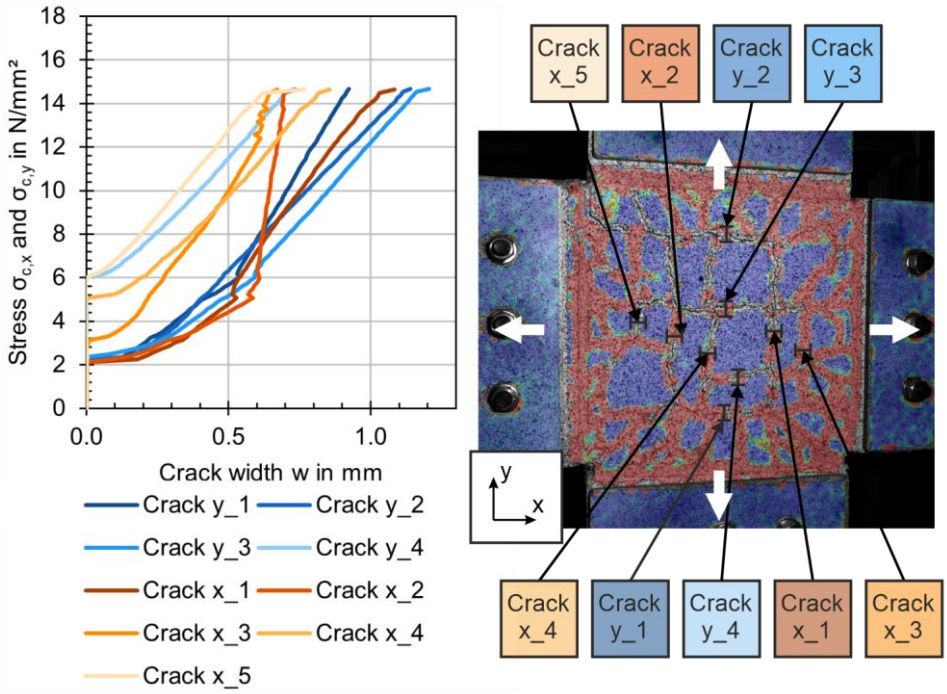


Fig. 5 Crack opening (left) and crack pattern (right) of the CRC slab at a load ratio of 1/1

The crack pattern of the five CRC slabs for each load ratio F_x/F_y was evaluated by considering the number of cracks per load direction and the mean crack width w_{mean} at maximum load. The mean crack width is shown in Fig. 6 depending on the three load ratios and the orientation of the cracks. A distinction is made between cracks perpendicular to load F_x and perpendicular to load F_y.

In the uniaxial tensile test, there were on average five cracks perpendicular to the load F_y. The number of cracks varied between 4 and 6 cracks in the CRC slabs, with no cracks occurring parallel to the y-direction in the test area. On average, the mean crack width w_{mean} was 0.76 mm at a maximum stress $\sigma_{c,y,max}$ of 15.8 N/mm².

At a load ratio F_x/F_y of 0.5/1, there were on average four cracks perpendicular to load F_y and three cracks perpendicular to load F_x. The mean crack width w_{mean} at maximum load for this load ratio was 0.84 mm for cracks perpendicular to the load F_y and 0.45 mm for cracks perpendicular to the load F_x. The load ratio F_x/F_y is closely reflected in the ratio of the mean crack widths $w_{mean,x}/w_{mean,y}$. The mean crack width is achieved at a maximum stress $\sigma_{c,y,max}$ of 16.2 N/mm² and $\sigma_{c,x,max}$ of 8.2 N/mm² on average.

The load ratio F_x/F_y of 1/1 resulted in an average of four cracks in x- and y-direction of the CRC slabs. The number of cracks varied between 3 and 5 cracks. At maximum load, a mean crack width of 0.94 mm for cracks perpendicular to the load F_y and 0.91 mm for cracks perpendicular to the load F_x was measured. At this load ratio, the CRC slabs failed on average at a maximum stress $\sigma_{c,x,max}$ of 14.1 N/mm² and $\sigma_{c,y,max}$ of 14.2 N/mm².

Overall, Fig. 6 shows a slight increase in mean crack widths with increasing transverse tensile force. The transverse tensile force causes cracks parallel to the main direction of stress (y-dir.), thereby contributing to deformation and crack width growth.

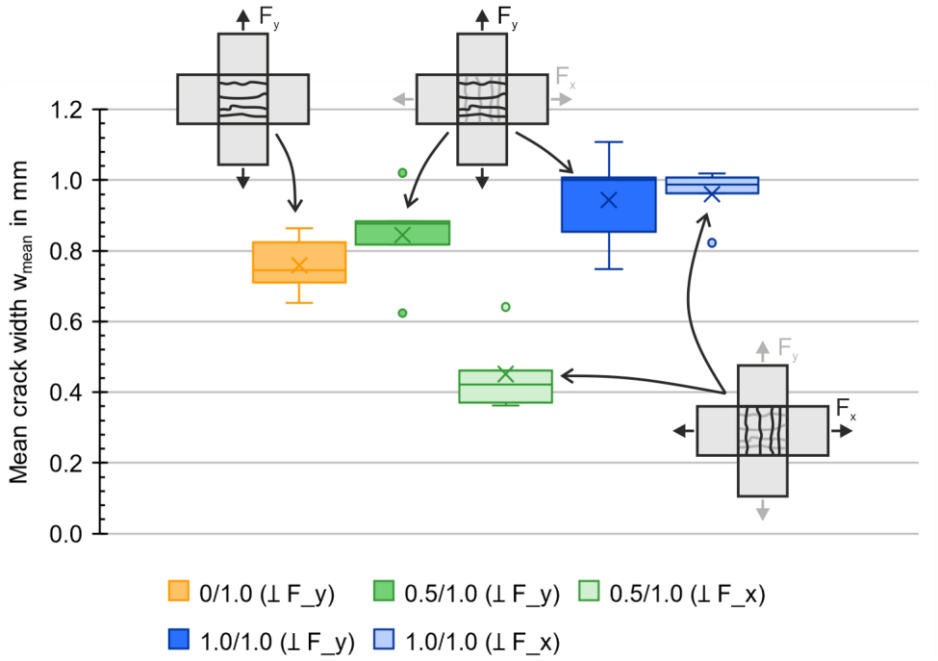


Fig. 6 Mean crack width of CRC slabs under uniaxial and biaxial tensile loading

The results of the tensile tests on CRC slabs to determine their crack behaviour were used to predict the expected mean crack width for the CRC covering layer for concrete pavements. For this purpose, a representative section of the CRC layer above the separating layer was selected. This CRC layer section measures 1210 mm and consists of a 10 mm wide joint and two 600 mm wide separating layers on both sides of the joint. In the case of uniaxial tensile loading of the CRC layer, 20 cracks occur across the entire CRC layer section. In the case of biaxial tensile stress with a load ratio F_x/F_y of 1/1, 16 cracks would occur in the CRC layer. For an existing concrete pavement with a slab length of 5 m, this results in a mean crack width of 0.08 mm under uniaxial tensile stress and 0.1 mm under biaxial tensile stress.

4 CONCLUSIONS

The CRC covering layer presented for repairing existing concrete pavements was examined with regard to its crack behaviour under uniaxial and biaxial tensile loads. The varying load ratios of biaxial tensile loads represent the varying joint opening of longitudinal and transverse joints as the temperature of the JPCP decreases. The crack behaviour of the CRC layer was examined on cross-shaped CRC slabs with two layers of carbon grid. DIC was used to measure crack widths and examine the crack pattern of the CRC slabs. The influence of the transverse tensile force on the crack behaviour was demonstrated on one CRC slab each for the load ratios 0/1, 0.5/1 and 1/1.

The CRC slabs under uniaxial tensile loading (5 cracks) had on average one more crack than the CRC slabs under biaxial tensile loading (4 cracks). In the tensile tests on CRC slabs, the smallest crack widths were found at a load ratio F_x/F_y of 0/1, with 0.76 mm for cracks perpendicular to the load F_y. The largest crack widths were observed at a load ratio F_x/F_y of 1/1, with 0.94 mm for cracks perpendicular to the load F_y. The experimental investigations thus demonstrated the increase in crack widths in CRC slabs as a result of transverse tensile force. The crack patterns in the CRC slabs reflect the load ratios of the biaxial tensile load. While the cracks extend parallel to each other and perpendicular to load F_y at a load ratio F_x/F_y of 0/1, crack networks occur at load ratios F_x/F_y of 0.5/1 and 1/1. The biaxial tensile load leads to cracks that extend in both load directions as well as diagonally. The results of the experimental investigations can be used to estimate the expected mean crack width for the presented configuration of the CRC layer under uniaxial and biaxial tensile loads.

Acknowledgements

The authors wish to acknowledge the support of the technicians at the Otto Mohr Laboratory and thank the German Research Foundation (DFG) for funding the research project 'Transformation of Singular Joint Deformations in Concrete Elements into Plural Cracks' (511403551).

References

[1] Breitenbücher, Rolf, and Fischer, Alexander. 2015. "Ausbildung und Abdichtung von Fugen in Betonfahrbahndecken – Aktuelle Studien." Paper presented at the Betonstraßentagung 2015 (FGSV B 32), Ulm, Germany, September 24–25.

[2] Curbach, M., Hegger, J., Bielak, J., Schmidt, C., Bosbach, S., Scheerer, S., et al. 2024. "New perspectives on carbon reinforced concrete structures—Why new composites need new design strategies." *Civil Engineering Design* 5(5–6):67–94. https://doi.org/10.1002/cend.202200008

[3] Wagner, J., Würgau, C., Schumann, A., Schütze, E., Ehlig, D., Nietner, L., and Curbach, M. 2022. "Strengthening of Reinforced Concrete Structures with Carbon Reinforced Concrete—Possibilities and Challenges." *CivilEng.* 3(2):400–426. https://doi.org/10.3390/civileng3020024

[4] Farwig, K., Neumann, J., Schneider, R., Breitenbücher, R., and Curbach, M. 2020. "Instandsetzung von gefugten Betonflächen mit einer dünnen Schicht aus Carbonbeton." *Beton- und Stahlbetonbau*, 115:768–778. https://doi.org/10.1002/best.202000048

[5] Schmidt, J., Weiß, M., Marx, S., Curbach, M., Breitenbücher, R., and Curoșu, I. 2025. "Fugenlose Betonfahrbahndecken mit Carbonbeton." *Beton- und Stahlbetonbau* 120(12):1030–1040. https://doi.org/10.1002/best.70020

[6] Weiß, M., and Curoșu, I. 2025. "Transformation of singular joint deformations into multiple cracks in carbon- reinforced concrete pavements." Paper presented at the Proceedings for 2025 FraMCoS XII, Vienna, Austria, April 23–25, 1442–1450. https://doi.org/10.21012/FC12.1163

[7] Papagiannakis, A. T., and Masad, Eyad. 2008. *Pavement design and materials.* Berlin: Wilhelm Ernst & Sohn. Wiley edition. https://doi.org/10.1002%2F9783433604090

[8] fib Special Activity Group, New Model Code, et al. 2013. *fib Model Code for Concrete Structures 2010.* Ernst & Sohn, Wiley. https://doi.org/10.1002/9783433604090

[9] American Association of State Highway and Transportation Officials (AASHTO). 1993. *AASHTO Guide for Design of Pavement Structures.* Washington, D.C.: AASHTO.

[10] Eisenmann, J., and Leykauf, G. 2006. "Verkehrsflächen aus Beton." *Beton-Kalender* 2007:93–263. Wiley. https://doi.org/10.1002/9783433600696.ch2

[11] solidian & kelteks. 2024. "solidian GRID Q95-C-EP-s38-F278." Accessed January 23. https://www.solidian-kelteks.com/en/products/construction/reinforcements/meshes/rigid-meshes/grid-carbon-detail

[12] Morales Cruz, C., and Raupach, M. 2019. "Influence of the surface modification by sanding of carbon textile reinforcements on the bond and load-bearing behavior of textile reinforced concrete." Paper presented at Concrete Solutions 2019 – 7th International Conference on Concrete Repair, Cluj-Napoca, Romania, September 30 – October 2. https://doi.org/10.1051/matecconf/201928904006

Towards a new generation of sustainable precast concrete: the use of limestone calcinded clay cement and reduced binder factors

Simone Rapelli, Denny Coffetti, Stefano Salvi, Leonardo Casali, Luigi Coppola

Department of Engineering and Applied Sciences,
University of Bergamo,
Via Marconi, 5 – 24044 Dalmine (BG), Italy

simone.rapelli@unibg.it

Summary
In the precast concrete sector, production efficiency and economic sustainability rely on rapid compressive strength development and very high flowability. These requirements are commonly achieved through high cement contents and using binders with high clinker factors, resulting in a significant embodied environmental impact. This study investigates the feasibility of designing sustainable room temperature-cured concretes for the production of precast panels and prestressed beams by using LC^3 binders and reduced cement factors. The concretes were evaluated in terms of flowability, compressive strength development from 16 hours to 28 days, environmental impact and production cost. The results demonstrate that the LC^3-based concretes fully met the performance targets even at reduced binder factors, confirming their suitability for industrial production. At the same time, a significant reduction in embodied environmental impact was achieved, with negligible variations in production costs.

1 INTRODUCTION

Today, climate change represents a critical challenge for several industrial sectors, where the development of more sustainable processes is essential to maintain market competitiveness. In this context, also the concrete industry, responsible for approximately 9% of global man-made CO_2 emissions [1], is called to find effective strategies to reduce its environmental impact while meeting the expected demand over the coming decades.

Considering that about 70-85% [2][3] of the total emissions associated with concrete manufacturing are related to cement production, considerable research efforts aimed at mitigating the carbon footprint of concrete are focused on reducing the impact of the binder by using Portland cements characterised by reduced clinker factors. This approach is also in accordance with current European standards (EN 197-1, EN 197-5 and EN 197-6), which promote the partial replacement of Portland clinker with supplementary cementitious materials (SCM) or mineral fillers.

Blended cements are already widely used in the production of ready-mix concretes due to their environmental benefits and their ability to enhance long-term durability through improved chloride binding capacity, increased sulphate resistance and reduced susceptibility to alkali-silica reaction [4]. Conversely, their slower strength development becomes a critical limitation in the precast concrete sector, where fast compressive strength development is essential to maintain production efficiency. For this reason, cements with high clinker factors are typically adopted in combination with steam curing or accelerating admixtures to ensure demoulding, handling and pre-stressing operations within 12-16 hours after casting.

In this context, ternary systems composed of ordinary Portland cement (OPC), calcined clay and limestone (LC^3) have recently gained increasing attention as a viable alternative to traditional blended binders. This growing interest is primarily due to the synergistic interaction between the limestone and the metakaolinite phase provided by the calcined clay. Such interaction promotes the formation of carboaluminate phases, which contribute to the formation of a denser microstructure, thereby enhancing mechanical performance compared to conventional blended cements [5]. This behaviour is supported by several studies [6] [7], demonstrating that LC^3 systems may increase long-term compressive strength by up to 20-25% compared to concretes produced with traditional Portland limestone cements at

equivalent clinker substitution rates. In addition, the refined pore structure of LC^3-based materials contributes to improved long-term durability [7], particularly with respect to chloride penetration, alkali-silica reaction (ASR) and sulphate attack. In line with this, several experimental investigations have reported reductions in chloride penetration depth of up to 75% compared to OPC-based concretes [5][8], along with a marked reduction in ASR and sulphate-induced expansion risk [9] [10].

Nevertheless, although LC^3 systems have been widely investigated for ready-mix concrete applications, where performance targets are typically required starting from 28 days after casting, a significant lack of knowledge still exists regarding their suitability for applications requiring high performance at very early ages (12-16 hours), such as in the precast concrete sector.

In this context, while the adoption of LC^3 binders represents an effective strategy to reduce the carbon footprint of concrete, further sustainability gains can be achieved by optimising the overall cement content of the mixture. Beyond its environmental benefits, a reduced binder content may also enhance long-term durability by mitigating issues related to shrinkage-induced cracking, acid attack, sulphate attack or alkali-silica reaction [11]. However, in precast applications, particularly for elements reinforced with a dense distribution of steel rebars, high flowability is often required to ensure adequate casting and compaction processes. Such workability is typically achieved through a high paste (cement and water) volume, which in turn limits the potential for reducing the cement factor [12].

Based on the aspects discussed above, the precast concrete industry represents a particularly challenging sector for the implementation of decarbonisation strategies. Within this context, the present study addresses this issue by assessing the feasibility of combining LC^3 binders with reduced cement factors for the production of sustainable precast panels and prestressed beams. The experimental program was divided into two main parts: the first focused on the development of LC^3-based concretes for prestressed beams, while the second addressed the optimisation of the mixtures for the production of more sustainable precast panels. In both cases, fresh and hardened-state properties were experimentally evaluated, together with an assessment of embodied environmental impact and production cost.

2 MATERIALS AND METHODS

2.1 Materials

To reflect current industrial practices, a commercially available ordinary Portland cement (CEM I 52.5 R) and a Portland limestone cement (CEM II/A-LL 42.5 R) were used. These cements were subsequently blended with commercially available calcined clay and limestone to produce the LC^3 binders. The main properties of these materials are summarised in Table 1.

Table 1 Main properties of the cements, calcined clay and limestone

	CEM I 52.5R	CEM II/A-LL 42.5R	Calcined Clay	Limestone
Specific surface area [m^2/kg]	1205	855	1186	1316
Dv (50) [μm]	11	21	9	7

Concrete mixtures were formulated using a blend of natural (N) and recycled aggregates classified into 4 grain size classes (maximum size: 12 mm). The recycled aggregates consisted of Construction and Demolition (C&D) materials obtained through recovery, sorting and crushing processes applied to waste generated from construction and demolition activities, mainly composed of concrete. The main properties of the aggregates are summarised in Table 2.

Table 2 Main physical properties of the aggregates

	N 0-4	N 4-8	N 8-12	C&D 4-12
Particle density [kg/m^3]	2650	2657	2662	2664
Water absorption [%]	1.70	1.70	1.70	1.62
Min-max size [mm]	0 - 4	4 - 8	8 - 12	4 - 12

To ensure consistent workability across all mixtures, a commercially available polycarboxylate ether-based superplasticizer (SP), specifically formulated for precast applications, was used. In addition, two types of accelerating admixtures were incorporated to enhance hydration kinetics and promote early-age strength development at room temperature. The first accelerating admixture, labelled AA1, is representative of those conventionally adopted in industrial precast production, while the second (AA2) was selected for its higher compatibility with blended binders. The main properties of the chemical admixtures are shown in Table 3.

Table 3 Main physico-chemical properties of the admixtures

	SP	AA1	AA2
Physical form	Brown liquid	White liquid	Brown liquid
Dry residue [%]	34%	31%	30%
Specific mass [kg/m^3]	1040 - 1080	1110 - 1170	1100 - 1120

2.2 Mix proportions – Prestressed beams

Four concrete mixtures were designed to meet the typical fresh and hardened-state targets required for the production of prestressed beams (B), specifically an S5 workability class and compressive strengths of 40 MPa at 16 hours and 65 MPa at 28 days. The reference mixture (REF), based on 460 kg/m^3 of CEM I 52.5 R and incorporating a high dosage of accelerating admixture (3 wt.% of CEM), reflects concrete mixtures commonly adopted at the industrial scale for prestressed elements, allowing adequate compaction and ensuring the achievement of early-age strength targets without steam curing.

The optimisation process primarily involved the partial replacement of ordinary Portland cement (CEM I) with an LC^3 system composed of 85% of CEM I, 10% calcined clay, and 5% limestone (B 460 15), classified as CEM II/A-M (Q-LL) according to EN 197-1. Subsequently, to further reduce the environmental impact, the binder content was reduced at 400 kg/m^3 (B 400 15) and 340 kg/m^3 (B 340 15), respectively, and replaced with an equivalent volume of calcareous filler. For all B mixtures, the water/binder ratio was kept constant at 0.42, while the superplasticizer dosage was properly adjusted to maintain the same workability class (S5). The detailed mix proportions are shown in Table 4.

Table 4 Mix design of the concretes for the production of prestressed beams (B)

Component [kg/m^3]	B -REF	B 460 15	B 400 15	B 340 15
N 0 – 4	885	885	920	956
N 4 – 8	280	280	295	310
N 8 – 12	385	385	400	415
C&D 4 – 12	120	120	125	125
CEM I 52.5R	460	391	340	289
Calcined clay	-	46	40	34
Limestone	-	23	80	137
Water	195	195	167	145
Super-plasticizer	3.25	3.70	5.75	6.35
Accelerating admixture 1	13.80	-	-	-
Accelerating admixture 2	-	9.20	8.00	6.80

2.3 Mix proportions – Precast panels

Three concrete mixtures were designed to evaluate the feasibility of reducing the environmental impact of precast panels (P). To reflect the concrete mixtures typically employed for the production of non-prestressed elements, the reference mixture (REF), targeting a S5 workability class and compressive strength of 20 MPa at 16 hours and 47 MPa at 28 days, was proportioned using a limestone cement (CEM II/A-LL) and a water/binder ratio of 0.49.

To reduce the environmental impact, in the P 360 15 mixture the limestone cement was first replaced with a ternary blended binder composed of 85% CEM II/A-LL 42.5 R, 10% calcined clay and

5% limestone, classified as CEM II/B-M (Q-LL) according to EN 197-1. Subsequently, the cement factor was reduced to 320 kg/m^3, corresponding to the minimum cement content required by the Italian standard UNI 11104 to ensure adequate carbonation resistance in concretes exposed to dry-wet cycles (XC4 exposure class). Notably, in all mixtures the water/binder ratio was kept constant at 0.49 and the superplasticizer dosage was adjusted to maintain the S5 workability class. The detailed mix proportions of the P concretes are reported in Table 5.

Table 5 Mix design of the concretes for the production of precast panels (P)

Component [kg/m^3]	P REF	P 360 15	P 320 15
N 0 – 4	1010	1010	1040
N 4 – 8	215	215	221
N 8 – 12	403	403	415
C&D 4 – 12	118	118	122
CEM II/A-LL 42.5R	360	306	272
Calcined clay	-	36	32
Limestone	80	98	136
Water	177	177	157
Super-plasticizer	3.00	3.50	4.20
Accelerating admixture 1	4.50	-	-
Accelerating admixture 2	-	7.20	6.40

2.4 Methods

All concrete mixtures were prepared in the laboratory under controlled environmental conditions and using a horizontal-axis mixer with a maximum capacity of 300 litres. The mixing procedure was carried out according to the following steps:

- Step 1: Mixing of aggregates with part of the mixing water (equivalent to the aggregates' absorption capacity) for 2 minutes;
- Step 2: Resting phase with the mixer sealed for 2 minutes;
- Step 3: Addition of cement and water and mixing for 2 minutes;
- Step 4: Addition of the admixtures (superplasticizer and accelerating admixture);
- Step 5: Final mixing for 2 minutes.

Flowability of the fresh concrete was assessed through slump tests (EN 12350-2). After fresh-state testing, 100 mm cubic specimens were cast in triplicate for compressive strength testing (EN 12390-3) at 16 hours, 1, 2, 3, 7 and 28 days. In accordance with EN 12390-2, for the first 24 hours all specimens were initially cured into their moulds covered with a plastic sheet and stored in a climatic chamber at 20 ± 2 °C. After demoulding, the specimens were cured in plain water at 20 ± 2 °C until testing.

The environmental impact of each concrete mixture was estimated in terms of Global Warming Potential (GWP), based on the corresponding mix designs and emissions data obtained from manufacturer-supplied Environmental Product Declarations (EPDs). The environmental assessment focused on the emissions associated with the production of raw materials (A1), which accounts for approximately 90% of the overall environmental impact of concrete. Production costs were estimated using average unit prices of raw materials used in precast concrete plants located in Northern Italy. The cost per m³ of concrete was obtained by multiplying the unit market price of each constituent by its corresponding dosage in the mixture.

3 RESULTS

The compressive strength development of the B mixtures is presented in Fig. 1. All tested concretes exhibited compressive strengths in the range of 48 - 50 MPa and 70 - 85 MPa at 16 hours and 28 days, respectively, thereby meeting the target requirements at both early and later ages and confirming their suitability for industrial applications.

Notably, at very-early ages all LC^3-based mixtures outperformed the reference concrete. This result demonstrates the effectiveness of the accelerating admixture AA2 in enhancing early-age strength development in concretes formulated with low-clinker binders. The strength gain ranged from approximately 5% at 16 hours to up to 20% at 28 days, indicating that the accelerating admixture

maintained its effect even at later ages. Focusing on the LC^3 concretes, the results reported in Fig. 1 indicate that, at a fixed water-to-cement ratio, the reduction in cement content did not significantly affect compressive strength development. This finding is consistent with Abrams' law [13], which correlates the mechanical performance of concrete with the gel-to-void ratio and thus to the water-to-cement ratio, despite the cement content.

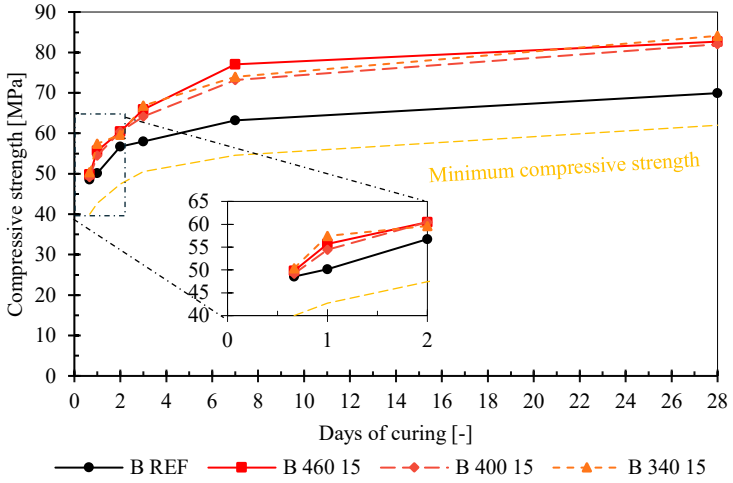


Fig. 1 Compressive strength development of the reference and optimised B concretes. The standard deviation of the results ranges from 0.25 MPa to 1.70 MPa, indicating that the observed variability is within the typical experimental scatter.

The results shown in Fig. 2 for the P concretes confirm the same trend, indicating that the compressive strength development of the concretes designed for the production of panels was not significantly influenced by binder content.

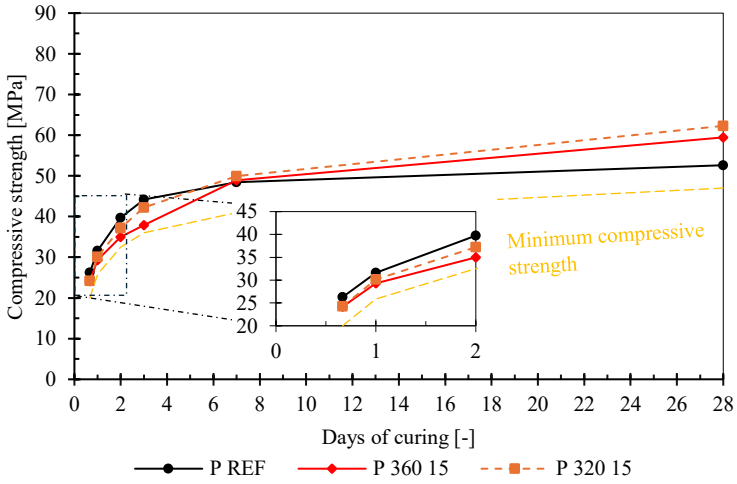


Fig. 2 Compressive strength development of the reference and optimised P concretes. The standard deviation of the results ranges from 0.10 MPa to 1.80 MPa, indicating that the observed variability is within the typical experimental scatter.

Notably, although the P LC^3-based concretes showed 6 - 8% lower compressive strength than the reference mixture after 16 hours of curing, they fully met the required strength targets at both early and later ages, confirming their suitability for the production of non-prestressed elements.

The results reported in Table 6, concerning slump values for B and P concretes and their corresponding superplasticizer dosages, show that, regardless of the concrete type, the partial replacement of cement with limestone and calcined clay required the addition of 0.5 l/m^3 of superplasticizer to ensure the S5 workability class at the same water content. This increase is mainly attributable to the higher fineness of the supplementary cementitious materials (Dv (50): 7 µm and 9 µm for limestone and calcined clay, respectively) with respect to the cements (Dv (50): 11 µm and 21 µm for CEM I and CEM II, respectively). Moreover, the reduction of cement factor at equal water-to-cement ratio determines a further increase of admixture content due to the limited mixing water.

Table 6 Slump values of the reference and optimised B and P concretes

	Prestressed beams				Precast panels		
	B REF	B 460 15	B 400 15	B 340 15	P REF	P 360 15	P 320 15
Slump [mm]	250	250	220	220	250	250	220
SP content [kg/m^3]	3.25	3.70	5.75	6.35	3.00	3.50	4.20

Once technical feasibility was demonstrated at lab scale, the suitability of the optimised concretes for industrial-scale production was further assessed in terms of environmental benefits and economic viability. A quantitative estimation of the environmental impact is reported in Fig. 3, which presents a comparative analysis of the global warming potential (GWP) of each mixture, divided into the contributions from binders, aggregates and chemical admixtures.

As expected, regardless of mixture composition, cement represents the main contributor to total greenhouse gas emissions. Accordingly, a comparative analysis of the reference concretes shows that the B REF concrete exhibits a higher environmental impact than the P REF, due to the combined effect of a higher cement content and the use of a cement with higher clinker factor.

Nevertheless, the progressive reduction in cement factor combined with the use of a low clinker binder led to a decrease in overall environmental impact of up to 32% and 17% for B and P concretes, respectively.

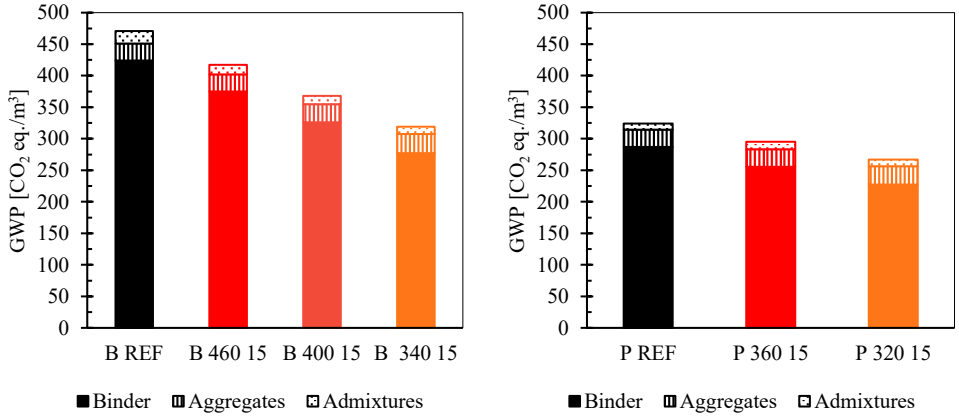


Fig. 3 Global warming potential of the reference and optimised concretes for prestressed beams (left) and precast panels (right)

The results of the cost analysis for the LC^3-based B and P concretes confirm their economic sustainability. As shown in Fig. 4, where the values are normalised with respect to the cost of 1 m^3 of

the reference concrete, the environmental benefits associated with the LC^3-based mixtures are achieved while maintaining production costs comparable to, or even lower than, those currently sustained in typical industrial processes.

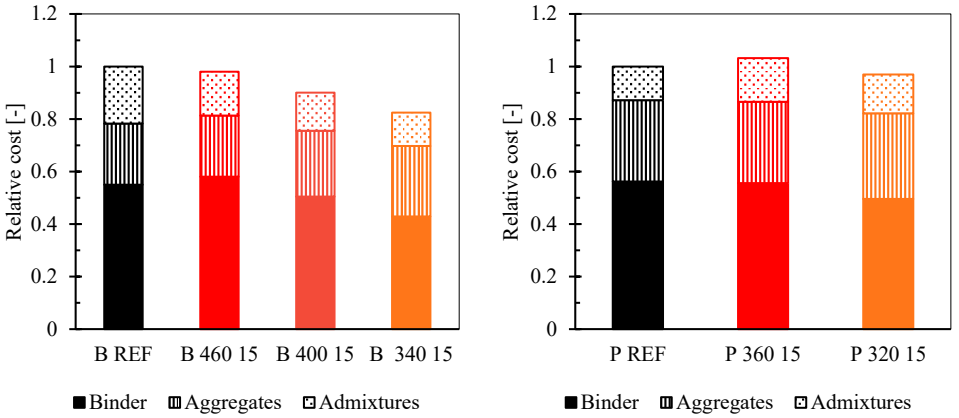


Fig. 4 Cost estimation of the reference and optimised concretes for prestressed beams (left) and precast panels (right)

4 CONCLUSIONS

The experimental investigation presented in this study evaluated the feasibility of using low-clinker blended cements in combination with reduced binder factors to design concretes suitable for the production of sustainable prestressed beams and precast panels. Starting from the reference mixtures representative of typical industrial precast production, *conventional* cements were replaced with LC^3 and the binder content was subsequently reduced by up to 120 kg/m^3.

Based on the results obtained, the following conclusions can be drawn:

- The LC^3-based mixtures achieved both early-age and 28 days compressive strength targets, confirming the technical feasibility of designing concretes for precast applications by combining ternary blended cements, reduced binder contents and a tailored selection of the accelerating admixture;
- To ensure an S5 workability class, the LC^3-based concretes required an increased superplasticizer dosage due to the higher fineness of the calcined clay. Moreover, the lower mixing water content in the mixtures with reduced cement factors further increased the demand for superplasticizer;
- Beyond technical feasibility, the proposed optimisation strategy led to a reduction in embodied environmental impact of up to 32% for prestressed beams and up to 17% for precast panels, without significantly affecting the production cost.

These findings provide a clear pathway for the effective implementation of decarbonisation strategies in the precast concrete sector. In order to validate the laboratory-scale results, the optimised mixtures are currently being tested at industrial scale in collaboration with a precast concrete manufacturer. Further studies are needed to assess the long-term durability performance of the optimised mixtures.

References

[1] Coffetti, Denny, Crotti, Elena, Gazzaniga, Gabriele, Carrara, Massimo, Pastore, Tommaso, and Coppola, Luigi. 2022. “Pathways towards sustainable concrete.” *Cement and Concrete Research* 154:106718 doi:10.1016/j.cemconres.2022.106718.

[2] Flower, David J M, and Sanjayan, Jay G. 2007. “Green House Gas Emissions due to Concrete Manufacture.” 12:282–288.

[3] Shamass, Rabee, Rispoli, Ottavia, Limbachiya, Vireen, and Kovacs, Robert. 2023. "Mechanical and GWP assessment of concrete using Blast Furnace Slag, Silica Fume and recycled aggregate." *Case Studies in Construction Materials* 18:e02164 doi:10.1016/j.cscm.2023.e02164.

[4] Neville, Adam. 2011. *Properties of Concrete*.

[5] Scrivener, Karen, Martirena, Fernando, Bishnoi, Shashank, and Maity, Soumen. 2018. "Calcined clay limestone cements (LC3)." *Cement and Concrete Research* 114:49–56 doi:10.1016/j.cemconres.2017.08.017.

[6] Antoni, Mathieu, Rossen, Jonh, Martirena, Fernando, and Scrivener, Karen. 2012. "Cement substitution by a combination of metakaolin and limestone." *Cement and Concrete Research* 42:1579–1589 doi:10.1016/j.cemconres.2012.09.006.

[7] Sharma, Meenakshi, Bishnoi, Shashank, Martirena, Fernando, and Scrivener, Karen. 2021. "Limestone calcined clay cement and concrete: A state-of-the-art review." *Cement and Concrete Research* 149:106564 doi:10.1016/j.cemconres.2021.106564.

[8] Maraghechi, Hamed, Avet, Francois, Wong, Hong, and Kamyab, Hadi. 2019. "Performance of Limestone Calcined Clay Cement (LC 3) with various kaolinite contents with respect to chloride transport." *Materials and Structures* 51:1–17 doi:10.1617/s11527-018-1255-3.

[9] Favier, Aurélie, and Scrivener, Karen. 2018. "Alkali Silica Reaction and Sulfate Attack: Expansion of Limestone Calcined Clay Cement BT - Calcined Clays for Sustainable Concrete."

[10] Nguyen, Quang Dieu, Kim, Taehwan, and Castel, Arnaud. 2020. "Mitigation of alkali-silica reaction by limestone calcined clay cement (LC3)." *Cement and Concrete Research* 137:106176 doi:https://doi.org/10.1016/j.cemconres.2020.106176.

[11] Coppola, Luigi, Beretta, Silvia, Bignozzi, Maria Chiara, Bolzoni, Fabio, Brenna, Andrea, Cabrini, Marina, Candamano, Sebastiano, Caputo, Domenico, Carsana, Maddalena, Cioffi, Raffaele, Coffetti, Denny, Colangelo, Francesco, Crea, Fortunato, De Gisi, Sabino, Diamanti, Maria Vittoria, Ferone, Claudio, Frontera, Patrizia, Gastaldi, Matteo Maria, Labianca, Claudia, Lollini, Federica, Lorenzi, Sergio, Manzi, Stefania, Marroccoli, Milena, Notarnicola, Michele, Ormellese, Marco, Pastore, Tommaso, Pedeferri, MariaPia, Petrella, Andrea, Redaelli, Elena, Roviello, Giuseppina, Telesca, Antonio, and Todaro, Francesco. 2022. "The Improvement of Durability of Reinforced Concretes for Sustainable Structures: A Review on Different Approaches." *Materials* 15 doi:10.3390/ma15082728.

[12] Kwan, Albert K H, and Li, Leo G. 2014. "Combined effects of water film , paste film and mortar film thicknesses on fresh properties of concrete." *Construction and Building Materials* 50:598–608 doi:10.1016/j.conbuildmat.2013.10.014.

[13] Coppola, Luigi. 2007. *Concretum*. Milano: McGraw-Hill.

The response of fully cracked solid reinforced concrete subjected to three-dimensional stress states

Julie Møller Schulz[1,2], Linh Cao Hoang[1], Peter Noe Poulsen[1], Jeff Larsen[1,2]

[1]Department of Civil and Mechanical Engineering,
Technical University of Denmark
Brovej 118, 2800 Kgs. Lyngby, Denmark

[2]Heavy Civil,
COWI A/S,
Parallelvej 2, 2800 Kgs. Lyngby, Denmark

Summary
The response of reinforced concrete panels subjected to in-plane stress conditions can be modelled by e.g. The cracked Membrane Model. A core part of the model is to determine the inclination of the compression field, which is done either by a direct approach or by use of the principle of minimum complementary energy. For solid concrete reinforced in three orthogonal directions and subjected to three-dimensional (3D) stress states, a similar analytical formulation cannot be established. This paper focuses on the fully cracked response of solid reinforced concrete and presents a numerical approach to determine the concrete stress field as well as the rebar stresses in the three orthogonal directions. The basic idea is to apply the principle of minimum complementary energy and formulate the problem as a convex optimization problem. Results are presented both 2D and 3D stress states, and it is shown that this general numerical approach reproduces the results of the analytical formulation.

1 INTRODUCTION

A sustainable development of the construction industry requires efforts toward reducing CO_2-emissions. One effective way to achieve this is by minimizing the use of construction materials and to achieve this, refined methods for designing and assessing concrete structures are needed.

Structures are designed to satisfy a number of limit state requirements. This includes the Ultimate Limit State (ULS) and the Serviceability Limit State (SLS) requirements. For SLS design, cracking in concrete structures is normally limited to a certain width.

Design-oriented crack width models for load-induced cracking of reinforced concrete exist in design standards [1-2]. The existing models are applicable for one-dimensional (1D) and two-dimensional (2D) stress states. A corresponding crack width model applicable for three-dimensional (3D) stress states is not developed. Therefore, when analysing cracked behaviour of solid concrete structures subjected to 3D stress states, engineers must rely on other methods that are often time consuming or overly conservative. One method to analyse crack widths is Non-Linear Finite Element Analysis (NLFEA). In NLFEA cracks can be modelled as smeared cracks [1] or in form of a discrete model [2]. Both modelling methods have its advantages; however, they are generally both time-consuming and convergence is not guaranteed. While crack modelling with NLFEA is useful in research, it can be impractical in design situations.

In the 2nd generation of the Eurocode 2 [3], crack width calculations for 2D stress states are based on The Cracked Membrane Model [4]. The model describes the response of orthogonally reinforced concrete panels. A core part of the model is to determine the inclination

of the compression field. This can be done by a direct approach or by use of the principle of minimum complementary energy. Both methods lead to an analytical formulation, where the inclination of the stress field is determined as the solution to a fourth-degree polynomial. For concrete with reinforcement in three orthogonal directions and subjected to 3D stress states, a similar analytical formulation of the compression field cannot be established in the same manner and therefore another method is required to produce similar results for 3D problems.

This paper presents a method suitable for 3D problems that, like the fourth-degree polynomial, solves for the stress inclination for a given stress state, assuming fully cracked reinforced concrete. A numerical method for determining the concrete stress field, as well as reinforcement stresses in all three orthogonal directions, is presented.

The numerical method introduced in this paper applies the principle of minimum complementary energy and formulates the problem as a convex optimization problem. In an efficient manner, it determines the stress distribution that fulfils equilibrium- and compatibility conditions. The numerical method is generalised for 3D and can replicate stress fields found with the Cracked Membrane Model in 2D cases.

2 REINFORCED CONCRETE AND STRESS FIELD DIRECTION

A cube of solid reinforced concrete is considered and represented by a three-dimensional RVE (Representative Volume Element). The RVE carries a triaxial stress state [σ_{xx}, σ_{yy}, σ_{zz}, τ_{xy}, τ_{xz}, τ_{yz}] and consist of concrete and smeared orthogonal reinforcement, ρ_x, ρ_y, and ρ_z. The concrete is assumed to have zero tensile strength and behave linear elastic in compression with Young's modulus, E_c. The Poisson effect is not considered. Reinforcement works linear elastic in tension and compression with Young's modulus, E_s.

$$\boldsymbol{\sigma}_{\square} = \boldsymbol{\rho}\, \boldsymbol{\sigma}_{\square s} + \boldsymbol{\sigma}_{\square c} \tag{1}$$

The applied total stress, $\boldsymbol{\sigma}_{\square}$, is a sum of concrete stress and equivalent reinforcement stress.

The equivalent reinforcement stresses $\boldsymbol{\rho}\, \boldsymbol{\sigma}_{\square s}$, concrete stresses $\boldsymbol{\sigma}_{\square c}$, are expressed in matrix form. Furthermore, concrete principal stresses $\boldsymbol{\sigma}_c^p$ and reinforcement stresses $\boldsymbol{\sigma}_s$ are expressed in tensor form

$$\boldsymbol{\rho} = \begin{bmatrix} \rho_x & 0 & 0 \\ 0 & \rho_y & 0 \\ 0 & 0 & \rho_z \end{bmatrix}, \quad \boldsymbol{\sigma}_{\square s} = \begin{bmatrix} \sigma_{s.xx} & 0 & 0 \\ 0 & \sigma_{s.yy} & 0 \\ 0 & 0 & \sigma_{s.zz} \end{bmatrix}, \quad \boldsymbol{\sigma}_s = \begin{bmatrix} \sigma_{s.xx} \\ \sigma_{s.yy} \\ \sigma_{s.zz} \end{bmatrix} \tag{2}$$

$$\boldsymbol{\sigma}_{\square c} = \begin{bmatrix} \sigma_{c.xx} & \tau_{xy} & \tau_{xz} \\ \tau_{xy} & \sigma_{c.yy} & \tau_{yz} \\ \tau_{xz} & \tau_{yz} & \sigma_{c.zz} \end{bmatrix} \tag{3}$$

$$\boldsymbol{\sigma}_c^p = \begin{bmatrix} \sigma_c^I \\ \sigma_c^{II} \\ \sigma_c^{III} \end{bmatrix}, \sigma_c^{III} \leq \sigma_c^{II} \leq \sigma_c^I \leq 0 \tag{4}$$

A membrane RVE is considered by disregarding the third dimension. For both the three-dimensional and membrane RVE, the concrete is considered fully cracked if the major principal stress of the concrete is zero. For a rotating crack model, where cracks are stress free and open orthogonally, the fully cracked concrete has cracks perpendicular to the major principal stress. Fig. 1 shows the two fully cracked RVEs considered.

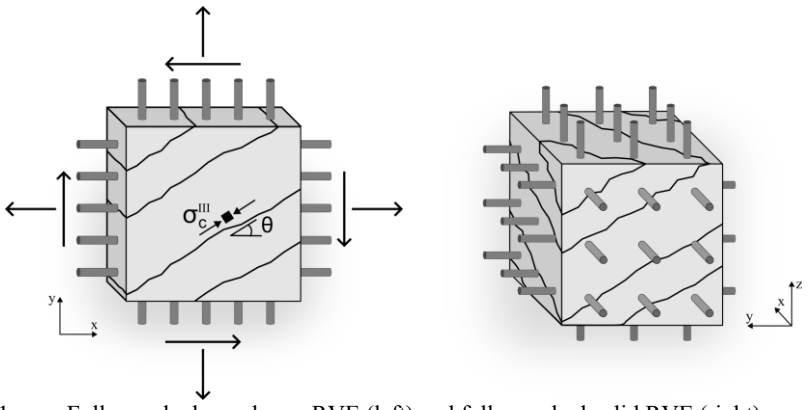


Fig. 1 Fully cracked membrane RVE (left) and fully cracked solid RVE (right)

The distribution of stresses in reinforcement and concrete changes with the inclination of the concrete principal stresses. For plane stress states, the stress field inclination is generally computed by a fourth-degree polynomial, see (5). This polynomial can be found in the 2nd generation of the Eurocode 2, EN1992-1-1 2023 [3] as well as the FIB model code 2020 [5]. The derivation of the polynomial is typically done analytically, using the principle of minimum complementary energy. The polynomial is derived under the same consideration mentioned for

$$(1+\rho_x n)\cot^4(\theta)+\frac{\sigma_x}{\tau_{xy}}\cot^3(\theta)-\frac{\rho_x}{\rho_y}\frac{\sigma_y}{\tau_{xy}}\cot(\theta)-\frac{\rho_x}{\rho_y}\left(1+\rho_y n\right)=0 \tag{5}$$

the considered RVEs in Fig. 1

Here θ describes the inclination of the concrete stress field as seen on Fig. 1 (left), ρ_x and ρ_y are reinforcement ratios in x and y direction, respectively, and $n = E_s/E_c$. Finally, σ_x, σ_y, and τ_{xy} are the applied stresses.

The focus of this paper is to produce a corresponding method, using same assumptions, to solve for the stress field inclination of three-dimensional stress states. The assumptions mentioned here are used in the following sections.

2.1 Minimum complementary energy of reinforced concrete

The principle of minimum complementary energy is a principle of least energy. The complementary energy for an elastic body can be calculated as:

$$\Pi_c = \int_\Omega C'(\boldsymbol{\sigma})\ \mathrm{d}\Omega - \int_{\Gamma_s} \bar{\mathbf{u}}^{\mathrm{T}}\mathbf{r}\ \mathrm{d}\Gamma_s \tag{6}$$

where Ω and Γ are the domain and boundary respectively, $C'(\boldsymbol{\sigma})$ is the complementary strain energy density, $\boldsymbol{\sigma}$ is the stress vector, $\bar{\mathbf{u}}$ is prescribed displacement vector, and $\mathbf{r}$ is the boundary load vector.

For a Representative Volume Element (RVE) a single point in a domain is considered, thereby eliminating the integral over the domain and boundary. Since prescribed displacements are zero for the RVE, (6) is simplified to containing only the complimentary energy density.

The complementary strain energy density is defined as

$$C'(\boldsymbol{\sigma}) = \int_{\boldsymbol{\sigma}} \boldsymbol{\varepsilon}(\boldsymbol{\sigma})\ \mathrm{d}\boldsymbol{\sigma} \tag{7}$$

which for a linear-elastic material with Young's modulus E is identical to:

$$C'(\boldsymbol{\sigma}) = \frac{1}{2E}\boldsymbol{\sigma}^2 \tag{8}$$

For an RVE of reinforced concrete, the strain energy consists of contributions from the reinforcement and the concrete, which can be expressed as follows:

$$C'\left(\boldsymbol{\sigma}_s, \boldsymbol{\sigma}_c^p\right) = {C_s}'(\boldsymbol{\sigma}_s) + {C_c}'\left(\boldsymbol{\sigma}_c^p\right) \tag{9}$$

The minimum complementary energy is attained when the function $C'\left(\boldsymbol{\sigma}_s, \boldsymbol{\sigma}_c^p\right)$ is minimized. Following the same assumptions as the fourth-degree polynomial (5), the complimentary energy density is here expressed using linear elastic material behaviour. The contribution from the reinforcement, is expressed as a function of reinforcement stresses in the three directions.

$${C_s}'(\boldsymbol{\sigma}_s) = \frac{1}{2E_s}(\boldsymbol{\sigma}_s)^{\mathrm{T}}\begin{bmatrix}\rho_x & 0 & 0\\ 0 & \rho_y & 0\\ 0 & 0 & \rho_z\end{bmatrix}\boldsymbol{\sigma}_s = \frac{1}{2E_s}\left(\rho_x {\sigma_{s.xx}}^2 + \rho_y {\sigma_{s.yy}}^2 + \rho_z {\sigma_{s.zz}}^2\right) \tag{10}$$

For the concrete, the energy is most conveniently expressed in terms of the principal stresses σ_c^I, σ_c^{II}, and σ_c^{III}:

$${C_c}'\left(\boldsymbol{\sigma}_c^p\right) = \frac{1}{2E_c}\left(\boldsymbol{\sigma}_c^p\right)^{\mathrm{T}}\begin{bmatrix}1 & 0 & 0\\ 0 & 1 & 0\\ 0 & 0 & 1\end{bmatrix}\boldsymbol{\sigma}_c^p = \frac{1}{2E_c}\left({\sigma_c^I}^2 + {\sigma_c^{II}}^2 + {\sigma_c^{III}}^2\right) \tag{11}$$

By reducing equation (1) and (9)-(11) to 2D, it is possible to derive the analytical expression for the fully cracked stress field inclination (5). The method presented in this paper applies the same equations generalised for three-dimensional stress state to express the minimum complementary energy. While the minimization of the complementary energy in 2D is done analytically, the three-dimensional problem will be done with help from convex optimization.

2.2 Convex Optimization

The minimum of the complementary energy can be determined by applying numerical optimization. It turns out that the problem can be cast as a convex optimization problem, as demonstrated in the following.

The program has nine stress components as primary unknowns: six parameters for concrete stresses and one parameter for each reinforcement stress in direction *x*, *y*, and *z*. Derived from these primary unknown are principal concrete stresses and auxiliary parameters used to express the energy in the correct format.

The minimisation problem may be stated as follows:

$$\begin{aligned}
\min_{\boldsymbol{\sigma}_s, \boldsymbol{\sigma}_c^p} \quad & C'\left(\boldsymbol{\sigma}_s, \boldsymbol{\sigma}_c^p\right)\\
\text{s.t.} \quad & \boldsymbol{\sigma}_{\square} = \boldsymbol{\rho}\,\boldsymbol{\sigma}_{\square s} + \boldsymbol{\sigma}_{\square c}\\
& -(\boldsymbol{\sigma}_{\square c} - \mathbf{I}\sigma_c^I) \succcurlyeq \mathbf{0}\\
& (\boldsymbol{\sigma}_{\square c} - \mathbf{I}\sigma_c^{III}) \succcurlyeq \mathbf{0}\\
& \sigma_c^{III} \le \sigma_c^{II} \le \sigma_c^I \le 0
\end{aligned} \tag{12}$$

Here, the first constraint corresponds to the stress equilibrium conditions while the two semidefinite restrictions containing the major and minor principal concrete define the concrete principal stresses used in the expression for the energy.

Per definition, the major principal stress σ_c^I is the largest eigenvalue of $\boldsymbol{\sigma}_c$, thus all other eigenvalues must be smaller than σ_c^{III} and thereby $-(\boldsymbol{\sigma}_c - \mathbf{I}\sigma_c^I)$ must be positive semidefinite. This condition together with the minimization of energy and $\sigma_c^I \le 0$, ensures that the major

principal stress is limited to non-positive values. For a more detailed explanation of the bounded eigenvalues see [6].

Though the principal stress components are found directly via the minimisation problem (12), the eigenvectors belonging to the principal stresses are not found. Therefore, a post-processing calculation is used to find the eigenvectors. For a principal stress of zero, the corresponding eigenvector is a normal vector to the crack plane $\boldsymbol{n_{cr}}$. For a 2D stress states, the eigenvector belonging to the major principal stress can be interpreted into the angle θ, used in equation (5).

For any convex optimization problem, a dual problem to the stated primal problem exists. The optimization algorithm solves both problems simultaneously. The dual problem to the minimum complementary energy optimisation problem is the minimum potential energy optimisation problem. Therefore, dual variables of the primal problem (12) can be interpreted as strains, see [6]. Thus, both the stress field and the strain field is found by the optimization problem.

For a correctly scaled optimisation problem, the optimisation algorithms are very stable and guarantee a solution. Therefore, the proposed method is effective and reliable, with little room for error. The optimization algorithm used in these investigations is commercially produced by MOSEK [7].

3 RESULTS

Results are produced using the convex optimization approach presented. A numerical program, generalized for 3D, has been made and produce the results presented here.

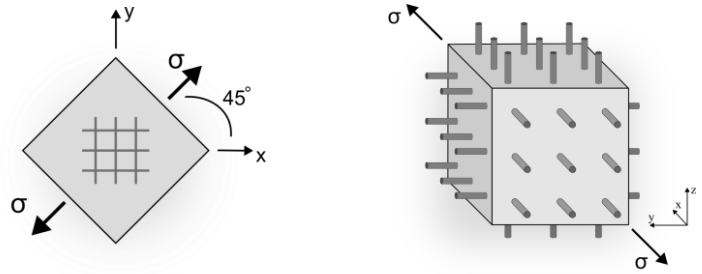


Fig. 2 Load for plane stress (left) and load on three-dimensional RVE (right)

Selected examples of both 2D and 3D are used to showcase the capabilities of the program. All examples consist of a RVE subjected to a uniaxial tensile load, at 45 degrees to all reinforcement directions. Figure 2 illustrates the applied load for a plane stress and three-dimensional stress state, respectively.

Results are first presented for plane stress states. It is shown that the plane stress examples give the expected results and compare with the analytical approach. Thereafter the method is used to find responses for three-dimensional stress fields.

3.1 Plane stress states

The selected examples are loaded with stresses given in (13) and calculated in the 3D optimisation program. Table 1 shows the complete input parameters for the two plane stress examples performed. In Example 2D-a, reinforcement is isotropic, while in Example 2D-b, the amount reinforcement in the x-direction is triple the amount of reinforcement in the y-direction. Both examples have same total reinforcement.

$$\begin{bmatrix}\sigma_{xx}\\ \sigma_{yy}\\ \sigma_{zz}\\ \tau_{xy}\\ \tau_{xz}\\ \tau_{yz}\end{bmatrix} = \begin{bmatrix}0.5\,\sigma\\ 0.5\,\sigma\\ 0\\ 0.5\,\sigma\\ 0\\ 0\end{bmatrix} \tag{13}$$

Table 1 Input parameters for plane stress investigations: Example 2Da (symmetric reinforcement) and Example 2Db (asymmetric reinforcement)

	E_c	E_s	ρ_x	ρ_y	ρ_z	σ
Example 2D-a	20 GPa	200 GPa	0.01	0.01	0	2 MPa
Example 2D-b			0.015	0.005		

3.1.1 Example 2D-a

With the given parameters of Table 1Table 2, the convex optimization program gives the following results:

$$\begin{bmatrix}\sigma_{c.xx}\\ \sigma_{c.yy}\\ \sigma_{c.zz}\\ \tau_{xy}\\ \tau_{xz}\\ \tau_{yz}\end{bmatrix} = \begin{bmatrix}-1.00\\ -1.00\\ 0\\ 1.00\\ 0\\ 0\end{bmatrix}\text{MPa}, \qquad \begin{bmatrix}\sigma_c^I\\ \sigma_c^{II}\\ \sigma_c^{III}\end{bmatrix} = \begin{bmatrix}0\\ 0\\ -2.00\end{bmatrix}\text{MPa}, \qquad \begin{bmatrix}\sigma_{s.xx}\\ \sigma_{s.yy}\\ \sigma_{y.zz}\end{bmatrix} = \begin{bmatrix}200\\ 200\\ 0\end{bmatrix}\text{MPa} \tag{14}$$

$$\begin{bmatrix}\varepsilon_{xx}\\ \varepsilon_{yy}\\ \varepsilon_{zz}\\ \gamma_{xy}\\ \gamma_{xz}\\ \gamma_{yz}\end{bmatrix} = \begin{bmatrix}0.0010\\ 0.0010\\ 0\\ 0.0022\\ 0\\ 0\end{bmatrix}, \qquad \boldsymbol{n}_{cr} = \begin{bmatrix}0.7071\\ 0.7071\\ 0\end{bmatrix} \tag{15}$$

As expected, the results show symmetry in x and y. The crack normal $\boldsymbol{n}_{cr}$ correspond to an angle of $\theta = -45°$ relative to the *x*-axis. This coincides with the direction of the load applied.

3.1.2 Example 2D-b

With the given parameters of Table 1, the optimization program gives the following results:

$$\begin{bmatrix}\sigma_{c.xx}\\ \sigma_{c.yy}\\ \sigma_{c.zz}\\ \tau_{xy}\\ \tau_{xz}\\ \tau_{yz}\end{bmatrix} = \begin{bmatrix}-1.41\\ -0.71\\ 0\\ 1\\ 0\\ 0\end{bmatrix} \text{MPa} \qquad \begin{bmatrix}\sigma_c^I\\ \sigma_c^{II}\\ \sigma_c^{III}\end{bmatrix} = \begin{bmatrix}0\\ 0\\ -2.12\end{bmatrix} \text{MPa} \qquad \begin{bmatrix}\sigma_{s.xx}\\ \sigma_{s.yy}\\ \sigma_{y.zz}\end{bmatrix} = \begin{bmatrix}161\\ 342\\ 0\end{bmatrix} \text{MPa} \tag{16}$$

$$\begin{bmatrix}\varepsilon_{xx}\\ \varepsilon_{yy}\\ \varepsilon_{zz}\\ \gamma_{xy}\\ \gamma_{xz}\\ \gamma_{yz}\end{bmatrix} = \begin{bmatrix}0.0008\\ 0.0017\\ 0\\ 0.0026\\ 0\\ 0\end{bmatrix}, \qquad \boldsymbol{n}_{cr} = \begin{bmatrix}0.5779\\ 0.8161\\ 0\end{bmatrix} \tag{17}$$

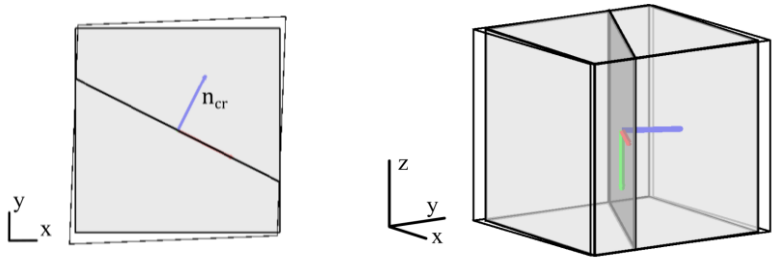


Fig. 3 Results of Example 2D-b, showing the cracked plane and deformations from strains. View of the *xy*-plane (left) and a perspective view (right)

The deformed RVE, showed with crack normal and the cracked plane is visualised on Fig. 3. The orthotropic reinforcement of this example, $\rho_x = 3\,\rho_y$, produces a crack normal $\boldsymbol{n}_{cr}$ corresponding to an angle of $\theta = -32.6°$. Since more force is attracted by the stiffer x-reinforcement, the concrete compression, parallel to the crack, is oriented more toward this direction. The reinforcement configuration gives a slightly higher concrete compressive stress compared to example 2D-a and a larger maximum reinforcement stress, indicating a less optimal reinforcement configuration compared to Example 2D-a.

3.2 Three-dimensional stress states

The two three-dimensional examples are performed similar to the plane stress examples. The applied load is shown in (18) and represent a pure tensile force, see Fig. 2 (right). Example 3D-a have isotropic reinforcement and Example 3D-b have orthotropic reinforcement $\rho_x = 3\,\rho_y = 2\,\rho_z$. Input parameters are found in Table 2.

$$\begin{bmatrix}\sigma_{xx}\\ \sigma_{yy}\\ \sigma_{zz}\\ \tau_{xy}\\ \tau_{xz}\\ \tau_{yz}\end{bmatrix} = \begin{bmatrix}1/3\ \sigma\\ 1/3\ \sigma\\ 1/3\ \sigma\\ 1/3\ \sigma\\ 1/3\ \sigma\\ 1/3\ \sigma\end{bmatrix} \tag{18}$$

Table 2 Input parameters for three-dimensional stress investigations: Test 3Da (symmetric reinforcement) and Test 3Db (asymmetric reinforcement)

	E_c	E_s	ρ_x	ρ_y	ρ_z	σ
Example 3D-a	20 GPa	200 GPa	0.01	0.01	0.01	2 MPa
Example 3D-b			0.015	0.005		

3.2.1 Example 3D-a

With the given load (18) and parameters of Table 2, the optimization program gives the following results of Example 3D-a:

$$\begin{bmatrix}\sigma_{c.xx}\\ \sigma_{c.yy}\\ \sigma_{c.zz}\\ \tau_{xy}\\ \tau_{xz}\\ \tau_{yz}\end{bmatrix} = \begin{bmatrix}-1.33\\ -1.33\\ -1.33\\ 0.67\\ 0.67\\ 0.67\end{bmatrix}\text{MPa} \qquad \begin{bmatrix}\sigma_c^I\\ \sigma_c^{II}\\ \sigma_c^{III}\end{bmatrix} = \begin{bmatrix}0\\ -1.99\\ -2.01\end{bmatrix}\text{MPa} \qquad \begin{bmatrix}\sigma_{s.xx}\\ \sigma_{s.yy}\\ \sigma_{y.zz}\end{bmatrix} = \begin{bmatrix}200\\ 200\\ 200\end{bmatrix}\text{MPa} \tag{19}$$

$$\begin{bmatrix}\varepsilon_{xx}\\ \varepsilon_{yy}\\ \varepsilon_{zz}\\ \gamma_{xy}\\ \gamma_{xz}\\ \gamma_{yz}\end{bmatrix} = \begin{bmatrix}0.0010\\ 0.0010\\ 0.0010\\ 0.0022\\ 0.0022\\ 0.0022\end{bmatrix}, \qquad \boldsymbol{n}_{cr} = \begin{bmatrix}0.5774\\ 0.5774\\ 0.5774\end{bmatrix} \tag{20}$$

The results show a symmetric response where strains and stresses are the same in *x*, *y*, and *z*. Second and third principal concrete stresses are -2 MPa, showing a homogenic concrete stress in the cracked plane. The crack normal, $\boldsymbol{n}_{cr}$, has equal inclination in *x*, *y*, and *z*, corresponding to the direction of the applied load.

3.2.2 Example 3D-b

With the given load (18), visualised in Fig. 4 (left), and parameters of Table 2, the optimization program gives the following results for Example 3D-b.

$$\begin{bmatrix}\sigma_{c.xx}\\ \sigma_{c.yy}\\ \sigma_{c.zz}\\ \tau_{xy}\\ \tau_{xz}\\ \tau_{yz}\end{bmatrix} = \begin{bmatrix}-1.69\\ -1.01\\ -1.42\\ 0.67\\ 0.67\\ 0.67\end{bmatrix} \text{MPa} \qquad \begin{bmatrix}\sigma_c^I\\ \sigma_c^{II}\\ \sigma_c^{III}\end{bmatrix} = \begin{bmatrix}0\\ -1.87\\ -2.25\end{bmatrix} \text{MPa} \qquad \begin{bmatrix}\sigma_{s.xx}\\ \sigma_{s.yy}\\ \sigma_{y.zz}\end{bmatrix} = \begin{bmatrix}157\\ 335\\ 208\end{bmatrix} \text{MPa} \tag{21}$$

$$\begin{bmatrix}\varepsilon_{xx}\\ \varepsilon_{yy}\\ \varepsilon_{zz}\\ \gamma_{xy}\\ \gamma_{xz}\\ \gamma_{yz}\end{bmatrix} = \begin{bmatrix}0.0008\\ 0.0017\\ 0.0010\\ 0.0025\\ 0.0020\\ 0.0028\end{bmatrix}, \qquad \boldsymbol{n}_{cr} = \begin{bmatrix}0.4845\\ 0.6820\\ 0.5479\end{bmatrix} \tag{22}$$

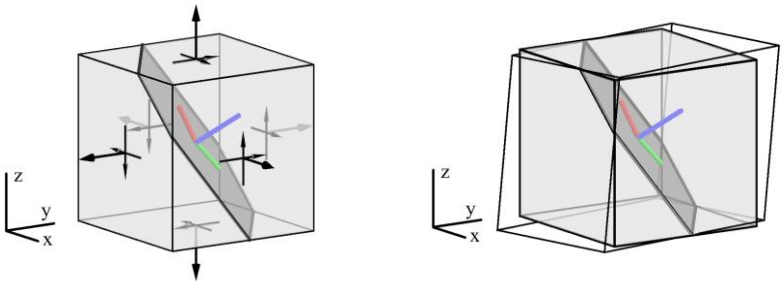


Fig. 4 Results of Example 3D-b, showing the cracked plane and stress field direction, with the applied load (left) and deformations from strains (right)

Compared to example 3D-a, the crack normal, $\boldsymbol{n}_{cr}$, of this example is rotated away from the stiffer *x*-axis and toward the less stiff *y*-axis. The crack normal has only shifted slightly in the direction of the unchanged *z*-direction. This response is comparable to Example 2D-b and indicates that the 3D response shown here is as expected. As with Example 2D-b, the total stresses of the concrete and the reinforcement, respectively, has increased compared to Example 3D-a, indicating a less optimal reinforcement configuration to the applied load. These considerations indicate a correct response.

The strains are visualised as deformation on in Fig. 4 (right), and show elongation in the tensile load direction.

Both stresses and strains are simultaneously found by the optimisation method, making this method a convenient first step for analysing crack widths of solid reinforced concrete subjected to 3D stress states. Further research toward this goal should investigate the crack spacing in solid reinforced concrete, expanding and building on the established relationships for plane stress cases. A crack spacing model would have to consider the effect of reinforcement in all 3 directions and include a bond model of the interactions between the concrete and reinforcement.

4 CONCLUSION

This paper has introduced an effective method that allows the user to evaluate fully cracked solid reinforced concrete subjected to 3D stress states. Rather than expressing the minimum complementary energy analytically, it is shown that it is possible to formulate the same problem using convex optimization. The analytical method involves solving a fourth-degree

polynomial, whereas the optimisation method requires the use of a semidefinite optimization algorithm.

The presented method uses same input parameters as the analytical method, keeping the overall formulation simple. For plane stress problems, the presented method yields results consistent with those obtained by the analytical method, confirming its validity rather than extending the state of the art. However, the strength of the presented method lies in the ability to analyse 3D problems, which is likely not solvable by the method used for plane stress problems. The examples performed show convincing results for 3D problems. The results are given in stresses and strains that could, with further post-processing, provide the variables needed to analyse tension stiffening effect and crack widths. Thus, the method presented is a first step for analysing crack widths and tension stiffening for solid reinforced concrete subjected to 3D stress states. Further research should involve investigating the bond behaviour of these structures, which potentially leads to a model for crack spacings and widths for 3D stress states.

REFERENCES

[1] Maekawa, Koichi, Okamura, Hajime, and Pimanmas, Amorn. 2003. *Non-Linear Mechanics of Reinforced Concrete*. London: CRC Press. doi:10.1201/9781482288087.

[2] Jirásek, Milan. 2000. "Comparative Study on Finite Elements with Embedded Discontinuities." *Computer Methods in Applied Mechanics and Engineering* 188 (1): 307–330. doi:10.1016/S0045-7825(99)00154-1.

[3] CEN-TC250-SC2. *EN 1992-1-1:2023, Eurocode 2: Design of concrete structures – Part 1-1: General rules and rules for buildings, bridges and civil engineering structures*. European Committee for Standardization, Brussels, 402 p., 2023.

[4] Kaufmann, Walter. 1998. "Strength and Deformations of Structural Concrete Subjected to In-Plane Shear and Normal Forces." PhD diss., Swiss Federal Institute of Technology Zurich (ETH Zürich). doi:10.1007/978-3-0348-7612-4.

[5] fib Task Group 10.1. *fib Model Code for Concrete Structures - 2020*. Fédération Internationale du Béton/ International Federation for Structural Concrete, Lausanne, 748 p., 2023.

[6] Poulsen, Peter Noe, and Olesen, John Forbes. 2025. "Unified Finite Element Limit Analysis for Solid Reinforced Concrete Structures." *International Journal of Solids and Structures* 314:113307. doi:10.1016/j.ijsolstr.2025.113307.

[7] MOSEK ApS. *MOSEK for MATLAB*, version 10.2.17. Computer software

Microstructural evolution and hardened properties of plain concrete with coal mine overburden sand and ternary binder

Vijay Gundala, Sivakumar M. V. N, Tezeswi T. P.

Department of Civil Engineering,
National Institute of Technology Warangal,
Warangal 506004, Telangana, India

Summary
The feasibility of employing coal mine overburden (CMOB) sand as a partial replacement for natural fine aggregate in concrete produced with a ternary binder is examined. The binder integrates ground granulated blast-furnace slag, Class F fly ash and Alccofine 1203, through which 58% of the ordinary Portland cement is displaced by mass. Grades M20 and M25 were investigated at CMOB dosages of 0, 20, 40, 60, 80 and 100%, each reported strength being the mean of three specimens. The compressive, splitting-tensile and flexural programme was complemented by ultrasonic pulse velocity, rebound hammer, FESEM-EDS, FTIR and XRD. The most favourable response was obtained at 40% CMOB, at which the M25 mix attained 40.1 MPa at 28 d (an increase of 20.8% over the control), the Ca/Si ratio was reduced from 1.72 to 1.64, the interfacial transition zone was narrowed by 36-42%, and the portlandite intensity was lowered by 66-67%, thereby conserving both binder and natural sand.

1 INTRODUCTION

Annual concrete production worldwide is estimated at approximately 25 billion tonnes, and the clinker on which it depends accounts for 5-8% of anthropogenic CO_2 emissions [1], [2]. In India, the second-largest cement producer, close to 7% of the national CO_2 footprint is attributable to clinker. At the same time, the Bhupalapally open-cast operations of Singareni Collieries Company Limited in Telangana, India, generate substantial volumes of coal mine overburden, the majority of which is consigned to external dumps [3], [4]. A material strategy that reduces clinker consumption while converting this overburden into a load-bearing constituent therefore addresses two interrelated engineering imperatives simultaneously [5], [6].

GGBS, being latently hydraulic, generates additional C-S-H once alkaline activation is established [7]. Class F fly ash reacts comparatively slowly, consuming $Ca(OH)_2$ through a pozzolanic mechanism and continuing to densify the matrix beyond 28 days [8]. Alccofine 1203 refines the early-age pore network and promotes the nucleation of C-S-H [7],[9], [10]. The three constituents are mutually complementary, the limited early-age strength development of GGBS is offset by Alccofine, while the pozzolanic activity of fly ash is sustained well beyond the first month [9],an [11]. Microstructural investigations have confirmed that such multi-SCM blends couple pore refinement with progressive pozzolanic phase formation [12],[13],[14].

For plain OPC systems, Jena et al. [3] reported the retention of strength at CMOB substitution levels as high as 60%, while Mishra et al. [4] located the plain-OPC mortar optimum within the 40-60% range. To the authors knowledge, no previous investigation has combined a ternary SCM binder with CMOB sand while monitoring the complete mechanical, non-destructive and microstructural response across a parabolic dosage range. The present study addresses this gap through a six-mixes mortar pre-trial, followed by mechanical confirmation of the optimum at grades M20 and M25, with proportioning conducted in accordance with IS 10262:2019 [3].

2 MATERIALS AND METHODS

2.1 Constituents

OPC 53 was the principal binder. The ternary SCM system comprised GGBS (specific gravity 2.90), Class F fly ash (specific gravity 2.20, reactive oxides 87.6%) and Alccofine 1203 (specific gravity 2.86). Oxide compositions by X-ray fluorescence are given in Table 1. Fine aggregate was Zone II river sand. CMOB sand from the Singareni Collieries Company Limited Bhupalapally, Telangana, India

open-cast workings was wet-screened through 4.75 mm and satisfying Zone III of IS 383:2016. Physical properties and chemical composition of both fine aggregates are compared in Fig. 1. Coarse aggregate was crushed granite (20 and 12.5 mm). Polycarboxylate-ether superplasticiser (ASTM C494 Type F) was added at 0.8-1.2% binder mass for a 75-125 mm slump.

Table 1 Oxide composition of the cementitious constituents (mass-%). OPC = ordinary Portland cement; GGBS = ground granulated blast-furnace slag; LOI = loss on ignition.

Oxide	OPC 53	GGBS	Fly ash	Alccofine
SiO2	20.85	34.20	58.60	33.10
Al2O3	5.42	18.50	24.30	22.40
CaO	62.30	38.60	3.20	32.50
Fe2O3	3.78	0.80	4.70	1.60
MgO	2.10	5.80	1.80	6.20
LOI	1.80	0.80	2.40	1.20

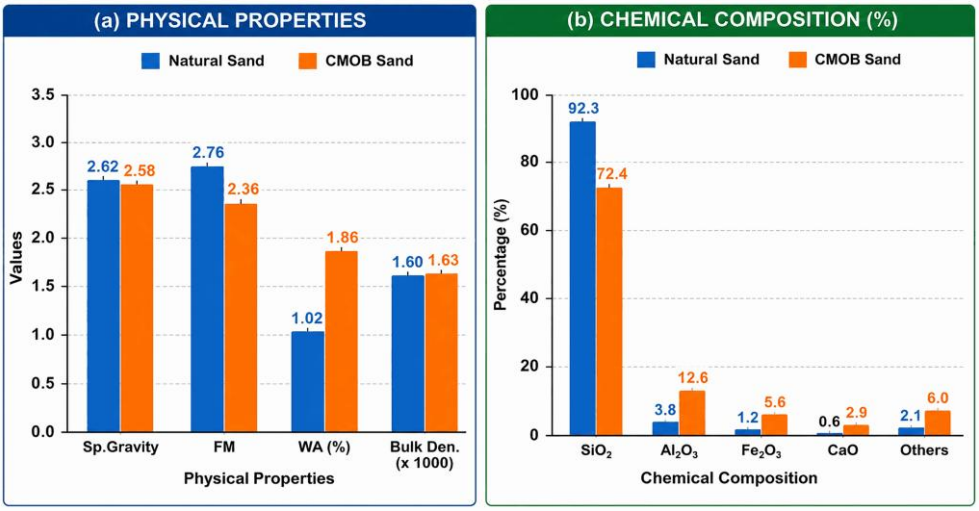


Fig. 1 Comparison of natural sand and CMOB sand:(a) physical properties, (b) oxide composition.

2.2 Mix proportioning per IS 10262:2019

Mix design followed IS 10262:2019 [3]. The target mean strength $f'_{ck} = f_{ck} + 1.65\sigma$ gave 26.6 and 31.6 MPa for M20 and M25 (σ = 4.0 MPa). Entrapped air was taken as 1.0 % for 20 mm aggregate, and the free water (186 kg/m^3 baseline) was corrected +6 % for the 100 mm slump and reduced for the superplasticiser. The coarse-aggregate volume fraction was 0.62, adjusted +0.01 per 0.05 decrement in w/b and corrected for the Zone III CMOB blend. Ternary SCM proportions were fixed at 30% GGBS, 20 % fly ash and 8% Alccofine (58% OPC replacement by mass). CMOB sand was introduced at six levels (0, 20, 40, 60, 80 and 100% by mass of river sand), designated CM-0 to CM-100. Combined M20 and M25 quantities are given in Table 2.

Specimens comprised 150 mm cubes, 150 × 300 mm cylinders and 100 × 100 × 500 mm prisms (tension and flexure) per IS 516 :1959 and IS 5816 :1999. The programme comprised 372 specimens : 144 cubes (12 mixes × 4 ages × 3), 36 cylinders, 36 prisms, 72 NDT cubes and 84 mortar cubes.

Table 2 Combined M20 and M25 mix quantities (kg/m^3) for the six CMOB levels.

Mix	Grade	OPC	GGBS	FA	AF	NRS	CMOB	CA	W
CM-0	M20	155.4	111	74	29.5	680	0	1177	185
	M25	176.4	126	84	33.6	660	0	1190	190
CM-20	M20	155.4	111	74	29.5	544	136	1177	185
	M25	176.4	126	84	33.6	528	132	1190	190
CM-40	M20	155.4	111	74	29.5	408	272	1177	185
	M25	176.4	126	84	33.6	396	264	1190	190
CM-60	M20	155.4	111	74	29.5	272	408	1177	185
	M25	176.4	126	84	33.6	264	396	1190	190
CM-80	M20	155.4	111	74	29.5	136	544	1177	185
	M25	176.4	126	84	33.6	132	528	1190	190
CM-100	M20	155.4	111	74	29.5	0	680	1177	185
	M25	176.4	126	84	33.6	0	660	1190	190

OPC = ordinary Portland cement; GGBS = ground granulated blast-furnace slag; FA = Class F fly ash; AF = Alccofine 1203; NRS = natural river sand; CMOB = coal mine overburden sand; CA = coarse aggregate; W = water; w/b = water-to-binder ratio = 0.50 (M20) and 0.45 (M25).

2.3 Test methods and replication

Fresh-state consistency followed the IS 1199 slump-cone procedure, targeting 75-125 mm. Hardened testing used IS 516:1959 for compression on 150 mm cubes, EN 12390-5:2019 flexure on 100 × 100 × 500 mm prisms, and EN 12390-6:2009 for splitting tension on 150 × 300 mm cylinders. For each mix, age (7, 28, 56, 90 d) and test type, three nominally identical specimens were tested; all reported strengths are the mean of these triplicates, with the standard deviation and coefficient of variation (CV) quantifying experimental variability. Direct-transmission ultrasonic pulse velocity and Schmidt rebound-hammer measurements were conducted at 28 days in accordance with IS 13311-1&2. Microstructural characterisation was performed on fragments recovered from the 90-day cubes. Field-emission scanning electron microscopy was carried out on a JEOL JSM-IT800 operated at 15kV, with EDS acquired at no fewer than ten points per specimen. Attenuated-total-reflectance FTIR spectra were recorded on a Bruker Alpha-II instrument across 400-4000 cm^{-1} at a resolution of 4 cm^{-1}, from which the silicate polymerisation index (SPI) was obtained by deconvolution of the Si-O ν3 envelope following Yu et al. [13]. X-ray diffraction was undertaken on a PANalytical X'Pert Pro diffractometer (Cu-Kα, 5-70° 2θ). The reported Ca/Si value represents the mean of ten EDS points, whereas the FTIR SPI and XRD intensities are each averaged over three patterns.

3 RESULTS AND DISCUSSION

3.1 Mortar pre-trial and optimum CMOB content

The plain-OPC mortar developed 16.5 MPa at 7 d and 30.5 MPa at 90 d. The introduction of the ternary binder with standard sand raised the 90-day strength to 39.2 MPa, corresponding to a 28.5% gain over the OPC baseline. The value increased further to 40.2 MPa at 20% substitution and attained a maximum of 41.8 MPa at 40%, exceeding the OPC control by 37.0%. Beyond this dosage the strength decreased progressively, to 37.8 MPa at 60%, 34.8 MPa at 80% and 31.6 MPa at 100% (Fig. 2). At substitution levels above the optimum, the elevated absorption of the angular CMOB grains, in combination with adherent silt films, increases the effective water demand and impairs the paste-aggregate bond [3]. This optimum lies below the 60% reported by Jena et al. [3] for plain-OPC concrete, consistent with the densifying action of the ternary binder, which saturates the packing benefit at a lower dosage.

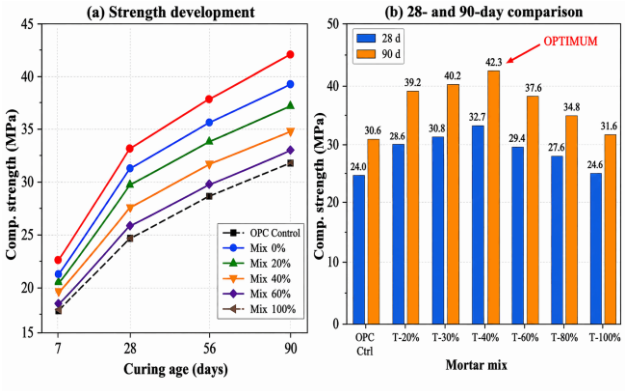


Fig. 2 Mortar compressive strength: left (a) development with curing age; Right (b) 28-day and 90-day values, with the 40% optimum highlighted.

3.2 Compressive strength of concrete

The cube compressive strengths at 28 and 90 days are presented in Table 3, with the standard deviation of the triplicate specimens given in parentheses. At 28 d, the CM-40 mix attained 32.6 ± 1.0 MPa for M20 (CV 3.1%) and 40.1 ± 1.2 MPa for M25 (CV 3.0%), representing gains of 21.6 and 20.8% over the respective controls. The corresponding 90-day strengths increased to 41.4 ± 1.3 MPa (+25.1%) and 50.8 ± 1.5 MPa (+23.3%). All CV remained within 3.0-5.4%, and the parabolic dosage-strength relationship observed in mortar was reproduced in both grades, with the 40% peak preserved.

Table 3 Cube compressive strength (MPa) at 28 and 90 days, reported as mean (standard deviation).

Mix	M20 28 d	M20 90 d	M25 28 d	M25 90 d
CM-0	26.8 (1.1)	33.1 (1.3)	33.2 (1.0)	41.2 (1.4)
CM-20	29.8 (0.9)	37.2 (1.2)	36.8 (1.1)	46.4 (1.5)
CM-40	32.6 (1.0)	41.4 (1.3)	40.1 (1.2)	50.8 (1.5)
CM-60	28.4 (1.0)	35.8 (1.2)	35.1 (1.1)	44.2 (1.4)
CM-80	25.2 (0.9)	31.4 (1.1)	31.2 (1.0)	39.2 (1.3)
CM-100	22.1 (1.2)	27.8 (1.3)	27.4 (1.1)	34.6 (1.4)

3.3 Tensile, flexural and non-destructive results

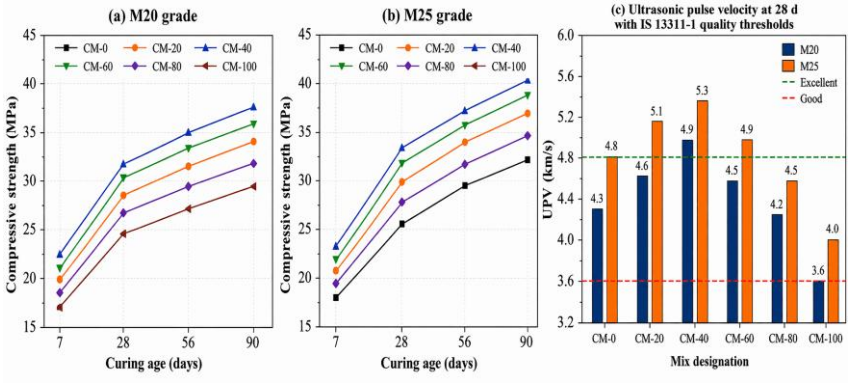


Fig. 3 Compressive strength against curing age: (a) M20 grade, (b) M25 grade; (c) ultrasonic pulse velocity for the M20 and M25 mixes at 28 d with IS 13311-1 quality-class thresholds.

At 28 d, CM-40 attained splitting tensile strengths of 2.94 ± 0.12 MPa (M20, +22.0 %) and 3.61 ± 0.15 MPa (M25, +20.8 %), and flexural strengths of 5.17 ± 0.20 MPa (+21.9 %) and 6.36 ± 0.24 MPa (+20.9 %). The tensile-to-compressive (8.5-9.2 %) and flexural-to-compressive (15.4-16.2 %) ratios fell within normal ranges. The 28-d UPV reached 4.52 km/s (M20) and 4.72 km/s (M25), both rated "Excellent" per IS 13311-1 (≥ 4.5 km/s), against 4.28 and 4.46 km/s ("Good") for CM-0 and above 3.9 km/s for CM-100. Rebound numbers tracked destructive cube strengths within an 8-10 % envelope (Fig. 3).

3.4 FESEM-EDS evidence on paste and ITZ

In CM-0, the paste was comparatively open, with the C-S-H occurring as loosely interconnected wisps and the hexagonal portlandite (CH) plates projecting into unfilled voids. In CM-40, by contrast, a densely interwoven fibrous C-S-H gel predominated, accompanied by only scattered ettringite needles and minimal residual CH, and the ITZ was reduced to 10-13 µm (M20) and 8-10 µm (M25), corresponding to contractions of 42 and 36%. EDS analyses (n = 10) returned mean Ca/Si ratios of 1.72 ± 0.08 (CM-0) and 1.64 ± 0.07 (CM-40). This decrease is consistent with the Taylor-Richardson framework for SCM-modified C-S-H [14], high-volume fly-ash–GGBFS ternary systems[15] (Fig. 4).

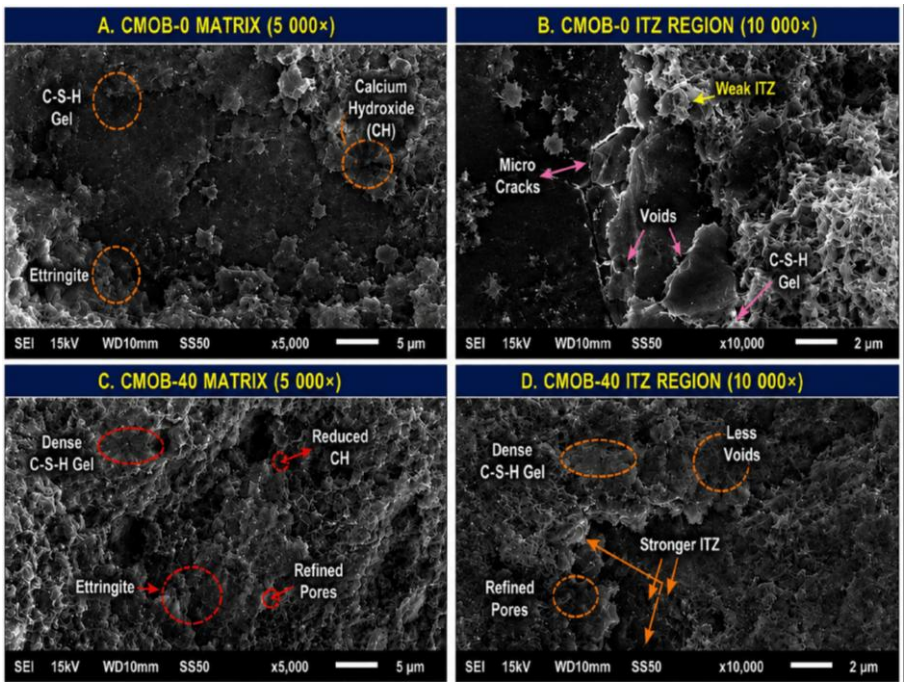


Fig. 4 FESEM images at 90 days: (A) CM-0 matrix at 5000×, (B) CM-0 ITZ at 10000×, (C) CM-40 matrix at 5000×, (D) CM-40 ITZ at 10000×.

3.5 FTIR and XRD evidence of hydration-phase evolution

The dominant Si-O-Si asymmetric stretching band, located at 970 cm^{-1} in CM-0, was displaced upward to between 1010 and 1025 cm^{-1} in CM-40. The portlandite O-H stretch at 3640 cm^{-1} was markedly attenuated, while the carbonate ν3 band spanning 1420-1497 cm^{-1} remained of low intensity. In the diffraction patterns, the principal portlandite reflections in the vicinity of $2\theta \approx 18.0°$, 34.1° and 47.1° were reduced by 66-67%, whereas the ettringite reflections were intensified by 92-95%. The amorphous C-S-H halo between 25° and 35° 2θ was more prominent in CM-40 than in CM-0 (Table 4, Fig. 5).

Table 4 Reference FTIR band and XRD peak assignments adopted in this study.

Technique	Band / 2θ	Assignment	Ref.
FTIR	3640 cm-1	O-H stretch, portlandite Ca(OH)2	[13]
FTIR	1420-1497 cm-1	C-O ν3 (carbonate marker)	[13]
FTIR	950-1025 cm-1	Si-O ν3 stretch (C-S-H)	[13]
FTIR	525 cm-1	Si-O bending	[13]
XRD	9.1°	Ettringite (AFt)	[14]
XRD	18.0/34.1/47.1°	Portlandite (CH)	[14]
XRD	20.8/26.6°	Quartz (CMOB)	[3]
XRD	25-35°	C-S-H halo	[14]
XRD	32.0-32.5°	Alite C3S, belite C2S	[14]

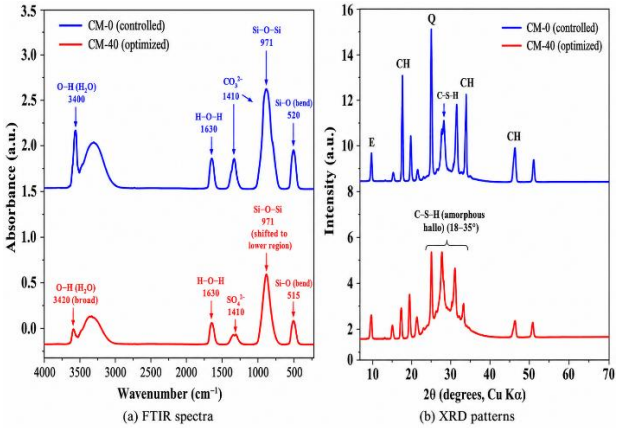


Fig. 5 Left (a) FTIR spectra of the CM-0 and CM-40 mixes with key band assignments labelled; Right (b) XRD patterns of the CM-0 and CM-40 mixes, peak positions per Table 4.

3.6 Comparison with prior studies

Table 5 Comparison with prior studies. CS = compressive strength; SCM = supplementary cementitious material.

Study	Binder	Fine aggregate	Optimum / 28-d CS
Narender Reddy & Meena [7]	OPC+20%GGBS+8%AF	River sand	8% AF, ~38-42 MPa
Sajan et al. [16]	OPC + industrial waste	Mixed	55% replacement viable
Jena et al. [3]	Plain OPC	CMOB (0-100%)	60% CMOB, +22% CS
Present study	OPC+30GGBS+20FA+8AF	CMOB (0-100%)	40% CMOB; 32.6 & 40.1 MPa

Table 5 positions the present CM-40 outcomes within the literature on ternary OPC–GGBS–ultrafine binders and CMOB-bearing concretes. The optimum determined here (40%) is lower than the 60% reported by Jena et al. [3] for plain-OPC concrete and the 40–60% band of Mishra et al. [4] for plain-OPC mortar, this is interpreted as an effect of the ternary binder, whose supplementary phases densify the matrix and saturate the packing benefit at a lower dosage, so the strength penalty from the higher water demand of angular CMOB grains appears earlier than under plain OPC. The 28-day strength of

CM-40/M25 (40.1 MPa) lies at the upper end of the OPC + 20% GGBS + 8% Alccofine window of Narender Reddy and Meena [7], and the Ca/Si reduction and ITZ contraction are consistent with the high-volume fly-ash–GGBFS systems of Jeong et al. [15]. The novelty of this work lies in coupling a three-component SCM binder with CMOB fine aggregate across a full parabolic dosage range, assessed by combined mechanical, non-destructive and microstructural methods a combination not previously reported.

3.7 Durability outlook, scale-up and carbon balance

A 90-day horizon encompasses early- and intermediate-age behaviour but does not extend to the longer durations over which the principal durability mechanisms develop. The measured reduction of 66-67 % in portlandite content, together with the dense C-A-S-H network observed under FESEM, is expected to enhance chloride binding and to retard chloride ingress, in agreement with reports on ternary OPC–FA–pozzolan systems [17]. The densified ITZ is likewise expected to enhance sulphate resistance, while analogous ternary GGBS–fly-ash Portland cements have exhibited well-controlled carbonation under natural exposure [18]. Recommended verification comprises RCPT (ASTM C1202), accelerated carbonation and sulphate immersion (ASTM C1012), with feedstock qualification by a wash-sediment-screen sequence. An indicative embodied-CO_2 estimate from published emission factors (kg CO_2/kg: OPC 0.93, GGBS 0.052, fly ash 0.027, Alccofine 0.060, river sand 0.0048, CMOB sand 0.0026, coarse aggregate 0.0075) yields ≈167 kg CO_2/m^3 for CM-40 against ≈330 kg CO_2/m^3 for a 100% OPC plus river-sand control of equal grade, consistent with the embodied-carbon benchmarks for concrete [19] and the eCO_2-per-strength gains reported for low-carbon ternary binders [5], [11], [20].

4 CONCLUSIONS

Six concrete mixes incorporating CMOB sand at 0-100% replacement were prepared on a ternary binder of 30% GGBS, 20% Class F fly ash and 8% Alccofine (58% OPC replacement) and evaluated at M20 and M25 grade. The principal findings are:

(1) A 40% CMOB optimum was identified by the mortar pre-trial, exceeding the OPC baseline by 37.0% at 90 d (41.8 against 30.5 MPa).

(2) At 28 days CM-40 delivered 32.6 ± 1.0 MPa (M20, +21.6%) and 40.1 ± 1.2 MPa (M25, +20.8%), with splitting-tensile strengths of 2.94/3.61 MPa and flexural strengths of 5.17/6.36 MPa, and CV within 3.0-5.4%.

(3) CM-40 reached the "Excellent" IS 13311-1 quality bracket (UPV 4.52-4.72 km/s), with rebound numbers within an 8-10% envelope.

(4) FESEM-EDS recorded a Ca/Si reduction from 1.72 ± 0.08 to 1.64 ± 0.07 and ITZ contractions of 42% (M20) and 36% (M25). The measured reduction of 66-67% in portlandite content, together with the dense C-A-S-H network observed under FESEM.

(5) FTIR recorded a 52-55% SPI rise with the Si-O v3 band shifting from 970 to 1010-1025 cm^{-1}, and XRD confirmed a 66-67% portlandite reduction with 92-95% ettringite growth. The optimised composite conserves binder and natural fine aggregate while approximately halving embodied CO_2.

Acknowledgements

The Department of Civil Engineering and the Central Research Instrumentation Facility of NIT Warangal are gratefully acknowledged for laboratory access and analytical support, as is the supply of GGBS, Alccofine and fly ash by industry partners.

References

[1] Monteiro, Paulo J.M., Miller, Sabbie A., and Horvath, Arpad. 2017. "Towards sustainable concrete." Nat. Mater. 16(7):698–699. https://doi.org/10.1038/nmat4930.

[2] Flower, David J.M., and Sanjayan, Jay G. 2007. "Greenhouse gas emissions due to concrete manufacture." Int. J. Life Cycle Assess. 12:282–288. https://doi.org/10.1065/lca2007.05.327.

[3] Jena, Biswajit, Zade, Nikhil P., Sarkar, Pradip, and Karak, Swapan Kumar. 2024. "Sustainable integration of coal mine overburden as a substitute for natural sand in concrete to enhance its mechanical and durability properties." Constr. Build. Mater. 411:134488. https://doi.org/10.1016/j.conbuildmat.2023.134488.

[4] Mishra, Anshumali, Das, Sarat Kumar, and Reddy, Krishna R. 2023. "Use of coal mine

overburden as sustainable fine aggregate in cement mortar." J. Mater. Civ. Eng. https://doi.org/10.1061/JMCEE7.MTENG-15424.
[5] Shubbar, Ali Abdulhussein, Sadique, Monower, Kot, Patryk, and Atherton, William. 2019. "Future of clean energy for the cement industry and a low carbon binder: development of a low carbon binder from ternary blending of cement, GGBS and high-calcium fly ash." Constr. Build. Mater. 195:660–670. https://doi.org/10.1016/j.conbuildmat.2018.11.081.
[6] Juenger, Maria C.G., Snellings, Ruben, and Bernal, Susan A. 2019. "Supplementary cementitious materials: new sources, characterization, and performance insights." Cem. Concr. Res. 122:257–273. https://doi.org/10.1016/j.cemconres.2019.05.008.
[7] Narender Reddy, A., and Meena, T. 2018. "A study on compressive behaviour of ternary blended concrete incorporating Alccofine." Mater. Today: Proc. 5(5):11356–11363. https://doi.org/10.1016/j.matpr.2018.02.102.
[8] Chindaprasirt, Prinya, and Rukzon, Sumrerng. 2008. "Strength, porosity and corrosion resistance of ternary blend Portland cement, rice husk ash and fly ash mortar." Constr. Build. Mater. 22(8):1601–1606. https://doi.org/10.1016/j.conbuildmat.2007.06.010.
[9] Juenger, Maria C.G., and Siddique, Rafat. 2015. "Recent advances in understanding the role of supplementary cementitious materials in concrete." Cem. Concr. Res. 78(A):71–80. https://doi.org/10.1016/j.cemconres.2015.03.018.
[10] Jena, Biswajit, Zade, Nikhil P., Sarkar, Pradip, and Karak, Swapan Kumar. 2024. "Experimental studies on coal mine overburden incorporated concrete as a sustainable substitute for fine aggregate." Int. J. Mater. Res. 115(7–8):512. https://doi.org/10.1515/ijmr-2024-0054.
[11] Yang, Keun-Hyeok, Jung, Yeon-Back, Cho, Myung-Sug, and Tae, Sung-Ho. 2015. "Effect of supplementary cementitious materials on reduction of CO2 emissions from concrete." J. Clean. Prod. 103:774–783. https://doi.org/10.1016/j.jclepro.2014.03.018.
[12] Nedunuri, Sai Surya Sree Aparna, Sertse, Seifemichael Getachew, and Muhammad, Salman. 2020. "Microstructural study of Portland cement partially replaced with fly ash, GGBS and silica fume as determined by pozzolanic activity." Constr. Build. Mater. 238:117561. https://doi.org/10.1016/j.conbuildmat.2019.117561.
[13] Yu, Ping, Kirkpatrick, R. James, Poe, Brent, McMillan, Paul F., and Cong, Xiandong. 1999. "Structure of calcium silicate hydrate (C-S-H): near-, mid-, and far-infrared spectroscopy." J. Am. Ceram. Soc. 82(3):742–748. https://doi.org/10.1111/j.1151-2916.1999.tb01826.x.
[14] Taylor, Rhys, Richardson, Ian G., and Brydson, Rik M.D. 2010. "Composition and microstructure of 20-year-old ordinary Portland cement–ground granulated blast-furnace slag blends containing 0 to 100% slag." Cem. Concr. Res. 40(7):971–983. https://doi.org/10.1016/j.cemconres.2010.02.012.
[15] Jeong, Yeonung, Park, Hyeoneun, Jun, Yubin, Jeong, Jin-Hoon, and Oh, Jae Eun. 2015. "Microstructural verification of the strength performance of ternary blended cement systems with high volumes of fly ash and GGBFS." Constr. Build. Mater. 95:96–107. https://doi.org/10.1016/j.conbuildmat.2015.07.158.
[16] K.C., Sajan, Adhikari, Rabindra, Mandal, Bharat, and Gautam, Dipendra. 2022. "Mechanical characterization of recycled concrete under various aggregate replacement scenarios." Clean. Eng. Technol. 7:100428. https://doi.org/10.1016/j.clet.2022.100428.
[17] Thomas, Michael D.A., and Bamforth, Phil B. 1999. "Modelling chloride diffusion in concrete: effect of fly ash and slag." Cem. Concr. Res. 29(4):487–495. https://doi.org/10.1016/S0008-8846(98)00192-6.
[18] Rivera, Rosa Abnelia, Sanjuán, Miguel Ángel, Martín, Domingo Alfonso, and Costafreda, Jorge Luis. 2021. "Performance of GGBS and coal fly ash ternary Portland cements exposed to natural carbonation." Materials 14(12):3239. https://doi.org/10.3390/ma14123239.
[19] Anderson, Jane, and Moncaster, Alice. 2020. "Embodied carbon of concrete in buildings, Part 1: analysis of published EPD." Buildings and Cities 1(1):198. https://doi.org/10.5334/bc.59.
[20] Radwan, Mohammed K.H., Onn, Chiu Chuen, Mo, Kim Hung, Yap, Soon Poh, Chin, Ren Jie, and Lai, Sai Hin. 2022. "Sustainable ternary cement blends with high-volume GGBS–fly ash." Environ. Dev. Sustain. 24(4):4751–4785. https://doi.org/10.1007/s10668-021-01633-4.

Compression Behavior of Preloaded Carbon Fiber-Reinforced Polymer-Confined Concrete Using Digital Image Correlation

Nima Kian, Nguyen Duc Tung

Chair of Structural Concrete,
Helmut Schmidt University/University of the Federal Armed Forces,
Hamburg (22159), Germany

Summary
In practice, reinforced concrete structures are retrofitted under service loads, although most confinement models neglect this effect. This study experimentally investigates the influence of preloading on the compressive behavior of CFRP-confined concrete cylinders. Ten specimens with two concrete strength levels were tested under uniaxial compression, including unconfined, confined, and preloaded-then-confined configurations. A preloading ratio of 85% of the axial capacity was applied prior to retrofitting, and three-dimensional digital image correlation was used to monitor axial and lateral strains. The results indicate that preloading slightly reduces the ultimate confined compressive strength of specimens with high concrete strength and decreases deformation capacity by up to 30%, particularly at low confinement ratios. The effect of preloading was more pronounced in high-strength specimens retrofitted with a single CFRP layer, which exhibited only a descending post-peak branch.

Keywords: Carbon Fiber Reinforced Polymer (CFRP), Concrete, Confinement, Preloading, Retrofitting, Uniaxial stress.

1 INTRODUCTION

There are myriad studies investigating the confinement effect stemming from external jacketing. The most popular and widely used material among the scientific community is Carbon fiber reinforced polymer (CFRP). Research has shown that FRP can grant and provide significant confinement, resulting in increased ductility and load-carrying capacity of structural elements.

There are many studies proposing analytical or empirical models for the axial stress-strain behavior of confined concrete [1]–[11]. However, a neglected matter common among all previous studies is the effect of preloading. It is transparent that all structural elements including columns are retrofitted while sustaining the existing loads such as service loads and gravity loads stemming from dead and live loads, self-weight, etc. However, all the aforementioned proposed axial stress-strain models were derived from tests on specimens retrofitted with FRP before loading began, thus neglecting the influence of any prior loading.

There are few studies focusing on the effect of preloading prior to retrofitting on confined columns [12]–[21]. He et al. [13], [14] performed 29 tests on circular plain and reinforced concrete columns with diameter (D) and height (H) of 150 mm × 450 mm and 100 mm × 450 mm, subjected to various preloading ratios ($0.2 \leq n_0 \leq 0.85$), defined as the ratio of the initial applied load (P_0) to the axial capacity ($f_{co}A_c$) of the column, where f_{co}, and A_c represent the unconfined concrete compressive strength and the gross cross-sectional area, respectively. Their findings indicated that short-term preloading slightly improved the axial capacity of the specimens compared to those tested without prior loading. Pan et al. [15], [16] conducted 42 tests on circular and square confined columns with preloading ratios (n_0) ranging from 0.22 to 0.71. The cylindrical specimens had a diameter and height of 110 mm and 200 mm, respectively. Contrary to He et al. [13], [14], their results demonstrated that confinement effectiveness diminished with increasing preloading ratio (n_0). Ferrotto et al. [17] investigated the behavior of 19 preloaded circular confined concrete columns (150 mm diameter × 600 mm height) and proposed an analysis-oriented stress-strain model derived solely from their test matrix [18]. Aligning with He et al. [13], [14] but differing from Pan et al. [15], [16], they found that preloading did not affect the ultimate axial load or strain of confined columns. Micelli et al. [19], [20] tested 25 CFRP-confined cylindrical specimens (100 mm diameter × 200 mm height) under preloading ratios (n_0) ranging from 0.2 to 0.8. Consistent with Pan et al. [15], [16], they concluded that preloading lowered confinement efficiency.

Lu et al. [21] carried out numerical simulations of preloaded FRP-retrofitted concrete columns under compression and proposed models for dilation and axial stress-strain behavior under preloaded conditions. Their analyses showed that preloading had a minor adverse effect on axial capacity enhancement.

As evidenced by the controversial results reported in previous studies, further investigation into the effects of preloading prior to retrofitting is deemed indispensable. In addition, limited information is available regarding the influence of preloading on full-field strain development and post-peak behavior of CFRP-confined concrete. To this end, ten concrete specimens were tested, with nominal confinement ratios (f_l/f_{co}) ranging from 0.11 to 0.54 and a preloading ratio (n_0) of 0.85. The experimental program included two concrete strength levels, unconfined reference specimens, and CFRP-confined specimens with one and three layers, tested both with and without preloading. A high preloading level of 85% of the unconfined axial capacity was applied prior to retrofitting to simulate real in-service conditions. Three-dimensional digital image correlation (3D-DIC) was utilized to monitor full-field axial and lateral strain distributions in conjunction with conventional linear variable differential transducers (LVDTs).

Results show that preloading notably reduces deformation capacity, especially at lower confinement ratios and higher concrete strengths. Increasing the confinement level helps mitigate these adverse effects. Moreover, 3D-DIC provided valuable insights into localized strain concentrations beyond conventional measurements.

2 EXPERIMENTAL PROGRAM

2.1 Specimens and instrumentation

Ten cylindrical concrete specimens with H and D of 670 mm and 200 mm were tested under compression using a 10 MN hydraulic compression machine. Specimens were named as follows: L0, and H0 are reference specimens. In the specimen nomenclature, L and H denote low and high concrete compressive strength (f_{co}), respectively; the digit following these letters indicates the preloading ratio prior to retrofitting (0 or 85% of the axial capacity), and the term preceding L/H represents the number of CFRP plies applied after preloading. The specimen matrix comprises the following parameters: cylindrical concrete compressive strength (f_{co}), preloading ratio (n_0), nominal confinement ratios (f_l/f_{co}), and number of FRP plies (n). All specimens were retrofitted using a woven unidirectional carbon fiber fabric (SikaWrap-230 C) in combination with a two-component epoxy impregnation resin (Sikadur-330). The CFRP has an elastic modulus (E_f), tensile strength (f_f), rupture strain (ε_f) and a nominal thickness (t_f) of 230 GPa, 4000 MPa, 1.7%, and 0.129 mm, respectively, as provided by the manufacturer. The standard cylindrical concrete compressive strengths of the first and second groups were 21.60 MPa and 50.71 MPa, respectively.

The L0 and H0 specimens served as control specimens and were tested without retrofitting or preloading. The subsequent specimens with retrofitting and without preloading were first retrofitted and then tested until failure. The specimens with retrofitting and preloading were first loaded to 85% of the axial capacity of their corresponding control specimens (i.e., L0/H0). The load was then kept constant, and the specimens were retrofitted under this constant load and left 48-56 hours at laboratory temperature. After approximately 48 hours, testing was resumed until failure. Furthermore, a 3D-DIC system was utilized as a tool to meticulously monitor micro cracks initiation and propagation, as well as the distribution of axial and lateral strains over the circumferential surface of the cylinders.

Fig. 1 shows the test setup and the LVDTs and strain gauges mounted on the specimens. To measure axial strains, two steel rings compatible with the specimen dimensions were devised. Three LVDT with a stroke range of 100 mm were attached to the top ring to measure axial deformations relative to the bottom ring. The measuring distance was set to 300 mm. These LVDTs were used to plot axial stress-strain curves. Moreover, two horizontal LVDTs with a stroke range of 100 mm were installed to measure lateral deformation of the specimens at mid-height (~335 mm). In addition, two strain gauges with a gauge length of 60 mm were attached at mid-height of the specimens (~335 mm) to measure lateral strain, corresponding to the FRP rupture strain (ε_{fe}) as shown in Fig. 1 (right).

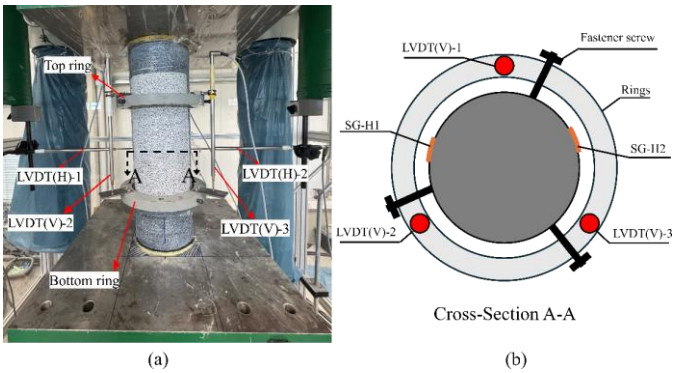


Fig. 1 Test setup and instrumentation a) side view, b) cross-section and position of vertical LVDTs and horizontal strain gauges (SG-H1 and SG-H2)

Furthermore, to implement and set up 3D-DIC, the following procedure was carried out: a) the specimens were painted white, b) using a black spray, fine black dots were randomly dispersed over the surface to create a speckle pattern, and c) three-dimensional calibration was perfomed to provide geometrical information of the specimen being imaged. It should be noted that the finer and more numerous the black dots on the surface, the greater the number of points detected by the DIC cameras. Fig. 2 shows the DIC installation procedure. As seen in Fig. 1 (left), the area covered by DIC cameras is smaller than the full specimen surface.

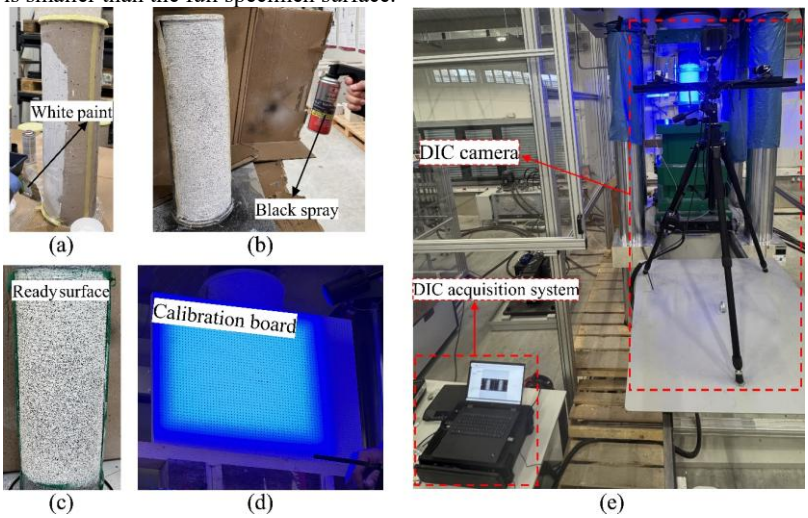


Fig. 2 DIC installation: a) painting with white color, b) distribution of black dots by spraying, c) prepared surface, d) calibration, e) general overview

2.2 Test results

2.2.1 Axial stress vs. axial and lateral strains

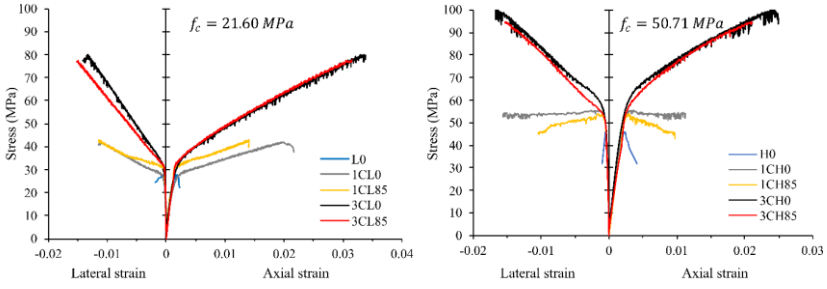
Table 1 summarizes the test results in terms of axial stress, axial strain, and lateral strain, where the strains measurements were obtained using the mounted LVDTs, as shown in Fig. 1. Fig. 3 (left) and (right) present the axial stress-axial strain and axial stress-lateral strain curves of the tested cylinders with low and high concrete compressive strength, respectively. In this study, f_c denotes the concrete compressive strength measured from standard cylinders with H and D of 300 mm and 150 mm, respectively, whereas f_{co} refers to the unconfined concrete compressive strength of the test cylinders with a H and D of 670 mm and 200 mm.

Table 1 Test results.

Specimens	f_{co} (MPa)	ε_{co} (%)	ε_{lo} (%)	n	f_l/f_{co}	f_{cc} (MPa)	ε_{cc} (%)	ε_{fe} (%)
L0	27.77	0.19	0.06	-	-	-	-	-
1CL0				1	0.18	41.99	1.93	1.15
1CL85				1	0.18	42.93	1.42	1.13
3CL0				3	0.54	80.09	3.38	1.35
3CL85				3	0.54	77.92	3.10	1.50
H0	45.88	0.27	0.39	-	-	-	-	-
1CH0				1	0.11	55.48	1.10	1.56
1CH85				1	0.11	53.94	0.30	1.08
3CH0				3	0.33	100.71	2.40	1.64
3CH85				3	0.33	94.83	2.10	1.52

For the first group with low concrete compressive strength, the control specimen L0 exhibited an unconfined compressive strength (f_{co}) of 27.77 MPa and a corresponding axial strain (ε_{co}) of 0.0019. Specimens 1CL0 and 3CL0, retrofitted with one and three CFRP layers without preloading, achieved strength increases of 51.2% and 188.4%, respectively, relative to the unretrofitted specimen L0. Among the preloaded specimens, specimen 1CL85 exhibited no change in confined compressive strength (f_{cc}), whereas specimen 3CL85 showed a minor reduction of 2.7% compared to 3CL0, which can be considered negligible. In contrast, preloading had a more pronounced effect on deformation capacity. For specimen 1CL85, the ultimate axial strain (ε_{cc}) was reduced by 26.4% relative to 1CL0 (Fig. 3 (left)), while specimen 3CL85 showed a smaller reduction of 8.3% in ε_{cc}. In addition, the FRP rupture strain (ε_{fe}) was not affected by preloading.

For second group with high concrete compressive strength, specimen H0 had an unconfined compressive strength (f_{co}) of 45.88 MPa and a corresponding axial strain (ε_{co}) of 0.0027. Specimens 1CH0 and 3CH0, which were retrofitted with one and three CFRP layers without preloading, showed strength increases of 20.9% and 119.5%, respectively, compared to their unretrofitted counterpart (H0). As expected, the confinement efficiency was reduced as the concrete compressive strength increased compared to the first group. Specimen 1CH85 exhibited 2.8% reduction in confined compressive strength (f_{cc}). Furthermore, the ultimate axial strain (ε_{cc}) and FRP rupture strain (ε_{fe}) were reduced by 72.7% and 30.8%, respectively, compared to 1CH0 (Fig. 3 (right)). For specimen 1CH85, the ultimate axial strain (ε_{cc}) was defined as the strain corresponding to $0.85f_{cc}$ on the descending branch, since a softening response was observed immediately after the peak stress. For specimen 3CH85, f_{cc} was reduced by 5.8% compared to 3CH0, which is higher than that observed in the first group. Moreover, for this specimen, ε_{cc} and ε_{fe} were reduced by 12.5% and 7.3%, respectively.



(a) (b)

Fig. 3 Axial stress-axial and lateral strain curve, a) low concrete compressive strength of 21.60 MPa, b) high concrete compressive strength of 50.71 MPa

2.2.2 DIC results

The merit and preponderance of DIC system over other measuring instruments, such as LVDTs and strain gauges, is that it can provide a comprehensive insight into both local and overall axial and lateral strain values of the specimens. Furthermore, due to the widening and propagation of cracks during the loading stages, the specimens tend to exhibit large lateral expansion and a drastic increase in volumetric strain (ε_v); under such conditions, LVDTs and strain gauges may fail to measure objective and reliable values.

Fig. 4 and Fig. 5 show the ultimate axial and lateral strain distribution of all tested specimens for the first and second groups, respectively. For instance, as seen in Fig. 4 (left), specimen 1CL85, with numerous local red and orange areas indicating low strain levels, could not reach higher axial strains compared to 1CL0 due to the preloading effect. However, for specimen 3CL85 owing to the higher confinement level, preloading did not have any noticeable impact on the development of axial and lateral strains (Fig. 4). In Fig. 5 (left), the axial strain rate of specimen 1CH85 remains lower than that of 1CH0 due to the preloading effect, which is also visible in Fig. 3.

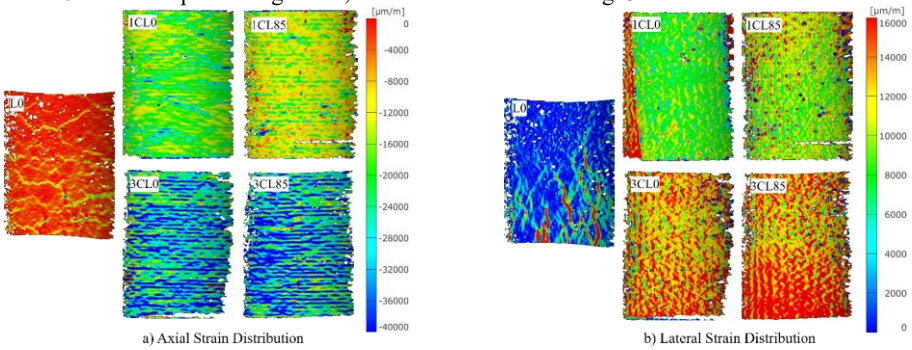


Fig. 4 DIC results for first group of specimens with low concrete compressive strength, a) axial strain distribution, b) lateral strain distribution

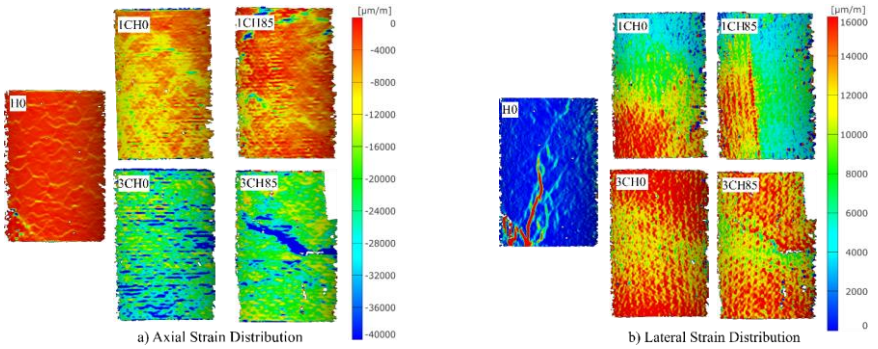
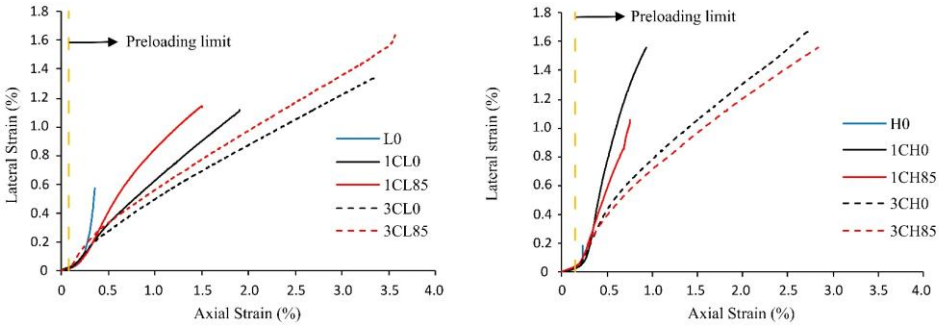


Fig. 5 DIC results for second group of specimens with high concrete compressive strength, a) axial strain distribution, b) lateral strain distribution

Fig. 6 presents the lateral-axial strain relationships for all tested specimens. As shown in Fig. 6 (left), specimen 1CL85 exhibits lower axial strain than 1CL0, which can be attributed to the effect of preloading. In contrast, for specimen 3CL85, where the confinement level is higher due to the increased number of CFRP layers, the influence of preloading is essentially vanished. In Fig. 6 (right), both axial and lateral strains of 1CH85 remain significantly lower than those of 1CH0, primarily due to the combined effects of preloading and a low confinement ratio. Similarly, when the confinement ratio increases with additional FRP layers, the effect of preloading essentially disappears. The vertical yellow dashed line indicates the preloading threshold, corresponding to the axial strain level at which preloading was applied prior to retrofitting.



(a) (b)

Fig. 6 Lateral-axial strain curves obtained by DIC, a) first group with low concrete compressive strength, b) second group with high concrete compressive strength.

Fig. 7 presents the lateral strain-time curve of specimen 1CL0 to compare the measured lateral strains, corresponding to the FRP rupture strain (ε_{fe}), obtained using three different methods (i.e., DIC, two horizontal LVDTs placed in opposite directions at 180°, and horizontal strain gauges). As observed, the results from the two LVDTs are the highest, as they measured ε_{fe} at the mid-height of the specimen, which is the critical location where local damage is concentrated. The strain gauges (SG-H1 and SG-H2) show lower strain values, as they measure strains over a relatively short gauge length (~60 mm). Finally, the DIC method provides an average lateral strain (ε_{fe}) over the captured specimen surface between the two rings, yielding more reliable and objective values.

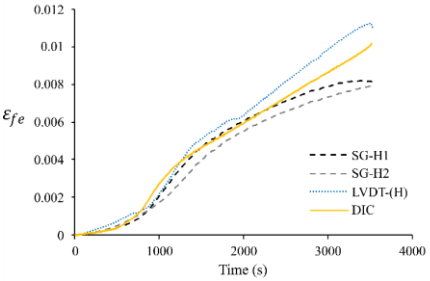
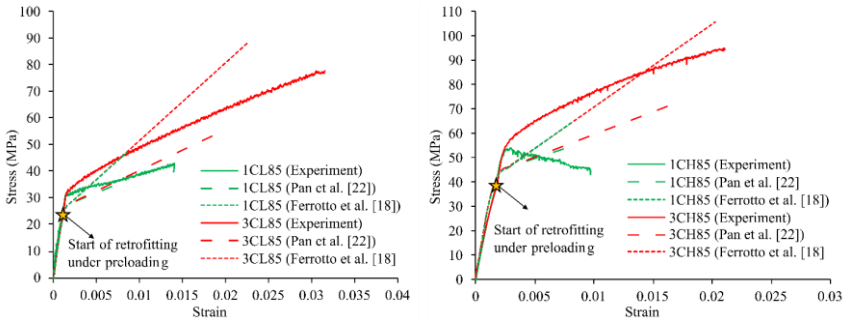


Fig. 7 Comparison of lateral strain-time curve of 1CL0 by three measuring instruments of DIC, horizontal LVDTs and strain gauges.

2.3 Axial stress-strain predictions

There are analysis-oriented models available for predicting the axial stress-strain behavior of CFRP-confined concrete cylinders under preloading conditions [18], [22]. Fig. 8 compares the predictions of the models proposed by Ferrotto et al. [18] and Pan et al. [22] with the experimental axial stress-strain responses of CFRP-confined specimens subjected to preloading for both low- and high-strength concrete groups. The comparison indicates that the two models exhibit different predictive characteristics with respect to the confined compressive strength (f_{cc}). Specifically, the model by Pan et al. [22] tends to produce conservative estimates, underestimating f_{cc}. In contrast, the model by Ferroto et al. [18] provides predictions closer to the experimental peak strength, with a maximum overestimation of 20.9%. For specimens with low confinement ratios subjected to preloading (e.g., 1CH85), both models failed to reproduce the experimentally observed strain-softening response and significantly overestimated the deformation capacity.



(a) (b)

Fig. 8 Comparison of experimental axial stress-strain curves with predictions proposed by Ferrotto et al. [18] and Pan et al. [22]

3 CONCLUSIONS

This study experimentally examined the effect of preloading on the compressive behavior of CFRP-confined cylindrical concrete columns by testing ten specimens with different concrete strengths and confinement levels. A high preloading level of 85% of the axial capacity was applied prior to retrofitting to simulate realistic in-service strengthening conditions, and a 3D-DIC system was employed for detailed strain measurements.

The experimental results showed that the deformation capacity was clearly affected, as preloaded specimens exhibited reductions in ultimate axial strain of up to 30% and ultimate lateral (FRP rupture) strain of up to 12% compared to non-preloaded specimens. This adverse effect became more pronounced at lower confinement ratios and higher concrete compressive strength (e.g., up to 72.7% decrease in ε_{fe} for 1CH85), while increasing the confinement level was found to partially mitigate the strain reduction induced by preloading. The 3D-DIC measurements provided reliable spatial strain distributions, revealing localized strain concentrations and highlighting the limitations of conventional point-based instrumentation in capturing ultimate strain behavior. Comparison with existing analytical models indicated that the model proposed by Ferrotto et al. predicts the ultimate confined compressive strength of preloaded specimens closer to the experimental values than the model by Pan et al. model; however, both models showed limitations in reproducing the post-peak response, particularly for specimen exhibiting strain-softening behavior (1CH85). Although minor experimental variability associated with material heterogeneity, CFRP installation, and strain measurements is inevitable, the overall trends observed in the tests were consistent for different confinement levels and concrete strengths.

Overall, the findings indicate that while CFRP confinement effectively preserves strength enhancement in preloaded columns, preloading can significantly reduce deformation capacity. This highlights the importance of explicitly considering preloading effects in confinement models and design recommendations, especially for performance-based and seismic retrofit applications.

References

[1] Ilki, Alper, Kumbasar, Nahit, and Koc, Volkan. 2002. “Strength and deformability of low strength concrete confined by carbon fibre composite sheets.” In: Proc. 15th Eng. Mech. Conference. New York: Columbia Univ.

[2] Jiang, T. and Teng, Jinguang. 2006. “Strengthening of short circular RC columns with FRP jackets: a design proposal.” In: Proc. 3rd Int. Conf. on FRP Compos. in Civ. Eng. Miami, Florida, USA.

[3] Berthet, J.F., Ferrier, Emmanuel, and Hamelin, Patrice. 2006. “Compressive behavior of concrete externally confined by composite jackets.” *Construction and Building Materials* 20:338–47. https://doi.org/10.1016/j.conbuildmat.2005.01.029.

[4] Tamuzs, V., Tepfers, R., and Sparnins, E. 2006. “Behavior of concrete cylinders confined by carbon composite 2. Prediction of strength.” *Mechanics of Composite Materials* 42:109–18. https://doi.org/10.1007/s11029-006-0022-7.

[5] Tamuzs, V., Tepfers, R., Zile, E., and Ladnova, O. 2006. "Behavior of concrete cylinders confined by a carbon composite 3. Deformability and the ultimate axial strain." *Mechanics of Composite Materials* 42:303–14. https://doi.org/10.1007/s11029-006-0040-5.

[6] Wu, Gang, Lü, Z.T., and Wu, Z.S. 2006. "Strength and ductility of concrete cylinders confined with FRP composites." *Construction and Building Materials* 20:134–48. https://doi.org/10.1016/j.conbuildmat.2005.01.022.

[7] Lam, Lik, and Teng, Jin-Guang. 2003. "Design-oriented stress–strain model for FRP-confined concrete." *Construction and Building Materials* 17:471–89. https://doi.org/10.1016/S0950-0618(03)00045-X.

[8] Binici, Baris. 2005. "An analytical model for stress–strain behavior of confined concrete." *Engineering Structures* 27:1040–51. https://doi.org/10.1016/j.engstruct.2005.03.002.

[9] Ozbakkaloglu, Togay, Lim, Jian C., and Vincent, Thomas. 2013. "FRP-confined concrete in circular sections: Review and assessment of stress–strain models." *Engineering Structures* 49:1068–88. https://doi.org/10.1016/j.engstruct.2012.06.010.

[10] Tung, Nguyen Duc, and Tue, Nguyen Viet. 2016. "A fracture mechanics-based approach to modeling the confinement effect in reinforced concrete columns." *Construction and Building Materials* 102:893–903. https://doi.org/10.1016/j.conbuildmat.2015.11.031.

[11] Tung, Nguyen Duc, and Tue, Nguyen Viet. 2013. "Deformation-based approach for determination of the efficiency of the confinement in R/C members." in: Proceedings of the Thirteenth East Asia-Pacific Conference on Structural Engineering and Construction (EASEC-13), Sapporo, Japan, September 11-13.

[12] Kian, Nima, Farzam, Masood, and Oshtolagh, M. Rezaie. 2021. "Carbon fiber reinforced polymer strengthened reinforced concrete square columns under pre-existing eccentric loads." *Advances in Structural Engineering* 24:3420–32. https://doi.org/10.1177/13694332211029730.

[13] He, Zheng, Jin, Jian-ping, Song, Ji-guang. 2009. "Experimental study on the expansion ratio of preloaded circular concrete columns with CFRP confinement." *Engineering Mechanics* 26:145–51.

[14] He, Zheng, and Jin, Jian Ping. 2011. "Axial Compressive Behavior of CFRP-Confined Concrete Columns Subject to Short-Term Preloading." *Advanced Materials Research* 163:3830–37. https://doi.org/10.4028/www.scientific.net/AMR.163-167.3830.

[15] Pan, Yi, Rui, Gou, Li, Hongyi, Tang, Hongyuan, and Xu, Long. 2017. "Study on stress-strain relation of concrete confined by CFRP under preload." *Engineering Structures* 143:52–63. https://doi.org/10.1016/j.engstruct.2017.04.004.

[16] Pan, Yi, Cao, Shuang Yin, Jing, Deng Hu, and Zhao, Shi Chun. 2011. "Experimental Research on Axially Loaded Circular Concrete Columns Confined by CFRP under Preload." *Advanced Materials Research* 255–260:694–98. https://doi.org/10.4028/www.scientific.net/AMR.255-260.694.

[17] Ferrotto, Marco Filippo, Fischer, Oliver, and Niedermeier, Roland. 2018. "Experimental investigation on the compressive behavior of short-term preloaded carbon fiber reinforced polymer-confined concrete columns." *Structural Concrete* 19:988–1001. https://doi.org/10.1002/suco.201700072.

[18] Ferrotto, Marco Filippo, Fischer, Oliver, and Cavaleri, O. L. "Analysis-oriented stress–strain model of CRFP-confined circular concrete columns with applied preload." *Materials and Structures* 51:44. https://doi.org/10.1617/s11527-018-1169-0.

[19] Micelli, Francesco, Cascardi, Alessio, and Aiello, Maria Antonietta. 2021. "Pre-Load Effect on CFRP-Confinement of Concrete Columns: Experimental and Theoretical Study." *Crystals* 11:177. https://doi.org/10.3390/cryst11020177.

[20] Micelli, Francesco, Cascardi, Alessio, and Aiello, Maria Antonietta. 2018. "A study on FRP-confined concrete in presence of different preload levels." In: Proceedings of the 9th International Conference on Fibre-Reinforced Polymer (FRP) Composites in Civil Engineering-CICE, Paris, France.

[21] Lu, Shiwei, Wang, Jizhong, Yang, Junlong, and Wang, Licheng. 2022. "Numerical analysis of preloaded FRP-strengthened concrete columns under axial compression." *Construction and Building Materials* 357:129297. https://doi.org/10.1016/j.conbuildmat.2022.129297.

[22] Pan, Yi, Rui, Gou, Li, Hongyi, Tang, Hongyuan, and Huang, Jingxiang. 2017. "Analysis-oriented stress–strain model for FRP-confined concrete with preload." *Composite Structures* 166:57–67. https://doi.org/10.1016/j.compstruct.2017.01.007.

Key Challenges in Designing and Evaluating Lined Rock Caverns for Hydrogen Storage

Aida Sabbaghian Toosi, Gabriele Della Vecchia, Giovanni Muciaccia, Liberato Ferrara

Department of Civil and Environmental Engineering,
Politecnico di Milano,
Piazza Leonardo da Vinci, Milan 20133, Italy

Aida.sabbaghian@polimi.it

Summary
Underground hydrogen storage in lined rock caverns (LRCs) is critical for decarbonisation. While successful for natural gas (Sweden, South Korea), hydrogen adaptation faces distinct challenges. Uncertainties persist in liner-rock coupled behaviour under hydrogen-specific demands: elevated pressures, thermal fluctuations, cyclic loading, and degradation. Existing frameworks inadequately account for hydrogen's enhanced diffusion, embrittlement, and thermomechanical dynamics. Three analytical approaches were developed, ranging from an energy-weighted averaging method to a Peng-Robinson real-gas formulation with iterative coupling. Results show that ideal-gas assumptions introduce substantial errors in predicted temperature and storage capacity, potentially altering thermal safety assessments, while structural analysis identifies rock confinement as a key factor for viability. Findings establish validated methods and hydrogen-specific design priorities.

1 INTRODUCTION: THE KNOWLEDGE GAPS

1.1 Current State of LRC Technology

Natural gas storage in lined rock caverns has operated successfully for over three decades. The Skallen facility in Sweden (operational since 1989) and multiple South Korean installations demonstrate the technical viability of this approach. However, these systems were designed for natural gas; therefore, transferring these design assumptions to hydrogen storage requires careful validation [1].

1.2 Why Hydrogen Requires a Dedicated Assessment

The adaptation of LRC technology to hydrogen storage introduces several critical challenges that existing design frameworks do not adequately address. Thermal Loading (Primary Gap): Hydrogen's negative Joule-Thomson coefficient causes heating during compression rather than cooling, opposite to natural gas. Combined with hydrogen's exceptionally high specific heat capacity (6.4 times more than that of methane), this creates temperature rises significantly larger than in natural gas systems [2]. Current design approaches typically assume ideal gas behaviour and treat thermal effects as secondary, but the validity of these assumptions for hydrogen at 20-30 MPa storage pressures remains unquantified [3].

Structural Response Under Thermal-Mechanical Coupling: The interaction between thermal stresses from temperature gradients and mechanical stresses from internal pressure is poorly understood. Existing natural gas designs focus primarily on mechanical loading, potentially underestimating the importance of thermal effects for hydrogen [4].

Operational Trade-offs: The relationship between charging rate, peak temperature, storage capacity, and economic throughput has not been systematically mapped for hydrogen systems. This gap prevents optimisation of operational strategies [5].

Rock-Liner Interaction: While rock confinement is qualitatively understood to be important, quantitative assessment of how rock stiffness affects liner stresses and overall system viability is lacking. [4].

1.3 Research Objective

To address these knowledge gaps, validated thermal analysis methods were developed that can: (1) quantify the errors introduced by conventional ideal gas assumptions; (2) accurately predict temperature evolution during hydrogen charging; (3) map trade-offs between charging speed, thermal safety, and economics; and (4) evaluate, within the adopted idealised framework, the role of rock confinement in structural response. This paper presents the systematic development of three modelling approaches and discusses the implications of key assumptions on predicted temperature evolution and storage performance.

2 METHODOLOGY: THREE APPROACHES TO THERMAL ANALYSIS

2.1 Approach 1: Energy-Weighted Average

Initially, a simplified method was adapted from hydrogen vehicle refuelling literature. Implementation: Empirical correlation with weighted averaging; Three configurations were tested (adiabatic: ΔT = 84.7°C; steel liner: ΔT = 46.6°C; concrete liner: ΔT = 39.1°C); Daily time steps were employed; Ideal gas assumption (Z = 1.0) was maintained. Key findings: The thermal mass of the lining was found to significantly reduce the predicted temperature rise; in particular, the concrete layer reduced the peak temperature by approximately 45.6°C compared to adiabatic conditions [6].

Limitations: Explicit multi-layer heat conduction was required to understand hour-by-hour temperature evolution.

2.2 Approach 2: Transient Heat Transfer + Ideal Gas

In the second approach, a transient heat transfer model was developed to account for multilayer conduction through steel, concrete, and surrounding rock. The cavern was idealised as a cylindrical system with radius 17.5 m and length 50 m (V = 48,000 m³), including a 12 mm steel liner, a 1.0 m concrete ring, and 30 m of surrounding rock. The adopted geometry, liner thicknesses, and surrounding rock extent were selected to represent a simplified but representative lined rock cavern configuration for comparative analysis. The thermal boundary conditions and material properties were taken from available literature and previous hydrogen storage studies, and the 95°C threshold was used as a conservative operational limit for comparing the charging scenarios considered here. The simulation was performed using a time step of 1 hour, assuming a polytropic compression exponent n = 1.2 and inlet conditions T_{in} = 20°C and $\dot{m}_{in}$ = 3.54 kg/s. The gas behaviour was initially modelled as ideal (Z = 1). For a 10-day charging scenario, the model predicts a final temperature of 86.7°C and a final stored mass of 1,034 tonnes. Under these assumptions, the thermal limit of 95°C is satisfied; however, the applicability of the ideal-gas approximation at 30 MPa should be interpreted with caution and checked against a real-gas formulation [8].

2.3 Approach 3: Peng-Robinson Real Gas

In the final approach, the Peng-Robinson equation of state was implemented to capture real gas effects through the compressibility factor Z [7].

2.3.1 Peng-Robinson equation:

$$p = RT/(Vm - b) - a\cdot\alpha(T)/[Vm(Vm + b) + b(Vm - b)] \quad (1)$$

This equation was rearranged into cubic form for Z :

$$Z^3 + (B-1)Z^2 + (A-2B-3B^2)Z - (AB-B^2-B^3) = 0 \quad (2)$$

2.3.2 Iterative coupling algorithm:

A coupled iterative algorithm was implemented to account for the dependence of the compressibility factor Z on pressure and temperature. At each time step (Δt = 5 min), the Peng–Robinson cubic equation was solved for Z, which was then used to update density and stored mass. The updated state variables were inserted into the energy balance to compute the new gas temperature. Iteration continued until convergence was achieved ($|T_{new} - T_{old}| < 0.01$ K), typically within 2–5 iterations.

2.3.3 Results for 10-day charging to 30 MPa:

For the 10-day charging case, the Peng-Robinson model predicts a final gas temperature of 96.0°C and a stored mass of 849.7 tonnes. The corresponding compressibility factor reaches Z = 1.116, indicating a noticeable deviation from ideal behaviour. Under the adopted thermal limit of 95°C, this scenario marginally exceeds the allowable threshold [9].

Table 1 Nomenclature:

Symbol	Definition
p	Pressure (Pa or MPa)
T	Temperature (K)
V_m	Molar volume (m³/mol)
R	Specific gas constant for hydrogen = 4,124 J/(kg·K)
Z	Compressibility factor (dimensionless)
a	Peng-Robinson parameter for intermolecular attraction
b	Peng-Robinson parameter for molecular volume
α(T)	Temperature-dependent function: $\alpha(T) = [1 + \kappa(1 - \sqrt{(T/Tc)})]^2$
κ	Parameter function: $\kappa = 0.37464 + 1.54226\omega - 0.26992\omega^2$
Tc	Critical temperature = 33.145 K (for hydrogen)
pc	Critical pressure = 1.2964 MPa (for hydrogen)
ω	Acentric factor = -0.219 (for hydrogen)
A	Dimensionless parameter: $A = a \cdot \alpha(T) \cdot p/(R^2T^2)$
B	Dimensionless parameter: $B = b \cdot p/(RT)$
ρ	Density (kg/m³)
m	Mass (kg)
V	Volume = 48,000 m³ (cavern storage volume)
ṁin	Mass flow rate (kg/s)
cp	Specific heat capacity = 14,300 J/(kg·K) (for hydrogen)

3 CRITICAL FINDING: IMPACT OF IDEAL-GAS ASSUMPTIONS ON SAFETY ASSESSMENT

3.1 Day-by-Day Temperature Comparison

Temperature predictions were monitored on a daily basis to identify when and why the approaches diverge; the results are summarized in Table 2 and illustrated in Fig.1.

Table 2 Temperature Evolution: Ideal Gas vs. Real Gas (10-day charging)

Day	Pressure (MPa)	Approach 2: Ideal Gas	Approach 3: Real Gas	Temperature Difference	Z-factor
0	0.1	20.0°C	20.0°C	0.0°C	1.000
1	3.0	38.2°C	28.7°C	-9.5°C (cooler)	1.015
5	15.0	68.1°C	68.1°C	0.0°C (convergence)	1.077
10	30.0	86.7°C	96.0°C	+9.3°C (hotter)	1.116

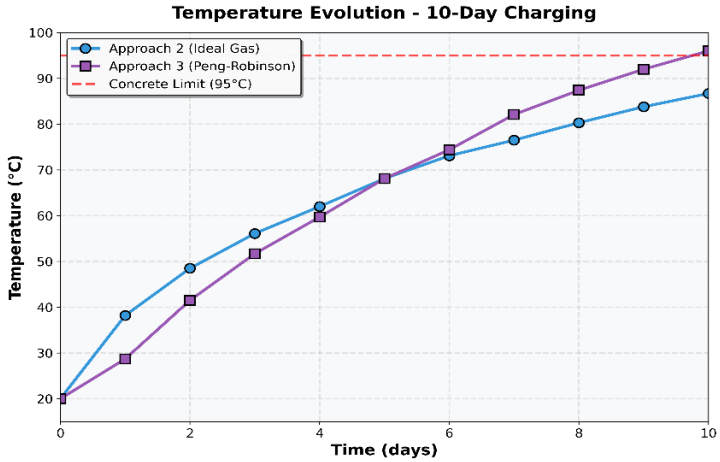


Fig. 1 Comparison of ideal gas (Approach 2) versus Peng-Robinson real gas (Approach 3) predictions for a 10-day charging cycle.

3.1.1 Physical interpretation:

Early stage (0-1 day): At low pressure, attractive intermolecular forces dominate, resulting in the real gas being cooler by 9.5°C.

Mid-stage (~5 days): Attractive and repulsive forces balance, causing the approaches to converge.

Late stage (7-10 days): At high pressure, repulsive forces dominate, resulting in the real gas being hotter by 9.3°C.

The compressibility factor systematically increases from 1.000 to 1.116, confirming significant deviation from ideal behaviour.

3.2 The Design Consequence

The ideal-gas model suggests compliance with the 95°C limit, whereas the real-gas model predicts a marginal exceedance (96.0°C), which changes the outcome of the thermal safety check." The 9.3°C difference—arising entirely from real gas effects determines whether the design passes or fails thermal criteria.

3.3 Storage Capacity Error

Temperature affects density, directly impacting storage capacity (Fig. 2):

- Approach 2 prediction: 1,034 tonnes
- Approach 3 prediction: 849.7 tonnes
- Error: +184 tonnes (+21.7% overestimate)

Economic impact: If the design is based on ideal gas assumptions, 1,034 tonnes will be promised, but only 850 tonnes will be delivered. Such overestimation may lead to non-conservative planning of operational capacity and facility performance [10].

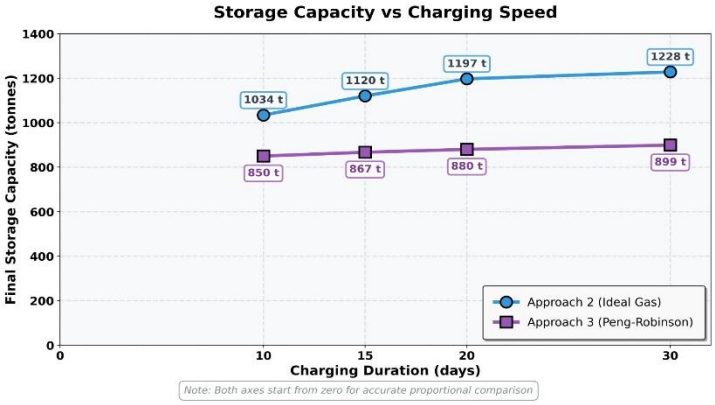


Fig. 2 Capacity of the storage in 4 scenarios of charging in 2 approaches

3.4 Recommendation on Approach Selection

Table 3 Comparison of Analytical Approaches

Approach	Complexity	Computational Cost	Accuracy at 30 MPa	Recommendation
1: Energy-weighted	Low	Seconds	Rough estimate only	Screening studies only
2: Ideal gas + HT	Medium	Minutes	Systematic error	Not acceptable for H_2
3: Peng-Robinson	High	<1 minute	Required accuracy	Recommended for high-pressure hydrogen storage

For hydrogen storage at 20–30 MPa, Approach 3 (or an equivalent real-gas treatment) is necessary for reliable predictions under the conditions examined. As shown in Table 3, simplified approaches introduce errors that can reverse fundamental design conclusions from “safe” to “unsafe”.

4 CHARGING RATE OPTIMISATION: MAPPING THE TRADE-OFF SPACE

4.1 Multi-Scenario Analysis

To evaluate operational flexibility, four charging durations were analysed using Approach 3 (Peng–Robinson). The corresponding results are presented in Table 4 and visualized in Fig. 3.

4.2 The Safety vs. Economics Trade-Off

4.2.1 From a thermal safety perspective:

- 10 days: FAIL (96.0°C > 95°C limit)
- 15 days: MARGINAL (87.9°C, only 7°C safety margin)
- 20 days: SAFE (82.1°C, comfortable margin)
- 30 days: VERY SAFE (74.2°C, large margin)

4.2.2 From an economic perspective:

- 10 days: Optimal (maximum throughput = baseline)
- 15 days: Reduced (-31% annual revenue)
- 20 days: Severely reduced (-48% annual revenue)
- 30 days: Significantly reduced throughput (-64% annual revenue)

Table 4 Multi-Scenario Analysis Results

Scenario	Duration	Flow Rate (kg/s)	Peak Temp (°C)	Final Mass (ton)	Z-factor
Fast	10 days	3.54	96.0	849.7	1.116
Moderate-Fast	15 days	2.36	87.9	867.2	1.118
Moderate	20 days	1.77	82.1	880.2	1.119
Slow	30 days	1.18	74.2	898.8	1.121

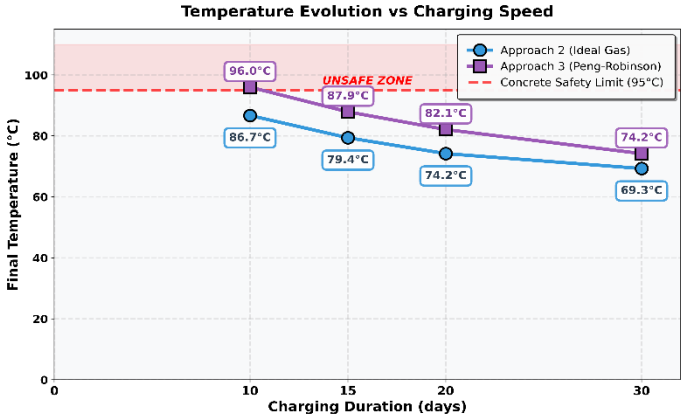


Fig. 3 Effect of charging duration on hydrogen temperature based on ideal gas (Approach 2) versus Peng-Robinson real gas (Approach 3). Four scenarios (10, 15, 20, and 30 days).

4.3 Design Implications

This trade-off shows that faster charging improves throughput but can raise thermal risk, whereas slower charging improves thermal safety at the expense of economic performance.

4.3.1 Resolution strategies:

1. A practical compromise may be a charging duration of about 15-20 days, or the use of thermal mitigation measures to support faster charging. (compromise between safety and economics)

2. Implement thermal mitigation to enable faster charging:

- Pre-cool inlet hydrogen (20°C → 5°C reduces peak by ~15°C)
- Active cooling systems in the liner
- Use high-performance concrete with elevated temperature tolerance (90-95°C)

3. Install real-time monitoring:

- Distributed temperature sensing (fibre optic DTS)
- Pressure-temperature correlation tracking
- Automatic flow rate adjustment based on thermal response

5 STRUCTURAL ANALYSIS: THE CRITICAL ROLE OF ROCK CONFINEMENT

5.1 Parametric Study Design

To quantify rock confinement effects, Lamé analysis for thick-walled cylinders was performed under two boundary conditions:

Scenario A: No rock confinement - Free-standing cylinder with external pressure po = 0
Scenario B: Stiff rock confinement - Rock prevents radial displacement at outer boundary (u(ro)=0)
Both scenarios were analysed for three concrete thicknesses: 0.5 m, 2.0 m, and 3.0 m (Table 5).

5.2 Results: Rock Confinement Changes Everything

Table 5 Steel Liner Stress at 30 MPa Internal Pressure

Concrete Thickness	No Rock Confinement	With Stiff Rock	Stress Reduction Factor
0.5 m	5,500 MPa	5.17 MPa	1,064×
2.0 m	2,293 MPa	11.85 MPa	193×
3.0 m	1,229 MPa	29.76 MPa	41×

Reference: Steel yield strength ≈ 355 MPa

It should be noted that these values represent an idealised analytical estimate intended to highlight the sensitivity to confinement, rather than a full structural design calculation

5.3 Physical Interpretation

5.3.1 Without rock confinement:

- Even 3 meters of concrete produces 1,229 MPa in steel
- This is 3.5× above yield strength → immediate failure
- To achieve safe stress levels (<355 MPa), steel walls several meters thick would be required
- The simplified analysis indicates that the system would be highly unfavourable without rock support and that rock confinement is likely essential in practical designs.

5.3.2 With rock confinement:

- 0.5 m concrete produces 5.17 MPa steel stress (perfectly safe)
- 3.0 m concrete produces 29.76 MPa steel stress (still safe)
- Rock stiffness provides the mechanical restraint that enables the use of a thin steel liner

Key insight: In the simplified framework adopted here, rock confinement plays a decisive mechanical role in enabling the use of a thin steel liner. The rock's role is not passive excavation space, it is active mechanical support. Without adequate rock stiffness, the project is not viable regardless of liner design improvements.

5.4 Thermal vs. Mechanical Stress Comparison

Both stress sources were calculated for comparison:

Mechanical stress (Lamé solution for 30 MPa internal pressure):

$\sigma\theta, mech = 15 - 20\ MPa$ (hoop stress at inner concrete surface)

Thermal stress (constrained expansion, $\Delta T = 60°C$ across 1.0 m concrete):

$$\sigma th = E \cdot \alpha \cdot \Delta T/(1-\nu) = 26.3\ MPa$$

where $E = 30\ GPa$ (concrete elastic modulus), $\alpha = 10 \times 10^{-6}\ /K$ (thermal expansion coefficient), ν = 0.2 (Poisson's ratio).

Critical finding: Thermal stress (26.3 MPa) exceeds mechanical stress (15-20 MPa) by a factor of 1.3-1.8×.

Design implication: For natural gas LRCs, thermal effects are secondary and often ignored. For hydrogen LRCs, thermal loading is the primary design driver. Current design practice should explicitly account for thermal effects when assessing hydrogen LRCs. [11].

The present study is based on idealised geometry, simplified boundary conditions, and selected material parameters from the available literature. The structural assessment is intended as an illustrative analytical comparison rather than a full design verification, and further validation with more detailed multiphysics and experimental data is recommended.

6 CONCLUSIONS

This study addresses important gaps in hydrogen LRC design through a set of simplified thermal and structural analyses. The main conclusions are as follows:

1. Real-gas modelling is required to achieve reliable predictions at 30 MPa: At 30 MPa, Z = 1.116. An ideal gas introduces a 9.3°C temperature error and 184 tonne capacity error, changing the design from 'safe' to 'unsafe.'

2. Thermal effects dominate: Thermal stresses (26.3 MPa) exceed mechanical stresses (15-20 MPa) by 1.3-1.8×. Current design practice must be revised—thermal management is primary.

3. Charging rate optimisation is critical: Fast charging violates thermal limits; slow charging destroys economics. Target 15-20 days OR implement thermal mitigation.

4. Rock confinement appears to be a major contributor to structural viability in the simplified analysis, with steel stress reduced by roughly 40- to 1,000-fold depending on the assumed concrete thickness. Without rock, even 3 m of concrete cannot prevent failure. Site selection must prioritise rock stiffness (E > 30 GPa).

5. Direct transfer of natural-gas design assumptions to hydrogen should be done cautiously: Hydrogen's unique properties create different thermal conditions. Direct extrapolation is inappropriate, hydrogen requires bespoke analysis.

Acknowledgements

This research is funded by Politecnico di Milano/Fondazione Politecnico di Milano - JRP Hydrogen through the project: 'Lined/reinforced caverns for hydrogen storage: materials and technologies for structural stability and analysis of plant facilities.' The author thanks supervisors Prof. Liberato Ferrara, Prof. Giovanni Muciaccia, and Prof. Gabriele Della Vecchia.

References

[1] Federal Energy Technology Centre. 1999. "Commercial Potential of Natural Gas Storage in Lined Rock Caverns (LRC)." https://doi.org/10.2172/774913

[2] Liu, Zhongzhong, Liu, Yuxuan, and Wang, Zonghao. 2024. "Comparative Study of Temperature and Pressure Variation Patterns in Hydrogen and Natural Gas Storage in Salt Cavern." *Applied Sciences* 14:9005. https://doi.org/10.3390/app14199005

[3] Masoudi, Mohammad, Hassanpouryouzband, Aliakbar, Hellevang, Helge, and Haszeldine, R. Stuart. 2024. "Lined Rock Caverns: A Hydrogen Storage Solution." *Journal of Energy Storage* 84:110927. https://doi.org/10.1016/j.est.2024.110927

[4] Zhao, Chenxi, Yu, Haiyang, Zhang, Zixin, and Lei, Qinghua. 2025. "Modelling Lined Rock Caverns Subject to Hydrogen Embrittlement and Cyclic Pressurisation in Fractured Rock Masses." *arXiv preprint*. https://doi.org/10.48550/arXiv.2503.09429

[5] Ghorbani, Bahram, Zendehboudi, Sohrab, Saady, Noori M., Duan, Xili, and Albayati, Talib M. 2023. "Strategies To Improve the Performance of Hydrogen Storage Systems by Liquefaction Methods: A Comprehensive Review." *ACS Omega 8*. https://doi.org/10.1021/acsomega.3c01072

[6] Xiao, Jinsheng, Bénard, Pierre, and Chahine, Richard. 2017. "Estimation of Final Hydrogen Temperature from Refueling Parameters." *International Journal of Hydrogen Energy* 42:7521–28. https://doi.org/10.1016/j.ijhydene.2016.05.213

[7] Peng, Ding-Yu, and Robinson, Donald B. 1976. "A New Two-Constant Equation of State." *Industrial & Engineering Chemistry Fundamentals* 15:59–64. https://doi.org/10.1021/i160057a011

[8] Mohamed, Abdel-Mohsen Onsy, and El Gamal, Maisa. 2024. "A Novel Polymerized Sulfur Concrete for Underground Hydrogen Storage in Lined Rock Caverns." *Sustainability* 16:8595. https://doi.org/10.3390/su16198595

[9] Liu, Hongtao, Li, Peng, Wang, Tao, Tang, Xibo, Wang, Ziyu, Liu, Luyao, Luo, Jing, and Tang, Jiguo. 2025. "Thermodynamic Performance of Hydrogen in Lined Rock Caverns for Large-Scale Underground Storage: Short-Term and Long-Term Analyses." *Journal of Energy Storage* 117:116149. https://doi.org/10.1016/j.est.2025.116149

[10] Papadias, Dionissios D., and Ahluwalia, Rajesh K. 2021. "Bulk Storage of Hydrogen." *International Journal of Hydrogen Energy*. https://doi.org/10.1016/j.ijhydene.2021.08.028

[11] Qiu, Kai, Li, Shuchen, Liu, Zhongzhong, Yuan, Meng, Zhao, Shisen, and Wan, Zeen. 2024. "An Elastoplastic Solution for Lined Hydrogen Storage Caverns During Excavation and Operation Phases Considering Strain Softening and Dilatancy." *International Journal of Rock Mechanics and Mining Sciences* 183:105949. https://doi.org/10.1016/j.ijrmms.2024.105949

Drying Shrinkage and Compressive Strength of Mortars Incorporating Low-Kaolinitic Calcined Clay and Limestone Powder

Niraporn Pornsiri[1], Shingo Asamoto[1], Keisuke Takahashi[2], Somnuk Tangtermsirikul[3], and Warangkana Saengsoy[3]

[1]Department of Civil and Environmental Engineering
Saitama University,
Shimo-okubo, Sakura-ku, Saitama City 338-8570, Japan

[2]Innovation Design Institute,
Kagawa University,
Hayashi-cho, Takamatsu-shi, Kagawa 761-0396, Japan

[3]Construction and Maintenance Technology Research Center,
School of Civil Engineering and Technology
Sirindhorn International Institute of Technology, Thammasat University,
Pathum Thani 12120, Thailand

Summary
Low-kaolinitic calcined clay exhibits limited pozzolanic reactivity and is less commonly used as a standalone supplementary cementitious material. When combined with limestone powder, it may enhance concrete performance through synergistic effects. However, cementitious systems incorporating calcined clay often experience increased shrinkage. This study investigates the effects of Thai calcined clay (25 % kaolinite) and limestone powder on drying shrinkage and compressive strength across five mortar mixtures. Results show that calcined clay (CC30), limestone powder (LP10), and control mixtures reached the same ultimate drying shrinkage after 28 days of drying. The transformation of ettringite to monosulfate was identified as a partial cause of the high initial drying shrinkage of CC30. While the CC30 binary mixture had the lowest compressive strength, the inclusion of limestone powder enhanced the strength of calcined clay-based mixtures through the formation of carboaluminate phases.

1 INTRODUCTION

Clay minerals are abundant within the Earth's crust, with particularly high concentrations found in equatorial regions [1]. Various clay types, including illite, montmorillonite, and kaolinite, become chemically reactive pozzolans following calcination at temperatures ranging from 600 to 850 °C [2]. By facilitating the significant reduction in clinker, calcined clay is emerging as an alternative to traditional supplementary cementitious materials (SCMs) similar to fly ash and ground granulated blast furnace slag. The integration of calcined clay in the systems offers a production of sustainable cement by lowering the CO_2 emissions of the construction industry.

Among these three clay minerals, kaolinite is the most reactive [3], and its concentration in raw clay determines the resulting reactivity of the calcined clay. Calcined kaolinitic clays are generally categorized into three grades: high, medium, and low. High-grade clays (60–90 % kaolinite) are often processed into metakaolin for use in binary blends at 10–15 % replacement levels to enhance compressive strength and durability [4]. Intermediate-grade clays, containing 40–60 % kaolinite, are considered suitable for concrete [5]. According to Avet and Scrivener [6], a kaolinite content of at least 40 % is required for LC^3-50 blends to achieve mechanical strength equivalent to Ordinary Portland cement. In contrast, low-grade kaolinitic clays, those with less than 40 % kaolinite, remain the most globally abundant and widely available. In Thailand, most available clay resources are low-grade kaolinitic clays with a kaolinite content of 25–35 %. Despite their availability, these clays often contain higher levels of impurities and have historically been neglected in favor of higher-grade sources that offer faster

reaction kinetics and higher reactivity [7]. Recent studies on mixed clay, such as London clay with low kaolinite content (10–30 %), show its great potential as SCM after proper thermal calcination [8].

Calcined clay is frequently blended with limestone powder, another sustainable material, to create a ternary system known as Limestone Calcined Clay Cement (LC^3) [9]. This combination triggers a synergistic reaction between the alumina from the calcined clay and the calcium carbonate in the limestone. This interaction improves the degree of reaction and helps in further refining the pores [10].

Even though blending calcined clay and limestone powder is beneficial, there is not enough information on whether using low-grade kaolinitic clay can provide high strength and durability over time. Moreover, with a kaolinite content of 40 %, the calcined clay mixture showed higher autogenous and total shrinkage than the reference cement mixture [11]. In existing literature, Nguyen et al. [12] reported that the increased autogenous and drying shrinkage of calcined clay-limestone mixture is attributed to the refinement of the pore structure. Apart from the physical mechanisms, it is suggested that the chemical aspects, such as hydration products and morphology, also play a role in the shrinkage of limestone-calcined clay mixture [13]. It is unclear if these mechanisms apply to low-grade kaolinitic clay.

The present study aims to investigate the drying shrinkage behavior of mortars using a low-grade kaolinite content clay (approximately 25 % kaolinite) sourced from Thailand in binary (calcined clay-cement) and ternary (calcined clay-limestone-cement) systems. The stoichiometric balance between calcined clay and limestone powder is evaluated through the evolution of hydration products, specifically alumino-ferrite-tri substituted (AFt) and alumino-ferrite-mono substituted (AFm) phases. Their relation to drying shrinkage and compressive strength is subsequently discussed. This paper seeks to couple the macroscopic mechanical properties with the microscopic precipitation of hydration products.

2 MATERIALS

In this study, three binders were investigated. High-early-strength Portland (HPC) cement from Japan, conforming to JIS R 5210 (equivalent to EN 197-1 CEM I 52.5 R and ASTM C150 Type III), was used as the sole cement type. Owing to its high clinker content and the absence of mineral admixtures, this cement is suitable for clearly evaluating the effects of calcined clay and limestone powder. The other two binders were low-kaolinite calcined clay (CC), containing approximately 25 % kaolinite and sourced from Thailand, and limestone powder (LP) from Japan. The calcined clay was supplied by Siam Cement Group Co., Ltd. (Thailand). The major chemical oxide compositions of all binders, determined by X-ray fluorescence (XRF) analysis, are presented in Table 1. River sand was used as the fine aggregate in the preparation of mortar specimens. The sand has a fineness modulus (FM) of 3.47, a maximum particle size (D_{max}) of 4.75 mm, a saturated surface-dry (SSD) specific gravity of 2.57 g/cm^3, and a water absorption of 2.16 %.

Table 1 Major chemical oxide compositions of the tested binders (% by weight)

Binder	SiO_2	Al_2O_3	Fe_2O_3	CaO	MgO	SO_3	LOI
HPC	20.21	5.37	2.68	65.6	0.97	3.02	0.87
CC	60.53	25.57	7.06	0.45	0.55	0.24	2.62
LP	0.01	-	-	55.4	0.2	-	43.7

Note: The total content of minor oxides (Na_2O, K_2O, TiO_2, P_2O_5, and MnO) is 1.14 wt.% for HPC, 2.94 wt.% for CC, and was not acquired for LP.

3 TEST PROGRAMS

3.1 Mix Proportions

Mortar specimens were prepared for drying shrinkage and compressive strength tests, while paste specimens were prepared for X-ray diffraction (XRD) analysis. For both mortar and paste mixtures, a water-to-binder ratio of 0.5 was used. In total, five mixtures were produced for both mortars and pastes: one cement-only control mixture, two binary mixtures, and two ternary mixtures. In one binary mixture, calcined clay replaced 30 % of the cement. In the other binary mixture, limestone powder replaced

10 % of the cement. The ternary mixtures consisted of cement, calcined clay, and limestone powder with two calcined clay-to-limestone powder ratios of 2:1 and 1:1. For the mortar mixtures, a fixed sand-to-binder ratio of 2:1 by weight was adopted. The tested mix proportions are summarized in Table 2.

3.2 Drying Shrinkage

Prismatic specimens with dimensions of 160 × 40 × 40 mm³ were prepared for the drying shrinkage test. For each mixture, three specimens were cast from a single 0.84-liter batch. The binders were mixed using a mechanical mixer at room temperature. The mixing sequence consisted of 30 seconds of dry mixing, followed by 2 minutes and 10 seconds of wet mixing after the addition of water. Immediately after mixing, the mortar was cast into the molds. The specimens were stored in a controlled environment at 20 °C and 60 % relative humidity for 24 hours, sealed in the molds with the top surface covered with plastic wrap. After demolding, four steel pins were attached to two opposite sides of each specimen, with two pins on each side. The initial distance between the opposing pins was set to approximately 100 mm. The specimens were then submerged in tap water for 14 days.

Before the drying shrinkage test, the reference mass and reference length of each specimen were measured. Drying shrinkage measurements were conducted in accordance with JIS A 1129 by storing the specimens in a controlled environment maintained at 20 °C and 60 % relative humidity. Length change measurements were taken at drying ages of 1, 3, and 7 days, and subsequently at 7-day intervals up to 28 days. The reported drying shrinkage values represent the average of three to six specimens for each mixture, and error bars represent the standard deviation (SD). Three mixtures (C100, CC30, and CC20LP10) required specimen reproduction due to pin attachment adhesion failures observed during the pre-drying stage.

Table 2 Mix proportions of tested mortars (kg/m³) with binder replacement percentages by weight in the brackets

Mixture ID	HPC	CC	LP	Water	Sand	w/b	s/b	Ratio of CC:LP
C100	643 (100 %)	-	-	321	1286	0.5	2.0	-
CC30	450 (70 %)	193 (30 %)	-	321	1286	0.5	2.0	-
LP10	579 (90 %)	-	64 (10 %)	321	1286	0.5	2.0	-
CC20LP10	450 (70 %)	129 (20 %)	64 (10 %)	321	1286	0.5	2.0	2:1
CC15LP15	450 (70 %)	96 (15 %)	96 (15 %)	321	1286	0.5	2.0	1:1

3.3 Compressive Strength Test

After mixing, the fresh mixtures (each mixture with a batch volume of 2.58 liters) were cast directly into cylindrical molds with a height of 100 mm and a diameter of 50 mm. The specimens were kept in the molds for 24 hours after casting. After demolding, the specimens were submerged in tap water and cured under controlled conditions at 20±1 °C until the testing age. The mixing and casting procedures complied with JIS A 1132 (Method of making and curing concrete specimens). Compressive strength tests were conducted at ages of 7 and 28 days in accordance with JIS A 1108 (Method of Test for Compressive Strength of Concrete). For each testing age, the reported values represent the average of three specimens, and error bars represent the standard deviation (SD).

3.4 X-ray Diffraction (XRD) Test

Paste specimens were prepared for X-ray diffraction (XRD) analysis. After mixing, the fresh pastes were sealed in zip-lock bags for approximately 2 hours at 20±1 °C to prevent bleeding prior to casting

into molds. The specimens were kept in the molds for 24 hours under controlled conditions at 23 °C and 55 % relative humidity. After demolding, the specimens were stored in tap water until the designated testing ages. After 7 days, one set of specimens was subjected to a water-cured condition, while the other set was subjected to a drying condition at 20 °C and 60 % relative humidity. XRD measurements were conducted at ages of 7,10, and 14 days.

X-ray diffraction (XRD) analysis was performed using a Bruker diffractometer with Cu Kα radiation (λ = 1.5406 Å), operated at 40 kV and 15 mA. Data were collected over a 2θ range of 3–35° with a step size of 0.01° and a scanning rate of 10.0°/min.

4 RESULTS

4.1 Compressive Strength

Fig. 1 illustrates the compressive strength development at ages of 7 and 28 days for the tested mixtures. At 7 days, the CC30 binary mixture exhibited the lowest strength. While the incorporation of LP enhanced the performance of all CC-based mixtures, their strengths remained below those of the C100 and LP10 systems. Among the ternary blends, the 2:1 (CC:LP) ratio demonstrated higher compressive strength compared to the 1:1 ratio. At this early age, C100 demonstrated the highest strength, followed closely by LP10.

At 28 days, all mixtures showed an increase in compressive strength while maintaining consistent relative trends with those at 7 days. A notable exception occurred in the binary systems. LP10 slightly surpassed C100 to achieve the highest strength. This indicates the late-age filler effect of LP and the stabilization of carboaluminate phases, where the presence of limestone powder allows the conversion of monosulfate to the more stable monocarboaluminate, leading to the ettringite stabilization and a densified matrix of LP10 mixture [14]. The ternary LC^3 systems in this study show that the 2:1 ratio is more effective for strength gain than the 1:1 ratio, likely due to the more extensive formation of space-filling carboaluminate phases [15].

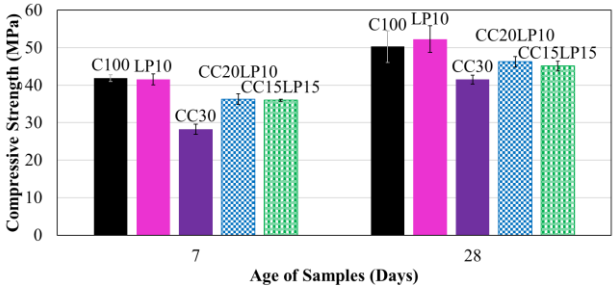


Fig. 1 Compressive strength results of tested mixtures at 7 and 28 days

4.2 Drying Shrinkage and Mass Loss

Fig. 2 (left) presents the drying shrinkage strains for the tested mixtures over a 28-day drying period. The CC30 binary mixture exhibited the highest initial shrinkage rate, especially during the first 7 days. This rapid early-age contraction can be due to self-desiccation of the calcined clay mixture, suggesting the rapid pozzolanic reactivity of calcined clay, even with a low kaolinite content. After 7 days of drying, the shrinkage rate for CC30 decelerated, reaching a plateau after 21 days, resulting in a similar ultimate shrinkage to the C100 and LP10.

The ternary calcined clay-limestone systems displayed different behaviors based on the calcined clay-to-limestone ratio. The 2:1 (CC:LP) mixture showed reduced shrinkage compared to the CC30 binary blend, and eventually converged with the CC30 values at 21 days. In contrast, the 1:1 (CC:LP) mixture initially exhibited lower shrinkage than CC30 during the first week; however, it showed continuous contraction through 28 days, ultimately resulting in the highest drying shrinkage among all five mixtures.

The weight loss of the control C100 and the LP10 binary system exhibited similar trends (Fig. 2 (right)), suggesting a relatively comparable pore structure in these mixtures. In contrast, the incorporation of calcined clay resulted in a significant increase in weight loss. When comparing the calcined clay-based mixtures, the CC30 mixture demonstrated the maximum weight loss. This

phenomenon is attributed to the high specific surface area (SSA) of the calcined clay of 35.53 m^2/g, which provides a larger reservoir for adsorbed evaporable water during water curing. During water curing before drying, all calcined clay-based mixtures showed higher weight gain (more than 1.50 % at 14 days, relative to initial weight before water curing) than the control C100 and LP10 (1.35 % and 1.29 %, respectively). This suggests the loss of water from either the clay's surfaces or the macropores present in the CC30 mixture due to the use of the low-kaolinitic clay. As reported by Avet and Scrivener [6], calcined clay with higher kaolinite content exhibits a greater degree of pore refinement. The ternary systems showed less weight loss compared to the CC30 binary blend. This indicates that the synergistic reaction between the calcined clay and limestone facilitates a greater degree of refinement of the pore structure than the calcined clay-cement system, as indicated by compressive strength.

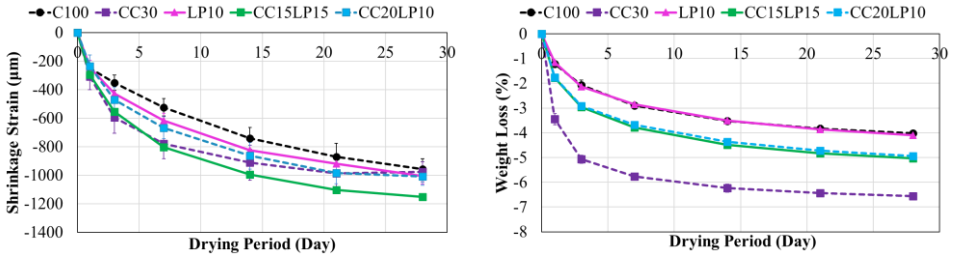


Fig. 2 Drying shrinkage results and weight loss of tested mixtures over 28 days of drying

4.3 XRD Analysis and Phase Identification

The XRD patterns for the pastes of the tested mixtures at 7, 10, and 14 days are illustrated in Fig. 3 (water-cured condition) and Fig. 4 (drying condition). In the water-cured condition, the C100 paste exhibited the highest intensity peaks of calcium hydroxide (CH), along with ettringite (Ett) (9.1° 2θ) and traces of monosulfate (Ms) at approximately 9.9° 2θ. In the calcined clay systems, apart from the phases observed in C100, quartz is visible as an inert component from the raw calcined clay. When limestone powder is added to the system, additional carboaluminate phases are formed, beginning with hemicarboaluminate (Hc), appearing at approximately 10.5°–10.8° 2θ, followed by monocarboaluminate (Mc) at 11.7° 2θ. Additionally, the calcite peak (29.4° 2θ) remains high in the limestone-calcined clay mixtures. On the other hand, the pastes in the drying condition demonstrated similar trends to those in the water-cured condition, except for the CC30 mixture. In this mixture, upon drying, the monosulfate peak increased while the ettringite peak diminished.

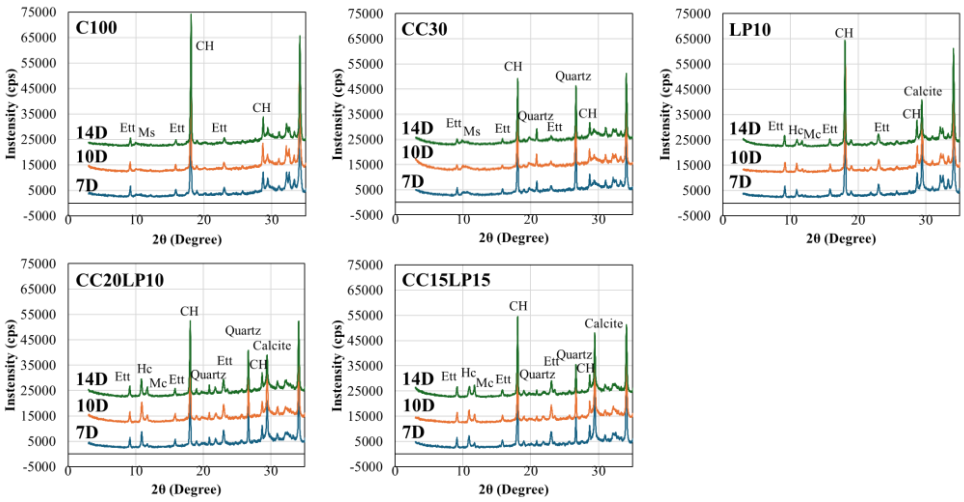


Fig. 3 XRD pattern of paste of the tested mixture under water-cured condition at 7, 10, and 14 days

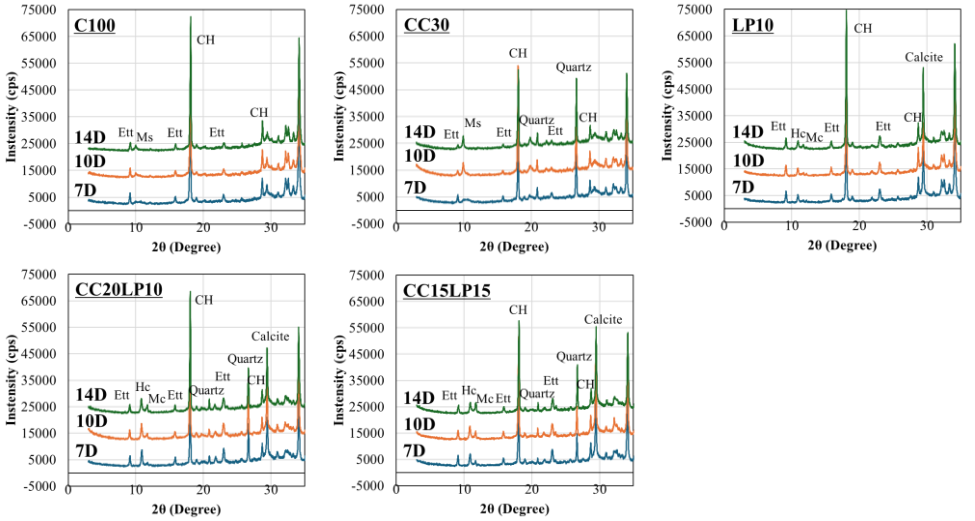


Fig. 4 XRD pattern of pastes of the tested mixtures under drying conditions at 7, 10, and 14 days

5 DISCUSSIONS

5.1 Correlation between Hydration Products and Strength

The development of compressive strength in the tested mixtures is fundamentally governed by the evolution of hydration products and the densification of the cementitious matrix. The CC30 binary mixture exhibited the lowest compressive strength. The limited CH content in the low-kaolinitic calcined clay system may restrict the extent of the pozzolanic reaction, causing the lowest compressive strength shown.

The introduction of LP to the calcined clay system results in a significant enhancement of compressive strength. This is evidenced by the precipitation of carboaluminate phases, with characteristic hemicarboaluminate (Hc) peaks and monocarboaluminate (Mc) peaks. As reactive alumina from the CC reacts with the calcium carbonate from LP, these Hc and Mc phases precipitate within the capillary voids. This space-filling mechanism increases the solid fraction of the paste, leading to a refinement of the pore structure [7].

The synergistic mechanism is governed by the stoichiometric balance between the reactive alumina from the CC and the carbonate from the LP. The 2:1 ratio represents a balanced condition in which sufficient alumina is available to react with limestone, promoting the formation of carboaluminates (Hc and Mc). In contrast, the 1:1 mixture reflects an excess-carbonate condition. Owing to the limited reactive alumina provided by the low-kaolinitic clay, a significant portion of limestone remains unreacted in the 1:1 system, as evidenced by the high-intensity calcite peaks observed in the XRD patterns. This imbalance results in a lower compressive strength at 28 days compared to the more chemically efficient 2:1 system.

5.2 Correlation Between Hydration Products and Drying Shrinkage

The drying shrinkage behavior can be further elucidated through the evolution of the hydration products. In the CC30 binary mixture, a distinct precipitation of monosulfate (Ms) is observed from the XRD pattern of the dried paste sample. This indicates that under drying conditions and high reactive alumina availability, the initially formed ettringite becomes unstable and transforms into lower-volume monosulfate, leading to shrinkage after expansion [15]. This transformation results in the creation of additional internal voids, which may accelerate drying shrinkage of calcined clay at early ages. This effect is further exacerbated by the high specific surface area of the calcined clay and self-desiccation that may happen before the drying process even occurs, due to the high pozzolanic reactivity that calcined clay possesses [16].

The authors notice that the role of the C-S-H and C-A-S-H phases must be considered to explain the shrinkage behavior more comprehensively. While the XRD patterns confirm the amorphous halo

during drying, indicating that the C-S-H and/or C-A-S-H remain in the system, XRD cannot directly detect the structures of C-A-S-H. Previous studies [17], [18] reported that drying shrinkage of cement paste was due to the rearrangement and densification of C-S-H structures after the removal of water from gel and interlayer pores. Further investigation is required to characterize the structural rearrangements of C-A-S-H and/or C-S-H in the calcined clay system. In addition, as shown in the weight loss results, the pore structure of the system incorporating low-kaolinitic calcined clay should be examined alongside the precipitated hydration products to clarify the shrinkage mechanism of the calcined clay-based system.

6 CONCLUSIONS

This study investigated the influence of low kaolinitic-calcined clay and the synergistic reaction between clay and limestone powder on compressive strength and drying shrinkage. Based on the experimental results and the analysis of hydration products, the following conclusions are drawn:

1. The ternary mixtures incorporating LP in the CC-based mixtures demonstrated higher compressive strength than the binary blend of CC30. This improvement is attributed to the precipitation of carboaluminate phases (Hc and Mc) that densify the microstructure of the mixture by filling up the voids, coupled with the physical filler effect from limestone powder itself.
2. The CC-to-LP ratio of 2:1 represents an optimized stoichiometric balance for the clay-limestone system. In the 1:1 (CC:LP) mixture, the reactive alumina content is insufficient to react with available calcium carbonate, leaving more leftover calcite in the system, leading to a lower compressive strength at 28 days compared to the 2:1 (CC:LP) mixture.
3. The addition of limestone powder stabilizes ettringite, preventing its transformation into monosulfate under drying conditions. While the CC30 mixture experienced high early shrinkage due to this transformation and the loss of evaporable water from the clay's high specific surface area, the 1:1 ternary mixture showed the highest ultimate shrinkage. The mechanisms driving this behavior remain unclear and require further study.
4. Although XRD confirmed the presence of amorphous C-S-H and/or C-A-S-H in all calcined clay-based mixtures, the needs of further investigation into the structural rearrangement of the gel upon drying is necessary.

Although the shrinkage mechanisms and the structural evolution of the C-S-H and C-A-S-H gel under drying conditions require further research, these findings caution that LP addition into CC-based mixtures should not be evaluated solely on compressive strength. Under the conditions examined, LP addition enhances compressive strength, but may also increase ultimate drying shrinkage. The optimized CC:LP ratio of 2:1 provides a practical reference to balance both properties. Comprehensive investigation is mandatory in the future, such as the effects of elevated curing temperatures.

Acknowledgements

The first author would like to express sincere gratitude to the Ministry of Education, Culture, Sports, Science and Technology (MEXT), Japan, for being awarded the Monbukagakusho scholarship at Saitama University. The authors gratefully acknowledge the great support received from the Construction and Maintenance Technology Research Center, Sirindhorn International Institute of Technology (SIIT), Thammasat University, and SCG Co., Ltd, Thailand.

References

[1] Scrivener, Karen, Martirena, Fernando, Bishnoi, Shashank, and Maity, Soumen. 2018. "Calcined clay limestone cements (LC^3)." *Cement and Concrete Research* 114: 49–56. doi:10.1016/j.cemconres.2017.08.017.

[2] Jaskulski, Roman, Jóźwiak-Niedźwiedzka, Daria, and Yakymechko, Yaroslav. 2020. "Calcined clay as supplementary cementitious material." *Materials 13*, no. 21: 4734. doi:10.3390/ma13214734.

[3] Fernandez, Rodrigo, Martirena, Fernando, and Scrivener, Karen. 2011. "The origin of the pozzolanic activity of calcined clay minerals: A comparison between kaolinite, illite and montmorillonite." *Cement and concrete research* 41, no. 1: 113–122. doi:10.1016/j.cemconres.2010.09.013.

[4] Siddique, Rafat, and Klaus, Juvas. 2009. "Influence of metakaolin on the properties of mortar and concrete: A review." *Applied Clay Science* 43, no. 3–4: 392–400. doi:10.1016/j.clay.2008.11.007.

[5] Sharma, Meenakshi, Bishnoi, Shashank, Martirena, Fernando, and Scrivener, Karen. 2021. "Limestone calcined clay cement and concrete: A state-of-the-art review." *Cement and Concrete Research* 149: 106564. doi:10.1016/j.cemconres.2021.106564.

[6] Avet, François, and Scrivener, Karen. 2018. "Investigation of the calcined kaolinite content on the hydration of Limestone Calcined Clay Cement (LC^3)." *Cement and Concrete Research* 107: 124–135. doi:10.1016/j.cemconres.2018.02.016.

[7] Dhandapani, Yuvaraj, Santhanam, Manu, Kaladharan, Gopakumar, and Ramanathan, Sivakumar. 2021. "Towards ternary binders involving limestone additions—A review." *Cement and Concrete Research* 143: 106396. doi:10.1016/j.cemconres.2021.106396.

[8] Dhandapani, Yuvaraj, Marsh, Alastair T.M., Rahmon, Suraj, Kanavaris, Fragkoulis, Papakosta, Athina, and Bernal, Susan A. 2023. "Suitability of excavated London clay as a supplementary cementitious material: mineralogy and reactivity." *Materials and Structures* 56, no. 10: 174. doi:10.1617/s11527-023-02260-3.

[9] Cheng, Danyang, Reiner, David M., Yang, Fan, Cui, Can, Meng, Jing, Shan, Yuli, Liu, Yunhui, Tao, Shu, and Guan, Dabo. 2023. "Projecting future carbon emissions from cement production in developing countries." *Nature Communications* 14, no. 1: 8213. doi:10.1038/s41467-023-43660-x.

[10] Antoni, Mathieu, Rossen, John, Martirena, Fernando, and Scrivener, Karen. 2012. "Cement substitution by a combination of metakaolin and limestone." *Cement and concrete research* 42, no. 12: 1579–1589. doi:10.1016/j.cemconres.2012.09.006.

[11] Sudswong, Chanachon, Saengsoy, Warangkana, Sinthupinyo, Sakprayuth, Tangtermsirikul, Somnuk, "Study on properties of mortars and concretes containing calcined clay in combination with fly ash and limestone powder," Paper presented at the 3rd ACF Symposium 2019: Assessment and Intervention of Existing Structures, organized by the Japan Concrete Institute, Sapporo, Japan, September 10–11.

[12] Nguyen, Quang Dieu, Afroz, Sumaiya, Zhang, Yingda, Kim, Taehwan, Li, Wengui, and Castel, Arnaud. 2022. "Autogenous and total shrinkage of limestone calcined clay cement (LC^3) concretes." *Construction and Building Materials* 314: 125720. doi:10.1016/j.conbuildmat.2021.125720.

[13] Hay, Rotana, Li, Liang, and Celik, Kemal. 2022. "Shrinkage, hydration, and strength development of limestone calcined clay cement (LC^3) with different sulfation levels." *Cement and concrete composites* 127: 104403. doi:10.1016/j.cemconcomp.2021.104403.

[14] Lee, Jihoon, Lothenbach, Barbara, and Moon, Juhyuk. 2024. "Performance improvement of Portland-limestone cement by mechanochemical activation." *Cement and Concrete Research* 176: 107411. doi:10.1016/j.cemconres.2023.107411.

[15] García Calvo, José Luis, Carballosa, Pedro, Pedrosa, Filipe, and Revuelta, David. 2022. "Microstructural phenomena involved in the expansive performance of cement pastes based on type K expansive agent." *Cement and Concrete Research* 158: 106856. doi:10.1016/j.cemconres.2022.106856.

[16] Du, Hongjian, and Pang, Sze Dai. 2020. "High-performance concrete incorporating calcined kaolin clay and limestone as cement substitute." *Construction and Building Materials* 264: 120152. doi:10.1016/j.conbuildmat.2020.120152.

[17] Asamoto, Shingo, Takahashi, Keisuke, Sakamoto, Naoki, Sampei, Tokio, and Matsui, Kunio. 2025. "Multiscale analysis on microstructural changes in hardened cement paste dried under different relative humidity levels: A comparison with cement paste containing water-dispersible polyurethane ether compound." *Cement and Concrete Research* 194: 107896. doi:10.1016/j.cemconres.2025.107896.

[18] Maruyama, Ippei, Sakamoto, Naoki, Matsui, Kunio, and Igarashi, Go. 2017. "Microstructural changes in white Portland cement paste under the first drying process evaluated by WAXS, SAXS, and USAXS." *Cement and Concrete Research* 91: 24–32. doi:10.1016/j.cemconres.2016.10.002.

A model for restrained shrinkage in rebar-reinforced Ultra-High Performance Fibre-Reinforced Concrete

Sina Yüksel, Torsten Leutbecher

Chair of Structural Concrete,
University of Siegen,
Paul-Bonatz-Straße 9-11, 57076 Siegen, Germany

Summary
Ultra-high performance concrete (UHPC) exhibits pronounced shrinkage that, in rebar-reinforced UHPFRC (R-UHPFRC) members, can induce residual stresses and pre-curvature prior to loading. This paper proposes an equivalent-load model to quantify shrinkage-induced reinforcement pre-strains and axial shortening and, for non-uniform restraint, the induced pre-curvature, assuming time-dependent linear elasticity, uncracked sections and the Bernoulli hypothesis. Seven R-UHPFRC specimens with different section depth, reinforcement ratio and fibre volume fraction were instrumented with foil strain gauges to monitor shrinkage-induced rebar strains over 40 days. Final strains calibrated the free-shrinkage strain and effective modulus, giving $\varepsilon_{cs} \approx$ -1,015 µm/m and $E_{c,eff} \approx$ 4,700 MPa (CV = 0.035) over the shrinkage period. The calibrated parameters support interpretation of bending tests by separating pre-curvature from load-induced response.

1 INTRODUCTION

Owing to its high cement content, ultra-high performance concrete (UHPC) exhibits pronounced autogenous shrinkage while long-term drying shrinkage is of minor relevance [1]. A significant part of the autogenous shrinkage strain develops within the first 24 to 48 h parallel to increasing strength and stiffness. For structural members made of ultra-high performance fibre-reinforced concrete (UHPFRC) with or without conventional reinforcement, reliable quantification of shrinkage strain and shrinkage-induced stresses is essential for serviceability assessment (crack control, deflections, long-term curvature, loss of prestress) [2].

In rebar-reinforced UHPFRC members (R-UHPFRC), shrinkage is partially restrained by the embedded reinforcement, leading to a self-equilibrated internal stress state (tension in the concrete and compression in the rebar) even before external loading. Restraint produces shrinkage-induced axial pre-strain (sectional shortening) and residual stresses that influence the stress and deformation state prior to loading. If restraint is non-uniform over the depth of a cross-section (e.g., due to asymmetric arrangement of reinforcement or through-thickness shrinkage gradients), restrained shrinkage additionally induces bending moments and thus an initial curvature (pre-curvature) that can affect the measured response in bending tests, the in-service deformation behaviour, and potentially the available deformation capacity.

Experimental studies have documented the magnitude and evolution of autogenous and drying shrinkage in UHPC and its sensitivity to the curing regime and environmental conditions [3], [4]. Under restraint, early-age cracking and stress development have been reported for UHPC/UHPFRC elements [5], [6], while composite and overlay configurations provide direct evidence that restraint and shrinkage gradients can generate pronounced curvature [7], [8]. For mild reinforced UHPC members, test and evaluation approaches to quantify restrained shrinkage effects have also been proposed [9]. At the member level, restraint effects can be measured through reinforcement strains; direct-tension studies on rebar-reinforced UHPC highlight that shrinkage-induced strains can influence the apparent cracking load and early post-cracking behaviour [10]–[12]. Importantly, shrinkage-induced restraint stresses do not develop purely elastically: they are partially relaxed by (early-age) creep and viscoelastic stress relaxation [13]–[15], implying that residual stresses and any pre-curvature evolve in time.

Against this background, this paper presents an equivalent-load based sectional approach to determine the shrinkage-induced pre-strains in the reinforcement, the associated residual stresses, and — where applicable — the induced bending moment and pre-curvature of R-UHPFRC flexural members. Seven specimens with varying section depth, fibre volume fraction, and longitudinal reinforcement ratio are investigated. Restrained shrinkage is measured in each specimen using strain gauges mounted on two reinforcing bars. The measured steel strains are used to evaluate the shrinkage-

induced axial force and, where present, the induced bending moment via equilibrium and compatibility relationships. The resulting framework supports consistent interpretation of member tests and serviceability response by distinguishing shrinkage-induced pre-strains and pre-curvature present prior to loading from effects induced by external loading.

2 EQUIVALENT-LOAD MODEL

This section presents an equivalent-load model to quantify shrinkage-induced effects in rebar-reinforced UHPFRC members. Shrinkage is represented as a fictitious external action, not because it is externally applied, but because this representation enables a direct sectional analysis based on equilibrium and compatibility.

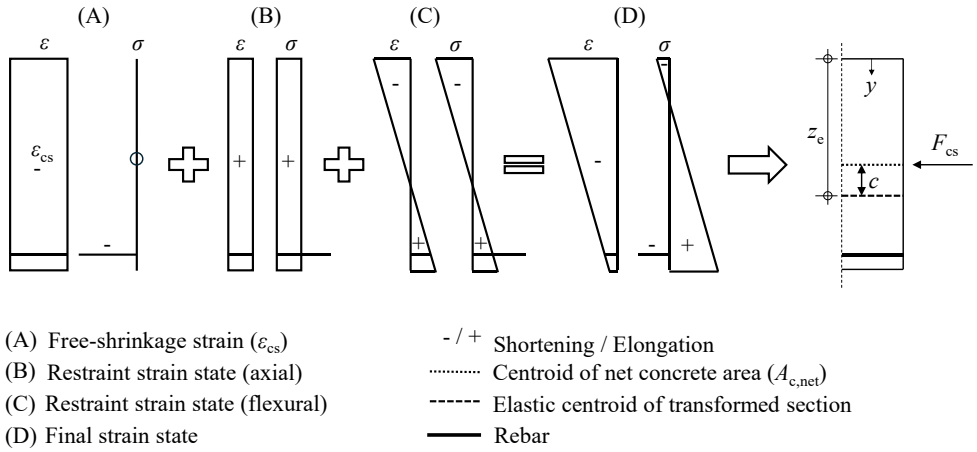


Fig. 1 Equivalent-load model concept: strain and stress superposition (states A–D) (left) and equivalent compressive force F_{cs} acting at $A_{c,net}$ with eccentricity c (right).

Figure 1 (left) illustrates the underlying superposition assuming rigid bond between UHPFRC and bar reinforcement. In state A, the UHPFRC matrix undergoes the free-shrinkage strain ε_{cs} (shortening taken as negative), assumed uniform over the section depth; this strain state is stress-free for the matrix. However, in a reinforced section shrinkage strain induces compressive stress in the reinforcement. Thus, equilibrium is not fulfilled by state A. The reinforcement restrains free shortening and induces additional strain components that generate internal stresses: a uniform axial component (state B) and, when restraint is non-uniform over the depth, a flexural component (state C). The final strain and stress state due to shrinkage (state D) is obtained by superposing the strain states (D = A + B + C). For symmetric reinforcement, state C does not apply, but state B remains and governs the shrinkage-induced axial response.

A key point is that in state A the concrete strain must not be converted into stress, since shrinkage is stress-free. Therefore, equilibrium is established between (i) the compressive force in the reinforcement obtained from stress states A + B + C and (ii) the tensile force in the concrete obtained from the restraint strains (stress states B + C).

This observation leads to the equivalent-load interpretation shown in Figure 1 (right): the shrinkage problem can be treated as a composite cross-section subjected to a fictitious compressive force F_{cs} acting at the centroid of the net concrete area $A_{c,net}$. The eccentricity between this centroid and the elastic centroid of the transformed section is denoted by c.

An equivalent compressive force F_{cs} is introduced producing a uniform shortening strain equal to ε_{cs} when acting on the net concrete section:

$$F_{cs} = \varepsilon_{cs} \cdot E_{c,eff} \cdot A_{c,net} \tag{1}$$

where $E_{c,eff}$ is the effective elastic modulus of UHPFRC accounting for creep-related stress relaxation during shrinkage, and $A_{c,net}$ is the net concrete area (sectional area excluding reinforcement).

Taking this force with respect to the elastic centroid of the transformed section gives the corresponding equivalent moment:

$$M_{cs} = \varepsilon_{cs} \cdot E_{c,eff} \cdot A_{c,net} \cdot c = \varepsilon_{cs} \cdot E_{c,eff} \cdot S_c \tag{2}$$

where $S_c = A_{c,net} \cdot c$ is the first moment of the net concrete area about the elastic centroid.

Since the elastic centroid is defined such that the sum of the first moments of the transformed section is zero, the first moment of the net concrete area (S_c) and that of the reinforcement (S_s) cancel each other about this point. Hence:

$$|S_c| = \frac{E_s \cdot S_s}{E_{c,eff}} \tag{3}$$

where E_s is the elastic modulus of the reinforcement. Substituting Eq. (3) into Eq. (2) yields:

$$M_{cs} = \varepsilon_{cs} \cdot E_s \cdot S_s \tag{4}$$

Accordingly, the shrinkage-induced pre-curvature of the section is:

$$\kappa_{cs} = \frac{M_{cs}}{E_{c,eff} \cdot I_E} = \frac{\varepsilon_{cs} \cdot E_s \cdot S_s}{E_{c,eff} \cdot I_E} = \varepsilon_{cs} \cdot \alpha_E \cdot \frac{S_s}{I_E} \tag{5}$$

where I_E is the transformed second moment of area of the composite section about the elastic neutral axis. Eq. (5) is identical to the Eurocode 2 [16] expression for pre-curvature of reinforced concrete members due to shrinkage.

The final strain distribution (state D) follows from linear-elastic sectional analysis of the transformed section as:

$$\varepsilon(y) = \kappa_{cs} \cdot (z_e - y) + \frac{F_{cs}}{E_{c,eff} \cdot A_E} = \frac{\varepsilon_{cs} \cdot \alpha_E \cdot S_s \cdot (z_e - y)}{I_E} + \frac{\varepsilon_{cs} \cdot A_{c,net}}{(A_{c,net} + \alpha_E \cdot A_s)} \tag{6}$$

where y is the distance of the investigated layer from the top face, z_e is the depth of the elastic neutral axis (from the top face), and A_E is the transformed area of the composite section. The second term in Eq. (6) represents the uniform axial component of the final shrinkage-induced strain state and corresponds to the superposition of states A and B in Fig. 1, whereas the first term represents the flexural component associated with state C. Using Eqs. (5) and (6), the shrinkage-induced pre-curvature and the final strain state (including reinforcement pre-strains and sectional shortening) can be computed.

In this formulation, ε_{cs} and $E_{c,eff}$ are treated as empirical inputs and should be calibrated from experimental data. Once calibrated, the equivalent-load model is not material-specific and can be applied to reinforced members made of conventional concrete, fibre-reinforced concrete, or UHPFRC. For the assessment of concrete stresses due to restraint, the restraint strain is obtained by subtracting the free-shrinkage strain state (state A) from the final strain state (state D):

$$\varepsilon_r(y) = \varepsilon(y) - \varepsilon_{cs} \tag{7}$$

Concrete stresses due to restraint are then given by:

$$\sigma_r(y) = E_{c,eff} \cdot \varepsilon_r(y) \tag{8}$$

3 EXPERIMENTAL PROGRAMME AND RESULTS

3.1 Experimental programme

As stated in the previous section, calibration of the free-shrinkage strain ε_{cs} and the effective elastic modulus $E_{c,eff}$ requires experimental data. For this purpose, seven prismatic R-UHPFRC specimens were cast. All specimens were 50 cm long representing short beam segments. The length provides sufficient transmission length for restraint strains to fully develop in the reinforcement.

Two UHPFRC mixtures were used with steel fibre volume fractions V_f = 1.0% and 2.0%. The mixtures consisted of Portland cement (C), silica fume (SF), quartz powder (QP), quartz sand (QS), superplasticiser (SP), water (W), and 14 mm long micro steel fibres (F). The ingredient quantities (by mass) are summarised in Table 1.

Figure 2 illustrates the layout of cross-sections and provides an example of the arrangement of reinforcement and measurement equipment (strain gauges) in the formwork (specimen B25.15–F2–6D12). Table 2 summarises the test programme. The test matrix was selected to isolate the influence of reinforcement ratio (specimens 1–3), fibre volume fraction (pairs 3/5 and 4/6), and section stiffness due to varying member depth (specimens 5–7).

Table 1 Mix proportions of the UHPFRC mixtures.

Mixture	C	SF	QP	QS	SP	W	F
	[kg/m^3]						
UHPFRC1 (V_f = 1.0%)	778	163	198	966	27	198	78.5
UHPFRC2 (V_f = 2.0%)	780	162	196	956	26	196	157

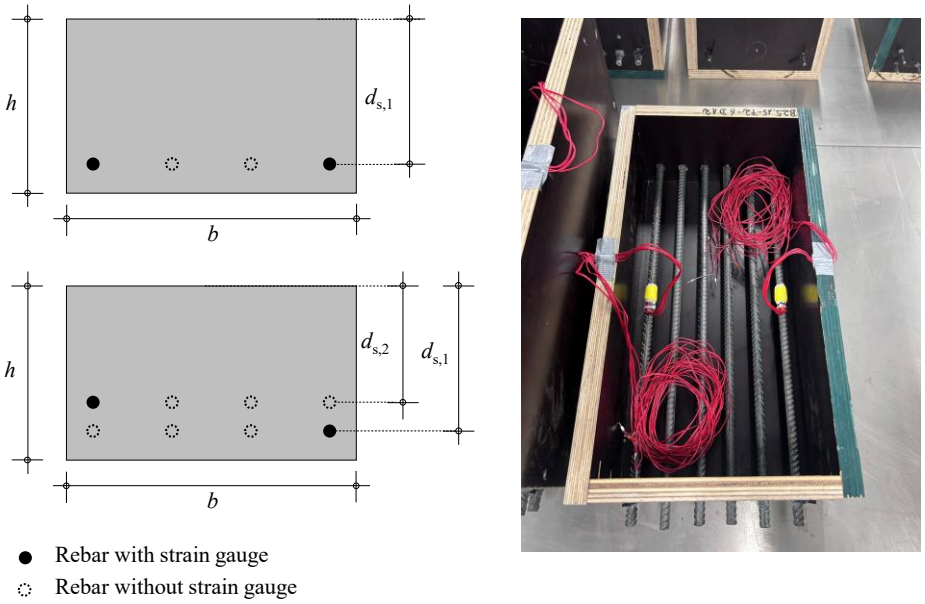


Fig. 2 Cross-section layout and instrumentation: single-/two-layer reinforcement arrangement (left) and formwork of specimen B25.15–F2–6D12 with strain-gauged reinforcing bars (right).

The specimen ID indicates the cross-section dimensions b and h in centimetres, the fibre volume fraction (F1: V_f = 1.0%, F2: V_f = 2.0%), and the number and diameter of reinforcing bars ϕ_s. For example, B25.15–F2–6D12 denotes b = 25 cm, h = 15 cm, V_f = 2.0%, and six reinforcing bars with ϕ_s = 12 mm.

Table 2 Test programme.

No.	Specimen ID	b [cm]	h [cm]	$A_{s,1}$ [cm^2]	$A_{s,2}$ [cm^2]	A_s [cm^2]	$d_{s,1}$ [cm]	$d_{s,2}$ [cm]	$d_{s,mean}$ [cm]	ρ_s [%]	V_f [%]
1	B25.15-F1-2D6	25	15	0.57	0.00	0.57	11.50	0.00	11.50	0.20	1.0
2	B25.15-F1-10D6	25	15	1.41	1.41	2.82	13.00	10.00	11.50	0.98	1.0
3	B25.15-F1-6D12	25	15	6.79	0.00	6.79	11.50	0.00	11.50	2.36	1.0
4	B15.30-F1-8D12	15	30	4.52	4.52	9.04	27.50	23.50	25.50	2.36	1.0
5	B25.15-F2-6D12	25	15	6.79	0.00	6.79	11.50	0.00	11.50	2.36	2.0

6	B15.30-F2-8D12	15	30	4.52	4.52	9.04	27.50	23.50	25.50	2.36	2.0
7	B15.50-F2-10D14	15	50	7.70	7.70	15.40	47.50	42.50	45.00	2.28	2.0

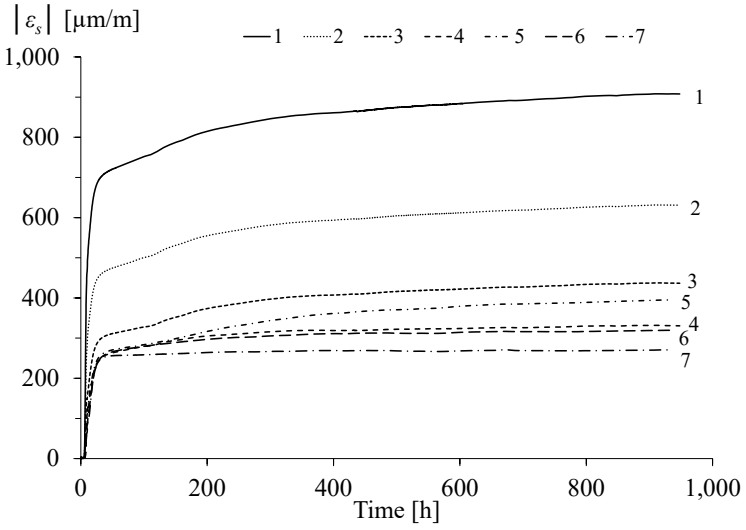
Table 2 further reports $A_{s,1}$ and $A_{s,2}$, the total reinforcement area $A_{s,tot}$, the corresponding effective depths $d_{s,1}$ and $d_{s,2}$, and the mean effective depth $d_{s,mean}$ used to calculate the reinforcement ratio ρ_s. Depending on the number of reinforcing bars, the reinforcing bars were arranged in one or two layers.

Reinforcement strains were measured using standard foil strain gauges with temperature compensation, wired in full-bridge circuits. In each specimen, strain gauges were bonded at mid-length to two reinforcing bars (Fig. 2). For single-layer reinforcement, gauges were installed on the two outermost reinforcing bars (left and right). For two-layer reinforcement, gauges were installed on one bar in each layer, located on opposite sides of the section (left bar in the upper layer and right bar in the lower layer), as indicated in Figure 2.

3.2 Results

After casting, shrinkage-induced strains in the reinforcement were monitored. Measurements were started immediately after casting and continued until the recorded strains had stabilised. Figure 3 (left) shows the development of the mean compressive strain from the two instrumented reinforcing bars for each specimen over time. Compressive strains are negative by the adopted sign convention; for readability, Figure 3 reports absolute values. The monitoring period was approximately 950 h (about 40 days), after which the measurement was stopped. For clarity, the curves are labelled according to the specimen numbering given in Table 2.

Figure 3 (right) summarises, for each specimen, the final mean reinforcement strain together with the mechanical effective depth d_{mech}. The parameter d_{mech} denotes the distance from the top face of the section to the line of action of the resultant reinforcement force associated with the measured strains. For single-layer reinforcement, this is identical to the depth of that layer. For two-layer reinforcement, the two instrumented reinforcing bars are located in different layers; the measured strains therefore correspond to two reinforcement forces acting at two depths. Their resultant acts at an intermediate depth, which is expressed by d_{mech}. In other words, d_{mech} is the force-weighted effective depth of the measured reinforcement forces. The parameter d_{mech} is used in the subsequent evaluation to relate the measured reinforcement strains to the shrinkage-induced axial force and bending moment.



No.	ε_s [µm/m]	d_{mech} [cm]
1	-908	11.5
2	-631	11.4
3	-437	11.5
4	-331	25.1
5	-396	11.5
6	-320	25.2
7	-271	44.6

Fig. 3 Shrinkage-induced reinforcement strains: time histories (left); final mean strain values and mechanical effective depth d_{mech} (right).

3.3 Discussion of results

Specimens 1–3 allow the effect of reinforcement ratio to be assessed in isolation, since ρ_s is the only varying parameter within this group. The measured compressive reinforcement strains decrease with increasing ρ_s: since the reinforcement increases the composite stiffness, a smaller compressive strain develops in the reinforcing bars for a given shrinkage strain.

Pairs 3/5 and 4/6 enable comparing the influence of fibre volume fraction (V_f = 1.0% vs. 2.0%) at otherwise identical geometry and reinforcement. The difference between specimens 3 and 5 is about 10%, whereas specimens 4 and 6 show almost identical final strains; overall, no clear influence of fibre volume fraction can be identified from this comparison.

All seven strain histories increase continuously over the measurement period, with no indication of a strain drop. This suggests that the monitored regions remained uncracked, since shrinkage-induced cracking would be expected to relax restraint and reduce the reinforcement strain. The uncracked response is consistent with the linear-elastic, uncracked-section assumption adopted in the evaluation and may also explain why no clear impact of fibre volume fraction is observed in the present dataset.

Finally, specimens 5–7 highlight the influence of section stiffness: these specimens have similar reinforcement ratio and identical fibre volume fraction, while the section depth (and thus axial and flexural stiffness of the concrete section) increases. The measured compressive reinforcement strains decrease with increasing section stiffness.

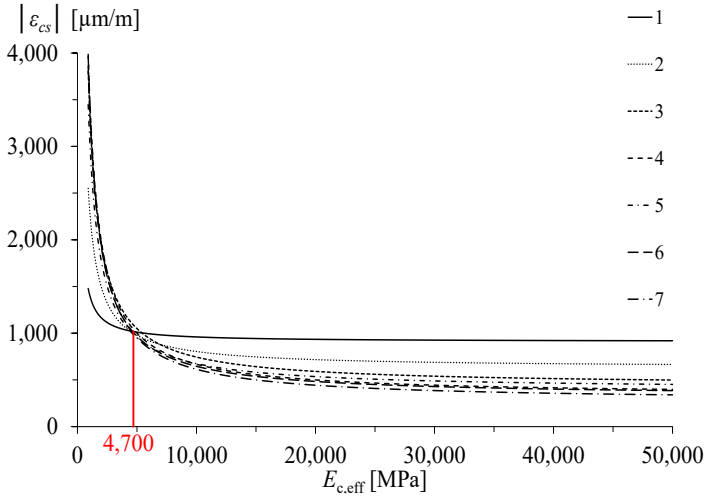
3.4 Calibration of ε_{cs} and $E_{c,eff}$

Based on the model in Section 2 and the reinforcement strain measurements in Section 3.2, the free-shrinkage strain ε_{cs} and the effective elastic modulus $E_{c,eff}$ can be calibrated. The calibration is performed using the final measured reinforcement strains, as ε_{cs} represents the long-term free shrinkage (that is, the stabilised value at large time).

With the final mean strain values ε_s and the mechanical effective depths d_{mech}, Eq. (6) can be evaluated at $y = d_{mech}$ and rearranged for ε_{cs}, which gives Eq. (9). Since α_E, S_s, z_e and I_E depend on $E_{c,eff}$, Eq. (9) provides a relationship $\varepsilon_{cs}(E_{c,eff})$ for each specimen by inserting trial values of $E_{c,eff}$.

$$\varepsilon_{cs} = \frac{\varepsilon_s}{\left(\frac{\alpha_E \cdot S_s \cdot (z_e - d_{mech})}{I_E} + \frac{A_{c,net}}{(A_{c,net} + \alpha_E \cdot A_s)} \right)} \tag{9}$$

Figure 4 (left) shows $\varepsilon_{cs}(E_{c,eff})$ for all specimens. Assuming a uniform ε_{cs} for the test series, the calibrated parameter pair corresponds to the intersection of all curves. The curves intersect at $E_{c,eff} \approx$ 4,700 MPa, which yields ε_{cs} values close to -1,000 µm/m. Figure 4 (right) summarises the resulting ε_{cs} per specimen, giving a mean value of -1,015 µm/m with a coefficient of variation CV = 0.035. With the calibrated values $E_{c,eff}$ and ε_{cs}, the shrinkage-induced pre-curvature, reinforcement pre-strains and concrete stresses of the R-UHPFRC members can be calculated using Eqs. (5)–(8).



No.	ε_{cs} [µm/m]
1	-1,017
2	-997
3	-1,083
4	-1,036
5	-981
6	-1,001
7	-987
µ	-1,015
CV	0.035

Fig. 4 Calibration of ε_{cs} and $E_{c,eff}$: $\varepsilon_{cs}(E_{c,eff})$ curves (left) and resulting ε_{cs} per specimen (right).

Figure 5 exemplifies the application of the equivalent-load concept introduced in Section 2 and illustrated in Fig. 1 for specimen 7, which represents the case with the largest restraint. Based on the calibrated values ε_{cs} = -1,015 µm/m and $E_{c,eff}$ = 4,700 MPa, the strain and stress distributions associated with states A–D are shown for the transformed section. The calculated tensile stress at the extreme tensile fibre of the UHPFRC section is 4.05 MPa, which remains below a representative matrix tensile strength level for UHPFRC (≈ 8 MPa). This supports the assumption that the monitored sections remained uncracked during the shrinkage process. For the mixtures used here, the mean elastic modulus was measured as 40,000 MPa for both UHPFRC1 and UHPFRC2. The relatively low value of $E_{c,eff}$ compared with the measured 28-day elastic modulus reflects stress relaxation due to creep during shrinkage, where $E_{c,eff}$ corresponds to about 11–12% of the nominal modulus after 28 days.

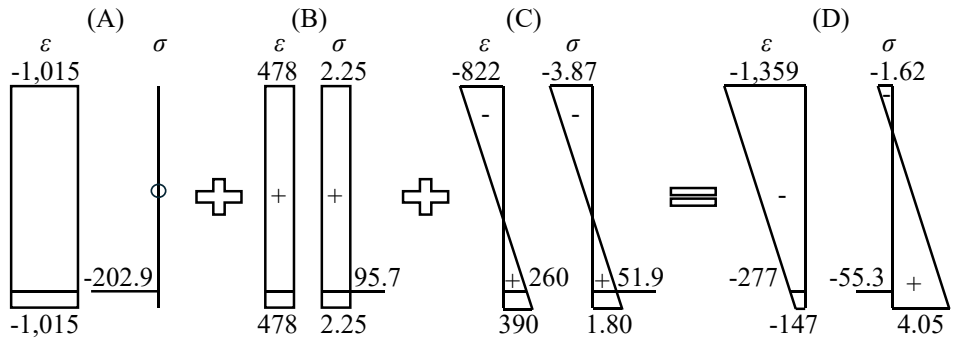


Fig. 5 Application of the equivalent-load model to specimen 7: strain and stress distributions for states A–D defined in Fig. 1. Strains are given in µm/m and stresses in MPa.

4 CONCLUSIONS

This study developed an equivalent-load formulation to quantify shrinkage-induced effects in rebar-reinforced ultra-high performance fibre-reinforced concrete (R-UHPFRC) members assuming linear elasticity, uncracked sections, and plane sections remain plane.

- The model provides a consistent way to determine shrinkage-induced reinforcement pre-strains, sectional shortening, concrete stresses and, when restraint is non-uniform over the depth, the induced pre-curvature.
- Reinforcement strain measurements on seven prismatic R-UHPFRC specimens showed (i) decreasing compressive steel strains with increasing reinforcement ratio, and (ii) decreasing compressive steel strains with increasing section height (and stiffness), whereas no consistent trend caused by varying fibre volume fraction (V_f =1.0% vs. 2.0%) could be identified.
- All measured strain histories increased monotonically over the monitoring period, indicating that the monitored regions remained uncracked; this supports the use of an uncracked, linear-elastic sectional evaluation for calibration and subsequent analysis.
- Calibration using the final measured steel strains yielded a free-shrinkage strain $\varepsilon_{cs} \approx$ -1,015 µm/m (CV = 0.035) and an effective elastic modulus $E_{c,eff} \approx$ 4,700 MPa. The calibrated $E_{c,eff}$ corresponds to about 11–12% of the measured nominal elastic modulus after 28 days, consistent with significant stress relaxation due to creep during shrinkage.
- With these calibrated inputs, the proposed framework can be applied to compute shrinkage-induced pre-strains, concrete stresses and, where relevant, pre-curvature in reinforced members. This enables shrinkage-induced axial and flexural effects to be separated from the load-induced response and thereby improves the interpretation of member tests and serviceability assessments under restrained shrinkage.

Acknowledgements

Funded by the Deutsche Forschungsgemeinschaft (DFG, German Research Foundation) – 551949869.

References

[1] Xie, Tianyu, Fang, Chengfeng, Mohamad Ali, Mohamed Sadakkathulla, and Visintin, Phillip. 2018. "Characterizations of autogenous and drying shrinkage of ultra-high performance concrete (UHPC): An experimental study." *Cement and Concrete Composites* 91:156–173. doi:10.1016/j.cemconcomp.2018.05.009.

[2] Russell, Henry G., and Graybeal, Benjamin A. 2013. *Ultra-High Performance Concrete: A State-of-the-Art Report for the Bridge Community.* Report FHWA-HRT-13-060. McLean, Virginia: Federal Highway Administration, June.

[3] Al Moman, Abdullah, Sundar, Deepika, Zeng, Kun, Tatar, Jovan, Radlińska, Aleksandra, and Rajabipour, Farshad. 2025. "Autogenous and drying shrinkage in Ultra-High-Performance Concrete (UHPC) and the effectiveness of internal curing." *Construction and Building Materials* 464:140217. doi:10.1016/j.conbuildmat.2025.140217.

[4] Zhang, Xiuzhen, Liu, Zhichao, and Wang, Fazhou. 2019. "Autogenous shrinkage behavior of ultra-high performance concrete." *Construction and Building Materials* 226:459–468. doi:10.1016/j.conbuildmat.2019.07.177.

[5] Yoo, Doo-Yeol, Min, Kyung-Hwan, Lee, Joo-Ha, and Yoon, Young-Soo. 2014. "Shrinkage and cracking of restrained ultra-high-performance fiber-reinforced concrete slabs at early age." *Construction and Building Materials* 73:357–365. doi:10.1016/j.conbuildmat.2014.09.097.

[6] De la Varga, Igor, Spragg, Robert P., El-Helou, Rafic G., and Graybeal, Benjamin A. 2019. "Shrinkage Cracking Propensity of Ultra-High Performance Concrete." Paper presented at the Second International Interactive Symposium on Ultra-High Performance Concrete, Albany, New York, June 2–5. doi:10.21838/uhpc.9695.

[7] Guo, Weiqiang, Wei, Ya, and Ma, Lei. 2022. "Shrinkage-induced warping of UHPC overlay cast on hardened NSC substrate under various conditions." *Cement and Concrete Composites* 134:104772. doi:10.1016/j.cemconcomp.2022.104772.

[8] Zhu, Yanping, Zhang, Yang, Hussein, Husam H., Liu, Jianhui, and Chen, Genda. 2020. "Experimental study and theoretical prediction on shrinkage-induced restrained stresses in UHPC-RC composites under normal curing and steam curing." *Cement and Concrete Composites* 110:103602. doi:10.1016/j.cemconcomp.2020.103602.

[9] Tahat, Mohammad, Binard, JP, Davis, Rodney, and Maguire, Marc. 2023. "Restrained Shrinkage in Mildly Reinforced Ultra-High Performance Concrete (UHPC) Structural Members." Paper presented at the Third International Interactive Symposium on Ultra-High Performance Concrete, Wilmington, Delaware, June 4–7. doi:10.21838/uhpc.16720.

[10] Luo, Xianzhi, Zhang, Sumei, Zhang, Yuchen, and Jiang, Yuexin. 2025. "Mechanical properties and cracking behavior of rebar reinforced UHPC (R-UHPC) under uniaxial tension: Evaluation and design." *Case Studies in Construction Materials* 22:e04243. doi:10.1016/j.cscm.2025.e04243.

[11] Tu, Lei, Zhao, Hua, Tan, Chengjun, Hu, Junde, Cao, Jingqi, and Wu, Suiwen. 2025. "Tensile behavior of reinforced UHPC: Effects of autogenous shrinkage and model of tensile capacity via deep learning-based symbolic regression." *Cement and Concrete Composites* 160:106019. doi:10.1016/j.cemconcomp.2025.106019.

[12] Shi, Zhanchong, Liang, Minfei, Su, Qingtian, Kanstad, Terje, and Ferrara, Liberato. 2024. "Tensile behavior of rebar-reinforced coarse aggregate ultra-high performance concrete (R-CA-UHPC) members: Experiments and restrained shrinkage creep effect." *Cement and Concrete Composites* 151:105574. doi:10.1016/j.cemconcomp.2024.105574.

[13] Switek-Rey, Agnieszka, Denarié, Emmanuel, and Brühwiler, Eugen. 2016. "Early age creep and relaxation of UHPFRC under low to high tensile stresses." *Cement and Concrete Research* 83:57–69. doi:10.1016/j.cemconres.2016.01.005.

[14] Garas, Victor Y., Kahn, Lawrence F., and Kurtis, Kimberly E. 2009. "Short-term tensile creep and shrinkage of ultra-high performance concrete." *Cement and Concrete Composites* 31(3):147–152. doi:10.1016/j.cemconcomp.2009.01.002.

[15] Park, Jung Jun, Yoo, Doo Yeol, Kim, Sung Wook, and Yoon, Young Soo. 2012. "An Evaluation on the Restrained Shrinkage of Ultra-High Performance Concrete." *Key Engineering Materials* 525–526:449–452. doi:10.4028/www.scientific.net/KEM.525-526.449.

[16] European Committee for Standardization (CEN). 2004. *Eurocode 2: Design of Concrete Structures—Part 1-1: General Rules and Rules for Buildings* (EN 1992-1-1). Brussels: CEN.

Evolution of Stress Transfer in the Compression Zone of Reinforced Concrete Beams Under Shear-Fatigue Loading

Christian Linden, Jan Hendricks, Martin Claßen

Institute of Structural Concrete,
RWTH Aachen University,
Im Süsterfeld 9, 52072 Aachen, Germany

Summary
Fatigue-induced damage leads to a reduction in the service life of reinforced concrete (RC) structures. Shear and combined flexural shear are critical fatigue modes in slender RC members without shear reinforcement. Under monotonic loading, shear transfer involves interacting mechanisms, including stress transfer in the uncracked compression zone, aggregate interlock, dowel action, and stress transfer in the fracture process zone. The Shear Crack Propagation Theory (SCPT) integrates these mechanisms for static conditions, but its extension to fatigue requires understanding their degradation under cyclic loading. This study presents high-resolution fatigue tests on slender RC beams without shear reinforcement, using distributed fibre-optic sensors (FOS) to capture longitudinal strain profiles, complemented by digital image correlation (DIC) for crack kinematics. Regression-based analysis of the FOS data enables robust derivation of longitudinal stress and shear stress distributions over the fatigue history.

1 INTRODUCTION

1.1 Motivation and Shear Transfer Mechanisms

Shear fatigue in RC members without shear reinforcement remains an important issue in structural engineering. Many existing bridges are exposed to increasing traffic volumes [1], which may cause progressive damage accumulation and ultimately shorten their service life. Repair and strengthening interventions are often costly and are associated with considerable environmental impacts, particularly due to the CO_2 emissions. Consequently, improving the durability of existing infrastructure requires a deeper understanding of the mechanisms responsible for shear fatigue.

For monotonic loading conditions, it is generally accepted that the shear capacity of RC members arises from the combined action of several stress transfer mechanisms [2]–[5]. In members without transverse reinforcement, shear is carried through mechanisms such as shear transfer in the uncracked compression zone, aggregate interlock along the crack surfaces, dowel action of the longitudinal reinforcement, and stress transfer within the fracture process zone. The relative contribution of each mechanism is still debated among researchers. Furthermore, [6] highlights that the contribution of the individual stress transfer mechanisms depend on the shape and position of the shear crack.

1.2 Shear Fatigue and Aim of the Study

While the shear behaviour of reinforced concrete under static loading is relatively well understood, the mechanisms governing shear fatigue are still not fully clarified. Previous studies have investigated shear fatigue in reinforced concrete beams without shear reinforcement [7]–[9]. However, the measurement techniques applied in these studies were mostly limited to displacement transducers and strain gauges. Consequently, the deformation response and crack kinematics during fatigue loading could not be captured with sufficient spatial resolution to enable a detailed assessment of the individual stress transfer mechanisms.

Recent experimental investigations under static loading have demonstrated that advanced measurement techniques such as digital image correlation (DIC) and fibre optic sensing (FOS) enable a much more detailed analysis of crack kinematics and the underlying load transfer mechanisms [2], [10], [11]. These measurement techniques also offer significant potential for fatigue experiments, as they enable continuous monitoring of the structural response and the evolution of key mechanisms during cyclic loading. In particular, FOS is increasingly applied in RC experiments, as it provides high

spatial resolution while maintaining comparatively low data volumes, making it well suited for long-term monitoring of structural behaviour [12].

The experimental investigations presented in this study were designed to capture the deformation behaviour and crack development of reinforced concrete beams under fatigue loading without shear reinforcement with high spatial resolution. Within the scope of this paper, the analysis focuses primarily on the behaviour of the concrete compression zone during fatigue loading. For this purpose, FOS is used to evaluate the strain development in the compression zone and is complemented by additional information obtained from DIC measurements.

2 EXPERIMENTAL PROGRAM

2.1 Specimens and General Test Concept

The experimental programme is based on fatigue tests on slender reinforced concrete beams without shear reinforcement in the investigated shear spans. To promote shear-governed failure, beams with a shear span-to-depth ratio of $a/d = 3.7$ and a longitudinal reinforcement ratio of 1.05% were used. Two shear spans without transverse reinforcement were arranged on opposite sides of each beam, allowing two consecutive partial tests to be performed on the same specimen while the non-investigated span remained unloaded (see Fig. 1). Outside the monitored regions, shear reinforcement was provided to prevent unintended failure mechanisms.

All beams were cast using normal-strength concrete (C30/37) with a maximum aggregate size of 16 mm and reinforced with ribbed steel bars of grade B500B. After casting, the beams were stored dry under laboratory conditions until testing. During testing, the compression zone was located on the top-as-cast side of the beams. The concrete properties of the beams investigated in this study are summarized in Table 1. Material properties were obtained from standard test specimens, including cylinders with a height of 300 mm and a diameter of 150 mm as well as cubes with an edge length of 150 mm.

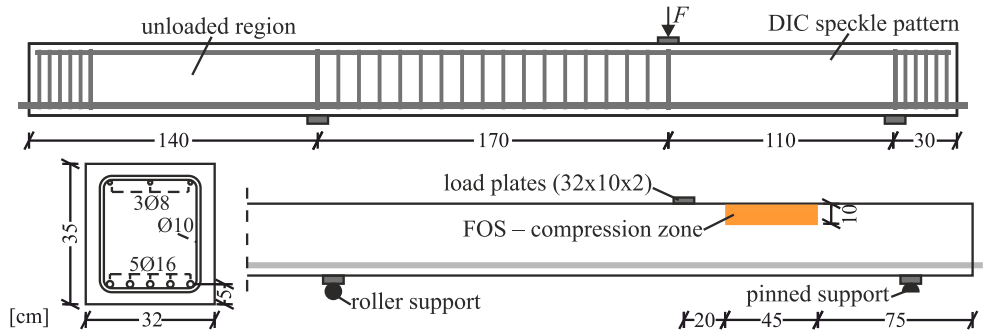


Fig. 1 Overview of the test specimen including geometry, reinforcement layout, loading and support conditions, and selected measurement instrumentation

2.2 Test Setup and Instrumentation

All experiments were conducted in a three-point bending configuration with an asymmetric support layout to increase the shear demand in the investigated span. Steel bearing plates were installed at the supports and at the load application point to ensure uniform load transfer. Global deflections were measured using linear variable displacement transducers (LVDTs) placed under the load application points and at midspan.

The key instrumentation used in this study was a FOS system installed in the compression zone of the investigated shear span. A glass fibre with an acrylate coating was used. Prior to installation, the concrete surface was primed, and the fibre was subsequently bonded using epoxy resin. This installation procedure has previously been validated in [12]. The fibre was applied in the shear-critical region (see Fig. 1) near the top of the beam, corresponding approximately to the expected compression zone. It was arranged in a serpentine pattern, creating ten horizontal segments. They run parallel to the top surface of the beam and are spaced 1 cm apart. The uppermost fibre is located 1 cm below the beam surface, while the lowest segment is positioned 10 cm below the top surface. The segments were defined using

the gage and segmentation features of the fibre-optic system, resulting in ten segments with a length of 45 cm each.

This arrangement allows continuous monitoring of longitudinal strain profiles in the compression chord with high spatial resolution over a significantly larger length than achievable with conventional strain gauges and with lower scatter compared to DIC for very small strains [13]. The FOS measurements were synchronized with the global load and displacement data, enabling the evaluation of the evolution of compressive strain distributions throughout the fatigue process. In addition, DIC was applied to the entire shear field (see Fig. 1), primarily to capture crack kinematics and their evolution during the loading process.

Table 1 Mean concrete properties on the days of testing

Specimen	Testing Age (d)	$f_{cm,cube}$ (MPa)	$f_{cm,cyl}$ (MPa)	$E_{cm,cyl}$ (MPa)	$f_{ctm,sp,cyl}$ (MPa)
V1–TV1[1)]	29	50.1	40.4	31528	3.5
V1–TV2	30	50.6	40.7	31649	3.5
V4–TV1	25	46.9	39.2	29971	3.2

[1)] Concrete strength values were obtained by linear interpolation between adjacent test days.

2.3 Loading Protocol

Two static reference tests were conducted under displacement control up to failure to determine the reference shear capacity. The fatigue tests were performed under force-controlled sinusoidal loading at a frequency of 2 Hz. The upper and lower load levels, S_{max} and S_{min}, were defined as fixed percentages of the maximum load obtained from the corresponding static tests.

Each cyclic test started with one displacement-controlled loading cycle at a rate of 1 mm/min up to the prescribed upper load level, followed by unloading to S_{min} and reloading to the mean load level. Subsequently, force-controlled cyclic loading was applied. At the beginning of each fatigue test, the load amplitude was increased gradually during a short ramp-up phase. The loading regime is illustrated schematically in Fig. 2 (right). The reported number of cycles includes this ramp-up phase.

3 RESULTS AND DEFORMATION ANALYSIS

3.1 General

This paper focuses on one representative cyclic fatigue test with an upper load level of $S_{max} = 85\%$ and a lower load level of $S_{min} = 40\%$ (specimen V4–TV1). The specimen was selected because it exhibits a typical and well-documented damage evolution. A comprehensive presentation and discussion of the complete experimental programme will be reported elsewhere.

Fig. 2 (left) presents the shear force–deflection relationship measured below the load introduction point for the two static reference tests and for the investigated cyclic test. At the beginning of loading, all three tests exhibit an almost identical stiffness. Minor differences become visible from a deflection of approximately 2.5 mm onwards and can be attributed to the usual scatter in material properties.

The two static reference tests reach very similar maximum loads and fail at comparable maximum deflections. While specimen V1–TV1 shows a limited post-peak response with decreasing load, specimen V1–TV2 fails in a brittle manner, which is typical for shear-governed failure of reinforced concrete members without shear reinforcement.

The cyclic test was performed between 85 % and 40 % of the reference shear resistance and reached 353 load cycles. Compared to the static reference tests, the onset of the final failure process is associated with a slightly larger deflection. This increased deformation prior to failure is consistent with commonly observed fatigue effects in reinforced concrete and reflects the progressive stiffness degradation under repeated loading [9], [14].

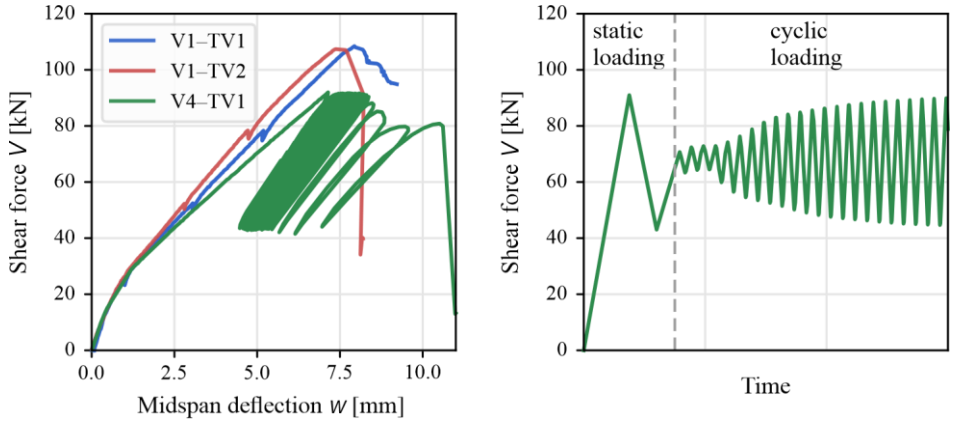


Fig. 2 (left) Shear force versus midspan deflection; (right) shear force versus time illustrating the exemplary loading regime

3.2 Crack States

Fig. 3 summarises selected crack states observed during the investigated fatigue test (specimen V4–TV1) and provides the qualitative basis for interpreting the subsequent deformation analyses. At the beginning of loading, the beam exhibits predominantly flexural cracking in the investigated shear span. These cracks are steeply inclined and mainly governed by bending. With increasing load, particularly when approaching the upper load level of the first cycle, several of these flexural cracks extend and progressively flatten towards the load introduction point, forming the initial shear-critical crack pattern.

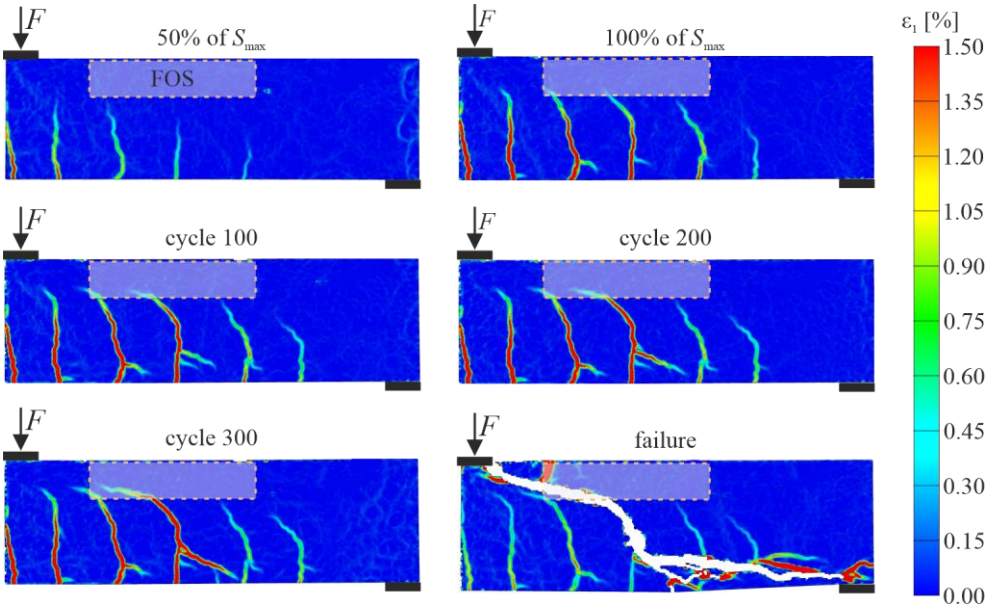


Fig. 3 Damage evolution of the investigated beam at selected stages of static and cyclic loading obtained from DIC, with the position of the FOS measurement field indicated

During the early phase of cyclic loading, secondary cracks initiate at the level of the longitudinal reinforcement and propagate towards the support. These cracks mark the onset of dowel-related cracking and indicate increasing interaction between the inclined shear crack and the longitudinal reinforcement.

With ongoing cyclic loading, one dominant shear crack localises and develops additional secondary branches in its vicinity. At this stage, the overall crack pattern remains stable, while the governing crack system becomes increasingly pronounced.

In the final crack state prior to failure, a single dominant crack path controls the structural response, connecting the compression zone near the load application point with the reinforcement level and the support region. This crack system defines the critical shear crack used as a reference in the following analyses.

The location of the FOS measurement field is indicated in Fig. 3. At the maximum load level (100% S_{max}), the dominant shear crack and an adjacent crack reach the region instrumented with FOS. With increasing number of cycles, both cracks propagate approximately horizontally towards the load introduction point, extending through the FOS measurement field.

3.3 Compression Zone and Shear Stress Evaluation

Fig. 4 shows the distributed longitudinal strain measurements obtained from FOS in the compression zone at 300 load cycles, i.e., shortly before failure. The diagram presents the raw microstrain data (in µm/m) along the 450 mm measurement length for all ten horizontally arranged fibre segments. Segment 1 is the topmost segment, while segment 10 is located 10 cm below the top surface of the beam.

The general strain distribution is consistent with the expected structural behaviour. The uppermost segment records the largest compressive strains, and the strain magnitude decreases continuously with increasing distance from the top surface. In addition, a clear trend is observed in longitudinal direction along the beam, where the compressive strains decrease with increasing distance from the load introduction point in segments not intersected by cracks. These trends are observed across all investigated load stages. It should be emphasised that the presented FOS data are unfiltered raw measurements. In contrast to DIC-based strain fields, no smoothing or interpolation is required to visualise meaningful trends at very small strain levels, representing a major advantage of the FOS technique for investigating the compression zone.

Several pronounced local peaks can be identified in the strain profiles. Peaks in the tensile strain range correspond to cracks crossing the fibre. In Fig. 4, the peaks of the ultimately critical shear crack are indicated by black dots. In combination with the crack states presented in the previous section, it is evident that the critical shear crack propagates towards the load introduction point. Consequently, the crack intersects individual fibre segments at different longitudinal positions, which explains the systematic shift of the corresponding peaks with decreasing vertical distance from the top of the beam.

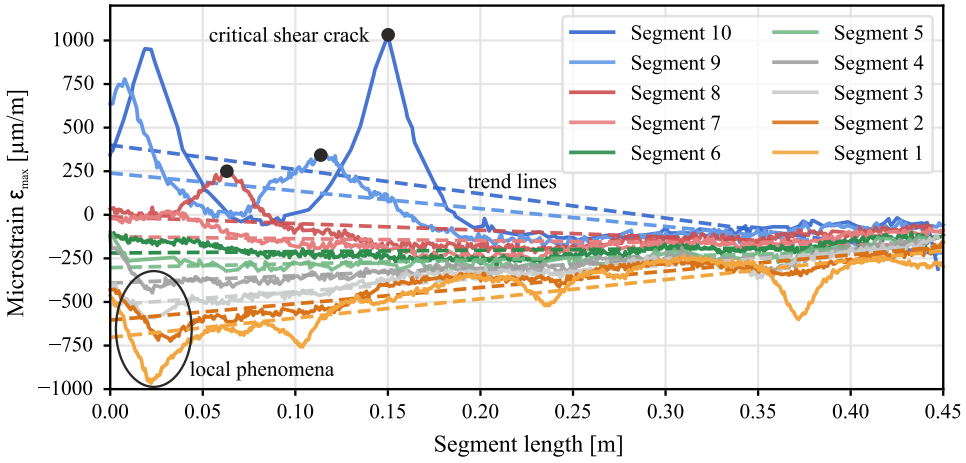


Fig. 4 Microstrain over segment length for FOS in the compression zone at maximum load at cycle 300

Additional, unmarked peaks originate from a neighbouring shear crack located to the left of the governing crack. Although this crack does not become critical, it intersects the fibre segments and progressively leaves the measurement window as it propagates further towards the load introduction. It is further observed that the strain peaks are distributed over a relatively wide longitudinal region. This

spatial smearing is a known characteristic of FOS with acrylate coating [12], [13] and results from the strain transfer behaviour of the soft coating. While this coating effectively prevents early rupture of the fibre and allows strain measurements even in cracked regions, it limits the spatial localisation of very sharp strain gradients, restricting highly localised evaluations.

Several smaller peaks are also visible in the segments in compression, even though no visible cracking occurs in this region. While these peaks might initially be interpreted as measurement noise, closer inspection reveals similar, although less pronounced, fluctuations in neighbouring fibre segments at comparable longitudinal positions. Since the fibre segments are only locally bonded and mechanically independent, mutual interaction between the segments can be excluded. These localised strain concentrations therefore indicate real structural effects, most likely associated with local heterogeneities of the concrete, such as aggregate particles or small material imperfections. Notably, the uppermost segment exhibits these local peaks more clearly than deeper segments, possibly due to edge effects or the higher strain level.

The FOS system captures highly local strain phenomena. Since the measurements are restricted to the concrete surface and do not represent an average over the full beam depth of 320 mm, a purely local evaluation leads to considerable scatter between different load stages and sensor heights. The strain smearing mentioned above furthermore limits localised evaluation.

To obtain a robust and representative description of the compression zone behaviour, trend lines were fitted to the strain data of each segment over the full measurement length (see Fig. 4). These trend lines are significantly less sensitive to local effects and provide a more stable representation of the average longitudinal strain state at the respective height.

The subsequent evaluation procedure follows the approach proposed by [15], which was recently applied to DIC measurements in [4], and is here applied to the FOS data. Based on these strain regression lines and the measured elastic modulus of the concrete specimens, the longitudinal stress gradient at each segment height was derived. From this, the shear stress distribution $\tau(z)$was calculated. Since FOS measurements cover only the upper 10 cm of the beam, values exceeding this height were extrapolated using a second-degree polynomial. The resulting shear stress distributions are presented in Fig. 5 (left) for several load stages. The end of the shear stress profile was defined at the crack tip, as in the Shear Crack Propagation Theory [16]. The crack tip was identified using DIC and defined as the location where the principal strain exceeds 0.1‰ for the ultimately critical shear crack.

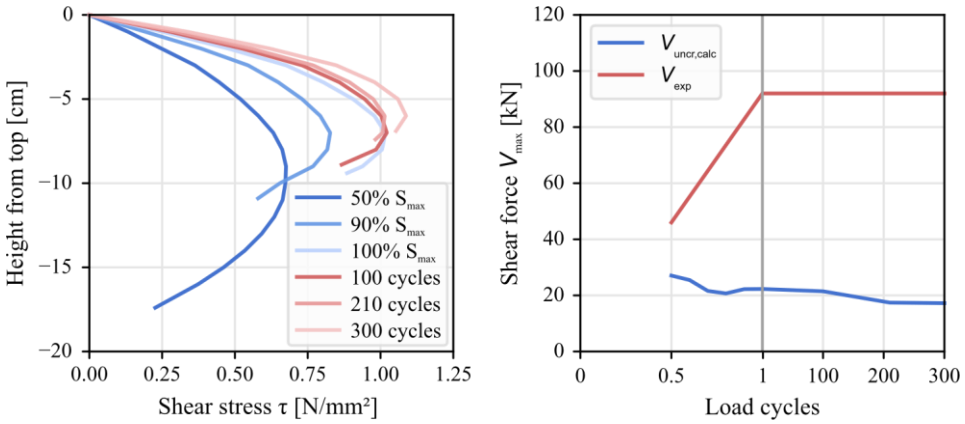


Fig. 5 (left) Shear stress distribution over the beam height at selected load levels; (right) Calculated shear force of the uncracked compression zone over the load cycles

It is observed that, with increasing load and number of cycles, the height of the compression zone above the crack tip decreases, while the local shear stresses increase. Fig. 5 (right) presents the corresponding shear force transferred by the uncracked compression zone over the applied fatigue cycles. The shear force was calculated by integrating the shear stress distribution over the beam height. The experimentally applied total shear force V_{exp} is also shown for comparison. The absolute shear force carried by the uncracked compression zone shows a slight decreasing trend over the cyclic loading history. In the initial loading phase, the relative contribution of the uncracked compression zone decreases. This observation is consistent with the assumption that, in the initially uncracked state, nearly

the entire shear force is carried by the uncracked concrete, while progressively, as cracks open, additional stress transfer mechanisms such as aggregate interlock and dowel action become activated.

4 CONCLUSION

This study investigated the shear fatigue behaviour of slender reinforced concrete beams without shear reinforcement, in this paper with a particular focus on the compression zone. FOS were successfully applied to capture longitudinal strain profiles with high spatial resolution, complemented by DIC to track crack kinematics.

Localised strain fluctuations detected by FOS reveal concrete heterogeneities, which necessitated the application of regression analysis to obtain robust strain trends. The regression-based strain data, combined with stress analysis, enabled the derivation of shear stress distributions, showing the progressive reduction of the effective compression height and the corresponding increase in shear stresses with fatigue loading.

Overall, the combination of FOS and DIC provides detailed insight into the mechanisms governing shear fatigue and the evolution of stress transfer in RC members. These findings contribute to a deeper understanding of fatigue-induced damage and can support the development of more accurate predictive models for structural performance under repeated loading. It should be noted that the presented results represent first outcomes of an ongoing research campaign, and a more comprehensive analysis will be provided in fortcoming full paper.

Acknowledgements

This work was funded by the Deutsche Forschungsgemeinschaft (DFG, German Research Foundation) - Project number 541376417.

References

[1] Bundesministerium für Digitales und Verkehr (BMDV). 2024. "Verkehr in Zahlen 2024/2025: 53. Jahrgang." Accessed January 7, 2026. https://www.bmv.de/SharedDocs/DE/Anlage/G/verkehr-in-zahlen24-25-pdf.pdf?__blob=publicationFile.

[2] Autrup, Frederik. 2022. "Shear Behaviour of Reinforced Concrete Beams without and with Small Amounts of Shear Reinforcement." PhD diss., University of Southern Denmark.

[3] Cavagnis, Francesco. 2017. "Shear in reinforced concrete without transverse reinforcement: from refined experimental measurements to mechanical models." PhD diss., Ecole Polytechnique Fédérale de Lausanne.

[4] Schmidt, Maximilian. 2025. "New insights into the fundamentals of shear behaviour in reinforced concrete members without shear reinforcement." PhD diss., RWTH Aachen University.

[5] Tung, Nguyen Duc, and Tue, Nguyen Viet. 2016. "A new approach to shear design of slender reinforced concrete members without transverse reinforcement." Engineering Structures 107:180–194. doi:10.1016/j.engstruct.2015.04.015.

[6] Cavagnis, Francesco, Fernández Ruiz, Miguel, and Muttoni, Aurelio. 2018. "An analysis of the shear-transfer actions in reinforced concrete members without transverse reinforcement based on refined experimental measurements." Structural Concrete 19:49–64. doi:10.1002/suco.201700145.

[7] Ueda, Tamon. 1982. "Behavior in Shear of Reinforced Concrete Beams under Fatigue Loading." PhD diss., University of Tokyo.

[8] Rombach, Günter Axel, and Kohl, Matthias. 2016. "Fatigue Strength of Reinforced Concrete Beams without Links under Shear Loads." ACI Structural Journal 113:941–950. doi:10.14359/51688924.

[9] Zanuy, Carlos, Gallego, Juan M., and Albajar, Luis. 2015. "Fatigue Behavior of Reinforced Concrete Haunched Beams without Stirrups." ACI Structural Journal 112:371–382. doi:10.14359/51687411.

[10] Schmidt, Maximilian, Schmidt, Philipp, Wanka, Sebastian. and Classen, Martin. 2021. "Shear Response of Members without Shear Reinforcement—Experiments and Analysis Using Shear Crack Propagation Theory (SCPT)." Applied Sciences 11:1–16. doi:10.3390/app11073078.

[11] Muttoni, Aurelio, Fernández Ruiz, Miguel, and Cavagnis, Francesco. 2018. "From detailed test observations to mechanical models and simple shear design equations." In Towards a Rational Understanding of Shear in Beams and Slabs: fib Bulletin 85: Workshop in Zürich, Switzerland, September 2016, edited by Oguzhan Bayrak, Miguel Fernández Ruiz, Walter Kaufmann, et al., 17–32. Lausanne: Fédération internationale du béton (fib).
[12] Becks, Henrik, Högemann, Matthias, Hegger Josef, and Classen, Martin. 2025. "Assessing crack formation and strain distribution in concrete structures using externally installed fiber optic sensors." Case Studies in Construction Materials. doi:10.1016/j.cscm.2025.e04744.
[13] Mata-Falcón, Jaime, Haefliger, Severin, Lee, Minu, Galkovski, Tena, and Gehri, Nicola. 2020. "Combined application of distributed fibre optical and digital image correlation measurements to structural concrete experiments." Engineering Structures 225:111309. doi:10.1016/j.engstruct.2020.111309.
[14] Fathalla, Eissa, and Mihaylov, Boyan. 2023. "Fatigue behavior of deep concrete beams with critical shear cracks." Structural Concrete 24:7314–7333. doi:10.1002/suco.202300603.
[15] Sherwood, Edward G. 2008. "One-Way Shear Behaviour of Large, Lightly-Reinforced Concrete Beams and Slabs." PhD diss., Universtity of Toronto.
[16] Classen, Martin. 2020. "Shear Crack Propagation Theory (SCPT) – The mechanical solution to the riddle of shear in RC members without shear reinforcement." Engineering Structures 210. doi:10.1016/j.engstruct.2020.110207.

Finite Element Analysis of Cementitious Layer Strengthened Reinforced Concrete Beams Using Different Configurations

Cecília Nemessányi, Anikó Pluzsik

Department of Mechanics, Materials and Structures, Faculty of Architecture,
Budapest University of Technology and Economics,
K. II. 61, Műegyetem rkp. 3, H-1111 Budapest Street, Hungary

Summary
Ultra high-performance fibre-reinforced concrete (UHPFRC) is a promising material for strengthening reinforced concrete (RC) structures due to its superior mechanical properties and durability. However, limited studies have compared how different strengthening configurations affect the failure behaviour and ductility of RC beams. This study employs finite element (FE) modelling to examine the influence of strengthening geometry, material strength, and steel reinforcement ratio within the strengthening layer. The findings showed that while adequate anchorage generally provides sufficient bonding between the layers, the behaviour of the strengthened beam differs from that of a monolithic structure, and conventional cross-sectional analytical models assuming perfect bond do not always yield conservative results. These findings provide valuable insights for optimising UHPFRC strengthening designs and enhancing the service life of existing RC structures.

1 INTRODUCTION

Ultra-High Performance Fibre Reinforced Concrete (UHPFRC) is characterised by low permeability, high tensile strength, and fibre-induced crack-bridging capacity, resulting in enhanced durability and ductility [1] – [4]. When applied to the tensioned side of reinforced concrete (RC) beams, UHPFRC improves flexural performance, and provides protection for steel bar reinforcement [3].

Experimental studies have investigated the bond behaviour between UHPFRC and normal strength concrete (NSC), demonstrating that surface preparation plays an important role in achieving adequate bond strength between the materials [1] – [3]. Although, bond behaviour is also influenced by material properties, loading conditions, and structural configuration [2]. In-situ UHPFRC strengthening layers where anchorage provided by the supports, often leads to effective composite action when sufficient surface roughening was applied, therefore debonding is generally not observed [1], [4] – [9]. In contrast, precast UHPFRC laminates are prone to debonding unless additional anchorage measures are used [10] – [11]. When the UHPFRC layer terminates before the supports, debonding frequently governed the failure mechanism, even when surface treatments were employed [7], [12] – [13].

Increasing thickness of the UHPFRC layer or the reinforcement ratio within the strengthening layer generally enhances flexural stiffness and ultimate load-bearing capacity; however, excessive stiffness may reduce ductility and promote brittle failure [4], [14]. Strengthening length also influences both debonding behaviour and structural performance, with longer strengthening layers reducing the likelihood of debonding up to a certain effective length [7], [11]. Effective anchorage methods include mechanical connectors, bent steel bars, or external anchorage systems. [7], [11].

Many analytical cross-sectional models for UHPFRC-strengthened RC beams assume perfect bond between the surface of the RC beam and the strengthening layer [4], [15]. Such assumptions may lead to overestimated predictions when anchorage is insufficient [7], [11]. Although several numerical studies have introduced interface models to capture bond imperfections – using cohesive zone models [6], [11], [14], frictional contact [7], or equivalent elements [16] – the combined effects of strengthening geometry, anchorage configuration, and strengthening stiffness remain insufficiently understood.

Therefore, further investigation is required to clarify how geometric and stiffness-related parameters influence the structural contribution of strengthening layers. In this study, a finite element modelling approach was adopted to assess the effects of strengthening length and anchorage type for strengthening layers with different stiffness characteristics.

2 NUMERICAL MODEL AND CALIBRATION

Finite element (FE) analyses were performed using the ATENA software. Structured quadratic elements were used in all cases. For strengthened beams, the bond between the concrete of the RC beam and the strengthening layer was modelled using fixed surface contact to isolate the effect of geometry and anchorage. Master-slave contact was determined automatically by ATENA.

2.1 Material Model Calibration and Mesh sensitivity Analysis

The material model parameters were adopted from experimentally determined values reported in the references [5], [17] – [18]. The strength values and material models are shown in Table 1.

The tensile softening behaviour of the UHPFRC material model was calibrated using experimental results [18] from a four-point bending test on a UHPFRC beam (Fig. 1 (left)). Furthermore, a mesh sensitivity study was conducted to assess the effect of element size on the numerical predictions. Mesh sizes of 25, 16.67, and 12.5 mm in all direction (corresponding to two to four elements across the strengthening layer thickness) were investigated. An element size of 25 mm provided good agreement with the experimental force-displacement response [18] (Fig. 1 (right)), while maintaining computational efficiency and was therefore adopted for all subsequent simulations.

Table 1 Finite element material settings

Material, reference	Compressive strength	Tensile strength	Material parameters used	Material models used in ATENA
NSC, [17]	39.5 MPa	2.5 MPa	NSC strengthened beams NSC strengthening + parametric study	3D fracture-plastic concrete model (CC3DNonLinCementious2)
NSC, [5]	25 MPa	2 MPa	UHPFRC strengthened beams	
UHPFRC [18]	164 MPa	11.5 MPa	calibration of UHPFRC + parametric study	3D fracture-plastic concrete model for fibre-reinforced concrete (CC3DNonLinCementious2SHCC)
UHPFRC [5]	136.5 MPa	11.5 MPa	UHPFRC strengthening	
Inserted steel bars, [5], [17]	500 MPa, hardening up to 650 MPa		for calibration	Uniaxial bilinear elastic–plastic model with yielding and optional hardening (embedded 1D elements; *CCReinforcement)*
	500 MPa, without hardening		parametric study	

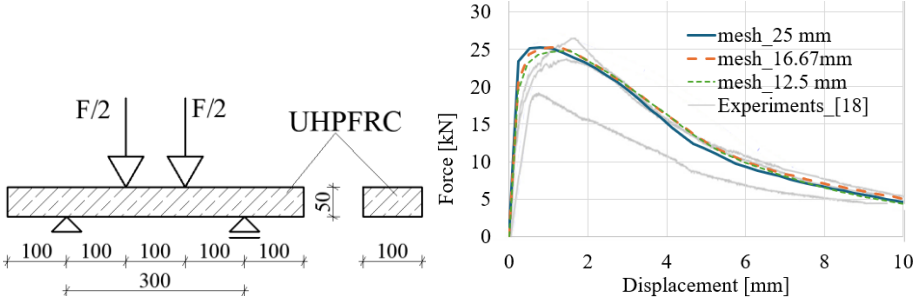


Fig. 1 UHPFRC beam geometry used for calibration [18] (left), comparison of the experimental [18] and numerical responses of UHPFRC beams using different mesh sizes (right)

2.2 Reference Configuration for Unstrengthened and Strengthened RC Beams

The applied geometry was matched as a reference to the four-point bending experiments of full and partial length NSC strengthened beams in [17] (Fig. 2 a-d) and full length UHPFRC strengthened beams in [5] (Fig. 2 a, e and f) resulting in five investigated cases including the unstrengthened beams.

2.3 Validation of Unstrengthened and Strengthened RC Beams

The cracking pattern and failure mode of the unstrengthened beams showed close correspondence between the numerical and experimental results (Fig. 2b and e).

In the FE models of the strengthened beams, fixed surface contact was used which enforces full displacement compability across the interface, corresponding to a perfect bond assumption. Consequently, any interface failure is governed by the material response rather than bond degradation. Using this assumption and the material parameters listed in Table 1, the numerically predicted crack patterns showed good agreement with the experimental observations (Fig. 2c, d and f).

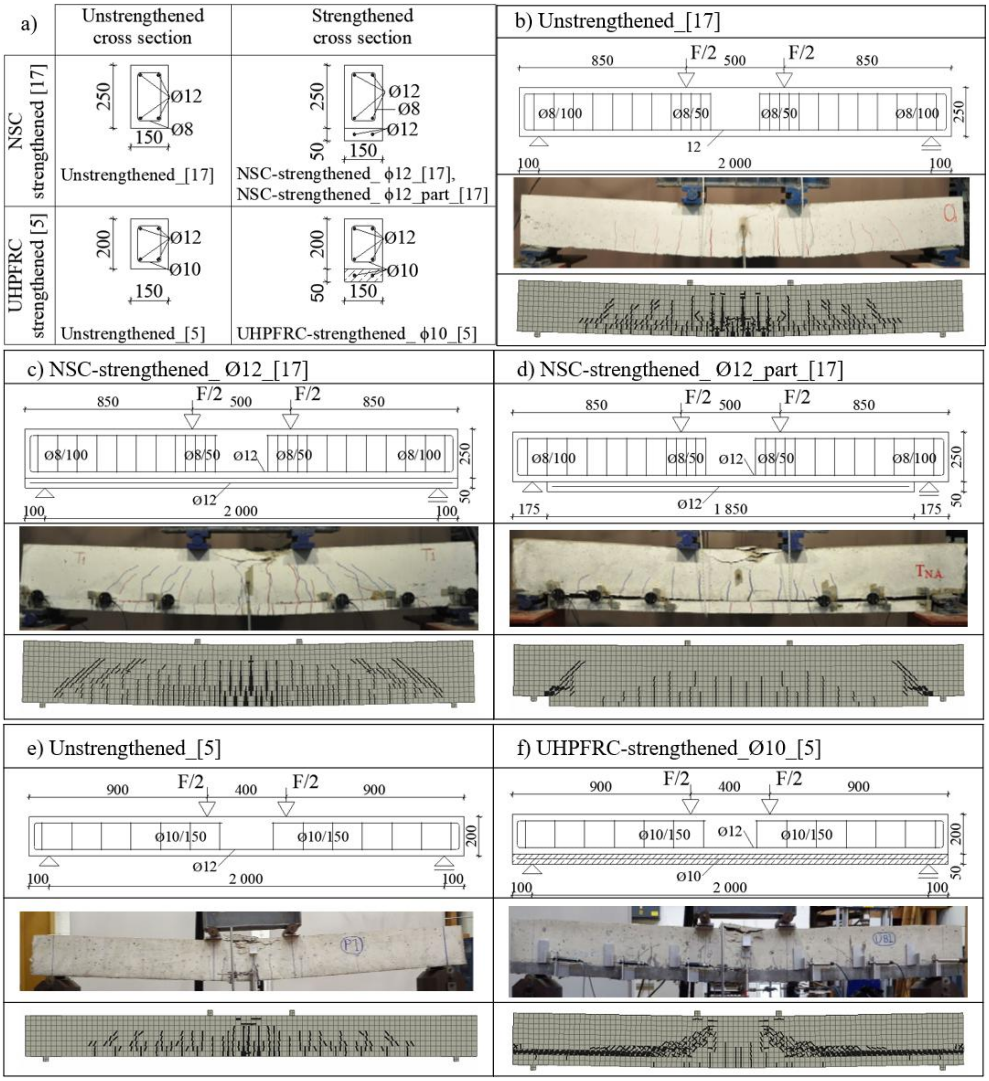


Fig. 2 Geometry and cracking patterns: a) cross sectional geometry, b)-f) comparison between experimental [5, 17] and numerical results. All dimensions are in [mm]

To complement the experimental validation of the numerical model, an analytical cross-sectional model was employed to evaluate the load-bearing capacity. The analytical model assumes plane sections with perfect bond between the layers, and is based on conventional reinforced concrete strength equilibrium, consistent with standard RC design procedures and previous studies [4], [15]. Concrete tensile properties were neglected, while UHPFRC was considered to have constant tensile strength defined as 85% of its ultimate tensile strength to represent strain-hardening behaviour. For steel material no strain hardening was assumed.

A comparison of analytical ($F_{max,calc}$), numerical ($F_{max,num}$), and experimental ($F_{max,exp}$) results is presented in Table 2, where $F_{max,exp}$ denotes the experimental ultimate load reported by Tsioulou (2013) [17] for specimens 1– 3 and by Paschalis (2018) [5] for specimens 4– 5. For cases without debonding, the analytical model underestimated the experimental load-bearing capacity due to the neglect of steel strain hardening, resulting in maximum difference from -18.77 to -25.46%. In contrast, for cases with debonding, the analytical model overestimated the load-bearing capacity, because interface failure was not considered, resulting in differences of 63,43% and 3,37% for specimens 3 and 5. The FE model showed good agreement with the experimental results slightly underestimating the load-bearing capacity in all cases. The maximum difference compared to the experimental results was -9,89% for the unstrengthened case and -2,95% for the strengthened case.

Table 2 Comparison of load-bearing capacities of reference beams

Specimen		Beam Geometry	Strengthening	$F_{max,exp}$ [kN]	$F_{max,calc}$ [kN]	$F_{max,num}$ [kN]
1	Unstrengthened_[17]	250 mm × 150 mm× 2200 mm	-	75	60.76	74.68
2	NSC-strengthened_Ø12_[17]		full length 50 mm thick NSC layer with two Ø12 steel bars	167	135.65	163.43
3	NSC-strengthened_Ø12_part_[17]		1850 mm length 50 mm thick NSC layer with two Ø12 steel bars	83	135.65	82.55
4	Unstrengthened_[5]	200 mm × 150 mm× 2200 mm	-	54.6	40.7	49.2
5	UHPFRC-strengthened_Ø10_[5]		full length 50 mm thick UHPFRC layer with two Ø10 steel bars	103.5	106.99	100.45

Overall, load-displacement diagrams from the numerical simulations showed good agreement with the experimental results, although the ductility was slightly underestimated (Fig. 3). For the partially strengthened NSC beam (NSC-strengthened_Ø12_part), the FE model captured the onset of debonding at load and displacement levels close to the experimental values (Fig. 3 (left), Table 2 Specimen 3). After debonding, the experimental response converged to that of the unstrengthened beam, indicating complete debonding (Fig. 2d and Fig. 3 (left)), while the numerical results were not reliable beyond this stage due to the fixed contact assumption and were therefore not presented.

For the full-length UHPFRC-strengthened beam (UHPFRC-strengthened_Ø10) the experimental load-bearing capacity was slightly lower than the analytical prediction, indicating debonding (Table 2 specimen 5). The FE model captured this behaviour conservatively by predicting a lower load-bearing capacity than the experimental value and reproducing the observed debonding pattern (Fig. 2f and Fig. 3 (right)). Although differences were observed in the load–displacement response, the displacement corresponding to the maximum load was similar.

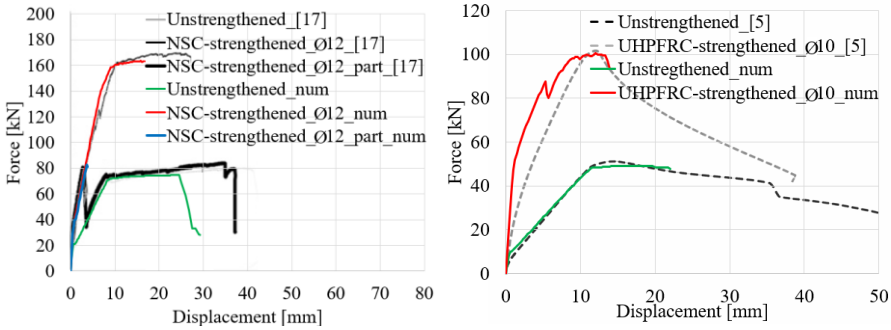


Fig. 3 Calibration of the FE model for NSC strengthened RC beams [17] (left), calibration of the FE model for UHPFRC strengthened RC beams [5] (right)

While the FE model accurately predicted the load-bearing capacity and indicated the onset of debonding, the detachment of the strengthening layer was not explicitly modelled. Consequently, the post-debonding response was not accurately captured and was not included in the load–displacement diagrams. Nevertheless, the FE model reproduced the overall structural response with slightly lower ductility and load-bearing capacity than observed experimentally.

3 PARAMETRIC STUDY

A parametric study was conducted using the calibrated FE model to evaluate the effects of strengthening geometry, anchorage configuration, material type, and reinforcement ratio. The material parameters listed in Table 1 were used throughout. To enable direct comparison with analytical results, steel strain hardening was neglected in the numerical model, differing from the calibration setup. The beam geometry was identical to that reported in Tsioulou (2013) [17]. Four anchorage configurations were considered for both NSC and UHPFRC strengthening: full-length strengthening anchored by supports, partial-length strengthening without support anchorage, and both configurations with and without connecting elements (Fig. 4). The connecting elements were modelled using Ø8 steel bar similarly to the stirrups. In the full-length strengthening configuration, they were distributed uniformly at 100 mm spacing along the beam length, whereas in the partial-length strengthening configuration they were placed more densely, at 50 mm spacing near the strengthening ends (Fig. 4 (right))

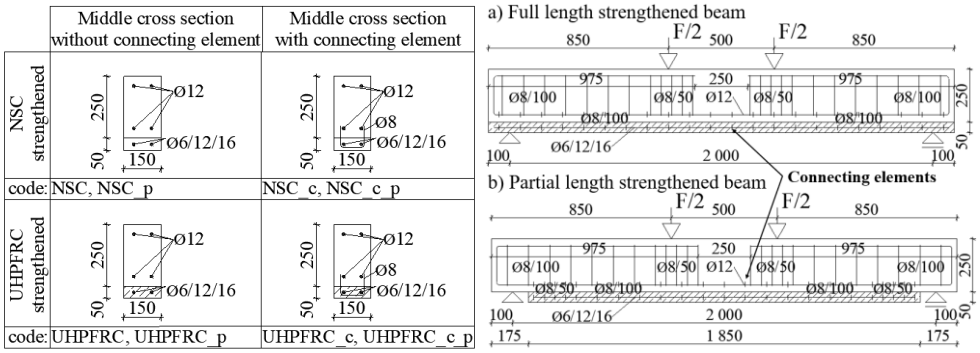


Fig. 4 Middle cross-sectional variations for parametric study (left), strengthened beam geometry. Connecting elements are indicated with dotted lines. All dimensions are in [mm] (right)

The results are summarised in Table 3-4, and Fig. 5-6, where NSC and UHPFRC denote the material of the strengthening material; Ø6/ Ø12/ Ø16 indicate the diameter of the reinforcement bars in the strengthening layer; "c" denotes the use of connecting elements while its absence indicates that none were used, and "p" refers to partial strengthening while its absence implies full-length strengthening.

Table 3 Comparison of numerically ($F_{max,num}$) and analytically ($F_{max,calc}$) determined load-bearing capacities of NSC strengthened RC beams (legend per Section 3)

Specimen	$F_{max,num}$ [kN]	$F_{max,calc}$ [kN]	Difference [%]	Specimen	$F_{max,num}$ [kN]	$F_{max,calc}$ [kN]	Difference [%]
NSC	61.82	60.76	1.76	NSC_Ø12	135.72	135.06	0.48
NSC_c	61.44	60.76	1.12	NSC_Ø12_c	137.31	135.06	1.66
NSC_p	61.86	60.76	1.81	NSC_Ø12_p	82.55	135.06	-38.88
NSC_c_p	61.26	60.76	0.82	NSC_Ø12_c_p	135.95	135.06	0.66
NSC_Ø6	80.16	79.87	0.36	NSC_Ø16	170,67	188.87	-9.64
NSC_Ø6_c	80.31	79.87	0.55	NSC_Ø16_c	192.52	188.87	1.93
NSC_Ø6_p	80.27	79.87	0.50	NSC_Ø16_p	80.11	188.87	-57.58

NSC_Ø6_c_p	85.20	79.87	6.68	NSC_Ø16_c_p	169.95	188.87	-10.02

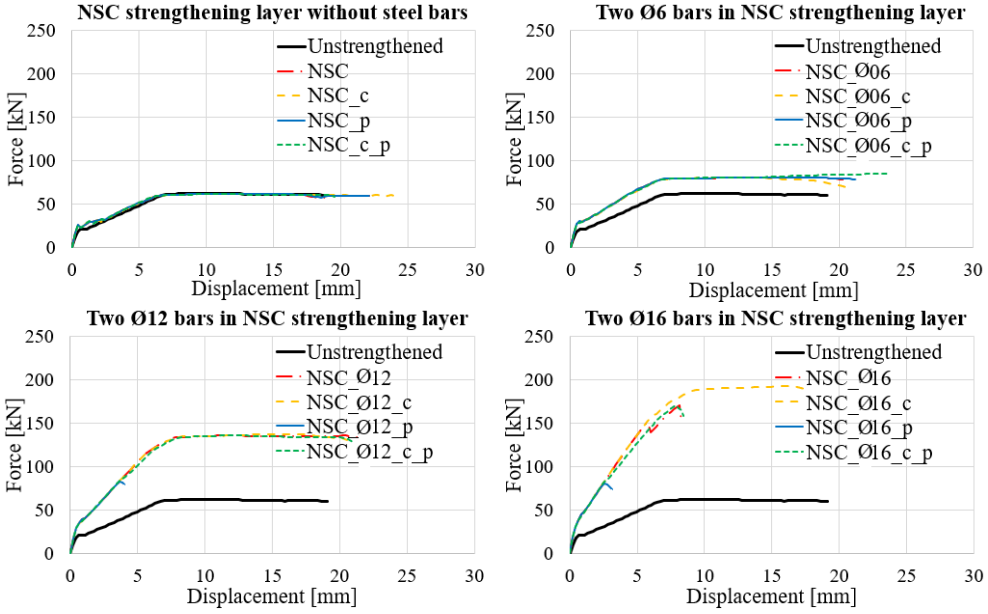


Fig. 5 Comparison of FE-derived load–displacement curves for NSC-strengthened RC beams: (legend per Section 3)

For NSC-strengthened beams, unreinforced layers provided negligible improvement. Inserted Ø6 reinforcement ensured stable composite behaviour even without support anchorage. In contrast, inserted larger bars (Ø12 and Ø16) required proper anchorage to prevent premature debonding. Optimal strength calculated from the analytical model and ductility was achieved for Ø12 in all anchored cases and for Ø16 only in full-length strengthening with connecting elements.

For UHPFRC-strengthened beams, partial-length strengthening without anchorage consistently resulted in debonding, regardless of reinforcement ratio. Anchored configurations in most cases reached the analytically predicted load-bearing capacity, except for the Ø16 reinforcement case, where only fully anchored, full-length strengthening provided the expected performance. Although UHPFRC strengthening improved stiffness, crack resistance, and load-bearing capacity compared to NSC, its higher stiffness increased interface stresses, making effective anchorage essential - such as connecting elements, steel plates, or FRP systems. Furthermore, UHPFRC-strengthened beams exhibited lower ductility compared to NSC-strengthened beams, even when effective anchorage was provided.

Table 4 Comparison of numerically (Fmax,num) and analytically (Fmax,calc) determined load-bearing capacities of UHPFRC strengthened RC beams (legend per Section 3)

Specimen	$F_{max,num}$ [kN]	$F_{max,calc}$ [kN]	Difference [%]	Specimen	$F_{max,num}$ [kN]	$F_{max,calc}$ [kN]	Difference [%]
UHPFRC	111,10	109.58	1.39	UHPFRC_Ø12	183.52	180.15	1.87
UHPFRC_c	112,76	109.58	2.90	UHPFRC_Ø12_c	183.72	180.15	1.98
UHPFRC_p	78.31	109.58	-28.54	UHPFRC_Ø12_p	76.93	180.15	-57.30
UHPFRC_c_p	109,08	109.58	-0.46	UHPFRC_Ø12_c_p	181.25	180.15	0.61
UHPFRC_Ø6	130.88	127.76	2.44	UHPFRC_Ø16	194.65	231.06	-15.76
UHPFRC_Ø6_c	131.23	127.76	2.71	UHPFRC_Ø16_c	234.99	231.06	1.70
UHPFRC_Ø6_p	78.02	127.76	-38.93	UHPFRC_Ø16_p	76.18	231.06	-67.03

UHPFRC_Ø6_c_p	130.98	127.76	2.52	UHPFRC_Ø16_c_p	175.84	231.06	-23.90

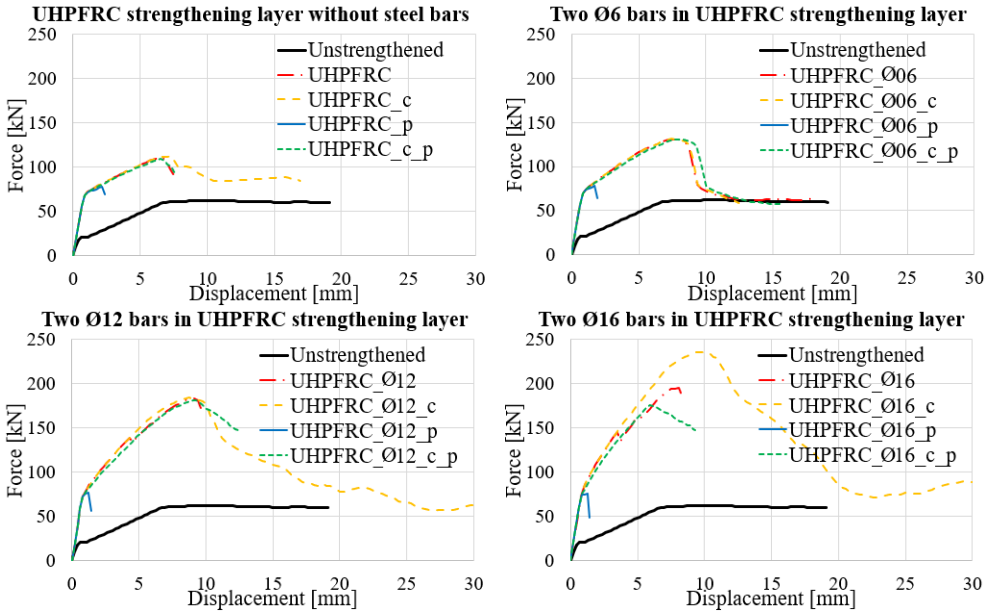


Fig. 6 Comparison of FE-derived load-displacement curves for UHPFRC-strengthened RC beams (legend per Section 3).

4 CONCLUSIONS

This study combined analytical cross-sectional analysis with nonlinear FE modelling to investigate tension-side strengthening of RC beams using a cementitious layer. The FE model was calibrated based on experimental results from literature. The results demonstrated that strengthening effectiveness depends strongly on geometry, anchorage conditions, material stiffness, and reinforcement ratio. In cases of insufficient anchorage, the cross-sectional analytical model assuming perfect bond overestimated load-bearing capacity of the strengthened beams.

References

[1] Al-Osta, Mohammed Ali, Isa, Muhammad Nura, Baluch, Mohammed Hussain, and Rahman, Muhammad Kalimur. 2017. "Flexural behaviour of reinforced concrete beams strengthened with ultra-high performance fibre reinforced concrete." *Construction and Building Materials* 134;279–296. https://doi.org/10.1016/j.conbuildmat.2016.12.094.

[2] Lampropoulos, Andreas, Tsioulou, Ourania, Nicolaides, Demetris, and Petrou, Michael F. 2023. "Strengthening of Existing Structures with UHPFRC: Concrete-To-UHPFRC Interfaces." *Lecture Notes in Civil Engineering*, 856–866. https://doi.org/10.1007/978-3-031-32511-3_88.

[3] Bahraq, Ashraf Awadh, Al-Osta, Mohammed Ali, Ahmad, Shamsad, Al-Zahrani, Mesfer Mohammad, Al-Dulaijan, Salah Othman, and Rahman, Muhammad Kalimur. 2019. "Experimental and Numerical Investigation of Shear Behaviour of RC Beams Strengthened by Ultra-High Performance Concrete." *International Journal of Concrete Structures and Materials*, 13(1). Accessed January 14. 2026. https://doi.org/10.1186/s40069-018-0330-z.

[4] Nugroho, Laurencis, Haryanto, Yanuar, Hsiao, Fu-Pei, Hu, Hsuan-Teh, Weng, Pu-Wen, Lin, Chia-Chen, Kristiawan, Stefanus Adi, and Sangadji, Senot. 2025. "Effectiveness of UHPC reinforced with steel rebars for flexural strengthening of RC T-beams in an idealized negative moment region." *Structures*, 80;109728–109728. https://doi.org/10.1016/j.istruc.2025.109728.

[5] Paschalis, Spyridon A., Lampropoulos, Andreas P., and Tsioulou, Ourania T. 2018. "Experimental and numerical study of the performance of ultra high performance fibre reinforced concrete for the flexural strengthening of full scale reinforced concrete members."

Construction and Building Materials, 186;351–366. https://doi.org/10.1016/j.conbuildmat.2018.07.123.

[6] Luu, Xuan-Bach. 2024. "Finite element modelling of reinforced concrete beam strengthening using ultra-high performance fibre-reinforced shotcrete combined with reinforcing bars." *Structures*, 60;105794–105794. https://doi.org/10.1016/j.istruc.2023.105794.

[7] Ahmed, Sayed, Mohamed, Eman Yehia, Mohamed, Heba A., and Emara, Mohamed. 2024. "Bending performance of RC beams reinforced with UHPFRC strips with different geometry and positions." *Structural Concrete*, 26(1);621–642. https://doi.org/10.1002/suco.202400470.

[8] Nemessányi, Cecília, and Pluzsik, Anikó. 2024. "Effect of Bonding Type on the Failure of Reinforced Concrete Beam Strengthened with In-Situ High Performance Fibre Reinforced Concrete Layer." *Építés- építészettudomány*, 52(1-2);49–73. https://doi.org/10.1556/096.2024.00113.

[9] Martinola, Giovanni, Meda, Alberto, Plizzari, Giovanni A., and Rinaldi, Zila. 2010. "Strengthening and repair of RC beams with fibre reinforced concrete." *Cement and Concrete Composites*, 32(9);731–739. https://doi.org/10.1016/j.cemconcomp.2010.07.001.

[10] Garg, Varun, Bansal, Prem Pal, and Sharma, Raju. 2019. "Retrofitting of Shear-Deficient RC Beams Using UHP-FRC." *Iranian Journal of Science and Technology, Transactions of Civil Engineering*, 43(3);419–428. https://doi.org/10.1007/s40996-019-00241-7.

[11] Hekal, Ghada M., Salama, Magdy I., Elsamak, Galal, and Almaadawy, Ahmed H. 2022. "Shear behaviour of RC beams strengthened with ultra-high-performance fibre-reinforced concrete using finite-element analysis." *Asian Journal of Civil Engineering*. https://doi.org/10.1007/s42107-022-00489-x.

[12] Tanarslan, Hasan Murat, Alver, Ninel, Jahangiri, R. Yalçınkaya, Çağlar, and Yazıcı, Halit. 2017. "Flexural strengthening of RC beams using UHPFRC laminates: Bonding techniques and rebar addition." *Construction and Building Materials*, 155;45–55. Accessed January 14. 2026. https://doi.org/10.1016/j.conbuildmat.2017.08.056.

[13] Zhang, Yang, Wang, Hao, Qin, Yanyue, Huang, Songling, and Fan, Wei. 2023. "Experimental and analytical studies on the flexural behaviour of steel plate-UHPC composite strengthened RC beams." *Engineering structures/Engineering structures* 283;115834–115834. Accessed January 14. 2026. https://doi.org/10.1016/j.engstruct.2023.115834.

[14] Zhu, Yanping, Zhang, Yang, Li, Xiangliang, and Chen, Genda. 2021. "Finite element model to predict structural response of predamaged RC beams reinforced by toughness-improved UHPC under unloading status." *Engineering Structures*, 235;112019. https://doi.org/10.1016/j.engstruct.2021.112019.

[15] Habel, Katrin, Denarié, Emmanuel, and Brühwiler, Eugen. 2006. "Structural Response of Elements Combining Ultrahigh-Performance Fibre-Reinforced Concretes and Reinforced Concrete." *Journal of Structural Engineering-asce*, 132(11);1793–1800. https://doi.org/10.1061/(ASCE)0733-9445(2006)132:11(1793).

[16] Yin, Hor, Shirai, Kazutaka, and Teo, Wee. 2019. "Numerical model for predicting the structural response of composite UHPC–concrete members considering the bond strength at the interface." *Composite Structures*, 215;185–197. Accessed January 14. 2026. https://doi.org/10.1016/j.compstruct.2019.02.040.

[17] Tsioulou, Ourania T., Lampropoulos, Andreas P., and Dritsos, Stephanos E. 2013. "Experimental investigation of interface behaviour of RC beams strengthened with concrete layers." *Construction and Building Materials*, 40;50–59. https://doi.org/10.1016/j.conbuildmat.2012.09.093.

[18] Lampropoulos, Andreas P., Paschalis, Spyridon A., Tsioulou, Ourania T., and Dritsos, Stephanos E. 2016. "Strengthening of reinforced concrete beams using ultra high performance fibre reinforced concrete (UHPFRC)." *Engineering Structures*, 106;370–384. https://doi.org/10.1016/j.engstruct.2015.10.042.

Shrinkage prediction using small concrete specimens

Lenka Dohnalová, Petr Havlásek and Vít Šmilauer

Faculty of Civil Engineering,
Czech Technical University in Prague,
Thákurova 7/2077, 166 29 Praha 6 – Dejvice, Czech Republic

Summary
Shrinkage prediction using experimental data remains highly challenging due to the slow development of shrinkage. The new fib MC2020 methodology improves prediction accuracy by calibrating the model using short-term measurements, but the necessary monitoring duration for standard 100 × 100 mm specimens is too long for engineering practice. This study investigates the possibility of using smaller specimens to obtain sufficiently representative shrinkage development within a significantly reduced time. An experimental program was carried out on cast and cut-out specimens of different sizes to quantify the influence of specimen size and the near-surface region. The results show that smaller specimens allow a substantial reduction of the initial measurement period, while the behaviour of cut-out specimens differs from that of cast specimens, indicating the need for further analysis before they can be reliably used to improve shrinkage prediction.

1 MOTIVATION

Shrinkage of concrete members is a phenomenon whose accurate prediction remains highly challenging. Both the kinetics and the ultimate magnitude of shrinkage are influenced by a wide range of factors, including the composition of the concrete mix, curing conditions during hydration, and the environmental exposure to which the member is subjected throughout its service life.

The difficulty of reliably predicting shrinkage becomes particularly critical for structures sensitive to time-dependent effects such as creep and shrinkage, especially when modern concretes with a high content of mineral additions and chemical admixtures are used. In such cases, capturing the influence of all these material constituents within a standardized calculation model is highly challenging, if not practically impossible.

In addition to code-based approaches, advanced academic models have been developed that describe the behaviour of concrete using detailed physical and rheological formulations [1], [2]. These models aim to capture the underlying physical and chemical processes within the cementitious composite and can account for a wide range of material and environmental factors. However, this increased level of detail requires extensive input data and can make the models highly sensitive to numerous parameters, which does not always lead to improved predictive accuracy in practical applications. For these reasons, such models are generally unsuitable for routine engineering practice due to their high demand for numerous detailed input parameters, and are mainly used in research.

Modern design codes, such as the *fib* Model Code 2020 [3] and Eurocode 2 [4], adopt a different strategy in their current formulations to improve the accuracy of shrinkage prediction. Instead of increasing model complexity, these codes use calibration coefficients, determined from experimental measurements on specimens prepared from the same material as the designed structure. This approach enables the overall behaviour of the specific concrete to be effectively captured, while keeping the number of input parameters practical for engineering applications.

The calibration and validation of code-based predictions of creep and shrinkage against observed material behaviour has long been recognized as an important step toward improved predictive accuracy. A recent study [5] demonstrates that adjusting model predictions using laboratory data from experimental databases leads to significantly improved accuracy compared to the use of standard, uncalibrated code-based formulations. This finding provides indirect support for the principle adopted in the *fib* Model Code 2020.

2 SHRINKAGE PREDICTION USING THE NEW MC 2020 METHODOLOGY

The shrinkage calculation according to the *fib* Model Code 2020 introduces a total of four calibration coefficients ξ. Two of them, namely ξ_{bs1} and ξ_{bs2}, are applied in the expressions for the basic shrinkage component, while the remaining two coefficients, ξ_{ds1} and ξ_{ds2}, are used in the calculation of drying shrinkage. In both cases, the first coefficient of the respective pair governs the final magnitude of the shrinkage component, whereas the second coefficient controls its time-dependent development.

The form in which the calibration coefficients are incorporated into the calculation is illustrated by the following expressions.

For the basic shrinkage component (previously referred to as autogenous shrinkage), the following relationship applies

$$\varepsilon_{\mathrm{cbs}}(t) = -\alpha_{\mathrm{bs}} \left(\frac{f_{\mathrm{cm},28}}{60 + f_{\mathrm{cm},28}} \right)^{2.5} \cdot 10^{-6} \cdot \beta_{\mathrm{bs}}(t) \tag{1}$$

where t refers to the concrete age (expressed in days), α_{bs} is a parameter reflecting the early-age strength development, and $f_{\mathrm{cm},28}$ is the 28-day compressive strength. The time function β_{bs}, which governs the kinetics of basic shrinkage, is given by

$$\beta_{\mathrm{bs}}(t) = 1 - \exp(-0.2\, \xi_{\mathrm{bs2}} \cdot \sqrt{t}\,) \tag{2}$$

For drying shrinkage, the following expression applies

$$\varepsilon_{\mathrm{cds}}(t - t_{\mathrm{s}}) = (220 + 110\, \alpha_{\mathrm{ds}}) \cdot \exp\left(-0.012\, f_{\mathrm{cm},28}\right) \cdot 10^{-6} \cdot \beta_{\mathrm{RH}} \cdot \beta_{\mathrm{ds}}(\mathrm{t} - \mathrm{t_s}) \tag{3}$$

with the corresponding time function

$$\beta_{\mathrm{ds}}(t - t_{\mathrm{s}}) = \sqrt{\frac{t - t_{\mathrm{s}}}{0.035\, \xi_{\mathrm{ds2}} \cdot h^2 + (t - t_{\mathrm{s}})}} \tag{4}$$

where t_s specifies the time at which drying begins, α_{ds} is a parameter reflecting the early-age strength development, and β_{RH} accounts for the influence of ambient relative humidity. The notional member size is given by $h = 2A/u$, meaning twice the ratio of the cross-sectional area to its perimeter, expressed in millimetres.

The total shrinkage strain is subsequently obtained as the sum of the basic and drying shrinkage components.

$$\varepsilon_{cs}(t, t_s) = \xi_{bs1} \cdot \varepsilon_{cbs}(t) + \xi_{ds1} \cdot \varepsilon_{cds}(t, t_s) \tag{5}$$

The role of each calibration coefficient and its influence on the shape of the predicted shrinkage curve are illustrated in [6].

The calibration coefficients ξ are to be determined using the method of least squares to achieve agreement with the results of short-term experimental measurements. The experimental data should be recorded at constant time intervals on a logarithmic time scale.

2.1 Duration of experimental measurements

The duration of measurements is not explicitly prescribed. It should be at least 90 days, and an observation period of several months is generally assumed.

In the case of shrinkage, a sufficiently long monitoring period is necessary in order to reliably distinguish between the effects governing the kinetics and the final value of shrinkage.

It is well known that shrinkage prediction based on short-term measurements is highly uncertain [7]. This represents an ill-conditioned problem, in which very different final shrinkage values may be obtained while still achieving an excellent fit to short-term experimental data [8]. The length of the initial observation period therefore plays a crucial role in improving shrinkage prediction.

When measurements are performed on standard laboratory specimens (e.g. prisms with a cross-section 100 × 100 mm), the time required to reliably identify the final shrinkage value typically exceeds one year. Such durations are hardly compatible with the practical requirements of structural design.

While the benefit of the newly introduced calibration methodology is evident, the conflicting requirements of design codes and engineering practice regarding the duration of initial measurements introduce a certain risk. In particular, calibration based on an excessively short observation period may not necessarily result in improved predictive accuracy.

To illustrate the above-mentioned risk, Fig. 1 presents an example of model calibration based on data from the first 90 days, corresponding to the minimum required observation period. This example is purely illustrative. First, shrinkage was calculated using the standard formulations of the *fib* Model Code 2020 for parameters representative of a typical structural concrete. The resulting drying shrinkage evolution over the first 90 days was then used as input data, and a manual fitting procedure was performed to obtain different shrinkage curves. These curves differ in their final shrinkage values while perfectly reproducing the known initial development. The two fitted curves differ solely in the values of the calibration coefficients ξ_{ds1} and ξ_{ds2} associated with the drying shrinkage component.

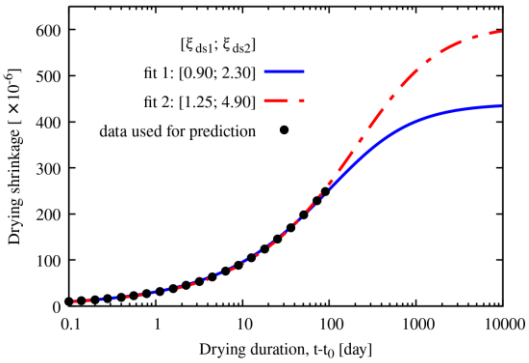


Fig. 1 A theoretical illustration of drying shrinkage calibration based on data from the initial 90 days. Different sets of calibration coefficients provide an excellent fit to the initial evolution while resulting in significantly different long-term shrinkage predictions.

The application of the new methodology to a real experiment is illustrated in the two graphs in Fig. 2. The experimental data originate from the NU database, which was later extended and is currently maintained in a MySQL format at CTU in Prague [9]. The dataset corresponds to the study by Hammer [10], in which high-strength concrete was used, providing a suitable example for assessing the new methodology, as verifying the prediction based on actual material behaviour is especially important for mixtures with more specific material behaviour. The specimen dimensions were 100 × 100 × 500 mm. Specimens for basic shrinkage measurements were sealed with aluminium foil.

Mixture designated as #1 has a water-to-cement ratio $w/c = 0.35$ and a 28-day compressive strength $f_{cm} = 79.4$ MPa, while mixture designated as #2 has $w/c = 0.30$ and $f_{cm} = 96.2$ MPa. This experiment was selected as an example using specimens whose size complies with the requirements of design codes. The specimens were monitored for one year, and both basic shrinkage and total shrinkage data were available.

The parameter fitting was carried out in two stages. First, the coefficients ξ_{bs1} and ξ_{bs2} were determined from the basic shrinkage data and subsequently kept fixed for the second stage. In the second stage, the remaining coefficients ξ_{ds1} and ξ_{ds2} were identified based on agreement with the total shrinkage data.

The fitting procedure was initially performed using only the first three months of experimental data, and the resulting curves together with the fitted values of all coefficients are shown in the left-hand graph in Fig. 2. The right-hand graph presents the results obtained from fitting based on the full one-year dataset. A comparison of the two graphs clearly demonstrates the improvement in predictive capability when a longer initial development is known.

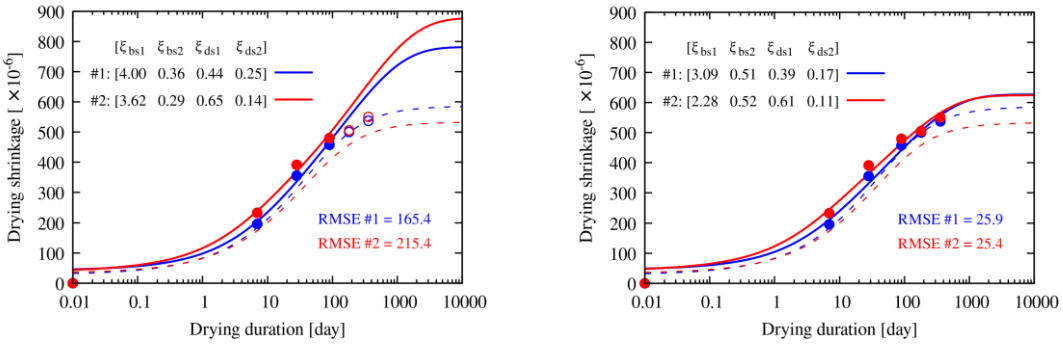


Fig. 2 Prediction of total shrinkage according to the new MC2020 methodology using calibration coefficients ξ. Calibration using experimental data from Hammer's study over the first three months (left) and over the one-year monitoring period (right). Empty markers in the left graph denote data points not used for shrinkage calibration. The curves were fitted separately to basic shrinkage and total shrinkage data. Dashed curves correspond to calculations performed with all calibration coefficients equal to 1. The quality of the prediction is quantified by the RMSE values calculated for each curve using all available experimental data.

For the basic shrinkage component, the fitted values of the coefficients are significantly higher than the reference value of 1. This may be attributed to a substantially different evolution of basic shrinkage compared with the assumptions of the computational model.

Since compressive strength is one of the input parameters of the *fib* MC2020 computational model, the values obtained from the two-stage fitting procedure remain higher than would be expected. The underlying cause is not entirely clear, one possible explanation is the difficulty in capturing the very early development of shrinkage, where partial drying prior to or during the sealing of the specimens may not have been fully eliminated.

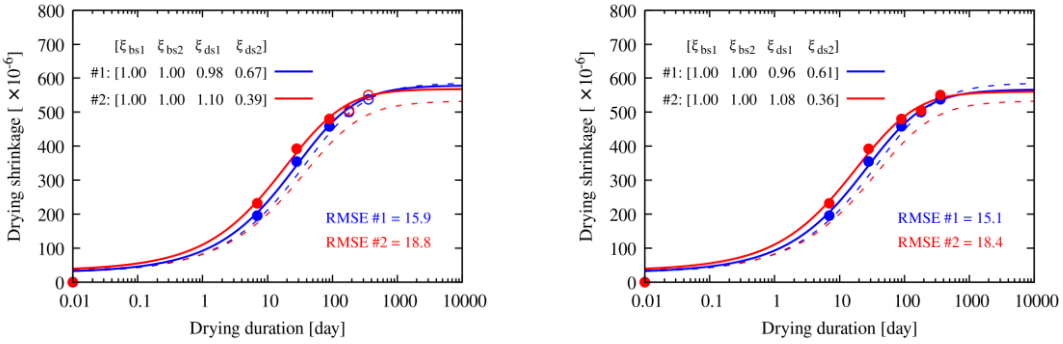


Fig. 3 Prediction of total shrinkage according to the new MC2020 methodology on Hammer's experimental data over the first three months (left) and over the full one-year monitoring period (right). All four calibration coefficients were fitted simultaneously to total shrinkage data, without separate fitting of the basic and drying components. Dashed curves correspond to all coefficients equal to 1.

Therefore, an alternative calibration of the computational model was performed. A one-stage fitting procedure was used, in which all four coefficients were calibrated simultaneously to match the total shrinkage data. Without imposing any constraints on the coefficient values, the optimisation surprisingly converged to zero values for coefficients ξ_{bs1} and ξ_{bs2} associated with the basic shrinkage component. Since basic shrinkage plays a significant role in cementitious materials with a low water-to-cement ratio, a lower bound equal to 1 was imposed on both coefficients. The upper bound

was set to 10, however, as evident from the results in Fig. 3, the fitted values remained at the lower limit.

Additional examples of the verification of the new methodology on specimens of standard size can be found in [6].

The number of experimental studies suitable for verifying the new methodology is rather limited. Most available studies do not provide both basic and total shrinkage data, and one of the most common issues is the insufficient duration of the experiments, which makes it impossible for the shrinkage prediction according to the new MC2020 methodology to be validated against the real long-term behaviour.

2.2 Use of small specimens for shrinkage prediction

As noted and clearly demonstrated in the previous section, obtaining a sufficiently long initial shrinkage development for reliable prediction improvement requires a very long measurement duration when standard laboratory specimens are used.

A possible way to reduce the required duration of the initial measurements is the use of smaller specimens, in which drying and the associated shrinkage develop significantly faster. However, this approach is not without complications. For smaller specimens, it is often necessary to slightly modify the mixture composition (e.g. due to limitations on the maximum aggregate size), or to use mortar specimens instead of concrete specimens. When mortar specimens are used, the shrinkage of concrete can be determined from the shrinkage of mortar (or paste) by taking into account the aggregate volume fraction in the mixture. This conversion is based on the fact that the difference in shrinkage between mortar and concrete is primarily a consequence of the differing aggregate volume fraction, which restrains the shrinkage of the cement paste [11].

One of the key issues when using smaller specimens is that shrinkage does not develop identically in specimens of different sizes. There is no consensus in the literature as to whether specimen size affects only the kinetics of shrinkage or also its ultimate value. Although the fib Model Code 2020 does not consider the influence of specimen size on ultimate shrinkage (possibly because the model does not expect the use of specimens with a cross-section smaller than 100 × 100 mm), previous experimental research [12] has demonstrated the existence of a so-called size effect on ultimate shrinkage.

An important aspect that may be responsible for the different behaviour of specimens of various sizes is that, in smaller specimens, the layer of material near the surface plays a more significant role. It is evident that the distribution of material (the ratio of aggregate to cement paste) will differ between the surface layer and the core of the specimen. The surface region has a higher proportion of cement paste, in which shrinkage occurs, and it can therefore be expected that the material in this area will exhibit a greater tendency to shrink during drying, although this is restrained by the core of the specimen. In addition, the surface of the specimens, which was in contact with the formwork during casting, may have a different structure and pore openness compared to the core.

It is very difficult to predict how the above-described heterogeneity could affect shrinkage. Therefore, a new experiment was designed and subsequently carried out, in which the drying shrinkage of cast specimens and specimens obtained by cutting from a larger concrete block was measured. Both types of specimens were prepared from a single batch of self-compacting concrete (495 kg/m^3 of CEM I 42.5 R, $w/c = 0.42$, aggregate-to-cement ratio $a/c = 3.21$, $f_{cm} = 45$ MPa). The specimens were exposed to drying after 28 days of age (at approximately 50% relative humidity and 20°C) in order to largely eliminate the influence of basic shrinkage during the drying process. From day 1 after casting, the specimens were stored together in an environment with 100% relative humidity. Cutting of the specimens was carried out at approximately 20 days of age, sufficiently in advance of drying to allow the saturation to equilibrate, which may have been affected by wet cutting.

Prediction of shrinkage using specimens of significantly smaller dimensions is illustrated in Fig. 4. The specimens considered are three cast concrete prisms with dimensions of 30 × 30 × 500 mm. Only drying shrinkage is taken into account, while basic shrinkage is neglected, as the most significant part of the basic shrinkage had already occurred during the 28 days prior to the start of the experiment. The quality of the experimental measurements is confirmed by the minimal differences observed between the individual specimens.

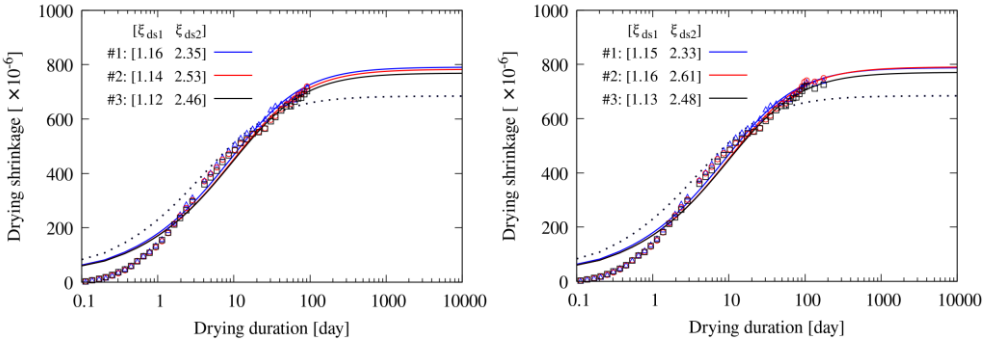


Fig. 4 Prediction of drying shrinkage using calibration coefficients fitted to data obtained over the first 3 months (left) and over 6 months (right) of measurements for cast concrete prisms of 30 × 30 × 100 mm. The dotted curve corresponds to the drying shrinkage prediction with the coefficient values equal to 1.

The prediction curves obtained by fitting the data from the first three months (Fig. 4 left) and those obtained by fitting the data from six months (Fig. 4 right) are almost identical; the same applies to the identified values of the coefficients ξ_{ds1} and ξ_{ds2}. Monitoring of the specimens still continues, and it will later be possible to verify the long-term predictive accuracy. However, it is already evident that the use of smaller specimens has significantly reduced the required duration of the initial measurements.

In the case of cut-out specimens, shrinkage developed faster than in the case of cast specimens. For almost the entire duration of the measurements, the shrinkage of the cut-out specimens was higher than that of the cast specimens. The only exception is represented by the prisms with a cross-section of 70 × 70 mm, for which the shrinkage of the cast specimens was initially slightly higher; however, even for this size, higher shrinkage values were observed for the cut-out specimens from approximately one week onwards.

A comparison of the experimentally measured shrinkage of both specimen types with cross-sections of 30 × 30, 50 × 50, and 70 × 70 mm is shown in Fig. 5. The open circle symbols correspond to the cut-out specimens, while the filled triangles represent the cast specimens. Individual specimen sizes are distinguished by colour. In each case, the plotted values represent the averages for the given group of specimens, as the differences in the measured values within each group were minimal.

Using these experimental data, the two calibration coefficients for the drying shrinkage component were subsequently identified. The left-hand graph in Fig. 5 shows the result of the fitting based on the first 3 months of measurements, while the right-hand graph presents the fitting based on the entire measurement period to date, i.e. 6 months. The solid curves correspond to the cast specimens, while the dashed curves represent the cut-out specimens. The dotted curves correspond to the default *fib* MC2020 drying shrinkage prediction for the respective specimen size, distinguished by colour.

The unexpected deviation in the experimental shrinkage development observed after approximately 90 days of drying was caused by a temporary drop in laboratory humidity resulting from an interruption in the operation of the humidifier. Since the shrinkage development returned to the expected trend after a relatively short period, the fitting results shown in the right-hand graph in Fig. 5 indicate that this disturbance had no significant effect on the identified coefficients. The fitted shrinkage curves do not differ substantially between the left- and right-hand graphs. Nevertheless, higher accuracy may be expected for the fitting based on the shorter three-month period, where this disturbance is absent.

The different behaviour of cast and cut-out specimens was well captured by the new MC2020 methodology. Interestingly, although the method does not account for specimen preparation in the calculations, it assigned essentially the same final shrinkage value to all specimens of a given type. This is particularly evident from the left-hand graph in Fig. 5, as well as from the graph in Fig. 6. Whether the individual groups will actually reach similar ultimate shrinkage values regardless of specimen size may later be confirmed or disproved based on experimental results obtained over a considerably longer monitoring period.

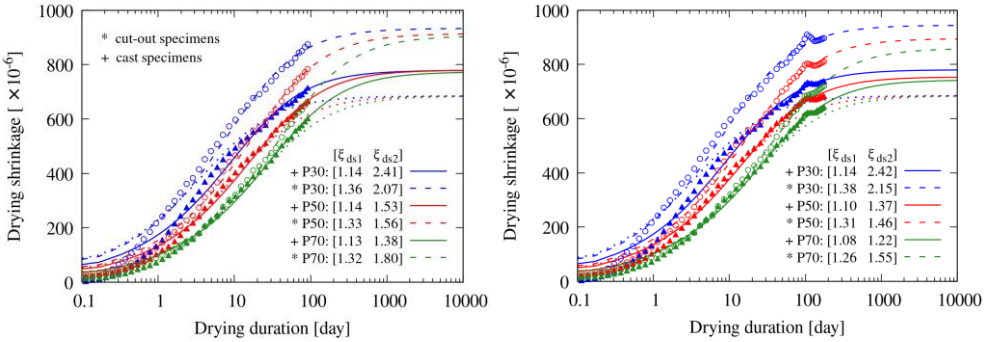


Fig. 5 Prediction of drying shrinkage using calibration coefficients fitted to data obtained over the first 3 months (left) and over 6 months (right) of measurements for cast and cut-out concrete prisms of different sizes. The dotted curves correspond to the drying-shrinkage prediction according to MC2020 with the coefficient values equal to 1.

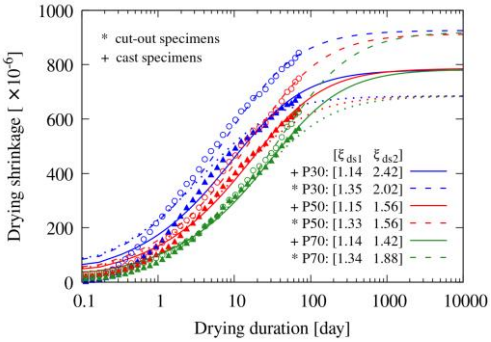


Fig. 6 Prediction of drying shrinkage using calibration coefficients fitted to data obtained over the first 60 days of measurements for cast and cut-out concrete prisms of different sizes.

The possibility of further reduction of the initial measurement period was also examined by fitting drying shrinkage to data obtained over an even shorter period than the required three months. The results shown in Fig. 6 demonstrate that the fitting procedure produced very similar outcomes even when only 60 days of experimental data were used. Naturally, the intention is not to shorten the monitoring period below the prescribed 90 days. The aim was to verify how consistent the prediction remains when calibrated using very short-term data.

3 CONCLUSIONS

This study has evaluated the performance of the new MC2020 calibration approach through experimental verification on both standard-size and small specimens, with the objective of determining whether smaller specimens can reduce the necessary duration of initial measurements while still enabling accurate shrinkage prediction, thereby demonstrating their potential for practical use.

The new calibration methodology introduced in the fib Model Code 2020 represents a significant step forward in shrinkage prediction. Adjusting the model using experimental data enables the specific behaviour of the material to be captured more accurately.

The long duration typically required to obtain a sufficiently representative initial shrinkage development can be reduced by using specimens smaller than the standard 100 × 100 mm size.

The use of smaller specimens requires further examination of the potential size effect, which may influence not only the kinetics but also the ultimate shrinkage value.

The experiment comparing the drying shrinkage of cast and cut-out small specimens revealed several important findings. Shrinkage in cut-out specimens developed more rapidly than in cast specimens, and higher ultimate shrinkage values can be expected.

Cut-out specimens cannot be considered a direct substitute for large structural members when assuming only an accelerated shrinkage development. Current results indicate a substantial difference also in the ultimate shrinkage. Nevertheless, the use of cut-out specimens appears promising, as cutting removes the influence of the near-surface region, where the material composition differs from the core.

Further research is required to obtain more precise conclusions and to assess whether adjustments to the computational model may be justified once the behaviour of cut-out specimens is sufficiently described.

The pilot experiment comparing cast and cut-out specimens is still ongoing, and two additional experimental series with different self-compacting concrete mixtures have already been initiated. These measurements will provide the data necessary for further analysis and for refining the understanding of the shrinkage behaviour of cast and cut-out concrete specimens of different sizes.

Acknowledgements

We gratefully acknowledge the financial support of the Czech Science Foundation under the project 25-17557J and from Student grant competition of Czech Technical University in Prague SGS26/038/OHK1/1T/11.

References

[1] RILEM Technical Committee TC-242-MDC. 2015. “Model B4 for Creep, Drying Shrinkage and Autogenous Shrinkage of Normal and High-Strength Concretes with Multi-Decade Applicability.” *Materials and Structures* 48:753–770. doi:10.1617/s11527-014-0485-2.

[2] Rahimi-Aghdam, Saeed, Bažant, Zdeněk P., and Cusatis, Gianluca. 2019. “Extended Microprestress-Solidification Theory for Long-Term Creep with Diffusion Size Effect in Concrete at Variable Environment.” *Journal of Engineering Mechanics* 145(2):04018131. doi:10.1061/(ASCE)EM.1943-7889.0001559.

[3] fib – International Federation for Structural Concrete. 2021. *fib Model Code 2020 for Concrete Structures*. Lausanne: fib.

[4] European Committee for Standardization (CEN). 2023. *EN 1992-1-1: Eurocode 2: Design of Concrete Structures – Part 1-1: General Rules and Rules for Buildings*. Brussels, CEN.

[5] Shurbert-Hetzel, Cole, Daneshvar, Dana, Robisson, Agathe, and Shafei, Behrouz. 2023. “Data-enabled Comparison of Six Prediction Models for Concrete Shrinkage and Creep.” *Case Studies in Construction Materials* 19(3):e02406. doi: 10.1016/j.cscm.2023.e02406

[6] Dohnalová, Lenka, Šmilauer, Vít, and Havlásek, Petr. 2026. “Influence of Specimen Size on Shrinkage Prediction Using Short-Term Data.” Paper presented at the 15th International Conference Modern Building Materials, Structures and Techniques, Vilnius, Lithuania, May 12–15.

[7] Meyers, Bernard L., Branson, Dan E., and Schumann C. G. 1972. “Prediction of Creep and Shrinkage Behavior for Design from Short Term Tests.” *PCI Journal* 17:29–45.

[8] Bažant, Zdeněk P., and Jirásek, Milan. 2018. *Creep and Hygrothermal Effects in Concrete Structures*. Dordrecht: Springer. doi:10.1007/978-94-024-1138-6.

[9] Šmilauer, Vít, Havlásek, Petr, Dohnalová, Lenka, Wan-Wendner, Roman, and Bažant, Zdeněk P. 2021. “Revamp of Creep and Shrinkage NU Database.” Paper presented at the Biot–Bažant Conference on Engineering Mechanics and Physics of Porous Materials, Evanston, Illinois, USA, June 1–4.

[10] Hammer, Tor A. 1993. “The Maturation of Mechanical Properties of High-Strength Concrete Exposed to Different Moisture Conditions.” *Proceedings of the Third International Symposium on Utilization of High-Strength Concrete*, Lillehammer: Norwegian Concrete Association, 1084–1091.

[11] Neville, Adam M. 2011. *Properties of Concrete.* Harlow: Pearson.

[12] Dohnalová, Lenka, Havlásek, Petr, Šmilauer, Vít, Reiterman, Pavel, and Davidová, Vendula. 2021. “Size Effect on the Ultimate Drying Shrinkage of Cement Mortar: 1-Year Experiment and Numerical Modeling.” *NMM 2020 Nano & Macro Mechanics*, Acta Polytechnica CTU Proceedings 30:1–6.

Shrinkage and Mechanical Performance of Cement Pastes Incorporating Cellulose Nanocrystals

Ali Satar Jaber Al-Askary[ab], Katalin Kopecskó[c]

[a] *Department of Construction Materials and Technologies, Faculty of Civil Engineering, Budapest University of Technology and Economics, Műegyetem rkp. 3., H-1111 Budapest, Hungary.*

[b] *Department of Building and Construction Technologies Engineering, Technical Engineering College - Baghdad, Middle Technical University, Muasker Al Rashid Street, 10074 Baghdad, Iraq*

[c] *Department of Engineering Geology and Geotechnics, Faculty of Civil Engineering, Budapest University of Technology and Economics, BME rkp. 3., H-1111 Budapest, Hungary.*

Summary

This research investigates the influence of sustainable, bio-based cellulose nanocrystals (CNCs) on the performance of three cement types (CEM I R, CEM I N-SR0, CEM II/B-LL). The objective is to evaluate how CNCs modify fresh-state, mechanical, and durability properties. An experimental programme assessed cement pastes incorporating 0.25%, 0.50%, and 0.75% CNC by weight, testing workability, compressive/flexural strength, and drying shrinkage. Results revealed that while CNCs decreased workability, they significantly enhanced mechanical strength by providing nucleation sites that accelerate hydration and refine the pore structure. Furthermore, CNCs effectively mitigated drying shrinkage by acting as internal curing agents. Crucially, a 0.50% dosage was identified as the optimum, balancing substantial strength gains and shrinkage reduction with acceptable flowability. Ongoing research will extend these findings to mortar scales to evaluate superplasticiser integration.

1 INTRODUCTION

Cellulose nanocrystals (CNCs) have recently emerged as a promising class of bio-based additives in cement and concrete technologies. In conventional construction practice, most chemical admixtures are synthesised from non-renewable or energy-intensive chemical sources, which raises concerns regarding environmental impact, long-term sustainability, and carbon footprint [1, 2]. In contrast, CNCs are derived from cellulose, the most abundant biopolymer on Earth, and are characterised by renewability, biodegradability, and low environmental burden [3]. Cellulose can be extracted not only from virgin wood resources but also from a wide range of waste streams, including industrial wood residues [4], agricultural by-products, waste paper [5], and food-processing waste [6]. This availability from secondary resources further strengthens the sustainability potential of CNCs and aligns their use with circular-economy principles in construction materials.

The increasing pressure on the construction sector to reduce greenhouse gas emissions and resource consumption has motivated research into alternative, bio-based materials capable of partially replacing or complementing traditional chemical admixtures. In this context, CNCs have attracted attention due to their unique physicochemical characteristics, such as extremely high specific surface area, high stiffness and tensile strength at the nanoscale, good elasticity, hydrophilicity, and a high density of hydroxyl functional groups on their surface [7, 8]. These hydroxyl groups enhance water affinity and promote interactions with cement hydration products, particularly calcium silicate hydrate (C-S-H), suggesting that CNCs may influence both hydration kinetics and microstructural development in cementitious systems [9].

Systematic research on the application of CNCs in cement-based materials began around 2015 by Cao et al. [10], with early studies primarily focusing on cement paste systems [11]. These initial investigations concentrated on hydration chemistry, calorimetric behaviour, phase evolution, and early-age mechanical performance. As research progressed, CNC incorporation was gradually extended to mortar systems, while studies at the concrete scale remain relatively limited. Although concrete-level

investigations are ultimately required for practical implementation, fundamental understanding at the cement paste scale remains essential. Cement paste studies allow the isolation of CNC–cement interactions without the complexity introduced by aggregates, enabling clearer interpretation of hydration, moisture transport, and microstructural mechanisms before upscaling to mortar and concrete systems.

Despite the growing body of literature on CNC-modified cement pastes, most existing studies have focused on chemical and microstructural evaluation, hydration enhancement, and strength development. In contrast, the influence of CNCs on drying shrinkage, one of the most critical parameters governing cracking susceptibility, dimensional stability, and long-term durability, has received limited and fragmented attention. Shrinkage-related phenomena are particularly relevant in modern cementitious systems, especially those incorporating supplementary cementitious materials or limestone fillers, where changes in pore structure and moisture transport can significantly affect volume stability. Given the hydrophilic nature of CNCs, their ability to retain water, and their interaction with hydration products through surface hydroxyl groups, CNCs may play a dual role in cement paste systems by modifying internal moisture distribution and influencing microstructural refinement. These mechanisms suggest a potential for shrinkage mitigation, particularly at early and intermediate ages, yet systematic experimental evidence across different cement types remains scarce.

This study investigates the effect of CNC incorporation on the shrinkage behaviour of cement pastes produced using three different cement types, including ordinary Portland cement (CEM I) and a limestone-blended cement (CEM II/B-LL). CNCs were incorporated at varying dosages, and the resulting shrinkage behaviour was evaluated up to mid-term ages. To support the shrinkage analysis, fresh-state properties and mechanical performance were also assessed, providing a comprehensive evaluation of CNC influence at the cement paste scale. This contribution represents part of an ongoing PhD research program, with future work focusing on long-term shrinkage, hydration degree quantification, durability performance, and detailed microstructural characterisation.

2 MATERIALS, EXPERIMENTS, AND METHODOLOGIES

CEM I 42.5 R and CEM I 42.5 N-SR0 were supplied by Danucem Kft., while CEM II/B-LL was obtained from Duna-Dráva Kft. The appearance of the three cement types is shown in Fig. 1b. Cellulose nanocrystals (CNCs) were supplied by CelluForce Canada. CNCs were extracted from wood pulp via sulfuric acid hydrolysis, and only dry powder-like products were used in this study (Fig. 1a, left). All aqueous CNC dispersions were prepared in-house following the dispersion procedure described below (Fig. 1a, right).

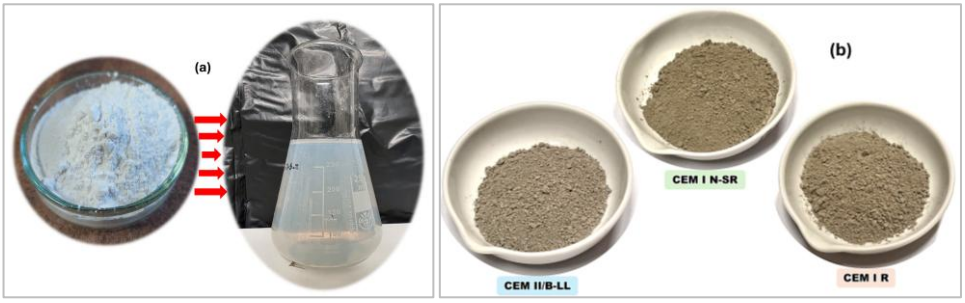


Fig. 1 a) CNCs powder (left) and the dispersed CNCs (right), b) CEM II/B-LL, CEM I N-SR0, and CEM I R

CNC dispersions were prepared by gradually adding the CNC powder to distilled water under gentle stirring, followed by high-shear mixing at 1300 rpm for 10 min. The suspension was then allowed to rest for 5 min, ultrasonicated for 30 min, and rested again for 5 min before being incorporated into the cement mixtures. According to the supplier's data, the CNCs exhibit an average diameter of 2.3–2.4 nm and a length ranging from 44 to 108 nm, as determined by atomic force microscopy (AFM).

Mixing of cement pastes was carried out in accordance with EN 196-1. The mix proportions and sample codes are summarised in Table 1. The reference mixtures for each cement type were denoted as OR, OSR, and OBL for CEM I 42.5 R, CEM I 42.5 N-SR0, and CEM II/B-LL, respectively. CNCs were incorporated at dosages of 0.25%, 0.50%, and 0.75% by weight of cement. The corresponding

mixtures were denoted as CR, CSR, and CBL for CNC-modified CEM I 42.5 R, CEM I 42.5 N-SR0, and CEM II/B-LL pastes, respectively. A constant water-to-cement ratio (w/c) of 0.35 was maintained for all mixtures.

Table 1 Mixture codes and mix proportions for cement paste samples.

Code	Cement (g)	CNC (g)	CNC% by wt. of cement	Water (g)
OR/OSR/OBL	1500	0	0	525
0.25CR/CSR/CBL	1500	3.75	0.25	525
0.50CR/CSR/CBL	1500	7.5	0.50	525
0.75CR/CSR/CBL	1500	11.25	0.75	525

Fresh properties were evaluated using consistency (penetration) and flow table tests in accordance with EN 196-1. Hardened properties, including compressive and flexural strength, were measured at 7 and 28 days following the same standard curing and testing procedures. Drying shrinkage was measured on prismatic specimens with dimensions of 40 × 40 × 160 mm, prepared using shrinkage moulds equipped with stainless-steel pins. Shrinkage measurements were conducted at specimen ages of 3, 7, 14, 28, 48, and 56 days. After demolding, all specimens were stored under curing conditions of 100% relative humidity to prevent premature drying and surface cracking prior to testing. Figure 2 presents an overview of the sample preparation and testing procedures for fresh properties, cured properties, and drying shrinkage.

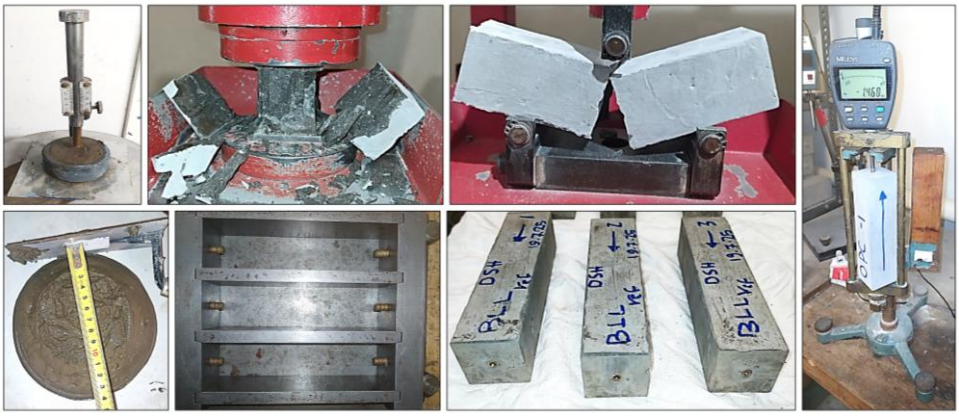


Fig. 2 From left to right: sampling and testing of fresh properties, hardened properties, and drying shrinkage sampling

3 RESULTS AND DISCUSSIONS

Fresh properties of cement pastes incorporating CNCs were evaluated using consistency (penetration) and flow table tests for three cement types, as represented in Fig. 3, where the columns refer to consistency and the line curves refer to flowtable diameters. For all reference pastes, the incorporation of CNCs resulted in a clear reduction in penetration depth with increasing dosage. In the OR system, penetration decreased from 40 mm to 26 mm at 0.75% CNC, corresponding to a reduction of approximately 35%. A similar reduction was observed for OSR paste, where penetration decreased by about 33%. The most pronounced effect was recorded for the limestone cement system (0.75CBL), where penetration was reduced by 50%. Flow table results exhibited the same trend. For OR paste, the flow diameter decreased from 23.25 cm to 14 cm, representing a reduction of approximately 40%. In

the OSR paste, the flow diameter decreased from 19.87 cm to 13.35 cm (33% reduction), while the OBL paste decreased from 17.75 cm to 12.9 cm (27% reduction). Across all cement types, increasing CNC content consistently reduced flowability. The reduction in workability is primarily attributed to the high specific surface area and hydrophilic nature of CNCs, which promote water adsorption and reduce the availability of free water for flow. Additionally, the abundance of hydroxyl groups on CNC surfaces enhances physical interactions with cement particles, leading to increased cohesion and viscosity of the fresh paste, which is confirmed by Montes et al. [12]. The stronger reduction observed in the limestone cement system suggests that the presence of fine limestone particles intensifies water demand and amplifies the effect of CNC incorporation [13].

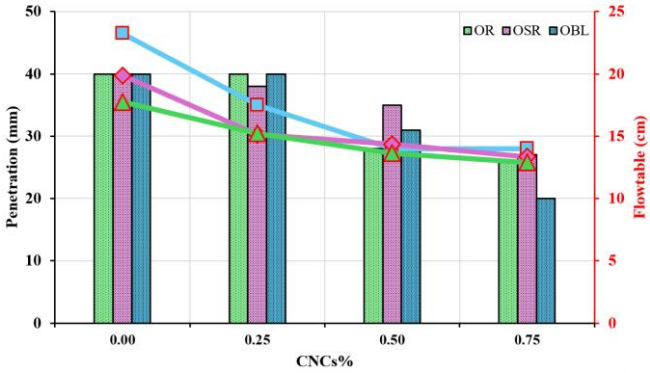


Fig. 3 Effect of CNCs on fresh properties of cement pastes: penetration (bars, left axis) and flow diameter (lines, right axis)

Fig. 4 presents the compressive and Fig. 5 presents the flexural strength development of cement pastes incorporating CNCs at 7 and 28 days. For all cement types, CNC addition resulted in a clear enhancement of mechanical performance, with the degree of improvement dependent on dosage and cement composition. In ordinary OR, compressive strength increased from 65.22 MPa at 28 days for the reference paste to 79.79 MPa and 81.57 MPa at 0.50% and 0.75% CNC, corresponding to improvements of approximately 22% and 25%, respectively. The trend agrees with the results of Al-Askary et al. [14], who reported compressive strength improvements of 20-35% in CNC-modified cement systems. Similar behaviour was reported by Lee et al. [15], who observed a 24% increase in compressive strength at 28 days for cement pastes incorporating 0.8% CNCs, and by Nassiri et al. [16], who reported a 21% strength enhancement at an optimal CNC dosage of 0.40%. For OSR, the highest compressive strength was achieved at 0.50CSR, reaching 88.68 MPa at 28 days, representing an increase of approximately 19% compared to the reference. At higher CNC content (0.75%), compressive strength decreased to 83.23 MPa, indicating the presence of an optimal dosage. This dosage-dependent behaviour is consistent with the findings of Fu et al. [17], who reported optimal CNC contents between 0.5% and 1.0% for maximising strength development in cement paste systems. In limestone cement (OBL), compressive strength increased from 65.04 MPa to 75.11 MPa at 0.75CBL, corresponding to an improvement of approximately 15%. This behaviour is consistent with the structural classification of CEM II/B-LL binders reported by Elisa et al. [18], where strength development remains effective despite limestone substitution. The accompanying reduction in workability suggests that CNC-induced water adsorption and viscosity enhancement contribute to a denser microstructure, explaining the concurrent strength improvement. Specifically, the extremely high specific surface area of the CNCs provides abundant nucleation sites for the precipitation of hydration products, such as calcium silicate hydrate (C-S-H) gel
. This seeding effect accelerates early-age hydration and promotes the filling of capillary pores, ultimately leading to a more refined and less permeable pore structure. Flexural strength (Fig. 5) exhibited more pronounced relative improvements than compressive strength. For OR paste, flexural strength at 28 days increased from 3.21 MPa to 5.12 MPa at 0.75% CNC, corresponding to an increase of approximately 60%. Comparable enhancements in flexural performance were reported by Lee et al. [15], who observed flexural strength increases of up to 58% at 28 days. In OSR paste, flexural strength increased from 2.13 MPa to 2.68 MPa (26%) at 0.50-0.75% CNC, while OBL paste showed an increase from 3.34 MPa to 4.71 MPa (41%), confirming the strong influence of CNCs on crack resistance and

tensile-related properties, further supporting the role of CNCs in enhancing cohesion and crack resistance at reduced fresh-state flowability.

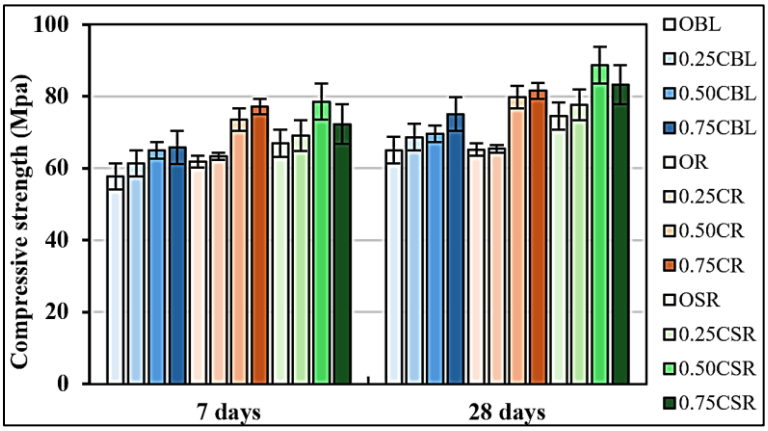


Fig. 4 Compressive strength of cement pastes incorporating different CNC dosages at 7 and 28 days

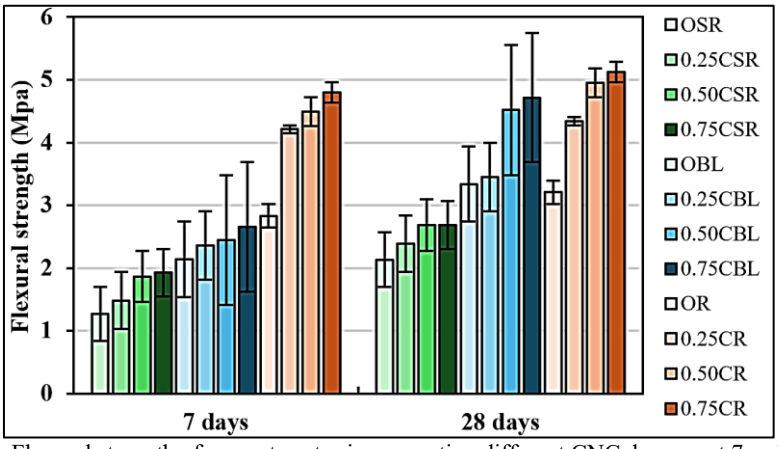


Fig. 5 Flexural strength of cement pastes incorporating different CNC dosages at 7 and 28 days

Fig. 6a illustrates the drying shrinkage evolution of the cement pastes up to 56 days. For all mixtures, shrinkage developed rapidly at early ages and gradually approached stabilisation after approximately 28 days, which corresponds well with the period of intensified moisture mass loss shown in Fig. 6b. The incorporation of CNCs modified both the rate and magnitude of shrinkage, with the response strongly dependent on cement type and CNC dosage. For ordinary Portland, OR, at 56 days, 0.50CR resulted in a systematic reduction in shrinkage, with the most effective mitigation of approximately 21%. This reduction coincided with a noticeable decrease in mass loss, which was reduced from −25.6% in the OR paste to −22.1% at 0.50CR. The simultaneous reduction in mass loss and shrinkage indicates that CNCs effectively limit moisture evaporation, acting as internal curing agents through their hydrophilic surface and high water-retention capacity. Specifically, the abundant hydroxyl groups on the surface of the CNCs absorb water during the initial mixing phase and gradually release it as the surrounding cement paste dries. This slow moisture release promotes the delayed hydration of previously unreacted cement particles and reduces the development of internal capillary stresses, which are the primary drivers of drying shrinkage. Similar dosage-dependent behaviour was reported by Lee et al. [19], who observed a 55% reduction in drying shrinkage at 60 days for cement composites incorporating 0.8% CNC, while higher CNC contents led to reduced efficiency due to dispersion limitations. The SR series, the reference paste, showed lower shrinkage than OR at all ages; however, the incorporation of CNC still resulted in a measurable reduction in shrinkage. At 56 days, shrinkage

decreased to 0.75CSR, approximately 22.6%. Mass-loss measurements showed the lowest than all other cements, indicating reduced moisture evaporation in CNC-modified pastes. Nevertheless, the magnitude of shrinkage reduction was smaller than that observed for OR, suggesting that shrinkage in SR systems is less governed by internal curing effects and more influenced by the reduced C_3A content and slower hydration kinetics, which promote the formation of a denser, less permeable microstructure. This is further supported by the significantly lower mass loss measured for SR pastes, indicating reduced moisture evaporation and capillary stress development [20, 21]. In contrast, limestone cement exhibited a distinctly different response. Although shrinkage decreased by 0.75CBL (12% reduction), the effect was notably weaker than in OR systems. Mass-loss data indicate that CNCs still reduced moisture evaporation in BLL pastes; however, this reduction did not translate into a proportional shrinkage mitigation. This behaviour is consistent with the findings of Blasi et al. [18], who demonstrated that shrinkage in CEM II/B-LL systems is primarily governed by clinker dilution and limestone-controlled pore-structure effects rather than by internal curing mechanisms. As a result, additives that act mainly through water retention, such as CNCs, exhibit limited efficiency in reducing shrinkage in limestone-blended cements. A 0.50% CNC dosage emerges as optimal, delivering 19–22% compressive strength gains and up to 21% shrinkage reduction without the severe 50% flowability loss seen at 0.75%. While applying these paste results to concrete will require superplasticisers to maintain workability, the internal curing of CNCs could provide significant structural benefits by mitigating shrinkage-induced micro-cracking at the interfacial transition zone (ITZ).

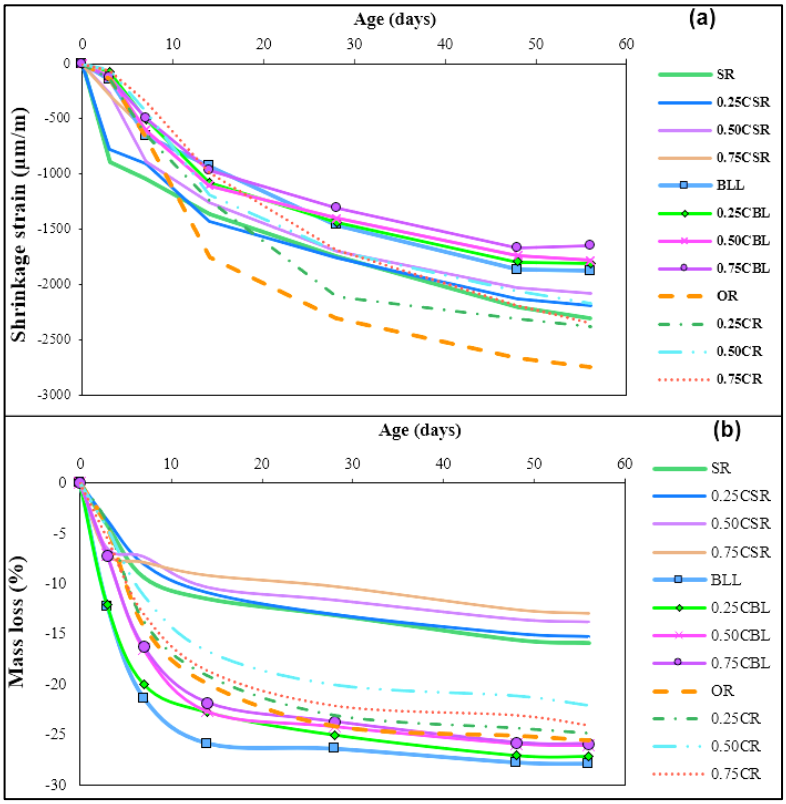


Fig. 6 (a) Drying shrinkage strain and (b) corresponding mass loss of cement pastes incorporating Figures and Tables

4 CONCLUSIONS

This study investigated the fresh, mechanical, and shrinkage behaviour of cement pastes (CEM I 42.5 R, CEM I 42.5 N-SR0, and CEM II/B-LL) modified with cellulose nanocrystals (CNCs). Based on the experimental results, the following conclusions can be drawn:

- Workability and Cohesion: CNC incorporation consistently reduced workability due to high water adsorption, which was most pronounced in the limestone cement series (OBL). However, this viscosity enhancement contributed to improved matrix cohesion and pronounced improvements in flexural strength across all types.
- Compressive Strength and Optimum Dosage: CNC addition enhanced compressive strength for all systems. While optimal strength for some cements was reached at 0.75%, 0.50% by weight serves as the optimal practical dosage. This concentration balances significant compressive strength gains (up to 19% in OSR) and drying shrinkage reduction without the severe flowability loss observed at higher dosages.
- Drying Shrinkage: CNCs effectively mitigated drying shrinkage by acting as internal curing agents that limit moisture evaporation. This reduction was highly efficient in OR and OSR systems, but more limited in OBL pastes where shrinkage is primarily governed by limestone-controlled pore structures rather than internal curing.

CNCs demonstrate high potential as sustainable, bio-based nano-additives. Ongoing research will scale these findings to mortar and concrete systems to specifically evaluate the necessary integration of superplasticisers (to regain workability) and to investigate the potential of CNCs to mitigate shrinkage-induced micro-cracking at the interfacial transition zone (ITZ)

References

1. Al-Askary, Ali, Satar, Jaber; Kopecsko, Katalin, and Oktay, Didem. (2025) Cellulose nanocrystals and their utilization in cement-based composites: A comprehensive review. Case Studies in Construction Materials 23:e05550. https://doi.org/10.1016/J.CSCM.2025.E05550
2. Guo, Aofei; Sun, Zhihui; Sathitsuksanoh, Noppadon; and Feng, Hu. (2020) Review a review on the application of nanocellulose in cementitious materials. Nanomaterials 10:1–25. https://doi.org/10.3390/nano10122476
3. George, Johnsy, and Sabapathi SN. (2015) Cellulose nanocrystals: synthesis, functional properties, and applications. Nanotechnol Sci Appl 8:45. https://doi.org/10.2147/NSA.S64386
4. Couret, Laetitia; Irle, Mark; Belloncle, Christophe, and Cathala, Bernard. (2017) Extraction and characterization of cellulose nanocrystals from post-consumer wood fiberboard waste. Cellulose 2017 24:5 24:2125–2137. https://doi.org/10.1007/s10570-017-1252-7
5. Nasir, Muhammad; Aziz, Muhammad Arif, and Zubair, Mukarram et al. (2022) Engineered cellulose nanocrystals-based cement mortar from office paper waste: Flow, strength, microstructure, and thermal properties. Journal of Building Engineering 51:104345. https://doi.org/10.1016/j.jobe.2022.104345
6. Abbas, Mazhar; Hussain, Tariq, and Arshad, Muhammad et al. (2024) Agricultural waste-derived cellulose nanocrystals for sustainable active food packaging applications. Food Hydrocoll 154:110141. https://doi.org/10.1016/j.ijbiomac.2019.08.153
7. Trache, Djalal; Hussin, M. Hazwan; Haafiz, M. K.Mohamad, and Thakur, Vijay Kumar. (2017) Recent progress in cellulose nanocrystals: sources and production. Nanoscale 9:1763–1786. https://doi.org/10.1039/C6NR09494E
8. Habibi, Youssef; Lucia, Lucian A., and Rojas, Orlando J. (2010) Cellulose nanocrystals: Chemistry, self-assembly, and applications. Chem Rev 110:3479–3500. https://doi.org/10.1021/CR900339W/ASSET/CR900339W.FP.PNG_V03
9. Bai, Shuai; Guan, Xinchun; Li, Hui, and Ou, Jinping. (2023) Effect of nanocellulose on early hydration and microstructure of cement paste under low and high water-cement ratios. Constr Build Mater 409:133963. https://doi.org/10.1016/J.CONBUILDMAT.2023.133963
10. Li, Wengui; Huang, Zhengyu, and Cao, Fangliang et al. (2015) Effects of nano-silica and nano-limestone on flowability and mechanical properties of

ultra-high-performance concrete matrix. Constr Build Mater 95:366–374. https://doi.org/10.1016/J.CONBUILDMAT.2015.05.137

11. Al-Askary, Ali,Satar, Jaber, and Kopecsko, Katalin. (2024) Role of Cellulose Nanocrystals and Their Utilization in Cement-Based Composites. In: György L. Balázs, Sólyom Sándor, Foster Stephen (eds) 15th fib International PhD Symposium in Civil Engineering. International Federation for Structural Concrete (fib), Budapest, pp 577–584
12. Montes, Francisco, Fu, Tang, Youngblood JP, Weiss, Jason. (2020) Rheological impact of using cellulose nanocrystals (CNC) in cement pastes. Constr Build Mater 235:117497. https://doi.org/10.1016/j.conbuildmat.2019.117497
13. Pipilikaki P, and Beazi-Katsioti M. (2009) The assessment of porosity and pore size distribution of limestone Portland cement pastes. Constr Build Mater 23:1966–1970. https://doi.org/10.1016/j.conbuildmat.2008.08.028
14. Al-Askary, Ali, Satar, Jaber; and Oktay, Didem; Kopecskó, Katalin. (2025) Utilization of cellulose nanocrystal as a bio-based material and nanosilica in cement-based systems: A comparative study. Structural Concrete 2025:1–26. https://doi.org/10.1002/SUCO.70206
15. Lee, Hyung Joo, and Kim Woosuk. (2020) Long-term durability evaluation of fiber-reinforced ECC using wood-based cellulose nanocrystals. Constr Build Mater 238:117754. https://doi.org/10.1016/j.conbuildmat.2019.117754
16. Nassiri, Somayeh; Chen, Zhen; Jian, Guoqing et al. (2021) Comparison of unique effects of two contrasting types of cellulose nanomaterials on setting time, rheology, and compressive strength of cement paste. Cem Concr Compos 123:104201. https://doi.org/10.1016/j.cemconcomp.2021.104201
17. Fu, Tang; Montes, Francisco; Suraneni, Prannoy et al. (2017) The influence of cellulose nanocrystals on the hydration and flexural strength of Portland cement pastes. Polymers (Basel) 9:. https://doi.org/10.3390/polym9090424
18. Blasi, Elisa; Mobili, Alessandra, and Choorackal, Eldho et al. (2025) Valorisation of Limestone in Sustainable Cements. Sustainability 2025, Vol 17, Page 2402 17:2402. https://doi.org/10.3390/su17062402
19. Lee, Hyung Joo; Kim, Seung Ki; Lee, Heon Seok, and Kim Woosuk. (2019) A Study on the Drying Shrinkage and Mechanical Properties of Fiber Reinforced Cement Composites Using Cellulose Nanocrystals. Int J Concr Struct Mater 13:. https://doi.org/10.1186/s40069-019-0351-2
20. Ke, Guoju; and Zhang, Jun, and Liu, Yuzhang. (2022) Shrinkage characteristics of calcium sulphoaluminate cement concrete. Constr Build Mater 337:127627. https://doi.org/10.1016/j.conbuildmat.2022.127627
21. Liu, Hui; Lin, Hui; Liu, Xiaoyong et al. (2021) Effects of triethanolamine on autogenous shrinkage and drying shrinkage of cement mortar. Constr Build Mater 304:124620. https://doi.org/10.1016/j.conbuildmat.2021.124620

Assessment of corrosion effects on the residual capacity of post-tensioned concrete road bridges

Aleš Mezera, Milan Holý, Petr Kněž

Klokner Institute,
Czech Technical University in Prague,
Solinova 7, Prague - 160 00, Czech Republic

Summary
The article deals with the assessment of the influence of corrosion on the residual load-bearing capacity of post-tensioned concrete road bridges from the second half of the 20th century, which were often operated without proper maintenance and show signs of degradation due to long-term leakage and corrosion of reinforcement and prestressing reinforcement. The subject of the work is a case study of a bridge from 1964 made of prefabricated KA73 beams with a span of 15 m, with the analysis focusing on the edge beam as the most exposed element. Nonlinear analysis was used to model the deterioration of the structure due to corrosion initiated by chloride penetration into the concrete, considering different chloride diffusion rates and corrosion ranges based on the results of extensive diagnostic surveys. The residual load-bearing capacity of the beam is determined for individual scenarios, which serves as a foundation for an objective assessment of the actual condition of the structure and decisions regarding its further operation or renovation.

1 INTRODUCTION

In the second half of the 20th century, a large number of road bridges made of post-tensioned concrete were built in Central Europe, often using prefabricated beams [15]. At the time of their construction, these structures represented an effective and economical solution for crossing medium spans, but a significant part of them is now past half of their designed service life. Long-term operation without systematic inspection and maintenance leads to the development of degradation processes, primarily corrosion of reinforcement and prestressing reinforcement, and can negatively affect the reliability of the structure [16].

Corrosion of prestressing reinforcement is a serious problem, especially in post-tensioned bridges, as it can lead to a loss of prestressing force, changes in deformation behavior, and a decrease in the residual load-bearing capacity of the structure. Older bridges are also often affected by technological deficiencies from the time of construction, such as insufficient grouting of cable ducts, which, combined with long-term exposure to moisture and de-icing salts, significantly increases the risk of degradation and corrosion. Bridge collapses in Europe, including the Troja footbridge in the Czech Republic, have raised concerns about the condition of prestressed bridges. As a result, many diagnostic surveys and recalculations of the load-bearing capacity of prestressed bridge structures have been carried out in the Czech Republic in recent years, which we are now able to evaluate collectively.

2 CONCRETE DEGRADATION PROCESSES

Concrete degradation processes are one of the main factors affecting the long-term durability and reliability of concrete structures. Some of the most significant are concrete carbonation and chloride penetration, which can result in the depassivation of steel reinforcement and subsequent corrosion. The main factor in the corrosion of steel reinforcement is loss of cross-section. This loss of cross-section leads to a reduction in the mechanical properties of the prestressing reinforcement (strength, ductility, etc.). Weakening of the prestressing reinforcement can lead to loss of prestressing force, cracking, and deformation. These problems shorten the overall (residual) service life of the structure.

2.1 CARBONATION OF CONCRETE

Concrete carbonation is a chemical process that can result in corrosion of steel reinforcement. Corrosion is an electrochemical process involving anodic and cathodic reactions. Under normal circumstances, steel reinforcement in concrete is protected by a thin passive layer of oxides formed due to the high alkalinity (pH ~ 13) of the pore solution [2]. The basic principle of concrete carbonation is the

penetration of carbon dioxide into concrete, which reacts with calcium hydroxide and turns into calcium carbonate and water.

$$CO_2 + Ca(OH)_2 \rightarrow CaCO_3 + H_2O \quad (1)$$

Calcium hydroxide in concrete works as an alkalinity carrier (prevents pH changes). Due to the change to calcium carbonate, an alkaline environment is not provided in the concrete and the steel changes from a passive to an active state (pH < 9). As a result of carbonation and subsequent corrosion, the prestressing reinforcement is weakened (loss of cross-section).

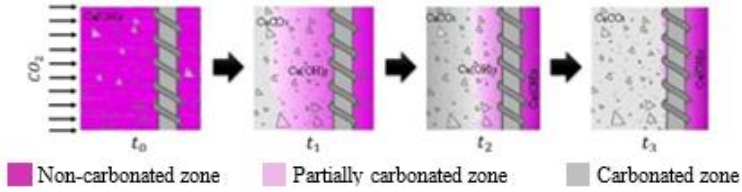


Fig. 1 Schematic representation of the carbonation of concrete. Adapted from [9]

2.2 PENETRATION OF CHLORIDE IONS

Chloride ions penetrate concrete in several ways, including capillary absorption, diffusion, and penetration through the pore system. The speed of this process is influenced by several factors, primarily the water coefficient of concrete and the presence of cracks, which significantly accelerate transport [2]. However, chloride ions can locally damage this passive layer even when the pH remains high. The trigger for corrosion is the attainment of a critical ratio of chloride and hydroxide ion concentrations on the surface of the reinforcement [6], [10].

The process of chloride-induced corrosion can be divided into two phases. The first is the initiation phase, in which aggressive substances such as chloride ions penetrate the concrete cover layer to the surface of the steel reinforcement. The second phase is the propagation phase (Fig. 2), which begins after a critical concentration of these substances is reached in the reinforcement (depassivation of the reinforcement). In this phase, an active electrochemical corrosion process takes place, leading to the formation of corrosion products, a reduction in the cross-section of the reinforcement, and subsequent cracking and spalling of the concrete [2]. Predicting the initiation phase is the most effective preventive step, as it allows you to influence the concrete mix design or the thickness of the cover layer. A crack with a width of 0.1 mm can reduce the length of the initiation phase by approximately 3 times [8].

Unlike uniform corrosion caused by carbonation, chloride-induced corrosion is typically uneven and localized. It occurs itself as pitting corrosion, which causes rapid material loss in small areas [11]. This non-uniformity is mainly caused by two factors: the variable distance between the steel surface and the outer surface of chloride-contaminated concrete, and local inhomogeneities at the steel-concrete interface, such as differences in concrete porosity or metallurgical defects on the steel surface [3].

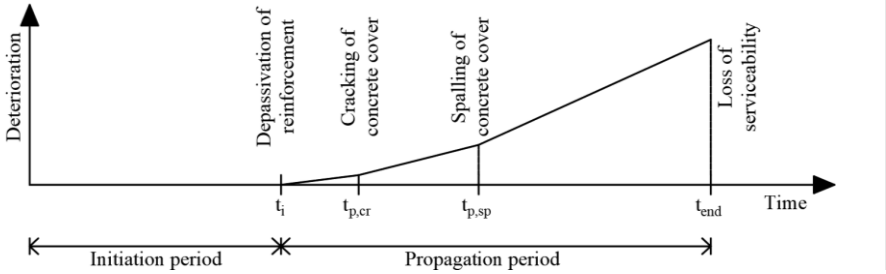


Fig. 2 Initiation and propagation periods [7]

Many prediction models for the service life of reinforced concrete structures are based on Fick's second law of diffusion, which describes non-stationary mass transport [1]. Mathematically, this law is expressed by a partial differential equation:

$$\frac{\partial C}{\partial t} = D\frac{\partial^2 C}{\partial x^2}, \quad (2)$$

where C is the chloride concentration [kgm^{-3}], t is time [s], D je is the diffusion coefficient (defines the amount of substance that passes through a unit area in a given time) depending on the properties, age of the concrete, and cracks [m^{2}s^{-1}] and x is the penetration depth (distance from the surface) [m].

The principle of these models is based on modeling the penetration of chlorides through the concrete cover layer. Corrosion initiation is defined as the moment when the chloride concentration on the surface of the reinforcement reaches a critical limit. The critical chloride limit for prestressed concrete is defined in [14] as 0.2% of the cement weight. The time to corrosion initiation is then the key output of these models [1].

3 NUMERICAL ANALYSIS

Numerical analysis was performed using non-linear software, which allows predicting the effect of carbonation and chloride ions penetration. The depth of carbonation is calculated in non-linear software according to [12] depending on the effective diffusivity of CO_2, the composition of the concrete mix, and moisture. Chloride corrosion is modeled in the software using the error function e*rf* and the scaling function f(w), which modifies the diffusion of chloride ions depending on the width of cracks in the concrete.

This study focused on comparing the load-bearing capacity of an additional prestressed KA beam that is not affected by chlorides (only carbonation) – the reinforcement is not corroded. In the second case, the beam was analyzed with the influence of chloride ions. The load-bearing capacity was analyzed using a 4-point bending simulation.

The software methodology focuses on determining the moment of reinforcement depassivation, which is a key point for predicting the overall service life of a structure t_l. All calculations and outputs in the software system are related to the initial time $t_0 = 0$. The overall service life is defined as the sum of phases [8]:

$$t_l = t_c + t_i + t_p + t_r, \tag{3}$$

where t_c is construction phase, t_i is initiation phase, t_p is propagation period and t_r is post-repair period.

3.1 NUMERICAL MODEL

Numerical analysis was performed for one post-tensioned KA73 beam with a length of 14.96 m and a span of 14.4 m. Concrete of class B500 (corresponding to C35/45) was used for the precast beams. The joints between the beams are made of concrete class B330 (C20/25). Mild reinforcement is of class 10 425(V) and 4.5 mm diameter plain patented wires were used as prestressing reinforcement, the number of wires in each cable (tendon) can be seen in Figure 3 and Figure 4. The beams were longitudinally made of 3 segments and thus contain 2 unreinforced transverse joints of 20 mm width filled with mortar.

The beam was designed using solid elements, including transverse joints without concrete reinforcement. The numerical model includes concrete reinforcement and prestressing reinforcement. The input material characteristics of the beam used for the numerical analysis are shown in Tables 1 and 2. For the material model of steel reinforcement, a bilinear working diagram of steel with hardening was considered.

Table 1 Input material characteristics for numerical analysis – concrete

	E [GPa]	ν [-]	f_{cm} [MPa]	f_{ctm} [MPa]
KA 73/15	34	0.2	43	3.2
Transverse Joint	30	0.2	28	2.2

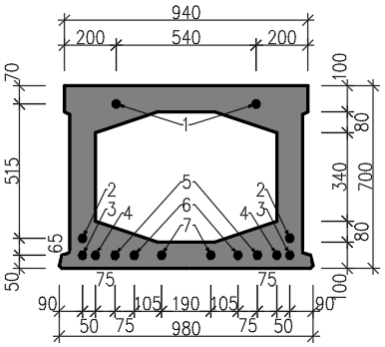
E – Young´s modul of elasticity
ν – Poissonn´s ratio
f_{cm} – mean value of compressive strength
f_{ctm} – mean value of tensile strength

Table 2 Input material characteristics for numerical analysis – steel

	E [GPa]	f_{yk} [MPa]	ε_{uk} [-]	k [-]

Reinforcement 10 425(V)	200	410	0.05	1.08
Patented wire PD 4.5	195	1262	0.05	1.08

f_{yk} – characteristic yield strength
ε_{uk} – characteristic value of ductility ($\varepsilon_{ud} = 0.9\varepsilon_{uk}$)
k – ratio $f_{pk}/f_{p0,1k}$ (f_{pk} – guaranteed ultimate strength ; $f_{p0,1k}$ – yield strength)



Cable	
1	2x6ø4.5
2	2x12ø4.5
3	2x12ø4.5
4	2x12ø4.5
5	2x12ø4.5
6	2x12ø4.5
7	2x6ø4.5

Fig. 3 Position of prestressing reinforcement in cross section –midspan (left); number of wires in individual bundles – cables (right) [5]; (dimensions in mm)

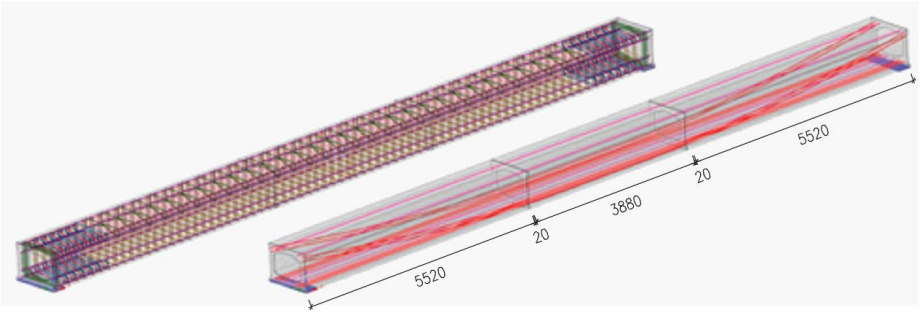


Fig. 4 Numerical model of a KA beam with visible concrete reinforcement (left); prestressing reinforcement (right); (dimensions in mm)

3.2 BEAM WITHOUT CHLORIDE CORROSION

For the reference calculation, an analysis of the beam without chloride effects was performed. In this case, the degradation of the beam was caused by the carbonation process. The results were evaluated for a time of 50 years (half of the design life of the beam) for a quasi-static load combination. Figure 5 shows the stress in the prestressing reinforcement. Even though the yield strength was exceeded, the structure did not collapse. Figure 6 shows the main compressive stress in the concrete, with a maximum value of 39 MPa in the center of the span in the upper slab of the beam. The maximum deflection of the beam in the middle of the span was evaluated at 5.7 mm (Figure 7), and the detail of the joint opening during deflection is shown in Figure 8.

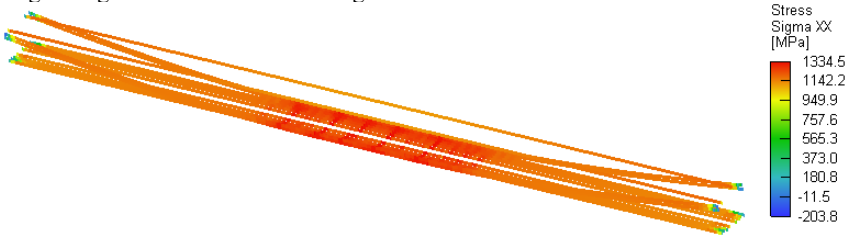


Fig. 5 Stress in prestressing reinforcement under loading corresponding to a quasi-static load combination at an age of 50 years

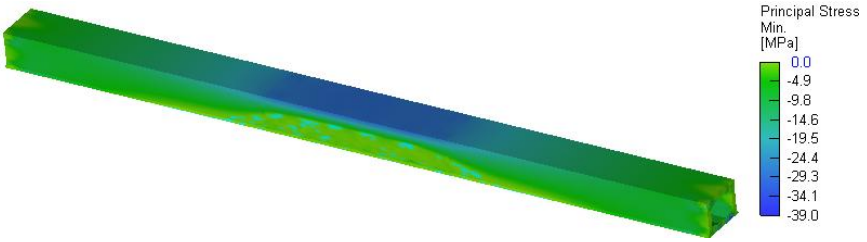


Fig. 6 Main compressive stress in concrete under loading corresponding to quasi-static load combination at an age of 50 years

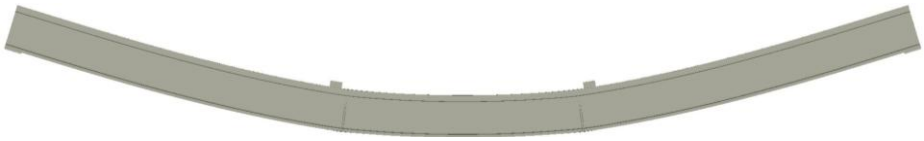


Fig. 7 Beam deflection of 5.7 mm under a load corresponding to quasi-steady load combination at 50 years of age (100x zoom)

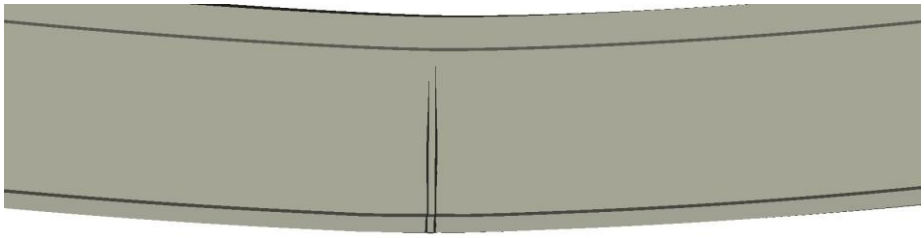


Fig. 8 Detail of joint opening (opening width approx. 0.8 mm under load corresponding to quasi-steady load combinationat 50 years of age)

3.3 BEAM WITH CHLORIDE CORROSION

This chapter describes the numerical analysis of post-tensioned beam exposed to degradation caused by carbonation and the effects of chloride ions. Two variants were selected as values for the diffusion coefficient of chloride ions for the numerical analysis: D_1 = 2.0e-13 m^2s^{-1} a D_2 = 2.5e-13 m^2s^{-1}. The chloride penetration was applied to the model through the bottom and one vertical surface of the beam; these application surfaces are shown in Figure 9.

The main subject of the analysis was to determine the corrosion weakening of the prestressing reinforcement area because of chloride ions. The effect of reduced ductility with increasing corrosion loss was not considered in this analysis. From the point of view of the analyzed beam, the weakening of the prestressing reinforcement area is the factor with the greatest impact on the residual load-bearing capacity.

In the first case (calculated with D_1), corrosion loss of approximately 26% was evaluated. In the second case (for D_2), corrosion loss was approximately 32%. The article shows only the results for the second case with a higher diffusion coefficient; the results of all analyses are summarized in the final Table 3.

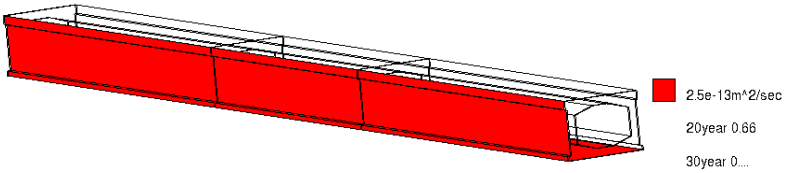


Fig. 9 Applied effect of chloride ions in the computational model (red surfaces)

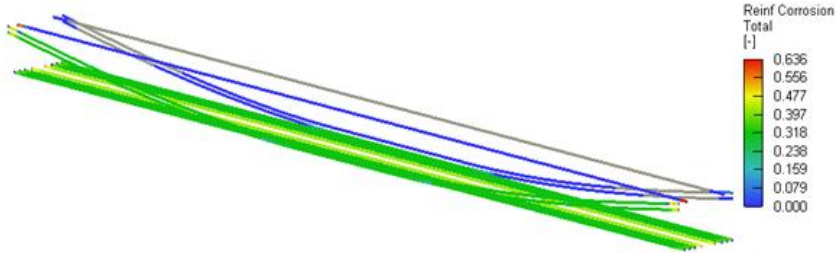


Fig. 10 Corrosion loss of prestressing reinforcement after 50 years of chloride exposure

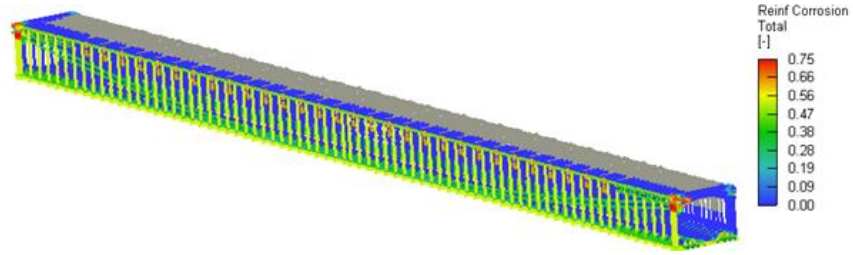


Fig. 11 Corrosion loss of all reinforcement after 50 years of chloride exposure

Figure 10 shows a weakening of the prestressing reinforcement area by approximately 32% (simplified, it can be assumed that the bending capacity of the cross-section will decrease by approximately the same value due to this weakening). Figure 11 shows that the weakening of the concrete reinforcement is around 46%. The resulting average chloride concentration in the cover layer was evaluated as 0.96% of the cement weight. In the anchor areas directly exposed to chloride, a local concentration of up to 2.26% was calculated. The anchor areas were not further addressed due to the assumption of functioning cohesion due to grouting.

4 DISCUSION

Numerical analysis of the prestressed KA beam after 50 years of operation showed that corrosion loss of reinforcement area (26% for variant I and 32% for variant II) caused by a combination of chlorides and carbonation leads to a decrease in stiffness and an increase in vertical deflection from the original value of 5.7 mm to 12.3 mm (an increase of 116%). Although the yield strength of the reinforcement was exceeded in all simulated scenarios due to the load, the nonlinear calculation in the software did not confirm total failure or collapse of the structure, with the main compressive stresses in the concrete around 38 MPa. The analysis, using a bilinear working diagram of steel with reinforcement, focused primarily on the effect of reducing the cross-sectional area of the prestressing reinforcement, which emphasizes the key influence of geometric degradation on the deformation characteristics of the beam.

Table 3 Summary of numerical analysis

	Corrosion loss PD 4.5	Corrosion loss 10 425(V)	Displacement u_z [mm]	Chloride concentration [-]
Beam without chlorides	0	0	5.7	0
Beam with corrosion I (D_1 = 2e-13 m^2s^{-1})	0.26	0.46	10.6	0.0083
Beam with corrosion II (D_2 = 2.5e-13 m^2s^{-1})	0.32	0.50	12.3	0.0096

Further analyses are currently being finalized, focusing on the global behavior of the entire bridge structure, which consists of 10 KA beams connected by hinge joints, and will take into account the interaction of these beams when only one beam is weakened.

The maximum corrosion loss of prestressing reinforcement in the numerical simulation was evaluated as a 32% weakening of the reinforcement area (the usual weakening of prestressing reinforcement in these structures is around 10% based on visual inspection of the reinforcement using destructive probes). The maximum chloride concentration in the simulation was 0.96% at a depth of 0–15 mm. Below is a comparison with the actual chloride content values from diagnostic surveys of nine bridge structures made of KA girders with an average age of 47 years. The measured values from actual structures generally show lower chloride concentrations, which is most likely due to the fact that the structures are actually exposed to chloride ions mainly in winter, while in the numerical analysis, the effect of chlorides was simulated continuously. Nevertheless, one of the diagnosed bridges achieved a similar value to that from the numerical simulation ~ 0.9% (Figure 12).

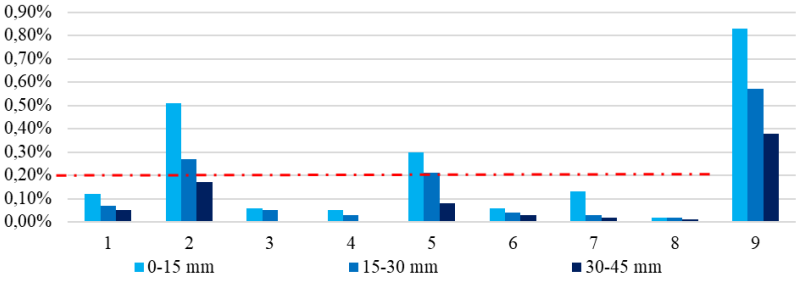


Fig. 12 Evaluation of chloride concentrations on bridge structures made of KA beams at various depths of the covering layer

5 CONCLUSION

The article presented the possibility of simulating the effect of chloride ions on post-tensioned prefabricated bridge beams. A parametric study was performed in the non-linear software using the example of KA73 type beams, which were widely used in the Czech Republic in the second half of the last century for the construction of road bridges. The study simulated three different cases of environmental impact and evaluated the effect on the corrosion state of the prestressing reinforcement over time. In the first case, a beam without the effect of chloride ions was simulated, with only the effect of carbonation. The remaining two cases also included the effect of chloride ions with different values of the diffusion coefficient, which indicates the rate of chloride ion diffusion in concrete. Finally, a comparison was made with the results of diagnostic surveys of actual structures.

Numerical analysis has shown that corrosion weakening of prestressing reinforcement, caused by chloride ions and the effect of prestressing force losses over time can theoretically cause an increase in deflection of more than 100% and a joint opening of 0.8 mm at a load corresponding to quasi-static load combination at an age of 50 years when the cross-sectional area of the reinforcement decreases by 32%. However, this effect would not appear to the same extent in an actual structure, because the global interaction of the beams would significantly reduce the effect of the weakening of a single beam, and the effect of deformation might not indicate corrosion damage to the reinforcement during a visual inspection. Further research will therefore focus on this global interaction of beams, and the analysis of degradation processes will be performed on a global model of the bridge, where interaction will be ensured.

Acknowledgements

The study has been supported by the Czech Technical University in Prague under Grant SGS25/113/OHK1/2T/31. Findings of Grant 24-10892S supported by the Czech Science Foundation has been utilised when developing a numerical model of the concrete bridge.

References

[1] Gettu, Ravindra, Pillai, Radhakrishna, Santhanam, Manu; Rathnarajan, Sundar; Basavaraj, Anusha; Raju, Sripriya; and Dhandapani, Yuvaraj. 2019. Service Life and Life-Cycle

Assessment of Reinforced Concrete with Fly ash and Limestone Calcined Clay Cement. International Conference on Durability of Concrete Structures. 1.

[2] Hu, Jiyue, Chen, Xu, Zhang, Shisun, and Wngui Li. 2024. A review on corrosion detection and protection of existing reinforced concrete (RC) structures, Construction and Building Materials, Volume 325, 126718, ISSN 0950-0618, https://doi.org/10.1016/j.conbuildmat.2022.126718.

[3] Korec, Evžen, Jirásek, Milan, Wong, Hong and Martínez-Pañeda, Emilio. 2023. Phase-field chemo-mechanical modelling of corrosion-induced cracking in reinforced concrete subjected to non-uniform chloride-induced corrosion, Theoretical And Applied Fracture Mechanics. https://doi.org/10.1016/j.tafmec.2023.104233

[4] Vítek, Jan. 2016. Historie předpjatého betonu (History of prestressed concrete, in Czech), ISBN 978-80-87438-84-8.

[5] Konštrukcie cestných a diaľničných mostov z prefabrikátov KA-73 dľžky 9-12-15-18 m. 1973. (Construction of road and highway bridges from KA-73 prefabricated elements with lengths of 9-12-15-18 m, in Slovak), Dopravoprojekt Bratislava.

[6] Alonso, Cruz, Andrade, Carmen, Castellote, Marta, and Castro, Pedro. 2000. Chloride threshold values to depassivate reinforcing bars embedded in a standardized OPC mortar, Cement and Concrete Research, 30(7):1047-1055 https://doi.org/10.1016/S0008-8846(00)00265-9

[7] Hajkova, Karolína, Šmilauer, Vít, Jendele, Libor, and Červenka, Jan 2018. Prediction of reinforcement corrosion due to chloride ingress and its effects on serviceability, Engineering Structures, Volume 174, Pages 768-777, ISSN 0141-0296, https://doi.org/10.1016/j.engstruct.2018.08.006.

[8] Červenka, Vladimír, Jendele, Libor, and Červenka, Jan. 2025. ATENA Program Documentation, Theory, Prague.

[9] Emerson, Felix, Rogério, Carrazedo, and Edna, Possan. 2017. Parametric analysis of carbonation process in reinforced concrete structures through Artificial Neural Networks. 7. 302-316.

[10] Gouda, Venice. 1970. Corrosion and corrosion inhibition of reinforcing steel I. immersed in alkaline solutions. British Corrosion Journal. 5(5):198-203. doi:10.1179/000705970798324450

[11] Wong, H. S., Zobel, M., Buenfeld, N. R., & Zimmerman, R. W. 2009. Influence of the interfacial transition zone and microcracking on the diffusivity, permeability and sorptivity of cement-based materials after drying, Magazine of Concrete Research, ISSN:0024-9831

[12] Papadakis, Vagelis, and Tsimas, Stamatis. 2002. "Supplementary Cementing Materials in Concrete. Part I: Efficiency and Design." Cement and Concrete Research 32(10): 1525–1532.

[13] *fib Bulletin No. 34 Model Code for Service Life Design*. 2006. Lausanne, Switzerland: International Federation for Structural Concrete *(fib)*

[14] ČSN EN 206+A2 Beton – Specifikace, vlastnosti, výroba a shoda. 2021. (Concrete – Specification, performance, production and conformity, in Czech), Pragu: ÚMNZ

[15] Řeháček, Stanislav, Čítek, David, Holý, Milan, Kryštov, Martin, Čítek, Adam, Mezera, Aleš. 2025. Diagnostic Survey of prestressed concrete bridges in Prague. *Civil and Environmental Engineering*, *0*(0). https://doi.org/10.2478/cee-2026-0049

[16] Ponechal, Radoslav, Koteš, Peter, Michálková, Daniela, Kraľovanec, Jakub, and Bahleda, František. 2021. Effect of Water Condensate on Corrosion of Wires in Ungrouted Ducts. Materials 14, 7765. https://doi.org/10.3390/ma14247765

Techniques for Measuring CO_2 Sequestration in Concrete: A Review of Key Methods

Muhammad Akbar Rafique, Amandeep Singh Sidhu, Flora Faleschini, Carlo Pellegrino

Department of Civil, Environmental and Architectural Engineering,
University of Padova,
Via Francesco Marzolo 9, 35131, Padova, Italy

Summary
Concrete production is a significant source of CO_2 emissions, especially the cement manufacturing process. To address this challenge, many studies focus on the process of capturing and storing CO_2 within concrete to reduce the carbon footprint of the construction industry. The present review focuses on various methods for measuring carbon sequestration in concrete. This study reviews and compares methods for measuring CO_2 uptake in concrete. Experimental techniques, including both qualitative and quantitative methods such as thermogravimetric analysis (TGA), X-ray diffraction (XRD), mass gain measurements, phenolphthalein indicator tests, scanning electron microscopy (SEM), ultrasonic pulse velocity (UPV), Gammadensitometry, Calcimetry, and Fourier transform infrared (FTIR) spectroscopy, are discussed. Analysis of various studies indicated that an integrated approach that couples multiple test methods provides the best understanding of CO_2 sequestration.

1 INTRODUCTION

Carbonation occurs naturally and slowly over the lifespan of a concrete structure. Carbonation can reduce the lifespan of the structure by lowering its pH, primarily by reacting with $Ca(OH)_2$, which is responsible for the high pH of concrete and hence provides protection to the reinforcement present in RCC structures [1]. It is crucial to have accurate carbonation measurements within a reasonable time frame, especially when dealing with older concrete structural samples. Researchers have commonly used accelerated carbonation techniques by exposing concrete specimens to CO_2-rich chambers with controlled CO_2 concentrations, relative humidity, temperature, and pressure [2]. This limited-time carbonation process has been identified as a viable Carbon capture and storage (CCS) method for sequestering carbon in concrete by forming $CaCO_3$ and densifying its microstructure, particularly in the outermost layers [3], without severely affecting the long-term performance, as in the case of natural carbonation of concrete.

Several techniques are available to assess carbonation in concrete, including pH measurement, TGA, UPV, FTIR, and XRD, which are key for detecting carbonation. However, accurate quantification is challenging, as many methods examine only a limited portion of the specimen rather than the bulk material. Each technique has distinct advantages and limitations that must be carefully evaluated for test specimens [4]. This study examines these methods in brief and compares them to provide a comprehensive overview of current carbonation assessment techniques.

2 QUALITATIVE TECHNIQUES

2.1 pH INDICATOR (PI) METHOD

Carbon dioxide penetration causes calcium carbonate to form by reacting with calcium hydroxide in concrete. For carbonation measurement using an indicator, the sample is split into two parts, and a pH indicator solution is sprayed on the split surface to reveal a colour change (see Fig. 1, left). The carbonation depth (minimum, maximum, and average) is then measured with a Vernier caliper [5]. A 1% phenolphthalein solution (1 g phenolphthalein and 99 g [5] ethanol or 1% ethynol+70% ethyl alcohol [6]) serves as the indicator, distinguishing the colourless carbonated zone from the pink high-pH non-carbonated zone to determine the perpendicular carbonation depth from the sample surface [7,8].

Phenolphthalein is the most commonly used indicator, while other indicators such as Thymolphthalein, Tropaeolin O, and Alizarine Yellow R have also been employed [9]. Table 1 presents

the estimated carbonation degree for different pH values. The pH indicator method is convenient and rapid; however, it lacks sufficient accuracy for engineering research requiring precise determination of the concrete carbonation degree. While pH indicators clearly delineate fully carbonated zones, they fail to detect partially carbonated zones [7].

Table 1 Carbonation degree estimation from pH value [2]

pH	Carbonation Degree (%)
< 7.5	100
7.5 – 9.0	-33.33pH + 349.98
9.0 – 11.5	-20pH + 230
> 11.5	0

The pH analysis can be combined with image analysis to more accurately measure carbonation depth as it can vary due to aggregate presence in concrete, therefore depicting maximum and minimum depths of penetration at the borders of carbonated areas. Image analysis software, such as "J Image", can be employed to facilitate measurement of the carbonation depth using various in-built tools [8]. Choi et al. [10] developed a novel image processing technique for easy detection of the carbonation region using a phenolphthalein solution spray and a "green-intensity" image extraction process. The authors demonstrated that simple grayscale or thresholding methods were inaccurate for phenolphthalein-based testing, which relies on colour change. The developed image processing approach successfully detected aggregates with colour similar to the cement paste and correctly identified them as non-carbonated.

2.2 Scanning Electron Microscopy (SEM) and Energy-Dispersive X-ray Spectroscopy (EDS) Analysis

The SEM technique is a qualitative method used to observe carbonation in concrete samples by examining the formation of carbonates ($CaCO_3$) [11] or, in some cases, by observing the denser microstructure and increased porosity of the CSH gel resulting from decalcification of the cement matrix [12]. The contrast of the SEM image for carbonated samples is expected to be brighter than that of the reference uncarbonated cement sample due to the formation of various calcium-carbonate polymorphs, which intermix with the silica gel [13]. SEM analysis can provide information on C–S–H gel modification due to carbonation, even when the direct formation of crystalline carbonates is not observed through the EDS spot analysis of the C–S–H gel. Additionally, carbonated cement paste appears finer in texture in SEM micrographs [14]. Jafari and Dorafshan [12] also suggested that EDS (elemental analysis) can be used to identify carbonation in samples by measuring increases in calcium and oxygen content. These EDS observations from the sample can be verified and supported by other techniques, such as thermogravimetric analysis and X-ray diffraction (XRD) [14]. Fig. 1 (right) shows the carbonated SEM micrograph and the EDS analysis of the concrete sample.

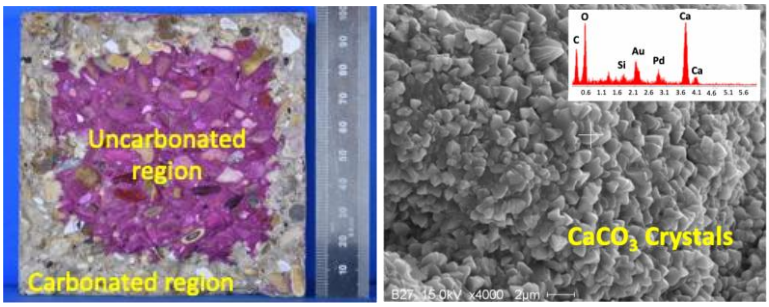


Fig. 1 (Left) Carbonation depth measurement by Phenolphthalein indicator (Adapted from [15]) (Right) SEM image of $CaCO_3$ crystals after 18 h carbonation with corresponding EDS confirming Ca and O [16]

2.3 Ultrasonic Pulse Velocity (UPV)

Several researchers have used Ultrasonic Pulse Velocity (UPV) to estimate microstructural changes in concrete [17]. UPV can help assess the internal structural properties of concrete, such as porosity, density, and crack development. This technique has also been applied to detect concrete carbonation, as wave velocity increases due to microstructural densification [8]. While linear UPV has been widely used, it has a limitation: it is less sensitive to carbonation at early stages and, in some cases, cannot distinguish between carbonation [1]. The aggregate type also affects the measurement sensitivity of the carbonation results [1]. Also, it has been shown that UPV values fluctuate in the initial carbonation stages and increase in the later stages [18]. Fig. 2 shows a schematic representation of ultrasonic and coda wave propagation in the concrete sample. A study by Kim et al. [19] on harmonic generation demonstrated that nonlinear ultrasonic techniques based on second-harmonic generation are highly effective for detecting carbonation in concrete. Carbonation markedly reduces the acoustic nonlinearity parameter due to pore and microcrack densification, whereas linear ultrasonic parameters exhibit minimal change. This confirms the greater sensitivity of nonlinear ultrasonic methods for early, non-destructive detection of carbonation. By analysing scattered, late-arriving ultrasonic waves in a moving reference frame, Sun et al. [18] demonstrated a strong linear correlation between relative velocity changes and carbonation depth. This approach enables robust, non-destructive carbonation monitoring at all stages and depths beyond the surface.

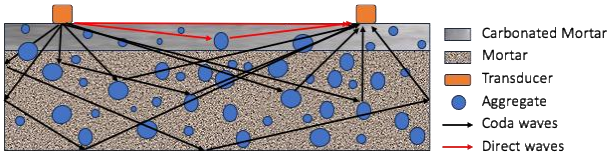


Fig. 2 Coda wave propagation v/s the direct Ultrasonic waves (Adapted from [18])

2.4 Gammadensitometry

The gamma-ray measurement technique (Gammadensitometry) has also been used for carbonation measurement by determining density changes associated with CO_2 penetration and subsequent $CaCO_3$ formation in the concrete [20]. It is a non-destructive technique that uses a Cs-137 source to measure density variations in concrete resulting from drying and carbonation. The method relies on gamma-ray absorption to quantify density changes throughout the samples, with corrections for moisture-induced variations in absorption. Results showed that gammadensitometry effectively tracks CO_2 penetration and carbonation progression with high precision, complementing conventional techniques such as thermogravimetric analysis [20]. The advantage of this technique is the short testing time (under 3 hours) and the continuous monitoring of the samples without damaging them [20]. Fig. 3 (Left) shows the test setup of gammadensitometry. The density measurement is based on Lambert's law (the absorption of gamma rays is measured). Refer to (1) [21]:

$$N = N_0 \exp(-\mu \rho l) \quad (1)$$

Where N_0 represents the number of photons in the air, and N denotes the number of photons transmitted through a sample with thickness l m and density ρ (kg/m³). The parameter μ (m²/kg) is the material's mass absorption coefficient. Knowing the value of μ and measuring N, N_0 and l parameters, the density can be calculated from the following (2):

$$\rho = \frac{-1}{\mu l} \ln\left(\frac{N}{N_0}\right) \quad (2)$$

3 QUANTITATIVE TECHNIQUES

3.1 Calcimetry

Calcimetry is based on the principle that the $CaCO_3$ produced after the carbonation of concrete, when reacted with hydrochloric acid (HCl), releases CO_2 gas. The pressure induced by the released CO_2 gas is measured by a calibrated CO_2 pressure sensor, which helps determine the amount of $CaCO_3$ present and the degree of carbonation [7]. The procedure consists of using a powdered concrete sample (about 1 g) at a controlled temperature of 20±2 ºC in a glass bottle, along with another glass bottle containing 20 ml of HCl solution (1 mol/L). Both glass bottles are placed in a vertical orientation in a speed-

regulated oscillator, which helps drive the reaction of HCl with the powdered sample, CO_2 is gradually released, increasing the pressure, which is measured [7]. Fig 3 (Right) shows the Calcimetry test setup.

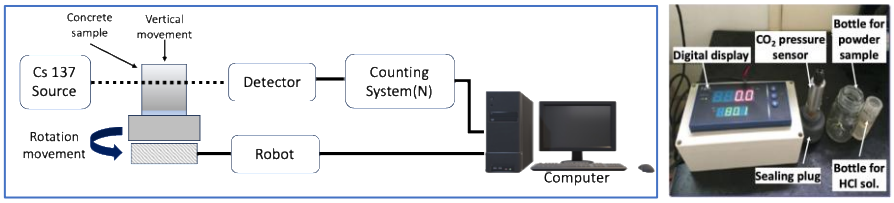


Fig. 3 (Left) Gammadensitometry instrumentation (Adapted from [20]) (Right) The test setup of the carbonation measurement (Calcimetry)[7]

3.2 X-ray diffraction (Phase analysis technique)

Several researchers have successfully used the X-ray diffraction technique to evaluate the extent of carbonation in concrete by measuring the relative peak intensities of $CaCO_3$ and $Ca(OH)_2$ in cementitious mixes. XRD can also be used as an auxiliary qualitative tool for characterising carbonation properties in concrete samples [7]. The accelerated carbonation of the concrete samples can be identified at various depths of the sample. However, it is difficult to quantify the absolute degree of carbonation in concrete samples due to the presence of sand and aggregate particles, which vary from sample to sample and may contribute overlapping XRD peaks. Jafari and Dorafshan [12] followed an identical procedure to minimise the effect of aggregate particles on the intensities of $CaCO_3$ and $Ca(OH)_2$ (CH) peaks in carbonated and non-carbonated samples. The authors suggested using only the surface mortar samples (0-2 mm), which were slow-speed micro-drilled and visibly checked to remove any aggregate particles. The samples were hand-ground and passed through a fine sieve to obtain a homogeneous fraction, which was then examined under a stereomicroscope to remove any aggregates visible to the naked eye. The reference diffraction peaks were calibrated using peak positions from a well-characterised standard material, which also aided phase identification for semi-quantitative comparison. This process of quantification can also be performed using the Rietveld refinement procedure [13]. Fig. 4 shows the XRD spectra of samples subjected to various carbonation conditions. The XRD results indicate a carbonation depth about twice that of the pH indicator test on similar samples [2].

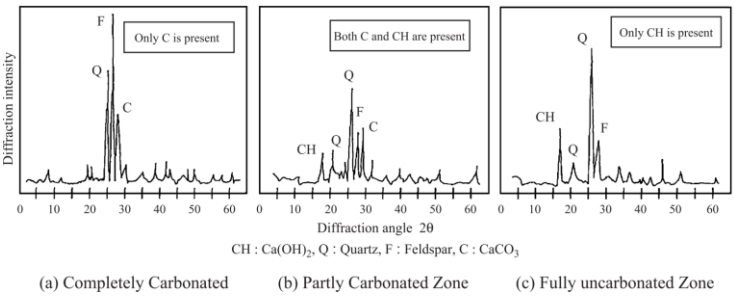


Fig. 4 X-ray diffraction peaks in accelerated carbonation test samples [2]

3.3 Thermogravimetric Analysis (TGA)

TGA is one of the most common carbonation measurement techniques used in several studies [2]. The thermogravimetric analysis for measuring the degree of carbonation requires heating at a high temperature (0–1000 ºC) under an inert environment, using a powdered sample [2], [13]. The typical TGA curve for the cementitious material is shown in Fig. 5 (Left). The peak corresponding to $Ca(OH)_2$ dehydration in the thermogravimetry plot is observed in the range 425-550 °C [2]. The samples undergo mass loss during heating due to the decomposition of $CaCO_3$ into CO_2 gas at 580-710 °C, which can help quantify the carbonate formed and, hence, the degree of carbonation in the samples. The TGA sample is obtained from the outer periphery towards the center of the carbonated concrete. The calcium

carbonate content varies with sample depth due to reduced carbon dioxide penetration [22]. However, the presence of calcium carbonate from the aggregate (limestone) used in concrete can alter the results, as such aggregate decomposes in the same range as the $CaCO_3$ and provides wrong results, which needs to be considered for this type of analysis technique [7].

TGA also inherently has limitations in measurement accuracy because the temperature limits for the decomposition of various constituents in a sample are unclear during high-temperature heating [7]. However, thermogravimetric analysis (TGA) is expected to provide greater accuracy than the phenolphthalein (pH) test regarding the measured carbonation depth, which may be approximately 2-2.5 times greater, indicated by the PI test [2], [7]. The TGA is accompanied by mass spectrometry (TGA-MS) or infrared spectrometry (TGA-IR) to achieve comprehensive analysis of the gases released during the heating of the concrete sample [11]. When heating the carbonated concrete sample, the primary $Ca(OH)_2$ gradually reacts with CO_2 (Refer to (3) and (4)). These changes are reflected in the TGA graph as percentage weight loss during $Ca(OH)_2$ dehydration and the decomposition of $CaCO_3$.

From (3) and (4), multiplying the two weight losses by the molecular proportions $M_{Ca(OH)2}/M_{H2O}$ *and* M_{CaCO3}/M_{CO2}, respectively, yields $M_{Ca(OH)2}$, M_{H2O}, M_{CaCO3}, and M_{CO2}, which are the masses of 1 mol of $Ca(OH)_2$, H_2O, $CaCO_3$, and CO_2, respectively. The weight of $Ca(OH)_2$ and $CaCO_3$ in the sample can thus be calculated [2]. The degree of carbonation can be calculated by (5).

$$\mathrm{Ca(OH)_{2(S)} \rightarrow CaO_{(S)} + H_2O_{(g)}} \quad (3)$$

$$\mathrm{CaCO_{3(S)} \rightarrow CaO_{(S)} + CO_{2(g)}} \quad (4)$$

$$D_c(\%) = (C - C_o)/(C_{max} - C_o) \times 100 \quad (5)$$

3.4 Fourier Transform Infrared (FTIR) Spectroscopy

FTIR is a semi-quantitative technique for measuring the relative carbonation level in concrete. The characteristic peaks of the C-O functional group in FTIR spectra can be used to identify carbonation in concrete samples [7]. The procedure for the FTIR analysis involves a powdered paste sample from the different depths of the sample to be tested for the carbonation [5]. The powdered cement sample (20 mg) is mixed with KBr (~200 mg) and formed into pellets using a high-pressure injection mould apparatus [5]. The scan frequency is generally set to 32 times/sec, with a resolution of 4 cm^{-1} and a measurement range of 400-4000 cm^{-1} [5]. The characteristic C–O stretching peak of $CaCO_3$ appears in the 1410–1510 cm^{-1} region, and its increase in intensity (corresponding to lower transmittance at about 1415 cm^{-1}) indicates a higher degree of carbonation in the concrete [2]. The O-H bond peaks in the $Ca(OH)_2$ spectrum in the FTIR are observed to reduce with the increased carbonation degree and disappear at the 100% $CaCO_3$ [5]. The FTIR mapping of the carbonated sample is shown in Fig. 5 (Right)

The increase in the peak absorptive value corresponds to the rise in the $CaCO_3$ content present in the test samples [7]. The FTIR technique can help determine the linear distribution of carbonation in concrete, including the boundary positions of the carbonated and non-carbonated areas [23]. This technique has been shown to reveal a carbonation zone extending to depths approximately two to three times greater than those identified by the phenolphthalein pH indicator test discussed earlier [7,23]. This is because the pH indicator (phenolphthalein) measures carbonation up to pH 9; therefore, areas with partial carbonation beyond this pH cannot be tested [2]. The FTIR method measures the vibrational modes of characteristic functional groups. It is not dependent on the crystallinity of the sample components, making it more suitable than techniques such as XRD, Raman spectroscopy, and quantitative phase analysis methods that rely on crystalline phase identification for carbonation assessment [11]. However, several factors, such as the stability of the light source, efficiency of the beam splitter due to variation in humidity in the FTIR test sample, makes the quantification of the results difficult to compare to the TGA results, which is based on direct mass measurement of the sample [5].

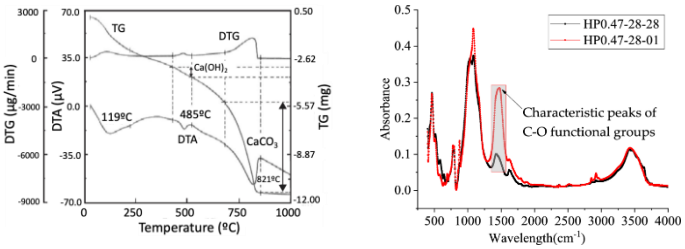


Fig. 5 (Left) Concrete characteristic curves of thermogravimetric analysis with temperature [2] (Right) FTIR mapping of carbonated sample [7]

3.5 Direct weight gain measurement

The measurement of carbonation by CO_2 uptake provides the theoretical amount of CO_2 sequestered in the concrete. The net CO_2 uptake is measured as the percentage of the dry binder. The mass loss due to moisture during cement carbonation (an exothermic process) should be excluded from calculations. Therefore, it is important to add the lost water back to the measured mass of the carbonated concrete sample, treating the system as closed, since this water was part of the sample's original mass [24]. The water generated during carbonation can be collected using absorbent paper [24]. The general expression for the CO_2 uptake is shown in (6) [25] or (7) [26].

$$CO_2 \text{ uptakes } (\%) = \frac{\text{Mass}_{\text{post } CO_2} + \text{Mass}_{\text{lost water}} - \text{Mass}_{\text{pre } CO_2}}{\text{Mass}_{\text{binder}}} \quad (6)$$

$$CO_2 \text{ uptake}, \% = \frac{\text{mass of reacted } CO_2}{\text{mass of } CO_2 \text{ reactive materials}} \times 100\% \quad (7)$$

It is important to note that not all water can be collected, as some remains in vapour form; thus, this method underestimates uptake and yields conservative results [24]. Therefore, it is recommended to obtain measurements from an independent sample to improve the accuracy of the results.

4 COMPARATIVE ANALYSIS

The current practices and detection and measurement techniques for carbon sequestration in concrete were reviewed and compared. Table 2 shows the pros and cons of the various techniques.

Table 2 Comparison of various concrete carbonation measurement techniques

Technique	Type	Pros	Cons	Suitable application
pH indicators	Qualitative	Simple, visual, field-applicable	Surface-only, threshold-based (pH ~9), destructive sampling, does not show carbonation gradient.	Initial carbonation depth mapping; routine lab/field screening
Image Analysis	Semi-Quantitative	Digital, objective depth measurement	Destructive, requires high-quality imaging and calibration via pH or chemical staining	Carbonation front mapping; comparative lab studies, restriction in the carbonation in the concrete interior depth
SEM-EDS	Semi-quantitative	Microstructural and elemental insight; high magnification	Localised, expensive, destructive	Microscale phase analysis; ITZ examination
Calcimetry	Quantitative	Direct $CaCO_3$ quantification via CO_2	Destructive; no spatial resolution;	Total carbonation degree: method validation

		measurement; simple setup	measures total carbonate only	
TGA	Quantitative	Precise $CaCO_3$ and portlandite quantification; good reproducibility	Requires powdering the sample, needs chemical analysis correction for concrete	Quantifying carbonation extent: phase decomposition studies
XRD	Qualitative/Semi-Quantitative	Identifies crystalline phases (calcite, vaterite, aragonite)	Misses amorphous phases; requires sample preparation; semi-quantitative with internal standards	Phase identification; carbonation product evolution
FTIR	Semi-Quantitative	Detects carbonates early; sensitive to molecular bonds	Surface-sensitive in ATR mode; transmission mode requires powder; peak overlap possible	Early carbonation detection; functional group analysis
Direct Weight Gain Method	Quantitative	Simple mass-based, continuous carbonation measurement possible	Affected by moisture loss/gain; not specific to carbonation alone	Carbonation curing studies; CO_2 sequestration monitoring
Ultrasonic pulse velocity	Indirect / Qualitative	Non-destructive; in-situ monitoring; covers large volumes	Not carbonation-specific; influenced by moisture, cracking, and porosity	Supplementary assessment
Gammadensitometry	Quantitative (Indirect)	Non-destructive; provides a complete CO_2 uptake profile; in situ capable	Radiation safety; equipment access; requires calibration for concrete density	Depth-wise carbonation profiling; in-situ monitoring in lab settings

5 CONCLUSIONS

The present study reviewed several techniques for determining the degree of concrete carbonation, which can be used to assess carbonation sequestration. Based on the several studies evaluated, the following conclusion can be made:

1. The pH indicator method is widely used for rapid carbonation detection; however, it cannot quantify carbonation degree or identify partially carbonated zones. Digital image analysis of pH indicator-stained samples enables a more accurate determination of the carbonation front. SEM analysis reveals microstructural changes in the concrete and helps identify the formation of $CaCO_3$ crystals from sample carbonation; this process is very localised.

2. Calcimetry provides the accurate determination of the carbonation degree at the required depth of the samples. The carbonation level at various depths within the sample can be accurately measured.

3. The use of the TGA technique provides a direct weight measurement of the calcium carbonate in the test sample; however, the presence of the aggregate, such as limestone, can alter results and should be considered during the testing and analysis procedure.

4. The use of direct weight measurement of the samples before and after the carbonation is also a common technique for the direct carbonation assessment; however, the role of ambient humidity and temperature should be carefully considered and taken into account for accurate analysis.

5. The FTIR technique effectively identifies concrete carbonation by monitoring C–O and O–H peaks, providing accurate depth profiling beyond pH indicators, such as phenolphthalein.

6. The XRD analysis can provide information about the crystalline phases; further study may be required to evaluate the degree of carbonation using techniques such as Rietveld refinement.

7. Based on the analysis of various studies, it can be stated that an integrated approach combining multiple test methods is essential for a precise understanding of CO_2 sequestration in concrete.

References

[1] Bouchaala, Fateh, Payan, Cédric, Garnier, Vincent, and Balayssac, Jean-Paul, 2011. "Carbonation assessment in concrete by nonlinear ultrasound." *Cement and Concrete Research* 41 557–9

[2] Chang, Cheng-Feng, and Chen, Jing-Wen, 2006. "The experimental investigation of concrete carbonation depth." *Cement and Concrete Research* 36 1760–7

[3] Kashef-Haghighi, Sormeh, and Ghoshal, Subhasis, 2010. "CO2 Sequestration in Concrete through Accelerated Carbonation Curing in a Flow-through Reactor." *Industrial & Engineering Chemistry Research* 49 1143–9

[4] Matschei, Thomas, Braymand, Sandrine, Garg, Nishant, Huet, Bruno, Jansen, Daniel, Myers, Rupert J, Scruggs, Bruce, Bernard, Ellina, Bertola, Julie, Cazacliu, Bogdan, Ellwood, Lucy, Felten, Christian, Ferrara, Giuseppe, Garboczi, Edward, Gholizadeh Vayghan, Asghar, Hafez, Hisham, Hanein, Theodore, Kanavaris, Fragkoulis, Mahoutian, Mehrdad, Maruyama, Ippei, Roux, Sébastien, Turcry, Philippe, Skibsted, Jørgen, Snellings, Ruben, Srivastava, Sumit, Vial, Virginie, Wei, Jinxin, Zajac, Maciej, Zhang, Zhidong, and Suraneni, Prannoy, 2026. "Test methods for CO2 mineralization in cement-based materials: A review by RILEM TC 309-MCP." *Materials and Structures* 59 175

[5] Lee, Ho Jae, Kim, Gyeum Do, Lee, Jang Hwa, and Cho, Myoung Suk, 2012. "A Study for Carbonation Degree on Concrete using a Phenolphthalein Indicator and Fourier-Transform Infrared Spectroscopy." *International Journal of Architectural, Civil and Construction Sciences* 6 152–8

[6] CPC-18, 1988. "Measurement of hardened concrete carbonation depth." *Material and Structures, RILEM* 453–5

[7] Li, Bei, Tian, Ye, Zhang, Guoyi, Liu, Yu, Feng, Huiping, Jin, Nanguo, Jin, Xianyu, Wu, Hongxiao, Shao, Yinzhe, Yan, Dongming, Zhou, Zheng, Wang, Shenshan, Zhang, Zhiqiang, Chen, Jin, Chen, Xiaodong, Lu, Yunjun, Li, Xinyi, and Wang, Jiaxi, 2023. "Comparison of detection methods for carbonation depth of concrete." *Scientific Reports* 13 19980

[8] Bui, Huyen, Delattre, Francois, and Levacher, Daniel, 2023. "Experimental Methods to Evaluate the Carbonation Degree in Concrete—State of the Art Review." *Applied Sciences* 13 2533

[9] Yu, Myoung-Youl, Lee, Jae-Yong, and Chung, Chul-Woo, 2010. "The Application of Various Indicators for the Estimation of Carbonation and pH of Cement Based Materials." *Journal of Testing and Evaluation* 38 534

[10] Choi, Jeong Il, Lee, Yun, Kim, Yun Yong, and Lee, Bang Yeon, 2017. "Image-processing technique to detect carbonation regions of concrete sprayed with a phenolphthalein solution." *Construction and Building Materials* 154 451–61

[11] Medvedev, Vyacheslav, and Pustovgar, Andrey, 2023. "A Review of Concrete Carbonation and Approaches to Its Research under Irradiation." *Buildings* 13 1998

[12] Jafari, Faezeh, and Dorafshan, Sattar, 2026. "Noncontact surface carbonation detection and monitoring in concrete structures." *Measurement* 266 120399

[13] Shah, Vineet, Scrivener, Karen, Bhattacharjee, Bishwajit, and Bishnoi, Shashank, 2018. "Changes in microstructure characteristics of cement paste on carbonation." *Cement and Concrete Research* 109 184–97

[14] Rostami, Vahid, Shao, Yixin, Boyd, Andrew J, and He, Zhen, 2012. "Microstructure of cement paste subject to early carbonation curing." *Cement and Concrete Research* 42 186–93

[15] Forsdyke, Jessica C, and Lees, Janet M, 2023. "Model fitting to concrete carbonation data with non-zero initial carbonation depth." *Materials and Structures* 56 22

[16] Xian, Xiangping, Logan, Chad, and Shao, Yixin, 2022. "Dimensional stability of cement paste and concrete subject to early-age carbonation curing." *Materials and Structures/Materiaux et Constructions* 55 94

[17] Terzić, Anja M, and Pavlović, Ljubica M, 2010. "Application of Results of Nondestructive Testing Methods in the Investigation of Microstructure of Refractory Concretes." *Journal of Materials in Civil Engineering* 22 853–7

[18] Sun, Xiangtao, Yi, Shanchang, Li, Xiuquan, Cui, Yongxiang, Zhang, Minghui, Jiang, Tianyong, Wang, Lei, and Kong, Qingzhao, 2026. "A novel ultrasonic-velocity-based concrete carbonation monitoring method based on step-wise stretching technique." *Structural Health Monitoring* 25 117–30

[19] Kim, Gun, Kim, Jin Yeon, Kurtis, Kimberly E, Jacobs, Laurence J, Le Pape, Yann, and Guimaraes, Maria, 2016. "Quantitative evaluation of carbonation in concrete using nonlinear ultrasound." *Materials and Structures/Materiaux et Constructions* 49 399–409

[20] Villain, Géraldine, and Platret, Gérard, 2006. "Two Experimental Methods to Determine Carbonation Profiles in Concrete." *ACI Materials Journal* 103 265–71

[21] Villain, Géraldine, and Thiery, Mickaël, 2006. "Gammadensimetry: A method to determine drying and carbonation profiles in concrete." *NDT and E International* 39 328–37

[22] Yahui, Yang, Gang, Xu, and Bin, Tian, 2021. "Carbonation characteristics of cement-based materials under the uniform distribution of pore water." *Construction and Building Materials* 275 121450

[23] Li, Bei, Jin, Nanguo, Tian, Ye, Jin, Xianyu, Li, Xinyi, and Zhao, Ruoyi, 2021. "Application of Infrared Spectroscopy in the Measurement of Carbonation Depth of Concrete." *Journal of Applied Science and Engineering* 24 1041–9

[24] El-Hassan, Hilal, Shao, Yixin, and Ghouleh, Zaid, 2013. "Reaction Products in Carbonation-Cured Lightweight Concrete." *Journal of Materials in Civil Engineering* 25 799–809

[25] Ahmad, Shamsad, Assaggaf, Rida Alwi, Maslehuddin, Mohammed, Al-Amoudi, Omar S Baghabra, Adekunle, Saheed Kolawole, and Ali, Syed Imran, 2017. "Effects of carbonation pressure and duration on strength evolution of concrete subjected to accelerated carbonation curing." *Construction and Building Materials* 136 565–73

[26] Zhang, Duo, Ghouleh, Zaid, and Shao, Yixin, 2017. "Review on carbonation curing of cement-based materials." *Journal of CO2 Utilization* 21 119–31

Effects of retrofitting interventions on risk and safety in existing bridges: a case study

Eleni Mariolopoulou, Marco Carlo Rampini, Marco di Prisco

Department of Civil and Environmental Engineering (DICA),
Politecnico di Milano,
Piazza Leonardo da Vinci 32, 20133 Milano, Italy

Summary
Infrastructures worldwide face challenges due to aging or lack of maintenance. In recent years, a series of bridge collapses has depicted the urgent need of restorations to ensure safety and seamless operation. The new Italian guidelines for risk classification and management, safety assessment and monitoring of existing bridges provide the procedure to define the class of attention of each bridge, acting as an alert when maintenance is required. Combined with the safety class defined by the European norms, an overview of the condition of a bridge can be offered. In this context, the study focuses on a highway bridge crossing a river in Northern Italy built 65 years ago and subjected to two significant interventions since its completion. Special attention is given to the 11 beams supported by half-joint saddles. Both safety coefficients for shear and bending failure of the beams are evaluated. The methodology demonstrates the value of risk definition by safety assessments for effective bridge maintenance planning.

1 INTRODUCTION

In recent years in the field of bridge engineering the focus has shifted on the safety assessment of the existing bridges [1], [2] with the goal to ensure their prominent use under any conditions [3]. In many cases, aging, change of the traffic demand and updated regulatory requirements often lead to obligatory intervention to improve safety performance. One big challenge engineers face is understanding how the evolving conditions (e.g., loads, material deterioration) and successive interventions affect the structural safety and risk classification of such structures over time. Some studies focus on verifications though safety coefficients considering the overall infrastructure [4] or specific parts of the bridge [5], while others keep a more general approach of safety assessment [6]. Although new regulations provide exact procedures for ultimate limit state verification, a lot of older bridges were built using previous standards, which makes direct comparison of safety levels difficult.

In Italy, the new Guidelines for Risk Classification and Management, Safety Assessment and Monitoring of Existing Bridges introduced a multi-level approach for bridge assessment [7]. On this frame, the assessment of risk levels [8] and risk elimination of the current bridges are also investigated [9]. Therefore, detailed analyses of critical structural elements can improve the reliability of the assessment.

This study analyses a 65-year-old Gerber bridge crossing the Po River in Northern Italy. The bridge has undergone two major interventions, and the present work can be considered as a Level 3 analysis proposed by the Italian guideline, providing examination and verification of critical elements. In all computations the degradation of materials was neglected with the analysis focused on the suspended beams supported by half-joint saddles. The shear capacity of the half-joints is evaluated using a strut-and-tie model, while the bending capacity at mid-span is assessed according to Eurocode 2.

The paper is a part of the ongoing research to determine the reliability of the bridge based on the entire course of its life, with respect to the various retrofitting carried out and the progression of loads over time. The objective of the study is to evaluate and compare safety coefficients for bending and shear both before and after the first intervention, to assess the effectiveness of the retrofit and identify the governing structural mechanisms that have the most influence on the global safety of the bridge.

2 CASE STUDY DESCRIPTION

2.1 Bridge and Materials Characteristics

The Po River bridge near Corana, in the Province of Pavia, was completed in 1960 as part of the Serravalle–Milan motorway project. Today, it forms part of the A7 highway, operating alongside a

parallel bridge that carries traffic in the opposite direction. The structure has an overall length of about 760 m, developed on a straight alignment and subdivided into 11 spans, each with an average length of 69.32 m. The spans are alternately composed of multi-cell box elements with variable height and cantilever elements, also box-type, with a length of 17.66 m, whose ends rest on Gerber saddles, supporting beams with an open section and a span length of 34.60 m (Fig.1). There are a total of six caissons and five buffer beams. The end spans feature a counterweight with a span of approximately 15 m cantilevered on the side of the abutment to compensate for the absence of the buffer beam.

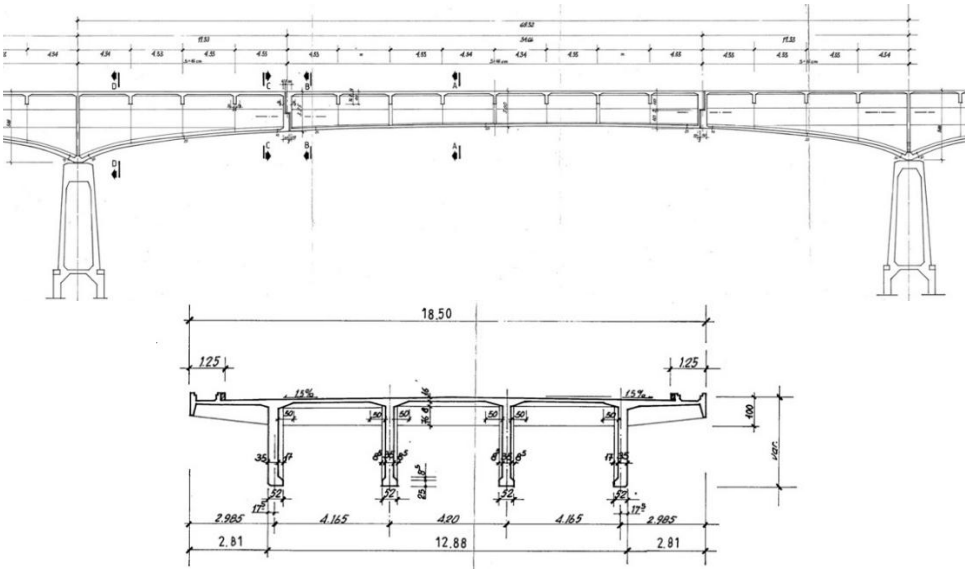


Fig. 1 Schematic of the central part of the bridge (top) and longitudinal section of the buffer beams (bottom).

The bridge was built with ordinary reinforced concrete. Only few construction drawings are still available, while the design report is missing. Concrete specifications are unknown, and the steel is noted with an old Italian notation "acciaio fer" likely mild steel (assumed as f_{yk} = 315 MPa). At that time, the 1939 standards (Decree Law no. 2229) classified steels as mild (42–50 kg/mm², allowable stress 1400 kg/cm²), medium (50–60 kg/mm², 2000 kg/cm²), and hard (60–70 kg/mm², 2000 kg/cm²). The mild steel corresponds roughly to FeB32K steel, with an allowable stress of 1600 kg/cm². However, from the design report of the first intervention in 1993, some properties of the original materials can be assumed: Concrete R_{ck} = 300 kg/cm² (allowable cubic compressive stress σ_c = 83.3 kg/cm², maximum allowable shear stress without reinforcement τ = 4.00 kg/cm², and with reinforcement τ = 14.00 kg/cm²). These concrete and steel properties are the ones considered for the following analysis.

2.2 History of Interventions

The bridge is subject to two main rehabilitation interventions though its lifetime: the first one in 1993, and the last one in 2023, ensuring its continued functionality and safety.

2.2.1 First intervention

In 1993, structural restoration and strengthening works were carried out on the bridge to comply with updated design and testing standards for road bridges. The project included reinforcement of the slabs, partial prestressing of the cantilever beams using external unbonded tendons to enhance load-bearing capacity (2 cables with 12 strands of 0.6" for each of the 4 beams, σ_{spi} = 9000 kg/cm²), and additional prestressing in the negative and positive moment regions of the main box spans. The Gerber saddles were also enlarged to replace the bearings, and end anchorages with prestressing ducts were installed in preparation for future tendon installation.

2.2.2 Second intervention

Following recent investigations, the structure had been categorized according to the new Italian guidelines for risk classification and management, safety assessment and monitoring of existing bridges. The Level 1 inspection by the motorway operator in 2021 indicated a widespread degradation of the structural elements and concrete. The bridge was found to be on the high class of risk, both for the structural-foundations and seismic categories, showing the need for immediate actions.

A full rehabilitation and strengthening program were launched in 2023. Works included removal of obsolete post-tensioning, slab reinforcement with steel bars, strengthening of external beams using stainless-steel FRCM strips, and concrete restoration on damaged surfaces. The Gerber saddles underwent complete reconstruction, including lifting of cantilever spans, hydro-demolition, reinforcement treatment, thixotropic mortar restoration, bearing replacement, and installation of new expansion joints (Fig. 2). Additional repairs addressed slab soffits, box girders, piles, and abutments. Seismic upgrades incorporated isolation bearings, hydraulic shock transmitters, shear keys, and drainage improvements. The intervention restored the bridge's structural capacity, durability, and seismic safety in compliance with modern highway standards. The exact details of the used materials are under investigation.

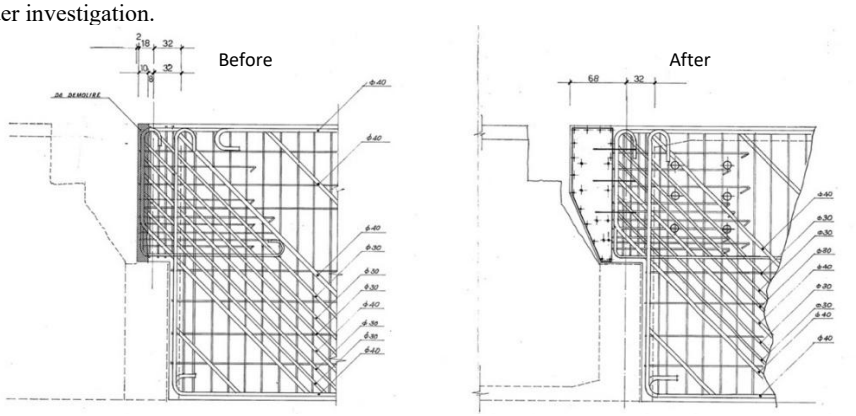


Fig. 2 Demolition scheme of the Gerber support and integration of the tooth (buffer beam side) before (left) and after (right) the first intervention.

3 SAFETY ASSESSMENT OF THE SUSPENDED GERBER BEAM

This study presents the safety assessment of the bridge with specific reference to the Gerber structural system by the original design and after the first intervention (adding of prestress). In both cases the material properties on the computations are the ones from the original bridge design. The analysis focuses on the suspended beams located between the two half-joints. All verifications are carried out with reference to the Ultimate Limit State (ULS) according to Eurocode 2, neglecting materials degradation.

3.1 Internal actions

The suspended Gerber beam is a simply supported element between the two half-joints. Based on this structural scheme, the most relevant internal actions for the beam design and verification are evaluated by determining the shear forces at the supports and the bending moment at mid-span. The analysis considers the combinations of permanent, variable, and accidental loads, as indicated by the original report of the first intervention. Loads are then amplified following the ULS design rules.

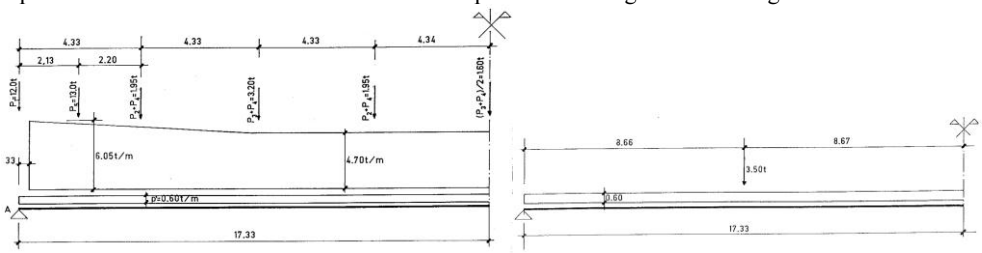


Fig. 3 Self-weight loads (left) and added weight distribution (right).

For the evaluation of the internal actions the used loads were the self-weight $R_{A\,pp1} = 129.62\,t$, the added loads $R_{A\,pp2} = 13.9\,t$, the permanent $R_{perm} = 17.33\,t$ and the accidental loads $R_{acc} = 80.60\,t$. The load computation was consistent with the Italian DM 1980 standard, as indicated in the design report of the first intervention. Following the loads distribution of Fig. 3, the resulting support reaction and the design mid-section bending moment obtained using the partial safety factors for permanent and variable actions are presented below. In addition, the same internal action at serviceability is reported. The design and service bending moments are evaluated at the mid-span section.

$$R_{Ed} = \gamma_{G1} \cdot G1 + \gamma_{G2} \cdot G2 + \gamma_Q \cdot Q = \gamma_{G1} \cdot \left(R_{A\,pp1} + R_{A\,pp2}\right) + \gamma_{G2} \cdot R_{perm} + \gamma_Q \cdot R_{acc} = 1.35 \cdot (129.62 + 13.9) + 1.5 \cdot 17.33 + 1.35 \cdot 80.60 = 3223.14\ \text{kN} \quad (1)$$

$$M_{Ed} = \gamma_{G1} \cdot \left(M_{pp1} + M_{pp2}\right) + \gamma_{G2} \cdot M_{perm} + \gamma_Q \cdot M_{acc} = 2386.76\ \text{tm} = 23.41\ \text{MNm} \quad (2)$$

$$R_{SLS} = G1 + G2 + Q = 241.45\ \text{t} = 2368.62\ \text{kN} \quad (3)$$

$$M_{SLS} = M_{pp1} + M_{pp2} + M_{perm} + M_{acc} = 1766.04\ tm = 17.32\ \text{MNm} \quad (4)$$

3.2 Effect of post-tension

In the capacity evaluation of the beams after the first intervention, the effective post-tensioning force $N_P = 2.6173\ MN$ (with prestress losses) is also taken into consideration following the scheme reported in Fig. 4. At mid-span, this effect can be represented as a counteracting moment M_p, while the effect of post-tension in the half-joined capacity is analysed in section 4. The horizontal component of the force is N_H, the vertical N_V and the angle α = 10.5°.

$$M_{Rd} = M_{Rd}(N_P) + N_P e = 28.46 + 3.12 = 31.58\ \text{MNm} \quad (5)$$

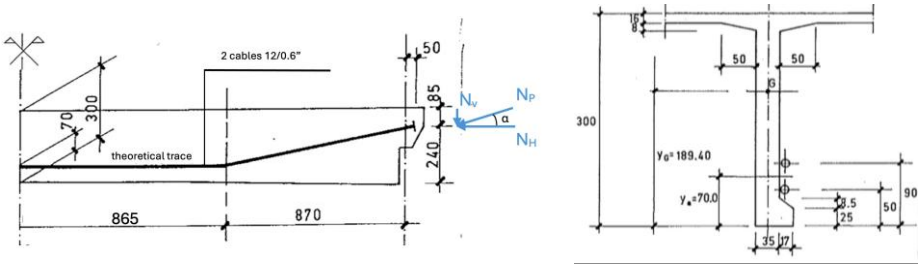


Fig. 4 Scheme of post-tension action at buffer beam support (left) and the position in the cross-section (right).

4 HALF JOINT CAPACITY

The load-bearing capacity of the half-joint (Gerber) saddle is evaluated by analysing the internal force transfer mechanisms activated ULS conditions. The half-joint depicts a key role in the structural behaviour of the bridge, so a strut-and-tie modelling is selected with the goal to represent the flow of forces within the discontinuity region.

The Strut and Tie method consider the external beam (i.e., section geometry and reinforcement distribution) of the deck, which is typically the most stressed under loading conditions. The Strut and Tie models presented in this document are based on those proposed in Eurocode 2 (EN 1992-1, 2004) and have been modified in accordance with several studies and guidelines available in the literature [10]-[13]. As a result, two resisting mechanisms are identified (Fig. 5) and analysed to determine the overall shear capacity of the half-joint and to verify its safety level. The assessment considers the combined effects of permanent, variable, and accidental actions acting on the suspended beam, as well as the contribution of prestressing forces without considering the effect of oxidation [14], [15].

4.1 Strut and tie mechanism 1

The first mechanism (Fig. 5) considers an inclined tie (Z_1) carried by the diagonal rebar (A_{s1}), and a vertical compressive strut (C_1). The horizontal component of the tie (Z_1) is equilibrated by a compressive horizontal strut (C_3). On this mechanism the resistance is governed by the diagonal rebars.

It is also worth mentioning that the significant compression activated in strut C_1 by the diagonal reinforcement Z_1 overlapped by mechanism 2, compensates the shorter A_{s2} reinforcement that remains active mainly as shear connection along the vertical critical section to prevent a Mattock's failure.

$$P_1 = Z_1 \cdot \sin\beta = A_{s1} \cdot f_{yd} \cdot \sin\beta = 15865.2 \cdot 273.913 \cdot \sin 45° = 3072.83 \text{ kN} \quad (6)$$

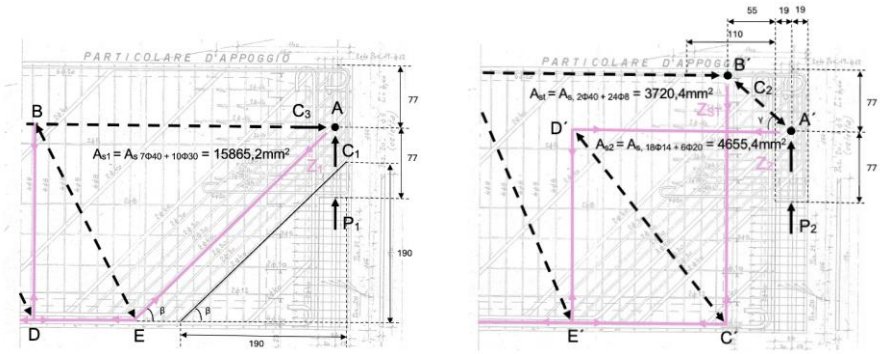


Fig. 5 Strut-and-tie model resisting mechanism 1 (left) and mechanism 2 (right).

4.2 Strut and tie mechanism 2

The second mechanism (Fig. 5) consists of an inclined compressive strut (C_2), and a horizontal tie (Z_2) resisted by the U-shape bars (A_{s2}). The vertical component of the inclined strut is equilibrated by a vertical tie (Z_{st}) resulting from the contribution of the first stirrups (A_{st}). The angle γ between the strut $C_{A'B'}$ and the horizontal axis is 43.78°. The equilibrium of forces is established at the nodes A′ and B′ of the strut-and-tie model and the following equations occur:

$$Z_2 = C_2 \cdot \cos\gamma \quad (7) \qquad P_2 = Z_{st} = Z_2 \cdot \tan\gamma \quad (8)$$

$$Z_{st} = C_2 \cdot \sin\gamma \quad (9) \qquad Z_2 = Z_{st} \cdot \cot\gamma \quad (10)$$

The applied load according to Eq. (7-8) is equilibrated either by the vertical tie ($Z_{R,st} = A_{st} \cdot f_{yd} = 1019.07\ kN$) and by the horizontal tie ($Z_{R,2} \cdot \tan\gamma = A_{s2} \cdot f_{yd} \cdot \tan\gamma = 1221.99\ kN$). It is to note also that the horizontal tie is overlapped to the strut C_3 of mechanism 1. Therefore, for this mechanism:

$$P_{2before} = 1019.07\ kN \quad (11)$$

The introduction of post-tensioning as shown in Fig. 4 modifies the equilibrium at node A′ through its horizontal and vertical components, and it gives:

$$P'_{2,ZR,st} = Z_{st} + N_v = 1496.03\ kN \quad (12)$$

$$P'_{2,ZR,2} = (N_h + Z_2)\tan\gamma + N_v = 3211.18\ kN \quad (13)$$

$$P_{2after} = \min(P'_{2,ZR,st}, P'_{2,ZR,2}) = 1496.03\ kN \quad (14)$$

The effect of post-tensioning on this mechanism is indirect, as it modifies the global stress state, but it does not change the governing mechanism and continues to be controlled by the vertical reinforcement.

The comparison between the two possible limits of mechanism 2, before and after the intervention, without considering the overlapping with the strut C_3 of the mechanism 1 is presented in Fig. 6. In the pre-intervention configuration, the horizontal tie mechanism provides a resistance of approximately

1222 kN, while the vertical tie mechanism reaches 1019 kN, thus governing the capacity. After the introduction of prestressing, the horizontal contribution increases to roughly 3200 kN, whereas the vertical tie capacity to almost 1500 kN.

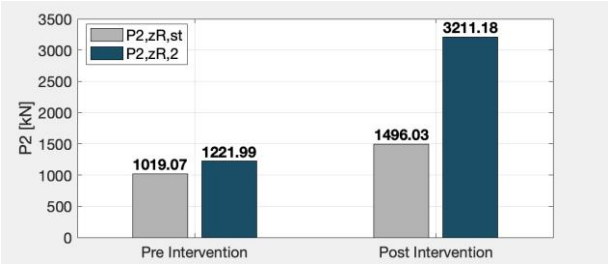


Fig. 6 Comparison of the shear capacity of the half-joint mechanism 2, before and after the first intervention: vertical tie (Z_{st}) and horizontal contribution (Z_2).

The total shear resistance of the half-joint due to the unchanged governing mechanisms P_1 and P_2 before ($R_{Rd,before} = 4091.90\ kN$) and after ($R_{Rd,after} = 4568.86\ kN$) with the value coming from:

$$R_{Rd} = P_1 + P_2 \tag{15}$$

gives a safety coefficient for the half joint γ_V that increases from 1.27 to 1.42 with the intervention.

5 MID-SECTION CAPACITY

The evaluation of the capacity of the midsection will be made in two ways. The first will follow the current Eurocode approach at Ultimate Limit State (ULS), while the second will follow the way the calculations were made before the first intervention using the 1982 regulations with the allowable stress method in the view of serviceability assessment. In both cases, the applied load was the same reported in Section. 3. In all computations no material degradation got assumed.

5.1 ULS assessment

The ULS verification was carried out in accordance with Eurocode 2 and the internal force equilibrium was established using the Eurocode stress block parameters (η=1.0, λ=0.8). In the evaluation of the overall midsection capacity (Fig. 7), the acting prestress was not taken into consideration due to the effective prestress losses and only the ordinary reinforcements positioned in the tensile zone are considered. These assumptions result in a conservative estimation of the bending resistance.

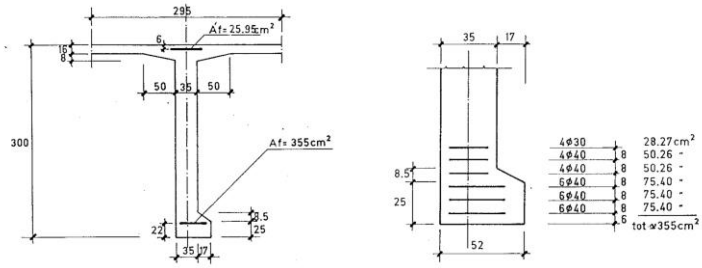


Fig. 7 Cross-section of the T-beam with the reinforcement position (left) and detail of the bottom ordinary steel reinforcement arrangement (right).

Imposing equilibrium $C = T$ yields a neutral axis depth $x = 0.781$ m, where $\lambda \cdot x > h_f$. Consequently, the design bending resistance is equal to $M_{Rd} = 25.55$ MNm before the intervention and 31.58 MNm after the intervention due to the post-tensioning. Using M_{Rd} and M_{Ed} we compute the safety coefficient before the first intervention ($\gamma_{M,before} = 1.09$) and after ($\gamma_{M,after} = 1.35$).

5.2 Serviceability Limit State (SLS) Assessment

Steel stress at SLS was evaluated using an elastic transformed-section approach, accounting for post-tensioning contribution through an effective force N_p applied. The transformed section properties were computed considering passive reinforcement only:

$$A_{id} = A_c + \alpha_E \sum_i A_{s,i} \tag{16}$$

$$I_{id} = I_c + A_c(y_c - y_{id})^2 + a_E \sum_i A_{s,i}(y_i - y_{id})^2 \tag{17}$$

For $\alpha_E = 15$, $A_{id} = 2.127$ m^2, $I_{id} = 2.74$ m^4, $y_{id} = 1.523\ m, e = 0.777\ m$, $y_s = 1.257\ m$, $N_p = 2.6173\ MN$ and $M_{SLS} = 17.32\ MNm$, the tensile stress in the bottom reinforcement results in:

$$\sigma_{s,SLS} = \alpha_E \left[-\frac{N_P}{A_{id}} + \frac{M_{SLS} - N_P\, e}{I_{id}} ys \right] = 86.7 \text{ MPa} \tag{18}$$

To enable comparison with allowable-stress approaches, the safety margin at SLS is defined as:

$$\gamma_{SLS,after} = \frac{0.8 \cdot f_{yk}}{\sigma_{s,SLS}} = \frac{252}{86.7} = 2.91 \tag{19}$$

Analysing the same SLS condition before the intervention, the safety margin was lower and can be computed as:

$$\gamma_{SLS,before} = \frac{0.8 \cdot f_{yk}}{\sigma_{s,SLS}} = \frac{252}{119.2} = 2.11 \tag{20}$$

6 RESULTS AND DISCUSSION

The analysis of the suspended Gerber beams provides a clear evaluation of the structural safety of the bridge in its original and retrofitted configuration. It should be noted that the results refer to an idealized condition, as material degradation was neglected to isolate the structural effects of the intervention. Regarding the Strut and Tie mechanisms verification in compression are not critical.

At the mid-span section, the comparison between the acting bending moment M_{Ed} and the resistant bending moment M_{Rd} shows that the original configuration of the bridge exhibits a safety coefficient equal to $\gamma_{M,before} = 1.09$. After the first intervention and the adding of post-tension, the bending resistance increases, leading to a safety coefficient of $\gamma_{M,after} = 1.35$ confirming the effectiveness of the intervention in enhancing the flexural capacity of the suspended beams.

Accordingly, in the half-joint region, in the original state, the shear verification shows a safety coefficient of $\gamma_{V,before} = 1.27$ and in the state after the first intervention $\gamma_{V,after} = 1.42$. Despite the increase in the horizontal contribution due to post-tensioning, the analysis of the second strut-and-tie mechanism reveals that the vertical tie governs the failure mechanism, in both cases.

As expected by adding an unbonded post-tensioning, a comparison between SLS and ULS with reference to the intervention highlights a higher increase of the safety margin for Serviceability: it changes from 2.11 to 2.91. These results underline that the apparent differences in safety levels are not necessarily indicative of overdesign but rather reflect the transition from a stress-based verification framework to a failure-based reliability approach.

7 CONCLUSIONS

This study investigated a 65-year-old Gerber bridge that has undergone two major interventions, focusing on the suspended beams and the half-joint regions. The analysis followed the framework of a Level 3 procedure according to the Italian Guidelines for risk classification and management of existing bridges. The degradation of materials was not considered in this paper.

The results confirm the investigated beam meets current Eurocode requirements. The first intervention improves bending capacity, increasing γ_M from 1.09 to 1.35, confirming the effectiveness of post-tensioning in improving flexural capacity. Shear behaviour at the half-joint does not change the resistant mechanisms, although it increases the safety margin from $\gamma_{V,before} = 1.27$ to $\gamma_{V,after} = 1.42$. As expected by introducing an unbonded post-tensioning the increase of the margin at serviceability is larger, passing from 2.11 to 2.91.

In the course of further work, the degradation of the materials will be included, and the analysis will also be extended to the latest intervention, enabling the definition of a time-dependent evolution of structural safety and reliability.

References

[1] Pregnolato, Maria. 2019. "Bridge safety is not for granted – A novel approach to bridge management." *Engineering Structures* 196:109193. doi:10.1016/j.engstruct.2019.05.035.

[2] di Prisco, Marco. 2019. "Critical infrastructures in Italy: State of the art, case studies, rational approaches to select the intervention priorities." *Proceedings of the fib Symposium 2019: Concrete – Innovations in Materials, Design and Structures*, 49–58.

[3] Arena, Marika, Azzone, Giovanni, Urbano, Valeria Maria, Secchi, Piercesare, Torti, Agostino, and Vantini, Simone. 2022. "Development of a functional priority index for assessing the impact of a bridge closure." *Bridge Safety, Maintenance, Management, Life-Cycle, Resilience and Sustainability*, 1817–22. CRC Press. doi:10.1201/9781003322641-225.

[4] Ferro, Giuseppe Andrea, Restuccia, Luciana, Falliano, Devid, Devitofranceschi, Achille, and Gemelli, Angelo. 2022. "Collapse of Existing Bridges: From the Lesson of La Reale Viaduct to the Definition of a Partial Safety Coefficient of Variable Traffic Loads." *Journal of Structural Engineering* 148(11):04022181. doi:10.1061/(ASCE)ST.1943-541X.0003458.

[5] Faleschini, Flora, Bonora, Riccardo, Zanini, Mariano Angelo, and Pellegrino, Carlo. 2026. "Ultimate capacity assessment of reinforced concrete half-joints." *Engineering Structures* 350:121971. doi:10.1016/j.engstruct.2025.121971.

[6] Ferrara, Mario, Gino, Diego, Miceli, Elena, Giordano, Luca, Malavisi, Marzia, and Bertagnoli, Gabriele. 2024. "Safety assessment of existing prestressed reinforced concrete bridge decks through different approaches." *Structural Concrete* 25(3):1637–57. doi:10.1002/suco.202301049.

[7] Ministero delle Infrastrutture e della Mobilità Sostenibili. 2022. *Linee guida per la classificazione e gestione del rischio, la valutazione della sicurezza ed il monitoraggio dei ponti esistenti.* D.M. 204, July 1, 2022. Rome, Italy.

[8] Santarsiero, Giuseppe, Masi, Angelo, Picciano, Valentina, and Digrisolo, Andrea. 2021. "The Italian Guidelines on Risk Classification and Management of Bridges: Applications and Remarks on Large Scale Risk Assessments." *Infrastructures* 6(8):111. doi:10.3390/infrastructures6080111.

[9] Rampini, Marco Carlo, Cornaggia, Greta, Zani, Giulio, Martinelli, Paolo, and di Prisco, Marco. 2026. "Comparative risk estimation of bridges under fire, impact, and blast hazards: Groundwork for prioritisation criteria in the Italian guidelines." *Structure and Infrastructure Engineering*, 1–20. doi:10.1080/15732479.2026.2617922.

[10] Granata, Michele Fabio, La Mendola, Lidia, Messina, Davide, and Recupero, Antonino. 2023. "Assessment and strengthening of reinforced concrete bridges with half-joint deterioration." *Structural Concrete* 24(1):269–87. doi:10.1002/suco.202200367.

[11] Palmisano, Fabrizio, Asso, Rebecca, Chiaia, Bernardino, Marano, Giuseppe Carlo, and Pellegrino, Carlo. 2023. "Structural assessment of existing R.C. half-joint bridges according to the new Italian guidelines." *Journal of Civil Structural Health Monitoring* 13:1551–75. doi:10.1007/s13349-022-00652-7.

[12] Highways England. 2020. *Risk management and structural assessment of concrete half-joint deck structures.* CS 466, Revision 0. United Kingdom.

[13] di Prisco, Marco, and Flores Ferreira, Katherina. 2025. "The half-joint in the Italian bridges: Residual bearing capacity and smart solutions for retrofitting." *Capacity Assessment of Corroded Reinforced Concrete Structures: From Research to Daily Engineering Evaluation*, 300–09.

[14] di Prisco, Marco, Colombo, Matteo, and Martinelli, Paolo. 2023. "Structural Aspects of the Collapse of a RC Half-Joint Bridge: Case of the Annone Overpass." *Journal of Bridge Engineering* 28(11):05023007. doi:10.1061/JBENF2.BEENG-6063.

[15] Martinelli, Paolo, Colombo, Matteo, and di Prisco, Marco. 2024. "Robustness assessment of half-joint RC girder bridges." *Engineering Structures* 306:117712. doi:10.1016/j.engstruct.2024.117712.

Structural Performance

Bond behaviour of concrete members with fibre-reinforced polymer reinforcement and its influence on cracking behaviour

Kay Lengert, Stephan Görtz

Institute of Civil Engineering,
Kiel Universtity of Applied Sciences,
Grenzstraße 3, 24149 Kiel, Germany

Summary
Within this research bond behaviour of FRP rebars in concrete is being investigated. Experimental investigations are carried out on steel and FRP reinforcement elements embedded in concrete in order to determine experimental bond-stress-slip curves and to outline differences in bond behaviour and bond-failure. The factors influencing bond behaviour are investigated by calculating non-linear finite elements in which concrete strength, bar diameter and bar surface formation are varied. Based on these results, a generally applicable comprehensive bond model will be derived that represents the transfer of bond stress and load transfer into the surrounding concrete. This model is evaluated by creating a database contaning bond test currently available in literatur. The model developed is used to investigate cracking behaviour of reinforced concrete members. These theoretical findings were applied to real structures.

1 INTRODUCTION

The load transfer between reinforcement and concrete via bond is the basis for the functioning of reinforced concrete members. The bond behaviour of frp rebars in concrete differs from that of reinforcing steel in concrete, which is due to the fact that frp reinforcement has different material and bond properties. Therefore, specific investigation of the bond behaviour is necessary. By means of experimental and numerical investigation, a comprehensiv bond model for frp rebars shall be developed that allows to determine the parameters such as the maximum bond strength by calculating it from basic parameters such as concrete compressive strength. The results of these investigations can then be apllied to approaches for determining the concrete cover, the anchorage and overlap length and for calculating deflections and crack widths.

2 THEORETICAL FOUNDATION

Bond behaviour can be defined as the transfer of force between rebar and concrete, which is an essential prerequisite for the functioning of reinforced concrete structures. A distinction is made between the bond mechanisms of adhesive bond, shear and friction. The main parameters influencing bond behaviour are relative rib area, concrete strength, external transverse pressure, concrete composition, concrete cover, bar diameter and position of the bar during pouring. Especially for FRP-reinforcement various surface charakteristics are available (see Fig. 1 and table 1).



Fig. 1 frp-rebars with different surface characteristics

2.1 Bond-stress-slip relation

A bond stress-slip relationship can be used to describe bond behaviour via the ratio of bond stress $\tau(s)$, and relative displacement s between reinforcement and concrete. If small relative displacements occur at high bond stresses, this is referred to as good bond behaviour [1]. Over time, various formulations for the bond stress-slip relationship have been developed for FRP reinforcement [2; 3]. The mBPE model, which is described in ModelCode 2010 [4] is preferable due to its simple mechanical interpretation (1).

$$\tau_b(s) = \begin{cases} \tau_{bm} \cdot \left(\frac{s}{s_m}\right)^{\alpha} \text{ for } 0 \le s \le s_m \\ \tau_{bm} - \tau_{bm} \cdot p \cdot \frac{s - s_m}{s_m} \text{ for } s_m < s \le s_u \end{cases} \quad (1)$$

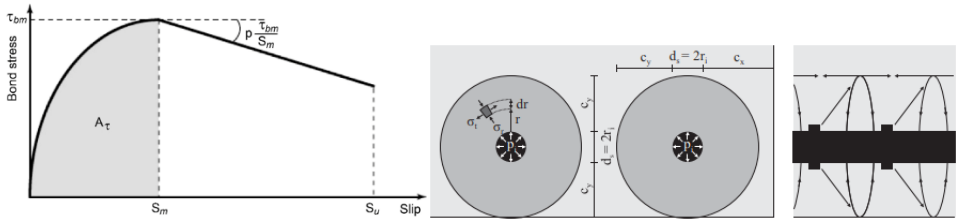


Fig. 2 Bond-Stress-Slip-Relation from [4] (left) and Ring-Model [5] adapted from [6] (right)

2.2 The tensile ring model

The tensile ring model, which was first introduced by Tepfers [5], is used to describe the splitting resistance of concrete cover (Figure 2 right). Three possible stress states are distinguished, for which Tepfers provides equations for calculating the internal pressure. The capacity depends directly on the tensile strength of the concrete. A distinction is made between elastic, plastic, elastically cracked and cohesively cracked tensile ring models. According to Ritter [6], the plastic tensile ring model provides the best correlation with test results. Based on the plastic tensile ring model and the differential equation of bond, Caspari [7] developed an approach for calculating the anchorage length and required concrete cover.

2.3 Failure modes

Typical types of failure of steel-reinforced concrete regarding bond failure are failure due to cracking of the concrete cover and failure due to pull-out, whereby the concrete consoles shear off , For components reinforced with FRP, these types of failure must be extended [8; 9]:

- Pull-Out with shearing of the concrete console
- Pull-Out with shearing of the profile of the FRP bar
- push through the FRP bar core
- Combined failure
- Split fracture

2.4 Differential equation of bond

If the stress state resulting from the bond force transmission is reduced to a one-dimensional problem, it can be described using the differential equation of bond. The differential stress change results from the force equilibrium between the concrete, reinforcement and composite stresses. The stress curve over the development length is determined for a known bond stress-slip relation $\tau(s) \Rightarrow P(w)$. This allows calculating the crack width for a specific stress level [10; 11].

3 EXPERIMENTAL INVESTIGATION

In a first step an overview of available FRP-rebars in Germany (Table 1, Fig. 1) was created to see the span of bar characteristics. In genral frp rebars can be characterised by its fibre material, modulus of elasticity, tensile strength and by its surface characteristics.

Table 1 Overview frp reinforcing bars

Product	Label (Fig 1)	Material	Dimension	Surface	Comment
Rebar 1	a)	GFRP	Ø 8 – 32 mm	cut-in profile	
Rebar 2	b)	GFRP	Ø 4 – 20 mm	braided rib	Outdated
Rebar 3	c)	CFRP	Ø 4 – 12 mm	braided rib	
Rebar 4	d)	CFRP	[ ] 32	plastic profil	Rectangular crosssection
Rebar 5	e)	BFRP	[ ] 27, 32	plastic profil	Rectangular crosssection
Rebar 6	f)	BFRP	Ø 5 – 12 mm	sanded	

Pull-Out-Tests, according to [12] have been carried out in order to investigate the bond behavior of each frp bar and to compare them to each other. The experimental bond stress slip relations (BSR) are given for a serie as an example (Fig. 3 left). The bond stress $\tau_b$is calculated as shown in (2) for bars with a circular crossection and for rectangular crosssections with dimesions a and b as in (3). Furthermore, an analytic model as given in (1) was calibrated using the test data (see Fig. 3 red graph).

$$\tau_b = F/(\pi \cdot d_{nm} \cdot l_b) \quad (2)$$

$$\tau_b = F/(2 \cdot (a+b) \cdot l_b) \quad (3)$$

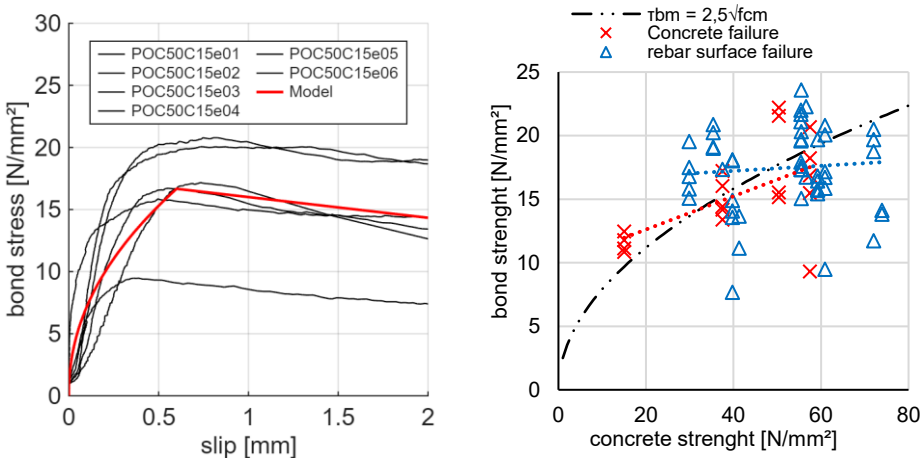


Fig. 3 BSR from Pull-Out-Tests with calibrated mBPE-model (left) and bond strength over concrete compression strength (right)

The tested bar types B500, Rebar 1 and Rebar 2 can be clearly classified in terms of their failure, regardless of the concrete strength. As expected, the concrete console sheared off in the case of the reinforcing steel. Similar behaviour was also observed with Rebar 1, although the damage to the bar surface was negligible. In case of Rebar 2 the reinforcement wrapping failed by detaching from the bar core (Fig. 4). Looking at the failure modes of the Rebar 5-C15 and C35 (Fig. 5), it can be seen that the type of failure depends on the concrete strength. With high concrete strength, the pronounced ribbing of the bars shears off. If the concrete strength is lower the concrete console fails.

Figure 3 (right) lines out that the concrete compressive strength is a major parameter to disribe bond strength if failure is initiaded by concrete. If failure is initiaded by shearing of rebar surface the strenght of the bar surface defines an upper threshold. An approach to discribe bond strenght is given in (4). The crucial point here is to determine the strenght of the surface $f_{nm,surface}$.

$$\tau_{b,m} = min\begin{cases} 2.5 \cdot \sqrt{f_{cm}} \\ f_{nm,surface} \end{cases} \quad (4)$$



Fig. 4 Sawn test specimen with carbon reinforcement Rebar 5 Shear-failure of the concrete console (left) and shear-failure of bar profile (right)

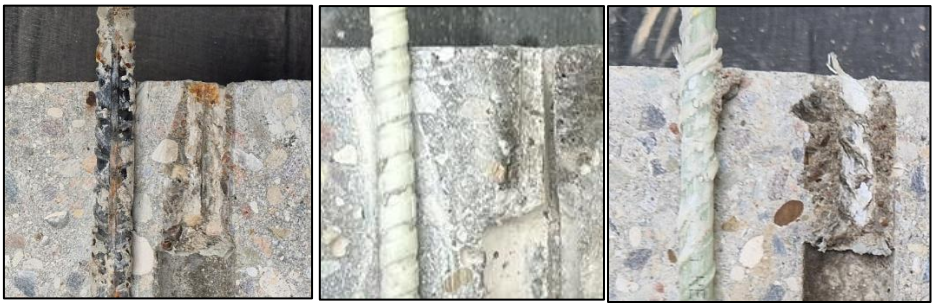


Fig. 5 Sawn test specimens with reinforcing steel B500 (left), Rebar 1 (centre) and Rebar 2 (right)

4 CRACK WIDTH CALCULATION

As mentioned in section 2 the differential equation of bond can be used to calculate crack width when a BSR is given. In order to determine which characteristic parameters of bond have a decisive influence on crack formation of FRP-reinforced members, calculations were performed on the basis of the numerical solution of the differential equation of bond, in which the modulus of elasticity of the reinforcement (E_{nm}), the maximum bond stress (τ_{bm}) and the bond stiffness (α) were varied (see Fig. 6).

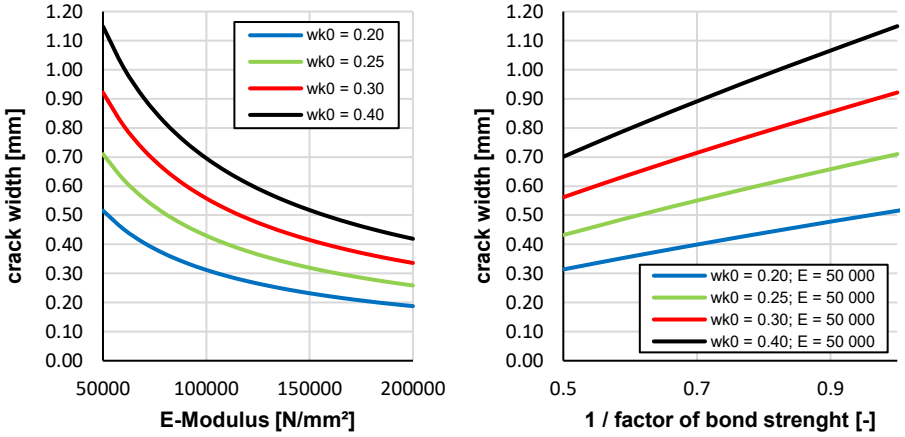


Fig. 6 Influence of the modulus of elasticity and bond strength on crack width

The subsequent section summarizes the results of the investigation. A reduction in modulus of elasticity leads to an increase in crack width. A reduction in modulus of elasticity by a factor of 0.25 results in increased crack width by a factor of 2.7. An increase in the bond strength reduces the crack width. If, for example, the bond stiffness is doubled, the crack width decreases by a factor of 0.6. From this, it can be concluded that the lower modulus of elasticity typical for glass and basalt fibre rebars can be compensated by good bond properties such as high bond strength and stiffness. It should be considerd that the transfer of high loads via bond requires a bigger concrete cover.

5 FINITE ELEMENT ANALYSIS

In order to simulate Pull-Out tests to visualize inner forces, a nonlinear finite element model was created using the software package ATENA Science [13]. A 3D-Modell with reference to [14] was created using isoparametric tetrahedra elements, material models shown in table 2 and the geometry and boundary conditions given in Fig. 7. The profile of the rebar is modelled discrete with a rib hight of $r_h = 0.65\ mm$ and a clear distance of $c = 6.5\ mm$ leading to a bond factor of $f_R = 0.1$. Furtehrmore, a bar with rectangular crosssection was modelled with a rib hight of $r_h = 1.5\ mm$ and a clear distance of $c = 4\ mm$ leading to a bond factor of $f_R = 0.375$. Compared to testdata it can be concluded that bond-stress-slip relations can be derived by FEA in a proper manner. Further, the FE-models will be used to conduct a parameter study.

Table 2 material models for finite element modell of bond

Material model	Material law	Implementation in ATENA
Concrete	Menetrey-Willam in compression Rankine-Criterum in tension	CC3DNonLinCementitios
Steel	Elastic-plastic material with von Mises failure criterion	CC3DBiLiniearSteelvon Mises
FRP	Linaer-elastic	CC3DElastIsotropic
Bond	Mohr-Coulomb failure criterion with tensile strength and residual friction	CC3DInterface

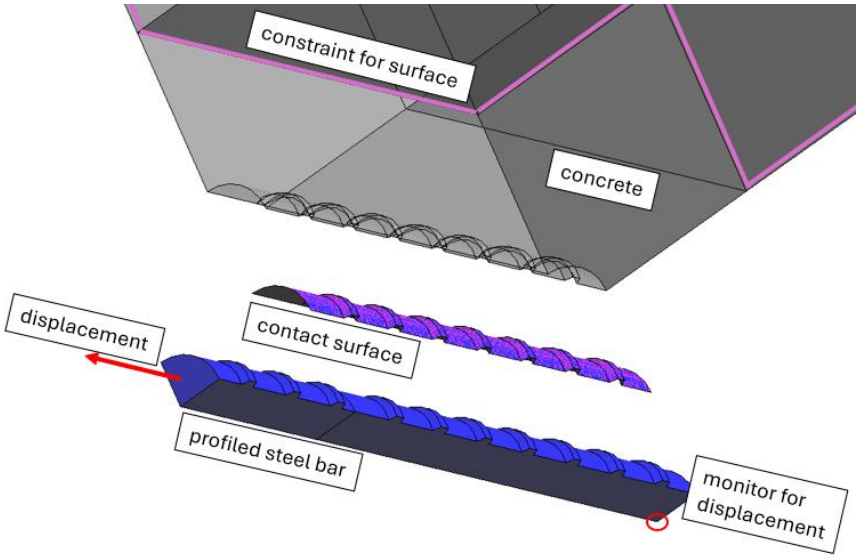


Fig. 7 three-dimensional finite element model

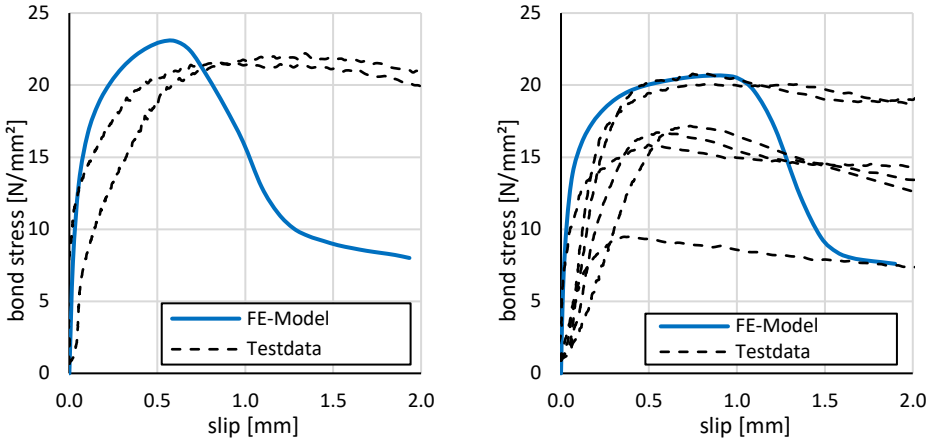


Fig. 8 comparison of FEA-bond-slip-relation and testdata for reinforcement steel like geometry (left) and Rebar 5-like bar geometry

6 BOND DATABASE

The database contains test data from 996 bond tests conducted between 2002 and 2023 from 15 different sources. Where possible, information on reinforcement (as bar diameter, strength and modulus of elasticity), on concrete (as compressive and tensile strength) on the test setup and results (as bond strength, slip and failure mode) were recorded. Missing data was calculated appropriatly when possible. The database was used to verify the own tests (Fig 9 left). In an initial evaluation, certain test parameters were examined with regard to their influence on the bond behaviour. Further, the database has been used to find a general approach for the parameters of a bond stress-slip relationship (such as $\tau_{b,max}$) for FRP-bars using a linear approximation with multiple parameters for a subset of the database (5) and Fig. 9 right).

$$\tau_{b,max} = 5.704 + 0{,}239 d_{nm} + 24.107 f_R + 0{,}159 f_{cm} - 0{,}036 l_b - 0{,}033\, c_{nom} \quad (5)$$

with:

$\tau_{b,max}$ – bond strenght
d_{nm} – diameter of FRP bar
f_R – bond ratio
f_{cm} – mean concrete strength
l_b – embedded length
c_{nom} – concrete cover

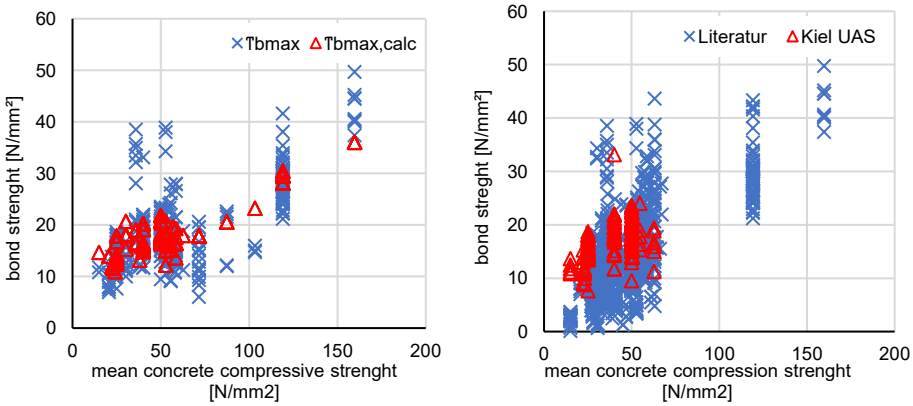


Fig. 9 Verification of test results at Kiel UAS (left) and calculation results of developed approach for bond strength in comparison with the database (right)

7 APPLICATION

7.1 Bridge Cap with BRFP

Due to chloride-induced corrosion of the reinforcement, bridge caps need to be replaced more frequently than planned. To overcome this problem, non-metallic reinforcement made of basalt fibre-reinforced polymer is to be used for the construction of bridge caps. Within the design of the bridge cap crack width calculation and anchorage were impotant issues which require knowledge of the bond behaviour of the rebars [15].

The mBPE model was calibrated for the basalt fibre bar using Pull-Out tests. Furthermore, based on the failure mode of the Pull-Out tests, the required concrete cover was determined. Using the differential equation of bond, a BSR can be transferred to long bond lengths. This also allows crack width and anchorage length to be calculated.

7.2 Shore Wall

As part of the repair of a shore wall in Kiel-Hasselfelde, BFRP reinforcement bars were used to manufacture two precast elements of the concrete facing [16]. As part of the design process, crack width was set to be a maximum of 0.20 mm. The calculation of the crack width was based on the results of Pull-Out tests carried out at Kiel UAS and the differential equation of bond.

With regard to production in the precast plant (Fig. 10, right) and installation on the construction site (Fig. 10, left), there were no negative deviations compared to steel reinforced concrete construction.



Fig. 10 Shore wall being lifted at the construction site (left) Reinforcement mesh at precast plant (right)

8 CONCLUSIONS AND OUTLOOK

In order to derive a generally applicable comprehensive bond model for frp rebars the following steps were carried out:

In a first step a literatur review has been conducted and common methods to describe bond behaviour have been outlined (Section 2). An overview of available frp rebars has been gathered to record the range of properties of frp reinforcement. Further, experimental investigations have been conducted to derive BSRs and studiy the failure modes of frp rebars (section 3). Further tests are planned in order to expand the range of parameters considered and to verify the results on larger test specimen. Nonlinear FE models have been created (section 5), which will be refined and used to conduct a parameter study to derive the general parameters influencing bond bahviour. The bond database (section 6) has been used to outline influencing parameters of bond and to verify the own test results. Further, it can be used to verify the comprehensive bond model. The derived model will be applied to crack width calculation, similar to the investigation in section 3, with the advantage that the direct influence of basic parameters like concrete strenght, bond ratio and surface profile of rebar can be taken into account. This will also allow an optimisation of e. g. the bar surface or rib area / clear space between ribs depending on the use case. In section 7 possible use cases have been presented and the applicability of frp reinforcement has been proved.

Acknowledgements

I would like to thank my supervisors Prof. Dr. Stephan Görtz and Prof. Dr. Raphael Kampmann and LAP Consult for the support.

References

[1] König, Gert; Tue, Nguyen V. 2003 *Grundlagen des Stahlbetonbaus – Einführung in die Bemessung nach DIN 1045-1*. 2. Aufl. Wiesbaden: Vieweg+Teubner Verlag.

[2] Cosenza, Edoardo; Manfredi, Gaetano; Realfonzo, Roberto 1997 *Behavior and Modeling of Bond of FRP Rebars to Concrete* in: Journal of Composites for Construction 1, H. 2, S. 40–51. https://doi.org/10.1061/(ASCE)1090-0268(1997)1:2(40)

[3] Malvar, L. J. 1994 *Bond Stress-slip characteristics of frp rebars*.

[4] fédération internationale du béton / International Federation for Structural Concrete 2013 *fib Model Code for Concrete Structures 2010*. Hoboken: Wiley.

[5] Tepfers, Ralejs 1973 *A theory of bond applied to overlapped tensile reinforcement splices for deformed bars* [Dissertation]. Chalmers Tekniska Högskola.

[6] Ritter, Laura 2013 *Der Einfluss von Querzug auf den Verbund zwischen Beton und Betonstahl* [Dissertation]. Technische Universität Dresden. https://nbn-resolving.org/urn:nbn:de:bsz:14-qucosa-132733.

[7] Caspari, Christian 2022 *Zur Verbundverankerung von Glasfaserkunststoffbewehrungsstäben in Betonbauteilen unter Kurzzeit- und Langzeitbeanspruchung* [Dissertation]. Technischen Universität Kaiserslautern.

[8] Schumann, Alexander 2020 *Experimentelle Untersuchungen des Verbundverhaltens von Carbonstäben in Betonmatrices* [Dissertation]. Technische Universität Dresden.

[9] Füllsack-Köditz, Raimo 2004 *Verbundverhalten von GFK-Bewehrungsstäben und Rissentwicklung in GFK-stabbewehrten Betonbauteilen*. Weimar: Univ.-Verl.

[10] Empelmann, Martin 1995 *Zum nichtlinearen Trag- und Verformungsverhalten von Stabtragwerken aus Konstruktionsbeton unter besonderer Berücksichtigung von Betriebsbeanspruchungen*. Aachen: Eigenverl.

[11] Martin, Horst 1973 *Zusammenhang zwischen Oberflächenbeschaffenheit, Verbund und Sprengwirkung von Bewehrungsstählen unter Kurzzeitbelastung*. Berlin: Ernst.

[12] Deutscher Ausschuss für Stahlbeton e. V. 2026 *DAfStb-Richtlinie Betonbauteile mit nichtmetallischer Bewehrung – (2. Fassung, Entwurf vom 04.02.2026)*.

[13] *ATENA Science (GiD 16.1 + ATENA Studio x64 V 5.9.1)* [Software].

[14] Jakubovskis, Ronaldas; Kaklauskas, Gintaris 2019 *Bond-stress and bar-strain profiles in RC tension members modelled via finite elements* in: Engineering Structures 194, S. 138–146. https://doi.org/10.1016/j.engstruct.2019.05.069

[15] Görtz, Stephan et al. 2025 *Dauerhafte und nachhaltige Brückenkappen aus nichtmetallischer Bewehrung und Recyclingbeton* in: Beton- und Stahlbetonbau 120, H. 2, S. 137–149. https://doi.org/10.1002/best.202400035

[16] Görtz, Stephan et al. 2025 *Anwendung von nichtmetallischer Bewehrung bei der Instandsetzung von Uferwänden* in: Konstruktiver Ingenieurbau, 1/2025, S. 21–29.

Bond Performance in Horizontally and Vertically Cast Ultra-High-Performance Fibre-Reinforced Concrete Overlays

Malena Thomassen[1], Ingrid Lande[1],

[1]Department of Engineering Sciences
University of Agder
Jon Lilletuns vei 9, 4879 Grimstad, Norway

1 SUMMARY

This study investigates the potential of Ultra-High-Performance Fibre-Reinforced Concrete (UHPFRC) as a standardized method for bridge rehabilitation in Norway. The primary objective is to evaluate the bond strength of an industrially cast bridge deck with a UHPFRC overlay. To assess the applicability of the casting technique for large-scale implementation, two specimens will be tested: one cast horizontally and one cast vertically. In Norway, vertical casting of UHPFRC in rehabilitation projects has yet to be attempted; therefore, this study aims to evaluate whether bond strength is influenced by the casting direction. Bond strength between the UHPFRC layer and the substrate will be measured through a pull-off test and a direct tensile test. The direct tensile test was used to provoke fracture, as the bond strength exceeded the capacity of the pull-off equipment. The results shows that the vertical cast specimens exhibit at least 35 % higher bond strength compared to the horizontally casted specimens.

2 BACKGROUND

The concrete infrastructure in Norway is aging and requires extensive rehabilitation [1]. Many bridges have already exceeded their intended service life, creating a significant backlog of maintenance needs. Conventional rehabilitation of concrete bridges is both time-consuming and material-inefficient, typically involving the removal of damaged asphalt and concrete followed by the application of a new layer of reinforced concrete. Several bridges are located in marine environments, where pillars and bridge decks are directly exposed to seawater. As a result, these structures suffer from chloride-induced corrosion, spalling caused by freeze–thaw cycles, and mechanical damage. Conventional concrete is still widely used for both bridge decks and pillars, but its long-term durability in such conditions is limited.

In countries such as Switzerland and the United States, Ultra-High-Performance Fibre-Reinforced Concrete (UHPFRC) has become a standard material for bridge rehabilitation [2]. The conceptual design applied in Switzerland involves removing the uppermost layers of asphalt and damaged concrete from the bridge deck [3, 4]. To ensure sufficient bonding, the surface is treated with water jetting before applying a new UHPFRC layer. Depending on the purpose, the UHPFRC overlay may be as thin as 20 mm for surface protection or a minimum of 40 mm for structural enhancement and the restoration of structural integrity. UHPFRC offers clear advantages over conventional concrete [5]. It exhibits very high compressive strength, tensile strength exceeding 7 MPa depending on the steel fibre content, low porosity, and excellent durability. Furthermore, its low permeability makes it highly resistant to environmental degradation, thereby extending the service life of rehabilitated structures.

Despite the frequent international use of UHPFRC, the material has yet to be widely adopted in the Norwegian construction industry. Some contractors have begun exploring its application in projects such as salmon farms and are planning pilot studies on local bridges. In practice, UHPFRC is typically cast by gravity in conventional formwork, and while contractors are optimistic about its use in bridge decks, in many cases the more critical challenges lie in deteriorated bridge pillars. These require rehabilitation through jacketing techniques or horizontal casting of bridge deck overlay. A clear gap has been identified between academic research on UHPFRC and current industrial best practices in Norway. This paper seeks to address this gap by investigating the feasibility of casting UHPFRC with conventional Norwegian equipment, both horizontally and vertically. The objective is to examine whether casting direction affects fibre distribution and, in turn, the bending and bond properties of composite structures combining UHPFRC and normal concrete.

3 RESEARCH QUESTION

How does the casting direction (horizontal vs. vertical) of UHPFRC overlays affect the bond strength between UHPFRC and an industrially casted concrete decks in Norway?

4 METHODS

Two reinforced C35/45 concrete decks from an airfield in the Norway were used as an existing concrete structure for the horizontally and vertically cast bridge decks (750 mm x 1450 mm). The tests were carried out in cooperation with a representative from a Norwegian contractor. Since the materials were supplied by the contractor, the UHPFRC used in this study is a patent-restricted product, and its mix design is therefore not disclosed. A spreading test was conducted to verify that the consistency of the material corresponded with the values specified by the producer. The fibre type used is straight wire steel micro fibres (DM) 12.5 mm/0.175 mm with tensile strength of 2800 MPa.

Prior to casting, the C35/45 decks were water-jetted with 400 Bar and covered with plastic for 24 hours to ensure sufficient bond. The roughness depth was not measured prior to casting. Two different formwork setups were applied: one with the deck positioned horizontally and one with the deck positioned vertically. In both cases, the specimens were covered with plastic immediately after casting, as shown in Fig.1.



Fig. 1 Casting of the vertical and horizontal layer of UHPFRC.

Compressive strength of the UHPFRC layer was measured according to NS-EN 12390-3 of six 100 mm cubes, and flexural strength at first crack according to NS-EN 196-1 of three prisms of 40 mm × 40 mm × 160 mm.

4.1 Preparation of test specimen

A total of 5 beams (B1–B5) and 4(5) pull-off tests (P1–P4(5)) were cut out from each deck. Test specimens taken from the vertical casting surface are designated with V, while those from the horizontal surface are designated with H. The specimens were taken from the decks as shown in Fig. 2. The beams (150 mm ×150 mm × 600 mm) are to be tested in the next stage. For the vertical cast deck, VP3-VP5 represent the bottom of the formwork, and thus may be more compacted and beneficial for bond strength.

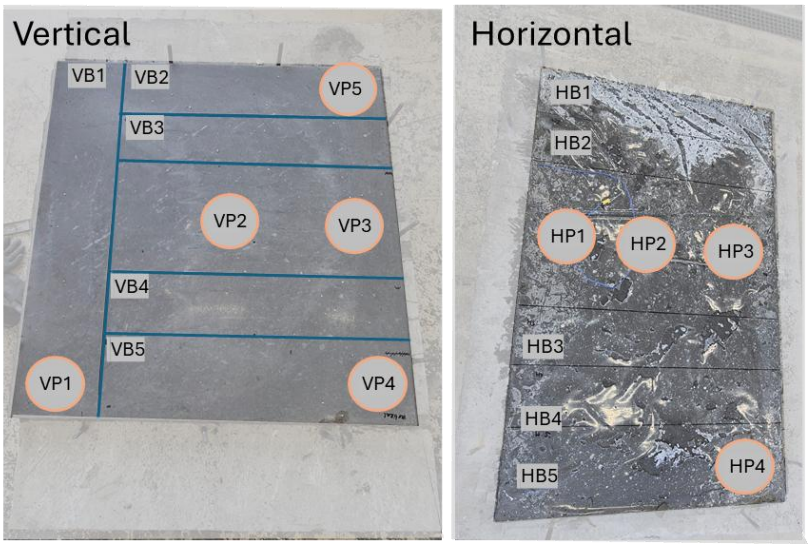


Fig. 2 Extraction of test specimens from the decks.

4.2 Bond strength

Bond strength was evaluated using a Proceq DY-225 pull-off tester, which has a maximum capacity of 3.06 MPa when using 50 mm cores. According to the Federal Highway Administration (FHWA) [6], interface bond strengths typically range between 2.4 and 4.12 MPa, which may exceed the capacity of the Proceq DY-225. Consequently, some specimens did not fail during testing with this device. To enable evaluation of the fracture surfaces and determine the bond strength beyond the device limit, selected specimens were subsequently loaded to failure using alternative equipment. A direct tensile testing machine (Zwick) was used to fracture the samples and measure the bond strength.

To ensure comparability with results obtained using the Proceq DY-225, a total of 20 C20/25 specimens with cast-on UHPFRC layers were tested. All specimens were produced following Norwegian industrial practice [7]. Ten specimens were tested using the Proceq DY-225, while the remaining ten were tested using the Zwick machine. The results were then compared to assess the compatibility of the Zwick setup for pull-off bond testing.

5 RESULTS AND DISCUSSION

The fresh properties of the UHPFRC mix showed a maximum spreading of 255 mm on the horizontally cast deck and 265 mm on the vertically cast deck. The average compressive strength, determined according to NS-EN 12390-3, was 172.65 MPa. In addition, the average flexural strength at first crack, measured on a 40 mm × 40 mm × 160 mm prism in accordance with NS-EN 196-1, was 20.8 MPa.

When using the direct tensile testing equipment, the results showed considerable variability, likely caused by misalignment and eccentricities in the test setup. The average bond strength measured using the Zwick machine was 1.58 MPa, compared to 2.13 MPa obtained with the Proceq pull-off tester. Due to this division and the large scatter in the results, the direct tensile equipment was considered unreliable for quantitative bond strength determination. Consequently, it was used only to pull off specimens that had already exceeded the capacity of the Proceq device. For these specimens, the failure surfaces were

examined to qualitatively assess the bond performance based on the location and mode of failure rather than on numerical strength values.

Using the Proceq DY-225 pull-off testing device, the maximum measured bond strength for a 50 mm diameter core was 3.06 MPa. One specimen (V2) exhibited a bond strength of 2.57 MPa, with failure occurring within the C35/45 conventional concrete substrate, as presented in Table 1. The remaining specimens did not reach failure due to the limited capacity of the testing equipment, indicating a minimum bond strength of 3.06 MPa. For the vertical specimens, the results also indicate that no clear relationship could be established showing that tests taken from the bottom location of the cast exhibit higher capacity. This aspect may be further evaluated in future research, particularly by using a pull-off device with a higher capacity. Core specimens were extracted from the bridge deck, and failure consistently occurred within the conventional concrete for all samples except one, see Fig. 3. This failure mode indicates that the bond strength at the UHPFRC–conventional concrete interface exceeds the tensile strength of the C35/45 concrete, demonstrating an excellent bond performance.

Table 1 Capacity and failure surface for the tested specimens

Specimen	Maximal capacity [MPa]	Average	Failure surface
VP1	>3.06	>2.956	C35/45 (existing concrete)
VP2	2.57		C35/45 (existing concrete)
VP3	>3.06		C35/45 (existing concrete)
VP4	>3.06		Interface, 85 % in C35/45 15 % in UHPFRC
VP5	>3.06		C35/45 (existing concrete)
HP1	2.01	2.193	C35/45 (existing concrete)
HP2	2.46		C35/45 (existing concrete)
HP3	1.75		C35/45 (existing concrete)
HP4	2.55		C35/45 (existing concrete)



Fig. 3 Extraction of test specimens from the decks.

Specimen VP2 exhibited a mixed failure mode, with approximately 85% of the fracture surface located in the substrate concrete and 15% within the UHPFRC layer, see Figure 4. This specimen had a comparatively thick UHPFRC overlay, which became locally indented due to excessive formwork deformation caused by the hydrostatic pressure of the fresh UHPFRC during casting. As a consequence, the core was not drilled to a sufficient depth, and the failure plane coincided with the bottom of the drilled core. This suggests that the observed fracture may have been artificially induced by geometric and testing constraints rather than representing the true bond capacity, thereby preventing a pure failure within the conventional concrete layer.



Fig. 4 Fracture surface of specimen VP2

For the horizontally cast specimens, the Proceq DY-225 was able to pull off all samples, indicating a lower capacity compared to the vertically cast specimens. The fracture occurred close to the interface between UHPFRC and NC for the horizontally casted beams, but deeper inside the NC layer for the vertically casted beams. The average measured bond strength for the horizontally cast specimens was 2.19 MPa, which is significantly lower than that observed for the vertically cast specimens, which exhibited an average minimum bond strength of 2.96 MPa. The observed difference in bond strength maybe influenced by fibre orientation effects within the UHPFRC layer, due to the fact that the failure happened close to the interface. Rojas et al.[8] reported that investigations of vertically cast walls and slabs show a preferential fibre alignment within the horizontal (XY) plane. Such fibre orientation may result in a higher likelihood of fibres intersecting the UHPFRC–conventional concrete interface, thereby enhancing mechanical interlocking and bond strength if fibres become anchored within the pore structure of the substrate concrete. However, this hypothesis requires further experimental verification, for instance through inductive testing methods capable of quantitatively assessing fibre orientation in the tested specimens.

Field pull-off tests conducted by Alvarez et al. [9] on a bridge structure in Socorro, New Mexico provide additional context for the present results. The bridge was constructed using a configuration similar to that employed in this study, consisting of a conventional concrete substrate overlaid with UHPFRC. The results demonstrated excellent bond performance, with the majority of specimens failing within the conventional concrete rather than at the interface. According to the evaluation criteria outlined in ACI 546S, the measured bond strength exceeded the minimum requirement of 1.72 MPa, thereby classifying the bond as excellent and supporting the findings of the present experimental investigation.

Despite the sufficient bond strength obtained in this research, it should be noted that pull-off tests represent only part of the overall performance. In real applications, shear transfer is typically the governing mechanism for bond behaviour and is therefore more critical to evaluate. Failure by direct pull-off rarely occurs in practice and is mainly used to verify that the materials act compositely. In the next stage of this research, evaluating the flexural bending strength will provide insight into potential delamination, as well as the composite behaviour under bending moments and shear forces. Although shear transfer is the most common failure mode with regard to bond performance, the Norwegian industry still commonly relies on pull-off testing as a practical method for post-casting quality assessment. Future research will also involve using an inductive test equipment for evaluating the fibre content and direction of fibres, both with regard to the pull-out test and the flexural bending test.

6 CONCLUSION

The aim of this study was to evaluate the influence of casting direction on the bond strength between UHPFRC overlays and industrially cast C35/45 concrete decks under Norwegian conditions. Based on the experimental results and observed failure modes, the following conclusions are drawn:

- UHPFRC exhibited excellent bond strength to the existing concrete for both casting directions, with failure predominantly occurring within the C35/45 substrate rather than at the interface, indicating that the bond strength exceeded the tensile capacity of the conventional concrete.
- The bond strength could not be directly evaluated, as failure consistently occurred within the substrate concrete rather than at the interface between the substrate and the UHPFRC overlay. However, the vertical casting configuration was subjected to higher loading, as the substrate concrete did not fail within the measurable range of the testing equipment.
- The capacity of the failure surface exceeded 2.956 MPa for vertically cast specimens and 2.193 MPa for horizontally cast specimens, indicating that the vertical configuration sustains higher stresses despite the governing failure mode being located in the substrate rather than at the interface.
- A superior bond performance of vertically cast overlays may be attributed to favourable fibre orientation and enhanced mechanical interlocking at the interface, although this mechanism was not directly verified and requires further investigation.

Acknowledgements

The authors also gratefully acknowledge the contribution and efforts of UiA student Aram Akhte for conducting some of the laboratory experiments. As an alternative to language editing services, Copilot was used during the preparation of the draft of this manuscript to improve readability and for spell-check, for some parts of the text.

References

[1] RIF Engineers, "State of the Nation - Norges Tilstand 2021," RIF, Oslo, 2021.

[2] Brühwiler, Eugene, “STRUCTURAL UHPFRC” TO ENHANCE BRIDGES," in *Proceedings of the 2nd International Conference on UHPC Materials and Structures UHPC* China, 2018 2018, vol. PRO 129: RILEM Publications S.A.R.L., pp. 140–158. [Online]. Available: https://infoscience.epfl.ch/handle/20.500.14299/151362. [Online]. Available: https://infoscience.epfl.ch/handle/20.500.14299/151362

[3] Bertola, Numa, Schiltz, Philippe, Denarié, Emmanuel, and Brühwiler, Eugene (2021) A Review of the Use of UHPFRC in Bridge Rehabilitation and New Construction in Switzerland. *Frontiers in Built Environment*.

[4] Brühwiler, Eugene, Denarié, Emmanuel, and Habel, Katrin "Ultra-High Performance Fibre Reinforced Concrete for Advanced Rehabilitation of Bridges," in *Fib Symposium "Keep Concrete Attractive"*, Budapest, 2005.

[5] Brühwiler, Eugene, *"Structural UHPFRC": Welcome to the post-concrete era!* 2016.

[6] Federal Highway Administration, "Design and Construction of UHPC-Based Bridge Preservation and Repair Solutions," 2022.

[7] Lande, Ingrid, Thorstensen, Rein Terje, Petersen, Berit Gudding, and Kanstad, Terje "Full-scale Production and Material Properties of Ultra-High-Performance Fiber-Reinforced Concrete (UHPFRC) for Rehabilitation of Bridge Decks in Norway," *Frontiers in Built Environment,* vol. 11, p. 1570920, 2025.

[8] Rojas, Guillem, Mena-Alonso Alvaro, Muñoz, Álvaro, Kanstad, Terje and Vicente, Miguel "Experimental study of the fibre distribution in SFRC: a comparison between CT-scanning techniques and the inductive method," *Materials and Structures,* vol. 58, 09/19 2025, doi: 10.1617/s11527-025-02784-w.

[9] Alvarez, Andres, Toledo, William, Weldon, Brad, and Newtson, Craig, "Construction Methods and Lessons Learned for a Non-Proprietary Ultra-High Performance Concrete Overlay," *Construction materials 2024,* pp. 271–291, 2024.

Influence of planted columns on shear resistance of transfer slabs without transverse reinforcement

Jiayu Long, Robert Vollum, Lorenzo Macorini

Department of Civil and Environmental Engineering
Imperial College London
Exhibition Rd, South Kensington, London SW7 2AZ

Summary
Transfer slabs are widely used in multistorey reinforced concrete buildings to accommodate changes in column layout between floors. Despite this, the shear resistance of transfer slabs supporting planted columns remains uncertain due to the complexity of the failure mode which can be punching shear, linear shear or a combination of the two. Current best practice is to use linear elastic shear field analysis to determine the design shear forces in transfer slabs. This paper uses nonlinear finite element analysis (NLFEA) with three-dimensional solid elements to determine both the shear field and failure load of representative transfer slabs failing in shear. Comparisons are made between the failure loads obtained with NLFEA and linear elastic shear field analysis carried out in accordance with Eurocode 2: 2023 (EC2-23). Significantly, the linear shear check in EC2-23 is found to be overly conservative for the considered slabs.

1 INTRODUCTION

In the UK, the adoption of transfer slabs increased markedly in the early 2000s following the widespread adoption of elastic finite element analysis for slab design. In the absence of specific codified guidance, the shear design of transfer slabs has historically relied on engineering judgement, resulting in considerable variations in slab thickness and detailing across the existing UK building stock. A key challenge in the design and assessment of transfer slabs is the verification of shear resistance. The shear force distribution around columns can be highly non-uniform in transfer slabs due to planted column loading. This nonuniformity is not captured by code-based shear enhancement factors β which relate the design shear force to the eccentricity $e = M/V$ of the design shear force. Based on the recommendations of Eurocode 2 (EC2-23) [1], the recently published IStructE guidance for the design of transfer slabs [2] recommends that the design shear force should be determined using elastic shear field analysis [3]. The IStructE guidance is currently based on EC2-04 [4] but will in due course be updated to EC2-23. As shown by Natário [3], the design shear force obtained with LFEA using shell elements can depend significantly on the choice of shear modulus as well as the averaging width on each side of the peak shear force which EC2-23 limits to $2d$ where d is the slab effective depth. This paper investigates the influence of through thickness shear stiffness on the shear verification of transfer slabs designed to EC2-23 using LFEA with shell elements. Nonlinear finite element analysis (NLFEA) using 3D solid elements is used to determine the planted column failure load, failure mechanism and shear force distribution before cracking and at failure. The results of NLFEA are subsequently used as a benchmark against which shear forces obtained from LFEA are compared. The shear fields obtained with NLFEA and LFEA are broadly similar. However, contrary to previous findings the design shear force is found to be relatively insensitive to the choice of through thickness shear modulus in the LFEA. This suggests that the design shear force obtained with LFEA is dependent not only on modelling considerations such as element size but also the element formulation which is dependent on the choice of design software.

2 NLFEA VALIDATION

Reinforced concrete shows pronounced nonlinear behaviour, meaning that the results of NLFEA are strongly influenced by the adopted modelling assumptions and material parameters. Consequently, these parameters must be carefully calibrated and validated using appropriate experimental evidence. In the NLFEA, concrete is simulated in ATENA [5] with the CC3DNonLinCementitious2 constitutive model and three-dimensional solid elements. A fully rotating crack approach is employed. The reinforcement is modelled by embedded truss elements under the assumption of perfect bond, whereas

steel components are represented by elastic tetrahedral elements. Following calibration studies conducted by Wang [6] on corbels [7], punching shear specimens [8] and experimental work on transfer slabs [9], the modelling strategy outlined in Table 1 is adopted. The author further validated these modelling parameters by simulating a series of internal punching specimens tested by Sagaseta et al. [10] and a series of simply supported one-way spanning slabs, subject to concentrated loading, tested by Reissen et al. [11]. The punching specimens were chosen due to their one-way loading arrangement, and elongated support, which leads to a greater concentration of shear force around the support than in standard punching shear tests. The slabs of Reissen et al. were chosen due to their varying width which caused the failure mode to shift from one-way shear to punching shear.

Table 1 Material parameters adopted in ATENA.

Parameter	Value/Reference
Concrete constitutive model	
Concrete elastic modulus	Model code 2010
Fracture energy	Model code 2010
Concrete tensile strength	Model code 2010
Smeared crack model	Fully rotating crack
Critical compressive displacement w_d	0.2mm
Limit of compressive strength reduction due to cracking	$0.5r_c$
Eccentricity (defining the shape of the failure surface)	0.52
Volume dilation plastic factor	0
Reinforcement bar model	
Stress-strain relationship	Bilinear with strain hardening
Bond-slip model	Perfect bond
Loading procedure and convergence criteria	
Loading procedure	Static (force-controlled)
Solution procedure	Arc-length method
Convergence criteria for displacement, residual force and absolute residual force error	1%
Convergence criterion for energy error	0.01%
Mesh properties	
Mesh size of slab along thickness	25mm
Mesh size of slab in plan	25mm
Mesh element for concrete slab	linear hexahedral element
Mesh element for loading apparatus	Linear tetrahedral or hexahedral element
Mesh element for support	Linear tetrahedral or hexahedral element
Mesh element for reinforcement bar	Embedded 2-noded truss element

Table 2 Additional validation in ATENA.

Test	b	b/d	h	a_v/d	Loading	P_{test}	Failure (test)	P_{ATENA}	$\frac{P_{test}}{P_{ATENA}}$	Failure (ATENA)
AM01	3.0	14.0	0.25	-	1-way	950	Punching	887	1.07	Punching
AM02	3.0	14.4	0.25	-	1-way	919	Punching	820	1.12	Punching
AM03	3.0	14.8	0.25	-	1-way	883	Punching	834	1.06	Punching
AM04	3.0	14.9	0.25	-	2-way	1067	Punching	943	1.13	Punching
S5B-1	0.5	2.1	0.28	4.2	1-way	183	Shear	261	0.70	Shear
S15B1	1.5	6.3	0.28	4.2	1-way	543	Shear	548	0.99	Shear
S25B1	2.5	10.4	0.28	4.2	1-way	664	Punching	678	0.98	Punching
S35B1	3.5	14.6	0.28	4.2	1-way	985	Punching	991	0.99	Punching

Table 2 shows that the ATENA simulations provide good estimates of the failure load of all the investigated specimens apart from S5B1 which was only 500 mm wide and hence unrepresentative of

transfer slabs supporting planted columns. Overall, $\frac{V_{test}}{V_{ATENA}} = 1.01$ for the specimens in Table 2 with a coefficient of variation of 0.14.

3 BACKGROUND OF SHEAR FIELD ANALYSIS

The punching shear provisions in EC2-23 are derived from the Critical Shear Crack Theory (CSCT) [12], which represents a significant departure from the semi-empirical approaches adopted in EC2-04. The CSCT is based on the premise that the shear resistance of reinforced concrete members depends on the width of the critical shear crack, which is assumed to be proportional to the product of the slab effective depth d and the slab rotation ψ. The design shear force can be determined with shear field analysis as first proposed by Vaz Rodrigues et al. [13] who recommended that the effective control perimeter for punching shear failure should be calculated as:

$$b_0 = \frac{V}{v_{max}} \tag{1}$$

Although adopted in fib MC2010 [14] comparisons with experimental results indicate that equation (1) leads to overly conservative predictions of punching resistance. Sagaseta et al. [10] attributed this to LFEA not capturing the redistribution of shear forces from failing to non-failing regions. EC2-23 allows for shear redistribution of this type by allowing shear forces from elastic analysis to be averaged on each side of the peak by up to $2d$. Natário [3] obtained realistic estimates of the reactions measured in his cantilever slab tests when using a reduced through thickness shear stiffness of $G = E_c/16$ in LFEA with SAP2000 [15].

4 MODELLING OF A TYPICAL TRANSFER SLAB STRUCTURE

Based on the work of Wang [6], this study considers the five-storey building shown in Fig. 1(a). The transfer slab at level 1 supports the interior columns of floors 2 to 5, which are offset from the columns below by a clear distance a_v, modelled as $2d$, $3d$ and $4d$. All the internal columns measure 400×400 mm^2 in cross-section with a storey height of 3.6 m. The transfer slab thickness was taken as 450 mm, for comparison with the results in [6]. At ground-floor level, the bottom columns were spaced at 6 m in the direction parallel to the column offset. The bay width b was taken as 2.7 m, 4.5 m and 6.0 m, giving b/d ratios of approximately 6.8, 11.3 and 15.0 like the slabs of Reissen et al. [11]. Such a variation in b/d can also arise for constant bay width due to increases in slab depth arising from increased planted column loading.

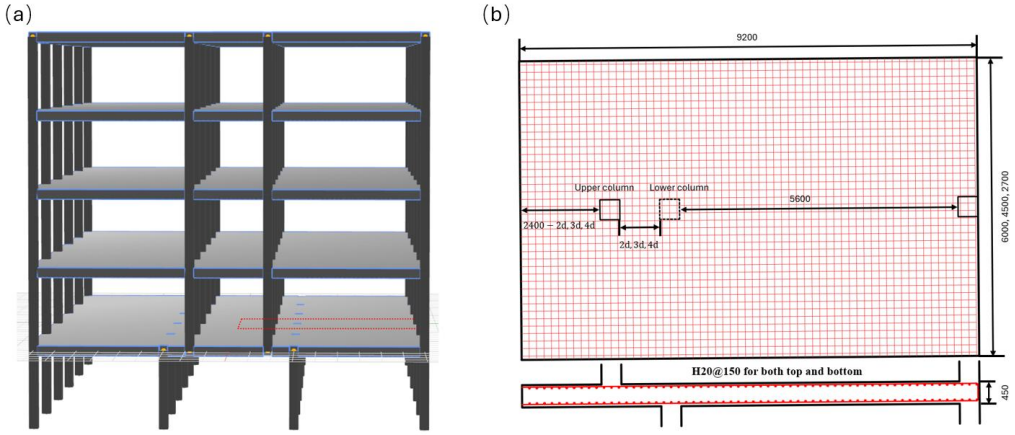


Fig. 1 The model used for research: (a) The whole building model and extraction of small subassembly; (b) the geometry and reinforcement layout.

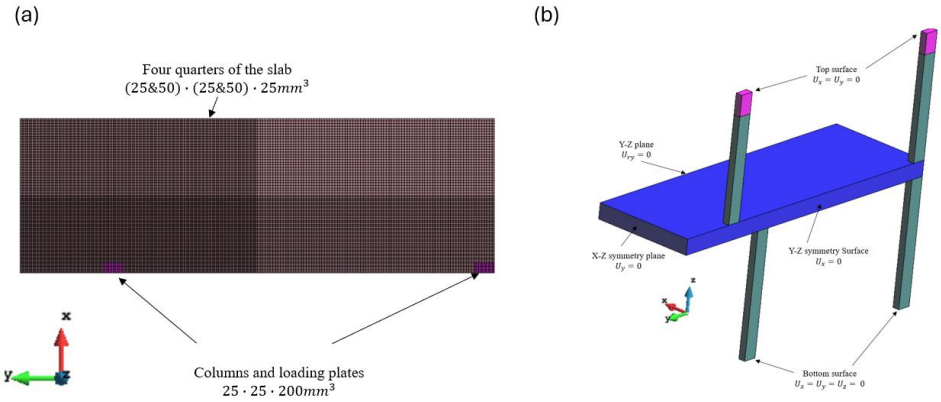


Fig. 2 The ATENA model: (a) The mesh assigned in the model; (b) boundary conditions.

The mean effective depth d of the slab reinforcement was 400 mm for both the top and bottom reinforcement layers. A characteristic concrete cylinder strength of 32 MPa, and Grade 500 reinforcement ($f_{yk} = 500$ MPa, $E_s = 200$ GPa) were adopted throughout. For detailed structural modelling, a one bay wide subassembly was modelled as shown in Figs. 1 and 2. The top and bottom flexural reinforcement was taken as $B20@150\,mm$ ($\rho = 0.52\%$) in both directions to ensure that shear failure was critical. The failure load was determined under i) pure UDL (field shear); ii) pure upper column load and iii) combinations of i) and ii) with the UDL applied first.

This paper examines the influence of reducing the through thickness element stiffness on one-way and punching shear resistances calculated with EC2-23 using shear field analysis. Shear forces arising from uniform loading on the transfer slab are depicted "field" shear. The LFEA was carried out using OASYS GSA [16] using linear elastic $25 \times 25\,mm^2$ elastic shell elements. The shell element formulation allows for shear deformation. Both MITC and Mindlin-Reissner formulations are available in GSA but this choice was not found to significantly affect the obtained results. The columns were modelled with beam-column elements connected to the slab around the column perimeter using rigid links. The long edges of the model were rotationally restrained. Two choices of through thickness shear modulus were considered i) $G = 100\%$ of the elastic value with Poisson's ratio $\nu = 0.2$; and ii) $G = 12.5\%$ of the elastic value with Poisson's ratio $\nu = 0$ as recommended by Natário [3]. For linear shear, the shear force was averaged over $2d$ on each side of the peak as shown in Fig. 3a. For punching, the shear force was averaged around i) ½ of the control perimeter which is the maximum permissible according to EC2-23 for the considered transfer slab geometry and ii) ¼ of the control perimeter as shown in Fig. 3b.

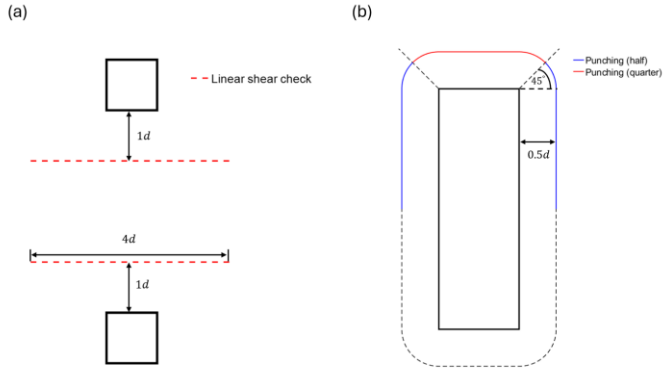


Fig. 3 (a) Averaging length of $4d$ for linear shear check; (b) the two averaging lengths "punching (half)" and "punching (quarter)" for punching shear check.

5 INFLUENCE OF SHEAR STIFFNESS ON SHEAR FIELD

In the ATENA simulations, all slabs failed in a brittle manner, with most exhibiting load-displacement responses like that shown in Fig. 4. The interaction between the planted column failure loads determined with ATENA and EC2-23 and field shear is illustrated in Fig. 5 which also indicates the failure mode in ATENA. The EC2-23 punching shear check is seen to become progressively less conservative as the field shear is reduced. The linear shear check in EC2-23 is seen to be overly conservative except for the 2.7 m wide slabs with $a_v = 3d$ and $4d$ where failure either occurred in linear shear or a mixed mode. The failure mode in the NLFEA was determined from observations of the cracking pattern and contour plots of the increase in slab thickness at failure. All the slabs failed in punching shear, linear shear, or a combination of the two.

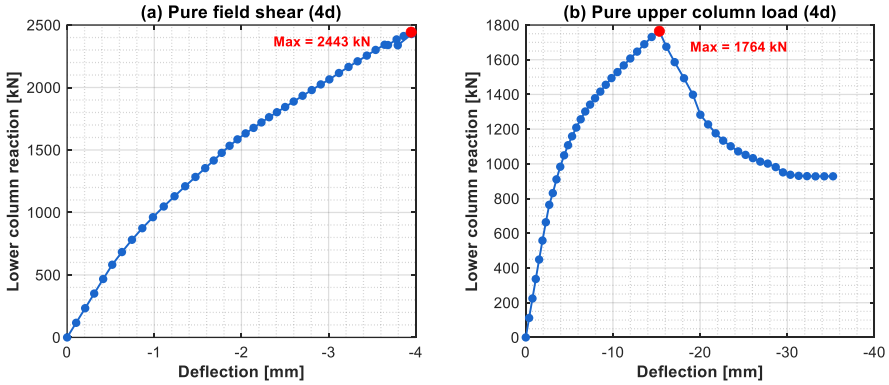


Fig. 4 Load-displacement response of $6m$ wide bay for a gap of $4d$.

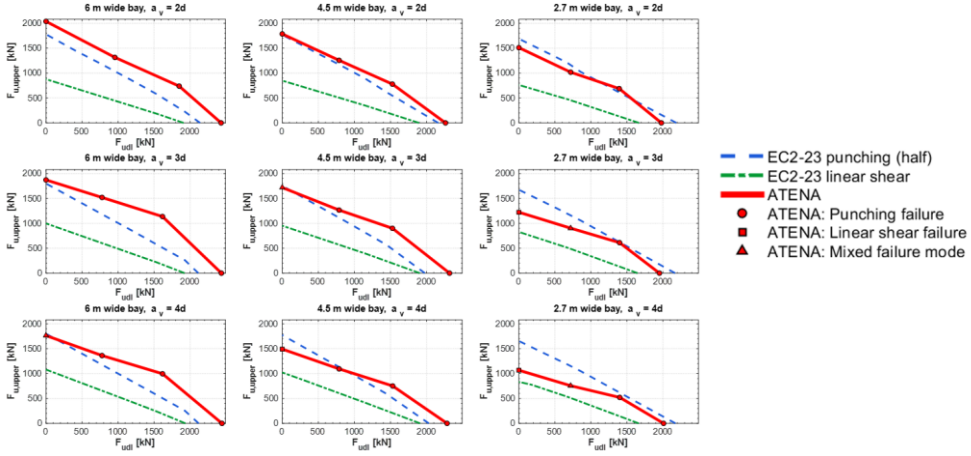


Fig. 5 Interaction diagrams.

Fig. 6 compares the shear fields obtained from LFEA with G=100% and G=12.5% and ATENA i) before cracking and ii) at failure. The ATENA shear field was obtained by post-processing the three-dimensional stress output from the analysis. The shear stress components τ_{xz} and τ_{yz}were extracted from the element output and averaged over all integration-point records within each element. The averaged stresses were then integrated through the slab thickness over slab thickness to obtain the through-thickness shear force components q_x and q_y. The resulting shear field was interpolated onto a regular two-dimensional grid and visualised as filled contour plots of the shear-flow magnitude $| q_{max} | = \sqrt{q_x^2 + q_y^2}$. For both linear shear and punching shear checks, the shear fields were normalised with respect to a 1 kN axial force in the internal lower column. The shear forces along the critical control sections for one-way and punching shear are compared in Fig. 7 and numerical values of the design shear forces are listed in Table 3.

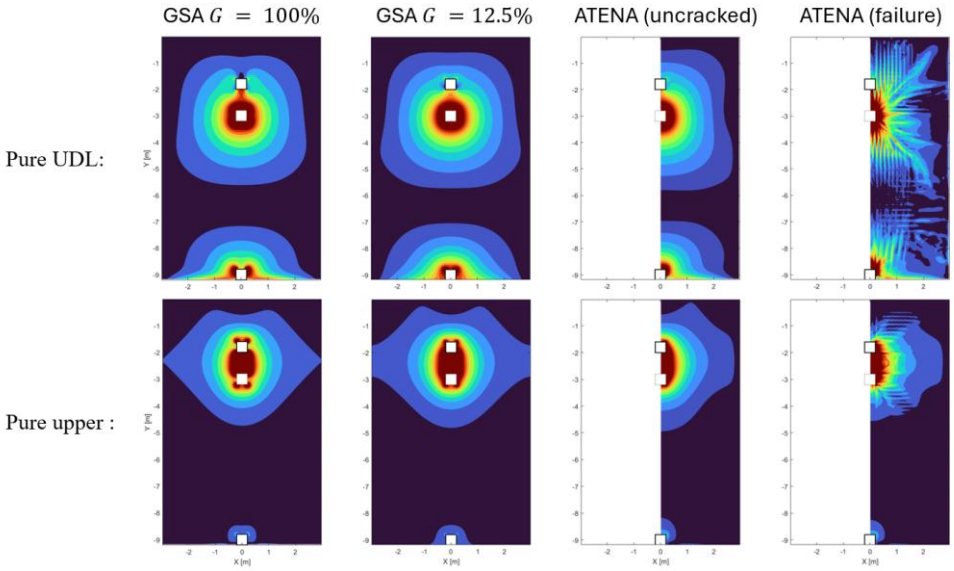


Fig. 6 Comparison of shear field between LFEA and NLFEA.

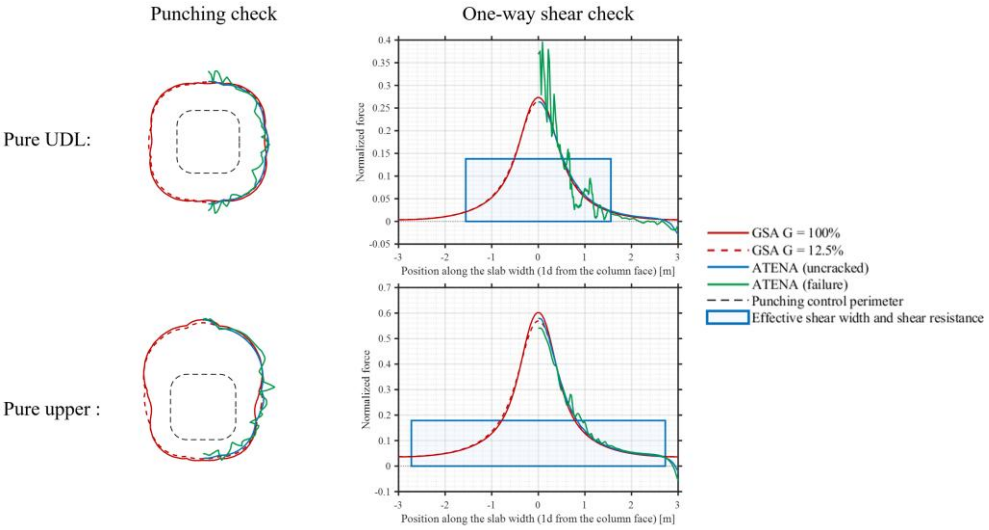


Fig. 7 Influence of shear stiffness on shear force (Normalized to $1kN$ lower column axial force) at critical control sections around internal lower column.

As shown in Fig. 7, the shear fields obtained from LFEA using the default shear modulus (G = 100%, $\nu = 0.2$) and the reduced shear modulus (G = 12.5%, $\nu = 0$) are both very similar to the uncracked shear field obtained with ATENA, particularly for the pure field shear case. This observation is confirmed quantitatively in Table 3, where the normalised design shear forces for both linear shear and punching shear checks differ by less than 2% between the two GSA solutions and the reference uncracked ATENA solution. The coefficients β in Table 3 represent the ratio of the design shear force to the average shear force around the control perimeter in kN/m. The design shear force is the average shear force along the depicted averaging length. Greater differences are observed for the pure upper column load case, where the shear field is highly concentrated around the internal lower column. Fig. 6 shows that the peak linear shear force obtained with GSA using the default shear modulus is slightly greater than obtained with ATENA before cracking. Very good agreement is obtained between the GSA results and ATENA when the through-thickness shear modulus is reduced to 12.5% of the default elastic

value. Significantly, the ATENA normalised design shear forces in Table 3 tend to be greater at failure than before cracking indicating that shear redistribution did not occur in the analysis as assumed in the CSCT [12]. A similar observation is made by Setiawan et al. in [17]. It is unclear whether this reflects reality or is a consequence of the adopted modelling parameters in ATENA. The blue boxes in the right-hand graphs of Fig. 7 indicate the the width over which the linear shear force needs to be averaged for the EC2-23 linear shear check not to be critical at d from the lower column. The area inside the blue box equals that under the other curves. Consideration of Fig. 7 suggests that undertaking a linear shear check at d from the support over an averaging length of $4d$ (i.e. 1.6 m for the considered slab) as suggested in EC2-23 based on [3] is overly conservative. It seems more appropriate to use an enhanced shear resistance within say $2d$ of the column that varies with distance from the support centreline. This would be more consistent with the ATENA shear force distribution at failure. However, it should be noted that Fig. 7 does not account for shear enhancement due to direct strut action which is neglected in EC2-23 for $a_v > 2d$ even though Natário [3] suggests that shear enhancement occurs for gaps as great as $2.75d$.

Table 3 Comparison of normalised design shear forces obtained using shear field analysis.

	GSA (G = 100%)	GSA (G = 12.5%)	ATENA (uncracked)	ATENA (failure)
Pure field shear:				
$\frac{V_{Ed,shear\ (4d)}}{V_{Ed,shear\ (full\ width)}}$	0.76	0.76	0.76	0.85
β for "punching (half)" check	1.02	1.01	1.02	1.00
β for "punching (quarter)" check	1.03	1.02	1.02	1.14
Pure upper column load:				
$\frac{V_{Ed,shear\ (4d)}}{V_{Ed,shear\ (full\ width)}}$	0.66	0.67	0.67	0.65
β for "punching (half)" check	1.30	1.30	1.33	1.40
β for "punching (quarter)" check	1.71	1.62	1.63	1.71

6 CONCLUSIONS

The paper considers the design of transfer slabs for shear using EC2-23. The design shear force is obtained using LFEA with shell elements in OASYS GSA and for comparison with NLFEA using 3D solid elements in ATENA. Very similar shear force distributions were obtained using LFEA and ATENA before cracking. At failure, the peak normalised shear forces obtained with NLFEA increased relative to the shear force before cracking. This was both unexpected and inconsistent with the CSCT which assumes that shear is redistributed from failing to non-failing sections. Reducing the through thickness shear stiffness to 12.5% of the default elastic value was found to have little influence on the design shear forces obtained with OASYS GSA. This finding is contrary to the findings obtained with linear elastic shell elements by Natário [3] using SAP2000 and Setiawan et al. [18] using ETABS [19]. Consequently, it appears that the effect of reducing the through thickness shear stiffness on the design shear force may be software dependent. It also seems likely that the degree of shear redistribution in ATENA may depend on the adopted material parameters. However, despite this, the NLFEA suggests an improbable degree of averaging for linear shear failure not to be critical for the slabs in Fig. 5 that failed in punching. Hence, instead of averaging the linear shear force over an increased effective width as done in Fig. 7. it seems more appropriate to use an enhanced shear resistance within say $2d$ of the column as suggested by the ATENA results at failure. Future work will focus on developing an improved method for modelling linear shear failure in transfer slabs using EC2-23.

References

[1] European Committee for Standardization. 2023. EN 1992-1-1: Eurocode 2 – Design of Concrete Structures – Part 1-1: General Rules and Rules for Buildings. Brussels: European Committee for Standardization.

[2] Penellum, Matthew, Vollum, Robert, Jones, Tony, and Hayes, Patrick. 2024. Design of Transfer Slabs. First edition. London: The Institution of Structural Engineers.

[3] Natário, Francisco Manuel Maciel. 2015. "Static and Fatigue Shear Strength of Reinforced Concrete Slabs Under Concentrated Loads Near Linear Supports." PhD thesis, École Polytechnique Fédérale de Lausanne, Lausanne.

[4] European Committee for Standardization. 2004. EN 1992-1-1: Eurocode 2 – Design of Concrete Structures – Part 1-1: General Rules and Rules for Buildings. Brussels: European Committee for Standardization.

[5] Červenka Consulting s.r.o. 2024. ATENA – Advanced Tool for Engineering Nonlinear Analysis. Prague: Červenka Consulting.

[6] Wang, Zeyu. 2024. "Development of a Design-Oriented Analytical Method for Reinforced Concrete Transfer Slabs Loaded with Closely Offset Planted Columns." PhD thesis, Imperial College London, London.

[7] Khosravikia, Farid, Kim, Hyun Su, Yi, Yousun, Wilson, Heather, Yousefpour, Hossein, Hrynyk, Trevor, and Bayrak, Oguzhan. 2018. "Experimental and Numerical Assessment of Corbels Designed Based on Strut-and-Tie Provisions." Journal of Structural Engineering 144:04018138. doi:10.1061/(ASCE)ST.1943-541X.0002137.

[8] Lips, Stefan, Fernández Ruiz, Miguel, and Muttoni, Aurelio. 2012. "Experimental Investigation on Punching Strength and Deformation Capacity of Shear-Reinforced Slabs." ACI Structural Journal 109:889–900. doi:10.14359/51684132.

[9] Wang, Zeyu, and Vollum, Robert L. 2025. "Punching Resistance of Flat Slabs Loaded with Closely Offset Planted Columns." Engineering Structures 322:119038. doi:10.1016/j.engstruct.2024.119038.

[10] Sagaseta, Juan, Muttoni, Aurelio, Fernández Ruiz, Miguel, and Tassinari, Loris. 2011. "Non-Axis-Symmetrical Punching Shear around Internal Columns of RC Slabs without Transverse Reinforcement." Magazine of Concrete Research 63:441–457. doi:10.1680/macr.10.00098.

[11] Reißen, Karin, Claßen, Martin, and Hegger, Josef. 2018. "Shear in Reinforced Concrete Slabs — Experimental Investigations on the Effective Shear Width of One-Way Slabs under Concentrated Loads and with Different Degrees of Rotational Restraint." Structural Concrete 19:36–48. doi:10.1002/suco.201700067.

[12] Muttoni, Aurelio. 2008. "Punching Shear Strength of Reinforced Concrete Slabs without Transverse Reinforcement." ACI Structural Journal 105:440–450. doi:10.14359/19858.

[13] Vaz Rodrigues, Rui, Fernández Ruiz, Miguel, and Muttoni, Aurelio. 2008. "Shear Strength of R/C Bridge Cantilever Slabs." Engineering Structures 30:3024–3033. doi:10.1016/j.engstruct.2008.04.017.

[14] Fédération Internationale du Béton. 2013. fib Model Code for Concrete Structures 2010. Lausanne: Fédération Internationale du Béton.

[15] Computers and Structures, Inc. 2014. SAP2000 – Integrated Structural Analysis and Design Software. Berkeley, CA: Computers and Structures, Inc.

[16] Oasys Ltd. 2024. GSA – General Structural Analysis Software, Version 10.2. London: Oasys, Arup Group.

[17] Setiawan, Andri, Cantone, Raffaele, Fernández Ruiz, Miguel, and Muttoni, Aurelio. 2024. "Verification of Shear Failures of Cantilever Bridge Deck Slabs Subjected to Concentrated Loads." Engineering Structures 303:117491. doi:10.1016/j.engstruct.2024.117491.

[18] Setiawan, Andri, Vollum, Robert L., Macorini, Lorenzo, and Izzuddin, Bassam A. 2020. "Punching Shear Design of RC Flat Slabs Supported on Wall Corners." Structural Concrete 21:859–874. doi:10.1002/suco.201900514.

[19] Computers and Structures, Inc. 2014. ETABS – Integrated Building Design Software. Berkeley, CA: Computers and Structures, Inc.

Load bearing capacity of hollow core floors subjected to free edge concentrated loads – experimental study

Miłosz Jeziorski, Wit Derkowski

CUT Doctoral School, Faculty of Civil Engineering, Chair of Reinforced and Prestressed Concrete Structures
Cracow University of Technology, Cracow, Poland

Summary
Precast prestressed hollow core floors are often subjected to concentrated loads on the free edge. Because of the inter connection between floor elements, a load applied to the outer element is expected to be distributed to adjacent elements, increasing the load-bearing capacity compared to that of a single unit. However, the complex stress state in the directly loaded unit can cause local brittle failure of slabs without transverse or shear reinforcement. To study this, tests were performed on three single elements (150, 320 and 500 mm height) and three full-scale floor assemblies with spans of 4.4, 9.4 and 14.94 m. Single elements failed in flexure and shear exhibiting significant ductility, whereas floors showed brittle failure governed by torsion and transverse flexure, with minor local effects and different modes observed in shallow and deep sections. Despite damage localized in the loaded element and brittle behaviour, full-scale tests showed increased capacity, varying between cases. Importantly, complete, uncontrolled collapse did not occur.

1 INTRODUCTION

Precast prestressed hollow core (HC) floors are commonly designed for distributed loads of constant intensity throughout the surface of the element. In such case, the load bearing capacity is mainly governed by flexure and shear, with later being largely dependent on the tensile strength of concrete due to the lack of transverse and vertical reinforcement [1]. It is yet not uncommon for hollow core floors to be subjected to concentrated loads. These types of actions induce, apart from flexure and shear, torsional, transverse flexural and local effects that can govern the floor capacity which, similarly as in case of shear, is largely dependent on the tensile strength of concrete [2]-[3]. The specific problem of a concentrated load applied on the free edge of the floor raises significant concerns regarding floors' reliability as it is expected that a brittle, sudden failure largely influenced by local effects will limit floors' capacity, yet due to the presence of adjacent precast elements interconnected by cast on site joints, peripheral tying limiting the transverse movement and torsional stiffness of HC, concentrated load applied to the floors' outer element is expected to be distributed to further elements and the actual capacity of full floor is expected to exceed the capacity of a single element. The phenomenon of load distribution is recognized and included in design standards and provisions [4]-[5] as well as analytical models [6]-[7], which despite having similar assumptions can lead to contradictory results [8], the above mentioned methods are also based on the theory of elasticity therefore their application in ultimate limit state is questionable. The problem of proper evaluation of the discussed phenomena stems from the fact that, in contrast to vast research conducted on single HC units, experimental data concerning floors subjected to concentrated loads is very limited [8].

This paper presents novel research conducted on three full scale hollow core floors subjected to concentrated loads applied on the free edge of the floor. The full floor experiments were accompanied by single element tests, performed on HC of the same cross section, geometry and loading conditions as in full floor experiments. Having performed experiments till failure on both single specimens and full floors, the effect of adjacent elements on the failure mode and load bearing capacity is directly evaluated.

2 EXPERIMENTAL SETUP

The shape and prestressing layout of the cross sections of the three HC elements used in single element and full floor tests are presented on Figure 1. A 150 mm deep SP150 section was used in Floor 1 experiment, 320 mm AVU320 in Floor 2 and 500 mm HC500 in Floor 3.

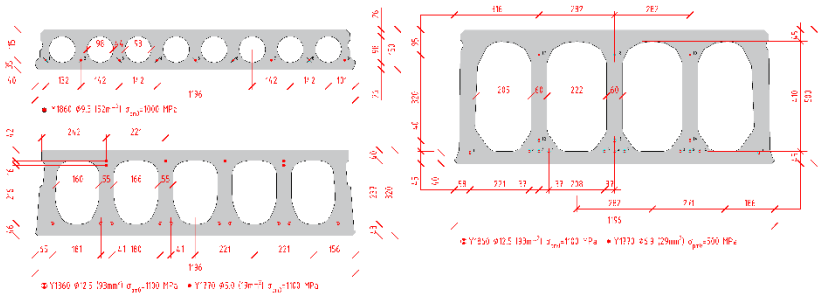


Fig. 1 Cross-sections of HC elements used in the experimental program

Figure 2 illustrates a sketch of the test setup of the single element tests. The SP150, AVU320 and HC500 elements measured 4527, 9555 and 15034 mm, respectively. The experiments began with single element tests in which specimens were supported on roller and fixed bearings through a 100x8 mm neoprene pad. Eccentric loading was applied onto two webs simultaneously through a spreader beam resting on two steel plates measuring 300x20x150 mm which were placed over the central and outer webs of the specimens through a high strength levelling mortar. Load was applied to the centre of the spreader beam by a hydraulic jack. A set o 9 vertical transducers was used to measure vertical displacements.

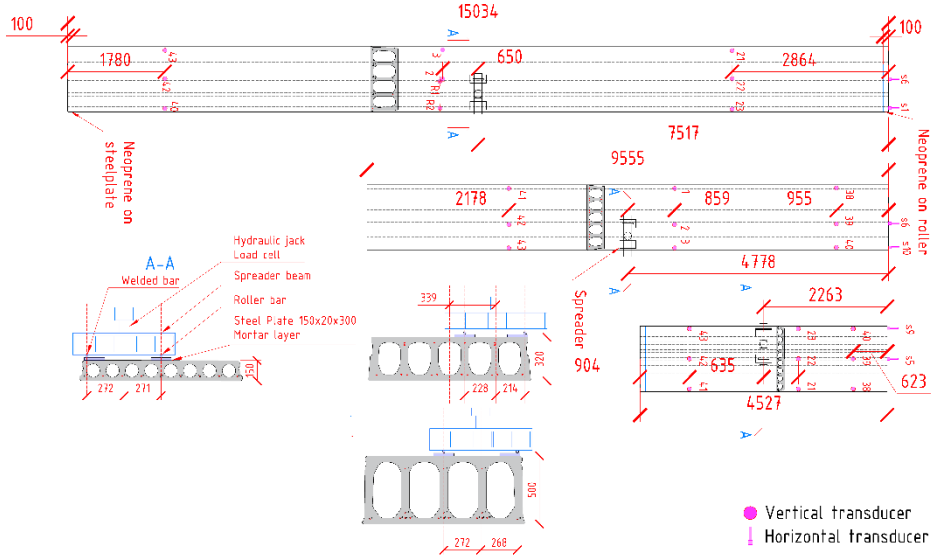


Fig. 2 Sketch of the experimental setup – single element tests

Figure 3 illustrates a sketch of the test setup of the full floor experiments. Each experiment was built of six identical HC elements supported on an individual steel plate measuring 100x40x1196 mm. A 100x8 mm neoprene pad was placed between the steel plate and HC. Each steel plate was supported on one side of the floor on three load cells with spherical bearings, on the other side of the floor the load cells were replaced with circular roller bars. The load cells and roller bars were supported on inverted precast T-beam anchored to the laboratory floor, see sections A-A and B-B of Figure 3. The cast-on-site joints were casted first and mechanically precracked, details of the mechanical precracking can be found in [9]. Precracking was followed by casting of the reinforced concrete tying beams on

both supports and free edges of the floor. The tying beams were reinforced with longitudinal rebars ma lapped them with L – shaped bars placed in floors' corners, the longitudinal bars at supports were placed in the corners of C – shaped bars protruding from joints. Distributed Fibre Optic Sensors (DFOS) glued to the top and the bottom of the floors provided linear strain measurements in both longitudinal (X) and transverse (Y) direction of the floor. Set of potentiometric position transducers with return springs, attached to light aluminium frames spanning across the floor were used to measure vertical displacements. Loads were applied to the midspan of the outermost element of the floor, indicated as position F1 on Figure 3. Hydraulic jack was attached to the steel frame spanning across the floor, the jack was used in Floor 1 to load the spreader beam in a similar manner to single specimen test. In Floor 2, a set of three hydraulic jacks was used to load three webs simultaneously, in Floor 3 set of six jacks was used, see Figure 4. Arrangement of loads applied on several webs was chosen in favour of a single point load in order to avoid possible stress concentrations leading to premature, local failure.

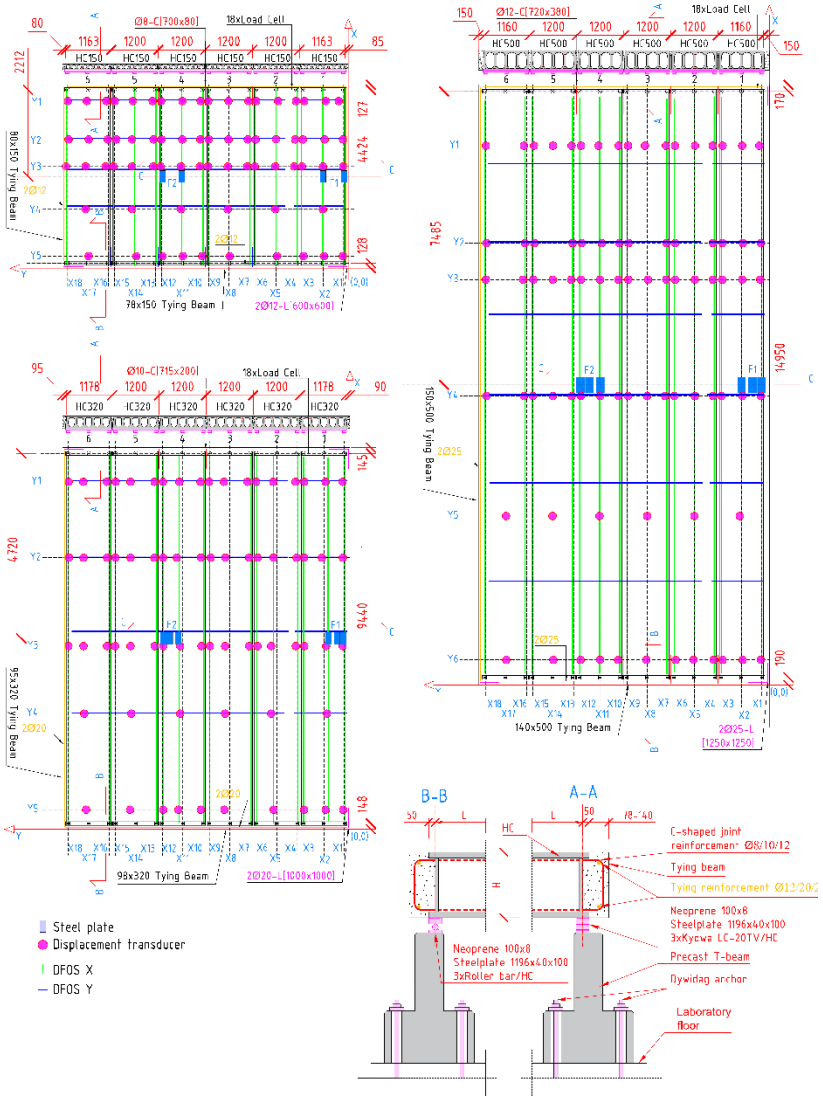


Fig. 3 Sketch of the experimental setup – full floor experiments.

(a) (b)

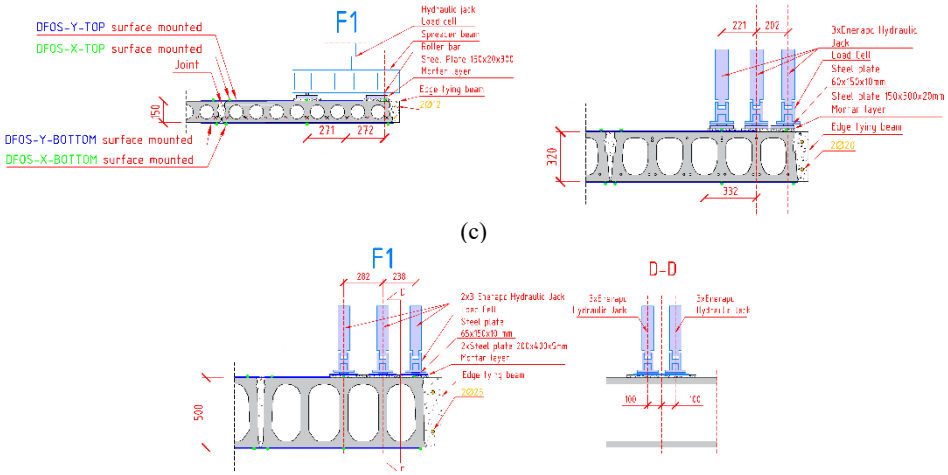


Fig. 4 Section C-C: Sketch of the load arrangement – full floor tests: (a) Floor 1, (b) Floor 2, (c) Floor 3

3 SELECTED RESULTS

Results of the single element and full floor tests are illustrated on load – displacement curves presented on Figure 5. In case of single elements, data from transducers 23, 3 and R2 is plotted for SP150, AVU320 and HC500, respectively on Figure 5 a, data from transducers at the intersection of X1 and Y3 axes (see Figure 3) is plotted for Floor 1 and 2, in case of Floor 3 transducer at the intersection of X1 and Y4 axis is plotted on Figure 5 b. Figures 6 – 8 illustrate selected cracks observed in floor and single specimen experiments.

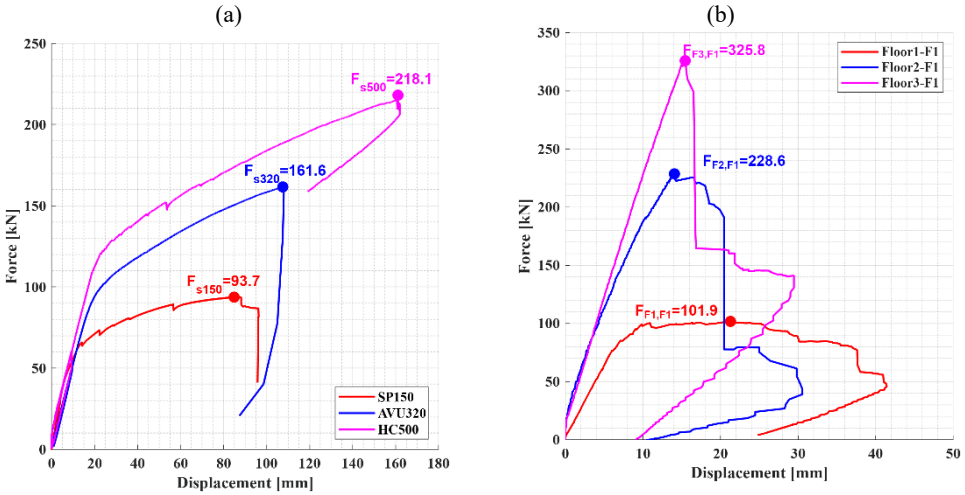


Fig. 5 Load-displacement curves: (a) Single specimen experiment, (b) Full floor experiment

(a) (b)

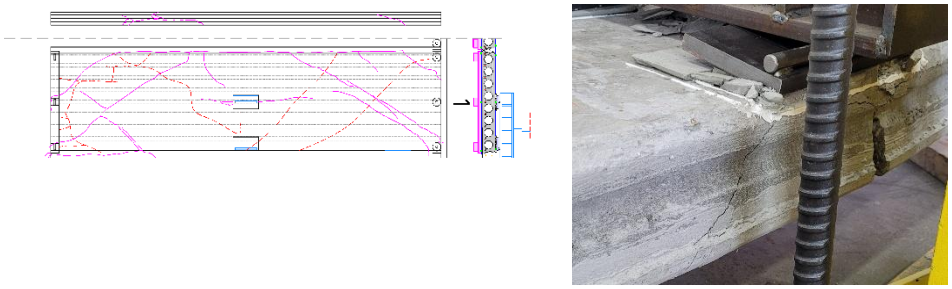
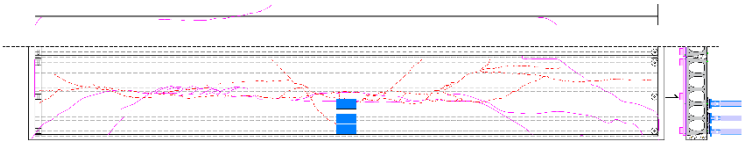


Fig. 6 Crack patterns: (a) Floor 1, sketch of cracks on bottom (dashed red line), top (magenta line) and outer web surface, (b) SP150, outer loaded web pictured after failure,

(a)



(b)



Fig. 7 Crack patterns: (a) Floor 2, sketch of cracks on bottom (dashed red line), top (magenta line) and outer web surface, (b) AVU320, shear crack on the outermost, loaded web pictured shortly before failure.

4 ANALYSIS

The three single specimens behaved in a similar manner, after first flexural cracking a visible change in stiffness was observed, gradual crack development was observed as flexural cracks propagated onto webs causing a sudden flexural (SP150) and shear – flexural failure (AVU320 and HC500), see Figures 6 b, 7 b and 8 b. No inclined skew and longitudinal cracks were observed on the surface of the single specimens, despite load being applied with a considerable eccentricity. The torsional effects were therefore limited and did not affect the failure mode. The eccentricity did affect the element behaviour slightly as damage was more pronounced on the directly loaded webs while outer, unloaded webs were considerably less damaged, especially in case of AVU320.

The behaviour of floor specimens was significantly different from corresponding single elements. Floors failed in much more brittle manner as peak displacements at which failure occurred were considerably lower than the ones observed in single element tests, compare Figures 5 a and b. A difference was observed between Floor 1 and Floors 2 and 3 where latter two behaved in a similar manner – failure was not preceded by a visible change in stiffness, after peak load was reached, a sudden opening of cracks was observed and load decreased significantly. In contrast, a visible change in stiffness and gradual evolution of damage was observed in Floor 1.

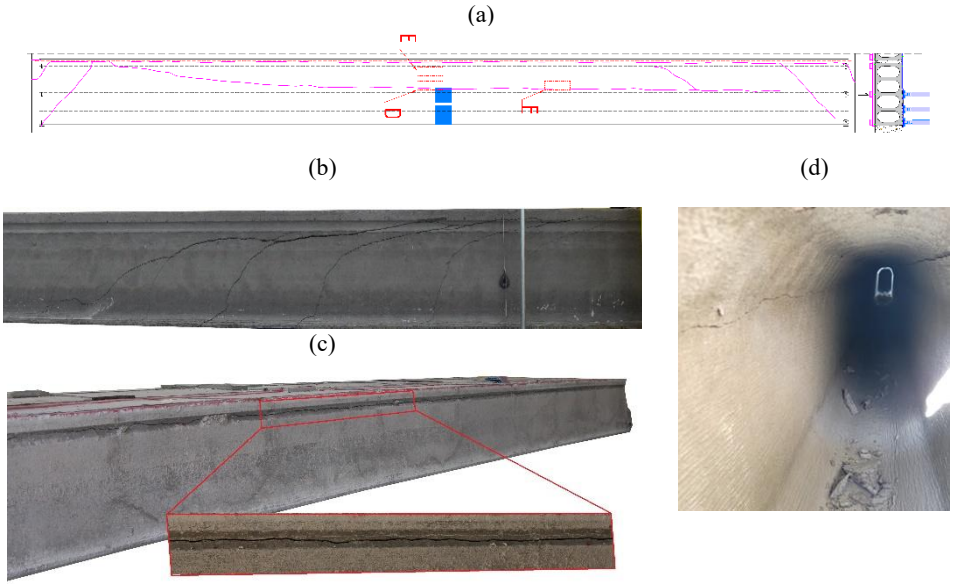


Fig. 8 Crack patterns: (a) Floor 3, sketch of cracks on top (magenta line), (b) HC500, shear crack on the outermost, loaded web pictured after failure, (c) Floor 3, horizontal crack in the joint groove, (d) Horizontal web cracks seen through hole made in point E

Failure modes of floor specimens differed significantly from single elements. In contrast to single specimens failing in flexure and shear, the floor specimens failed due to torsion (Floor 1) and transverse flexure (Floor 2 and 3). The torsional failure of Floor 1 was characterized by vast skew cracking on both top and bottom surface of the floor, with bottom cracks propagating through webs onto top surface of the elements creating a spiral, spatial patterns associated with torsional stresses. Large horizontal damage was observed in the outermost web, following the joint groove, this indicates large stress concentration in the groove which primarily transfers the shear forces to further elements. Transverse flexural failure of Floors 2 and 3 was characterized by predominant longitudinal cracks observed on both top and bottom surface (Floor 2) and top cracks (Floor 3) propagating throughout the entire length of the specimen, see Figures 7 a and 8 a. Inclination of longitudinal cracks in support (Floors 2 and 3) and midspan (Floor 2) vicinity indicates torsional effects – more pronounced in case of Floor 2, less visible in Floor 3. Horizontal web cracks, associated with transverse flexural effects similar to ones observed in Vierendeel trusses, were observed through openings made in the top flange of Floor 3, see Figure 8 (d). The difference between floors behaviour can be explained by the shape of the HC cross sections. The shallow SP150 section with circular voids is much more rigid in torsion, the specific shape of the web is more rigid when subjected to transverse and vertical loads – in contrast to slender webs of AVU320 and HC500 which are more slender and thus prone to transverse flexural effects. Horizontal crack in the joint groove observed in Floor 3, see Figure 8 c, indicates, similarly as in case of Floor 1, significant stress concentrations in the joint groove that can potentially impact the floor capacity.

Even though cracks were only observed in directly loaded specimens, the load bearing capacity of floor was significantly higher than the single elements – in case of Floors 2 and 3 the failure load was 1.41 and 1.49 higher than the load measured in single specimens, respectively. In case of Floor 1, even though the failure mode was completely different from a single specimen, the improvement in capacity was negligible as floor specimen failed at a load approximately 9% higher than the corresponding single specimen. Despite the brittle behaviour of floor specimens, the experiments did not result in a complete collapse of the floor. After unloading, specimens remained in place allowing safe post failure inspection.

5 CONCLUSIONS

The conducted experiments on both single HC specimens and full-floor systems provided valuable and novel insights into the behaviour of precast floors at a natural scale. The results clearly demonstrated that full floors subjected to edge-concentrated loads may behave substantially differently from individual specimens, suggesting that tests performed on single HC units may not always accurately represent the actual behaviour of complete floor systems. Following conclusions were drawn from the presented results and their subsequent analysis:

- Results obtained from single element tests suggest that the local stress concentrations and torsional effects induced by eccentric point loads have a marginal influence on the HC load-bearing capacity as failure is mainly governed by shear and flexure. This holds provided that the eccentric concentrated load applied to HC is spread on a sufficiently big area or the load is distributed properly onto several webs and that it is applied in elements midspan where flexural effects are more pronounced. This observation contrasts with findings reported by Pajari [10], whose experiments involved similarly applied loads but located near the supports.
- Behaviour of full floors is largely different from single elements. The effects of torsion, transverse flexure and local stress concentrations in joint grooves cannot be neglected. In contrast to single specimens behaving ductile, full floors are much stiffer which can lead to brittle failures.
- Failure mode of HC floors is largely dependent on the shape of the cross section as deep elements characterized by slender webs are especially prone to transverse flexural effects. The deep HC undergo effects that can be associated with Vierendeel truss behavior. Transverse flexural effects are less pronounced in shallow elements which are predominantly affected by torsion.
- If the load is spread onto several webs or distributed on a significant area, the load bearing capacity of HC subjected to point loads is not largely affected by local punching effects – in contrast to observations made in previous experiments where loads were applied on relatively small area [11]-[12]. This observation aligns with authors' previous numerical research [13].
- Although the damage did not propagate to adjacent elements, floor assemblies subjected to edge-concentrated loads can exhibit a significantly higher load-bearing capacity than single elements. This may be attributed to additional confinement provided by tying systems, which positively influences the stress state in the HC webs and flanges. Furthermore, load redistribution is expected to substantially reduce the bending moment in the directly loaded element. However, the increase in capacity is not consistent, even among floors of the same scale. The observed improvement may be related to both cross-sectional geometry and floor span, although further research is required to fully clarify these effects.
- Despite the brittle and sudden nature of the failure observed in the floor specimens, the applied load did not result in a complete, uncontrolled progressive collapse of the floor. This behaviour can be attributed to the proper design of the continuous tying system, which helped maintain the overall structural integrity of the floor.

Acknowledgements

This paper contributes to the "HOLCOLODIS" project led by IPHA – International Prestressed Hollowcore Association. The project aims to address questions and ambiguities surrounding load distribution through new experimental tests on hollow core floor fields and advanced numerical modeling. The financing and support by IPHA are gratefully acknowledged.

Authors wish to acknowledge the valuable contribution of the staff of the Construction Engineering Research Group (CERG), Application Centre for Concrete and Construction of Hasselt University: Rik Steensels, Dan Dragan, Herve Degee, Bram Vandoren, Rajarshi Das, Jan Leuraers and Niels Blocken, Hasselt University PhD candidates: Luke van Ratingen, Tine Engelen and Dries Byloos in planning, design, preparation and execution of the experiments as well as their hospitality and helpfulness during the course of the authors stay in Belgium. Authors gratefully acknowledge valuable contribution of

Karolina Makowska, Rafał Sieńko, Tomasz Howiacki, Maciej Frankowski, Jakub Wojtyczek, Mariusz Kapcia, Piotr Śmiertka and Szymon Długosz, of SHM System and Nerve-Sensors in planning, design, preparation and execution of the DFOS measurements as well as valuable insights into post-processing and analysis of obtained results.

References

[1] Pajari, Matti. 2009. "Web Shear Failure in Prestressed Hollow Core Slabs." *J Struct Mech* 42:297–317.

[2] Broo, Helén, Karin Lundgren, and Björn Engström. 2005. "Shear and Torsion Interaction in Prestressed Hollow Core Units." *Mag Concr Res* 57:521–33. Accessed January 28, 2026. doi:10.1680/macr.2005.57.9.521.

[3] Derkowski, Wit, and Mateusz Surma. 2015. "Torsion of Precast Hollow Core Slabs." *Tech Trans Civ Eng* 3-B/2015:32–43.

[4] European Committee for Standardization (CEN). 2011. *EN 1168:2005+A3:2011 Precast Concrete Products—Hollow Core Slabs.* Brussels: CEN.

[5] Precast/Prestressed Concrete Institute. 2015. *PCI Manual for the Design of Hollow Core Slabs and Walls.* 3rd ed. MNL-126-15.

[6] Bernardi, Patrizia, Roberto Cerioni, Filippo Leurini, and Elena Michelini. 2016. "A Design Method for the Prediction of Load Distribution in Hollow-Core Floors." *Eng Struct* 123:473–81. Accessed February 3, 2026. doi:10.1016/j.engstruct.2016.06.008.

[7] Stanton, John F. 1992. "Response of Hollow-Core Slab Floors to Concentrated Loads." *PCI J* 37:98–113. Accessed December 18, 2025. doi:10.15554/pcij.07011992.98.113.

[8] Jeziorski, Milosz, Wit Derkowski, and Elena Michelini. 2024. "Vertical Load Distribution in Precast Hollow Core Floors: State of the Art and Future Perspectives." *Struct Concr* 25:3412–29. Accessed February 11, 2026. doi:10.1002/suco.202301150.

[9] Jeziorski, Milosz, and Wit Derkowski. 2025. "Experimental Evaluation of Load Distribution in a Full Scale Hollow Core Floor." Paper presented at the fib Symposium 2025, *Concrete Structures: Extend Life Span, Limit Impacts*, Antibes, France, June 16-18.

[10] Pajari, Matti. 2004. *Shear-Torsion Interaction Tests on Single Hollow Core Slabs.* Finland: VTT Technical Research Centre of Finland.

[11] Huovinen, Seppo, and Heikki Lintunen. 1991. *RAT12538/91—The Performance of Point-Loading Tests on Deck Consisting of Six Variax 4 Slabs (in Finnish).* Finland: VTT Technical Research Centre of Finland.

[12] Aswad, Alex, and Francis Jacques. 1992. "Behavior of Hollow-Core Slabs Subjected to Edge Loads." *PCI J* 37:72–83. Accessed January 9, 2026. doi:10.15554/pcij.03011992.72.84.

[13] Jeziorski, Milosz, and Wit Derkowski. 2025. "Comprehensive Numerical Investigation of the Concentrated Load Capacity in Prestressed Hollow Core Floors." *Eng Struct* 335:120208. Accessed February 14, 2026. doi:10.1016/j.engstruct.2025.120208.

Efficient Implementation of the Shear Crack Propagation Theory Using Algorithmic Differentiation

Jan Hendricks, Christian Linden, Martin Classen

Institute of Structural Concrete,
RWTH Aachen University,
Im Süsterfeld 9, 52072 Aachen, Germany
(Jan Hendricks, Christian Linden, Martin Classen)

Cluster of Excellence CARE,
TU Dresden and RWTH Aachen,
Helmholtzstraße 10, 01069 Dresden, Germany
(Jan Hendricks, Martin Classen)

Summary
Shear failure of reinforced concrete members without shear reinforcement remains difficult to predict because several interacting transfer mechanisms govern crack propagation and load redistribution. This paper presents a numerically efficient implementation of the Shear Crack Propagation Theory (SCPT) using a Newton–Raphson solution strategy combined with algorithmic differentiation. The approach reformulates each crack propagation step as a nonlinear root-finding problem and evaluates the Jacobian consistently and automatically. A representative beam example demonstrates stable convergence, realistic shear crack patterns and a substantial reduction in computational effort compared with previous grid-based solution strategies. The framework provides a basis for systematic validation and future parametric studies.

1 SHEAR CRACK PROPAGATION THEORY – CONCEPTUAL AND NUMERICAL BACKGROUND

The Shear Crack Propagation Theory (SCPT), developed by Classen, describes the mechanical behavior of reinforced concrete members without shear reinforcement during the formation and propagation of shear-critical cracks [1], [2]. In contrast to empirical or single-mechanism approaches, SCPT represents a mechanically consistent framework that explicitly accounts for all relevant shear transfer mechanisms, including crack propagation, cantilever action, shear transfer in uncracked concrete, aggregate interlock, dowel action, and crack bridging.

The complete theoretical formulation of SCPT, including the derivation of governing equations and constitutive relationships, is provided in the original publication and is therefore not repeated here [1]. Instead, this section summarizes the conceptual structure and numerical characteristics of SCPT that are essential for its computational implementation and for understanding the challenges addressed in this paper.

1.1 Incremental analysis of a cross-section

SCPT is applied to a predefined cross-section of a reinforced concrete beam. For this section, the theory incrementally determines the geometry of the propagating shear crack and the corresponding forces transferred across the cross section. The analysis starts from an initial state with an infinitesimally small crack and proceeds through successive load increments until the state of shear failure is reached.

The shear crack is idealized by two straight crack segments: an upper branch with inclination angle β_1 and vertical height y_1, and a lower branch with inclination angle β_2 and vertical height y_2. The geometry of the crack at a representative load increment, together with the acting internal forces and their lever arms, is illustrated in Fig. 1. The reference point (colored red) for all lever arms is the longitudinal reinforcement (colored gray) intersecting the crack, which undergoes deformation due to crack opening.

Crack kinematics are governed by a single rotational degree of freedom φ, representing the relative rotation of the two concrete teeth about a center of rotation (CR is colored black). Depending on the stress state at the crack tip, the CR may be located either above or below the crack tip. The crack

opening shown results from the rotation of the crack around the CR. In Fig. 1, the left crack tooth is shown in a horizontal position for visual clarity, although this does not occur in real beams.

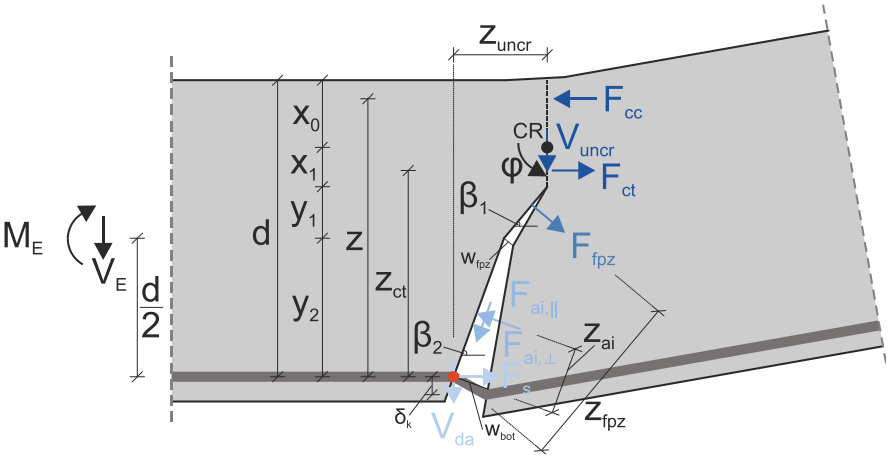


Fig. 1 A side view of a reinforced concrete beam section with the geometry properties of an approximated SCPT shear crack, showing the contributing forces and their lever arms adapted from [1]

1.2 Governing variables and coupling of mechanisms

For each crack propagation step, SCPT introduces four governing variables, which are treated as unknowns of the problem and collected in the vector shown in Equation (1).

$$x = \begin{pmatrix} \Delta y \\ \beta \\ \sigma_{z0} \\ \varphi \end{pmatrix} \tag{1}$$

Here Δy denotes the incremental increase of the crack height ($y_1 + y_2$) in relation to the previous crack propagation step, β the combined crack angle, σ_{z0} the vertical stress at the crack tip, and φ the rotation governing crack opening and sliding.

Based on these variables, SCPT evaluates the individual shear transfer mechanisms and enforces equilibrium and compatibility conditions to obtain corresponding calculated values Δy_{calc}, β_{calc}, $\sigma_{z0,calc}$, and φ_{calc}. From a numerical perspective, SCPT thus represents a strongly coupled nonlinear system, in which crack geometry, stress redistribution, and kinematic compatibility mutually depend on each other.

1.3 Iterative structure of the SCPT algorithm per load increment

For each crack propagation step of the crack, the following sequence of the SCPT algorithm is executed. The assumed values of the crack increment Δy and the crack angle β, together with the results from the previous load increment, are used to determine the current crack geometry.

Based on the crack geometry and the vertical stress at the crack tip σ_{z0}, the required horizontal normal stress σ_{x0} and shear stress τ_0 at the crack tip are determined such that crack propagation occurs. While the vertical stress component must always be tensile, the horizontal stress component may correspond either to compression (negative) or tension (positive). As the fracture criterion governing crack initiation and propagation, the biaxial concrete fracture criterion proposed by Kupfer [3] combined with the cohesive crack approach from Hillerborg [4] is employed.

The horizontal normal stress σ_{x0} is subsequently used to determine the position of the center of rotation (CR). If σ_{x0} is negative, the CR must be located below the crack opening, if σ_{x0} is positive, the CR is located above the crack opening. Once the position of the CR is known, the rotation φ can be used to determine the opening of the shear crack.

Based on the assumed crack geometry and kinematics, the internal force contributions are then determined. In the uncracked concrete above the crack, a compressive force F_{cc} develops, and depending on the position of the CR, a tensile force F_{ct} may additionally arise. Furthermore, a shear force V_{uncr} is transferred through the uncracked concrete zone. This contribution is obtained by integrating the shear stress distribution $\tau(x)$ over the height of the uncracked cross section. The shear stress $\tau(x)$ follows a parabolic distribution, characterized by a zero value at the top fiber, a maximum at the level of the center of rotation, and the value τ_0 at the crack tip.

In the upper part of the crack, corresponding to the fracture process zone (FPZ), a tensile force F_{fpz} acting perpendicular to the crack develops. This force is likewise obtained by integrating the stresses along the length of the crack. The stress–crack opening relationship within the FPZ is evaluated using constitutive models established in previous experimental and analytical investigations, for example from Jirásek [1], [5].

For the lower part of the crack, the orthogonal and parallel forces $F_{ai,\parallel}$, $F_{ai,\perp}$ arise from aggregate interlock. These contributions are determined using existing aggregate interlock models reported in the literature (e.g. from Walraven & Reinhardt [6]) and adopted in the SCPT framework.

The dowel action of the longitudinal reinforcement results in the vertical force V_{da}. In the present implementation, this contribution follows the formulation adopted in the SCPT framework [1], while the dowel-action mechanism itself is supported by established experimental investigations by Baumann and Rüsch [7].

After all internal force contributions have been determined, equilibrium conditions are enforced to compute the total transferable shear force V_E, defined as the sum of all vertical force components, as well as the horizontal force F_s in the longitudinal reinforcement, defined as the sum of all horizontal force components. The shear force V_E represents the transferable shear capacity of the cross section for the current crack propagation step.

Subsequently, a feedback procedure is applied to update the four governing variables. The force F_s in the longitudinal reinforcement is first used, together with the stress–strain relationship of the reinforcement (with or without consideration of tension stiffening effects), to determine the reinforcement strain. Based on the crack geometry, this strain is then used to compute the corresponding rotation φ_{calc}.

The vertical stress at the crack tip $\sigma_{z0,\,calc}$ is determined by modeling the concrete region between two adjacent shear cracks as a concrete tooth subjected to cantilever action. A clamping moment is calculated for this concrete tooth, which is subsequently used to evaluate the vertical stress $\sigma_{z0,\,calc}$ at the crack tip.

Finally, the crack angle β_{calc} is obtained from moment equilibrium, and the crack increment Δy_{calc} is updated from the geometry of the newly propagated crack. The fundamental concept of SCPT is that the assumed values of the governing variables must coincide with their corresponding calculated values. If this condition is satisfied, equilibrium has been achieved and the load increment is accepted. If discrepancies remain, the algorithm is repeated with adjusted input variables until convergence is reached. The algorithmic structure of a single crack propagation step can be summarized as follows [1]:

1. Assume Δy, β, σ_{z0}, φ for the current step
2. Discretize updated crack geometry using Δy and β
3. Evaluate crack propagation criterion using σ_{z0}
4. Determine the position of the center of rotation and crack kinematics using φ
5. Compute force contributions in uncracked concrete (V_{uncr}, F_{cc}, F_{ct})
6. Compute force contributions within the shear crack (F_{fpz}, $F_{ai,\parallel}$, $F_{ai,\perp}$, V_{da})
7. Enforce equilibrium to obtain (V_E, F_s)
8. Use force in reinforcement to calculate φ_{calc}
9. Use cantilever action to calculate $\sigma_{z0,\,calc}$
10. Calculate Δy_{calc} and β_{calc} with equilibrium and geometry
11. Check convergence of assumed and calculated variables.
12. If converged, return Δy, β, σ_{z0}, φ, otherwise go back to 1.

2 NUMERICAL CHALLENGES OF SCPT AND CONVENTIONAL SOLUTION STRATEGIES

From a numerical point of view, SCPT poses significant challenges. The four governing variables are strongly interdependent, and the underlying relationships are highly nonlinear. In early implementations, the convergence problem was addressed by performing systematic grid searches over the four-dimensional parameter space. Although robust, this approach results in a prohibitively large number of evaluations of the SCPT algorithm.

Due to the exponential growth of required iterations with increasing resolution, such brute-force strategies lead to excessive computational costs. In practice, execution times of several hours were observed even on high-performance computing systems. This severely limits the applicability of SCPT for parametric studies, benchmark analyses, or practical engineering use.

To render SCPT computationally efficient and practically usable, a more systematic and mathematically consistent solution strategy is required.

3 NEWTON–RAPHSON FORMULATION OF THE SCPT PROBLEM

The SCPT problem can be reformulated as a root-finding problem. This is because the four governing variables and their corresponding calculated variables must converge.

3.1 Newton–Raphson Method

The Newton–Raphson method can be used to solve such root-finding problems. In civil engineering, for instance, it is a well-known method of applying second-order theory to structures under load. It is suitable for iteratively determining the zero points of functions. The method starts with an initial value and uses the first derivative of the function to get closer to the zero point. Fig. 2 shows the conceptual procedure for the one-dimensional function f(x).

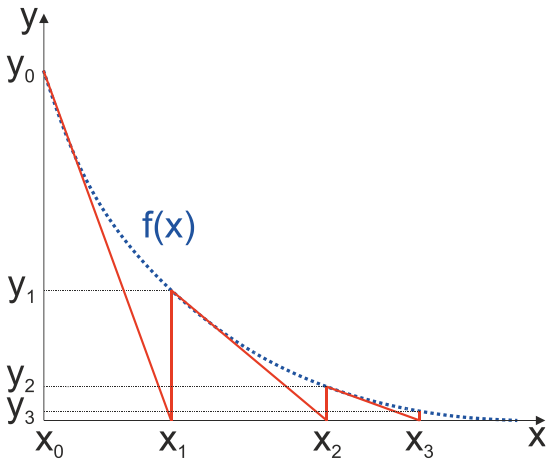


Fig. 2 Visualization of the Newton-Raphson method for a one-dimensional function f(x) with start point $x_0 = 0$.

The methodology starts with the value x_0 (here $x_0 = 0$) and determines the value $y_0 = f(0)$ and the slope $f'(0)$. The slope is shown in red in Fig. 2 in the form of the tangent. Now the Newton-Raphson approach from Equation (2) can be used to improve the estimate.

$$x_{n+1} = x_n - \frac{f(x_n)}{f'(x_n)} \tag{2}$$

From Equation (2), the value x_1 is obtained, which is already closer to the zero point. For the value x_1, $f(x_1)$ and $f'(x_1)$ are now determined again, and the Newton-Raphson method can be used to get closer and closer to the zero point. The more iterations are performed, the closer the final estimation is to the zero point being sought.

3.2 Residual formulation

For the SCPT in each crack propagation step, a residual vector R(x) is defined as the difference between assumed and calculated values of the governing variables according to Equation (3):

$$R(x) = \begin{pmatrix} \Delta y_{calc} - \Delta y \\ \beta_{calc} - \beta \\ \sigma_{z0,calc} - \sigma_{z0} \\ \varphi_{calc} - \varphi \end{pmatrix} \tag{3}$$

Equilibrium and compatibility are achieved when R(x) = 0. Although the SCPT algorithm itself is complex, the calculated quantities can be interpreted as implicit nonlinear functions of the input variables, which enables the use of a Newton–Raphson solution strategy.

3.3 Multidimensional Newton–Raphson scheme

In contrast to the one-dimensional case, the Newton–Raphson method for SCPT requires the evaluation of a Jacobian matrix $J_R(x)$ (shown in Equation (4)) consisting of all partial derivatives of the residual components with respect to the governing variables. Instead of one derivative in the one-dimensional case, thus 16 partial derivatives are now required.

$$J_R(x) = \begin{pmatrix} \frac{\partial \Delta y_{calc}}{\partial \Delta y} - 1 & \frac{\partial \Delta y_{calc}}{\partial \beta} & \frac{\partial \Delta y_{calc}}{\partial \sigma_{z0}} & \frac{\partial \Delta y_{calc}}{\partial \varphi} \\ \frac{\partial \beta_{calc}}{\partial \Delta y} & \frac{\partial \beta_{calc}}{\partial \beta} - 1 & \frac{\partial \beta_{calc}}{\partial \sigma_{z0}} & \frac{\partial \beta_{calc}}{\partial \varphi} \\ \frac{\partial \sigma_{z0,calc}}{\partial \Delta y} & \frac{\partial \sigma_{z0,calc}}{\partial \beta} & \frac{\partial \sigma_{z0,calc}}{\partial \sigma_{z0}} - 1 & \frac{\partial \sigma_{z0,calc}}{\partial \varphi} \\ \frac{\partial \varphi_{calc}}{\partial \Delta y} & \frac{\partial \varphi_{calc}}{\partial \beta} & \frac{\partial \varphi_{calc}}{\partial \sigma_{z0}} & \frac{\partial \varphi_{calc}}{\partial \varphi} - 1 \end{pmatrix} \tag{4}$$

The Newton–Raphson update h_n is obtained by solving Equation (5), whereby n indicates the iteration of the SCPT logic described in Chapter 1.3.

$$J_R(x) \cdot h_n = -R(x_n) \tag{5}$$

After each Newton step, the variable vector x can now be adjusted with the vector h_n according to Equation (6).

$$x_{n+1} = x_n + h_n \tag{6}$$

The algorithm terminates as soon as h_n falls below a predefined limit value and thus complies with the desired tolerance. The variables in vector x are now the results of one crack propagation step. The Newton-Raphson method must be performed individually for each crack propagation step.

4 ALGORITHMIC DIFFERENTIATION FOR SCPT

The Newton–Raphson solution strategy introduced in the previous section requires the consistent evaluation of the Jacobian matrix of the SCPT residual function. Due to the highly nonlinear and strongly coupled structure of SCPT, the analytical derivation of all partial derivatives is impractical, while numerical differentiation would lead to significant inaccuracies and poor convergence behavior.

Algorithmic Differentiation (AD) provides the exact derivatives of functions by breaking them down into elementary operations [8]. In the case of numerical simulations as often seen in engineering problems, AD can be used to determine derivatives needed for optimization highly efficiently [9], [10].

In the context of SCPT, AD is particularly advantageous because the calculated quantities of each crack propagation step are obtained through a deeply nested algorithm.

To enable the use of AD, the existing SCPT implementation was reformulated into a fully differentiable computational framework. The original Python implementation was restructured using a

differentiation-capable numerical code, allowing all operations within the SCPT algorithm to be traced and differentiated consistently. This reformulation does not alter the mechanical formulation of SCPT but ensures that the entire residual evaluation can be differentiated.

Within the proposed framework, the evaluation of the residual vector and the corresponding Jacobian matrix are performed simultaneously. As a result, the additional computational cost associated with derivative evaluation is marginal compared to the evaluation of the SCPT algorithm itself. The computed Jacobian is then directly used in the Newton–Raphson scheme.

By combining algorithmic differentiation with the Newton–Raphson method, a numerically robust and efficient solution strategy for SCPT is obtained. This approach transforms SCPT from a mechanically comprehensive but computationally demanding theory into a practically applicable numerical model, while fully preserving its theoretical consistency.

5 RESULTS

The proposed numerical framework was implemented in a Python-based environment using a framework suitable for AD (JAX, Google Research). To demonstrate the functionality and robustness of the implementation, a representative reinforced concrete beam without shear reinforcement was analyzed as an example case.

The beam geometry was defined as follows: width b = 250 mm, total height h = 600 mm, half-span l/2 = 3850 mm. The material properties correspond to typical concrete and steel with characteristics of a concrete with compressive strength $f_{cm,cyl}$ = 33 MPa, a maximum aggregate size of 16 mm, and a longitudinal reinforcement consisting of two bars with a diameter of 28 mm and a yield strength f_y = 713 MPa. The concrete cover was set to 30 mm.

The analysis was performed by applying the described SCPT algorithm for nine different cross-sections. The locations of the cross-sections are defined by a crack spacing of 0.7·d.

Fig. 3 illustrates the simulated shear crack configurations obtained for the analyzed beam. The static system corresponds to a simply supported single-span beam subjected to a concentrated load; for clarity, only one half of the beam is shown. The support is located at the origin (0 mm, 0 mm) while the point load is applied at (3850 mm, 600 mm).

The results show that shear cracks forming close to the support exhibit an early deviation from a steep crack inclination, whereas cracks located closer to the load application point initially propagate almost vertically before bending towards flatter inclinations at higher load levels. Among the simulated cracks, the red crack was identified as the decisive shear crack, governing the lowest maximum transferable shear force $V_{\max}$. Cracks associated with higher shear capacities are visualized such that crack segments developed up to $V_{\max}$ are shown in black, while additional crack propagation beyond this load level is indicated by gray extensions.

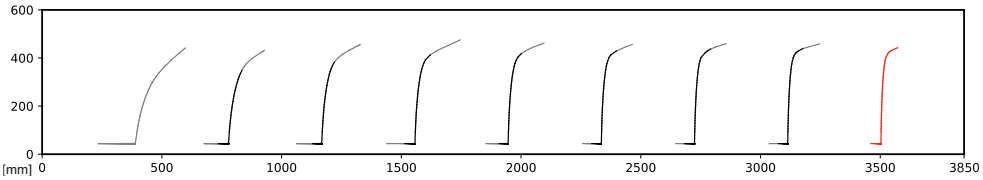


Fig. 3 Simulated shear cracks obtained from the SCPT analysis assuming a crack spacing of 0.7·d. The red crack indicates the decisive shear crack governing the maximum transferable shear force $V_{\max}$. Black cracks represent crack configurations corresponding to load levels below $V_{\max}$, while gray extensions illustrate simulated crack propagation beyond $V_{\max}$.

All computations were carried out on a standard laptop computer using a single processing core. The complete analysis of the beam, including all crack propagation steps and the evaluation of the corresponding internal force contributions, required approximately 15 minutes of computation time. This represents a substantial reduction in computational effort compared to previous grid-based solution strategies, which required several hours of computation on high-performance computing systems.

Although the presented results are limited to a single representative example and should be regarded as preliminary, they demonstrate that the proposed implementation enables the efficient and stable evaluation of the SCPT. The obtained crack patterns appear promising and indicate that the framework is well suited for more extensive parametric studies and systematic validation efforts in future work.

6 CONCLUSIONS

This paper presented an efficient and robust implementation of the Shear Crack Propagation Theory (SCPT) using a Newton–Raphson solution strategy combined with algorithmic differentiation. While SCPT provides a mechanically comprehensive framework for describing the shear behavior of reinforced concrete members without shear reinforcement, its practical applicability has so far been limited by the high computational effort required to solve the strongly coupled nonlinear problem.

By reformulating the SCPT algorithm as a root-finding problem and employing algorithmic differentiation for the consistent evaluation of the Jacobian matrix, the proposed implementation significantly improves numerical stability and convergence behavior. The resulting framework enables the reliable solution of each crack propagation step with manageable computational effort, thereby allowing the full shear crack evolution and load–deformation response to be traced efficiently.

The results presented for a representative beam example demonstrate that the implemented approach is capable of reproducing physically plausible shear crack geometries and force contributions. Although the current implementation should be regarded as prototypical, the obtained results indicate that the numerical formulation preserves the mechanical consistency of the original SCPT while substantially reducing computational cost.

Future work will focus on a systematic validation of the implementation against experimental data and on detailed investigations of the individual shear transfer mechanisms within the SCPT framework. In addition, parametric studies will be conducted to assess the influence of material properties, geometry, and loading conditions on the predicted shear response. The numerical framework presented in this paper forms a necessary basis for such investigations and constitutes a key step towards making SCPT a practical tool for advanced shear analysis of reinforced concrete structures.

Acknowledgements

This work was funded by the European Union and the State of North Rhine-Westphalia under the project “CirCoRo” (funding code EFRE-20800768) within the EFRE.NRW program, and by the Deutsche Forschungsgemeinschaft (DFG, German Research Foundation) under Germany’s Excellence Strategy – EXC 3115 – 533767731.

References

[1] Classen, Martin. 2020. Shear Crack Propagation Theory (SCPT) – The mechanical solution to the riddle of shear in RC members without shear reinforcement. Engineering Structures 210. https://doi.org/10.1016/j.engstruct.2020.110207.

[2] Schmidt, Max and Schmidt, Philipp; et al. 2021. Shear Response of Members without Shear Reinforcement—Experiments and Analysis Using Shear Crack Propagation Theory (SCPT). Applied Sciences 11:1–16. https://doi.org/10.3390/app11073078.

[3] Kupfer, Helmut and Hilsdorf, Hubert; et al. 1969. Behavior of Concrete Under Biaxial Stresses. ACI Journal 66(8):656–666.

[4] Hillerborg, Arne, and Modéer, Matz; et al. 1976. Analysis of Crack Formation and Crack Growth in Concrete by Means of Fracture Mechanics and Finite Elements. Cement and Concrete Research 6:773–781. https://doi.org/10.1016/0008-8846(76)90007-7.

[5] Jirásek, Milan. 2011. Damage and smeared crack models. Numerical Modeling of Concrete Cracking. Vienna: Springer Vienna, pp 1–49

[6] Walraven, Joost and Reinhardt, Hans-Wolf. 1981. Theory and Experiments on the Mechanical Behaviour of Cracks in Plain and Reinforced Concrete Subjected to Shear Loading. HERON 26:1–68

[7] Baumann, Theodor and Rüsch, Hubert. 1970. Schubversuche mit indirekter Krafteinleitung. Versuche zum Studium der Verdübelungswirkung der Biegezugbewehrung eines Stahlbetonbalkens: DAfStb-Heft 210. Ernst & Sohn.

[8] Griewank, Andreas and Walther, Andrea. 2008. Evaluating derivatives: principles and techniques of algorithmic differentiation. Society for Industrial and Applied Mathematics.

[9] Corliss, George; et al. 2013. Automatic Differentiation of Algorithms: From Simulation to Optimization. Springer Science & Business Media.

[10] Naumann, Uwe. 2011. The art of differentiating computer programs: an introduction to algorithmic differentiation. Society for Industrial and Applied Mathematics.

Prediction and Measurement of Slab Construction Load and Deflection of Wall-Type Residential Building

Jong-Min Lee, Hyeon-Jong Hwang, Han-Se Moon and Hong-Gun Park

Department of Architecture and Architectural Engineering,
Seoul National University,
Gwanak-ro 1, Seoul (08826), Republic of Korea

Summary
This study proposes a modified analytical model for construction loads and slab deflections in wall-type residential buildings using aluminum form systems. The model distinguishes regular and temporary supports, accounts for load redistribution during temporary support removal, and uses an effective supporting area to represent irregular shore layouts. The model was validated using 57 days of shore-load measurements from four consecutive floors and 101 days of deflection measurements from a representative slab. The model reproduced the key construction-stage load-transfer mechanisms and the long-term deflection trend observed in the field.

1 INTRODUCTION

1.1 Research Background

Structural design generally assumes that concrete has reached its design strength and that slabs support only self-weight, finishing loads, and live loads. During multistory construction, however, early-age slabs also carry upper-floor construction loads through shoring systems, which may cause cracking, excessive deflection, or collapse [1]. This risk is more pronounced in Korean wall-type residential buildings using aluminum forms, where temporary supports are removed early and loads are rapidly redistributed to the remaining regular supports.

1.2 Literature Review

Construction-load prediction has commonly relied on the Simplified Method by Grundy and Kabaila and ACI 347, which assume infinitely stiff shores and distribute loads according to slab stiffness [2], [3]. Later refined models considered finite shore stiffness, concrete aging, cracking, and stiffness degradation [4]-[6]. However, these studies mainly addressed beam-column frame or flat-plate systems with uniform shore layouts and therefore do not sufficiently capture wall-type residential buildings where bearing walls create irregular shore arrangements and regular and temporary supports are installed and removed separately.

1.3 Objectives

This study develops and validates a prediction model for construction loads and slab deflections in wall-type residential buildings by reflecting the floor-by-floor construction sequence, irregular shore arrangement, and separate removal of regular and temporary supports. The model incorporates load redistribution during temporary support removal and introduces the Effective Supporting Area (A_{eff}) to calculate equivalent stiffness. Validation was performed using 57 days of shore-load measurements from four consecutive floors and 101 days of deflection monitoring from a representative slab at an actual wall-type apartment construction site.

2 PREDICTION MODELS FOR CONSTRUCTION LOAD AND DEFLECTION

2.1 Existing Prediction Methods

Representative methods for predicting construction loads include the Simplified Method adopted by ACI 347 and the Refined Method, which considers shore stiffness and concrete aging effects [3].

2.1.1 Simplified Method

The Simplified Method proposed by Grundy and Kabaila assumes infinitely stiff shores and identical slab flexural stiffness [2]. Although simple and widely used, it neglects finite shore stiffness and time-dependent changes in the concrete elastic modulus (E_c), which may cause errors in estimating maximum slab loads during construction.

2.1.2 Refined Method

The Refined Method represents shores as elastic elements with finite stiffness and distributes loads according to the relative stiffness of the slabs and shores [4], [5]. However, existing refined models generally assume uniform shore layouts, limiting their direct application to wall-type structures with irregular shore arrangements caused by bearing walls and the omission of shores to secure workspace.

2.2 Proposed Model: Effective Supporting Area and Equivalent Stiffness

The Effective Supporting Area (A_{eff}) is introduced to represent irregular shore arrangements in the equivalent beam model by converting the average load-sharing area of each shore into equivalent stiffness.

2.2.1 Effective Supporting Area (A_{eff})

The Effective Supporting Area (A_{eff}) supported by a single shore is defined from the total slab area (A_{slab}) and the number of shores (n_{sh}), as given in Eq. (1). It is then converted into an effective shore spacing ($(S_1)_{eff}$) for the unit-width slab-shore model using Eq. (2).

$$A_{eff} = \frac{A_{slab}}{n_{sh}} \tag{1}$$

$$(S_1)_{eff} = \sqrt{A_{eff}} \tag{2}$$

2.2.2 Effective Stiffness of the Equivalent Beam Model

The shoring system is modeled as elastic supports, and the axial stiffness of each shore is converted into an effective stiffness per unit length ($(k_{sh})_{eff}$) using the effective shore spacing ($(S_1)_{eff}$), as shown in Eq. (3). This stiffness is used to construct the system stiffness matrix in the step-by-step construction analysis.

$$(k_{sh})_{eff} = \frac{E_S A_S}{(S_1)_{eff} H} = \frac{E_S A_S}{\sqrt{A_{eff}} H} \tag{3}$$

2.3 Structural Analysis Procedure

A step-by-step stiffness matrix analysis is used to simulate changes in stiffness and load distribution during slab casting, temporary support removal, and lowest shore removal, as illustrated in Fig. 1.

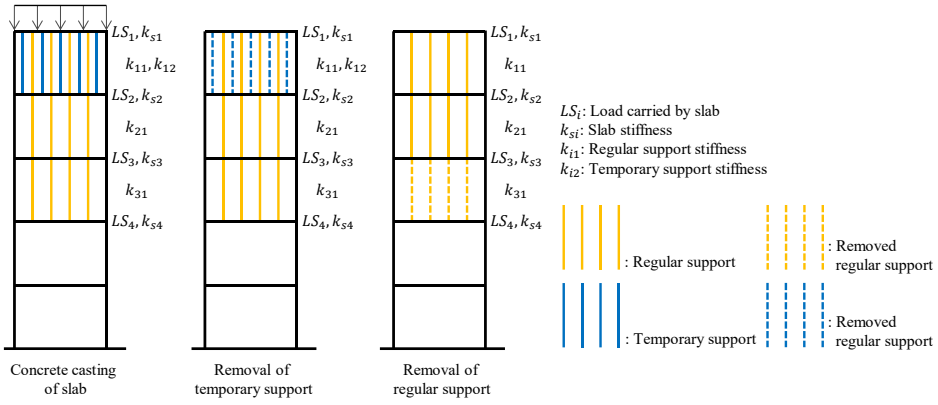


Fig. 1 Schematic illustration of the step-by-step construction analysis procedure

2.3.1 Step 1: Slab Casting (Top Slab)

During slab casting, the newly cast top slab is assumed to have negligible flexural stiffness ($k_{s1} \approx 0$). The casting load is transferred to the hardened lower slabs through the shoring system, and the load vector carried by each slab is calculated using the condensed stiffness matrix in Eqs. (4) and (5).

$$[K_{ff}]\{v\} = \{P_{cast}\} \tag{4}$$

$$\begin{aligned} &\{LS\}_{step1} = [K_{fsl}]\{v\} = [K_{fsl}][K_{ff}]^{-1}\{P_{cast}\} \\ &[K_{fsl}] = \begin{bmatrix} k_{s2} & 0 & 0 \\ 0 & k_{s3} & 0 \\ 0 & 0 & k_{s4} \end{bmatrix}, \\ &[K_{ff}] = \begin{bmatrix} k_{s2}+k_{21} & -k_{21} & 0 \\ -k_{21} & k_{s3}+k_{21}+k_{31} & -k_{31} \\ 0 & -k_{31} & k_{s4}+k_{31} \end{bmatrix}, \{P_{cast}\} = \begin{Bmatrix} Load_c \\ 0 \\ 0 \end{Bmatrix} \end{aligned} \tag{5}$$

2.3.2 Step 2: Removal of Temporary Supports

Temporary support removal is modeled as unloading followed by redistribution. The Temporary Support Stiffness Ratio in Eq. (6) defines the load share carried by temporary supports. The unloading load is calculated using Eq. (7), redistributed to the system supported by regular shores using Eqs. (8) and (9), and superimposed with the Step 1 load to obtain the slab load after removal in Eq. (10).

$$\alpha_{temp} = \frac{k_{temp}}{k_{total}} = \frac{k_{temp}}{k_{reg}+k_{temp}} \tag{6}$$

$$\Delta\{LS\}_{unload} = [K_{fsl}][K_{ff}]^{-1}\begin{Bmatrix} -(DL \cdot \alpha_{temp} + CLL) \\ 0 \\ 0 \end{Bmatrix} \tag{7}$$

$$\{P_{redist}\} = \begin{bmatrix} DL \cdot \alpha_{temp} \\ 0 \\ 0 \\ 0 \end{bmatrix} \tag{8}$$

$$\begin{aligned} &\Delta\{LS\}_{redist} = [K_{fsl}][K_{ff}]^{-1}\{P_{redist}\} \\ &[K_{fsl}] = \begin{bmatrix} k_{s1} & 0 & 0 & 0 \\ 0 & k_{s2} & 0 & 0 \\ 0 & 0 & k_{s3} & 0 \\ 0 & 0 & 0 & k_{s4} \end{bmatrix}, \\ &[K_{ff}] = \begin{bmatrix} k_{s1}+k_{11} & -k_{11} & 0 & 0 \\ -k_{11} & k_{s2}+k_{11}+k_{21} & -k_{21} & 0 \\ 0 & -k_{21} & k_{s3}+k_{21}+k_{31} & -k_{31} \\ 0 & 0 & -k_{31} & k_{s4}+k_{31} \end{bmatrix} \end{aligned} \tag{9}$$

$$\{LS\}_{step2} = \{LS\}_{step1} + \Delta\{LS\}_{unload} + \Delta\{LS\}_{redist} \tag{10}$$

2.3.3 Step 3: Removal of Lowest Shores

When the lowest regular supports are removed, the load previously carried by those shores is redistributed to the remaining slab-shore system above. This redistribution is modeled using an equivalent load opposite to the shore reaction force, and the resulting slab load is calculated using Eq. (11).

$$\Delta\{LS\}_{step3} = [K_{fsl}][K_{ff}]^{-1}\{0, 0, 0, -R_{shore}\}^T \tag{11}$$

2.4 Deflection Prediction Model

A three-step deflection analysis using a grid beam model is performed to account for construction-stage load variation, early-age cracking, and long-term effects due to creep and shrinkage.

2.4.1 Grid Beam Model

A grid beam model is adopted to efficiently account for stiffness reduction and moment redistribution caused by early-age cracking [6]. The slab is idealized as orthogonal beam elements in the x- and y-directions, and distributed loads are applied to each element. The global stiffness matrix is constructed

using the concrete elastic modulus ($E_c(t_0)$) and moment of inertia ($I(t_0)$) at the time of loading. The element stiffness relationship is given in Eq. (12), and cracking is reflected by updating the effective moment of inertia ($I(t)$) at each construction stage.

$$\begin{Bmatrix} F_{z1} \\ M_{y1} \\ F_{z2} \\ M_{y2} \end{Bmatrix} = \frac{E_c(t_0)I(t_0)}{L_x^3} \begin{bmatrix} 12 & 6L_x & -12 & 6L_x \\ 6L_x & 4L_x^2 & -6L_x & 2L_x^2 \\ -12 & -6L_x & 12 & -6L_x \\ 6L_x & 2L_x^2 & -6L_x & 4L_x^2 \end{bmatrix} \begin{Bmatrix} w_1 \\ \theta_1 \\ w_2 \\ \theta_2 \end{Bmatrix} \tag{12}$$

2.4.2 Effective Moment of Inertia and Analysis Procedure

Cracking caused by construction loads reduces the flexural stiffness of early-age slabs. The effective moment of inertia (I_e) is calculated using the Bischoff and Scanlon equation in Eq. (13), which is suitable for lightly reinforced slabs [7]. Because effective stiffness depends on the applied moment (M_a), iterative calculation is used. During unloading caused by shore removal, elastic recovery is evaluated using the gross moment of inertia (I_g) to reflect the irreversible deflection behavior associated with load history [8].

$$I_e = \frac{I_{cr}}{1-\left(\frac{M_{cr}}{M_a}\right)^2\left(1-\frac{I_{cr}}{I_g}\right)} \leq I_g \tag{13}$$

2.4.3 Long-term Deflection Calculation

The final long-term deflection (Δ_T) is obtained by summing the creep deflection, calculated by applying the creep coefficient (v) to the immediate deflection increment (ΔI_i) occurring at each construction stage, and the shrinkage deflection (Δ_sh), as shown in Eq. (14). The creep and shrinkage models follow ACI 209R-92 [9].

$$\Delta_T = \sum\left[1 + v\left(t, t_{0,i}\right)\right]\Delta I_i + \Delta_{sh} \tag{14}$$

At this time, $(1 + v)$ is multiplied and accumulated for deflection increments in stages where load increases. In stages where load is removed (Unloading), the amount of elastic recovery is subtracted from the long-term deflection, but the creep coefficient is not applied to the recovered deflection.

3 FIELD MEASUREMENT

3.1 Description of the Measured Building

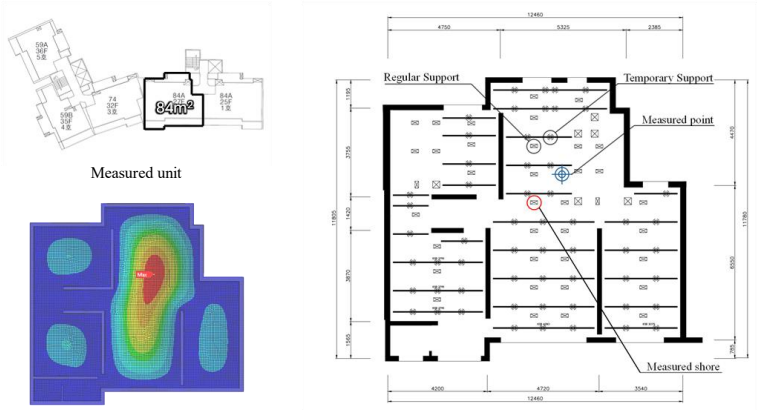


Fig. 2 Measured unit (top left), predicted deflection distribution (bottom left), and support and measurement layout (right)

The building subject to field measurement is a 27-story wall-type residential building under construction in South Korea. Among various floor plan types at the site, the 84 m² unit, representing the largest floor type and expected to be most critical with respect to construction loads, was selected as the measurement section. Prior to the field measurement, a finite element analysis was conducted for

the target unit to identify the location of maximum expected deflection. The selected measurement unit is shown in Fig. 2 (top left), the predicted deflection distribution used to select the monitoring point in Fig. 2 (bottom left), and the support and measurement layout, including the measured shore and deflection monitoring point, in Fig. 2 (right). The major design information of the measured slab is summarized in Table 1.

Table 1 Slab design information

Thickness [mm]	28-day strength [MPa]	Reinforcement Information		
		Diameter [mm]	Yield strength [MPa]	Spacing [mm]
210	40	9.53	500	300

3.2 Measurement Method

In this study, shore axial loads were measured to evaluate construction loads, and slab deflections were measured to investigate the immediate and long-term behavior of the structure.

3.2.1 Shore Load Measurement

To verify the proposed model, shore axial forces were measured over a total period of 57 days across four consecutive floors, from the 3rd to the 6th floors. Shore axial forces were measured using load cells installed beneath the regular supports located closest to the expected maximum slab deflection point. Although temporary supports were not instrumented, continuous monitoring of axial load variations in the selected regular supports enabled evaluation of load redistribution caused by the removal of temporary supports, as well as the load transfer mechanism throughout the entire construction cycle.

3.2.2 Slab Deflection Measurement

To evaluate slab deflection induced by construction loads and the subsequent long-term behavior due to creep and shrinkage, vertical deflection at the slab center was measured using an LVDT (Linear Variable Differential Transformer). The measurement was conducted over a total period of 101 days, allowing observation of both deflection development during construction stages and long-term deflection behavior after construction loading.

3.3 Material Testing

To reflect the material properties of the actual structure in the construction load and deflection analysis, cylindrical concrete specimens with dimensions of $\phi 100 \times 200$ mm were prepared at the time of slab casting. The specimens were cured under the same temperature and humidity conditions as the slabs at the construction site. Compressive strength and elastic modulus tests were conducted at concrete ages of 7, 14, and 28 days. The average values of the measured compressive strength and elastic modulus are summarized in Table 2.

Table 2 Compressive strength and elastic modulus of concrete

Floor	7-day f_c [MPa]	14-day f_c [MPa]	28-day f_c [MPa]	7-day E_c [MPa]	14-day E_c [MPa]	28-day E_c [MPa]
4F	40.3	53.4	53.9	18,763	31,979	22,862
5F	49.8	54.8	64.6	28,185	25,852	25,079
6F	42.6	47.7	54.3	25,188	28,661	30,207
7F	29.6	52.1	55.9	18,689	27,307	28,139

3.4 Construction Sequence and Environment

The construction site adopted a 7-day construction cycle per floor. Temporary shores and formwork were planned to be removed approximately 2–3 days after slab casting, and the lowest shores were planned to be removed approximately 5 days after casting. However, the actual construction schedule varied depending on weather conditions and site-specific circumstances. In this study, the analysis model incorporates the actual construction sequence observed on site to reflect site conditions. The detailed slab casting and shore removal schedules for each floor are summarized in Table 3.

Table 3 Construction schedule for concrete casting and shoring

Floor	Concrete casting	Regular support		Temporary support	
		Installation	Removal	Installation	Removal
3F	Aug 16	Aug 22	Sep 24	Aug 22	Aug 29
4F	Aug 23	Aug 30	Oct 4	Aug 30	Sep 3
5F	Sep 2	Sep 16	Oct 11	Sep 16	Sep 22
6F	Sep 20	Sep 26	Oct 18	Sep 26	Sep 29
7F	Sep 28	Oct 5	Oct 26	Oct 5	Oct 8

4 RESULTS AND DISCUSSION

4.1 Construction Load Comparison

4.1.1 Conversion of Measured Data

While the prediction model proposed in this study calculates the distributed load (w_{slab} , DL) carried by the slab, the load cells installed at the site measure the axial load (P_{shore} , kN) of individual shores. Therefore, to compare the measured point loads with the construction load carried by the slab, a two-step conversion process is required.

First, the measured shore axial load (P_{shore}) is divided by the Effective Supporting Area (A_{eff}) defined in Section 2.2 to convert it into shore load per unit area (Sh_i) for the corresponding floor.

$$Sh_i = \frac{P_{shore,i}}{A_{eff}} \tag{15}$$

Second, the converted shore load (Sh_i) is substituted into the equilibrium relationship of the slab–shore system, expressed in Eq. (16), to derive the construction load actually carried by the slab at the i-th floor.

$$w_{slab,i} = Sh_i + DL - Sh_{i-1} \tag{16}$$

Here, $w_{slab,i}$ is the construction load carried by the slab at the i-th floor, Sh_i is the load intensity of the shores supporting the slab from below (i-th floor), and Sh_{i-1} is the load intensity transmitted to the slab from the shores above. DL denotes the self-weight of the slab. Equation (16) represents the vertical force equilibrium of the slab, where the net load carried by the slab is obtained by subtracting the load transferred upward through the shoring system from the load supported below.

4.1.2 Comparison Analysis

Existing construction load calculation methods, such as the Simplified Method, assume that shores are uniformly installed and removed across all floors. As a result, these methods cannot represent the complex construction sequence of the present site, where temporary supports and regular supports are operated independently. Therefore, in this section, existing methods are excluded, and only the construction loads predicted by the proposed model are compared with the field measurement results.

Fig. 3 presents the variation of construction loads acting on the 4th floor slab (top left), 5th floor slab (top right), and 6th floor slab (bottom left) throughout the construction process. The horizontal axis represents the elapsed time after slab casting, while the vertical axis indicates the construction load normalized by the slab self-weight (DL). Major construction events are marked by Steps (1)–(17).

For the measured floors, the proposed model captured the timing and magnitude of peak construction loads observed during upper-floor casting.

In addition, the load variation associated with the removal of temporary supports (Steps 2, 5, 8, and 11), which is a key focus of this study, was clearly identified.

The load increase–decrease behavior associated with temporary support removal and subsequent load redistribution was consistently captured by the proposed model.

Furthermore, when the lowest regular supports were removed (Steps 3, 6, and 9), a stepwise increase in construction load due to load transfer to the upper slabs was observed.

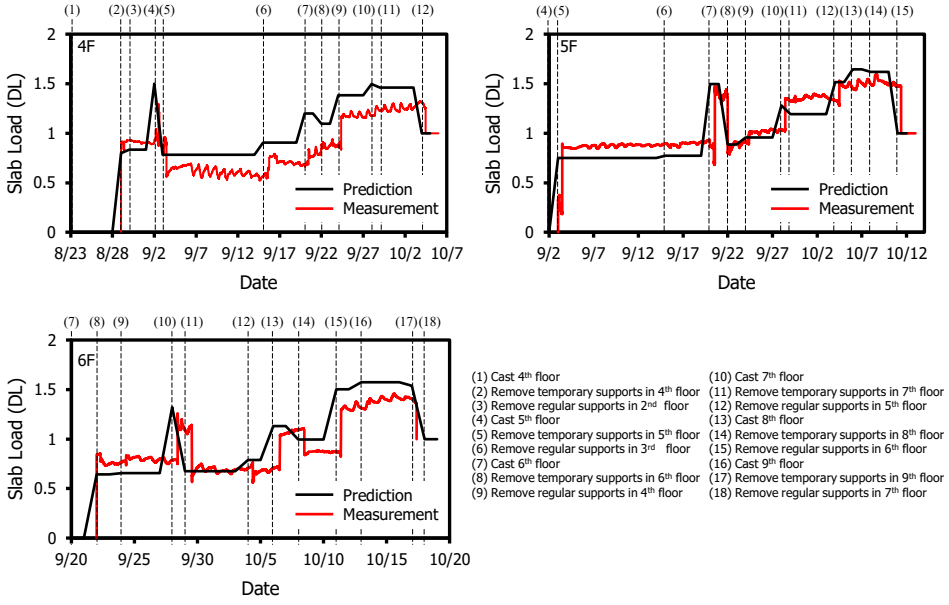


Fig. 3 Comparison of measured and predicted construction loads: 4th floor slab (top left), 5th floor slab (top right), and 6th floor slab (bottom left)

4.2 Deflection Comparison

4.2.1 Immediate Deflection

The comparison of measured and predicted slab deflections over 120 days is shown in Fig. 4 (left). The proposed model captured the measured immediate deflection response during construction stages.

4.2.2 Long-term Deflection Behavior

Even after all shores were removed, the slab deflection continued to increase during the 101-day measurement period due to concrete creep and shrinkage. The extended prediction up to 365 days is shown in Fig. 4 (right).

The proposed model captured the measured long-term deflection trend after shore removal.

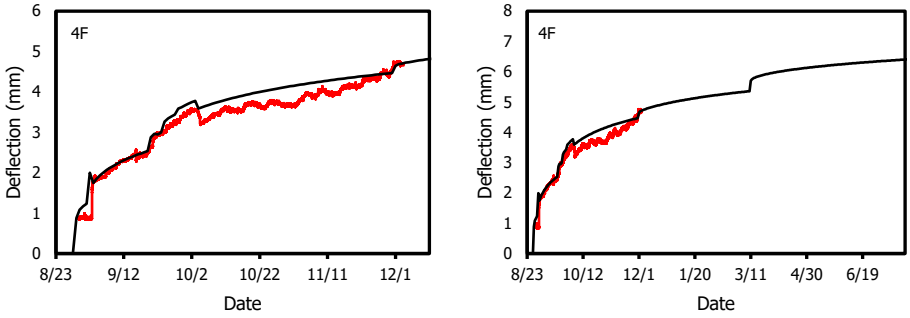


Fig. 4 Comparison of measured and predicted slab deflections: 120-day response (left) and 365-day response (right)

5 CONCLUSION

In this study, a modified analytical model was proposed to predict slab construction loads and deflections by explicitly considering the construction characteristics of wall-type residential buildings employing aluminum form systems. The proposed model distinguishes regular and temporary supports, incorporates the load redistribution process associated with temporary support removal, and introduces the effective supporting area concept to represent irregular shore arrangements in wall-type structures.

Field measurements, including shore-load monitoring over four consecutive floors and deflection monitoring of a representative slab, were used to verify the proposed model. The results showed that the model captured the main construction-stage load-transfer mechanisms, including peak-load development and the load increase–decrease behavior induced by the installation and removal of temporary and regular supports.

The results showed that the measured slabs experienced a peak construction load of approximately 1.5 times their self-weight during the casting of the immediately upper floor slab, occurring at an early-age stage when concrete stiffness was insufficiently developed. In addition, construction loads applied at early ages were found to increase long-term deflection through subsequent creep and shrinkage. These findings indicate that construction-load prediction and management are important for ensuring construction-stage safety and long-term serviceability of wall-type residential buildings.

Acknowledgements

This research was supported by a grant (RS-2022-00143493) from Digital-Based Building Construction and Safety Supervision Technology Research Program funded by Ministry of Land, Infrastructure and Transport of Korean Government.

References

[1] Chun, Sung-Chul, and Ha, Taehun. 2016. “Safety and Serviceability of Reinforced Concrete Beam-Column Joints Supported by Shores and Reshores during Construction.” *Journal of Structural Engineering* 142(7):04016034. doi:10.1061/(ASCE)ST.1943-541X.0001494.

[2] Grundy, Peter, and Kabaila, Alexander. 1963. “Construction Loads on Slabs with Shored Formwork in Multistory Buildings.” *ACI Journal Proceedings* 60(12):1729–1738.

[3] ACI Committee 347. 2014. *Guide to Formwork for Concrete (ACI 347R-14).* Farmington Hills, MI: American Concrete Institute.

[4] Liu, Xiaodong, Chen, Wai-Fah, and Bowman, Mark D. 1985. “Construction Load Analysis for Concrete Structures.” *Journal of Structural Engineering* 111(5):1019–1036. doi:10.1061/(ASCE)0733-9445(1985)111:5(1019).

[5] Park, Hong-Gun, Hwang, Hyun-Jong, Hong, Gyu-Hong, Kim, Young-Nam, and Kim, Jae-Yo. 2011. “Slab Construction Load Affected by Shore Stiffness and Concrete Cracking.” *ACI Structural Journal* 108(6):679–688. doi:10.14359/51683366.

[6] Hwang, Hyun-Jong, Park, Hong-Gun, Hong, Gyu-Hong, Kim, Jae-Yo, and Kim, Yong-Nam. 2016. “Time-Dependent Deflection of Slab Affected by Construction Load.” *ACI Structural Journal* 113(3):557–566. doi:10.14359/51687943.

[7] Bischoff, Paul H., and Scanlon, Andrew. 2007. “Effective Moment of Inertia for Calculating Deflections of Concrete Members Containing Steel Reinforcement and Fiber-Reinforced Polymer Reinforcement.” *ACI Structural Journal* 104(1):68–75.

[8] Park, Hong-Gun, Hwang, Hyun-Jong, Hong, Gyu-Hong, Kim, Yong-Nam, and Kim, Jae-Yo. 2012. “Immediate and Long-Term Deflections of Reinforced Concrete Slabs Affected by Early-Age Loading and Low Temperature.” *ACI Structural Journal* 109(3):413–422.

[9] ACI Committee 209. 1992. *Prediction of Creep, Shrinkage, and Temperature Effects in Concrete Structures* (ACI 209R-92). Farmington Hills, MI: American Concrete Institute.

Experimental Investigation on the Structural Behaviour of Reinforced Concrete Dapped-End Beams with Bars Subjected to Pitting Corrosion

Elisa Carleschi, Adriano Reggia, Giovanni A. Plizzari

Department of Civil, Environmental, Architectural Engineering and Mathematics (DICATAM)
University of Brescia,
via Branze n.43, Brescia (25123), Italy

Summary
The ageing of existing bridges represents a significant risk for road transportation networks. Evaluating structural reliability and bridge safety is crucial, particularly regarding material decay caused by environmental conditions and lack of maintenance. This research investigates pitting corrosion induced by de-icing salt (chlorides) on dapped-end beams (Gerber girders). This member type is prone to localized corrosion due to service-load cracks that promote chloride penetration and corrosion initiation. Accordingly, this research examines reinforcing steel affected by pitting corrosion, focusing on residual tensile strength and ductility loss, and its influence on bridge girders. A heavily damaged RC girder is tested to assess global structural behaviour and to correlate reinforcement deterioration with load capacity reduction. With a 30% loss of cross-sectional area in longitudinal rebars, beams show a significant reduction in ductility, highlighting the critical role of localized corrosion in structural performance.

1 INTRODUCTION

1.1 Dapped-end Beams

Dapped-end beams (DEBs) are reinforced concrete structural elements historically used in precast bridge construction. They are characterized by a notched, "dapped", end designed to reduce member depth and facilitate structural connections. This structural detail is particularly common in half-joint systems, in which a continuous beam is subdivided into statically determinate spans connected through regions with reduced cross sections at intermediate supports. Therefore, Dapped-end beams have two different structural zones. The central portion behaves as a B-region, where the Bernoulli-Navier assumptions remain valid and strain distribution is approximately linear. In contrast, the two regions near the supports form D-regions (i.e., discontinuty regions), where geometric changes cause highly disturbed stress fields.

Because standard beam theory is not applicable in these areas, analytical approaches such as the Strut-and-Tie (S&T) method and detailed finite element modeling (FEM) are commonly employed. Although the dapped-end configuration offers structural and construction advantages, it also creates critical vulnerabilities. The stress concentration and complexity of the reinforcement detailing make these regions particularly sensitive to deterioration processes, especially reinforcement corrosion. The consequences of such degradation have been highlighted by past bridge failures, including the collapse of the De la Concorde Gerber Bridge in Canada, where corrosion of reinforcing steel played a major role [3].

Experimental research in recent years has confirmed the severe impact of corrosion on the structural performance of dapped-end beams. Several studies have simulated corrosion damage by intentionally removing or reducing key reinforcement components, such as diagonal bars or U-shaped stirrups, demonstrating how the loss of these elements can significantly compromise load transfer mechanisms and promote brittle failure modes [4]. Other investigations [5] have reproduced localized corrosion mechanically, again showing pronounced reductions in both strength and ductility.

Tests involving artificially corroded reinforcement have reported load capacity losses reaching approximately 40–45% compared to undamaged specimens [6]. These studies clearly demonstrate that reinforcement corrosion significantly threatens the structural safety of dapped-end beams, substantially altering their structural behaviour by reducing load capacity, ductility and, in many cases, changing failure mechanisms.

1.2 Pitting Corrosion

Corrosion is one of the most relevant forms of degradation in the reinforced concrete structures. In contrast to uniform corrosion, which progressively deteriorates the material along the entire length of the rebar, this localized type (pitting corrosion) compromises durability by creating deep cavities, or "pits", with a relativerly small overall material loss. Chloride ingress, originating from de-icing salts, seawater exposure or contaminated aggregates or mixing water, is the most important external cause of the pitting corrosion.

Concrete's capillarity pores and microcracks allow chlorides to penetrate until they reach the surface of steel. When the chloride concentration reaches a critical threshold, the passive layer that protects the rebars breaks down and localized corrosion begins. After the initiation of pitting corrosion, distinct morphological features develop that can affect its propagation and structural significance. Research [8] on reinforced concrete subjected to a marine environment have identified two principal types of pits:

- **Wide-shallow pits**: pits are wider and more superficial, and they grow laterally rather than vertically.
- **Narrow-deep pits**: pits are small and deep, with predominantly vertical growth.

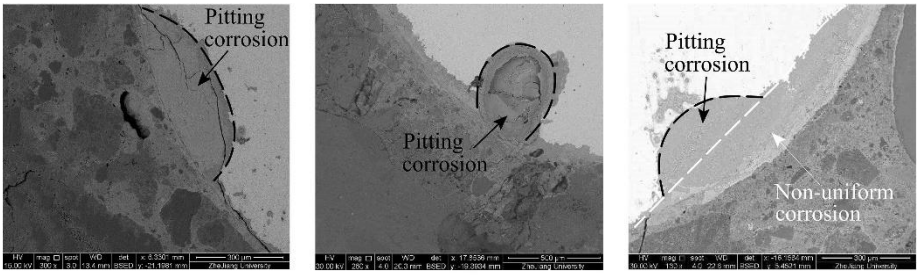


Fig. 1 Pitting corrosion in reinforcement steel bars: shallow pit (left), deep pit (middle) and, shallow deep (right). Reproduced from [8].

While the percentage of material loss due to pitting may be relatively low as compared to the total material volume, the impact of the non-uniform corrosion on the structure remains significant. This is because the depth of the pits can severely reduce the effective cross-sectional area of the reinforcing bars, leading to stress concentration and a reduction in load-bearing capacity. In addition, the presence of such pits accelerates concrete cracking and spalling, as well as the loss of bond between the concrete and the reinforcing bars, due to the volumetric expansion of the corrosion products.

2 RESEARCH SIGNIFICANCE

This study investigates the effects of pitting corrosion on reinforced concrete beams with dapped ends by examining the mechanical response of the reinforcing bars and of full-scale beams incorporating them. Pitting corrosion was simulated mechanically by locally removing material to achieve section losses ranging from 0% to 30%. The artificial damage was applied to the longitudinal reinforcement in the dapped-end region, at the location of the inclined crack that typically forms in the support zone and initiates from the inner edge of the bearing. This controlled approach enabled a systematic assessment of localized corrosion on structural performance, with particular attention to reductions in peak load and displacement capacity. The results show that even highly localized damage can have substantial consequences, highlighting the need for a thorough understanding to support advanced safety assessment of these structural systems.

3 MECHANICAL SIMULATION OF PITTING CORROSION

The study by Haefliger and Kaufmann [9] investigates the microstructural composition of Tempcore reinforcing bars. Three concentric layers define the bar cross section: an external martensitic shell produced by a short-duration water quenching followed by tempering, an intermediate bainitic layer, and a ferrite-pearlite core. The ferrite-pearlite zone shows the greatest ductility, while the outer ring exhibits the highest yield and ultimate strength. The bainitic zone provides mechanical characteristics intermediate between the two.

Tensile test results on reduced-diameter bars show that the removal of the outer martensitic ring results in a loss of load-bearing capacity that is not proportionate to the decrease in cross-sectional area because the ferrite-pearlite core's contribution to strength is much lower.

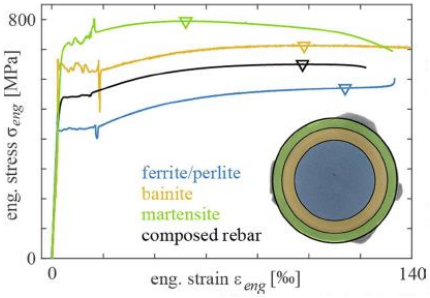


Fig. 2 Stress strain curve of each layer in reiforcing rebar. Taken from[9]

As a result of the bar microstructure, pit morphology has different implications for the overall structural response of the reinforcing bar. While a deep pit penetrates the bainitic layer and eventually the ferrite-pearlite core, resulting in a reduction in both strength and ductility, a shallow cavity primarily affects the martensitic annulus, resulting in a significant strength reduction.

Pitting corrosion can be mechanically reproduced by introducing a notch with a cilyndrical tip into the rebar, thereby simulating material loss in specific layers. The diameter of the milling tool controls which layers are affected. A shallow notch is produced using a tool with a diameter equal to that of the reinforcing bar, resulting in material removal limited to the outer layers. In contrast, a deeper notch is generated using a tool with a diameter equal to half that of the bar, allowing the cut to penetrate into the bainitic region and potentially reach the ferrite–pearlite core (see Fig. 3)

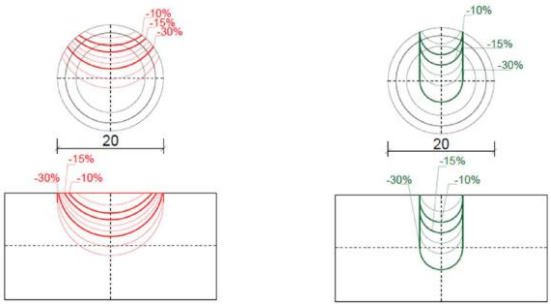


Fig. 3 Pit morphology: shallow pit (left) and, deep pit (right).

Yilmaz et al. (2024) [10] documented more than 600 chloride-induced corrosion attacks and found that the attacks are almost always shallow and laterally extensive rather than deep. All corrosion attacks were clearly wider and longer than deep, not clearly related to the manufacturing conditions, the materials, the exposure, and age of the structures. For this reason, the experimental campaign was designed using a milling tool with a diameter equal to that of the reinforcing bar to simulate shallow pitting corrosion. The pit was created between two ribs.

To realistically reproduce natural corrosion, different percentages of cross-sectional area reduction were investigated. The considered reductions in cross-section area were 5%, 10%. 15%, 20%, 25%,

30%, and 50% relative to the nominal cross-section area. For each corrosion level, two specimens were tested. The penetration depth of the spherical tip was easily calculated through geometric considerations.



Fig. 4 Simulation of pitting corrosion: mechanical tooling (left), detail of the indented reinforce ment bar (right).

4 EXPERIMENTAL TEST ON PITTING REBARS

4.1 Experimental Program and Specimens

An experimental program was carried out involving a series of tensile tests on twenty reinforcing bars, each characterized by varying degrees of pitting corrosion located at the mid-lenght of the specimen. Each specimen measured 600 mm in length and had a nominal diameter of 20 mm. The The ribbed steel bar was B450C Tempore ribbed steel, with a mean yield strength (fsy) of 520 MPa and a mean ultimate strength (fsu) of 620 MPa.

The load was applied under displacement control by gripping the bar ends in the testing machine. The test was carried out using an Instron 1274/8500 testing machine at at the Laboratory of the University of Brescia. Rebar deformation was measured using four displacement transducers. One displacement transducer (Linear Variable Differential Transformer, LVDT) was applied at the middle of the specimen with a gauge lenght of 50 mm, in correspondence with the damaged region. Two LVDTs were positioned to measure the displacement in the upper and lower portions of the specimen, while a fourth LVDT measured the overall elongation along the entire specimen length (see Fig. 5).



Fig. 5 Experimental set-up of tensile test.

4.2 Experimental Results

Figure 6 (left) shows the load–displacement curves for 20 mm diameter rebars with different levels of cross-sectional area reduction.

The reference bar (black curve) follows the classic tensile response of ribbed rebars: an elastic behaviour up to the 160 kN, a yield plateau (Phase II) reflecting the onset of yielding and strain hardening, followed by a hardening phase reaching a maximum load of 200 kN. Corroded rebars exhibited a different behavior: an initial elastic phase followed by early yielding, a minimal or absent yield plateau, brittle failure at peak load, and pronounced post-peak softening. Figure 6 (right) clearly demonstrates a linear correlation between damaged area and ultimate strength. A reduction of 10%, 20%, and 30% in cross-sectional area resulted in a 6.1%, 15.7%, and 23.4% decrease in ultimate strength, respectively.

Particularly significant is the severe loss of ductility in pitted rebars due to deformation concentrating in the pit area. Fig. 6 (right) shows an exponentially decreasing relationship between increasing pitting corrosion and ultimate displacement reduction. For the same corrosion levels (10%, 20%, 30%), ultimate displacement dropped to 47.5%, 25.4%, and 28.7% of the reference bar values, respectively.

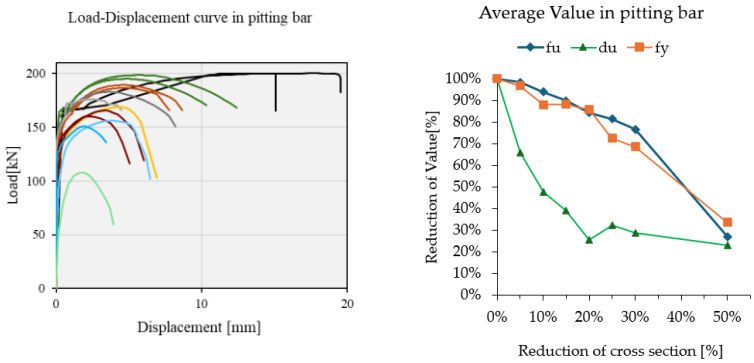


Fig. 6 displacement curve in pitting rebars (left); schematical results (right).

Unlike uncorroded bars, where fracture occurs randomly at the weakest section (due to physico-chemical or mechanical defects, often between ribs), in damaged bars the rupture consistently happens at the pitted zone. Fig. 7 shows the fracture surfaces of a damaged bar with 30% cross-sectional loss.

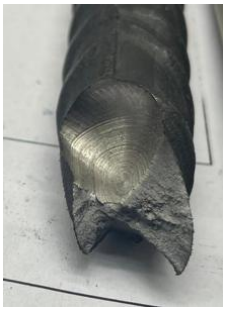


Fig. 7 Fracture surfaces on corroded rebar.

5 EXPERIMENTAL TEST ON GIRDERS

5.1 Geometry and Material Properties of Beams

Two full-scale RC dapped-end beams were tested under three-point bending (3PBT): the first was the reference un-corroded beam (REF) and the second was characterized by 30% pitting corrosion of the longitudinal reinforment of the dapped end (L30). Globally, the research included ten girders with different level of corrosion (10%, 15%, 30%), and different positions of pitting corrosion (longitudinal, diagonal and stirrup).

Each beam had a length of 5500 mm, a depth of 1000 mm, and a thickness of 240 mm, while the dapped-end region was reduced to 500 mm in length, 450 mm in depth, and 240 mm in width. In the reinforcement layout (Fig. 8), the longitudinal bars selected for artificial pitting corrosion are marked in red. Beam L30 included an artificial notch placed close to the inner edge of the bearing to simulate an existing crack.

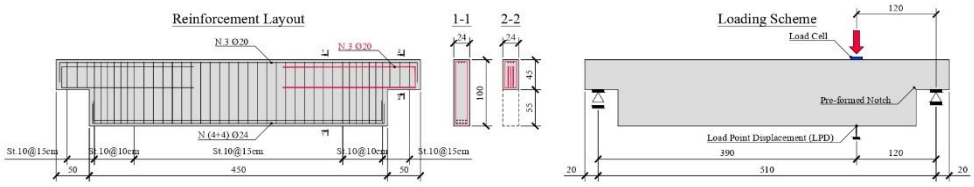


Fig. 8 Three point bending test: reinforcement layout and loading scheme.

Concrete strength class was C50/60 and steel designation was B450C according to Italian standards. Concrete compressive strength measured on cubes was 59.8 MPa after 28 days from casting.

5.2 Testing Set-up

Tests were carried out under displacement control using an electromechanical actuator over a 1.20 m shear span, adopting an asymmetric load configuration to promote a shear failure in the half joint.

The end restraints were configured as a steel hinge at the loaded support and a roller at the opposite end, ensuring statical determinacy of the setup. Instrumentation monitored crack initialiation, propagation, opening widths, as well as vertical deflections, and global deformations (Fig. 9).

A 100 mm LVDT measured load point displacement (LPD) below the loading point and midspan displacement (MPD) at the beam center. Four potentiometers tracked main crack propagation, while a load cell beneath the jack measured vertical forces, with shear loads derived from static equilibrium.

Additionally, Digital Image Correlation (DIC) was utilized on the opposite side of half-joint, where no other devices were placed, to capture crack patterns and surface deformations.

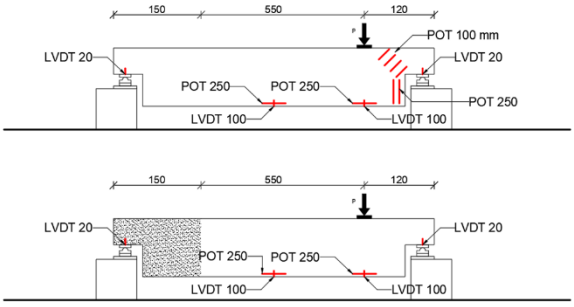


Fig. 9 Instrumentation

5.3 Experimental Results

Fig. 10 (left) illustrates the structural behavior of the dapped-end beams through shear force against Load Point Displacement (LPD) curves.

Specimen REF initially exhibited elastic, uncracked behaviour up to 50 kN. After crack initiation, a gradual reduction in stiffness due to tension stiffening effects was observed to 200 kN, followed by strong non-linearity up to 350 kN. At this point, yielding of the reinforcement produces a load plateau before reaching a peak load of 370 kN at 34 mm displacement, with minimal post-peak capacity.

The corroded beam L30 (with 30% pitting) followed the reference specimen's response up to 200 kN. Thereafter, it displayed accelerated stiffness loss compared to the undamaged beam. Brittle failure occurred at 340 kN, resulting a complete loss of load capacity.

Experimental results revealed that pitting corrosion in the longitudinal reinforcement of dapped-end beams significantly altered structural behavior. The Fig. 10 (right) clearly summarizes the effect of a 30% reduction in cross-section area: -6% in load capacity and -43% reduction in displacement capacity.

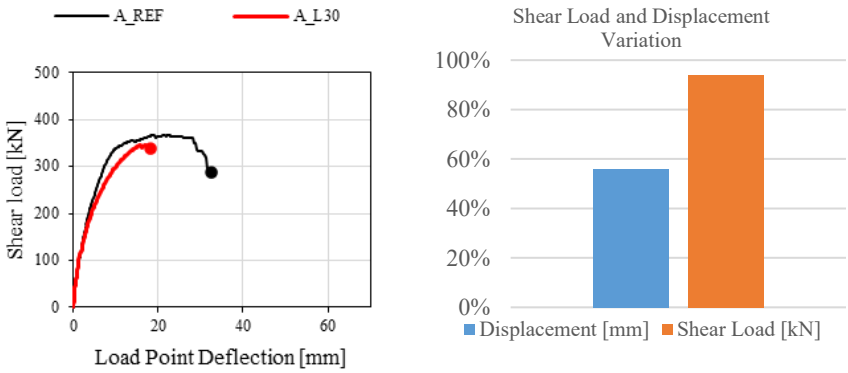


Fig. 10 Load-displacement in dapped-end beam (left); Maximum Load-reduction and displacement reduction on beam with pitting corrosion (right).

6 CONCLUSIONS

Experimental results demonstrate that localized corrosion significantly degrades the mechanical property of reinforcement bars. Tensile tests confirmed the expected reduction in maximum load, but also revealed a drastic loss of ductility.

When artificial pitting corrosion was applied to the dapped-end beam, the load-bearing capacity decreased modestly (~6%), while deformation capacity was severely compromised (-43%). These result highlight how rebar corrosion critically impairs the performance of RC structure, particularly dapped-end beams, and can affect the safety of existing bridges.

Acknowledgements

The project was funded by the PNRR through the PRIN 2022 project “New perspectives for the assessment, control and retrofitting of damaged reinforced concrete bridges” and by the European Union-NextGeneration EU, Mission 4, Component 1 (CUP D82B23003170001). This study was conducted as part of the program of activities carried out as part of the agreement between the ReLUIS Interuniversity Consortium and the Superior Council of Public Works stipulated pursuant to art. 3 of the Decree of the Minister of Infrastructure no. 578 of 17 December 2020; however, this publication does not necessarily reflect the Council's position and assessments.

A special thank goes to Andrea del Barba and Luca Martinelli, technicians at the University of Brescia, for their valuable support during the experimental campaign.

References

[1] Iori, Tullia. 2006. “L’autostrada del Sole”. Storia dell’Ingegneria 2: 1111-1120.

[2] Ahmad, Shamsad. 2003. “Reinforcement Corrosion in Concrete Structures, Its Monitoring and Service Life Prediction—A Review.” Cement and Concrete Composites 25:459–471. 10.1016/S0958-9465(02)00086-0.

[3] Johnson Johnson, Pierre Marc. 2007. Commission of Inquiry into the Collapse of a Portion of the De la Concorde Overpass, October 3, 2006–October 15, 2007: Report. Québec, QC: Commission d’enquête sur le viaduc de la Concorde.

[4] Desnerck, Pieter, Jeffrey M. Lees, and Christopher T. Morley. 2016. “Impact of the Reinforcement Layout on the Load Capacity of Reinforced Concrete Half-Joints.” Engineering Structures 127:227–239. DOI: 10.1016/j.engstruct.2016.08.061

[5] Tambusay, Asdam, Benny Suryanto, Priyo Suprobo, Fiona S. Grieve, Michael W. Aitken, and Warren Don. 2024. “Influence of Reinforcement Reductions on the Response of Reinforced Concrete Half-Joints.” Engineering Structures 321:118934. doi:10.1016/j.engstruct. 2024.118934.

[6] Menichini, Giovanni, Federico Gusella, Salvatore Giacomo Morano, and Maurizio Orlando. 2025. “RC Dapped-End Beams with Various Reinforcement Layouts: An Experimental Investigation.” Engineering Structures 322:119043. doi:10.1016/j.engstruct.2024.119043.

[7] Cairns, John, Giovanni A. Plizzari, Yong Du, David W. Law, and Carla Franzoni. 2005. “Mechanical Properties of Corrosion-Damaged Reinforcement.” ACI Materials Journal 102:256–264.

[8] Zhao, Yang, Xiaoyan Xu, Yan Wang, and Jian Dong. 2020. “Characteristics of Pitting Corrosion in an Existing Reinforced Concrete Beam Exposed to Marine Environment.” Construction and Building Materials 234:117392. doi:10.1016/j.conbuildmat.2019.117392.

[9] Haefliger, Simon, and Walter Kaufmann. 2021. “Influence of Cross Section Loss on the Stress–Strain Characteristics of Corroded Quenched and Self-Tempered Reinforcing Bars.” Construction and Building Materials 282:122598. doi:10.1016/j.conbuildmat.2021.122598.

[10] Yilmaz, D., E. Rossi, and U. Angst. 2025. “Assessment of Corrosion Attack Morphology on Reinforced Concrete Structures Exposed to Chlorides.” Structural Concrete 26(2):2124–2141. doi:10.1002/suco.202401161.

Fibre Optic Sensing in Formed Carbon Reinforcement: Separation of Longitudinal Strain and Transverse Pressure

Berk Gündogdu, Birgit Beckmann and Steffen Marx

Institute of Concrete Structures
Dresden University of Technology,
George-Bähr Straße 1, 01069, Germany

Summary
Formed carbon reinforcement develops a multiaxial stress state in the curved region, where longitudinal tension is superimposed with transverse pressure. Distributed fibre optic sensing (DFOS) is well suited to resolve the longitudinal strain, but optical fibres are also sensitive to transverse pressure, which couples into the signal as an apparent strain. This contribution presents a differential DFOS approach in which fibres are applied on both the convex and the concave side of the yarn. The outer fibre records longitudinal strain only and provides the local force distribution, while the difference between inner and outer fibre isolates the pressure-induced apparent strain. The method is demonstrated on five formed loop specimens loaded around a mandrel without concrete and provides the basis for future investigations of the load transfer between curved reinforcement and concrete.

1 INTRODUCTION

The growing application of carbon reinforcement in concrete construction has created demand for shaped elements such as stirrups, end hooks and freely formed structures [1, 2]. Unlike steel, non-metallic reinforcement cannot be bent on site; shaped elements are produced during fabrication, introducing a curved region in which the load-bearing behaviour differs substantially from that of the straight material [3]. Carbon fibres exhibit high stiffness and strength in the fibre direction but considerably lower transverse properties, so that in the bent region the superposition of longitudinal tension and transverse pressure against the forming radius governs the load-bearing capacity of the element [4]. A detailed understanding of this behaviour requires spatially resolved measurement of the strain distribution along the curved region. Distributed fibre optic sensing (DFOS) based on Rayleigh backscattering provides continuous strain profiles at millimetre resolution and has been applied to both reinforced concrete members and FRP reinforcement, though almost exclusively in straight configurations [5, 6]. Optical fibres are, however, also sensitive to transverse loading: lateral pressure couples into the Rayleigh signal as an apparent strain through the photoelastic effect, with a magnitude that depends on the fibre coating, bonding configuration and pressure direction, so that sensitivity coefficients cannot readily be transferred between set-ups [7]. The combination of spatially resolved DFOS measurements with the mechanical description of formed elements and in particular the separation of the pressure-induced apparent strain from the true longitudinal strain, has not yet been addressed.

This contribution presents an experimental method for separating transverse pressure effects from the longitudinal strain response in formed carbon reinforcement. The investigation is based on tensile tests on formed loop specimens loaded around a cylindrical mandrel without surrounding concrete, so that the transverse pressure originates solely from the well-defined contact between yarn and mandrel. Optical fibres are applied on both the convex and the concave side of the yarn: the outer fibre experiences longitudinal strain only, while the inner fibre additionally undergoes transverse pressure. This differential arrangement is used to isolate the pressure-induced apparent strain and to reconstruct the local force distribution along the curved region, providing the basis for future investigations of the load transfer between curved reinforcement and concrete.

2 EXPERIMENTAL PROGRAMME

The investigation comprises five tensile tests on closed loop specimens made of carbon reinforcement. Each loop was fabricated from two U-shaped elements produced from a single weft yarn of HTC 21/21-80 by HiTexbau, with a cross-sectional area of A = 1.81 mm², a width of approximately 2 mm and a

longitudinal modulus of elasticity of E ≈ 180 000 N/mm². The U-shaped elements were separated from the grid to obtain individual yarns. Two such yarns were then joined along the straight shanks using 2K-Epoxy and fixed with shrink tubing, resulting in one lap joint of 100 mm length in each of the two shanks. The fabrication sequence is illustrated in Fig. 1.

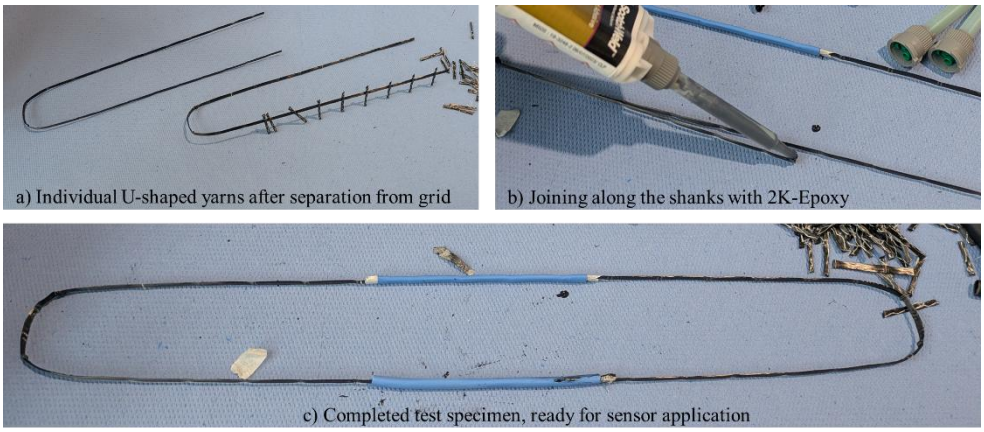


Fig. 1 Steps a) to c) for Specimen preparation

2.1 Test set-up and loading

The tests were carried out on a Zwick ZD250 testing machine under displacement control at a rate of 1 mm/min. The load was introduced symmetrically through the upper mandrel at the loop head, with the lower mandrel providing the reaction. Prior to each test, the specimens were preloaded to 100 N in order to establish defined contact with the mandrels and to provide the reference state for the strain measurement. The closed loop was loaded around two cylindrical steel mandrels of 40 mm diameter, one at the loop head for load introduction and one at the loop foot acting as support, each enclosed over a wrap angle of 180°. Loading was applied without surrounding concrete, so that the transverse pressure in the curved regions originated solely from the well-defined contact between yarn and mandrel. Due to the symmetry of the set-up, both shanks carry equal force, and the tensile force along each curved region is governed by the equilibrium discussed in Section 3. The test setup is shown in Fig. 2



Fig. 2 Test setup: closed loop specimen loaded around two cylindrical mandrels (40 mm diameter) ready for testing a) + b). Close-Up on the upper mandrel with bulges on the yarn c).

2.2 Fibre optic instrumentation

Strain measurements were performed using a LUNA ODiSI distributed fibre optic sensing system based on Rayleigh backscattering, with a gauge pitch of 0.67 mm. Optical fibres (polyimide-coated single-mode fibre) were first fixed in place with spot applications of a cyanoacrylate gel (Loctite) and subsequently bonded over their full length with a two-component epoxy adhesive. The bonded length covers the straight shank, the forming bow and the adjacent straight shank; each fibre extends from the end of one lap joint to the beginning of the next, so that one forming region is instrumented per fibre, flanked by two straight reference segments.

On each specimen, two separate fibres were applied, one on the convex (outer) and one on the concave (inner) side of the yarn. The outer fibre, which is not in contact with the mandrel, is subjected to longitudinal strain only. The inner fibre, located between yarn and mandrel, additionally experiences the transverse pressure of the contact. It was applied centrally on the concave surface of the yarn by visual alignment, without a guiding groove. The straight shank segments, in which both fibres must record identical longitudinal strains, serve as an in-situ reference for the determination of sensor-specific offsets.

2.3 Measurements and failure documentation

For each test, the continuous longitudinal strain distribution along both the inner and the outer fibre was recorded throughout loading up to failure, together with the synchronously logged force and machine displacement. The failure location was identified directly from the strain peaks in the DFOS profiles, and the maximum force and corresponding displacement were determined for each specimen.

3 ANALYTICAL FRAMEWORK

3.1 Force equilibrium in the curved region

In the curved region, the yarn is wrapped around a mandrel of radius R = 20 mm over a wrap angle of 180°. The arc length coordinate s is measured from the transition between the straight shank and the bow (s = 0) to the apex (s ≈ 31.4 mm). Radial equilibrium of an infinitesimal arc segment relates the local yarn force $F(s)$to the radial line load $q_r(s)$ acting between yarn and mandrel:

$$q_r(s) = \frac{F(s)}{R} \tag{1}$$

This relation is exact and independent of any assumption regarding the distribution of F along the arc. Tangential equilibrium introduces the friction interaction at the contact interface:

$$\frac{dF}{ds} + \tau_{lin}(s) = 0 \tag{2}$$

where τlin(s) is the tangential friction line load, limited by the Coulomb condition $\tau_{lin}(s) \leq \mu \cdot q_r(s)$ with the friction coefficient μ between yarn and mandrel.

3.2 Limiting cases and characteristic length

Two limiting cases bracket the expected behaviour. In the frictionless limit, *F* remains constant along the arc and $q_r = \frac{F}{R}$ is uniform. In the limit of fully mobilised friction, integration of Eq. (2) with the boundary condition$F(0) = F_{shank}$ yields the classical Euler–Eytelwein relation:

$$F(s) = F_{shank} \cdot \exp\left(-\frac{\mu s}{R}\right) \tag{3}$$

For friction coefficients in the range μ = 0.1 to 0.3, the apex force is thereby reduced to between 85 % and 62 % of the shank force, so that the transverse pressure decreases from the shank transition towards the apex. The actual degree of friction mobilisation is one of the quantities to be determined experimentally. A second-order influence arises from the finite bending stiffness of the yarn, which introduces a boundary layer of characteristic length $\lambda = \sqrt{\frac{EI}{F}}$ at the entry and exit of the contact region. With

EI ≈ 1.5 × 10⁴ N·mm² obtained from three-point bending tests on a single yarn and expected loop loads

of 1 to 2 kN, λ amounts to approximately 0,35 to 0,48 mm, which is small compared to the half-arc length of 31.4 mm. The bending-induced transition zones are therefore short, and the redistribution of force along the arc is dominated by friction rather than by bending stiffness.

3.3 Ondulation effects in the measurement signal

The yarn under investigation is a weft yarn embedded in a woven structure with a mesh width of 25 mm. At each crossing point with a warp yarn, the weft yarn follows a curved path around the transverse fibre, producing a local undulation (ondulation) as seen in Fig. 3.

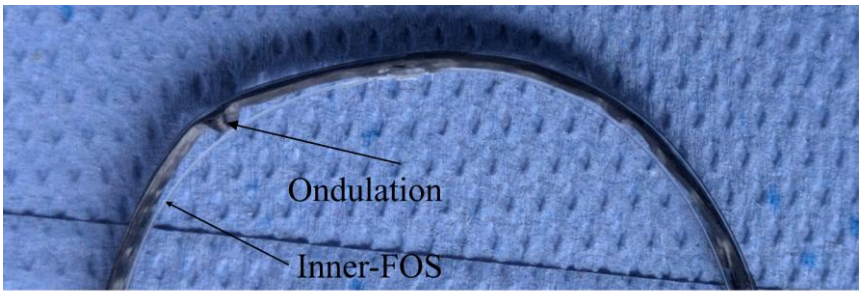


Fig. 3 Ondulation of the weft yarn at the crossing points with the warp yarns (mesh width 25 mm).

These ondulations introduce a periodic bending deformation with a spatial period equal to the mesh width, which is superimposed on the global axial strain field. Because the two optical fibres are bonded on opposite sides of the yarn cross-section, the local bending at each crossing point affects the two sensors with opposite sign:

$$\varepsilon_a^{raw}(s) = \varepsilon_{axial}(s) + \varepsilon_{ond}(s) \quad \textbf{(4)}$$

$$\varepsilon_i^{raw}(s) = \varepsilon_{axial}(s) - \varepsilon_{ond}(s) + \varepsilon_{press}(s) \quad \textbf{(5)}$$

where $\boldsymbol{\varepsilon_{axial}(s)}$ is the longitudinal strain due to the yarn force, $\boldsymbol{\varepsilon_{ond}(s)}$ is the symmetric bending contribution from the ondulation (positive on the convex outer side, negative on the concave inner side), and ε_press(s) is the apparent strain induced by transverse pressure, present only in the contact zone. A naive subtraction of the two raw signals would yield:

$$\varepsilon_i^{raw} - \varepsilon_a^{raw} = -2\varepsilon_{ond}(s) + \varepsilon_{press}(s) \quad \textbf{(6)}$$

rather than isolating the pressure contribution alone. The ondulation component would not cancel but double. Direct application of the equilibrium relations to the raw signal is therefore not admissible. The ondulation is experimentally confirmed by the presence of periodic peaks at exactly 25 mm intervals in both the straight shank region (where no mandrel contact exists) and the curved region. The consistency of the peak spacing across all zones verifies that the periodicity originates from the textile architecture and not from the loading or the contact mechanics. To separate the slowly varying axial strain from the rapidly oscillating ondulation, a spatial averaging over one full ondulation period is applied to each sensor signal independently:

$$\varepsilon_a(s) = \frac{1}{L_p}\int_{s-\frac{L_p}{2}}^{s+\frac{L_p}{2}} \varepsilon_a^{raw}(s')ds' \quad \textbf{(7)}$$

with L_p = 25 mm corresponding to 38 measurement points at the gage pitch of 0.65 mm. Because $\varepsilon_{ond}(s)$ has zero mean over one full period, the averaging eliminates the ondulation contribution and yields a signal that represents the local axial strain only. The same operation is applied to the inner sensor signal.

3.4 Reconstruction of the local force distribution

After spatial averaging according to Eq. (6), the outer fibre signal represents the longitudinal strain free of ondulation artefacts. Since the outer fibre is not in contact with the mandrel, it records only the axial strain, from which the local yarn force follows as:

$$F(s) = E \cdot A \cdot \varepsilon_a(s) \tag{8}$$

with E ≈ 180 000 N/mm² and A = 1.81 mm². The local radial line load $q_r(s)$ is then obtained from Eq. (1). Consistency of the reconstruction is verified against the global equilibrium of the bow:

$$2 \cdot F_{shank} = \int_0^{\pi} q_r(\varphi) \cdot R \cdot sin\varphi \; d\varphi \tag{9}$$

which relates the integrated vertical component of the contact pressure to the externally applied force and holds for any pressure distribution.

3.5 Separation of the apparent strain

The spatially averaged inner fibre signal contains the same axial strain as the outer fibre, superimposed with the pressure-induced apparent strain. After subtraction of sensor-specific offsets determined in the straight shank segments, where both fibres must record identical averaged strains in the absence of transverse pressure, the difference of the two averaged signals isolates the pressure contribution:

$$\varepsilon_{app}(s) = \varepsilon_i(s) - \varepsilon_a(s) = k_p \cdot q_r(s) \tag{10}$$

where k_p is an effective pressure sensitivity coefficient for the present combination of fibre, adhesive, and contact geometry. With $q_r(s)$ known from the outer fibre via Eqs. (6) and (1), the coefficient k_p is determined as the slope of $\varepsilon_{app}(s)$ plotted against $q_r(s)$. A constant slope indicates a well-defined sensitivity, whereas a systematic deviation would point to a position- or pressure-dependent sensitivity associated with the local contact conditions.

4 RESULTS AND DISCUSSION

4.1 Failure loads and failure location

The five specimens failed at ultimate forces ranging from 1640 N to 2830 N (mean: 2058 N, coefficient of variation: 24 %). The displacement at failure ranged from 3.6 to 5.0 mm. The considerable scatter in failure loads is attributed to the manual fabrication of the loop specimens and the sensitivity of the formed region to local fibre arrangement. In all specimens, failure occurred consistently at the first ondulation point inside the curved region at the entry from the straight shank into the forming zone, as identified from the abrupt signal loss in the DFOS profiles immediately prior to failure. This location coincides with the transition where the yarn first comes into contact with the mandrel and where both longitudinal tension and transverse pressure from the mandrel contact act simultaneously on the cross-section. The DFOS signals provided reliable, interpretable strain measurements up to yarn forces of approximately 330 to 510 N, depending on the specimen. Beyond this level, signal quality deteriorated progressively due to increasing spectral shift correlation losses in the highly strained curved region. The subsequent evaluation is therefore based on load levels below this threshold.

4.2 Ondulation signature and spatial periodicity

Fig 4 shows the strain distribution recorded by the outer sensor along the measurement length for specimen PK5 at multiple load levels. Both in the straight shank segments and in the curved region, the signal exhibits periodic oscillations at a spatial period of exactly 25 mm, corresponding to the mesh width of the woven reinforcement. The periodicity is present in the straight shank segments, where no mandrel contact exists, as well as in the curved region, confirming that the oscillations originate from the textile architecture rather than from the loading or the contact mechanics.

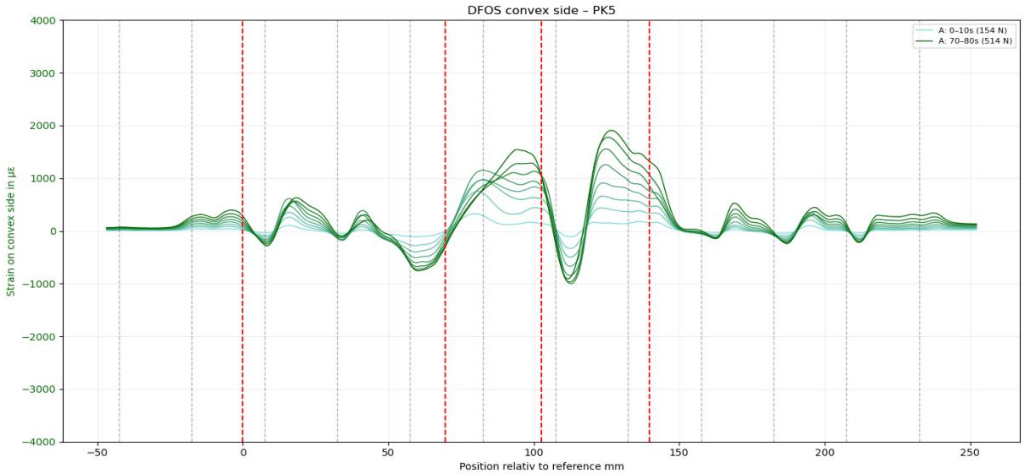


Fig 4. Strain distribution of the outer sensor along the measurement length for specimen PK5 at multiple load levels, showing periodic oscillations at the 25 mm mesh width.

In the straight shank, the oscillation amplitude remains approximately constant across all load levels, indicating that the ondulation-induced local bending scales weakly with the global yarn force at the investigated loads. In the curved region, the periodic oscillation is superimposed on a broader strain distribution that grows with applied force, reaching peak values in excess of 3000 με at the highest reliable load level. Prior to applying the analytical framework, a spatial averaging over one full ondulation period (25 mm, corresponding to 39 measurement points at the gage pitch of 0.65 mm) is applied to eliminate the periodic component and to obtain the underlying strain distribution.

4.3 Strain distribution along the curved region

Fig. 5 shows the spatially averaged strain profile of the outer sensor for the highest reliable load level (514 N applied force, corresponding to a yarn force of approximately 257 N in the straight shank). In the straight shank segment between the reference marker and the entry marker, the averaged strain is approximately uniform and corresponds to an axial force consistent with the expected value of $F_{applied/2}$. In the curved region between the entry and exit markers, the spatially averaged outer sensor signal increases substantially, reaching peak values that correspond to an apparent force of approximately 700 N when converted using the relation $F = E \cdot A \cdot \varepsilon_a$.

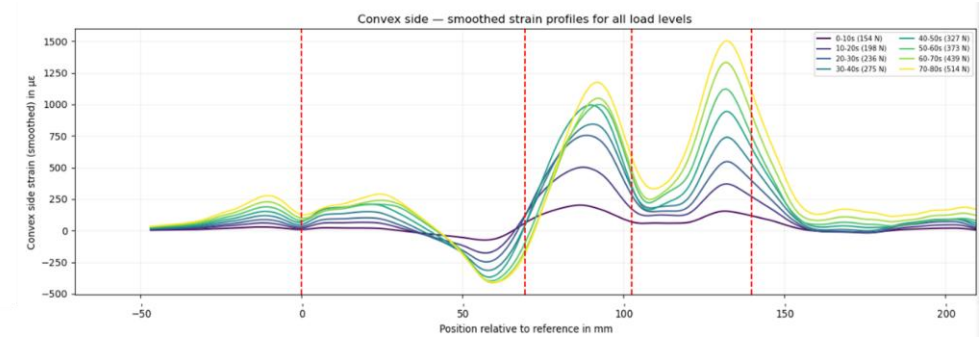


Fig. 5 Spatially averaged strain profile of the outer sensor (PK5) at the highest reliable load level.

This value exceeds the total applied force and is physically inadmissible as a yarn tension, since the yarn force in the bow must be equal to or less than the shank force according to the equilibrium relations of the analytical framework. The outer sensor in the curved region therefore does not record the axial yarn force alone.

4.4 Limitations of the force reconstruction

The force reconstruction according to the analytical framework assumes that the outer fibre, bonded to the convex surface of the yarn away from the mandrel, records only the longitudinal strain from the yarn force. The results demonstrate that this assumption is not satisfied in the curved region. The outer sensor in the bow records strains approximately four times higher than in the straight shank at the same applied load, indicating that additional strain contributions beyond the axial yarn force are present. Several mechanisms may contribute to the elevated outer sensor response in the curved region. First, the transverse compression of the yarn cross-section under radial pressure from the mandrel contact may cause a Poisson expansion on the outer surface, producing a positive strain contribution on the outer fibre. Second, the local curvature change at each ondulation within the bow may interact with the global curvature of the mandrel, amplifying the bending contribution at the crossing points. Third, the bonding geometry between the optical fibre and the yarn surface may introduce parasitic sensitivity to the radial contact pressure even on the outer side, if the adhesive layer transmits a portion of the through-thickness stress to the sensor. Regardless of the specific mechanism, the consequence is that the outer sensor signal in the bow cannot be interpreted as a pure measure of axial yarn force. The separation approach based on the analytical framework, which relies on the outer sensor providing an independent measurement of the yarn force and is therefore not directly applicable in its present form.

4.5 Qualitative observations

Despite the limitation of the quantitative separation, several qualitative conclusions can be drawn from the measurements. First, the strain response in the curved region increases monotonically with applied force and is spatially confined to the zone between the entry and exit markers, confirming that the mandrel contact produces a clearly identifiable and localised signal. Second, the signal in the straight shank segments remains consistent between specimens and proportional to the applied force, demonstrating that the measurement system functions reliably outside the contact zone. Third, the ondulation signature provides an inherent spatial reference that allows precise identification of the crossing points and verification of the sensor positioning along the yarn.

5 CONCLUSION AND OUTLOOK

This contribution investigated the separation of transverse pressure effects from the longitudinal strain response in formed carbon reinforcement using distributed fibre optic sensing based on Rayleigh backscattering. Loop specimens fabricated from carbon reinforcement were loaded around a cylindrical mandrel and instrumented with optical fibres on both the convex and the concave side of the yarn. The strain distribution recorded by the outer fibre in the straight shank shows a clear load-proportional response with the characteristic ondulation signature at 25 mm spatial period. However, the yarn force measured at the load cell could not be fully recovered from the DFOS signal. The spatial averaging over one ondulation period reduces the periodic oscillations but does not completely eliminate their influence on the underlying strain level. In the curved region, the ondulation crossing points assume a considerably more critical role. The combination of global curvature from the mandrel and local curvature at each crossing point produces extreme strain concentrations that dominate the signal. Determining the strain distribution in the formed region is in principle possible, but the individual influence parameters—axial tension, transverse pressure, global bending, and local ondulation bending—must be more rigorously separated to isolate their respective contributions, which the present superposition prevents. The strong local ondulations within the formed region caused early failure of the yarn and simultaneous destruction of the DFOS through excessive local transverse pressure, limiting reliable measurements to approximately one sixth of the ultimate load capacity (330 to 510 N of failure loads of 1640 to 2830 N). Furthermore, the forming was not perfectly symmetric: the DFOS profiles reveal a visible strain anomaly between the two sides of the apex, indicating different contact conditions and complicating comparison with the symmetric analytical model. Future work should focus on the following aspects. First, these experiments should be conducted on a specially manufactured carbon yarn without woven architecture, eliminating ondulation-induced stress concentrations and enabling

unbiased measurements over the full load range. Second, the mechanism responsible for the elevated outer sensor response in the curved region should be identified through finite element modelling of the yarn cross-section under combined tension and radial pressure. Third, the experimental configuration should be modified to provide an independent reference for the yarn force in the bow, for example through instrumented mandrel surfaces. Fourth, the method should be extended to specimens embedded in concrete, where the quantitative separation of strain and pressure is ultimately required for structural assessment.

Acknowledgements

This Project is supported by the Federal Ministry for Economic Affairs and Climate Action (BMWE) on the basis of a decision by the German Bundestag: KK5524603EB4
The authors gratefully sincerely thank their colleagues at the Otto-Mohr-Laboratory for their valuable assistance in conducting the experimental testing.

References

[1] Apitz, Alexander, Schmitz, Jonas, and Schlaich, Mike. 2022. "New Thermoplastic Carbon Fibre Reinforced Polymer Rebars and Stirrups." *Structural Concrete* 23:923–938. Accessed July 15, 2026. doi:10.1002/suco.202100434.

[2] Schlaich, Mike, Apitz, Alexander, and Jesse, Frank. 2020. "Brücken aus vorgespanntem Carbonbeton." *Beton- und Stahlbetonbau* 115:684–696. Accessed July 15, 2026. doi:10.1002/best.202000018.

[3] Rettinger, Martin, Hückler, Alex, and Schlaich, Mike. 2024. "A Modular Precast Segmental Bridge with Thermally Formed CFRP Reinforcement – Modularisation Approach and Precast Concrete Production." *Beton- und Stahlbetonbau*. Accessed July 15, 2026. doi:10.1002/best.202400051.

[4] Spelter, Arne et al. 2019. "Long-Term Durability of Carbon-Reinforced Concrete: An Overview and Experimental Investigations." *Applied Sciences* 9:1651. Accessed July 15, 2026. doi:10.3390/app9081651.

[5] Richter, Bertram, Herbers, Max, and Marx, Steffen. 2024. "Crack Monitoring on Concrete Structures with Distributed Fiber Optic Sensors—Toward Automated Data Evaluation and Assessment." *Structural Concrete*. Accessed July 15, 2026. doi:10.1002/suco.202300100.

[6] Bielak, Jan et al. 2021. "Application of Fibre Optic Measurement in Textile-Reinforced Concrete Testing." *Structural Concrete* 23:2600–2614. Accessed July 15, 2026. doi:10.1002/suco.202100252.

[7] Gafsi, Rachid, and El-Sherif, Mahmoud A. 2000. "Analysis of Induced-Birefringence Effects on Fiber Bragg Gratings." *Optical Fiber Technology 6*:299–323. Accessed July 15, 2026. doi:10.1006/ofte.2000.0333.

Prestressed Ultra High-Performance Concrete-Steel Composite Beams with Continuous Shear Connectors in the Tension Zone

Peter Harsányi*, Norbert Randl* and Nguyen Viet Tue**

**Faculty of Civil Engineering and Architecture*
Carinthia University of Applied Sciences (CUAS)
Villacher Straße 1, A-9800 Spittal an der Drau, Austria

***Institute of Structural Concrete*
Graz University of Technology
Lessingstraße 25, A-8010 Graz, Austria

Summary
Prestressed UHPFRC-steel composite beams with continuous shear connectors in compression and tension zones were investigated using push-out tests, large-scale bending tests and 3D FE analyses. DIC-based push-out tests identified concrete pry-out, vertical splitting and steel shear-bending as interacting connector mechanisms. Large-scale beams reached ultimate loads up to ~1360 kN and mid-span deflections exceeding 100 mm. Prestressing delayed cracking of the tensile UHPFRC flange, while continuous shear connection maintained composite action after cracking. Adequately reinforced beams failed by rupture of prestressing strands; the beam without transverse reinforcement exhibited splitting failure. FE analyses reproduced the load-deflection response and failure sequence, including stress redistribution and Inter-dowel Web Yielding. The results demonstrate the feasibility of activating both UHPFRC flanges in prestressed composite beams with continuous connectors in the tension zone.

1 INTRODUCTION

Steel–concrete composite structures are traditionally designed by assigning the concrete to the compression zone and the steel to the tension zone, while the shear connection is primarily required to transfer longitudinal shear forces at the interface. In conventional composite beams, headed studs or similar discrete connectors are commonly used to activate the concrete slab in compression [1], whereas the tensile resistance is provided almost exclusively by the steel section.

The increasing use of ultra high-performance fibre-reinforced concrete (UHPFRC) challenges this traditional separation of structural roles. Due to its high compressive strength, significant post-cracking tensile capacity and enhanced durability, UHPFRC enables the design of slender structural elements with reduced material consumption. However, the combination of UHPFRC with conventional shear connectors often leads to unfavourable failure modes [2]. In particular, headed studs embedded in UHPFRC tend to fail in a brittle manner or do not satisfy the ductility criterion specified for composite structures according to Eurocode 4, EN 1994-1-1, Annex B.2.5.(4) [3], even when high-strength steel grades or increased stud diameters are used. This limitation becomes critical when UHPFRC is intended to contribute not only in compression, but also to the overall structural performance of the cross-section.

Continuous shear connectors represent an alternative to discrete connectors, as they allow a more uniform shear flow and reduce local stress concentrations. Previous studies have shown that puzzle-shaped or clothoid-shaped continuous connectors can achieve higher load-bearing capacities and improved deformation capacity when combined with high-performance concretes [4], [5]. Nevertheless, existing applications and investigations are largely restricted to the compression zone of composite members. The potential of continuous shear connectors in a prestressed tension zone has not been systematically explored, with limited research available in cracked concrete and under tension without prestressing [6], [7].

Introducing a shear connection into the tension zone fundamentally changes the structural concept of a composite beam. In such a configuration, the concrete flange is subjected to tensile stresses and cracking becomes inevitable. To ensure a controlled and ductile structural response, additional measures are required. Prestressing of the tensile concrete flange provides an effective means to delay crack initiation, limit crack widths and promote a more uniform stress distribution. When combined

with UHPFRC containing high-strength steel fibres, the prestressed tensile zone can contribute significantly to the load-bearing capacity and deformation behaviour of the composite cross-section.

The steel web is fabricated from high-strength S460 ML steel, while both the compression and tensile flanges are made of UHPFRC reinforced with high-strength fibres. The tensile flange is prestressed using bonded strands, allowing for a slender cross-section with full activation of all constituent materials.

The research campaign follows a multi-scale approach. First, the local shear transfer mechanisms of continuous shear connectors embedded in UHPFRC are investigated in small-scale push-out tests using digital image correlation (DIC), allowing a detailed identification of governing failure modes [8]. Second, large-scale bending tests on prestressed I-shaped composite beams are conducted to study the global structural behaviour and failure sequence at system level [9]. Based on the experimental observations, a simplified engineering model for the ultimate limit state is developed. Finally, a three-dimensional finite element model is used to validate the proposed structural concept and to interpret internal stress redistributions and failure mechanisms that cannot be directly captured experimentally.

By linking connector-related local mechanisms, system-level behaviour and numerical validation, this study aims to demonstrate the feasibility and structural efficiency of such prestressed UHPFRC–steel composite beams with continuous shear connectors in the tension zone, and to provide a coherent framework for understanding their load bearing behaviour and structural design.

2 RESEARCH CONCEPT AND METHODOLOGY

The structural concept investigated in this study is based on the assumption that a composite I-shaped cross-section, with UHPFRC compression and tensile flanges, can be fully activated if the shear transfer between steel and concrete is ensured in both the compression and the tension zone. To achieve this, puzzle- and clothoid-shaped continuous shear connectors are combined with prestressing strands, high-performance materials and conventional reinforcement, allowing also the concrete flange in tension to participate in load transfer in a controlled and ductile manner. The research methodology follows a bottom-up approach, starting from local shear transfer mechanisms and progressing towards global structural behaviour and numerical interpretation. The individual stages of the investigation are closely linked and build upon each other, ensuring that the observed system behaviour can be traced back to well-understood local mechanisms.

2.1 Investigation of local shear transfer mechanisms

The local shear transfer behaviour of the continuous connectors embedded in UHPFRC (mean compressive strength 160 N/mm², modulus of elasticity 46 GPa) was investigated by means of 25 small-scale push-out tests, covering variations in connector geometry, reinforcement layout, fibre content and concrete cover. The tests were designed to isolate the interaction between the steel connector and the surrounding UHPFRC, as well as the reinforcement, and to identify the governing failure mechanisms under monotonic loading.

Digital image correlation (DIC) was employed as the primary measurement technique to capture full-field surface displacements and strain distributions. This allowed to investigate the different failure mechanisms and their interaction in detail, including concrete pry-out, vertical splitting, as well as their combined occurrence. Compared to conventional measurement techniques, DIC enabled a more thorough interpretation of the connector behaviour and provided insight into the transition from elastic response to ductile failure.

Based on these investigations, puzzle-shaped continuous shear connectors were identified as particularly suitable for use in slender UHPFRC composite members, as they showed sufficient deformation capacity and adequate failure behaviour. A detailed description of the test program, measurement setup and observed failure mechanisms is given in [8].

2.2 Conceptual design and manufacturing considerations

The investigated composite beams were designed as I-shaped members consisting of a planar steel web and two UHPFRC flanges (mean compressive strength between 152,7 and 154,7 N/mm², 2 Vol% steel fibres). The steel web was fabricated from high-strength S460 ML steel plates, in which puzzle-shaped continuous shear connectors were integrated by thermal cutting. This approach allowed the web and connectors to be manufactured as a single component, avoiding additional welding or mechanical fastening.

Both the compression and tensile flanges were cast from UHPFRC reinforced with high-strength steel fibres. In contrast to conventional composite beams, the tensile flange was connected to the steel web by puzzle-shaped continuous shear connectors and prestressing using bonded strands. Prestressing was introduced to delay crack initiation in the tensile flange, to optimize the load bearing contribution of the UHPFRC flange and to promote a more uniform stress distribution along the beam length. The combination of prestressing and fibre reinforcement enabled the tensile flange to contribute to the load-bearing capacity beyond first cracking, while maintaining a stable and ductile response.

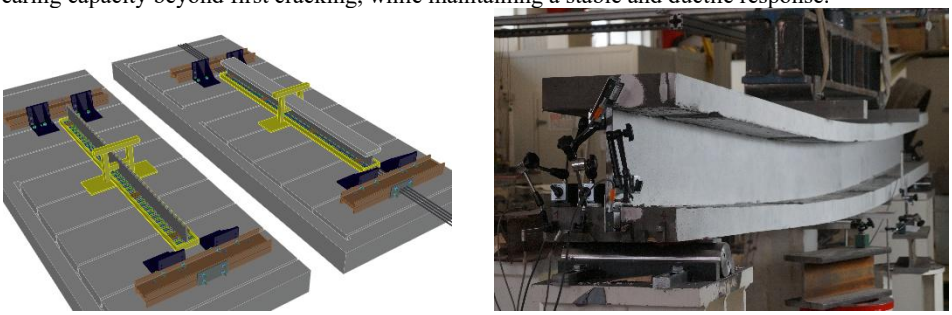


Fig. 1 Production method of I-shaped beams (left); prestressed I-shaped UHPFRC composite beam test (right)

Special attention was given to manufacturing aspects (see Fig. 1), as the structural concept relies on precise positioning of the steel web, connectors and prestressing strands. The beams were produced in a controlled laboratory environment using a two-stage casting process, ensuring proper bond conditions and reproducibility. The chosen manufacturing method is intended to be compatible with practical production processes and does not rely on complex or highly specialized equipment (see [9] for more details).

2.3 Setup of large-scale tests on prestressed composite beams

Building on the findings from the push-out tests, four large-scale bending tests were conducted on prestressed I-shaped composite beams in order to assess whether the favourable local behaviour of the continuous shear connectors could be transferred to the structural system level. The beams were tested under monotonic loading in three-point and four-point bending configurations, in order to identify the influences of stress localisations on the global behaviour, with varying degrees of internal reinforcement, a total length of 5,47 m and a free span of 5 m (see Fig. 2).

The global load–deflection response, strain development and failure sequence were recorded. DIC was again used to monitor surface strains and crack patterns, allowing a direct comparison between local connector mechanisms and global structural behaviour. Particular attention was paid to the interaction between prestressing, tensile behaviour of UHPFRC and shear transfer in the tension zone. Details of the experimental program and the observed global behaviour are reported in [9].

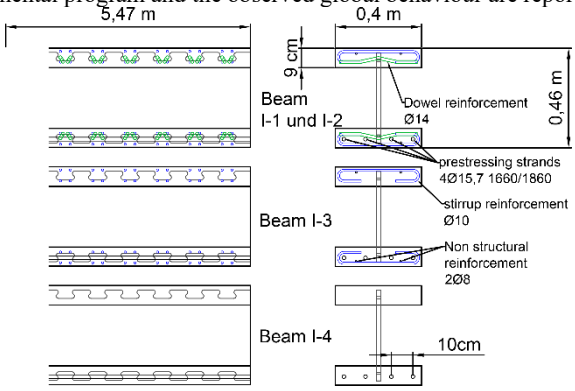


Fig. 2 Size of the prestressed I-shaped beams [mm], reinforcement details according to [9]

3 CONNECTOR MECHANISMS IDENTIFIED BY DIC

The structural performance of composite members with continuous shear connectors is governed by the local interaction between the steel connector, the surrounding concrete matrix and the internal reinforcement. In the present study, this interaction was investigated using a dedicated series of small-scale push-out tests with continuous puzzle- and clothoid-shaped shear connectors embedded in UHPFRC (see Fig. 3). The objective was not only to quantify load–slip behaviour, but primarily to identify the governing failure mechanisms and their interaction.

The experimental investigations revealed that shear transfer in continuous connectors embedded in UHPFRC is not controlled by a single failure mode. Instead, a combination of mechanisms develops progressively with increasing load. Based on the DIC measurements, three dominant mechanisms were consistently observed: concrete pry-out in front of the connector (see Fig. 3), vertical splitting of the surrounding UHPFRC and steel shear-bending of the connector web. Depending on connector geometry, reinforcement layout and fibre content, these mechanisms occurred either sequentially or simultaneously.

Digital image correlation proved essential for resolving the spatial and temporal development of these mechanisms. Full-field strain measurements allowed the initiation and propagation of cracking to be identified at an early stage, long before visible surface cracks formed. In particular, DIC revealed that vertical splitting cracks often developed in combination with concrete pry-out, while steel shear-bending contributed to stress redistribution and delayed sudden loss of load-carrying capacity. This kind of combined response explains the observed ductile behaviour of properly detailed continuous connectors in UHPFRC.

A comparison between puzzle-shaped and clothoid-shaped connectors showed that puzzle-shaped geometries provide a more favourable stress distribution in the surrounding UHPFRC matrix. For otherwise comparable configurations, puzzle-shaped connectors exhibited a more stable post-peak response and a higher deformation capacity, especially when combined with transverse reinforcement and high-strength fibres. These characteristics are of particular relevance for applications in slender composite members, where controlled cracking and ductility are essential.

The insights gained from the push-out tests formed the basis for selecting the connector geometry and detailing used in the subsequent large-scale beam tests. Rather than optimising connectors solely for maximum shear resistance, the design emphasis was placed on achieving a robust and ductile failure behaviour compatible with tensile concrete participation. A comprehensive description of the experimental programme, test parameters and detailed DIC-based failure analyses is provided in [8].

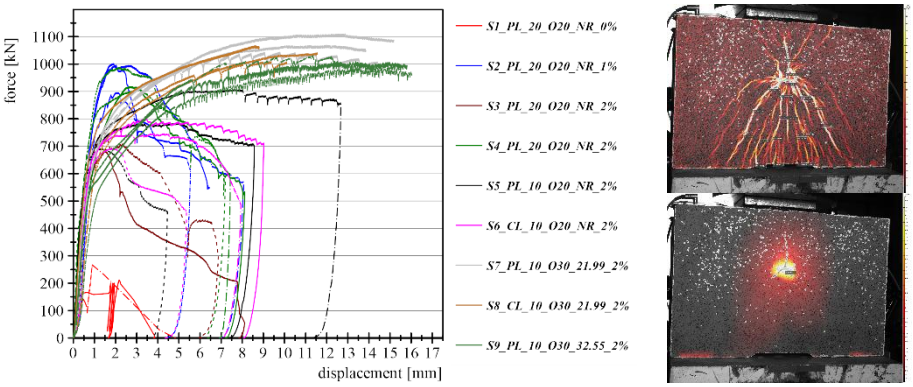


Fig. 3 Load deflection curves of small scale push-out test series (left); example for DIC evaluation of failure modes with crack visualisation and concrete pry-out failure (right)

4 GLOBAL BEHAVIOUR OF PRESTRESSED COMPOSITE BEAMS

The investigated I-shaped composite beams exhibited a stable response under monotonic loading. In the initial loading phase, the behaviour was governed by elastic action of the composite cross-section, with the prestressing effectively reducing tensile stresses in the UHPFRC flange. First cracking in the tensile flange was delayed. Once cracking had initiated, the combination of fibre reinforcement and prestressing ensured a gradual stiffness reduction rather than a sudden loss of load-carrying capacity (see Fig. 4)

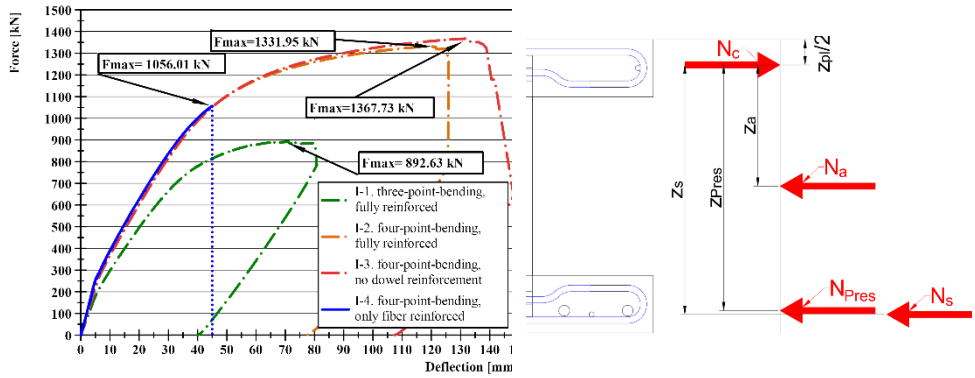


Fig. 4 Load deflection curves of large-scale tests in prestressed UHPFRC-steel composite beams (left); Harsányi et al. [9], CC BY 4.0, Internal lever arms and equilibrium

Throughout the loading process, the continuous shear connectors in the tension zone remained fully engaged, enabling effective force transfer between the steel web and the UHPFRC tensile flange. No premature connector failure was observed. Instead, the load–deflection response was characterised by a pronounced plastic range, indicating that the composite action was maintained even after cracking of the tensile UHPFRC. This confirms that the shear connection in the tension zone is capable of sustaining load transfer under cracked concrete conditions.

Digital image correlation measurements provided detailed insight into the global deformation behaviour and crack development and allowed to identify a new failure mode called Inter-dowel Web Yielding [9], where the steel in the web between two adjacent shear dowels in the tensile zone yields progressively towards the compression zone. Strain fields and crack patterns showed a uniform distribution along the beam length, with localisation of damage only at later stage in the test, combined with large mid-span deflections of more than 100 mm. The observed crack spacing and orientation were consistent with a well-distributed tensile stress state, with relatively constant crack spacings of ~10 to 15 cm in the tensile UHPFRC flange, demonstrating the beneficial interaction between prestressing, fibre reinforcement and continuous shear transfer.

All tested beams failed at high load levels, ranging from ~1050 kN to ~1360 kN, after extensive deformation. For specimens with sufficient internal reinforcement, failure was governed by rupture of at least one prestressing strand, indicating full utilisation of the prestressing system and the surrounding UHPFRC matrix. In the beam without internal conventional reinforcement, splitting of the tensile UHPFRC flange occurred along the connector axis, highlighting the importance of adequate transverse reinforcement and fibre content for ensuring a ductile failure mode. In all cases, failure occurred only after the steel web had reached significant non-linear deformation, confirming that the composite cross-section was fully activated.

To provide a simplified design-oriented interpretation of the experimental results, an engineering model based on internal force equilibrium was applied. The model assumes full composite action between the steel web and both UHPFRC flanges and considers the internal lever arms of the compressive force in the upper flange and the tensile force contributions of the lower flange, steel web and prestressing strands. As illustrated in Fig. 4, this approach allows the global load-bearing behaviour to be related to the activated cross-sectional components and provides a transparent mechanical explanation for the high ultimate loads observed in the tests. A detailed derivation, validation and discussion of the model are provided in Harsányi et al. [9].

The experimental results demonstrate that extending the shear connection into the tension zone fundamentally changes the structural behaviour of the composite beam. Rather than acting as a conventional steel beam with a passive concrete compression flange, the system behaves as a fully composite member in which both UHPFRC flanges contribute to load-bearing capacity. Prestressing plays a key role in enabling this behaviour by controlling cracking and ensuring compatibility of deformations between steel and concrete. A detailed presentation of the experimental programme, measurement setup and quantitative results of the large-scale bending tests is provided in [9].

5 FINITE ELEMENT ANALYSIS AND MECHANISM-BASED INTERPRETATION

A three-dimensional finite element (FE) model of the tested fully reinforced I-beam was developed with ATENA Science in order to complement the experimental investigations and to provide insight into internal stress redistributions and failure mechanisms that cannot be directly observed in laboratory tests.

The composite beam was modelled in 3D, including the steel web with integrated continuous shear connectors, the UHPFRC compression and tensile flanges, the prestressing strands and the conventional reinforcement (Fig. 5). Due to geometric symmetry, only half of the beam was represented in the numerical model in order to reduce computational effort. Nonlinear material behaviour was considered for UHPFRC, structural steel and prestressing strands. Bonded interaction between prestressing strands and UHPFRC was accounted for by appropriate material modelling. The material parameters were derived from an extensive material and bond test campaign [10] and were not calibrated on the basis of the global beam response.

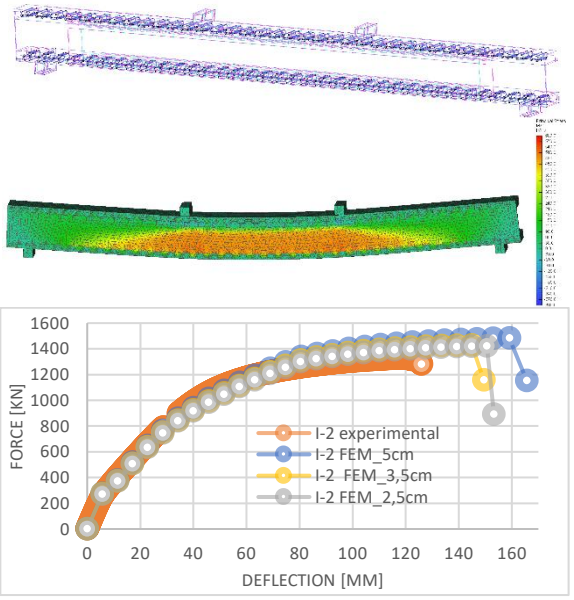


Fig. 5 Finite element model of the prestressed UHPFRC–steel composite beam (top); half model with symmetry plane (middle) and comparison of experimental and numerical load–deflection response (bottom)

The numerical simulations reproduced the characteristic features of the experimentally observed structural behaviour. In the initial loading stage, stresses were distributed over the full composite cross-section, with the prestressing effectively reducing tensile stresses in the UHPFRC flange. After crack initiation in the tensile flange, load transfer between the steel web and the UHPFRC continued through the shear connectors, resulting in a gradual redistribution of stresses rather than abrupt localisation.

With increasing load, plastic deformation developed in the steel web between adjacent connectors, while progressive cracking and crushing occurred in the surrounding UHPFRC. The simulations showed that the continuous shear connectors in the tension zone remained active throughout the loading process, ensuring compatibility of deformations between steel and concrete even after cracking of the tensile flange. This observation from the numerical simulation is consistent with the experimentally observed absence of premature connector failure and with the extended plastic range of the load–deflection response.

Failure in the numerical model was governed by rupture of the prestressing strands after significant plastic deformation of the composite cross-section. This failure mode corresponds to the dominant experimental observation for beams with sufficient internal reinforcement and confirms that the high-performance materials were fully activated up to ultimate load. Local concrete crushing in front of the connector roots, and the corresponding damage locations could be identified in the simulation, thus closing a gap in the experimental campaign.

The FE analysis therefore supports the experimental findings by demonstrating that the favourable local connector mechanisms identified in the push-out tests are preserved at structural level and remain effective after cracking of the tensile UHPFRC flange. The numerical results provide a consistent explanation for the observed sequence of cracking, stress redistribution and final failure, and confirm the structural feasibility of extending the shear connection into the tension zone of prestressed UHPFRC–steel composite beams.

6 CONCLUSIONS

This study investigated a prestressed UHPFRC–steel composite beam in which continuous shear connectors are applied in both the compression and in the tension zone. The objective was to demonstrate that this configuration enables a fully activated and slender composite cross-section and to quantify high-level structural performance.

- Small-scale push-out tests monitored in detail by digital image correlation showed that shear transfer in continuous connectors embedded in UHPFRC is governed by a combined action of concrete pry-out, vertical splitting and steel shear-bending. When appropriate connector geometry, fibre content and transverse reinforcement are provided, these mechanisms interact progressively and lead to a stable and ductile response. Puzzle-shaped connectors exhibited the most favourable deformation capacity and were therefore selected for the structural application.
- Large-scale bending tests on slender prestressed I-shaped composite beams confirmed that this favourable local behaviour can be transferred to the structural system level. Ultimate loads of up to ~1360 kN with a 5 m span were reached, depending on the reinforcement configuration, with mid-span deflections exceeding 100 mm prior to failure. First cracking in the tensile UHPFRC flange was significantly delayed by prestressing, and composite action was maintained after cracking due to the continuous shear connection in the tension zone. For beams with sufficient internal reinforcement, failure was governed by rupture of at least one prestressing strand, indicating full utilisation of the prestressing system, the UHPFRC flanges and the steel web. In the specimen without conventional transverse reinforcement, splitting of the tensile UHPFRC flange occurred at an early stage along the connector axis, highlighting the importance of adequate detailing for ensuring ductile behaviour.
- A three-dimensional finite element model was established to provide a mechanism-based interpretation of the experimental observations. The simulations reproduced the characteristic load–deflection behaviour and failure sequence, including progressive cracking of the tensile UHPFRC flange, plastic deformation of the steel web between adjacent connectors and final rupture of the prestressing strands. Additionally, it confirmed the finding of a so-called failure mode “Inter-dowel Web Yielding” [9] in the experimental campaign. The numerical model was calibrated using an extensive database of independently determined material and bond properties for UHPFRC, high-strength steel and prestressing strands. This material database forms a robust basis for future parametric numerical investigations and for the development of refined design-oriented modelling approaches.

Overall, the results demonstrate that extending the shear connection into the tension zone, in combination with prestressing and high-performance materials, fundamentally changes the behaviour of such high-performance composite beams and enables slender members with high load-bearing capacity and large deformation capacity. By linking connector-level mechanisms, system-level experiments, an engineering model and validated numerical simulations, a coherent framework for understanding and designing such members is established. Future work should focus on parametric numerical studies, on refining the engineering model to further support practical design, and on comparative assessments against conventional prestressed concrete, steel and full-UHPFRC beams regarding structural efficiency, material use and economic feasibility.

Acknowledgements

This work was financially supported by the Austrian Research Promotion Agency (FFG) through grant No. 846023 (2014). The authors gratefully acknowledge MCE GmbH for the fabrication of the steel components, voestalpine Special Wire GmbH for supplying the prototype steel fibres, KB Vorspann-Technik GmbH for providing the prestressing systems, and Kirchdorfer Industries GmbH together with w&p Zement GmbH for supplying the cement-based materials used in the experimental programme.

Declaration of generative AI and AI-assisted technologies in the writing process

During the preparation of this work the authors used Chat GPT in order to enhance the linguistic and editorial style and clarity of the manuscript. After using this tool/service, the authors reviewed and edited the content as needed and take full responsibility for the content of the publication.

References

[1] Lowe, Daniel, Roy, Krishanu, Das, Raj, Clifton, Charles G., and Lim, James B. P. 2020. "Full Scale Experiments on Splitting Behaviour of Concrete Slabs in Steel–Concrete Composite Beams with Shear Stud Connection." Structures 23:126–138. doi:10.1016/j.istruc.2019.10.008.

[2] Hu, Yuqing, Yin, Huiguang, Ding, Xiaomeng, Li, Shuai, and Wang, Jingquan. 2020. "Shear Behavior of Large Stud Shear Connectors Embedded in Ultra-High-Performance Concrete." Advances in Structural Engineering 23:3401–3414. doi:10.1177/1369433220939208.

[3] European Commission, Joint Research Centre. n.d. "Eurocode 4: Design of Composite Steel and Concrete Structures." Accessed May 12, 2026. https://eurocodes.jrc.ec.europa.eu/EN-Eurocodes/eurocode-4-design-composite-steel-and-concrete-structures

[4] Lorenc, Wojciech. 2016. "The Design Concept for the Steel Part of a Composite Dowel Shear Connection." Steel Construction 9:89–97. doi:10.1002/stco.201610014.

[5] Hegger, Josef, Gallwoszus, Jörg, and Rauscher, Sabine. 2009. "Load-Carrying Behaviour of Connectors under Shear, Tension and Compression in Ultra High Performance Concrete." Paper presented at the Nordic Steel Construction Conference 2009, Malmö, Sweden, September 2–4.

[6] Classen, Martin, and Hegger, Josef. 2017. "Assessing the Pry-Out Resistance of Open Rib Shear Connectors in Cracked Concrete—Engineering Model with Aggregate Interlock." Engineering Structures 148:254–262. doi:10.1016/j.engstruct.2017.06.050.

[7] Christou, Georgios, Wolters, Kevin A., Ungermann, Jan, Classen, Martin, and Hegger, Josef. 2022. "Combined Shear-Tension Loading of Composite Dowels in Cracked Concrete—Experimental Investigations and Design." Applied Sciences 12:1449. doi:10.3390/app12031449.

[8] Harsányi, Peter, Randl, Norbert, and Tue, Nguyen Viet. 2021. "DIC-Based Failure Analysis of High-Strength Continuous Steel Shear Dowels for Composite UHPFRC–Steel Construction." Engineering Structures 247:113093. doi:10.1016/j.engstruct.2021.113093.

[9] Harsányi, Peter, Randl, Norbert, and Tue, Nguyen Viet. 2025. "Structural Performance of Prestressed I-Shaped Fibre-Reinforced UHPC–Steel Composite Beams with Puzzle-Shaped Continuous Shear Connectors." Composites Part B: Engineering 307:112880. doi:10.1016/j.compositesb.2025.112880.

[10] Vojvodic, Goran. 2016. "Verbundverhalten von Litzen im UHPC." Paper presented at Beton Graz '16: 3. Grazer Betonkolloquium, Graz, Austria, September 29–30, 273–282.

Punching shear strengthening of already shear reinforced structures by use of additionally installed concrete screws

Ludwig Fröschl, Rupert Walkner, Jürgen Feix

Unit of Concrete Structures and Bridge Design,
Department of Structural Engineering and Material Sciences,
University of Innsbruck,
Technikerstraße 13, 6020 Innsbruck, Austria

Summary
Concrete screws provide an efficient and practical solution for increasing the punching shear resistance of existing reinforced concrete structures. In most cases, punching shear reinforcement is already present in the punching shear zone of a slab. However, the existing design approach for determining the required quantity of concrete screws does not allow existing punching shear reinforcement to be taken into account, which leads to an uneconomical approach. For this reason, a series of tests was carried out to better understand the interaction between existing punching shear reinforcement and concrete screws. The main result is, that the punching shear resistance still can be significantly increased by concrete screws when reinforcement is already in place. In addition, concrete screws increase the deformation capacity and make failure mode more ductile. A numerical model was also created that accurately reflects the laboratory tests with the aim of conducting a parameter study.

1 INTRODUCTION

The Paris Climate Agreement, which has now been ratified by 195 countries, has set the goal of limiting global warming to significantly below two degrees compared to pre-industrial levels [1]. To achieve this goal, the European Community has committed to reducing net greenhouse gas emissions to zero by 2050 and therefore becoming climateneutral [2]. In Austria, infrastructure operators in particular have a responsibility in this regard, as the construction sector accounts for almost 40% of energy-related global CO2 emissions [3]. Nevertheless, the planned reduction in greenhouse gas emissions is complicated by the high age of existing structures and the resulting projected number of replacements required. For example, the average age of bridges managed by ASFINAG is over 40 years [4]. To counteract this, one of the core objectives is to increase the remaining service life of existing bridges as much as possible through maintenance and reinforcement measures. This would significantly reduce the number of bridge replacements required in the coming decades [5]. Also in building construction, conversions or renovations can lead to increased loads, which require reinforcement measures.

The use of concrete screws as reinforcement is a resource-efficient and economical method for increasing punching shear resistance in existing structures. A key advantage of concrete screws is that the supporting structure only needs to be accessible from one side of the structural element. This allows their installation for example in bridge structures even during ongoing operation without traffic restrictions. The effectiveness of concrete screws has already been demonstrated in earlier work at the University of Innsbruck [6]-[8], which led to an official building approval as a punching shear reinforcement element [9]. However, according to the current approval [9], existing punching shear reinforcement must not be considered in the structural design. Therefore, the required punching shear resistance must be provided exclusively by the concrete screws. This leads in some cases to an uneconomical solution. Many slabs requiring an increase in punching shear resistance already contain punching shear reinforcement elements. This raises the question of how the existing punching shear reinforcement interacts with the additionally added concrete screws. To address this issue, six component tests were carried out in which concrete screws were combined with double-headed studs, bent-up bars, and hooks. In addition, a numerical model was developed with the aim of accurately reproducing the experimental results.

2 EXPERIMENTAL INVESTIGATIONS

In order to investigate the reinforcement potential of concrete screws in slabs in combination with existing punching shear reinforcement in the form of bent-up bars, double-headed studs or hooks, a series of punching shear tests was carried out in 2024. Six component tests were performed as part of the test series. A detailed description and evaluation are documented in [10].

2.1 Test setup and material properties

The component tests were conducted on circular slabs with a diameter of 2.7 m and a slab thickness of 20 cm. A circular column stub with a diameter of 25 cm was cast integrally with the test slabs. The load was applied by a hydraulic press positioned centrally between the test slab and the counter slab. Twelve bar anchors, arranged around the perimeter of the slab, were used to anchor the test slab to the counter slab. Fig. 1 shows the test setup (left) and the implemented flexural reinforcement (right).

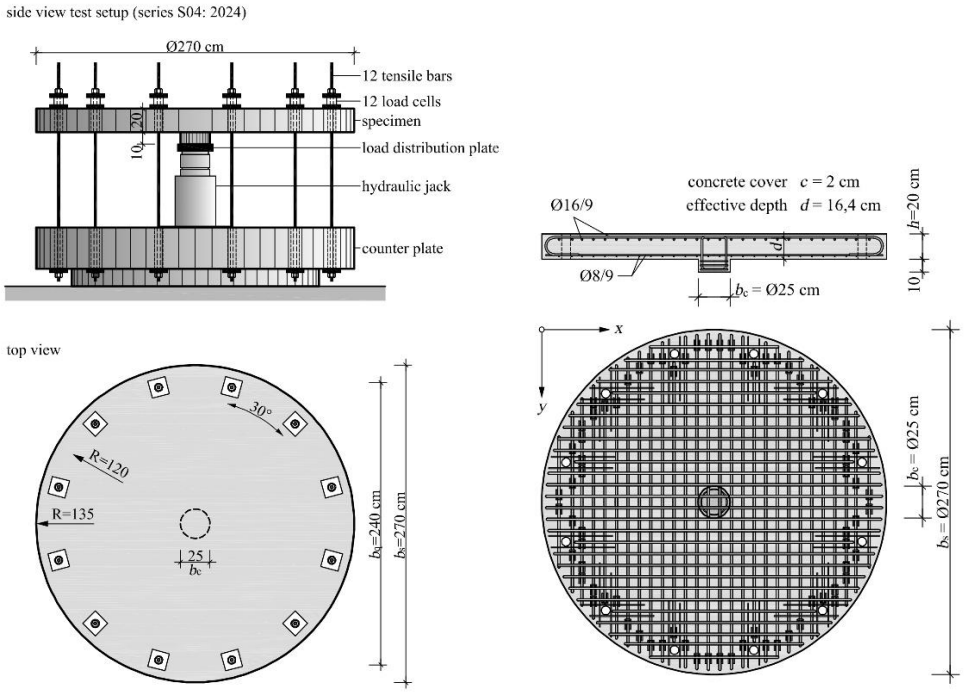


Fig. 1 Test setup and specimen (left) and the Reinforcement arrangement in the slab (right)

The test slabs were reinforced in the x- and y-directions with 16 mm diameter flexural reinforcement spaced at 90 mm intervals. With a nominal concrete cover of 20 mm, this results in an average effective depth of d = 164 mm and an average flexural reinforcement ratio of ρ_m = 1.37%. In the flexural compression zone, reinforcement bars with a diameter of 8 mm were arranged at 90 mm intervals. The steel grade was B550 throughout.

The key material properties of the concrete and reinforcement are listed in Table 1. All hardened concrete tests were carried out in the same laboratory. The cylinder compressive strength was tested in parallel with each individual test. In addition, the cube compressive strength was determined on the test days of specimens P01, P04, and P06. The hardened concrete tests for splitting tensile strength and modulus of elasticity were each carried out only once, on the test day of specimen P04 and P06, respectively. To ensure comparability, all test specimens were cast using ready-mixed concrete from the same batch.

2.2 Punching shear reinforcement and experiment execution

The test series consisted of six test slabs, with the arrangement of the punching shear reinforcement shown in Fig. 2. In slabs S04-P01 and S04-P02, twelve PSB double-headed studs with a shaft diameter of 12 mm and an anchor length of 165 mm from the company Peikko were arranged in two rows, each consisting of 6 elements. In tests S04-P03 and S04-P04, ribbed bent-up bars with a diameter of 16 mm in steel grade B550 were selected as existing punching shear reinforcement. Four bars were arranged in each reinforcement direction. The slabs S04-P05 and S04-P06 were reinforced with 32 stirrup hooks with a diameter of 8 mm in two rows. This reinforcement was also made of B550 steel.

The test specimens S04-P02, S04-P04, and S04-P06 were additionally reinforced with TSM BC SB concrete screws of the RELAST system manufactured by Würth. The screws had a drill hole diameter of 16 mm and an M16 connection thread. The individual components of the concrete screw are shown in Fig. 3. The arrangement of the screws was carried out in accordance with the currently valid approval for concrete screws [9]

The tests were conducted at a piston stroke rate of approximately 0.9 mm/min, with pauses at load levels of 208 kN and 383 kN to document crack formation on the top surface of the slab. The applied load was then reduced to 100 kN, after that it was increased again until failure.

Table 1 Material properties

	Test ID	Age at testing	$f_{c,cube,28}$ [MPa]	$f_{c,cube}$ [MPa]	f_c [MPa]	$f_{ft,sp}$ [MPa]	E_c [GPa]
Concrete	S04-P01	82	42,0	45,1	40	-	-
	S04-P02	83		-	41,3	-	-
	S04-P03	84		-	39,1	-	-
	S04-P04	88		42,9	40,6	-	34,8
	S04-P05	89		-	39,2	-	-
	S04-P06	90		43,7	39,2	3,4	-

		f_y [MPa]	f_t [MPa]	E_s [GPa]
Steel	Reinforcement B550	590	686	210
	Double headed studs	532	636	206
	Bent up bars	590	686	210
	Hooks	539	643	208
	Screws	761	780	210

$f_{c,cube,28}$	cube compressive strength after 28 days of standard storage	f_y	yield strength of the steel component
$f_{c,cube}$	cube compressive strength at testing age	f_t	tenstile strength of the steel component
f_c	cylindrical compressive strength at testing age	E_s	elastic modulus of the steel component
$f_{ft,sp}$	splitting tensile strength at testing age		
E_c	elastic modulus of the concrete at testing age		

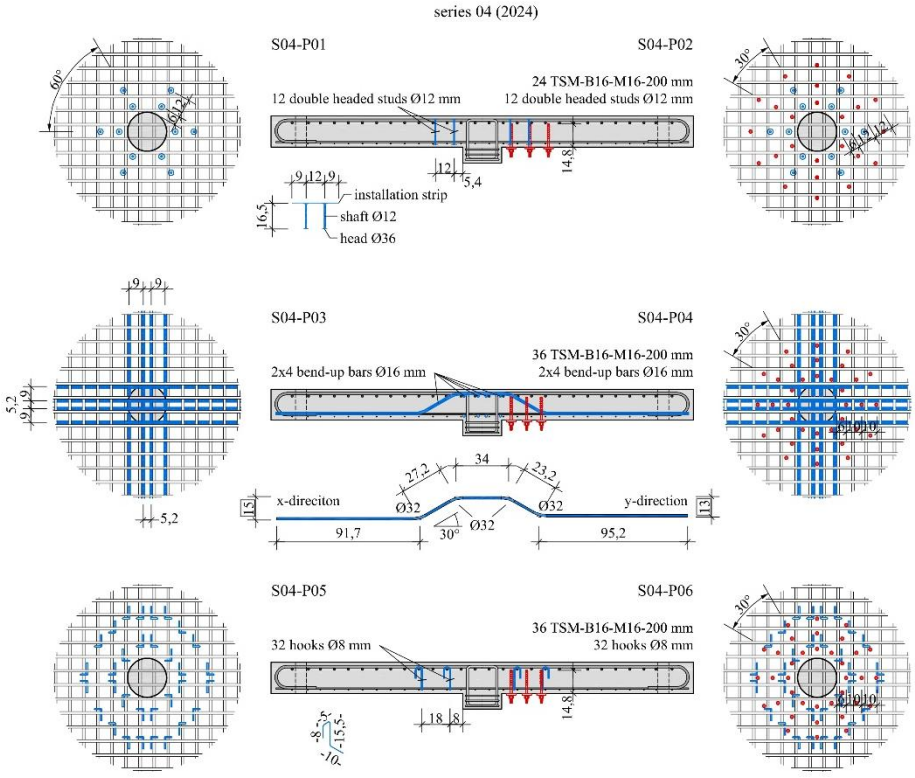


Fig. 2 Arrangement of punching shear reinforcement and RELAST concrete screws

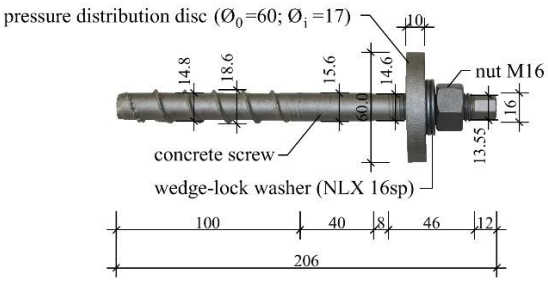


Fig. 3 Dimensions of the composite anchor bolts used

3 EXPERIMENTAL RESULTS

Fig. 4 shows on the left side the load-displacement curves for the individual tests, with the abscissa describing the measured vertical displacement at the center of the slab w_c and the ordinate describing the press force V. The maximum loads reached in each test are additionally indicated in the legend. The strengthened test S04-P02 reached a failure load of 1122 kN, corresponding to 131% of the failure load of the unstrengthened test S04-P01. A similar increase in load capacity was achieved in the tests with bent-up bars. In test S04-P04, the punching shear capacity was increased by 34% to 1253 kN compared to test S04-P03. Likewise, in test S04-P06, the strengthening with concrete screws resulted in a substantial increase in punching shear capacity, reaching 1067 kN, which corresponds to an increase of 37% compared to the unstrengthened test S04-P05. When comparing the unstrengthened slabs with the corresponding strengthened test specimens, it can be seen that in all three cases the concrete screws

lead to a significant increase in the deformation capacity. In addition, a strong flattening of the load-displacement curves can be observed in the strengthened slabs, which indicates a significantly more ductile behavior.

The saw-cut images of the individual test specimens are shown in Fig. 4 on the right side. In the case of the unrestrengthened slab with double-headed studs (S04-P01), punching shear failure can be observed outside of the punching shear reinforcement zone. Strengthening with concrete screws changed the type of failure and the critical shear crack formed in S04-P02 in the punching shear reinforced area. A comparison between tests S04-P03 and S04-P04 likewise reveals a change in failure mode due to the additional reinforcement. In the specimen without concrete screws (S04-P03), the critical shear crack propagated at a shallow angle from the column edge towards the top surface of the slab, whereas in test S04-P04 the shear crack initiated at the outermost row of concrete screws. In test S04-P05, the shear crack developed in a fan-shaped pattern upwards from the column edge. Due to the additional effect of the concrete screws in S04-P06, the critical shear crack runs more steeply away from the column edge.

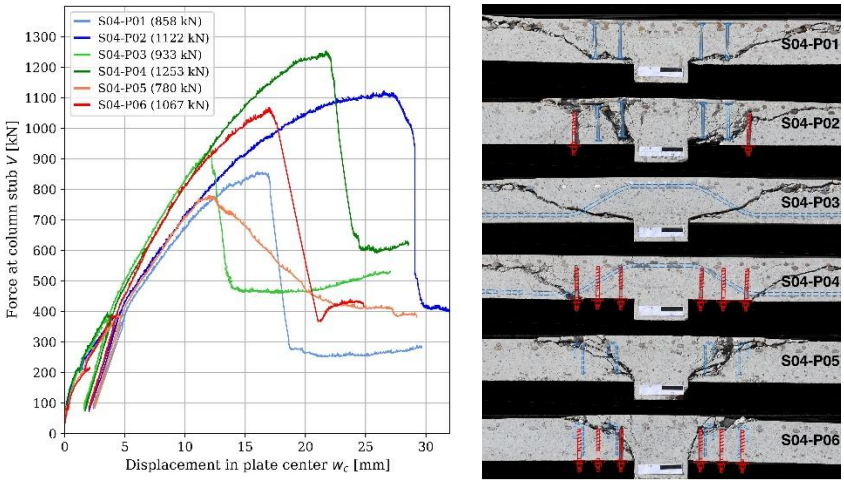


Fig. 4 Load-deflection curves of the test series (left) and Saw-Cuts of the tested slabs (right)

4 NUMERICAL MODEL

A three-dimensional numerical model was developed using the ATENA software to reproduce the experimental tests. By exploiting the symmetry of the slab, only one quarter of the specimen was modeled. The geometric model is shown in Fig. 5. The slab was discretized using eight-node, isoparametric, Gauss-integrated hexahedral elements with a linear displacement formulation (CCIsoBrick type). To adequately capture the qualitative development of the critical shear crack and the associated shear stress distribution, eight elements were defined across the slab thickness, resulting in an element size of 25 mm.

The CC3DNonLinCementitious2 material model implemented in ATENA was used to simulate the concrete behavior. This model is based on the SBETA material model [11] and the three dimensional combined fracture-plastic model [12]. The total strain is divided into elastic, plastic and fracture-mechanical components, taking into account various types of material damage and failure mechanisms. In tension the Rankine criterion for tensile fracture with exponential softening of Hordijk [13] is used, whereby cracking is represented using a smeared crack approach. Tensile and compressive softening is modeled consistently using the crack band concept [14]. A detailed description of the material model can be found in [15]. The material parameters determined from the experimental tests were adopted into the model, while the remaining parameters were calculated according to Model Code 2010 [16].
The flexural reinforcement was modeled using truss elements with uniaxial stiffness. The bond–slip relationship between the concrete and the reinforcement was defined according to Model Code 2010 [16].

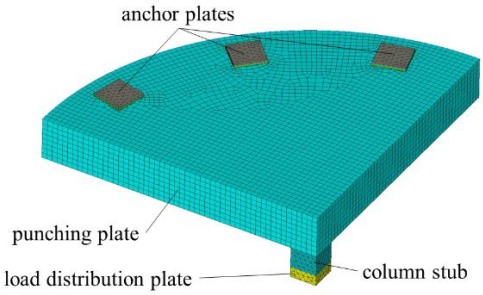


Fig. 5 Meshing distribution of the simulation model

The concrete screws were simulated using truss elements, assuming that the bond only acts over the 10 cm long thread. The bond slip relationship used was derived from conducted pull-out tests [17]. On the concrete surface the concrete screws are anchored by an anchor plate, which is connected to the component surface by means of fixed contact. To model the existing reinforcement, vertical truss elements were used for the double-headed studs, which are connected to the concrete on both ends using fixed contact. This approach adequately represents the effective end anchorage of the double-headed studs. The diagonal bends were defined in the same way as the flexural reinforcement. For the hooks the focus was to correctly represent the bond slip relationship for the end anchors. Direct geometric modeling of the stirrups resulted in unrealistic numerical responses. Therefore, the hooks were represented in a simplified manner using vertical truss elements, with an anchorage slip relationship at the ends adopted from [18].

In the Simulation it was observed that the transition from the uncracked to the cracked state occurs at a significantly too high load in the FE-Model. According to [19], this is due to the fact that the numerical model does not account for tensile stresses in concrete resulting from restrained shrinkage. To account for shrinkage effects in the numerical model, an initial compressive strain of $\varepsilon_0 = 0.15‰$ was applied to all solid elements. The imposed compressive strain in the concrete induces compressive stresses in the flexural reinforcement and consequently tensile stresses in the concrete. It was observed that the applied initial concrete compressive strain had no effect on either the failure mode or the punching shear resistance in the simulations. For the present simulations, the initial compressive strain was calibrated such that the resulting load–displacement response of the numerical model approximated the experimentally observed behaviour. In future experimental investigations, the authors intend to measure the compressive stresses developing in the flexural reinforcement due to restrained shrinkage in order to compare the measured stresses with those assumed in the numerical simulations.

In the following, the simulations of the tests with bent-up bars as existing punching shear reinforcement, namely S04-P03 and S04-P04, are discussed in detail. Due to space limitations, only these two experimental tests are presented. As observed in the laboratory tests, punching shear failure also occurred in the simulations. Fig. 6 shows a comparison of the load-displacement curves from the laboratory test and the corresponding FEM calculation for the experimental tests S04-P03 (left) and S04-P04 (right). It can be seen that the curves from the FE calculation correspond very well with those from the laboratory tests. Both the maximum punching shear force and the corresponding vertical displacement of the slab are accurately reproduced by the simulations. In test S04-P03, the simulation predicted a failure load of 979 kN, corresponding to 104.9 % of the experimentally measured failure load of 933 kN. Likewise, in test S04-P04, the numerical model predicted a slightly higher failure load than observed experimentally, reaching 1312 kN compared to 1253 kN, corresponding to 104.7 %. For both tests, the transition from the uncracked to the cracked state occurs at slightly higher load levels in the numerical models than in the experiments. A further adjustment of the assumed initial compressive strain may lead to an improved agreement between the simulated and experimentally observed behaviour. In test S04-P04 (right), which was strengthened with concrete screws, the simulation exhibits a slightly stiffer response in the cracked regime. This can be explained by the fixed contact between the holding plates of the screws and the concrete surface, as this prevents the adjacent FE elements of the concrete from being compressed. The Simulation of test S04-P04 likewise shows a

noticeable flattening of the load–displacement curve prior to reaching the maximum punching shear capacity.

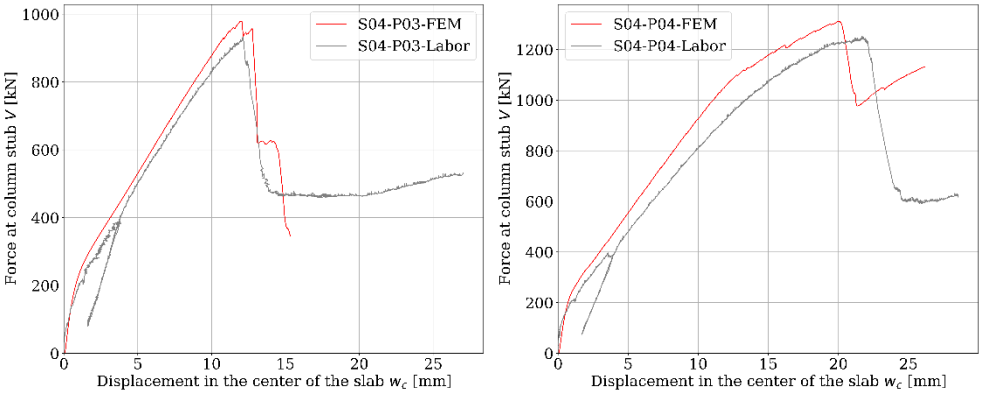


Fig. 6 Force-deflection diagrams of the tests S04-P03 (left) and S04-P04 (right) compared with the corresponding finite element simulations

5 CONCLUSION

Six component tests were conducted to investigate the extent to which the punching shear resistance of slabs with existing punching shear reinforcement can be further enhanced by retrofitting concrete screws. Double-headed studs, bent-up bars, and hooks were considered as existing punching shear reinforcement systems. The main findings can be summarized as follows:

- For each of the three types of existing punching shear reinforcement tested, the punching shear resistance can be increased by approximately one third with the post-installation of concrete screws, assuming a punching shear reinforcement level that is common in construction practice.
- The failure mode, as well as the position and inclination of the punching shear cone, can be favorably influenced by the application of concrete screws.
- The deformation capacity of the slabs increases with the arrangement of composite anchor bolts, and the load-deformation curve flattens noticeably before punching failure, indicating improved failure warning behavior.

In addition, a numerical model was developed with the aim of reproducing the laboratory tests as closely as possible. The main findings can be summarized as follows:

- The load displacement curves from the simulations correspond very closely to those from the laboratory tests.
- Both the punching shear resistance and the associated vertical displacement can be reproduced very well by the simulations.

References

[1] United Nations Environment Programme. 2023. Broken Record – Emissions Gap Report 2023 – Temperatures hit new highs, yet world fails to cut emissions (again). Nairobi https://doi.org/10.59117/20.500.11822/43922.

[2] Umweltbundesamt. 2024. Klimaschutzbericht 2024. Wien. ISBN: 978-3-99004-757-6.

[3] United Nations Environment Programme. 2020. 2020 Global Status Report for Buildings and Construction: Towards a Zero-emission, Efficient and Resilient Buildings and Construction sector. Nairobi.

[4] ASFINAG. 2023. Netzzustandsbericht 2023. Wien.

[5] Kleiser, Michael. 2023. “Zurück in die Zukunft - Brückenbau im Zeichen des Klimawandels neu denken und lenken.” Presentation Brückentagung. Wien.

[6] Wörle, Patrick. 2013. “Entwicklung eines neuen Systems zur Steigerung der Tragfähigkeit durchstanzgefährdeter Stahlbetonbauteile.” PhD diss., Leopold-Franzens-Universität Innsbruck.

[7] Spiegl, Matthias. 2020. “Erweiterte Untersuchungen zur Durchstanzertüchtigung mittels Betonschrauben unter Berücksichtigung zyklischer Belastung.” PhD diss., Leopold-Franzens-Universität Innsbruck.

[8] Feix, Jürgen, Lechner, Johannes, Spiegl, Matthias, and Walkner, Rupert. 2021. “Nachhaltige Bauwerksverstärkung mit Betonschrauben.” in Beton-Kalender 2021. 110:953-1005. https://doi.org/10.1002/9783433610206.ch11

[9] Z-15.1-340. 2024. TOGE TSM BC SB reLAST für die Durchstanzverstärkung. Berlin: DIBt - Deutsches Institut für Bautechnik.

[10] Walkner, Rupert, Fröschl, Ludwig, and Feix, Jürgen. 2025. “Durchstanzverstärkung mit Betonschrauben in Kombination mit einer bestehenden Durchstanzbewehrung.” Beton- und Stahlbetonbau. 121:49-59. https://doi.org/10.1002/best.70033.

[11] Cervenka, Vladimir, and Bergmeister, Konrad. 1999. “Nichtlineare Berechnung von Stahlbetonkonstruktionen - Finite-Elemente-Simulation unter Bemessungsbedingungen.” Beton- und Stahlbetonbau. 94:413-19. https://doi.org/10.1002/best.199901440.

[12] Červenka, Jan, and Papanikolaou, Vassilis K. 2008. “Three dimensional combined fracture–plastic material model for concrete.” International Journal of Plasticity. 24:2192–2220. https://doi.org/10.1016/j.ijplas.2008.01.004.

[13] Hordijk, Dick. 1991. “Local approach to fatigue of concrete.” PhD diss., University of Technology Delft.

[14] Červenka, Jan, Červenka, Vladimir, and Laserna, Santiago. 2018. “On crack band model in finite element analysis of concrete fracture in engineering practice.” Engineering Fracture Mechanics. 197:27–47. https://doi.org/10.1016/j.engfracmech.2018.04.010.

[15] Červenka, Vladimir, and Jendele, Libor. 2021. “ATENA Program Documentation Part 1 – Theory.”

[16] CEB-FIP. 2010. Model Code 2010 – Volume 1. International Federation for Structural Concrete (fib).

[17] Lechner, Johannes et al. 2017. “Zum Verbundverhalten von Betonschraubdübeln mit großem Durchmesser.” Beton- und Stahlbetonbau 112:589–600. https://doi.org/10.1002/best.201700043

[18] Brantschen, Fabio. 2016. “Influence of bond and anchorage conditions of the shear reinforcement on the punching strength of RC slabs.” PhD diss., École polytechnique fédérale de Lausanne.

[19] Pryl, Dobromil and Červenka, Jan. 2017. “ATENA Program Documentation Part 11: Troubleshooting Manual.”

Energy-Based Evaluation of Regular Reinforced Concrete Shear Wall Building

Dr. Mohamad Issa and Aleen Al-Dali

Department of Structural Engineering, Faculty of Civil Engineering,
Homs University, Syria

Summary
Force-based seismic design neglects inelastic displacement, plastic behaviour, and ground motion duration, often leading to inadequate performance. Energy-based seismic design offers a more comprehensive framework by incorporating these effects. In this approach, input energy dissipates through damping and hysteretic energy. Quantifying story-wise and component-wise hysteretic energy distribution is essential for developing energy-based design tools. This study evaluates the seismic performance of reinforced concrete shear wall buildings using an energy-based methodology. Four regular models (6, 10, 14, and 20 stories) were analysed under 11 ground motion using Nonlinear Time History Analysis (NLTHA). The distribution of hysteretic energy across stories and structural elements was examined, assessing the influence of ground motion characteristics and structural properties on energy dissipation. Results show potential for practical design rules based on hysteretic energy distribution.

1 INTRODUCTION

The energy-based seismic design paradigm, first established by Housner (1956), asserts that structural safety requires earthquake input energy (Ei) to remain below the system's dissipation capacity. Initial formulations addressed SDOF systems (Housner, 1956), with subsequent research extending the methodology to MDOF configurations [3],[5],[6],[9],[11]. Within this framework, (Ei) partitions into: Kinetic energy (Ek) from inertial forces, Elastic strain energy (Es) stored in elastic deformations, damping energy (Ed) dissipated by damping material, Hysteretic energy (Eh) dissipated through cumulative plastic deformation [8]. Energy balance equation can be written as

$$Ei = Ek + Ed + Es + Eh \quad (1)$$

Considering the inelastic behaviour of the structure, Ek and Es are very small compared to Ed and Eh during seismic action.

It is possible to state that almost all the input energy of the earthquake is dissipated by damping energy and hysteretic energy at the end of the earthquake [11].

$$Ei \cong Ed + Eh \quad (2)$$

While (Ei) estimation dominates energy-based literature, (Eh) quantification—critical for damage assessment—remains understudied, particularly its spatial distribution. Although (Eh) distribution in reinforced concrete (RC) systems have seen limited exploration [7],[15],[10], prior detailed investigations focused exclusively on steel frames [1],[2],[16].

This study aims to carry out an energy-based evaluation of reinforced concrete shear wall buildings, with estimation of hysteretic energy and its story-wise and member-wise distribution. For this reason, regular models with varying heights (6, 10, 14, and 20 stories) are selected, and their energy response under 11 ground motions are evaluated.

2 STRUCTURAL MODELS CONSIDERED

Four regular reinforced concrete building models with shear walls were developed to investigate the influence of building height on the distribution of hysteretic energy under seismic excitation. The models vary in height, comprising 6, 10, 14, and 20 stories.

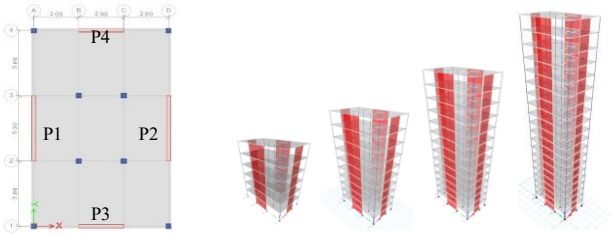


Fig. 1 Floor plan and Dimensional (left) and 3D Models of the studied structures (right).

2.1 Model Description and Design Parameters

Four regular reinforced concrete shear wall building models with varying heights (6, 10, 14, and 20 stories) were analysed. The story height was 3.5 m, with shear walls serving as the lateral force-resisting system. According to the Syrian seismic code, the site was classified as soil type C with an importance factor I = 1. Seismic spectral coefficients Ca = 0.38 and Cv = 0.29 were adopted to generate the design response spectrum for scaling ground motion records. Material strengths corresponded to C25 concrete and T400 reinforcement steel. Design loads included a dead load of 3 kN/m², a live load of 2 kN/m², and a seismic load derived from the response spectrum using a response modification factor R = 4.5. Load combinations followed UBC 1997, consistent with Syrian code provisions. All modelling, analysis, and design were performed using ETABS 2020.The structural models were developed under combined vertical and seismic loading, and the slab thickness was set at 20 cm, with a drop panel thickness of 15 cm at columns for all buildings, satisfying all strength and deflection requirements. Section Dimensions and reinforcement details are summarized in Table 1.

Table 1 Member Section Design Summary

Building Type	Floor Number	Column size (cm)	Column Rebar	Floor Number	Shear Wall size (cm)		Shear Wall Rebar			
							Longitudinal Reinforcement			
							P1,P2		P3,P4	
					P1,P2	P3,P4	AS Boundary zone (2t,t) cm	AS wall	AS Boundary zone (2t,t) cm	AS wall
6-Story, Regular	1,2,3,4,5,6	45 × 45	8T18 , 1CØ8/150 mm	1,2,3,4,5,6	25 × 500	25 × 300	14T14	14T/150	12T18	18T/150
10-Story, Regular	1,2,3,4	60 × 60	16T20 , 3CØ10/100 mm	1,2,3,4	35 × 500	35 × 300	20T18	T14/150	20T20	T20/150
	5,6,7	50 × 50	12T20 , 3CØ10/100 mm	5,6,7	30 × 500	30 × 300	12T14	T12/150	12T14	T12/150
	8,9,10	40 × 40	8T20 , 1CØ10/100 mm	8,9,10	25 × 500	25 × 300	10T14	T12/150	10T14	T12/150
14-Story, Regular	1,2,3,4	60 × 60	12T22 , 3CØ10/100 mm	1,2,3,	40 × 500	40 × 300	20T20	T18/150	10T25/m	
	5,6,7	50 × 50	12T22 , 3CØ10/100 mm	4,5,6	35 × 500	35 × 300	12T18	T14/150	10T14/m	
	8,9,10	40 × 40	8T22 , 1CØ10/100 mm	7,8,9,10	30 × 500	30 × 300	12T14	T12/150	7T12/m	
				11,12,13,14	25 × 500	25 × 300	10T14	T12/150	7T12/m	
20-Story, Regular	1,2,3,4,5	70 × 70	16T25 , 3CØ10/100 mm	1	50 × 500	50 × 300	28T22	T18/150	12T25/m	
	6,7,8,9,10	60 × 60	12T25 , 3CØ10/100 mm	2,3,4	45 × 500	45 × 300	24T20	T18/150	12T22/m	
	11,12,13,14,15	50 × 50	12T25 , 3CØ10/100 mm	5,6,7,8	40 × 500	40 × 300	16T18	T12/150	7T14/m	
				9,10,11,12	35 × 500	35 × 300	16T14	T12/150	7T12/m	
	16,17,18,19,20	40 × 40	8T25 , 1CØ10/100 mm	13,14,15,16	30 × 500	30 × 300	12T14	T12/150	7T12/m	
				17,18,19,20	25 × 500	25 × 300	10T14	T12/150	7T12/m	

3 NLTH ANALYSIS

In order to investigate the energy-based seismic response of reinforced concrete shear wall models under seismic action, nonlinear time history analysis is essential since it is possible to monitor the force-deformation relationship of all elements in each time step of ground motion record with NLTH analysis. ETABS (2020) structural analysis and design software is used for all linear and nonlinear analysis of this work.

3.1 Modelling

The modelling methodology adhered to the specifications of ASCE 41-13, incorporating the following protocols:

3.1.1 Plastic Hinges

Plastic hinges were assigned to columns and shear walls to simulate nonlinear seismic behaviour. For columns, automatic plastic hinges were placed at both ends, with properties derived from section geometry, reinforcement details, and element length. For shear walls, fiber-based hinges were employed; cross-sections were discretized into concrete and steel fibers, with reinforcement explicitly modelled in layers. This approach captures nonlinear effects such as cracking, crushing, and rebar buckling. The concrete was represented using the "Concrete Hysteretic" material model, and the steel reinforcement with the "Kinematic" model, ensuring accurate simulation of force transfer and stress distribution.

3.1.2 Material Properties

Material strengths were amplified per ASCE 41-13 recommendations to avoid underestimating structural capacity, Concrete strength was increased by a factor of 1.3, and steel strength by 1.1, achieving a realistic yet safe design approach.

3.1.3 Damping

Rayleigh damping (2.5% for fundamental modes) was employed to distribute damping between the first and second modes, aligning with the actual dynamic characteristics of the structure. was applied via mass and stiffness proportionality:

$$[C] = \alpha [M] + \beta [K] \quad (3)$$

where ($\alpha = 2\zeta \frac{\omega_1 * \omega_2}{\omega_1 + \omega_2}$, $\beta = 2\zeta \frac{1}{\omega_1 + \omega_2}$), and ($\zeta = 0.025$) (($\omega_1, \omega_2$): primary modal frequencies).

3.2 Ground motion records

For energy calculations and NLTHA, eleven ground motion records were selected to ensure variability in duration, PGA (0.18g–0.7g), and dominant frequency content (0.2–4 Hz).

Table 2 Characteristics of the selected ground motion record

No.	Label	Event_Country	Year	Magnitude	PGA (g)	PGV (cm/s)
1	EQ1	Friuli, Italy-01	1976	6.5	0.36	30.5
2	EQ2	Loma Prieta, USA	1989	6.93	0.25	21.78
3	EQ3	Landers, USA	1992	7.28	0.274	42.57
4	EQ4	Manjil, Iran	1990	7.37	0.51	50.56
5	EQ5	Hector Mine, USA	1999	7.13	0.182	27.6
6	EQ6	Cape Mendocino, USA	1992	7.01	0.265	35.5
7	EQ7	Chuetsu-oki, Japan	2007	6.8	0.2	22.1
8	EQ8	Chuetsu-oki, Japan	2007	6.8	0.45	51.8
9	EQ9	Iwate, Japan	2008	6.9	0.536	69.6
10	EQ10	Iwate, Japan	2008	6.9	0.7	48.7
11	EQ11	Darfield, New Zealand	2010	7	0.63	42.3

The ground motion records were scaled to the Syrian code target spectrum using the PEER database per ASCE 7-16. Scaling required the geometric mean spectrum of the scaled components to match or exceed the target spectrum and not fall below 90 % of its values within the period range $0.2T_1$ to $2T_2$,

where T_1 and T_2 are the smaller and larger fundamental periods in the orthogonal directions, respectively.

Table 3 Fundamental periods (T_1 and T_2) of the studied models

Building Type	First Period (s)	Second Period (s)
6-Story, Regular	0.56	0.41
10-Story, Regular	0.997	0.797
14-Story, Regular	1.514	1.265
20-Story, Regular	2.304	2.009

4 ENERGY CALCULATIONS AND RESULTS

Following NLTH analysis, the energy parameters for the selected RC shear wall buildings subjected to a set of ground motion records are calculated. In order to contribute to the development of a practical energy-based design or assessment method, three primary steps are considered, which are: estimation of input energy, calculating the ratio of hysteretic energy to input energy (Eh/Ei) and evaluation of the distribution of hysteretic energy among stories and structural members. Estimation of the input energy is spotlighted by many studies while determination of the hysteretic energy of RC buildings has been taken into account in fewer previous work. Estimation of hysteretic energy and its distribution through stories and elements are the main focus of this study, and it is discussed in more detail.

4.1 Time History of the Energy Parameters

As mentioned earlier, input energy is dissipated within the structure through recoverable elastic strain energy, kinetic energy, damping energy and irrecoverable plastic hysteretic energy. In this section, the time history of input energy and its components are plotted for selected cases. Since there are 44 analysis cases, it would take pages to show all energy time histories. So, the following presents representative results for the 6-story model, with a selected ground motions illustrating energy dissipation behaviour. Fig. 2 shows the plotted energy time histories.

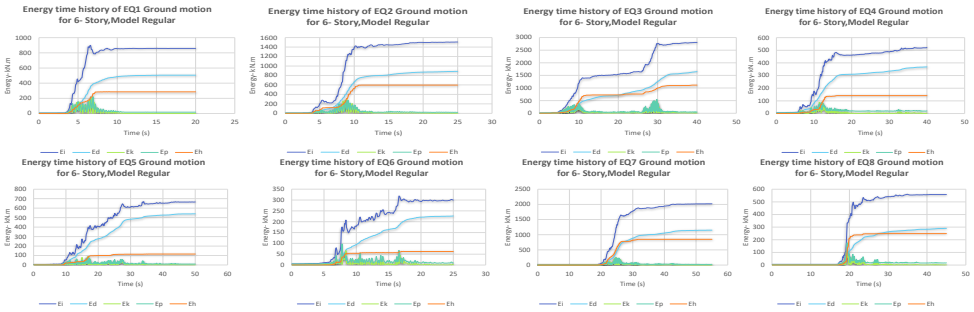


Fig. 2 Energy time history of EQ1,2,3,4,5,6,7,8 Ground motions for 6-Story model.

The energy time histories demonstrate that contributions from elastic strain energy (Es) and kinetic energy (Ek) are insignificant relative to damping energy (Ed) and hysteretic energy (Eh). (Es) and (Ek) dissipate fully upon cessation of ground shaking, with input energy (Ei) irreversibly absorbed by (Ed) and (Eh) – consistent with (2). Critically, both damping and hysteretic components exhibit non-recoverable accumulation throughout seismic excitation. Divergence in the disparity between (Eh) and (Ed) trajectories across histories confirms that their proportional distribution relative to (Ei) varies per analysis scenario. Hence it is a function of both ground motion and structural parameters.

4.2 Input Energy Results

Accurate estimation of input energy is essential for advancing energy-based design methodologies. Structures exhibiting nonlinear behaviour under strong ground motions experience significant stiffness and strength degradation. In such systems, ground motion characteristics critically influence seismic

input energy. Notably, the number of high-amplitude cycles and presence of long-duration acceleration pulses are key seismic features that govern substantial energy input and precipitate structural degradation [12].

The input energy of each model is calculated for eleven ground motion records. The results are illustrated and compared to each other and the effect of ground motion characteristics and structural properties on input energy is discussed. Fig.3 shows input energy of each ground motion for all the studied models.



Fig. 3 Input energy of all ground motions for the studied models

Comparative analysis of input energy across identically excited shear wall structures reveals substantial variations in energy absorption despite identical ground motion excitation. Input energy demonstrates pronounced period-dependency, confirming its dual dependence on ground motion characteristics and structural properties. As quantified in Fig. 3, the EQ9 (Iwate 2008) record generates peak input energy for 14-story and 20-story systems, while ranking second for the 10-story model after EQ3 and producing moderate energy levels in the 6-story structure. Notably, EQ9's original PGA (0.536g) and PGV (69.6 cm/s) are lower than EQ10 (0.7g) per Table 2. However, Fig. 4 establishes that EQ9's extended duration (≥40s) with repeated high-amplitude acceleration cycles (≥0.4g) drives exceptional energy demand. It is possible to conclude that PGA and PGV are inadequate ground motion parameters to represent earthquake damage potential; other characteristics like duration and number of high-amplitude acceleration cycles must be considered.

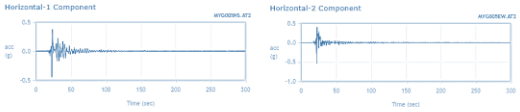


Fig. 4 EQ9 (Iwate 2008) ground motion record.

4.3 The Ratio of Hysteretic to Input Energy

To develop practical energy-based design or assessment methodologies, hysteretic energy (Eh), which is the representative of the damage potential of the structure, Fajfar et al. (1990) demonstrated that (Eh) demand can be estimated via the (Eh/Ei) ratio.

For all shear wall models under 11 ground motion records, (Eh/Ei) and (Ed/Ei) ratios were calculated as shown in Table 4. Mean values of these ratios are summarized in the table's final row. To evaluate the influence of ground motion characteristics and structural parameters on (Eh), the (Eh/Ei) percentages for all records are plotted per model in Fig. 5.

Table 4 Eh/Ei and Ed/Ei ratios of all ground motion records for the studied models

Ground Motion Labels	6-Story, Regular Model		10-Story, Regular Model		14-Story, Regular Model		20-Story, Regular Model	
	Eh/Ei	Ed/Ei	Eh/Ei	Ed/Ei	Eh/Ei	Ed/Ei	Eh/Ei	Ed/Ei
EQ1	33.4%	58.9%	21.4%	72.4%	17.0%	72.0%	5.8%	78.9%
EQ2	39.7%	58.8%	12.0%	84.6%	17.4%	76.1%	4.8%	87.2%
EQ3	39.7%	58.7%	38.7%	58.8%	10.1%	84.9%	6.7%	82.0%
EQ4	27.1%	70.6%	5.6%	89.8%	4.3%	90.6%	24.2%	71.3%
EQ5	17.2%	80.7%	11.0%	87.3%	43.7%	53.8%	4.2%	79.0%
EQ6	19.8%	71.2%	9.8%	82.9%	22.3%	66.2%	28.2%	52.7%
EQ7	42.1%	56.9%	8.5%	88.3%	9.6%	85.4%	5.6%	88.6%
EQ8	44.6%	52.1%	34.5%	64.4%	24.7%	70.2%	15.3%	72.6%
EQ9	31.3%	65.6%	16.6%	79.8%	29.8%	69.4%	44.9%	54.0%
EQ10	24.9%	73.7%	8.8%	89.5%	6.6%	90.1%	8.3%	89.1%
EQ11	15.4%	79.7%	6.1%	92.7%	4.4%	94.1%	9.2%	88.4%
MEAN	30.5%	66.1%	15.7%	80.9%	17.3%	77.5%	14.3%	76.7%

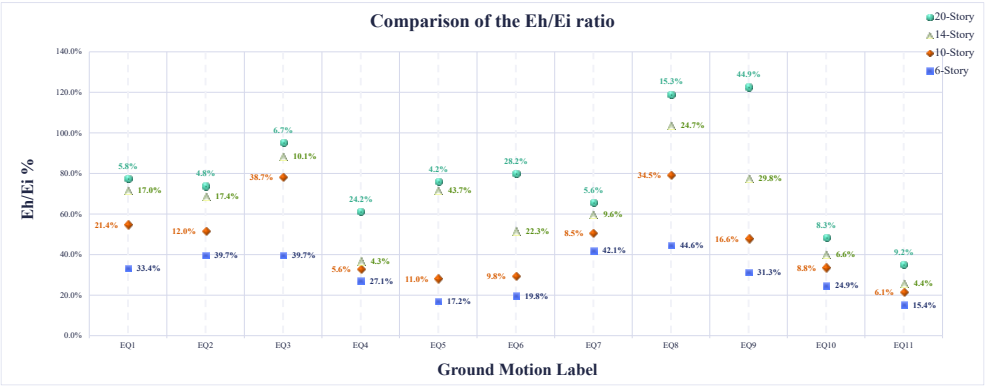


Fig. 5 Comparison of the Eh/Ei ratio shown as percentage for each studied model for all ground motion records

Table 4 validates the energy equilibrium principle, confirming that the summation of hysteretic energy (Eh) and damping energy (Ed) consistently equals the total seismic input energy (Ei) at ground motion cessation. Quantitative analysis reveals significant variation in the hysteretic-to-input energy ratio (Eh/Ei) across structural heights: 6-story: 30.5% (range: 15.4–44.6%), 10-story: 15.7% (range: 6.1–38.7%), 14-story: 17.3% (range: 4.4–43.7%), 20-story: 14.3% (range: 4.2–44.9%). The wide range of Eh/Ei ratios highlights the strong influence of ground motion characteristics, Therefore, a single mean value is not sufficient for design purposes. The mean values presented here are only intended to show the general trend across the studied models.

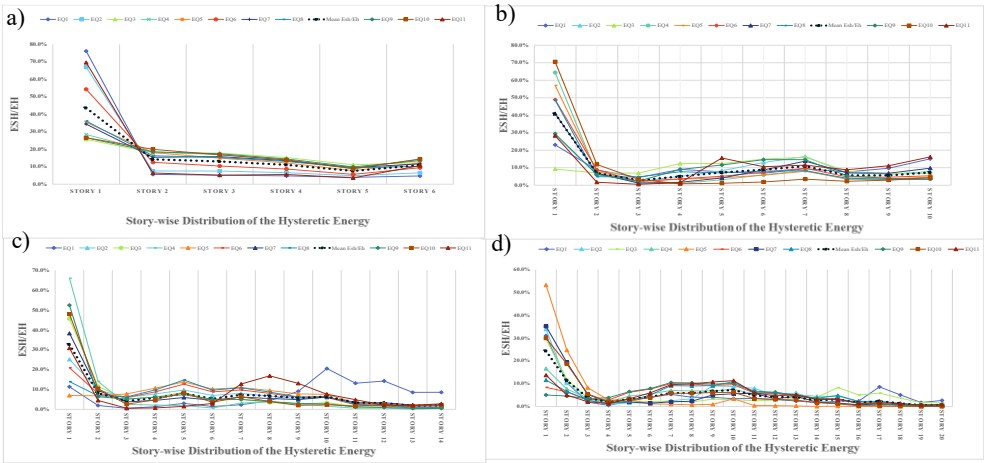
A pronounced inverse relationship emerges between structural height and the mean (Eh/Ei) ratio, where the damping energy component constitutes a larger share of the total dissipated energy ((Ed/Ei) ≈ 66.1–80.9%). The decline in the relative contribution of hysteretic dissipation in taller structures suggests a shift in energy dissipation mechanisms, likely influenced by their altered dynamic characteristics and modal responses under seismic excitation.

Analysis of Fig. 5 reveals (Eh/Ei) remains relatively stable for low-rise structures (6 stories) but exhibits heightened sensitivity to ground motions as height increases. This signifies stronger dependence on ground motion characteristics with longer fundamental periods. Vertical grid-line comparisons in Fig. 5 show (Eh/Ei) variations across studied models for the same ground motion record.

In summary, hysteretic demand depends on both structural and ground motion characteristics, with ground motion characteristics demonstrating dominant influence within the studied model set.

4.4 Distribution of Hysteretic Energy

Understanding hysteretic energy distribution across stories and structural elements is essential for developing energy-based design and assessment methodologies. Consequently, hysteretic energies at



all plastic hinges were computed for the studied four shear wall regular models under 11 ground motion records. Results are presented through story-wise and member-wise distributions of hysteretic energy.

4.4.1 Story-wise Distribution of the Hysteretic Energy

Hysteretic energy dissipated at shear wall and column hinges was summed per story and divided by total structure hysteretic energy to determine cumulative story demands (Esh/Eh). The distribution of story-wise hysteretic energy to total hysteretic energy ratio (Esh/Eh) over the height of the structures for different ground motion record are shown for ground motion set in Fig. 6 in which "Mean" represent mean value of the results for records.

Fig. 6 Esh/Eh % for: a) 6-story b) 10-story c) 14-story d) 20-story

General trends indicate that hysteretic energy distribution over the building height depends on both ground motion characteristics and structural properties. For low-rise buildings (6 stories), (Esh/Eh) ratios were consistent across all ground motions, whereas higher models exhibited greater scatter. This demonstrates reduced sensitivity to seismic inputs in story-wise energy distribution for low-rise structures. The results show that about 70% of the hysteretic energy is dissipated in Stories 1–2 (6-story building). This percentage decreases to: 45% in Stories 1–3 (10-story), 25% in Stories 6–12 (14-story), 15% in Stories 8–16 (20-story).

It means that as the fundamental period increases, hysteretic energy shifts from lower to mid and upper stories.

4.4.2 Member-wise Distribution of Hysteretic Energy

The dissipated hysteretic energy at each shear wall and column hinge is divided by the total hysteretic energy to obtain the ratio of member-wise (shear wall or column) hysteretic energy to total hysteretic energy (Emh/Eh) for all ground motions as a measure. Total hysteretic energy percentage dissipated by the columns (sum of Emh/Eh% at columns) and shear walls (sum of Emh/Eh% at shear walls) for all records and presented in Fig. 7. Also, the mean values of hysteretic energy percentage dissipated by the shear wall and column members are obtained for all records. The results are presented in Fig. 8.

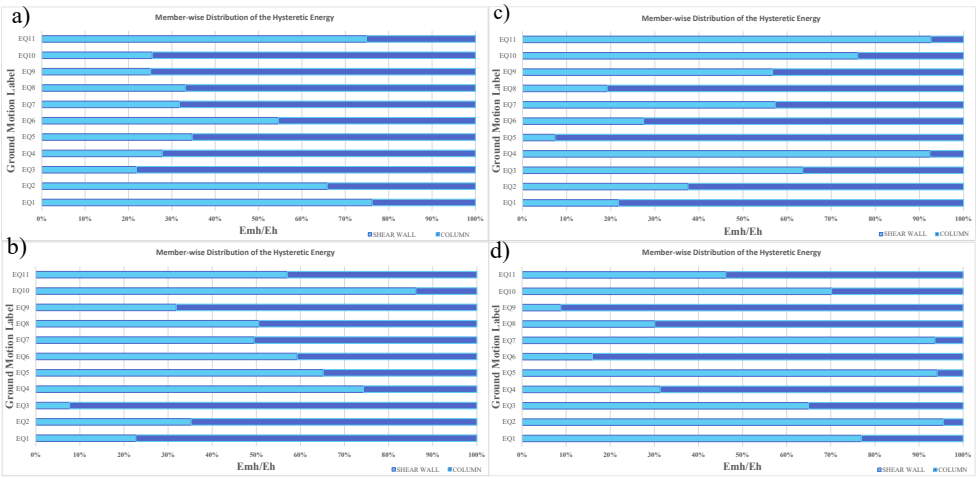


Fig. 7 Emh/Eh % for : a) 6-story b) 10-story c) 14-story d) 20-story

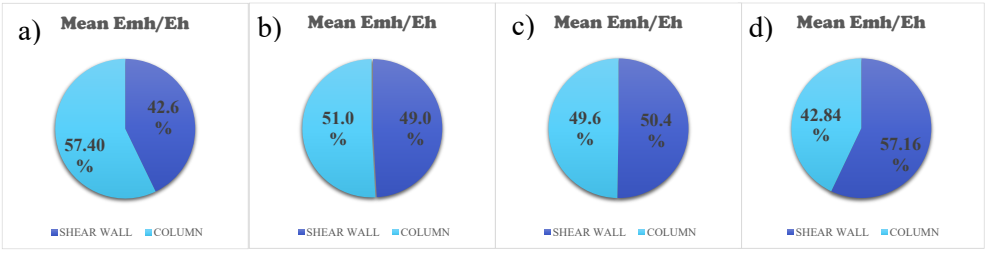


Fig. 8 Mean values of Emh/Eh % for: a) 6-story b) 10-story c) 14-story d) 20-story

Calculated mean values of hysteretic energy dissipated by column and shear wall hinges for all analysis cases show that 49.8% of total hysteretic energy is dissipated by shear wall hinges whereas 50.2% is dissipated by column hinges. It seems that the ratio of dissipated hysteretic energy by columns to dissipated hysteretic energy by shear walls is sensitive to the relative stiffness and strength of these elements. Although shear walls are designed to be the primary lateral-load-resisting elements, columns still exhibit significant hysteretic behaviour, indicating that energy dissipation is shared between both components. From the results, it is observed that as fundamental period of the structure increases (with building height), dissipated hysteretic energy shifts from columns to shear walls, with shear walls dissipating up to 57.2% in 20-story structure.

Member-wise distribution of hysteretic energy is directly influenced by the geometric and reinforcement properties of shear walls and columns. The observed variation across records (e.g., opposite shares for EQ4 and EQ5 in Fig.8.c) is related to the distribution of hysteretic energy, which depends on both ground motion characteristics and building height. This distribution determines which stories and elements participate in energy dissipation. Moreover, stiffness degradation and force redistribution further alter the contribution of each member. This demonstrates that practical energy-based design rules can be established to control inelastic action distribution in shear wall structures, ensuring optimal seismic performance by leveraging the complementary roles of shear walls and columns.

5 CONCLUSIONS

Based on a comprehensive energy-based evaluation of regular reinforced concrete shear wall buildings using Nonlinear Time History Analysis (NLTHA) for 6-, 10-, 14-, and 20-story models under 11 ground motions, the following conclusions are drawn:

1. Input Energy (Ei) depends on both structural properties (e.g., height, fundamental period) and ground motion characteristics (e.g., duration, frequency content, amplitude cycles).
2. The influence of ground motion characteristics on the Esh/Eh ratio becomes increasingly pronounced with longer fundamental periods of the structure.
3. Story-Wise Hysteretic Energy Distribution:

- In low-rise buildings (6-story), approximately 70% of (Eh) is concentrated in the first two stories.
- In mid- and high-rise models, hysteretic energy shifts upward due to the influence of higher vibration modes: 45% in Stories 1–3 (10-story), 25% in Stories 6–12 (14-story), 15% in Stories 8–16 (20-story).
- This upward shift highlights the importance of considering modal contributions beyond the fundamental mode in energy-based design.

4. Member-Wise Hysteretic Energy Distribution

- On average, columns and shear walls share hysteretic energy dissipation nearly equally: 50.2% and 49.8%, respectively.
- In taller buildings, shear walls absorb a larger portion of (Eh) (up to 57.2% in 20-story model).
- The distribution is governed primarily by member geometry, reinforcement detailing, and design intent.
- Although shear walls were designed as the primary energy-dissipating elements, columns exhibited significant inelastic behaviour, indicating shared dissipation roles.

The observed energy distribution patterns help identify critical zones—especially lower stories and shear walls—that require targeted reinforcement to enhance the seismic performance of the structure.

This study focused on regular reinforced concrete buildings with shear walls. To broaden the applicability of the findings, future research should investigate irregular configurations, dual systems combining shear walls and moment-resisting frames, and experimental and analytical studies to establish energy capacity limits for individual structural components.

References

[1] Akbaş, Bülent, Akşar, Bora, Doran, Bilge, and Alacalı, Sema. 2016. "Hysteretic energy to energy input ratio spectrum in nonlinear systems." *Dokuz Eylul University Faculty of Engineering Journal of Science and Engineering* 18(2):239-254. doi:10.21205/deufmd.20165318384.

[2] Akbaş, Bülent, Shen, J., and Hao, Hong. 2001. "Energy approach in performance-based seismic design of steel moment resisting frames for basic safety objective." *The Structural Design of Tall Buildings* 10(3):193-217. doi:10.1002/tal.172.

[3] Akiyama, Hiroshi. 1985. *Earthquake-resistant limit-state design for buildings*. Tokyo: University of Tokyo Press.

[4] American Society of Civil Engineers. 2013. *ASCE/SEI Standard 41-13, Seismic Rehabilitation of Existing Buildings*. Reston, VA: ASCE.

[5] Amiri, Gholamreza Ghodrati, Amiri, Javad Vaseghi, and Ganjavi, Behnoud. 2008. "Seismic vulnerability assessment of multi-degree-of-freedom systems based on total input energy and momentary input energy responses." *Canadian Journal of Civil Engineering* 35(1):41-56. doi:10.1139/L07-085.

[6] Chou, Chung-Che, and Uang, Chia-Ming. 2003. "A procedure for evaluating seismic energy demand of framed structures." *Earthquake Engineering & Structural Dynamics* 32(2):229-244. doi:10.1002/eqe.221.

[7] Du, Hongbiao, and Guan, Minsheng. 2013. "Energy-based seismic performance of reinforced concrete frame structures." *Magazine of Concrete Research* 65(8):494-505. doi:10.1680/macr.12.00149.

[8] Khashaee, Payam, Gross, John L., Lew, Hai S., Mohraz, Bijan, and Sadek, Fahim. 2003. Distribution of earthquake input energy in structures. Gaithersburg, MD: US Department of Commerce, National Institute of Standards and Technology.

[9] Manfredi, Gaetano. 2001. "Evaluation of seismic energy demand." *Earthquake Engineering & Structural Dynamics* 30(4):485-499. doi:10.1002/eqe.17.

[10] Okur, Abdullah, and Erberik, Murat Altug. 2014. "Adaptation of Energy Principles in Seismic Design of Turkish RC Frame Structures. Part II: Distribution of Hysteretic Energy." Paper

presented at the 2nd European Conference on Earthquake Engineering and Seismology, Istanbul, Turkey, August 25–29.

[11] Shen, J., and Akbaş, Bülent. 1999. "Seismic energy demand in steel moment frames." Journal of Earthquake Engineering 3(04):519-559. doi:10.1080/13632469909350358.

[12] Sucuoğlu, Haluk, and Erberik, Murat Altug. 2004. "Energy-based hysteresis and damage models for deteriorating systems." *Earthquake Engineering & Structural Dynamics* 33(1):69-88. doi:10.1002/eqe.338.

[13] *The Syrian Arab Code for Design & Construction of Reinforced Concrete Structures*. 2022. Damascus: Syrian Arab Republic.

[14] *The Syrian Arab Code – Appendix 2. Design and Check of Seismic Resistant Buildings and Constructions*. 3rd ed. 2019. Damascus: Syrian Arab Republic.

[15] Tu, Bing Bing, and Zhao, Dong. 2018. "Distribution of accumulated irrecoverable hysteretic energy in MDOF structures." *Multidiscipline Modeling in Materials and Structures* 14(2):202-215. doi:10.1108/MMMS-05-2017-0028.

[16] Uang, Chia-Ming, and Bertero, Vitelmo V. 1990. "Evaluation of seismic energy in structures." *Earthquake Engineering & Structural Dynamics* 19(1):77-90. doi:10.1002/eqe.4290190108.

Comparative experimental study of test setups for bond testing of textile reinforcements in concrete

Jonas Wachter[1], Julian Konzilia[1], Jürgen Feix[1], Philipp Preinstorfer[2]

[1]Unit of Concrete Structures and Bridge Design,
Department of Structural Engineering and Material Sciences,
University of Innsbruck,
Technikerstraße 13, 6020 Innsbruck, Austria

[2]Research Unit Structural Concrete,
Institute of Structural Engineering,
TU Wien,
Karlsplatz 13, E212-2, 1040 Vienna, Austria

Summary
Reliable test setups for characterising the bond behaviour of textile-reinforced concrete (TRC) are important for the design of TRC members and application in civil engineering. Existing configurations often involve fragile specimens, limited handling precision, and variable failure modes, which affect the reliability of the results. This study introduces a new specimen configuration for TRC single sided pull-out test to enhance the robustness and consistency of TRC bond tests. A total of 55 bond tests with carbon-fibre reinforcements were conducted to compare the bond performance obtained from the new configuration with the results from conventional configurations. Specimens with separation elements showed comparable splitting failure patterns and were simple to produce and handle, thus clearly demonstrating their effectiveness. These findings foster the development of standardised assessment methods for TRC bond behaviour that are easy to handle and yield reliable results.

1 INTRODUCTION

Reinforced concrete is the most widely used construction material due to its good mechanical properties and high versatility. However, the cement and concrete industry is responsible for approximately 8% of annual global CO2 emissions [1], and corrosion of steel reinforcement poses a major durability issue [2]. Non-metallic reinforcements made of fibre-reinforced polymers (FRP) offer a sustainable alternative with high tensile strength [3], combined with low crack widths [4] and good corrosion resistance [5]. Despite the successful realisation of several pilot projects [6], the lack of uniform testing procedures is hampering a broader implementation of these alternative reinforcement methods. For example, bond behaviour between reinforcement and concrete is currently characterised according to German guideline [7] using a test setup, based on the principles summarised by Lorenz et. al. [8]. These configurations have been established to mimic realistic conditions, but often have limitations in terms of specimen configuration, handling, and evaluation of failure mechanisms. In addition, a wide variety of reinforcement configurations are available on the market [9], with differing fibre and impregnation materials that influence the interaction between concrete and reinforcement. This study investigates the robustness and reliability of bond tests for TRC. In total, four configurations were experimentally tested, three of which are provided in the German guideline [7] and a novel configuration that the authors first introduced in this manuscript.

The bond between carbon rovings and mineral matrices is described by relationships linking the transferred load to either crack opening or roving slip, depending on the governing deformation mechanism. These mechanisms and their boundary conditions are summarised in [10].

2 MATERIALS AND METHODS

2.1 Material properties

All specimens were produced using fine-grained concrete with a maximum aggregate size of 2 mm (diabase 0/2), following the mixture by Konzilia et al. [11]. To determine compressive and flexural strength, six prisms (40×40×160 mm) were produced. Specimens were demolded after 24 hours. Three

were stored in water at 20 °C until testing according to EN 196-1:2016, while the remaining three were conditioned like the test specimens, kept in water until day 7 and then at 20 °C and 65 % relative humidity. Corresponding mechanical properties are given in Table 1.

Table 1 Concrete properties for the used concrete according to [11]

Curing	Mortar density [kg/m³]	Compressive strength [MPa]	Flexural strength [MPa]
EN 196-1:2016	2212.0	75.6	12.5
Specimen curing	2272.8	68.5	10.6

All reinforcements used in this study consisted of epoxy-impregnated, embroidered carbon fibre rovings manufactured using tailored fiber placement (TFP) technology, with a fineness of 6400 tex. The reinforcement was configured as a two-dimensional grid with a mesh size of 27 mm in both principal directions. For this study, only the longitudinal (L) rovings were examined. Relevant mechanical properties were obtained from uniaxial tensile tests on individual rovings, conducted according to the German guideline [7], from which the stress–strain response and Young's modulus were determined. The results are given in Table 2.

Table 2 Mechanical Properties of the textile reinforcement

Reinforcement	Breaking stress $f_{f,nm,u}$ [MPa]	Breaking strain $\varepsilon_{f,nm,u}$ [mm/m]	Young's modulus $E_{f,nm}$ [GPa]
2D-6400-L	3502	14.01	252

2.2 Specimen dimensions

The specimens followed designs in accordance with the German DAfStb Guideline on design and construction with non-metallic reinforcement [7]. Three different geometries were investigated to compare different approaches for defining the embedded length (see Fig. 1).

- **Geometry A** featured recesses in the concrete to define the bonded area, enabling observation of splitting failure. The recesses were formed using pre-prepared cubes of non-absorbent hard foam, and the intended crack joint was achieved by manually weakening the cross-section with a spatula. The corresponding longitudinal roving was cut in advance to determine the embedment length, following the approach of [12]. Within the bonded zone, only a single longitudinal roving remains active, effectively preventing lateral stress transfer to adjacent rovings and thus representing the intended reinforcement ratio without artificial contributions from neighbouring rovings. The geometry is shown in Fig. 1a.
- **Geometry B** corresponds largely to [8] and is the most common method for determining the bond behaviour between concrete and textile reinforcement. The anchoring length in the upper part of the test specimen is defined by saw cuts on both sides below the clamp, severing the rovings to be tested. Two variants were investigated: Lorenz's setup [8] was used as a reference to separate bonded and unbonded areas (B.1), whilst a novel approach introduced by the authors employed T-shaped separating elements placed in the formwork (B.2). In B.2, the leg of each insert is arranged parallel to the longitudinal rovings along the embedment length, ranging to the center distance between middle and outer longitudinal yarn from each side, forming a predefined separation between front and back face of the specimen to reduce overly large splitting resistance. Details of the inserts are shown in Fig. 4b and 4c.

  In both variants, the full concrete cross-section remains intact within the embedment zone, permitting a degree of lateral force transfer from the central roving to the adjacent rovings over the bonded length.
- **Geometry C** consists of a single roving embedded in a concrete block, with a sleeve cast into the specimen to define the embedment length and confine stress transfer to the bonded zone. The sleeve type and embedment length were varied to study their influence on bond behaviour and failure mechanisms. To introduce the tensile force into the reinforcement, a concentric block of epoxy resin was cast onto the free end of the roving, which was subsequently installed in the testing machine.

Unlike configurations A and B, the concrete block in configuration C is subjected to compressive stresses during testing, as the specimen's end face bears directly against the steel loading plate. This produces a different stress state within the bonded zone compared to the single sided pull-out configurations, a distinction that warrants careful consideration when comparing bond stresses across all three configurations.

Across all configurations, the embedded length was the key parameter used to calculate the average bond stress. A uniform specimen thickness of 20 mm was used, providing approximately 10 mm of concrete cover on each side. Specimens were produced by a conventional casting method, with the formwork filled vertically from the side.

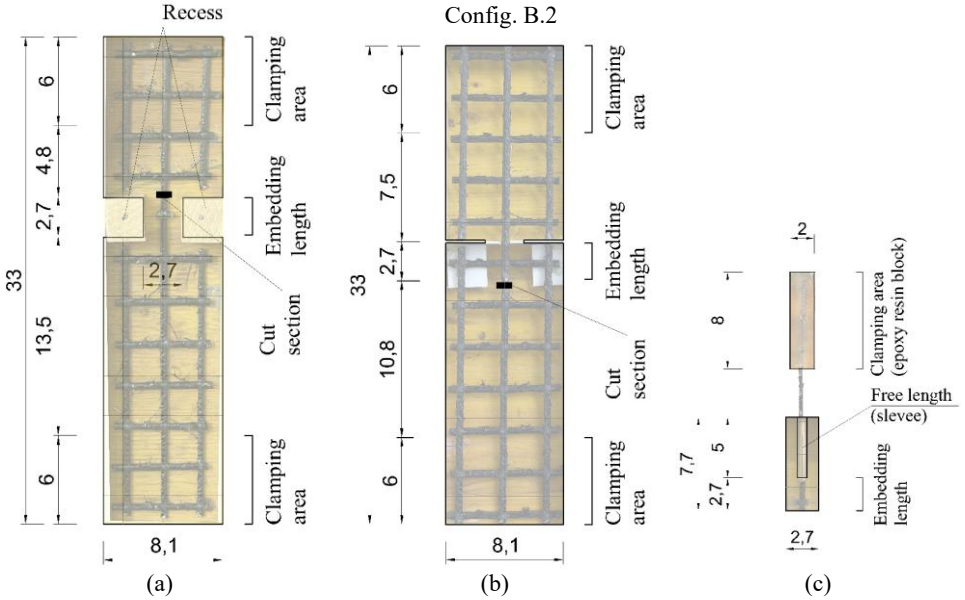


Fig. 1 Configuration A showing a recess defining the composite area (a), configuration B with a cut or inlay to separate bonded and unbonded zones (b), and configuration C with a single roving and optional sleeve embedded in the concrete block (c). Dimensions are given in Centimetres.

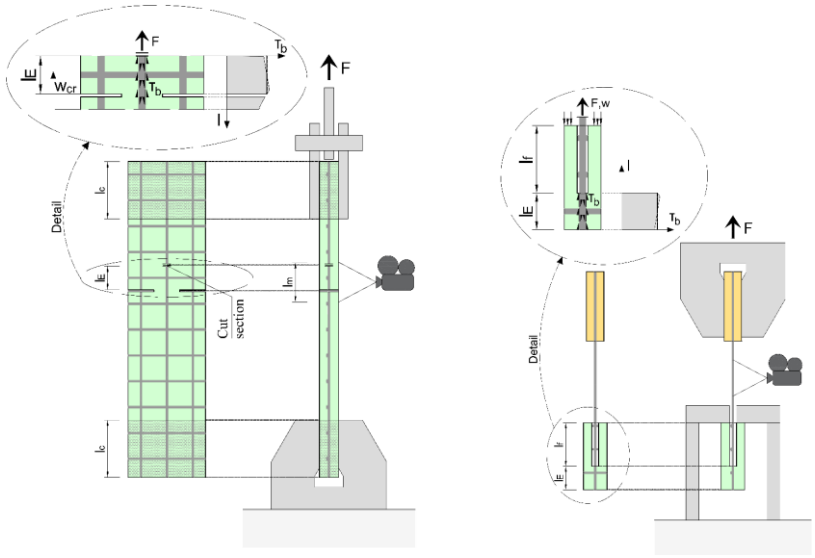
2.3 Test setup

For configurations A and B, the asymmetric single sided pull-out configuration (SSPO) was used in accordance with the DAfStb guideline [7] and the method proposed by Lorenz et al. [8]. In general, the measurement method involves measuring the machine force (F_{red}) and the displacement (Δl). For the experiments performed, crack opening (Δl) was monitored using a three-dimensional digital image correlation (DIC) system. Crack opening was obtained by averaging displacements measured with optical extensometers on the specimen's front and rear faces, accounting for local eccentricities and inclined crack formation. A schematic of the test setup is shown in Fig. 2a.

Configuration C was tested using a single-strand pull-out setup based on the RILEM [13] recommendation. In this configuration, the load was introduced without any mechanical gripping of the reinforcement. Instead, the specimen's end face was placed directly against a steel loading plate. For measurement, a 2D-DIC system was used for this setup. The machine load (F_{red}) and the displacement of the pulled roving (Δl) were recorded, capturing the slip response without measuring strain in the textile. A simplified diagram of the experimental setup is shown in Fig. 2b.

All specimens were tested under identical boundary conditions to ensure comparability. Machine load and roving displacement were recorded continuously. The corresponding frequency was 5 Hz.

After each test, the embedded length (l_E) of the roving was measured on the fractured specimen. Based on this measured embedment length, the average shear flow acting along the bonded length was determined from the recorded machine load.



(a) (b)

Fig. 2 Schematic test setup for asymmetric pull-out testing for configuration B (analogous to A) (a), and the test setup for configuration C (b) in reference to [10].

The whole investigation is divided into eight test series. They differ in terms of sample configuration, installation length and the type of separation or sleeve used to control the stress transfer zone. Specifically, configurations A, B.1 and B.2 were tested with a constant installation length of 27 mm and three alternative separation methods (recess, saw cut and insert), which allowed a direct comparison of their influence on the composite behaviour.

Configuration C included five variants with different sleeve materials and two embedding lengths (27 mm and 81 mm), allowing the effects of the enclosure and the bonded length on the pull-out behaviour to be systematically evaluated. The series are summarised in Table 3.

Table 3 Summary of the test configurations and the planned embedment length

Series	Configuration	Number of specimens	Separation / Sleeve type	Embedment length [mm]
A-27-REC	A	10	Recess	27
B-27-CUT	B.1	10	Saw cut	27
B-27-INL	B.2	10	Inlay	27
C-27-BRS	C	5	Brass sleeve	27
C-81-BRS	C	5	Brass sleeve	81
C-27-PVC	C	5	PVC sleeve	27
C-27-SHT	C	5	Shrink tube	27
C-27-NON	C	5	None	27

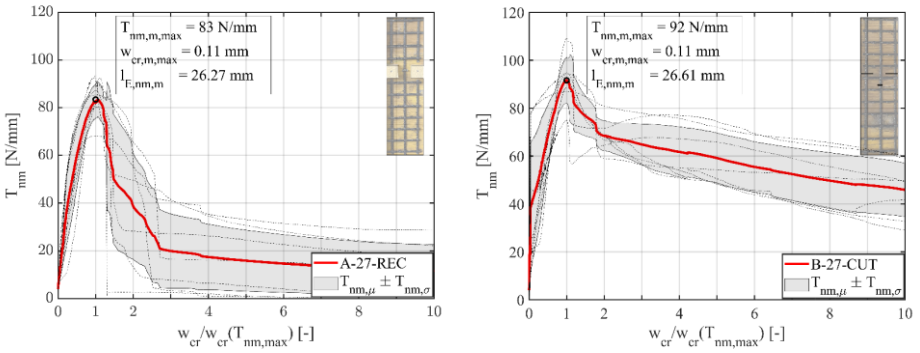
3 RESULTS

In the present study, the shear flow T_{nm} along the embedment length was determined according to the following equation:

$$T_{nm} = \frac{F_{red}}{l_E} \quad (1)$$

For the configurations A and B, the pull-out response is represented by a bond-flow and crack width relationship because the deformation response is governed by the crack opening in the notched region. For configuration C, the shear flow T_{nm} is calculated in the same manner (see equation (1)), but the corresponding relationship is expressed with the slip of the pulled roving.

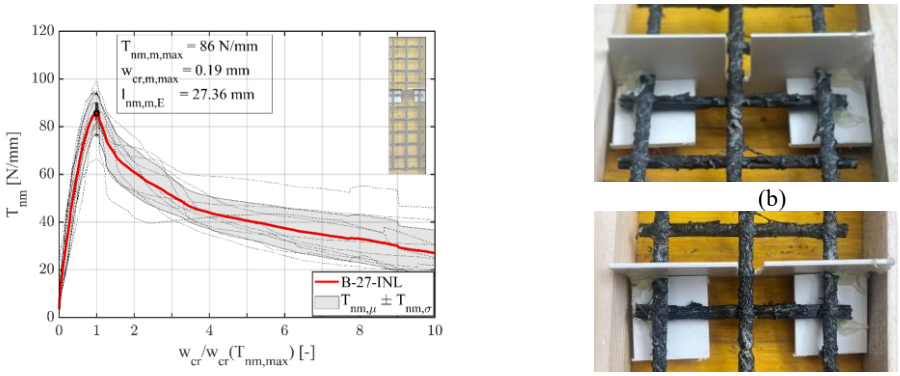
To enable a consistent comparison across specimens for configurations A and B, the shear flow is presented as a function of the normalised crack width. The measured crack opening was divided by the crack width at maximum shear flow. This procedure yields a maximum value of x=1 for each specimen and allows a statistical evaluation across the examined series. The results for the configurations with geometries A and B.1 are shown in Fig. 3a and Fig. 3b:



(a) (b)

Fig. 3 Shear flow – crack width curve for the specimens with configuration A (a) and configuration B.1 with cut-ins to determine the notched area (b)

For specimens of configuration A (series A-27-REC), the average maximum shear flow reached 83 N/mm, accompanied by a mean maximum crack width of 0.11 mm. The corresponding mean embedment length for this series was 26.27 mm. Fig. 3b presents the averaged results for configuration B.1 specimens where the notch was cut (series B-27-CUT). These specimens exhibited a peak shear flow of 92 N/mm with a mean maximum crack width of 0.11 mm, and the mean embedment length was 26.61 mm.



(a) (b) (c)

Fig. 4 Shear flow – crack width curve for the Series B-27-INL (a) and the used inlay part perspective view (b) and top view (c)

For configuration B.2 with the inlays (series B-27-INL), the maximum average shear flow was 86 N/mm, with a maximum crack width of 0.19 mm. The mean embedment length was 27.36 mm. The resulting shear flow – crack width relationship is shown in Fig. 4a.

For all five test series of configuration C, shear flow and embedment length were post-processed from the measured data and presented as boxplots with individual measurements in Fig. 5.

Configuration C generally exhibited higher bond stresses than configurations A and B, as summarised in Fig. 5. The highest mean shear flow was observed for C-27-BRS at 128 N/mm, whilst C-27-NON showed the lowest performance at 69 N/mm. Increasing the embedment length in C-81-BRS reduced the apparent shear flow, consistent with expected redistribution along longer anchorage zones.

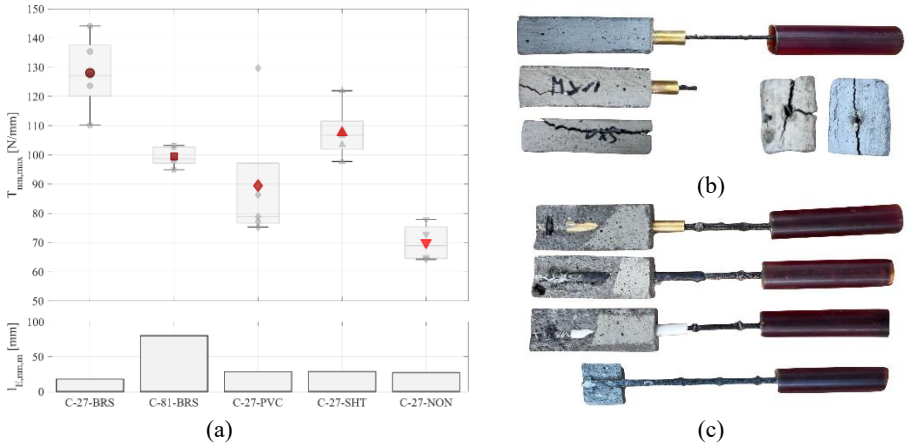


Fig. 5 Boxplot of maximum shear flow for all series with configuration C. The corresponding mean embedment lengths are shown below, allowing direct comparison between bonded length and measured shear flow (a). Typical failure pattern of specimens with configuration C. After reaching maximum bond stress, longitudinal splitting cracks developed along the embedment zone, resulting in complete bond loss (b). The crack pattern and surface detachment vary with the applied sleeve type, as shown by representative specimens (c).

4 DISCUSSION

The comparative evaluation of the eight test series revealed distinct differences in bond behaviour and failure mechanisms across the investigated configurations. Configuration A exhibited the most brittle failure behaviour of all SSPO test setups shown in Fig. 2a. Before triggering failure due to pull-out of the textile reinforcement, tensile failure of the concrete occurred, accompanied by diagonal shear cracks in the narrowed area near the recesses. Both mechanisms led to an abrupt drop in load after the peak value, with a very limited residual load-bearing capacity. The increased scatter observed in this series is attributed to the sensitivity of the recess geometry to manual preparation, as slight variations in the spatula-induced crack joint directly influence the failure initiation and the subsequent load-bearing response.

Configuration B.1 showed a more ductile failure behaviour, with noticeable differences between the two methods used to create the notched region. In specimens with lateral saw cuts (series B-27-CUT), cracking initiated at the cut section and propagated through the concrete cover, followed by delamination and spalling of the cover within the embedment zone of the central roving. Due to the saw cuts, the two outer rovings are stress-free within the notched region, as the cut prevents force transfer to the surrounding concrete. The concrete cross-section, however, is unchanged. Hence, the concrete attributed to the outer rovings still resists splitting forces, artificially increasing splitting resistance. Consequently, splitting behaviour in saw-cut specimens may not represent realistic structural conditions, since the reinforcement ratio affects the initiation and propagation of splitting cracks. As shown in [14], lower reinforcement ratios tend to promote splitting due to larger crack spacing and higher local bond stresses, independent of the reinforcement surface properties.

The T-shaped inlay parts introduced in this paper for configuration B.2 (B-27-INL series) were designed for decoupling the lateral rovings and ensuring the effective concrete cross-section matches the intended reinforcement area. For specimens with inlays, the shear flow–crack width response (Fig. 4a) shows predominantly splitting-type failure along the insert plane. This configuration produced reproducible results and avoided the artificial stiffening seen in saw-cut specimens. Post-peak behaviour was abrupt but is considered to be more consistent with realistic boundary conditions, as the reinforcement ratio and concrete contribution remained as intended. Both inlay variants exhibited a narrower scatter band compared to the saw-cut specimens, indicating more reproducible post-peak behaviour under the given test conditions.



(a) (b) (c)

Fig. 6 Overview of the three characteristic failure modes observed. (a) Configuration A: tensile cracking and diagonal shear in the notched region, causing an abrupt post-peak load drop (Fig. 3a). (b) Configuration B.1 with saw cuts: crack initiation at the node followed by delamination and spalling of the concrete cover, leading to a more gradual post-peak decline (Fig. 3b). (c) Configuration B.2 with inlay components: defined splitting along the inlay plane, resulting in a controlled and realistic bond failure mode (Fig. 4a).

In configuration C, the type of sleeve influenced force transfer and failure behaviour. Embedded sleeves ensured a more evenly distributed load along the bonded length, resulting in comparatively high shear flows for short embedment lengths (C-27-BRS), whilst increasing the bonded length (C-81-BRS) reduced the apparent shear flow. Specimens without a sleeve (C-27-NON) exhibited the lowest bond strength and irregular cracking, whilst the heat-shrink sleeve (C-27-SHT) improved mechanical interlocking through surface irregularities, leading to increased bond stresses. The comparatively higher bond stresses observed in configuration C are partly attributable to the different stress distributions within the concrete block, which were caused by the support conditions during the test. Further factors and the influence of lateral specimen deformation cannot be fully deduced from the current data set and require further investigation.

Taken together, the results highlight that the choice of test configuration has a considerable influence on both the measured bond response and the associated failure mechanisms. The three configurations differ not only in specimen geometry but also in the mechanical boundary conditions governing stress transfer within the bonded zone. In configuration A, the recesses ensure that only a single longitudinal roving is active over the embedment length, isolating the bond response without lateral interaction between neighbouring rovings. However, this approach is inherently limited to lower force levels, as the absence of continuous reinforcement at the upper boundary of the recess, where the central roving is severed, means that global tensile forces exceeding the local concrete tensile capacity will produce invalid failure in this region rather than the intended bond failure. In configurations B.1 and B.2, bond behaviour is assessed within the textile grid rather than on an isolated roving, which represents a more robust test condition. The full concrete cross-section remains intact within the embedment zone, permitting a degree of lateral force transfer from the central roving to the adjacent rovings, effectively creating a lap-like stress transfer condition. Configuration B.2 with the inlay element additionally reduces splitting resistance and the tensile contribution of the surrounding concrete, making it the most realistic representation of in-situ conditions among the configurations studied. In configuration C, the concrete block is subjected to compressive stresses during testing, resulting in a different stress state compared to configurations A and B.

5 CONCLUSIONS

The comparative evaluation of the eight test series revealed differences in bond behaviour and failure mechanisms between the investigated configurations. The failure modes for configurations A, B.1 and B.2 are shown in Fig. 6. Although all three configurations are permitted under the DAfStb guideline [7], the results indicate that the underlying boundary conditions and stress states differ between test setups. Configuration A exhibited high sensitivity to the test setup, resulting in an abrupt post-peak response and increased scatter. The inlay-based configuration B.2 showed promising performance by avoiding artificial confinement effects and enabling reproducible splitting failure, though further testing is required to fully characterise its behaviour relative to saw-cut specimens. Configuration C tended to

reach higher bond stresses, but it remains unclear whether this is due to the test configuration, sleeve–matrix interaction, or inherent load-transfer mechanisms. Further investigations under controlled and harmonised conditions are needed to assess the influence of stress fields, confinement, and measurement methods, improving the comparability of SSPO and yarn pull-out (YPO) results and clarifying how the test setup affects bond behaviour in TRC.

Acknowledgements

The authors gratefully acknowledge the support of the Austrian Society for Construction Technology (ÖBV) and the Austrian Research Promotion Agency (FFG) for funding the research project "SusDeCon – Sustainable Design and Construction with non-metallic reinforcement".

References

[1] Wietek, Bernhard. 2024. „Bedeutung für die Umwelt." In *Beton – Stahlbeton – Faserbeton: Eigenschaften und Unterschiede*, 33–34. Springer Fachmedien Wiesbaden. doi:10.1007/978-3-658-44752-6_8.

[2] Schießl-Pecka, Angelika, Rausch, Anne, Zintel, Marc, and Linden, Christian. 2019. „Lebenszykluskostenbetrachtungen für chloridexponierte Bauteile von Brücken- und Tunnelbauwerken." *Beton- und Stahlbetonbau* 114:767–75. doi:10.1002/best.201900038.

[3] Konzilia, Julian, Wachter, Jonas, Egger, Matthias, Waltl, Christoph, Fröis, Thomas, Bechtold, Thomas, and Feix, Jürgen. 2023. "Embroidered Carbon Reinforcement for Concrete." *Buildings* 13:2293. doi:10.3390/buildings13092293.

[4] Hansl, Mario, and Feix, Jürgen. 2015. „Untersuchung der Rissbreiten in textilbewehrten Betonen." *Beton- und Stahlbetonbau* 110 (6):410–18. doi:10.1002/best.201400122.

[5] Hollaway, Leonhard C. 2010. "A Review of the Present and Future Utilisation of FRP Composites in the Civil Infrastructure with Reference to Their Important In-Service Properties." *Construction and Building Materials* 24 (12):2419–45. doi:10.1016/j.conbuildmat.2010.04.062.

[6] Feix, Jürgen, Konzilia, Julian, Waltl, Christoph, Egger, Matthias, and Plattner, Norbert. 2023. „Textilbetonverstärkung für ein typisches Brückenbauwerk aus den 1980er-Jahren." *Bauingenieur* 98:207–16. doi:10.37544/0005-6650-2023-07-08-29.

[7] DAfStb. 2024. *Concrete Components with Non-Metallic Reinforcement*. Heft 660. Berlin: Deutscher Ausschuss für Stahlbeton.

[8] Lorenz, Enrico, Schütze, Elisabeth, Schladitz, Frank, and Curbach, Manfred. 2013. „Textilbeton – Grundlegende Untersuchungen im Überblick." *Beton- und Stahlbetonbau* 108 (10):711–22. doi:10.1002/best.201300041.

[9] Reichenbach, Sara, Preinstorfer, Philipp, Hammerl, Mathias, and Kromoser, Benjamin. 2021. "A Review on Embedded Fibre-Reinforced Polymer Reinforcement in Structural Concrete in Europe." *Construction and Building Materials* 307:124946. doi:10.1016/j.conbuildmat.2021.124946.

[10] Preinstorfer, Philipp, El Kadi, Michael, Dittel, Gözdem, Ghiassi, Bahman, Müller, Steffen, Mansur de Castro Silva, Rebecca, Mobasher, Barzin, de Andrade Silva, Flavio, and Peled, Alva. 2024. "RILEM TC 292-MCC: Bond Behaviour of Textile-Reinforced Concrete—A Review." *Materials and Structures* 57 (4):97. doi:10.1617/s11527-024-02339-5.

[11] Konzilia, Julian, Egger, Matthias, and Feix, Jürgen. 2022. "Experimental Investigation on Salt Frost Scaling of Textile-Reinforced Concrete." *Structural Concrete* 23 (2):954–69. doi:10.1002/suco.202100481.

[12] Preinstorfer, Philipp, Kromoser, Benjamin, and Kollegger, Johann. 2018. „Einflussparameter auf die Spaltrissbildung in Textilbeton." *Beton- und Stahlbetonbau* 113 (12):877–85. doi:10.1002/best.201800071.

[13] RILEM TC. 1994. "RC 6: Bond Test for Reinforcement Steel. 2. Pull-out Test." In *RILEM Recommendations for the Testing and Use of Constructions Materials*, 218–20. London: E & FN Spon. doi:10.1617/2351580117.081.

[14] Preinstorfer, Philipp, Yanik, Serdar, Kirnbauer, Johannes, Lees, Janet M., and Robisson, Agathe. 2023. "Cracking Behaviour of Textile-Reinforced Concrete with Varying Concrete Cover and Textile Surface Finish." *Composite Structures* 312:116859. doi:10.1016/j.compstruct.2023.116859.

Experimental Investigation of the Shear Capacity of Reinforced Concrete Beams with Bent-up Bars

Esra Jespersen[1,2], Henrik Brøner Jørgensen[1] and Frederik Autrup[2]

[1]SDU Structures, Civil and Architectural Engineering, Department of Technology and Innovation, University of Southern Denmark, Denmark

[2]Department of Monitoring and Analyses of Existing Structures, Rambøll Denmark A/S, Denmark

Summary

Many existing concrete bridges are reinforced with bent-up bars. When the structural capacity of these bridges is assessed according to current design standards, it is often the shear capacity that is critical. However, limited research has been carried out on the shear behaviour of reinforced concrete beams with bent-up bars. Therefore, this paper presents an experimental programme consisting of 30 shear tests of beams with bent-up bars. The programme varies different important design parameters, such as the yield strength, the diameter, the longitudinal spacing, the surface type and the angle of the bent-up bars, as well as the concrete compressive strength. The shear behaviour and the crack development are measured during testing by applying Digital Image Correlation (DIC). The test results show that an increase in the yield strength, the diameter, and the angle of the bent-up bars, results in an increase in the shear capacity.

1 INTRODUCTION

Many existing concrete bridges are reinforced with bent-up bars. When the structural capacity of these bridges is assessed according to current design standards, it is often the shear capacity that is critical when determining whether the bridge should be kept in service, strengthened or demolished and rebuilt. However, limited experimental research has been carried out in the recent years on the shear behaviour of reinforced concrete beams with bent-up bars. In [1] shear tests were performed on beams with both plain and ribbed bent-up bars of varying diameter, in [2] the position of the bends and the point of the load were varied and in [3] full scale bridge slabs were tested. In [4] beams with shallow angled bent-up bars between 20° and 25° were tested. In an attempt to fill the gap in the literature, an experimental programme consisting of 30 shear tests of beams with and without bent-up bars is designed and conducted. The design of the experimental programme is based on the design of existing concrete bridges constructed with bent-up bars. When determining the shear capacity of these types of bridges, they must comply with a set of detailing requirements according to the current design standards Eurocode 2 [5] and *fib* Model Code 2020 [6] to be classified as shear reinforced. If the bridges do not comply with the requirements, their shear capacity must be calculated as if they were non-shear reinforced. This sometimes leads to a shear capacity that is too low for the bridges to be kept in service. To investigate whether the detailing requirements are too conservative, the experimental program contains beams that are both compliant and non-compliant with the detailing requirements. The detailing requirements are; the minimum shear reinforcement ratio, $\rho_{\mathrm{b,min}}$, the minimum angle of the bent-up bar, $\alpha_{\mathrm{b,min}}$, and the maximum spacing between the bent-up bars, $s_{\mathrm{b,max}}$.

Table 1 The detailing requirements defined by Eurocode 2 and *fib* Model Code 2020.

	$\rho_{\mathrm{b,min}}$	$\alpha_{\mathrm{b,min}}$	$s_{\mathrm{b,max}}$
Eurocode 2	$0.08\frac{\sqrt{f_c}}{f_{yw}}$	45°	$0.6\,d\,(1+\cot(\alpha_b))$
fib Model Code 2020		30°	$\min(0.75\,d, 500\,mm)$

Notation: d is the effective height of the beam and α_b is the angle of the bent-up bar.

2 EXPERIMENTAL PROGRAMME

The experimental programme consists of 15 reinforced concrete beams, designed to investigate the shear behaviour of beams with bent-up bars. Fig. 1 shows the dimensions of the beams, which are designed to allow two shear tests to be performed on each beam, resulting in 30 shear tests in total. The beams are divided into three equally sized shear zones; A, B and a middle shear zone. The shear span is 1500 mm in all tests with an a/d ratio of 3.4. The end-zones of the beams are 600-900 mm long and are designed to ensure full anchorage of the bent-up bars. This includes bending the ends of the plain bars, to ensure anchorage. The middle shear zone is reinforced with conventional shear reinforcement to avoid shear failure outside zone A and B. Three Φ32 Y950 reinforcement bars are used as longitudinal reinforcement to avoid flexural failure. Most of the beams have the same design of the bent-up bars as shown on Fig. 1. The reinforcement design of the beams with a different number of bent-up bars or bent-up bars with a different angle is shown in Fig. 2. The beams were tested 34-71 days after casting. Table 2 shows an overview of the conducted tests and shows that the varied design parameters in the experimental programme are; the yield stress of the bent-up bars, the diameter and surface type of the bent-up bars, the concrete compressive strength, the longitudinal spacing between bent-up bars and the angle of the bent-up bars.

2.1 Experimental setup and instrumentation

Fig. 1 shows the three-point bending experimental setup. To ensure free horizontal movement, the beams were placed on two 6 mm teflon plates, and to ensure free rotation, a 20 mm steel plate on top of a piece of round steel was placed between the teflon plates and a steel support. The load was applied by a displacement-controlled hydraulic actuator with a displacement rate of 0.5 mm per minute until the critical shear crack had formed, after which the rate was set to be 2 mm per minute. The load was measured by an external load cell placed between the actuator and the beams and the displacement at the middle of the beams was measured using a Linear Variable Differential Transformer (LVDT). Digital Image Correlation (DIC) was applied to the front and back surfaces of the beams, to measure the displacement and crack formation in the testzone. To enable this, the surfaces were painted with a randomised speckle pattern. One surface was photographed using two 12MP cameras at a rate of 1 Hz, and both surfaces were photographed using a DSLR camera at a rate of 2 Hz. For the shear tests B.25.275.53.2 and B.25.275.53.3, the strains along the bent-up bars were measured using fibre optical sensors. To protect the sensors, two 2 mm x 2 mm grooves were cut into the bar, and the sensors were glued in place in the grooves. The results of the fibre optical measurements will not be reported on in this paper.

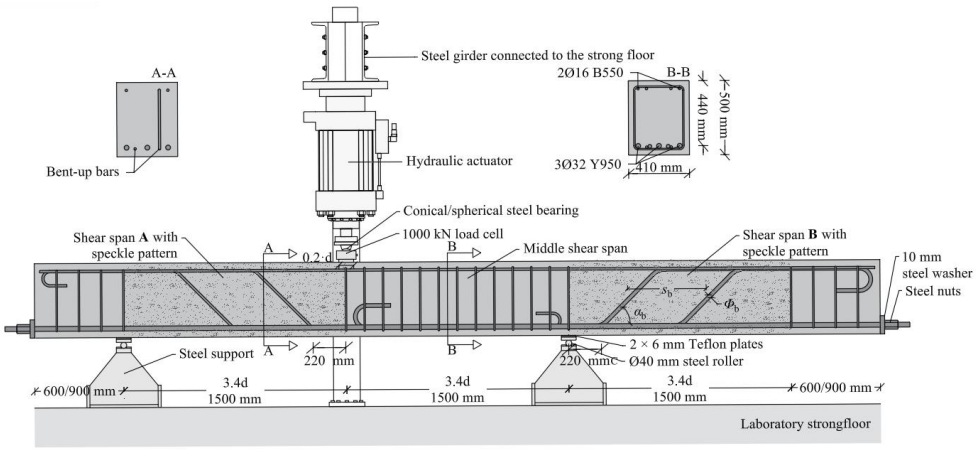


Fig. 1 Experimental setup showing the geometry and the reinforcement of a beam. Φ_b is the diameter of the bent-up bar, α_b is the angle of the bent-up bar, and s_b is the longitudinal spacing between bent-up bars.

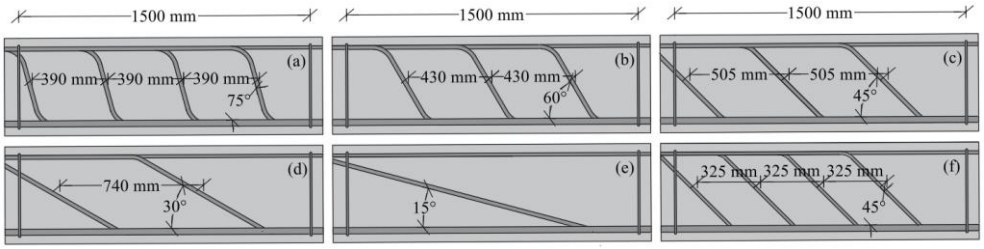


Fig. 2 Reinforcement design for the beams **(a)** B.20.275.39.a4, **(b)** B.20.275.43.a3, **(c)** B.20.275.51, **(d)** B.20.275.39.a2, **(e)** B.20.275.150.a1 and **(f)** B.16.275.33.

2.2 Material properties

For every beam, six cylinders measuring 100x200 mm were cast using concrete from the same batch as the beam. The cylinders were stored together with the beams and were tested on the same day as the shear tests were performed. Three cylinders were tested for each shear test. The average of the six measured concrete compressive strengths for each beam was converted to a standard Ø150x300 mm cylinder by a factor of 0.97, according to [7 p.8].

Three concrete mixtures are used in the programme, P20, P30 and P40, with a target compressive strength of 20 MPa, 30 MPa and 40 MPa and a water-cement ratio of 0.85, 0.85 and 0.50, respectively. All mixtures have a maximum aggregate size of 16 mm. The concrete compressive strength corresponding to each test is found in Table 2.

The type of reinforcement used as bent-up bars vary in the experimental design and includes two types of plain reinforcement, S275JR+AR (S275) and S355JR+AR steel (S355) and one type of ribbed reinforcement B550C (B550). The material properties of the bent-up bars and the longitudinal reinforcement were determined by performing tensile tests on 600 mm bars of the reinforcement. The results of the tensile tests are shown in Table 1.

Table 1 Mechanical properties of the reinforcement.

Steel grade	S275				S355			B550			Y950
Φ_b [mm]	16	20	25	25*	16	20	25	16	20	25	32
f_y [MPa]	338	335	314	306	406	403	400	579	571	596	996
f_u [MPa]	462	446	436	421	555	530	542	671	666	698	1112
E_k [GPa]	202	225	219	205	225	213	220	198	221	195	213
ε_{s0} [%]	19.8	20.6	20.4	18.8	16.5	16.3	16.8	9.4	10.3	8.8	6.5
ε_{su} [%]	29.7	30.6	26.1	22.3	23.5	26.4	22.6	12.6	15.0	12.9	7.7

Notations: f_y and f_u are the yield stress and tensile strength of the reinforcement, E_s is the modulus of elasticity and ε_{s0} and $\varepsilon_{su}$are the strains corresponding to the maximum stress and rupture, respectively.
*Mechanical parameters of the plain bars that were cut with a groove to lay fibre optical sensors.

3 EXPERIMENTAL RESULTS

In the following, the results of the shear tests will be presented. Table 2 presents the experimental results alongside the measured values of the geometry and the parameters of the test series.

Table 2 Overview of the parameters and test results of the shear tests.

ID	Steel grade	Φ_b [mm]	s_b [mm]	f_c [MPa]	α_b [°]	ρ_b [%]	ρ_l [%]	$V_{u,exp}$ [kN]
B.00.000.00.c1	-	-	-	28.6	-	0.00	1.18	206
B.00.000.00	-	-	-	40.1	-	0.00	1.18	208
B.00.000.00.c2	-	-	-	53.9	-	0.00	1.18	305
B.16.275.33	275	16	325	40.1	45	0.21	1.57	301
B.16.275.53	275	16	530	28.9	45	0.13	1.37	226
B.16.275.79	275	16	790	37.6	45	0.09	1.37	214
B.20.275.51	275	20	505	37.6	45	0.21	1.64	275
B.20.275.53.1	275	20	530	38.8	45	0.20	1.48	294
B.20.275.53.2	275	20	530	36.3	45	0.20	1.48	249
B.20.275.62	275	20	615	40.6	45	0.18	1.48	269
B.20.275.71	275	20	705	40.6	45	0.15	1.48	256
B.20.275.79	275	20	790	38.3	45	0.14	1.48	251
B.25.275.53.1	275	25	530	28.9	45	0.32	1.66	305
B.25.275.53.2	275	25	530	38.8	45	0.32	1.66	291
B.25.275.53.3	275	25	530	39.8	45	0.32	1.66	317
B.25.275.79.1	275	25	790	37.6	45	0.21	1.66	258
B.25.275.79.2	275	25	790	36.3	45	0.21	1.66	248
B.16.355.53	355	16	530	39.8	45	0.13	1.37	249
B.20.355.53	355	20	530	26.8	45	0.20	1.48	272
B.25.355.53	355	25	530	26.8	45	0.32	1.66	299
B.16.550.53	550	16	530	33.5	45	0.13	1.37	246
B.20.550.53	550	20	530	32.2	45	0.20	1.48	314
B.25.550.53.1	550	25	530	32.2	45	0.32	1.66	395
B.25.550.53.2	550	25	530	33.5	45	0.32	1.66	377
B.20.275.150.a1	275	20	1500	39.8	15	0.20	1.33	200
B.20.275.75.a2	275	20	750	39.8	30	0.20	1.48	256
B.20.275.43.a3	275	20	430	37.6	60	0.21	1.64	302
B.20.275.39.a4	275	20	385	38.3	75	0.21	1.79	316
B.25.275.53.c1	275	25	530	28.6	45	0.32	1.66	271
B.25.275.53.c2	275	25	530	53.9	45	0.32	1.66	319

Notations: Φ_b is the rebar diameter of the bent-up bars, s_b is the longitudinal spacing between the bent-up bars, f_c is the tested concrete compressive strength, converted to a Ø150x300 mm standard cylinder according to [7 p.8], α_b is the angle of the bent-up bar, ρ_b is the shear reinforcement ratio for the bent-up bars, ρ_l is the longitudinal reinforcement ratio found at the section at the point load and $V_{u,exp}$ is the tested shear capacity.

3.1 Load-displacement curves

Load-displacement curves for selected shear tests are shown in Fig. 3 and Fig. 4. Fig. 3 shows the load-displacement curves for the shear tests of beams with different diameter and yield stress of the bent-up bars. The load-displacement curves for the beams with plain reinforcement, shown in Fig. 3(a), all follow a similar pattern. The first peak corresponds to the opening of the critical shear crack, whereas the second peak corresponds to tensile failure in the bent-up bar activated by the shear crack. Fig. 3(c) shows the curves for the beams with ribbed reinforcement and shows that the curve for the beam with bent-up bars with diameters of 25 mm only has one peak. On the other hand, the other beams in Fig. 3(c) seem to have similar load-displacement curves as those with plain reinforcement, i.e. similar stiffness and peak displacement.

Fig. 4 shows the load-displacement curves for the shear tests of beams with varying concrete compressive strength. Both the curves for the shear reinforced and non-shear reinforced beams are shown. It can be seen that the curves are similar up until the shear capacity of the non-shear reinforced beams. Here, the curves for the non-shear reinforced beams peak and drop off around a displacement of 5-6 mm, while the curves for the shear reinforced beams continue to rise and exhibit the same behaviour as the curves shown in Fig. 3.

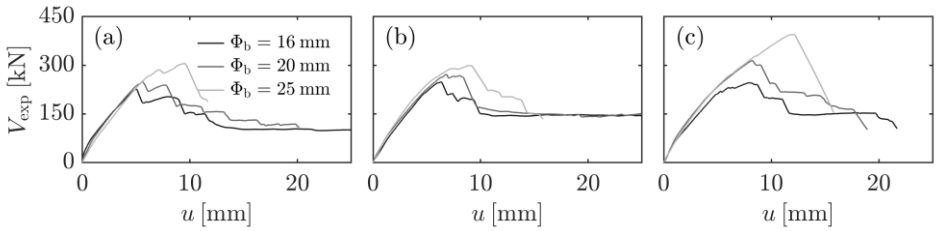


Fig. 3 Load-displacement curves for beams with varying diameter, Φ_b, of the bent-up bars, for: **(a)** S275 plain bars, **(b)** S355 plain bars and **(c)** B550 ribbed bars.

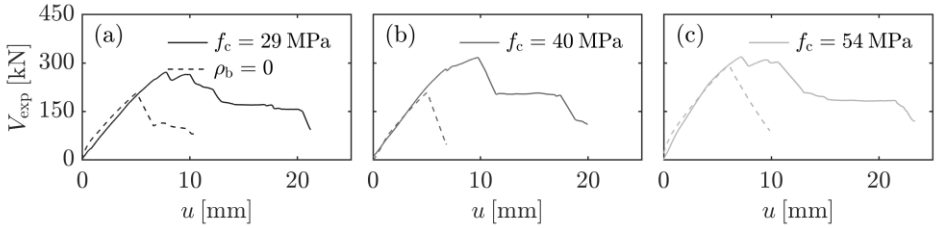


Fig. 4 Load-displacement curves for beams with varying concrete compressive strength, f_c, with and without bent-up bars, for beams cast with the concrete mixture **(a)** P20, **(b)** P30 and **(c)** P40.

3.2 Shear capacity compared to parameters

Fig. 5 shows the maximum tested shear capacities, $V_{u,exp}$, compared to the tested parameters of the beams. Fig. 5a shows that an increase in both the yield stress and the diameter of the bent-up bar results in an increase in the shear capacity. Similarly, Fig. 5b shows that an increase in the angle of the bent-up bar, results in an increase in the shear capacity. It is also shown that, even though the beam with bent-up bars with an angle of 30° does not comply with the minimum angle in Eurocode 2 [1], it still achieves a larger shear capacity than that of the beam with a 15° bent-up bar. The beam with a bent-up bar with an angle of 15° achieved a shear capacity comparable to that of the non-shear reinforced beam shown in Fig. 5c. Fig. 5c further shows that an increase in concrete compressive strength results in a slight increase in shear capacity. Comparing the non-shear reinforced beams to the shear reinforced beams, it can be seen that the non-shear reinforced beams with a concrete strengths of 29 MPa and 40 MPa have far lower capacities than the reinforced beams with the same concrete strength, whereas the non-shear reinforced beam with a concrete strength of 54 MPa achieves a capacity comparable to that of the reinforced beam. Fig. 5d shows shear capacities of the beams with a constant shear reinforcement

ratio but varying diameter and spacing of the bent-up bars. It can be seen that decreasing the diameter and spacing between the bars results in an increase in shear capacity. It should be noted that although the beams with 25 mm diameter bent-up bars and a spacing of 790 mm far exceed the maximum spacing requirement of both design standards, they still achieve a higher shear capacity than the beams without bent-up bars with the same parameters. The same trend can be seen in Fig. 5e. Here, it is shown that an increase in the spacing of the bent-up bars does not result in any significant decrease in shear capacity, even though most of the beams do not comply with the maximum spacing requirement of the design standards. Fig. 5f shows that an increase in the shear reinforcement ratio leads to an increase in the shear capacity, even when the beams do not comply with the minimum shear reinforcement ratio, which is calculated using the average of the material parameters of the beams shown in Fig. 5f. It is also shown that beams with a spacing of 790 mm achieve shear capacities similar to those of beams with a spacing of 530 mm when the shear reinforcement ratio is similar, despite exceeding the maximum spacing requirements of both design standards.

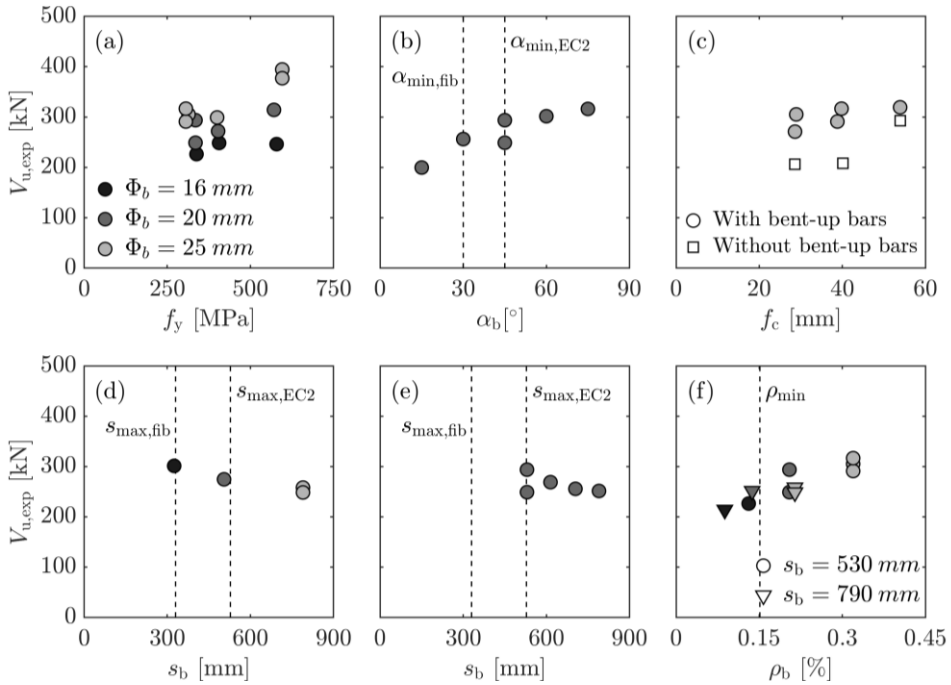


Fig. 5 Comparison of the experimental parameters on the y-axis and the test results with the **(a)** yield stress of the bent-up bars, f_y, **(b)** the angle of the bent-up bars, α_b, **(c)** the concrete compressive strength, f_c, **(d-e)** the longitudinal spacing of the bent-up bar, s_b, and **(f)** the shear reinforcement ratio, ρ_b on the x-axes.

3.3 Failure mechanism

Digital Image Correlation (DIC) was applied on the surface in shear zone A and B, to measure the displacement and strains during testing. Fig. 6 and Fig. 7 show major tensile strain plots placed on top of shear zone A or B. The strain plots are taken at the time where the critical shear crack just formed. Fig. 6 shows the shear tests with a varying spacing between the bent-up bars. For all four tests, the critical shear crack seems to cross one bent-up bar and cross the second one close to the bent part, even though the requirement of the maximum spacing is exceeded. For the tests where the spacing is 530 mm and 615 mm the critical shear crack is shown to cross the bent-up bar closest to the support. However, when the spacing increases to 705 mm and 790 mm, the critical shear crack crosses the bent-up bar closest to the applied load.

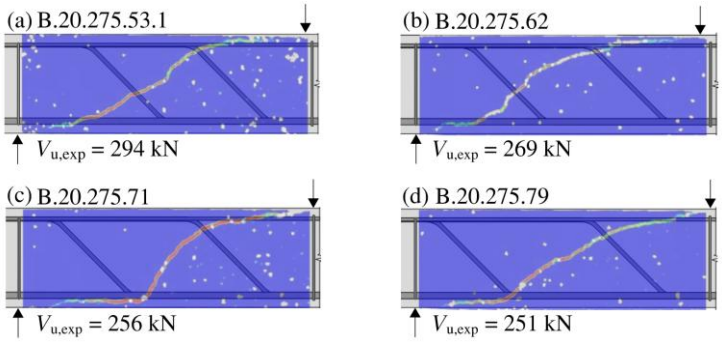


Fig. 6 Major strain plots on top of a sketches of beam **(a)** B.20.275.53.1 where s_b = 530 mm, **(b)** B.20.275.62.1 where s_b = 615 mm **(c)** B.20.275.71.1 where s_b = 705 mm and **(d)** B.20.275.79.1 where s_b = 790 mm.

Fig. 7 shows the strain plots for three shear tests where the diameter and spacing between the bent-up bars vary while the shear reinforcement ratio is kept at 0.21%. It is shown that the number of bars that the critical shear crack crosses increases as the diameter decreases. Table 3 gives an overview of the number of bent-up bars that are crossed by the shear crack, as well as the total area of the reinforcement that is assumed to be activated. The table also shows the tested shear capacities for the three beams. It is shown that the total area crossed by the shear crack is not proportional to the number of bars crossed nor the tested shear capacities, as beam B.20.275.51 has a higher total area than B.16.275.33, but a lower shear capacity.

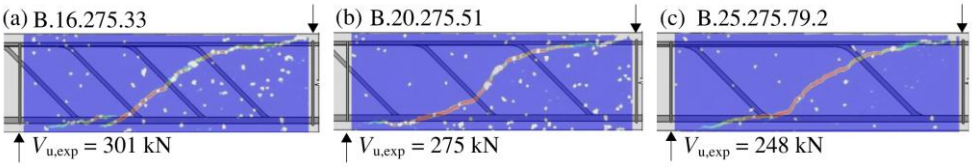


Fig. 7 Major strain plots on top of sketches of beam **(a)** B.16.275.33 where s_b = 325 mm and Φ_b = 16 mm, **(b)** B.20.275.51 where s_b = 505 mm and Φ_b = 20 mm, **(a)** B.25.275.79 where s_b = 790 mm and Φ_b = 25 mm.

Table 3 Overview of how many bent-up bars the shear crack seems to cross as well as the total area of the bent-up bars that is assumed to be activated, $A_{b,tot}$, and the tested shear capacity, $V_{u,exp}$.

		B.16.275.33	B.20.275.51	B.25.275.79.2
Crossed bars	[pcs.]	3	2	1
$A_{b,tot}$	[mm^2]	603	628	491
$V_{u,exp}$	[kN]	301	275	248

4 CONCLUSIONS

The paper presents a comprehensive experimental programme comprising 30 tests of the shear capacity of beams with and without bent-up bars. The experimental programme varied the yield strength, the cross-sectional diameter, the longitudinal spacing, the surface type and the angle of the bent-up bars, as well as the concrete compressive strength of the beams. The experimental programme was designed to investigate the shear capacity contribution of the bent-up bars, when the number of bent-up bars is low and close to the detailing requirements of Eurocode 2 and *fib* Model code 2020.

The experimental results show that increasing the diameter, yield stress, and angle of the bent-up bar increases the shear capacity. Furthermore, increasing the spacing between the bent-up bars results in a small decrease in the shear capacity. However, the tests show that even for beams where the requirements for the maximum spacing of the bent-up bars are exceeded, the shear capacity is observed to be larger than similar beams without bent-up bars.

The shear failure mechanism is studied on the basis of Digital Image Correlation and shows that the critical shear crack has a similar form in beams with different spacing and number of bent-up bars. It is also shown that the critical shear crack intersects and activates the bent-up bars in beams that do not comply with the detailing requirements, e.g. in beams with larger spacing between the bent-up bars than allowed by the standards.

Acknowledgements

The experimental work was conducted with the help of BSc. Stefán Torfi Torfason, BSc. Frederik Oldengaard Nielsen and BSc. Oliver Lund Henningsen. The project is financially supported by the Ramboll Foundation, Innovation Fund Denmark and the Danish Road Directorate. The authors gratefully acknowledge these contributions.

References

[1] Huber, Tobias. Franz Untermarzoner and Johann Kollegger. 2023. „Experimental investigation and mechanical modelling of shear failure in reinforced concrete members with plain and ribbed bent-up bars.“ *Engineering structures.* 283:1-15

[2] Huber, Tobias. et al. 2017 “Load carrying behaviour of beams with bent-up bars as shear reinforcement”. *IABSE Conference, Vancouver 2017: Engineering the Future - Report*. Vol 109:96-101.

[3] Huber, Tobias. et al. 2024. “Shear tests on full-scale bridge slabs with bent-up reinforcing bars.” *Engineering structures*. 308:1-16.

[4] Teo, Wee, and Gerald Müller. 2014. “Shear effectiveness of shallow-angle bent-up bars for reinforced concrete beams”. *Proceedings of the Institution of Civil Engineers. Structures and buildings.* 167(7):398–413.

[5] EN:1992-1-1. 2023. Eurocode 2: Design of concrete structures - Part 1-1: General rules - rules for buildings, bridges and civil engineering structures

[6] *fib* Model Code 2020. 2023. Fédération Internationale du Béton, fib Model Code for concrete structures 2020.

[7] Nielsen, Mogens Peter. 2005. *Beton 1-del 1: Materialer*, 2nd ed. Lyngby: Technical University of Denmark.

Effect of reinforcement configuration on shear capacity of aged reinforced autoclaved aerated concrete roof panels

Siavash Soleimani Amiri [1], Chris Ian Goodier [1], Karen Blay [1], Chris Gorse [1], Kevin Waters [2]

[1] School of Architecture, Building and Civil Engineering,
Loughborough University,
Epinal Way, Loughborough LE11 3TU, United Kingdom
[2] RAAC Consulting Solutions (RCS),
CM1 1DB, United Kingdom

Summary
Reinforced autoclaved aerated concrete (RAAC) roof panels were widely used in UK buildings in the 1960s and 1970s, and many are now past their service life, raising concerns over brittle shear failure. This study investigates how transverse reinforcement configuration affects the shear capacity of aged RAAC panels. Three closely matched panels, differing only in transverse reinforcement ratio, were tested under four-point bending. Increasing this ratio from 503 mm² to 1810 mm² raised the shear capacity from 5.4 kN to 7.5 kN and increased mid-span deflection at peak load by 46.7%. This improvement is attributed to enhanced confinement and restraint of the longitudinal bars, which increased their dowel action. The transverse reinforcement's contribution to this is also described and a conceptual model presented. The findings show reinforcement configuration strongly influences the residual shear performance of aged RAAC panels.

1 INTRODUCTION

Reinforced autoclaved aerated concrete (RAAC) was widely adopted as a structural material for roof, floor, and wall panels in UK public and commercial buildings from the 1950s onwards, owing to its lightweight nature, ease of installation, and cost-effectiveness [1]. Among the various types of RAAC elements, roof panels are of particular concern as they may pose a critical risk to occupant safety [2]. Despite having remained in service for several decades, a small number of sudden collapses without prior warning have been reported, intensifying concerns regarding the residual structural safety of these elements [3].

Between the potential failure modes for reinforced concrete structures, RAAC panels are inherently more susceptible to brittle shear failure. Unlike conventional concrete, RAAC lacks coarse aggregate. This means that aggregate interlock, one of the primary shear transfer mechanisms in normal-weight concrete, is either absent or negligible [4], [5]. Furthermore, material degradation over time, including carbonation, moisture ingress, and potential reinforcement corrosion, progressively reduces the residual load-carrying capacity of these panels [1].

RAAC roof panels typically contain longitudinal reinforcement arranged in two layers, near the top and bottom faces. The transverse bars are welded to the longitudinal bars perpendicularly and horizontally; however, no reinforcement is provided through the panel depth in a vertical direction (as is typical in deeper conventional reinforced concrete sections), and the transverse bars do not function as closed stirrups. In normal reinforced concrete members without stirrups, the recognised shear transfer mechanisms include residual tensile stress across cracks, shear carried by the uncracked compression zone, aggregate interlock, and dowel action of the longitudinal reinforcement [5]-[8]. In RAAC, however, the absence or minimal contribution of aggregate interlock suggests that the remaining mechanisms, particularly the uncracked concrete zone shear transfer and dowel action play a proportionally greater role in shear resistance.

At present, many asset owners across the UK keep ageing RAAC panels in service, yet limited understanding of the structural behaviour of these panels makes it difficult to manage them effectively over an extended period or to make informed decisions regarding the timing of replacement. The

variability in material properties and reinforcement layout across panels of similar specification adds further uncertainty to structural assessments, increasing concerns among building owners and engineers. One parameter that varies considerably between panels is the amount of transverse welded reinforcement per unit length, which may influence shear capacity indirectly by affecting load transfer, and crack development and distribution, although the bars do not act as conventional shear reinforcement.

This paper presents an experimental investigation on the influence of transverse reinforcement ratio on the shear capacity and the load–deflection behaviour of aged RAAC roof panels. 34 RAAC roof panels, more than 50 years old, were extracted from an office building in the United Kingdom. Based on geometric measurements and cover-meter mapping of the longitudinal and transverse reinforcement, three panels were selected for four-point bending tests [9]. The selected panels had comparable AAC compressive strength, panel depth, effective depth, longitudinal tensile reinforcement ratio, and shear span-to-effective depth ratio, *a/d*, but differed in transverse reinforcement ratio, allowing the effect of this parameter to be isolated and hence investigated.

2 EXPERIMENTAL METHODOLOGY

2.1 Specimen details and material properties

The geometric and reinforcement properties of the three selected panels are summarised in Table 1. All three panels had a cross-sectional depth of 100 mm and a width of 600 mm. RAAC-T1 denotes the panel with the lowest ratio of transverse reinforcement, RAAC-T2 represents the panel with medium ratio, and RAAC-T3 has the highest ratio. The effective depth was 80 mm for all specimens, and the consistent longitudinal tensile reinforcement ratio (ρ_s) was 0.31 %.

Table 1 Geometric and reinforcement properties of RAAC panels

Beam	Total length (mm)	Support length (mm)	Effective depth (mm)	Longitudinal tensile reinforcement ratio (%)	Transverse reinforcement ratio (mm^2)	a/d
RAAC-T1	2145	35	80	0.31	503 (low ratio)	6.6
RAAC-T2	2150	35	80	0.31	704 (medium ratio)	6.6
RAAC-T3	2145	35	80	0.31	1810 (high ratio)	6.6

The reinforcement layout of the bottom face of each panel is illustrated in Fig. 1. All three panels contained three 8 mm diameter longitudinal bars at the bottom (tension zone) and two 8 mm diameter longitudinal bars at the top (compression zone). The transverse reinforcement was also 8 mm. All bars were smooth (not ribbed) and had a thin cementitious coating, as is typical for RAAC panels. The key difference between the specimens lies in the spacing and number of transverse reinforcement bars. Fig. 1(a) shows the low reinforcement ratio (RAAC-T1), Fig. 1(b) the medium reinforcement ratio (RAAC-T2), and Fig. 1(c) the high reinforcement ratio (RAAC-T3).

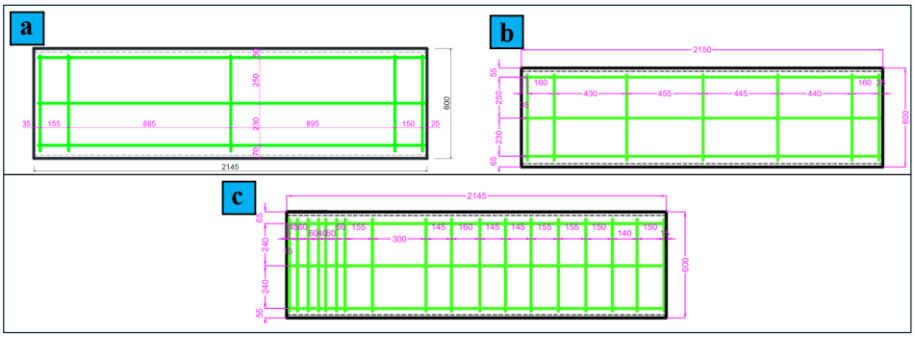


Fig. 1 Reinforcement configurations of the bottom face of the three panels: (a) RAAC-T1; (b) RAAC-T2; (c) RAAC-T3

After the bending tests, cores were extracted from each panel to determine the compressive strength of the AAC material. The measured compressive strengths ranged from 2.27 to 2.45 MPa, with an average of 2.38 MPa. These values are consistent across the three specimens, confirming that the material properties were sufficiently comparable to attribute any differences in structural response to the reinforcement configuration [10].

2.2 Test setup and instrumentation

The four-point bending test setup used for all three panels is shown in Fig. 2. Each panel was placed on simple supports with a bearing length of 35 mm on each side, representative of typical in-service support conditions for RAAC roof panels. The clear span between supports was 2075 mm for RAAC-T1 and RAAC-T3, and 2080 mm for RAAC-T2, reflecting the minor differences in panel length.

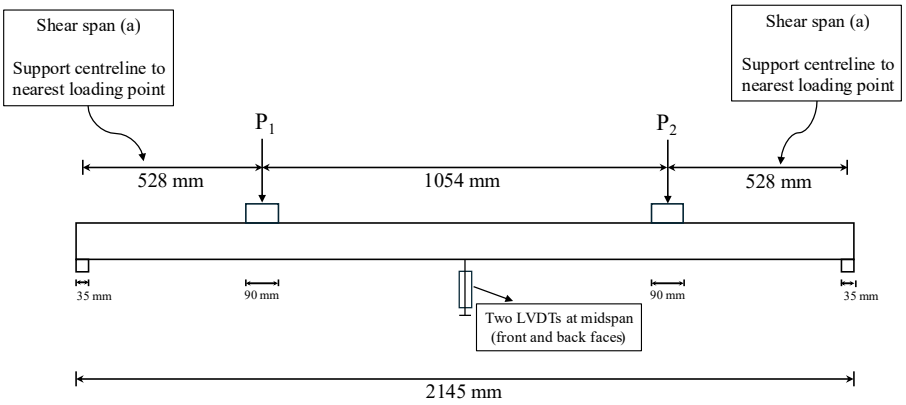


Fig. 2 Four-point bending test setup

Loading was applied through a steel spreader beam to generate two equal point loads, with the shear span (a) set to produce a constant shear slenderness ratio (a/d) of 6.6 for all three specimens. This relatively high a/d ratio is representative of the loading conditions experienced by long-span RAAC roof panels in service, where shear span-to-dept ratios are typically well above those associated with deep beam behaviour.

Mid-span deflection was measured using two linear variable differential transformers (LVDTs) positioned at the centre of the panel, and the average of the two readings is reported. The applied load was recorded using two load cells. Loading was applied under load control at a rate of 1 kN/min and continued until failure. Throughout each test, load–deflection data was

recorded continuously, and the shear span was video recorded to capture the full progression of cracking up to and including the formation of the critical shear crack and subsequent failure.

3 RESULTS AND DISCUSSIONS

3.1 Load–deflection behaviour, crack patterns and failure mode

The load–mid-span deflection curves for the three RAAC panels tested under four-point bending are presented in Fig. 3, and the corresponding experimental results are summarised in Table 2. All three panels exhibited broadly similar initial stiffness in the early stages of loading, which is consistent with their comparable material properties, cross-sectional geometry, and longitudinal reinforcement ratio.

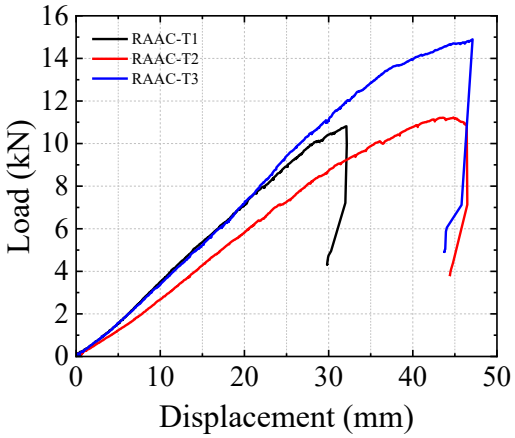


Fig. 3 Load–mid-span deflection curves for the three RAAC panel specimens

Table 2 Summary of experimental results

Beam	Peak load, P (kN)	Shear force, V (kN)	Deflection at peak load (mm)	Failure mode
RAAC-T1	10.8	5.4	32.1	Flexure-shear
RAAC-T2	11.2	5.6	44.8	Flexure-shear
RAAC-T3	14.9	7.5	47.1	Flexure-shear

As loading progressed, the first cracks initiated and propagated in the constant-moment region between the load points, followed by additional cracks developing within the shear spans. However, the number of flexural cracks that developed prior to failure was notably limited in all three specimens. This can be attributed to the characteristically weak bond between the reinforcement bars and the AAC matrix, which restricts the transfer of tensile stresses and consequently limits the formation of distributed cracking [5], [11]. This behaviour is a recognised feature of RAAC members, and distinguishes them from conventional reinforced concrete, where more extensive crack patterns typically develop before failure.

Despite the differences in transverse reinforcement ratio, all three panels ultimately failed in a flexural-shear mode, as illustrated in Fig. 4. In each case, failure was initiated by the sudden propagation of an inclined crack originating from a pre-existing flexural crack at the tension zone and extending diagonally toward the loading point. The failure was brittle and occurred immediately following the formation of this critical inclined crack, with no significant post-peak load-carrying capacity observed. This sudden and brittle response is consistent with the behaviour reported for reinforced concrete members without conventional shear links, where the absence of vertical stirrup legs means that once the inclined crack forms, no reinforcement crosses the failure

plane to provide residual shear resistance [5], [12]–[14]. In the case of aged RAAC, this vulnerability is further compounded by the low tensile strength of the AAC matrix, which has likely deteriorated over the panels' extended service life.



Fig. 4 Crack patterns at failure: (a) RAAC-T1; (b) RAAC-T2; (c) RAAC-T3

Although the failure mode was consistent across all three specimens, the shear capacity and deformation behaviour differed markedly. RAAC-T3, the panel with the highest transverse reinforcement ratio, resisted a shear force of 7.5 kN, representing a 38.9% increase over RAAC-T1, which had the lowest transverse reinforcement ratio and resisted 5.4 kN. The mid-span deflection at peak load also increased substantially, from 32.1 mm for RAAC-T1 to 47.1 mm for RAAC-T3; an improvement of 46.7%. RAAC-T2, with medium transverse reinforcement ratio, exhibited a 39.6% increase in deflection at peak load compared to RAAC-T1; however, the corresponding increase in shear capacity was insignificant, at approximately 3.7%. These results indicate that while transverse reinforcement density has a pronounced effect on both shear capacity and deformation behaviour, the relationship between the two is not necessarily linear, and the mechanisms through which transverse reinforcement contributes to shear resistance warrant closer examination.

3.2 Influence of transverse reinforcement on shear capacity

In reinforced concrete members without stirrups (shear links), four shear transfer mechanisms are generally recognised, namely aggregate interlock, residual tensile stresses across cracks within the fracture process zone, shear transfer through the uncracked compression zone, and dowel action of the longitudinal reinforcement [5]. RAAC however, does not contain coarse aggregate. So, aggregate interlock which in conventional concrete relies on the mechanical interlocking of aggregate particles along crack faces is either absent or negligible in RAAC. This leaves the remaining three mechanisms as the primary contributors to shear resistance in RAAC panels.

In this study, the AAC compressive strength, effective depth, a/d ratio, and longitudinal tensile reinforcement ratio were held approximately constant across the three test specimens. Under these dictated conditions, the observed differences in shear capacity and deformation behaviour can be attributed primarily to the variation in transverse reinforcement's configuration. The uncracked compression zone contribution is governed by the AAC's compressive strength and the depth of the neutral axis, both of which are similar across the three panels. Also, the residual tensile stress contribution is a function of the AAC tensile properties, which were also consistent across the three specimens. Therefore, the most likely explanation for the observed differences lies in the enhanced contribution of dowel action in panels with a higher transverse reinforcement ratio.

This interpretation is consistent with the established mechanics of dowel action in reinforced concrete [15]–[17]. Longitudinal reinforcement crossing an inclined crack can provide a resisting shear force through dowel action; however, the magnitude of this contribution depends strongly on the concrete cover beneath the bars and on the extent to which vertical displacement of the longitudinal bars at the crack is restrained. In members with little or no transverse reinforcement, especially when the longitudinal bars are close to the tension face, dowel action is often limited by splitting of the surrounding concrete matrix, and only a small proportion of the potential dowel resistance can be mobilised. In the present panels, the transverse bars are welded to the longitudinal bars; therefore, increasing the number of transverse bars improves the confinement of the longitudinal reinforcement and provides more frequent restraint against vertical displacement at the inclined crack. As illustrated conceptually in Fig. 5, sparse transverse reinforcement allows larger vertical movement of the stressed longitudinal bar at the crack, leading to a smaller dowel force, V_d. Conversely, more transverse reinforcement bars provide closer restraint, reduces vertical displacement, improves bond and anchorage along the

longitudinal bars, and delays longitudinal splitting. As reported in [15]–[17], this enhanced restraint enables the longitudinal bars to mobilise a greater proportion of their potential dowel capacity, thereby increasing their contribution to the overall shear resistance of the section. Consequently, panels with a higher number of transverse reinforcement are able to sustain greater shear forces before the critical inclined crack widens and propagates unstably. This mechanism also explains the observed increase in deformation capacity. Improved confinement provided by the welded transverse reinforcement delays the initiation of splitting cracks along the longitudinal reinforcement, allowing the panel to undergo greater deflection before the critical flexural-shear crack fully develops and propagates. The crack patterns shown in Fig. 4 are consistent with this interpretation. RAAC-T3 exhibited narrower (shear) crack widths compared to RAAC-T1, suggesting more effective mobilisation of the longitudinal tensile reinforcement through enhanced dowel action.

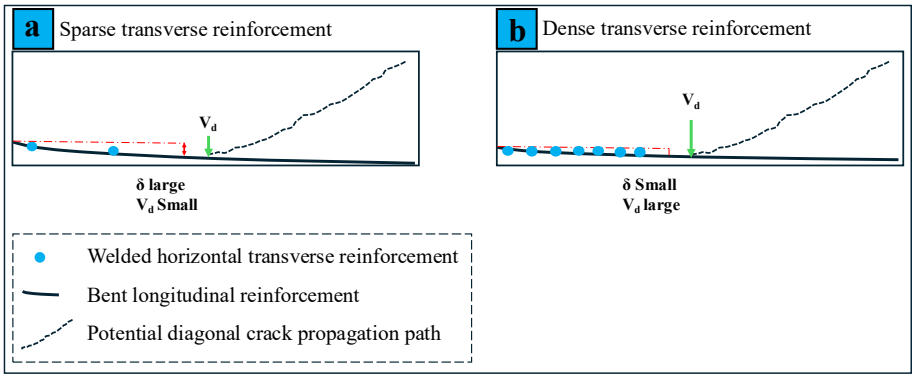


Fig. 5 Conceptual model of the effect of transverse reinforcement configuration on longitudinal bar confinement and dowel action

It is important to note that the bond between the AAC matrix and reinforcement bars is inherently weaker than in conventional concrete, owing to the aerated microstructure of AAC, the coating, and lack of ribs. Consequently, any factor that improves confinement and bond conditions such as increased transverse reinforcement density is likely to have a proportionally greater influence on shear capacity than would be observed in normal-weight concrete, where the baseline bond strength is already substantially higher [16], [17]. This may explain the considerable 38.9% increase in shear capacity observed between RAAC-T1 and RAAC-T3 and highlights the importance of accounting for reinforcement configuration and density in the structural assessment of aged RAAC panels. While the present findings are based on a limited number of specimens, they provide preliminary experimental evidence that transverse reinforcement density is a significant parameter influencing the residual shear capacity and deformation behaviour of aged RAAC roof panels. Further experimental testing across a wider range of reinforcement configurations and panel ages, complemented by numerical modelling, is planned to validate and extend these findings.

4 CONCLUSIONS

This paper has presented an experimental investigation into the influence of transverse reinforcement density on the shear capacity and load–deflection behaviour of aged RAAC roof panels, exceeding 50 years in service, extracted from a building in the United Kingdom. Three panels with comparable AAC compressive strength, effective depth, shear slenderness, and longitudinal reinforcement ratio were tested under four-point bending, isolating the transverse reinforcement ratio as the sole variable. The principal findings are as follows:

- All three panels failed in a brittle flexural-shear mode. Failure occurred suddenly and immediately following the formation of a critical inclined crack, with no significant post-peak load-carrying capacity. This confirms that aged RAAC panels of this

configuration remain highly susceptible to brittle shear failure, whatever the amount or transverse bars.

- Increasing the transverse reinforcement area by approximately 260% (from 503 mm^2 to 1810 mm^2) resulted in a 38.9% increase in shear capacity (from 5.4 kN to 7.5 kN) and a 46.7% increase in mid-span deflection at peak load (from 32.1 mm to 47.1 mm). These results demonstrate that the transverse reinforcement quantity and configuration have a substantial influence on both the residual shear resistance and the deformation capacity.
- The enhanced shear performance of panels with higher transverse reinforcement ratio is attributed to the improved contribution of dowel action. A higher number of welded transverse bars provides more frequent confinement and restraint points along the longitudinal reinforcement, thereby improving bond, anchorage, and resistance to vertical displacement at inclined cracks. This enables the longitudinal bars to contribute more effectively to shear resistance through dowel action; a mechanism of particular significance in RAAC, where aggregate interlock is limited or absent due to the porous microstructure of the material.
- These findings highlight the need to consider transverse reinforcement number, position and density in the structural assessment of aged RAAC roof panels, as panels with otherwise comparable (dimensional and longitudinal reinforcement) properties can exhibit markedly different shear capacities depending on their reinforcement layout. Further experimental and numerical investigation is recommended to extend these findings across a broader range of reinforcement configurations, panel geometries, AAC mechanical properties, support bearing lengths, and degradation levels.

References

[1] Di Sarno, Luigi, and Albuhairi, Danah. 2024. "Reinforced Autoclaved Aerated Concrete: Structural Assessment and Retrofitting." Buildings 14, no. 8: 2570. doi:10.3390/buildings14082570.

[2] Saad, Ali M., Gorse, Chris, Goodier, Chris I., Blay, Karen, and Cavalaro, Sergio. 2024. "Autoclaved Aerated Concrete in Reinforced Building Applications: A Systematic Review of AAC/RAAC in the Last 40+ Years." Results in Engineering 24:103431. doi:10.1016/j.rineng.2024.103431.

[3] SCOSS. 2019. "Failure of Reinforced Autoclaved Aerated Concrete (RAAC) Planks." Standing Committee on Structural Safety Alert, May. Accessed July 4, 2024. https://www.cross-safety.org/uk/safety-information/cross-safety-alert/failure-reinforced-autoclaved-aerated-concrete-raac-planks.

[4] Hwang, Seongha, Blay, Karen, Goodier, Chris, Gorse, Chris, and Cavalaro, Sergio. 2025. "Advanced Crack Detection in Reinforced Autoclaved Aerated Concrete Using Generative Data Augmentation and Enhanced Segmentation." Journal of Computing in Civil Engineering 39, no. 5: 04025055. doi:10.1061/JCCEE5.CPENG-6572.

[5] Yang, Yuguang, Walraven, Joost, and den Uijl, Joop. 2017. "Shear Behavior of Reinforced Concrete Beams without Transverse Reinforcement Based on Critical Shear Displacement." Journal of Structural Engineering 143, no. 1: 04016146. doi:10.1061/(ASCE)ST.1943-541X.0001608.

[6] British Standards Institution. 2016. BS EN 12602:2016: Prefabricated Reinforced Components of Autoclaved Aerated Concrete. London: British Standards Institution.

[7] ACI-ASCE Committee 426. 1973. "The Shear Strength of Reinforced Concrete Members." Journal of the Structural Division, ASCE 99, no. 6: 1091–1187. doi:10.1061/JSDEAG.0003532.

[8] ACI-ASCE Committee 445. 1998. "Recent Approaches to Shear Design of Structural Concrete." Journal of Structural Engineering 124, no. 12: 1375–1417. doi:10.1061/(ASCE)0733-9445(1998)124:12(1375).

[9] British Standards Institution. 1988. BS 1881-204:1988: Testing Concrete: Recommendations on the Use of Electromagnetic Covermeters. London: British Standards Institution.

[10] British Standards Institution. 2015. BS EN 771-4:2011+A1:2015: Specification for Masonry Units—Part 4: Autoclaved Aerated Concrete Masonry Units. London: British Standards Institution.

[11] Leonhardt, Fritz, and Walther, René. 1962. Schubversuche an einfeldrigen Stahlbetonbalken mit und ohne Schubbewehrung [Shear Tests on Single-Span Reinforced Concrete Beams with and without Shear Reinforcement]. Bulletin 151. Berlin: Ernst. In German.

[12] Cavagnis, Francesco, Fernández Ruiz, Miguel, and Muttoni, Aurelio. 2015. "Shear Failures in Reinforced Concrete Members without Transverse Reinforcement: An Analysis of the Critical Shear Crack Development on the Basis of Test Results." Engineering Structures 103:157–73. doi:10.1016/j.engstruct.2015.09.015.

[13] Cavagnis, Francesco, Fernández Ruiz, Miguel, and Muttoni, Aurelio. 2018. "A Mechanical Model for Failures in Shear of Members without Transverse Reinforcement Based on Development of a Critical Shear Crack." Engineering Structures 157:300–315. doi:10.1016/j.engstruct.2017.12.004.

[14] Chana, Pal S. 1987. "Investigation of the Mechanism of Shear Failure of Reinforced Concrete Beams." Magazine of Concrete Research 39, no. 141: 196–204. doi:10.1680/macr.1987.39.141.196.

[15] Autrup, Frederik, and Joergensen, Henrik B. 2021. "Shear Capacity of RC Members without Shear Reinforcement: A Modified Crack Sliding Model." Engineering Structures 239:112147. doi:10.1016/j.engstruct.2021.112147.

[16] Kim, Hyeong-Gook, Jeong, Chan-Yu, Kim, Min-Jun, Lee, Young-Jun, Park, Jung-Han, and Kim, Kil-Hee. 2018. "Prediction of Shear Strength of Reinforced Concrete Beams without Shear Reinforcement Considering Bond Action of Longitudinal Reinforcements." Advances in Structural Engineering 21, no. 1: 30–45. doi:10.1177/1369433217706778.

[17] Hawkins, Neil M., Kuchma, Daniel A., Mast, Robert F., Marsh, M. Lee, and Reineck, Karl-Heinz. 2005. Simplified Shear Design of Structural Concrete Members: Appendixes. NCHRP Web-Only Document 78 (Project 12-61): Contractor's Final Report—Appendixes. Washington, DC: Transportation Research Board, National Research Council. doi:10.17226/13555.

Effect of Bond of Post-tensioned Reinforcement on Cracking and Deflection Development of Post-Tensioned Concrete Beams

Tomáš Vízner, Jan L. Vítek

Czech Technical University in Prague,
Faculty of Civil Engineering,
Thákurova 7/2077, 166 29 Praha 6, Czech Republic

Summary

Post-tensioned reinforcement can be used in different structural arrangements. Classical bonded tendons are usually grouted with cement mortar. Alternatively, internal or external tendons grouted with wax or grease are unbonded tendons. This has a significant effect on cracking and deflection development as well as on the load carrying capacity of the structure. The prestressed beams with a span of 10.8 m, subjected to short-tem and long-term 4-point bending test, had identical prestressing but different mild steel reinforcement. Series 1 has bonded prestressing (using cement grout) and no mild reinforcement. This series illustrates the effect of the bond of prestressed reinforcement on cracking and deflections. Series 2 has unbonded prestres-sing and no mild reinforcement. Series 3 has unbonded prestressing and also reinforcement by mild steel. Mild steel reinforcement guarantees a reasonable crack distribution and improves the structural performance in comparison with the beams of Series 2.

1 DESCRIPTION OF THE EXPERIMENT

The aim of the experiment is to compare the influence of tendon bond on the behaviour of beams. The type of prestressing reinforcement in terms of bonding has a fundamental impact on the initiation and development of cracks. In elements reinforced with bonded tendons, the bond between the reinforcement and concrete leads to the formation of a higher number of smaller cracks. On the contrary, structures reinforced with unbonded tendons develop fewer cracks with larger widths; therefore, unbonded reinforcement cannot be considered for crack width control. Since the formation of large cracks after the loss of compression reserve is undesirable, unbonded systems are typically supplemented with bonded non-prestressed reinforcement, which can be designed to limit crack widths under a given load.

To evaluate these effects, three series of beams were designed:

- **Series S01:** Beams prestressed with bonded tendons (grouted with cement grout).
- **Series S02:** An extreme case reinforced only with unbonded tendons (grouted with viscous gel) without any additional bonded reinforcement. This configuration would not be feasible for real structural designs.
- **Series S03:** Beams reinforced with unbonded tendons (grouted with viscous gel) and supplemented with bonded mild steel reinforcement to ensure proper crack distribution.

All beams feature the same cross-sectional area of prestressing steel, the same tendon profile geometry, and were prestressed with an identical initial prestressing force. Each series contained 4 identical beams.

Three beams from each series were subjected to short-term four-point bending test until reaching the ultimate limit state and following collapse. From each series, one beam was selected for long-term testing. It was first loaded to the cracking point, and after 14 days, a permanent load was applied to monitor the long-term cracks and deflection development.

Short-term tests were conducted approximately 30 days after casting. The long-term load consisted of concrete blocks weighing 4.7 tonnes. These loads were placed in thirds of the span.

2 DESCRIPTION OF THE BEAMS

2.1 Materials

The beams were designed using concrete grade C35/45, with B500B reinforcing steel and Y1860S7-15.7 prestressing tendons. To ensure the accuracy of the structural analysis, the calculations incorporate the actual measured properties of the materials rather than just the nominal design values. [1] [2]

The compressive strength of the concrete was determined through cylindrical tests. The measured values for each series are as follows:

- **Series S01:** 45 MPa
- **Series S02:** 46 MPa
- **Series S03:** 49 MPa

The tensile strength of the concrete was measured for the second and third variants, yielding an identical value of 2.5 MPa for both series.

For the structural calculations and analytical verification, the following characteristic values of steel were adopted: a characteristic yield strength of f_{yk} = 500 MPa for the reinforcement and a characteristic tensile strength of f_{pk} = 1860 MPa for the prestressing reinforcement. [3]

2.2 Geometric characteristics

The test beams were designed with a span of L = 10.8 m. The cross-sectional dimensions were defined as follows:

- Section depth d = 0.5 m
- Top flange width b = 0.5 m
- Top flange thickness t_d = 0.15 m
- Web thickness t_s = 0.2 m

The cross-sectional dimensions and the overall geometry of the T-section are detailed in Fig. 1 (left), while the actual beams positioned in the laboratory environment prior to testing are displayed in Fig. 1 (right).

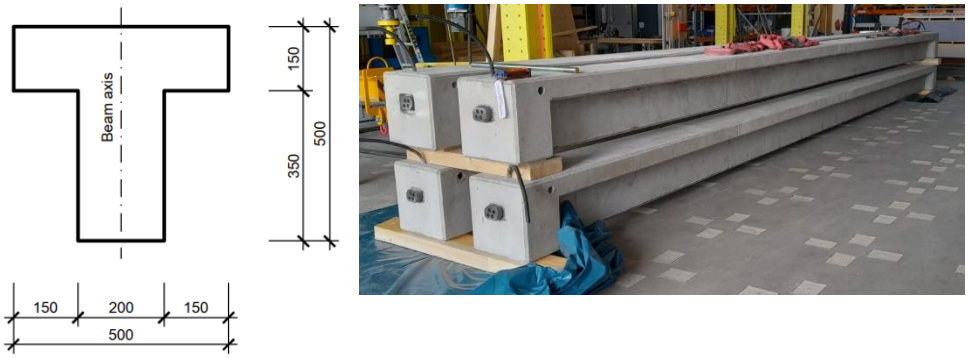


Fig. 1 Geometry of the T-section concrete beam (left) and concrete beams prior to testing (right)

2.3 Design of the Beams

The beams were designed to ensure that the ultimate limit state could be reached within the maximum loading capacity of the testing equipment. Furthermore, the design allowed for the production of concrete blocks for long-term testing of a specific size, capable of inducing both the initiation and development of cracks.

The critical moment M_{cr} at the crack initiation limit was calculated for an ideal cross-section unaffected by cracking, in which the tensile strength of concrete was considered. First, the position of the neutral axis x was determined from the equilibrium condition of forces acting on the cross-section, and subsequently the sectional characteristics of the ideal cross-section were calculated (moment of inertia I_i). The crack initiation moment M_{cr} was calculated according to the following equation (1),

including the acting normal stress due to prestressing in absolute value $\sigma_{P,bot}$ and the tensile strength of concrete f_{ctm}.

$$M_{cr} = \frac{(f_{ctm} + \sigma_{P,bot})}{(h - x)} \cdot I_i \quad (1)$$

The ultimate moment capacity of the individual beams was determined according to the theory of ultimate strains, including the initial stresses in the concrete cross-section and in the prestressing reinforcement. Characteristic values of material strengths were considered. For concrete, the measured strength values were used. A bilinear stress–strain diagram was adopted for concrete. For the prestressing reinforcement, tensile hardening was considered, with failure of the reinforcement occurring at a relative strain in the prestressing steel ε_{uk} = 20.0 ‰. The maximum stress in unbonded prestressing tendons was taken as the stress in the tendon after deduction of losses, increased by 100 MPa in accordance with Eurocode 2. The calculations were performed manually. Prestressing losses, including both short-term effects and long-term effects (creep, shrinkage, and relaxation), were calculated to find the effective prestressing force at the time of testing. [4] [5]

The prestressing reinforcement was designed as two strands (A_{p1} = 150 mm^2) with an initial stress of 1300 MPa after anchorage. The prestressing tendons are designed in the distance of 100 mm from the bottom fibers in the central part of the beams. In beams with unbonded tendons and with non-prestressed reinforcement, longitudinal reinforcement consisting of 3x Ø10 bars was designed at the bottom fibers. This reinforcement is designed to ensure that the crack width is appropriate for the given load level at the serviceability limit state (SLS) and is displayed in Figure 2.

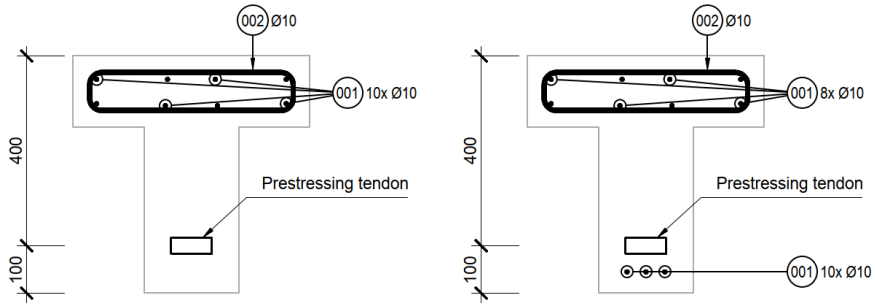


Fig. 2 Reinforcement layout at mid-span – Series 1 and 2 (left), Series 3 (right)

3 LOADING

3.1 Short-term static loading test

Static loading tests were performed for each series on three specimens until the collapse of the beam, and on one additional beam from each series only beyond the cracking limit. During the tests, the deflection was monitored at the mid-span and under both loading points. To measure the deflection, potentiometric cable extension sensors with a measurement range of 300 mm were used. The loading was applied at two locations on the beam according to the schematic view shown in Fig. 3.

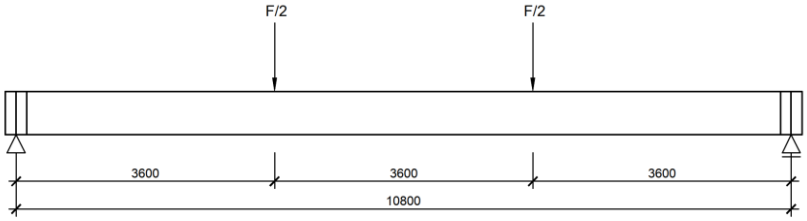


Fig. 3 Static loading test configuration

The loading was controlled by the increase in displacement of the loading cylinder. In the first loading step, the beam was loaded beyond the cracking point and then subsequently unloaded. In the next step, the beams were loaded until the maximum possible extension of the cylinder was reached. At this point, the deformation of the beams was held constant to allow for the resetting of the cylinder,

after which loading continued until the collapse of the beam. A 630 kN INOVA hydraulic cylinder with a maximum stroke of 300 mm was used for the static loading test.

3.2 Long-term loading test

A long-term static loading is executed on only one beam from each series. Each beam was initially loaded just beyond the cracking limit using a hydraulic cylinder, following the same loading configuration as the short-term tests. For all beams, this initial loading corresponded to a displacement of 30 mm at the location of the loading cylinder. The beams for the long-term test were equipped with four vibrating wire strain gauges. Three of these gauges were positioned near the bottom surface of the beam: one at the mid-span and two located approximately 1 m on either side of the centre. The fourth strain gauge was placed at the mid-span near the top surface of the beam.

Fourteen days after the initial laboratory loading, the beams were moved to an outdoor area where concrete blocks weighing approximately 4,700 kg were suspended from them. The loading arrangement corresponded to the configuration used in the short-term tests (Fig. 5). Both the deflection and the relative strain are being monitored on the beams using the vibrating wire strain gauges.



Fig. 5 Long-term static loading test, suspended weights

4 RESULTS AND EVALUATION

4.1 Short-term static loading test

4.1.1 Series S01

Series S01 consists of beams prestressed with bonded tendons without the use of non-prestressed reinforcement. For these specimens, the theoretical cracking moment was calculated as M_{cr} = 136.9 kNm, which corresponds to a cylinder load of F_{cr} = 46.7 kN.

The experimental results for the S01 series, showing the force required for the initiation of the first five cracks, are summarized in Table 1.

Table 1 Cylinder force at the initiation of the 1st to 5th cracks for Series S01

Beam	1. crack	2. crack	3. crack	4. crack	5. crack
	F				
	[kN]				
S01/1	41.3	42.1	42.8	43.3	45.1
S01/2	42.5	43	43	46	46.3
S01/3	38.1	39.2	39.6	40.1	40.4
S01/4	41.5	41.5	42.1	44.7	45.4

Ø S01	**40.9**	**41.5**	**41.9**	**43.5**	**44.3**

The results indicate that the first crack occurs at an average force of F_{cr} = 40.9 kN. Subsequent cracks appear with relatively small increments in load, specifically at an average increase of ΔF = 0,9 kN.

The crack widths at specific cylinder displacements are shown in the Table 2. The final row summarizes the maximum crack width at the given cylinder displacement, alongside the average force at which this displacement was reached.

Table 2 Maximum crack width at specific cylinder displacements for Series S01

Displacement [mm]	**15**		**20**		**25**		**30**		**35**		**40**	
Beam	F	w	F	w	F	w	F	w	F	w	F	w
	kN	mm	kN	mm	kN	mm	kN	mm	kN	mm	kN	mm
S01/1	42.3	0.2	45.5	0.3	48.0	0.6	51.8	1.0	-	-	-	-
S01/2	-	-	-	-	48.0	0.6	50.7	1.0	54.0	1.3	57.2	1.5
S01/3	-	-	43.2	0.2	46.2	0.4	48.5	0.4	-	-	-	-
S01/4	43.7	0.1	45.7	0.4	48.7	0.5	51.3	0.8	-	-	-	-
Ø F/max w	**43.0**	**0.2**	**44.8**	**0.4**	**47.7**	**0.6**	**50.6**	**1.0**	**54.0**	**1.3**	**57.2**	**1.5**

4.1.2 Series S02

Series S02 consists of beams prestressed solely with unbonded tendons.

For the specimens in this series, the theoretical cracking moment was calculated as M_{cr} = 132.9 kNm, which corresponds to a cylinder load of F_{cr} = 44.5 kN. The crack distribution is displayed in Figure 6. The experimental results for the S02 series, showing the force required for the initiation of the first five cracks, are summarized in Table 3.



Fig. 6 Short-term static loading test of series S02 – cracks exhibit large widths and wide spacing, which is caused by the absence of bonded reinforcement

Table 3 Cylinder force at the initiation of the 1st to 5th cracks for Series S02

Beam	1. crack	2. crack	3. crack	4. crack	5. crack
	F				
	[kN]				
S02/1	41.6	45	47.3	49.3	51.3
S02/2	45	50	50	52.9	-

S02/3	41	42.4	48.5	56.5	66
S02/4	42.6	-	-	-	-
Ø S02	**42.6**	**45.8**	**48.6**	**52.9**	**58.7**

According to the measurements, the initiation of the first crack occurred at a force of F_{cr} = 42.6 kN, which is very close to the predicted value. Subsequent cracks formed with an average load increment of ΔF = 4.0 kN. This represents a load increase approximately four times greater than that observed for the variant with bonded prestressing reinforcement. The crack widths at specific cylinder displacements are shown in the Table 4.

Table 4 Maximum crack width at specific cylinder displacements for Series S02

Displacement [mm]	**15**		**20**		**25**		**30**		**35**		**40**	
Beam	F	w	F	w	F	w	F	w	F	w	F	w
	kN	mm	kN	mm	kN	mm	kN	mm	kN	mm	kN	mm
S02/1	40.0	0.8	43.4	1.7	44.2	3.0	46.6	3.0	46.6	3.5	46.7	3.5
S02/2	41.5	0.6	45.3	3.0	47.2	3.5	49.0	5.0	50.6	5.0	50.5	5.0
S02/3	39.6	0.8	44.0	1.7	44.5	2.0	47.0	2.5	48.5	3.5	49.4	3.5
Ø F/max w	**40.4**	**0.8**	**44.2**	**3.0**	**45.3**	**3.5**	**47.5**	**5.0**	**48.6**	**5.0**	**48.9**	**5.0**

Maximum crack width for series S02 at a cylinder displacement of 40 mm is w = 5.0 mm.

4.1.3 Series S03

Series S03 consists of beams prestressed with unbonded tendons and reinforced with mild steel reinforcement.

For this series, the theoretical cracking moment was calculated as M_{cr} = 138.2 kNm, which corresponds to a cylinder load of F_{cr} = 47.4 kN. This represents the highest value among all the tested series. The crack distribution is displayed in Figure 7. The experimental results for the S03 series, showing the force required for the initiation of the first five cracks, are summarized in Table 5.



Fig. 7 Short-term static loading test of series S03 – cracks exhibit small widths and narrow spacing; the cracks are distributed by the bonded reinforcement

Table 5 Cylinder force at the initiation of the 1st to 5th cracks for Series S03

Beam	1. crack	2. crack	3. crack	4. crack	5. crack
	F				

	[kN]				
S03/1	47	47.5	47.5	47.5	51.5
S03/2	44.9	46.4	47.1	48	49.7
S03/4	48.7	49.2	50.1	50.1	51.5
Ø S03	**46.9**	**47.7**	**48.2**	**48.5**	**50.9**

According to the measurements, the initiation of the first crack occurred at a force of F_{cr} = 46.9 kN. This value is practically identical to the predicted value. Subsequent cracks formed with an average load increment of ΔF = 1,0 kN, which is very similar to Series S01, where bonded reinforcement was also used.

The crack widths at specific cylinder displacements are shown in the Table 6.

Table 6 Maximum crack width at specific cylinder displacements for Series S03

Displacement [mm]	**15**		**20**		**25**		**30**		**35**		**40**	
Beam	F	w	F	w	F	w	F	w	F	w	F	w
	kN	mm	kN	mm	kN	mm	kN	mm	kN	mm	kN	mm
S03/1	47.0	0.1	51.5	0.1	52.7	0.3	56.7	0.3	59.5	0.4	62.3	0.5
S03/2	47.1	0.1	51.3	0.1	55.8	0.2	58.3	0.2	60.0	0.3		-
S03/4	50.1	0.1	54.0	0.1	57.1	0.2	59.6	0.3	-	-	-	-
Ø F/max w	**48.1**	**0.1**	**52.3**	**0.1**	**55.2**	**0.3**	**58.2**	**0.3**	**59.8**	**0.4**	**62.3**	**0.5**

The maximum crack width at a displacement of 40 mm is only 0.5 mm. In Series S03, the crack widths develop slowly; furthermore, on the contrary to Series S02, a higher number of cracks form with smaller spacing between them.

4.1.4 Load-displacement diagram

Figure 8 shows the load-displacement diagrams for all nine beams tested during the short-term static loading test. The shapes of all diagrams are very similar at the beginning of the loading process, as no cracks have formed in concrete yet; the entire concrete cross-section remains effective, and the reinforcement does not play a significant role at this stage.

As expected, Series S02 without bonded reinforcement reached the lowest load-bearing capacity, with collapse occurring at an average cylinder load of F_{S02} = 89.7 kN. On the contrary, Series S03 achieved the highest load-bearing capacity, where collapse occurred at an average applied force of F_{S03} = 110.3 kN. Furthermore, the load-displacement diagram for Series S03 is the longest. It is also observed that Series S01 exhibits better performance than Series S03 at a certain stage of loading.

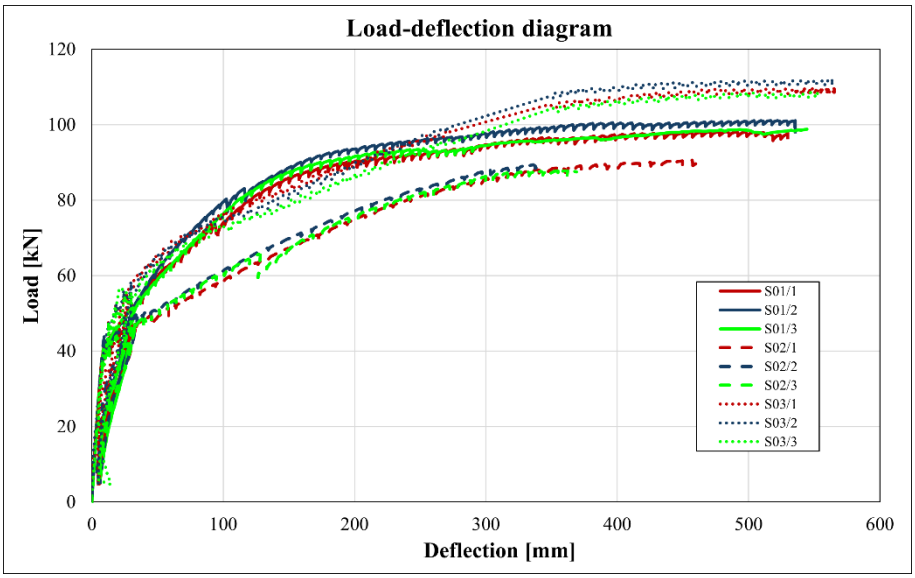


Fig. 8 Comparison of load-displacement diagrams for individual series

4.1.5 Crack spacing

After completion of the short-term tests, the distances between individual cracks were also measured. For Series S01, with bonded prestressing reinforcement, the average crack spacing was 573 mm. In Series S02, featuring unbonded prestressing reinforcement, the spacing was 697 mm, whereas for Series S03, with unbonded prestressing and supplemental non-prestressed reinforcement, the average spacing was only 266 mm.

In Series S03, the presence of mild steel reinforcement resulted in significantly smaller crack spacing compared to Series S02.

4.1.6 Failure Mode

In all series, the collapse was caused by concrete crushing, which represents a compression failure of the concrete. Figure 9 illustrates the beams failure.



Fig. 9 Failure of Series S02 (left) and failure of Series S03 (right)

The ultimate limit state was calculated for each series. For Series S01, the calculated moment of resistance was $M_{Rd,S01} = 209.3$ kNm, which corresponds to a hydraulic cylinder force of $F_{S01} = 86.9$ kN. The average measured force at failure was $F_{S01} = 97.0$ kN. For Series S02, the calculated moment was $M_{Rd,S02} = 162.0$ kNm with a corresponding force of $F_{S02} = 60.6$ kN, while the average measured force was $F_{S02} = 89.7$ kN. For Series S03, the calculated moment of resistance was $M_{Rd,S03} = 210.0$ kNm, corresponding to a force of $F_{S03} = 87.3$ kN; the average measured force at the point of concrete failure was $F_{S03} = 110.3$ kN. The results show that the load at the first crack was estimated by a simple analysis

rather accurately, the ultimate load was significantly underestimated by a simple analysis, in case of the Series 2 in particular.

5 CONCLUSION

In all tested series, two prestressing tendons with identical prestressing levels were designed, differing only in their bond conditions. Series S03 was further supplemented with non-prestressed reinforcement.

When comparing crack spacing, the difference between Series S01 and S02 is not particularly significant, while the series 3 exhibited much smaller crack spacing. It clearly demonstrates that mild steel reinforcement is always necessary to ensure optimal crack distribution. In Series S02, only a small number of cracks with large widths formed. This indicates that current cracks open significantly before a subsequent crack can initiate. In such cases, the prestressing steel is not protected by the concrete cover, leading to a reduction in the structure's durability.

Due to the bond effects in Series S01 and S03, cracks form uniformly with small increments in force. The primary difference between these series lies in the absence of mild steel reinforcement in S01, resulting in a smaller overall reinforcement area.

In Series S02, collapse occurred during a steady increase in the loading force, suggesting that the reinforcement did not reach a plastic state. This is likely because the large crack widths caused premature concrete crushing in the compression zone. Simultaneously, it is evident that a certain degree of "pseudo-bond" exists between the tendon and the concrete section due to the beam's deflection.

The greatest discrepancy between the calculated load-bearing capacity and the values achieved during testing was observed in Series S03. This is because, according to Eurocode, the calculation of cross-sectional capacity with unbonded tendons assumes a stress increase in the tendon of only 100 MPa. This does not reflect reality, as the stress in the tendon increases significantly more, partly due to the aforementioned bond effects during deflection.

Based on the results, Series S03 (unbonded tendons with supplementary mild steel reinforcement) appears to be the most optimal design among those which were tested. However, in a real-world design, a design with bonded tendons would also include mild steel reinforcement, and such a configuration would likely achieve the highest load-bearing capacity and the smallest crack widths.

The initial findings from this experiment can be utilized in the design of prestressed concrete structures with respect to their durability and safety. Furthermore, the experiment has contributed to a better understanding of how the bond of prestressing reinforcement influences the initiation and propagation of cracks. The long-term tests will continue and both short-term and long-term tests will be evaluated more in detail and experimental results will be compared with the results of different numerical analyses.

Acknowledgements

This paper was supported by the Technological agency of the Czech Republic (Project No. TS01030114 Quality Management System for the Construction of New Nuclear Power Plant Concrete Structures under local conditions in the Czech Republic).

References

[1] EN 1992-1-1. 2006. *Eurocode 2: Design of concrete structures - Part 1-1: General rules and rules for buildings*

[2] EN 1991-1-1. 2006. *Eurocode 1: Actions on structures - Part 1-1: General actions - Densities, self-weight, imposed loads for buildings*

[3] EN 1990. 2011. *Eurocode: Basis of structural design*

[4] EN 1992-2. 2007. *Eurocode 2: Design of concrete structures - Part 2: Concrete bridges - Design and detailing rules*

[5] Bílý, Petr. 2025. *Examples of Designing Reinforced Concrete Structures According to the Second Generation of Eurocode (in Czech). Prague: Czech Technical University in Prague*

Punching shear in unbonded post-tensioned steel fibre reinforced concrete slabs: the role of fibre distribution

Chiara Gaddi, Matteo Colombo and Marco di Prisco

Department of Civil and Environmental Engineering,
Politecnico di Milano,
Piazza Leonardo da Vinci 32, Milano (20133), Italy

Summary
The use of steel fibres is an effective method for enhancing the punching shear capacity of flat slabs. However, further experimental data are needed to assess the fibre contribution when fibres serve as the primary flexural reinforcement. To address this, the research investigates the punching shear behaviour of unbonded post-tensioned steel fibre reinforced concrete slabs without conventional reinforcement. As the structural response depends on the spatial distribution and orientation of fibres, the experimental programme includes geometrically identical slabs made with self-compacting and S4 concrete. The fibre contribution is analysed in relation to failure modes observed for slabs with varying fibre contents and to data on fibre distribution and orientation in the punching cone region. Finally, the paper discusses the reliability of current formulations in predicting the fibre contribution to the punching shear resistance, highlighting the physical meaning of the reduction coefficient η_F introduced in Eurocode 2.

1 INTRODUCTION

The use of steel fibres represents a valuable solution for elevated slabs, as it is effective in improving the flexural capacity of statically redundant members, while limiting deflections and enhancing durability under serviceability conditions. At the same time, it provides an alternative to punching shear reinforcement, addressing a failure mode that is often critical for this type of structural members.

Despite experimental evidence supporting the role of fibres in increasing punching shear resistance and deformation capacity [1]-[2], the quantitative assessment of their resisting contribution is still debated, with the major difference between the *fib* Model Code 2020 (MC2020) [3] and the new generation of Eurocode 2 (EC2) [4] lying in the fibre reduction coefficient η_F. Since the performance of steel fibre reinforced concrete (SFRC) is strongly influenced by the fibre spatial distribution and orientation, it is important to establish a correlation between the fibre arrangement in specimens used for material characterisation and the actual fibre distribution within the investigated slabs [5]-[6].

In this framework, the presented research investigates the punching shear behaviour of unbonded post-tensioned SFRC elevated slabs without conventional reinforcement. As existing design formulations for punching shear do not apply to slabs without bonded reinforcement, the aim of the research is to assess the fibre contribution and to develop analytical expressions for the punching resistance of slabs where fibres act as the primary flexural reinforcement. To investigate the role of design parameters and construction details, the research includes an extensive experimental campaign on full-scale slab specimens characterised by different fibre contents [7], post-tensioning configurations, and additional reinforcement (integrity rebars and headed shear studs).

Among the investigated parameters, the paper focuses on the influence of concrete workability to the punching shear behaviour, presenting the results of punching tests and fibre arrangement for slabs cast with self-compacting concrete (SCC) and vibrated concrete. The experimental fibre contribution is compared with predictions according to EC2, focusing on the physical meaning of the coefficient η_F, in light of the observed fibre arrangement and failure mode.

2 EXPERIMENTAL PROGRAMME

Two pairs of geometrically identical slabs with 35 kg/m³ of fibres were investigated. The first pair (slab specimens SS35-a and SS35-b) was produced using SCC, whereas the second pair (specimens SS35S4-a and SS35S4-b) was cast with an S4 consistency class concrete. For both concrete types, image analysis and Montevideo tests were performed on cubic specimens extracted from reduced-scale slabs reproducing the region affected by punching, in order to characterise the fibre arrangement.

2.1 Slab specimens and punching test set-up

Square slabs with side length of 2000 mm and thickness of 200 mm were investigated (Fig. 1a). For each slab, the post-tensioning system consisted of six 0.5" straight strands for each direction arranged according to a distributed-banded layout. The banded tendons were centred to the slab thickness, while the uniformly distributed tendons were centred at the slab edges and have a downward eccentricity of approximately 17 mm at the centre, corresponding to the duct diameter. The tendons were unbonded and post-tensioned in order to achieve an average concrete compressive stress of 0.9 MPa after losses. Conventional reinforcement consisting of 5ϕ18 with a spacing of 100 mm and an average bottom concrete cover of 31 mm was provided at the slab perimeter to limit the propagation of the flexural cracks, thus fostering a punching shear failure without interfering with the formation of the punching cone [8]. Additional rebars were added at the anchorage location to prevent bursting failure.

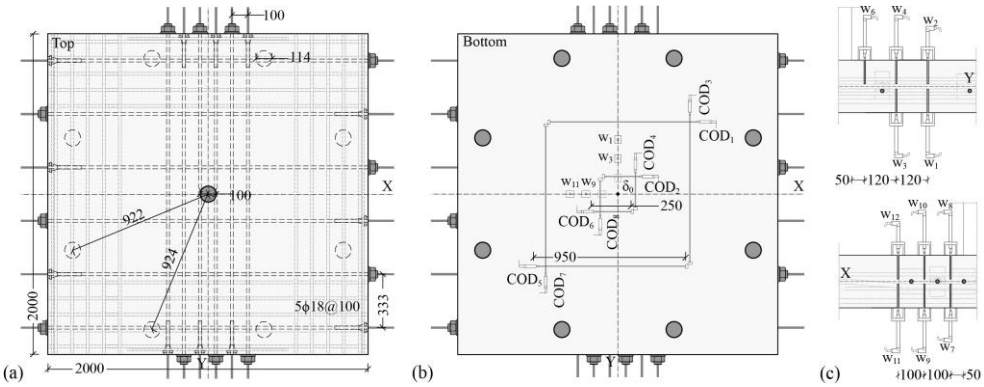


Fig. 1 Geometry of slab specimens (a); instrumentation of slab SS35-b and SS35S4-b (b); LVDTs measuring the propagation of the punching cone (c). Dimensions in mm. Adapted from [7].

To simulate the hogging moment area around a column, the slabs were simply supported on eight 114 mm diameter spherical supports symmetrically located along the slab perimeter. The load was applied under displacement control by means of a circular punch, whose diameter was set to 100 mm in order to foster the punching failure. The applied force was also measured by load cells placed at the supports. A 2 mm thick neoprene pad was placed between the loaded area and the slab surface.

For each test, one displacement transducer (indicated with "δ_0" in Fig. 1b) was used to monitor the vertical displacement at the slab centre. The symmetry of the structural response was monitored by further displacement transducers and inclinometers located along the centrelines. For one specimen of each set, the cumulative crack opening displacement (COD) of flexural radial cracks was monitored using eight displacement transducers (labelled as "COD_i") installed on the slab underside as shown in Fig. 1b, while on the other slabs, the formation of tangential cracks was measured by displacement transducers arranged radially. For all specimens, the propagation of the punching cone inside the slab was measured by Linear Variable Displacement Transducers (LVDTs) installed in holes that were drilled along the two centrelines (Fig. 1c). Further details about the test set-up can be found in [7].

2.2 Tests on cubes for fibre distribution

To determine the possible fibre spatial distribution and orientation of the tested slabs, two slab specimens, representative of the central region affected by the formation of the punching cone (1400×1400×200 mm), were cast. This allowed to characterise the material properties without interferences from cracking. Since the fibre distribution is influenced by the presence of reinforcement and tendons, plastic tubes with 16 mm diameter were embedded to simulate the post-tensioning strands. From each slab, 2×24 cubes with side of about 95 mm were cut (Fig. 2a). In addition, two pairs of beams were extracted from each slab to perform four point bending tests.

Image analysis was performed on the cubes to determine fibre orientation (angles θ and ϕ in Fig. 2b) and their spatial distribution for each slab section considered [9]. Subsequently, the cubic specimens were notched and Montevideo tests [10] were performed to obtain a correlation with the image-based results (Fig. 2c). The location of the notches was defined based on the punching cone dimensions (Fig. 4). Vertical notches were introduced to reproduce flexural cracks, while horizontal notches were cut to simulate diagonal cracking due to punching. The tests were conducted by

controlling the stroke displacement, at a rate of 6.25 μm/s and up to a stroke displacement of 10 mm, which ensured a crack opening of at least 2.5 mm. Steel angular profiles were placed across the notch to reduce friction between wedge and concrete. The relationship between stroke displacement and crack opening was obtained by installing two clip gauges across the notch. Since a good correlation between the two measurements was observed, only ten cubes per concrete type were instrumented, in order to reduce preparation time.

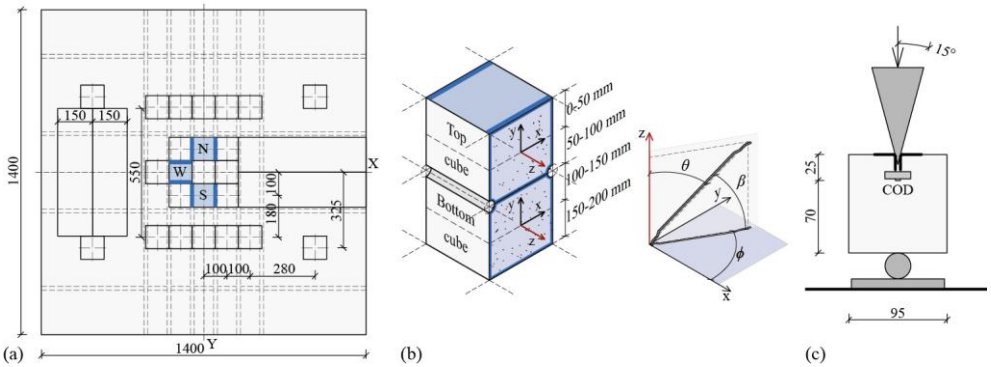


Fig. 2 Geometry of reduced-scale slab specimens and location of investigated cubes, with the cube pairs discussed in Section 4 highlighted in blue (a); orientation state of a single fibre and indication of layers used to investigate the fibre distribution over the slab thickness (b); set-up of Montevideo test (c).

2.3 Material properties and specimen production

The nominal mix design adopted for the concrete matrix of both concrete types is reported in Tab. 1. Double hooked-end steel fibres 60 mm long and with a diameter of 0.75 mm were added to each SFRC at a dosage of 35 kg/m³.

For every concrete batch, a volume of about 2.5 m³ has been mixed at the batching plant. For each slab specimen, the SCC was poured from the slab centre using the chute of a truck mixer, thus allowing concrete to radially flow and fill the formwork. No vibration was applied. For the S4 concrete specimens, concrete pouring began at the centre of the formwork. The truck mixer chute was subsequently repositioned to ensure even distribution of the concrete across the formwork. To achieve proper consolidation, a poker vibrator was employed throughout the casting process.

Table 1 Nominal mix design adopted for the concrete matrices.

	CEM IV/A (V) 42.5 R [kg/m³]	Sand 0/5 [kg/m³]	Gravel 5/15 [kg/m³]	Shrinkage reducing admixture [l/m³]	Superplasticizer [l/m³]	Filler [kg/m³]	Water [kg/m³]
SCC	450	942	630	5.00	5.00÷6.50	70	200
S4-concrete	420	775	974	5.00	2.52	-	186

Table 2 Results from uniaxial compression tests and three point bending test.

	f_{cm} [MPa]	f_{ck} [MPa]	$f_{ct,flm}$ [MPa]	$f_{ct,flk}$ [MPa]	$f_{R1,m}$ [MPa]	$f_{R1,k}$ [MPa]	$f_{R3,m}$ [MPa]	$f_{R3,k}$ [MPa]
SCC slabs	47.29	41.91	4.70	3.49	7.10	4.22	7.64	4.96
SCC cubes	45.89	43.37	4.54	3.81	3.96	2.35	5.24	3.44
S4-concrete	46.56	43.14	5.21	4.17	4.78	3.27	5.44	3.57

The concrete properties reported in Tab. 2 were measured on the days of the tests (28-35 days) on specimens that were cast from the same concrete batches of the slabs. The post-cracking behaviour of

the SFRC was assessed according to EN 14651. The SCC used to cast the tested slabs and the slab from which the cubes were extracted does not coincide, as they were poured on different days.

The post-tensioning tendons are 7-wire low relaxation strands ($A_p = 100$ mm^2) with average 0.1% proof-strength equal to 1709 MPa and average ultimate tensile strength of 1940 MPa. The rebars are characterised by a mean yield strength of 532 MPa and a mean ultimate tensile strength of 668 MPa.

3 PUNCHING TEST RESULTS

Figure 3a reports the load-deflection curves obtained from the punching tests. All the investigated slabs failed in punching shear, with average peak load of 572 kN for the SCC slab and 566 kN for the S4 concrete slabs. Overall, a stiffer structural response was observed for the S4 concrete slabs.

The final crack patterns are shown in Fig. 4. In all slab specimens, flexural radial cracks first developed on the tension surface, from the region underneath the loading area. At failure, an average cumulative COD of about 2.42 mm and 2.19 mm was measured from the inner and outer displacement transducers of slab SS35-b (Fig. 1b), while for slab SS35S4-b, they were respectively equal to 1.44 mm and 1.46 mm. The onset of tangential cracks was visible after the peak load was reached. Despite the pronounced asymmetry of the crack patterns, it should be pointed out that, at the end of the test, the propagation of the punching cone inside the slab was complete in all directions for each specimen.

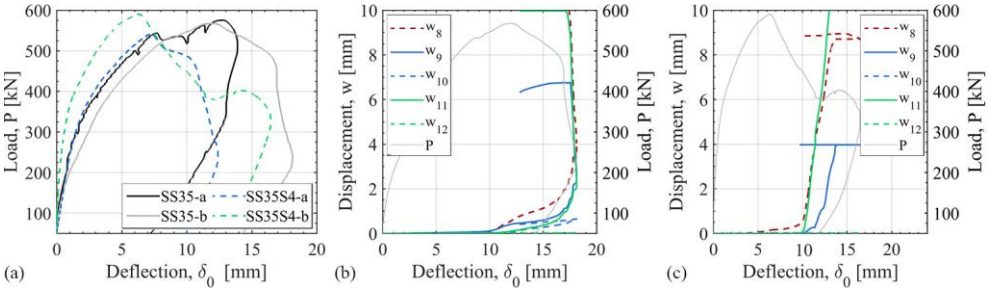


Fig. 3. Load-deflection curves from punching tests on SCC and S4 concrete slabs (a); vertical component of shear crack opening in x-direction vs deflection curves for slab SS35-b (b) and slab SS35S4-b (c).

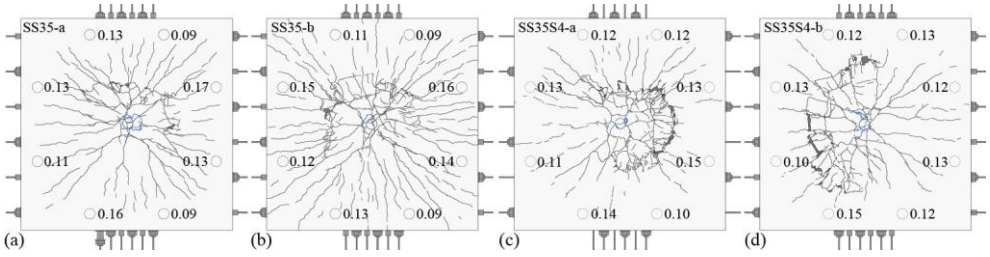


Fig. 4 Final crack patterns for slabs SS35-a (a), SS35-b (b), SS35S4-a (c), and SS35S4-b (d). Black lines represent bottom face cracks; blue lines mark top face cracks. Values at the supports indicate the fraction of failure load. Subfigures (a) and (b) are adapted from [7].

As indicated by the evolution of the vertical component of the punching shear crack opening (Fig. 3b-c), the first crack openings due to punching shear were recorded by the LVDTs installed on the top side of the slabs near the loading area (instrument w_8, Fig. 1c). These measurements are indicative of a failure mode which, based on the crack opening values and peak loads, can be classified for both slab typologies as intermediate between a splitting failure of the concrete strut and a shear-compression failure. Further details on the test results and on the failure modes of slabs SS35-a and SS35-b can be found in [7] and will be discussed in Section 5.

4 RESULTS ON FIBRE DISTRIBUTION AND ORIENTATION

Figures 5-6 present the results of the image analyses performed to determine the fibre arrangement, referring respectively to the angles β and ϕ. The angle β represents the inclination of the fibres with respect to the analysed x-y plane, and is complementary to angle θ. The angle ϕ denotes the angle between the local x-axis and the projection of the fibre onto the x-y plane (Fig. 2b). Fibre orientation distributions were evaluated considering 10° intervals for angle β and 20° intervals for angle ϕ.

Fibre segregation and variations in fibre orientation through the slab thickness were assessed by dividing, for each sampling location, the cube pairs (top and bottom cubes) into layers of approximately 50 mm, starting from the top surface of the slab (Fig. 2b). The resulting fibre distributions were compared with theoretical curves corresponding to an isotropic fibre orientation [6], [11].

Since the formation of the punching cone occurred near the loading region, each plot in Fig. 5-6 refers to cube pairs extracted approximately 100 mm from the slab centre and highlighted in blue in Fig. 2a. For each pair, the reported results correspond to the average fibre orientation measured on two parallel faces oriented radially with respect to the slab centre and indicated with blue lines in Fig. 2a-b, with the local x-axis defined as positive outward from the slab. Consequently, for the investigated planes, β angles approaching 90° indicate the highest effectiveness of the fibres in limiting the opening of radial flexural cracks, as the fibres are orthogonal to the radial planes (x-y in Fig. 2b). Conversely, fibres with β angles close to 0°, combined with ϕ values of 45°, provide the greatest contribution to punching shear resistance, as they are orthogonal to the theoretical profile of the punching cone.

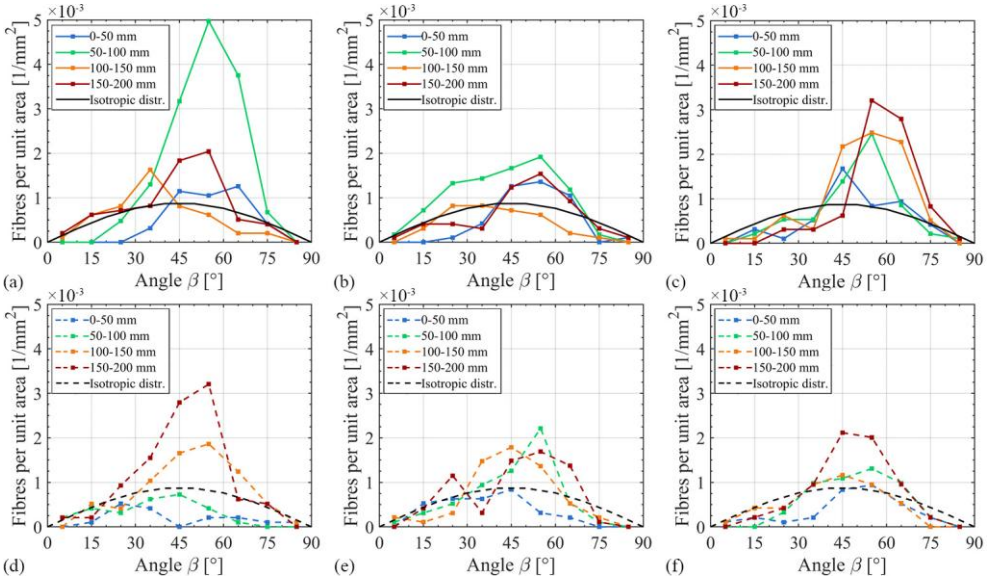


Fig. 5 Distribution of fibre orientation relative to the vertical plane, evaluated by horizontal layers: cubes N (a), S (b) and W (c) of SCC slab; and cubes N (d), S (e) and W (f) of S4 slab.

As shown in Fig. 5, the distribution of fibre orientation with respect to the vertical plane exhibits variations depending on both the spatial location and the depth considered. For all the investigated specimens, the fibre distribution is non-isotropic, with fibres predominantly aligned between 40° and 70° relative to the radial vertical planes (x-y plane in Fig. 2b). In the case of the SCC slab, such a distribution is likely influenced by the adopted casting procedure and by the tendency of fibres to align orthogonally to the direction of concrete flow [12]. A comparable orientation pattern was also identified in the cubic specimens positioned along the global Y-axis, at 280 mm from the slab centre (Fig. 2a).

Regarding the vertical orientation of the fibres, represented by the angle ϕ, the measured values generally oscillate around the theoretical curve corresponding to an isotropic fibre distribution, with no predominant orientation (Fig. 6). However, in the bottom and top layers of the S4 concrete slab, a flatter fibre distribution can be identified.

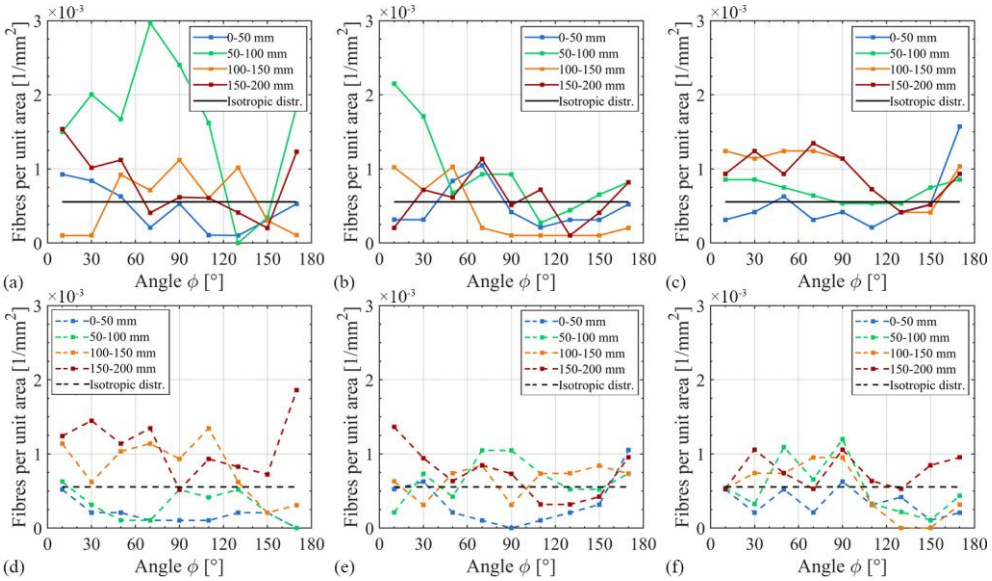


Fig. 6 Distribution of fibre vertical orientation, evaluated by horizontal layers: cubes N (a), S (b) and W (c) of SCC slab; and cubes N (d), S (e) and W (f) of S4 slab.

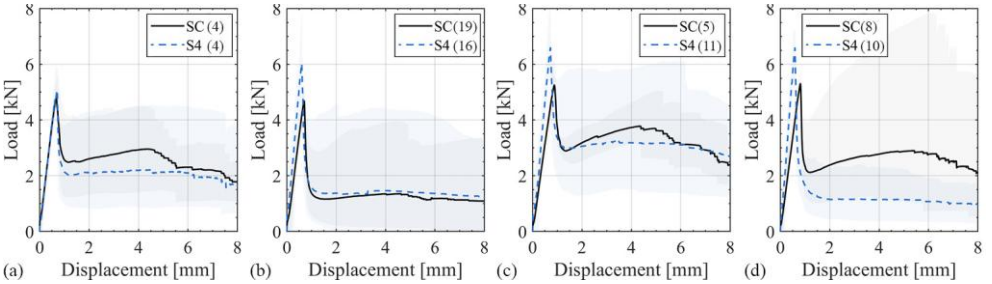


Fig. 7 Average load-displacement curves from Montevideo tests: top cubes with vertical (a) and horizontal notch (b); bottom cubes with vertical (c) and horizontal notch (d). Shaded areas represent the envelopes of all tests. Numbers in parentheses indicate the tests considered.

The distribution of fibres through the slab thickness indicates a moderate fibre segregation in the slab cast with S4 concrete. For this slab, the average number of fibres in the layers between 100-150 mm and 150-200 mm respectively corresponds to 23% and 36% of the total number of fibres, with coefficients of variation (CoV) of 0.15. For the SCC slab, the percentages of fibres within the same depth intervals are 23% and 29%, with CoV values of 0.21 and 0.16, respectively. The higher concentration of fibres in the lower portion of the S4 concrete slab may explain the smaller crack openings measured in slab SS35S4-b compared to slab SS35-b.

With reference to the vertical faces of the cube pairs, the average number of fibres per unit area (N_f) measured in the cubes located between the two central uniform tubes is higher than that recorded in the outer cubes, consistent with the observations reported in [6]. For the SCC slab, the average value of N_f is 0.0064 (CoV 0.13) in the central cubes and 0.0051 (CoV 0.14) in the outer ones, whereas for the S4 concrete slab these values are 0.0053 (CoV 0.10) and 0.0049 (CoV 0.16), respectively. It is worth noting that the theoretical value of N_f assuming two parallel boundaries at a distance equal to the slab thickness is 0.0045 [13], while for the notched beams used in three-point bending tests it is 0.0059 [11].

The spatial variability of fibre distribution is also reflected in the scatter of the Montevideo test results (Fig. 7). Overall, specimens with horizontal notches exhibit lower performance, suggesting a greater fibre efficiency in flexure than in punching. This trend is more evident for S4 concrete cubes, for which similar average results were obtained for top and bottom cubes despite the fibre segregation.

5 RESULT DISCUSSION

Figure 8 compares the experimental ($V_{Rf,exp}$) and theoretical fibre contribution ($V_{Rf,th}$) to the punching shear resistance, considering both the slab pairs discussed so far and geometrically identical slabs cast using SCC with the same nominal mix design, but fibre contents of 25 kg/m³ (specimens SS25) and 45 kg/m³ (specimens SS45). The test results obtained for these slabs are discussed in [7]. The experimental contribution of fibres is calculated according to Eq. 1, based on the experimental punching shear resistance ($V_{R,exp}$) and EC2 formulations. Because of the inapplicability of design equations in absence of bonded reinforcement, the contribution of the concrete matrix is assumed equal to the experimental punching resistance $V_{R,PC}$ obtained for analogous plain concrete slabs cast with SCC [7], corrected by a factor accounting for the different compressive strength ($f_{ck,PC}$ equal to 39.76 MPa).

$$V_{Rf,exp} = V_{R,exp} - \eta_c \cdot (f_{ck}/f_{ck,PC})^{1/3} \cdot V_{R,PC} \quad (1)$$

where the reduction coefficient for the concrete matrix contribution (η_c) is defined as follows:

$$\eta_c = (f_{ck}/f_{ck,PC})^{1/3} \cdot V_{R,PC}/V_{R,exp} \quad (2)$$

The theoretical fibre contribution is calculated according to Eq. 3, both adopting a reduction coefficient η_F equal to 0.4 as prescribed by the EC2, and equal to 1, following the MC2020 approach:

$$V_{Rf,th} = \eta_F \cdot (0.33 f_{R3,k} \cdot b_{0.5} \cdot d_v) \quad (3)$$

where $b_{0.5}$ is the shear-resisting control perimeter taken at a distance of 0.5d from the loading area and d_v is the shear resisting effective depth. Since the area interested by the formation of the punching cone is free from longitudinal reinforcement, the effective depth is assumed equal to the depth of the slabs.

As shown in Fig. 8, the comparison between slab specimens with different residual tensile strengths allows to identify an upper bound for the punching resistance of the tested specimens. This limit is associated with the splitting of the concrete strut in slabs SS25 and with the shear-compression failure of the compressed chord in slabs SS45, while slabs SS35 and SS35S4 exhibited an intermediate failure mode. It is worth noting that the residual tensile strength obtained for the S4 concrete is considered poorly representative of the actual mechanical performance of the material used in slabs SS35S4. Indeed, the beams used to characterise the residual strength of the S4 concrete had an average N_f value of 0.0052, whereas for the concrete used in slabs SS35 this value was 0.0067.

Beside of the failure mode, the reduced fibre contributions compared to those predicted when assuming a unit value for η_F can also be attributed to the topological variability of the SFRC within the slab (Fig. 7) and to fibre orientations that differ from those in beams for material characterisation. For these reasons and due the brittleness of the failure, the use of characteristic values rather than mean values of material properties is deemed more representative even for comparison with experimental results, whereas the coefficient accounting for structural redundancy k_G is assumed equal to 1 [4].

Additional factors include the uneven distribution of the reaction forces at the supports, with CoV values at peak load ranging from 0.12 for slab SS35S4-a to 0.24 for slab SS35-a (Fig. 4), as well as the inherent asymmetry of the failure mode. At peak load the propagation of the punching cone differ based on the considered direction, with non-uniform crack openings (Fig. 3) that are generally smaller than those assumed by EC2 (2.5 mm) or MC2020 (1.5 mm) for the computation of the fibre contribution.

The underestimation of the fibre contribution when adopting η_F equal to 0.4 is attributable to the calibration procedure used to derive this value [2], which was formulated using mean material properties and to ensure agreement with analytical models rather than experimental resistance data.

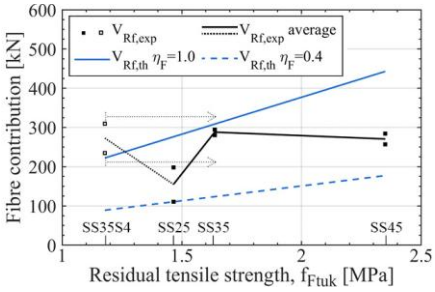


Fig. 8 Experimental and theoretical fibre contribution to the punching shear resistance for slabs with varying fibre dosages and consistency classes.

6 CONCLUSIONS

The paper presents the results of an experimental campaign aimed at investigating the influence of concrete workability on the punching shear resistance of post-tensioned SFRC slabs, focusing on fibre spatial distribution and orientation. Based on the test results, the following conclusions can be drawn:

- For both SCC and S4 concrete slab, punching is associate to a transitional failure mode between splitting of the concrete strut and shear-compression failure, and occurs at comparable failure loads. The structural response of the S4 concrete slabs is stiffer than that of the SCC slabs due to a partial segregation of fibres.
- The spatial distribution of fibres is non-uniform and varies with depth and with distance from the casting point, where the highest fibre concentration is observed.
- Fibres tend to orient orthogonally to the flow direction both in SCC and S4 concrete slabs, with most of the fibres in the interval 50°-60°. Although no predominant vertical orientation can be identified, the results of Montevideo tests indicate a higher efficiency of the fibres in limiting the opening of radial flexural cracks rather than diagonal cracks associated with punching shear.

With regard to the calculation of the fibre contribution, the results highlight the need for design codes to introduce upper bounds to the punching shear resistance of SFRC slabs associated with shear-compression failure. Given the topological variability of SFRC and the brittle nature of punching, the findings also indicate the importance of calibrating the reduction coefficient η_F on the basis of characteristic values of material properties, assuming a unit value for the coefficient k_G.

Acknowledgements

The authors thank MSc student Chiara Saligari for her contribution to the image analyses and the execution of the Montevideo tests. The punching tests were funded by Bekaert and CCL.

References

[1] Maya, Luis F., Miguel Fernández Ruiz, Aurelio Muttoni, and Stephen J. Foster. 2012. "Punching shear strength of steel fibre reinforced concrete slabs." *Engineering Structures* 40:83–94.

[2] Faccin, Enrico. 2022. "Experimental and analytical study on punching shear strength of steel fibre reinforced concrete flat slabs," PhD diss., Università degli Studi di Brescia.

[3] fib. 2022. *fib Model Code 2020 - 2nd draft*. Lausanne: Fédération internationale du béton.

[4] EN 1992-1-1. 2022. *Eurocode 2: Design of concrete structures - Final draft*, August, 1.

[5] Nguyen, Thuc N., Tung T. Nguyen, and Withit Pansuk. 2017. "Experimental study of the punching shear behavior of high performance steel fiber reinforced concrete slabs considering casting directions." *Engineering Structures* 131:564–73.

[6] Hernández Fraile, Diego, Enrico Faccin, Fausto Minelli, Giovanni Plizzari, and Aurelio Muttoni. 2024. "Fibre orientation in SFRC slabs and consequences for punching shear and flexural resistance." *Engineering Structures* 302:117364.

[7] Gaddi, Chiara, Matteo Colombo, and Marco di Prisco. 2026. "Punching shear of unbonded post-tensioned steel fiber reinforced concrete slabs: the fiber contribution." *Structural Concrete* (in press).

[8] Gaddi, Chiara, Matteo Colombo, and Marco di Prisco. 2024. "Preliminary analyses on punching strength of post-tensioned SFRC slabs." Paper presented at the Italian Concrete Conference 2024, Firenze, Italy, June 19-21.

[9] Mlekusch, Bernd. 1999. "Fibre orientation in short-fibre-reinforced thermoplastics II. Quantitative measurements by image analysis." *Composites Science and Technology* 59(4):547–60.

[10] Segura-Castillo, Luis, Renata Monte, and Antonio D. de Figueiredo. 2018. "Characterisation of the tensile constitutive behaviour of fibre-reinforced concrete: A new configuration for the Wedge Splitting Test." *Construction and Building Materials* 192:731–41.

[11] Dupont, David, and Lucie Vandewalle. 2005. "Distribution of steel fibres in rectangular sections." *Cement and Concrete Composites* 27(3):391-98.

[12] Blanco, Ana, Pablo Pujadas, Albert de la Fuente, Sergio H. P. Cavalaro, and Antonio Aguado. 2015. "Assessment of the fibre orientation factor in SFRC slabs." *Composites: Part B* 68:343-54.

[13] Soroushian, Parviz, and Cha-Don Lee. 1990. "Distribution and orientation of fibers in steel fiber reinforced concrete." *ACI Materials Journal* 87(5):433–39.

Numerical Modelling

Development of constitutive models for masonry structures

Krisztian Fekete, János Szép

Department of Structural and Geotechnical Engineering,
Széchenyi István University,
Egyetem tér 1, 9026 Győr, Hungary

Summary
Initially, the vaulted structures were built empirically, but as technology advanced and theoretical knowledge grew, they were constructed using increasingly sophisticated design methods. The thrust-line theory satisfies the problems of geometric stability but cannot consider the failure of the materials due to material imperfections and insufficient material strength. The Mohr-Coulomb failure theory, formulated at the beginning of the 20th century and the Drucker-Prager constitutive model already considered material non-linearity but did not yet handle geometric issues and initial damage. The Willam-Warnke plasticity constitutive model accounts for tension, enabling a more effective approach, but failure is tied to a specific point in time.

This article describes material models, their scope of applications, limitations, and additional research opportunities in this topic.

1 INTRODUCTION

Masonry structures and vaults built using traditional methods have been used for centuries in both Western and Eastern architecture. Vaults are an important element of medieval and early modern sacred architecture in Hungary, and their maintenance and renovation are tasks of paramount importance today, both from a monument protection and structural engineering perspective. The protection, maintenance, and restoration of our built heritage is our duty not only as engineers but also as worthy successors.

Understanding the structural behavior of masonry vaults is a complex task. In addition to constitutive models, the methodsfor designing structures also vary greatly, and their development provides us with increasingly accurate information about structures.

The difficulty of static dimensioning is caused by the heterogeneity of masonry structures. Both the masonry elements (stone, brick) and the mortar have different mechanical properties. Based on early empirical results, researchers have attempted to determine the stability of this heterogeneous structure in a number of ways, beyond the basic mechanical equilibrium equations.

According to the technical regulations used in Hungary, a building can be classified as "suitable" if, based on at least 20 years of use, it has fulfilled its intended function, has not suffered any significant structural damage, and will not be subject to any adverse effects during its remaining lifetime. This simple engineering assumption can be interpreted as a test load, but it does not exempt the structure from actual dimensioning. Huerta [1] stated that damage can also be caused by incorrect design or inappropriate repair work.

Therefore, a theoretical review is necessary to design these elements and determine future research directions.

The aim of this article is to summarize, based on the available literature, the constitutive models and scaling theories that can be used to verify the stability of vaults.

2 BIBLIOMETRIC STUDY

We analyzed articles on the study of historic buildings based on Bertolesi's [2] research. The article identified the most important keywords and then examined their frequency of occurrence based on Scopus data. Bertolesi analyzed the period between January 1960 and August 2018 in the article.

We considered three periods for searching for the specified keywords. The first period was 1960–2000, the second was 2001–2019, and the last interval was 2020–2026. The analysis focused on journal articles indexed in Scopus and conference publications.

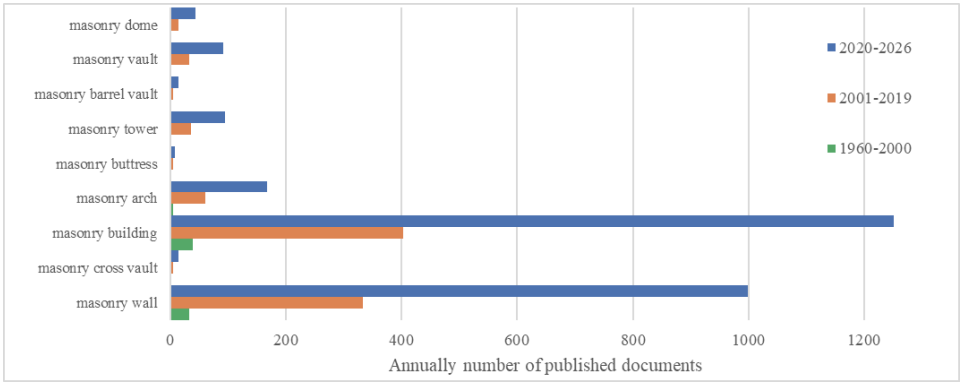


Fig. 1 Number of published documents on research topics registered in the Scopus database by period (updated: January 5, 2026)

Figure 1 was created by dividing the number of documents by the number of years in the time interval, thus obtaining a document/year ratio, which I then marked.

Based on the results of the research, it can be stated that a significant number of publications have been published in the field of research on masonry structures and the characteristics and mechanical behavior of masonry. Over the past six years, 6,255 and 4,994 articles have been published on the subject. The number of articles published on arches and, in summary, on vaulted structures has increased significantly, with a total of 1,954 articles and conference papers published on the subject.

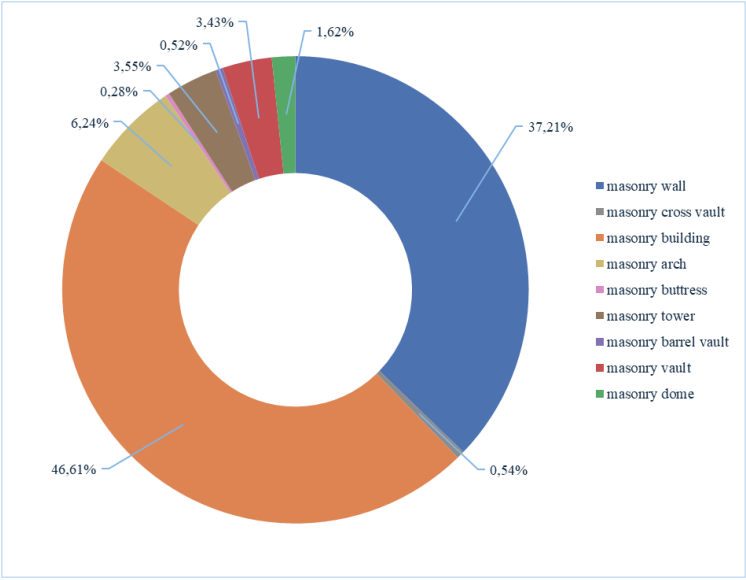


Fig. 2 Documents published between 2020 and 2026

What is the reason for the significant increase in publications on this topic in recent years? For one thing, researchers previously worked experimentally and with software using finite element methods, but recently, discrete element modeling has opened the door to solving more complex problems. On the other side, our built heritage has reached a state where its maintenance and reinforcement can no longer be postponed. Only the third factor is the lower financial cost of research using numerical methods, as they do not require models or test specimens to be physically constructed.

3 EARLY DIMENSIONING THEORIES

Vaults were first used in Egypt, but they reached their most advanced form during the Roman era. In fact, they were not yet measured, but specific empirical guidelines were established. The earliest description of this subject is Vitruvius' Ten Books on Architecture, but even this does not contain clear instructions on vaults.

However, medieval writings provide us with much more information. From the 13th to the 17th century, master builders tried to preserve their knowledge in some form, so they created sketchbooks containing drawings of the necessary machines and construction and editing methods. However, even here, theoretical information was lacking, and the necessary dimensions of buildings were determined by editing.

The first milestone was Giovanni Poleni's investigation in 1743. Over the years, large cracks had appeared in the domes of St. Peter's Basilica in Rome, which rightly scared the public. At the request of Pope Benedict XIV, Poleni divided the dome into 50 meridian segments and built a scaled-down model of one segment. He loaded each part of the segment with weights, which determined a chain of rods. He fitted the resulting shape to the segments of the vault and concluded that if the resulting shape fell between the intrados and extrados of the vault, the segments of the vault were stable on their own, and the visible cracks were not dangerous.

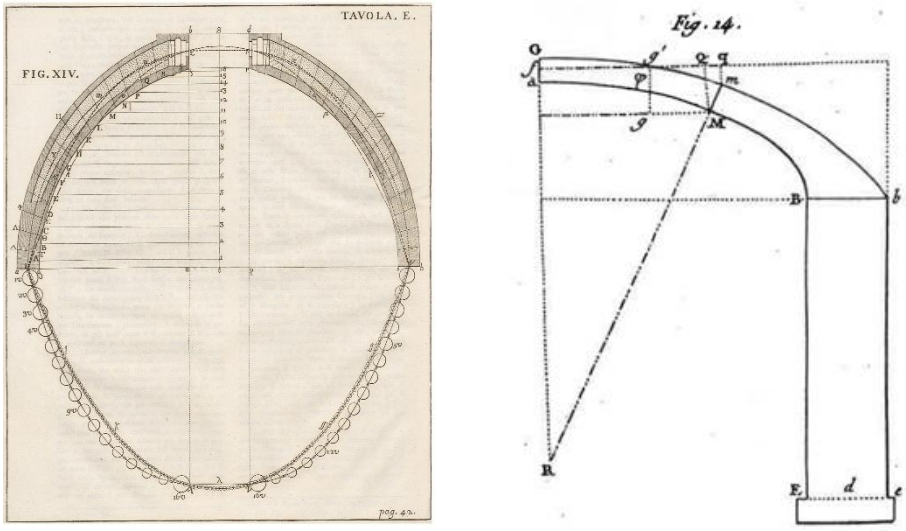


Fig. 3 Left: Poleni's experiment diagram [3]; right: Coulomb's sketch for determining the minimum-maximum problem of the arch [4]

The development of mathematics and engineering in the 18th century reached a level that laid the foundations for the static analysis of arches and vaults. In 1773, Coulomb was already working on the dimensioning of major supporting structures, such as the compressive failure of stone and brick walls, curved supports, arches, retaining walls, and the theory of earth pressure [4].

In his work "Essai sur une application des regles des maximis et minimis à quelques problémes de statique relativs a l'arquitecture", Coulomb investigated the stability of arches using mathematical methods. When describing the system, he also took into account the rotation and slippage between the components. He developed a maximum-minimum method for determining the position of the joints, the fundamental equation of which can be written as follows:

$$W\frac{\overline{gM}}{\overline{QM}} < H < W\frac{\overline{Gq}}{\overline{qm}} \tag{1}$$

The sections appearing in the equation and the mass of the arch section corresponding to the position of the hinge are shown in Figure 3 on the right. During the computation, the possible location of the hinge is determined using variable angle values, and the limits of the crown thrust for a given angle closure are calculated for each characteristic position. Taking into account the narrowest limits, the maximum joint force can be obtained, and the corresponding internal angle gives the location of the fracture cross-section [5].

Coulomb's theory made it possible to dimension arches using graphostatic methods. In 1823, Lamé and Clapeyron stated that, in symmetrical arches, the lateral pressure is maximum at the cross-sectional point where the sum of the horizontal force of the arch and the weight force touches the intrados.

Alfred Durand-Claye's graphostatic method is still the subject of research today [6],[7]. The essence of the principle is to define a stability region on the crown of a symmetrical arch, and then to determine all crown pressures and eccentricities that satisfy the equilibrium equations. The boundary equilibrium state is achieved when the stability region shrinks to a single point. Modern research has found that the method only works for rotationally symmetric domes and if three conditions formulated by Heyman are satisfied.

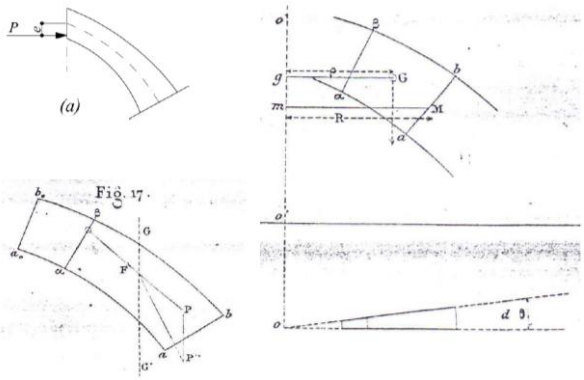


Fig. 4 Depiction of Durand-Claye's compilation [6], [7]

4 CONSTITUTIVE MODELS

According to Mohr-Coulomb failure theory, masonry structures fail when the shear stress reaches a certain value supplemented by cohesion.

$$\tau \geq \sigma \cdot \tan\phi + c \tag{2}$$

where τ is the shear stress, σ is the normal stress, ϕ is the friction angle, and c is the cohesion. In masonry, cohesion is not only the adhesive strength between the brick and the mortar, but also an experimentally determined effective parameter. In addition to the adhesive strength, other determining factors include the angle of rotation of the masonry elements relative to each other, the micro-roughness of the masonry and mortar, its moisture content, etc. The model allows for slippage, but assumes pressure at all points of the structure, not tension.

The Mohr-Coulomb theory describes the behavior of the structure in terms of shear and normal stresses, but according to Rankine's logic, it is advisable to define the limits of principal stresses, which resulted in the modified Mohr-Coulomb failure mechanism supplemented by Rankine's cut-off. Accordingly, in the model, the appearance of tension is indicated by the contact of the Mohr circle on the left side with the σ=0 limit, which indicates the formation of a crack due to the elimination of normal stress, which can be interpreted as a hinge in vaults.

For both brick and mortar, the compressive strength of the component is determined by adding the tensile strength limit (f_b^s) to the Mohr-Coulomb strength (f_b^t) (Equation 3).

$$f_b^s = -\sigma_1 + \sigma_3 \cdot N_\phi - f_{cb} \tag{3a}$$

$$f_b^t = \sigma_3 - f_{tb} \tag{3b}$$

where f_{cb} and f_{tb} are uniaxial compressive and tensile strengths [8].

While earlier constitutive models allowed for infinite compressive strength [9], considered finite compressive strength. Although the article was written from a soil mechanics perspective, its application to masonry later proved to be a fundamental model [10], [11]. According to the model, the yield condition of an elastic, perfectly plastic material can be determined by equation (4):

$$\sqrt{J_2'} + 3\alpha p - c \leq 0 \tag{4}$$

where α and c are factors dependent on the friction angle, p is the hydrostatic stress, and J2' is the second invariant of the stress deviation.

The Drucker-Prager model (Figure 5) presents a non-elastic hardening fracture theory that also accounts for material plastic deformation. The first section of the curve is modeled as a straight line

representing the shear failure surface, followed by the covering surface, which describes the hardening of the material [12].

The linear section is described by equation (5), and the envelope curve by equation (6).

$$F_s = q - d - p \cdot \tan\beta = 0 \tag{5}$$

where q is the von-Mises effective stress, p is the hydrostatic stress, d is the cohesion, and β is the angle of inclination of the fracture line.

$$F_c = \sqrt{(p - p_a)^2 + (Rq)^2} - R \cdot (d + p_a \cdot \tan\beta) = 0 \tag{6}$$

where R is the eccentricity of the ellipse, p_a is the point on the horizontal axis where the line becomes an ellipse, and p_b is the hydrostatic flow stress.

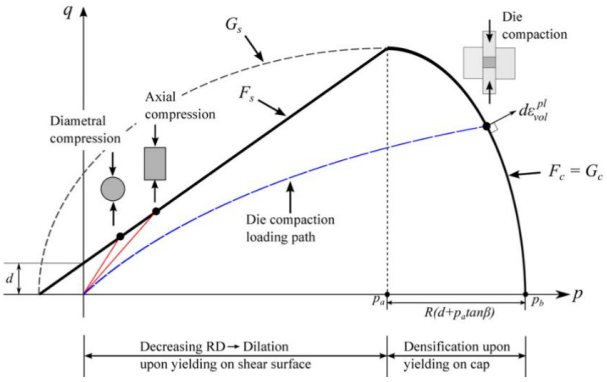


Fig. 5 Drucker-Prager failure mechanism [12]

Heyman concluded that plastic limit state analysis can also be applied to masonry structures [13]. In his work, he formulated three basic conditions under which the theorem can be applied:

- The compressive strength of the masonry element is infinite.
- There is no slippage between the elements.
- The tensile strength of the masonry structure is zero.

Willam and Warnke published their constitutive model in 1975, which described the triaxial behavior of concrete (Figures 6 and 7). The model determines the elastic-brittle stress norm based on five parameters. The deviatoric shape of the fracture surface consists of three intersecting ellipses that form a Rankine triangle. The three ellipses are tangent to the Drucker-Prager circle. We emphasize two main meridians. The compression meridian contains the uniaxial compressive strength f_c, while the tension meridian contains the uniaxial tensile strength f_t and the biaxial compressive strength f_{cc}. The shape of the deviatoric cross-section of the surface is rotated by a Lode angle of 60°. The inscribed meridians intersect at a point determined by the triaxial tensile strength f_{ttt}. The extreme values of the two meridians can be determined by the values $f_{1.max}$ and $f_{2.max}$. [14].

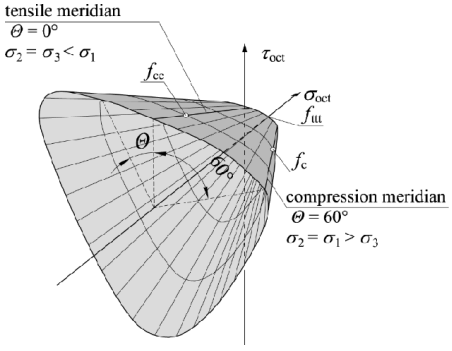


Fig. 6 Willam-Warnke (WW-5) fracture surface stress criterion [14]

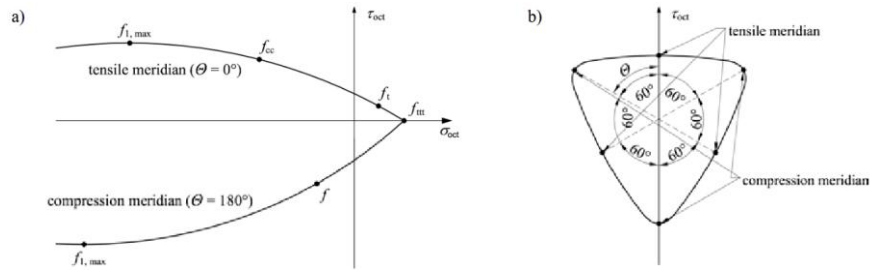


Fig. 7 Meridians of the Willam-Warnke fracture surface [14]

When cracks form, materials that were initially considered isotropic take on orthotropic properties, as the tensile strength in the direction perpendicular to the crack decreases in proportion to a weakening coefficient.

The general shape of the model is described by equation 7:

$$F = A \cdot I_1 + B \cdot \sqrt{J_2} + C \cdot \frac{J_3}{J_2} \leq 0 \tag{7}$$

where A, B, and C are material parameters determined experimentally,

$$I_1 = \sigma_1 + \sigma_2 + \sigma_3 \tag{8}$$

$$J_2 = \frac{1}{6} \cdot [(\sigma_1 - \sigma_2)^2 + (\sigma_2 - \sigma_3)^2 + (\sigma_3 - \sigma_1)^2] \tag{9}$$

$$J_3 = (\sigma_1 - \sigma_2) \cdot (\sigma_2 - \sigma_3) \cdot (\sigma_3 - \sigma_1)/27 \tag{10}$$

The Lode angle determines whether we are in the vicinity of uniaxial compressive strength, shear, or uniaxial tensile strength in the deviatoric plane. The value of the Lode angle is specified by equation (11).

$$\Theta = \frac{1}{3} \cdot cos^{-1}\left(\frac{3\sqrt{3}}{2} \cdot \frac{J_3}{J_2^{3/2}}\right) \tag{11}$$

If the F value calculated according to equation (7) is less than 0, the vault is safe; if it is greater than 0, the structure is likely to collapse.

The Willam–Warnke constitutive model is used by the most complex, nonlinear software currently available. In addition, more complex constitutive models are presently being developed, which not only summarize the properties of individual components but also represent the components of a heterogeneous structure in a unified model.

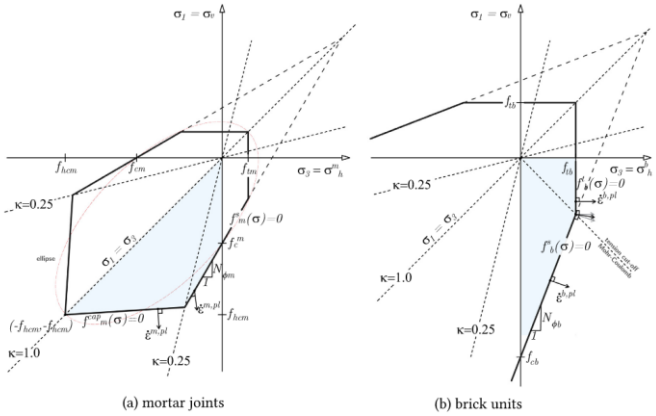


Fig. 8 Multi-surface fracture theory defined for masonry components [8]

The multi-surface fracture theory masonry model shown in Figure 8 is based on the mechanical properties of mortar and block elements. It is capable of demonstrating the elastoplastic behavior of the masonry units and mortar, the nonlinear behavior of the mortar, the fracture of the mortar and masonry

units according to the multi-surface fracture range, and the elastic fracture state of the heterogeneous structure [8].

Knowledge of dimensional methods, supplemented by familiar constitutive models, enables us to understand the deformation and safety of structural forces.

No-Tension material models are based on Heyman's theory and form the basis for the dimensioning of arches. Thrust Line Analysis, which is based on this model, is a rigid-plastic theory that is still used today.

The lines of thrust representing the stresses within the arches of the vault are a series of straight lines [16]. If we discretize the lines of thrust of the three-dimensional vault into a series of point loads applying to the arch, we can define a funicular polygon. The force distribution of the vault can be modeled as a force network connecting the nodes of this polygon. Taking Heyman's principles into account, it is acceptable that all forces in the structure appear as compressive forces [17].

During Thrust Network Analysis, this force system must be determined on the static model of the vault. The analysis is intended to verify the basic principle applied by Poleni, according to which if the thrust line lies between the intrados and extrados of the vault and does not extend beyond the geometry of the structure, it must be considered stable. In the case of a two-dimensional arch, if the thrust line is a curve, the three-dimensional structure defines a thrust surface that also does not deviate from the two boundary surfaces [18].

By evaluating a two-dimensional arch, it was determined that if three joints (cracks) form on the arch, the structure remains stable. However, if four joints form, stability is lost and the structure collapses [1].

There are currently three types of computer simulations [19]. In macro modeling, the masonry structure is considered as a single-phase material. In simplified micro-modeling, the structures appear as two-phase elements, and the actual joint width between the individual bricks is shown. In this case, the calculation model is more complex and the dimensioning takes more time. The third dimensioning method is detailed micro-modeling, in which bricks and mortar are defined as elements with actual specified properties. Due to its computational requirements, it is not suitable for examining larger models, but the results obtained with this method most closely approximate the behavior of the actual structure.

Which method and under what conditions the specialist applies is determined by the specific task and the desired result. Some software already supports the most modern constitutive models, while simpler finite element applications are still under development, so future research opportunities remain to be explored.

5 CONCLUSIONS

When dimensioning structures, the basic requirement for testing is to use a constitutive model that accurately describes the structure's behavior. The development of mathematics and technology over the past two centuries has greatly assisted the structural engineers' work.

In our article, we have summarized the most characteristic constitutive models of this period, which illustrate the thinking behind the operation of software that uses finite element and discrete methods, which are still in use today. In addition to the models described, the development of dimensioning methods provides a complete overview of the in-depth study of structures. However, current research does not approach vaults exclusively from the perspective of material properties.

Our task is to continuously refine the constitutive models currently in use and apply them in our everyday work using the software available to us. The aim of our research is to become as familiar as possible with the vaults of historic buildings by homogenizing masonry structures and comparing constitutive models. In the next phase of our research, we will conduct a sensitivity analysis of the structure based on the material models we have developed and identify the boundary conditions that affect stability. Understanding the behavior of vaults allows us to choose the most economical and sustainable solution for reinforcing centuries-old structures using a physics-informed neural network (PINN).

We approach the investigation not only from the material side, as knowledge of the equilibrium and stress potential of the curved shell structure and the ideal membrane shape it determines, but also enables us to understand the behavior of historic buildings. With the support of PINN, it is possible to more effectively identify damage to vaults, their underlying causes, and the development of suboptimal vault geometry.

References

[1] Huerta, Santiago. 2008. „Static analysis of masonry vaults, constitutive model, and numerical analysis." *Architectural Science Review* 51: 297–328.

[2] Bertolesi, E., Adam, J.M., Rinaudo, P., Calderón, P.A. 2019. „Research and practice on masonry cross vaults – A review." *Engineering Structures* 180: 67–88. doi: 10.1016/J.ENGSTRUCT.2018.10.085

[3] Poleni, Giovanni. 1748. *Memorie Istoriche Della Gran Cvpola Del Tempio Vaticano.* Nella Stamperia del Seminario, Padova. http:// https://catalog.hathitrust.org/Record/102825511

[4] Coulomb, Charles-Augustin. 1773. *Essai sur une application des règles des maximis et minimis à quelques problèmes de statique relatifs à l'arquitecture. Mémoires de mathématique et de physique, présentés à l'académie royal des sciences per divers savants et lus dans ses assemblées*, Paris (1776), vol. 7 :343–382

[5] Peck Tiborné 2003. „Falazott boltívek hagyományos elmélete." *Építés- Építészettudomány* XXXI:69–104.

[6] Aita, D., Bersotti, R., and Bennati, S. 2019. „A parametric study of masonry domes equilibrium via a revisitation of the Durand-claye method" Paper presented at COMPDYN Proceedings. National Technical University of Athens, pp. 663–672. doi: 10.7712/120119.6947.19313

[7] Ascione, L., Berardi, V., Feo, L., Fraternali, F., Tralli, A.M., Aita, D., Barsotti, R., Bennati, S. 2017. „A modern reinterpretation of Durend-Claye's method for the study of equilibrium conditions of masonry domes." Paper presented at AIMETA 2017.

[8] da Silva, L.C.M., Milani, G., Grande, E., Funari, M.F. 2024. „Mechanistic model for the compression strength prediction of masonry columns strengthened with fibre–polymer composites." *Composite Structures 338.* doi: 10.1016/j.compstruct.2024.118088

[9] Drucker, Daniel Charles, Prager, William. 1952. „Soil mechanics and plastic analysis for limit design." *Quarterly of Applied Mathematics* 10:157–165. doi: 10.1090/qam/48291

[10] Lourenço, Paulo José Brandão Barbosa, 1996. „Computational strategies for masonry structures." PhD Dissertation. Delft Univ. Press, Delft.

[11] Lourenço, Paulo B. and Rots, Jan G. 1997. „Multisurface Interface Model for Analysis of Masonry Structures." *Journal of Engineering Mechanics.* 123:660–668. doi: 10.1061/(ASCE)0733-9399(1997)123:7(660)

[12] Garner, S., Strong, J., and Zavaliangos, A. 2015. „The extrapolation of the Drucker–Prager/Cap material parameters to low and high relative densities." *Powder Technology* 283:210–226. doi: 10.1016/j.powtec.2015.05.027

[13] Heyman, Jaques. 1966. „The stone skeleton." *International Journal of Solids and Structures* 2:249–279. doi: 10.1016/0020-7683(66)90018-7

[14] Drobiec, Łukasz, and Jasiński, Radosław. 2017. „Adoption of the Willam-Warnke Failure Criterion for Describing Behavior of Ca-Si Hollow Blocks" Paper presented at Procedia Engineering. Elsevier Ltd. doi: 10.1016/j.proeng.2017.06.239

[15] Jasiński, Radosław. 2020. „Numerical analysis of the strains and stress states reinforced clay brick masonry walls horizontally sheared." *The International Journal of Engineering Technologies and Management Research* 5:20–37. doi: 10.29121/ijetmr.v5.i8.2018.277

[16] O'Dwyer, Dermot. 1999. „Funicular analysis of masonry vaults." *Computers & Structures* 73:187–197. doi: 10.1016/S0045-7949(98)00279-X

[17] Roca, P., Cervera, M., Gariup, G., Pela', L. 2010. „Structural analysis of masonry historical constructions. Classical and advanced approaches." *Archives of Computational Methods in Engineering* 17:299–325. doi: 10.1007/s11831-010-9046-1

[18] Block, P., Ciblac, T., and Ochsendorf, J. 2006. „Real-time limit analysis of vaulted masonry buildings." *Computers and Structures* 84:1841–1852. doi: 10.1016/j.compstruc.2006.08.002

[19] Asteris, P.G., Plevris, V., Sarhosis, V., Papaloizou, L., Mohebkhah, A., Komodromos, P., Lemos, J.V. eds. 2015. „Numerical modeling of historic masonry structures, in: Handbook of Research on Seismic Assessment and Rehabilitation of Historic Structures." *Advances in Civil and Industrial Engineering. IGI Global*, 213–256. doi: 10.4018/978-1-4666-8286-3

Modelling of Flexural Hinge Property of Equivalent Beams for Pushover Analysis of a Building with Flat Slabs

Prem Kumar Akula and Amlan Kumar Sengupta

Indian Institute of Technology Madras,
Adyar, Chennai (600036), India

Summary
A pushover analysis of a building with flat slabs can be carried out by modelling slabs as one-dimensional equivalent slab–beam members using the Effective Beam Width Method (EBWM). This approach requires appropriate hinge properties to represent the nonlinear slab response. The present study aims to develop a mechanics-based flexural hinge property. The slab response near an interior slab–column joint was investigated. A nonlinear finite element model was first validated using a test building with flat slabs reported in the literature. The modelling approach was then applied to a proposed slab–column sub-assemblage under lateral load. The bending and twisting moment fields and their azimuthal variations (Ø) around the column centreline were examined. Fourier analysis showed that the bending and twisting moments follow sin(Ø) and cos(3Ø) patterns, respectively. These results will be used to formulate flexural hinge properties for equivalent slab–beam members.

1 INTRODUCTION

Flat slabs are widely used in multi-storeyed reinforced concrete buildings due to their architectural flexibility and ease of construction. In engineering practice, seismic analysis and design of such buildings are commonly carried out using linear equivalent frame or finite element models. However, performance-based evaluation under earthquake loading requires modelling of nonlinear behaviour of the members to capture stiffness degradation, strength redistribution, and deformation capacity. A pushover analysis is a static method where lumped plasticity can be assigned at critical sections of the members to model the material nonlinearity.

The present study investigates the behaviour of a slab around the supporting interior column when the structure is subjected to increasing lateral drift. First, from the reviewed literature, a building specimen with columns and flat slabs tested only under lateral loads, was numerically simulated. A finite element model of the slab was developed using nonlinear layered shell elements. Quadratic displacement interpolation and Gaussian integration through the shell thickness were adopted to capture coupled membrane, flexural, and twisting behaviour. The model was validated against the reported total lateral load versus roof drift data.

Next, the same modelling approach was used to investigate the flexural and twisting moment fields around the joint of a slab–column sub-assemblage specimen which will be tested under lateral load. The paper presents the salient results from this analysis. The results will be used to formulate flexural hinge properties for equivalent slab-beam members in pushover analysis of buildings with flat slabs.

2 LITERATURE REVIEW

For analysing the behaviour of flat slab structures subjected to lateral loading, various analytical approaches have been developed based on simplified structural idealisations. Most of these methods are based on the Equivalent Frame Method (EFM) and its extensions, in which the three-dimensional slab–column system is represented as an assemblage of two-dimensional frames for analysis in each horizontal direction at a time.

2.1 Equivalent Frame Method

For flat slab buildings with columns arranged in a regular grid, the three-dimensional slab–column system is idealized as a set of two-dimensional equivalent frames acting independently in each orthogonal direction [8]. Each equivalent frame is considered along a column line and bounded by the centerlines of adjacent slabs. While this idealization was originally developed for gravity load analysis,

its application to lateral loading has been shown to be sensitive to the assumed stiffness of slab–column connections [9].

2.1.1 Equivalent Column Method

In the Equivalent Column Method (ECM), slab portions attached to the transverse faces of a column are idealized as torsional members that transfer moments between the slab and the column. The rotational stiffness at the slab–column joint is represented through the combined effect of column flexural stiffness and slab torsional resistance. This approach is primarily applicable to analysis under gravity and monotonic lateral loading [1], [4].

2.1.2 Effective Beam Width Method

In the Effective Beam Width Method (EBWM), the slab is represented as an equivalent beam of reduced width to approximate the rotational response at slab–column connections within a two-dimensional frame idealization. The effective width is defined based on stiffness considerations of the slab–column connection, with refinements proposed for lateral and seismic loading conditions. In this approach, the slab–column behavior is described primarily through stiffness-based representation [2], [5]-[6].

The above methods estimate the flexural and punching shear demands or capacities, which are necessary for the design of a flat slab. The present study aims to extend the EBWM for estimating the rotation of the slab in the vicinity of an interior slab–column joint.

2.2 Validation of Numerical Simulation

A numerical simulation was performed on a two-bay, three-story prototype building subjected to monotonically increasing static lateral loads, as tested by [3]. The specimen was selected since no punching failure occurred in the slabs up to the peak load. Symmetry allowed for modeling only half of the building. Fig. 1 shows the building dimensions.

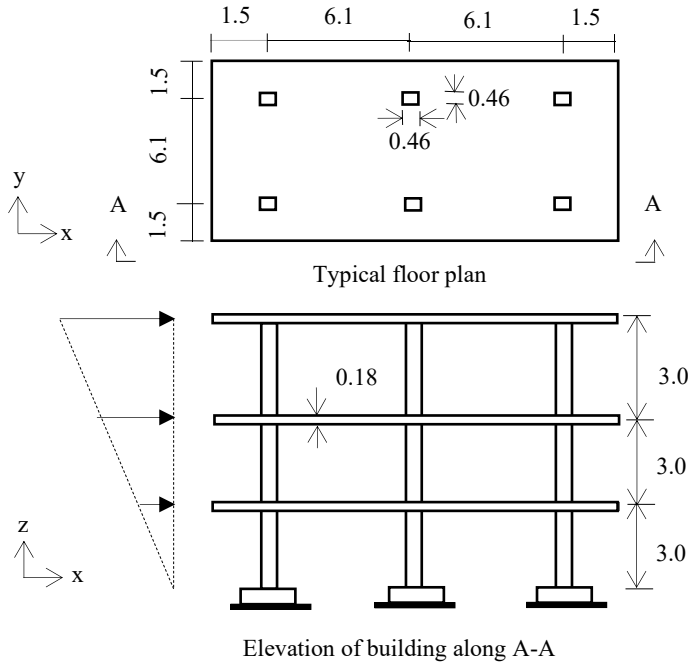


Fig. 1 Plan and elevation of prototype building (dimensions in meters) [3]

The slab and column reinforcement details, material properties, loading protocol, and boundary conditions, including the fixed column base, were adopted directly from the reference experimental

study. Soil effects were not considered in this study. Superimposed dead load was applied on the slabs, followed by monotonic lateral loading along the longer plan (x-axis) direction, with load distribution varying linearly with height.

The material nonlinearity was assigned to the constitutive relationships of concrete and reinforcing steel. Since the columns were stiff, they were modeled using linear line elements. A uniform mesh size of 200 mm was applied throughout the slab. A displacement-controlled pushover analysis was performed in the lateral direction, targeting a roof displacement of 0.25 m, applied in 12 increments. The experimental and numerical pushover curves (total lateral load termed as base shear, versus roof displacement) are illustrated in Fig. 2. The numerical model reproduced the initial stiffness reasonably well, while slightly higher stiffness and strength were observed at larger displacements, which may be attributed to the assumed column base fixity. Following validation at the prototype building level, the same modelling approach was subsequently applied to the study of slab–column sub-assemblage behaviour under lateral loading.

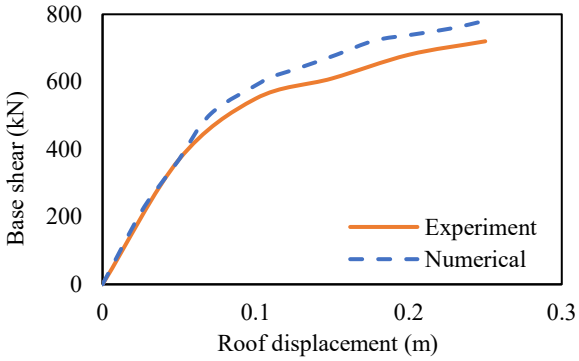


Fig. 2 Comparison of pushover curves

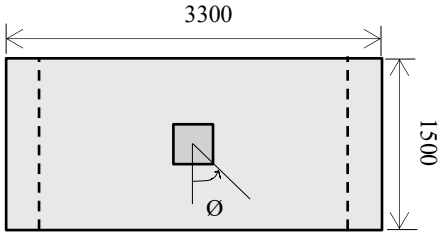
3 ANALYSIS OF THE PROPOSED SUB-ASSEMBLAGE SPECIMEN

The proposed interior slab–column subassemblage consisted of a rectangular slab with a centrally positioned square column. Uniform top and bottom reinforcement was provided in both directions, resulting in an approximately isotropic reinforcement configuration. The geometric configuration and reinforcement layout are shown in Fig. 3, and the corresponding details are summarized in Table 1. Lateral loading was applied in the x-direction. The column was modeled as linear elastic to maintain a relatively rigid column response, thereby enabling nonlinear behaviour of the slab under lateral loading. A hinged support condition was assigned at the column base to permit rotation. The slab edges perpendicular to the direction of loading were restrained against vertical movement, consistent with the adopted boundary conditions. Lateral load was applied at the top of the column using a displacement-controlled procedure, with incremental displacement steps of 3.5 mm, up to a maximum lateral displacement of 35 mm.

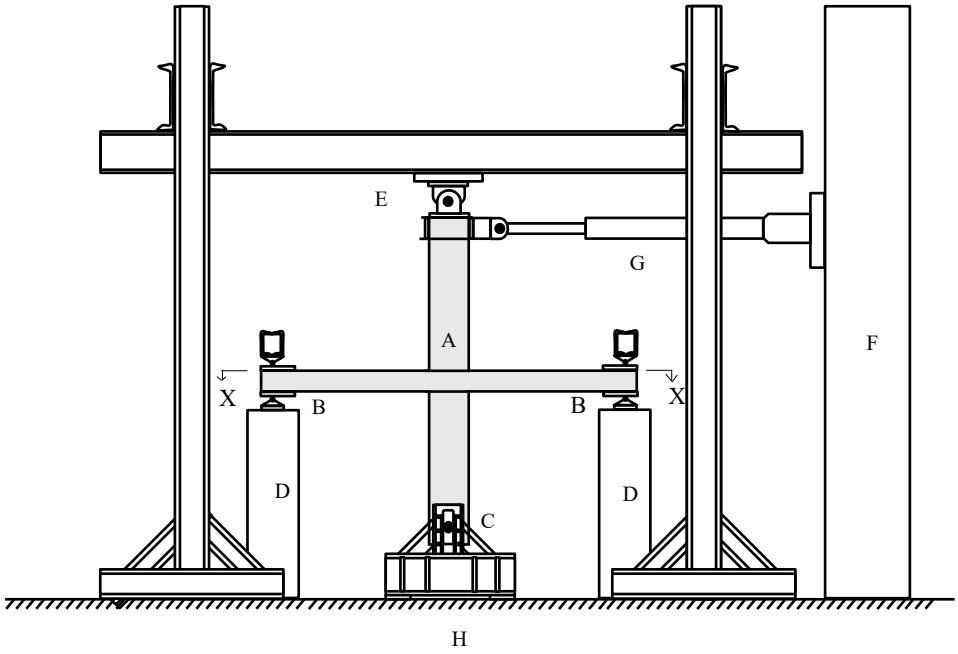
Material nonlinearity was incorporated corresponding to concrete compressive strength of 25 MPa and steel yield strength of 550 MPa. A uniform finite element discretisation of 100 mm × 100 mm was adopted for the slab, and mesh sensitivity was checked to ensure that the predicted response was not significantly affected by element discretization. Shell elements within the column section were assigned higher stiffness to simulate the rigid joint behaviour. An angular (azimuthal) coordinate, Ø, was defined around the column to extract response quantities of the slab. The response quantities presented here include contours of bending and twisting moments in the slab at peak lateral load.

Based on the recommendation of Muttoni [7], the critical region of response in the slab was considered to be within a radial distance of approximately 0.22 l around the column centre-line. Here, l is the length of the slab between the supports.

In a frame idealisation, this (0.22 l) is the same as the span of a slab between the column centre-lines. Therefore, results in the present study are reported within this critical region (1500 mm × 1500 mm) rather than over the entire slab area.



Plan at Level X-X



Schematic test setup

A	Specimen	E	Horizontal sliding cum rocker
B	Roller support	F	Reaction wall
C	Pin insert	G	Actuator
D	Pedestal	H	Strong floor

Fig. 3 Investigated sub-assemblage specimen

Table 1 Geometry and material properties of the investigated sub-assemblage

Parameter	Details
Slab	
Dimensions	3300 mm (length) × 1500 mm (width) × 150 mm (thickness)
Longitudinal reinforcement	8 mm ϕ @ 125 mm c/c (top and bottom)
Transverse distribution reinforcement	8 mm ϕ @ 125 mm c/c (top and bottom)
Column	
Section dimensions	350 mm × 350 mm
Longitudinal reinforcement	4 bars of 25 mm ϕ
Transverse tie bars	8 mm ϕ @ 75 mm c/c
Height of the column from mid-depth of slab	1100 mm (above and below)
Mechanical properties of materials	
Cylinder compressive strength of concrete	25 MPa
Elastic modulus of concrete	25000 MPa
Yield strength of reinforcing bars	550 MPa
Elastic modulus of reinforcing bars	200000 MPa

4 RESULTS AND DISCUSSIONS

Here, local responses in terms of flexural and twisting moments per unit width are presented.

4.1 Variations of Bending Moment (m_{xx})

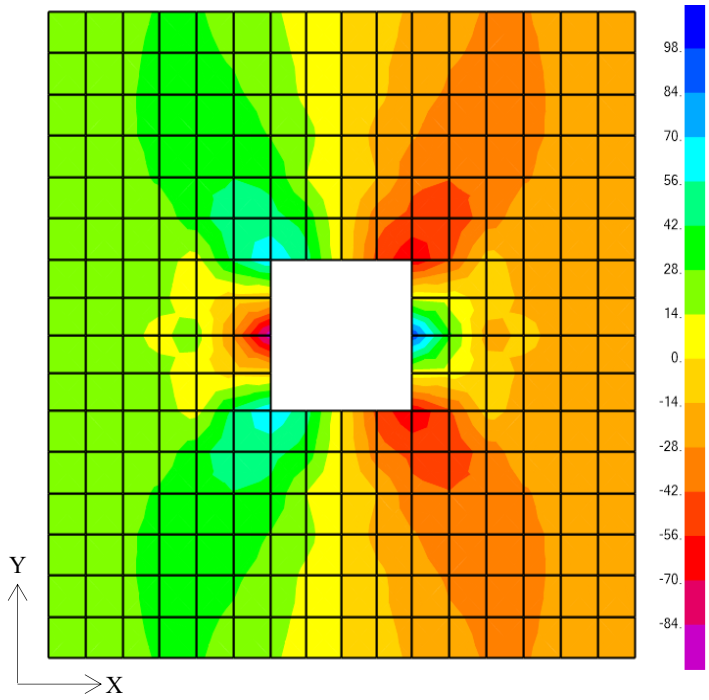
The distribution of bending moment per unit width in the slab along the direction of loading (m_{xx}) at the peak load is shown in Fig. 4 (top). The response exhibits an antisymmetric pattern about the column axes.

The azimuthal variation of m_{xx} at a radial distance of 0.22*l* from the column centreline, shown in Fig. 5 (top), increases from zero at Ø = 0°, attains high values along the loading direction, and returns to zero at Ø = 180°, with a subsequent reversal of sign. The Fourier decomposition indicates that the response is dominated by the first harmonic component, while the next higher-order component has relatively smaller amplitude. Accordingly, the variation of bending moment may be reasonably approximated using a sinusoidal function for the formulation of hinge properties.

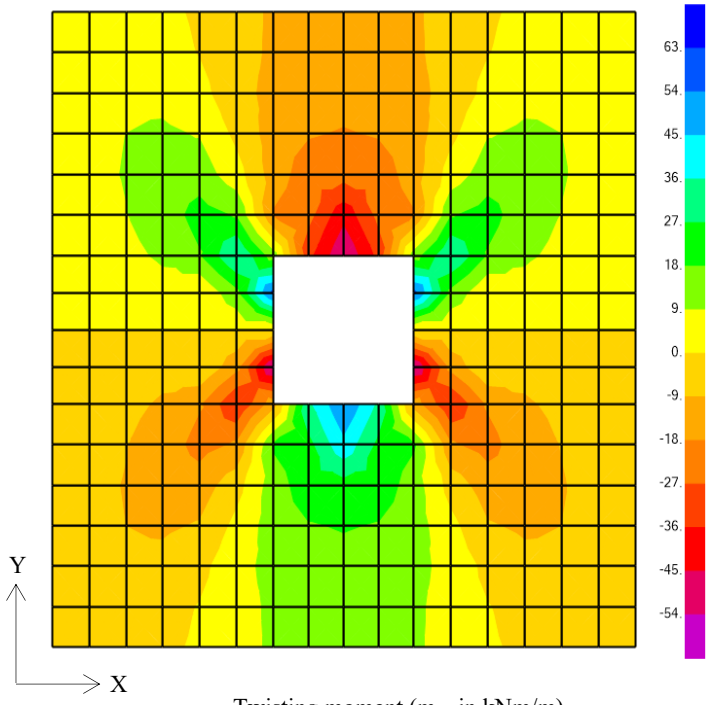
4.2 Variation of Twisting Moment (m_{xy})

The distribution of twisting moment per unit width of the slab (m_{xy}) at the peak load is shown in Fig. 4 (bottom). Alternating positive and negative twisting regions develop around the column, predominantly along the diagonal directions, exhibiting antisymmetric behaviour about the column axes.

The azimuthal variation shown in Fig. 5 (bottom) exhibits peak values along the transverse axis (at Ø = 0° and 180°). High values occur near 45°, 135°, 225°, and 315°. Fourier decomposition indicates that the variation of the twisting moment is governed by the third harmonic component, supporting a cos(3Ø) type representation.



Bending moment along the x-axis (m_{xx} in kNm/m)



Twisting moment (m_{xy} in kNm/m)

Fig. 4 Contours of bending moment and twisting moment per unit width at peak load (joint region is unshaded)

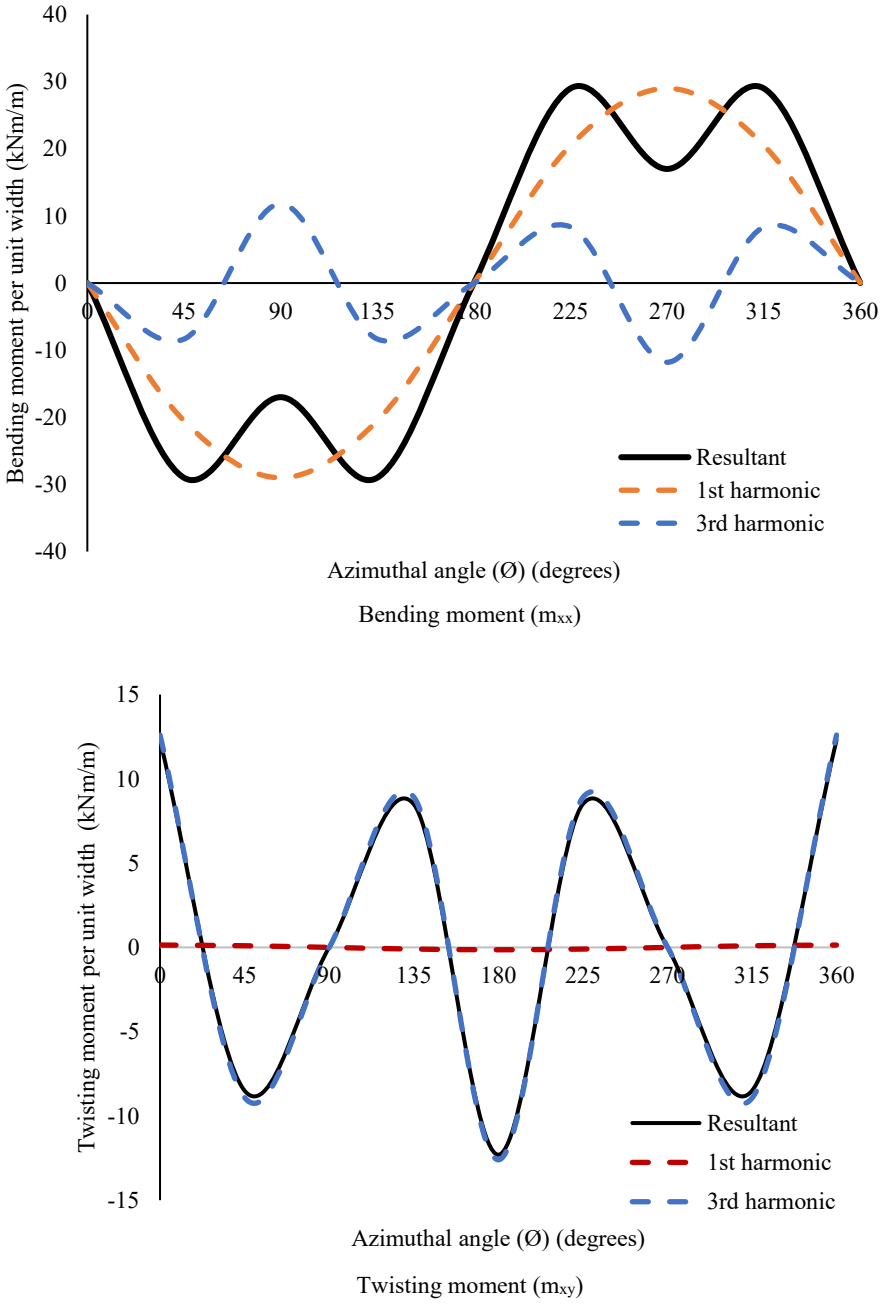


Fig. 5 Azimuthal variations and Fourier decompositions of bending and twisting moments in slab

5 CONCLUSIONS

This study examined the response of a flat slab around an interior joint of a slab–column sub-assemblage subjected to lateral load. Emphasis was placed on investigating the azimuthal variations of bending and twisting moments around the column centreline. The numerical modelling approach was first validated using experimental data reported for a test building with flat slabs. Next, a proposed slab–column sub-assemblage specimen to be tested under lateral load was analysed.

Based on the numerical results for the sub-assemblage specimen, the following conclusions are drawn:

- The azimuthal variation of the bending moment in the slab along the direction of loading is antisymmetric with a dominant first harmonic component. It can be idealised as a sin(Ø) pattern, where Ø is the azimuthal angle.
- The azimuthal variation of the twisting moment shows alternating positive and negative values with a dominant third harmonic component. This can be idealised as a cos(3Ø) pattern.
- The results of the present study indicate that the coupling between the bending and twisting moments in the slab around the column needs to be considered in the development of the flexural hinge property for the slab–beam member. For precise estimation of the rotation, the hinge property cannot be based only on one-dimensional bending of the slab by neglecting the twisting moment.

The results from the present study can be used in the formulation of flexural hinge properties for equivalent slab–beam members. The detailed hinge formulation is presently kept in abeyance. The proposed hinge properties will be demonstrated in a pushover analysis of a building with flat slabs.

Acknowledgements

This research was supported by the Indian Institute of Technology Madras and the Prime Minister Research Fellowship funded by the Ministry of Education, Government of India.

References

[1] Corley, W. Gene, and Jirsa, James O. 1970. “Equivalent Frame Analysis for Slab Design.” *ACI Journal Proceedings* 67:875–884. doi:10.14359/7317.

[2] Dovich, Laurel M., and Wight, James K. 2005. “Effective Slab Width Model for Seismic Analysis of Flat Slab Frames.” *ACI Structural Journal* 102:868–875. doi:10.14359/14795.

[3] Fick, Damon R., Sozen, Mete A., and Kreger, Michael E. 2017. “Response of Full-Scale Three-Story Flat-Plate Test Structure to Cycles of Increasing Lateral Load.” *ACI Structural Journal* 114:1507–1517. doi:10.14359/51689502.

[4] Luo, Y. H., Durrani, Ahmad J., and Conte, Joel P. 1994. “Equivalent Frame Analysis of Flat Plate Buildings for Seismic Loading.” *Journal of Structural Engineering* 120:2137–2155. doi:10.1061/(ASCE)0733-9445(1994)120:7(2137).

[5] Luo, Y. H., and Durrani, Ahmad J. 1995. “Equivalent Beam Model for Flat-Slab Buildings—Part I: Interior Connections.” *ACI Structural Journal* 92:115–124. doi:10.14359/1534.

[6] Luo, Y. H., and Durrani, Ahmad J. 1995. “Equivalent Beam Model for Flat-Slab Buildings—Part II: Exterior Connections.” *ACI Structural Journal* 92:250–261. doi:10.14359/1154.

[7] Muttoni, Aurelio. 2008. “Punching Shear Strength of Reinforced Concrete Slabs Without Transverse Reinforcement.” *ACI Structural Journal* 105:440–450. doi:10.14359/19858.

[8] Pillai, S. Unnikrishna, and Menon, Devdas. 2021. *Reinforced Concrete Design*. Fourth edition. New Delhi: Tata McGraw Hill Education.

[9] Vanderbilt, M. Daniel, and Corley, W. Gene. 1983. “Frame Analysis of Concrete Buildings.” *Concrete International* 5:33–43.

Numerical Modelling of Hydration Heat and Shrinkage in Gravity Dam

Simona Potůčková, Petr Kněž, Milan Holý, Jiří Kolísko

Klokner Institute,
CTU in Prague,
Šolínova 7, Prague 166 08, Czech Republic

Summary

Massive concrete structures are highly sensitive to early-age thermal and shrinkage effects, which may lead to cracking and long-term durability issues. This research investigates the coupled interaction of hydration heat, shrinkage, and moisture transport using advanced numerical simulations. The proposed modelling framework accounts for heat conduction, moisture diffusion, and creep–shrinkage behaviour, providing a more realistic representation of the structural response during and after construction. Parametric analyses on a representative dam section were conducted to examine the influence of curing conditions, ambient climate, and construction scheduling. The study demonstrates that moisture-related processes significantly affect stress development and long-term deformation, underlining their importance for reliable design and crack risk assessment. The presented approach contributes to the optimization of construction strategies for gravity dams and other massive concrete structures.

1 INTRODUCTION

Gravity dams and other massive concrete structures are characterized by large volumes, limited reinforcement, and significant restraint, which makes them particularly vulnerable to early-age thermal and shrinkage effects [1], [3]. The exothermic hydration of cement leads to elevated internal temperatures, while subsequent cooling and moisture loss induce tensile stresses that may exceed the low tensile strength of young concrete [4], [9]. Resulting cracks can compromise watertightness, durability, and long-term performance of the structure [2], [3].

Traditional design approaches relied on empirical rules, temperature limits, and conservative construction procedures [3], [5]. Although these methods have proven effective in many historical projects, they generally treat hydration heat, shrinkage, creep, and moisture effects in a simplified or decoupled manner [1], [6]. Contemporary dam engineering increasingly relies on advanced numerical modelling to explicitly simulate coupled thermo–hygro–mechanical behaviour and to support rational optimization of construction technology [1], [2], [8].

This paper presents a comprehensive numerical study of hydration heat, shrinkage, and moisture transport in a gravity dam. Emphasis is placed on the modelling procedure and verification of material models, rather than on project-specific results, in order to provide a transferable methodology applicable to a wide range of massive concrete structures.

2 HISTORICAL DEVELOPMENT OF MODELLING APPROACHES FOR MASS CONCRETE DAMS

Early analyses of thermal behaviour in concrete dams were based on analytical solutions of heat conduction and empirical estimates of temperature rise [3], [5]. Crack risk was assessed indirectly, typically by limiting maximum temperatures or temperature differences between the core and surface [3]. Shrinkage and creep were often considered only qualitatively.

With the development of finite element methods in the second half of the twentieth century, numerical simulation of temperature fields became standard practice [5], [7]. However, early FE models typically addressed thermal analysis and structural analysis separately, with shrinkage introduced as prescribed strains and moisture effects neglected [6].

In recent decades, advances in computational power and material modelling have enabled fully coupled thermo–hygro–mechanical simulations [1], [4], [8]. Modern approaches explicitly consider hydration kinetics, moisture diffusion, autogenous and drying shrinkage, and creep, allowing more realistic prediction of stress development and cracking. Such methods are particularly relevant for

massive concrete dams, where construction spans multiple seasons and long-term environmental exposure governs structural response [1], [2].

3 NUMERICAL MODELLING FRAMEWORK

The analysis was performed using nonlinear numerical software, which concerns nonlinear finite element modelling with coupled transport and mechanical analyses. The calculation procedure was divided into two main stages:

- Transport analysis, simulating the evolution of temperature and moisture fields due to cement hydration, environmental exposure, and boundary conditions.
- Mechanical (creep) analysis, in which the temperature and moisture evolution obtained from the transport analysis were applied as loads to evaluate stress development and crack risk. Material parameters were calibrated using laboratory measurements of hydration heat and shrinkage to ensure consistency between numerical predictions and experimentally observed behavior.

Sensitivity analysis to define the size of the mesh element was also carried out – it takes into consideration computation speed and memory requirements. Element size of 1,0 m was found too inaccurate for the areas where cracking appeared. In contrary, using the mesh size of 0,5 m for the whole construction proved to be ineffective. Subsequently, a final transport and creep analysis was performed on a model with a refined mesh in areas with an increased risk of cracking – the size of the mesh elements was set to 1.0 m outside the risk areas and 0.5 m in the risk areas.



Fig. 1 Final global model with a refined mesh size [17]

3.1 Transport Analysis

The transport analysis solves coupled heat conduction and moisture diffusion. Heat generation due to cement hydration is modelled using an affinity-based hydration model calibrated against laboratory measurements. The analyses employed the CCTransport materialLevel7 model [10], [11], which allows direct input of experimentally measured moisture-related and thermal properties. The model simulates both cement hydration heat development and moisture transport within the concrete. Moisture transport accounts for diffusion and surface exchange driven by ambient temperature and relative humidity.

Variable ambient temperature and humidity conditions were derived from Czech Hydrometeorological Institute (CHMI) data for the Krnov area. Individual values were taken as weekly average temperatures and implemented in the numerical model as time-dependent boundary conditions.

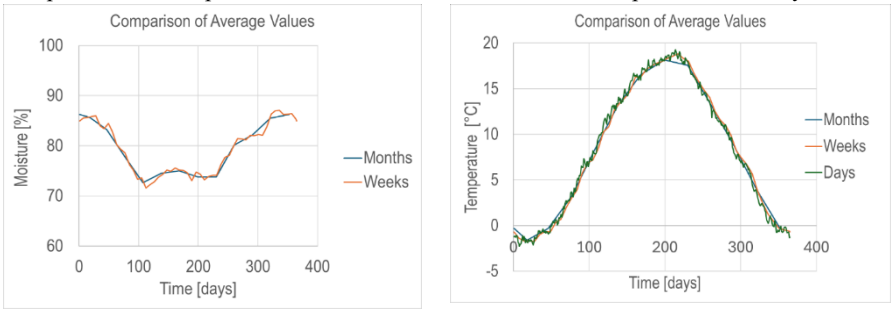


Fig. 2 Ambient temperature and moisture values [17]

3.2 Mechanical Analysis

The mechanical response of concrete is described using a nonlinear constitutive model incorporating creep, autogenous shrinkage, and drying shrinkage. For the concrete structure, the CCModelB4 material model was employed [10], [11]. Application of this model requires the definition of a number of parameters dependent on the geometry of the structure and the concrete mix composition. The creep material model simulates the time-dependent development of concrete strength and shrinkage. Shrinkage develops naturally as a consequence of moisture loss, while creep provides stress relaxation under sustained loading. Temperature- and moisture-dependent evolution of mechanical properties is considered throughout the analysis.

3.3 Verification of Material Models

Reliable numerical prediction of thermal and shrinkage-related behaviour of massive concrete structures requires not only advanced constitutive models, but also a transparent verification strategy [1], [2]. Material parameters were calibrated against laboratory measurements: hydration kinetics using semi-adiabatic tests and moisture transport via mass-loss monitoring of specimens under controlled relative humidity (50% and 75%).

In this study, a hierarchical modelling strategy was adopted, consistent with recommendations by RILEM and ICOLD [1,2]. The procedure comprised:

1. verification of thermal and moisture-related material parameters using laboratory-scale experiments [9], [12],
2. verification of shrinkage and time-dependent deformation models on simplified structural elements [4], [13],
3. application of verified material models to sectional and global dam models [1], [2].

This stepwise approach was chosen to reduce modelling uncertainty and ensure physical consistency of coupled analyses.

3.3.1 Verification of Hydration Heat Model

The hydration heat model was calibrated using a numerical simulation of a 300 mm concrete cube, corresponding to laboratory temperature measurements performed during cement hydration. A transient heat transfer analysis was conducted, accounting for the concrete mix composition, thermal properties of individual constituents, and insulation conditions used during the experiments.

A numerical model reproducing the test geometry and boundary conditions was used to calibrate hydration kinetics parameters, ensuring good agreement between measured and simulated temperature–time curves.



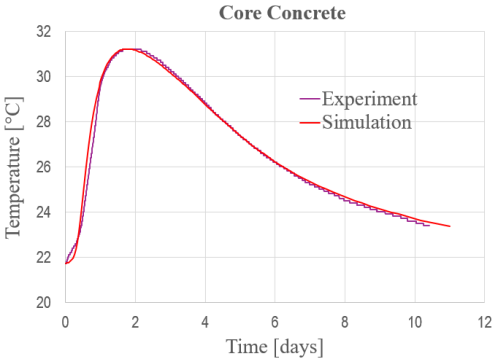


Fig. 3 Example of core concrete temperature verification [17]

3.3.2 Verification of Moisture Transport Parameters

Moisture transport plays a key role in long-term deformation and stress development of massive concrete structures. Moisture transport parameters were therefore verified using experimental observations of drying behaviour under controlled environmental conditions.

Laboratory specimens were exposed to defined relative humidity levels, and their mass loss and deformation were monitored over time [1], [14]. The numerical moisture transport model was applied to the same specimen geometry, and moisture diffusivity and surface exchange coefficients were adjusted to reproduce the experimentally observed drying kinetics. Similar verification approaches have been reported in previous studies dealing with moisture-driven shrinkage in concrete [8], [14].

This step ensured that moisture gradients and drying rates predicted by the model are physically realistic, which is essential for reliable simulation of drying shrinkage.

3.3.3 Verification of Shrinkage Behaviour

Shrinkage behaviour was verified by comparing numerical predictions with laboratory shrinkage measurements performed on prismatic specimens subjected to controlled humidity conditions (50% and 75%). Both autogenous and drying shrinkage components were considered, in accordance with current modelling concepts for early-age concrete [8], [13].

In contrast to simplified approaches where shrinkage is prescribed as a time-dependent strain, shrinkage in the present model resulted directly from the evolving moisture field. This coupling reflects the physical origin of drying shrinkage and is consistent with modern modelling recommendations.

Creep behaviour was represented using a time-dependent constitutive model based on established formulations, such as Model B4 [1]. The inclusion of creep is essential for realistic stress relaxation under sustained thermal and shrinkage-induced loading [15], [16].

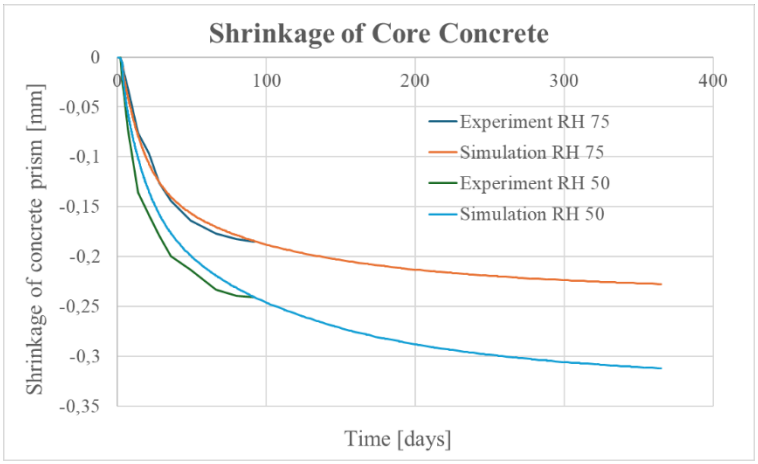


Fig. 4 Example of core concrete shrinkage verification [17]

3.3.4 Verification on Simplified Structural Models

Following material-level verification, the calibrated models were applied to simplified three-dimensional structural models representing a characteristic section of the gravity dam. This intermediate step allowed assessment of the interaction between temperature evolution, moisture transport, shrinkage, and mechanical restraint under controlled conditions and reduced computational effort.

The results obtained from the sectional models were evaluated in terms of temperature gradients, stress development, and crack initiation patterns. This approach is consistent with recommendations to verify coupled material models on representative structural elements prior to full-scale application.

3.3.5 Application to the Global Dam Model

Only after successful verification at the material and sectional levels were the calibrated models applied to the global three-dimensional model of a gravity dam block. The global model incorporated staged construction, activation and deactivation of construction phases, long-term climatic boundary conditions, and reservoir impoundment.

By following this hierarchical modelling and verification strategy, uncertainties associated with complex coupled analyses were significantly reduced, and the numerical predictions of stress development and crack risk could be interpreted with greater confidence.

4 PARAMETRIC ANALYSES ON A REPRESENTATIVE DAM SECTION

Following verification of the material models, a series of parametric analyses was performed on a representative three-dimensional section of the gravity dam. The objective of this step was not to reproduce the complete structural behaviour, but to identify the governing parameters influencing thermal gradients, moisture loss, and shrinkage-induced stresses under controlled and computationally efficient conditions [5], [6].

The analysed section was selected to represent regions with large concrete volumes and significant restraint, where the risk of cracking is typically highest. The parametric analyses focused on technological and environmental parameters that can be influenced during design and construction, namely:

- initial temperature of fresh concrete,
- duration and intensity of surface curing,
- ambient temperature and relative humidity,
- time intervals between successive concrete placements.

Each parameter was varied independently while maintaining identical material properties and boundary conditions for the remaining variables. This approach allowed direct comparison of individual effects and facilitated interpretation of their influence on temperature evolution, moisture gradients, and stress development.

The results showed that thermal effects dominate the early-age behaviour, particularly during the first weeks after placement, whereas moisture-driven shrinkage becomes increasingly significant at later ages. Extended curing effectively reduced early moisture loss and delayed the onset of drying shrinkage; however, long-term moisture gradients persisted even under favourable curing conditions. These findings confirmed the necessity of including moisture transport in subsequent global analyses.

- Variation of curing time:

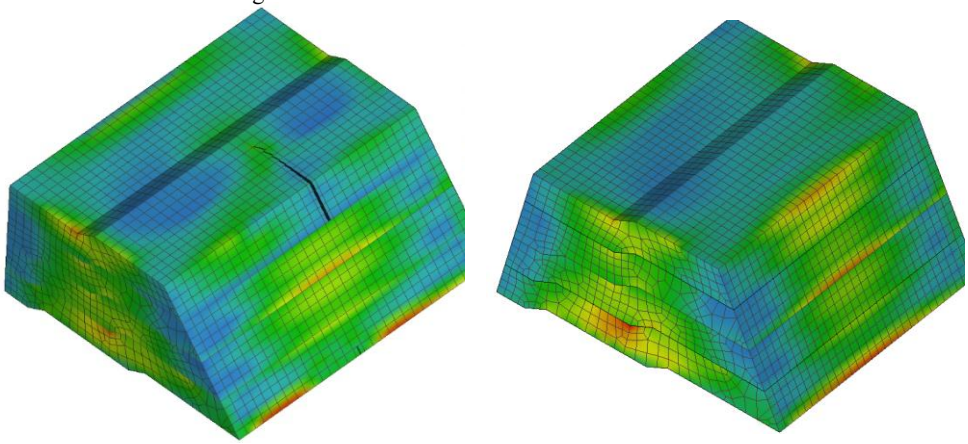


Fig.5 Left: default model (curing until overlying block is concreted), right: extended curing throughout the entire construction of the block [17]

5 GLOBAL 3D MODELLING OF STAGED CONSTRUCTION

5.1 Construction Phase

Based on the insights gained from the parametric study, a three-dimensional global model of a complete gravity dam block was developed. The model explicitly simulated staged construction, with individual

concrete sections activated according to the construction schedule. Adjacent blocks were included to represent realistic restraint conditions [2].

The construction phase analysis demonstrated that hydration heat leads to elevated temperatures in the structural core for several months after placement. Due to the large dimensions of the block, heat dissipation was relatively slow, resulting in pronounced temperature gradients between the core and exposed surfaces during cold periods. At the same time, progressive drying of surface layers led to non-uniform moisture distribution, which significantly influenced shrinkage development.

The combined effect of thermal contraction and moisture-driven shrinkage governed the evolution of tensile stresses near the surfaces. The results confirmed that the most critical stress states did not necessarily coincide with peak hydration temperatures, but often occurred later, when thermal gradients combined with ongoing drying.

5.2 Operational Phase and Reservoir Impoundment

Reservoir impoundment altered thermal and moisture boundary conditions on the upstream face, suppressing moisture exchange and damping temperature fluctuations. This resulted in asymmetric long-term behaviour, with stress redistribution rather than uniform stress reduction.

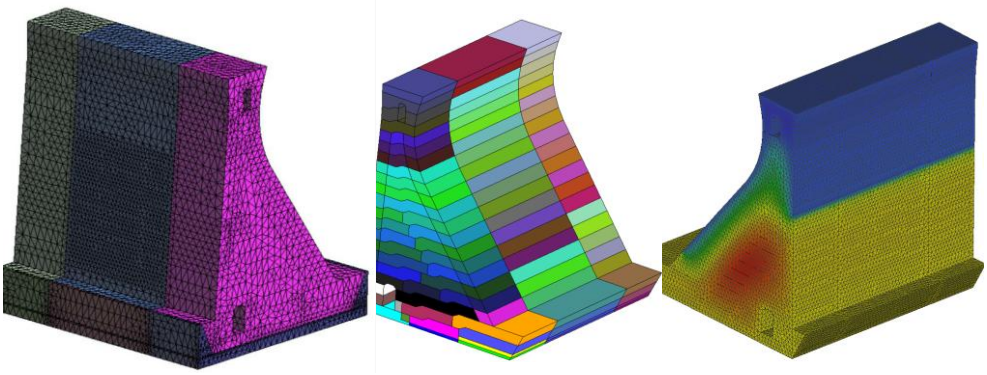


Fig. 6 Left: Final global model with a refined mesh size – sensitivity analysis was performed [17], middle: Global 3D model of the expansion block and adjacent structures – colour-coded individually concreted blocks/layers [17], right: Operation phase – water-air level at blue-yellow interface [17]

6 CRACK RISK ASSESSMENT AND INTERPRETATION OF RESULTS

The numerical analyses provided a comprehensive insight into the coupled thermo–hygro–mechanical behaviour of the gravity dam during construction and early operation. The results confirmed that hydration heat governs the early-age temperature evolution, while moisture transport and associated shrinkage progressively control long-term stress development [1], [2].

The parametric analyses on the representative dam section demonstrated that peak temperatures and thermal gradients are strongly influenced by technological parameters such as initial concrete temperature, curing duration, and construction scheduling. Reduced initial mix temperatures and extended curing effectively limited early thermal gradients and delayed moisture loss from exposed surfaces. Nevertheless, even under favourable curing conditions, long-term drying effects remained significant, underlining the importance of explicitly modelling moisture transport.

The global three-dimensional analyses showed that elevated temperatures persist in the structural core for several months after placement, whereas surface layers experience progressive cooling and drying. As a result, critical tensile stresses did not necessarily coincide with peak hydration temperatures but often developed later, when thermal contraction interacted with ongoing moisture-driven shrinkage. This finding highlights a limitation of simplified thermal-only analyses, which may underestimate delayed crack risk [1], [7].

Reservoir impoundment significantly altered the boundary conditions on the upstream face of the dam. Moisture exchange was suppressed and temperature fluctuations were reduced, leading to asymmetric long-term behaviour of the structure. While stresses near the upstream face partially

relaxed, the downstream face remained exposed to drying, resulting in stress redistribution rather than uniform stress reduction. Such effects cannot be captured without coupled moisture transport modelling.

Crack risk assessment indicated that cracking is most likely to initiate in near-surface regions where restraint, temperature gradients, and moisture loss act simultaneously [1], [3]. The predicted cracking remained localized and predominantly oriented perpendicular to the dam axis. Seasonal behaviour was observed, with partial crack closure during warmer periods and reopening during colder seasons. Importantly, cracking did not propagate through the entire dam cross-section and did not compromise global structural stability.

Overall, the results demonstrate that verification of material models and explicit coupling of thermal, moisture, and mechanical processes are essential for reliable interpretation of numerical predictions. The adopted hierarchical modelling strategy enabled consistent evaluation of both early-age and long-term behaviour and provided a transparent basis for assessing crack risk.

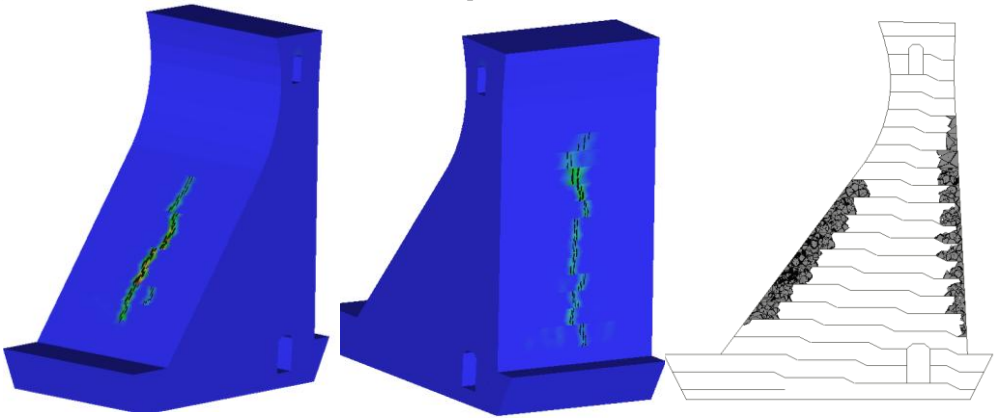


Fig. 7 Areas with predicted risk of cracks > 0.2 mm during the second winter period – 2 years after the start of construction in March; the upstream face and potential depth of cracks in cross-section are shown [17]

7 CONCLUSIONS

The presented study confirms that a reliable assessment of the thermal and shrinkage-related behavior of massive concrete structures requires a modelling approach that explicitly accounts for the coupled interaction of hydration heat, moisture transport, creep, and shrinkage. The research yielded several critical findings:

- Dominance of Moisture in Long-Term Response: While hydration heat governs early-age temperature evolution, moisture transport and associated drying shrinkage progressively control long-term stress development.
- Timing of Critical Stress States: Numerical analyses demonstrated that the most critical tensile stress states do not necessarily coincide with peak hydration temperatures; instead, they often occur later when thermal contraction interacts with ongoing moisture-driven shrinkage.
- Optimization of Construction Strategies: Parametric studies showed that peak temperatures and thermal gradients are strongly influenced by technological parameters such as the initial concrete temperature, curing duration, and construction scheduling. While extended curing effectively delays moisture loss, long-term drying effects remain significant even under favorable conditions.
- Reinforcement vs. Curing Effectiveness: During the parametric analysis, a variant with surface reinforcement was also investigated. However, the results indicated that the addition of reinforcement to the structure had a significantly lower impact on mitigating the amount of cracking compared to the optimization and extension of surface curing periods.

Overall, the key contribution of this work lies not only in the implementation of coupled modelling, but in the identification and quantification of governing mechanisms controlling crack formation in

massive concrete dams. The results provide a rational basis for optimizing construction technology and improving crack control strategies beyond traditional empirical approaches.

Acknowledgements

The authors gratefully acknowledge the cooperation of the state enterprise Povodí Odry and the company AQUATIS, a.s. for their collaboration and for granting permission to publish the results. This work was supported by the Czech Science Foundation under Grant GAČR 24-10892S and Grant SGS25/113/OHK1/2T/31.

References

Each journal article, conference paper, book or book chapter, thesis, research report etc. must be referred to at least once in the text. Below are a few typical examples of how to provide references. You do not have to leave a blank line between each reference. Please add DOI of the references if they exist.

[1] RILEM TC 254-CMS. 2018. *Thermal Cracking of Massive Concrete Structures – State of the Art Report*. Cham: Springer. doi:10.1007/978-3-030-21359-3.

[2] ICOLD. 2016. *Thermal Behaviour of Concrete Dams*. Paris: International Commission on Large Dams. icold-cigb.org.

[3] ACI Committee 207. 2014. *Guide to Mass Concrete (ACI 207.1R-14)*. Farmington Hills: American Concrete Institute.

[4] Ulm, Franz-Josef, and Coussy, Olivier. 1995. "Modeling of Thermo-Chemical–Mechanical Couplings of Early-Age Concrete." *Journal of Engineering Mechanics* 121:785–94. doi:10.1061/(ASCE)0733-9399(1995)121:7(785).

[5] CIRIA. 2007. *Early-Age Thermal Crack Control in Concrete (C660)*. London: Construction Industry Research and Information Association. doi: n/a.

[6] fib. 2013. *fib Model Code for Concrete Structures 2010*. Berlin: Ernst & Sohn. doi:10.1002/9783433604090.

[7] Hansen, Knud D., and Erik J. Pedersen. 1983. "Thermal Stress Analysis of Mass Concrete Structures." *Journal of Engineering Mechanics* 109:804–20. doi:10.1061/(ASCE)0733-9399(1983)109:3(804).

[8] Lura, Pietro. 2003. *Autogenous Deformation and Internal Curing of Concrete*. PhD diss., Delft University of Technology.

[9] EN 196-9. 2010. *Methods of Testing Cement – Part 9: Heat of Hydration – Semi-Adiabatic Method*. Brussels: CEN.

[10] Červenka, Vít, Červenka, Jan, and Pukl, Robert. 2004. "ATENA – A Tool for Engineering Analysis of Fracture in Concrete." *Engineering Fracture Mechanics* 71:1235–49. doi:10.1016/j.engfracmech.2003.11.003.

[11] Červenka, Vít, et al. 2018. *ATENA Program Documentation, Part 1 – Theory*. Prague: Červenka Consulting.

[12] Schindler, Anton K., and Kevin J. Folliard. 2005. "Heat of Hydration Models for Cementitious Materials." *ACI Materials Journal* 102(1):24–33.

[13] Wittmann, Folker H. 1978. "Drying Shrinkage and Creep of Concrete." *Materials and Structures* 11:163–173. doi:10.1007/BF02480479.

[14] Bažant, Zdeněk P., and Jirásek, Milan. 2018. *Creep and Hygrothermal Effects in Concrete Structures*. Cham: Springer. doi:10.1007/978-94-024-1138-6.

[15] Baroghel-Bouny, Véronique. 2007. "Water Vapour Sorption Experiments on Hardened Cementitious Materials." *Cement and Concrete Research* 37:414–37. doi:10.1016/j.cemconres.2006.11.019.

[16] Neville, Adam M. 2011. *Properties of Concrete*. 5th ed. Harlow: Pearson Education.

[17] Klokner Institute CTU in Prague. 2022. "VD Orlík – SO 03 open Chute Spillway – Partial Report on the experimental measurement and numerical analysis of the impact of hydration heat on the formation of cracks on the experimental block ZB4 at Orlik Reservoir." Expert Report No. 2100J359

Estimation of Punching Shear Strengths of Overlay Slabs Based on Dual Potential Capacity Model

Yeongtaek Yoon[1], Jae Min Kim[1], Jinseok Kang[1], Hoseong Jeong[2], Kang Su Kim[1]

Department of Architectural Engineering and Smart City Interdisciplinary Major Program
University of Seoul
163 Seoulsiripdaero, Dongdaemun-gu, Seoul 02504, Republic of Korea

School of Architecture and Architectural Engineering
Hankyong National University
327 Jungang-ro, Anseong-si, Gyeonggi-do 17579, Republic of Korea

Summary
Recent incidents of punching shear failure in flat-plate slabs of large-scale apartment parking lots in South Korea have raised safety concerns. This study investigates the punching shear behavior of two-way slabs strengthened with an overlay and proposes an analytical model for predicting their shear strengths. Two specimens were tested under quasi-static loading, varying slab dimensions and shear connector spacing. Failure patterns, load-displacement responses, and the behavior of shear connectors were analyzed to identify key characteristics. The proposed model classified failure modes based on the horizontal shear strength governed by interfacial properties, and the punching shear strength for each failure mode is evaluated using the dual potential capacity model (DPCM). Validation against two test specimens and eight specimens reported in previous studies demonstrates that the model reliably predicts the strength of overlay-strengthened slabs.

1 INTRODUCTION

Flat plate structures, in which slabs are directly supported by columns without the use of beams, offer construction simplicity and efficient floor-to-floor height, making them widely adopted in high-rise buildings and large-scale parking facilities. However, this structural simplicity can lead to stress concentrations at slab-column connections, which may result in punching shear, a brittle failure mechanism [1], [2]. Punching shear failure typically occurs suddenly after the initiation of localized cracks, before the formation of yield lines in the slab, and can pose significant safety risks if not properly accounted for in the design stage [3], [4].

Moreover, the aging of existing structures and increased service loads can further compromise structural safety, necessitating reinforcement measures to enhance the punching shear capacity of slab-column connections. Common strengthening strategies include shear strengthening, flexural strengthening, column head strengthening, and prestressing [5], [6]. Among these methods, the overlay technique, which involves casting an additional concrete layer on the top surface of the slab, has been found particularly effective for flat plates located in underground parking or top-floor slabs. This method can simultaneously improve both flexural and shear resistance, and when the overlay layer acts integrally with the existing slab, improvements in both strength and stiffness can be expected [7].

The overlay method is a practical strengthening solution as it imposes minimal geometric constraints on slab-column connections and interferes little with equipment beneath the slab. However, to ensure that the overlay slab behaves integrally with the existing slab, sufficient interfacial shear resistance must be provided. This requires careful consideration of shear connector behavior, interface roughness, and the performance of bonding materials such as epoxy adhesives [8]. In this study, punching shear tests were conducted on slabs strengthened with overlays to quantitatively evaluate the effectiveness of the strengthening method. Two specimens with different strengthening conditions were fabricated, and the effect of interfacial characteristics on the strengthening performance was closely analyzed. A predictive model for the punching shear capacity of strengthened slabs was developed using the dual potential capacity model (DPCM), and the accuracy of the proposed model was validated against a total of ten specimens, including eight specimens reported in the literature.

2 EXPERIMENTAL STUDY

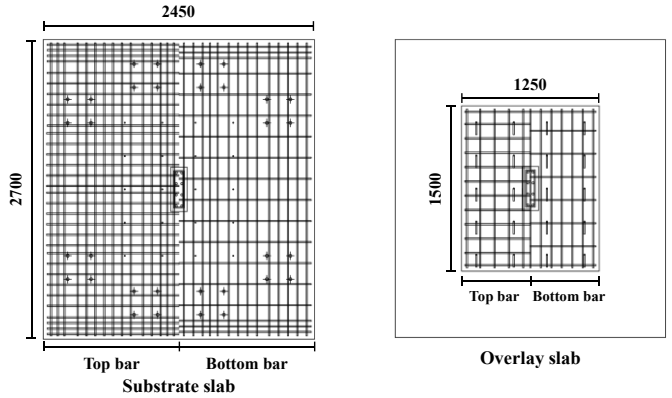
2.1 Details of test specimens

Two specimens were planned to evaluate the performance of the strengthened overlay slab. Table 1 and Fig. 1 present the experimental variables and detailed design of the specimens, respectively. For all specimens, the substrate slabs had plan dimensions of 2,450 × 2,700 mm with a thickness of 225 mm, and were simply supported at eight points to simulate the contraflexure points of a continuous slab. The slabs were supported at the center by a stub column measuring 150 × 400 mm.

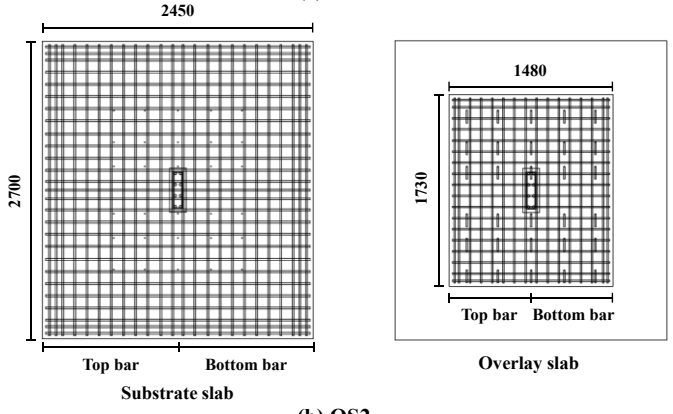
The two specimens differed in terms of the dimensions of the overlay slab, the reinforcement detailing of both the substrate and overlay slabs, and the arrangement of the shear connectors. The overlay slabs of specimens OS1 and OS2 measured 1,250 × 1,500 × 125 mm and 1,480 × 1,730 × 140 mm, respectively, with 20 and 30 shear connectors installed in each case.

Table 1 Specifications of test specimens

Specimen	Dimensions (mm)						Shear Connectors (EA)	
	Substrate			Overlay				
	Width	Length	Depth	Width	Length	Depth	Short span	Long span
OS1	2,450	2,700	225	1,250	1,500	125	4	5
OS2				1,480	1,730	140	5	6



(a) OS1



(b) OS2

Fig. 1 Dimensional details of test specimens

Table 2 presents the key design parameters of the concrete and reinforcement used in the two specimens. The compressive strength of the overlay slab concrete in all specimens was designed to be higher than that of the substrate slab concrete, and the longitudinal reinforcement ratio of specimen OS2 was designed to be higher than that of specimen OS1. Only the longitudinal reinforcement of the substrate slab in specimen OS2 utilized D16 reinforcements, while all other longitudinal reinforcements were D13 bars, with yield strengths of 655.7 MPa and 594.9 MPa, respectively. For both specimens, the shear connectors were made of D13 bars with a yield strength of 502.3 MPa.

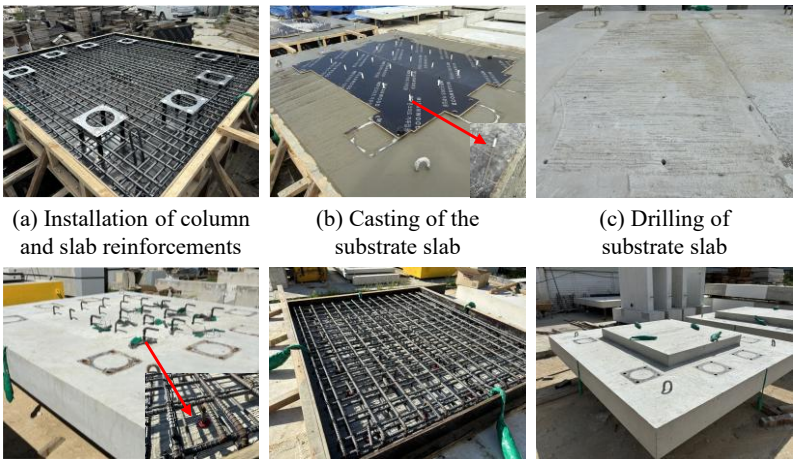
Table 2 Concrete and steel reinforcement details of specimens

Specimen	Compressive strength of Concrete $f_c^{'}$ (MPa)		Reinforcement ratio of substrate slab ρ_{sub} (%)		Reinforcement ratio of overlay slab ρ_{over} (%)		Average effective depth of reinforcement d_{avg} (mm)	
	Substrate	Overlay	Short side	Long side	Short side	Long side	Substrate	Overlay
OS1	21.7	30.8	0.79	0.86	1.15	1.15	185	310*
OS2			0.98	0.98	1.27	1.27		325*

* Average effective depth measured from the bottom surface of the substrate slab to the tensile reinforcement of the overlay slab

2.2 Fabrication of test specimens

Fig. 2 illustrates the sequence of specimen fabrication. The stub columns and the substrate slab were cast monolithically, and the top surface of the slab was roughened before the concrete fully hardened. Additionally, pipes with smaller diameters than the shear connectors were inserted to secure the exact locations of the shear connectors. 13 days after casting, the pipes were removed, drilling and epoxy injection were carried out, and the shear connectors were installed. Finally, 15 days after casting, any debris on the top surface of the substrate slab was removed, a concrete bonding agent was applied, and the reinforcement and casting of the overlay slab were carried out.



(a) Installation of column and slab reinforcements (b) Casting of the substrate slab (c) Drilling of substrate slab

(d) Installation of shear connector (e) Installation of reinforcement for overlay slab (f) Casting and curing of overlay slab

Fig. 2 Fabrication process of specimens

2.3 Test setup

As shown in Fig. 3, hinges were arranged on the slab to simulate the contraflexure points, with the distance from the column face to each hinge set at 825 mm. Loading was applied at the bottom of the central column of the specimen, and the deflection under applied load was measured using LVDTs installed at the center of the slab.

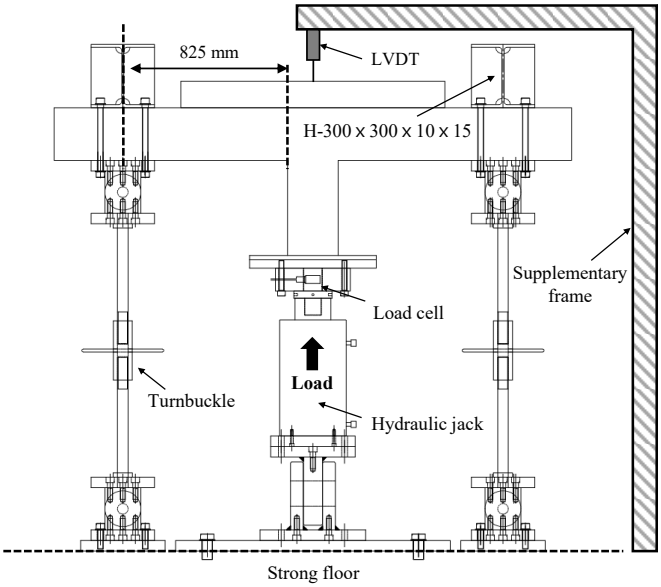


Fig. 3 Test setup

3 TEST RESULTS AND DISCUSSION

3.1 Ultimate loads and deflections

Fig. 4 shows the load-displacement relationships of the specimens, while Table 3 summarizes the loads and displacements at key points. The test results indicate that specimen OS2 exhibited higher strength than specimen OS1. In addition, both specimens exhibited a brittle failure mode before the yielding of the longitudinal reinforcement, and the shear connectors yielded prior to punching shear failure.

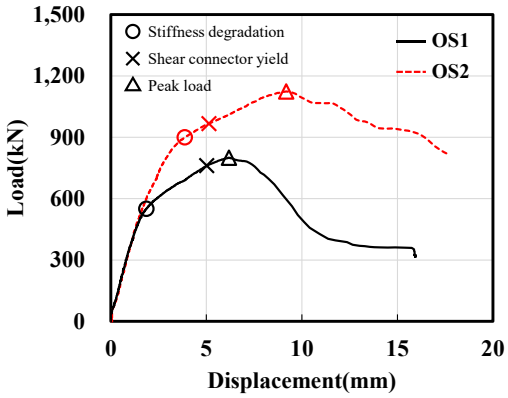


Fig. 4 Load-displacement relationship of slabs OS1 and OS2

Table 3 Summary of test results

Specimen	Peak load		Post-peak load at 80% load	
	Load (kN)	Displacement (mm)	Load (kN)	Displacement (mm)
OS1	800	6.2	640	8.7
OS2	1124	9.2	899	16.4

4 ANALYTICAL MODEL FOR OVERLAY SLAB USING DUAL POTENTIAL CAPACITY MODEL

In this study, an analytical model based on DPCM was developed to accurately predict the strength of specimens strengthened with overlays. Unlike conventional assumptions in which the shear-resisting mechanism of reinforced concrete (RC) members is considered to act only in a specific region, DPCM is based on the concept that both the tension cracked concrete and the uncracked compression concrete contribute simultaneously to shear resistance [9], [10], and the total applied shear force, V_{tot} is calculated as shown in Eq. (1). Furthermore, failure is assumed to occur at the point where the shear demand curves and potential capacity curves of the two regions intersect, and the ultimate shear strength is calculated as presented in Eq. (2).

$$V_{tot} = V_{ci,req} + V_{cc,req} \tag{1}$$

$$V_{n,cc} = V_{cc,req} + V_{ci,req} \text{ when } V_{cc,req} \geq V_{cc,cap} \text{ before } V_{ci,req} \geq V_{ci,cap} \tag{2a}$$

$$V_{n,ci} = V_{cc,req} + V_{ci,req} \text{ when } V_{ci,req} \geq V_{ci,cap} \text{ before } V_{cc,req} \geq V_{cc,cap} \tag{2b}$$

Where, $V_{cc,req}$, and $V_{cc,cap}$ denote the shear demand and potential capacity in the compression zone, respectively, while $V_{ci,req}$ and $V_{ci,cap}$ denote the shear demand and potential capacity in the cracked tension zone, respectively.

According to ACI 318-19, when the top surface of the existing slab is intentionally roughened and the minimum shear connectors are provided as specified in Eq. (3), the nominal horizontal shear strength (V_{nh}) at the interface of a composite concrete member can be calculated using Eq. (4). When no shear connectors are present, the V_{nh} can be considered as shown in Eq. (5) [11]. Furthermore, the horizontal shear force (V_{uh}) acting on the interface due to increasing load at the center of the slab can be determined using Eq. (6). In this case, M_d is calculated based on the equivalent effective depth determined under the assumption of full composite action [12]. If the nominal shear strength is lower than the applied load, cover separation may occur at the interface, reducing the composite action between the two slabs. Under such conditions, any additional load is assumed to be resisted solely by the existing slab.

$$A_{v,min} = max\ (0.0625\sqrt{f_{ck}}\frac{b_v s}{f_{yt}}, 0.35\frac{b_v s}{f_{yt}}) \tag{3}$$

$$V_{nh} = \lambda(1.8 + 0.6\rho_v f_{yt}) b_v d \tag{4}$$

$$V_{nh} = 0.55 b_v d \tag{5}$$

$$V_{uh} = \frac{M_d}{0.9d} \tag{6}$$

Where, b_v denotes the width of the contact surface(i.e., the width of the overlay slab), s denotes the spacing of the shear reinforcement in the direction parallel to the longitudinal reinforcement, and ρ_v denotes shear reinforcement ratio resisting horizontal shear, f_{yt} denotes the yield strength of the shear connectors, and d denotes effective depth of the composite section, and M_d denotes the moment

induced by punching shear. Furthermore, to predict the cover separation strength of overlay-strengthened specimens, the concrete tooth model proposed in previous studies was integrated into the DPCM to develop a punching shear strength prediction model suitable for overlay slabs [13]. In the proposed model, the distance from the edge of the strengthening layer toward the slab center to the critical crack is sequentially assumed, and at each assumed location, the punching shear strength of the substrate slab alone, excluding the overlay slab, is compared with the cover separation strength. If the punching shear strength is lower than the cover separation strength, the slab is considered to fail in punching shear. In case of the specimens with sufficiently provided horizontal shear strength, the punching shear strengths are calculated assuming full composite action.

Fig. 5 shows the failure strengths of the 8 specimens collected from previous studies [14], along with the OS1 and OS2 specimens, compared with the predicted values obtained from the proposed model. The results indicate the ratio of experimental to predicted values is 1.09, with a correlation coefficient of 0.89, demonstrating that the proposed model reasonably captures the observed strength.

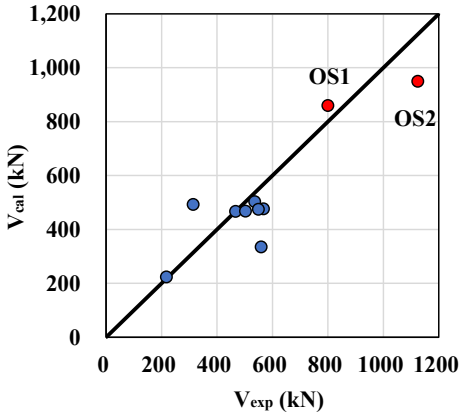


Fig. 5 Comparison of measured and calculated strengths

5 CONCLUSIONS

In this study, an analytical model based on the DPCM was proposed to quantitatively evaluate the punching shear strength of two-way slabs strengthened by the overlay technique. To this end, two specimens were fabricated and tested under quasi-static loading. The ultimate failure strengths of the specimens were evaluated based on the proposed model, and the main conclusions of this study are summarized as follows.

- Two specimens were designed by varying key parameters, including the shear connectors, longitudinal reinforcement ratio, and the dimensions of the overlay slab. The shear connectors were installed using epoxy after the existing slab had fully cured. The contraflexure points of the slabs were simulated using eight hinge supports, and a quasi-static load was applied through a centrally located column.
- Both specimens exhibited brittle failure behavior, and the shear connectors yielded before the slabs reached their maximum load. As a result, specimen OS2 demonstrated higher load-carrying capacity and larger displacement at failure compared to specimen OS1.
- The failure modes of the slabs were classified based on the horizontal shear strength at the interface. For specimens that did not secure sufficient horizontal shear capacity, the failure load was determined by comparing the cover separation strength of the overlay with the punching shear strength of the substrate slab alone. Overall, the proposed model showed good agreement with the experimental results, with a ratio of experimental to predicted values of 1.09 and a correlation coefficient of 0.89, indicating that the model can reasonably predict the punching shear strength of overlay-strengthened slabs.

Acknowledgements

This work was supported by the National Research Foundation of Korea(NRF) grant funded by the Korea Goverment(MSIT) (No. RS-2024-00343740).

References

[1] Chavan, Madhura Sanjay, Hueste, Mary Beth Deisz, and Genikomsou, Aikaterini S. 2025. "Two-Way Shear in Nonprestressed Slabs: Flexural Reinforcement Ratio Effects." *ACI Structural Journal* 122(1).

[2] Broms, Carl Erik. 2000. "Elimination of Flat Plate Punching Failure Mode." *ACI Structural Journal* 97(1):94–101.

[3] Ju, Hyunjin, Cheon, Na-Rae, Lee, Deuck Hang, Oh, Jae-Yuel, Hwang, Jin-Ha, and Kim, Kang Su. 2015. "Consideration on Punching Shear Strength of Steel-Fiber-Reinforced Concrete Slabs." *Advances in Mechanical Engineering* 7(5):1687814015584251.

[4] Marzouk, Hesham, and Hussein, Ahmed. 1992. "Experimental Investigation on the Behavior of High-Strength Concrete Slabs." *ACI Structural Journal* 89(6):701–713.

[5] Lapi, Massimo, Ramos, António Pinho, and Orlando, Maurizio. 2019. "Flat Slab Strengthening Techniques against Punching-Shear." *Engineering Structures* 180:160–180.

[6] Ramos, António Pinho, Lúcio, Valter José da Guia, and Regan, Paul Erskine. 2011. "Punching of Flat Slabs with In-Plane Forces." *Engineering Structures* 33(3):894–902.

[7] Lapi, Massimo, Fernandes, Hugo, Orlando, Maurizio, Ramos, António, and Lúcio, Válter. 2018. "Performance Assessment of Flat Slabs Strengthened with a Bonded Reinforced-Concrete Overlay." *Magazine of Concrete Research* 70(9):433–451.

[8] Sirimontree, Sayan, Witchayangkoon, Boonsap, Lertpocasombut, Krittiya, and Sornchomkaew, Phongphoom. 2018. "Strengthening of Reinforced Concrete Slab by Concrete Overlay." *MANZAR, the Scientific Journal of Landscape* 10(44):60–67.

[9] Lee, Deuckhang, Han, Sun-Jin, and Kim, Kang Su. 2016. "Dual Potential Capacity Model for Reinforced Concrete Beams Subjected to Shear." *Structural Concrete* 17(3):443–456.

[10] Ju, Hyunjin, Lee, Deuckhang, Park, Min-Kook, and Memon, Shazim Ali. 2021. "Punching Shear Strength Model for Reinforced Concrete Flat Plate Slab–Column Connection without Shear Reinforcement." *Journal of Structural Engineering* 147(3):04020358.

[11] ACI Committee 318. 2019. *Building Code Requirements for Structural Concrete (ACI 318-19) and Commentary. Farmington Hills, MI: American Concrete Institute*.

[12] Roh, Yu-Jin, Kim, Hui-do, Yune, Dai-Young, Eom, Tae-Sung, Kang, Su-Min, and Kim, Sung-Hyun. 2025. "Existing Reinforced Concrete Slab Strengthening by Reinforced Spray Mortar and Shear Connectors." *Engineering Structures* 343:121030.

[13] Zhang, Dawei, Ueda, Tamon, and Furuuchi, Hitoshi. 2012. "Concrete Cover Separation Failure of Overlay-Strengthened Reinforced Concrete Beams." *Construction and Building Materials* 26(1):735–745.

[14] Fernandes, Hugo Daniel Pereira. 2019. "*Strengthening of Flat Slabs with Reinforced Concrete Overlay–Analysis and Development of the Solution.*" PhD diss., Universidade NOVA de Lisboa

Numerical Modelling Strategies for Textile Reinforced Concrete

Chiara Saccomanno[1], Marco C. Rampini[2], Giulio Zani[2], Francesco Romeo[1]

[1] Department of Structural and Geotechnical Engineering,
Sapienza Università di Roma,
Via Eudossiana 18, Rome 00184, Italy

[2] Department of Civil and Environmental Engineering,
Politecnico di Milano,
Piazza Leonardo Da Vinci 32, 20133 Milano, Italy

Summary
In shell structures geometry governs structural efficiency and architectural expression establishing a close relationship between form and performance. While concrete has traditionally been the reference material for such systems, increasing demands for sustainability, durability and construction efficiency are challenging its use. In this context, Textile Reinforced Concrete (TRC) represents a promising alternative material. This study compares different numerical modelling strategies for TRC as an intermediate step toward shell analysis, focusing on material-level behaviour through tensile and flexural tests. Three strategies are considered: a smeared model, a discrete model with explicit representation of the reinforcement, and a composite layup model. All approaches are implemented within a nonlinear finite element framework, and their numerical responses are compared with experimental results. The comparison highlights advantages and limitations of the modelling strategies.

1 INTRODUCTION

The use of Textile Reinforced Concrete (TRC) has steadily expanded in thin structural applications [1]. As a composite material consisting of a cementitious matrix reinforced with synthetic or natural textiles, TRC enables the design of slender structural elements combining high mechanical performance with reduced thickness, enhanced durability, and lower environmental impact compared to conventional reinforced concrete.

Extensive experimental research has investigated the tensile and flexural response of TRC at the material scale [2, 3], providing valuable insight into the composite's global behavior. However, despite these advances, a consolidated and widely accepted numerical modelling framework for TRC is still lacking. This limits the reliable analysis and design of TRC structures, especially in cases where variations in cross-section, textile orientation, and reinforcement positioning are significant.

Numerical models capable of accurately reproducing TRC mechanical behaviour while enabling systematic parametric investigations without user-defined subroutines or excessive computational cost are therefore highly desirable. To address this gap, the present study compares three numerical modelling approaches aimed at reproducing the results of a previous experimental campaign [4], which comprised meso-scale tensile and flexural tests as well as full-scale structural ones. All approaches are implemented within a nonlinear finite element framework.

2 EXPERIMENTAL DATA

The experimental programme considered in this study is part of a broader research activity focused on the development of an innovative slab system combining very-high-performance cementitious fibre-reinforced concrete beams with stay-in-place TRC formworks [4]. The investigated TRC consists of a fine-grained cementitious matrix reinforced with a single layer of alkali-resistant glass textile. The reinforcement features an orthogonal arrangement of yarns with different spacing in the warp and weft directions (4.9 mm and 10.1 mm, respectively) and different tensile capacities, approximately 157 kN/m in the warp direction and 39 kN/m in the weft direction, resulting in an orthotropic response of the composite material.

At the meso-scale, the experimental campaign included uniaxial tensile tests and four-point bending tests performed on specimens measuring 9×70×400 mm³ and 15×70×500 mm³, respectively, with the

aim of characterizing the mechanical behaviour of TRC at the material level (Fig. 1). Considering the non-symmetrical mechanical properties of the reinforcement, specimens were tested separately according to fibre orientation, distinguishing between TRC coupons reinforced along the warp and the weft direction.

Direct tensile tests on TRC specimens were used to investigate crack initiation, multiple cracking development, and post-cracking stiffness governed by the textile reinforcement under in-plane loading. Four-point bending tests provided complementary information on the flexural response of the material and on the influence of the reinforcement position within the cross-section against out-of-plane actions.

The present study primarily focuses on the numerical analyses of the flexural tests. The numerical results related to tensile loading, which have been investigated in earlier work [5], are recalled here in to provide a comprehensive framework for the assessment of the advantages and limitations of the three adopted modelling approaches.

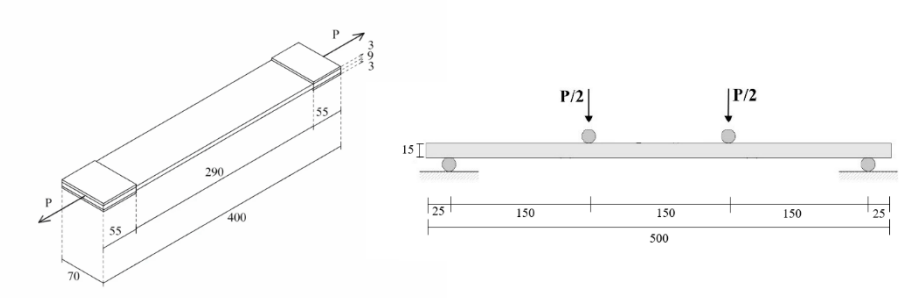


Fig. 1 Schematic representation, adapted from [6], of the tensile (left) and flexural (right) tests.

3 NUMERICAL MODELLING STRATEGIES

The numerical investigation is based on three alternative modelling strategies, characterised by different levels of material idealisation, computational cost and complexity. The strategies range from simplified homogenised material models to approaches explicitly accounting for the presence and position of the textile reinforcement. All simulations were carried out using the finite element software Abaqus 6.14-5, adopting a static general solution procedure under displacement-controlled loading. The material properties and modelling assumptions adopted for each strategy are described in the following sections and summarised in table 1 and table 2.

3.1 Smeared model (A)

The smeared modelling approach represents the TRC as an equivalent homogeneous composite, assuming a uniform stress–strain response over the entire cross-section. Within this framework, the composite behaviour is described by a single equivalent tensile law, without explicitly modelling the textile reinforcement or its position through the thickness. Consequently, the model can only reproduce an identical mechanical behaviour in the different directions of the composite. This limitation is particularly significant for strongly unbalanced textiles, such as the one investigated in this study.

The material behaviour was implemented in Abaqus using the Concrete Damaged Plasticity (CDP) model, calibrated to reproduce the asymmetric response of the composite under tensile and compressive loading. The compressive behaviour was defined according to the recommendations of Model Code 2010, while the tensile response was described by a trilinear constitutive law by fitting the average normalized stress ($P/(b \cdot t)$; P = tensile load, b = specimen width, t = specimen thickness) vs. normalized displacement ($Stroke/L_0$; L_0= initial specimen length) experimental response [3]. Separate tensile constitutive laws were defined for the warp and weft directions to account for their different stiffness and strength. The same constitutive relationships were adopted for the numerical simulation of both uniaxial tensile tests and flexural tests. In the former, the smeared model reproduces the experimental response with good agreement, as shown in Fig. 2. Conversely, the flexural behaviour cannot be captured consistently. This limitation is primarily related to the calibration of the constitutive laws on tensile tests, which do not adequately reflect the different stiffness ratios and anchorage conditions governing the response under bending.

3.2 Discrete model (B)

The discrete modelling approach explicitly represents the two components of the Textile Reinforced Concrete (i.e., matrix and textile), providing a more realistic description of internal stress transfer and reinforcement effects, at the expense of increased modelling complexity and computational cost.

The cementitious matrix is modelled using solid finite elements governed by the CDP model, calibrated on the experimentally determined compressive strength and defined in accordance with the recommendations of Model Code 2010 [7]. The textile reinforcement is represented by truss elements assuming a linear-elastic brittle behaviour in both the warp and weft directions. The interaction between matrix and textile is introduced through an embedded region formulation, assuming perfect bond. Bond-related phenomena observed experimentally, such as partial filament sliding, are indirectly considered by introducing a reduced effective elastic stiffness for the textile reinforcement. This reduction is defined through the TRC efficiency factor $EF_{\mathrm{TRC},f}$, evaluated from uniaxial tensile tests and defined as the ratio between the maximum tensile stress attained in the textile during tests on TRC specimens and the nominal tensile strength of the alkali-resistant glass filaments [3].

In the case of the uniaxial tensile tests considered in this study, experimental observations revealed bond imperfections and partial filament sliding; therefore, a reduced effective stiffness was adopted in the numerical simulations. The effective stiffness of the textile reinforcement was approximately 40% of the nominal value, corresponding to an elastic modulus in the range of 28.0-33.4 GPa. This reduction reflects the loss of mechanical efficiency associated with bond-related phenomena.

Conversely, such effects were not observed in the flexural tests thanks to the longer matrix-textile anchoring length (shear span of around 150 mm between maximum bending moment and end sections). In this case, the discrete modelling approach is particularly advantageous, as it allows the explicit representation of the reinforcement position within the cross-section, a key parameter governing the flexural response as discussed in Sec 4, and the non-symmetrical textile behaviour.

3.3 Composite model (C)

The composite layup modelling approach combines features of both the smeared and the discrete strategies, providing an explicit description of the composite constituents while limiting the associated modelling effort. As in the discrete approach, the cementitious matrix and the textile reinforcement are treated as separate components; however, the textile is represented as a continuous layer rather than through explicitly meshed roving, leading to a significant reduction in computational cost while retaining the essential characteristics of the composite behaviour.

The model is implemented in Abaqus using the built-in *composite layup* module, which allows the definition of multiple layers called *ply* characterised by specific material properties, thicknesses, and fibre orientations. The cementitious matrix is described using the same constitutive model adopted for the discrete approach. The textile reinforcement is modelled as an orthotropic lamina material (engineering material when solid elements are adopted), with distinct mechanical properties assigned to the warp and weft directions to represent anisotropic stiffness effects. The thickness and elastic properties of the textile ply are defined by recalibrating the Young's modulus so that the resulting flexural stiffness of the ply is equivalent to that of the discrete reinforcement in both directions.

4 RESULTS OF TRC TEST MODELLING

4.1 Tensile test results

The numerical simulation of the uniaxial tensile tests was investigated in detail in a previous study [4] and is therefore only briefly recalled here (Fig. 2). The smeared modelling approach can reproduce all three phases of the tensile response with good agreement and at a very low computational cost. However, its main limitation lies in the strong dependence on a single cross-sectional configuration, which requires the constitutive description to be reformulated whenever the geometry or reinforcement layout is modified. For both the discrete and the composite layup approaches, the matrix tensile strength f_{ctm} (Tab. 1) was defined according to the compressive strength class of the cementitious matrix. Experimental evidence from bending tests suggests that higher tensile strength values could be expected, which likely contributes to the underestimation of the stress level associated with crack initiation and multiple cracking in the warp direction. Among the investigated strategies, the discrete model provides the most accurate reproduction of the experimental tensile response, at the expense of a significantly higher computational cost. The composite layup approach, on the other hand, can

reproduce the overall tensile behaviour and all three response phases with satisfactory accuracy, while exhibiting a more stable response and a substantially reduced computational effort compared to the discrete model.

Table 1 Comparative discussion of material scale models: input parameters for tensile test

Strategy	Input material Data	Element type	Nodes	Computational cost
Smeared model (A)	E_m=46 GPa	S4R (shell)	915	Low
Discrete model (B)	f_{ctm}=4.7 MPa E_m=46 GPa $E_{f,warp}$=27.957 GPa $E_{f,weft}$=33.427 GPa	S4R (shell) T3D2 (truss)	3630	Medium
Composite model (C)	f_{ctm}=4.7 MPa E_m=46 GPa $E_{f,warp}$=27.957 GPa $E_{f,weft}$=33.427 GPa	S4R (shell)	915	Low

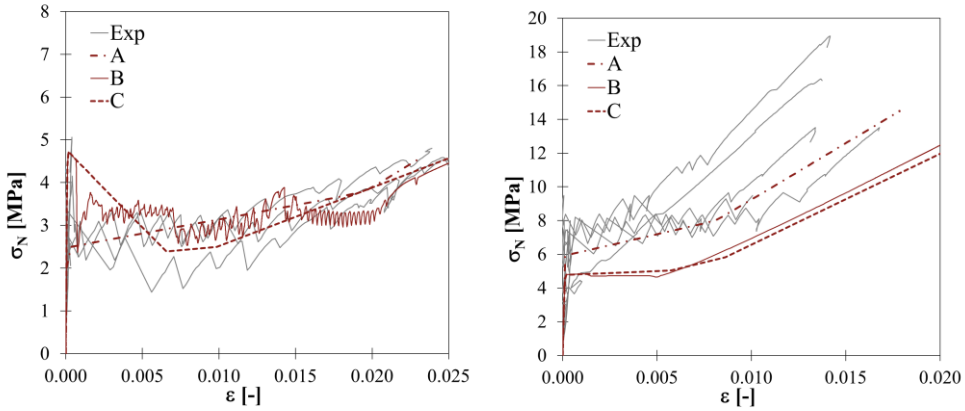


Fig. 2 Comparison between numerical and experimental TRC specimens' curves (left) in weft and warp (right) reinforcing directions (reproduced from [5]).

4.2 Bending test

The numerical analyses carried out on the flexural tests provide additional insight into the modelling of TRC elements and highlight aspects that cannot be fully captured through tensile simulations alone. As previously discussed in section 3.1, the smeared modelling approach proves to be unsuitable for the simulation of bending-dominated behaviour, for this reason, the following discussion focuses on the results obtained using the discrete and the composite layup modelling approaches.

In the numerical model developed in Abaqus, the specimen was supported by a pinned support and a roller support positioned at 25 mm from the specimen edges. The load was applied through displacement control and distributed along the entire cross-section at 150 mm from the supports, consistently with the experimental configuration. In the discrete modelling approach, the cementitious matrix was discretized using three-dimensional solid elements (C3D8R), while the reinforcement was explicitly represented by truss elements (T3D2). Conversely, in the composite layup model, the specimen was discretized using solid elements only (C3D8R), assuming a homogenized representation of the composite behaviour. Displacement control was adopted to ensure numerical stability and to accurately capture the flexural response.

Table 2 Comparative discussion of material scale models: input parameters for bending test

Strategy	Input material Data	Element type	Nodes	Computational cost

Discrete model (B)	f_{ctm}=4.7 MPa E_m=46 GPa $E_{f=}$ 70 GPa	C3D8R (solid) T3D2 (truss)	7524	High
Composite model (C)	f_{ctm}=4.7 MPa E_m=46 GPa $E_{f,warp}$=15.54 GPa $E_{f,weft}$= 62.79 GPa	C3D8R (solid)	6060	Low

4.2.1 Discrete model

In the experimental programme, due to the absence of spacers, the position of the textile reinforcement within the cross-section was not perfectly controlled. As a result, the flexural specimens exhibited different reinforcement positions, which were quantified after testing by measuring the distance of the textile from the bottom face at the failing cross-sections. To account for this variability, a series of numerical analyses was carried out by varying the reinforcement depth within the cross-section. The simulations were performed considering two different assumptions for the elastic response of the textile reinforcement: (i) a reduced Young's modulus E_r, using efficiency factors $EF_{\mathrm{TRC},f}$ as for tensile tests, to indirectly account for possible slip effects; and (ii) the nominal Young's modulus of the fibres (70 GPa), assuming the adequate anchoring length allows the full utilization of the available textile stiffness. As shown in Fig. 3, the numerical simulations of specimens reinforced in the warp direction with the full textile stiffness exhibit good agreement with the experimental results, successfully reproducing the different flexural responses associated with the varying reinforcement positions. Conversely, the analyses performed using the reduced elastic modulus E_r tend to underestimate the experimental response. This can be attributed to the fact that, unlike in tensile tests affected by a limited anchorage length (50 mm) in the clamping regions, the anchorage length in the flexural specimens was enough to prevent significant slip between textile and matrix.

For specimens reinforced in the weft direction, the influence of the assumed elastic modulus is significantly less pronounced, as shown in Fig. 4. This is mainly due to the lower reinforcement ratio in the weft direction, which results in a flexural response largely governed by the cementitious matrix. Consequently, the third branch of the trilinear tensile law associated with textile activation is either very limited or nearly flat, reflecting the reduced contribution of the reinforcement to the overall response. As shown in Fig. 5 and Fig. 6, the contour plots of equivalent plastic strain (PEEQ) indicate that the model correctly reproduces the localization of irreversible deformations and the crack patterns observed at displacements of 10 mm and 30 mm, corresponding to the end of the second and third stages, respectively.

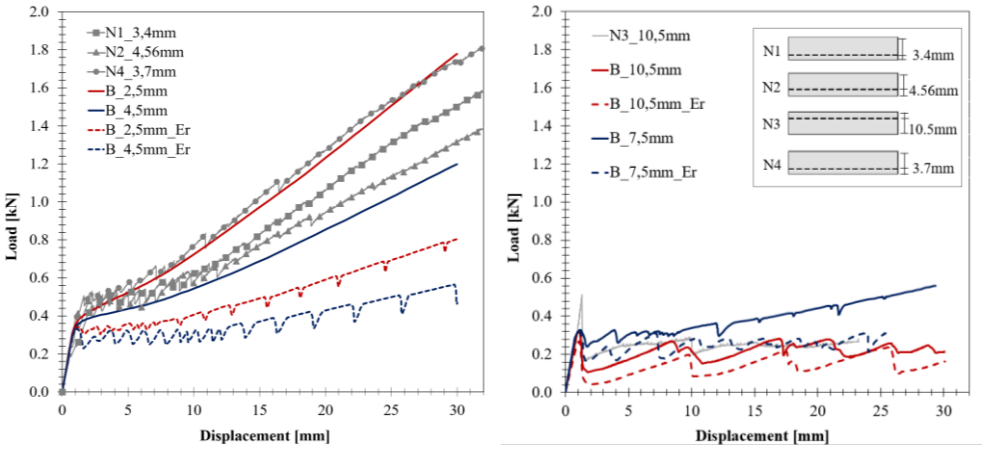


Fig. 3 Comparison between numerical and experimental TRC coupons curves in warp direction.

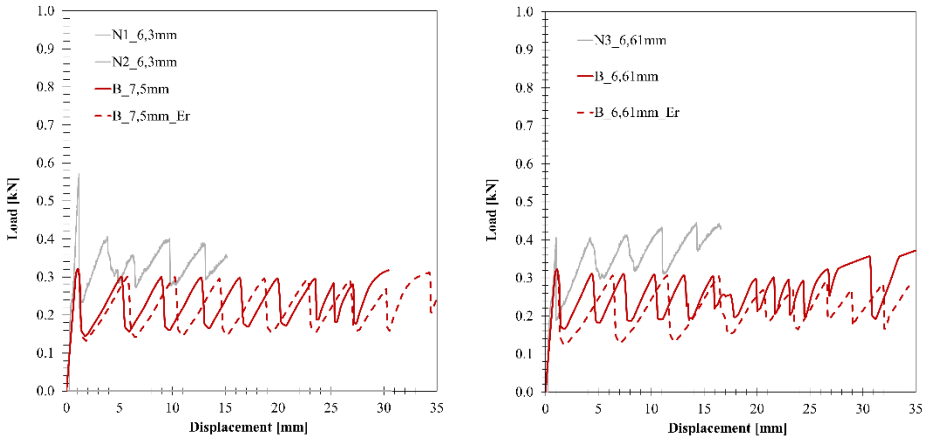


Fig. 4 Comparison between numerical and experimental TRC coupons curves in weft direction.

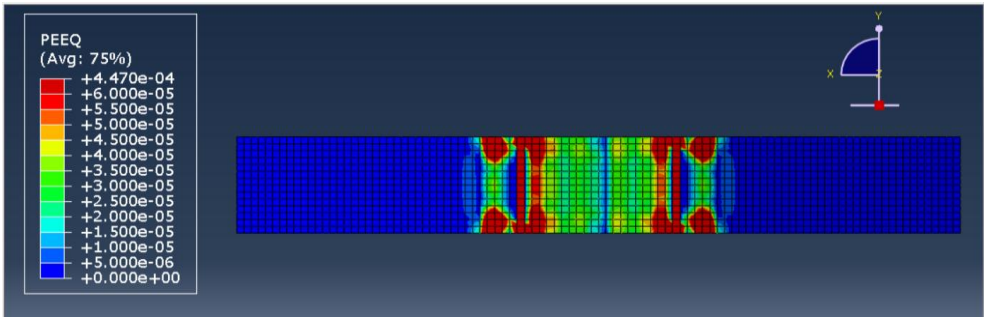


Fig. 5 Model B_7.5mm, warp direction: principal equivalent plastic tensile strains (PEEQT) at 10 mm displacement.

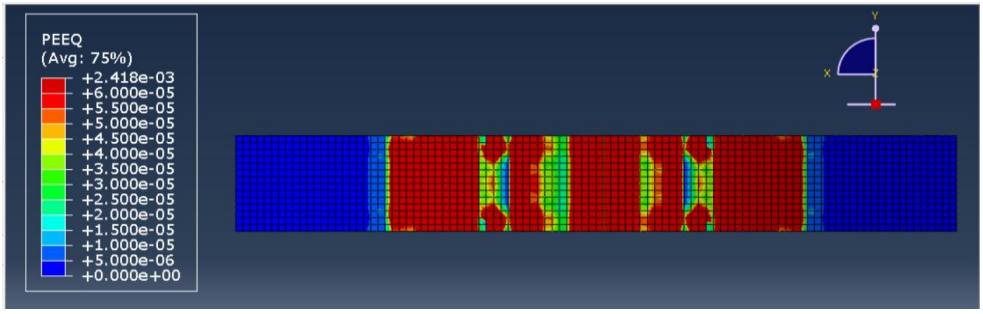


Fig. 6 Model B_7.5mm, warp direction: principal equivalent plastic tensile strains (PEEQT) at 30 mm displacement.

4.2.2 Composite layup model

The composite layup modelling strategy was adopted to represent the layered configuration of the TRC specimen with reduced modelling complexity. As outlined in Section 3.3, the Young's modulus in the two principal directions (E1 and E2) was calibrated to ensure that the reinforcement ply provided an equivalent flexural stiffness to that of the experimental system. Based on the verification reported in Section 4.2.1, which confirmed that the unreduced textile modulus is appropriate for four-point bending conditions, all analyses were performed using the nominal (non-reduced) elastic properties.

The simulations revealed an inherent limitation of the composite layup approach, which in its current configuration does not allow explicit representation of varying reinforcement positions within the specimen cross-section. Consequently, the modelling strategy is best suited to configurations where the textile reinforcement is located at the mid-depth of the section, although further investigations are currently ongoing to rule out potential numerical artefacts related to the finite elements adopted to model the cementitious matrix. Under this assumption, the numerical results show good agreement with the experimental behaviour, as illustrated in Figure 7 for both specimens with textile reinforcement oriented along the warp and the weft directions.

As illustrated in Fig. 8 and Fig. 9, the equivalent plastic strain (PEEQ) contours show that the model captures well the localization of irreversible deformations and the crack distribution at a displacement of 10 mm, corresponding to the end of the second stage; however, at 30 mm displacement (end of the third stage), the response appears to be strongly underestimated.

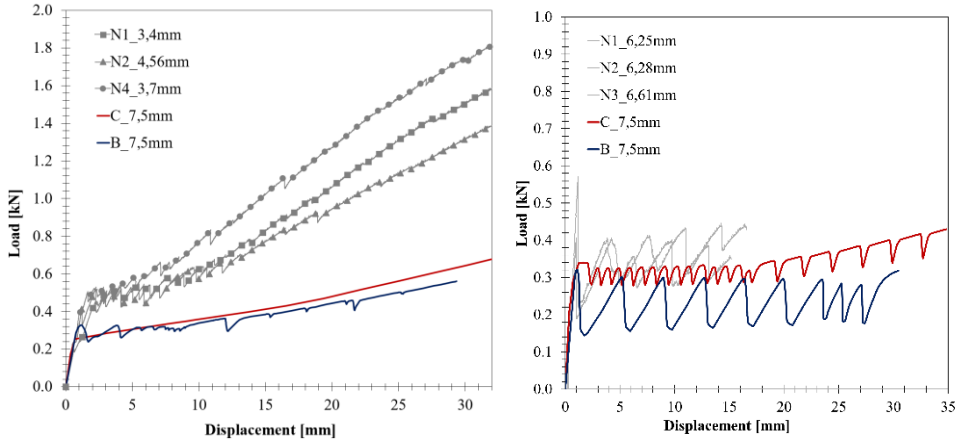


Fig. 7 Comparison between numerical and experimental TRC coupons curves in warp direction (left) and weft direction (right).

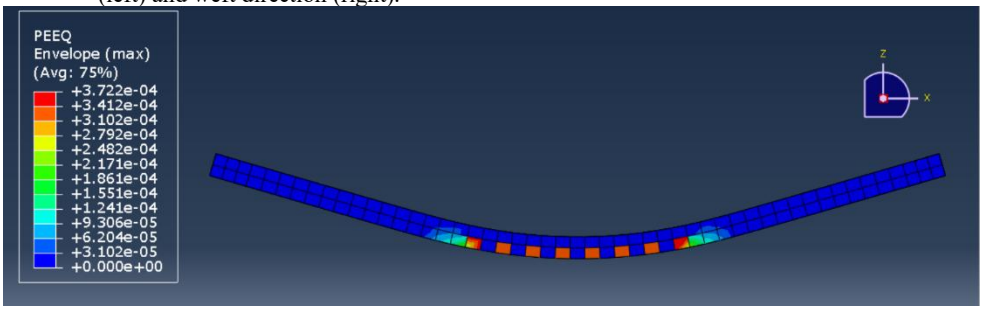


Fig. 8 Model C_7.5mm, warp direction: principal equivalent plastic tensile strains (PEEQT) at 10 mm displacement

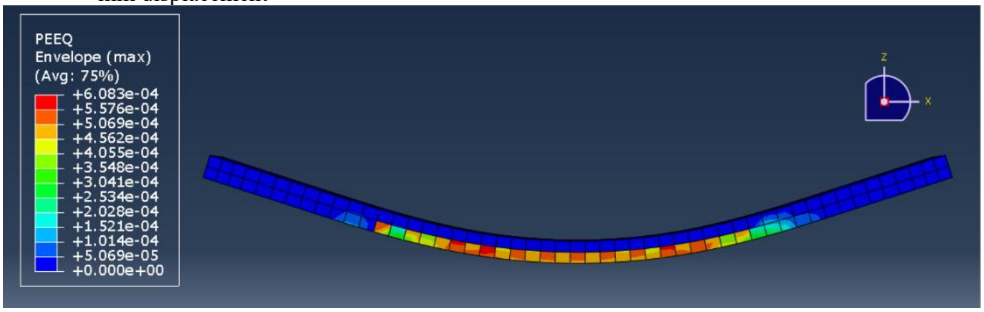


Fig. 9 Model C_7.5mm, warp direction: principal equivalent plastic tensile strains (PEEQT) at 30 mm displacement

5 CONCLUSIONS

This study compared three numerical modelling strategies for Textile Reinforced Concrete (TRC) at the material scale, with particular focus on flexural behaviour as a key step towards structural applications.

The comparison shows that the nonlinear numerical response is sensitive to selected material and geometrical parameters, particularly the effective Young's modulus of the textile reinforcement and the reinforcement position within the specimen thickness. These parameters mainly affect the second and third branches of the response and therefore require careful calibration against experimental evidence.

Overall, the results indicate that no single modelling strategy can be regarded as universally superior. The smeared approach is appropriate for preliminary simulations of the global tensile response and for low-cost parametric studies, but it is not recommended for bending-dominated problems where reinforcement position and anisotropy govern the response. The discrete model provides the most accurate representation of the experimental behaviour and should be preferred when the local reinforcement position, anchorage conditions, and matrix-textile interaction are of primary interest, although this comes at a higher computational cost. The composite layup model appears to be the most balanced and versatile strategy for future structural-scale applications, as it captures the orthotropic material response while keeping the computational effort limited. The limitations observed for this model are currently being further investigated, with particular attention to refinements of the finite element modelling strategy aimed at achieving a more detailed discretisation of the reinforcement layer. Preliminary results represent encouraging steps in this direction.

The numerical modelling approaches presented in this work (uniaxial tensile and flexural simulations) will be extended to the interpretation of biaxial behaviour, with the aim of establishing the basis for the structural-scale analysis of TRC shells, whose mechanical response is governed by the interplay between membrane and flexural stress states.

References

[1] Scheerer, Silke, and Chudoba, Rostislav, and Garibaldi, Maria Patricia, and Curbach, Manfred 2017. "Shells made of textile reinforced concrete–applications in Germany*." Journal of the international association for shell and spatial structures* 58(1):79–93, 2017.

[2] Valeri, Patrick, and Ruiz, Miguel Fernàndez, and Muttoni, Aurelio 2020. "Tensile response of textile reinforced concrete". *Construction and Building Materials*, *258*, 119517.

[3] Rampini, Marco Carlo, and Zani, Giulio, and Colombo, Matteo, and di Prisco, Marco 2019. "Mechanical behaviour of TRC composites: experimental and analytical approaches". *Applied Sciences*, *9*(7), 1492.

[4] Rampini, Marco Carlo, Zani, Giulio, and Colombo, Matteo, and di Prisco, Marco 2024. "Advancing construction techniques: Textile reinforced concrete shells and high-performance fiber-reinforced concrete beams for partially prefabricated elevated slabs*". In Structures* (Vol. 70, p. 107710). Elsevier.

[5] Saccomanno, Chiara, Rampini, Marco Carlo, and Zani, Giulio, and Romeo, Francesco 2025. "Numerical Modelling of TRC Shell Formworks: From Homogenized Approaches to Explicit Textile Simulation". Paper accepted for RILEM Spring Convention 2026, Ghent, Belgium, April 13 -17

[6] Marchetti, Ezio. 2016. "Caratterizzazione sperimentale di un cassero a perdere in Textile Reinforced Concrete per solai leggeri prefabbricati". Master Thesis, Politecnico di Milano.

[7] CEB-FIP (2010) Model Code 2010 – Volume 1. CEB-FIP, Lausanne.

Numerical Investigation of Post-Installed Screw Anchors for Shear Retrofitting of RC Beams

Rawand Alnsour, Giovanni Muciaccia

Department of Civil and Environmental Engineering,
Politecnico di Milano,
Piazza Leonardo da Vinci, Milan 20133, Italy

Summary
Retrofitting shear-deficient reinforced concrete (RC) elements is a critical challenge for existing structures designed according to outdated standards. This study numerically investigates post-installed concrete screws as a minimally invasive shear-strengthening solution for RC beams using a mechanically equivalent bar-based representation. Since concrete screws cannot be directly modelled as conventional reinforcement, their anchorage behavior is reproduced by embedded bars with calibrated bond–slip properties. Nonlinear finite-element models were developed and calibrated to match the experimental load–deflection response. The results demonstrate that the assumed bond–slip law governs the predicted shear behavior, significantly affecting both peak load and post-peak softening. The proposed modelling strategy provides a solid framework for assessing screw-based shear retrofitting systems.

1 INTRODUCTION

A large portion of the existing reinforced concrete (RC) buildings and bridges stock worldwide was designed according to outdated codes and often exhibits inadequate shear capacity when assessed against current safety and seismic requirements. Shear-deficient RC beams represent a critical vulnerability, as shear failures are typically brittle and associated with limited warning before collapse [1–3]. Consequently, effective and reliable shear strengthening and retrofitting techniques are essential to enhance the safety and service life of existing structures.

Conventional shear strengthening solutions include the addition of external concrete jacketing [4–6], externally bonded steel plates [7,8], and fibre-reinforced polymer (FRP) systems. Although FRP-based techniques are widely used due to their high strength-to-weight ratio and ease of installation, they are susceptible to premature debonding, exhibit reduced performance at elevated temperatures, and face practical limitations in confined spaces [9–12]. In recent years, post-installed mechanical fasteners, particularly screw anchors, have emerged as a promising alternative for shear retrofitting applications [13–15]. These systems enable rapid installation with minimal surface preparation and cause only limited disturbance to the existing structure, making them well-suited for retrofit interventions. Moreover, their compact installation requirements allow effective application in confined spaces, while maintaining compatibility with existing concrete members.

Experimental investigations [16,17] have shown that post-installed screw anchors can effectively function as transverse shear-resisting elements, leading to increased shear capacity and improved crack control in strengthened RC beams. Nevertheless, the load-transfer mechanism of concrete screws is governed by complex local interactions between the fastener and the surrounding concrete, including mechanical interlock, bearing, friction, and confinement effects, which result in a highly non-uniform stress distribution along the embedment length.

The objective of this study is to numerically investigate the influence of bond stress–slip modelling on the global shear response of RC beams strengthened with post-installed screw anchors. Since concrete screws cannot be directly represented using standard reinforcement assumptions due to their mechanically governed anchorage and non-uniform stress transfer along the embedment length, an equivalent bar-based representation is adopted. In this approach, the bond stress–slip properties of embedded bars are systematically calibrated to reproduce the mechanical behaviour of screw anchors. Special attention is devoted to the identification and calibration of local bond stress–slip parameters and to evaluating their influence on the load–deflection response, peak shear capacity, and post-peak softening of the strengthened RC beams.

2 BACKGROUND AND RESEARCH GAP

Previous research on the shear strengthening of RC beams has primarily focused on externally bonded FRP systems [18–20] and traditional post-installed reinforcement techniques, such as embedded through-section bars [21–23]. These studies have consistently highlighted the critical role of bond behaviour in governing failure modes, load redistribution, and deformation capacity. For post-installed screw anchors, experimental investigations have identified multiple potential failure mechanisms, including concrete cone breakout and pull-out, depending on the embedment depth, concrete strength, and confinement conditions [15,24].

Despite this experimental progress, numerical investigations on screw-anchor-strengthened RC beams remain limited. Most finite-element (FE) studies adopt simplified perfect-bond assumptions or generic bond–slip laws developed for conventional reinforcement, which are not able to represent the mechanically governed anchorage behaviour of concrete screws. As a result, the influence of anchor–concrete interaction on the global shear response of strengthened beams is not adequately captured.

The main research gap addressed in this study is the absence of numerical investigations that provide a mechanically consistent representation of post-installed concrete screws through equivalent reinforcing bars with calibrated bond–slip behaviour. Owing to their mechanically governed anchorage and non-uniform stress transfer, concrete screws cannot be modelled using conventional reinforcement assumptions. Consequently, their local anchorage response must be reproduced through an equivalent bar-based formulation in which the bond–slip parameters are systematically calibrated to reflect the mechanical behaviour of screw anchors.

3 NUMERICAL MODELLING FRAMEWORK

3.1 Mechanical Representation of Screw Anchors

The FE modelling of RC beams strengthened using post-installed shear reinforcement is based on the experimental approach adopted by Buhler and Vilotijevic [16] for a hybrid bonded concrete screw anchor system. The adopted system combines a self-tapping concrete screw anchor with an injectable organic adhesive, allowing load transfer through a combined mechanism of mechanical interlock provided by the threads and adhesive bonding at the steel–concrete interface. Due to the mechanically governed anchorage and non-uniform stress transfer along the embedment length, concrete screws cannot be represented using conventional reinforcement assumptions. Therefore, the screws are mechanically represented by equivalent embedded bars whose local bond–slip behaviour is calibrated to reproduce the global experimental response of beams strengthened using embedded through-section bars.

3.2 Reference Experimental Programme and Geometry

Fig. 1 shows large-scale four-point bending tests on RC beams, which were used as the reference for numerical model calibration. The experimental programme investigated the effectiveness of post-installed concrete screw anchors acting as transverse shear reinforcement. The anchors were installed at the soffit of the beams and oriented vertically to intersect the critical shear crack region.

Due to geometric and loading symmetry, only half of the beam was modelled in the numerical analysis to reduce computational cost while preserving the accuracy of the global response.

The beam geometry adopted in the model corresponds to the experimental specimens and includes a width of 220 mm, an overall height of 320 mm, and a total length of 3500 mm. The longitudinal reinforcement layout consisted of two top bars of a diameter of 20mm and four bottom bars of a diameter of 20 mm, and the screw anchors of 20 mm were placed at a spacing of 250 mm and with an effective embedment depth of 290 mm, as defined in accordance with the original test configuration.

3.3 Material and Geometric Properties

The concrete in the numerical model was defined as strength class C25/30, with a tensile strength of 1.96 MPa and a modulus of elasticity of 29090 MPa. The longitudinal reinforcement was modelled using steel grade B with a yield strength of 500 MPa.

For the post-installed shear reinforcement, the mechanical and geometric properties of the concrete screw anchors were adopted. In particular, a commercially available M20 concrete screw anchor was used for strengthening. The anchor has an external diameter of 24.3 mm, a core diameter of 16.93 mm,

and a cross-sectional area of 3.3 cm². The screws were modeled with an equivalent yield strength of 500 MPa and modulus of elasticity of 200000 MPa.

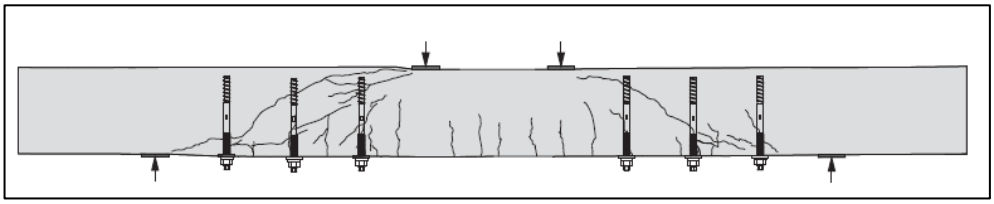


Fig. 1 Shear strengthening of RC beam using post-installed screw anchors [16].

3.4 Finite Element Discretization and Boundary Conditions

The FE models were developed using ATENA software. Concrete was discretized using three-dimensional solid elements with a structured mesh. The beam domain was divided into elements of approximately 50 mm along the longitudinal direction, 32 mm through the depth, and 33 mm across the width, as shown in Fig. 2. A mesh sensitivity study was performed to ensure that further refinement did not significantly affect the global load–deflection response.

Simply supported boundary conditions were applied, and monotonic vertical loading was imposed through displacement control to reproduce the experimental four-point bending configuration. Three modelling approaches were considered, including a perfect-bond assumption between the screws and concrete, a reference model employing standard local bond-slip values available in ATENA, and modified models incorporating calibrated bond–slip relationships.

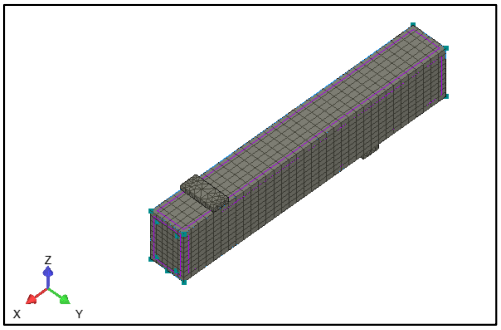


Fig. 2 FE mesh of the RC beam half-domain model due to geometric and loading symmetry.

4 BOND–SLIP MODELLING AND CALIBRATION

4.1 Reference Bond–Slip Model

To mechanically represent the behaviour of post-installed screw anchors within the finite element framework, an equivalent embedded bar formulation was adopted. As a reference, the local bond–slip relationship implemented in ATENA was based on the fib Model Code, assuming ribbed reinforcement and good bond quality. This reference model represents conventional deformed reinforcement behaviour and served as a baseline.

4.2 Calibrated Bond –Slip Law

To reproduce the mechanically governed anchorage of concrete screws, the standard bond stress and slip values defined in ATENA for the conventional bars model were modified through a user-defined stress–slip function. Since the original experimental programme did not include single-anchor pull-out tests, the bond–slip relationship could not be directly derived from measured local load–slip data. Therefore, starting from a generic bond–slip formulation, the bond–slip values were iteratively calibrated to match the experimental load–deflection response of the strengthened beam. Given that the

adopted system combines a self-tapping concrete screw with adhesive bonding, an equivalent local bond–slip law was assumed to represent the combined anchorage behaviour. Particular attention was given not only to the peak load but also to the post-peak response and overall structural behaviour. The best agreement with the experimental response was obtained using a nominal bond strength parameter (Bond Fcu) of 30 MPa in ATENA. This value represents an internal input parameter in the CEB-FIB bond formulation and does not directly correspond to the peak bond stress in the generated bond–slip curve. The bond–slip relationship adopted for the equivalent bar representation of the concrete screw is shown in Fig. 3. The curve exhibits a steep initial ascending branch, reaching a peak bond stress of 15 MPa at a slip of approximately 3 mm, representing the rapid activation of mechanical interlock between the screw threads and the surrounding concrete. This is followed by a gradual softening branch and a non-zero residual stress at large slip, indicating progressive degradation of the anchorage while maintaining frictional resistance. Although the anchor system consists of different connection regions along its length, an equivalent bond–slip relationship was adopted along the embedded bar to represent the combined contribution of adhesive bonding and mechanical interlock. The screw head region was represented as a fixed anchorage in the FE model. This representation provided improved agreement with the experimental post-peak response.

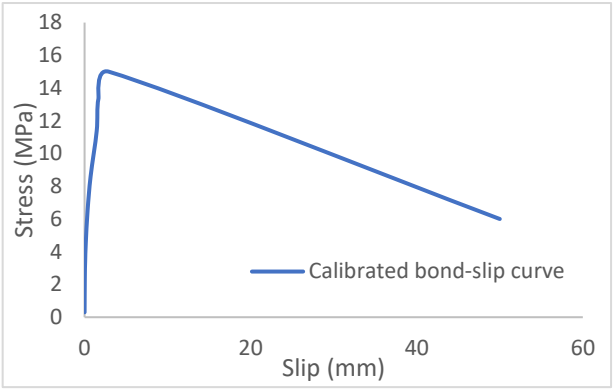


Fig. 3 The adopted bond stress-slip curve

5 NUMERICAL RESULTS

5.1 Load–Deflection Response

Fig. 4 compares the experimental load–deflection response of both the strengthened and unstrengthened RC beams with the numerical predictions. For the strengthened beam, three different modelling approaches were considered: perfect bond, standard ATENA bond stress–slip, and the modified bond–slip model. In addition, the experimental and numerical responses of the unstrengthened reference beam are included to assess the predictive capability and general quality of the FE model prior to modelling the strengthening system.

The perfect bond assumption significantly overestimates the peak load. This behaviour reflects an unrealistically rigid force transfer mechanism between the screw and the surrounding concrete, neglecting the effect of slip at the interface, which is not representative of the mechanically governed anchorage of concrete screws.

The model employed on the standard ATENA bond stress-slip values fails to capture the experimental response, underestimating the peak load and exhibiting premature strength degradation. This indicates that generic bond stress–slip relationships developed for conventional reinforcement are not suitable for representing screw anchors.

In contrast, the calibrated bond–slip model shows a significantly improved agreement with the experimental curve compared to the perfect-bond and standard bond assumptions. The model captures the general trend of the response, including the peak load level and the post-peak softening behaviour. However, the numerical response remains slightly stiffer than the experimental curve in the peak load. This difference is attributed to idealizations in the material models and boundary conditions, and the fact that the hybrid bonded post-installed concrete screw system is represented through an equivalent

bar with modified bond stress–slip properties. Nevertheless, the calibrated model provides a substantially more realistic prediction of the global shear response than the uncalibrated approaches.

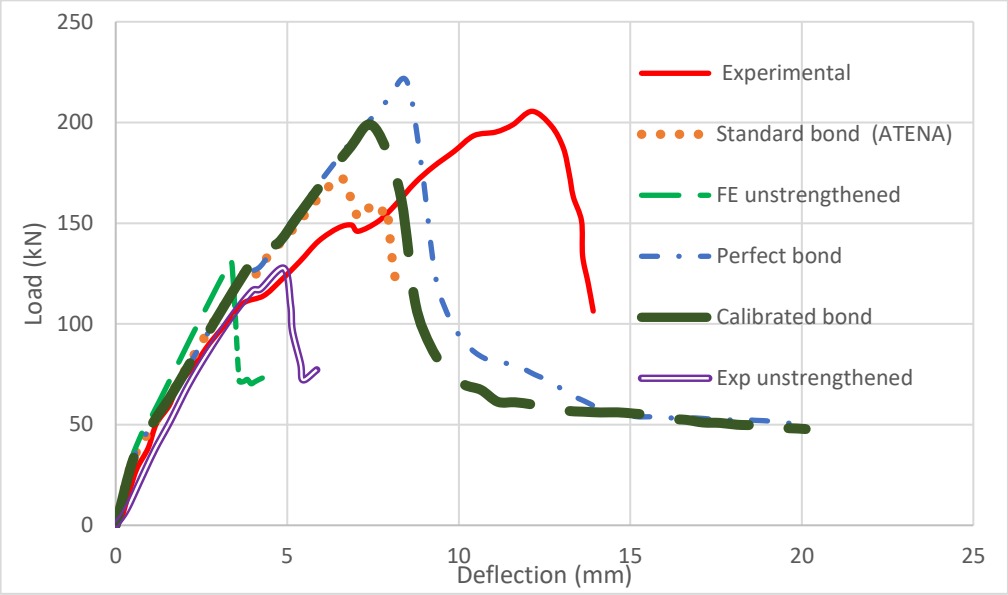


Fig. 4 Load-deflection response.

5.2 Crack Pattern, Failure Mode, and Stress Distribution

Fig. 5 presents the predicted damage pattern and internal force transfer mechanism obtained from the calibrated bond–slip model at peak load. The figure shows the crack-width contour in the strengthened RC beam and the experimental failure pattern of the tested beam [16].

The numerical crack pattern is characterized by a dominant diagonal shear crack developing in the shear-critical region, extending from the loading point toward the support. The highest crack widths are localized around the screw-anchor zone, indicating strong interaction between the anchors and the surrounding concrete and confirming that the applied shear force is effectively transferred through the screw system. The inclination and localization of the crack are consistent with a shear-controlled failure mode governed by a splitting bond mechanism.

A close agreement is observed between the numerical crack pattern and the experimentally observed failure mode. Both exhibit an inclined shear crack accompanied by localized concrete damage in the screw installation region, confirming a shear-controlled failure mode governed by a splitting bond mechanism. This agreement demonstrates that the proposed bond–slip modelling approach is able to realistically capture the governing failure mechanism of the strengthened beam.

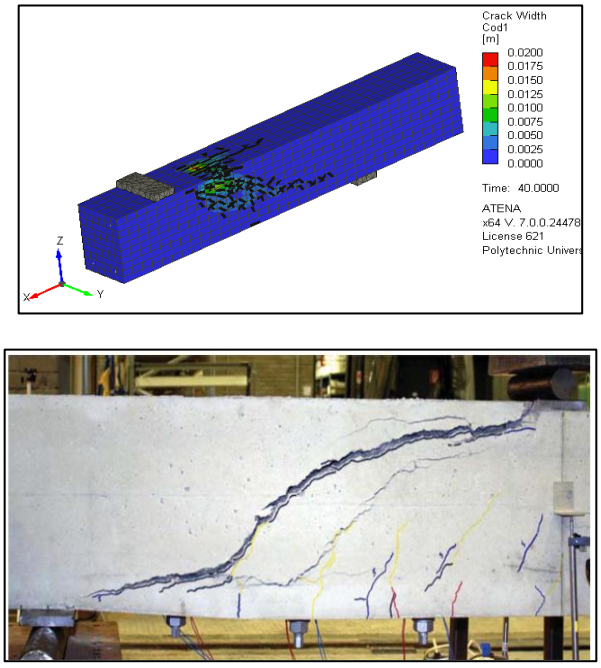


Fig. 5 Predicted damage pattern of the strengthened RC beam and experimental failure mode.

6 CONCLUSIONS

This study developed and applied an equivalent numerical modelling approach to evaluate the influence of anchor–concrete bond behaviour on the shear response of RC beams strengthened with post-installed concrete screws. The adopted bond–slip relationship was calibrated against the global beam response and provided a reasonable representation of the experimental behaviour; however, further validation against local load–slip data and additional beam configurations is required for broader applicability. Based on the numerical investigations, the following conclusions are drawn:

1. A mechanically equivalent modelling strategy based on embedded bars with modified bond–slip behaviour represents an appropriate solution to represent concrete screws, as their anchorage is governed by mechanical interlock and non-uniform stress transfer rather than by conventional reinforcement bond mechanisms.

2. The perfect-bond model significantly overestimated the stiffness and peak load, while the standard ATENA bond stress and slip values underestimated the capacity and failed to capture the post-peak behaviour.

3. The proposed modified bond–slip law provided a substantially improved prediction of the experimental load–deflection response and reproduced the progressive post-peak softening observed in the tests, although a slightly stiffer response before peak load remained.

4. The global shear behaviour of the strengthened beam was shown to be highly sensitive to local bond–slip properties, confirming that accurate modelling of anchor–concrete interaction is essential for reliable numerical assessment.

5. Stress results in the reinforcement indicated that the failure was not steel-controlled, confirming that the governing mechanism was associated with concrete cracking and bond degradation rather than with the strength of the steel components.

6. The proposed FE framework provides a basis for a forthcoming experimental program on full-scale screw-strengthened RC beams, as well as for systematic parametric studies on anchor spacing, embedment depth, and concrete strength to support future design recommendations.

Acknowledgements

This paper was produced while attending the PhD programme in Structural, Seismic, and Geotechnical Engineering at the Politecnico di Milano, Cycle XL, with the support of a scholarship co-financed by the Ministerial Decree no. 630 of 24th April 2024, based on the NRRP - funded by the European Union - NextGenerationEU - Mission 4 "Education and Research", Component 2 "From Research to Business", Investment 3.3.

References

[1] Jin, Liang, Du, Xilin, Li, Dong, and Su, Xiaotong. 2016. “Seismic Behavior of RC Cantilever Beams under Low Cyclic Loading and Size Effect on Shear Strength: An Experimental Characterization.” *Engineering Structures* 122:93–107. doi:10.1016/j.engstruct.2016.04.048.

[2] Wang, Guo Lin, Dai, Jianguo, and Teng, Jinguang. 2012. “Shear Strength Model for RC Beam–Column Joints under Seismic Loading.” *Engineering Structures* 40:350–360. doi:10.1016/j.engstruct.2012.02.038.

[3] Das Adhikary, Satadru, Li, Bing, and Fujikake, Kazunori. 2013. “Strength and Behavior in Shear of Reinforced Concrete Deep Beams under Dynamic Loading Conditions.” *Nuclear Engineering and Design* 259:14–28. doi:10.1016/j.nucengdes.2013.02.016.

[4] Hong, Sung-Gul, and Lim, Woo-Young. 2023. “Strengthening of Shear-Dominant Reinforced Concrete Beams with Ultra-High-Performance Concrete Jacketing.” *Construction and Building Materials* 365:130043. doi:10.1016/j.conbuildmat.2022.130043.

[5] Raval, Sachin S., and Dave, Urmil V. 2013. “Effectiveness of Various Methods of Jacketing for RC Beams.” *Procedia Engineering* 51:230–239. doi:10.1016/j.proeng.2013.01.032.

[6] Shabani Attar, Hamed, Esfahani, Mohammad Reza, and Ramezani, Ahmadreza. 2020. “Experimental Investigation of Flexural and Shear Strengthening of RC Beams Using Fiber-Reinforced Self-Consolidating Concrete Jackets.” *Structures* 27:46–53. doi:10.1016/j.istruc.2020.05.032.

[7] Thamrin, Rinaldi, Zaidir, and Wahyuni, Admi. 2023. “Shear Capacity of Reinforced Concrete Beams Strengthened with Web Bonded Steel Bars or Steel Plates.” *Results in Engineering* 17:100953. doi:10.1016/j.rineng.2023.100953.

[8] Barnes, Richard A., Baglin, Peter S., Mays, Gordon C., and Subedi, Narayan K. 2001. “External Steel Plate Systems for the Shear Strengthening of Reinforced Concrete Beams.” *Engineering Structures* 23:1162–1176. doi:10.1016/S0141-0296(00)00124-3.

[9] Abdel-Jaber, Mu'tasim, Al-Nsour, Rawand, Almahameed, Aseel, and Ashteyat, Ahmed. 2025. “Comparative Analysis of Shear Behavior in Continuous Low-Strength RC Beams Strengthened with BFRP and CFRP: An Experimental and Numerical Investigation.” *Composites Part C: Open Access* 16:100575. doi:10.1016/j.jcomc.2025.100575.

[10] Kotynia, Renata, Oller, Eduard, Marí, Antonio, and Kaszubska, Monika**.** 2021. “Efficiency of Shear Strengthening of RC Beams with Externally Bonded FRP Materials – State-of-the-Art in the Experimental Tests.” *Composite Structures* 267:113891. doi:10.1016/j.compstruct.2021.113891.

[11] Lee, Deuck Hang, Han, Sun-Jin, Kim, Kang Su, and LaFave, James M. 2017. “Shear Strength of Reinforced Concrete Beams Strengthened in Shear Using Externally-Bonded FRP Composites.” *Composite Structures* 173:177–187. doi:10.1016/j.compstruct.2017.04.025.

[12] Mhanna, Haya H., Hawileh, Rami A., and Abdalla, Jamal A. 2019. “Shear Strengthening of Reinforced Concrete Beams Using CFRP Wraps.” *Procedia Structural Integrity* 17:214–221. doi:10.1016/j.prostr.2019.08.029.

[13] Randl, Norbert, Harsányi, Peter, and Kunz, Jürgen. 2023. “Innovative Shear Strengthening with Post-Installed Undercut Anchors.” In *Life-Cycle of Structures and*

Infrastructure Systems: Proceedings of the 8th International Symposium on Life-Cycle Civil Engineering (IALCCE 2023), 1097–1104. doi:10.1201/9781003323020-134.

[14] Dondrea, Anthony, and Bayrak, Oguzhan**.** 2019. "Undercut and Grouted Anchors as Post-Installed Shear Reinforcement." *ACI Structural Journal* 116:27–37. doi:10.14359/51715504.

[15] Buhler, Jochen, and Crisolo, Ramil. 2020. "Post-Installed Retrofitting System for Improving the Punching Shear and Shear Capacity of Reinforced Concrete Elements." In *Proceedings of the Australian Structural Engineering Conference (ASEC 2020)*. Barton, ACT: Engineers Australia. doi:10.3316/informit.720611548600418.

[16] Buhler, Jochen, and Vilotijević, Danijel. 2022. "Improving the Punching Shear and Shear Capacity of Reinforced Concrete Elements with a New Post-Installed Retrofitting System." *Građevinski Materijali i Konstrukcije* 65:37–45. doi:10.5937/grmk2201037b.

[17] Lechner, Johannes, and Feix, Jürgen. 2022. "Enhanced Service Life of Existing Infrastructure Buildings by Use of Concrete Screw Anchors as Post-Installed Shear Reinforcement." *Acta Polytechnica CTU Proceedings* 33:322–328. doi:10.14311/APP.2022.33.0322.

[18] Junaid, Muhammad Tayyab, Karzad, Ahmad S., Elbana, Ashraf, and Altoubat, Samer. 2022. "Experimental Study on Shear Response of GFRP Reinforced Concrete Beams Strengthened with Externally Bonded CFRP Sheets." *Structures* 35:1295–1307. doi:10.1016/j.istruc.2021.10.089.

[19] Li, An, Assih, Jacques, and Delmas, Yves. 2001. "Shear Strengthening of RC Beams with Externally Bonded CFRP Sheets." *Journal of Structural Engineering* 127(4):374–380. doi:10.1061/(ASCE)0733-9445(2001)127:4(374).

[20] Islam, Mohammad R., Mansur, Mohd A., and Maalej, Mohamed. 2005. "Shear Strengthening of RC Deep Beams Using Externally Bonded FRP Systems." *Cement and Concrete Composites* 27:413–420. doi:10.1016/j.cemconcomp.2004.04.002.

[21] Barros, Joaquim A. O., and Dalfré, Gislaine M. 2013. "Assessment of the Effectiveness of the Embedded Through-Section Technique for the Shear Strengthening of Reinforced Concrete Beams." *Strain* 49:75–93. doi:10.1111/str.12016.

[22] Breveglieri, Marco, Aprile, Andrea, and Barros, Joaquim A. O. 2014. "Shear Strengthening of Reinforced Concrete Beams Strengthened Using Embedded Through Section Steel Bars." *Engineering Structures* 81:76–87. doi:10.1016/j.engstruct.2014.09.026.

[23] Breveglieri, Marco, Aprile, Andrea, and Barros, Joaquim A. O**.** 2016. "RC Beams Strengthened in Shear Using the Embedded Through-Section Technique: Experimental Results and Analytical Formulation." *Composites Part B: Engineering* 89:266–281. doi:10.1016/j.compositesb.2015.11.023.

[24] Lechner, Johannes, and Feix, Jürgen. 2019. "First Experiences with Concrete Screw Anchors as Post-Installed Shear Reinforcement in Concrete Bridges." *Civil Engineering Design* 1:17–27. doi:10.1002/cend.201800004.

Numerical simulation of corrosion-induced rust expansion with crack influence

Gonzalo Garcia Noxpanco, Ireneusz Marzec

Faculty of Civil and Environmental Engineering, Department of Engineering Structures,
Gdańsk University of Technology,
Gabriela Narutowicza 11/12, 80-233, Gdańsk, Poland

Summary
Corrosion-induced cracking constitutes a predominant mechanism of durability degradation in reinforced concrete structures subjected to chloride-rich environments. Conventional numerical methodologies inadequately represent spatially heterogeneous corrosion by assuming uniform rust expansion or temporally decoupled processes. This investigation introduces a finite element framework integrating chloride transport with mechanical fracture mechanics, incorporating concentration-dependent rust expansion and crack-facilitated diffusion. Implemented via thermal analogy in Abaqus with user subroutines, the methodology enables natural evolution of non-uniform corrosion patterns based on local chloride distributions. The framework employs bidirectional coupling where mechanical cracking enhances chloride penetration through crack width-dependent diffusion, creating self-reinforcing deterioration. A continuous activation function characterizes progressive porous zone saturation before expansive pressure development.

1 INTRODUCTION

Durability degradation in reinforced concrete structures stems predominantly from corrosion-induced cracking, a phenomenon particularly pronounced in chloride-laden marine environments where aggressive ion penetration expedites material deterioration. Upon reaching the steel reinforcement through the concrete cover, chloride ions compromise the protective passive film on the steel surface, thereby initiating the corrosion mechanism [1]. The critical chloride concentration threshold - defined as the minimum chloride content at the reinforcement interface necessary to destabilize the passive layer and trigger corrosion [2]exhibits considerable variability. Following corrosion initiation, rust products progressively occupy the interfacial porous zone surrounding the reinforcement [3] Subsequent rust accumulation between this porous zone and the concrete matrix generates volumetric expansion, inducing mechanical stress on the surrounding concrete that may culminate in crack formation. These corrosion products demonstrate substantial volumetric expansion relative to the steel - typically two to six-fold, contingent upon oxygen and moisture availability during rust formation [4] - [5].

Robust numerical characterization of this degradation mechanism necessitates the integration of two interdependent physical processes: transient chloride transport through the concrete matrix and the mechanical response of concrete subjected to rust-induced volumetric expansion. Various computational methodologies have emerged to simulate corrosion-induced deterioration in reinforced concrete systems, being the most popular: internal pressure, displacements, and thermal strains. The thick-walled cylinder model introduced by [6] constitutes one of the seminal and most extensively utilized frameworks. Despite its computational simplicity, this approach necessitates predetermined assumptions regarding pressure distribution and fails to inherently represent localized expansion patterns arising from spatially heterogeneous corrosion. Furthermore, [7] demonstrated that this model systematically underestimates crack initiation timing under realistic exposure scenarios.

More recently, thermal analogy approaches have gained popularity, where corrosion - induced strain is represented as equivalent thermal expansion in the steel or rust region [8]. Within this framework, several implementation strategies exist. Some researchers have defined the rust region explicitly with its own mechanical properties, others have employed cohesive elements to define the interface between rust and rebar or between rust and concrete [8] - [9].

A fundamental deficiency in numerous existing computational frameworks concerns the inadequate representation of bidirectional coupling between chloride transport and mechanical fracture processes. The literature unequivocally establishes that crack formation substantially accelerates chloride penetration by creating preferential diffusion pathways [10], with multiple investigations proposing and

validating crack width-dependent diffusion coefficient relationships [10] - [13]. Nevertheless, relatively few models incorporate this feedback mechanism in a fully coupled spatiotemporal manner within comprehensive corrosion simulations.

The presented framework operationalizes bidirectional coupling between mechanical deterioration and chloride transport phenomena. As fractures propagate consequent to rust-induced expansion, local diffusion coefficients are augmented as a function of crack aperture width according to the formulation established by [10]. Upon exceeding a critical crack width threshold, diffusion coefficients within the fractured zone may increase by over two orders of magnitude, asymptotically approaching free solution diffusion conditions. This mechanism establishes a self-reinforcing deterioration cycle wherein mechanical damage expedites chloride penetration, subsequently promoting additional corrosion and crack propagation.

2 METHODOLOGY

2.1 Chloride Transport

Chloride-ion transport through the porous concrete matrix toward steel reinforcement constitutes the fundamental mechanism governing deterioration in chloride-exposed reinforced concrete structures. Fick's law describes the spatio-temporal evolution of the chloride concentration $C(x,t)$:

$$\frac{\partial C}{\partial T} = \nabla \cdot (D(C,t)\nabla C) \tag{1}$$

where $C(x,t)$ represents chloride concentration at position x and time t, while $D(C,t)$ denotes the effective diffusion coefficient, dependent on concrete age and environmental exposure conditions. An aging function characterizes the time-dependent diffusion coefficient:

$$D(t) = D_0(\frac{t}{t_0})^n \tag{2}$$

where D_0 represents the initial diffusion coefficient at reference time t_0. The exponent n quantifies diffusivity reduction rate, reflecting continuous hydration and pore structure refinement within the concrete matrix.

2.2 Corrosion initiation

Corrosion initiation occurs when chloride concentration at the reinforcement surface reaches a critical threshold value C_{th}. This threshold denotes the minimum chloride content required to compromise the protective passive oxide film on the steel surface within concrete's alkaline environment. A smooth activation function $s(C)$ characterizes the progressive corrosion development within the porous zone during the initial phase:

$$(C) = \begin{cases} 0\,, & C \le C_{th} \\ x^2(3-2x)\,, & C_{th} < C < C_{hi} \text{ with } x = \dfrac{C - C_{th}}{C_{hi} - C_{th}} \\ 1\,, & C \ge C_{hi} \end{cases} \tag{3}$$

where C_{hi} represents the chloride content at full corrosion process activation. The cubic Hermite polynomial function guarantees continuity for both the activation function $s(C)$ and its derivative ds/dC, yielding numerically stable and physically realistic transitions between passive and fully corroded states. The activation function restricts expansion to conditions exceeding the critical threshold, increasing progressively as corrosion products fill the porous zone.

2.3 Corrosion induced expansion

Once the porous zone surrounding the steel reinforcement becomes saturated with corrosion products, continued rust formation generates volumetric expansion that exerts mechanical pressure on the surrounding concrete. The resulting corrosion products occupy significantly larger volume than the original steel elements. The magnitude of rust-induced expansion at any location depends on the local

corrosion state, which in turn is governed by the local chloride concentration. The normal radial strain generated by rust accumulation can be expressed through an incremental formulation:

$$d\varepsilon^{cor} = \alpha \cdot s(C) \cdot dC \tag{4}$$

where ε^{cor} denotes strain from rust-induced volumetric growth, α represents the expansion coefficient correlating chloride concentration increase with volumetric strain, and $s(C)$ is the activation function from Equation (3). Temporal integration of incremental strains over the concentration history yields the accumulated thermal strain:

$$\varepsilon^{cor}(t) = \alpha \int_{C_{th}}^{C(t)} s(\xi) d\xi \tag{5}$$

This integral formulation incorporates the complete loading history at each material point, ensuring total expansion reflects cumulative chloride accumulation effects over time. It is worth noting that the rust products are assumed to be solely at the concrete-rebar interface, rust products filling the cracks are not considered in the present model as in [8], [14]. Furthermore, the extent of corrosion products penetrating the cracks remains under discussion, and only very limited experimental data have been reported to quantify the amount of rust that flows into the cracks [9].

2.4 Mechanical model

For the constitutive description of concrete behavior under corrosion-induced loading, this study employs the Concrete Damaged Plasticity (CDP) framework implemented in Abaqus. This constitutive model captures concrete's characteristic response by integrating damage mechanics with plasticity theory, accounting for both tensile and compressive inelastic deformation modes.

Throughout the numerical simulation, the equivalent plastic strain in tension ε_t^{pl} serves as the primary indicator for monitoring crack development. According to the crack band approach, a material point is considered cracked when ε_t^{pl} exceeds zero, signifying the onset of inelastic tensile deformation. The characteristic crack opening displacement w_{cr} can be related to the equivalent plastic strain and the finite element characteristic length h_e through:

$$w_{cr} = \varepsilon_t^{pl} \cdot h_e \tag{6}$$

Experimental investigations have consistently demonstrated monotonic increase of the local diffusion coefficient with increasing crack width, exhibiting distinct threshold behavior [11] - [10]. For narrow cracks below a lower threshold, the diffusion coefficient remains approximately equal to that of sound concrete. As crack width increases beyond this lower threshold, the diffusion coefficient rises progressively, with the rate of increase governed by a smooth transition function that reflects the gradual opening of interconnected pathways through the damaged concrete matrix.

2.5 Numerical implementation

The coupling between chloride diffusion and mechanical expansion presented in preceding sections requires numerical implementation within a finite element framework. Abaqus lacks native capabilities for directly solving mass transport problems coupled with mechanical analysis. To circumvent this limitation, the mathematical analogy between diffusion-governed chloride transport and heat conduction physics is incorporated. This approach, widely adopted in the literature, permits utilization of Abaqus's established thermo-mechanical coupling capabilities for simulating chloride-induced deterioration.

Within this implementation strategy, the temperature field *T* acts as a surrogate for representing chloride concentration *C*, while volumetric strains arising from rust formation are modeled through the thermal expansion mechanism. User-defined subroutines enable representation of the complex physical phenomena characterizing the corrosion process. Specifically, USDFLD (user-defined field variable) manages temporal evolution of the chloride diffusion coefficient per Equation (2), with updates at each increment reflecting both aging effects and crack width influence via the enhanced diffusion

relationship. The UEXPAN (user-defined thermal expansion) subroutine imposes incremental strains representing mechanical pressure from expanding rust products on the surrounding concrete matrix

The bidirectional coupling between mechanical fracture and chloride ingress represents a critical component of the computational framework. Following formulation by [10], the relationship linking crack aperture to local diffusivity captures the transition from sound concrete to free solution conditions:

$$D_{cr} = \begin{cases} D_c\,, & w_{cr} \le w_1 \\ \dfrac{D_c + D_0}{2} + \dfrac{D_0 - D_c}{2} sin\left[\dfrac{\pi}{w_2 - w_1}\left(w_{cr}\dfrac{w_2 + w_1}{2}\right)\right], & w_1 \le w_{cr} \le w_2 \\ D_0\,, & w_{cr} \ge w_2 \end{cases} \tag{7}$$

where D_{cr} denotes cracked concrete diffusion coefficient, D_c represents sound concrete diffusion coefficient, D_0 is free solution diffusion coefficient (approximately 2×10^{-3} mm²/s for chloride ions in water), and w_{cr} is local crack width. Lower crack width threshold w_1 and upper crack width threshold w_2 define the transition zone where the diffusion coefficient increases from sound concrete to free solution values. For this simulation, values for w_1 and w_2 are set as 0.03 mm and 0.10 mm, respectively.

It should be noted that the threshold values w_1 and w_2, reported in the literature vary considerably depending on experimental conditions, environmental exposure, and concrete composition.

3 RUST EXPANSION SIMULATION

3.1 Experimental setup

The numerical model presented in Section 2 was validated using experimental data from [15], who performed accelerated corrosion tests on reinforced concrete beams to quantify and characterize the non-uniform rust distribution around steel rebars. After the corrosion exposure, the whole beam was divided into three longitudinal sections: left(L), middle(M) and right(R) (Fig.1). Each section was then subdivided into multiple transverse panels, and each panel was examined individually to document spatial variation in rust thickness and associated crack patterns. For this numerical model, section R was used, specifically panel R-1, which exhibited significant damage.

Experimental results were solely focused on the rust thickness, its distribution and some cracking patterns, further details on the crack width were not reported.

3.2 Model description

The mechanical behaviour of concrete is characterized using the Concrete Damaged Plasticity (CDP) model implemented in Abaqus, as detailed in Section 2.5. Diffusion parameters and mechanical properties were calibrated using experimental data from [15] and supplemented with literature values when direct measurements were unavailable.

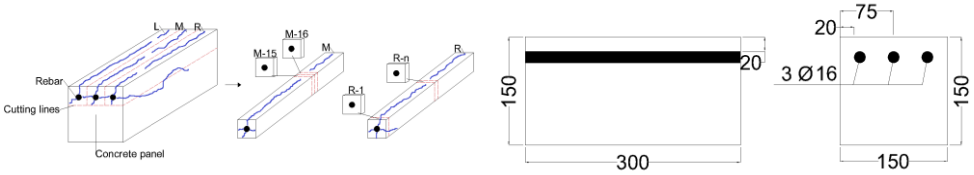


Fig. 1 Set up from experiment: sliced panels (left) and cross-section (right).

Fig. 2 (right) illustrates the boundary conditions applied in the simulation, including the surfaces exposed to chloride ingress and the mechanical constraints. Fig. 2 (left) presents the finite element discretization of the cross-section. Four-node plane strain elements with temperature degree of freedom (CPE4T) were used for the concrete domain. A mesh size of 1 mm was adopted near the rebar to accurately capture steep gradients in chloride concentration and the stress field. The analysis period

was set to two years to enable visualization of crack initiation and propagation at various stages of the corrosion process.

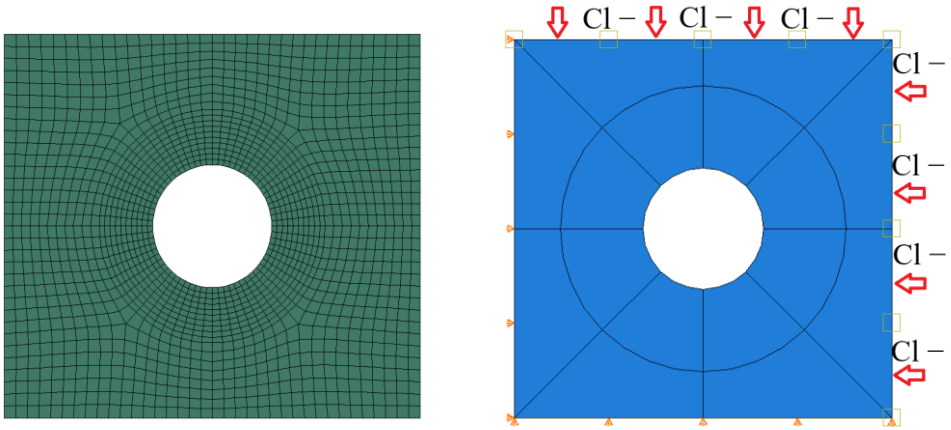


Fig. 2 FEM mesh discretization (left) and boundary conditions (right).

Concrete is modelled as a homogeneous material, without explicit representation of aggregates, interfacial transition zones, or other meso-scale heterogeneities. As a result, the calculated crack pattern may differ from the actual crack morphology observed in experiments, where aggregates and material heterogeneities influence the specific crack path. The crack-enhanced diffusion mechanism remains active throughout the simulation, which enables mechanical damage to accelerate chloride ingress and results in the coupled deterioration process observed experimentally.

4 RESULTS AND DISCUSSION

Fig. 3 (right) shows that the widest crack develops vertically toward the top of the concrete cover, consistent with the behaviour observed in most corrosion-induced cracking simulations and experiments reported in the literature. The calculated width of this primary crack is approximately 0.1 mm, exceeding the lower threshold for crack-enhanced diffusion defined in Section 2. As a result, the diffusion coefficient in this region increases substantially, establishing a preferential pathway for accelerated chloride ingress. This feedback mechanism facilitates more rapid chloride penetration toward the steel surface near the crack, thereby promoting additional corrosion and further crack propagation in adjacent areas. The increased D_{eff} inside the cracks can be seen in Fig. 3 (middle), whereas Fig. 3 (left) shows the absence of this crack-enhancement feature, remarking the importance of these pathways created by the cracks.

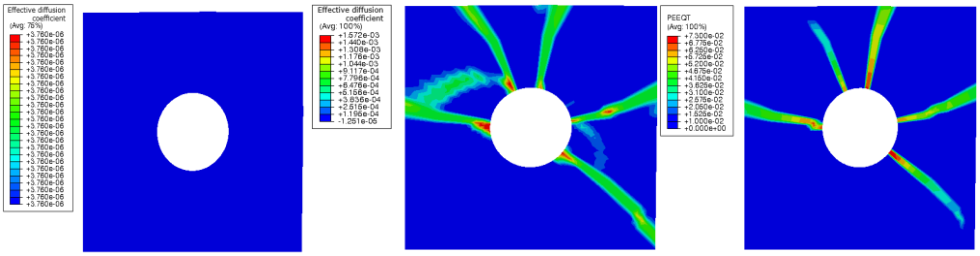


Fig. 3 Effective diffusion coefficient and cracking: without crack coupling (left), with crack coupling (middle), and cracking patterns (right).

As described in Section 2, the D_{eff} changes occur dynamically during the analysis; therefore, the concentration values will change accordingly. Fig. 4 (left) shows how the concentration contours

change due to the higher diffusion inside the cracks. It can be noted that the contour presents some distortion due to this effect. Moreover, Fig. 4 (right) shows the global concentration levels around the steel-concrete interface, where the crack-enhanced model yields higher concentrations, indicating more severe damage. Due to the local increase of D_{eff} the crack coupled model also shows a rather irregular concentration curve. It is worth mentioning that the concentration plot was measured using polar coordinates, where π is located at the top-right corner, to match the exposure boundary conditions.

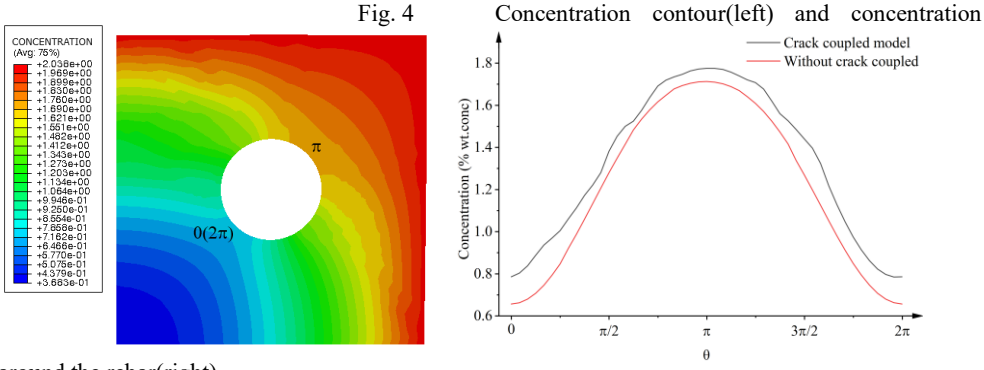


Fig. 4 Concentration contour(left) and concentration around the rebar(right).

Fig. 5 illustrates the evolution of expansive strains associated with rust-induced volumetric growth. Initially, expansive strains are zero across the concrete domain because the chloride concentration at the steel surface remains below the critical threshold for corrosion initiation. Strain accumulation begins at approximately 0.4 to 0.6 years, which corresponds to the point when the local chloride concentration at the rebar surface surpasses the threshold value C_{th}.

After the threshold is exceeded, the activation function increases from zero, and expansive strains begin to accumulate gradually according to Equations (4) and (5). The initial growth rate of expansive strains remains slow, indicating the progressive filling of the porous zone around the rebar with corrosion products. During this stage, rust accumulates within the available porosity without producing significant mechanical pressure. As the chloride concentration rises beyond the threshold and approaches the full activation level, the activation function approaches unity, resulting in a more rapid increase in expansive strains. This accelerated growth ultimately generates sufficient expansive pressure to surpass the concrete tensile strength and initiate cracking in the surrounding concrete.

Furthermore, as discussed previously, the local increase in diffusion also affects the strains that eventually lead to damage, as these depend on the local concentration. Thus, the crack-coupled model will show more damage.

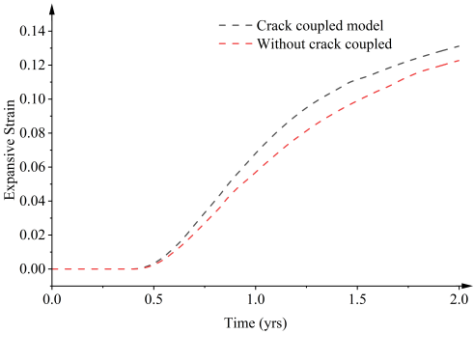


Fig. 5 Expansive strains evolution with time.

The final crack pattern for the panel R-1 obtained from the numerical simulation is compared with experimental observations and with other models from different authors in Fig. 6. The specific crack path in concrete is known to depend on the local mesostructure, including aggregate distribution and interfacial transition zone properties. Despite this, the finite element model shows good agreement with the experimental crack pattern and with the model in [16], which used a 3D mesoscale approach and validated it against the same experimental dataset from [15]. Both the simulation and experiment display a dominant vertical crack extending from the rebar to the top surface, along with four cracks propagating in various directions. The general crack distribution and failure mode are effectively captured by the homogenized continuum approach used in the present model.

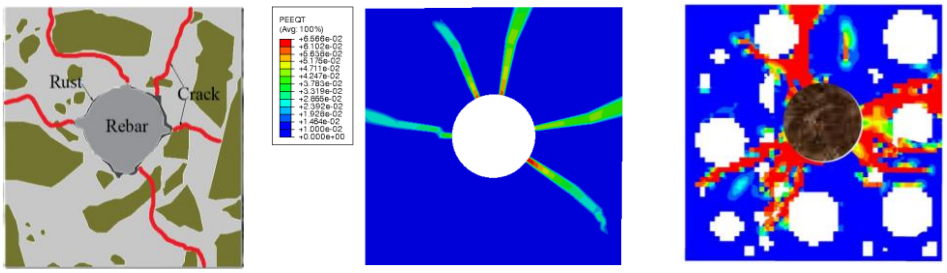


Fig. 6 Experimental final cracking (left), FEM simulation final cracking (middle), and FEM simulation final cracking (right) from [16].

5 CONCLUSIONS

This study presents a finite element modelling framework for corrosion-induced cracking in reinforced concrete, which has been validated against experimental results. Rust expansion is simulated using a thermal analogy, where the temperature field represents chloride concentration and thermal strains correspond to volumetric expansion resulting from corrosion products. The implementation of a smooth activation function with a critical chloride threshold allows for a realistic depiction of the gradual initiation of the corrosion process, effectively capturing the physical delay between corrosion initiation and the onset of mechanically significant expansion.

A principal feature of the proposed model is the explicit bidirectional coupling between mechanical cracking and chloride transport. As cracks form due to rust expansion, the local diffusion coefficient increases with crack width, establishing a mechanism in which mechanical damage accelerates additional chloride ingress, thereby leading to higher concentrations and overall damage. Furthermore, the model with the crack enhancement feature shows slightly more damage, underscoring the importance of accounting for increased local diffusion within cracks. Overall, the numerical results show satisfactory agreement with experimental observations regarding crack patterns and rust distribution.

Future developments of the framework may include three-dimensional analysis and explicit representation of the concrete mesostructure to enable more detailed predictions of crack trajectories as well as to investigate the possible influence of the aggregates and ITZ in the expansion process. Although actual corrosion kinetics involve complex electrochemical processes, the simplified approach presented in this study has demonstrated the ability to reproduce essential features of corrosion-induced deterioration. Therefore, for engineering applications focused on structural performance and service life assessment, the proposed framework provides a practical balance between model complexity and predictive accuracy.

Acknowledgements

Calculations were carried out at the Centre of Informatics Tricity Academic Supercomputer and Network. This research was partially funded by the National Centre for Research and Development and Clean Energy Transition Partnership (CETP) co-funded by the European Union within project WECHULL+ “Sustainable Concrete Material Leading to Improved Substructures for Offshore Renewable Energy Technologies” (CETP-2022-00127).

Generative AI tools were used solely to improve the clarity and grammar of the English text. All scientific content (including figures and graphs) was exclusively made, written and verified by the authors.

References

[1] Gareth K. Glass and Nicholas R. Buenfeld, "The influence of chloride binding on the chloride induced corrosion risk in reinforced concrete," 1997.

[2] Ki Yong Ann and Ha Wong Song, "Chloride threshold level for corrosion of steel in concrete," *Corrosion Science*, vol. 49, no. 11, pp. 4113–4133, Nov. 2007, doi: 10.1016/j.corsci.2007.05.007.

[3] Samanta Robuschi *et al.,* "A closer look at corrosion of steel reinforcement bars in concrete using 3D neutron and X-ray computed tomography," *Cement and Concrete Research*, vol. 144, Jun. 2021, doi: 10.1016/j.cemconres.2021.106439.

[4] Lin An, Ryosuke Saito, Satoshi Takaya, and Toyoaki Miyagawa, "DETERMINATION OF YOUNG`S MODULUS OF RUST-LAYER BY BENDING EXPERIMENT."

[5] Shuxian Hong *et al.*, "Quantification of rust penetration profile in reinforced concrete deduced by inverse modeling," *Cement and Concrete Composites*, vol. 111, Aug. 2020, doi: 10.1016/j.cemconcomp.2020.103622.

[6] Zdenek P. Bazant, M. ASCE, "Physical Model for Steel Corrosion in Concrete Sea Structures," 1979.

[7] Tamer El Maaddawy and Khaled Soudki, "A model for prediction of time from corrosion initiation to corrosion cracking," *Cement and Concrete Composites*, vol. 29, no. 3, pp. 168–175, Mar. 2007, doi: 10.1016/j.cemconcomp.2006.11.004.

[8] Magdalena German and Jerzy Pamin, "Cracking in Reinforced Concrete Cross-Sections Due to Non-Uniformly Distributed Corrosion," *Materials*, vol. 16, no. 18, Sep. 2023, doi: 10.3390/ma16186331.

[9] C. Van Steen, T. Van Beirendonck, R. Vrijdaghs, M. A. N. Hendriks, and E. Verstrynge, "A two-phased modelling approach for corrosion-induced concrete cracking and bond deterioration in reinforced concrete," *Engineering Structures.*, vol. 294, Nov. 2023, doi: 10.1016/j.engstruct.2023.116624.

[10] Renbo Zhang, Liu Jin, Mengjia Liu, Xiu Li Du, and Yue Li, "Numerical investigation of chloride diffusivity in cracked concrete," *Magazine of Concrete Research*, vol. 69, no. 16, pp. 850–864, Aug. 2017, doi: 10.1680/jmacr.16.00511.

[11] Seung Yup Jang, Bo Sung Kim, and Byung Hwan Oh, "Effect of crack width on chloride diffusion coefficients of concrete by steady-state migration tests," *Cement and Concrete Research*, vol. 41, no. 1, pp. 9–19, Jan. 2011, doi: 10.1016/j.cemconres.2010.08.018.

[12] Assia Djerbi, Stephanie Bonnet, Abdelhafid Khelidj, and Veronique Baroghel-Bouny, "Influence of traversing crack on chloride diffusion into concrete," *Cement and Concrete Research*, vol. 38, no. 6, pp. 877–883, 2008, doi: 10.1016/j.cemconres.2007.10.007.

[13] Bong Seok Jang and Byung Hwan Oh, "Effects of non-uniform corrosion on the cracking and service life of reinforced concrete structures," *Cement and Concrete Research*, vol. 40, no. 9, pp. 1441–1450, Sep. 2010, doi: 10.1016/j.cemconres.2010.03.018.

[14] Fan Xiu Chen *et al.*, "Non-uniform model of relationship between surface strain and rust expansion force of reinforced concrete," *Scientific Reports.*, vol. 11, no. 1, Dec. 2021, doi: 10.1038/s41598-021-88146-2.

[15] Yuxi Zhao, Bingyan Hu, Jiang Yu, and Weiliang Jin, "Non-uniform distribution of rust layer around steel bar in concrete," *Corrosion Science*, vol. 53, no. 12, pp. 4300–4308, Dec. 2011, doi: 10.1016/j.corsci.2011.08.045.

[16] Liu Jin, Mengjia Liu, Renbo Zhang, and Xiuli Du, "Cracking of cover concrete due to non-uniform corrosion of corner rebar: A 3D meso-scale study," *Construction and Building Materials,* vol. 245, Jun. 10, 2020, doi: 10.1016/j.conbuildmat.2020.118449.

Numerical Analysis of Pull-Out Test Using a Realistic Ribbed Rebar Geometry Model

Marcin Burdziński, Maciej Niedostatkiewicz

Faculty of Civil and Environmental Engineering
Gdańsk University of Technology
Narutowicza 11/12, 80-233 Gdańsk, Poland

Summary

The bond between reinforcement and concrete is fundamental to the performance of reinforced concrete structures. This paper evaluates the influence of incorporating realistic, 3D-scanned ribbed bar geometry on the fidelity of Finite Element Method (FEM) simulations of pull-out test. The numerical analysis, performed in ABAQUS using the Concrete Damaged Plasticity (CDP) model, was validated against experimental results. The simulation utilized a complex bar shape obtained via optical scanning, in contrast to typical simplified geometric models. Results demonstrated strong agreement for peak bond stress and corresponding slip, with relative errors below 11%. However, significant discrepancies were observed in residual stresses, attributed to distinct failure modes: pull-out failure in experiments versus a combined failure mode in the numerical model. The study highlights the limitations of standard continuum models in reproducing micro-scale shearing under high confinement.

1 INTRODUCTION

Bond is the mechanism that enables the interaction between reinforcement and concrete during the load transfer process, forming the fundamental basis for the behaviour of reinforced concrete elements. It determines key parameters related to structural capacity, such as anchorage and lap lengths, and influences serviceability aspects, including cracking and deflection. The most frequently conducted bond test is the pull-out test (POT). This test typically represents bond observation at the rib scale, which – alongside the bar and member scales – was defined by Cox and Herrmann [1]. The test involves pulling a bar directly out of a concrete block while recording the applied force and the relative displacement of the bar. The primary output of the test is the bond-slip curve, which is treated as the constitutive bond law, analogous to the stress-strain curve obtained from uniaxial tensile testing of steel [2]. One of the first analyses using this method was conducted by Abrams [3] at the beginning of the 20th century. In recent years, the focus of research has shifted from general bond mechanics to assessing the impact of unconventional materials on the reinforcement-concrete interaction.

Currently, pull-out tests are primarily applied in research on new-generation concretes, including self-compacting concrete [4], [5], recycled aggregate concrete [6], [7], fibre-reinforced concrete [8], [9], and hybrid concretes that combine features of various materials, such as steel-fibre-reinforced self-compacting concrete [10]. This method is also commonly used to evaluate the interaction between concrete and non-metallic reinforcement, such as FRP bars [11], [12]. Despite the growing interest in new materials, fundamental research into bond mechanics using the POT method, though still active (e.g., [13–15]), has become relatively rare.

Experimental research, which forms the foundation of reinforced concrete structural analysis, is complemented by numerical simulations, most performed using the Finite Element Method (FEM). A key advantage of the numerical approach is the ability to obtain data that is difficult or impossible to measure in a laboratory environment, such as stress and strain fields. Simulations offer extensive post-processing capabilities, enabling the analysis of the state of any point in the model at a given time step. Furthermore, numerical methods facilitate parametric studies, including the investigation of elements with varying geometries and scales, without the need to fabricate physical specimens. The ease of modifying input data and the repeatability of calculations make this method cost-effective compared to expensive and labour-intensive destructive experiments. However, certain limitations of numerical simulations must be acknowledged, mainly related to the time-consuming nature of the processes and the demand for significant computational power, particularly in the case of highly complex models. This computational cost is directly correlated with the type and density of the finite element mesh, the required solution accuracy, and the available hardware resources.

In numerical simulations of pull-out tests, two main approaches to modelling the bar-concrete interaction are distinguished. The first utilizes a plain bar, where the interaction with the surrounding concrete is modelled through a defined contact interface. This interface is typically implemented using cohesive elements or surfaces assigned properties appropriate for the specific method [16–19]. The primary advantage of this approach is the

relative simplicity of defining the bar-concrete interaction. However, its main drawback is a significant oversimplification of the underlying physics, as mechanical interlocking is replaced by contact parameters. This prevents the analysis of localized processes in the vicinity of the ribs, limiting the evaluation of the bond mechanism to the global response of the system.

The second approach relies on the use of a detailed ribbed bar model. This allows for a faithful reproduction of the actual source of the bond, which arises primarily from the mechanical interlocking of the ribs within the concrete matrix. This method eliminates the limitations of plain bar models, enabling a more detailed analysis of the material interaction in the immediate vicinity of the ribs – the very essence of research at this scale. However, this introduces significant geometric complexity and necessitates a highly refined finite element mesh. This results in extended computation times and a higher risk of convergence issues.

Existing ribbed bar models in POT simulations have typically been based on either idealized geometry, which reproduces the nominal shape of a given bar type [20], [21], or simplified geometry, which represents ribs in the form of regular lugs [22], [23] or spirals [24]. This paper presents numerical simulations using actual bar geometry obtained via 3D scanning, representing a novel approach compared to existing solutions found in the literature. The aim of this study is to assess the influence of the geometry defined in this manner on the fidelity of the simulated bond mechanism, validated against the authors' own experimental data reported in [25]. Beyond validating numerical accuracy, establishing this high-resolution modelling framework lays the groundwork for practical engineering applications, particularly in design (e.g., determining the anchorage length) and expert technical assessments within structural diagnostics.

2 DETAILS OF NUMERICAL ANALYSIS

Numerical simulations were performed using the ABAQUS software [26], which enabled the inclusion of both geometric and material nonlinearities in the analysis. To capture concrete behaviour, the Concrete Damaged Plasticity (CDP) model was utilized. It combines an elastic degradation model with a constitutive elastoplastic law, providing a versatile framework for modelling quasi-brittle materials such as concrete. The selection of CDP model parameters for the uniaxial stress state was guided by the fib Model Code 2010 guidelines [27] and the software documentation [26]. The 2010 edition was utilized as the source of constitutive relations because the final version of the fib Model Code 2020 [28] had not yet been officially published when these numerical analyses were conducted. For uniaxial tension, linear-elastic material behaviour was assumed until the tensile strength was reached. Beyond this point, linear softening was implemented, characterized by the fracture energy G_F, which was determined according to the formula provided in [27]. The compressive strength f_c and tensile strength f_{ct} values were adopted directly from the authors' own tests. These tests were performed on companion specimens cast from the same concrete batch as the elements subjected to the pull-out tests, demonstrating that the concrete satisfies the criteria for strength class C35 according to the fib Model Code 2010 [27]. Other mechanical properties and parameters describing concrete behaviour under complex stress states were established in accordance with CDP model recommendations and fib guidelines [27]. The adopted concrete material parameters are summarized in Table 1. The chosen concrete density (ρ_c = 2500 kg/m^3) conforms to the standard range of 2000 to 2600 kg/m^3 defined for normal-weight concrete in Section 5.1.3 of the fib Model Code 2010 [27]. For comparison, the corresponding symbols and values from Eurocode 2 [29] that differ from those in [27] are shown in brackets.

Table 1 Parameter values for the concrete material model adopted in the FEM simulation

density ρ_c	Poisson's ratio υ_c	Young's modulus E_c	compressive strength f_c	tension strength f_{ct}	fracture energy G_F	strain in compressive strength ε_{c1}	ultimate strain in compression $\varepsilon_{c,lim}$ (ε_{cu})
[kg/m^3]	[-]	[GPa]	[MPa]	[MPa]	[N/mm]	[‰]	[‰]
2500	0.20	30.82	40.20	3.38	0.1419	2.3 (2.25)	3.5

dilation angle	eccentricity	f_{b0}/f_{c0}	Kc	viscosity parameter [s]
31°	0.1	1.16	0.67	0

A linear-elastic model was used to describe the reinforcing steel; consequently, the steel's ductility class was of no consequence to the numerical simulation results. Material density ρ_s was assumed to be 7850 kg/m^3,

and Poisson's ratio υ_s was set to 0.33. Young's modulus E_s was determined experimentally, yielding a value of 211 GPa.

By utilizing a ribbed bar model, the bond resulting from mechanical interlocking is directly accounted for. For the direction normal to the contact surface, a "hard contact" relationship was adopted, while a friction coefficient of 0.075 was defined for the tangential direction. This value was determined during the calibration of the numerical model by matching the simulated peak bond stress with experimental results. The effect of adhesion on the bar-concrete interaction was neglected as it had an insignificant impact on the global system response, which allowed for model simplification without a notable loss of simulation accuracy.

The realistic bar geometry was acquired via 3D optical scanning. The initial scan of a 70 mm long bar segment with a 12 mm diameter yielded a point cloud of 589,208 points. This high point density, while ensuring excellent surface reproduction, was unnecessary to faithfully recreate the rib geometry. Furthermore, importing such a large number of points would generate an excessively dense finite element mesh, leading to disproportionately long computation times. Consequently, a reduction in the number of points forming the scanned bar geometry was necessary. The influence of this reduction level on the fidelity of the bar shape reproduction is shown in Fig. 1.



Fig. 1 Reduction of 3D scan points for a 70 mm bar section

Visual analysis showed that with a 50%-point reduction, differences relative to the original geometry were imperceptible, and the first significant deviations appeared only at a reduction of 97.5% (at 99.9%, only a coarse volume was preserved). Based on this analysis, the geometry reduced by 99.5% was selected for the simulation, limiting the number of points describing the bar segment to 2,946. The remaining portion of the bar, which was not in contact with the concrete, was modelled by extruding the end contour of the scan, thereby creating a smooth surface.

The numerical model accurately replicated the geometry and boundary conditions of the specimen subjected to the pull-out test (see Fig. 2). The system comprised a 12 mm diameter steel bar with a total length of 170 mm, centrally embedded within a cubic concrete block with a side length of 160 mm. The anchorage length was 60 mm (i.e., five times the bar diameter), thereby satisfying the requirements for a short specimen typical of pull-out tests [30]. Along the remaining section inside the block, contact between the steel and concrete was prevented. Due to the irregular shape of the bar, it was not possible to exploit symmetry in the numerical model.

Calculations were performed using the ABAQUS Explicit solver. This tool is highly efficient in simulating complex contact problems owing to the stability of the explicit time integration method and its full support for geometric and material nonlinearities. The model was discretized using C3D4 finite elements (four-node tetrahedral elements) and C3D8R elements (eight-node hexahedral elements with reduced integration). C3D4 elements were used in zones with complex geometry (the bar ribbing and adjacent concrete), while C3D8R elements were applied in the remaining regions of the model. The global element size was set to 3 mm for the contact zone and 6 mm for the rest of the model, with local mesh refinement governed by the rib geometry. The adopted discretization strategy represented a trade-off between computational efficiency, numerical stability, and the accuracy of capturing the steel-concrete interaction. Fig. 3 illustrates the numerical model with the applied finite element mesh.

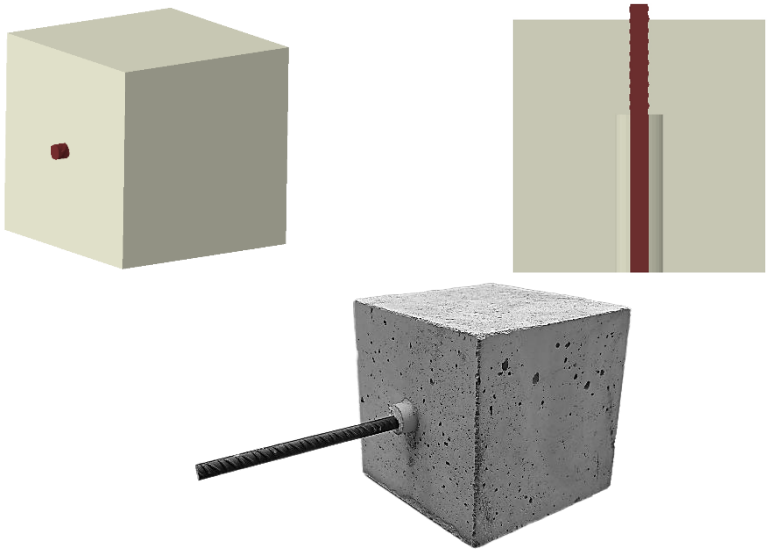


Fig. 2 Test specimen for the pull-out test: numerical model (top left), cross-section of the numerical model (top right), view of the specimen used in the experiment (bottom)

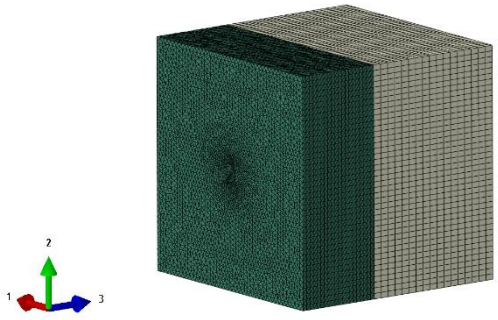


Fig. 3 Numerical model with the finite element mesh

3 ANALYSIS OF RESULTS

Table 2 summarizes the FEM simulation results alongside the experimental POT results described in detail in [25]. The comparison includes the values of the peak bond stress $\tau_{b,max}$, the corresponding slip s_1, the residual bond stress $\tau_{b,f}$, and the identified bond failure mode. Fig. 4 presents the bond-slip relationships τ_b-s obtained from both the simulation and laboratory tests. The experimental curve constitutes a representative response for the entire test series (comprising six specimens) and is plotted alongside the experimental results envelope.

Table 2 Results of FEM simulation and experiment

	$\tau_{b,max}$ [MPa]	s_1 [mm]	$\tau_{b,f}$ [MPa]	Failure mode
FEM Simulation	27.34	1.52	1.48	combined
Experiment	26.35	1.37	8.73	pull-out

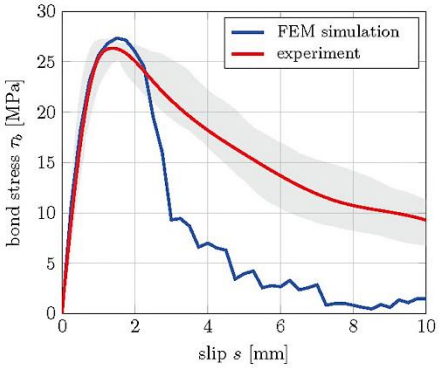


Fig. 4 Bond-slip curves from FEM simulation and experiment

The peak bond stress and the corresponding slip determined via numerical simulation show strong agreement with the experimental values, with relative errors of 3.7% and 10.4%, respectively. This close agreement in $\tau_{b,max}$ and s_1 can be attributed to the faithful reproduction of the bar rib geometry. For the peak stresses, the proper selection of the friction coefficient at the material interface also proved crucial. However, significant discrepancies were noted for the residual bond stresses $\tau_{b,f}$, defined in this study as the stress at an ultimate slip of 10 mm. In this region, the difference amounted to 142.0%. Such a pronounced discrepancy stems from the distinct bond failure mechanisms observed in the FEM simulation versus the experimental tests. Analysis of the τ_b-s curves indicates that in the experiment, failure occurred via pull-out (POF), whereas the numerical model exhibited a splitting-pull-out failure, alternatively designated as a combined failure (CF) mode. In the POF mechanism, bond degradation occurs due to the shearing-off of the concrete keys contained between the bar ribs. Conversely, partial splitting of the concrete block occurred in the numerical model. The appearance of splitting cracks leads to a reduction in bar confinement, resulting in a rapid drop in bond stresses. This difference in the failure patterns is confirmed by Fig. 5, which compares the concrete tensile damage distribution at the end of the simulation (variable DAMAGET, representing cracking) with the physical specimen after testing.

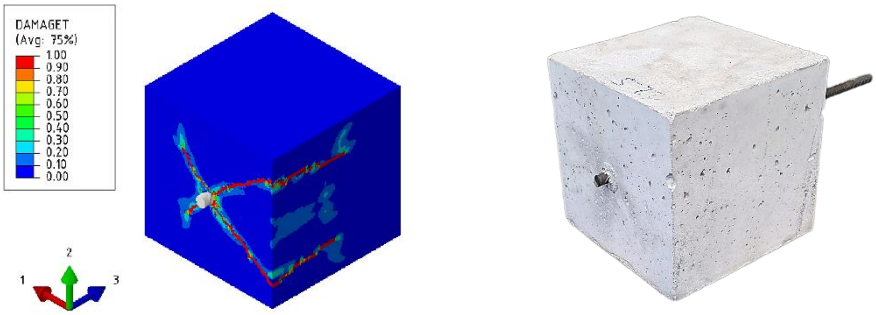


Fig. 5 Illustration of obtained bond failure modes: numerical model (CF) (left), experiment (POF) (right)

The divergence in the identified failure mechanisms is rooted in the limitations of the applied material model. One primary reason is the difficulty in reproducing concrete shearing at the micro-scale (between ribs) using a macroscopic constitutive model. As noted in [1], the fidelity of simulations at the rib scale depends heavily on the model's ability to capture aggregate cracking and crushing processes. The Concrete Damaged Plasticity model describes concrete behaviour in a volumetric (averaged) manner, whereas shearing-off is a process highly localised within the contact zone. It should be noted that the application of continuum material models for concrete is an idealisation. In reality, concrete is highly heterogeneous, and aggregate particle dimensions may exceed the size of a single bar rib, thereby challenging the assumption of material homogeneity.

An additional factor influencing the FEM results is the specific formulation of the CDP model. According to Seok et al. [22], the CDP model tends to predict excessively high concrete strength under conditions of high confinement, such as those encountered in the pull-out test. This leads to an overestimation of bond stresses, particularly prior to and during the attainment of $\tau_{b,max}$. This observation justifies the necessity of adopting a relatively low friction coefficient of 0.075 in the calibration process. This value enabled good agreement along the pre-peak branch of the τ_b-s curve, despite literature suggesting that the friction coefficient between steel reinforcement and concrete typically ranges from 0.3 to 0.5 [21], [22].

Another limitation of the CDP model lies in the definition of its yield surface, which can lead to an inaccurate prediction of the bond failure mechanism. This limitation is less pronounced when the numerical simulation is intended to reflect an experiment where bond failure genuinely occurred via splitting, as seen for instance in [21], [22]. In such cases, obtaining a DAMAGET distribution indicating splitting, analogous to that presented in Fig. 5 (left), would align with the experimental observations.

To provide a comprehensive overview of the stress state, Fig. 6 illustrates the distributions of the principal compressive and tensile stresses within the concrete block, extracted at the time step corresponding to the peak bond stress.

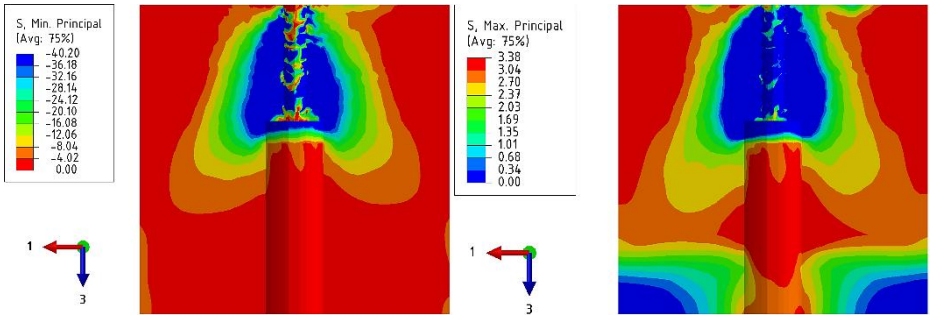


Fig. 6 Principal stress distributions in concrete at peak bond stress: compressive (left), tensile (right)

The observed asymmetry of the principal stress distributions is a direct consequence of the irregular geometry of the scanned bar model. The fact that stresses reach the tensile strength across a substantial portion of the concrete block indicates the formation of splitting cracks, as illustrated in Fig 5 (left). This finding aligns with the bond failure mechanism identified through the analysis of both the τ_b-s curve and the distribution of the tensile damage parameter.

4 SUMMARY AND CONCLUSIONS

- Properly calibrated numerical models of pull-out tests provide a valuable complement to experimental research. FEM simulations enable a detailed analysis of the stress state across any cross-section of the specimen, allowing for the prediction of bond failure mechanisms that are often difficult to unequivocally identify under laboratory conditions.
- Incorporating the realistic geometry of the ribbed bar into the FEM framework enables the extraction of detailed localized data, such as principal stress distributions and concrete damage propagation fields. This facilitates a deeper insight into the interaction at the steel-concrete interface.
- Using the adopted material models, strong agreement was achieved regarding the peak bond stress and the corresponding slip, with relative errors compared to the experimental data remaining below 11%.
- Significant discrepancies were observed in the residual stress range. These stem from the occurrence of distinct bond failure modes in the simulation versus the experiment. The primary cause lies in the limitations of the CDP model in reproducing localized concrete shearing between the bar ribs (the shearing of concrete keys) and capturing concrete behaviour under high confinement.
- Future research will focus on evaluating model sensitivity to variations in material parameters and investigating the suitability of alternative concrete constitutive models for simulating these contact phenomena.

References

[1] Cox, James V., and Leonard R. Herrmann. 1998. "Development of a Plasticity Bond Model for Steel Reinforcement." Mechanics of Cohesive-Frictional Materials 3 (2): 155–80. https://doi.org/10.1002/(SICI)1099-1484(199804)3:2%253C155::AID-CFM45%253E3.0.CO;2-S.

[2] Rehm, Gallus. 1961. The Basic Principle of the Bond between Steel and Concrete. Cement and Concrete Association.

[3] Abrams, Duff A. 1913. "Tests of Bond Between Concrete and Steel." University of Illinois 11 (15).

[4] Zhu, W., M. Sonebi, and P. J. M. Bartos. 2004. "Bond and Interfacial Properties of Reinforcement in Self-Compacting Concrete." Materials and Structures 37 (7): 442–48. https://doi.org/10.1007/BF02481580.

[5] Almeida Filho, Fernando Menezes de, Mounir K. El Debs, and Ana Lúcia H. C. El Debs. 2008. "Bond-Slip Behavior of Self-Compacting Concrete and Vibrated Concrete Using Pull-out and Beam Tests." Materials and Structures 41 (6): 1073–89. https://doi.org/10.1617/s11527-007-9307-0.

[6] Seara-Paz, Sindy, Belén González-Fonteboa, Javier Eiras-López, and Manuel F. Herrador. 2014. "Bond Behavior between Steel Reinforcement and Recycled Concrete." Materials and Structures 47 (1): 323–34. https://doi.org/10.1617/s11527-013-0063-z.

[7] Kim, Sun-Woo, Hyun-Do Yun, Wan-Shin Park, and Young-Il Jang. 2015. "Bond Strength Prediction for Deformed Steel Rebar Embedded in Recycled Coarse Aggregate Concrete." Materials & Design 83 (October): 257–69. https://doi.org/10.1016/j.matdes.2015.06.008.

[8] Ganesan, N., P. V. Indira, and M. V. Sabeena. 2014. "Bond Stress Slip Response of Bars Embedded in Hybrid Fibre Reinforced High Performance Concrete." Construction and Building Materials 50 (January): 108–15. https://doi.org/10.1016/j.conbuildmat.2013.09.032.

[9] Li, L. G., Z. P. Chen, Y. Ouyang, J. Zhu, S. H. Chu, and A. K. H. Kwan. 2019. "Synergistic Effects of Steel Fibres and Expansive Agent on Steel Bar-Concrete Bond." Cement and Concrete Composites 104 (November): 103380. https://doi.org/10.1016/j.cemconcomp.2019.103380.

[10] Majain, Nelly, Ahmad Baharuddin Abd. Rahman, Azlan Adnan, and Roslli Noor Mohamed. 2022. "Bond Behaviour of Deformed Steel Bars in Steel Fibre High-Strength Self-Compacting Concrete." Construction and Building Materials 318 (February): 125906. https://doi.org/10.1016/j.conbuildmat.2021.125906.

[11] Achillides, Zenon, and Kypros Pilakoutas. 2004. "Bond Behavior of Fiber Reinforced Polymer Bars under Direct Pullout Conditions." Journal of Composites for Construction 8 (2): 173–81. https://doi.org/10.1061/(ASCE)1090-0268(2004)8:2(173).

[12] Hao, Qing-duo, Yan-lei Wang, Zhi-chun Zhang, and Jin-ping Ou. 2007. "Bond Strength Improvement of GFRP Rebars with Different Rib Geometries." Journal of Zhejiang University-SCIENCE A 8 (9): 1356–65. https://doi.org/10.1631/jzus.2007.A1356.

[13] Metelli, Giovanni, and Giovanni A. Plizzari. 2014. "Influence of the Relative Rib Area on Bond Behaviour." Magazine of Concrete Research 66 (6): 277–94. https://doi.org/10.1680/macr.13.00198.

[14] Cairns, John. 2015. "Bond and Anchorage of Embedded Steel Reinforcement in Fib Model Code 2010." Structural Concrete 16 (1): 45–55. https://doi.org/10.1002/suco.201400043.

[15] Plizzari, Giovanni, Giovanni Metelli, and John Cairns. 2022. An Overview of Enhancements to Provisions for Bond in the Draft Fib Model Code 2020. https://iris.unibs.it/handle/11379/563004.

[16] Senthil, K, S Aswa, and Cp Aswin. 2018. "Influence of Concrete Strength and Diameter of Reinforcing Bar on Pullout Tests Using Finite Element Analysis." Journal of Structural Engineering & Applied Mechanics 1 (3): 105–16. https://doi.org/10.31462/jseam.2018.03105116.

[17] Rolland, Arnaud, Pierre Argoul, Karim Benzarti, Marc Quiertant, Sylvain Chataigner, and Aghiad Khadour. 2020. "Analytical and Numerical Modeling of the Bond Behavior between FRP Reinforcing Bars and Concrete." Construction and Building Materials 231 (January): 117160. https://doi.org/10.1016/j.conbuildmat.2019.117160.

[18] Burdziński, Marcin, and Niedostatkiewicz, Maciej. 2022. "Experimental-Numerical Analysis of the Effect of Bar Diameter on Bond in Pull-Out Test." Buildings 12 (9). https://doi.org/10.3390/buildings12091392.
[19] Abbas, Mohammad, Benoît Bary, and Ludovic Jason. 2023. "A 3D Mesoscopic Frictional Cohesive Zone Model for the Steel-Concrete Interface." International Journal of Mechanical Sciences 237 (January): 107819. https://doi.org/10.1016/j.ijmecsci.2022.107819.
[20] Abbas, Mohammad, Benoît Bary, and Ludovic Jason. 2023. "3D Mesoscale Analysis of the Effects of Steel Bar Ribs Geometry on Reinforced Concrete Bond Strength." Finite Elements in Analysis and Design 219 (July): 103928. https://doi.org/10.1016/j.finel.2023.103928.
[21] Zhao, Yazhou, Yuhang Li, Xinwei Li, Xinguo Sun, and Lu Lu. 2025. "Experimental and Numerical Investigation on Bond Behavior of Deformed Rebar in Concrete with Triethanolamine Derivatives: A Rib-Scale Study." Materials and Structures 58 (5): 196. https://doi.org/10.1617/s11527-025-02722-w.
[22] Seok, Seungwook, Ghadir Haikal, Julio A. Ramirez, Laura N. Lowes, and Jeehee Lim. 2020. "Finite Element Simulation of Bond-Zone Behavior of Pullout Test of Reinforcement Embedded in Concrete Using Concrete Damage-Plasticity Model 2 (CDPM2)." Engineering Structures 221 (October): 110984. https://doi.org/10.1016/j.engstruct.2020.110984.
[23] Shoaib Karam, Muhammad, Hikaru Nakamura, Yoshihito Yamamoto, Muhammad Tahir, and Rashid Hameed. 2024. "Mesoscopic Evaluation of the Bond Behavior of Concrete with Deformed Rebar Subjected to Passive Confinement Employing 3D Discrete Model." Engineering Fracture Mechanics 295 (January): 109790. https://doi.org/10.1016/j.engfracmech.2023.109790.
[24] Jin, Liu, Xiaoya Li, Renbo Zhang, and Xiuli Du. 2022. "Modelling of Bond Behavior of Deformed Bar Embedded in Concrete after Heating to High Temperatures: A Mesoscale Study." Construction and Building Materials 334 (June): 127456. https://doi.org/10.1016/j.conbuildmat.2022.127456.
[25] Burdziński, Marcin. 2026. "Experimental and Numerical Analysis of the Effect of Reinforcing Bar Confinement in Concrete on Bond Behavior in the Pull-Out Test." PhD diss., Gdańsk University of Technology.
[26] Dassault Systèmes SIMULIA. 2025. ABAQUS.
[27] Fédération internationale du béton (fib), 2013. *fib Model Code for Concrete Structures 2010*. Lausanne, Switzerland: International Federation for Structural Concrete (fib).
[28] Fédération internationale du béton (fib), 2024. *fib Model Code for Concrete Structures 2020*. Lausanne, Switzerland: International Federation for Structural Concrete (fib).
[29] European Committee for Standardization. 2023. EN 1992-1-1:2023 Eurocode 2 – Design of concrete structures – Part 1-1: General rules and rules for buildings, bridges and civil engineering structures.
[30] CEB-FIP. 2000. fib Bulletin No. 10 - Bond of Reinforcement in Concrete: State-of-Art Report.

Anisotropic Nonlinear Analysis of Timber-Concrete Composite Structures

Thilakshi Gamage and Ali Abbas

School of Architecture, Computing and Engineering,
University of East London,
University Way, London E16 2RD, United Kingdom

Summary
This study forms part of a broader investigation into Timber–Concrete Composites (TCC), which combine timber and concrete into a single structural element, with shear connectors ensuring effective interaction. As timber provides net carbon storage, TCC systems can significantly reduce embodied carbon compared with conventional concrete structures by reducing concrete use. Despite the predominantly nonlinear behaviour of TCC joints and materials, current analytical approaches commonly adopt linear elastic assumptions and often neglect the anisotropic mechanical behaviour of timber. This research focuses on the numerical simulation of TCC beams to realistically capture anisotropic nonlinear behaviour and associated failure mechanisms. Reliable simulations require robust timber models, which remain limited. In this study, an anisotropic timber constitutive model was developed in ADINA and validated against published experimental results under compressive, tensile and flexural loading.

1 INTRODUCTION

The construction sector is a major contributor to greenhouse gas emissions, primarily due to the extensive use of carbon-intensive construction materials such as concrete and steel. For every ton of cement produced, nearly 1 ton of CO_2 is released [1]. The production of steel emits approximately 1.8 to 2.2 tons of CO_2 per ton of steel [2]. During the past few decades, there is an increased interest in timber as a structural material. Timber–Concrete Composite floors represent an effective compromise between structural performance and environmental impact, combining the compressive capacity and durability of concrete with the low embodied carbon and carbon storage benefits of timber. In addition, TCC structures enhance load-bearing capacity, thermal and acoustic insulation, fire resistance and vibration performance compared with traditional timber structures. TCC structures can therefore expand the use of timber in high-rise buildings, complex structures and renovations. Many structures have already been constructed using the TCC floor system.

TCC structures are more in the range of research and development. The TCC approach is similar to that of steel-concrete composite structures (Fig. 1), the concrete slab is cast over a series of individual timber beams. The timber component is commonly composed of glued laminated timber (GLT), cross laminated timber (CLT) or laminated veneer lumber (LVL). The two materials timber and concrete are connected using shear connectors. Various types of shear connectors have been investigated in research, including dowel-type fasteners, notches combined with fasteners, steel plates and glued-in rods. Among these, dowel-type fasteners and notches combined with fasteners are the most widely used [3],[4].

1.1 Structural behaviour of a TCC beam

This structural system is designed to exploit the complementary mechanical characteristics of its constituent materials. The concrete layer contributes high compressive strength and stiffness, while the timber member provides efficient load bearing capacity together with a low self-weight. TCC structures exhibit nonlinear behaviour due to partial or full composite action between timber and concrete, nonlinear behaviour of the shear connections and material nonlinearity [5]. The composite action of TCC structures is mostly rely on this connection system that transfers the stresses between the two materials and provide ductile and safe structure.

1.2 Current design methods and limitations

Currently, countries adopt different approaches to the design of TCC systems. Globally, the design of TCC structures lacks a comprehensive regulatory framework and is often based on principles from existing timber and concrete standards. In the European approach, the technical specification PD CEN/TS 19103:2021[6], published by the British Standards Institution (BSI) in July 2021 and valid for

three years, provides a framework for the structural design of TCC systems in accordance with Eurocode 5. It was under review at the time of writing this paper. It assumes a linear-elastic shear force–slip relationship for the connection and linear-elastic stress–strain behaviour for timber and concrete. Consequently, linear-elastic methods tend to overestimate the ultimate capacity of TCC sections, as the actual structural behaviour transitions from linear to nonlinear response prior to failure [7],[8].

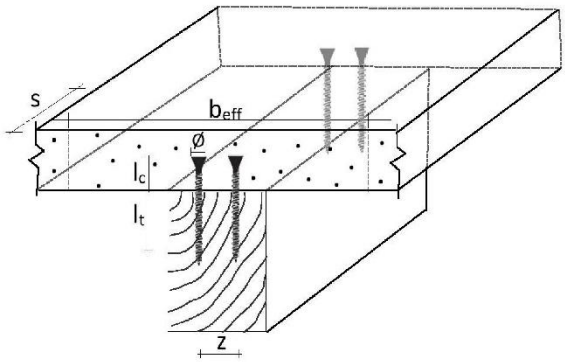


Fig. 1 Primary configuration of timber-concrete composite beam

1.3 Numerical analysis of TCC structures

Numerical analysis offers a more accurate representation of the timber–concrete interaction by capturing nonlinear behaviour and providing detailed insights into load-bearing capacity, ductility and failure modes, thereby enabling more accurate design of TCC elements and addressing the limitations of current design methods. Finite element analysis (FEA) of TCC requires material models for both timber and concrete. While constitutive material models for concrete are well established, those for timber are not as readily available [9]. This is primarily due to timber's complex anisotropy, species variability and diverse product types. Several research works had been carried out in the recent past to address this.

Early studies on the numerical modelling of timber primarily employed two-dimensional finite element formulations with simplified material assumptions, restricting their use to thin members and idealised joint configurations [9],[10]. Subsequent developments introduced three-dimensional models, yet these often assumed linear elastic–brittle behaviour or relied on fracture mechanics concepts, which are insufficient to represent the nonlinear response of timber under general stress states [11],[12]. More advanced approaches incorporated anisotropic plasticity, continuum damage mechanics, or coupled plasticity damage formulations to capture key features such as tension–compression asymmetry, brittle tensile failure, and compressive densification [13]-[15]. Despite these advances, many models employ simplified yield or damage criteria, or assume isotropic damage evolution, limiting their ability to accurately represent the inherently anisotropic behaviour of timber [16]. In addition, many constitutive formulations are implemented via user defined material subroutines, requiring advanced numerical expertise and reducing their applicability in engineering practice.

2 TIMBER MODEL DEVELOPMENT FOR NUMERICAL SIMULATION OF TCC

The inherent anisotropy of timber makes it more challenging to accurately simulate its material behaviour. The fact that most materials exhibit some degree of internal organisation allows the stress–strain relationship to be further simplified [17]. Most timber composites are symmetric about three mutually perpendicular planes, which makes it an orthotropic material. Orthotropic materials are characterised by their directional properties. Timber can be referenced to a cylindrical coordinate system in which the longitudinal direction (L) corresponds to the grain, the tangential direction (T) follows the curvature of the growth rings and the radial direction (R) aligns with the wood rays. From a theoretical perspective, the mechanical behaviour of timber is analysed using a rectangular coordinate system, where the curved growth rings are considered as planner layers [18].

In this study, an orthotropic plastic material model for timber is implemented in the nonlinear finite element analysis software ADINA. Elastic and plastic properties are defined independently in the L, T, and R directions to represent anisotropy.

2.1 Anisotropic yielding and plastic behaviour of timber

Hill [19] developed a theory describing the yielding and plastic flow behaviour of anisotropic metals. In this study, this theory is adopted to model the anisotropic yielding of timber within the plastic regime. As presented by Hill (1948), this theory is based on the concept of plastic distortion in crystals, first proposed by von Mises (1928) and subsequently detailed by Geiringer (1937), in which yielding and plastic flow are governed by a quadratic stress potential. Within Hill's framework, the stress increment function at a given time step is constant, and plastic strain evolution is driven by the energy conjugacy between stress and strain increments. The Hill yield condition is given by:

$$2f \equiv F\left(\sigma_{yy} - \sigma_{zz}\right)^2 + G(\sigma_{zz} - \sigma_{xx})^2 + H\left(\sigma_{xx} - \sigma_{yy}\right)^2 + 2L\sigma_{yz}^2 + 2M\sigma_{zx}^2 + 2N\sigma_{xy}^2 = 1 \qquad (1)$$

Here, (x, y, z) denote the principal orthotropic material axes, while F, G, H, L, M, and N represent material constants.

2.1.1 Strain hardening model

In ADINA, the plastic behaviour of a material is characterised through the definition of a strain hardening model [20]. Once the material reaches its yield point, associated flow rule is applied in conjunction with the proportional hardening rule to simulate the evolution of plastic deformations. For the numerical simulation of the plastic behaviour of timber in ADINA, a hardening model was developed using the bilinear strain-hardening modulus, accounting for all three orthogonal directions and planes. Hill's plasticity theory was incorporated to capture the anisotropic yielding characteristics, making the model well-suited for simulating timber's direction-dependent plastic behaviour. The compressive behaviour of timber exhibits an initial strain-hardening phase following yielding. The extent of this strain hardening varies considerably between the three principal material directions. Consequently, accurate modelling of compressive behaviour requires careful consideration of associated variation in plastic response across the three directions. Therefore, it is recommended to use the option available in ADINA that allow the specification of different bilinear strain hardening moduli E_x^T , E_y^T and E_z^T in the three orthogonal directions x,y and z and E_{xy}^T , E_{xz}^T and E_{yz}^T for the three planes (x,y), (x,z) and (y,z), in order to accurately simulate the plastic behaviour of timber. Then, the universal plastic modulus, E_u^P is given by:

$$\sqrt{\frac{1}{2}\left(\frac{1}{3}\left(E_x^{p\,2} + E_y^{p\,2} + E_z^{p\,2}\right) + E_{xy}^{p\ 2} + E_{xz}^{p\ 2} + E_{yz}^{p\ 2}\right)} \qquad (2)$$

where,

$$E_i^p = \frac{E_i E_i^T}{E_i - E_i^T} \qquad i = x, y, z$$

And

$$E_{ij}^p = \frac{E_{ij} E_{ij}^T}{E_{ij} - E_{ij}^T} \qquad i = xy, xz, yz$$

2.2 Failure criterion

Failure was defined by prescribing a maximum effective plastic strain. The accumulated effective plastic strain, e_a^{-p}, is defined based on the principle of equivalence of plastic work, dW^p, expressed as:

$$dW^p = \bar{\sigma}_a de_a^{-p} \quad (3)$$

Where, $\bar{\sigma}$ is the Hill effective stress. The expression for the increment of orthotropic effective plastic strain differs from that used in isotropic plasticity. In particular, under uniaxial tension or compression, the accumulated effective plastic strain generally does not coincide with the corresponding uniaxial plastic strain.

2.3 Validation of timber model

To validate the developed timber material model, it is essential to accurately reproduce the anisotropic behaviour of timber. In this study, initial numerical simulations were performed under uniaxial compression in the three principal material directions, L, T and R, based on published experimental data:

- Longitudinal compression test – parallel to the grain (L)
- Tangential compression test – perpendicular to the grain, along the growth rings (T)
- Radial compression test – perpendicular to the grain, perpendicular to the growth rings (R)

Under compressive loading, timber exhibits linear elastic behaviour up to the yield point in the three principal direction. Beyond this point, the material enters a ductile phase characterised by distinct, direction-dependent failure mechanisms. For this study, the softwood species Nordic spruce (Picea abies) was selected, as it is the most widely used softwood species in Nordic glulam production. The results were compared with the experimental data to validate the numerical analyses.

2.3.1 Longitudinal compression test (L)

Experimental compression tests parallel to the grain on Nordic spruce (Picea abies), conducted by Saad, Pintér and Lengyel [21] was referenced in this study to validate the compressive behaviour in the L direction. Average values of the longitudinal modulus of elasticity, $E_L = 7215$ MPa, compressive yield stress $\sigma_L = 34.66$ MPa and ultimate strain $\varepsilon_{uL} = 0.016$ were obtained from the experimental results for FEA. The modulus of elasticity in the transverse and radial directions, E_R = 577 MPa and $E_T = 361$ MPa , along with the shear moduli $G_{TR} = 51.54$ MPa, $G_{TL} = 484.44$ MPa and $G_{RL} = 515.36$ MPa , were calculated using the established interrelationships among the elastic moduli and shear moduli in the three principle material directions L,T and R, as well as the relationship between E_L and G_{LR} [18]. The Poisson's ratios $\vartheta_{TR} = 0.29, \vartheta_{TL} = 0.01$ and ϑ_{RL} = 0.02 for Nordic Spruce timber were determined by referring to published experimental and literature data. The strain hardening modulus in the three principal material directions ($n_T = 0.4741, n_R = 0.0977, n_L = 0.6386$) and in the three shear planes ($n_{TR} = 0.4197, n_{TL} = 0.5117, n_{RL} = 0.5884$) were calculated by applying power-law relationship to the plastic portion of the stress–strain curve. For the T and R directions, the stress–strain data from the other two selected experimental studies were used [22],[23]. In this study, this modulus was assumed to be the same across all Nordic spruce material models, reflecting a species-specific property. This assumption is further supported by the fact that each timber model is subjected to uniaxial compressive loading, and the strain hardening modulus in the respective direction corresponds to the hardening behaviour observed in the specific test specimen. To satisfy the Hill yield condition and ensure positive values of the material constants (Equations 1) and given that the yield stress values in the tangential (T) and radial (R) directions are close, a single yield stress equal to the minimum of the two was adopted for both the T and R directions ($\sigma_T = \sigma_R = 1.73$ MPa) in the developed timber model.

A three-dimensional finite element model was developed in ADINA using 3D solid hexahedral elements for the timber specimen and steel plates. Boundary conditions were applied to the bottom face of the lower steel plate with a user-defined fixity condition, in which only the translational degrees of freedom in the loading direction (L) was constrained. To simulate the application of compressive loading, the load was imposed as a gradually increasing displacement applied at the top surface of the upper steel plate of the specimen. The mesh sensitivity analysis showed identical results for 10 mm and 5 mm mesh sizes. A finer 5 mm mesh was adopted to better capture the failure mode.

The numerical analysis showed good agreement with the experimental stress–strain response and failure mode under L-direction compression, with the FE-predicted peak stress 2% higher than the experimental value (Fig. 2). Once the material reaches the initial yield point, it enters the incipient

kinking phase, which is characterised by the formation of a continuous kink band. The numerical analysis captured kink band formation through progressive element deletion at the predefined accumulated maximum plastic strain, successfully simulating compressive failure development (Fig 3).

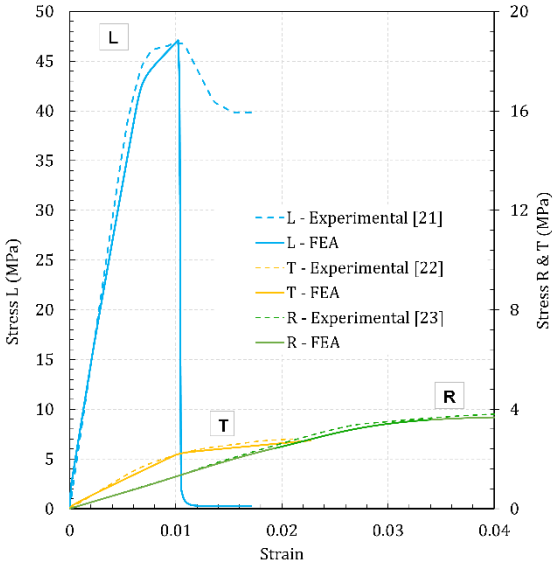


Fig. 2 Experimental and FEA stress–strain responses under uniaxial compression in L, T and R directions

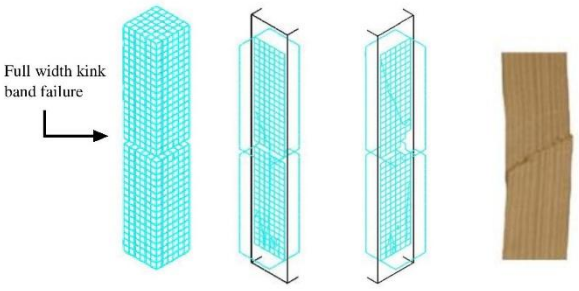
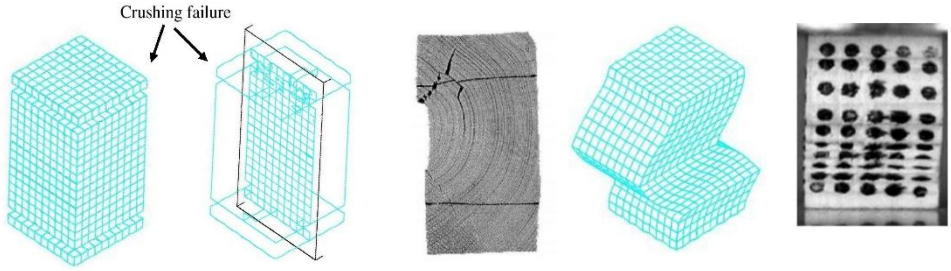


Fig. 3 Comparison between numerical and experimental failure modes in the L direction [21]

2.3.2 Tangential compression test (T)

Timber exhibits pronounced anisotropy, with compressive strength perpendicular to the grain (T and R) significantly lower than parallel to the grain (L) due to its cellular structure [23],[24]. Perpendicular to grain compression is characterised by linear elastic and nonlinear plastic behaviour without a distinct ultimate strength. Instead, the stress–strain curve demonstrates a gradual and continuous increase in stress with increasing deformation (Fig. 2), extending far beyond the range of practical relevance [22],[24]. This behaviour complicates experimental interpretation and failure criterion definition. To account for this behaviour, BS EN 408 [25] defines the maximum compressive stress perpendicular to the grain as the stress corresponding to 1% strain. This definition was used to determine the timber elastic limit from the experimental results [22]. The FEA response shows good agreement with the

experimental stress–strain behaviour over the entire loading range. In the initial linear region, both curves exhibit nearly identical stiffness, indicating accurate prediction of the elastic response. At approximately 0.01 strain, the FEA prediction agrees closely with the experimental result with a



(a) (b) (c) (d) (e)

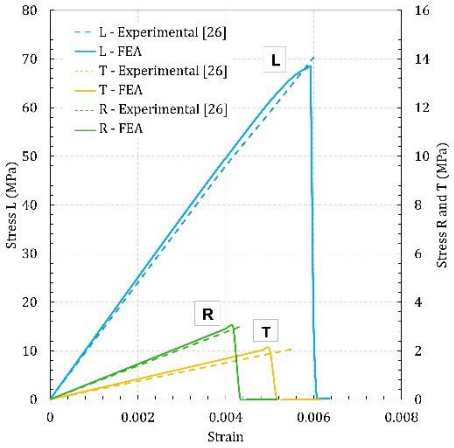
deviation below 2%. Beyond this point, the model slightly underpredicts strain hardening, with a maximum deviation of 6% at 0.02 strain. The numerical results also reproduce localised crushing at the specimen ends under tangential compression (Fig.4), consistent with experimental observations [22].

Fig. 4 Comparison between numerical and experimental failure modes: (left a – c) crushing failure in the T direction [22] and (right d - e) large-deformation failure in the R direction [23]

2.3.3 Radial compression test (R)

The radial compression stress–strain curve was also evaluated following BS EN 408 to determine the yield stress. After yielding, a short plateau-like strain-hardening phase is observed, followed by a reduction in stiffness and large plastic deformation up to a maximum stress, indicating near-complete failure. This behaviour was well captured in the FEA (Fig. 2 and Fig. 4). The model accurately captures the initial linear response with identical stiffness and the subsequent nonlinear plastic response, with an average underprediction of approximately 3%.

2.3.4 Tensile test in L,T and R directions



(d)

Fig. 5 Experimental and FEA stress–strain responses under uniaxial tension in L, T and R direions

The developed timber model was further validated against tensile loading. Tensile test in the L direction was performed on dog-bone specimen measuring 50 × 10 × 443 mm, with a minimum central thickness of 10 mm. Special consideration was given to the mesh subdivision, particularly at geometric transitions, to maintain continuity and compatibility throughout the specimen. Tensile tests in the T and R directions were carried out on square prismatic specimens with nominal dimensions of 20 × 20 × 120

mm. All specimen sections were modelled as 3D solid hexahedral elements, while the top and bottom gripping sections were modelled as rigid bodies to better approximate the experimental setup.Under tensile loading, timber exhibits higher strength and stiffness parallel to the grain (L direction), with predominantly linear elastic behaviour up to failure. The FEA results show close agreement with the experimental stress–strain responses [26] in all three directions (Fig. 5) with a maximum deviation of 2% (L) and 1% (T and R) at peak load.

2.3.5 Bending test



Fig. 6 Experimental three point bending test configuration (left) [27] and finite element model (deflected shape) (right)

Fig. 6 presents the numerical simulation of a three-point bending test in the TL plane. Results showed good agreement with the experimental load–displacement response accurately capturing the non-linear bending behaviour of timber. The FEA prediction is conservative relative to the experimental lower bound, with the FEA curve approximately 5–8% lower in the pre-peak region and 1–2% lower at the peak load. The numerical results further indicate that the beam failed in compression, which is one of the most observed failure modes in timber beams subjected to bending [28]. This failure behaviour is consistent with the experimental observations and supports the validity of the adopted material model and failure criterion. The study further indicates that the maximum compressive failure strain for Nordic spruce as 0.027.

3 CONCLUSIONS

The numerical results are consistent with the expected mechanical response of timber under compressive, tensile, and flexural loading, demonstrating acceptable accuracy. The developed model captures the anisotropic elastic and plastic behaviour of timber with good fidelity and provides a computationally efficient framework for nonlinear analysis of timber elements. Future work will focus on investigating the nonlinear structural response of TCC beams, with the objective of numerically evaluating their behaviour and providing recommendations for more efficient design approaches. This will address the limitations of current design methods, which commonly assume linear elastic behaviour in TCC systems. Furthermore, the developed material model can be applied to timber structural elements to capture anisotropic plastic behaviour, thereby supporting the development of optimised timber design solutions.

References

[1] Lehne, J. and Preston, F. Making concrete change innovation in low-carbon cement and concrete, The Royal Institute of International Affairs, Chatham House Report Series, p. 138, 2018.

[2] International Energy Agency, Iron and Steel Technology Roadmap: Towards more sustainable steelmaking, OECD Publishing, Paris, France, 2020.

[3] Dias, A. Design of timber-concrete composite structures: A state-of-the-art report by COST Action FP1402/WG 4*, European Journal of Wood and Wood Products*, 2018.

[4] Cuerrier-Auclair, S. C. Design guide for timber-concrete composite floors in Canada. Pointe-Claire, QC, Canada: *FPInnovations*, 2020.

[5] Dias, Alfredo M.P.G., Jorge, L.F.C. The effect of ductile connectors on the behaviour of timber-concrete composite beams, *Engineering Structures*, 33(1), pp. 1–14, 2011.

[6] British Standards Institution. PD CEN/TS 19103:2021 – Eurocode 5: Design of Timber Structures – Structural design of timber-concrete composite structures – Common rules and rules for buildings. London: BSI [Under review – not currently valid]. 2021.
[7] Cuerrier-Auclair, S., Dagenais, C. and Gagnon, S. Technical design guide for timber-concrete composite floors – A Canadian approach. In: Proceedings of the World Conference on Timber Engineering (WCTE 2023), Oslo, Norway, 19–22 June 2023.
[8] Töpler, J., Schweigler, M., Lemaître, R., Palma, P., Schenk, M., Grönquist, P., Tapia, C., Hochreiner, G. and Kuhlmann, U. 2023a. *Finite element based design of timber structures,* 2023.
[9] Sawata, K. and Yasumura, M. Estimation of yield and ultimate strengths of bolted timber joints by nonlinear analysis and yield theory, Journal of Wood Science, 49(4), pp. 383–391, 2003.
[10] Daudeville, L. Fracture in spruce: experiment and numerical analysis by linear and nonlinear fracture mechanics. Holz als Roh und Werkstoff, 57(6), pp. 425–432, 1999.
[11] Serrano, E. Glued-in rods for timber structures — a 3D model and finite element parameter studies. International Journal of Adhesion & Adhesives, 21(2), pp. 115–127, 2001.
[12] Smith, I. and Vasic, S. Fracture behaviour of softwood. Mechanics of Materials, 35(8), pp. 803–815, 2003.
[13] Sandhaas, C. and van de Kuilen, J.W.G. Material model for wood. Heron, 58(2-3), pp.179–199, 2013.
[14] Gharib, M., Hassanieh, A., Valipour, H. & Bradford, M.A. Three dimensional constitutive modelling of arbitrarily orientated timber based on continuum damage mechanics. Finite Elements in Analysis and Design, 135, pp.79–90, 2017.
[15] Khelifa, M., Khennane, A., El Ganaoui, M. & Celzard, A. Numerical damage prediction in dowel connections of wooden structures. Materials and Structures, 49(5), pp.1829–1840, 2016.
[16] Sirumbal Zapata, L.F., Málaga Chuquitaype, C. & Elghazouli, A.Y. A three dimensional plasticity damage constitutive model for timber under cyclic loads. Computers & Structures, 195, pp.47–63, 2018.
[17] Hosford, W.F. Mechanical Behavior of Materials. Cambridge University Press, Cambridge, 2009.
[18] Bodig, J. and Jayne, B.A. Mechanics of wood and wood composites. Van Nostrand Reinhold, New York, 1982.
[19] Hill, R. A theory of the yielding and plastic flow of anisotropic metals. Proceedings of the Royal Society of London. Series A, Mathematical and Physical Sciences, 193(1033), pp. 281–297, 1948.
[20] ADINA R & D, Inc. Theory and Modeling Guide, Volume I: ADINA. Report ARD 12-8. ANSYS, Inc. (2018) LS-DYNA® Keyword User's Manual, Volume II: Material Models. LS-DYNA Dev, 2012.
[21] Saad, K., Pintér, E. and Lengyel, A. Comparative study on complete characterisation of elastic–ductile compressive behaviour of aged and new Norway spruce timber. International Journal of Architectural Heritage, 19:4, 485–495, 2025.
[22] Hoffmeyer, P., Damkilde, L. and Pedersen, T.N. Structural timber and glulam in compression perpendicular to grain. Holz als Roh- und Werkstoff, 58, 73–80, 2000.
[23] Reiterer, A. & Stanzl Tschegg, S.E. Compressive behaviour of softwood under uniaxial loading at different orientations to the grain. Mechanics of Materials, 33:12, 705–715, 2001
[24] Leijten, A.J.M. The bearing strength capacity perpendicular to grain of Norway spruce – Evaluation of three structural timber design models. Construction and Building Materials, 105, pp. 528–535, 2016.
[25] British Standards Institution. Timber structures. Structural timber and glued laminated timber. Determination of some physical and mechanical properties (BS EN 408:2010+A1:2012). London: BSI, 2012.
[26] Gambarelli, S., Bošnjak, J., Fararoni Platas, R.N. & Jin, K. Experimental study on mechanical properties of European oak and Norway spruce clear wood, Materials, 18(14), article 3257, 2025.
[27] Fajdiga, G., Rajh, D., Nečemer, B., Glodež, S. and Šraml, M. Experimental and numerical determination of the mechanical properties of spruce wood. Forests, 10:12, article 1140, 2019.
[28] ASTM International. Standard test methods for small clear specimens of timber (ASTM D143-14). West Conshohocken, PA: ASTM International, 2014.

Conceptual study on the material-saving potential of prestressed concrete industrial floors

Efim Griniov, Rewi Yolcu Sever and Dirk Schlicke

Institute of Structural Concrete,
Graz University of Technology,
Lessingstraße 25, Graz 8010, Austria

Summary
This study is motivated by the demand for thin, crack-controlled industrial floor slabs with reduced material consumption and environmental impact. The objective is to compare a conventional reinforced concrete slab with an innovative prestressed slab concept, both with slab thicknesses of up to 25 cm. Numerical analyses are conducted using the finite element software SOFiSTiK to evaluate global stress distributions and soil-industrial floor interaction, the latter being modeled as a linear elastic half-space. The results demonstrate that prestressing significantly reduces tensile stresses due to both imposed and restrained strains as well as loads, thereby ensuring an uncracked state in service. This enables the realization of jointless and watertight floor systems and permits a reduction in slab thickness and concrete volume, ultimately resulting in lower material consumption, reduced logistical effort, and decreased CO_2 emissions.

1 MOTIVATION

Concrete industrial floors have been successfully designed and constructed for many centuries. They serve as traffic surfaces, storage areas, and structural foundation elements, for example in high-rack warehouses, and must meet demanding performance requirements, including flatness, wear resistance, resistance to chemical attack, durability, and structural stability. However, even with the continuous development of concrete materials and well-established design approaches [1], [2], recent years have shown a growing number of damage cases in industrial concrete floors, especially under the combined action of imposed and restrained strains as well as heavy forklift traffic and storage rack loads.

Industrial concrete floors are typically constructed as large-area slab systems. To accommodate imposed strains, such slab configurations must be designed with dilatation joints. These joints serve to limit restraint stresses resulting from variations in mean temperature, drying shrinkage and swelling, as well as differential thermal gradients over the slab thickness. The restraint stresses that develop due to these imposed strains have a decisive influence on the structural behavior and crack formation of industrial floors. In engineering practice, restraint stresses are mitigated by subdividing the slab into defined fields using regularly spaced dilatation joints, thereby limiting external restraint effects.

In this case study, different design variants of industrial floor slabs subject to water protection regulations are investigated. Such regulations exist in many countries worldwide, for example the Austrian Water Rights Act (WRG) [3] and the German Water Act (WHG) [4]. These structures are subject to particularly stringent requirements regarding crack width limitation in order to prevent environmental damage. For such applications very small allowable crack widths, typically limited to 0.2 mm, must be ensured in accordance with guidelines such as DAfStb guideline: Watertight Concrete Structures [5]. In the case of watertight industrial floors, this requirement results in significantly increased reinforcement ratios in conventionally reinforced systems and higher fiber dosages in steel fiber reinforced concrete systems. In addition, minimum requirements regarding the height of the compression zone must be satisfied.

A key issue in this context is the formation of joints in industrial floors resulting from temperature-induced strains and drying shrinkage. Another critical aspect affecting service life is the continuous traffic of forklifts, which generate dynamic loads. These repeated load cycles often cause damage, particularly edge spalling and deterioration in dilatation joints. As a result, such damage mechanisms lead to increased maintenance requirements and higher life-cycle costs for these structures [6].

In contrast, prestressing of industrial floors often results in significantly improved structural performance. Compliance with the specified crack width limits can be reliably achieved and, in many cases, even entirely crack-free behavior can be attained. A further major advantage lies in the possibility of jointless slab construction, which substantially reduces the risk of construction defects as well as the

occurrence of cracking and edge spalling caused by continuously acting forklift loads during the service life. Furthermore, prestressed industrial floors offer considerable material-saving potential, as they can typically be designed with reduced slab thickness and without conventional reinforcement. Due to the applied prestressing forces, the concrete cross-section is often subjected predominantly to compressive stresses, or the resulting tensile stresses remain below the characteristic tensile strength of the concrete.

This paper presents and compares the key characteristics of two types of concrete industrial floors, namely conventionally reinforced and prestressed floor systems, based on selected technical and economic criteria. The evaluation is carried out using a numerical finite element (FE) analysis, which enables a detailed assessment of structural behavior under service conditions. A holistic consideration of the planning and construction process, including the soil-industrial floor interaction, is particularly important to achieve an economical design with low initial construction costs and reduced maintenance requirements.

2 HOLISTIC FINITE ELEMENT SIMULATIONS

2.1 FE Model of the concrete industrial floor

In accordance with the Austrian WRG [3] or German WHG [4], industrial halls that store hazardous substances must ensure that these substances do not infiltrate the subsoil or reach the groundwater.

These requirements generally include a minimum slab thickness h of 0.25 m, strict limitations on crack width, and detailed control of dilatation joints. However, dilatation joints are highly susceptible to damage under service loading conditions and represent a critical weak point in terms of durability and long-term maintenance requirements. For this reason, the feasibility of a prestressed floor slab is investigated, as prestressing enables jointless construction and thereby eliminates this primary source of deterioration. In this configuration, the slab thickness is reduced to 18 cm while adopting a predefined prestressing tendon grid with a spacing of 65 × 65 cm. The FE analysis was performed using the software SOFiSTiK [7].

The proposed modeling approach incorporates stresses resulting from forklift traffic and storage rack loads, as well as restraint stresses induced by drying shrinkage during the service life as well as soil-structure interaction. The numerical model represents an embedded industrial floor slab, discretized using 2D shell elements with a finite element size of 0.35 x 0.35 m. For industrial floor configurations, concrete of strength class C30/37 was assumed, including an elastic modulus E of 33000 MN/m². The industrial floor was simulated with linear elastic material behavior.

The plan dimension of the industrial floor was $L_y = 62.3$ m in the y-direction and $L_x = 39.2$ m in the x-direction, see Fig. 1 (left). Since the structure represents an industrial hall, column openings that are structurally decoupled and supported on footings were included in the model at regular spacings of 7.0 m in both directions. The openings for the footing supported columns have plan dimensions of 0.70 x 0.70 m.

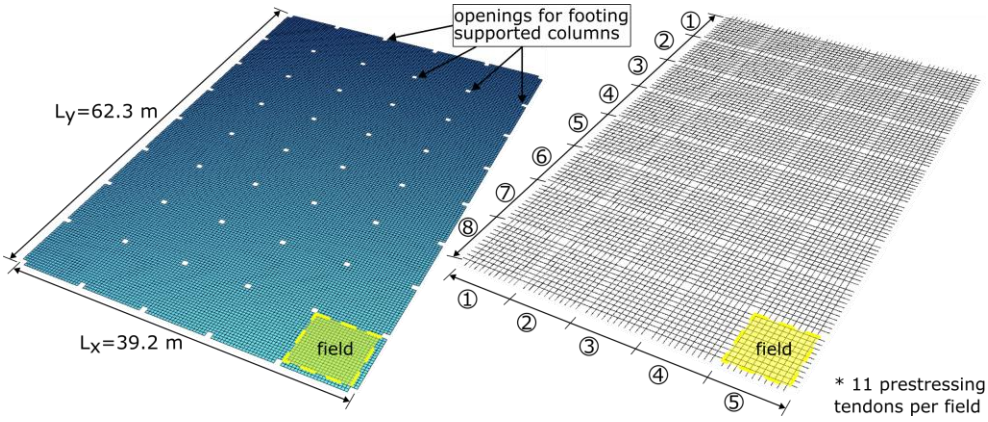


Fig. 1 FE model of the industrial floor (left) and representation of the discrete prestressing tendons (right)

The prestressed slab was designed in accordance with [8], using unbonded monostrands made of prestressing steel grade St 1660/1860. In the FE model, the monostrands were implemented using the dedicated tendon functionality of the SOFiSTiK module "Tendon*"* apply the prestressing forces to the structural model. The FE module accounts for the effects of elastic concrete deformation, friction losses, anchorage slip losses, and time-dependent prestress losses, which were assumed to amount to approximately 10%. Due to the column layout of the superstructure, the grid is locally interrupted in the column regions. Within each 7 × 7 m field, 11 tendons were arranged in both directions. These geometric discontinuities were explicitly considered in the numerical model to accurately represent the structure, see Fig. 1 (right).

The interaction between the industrial floor and the soil was represented by a linear elastic half-space beneath the slab. The half-space was modeled with a depth of 50 m and consisted of two soil layers: a 0.20 m thick gravel base layer with a constrained modulus E_s of 100 MN/m², underlain by a 49.8 m thick soil layer with a constrained modulus E_s of 40 MN/m².

2.2 Applied loads

2.2.1 Self-weight

The self-weight of the floor slab was automatically calculated within the FE software SOFiSTiK [7] based on a concrete unit weight γ_c of 25.0 kN/m³ and included in the numerical model.

2.2.2 High-rack storage

To determine internal forces resulting from high-rack storage, double-row racks were considered with a spacing of 1.20 m between base plates in the transverse direction and 2.80 m in the longitudinal direction. The maximum height of the racks is 7.50 m. The base plates measure 15 × 15 cm, with a maximum load of 75 kN per plate, see Fig. 2. Load distribution over the floor slab was assumed at an angle of 45°, in accordance with [9]. The high-rack rows are oriented along the longitudinal axis of the floor slab. At the edges of the slab, a single row of racks is provided, whereas in the interior region, double-row racks are arranged with an aisle width of approximately 3.70 m. The center-to-center distance between the double-row racks is 2.80 m.

To realistically capture the influence of forklift positioning, three representative load cases were modeled: (i) the forklift positioned at the center of the aisle, laterally offset from a single high-rack row; (ii) the forklift positioned at the center of the aisle, located between the base plates of the opposing high-rack rows and (iii) an isolated position without the influence of adjacent high-rack storage areas, see Fig. 2.

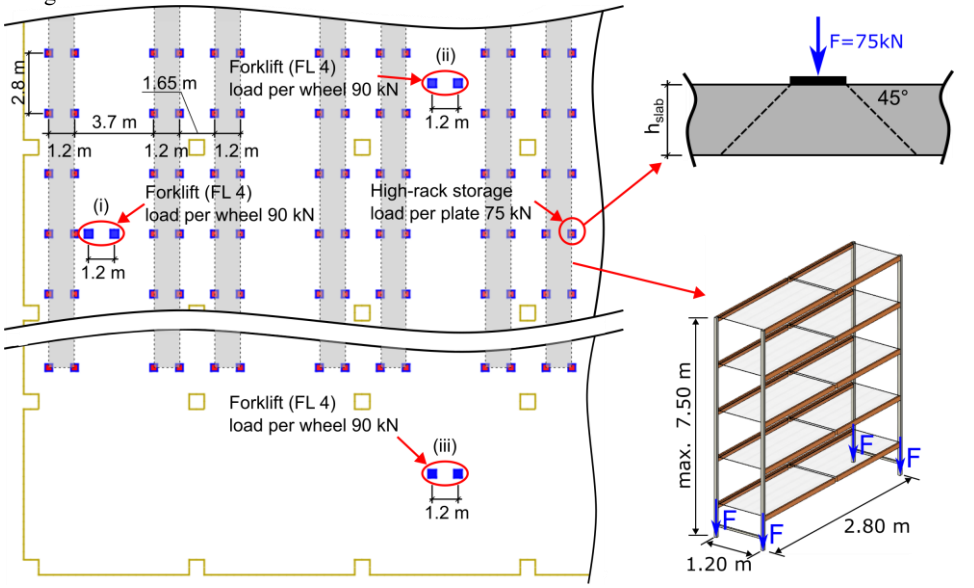


Fig. 2 Plan view single high-rack storage system and forklift loads (left) and representation of the high-rack storage system (right)

In the investigated warehouse, high-rack storage induces highly concentrated local point loads. These point loads result in elevated stress peaks in limited regions, necessitating careful modeling and appropriate evaluation of the simulation results. To avoid smearing of local loads due to the discretization of the FE mesh and resulting in unrealistic stress evaluation, a refined mesh with an element size of 0.35 × 0.35 m was adopted. This is consistent with the investigations presented in [10], which indicate that such a mesh density is sufficiently fine for modeling local loads such as single rack base plates or forklift wheel loads.

2.2.3 Block storage load

The block storage loads were arranged in a uniform grid with an aisle spacing of 2.0 m and an edge offset of 0.70 m, distributed over the entire floor area. Each block storage field measures 2.50 × 2.50 m and is subjected to an area load of 50 kN/m².

To realistically capture the influence of forklift positioning, four representative load cases were defined. These comprised: (i) the forklift positioned at the center of the aisle between block storage areas; (ii) the forklift positioned at the center of the aisle at the intersection of the longitudinal and transverse aisles; (iii) the forklift positioned in the transverse aisle between block storage areas and (iv) the forklift positioned in the transverse aisle at the location of a column opening, see Fig. 3.

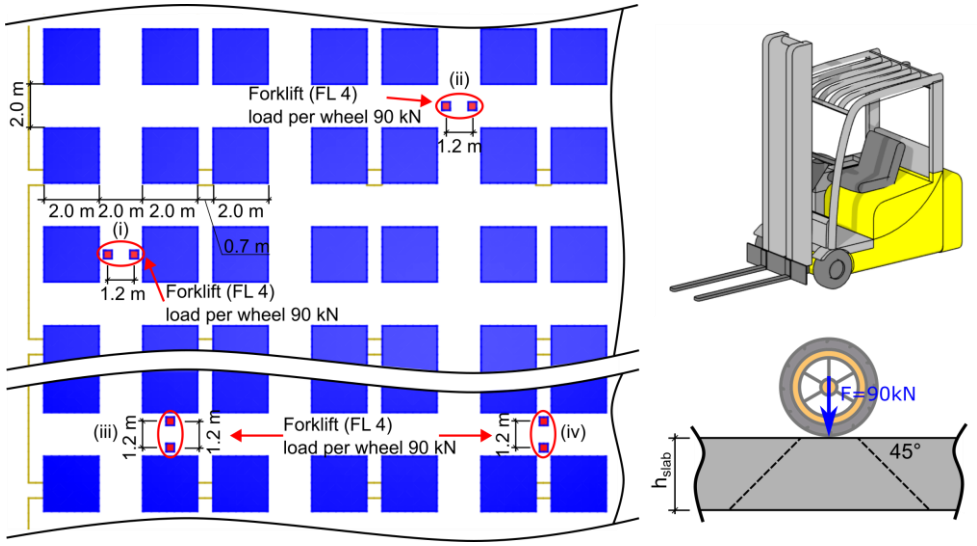


Fig. 3 Plan view block storage load and forklift loads (left) and representation of the forklift (right)

2.2.4 Forklift load

To represent dynamic loading from forklift traffic, a Class 4 (FL4) forklift with a wheelbase of 1.20 m was considered. In the FE model, only the front wheels were accounted for, each with an axle load of 90 kN, as prescribed in [11]. To capture dynamic effects due to acceleration and deceleration, the axle load used for internal force calculations was increased by a dynamic amplification factor of $\varphi = 2.0$, following [11].

The resulting wheel load corresponds to half of the axle load and was therefore 90 kN per wheel, see Fig.3 (right). In the FE model, this load was applied as an equivalent distributed area load over the wheel contact area of 0.20 m × 0.20 m, aligned along the slab centerline with a 45° distribution in accordance with [9].

2.2.5 Drying shrinkage during the service life

Imposed deformations were regarded with respect to drying shrinkage $\Delta\varepsilon_{cds}$ strain during the service life. With respect to rather sealed conditions at the bottom and free drying at the top surface the drying shrinkage was considered as a linear gradient ranging from 0.0 ‰ at the bottom surface to -0.10 ‰ at the top surface exposed to air.

3 RESULTS FROM THE FE-ANALYSES

In this chapter, the numerical results are given with focus on the development of principal stresses. A central aspect of the analysis is the evaluation of the principal tensile stresses to identify any potential risk of harmful cracking during service life of the industrial floor. The assessment of the principal tensile stresses was carried out using the SLS rare load combination in accordance with [12].

3.1 Results for the industrial floor system without prestressing tendons

Fig. 4 presents the principal tensile stresses of the concrete industrial floor model with the slab thickness h of 0.18 m, without prestressing tendons. The principal tensile stresses are shown for both the bottom and top surfaces of the slab under the loading conditions described in Section 2.2.

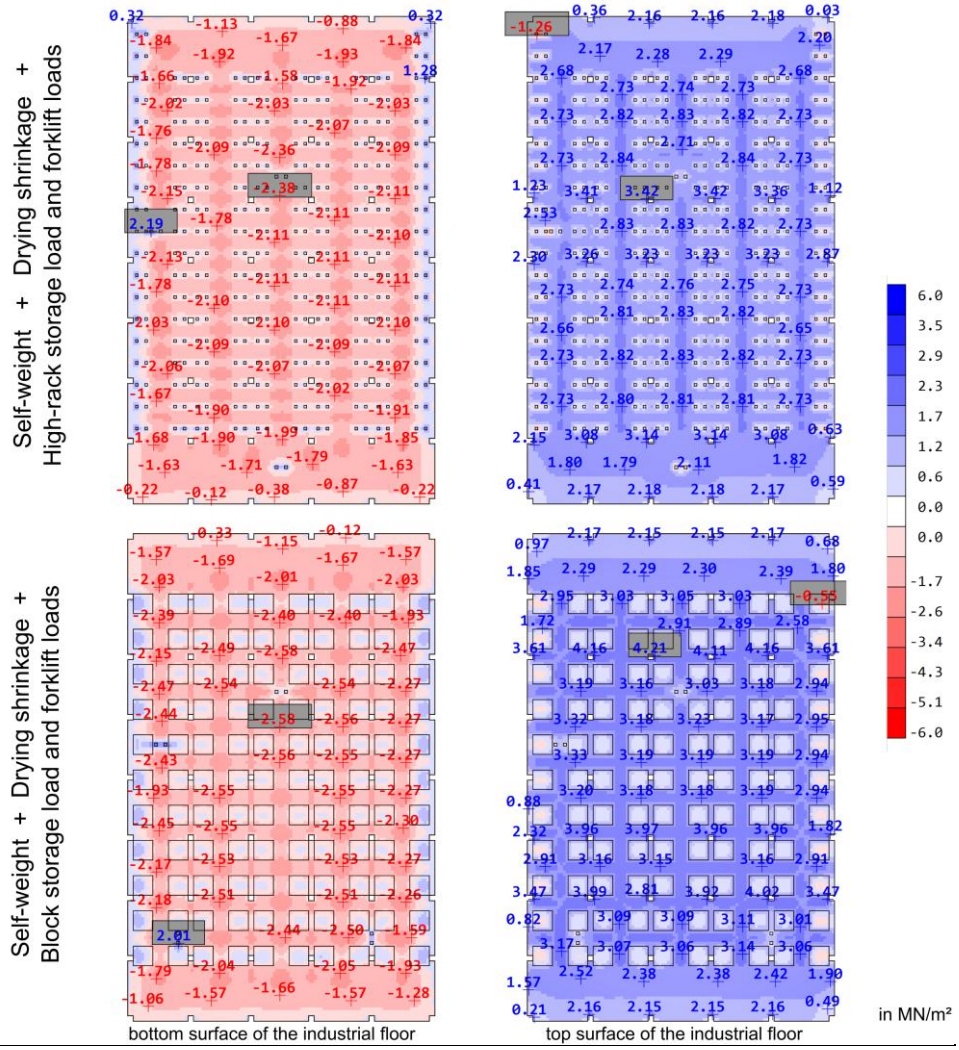


Fig. 4 Principal tensile stresses the industrial floor: bottom surface (left) and top surface (right)

As can be seen in Fig. 4, the load case with "Block storage load and forklift loads" produces a principal tensile stress of 4.21 MN/m² at the top of the concrete industrial floor. Consequently, the mean tensile strength of the concrete f_{ctm} of 2.90 MN/m² is exceeded, indicating a risk of cracking. The high tensile stress levels primarily result from drying shrinkage effects.

In practice, the stresses caused by drying shrinkage are controlled by introducing dilatation joints. These joints allow the slab to deform freely and thereby reduce the tensile stresses that develop due to restrained shrinkage.

3.2 Results for the industrial floor system with prestressing tendons

For the same concrete industrial floor model, the prestressing tendons described in Section 2.1 are now activated. Fig. 5 presents the results for the governing load case "Block storage load and forklift load" of the prestressed industrial floor model.

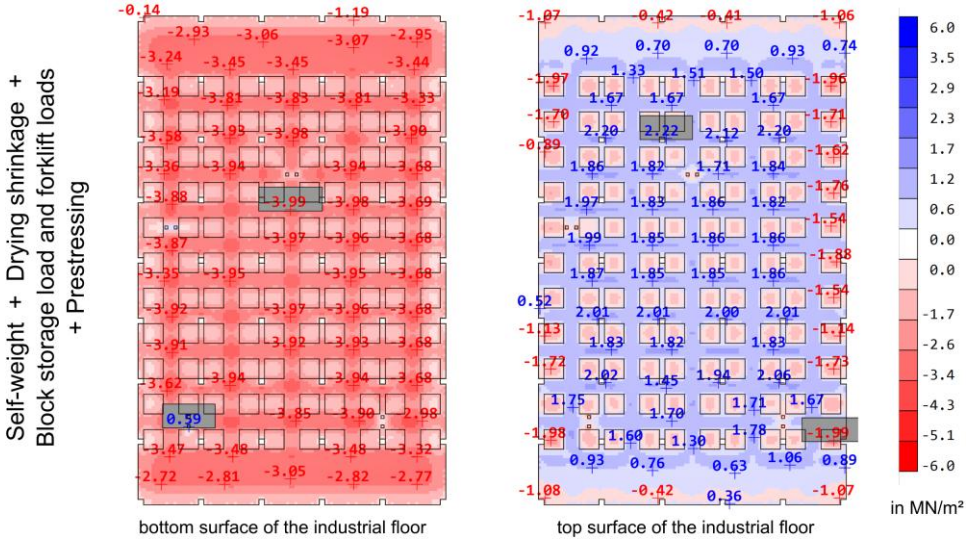


Fig. 5 Principal tensile stresses the industrial floor: bottom surface (left) and top surface (right)

For the prestressed industrial floor system in Fig. 5, the distribution of principal tensile stresses shows maximal values of 2.22 MN/m², indicating that the mean tensile strength of the concrete is not exceeded. As a result, the development of harmful cracks due to service loading is considered unlikely.

4 DISCUSSION

The study presents a numerical FE approach for evaluating the structural performance of prestressed industrial floor systems. By incorporating soil-structure interaction and serviceability limit state considerations, the model enables a realistic simulation of stress development over the service life and provides a reliable basis for performance comparison between structural alternatives.

As can be seen in Fig. 4 and Fig. 5, the principal tensile stresses can be significantly reduced by the application of prestressing in the industrial floor system. By limiting the principal tensile stresses below the tensile strength of the concrete, crack formation can be prevented and a watertight structure can be achieved.

In this conceptual study, the slab thickness was reduced to 18 cm to achieve a more efficient structural utilization compared to a minimum standard thickness of 0.25 m for such applications [5]. Although this approach is not formally in accordance with the DAfStb guideline [5], a verified crack-free behavior due to prestressing may also be considered as verification for ensuring impermeability.

Furthermore, no dilatation joints were modeled in the analysis. As a result, significant shrinkage-induced strains develop due to the restrained deformation of the slab. However, these tensile stresses can be effectively counteracted by the introduction of compressive stresses from prestressing.

This represents a major advantage of the prestressed system, as the imposed compressive stress state compensates for shrinkage effects and thereby reduces the risk of cracking even in jointless industrial floors. This reduces construction complexity, significantly lowers maintenance costs, and eliminates potential sources of failure associated with leaking of dilatation joints.

5 CONCLUSIONS

In the present study, a calculation approach was developed that realistically captures the overall slab behavior, including soil-industrial floor interaction. The numerical investigation was conducted using the finite element method. The results of the presented finite element analysis confirm that the prestressed industrial floor system represents a viable practical alternative to the conventional reinforced system. The FEA further indicates that designing for the serviceability limit state significantly reduces principal tensile stresses, thereby lowering the risk of crack initiation.

The application of prestressed tendons in industrial floor systems enables a reduction in slab thickness and the potential elimination of dilatation joints. This results in savings in material consumption, construction time, excavation work, and carbon emissions. By avoiding dilatation joints, maintenance requirements are reduced and potential serviceability problems caused by joint degradation are eliminated. Consequently, the prestressed system remains watertight and satisfies the required performance criteria in accordance with [5].

In this case study, the analysis demonstrates that under the given load assumptions the slab thickness can be reduced from 25 cm for the conventionally reinforced industrial floor to 18 cm for the prestressed system. This reduction of 7 cm per square meter corresponds to a concrete saving of approximately 175 kg per square meter of floor area. However, the advantages are not limited to material savings. Additional cost reductions result from less concrete transports and reduce on-site casting efforts. Further reduction of the slab thickness may be possible, provided that the punching shear capacity of the slab is verified.

By considering the entire structural system including the soil-industrial floor interaction, a more accurate simulation of stress development over the service life was achieved. This detailed analysis enables a well-founded assessment of the load-bearing behavior and provides valuable insights for further optimization of the industrial floor system. To further confirm the current findings, additional research is planned that will investigate the differential prestressing grid experimentally. Future studies should use the proposed method to systematically analyze different span lengths and grid configurations. Furthermore, attention should be given to punching shear performance and a comparative evaluation of fiber-reinforced and conventionally reinforced concrete slabs should be conducted.

References

[1] Deutscher Beton- und Bautechnik-Verein e.V. (DBV). *Industrieböden aus Beton / IndustrialConcrete Floors.* DBV-Merkblatt Bautechnik, Berlin: Deutscher Beton- und Bautechnik-Verein e.V. Accessed February 2017.

[2] Deutscher Beton- und Bautechnik-Verein e.V. (DBV). *Steel Fibre Reinforced Industrial Concrete Floors – Special Features of the Design and Detailing, Production and Conformity.* DBV-Merkblatt Bautechnik, Berlin: Deutscher Beton- und Bautechnik-Verein e.V. Accessed July 2013.

[3] Austria. Wasser Rights Act 1959 (Wasserrechtsgesetz 1959 – WRG). BGBl. Nr. 215/1959. https://www.bmluk.gv.at/themen/wasser/wasser-oesterreich/wasserrecht_national

[4] Germany. Water Resources Act (Wasserhaushaltsgesetz – WHG). Federal Law Gazette (Bundesgesetzblatt) I p. 2585 (2009), as last amended. https://www.gesetze-im-internet.de/whg_2009

[5] German Committee for Structural Concrete (DAfStb). Guideline: Watertight Concrete Structures (Wasserundurchlässige Bauwerke aus Beton – WU-Richtlinie), Deutscher Ausschuss für Stahlbeton e. V., Berlin, Germany. Accessed December 2017.

[6] Wörner, Johann-Dietrich, und Hans-Werner Nordhues. „Betonbau beim Umgang mit wassergefährdenden Stoffen." In *BetonKalender 2023: Wasserundurchlässiger Beton; Brückenbau*, herausgegeben von Konrad Bergmeister, Frank Fingerloos und Johann-Dietrich Wörner, 185-207. Berlin: Ernst & Sohn. Accessed 2023.

[7] SOFiSTiK, 2025, https://www.sofistik.com

[8] European Organisation for Technical Assessment (EOTA), Euro*pean Technical Assessment ETA-21/0765: ANP-FS Monostrand Post-tensioning System with 1 to 4 Strands*, Technical Assessment Body: OIB, 27 September 2021.

[9] Austrian Standards International. ÖNORM EN 1991-2: *Eurocode 1: Actions on structures – Part 2: Traffic loads on bridges*. Vienna: Austrian Standards International. Accessed March 02, 2012.

[10] Sever, Yolcu and Schlicke, Dirk. 2025. "*Finite-Elemente-Analyse von dünnen gebetteten Platten mit lokaler Lasteinleitung*". Beton- und Stahlbetonbau 120, H. 6,S. 426–433. https://doi.org/10.1002/best.202500013.

[11] Austrian Standards International. ÖNORM EN 1991-1-1: *Eurocode 1: Actions on structures – Part 1-1: General actions – Densities, self-weight, imposed loads for buildings*. Vienna: Austrian Standards International. Accessed December 01, 2011.

[12] Austrian Standards International. ÖNORM EN 1990: *Eurocode – Basis of structural design*. Vienna, Austria: Austrian Standards International. Accessed March 15, 2013.

Large-Scale Tests on Reinforced Concrete Shell Elements and Comparison to Multilayer Model Analyses

Yannick Kummer, Karel Thoma, Walter Kaufmann

Institute of Structural Engineering (IBK),
ETH Zürich,
Stefano-Franscini-Platz 5, 8093 Zürich, Switzerland

Summary
The complex load-bearing behaviour of reinforced concrete (RC) shells in the cracked elastic regime, relevant for serviceability and fatigue verification, remains an open topic of research. Capturing this behaviour requires demanding nonlinear finite element analyses, typically employing multilayer shell elements. Although these models have been extensively validated for their global load-deformation response, experimental test data providing insight at the local stress-strain level is scarce.

This paper presents two large-scale tests on RC shell elements subjected to combined loading. Strains measured along the reinforcing bars and on the surfaces of the specimens are compared with multilayer shell element analyses. The results will support the design of an experimental campaign aimed at validating the fundamental assumptions of these models at the stress-strain level in the cracked elastic regime, with particular emphasis on stresses in the reinforcement.

1 INTRODUCTION

An increasing number of bridges are approaching the end of their service life in the upcoming years. Since these bridges were built, the loads and the design codes have evolved. The current fatigue provisions in the design codes are intentionally conservative to prevent fatigue failure in new bridges over their service life. When these provisions are applied to existing RC bridge decks, which were typically designed without explicit consideration of fatigue, verification requirements for reinforcement stress amplitudes are frequently infringed. This particularly affects RC bridge decks, which are directly subjected to fatigue loading from heavy vehicle traffic, resulting in high fatigue demands. However, hardly any fatigue damage has been observed in RC bridge decks, suggesting unaccounted structural reserves [1] which should be utilised to prevent cost- and resource-intensive strengthening measures for existing structures and allow for more efficient designs of new bridge decks.

Although required for the fatigue verification of reinforcement in RC bridge decks, no experimentally validated analytical model currently exists to reliably determine the reinforcement stresses in RC shells subjected to general loading, i.e. in the cracked elastic regime. Designers commonly rely on simplified hand calculations that neglect membrane forces, often leading to incorrect, overly conservative results. Apart from trivial cases, such as pure bending in reinforcement directions, Marti's solution for pure torsion [2] and its generalisation to account for axial restraint proportional to the mid-plane strains [3] remain the only available closed-form solutions to determine reinforcement stresses in the cracked elastic regime. Recent investigations [4] indicate that establishing analytical solutions for more general cases may not be possible at all. Alternatively, numerical methods based on mechanically sound multilayer shell models can be used. However, these nonlinear finite element (NLFE) analyses are computationally demanding and rarely applied in practice. Moreover, multilayer shell models have not been sufficiently validated for RC shells subjected to general loading due to the scarcity of available experimental data, and hardly at all at the local stress-strain level.

The objective of the two large-scale RC shell element tests presented in this paper, along with a forthcoming experimental testing campaign comprising eight further large-scale shell element tests, is therefore to experimentally validate the fundamental assumptions of the multilayer shell model, summarised in Section 2, at the local stress-strain level in the cracked elastic regime. Section 3 outlines the experimental tests presented in this paper, including the instrumentation, test specimens, and loading of the large-scale shell element tests. In Section 4, the post-processing of the experimental data and the parameters of the nonlinear finite element (NLFE) analyses are detailed, followed by a comparison and discussion of the results in Section 5, and the conclusions in Section 6.

2 MULTILAYER SHELL MODEL

To capture the post-cracking behaviour of RC shells under general loading conditions, relevant to the fatigue verification of reinforcing bars, nonlinear analyses comprising multilayer shell elements are typically employed in research. The multilayer shell element models are based on the kinematic assumptions of either Kirchhoff-Love or Reissner-Mindlin, both assuming a linear distribution of the in-plane strain components (i.e., ε_x, ε_y, and ε_{xy}) across the thickness of the shell. Kirchhoff-Love kinematics are adequate to model slender RC slabs, such as bridge decks, assuming that out-of-plane shear strains may be neglected. With this additional assumption, six generalised strains – commonly defined as mid-plane strains ε_{x0}, ε_{y0}, and $\varepsilon_{xy0} = \gamma_{xy0}/2$ and curvatures χ_x, χ_y, and χ_{xy} shown in Fig. 1 (left) – are sufficient to model RC shells. Nonetheless, many multilayer shell models use the more general Reissner-Mindlin kinematics, which can also be used to model less slender RC shells.

In either case, shells are discretised into layers – representing, e.g., concrete or reinforcement (see Fig. 1 (right)) – which are coupled via the respective kinematic constraints. Each layer is subjected to plane stress conditions and is assigned its own nonlinear constitutive relationship. Using the latter, the resulting layer stresses can then be computed for any given combination of generalised strains, from which the stress resultants – the in-plane membrane forces n_x, n_y and n_{xy}, the normal moments m_x and m_y, and the torsional moment m_{xy} – are obtained by integration over all layers. Conversely, determining generalised strains and layer stresses from known stress resultants requires an iterative procedure.

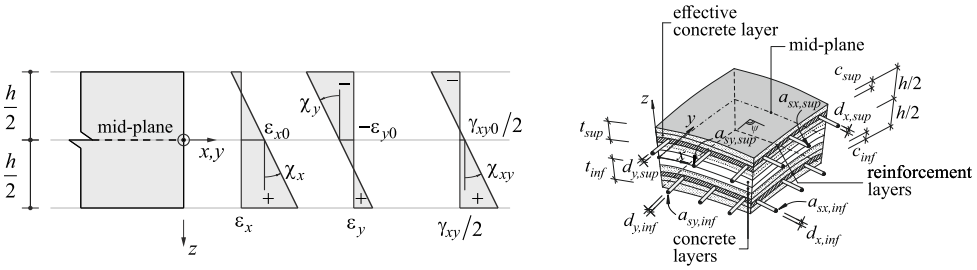


Fig. 1 Multilayer shell model: (left) kinematic constraints of Kirchhoff-Love, assuming linear strain distribution across the thickness of the shell element, adapted from [4]; (right) CMM-Usermat model including discrete reinforcing layers, adapted from [5]

Various multilayer shell models have been developed by different authors in the past (e.g., [6], [7], [8]). In order to obtain reliable results at a reasonable computational cost, numerically efficient yet mechanically sound constitutive relationships for the layers are essential. These prerequisites are met by the CMM-Usermat (see Fig. 1 (right)), a multilayer finite element model developed by Thoma et al. [9], implemented in ANSYS APDL [10]. This model is based on the Cracked Membrane Model (CMM) [11] with rotating cracks and Reissner-Mindlin kinematics, and has been proven to reliably account for tension stiffening. The latter is essential to accurately capture the behaviour of RC shells in the cracked elastic regime, and particularly relevant to reliably quantifying compressive membrane action (CMA). CMA develops when the mid-plane extensions of the shell elements – which occur after crack formation – are restrained by adjacent structural elements (e.g., uncracked surrounding elements or bridge decks restrained by the webs) and are considered a main source of reserve in the fatigue verification of reinforcing bars in bridge decks [1]. Importantly, neglecting tension stiffening ([6], [7]), which is usually conservative, leads to an overestimation of axial strains and consequently unrealistically high – hence unconservative – CMA.

Although the CMM-Usermat is based on mechanically sound models and has been experimentally validated for various structural elements such as girders [5], shear walls [12], and both one-way and two-way slabs [13], experimental data for combinations of membrane forces with normal and torsional moments, particularly at the local stress-strain level – i.e., where all applied stress resultants were known and resulting reinforcement stresses were measured – is scarce. The two large-scale RC shell element tests presented in this paper, address this research need, aiming at validating the fundamental assumptions of multilayer shell models at the stress-strain level, with particular emphasis on determining reinforcement stresses under fatigue loading including CMA.

3 EXPERIMENTAL TESTS

This section presents the two large-scale RC shell element tests conducted in the Large Universal Shell Element Tester (LUSET) at the Chair of Concrete Structures and Bridge Design of ETH Zurich. The LUSET provides a unique testing setup capable of carrying out large-scale shell element tests under general loading conditions, pertinent for the validation of the multilayer shell model. Detailed information on the components and functionality of the LUSET is provided in [14]. This test setup has already been successfully employed in several relevant experimental studies (e.g., [15], [16]).

3.1 Test Campaign Overview

The two LUSET tests were conducted as part of an expert consulting mandate to assess the serviceability of a planned structure, which defined the applied serviceability loading (LS1, see Section 3.5), as well as geometrical and material parameters of the specimens, and also required the brickwork-type pattern in three of four quarters on the front surface of the specimens (see Fig. 2 (right)).

The strains along the reinforcing bars and on the surfaces of the specimens were measured for comparison with predictions using the CMM-Usermat model. Since the subsequent large-scale shell element testing campaign aims to validate the model specifically for determining reinforcement stresses under fatigue loading, the load application and evaluations presented in this paper are restricted to the relevant cracked elastic regime.

3.2 Specimens

LUSET specimens generally measure 2.00 m × 2.00 m in plane (2.20 m × 2.20 m including load introduction blocks). Specimens BT1 and BT2 had a nominal concrete cover of 35 mm each, with thicknesses $t_{BT1} = 280$ mm and $t_{BT2} = 300$ mm, respectively. The reinforcement layout is shown in Fig. 2 (left). Both specimens were orthogonally reinforced, with outer (1st and 4th) vertical reinforcing layers of Ø20@133 mm and inner (2nd and 3rd) horizontal reinforcing layers of Ø12@200 mm. In Fig. 2 (centre), a specimen is shown during casting, with reinforcing bars connected to the LUSET blocks using high-strength connectors and shear keys to ensure shear transfer. Fig. 2 (right) shows Specimen BT1 installed in the LUSET, with the blocks connected to the yokes, and indicates the coordinate system used for the load application and measurement evaluation throughout this paper.



Fig. 2 Specimen BT1: (left) reinforcement layout; (centre) during casting; and (right) installed in the LUSET, including definition of the coordinate system

3.3 Material Properties

Class B500B ribbed reinforcing bars were employed in accordance with SIA 262:2013 (Switzerland). A total of 10 reinforcing bars per diameter, from the same batch used in the LUSET tests, were tested to failure in tension using a universal testing machine. These tensile tests were not intended to accurately capture the Young's Modulus. Therefore, the standard value of 205 GPa was adopted for the numerical analyses. Both specimens were cast using a high-strength concrete with a compressive strength of $f_c = 76.4$ MPa and a tensile strength of $f_{ct} = 5.2$ MPa.

3.4 Instrumentation and Measurement Systems

The load pins on the 100 actuators of the LUSET measured the applied loads at 1 Hz during the tests. For both tests, surface deformations on the front and back surfaces were measured at 0.1 Hz using 3D

digital image correlation (DIC) systems, with their setup parameters summarised in Fig. 3 (top). Both DIC systems consisted of two 24.6 Mpx Alvium 1800 U-2460 cameras with a resolution of 5328 × 4608 pixels and 25 mm focal length lenses. Due to the brickwork-type pattern, the DIC measurements on the front surface were restricted to the quarter on the top right. On both sides, the area of interest (AOI) was further reduced at the edges to mitigate load introduction effects.

The strains along the reinforcing bars were measured every 1.3 mm at intervals of 30 s and 24 s for BT1 and BT2, respectively, using a distributed optical fibre sensing (DOFS) system (i.e., Odisi 6104 from Luna Innovations Inc. [17]). The measurements were limited to approximately the central 1.15 meters of the reinforcing bars due to installation constraints. The respective glass fibres for both specimens, indicated in Fig. 3 (bottom left), were glued into 1 mm × 1 mm grooves along the reinforcing bars and positioned towards the inside of the specimen to protect them during casting.

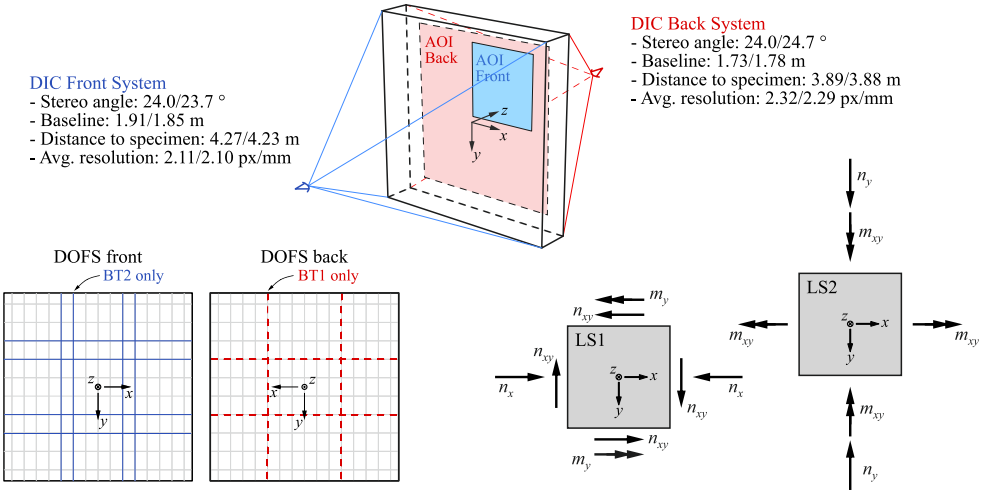


Fig. 3 (top) DIC setup parameters for BT1/BT2 and AOI on front and back surface; (bottom left) installed DOFS sensors on front (1st/2nd) and back (3rd/4th) reinforcing layers; and (bottom right) sign convention for the applied loads for LS1 and LS2, for magnitudes see Table 1

3.5 Loads

The tests were divided into two load stages (LS), with loads and load rates specified in Table 1. LS1 included longitudinal compression (n_x), in-plane shear (n_{xy}), and transverse bending (m_y), representing serviceability loads. In LS2, torsion (m_{xy}) was superimposed on LS1, and, in the case of the BT2, combined with transverse compression (n_y). The load components per LS (see Fig. 3 (bottom right)) were applied in proportion, while unspecified load components were held at zero.

Table 1 Load stages (LS) for BT1 and BT2, sign convention see Fig. 3 (bottom right)

Specimen	LS1	LS2
BT1	n_x = 980 kN/m (12.0 kN/min) n_{xy} = 952 kN/m (11.7 kN/min) m_y = 80 kNm/m (0.98 kNm/min)	n_y = 0 kN/m m_{xy} = 40 kNm/m (1.00 kNm/min)
BT2	n_x = 1290 kN/m (11.5 kN/min) n_{xy} = 1200 kN/m (10.7 kN/min) m_y = 62 kNm/m (0.55 kNm/min)	n_y = 25 kN/m (0.8 kN/min) m_{xy} = 40 kNm/m (1.33 kNm/min)

4 4 DATA PROCESSING AND NUMERICAL ANALYSES

4.1 Post-Processing of Measurement Data

The measurements of (i) the load pins of the LUSET, (ii) the DIC systems, and (iii) the DOFS systems were synchronised, processed, filtered, and visualised using the MATLAB software. The experimental data were filtered as described below, and the data points were subsequently reduced by a factor of 5.

To determine the stress resultants from the recorded measurements of the LUSET load pins, Lagrangian optimisation was applied, according to [18]. To further reduce potential noise, the stress resultants were filtered with a Gaussian-weighted moving average filter (*window size*: 50).

The displacement fields on the front and back surfaces of the specimens were obtained from the raw data of the DIC systems (i.e., speckle images taken with the DIC cameras) using the VIC-3D software [19], with the parameters *subset size* and *step size* set to 29 and 3, respectively. From every fifth measurement of the in-plane displacements, the best-fit homogeneous strains $\boldsymbol{\varepsilon}^*$ [20] were evaluated, for which a temporal moving average filter (*window size*: 10) was employed. The crack inclinations on the surfaces were analysed with the automated crack detection and measurement (ACDM) tool [20].

Outliers in the DOFS measurements were removed employing a Hampel filter, and the measurements were further filtered with a spatial moving average filter (*window size*: 7, 11) and a low-pass filter (*passband frequency*: 0.1 mm^{-1}, 0.066 mm^{-1}), approximately corresponding to the rib spacing of the Ø12 and Ø20 reinforcing bars, respectively.

4.2 Multilayer Model Analyses

Using the multilayer finite element model CMM-Usermat introduced in Section 2, NLFE analyses were carried out by dividing the shell into 50 layers and applying the geometrical and material parameters specified in Sections 3.2 and 3.3, respectively, and the loads defined in Section 3.5. The Young's Modulus of the concrete was calculated according to SIA 262, with $k_E = 10'000$. The parameters for the Tension-Chord Model [21] were set to the standard values of $\tau_{b0} = f_{ctm}$, $\tau_{b1} = 2 \cdot f_{ctm}$, and $\lambda = 0.67$, with $f_{ctm} = 0.3\ f_c^{2/3}$. The effective tensile strength of the concrete, used only to determine whether the respective layer has cracked, was set to $0.5 \cdot f_{ctm}$.

5 COMPARISON OF THE MULTILAYER MODEL WITH EXPERIMENTAL RESULTS

For both tests, the load-bearing behaviour observed in the experiments is compared with NLFE analyses using the CMM-Usermat. To this end, the experimentally obtained strains from the DIC and DOFS systems and the stress resultants of the LUSET throughout the load stages LS1 and LS2 are compared with the average strains predicted by the multilayer finite element model at the same applied loads.

5.1 Surface Strains

In Fig. 4, the best-fit homogeneous strains $\boldsymbol{\varepsilon}^*$ on the surfaces of the specimens are compared with the average concrete strains $\boldsymbol{\varepsilon}_{\text{CMM-U}}$ obtained from the CMM-Usermat analyses in the surface layers as a function of the applied loads. The analyses correctly predict the uncracked, closely linear response for BT1 and BT2, shown in Fig. 4 (top left and bottom left), respectively. The best-fit homogeneous strains on the front surface of Specimen BT1 (see Fig. 4 (top left)) indicate the onset of crack formation at $0.41 \cdot$LS1, whereas on the back surface, cracking was less pronounced and cannot be reliably determined. In the cracked elastic regime of LS1, the analysis accurately predicts the surface strains (see Fig. 4 (top centre)). While the shear strains (γ_{xy}) are again accurately captured in LS2, ε_x is over-, and ε_y is underpredicted, with increasing deviations at higher loads. The comparison of the normal strain components (ε_x and ε_y) in Fig. 4 (top right) on the back surface shows good agreement, while the magnitude of γ_{xy} is underpredicted.

The analysis of BT2 in Fig. 4 (bottom left) similarly shows good agreement with the best-fit homogeneous strains on the front surface. Cracking becomes visible on the front surface at $0.51 \cdot$LS1, whereas on the back surface, cracking is more pronounced than in BT1 and occurs at $0.56 \cdot$LS1. For BT2, the onset of cracking corresponds to the maximum deviation between the analysis and measurements on the front surface (see Fig. 4 (bottom centre)). The increasing deviation of the normal strain components, especially for ε_y, is more pronounced than for BT1. For the back surface (see Fig. 4 (bottom right)), the measurements indicate biaxial tensile strains (ε_x, ε_y), whereas the analysis predicts a fully compressed back surface layer and clearly underpredicts the magnitude of the shear strain (γ_{xy}).

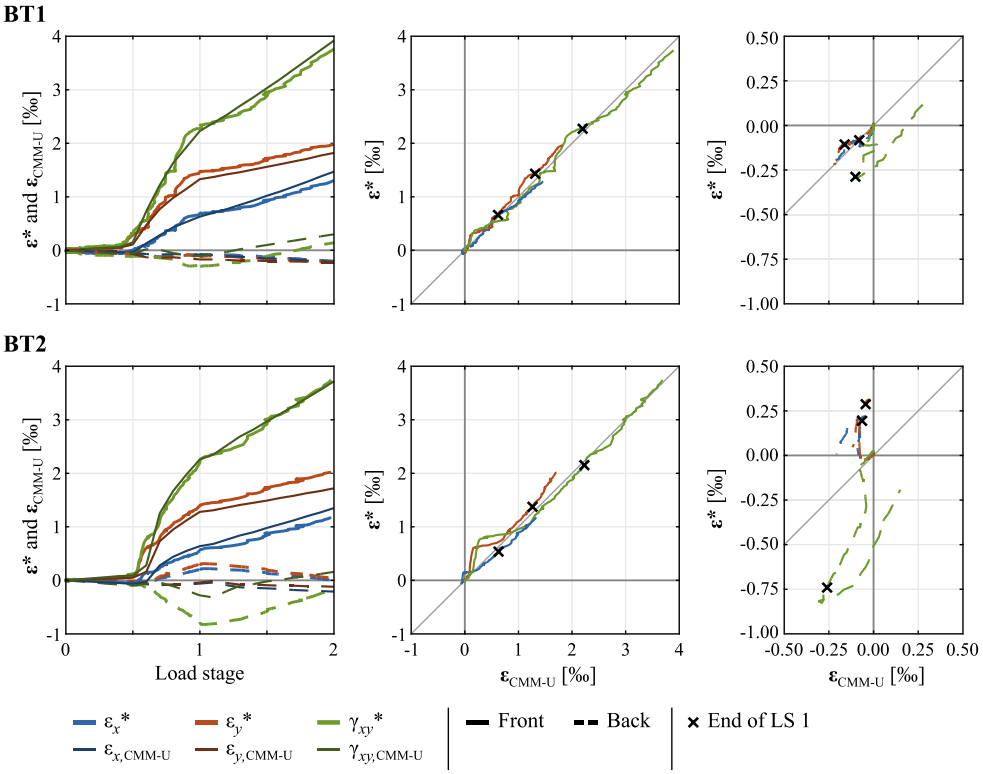


Fig. 4 Comparison of experimental best-fit homogeneous strains $\boldsymbol{\varepsilon}^*$ with predicted average surface strains $\boldsymbol{\varepsilon}_{CMM\text{-}U}$ for BT1 (top row) and BT2 (bottom row): (left) front and back surface strains as a function of the load stage; (centre) 45° plots for front surface strains; and (right) 45°plots for back surface strains

5.2 Reinforcement Strains

In Fig. 5 (top left and bottom left), the average measured strains $\varepsilon_{s,avg}$ per reinforcing layer (over the measurement length) of Specimens BT1 and BT2, respectively, are compared with the average reinforcement strains determined with CMM-Usermat $\varepsilon_{s,avg,CMM\text{-}U}$ as a function of the applied loads. The analyses correctly capture the experimental reinforcement strains in the uncracked elastic regime. The onset of cracking is consistent with the DIC measurements; for the back surface of BT1, where it could not be reliably determined with DIC, cracking clearly initiates at 0.53·LS1.

While the analyses of both specimens accurately predict the average reinforcement strains in the 1st layer ($\varepsilon_{s,avg,1Ly}$) in the cracked elastic regime of LS1 (see Fig. 5 (top centre and bottom centre)), they overpredict strains in the 2nd layer ($\varepsilon_{s,avg,2Lx}$). In LS2, the analyses underpredict $\varepsilon_{s,avg,1Ly}$ and overpredict $\varepsilon_{s,avg,2Lx}$, with the deviation increasing with the applied load. The strains of the back reinforcing layers ($\varepsilon_{s,avg,3Lx}$ and $\varepsilon_{s,avg,4Ly}$, in Fig. 5 (top right)) are generally well predicted in BT1, with smaller deviations than in the front layers. In the analysis of BT2, on the other hand, the predicted strains in the back reinforcing layers (see Fig. 5 (bottom right)) deviate more from the measured strains. Note that the measurements of $\varepsilon_{s,avg,4Ly}$ are based on a single fibre and should therefore be interpreted with caution.

5.3 Discussion of Results

The DIC and DOFS measurements show good agreement, and the average surface and reinforcement strains are generally well predicted by the CMM-Usermat. However, the average strains on the back surfaces of both specimens deviate more, particularly in BT2. This might be attributed to the fact that these surfaces were only partially cracked due to the high longitudinal compression force and transverse bending moment in LS1, combined with in-plane shear; it appears that the NLFE analyses and comparisons based on average strains are not appropriate for assessing this state.

For LS2, the NLFE analyses underpredict $\varepsilon_{s,avg,1Ly}$, while overpredicting $\varepsilon_{s,avg,2Lx}$, with deviations increasing for higher loads. The crack inclinations on the front surface, measured with ACDM, remain approximately constant in the cracked elastic regime, while the NLFE model assumes rotating cracks. To determine whether this explains the observed deviations, further investigations are required.

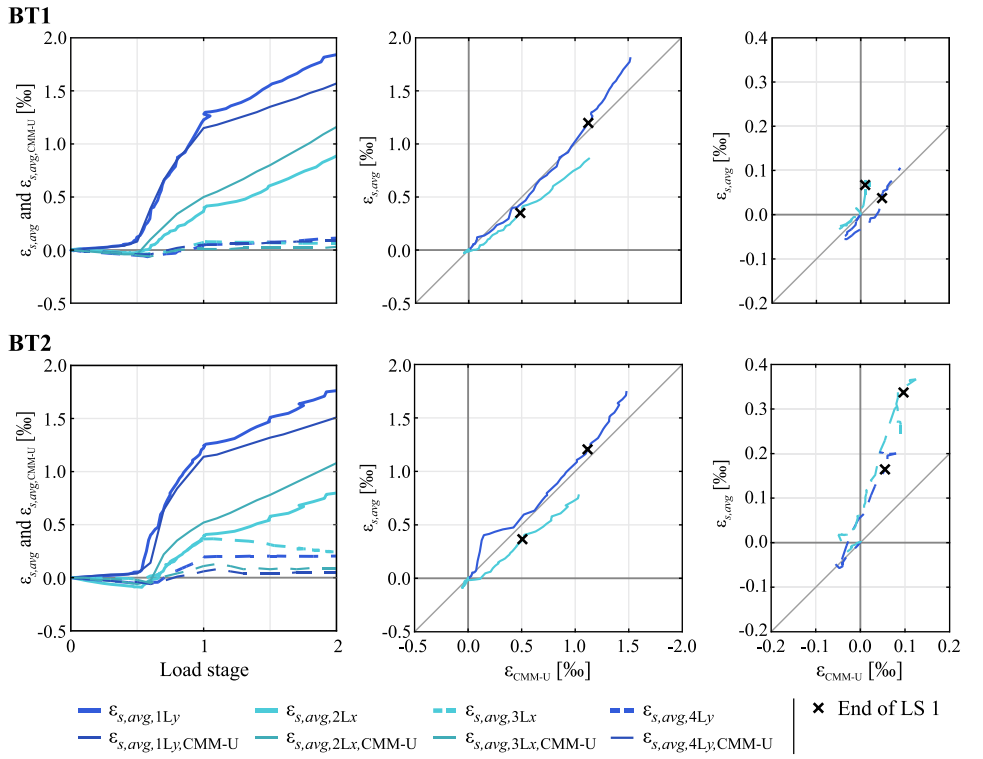


Fig. 5 Comparison of observed ($\varepsilon_{s,avg}$) and predicted ($\varepsilon_{s,avg,CMM-U}$) average reinforcement strains for BT1 (top row) and BT2 (bottom row): (left) strains in reinforcing layers as a function of the load stage; (centre) 45° plots for reinforcing bars on the front (1st/2nd layer); and (right) 45° plots for reinforcing bars on the back (3rd/4th layer)

6 CONCLUSION

The two presented large-scale RC shell element tests conducted in the LUSET under complex load combinations (i) address the scarcity of experimental data of RC shells at the stress-strain level by measuring the applied loads as well as surface and reinforcement strains and (ii) provide valuable insight into the load-bearing behaviour in the cracked elastic regime. The NLFE analyses employing the finite element multilayer shell model CMM-Usermat reliably predict the average strains in the reinforcement for given stress resultants. When the load path is changed, i.e. when torsion is added to the serviceability loads, the NLFE analyses deviate more from the experimental results. Further analyses are required to determine the underlying causes.

The comparisons of the experimental results with the NLFE analyses will form the basis for defining test parameters for a subsequent experimental testing campaign in the LUSET, aimed at validating the multilayer shell model at the stress-strain level for RC shells in the cracked elastic regime under general loading, including CMA, with a focus on reinforcement stresses under fatigue loading.

Acknowledgements

The tests presented were conducted as part of an expert consulting mandate to validate the serviceability (crack widths) of a planned structure. The authors acknowledge the possibility to define a separate load-stage (LS2) independent of the client's needs.

References

[1] Thoma, Karel, Kenel, Albin, and Borkowski, Gregor. 2019. “Fatigue strength of deck slabs loaded predominantly in bending.” AGB 2010/001. doi.org/10.3929/ethz-b-000404295.

[2] Marti, Peter, and Kong, Keith. 1987. “Response of Reinforced Concrete Slab Elements to Torsion.” J. Struct. Eng. 113 no. 5:976–993. doi: 10.1061/(ASCE)0733-9445(1987)113:5(976).

[3] Balmer, Vera, Thoma, Karel, and Kaufmann, Walter. 2024. “Design of Concrete Plates and Shells: A Solved Problem?.” Proceedings of the IASS 2024 Symposium. doi: 10.3929/ethz-b-000698486.

[4] Marti, Peter, Kaufmann, Walter, Seelhofer, Hans, and Karagiannis, Demis. 2022. “Kirchhoff–Love Plate Deformations Reinterpreted.” J. Eng. Mech. 148 no. 6:04022026. doi: 10.1061/(ASCE)EM.1943-7889.0002105.

[5] Thoma, Karel. 2018. “Finite element analysis of experimentally tested RC and PC beams using the cracked membrane model.” Eng. Struct 167:592–607. doi: 10.1016/j.engstruct.2018.04.010.

[6] Kirschner, Uwe, and Collins, Michael P. 1986. “Investigating the Behaviour of Reinforced Concrete Shell Elements.” Department of Civil Engineering, University of Toronto, Publication no. 86-09.

[7] Kollegger, Johann. 1991. “Algorithmus zur Bemessung von Flächentragwerkelementen unter Normalkraft- und Momentenbeanspruchung.” Beton- und Stahlbetonbau 86 no. 5:114–119. doi: 10.1002/best.199100230.

[8] Seelhofer, Hans. 2009. “Ebener Spannungszustand im Betonbau: Grundlagen und Anwendungen.” Doctoral thesis, ETH Zurich. doi: 10.3929/ETHZ-A-005901914.

[9] Thoma, Karel. 2021. “CMM-Usermat: Implementation of the Cracked Membrane Model (CMM) in ANSYS Mechanical APDL to analyse reinforced concrete structures.” Accessed Jan. 26. https://github.com/kfmResearch-NumericsTeam/CMM_Usermat.

[10] ANSYS 2024. *ANSYS 2024 R1 Mechanical APDL*, Canonsburg, USA.

[11] Kaufmann, Walter, and Marti, Peter. 1998. “Structural Concrete: Cracked Membrane Model.” J. Struct. Eng. 124 no. 12:1467–1475. doi: 10.1061/(ASCE)0733-9445(1998)124:12(1467).

[12] Thoma, Karel, Roos, Patrick, and Weber, Marius. 2014. “Finite-Elemente-Analyse von Stahlbetonbauteilen im ebenen Spannungszustand.” Beton- und Stahlbetonbau 109 no. 4:275–283. doi: 10.1002/best.201300087.

[13] Thoma, Karel, Roos, Patrick, and Borkowski, Gregor. 2014. “Finite Elemente Analyse von Stahlbetonplatten.” Beton- und Stahlbetonbau 109 no. 12:895–904. doi: 10.1002/best.201400047.

[14] Kaufmann, Walter, Beck, Alexander, Karagiannis, Demis, and Werne, Dominik. 2019. “The Large Universal Shell Element Tester LUSET.” Institute of Structural Engineering, ETH Zurich, IBK Report 506. doi: 10.3929/ethz-b-000379657.

[15] Karagiannis, Demis. 2021. “Effect of transverse bending on the shear capacity of concrete bridges.” Doctoral thesis, ETH Zurich. doi: 10.3929/ETHZ-B-000485497.

[16] Beck, Alexander. 2021. “Paradigms of shear in structural concrete: Theoretical and experimental investigation.” Doctoral thesis, ETH Zurich. doi: 10.3929/ethz-b-000482684.

[17] LUNA Innovations Inc. 2021. “LUNA ODiSI 6000 Data Sheet.” Roanoke, Virginia, USA. Accessed Jan. 26. https://lunainc.com/sites/default/files/assets/files/data-sheet/LUNA%20ODiSI%206000%20Data%20Sheet.pdf.

[18] Haefliger, Severin, and Kaufmann, Walter. 2022. “Load-deformation behavior of locally corroded reinforced concrete retaining wall segments: Experimental results." Structural Concrete 24 no. 1:288–317. doi: 10.1002/suco.202200405.

[19] Correlated Solutions Inc. 2021. “Vic-3D 9.” Irmo, South Carolina, USA. Accessed: Jan. 26. https://correlated.kayako.com/article/60-vic-3d-9-manual-and-testing-guide.

[20] Gehri, Nicola. 2024. “Exploring the shear behaviour of fibre-reinforced concrete.” Doctoral thesis, ETH Zurich. doi: doi.org/10.3929/ethz-b-000677209.

[21] Marti, Peter, Alvarez, Manuel, Kaufmann, Walter, and Sigrist, Viktor. 1998. "Tension Chord Model for Structural Concrete." Struct. Eng. International 8 no. 4:287–298. doi: 10.2749/101686698780488875.

Connections and Fastenings

Experimental Investigation of Uplift in a Reversibly Dry-Jointed Timber-Concrete Composite Ceiling System

Rebecca Müller, Christian Sorg, Felix Ruppert, Christian Glock

Institute of Concrete Structures and Structural Design
University of Kaiserslautern-Landau (RPTU),
Paul-Ehrlich-Straße 14, 67663 Kaiserslautern, Germany

Summary
Timber–concrete composite (TCC) ceiling systems offer significant potential for reducing embodied emissions. A joint project investigated a reversibly dry-jointed TCC ceiling system without uplift restraints, aiming to enable repeated (dis-)assembly. The composite action is achieved by a sawtooth-shaped notch geometry. The research methodology comprises small-scale prototype production to assess dimensional accuracy, beam tests to compare dry-jointed and directly concreted reference specimens and a real-scale ceiling strip test. The experimental results demonstrate sufficient dimensional accuracy when using appropriate formwork. The tests on beams and ceiling strip showed no uplift failure despite the absence of uplift restraints. The occurring minor uplift exhibits hints at possible correlations with known parameters, which are yet to further examine.

1 MOTIVATION

With regard to embodied emissions, timber-concrete composite ribbed slabs present a more ecological alternative to conventional reinforced concrete slabs [1]. Using composite action, a thin reinforced concrete slab primarily bears compressive stresses, while the divided tensile zone is regularly transferred to fibre-parallel engineered timber products. Depending on the chosen assessment scenario, this results not only in a decrease in GWP-total through reducing concrete consumption but also through its substitution with engineered timber products. Those usually display a negative GWP-total in the manufacturing phase (A1 – A3 [2]) due to biogenic carbon storage as shown in Fig. 1 (left). However, at the end of life of TCC ceilings, waste treatment (C3 [2]) adversely affects LCA. The stored carbon is again released as CO2 during thermal utilisation. Timber used in construction therefore only serves as a temporary CO2 sink for the duration of its life cycle.

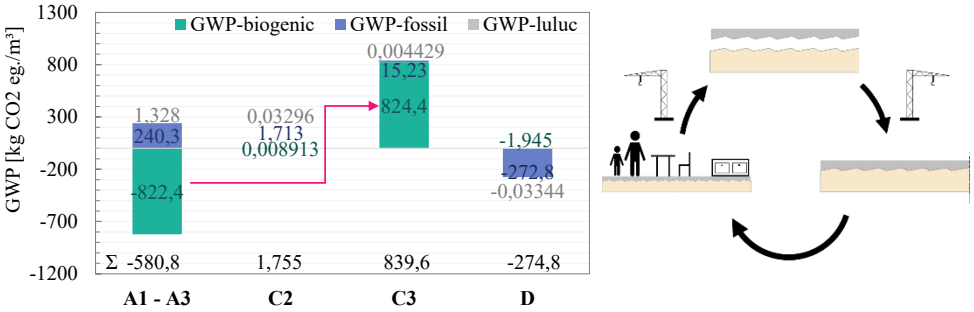


Fig. 1 GWP per m³ glued laminated timber according to a generic dataset in ÖKOBAUDAT [3] (left), schematic diagram of reversible TCC ceiling system (right) [4],[5]

The permanent preservation of biogenic carbon storage in timber by reuse at the construction component level is a significant lever for improving the ecological footprint of ceilings. Based on this idea, a joint research project on the development of reversible TCC ceiling system [4],[5] was carried out at RPTU's Institute of Concrete Structures and Structural Design and Institute of Steel Construction from 2023 to 2025. The cross-sections of this ceiling system are designed for multiple use, as shown in Fig. 1 (right). This paper presents experimental investigations into the dimensional accuracy as well as

the load-bearing and deformation behaviour of dry-jointed TCC components without metallic connectors.

2 PRINCIPLES AND PRELIMINARY INVESTIGATIONS

2.1 Introduction to reversibility

In the context of the investigated ceiling system, reversibility refers to the repeated jointability and separability of the concrete and timber cross-sections. This imposes special requirements on the composite joint, which is to be implemented in a form-fitting sawtooth geometry as indicated in Fig. 1 (right). The geometry is created by CNC milling on the timber cross-section or corresponding formwork elements for shaping the concrete cross-section. Consequently, the cross-sections of the composite system are prefabricated separately under increased requirements for dimensional accuracy. The design of the load-bearing sawtooth-shaped composite joint is based on notched connections. Small prototypes were initially produced to investigate the manufacturability of this geometry.

2.2 Connectors and uplift restraint

Notches are TCC connectors created by milling a groove in the timber cross-section which is then concreted. The shear force in the composite joint is transmitted by pressure contact on the flank of the notch [6]. According to CEN/TS 19103 [7], notched connections must be secured vertically to prevent the cross-sections from uplift. This is usually achieved by adding a cast screw, see Fig. 2 (left), but is not possible in a prefabricated reversible composite joint.

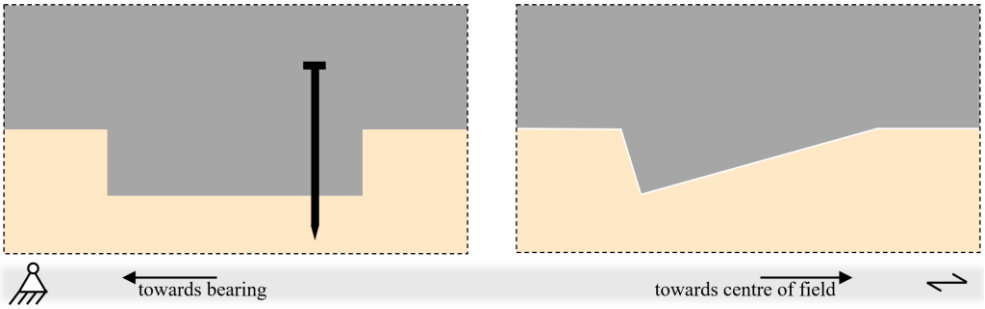


Fig. 2 Conventional notch (left), unidirectional sawtooth notch without uplift restraint (right)

Furthermore, the developed composite joint does not incorporate the inner notch flank which is not needed to transfer the shear force that is directed from the centre towards the bearing for single-span beams. With only the essentially required flank, dry jointing is simplified as shown in Fig. 2 (right). The maximum incision depth of the tapered notch is set at 20 mm in accordance with the recommendation in CEN/TS 19103 [7] for residential and office use. With a notch length of 160 mm, chosen as an analogy to existing research work [8], this results in an angle of inclination of ~8° to the vertical at notch flank with a right angle at its base. Based on the hypothesis that a greater inclination would result in less vertical tensile stress in the composite joint due to the orientation of the trajectory network, various angles of inclination were numerically investigated by the Institute of Steel Construction at RPTU. But since the uplift forces in the simulation results primarily correlated with the shear ratio of the connectors, the chosen inclination primarily serves to ensure the feasibility of dry jointing.

Moreover, another significant difference is the imperfect fit between concrete and timber, which is inevitable due to separate prefabrication. In conventional design, grouting results in a perfect match between the groove in the timber and the concrete cross-section and additionally provides adhesive bonding. A dry-jointed notch will inevitably have some misfit, leading to an unintended clearance that causes increased initial deformation in the system until all notch flanks experience pressure contact. In the worst case, a poor fit may even prevent dry jointing from being performed, or individual flanks may remain permanently inactive due to lack of contact. The extent of this clearance is therefore investigated experimentally through prototype production. In return, dry jointing can prevent increased moisture

ingress through contact with fresh concrete into areas of the notch geometry that are relevant to load-bearing capacity and stiffness.

2.3 Small-scale prototypes

To investigate the feasibility and achievable accuracy of fit, small test specimens were first produced as prototypes. For this purpose, CNC milling of the timber cross-sections and formwork elements was commissioned. As the optimisation of the sawtooth geometry had not yet been completed at this stage, flank angles of 0° (vertical) and 25° to the vertical (opening) were investigated. In addition, the composite joint was formed continuously, i.e. with a direct sequence of sawteeth, in this case 250 mm long, which later proved to be unnecessary milling work based on the performance of the connection.

As shown in Fig. 3 (left), the formwork elements were manufactured in glulam as the first prototype during the timber framing process and in PVC. By using those, concrete cross-sections in C20/25 were produced and combined with timber centre elements made of GL 24h in push-out tests (Fig. 3, right) after testing for dimensional accuracy. Because of the test setup that is supported against the cross-sections drifting apart, no relevant conclusions regarding uplift in the composite joint can be drawn from push-out tests. Nonetheless, an initial magnitude was obtained for the shear modulus of a sawtooth notch, ranging between 900 and 1.300 N/mm/mm. For comparison, CEN/TS 19103 [7] specifies 1.000 N/mm/mm for conventional notches. One of a total of three tests conducted with concrete cross-sections produced with glulam-formwork had to be excluded due to a lack of fit accuracy, which was evident in the lack of contact between the notch flanks [9].

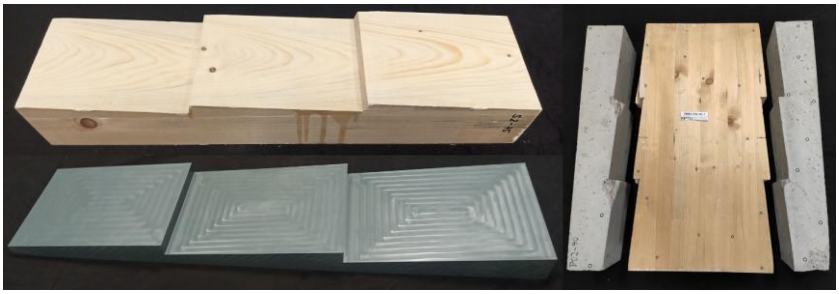


Fig. 3 25° glulam formwork element (left, top), 0° PVC formwork element (left, bottom) und tested push-out specimen (right)

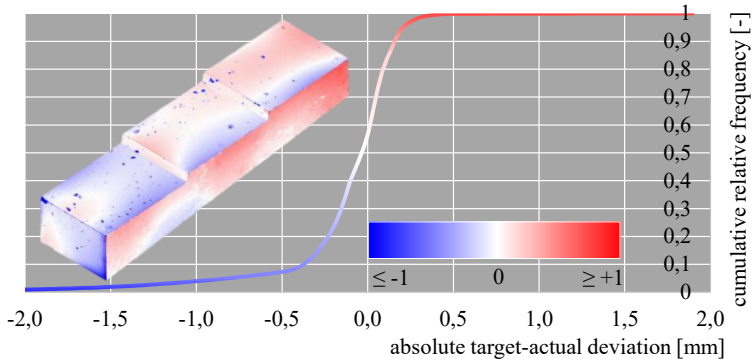


Fig. 4 Target/actual deviations [mm] on a prototypical concrete cross-section from PVC formwork, distances computed using CloudCompare [10]

To examine dimensional accuracy, the manufactured prototypes were digitised as polygonal meshes using a mobile 3D scanner and compared with ideal target models in CloudCompare [10]. Fig. 4 shows an example of the result of computed distances between target and actual geometry on a PVC-formwork concrete prototype. The colour scalar field placed on the test specimen shows the absolute deviations

in red when protruding from the target geometry and in blue when remaining under the measurements. The cumulative relative frequency distribution of the computed distances in Fig. 4, limited exclusively to the surface of the sawtooth geometry, shows that around 95% of the points have a target/actual deviation of less than +/- 1 mm. In the positive value range, there are almost no deviations from the target geometry of more than +0,5 mm. But this dimensional accuracy could only be achieved by using PVC formwork elements, which are also suitable for repeated use and do not swell when in contact with fresh concrete.

3 REAL-SCALE-CEILING TEST

3.1 Preliminary tests on beams

Given the critical requirements for dimensional accuracy, the ceiling test was preceded by beam tests with a span of 6 m. Fig. 5 shows the test setup for these 6-point bending tests, which included inductive displacement transducers at the notch flanks for measuring slip and uplift as well as in the middle of the field for measuring deflection. A total of four beams were tested, half of which were joined using fresh concrete grouting and dry jointing. The latter was implemented by wrapping the milled geometry on the glulam beam with a thin film before concreting to prevent adhesive bonding and moisture ingress. The concrete cross-sections were then exchanged between the test specimens to simulate an imperfect fit analogous to the use of a formwork system.

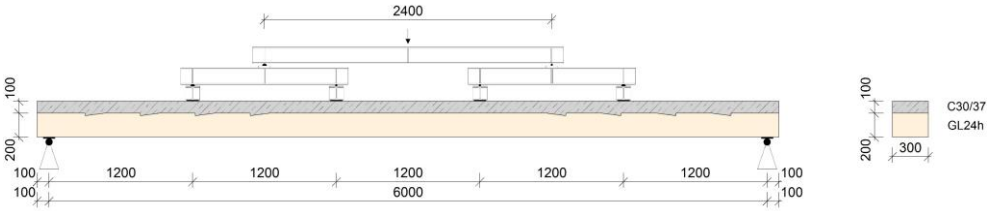


Fig. 5 Test setup for 6-point bending test [5]

As indicated by the gradient of the load-deflection diagram in Fig. 6 (left), the dry-jointed beams V03 and V04 exhibit reduced initial flexural stiffness but then align with the concreted reference beams V01 and V02 during the preloading cycles. Contrary to expectations, the concreted reference beams failed under lower loads and increased final deflections. After dismantling, compressive failure of the timber on the notch flanks was observed exclusively in the directly concreted beams. A possible explanation for this is the moisture-induced strength reduction in timber originating from contact with fresh concrete. In addition, restraint from restricted shrinkage caused cracks near the notch flanks before testing with this variant. The concrete cross-section apparently slips over the damaged material and glides up on the notch flank as the damage progresses, which leads to increased uplift in direct comparison with the dry-jointed variant (Fig. 5, right). The dry-jointed composite joints, on the other hand, show abrupt shear failure of the concrete notch.

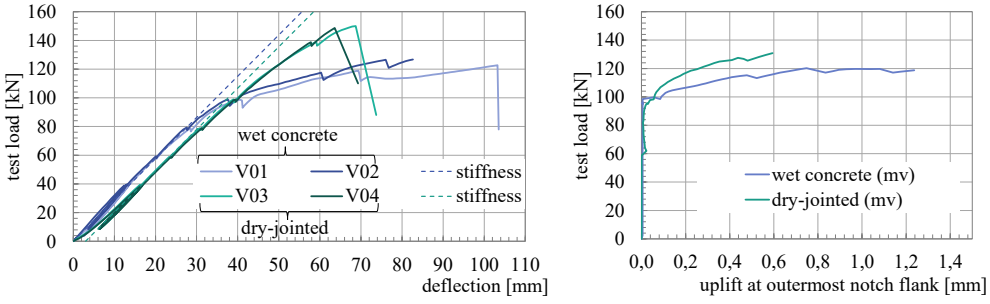


Fig. 6 Load-deflection- (left) and load-uplift-diagram (right) of beam tests

4

TEST ON CEILING STRIP

4.1.1 Pre-dimensioning

A realistic force-displacement law for sawtooth notches was derived from the beam tests, using sensor fibre optics to determine the normal force transmitted via the composite joint. The non-linear spring law was implemented into a framework-model in reference to [11] to represent the notches as discrete connectors, as schematically depicted in Fig. 7. Since this type of modelling rigidly couples the concrete and glulam cross-sections via pendulum rods to represent the composite behaviour with equal deflection, it is not possible to deduce information about uplift. The large-scale test aimed at composite joint failure, which, according to modelling, would occur at a test force of 280 kN in a 6-point bending test.

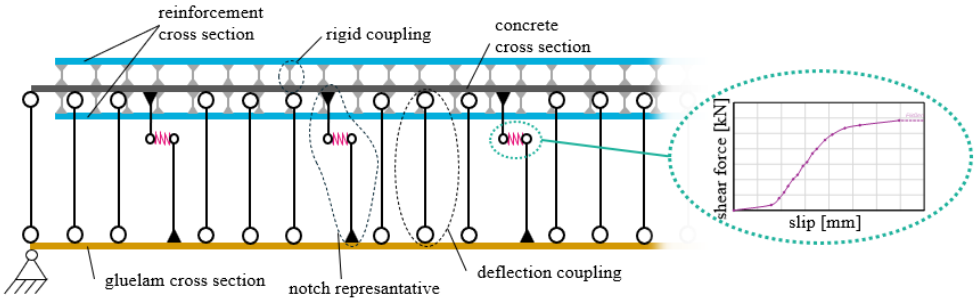


Fig. 7 Modelling scheme for framework-model of TCC with notches

4.1.2 Test specimen production

The difference to the beam tests described above lies in the design of the concrete cross-section as a 1,35 m wide slab, forming a TCC ceiling strip with two glulam beams, see Fig. 8. The film-method from producing the dry-jointed beams was again used to form the composite joint. For testing, the arrangement of the glulam beams was reversed compared to the concreting configuration. Separate transport and lifting from the formwork are decisive for the bending reinforcement and concrete strength of the slab, produced in C30/37.

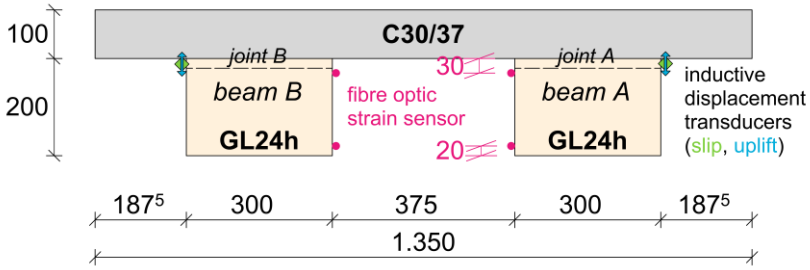


Fig. 8 Cross-section of ceiling strip test specimen [5] with labelling of beams and joints as in test

4.1.3 Experimental procedure

The test setup corresponds to that of the beam tests in Fig. 5. First, the glulam beams were placed on the supports and propped in the middle of the field with a square timber to compensate for the deflection due to their own weight. The dry jointing with the concrete slab was successful without damage or the need for reworking individual notch flanks. Fig. 9 shows a detail of a notch flank immediately before setting (left) and a view of the space between the beams (right) after the slab had been set. There was visible contact on all notch flanks, demonstrating the suitability of separate prefabrication with sufficient accuracy of fit for real scale.

The main test was preceded by two preloading tests, loading the ceiling strip with 30% of the predicted failure load in each of three load cycles with dis- and reassembly in various combinations in

between. By rotating the ceiling slab around its centre point, another joint configuration was examined besides from the beam replacement, which was not identical to the concreting configuration. This was also feasible without any signs of an inadequate fit.



Fig. 9 End of dry jointing

Finally, the concrete slab was placed in the first joint configuration and loaded to failure after two preloading cycles at 40% of the preliminary design load. At just under 350 kN, roughly six times ULS load level for residential and office use, the composite joint failed due to end shear failure of the timber at one end face, see Fig. 10 (left). Simultaneously, concrete breakout failure around the outer notch flanks occurred at the other end of the joint as shown in Fig. 10 (right). After that, a load of approx. 340 kN could still be maintained during a further displacement increase of just under 20 mm deflection before one of the glulam beams failed in bending tension. After dismantling, several glulam notch flanks displayed compressive failure.



Fig. 10 end shear failure and bending tension failure (left), concrete breakout failure (right)

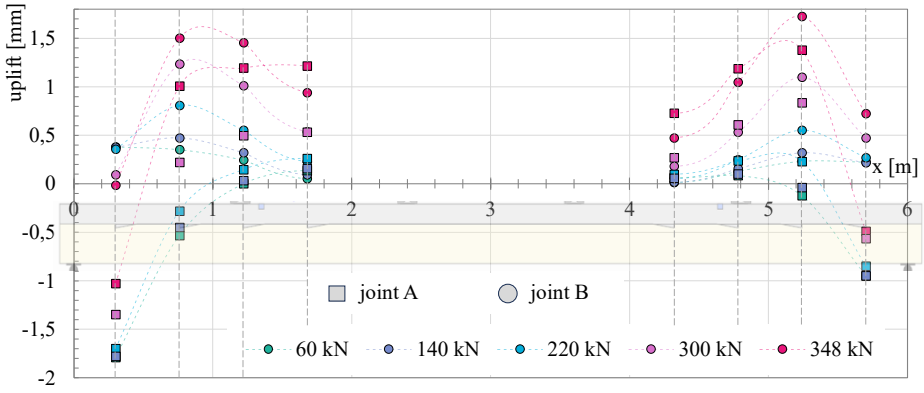


Fig. 11 Uplift at the measuring points (notch flanks) along the composite joints A and B at selected load levels

Firstly, it should be noted that despite the absence of any uplift restraints and the dry jointing without any adhesive bond, there was no uplift failure. Fig. 11 shows the detected uplift on each of the eight notch flanks per beam at selected load levels and under maximum load (348 kN). The maximum uplift measured is 1,8 mm and occurred on the second outermost notch flank in joint B. Overall, it is noticeable that the uplift at the innermost and outermost notch flanks tends to be significantly lower. In this context, it is worth noting that negative uplift is reported, which results from the dry-jointing leaving a vertical gap of approximately 2 mm towards the bearings of beam A. While removing the propping to release self-weight of the ceiling strip, the vertical gap closed, causing initially negative measuring values for uplift.

According to the model representation of composite structures with non-rigid connectors, the shear stress distribution and thus also the slip increases from the centre of the field towards the bearings. According to Fig. 12, the slip measurements of the bending test approve this hypothesis. This implies that, even in the full-scale test, there was a sufficiently evenly distributed fit on the notch flanks. Nevertheless, the graphs initially curving significantly to the left in the slip measurement are a symptom of relevant clearance on the notch flanks, allowing for increased slip at the beginning. At approx. 80 kN vertical load, all 4 measurement curves indicate an approximately linear-elastic force-slip behaviour. In the recalculation of the test, which was based on sensor fibre optical measurements on the glulam beams to determine the inner stress resultants, the normal force and deflection of the ceiling strip under investigation could be correctly predicted by adding 0.5 mm initial displacement before activation of a displacement modulus of 800 N/mm/mm at the notches in the framework-model shown in Fig. 7.

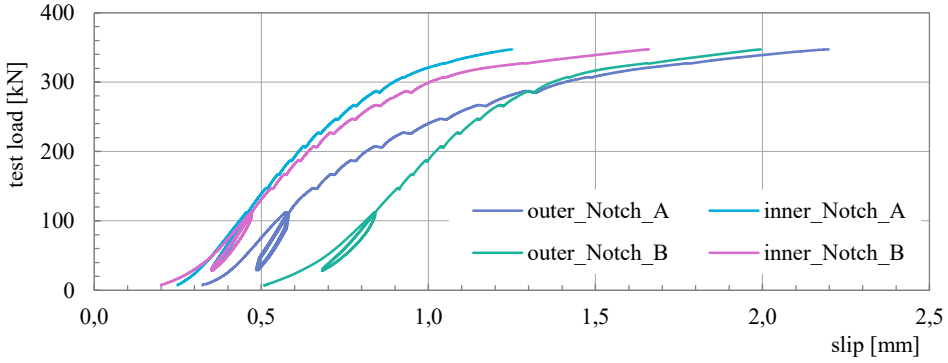


Fig. 12 Average load-slip-diagram at the innermost and outermost notch flanks of beam A and B

Similar to the observations in the beam tests, there appears to be a correlation between the tendency for uplift to increase from the middle of the field towards the outer sections of the beam analogous to the shear ratio and damage increase of the notch flanks. This is supported by the observation of compressive failure on the glulam notch flanks after dismantling the ceiling strip and the observed correlation between damaged compressive flanks and increasing uplift. In contrast, it is noticeable in Fig. 11 that the uplift on the outermost flanks is significantly lower than the values at the adjacent measuring points, while however slip increases towards the bearing. Although the timber cross-section is held in a vertical direction by the bearing in 30 cm horizontal distance to the notch flank, there is no comparable reduction in uplift at the second innermost notch flank, which is located directly below the load introduction structure. The fact that there is hardly any uplift at the outermost notch flank might be related to the transfer of the shear force coming from the centre of the beam being completed there. Assuming that the last diagonal concrete strut is transferred to the timber cross-section via the outermost flank and then into the bearing, there is no need for another vertical tension strut to further spread the load. At the bearing, the pressure trajectories of a monolithic beam extend downwards nearly vertically. In addition to that, the curvature as well as the deflection are minimal at the bearing and maximal at the centre of the field for single span beams. Uplift can be understood as a deviation from the principle of equal deflection of the cross-sections. Therefore, a direct correlation between uplift and the occurrence of deflection, which is prevented at the bearing, seems plausible. A precise connection between those variables and the uplift might be not directly identifiable because of interference with the noted tendency for uplift to increase simultaneously with the shear ratio of the connectors. Ultimately, the

possibility to receive negative measuring values for uplift due to the dry-jointed composite joint closing vertically after releasing the propping further complicates evaluating the results.

5 CONCLUSIONS AND PROSPECTS

The experimental investigations on prototypes and full-scale test specimens served to demonstrate the feasibility of a reversibly dry-jointed TCC ceiling system in terms of both dimensional accuracy and the absence of uplift restraints. There is inevitably some clearance at the notch flank due to separate prefabrication, which reduces the initial stiffness of the composite joint. By using suitable formwork, this can be limited to such an extent that all notch flanks of the tested ceiling strip could be activated despite imperfect form fit. At less than 10% of the incision depth, uplift was far from originally causing the ceiling strip to fail. However, there is currently no established modelling method to accurately estimate uplift, so this will be the subject of further investigation in the context of the hypotheses put forward. Furthermore, the composite joint geometry will be revised to reduce the increased initial deformations and therefore improve the ceiling system's serviceability, especially regarding increased service life.

Acknowledgements

This research is funded by the Federal Institute for Research on Building, Urban Affairs and Spatial Development on behalf of the Federal Ministry of Housing, Urban Development and Construction with funds from the "Zukunft Bau" program. The project team gratefully acknowledges Brüninghoff for the provision of the milled glulam beams.

References

[1] Hegger, Josef, Glock, Christian, Curbach, Manfred, Fischer, Oliver, Haist, Michael, Leutbecher, Torsten, Mark, Peter, Scheerer, Silke, Forman, Patrick, Sanio, David, Müller, Rebecca, Sinning, Annkathrin, and Schmidt, Christopher. 2025. "Innovativer Betonbau – Tradition und Zukunft." Bauingenieur 100(7-8):181-95. doi: 10.37544/0005-6650-2025-07-08-15.

[2] DIN EN 15643. Sustainability of construction works – Framework for assessment of buildings and civil engineering works; German version EN 15643:2021.

[3] Bundesministerium für Wohnen, Stadtentwicklung und Bauwesen. 2024. ÖKOBAUDAT dataset "Laminated timber planks coniferous wood (generic); Glued laminated timber. UUID 86138863-3c1c-4345-9ae9-03ba28a5f9a7. Accessed 09.02.2026.

[4] BBSR. 2023. "Zirkulare H(R)BV-Decke. Vollständig wiedereinsetzbare Holz-Beton-Verbund-Decke unter Verwendung von nachwachsenden und rezyklierten Baustoffen zur Umsetzung der Kreislaufwirtschaft im Bauwesen." Accessed 9.02.2026. https://www.zukunftbau.de/projekte/forschungsfoerderung/1008187-2209

[5] BBSR (Ed.). 2025. "Zirkulare H(R)BV-Decke. HBV-Decke mit formschlüssiger Verbundfuge ohne abhebungssichernde Verbindungsmittel." Unpublished final report (under examination), University of Kaiserslautern-Landau.

[6] Michelfelder, Birgit Christiane. 2006. "Trag- und Verformungsverhalten von Kerven bei Brettstapel-Beton-Verbunddecken." PhD diss., University of Stuttgart.

[7] DIN CEN/TS 19103. Eurocode 5: Design of Timber Structures – Structural design of timber-concrete composite structures – Common rules and rules for buildings; German version CEN/TS 19103:2021.

[8] Kudla, Katrin. 2017. "Kerven als Verbindungsmittel für Holz-Beton-Verbundstraßenbrücken." PhD diss., University of Stuttgart.

[9] Müller, Rebecca. 2024. "Reversible, kreislauffähige Holz-Beton-Verbunddecke." Presentation delivered at IAB-Tage "Beton", Weimar, November 13-14.

[10] CloudCompare (Version 2.12.4) [GPL-Software]. 2023. Retrieved from http://www.cloudcompare.org/

[11] Grosse, Marco, Hartnack, Ralf, Lehmann, Steffen, and Rautenstrauch, Karl. 2003. "Modellierung von diskontinuierlich verbundenen Holz-Beton-Verbundkonstruktionen / Teil 1:
Kurzzeittragverhalten." *Bautechnik* 80(8):534-41. doi: 10.1002/bate.200304120.

Evaluation and prioritisation of sealing elements in contact joints of precast lock chamber walls

Jacqueline Schmied[1], Stefan Lühr[1], Christoph Stephan[1], Matthias Pahn[2]

[1]Department of Structural Engineering,
Federal Waterways Engineering and Research Institute,
Kussmaulstrasse 17, 76187 Karlsruhe, Germany

[2]Department of Civil Engineering,
RPTU University Kaiserslautern-Landau,
Paul-Ehrlich-Straße, Gebäude 14, 67663 Kaiserslautern, Germany

Summary
The use of large-format precast elements in lock chamber walls is being investigated at the German Federal Waterways Engineering and Research Institute in order to make use of the known technical and economic advantages of precast construction in waterways engineering and to establish uniform principles for its use. One related issue is the technical design of the contact joints between the individual precast elements, taking into account the requirements of waterways engineering and precast construction. These combined requirements necessitate the identification of suitable joint constructions. This article presents the decision-making process for selecting the most suitable solution. The results of a comprehensive literature and product review informed a subsequent multi-criteria decision analysis including considerations of the sensitivity of the results. The analysis identified two preferred solutions: a filled elastomer hose and a reinforced grouting pocket with reinforcing bar. The following experimental procedure for testing the filled elastomer hose is outlined.

1 INTRODUCTION

Compared to conventional construction methods, building with precast elements in the sense of modular construction offers advantages in terms of manufacturing quality, construction time, waste production, CO2 emissions and water consumption, while also enabling the use of recycled materials. In order to demonstrate these advantages of a precast construction in a pilot project for structural waterway engineering and to apply them on a pilot basis, the German Federal Waterways Engineering and Research Institute (BAW) has been investigating the use of precast elements in a research and development project (R&D project) since 2020, using a lock chamber as an example [2].

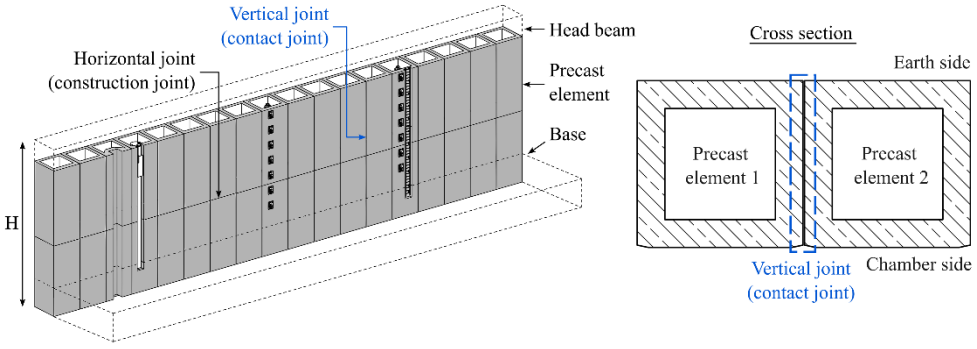


Fig. 1 Schematic representation of a section of a lock chamber with precast elements integrated into a head beam and a base

The specific use of precast elements in lock chamber walls raises the question of how the planned joints between the individual precast elements can be constructed in a manner that is robust enough to meet

the requirements of waterways engineering. As shown in Fig. 1, vertical joints always occur between the precast elements and, depending on the required height H, horizontal joints may also occur.

The use of precast concrete components in lock construction is currently found in new construction and repair work, either in the form of entire modules that are floated or lifted into place (e.g. [4]) or in the form of partially precast elements (e.g. [5]). The planned construction method for lock chamber walls using manageable, smaller precast elements weighing up to 100 tonnes without prestressing requires a new approach to joint construction. The contact joints must be re-evaluated, taking into account these specific requirements. This article assesses and prioritises suitable joint constructions.

2 METHOD

Searching for a product with a specified function and defined requirements is an everyday task in engineering. Solutions must be found, and a decision must be made on the most suitable one. According to Katicic and Ommeln [6], established approaches include intuitive methods for information gathering and discursive methods for solution evaluation, with empirical intuition consistently playing a role. One well-known discursive method is multi-criteria decision analysis (MCDA), which supports decision-making by providing a structured approach to a variety of solutions [7], [8].

The MCDA method can be applied to decision problems with a limited number of alternatives and a clearly defined objective. The alternatives represent possible solutions that are evaluated using relevant and independent criteria derived from the objective. These criteria may be quantitative or qualitative and can be scaled differently. In addition, criteria can be weighted to incorporate preferences into the decision-making process. Through normalization and aggregation, a comparable utility value is calculated for each alternative. The alternative with the highest utility value represents the preferred solution with respect to all evaluated criteria and best fulfils the defined objective [9], [10]. The main steps of the MCDA method are shown in Fig. 2. Detailed descriptions can be found in [7], [9], [10].

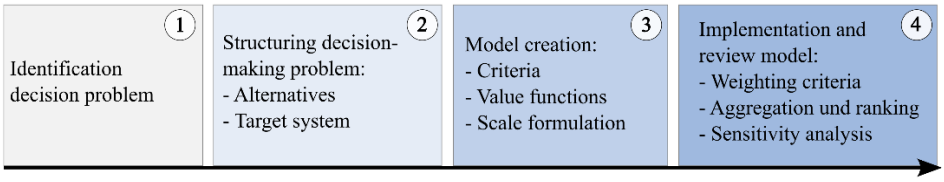


Fig. 2 Steps in the implementation of the MCDA method (based on Belton and Stewart [10])

The MCDA presented in this study to identify a design for contact joints of precast elements in waterway engineering was conducted with ten members of the steering and working group of the BAW R&D project. The group evaluated the weighting of the criteria, while seven members assessed the alternatives. This approach follows Miner [11], who showed that group averages provide a reliable basis for decision-making when the most qualified expert cannot be clearly identified.

3 APPLICATION OF THE METHOD

In order to find suitable joint designs for the precast construction of lock chamber walls and to describe defined alternatives, a literature and product review is first done. In the first step, the research serves to generate ideas freely and is initially subject to no evaluation. The research examines applications of precast concrete elements and other construction areas involving sealing systems. Key sectors include building and industrial construction, as well as bridge, tunnel, earthwork, and harbor projects. The study is complemented by expert and peer interviews on joint design and sealing solutions.

The next step requires structured decision-making because the chosen alternatives that differ in materials, shape and geometric arrangement, have advantages and disadvantages for the new waterways engineering application. At this point, the MCDA method provides structured support for the complex decision-making process leading to a preferred solution for the joint construction. Fig. 3 illustrates the individual steps and methods of this process.

To enable the respondents to analyse the individual alternatives, the specification of criteria is carried out and profiles are created for each joint construction. The criteria are developed in MCDA, taking

into account the properties required according to Belton and Stewart. For each criterion, a scale with clearly described verbal levels is defined (Fig. 4).

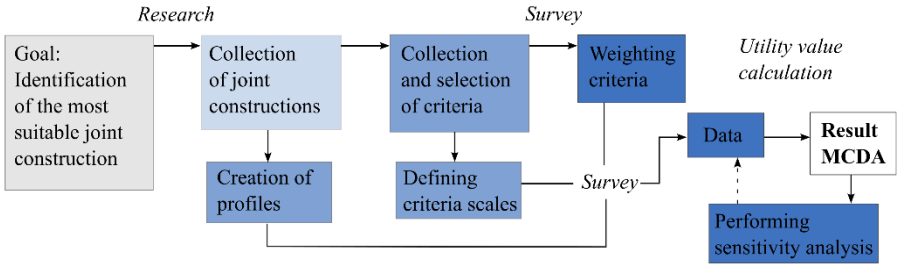


Fig. 3 Process model application of the MCDA method

Prior to the MCDA, the criteria are weighted by the respondents. The subjective weighting is collected via a web-based survey using three methods: (1) paired comparison in a preference matrix, (2) scoring on a defined point scale, and (3) direct rating by distributing a fixed number of points across all criteria. Respondents provide their assessment once to capture an unbiased opinion before discussion.

The data required for the utility value calculation is collected through individual queries using the input form shown in Fig. 4 left. In addition to evaluating each alternative, respondents also indicate the subjectively best option in terms of 'engineering intention'. The verbally defined criterion scales (e.g., Fig. 4 right) are then converted into numerical values for the utility calculation.

Alternatives	Criteria			
	C1	C2	C3	C4
1				
2			Simple	
3			Complex	
...			Difficult	
13				
14				
15				

C3: Manufacturing technologies		Value
Simple	Few components and no/simple joining technology	1
Complex	Few components and complex joining technology or multiple components and no/simple joining technology	2
Difficult	Many components and complex joining technology	3

Fig. 4 Form for evaluating alternatives (left) and example rating scale criterion C3 (right)

For this calculation, the values of the alternatives are first normalised for comparability. In a second step, the normalised values are combined using aggregation functions to present values from differently defined scales in a comparable manner. Four different normalisation methods are selected, which take into account the information about the quantitative performance differences (standardisation (Z-score), min-max, target, logistic). This is followed by a combination of five different aggregation functions (additive, geometric, harmonic, minimum, median). Since no method of normalisation or aggregation is preferred, several combinations are examined. Python scripts are used to evaluate each respondent individually, and the group evaluation is based on the mean value.

In order to evaluate the result of the MCDA with selected alternatives ranked according to utility value, the robustness of the result is finally examined using a sensitivity analysis. According to Belton and Stewart [10], the investigations can be grouped into three perspectives: technical, individual and group-related. In this application case, sensitivity considerations from the technical and individual perspectives are relevant. The technical perspective is already reflected in the utility calculation. In addition, the impact of percentage changes n in the highest-weighted criterion $W_{\max}$ is analyzed (1), while the remaining weights W_i are proportionally adjusted to maintain a total of 1 (2).

$$W_{\max,S} = W_{\max} \pm n\,\% \tag{1}$$

$$W_{\max,S} + \sum_{i=1}^{n} \frac{W_i}{x} = 1 \quad (2)$$

Following Więckowski and Salabun [12], this parameter modification approach is widely used in sensitivity analysis. To assess sensitivity at the individual level, MCDA results are compared with respondents' 'engineering intention'.

4 RESULTS

For the joint construction of precast elements in waterways engineering, 15 alternatives were collected. A key challenge is that the requirements and application context are not yet fully defined. The various joint constructions differ in terms of their position in the chamber wall, material and shape. They can be installed on the earth side or chamber side, as well as in the contact joint between the precast elements. Furthermore, they can be made out of plastics including elastomers, steel with and without concrete, as well as clay or clay-like materials. In terms of their shape, the constructions with sealing elements can be either flat or profiled, and can be effective with or without external prestressing. The following 15 hard and soft alternatives are being considered for the decision-making process.

- Contact joint: Flat console with compression sealing profile (CSP) (1), spatial console with CSP (2), CSP with hollow chambers (3), profiled prestressed CSP (e.g. lips, GINA) (4), filled elastomer hose (5), clay or swelling clay granulate core (7), swelling joint tape (10), reinforced grouting pocket with reinforcing bar (14), geometrically interlocked mortar joint (15)
- Earth side: Liquid soil (6), geosynthetic clay liner (8), polymeric geosynthetic barrier (11), sheet pile (12)
- Chamber side: Clamped joint tape (9), clamped steel sheet (13)

Five selected alternatives are described in detail below:

- (3) CSP with hollow chambers: There are recesses in the contact area of the precast elements. The elastic profile with hollow chambers is fixed in these recesses. The hollow chambers promote its sealing effect through external compression.
- (5) Filled elastomer hose: There are opposing recesses in the contact area of the precast elements. An elastomer hose is inserted into the centre of these recesses. It is then filled with a liquid or mortar and pressed into the recesses by applying internal pressure.
- (8) Geosynthetic clay liner (GCL): On the earth side, overlapping GCL can be installed over the entire surface to seal the precast walls. A GCL is a composite mat made of needled geotextiles and a swellable waterproof material. When exposed to water, the swelling process is activated and the GCL acts as a seal.
- (9) Clamped joint tape: A clamped joint tape can be installed on the chamber side, which is attached to the precast elements by means of steel tabs and screws and bridges the joint, sealing it spatially.
- (14) Reinforced grouting pocket with reinforcing bar: Opposite recesses are provided in the contact area of the precast elements, from which integrated stirrup reinforcement protrudes. When the precast elements are placed side by side, they overlap and are additionally secured with steel bars. The recesses are filled with mortar and sealed with joint filling plates.

Based on ZTV-W LB 215:2025 [13], two joint constructions are planned for each contact joint. The following four criteria (C) are selected for the implementation of the MCDA [14]:

- C1: Probability of damage occurrence
- C2: Number of work steps on the construction site
- C3: Manufacturing technologies
- C4: Inspection options, maintenance and early damage detection

The survey on the weighting of the four criteria shows the following result: C1 receives the highest weighting with an average value of 0.35. This is followed by C4 with 0.27. C2 and C3 are both weighted lowest with a value of 0.19.

The MCDA is based on the data sets of the respondents, in which each alternative is evaluated against all four criteria. Each combination of normalisation method and aggregation function generates a ranking of alternatives per person and is included in the MCDA as partial results [14]. In order to find preferred solutions, the best ranking is analysed comparatively across all combinations. Fig. 5 summarises how often an alternative achieves rank 1 or rank 2 for the group mean. The two alternatives – the filled elastomer hose (5) and the reinforced grouting pocket with reinforcing bar (14) – are the most frequently rated as the best option and are regarded as the preferred solution.

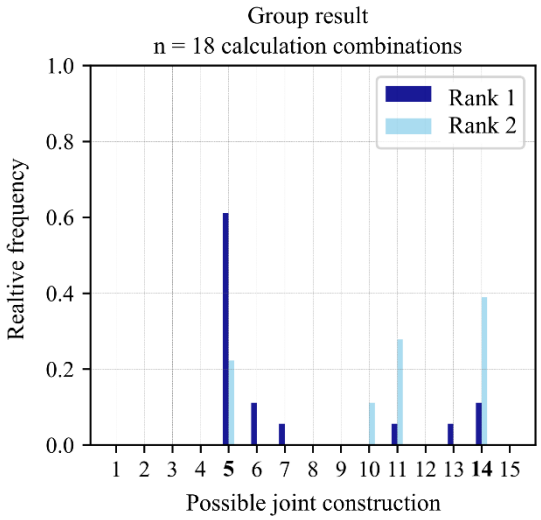


Fig. 5 Group result from the MCDA: relative frequency of rank 1 and 2 for each possible joint design

These solutions favour both a soft and a hard design option with a sealing element located in the contact joint between the precast elements. Fig. 6 shows detailed sketches of the joint designs to be pursued. The contact joint does not have to transfer any loads, as this is done via the base and the head beam (Fig. 1).

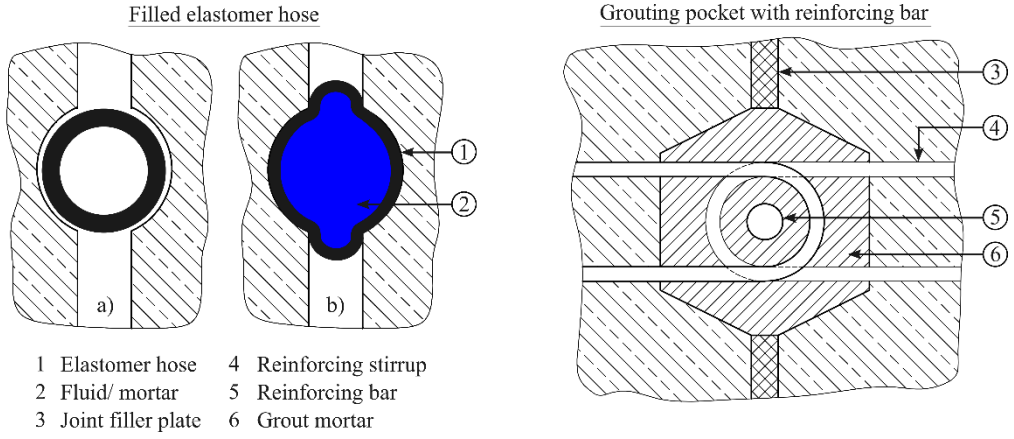


Fig. 6 Detailed sketch of filled elastomer hose in installed (a) and final state (b) (left) and reinforced grouting pocket with reinforcing bar (right)

The filled elastomer hose (Fig. 6 left) allows movement to be absorbed by the elastic properties of the hose itself and by possible elastic fillings. In the case of the reinforced grouting pocket with steel bars (Fig. 6 right), cracks would form in the grouting mortar when the precast elements move out of alignment, activating the existing joint reinforcement. The reinforcement would limit the crack width so that the water impermeability of the joint is maintained. The advantage is that the joint is not subjected to early stress in precast construction and the deformation stress is therefore considerably lower overall than in in-situ concrete construction.

In the final step, MCDA sensitivity is assessed by varying the highest-weighted criterion and comparing intuitive preferences with group results. For criterion C1, the weight is varied by ±5 percentage points (W1 = [0.38–0.48]). Two individuals show deviations, but the group mean remains unchanged. The comparison between the intuitive preferred solution and the group result of the MCDA in Fig. 7 reveals strong agreement: five of seven participants intuitively prefer alternatives 5 and 14. Compared to the MCDA result (Fig. 5), alternative 14 dominates here.

In light of these two considerations, the result of the MCDA can be described as robust.

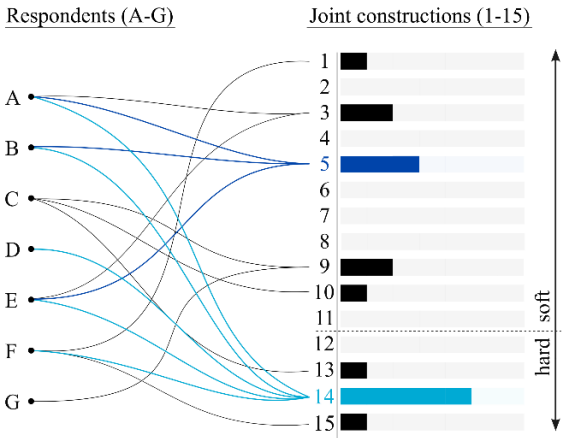


Fig. 7 Result of ‘engineering intention’ query

5 EXPERIMENTAL INVESTIGATIONS

The MCDA method is used to identify the most likely joint design. To further evaluate this solution, additional investigations are required. As a first step, the filled elastomer hose will be tested in an experimental setup to assess the performance of the system under predefined conditions.

Due to the environment of locks and the intended use, the sealing element is exposed to chemical, biological, and mechanical stresses. The hose material must withstand weathering, seasonal temperature variations and fluctuating humidity without significant changes of the material due to ageing, ideally over a service life of 100 years. An EPDM (ethylene propylene diene monomer) elastomer is therefore selected, offering good resistance to weathering, mechanical stress and temperature that is mainly used in expansion joints of underground structures [15].

For application in locks and precast concrete elements, the sealing element should be installed on site and positioned within the contact joint to protect it from mechanical damage. It must reliably seal water pressures for chamber wall heights up to 17 m enabling a drop height of 10 m [3]. At the same time the joint construction has to balance geometric differences caused by manufacturing tolerances and offset deformation, including a safety factor for the design load.

The experimental setup in Fig. 8, currently under construction, will test the sealing element at a geometrical scale of 2:3. To ensure circumferential watertightness, the EPDM hose is hot-vulcanised into a ring with connections for valves and placed in semicircular recesses in the lower and upper concrete plate (each plate: w/d/h = 120/80/12 cm). The upper concrete plate is positioned using spacers. The hose and the joint gap are filled with water, while pressure is controlled by a pump via two filling lines. Spindles mounted on the surrounding steel frame allow horizontal and vertical movement of the upper plate.

Initial tests will determine the hose pressure required for the design water pressure in the joint. In a second step, deformation will be manually increased until leakage occurs. Water pressure and displacement will be recorded by sensors.

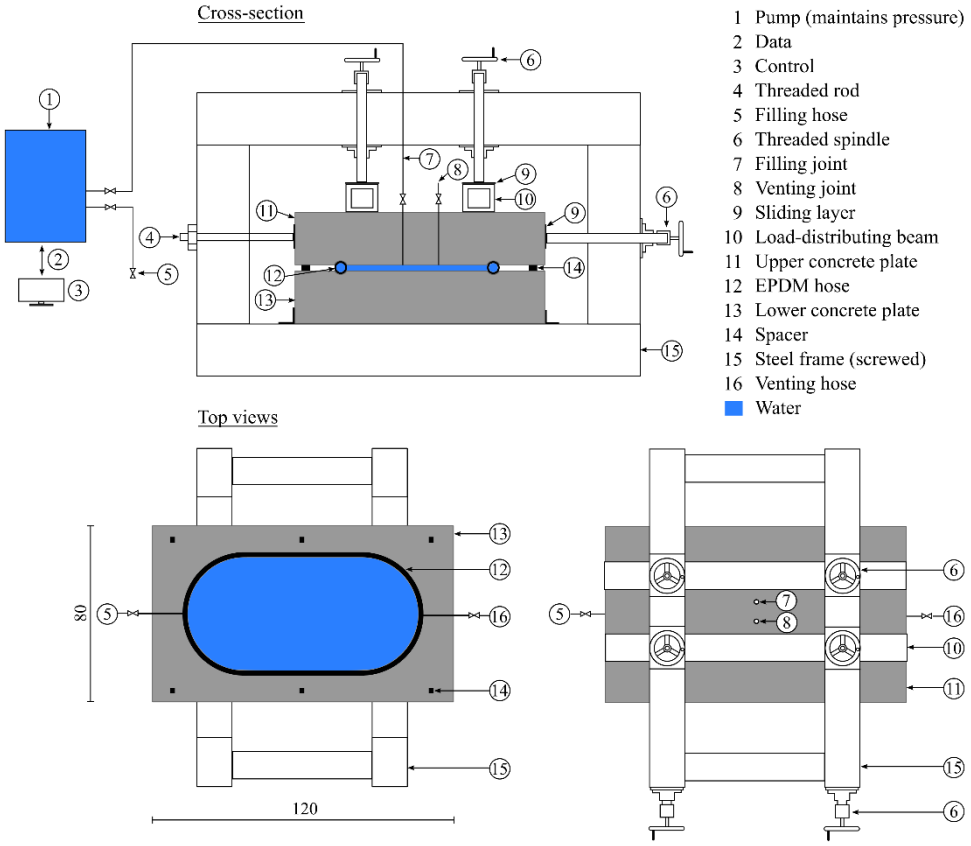


Fig. 8 Experimental setup to test the filled elastomer hose with waterpressure and displacement

6 DISCUSSION

The presented decision-making process is one possible approach for identifying preferred solutions from a wide range of alternatives. However, limited knowledge of alternatives and requirements, along with a reduced response rate, constrains the validity of the evaluation. As the results derived from the MCDA proved to be robust in the sensitivity analysis, the scope can be considered appropriate for this particular application.

For future use, a larger data basis and clearly defined requirements for the joint designs prior to the evaluation are recommended to improve evaluations. The approach is recommended in retrospect because the result allows the evaluation of known and innovative alternatives. The alternatives 5 and 14 are identified as preferred in both, the MCDA and according to the 'engineer intention', but in different order of preference. The MCDA methodology enables the integration of empirical knowledge, supports its structured use and at the same time protects the result from hasty and simplistic criticism, as the decision-making process is documented in a transparent and comprehensible manner.

The presented experimental setup will test the filled elastomer hose as one preferred solution under representative conditions. However, this setup will not test long-term performance, changing temperatures or the actual geometry. Despite these limitations, it is expected to generate data that will help to evaluate the system for real application.

7 CONCLUSIONS

This article presents a decision-making approach for a water-impermeable joint between precast elements in lock chamber walls, supported by MCDA. Ten members of the steering and working group of the BAW R&D project are interviewed. The alternatives identified are explained to the respondents using profiles so that they can be evaluated using criteria. The MCDA produces a ranking of the alternatives based on the group mean value. The robustness of the results is examined using known sensitivity analysis methods. When weighting the criteria, respondents prioritised damage occurrence and early detection during operation over production effort and required technologies. The MCDA identified two preferred solutions: filled elastomer hose and reinforced grouting pocket with reinforcing bar. The preferred solutions identified are considered the most likely to be suitable and are subjected to a detailed technical assessment with experimental investigations. The ability to combine these solutions and apply them multiple times within a contact joint is considered. For future applications of the MCDA method, an expanded database is recommended. The application of the methodology proved to be of added value, as it incorporates empirical knowledge. As a structured, transparent and experience-based approach, MCDA is recommended as support for decision-making in similar processes.

References

[1] Zohourian, Mohammadamin et al. 2025. “Modular Construction: A Comprehensive Review.” *Buildings* 15:12-2020.

[2] Lühr, Stefan et al. 2020. “Einsatz von Fertigteilen im massiven Verkehrswasserbau.” *Bautechnik* 97:6-404.

[3] Kaiser, Maximilian et al. 2025. “Innovative Schleusenkammerkonstruktion mit Einsatz von Fertigteilen.” Paper presented at 48. Dresdner Wasserbakolloquium. Technische Universität Dresden, Institut für Wasserbau und technische Hydromechanik, Dresden, March 6-7.

[4] PIANC. 2025. *Design of Navigation Locks – InCOM Working Group Report N° 206*. Brussels.

[5] ABAM Engineers. 1987. *Design of a Precast Concrete Stay-in-Place Forming System for Lock Wall Rehabilitation - Technical Report REMR-CS-7*. US Army Corps of Engineers. Washington.

[6] Katicic, Jurica, and Ommeln, Miriam. 2013. “Die Rolle der Intuition des Ingenieurs in der Designphase.” *Wirtschaft und Technologie im Dienst der Gesellschaft*. Sofia, S. 176–184.

[7] Cinelli, Marco et al. 2021. “MCDA Index Tool: an interactive software to develop indices and rankings.” *Environment systems & decisions* 41:1-82.

[8] Basílio, Marcio P. et al. 2022. “A Systematic Review of the Applications of Multi-Criteria Decision Aid Methods (1977–2022).” *Electronics* 11:11-1720.

[9] Geldermann, Jutta, and Lerche, Nils. 2014. *Leitfaden zur Anwendung von Methoden der multikriteriellen Entscheidungsunterstützung – Methode: Promethee*. Göttingen.

[10] Belton, Valerie, and Stewart, Theodor J. 2002. *Multiple criteria decision analysis: An integrated approach*. Dordrecht: Springer-Science+Business Media, B.V.

[11] Miner, Frederick C. 1984. “Group versus Individual Decision Making: An Investigation of Performance Measures, Decision Strategies, and Process Losses/Gains.” *Organizational behaviour and human performance* 33-112.

[12] Więckowski, Jakub, and Sałabun, Wojciech. 2023. “Sensitivity analysis approaches in multi-criteria decision analysis: A systematic review.” *Applied Soft Computing* 148:110915.

[13] ZTV-W LB 215 2025. Zusätzliche Technische Vertragsbedingungen - Wasserbau für Wasserbauwerke aus Beton und Stahlbeton (Leistungsbereich 215). Bundesministerium für Verkehr. Karlsruhe.

[14] Schmied, Jacqueline et al. 2026. “Vorgehensweise zur Bewertung von Lösungen für Fugenabdichtungen von Schleusenkammerwänden aus Fertigteilen.” *Bautechnik* 104:5.

[15] Klawa, Norbert, and Haak, Alfred. 1990. *Tiefbaufugen: Fugen und Fugenkonstruktionen im Beton- und Stahlbetonbau*. Berlin: Ernst & Sohn Verlag für Architektur und technische Wissenschaften.

Dry Interlocking Joint for CFRP-Reinforced Modular Component: Tensile Testing with Computed Tomography and Digital Image Correlation

Aya Ragab[1*], Frank Liebold[2], Szymon Grzesiak[3], Lore Zierul[4], Christoph de Sousa[3], Matthias Pahn[3], Birgit Beckmann[4], Viviane Adam[1]

[1]Institute of Structural Engineering, chair of Concrete Structures, Kassel University, Kurt-Wolters-Straße 3, 34125 Kassel, Germany*

[2]Institute of Photogrammetry and Remote Sensing, TUD Dresden University of Technology 01062 Dresden, Germany

[3]Department of Civil Engineering, RPTU University of Kaiserslautern-Landau Paul-Ehrlich-Straße 14, 67663 Kaiserslautern

[4]Institute of Concrete Structures, TUD Dresden University of Technology 01062 Dresden, Germany

Summary

The growing use of *Carbon Fiber Reinforced Polymers* (CFRPs) in concrete structures highlights limitations of yield-based design approaches. In discontinuity regions, plasticity-based Strut and Tie Models (STM) are challenged by the linear-elastic and brittle behavior of CFRPs, motivating the investigation of alternative stress transfer mechanisms. This study investigates the tensile behavior of a CFRP-reinforced dry interlocking concrete joint. Three carbon concrete beam specimens with an interlocking joint inspired by the *Osaka Jo Tsugite* timber joint were tested. Surface deformation was measured using *Digital Image Correlation* (DIC), while internal crack development and contact evolution were examined using *Computed Tomography* (CT). The results illustrate the progression of damage from crack initiation at geometric stress concentrations to changes in internal contact conditions and load transfer mechanisms. By correlating DIC measurements with ex situ CT observations, the study demonstrates the feasibility of a combined experimental methodology for investigating damage evolution in CFRP-reinforced dry interlocking concrete joints.

1 INTRODUCTION

Carbon Fiber Reinforced Polymer (CFRP) reinforcement enables slender, corrosion-resistant concrete members and supports material-minimized structural concepts. Recent research initiatives in *Carbon Reinforced Concrete* (CRC) have demonstrated its potential for efficient load-bearing systems and novel design strategies [1–3]. However, the predominantly linear-elastic and brittle behavior of CFRP-reinforced concrete fundamentally limits plastic stress redistribution compared to conventional steel-reinforced systems [4,5].

In discontinuity regions, where classical beam theory is no longer applicable, load transfer is described using *Strut and Tie Models* (STM) [4,5]. These plasticity-based models rely on reinforcement yielding to redistribute internal forces. For CFRP-reinforced members, the absence of yielding challenges these assumptions and motivates the investigation of alternative stress-transfer concepts that rely not on plastic redistribution but on geometry-controlled and contact-based load transmission.

In this context, dry kinematically interlocking joints represent a promising strategy, where tensile forces are transferred through compressive contact engagement and reinforcement tension rather than through monolithic continuity. However, the experimental characterization of the structural behavior of such systems remains challenging, as the processes governing stress transfer cannot be directly observed. A comprehensive understanding requires the integration of multiple measurement techniques to capture external deformation and cracking, internal damage development, and contact evolution, as well as reinforcement activation.

The objective of this study is to demonstrate the feasibility of a combined experimental methodology based on DIC and CT. By relating externally observed deformation and crack development to the internal damage state and contact conditions of a CFRP-reinforced dry interlocking joint, the methodology provides insight into the progression of damage from the surface to the internal

material state. Together with complementary reinforcement monitoring approaches presented in parallel studies [6,7].

2 EXPERIMENTAL PROGRAM

2.1 Joint concept and specimen geometry

The investigated specimens feature a dry interlocking concrete joint inspired by the Japanese Osaka-jo-otemon-hikae-bashira-tsugite timber joint [8], with a geometry governed by kinematic interlocking, as shown in Fig. 1c. The test specimens consisted of three prismatic CFRP-reinforced concrete beams, labeled *T1-1* to *T1-3*, each with a total length of 120 cm and a square cross-section of 15 × 15 cm (Fig. 1a,b). The dry interlocking joint is located at the mid-length of each beam, dividing the specimen into two reinforced concrete segments: joint right part (RP) and joint left part (LP), which are mechanically connected through geometric interlocking. Each segment is reinforced with custom-shaped CFRP-reinforcement elements, arranged to follow STM principles (Fig. 1d,e). Embedded anchorage elements are provided at both beam ends to enable axial tensile loading. A schematic overview of the specimen geometry, joint kinematics, reinforcement layout, and anchorage locations is shown in Fig. 1.

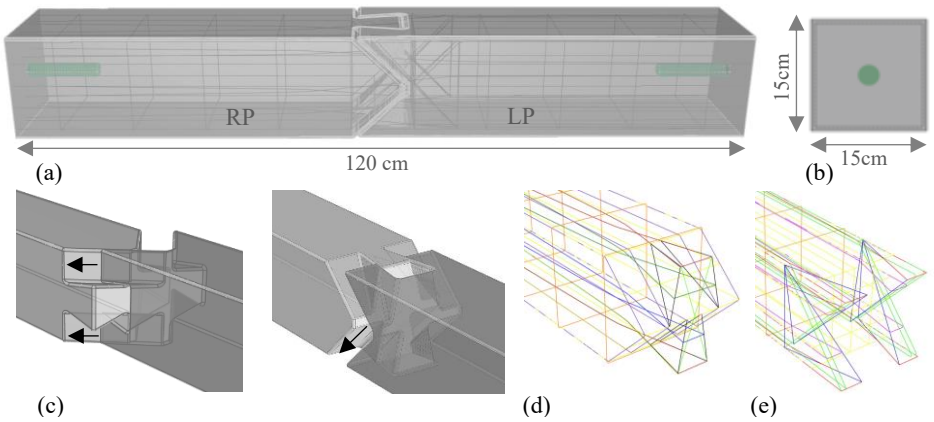


Fig. 13 CFRP-reinforced interlocking beam specimen: (a) interlocking joint geometry with left (LP) and right (RP) segments, and embedded anchors (green); (b) cross-section;(c) kinematic interlocking mechanism: (left) locking directions; (right) locking direction with respect to the test configuration; (d) RP reinforcement layout; (e) LP reinforcement layout

2.2 CFRP reinforcement layout and fabrication

Based on the joint kinematics and geometric characteristics, the CFRP reinforcement elements were individually custom-shaped (Fig. 2d,f) and locally adapted in the vicinity of the interlocking region, where the force transfer across the discontinuity is governed by geometric interlocking and contact mechanisms rather than reinforcement continuity. The resulting CFRP reinforcement cages for the right and left beam segments are illustrated in Fig. 2e,g. The reinforcement shapes differ between the two segments, reflecting the asymmetric geometry and kinematic constraints of the interlocking joint.

The CFRP reinforcement elements were manufactured as prefabricated components prior to concrete casting. Carbon fiber textiles (*Tenax-E HTS40 F13, 12K, 800 tex*) were cut according to the predefined lengths (Fig. 2a)and impregnated with a two-component epoxy resin system (*Epoxy Resin L*). Impregnation was performed to ensure full wet-out of the textile, after which excess resin was removed by rolling to achieve a uniform resin distribution (Fig. 2b).

The freshly impregnated CFRP textiles were subsequently suspended in shaping frames with end weights to obtain the required reinforcement shapes (Fig. 2c). The individual CFRP elements were then assembled to form the reinforcement layouts for each beam segment and placed into the formwork prior to concrete casting.

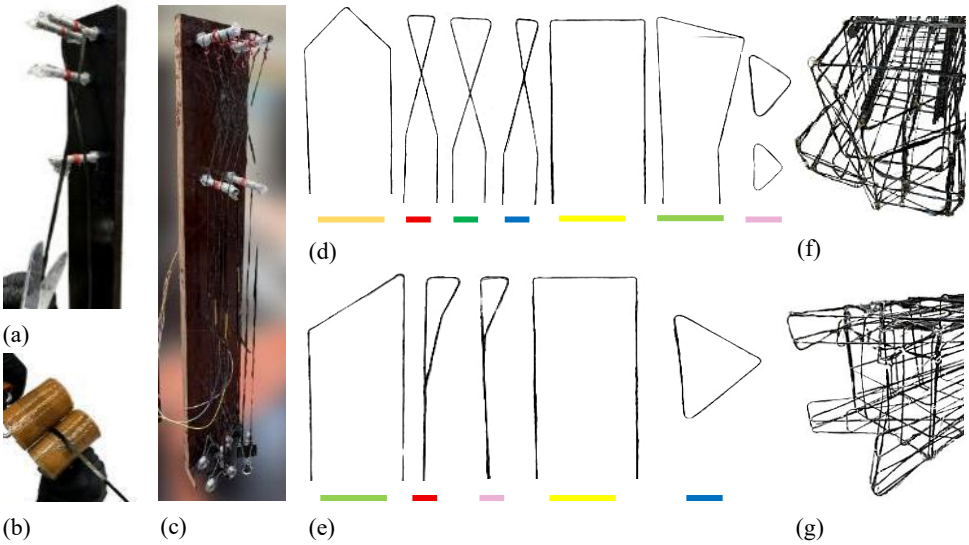


Fig. 14 Fabrication process and assembly of CFRP reinforcement elements: (a) cutting yarn to predefined lengths; (b) epoxy resin impregnation and resin removal by rolling; (c) drying stencil; (d-e) reinforcement elements for RP and LP, color-coded according to Fig. 1d,e; (f-g) assembled reinforcement cage

Uniaxial tensile tests were performed on nine CFRP textile specimens to characterize their mechanical properties. The CFRP exhibited an average tensile strength of approximately 4090 MPa, an elastic modulus of about 260 GPa, and an ultimate tensile strain of 11.63‰.

2.3 Concrete Mixture

A high-strength concrete mixture with a maximum aggregate size of 4 mm and a water-cement ratio of 0.30 was used for all specimens. Material properties were determined at 69 days from standardized tests. The corresponding mean values, specimen dimensions, and number of tests (n) are summarized in Table 1.

Table 1 Concrete mechanical properties at an age of 69 days

Property	Unit	Value	Specimen	Dimension [mm]
Mean compressive strength $f_{cm,69d}$	MPa	120.8	Cube (n=2)	150x150x150
Compressive strength $f_{cm,69d}$	MPa	103.2	Cylinder (n=1)	Ø150x300
Splitting tensile strength $f_{ct,sp,69}$	MPa	4.73	Cylinder (n=1)	Ø150x300
Elastic modulus $E_{c,69}$	GPa	44.5	Cylinder (n=1)	Ø150x300

2.4 Test setup

The specimens were tested under axial tensile loading using a custom-built test setup, as shown in Fig. 3. Tensile forces were introduced through threaded steel connected to the anchorage elements (M20, strength class 8.8) embedded at both beam ends. One end of the specimen was fixed to a rigid steel reaction frame (left end), while tensile loading was applied at the opposite end by manually rotating the threaded rod (right end). The symmetric alignment of the anchorage system ensured

predominantly axial force transfer across the dry interlocking joint, while unintended bending effects were minimized.

2.5 Loading protocol

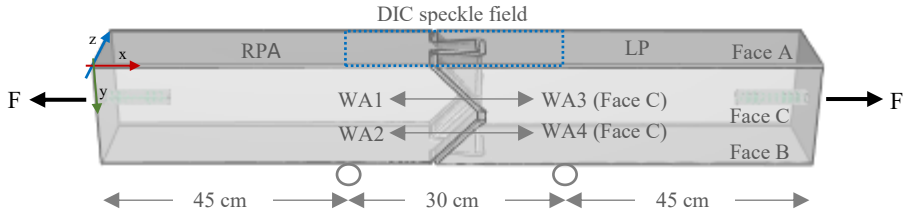


Fig. 15 Axial tensile test setup: Top (Face A); front Face B; opposite to B is Face C

The three specimens were tested under quasi-static, force-controlled loading, with average loading rates of 0.1 kN/min for T1-1 and 0.5 kN/min for T1-2 and T1-3. All specimens followed a staged loading protocol.

In the first loading stage (*Stage-1*), specimen *T1-1* was loaded to failure with intermittent pauses for inspection to determine the maximum tensile load capacity of the interlocking joint. Specimens *T1-2* and *T1-3* were loaded up to the onset of cracking or to a load level close to the maximum load identified in *T1-1*, after which loading was stopped.

Following completion of *Stage-1* for all specimens, all specimens were scanned using CT to capture internal crack development within the joint region. After scanning, specimens *T1-2 and T1-3* were reinstalled in the test setup and subsequently loaded under the same force-controlled conditions (*Stage-2*) until complete failure.

2.6 Measurement techniques

Relative axial displacement across the interlocking joint was measured using four linear variable displacement transducers (LVDTs). Two LVDTs (WA1 and WA2) were mounted on each lateral face B, and two LVDTs (WA3 and WA4) on the opposite lateral Face C of the specimen, aligned with the beam axis and arranged symmetrically around the joint region, as illustrated in Fig. 3.

Surface deformation and crack development in the joint region were monitored using two-dimensional DIC. The measurement field covered approximately 30 cm on the top surface of the specimen (Face A), as shown in Fig. 3, and was imaged using a single camera (*Pentax K70, 50 mm focal lens, measurement distance ≈ 2.18 m*) positioned perpendicular to the surface. Images were acquired at predefined load increments corresponding to the applied loading rates (0.1 kN for *T1-1* and 0.5 kN for *T1-2* and *T1-3*).

Internal damage and crack state within the joint region were investigated using ex-situ CT scanning. Scans were performed using the *Gulliver* tomography portal [9] at the RPTU in Kaiserslautern, equipped with a 9 MeV high-energy X-ray source and flat-panel detector (*Varex 4343HE*), between the two loading stages, enabling non-destructive three-dimensional imaging of the internal displacement and deformation state.

3 EXPERIMENTAL RESULTS

3.1 Load-displacement response and Surface Kinematics (DIC)

Load-displacement response and DIC-based surface deformation fields are evaluated jointly to relate mechanical behavior to crack evolution. Joint kinematics were obtained from LVDTs across the interface (section 2.6), while DIC data were post-processed using ZEISS INSPECT [10], enabled visualization of surface strain fields and crack initiation.

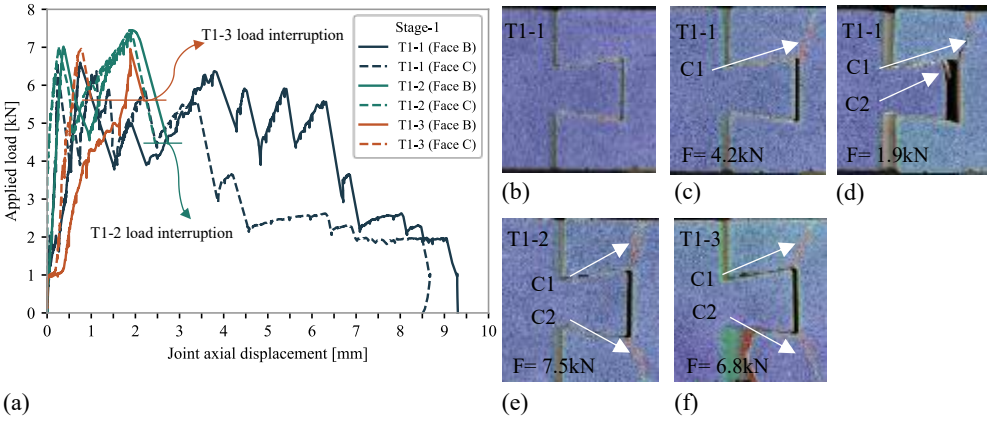


Fig. 16 Stage-1 tensile behavior: (a) load-displacement responses; (b-f) DIC crack evolution for different load stages and specimens

The load-displacement response of specimen *T1-1* (Fig. 4a) exhibits multiple load peaks associated with progressive joint engagement and crack development. An initial increase to approximately 2 kN was followed by a minor load drop without visible surface cracking, which is attributed to seating effects and frictional adjustment of the interlocking contact surfaces rather than concrete cracking.

Reloading led to a second peak at approximately 4 kN, accompanied by localized opening on Face B, indicating the onset of relative slip and partial redistribution of contact stresses within the joint. The maximum load of approximately 6.8 kN (Fig. 4b) was reached prior to visible surface cracking. The primary crack (C1) subsequently initiated at the re-entrant corner of the upper tooth (Fig. 4c).

Following crack initiation, stiffness degradation and asymmetric displacement development between Face B and Face C were observed. DIC measurements revealed slight rotation of the joint segments and modified contact engagement along the interlocking surfaces.

Despite progressive crack propagation, residual load-carrying capacity remained, attributed to continued tensile stress transfer through the CFRP reinforcement combined with partial compressive contact interaction within the interlocking geometry. At later stages, a secondary crack (C2) formed at the inner corbel region on the joint RP, coinciding with the final loss of load-carrying capacity (Fig. 4d).

For specimens *T1-2* and *T1-3* (*Stage-1*), comparable peak loads of approximately 7.5 kN and 6.8 kN were recorded, respectively (Fig. 4a). The pre-peak response showed stepwise load increases reflecting contact redistribution in *T1-2*, whereas in *T1-3,* they coincided with the initiation of crack C1 at the re-entrant tooth corner (LP) due to local tensile stress concentration.

In *T1-2*, crack C1 initiated near 7 kN at the re-entrant corner of the upper interlocking tooth, followed by a pronounced load drop and increased joint slip, indicating substantial stress redistribution and rotation. Reloading led to the peak load of 7.5 kN, at which a secondary crack (C2) formed in the lower tooth region (Fig. 4e). The displacement records indicate asymmetric joint opening and the development of relative segment rotation in accordance with the previous one.

In contrast, T1-3 exhibited earlier crack initiation (C1) at approximately 4 kN. This earlier onset is attributed to initial geometric imperfections and local pre-damage at the lower tooth. Although a slip event was observed during subsequent loading, crack C2 remained less developed at peak load (6.8 kN) compared to *T1-2* (Fig. 4f). Loading of both specimens was stopped after peak response for intermediate CT scanning compared to *T1-2* (Fig. 4f). Loading of both specimens was stopped after peak response for intermediate CT scanning.

For Stage-2, specimens T2-2 and T2-3 (reloading of T1-2 and T1-3 after CT scanning), exhibited reduced initial stiffness due to the widening of the pre-existing cracks C1 and C2.

The load-displacement curves (Fig. 5a) show gradual reloading accompanied by progressive slip and joint rotation observed in the DIC analysis. For T2-2 (Fig. 5a), the load reached an initial peak of ap-proximately 5.9 kN, followed by a drop associated with widening of C1 and C2 and a localized slip event. Subsequent stress redistribution enabled a second peak of about 6.0 kN (Fig. 5b).

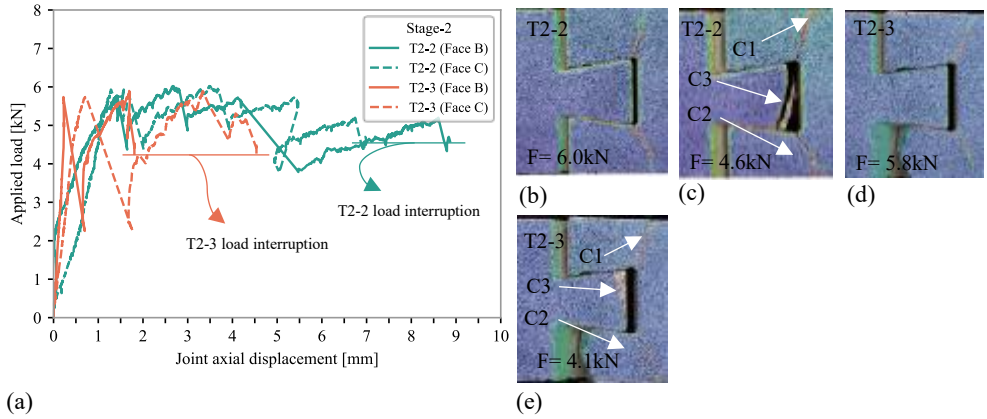


Fig. 17 Stage-2 tensile behavior: (a) load-displacement responses; (b-e) DIC crack evolution for different load stages and specimens

Continued degradation of compressive contact led to the formation of a new crack (C3) at the inner corbel of the joint RP (Fig. 5c), coinciding with rapid strength loss. Failure was governed by localized edge contact, pronounced rotation, concentrated stress transfer, and partial internal material detachment. For *T2-3* (Fig. 5a), the load increased to approximately 5.8 kN before a more pronounced drop due to major slip and reduction of effective contact. The specimen partially regained capacity and reached a second peak close to 5.8 kN (Fig. 5d). In contrast to *T2-2*, DIC observations (Fig. 5e) indicate damage remained more distributed, with slip-dominated deformation and less pronounced inner corbel crushing. The final capacity loss was governed by progressive crack opening and rotation rather than sudden material separation.

Overall, *Stage-2* behavior was controlled by widening of existing cracks, reduced compressive contact area, and rotation-induced slip. Compared to *Stage-1*, the mechanism shifted from distributed interlocking compression to localized edge contact and deformation-controlled resistance.

3.2 Internal cracks (CT-scans)

The internal crack pattern was evaluated using reconstructed CT volumes with a voxel size of 125.7 µm. Scans were performed after *Stage-1* loading to investigate internal cracking and the condition of the interlocking contact zones. The reconstructed volumes were visualized using ParaView [11]. For each specimen, multiple longitudinal slices (S1-S5), parallel to the x-axis, and transverse slices (S7-S9), parallel to the z-axis, were extracted at representative locations, as illustrated inFig. 6a.

All slices were systematically examined; only selected representative slices highlighting the most relevant crack features and contact conditions are presented in Fig. 6b-i.

For specimen T1-1, CT slices show that crack C1 penetrates the full thickness of the upper tooth, forming a full separation (Fig. 6b). In addition, a secondary crack (C3) is observed within the lower tooth on the same side (Face C), indicating that tensile stresses were transferred across both interlocking teeth on this joint side.

Crack C2 is identified at the inner corbel region (joint RP), propagating from the internal bearing interface into the surrounding concrete (Fig. 6c). Its location at the contact zone indicates a reduction of distributed compressive contact and stress concentration at the inner bearing region following crack-induced force redistribution.

Furthermore, slice S7 (Fig. 6d) may indicate localized material fragmentation, and crushed zones are at the corbel contact interfaces. This damage pattern indicates that, following tensile crack formation in the teeth, compressive stresses became concentrated at the corbel bearing zones, leading to localized compressive overstressing rather than purely tensile failure, and load transfer was no longer uniformly distributed across the full contact surface but instead occurred through reduced and localized contact areas.

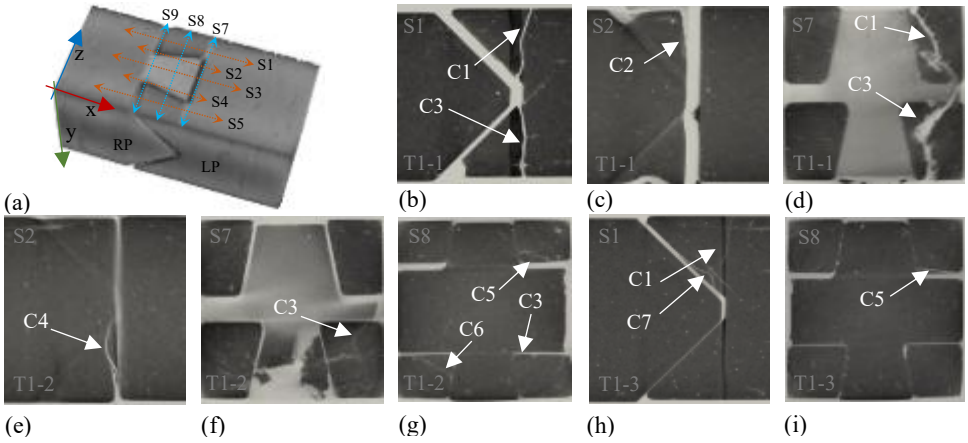


Fig. 18 CT-based internal crack assessment after *Stage-1*: (a) joint reconstructed 3D volume showing the slice locations (S1-S9); (b-d) *T1-1* representative slices; (e-g) *T1-2* representative slices; (h-i) *T1-3* representative slice

For specimen *T1-2*, CT slices reveal a more complex internal fracture network compared to *T1-1*. Crack C4 is observed at the inner corbel interface, propagating vertically along the bearing face (Fig. 6e), consistent with tensile splitting under concentrated contact stresses. In the lower tooth, crack C3 extends diagonally toward the contact region (Fig. 6f), accompanied by localized fragmentation. Slice S8 (Fig. 6g) further shows additional crack branches (C5, C6) within the tooth-corbel zone, evidencing non-uniform stress redistribution and localized contact edge loading.

Compared to *T1-1*, *T1-2* exhibits more pronounced internal crack branching at the inner bearing zone, indicating a more localized and unstable load transfer mechanism after initial tensile cracking, potentially influenced by geometric imperfections or uneven contact engagement.

For specimen *T1-3*, CT slices show that the primary crack C1 extends through the upper tooth thickness (Fig. 6h), consistent with *T1-1* and *T1-2*. In addition to C1, a secondary crack C7 is observed between the upper tooth and the adjacent corbel region (Fig. 6h), which follows a different orientation, indicating localized stress redistribution within the upper joint region rather than direct continuation of the primary tensile crack.

Transverse slices (Fig. 6i) reveal limited additional cracking within the upper tooth (C5), originating from the inner contact zone. Unlike T1-2, no pronounced fragmentation or crushing is observed at the inner corbel interface.

Compared to *T1-2*, internal branching is less extensive, and no pronounced fragmentation at the inner corbel interface is observed. Overall, *T1-3* exhibits the same primary tensile cracking mechanism at the re-entrant corner as *T1-1* and *T1-2*, but with less crack branching, reduced inner corbel damage, and more limited compressive crushing.

Taken together, the CT observations indicate that load transfer within the interlocking joint was not governed by uniformly distributed compressive contact across the full tooth surfaces. Instead, contact engagement occurred in localized zones, as evidenced by concentrated crushing at the corbel interfaces and asymmetric damage development. Following tensile crack formation in the teeth, force transmission became increasingly controlled by localized compressive bearing and rotation-induced tensile stresses. The combined tensile cracking of the teeth and compressive overstressing at the corbel interfaces governed the final failure mechanism. The asymmetric crack progression, particularly the more pronounced damage on Face C, further supports the presence of non-uniform contact engagement and rotation-driven load redistribution.

The results confirm that tensile forces can be transferred across a dry interlocking joint without reinforcement continuity through a hybrid mechanism of compressive contact within the interlocking geometry and axial tension in the CFRP reinforcement. Prior to cracking, load transfer is governed by distributed compressive engagement, while progressive cracking shifts the response toward localized

bearing, slip, and rotation-controlled interaction, making the system highly sensitive to effective contact conditions.

4 CONCLUSIONS

This study investigated the axial tensile load transfer of a dry, kinematically interlocking CFRP-reinforced concrete joint and evaluated a combined DIC-CT methodology for relating externally observed structural response to internal damage development and contact evolution.

The results demonstrate the applicability of the proposed methodology for investigating dry interlocking systems beyond the specific geometry considered in this study. The combined assessment of surface cracking (DIC) and internal damage development (CT) demonstrated the feasibility of relating externally observed structural response to the internal damage state and contact evolution within the joint, as well as the value of complementary measurement techniques for the reliable assessment of structural behavior. Although demonstrated using a specific interlocking geometry, the proposed methodology is not limited to this configuration and provides a basis for future systematic investigations of geometric effects, contact conditions, and structural performance in dry interlocking systems

Future research should therefore focus on geometric refinement and controlled contact-surface fabrication, including advanced manufacturing strategies (Robotic-assisted), as well as in-situ CT investigations under loading.

Acknowledgements

The authors acknowledge financial support from the Deutsche Forschungsgemeinschaft (DFG, German Research Foundation) within SFB/TRR 280 (Project-ID 417002380, C08) and express their gratitude to the student assistants and the technical staff of the Institute of Structural Concrete (IMB) for their assistance in preparing and conducting the tests, as well as the Institute for Textile Technology (ITA) of RWTH Aachen University.

References

[1] Beckmann, Birgit, Viviane Adam, Steffen Marx, Rostislav Chudoba, Josef Hegger, and Manfred Curbach. 2023. “Novel Design Strategies for Material-Minimized Carbon Reinforced Concrete Structures–Overview of the Research in CRC/TRR 280.” International Symposium of the International Federation for Structural Concrete, 2023, 1242–1251.

[2] Curbach, Manfred, Josef Hegger, Jan Bielak, Christopher Schmidt, Sven Bosbach, Silke Scheerer, Martin Claßen, et al. 2024. “New Perspectives on Carbon Reinforced Concrete Structures—Why New Composites Need New Design Strategies.” Civil Engineering Design 5 (5–6): 67–94.

[3] Curbach, Manfred, Josef Hegger, Frank Schladitz, Matthias Tietze, and Matthias Lieboldt. 2023. Handbuch Carbonbeton: Einsatz Nichtmetallischer Bewehrung. John Wiley & Sons.

[4] Abbood, Imad Shakir. 2023. “Strut-and-Tie Model and Its Applications in Reinforced Concrete Deep Beams: A Comprehensive Review.” Case Studies in Construction Materials 19 (December 2023): e02643. https://doi.org/10.1016/j.cscm.2023.e02643.

[5] Panjehpour, Mohammad, Abang Abdullah Abang Ali, Anwar Mohammed Parvez, Farah Nora Aznieta, and Yen Lei Voo. 2012. “An Overview of Strut-and-Tie Model and Its Common Challenges.” International Journal of Engineering Research in Africa 8 (2012): 37–45. https://doi.org/10.4028/www.scientific.net/JERA.8.37.

[6] Ragab, Aya, Till Janiak, Lore Zierul, Kira Heins, Birgit Beckmann, and Viviane Adam. 2026. “Fresh-in-Fresh Fiber Optic Sensor Embedding for Monitoring Yarn Behavior in Carbon-Fiber-Reinforced Concrete: A Feasibility Study.” Proceedings of SMAR 2026, 2026.

[7] Ragab, Aya, Lore Zierul, Birgit Beckmann, and Viviane Adam. 2026. “Interlocking Dry Joints to Assemble CFRP-Reinforced Modular Components: Pilot Study and Performance Testing.” Proceedings of the Fib Congress 2026, 2026.

[8] Seike, Kiyosi. 2025. The Art of Japanese Joinery. Shambhala Publications.

[9] Salamon, Michael, Nils Reims, Dimitri Prjamkov, Michael Schmitt, Jurij Makarov, Dennis Ak, Markus Kronenberger, et al. 2025. “Gulliver–A New Kind of Industrial CT.” Journal of Nondestructive Testing 30 (2025): 2.

[10] ZEISS Industrial Quality Solutions. 2026. “ZEISS INSPECT: Optical 3D Deformation Measuring and Inspection Software.”

[11] Ahrens, James, Berk Geveci, and Charles Law. 2005. “Paraview: An End-User Tool for Large Data Visualization.” The Visualization Handbook 717 (8).

Structural Exoskeletons for Sustainable Rehabilitation of European Cold War Sites.

Alessandra Vazzoler, Giovanni A. Plizzari, Olivia Longo, Alessandra Marini, Simone Labò

Dicacim (PhD in Civil, Environmental Engineering, International Cooperation and Mathematics),
University of Brescia,
Via Branze 43, Brescia (25123), Italy

alessandra.vazzoler@unibs.it

Summary
Cold War military sites represent an important but largely neglected component of European built heritage. Many former military bases have become abandoned and structurally vulnerable after decommissioning, while lacking systematic approaches for their preservation and adaptive reuse. This paper presents ongoing research combining the mapping of European Cold War military heritage with the case study of the former NATO base of Dosso dei Galli (Italy). A non-invasive rehabilitation strategy based on an external steel exoskeleton is proposed to improve the seismic performance of existing reinforced concrete buildings while simultaneously providing passive solar shading. Designed according to Life Cycle Thinking principles, the system promotes prefabrication, dry assembly and reversibility. The research aims to develop a transferable methodology integrating structural safety, sustainability and architectural conservation for the adaptive reuse of decommissioned military sites across Europe.

1 INTRODUCTION

Since the mid-1980s, defence authorities across Europe have progressively abandoned and decommissioned military areas and buildings, generating a growing number of "urban voids" [1]. This contraction of the military presence, particularly evident in Italy, has raised new challenges for urban management and stimulated new design demands for adaptive reuse. These sites, generally classified as nuclear weapon depots, communication and radar systems, airports, and naval or land defence structures, still lack a systematic and homogeneous body of knowledge, in particular regarding the former military network built during the Cold War.

One of the main challenges for designers today is the relationship with the existing built heritage, together with the pressing need to increase the sustainability of the construction sector. A deep, integrated renovation of the existing building stock should always be preferred to demolition and reconstruction, since it promotes safety, resilience and sustainability while overcoming structural vulnerabilities that may cause damage or collapse under natural hazards [2]. The advantage of such an approach over conventional retrofit actions emerges both during construction – avoiding the relocation of occupants – and when the analysis is extended to a full life-cycle perspective [3].

In recent years, structural upgrading through the addition of an exoskeleton has become one of the most widespread strengthening techniques for reinforced concrete buildings. The term originates from biology, where the exoskeleton is the external, protective structure of some invertebrates; the concept has since been transferred to medical biotechnology, as an aid for post-traumatic rehabilitation, and to civil engineering, where it defines a volumetric expansion, independent from the original structure but connected to it, that can be designed either adherent to the existing building or separated from it by a cavity, depending on urban constraints [4]. The exoskeleton generally consists of a steel structure with independent foundations, improving the dynamic response of the existing building and enabling an "integrated design" that involves several disciplines and professionals at once.

From a technical standpoint, the exoskeleton is a global strengthening technique: a new structure is added to the original one in the form of a double envelope, and it can be either over-resistant or dissipative depending on the initial stiffness of the building. This allows seismic improvement, energy retrofit and architectural restoration to be designed simultaneously, extending the service life of old,

highly vulnerable buildings [5], while reducing the use of raw materials and construction/demolition waste with respect to demolition-and-reconstruction scenarios [6]. Among others, Labò et al. (2021) [3] and Feroldi et al. (2014) [5] have investigated the relevance of this intervention for post-war reinforced concrete buildings.

2 AIM AND SCOPE OF THE RESEARCH WORK

The research starts from the analysis of the European network of Cold War architectural heritage. Figure 1 shows a first mapping of the military sites built during the Cold War in Europe, with reference to their NATO code. Since studies on how to preserve and reuse these sites are lacking both in Italy and in many other European countries, a systematic and homogeneous knowledge of these buildings is required. The main objective is the systematisation of the reuse processes of these places for a wide audience: the possibility of giving new life to these "urban voids" follows from the mapping of the different structural typologies present within the network, since these buildings have generally exceeded their service life and present structural and energy deficiencies.

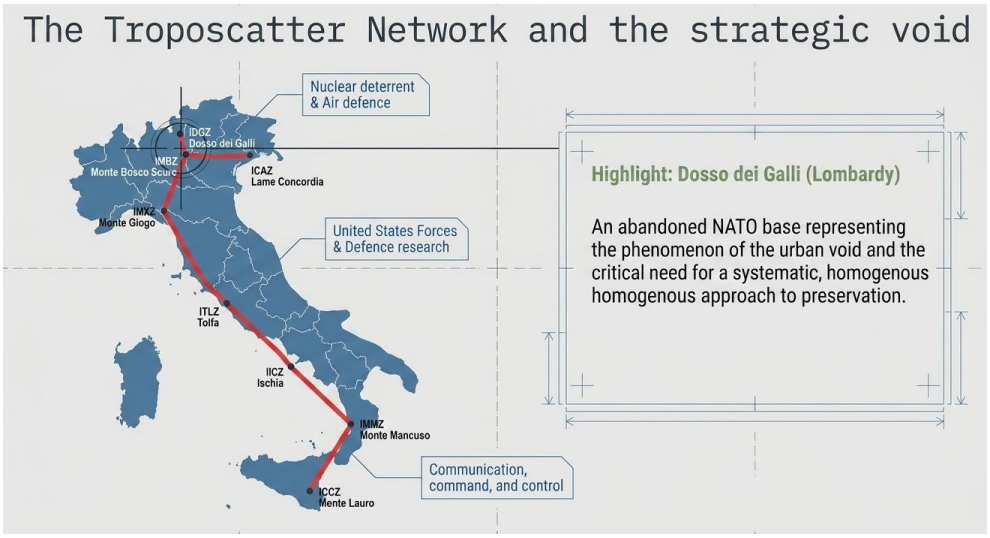


Fig. 1 Mapping of Cold War military sites

Building on this mapping, the aim is to provide an intervention and recovery proposal for a reference case study, later transferable to other mapped buildings belonging to different structural typologies, but modulated according to the geographic, urban and seismic-hazard context. The target is a solution that is a genuine alternative to conventional demolition and reconstruction, and that enables a multidisciplinary approach aimed at the structural, energy and architectural requalification of these buildings, with a focus on the enhancement of their urban context. Structural upgrading through an exoskeleton allows exactly this kind of approach, integrating structural safety with energy and architectural renovation.

To achieve maximum efficiency with minimum environmental impact, cost and life-cycle burden, the design must be accompanied by a study that considers not only the economic advantage of the intervention but also its environmental costs. Figure 2 summarises the Life Cycle Thinking criterion adopted in the research, according to which the structural design follows the principles of minimising environmental impact and cost through the use of eco-compatible and recyclable materials, prefabricated or dry technologies that are easy to disassemble, repair and adapt, together with the resolution of structural deficiencies and the provision of adequate seismic resistance [7]. In this way, the exoskeleton becomes a strategic design device, operating within a set of integrated and multidisciplinary interventions rather than as an isolated strengthening measure.

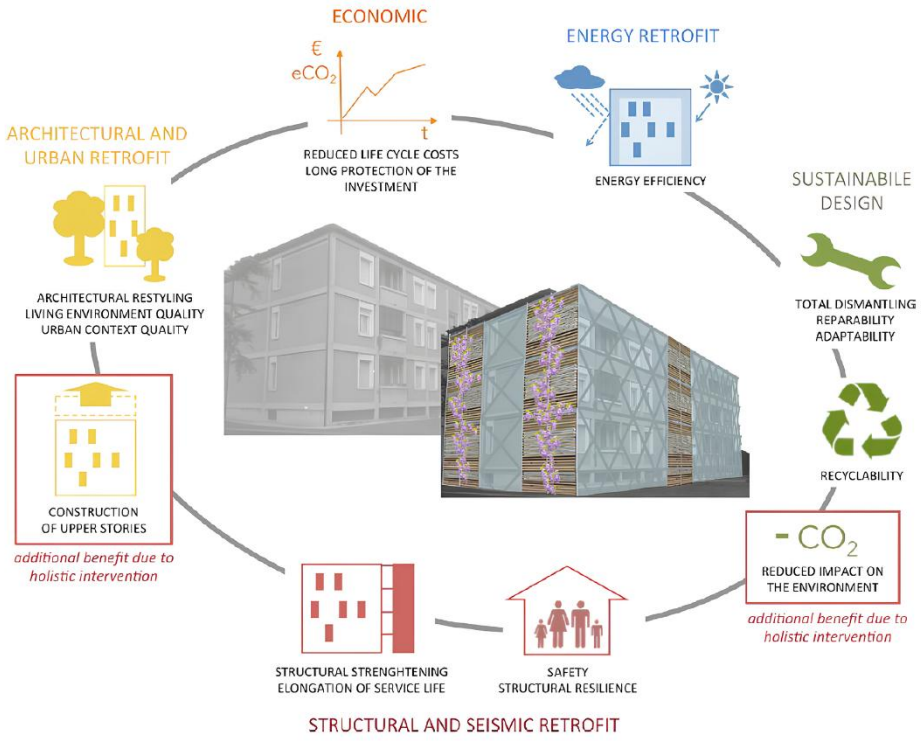


Fig. 2 Life Cycle Thinking design criterion (adapted from Bellini et al., 2018)

3 RESEARCH FRAMEWORK AND MULTIDISCIPLINARY APPROACH

The rehabilitation of decommissioned Cold War sites requires the integration of multiple disciplinary perspectives, owing to the intrinsic complexity of these environments. These complexes cannot be addressed solely as structural systems in need of strengthening, nor exclusively as architectural artefacts to be preserved: they must instead be interpreted as hybrid entities, in which structural performance, spatial configuration, environmental conditions and cultural value are deeply interconnected.

Within this context, the research adopts a multidisciplinary framework based on the interaction between architecture and structural engineering, supported by the principles of sustainability and Life Cycle Thinking. The proposed approach aims to overcome the traditional separation between disciplines by developing a unified design process, in which structural interventions are conceived simultaneously as architectural and environmental devices.

The methodological framework is articulated through a sequence of interconnected phases. First, an in-depth knowledge process is carried out, including geometric surveys, photographic documentation and preliminary material assessments, essential to understand the construction characteristics of the buildings and the main degradation phenomena. In parallel, historical and architectural analyses recognise the cultural and testimonial value of the complex, particularly in relation to its role within the Cold War military network.

Subsequently, structural assessments identify the main vulnerabilities of the existing buildings – insufficient lateral resistance, lack of seismic detailing and general structural obsolescence – which significantly compromise safety and resilience. At the same time, energy-related deficiencies and environmental discomfort are evaluated, especially considering the extreme climatic conditions of high-altitude sites.

Based on this integrated knowledge, the research explores the potential of external exoskeleton systems as a comprehensive rehabilitation strategy. Unlike conventional retrofit techniques, which often focus on isolated aspects of performance, the exoskeleton is conceived here as a multifunctional system able to address structural, architectural and environmental requirements simultaneously,

enhancing seismic behaviour without invasive interventions on the existing fabric, while offering opportunities for spatial reconfiguration, façade upgrading and climatic adaptation.

4 CASE STUDY: THE FORMER NATO BASE OF DOSSO DEI GALLI

The former NATO base of Dosso dei Galli, located in the province of Brescia, in Northern Italy, is a significant example of Cold War military infrastructure embedded within a high-altitude alpine environment. Built as part of the NATO communication and defence network, the site played a strategic role during the Cold War, functioning as a radar and transmission station within a broader European system of surveillance and control.

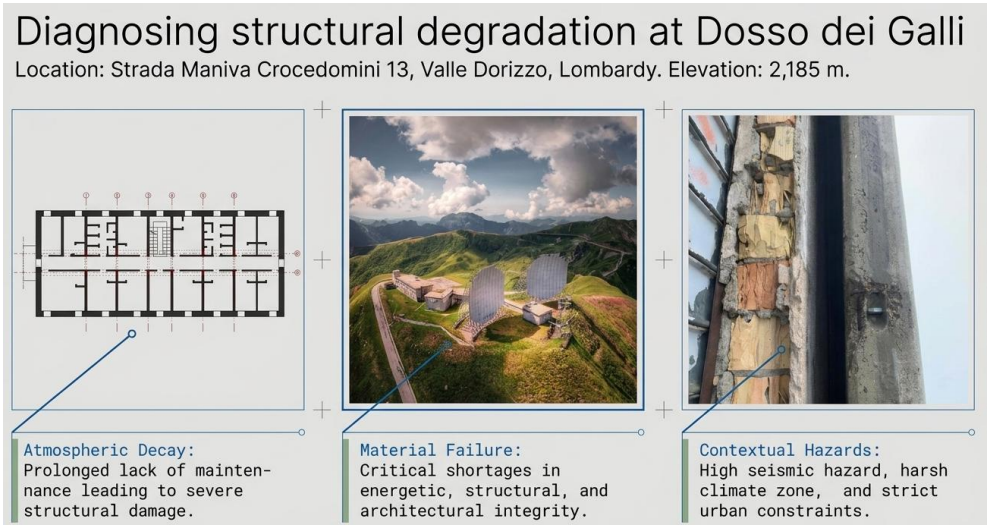


Fig. 3 Former NATO base of Dosso dei Galli: geographical context, current conservation state and structural degradation.

Positioned at an altitude of approximately 2000 m above sea level, the base is characterised by a strong relationship with the surrounding landscape. Extreme environmental conditions – low temperatures, thermal excursions, high wind exposure and seasonal snow loads – have influenced both the original construction techniques and the current state of conservation. Today the site appears partially abandoned, with several structures showing visible signs of decay and functional obsolescence.

Architecturally, the complex consists of reinforced concrete buildings designed according to functional and defensive criteria typical of Cold War military facilities: massive volumes, limited openings and a strong material presence, reflecting a design approach oriented towards durability, protection and operational efficiency. Despite their apparent rigidity, these buildings hold significant historical and cultural value, as physical testimonies of a geopolitical period that deeply influenced the European territory.

From a structural point of view, the buildings present evident vulnerabilities, mainly related to the absence of seismic design provisions, insufficient lateral resistance and material degradation over time – aspects particularly relevant considering the seismic hazard affecting the Italian territory. In addition, the site suffers from poor energy performance, since the original buildings were not designed according to contemporary energy standards, resulting in high thermal dispersion and limited indoor comfort, further worsened by the harsh alpine climate.

The remote location and high altitude also pose logistical challenges for construction, maintenance and future use, favouring prefabrication and dry-assembly techniques. As a former Cold War outpost, the site holds a strong symbolic and historical identity that must be carefully preserved: any intervention has to balance structural upgrading with the conservation of the original architectural character and the memory of the place. For these reasons, Dosso dei Galli is identified as a representative case through which to explore the potential of non-invasive exoskeleton systems, aiming to transform a fragile, abandoned military site into a resilient, sustainable and culturally meaningful environment.

5 EXOSKELETON-BASED REHABILITATION STRATEGY

In response to the critical issues identified in the case study, the research proposes a rehabilitation strategy based on a non-invasive external exoskeleton, conceived as an independent structural framework designed to enhance the seismic performance of the existing buildings while minimising interference with the original fabric. Unlike conventional strengthening techniques, which often require intrusive interventions within the existing structure, the proposed exoskeleton operates as an external support system: it is structurally connected to the building but maintains a degree of independence, preserving the original architectural configuration and reducing the need for demolition or invasive modifications – an aspect particularly relevant for Cold War heritage, where the conservation of material authenticity plays a central role.

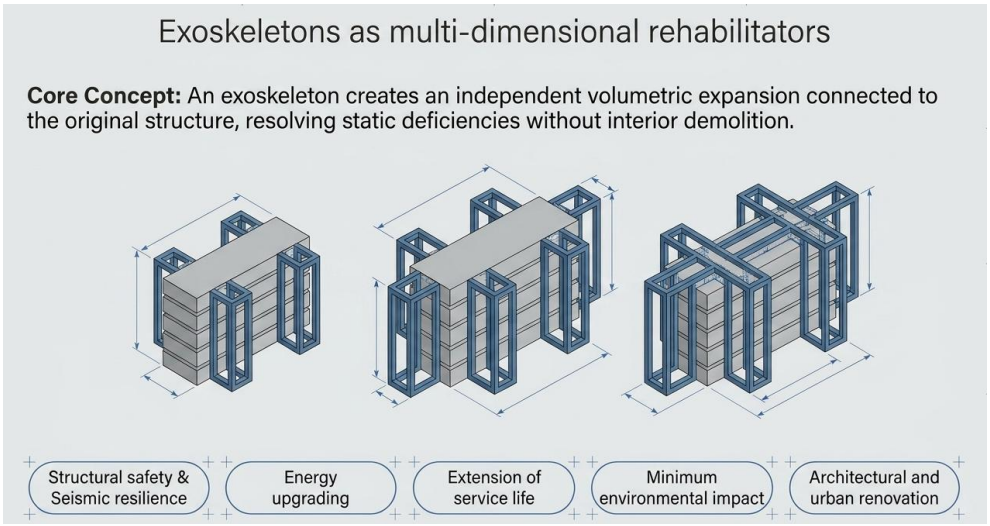


Fig. 4 Conceptual evolution of the external steel exoskeleton as a multifunctional rehabilitation system

The exoskeleton is designed as a steel structure composed of vertical, wall-like elements arranged around the perimeter of the existing buildings. Steel is selected for its high strength-to-weight ratio, durability, ease of prefabrication and recyclability; moreover, it enables dry construction techniques, particularly suitable for high-altitude sites, reducing construction time and logistical complexity.

A distinctive feature of the system is the geometric configuration of the structural elements: the exoskeleton is composed of inclined wall elements, whose orientation is defined not only by structural requirements but also by environmental considerations. Structurally, the inclination increases stiffness and improves the global seismic behaviour of the system; architecturally and environmentally, the same elements act as passive shading devices, reducing solar gains on the façades. This dual functionality highlights the integrated nature of the intervention, turning the exoskeleton into a mediating layer between the existing building and the external environment. Modularity and replicability are further key aspects: the exoskeleton is conceived as a system of standardised, prefabricated components assembled on site through dry connections, facilitating transportation and installation especially in remote locations such as Dosso dei Galli. Reversibility is a further fundamental design principle: bolted connections and independent structural systems ensure that the exoskeleton can be disassembled or modified over time without causing irreversible alterations to the existing buildings – an essential requirement in heritage contexts. In this way, the exoskeleton is conceived not only as a structural device but also as an architectural element capable of redefining the identity of the site, establishing a dialogue between past and present.

6 PRELIMINARY STRUCTURAL CONSIDERATIONS AND EXPECTED PERFORMANCE

The definition of the exoskeleton-based intervention is supported by preliminary structural assessments aimed at identifying the main deficiencies of the existing buildings and at evaluating the potential effectiveness of the proposed system. The analysed structures, typical of Cold War military facilities, were not originally designed according to modern seismic criteria: they exhibit significant vulnerabilities, including insufficient lateral stiffness, lack of ductile detailing and limited capacity to dissipate energy under seismic actions, further aggravated by material degradation and ageing effects.

Initial evaluations, based on geometric surveys and mass estimations of the existing buildings, provided a first approximation of the seismic demand and allowed the identification of the increase in stiffness and load-bearing capacity required to ensure an adequate structural performance. On this basis, preliminary seismic checks were performed to define the minimum structural requirements of the exoskeleton system: simplified models were adopted to estimate the contribution of the external structure in terms of lateral resistance and global stiffness, leading to a first identification of the minimum thickness and configuration of the wall-like elements needed to counteract horizontal loads.

A parametric approach is currently being developed to further investigate the influence of geometric variables – inclination angle, spacing, thickness and connection layout of the walls – on the structural behaviour of the system, in order to optimise the balance between structural performance, material use and architectural integration. The inclination of the elements, in particular, represents a key design variable, since it affects both the distribution of internal forces and the global stiffness of the system.

From a structural perspective, the exoskeleton can be interpreted as an independent load-bearing system, capable of significantly improving the dynamic response of the existing buildings: by introducing additional stiffness and strength, it reduces the demand on the original structure, limiting damage and enhancing overall safety. Depending on the adopted configuration, the system may behave either as an over-resistant structure or as a dissipative one, contributing to energy dissipation during seismic events, while also acting as an external protective layer that mitigates long-term degradation. Although the results presented at this stage are preliminary, they confirm the feasibility of the proposed approach; ongoing developments include refined numerical modelling and detailed design of connections, aimed at validating the solution in real contexts.

7 DISCUSSION AND CONCLUSIONS

The rehabilitation of decommissioned Cold War military heritage requires integrated design approaches capable of simultaneously addressing structural safety, architectural conservation and environmental sustainability. The proposed multidisciplinary framework demonstrates that these objectives should not be considered independently, but rather as complementary components of a unified rehabilitation strategy. Within this context, the adoption of a non-invasive steel exoskeleton represents an effective and scalable solution. Acting as an external structural system, it enhances the seismic performance of existing reinforced concrete buildings while preserving their historical identity. At the same time, its multifunctional configuration combines structural strengthening, passive solar control and architectural upgrading, supporting Life Cycle Thinking principles through prefabrication, dry assembly and reversibility. A key outcome of the research is the definition of a transferable intervention methodology that extends beyond the Dosso dei Galli case study and can be adapted to other abandoned Cold War sites sharing similar structural and conservation challenges. This shifts the focus from a single design solution to a broader framework for the sustainable regeneration of military heritage. The current work represents an initial stage of the research and is based on preliminary assessments. Future developments will include advanced numerical modelling, optimisation of the exoskeleton geometry and connection systems, and validation through detailed structural analyses. Particular attention will also be devoted to integrating passive biophilic strategies within the structural concept, with the ultimate objective of developing multidisciplinary design guidelines for the adaptive reuse of Cold War military heritage across Europe.

Acknowledgements

This study is part of a wider research on the former NATO bases in North-East Italy, started in 2017 by a group of researchers and teachers of the Department of Civil Engineering Architecture Territory Environment and Mathematics (DICATAM) of the University of Brescia.

References

[1] Gastaldi, Francesco, and Camerin, Federico. 2019. *Aree militari dismesse e rigenerazione urbana*, Saggi IUAV series. Siracusa: LetteraVentidue Edizioni.

[2] Casprini, Enrico, Passoni, Chiara, Marini, Alessandra, and Riva, Paolo. 2018. "Critical analysis of the models for the residual life evaluation of RC buildings." Proceedings of Italian Concrete Days, Lecco.

[3] Labò, Simone. 2021. Diagrid Exoskeletons for the Retrofit of RC Buildings. Holistic sustainable solutions to renovate post World War II RC buildings in a Life-Cycle Perspective. doi: 10.6092/978-88-97413-45-5

[4] Moramarco, Vincenzo. 2020. Studio di adeguamento sismico mediante esoscheletro di un edificio ad uso scolastico. Master's thesis.

[5] Feroldi, Francesca, Marini, Alessandra, and Belleri, Andrea. 2014. "Miglioramento e adeguamento sismico di edifici contemporanei mediante approccio integrato energetico, architettonico e strutturale con soluzioni a doppio involucro a minimo impatto ambientale." Progettazione Sismica 5(2):31–47. doi:10.7414/PS.5.2.31-47

[6] Thormark, Catarina. 2006. "The effect of material choice on the total energy need and recycling potential of a building." Building and Environment, 41(8), 1019–1026, 2006.

[7] Bellini, Oscar Eugenio, Marini, Alessandra, and Passoni, Chiara. 2018. Adaptive exoskeleton systems for the resilience of the built environment. TECHNE – Journal of Technology for Architecture and Environment, 71–80. doi:10.13128/TECHNE-22120

Wood meets minerals: Behaviour of timber-to-concrete joints

Ayşe Özdemir, Vinay Mahadik, Jan Hofmann

Institute of Construction Materials – Department of Fastening and Strengthening Methods, University of Stuttgart,
Breitwiesenstr. 3, 70565 Stuttgart, Germany

Summary
Experimental investigations were carried out in this study to realistically assess the load-bearing capacity and behaviour of connections between timber and mineral building materials. The investigation includes transverse load tests in which two different timber materials, spruce [Fi] and construction beech [BuLVL], were connected to various substrate materials, namely normal-strength concrete (C20/25), high-strength concrete (C50/60), and aerated concrete. Metal expansion anchors and bonded anchors were used as fastening systems. The aim of the tests was to investigate the influence of the anchoring depth, substrate material (different concrete types and concrete strength classes), fastening system, and timber material on the load-bearing capacity and deformation behaviour of the connections. The experimental results indicate that neither the timber material nor the fastening system had a significant influence on the load-bearing capacity, whereas the substrate material and the anchoring depth caused a significant increase in load-bearing capacity.

1 INTRODUCTION

In recent years, timber construction has gained increasing importance, particularly in the context of sustainable building and hybrid structural concepts. Composite structures consisting of timber and mineral building materials have been extensively studied, as the combination of these materials offers numerous advantages. Timber provides favourable strength-to-weight characteristics and ecological benefits, whereas concrete is characterised by high compressive strength and stiffness. The use of suitable fastening systems enables the formation of composite action, resulting in improved load-bearing capacity and serviceability of the overall structure.

Numerous experimental and numerical studies have investigated the load-bearing and deformation behaviour of timber-concrete composite systems. The primary focus lies on the composite interaction between the materials, system stiffness, and the failure behaviour of the fastening systems. These studies demonstrate that the composite effect is strongly influenced by the connection type, the stiffness of the individual components, and the quality of the interface between timber and the mineral substrate. The design of timber components and anchors in concrete is governed by the relevant standards of Eurocode 5 (EN 1995-1-1) [1] and Eurocode 2 (EN 1992-1-1) [2], which define the fundamental requirements for load-bearing capacity and serviceability. Composite structures are commonly designed using simplified analytical approaches, such as the γ-method or modified models accounting for composite stiffness.

Although numerous studies have been carried out, there are still gaps in research regarding the behaviour of direct timber-to-concrete connections using post-installed fasteners in different mineral substrates. To address this knowledge gap, the present study investigates the mechanical and stochastic behaviour of such connections using expansion anchors and bonded anchors in normal-strength concrete (C20/25), high-strength concrete (C50/60), and aerated concrete. Based on these findings, design approaches for cross-material connections are evaluated and discussed.

2 EXPERIMENTAL PROGRAM

To investigate the load-bearing and deformation behaviour of timber-concrete connections with post-installed fasteners, transverse shear tests were conducted using different substrate materials and attachment components. Table 1 provides an overview of the investigated test configurations. The fasteners used – expansion anchors and bonded anchors with 2K reaction resin mortar– were manufactured from A4 stainless steel. The aim of the test configurations was to identify the basic parameters influencing the load-bearing behaviour. To evaluate the effects of different substrate

materials, attachment components, and fastener types, two anchorage depths were considered. According to ETA-19/0520, these correspond to the minimum and maximum anchorage depths for expansion anchors [3].

Table 1 Test programme

Test combination	Mineral material	Timber component	Fastener type	Anchoring depth in mineral material [mm]
SAF-C20/25-Fi	C20/25	Spruce	Metal expansion anchor	40 / 100
SAF-C20/25-BuLVL	C20/25	Construction beech	Metal expansion anchor	40 / 100
SAF-C50/60-Fi	C50/60	Spruce	Metal expansion anchor	40 / 100
SAF-C50/60-BuLVL	C50/60	Construction beech	Metal expansion anchor	40 / 100
VDW-PB-Fi	Aerated concrete	Spruce	Bonded anchor	40 / 100
VDW-PB-BuLVL	Aerated concrete	Construction beech	Bonded anchor	40 / 100
VDW-C20/25-Fi	C20/25	Spruce	Bonded anchor	40 / 100
VDW-C20/25-BuLVL	C20/25	Construction beech	Bonded anchor	40 / 100
VDW-C50/60-Fi	C50/60	Spruce	Bonded anchor	40 / 100
VDW-C50/60-BuLVL	C50/60	Construction beech	Bonded anchor	40 / 100

2.1 Specimens and materials

Two different mineral materials were used as anchorage materials. On the one hand, aerated concrete of strength class PPW4 was investigated, while on the other hand, concrete with compressive strength classes C20/25 and C50/60 was used. The concrete test specimens, with dimensions of 128.5×128.5×20 cm, were produced in the concrete plant in accordance with the state of the art and the requirements of EN 206 [5]. The aerated concrete specimens, measuring 49.5×36.5×24.9 cm, were obtained from a commercial supplier. The compressive strengths of the materials were determined in accordance with the relevant standards: aerated concrete according to DIN EN 772-1 [4] and concrete according to DIN EN 12390-3 [9]. The measured compressive strengths are summarised in Table 2. The timber components, spruce and construction beech, had dimensions of 30.0×15.0×10.0 cm.

Table 2 Overview of compressive strengths

Mineral Material // Test date	Density ρ [kg/m³]	Compressive strength f_b/f_c [N/mm²]
PB // 10/2025	507.0	5.5
C20/25 // 08/2025	2202.4	29.2
C20/25 // 09/2025	2170.1	29.3
C50/60 // 08/2025	2284.6	62.2
C50/60 // 09/2025	2270.6	60.5

2.2 Test preparation and Test setup

The test specimens were prepared in the laboratory.

Central holes with a drill diameter of $d_0 = 12$ mm were drilled in the timber components. The boreholes in the concrete slabs were positioned to avoid edge effects (see Fig. 1). Due to the limited dimensions of the aerated concrete blocks, only one test specimen could be installed per block.

For the expansion anchors installed in concrete of strength classes C20/25 and C50/60, boreholes with a diameter of $d_0 = 10$ mm were drilling using drilling rig to ensure perpendicular alignment. After cleaning in accordance with ETA-19/0520 [3], the anchors were installed to the specified embedment depth. The timber component was then fixed using washer and nut, which were tightened to the prescribed installation torque before testing.

For bonded anchors, boreholes with a diameter of $d_0 = 12$ mm were prepared and cleaned according to the manufacturer´s instructions. The mortar was injected into the borehole, the threaded rod was installed, and, after the specified curing time, the timber component was attached and tightened to 10 Nm.

The test was carried out in accordance with DIN EN 26891 [6] to ensure comparability with timber engineering test procedures. The loading protocol was based on an estimated reference load according to Eurocode 2 [2] and consisted of cyclic loading and unloading at 20 %, 40 %, 60 % and 80 % of the reference load, followed by continuous loading until failure.

The timber component was clamped in a steel loading frame and supported on steel plates with Teflon sheets to minimize friction. Load was applied horizontally by a hydraulic cylinder, while horzontal displacement and vertical uplift of the timber component were recorded. The test setup is shown schematically in Fig. 1.

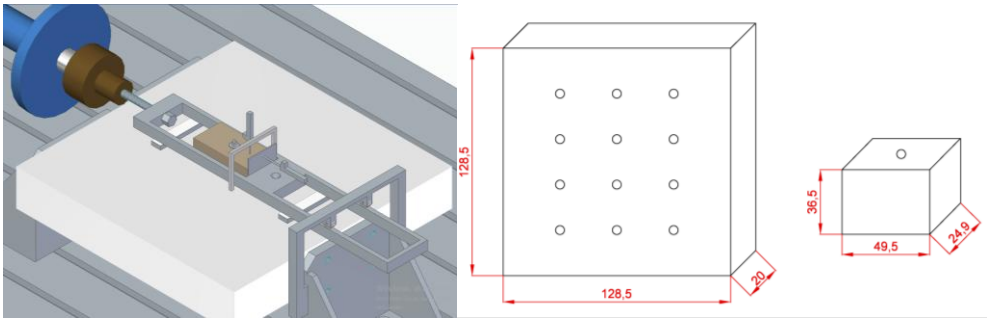


Fig. 1 Schematic shear test setup and anchor position: concrete slab (left): 12 anchors per slab and aerated concrete (right): one anchor per slab

3 RESULTS

3.1 Experimental results

The experimental results were evaluated with respect to fastener type, anchoring depth, attachment, and anchor base.

A comparison of all tests (Fig. 3) shows that the anchoring depth had the greatest influence on the load-bearing capacity. Speciments with an anchoring depth of $h_{ef} = 100$ mm reached the calculated load-bearing capacity and failed by steel shear of the fastener. At the reduced anchoring depth of $h_{ef} = 40$ mm, the load-bearing capacity decreased significantly, and failure occurred by pry-out of the fastening from the anchor base (Fig. 2).

The influence of the anchor base strength and the timber component on the ultimate load was comparatively small (Fig. 3). However, speciments with spruce (Fi) attachments exhibited approximately twice the displacement of thos with beech (BuLVL) attachments due to the lower timber density.

The bonded anchors installed in aerated concrete were also tested. Preliminary tests showed that the prescribed loading and unloading stages could not be completed because of the low compressive strength of the substrate. Therefore, the remaining tests were performed withour these stages. In all cases, failure occurred by levering the fastening out of the anchor base (rear concrete breakout), which identified as the governing failure mode (Fig. 2).



Fig. 2 Failure patterns of expansion anchors – Left – levering of fasteners out of the anchor base at h_{ef} = 40 mm; Right – shear failure of fasteners between the anchor base and attachment part at h_{ef} = 100 mm

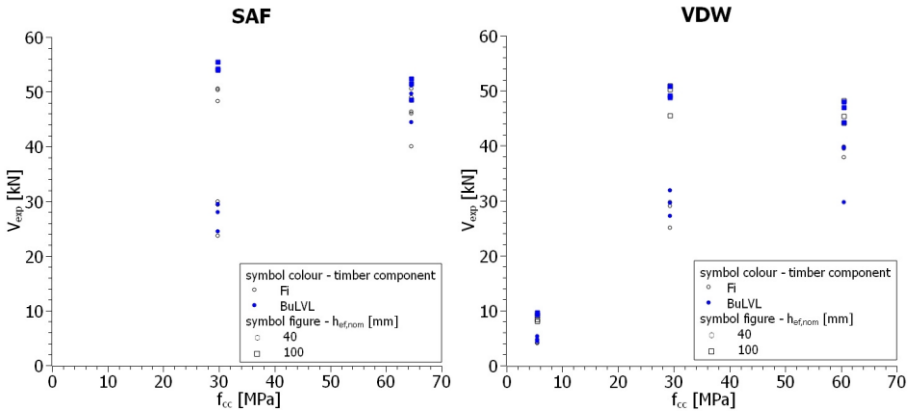


Fig. 3 Failure loads of all tests: Left - expansion anchors; Right – bonded anchors

3.2 Comparison of test results and design values

To compare the experimental results with the existing design models of Eurocode 2, the theoretical predictions were evaluated against the test data. The objective was to identify the most suitable design approach for further investigations. For this purpose, the test results were compared with three key calculation models [2], [7]: the bending capacity model based on a maximum bending angle of 10°, the lateral-load model considering the lever arm, and the lateral-load model without the lever arm.

To determine the lateral load resulting from bending at 10°, the plastic bending moment was first calculated according to Scheer, Peil and Nölle (1987) [8] using the material properties listed in Table 3 (Equation (1)). The equation for distance mounting was then used to determine the design torque (Equation (2)). This relationship was subsequently rearranged to express the lateral load load and linked to Equation (1). For the fixed clamping condition, a clamping ratio of α_B = 2.0 and a lever arm of l_a = 50 mm were assumed [8].

$$M_{u,S} = 1{,}7 \cdot W_{el} \cdot f_{uk} \tag{1}$$

where W_{el} section modulus for the threaded part calculated based on the net tensile area [mm³]

f_{uk} steel strength [MPa]

$$M_{u,S} = \frac{V_{B,10°} \cdot l_a}{\alpha_B} \tag{2}$$

where $V_{B,10°}$ lateral load at max. 10° bending angle [N]
l_a lever arm [mm]
α_B clamping force [-]

$$V_{B,10°} = \frac{M_{u,S}}{l_a} \cdot \alpha_B \tag{3}$$

where $M_{u,S}$ plastic bending Moment [Nmm]
l_a lever arm [mm]
α_B clamping force [-]

Table 3 Material properties of expansion anchors and bonded anchors

Anchor type	Stress cross-section A_s [mm²]	Resistance moment W_{el} [mm³]	Steel strength f_{uk} [MPa]
Metal expansion anchor	58.0	62.4	869.3
Composite anchor	58.0	62.4	798.5

After determining the theoretical shear forces resulting from bending at 10°, the actual clamping degrees (4) for each test were calculated by transforming Equation (3):

$$\alpha_B = \frac{V_{exp.}}{M_{u,S}} \cdot l_a \tag{4}$$

where $V_{exp.}$ experimental lateral force [N]
$M_{u,S}$ plastic bending Moment [Nmm]
l_a lever arm [mm]

The resulting diagrams indicate that, although the experimental results are on the safe side compared to prediction from Equation (3), a direct comparison is not possible (see Fig. 3, left). The diagram on the right-side in Fig. 3 shows the calculated clamping degrees. The results reveal that the initially assumed clamping degree of 2.0 does not apply for the conditions tested, as all determined values are significantly higher. This suggests that the load on the anchors with a soft attachment component, both spruce and construction beech, may promote the formation of two flow joints, and that the 10° bending criterion proposed by Scheer, Peil and Nölle (1987) [8] is no longer valid due to elastic bedding occurring in the wooden attachment area [8].

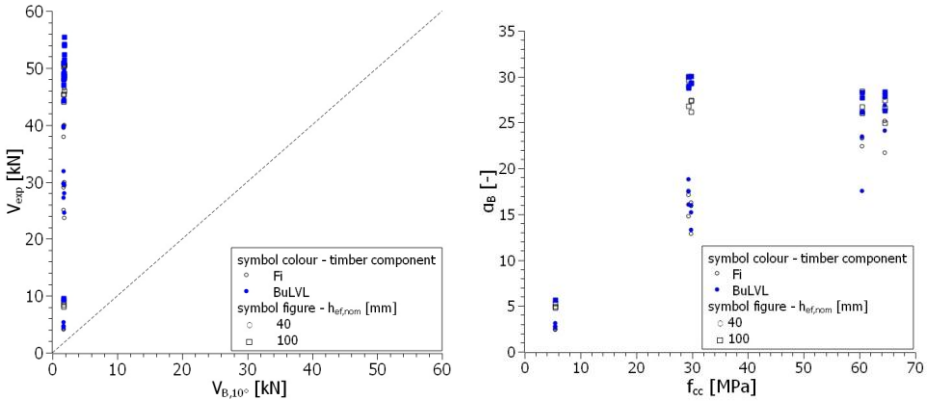


Fig. 4 Left: Comparison of experimental test results with Equation (3); Right: Calculated clamping degrees for each test according to Equation (4)

In the case of a transverse load with a lever arm (Equation (6)), the resulting stress is determined from the moment equilibrium of the static system (see Fig. 4):

$$V_E(h_{ef} + l_a) = V_{E,new} \cdot h_{ef} \tag{5}$$

$$V_{E,new} = V_E \frac{(h_{ef} + l_a)}{h_{ef}} \tag{6}$$

where
V_E applied lateral force [kN]
$V_{E,new}$ theoretical lateral force [kN]
h_{ef} effective embedment depth [mm]
l_a lever arm [mm]

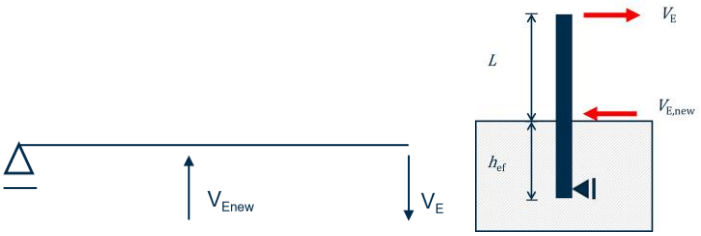


Fig. 5 Static system (left) and schematic representation of the system with lever arm

These calculations yield the theoretical shear forces in the shear plane immediately above the concrete surface, accounting for the existing lever arm. However, a comparison with the experimental results (Fig. 5) shows that the measured values are significantly higher. This indicates that the design according to Equation (6) provides a conservative estimate of the actual load-bearing capacity. Similar to the previous model for bending capacity, this approach does not account for the effects of elastic bedding or the rope effect.

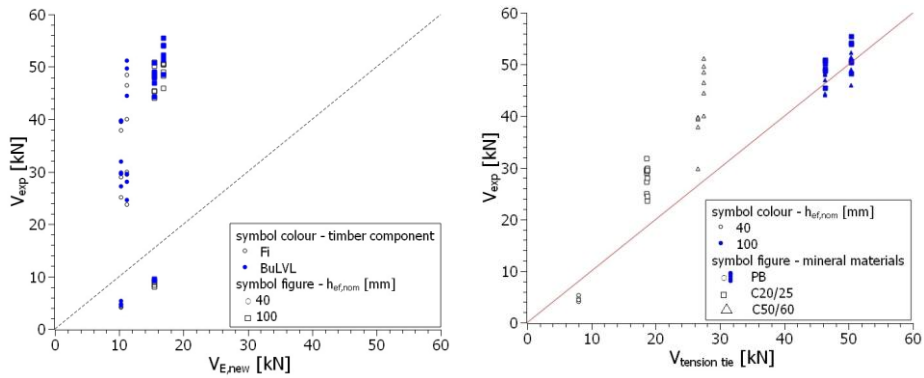


Fig. 6 Left: Comparison of experimental test results with theoretical predictions from Equation (6); Right: Comparison of test results with Equation (7) assuming $\alpha_Q = 1.0$

If, on the other hand, the test setup is considered to result in pure shear failure, it can be assumed that the transverse load acts without a lever arm (Equation (7)). In this case, the transverse load-bearing capacity is given by:

$$V_{without\ leverarm} = \alpha_Q \cdot A_S \cdot f_{uk} \tag{7}$$

where
α_Q 0,5 for for steel failure due to lateral load without a lever arm [mm]
A_s cross section [mm²]
f_{uk} steel strength [MPa]

Similar to the calculation of the shear load for bending failure, the α_Q coefficient was determined for each test (Equation (8)):

$$\alpha_Q = \frac{V_{exp.}}{A_S \cdot f_{uk}} \tag{8}$$

where $V_{exp.}$ experimental lateral force [N]
A_s cross section [mm²]
f_{uk} steel strength [MPa]

Fig. 6 (left) shows that assuming a lateral load failure without a lever arm provides a significantly better approximation of the test results than a bending failure, even though this approach is not fully compliant with Eurocode 2. Fig. 6 (right) indicates that a value $\alpha_Q = 0.5$ is a realistic assumption for design without a lever arm. However, this assumption does not apply for the lower anchoring depth of $h_{ef} = 40$ mm, where a pry-out failure was observed. For the higher anchoring depth, values in the range of $\alpha_Q = 0.8$ to 1.0 suggest that design according to Equation (7) is feasible with $\alpha_Q = 1.0$. This reflects the formation of a tension band, making the tensile load-bearing capacity of the anchor at $h_{ef} = 100$ mm the governing factor. The test results and observed failure patterns clearly confirm this behaviour (see Fig. 7).

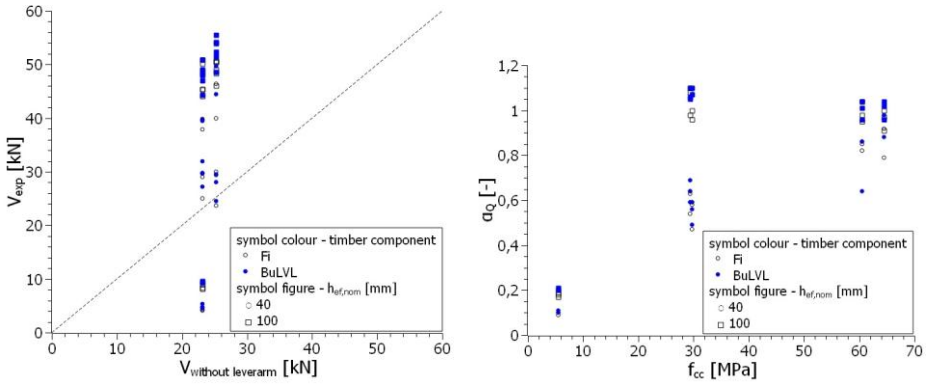


Fig. 7 Left: Comparison of experimental test results with Equation (7); Right: Calculated α_Q coefficients for each test according to Equation (8)

4 CONCLUSIONS

The results of this study show that the load-bearing capacity of timber-to-concrete connections under transverse loading is strongly influenced by the anchoring depth and the substrate material of the mineral base material. In all investigated cases, an increase in anchoring depth led to higher load-bearing capacity, as failure in the substrate could mostly be avoided. In contrast, the timber component (type, dimensions and density of the timber) and the type of fastening system had only a minor influence on the maximum load-bearing capacity. The influence of those parameters is more pronounces with respect to the displacement behaviour than ultimate load.

At lower anchoring depths, failures occurred due to the fastening being pulled out of the substrate, indicating limited force transmission in the mineral material (pullout of pryout failure). For larger anchoring depths, steel shear failure of the fastening was predominantly observed, allowing near-full utilisation of the load-bearing capacity.

Comparison with existing design approaches from Eurocode 2 [2,7] indicates that, for certain configurations, a simplified model without considering a lever arm provides a realistic approximation of the experimental results if the displacement could be neglected of is not limited to an inclination of 10°.

These findings provide a basis for the further development of design models for timber-mineral connections. The aim is to find a design equation that includs the current design of timber connections according to Eurocode 5 [1] and concrete connections according to Eurocode 2 [2,7]. Future

investigations will focus on varying the anchoring depth and examining the influence of substrate material and lever arm length in greater detail.

References

[1] "DIN EN 1995-1-1: Design of timber structures - Part 1-1: General - common rules and rules for buildings," Beuth Verlag GmbH, Berlin, 2010.

[2] "DIN EN 1992-1-1: Eurocode 2 - Bemessung und Konstruktion von Stahlbeton- und Spannbetontragwerken - Teil 1-1: Allgemeine Regeln - Regeln für Hochbauten, Brücken und Ingenieurwerke," Beuth Verlag GmbH, Berlin, 2021.

[3] ETA-19/0520: Mechanical fasteners for use in concrete," EOTA, Berlin, 2023.

[4] "DIN EN 772-1: Prüfverfahren für Mauersteine - Teil 1: Bestimmung der Druckfestigkeit," Beuth Verlag GmbH, Berlin, 2016.

[5] "DIN EN 206: Beton - Festlegung, Eigenschaften, Herstellung und Komformität," Beuth Verlag GmbH, Berlin, 2021.

[6] "DIN EN 26891: Holzbauwerke - Verbindungen mit mechanischen Verbindungsmitteln - Allgemeine Grundsätze für die Ermittlung der Tragfähigkeit und des Verformungsverhaltens," Beuth Verlag GmbH, Berlin, 1991.

[7] "DIN EN 1992-4: Eurocode 2 - Bemessung und Konstruktion von Stahlbeton- und Spannbetontragwerken - Teil 4: Bemessung der Verankerung von Befestigungen in Beton," Beuth Verlag GmbH, Berlin, 2019.

[8] Rolf Eligehausen and Rainer Mallée 2000, Befestigungstechnik im Beton- und Mauerwerksbau, Berlin: Ernst & Sohn, 2000.

[9] "DIN EN 12390-3: Prüfung von Festbeton - Teil 3: Druckfestigkeit von Probekörpern," Beuth Verlag GmbH, Berlin, 2019.

Numerical investigation of behaviour of connections between bonded laminates and concrete

Marta Burczyk, Vinay Mahadik, Jan Hofmann

Institute of Conctruction Materials (IWB),
University of Stuttgart,
Pfaffenwaldring 4, Stuttgart 70569, Germany

Summary
Carbon Fiber Reinforced Polymer (CFRP) laminates find extensive application in construction, especially for concrete repair and structural modifications. Strengthening of structural elements with bonded reinforcement can be carried out either by Near Surface Mounting (NSM) typically bonded in slots in the concrete surface or by External Bonded Reinforcement (EBR) bonded directly to the concrete surface. NSM CFRP laminates provide significantly better bond performance compared to EBR. In this study, available test data are used to validate the Finite Element (FE) model. Following the validation, the paper presents numerical simulations of the proposed reinforced concrete model, including extended analyses of additional configurations with NSM and EBR techniques. The validated FE approach is used to understand the efficiency of strengthening using different connection methods between concrete and the CFRP laminates.

1 INTRODUCTION

Reinforced concrete (RC) structures often require strengthening and rehabilitation because of numerous reasons, eg. functional changes, new demands, design corrections and limiting crackwidths [1]. Strengthening of concrete members with carbon fiber reinforced polymer (CFRP) is a popular and cost-effective method for increasing the durability and load-bearing capacity of structures. Concrete structures strengthened with CFRP laminates have a wide scope of application, eg., flexural, shear and axial strengthening [2].

Strengthening with CFRP laminates can be achieved either by bonding of the laminates into slots made in existing concrete members (method called NSM) or by direct bonding of the laminates on the concrete surface (method called EBR). The bond between the CFRP laminates and concrete for both NSM and EBR applications is know to be a critical factor influencing the efficacy of the strengthening solution. By bonding the laminate within grooves, a defined bond length can be achieved in case of NSM laminates, allowing the laminate to develop its maximum stress. NSM laminates, thus enable high force transfer even with relatively short anchorage lengths. In the case of EBR, bond strength is limited by the tensile strength of the cover concrete. One of the strengthening methods involve pre-stressing CFRP laminates. Approximately 60 % of the tensile strength of the CFRP is utilized, enabling the structural element to achieve its maximum reinforcement potential with full use of the composite material. However, pre-stressing is a relatively time-consuming and effort intensive technique. Hence in the context of ease of application, end anchorages without prestressing of laminates are preferred. The end anchorages are typically used, to ensure load transfer at the laminate ends. A research project aimed at optimization of the bond (anchorage) between the CFRP laminates and concrete is being carried out at the Institute of Construction Materials (IWB), University of Stuttgart. This paper presents the insights from an initial phase of this project undertaken to understand the influence of product dependent parameters on the strengthening efficacy of the NSM and EBR solutions. To this end, a validated Finite element (FE) analysis approach is employed.

2 RESEARCH MOTIVATION

One objective of this paper is to highlight the challenges in finite element modeling, explain the complexity of the process, and outline the requirements for reasonable simulation of RC strengthening using CFRP laminates. Since the bond between CFRP laminates and concrete is critical for the efficacy of the strengthening solution, the characteristics of the adhesive product (bond strength and stiffness) are investigated as influencing parameters in this study. The study provides an insight into comparable

behaviour of NSM and EBR strengthening solutions using bonded adhesives represented within a defined range of bond strength and bond stiffness.

3 VALIDATION OF FE MODELLING APPROACH

This study uses FE analysis as a tool to draw the required behaviourial insights on the NSM and EBR strengthening solutions. FE analysis enables a huge cost and time reduction compared to often expensive and time-consuming experimental tests. The numerical investigations in this study were carried out using commercial FE software ANSYS Mechanical 2024 R2 [3].

3.1 Benchmark Problem for FEA Validation

For validation of the FE modelling approach, available test data [4] on reference and strengthened (NSM) RC beam is used in this study. The reference specimen and the specimen strengthened using NSM laminates used as benchmark are schematically shown in Fig. 1. The 230×230 mm reference beam (Fig. 1a) consists of longitudinal reinforcement of 12 mm diameter and stirrup reinforcement of 10 mm diameter with a spacing of 95 mm. The NSM specimen was obtained by strengthening the reference beam with 8 units of 12.5×4.2 mm CFRP laminates as shown in Fig. 1b.

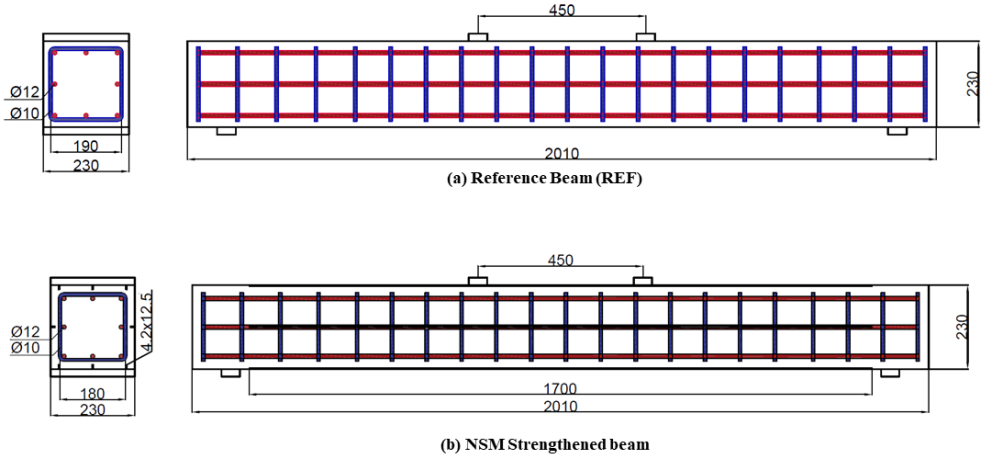


Fig. 1 Test specimens from [4] used for FE validation

The material parameters determined through testing [4] are summarized in

Table 1. The bond strength of the adhesive system used for bonding the CFRP laminates to the concrete was obtained in pull out experiments as 8.7 MPa. The detailed bond-slip curve was however not reported. Hence, a measure of bond stiffness was not available.

3.2 FE modelling approach and validation

To ensure meaningful simulation results, a precise description of the material properties is of decisive importance. Depending on the load, materials react differently, therefore their properties have to be defined as accurately as possible. A careful specification of the material parameters enables an accurate reflection of reality.

Table 1 presents the definition of material properties and parameters that have been defined for conducting the simulations discussed in this paper. For all steel elements, which were modelled in Simulations (longitudinal and stirrup reinforcement as well as loading and supporting pins) Young's Modulus was defined to 200 GPa and Poisson's Ratio to 0.3. Different FE modelling approaches are possible for simulation of the benchmark specimens shown in Fig. 1. In 3D FE analyses, concrete is modelled using solid elements. Reinforcements can be modelled either as bar elements or as solid elements. Bond between reinforcement and concrete can be modelled as perfect or as multilinear bond-slip relationship. The modelling of NSM laminates can be as bar elements or as solid elements, with or without due considerations to the bond behaviour. In FE analyses, the objective is to simulate the observed structural behaviour using an approach that is as simplified and computationally effecient as possible.

Table 1 Material parameters

		Concrete	Steel Reinforcement	CFRP
Compressive strength	[N/mm^2]	38	-	1400
Tensile strength	[N/mm^2]	2.9	620 (longitudinal) 632 (stirrup)	2300
Young's Modulus	[N/mm^2]	33000	200000	165000
Poisson's ratio	[-]	0.22	0.3	0.33
Yield strength	[N/mm^2]	-	512 (longitudinal) 503 (stirrup)	-

In the FE approach adopted in this study, concrete is modelled using 3D tetrahedral elements. To define the constitutive relation of concrete, Drucker-Prager plasticity model with Rankine's yield criteria in tension similar to [5] was used. The reinforcement bars and stirrups were modelled using Reinf elements. Bilinear stress-strain behaviour was adopted as constitutive law for steel reinforcement. A perfect bond condition was assumed between the reinforcing steel and concrete. The material parameter for concrete and steel were based on the experimental values shown in

Table 1.

A comparison between the test result with the FE result for the reference specimen (shown in

Fig. 2a.) indicates that the concrete and reinforcement modelling approaches adopted in this study provide a reasonably realistic representation of the structural behaviour. The FE results from the adopted modelling method for RC beam shows good agreement with the experimental observations. The approach can hence be considered as validated for RC beam simulations.

For modelling CFRP strengthening, laminates were defined using solid elements. In an initial model perfect bond condition between the laminate and concrete was assumed. This assumption ensures full transfer of stresses between the laminate and the concrete without any relative slip. A comparison of FE results with perfect bond condition (NSM_Perfect) with the test result (

Fig. 2b) shows that the FE approach overestimates the specimen strength. The failure of the test specimen was observed because of bond delamination. Hence, a realistic simulation of the strengthened NSM specimen requires due consideration of the bond-slip relation between the laminate and concrete.

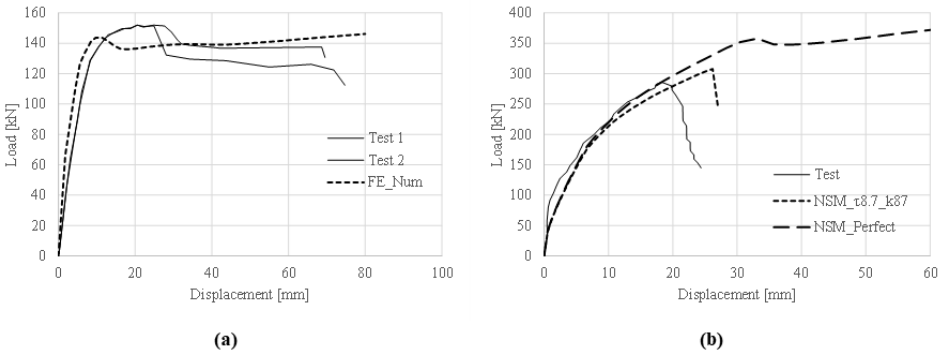


Fig. 2 Comparison of FE results with test observations [4]

In ANSYS, Cohesive Zone Model (CZM) can be used to define the bond behaviour between contacting solid surfaces. A mixed mode bilinear CZM model was used for definition of the bond behaviour. The bond slip curve is required for defining the CZM parameters. Since only the bond strength was available from the test data, several trials with different bond-slip curves were conducted in [6] in order to obtain the suitable CZM parameters representing the bond behaviour of the NSM-concrete contact. In this study, a wide range of bond stiffness (8.7 N/mm³, 87 N/mm³ and 870 N/mm³) was considered for the same bond strength. The Cohesive Zone Model (CZM) with a defined bond strength τ_m = 8.7 MPa and

bond stiffness $K_t = 87$ N/mm^2, was found to provide a reasonably realistic simulation of the strengthened NSM specimen as shown in

Fig. 2b. It is observed that the adopted CZM model for consideration of NSM-concrete bond, provides reasonable prediction of the specimen behaviour. Therefore, modeling the bond behaviour is the most important aspect for achieving accurate results. Since bond behaviour is inherently product dependant, a range of bond stiffness and bond strength is considered as representing different adhesion system in parametric studies. Furthermore, since the bond behavior between laminates and concrete has been validated, the EBR solution is also investigated in the parametric studies.

4 PARAMETRIC STUDIES

The objective of the parametric studies is to develop insights on the efficacy of strengthening for NSM and EBR solutions as a function of parameters representing the adhesive system used for bonding between the laminates and concrete. To this end the bond stiffness and bond strength are used as parameters to represent bond behaviour. The parameters are varied within a range representative of different products available on the market. Validated FE modelling approach is used for performing the analyses to obtain insights on the NSM and EBR configurations.

For EBR configuration, total reinforcement area was chosen to be equivalent to that of the NSM system. The specimen was strengthened using a single CFRP laminate, with its length and width adjusted such that the overall reinforcement area corresponded to the combined area of the embedded NSM laminates. The study thus compares NSM and EBR solutions implemented with different adhesive systems for a given cross sectional area of the laminates mounted on the tension side of the beam.

Table 2 Summary of parametric FE analyses and results

Model	Bond strength τ_m [MPa]	Bond stiffness K_t [N/mm³]	Max Load [kN]	Failure load [kN]
REF	-	-	146.14	146.14
NSM_τ8.7_k87	8.7	87	307.53	307.53
NSM_τ15_k87	15	87	319.37	319.37
NSM_τ15_k150	15	150	325.21	325.21
NSM_τ30_k87	30	87	327.19	327.19
NSM_τ30_k300	30	300	335.96	335.96
NSM_Perfect	-	-	478.53	357.67
EBR_τ8.7_k87	8.7	87	225.07	225.07
EBR_τ15_k87	15	87	230.85	230.85
EBR_τ15_k150	15	150	232.30	232.30
EBR_τ30_k87	30	87	233.87	233.87
EBR_τ30_k300	30	300	239.63	239.63
EBR_Perfect	-	-	273.20	273.20

Table 2 provides an overview of the parametric studies and the results. For both NSM and EBR solutions, adhesive system with bond strength 8.7 MPa, 15 MPa and 30 MPa were considered. The

benchmark specimens corresponded to bond strength of 8.7 MPa and bond stiffness of 87 N/mm^3. For the case of higher bond strengths, bond stiffness of 87 N/mm^3 and 10 times the corresponding bond strength were considered as varying parameters. This study aimed to investigate whether an increase in bond strength or bond stiffness leads to a noticeable improvement in the structural response of NSM systems, while identifying potential limitations in the case of EBR systems, even for high bond strength values. Furthermore, the cases with perfect bond assumption (i.e. no relative slip between concrete and laminate) are also included since they constitute an upper bound for the respective (NSM and EBR) strengthening solutions.

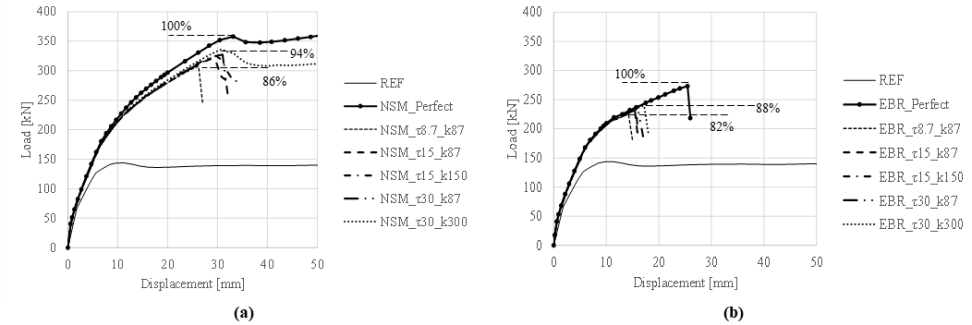


Fig. 3 Load displacement behaviour observed in different cases

The load-displacement curves for all the FE cases of NSM and EBR are plotted in

Fig. 3a and b respectively. In case of NSM_Perfect analysis, an initial drop was observed around 32mm displacement. The maximum load observed was much higher, and is attributed to numerical reasons. The failure load is hence assumed to be corresponding to the max load before the drop. In all other cases, the maximum load observed in the analysis is the failure load. The crack patterns observed on the front and soffit of the beam for REF specimen and representative NSM and EBR specimens are shown in Fig. 4.

The NSM_Perfect model represents a perfect bond situation. This correspond to an upperbound capacity achievable using the laminates employed on the tension side. It is noted here that the failure load for NSM_Perfect is lower than that corresponding to the analytical sectional capacity. This is attributed to the localized splitting effects because for the shorter load transfer length. All cases of NSM with bond modelling failed because of interface delamination at lower failure loads relative to the NSM_Perfect case. An increase in the bond strength and stiffness is observed to increase the failure load.

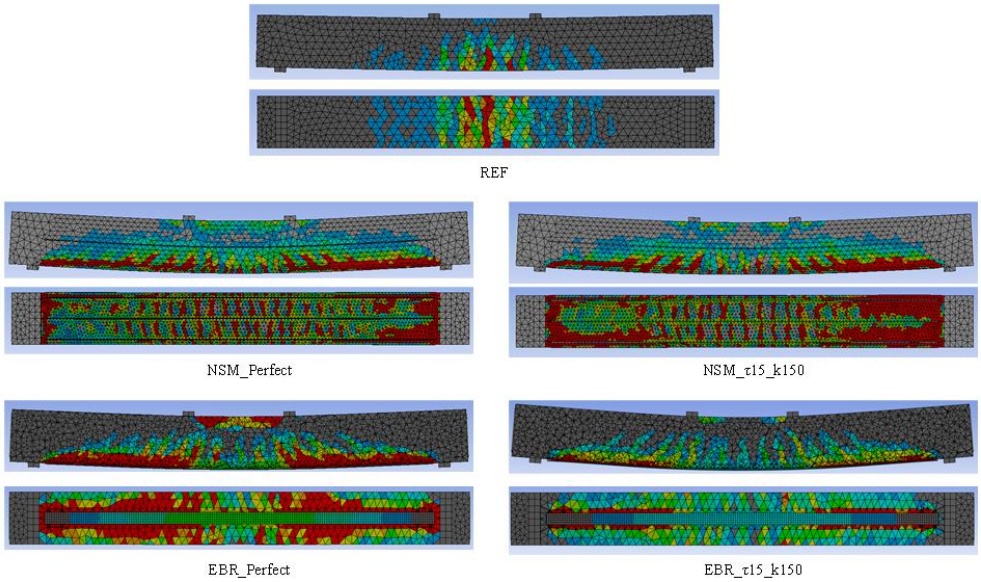


Fig. 4 Failure patterns observed in different cases

The EBR_Perfect specimen with the same laminate area in tension shows a much lower strength of the beam as compared to the NSM_Perfect. Thus inspite of a perfect bond assumption, EBR methodology results in lesser capacity relative to the NSM methodology. In case of EBR_Perfect, the tensile failure of concrete cover is observed in contrast to splitting failure in case of NSM_perfect specimen (see Fig. 4). This conclude that cover failure in concrete limits the capacity of EBR. This does not happen in case of NSM. This difference highlights the superior force transfer mechanism of the NSM system relative to the EBR system. Similar to the case of NSM, the different models for EBR considering bond are observed to fail pre-maturely relative to the perfect bond situation. An increase in the bond strength and stiffness is observed to increase the failure capacity.

5 DISCUSSION OF RESULTS

The fundamental difference between the NSM and EBR retrofitting solutions lies in the mechanism of force transfer between the CFRP and the concrete. In the NSM system, the tensile force is distributed into the surrounding concrete through the adhesive filled groove, resulting in a more robust bond behaviour thereby inducing splitting action in the cover region. In contrast, in EBR systems bond transfer results in tensile stresses in the concrete cover, making the bond performance more sensitive to the tensile strength of the concrete. The bond characteristics of the adhesive system employed are responsible for inductng the splitting and tensile stresses for the NSM and EBR cases respectively. The intensity of these stresses is a function of the bond characteristics (strength and stiffness). This leads to different failure capacities.

An overview of the failure loads in all the cases is summarized in Fig. 5a. Both NSM and EBR solutions result in gain in capacity in comparison to the reference beam. The effeciency of strengthening with NSM solutions is better than the EBR solution. In general an increase in the capacity is observed as a function of bond strength and the bond stiffness.

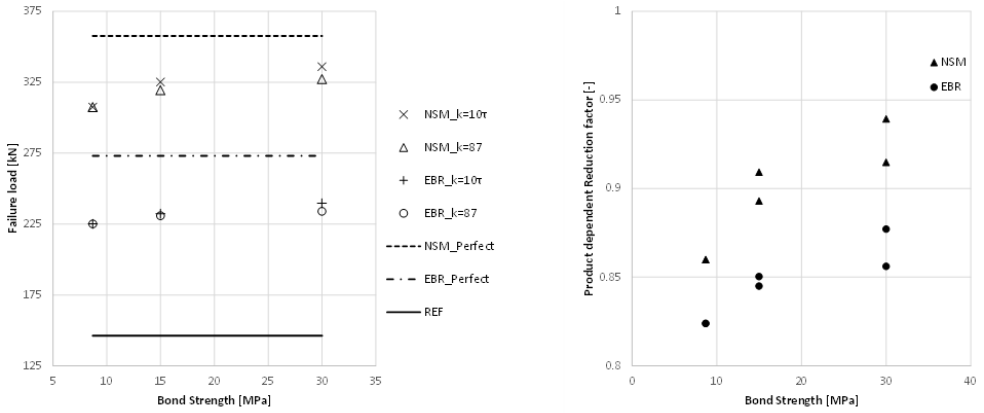


Fig. 5 Summary of influence of product dependency on NSM and EBR strengthening

An analytical estimate of the sectional capacity based on concrete properties is possible for both NSM and EBR solutions. This analytical estimate typically correspond to the respective cases with perfect bond assumption. A normalization of the NSM and EBR capacities with consideration of the bond behaviour is done relative to the corresponding perfect bond capacities. This provides a reduction factor which accounts for the influence of product dependent characteristics on the analytical sectional capacity. A perspective on these reduction factors is provided in Fig. 5b. The different combinations of bond strength and stiffness represent different adhesive products. Thus the product dependant reduction factors provide a method to evaluate a realistic capacity of the NSM and EBR solutions based on the actual bond behaviour. A careful combination of numerical and experimental program is possible to define a framework for evaluation of such product specific parameters.

6 CONCLUSION

This study presented a comparison of efficiency of the NSM and EBR methods for flexural strengthening of RC elements. A validated FE modelling approach for reasonable consideration of influencing parameters in simulation of specimen behaviour for the reference and strengthenedspecimens was discussed. This approach was employed to derive perspective on influence of product dependency on the efficiency of the strengthening solutions. The overall conclusions from this study is summarized in the following points.

1. EBR applications generate tensile stresses in the cover region. NSM applications generate splitting stresses because of shear transfer between the laminates and concrete. This fundamental difference in the load transfer mechanisms is responsibe for the lower efficiency of EBR solution relative to the NSM solution.
2. The bond strength and stiffness of the adhesion system were identified as product dependent influencing factors representing different adhesion systems.
3. An increase in the strengthening efficiency was observed with increase in bond strength.
4. For the same bond strength, a further increase in the strengthening efficiency was observed by increasing the bond stiffness.
5. A framework for definition of product dependent reduction factors as a function of bond strength and stiffness was discussed in this study. These reduction factors can be used to obtain an estimate of the capacity of the strengthened elements based on analytical sectional capacity evaluations.

This study was focussed on evaluation of structural capacity of the strengthening solution as a function of the product dependant parameters. However, for a complete engineering solution, the product specific durability and serviceability aspects are required to be accounted for development of product specific design theory in the future.

References

[1] Weidner, Jörg, Köhler Winfried, Krams Jürgen 2000 “Verstärken von Betonbauteilen mit geklebter Bewehrung. Bemessung und Ausführung”, *Beton- Stahlbetonbau*, vol. 95, no. 9, pp. 537–543, doi: 10.1002/best.200001050.

[2] Finckh, Wolfgang. 2024 *Verstärken von Betonbauteilen: Tragwerksplanung im Bestand*. Wiesbaden: Springer Fachmedien Wiesbaden. doi: 10.1007/978-3-658-45857-7.

[3] Ansys. 2026. “Ansys Help“ Accessed January 12. https://ansyshelp.ansys.com/public/account/secured?returnurl=//Views/Secured/corp/v252/en/ans_mat/mat_geomechanics.html%23matgeomechDPconc

[4] Chellapandian, Maheswaran. 2019 “Axial Compression – Bending Interaction Behaviour of Square RC Columns Strengthened Using Hybrid FRP Composites”, PhD diss, Indian Institute of Technology Hyderabad.

[5] Holder, Johannes; Lakhani, Hitesh and Hofmann, Jan. 2025 “Influence of the compressive fracture energy on the predicted breakout failure of fasteners”, Paper presented at 12th International Conference on Fracture Mechanics for Concrete and Concrete Structures, IA-FraMCoS, Austria, Vienna, April 23-25. doi: 10.21012/FC12.1238.

[6] Bilgic, Berkay. 2025 “Flexural strengthening of reinforced concrete beams using CFRP laminates” Master’s thesis, University of Stuttgart.

Validation concept for numerical simulations for the design of fastenings in reinforced concrete

Johannes Holder, Hitesh Lakhani, Jan Hofmann

Institute of Construction Materials,
University of Stuttgart,
Pfaffenwaldring 4, 70569 Stuttgart, Germany

Summary
Modelling concrete in FE-simulations is still a challenging topic due to the complex failure mechanism. Models need to be extensively validated before they can be used for design. The absence of guidelines for validation often hinders the widespread application of FE-simulations in design. The design of fastenings not covered by standards could massively benefit from design by simulation as this would replace expensive and time-consuming design by experiments. However, this is currently not yet the case due to the uncertainties in the results and the efforts needed for model validation. Therefore, a validation concept for the design of fasteners in concrete assisted by numerical simulation is presented in the paper. The concept considers the relevant failure modes and allows to assess the suitability and precision of a numerical modelling approach. Furthermore, a statistical evaluation concept for the computation of design values based on the accuracy of the simulation results is presented.

1 INTRODUCTION

The use of numerical simulations using the finite element (FE) method has increased significantly in various industries over the last decades. This trend is also visible in construction industry. But despite several decades of research, numerical modelling of concrete and reinforced concrete structures is still challenging. This is mainly due to the complex fracture mechanisms and the very elaborate material models which are required to describe this behaviour. Therefore, numerical models have to be validated thoroughly in order to achieve sufficient reliability of results. Only then they can be safely used in design of concrete structures.

In fastening technology, numerical simulations of anchorages to concrete are currently also rarely used in design. In cases of fastenings not covered by the governing standards, EN 1992-4 [1] in the European Union and ACI 318 [2] in North America, time- and cost-intensive experimental design is often required. Despite the large benefits of design by numerical simulation compared to experimental design, it is still not used in widespread application. This is due to the previously mentioned extensive validation processes, but also due to the fact that guidelines for model validation and application of numerical tools for the simulation of fasteners in concrete are still lacking.

Such guidelines for numerical model validation are required for fastening technology, as numerical results from different simulation approaches can vary massively, and even smaller changes to a numerical simulation can significantly affect the results [3]. In literature, a large variety of different modelling approaches for numerical simulation of fasteners in concrete can be found. Some of these modelling approaches were compared by Holder et al. [3] and Neupane et al. [4]. Most of these approaches are designed for the investigation of a very specific setting, e.g., a specific failure mode or anchor configuration. The numerical tools are usually validated with a set of experimental results for this setting and then used to extend this database with numerical results. This leads to the situation that only the performance of the numerical tool in this very specific field of application is known. For any fastening or structure outside this field, the precision of the model is unknown. For those cases, further validation is required.

Due to these usually very specific validations, approaches and procedures for general validation of numerical simulations have been proposed for structural design in different fields of construction. The aim of these methods is to provide a framework for the assessment of the precision of a numerical tool. Furthermore, these concepts provide methods to consider the precision of the numerical tool and safely use results from numerical simulation in design.

In concrete construction, one such framework is provided by the “estimate of coefficient of variation” (ECOV) method [5], [6]. The concept uses two safety factors γ_m and γ_{Rd} to reduce the numerical load bearing capacity to a design capacity. The factor γ_m is computed based on the ratio of

mean and characteristic structural resistances from the simulations. These resistances are computed by using mean and characteristic input parameters for material properties. The factor γ_{Rd} considers the precision of the numerical tool by comparing the numerical results with experimental results for cases with known capacity. Both factors apply the concepts of fib Model Code 2010 [7], which assumes log-normal distribution of structural resistance and numerical precision.

For the field of steel construction, such a concept is introduced by prEN 1993-1-14 [8], [9]. It gives a framework for the use of numerical simulation in steel construction. In the concept, a distinction is made between "numerical simulations" and "numerical design calculations". The first aim to reproduce mean level results comparable to experiments, while the latter aim to produce result quantities for design. The "numerical design calculations" are further divided into two cases: The first is the "analysis requiring subsequent design check", which utilizes numerical simulation only for computation of internal forces, while design is still performed by the rules of the other parts of EN 1993 [10]. The second case is the "direct resistance check", in which the numerical load-bearing capacities are utilized for design.

In standard cases, where the engineer has sufficient experience in the numerical simulation of such cases, prEN 1993-1-14 [8] allows for the direct application of numerical results. In this case, numerical load-bearing capacities from simulations with characteristic input data can be applied as characteristic load-bearing capacities. In other cases, a safety factor γ_{fe} has to be applied. This factor is computed by comparing numerical results to experimental results in similar cases. γ_{fe} computes a 5 %-fractile value of the numerical deviation by application of the safety concepts from EN 1990 [11], which assume normal distribution of numerical precision. Furthermore, concepts for verification of numerical tools are also given in prEN 1993-1-14.

For the field of timber construction, the concepts of prEN 1993-1-14 [8] are adjusted by Töpler et al. [12], [13]. The main components of these "guidelines for a finite element-based design of timber structures" remain very similar to prEN 1993-1-14 [8].

In the field of fastening technology, no such guidelines exist so far. In the following, a numerical model validation procedure designed for the special requirements of fastenings to concrete shall be derived.

2 REQUIREMENTS FOR A VALIDATION PROCEDURE FOR FASTENINGS IN REINFORCED CONCRETE

In this section, a validation procedure with a framework for the computation of design capacities shall be derived for the numerical simulation of fastenings to reinforced concrete. For this procedure, some aspects can be adapted from the previously presented validation methods (see section 1). However, there are some aspects, which are not compatible to the requirements of numerical simulations for fasteners in reinforced concrete. In this section, the characteristics of prEN 1993-1-14 [8] and the ECOV [5,6] are being discussed, and specific requirements for the new model validation procedure for fastenings are derived.

A favourable aspect is the application of well-established safety concepts in both prEN 1993-1-14 [8] and the ECOV [5], [6]. A reduction factor for the inaccuracy of the numerical result shall also be used in the newly derived validation procedure with design concept. Especially the definition of the factor γ_{fe} in prEN 1993-1-14 [8] is seen as a very good starting point for the definition of such a factor, as γ_{fe} depends on the number of simulations used in the model validation.

One difficulty in concrete construction is the large scatter of mechanical properties. In experimental investigations, large variation of results is common in this field. In Fig 1(a), concrete cone capacity tests from Eligehausen et al. [14]–[16] are shown in comparison to predicted capacity using the CCD (Concrete Cone Design) method at mean level [1,16]. It can be seen that large scatter up to +/- 50 % of the predicted load is not uncommon for the capacity of fasteners in concrete. When looking at the result scatter of reinforced concrete structures, even larger scatter is possible in some cases. Fig. 1(b) shows the peak shear stress of reinforced concrete beams without shear reinforcement. The experimental results [17]–[19] are normed towards a concrete strength of $f_{cm} = 28\ MPa$ and a degree of longitudinal reinforcement of $\rho_{sl} = 2$ % with the computation rule of EN 1992-1-1:2011-01 [20]. It can be seen that the result scatter is immense for low values of the beam slenderness a/d, and it reduces with increasing beam slenderness. While the use of other computation rules for norming may slightly change the results, the general trend and the large scatter remains. This large variation of experimental results induces additional challenges for the derivation of a numerical model validation procedure. This is especially

the case for the direct adaption of concepts from prEN 1993-1-14 [8] to fastening technology applications, as it comes from the field of steel construction, where result scatter is generally much smaller.

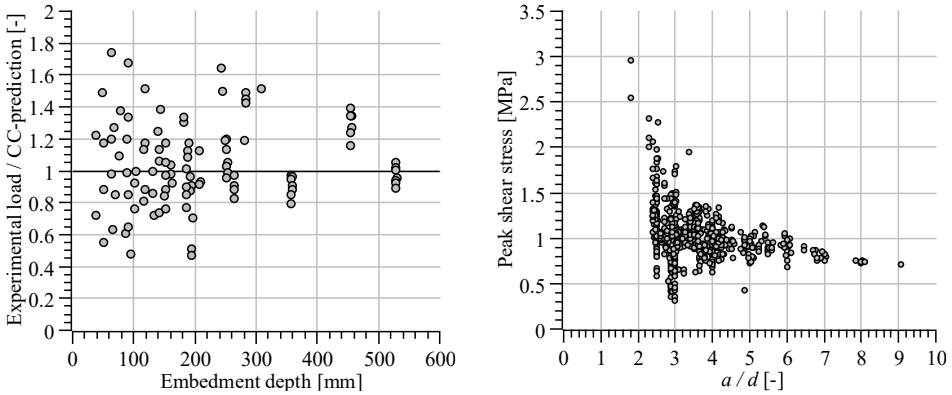


Fig. 1 *Result scatter in experiment: left Concrete cone capacity of headed studs compared to mean CC-capacity (left, data from*[14]–[16]*) and right Peak shear stress of reinforced concrete beams without shear reinforcement scaled to* $f_{cm} = 28\ MPa$ *and* $\rho_{sl} = 2\ \%$ *(right, data from* [17]–[19]*)*

One major issue with different validation approaches presented till date is that they all rely on validation against single experiment. Due to the large variation of experimental results (as shown in Fig. 1), experiments for validation have to be selected carefully. A validation with only experiments from the upper or lower end of the field of scatter can lead to possibly unsafe or too conservative results.

Furthermore, the different failure modes in fastening technology and reinforced concrete construction are sometimes governed by concrete failure and sometimes by steel failure. The numerical modelling of concrete is usually much more challenging than the modelling of steel. Thus, the numerical precision can have large differences between concrete failure and steel failure. This then translates to different model precisions for different failure modes. As a consequence, the different failure modes should be assessed separately. The ECOV [5], [6] does differentiate the different failure modes, but in the end, a global factor is computed by evaluation of all simulations from all failure modes. In the worked example by Červenka et al. [21], the global reduction factor is more conservative than the most unfavourable from a single failure mode. However, the global reduction factor can be less conservative than the most unfavourable from single failure mode for this type of computation. This can be the case for large differences in precision and uneven distribution of simulation quantity between the different failure modes.

Even within a failure mode, numerical precision can vary with different influencing parameters (e.g.,[22]). Thus, during the validation of a model, extensive variation of the main influencing parameters should be conducted. This should be prescribed by the validation procedure.

Additional to the consideration of numerical precision, a characteristic value has to be computed in order to consider the scatter of the structure and proceed with the design. prEN 1993-1-14 [8] simply prescribes the use of characteristic material properties for the numerical simulation. After reduction with the factor γ_{fe}, the numerical capacity is treated as characteristic capacity. Considering only the scatter of the material properties by using characteristic input values is not sufficient in concrete construction. The ECOV [5], [6] covers this by estimating the scatter of capacity from comparison of numerical capacity with mean and characteristic material input parameters. Based on the estimated scatter, a reduction factor γ_m is computed. However, even this can be not sufficient in some cases. Assuming that the numerical shear capacity of a reinforced concrete beam scales with the third root of concrete strength (as the EN 1992-1-1 [20] computation rule does), the factor γ_m becomes only 1.11 for a shear beam made of C40/50. Comparing this to the large scatter visible in Fig. 1 right, it becomes apparent that this factor does not sufficiently account for the ratio between experimental mean and lower 5 % fractile.

From the review of the two numerical model validation procedures, the following requirements for the new numerical model validation procedure could be derived:

- The validation should cover all failure modes and mechanical properties that are relevant for fastenings to reinforced concrete structures.
- The precision of the numerical tool in the different failure modes, mechanical properties etc. should be assessed separately. The most unfavourable case should govern the global adjustment factor.
- The validation should be made with experimental mean values as reference rather than single experimental results.
- The number of simulations used in the validation of one failure mode, mechanical property etc. should be considered in the computation of the reduction factor.
- Within the validation of one failure mode, mechanical property etc., the variation of influencing parameters should be prescribed.
- A suitable and safe concept, which considers the variation of the actual experimental capacities, should be included for the derivation of characteristic values.

3 VALIDATION CONCEPT

The proposed concept gives a framework for the validation of a numerical model and the derivation of design capacities from numerical simulation results generated with the validated model. The general structure is as following: Prior to the validation, a uniform numerical modelling approach is defined. With this modelling approach, a prescribed set of validation simulations has to be simulated. Based on the deviation of the simulation capacities from the reference capacities in the validation simulations, a factor $\eta_{fe,m}$ for consideration of numerical imprecision is computed. Using this factor, the mean level capacity R_m of a structure can be computed from the numerical capacity R_{NA}, which was generated by simulation with the same uniform numerical modelling approach as used in the validation process:

$$R_m = R_{NA} \cdot \eta_{fe,m} \quad (1)$$

Furthermore, the concept provides another reduction factor $\alpha_{5\%}$, which allows to further reduce the mean level capacity R_m to a characteristic capacity R_k:

$$R_k = R_m \cdot \alpha_{5\%} \quad (2)$$

The design value of resistance R_d can then be computed with the standard partial safety factor γ_c from EN 1992-1-1 [20]:

$$R_d = \frac{R_k}{\gamma_c} \quad (3)$$

3.1 Numerical modelling approach

The most important aspect of the validation is to use a uniform numerical modelling approach. As even slight changes of the numerical model can have large impact on the results [3], the resulting reduction factor $\eta_{fe,m}$ is only valid if a uniform numerical modelling approach is used throughout the validation process. Deviation from this uniform numerical modelling approach voids the validation and a repetition with the adjusted numerical modelling approach is necessary. The numerical modelling approach should be defined in detail prior to the validation and comprise the following aspects:

- The software used for the numerical analysis
- Further numerical details, such as element shape and element order in FE analysis
- The material models and the derivation of input parameters
- Specific implementation and modelling details, such as meshing, constraints, contact formulations etc.

3.2 Validation simulations

For the computation of the reduction factor $\eta_{fe,m}$ for numerical imprecision, the numerical modelling approach has to be tested in a set of validation simulations. The validation simulations should cover all relevant mechanical properties and failure modes for fasteners in reinforced concrete. Therefore, the validation is segmented in four main validation categories: “material validation” covers the behaviour

of plain concrete, "local validation" the behaviour of fasteners in plain concrete, "component validation" the behaviour of reinforced concrete structures and "interaction validation" the behaviour of anchors in reinforced concrete structures. Within one validation category, several validation cases are distinguished. Each validation case covers the test for a specific mechanical property or failure mode. The validation categories for the validation of fasteners in reinforced concrete structures are listed in Table 1 with their specific validation cases.

Table 1 Validation categories with their respective validation cases

Material validation	Local validation	Component validation	Interaction validation
Compression cube & cylinder	Tension headed studs	Beam bending	Interaction beam- anchor
Tensile splitting	Tension bonded anchors	Beam shear	
Size effect	Shear headed studs		
Shear	Shear bonded anchors		
	Bond uncracked		
	Bond cracked		

For each validation case, a set of simulations has to be given. These validation simulations must cover the important influencing parameters for this failure mode/mechanical property. Furthermore, the relevant geometrical and mechanical properties have to be given for each validation simulation alongside a reference value for the mean level ultimate load of the structure/anchorage/test specimen. These reference capacities can be derived by evaluation of experimental databases, from computation rules on mean level or from literature.

3.3 Statistical validation evaluation

When the validation simulations are simulated using the uniform numerical modelling approach, its precision can be considered by computation of the factor $\eta_{fe,m}$. As previously described, different failure modes, problem statements etc. should be assessed separately. Therefore, a validation-case-specific numerical reduction factor $\eta_{fe,m}^{i}$ has to be computed separately for all 13 validation cases i:

$$\eta_{fe,m}^{i} = m_{X,i} \cdot \left(1 - k_{n,i} \cdot V_{X,i}\right) \leq 1.0 \qquad (4)$$

The computation is based on the ratio of reference capacity to numerical capacity for all validation simulations in the validation cases. In Equation (4), $m_{X,i}$ is the mean value of these ratios within the validation cases i, and $V_{X,i}$ is the respective coefficient of variation. The factor $k_{n,i}$ is the characteristic fractile factor taken from EN 1990 [11].

The most unfavourable factor $\eta_{fe,m}^{i}$ from all 13 validation cases i is chosen as global reduction factor $\eta_{fe,m}$:

$$\eta_{fe,m} = min\left(\eta_{fe,m}^{i}\right) \qquad (5)$$

3.4 General suitability check

The factor $\eta_{fe,m}$ scales the numerically computed capacity based on the precision of the used numerical modelling approach. Nevertheless, it is not recommended to use a numerical modelling approach with very large deviation from the reference results. Therefore, two criteria for general suitability are defined. If any of the two criteria are violated, the numerical modelling approach has to be modified and the validation has to be repeated with the modified modelling approach. The first criterion is that the ratio of reference to simulation capacity must be within the range of 0.5 -2.0 for all validation simulations in all validation cases. The second criterion is that the fracture pattern of the numerical simulations must show characteristics of the (governing) reference failure mode. A mix of fracture pattern is still valid when at least some characteristics of the reference failure mode are visible. When the fracture pattern shows a completely different failure mode, the numerical modelling approach must be improved or discarded.

3.5 Reduction factor for characteristic capacities

The reduction factor $\alpha_{5\%}$ for the computation of characteristic capacities from the mean level capacities is based on evaluation of the reference capacities on both mean and characteristic level. The reference capacities are derived from empirical formulas on mean level, evaluation of experimental databases or from literature. For those values, usually values on characteristic level are also given for design purposes, or the statistical evaluation for characteristic capacity can be performed by oneself. This reduction factor is calculated separately for all simulations in all 13 validation cases. The most unfavourable ratio has to be used as global reduction factor $\alpha_{5\%}$ for the computation of characteristic capacities.

3.6 Limitations of validation procedure

The proposed validation procedure is designed for the validation with respect to the load-bearing capacity of fastenings in reinforced concrete structures. Only the ultimate capacity in simulation is evaluated in the statistical evaluation, which results in the reduction factor $\eta_{fe,m}$ for consideration of numerical imprecision. Other result quantities, such as displacements, are not evaluated. Thus, the validated numerical model may not be used for assessing the serviceability limit state without further validation with respect to the stiffness characteristics.

3.7 Simplification of validation procedure for special application

When only simpler systems are supposed to be designed with the validated numerical modelling approach, the effort for the validation process can be disproportionally large. Thus, the validation procedure can be simplified in special cases.

The validation should always include the validation cases from the material validation. When only fasteners in plain concrete are to be designed with the validated model, it is sufficient to only carry out the validation categories “material validation” and “local validation”. When only reinforced concrete structures without fastenings shall be designed with the validated model, it is sufficient to only carry out the validation categories “material validation” and “component validation”.

3.8 Optimization of numerical reduction factor

It is preferable to have a numerical reduction factor $\eta_{fe,m}$ close to the value of one in order to maximize the capacity. If the reduction imposed by $\eta_{fe,m}$ is seen as too large, it can be optimized in two ways: One option is certainly the modification and re-validation of the numerical modelling approach. An optimization within a certain range is also possible by extending the number of validation simulations in the validation case which yields the governing (lowest) $\eta_{fe,m}^{i}$. As the fractile factor $k_{n,i}$ scales with the quantity of simulations in the validation case, the value for $\eta_{fe,m}^{i}$ improves

4 CONCLUSION AND OUTLOOK

Design by numerical simulation could offer a quick and cost-efficient method for the design of fastenings which are not covered by current design standards. In order to use these advantages, reliable numerical models are required. Neither models with proven reliability in general scene (spanning across different failure modes and complex fracture mechanics of concrete) nor methods to assess the reliability of a model are currently available for the field of fastening technology. As a consequence, the scope of this work was to derive a framework for numerical model validation for the special requirements of fasteners in reinforced concrete structures. In a first step, approaches for model validation in literature were reviewed, and their suitability for the use with simulations of fasteners in reinforced concrete was discussed. Based on the identified advantages and challenges of the approaches from literature, requirements for a model validation procedure were defined. The framework for numerical model validation was then derived in a way that matches these requirements.

The proposed framework includes the following steps:

- The numerical modelling approach used in the validation procedure has to be defined precisely prior to the validation.
- A schedule of simulations, which include a variety of problem statements relevant for fastenings in reinforced concrete, has to be simulated.
- Based on the derivation of numerical results to given reference value, a capacity reduction factor for the numerical imprecision is computed.
- Design capacities can be computed from numerical results following the given framework.

For the practical application of this framework, the geometry details, material details and reference capacities for the validation simulations have to be defined. Once all the details are defined, the method can be used for the validation and optimization of numerical modelling approaches for the use with fasteners in reinforced concrete. The validated model can then be used for design of fastenings, especially in cases which would otherwise require design by experiment. The presented method focusses on the load-bearing capacity in the validation. However, the general concept is suitable for any other result that can be quantified. One possibility could be the stiffness parameters which are relevant for the serviceability limit state. Unfortunately, the experimental databases for displacements are much smaller, hindering the derivation of reference values.

References

[1] Eurocode 2 - Design of concrete structures - Part 4: Design of fastenings for use in concrete; German version EN 1992-4:2018. 2018.

[2] ACI 318-19 Building Code Requirements for Structural Concrete. 2019.

[3] Holder J, Lakhani H, Hofmann J. 2024. "Use of numerical simulations for the design of fasteners – limitations and way forward". Paper presented at the 15th fib PhD Symposium in Civil Engineering, Budapest, Hungary, August 28-30

[4] Neupane CC, Lee J, Pokharel T, Tsang H-H, Gad E. 2023."Development and challenges in finite element modelling of post-installed anchors in concrete". Structure and Infrastructure Engineering 2023. DOI: 10.1080/15732479.2023.2208567.

[5] Červenka V. 2008. "Global Safety Format for Nonlinear Calculation of Reinforced Concrete". Beton- und Stahlbetonbau 103:37–42. DOI: 10.1002/best.200810117

[6] Červenka V. 2013. "Reliability-based non-linear analysis according to fib Model Code 2010". Structural Concrete14:19–28. DOI: 10.1002/suco.201200022

[7] fib Model Code for concrete structures 2010. 2013; Ernst & Sohn Verlag, Berlin.

[8] Eurocode 3: Design of steel structures - Part 1-14: Design assisted by finite element analysis; German and English version prEN 1993-1-14:2023. 2023

[9] Dunai L, Kövesdi B, Gardner L, Al-Emrani M, Casafont M, Degée H, et al. 2023. "Design assisted by finite element analysis – Introduction to prEN 1993-1-14 and Technical Report". Ce/Papers 6:2677–2682. DOI: 10.1002/cepa.2574

[10] Eurocode 3 - Design of steel structures - Part 1-1: General rules and rules for buildings; German version EN 1993-1-1:2022. 2025.

[11] Eurocode: Basis of structural design; German version EN 1990:2002 + A1:2005 + A1:2005/AC:2010. 2021.

[12] Töpler J, Kuhlmann U, Buchholz L, Machanek S. 2022. "Guidelines for a Finite Element Based Design of Timber Structures". Institute Report. Institute of Structural Design, University of Stuttgart. DOI: 10.18419/opus-12769

[13] Töpler J, Buchholz L, Lukas J, Kuhlmann U. 2023. "Guidelines for a Finite Element Based Design of Timber Structures and Their Exemplary Application on Modelling of Beech LVL". Buildings MDPI 13:393. DOI: 10.3390/buildings13020393

[14] Eligehausen R, Fuchs W, Ick U, Mallee R, Reuter M, Schimmelpfennig K, et al. 1992. "Tragverhalten von Kopfbolzenverankerungen bei zentrischer Zugbeanspruchung" ("Load-bearing behavior of headed anchors under centric tensile load"). Bauingenieur 67:183–196.

[15] Eligehausen R, Bouska P, Červenka V, Pukl R. 1992. "Size effect of the concrete cone failure load of anchor bolts". Paper presented at FraMCoS I, Boulder, Colorado, June 1-5.

[16] Eligehausen R, Mallée R, Silva J. 2006 "Anchorage in Concrete Construction". Ernst & Sohn Verlag, Berlin.

[17] Reineck K-H, Kuchma DA, Fitik B. 2010. "Extended databases with shear tests on structural concrete beams without and with stirrups for the assessment of shear design procedures". Research Report. Institute for Lightweight Structures, Conceptual and Structural Design (ILEK), University of Stuttgart.

[18] Słowik M. 2014. "Shear failure mechanism in concrete beams". Paper presented at 20th European Conference on Fracture (ECF20), Trondheim, Norway, June 30-July 4. DOI: 10.1016/j.mspro.2014.06.318

[19] Sarkhosh R. 2014. "Shear resistance of reinforced concrete beams without shear reinforcement under sustained loading". PhD dissertation. Delft University of Technology.

[20] EN 1992-1-1:2011-01 Eurocode 2: Design of concrete structures – Part 1-1: General rules and rules for buildings 2011.

[21] Červenka V, Červenka J, Kadlec L. 2018 Model uncertainties in numerical simulations of reinforced concrete structures. Structural Concrete 9:2004–2016. DOI: 10.1002/suco.201700287

[22] Holder J, Lakhani H, Hofmann J. 2024. "Influence of different modelling approaches on the predicted concrete edge failure of fasteners". Paper presented at the 20th fib Symposium, Christchurch, New Zealand, November 11-13.

Connection failure of near surface steel mounts used for flexural strengthening

Baran Deniz Upcin, Vinay Mahadik, Jan Hofmann

Institute of Construction Materials,
University of Stuttgart,
Pfaffenwaldring 4, 70569 Stuttgart, Germany

Summary
This study investigates the flexural strengthening of reinforced concrete beams using steel plates mechanically fastened by post-installed anchors. Unlike bonded systems, anchored plates introduce discrete force transfer, which may trigger local splitting in the end anchorage zone before the theoretical bending capacity is reached. An experimental program combined with validated finite element simulations was conducted to analyse the governing mechanisms. Results show that the structural response is controlled by local stress concentrations around anchors rather than by global flexural resistance. Increasing anchor diameter in the critical zone or distributing the plate force over multiple plates enables a bending-governed response and mobilization of the theoretical sectional capacity. The findings provide a basis for a mechanics-based design approach for anchored plate strengthening systems.

1 INTRODUCTION

Externally attached steel plates are a well-established method for increasing the flexural capacity of reinforced concrete (RC) beams. In conventional applications, the plates are bonded to the concrete surface using epoxy adhesives, enabling continuous force transfer along the interface. When full composite action is achieved, the external plate acts as additional tensile reinforcement and the bending resistance can be determined from sectional equilibrium assuming strain compatibility.

However, bonded strengthening systems are often governed by interface-related failure mechanisms such as debonding or delamination. Since load transfer is limited to the concrete surface, premature bond failure may prevent mobilization of the theoretical sectional bending capacity.

Mechanical fastening using post-installed anchors represents an alternative approach in which the steel plate is directly connected to the concrete core. In contrast to bonded systems, the load transfer occurs discretely through individual anchors. Compared to externally bonded reinforcement, research on such mechanically fastened plate systems is still limited, particularly regarding their governing structural behaviour and possible failure mechanisms.

2 RESEARCH MOTIVATION

Mechanically fastened steel plate strengthening using post-installed anchors is not yet established as a standardized or codified strengthening technique. In contrast to externally bonded reinforcement systems, no comprehensive design concept currently exists that reliably describes the load transfer mechanism and governing failure modes of anchored plate systems.

The discrete force introduction through individual anchors fundamentally differs from the continuous interface behaviour of bonded systems. As a result, the internal stress state in the tension zone and particularly in the end anchorage region is significantly altered. A clear understanding of this load transfer mechanism is essential in order to define a suitable anchor configuration that enables efficient force redistribution and prevents premature anchorage-related failure.

The primary motivation of this study is therefore to (i) clarify the governing mechanical behaviour of anchored plate strengthening systems, (ii) identify the parameters controlling the anchorage zone response, and (iii) establish the basis for a mechanically consistent design concept.

The findings of this study are intended to contribute to the development of such a design approach for anchored steel plate strengthening systems.

3 CONCEPT OF FLEXURAL STRENGTHENING

This study investigates the flexural strengthening of reinforced concrete beams using externally attached steel plates mechanically fastened by post-installed anchors. Strengthening is most effective when the available shear resistance significantly exceeds the flexural resistance. Therefore, the difference between both resistances defines the strengthening potential. A beam configuration with an estimated shear resistance approximately 2.5 times its flexural resistance was selected to provide sufficient reserve for increasing the flexural capacity.

The objective is to identify anchorage configurations that provide sufficient force transfer for the strengthened beam to approach the flexural resistance of an equivalent bonded strengthening system.

The theoretical flexural resistance is determined using the design concept for externally bonded reinforcement, where the external steel plate is treated as additional tensile reinforcement. The bending resistance is obtained from internal force equilibrium assuming strain compatibility and plane sections remain plane (Fig. 1) [1]. The resulting sectional resistance represents the target resistance for the strengthening system and serves as a reference for the experimental and numerical investigations.

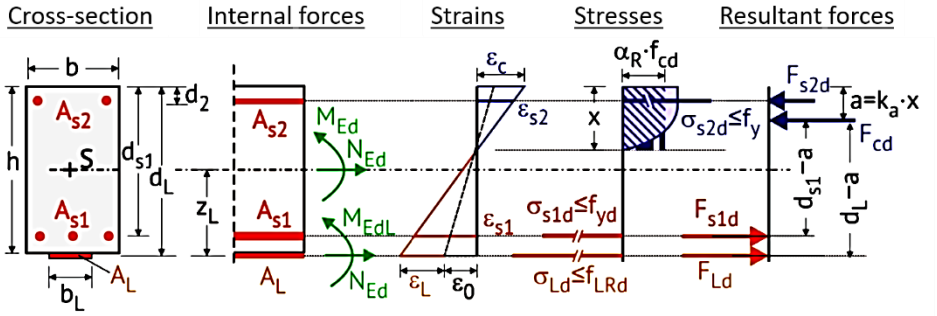


Fig. 1 Strain distribution, stress distribution and internal force equilibrium of a reinforced concrete cross-section strengthened with an external steel plate. A_{s1} and A_{s2} denote the tensile and compression reinforcement, respectively, while A_L denotes the external steel plate [1].

To investigate the ability of the anchorage system to mobilize the target resistance, the strengthening level was increased stepwise by increasing the steel plate cross-section, resulting in progressively higher anchor forces.

4 VALIDATION OF FE MODELLING APPROACH

For the numerical investigations, an experimental program conducted at the Institute of Construction Materials, University of Stuttgart [2], was used for validation.

A simply supported reinforced concrete beam (b =0.35 m, h = 0.20 m, total length 4.0 m, clear span 3.7 m) was tested under four-point bending with a 1.0 m constant moment region. The beam had tensile reinforcement (4Ø8), no shear reinforcement and concrete strength class C20/25 [2].

Steel plates were mounted at the soffit and connected by M16 post-installed anchors with 120 mm embedment depth, arranged in one row along the beam axis. An anchor-free region was provided in the constant moment zone.

Three configurations (SP-1, SP-2 and SP-3) were defined by increasing the plate cross-section while keeping the remaining parameters constant (Fig. 2). The plates were made of structural steel S235. Force transfer was achieved exclusively through the post-installed anchors.

The experimentally measured ultimate loads, analytically calculated target loads based on sectional theory, and the numerically obtained resistances in the bonded and anchored models are summarized in Table 1 for the three strengthened benchmark specimens. The reference beam reached an experimental ultimate load of 25.3 kN and a numerically predicted resistance of 24.8 kN. Compared with the reference beam, the strengthening configurations increased the ultimate load by 121–233%. All strengthened specimens failed after yielding of the tensile reinforcement [2]. The overall agreement between experimental and numerical results indicates that the model reliably captures the global load-bearing behaviour, particularly for low to moderate strengthening levels.

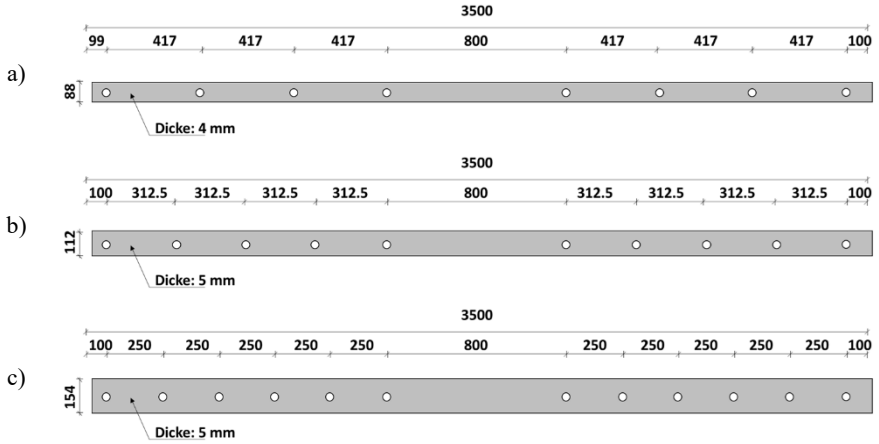


Fig. 2 Steel plate geometries of the strengthening configurations: (a) SP-1, (b) SP-2, (c) SP-3 [2].

FE simulations were performed in ANSYS 2024 R2 [3] using a half-model with symmetry to reduce computational effort. Concrete was modelled by a Drucker–Prager material with tensile and compressive softening, while reinforcement, steel plates and anchors were represented by bilinear elastoplastic elements. Frictional contact ($\mu = 0.2$) was assumed at all concrete–steel interfaces except for the anchored connection, where post-installed anchors were represented by cohesive zone elements (CZM) allowing debonding and separation. Interface properties were defined by normal and tangential strengths together with the corresponding separation and slip limits.

Additional bonded models represented the idealized upper limit with full bond between steel plate and concrete surface and continuous force transfer along the interface.

Table 1 Comparison of experimental ultimate loads, calculated bonded reference loads and numerical resistances for SP-1 to SP-3.

Specimen	Steel Plate [mm]	Failure Load [kN]			
		Test	Analytical	FE-bonded	FE-anchored
SP-1	88x4	56.0	55.2	53.0	51.3
SP-2	112x5	68.1	69.7	68.5	66.3
SP-3	154x5	84.2	83.6	83.9	72.1

For SP-1 and SP-2, the anchored configurations reached nearly the bonded reference level. The small deviations between analytical, experimental and numerical results indicate efficient force transfer and mobilization of the intended strengthening effect.

In contrast, SP-3 exhibited a pronounced reduction in load-bearing capacity because failure was governed by anchorage splitting rather than flexural resistance. FE results revealed high tensile strain concentrations at the end anchorage zone, indicating crack initiation before the theoretical flexural capacity was reached.

In Fig. 3, the colour scale shown on the left represents the maximum principal tensile strain obtained from the numerical simulation. A value of 0.01 corresponds approximately to a crack width of 0.3 mm. The same threshold definition was applied to all models to ensure consistent crack evaluation.

A longitudinal crack initiates between the last two anchors near the plate end and propagates along the anchor axis, differing from a typical flexural crack pattern (Fig. 3).

Such splitting could not be directly confirmed in the experimental tests. In the SP-3 specimens, the steel plate was not removed after testing and the crack development in the concrete cover along the anchor axis was therefore not inspected in detail. Moreover, the onset of flexural yielding and the predicted splitting-controlled capacity appear to be very close for SP-3. As a result, no pronounced load drop was clearly observed during the experiment.

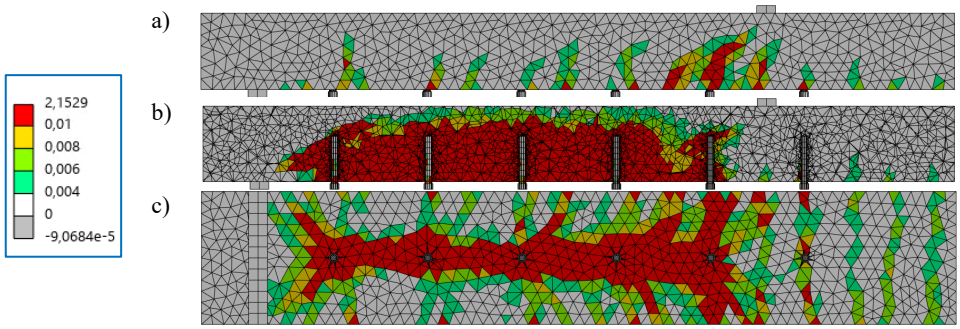


Fig. 3 Crack development and stress distribution in configuration SP-3 at the ultimate load level: (left) colour scale of maximum principal tensile stress (MPa); (right) numerical results for (a) side view, (b) midspan section, and (c) bottom view.

Consequently, the structural response of SP-3 observed in the FE simulation is governed by anchorage splitting rather than by sectional flexural resistance, preventing mobilization of the theoretical bending capacity.

The observed anchorage-controlled failure in SP-3 motivated a systematic parametric investigation to identify governing parameters and possible mitigation strategies.

5 PARAMETRIC INVESTIGATION

Based on the anchorage-controlled splitting failure observed in SP-3, a parametric study was conducted to identify the governing parameters influencing the stress state in the end anchorage zone and mitigation strategies for mobilizing the theoretical flexural resistance. Specimens are identified as n-d-hef-p (anchors per half beam - anchor diameter [mm] - embedment depth [mm] - number of plates). Thus, SP-3 corresponds to 6-16-120-1. Unless otherwise stated, all other parameters remain unchanged.

Because anchor number, diameter and embedment depth may affect shear resistance, the available shear resistance was checked using the approach proposed by Goertz [4]. Based on DIN 1045-1, the concrete contribution is calculated as

$$V_c = \gamma_c \cdot \eta \cdot \kappa \cdot \left(100 \cdot \rho_l \cdot f_{cm}\right)^{1/3} \cdot b_w \cdot d \tag{1}$$

where ρ_l is the longitudinal reinforcement ratio, f_{cm} is the mean concrete compressive strength, b_w is the web width, d is the effective depth, and κ is the size effect factor ($\kappa \leq 2.0$) [4]. In accordance with Goertz [4], a mean-value formulation was used (($\gamma c = 1.0$), ($\eta = 0.10$)). Furthermore, the steel plate was included in the longitudinal reinforcement ratio, while any direct contribution of the post-installed anchors to shear resistance was neglected.

For specimen SP-3, the estimated shear resistance is 119.7 kN, exceeding the bonded reference resistance (83.9 kN), which represents the maximum flexural capacity achievable by the strengthening system. Hence, even without considering a direct anchor contribution to shear resistance, shear failure is not expected to govern. The following parametric study therefore focuses on flexural and anchorage-related mechanisms.

5.1 Influence of the number of anchors

Starting from configuration 6-16-120-1, the number of anchors per half beam was increased to 7, 8, and 9 while keeping diameter, embedment depth and plate geometry constant. These configurations are denoted as 7-16-120-1, 8-16-120-1, and 9-16-120-1, respectively.

The load–displacement curves are shown in Fig. 4 (left) together with the bonded reference. Increasing the number of anchors leads to a gradual increase in load-bearing capacity, with the ultimate load rising from approximately 72 kN for configuration 6-16-120-1 to about 81 kN for configuration 9-16-120-1, thereby approaching the bonded reference solution. This improvement is attributed to a more uniform distribution of the plate force among the anchors, enabling a more complete mobilization of the theoretical flexural capacity. Accordingly, local anchorage-related cracking is reduced and the governing behaviour gradually shifts from anchorage-controlled splitting towards flexural behaviour, as illustrated by the crack patterns in Fig. 4 (right). However, local anchorage damage remains visible, indicating that the response has not yet fully converged to the bonded reference behaviour.

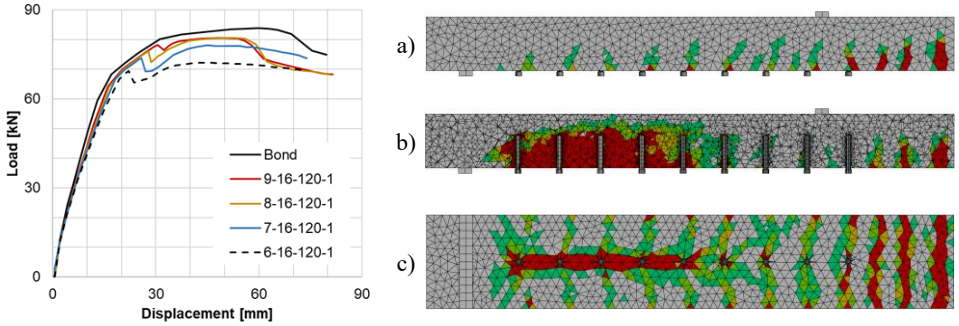


Fig. 4 Influence of anchor number on the structural response: (left) load–displacement curves for 6-16-120-1 to 9-16-120-1; (right) crack patterns of 9-16-120-1 at the ultimate load level: (a) side view, (b) midspan longitudinal section, (c) bottom view.

5.2 Influence of embedment depth

The embedment depth was increased from 120 mm to 180 mm for all configurations with 6 to 9 anchors per half beam, while keeping all other parameters constant.

For configurations with 6, 7 and 8 anchors, the increase in embedment depth led to a more stable response but did not eliminate splitting in the end anchorage zone. The structural behaviour remained governed by anchorage-related cracking.

A different response was observed only for nine anchors per half beam. Fig. 5 compares 9-16-120-1 and 9-16-180-1 ; the load level remains nearly unchanged, but the failure mode changes significantly.

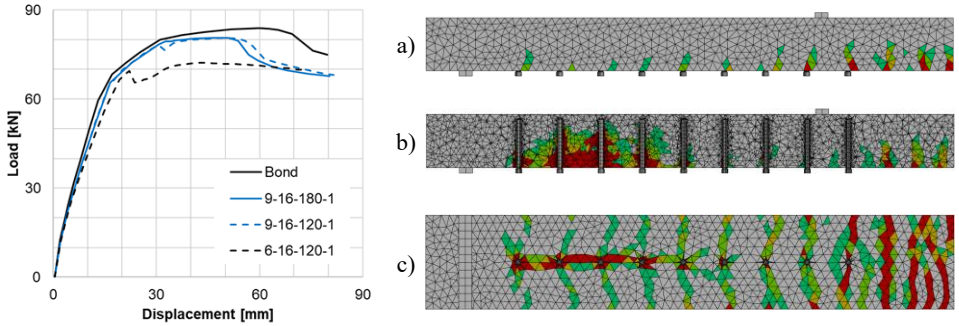


Fig. 5 Influence of embedment depth for configuration with nine anchors per half beam: (left) load–displacement curves; (right) crack patterns of 9-16-180-1 at the ultimate load level: (a) side view, (b) midspan longitudinal section, (c) bottom view.

While configuration 9-16-120-1 still exhibits longitudinal splitting in the end anchorage zone, configuration 9-16-180-1 shows an almost pure bending failure. Splitting cracks are largely eliminated and flexural cracks became dominant in the constant moment region (Fig. 5, right).

Increasing embedment depth alone is therefore insufficient when anchor force remains high. In combination with enough anchors, deeper embedment stabilizes the anchorage zone and allows mobilization of the sectional bending resistance.

5.3 Influence of anchor diameter

Since the splitting crack consistently initiates in the end anchorage zone, the local stress level in this region was reduced by increasing the anchor diameter.

Starting from configuration 6-16-120-1, two modification strategies were investigated :

- All anchors were replaced by M24 anchors (6-24-120-1).

- Only the three anchors located in the end anchorage region were replaced by M24 anchors, while the remaining anchors remained M16 (denoted as combination).

The load-displacement curves are shown in Fig.6 (left). Both configurations reach the bonded reference load level and exhibit a pure bending failure mode. No splitting crack develops in the end anchorage zone.

The crack patterns (Fig. 6, right) confirm that increasing the diameter only in the critical anchorage region is sufficient to suppress splitting. The response of the combination model is practically identical to the configuration with enlarged diameter for all anchors.

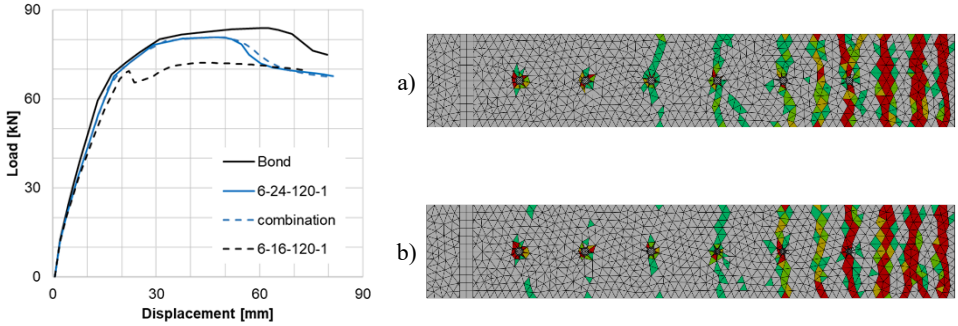


Fig. 6 Influence of anchor diameter: (left) load–displacement curves; (right) crack patterns at ultimate load: (a) 6-M24-120-1, (b) selective diameter increase (combination).

These findings show that local stress concentration in the end anchorage zone, rather than global anchorage capacity, governs splitting. Selectively increasing anchor diameter in the critical region is therefore an effective and mechanically consistent mitigation strategy.

5.4 Modification of the plate geometry

In a further step, the plate geometry was modified while keeping all anchorage parameters identical to configuration 6-16-120-1.

The single plate was replaced by two separate plates with equal total cross-sectional area. Each plate was connected using six anchors per half beam. As a result, the number of load introduction points increased. Thus, the theoretical flexural resistance remained unchanged, while only the load introduction mechanism was modified.

Figure 7 (left) compares the load–displacement curves of the single-plate and double-plate configurations. Although both configurations possess the same calculated flexural capacity, the structural response differs significantly.

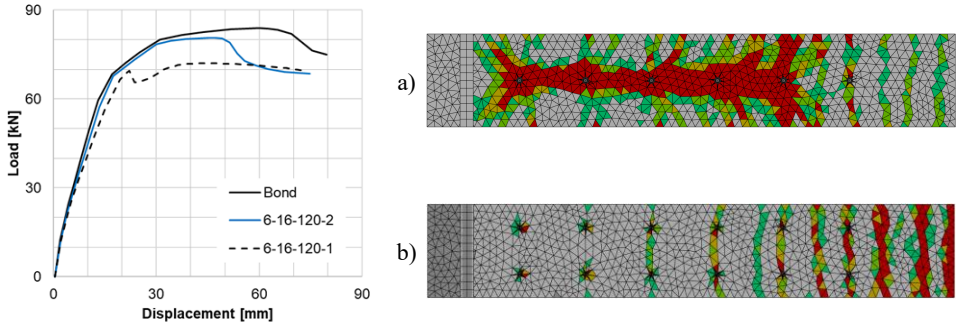


Fig. 7 Influence of plate geometry: (left) load–displacement curves for single- and double-plate configurations with equal total steel area; (right) crack patterns at ultimate load: (a) single plate, (b) two plates.

The crack patterns shown in Fig. 7 (right) further support this observation. The upper image corresponds to the single-plate configuration and shows longitudinal splitting in the anchorage zone. The lower image represents the double-plate configuration, where flexural cracking governs the response.

These results demonstrate that the governing parameter is not the global flexural resistance but the distribution of forces within the anchorage zone. Although both configurations possess the same theoretical flexural resistance, the ultimate load increases from approximately 72 kN to 81 kN, corresponding to an increase of about 11%. Increasing the number of load introduction points reduces local stress concentrations and prevents splitting without modifying anchor diameter or embedment depth.

5.5 Transferability to a higher strengthening level (SP-4)

To investigate whether the anchorage-controlled splitting failure observed in SP-3 also governs at a higher strengthening level, a new beam configuration (SP-4) with a fivefold larger plate cross-section (5×200 mm) was analysed.

A parametric study analogous to SP-3 was conducted by varying the anchor number, diameter, embedment depth and plate configuration while keeping all other parameters constant. Based on the results, critical configurations were selected for future experimental program (Table 2). The corresponding numerical results are summarized in Fig. 8.

Table 2 Test matrix of the experimental program for SP-4: plate geometry, number of plates, anchor configuration and embedment depth.

Specimen's name	Plate		Anchor configuration (per plate)	Anchor's embedment depth (mm)
	Dimensions t×w×l (mm)	No.		
S-P4-Ref	-	-	-	-
S-P4-1	5×200×3500	1	(8+8)×M16 5.8	120
S-P4-2	5×109×3500	2	(8+8)×M16 5.8	120
S-P4-3	5×105×3500	2	(8+8)×M12 5.8	120

The first configuration, consisting of a single plate with M16 anchors, is predicted to exhibit splitting failure in the end anchorage zone.

In configuration SP-4-2, the single plate was replaced by two plates while maintaining the total steel cross-sectional area constant. Consequently, the theoretical flexural resistance remains unchanged, while the number of load introduction points is increased. A bending-governed response is obtained and the ultimate load increases from approximately 81 kN to 96 kN, corresponding to an increase of about 19% compared with SP-4-1. The decisive modification between these two configurations is therefore the redistribution of load introduction points rather than a change in flexural capacity.

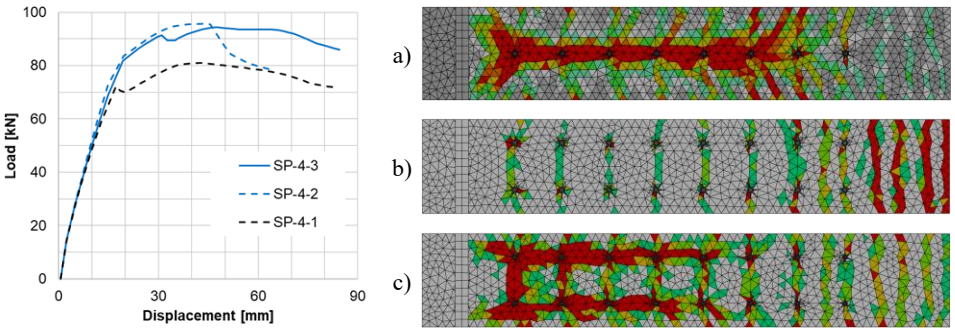


Fig. 8 Influence of plate geometry on SP-4 configurations. Left: load–displacement curves. Right: crack patterns at ultimate load — (a) SP-4-1 (single plate), (b) SP-4-2 (two plates, M16), (c) SP-4-3 (two plates, M12).

In SP-4-3, the anchor diameter was reduced while maintaining the two-plate arrangement. The ultimate load decreased slightly to approximately 94 kN (−2% compared with SP-4-2), whereas the failure mode changed to a mixed mechanism combining flexural cracking and local anchorage effects. This indicates that a smaller anchor diameter reduces local stress concentrations and delays anchorage splitting.

These results indicate that the anchorage-controlled splitting mechanism is not limited to SP-3 but remains relevant at higher strengthening levels. The present study therefore provides the basis for the experimental program on SP-4, which is currently under preparation.

6 DISCUSSION AND DESIGN IMPLICATIONS

The results show that mechanically fastened steel plate strengthening is governed by the local force transfer in the end anchorage zone rather than solely by sectional flexural resistance.

Unlike bonded systems with continuous interface stresses, anchored systems transfer plate forces discretely through individual anchors, generating transverse tensile stresses in the concrete cover. Once these exceed the tensile strength of concrete, longitudinal splitting develops along the anchor axis, preventing full mobilization of the theoretical bending capacity

The governing design parameter is therefore the local stress state around the anchors rather than the global strengthening ratio. The parametric study showed that redistributing the load introduction points and increasing the anchor diameter in the critical anchorage region effectively reduce local stress concentrations and suppress splitting. Increasing embedment depth was beneficial only when combined with a sufficient number of anchors.

Consequently, the design of mechanically fastened strengthening systems should include verification of the anchorage zone behaviour in addition to sectional bending resistance.

7 CONCLUSIONS

Based on the numerical investigations, the following conclusions can be drawn:

- Anchored plate strengthening may fail by longitudinal splitting in the end anchorage zone before reaching the sectional bending capacity.
- The governing mechanism is local stress concentrations caused by discrete force transfer through anchors.
- Increasing the number of anchors improves the structural response and increases the attainable load level but does not necessarily eliminate anchorage-controlled splitting.
- A bending-governed response is achieved only when the anchorage zone is sufficiently stabilized.
- Effective mitigation strategies include increasing the anchor diameter, redistributing the load introduction points, and using multiple plates.
- Increasing the embedment depth was found to be effective only when combined with a sufficiently large number of anchors.
- The identified mechanism is independent of the strengthening level and remains relevant for higher flexural capacities.

Future work will focus on experimental validation and the development of a mechanically based design model quantifying the splitting failure criterion as a function of anchor diameter.

References

[1] Finckh, Wolfgang. 2024. *Verstärken von Betonbauteilen*. Wiesbaden: Springer Vieweg

[2] Sadeghi, Nader, and Sharma, Akanshu. 2022.“Flexural Strengthening of Reinforced Concrete Beams Using Anchored and Bonded Steel Lates.” Unpublished Report, Institute of Construction Materials, University of Stuttgart, Stuttgart.

[3] ANSYS, Inc. 2024. ANSYS Academic Research Mechanical, Release 2024 R2.

[4] Görtz, Stephan. 2004. “Zum Schubrissverhalten von Stahlbeton- und Spannbetonbalken aus Normal- und Hochleistungsbeton.” PhD diss., Rheinisch-Westfälische Technische Hochschule Aachen.

Development of a ductile tension anchor in mid-rise timber-hybrid-buildings in context of a circular economy

Alexander Gerger, Alireza Fadai

Research Unit of Structural Design and Timber Engineering,
TU Wien,
Karlsplatz 13/E259-02, 1040 Vienna, Austria

Summary
The construction industry is currently facing a need for the implementation of separable connections, a development that is essential for facilitating the principles of a circular economy. In this paper the autors focus on ductile connectors for extreme events (e.g., earthquakes) to ensure durable load bearing building elements over several decades. This concept finds applicability in a wide range of building materials. The proposed anchor is a compression-based ductile tension anchor that yields within its own hollow core. This design limits plastic damage to the surrounding timber and remains demountable. The proposed approach is designed to address the limitations of conventional screw/dowel systems that impede the reuse of these components. The load-bearing behaviour of the tube connector is examined by finite element models, which illustrate stress paths and embedment weaknesses through lamella layout.

1 INTRODUCTION

The built environment is one of the most significant factors influencing climate change. Depending on the perspective adopted, the construction industry is responsible for between 21 % and 37 % of greenhouse gas emissions [1, p. 17]. In a linear economic model, the extraction of raw materials from the environment is a fundamental process ('take'), processed into energy sources or products ('make'), consumed during a short period of use ('use'), and returned to the environment as waste or emissions ('waste') [2, p. 4]. The goal of 'net zero emissions' requires transforming this linear economy into a circular economy, improving every area. Ten R-strategies have been defined for this transition [3, p. 28]. In the construction industry, following the reduction of operational (red) emissions, indirect (grey) emissions are now becoming the focus of sustainable construction. The load-bearing structure accounts for the largest share of these material-related emissions [4]. For this reason, reusing load-bearing elements is particularly important for the climate. The reuseability of components places new demands on designs: connections must be demountable and building parts must be 'reuseable' intact, even after the first cycle of use. These strategies are part of the Design for Disassembly and Adaptability (DfD/A) concept, which is a new design approach that focuses on implementing the circular economy through separable connections. These requirements differ depending on whether suitability is sought in the elastic working load range or the plastic load-bearing range. In the context of the working load range, a range of strategies can be employed for implementing reuseable connections.

By reusing components in several buildings, the consideration limit shifts from a planned service life of 50 years (building-based) to over 150 years (component-based). However, the reuse of timber components in several usage cycles increases the probability of extreme events (such as earthquakes) occurring during that extended lifespan. This makes handling plastic load-bearing capacities increasingly relevant in the context of a circular economy. Energy dissipation can reduce stress on structural elements. In timber construction, components alone cannot meet the energy dissipation requirement, so the formation of ductile areas in connections, joints, or targeted energy dissipation systems is necessary [5, p. 219].

The dissipation of energy occurs through the plastic deformation of the fastener's axis, resulting from the surpassing of the yield stress in specific areas. Bending the fastener axis makes dismantling and reusing load-bearing timber-hybrid-components difficult, creating a need in the context of the circular economy. The implementation of repeated reuse of load-bearing elements beyond the elastic working load range requires new strategies in the design of ductile connections. Current work presents the development of a ductile tension anchor for the reuse of timber-hybrid buildings elements.

2 BOUNDARY CONDITIONS FOR CONNECTIONS THROUGH CIRCULAR ECONOMY

Cross-laminated timber (CLT) is a solid building element characterised by a high load-bearing capacity and rigidity. In timber construction, unlike in reinforced concrete construction, the rigidity of the entire supporting structure is largely determined by the rigidity of the joints. Bracing wall panels transfer horizontal loads caused by wind or earthquakes to the foundation. Traditionally, the connection of wall and floor elements is achieved using tension anchors at the ends of the walls and shear angles along the joint (see Fig. 1). These multi-part metal connectors consist of metal plates or moulded metal parts combined with pin-shaped fasteners, such as screws, nails or dowels. While these pin-shaped connectors enable ductile behaviour in the timber-steel joint, they also lead to a significant reduction in the system stiffness of the overall structure. The mechanical properties are significantly influenced by the orientation of these fasteners. It is important to distinguish between connections that are predominantly subjected to tensile stress and those that are predominantly subjected to shear stress.

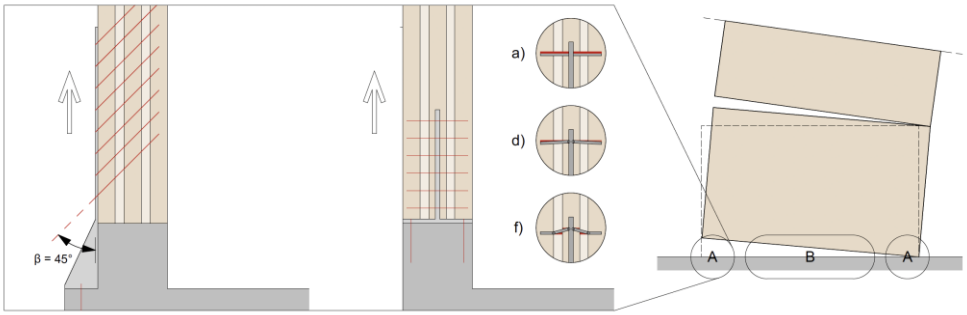


Fig. 1 Areas of connectors: A – tensile, B – shear (right); detail of a tensile anchor with metal angle and inclined screws (left); detail of a tensile anchor with metal plate and dowels (centre) and the possible failure mechanisms a) to f)

2.1 Screws / predominantly tensile stress

Traditionally, screws can be arranged at an angle (e.g. 45°) to break down the shear stress between the metal plate and timber components into tensile and normal forces. Stress is primarily transferred via form closure in the thread and force closure (friction) in the joint. The inclined arrangement of fully threaded screws has very low plastic potential and is classified as non-ductile. Studies show that the dismantlability of inclined screw connections depends on various parameters, including embedment length, stress type and corrosion susceptibility [6, p. 143]. If screws remain in the component during disassembly (e.g. due to turning down the head), they are classified as contaminants, which makes it difficult to reuse the component. If the fasteners can be unscrewed, it can be assumed that the threads remain in the component. The load-bearing capacity of the fastener when reusing the existing thread remains uncertain [6, p. 145].

2.2 Dowels / predominantly shear stress

Dowel type connections are primarily subjected to shear stress. Force is transferred between the metal and the timber in the form of embedment stress. The load-bearing capacity is determined by failure mechanisms, as described by Johansen [7, p. 169f]. There are three types of failure: failure of the fastener due to exceeding the plastic moment-bearing capacity; failure of the timber matrix due to plastic deformation; and combined failure (see Fig. 1, centre). Dowel type connections are well suited to energy dissipation. This should be achieved by exceeding the yield stresses due to bending stresses in the fastener (deformation energy) [5, p. 219]. Pin-shaped metallic fasteners are considered to be ductile/dissipative under stress normal to the fastener axis, but not under predominantly axial stress (e.g. inclined orientation). Due to the formation of flow joints, pin-shaped fasteners can achieve correspondingly high static ductility values ($Ds > 3$ or $Ds > 6$) [8, p. 27]. The activation of the fastener's ductile behaviour is linked to the formation of cavities (i.e. local plastic failure of the timber matrix).

From the point of view of circularity, this mechanism of action is particularly disadvantageous. Bending of the fastener axis due to the deformation of the pin-shaped fasteners when they are bent hinders

disassembly in the axial direction. Even if the fasteners can be removed, plastically deformed areas remain in the timber cross-section. Reuse without reconditioning can result in a 'pinching effect' [9, p. 16]. The dowel is not fully embedded in the timber matrix, which causes yield stresses due to shear stress to occur earlier, reducing the load-bearing capacity.

2.3 Strategies for circular connections

In summary, the following challenges can be identified when dealing with pin-shaped fasteners. New strategies are needed in the context of the circular economy.

Table 1 Summary of current challenges facing traditional fasteners in the context of circularity and strategies derived from this for increasing reuseability

	Challenge	Strategy
1)	The possibility of ductile load-bearing behaviour without restricting the separability of the connetions (bending deformations)	Capacity design with replaceable ductile elements refers to a design concept in which plastic deformation is deliberately concentrated in defined areas, while the load-bearing timber components remain within the elastic range.
2)	The ability to unscrew depends on many parameters (embeded length, type of stress, susceptibility to corrosion) and is difficult to control.	Achieving power transmission is typically achieved by utilising a higher number of short screws or by employing alternative methods.
3)	Ductile behaviour due to bending deformations causes the bar axis to bend in pin-shaped fasteners, making them difficult to remove.	The ability to unscrew can be improved by an axially dominated load due to radial arrangement.
		Ductile behaviour should be achieved through controllable bending deformations of a replaceable metal element.
4)	Ductile behaviour due to bending deformations leads to plastic deformations of the surrounding timber matrix in pin-shaped fasteners.	Energy dissipation through deformation should take place in defined minimal cavities without plastic deformation of the surrounding timber matrix.

3 CONCEPT OF A DUCTILE TENSION ANCHOR CONNECTION

There are already concepts that take these strategies into account for the transfer of shear forces between CLT surface elements: the usage of short screws; ductile behaviour is achieved through controlled bending of replaceable elements in defined minimal cavities (see Fig. 2). U-shaped Flexural Plate-connectors (UFP) consist of U-shaped, interchangeable metal plates that are fastened to timber components using short screws. A cavity is provided in the area of the plates to accommodate deformation. According to Schmid, contact connectors require even less cavity space (see Fig. 2, centre) [10, p. 11]. In accordance with Johansen's theory of pin-shaped connectors, areas of plastic timber deformation are milled out from the outset. This creates minimal deformation space for the metal plates. This concept corresponds to classic Johansen theory, but for linear rather than point-shaped fasteners.

In the field of tension anchors, there are currently no connectors that incorporate these concepts. Connectors for reuse in this field pursue Strategy 3) of avoiding bending deformation by applying as much axial stress as possible to the bolts (see Table 1). One example of a ring connector is the RING 90C from Rothoblaas [11]. It consists of a metal ring with axially arranged, double-inclined screws for connecting the fastener to the CLT wall element in the upper part of the ring, and a bolt on the lower edge of the ring for connecting the element joint. Due to their radial arrangement, the screws are primarily subjected to tensile stress. With a screw length of 200 mm, an elastic limit load of approximately 60 kN can be achieved. This gives the connector a low elastic load-bearing capacity, followed by a 'plastic' range due to the withdrawal failure of the top screws. The performance of the RING 90C connector is largely determined by the withdrawal capacity of the screws used. Ductile

behaviour is not caused by bending deformation, but by load redistribution between the screws and them being pulled out. The cavity in the centre of the connector is not used for deformation.

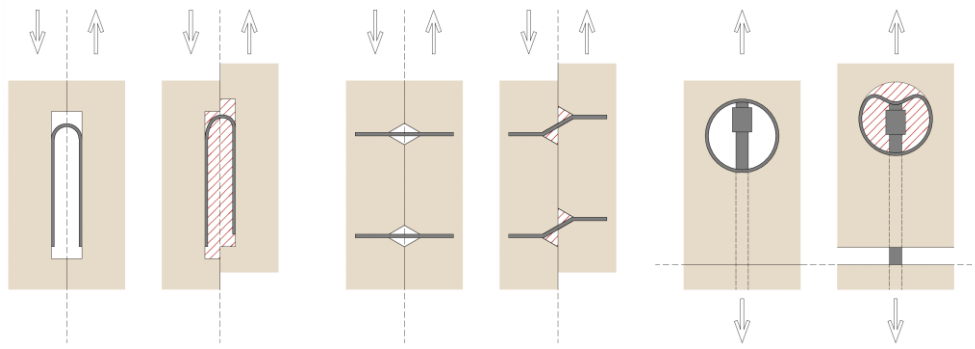


Fig. 2 Comparison of different connectors for reuse: UFP connectors for absorbing shear forces between elements (left), contact connectors for eliminating shear forces between solid timber elements (centre) and an innovative ductile tension anchor (right)

As part of the dissertation research, an alternative to the ring connector is currently being investigated. This involves a transition from a tension-based to a pressure-based approach. The approach under consideration consists of a metal ring with a threaded rod attached to the upper section (see Fig. 2, right). The fastener and the CLT element are designed to engage with one another exclusively through form-fit, pressure, and friction forces. The threaded rod's connection to the upper part of the ring enables ductile bending deformation within the existing cavity of the ring, while preventing plastic deformation of the surrounding timber matrix. The threaded rod is connected to the ring-shaped fastener by means of a sleeve, which ensures that the fastener can be dismantled even after plastic loading. In the present concept, three parameters are of interest for determining performance: the present study investigates the load-bearing and deformation behaviour of the ring connector as well as the function of the load. The load-bearing capacity of the surrounding timber matrix is a key consideration. The load-bearing capacity of the metal ring is of particular relevance, especially in the context of the plastic range.

3.1 Load-bearing behaviour

The general load-bearing behaviour of such a connector can be categorised into four phases [12]:

- Phase I: The material behaviour of the steel tube is linear elastic, with a rapid increase in load.
- Phase II: The material behaviour of the steel tube is characterised by yielding, with a decrease in stiffness of the connector.
- Phase III: The material behaviour of the steel tube is characterised by hardening.
- Phase IV: Local buckling of the steel tube occurs until the connector fails.

Finite element (FE) models have been created to provide a more detailed understanding of the stress distribution in the joint between the ring and the CLT wall element. To this end, a range of surface and volume models have been developed using the Dlubal's RFEM 6.12 software. The parameters are based on the test series conducted by Schneider for better calibration of the results [12]. The stress diagrams in and across the lamella stress direction demonstrate the load distribution of the system (see Fig. 3).

The precise fit of the ring results in stiff initial behaviour, as the ring is continuously supported by the timber matrix from the moment the load is applied. Phase I is characterised primarily by vertical load transfer via the lower half of the ring, without significant deformation of the ring. The situation is analogous to that of a dowel with a large diameter. The force is transmitted primarily via embedment stress in the lamella layers stressed parallel to the grain. As the load increases, the ring's behaviour shifts towards a configuration reminiscent of an arch structure, with a substantial proportion of the force concentrated in the global X-direction. The location of the lowest embedment strength is subject to variation depending on the selected material and geometric lamella composition of the cross-laminated timber wall, and shifts through the timber matrix. As illustrated in Figure 3, the reference configuration after Schneider is a three layers 3s CLT element, composed of spruce-pine-fir (32-35-32 mm) layers,

and a European five layers 5s CLT element, constructed with spruce (40-20-40-20-40 mm) layers, show significant differences depending on the calculation model. For a 30 mm dowel the area of lowest embedment strength varies between 50° (FprEN 1995), 65° (Model 2 Blaß for 32-35-32), and 90° to the vertical (Model 2 Blaß for 40-20-40-20-40). In this area, the ring exhibits the greatest degree of compression against the surrounding timber matrix. This range can be adjusted slightly depending on the number and thickness ratio of transverse to longitudinal layers. Wood exhibits significantly non-linear compressive strength depending on the angle to the grain. In contrast to the model according to FprEN 1995 (1), the model 2 by Blaß [13] takes into account the layer composition of the CLT elements (2).

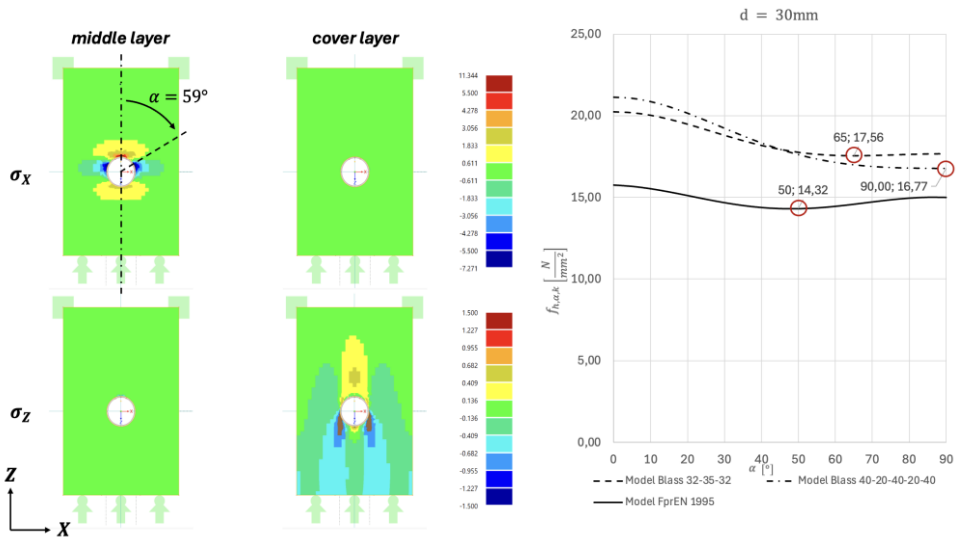


Fig. 3 Qualitative stress curves parallel and perpendicular to the grain direction in the middle layer and top layer (left), graph of average embedment strength as a function of angle and layer structure (right) [14]

This finding aligns with the outcomes of the FE-modelling (cf. Fig. 3). An analysis of the stresses, as a function of the layer position, reveals distinct patterns of load transfer behaviour. The middle layer is exposed to elevated compressive stress along the grain. The introduction of pressure on both sides of the material results in elevated, locally constrained tensile stresses along the grain in the upper quadrant of the ring. The middle layer can be described as a kind of 'load distributing layer'. The centre layer fulfils a function analogous to that of the screws in the RING 90C, thereby ensuring the distribution of loads over a more substantial area of the solid body. As the distance from the load introduction increases, the cover layers demonstrate reduced stresses perpendicular to the grain (see Fig. 3, centre top). In the upper quadrant of the tube, perpendicular tensile stresses are observed, which can result in the rupture of the lamella. The cover layers can be described as 'load transfering layers'. The distribution of the load is contingent upon the accuracy of fit of the fastener, the friction in the joint between the lower half of the ring and the hole lining, and the friction forces due to the deformation of the ring in the upper lateral area. Subsequent loading results in the ring undergoing deformation in the global Z-direction from the connection point of the threaded rod. The onset of a plastically safe deformation range is indicated. It is evident that, consequent to internal force redistribution due to increasing deformation, a brief period of work hardening commences in phase III prior to the occurrence of stability failure in phase IV.

3.2 Embedment strength of the surrounding timber matrix

The load-bearing behaviour of the ring is significantly influenced by the existing embedment strength of the surrounding timber matrix. However, this behaviour is particularly absent at the initiation of the loading process. Within the range of elastic working loads, the embedment situation is analogous to

that of a large-diameter dowel, with the embedment strength serving as the determining factor. The embedment strength can be determined according to either EN 383 or ASTM D5764 [15, 16]. It is evident that both standards were developed for small diameters. A comprehensive review of the extant literature revealed that prior calculation models and experimental series have predominantly focused on diameters ranging from 6 mm to 30 mm, with a conspicuous absence of coverage for diameters up to 150 mm. Depending on the calculation model employed, the embedment strength can reach negative values and vary by approximately 550 % (see Fig. 4). A more detailed analysis of the bedding behaviour of timber reveals that it is a combination of compressive stress parallel to the grain (extending over approximately 48 % of the diameter of the fastener) and friction caused by laterally displaced timber fibres [17]. In the case of the tube connector under investigation, it is expected that there will be no lateral displacement of fibres. The load transfer process should occur exclusively via compressive stress, oriented parallel to the grain.

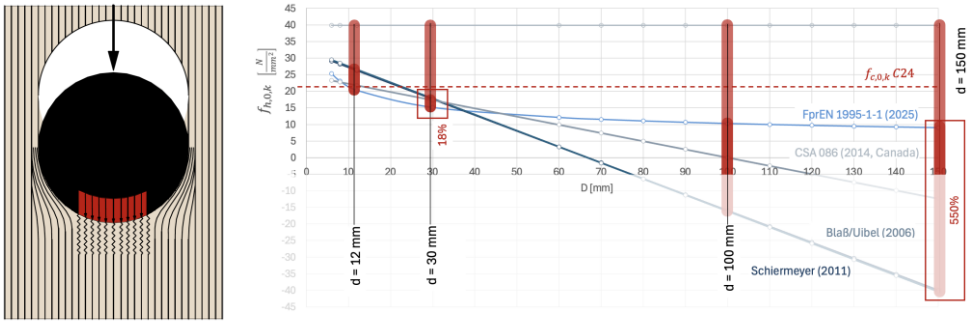


Fig. 4 Load-bearing behaviour due to embedment stress (left), comparison of different calculation models for the embedment strength of CLT depending on the fastener diameter (right) [18]-[20]

A comparison of the embedment situation of the tube with that of a bearing situation for CLT elements reveals a potential for an even wider range of values. ETA-06/0138 permits an increase in compressive strength parallel to the grain of up to 190 %, depending on the edge distance [21, p. 24]. In view of the wide range of variables, it is not possible to make reliable statements about the embedment strength. The present series of large-diameter dowel type tests is therefore being carried out in order to provide more reliable data on this important issue. In collaboration with holz.bau Forschungs GmbH, orientation tests are being conducted with diameters ranging from 30 mm to 150 mm at 30 mm intervals. The objective of this study is to verify the embedment strength in CLT elements for diameters in excess of 30 mm, and to make a recommendation for updating the formula for embedment strength in accordance with FprEN 1995-1-1 (2) [7, p. 176]. This formula is used to calculate the embedment strength for the entire element, without information about the lamellar composition. The only input parameters are the raw density, the fastener diameter and the angle between the stress and the grain direction of the cover layer. However, this model appears to be suitable for diameters over 30mm. Blaß's model 2 (1) takes the lamella composition into account but delivers negative strength values for large diameters and is therefore unsuitable for diameters above 30 mm [13].

$$f_{h,\alpha,k} = 0{,}032 \cdot (1 - 0{,}015 \cdot d) \cdot \rho_k^{1{,}2} \cdot \left[\frac{\sum_{i=1}^{n} t_{0,i}}{t \cdot \left(1{,}6 \cdot \sin^2(\alpha) + \cos^2(\alpha)\right)} + \frac{\sum_{j=1}^{n-1} t_{90,j}}{t \cdot \left(1{,}6 \cdot \cos^2(\alpha) + \sin^2(\alpha)\right)} \right] \quad (1)$$

$$f_{h,\alpha,k} = \frac{0{,}057 \rho_k^{1{,}12} d^{-0{,}32}}{1{,}075 \cdot \sin^2(2\alpha) + \cos^2(2\alpha) + 0{,}05 \left(\frac{\alpha}{90}\right)} \quad (2)$$

with

ρ_k	characteristic raw density of the CLT element
d	diameter of the dowel type fastener
α	angle between the load and the grain direction

$t_{0,i}$	layer thickness parallel to the grain
$t_{90,j}$	layer thickness perpendicular to the grain

3.3 Optimisation of the metal connector

After verifying the embedment strength of the tube, an FE-based parameterised optimisation of the connector is performed using RFEM and Grasshopper [22]. The objectives for the connector were defined in cooperation with the connector manufacturer SIHGA. The aim is to exceed the performance of current non-DfD/A connectors (elastic limit load 150 kN, static ductility >6) while also ensuring circularity. The parameters that are varied are the thickness and lamella composition of the CLT element, the steel grade, the ring diameter, and the thickness of the ring connector.

4 CONCLUSIONS

The dissertation research addresses a central field in timber engineering for a circular economy: connections must both dissipate energy under extreme actions and remain demountable to enable reuse across multiple life cycles, extending load-bearing components perspectives from 50 to over 150 years. Conventional screw and dowel type systems provide ductility primarily through bending, but this induces plastic deformation in the surrounding timber matrix and curvature of the fastener axis, hindering disassembly and degrading performance upon reuse.

The concept of a ductile tube connector advances the proposed circularity-aligned strategies. First, it limits reliance on long, inclined screws whose demountability and reuse remain uncertain. Second, it relocates ductility to a replaceable metal element with a defined deformation cavity, to avoid plastic deformation in the CLT element that undermines reuse.

Finite element studies (particularly using RFEM Software) have been employed to clarify stress paths and bedding phenomena at the tube–CLT interface. Calibrated against relevant experimental references, the models reveal the evolution of parallel- and perpendicular-to-grain stresses through different angles and CLT-configurations. The analyses highlight that the weakest bedding orientation in representative CLT layers migrates toward 50°–60° from the vertical.

The ring's performance is governed by the embedment strength of the surrounding CLT, yet established dowel type standards (EN 383, ASTM D5764) focus on small diameters and show wide scatter when extrapolated to large diameters. Because the connector aims to work in an elastic range of the timber matrix, a dedicated experimental campaign with large diameters (30–120 mm) is initiated to characterise embedment strength for large diameter dowels to support an update of design expressions.

Acknowledgements

The authors gratefully acknowledge the Austrian Research Promotion Agency (FFG) for the funding to enable the implementation of an orientation test series to verify the embedment strength of large diameters in CLT elements. Further-more the authors would like to thank the holz.bau Forschungs GmbH for the support in carrying out the tests and SIHGA GmbH for the excellent corporation and trust.

References

[1] United Nations Environment Programme. 2024. Global Status Report for Buildings and Construction, "Beyond foundations: Mainstreaming sustainable solutions to cut emissions from the buildings sector". Nairobi. doi: 10.59117/20.500.11822/45095.

[2] BMLUK. 2022. "Die österreichische Kreislaufwirtschaftsstrategie" BMLUK. Bericht, Wien.

[3] ISO 59004:2024-05. "Circular economy – Vocabulary, principles and guidance for implementation" Austrian Standards.

[4] Wermke, Christiane. 2020. „Graue Energie versus Betriebsenergie – Ein Vergleich von Leicht- und Massivbauweise", 16. Symposium Energieinnovation. Graz.

[5] prEN 1998-1-2:2023-10-01. „Eurocode 8 – Auslegung von Bauwerken gegen Erdbeben – Teil 1-2: Hochbauten" Austrian Standards.

[6] Graf et al. 2022. „Wandelbarer Holzhybrid für differenzierte Ausbaustufen". Bericht. Technische Universität Kaiserslautern. doi: 10.13140/RG.2.2.34197.81120.

[7] N2259 FprEN 1995-1-1:2025-05-01. "Eurocode 5: Design of timber structures – Part 1-1: General rules and rules for buildings" CEN.

[8] Krupka, Bernhard. 2025. „Einfluss der Federsteifigkeiten von Holzverbindungen im mehrgeschossigen Brettsperrholzbau unter Erdbebenlast". Thesis, Technische Universität Wien. https://repositum.tuwien.at/handle/20.500.12708/6333.

[9] Blaß, Hans Joachim, and Schädle, Patrick. 2011. „Verhalten einer Massivholzwand unter Erdbebenlasten". Band 18 aus Karlsruher Berichte zum Ingenieurholzbau. Karslruher Institut für Technologie (KIT).

[10] Schmidt, Tobias. 2018. „Kontaktverbindungen für aussteifende Scheiben aus Brettsperrholz". Band 33 aus Karlsruher Berichte zum Ingenieurholzbau. Karslruher Institut für Technologie (KIT). doi: 10.5445/KSP/1000083480.

[11] Rothoblaas RING. 2026. Accessed February 09. https://www.rothoblaas.de/produkte/verbindungstechnik/holzbauverbinder/winkel-und-verbinder-fur-gebaude/ring.

[12] Schneider, Johannes, and Tannert, Thomas, and Tesfamariam, Solomon, and Stiemer, Siegfried 2018. "Experimental assessment of a novel steel tube connector in cross-laminated timber", *Engineering Structures* 177:283-290. doi: 10.1016/j.engstruct.2018.09.058.

[13] Blaß, Hans Joachim und Uibel, Thomas. 2007. „Tragfähigkeit von stiftförmigen Verbindungsmitteln in Brettsperrholz". Forschungsbericht. Karslruher Institut für Technologie (KIT).

[14] Dlubal. 2026. Accessed February 09. https://www.dlubal.com/de/produkte/fem-statik-software-rfem/rfem/was-ist-rfem.

[15] ÖNORM EN 383:2007-03-01. „Holzbauwerke – Prüfverfahren – Bestimmung der Lochleibungsfestigkeit und Bettungswerte für stiftförmige Verbindungsmittel" Austrian Standards.

[16] ASTM D 5764-97a: "Standard Test Method for Evaluating Dowel-Bearing Strength of Wood and Wood-Based Products" ASTM International.

[17] Hochreiner et al. 2013. „Stiftförmige Verbindungsmittel im EC5 und baustatische Modellbildung mittels kommerzieller Statiksoftware" *Bauingenieur* 88:275-89.

[18] Schiermeyer, Volker. 2011. „Verbindungstechnik in der Brettsperrholzbauweise". 4. Europäischer Kongress für energieeffizientes Bauen mit Holz. Köln, Mai 4-5.

[19] CSA O86-14, "Engineering design in wood", CSA Group, Mississauga, Canada.

[20] Uibel, Thomas, and Blaß, Hans Joachim. 2006. "Load carrying capacity of joints with dowel type fasteners in solid wood panels" 39th CIB-W18 Meeting, Florence, August 28-31.

[21] ETA-06/0138. 2021. „Massive plattenförmige Holzbauelemente für tragende Bauteile in Bauwerken" OIB.

[22] Grasshopper. 2026. Accessed February 14. https://www.rhino3d.com/learn/?query=kind:%20grasshopper&modal=null

Effect of interface morphology on the behaviour of HSC dry joints subjected to concentric loading

Nguyen Duy Hung, Nguyen Duc Tung

Chair of Structural Concrete,
Helmut Schmidt University / University of the Federal Armed Forces Hamburg,
Holstenhofweg, 22043 Hamburg, Germany

Summary
The contact interfaces of dry joints in precast concrete structures are critical to the overall structural integrity and are strongly affected by surface imperfections. Although a great deal of research has focused on the shear and flexural mechanisms, the behaviour under axial compression in the presence of interfacial irregularities remains inadequately understood. To elucidate the influence of interface morphology on the compressive performance of dry joints, an experimental campaign of uniaxial compression tests was conducted on high-strength concrete (HSC) specimens with rectangular cross-sections. The interface morphologies of the dry joints were retrieved from the actual joint planes using 3D scanning technology. Two surface morphologies, namely waviness and hemispheres, were identified as the prominent shapes. In addition, a refined 3D finite element model was established and validated to simulate the behavior of a HSC dry joint with rough surface contact. The surface morphologies were artificially created, and the concrete damaged plasticity model in ABAQUS was employed to describe the nonlinear material behaviour of HSC. The numerical simulation showed good agreement with the experimental results regarding load displacement behaviour. The findings suggest that concrete surface morphology should be carefully controlled during the manufacturing process to avoid degradation of the load-bearing capacity of dry joints. This research provides valuable insights for the safety design of precast concrete structures.

1 INTRODUCTION

Indeed, clearance is unavoidable in dry joints of precast concrete structures due to the irregularity of the contact interface. Even when small, it may lead to loss of contact precision, different load tranfer regimes, and localized deformation. Numerous experimental studies have shown that the geometric imperfections of bed joints can significantly influence the compressive performance of dry joints. At low loading levels, interface roughness may cause abrupt changes in the load-displacement behaviour of the test prisms [1], known as the seating effect [2]. Moreover, it has been found that the ultimate strength decreases with increasing joint roughness amplitude [3]. To expand the database, numerical analysis models have been developed to study a wider range of parameters not considered in experiments. Thanoon et al. [4] proposed a mathematical model to describe the nonlinear progressive contact behaviour of dry joints in hollow block masonry. Theiler et al. [5] studied dry compression connections of C50/60 concrete wall panels, where surface unevenness was assumed to follow a sinusoidal wave. Martinez et al. [6] developed numerical models to reproduce the seating effect in compressive behaviour of dry-stacked prisms using different schematic representations of surface roughness. However, these studies either relied on plane stress two-dimensional (2D) continuum models or adopted simplifed representations of surface roughness [5], [6]. Variations in the concrete surfaces due to the manufacturing process, such as the aggregate component, the water-cement ratio, formwork type, and environmental conditions, are significant. Since 2D morphology cannot fully reproduce the geometric characteristic of contact surfaces, investigation of three-demensional (3D) surface morphology is essential for understanding the mechanical behaviour of the HSC dry joints, which is the primary focus of this work.

To address this research gap, the contact surfaces of large-scale concrete specimens were measured using a non-contact scanning technique prior to compression testing. The measured surfaces were classified according to their basic shapes, and the clearance distribution in dry joints was evaluated. Simultaneously, a finite element (FE) model was developed and validated, then used to elucidate the effect of surface morphology on the response of the dry joints. In the numerical simulation, the artificial rough surfaces were assumed as random field and generated in the MATLAB. FE analysis were performed using ABAQUS, which provides a graphical user interface (GUI) and the concrete damaged

plasticity (CDP) model, enabling realistic simulation of surface morphology and nonlinear behaviour of HSC. The results highlight the importance of interface morphology in governing the axial compressive performance of HSC dry joint.

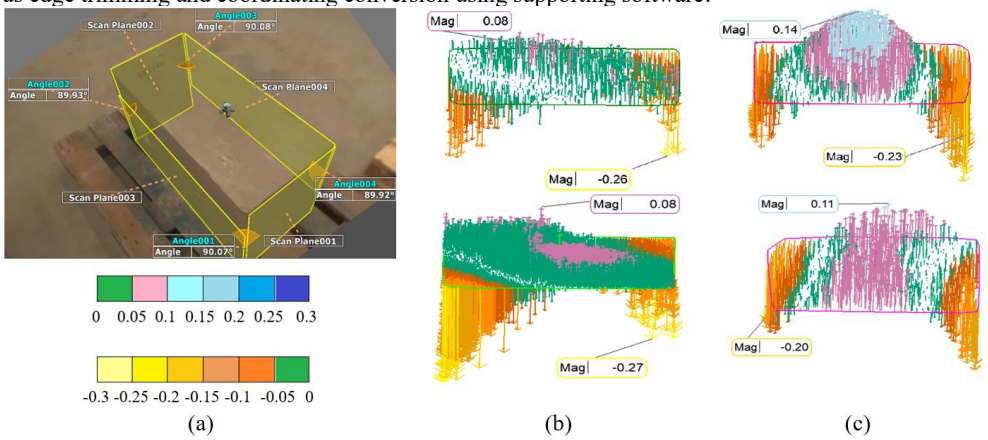
2 EXPERIMENTAL INVESTIGATION

2.1 Specimen preparation and test setup

The investigated HSC dry joints comprised two stacked concrete blocks without mechanical connection, using a rectangular cross-section of 320 mm × 400 mm. Due to the spatial limitations of the 10 MN Universal Testing Machine (UTM), a height of 710 mm was adopted for each concrete block. To facilitate lifting, two holes with a diameter of 25 mm were designed, located 218 mm from each end surface. The key mechanical properties of the material were determined using standard cylindrical specimens under the same curing condition, including a compressive strength of 114.5 MPa and an elastic modulus of 46,428 MPa. Full-scale tests were performed under different surface roughness combinations to investigate the compressive behaviour of the dry joints, with particular focus on the morphology of the contact interface. In the experiments, the hydraulic jact was operated using displacement-controlled mode, applying a vertical load to lower bearing plate of the UTM at a rate of 0.1 mm/min.

2.2 Surface morphology measurement

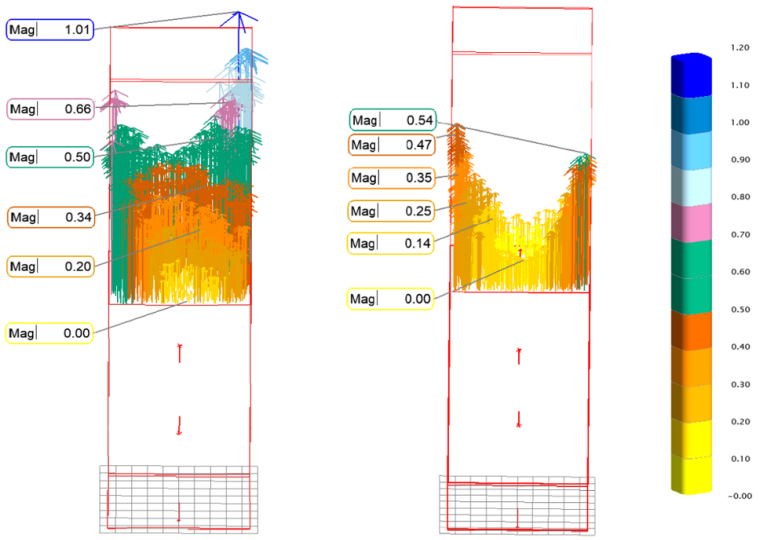
The surface morphology at the contact interface of specimens was measured using a Coordinate Measuring Machine (CMM) prior to the tests. A portable scanning device manufactured by Keyence was employed to acquire a set of 3D coordinates of a concrete block, reconstructing a three-dimensional model as shown in Fig. 1a. The 3D point database of target surface was extracted and processed, such as edge trimming and coordinating conversion using supporting software.



(a) (b) (c)

Fig. 1 Realistic surface profile of contact surface from 3D measurement

After processing the data obtained from the CMM and computer software, the amplitude of the measured surfaces are represented by vectors, as shown in Fig. 1b and 1c. The colour palette was applied to surface images to clearly distinguish the magnitudes of the vectors. A total of twelve color bands were used to visualize surface topography, with height increments of 0.05 mm over the vertical range from -0.3 mm to 0.3 mm. Within this visualization, the colors green, dark blue, and light yellow represent isoplanes corresponding to the arithmetic mean height, maximum peak height, and maximum valley depth, respectively. The graphical representation reveals a wavy appearance in the surface morphology of concrete. Furthermore, the surfaces also exhibit rough components and an irregular microstructure. Fig. 1 middle shows relatively homogeneous surfaces with an approximately uniform height distribution. The large flat regions are indicated by the green colour. Meanwhile, the surfaces in Fig. 1c have more heterogeneous appearance, with significant variations in height distribution. Based on geometric appearances, the morphology of measured concrete surfaces can be categorized into wavy and hemispherical shapes. Moreover, the maximum height of surfaces is very sensitive, in the range 0.3 mm to 0.4 mm.



(a) (b)

Fig. 2 The clearance distribution between two contact surfaces when stacked together.

Fig. 2 shows the clearance distribution between two surfaces when they are stacked on top of each other. There are twelve color bands on the colour palette, which are used to visualize the distance between corresponding points on two rough surfaces. The step size is 0.1 mm over the range from 0 mm to 1.2 mm. The colour palette represents the relative clearance between two surface points and indicates that the initial contact in dry joints occurs along the edges and around the central region of the surface. Furthermore, the contact characteristics of the surface pairs differ significantly. The clearance distribution shown in Fig. 2 left is symmetrical about the axis parallel to the surface edge, while that shown in Fig. 2 right is symmetrical about the center of the rectangular surface.

3 NUMERICAL SIMULATIONS

3.1 Modeling of concrete block with rough surface

3.1.1 Generation of randomly rough topography

The rough surface height (z_{ro}) can be modelled as the distribution of asperities using random field. The random field can be expressed by the spectral representation equation as follows:

$$z_{ro}(p,q) = \sum_{k=0}^{M-1}\sum_{l=0}^{N-1}\sqrt{\tilde{S}_{k,l}}exp\left(i2\pi\left[\varphi_{k,l}+\frac{kp}{M}+\frac{lq}{N}\right]\right) \quad \begin{matrix} p = 0,1,2,\dots,(M-1) \\ q = 0,1,2,\dots,(N-1) \end{matrix} \tag{1}$$

Where $\tilde{S}_{k,l}$ is the power spectral density function of the target roughness, $\varphi_{k,l}$ is a set of independent random phase angles, uniformly distributed between 0 and 2π. The term i is the imaginary unit. The $\tilde{S}_{k,l}$ can be obtained from autocorrelation function (ACF) $\tilde{R}_{r,s}$ based on Fast Fourier Transform (FFT):

$$\tilde{S}_{k,l} = \frac{1}{MN}\sum_{r=0}^{M-1}\sum_{s=0}^{N-1}\tilde{R}_{r,s}exp\left(-i2\pi\left[\frac{kr}{M}+\frac{ls}{N}\right]\right) \quad \begin{matrix} k = 0,1,2,\dots,(M-1) \\ l = 0,1,2,\dots,(N-1) \end{matrix} \tag{2}$$

As presented in equations 1 and 2, M, N are number of surface points in X, Y directions. k, l, p, q, r, s are variable integers. Detailed guidance on simulation of rough surfaces with FFT was provided in [7]. For engineering surface, the ACF is commonly used in exponential form.

$$\tilde{R}_{r,s} = \sigma^2 exp\left[-2.3\sqrt{\left(\frac{r\Delta_x}{d_x}\right)^2+\left(\frac{s\Delta_y}{d_y}\right)^2}\right] \tag{3}$$

Where, σ is the root mean square roughness. The grid size (Δ_x, Δ_y) and the autocorrelation lengths (d_x, d_y) in X and Y directions quantify the resolution and spatial similarity between different points on

the surface. Consequently, the autocorrelation length governs the shape and the relative location of the surface asperities, the desired morphology of surface can be achieved.

3.1.2 Volumetric 3D mesh of concrete block

The 3D FE model for each concrete block was divided into two parts in simulation due to its complexity. These are a non-uniform mesh part containing rough surface (part A) and a uniform mesh part with holes (part B), initially constructed in MATLAB and ABAQUS, respectively. For part A, a rectangular prism with dimensions of 320 mm × 400 mm × 60 mm was first created. The top surface corresponding to the cross-section and coinciding with the *OXY* plane was designated as the rough surface. The nodal coordinates on this surface were initially determined based on the grid of the generated surface. The surface roughening procedure simply involves moving each surface node point perpendicular to the *OXY* surface according to the roughness amplitude. Next, three layers with a uniform fine mesh were generated near the rough surface, with the element sizes approximately equal to the surface mesh size. In the remaining region, nodes and elements were treated using a mesh transition technique along the *Z*-direction. The application of the mesh transition technique is described in [8]. The components defining part A were specified by index and imported into ABAQUS/Standard as **.inp* file. For part B, a rectangular prism with dimensions of 320 mm × 400 mm × 650 mm containing two designed holes was created in ABAQUS and uniformly meshed with a mesh size of 10 mm. Parts A and B were then merged in the Assembly Manager using the Mesh operation. The mesh size of the concrete model was optimized by considering both accuracy and efficiency.

3.2 FE Modeling

The CDP model in ABAQUS was used to represent the nonlinear response of HSC. This model allows the concrete material properties under uniaxial compression and tension, along with damage variables, to be incorposated into the FE analysis, as illustrated in Fig. 3a and 3b. Three plasticity parameters of the CDP model, the biaxial-to-uniaxial compressive stress ratio, shape factor and eccentricity were set to the default values of 1.16, 0.667 and 0.1, respectively. Through sensitivity analysis, two other parameters, the dilation angle and viscosity constant, were set to 44° and 0.001 to achieve better computational accuracy and convergence. On the other hand, steel plates were modelled using a linear elasticity material model characterized by Young's modulus of 200 GPa and Poisson's ratio of 0.3.

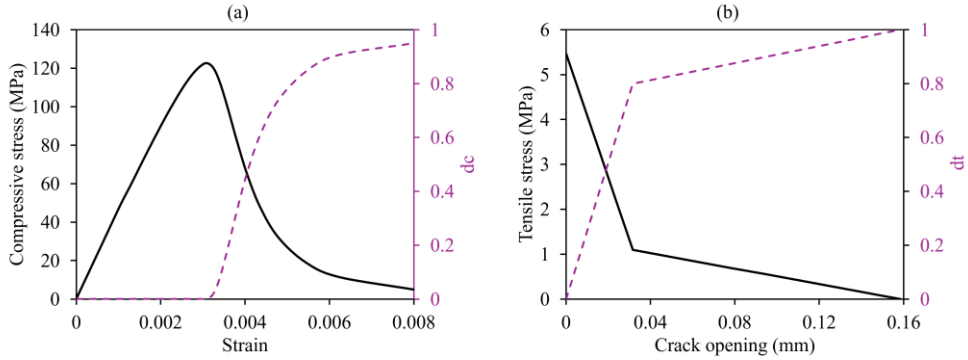


Fig. 3 (a) Compressive and (b) tensile behaviours of HSC used in the FE model.

In the modelling procedure, two concrete blocks and two steel plates in the test setup were included. The 8-node linear hexahedral element (C3D8R) from the ABAQUS library, which is commonly used to simulate concrete behaviour, was adopted. A uniform mesh size of 25 mm was used for the steel plates. To simulate the closure of the dry joint under compressive load, the surface-to-surface contact with finite sliding was employed in the contact behaviour. Hard contact and penalty function were used to define the behaviour in the normal and tangential directions between two surfaces. The friction coefficient based on Mohr-Coulomb model was set to 0.5. A similar contact definition was adopted for the interaction between concrete and steel plate, with a coefficient of friction of 0.3. Additionally, the *Nlgeom* setting in Step Manager was activated to account for geometric nonlinearity during contact. The boundary and loading conditions in the numerical simulation were defined according to the experiment setup. Each opposite side of the contact surface with concrete on each steel plate was

coupled to a reference point at its centre. Fixed support conditions were assigned to the reference points. To apply axial loading, an upward displacement was applied to the lower reference point.

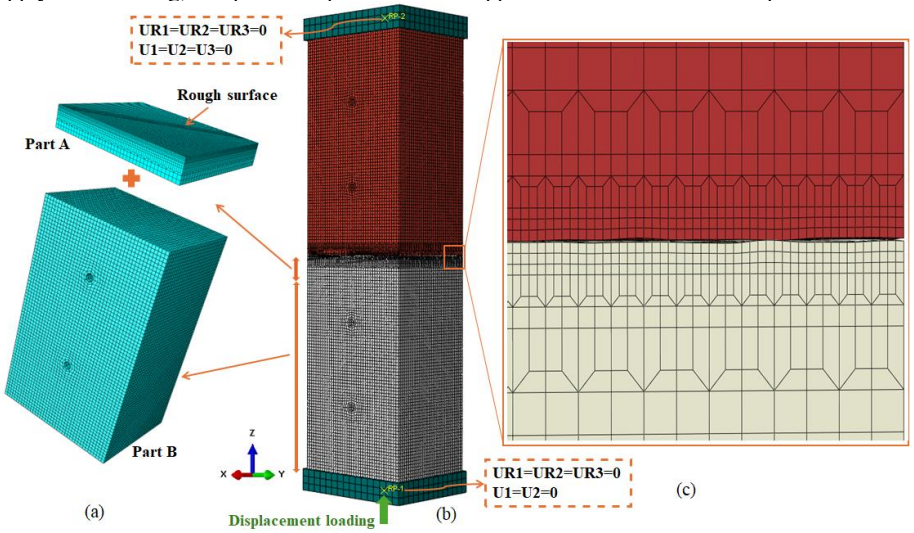


Fig. 4 FE model in ABAQUS.

4 INVESTIGATING THE EFFECT OF INTERFACE MORPHOLOGY

Since the interface morphology parameters of HSC are difficult to control experimentally and related studies remain limited, numerical simulations were employed to generate rough surfaces resembling the measured surface morphologies. The influence of interface morphology on the axial compressive performance of dry joints was investigated using FE analysis and validated against experimental results.

4.1 Representative surface morphologies for numerical analysis

Two kinds of surface morphologies were considered in simulation. The same parameters were used for the random generations, i.e. $\sigma = 0.1, \Delta_x = \Delta_y = 5mm, M = 65, N = 81$. Due to a lack of specific information of the field correlation of concrete surface, the correlation lengths $(d_x = d_y)$ of 150 mm and 350 mm were assumed for wavy and hemispherical shape surfaces, respectively.

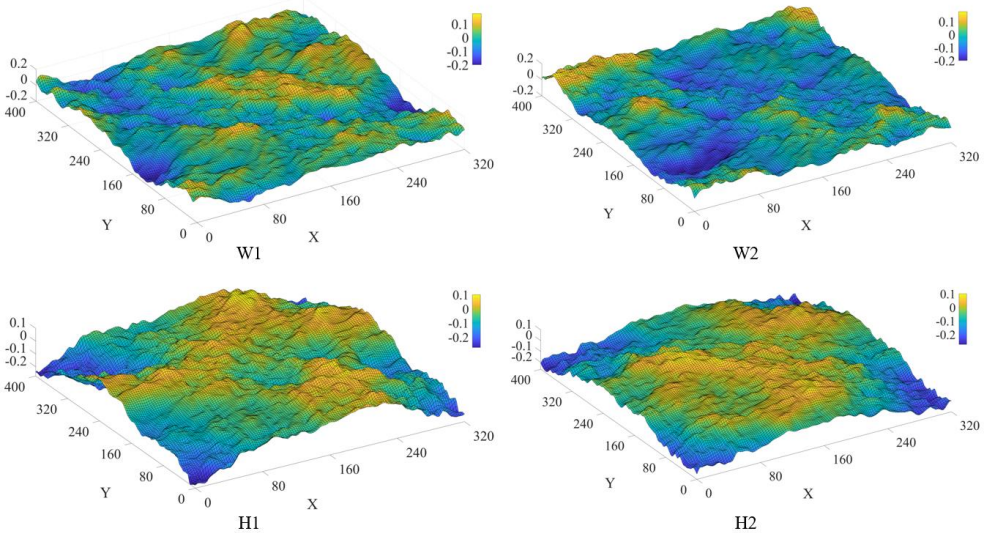


Fig. 5 The visualization of simulated surfaces with different base shapes

Fig. 5 shows the generated surfaces after adding the interpolated midpoints. The surfaces can be defined as the superposition of a base shape and surface roughness, denoted as W1, W2, H1, and H2. Surfaces W1 and W2 illustrate the base shape formed by short-wavelength components (simplifying as a wavy shape). Meanwhile, the base shape of surfaces H1 and H2 is governed by long-wavelength components (simplifying as a hemispherical shape). The simulated surfaces are consistent with the measured surfaces. The maximum surface heights were controlled to be approximately 0.37 mm.

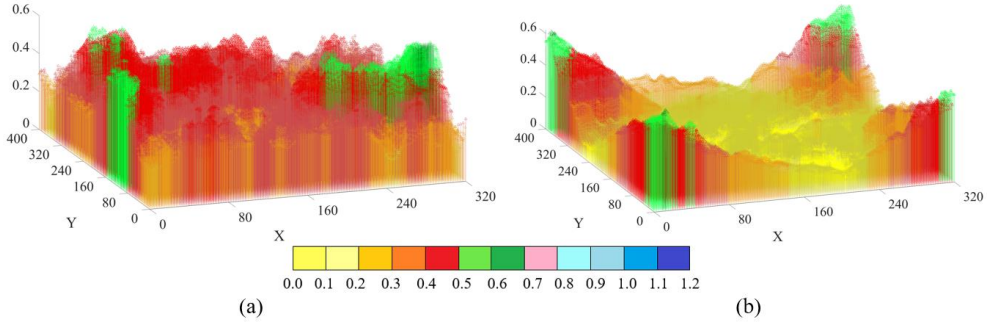


Fig. 6 The clearance distribution of joints (a) WV contact (b) HS contact.

Each dry joint forms a contact pair consisting of two rough surfaces. The combination of surfaces with diferent morphologies results in a relatively small actual contact area compared with the overall surface. To replicate the experiment, a deliberate combination was adopted. Surfaces W1 and W2 were paired to form the WV contact, while surfaces H1 and H2 were paired to form the HS contact. The clearance distributions of the WV and HS contacts are shown in Fig. 6, where the light yellow zone represents the contacting patches. Compared with Fig. 2, the clearance distributions obtained from numerical simulations show good qualitative similarity with the experiments.

4.2 Comparison of experimental and numerical results

To verify the accuracy of the FE model and examine the influence of the interface morphology on dry joint's capacity, the aforementioned WV and HS contact scenarios were used in the numerical analysis.

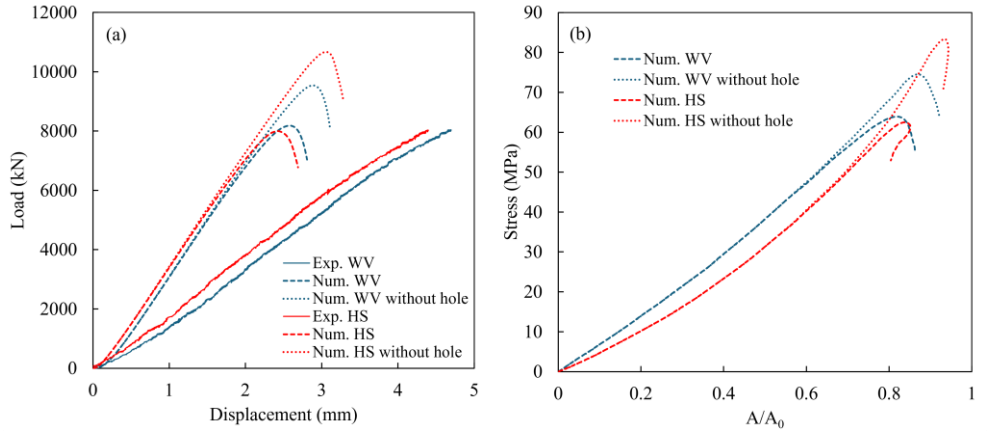


Fig. 7 (a) Comparison of load-displacement curves between experimental and numerical results. (b) Comparison of stress-dimensionless contact area curves in simulation.

Fig. 7 left shows the comparisons of load-displacement relationships between test results and FE predictions under different contact scenarios. Solid and dashed lines represent the experimental and numerical results of the concrete block with transportation holes, respectively. The numerical results of dry joints without transportation holes were depicted by dotted lines. It is observed that the FE model effectively capture the general trend and load bearing capacity of the dry joints in both contact scenarios. The low contact stiffness at the early stage of load-displacement curves indicates the closure of the dry joints due to the surface irregularities, known as the seating effect. The behaviour of the dry

joint with WV contact differs from that with HS contact, not only at the low load level but also at ultimate load. In the early stage, for the same axial deformation, the load bearing capacity of the dry joint with WV contact is lower than that with HS contact. This phenomenon can be adequately explained by Fig. 7 right, which illustrates the relationship between the stress and the non-dimensional contact area (where A_0 is apparent contact area). The HS contact has a larger contact area due to the lower slope of the stress-dimensionless contact area curve. Its larger contact area considerably improves the contact stiffness. At the ultimate stage, in the absence of transportation holes, the load bearing capacity of HS contact is significantly higher than that of WV contact. Conversely, it is noteworthy that the load-bearing capacity of HS contact is slightly smaller in the case of transportation holes. Based on the evolution of the contact area, the case without transportation holes still yields more convincing results. Therefore, it can be concluded that surface morphology significantly influences both the early stage behavior and the load bearing capacity of the dry joints.

4.3 Further discussion on numerical results

Due to limitations of processing and testing, four additional scenarios of dry joints were numerically investigated to further evaluate the influence of interface morphology. The same surfaces described in Section 4.1 were adopted in this study. These scenarios are denoted as W1-H1, W1-H2, W2-H1 and W2-H2 contact, representing the pairing of the corresponding surfaces. For example, Fig. 8 demonstrates the clearance distribution for the W1-H2 and W2-H1 contacts.

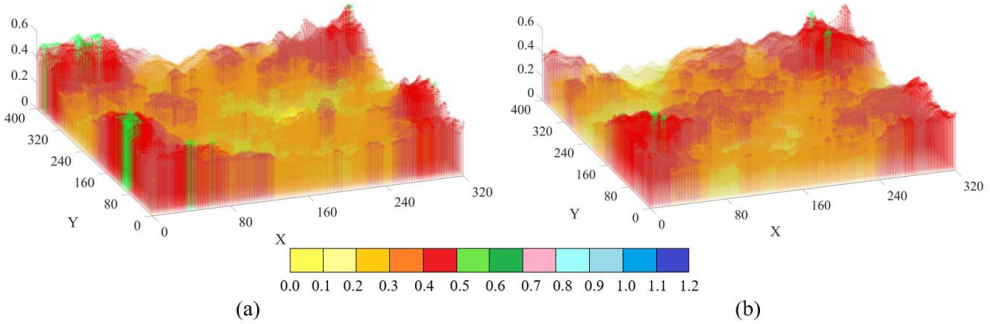


Fig. 8 The clearance distribution of joints (a) W1-H2 contact (b) W2-H1 contact.

Fig. 9 left shows the numerical load-displacement curves under six different contact scenarios. Differences in peak load and seating effect can be observed among contact scenarios, thereby highlighting the influence of surface morphology on the compressive response. Although the HS contact exhibits a higher initial contact stiffness, its load bearing capacity is lower than that of the W1-H2 contact.

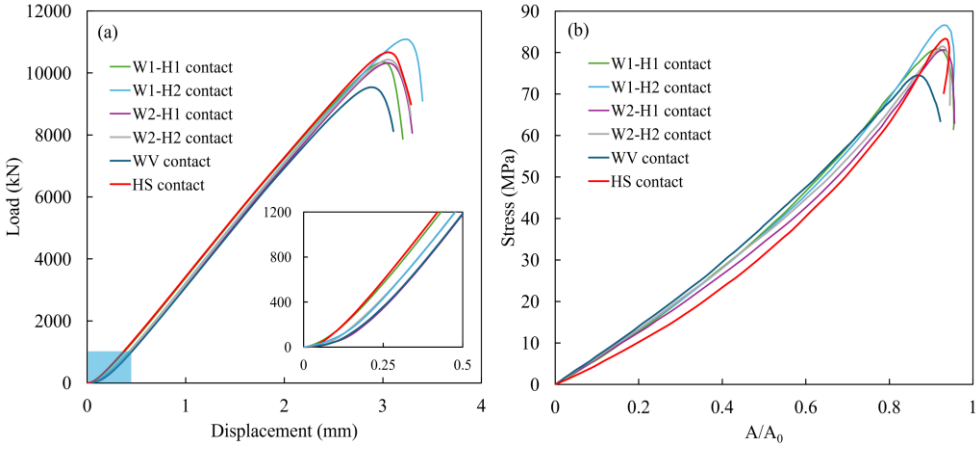


Fig. 9 (a) Comparison of numerical load-displacement curves. (b) Comparison of numerical stress-dimensionless contact area curves.

Fig. 9 right shows the stress versus the non-dimensional contact area for six different contact scenarios. As observed, stress increases nonlinearly with increasing contact area, indicating that compressive resistance improves as more interface regions participate in load transfer. At low contact ratios, the stress remains relatively small, and differences among contact scenarios are minor. This is because only a limited number of asperity peaks carry the applied load, resulting in inefficient load transfer. As A/A_0 increases, the slopes of the curves become steeper and the differences among contact scenarios become more pronounced, reflecting the transition from localized contact at discrete regions to a more continuous load-transfer mechanism over the interface. The W1-H2 contact exhibits the most efficient conversion of contact area into load resistance. In contrast, the WV contact shows poorer performance, reaching its peak stress at a lower contact ratio. These results demonstrate that the spatial distribution of contact area is critical for the compressive performance of dry joints.

5 CONCLUSIONS

This study investigated the effect of interface morphology on the concentric compressive behaviour of HSC dry joints. The experimental programme provided valuable insights into surface geometry through non-contact measurements and the load-displacement curves obtained from compression tests. In addition, a 3D FE-based simulation was performed to validate the experimental results and further examine the influence of surface features. The following conclusions can be drawn:

The developed FE model, combining the CDP model and simulated rough surfaces generated using a random field approach, successfully predicts the compressive behaviour of HSC dry joints with rough surface contact. The numerical model also captures the seating effect induced by interface morphology, particularly in terms of the initial contact stiffness observed in the load-displacement curves.

The case study results reveal that the compressive behaviour of HSC dry joint is strongly influenced by interface morphology. A larger contact area corresponds to greater initial contact stiffness, resulting in higher load bearing capacity and smaller axial displacement in the early loading stage.

The spatial distribution of interface morphology plays a significant role in the contact behaviour of dry joints, as different surface distributions can lead to substantially different mechanical responses. These findings are expected to contribute to the optimisation of tolerance design in precast concrete structures.

References

[1] Atamturktur, Sez, Ross, Brandon E., Thompson, Jason, and Biggs, David. 2016. “Compressive Strength of Dry-Stacked Concrete Masonry Unit Assemblies.” *Journal of Materials in Civil Engineering* 29:06016020. doi: 10.1061/(ASCE)MT.1943-5533.0001693.

[2] Al-Fakih, Amin, Mohammed, Bashar S., Al-Shugaa, Madyan A., Al-Osta, Mohammed A. 2022. “Experimental investigation of dry-bed joints in rubberized concrete interlocking masonry.” *Journal of Building Engineering* 58:105048. doi: 10.1016/j.jobe.2022.105048.

[3] Shi, Tingwei, Zhang, Xihong, Hao, Hong, and Hong, Chen. 2021. “Experimental and numerical investigation on the compressive properties of interlocking blocks.” *Engineering Structures* 228:111561. doi: 10.1016/j.engstruct.2020.111561.

[4] Thanoon, Waleed A.M., Alwathaf, Ahmed H., Nooryaei, Jamaloddin, Jaafar, Mohd. Saleh, and Abdulkadir, Mohd. Razali. 2008. “Finite element analysis of interlocking mortarless hollow block masonry prism.” *Computers and Structures* 86:520-528. doi: 10.1016/j.compstruc.2007.05.022.

[5] Theiler, Werner, Reicht, Oliver, and Tue, Nguyen Viet. 2015. “Auswirkungen von Unebenheiten bei trockenen Druckverbindungen von Betonbauteilen.” *Beton- und Stahlbetonbau* 110:687–698. doi:10.1002/best.201500003.

[6] Martinez, Marcos, Atamturktur, Sez, Ross, Brandon, Thompson, Jason. 2018. “Assessing the Compressive Behavior of Dry-Stacked Concrete Masonry with Experimentally and Informed Numerical Models.” *Journal of Structural Engineering* 144:04018080. doi: 10.1061/(ASCE)ST.1943-541X.0002056.

[7] Wu, Jiunn-Jong. 2000. “Simulation of rough surfaces with FFT.” *Tribology International* 33:47–58. doi: 10.1016/S0301-679X(00)00016-5.

[8] Zhang, Haibo, Liu, Shengli, and Wang, Wenzhong. 2024. “On contact spots details of rough surface contact using morphologic image processing.” *Mechanism and Machine Theory* 192:105546. doi: 10.1016/j.mechmachtheory.2023.115546.

Enhanced Analytical Model for Estimating Pull-Out Capacity of Power-Actuated Fasteners

Alhussain Yousef[1*], Panagiotis Spyridis [1]

Concrete Structures and Infrastructures Engineering,
University of Rostock,
Justus-von-Liebig-Weg 2, 18059 Rostock, Germany

Summary
Direct fastening systems based on power-actuated fasteners (PAFs) provide rapid anchorage in concrete without drilling or curing. However, their pull-out resistance exhibits pronounced scatter due to shallow embedment and concrete heterogeneity. This study investigates PAF behaviour through experimental testing and analytical modelling. Forty fasteners installed in normal concrete were tested in tension. Penetration depth, nail curvature, crack radius, and damaged concrete area were evaluated using measurements and MATLAB-based image analysis. Gerber's analytical model was refined by introducing a local tensile strength estimated from the measured crack radius and a geometry-dependent reduction factor accounting for curvature-induced reductions in effective embedment depth. The modified model improved the prediction of pull-out resistance and provided a more realistic representation of the observed experimental variability.

1 POWER-ACTUATED FASTENERS (PAFS): BACKGROUND AND RESEARCH OBJECTIVES

Power-actuated fasteners (PAFs) are direct fastening systems that drive hardened steel nails into concrete, masonry, or steel substrates using high-velocity energy sources. Depending on the system, driving may rely on powder cartridges, compressed gas, or spring actuators, reaching impact velocities of 50–100 m/s and enabling rapid, single-step installation [1]. Compared to conventional anchoring systems that require drilling, cleaning, and curing, PAFs achieve anchorage through direct impact, resulting in high productivity, particularly in time-critical, prefabricated, and modular construction applications [1]. PAF penetration into concrete can be interpreted using Cylindrical Cavity Expansion Theory (CET), which idealizes the installation process as a radially propagating stress field consisting of a plastic core, a cracked intermediate zone, and an outer elastic region [2] (Fig. 1). Anchorage resistance arises from combined thermal and mechanical mechanisms, including local bonding due to frictional heating, mechanical interlock between surface deformations and the cement matrix, and radial confinement of the surrounding concrete [1]. Owing to these characteristics, PAFs are widely used for suspended ceilings, conduits, partition tracks, and utility supports, particularly in repetitive but safety-relevant applications [1],[3],[4]. Recent studies have further demonstrated their applicability for retrofitting measures, such as anchoring steel plates or shape-memory alloys, thereby extending their use in repair and strengthening interventions [5,6].

Despite these advantages, PAF pull-out resistance exhibits significant variability due to the dynamic installation process and the heterogeneous nature of concrete. Aggregate size, orientation, and hardness strongly influence the local stress response and contribute to pronounced scatter in test results [7,8]. Installation-related defects, including fastener bending, incomplete embedment, and local surface spalling, may further reduce anchorage performance, especially in concretes containing coarse aggregates or discrete fibers [7]–[11]. In addition, material parameters such as compressive strength, porosity, and fiber content affect penetration resistance and mechanical interlock [7],[12],[13]. Given the shallow embedment depths and brittle failure modes typical of PAFs, extensive experimental investigation is required for reliable characterization. In practice, PAFs are therefore commonly used in redundant arrangements, allowing load redistribution and enhanced robustness in safety-relevant applications. Owing to their comparatively low individual load-bearing capacity and the associated variability in resistance, such systems are generally intended for applications where the load can be shared among multiple fasteners rather than transferred through a single fastening point [3],[8],[9].

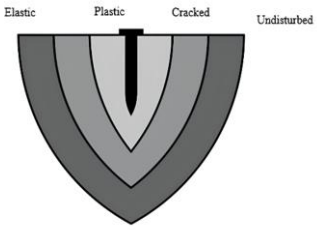


Fig. 1. CET: Three response regions according to Cavity Expansion Theory [2].

Although existing analytical approaches adequately describe the average relationship between pull-out resistance and embedment depth, they do not explicitly account for installation-induced geometric effects and local damage. Consequently, part of the experimentally observed scatter remains unexplained. The objective of this study is therefore to link measurable post-installation parameters, including nail curvature and concrete surface damage, to the analytical description of PAF anchorage behaviour. Experimental investigations are combined with analytical modelling to evaluate the influence of these parameters on pull-out resistance and to improve the prediction of the observed variability.

2 ANALYTICAL MODELING OF PAF PENETRATION AND PULL-OUT RESISTANCE

The mechanical behavior of power-actuated fasteners (PAFs) can be divided into penetration during installation and pull-out under loading, which together govern embedment conditions and anchorage resistance. Penetration into concrete can be interpreted using rigid projectile impact theory for quasi-brittle materials, where localized fracture, stress wave propagation, and embedment formation dominate. Analytical approaches include empirical models, cavity expansion theory (CET), hydrodynamic formulations, and wave-based models [2], all highlighting the role of concrete strength, stiffness, shear resistance, impact velocity, and projectile geometry. CET and its refined forms describe the concrete response through a plastic core, a cracked or tunnel zone, and an outer elastic region [14],[17], providing a physical framework for PAF penetration despite their lower impact energy.

For pull-out resistance, Gerber [7] proposed an analytical model accounting for concrete heterogeneity by distinguishing impacts on cement matrix and aggregates, which may cause fastener deflection, reduced embedment, and surface damage. Assuming an axisymmetric cylindrical stress field, the pull-out force is expressed as

$$F = \frac{4 \cdot \pi^2}{3} \cdot f_t \cdot \nu \cdot h^2, \quad (1)$$

where f_t is the concrete tensile strength, ν the Poisson's ratio, and h the penetration depth. The model reproduces the mean load–depth trend observed experimentally but does not capture the large scatter in pull-out resistance caused by material heterogeneity and dynamic installation effects. To address this limitation, the present study investigates whether measurable post-installation parameters can be incorporated into Gerber's analytical framework. Particular attention is given to crack radius, damaged surface area, embedment depth, and nail curvature, which may reflect local installation conditions and anchorage efficiency. Based on these parameters, the analytical model is refined and calibrated against experimental observations. The experimental programme described in the following section provides the basis for the proposed model development and validation.

3 EXPERIMENTAL PROGRAM

3.1 Concrete Mix, Fasteners, and Installation

A reinforced concrete slab (1500 × 2000 × 160 mm) made of C20/25 concrete was cast using Rhine River aggregates following the A16–B16 grading curve (0/2, 2/8, and 8/16 mm) and a mix with 235 kg/m³ CEM I 42.5 N cement and a water–cement ratio of 0.65. Concrete properties were determined from six cube compression tests and three splitting tensile tests on drilled cores. The measured compressive strengths were converted to equivalent cylinder strengths, yielding mean values of f_{cm} =

28.6 MPa and f_{ct} = 2.9 MPa after age correction. Forty power-actuated fasteners (Hilti X-P 27 MX) (Fig. 2) were installed using a Hilti DX 5 MX tool with red powder cartridges at an energy level of 2.5. The electro-galvanized steel nails had a 27 mm shank length and 4 mm diameter. A minimum spacing of 150 mm was maintained to avoid interaction between fasteners, and all PAFs were connected to the pull-out setup via a steel adapter (Fig. 2).

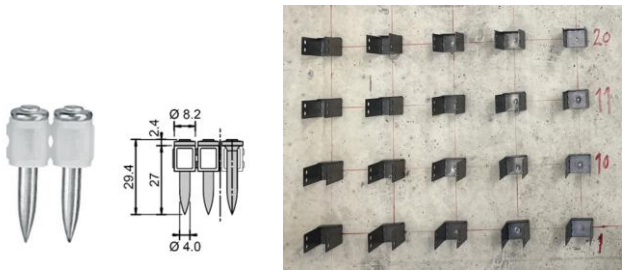


Fig. 2. Hilti X-P 27 MX fasteners; nominal fastener dimensions. Arrangement of the PAFs on the test specimen

3.2 Penetration Depth and Crack Radius

The penetration depth H_p was determined from the total PAF length minus the visible protrusion and fixture thickness, ranging from 21.9 to 26.1 mm (mean 24.6 mm, SD 0.83 mm). Greater penetration generally corresponded to higher pull-out resistance, consistent with Gerber's analytical model. The surface crack radius measured after installation varied between 25 and 80 mm (mean 38 mm, SD 9 mm). The steel adapter used for pull-out testing had a characteristic dimension of approximately 25 mm around the fastener. Consequently, only cracks extending beyond the adapter footprint were considered in the crack-radius evaluation. Since all measured crack radii exceeded this dimension, the crack patterns remained visible and could be measured directly. Moderate cracking showed no clear influence, whereas larger crack radii were occasionally associated with reduced pull-out resistance.

3.3 Pull-Out Testing and Post-Test Evaluation

Pull-out tests were performed under monotonic tension on all 40 PAFs, including setting failures. Measured pull-out forces ranged from 0.32 to 4.40 kN, with a mean value of 2.45 kN and a standard deviation of 0.98 kN (CoV = 44%), reflecting the pronounced scatter typical of power-actuated fasteners. The statistical distribution of the test results was represented using a three-parameter Weibull cumulative distribution function for descriptive representation of experimental scatter, in accordance with the European Assessment Document [3],[8],[9]. The fitted distribution showed close agreement with the experimental data (K–S p-value = 0.89, R^2 = 0.95) (Fig.3.a).

$$(F) = 1.99 \times \left[1 + \exp\left(1 - \left(\frac{F+0.99}{6.5}\right)^{1.96}\right)\right] \quad (2)$$

PAF curvature was classified according to [8] into four levels ranging from no curvature to setting failure. A strong inverse correlation (Pearson r = −0.70) was observed between curvature class and pull-out resistance.

Post-test concrete surface damage was quantified using MATLAB-based image analysis. The damaged surface area A_d ranged from 10.1 to 124.5 cm² (mean 43.8 cm², SD 27.1 cm²) (Fig.3.b).

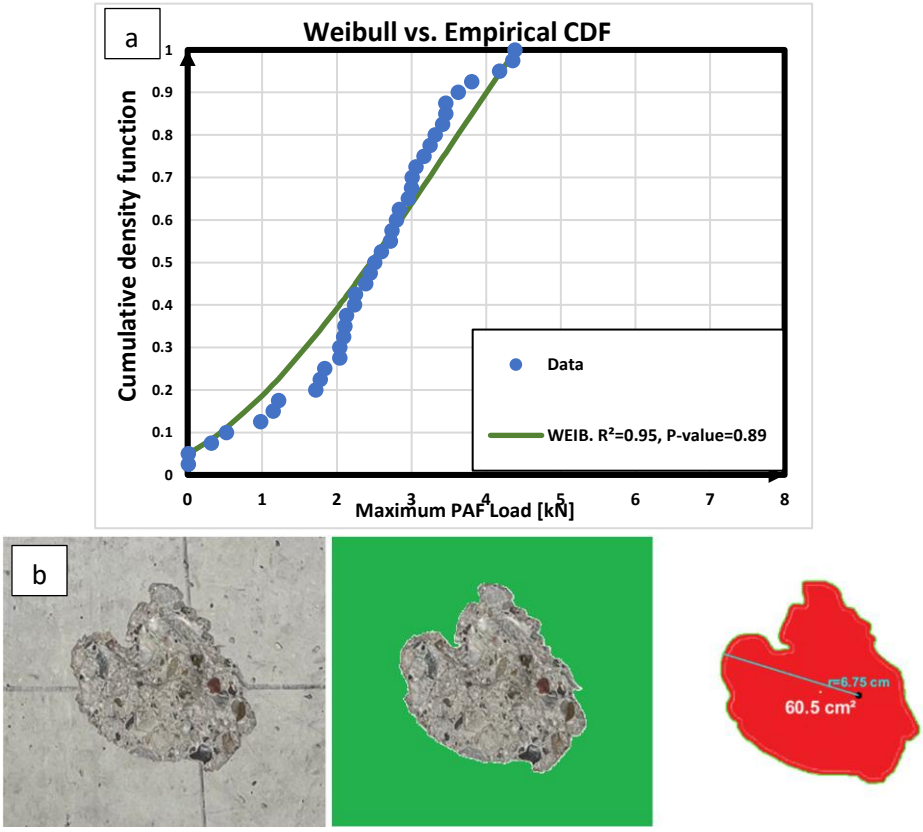


Fig. 3. a: Test data and fitted cumulative distribution function (CDF). b: damaged concrete surface; Defining the damaged area on the concrete; calculating of the damaged area A_d and the largest damage radius from the PAF installation point

4 ANALYTICAL MODEL CALIBRATION OF PAF PULL-OUT CAPACITY

Gerber's analytical model describes the pull-out capacity of power-actuated fasteners (PAFs) as a function of embedment depth, concrete tensile strength, and Poisson's ratio [7]. The formulation was originally validated for test series with varying embedment depths and showed good agreement with experimental results, particularly in reproducing the mean load–depth relationship. In the present experimental program, however, the embedment depth remained nearly constant across all tests (mean ≈ 24.6 mm, SD = 0.8 mm). As a consequence, the pull-out capacities predicted by the original formulation exhibited only minor variation and failed to reflect the pronounced scatter observed in the measured pull-out forces. This highlights a key limitation of the original model when applied to test series dominated by local material effects and installation-induced imperfections rather than by variations in embedment depth. To extend Gerber's formulation to the conditions of the present study, a two-stage calibration strategy was adopted. The first stage addresses local variations in concrete tensile behavior near the fastener, while the second accounts for geometric effects related to fastener curvature and effective embedment depth.

The observed variability in pull-out resistance is primarily attributed to the heterogeneous aggregate distribution and the resulting local variation in tensile strength near the concrete surface. Due to the projectile-type penetration mechanism of PAFs, the mechanical response is governed by the material immediately surrounding the fastener tip rather than by global concrete properties. To capture this effect, the surface crack radius formed during installation was used as an indirect indicator of the local tensile capacity. Following Gerber [7], the crack radius R_z is related to the fastener radius a, the radial stress acting on the shank σ_0, and the local tensile strength f_{ct} through

$$R_z = a \cdot (\sigma_o / f_{ct}) \quad (3)$$

The radial stress σ_0 depends on the concrete compressive strength and the relative density of the cement matrix, accounting for capillary and air porosity, and is expressed as:

$$\sigma_0 = f_c / \sqrt{\left(1 - \rho/\rho'\right)} \quad (4)$$

By rearranging the crack-radius relationship, a local tensile strength $f_{ct,local}$ can be calculated directly from the measured crack radius:

$$f_{ct,local} = (\sigma_o \cdot a)/R_{z\text{-measured}} \quad (5)$$

For the tested C20/25 concrete, a relative matrix density of approximately 70% was estimated based on the water–cement ratio [18]. As reported by Gerber [7], the material displaced during PAF penetration is mainly accommodated within air and capillary pores, while gel pores contribute negligibly due to their small volume. Using the measured compressive strength f_{cm}=28.6 MPa and a fastener radius a=2mm, the radial stress at the fastener shank was calculated as σ_0=50 N/mm², corresponding to an average crack radius of approximately 34 mm. These values were used to estimate the local tensile strength at each fastener position, allowing spatial variability in concrete properties to be reflected in the analytical model. In a second calibration step, the influence of fastener curvature on pull-out resistance was considered. Previous studies [8] have shown that curvature developing during penetration leads to a reduction in effective embedment depth and, consequently, to a decrease in anchorage capacity. Although curvature can only be identified after testing, it affects several measurable quantities, including the crack radius, the plastified and damaged concrete area, and the embedment deficit ΔH, defined as the difference between nominal shank length and actual embedment.

These parameters were therefore used to define a geometry-based reduction factor k for calculating an effective embedment depth $H_{eff}=k \cdot H_p$. Different functional forms relating k to the damaged area A_d , crack radius R, and embedment deficit ΔH were evaluated using an automated calibration routine in MATLAB. Model parameters were optimized using a genetic algorithm, and performance was assessed using statistical indicators including the coefficient of determination (R^2), root mean square error (RMSE), mean absolute error (MAE), and the Kolmogorov–Smirnov (K–S) p-value.

The best agreement with the experimental data was obtained using a logistic-type expression for the reduction factor :

$$K = c_1 + \frac{c_2}{1+\exp[-(c_3+c_4 \cdot A_d+c_5 \cdot {A_d}^2+c_6 \cdot R+c_7 \cdot R^2+c_8 \cdot \Delta H)]} \quad (6)$$

with the calibrated coefficients:

c_1= 0.7, c_2= 0.3, c_3= −5, c_4= 0.04, c_5= −0.0002, c_6= 0.26, c_7= −0.004, c_8= −0.5.

Each coefficient influences the reduction factor as follows:

- c_1, c_2 : define the lower and upper bounds of k (0.7–1.0).
- c_3: sets the reference position of the logistic curve.
- c_4, c_5 : describe the effect of the damaged area A_d, where larger areas tend to increase k up to a limit.
- c_6, c_7 : capture the influence of the crack radius R, where moderate cracking slightly enhances embedment efficiency but excessive cracking reduces it.
- c_8: represents the penalty associated with the embedment deficit ΔH; larger values correspond to stronger reductions in k.

Compared to the original Gerber model, the calibrated formulation significantly improved agreement with the experimental results, reducing RMSE and MAE by more than 50% and increasing R^2 from 0.3 to 0.6. The K–S p-value increased from 0 to 0.76, indicating a substantially improved representation of the statistical distribution of the measured pull-out capacities (Table 1) (Fig. 4).

Table 1: Statistical performance indicators for the Gerber and modified analytical models:

Model	RMSE	MAE	R^2	K-S P-value
Gerber	1.5	1.23	0.3	0
Modified Model	0.69	0.55	0.6	0.76

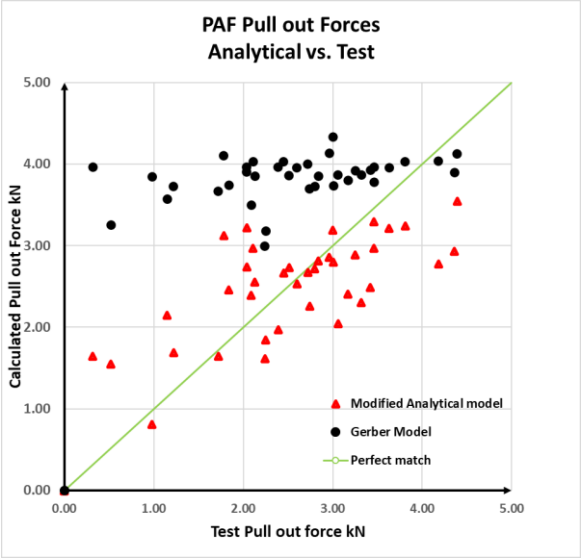


Fig. 4. PAF Pullout capacity: Gerber model vs. Modified analytical model

Fig. 4 compares the calculated pull-out forces from the analytical models with the experimental test results. The black markers represent the original Gerber model, while the red triangles correspond to the modified Gerber model, which incorporates the updated local tensile strength and the reduction in effective embedment depth caused by PAF curvature, estimated from the measured crack radius and damaged concrete area. The original Gerber model yields nearly constant calculated values, forming a horizontal cluster around 4 kN and therefore failing to reflect the overall trend of the experimental data. In contrast, the modified model shows a clear dependence on the measured parameters and aligns more closely with the test results, providing a more realistic representation of the variability in pull-out resistance.

5 CONCLUSION

An experimental investigation on 40 power-actuated fasteners (PAFs) installed in C20/25 concrete was conducted to examine the parameters governing pull-out resistance. Measured capacities ranged from 0.3 to 4.4 kN, with a mean value of 2.45 kN and a standard deviation of 0.98 kN, confirming the pronounced scatter typical of impact-driven fastening systems.

The original Gerber analytical model, while capable of reproducing mean load–depth trends, was unable to capture this variability due to the nearly constant embedment depth in the test series. By recalibrating the model using measurable geometric indicators—penetration depth, surface crack radius, and damaged concrete area—and by introducing a geometry-based reduction factor to account for curvature-induced reductions in effective embedment depth, the predictive accuracy was significantly improved. Compared to the original formulation, the modified model achieved substantially lower prediction errors and a closer agreement with the experimental distribution of pull-out capacities.

The results demonstrate that post-installation measurable parameters provide physically meaningful information on anchorage performance and can be effectively incorporated into analytical models. This

approach offers a more realistic representation of the mechanical behavior of shallow PAF anchorages and supports improved assessment of fastening performance in practical applications, where fasteners are typically used in redundant arrangements.

References

[1] Hilti Corporation: Direct Fastening Technology Manual 2019. Online manual of fastening technology, Schaan: Hilti Deutschland AG (10/2021).

[2] Fang, Qin, and Wu, Hao. 2017. Concrete Structures Under Projectile Impact. Singapore: Springer, 497–558.

[3] EAD 330083-02-0601. Power-actuated fastener for multiple use in concrete for non-structural applications. Brussels: EOTA; 2018.

[4] Gould, William, and Liechti, Drew. 2013. "Driving Power-Actuated Fastener (PAF) Code Provisions." STRUCTURE Magazine 20(3):51–52.

[5] Shan, Zhiwei, Looi, Daniel Ting-Wee, and Su, Ray Kai Leung. 2020. "A Novel Seismic Strengthening Method of RC Columns Confined by Direct Fastening Steel Plates." Engineering Structures 218:110838. https://doi.org/10.1016/j.engstruct.2020.110838

[6] Michels, Julien, Shahverdi, Moslem, and Czaderski, Christoph. 2018. "Flexural Strengthening of Structural Concrete with Iron-Based Shape Memory Alloy Strips." Structural Concrete 19(3):876–891.

[7] Gerber W. Theorie zum Eintreiben und Verankern von Bolzen in Beton. Bauingenieur. 1987; 62: 213–218.

[8] Yousef, A., & Spyridis, P. (2025). Structural and redundancy performance of power actuated fasteners as direct fastenings in fiber reinforced concrete. Structural Concrete. https://doi.org/10.1002/suco.70071

[9] Yousef, Alhussain, and Spyridis, Panagiotis. 2025. "Structural and Redundancy Performance of Power Actuated Fasteners as Direct Fastenings in Fiber Reinforced Concrete." *Structural Concrete* 26:8572–8587.

[10] Patzak, Manfred. 1979. "Zur Frage der Sicherheit von Setzbolzenbefestigungen in Betonbauteilen." Betonwerk + Fertigteil-Technik 5:308–314.

[11] Langenbeck, Anna Dorothea, Spyridis, P., Beßling, M., Orlowsky, J. (2023). Experimental investigations of power-actuated fastenings in TRC. Developments in the Built Environment, 14.

[12] Yousef, Alhussain, Mellios, Nikolaos, and Spyridis, Panagiotis. 2022. "Probabilistic Finite Elements of Direct Fixings in Concrete with Discrete Steel-Fibres." Proceedings of the 14th fib PhD Symposium, Rome, Italy, September 5–7, 879–886.

[13] Mellios, Nikolaos, Yousef, Alhussain, and Spyridis, Panagiotis. 2022. "Probabilistic Finite Elements of Direct Fixings in Concrete with Discrete Aggregates." Proceedings of the 14th fib PhD Symposium in Civil Engineering, Rome, Italy, September 5–7, 871–878.

[14] Forrestal, Michael J., and Luk, Vincent K. 1992. "Penetration into Soil Targets." International Journal of Impact Engineering 12(3):427–444.

[15] Li, Qing, Reid, Stephen R., Wen, H. M., and Telford, A. R.R. 2005. "Local Impact Effects of Hard Missiles on Concrete Targets." International Journal of Impact Engineering 32(1–4):224–284.

[16] Frew, Danny J., Forrestal, Michael J., and Hanchak, Stephen J. 2000. "Penetration Experiments with Limestone Targets and Ogive-Nose Steel Projectiles." Journal of Applied Mechanics 67(4):841–845.

[17] Zhang, Yanyan, Chen, Wanxiang, Cheng, Songsong, Zou, Huihui, and Guo, Zhikun. 2017. "Penetration of Rigid Projectiles into Concrete Based on Improved Cavity Expansion Model." Structural Concrete 18(6):974–985. doi:10.1002/suco.201600195.

[18] Czernin, W: Das Schwinden des Betons. In: Betonstein-Zeitung, (1960), pp. 460 - 464

3D Print

Durability assessment of 3D printable concrete under freeze and thaw

Sushmita Baral[1*], Gunnar Madsen[1], Ingrid Lande[1], and Dmitry Vysochinskiy[1]

*1University of Agder, Grimstad, 4879, Norway, sushmita.baral@uia.no, corresponding author**

Summary

Layer-by-layer concrete printing is gaining attention in construction due to reduced formwork, labor demand, and construction time. Despite these advantages, durability, mainly frost resistance, remains a key concern. This study compares the frost performance of a 3D printable ready mix with conventional B35 M40 concrete, named the reference mix of a similar water-to-binder ratio as casted concrete. Freeze and thaw resistance was evaluated according to NS-EN 12390-9 using slab and cube tests assessing mass loss. In addition, a strength test was also performed after 56 cycles of freeze and thaw, along with 28 days and 84 days for unexposed specimens. Slab test showed higher mass loss in the 3D ready mix, whereas the cube test showed greater loss for the reference mix. Although the reference mix exhibited higher overall strength, freeze and thaw exposure caused up to a 30% reduction in strength, compared to only 4% for the 3D printable mix. These contrasting outcomes underline the complexity of frost performance assessment and highlight the need for further targeted research.

1 INTRODUCTION

Three-Dimensional Concrete Printing (3DCP) is an additive manufacturing technology that is gaining widespread attention in the construction industry. Utilizing computer-aided software for designing and manufacturing structures, it is built layer by layer through the deposition of printable materials on a built platform. This technology has gained popularity by reducing the need for formwork, minimizing labor dependence, increasing construction speed, and enhancing architectural flexibility [1], [2]. Developments in printing technology, pump systems, and the availability of ready-mix dry powders have boosted its adoption in commercial construction. There are many projects ranging from low-rise housing to infrastructure components [3].

Despite growing interest, 3DCP remains a developing technology with several challenges that significantly restrict its structural applications. Among these, durability and long-term performance under environmental exposure are of particular concern [4].

In cold climates, freeze and thaw action is one of the most critical durability challenges for concrete. Repeated freezing and thawing induce internal hydraulic pressure and ice crystallization, which can lead to surface scaling, internal cracking, and progressive strength loss [5]. For conventional concrete, international standards include procedures for evaluating it, but for the 3DCP, whether these procedures are directly applicable remains unknown due to its unique microstructural behavior. It exhibits higher open porosity, layer-induced discontinuities, and weak interfacial transition zones (ITZ) compared to conventional concrete [4], [6], [7]. These differences suggest that frost durability may vary significantly from that of traditionally cast concrete, even though the mixtures share similar binder compositions and water-to-binder (w/b) ratios.

In recent research, many researchers have focused on the mechanical performance of 3D printed concrete, primarily on its compressive, interlayer strength, and flexural strength [8]. In many studies, it has been found that printing parameters, such as layer height, printing speed, time gap between printing layers, and nozzle geometry, have an impact on the mechanical behavior of the final structure [9], [10]. However, studies addressing frost resistance remain limited, and the available findings are inconsistent. Comparisons between mold-cast and 3D-printed concrete have produced mixed results [4]. Some researchers report higher mass loss in mold-cast concrete after freeze and thaw cycles due to increased porosity and microcracking [11], [12], while others observe greater mass loss in 3DCP. This increased

deterioration in 3DCP is often attributed to interlayer interfaces, which introduce interconnected pores that facilitate water ingress, promote crack formation during freezing, and ultimately lead to higher mass loss [13], [14].

Water transport and pore structure are the governing parameters in frost deterioration [3]. As in conventional concrete, freeze and thaw resistance is strongly linked to the entrained air void system and the connectivity of the capillary pores [15]. While in the case of the 3DCP, changes in the extrusion process, shear-induced particle alignment, and incomplete layer compaction change the pore structure [16], [17]. Research using X-ray computed tomography (X-CT) and digital image correlation in printed concrete reveals that interlayer zones contain larger, more interconnected pores and microcracks [18]. These features can accelerate moisture penetration and act as stress concentrators during freezing.

One of the important factors in durability is the w/b ratio. As in the conventional concrete with a lower w/b ratio, concrete has higher strength and better durability due to the reduced capillary porosity. While in 3DCP, to maintain printability, pumpability, and extrudability, concrete is dependent on the w/b ratio. This w/b ratio is also a governing parameter in frost resistance. Therefore, this study aims to evaluate the frost resistance of a 3D printable concrete mixture in comparison with a conventional C35/45 reference concrete with a similar w/b ratio under identical laboratory conditions. Freeze and thaw performance was assessed using standardized slab and cube tests in accordance with NS-EN 12390-9 [19], focusing on mass loss and compressive strength. The results provide insight on the durability assessment for different mix of concrete.

2 MATERIALS AND METHODS

2.1 Materials and mix proportion

In this study, a ready-mix 3DCP and conventional concrete of class C35/45 (B35/45, M40 as per Norwegian standard) were investigated. The 3DCP mix was an industrial product whose constituent details were not disclosed due to trade-secret restrictions. Since detailed material information was unavailable, a sieve analysis was conducted in the laboratory, which showed 38.3% of fines. For comparison, conventional concrete is referred as *Ref mix* and 3D printable mix is referred as *3D mix.* The w/b ratio is taken as the key comparison parameter. As for 3D printable mix exact amount of binders used in the mix is unknown, hence the water to powder (w/p) ratio is defined for this mix. The w/p ratio represented the mass ratio of water to all particles smaller than 0.125 mm, including cement, other binders, and fine sand fillers. Table 1 summarizes the properties of the reference materials used.

Table 1: Information on the materials used

Material	**Characteristics**	**Density (kg/m^3)**
Cement (CEM)	CEM I	3100
Fine Aggregates	Natural sand (0-8) mm	2670
Coarse aggregates	Natural aggregates (8-16) mm	2670

The study aimed to compare the 3D printable mix and the reference mix at the same w/b ratio. For the 3D printable mix, the maximum w/p ratio that allowed adequate flowability was 0.37. At this ratio, however, the reference mix could not be cast. Therefore, the w/b ratio for the reference mix was set to 0.4, which was considered sufficiently similar. Mix proportions were calculated for one cubic meter of concrete and later scaled down, as only 25 liters were required for testing which is shown in Table 2.

Table 2: Mix proportion (w/b = 0.4)

Component	**Quantity (kg) per 1000 liters**	**Quantity (kg) per 25 liters**
Cement	450	16.8

Water	180	6.9
Sand	1049	35.5
Coarse aggregate	700	23.7

2.2 Mixing and specimen fabrication

The reference concrete ingredients were made ready as seen in left of Figure 1 and mixed under standard laboratory conditions using a rotating pan mixer in accordance with NS-EN 206 [20]**.** The mixing dry ingredients was done for five minutes, then water was added and mixed for five minutes. While for the 3D printable industrial ready-mix bag of 25 kg as seen on right of Figure 1 were used and mixed with water on the rotating pan mixer same as the reference mix.



Figure 1: (Left) Ingredients for the Reference concrete and (Right) ready mix powder for 3D printing.

Immediately after mixing, a slump test was performed for both the reference mix and the 3D printable mix as seen in Figure 2. Subsequently,100 × 100 × 100 mm of 30 cube specimens were cast for both reference and 3D printable mix. All molds were lubricated with oil prior to casting. After casting, the molds were covered with plastic sheets to prevent moisture loss. After 24 hours, the specimens were demolded and cured in a water bath at a temperature of 20°C until testing.



Figure 2: Reference mix (left) and 3D mixes (right) and the corresponding slump tests.

2.3 Strength test

Compressive strength test for four cubes was conducted at 28 days of casting as seen in Figure 3 according to the standard *NS- EN 206* [20]. In addition, four specimens subjected to 56 freeze and thaw cycles were tested to evaluate strength degradation. For comparison, four specimens stored continuously in a water bath without freeze and thaw exposure were tested on the same day. The rate of loading on the specimens was 2400 N/s. Facture loads for each sample were recorded, followed by calculating the mean and deviation.



Figure 3: Compressive strength testing of reference specimens at 28 days (left) and after freeze and thaw exposure (middle) and 3D mix (left).

2.4 Freeze and thaw test

Freeze and thaw resistance was evaluated using two methods, the slab test and the cube (alternative) test as per standard *EN 12390-9:2006* [19].

2.4.1 Slab test

After 21 days of casting for the slab test, each 100 mm cube was diamond cut into two halves measuring 50 × 100 × 100 mm. The cut specimens were stored in a climate chamber at 20 ± 2 °C and 65 ± 5% relative humidity. At 25 days, each specimen was wrapped with a rubber sheet bonded to the concrete surface using adhesive, leaving the freshly cut face exposed. A thin line of glue was applied along the interface between the concrete and rubber to ensure sealing, keeping the glued area below 10% of the total exposed surface. After wrapping, the specimens were returned to the climate chamber. At 28 days, a 3 mm thick layer of deionized water (20 ± 2 °C) was added to the exposed surface. Before beginning the experiment, thermal insulation was applied around each specimen, and polypropylene sheets were placed on top as seen in Figure 4. The freeze and thaw test for four specimens started at 31 days of age.



Figure 4: Specimens before testing (left), during freezing inside the freezer (right).

When the freeze and thaw tester machine was on, all the specimens in the freezer were kept for 30 minutes from the start of the cycle as seen in Figure 4. The freezer temperature was recorded every hour, following the curve below as specified by the standard. After 7, 14, and 28 cycles of freeze and thaw, scaled materials were collected from the specimens. Scaled materials from specimens were removed gently with a brush and spray bottle of water. The cumulative mass loss after n freeze and thaw cycle is measured by Equation 1. After completing it again fresh freezing medium was applied to the test surface and kept in the freezer for other cycles.

$$M_{s,n} = m_{s,before} + (m_{v+s(+f)} - m_{v(+f)}) \quad (1)$$

where,

$m_{s,n}$ is the cumulative mass loss after n freeze and thaw cycles

$m_{s,before}$ is the cumulative mass loss of dried scaled material calculated before

$m_{v+s(+f)}$ is the mass of the vessel containing dried, scaled material and filter paper

$m_{v(+f)}$ is the mass of the empty vessel and the dry filter

2.4.2 Cube test

After 27 days of curing, the masses of four cube specimens were measured. The cubes were placed in two containers, with the cast faces oriented perpendicular to the container base as seen in Figure 5. A freezing medium consisting of 3% NaCl solution was added until the liquid level reached 25 mm above the bottom surface of the cubes. After 24 hours of immersion, the cubes were weighed again to determine liquid absorption, calculated using Equation 2.

$$L = \frac{m_{28d} - m_{27d}}{m_{27d}} * 100 \quad (2)$$

where,

m_{28d} is the mass of cube at 28 days of cast that is immersed in freezing medium for 1 day

m_{27d} is the mass of cube at 27 days of cast

The specimens were then returned to the freezing medium and subjected to freeze and thaw cycling following the temperature profile as mentioned on standard. Mass loss was measured after 7, 28, 42, and 56 cycles and calculated using Equation 3.

$$m_{s,n} = m_{s,before} + m_{c+f+b} \quad (3)$$

where,

$m_{s,n}$ is the cumulative mass of dried scaled material after n freeze and thaw cycles

$m_{s,before}$ is the cumulative mass of dried scaled material calculated before the current cycle

m_{c+f+b} is the mass of the dried scaled material



Figure 5: Cube specimens during testing (left) and their placement in the freezer (right)

3 RESULTS

3.1 Freeze and thaw performance

A freeze-thaw test was performed for both reference mix C35/45 and 3D printable ready mix, as per the standard [19], using two different methods. The first method was the slab test method, which is the surface scaling. Figure 6 shows the surface scaling from the specimens. A higher rate of surface scaling is seen in the 3D printable mix compared to the reference mix throughout the test duration as seen in Figure 7. After 7 cycles of freeze and thaw, scaling was 0.7 kg/m^2 in the 3D mix, while in the reference mix it was 0.1 kg/m^2. After 28 cycles of freeze and thaw scaling of the reference mix was 0.53 kg/m^2, while that of the 3D mix was 1.5 kg/m^2. These results indicate that the surface of the 3D printable

concrete is more vulnerable to freeze and thaw deterioration when exposed in slab form. It's likely due to the high content of fines in the mixture which promotes water ingress and scaling under cycling freezing.



Figure 6: Specimens of slab test (left) and cube test (right) after freeze and thaw exposure.

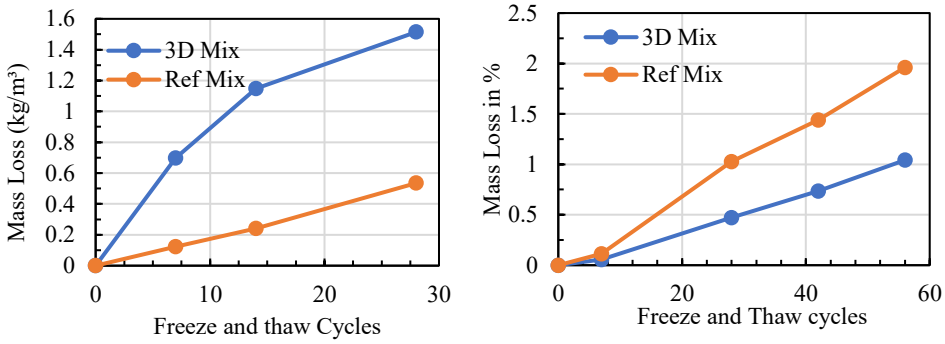


Figure 7: Mass loss per freeze and thaw from the slab test method (left) and cube test method (right)

The second method was the cube test, which also measured the scaled mass loss from the cube. For both the concrete mass loss increases progressively, showing that both concretes are vulnerable to freeze and thaw deterioration as seen in Figure 7. Figure 7 (right) indicates reference material has more mass loss compared to the 3D printable mix. After seven cycles of freeze and thaw percentage of mass loss in both the mix is around 0.1. However, in 56 cycles % of mass loss in the reference mix is 2, while in the 3D mix it is 1. These results suggest that, under the cube test conditions, the 3D mix demonstrates better resistance to frost induced mass loss than the reference concrete.

From Figure 8, it can be observed that the reference mix is stronger than the 3D printable mix. Strength of the 3D printable mix is 50 MPa, while that of the reference mix is 73 MPa after 28 days of casting. At 88 days, the strength increased by approximately 17% for the reference mix and 24% for the 3D mix, indicating continued strength development beyond 28 days for both concretes. Specimens when exposed to freeze and thaw cycles reduction in the strength of the 3D printable mix is 4% while that of the reference mix is 30%. This indicates that the 3D mix has retention over mechanical performance compared to the reference mix of exposure class XF1.

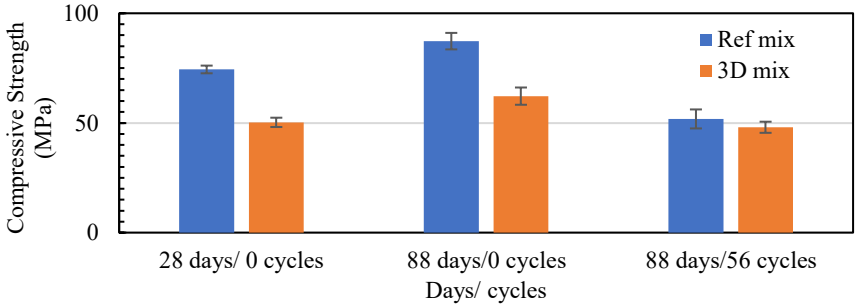


Figure 8: Mean compressive strength with standard deviation

4 DISCUSSIONS

The results obtained in this study show that the frost resistance of the investigated concrete is strongly influenced by the mix composition, as both concretes were mixed, cast, and cured using the same procedures in the lab. The 3D printable ready mix was an industrial mix combined with water at 0.37 w/p, while reference concrete C35 (B35 M40) had a w/b of 0.4. The 3D printable mix was originally developed for extrusion-based construction, but in this study, it is cast to determine how the materials behave in the standard durability test.

From the study, it is seen that the 3D printable mix and the reference mix exhibited different responses depending on the test configuration. The conventional concrete performed better in terms of surface scaling in the slab test while, the 3D ready mix showed lower cumulative mass loss in the cube test. This contrasting behaviour can be explained by using Particle Matrix Model (PPM) introduced by Mortsell (1997) [21] which describes concrete as a two-phase system consisting of a liquid matrix phase (particles smaller than 0.125 mm) and a solid particle phase (particles larger than 0.125 mm).

In the reference concrete, compaction during casting promoted the migration of fine particles toward the specimen surfaces, resulting in a matrix-rich outer layer on the cube specimens. During the cube freeze and thaw test, these fine rich surfaces were directly exposed to cyclic freezing and thawing, leading to increased surface deterioration and mass loss. In contrast, the slab test specimens were cut at a depth of approximately 50 mm, exposing an internal section where coarse aggregates and binder were more uniformly distributed. In these specimens, frost-induced erosion primarily initiated in the cement paste, however, the presence of coarse aggregates reduced the effective cement paste area, thereby limiting surface scaling and mass loss.

An increased fines content can enhance frost resistance by filling voids, increasing paste density, and reducing water mobility within the concrete [22]. However, excessive fines also raise water demand and may lead to the formation of a weaker surface layer with a higher proportion of detrimental pores, thereby reducing overall durability [23]. This shows that lower porosity has better resistance to freeze and thaw damage which explains the reference mix has better performance in the slab test.

The observed continued strength gain beyond 28 days for both mixtures further emphasizes the importance of long-term performance evaluation. The higher relative strength increase in the 3D mix suggests prolonged hydration or pozzolanic reactions, potentially influenced by the fine particle content and modified hydration kinetics. This ongoing densification may enhance resistance to frost damage over time, partially compensating for the lower early age strength of the 3D printable mix. The relatively stable strength of the 3D printable mix after freeze and thaw cycling indicates that its internal microstructure remained largely intact This behaviour may be associated with differences in fines content and pore structure; however, no direct pore characterization (e.g., air-void analysis or X-CT) was performed in this study. Therefore, these explanations should be regarded as plausible hypotheses rather than confirmed mechanisms.

Overall, this study demonstrates that frost resistance cannot be evaluated using single performance metrics. The differing outcomes observed in slab and cube tests indicate that durability assessment must consider both surface related damage and internal material degradation. Furthermore, in depth research with durability testing is necessary to develop clearer design guidelines and testing standards tailored specifically to 3D printed concrete.

5 CONCLUSIONS

This study investigated the freeze and thaw resistance of a 3D printable ready mix concrete designed for additive manufacturing and compared its performance with conventional concrete of strength class B35 and durability class of M40 XF1. Both materials were mixed, cast, and cured under identical laboratory conditions. The experimental work was conducted according to the standard NS-EN 12390-9 [19] which includes slab and cube freeze and thaw test as well as compressive strength test.

The results showed that the frost durability of the investigated concretes strongly depends on the test configuration. In the slab test, the reference concrete performed better than 3D mix. In cut slab specimens, the presence of coarse aggregates reduced the effective cement paste area exposed to freeze and thaw action, which limited surface erosion. This shows great results in favour of conventional concrete while in 3D mix absence of coarse aggregate increases the matrix area which leads to high erosion of masses. Thus, slab test is favourable for the reference mix. In contrast, the cube test showed less mass loss in 3D mix compared to reference mix as its rich fines outer layer limited the water ingress and internal frost damage. This test result shows the cube test method favorable for 3D mix concrete.

Although the reference concrete had higher strength, the 3D mix maintained mechanical integrity after freeze and thaw cycling, reflecting its stable internal microstructure and reduced vulnerability to internal cracking. These findings show that frost durability in 3D printed concrete cannot be assessed by a single test method. The findings are valid for cast 3D printable concrete and should not be directly generalized to printed elements without further experimental verification. Comprehensive evaluation of both surface and internal behavior is necessary, and customized assessment criteria and surface protection strategies are recommended for frost exposed applications.

6 REFERENCES

[1] Buswell, Richard Andrew, Wilson Ricardo Leal de Silva, Scott Z. Jones, and Justin Dirrenberger. 2018. "3D printing using concrete extrusion: A roadmap for research." *Cement and Concrete Research* 112:37-49.https://doi.org/10.1016/j.cemconres.2018.05.006.

[2] Wolfs, Rob J. M., Freek Paul Bos, and Theo A. M. Salet. 2019. "Hardened properties of 3D printed concrete: The influence of process parameters on interlayer adhesion." *Cement and Concrete Research* 119:132-40.https://doi.org/10.1016/j.cemconres.2019.02.017.

[3] Niu, Wenlong, Tiesheng Dou, Meng Li, and Shifa Xia. 2025. "Microscopic Deterioration Mechanism and Different Reinforcement Methods of Concrete Under Freeze–Thaw Environment: A Review." *Processes* 13(12):4064.https://doi.org/10.3390/pr13124064.

[4] Nodehi, Mehrab, Federico Aguayo, Shahab Edin Nodehi, Aliakbar Gholampour, Togay Ozbakkaloglu, and Osman Gencel. 2022. "Durability properties of 3D printed concrete (3DPC)." *Automation in construction* 142:104479.https://doi.org/10.1016/j.autcon.2022.104479.

[5] Guo, Jinjun, Wenqi Sun, Yaoqun Xu, Weiqi Lin, and Weidong Jing. 2022. "Damage Mechanism and Modeling of Concrete in Freeze–Thaw Cycles: A Review." Pp. 1317 in *Buildings*.

[6] Ler, Kee-Hong, Chau-Khun Ma, Chee-Loong Chin, Izni Syahrizal Ibrahim, Khairul Hazman Padil, Mohd Aminul Izmeer Ab Ghafar, and Alva Ami Lenya. 2024. "Porosity and durability tests on 3D printing concrete: A review." *Construction and Building Materials* 446:137973.https://doi.org/10.1016/j.conbuildmat.2024.137973.

[7] Kruger, Jacques, Anton du Plessis, and Gideon van Zijl. 2021. "An investigation into the porosity of extrusion-based 3D printed concrete." *Additive Manufacturing* 37:101740.https://doi.org/10.1016/j.addma.2020.101740.

[8] Cai, Jianguo, JingSong Wang, Qian Zhang, Caixia Du, Marco Meloni, and Jian Feng. 2024. "State-of-the-art of mechanical properties of 3D printed concrete." *Case Studies in Construction Materials* 21:e03847.https://doi.org/10.1016/j.cscm.2024.e03847.

[9] Salaimanimagudam, M. P., and J. Jayaprakash. 2023. "Effect of printing parameters on inter-filament voids, bonding, and geometrical deviation in concrete 3D printed structures." *Materials Letters* 349:134815.https://doi.org/10.1016/j.matlet.2023.134815.

[10] Tay, Yi Wei Daniel, Guan Heng Andrew Ting, Ye Qian, Biranchi Panda, Lewei He, and Ming Jen Tan. 2019. "Time gap effect on bond strength of 3D-printed concrete." *Virtual and Physical Prototyping* 14(1):104-13.https://doi.org/10.1080/17452759.2018.1500420.

[11] Du, Longyu, Jiehang Zhou, Jianzhong Lai, Kai Wu, Xuexiang Yin, and Yuanyuan He. 2023. "Effect of pore structure on durability and mechanical performance of 3D printed concrete." *Construction and Building Materials* 400:132581.https://doi.org/10.1016/j.conbuildmat.2023.132581.

[12] Mohan, Manu K., A. V. Rahul, Geert De Schutter, and Kim Van Tittelboom. 2022. "Salt Scaling Resistance of 3D Printed Concrete." Pp. 188-93 in *Third RILEM International Conference on Concrete and Digital Fabrication*, edited by Richard Buswell, Ana Blanco, Sergio Cavalaro, and Peter Kinnell. Cham: Springer International Publishing.

[13] Wang, Li, Wei Xiao, Qiao Wang, Hailong Jiang, and Guowei Ma. 2022. "Freeze-thaw resistance of 3D-printed composites with desert sand." *Cement and Concrete Composites* 133:104693.https://doi.org/10.1016/j.cemconcomp.2022.104693.

[14] Dong, Wei, Junfeng Wang, Meiyan Hang, and Shuqiang Qu. 2024. "Research on printing parameters and salt frost resistance of 3D printing concrete with ferrochrome slag and aeolian sand." *Journal of Building Engineering* 84:108508.https://doi.org/10.1016/j.jobe.2024.108508.

[15] Krstic, Marija, Julio F. Davalos, Emanuele Rossi, Stefan C. Figueiredo, and Oguzhan Copuroglu. 2021. "Freeze–Thaw Resistance and Air-Void Analysis of Concrete with Recycled Glass–Pozzolan Using X-ray Micro-Tomography." Pp. 154 in *Materials*.

[16] Das, Arnesh, Yu Song, Sara Mantellato, Timothy Wangler, David A. Lange, and Robert J. Flatt. 2022. "Effect of processing on the air void system of 3D printed concrete." *Cement and Concrete Research* 156:106789.https://doi.org/10.1016/j.cemconres.2022.106789.

[17] Zhang, Yu, Yunsheng Zhang, Lin Yang, Guojian Liu, Yidong Chen, Shiwei Yu, and Hongjian Du. 2021. "Hardened properties and durability of large-scale 3D printed cement-based materials." *Materials and Structures* 54(1):45.https://doi.org/10.1617/s11527-021-01632-x.

[18] Liu, Chao, Rongfei Zhang, Huawei Liu, Chunhui He, Youqiang Wang, Yiwen Wu, Shuhua Liu, Lin Song, and Fan Zuo. 2022. "Analysis of the mechanical performance and damage mechanism for 3D printed concrete based on pore structure." *Construction and Building Materials* 314:125572.https://doi.org/10.1016/j.conbuildmat.2021.125572.

[19] 2006. "Testing hardened Concrete Part 9: Freeze-Thaw Resistance Scaling 12390-9:2006."

[20] 2013. "NS-EN 206:2013+A2+NA Concrete - Specification, performance, production and conformity."

[21] Stefan. Jacobsen, Magne Maage, Sverre Smeplass, Knut O. Kjellsen, Erik Johan Sellevold, Jan Lindgård, Rolands Cepuritis, Roar Myrdal, Øyvind Bjøntegaard, and Mette Rica Geiker. 2010. *Concrete Technology*. Trondheim Norway.

[22] Kwan, Albert Kwok Hung, Po Lok Ng, and Ka Yu Huen. 2014. "Effects of fines content on packing density of fine aggregate in concrete." *Construction and Building Materials* 61:270-77.https://doi.org/10.1016/j.conbuildmat.2014.03.022.

[23] Wang, Zhuo, Zhichen Liu, Feng Zeng, Kun He, and Shuaicheng Guo. 2024. "Review on frost resistance and anti-clogging of pervious concrete." *Journal of Traffic and Transportation Engineering (English Edition)* 11(3):481-96.https://doi.org/10.1016/j.jtte.2023.05.008.

Experimental investigation of interlayer shear behaviour in 3D printed concrete under varying confinement conditions

Gianluca Giulivo, Antonio Mudadu, Costantino Menna

Department of Structures for Engineering and Architecture (DiSt),
University of Naples Federico II,
Via Claudio 21, 80125 Naples, Italy

Summary
This paper presents an experimental investigation on the shear behaviour of interlayer interfaces in 3D printed concrete at the material scale. A proper characterization of the mechanical parameters governing interlayer adhesion is crucial on the structural performance of printed elements. A novel experimental setup was developed to induce shear forces along interlayer surfaces under varying levels of confinement stress. Both direct shear tests and compression–shear tests were carried out on prismatic specimens with dimensions of 60 mm thickness, 70 mm width, and 140 mm length. The experimental results permit the identification of cohesion and friction parameters defining the Mohr–Coulomb failure envelope of printed interfaces. The findings provide a consistent experimental basis for numerical model calibration and support the definition of design-oriented parameters for the structural application of 3D printed concrete.

1 INTRODUCTION

Extrusion-based additive manufacturing of concrete, commonly named as 3D printed concrete (3DPC), has emerged as a promising construction technology, offering advantages in terms of automation, geometric freedom, and reduction of formwork and labour demand. Over the past decade, significant progress has been achieved in printing systems, material development, and full-scale demonstrators. Nevertheless, the structural application of 3DPC remains limited because of uncertainties related to its mechanical behaviour and the lack of standardized characterization procedures tailored to the layered nature of printed elements [1].

Concrete 3D printing is an additive manufacturing technology based on material extrusion, unlike traditional concrete pouring, 3DPC does not require the concrete to flow; rather, it requires the concrete to hold shape after extrusion. Thus, the properties and behaviour of 3DPC differ from the standard conventional concrete as the concrete is printed and stacked in layers of predefined width and thickness, resulting in interface formation (i.e. deposition interface), which leads to lower bond strengths between layers due to inadequate compaction and, finally, to a pronounced anisotropy in mechanical[2]. Experimental investigations prove that interlayer interfaces could represent preferential planes for crack initiation and failure, particularly under tensile- and shear-dominated loading conditions [3,4].

At the microstructural scale, printed interfaces are characterized by a dual hierarchical structure, with increased porosity and reduced micromechanical properties compared to the bulk material. This localized weakness governs damage initiation and propagation, confirming the critical role of interlayer regions in the overall mechanical response of 3D printed concrete [5].

On the other hand, at the structural scale, interlayer bond strength is governed by several factors such as the printing time interval, nozzle height, and layer thickness, highlighting the strong dependence of mechanical performance on the printing process. Among mechanical properties affected by interlayer interfaces, shear resistance combined with normal stress plays a key role for structural elements such as walls and panels subjected to in-plane actions, which are therefore subjected to a complex stress state. Initially, shear is transferred across printed interfaces based on a cohesive mechanism; once cracking occurs, frictional sliding happens. [6,7].

Within this scenario, 3D-printed concrete can be compared to jointed materials (i.e. masonry) in which the mechanical behaviour is governed by the interfaces between layers. In masonry structures, the shear response of mortar joints has been extensively investigated through triplet shear tests and is commonly described using a Mohr–Coulomb failure criterion, based on cohesion and friction parameters.

Recent experimental studies have refined this framework by combining traditional shear testing with advanced measurement techniques. Digital Image Correlation was adopted to investigate masonry triplets, enabling the identification of displacement fields, damage localization, and effective Mohr–Coulomb parameters at the joint level, while highlighting the role of asymmetric cracking and progressive joint activation [8]. Segura et al. [9] performed a systematic experimental comparison between triplet and couplet test configurations, demonstrating that test setup and boundary conditions significantly influence the identification of shear strength parameters. Results confirm that, despite inherent limitations, triplet tests remain a robust and widely adopted method for characterizing joint shear behaviour when interpreted within a Mohr–Coulomb framework. These findings provide a consolidated experimental and conceptual background that is directly relevant for extending similar approaches to interlayer interfaces in 3D printed concrete.

Inspired by this analogy, recent research has started to explore shear testing strategies for 3DPC interfaces. Licciardello et al. [10] proposed an experimental and numerical investigation of interlayer shear behaviour under combined shear and normal compression, demonstrating that the resulting failure envelope can be effectively interpreted using a Mohr–Coulomb criterion and providing parameters suitable for numerical modelling.

Within this context, the present study aims to experimentally characterize the **shear behaviour of interlayer interfaces in 3D printed concrete at the material scale**. A dedicated experimental programme is developed to investigate both direct shear and compression–shear loading conditions, in order to allow the assessment of the shear behaviour of the interlayer surface in terms of shear strength, shear stiffness, cohesion, and friction angle.

2 EXPERIMENTAL PROGRAMME

2.1 Materials and specimen preparation

The experimental program was carried out on specimens manufactured using an extrusion-based 3D concrete printing (3DCP) process. A 6-axis robot was connected to the M-Tec Duomix 2000 mixer-pump with a linear displacement pump, that feeds concrete through a Ø35 mm, 5 m length hose.

A commercially available dry printable mortar specifically developed for extrusion-based 3D concrete printing applications was adopted in the present investigation. The material consists of Portland cement, siliceous aggregates with a maximum particle size of 2 mm, and specific chemical admixtures designed to optimize pumpability, extrusion stability, thixotropic behaviour, buildability, and interlayer bonding. No fibers were included in the mixture.

According to the manufacturer specifications, the printable mortar is characterized by a fresh density of approximately 2150 ± 50 kg/m³, a water content ranging between 16% and 17%, and a workability time of about 20 ± 10 min. The hardened material exhibits a dry density close to 2000 kg/m³, with nominal mechanical strengths at 28 days higher than 45 MPa in compression and 7 MPa in flexure, evaluated on standard 40×40×160 mm specimens. In the present study, the average compressive strength measured at the testing age was approximately 50 MPa.

Printing operations were performed under controlled laboratory conditions using a continuous and regular layer deposition sequence in order to reduce process-induced variability and obtain reproducible interface conditions along the specimen height. The extrusion flow rate and nozzle travel speed were calibrated to minimize filament deformation after deposition and to ensure adequate interlayer adhesion between consecutive layers. The extrusion nozzle width was 20 mm, while the layer height was fixed at 10 mm to guarantee stable geometric buildability and regular filament deposition.

A unique continuous printing path frame with regular layer stacking was printed (Fig. 1a) under controlled laboratory conditions, to ensure reproducibility and a clear definition of material orientations with respect to the applied loading directions.

Specimens were cut by wet-sawing from the frame with a thickness of 60 mm, width of 70 mm and height of 140 mm (Fig. 1b). Specimens were cured under controlled conditions until the testing age, ensuring comparable hydration and mechanical development across all test series.



(a) (b) (c)

Fig. 1 Manufacturing of 3DPC specimens: (a) extrusion; (b) cutting; (c) specimen geometry, dimensions (mm), and printing direction.

Fig. 2 shows the cross-sectional shear resistant areas; as a result of the printing process, the cross-section of the specimens can have significant irregularities (Fig. 2b). Therefore, evaluation of the effective cross-sectional shear-resisting area is crucial in the determination of the shear strength of 3D-printed concrete specimens. For this purpose, an effective thickness, t_{eff}, was measured to represent the portion of material effectively engaged in resisting shear stresses at the interlayer interfaces. These irregularities lead to a reduction of the effective thickness with respect to the nominal maximum thickness, $t_{\max} = 60\text{mm}$, resulting in $t_{\text{eff}} < t_{\max}$.

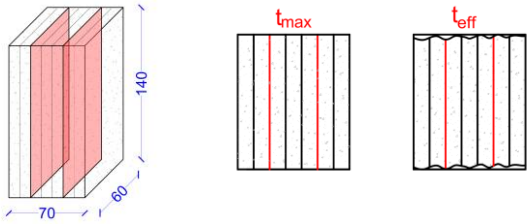
The specimen dimensions were therefore selected to promote shear failure along the interlayer interfaces, while minimizing the contribution of alternative failure mechanisms. Based on the effective thickness t_{eff}, the effective shear-resisting area was computed for each specimen as

$$A_{\text{eff}} = t_{\text{eff}} \cdot h, \tag{1}$$

where $h = 140$ mm is the specimen height. The corresponding average shear stress was then evaluated as

$$\tau = \frac{F_{max}}{2\ A_{\text{eff}}} \tag{2}$$

with F_{max} denoting the applied shear force. The values of t_{eff} and the corresponding effective areas for all tested specimens are reported in Table X.



(a) (b)

Fig. 2 Definition of the effective shear-resisting area: (a) activated interlayer surfaces; (b) effective thickness t_{eff} compared with the nominal thickness $t_{\max} = 60\text{mm}$.

3 TEST SETUPS

The interlayer shear strength was investigated using a dedicated testing methodology derived from EN 1052-3, originally developed to determine the shear strength of masonry elements. Tests were carried out on prismatic specimens with vertically oriented printing layers, adopting a three-point loading configuration.

A vertical load was applied at the center of the upper surface through a steel loading plate covering the central three layers of the specimen, while two steel plates placed at the sides of the lower surface acted as supports. It should be noted that the lateral steel plates restrain specimen rotation, allowing only vertical translation.

This configuration resulted in uniform compressive stresses under the loading plate and over the lateral supports, while shear failure was forced along the two symmetrical interlayer interfaces located between the loading point and the outer supports.

Tests were performed by increasing monotonically the vertical load until to reach failure on specimens tested under different confinement conditions. Two main configurations were considered: (i) tests without lateral confinement (0 MPa), aimed at characterizing the pure interlayer shear response; and (ii) tests with imposed lateral confinement, adopting two normal compressive stress levels (2.5 MPa and 5.0 MPa), corresponding to approximately 5% and 10% of the material compressive strength (i.e. 50 MPa). These values are representative of the compressive stress range acting in real structural applications of 3D printed vertical elements. More in details, the applied normal stresses reproduce the compressive stresses acting perpendicular to the interlayer interfaces due to the cumulative self-weight of overlying structural elements.

The vertical load was applied under displacement control at a constant loading rate of 0.05 mm/min by using a servo-controlled universal testing machine with a maximum capacity of 500 kN.

For the confined compression–shear tests, the lateral normal stress was applied by means of four threaded steel rods connected to lateral steel confinement plates. The confinement force was progressively introduced through controlled tightening of the nuts using a calibrated torque wrench.

Strain gauges and load cells installed on the threaded rods were used to continuously monitor the applied confinement force during the entire test. Before the beginning of each test, the target normal stress level was reached and stabilized. During loading, the confinement condition remained approximately constant, with only negligible variations due to local specimen deformation and interface cracking.On the front side of the specimen, displacements and strain fields were measured by means of a three-dimensional Digital Image Correlation (3D-DIC) system (ZEISS ARAMIS Adjustable 24M). The system consists of two synchronized 24-megapixel cameras capable of tracking full-field surface displacements and strain evolution during the test through stereoscopic image acquisition.

Images were acquired every 15 s and subsequently processed using the commercial software GOM Correlate. A stochastic speckle pattern was prepared by spraying black paint on the specimen surface previously coated in white in order to ensure accurate optical tracking during loading.

The speckle pattern was prepared by spraying black paint on the panel surface previously painted white (Fig. 3).

Moreover, optical markers were placed on each printed layer to measure both relative horizontal and vertical displacements between adjacent layers, thus allowing the measurement of crack opening (Mode I) and relative sliding (Mode II) at different locations along the specimen height. Digital Image Correlation proved fundamental for detecting crack initiation and propagation throughout the tests.



(a) (b)

Fig. 3 Shear test configuration and experimental setup: (a) test without lateral confinement (0 MPa); (b) test with lateral confinement applied normal to the interlayer interfaces.

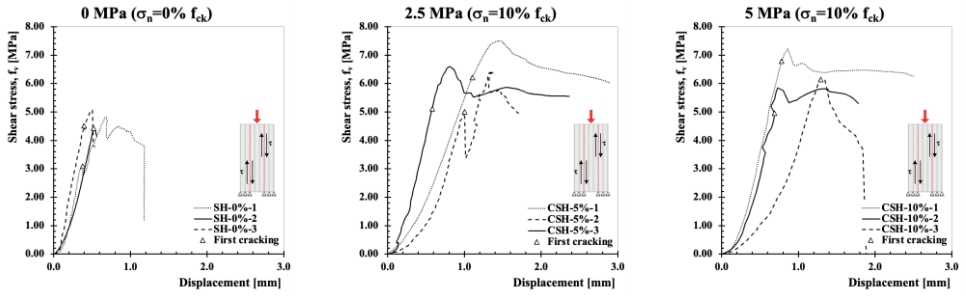
4 EXPERIMENTAL RESULTS

The experimental campaign comprised unconfined conditions (0 MPa) and two levels of imposed normal compressive stress: 2.5 MPa and 5.0 MPa, equal to 5% and 10% of the material compressive strength, respectively. For each confinement level, three nominally identical specimens were tested, resulting in a total of nine samples.

The combination of the previously mentioned parameters defines a specific series, identified according to the notation X–Y–Z, where: X represents the type of test (SH and CSH stands for SHear test and Confined SHear test, respectively); Y the level of confined compressive load (0%, 5%, 10%)

as a fraction of the compressive strength and Z the ID number of sample (-1, -2,-3) tested under the same configuration.

Fig. 4 reports shear stress vs. displacement experimental curve of the three groups of samples. Displacement was evaluated directly on the sample surface through the optic markers applied on the sample and tracked by DIC device; whereas the shear resistance was evaluated (according to Eq.2) at the onset of the first cracking thus at the activation of the governing interlayer failure mechanism. It should be noted that the post-cracking response shows a transition from interface-controlled sliding to a mixed sliding–matrix damage mechanism, leading to a subsequent increase in shear force and to a higher apparent peak load; hence it is of paramount importance to well defined the cracking stage.



(a) (b) (c)

Fig. 4 Shear stress–relative displacement curves of 3DPC specimens from push-out tests under different confinement levels: (a) unconfined condition (0 MPa), (b) moderate confinement (2.5 MPa, corresponding to 5% of the compressive strength), and (c) high confinement (5.0 MPa, corresponding to 10% of the compressive strength).

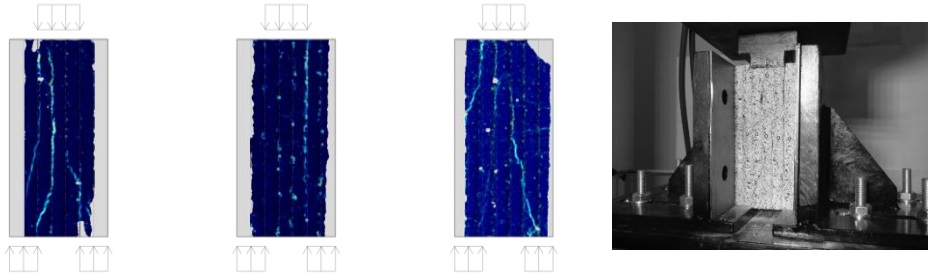
Results prove a strong dependence of the applied confinement on the interlayer shear capacity. The higher the applied normal compressive stress, the higher peak shear strengths and a more stable post-peak response. Compared to the unconfined condition (0%), average peak shear stress values increase significantly at 5% and 10% precompression levels, confirming the beneficial role of compressive normal stress in enhancing shear transfer across interlayer interfaces in 3D-printed concrete specimens.

A synoptic summary of the experimental results is reported in Table 1, which lists the specimen identification, the applied normal stress level, the load at the cracking stage (F_{cr}), the ultimate applied load (F_{max}), the corresponding peak shear stress (τ_u) and its correspondence relative displacement (Δ), the initial shear stiffness (K_s), and the effective shear-resisting area ($A_{\min}$) adopted for the shear stress evaluation.

For each test configuration, the final damage state is qualitatively documented through the final damage pattern obtained from Digital Image Correlation (DIC).

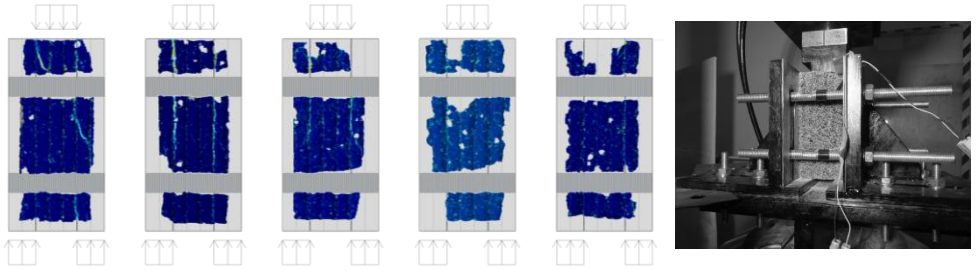
The DIC contour maps reported in Figs. 5 and 6 represent strain localization fields obtained during the tests, allowing the visualization of crack initiation and damage propagation mechanisms along the interlayer interfaces.

The DIC analyses allowed the identification of the dominant failure mechanism, either interface-controlled sliding or mixed sliding–matrix damage—and its spatial localization along the interlayer interfaces. In particular, the evolution and concentration of strain localization provide clear evidence of whether shear transfer is predominantly governed by relative sliding at the interlayer interface or by the progressive propagation of cracks within the surrounding cementitious matrix.



(a) (b) (c) (d)

Fig. 5 Failure modes from DIC analyses of unconfined shear (SH) push-out tests: (a) SH-0%-1, (b) SH-0%-2, (c) SH-0%-3, and (d) photograph of the shear push-out test. DIC maps show strain localization along the interlayer interface, indicating interface-controlled sliding.



(a) (b) (c) (d) (e) (f)

Fig. 6 Failure modes from DIC analyses of compression–shear (CSH) push-out tests: (a) CSH-5%-2, (b) CSH-5%-3, (c) CSH-10%-1, (d) CSH-10%-2, (e) CSH-10%-3, and (f) photograph of the compression–shear push-out test. Increasing confinement promotes a transition from interface-dominated sliding to mixed sliding–matrix damage.

Table 1 Summary of SH and CSH push-out test results for 3D-printed concrete specimens.

ID [-]	σ_N [MPa]	A_{eff} [mm^2]	F_{crack} [kN]	F_{max} [kN]	f_v [MPa]	D [mm]	K_s [N/mm^2/mm]	Failure mode [-]
SH-0%-1		15680	48.45	75.59	3.09	0.38	10.83	Sliding-Matrice
SH-0%-2	0	16100	71.32	71.39	4.43	0.52	9.97	Sliding
SH-0%-3		15960	72.14	80.75	4.52	0.40	13.59	Sliding-Matrice
	Mean value		63.97	75.91	4.01	0.43	11.46	
		(COV)	(0.21)	(0.06)	(0.2)	(0.18)	(0.16)	
CSH-5%-1		15960	99.27	119.70	6.22	1.10	6.26	Sliding-Matrice
CSH-5%-2	2.5	15960	79.80	102.31	5.00	1.00	3.57	Sliding-Matrice
CSH-5%-3		15960	81.56	105.48	5.11	0.58	7.87	Sliding
	Mean value		86.88	109.17	5.44	0.90	5.90	
		(COV)	(0.12)	(0.02)	(0.01)	(0.33)	(0.51)	
CSH-10%-1		15960	108.37	115.30	6.79	0.69	2.99	Sliding-Matrice
CSH-10%-2	5	15960	79.16	93.68	4.96	0.69	3.83	Sliding
CSH-10%-3		15960	97.99	99.06	6.14	1.29	3.37	Sliding
	Mean value		95.17	102.68	5.96	0.89	3.40	
		(COV)	(0.16)	(0.11)	(0.16)	(0.39)	(0.12)	

Assuming a linear Mohr–Coulomb failure criterion, the interface bond behavior can be expressed in terms of cohesion and friction angle for the deposition interfaces. The experimental data of shear stresses corresponding to different predefined precompression stress as axial stresses were extracted, and a best-fit linear curve was drawn to get these shear resistance parameters by using the expression $\tau = C + \sigma \tan\theta$ as shown in Fig. 7. The shear resistance parameters obtained for the deposition interface are a cohesion of 4 MPa and internal friction angle of 21.3°, supporting the applicability of a Mohr–Coulomb description for the interlayer shear behaviour.

The obtained results highlight a clear dependence of the interlayer shear response on the applied confinement level. Under unconfined conditions, failure was mainly governed by interface-controlled sliding, whereas increasing normal compressive stress promoted a progressive transition toward mixed sliding–matrix damage mechanisms, associated with higher peak shear stresses and more distributed strain localization fields.

This behaviour is consistent with previous studies on both masonry joints and 3D printed concrete interfaces, where compressive normal stresses enhance frictional resistance and delay interface debonding. In particular, the experimentally observed increase in shear strength with confinement confirms the applicability of a Mohr–Coulomb interpretation for the mechanical characterization of printed interfaces.

Compared to traditional masonry triplet tests, the obtained cohesion value is significantly higher, reflecting the higher intrinsic mechanical strength of the cementitious matrix used in 3D printed concrete. On the other hand, the identified friction angle remains comparable to values commonly reported for masonry interfaces. In this regard, standard masonry triplet tests generally provide cohesion and friction angle values of approximately 0.27 MPa and 19.8°, respectively [11], suggesting similarities in the friction-controlled post-cracking mechanisms governing layered materials.

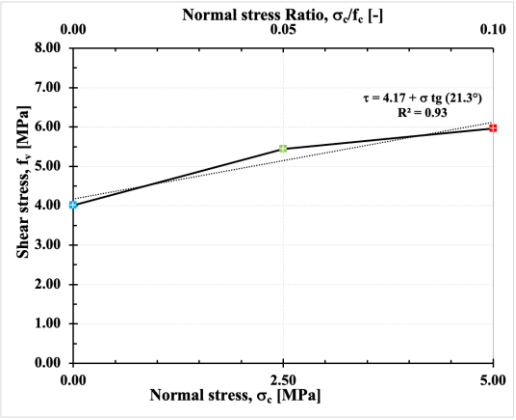


Fig. 7 Mohr–Coulomb failure envelope for the interlayer interface of 3D-printed concrete: peak shear stress versus applied normal stress. The linear regression provides cohesion c and friction angle φ.

5 CONCLUDING REMARKS

This study experimentally investigated the shear behaviour of interlayer interfaces in extrusion-based 3D printed concrete, with particular attention to the influence of normal compressive stress. A dedicated testing methodology, inspired by standardized procedures for masonry materials, was developed and applied to prismatic specimens extracted from printed elements, allowing a controlled activation of interlayer shear mechanisms.

The results confirm that interlayer interfaces represent the governing weakness of 3D printed concrete under in-plane loading. Under unconfined conditions, shear transfer is mainly controlled by cohesive mechanisms, leading to interface-dominated sliding and early crack localisation along the printed layers. The application of normal compressive stress significantly increases the shear capacity and alters the failure mode, promoting a progressive transition from pure interface sliding to mixed sliding–matrix damage, which is representative of stress states expected in real structural elements.

The combined analysis of shear and compression–shear tests enabled the identification of interlayer mechanical parameters within a Mohr–Coulomb framework. The experimentally derived cohesion and friction angle provide a consistent and physically meaningful description of the interlayer failure envelope, supporting their use in numerical modelling and design-oriented analyses of layered 3D printed concrete components.

Finally, Digital Image Correlation proved to be a valuable tool for tracking displacement fields, crack initiation, and damage evolution, offering insight into the governing failure mechanisms and their spatial localisation. The proposed experimental approach and the identified parameters establish a robust basis for the mechanical characterisation of interlayer interfaces and for the extension of masonry-inspired modelling strategies to 3D printed concrete.

Acknowledgements

This study was funded by the European Union – NextGenerationEU under the National Recovery and Resilience Plan (PNRR), Mission 4 "Education and Research", Component 2 "From Research to Business", Investment 1.1 – PRIN 2022 Call (D.D. No. 104 of 02/02/2022), Project TOMORROW (TOpology & Material Optimization using additive manuFactuRing to maximize stRuctural and thermal perfOrmances of building Walls). CUP: E53D23003760006.

References

[1] Buswell, R.A., Leal de Silva, W.R., Jones, S.Z., Dirrenberger, J. 3D printing using concrete extrusion: A roadmap for research. Cement and Concrete Research, 112, 2018, pp. 37–49.

[2] Bharti, M., Menon, A., Santhanam, M. Experimental study of hardened properties of 3D-printed concrete under compression, tension and shear considering interlayer influence. Materials and Structures, 2026, 59:48. https://doi.org/10.1617/s11527-025-02935-z

[3] Nerella, V.N., Krause, M., Mechtcherine, V. Effects of layer-interface properties on mechanical performance of concrete elements produced by extrusion-based 3D-printing. Construction and Building Materials, 205, 2019, pp. 586–601.

[4] Chan, L.-J., Padil, K.H., Chin, C.-L., et al. Strategies to enhance interlayer bonding in 3D printed concrete: A review. Journal of Building Engineering, 113, 2025, 114077.

[5] Geng, G., Li, Z., Zhang, J., Wang, Y. Layer-interface properties in 3D printed concrete: Dual hierarchical structure and micromechanical characterization. Cement and Concrete Research, 137, 2020, 106195.

[6] Wolfs, R.J.M., Bos, F.P., Salet, T.A.M. Hardened properties of 3D printed concrete: The influence of process parameters on interlayer adhesion. Cement and Concrete Research, 119, 2019, pp. 132–140.

[7] Tang, Y., Li, L., Feng, W., et al. Mechanical properties of extrusion-based 3D-printed concrete considering the thickness of printed layer and printing time interval. Construction and Building Materials, 256, 2020, 119455.

[8] Collin, L., Gatuingt, F., Giry, C., Hild, F. Exploring the shear behavior of masonry triplets via digital image correlation, damage quantification and Mohr–Coulomb criterion identification. Structures, 80, 2025, 109696.

[9] Segura, J., Bernat, E., Mendizabal, V., Pelà, L., Roca, P., Gil, L. Experimental comparison of two testing setups for characterizing the shear mechanical properties of masonry. Journal of Building Engineering, 44, 2021, 103277.

[10] Licciardello, L., et al. Experimental and numerical study on the inter-layer shear behavior of 3D printed concrete. Construction and Building Materials, 2025.

[11] Incerti, A., Rinaldini, V., Mazzotti, C. The evaluation of masonry shear strength by means of different experimental techniques: A comparison between full-scale and laboratory tests. Brick and Block Masonry – Trends, Innovations and Challenges, 2016, Taylor & Francis Group, London.

Load-bearing behaviour of 3D-printed concrete beams with a rationalised reinforcement approach for automated production

Fabian Fritz, Patrick Huber and Tobias Huber

Institute for Structural Engineering - Research Unit of Structural Concrete,
TU Wien,
Karlsplatz 13, 1040 Vienna, Austria

Summary
This study investigates rational reinforcement approaches for the automated production of 3D-printed concrete members (3DPC). To this end, six concrete specimens are produced and tested in three-point bending tests while material properties for the used concrete and reinforcement are determined. The varied parameters are reinforcement layouts (ribbed rebars and reinforcement mats) and printing directions relative to the load direction. The test results are evaluated with code provisions for cast concrete in order to evaluate their applicability for the produced members. Found results demonstrate a good applicability of current design models for shear and bending to 3DPC with the introduced layerwise reinforcement approach regardless of their printing orientation.

1 INTRODUCTION

Recent developments in additive manufactured concrete structures suggest a redefinition of the future construction industry [1]. Three-dimensional printed concrete (3DPC) is already being used for components under compression stresses, e.g. in the building sector as 3D printed walls in housing [2]. However, to enable 3DPC to be applied in structural contexts comparable to conventional reinforced concrete, strategies for integration and applicability of reinforcement to carry tensile stresses are still needed. Several reinforcement strategies emerged in academia over the last decade [3], but only a few show potential for automated integration during printing. Further research for rebars in beam structures, with the testing direction aligned to the printing direction, showed delamination of the bottom layers next to the reinforcement [4]. To counteract this the "flip method" is introduced, where members are rotated after printing, to evenly distribute the applied tensile stresses between all layers.

This paper describes three reinforcement layouts for automated layerwise integration during the printing process, consisting of ribbed rebars and reinforcement mats with a diameter of 4.2 mm. The load-bearing behaviour of six specimens featuring those layouts is investigated in three-point bending tests with the printing direction relative to the load direction being a parameter. Furthermore, the applicability of current standards for cast concrete [5] to the tested reinforced 3DPC members is evaluated through comparison to the experimental results. The investigations highlight the potential when aiming for rationality and material optimisation in an automated production. Based on these findings, future research on the robotic reinforcement integration into the 3D printing process for concrete structures will be conducted.

2 MATERIALS AND METHODS

2.1 Specimen design

2.1.1 Geometry

The chosen 3DPC geometry for all specimen depends on the printing setup and results as a multiple of the used inner nozzle diameter of 12 mm and the layer height of 8 mm. A total of eight beams (length = 1440 mm, width = 80 mm, height = 240 mm, see Fig. 1) are produced, of which six are reinforced to be analysed under bending tests (see Section 3.1) and two are unreinforced for obtaining the material properties (see Section 2.4).

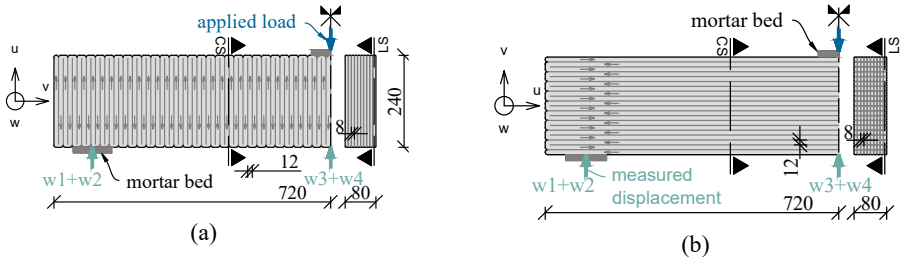


Fig. 1 Specimen geometry, shown partially from the support to the symmetry axis, and printing orientation (a) vertical and (b) horizontal with strand direction naming nomenclature after [6], position of the applied load axis and of the measured displacements (in mm)

2.1.2 Reinforcement

Three different reinforcement layouts are investigated, which include individual rebars as well as mats (see Fig. 2). The reinforcement consists of ribbed bars with a diameter of 4.2 mm that are positioned centric between the printed layers. The embedded distance is therefore determined by the chosen layer height of 8 mm (see Fig. 1).

The first reinforcement layout (B1, see Fig. 2a) consists of 13 straight rebars, which are positioned along the bottom over the entire beam length. A shear reinforcement is deliberately excluded.

The second layout (B2) follows a different approach by bending selected rebars (see Fig. 2b). Six rebars are positioned along the bottom to act as bending reinforcement and are subsequently bent up towards both ends of the beam to act as shear reinforcement (i - iii in Fig. 2b). The designed mandrel diameter with 55 mm is greater than the required $4Ø$ for $Ø \leq 16\,mm$ according to [5]. In addition, seven straight bars are placed along the bottom over the entire length of the beam (iv in Fig. 2b).

A third layout (B3) shifts the focus to reinforcement mats (see Fig. 2c), where three meshes (length = 1440 mm, height = 240 mm, axial grid = 100x100 mm) are placed every third layer and act both as bending and shear reinforcement (i in Fig. 2c). Additionally, three straight rebars are tied to each mesh between the lowest and middle longitudinal bar of the mesh (ii in Fig. 2c).

2.1.3 Printing Orientation

With the process of creating the geometry in layers by printing single strands, an anisotropic material behaviour is introduced. To observe a potential difference of the strand orientation to a given load, each reinforcement layout (B1-B3) is produced with a vertical (V) and a horizontal (H) strand orientation (see Fig. 1).

The printing direction nomenclature is adapted from [6] and describes the strand orientation as the u - axis as well as normal to the strand direction in the same layer as the v - axis. The direction, in which the layers align is called the w - axis and is aligned normal to the uv - plane.

The beams are designed to be printed and reinforced in their local uv - plane and advance vertically for each layer in their local w -axis, so they appear to be laying on their side. After hardening, the specimens are flipped along their longitudinal axis (u - or v - axis) and appear in their upright position.

2.2 Preparation and production

The straight rebars for all three reinforcement strategies are cut to desired length. The bent rebars are manually bended using a manual bending machine with exchangeable mandrel diameter. The mats are cut out of a large industrial manufactured, resistance welded mesh and the additional longitudinal rebars are tied to the cut mats by hand with a rebar wire.

The concrete printing setup consists of an ABB IRB 2600 articulated six - axis robot on an ABB IRT 510 linear track motion platform. The constituents of the concrete are weighed and mixed with a hand-held stirrer. A total of eight batches is produced. The material is pumped via a MAI Pictor pump to a self-built printing nozzle which is attached to the robot as an end effector, see [7] for further details.

The production of all eight beams is performed on the same day. To guarantee an uninterrupted printing process, two beams are produced next to each other in an alternating pattern. While the concrete layer for one beam is printing, the reinforcement for the other beam is placed by hand and vice versa.

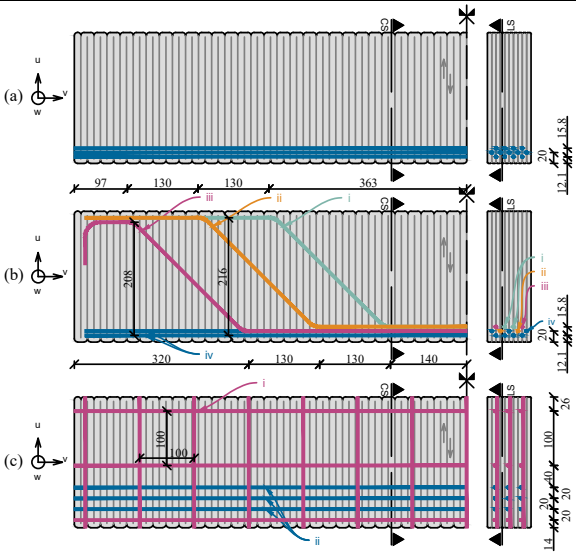


Fig. 2 Reinforcement layouts, shown partially from the support to the symmetry axis (a) B1: straight rebars, (b) B2: bent rebars and (c) B3: mesh, longitudinal section (left) and cross section (right) (in mm)

To assure a correct placement of the rebars, multiple purpose-built guides are used for each layer and rebar layout. These guides included grooves to indicate both outside edges of the concrete beam as well as the axis of the reinforcement bars for each layer. To minimize voids in the concrete and ensure an optimal bond the single rebars are pushed into the fresh concrete by half the diameter whereas the mesh is pushed in by a full diameter, since the mat consists of two bars crossing each other out of plane.

Each beam is covered with a foil one hour after the individual production and stays covered for 23 days. After hardening the specimens are flipped upright and vertically aligned making use of the single planar surface generated from the flat printing table. Afterwards, a 20 - 40 mm thick mortar bed (Pagel UM20) is cast at the positions of both supports as well as the load to compensate for the uneven surface caused by the 3D-printing process and assure a stable test setup.

2.2.1 Geometry deviation between designed and produced specimens

After the production of all specimens their real geometry is measured with a tape measure and compared to the designed geometry (see Table 1). All distances are measured on up to three different positions for each beam and displayed as a mean across all specimens of the same printing orientation.

After completion of all tests, a cross-section through each specimen is cut and the true position of each rebar d_1 is determined. The spacing d_1 between the bottom edge of the beam and the centre of gravity of all reinforcing bars in tension is determined, allowing the true effective depth d to be calculated as $d=h-d_1$.

2.3 Test setup and instrumentation

Three point bending tests are conducted for all six reinforced specimens. The beams rest on a half-shell shaped support on either side where the horizontal movement of one support is enabled by a PTFE-layer whereas the other support is blocked. The span length amounts to 1240 mm for all specimen except for B2H (bent bars, horizontal strand orientation) where it is 1300 mm.

Table 1 Description of the specimen, measured specimen geometry and calculated rebar centroid distance to the bottom edge d_1 in the upright position

Name	Reinforcement layout	Printing direction	Length (in mm)	Height (in mm)	Width (in mm)	d_1 (in mm)
B1V	Straight rebars	Vertical	1463 CV: 0.3%	272 CV: 3.7%	85 CV: 1.3%	31.9
B2V	Bent rebars					36.0
B3V	Mesh					84.6
B1H	Straight rebars	Horizontal	1464 CV: 0.2%	273 CV: 3.3%	85 CV: 0.7%	23.0
B2H	Bent rebars					25.6
B3H	Mesh					74.2

The load is applied vertically in the longitudinal beam centre on top of the mortar bed (see Fig. 1) with a 10 mm thick elastomer or an equivalent thick sand bed in between and is measured via a loading cell. Only for the specimen B2H an alternative layout under the load cell with a reduced mortar with of 40 mm and equivalent sand bed width is applied.

In the first stage of the testing cycle the load is applied through a controlled force rate of 0.05 kN / s with ten evenly distributed load steps up to 60 kN (B1V, B1H and B2V) or up to 100 kN (B2H, B3V and B3H). If the predefined force is reached, the program switches to a deflection-controlled mode at a rate of 1 mm / min until failure or until a maximum displacement of 20 mm is reached.

The vertical displacements for all six beams are measured via linear displacement transducers on both supports as well as in load axis both on the front and back side of the beams for a total of six measurement points (see Fig. 1).

2.4 Materials

The previously mentioned unreinforced specimens, one for each strand orientation, are cut in the transverse plane (uv - plane for vertical and vw - plane for horizontal strand orientation, see Fig. 1) and twelve cylindrical cores with a diameter of 60 mm and height of 120 mm are obtained perpendicular to the load direction (v - axis for vertical and u - axis for horizontal strand orientation). These specimens are used for compression and splitting tensile tests after 49 days to obtain the mechanical properties displayed in Table 2.

The reinforcement are cold-formed ribbed bars with a diameter of 4.2 mm, used for the production of reinforcing mats AQ42, which are usually used for crack control. Those beams, which make use of reinforcement mats, a mesh of type AQ42 (longitudinal and lateral bar diameter of 4.2 mm and bar axis distance 100 mm) is produced by resistance welding the above-mentioned straight bars into the grid-like pattern. The yield stress $f_{0.2}$ and tension stress f_t is obtained experimentally on three bars for straight rebars and the mesh in longitudinal direction and on two bars for the mesh in transverse direction (see Table 2)

3 RESULTS

3.1 Three-point bending test

Fig. 3 illustrates the load-deflection curves of the three reinforcement strategies for (a) vertical – and (b) horizontal printing orientation. The maximum applied load F_{max} and its corresponding vertical displacement in load axis w_F is shown in Table 3. The relative deflection w_F is calculated by subtracting the mean displacement on both supports from the mean displacement under the load. The observed crack patterns after testing are displayed in Fig. 4 for each reinforcement strategy and printing direction.

B1V increases linear to a maximum load of 47.7 kN (see blue in Fig. 3a) before failing by a single shear crack one side (see Fig. 4a top). B1H forms a first shear crack on one end of the specimen at a load of 39.4 kN, visible as a sudden deflection increase in the graph in Fig. 3b (blue line). Afterwards, the load increases again until the main failure shear crack appears on the other side of the beam (see Fig. 4a bottom) at a maximum load of 45.5 kN.

Table 2 Mean values of the mechanical properties for the concrete for a given load direction after 49 days as well as for the reinforcement

Specimen	Reinforcement type	f_{cm} (in MPa) | CV	$f_{ct,sp}$ (in MPa) | CV	$f_{0.2}$ (in MPa) | CV	f_t (in MPa) | CV
B1V	Straight rebars	Load dir.: v	Load dir.: u	733.0 | 2.1%	760.7 | 1.6 %
B2V	Bent rebars	69.94 | 3.6%	3.3 | 18.1 %		
B3V	Mesh			787.0 | 1.5 %	835.7 | 1.6 %
				801.0* | 0.4 %	821.5* | 0.9%
B1H	Straight rebars	Load dir.: u	Load dir.: v	733.0 | 2.1%	760.7 | 1.6 %
B2H	Bent rebars	77.6 | 2.6 %	3.4 | 7.4 %		
B3H	Mesh			787.0 | 1.5 %	835.7 | 1.6 %
				801.0* | 0.4 %	821.5* | 0.9%

* Determined in transverse direction

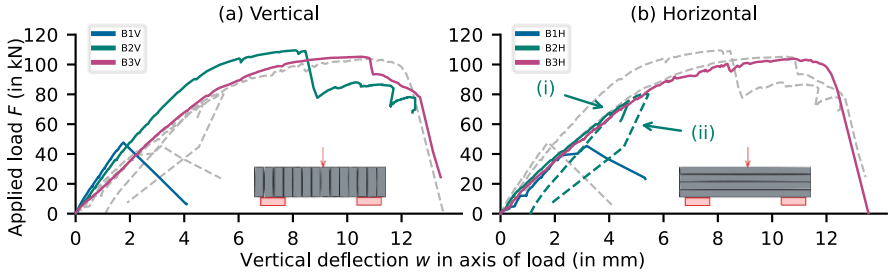
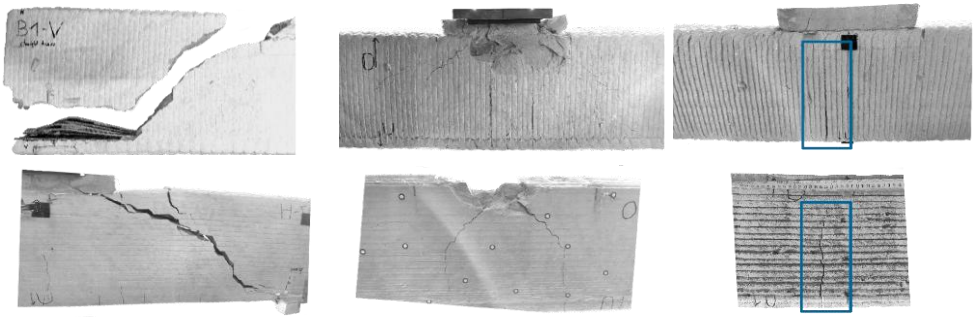


Fig. 3 Load - deflection curve of each reinforcement layout for (a) vertical - and (b) horizontal printing orientation with opposite orientation shown in grey for comparison. For B2H (i) initial load and (ii) reload.



(a) (b) (c)

Fig. 4 Crack pattern after the bending tests (a) shear crack on one side from the load for B1V (top) and B1H (bottom), (b) spalling under the load for B2V (top) and B2H (bottom) and (c) bending crack under the load, outlined with a rectangle, for B3V (top) and B3H (bottom)

B2V shows a linear load increase up until 55 kN where to curve flattens until it reaches a maximum load of 109.6 kN (see green in Fig. 3a). At this point one edge of the upper mortar bed bursts and the load drops to 77.7 kN before it increases again to a maximum of 88.0 kN and then fluctuates. A second load drop appears at 72.0 kN due to spalling of the side wall under the load introduction point (see Fig. 4b top) and the test is aborted. The first loading sequence of specimen B2H is aborted and in a

second attempt without a mortar bed on top reloaded. The corresponding green graphs in Fig. 3b are marked with (i) initial load as continuous and (ii) reload as dashed with both values presented in Table 3. The residual relative vertical deformation from the initial loading at the start of the reload is set to 1.1 mm and the reload curve (ii) intersects the initial load curve (i) at 74.1 kN before it starts rising to a maximum of 80.3 kN until spalling of the side wall under the load introduction area appears (see Fig. 4b bottom), the load drops under 50 kN and the test is terminated

The load curve of specimen B3V shows a linear pattern until 59 kN where it flattens and rises to a maximum load of 105.2 kN at a vertical deflection of 10.5 mm (see magenta in Fig. 3a). Afterwards the load drops to 93.3 kN before it decreases with an increasing deflection until a load of 79.5 kN at a deflection of 12.6 mm is reached and the reinforcement ruptures. For the specimen B3H the load increases to 103.9 kN at a relative vertical deflection of 10.8 mm (see magenta in Fig. 3b) before dropping to 91.1 kN and the reinforcement ruptures. Both specimens B3V and B3H perform up to their maximum load while showing a flexural crack with a simultaneous increasing crack width rate in the load axis starting from the bottom of the beam. For the horizontal printing orientation, the crack follows a small zig-zag pattern (see Fig. 4c bottom) whereas for the vertical printing direction the crack forms between two strands parallel to their orientation (see Fig. 4c top). On both specimens the bending reinforcement ruptured under a maximal load.

4 DISCUSSION

4.1 Load calculation using a current design code

The maximum possible load for both shear and bending resistance is calculated with the material properties f_{cm} and $f_{0.2}$ (see Table 2) for the given specimen geometry and reinforcement layout (see Table 1) and is listed in Table 3. The maximum stresses for the additional rebars (see ii in Fig. 2) of specimen B3V and B3H are selected equal to those of the mesh in longitudinal direction. It shall be noted that all calculations are based on f_{cm}, obtained on a cylinder with diameter 60 mm, and are not adapted to represent the compression resistance of a cylinder with diameter 150 mm.

The calculations for the bending resistance M_R (2) of all six specimens are based on a rectangular stress distribution [5]. The effective height of the compression zone and effective compression strength for the bending resistance result with the factors λ and η respectively for $50<f_{cm}\leq 90$ MPa, see (1).

After subtracting the moment M_g, caused by the dead weight, the maximal external load $F_{max,M}$ is calculated with (3).

$$\lambda=0.8-(f_{cm}-50)/400 \text{ and } \eta=1.0-(f_{cm}-50)/200 \tag{1}$$

$$M_R = F_c \cdot \left(d - 0.5 \cdot \underbrace{\lambda \cdot x}_{x_B} \right) = \underbrace{\lambda \cdot \frac{\overbrace{A_{eff} \cdot f_{0.2}}^{x_B}}{b \cdot \eta \cdot f_{cm}} \cdot b \cdot \eta \cdot f_{cm}}_{F_c} \cdot (d - 0.5 \cdot \lambda \cdot x) \tag{2}$$

$$F_{max,M}=\frac{(M_R-M_g)\cdot 4}{L}=\frac{\left(M_R-\frac{g\cdot(2\cdot a)^2}{8}\right)\cdot 4}{2\cdot a} \tag{3}$$

The shear resistance calculation (4) for specimens without shear reinforcement (B1V and B1H) is conducted according to [5] and the maximal load $F_{max,Vc}$ results to (6), where g·L denotes the vertical component of the dead weight. The empirical factor $C_{R,c}$ is set to 0.15 according to the recommendations for post-test analysis [8].

For those specimens with vertical as well as inclined shear reinforcement (B2V, B2H, B3V and B3H) the shear resistance calculation (5), with $\cot(\theta)=1.38$, is performed according to [5] and the resulting maximal load $F_{max,V}$ is determined by (6).

4.2 Comparison to a current design code

While both specimens B1V and B1H experience a shear failure for the given load, B1V outperforms the calculated maximum shear load without shear reinforcement, reaching 107.6% (see Table 3). B1H underperforms and only reaches 96.5 % of the predicted load. The calculated loads based on the flexural resistance are not representative for these specimens, since this failure mode is never reached.

Table 3 Maximum applied load F_{max} and its corresponding vertical deflection in load axis w_F, calculated maximum load for shear $F_{max,V}$ and bending $F_{max,M}$ with their respective deviation.

Specimen	Observed Failure	F_{max} (in kN)	w_F (in mm)	Bending (in kN)		Shear (in kN)	
				$F_{max,M}$	$\frac{F_{max}}{F_{max,M}}$	$F_{max,Vc}$, $F_{max,V}$	$\frac{F_{max}}{F_{max,V}}$
B1V	Flexural shear failure in concrete	47.7	1.8	73.1	65.2%	**44.3***	107.6%
B2V	Spalling of concrete at load introduction / yielding	109.6	8.5	**71.4**	153.5%	110.5	99.2%
B3V	Rupture of longitudinal reinforcement	105.2	10.5	**83.8**	125.6%	157.7	66.7%
B1H	Flexural shear failure in concrete	45.5	3.2	74.1	61.4%	**47.1**	96.5%
B2H	Spalling of concrete at load introduction	(i) 74.6 (ii) 80.3	(i) 4.6 (ii) 5.3	69.9	114.9%	115.8	69.3%
B3H	Rupture of longitudinal reinforcement	103.9	10.8	**88.3**	117.7	168.4	61.7%

* Bold values indicate the relevant strength for comparison according to the observed failure

$$V_{Rm,c} = \max\left[\begin{array}{c}\left[\underbrace{\frac{0.15}{\underbrace{\gamma_c=1{,}0}_{C_{Rm,c}}}}\cdot\left(\underbrace{1+\sqrt{200/d}}_{k}\right)\cdot\left(100\cdot\rho_l\cdot f_{cm}\right)^{\frac{1}{3}}+\underbrace{k_1\cdot\sigma_{cp}}_{=0}\right]\cdot b\cdot d\\ \left[\left(\underbrace{0.035\cdot k^{\frac{3}{2}}\cdot f_{cm}^{1/2}}_{v_{min}}\right)+\underbrace{k_1\cdot\sigma_{cp}}_{=0}\right]\cdot b\cdot d\end{array}\right] \quad (4)$$

$$V_{Rm} = \min\left[\begin{array}{c}V_{Rm,s}=a_{sw}\cdot z\cdot f_{0.2}\cdot(\cot\theta+\cot\alpha)\cdot\sin\alpha\\ V_{Rm,max}=\frac{\overbrace{\alpha_{sw}}^{=1}\cdot b\cdot z\cdot\overbrace{\left(0.6\cdot(1-f_{cm}/250)\right)}^{\nu_1=\nu}\cdot f_{cm}\cdot(\cot\theta+\cot\alpha)}{\left(1+\cot^2\theta\right)}\end{array}\right] \quad (5)$$

$$F_{max,Vc}=2\cdot V_{Rm,c}-g\cdot\underbrace{2\cdot a}_{L} \quad and \quad F_{max,V}=2\cdot V_{Rm}-g\cdot\underbrace{2\cdot a}_{L} \quad (6)$$

The specimens B2V and B2H both exceed the anticipated bending load, reaching 153.5 % and 114.9 % respectively, and, while B2V gets close to the calculated shear capability at 99.2 %, B2H utilizes only 69.3 % of its predicted shear load. When interpreting the load-deflection trend of specimen B2V it becomes apparent by the flattening of the curve that a flexural failure would have been the leading failure mode. Since the test on specimen B2H was reloaded due to a failure of the mortar bed and ultimately failed prematurely, it is excluded in this comparison.

Both specimens B3V and B3H show a flexural failure under the maximum load applied and outperform the calculation reaching 125.6 % and 117.7 %, respectively, of the predicted load. This represents a fitting accuracy between calculation and reality.

All specimens with a vertical printing direction show only a slightly higher maximum load then those with a horizontal printing direction. When excluding B2H form this analysis, this minimal deviation indicates that the strand orientation only plays a minor role for their load-bearing capacity. It should be noted that an effect on the load-deflection behaviour will be analysed in further investigations. Both specimens without a shear reinforcement B1V and B1H show, as confirmed by the calculations, a shear failure which supports the applicability of the analysed design formula [5] for the introduced 3D printed concrete. When comparing the specimens with shear reinforcement B2V, B3V and B3H, it

becomes apparent that shear resistance is not the limiting factor for the analysed reinforcement layouts. While all three beams show a flexural failure (B3V and B3H), or at least let it anticipate (B2V), they reach their calculated bending resistance, which further supports the applicability of the analysed design code [5] when being applied for flexural prediction of the presented reinforced 3D printed concrete specimen.

5 CONCLUSION

The investigation deals with the load-behaviour of 3D-printed concrete members with different rationalized approaches for in-layer reinforcement, which can be automatized in the future. From the test results and evaluations, the following conclusions can be drawn:

- The 3D-printed concrete beams with layerwise integrated reinforcement of this study can be assessed using conventional reinforced concrete code provisions for cast concrete. Specimens without shear reinforcement failed in shear as predicted, while specimens with inclined/mesh reinforcement were governed by flexure and matched the calculated flexural capacities. This indicates good transferability of current shear and bending design models to the presented reinforced 3DPC approach. It should be noted that further research is needed make reliable statements about the applicability when deviating from the presented material, printing- and testing setup.
- Rationalized shear reinforcement layouts (bent bars acting as combined bending and shear reinforcement as well as meshes placed every third layer) are considered suitable within an automated production workflow as they effectively shifted the limiting failure mode to flexure.
- Practical details of load introduction (e.g., mortar bed integrity) can govern test outcomes and should be controlled in future studies, but do not detract from the demonstrated structural viability of reinforced 3DPC.
- For the investigated geometries and reinforcement strategies, the printing direction (vertical vs. horizontal strand orientation) had only a minor effect on ultimate load-bearing capacity.

Acknowledgements

The authors acknowledge the funding (FFG grant number: 5138043) provided by the Federal Ministry for Innovation, Mobility and Infrastructure (BMIMI), Republic of Austria; Federal Ministry for Economy, Energy and Tourism (BMWET), Republic of Austria and Austrian Research Promotion Agency (FFG) and sponsors from industry.

References

[1] Dubey, Pratik K. and Maurya, Madan C. 2026 “A comprehensive review of 3D printing in construction: technology, materials, and digital workflow” *Innovative Infrastructure Solutions*, DOI: 10.1007/s41062-025-02432-w

[2] Nasir, Osama. “3D Concrete Printing in Construction: Applications, Benefits and Challenges“ *parametric architecture* August 07, 2024, Accessed February 14, 2026. https://parametric-architecture.com/3d-concrete-printing-in-construction-applications-benefits-and-challenges/

[3] Kloft, Harald et al. 2024 “Interaction of reinforcement, process, and form in Digital Fabrication with Concrete” *Journal of Building Engineering*, DOI: 10.1016/j.cemconres.2024.107640

[4] Ter Haar, Bjorn et al. “Off-site 3D printed concrete beam design and fabrication” *Journal of Building Engineering*, DOI: 10.1016/j.jobe.2024.109117

[5] European Committee for Standardization. 2004 “EN 1992-1-1, Eurocode 2: Design of concrete structures, Part 1-1: General rules and rules for buildings”

[6] Mechtcherine, Viktor et al. 2022 “A roadmap for quality control of hardening and hardened printed concrete” *Cement and Concrete Research*, DOI: 10.1016/j.cemconres.2022.106800

[7] Pfleger, Marc-Patrick et al. 2026 “Influence of variable strand orientation on the strength of 3D-printed concrete” *16th fib International PhD Symposium in Civil Engineering*

[8] König, Gert and Fischer, Jürgen. 1995 “Model uncertainties concerning design equations for the shear capacity of concrete members without shear reinforcement” *CEB Bulletin*

Influence of variable strand orientation on the strength of 3D-printed concrete

Marc-Patrick Pfleger[1,2], Elisabeth Radl[1,2], Patrick Huber[2] and Tobias Huber[2]

[1] Research Center for Building and Design, Hochschule Campus Wien, Favoritenstraße 226, 1100 Vienna, Austria

[2] Institute for Structural Engineering, Research Unit of Structural Concrete, TU Wien, Karlsplatz 13, 1040 Vienna, Austria

Summary

In the field of 3D concrete printing a wide range of research on the material behavior of extrudable mix-designs can be seen. This can be explained by the specific, anisotropic material behavior caused by the layered inner structure of 3D printed objects. These anisotropic properties can lead to unfavorable failure mechanisms in structural elements. A preliminary experimental study aims to demonstrate the influence of specifically arranged transverse strands on material strength of printed cube-shaped specimens. As part of this study, compressive strength tests are conducted on specimens with uniform layer orientation as a reference, and 2 variant studies with different transverse layer ratios are being investigated. The influence on strength is presented and discussed in relation to direction. It is shown, that the anisotropic behavior of the compressive strength of 3D printed concrete can be reduced by integrating transverse-oriented strands.

1 INTRODUCTION

Additive manufacturing with concrete is currently a topic of increasing research interest internationally [1]. The used materials and mix designs in the field of 3D concrete printing (3DCP) vary significantly from one another, because the printing material is often adjusted to suit a specific printing setup or equipment. It is therefore of special interest to characterize the material properties of hardened printed concrete using specific material tests or methods [2]. Compared to conventional testing, crucial questions concerning the influence of the print strand orientation on material strengths arise. It is known that printed concrete specimens show anisotropic material behavior, because these generally solid objects are built up by multiple material layers consisting of individual strands with a certain orientation.

The problem outlined above with regard to load direction-dependent strength values is also evident in the fracture behavior observed compressive strength tests performed on cubes. As shown in Fig. 1, the layer structure of the specimens can be traced in accordance with the fracture pattern. There is no uniform failure of the material, especially under loads introduced normal to the direction of printing.

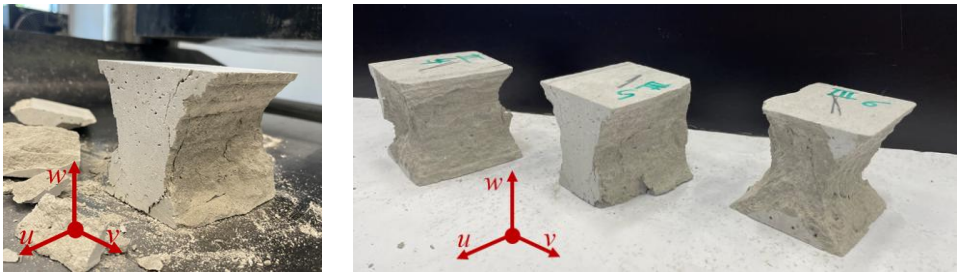


Fig. 1 Typical fracture pattern under load perpendicular to the material strands (*w*-direction) after testing (left), fracture patterns of *w*-test series (right)

Related observations can also be made during testing of structural elements. As shown in Fig. 2, crack propagation follows the layer structure and, for example in the node areas of truss structures, develops along the direction of the contact surfaces of the material strands.




Fig. 2 Delamination of parallel material strands observed in bending tests on different printed truss structures

This can be attributed to the resulting inhomogeneities, which arise not only from the layer structure and porosity of printed concrete, but also from the fact that the extrusion or pumping process causes additional segregation, which can lead to higher cement contents and water-binder values at the layer boundaries [3], [4]. Consequently, it should be investigated whether varying the orientation of the printed strands result in more homogeneous fracture behavior and thus to a harmonization of direction-dependent strengths. In the following, the influence on compressive strength through the arrangement of transverse layers will be investigated, to be considered in future designs of structural elements.

2 MATERIALS AND METHODS

2.1 Printing setup and materials

The printing system used is based on a 6-axis articulated arm robot mounted on an external axis which provides a build volume of approx. 1000 x 1000 x 7000 mm. The printed objects are produced on a height-adjustable printing table paneled with film-faced birch plywood for calibration purposes.

A standard printing setup was defined for sample production, using a 1 K-material and a matching extruder. The nozzle diameter (*dN*) was set at 12 mm, and the layer height (*hl*) at $dN / 1.5 = hl$, resulting in a printed layer height of 8 mm. The strand spacing of the adjacent layers was defined as 12 mm. The samples are produced in a single print job and as a continuous printed object out of a single batch of material for each test series. The printing material has been specially developed tailored to the printing system described and is based on clinker-reduced standard cement, CEM II C-M in accordance with EN 197 [5]. The additional components and their dry mass fractions can be found in Table 1.

Table 1 Overview of the main constituents of the extrudable concrete for specimen production

Type	Material	Weight percentage [wt. %]
Binder	CEM II C-M (S-LL) 42.5N	37
Aggregate	Quartz sand 0-1.0 mm	45
Property enhancer	Silica fume	3
-	Water	15
Additive	PCE-superplasticizer	< 0,1
Additive	VMA	< 0,01
Fibers	Glass fibers, 12 mm	< 0,02

Since the mixing process has a significant influence on the consistency and general behavior of the fresh concrete, the procedure is followed precisely and repeatedly. All dry components, with the exception of additives and fibers, are premixed for 3 min with a hand-held stirrer. The mixing water together with superplasticizer is then added in full quantity and mixed for 5 min. To adjust consistency, VMA (viscosity modifying agent) is added together with glass fibers and mixed for 2.5 min. After a

setting time of 10 min., the fresh concrete properties are determined in accordance with Perrot and Roussel and checked for conformity with the expected values [6] - [8].

Table 2 Fresh concrete properties of the printing material at various test times

Test type		T = 0 min.	T = 30 min.	T = 60 min.	T = 90 min.
Flow table (bucket), 15 drops	[mm]	140	125	117	-
Flow table (extruded) 15 drops	[mm]	150	155	-	-
Pocket penetrometer, 25 mm plunger	[kPa]	27.0	43.5	50.6	67.4
Pocket shear vane test, 47,5 mm vane	[kPa]	38.1	53.0	69.7	93.2
Slug test, 30 slugs	[g/slug]	46.7	-	-	-

As can be derived from the test values for the fresh concrete properties in Table 2, the used concrete mix shows typical properties of a 1K-material with a normal setting time. In order to achieve the desired structural properties (building height or stability properties for printing thin-walled cross-sections), the material consistency can be classified as stiff-plastic [9]. Unlike conventional concrete mixes, it is therefore not possible to easily place and compact the material in conventional test molds using a vibrating table. In order to achieve a representative material density compared to printing and a correspondingly homogeneous structure, the printing concrete is filled into the test specimen molds using the extrusion head. The nozzle remains immersed at least 10 mm into the already extruded material and is distributed until the molds are completely filled and can be smoothed on the upper surface. The nozzle diameter, hose length, material conveyor system including hose type, and feed rate are choosen in the same way as for the subsequent printing process. The samples are stored in accordance with EN 12390-2 until the strength tests are conducted [10]. Test cubes with an edge length of 150 mm and prisms measuring 40 x 40 x 160 mm are produced in steel molds. Each of these two described test series consist of three test specimens. The mean values of the strength tests can be taken from Table 3.

Table 3 Material strengths of the printing material on casted cube and prism specimens

Specimen type	Testing age [d]	f_{cm} [MPa] (CV)	$f_{ctm,fl}$ [MPa] (CV)	Density (mean) [g/cm^3]
Cube 150 x 150 x 150 mm	28	69.70 (5 %)	-	2.0489
Prism 40 x 40 x 160 mm	28	67.29 (3 %)	7.07 (6 %)	2.0561

2.2 Sample preparation and definition of specimen types and geometries

The study is based on cube samples that are subjected to compressive strength tests. The sample dimensions are defined so that a representative number of material strands and layers are included within a sample, thereby allowing the influence of the layer structure and layer composite on the material strength to be determined during the tests.

In order to obtain undisturbed, uniformly structured samples, three beam-shaped objects with dimensions of 130 x 104 x 900 mm are produced using the printing parameters specified in Section 2.1. The objects are covered with PE film (0.2 mm, 184 g/m^2) for 14 days and stored at approx. 20 °C. After further storage without cover, the samples are cut into cubes with an edge length of approx. 80 mm using a wet cutter after a further 14 days. The cubes are then ground on two opposite sides in several steps, to achieve parallel and smooth load areas, using a surface grinding machine. The printed objects

from which the individual test specimens are extracted are significantly larger than the specimens to exclude any influences from the material near the edges and possible differences in compaction.

Due to the layer and strand structure of 3D-printed objects, three different loading scenarios should be characterized for comparability (*u*,*v*,*w* in accordance with [2]) considering the applied load relative to layer or strand orientation (Fig. 3).

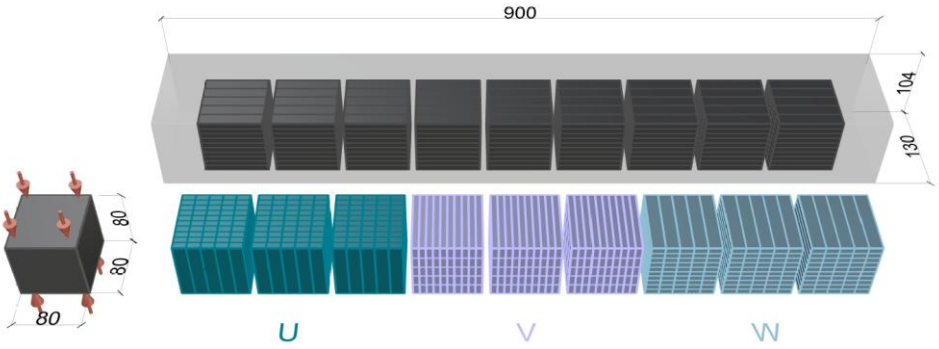


Fig. 3 Schematic visualization of specimen extraction from 3D printed concrete samples with uniform strand layout and the main test orientations *u*, *v* and *w*, dimensions in [mm]

As can be seen in Fig. 3, the printing objects for specimen preparation are manufactured with sufficient excess material to rule out possible influences from material layers and strands close to the edge. All nine specimens are obtained from a single printed object as shown.

2.3 Specimen composition, testing scope and procedure

To enable sufficient comparability and evaluation of the influences of transverse layers, variants of the layer and strand structure of the samples are specified. The basic variant (*100/0*) consists of uniformly aligned strands which run lengthwise along the printed samples (Fig. 4, left).

In addition, two sample variants are produced for performance comparison, which are printed with 20 % (*80/20*) and 40 % (*60/40*) of the layers in transverse direction (Fig. 4, right). The transverse layers are printed at 90° to the main strand orientation and arranged in height so that they are later positioned at a uniform distance from the specimen's outer edges.



Fig. 4 Design concept (left) and manufacturing of samples "80/20" and "60/40" with perpendicular strands in certain material layers (middle) and typical surface structure (right)

One 3D printed sample per strand layout variant and layer structure with the dimensions specified in 2.2 is produced and further processed for compressive strength testing. Nine cube specimens with an edge length of approx. 80 mm are cut in each case in order to examine the three main load configurations, according to Fig. 3. Thus, a total of 27 cube specimens are prepared and their compressive strength is determined [11]. The test parameters are kept the same for all test series and

specimens, with the loading rate defined as 7.1 kN/s so that the sample is likely to fail 45 – 60 s after the start of loading. All tests were started with a preload of 7.5 kN.

3 TESTING RESULTS

3.1 Strength testing of reference specimens with standard strand orientation

The reference series "100/0" represents a basic test series of nine cube specimens with the dimensions specified in Table 4. The uniaxial concrete compressive strength in all three main stress directions is determined on three specimens in each case, as shown in Fig. 5.

Table 4 Specimen properties, overview and results of test series *100/0*

Sample type (ratio of longitudinal to transverse strands)	Specimen ID	Testing age [d]	Dimensions [mm]			Loading area [mm²]	Mass [g]	Density [g/cm³]	f_c [MPa]
			l	w	h				
100 / 0-u	100/0-u-1	43	79.3	79.4	77.5	6296.4	1004.2	2.0579	74.85
	100/0-u-2		79.4	79.3	78.9	6296.4	1018.8	2.0508	71.97
	100/0-u-3		79.6	79.8	78.0	6352.1	1007.4	2.0333	70.50
100 / 0-v	100/0-v-1	43	79.9	80.2	76.9	6407.9	1023.6	2.0772	50.08
	100/0-v-2		80.2	80.5	76.0	6456.1	996.8	2.0315	57.75
	100/0-v-3		80.1	81.5	76.1	6528.2	1010.6	2.0345	47.58
100 / 0-w	100/0-w-1	43	79.4	79.5	76.7	6312.3	984.0	2.0324	63.22
	100/0-w-2		79.5	79.7	76.5	6336.2	993.3	2.0492	63.92
	100/0-w-3		81.6	81.9	78.5	6630.0	1079.6	2.0595	60.25

Determining the density of the reference samples should provide information about possible differences in compaction between different layer structure variants. No outliers are identified in Table 4. The determined material strengths show direction-dependent deviations on the mean compressive strength, -28 % for *v* and -14 % for *w* in relation to *u* direction. The results correspond to the general empirical values from reference tests [2].

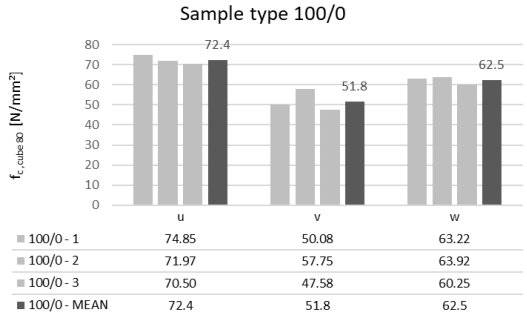


Fig. 5 Results of the compressive strength test of sample type *100/0* with individual test results and mean values for load directions *u, v, w*

3.2 Strength testing of specimens with alternated strand orientation

The specimen's dimensions and corresponding densities of the individual samples in the "80/20" and "60/40" variant series can be found in Table 5. Due to only slight changes in material density caused by the alternative layer structures, there is no indication of poorer compaction resulting from the integration of transverse layers compared to series "100/0". Lower densities could be related to changes in the ratio and volume of interfilament pores between the strands or layers [12].

Table 5 Specimen properties, overview and results of test series *80/20* and test series *60/40*

Sample type (ratio of longitudinal to transverse strands)	Specimen ID	Testing age [d]	Dimensions [mm]			Loading area [mm²]	Mass [g]	Density [g/cm³]	f_c [MPa]
			l	w	h				
80 / 20-u	80/20-u-1	45	81.3	81.9	77.1	6658.5	1065.2	2.0749	69.82
	80/20-u-2		81.3	81.4	77.9	6617.8	1075.5	2.0862	73.55
	80/20-u-3		81.2	81.7	79.1	6634.0	1095.4	2.0875	74.08
80 / 20-v	80/20-v-1	45	81.4	81.3	79.1	6617.8	1092.6	2.0872	62.59
	80/20-v-2		81.8	81.3	78.9	6650.3	1100.8	2.0979	61.46
	80/20-v-3		81.3	81.5	79.5	6625.9	1086.3	2.0622	64.40
80 / 20-w	80/20-w-1	45	81.3	81.4	78.5	6617.8	1078.7	2,0764	65.38
	80/20-w-2		81.1	81.5	78.9	6609.7	1077.0	2,0652	63.50
	80/20-w-3		80.8	81.6	81.6	6593.3	1073.3	1.9949	64.53
60 / 40-u	60 / 40-u-1	45	81.4	81.4	80.4	6625.9	1110.8	2.0851	68.35
	60 / 40-u-2		81.7	81.5	79.8	6658.6	1098.5	2.0673	57.19
	60 / 40-u-3		82.3	82.1	81.1	6756.8	1131.6	2.0650	53.70
60 / 40-v	60 / 40-v-1	45	81.2	81.3	80.4	6601.6	1100.8	2.0739	58.43
	60 / 40-v-2		81.5	82.1	81.1	6691.1	1131.7	2.0854	62.55
	60 / 40-v-3		82.2	81.7	79.6	6715.7	1112.7	2.0870	58.69
60 / 40-w	60 / 40-w-1	45	81.1	81.9	79.1	6642.1	1096.5	2.0870	66.82
	60 / 40-w-2		82.1	81.6	78.4	6699.4	1095.8	2.0863	67.93
	60 / 40-w-3		81.3	81.2	79.8	6601.6	1097.1	2.0825	66.80

The results of the compressive strength test of specimen types *80/20* and *60/40* are shown in Fig. 6.

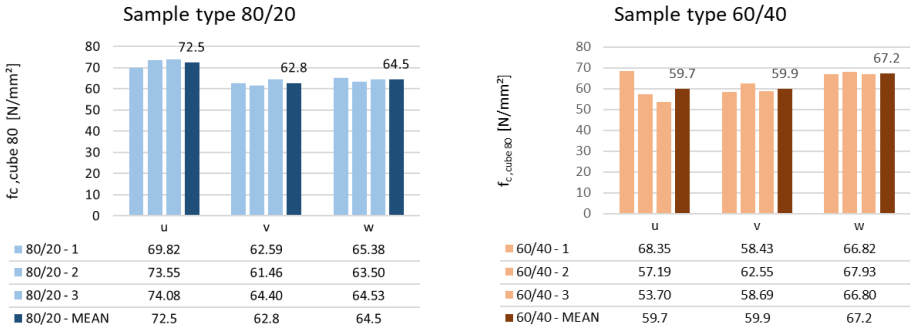


Fig. 6 Results of the compressive strength test of sample type *80/20* (left) and sample type *60/40* (right) with individual test results and mean values for load directions *u, v, w*



Fig. 7 Representative example of *60/40-w* specimens after compressive strength testing showing a uniform fracture pattern

4 DISCUSSION

The average values of the tested compressive strengths of all three variants in the *u*, *v*, and *w* directions are used as a basis for comparison of the material performance. As can be seen in Fig. 7, in the case of the arrangement of transverse strands, the fracture surfaces are more uniform, compared to the standard strand layout.

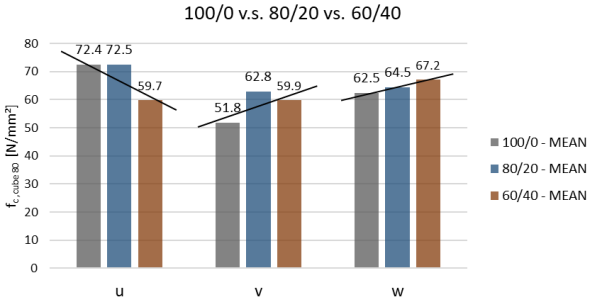
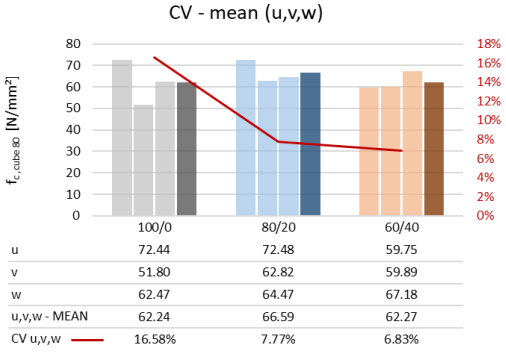


Fig. 8 Comparison of the compressive strength as mean values by load direction

Fig. 8 highlights the influence of the material strand orientation on the anisotropic properties of 3D-printed components in terms of their compressive strength. Particularly in the load directions *v* and *w*, where uneven failure of the samples occurs along the strand direction. This can be explained by a significant impact of the strand or layer contact surfaces. The compressive strength can be significantly increased compared to the reference layout (*100/0*) by arranging transverse layers with 20 % and 40 % of the total layer number. Presumed air voids in the interfilament area, which are created by the application of the transverse layers and remain as pores, cannot be observed, which is confirmed by only slight changes in material density. According to the presented study, the placement of transverse layers leads to a more uniform distribution of direction-depending strengths, which is composed of an increase in the values in *w*, a partial increase in *v*, and a decrease in *u* with a higher CV due to its approximation to *v-layout*. Fig. 9 shows the mean strengths for each sample type *100/0, 80/20* and *60/40* not taking the strand orientations into account. By determining the CV per sample type, it can be pointed out that the variation in strand orientation can lead to a reduction in dispersion of the compressive strengths.



	100/0	80/20	60/40
u	72.44	72.48	59.75
v	51.80	62.82	59.89
w	62.47	64.47	67.18
u,v,w - MEAN	62.24	66.59	62.27
CV u,v,w	16.58%	7.77%	6.83%

Fig. 9 Compariosn of CV of the mean values of *u, v, w* per sample type

In general, comparable compressive strengths can be observed for printed test specimens and those extruded in conventional molds (Table 3), provided that the material is extruded into the formwork so that similar material density is achieved. The basis for this comparison must be the direction of stress that is favorable in terms of strength. This circumstance arises even though the test specimens used for material testing differ greatly in terms of geometry and dimensions when comparing printed and cast samples. In accordance with Table 3, compressive strengths were therefore determined on different cast samples (150 mm and 40 mm cubes). The test values for compressive strength differ only slightly, which may be explained using only fine grain of max. 1 mm.

5 CONCLUSION

The orientation of the material strands has a significant influence on the compressive strength of 3D-printed concrete. With conventional, uniform orientation, there are large directional differences, resulting in a *CV* of 16.5 %, which confirm the anisotropy of compressive stresses described in the literature. This behavior can be explained, partly, by the fracture pattern and can be attributed to a failure of the material layer interfaces. By using 20 % and 40 % transverse layers within the specimens, these effects can be suppressed, as the results of the compressive strength tests show a homogenization of the strengths, with the favorable load direction *u* experiencing a reduction, while directions *v* and *w* show higher values, reducing the overall *CV* in case of specimens *60/40* to 6.8 %.

References

[1] Garcés, Gonzalo, García-Alvarado, Rodrigo, Bunster, Victor, and Muñoz-Sanguinetti, Claudia. 2026. "Additive Construction 4.0: A systematic review of 3D concrete printing for Construction 4.0." *Engineering, Construction and Architectural Management* 8:6539-6568. doi:10.1108/ECAM-07-2024-0875.

[2] Bos, Freek, Robens-Radermacher, Annika, Muthukrishnan, Shravan, Versteegen, Jelle, Wolfs, Rob, Santhanam, Manu, Menna, Costantino, and Mechtcherine, Viktor. 2024. "Database of the RILEM TC 304-ADC interlaboratory study on mechanical properties of 3D printed concrete (ILS-mech)." *Data set. Zenodo*. doi:10.5281/zenodo.12200570.

[3] Perrot, Arnaud, Rangeard, Damien, Mélinge, Yannick, Estellé, Patrice, and Lanos, Christophe. 2009. "Extrusion Criterion for Firm Cement-Based Materials." *Applied Rheology* 19:53042. doi:10.3933/ApplRheol-19-53042.

[4] Das, Arnesh, Song, Yu, Mantellato, Sara, Wangler, Timothy, Flatt, Robert J., and Lange, David. 2020. "Influence of pumping/extrusion on the air-void system of 3D printed concrete." *Second RILEM International Conference on Concrete and Digital Fabrication. Digital Concrete 2020* 28:417-427. doi:10.3929/ethz-b-000426811.

[5] Austrian Standards Institute. 2021. "ÖNORM EN 197-5: Cement - Part 5: Portland-composite cement CEM II/C-M and Composite cement CEM VI." *Wien: Austrian Standards*.

[6] Barry, Mamadou, Jacquet, Yohan, and Perrot, Arnaud. 2025. "Pocket vane and penetrometer as quality control tool for Extrusion 3D concrete printing." *Materials and Structures* 58:Article 297. doi:10.1617/s11527-025-02831-6.

[7] Roussel, Nicolas, Buswell, Richard, Ducoulombier, Nicolas, Ivanova, Irina, Kolawole, John T., Lowke, Dirk, Mechtcherine, Viktor, Mesnil, Romain, Perrot, Arnaud, Pott, Ursula, Reiter, Lex, Stephan, Dietmar, Wangler, Timothy, Wolfs, Rob, and Zuo, Wenqiang. 2022. Assessing the fresh properties of printable cement-based materials: "High potential tests for quality control." *Cement and Concrete Research* 158. doi:10.1016/j.cemconres.2022.106836.

[8] Ducoulombier, Nicolas, Mesnil, Romain, Carneau, Paul, Demont, Léo, Bessaies-Bey, Hela, Caron, Jean.-F., and Roussel, Nicolas. 2021. "The "Slugs-test" for extrusion-based additive manufacturing: Protocol, analysis and practical limits." *Cement and Concrete Composites* 121. doi:10.1016/j.cemconcomp.2021.104074.

[9] Kolawole, John T., De-Becker, Danny, Xu, Jie, Dobrzanski, James, Cavalaro, Sergio, Austin, Simon, and Buswell, Richard. "Selected Test Methods for Assessing Fresh and Plastic-State 3D Concrete Printing Materials." Third RILEM International Conference on Concrete and Digital Fabrication. Digital Concrete 2022.37:460–466. doi:10.1007/978-3-031-06116-5_68.

[10] Austrian Standards Institute. 2019. "ÖNORM EN 12390-2: Testing hardened concrete - Part 2: Making and curing specimens for strength tests." *Wien: Austrian Standards.*

[11] Austrian Standards Institute. 2019. "ÖNORM EN 12390-3: Testing hardened concrete - Part 3: Compressive strength of test specimens." *Wien: Austrian Standards.*

[12] Liu, Xingzi, Buswell, Richard, Cavalaro, Sergio Henrique Pialarissi, and Kolawole, John Temitope. 2026. "Influence of Inter-Filament Voids on the Failure Mechanism and Compressive Strength of 3D Printed Concrete." *Construction and Building Materials.* 510:145266. doi:10.1016/j.cemconres.2019.02.017.

Structural Monitoring

Existing tunnels monitoring, risk evaluation and rehabilitation: an overview of the Italian Guidelines

Giulia Brentana, Ivan Trabucchi, Giuseppe Tiberti, Giovanni A. Plizzari

DICATAM,
University of Brescia,
via Branze 43, Brescia 25123, Italy

Summary
After World War II, the Italian transport network underwent a rapid expansion, resulting in more than 9000 road tunnels, many of which are approaching or exceeding their service life. This condition highlights the need for a systematic regulatory framework for inspection, risk assessment and rehabilitation. This paper aims to review the evolution of Italian regulations for existing tunnels and to present typological structural intervantions. The first starts from the technical documents developed by "Autostrade per l'Italia" in 2020 to the comprehensive Guidelines promoted by Ministry of infrastructure and transport in 2022. These introduce a multilayered methodology integrating inspection protocols, defect classification, multi-risk analysis, safety assessment and intervention prioritisation. Building upon the decision-making criteria introduced in 2022, the paper discusses possible local and global rehabilitation strategies, focusing on technical solutions applicable to thickness deficiencies in existing tunnel linings.

1 INTRODUCTION

Due to its complex orography, dominated by the Alps and Apennine chains, Italy has developed an extensive transport infrastructure network with a very high number of tunnels, constructed with reinforced or unreinforced concrete linings. Many of these structures are now approaching or exceeding their original design service life.

Recent failures, including the collapse of the Berté tunnel on the A26 motorway, have highlighted the vulnerability of existing tunnel linings and triggered significant regulatory evolution. The Italian Ministry of Infrastructure introduced updated inspection manuals and guidelines, promoting systematic defect classification and intervention strategies. The Italian regulatory framework for tunnel maintenance has progressively evolved from an initial inspection-oriented approach towards a more structured and methodologically defined system. Early regulations were primarily focused on periodic checks and documentation [1], whereas recent developments have introduced a clearer connection between inspection outcomes, defect classification and risk management strategies. A significant step in this evolution was the publication of the 2020 "Manuale Ispezione Gallerie" [2], which established a standardised inspection procedure and introduced a defect-by-defect severity classification system. This approach was complemented by the requirement for systematic documentation through tunnel dossiers, enabling the continuous tracking of structural conditions over time and promoting a more consistent management of infrastructure assets.

Based on this framework, the 2022 Guidelines [3]further refined the regulatory scheme by structuring risk assessment into distinct categories, including global structural and geotechnical risks, local structural defects, seismic risk, as well as hydraulic and geological risks. This categorisation reflects an increased awareness of the multiple interacting mechanisms that can affect tunnel performance, moving beyond a purely descriptive census of defects towards a comprehensive risk-based approach.

Within this regulatory context, defects affecting tunnel linings are classified according to their origin, distinguishing between water-related degradation phenomena, ground–lining interaction processes, intrinsic material deterioration and structural or geometric deficiencies. Such a classification is not merely taxonomical, but directly influences the selection of intervention strategies and the evaluation of safety conditions. Among the various defect typologies, lining thickness deficiency, commonly referred to as sub-thickness, and detachments emerge as particularly critical, as they directly compromise the load-bearing capacity of the lining and may trigger local collapse mechanisms with potential implications for the overall structural behaviour of the tunnel.

The following sections examine the principal regulatory documents and subsequently outline some local and global rehabilitation strategies adopted for existing tunnels.

2 "MANUALE ISPEZIONE GALLERIE"

The 2020 Italian technical documents on existing road tunnels [2] promoted by Ministry of infrastructure and transport, represent a decisive transitional phase in the evolution of tunnel safety management, marking the shift from heterogeneous and experience-based maintenance practices to a more structured and process-oriented framework. Developed in response to growing awareness of infrastructure ageing and the need for harmonised procedures across operators, these documents anticipated several principles that were later formalised in the 2022 national Guidelines [3].

Rather than introducing new design rules, the 2020 framework focuses on the organisation of knowledge and decision-making processes. Its primary objective is to support safety management through structured inspection outcomes, traceable evaluation steps and qualitative–quantitative assessments. In this sense, the "Manuale Ispezione Gallerie" [2] should be interpreted as part of a broader technical culture in which inspection, defect classification and intervention planning are progressively standardised and interconnected.

A key issue addressed by the 2020 documents concerns the lack of uniform inspection criteria and the absence of a shared technical language for describing defects. Prior to their introduction, inspection outcomes were often influenced by operator-specific practices, limiting comparability between different tunnels and concessionaires. The manual responds to this limitation by formalising a standardised inspection procedure and introducing a defect-by-defect severity classification system. Visual inspection is no longer treated as a purely descriptive activity but as a diagnostic process, in which observed anomalies are systematically identified, classified and interpreted in light of potential structural implications.

This approach implicitly assumes that tunnel safety can be effectively managed when defects are detected early, consistently described and associated with plausible evolution mechanisms. Such an assumption places strong emphasis on inspection quality and inspector competence, while simultaneously justifying the need for structured catalogues capable of reducing subjectivity in defect identification. In this context, the conceptual and operational influence of the Autostrade per l'Italia (ASPI) defect catalogues [4] becomes particularly evident.

The 2020 framework adopts a classification logic that distinguishes defects according to their origin and nature, including material degradation, structural behaviour anomalies, construction-related deficiencies and environmental actions. This categorisation is not merely descriptive but serves as the basis for subsequent safety evaluation. Defects are considered within a broader interpretative framework that accounts for tunnel typology, age, construction technique and environmental context. Although the resulting safety assessment remains largely qualitative, the aggregation of inspection data into structured categories represents a significant improvement over purely experience-based judgements and anticipates the multilayered risk analysis introduced in 2022.

Parallel to defect classification, the framework implicitly promotes a structured link between observed anomalies and technically validated intervention strategies. Standardised intervention typologies, strongly aligned with the ASPI catalogues [4], enable a coherent defect–intervention logic, in which remedial actions are selected according to defect type, severity and expected evolution. This contributes to greater traceability, comparability and consistency in maintenance planning, reinforcing the transition from reactive repair to preventive and risk-informed management.

Nevertheless, the 2020 documents [2] retain a transitional character. They are based on the assumption that structured defect classification can sufficiently support safety decisions, an approach that raises open questions regarding hidden defects, time-dependent degradation mechanisms and complex soil–structure interaction phenomena. The limited formalisation of explicit risk metrics and the absence of fully integrated multi-risk assessment further highlight the evolutionary nature of the framework. These aspects, however, should be interpreted not as intrinsic weaknesses but as stepping stones towards the more comprehensive regulatory system established in 2022.

Within this evolving technical landscape, the ASPI defect [4] and intervention catalogues [i] play a central methodological role. The following section therefore examines these manuals in detail, analysing their structure, classification criteria and operational implications for tunnel rehabilitation strategies.

3 ASPI: "NUOVO CATALOGO DIFETTI"

The Technical-Illustrative Report of the New Defect Catalogue (NDC) [4] issued by "Autostrade per l'Italia" represents the operational core of the inspection system adopted for motorway tunnels. This catalogue includes the deteriorations and defects that may be observed in structures and serves as the practical guide for the inspector. The document has been prepared in accordance with the CETU (Centre d'Études des Tunnels) Guidelines 2015 [6]. The "Nuovo catalogo difetti" is conceived as a structured methodological tool that supports inspectors in identifying, interpreting and managing deterioration phenomena affecting tunnel linings and no-structural components. It provides a shared technical language and a standardised framework aimed at reducing subjectivity in inspection outcomes, ensuring consistency across different assets and operators.

The catalogue organises twelve identified defects into thematic categories based on prevailing causes or affected elements, such as water-related phenomena, ground–lining interaction, material deterioration, drainage malfunction, geometric irregularities and fire damage. This structure reflects a causal logic, linking observable manifestations to potential origins and structural implications. Each defect is assigned an alphanumeric code to ensure traceability in inspection reports and digital management systems.

Each defect sheet follows a consistent format, including description of the anomaly, inspection methods, characterisation parameters, associated defects, likely causes, aggravating factors, foreseeable consequences and potential risks for both users and the structure. Monitoring recommendations and corrective measures are also indicated. This scheme establishes a logical chain from observation to diagnosis and intervention, transforming inspection into an interpretative process.

The catalogue distinguishes clearly between visible symptoms and underlying mechanisms. For instance, water infiltrations are characterised in terms of flow, pressure and geological context, while defects in unlined sections are analysed with reference to stability and detachment mechanisms. Although primarily descriptive, the document introduces an evaluative dimension by differentiating between user hazards and structural risks and by linking observable indicators to severity levels.

However, the approach remains largely qualitative and assumes that defect classification based on visual inspection is sufficient to guide safety decisions. While interactions between multiple deterioration mechanisms are acknowledged, a fully integrated multi-risk framework is not explicitly formalised.

Overall, the ASPI Technical-Illustrative Report [4] constitutes a decisive step towards the rationalisation of tunnel inspection practice. By standardising terminology, structuring observation and linking defect identification to monitoring and intervention strategies, it establishes the methodological foundation for a coherent maintenance policy. Its influence extends beyond the descriptive domain, shaping the way in which safety is interpreted and managed within the broader regulatory evolution discussed in the previous chapter.

3.1 Defects affecting concrete linings - thickness reduction

Within the ASPI New Defect Catalogue [4], Chapter 7 is dedicated to defects affecting concrete linings, including cracking, spalling, honeycombing, voids, reinforcement exposure and shotcrete deterioration. The catalogue does not limit itself to a descriptive inventory of these phenomena, but systematically relates each observable anomaly to its likely causes and possible evolution, framing degradation within a broader structural context.

Nevertheless, while Chapter 7 provides a detailed classification of concrete lining defects, [4] does not explicitly quantify their structural impact. The assessment remains qualitative, based on severity indicators and observable criteria rather than on mechanical verification. This reflects the overall philosophy of the catalogue, which prioritises standardised identification and comparability over analytical structural evaluation. As a result, the transition from observation to structural capacity assessment is not fully formalised within the document itself and must be addressed through subsequent engineering analysis.

This gap becomes particularly relevant in the context of existing tunnels where multiple localised thickness reductions may coexist along extended stretches of lining. While each defect may individually fall within the category of a "local anomaly", their cumulative effect could influence global structural behaviour. The catalogue provides the necessary descriptive framework to detect and classify such defects, but it leaves open the question of how their structural significance should be quantified.

4 GUIDELINE FOR THE RISK CLASSIFICATION, SAFETY EVALUATION, AND MONITORING OF EXISTING TUNNELS

The Italian Decreto Ministeriale 247 of 1 August 2022 [3] approves the Guidelines for the classification and management of risk, the evaluation of safety and the monitoring of existing road tunnels along state roads and motorways managed by ANAS S.p.A. or concessionaires. The Guidelines are intended to provide a harmonised framework for tunnel safety assessment and risk-based decision-making across the national network.

The DM 247/2022 represents a methodological advance in infrastructure management by integrating, in a structured way, multiple dimensions of tunnel assessment: systematic data collection, risk classification, safety evaluation and continuous monitoring. This approach reflects a policy shift from reactive maintenance towards risk-informed prioritisation of inspection and intervention. The principal aim is not merely to catalogue defects, but to establish a procedural basis for assigning attention levels to tunnels, thereby enabling operators to plan inspections, detailed analyses, monitoring programmes and mitigation actions in a consistent and traceable manner.

The Guidelines introduce a multilevel analytical framework, summarized with the flowchart in Fig. 1, that organises the tunnel evaluation process into progressively refined stages. Each level corresponds to increasing analytical accuracy and investigation depth, with the objective of aligning inspection efforts with the severity and urgency of the risk profile.

By structuring the assessment process into levels, these guidelines offer a transparent and traceable basis for prioritising interventions. Attention classes derived from the multilayer process provide a rational framework for comparing tunnels with diverse characteristics and damage patterns. In this way, the Guidelines support not only classification and monitoring, but also the early identification of cases where detailed structural analysis and repair intervention planning are justified.

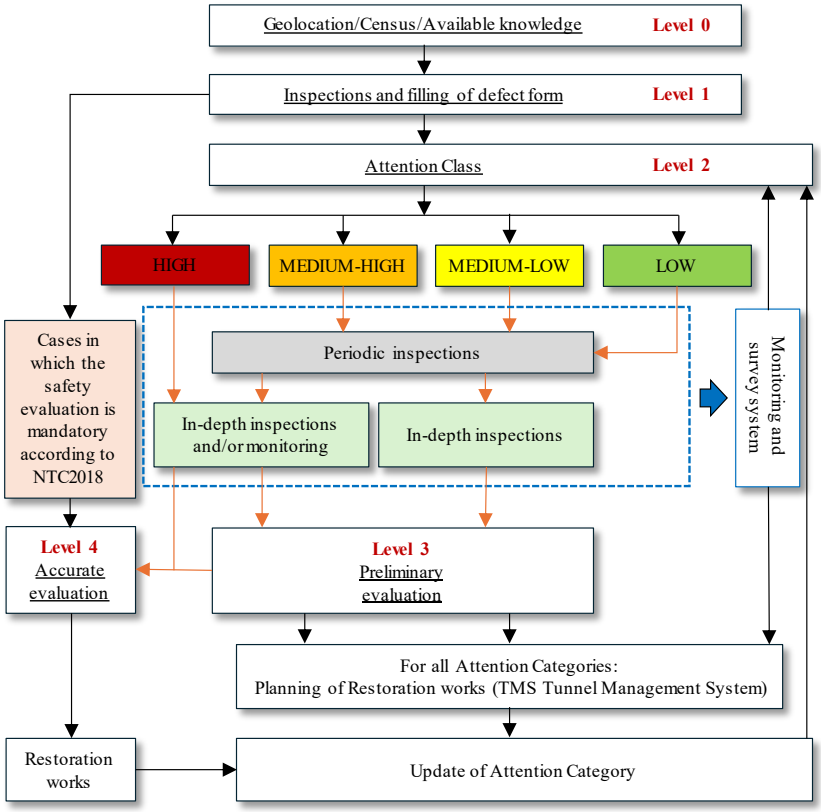


Fig. 1 Overall structure of 2022 Guidelines.

4.1 Level 0

The first stage, referred to as Level 0, is dedicated to the establishment of a comprehensive census of existing tunnels and the assembly of a basic knowledge base. At this level, the objective is to ensure that all relevant assets are accounted for and that fundamental information is gathered, including tunnel geometry, age, construction history and any available documentation on past inspections or interventions, as well as data relating to the road network and the geographical context in which each tunnel is located. This foundational dataset forms the basis for subsequent risk classification and is crucial for contextualising observed defects and anomalies within the tunnel.

The information gathered at Level 0 also supports the definition of priorities for initial visual inspections and the activation of Level 1 activities. Moreover, the combined use of census data and Level 1 inspections may directly identify cases requiring an in-depth safety assessment (Level 4), allowing the classification phase (Level 2) to be bypassed where necessary.

4.2 Level 1

Level 1 is based on systematic visual inspections to identify and document observable anomalies in the tunnel lining, utilities, drainage systems and other components. Through the use of standardised protocols and defect descriptors, such as those found in the ASPI defect catalogue [3], qualitative observations are translated into structured and comparable data, forming the basis for preliminary risk screening and for selecting cases that require more detailed investigation.

Initial inspections are carried out on all tunnels identified during the Level 0 census, taking into account their specific characteristics and the level of knowledge already available. The objective is to verify and integrate Level 0 information, document the actual geometric and structural features of the tunnel and its site conditions, and provide a first assessment of its conservation state. The inspection covers the intrados and all related components, including access areas and non-structural elements; where necessary, surface cleaning is performed to ensure proper detection of defects.

On the basis of the findings, the tunnel manager may update the Level 0 documentation and schedule more detailed investigations. Where uncertainties remain, this lack of knowledge contributes to increasing the attention class, which may be revised following more in-depth assessments according to the established priority level.

4.3 Level 2

Level 2 develops the outcomes of Level 1 through an analytical assessment aimed at classifying tunnels according to their overall risk profile at a territorial or network scale. Its purpose is to assign an Attention Class (CdA) to each tunnel, providing a composite indicator of current conditions and potential adverse scenarios, and supporting the prioritisation of further investigations, monitoring and rehabilitation measures.

The classification is based on an expert-based estimation of relevant risk factors identified during the census and inspection phases. Although it does not constitute a full quantitative risk analysis, it relies on a simplified evaluation of hazard, exposure and vulnerability derived from the information collected at Levels 0 and 1. Four Attention Classes are defined: High, Medium-High, Medium-Low and Low, reflecting increasing levels of concern.

Given the complexity of tunnel systems, risks are examined by category, including global structural and geotechnical risk related to ground-lining interaction, local structural risk affecting specific elements, seismic risk, road-related risk and external hazards such as landslide and hydraulic risk. Separate Attention Classes are determined for each category using parameters appropriate to the specific mechanism considered. These individual classifications are then combined to define the overall Attention Class of the tunnel, which guides subsequent decision-making processes and prioritisation of actions.

4.4 Level 3 and Level 4

After the attribution of Attention Classes at Level 2, the Guidelines introduce two advanced stages with increasing analytical depth. Level 3 is started for tunnels classified as Medium-High, while Level 4 applies to High CdA cases; for Medium-Low or Low classes, these stages are not mandatory.

Level 3 constitutes the first fully analytical phase and involves quantitative structural and geotechnical verifications where simplified assessments are insufficient. Mechanical models are developed using available geometric, material and historical data, supplemented, where necessary, by in situ tests, laboratory analyses and detailed surveys to reduce uncertainties. The aim is to verify the

fulfilment of required safety levels under relevant load combinations and to identify any need for strengthening or mitigation measures.

Level 4 is introduced when significant residual risk or high uncertainty remain. It establishes a structured monitoring strategy focused on controlling risk over time by monitoring key parameters related to the identified failure mechanisms, such as deformations, cracking or water pressures. Predefined thresholds and trigger criteria support timely intervention. Once the risk level is defined, and after the eventual necessary measures, the CdA is then redefined.

4.5 Annexes to the 2022 Guidelines

The Annexes to the 2022 Guidelines constitute the operational part of the methodology, providing the technical tools for its implementation. Together, Annexes A, B, C and D define how knowledge is structured, defects are identified and recorded, and inspections are organised.

Annex A introduces the Level 0 Census and Knowledge Sheet, a standardised form completed for each tunnel to systematise available documentation and technical information, including geometric characteristics, structural features, historical data and previous investigations. It supports the initial assessment of the tunnel knowledge level and the identification of potential hazard indicators. Although conceived as the starting point of the process and for the assignment of the Attention Class, the Knowledge Sheet must be continuously updated as new investigations, monitoring results and studies become available.

Annex B provides a defect catalogue organised by defect typology and underlying cause, including the most common deterioration and damage phenomena affecting tunnels. Each defect is geographically referenced along the tunnel alignment and characterised through three parameters. Extension (k1) describes the spatial development of the defect within a standard 20 m stretch, while intensity (k2) quantifies its magnitude (e.g., crack width or water inflow rate). The third parameter, severity (G), ranging from 1 to 4, is assigned by the Tunnel Officer considering the inspection findings and the interaction between defects and their context.

Annex C translates the classification framework into inspection sheets for each 20 m tunnel stretch. Inspectors record the corresponding k1 and k2 coefficients for each defect and assign the severity level. The sheets also identify conditions potentially affecting structural stability, distinguishing between defects that may compromise the global structural response (PSg) and those that may trigger local structural crises (PSl), both of which influence the Attention Class. They also specify whether a defect is absent, not applicable to the tunnel typology or not detectable under inspection conditions. Photographic documentation is an integral part of the record.

Finally, Annex D defines the inspection types within tunnel lifecycle management: initial inspections, carried out at the first application of the Guidelines, at the opening of new tunnels or after major interventions; detailed inspections involving advanced investigations; routine periodic inspections; and post-event inspections following earthquakes, fires or accidents. This structured system ensures continuous knowledge updating, condition assessment and risk control, maintaining consistency between data collection, defect classification and safety management.

5 EXISTING TUNNEL REFURBISHMENT

The regulatory and risk-based framework described in the previous chapters naturally leads to the definition of intervention strategies. Once defects have been classified and prioritised through the Attention Class system, the selection of appropriate remedial measures becomes a technically driven process. In this context, it is useful to distinguish between local interventions, typically aimed at repairing limited portions of the lining affected by specific defects, and global interventions, which address more extensive structural deficiencies or overall performance upgrading.

5.1 Local Interventions

Within the scope of this research, particular attention is dedicated to interventions related to detachments, sub-thickness conditions and lining thickness reduction. The ASPI technical report [5] identifies several typological interventions (A, B, C, D, E, F, H, I), differentiated according to the depth of degradation, the presence of water inflow, the existence of cavities behind the lining, and the condition of reinforcement.

Interventions of type C1 and C2 concern deep detachments and deterioration of the lining in the absence of water inflow, with depths up to 20 cm (C1) or between 20 and 40 cm (C2), typically in unwaterproofed concrete linings in rock masses. The standard procedure involves removal of unstable

portions, surface regularisation through hydro-demolition or controlled mechanical demolition, and reconstruction of the original thickness using fibre-reinforced shotcrete combined with welded steel mesh. In cases with greater depth (20-40 cm), mechanical connectors are introduced to ensure composite action between the existing and the newly concrete.

When detachments and degradation are associated with diffuse or concentrated water inflow, as in E1 and E2, the repair of the lining must be integrated with drainage systems. In addition to the removal of damaged material and thickness restoration, water management measures such as discharge pipes and corrugated steel sheets for water conveyance are implemented.

More complex scenarios arise in the presence of cavities at the ground-lining interface, classified as F1 and F2, with or without water inflow. In these cases, the intervention is preceded by endoscopic investigations to delimit the affected area and define the geometry of the voids. The lining restoration is combined with injections of lightweight cementitious materials to fill the cavities and re-establish contact between the lining and the surrounding ground. Where water is present, drainage provisions are again incorporated.

Interventions H1 and H2 address reinforcement corrosion and cover concrete deterioration up to 20 cm, respectively without and with water inflow. A preliminary assessment of the reinforcement condition is required to determine whether cleaning and passivation of the steel bars are sufficient or whether partial replacement is necessary.

In addition to the typological intervention proposed by ASPI, the Handbook on Tunnels and Underground Works [7] also describes a local intervention applicable to significant voids within the lining thickness at the ground-lining interface, Fig. 2 (left). This situation refers to cavities caused by incomplete filling during casting or by voids developing at the lining-ground interface and with a residual lining thickness greater than 30 cm. The intervention consists of removing unstable portions of the lining and investigating the cavity through video-endoscopy to determine its geometry and extent. Then, PVC pipes are installed to enable staged injections. The restoration of the lining thickness is then carried out through concrete injections in successive layers, while any cavities extending beyond the design thickness at the lining-ground interface are filled with lightweight cementitious materials.

5.2 Global Interventions

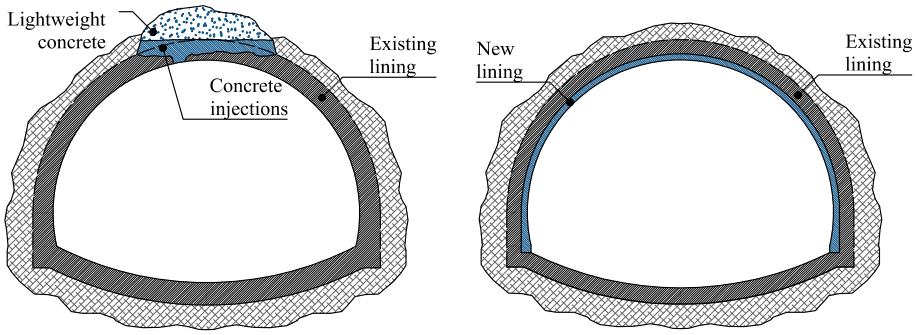


Fig. 2 Treatment of cavities at the ground-lining interface (left). Concrete casting with prefabricated and mobile formworks (right).

When defects affect extensive portions of the lining or when structural deficiencies cannot be resolved through localised repairs, global interventions may be required. These techniques involve the partial or total replacement and strengthening of the tunnel lining.

One possible approach consists of the complete demolition of the existing deteriorated lining followed by a new in situ concrete casting. Alternatively, the use of precast slabs equipped with starter bars involves deep milling of the existing concrete lining, followed by the execution of a completion back-casting [7]. Another global strengthening method consists of steel rib installation, with or without prior milling of the existing concrete, often combined with shotcrete application to ensure structural continuity.

An alternative solution is partial milling of the lining, followed by reconstruction using different techniques depending on design requirements. These include the application of shotcrete, in situ casting with modular formworks, Fig. 2 (right), the installation of prefabricated segments with backfilling of

the annular gap using mortar [8], or steel plate lining. The latter consists of steel plates with thickness ranging in 15-30 mm according to static requirements, connected to the existing lining by steel bolts [9].

With regard to in situ casting using modular formworks, recent technological developments aim to accelerate relining through continuous extrusion systems [8]. This automated lining technique is based on steel formworks designed to cast concrete in place through a continuous extrusion process.

Strengthening interventions aimed at increasing the load-bearing capacity of tunnel linings may also involve the use of high-performance materials, such as ultra-high tensile strength steel textiles (UHTSS) [9].

6 CONCLUSIONS

The evolution of the Italian regulatory framework for existing tunnels reflects a progressive shift from inspection-based practices towards a structured, risk-informed management approach. The 2020 technical documents introduced standardised defect classification and intervention logic, while the 2022 Guidelines established a harmonised methodology integrating census, inspection, multi-risk analysis and prioritisation criteria. Within this framework, lining defects such as sub-thickness and thickness reduction emerge as critical issues due to their structural implications and interaction with ground conditions. The analysis of defect catalogues and technical references highlights the importance of linking observed degradation mechanisms to appropriate intervention strategies. Both local and global rehabilitation techniques offer viable solutions, ranging from targeted repairs to complete relining systems. Overall, the integration of regulatory evolution, defect characterisation and intervention technologies provide a coherent basis for improving the safety and durability of existing tunnel infrastructure.

References

[1] Ministero dei Lavori Pubblici. 1967. "Circolare n. 6736-61-A1 del 19 luglio 1967: Controllo delle condizioni di stabilità delle opere d'arte stradali." Rome, Italy..

[2] Ministero delle Infrastrutture e dei Trasporti. 2020. *Manuale di Ispezione Gallerie*. Rev. 01, May 25, 2020. Rome, Italy.

[3] Ministero delle Infrastrutture e della Mobilità Sostenibili. 2022. "Decreto Ministeriale n. 247/2022. Approvazione delle Linee Guida per la classificazione e gestione del rischio, la valutazione della sicurezza e il monitoraggio delle gallerie esistenti lungo le strade statali o autostrade gestite da ANAS S.p.A. o da concessionari autostradali." *Gazzetta Ufficiale della Repubblica Italiana*, no. 196, August 23, 2022.

[4] Autostrade per l'Italia. 2020. *Gallerie autostradali rivestimenti - Ispezioni Servizi di ingegneria per indagini e progettazione - Nuovo catalogo difetti.*

[5] Autostrade per l'Italia. 2020. *Gallerie autostradali rivestimenti - Ispezioni - Servizi di ingegneria per indagini e progettazione - Interventi tipologici di messa in sicurezza Gallerie a 3 corsie.*

[6] Centre d'Études des Tunnels (CETU). 2015. *Guide de l'inspection du genie civil des tunnels routiers.* Bron, Francia: Centre d'Études des Tunnels.

[7] Damiani, Andrea, and Enrico Crippa. 2023. "Tunnel Refurbishment." In *Handbook on Tunnels and Underground Works*, 497-525. CRC Press. doi:10.1201/9781003306467-7.

[8] Alessio, Carlo, Lapo Baccolini, Daniele Di Fiore, Marilisa Conte, Mariangela Cicolani, Daniele Peila, and Andrea Carigi. 2024. "The 365 km Tunnels Assessment along ASPI Motorways Network – Key Findings Addressing Risk Analysis Procedures and Structural Conditions Evaluation and Strategy of Interventions." *Procedia Structural Integrity* 62:1077-1088. II Fabre Conference - Existing Bridges, Viaducts and Tunnels: Research, Innovation and Applications (FABRE24). doi: 10.1016/j.prostr.2024.09.143.

[9] Gatti, Martino, Giorgio Giacomin, Gilberto Masnaghetti, and Giuseppe Lunardi. 2019. "Refurbish and Static Reinforcement of Tunnels: Innovative Construction Methods and Materials." Paper presented at the XVIII Convegno ANIDIS - *L'Ingegneria Sismica in Italia*, Ascoli Piceno, Italy, September 15-19.

Rod Shape Monitoring Based on Strain Measurements from Fibre Optic Sensors

Bohumil Šplíchal[1], Damjan Grba[2], David Lehký[1], Alfred Strauss[2]

[1]Faculty of Civil Engineering,
Brno University of Technology,
Veveří 331/95, 602 00 Brno, Czechia

[2]Department of Landscape, Water and Infrastructure,
BOKU University,
Peter-Jordan-Straße 82, 1190 Vienna, Austria

Summary
This paper presents an experimental–computational methodology to reconstruct the shape of a deformed rod using only axial strain measurements from fibre optic sensors. A 4 m-long strain monitoring rod containing three optical fibres arranged at 120° was tested inthe laboratory, producing experimental data of motor-controlled rod displacements and the corresponding strain profiles. An Artificial Neural Network (ANN) was trained on these measurements to map the inverse relationship between the imposed rod geometry and the measured strains. The model was then validated using additional test samples with previously unseen deformation cases. The results show that the ANN can accurately predict the rod's position using strain data alone. This confirms that reliable shape reconstruction can be achieved using a purely experimental dataset. This approach provides a practical tool for detecting subsurface movements and supporting stability assessments in bridge construction and maintenance.

1 INTRODUCTION

In bridge engineering, structural safety is strongly influenced not only by the superstructure but also by the performance of foundations and surrounding soil. Bridge abutments, piers, piles, and anchorage systems can be exposed to settlement, lateral soil movement, and progressive slope deformation, which may lead to serviceability issues or even structural damage if not detected early. Therefore, monitoring subsurface displacement and ground–structure interaction is an essential part of modern Structural Health Monitoring (SHM) strategies for bridge infrastructure, particularly in areas prone to instability [1], [2].

Fibre optic sensors (FOS) provide a robust and reliable solution for continuous strain monitoring, enabling early detection of ground movement [3]. In this study, a strain-monitoring rod equipped with three optical fibres spaced at 120° is used to obtain strain measurements along its length. From these strain profiles, the local curvature and shape of the rod can be reconstructed, providing valuable insight into subsurface deformation.

This study develops a data-driven model for reconstructing the rod's shape directly from strain measurements using an Artificial Neural Network (ANN). Recent advances show that ANN-based surrogate models can effectively approximate complex structural or mechanical responses [4], motivating their use for geotechnical monitoring. The proposed method is trained on experimental measurements of a 4 m long rod specimen. The controlled testing equipment allows precise shaping of the rod into known shapes, enabling the generation of a comprehensive experimental dataset linking strain responses to corresponding motor-controlled displacements.

After training on these experimental samples, the ANN is validated using separate experimental measurements with previously unseen deformation cases. Despite being trained without any simulated data, the ANN successfully predicts the rod's shape and accurately estimates motor positions from strain input alone. This demonstrates that an experimental training strategy is sufficient to build a reliable surrogate model for monitoring rod shape, providing a practical and efficient tool for detecting shifts in soil layers and improving assessment of slope stability in situ [5].

Overall, this work aims to (i) establish an experimental dataset linking FOS strain profiles to rod deformation, (ii) train an ANN to reconstruct rod shape directly from the measured strains, and (iii) validate the approach on unseen deformation cases. The resulting data-driven model provides a

practical basis for reliable subsurface displacement monitoring and supports stability assessment in geotechnical and bridge-related applications.

2 METHODOLOGY

The selected experimental approach combines a fibre-optic strain sensing rod with a motor-controlled deformation rig to create a direct and reproducible link between measured strain profiles and the corresponding rod shape. This method was chosen because it enables the generation of high-quality training and validation data under well-defined boundary conditions, which is essential for developing reliable data-driven reconstruction model. Unlike purely numerical simulations, the laboratory setup inherently captures real-world effects such as imperfect bonding, sensor noise, manufacturing tolerances, and material non-linearities, all of which influence strain measurements in practical monitoring applications. Moreover, the use of three fibres arranged at 120° provides sufficient information to estimate bending direction and curvature along the rod while keeping the sensing layout mechanically simple and scalable. The motor-based actuation allows the rod to be deformed into a wide range of repeatable shapes with known displacement inputs, making it particularly suitable for training an ANN that maps the strain-to-shape relationship directly from experiments. Overall, this configuration offers a practical balance between measurement accuracy, experimental controllability, and applicability to field-scale slope and foundation monitoring scenarios.

2.1 Experimental Setup

The experimental setup is based on an 18 m long glass-fibre-reinforced polymer (GFRP) rod with a diameter of 8 mm. The rod includes three integrated grooves for the optical fibres, which are bonded to the rod and protected with a shrink tube. The fibres are arranged at 120° intervals around the circumference, and each contains Fibre Bragg Grating (FBG) sensors placed at 2 m spacing, enabling strain measurements along the rod. As shown in Fig. 1, the cross-section of the GFRP rod is displayed on the left, while the detail of the fibre-to-rod connection is shown on the right.

To acquire strain data, the experiment uses the FS22 Industrial BraggMETER interrogator, designed specifically for FBG-based sensing [6]. The FS22 operates with sampling rates from 1 S/s up to 1000 S/s and employs continuous swept-laser scanning together with a traceable wavelength reference to ensure accurate and stable measurements. In this configuration, the FS22 records strain from all three fibres embedded in the GFRP rod. FBG sensors reflect specific wavelengths of light that shift in response to strain-induced changes in the fibre's refractive index, allowing precise reconstruction of the strain field along the rod.

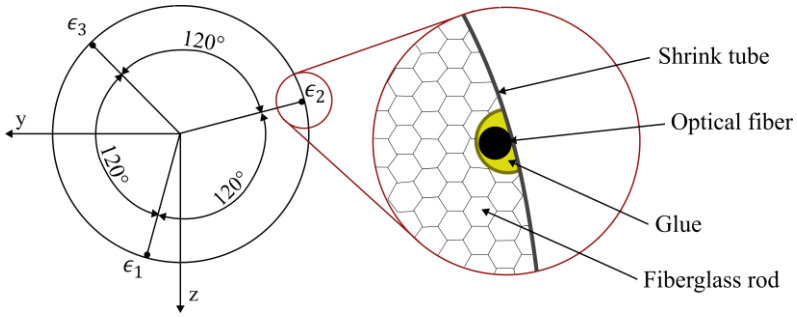


Fig. 1 Cross-section of the GFRP rod is displayed on the left, the detail of the fibre-to-rod connection is shown on the right.

The test setup, located at the Vienna University of Technology, consists of a 21 m table and a deformation system using linear guide rails, spindles, 3D-printed connectors, stepper motors, and Arduino controllers. This system enables controlled deformation of the rod at predefined points, up to 40 cm.

The experimental setup investigated in this paper focuses on a 4-meter section of the rod. Seven motors are used to define the rod's position, spaced approximately 66 cm apart. Sensor measurements are taken at three locations along the 4-meter span, specifically at the positions of the 1st, 4th, and 7th

motors, which are spaced 2 m apart. These motors are shown in black in Fig. 2, while the remaining motors without sensors are shown in red.

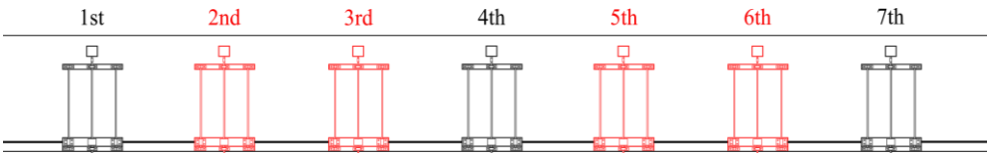


Fig. 2 Schematic of the 4-meter experimental setup with seven motors. Motors equipped with sensors are shown in black, and motors without sensors are shown in red.

2.2 Data preparation and Training Datasets

2.2.1 Deformation patterns and control sequence

The surrogate model was trained using 200 input–output samples, each consisting of nine strain measurements and the corresponding five motor positions. The training set was generated by controlled rod deformations with a predefined movement pattern. All motor commands and deformation sensor readings were performed automatically using a special Python script, ensuring accuracy and eliminating operator variability.

The central (4th) motor was assigned the maximum displacement, while the surrounding motors followed proportional movements: motors 3 and 5 were set to two-thirds of the central displacement, motors 2 and 6 to one-third, and motors 1 and 7 remained fixed at 0 mm throughout all samples.

To cover the operating range of the system, the displacement of the central motor was varied from 0 mm to 20 mm in 1 mm increments, alternating between positive and negative directions. For each target level, the motors were moved sequentially from motor 2 to motor 6: starting with motor 2, then 3, 4, 5, and finally 6, until the full proportional displacement profile was established. After reaching the target configuration, the system returned to the zero state in the same order (2 → 3 → 4 → 5 → 6). Fig. 3 shows an example sequence corresponding to a target displacement of 19 mm applied to the central motor, where each motor has its own color.

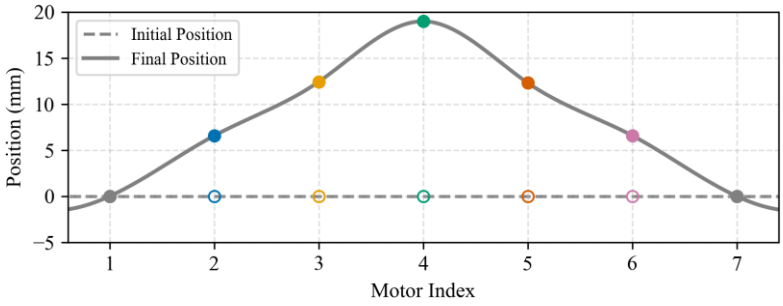


Fig. 3 Example of a training sample with a 19 mm displacement applied to the central (4th) motor. The neighboring motors follow the proportional displacement pattern used during dataset generation: motors 3 and 5 move at two-thirds of the central displacement, motors 2 and 6 at one-third, while motors 1 and 7 remain fixed at 0 mm.

2.2.2 Strain measurement

At each time step, nine strain measurements were recorded from the three optical fibres installed at the three instrumented cross-sections of the rod (located at motors 1, 4, and 7). Since the aim of the study was to assess whether an ANN can learn the strain-to-position relationship directly from experimental data, the raw strain signals were used without any filtering or normalization.

Each 9-element strain vector (s_{1-9}), as defined in Fig. 4, was paired with the corresponding motor-position vector (p_{1-5}). The indexing of p_1 to p_5 follows the convention introduced in Fig. 4, where each p_i denotes the position of one of the five actively controlled motors (motors 2–6). Together, each (s, p) pair forms a single input–output training sample for the ANN.

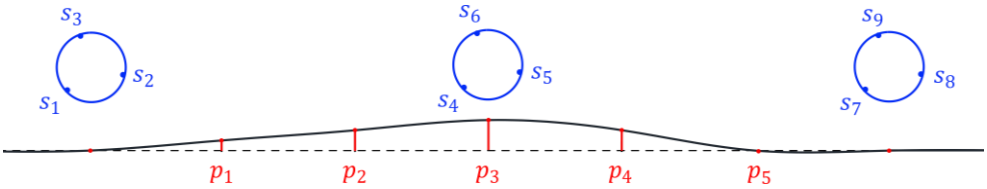


Fig. 4 Scheme of input-output training pairs of strain vector (s_{1-9}) and the corresponding motor-positions (p_{1-5}) for a single time step of rod shape.

2.3 Surrogate model

The surrogate model used in this study is an Artificial Neural Network designed to map the nine measured strain values to the corresponding positions of the five actuated motors (motors 2–6) [7]. The network architecture consists of an input layer with 9 neurons, corresponding to the strain inputs (s_{1-9}), followed by two fully connected hidden layers with 32 and 64 neurons, respectively. Both hidden layers use the hyperbolic tangent (tanh) activation function, while the output layer with 5 neurons employs a linear activation to allow unrestricted prediction of motor positions (p_{1-5}), see Fig. 4.

The model was trained for a maximum of 10 000 epochs using the Adaptive Estimation Moment (AdaM) optimizer and a mean absolute error (MAE) loss function, with early stopping enabled to prevent overfitting. The overall ANN architecture is presented in Fig. 5. All training and evaluation routines were implemented in Python.

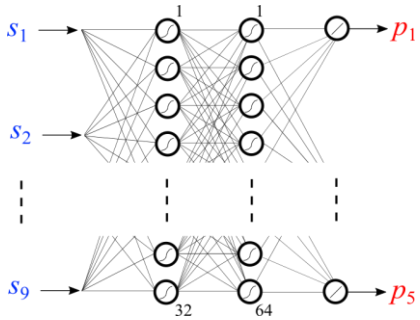


Fig. 5 Scheme of architecture of surrogate model (ANN), input layer of 9 paramters, two hidden layers of 32 neurons and 5 neurons in output layer.

3 RESULTS AND DISCUSSION

To test the ANN on previously unseen deformation levels, eight random displacement values of the middle motor were selected (3, 4.9, −6, 9, −12, 15, 13.8 and 17.9 mm). For each of these values, the motors were moved using the same sequence as in the training procedure, starting with motor 2, followed by motors 3, 4, 5, and 6, and then returning to zero in the same order resulting in 80 test datasets. During this procedure, strain measurements were recorded and subsequently used as inputs to the ANN in an inverse-modeling framework, where the network predicted the corresponding motor positions. This approach preserved the motion pattern learned during training while introducing new displacement amplitudes for validation.

The predicted positions closely followed the expected trends: the middle motor exhibited the largest displacement, and the plateaus corresponding to the holding phases were clearly visible (see Fig. 6). In this figure, the target motor positions are shown with dashed lines, while the ANN predictions are displayed with solid lines, with each motor represented by its own distinctive color.

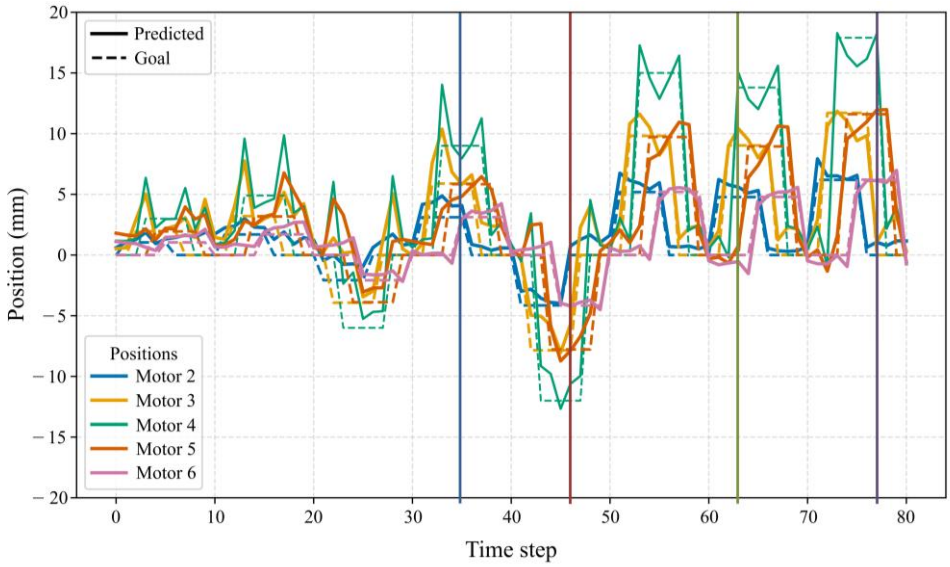


Fig. 6 Comparison of goal and predicted motor positions for the laboratory configuration. Dashed lines indicate goal positions; solid lines show ANN predictions. Each motor is represented by a different color.

To better highlight the behavior of each actuator, Fig. 7 divides the combined results from Fig. 6 into five individual plots. Each plot compares the goal trajectory (dashed line) with the ANN-predicted position (solid line) for one motor, enabling a clearer visual assessment of their differences. The color assignment for each motor remains consistent with Fig. 6.

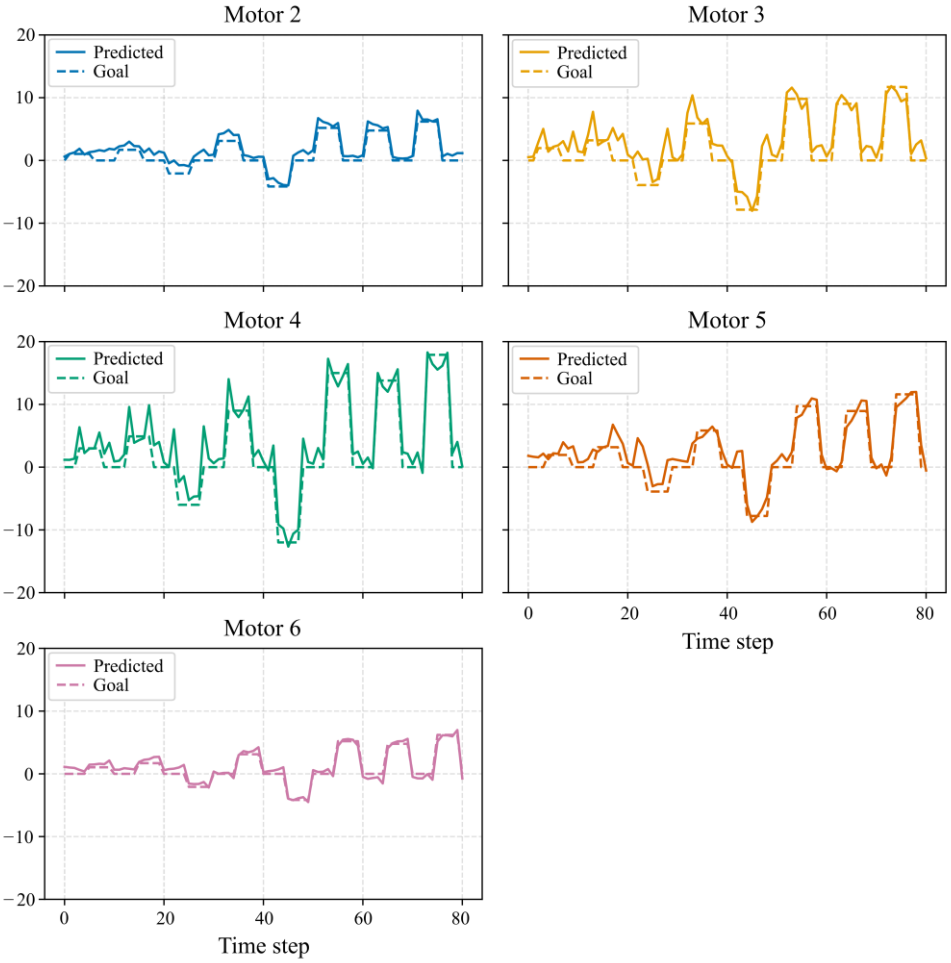


Fig. 7 Comparison of goal and predicted motor positions for the laboratory configuration in five separate figures. Dashed lines indicate goal positions; solid lines show ANN predictions. Each motor is represented by a different color.

To provide a clearer illustration of the rod shape reconstruction, four representative time steps were selected and are shown in Fig. 8. These time steps correspond to specific moments within the controlled sequence and are highlighted in Fig. 6 by colored lines, using the same colors as the frames surrounding the plots in Fig. 8. This presentation enables direct comparison between the goal and predicted configurations: filled markers indicate the ANN-predicted motor positions, while open markers indicate the goal positions, following the same color scheme used in the previous figures. The corresponding rod shapes are shown as solid (predicted) and dashed (goal) curves. Together, these visual elements reveal how accurately the ANN captures the deformation state of the rod at each selected moment.

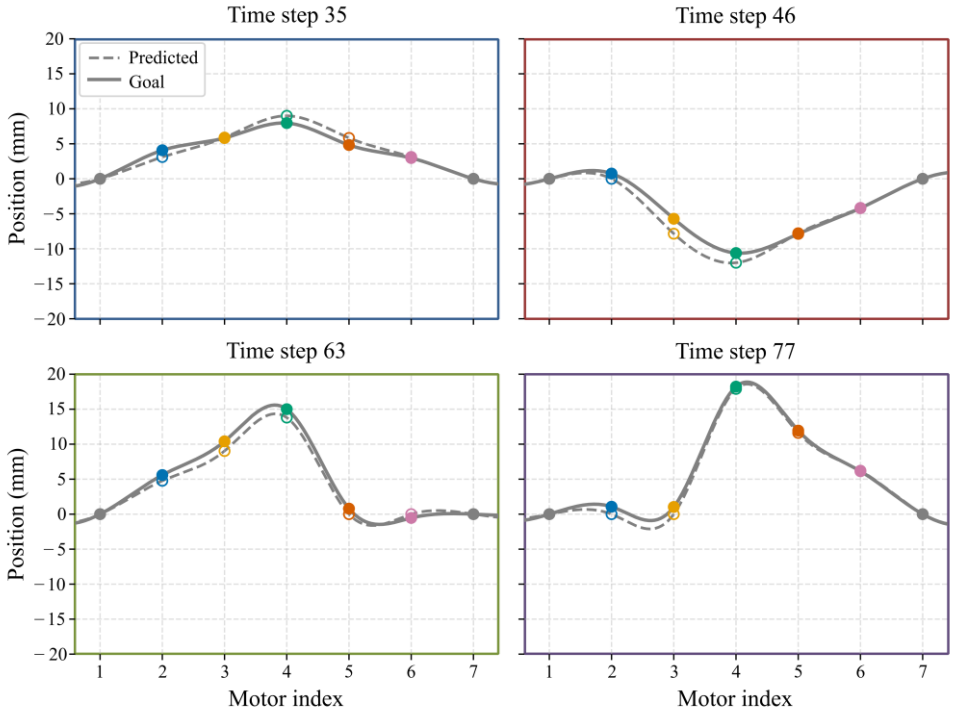


Fig. 8 Comparison of goal and predicted shape of rod from motor positions for the laboratory configuration in four different time steps.

4 CONCLUSIONS

This study demonstrated that a three-fibre strain-monitoring rod combined with an experimentally trained ANN can reliably estimate the deformation state and shape of the rod. Using only experimental strain measurements and corresponding motor-position data, the surrogate model successfully learned the relationship between strain profiles and rod geometry.

The trained ANN was validated using independent experimental measurements. The model accurately reproduced the relative movement of the motors, including the characteristic plateaus caused by the sequential activation process, and captured the overall deformation pattern of the rod. These results confirm that the nine strain inputs obtained from three cross-sections contain sufficient information for robust shape reconstruction, even when the training dataset is limited but well structured.

The findings demonstrate the feasibility of purely experimental, data-driven rod shape monitoring and provide an important basis for transferring the concept to real-world monitoring tasks. In field applications, such as slope stability assessment and subsurface displacement detection, the method could enable continuous deformation tracking of soil layers where direct observation is not possible. Since the model operates directly on strain measurements, it provides a practical pathway for interpreting real fibre optic sensor data in terms of meaningful displacement and deformation patterns.

Future research will focus on extending the approach to longer rods, more complex deformation modes, and realistic boundary conditions, including in situ field conditions and real-time implementation. A key next step is the development of a dedicated finite element model of the rod to generate synthetic strain–displacement datasets. This will enable training on a much wider range of scenarios and support improved generalization for laboratory tests and long-term field monitoring campaigns.

Acknowledgements

The Czech authors thank for the financial support of the project No. 26-20456S supported by the Czech Science Foundation and the project INODIN No. CZ.02.01.01/00/23_020/0008487 co-funded by European Union. The Austrian authors gratefully acknowledge the financial support provided by the Austrian Research Promotion Agency (FFG) under Project FO999924206 ("3D Optic Sensor"). The project was funded as a non-repayable grant within the Innovation Voucher scheme (De-Minimis aid).

References

[1] Yassin, Mohammad H., Farhat, Mohamad H., Soleimanpour, Reza, and Nahas, Michel. 2024. "Fiber Bragg grating (FBG)-based sensors: a review of technology and recent applications in structural health monitoring (SHM) of civil engineering structures." *Discover Civil Engineering* 1:151. doi: 10.1007/s44290-024-00141-4.

[2] Gharehbaghi, Vahid R., Noroozinejad Farsangi, Ehsan, Noori, Mohammad, Yang, T.Y., Li, Shaofan, Nguyen, Andy, Málaga-Chuquitaype, Christan, Gardoni, Paolo, and Mirjalili, Seyedali. 2022. "A Critical Review on Structural Health Monitoring: Definitions, Methods, and Perspectives." *Archives of Computational Methods in Engineering* 29:2209–35. doi: 10.1007/s11831-021-09665-9

[3] Acharya, Ashis, and Tetsuya, Kogure. 2025. "Advances in fibre-optic-based slope reinforcement monitoring: A review." *Journal of Rock Mechanics and Geotechnical Engineering,* 17:1263–84. doi: 10.1016/j.jrmge.2024.03.022

[4] Šplíchal, Bohumil, Lehký, David, and Lamperová, Katarína. 2025. "Structural damage identification of existing bridges using machine learning-aided nested sequential optimization. " *Neural Computing and Applications* 37:27301–24. doi: 10.1007/s00521-025-11673-w

[5] Showkat, Majid, and Ghani, Sufyan. 2025. "Surrogate modeling for slope stability: integrating limit equilibrium method with machine learning." *Multiscale and Multidisciplinary Modeling, Experiments and Design.* 8:253. doi: 10.1007/s41939-025-00853-9

[6] Hottinger Brüel & Kjær (HBK). 2024. FS22 Industrial BraggMETER Optical Interrogator. Technical Data Sheet B04203. Accessed September 19, 2024 https://www.hbm.com/fileadmin/mediapool/hbmdoc/technical/B04203.pdf

[7] Samadian, Delbaz, Muhit, Imrose, B., and Dawood, Nashwan. 2025. "Application of Data-Driven Surrogate Models in Structural Engineering: A Literature Review." *Archives of Computational Methods in Engineering.* 32:735–84. doi: 10.1007/s11831-024-10152-0

Structural Behaviour and Crack Evolution of Full-Scale RC Dapped-End Beams with Orthogonal Reinforcement

Luke van Ratingen[1], Andras Vanquaille[2], Nadia Amin[3], Els Verstrynge[2], Boyan Mihaylov[3], Eline Vereecken[1], Hervé Degée[1]

[1] Construction Engineering Research Group, Hasselt University, Diepenbeek, Belgium
[2] Materials and Constructions Division, Civil Engineering Department, KU Leuven, Leuven, Belgium
[3] Urban and Environmental Research Unit (UEE), Univ. of Liège, Liège, Belgium

Summary
Ageing reinforced concrete bridges from the 1970s and 1980s increasingly exhibit deterioration in critical structural details, such as dapped-end regions in Gerber-type bridge systems. These regions are prone to early cracking, which accelerates reinforcement corrosion and compromises structural safety. This study presents the first phase of an ongoing research programme investigating the interaction between mechanical loading, sustained loading and corrosion. Full-scale dapped-end beams with varying orthogonal reinforcement layouts were tested under static loading until failure to establish a mechanical reference state. Crack development, load-displacement behaviour and failure mechanisms were monitored, with particular emphasis on service-relevant load levels around 50% of the ultimate capacity. The results show a transition from flexural, reinforcement-controlled behaviour to concrete-governed mixed flexural–shear failure with increasing reinforcement. The findings provide a robust experimental baseline for subsequent long-term creep and corrosion experiments and for validating numerical models.

1 BACKGROUND AND MOTIVATION

A significant proportion of reinforced concrete bridge infrastructure in Europe was constructed during the 1970s and 1980s and is now approaching or exceeding its intended service life. Ageing-related deterioration processes such as reinforcement corrosion, concrete cracking and material degradation increasingly threaten structural safety and durability. Recent bridge failures have demonstrated that local weaknesses in critical structural details can trigger global collapse, highlighting the need for improved assessment tools supported by experimentally validated evidence. Well-documented examples include the collapse of the de la Concorde overpass in Canada [1] and the Annone Brianza bridge in Italy [2]

One particularly vulnerable structural detail is the reinforced concrete dapped-end (DE) beam, commonly used in Gerber-type bridge systems (Fig. 1). The geometric discontinuity at the dapped end causes highly disturbed stress distributions and pronounced tensile stresses near the re-entrant corner, leading to early crack formation under service loads. These cracks tend to open relatively wide and act as preferential pathways for water and chlorides, accelerating reinforcement corrosion and the associated loss of load-bearing capacity. Field inspections of existing bridges in Belgium and elsewhere frequently reveal severe cracking and advanced corrosion damage in dapped-end regions.

Previous experimental and analytical studies have substantially advanced the understanding of the short-term mechanical behaviour of dapped-end beams under monotonic loading, identifying characteristic shear and flexural failure mechanisms [3-9]. In particular, large-scale experimental campaigns by Rajapakse [8] demonstrated that failure is often governed by the initiation and propagation of the re-entrant corner crack. However, most available studies focus on undamaged specimens and do not address the interactions among mechanical loading, time-dependent effects, and corrosion-induced degradation. Experimental data capturing this coupled behaviour therefore remain scarce, despite their relevance for the assessment of existing bridge infrastructure.

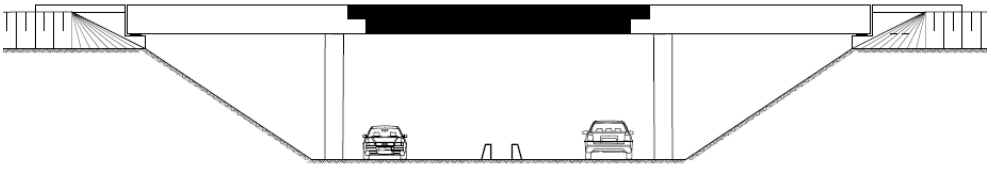


Fig. 1 Gerber-type bridge design with DE-beams

To address this gap, a multi-phase experimental programme has been initiated. This contribution reports on the first phase, consisting of short-term static tests on full-scale dapped-end beams under non-corrosive conditions. The objective is to establish a reliable mechanical reference prior to the introduction of sustained loading and environmental exposure. Emphasis is placed on the load–deformation response, crack development at service-relevant load levels (approximately 50% of the ultimate capacity), and the identification of governing failure mechanisms. The experimental results are further used to validate finite element models for subsequent parametric and long-term studies.

2 EXPERIMENTAL PROGRAMME

2.1 Test setup and instrumentation

The static tests up to failure were conducted using a test setup similar to that previously applied by Rajapakse [8], as shown in Fig. 2, allowing direct comparison with earlier experimental results. A comparable instrumentation scheme was adopted, including linear transducers (LTs) to monitor global and local deformations, strain gauges on selected reinforcement bars, and manual crack width measurements using a digital microscope camera at intermediate load levels.

In contrast to earlier studies at UHasselt and ULiège, which investigated beams with dapped ends at both extremities, the present programme uses beams with a single-sided dapped end. The opposite end was detailed as a straight end, with longitudinal reinforcement extending beyond the concrete surface to connect measurement equipment. Specimen dimensions and support conditions were selected to match those used in previous experimental campaigns ensuring consistent boundary conditions [8, 9].

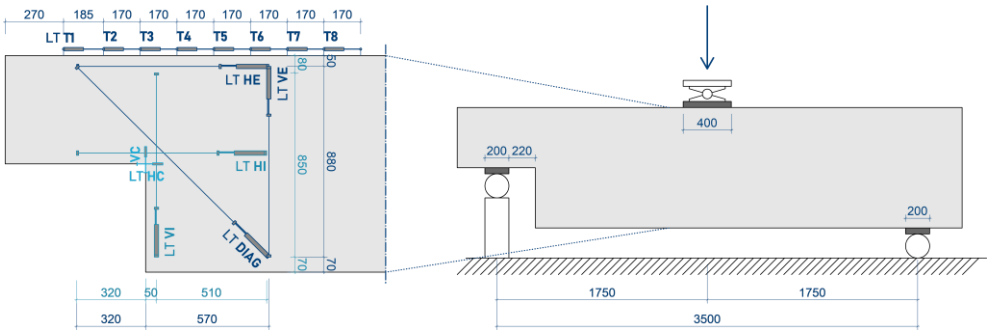


Fig. 2 Test setup and instrumentation position in mm retrieved from Rajapakse [8]

2.2 Test specimens and reinforcement layouts

The experimental programme comprises three full-scale reinforced concrete dapped-end (DE) beams representative of bridge construction practice from the 1970s and 1980s, when orthogonal reinforcement layouts were commonly applied. The beams differ only in the amount and detailing of reinforcement in the dapped-end region and are classified as lightly reinforced (RE-L), moderately reinforced (RE-M), and heavily reinforced (RE-H). The selected reinforcement configurations are based on layouts previously investigated by Rajapakse [8]. Concrete material properties were

determined from compressive strength and Young's modulus tests on cylinders, supplemented by cube tests, as summarised in Table 1

Table 1. Beam identification and concrete properties. The coefficient of variation (CV), expressed as a percentage, is given in parentheses for averaged quantities

Beam type	Reinforcement level	Name	$f_{c,cyl}$ [MPa]	E_c [Mpa]
L	Low	RE-L	46.2 (5.6)	43 667 (13.6)
M	Moderate (standard)	RE-M	41.7 (20.3)	39 100 (5.6)
H	High	RE-H	41.3 (7.2)	35 433 (0.9)

Beam RE-L has the least shear reinforcement. In the full-depth region adjacent to the dapped end, shear reinforcement is limited to three sets of four-legged Ø8 stirrups, while the stirrup spacing in the remainder of the full-depth portion of the beam is increased compared to the other specimens (Fig. 3). This detailing results in limited confinement near the re-entrant corner and a reduced overall shear reinforcement ratio in the critical region.

Beam RE-M is characterised by a more balanced reinforcement layout relative to the concrete capacity. In the vicinity of the dapped end and the re-entrant corner, five sets of closely spaced four-legged Ø10 stirrups are provided, significantly enhancing confinement and shear resistance.

Beam RE-H contains the highest level of shear reinforcement among the tested specimens. While the number and spacing of stirrups in the dapped-end and re-entrant corner region are identical to those of beam RE-M, the stirrup diameter in this region is increased to Ø12. This results in a higher shear reinforcement ratio and increased confinement in the critical zone, deliberately targeting a transition from reinforcement-controlled behaviour towards concrete-governed failure mechanisms.

Compared to earlier experimental campaigns, the present study adopts a uniform stirrup diameter throughout the beam depth. Whereas previous designs combined stirrups of different diameters, all specimens in this programme employ Ø12 stirrups in the full-depth region. In the dapped-end region, local variations in stirrup spacing are retained to reflect increased reinforcement demand near the re-entrant corner and to investigate its influence on crack development and failure behaviour (Fig. 3).

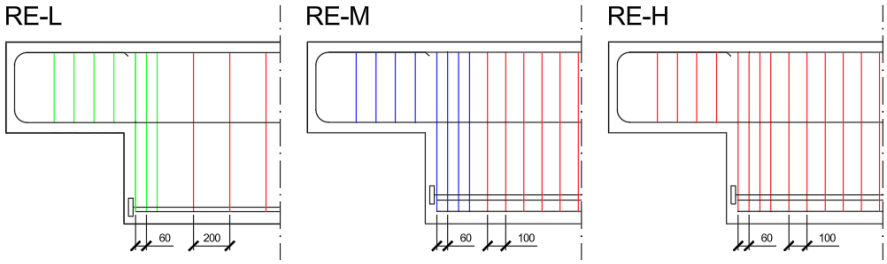


Fig. 3 Construction drawing dapped-end beams; RED = ø 12, BLUE = ø 10, GREEN = ø 8

The mechanical properties of the reinforcing steel were obtained from tensile tests on three specimens per bar diameter. Average values of yield strength, ultimate strength, Young's modulus and rupture strain are reported in Table 2 and are used throughout this study for the interpretation of the experimental results.

3 EXPERIMENTAL SETUP AND MONITORING STRATEGY

3.1 Test configuration and loading protocol

The static tests were conducted under controlled laboratory conditions using a loading configuration designed to reproduce the force transfer mechanisms characteristic of dapped-end regions in Gerber-type bridge systems. Load was applied incrementally in constant steps of 100 kN until failure, allowing intermediate observation of crack development and deformation behaviour. Up to a load level of 500 kN, each load step was followed by partial unloading equal to 10% of the applied load to enable manual

crack measurements. Beyond 500 kN, unloading was limited to a fixed reduction of 50 kN. This loading–unloading sequence was maintained until unstable behaviour occurred, after which crack measurements were discontinued and loading proceeded monotonically to failure.

Table 2. Average mechanical properties of reinforcing steel. The coefficient of variation (CV), expressed as a percentage, is given in parentheses for averaged quantities; ε_r is reported as the measured range.

Bar diameter	$f_{y,avg}$ [MPa]	$f_{u,avg}$ [MPa]	E_{avg} [MPa]	ε_r [‰]
Ø8	469 (3.8)	568 (0.1)	194 490 (3.4)	14-20
Ø10	522 (1.5)	650 (0.1)	214 530 (13.3)	114-120
Ø12	535 (1.6)	653 (0.1)	175 480 (6.7)	95-108
Ø14	547 (2.9)	672 (0.1)	206 800 (2.4)	106-114
Ø16	604 (0.5)	731 (0.3)	204 560 (10.7)	75-85
Ø20	523 (1.3)	667 (0.3)	215 360 (14.2)	110-112

3.2 Monitoring strategy

A comprehensive monitoring scheme was employed to capture both global and local structural responses. Linear transducers (LTs) were used to measure global displacements and diagonal deformations governing the force–displacement behaviour of the dapped-end region. In total, fifteen LTs were installed: eight arranged along the top surface to monitor concrete compression and deformation, five positioned to record global surface displacements, and two placed near the re-entrant corner to measure local crack opening and displacement (Fig. 2). Strain gauges were installed on selected stirrups and longitudinal reinforcement bars prior to concrete casting to record internal strain development. In addition, crack widths were measured manually at each load step using a high-resolution crack camera.

4 EXPERIMENTAL RESULTS

4.1 Global mechanical behaviour

All three beams were tested individually under static loading until failure. The force–displacement response derived from the diagonal LT measurements (Fig. 4) illustrates the global mechanical behaviour and governing deformation of the dapped-end region for each beam type. All specimens exhibited a ductile response governed by reinforcement yielding at the re-entrant corner, although the beam with the highest reinforcement level showed reduced ductility due to increased concrete compression demands. Load levels around 50% of the ultimate capacity were identified as representative of long-term service conditions and of particular relevance for subsequent creep and corrosion experiments, as they correspond to crack widths favourable for capillary suction. The static tests thus provide a reliable mechanical reference linking applied load levels to the structural response of the different beam types.

4.2 Crack development and failure mechanisms

Crack development was monitored throughout loading, with particular emphasis on crack patterns and crack widths at approximately 50% of the ultimate load. This load level is relevant for comparing specimens and is representative of service conditions in the subsequent creep and corrosion tests. Eurocode 2 specifies a maximum allowable crack width of 0.3 mm for durability under serviceability limit state conditions [10], which is used here as a normative reference. Experimental studies have shown that larger crack widths are particularly relevant for corrosion processes; Poursaee reports that crack widths in the range of approximately 0.3–0.7 mm are favourable for capillary suction of moisture and chlorides [11]. The static test results were therefore used to identify the load levels at which such crack widths occur for each beam type, while the associated failure mechanisms were documented and related to the respective reinforcement layouts.

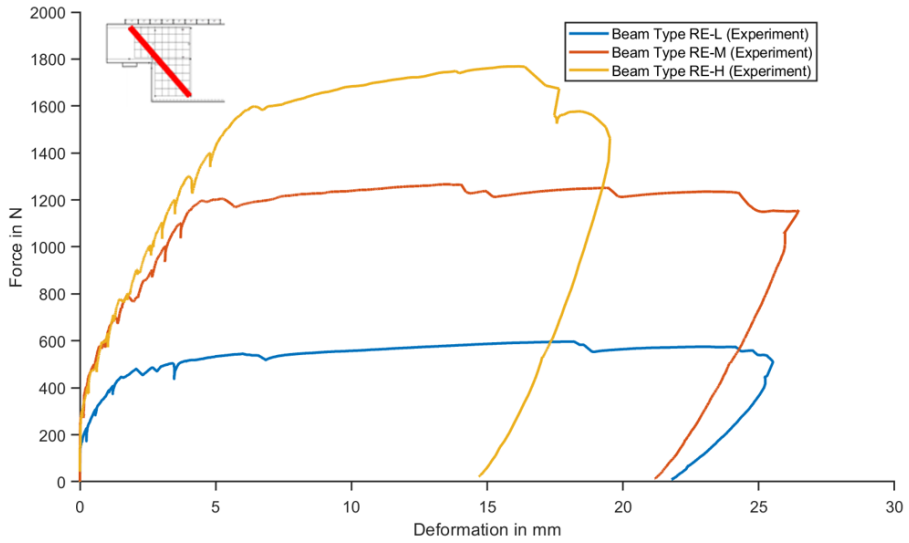


Fig. 4 Diagonal LT force-displacement graph

4.2.1 Beam RE-L

At approximately 50% of the peak load (300 kN), beam RE-L exhibited pronounced crack localisation at the re-entrant corner (Fig. 5 left). A dominant crack developed, reaching a maximum width of about 0.8 mm near the concrete surface. With further loading, this crack widened and propagated, leading to failure at a load of 597.4 kN. Failure was governed by yielding of the horizontal and vertical reinforcement crossing the re-entrant corner crack, resulting in large plastic rotations of the dapped end. Partial rupture of vertical reinforcement occurred at higher load levels (around 480 kN) and contributed to the ultimate failure. This behaviour is classified as flexural failure, characterised by rotation of the dapped end relative to the full-depth section along the re-entrant corner crack (Fig. 5 right).

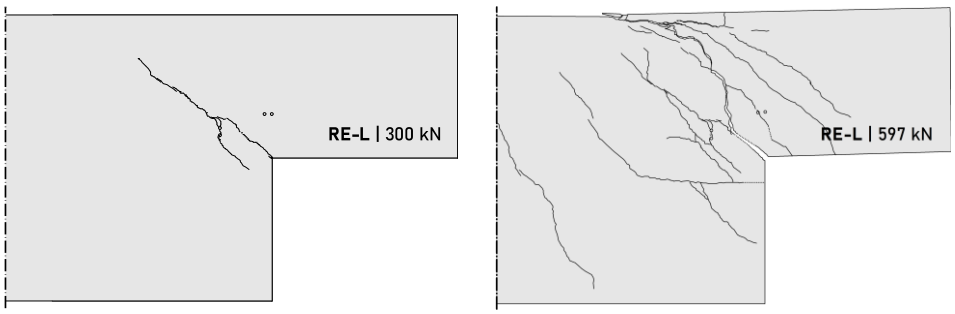


Fig. 5 (left) RE-L crack pattern at approx. 50% peak load (right) RE-L crack pattern at failure

4.2.2 Beam RE-M

At a load level of 700 kN (55.3% of the peak load), beam RE-M showed a more distributed cracking pattern in the dapped-end region compared to RE-L, while a clearly defined re-entrant corner crack was still present (Fig. 6 left). The measured crack width at this stage was approximately 0.56 mm. Continued loading led to crack propagation and widening, with failure occurring at a maximum load of 1266.5 kN. Similar to RE-L, failure was governed by plastic rotations along the re-entrant corner crack due to yielding of the reinforcement. Concrete crushing in the compression zone and local rupture of vertical reinforcement occurred during the plastic plateau, reducing ductility but having only a limited influence

on peak strength. The failure mode is therefore classified as flexural, although local concrete crushing may have been influenced by shear cracking extending from the dapped-end region (Fig. 6 right).

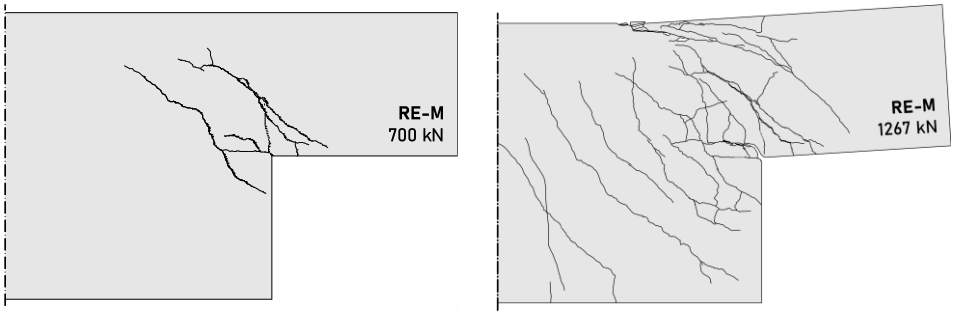


Fig. 6 (left) RE-M crack pattern at approx. 50% peak load (right) RE-M crack pattern at failure

4.2.3 Beam RE-H

At approximately 50% of the peak load (900 kN), beam RE-H exhibited a significantly more distributed cracking response, with multiple shear cracks extending from the dapped end into the full-depth region of the beam (Fig. 7 left). The crack width at the re-entrant corner at this load level reached approximately 1.01 mm. With increasing load, the beam failed at a maximum load of 1768 kN due to spalling of the concrete cover in the compression zone (Fig. 7 right). Although the reinforcement crossing the re-entrant corner crack yielded prior to failure, reinforcement rupture did not occur. Compared to RE-M, earlier crushing of the concrete in the compression zone limited ductility. Owing to the diffuse crack pattern and the combined influence of flexural deformation and shear cracking, the failure mode of beam RE-H is characterised as mixed flexural–shear.

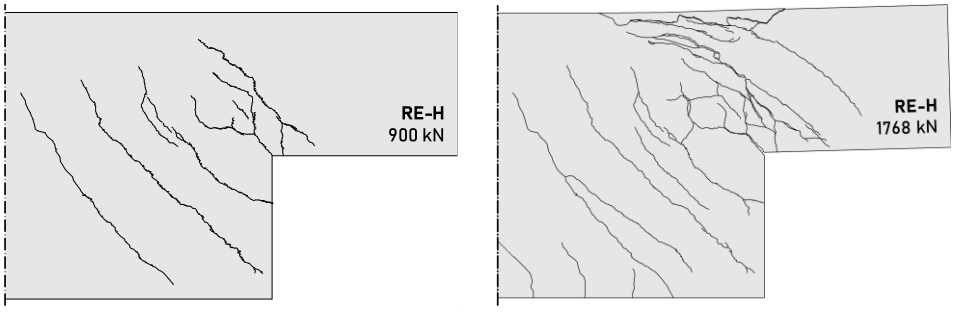


Fig. 7 (left) RE-H crack pattern at approx. 50% peak load (right) RE-H crack pattern at failure

5 DISCUSSION AND CONCLUSIONS

The experimental programme clearly demonstrates that the amount and detailing of orthogonal reinforcement in the dapped-end region govern crack development, load-carrying capacity and the ultimate failure mechanism of full-scale beams. A systematic transition in structural response is observed from beam RE-L to RE-H, reflecting a shift from reinforcement-controlled behaviour towards concrete-governed limitations. At service-relevant load levels around 50% of the ultimate capacity, all specimens exhibited pronounced cracking at the re-entrant corner, confirming this region as the critical zone for both structural performance and durability, although significant differences in crack patterns and widths were observed.

Beam RE-L exhibited early crack localisation, with a dominant re-entrant corner crack reaching relatively large widths. This behaviour reflects the limited reinforcement provided and resulted in a flexural failure mechanism governed by yielding and partial rupture of reinforcement crossing the corner crack, accompanied by large plastic rotations of the dapped end (Fig. 8 left).

In beam RE-M, the increased reinforcement led to a more distributed cracking response and a substantial increase in load-carrying capacity. Although a clearly defined re-entrant corner crack remained dominant, crack development was more gradual and an extended plastic response was observed. Failure was again flexural in nature, controlled by reinforcement yielding, while concrete crushing in the compression zone and local reinforcement rupture reduced ductility without significantly affecting peak strength (Fig. 8 middle).

For beam RE-H, further increasing the reinforcement resulted in a markedly different response. Cracking became more diffuse, with multiple shear cracks extending into the full-depth region of the beam. Despite reinforcement yielding at the re-entrant corner, failure was governed by concrete-related mechanisms, including early crushing of the compression zone and spalling of the concrete cover. Consequently, the failure mode is classified as mixed flexural–shear, with concrete capacity rather than reinforcement strength governing the ultimate behaviour. The reduced ductility of this specimen indicates that increasing reinforcement beyond a certain level does not necessarily enhance structural robustness (Fig. 8 right).

Overall, the experimental results provide a robust mechanical reference for the behaviour of dapped-end beams under static loading. They confirm the re-entrant corner as the governing region for crack development and failure and form a reliable basis for subsequent long-term investigations focusing on sustained loading, crack width evolution and reinforcement corrosion.



Fig. 8 (left) Failure of RE-L (middle) Failure of RE-M (right) Failure of RE-H

Acknowledgements

The authors gratefully acknowledge the financial support of the Research Foundation,Full de Flanders (FWO) under project number G0A3H24N. The experimental work was carried out in the ACB² laboratory at Hasselt University. The authors further acknowledge the collaboration with KU Leuven and the University of Liège, whose expertise in materials, structural behaviour, and numerical modelling significantly contributed to the execution and interpretation of the research.

References

[1] Jennifer, Golden, Elizabeth, Gomes, Anurag, Roy, and Ying Tsun Su, "De La Concorde Overpass Bridge Collapse: Analysis of a Historical Failure." 2018.

[2] Marco, Angelo *et al.*, "Bridge collapses in Italy across the 21st century: survey and statistical analysis," *Structure and Infrastructure Engineering,* 04/02 2025, doi: 10.1080/15732479.2025.2483500.

[3] Pieter, Desnerck, Janet, Lees, and Chris, Morley, "Reinforcement Layout Implications for Reinforced Concrete Half-Joint Structures." 2016.

[4] Pieter, Desnerck, Janet, Lees, and Chris, Morley, "Assessment of reinforced concrete half-joint structures: dealing with deterioration," in *Proceedings of the 2014 PCI Convention and National Bridge Conference*, 2014, p. 16.

[5] Pieter, Desnerck, Janet, Lees, and Chris, Morley, "Impact of the reinforcement layout on the load capacity of reinforced concrete half-joints," *Engineering Structures,* v ol. 127, pp. 227-239, 2016/11/15/ 2016, doi: https://doi.org/10.1016/j.engstruct.2016.08.061.

[6] Pieter, Desnerck, Janet, Lees, and Chris, Morley, "The effect of local reinforcing bar reductions and anchorage zone cracking on the load capacity of RC half-joints," *Engineering Structures,* vol. 152, pp. 865-877, 2017/12/01/ 2017, doi: https://doi.org/10.1016/j.engstruct.2017.09.021.

[7] Boyan, Mihaylov, Chathura, Rajapakse, and Herve, Degee, "Towards Crack-Based Assessment of Dapped-End Connections," 2023, pp. 352-360.

[8] Chathura, Rajapakse, Herve, Degee, and Boyan, Mihaylov, "Assessment of Failure along Re-Entrant Corner Cracks in Existing RC Dapped-End Connections," *Structural Engineering International,* 03/10 2021, doi: 10.1080/10168664.2021.1878975.

[9] Chathura, Rajapakse, Herve, Degée, and Boyan, Mihaylov, "Investigation of shear and flexural failures of dapped-end connections with orthogonal reinforcement," *Engineering Structures,* vol. 260, p. 114233, 2022/06/01/ 2022, doi: https://doi.org/10.1016/j.engstruct.2022.114233.

[10] (2014). *Eurocode 2: Design of concrete structures – Part 1-1: General rules and rules for buildings*.

[11] Amir, Poursaee, and Brandon, Ross, "The Role of Cracks in Chloride-Induced Corrosion of Carbon Steel in Concrete—Review," *Corrosion and Materials Degradation,* vol. 3, pp. 258-269, 06/10 2022, doi: 10.3390/cmd3020015.

Monitoring Crack Initiation and Propagation in Reinforced Concrete Using 2D-FOS

Till Wellmann, Henrik Becks, Martin Classen

Institute of Structural Concrete,
RWTH Aachen University,
Im Süsterfeld 9, 52072 Aachen, Germany

Summary
To ensure reliable service life prediction of reinforced concrete (RC) structures, an in-depth understanding of damage progression under repetitive subcritical loading is essential. As computational structural assessments are demanding and subject to uncertainties in loading history and material properties, remaining service life is often assessed through visual inspection. To overcome this time-intensive process, continuous information on the structural damage state from autonomous strain measurements can be integrated into prediction models, improving safety assessments. Based on this premise, a monitoring strategy using two-dimensional distributed fibre optic sensors (2D-FOS) on concrete surfaces was developed at the authors' institute, enabling accurate two-dimensional strain monitoring. Following crack initiation, the focus shifts to evaluation methods regarding crack initiation and propagation, which are presented in this study as essential components in service life prediction models of RC structures.

1 INTRODUCTION

Transport infrastructure in Germany and many other industrialized countries is increasingly challenged by growing freight traffic and ageing structures. In the German federal highway network alone, approximately 52,000 bridges are in service, of which around 20 % require significant modernization or replacement [1]. A large share of these structures was constructed between the 1960s and mid-1980s, resulting in an ageing bridge stock designed according to outdated load models and design standards [2]. Increasing freight traffic, combined with more stringent modern requirements, particularly with regard to shear and torsional resistance, has further widened the gap between existing structural capacity and current demands [1], [3]. In view of limited financial resources, sustainability goals, and the challenges posed by climate change, condition-based and resource-efficient maintenance strategies are gaining increasing importance. A prerequisite for such strategies is a reliable assessment of the structural damage state and a robust estimation of the remaining service life. In current engineering practice, bridge condition assessment in Germany is largely based on periodic visual inspections according to DIN 1076. While this approach is well established, it is inherently subjective, labour-intensive, and only provides limited insight into internal damage mechanisms such as crack initiation, crack propagation, and fatigue-induced degradation. Consequently, damage processes often remain undetected until they reach an advanced stage.

Structural Health Monitoring (SHM) offers a promising complement to conventional inspection methods by providing continuous, objective, and quantitative information on the structural condition. In reinforced and prestressed concrete structures, strain- and deformation-based monitoring is particularly suitable, as their measurements are directly linked to structural deterioration phenomena like cracking, stiffness degradation, and fatigue damage accumulation.

Among the available sensing technologies, fibre optic sensors (FOS) have gained increasing relevance in SHM applications over the past decades. They are widely used in large-scale infrastructure monitoring, including pipelines [4], railway embankments [5], and civil engineering structures such as bridges [6], [7] and tunnels [8]. Originating from developments in telecommunications [9], fibre optic sensing technology has evolved into a versatile measurement approach capable of capturing a wide range of physical quantities, including strain, temperature, pressure, and moisture. Compared to conventional point-based strain gauges (SG) or linear variable displacement transducers (LVDT), FOS offer several advantages: small dimensions, high durability, immunity to electromagnetic interference, corrosion resistance, and most importantly the capability for quasi-continuous measurements over long distances.

In reinforced concrete applications, fibre optic sensors have been installed in various ways, including embedding within the concrete matrix [10], attachment to reinforcement bars [11], and external bonding to the concrete surface [12]. For existing structures, surface-mounted installation is particularly attractive, as it allows application without intrusive interventions. Previous studies conducted at the authors' institute have demonstrated that externally bonded fibre optic sensors are capable of reliably detecting crack formation, estimating crack widths, and continuously monitoring fatigue-induced strain development under static and cyclic loading [13].

However, FOS inherently provides one-dimensional strain measurements along the fibre axis. Consequently, existing monitoring applications for reinforced concrete structures have been mostly limited to uniaxial measurements. As a result, complex multi-directional strain states and two-dimensional crack patterns – such as inclined shear cracks, intersecting crack networks, or spatially distributed fatigue damage – cannot be fully captured using conventional single-fibre layouts.

To overcome this limitation, an externally installed two-dimensional distributed fibre optic sensing concept (2D-FOS) has been developed in recent studies at the authors' institute [14], [15]. By arranging one or multiple sensing fibres in three distinct orientations to form a surface-mounted sensor network, the proposed approach enables spatially resolved strain measurements over a defined measurement area. Building on this concept, the present study develops and validates automated strain-based methods for crack detection and crack width estimation, which form the basis for subsequent two-dimensional crack visualisation. The capability of the developed methods is validated by uniaxial tensile tests on octagonal reinforced concrete specimens, specifically designed to investigate the performance of the sensor network under varying sensor orientations and loading directions. The paper presents the 2D-FOS sensing concept, the associated experimental setup, and the automated procedures for crack detection, crack width estimation, and two-dimensional crack visualisation. The results demonstrate that 2D-FOS is capable of capturing two-dimensional crack formation and propagation, highlighting its potential as an image-based SHM tool for damage assessment in shear-critical regions of bridge structures.

2 MONITORING CONCEPT: 2D-FOS

2.1 Basic principle of the 2D-FOS concept

To enable continuous strain measurement within a two-dimensional zone, the 2D-FOS concept employs a multidirectional arrangement of FOS on the concrete surface. Fig. 1 illustrates the proposed fibre arrangement. Two fibres are aligned horizontally and vertically, respectively, and are oriented orthogonally to each other. A third fibre is arranged diagonally at an angle of 45° and connects the intersection points of the horizontal and vertical fibres. This configuration enables strain measurements in three discrete directions (ε_x, ε_y, ε_{xy}) within the same measurement area and forms the basis of the two-dimensional sensing concept. The fibre layout shown corresponds to the configuration used in the experimental investigations presented in this paper. However, the network geometry can be adapted with respect to grid spacing (s_h, s_v), number of segments, and overall dimensions, provided that the fundamental principle of strain measurement in three distinct directions (x, y, xy) is maintained.

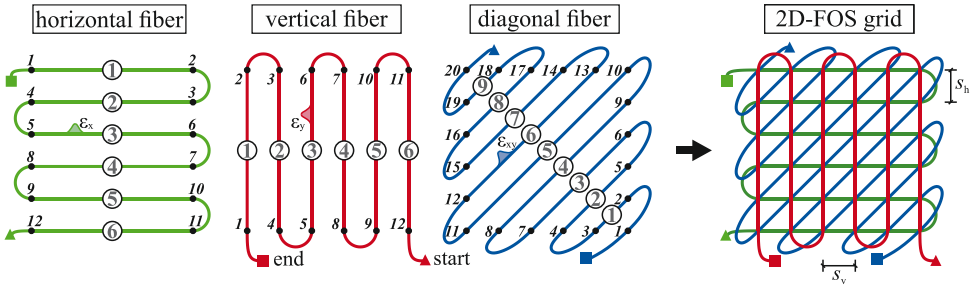


Fig. 1 2D-FOS Concept.

The sensing concept is combined with an automated processing tool that enables several post-processing functions of the measured data, including two-dimensional strain visualisation as well as the

crack related analysis methods, which are presented in detail in this paper. To derive two-dimensional strain fields from raw FOS measurements, the strain data are processed segment-wise. Each fibre is subdivided into segments (grey, circled numbering) between predefined measurement points (gages, black numbering) and mapped into a matrix that represents the physical layout of the sensor network. In a first step, the strain data from the three fibre orientations are post-processed separately. Within each orientation, interpolation between adjacent segments is performed, resulting in three individual directional strain matrices. As long as the concrete remains uncracked, these matrices are used as a basis for a principal axis transformation to obtain two-dimensional fields of principal strains. This principal strain matrix can then serve as input for service life prediction models of concrete until crack formation. Results on two-dimensional strain visualisation, as well as preliminary investigations on different application methods, fibre coatings, and post-processing strategies for one-dimensional FOS strain measurements are reported in [13], [15]. After crack formation, further post-processing steps are required to autonomously detect cracks, calculate crack widths, and visualise them in a two-dimensional field. These procedures are described in more detail in the following sections.

2.2 Automated crack detection

Automated crack detection and localisation is based on a segment-wise evaluation of the FOS strain data and follows an automated four-stage algorithm, as illustrated in Fig. 2. In the first step, potential crack time steps are identified by analysing abrupt changes in the strain development within individual fibre segments. For each segment, the temporal evolution of the mean strain and its standard deviation is evaluated and compared with predefined limit values (steps 1 and 2). Crack formation is considered possible if a significant relative increase in the segment mean strain occurs simultaneously with an increased strain scatter σ within the segment. At the same time, this strain scatter must not exceed a defined upper limit to ensure adequate data quality. These two preselection steps efficiently filter relevant time stamps for further analysis.

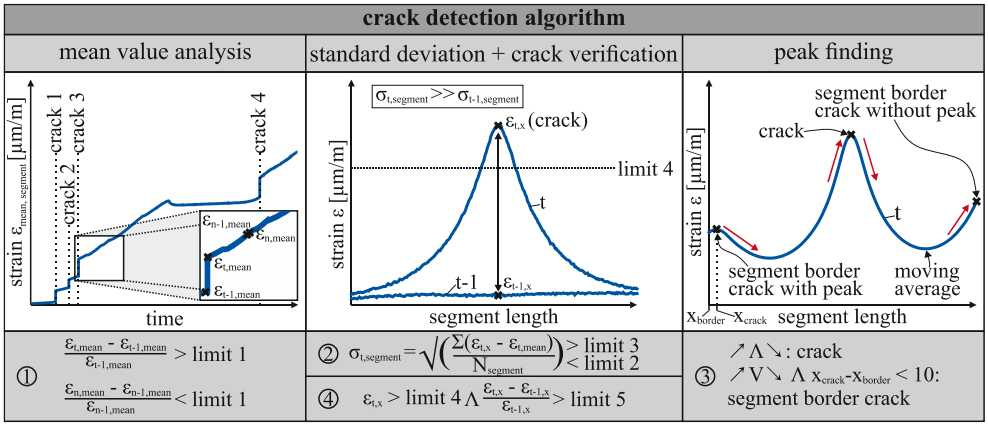


Fig. 2 Schematic illustration of the developed crack detection algorithm.

Subsequently, the preselected time stamps are examined for the presence of local strain peaks within the corresponding segments (step 3). To improve robustness against measurement noise, the peak search is performed on a moving-average representation of the strain signal. Finally, in step 4, a crack is confirmed if the detected local strain maximum exceeds a predefined minimum strain threshold (limit 4) and the relative local strain increase at the peak exceeds limit 5. These two limits ensure that the detected strain maximum corresponds to valid concrete crack strains and that the observed segment-wise strain increase is associated with a local strain concentration at the peak position. Special consideration is given to segment-border cracks, which are classified separately depending on whether a local peak is fully captured within the measurement range. Only if all described criteria are fulfilled is the event classified as a crack, and its position along the fibre and time of initiation are stored.

The definition of the five limit values has so far only been investigated within the tensile tests presented in section 3, and further studies are therefore required for a general validation of the thresholds. This combined automated evaluation strategy enables a reliable discrimination between

crack-induced strain peaks and non-damage-related strain fluctuations and forms the basis for the subsequent crack width calculation and two-dimensional crack visualisation.

2.3 Automated crack width estimation

Automated crack width estimation is performed based on the cracks detected by the crack detection algorithm and is carried out segment-wise for all available measurement time stamps. For a given time index, all cracks that have occurred up to this point are identified and classified as active. Subsequent calculations are restricted to these active cracks, which reduces computational effort and ensures temporal consistency of the crack width evaluation. For each segment, the positions of all detected cracks, as well as the positions of potential neighbouring cracks, are collected. Following an established approach [13], crack widths are calculated by integrating the strain within the crack influence zone, as schematically illustrated in Fig. 3. A prerequisite for this integration is the determination of the left and right integration boundaries for each crack. Cracks located at the segment boundaries are treated separately, as a reliable determination of the crack influence zone is not possible in these cases. Consequently, such cracks are therefore excluded from crack width calculation.

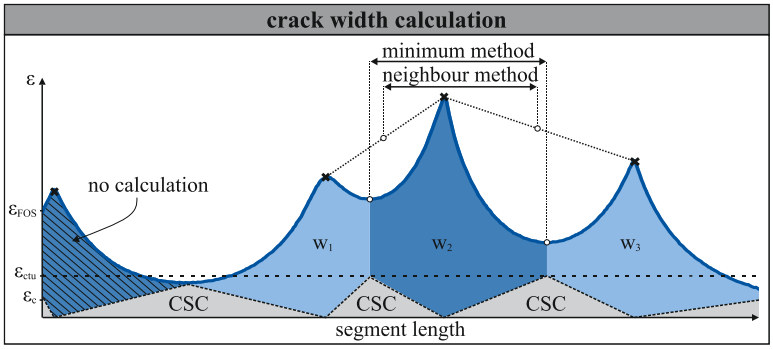


Fig. 3 Schematic illustration of the crack width calculation method based on [13].

For cracks fully located within a segment, the integration boundaries are defined either by the positions of neighbouring cracks or by local minima in the strain distribution. Two approaches are implemented: a *minimum method*, in which the integration boundary is defined by the minimum strain value between previously identified neighbouring cracks, and a *neighbour method*, in which the boundary is defined by the midpoint between two neighbouring cracks. Both approaches are illustrated in Fig. 3 and allow flexibility depending on the strain distribution and crack spacing. Once the integration boundaries are defined, the crack width is obtained by integrating the strain values between the boundaries using the spatial sampling of the FOS measurements. Finally, the concrete strain contributing (CSC) is calculated linearly based on the approach presented in [10] (grey area in Fig. 3) and subtracted from the calculated crack width. The resulting crack widths are stored segment-wise and serve as input for subsequent two-dimensional crack visualisation and validation.

2.4 Two-dimensional crack visualisation

Two-dimensional crack visualisation is performed by combining the cracks detected in the individual segments of the fibres forming the 2D-FOS network into a common crack field, as illustrated in Fig. 4. For all available time stamps, crack detection and crack width estimation are first carried out independently for each fibre orientation, as described in the previous sections. The detected cracks and their associated crack widths are then mapped into three separate matrices according to the physical layout, orientation, and spacing of the corresponding fibre segments, as previously shown in Fig. 1. Cracks classified as segment-border cracks are excluded from the visualisation, as the crack width calculation is not reliable.

In a subsequent step, the three fibre-specific crack matrices are scaled to a common matrix size and combined into a single two-dimensional crack matrix. If multiple cracks overlap at the same matrix position, the larger crack width is retained as the angle between fibre orientation and occurred crack influences the measured strain and consequently calculated crack width. To avoid multiple and false

connections, closely spaced crack entries are interpreted as a single crack point and filtered prior to further processing. Finally, individual crack points are connected to continuous crack paths using a distance-based linking strategy, subject to predefined geometric constraints derived from the applied fibre layout. The crack paths are generated using a line-connection algorithm based on the method proposed by Jack Bresenham [16], and crack widths are interpolated along the connected paths. To account for oblique intersections between fibre orientation and crack direction, the interpolated crack widths are adjusted using an angle-dependent correction factor, which adopts the orthogonal intersection between fibre and crack as a reference baseline. This correction factor has been developed based on a limited number of uniaxial tension tests and is therefore the subject of ongoing experimental investigations at the authors' institute. The final output is a continuous two-dimensional representation of crack patterns and crack widths, which forms the basis for qualitative assessment and quantitative comparison with reference measurements.

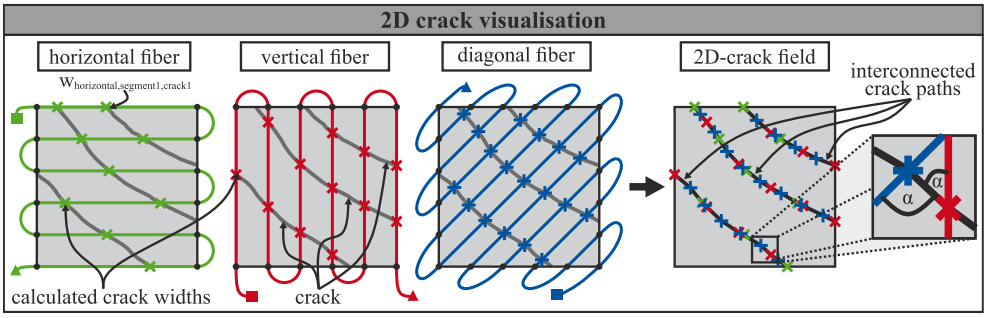


Fig. 4 Schematic illustration of the two-dimensional crack visualisation.

3 EXPERIMENTAL VALIDATION

3.1 Test setup

An experimental programme was developed to validate the proposed 2D-FOS concept and the associated algorithms for automated crack detection, crack width estimation, and two-dimensional crack visualisation. The investigation focused on the performance of the 2D-FOS network under varying loading directions. For this purpose, uniaxial tensile tests were performed on octagonal concrete specimens. The octagonal specimens and the experimental setup are illustrated in Fig. 5. The specimens have a side length of 25 cm and a thickness of 5 cm and are reinforced with a grid of Ø6 rebars. The target concrete strength class was C30/37.

A surface-bonded 2D-FOS network was applied to the front face of each specimen. The horizontal and vertical fibre directions comprised six segments each, while the diagonal fibre consisted of nine segments, resulting in a dense sensor network with 36 intersection points and 21 segments.

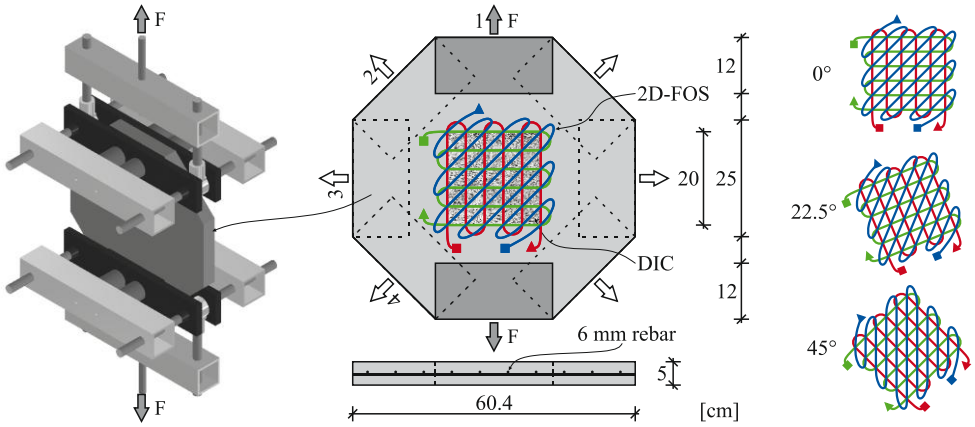


Fig. 5 Test setup and instrumentation.

The grid spacing in both directions (s_h and s_v) was 4 cm. The sensing fibres featured acryl and polyimide coatings and were bonded to the primed concrete surface using a two-component epoxy adhesive. The orientation of the 2D-FOS network on the concrete surface was varied between specimens (0°, 22.5°, and 45°) to investigate performance under different alignment conditions between fibre directions and the applied load. For validation purposes, the instrumented area was additionally monitored using a digital image correlation (DIC) system.

In addition, each octagonal specimen was tested in multiple sub-tests by rotating the specimen within the test setup, enabling uniaxial loading from four different directions relative to the sensor network. With the exception of the 22.5° network orientation, it was ensured that at least one fibre was aligned parallel to the loading direction, allowing theoretically optimal strain measurement. Furthermore, different loading scenarios were applied across the tests and sub-tests, including a static load case and a fatigue load case with constant amplitude loading. Further details on the load application and the fibre installation procedure are provided in [13]. During each loading direction, FOS strain fields and DIC measurements were recorded and subsequently compared with respect to crack detection time, crack localisation, crack width evolution, and the resulting two-dimensional crack patterns

3.2 Results and validation

The validation of the proposed concepts was carried out on multiple levels. With regard to the functionality of the automated crack detection and crack width estimation algorithms, crack widths obtained using 2D-FOS were first compared with reference measurements derived from DIC. In this initial evaluation, only cracks for which the fibre was aligned parallel to the loading direction, and thus perpendicular to the resulting crack, were considered. The analysis included both the octagonal specimens presented in this paper and additional rectangular tensile specimens described in [13], [15]. The results of this comparison are summarised in Table 1.

In total, crack widths of 52 cracks formed under static loading scenarios were compared between 2D-FOS and DIC. The mean deviation over all cracks was 0.028 mm with a standard deviation of 0.019 mm, for maximum crack widths of up to 0.8 mm. It was observed that the mean deviation decreased to 0.008 mm when only cracks smaller than 0.4 mm located in the centre of the respective fibre segments were considered. This indicates that both the measurement accuracy and the presented crack width estimation approach perform very well, with increasing deviations occurring mainly at larger crack widths or when cracks are located close to segment boundaries. In these cases, the strain-influenced zone extends beyond the considered segment, leading to an underestimation of the crack width due to incomplete strain integration.

Table 1 Mean deviation of crack widths calculated using 2D-FOS compared to results obtained from DIC for static and fatigue loading.

crack width deviation [mm]	static load: 52 cracks (mean value/standard deviation)	fatigue load: 24 cracks (mean value/standard deviation)
cracks in segment centre	0.008 / 0.004	0.011 / 0.012
cracks near segment border	0.046 / 0.029	0.018 / 0.005
total cracks	0.028 / 0.019	0.013 / 0.010

For fatigue loading scenarios, a similar behaviour was observed. Based on the evaluation of 24 cracks, a mean deviation of 0.013 mm with a standard deviation of 0.010 mm was obtained. For cracks located in the segment centre, the deviation was reduced to 0.011 mm. It should be emphasised that the calculation was performed fully automatically using the algorithms presented in this paper. This includes both automated crack detection and subsequent automated crack width calculation. In the presented evaluation, the minimum-based integration method was applied, as it proved to be more accurate than the neighbour-based method, particularly in cases where adjacent cracks exhibit significantly different strain levels at the peak [13]. Overall, the results demonstrate that the proposed algorithms are well suited for automated crack detection and crack width estimation under different

loading scenarios. Limitations mainly arise when data quality decreases at very high strain levels, leading to an increased occurrence of missing measurement points and signal anomalies.

With regard to the automated two-dimensional crack visualisation, Fig. 6 presents three representative examples considering different network orientations and loading directions. In each case, the crack patterns obtained from 2D-FOS are directly compared with those derived from DIC. A very good agreement between the two measurement systems is observed, even in cases where none of the fibres is aligned parallel to the loading direction, as illustrated by the middle example in Fig. 6. The presented crack images correspond to the final crack patterns observed on the specimens and show a high level of consistency with the experimentally observed cracking. The generation of these two-dimensional crack images was performed fully automatically based on the raw measurement data of the three fibre orientations. As the algorithms process the data for each measurement time step, the successive formation and propagation of cracks can be visualised over time. It should be noted that DIC provides strain fields rather than explicit crack images. This highlights a further advantage of 2D-FOS, as crack images can be generated directly from the raw strain measurement data. In summary, the results confirm that 2D-FOS reliably detects crack initiation and propagation in a defined area and represents an image-based monitoring technique with significant potential for the damage assessment of concrete surfaces.

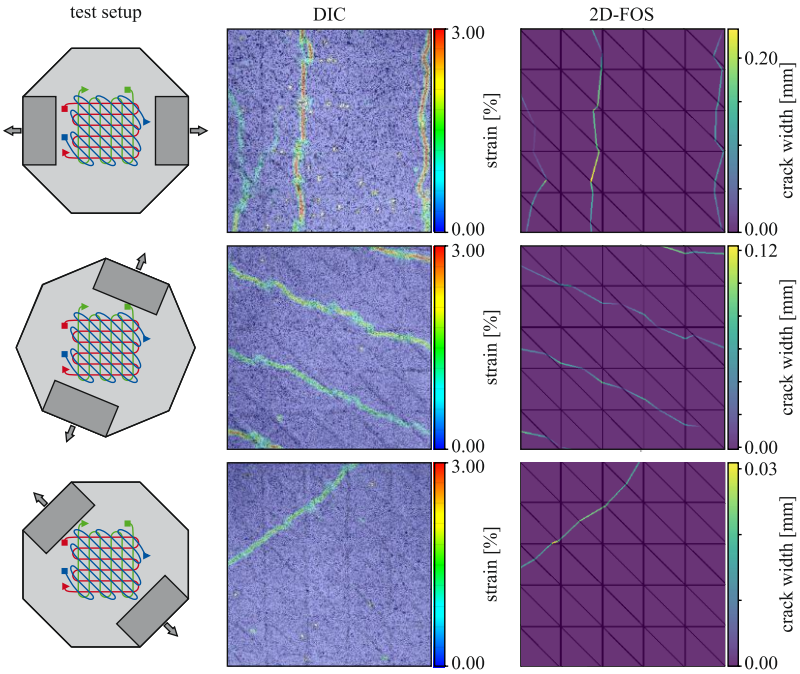


Fig. 6 Two-dimensional crack fields created with 2D-FOS and comparison with results created with DIC for different test setups.

4 CONCLUSIONS AND OUTLOOK

This paper presented a two-dimensional distributed fibre optic sensing concept (2D-FOS) for monitoring strain fields and crack development on concrete surfaces. By combining a surface-bonded fibre network in three orientations with automated algorithms for crack detection, crack width estimation, and two-dimensional crack visualisation, the approach enables image-like representations of crack patterns derived directly from FOS data. Validation on octagonal reinforced concrete tensile specimens demonstrated reliable detection of crack formation under varying loading directions and good agreement with DIC-based reference measurements. Current research aims to improve the angle-dependent correction for crack width estimation when cracks are recorded under oblique fibre orientations, to compensate for temperature effects, and to combine the developed algorithms for strain and crack visualisation with service-life prediction models until and after crack initiation.

Acknowledgements

The authors gratefully acknowledge the support for this research by the Deutsche Forschungsgemeinschaft (DFG, German Research Foundation) within the scope of the Priority Program SPP2388 "100+" (Project number: 501771082) and the Bundesanstalt für Straßen- und Verkehrswesen (BASt, Federal Highway Research Institute) within the Projekt "VLASDA" (Project number: FE 88.0229/2024/AE09).

References

[1] Marzahn Gero. 2022. Brücken an Bundesfernstraßen - Bilanz und Ausblick. In: Krieger J, Isecke B, editors. 5. Brückenkolloquium - Fachtagung für Beurteilung, Planung, Bau, Instandhaltung und Betrieb von Brücken. Ostfildern: Technische Akademie Esslingen; p. 17–35.

[2] Bundesanstalt für Straßen- und Verkehrswesen (BASt). 2026. Brückenstatistik. [January 07, 2026]; Available from: https://www.bast.de/fokusbruecken.

[3] Bundesministerium für Digitales und Verkehr. 2024. Verkehr in Zahlen 2024/2025: 53. Jahrgang. [January 07, 2026]; Available from: https://www.bmv.de/SharedDocs/DE/Anlage/G/verkehr-in-zahlen24-25-pdf.pdf?__blob=publicationFile.

[4] Baldwin Christopher. 2018. Fibre Optic Sensors in the Oil and Gas Industry: Current and Future Applications. In: Alemohammad H, editor. Opto-Mechanical Fibre Optic Sensors: Butterworth-Heinemann; p. 211–236.

[5] Chuang Shun Lien, Hsu Alan, Young Erik. 2003. Fibre Optical Sensors for High-Speed Rail Applications: Final Report for High-Speed Rail IDEA Project 19.

[6] Herbers Max, Bartels Jan-Hauke, Richter Bertram, Collin Fabian, Ulbrich Lisa, Al-Zuriqat Thamer et al. 2024. openLAB – Eine Forschungsbrücke zur Entwicklung eines digitalen Brückenzwillings. Beton und Stahlbetonbau; 119(3):169–180.

[7] Lila Kleo, Herbers Max, Richter Bertram, Agreiter Andrea, Kreslin Maja, Triller Petra et al. 2025. DFOS-Based Monitoring of Prestressed Concrete Bridge Girders. In: 13th International Conference on Structural Health Monitoring of Intelligent Infrastructure, SHMII-13, Graz, 01.09.-05.09.

[8] Vorwagner Alois, Kwapisz Maciej, Lienhart Werner, Winkler Madeleine, Monsberger Christoph, Prammer Dominik. 2021. Verteilte Rissbreitenmessung im Betonbau mittels faseroptischer Sensorik – Neue Anwendung von verteilten faseroptischen Messsystemen. Beton und Stahlbetonbau; 116(10):727–740.

[9] Künzel Andreas. 2016. Parameteridentifikation auf Basis faseroptisch gemessener quasi-kontinuierlicher Dehnungssignale. Dissertation. Berlin.

[10] Fischer Oliver, Thoma Sebastian, Crepaz Simone. 2019. Distributed fibre optic sensing for crack detection in concrete structures. Civil Engineering Design; 1(3-4):97–105.

[11] Richter Bertram, Herbers Max, Marx Steffen. 2023. Crack monitoring on concrete structures with distributed fibre optic sensors—Toward automated data evaluation and assessment. Struct Concrete;25(2):1465–1480.

[12] Becks Henrik, Hegger Josef, Classen Martin. 2024. Measuring Strain and Crack Evolution in Reinforced Concrete under Monotonic and Fatigue Tension using Fibre Optic Sensors. In: Motavalli M, editor. Proceedings of the 7th International Conference on Smart Monitoring, Assessment and Rehabilitation of Civil Structures (SMAR2024); 1279-1286.

[13] Becks Henrik, Högemann Matthias, Hegger Josef, Classen Martin. 2025. Assessing crack formation and strain distribution in concrete structures using externally installed fibre optic sensors. Case Studies in Construction Materials 2025(22).

[14] Becks Henrik, Lippold Lukas, Winkler Paul, Moeller Max, Rohrer Maximilian, Leusmann Thorsten et al. 2024. Neuartige Konzepte für die Zustandsüberwachung und -analyse von Brückenbauwerken – Einblicke in das Forschungsvorhaben SPP100+. Bauingenieur 2024;99(10):327–338.

[15] Becks Henrik, Hegger Josef, Classen Martin. 2025. Two-dimensional strain measurement and crack detection of reinforced concrete using fibre optic sensors. In: Proceedings of the IABSE Congress Ghent 2025: The Essence of Structural Engineering for Society, Ghent, Belgium, 27.08.-29.08.

[16] Bresenham Jack. 1965. Algorithm for computer control of a digital plotter. IBM Systems Journal; 4(1):25–30.

Monitoring of Reinforced Concrete Beams with Thermoplastic Bars Using Digital Image Correlation and Optical Fibers

Christian Renato Mendoza, Galo Ortiz, Eva Oller, Juan Murcia-Delso

Department of Civil and Environmental Engineering,
Universitat Politècnica de Catalunya (UPC-BarcelonaTech),
Jordi Girona 1-3, Building C1, 08034 Barcelona, Spain

Summary
Thermoplastic Glass Fibre-Reinforced Polymer (GFRP) bars constitute a recyclable and bendable innovative alternative for the reinforcement of concrete structures. This paper analyses the shear behaviour of concrete beams reinforced with longitudinal and transverse thermoplastic GFRP bars through an integrated monitoring approach that combines Digital Image Correlation (DIC) and optical fibre monitoring. Both techniques were applied to measure the shear response and record the cracking process. DIC was used on one face of each beam to capture full-field surface strains and crack evolution, while optical fibres were bonded to the external surface of the same or opposite face in the region where shear failure was expected to occur. This configuration enables simultaneous monitoring of strain and crack development during loading. The combined use of DIC and optical fibre monitoring enhances the assessment of shear behaviour in thermoplastic FRP reinforced concrete members.

1 INTRODUCTION

The use of Fibre Reinforced Polymer (FRP) bars as internal reinforcement in reinforced concrete structures has increased significantly in recent decades due to their high corrosion resistance, low specific weight, and durability in aggressive environments. Among these materials, glass fibre reinforced polymer (GFRP) bars have been widely investigated as an alternative to conventional steel reinforcement. Unlike steel, FRP bars exhibit a linear-elastic behaviour up to failure and a limited stress redistribution capacity, which may influence the structural response, particularly in brittle failure modes such as shear. Most commercially available FRP systems are based on thermosetting matrices, such as vinyl ester resins. However, thermoplastic FRP bars have recently emerged as an alternative solution, offering potential advantages in terms of recyclability, formability, and manufacturing efficiency. Thermoplastic matrices allow post-forming, recyclability, and improved deformability [1]. New thermoplastic CFRP bars with engraved surface profiles increased the strength of bent bars by up to 71% compared to previous investigations [2], while bendable thermoplastic basalt fibre reinforced polymer (BFRP) bars exhibited superior ductility under interlaminar shear stresses compared to thermoset-matrix bars [3]. In addition, thermoplastic-matrix bars exhibit improved resistance to alkaline environments and allow complete recyclability due to their remelting capability [4]. Bendable thermoplastic CFRP bars exhibit a linear-elastic tensile behaviour up to failure and demonstrate feasibility for applications involving bent configurations [5]. The tensile and compressive behaviour of thermoset and thermoplastic GFRP bars showed that the compressive strength ranges between 50% and 60% of the tensile strength, while the elastic modulus remains similar in both tension and compression [6]. More recently, Bertolli, Pisani and D'Antino [7] experimentally compared reinforced concrete beams reinforced with thermoset and thermoplastic GFRP bars subjected to flexural and shear loading. Their results showed an overall comparable structural behaviour between both systems, although differences were observed in terms of bond performance and ultimate capacity.

In parallel, advanced monitoring techniques have enabled a more detailed investigation of strain localisation and crack development. Digital image correlation (DIC) provides full-field surface strain measurements, while distributed fibre optic sensing (DFOS) enables continuous strain monitoring along extended regions of structural elements. DFOS systems overcome the limitations of conventional mechanical strain gauges [8]. The combined DFOS-DIC instrumentation applied to reinforced concrete beams reinforced with steel bars provides a high-resolution strain map that enables the experimental verification of shear-transfer kinematic mechanisms in complex cracked elements [9]. More recently, Cavagnis et al. [10] investigated the shear behaviour of reinforced concrete beams without transverse

reinforcement using three-dimensional DIC, demonstrating that shear failure is not governed by a single isolated resisting mechanism, but rather by the interaction of multiple shear-transfer mechanisms.

The combined application of the above-mentioned monitoring techniques represents a promising strategy for improving the understanding of damage evolution and structural behaviour in FRP-reinforced elements. This paper studies the shear response of beams reinforced with thermoplastic and thermoset GFRP bars, focusing on the use of DIC and DFOS to elucidate strain evolution and crack propagation in the failure regions.

2 EXPERIMENTAL PROGRAM

2.1 General description

The experimental program was designed to evaluate the applicability of an integrated monitoring strategy for reinforced concrete beams reinforced with GFRP bars, comparing thermoplastic and thermoset matrix. All tested beams feature the same general geometry, while controlled variations are introduced in the type of longitudinal reinforcement, concrete strength, and the transverse reinforcement ratio. The experimental response was monitored by combining conventional displacement instrumentation, DIC and DFOS.

2.2 Test specimens and materials

The experimental program included five beams with a total length of 3.20 m and a rectangular cross-section of 0.20 m × 0.25 m (see Figure 1). Two target specified concrete compressive strengths were used (30 MPa and 60 MPa) to analyse their influence on shear behaviour and cracking evolution. The thermoplastic GFRP bars had a nominal diameter of 12.7 mm, an elastic modulus of approximately 53 GPa and an ultimate tensile strength of 977 MPa. The thermoset GFRP bars had a nominal diameter of 12 mm and an elastic modulus of approximately 46 GPa, an ultimate tensile strength of 850 MPa. The main geometric, mechanical, and reinforcement characteristics of the specimens are summarized in Table 1. The measured average compressive strengths at the testing age of 28 days were approximately 48.3 MPa and 57.7 MPa, respectively.

Table 1 Matrix of the tests considered in the experimental program

Item	Beam ID	Matrix Type	f_{cm} (MPa) test day	Stirrup Spacing	Long. bottom reinfor.	Ultimate Load (kN)	V_u (kN)
1	ST2w1_30	Thermoplastic	54.7	φ8 @250	3φ12.7	115.4	88.47
2	ST2w2_60	Thermoplastic	65.2	φ8 @150	3φ12.7	91.7	70.30
3	SCV2w2_60	Vinylester	65.2	φ8 @150	3φ12.7	112.5	86.25
4	ST3w2_30	Thermoplastic	54.7	φ8 @150	4φ12.7	72.3	55.43
5	SCV3w2_30	Vinylester	54.7	φ8 @150	4φ12.7	93.6	71.76

2.3 Test setup and loading protocol

The tests were performed using a point load applied at a distance of 700 mm from the support, creating a clearly defined critical shear span between the loading point and the nearest support. During the tests, four successive load cycles were applied. In each cycle, once the predefined load level was reached, the beam was completely unloaded and subsequently reloaded in order to record its structural response at different representative stages of behaviour.

The load levels corresponded approximately to 20%, 40%, and 60% of the estimated failure load in the first three cycles, respectively. The first cycle aimed to identify crack initiation, while the following cycles were used to analyse strain evolution and crack propagation. In the final cycle, the load was continuously increased until failure.

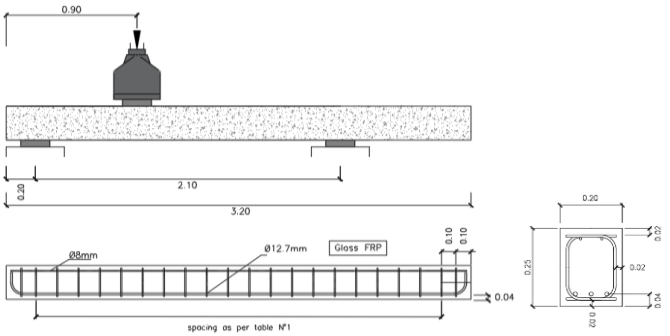


Fig. 1 General test configuration of the experiments, including loading arrangement, beam geometry and representative reinforcement layout.

The structural response of the beams was monitored through a combination of conventional instrumentation and advanced measurement techniques, aiming to capture both global behaviour and local mechanisms associated with shear. Conventional instrumentation included four magnetostrictive displacement transducers (Temposonic) and six LVDTs for monitoring vertical displacements. The sensors were distributed along the beam to capture both global deflections and local displacement variations associated with diagonal crack development.

2.3.1 Digital Image Correlation

All beams were monitored using Digital Image Correlation (DIC), applied to one of the lateral faces. A stochastic speckle pattern was prepared on the monitored surface in order to enable full-field surface strain measurements throughout the loading process, as shown in Fig. 2(right). The camera was positioned at an approximate distance of 1 m from the monitored beam surface, and images were acquired at a frequency of 0.1 Hz during testing. DIC measurements were processed using GOM Correlate Pro 2021 software under a 2D DIC configuration. The analysis was conducted using a subset size of 15 pixels and a step size of 9 pixels under high-precision correlation settings.

To quantify local strain evolution, virtual extensometers were defined within the DIC analysis. Five virtual extensometers were positioned 40 mm above the bottom fibre, covering the first five cracks identified during the test. Two additional virtual extensometers were placed directly below the loading point: one located along the geometric axis of the beam and another positioned 40 mm below the top fibre. Furthermore, virtual reference points were defined at the same locations as the Temposonic displacement transducers, allowing direct comparison between optically measured displacements and conventional instrumentation, as shown in Fig. 2 (left). In specimen ST3w2_30, the DIC system was installed on the same face as the distributed optical fibre sensors to establish a direct comparison. In the remaining specimens, the systems were placed on opposite faces to obtain complementary data.

2.3.2 Distributed Fibre Optic Sensing (DFOS)

The beams were instrumented with distributed fibre optic sensors locally arranged within the critical shear span region, specifically between the support and the load application point. The distributed fibre optic system was employed to record the spatial distribution of strain within the shear region, enabling the identification of localised strain concentrations associated with crack initiation and propagation. Distributed Fibre Optic Sensing (DFOS) measurements were performed using a Luna Innovations ODiSI 6102 interrogator based on Optical Frequency Domain Reflectometry (OFDR) and Rayleigh backscattering. The system employed high-definition polyimide-coated low bend loss optical fibre sensors with a fibre diameter of approximately 155 µm and a gauge pitch of 5.2 mm. Measurements were acquired at a frequency of 2 Hz using the ODiSI software platform. In all specimens, the fibre was arranged in a two-dimensional grid configuration composed of longitudinal segments (L1–L4) and vertical segments (V0–V4), enabling strain monitoring in two orthogonal directions within the critical shear region, as shown in Fig. 3. Depending on the specimen, the fibre was bonded to the concrete surface using cyanoacrylate or two-component epoxy adhesive, with and without prior surface grooving, in order to evaluate the influence of bonding conditions on strain transfer and data quality.

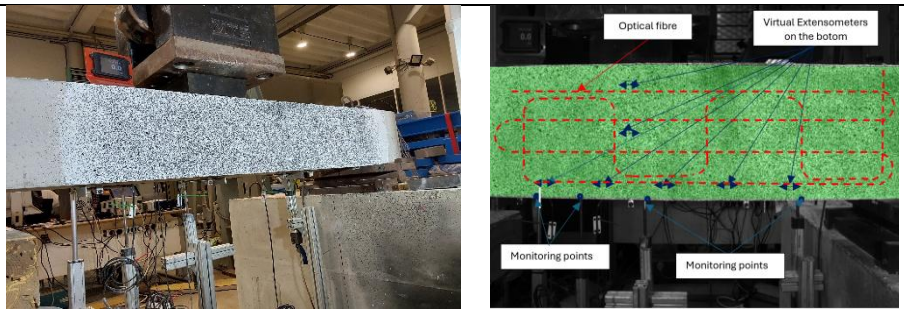


Fig. 2 Monitoring configuration of specimen ST3w2_30: (left) speckle pattern applied for DIC measurements; (right) distribution of virtual extensometers, monitoring points and distributed fibre optic (DFOS) layout.



Fig. 3 DFOS monitoring configuration: (left) experimental setup with fibre bonded on the monitored face; (right) longitudinal (L1–L4) and vertical (V0–V4) segments.

3 PRELIMINARY RESULTS

The maximum load-carrying capacities and corresponding shear forces at failure of the tested beams are presented in Table 1. The highest shear capacities were obtained for beams SCV2w2_60 and ST2w1_30, corresponding to specimens reinforced with thermoset and thermoplastic bars, respectively. Differences in the structural response were mainly associated with the concrete compressive strength and the type of longitudinal reinforcement used. In both reinforcement systems, the beams with higher concrete compressive strength exhibited higher ultimate loads, suggesting a significant contribution of concrete compressive strength to the shear capacity of the tested beams. When comparing specimens with similar reinforcement configurations and geometry, the beams reinforced with vinylester GFRP bars exhibited higher load-carrying capacities than those reinforced with thermoplastic GFRP bars. This tendency was observed in specimens SCV2w2_60 and SCV3w2_30, which showed ultimate loads approximately 22–29% higher than their thermoplastic counterparts ST2w2_60 and ST3w2_30, respectively. No clear increase in shear capacity associated with the reduction in stirrup spacing was observed between specimens ST2w1_30 and ST3w2_30. This behaviour may be related to differences in cracking pattern and failure mode, possibly promoting an arching action within the shear span.

The force-displacement curves obtained for each of the five beam specimens are shown in Fig. 4. The envelope of the curves follows a practically bilinear response, corresponding to the uncracked and cracked stages of the beams. Once the maximum load was achieved, the load-carrying capacities dropped suddenly in all cases due to the shear failures. Additionally, the load-displacement curves showed a predominantly linear response up to failure, characteristic of the elastic behaviour of FRP reinforcement, without a clearly defined plastic stage. Although the thermoplastic GFRP bars individually presented an ultimate tensile strength approximately 14% higher than the vinylester GFRP bars, this increase was not directly reflected in the global structural capacity of the tested beams.

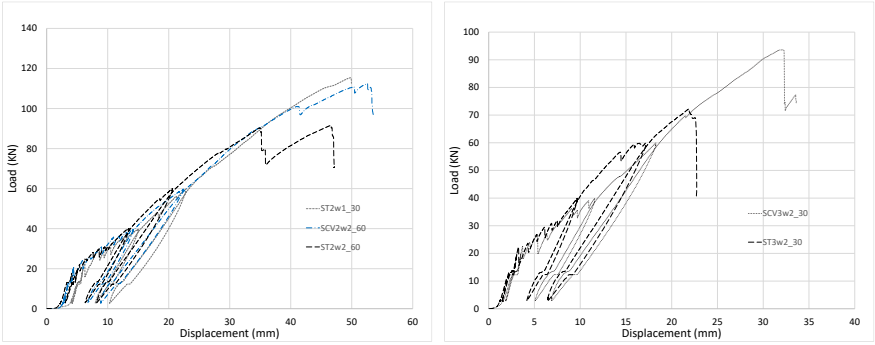


Fig. 4 Load-displacement of tested beams, (left) 3Ø12 beams; (right) 4Ø12 beams.

Table 2 Summary of crack widths measured by Digital Image Correlation (DIC) for the first five cracks identified during the tests, corresponding ultimate load (ULS) for each beam.

Beam ID	Crack 1 (mm)	Crack 2 (mm)	Crack 3 (mm)	Crack 4 (mm)	Crack 5 (mm)	Deflection at Load Point (mm)	Ultimate Load (kN)
ST2w1_30	1.24	1	2.06	0.9	5.57	41.38	115.4
SCV2w2_60	0.12	1.35	1.04	3.41	7.58	45.71	112.5
ST2w2_60	0	0.98	5.19	5.51	0.09	41.45	91.7
SCV3w2_30	0.61	1.45	1.68	1.18	1.29	22.47	93.6
ST3w2_30	1	1.27	1.01	1.02	0.85	19.15	72.3

3.1 Digital Image Correlation (DIC)

Digital Image Correlation (DIC) was used to monitor crack development and strain localisation in all tested beams. The strain fields enabled the identification of the transition from an initially flexure-dominated response towards a shear-governed behaviour characterised by the formation of dominant diagonal cracks within the critical shear span. At approximately 20–30% of the ultimate load, vertical flexural cracks developed. At higher load levels (40–60% of the ultimate load), strain localisation became evident within the shear region, with the progressive formation of an inclined strain band associated with the initiation of the dominant diagonal crack, as shown in Fig.5.

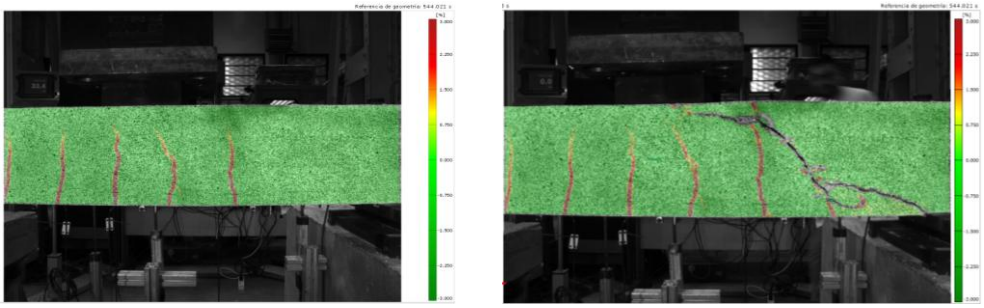


Fig. 5 Crack pattern obtained by Digital Image Correlation (DIC) for specimen ST3w2_30: (left) strain field at approximately 20–30% of the ultimate load, (right) strain field at ultimate load (ULS)

In the final loading stages, all specimens exhibited pronounced strain localisation and failure governed by the propagation of a dominant diagonal crack extending between the support and the load application point, accompanied by secondary cracks of smaller width, as shown in Fig. 5 (right). Table 2 summarises the crack widths measured by DIC, the vertical displacements beneath the load application point, and the ultimate loads of the tested beams. Specimens SCV2w2_60 and ST2w1_30 exhibited the highest ultimate loads and the largest crack widths prior to failure, indicating strong damage localisation within the shear span. In contrast, specimen SCV3w2_30 showed a more distributed crack pattern, whereas ST2w2_60 and ST2w1_30 exhibited a more localised response characterised by dominant cracks with larger openings. When comparing specimens SCV3w2_30 and ST3w2_30, as well as SCV2w2_60 and ST2w2_60, similar global deflections were observed beneath the load application point. However, the beams reinforced with vinylester GFRP bars reached higher ultimate loads than those reinforced with thermoplastic GFRP bars, suggesting differences in stress transfer and crack distribution mechanisms. In specimen ST2w1_30, the crack pattern and failure configuration may have promoted an arching action, contributing to its higher shear capacity despite the lower transverse reinforcement ratio.

3.2 Distributed Fibre Optic Sensing (DFOS)

The analysis of DFOS results focuses on specimen ST3w2_30, in which both monitoring systems (DIC and DFOS) were installed on the same lateral face, enabling direct spatial comparison between the surface strain measurements and those recorded by the distributed optical fibre.

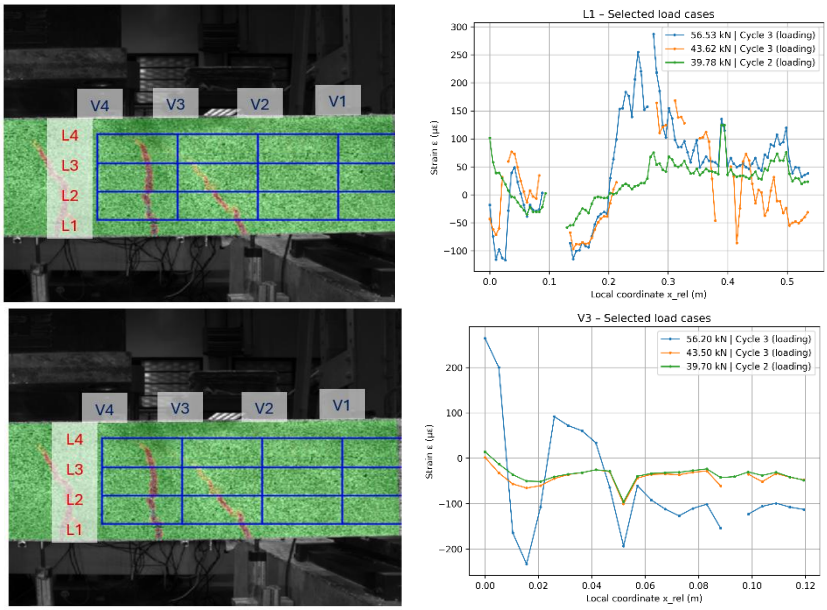


Fig.6 Comparison between DIC and DFOS measurements at load levels associated with the initiation of the dominant diagonal crack: (left) full-field strain distribution obtained by DIC at the load stage marking the onset of diagonal cracking; (right) DFOS strain profiles along longitudinal segment L1 and vertical segment V3 at 39.78 kN (second loading cycle) and 43.62 kN and 56.53 kN (third loading cycle).

Three representative load levels were selected for the analysis of DFOS data: one corresponding to the second cycle (39.7 kN), where flexural cracks were predominant, and two from the third cycle (43.5 kN and 56.2 kN), close to the initiation and development of the dominant diagonal crack. These levels were chosen to evaluate the evolution of the strain distribution within the shear region (Fig. 6). In the longitudinal segment L1, the tensile strains recorded by the optical fibre increased progressively with the applied load level, showing a localised concentration in the region associated with the diagonal crack identified by DIC. At the highest analysed applied load level, a partial loss of valid data points was observed in the zone where DIC clearly indicated the presence of the crack. This behaviour may

be attributed to high strain concentrations and possible local debonding effects between the optical fibre and the concrete substrate, limiting the continuity of the measurement at the exact crack location. In some segments, isolated strain peaks were recorded that did not show direct correspondence with crack locations observed by DIC and were not consistently repeated in adjacent segments. These outlier values are likely associated with instrumental noise or anomalous readings from the ODISI system rather than representing a structural phenomenon. The longitudinal segment L4 exhibited predominantly compressive behaviour throughout all analysed loading cycles. The recorded strains were negative and showed consistent evolution with increasing load, which agrees with the expected behaviour of the compression zone of the beam within the shear-resisting mechanism (Fig.7). Overall, the general strain localisation patterns recorded by DFOS show qualitative agreement with the strain fields obtained from DIC, particularly regarding the initiation and propagation zone of the dominant diagonal crack. Nevertheless, the limitations of distributed measurements under high strain gradients, as well as the potential presence of isolated outlier readings, should be considered when interpreting the results.

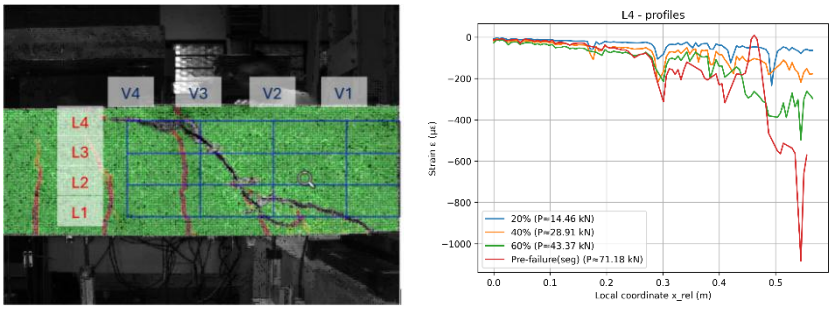


Fig.7 Comparison of DIC and DFOS results at different load levels (left) DIC strain field after structural failure, illustrating the final crack configuration; (right) DFOS strain profiles extracted from longitudinal segment L4 at 20%, 40% and 60% of the ultimate load, and at the pre-failure load level (last valid measurement stage before partial data loss)

4 CONCLUSIONS

The present study investigated the applicability of an integrated monitoring strategy based on Digital Image Correlation (DIC) and Distributed Fibre Optic Sensing (DFOS) for tracking strain evolution and crack development in reinforced concrete beams reinforced with thermoset and thermoplastic GFRP bars.

Five beams reinforced with thermoplastic GFRP were tested up to failure. All the beams exhibited shear-governed failure characterised by the formation of a dominant diagonal crack between the support and the load application point, preceded by vertical flexural cracking. Although differences in reinforcement configuration led to variations in ultimate load, the failure mode was consistent, with progressive strain localisation within the critical shear span. Differences in ultimate load, crack distribution, and strain localisation were observed among the tested beams.

The beams reinforced with vinylester GFRP bars developed higher load-carrying capacities than those reinforced with thermoplastic GFRP bars for comparable reinforcement configurations and similar levels of global deformation.

The DIC system successfully identified crack initiation and propagation, providing full-field strain measurements up to failure. Virtual extensometers enabled quantitative tracking of crack development, in agreement with conventional displacement measurements.

The DFOS system captured localised strain concentrations along the monitored segments within the shear span, reflecting the evolution of the dominant diagonal crack. In beam ST3w2_30, where both monitoring systems were installed on the same lateral face, a clear spatial correspondence was observed between the crack pattern identified by DIC and the strain concentrations measured by DFOS. More stable and continuous strain profiles were obtained in compression-dominated regions than in cracked tension zones, indicating a more reliable DFOS response under compressive stress states.

A progressive loss of valid sensing points was observed near ultimate conditions, likely associated with large crack openings, high localised strain concentrations, and possible fibre–concrete debonding

effects. In addition, isolated strain peaks not directly correlated with visible cracking were detected and are likely related to instrumental noise or acquisition anomalies.

Overall, the combined use of DIC and DFOS proved complementary for monitoring shear-critical regions in FRP-reinforced concrete beams. DIC enabled full-field visualisation of crack propagation, while DFOS provided continuous strain measurements along predefined monitoring paths, enabling the early detection of localised strain concentrations associated with crack development. Further quantitative correlation between both monitoring techniques is currently under investigation.

Acknowledgements

The authors gratefully acknowledge the financial support provided by the research projects PCI2023-143361. The experimental programme was carried out at the Structural Laboratory of UPC-BarcelonaTech. The authors also thank Sireg for supplying the GFRP bars used in this study.

References

[1] Benmokrane, Brahim, Mousa, Salaheldin, Mohamed, Khaled, and Sayed-Ahmed, Mahmoud. 2021. "Physical, Mechanical, and Durability Characteristics of Newly Developed Thermoplastic GFRP Bars for Reinforcing Concrete Structures." *Construction and Building Materials* 276:122200. doi:10.1016/j.conbuildmat.2020.122200.

[2] Apitz, Andreas, Schmitz, Jonas, Hückler, Alex, and Schlaich, Mike. 2022. "New Thermoplastic Carbon Fiber Reinforced Polymer Rebars and Stirrups." *Structural Concrete* 23 (2): 923–38. doi:10.1002/suco.202100434.

[3] Wang, Xin, Peng, Zheqi, Ding, Lining, Lu, Jing, Zhu, Zhongguo, and Wu, Zhishen. 2021. "Mechanical and Bonding Behavior of a Bendable Fiber-Reinforced Thermoplastic Rebar." *Construction and Building Materials* 302:124222. doi:10.1016/j.conbuildmat.2021.124222.

[4] Zeng, Jun-Jie, Feng, Sheng-Zhao, Zhao, Bin, Wu, Feng-Yi, Zhuge, Yan, and Wang, Hao. 2024. "Recyclable Thermoplastic FRP Bars for Reinforced Concrete Structures: Current Status and Future Opportunities." *Composite Structures* 348:118438. doi:10.1016/j.compstruct.2024.118438.

[5] El-Tahan, Mossab, Galal, Khaled, and Hoa, Van Suong. 2013. "New Thermoplastic CFRP Bendable Rebars for Reinforcing Structural Concrete Elements." *Composites Part B: Engineering* 45:1207–15. Accessed February 16, 2026. doi:10.1016/j.compositesb.2012.09.025.

[6] D'Antino, Tommaso, and Pisani, Marco Andrea. 2023. "Tensile and Compressive Behavior of Thermoset and Thermoplastic GFRP Bars." *Construction and Building Materials* 365:130104. doi:10.1016/j.conbuildmat.2022.130104.

[7] Bertolli, Veronica, Pisani, Marco Andrea, and D'Antino, Tommaso. 2025. "Use of Thermoset- and Thermoplastic-Resin GFRP Bars as Internal Flexural and Shear Reinforcement of Concrete Beams." *Engineering Structures* 343:120986. doi:10.1016/j.engstruct.2025.120986.

[8] Bado, Mattia Francesco, Casas, Joan R., and Kaklauskas, Gintaris. 2021. "Distributed Sensing (DOFS) in Reinforced Concrete Members for Reinforcement Strain Monitoring, Crack Detection and Bond-Slip Calculation." *Engineering Structures* 226:111385. doi:10.1016/j.engstruct.2020.111385.

[9] Poldon, Jack J., Hoult, Neil A., and Bentz, Evan C. 2022. "Understanding Shear-Resistance Mechanisms in Concrete Beams Monitored with Distributed Sensors." *ACI Structural Journal* 119:235–45. doi:10.14359/51734479.

[10] Cavagnis, Francesco, Fernández Ruiz, Miguel, and Muttoni, Aurelio. 2017. "An Analysis of the Shear-Transfer Actions in Reinforced Concrete Members Without Transverse Reinforcement Based on Refined Experimental Measurements." *Structural Concrete* 19:49–64. doi:10.1002/suco.201700145.

Thermal Imaging–Based Automated Fatigue Monitoring for Concrete Anchorages

Nikolaos Mellios, Mohamad Ahmad, Theodoros Rousakis, Panagiotis Spyridis

University of Rostock,
Justus-von-Liebig-Weg 2, 18059 Rostock, Germany

Summary
Concrete anchorages play a critical role in modern construction by enabling flexible and rapid structural assembly. This study investigates an automated system for early detection of fatigue-induced failures in safety-critical chemical fastening systems under cyclic loading using infrared thermography and computer vision. Twenty-one tensile tests (nineteen fatigue and two static) were conducted. A real-time monitoring algorithm was developed to identify thermal anomalies and correlate them with fatigue progression. In all cross-validated experiments, the system successfully issued early warnings before failure. The thermal imaging-based monitoring approach demonstrated high accuracy, robustness, and low sensitivity to environmental noise. The proposed method advances automated inspection and failure-warning technologies, supporting predictive maintenance, lifecycle monitoring, and safer infrastructure through non-contact structural health monitoring.

1 INTRODUCTION

1.1 General

Concrete anchorages are critical structural connection technologies in modern construction, enabling flexible and rapid assembly of prefabricated components. These anchors, embedded in concrete, provide secure fastening points for bolts, hooks, and threaded rods, and are manufactured from materials such as steel, stainless steel, and polymers. Common types include cast-in rebars, chemical bonded anchors, concrete screws, undercut anchors, and expansion anchors. Among them, steel threaded rods bonded with chemical adhesives, such as epoxy, offer high static resistance, durability, ease of installation, and cost efficiency [1], [2].

In recent decades, fatigue-related live loads have increased due to leaner structural designs and the use of high-performance materials. Fatigue is often a governing design criterion, particularly in structures exposed to cyclic loading such as seismic activity, traffic loads, industrial machinery, cranes, and ventilators [3], [4]. Fatigue failure is particularly critical because it occurs suddenly and without clear warning signs, posing significant safety and economic risks. Early detection of fatigue damage is therefore essential to ensure structural reliability.

Conventional inspection techniques, including visual inspection and ultrasonic testing, are often time-consuming and may fail to detect early-stage damage [5]. Consequently, advanced non-destructive evaluation methods have gained attention, particularly infrared thermography, which enables temperature-based monitoring of stress concentrations and fatigue processes in metals [6]–[7]. Fatigue crack initiation in steel is typically associated with localized temperature increases, even before visible cracking occurs [7], highlighting temperature monitoring as a promising indicator of structural degradation.

This study evaluates a fatigue warning system that combines thermocouples, thermal cameras, and computer vision techniques to continuously monitor temperature variations in fastening elements. Thermal cameras capture infrared radiation to provide spatial temperature distributions [8], while deep learning approaches, particularly convolutional neural networks (CNNs), enable automated anchor detection and temperature extraction from thermal imagery [9]. In parallel, thermocouples provide direct, point-based temperature measurements from the anchor surface [10].

Recent research demonstrates increasing integration of sensing technologies, IoT frameworks, and digital twin concepts for infrastructure monitoring [11]–[12]. These approaches emphasize multi-sensor fusion, real-time analytics, and lifecycle asset management. Building on these developments, this study focuses on fatigue monitoring of safety-critical chemical anchors, an application that remains largely unexplored in thermal monitoring research.

The proposed framework introduces a low-cost, retrofittable early-warning methodology based on dual-region thermal evaluation and smoothed derivative thresholding ($\Delta = 0.01$), reducing environmental noise without requiring pre-trained models. Furthermore, the study provides a systematic comparison between thermocouple-based and image-based temperature monitoring, demonstrating the limitations of single-point sensing and the improved robustness of spatial thermal monitoring. The findings aim to support the development of scalable and reliable monitoring solutions for fastening systems in real-world infrastructure.

1.2 Thermodynamic Background and Application to Concrete Anchors

Fatigue is a dissipative process in which part of the mechanical energy is converted into heat, causing measurable temperature increases. Schaefer et al. [13] proposed a thermometric approach to estimate fatigue limits by monitoring temperature evolution during cyclic loading, which can also be applied to concrete anchors. The fatigue process can be described by a thermodynamic heat balance equation. Assuming fatigue is mainly dissipative and that surface temperature represents internal temperature distribution, the equation simplified. More profound information can be found in [14] The resulting temperature field can be measured using thermocouples and infrared thermography, enabling estimation of heat generation per load cycle and early fatigue detection. Further theoretical details are provided in [13].

2 MATERIALS AND EXPERIMENTAL SETUP

Fatigue tests were conducted on two lightly reinforced concrete slabs (1.60 × 1.60 × 0.25 m), each containing twelve chemical bonded anchors for fatigue testing and one for static testing. Three anchors failed prematurely under static loading, resulting in twenty-one fatigue and two static tests evaluated. The slabs were reinforced with a B12/230 S500 mesh and perimeter stirrups, and were fixed to the laboratory strong floor to minimise vibration. Anchors were installed with a spacing of 250 mm.

The concrete consisted of CEM I 42.5 R Portland cement with natural aggregates and a water–cement ratio of 0.52, complying with bonded anchor certification guidelines [15]. Specimens were vibrated, foil-cured for 28 days, and companion cubes were cast to determine compressive strength. Reinforcement steel BSt 500 S+M (Ø12 mm) was used.

Post-installed M16 threaded rods (strength class 8.8) were bonded using FIS EM Plus 390 S epoxy mortar in hammer-drilled boreholes, with an embedment depth of at least 100 mm. Alignment was controlled within ±2°.

The monitoring system included a load cell, displacement transducers, K-type thermocouples attached to anchor heads, and a FLIR E8-XT infrared camera positioned approximately 1 m from the specimen. Thermocouples provided continuous temperature measurements, while thermal imaging enabled spatial monitoring of temperature development. Thermocouples were pre-calibrated and data were recorded at 25–30 s intervals. A dual-region evaluation approach was used to reduce environmental effects. All tests were performed under controlled laboratory conditions (Fig. 1). A more detailed explanation of the materials used and the monitoring methodology can be found in [14].

3 PHYSICAL ANCHOR TEST EXECUTION

Fatigue behaviour was characterised using S–N (Wöhler) curves describing the relationship between stress amplitude and number of load cycles [16], [17]. The S–N curve was progressively refined during testing, starting from an initial estimate based on experience and static tensile resistance of the threaded rods. The curve supported (i) selection of representative stress amplitudes and (ii) timely activation of the thermal camera shortly before expected steel failure, reducing unnecessary data acquisition and equipment usage (Fig. 1). The measured static tensile strength was 148 kN. Fatigue tests primarily targeted the high-cycle fatigue regime, with failures typically occurring between approximately 104 and 106 load cycles. After approximately five to six tests, the S–N curve parameters stabilised, providing reliable failure predictions. In total, 21 fatigue tests and 2 static tests were conducted, resulting in 18 usable thermocouple datasets and 14 high-quality thermal imaging datasets. A more detailed overview of the test results is presented in [14]. Tests were performed at varying stress amplitudes and loading frequencies to evaluate fatigue performance and temperature development leading to failure (Fig. 2).

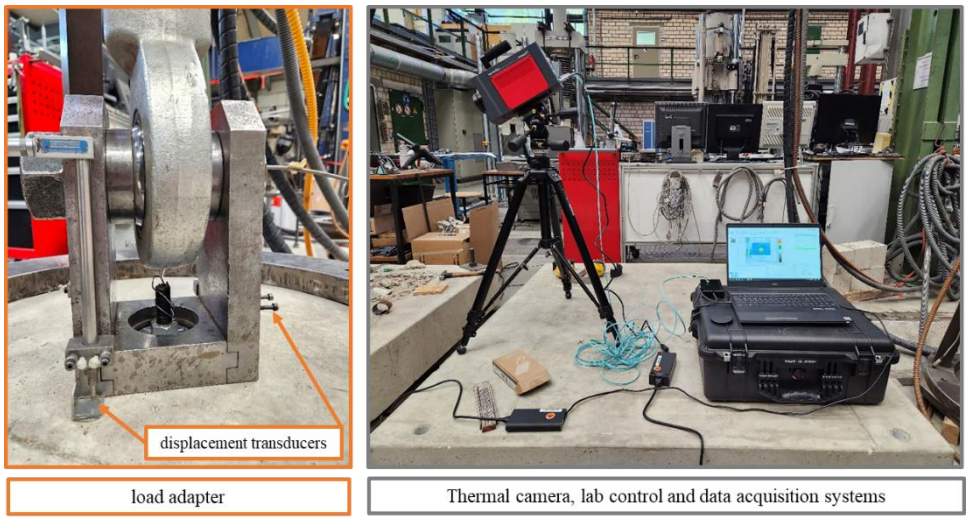


Fig. 1 Test Setup. Load adapter with two displacement transducers (left), thermal camera (right).

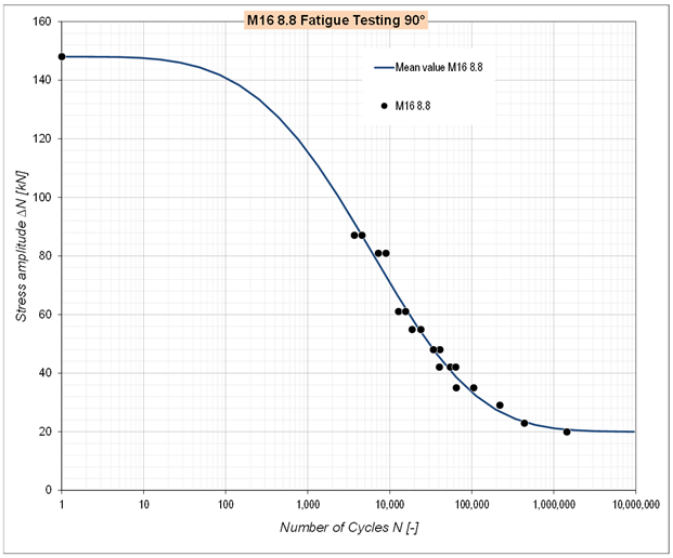


Fig. 2 S-N Curve of the testing series for 21 experiments.

4 DATA PROCESSING

4.1 Computational Algorithm for Thermal Camera Data Processing

Thermal images and corresponding ASCII files provide spatial temperature distributions for each pixel of the recorded infrared images. Each image contains approximately 1.37 million temperature data points. The processing algorithm extracts temperature information using a four-step automated routine. First, the program imports thermal images and associated ASCII temperature matrices and organises them for sequential processing. Two circular Regions of Interest (ROIs) are defined: one centred on the anchor and one representing the surrounding environment. Binary masks isolate temperature data within each region, and mean temperatures are stored in dedicated arrays (see Fig. 3).

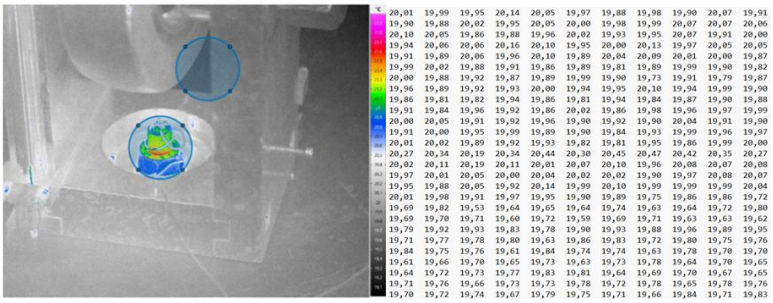


Fig. 3 Thermal image including Regions Of Interest (ROI) in binary masking and temperature contour indicators (left), and exemplary excerpt of ASCII file indicating corresponding temperatures in °C per pixel (right)

Second, the algorithm iteratively processes each image–ASCII pair, updating anchor and environmental temperature histories while maintaining synchronization with test progression. Third, temperature data are smoothed using a moving-average method based on predefined frame and window sizes to reduce noise and highlight meaningful thermal trends. Finally, an early-warning logic is applied once sufficient data is available. The system evaluates the derivative of the temperature difference between anchor and environment, applies additional smoothing through convolution, and compares the resulting signal with a predefined threshold ($\Delta = 0.01$). When exceeded, the algorithm triggers a warning indicating imminent fatigue failure and identifies the corresponding monitoring frame. This automated monitoring framework enables real-time detection of localized fatigue-induced heating and provides a robust early-warning tool for anchor failure prediction.

4.2 Temperature–Stress–Frequency (TSF) Relation

Experimental results consistently showed that rapid temperature increases preceded fatigue failure, confirming thermodynamic fatigue behaviour reported in literature. The duration and magnitude of this temperature rise depended on the applied stress and loading frequency. Tests were conducted at stress levels between 20 and 87 kN and frequencies between 1 and 10 Hz. For interpretation, frequencies were grouped as low (1 Hz), high (5 Hz), and very high (10 Hz), while stress levels were classified as low (< 42 kN), medium (42–60 kN), and high (> 60 kN).

Fig. 4 presents representative temperature histories from thermal imaging measurements. In all cases, a clear temperature increase was observed shortly before fatigue failure, highlighting the strong relationship between thermal behaviour and anchor degradation. Similar trends were also observed in static testing, indicating that temperature rise can serve as a reliable failure indicator even without cyclic loading. Thermal imaging measures combined temperature fields of the anchor and surrounding environment. By introducing a reference environmental measurement, differential temperature evaluation significantly reduced noise and improved signal clarity. In comparison, thermocouple measurements, although directly attached to the anchor, exhibited higher noise levels, limiting their reliability for automated early-warning detection.

4.3 Differentiation and Smoothing of the Data Set

To improve warning reliability and reduce noise, the derivative of the temperature difference between the anchor and its environment was calculated and smoothed using a multi-step filtering approach. Subtracting environmental temperature from anchor temperature removed common-mode noise, such as ambient fluctuations and sensor drift, isolating the anchor's local thermal response. The resulting difference signal was differentiated to highlight rapid temperature changes associated with fatigue damage. Residual noise was reduced using a 15-point moving average filter applied via convolution, preserving gradual thermal build-up preceding failure.

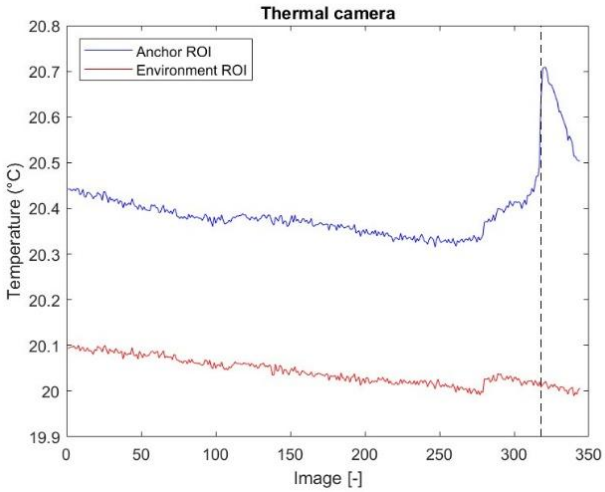


Fig. 4 Mean recorded temperatures in the ROIs using thermal camera for T-61/01/14 for a load frequency of 1 Hz (right).

An empirical threshold was then applied to the smoothed derivative signal to trigger the warning system. Three thresholds (0.005, 0.01, and 0.015) were evaluated. A threshold of 0.005 produced frequent false positives, while 0.015 delayed warnings until near or after failure. The intermediate threshold of 0.01 provided the best balance between early detection and reliability, achieving accurate failure prediction while maintaining practical lead time for intervention.

5 SYSTEM APPLICATION AND PERFORMANCE VALIDATION

5.1 Thermal Camera System

In contrast to the thermocouple setup, the thermal camera system, supported by computer vision and automated processing algorithms, demonstrated high consistency and predictive accuracy in both static and fatigue tests. By analysing the temperature difference between the anchor and its surroundings, the system effectively isolated anchor-specific heat development and reliably triggered warnings prior to failure, with lead times dependent on stress and frequency levels.

Fig. 6 presents representative outputs of the differentiated and smoothed temperature difference used for warning activation. The threshold level ($\Delta = 0.01$) and actual failure points are indicated, alongside thermocouple temperature and deformation data for comparison. Selected thermal images in Fig. 5 confirm localized temperature increases in the anchor region before failure, demonstrating the spatial monitoring capability of the system. Overall, the image-based monitoring approach provided improved spatial resolution and more robust early-warning performance. The results validate the effectiveness of dual-region thermal monitoring and highlight its potential extension to multi-sensor thermocouple systems.

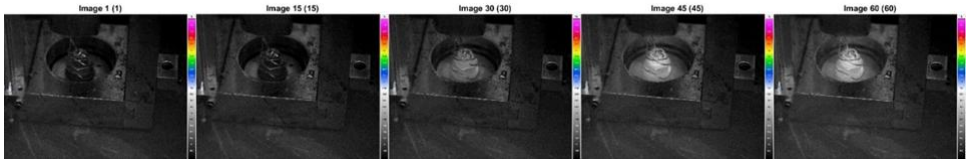


Fig. 5 Extract of thermal camera images with temperature contours for a selected series of fatigue test and failure results, corresponding to T-81/05/19.

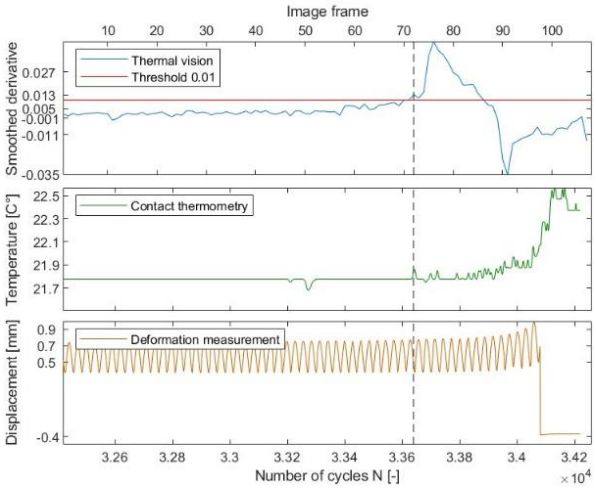


Fig. 6 Trigger sequences using thermal camera image analysis for a selected series of fatigue test and failure results T-48/01/08. The trigger point is highlighted with a dashed line.

5.2 Thermal Signal Amplification

After the validation of the system with the thermal camera, it was decided to investigate methods to amplify the thermal signal. For this, a typical thermal paste, which is commonly used in computers, was considered. This is a special type of paste or gel that is applied between two surfaces to improve heat transfer between them. In the present application, the thermal paste was applied between the anchor and the nut or washer (see Fig. 7). This allows the heat generated by the anchor to be transferred faster and more effectively, thereby improving the accuracy of thermal imaging using a thermal camera.



Fig. 7 ExtracNut with thermal paste (Arctic MX-4)

An additional cyclic test was conducted with the configuration with thermal paste. By using thermal paste, it becomes possible to measure the temperature emitted by a cyclically loaded anchor more precisely and comprehensively. This supports the early detection of fatigue damage that may occur as a result of repeated loading.

A particular advantage is that the combination of thermal paste and thermal imaging enables visualization of the load acting on the anchor. Every frequency applied to the anchor generates an impulse that becomes visible as a temperature difference. Through the application of thermal paste, it is possible not only to determine whether an anchor is under load, but also to identify whether certain anchors are subjected to higher or lower loads compared to others.

Furthermore, the use of a thermal camera in combination with thermal paste makes it possible to identify the exact frequency at which the load occurs. This is particularly important because it allows targeted measures to be taken to optimize load distribution, thereby improving the service life and performance of the overall system.

6 CONCLUSIONS

This study investigated a thermal-based early-warning system for detecting fatigue failure in steel anchors through an experimental programme including fatigue and static loading tests. Two monitoring approaches were evaluated: a single-sensor thermocouple system and a spatial thermal imaging system supported by computer vision and automated data processing.

The thermal camera system, employing a dual-region temperature comparison, provided consistent and accurate early warnings. The monitoring algorithm used differentiation and smoothing techniques with an empirically defined threshold ($\Delta = 0.01$), successfully predicting fatigue failure several seconds to minutes before occurrence, depending on loading conditions.

The results demonstrate the strong potential of continuous thermal monitoring for improving the safety and reliability of fatigue-sensitive fastening systems. Thermal imaging showed high robustness across different loading scenarios.

The application of thermal paste significantly improves heat transfer between the anchor and surrounding components, enabling more accurate thermal imaging for detecting load conditions and early fatigue damage.

Future work should consider the adaptation of the algorithm for simultaneous monitoring of multiple anchors. Integration with wireless communication technologies and data-driven methods, such as adaptive thresholding or machine learning, could further enhance detection reliability and system scalability. Additional research is also required to assess longterm sensor durability, environmental influences, and operational constraints.

Overall, the study confirms the effectiveness of automated thermal monitoring as a non-contact, real-time inspection method for fatigue-critical fastening systems. The implementation of such monitoring technologies supports improved maintenance strategies and contributes to safer and more resilient structural infrastructure.

References

[1] Spyridis, Panagiotis. 2019. “Fastening technology as an interface and integration element of architectural, structural, and building engineering.” In Structures and Architecture – Bridging the Gap and Crossing Borders: Proceedings of the Fourth International Conference on Structures and Architecture (ICSA 2019), edited by Paulo J. S. Cruz, 296–303. CRC Press. doi:10.1201/9781315229126-36.

[2] Epackachi, Siamak, Esmaili, Omid, Mirghaderi, Seyed Rasoul, and Behbahani, Ali Asghar Taheri. 2015. “Behavior of adhesive bonded anchors under tension and shear loads.” Journal of Constructional Steel Research 114:269–280. doi:10.1016/j.jcsr.2015.07.022.

[3] Lazzarin, Paolo, Grün, Jürgen, Mutignani, Francesco, and Ronchi, Roberto. 2010. “Fatigue behaviour of bonded anchors subjected to tensile loads.” Materialwissenschaft und Werkstofftechnik 41(5):372–377. doi:10.1002/mawe.201000611.

[4] Tóth, Máté. 2020. Fatigue behaviour of fasteners: Numerical and experimental investigations on the concrete cone failure mode. PhD diss., Universität Stuttgart, Stuttgart. doi:10.18419/opus-10815.

[5] Peng, Kunhong, Zhang, Yi, Xu, Xian, Han, Jinsong, and Luo, Yaozhi. 2022. “Crack detection of threaded steel rods based on ultrasonic guided waves.” Sensors 22(18):6885. doi:10.3390/s22186885.

[6] Kortmann, Lukas, Höpfner, Marvin, and Spyridis, Panagiotis. 2020. “Die elektrische Widerstandsmessung zur zerstörungsfreien Prüfung von Betonstählen im Beton unter ermüdungsrelevanter Belastung.” Bautechnik 97(10):729–736. doi:10.1002/bate.202000013.

[7] Liaw, Peter K., Wang, Heda, Jiang, Leiwen, Yang, Bing, Huang, Jiunn-Yuan, Kuo, Roang-Ching, and Huang, J. G. 2000. “Thermographic detection of fatigue damage of pressure vessel steels at 1,000 Hz and 20 Hz.” Scripta Materialia 42(4):389–395. doi:10.1016/S1359-6462(99)00358-9.

[8] Gade, Rikke, and Moeslund, Thomas B. 2014. “Thermal cameras and applications: A survey.” Machine Vision and Applications 25(1):245–262. doi:10.1007/s00138-013-0570-5.

[9] Liu, Li, Ouyang, Wanli, Wang, Xiaogang, Fieguth, Paul, Chen, Jie, Liu, Xinwang, and Pietikäinen, Matti. 2020. “Deep learning for generic object detection: A survey.” International Journal of Computer Vision 128(2):261–318. doi:10.1007/s11263-019-01247-4.

[10] Bentley, John P. 1984. “Temperature sensor characteristics and measurement system design.” Journal of Physics E: Scientific Instruments 17(6):430. doi:10.1088/0022-3735/17/6/002.

[11] Hakimi, Obaidullah, Liu, Hexu, Abudayyeh, Osama, Houshyar, Azim, Almatared, Manea, and Alhawiti, Ali. 2023. “Data fusion for smart civil infrastructure management: A conceptual digital twin framework.” Buildings 13(11):2725. doi:10.3390/buildings13112725.

[12] Mardanshahi, Ali, Sreekumar, Abhilash, Yang, Xin, Barman, Swarup Kumar, and Chronopoulos, Dimitrios. 2025. “Sensing techniques for structural health monitoring: A state-of-the-art review on performance criteria and new-generation technologies.” Sensors 25(5):1424. doi:10.3390/s25051424.

[13] Schaefer, Florian, Rosar, Jan, Wu, Haoran, Starke, Peter, and Marx, Michael. 2022. “Obtaining a lower estimate of the fatigue limit of metals by a simplified quantitative thermometric approach in a low-cost one-specimen test.” International Journal of Fatigue 159:106729. doi:10.1016/j.ijfatigue.2022.106729.

[14] Mellios, Nikolaos, Ahmad, Mohamad, Rousakis, Theodoros, and Spyridis, Panagiotis. 2025. “Smart sensing and automated fatigue warning in concrete anchorages using thermocouples and thermal imaging.” Developments in the Built Environment 24:100778. doi:10.1016/j.dibe.2025.100778.

[15] European Organisation for Technical Assessment (EOTA). n.d. EAD 330250-00-0601. Brussels: EOTA.

[16] Höpfner, Marvin, and Spyridis, Panagiotis. 2018. “Early damage detection of fastening systems in concrete under dynamic loading: Model details and health monitoring framework.” In Life-Cycle Analysis and Assessment in Civil Engineering: Towards an Integrated Vision – Proceedings of the 6th International Symposium on Life-Cycle Civil Engineering (IALCCE 2018), edited by Dan M. Frangopol, Robby Caspeele, and Luc Taerwe, 1857–1864. CRC Press/Balkema. doi:10.1201/9781315228914.

[17] Kessler, Sylvia, Mellios, Nikolaos, Takriti, Ahmad, and Spyridis, Panagiotis. 2023. “Redundancy of concrete fastenings under combined fatigue and corrosion: A probabilistic study on catenary system installations.” In Life-Cycle of Structures and Infrastructure Systems, edited by Fabio Biondini and Dan M. Frangopol, 2967–2974. CRC Press. doi:10.1201/9781003323020-361.

Reliability Assessment of Structural Health Monitoring using Model-Assisted Probability of Detection

Yogi Jaelani, Jan Grashorn, Francesca Marsili, Sylvia Keßler

Chair of Engineering Materials and Building Preservation,
Faculty for Mechanical and Civil Engineering,
Helmut Schmidt University/University of the Federal Armed Forces Hamburg,
Holstenhofweg 85, 22043 Hamburg, Germany

Summary
This study evaluates the reliability assessment of Structural Health Monitoring (SHM) system using temperature-dependent Model Assisted Probability of Detection (MAPOD) based on calibrated finite element (FE) models. Bayesian inverse methods are used for FE model calibration, and generalized Polynomial Chaos Expansion (gPCE) surrogate models are applied to reduce computational cost. The approach is demonstrated through large-scale field tests with multiple sensing modalities and damage-sensitive features, thereby capturing practical complexity and variability. The results indicate that temperature-dependet MAPOD offers a feasible and rigorous pathway for assessing SHM system reliability under realistic environment conditions. They highlight both the strengths and current limitations of the approach, including sensitivity to modeling assumptions and feature selection. More importantly, the findings underscore the potential of combining physics-based modeling, probabilistic frameworks, and surrogate techniques to establish a reliable foundation for quantitative reliability assessment of SHM system.

1 INTRODUCTION

Structural Health Monitoring (SHM) is important for assessing the condition and integrity of civil infrastructure through continuous or periodic data acquisition. By deploying sensor networks, SHM systems enable the detection and localization of damage and/or changes in the structural response, thereby supporting maintenance strategies and potentially extending service life. SHM damage identification approaches are commonly classified into physics-based methods, which utilize numerical models e.g., finite element (FE) models, and data-driven methods, which are based on statistical inference, and machine learning techniques [1].

A key limitation in SHM is the lack of availability of damaged-state data, which complicates the validation and quantitative performance assessment. In contrast, Non-Destructive Testing (NDT) techniques benefit from well-established reliability assessment procedures, such as Probability of Detection (POD) [2]–[4]. For SHM, however, standardized framework for quantifying system reliability is still under development.

To address this gap, the present study proposes a reliability assessment framework for SHM based on Probability of Detection (POD) and Model-Assisted POD (MAPOD). The framework is enhanced through simulated data generated from calibrated finite element (FE) models. MAPOD has been successfully investigated in several NDT-related studies [5]–[7].

In vibration-based SHM, the application of MAPOD is particularly challenging under real operational conditions, since modal parameters are strongly influenced by environmental effects such as temperature, which may mask damage-induced changes. This study proposes a MAPOD-based reliability assessment framework for vibration-based SHM, supported by Bayesian FE model calibration and uncertainty quantification. Furthermore, to reduce the computational burden associated with high-fidelity simulations, generalized Polynomial Chaos Expansion (gPCE) surrogate models are employed. Two stochastic inverse approaches are employed in this study: Markov Chain Monte Carlo (MCMC) sampling and a Polynomial Chaos Expansion-based Kalman Filter (PCE-KF). Both methods are successfully validated through a laboratory-scale experiment on a four-degree-of-freedom (4-DOF) wooden frame, using vibration-based measurements under controlled and constant room environment condition. The measurements included both reference (undamaged) and changed (damaged) states, with controlled mass variations [8].

In the present study, the framework is extended to full-scale field test data from the Test Bridge at the University of the Bundeswehr Munich [9]. Temperature-dependent calibration is performed by

subdividing the reference dataset into discrete temperature intervals, enabling the derivation of temperature-dependent MAPOD curves for a concentrated mass-addition scenario. The results quantify the influence of temperature on detectability and confirm the applicability of MAPOD under realistic environmental variability.

2 METHODOLODY

The overall workflow proposed for the temperature dependent MAPOD construction is illustrated in Figure 1.

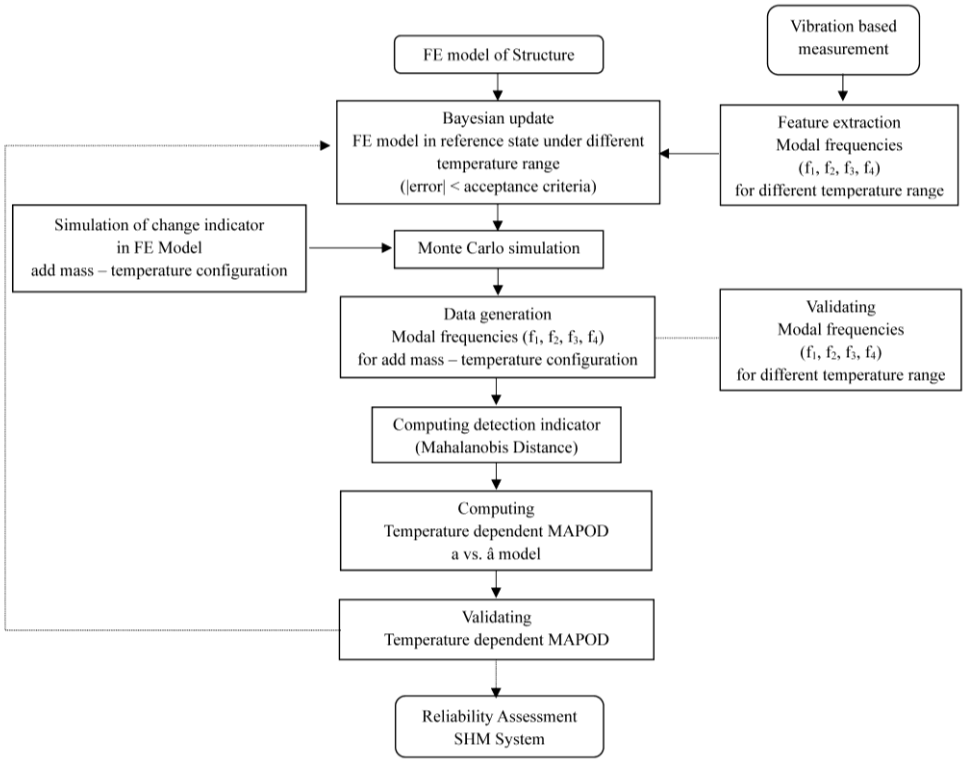


Fig. 1 Temperature dependent MAPOD model building process.

2.1 Bridge Description

The test bridge at the University of the Bundeswehr Munich was constructed in 2007 and is a steel-concrete composite structure with a span of 30 m and a width of 4 m. It consists of two primary steel girders (HEB1000), seven transverse braces along the span (HEB120), and two additional transverse braces at both abutments (HEB240). The concrete deck is segmented into 11 elements of varying length (1.4–3.0 m), 4m wide and 0.2 m of thickness, with gaps filled by partially cracked cement paste. The concrete has a compressive strength of C30/37, and the steel material is grade S235. The composite action is achieved through bolted connections between the steel girders and the inverted T-shaped steel beams embedded in the lower part of the concrete segments, with bolts spaced at 50 cm intervals.

For the measurement campaign, the bridge is configured as a two-span sturcture by installing a temporary mid support.

2.2 Measurement system and Measurement Campaign

The bridge is instrumented with accelerometers, strain gauges, inclinometers, load cells and a weather station. Accelerometers are installed along the beam centerline and beneath the steel girder flanges to capture vertical and transverse vibrations. Inclinometers are placed on the main girders and transverse braces to measure rotational responses. Strain gauges are located at expected maximum stress points,

including the top flanges over middle supports and at midspan. Load cells are installed at the middle support to measure reaction forces. A schematic of the sensor placement is provided in Figure 2.

Dynamic excitation is induced by a shaker with a total weight of 140 kg, which generated vertical white noise vibration over a frequency bandwidth between 2 Hz -100 Hz with a maximum acceleration of 1.5 m/s². The shaker is placed in the midspan region between axes 2 and 3, directly above the primary girder A (see Fig. 1). The measurements are conducted under both reference (undamaged) and changed (damaged) conditions. Detail information on the measurement campaign can be found in [9].

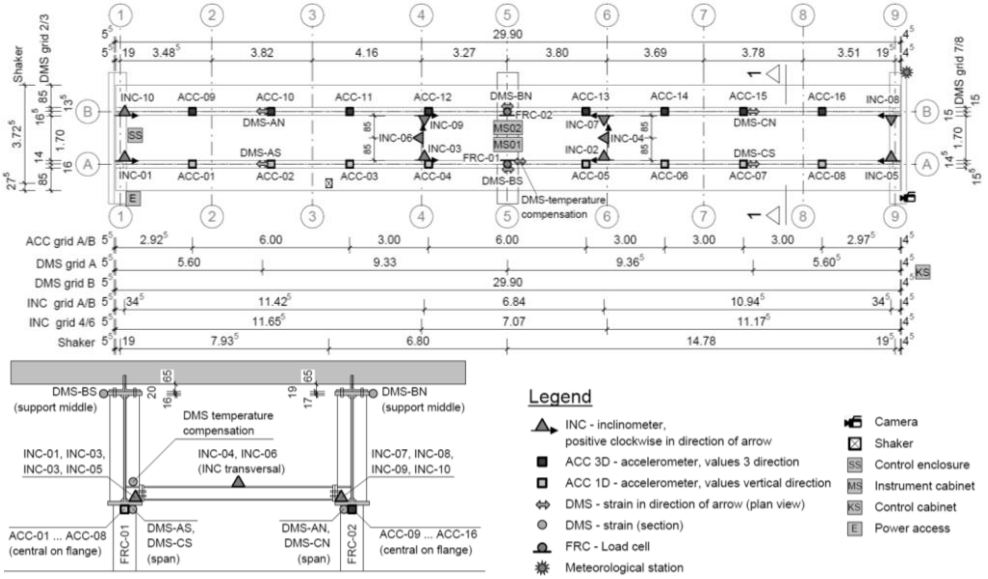


Fig. 2 Instrumentation plan of the test bridge at the University of Bundeswehr Munich

2.3 Finite element model

A three-dimensional finite element (FE) model of the bridge is developed in ANSYS to simulate its modal dynamic behaviour. The model geometry reflects the actual physical structure, shell elements are used to represent the thin structural components and supports were modeled as pinned–rolled to replicate boundary conditions. Material properties were initially assigned based on typical engineering values for steel and concrete and cross-checked with design documentation. The elastic moduli of steel and concrete were treated as uncertain parameters for Bayesian updating.

2.4 Bayesian model updating framework

The FE models are calibrated using Bayesian model updating, where uncertain parameters (elastic modulus of steel and concrete) are treated as random variables. The objective of Bayesian updating is to estimate the posterior distribution $p(\theta|\mathcal{D})$ of the parameter vector θ in the FE-model based on responses $\mathcal{D}$ from measurements, according to Bayes' theorem:

$$p(\theta|\mathcal{D}) = \frac{p(D|\theta) \cdot p(\theta)}{p(\mathcal{D})} \tag{1}$$

where $p(\theta)$ denots the prior distribution, $p(D|\theta)$ the likelihood function, and $p(\mathcal{D})$ is the evidence. The likelihood function is often assumed to follow a Gaussian distribution expressed as :

$$p(D|\theta) = \frac{1}{\sqrt{2\pi\sigma_{\mathcal{D}}^2}} \exp\left[-0.5\left(\mathcal{D} - \mathcal{M}(\theta)\right)^2 \bar{\sigma_{\mathcal{D}}}^2\right] \tag{2}$$

where $\sigma_{\mathcal{D}}$ represents the standard deviation of the error and $\mathcal{M}(\theta)$ is the corresponding model prediction.

2.5 Surrogate model using gPCE

To reduce the computational costs associated with repeated FE simulations during Bayesian model updating, a generalized Polynomial Chaos Expansion (gPCE) is employed to construct a surrogate model. The gPCE framework approximates the model response by expanding it in a polynomial basis that is selected according to the probability distributions of the input parameters. The gPCE approach approximates the model output of interest $\hat{Y}$, such as natural frequencies and is formulated as:

$$\hat{Y} = \mathcal{M}^{\mathcal{PCE}}(\theta) = \sum_{\alpha} a_\alpha \, \Psi(\theta) \tag{3}$$

The coefficients a_α are found by least-squares optimization using a set of training points $(\hat{Y}, \hat{\theta})$ and $\Psi(\theta)$ is the orthogonal polynomial basis function. For more detail of gPCE refer to Rosic et al. (2012) and Rosic et al. (2013).

2.6 POD estimation and reliability metrics

The *a vs. â* model POD model is widely used in NDT to evaluate a system's detection capability using continuous damage indicators. Here, a represents the actual damage size or severity, while $\hat{a}$ denotes the measured response or damage-sensitive indicator estimated from the monitoring system. Unlike classical hit/miss POD methods based on binary outcomes, the *a vs. â* approach uses continuous response data, enabling a more detailed assessment of detection performance. In vibration-based monitoring, $\hat{a}$ is typically derived from changes in modal properties such as natural frequencies or mode shapes.

When multiple response features are available, it is necessary to consolidate them into a representative scalar indicator. In this study, the local Mahalanobis distance (LMD) is used as the fault indicator. The Mahalanobis distance accounts for correlations between variables and measures the statistically normalized distance of an observation from a reference distribution. For an observation vector x_i (e.g., the measured eigenfrequencies of a structure at a specific condition), and a reference data set with mean μ and covariance matrix Σ, the Mahalanobis distance $D_M(x_i)$ at a specific condition is defined as:

$$D_M(x_i) = \sqrt{(x_i - \mu)^T \, \Sigma^{-1} \, (x_i - \mu)} \tag{4}$$

In its localized form, LMD is computed using a subset of the reference data (e.g., via a k-nearest neighbour approach), making it more sensitive to local variations and non-Gaussian distributions in the feature space. This localized metric effectively distinguishes between baseline and anomalous structural states and is widely used in data-driven fault detection frameworks [1].

If the covariance matrix Σ is highly correlated or nearly singular, the Mahalanobis distance may become unstable due to numerical issues in the matrix inversion. To mitigate this, covariance regularization is applied using the Ledoit–Wolf shrinkage estimator [12]. The regularized covariance matrix Σ_{LW} is defined as:

$$\Sigma_{LW} = (1 - \alpha)\Sigma + \alpha I \tag{5}$$

where α is the shrinkage intensity and I is the identity matrix. This approach stabilizes the inverse covariance matrix and improves the robustness of the distance metric. The corresponding regularized Mahalanobis distance is computed as:

$$D_M(x_i) = \sqrt{(x_i - \mu)^T \, \Sigma_{LW}^{-1} \, (x_i - \mu)} \tag{6}$$

To determine the decision threshold, the confidence interval approach based on the assumption of normally distributed data can be applied. The threshold is calculated as follow:

$$T = \mu_{D_M} + Z \cdot \sigma_{D_M} \tag{7}$$

where μ_{D_M} and σ_{D_M} is the mean value and standard deviation of the Mahalanobis distance at reference state. Z is a z-score corresponding to the desired confidence level. This formulation allows the threshold to reflect the probabilistic boundary beyond which a decision can be made with a specified level of confidence. For instance, at a 95% confidence level in a one-tailed test, the z-score is approximately 1.645, yielding a threshold that captures the upper 5% of the false alarm.

The POD for a damage size a is then calculated as:

$$POD(a) = 1 - \Phi\left(\frac{T - \mu(a)}{\sigma(a)}\right) \tag{8}$$

where $\Phi(\cdot)$ is the standard normal CDF, and $\mu(a)$ and $\sigma(a)$ denote the mean and standard deviation of the damage size a. The POD curve provides performance metrics such as:

- a_{90} is the flaw size corresponding to 90% detection probability.
- $a_{90/95}$ is the flaw size with 90% POD at 95% confidence (derived from confidence bounds).

Confidence intervals can be computed using either statistical bootstrapping technique or model-based variance propagation [13,14]. These metrics enable a quantitative assessment and comparison of the detection performance of the SHM system. Using the same methodology, POD results are also derived from synthetic data generated with the calibrated FE model.

3 ANALYSIS

The analysis is conducted in three stages:

- Reference state vibration analysis:

  Modal parameters were identified from 18 days of vibration measurements using Operational Modal Analysis (OMA). Four modes are tracked, and mode similarity is verified using MAC greater than 0.8. The results reveal clear temperature-dependent frequency shifts.

- Temperature-dependent model updating:

  Since the identified modal frequencies showed a clear temperature dependency, the reference data are grouped into temperature intervals from −5 °C to +19 °C with a 2 °C interval size. Separate Bayesian model updating is performed for each interval, resulting in 13 temperature-dependent FE models

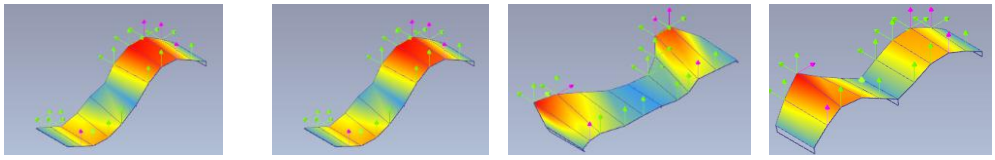
- Temperature-dependent MAPOD reliability assessment:

  For each updated FE model, structural changes are simulated by introducing concentrated masses from 200 kg to 1200 kg in 200 kg increments. The masses are applied at the bridge midspan near the deck edge above longitudinal girder A (Fig. 2). Posterior parameter samples are then used to generate modal frequency ensembles, with at least 100 simulations per temperature–mass configuration. Mahalanobis distance-based indicators are computed and used to construct the temperature-dependent MAPOD curves.

3.1 Reference state vibration analysis

The reference-state vibration data, acquired over 18 continuous days under ambient conditions and shaker excitation, are analyzed using Operational Modal Analysis (OMA). By using Artemis Modal Pro 7.2 Software the OMA is performed and allows for extraction of modal parameters such as natural frequencies, damping ratios, and mode shapes.

Four dominant modes of the bridge are identified, corresponding to the primary translational and torsional behaviors of the structure (Figure 3). Mode tracking across all datasets is performed using the Modal Assurance Criterion (MAC)**,** with a threshold of 0.8 to ensure consistent mode matching (Figure 4a). The development of the tracked resonance frequencies over time revealed a clear correlation with temperature, indicating environmental sensitivity of the bridge's dynamic response (Figure 4b). These reference-state modal parameters served as baseline data for the subsequent Bayesian model updating of the FE models.



Mode 1 Mode 2 Mode 3 Mode 4

Fig. 3 Identified mode shapes of the bridge in its reference state.

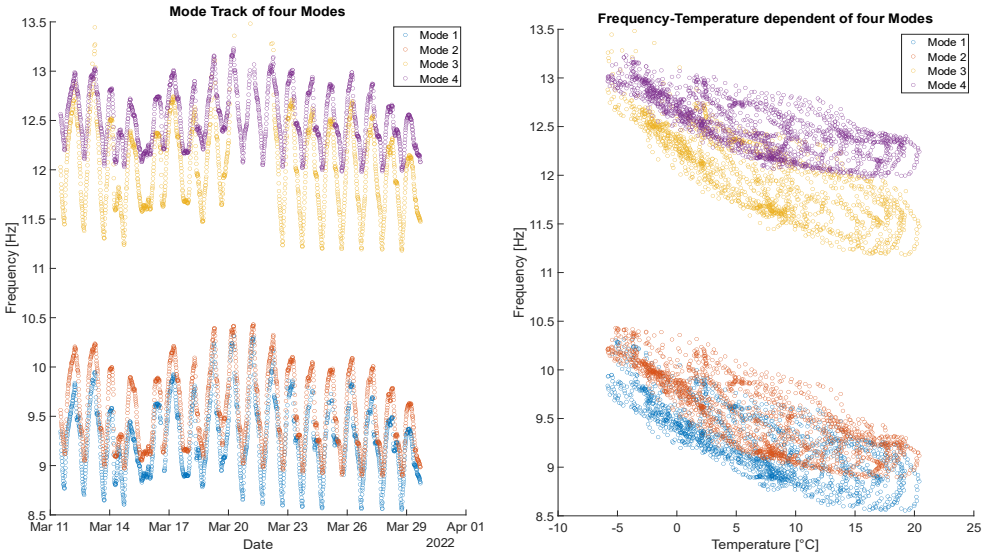


Fig. 4 Tracked frequency development (MAC > 80%) for the reference state

3.2 Temperature-Dependent Model Updating

FE model of the bridge is developed in ANSYS Mechanical. In this study, two key parameters are considered: the elastic modulus of the steel and elastic modulus of concrete. The prior distributions of the uncertain FE model parameters are defined by their mean (μ) and standard deviation (σ), reflecting initial assumptions and associated uncertainty. Posterior distributions are then obtained through Bayesian updating using the generalized Polynomial Chaos Expansion-based Kalman Filter (gPCE-KF) and Markov Chain Monte Carlo (MCMC) [11], [12]. These approaches incorporate measurement uncertainty and enable efficient exploration of the parameter space. Figure 6 illustrates the resulting posterior distributions. The updated results show a clear reduction in standard deviation, indicating reduced uncertainty and successful model calibration.

After updating, the posterior mean elastic modulus of steel varies between 164 GPa and 184 GPa across temperature intervals, while the elastic modulus of concrete ranges from 27 GPa to 43 GPa. These values are lower than typical nominal material properties for structural steel and concrete within the considered temperature range (-5°C to 19°C). However, they should not be interpreted as true physical material constants. Instead, they represent effective (virtual) parameters that compensate for unmodelled temperature-dependent effects, enabling the FE model to accurately reproduce the observed modal behaviour under varying environmental conditions. Despite this interpretation, the calibrated FE model achieved high accuracy, with a maximum absolute relative error of 1.9% across all temperature intervals.

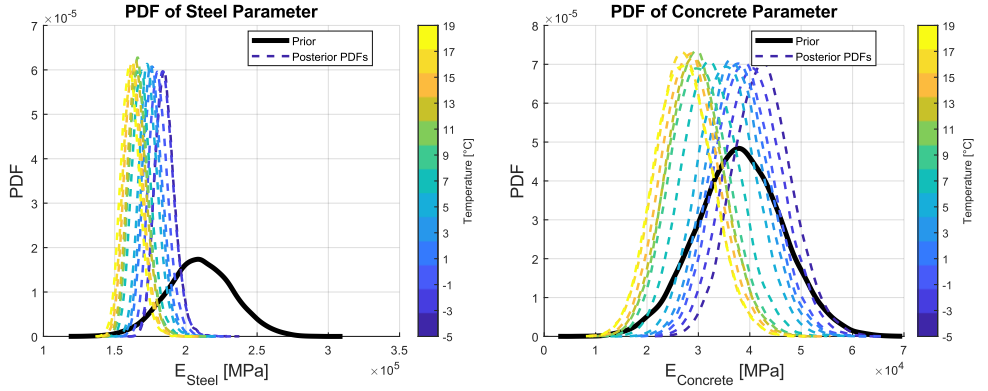


Fig. 5 Prior and posterior PDFs of the model parameters

3.3 Temperature-dependent reliability assessment MAPOD

Following model calibration, temperature-dependent MAPOD analyses are performed using the updated FE models. For each calibrated temperature-dependent FE model, structural changes are simulated by introducing concentrated masses from 200 kg to 1200 kg in 200 kg increments. Posterior parameter samples were combined with these mass levels to generate modal frequency ensembles for each temperature–mass configuration, with at least 100 simulations conducted per case to account for uncertainty propagation.

For each simulation, the Mahalanobis distance based on modes 1–4 was computed to quantify deviations from the undamaged reference state and to construct the MAPOD curves. The analyses showed that lower-order modes were generally more sensitive to added mass, while higher-order modes exhibited reduced sensitivity, consistent with expected structural dynamic behavior [15]. The resulting temperature-dependent MAPOD analysis revealed a clear improvement in detection sensitivity with increasing temperature. The $a_{90/95}$value decreased from 1064 kg at -5 °C to 752 kg at 19°C (Figure 6), indicating that smaller structural changes could be detected at higher temperatures.

The simulation-based MAPOD results demonstrate that the updated temperature-dependent FE models provide a consistent and robust framework for predicting detection performance under varying environmental conditions.

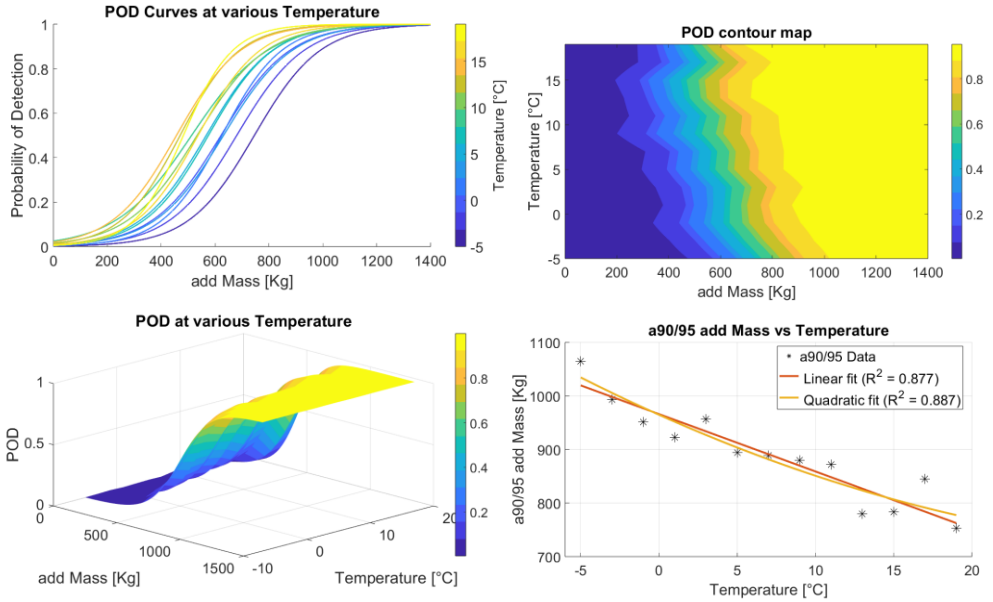


Fig. 6 Temperature-dependent MAPOD

4 CONCLUSIONS AND OUTLOOK

This study presents a framework for evaluating the reliability of SHM systems using MAPOD approaches under variying temperature conditions. A full-scale composite bridge at the university of the Bundeswehr Munich is used as the case study. The vibration data from the reference state are used to calibarate temperature dependent FE-Models through Bayesian model updating. The calibrated FE-Model served as the basis for Monte Carlo simulations under different mass scenarios, enabling the construction of temperature-dependend MAPOD curves.

The comparison between OMA results and calibrated FE-model predictions shows strong agreement, with relative deviations below 2%. The temperature-dependent MAPOD results at -5°C and 19°C reveal a clear influence of temperature on detectability, with $a_{90/95}$values decreasing as temperature increases, indicating improved detection performance at higher temperatures. Overall, the simulation-based MAPOD framework provides a consistent and efficient approach for predicting SHM detection capability under uncertainty, while significantly reducing the need for extensive physical testing.

Future work should extend the framework to more complex damage scenarios, incorporate additional SHM sensing techniques and increase the number of response features; beyond the four considered in this study, including potential fusion of vibration-based and static measurement. Furthermore, integrating historical temperature variations could also enable the analysis of thermal cycling effects over time. Finally, validation on additional full-scale structures will be essential for broader practical implementation in SHM applications.

Acknowledgements

This research is funded by dtec.bw - Digitalization and Technology Research Center of the Bundeswehr. dtec.bw is funded by the European Union - NextGenerationEU. We thank all DTEC Project supporters.

References

[1] Farrar, Charles. R., and Worden, Keith. 2012. *Structural Health Monitoring: A Machine Learning Perspective*. Chichester, UK: Wiley.

[2] U.S. Department of Defense. 2009. *Nondestructive Evaluation System Reliability Assessment, MIL-HDBK-1823A*.

[3] Deng, Yiming, Liu, Xin, and Udpa, Lalita. 2012. "Magneto-Optic Imaging for Aircraft Skins Inspection: A Probability of Detection Study of Simulated and Experimental Image Data." *IEEE Transactions on Reliability* 61(4):901–908. doi:10.1109/TR.2012.2221613.

[4] Berens, Alan P. 1989. "NDE Reliability Data Analysis." *ASM Handbook,* Vol. 17, 689–701.

[5] Knopp, Jerremy S., Aldrin, John C., Lindgren, Eric A., and Annis, Charles. 2007. "Investigation of a Model-Assisted Approach to Probability of Detection Evaluation." *AIP Conference Proceedings* 894:1775–1782. doi:10.1063/1.2718178.

[6] Smith, Kevin, Thompson, Bruce, Meeker, Bill, Gray, Tim, and Brasche, Larry. 2007. "Model-Assisted Probability of Detection Validation for Immersion Ultrasonic Application." *AIP Conference Proceedings* 894:1816–1822. doi:10.1063/1.2718184.

[7] Calmon, Pierre., Mesnil, Olivier, Miorelli, Roberto, Artusi, Xavier, Chapuis, Bastien, and d'Almeida, Oscar. 2019. "Model Assisted Probability of Detection for Guided Wave Imaging Structural Health Monitoring." *Proceedings of SHM* 2019. doi:10.12783/shm2019/32190.

[8] Jaelani, Yogi, Marsili, Francesca, Grashorn, Jan, Knoth, Sven, and Keßler, Sylvia. 2025. "Reliability Assessment of Structural Health Monitoring Systems Using Model-Assisted Probability of Detection and Bayesian Model Updating." Paper presented at the 13th International Conference on Structural Health Monitoring of Intelligent Infrastructure (SHMII-13), Graz, Austria, September 01–05.

[9] Jaelani, Yogi, Klemm, Alina, Wimmer, Johannes, Seitz, Fabian, Köhncke, Martin, Marsili, Francesa, Mendler, Alexander, von Danwitz, Max, Henke, Sasca, Gündel, Max, Braml, Thomas, Spannaus, Max, Popp, Alexander, and Keßler, Sylvia. 2023. "Developing a Benchmark Study for Bridge Monitoring." *Steel Construction* 16. doi:10.1002/stco.202200037.

[10] Rosić, Bojana V., Litvinenko, Alexander, Pajonk, Oliver, and Matthies, Hermann G. 2012. "Sampling-Free Linear Bayesian Update of Polynomial Chaos Representations." *Journal of Computational Physics* 231(17).

[11] Rosić, Bojana V., Kučerová, Anna, Sýkora, Jan, Pajonk, Oliver, Litvinenko, Alexander, and Matthies, Hermann G. 2013. "Parameter Identification in a Probabilistic Setting." *Engineering Structures* 50.

[12] Ledoit, Olivier, and Wolf, Michael. 2004. "A Well-Conditioned Estimator for Large-Dimensional Covariance Matrices." *Journal of Multivariate Analysis* 88(2):365–411. doi:10.1016/S0047-259X(03)00096-4.

[13] Efron, Bradley. 1979. "Bootstrap Methods: Another Look at the Jackknife." *The Annals of Statistics* 7(1):1–26. doi:10.1214/aos/1176344552.

[14] Wehling, Paul, LaBudde, Robert A., Brunelle, Sharon L., and Nelson, Maria T. 2011. "Probability of Detection (POD) as a Statistical Model for the Validation of Qualitative Methods." *Journal of AOAC International* 94(1):335–347.

[15] Chopra, Anil. K. 2012. *Dynamics of Structures: Theory and Applications to Earthquake Engineering*. 4th ed. Upper Saddle River, NJ: Pearson.

Integrated Experimental–Numerical Study on Prestressed Concrete Girders for Structural Health Monitoring

Amir Shamsaddinlou[1], Dario De Domenico[1], Antonino Recupero[1], Mohammad Rezaie Oshtolagh[1], Natale Maugeri[1], Paolo Longo[1], Dario La Mazza[2], Monica Longo[2], Giuseppe Mancini[2]

[1]Department of Engineering, University of Messina
Contrada Di Dio, Villaggio S. Agata, 98166 Messina (ME), Italy
[2]Sacertis Ingegneria s.r.l.
C.so M. D'Azeglio 118, 10126 Turin, Italy

Summary

This study combines full-scale testing with nonlinear FE modelling to develop SHM indicators for prestressed concrete bridge girders. Twelve 8 m beams (with bonded and unbonded tendons) were tested with a transverse diaphragm and a distributed dead load to simulate girder interaction. Progressive damage was introduced by staged strand cutting at the L/4, L/3, and L/2 spans. MEMS inclinometers provided direct tilt (rotation) profiles during loading and unloading. Damage localisation is inferred from the migration of the zero-tilt crossing and the concentration of rotation gradients near the damaged section. MEMS/piezoelectric accelerometers were used for operational modal analysis to track frequency and mode-shape trends. A 3D ATENA nonlinear model reproduced the test sequence and supported the interpretation of damage effects. Results show that tilt-based signatures are highly sensitive to damage location and severity, while frequency shifts under service loads remain modest.

1 INTRODUCTION

Many prestressed concrete bridges built in the mid-20th century are now ageing and exhibiting deterioration of their structural components [1], [2]. In particular, corrosion-induced damage to internal prestressing tendons is a critical concern because it remains hidden until advanced stages and can significantly reduce effective prestress, stiffness, and load-bearing capacity [3]. Ensuring the safety and serviceability of such structures has become an important challenge for infrastructure management. Structural health monitoring (SHM) offers a promising approach to detect and assess damage in prestressed concrete (PC) girders by linking measured structural responses to damage indicators. Traditionally, two complementary SHM approaches have been adopted: (i) dynamic (vibration-based) methods [4], especially Operational Modal Analysis (OMA), to track changes in global modal properties (frequencies, mode shapes, damping) that may indicate damage; and (ii) static or quasi-static measurements of displacements, rotations, and crack openings that directly reflect stiffness and capacity changes [5]. However, monitoring prestressed members presents unique difficulties. Changes in natural frequency due to moderate prestress loss are typically very small and often undetectable until severe cracking or failure occurs. On the other hand, static deflection or rotation metrics can capture localised stiffness reductions but require dense sensor information and careful interpretation.

Motivated by the need for more effective monitoring strategies, this paper presents a concise experimental–numerical study of 12 full-scale prestressed beams tested under controlled, progressive tendon-cut scenarios, coupled with FE modelling, aimed at gaining deeper insight into the measurable signs of damage in these structures [6]. The ultimate goal is to leverage both dynamic identification and static deformation monitoring to enhance damage-detection capabilities for prestressed concrete bridges. The following sections present the tools and methods used, detail the experimental programme, discuss key findings from static and dynamic tests, and present the numerical simulations used to interpret the results and plan for future SHM applications.

2 EXPERIMENTAL PROGRAMME

2.1 Specimens and damage scenarios

The campaign includes twelve 8.0 m beams (7.0 m clear span) with rectangular 300 × 250 mm cross-section, with precast inspection windows for access to the bottom strands depicted in Fig. 1. The beams

were reinforced with six straight 0.5″ seven-wire strands (five at the soffit, one near the top), and ordinary reinforcement included steel longitudinal rebars (4 ø10 at the corners) and stirrups (ø8/30 cm). The adopted concrete class was C50/60 (characteristic cubic strength of 60 MPa), and strands were released approximately 16 hours after casting, when the concrete reached about 35 MPa in compression.

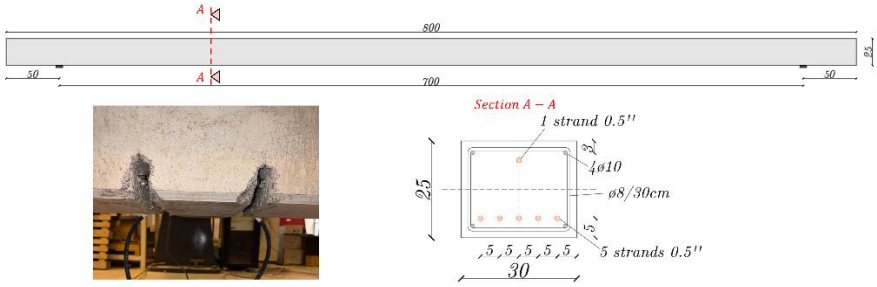


Fig. 1 Specimen geometry and construction details: beam cross-section, reinforcement/prestressing layout, and the precast inspection windows

Nine beams were produced with bonded tendons, and three with unbonded tendons, placed in ducts along the clear span. Damage was simulated by cutting strands through pre-cast inspection windows located at prescribed positions along the span, allowing staged interventions at L/4, L/3, and L/2 (L = clear span). Among the bonded specimens, three beams featured inspection windows at mid-span (L/2), while the remaining six were divided equally, with windows located at L/3 and L/4 along the clear span. All specimens were produced within the same casting campaign within a casting slot of 100 m using steel formworks and pretensioned strands, shown in Fig. 2.



Fig. 2 Photograph of the prestressing plant for manufacturing the pretensioned PC beams

2.2 Load-sharing simulation, instrumentation, and measurements

To reproduce the load-sharing mechanism typical of girder systems, a transverse steel diaphragm was installed at mid-span during the service-level protocol. During service tests, the transverse IPE80 is present; therefore, the live load is capped to prevent yielding in the diaphragm. The diaphragm yielding moment is estimated as $M_y = f_{yk}\, W_k$ with $f_{yk} = 275$ MPa (S275 steel) and $W_k = 20{,}000\, mm^3$, giving $M_y \approx 5.5$ kN·m, which corresponds to an estimated yielding load of about 20 kN. Applying a safety factor, the elastic threshold load is set to $F_{\text{lim}} = 17.5$ kN, which is therefore not exceeded in service conditions. The service jack load was 15 kN, corresponding to 15% of the design ULS load of 100 kN; including the actuator self-weight, the total effective service load was 17.5 kN, corresponding to 17.5%. Distributed steel blocks were placed along the span to represent superimposed dead load of a concrete deck self-weight and achieve a realistic dead-to-live action ratio (50:50) under laboratory conditions illustrated in Fig. 3. The welded steel blocks were distributed uniformly along the span, providing an additional load of approximately 3.3 kN/m. Each block consisted of eight plates, each 5 cm thick, 40 cm wide and 12 cm high, with 2 cm anti-slip teeth on both sides.



Fig. 3 Schematic and test setup of the prestressed-concrete beam with a transverse IPE80 diaphragm and steel-block system, ensuring a 50:50 dead-to-live load ratio

Each specimen was instrumented with MEMS inclinometers for direct tilt measurement along the span and for damage localisation from tilt profile signatures; MEMS and piezoelectric accelerometers for vibration response and OMA; and displacement transducers (laser/LVDT) to quantify global vertical response and track service/ultimate behaviour. Fig. 4 shows the complete test setup, while Table 1 lists the number and positions of the sensors.

Table 1 Sensor arrangement in the final laboratory test configuration

Sensor type	Quantity	Positions from mid-span (m)
MEMS (3D accelerometers + 2D inclinometers)	8	$\pm 0.25, \pm 1, \pm 1.75, \pm 2.75$
PCB piezoelectric sensors (1D accelerometers)	8	$\pm 0.25, \pm 1, \pm 1.75, \pm 2.75$
Laser sensors (deflection and rotation)	4	$\pm 1.1, \pm 2.1$
LVDT (mid-span deflection)	1	0

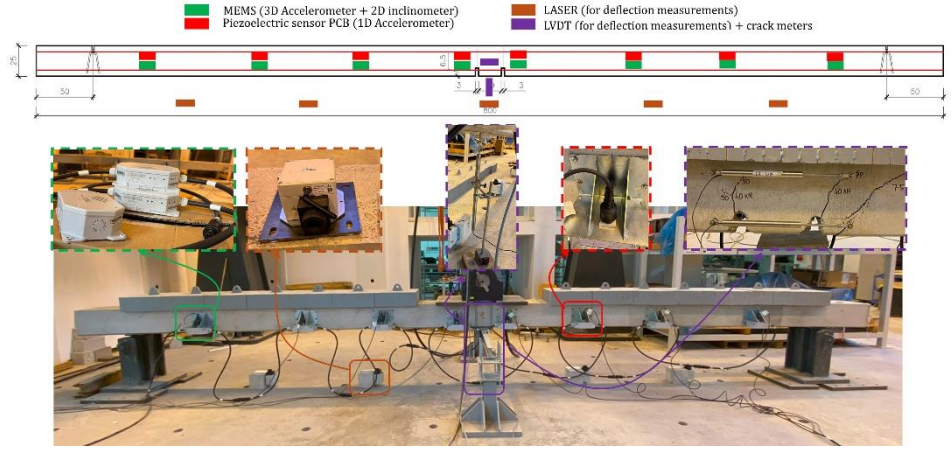


Fig. 4 Full-scale test setup and instrumentation: transverse diaphragm for load sharing, dead-load blocks, actuator, and sensor layout (MEMS inclinometers, accelerometers, and displacement transducers)

2.3 Loading protocol and damage sequence

In the experimental protocol for the serviceability limit state (SLS), each specimen was subjected to a three-point bending loading-unloading cycle up to 17.5 kN, returning to 0 kN. After each tendon cut, the same 0-17.5-0 kN cycle was repeated to quantify the incremental stiffness loss; immediately after unloading, vibration data were acquired for OMA identification. The experimental programme involved two primary damage levels: Scenario 1, consisting of four progressive tendon cuts, and Scenario 2, which extended the damage to six cuts. In Scenario 1, Cut 1 severed the first bottom strand through the

left inspection window (farther from mid-span), while Cut 2 severed the same strand through the right window. This alternating left-right sequence was repeated for a second strand during Cuts 3 and 4. For Scenario 2, the procedure followed the same pattern but was extended to a third strand, encompassing Cuts 5 and 6. At the ultimate limit state (ULS), after completing the SLS damage sequence, the transverse diaphragm was removed, and the beam was loaded to failure according to the ultimate loading. For the beams with a 2-tendon-damaged scenario, cycles of 27.5, 52.5, 77.5, 102.5 kN, and for the beams with a 3-tendon-damaged scenario, cycles of 17.5, 32.5, 47.5, 62.5 kN were applied up to failure. The terminology and interpretation of serviceability and ultimate conditions follow the Eurocode limit-state framework (EN 1990) and concrete design provisions (EN 1992-1-1) [7], [8].

3 STATIC–DYNAMIC PROCESSING AND MODALYZER (OMA)

3.1 Tilt rotation measurements and indicators

The MEMS inclinometers provide direct tilt (rotation) measurements at discrete positions along the span during loading and unloading. In this paper, damage assessment is primarily based on measured tilts. Displacement transducers (laser/LVDT) are used to quantify the global vertical response and support the interpretation of stiffness changes. At the same time, the inclinometers provide spatially informative signatures for localisation (migration of the zero-tilt crossing and concentration of rotation gradients).

3.2 OMA workflow and quick Modalyzer overview

OMA was used to extract natural frequencies and mode shapes from output-only vibration data. In this research, modal identification was supported by Modalyzer, a Python-based framework that integrates preprocessing and multiple OMA algorithms within a consistent workflow (e.g., frequency-domain decomposition and stochastic subspace identification) [9]. A full description and benchmarking of the library are reported elsewhere; in the present paper, Modalyzer is mentioned to clarify the repeatable pipeline adopted to track modal parameters across damage states while keeping the focus on the beam campaign results.

4 NUMERICAL MODELLING IN ATENA

A 3D finite-element model of the tested girder system was developed using ATENA to simulate the global static and dynamic response of the specimens under the same boundary conditions as those adopted in the laboratory, as shown in Fig. 5. The numerical model consists of: (i) a prestressed concrete girder modelled with solid finite elements, (ii) distributed dead-load blocks represented as applied masses and loads, and (iii) a transverse steel diaphragm introduced to account for load redistribution under service conditions. Prestressing was applied by imposing an initial strain in the prestressing tendons, modelled as line elements, after accounting for prestress losses due to concrete shrinkage, creep, and elastic relaxation in accordance with Eurocode 2 [8]. The staged loading procedure implemented in ATENA was used to reflect the prestressing and subsequent loading and unloading phases. Progressive damage was introduced by selectively deactivating prestressing tendons at the inspection windows, following the same damage sequence imposed during the experimental programme. For comparison with experimental measurements, the ATENA model was employed to evaluate: (a) load–deflection responses under serviceability and ultimate loading conditions; and (b) modal characteristics, including natural frequencies and corresponding mode shapes, for both undamaged and damaged states.

For the beam cross-section, ten finite elements were adopted in each transverse direction, resulting in a minimum element size of 0.025 m. Along the longitudinal axis of the beam, the maximum element length was limited to 0.075 m. The beams were subjected to a limited number of loading cycles, with each loading–unloading cycle applied explicitly in the numerical model. Accordingly, in line with the ATENA documentation [10], the CC3DNonLinCementitious2 and CCCyclingReinforcement material models were employed to represent the concrete and reinforcement, respectively.

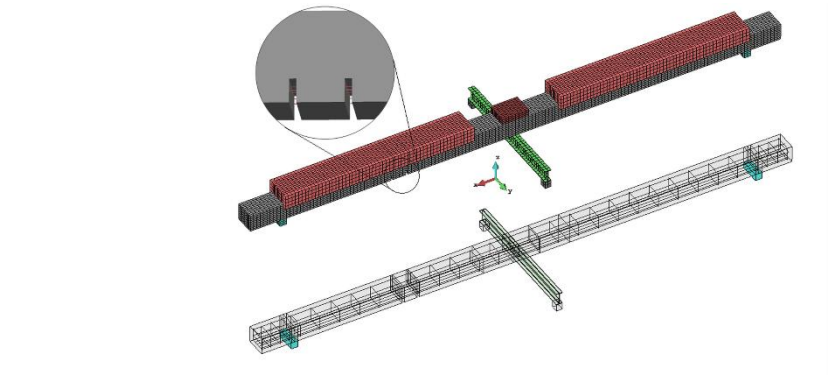
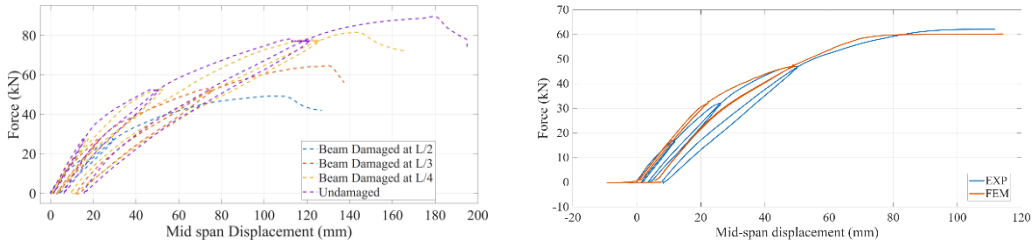


Fig. 5 3D ATENA finite-element model of the tested girder system, including supports, transverse diaphragm, and dead-load blocks (service configuration)

5 EXPERIMENTAL RESULTS AND DISCUSSION

5.1 Static response, ultimate capacity, and finite-element model validation

Progressive tendon cuts resulted in measurable stiffness degradation during service-level cycles and systematic reductions in ultimate strength. The influence of the damage location is clear in Fig. 6(a): tendon loss closer to the high-moment region (L/2) leads to stronger reductions in capacity than off-centre damage (L/3 and L/4). Capacity reductions of roughly 9%, 28%, and 45% were recorded for beams with strand damage located at L/4, L/3, and L/2, respectively. In each case, the decrease in peak strength was accompanied by a corresponding loss in displacement capacity at failure. These findings underscore the governing role of damage location in determining the residual performance of bonded prestressed girders. The numerical model's reliability is further demonstrated in Fig. 6(b), which compares the experimental and FE force–displacement responses for a bonded beam subjected to a three-strand damage scenario at L/4. The FEM accurately captures the initial elastic stiffness, the onset of cracking, and the subsequent nonlinear softening phase. Furthermore, the model effectively reproduces the hysteretic behaviour observed during the loading–unloading cycles, confirming that the adopted constitutive laws for concrete and reinforcement correctly simulate energy dissipation and residual plastic deformations.



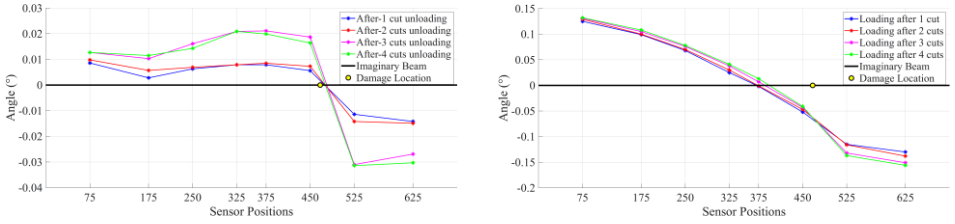
(a) (b)

Fig. 6 Force–displacement response of bonded beams: (a) two-cut scenarios at different damage locations and (b) validation of the finite-element model against the experimental response

5.2 Deformation-shape indicators for SHM

Rotation-based shape reconstruction provides an interpretable SHM quantity: residual deformation after unloading increases with tendon loss. For off-centre damage, the “shape signature” tends to concentrate near the damaged region. This supports a physics-based localisation indicator under controlled load cycles. As shown in Fig. 7, although the external load is applied at mid-span, the measured tilt profiles reveal a clear shift in the sign change toward the damage location (inspection window at L/3). In an undamaged and symmetric three-point bending case, this sign inversion is expected close to mid-span; here, after strand cutting, the local stiffness reduction attracts curvature,

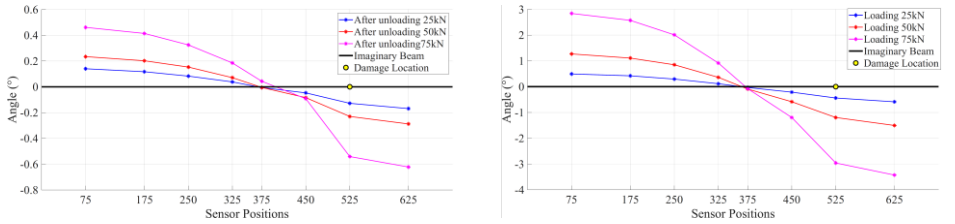
and the rotation field becomes asymmetric, shifting the "rotation reversal" section toward the weakened region. During the loading phase (Fig. 7b), the curves progressively shift toward the damaged section, and the steepest rotation gradient concentrates around the sensors closest to the cut region, providing a direct damage-localisation indicator from the inclinometers. During unloading (Fig. 7a), a growing residual rotation/offset develops and remains spatially concentrated near the same region, consistent with reduced effective prestress and accumulated local cracking. Overall, tracking (i) the position of the zero-tilt crossing and (ii) the concentration of rotation gradients across sensor stations offers a robust, interpretable localisation metric, complementary to global deflection-based indicators.



(a) (b)

Fig. 7 Measured rotation profiles for bonded specimen with damage at L/3: (a) residual tilt during unloading and (b) instantaneous tilt during loading

As shown in Fig. 8, the ULS stages lead to a distinctly nonlinear response, with pronounced hysteresis and greater residual deformation than the SLS cycles. In the loading branches (Fig. 8b), the rotation profiles become progressively more asymmetric as the demand level increases, and the steepest changes in tilt concentrate toward the inspection window at L/4, where stiffness has been reduced by tendon loss. Although the external load is applied at mid-span, the rotation reversal does not remain centred. Instead, it shifts toward the damaged section, indicating redistribution of curvature and the formation of a dominant flexural mechanism in the weakened region. In the unloading branches (Fig. 8a), the curves do not return to the original baseline, and a clear residual rotation field persists, which is consistent with cracking and irreversible stiffness degradation at ULS. Overall, Fig. 8 suggests that tracking both the migration of the zero-tilt crossing and the local concentration of rotation gradients provides a practical deformation-shape indicator of damage location and severity under ultimate-level actions.



(a) (b)

Fig. 8 Ultimate limit state (ULS) rotation profiles for bonded specimen with damage at L/4: (a) residual tilt during unloading and (b) instantaneous tilt during loading

5.3 Dynamic indicators (OMA)

5.3.1 FEM validation against experimental results

To establish a reliable numerical baseline for the dynamic response, the ATENA FE model was first validated for the isolated beam's initial condition. This validation considers the girder's self-weight and 240 days of concrete time evolution to account for shrinkage and creep effects before the experimental campaign. As shown in Table 2, the model demonstrates high accuracy in predicting the fundamental dynamic properties, with the numerical Mode-1 frequency (8.91 Hz) closely matching the experimental value (8.73 Hz) identified at the same time interval. This strong correlation confirms the model's fidelity

in representing the initial stiffness and mass distribution of the beams before the introduction of secondary loads or damage scenarios.

Table 2 Numerical and experimental natural frequencies used for service-level model validation

Condition	Mode-1 *f(Hz)*	Mode-2 *f(Hz)*	Mode-3 *f(Hz)*	Mode-4 *f(Hz)*	Mode-5 *f(Hz)*
FEM after 240 days from construction	8.91	9.66	32.12	33.12	66.50
Experimental after 240 days	8.73	9.21	31.23	33.79	64.04

5.3.2 Influence of prestress damage on natural-frequency shifts

The evolution of natural frequencies across progressive damage states shows a clear difference between service and ultimate conditions, as reported in Table 3 and Table 4.

Table 3 Experimentally identified SLS natural frequencies for Scenario 2 (L/4)

Condition	Mode-1 *f(Hz)*	Mode-2 *f(Hz)*	Mode-3 *f(Hz)*	Mode-4 *f(Hz)*	Mode-5 *f(Hz)*
SLS – undamaged	7.27	7.59	17.89	18.76	43.44
SLS – 1 cut at L/4	7.17	7.53	17.80	18.57	42.90
SLS – 2 cuts at L/4	7.17	7.53	17.70	18.54	43.34
SLS – 3 cuts at L/4	7.14	7.50	17.62	18.51	43.34
SLS – 4 cuts at L/4	7.11	7.47	17.55	18.46	43.26
SLS – 5 cuts at L/4	7.11	7.40	17.47	18.46	43.11
SLS – 6 cuts at L/4	7.09	7.32	17.40	18.47	42.90
SLS – reduction percentage (%)	-2.47	-3.55	-2.73	-1.54	-1.24

Table 4 Experimentally identified ULS natural frequencies for Scenario 2 (L/4)

Condition	Mode-1 *f(Hz)*	Mode-2 *f(Hz)*	Mode-3 *f(Hz)*	Mode-4 *f(Hz)*	Mode-5 *f(Hz)*
ULS – undamaged	5.11	5.57	18.61	19.76	44.94
ULS – 6 cuts at L/4	5.05	5.57	18.46	19.61	44.79
ULS – 15 kN	4.95	5.41	18.08	18.99	43.57
ULS – 30 kN	4.73	5.34	18.00	19.00	42.80
ULS – 45 kN	4.49	5.18	17.95	18.92	42.57
ULS – reduction percentage (%)	-12.13	-7.0	-3.54	-4.25	-5.27

During the SLS phase at L/4, frequency shifts remain small, with a first-mode reduction of only 2.47% even after six tendon cuts. This limited variation is consistent with the observed crack pattern under service loading, which consisted mainly of narrow and localised flexural cracks near the inspection-window region, while most of the span remained essentially uncracked. Consequently, the reduction in global bending stiffness was modest, and the corresponding frequency changes remained small, confirming the limited sensitivity of frequency-based indicators under moderate service-level damage. In contrast, the ULS cyclic loading stages produced more pronounced nonlinear degradation, leading to a 12.13% drop in the first natural frequency as crack widening and irreversible stiffness loss became dominant.

6 CONCLUSIONS

This study combined full-scale experiments and nonlinear finite-element modelling to evaluate structural-health-monitoring indicators for twelve prestressed concrete girders with staged strand cuts. Damage location strongly governed residual performance: bonded beams damaged at mid-span lost up to 45% of capacity, compared with about 9% for quarter-span damage. Service-level natural-frequency changes remained below 3%, showing that frequency shifts alone are not sufficiently sensitive to moderate prestress loss. In contrast, tilt profiles provided clear spatial indicators through migration of the zero-tilt crossing, concentration of rotation gradients near the damaged section, and residual rotations after unloading. The calibrated ATENA model reproduced the measured static and dynamic response and provides a basis for investigating damage scenarios that are difficult to reproduce experimentally. For bridge applications, the results support combining inclinometers, deformation sensors, and model-based interpretation rather than relying on modal frequencies alone. Future work will transfer these indicators to in-service bridges and integrate them with automated anomaly detection.

Acknowledgements

The study presented was supported by the Research Project of Relevant National Interest (PRIN) DATAGRAM, “DATa and strAteGies for Resilience AssessMent of Existing Road Networks: A Bridge-Based Application in Italy”, CUP C53C24000910006.

References

[1] Cosenza, Edoardo, and Losanno, Daniele. 2021. “Assessment of Existing Reinforced-Concrete Bridges Under Road-Traffic Loads According to the New Italian Guidelines.” *Structural Concrete* 22:2868–81. doi:10.1002/suco.202100147.

[2] De Domenico, Dario, Messina, Davide, and Recupero, Antonino. 2022. “Quality Control and Safety Assessment of Prestressed Concrete Bridge Decks Through Combined Field Tests and Numerical Simulation.” *Structures* 39:1135–57. doi:10.1016/j.istruc.2022.03.086.

[3] Recupero, Antonino, and Spinella, Nino. 2019. “Experimental Tests on Corroded Prestressed Concrete Beams Subjected to Transverse Load.” *Structural Concrete* 20:2220–29. doi:10.1002/suco.201900242.

[4] Gandelli, Emanuele, Rossini, Giulia, Mantelli, Stefano Giuseppe, and Minelli, Fausto. 2024. “Damage Detection of Prestressed Concrete Beams Affected by Shear and Flexure Cracks Through Vibration Monitoring.” *Engineering Structures* 304:117572. doi:10.1016/j.engstruct.2024.117572.

[5] Shamsaddinlou, Amir, De Domenico, Dario, and Recupero, Antonino. 2026. “Experimental Investigation on Prestressed Concrete Beams with Localized Strand Damage: Tilt-Based Deflection Mapping and Damage Indicators.” Engineering Structures 365:123270. doi:10.1016/j.engstruct.2026.123270.

[6] De Domenico, Dario, Shamsaddinlou, Amir, La Mazza, Dario, Longo, Monica, Maugeri, Natale Antonio, Longo, Paolo, Messina, Davide, and Recupero, Antonino. 2025. “Prestressed Concrete Beams with Artificially Damaged Strands: Plan of Experimental Tests and Numerical Modeling.” Paper presented at COMPDYN 2025, Rhodes Island, Greece, June 15–18. doi: 10.7712/120125.12568.24757.

[7] European Committee for Standardization. 2002. *Eurocode 0: Basis of Structural Design—EN 1990:2002+A1:2005*. Brussels: European Committee for Standardization.

[8] European Committee for Standardization. 2005. *Eurocode 2: Design of Concrete Structures—Part 1-1: General Rules and Rules for Buildings (EN 1992-1-1:2004)*. Brussels: European Committee for Standardization.

[9] Shamsaddinlou, Amir, Nikoofaraz, Mehrab, De Domenico, Dario, and Longo, Monica. 2026. “Computationally Efficient Python-Based Operational Modal Analysis of Structures: Modalyzer.” *Journal of Vibration and Control*. Published electronically January 16. doi:10.1177/10775463251410790.

[10] Červenka, Vladimír, Červenka, Jan, Janda, Zdeněk, and Pryl, Dobromil. 2017. *ATENA Program Documentation, Part 8: User’s Manual for ATENA-GiD Interface*. Prague: Červenka Consulting.

AI Knowledgebased Modelling

Predicting mechanical response of discrete lattice unit cells using neural networks

Jan Raisinger, Jan Eliáš

Institute of Structural Mechanics,
Brno University of Technology,
Veveří 331, Brno 60200, Czech Republic

Summary
Discrete lattice particle models effectively capture the nonlinear behaviour of quasibrittle materials such as concrete, but their high computational cost limits large-scale applications. This work introduces a data-driven framework that uses specialized recurrent neural network, the Linearized Minimal State Cell (LMSC), to predict the homogenized stress response of a unit cell modelled with a mesoscale discrete lattice model, with significant speed-up compared to the full lattice model. Two approaches for generating random strain paths are discussed: Gaussian process and Brownian motion. The surrogate trained on these paths accurately reproduces path-dependent behaviour while maintaining consistency across load step sizes thanks to the LMSC architecture. When integrated into macroscopic finite element simulations as a constitutive model, the approach shows good agreement under both monotonic and unloading–reloading regimes.

1 INTRODUCTION

Simulating the complex nonlinear fracture behaviour of quasibrittle materials, most commonly concrete in structural engineering, presents a significant challenge. Commonly used methods, such as Cohesive Zone and Phase-Field models, suffer from nontrivial parameter calibration or struggle to reproduce complex crack patterns. In the discrete lattice particle models, which use simple vectorial constitutive functions, the fracture patterns naturally arise from their heterogenous geometry representing concrete at mesoscale. However, applying such models at the scale of civil structures is impractical, as simulating an entire structure at the resolution of individual concrete grains is prohibitively expensive.

To address the computational challenges posed by complex microstructures in large-scale structures, multiscale analysis offers an effective modelling strategy. It considers only a small but representative sample of the heterogeneous microstructure, called the representative volume element (RVE), and upscales its behaviour to the macroscale. In the case of softening the existence of RVE is disputable due to strain localization and deterministic size effect [1]. This, however, does not prevent successful practical use of softening materials in multi-scale simulations, as demonstrated by relevant studies, using lattice discrete mesoscale models [2], [3]. Here, a fine-scale lattice discrete model with periodic boundary conditions and geometry serves as an RVE in multiscale numerical simulation.

In the coupled-volume approach, where the size of the fine-scale model is defined by the size of the macroscopic finite elements, the combined size of the fine-scale models is effectively equal to the macroscale model [4]. Therefore, the computational demands of such multiscale calculation remain large. However, partitioning the full model into a number of fine-scale periodic models enables the use of data-driven surrogates to approximate the behaviour of the fine-scale regions and lower the computational demands at the cost of some accuracy loss.

In the presented approach, the data-driven surrogate takes strain as input and outputs homogenized stress, effectively serving as a constitutive model. Predicting the stress response of history-dependent materials and fine scale models is a well-established in the recent literature. Existing studies predominantly address non-softening plasticity [5], [6] or consider softening only under highly restricted loading conditions [7].

In this work, the aim is to develop a neural network (NN) model capable of approximating the response of a discrete lattice model with softening under arbitrary loading path within predefined bounds. Models for history-dependent stress prediction in the literature can be classified in two independent ways:
(i) whether the state evolution is *known* or *unknown*, and
(ii) whether the state is updated through a *continuous evolution function* or a *step-wise update* [5]-[8].
If the state evolution is known, the material or fine-scale model state can be included in the training data and predicted with the stress. In the case of the presented fine-scale model, which contains

thousands of contacts with history variables, the inclusion of state variables in the training data is computationally impractical. In such cases, neural-network models that infer a latent state evolution solely from strain–stress data are used.

In both cases, when predicting a stress based on a given strain and previous state, the state must be updated to correspond with the new stress. Neural Ordinary Differential Equation approaches model the state evolution as a continuous function and typically rely on numerical integration for state updates. Although this enables time-step size invariant prediction, it is computationally costly and harder to train, compared to the stepwise update provided by recurrent neural networks (RNNs), especially in the case of unknown state evolution. The widely used Gated Recurrent Unit (GRU) and Long Short-Term Memory (LSTM) RNN variants suffer from time-step size dependent prediction. To address this limitation, the Linearized Minimal State Cell (LMSC) was developed in [7] and is, in an altered form, used here.

Effective training of RNN requires a representative dataset of input–output sequences, here strain–stress histories obtained from fine-scale simulations. To cover a wide range of loading scenarios, non-proportional random strain paths must be generated. The two most common approaches are Gaussian process (GP) and Brownian motion (BM)-based paths, differing in the temporal correlation present in GP.

In this work, the GP and BM are used to generate random strain paths dataset, on which a LMSC model is trained. The parameters of both methods and the differences of the datasets are discussed. Then, the LMSC model's performance is compared to the original fine-scale model in both single integration-point predictions and macroscopic model simulations. Finally, the challenges and advantages of using the LMSC as constitutive model in FEM simulations are discussed.

2 DISCRETE FINE-SCALE MODEL AND HOMOGENIZATION

2.1 Periodic fine-scale discrete model

The discrete lattice model is an assembly of contact elements connecting rigid particles, representing concrete aggregates and surrounding binder. It is generated inside a cube of size 30 mm, see an example shown in Fig. 1. When generating the geometry, aggregates are randomly distributed according to prescribed volume fractions and size distributions. Weighted Delaunay triangulation and power tessellation define the rigid bodies and their connecting contact elements. Each contact element links two particles and is characterized by its area, length, and local coordinate system, with nodal displacements and rotations serving as the degrees of freedom (DoFs). The boundary geometry of the model is nonuniform and periodic to avoid the boundary wall effect. The model behaviour is governed by balance equations for linear and angular momentum, accounting for contact tractions and couple tractions. The kinematic equation gives the element strain vector from displacements and rotations of the end nodes. The constitutive model, providing inelastic response based on a non-decreasing scalar damage parameter, is based on the model formulated in [10]. All the governing equations can be found in [11]. The material parameters used in the presented model are: $E_0 = 60$ GPa, $\alpha = 0.25$, $f_t = 3.4$ MPa, $G_t = 49$ J/m^2

2.2 Asymptotic homogenization of discrete model

The asymptotic homogenization of the discrete model is analogous to the homogenization of standard continua, with the difference being the inclusion of rotational DoFs in the discrete model. The homogenization techniques for the discrete systems composed of ideally rigid particles were introduced in [3], [12] and finalized in [13], with the coarse scale here considered as Cauchy continuum. During calculation, the symmetric coarse-scale strain tensor is projected as an eigen-strain vector on individual discrete contacts. After equilibrium is reached, the coarse-scale stress tensor is calculated by summing the tractions over all discrete contacts. The periodic boundary conditions are applied both to rotational and displacement DoFs.

In the presented work, size of the cube fine-scale model directly dictates the size of the macro-scale cube trilinear finite elements, such that the element consists of 8 adjacent fine-scale models, resulting in element of size 60 mm for the presented fine-scale model of size 30 mm. No additional regularization method is used. Generalization to different element sizes is an area of future research. The elements in which localization does not occur do not require this size consistency.

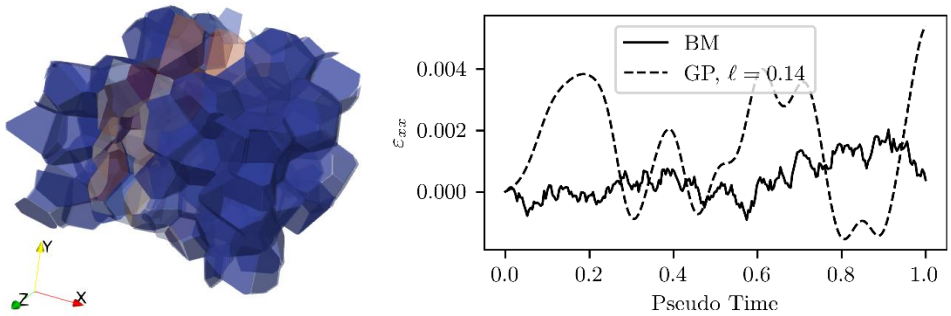


Fig. 1 Discrete fine-scale model loaded with uniaxial strain in x direction with fracture perpendicular to the load (left), Example of the ε_{xx} component of random strain path generated with Gaussian Process (GP) and Brownian motion (BM) (right)

3 GENERATION OF RANDOM STRAIN-STRESS PATHS

3.1 Gaussian process and Brownian motion

The random strain load paths are generated using two methods, the Gaussian process (GP) and Brownian motion (BM), also called Random walk. In both cases, the 6 strain vector components are considered uncorrelated, if not stated otherwise, therefore, for each component an independent 1D random path is generated. The GP is defined by the covariance or kernel function and mean function [8]. Here the squared exponential kernel defined by the variance parameter σ and correlation parameter ℓ is used, together with constant mean function with value μ. The GP is sampled at n points in pseudotime, with constant time step T/n and is conditioned with the point (0,0) imposing the paths to start at zero strain.

The Brownian motion approach generates the random path by adding random strain to the previously recorded value at each predefined pseudotime step, with the first step defined with 0 strain. The increments are sampled from normal distribution $N(\mu, \sigma)$ defined by μ and σ parameters. The spread and mean value of the strain values distribution depends also on n. Brownian motion can be interpreted as a Gaussian process with covariance kernel $k(s,t) = \sigma^2 \min(s,t)$ [9]. Based on this equivalence, approximate relations between the parameters of a discretized GP and a BM with matching mean and variance over a finite horizon can be derived. For $T^{BM} = 1$, this yields

$$\mu^{BM} = \frac{2\mu^{GP}}{n}, \qquad \sigma^{BM} = \frac{\sqrt{2}\sigma^{GP}}{\sqrt{n}} \tag{1}$$

The correlation ℓ can be manually tuned to obtain similar strain increment distributions.

3.2 Dataset properties

The datasets comprise strain-stress sequences evolving in pseudotime, with each step described by the 6-component strain and stress vector. The strain sequence load is applied to the fine-scale model, its response is calculated in the OAS software, open source at https://gitlab.com/kelidas/OAS, and recorded in the stress sequence. All sequences are composed of $n = 250$ steps. The GP paths are generated with parameters: $\sigma^{GP} = 0.0013$, $\mu^{GP} = 0.002$,$T = 3$, $\ell = 0.14$. The positive μ^{BM} is motivated by the properties of the fine-scale model. During and after strain localization, the model can be subjected to very large positive strains while producing small to none stress response. This is not true for compression however, where equivalent strain values would produce excessively large stress, skewing the dataset and the model's prediction. The μ^{GP}, σ^{GP} values were tuned, such that the strain distribution covers maximum strains recorded in the macroscopic simulations, while preventing the compressive stress domination in dataset. The BM parameters were obtained from μ^{GP}, σ^{GP} according to (1).

To improve predictions under correlated strain components, such as in uniaxial or biaxial loading, the datasets are augmented with corresponding paths. In both GP and BM, 5000 paths are generated without any spatial correlation, and 1600 are generated as uniaxial, biaxial or triaxial, by randomly generating the load directions and keeping it constant during loading, with the magnitude of loading

controlled by the random path. This results in two datasets: D^{GP}, D^{BM}. Due to the almost plane-stress like loading conditions in x, z plane in the macromodels used for verification, large portions of the strain paths are irrelevant for the micromodel predictions. Therefore, a specialized version of the datasets is defined, in which the almost zero-stress directions of the strain paths $\varepsilon_{yy}, \varepsilon_{yz}, \varepsilon_{xz}$ are divided by 10 and denoted ${D_{2D}}^{GP}$, ${D_{2D}}^{BM}$.

4 NETWORK ARCHITECTURE AND TRAINING

4.1 Network architecture

The network architecture comprises two blocks: the state update block R and stress prediction block F. At each step, the input to the network is current strain vector $\varepsilon^{(t)}$ and previous state vector h^{t-1}. These are processed by the state update block, in this case the LMSC, or GRU for comparison, predicting current state $h^{(t)}$. Current state, together with current strain are then processed by a feed-forward neural network (FFNN), predicting a scalar value $\Psi(\varepsilon, h)$. This value is analogous to the Helmholtz free energy, so its strain derivative gives stress. Prediction of stress as derivation of a scalar potential was shown to produce NN constitutive models with great generalization ability and thermodynamically stable predictions [4][5]. Additionally, the dissipative forces d can be obtained by differentiating the potential by the state vector and used to calculate dissipation rate $\Delta D = -d^{(t)} \cdot \Delta h$.

$$h^{(t)} = R\left(h^{(t-1)}, \varepsilon^{(t)}\right), \qquad \Psi^{(t)} = F\left(h^{(t)}, \varepsilon^{(t)}\right), \qquad \sigma^{(t)} = \frac{\partial \Psi}{\partial \varepsilon}\bigg|_{\varepsilon = \varepsilon^{(t)}}, \qquad \mathrm{d}^{(t)} = \frac{\partial \Psi}{\partial \mathrm{h}}\bigg|_{h = h^{(t)}} \tag{2}$$

During training, the initial state $h^{(0)}$ is set to zero vector. In case of LMSC used as R, h is chosen to have 10 elements, meaning the hidden size parameter of the network is set to 10. while GRU models use state sizes of 10 and 50, reflecting their higher state-dimension requirements [7]. In LMSC, both $\varepsilon^{(t)}$ and $\Delta\varepsilon^{(t)}$ are used as its input, in contrast to the original definition. The LMSC network has approximately 23000 parameters and GRU 20000 and 32000 for h with size 10 and 50 respectively.

4.2 Training parameters

Both models are trained for 3000 epochs using the Adam optimizer without weight decay and a learning rate of 0.001. Training employs a custom weighted mean-squared-error loss (wMSE), which scales the MSE by the average amplitude of each stress component in the sequence. This weighting has been shown to improve prediction accuracy compared to standard MSE. The improvement arises for two main reasons. First, wMSE increases the relative accuracy at low strain and stress levels, which are otherwise dominated by errors at larger stresses. Second, under plane-stress-like loading, some stress components remain near zero while others are large; the weighting better promotes accurate prediction of these small components. In addition to the wMSE term for stress prediction, negative dissipation is penalized through an additional loss term.

5 RESULTS

5.1 Test dataset prediction

The datasets are randomly shuffled and divided into training, validation and test datasets in 72:13:15 ratio. Table 1 shows Mean absolute error (MEA) between the correct and predicted values of different test sets, with the predictions calculated by the LMSC and GRU models, trained on different datasets denoted in brackets. The error is calculated on normalized stress values. The 3PB dataset contains loading paths form IPs of the macroscopic model simulation and is used to test the generalization power of the models, as it contains paths differing from those in both datasets.

The models trained on the BM datasets can predict paths from GP dataset with comparable accuracy as the models trained on these GP paths, but the opposite is not true. This shows that the BM datasets lead to models with significantly better generalization. The 2D like variants of the datasets lead to models better predicting these 2D like paths and failing to generalize to the 3D paths, both of which is expected. The GRU models with h size 10 can achieve similar results to the LMSC models and the GRU models with h size 50 surpass them slightly. The accuracy of the predictions on the test set is, however, not a completely reliable indicator of the generalization power of the models, as is seen on the MAE values calculated on the 3PB dataset. Here, the LMSC trained on ${D_{2D}}^{BM}$ produces best results

and is only matched by GRU($D_{2D}{}^{GP}$). This demonstrates the need for bigger h size for GRU compared to LMSC, and shows the influence of the interaction between model architecture and dataset properties.

Table 1 MAE of prediction on different test datasets of different models trained on different datasets

Dataset Model	D^{GP}	D_{2D}^{GP}	D^{BM}	$D_{2D}{}^{BM}$	3PB
LMSC(D^{GP})	0.012	0.017	0.110	0.094	0.005
LMSC($D_{2D}{}^{GP}$)	0.119	0.009	0.205	0.058	0.003
LMSC(D^{BM})	0.015	0.016	0.024	0.033	0.006
LMSC($D_{2D}{}^{BM}$)	0.113	0.011	0.176	0.015	0.002
GRU($D_{2D}{}^{GP}$)	0.085	0.007	0.154	0.043	0.002
GRU($D_{2D}{}^{BM}$)	0.140	0.007	0.190	0.012	0.004
GRU$_{10}$($D_{2D}{}^{BM}$)	0.077	0.011	0.169	0.017	0.005

5.2 Fine-scale response prediction

As seen in Table 1, the models trained on the 2D-like versions of the datasets show the best generalization power, when tested on the 3PB paths. The comparison to models trained on 3D data is shown in Fig. 2. It shows the strain path recorded in integration point 0 of the notched model, seen in Fig. 4, together with the stress path calculated on the fine-scale periodic model, denoted as "Reference", and the prediction of several NN models. The loading of the model stops at pseudotime 0.2 and is unloaded to (almost) zero load. Then it is loaded back, reaching the load level at which the unloading started at pseudotime 0.45 and then loaded further. The linear elastic unloading-reloading response of the CSL material model results in the linear strain in this regime recorded in the integration point 0. The peak strength together with reloading and late softening phases show underprediction of stress with the 3D datasets. The 2D-like datasets allow the NN models to learn the response with better accuracy, as they sample the plane-stress like loading paths more densely. This should be possible to improve with better data and potentially by larger and better trained models and is the aim of further research.

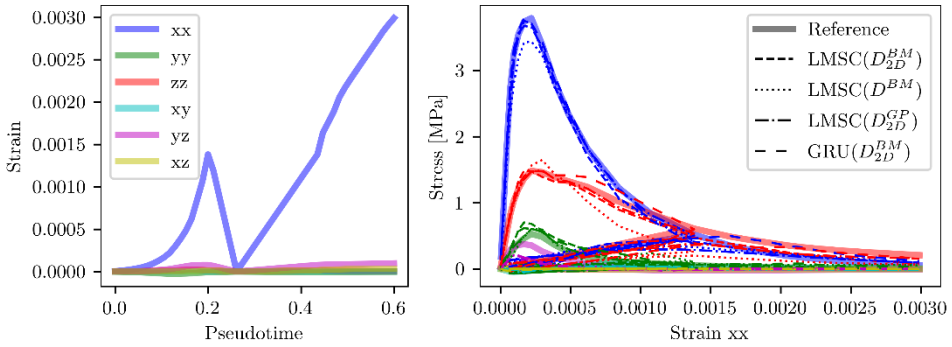


Fig. 2 Strain path recorded in integration point 0 of the macroscale notched model loaded in three-point bending and corresponding stress path calculated on the Reference fine-scale periodic model and predicted by neural network models

From the test and 3PB dataset's analysis, the LMSC($D_{2D}{}^{BM}$), together with GRU($D_{2D}{}^{GP}$), was deemed as the best model for use in macroscopic simulations. However, it was found to be susceptible to underprediction of stress in case of large strain increments stepping above the peak strength. The other models do not suffer from this issue, as shown in case of LMSC($D_{2D}{}^{GP}$) in Fig. 3. If the same path is sampled with smaller strain increments ensuring sampling of the peak, the LMSC($D_{2D}{}^{BM}$) predicts correct response. This is exploited in a modified variant LMSCs($D_{2D}{}^{BM}$), in which a maximum

allowable strain-increment size is defined. Increments exceeding this threshold are subdivided into smaller steps, which are evaluated sequentially, with only the final response retained.

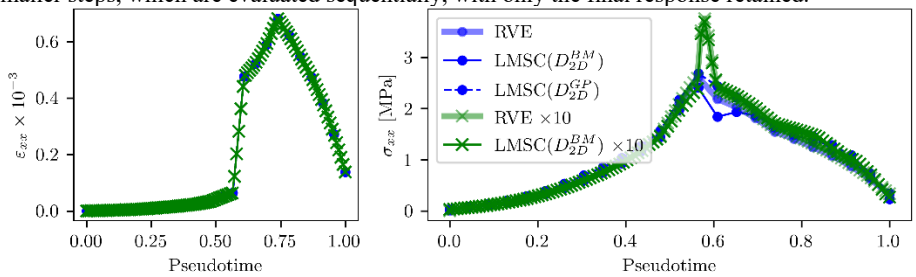


Fig. 3 Large strain increment stepping above peak, causing underprediction with LMSCs($D_{2D}{}^{BM}$) model, and the same path sampled with 10 times shorter pseudotime step

5.3 Macroscopic three-point bending test

In case of macroscopic FEM models, where the NNs are employed as constitutive models, small inaccuracies in NN's predictions can lead the models to unknown strain states during the iterative search of equilibrium. This reveals generalization insufficiencies otherwise hidden in the fine-scale analysis. Here, a three-point bending test of a beam of single element thickness with a notch is subjected to displacement of its upper surface central nodes. The model is considered in two variants: In the first, shown in Fig. 4, only a small region of the beam, where the crack is expected, uses the fine-scale model or NN response, with the rest of the model using a linear elastic material with elastic properties homogenized from the fine-scale periodic model.

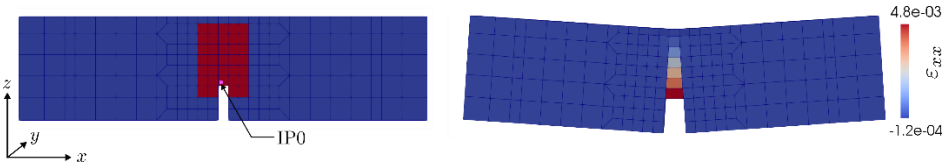


Fig. 4 Left: Geometry of the single-element-wide notched beam subjected to a three-point bending test. The red region indicates the domain where either the fine-scale periodic model or the neural network is used. Right**:** Strain-localization pattern at the end of the test.

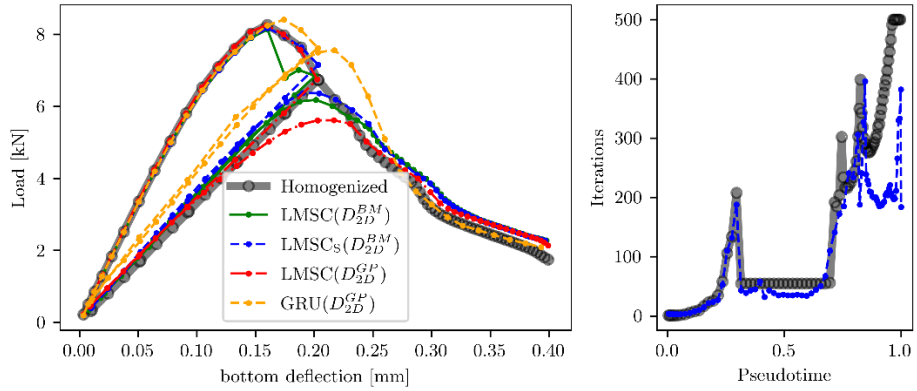


Fig. 5 Three-point bending test with unloading-reloading regime: Left: Reaction at the nodes loaded by vertical displacement plotted against deflection of the bottom middle node. Right: Iterations needed for convergence during calculation

Fig. 5 (left) shows the deflection of the middle bottom node plotted against the reaction force measured in the loaded upper middle nodes. At deflection 0.2 mm, the model is unloaded to (almost) zero load and reloaded back, resulting in linear response with lower stiffness compared to the initial caused by the accumulated damage. All the tested NN models capture the general trend of the response,

however, they significantly differ in its accuracy. The LMSC($D_{2D}{}^{BM}$) model's issue of stress underprediction discussed in Section 5.2 is clearly manifested in the abrupt decrease in response at peak. The LMSCs($D_{2D}{}^{BM}$) does not suffer by this inaccuracy. The LMSC($D_{2D}{}^{GP}$) model produces better results up until the reloading phase, where it fails to return to the softening phase correctly. The exact reason is the aim of future research, with likely cause being non-ideal sampling of the GP paths. Interestingly, the GRU($D_{2D}{}^{GP}$) model does not show this issue, however, the overall accuracy of the prediction is significantly lower. In Fig. 5 (right), the iterations needed for convergence during calculation are plotted. Up until the late postpeak, the NN model needs similar number of iterations as the homogenized model, then, likely due to its smoother predictions, it surpasses the homogenized model, which fails to converge. The total number of iterations and computational time are reported in Table 2.

Table 2 Calculation statistics of the three-point bending simulation of the model in Fig. 4

Model	Total number of iterations	Calculation time [s]
Homogenized	18258	101909
LMSCs($D_{2D}{}^{BM}$)	10744 (58.8%)	299 (0.29%)

The second variant of the three-point bending test is done on a model consisting entirely of FEs with fine-scale model response or NN as material model. Additionally, the prescribed load path is different, as seen in Fig. 6 (right). The quality of the response prediction of LMSCs($D_{2D}{}^{BM}$) remains the same.

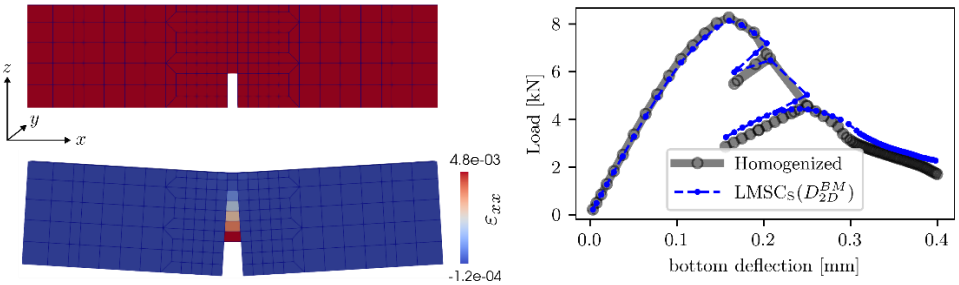


Fig. 6 The second variant of the three-point bending test, using NN in all integration points: Left: model geometry and strain localization at the end the simulation calculated with LMSCs($D_{2D}{}^{BM}$) model. Right: Load-deflection diagram

6 CONCLUSIONS

Using a Gaussian process (GP) and Brownian motion (BM) with comparable parameters, two sets of random strain paths were generated. These paths were prescribed as macroscopic load paths to a periodic discrete model of concrete at mesoscale, capturing its softening behaviour. Its homogenized stress response was recorded and combined with the strain paths into strain-stress sequence datasets. A recurrent neural network (RNN) with an architecture specialized to history-dependent constitutive modelling, the Linearized minimal state cell (LMSC), was trained on these datasets. Model performance for different training datasets was evaluated and compared against neural networks based on the conventional Gated Recurrent Unit (GRU) RNN architecture.

Models trained on BM strain paths were shown to generalize well to GP paths, whereas the reverse was not observed. Although alternative GP formulations with different kernel choices and parameters might improve this behaviour, they could introduce additional tuning requirements. Given its smaller number of parameters and superior generalization, BM appears to be the more suitable option.

Both the GRU and LMSC models can achieve good overall accuracy on synthetic test sets and on strain paths recorded in macroscopic simulations of concrete structures. However, when applied in macroscopic structure as a constitutive model, significantly different results are obtained. This was demonstrated on a simulation of a three-point bending test of a notched beam. There the LMSC model trained on BM paths and slightly modified to prevent peak stress underprediction can accurately predict all the elastic, hardening and softening regimes. The elastic unloading and reloading is also captured

well. Significant time savings were achieved compared to reference simulations using the discrete model's response of a periodic unit cell.

The traditional GRU models show inferior accuracy in predicting the peak and postpeak response, despite a higher parameter count and good accuracy on test data. This indicates poorer generalization compared to the LMSC-based model. Furthermore, the LMSC has lower memory requirements thanks to the lower size of its hidden state vector.

The LMSC-based model presented in this work is not without limitations. At present, it is accurate primarily for plane-stress-like loading conditions in macroscopic models and shows reduced accuracy when returning to the softening regime after unloading. Addressing these limitations will require further optimization of the dataset generation strategy, network architecture, and training procedure, followed by validation on a broader range of macroscopic problems. Nevertheless, even in its current form, the model demonstrates strong potential for use in a machine-learning-accelerated approach for simulating large-scale structures exhibiting strain localization.

Acknowledgements

Authors gratefully acknowledge financial support from the Czech Science Foundation under project number GA24-11845S.

References

[1] Gitman, Inna; Askes, Harm, and Sluys, Bert. 2007. "Representative volume: Existence and size determination." *Engineering Fracture Mechanics* 74(16), 2518–2534. doi: 10.1016/j.engfracmech.2006.12.021

[2] Eliáš, Jan, and Cusatis, Gianluca. 2022. "Homogenization of discrete mesoscale model of concrete for coupled mass transport and mechanics by asymptotic expansion." *Journal of the Mechanics and Physics of Solids* 167. doi: 10.1016/j.jmps.2022.105010

[3] Rezakhani, Roozbeh, and Cusatis, Gianluca. 2016. "Asymptotic expansion homogenization of discrete fine-scale models with rotational degrees of freedom for the simulation of quasi-brittle materials." *Journal of the Mechanics and Physics of Solids* 88. doi: 10.1016/j.jmps.2016.01.001

[4] Gitman, Inna; Askes, Harm, and Sluys, Bert. 2008. "Coupled-volume multiscale modelling of quasi-brittle material." *European Journal of Mechanics - A/Solids* 27(3), 302–327. doi: 10.1016/j.euromechsol.2007.10.004

[5] Masi, Filippo, and Stefanou, Ioannis. 2023. "Evolution TANN and the identification of internal variables and evolution equations in solid mechanics." *Journal of the Mechanics and Physics of Solids* 174. doi: 10 .1016/j jmps.2023.105245

[6] Flaschel, Moritz; Steinmann, Paul; De Lorenzis, Laura, and Kuhl, Ellen. 2025. "Convex neural networks learn generalized standard material models." *Journal of the Mechanics and Physics of Solids.* doi: doi.org/10.1016/j.jmps.2025.106103.

[7] Zhu, Yingbo; Brigham, John, and Fascetti, Alessandro. 2025. "Data-driven multiscale lattice discrete particle model for digital twin modeling of concrete structures." *Computer Methods in Applied Mechanics and Engineering* 445. doi: 10.1016/j.cma.2025.118183

[8] Bonatti, Colin, and Mohr, Dirk. 2021. "On the Importance of Self-consistency in Recurrent Neural Network Models Representing Elasto-plastic Solids." *Journal of the Mechanics and Physics of Solids*. doi: 10.1016/j.jmps.2021.104697.

[9] Rasmussen, Carl Edward, and Williams, Christopher K. I. 2005. *Gaussian Processes for Machine Learning*, Publisher: The MIT Press. doi: 10.7551/mitpress/3206.001.0001

[10] Cusatis, Gianluca, and Cedolin, Luigi. 2007. "Two-scale study of concrete fracturing behavior." *Engineering Fracture Mechanics*. 74. 3-17. doi: 10.1016/j.engfracmech.2006.01.021.

[11] Raisinger, Jan; Zhang, Qiwei; Bolander, John E. and Eliáš, Jan. 2025. "Simulating heterogeneity within elastic and inelastic discrete mechanical models." *Engineering Fracture Mechanics* 32. doi: 10.1016/j.engfracmech.2025.111362

[12] Eliáš, Jan, and Cusatis, Gianluca. 2022. "Homogenization of discrete mesoscale model of concrete for coupled mass transport and mechanics by asymptotic expansion." *Journal of the Mechanics and Physics of Solids.* 167. doi: 10.1016/j.jmps.2022.105010.

[13] Eliáš, Jan, and Cusatis Gianluca. 2025. "Do discrete fine-scale mechanical models with rotational degrees of freedom homogenize into a Cosserat or a Cauchy continuum?" *Journal of the Mechanics and Physics of Solids.* 207. doi: 10.1016/j.jmps.2025.106422.

Automated Characterisation of Subsequently Cut Surfaces of Reused RC-Elements Using Optical 3D Scans

Swantje Pieplow, David Sanio, Peter Mark

Institute of Concrete Structures,
Ruhr University Bochum,
Universitätsstraße 150, 44801 Bochum, Germany

Summary
Reuse of reinforced concrete (RC) elements is a key strategy for sustainable construction. Elements recovered during deconstruction are reassembled into new structures using new connections. For transferring compressive axial forces, dry joints between RC elements are a promising approach. Their load-bearing capacity depends largely on the properties of the cut interfaces resulting from the cutting process. However, there is currently no standardised procedure for surface characterisation that enables quantification of the influence of the surface condition on the compressive load-bearing capacity. This paper presents an evaluation routine for deriving areal and volume parameters from point clouds obtained by optical 3D scans. Implemented filters enable targeted analysis of waviness and roughness components. A systematic preprocessing is presented, and the choice of a suitable reference plane is discussed. The routine was applied to subsequently cut RC elements.

1 INTRODUCTION

For sustainable construction, the reuse of reinforced-concrete (RC) elements is a key strategy. Structural elements are extracted during deconstruction, characterised regarding their load-bearing capacity, processed, and retrofitted, and then assembled into new structures. The aim is to reuse them as load-bearing components rather than downcycling them to low-grade applications or disposing of them as wast.

Modular reuse concepts require reliable connections between the elements. These connections must be detachable to enable dismantling of the structure at the end of its service life and reuse of the components. This approach is motivated by the cradle-to-cradle principle, whereby components are repeatedly returned to the material cycle at a high value level [1,2]. In [3,4], a concept for the automated fine processing of reused elements for new connections is presented. In this context, concrete sawing and water-jet cutting are considered. The resulting surfaces form the contact interfaces of the dry joints. Previous research has shown that the load-bearing capacity of such concrete compression joints is influenced by surface characteristics [5–7]. Currently, there is no method available for the rapid and systematic evaluation of concrete surfaces based on 3D scans. Initial approaches are reported in [8].

This paper presents a method that automatically derives characteristic surface parameters from point clouds of test specimens, which is then applied to an experimental program. Section 2 describes the workflow for the automated evaluation of surface properties. This includes the requirements for input data, a density-based cutting procedure for removing side faces, initial alignment and resampling of the point cloud. The roughness and waviness components are then separated using a Gaussian filter and a set of characteristic surface parameters is computed. Section 3 applies the routine to the experimental program, while Section 4 discusses the chosen approach based on the evaluation of results.

2 METHOD FOR AN AUTOMATED SURFACE CHARACTERISATION

The following section provides a general description of the methodological approach for the automated evaluation of characteristic surface parameters, defines the limits of its application, and explains the preprocessing of the 3D point clouds. In [9], this is implemented in a Python routine.

2.1 Input data and preprocessing through density-based cutting

The input data consist of point clouds from 3D scans that contain point coordinates and their normal vector (x, y, z, n_x, n_y, n_z) and are exported in ASCII format (.asc/.txt). The developed routine [9] is designed for automated batch processing of an arbitrary number of point clouds in a single run. The surface parameters determined for each surface are written to a consolidated text file. The method is applicable to test specimens with a rectangular base area.

Before applying the routine, the point cloud must be manually cleaned of points or point clusters located outside the component geometry (e.g., from the measurement setup). The point cloud is then oriented such that the rectangular base of the component is parallel to the global xy-plane and any side faces are parallel to the xz- and yz-planes. An approximate alignment is sufficient. Then the routine automatically determines a minimum-area bounding rectangle enclosing the convex hull of the points in the xy-projection and performs an initial alignment by computing the angle between one edge of this rectangle and the x-axis, then rotating the point cloud about the z-axis accordingly.

Subsequently, the surface of interest, including the adjacent edge regions, is pre-separated by z-coordinate based cutting (Fig. 1a and b). All points whose z -coordinates lie within a defined threshold Δz of z_{min} or z_{max} are assigned to the respective surface (orange in Fig. 1a). Points with $z \geq z_{max} - \Delta z$ are assigned to the upside and points with $z \leq z_{min} + \Delta z$ to the downside, where z_{max} and z_{min} are the maximum and minimum z-values of all points in the point cloud.

To remove the remaining points belonging to the side faces, an adaptive density-based cutting is applied. For this purpose, a regular orthogonal grid is defined in the xy-plane, and the density s is computed as the number of points per cell. Regions containing side faces typically exhibit significantly higher densities, as visualised in the density heat map in Fig. 1c. From an inner reference region of the grid, the reference density s_{ref} (mean) and its standard deviation $\sigma_{x,ref}$ are calculated. The inner reference region (see Fig. 1c) is obtained by excluding an edge strip of width B_{max} from the grid. Within this edge strip, cells whose density s exceeds a threshold t, and thus show a significantly increased density, are detected as side faces. The threshold is computed as the 99% quantile based on a normal distribution, with $t = s_{ref} + k \cdot \sigma_{x,ref}$ and $k = 2.326$.

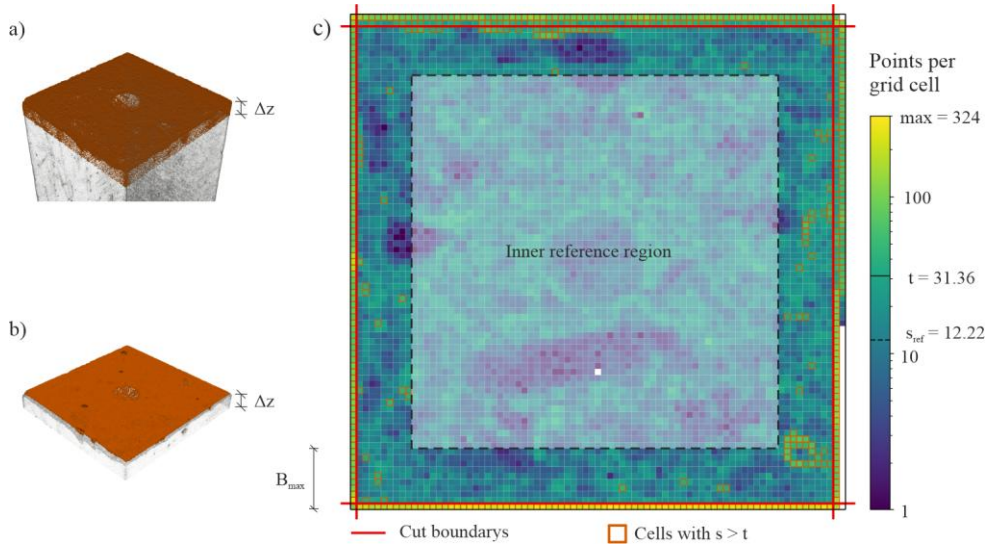


Fig. 1 Exemplary isolation of the surface: a) separation based on the z-coordinate; b) result after density-based cutting; c) density heat map.

The edge cutting is performed separately for each side by successively checking boundary strips. Strips are removed only in their entirety and if both criteria are met, $e \geq m_{\text{abs}}$ and $e \geq n \cdot m_{\text{frac}}$. Here, n denotes the total number of occupied cells in a strip ($s > 0$), and e is the number of cells with $s > t$. The parameters m_{abs} and m_{frac} are specified by the user and define the minimum absolute and relative number of cells whose density must exceed the threshold. The remaining point cloud of the separated surface is shown in Fig. 1b in orange.

2.2 Surface alignment and resampling

The computation of characteristic surface parameters requires the distance $z(x, y)$ to a reference plane. Two methods are used to determine this reference plane: principal component analysis (PCA) [10] and random sample consensus (RANSAC) [10–12].

Using PCA, a best-fit plane is determined according to the total least squares (TLS) principle. The plane is obtained by minimising the sum of squared orthogonal distances of all points to the plane [10]. This corresponds to the least-squares reference plane defined for flatness parameters in [13].

RANSAC-based plane fitting iteratively identifies a plane that represents a dominant planar region [11]. In each iteration, the algorithm randomly selects three points (a point triplet) from the point cloud, defines a plane through them, and then evaluates the orthogonal distance of all remaining points to this plane [12]. Points with a distance less than or equal to a prescribed threshold are classified as inliers [12]. The procedure is repeated up to a predefined iteration limit. The plane with the largest number of inliers is retained and accepted only if it reaches a specified minimum number of inliers [12]. Because the selection of point triplets is random, the result is not uniquely reproducible. Both methods yield a reference plane defined by a support point $\overline{\mathrm{p}}$ and a normal vector **n**. **n** is defined as positive when it points away from the element's surface.

The RANSAC plane is considered more robust to outliers [10] and is therefore selected as the reference plane for subsequent computations. The PCA plane is analysed for comparison. After the reference plane has been defined, the point clouds are transformed such that the resulting height field $z'(x, y)$ corresponds to the signed orthogonal distance $\Delta z(x, y)$ to the RANSAC plane. Then, for the subsequent evaluation, remaining outliers and voids (e.g., air pores) with $|\Delta z| >$ threshold are eliminated to reduce their influence on the parameters. For example, in pressure contact, air voids do not contribute to force transmission, regardless of their size.

3D scans yield irregular point clouds (blue points in Fig. 2a). However, the subsequent application of 2D Gaussian filters for separating roughness and waviness requires a regular height field [14]. Therefore, as a first step, a triangulated irregular network (TIN) surface is generated by Delaunay triangulation of the point projections in the xy-plane [15] (Fig. 2a). This yields a piecewise linear surface approximation and is well suited for local interpolation [16]. The interpolation is performed by defining a regular xy-grid with spacing h on the surface (Fig. 2b). For each grid node, z is interpolated within the corresponding triangle, resulting in the resampled point cloud (Fig. 2c). The resulting z coordinates are interpreted as residuals with respect to the previously determined reference plane. No additional plane fitting is performed after resampling, because resampling does not introduce a new reference geometry but merely generates an equidistantly sampled height field from the same measurement data. The grid spacing h is selected based on the point density as $h = max(h_{dens}, h_{nn})$, with $h_{dens} \approx \sqrt{A/N}$ and $h_{nn} \approx 0{,}8 \cdot \mathrm{median}(d_{\mathrm{NN}})$. Here, h_{dens} represents an average point spacing derived from the evaluated area A and the number of measurement points N. h_{nn} is a robust estimate of the local nearest-neighbour spacing d_{NN}, computed as the distance from each point to its nearest neighbour in the xy-plane. This ensures that the grid is not finer than the available point spacing and that the resampled height values are predominantly based on measured points rather than interpolation.

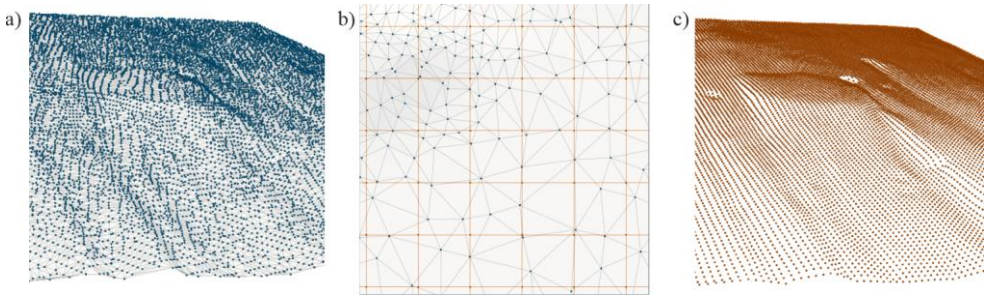


Fig. 2 Point cloud from the 3D scan before and after resampling: a) Delaunay triangulation of the surface; b) resampling on the surface using a regular grid; c) resampled point cloud.

2.3 Filtering and determination of surface and volume parameters

For the characterisation of concrete surfaces, waviness and roughness must be distinguished. Roughness describes short-wavelength components of a profile, whereas waviness refers to long-wavelength components (see Fig. 6). These terms are generally used to describe profiles and cannot be transferred directly to 2D surfaces, because a surface can exhibit short- and long-wavelength components simultaneously in different directions [17]. Therefore, the terms SF surface and SL surface are commonly used, where the letters denote the applied filtering operations (S: short-wavelength S-filter; F: form removal; L: long-wavelength L-filter)[18]. Nevertheless, in this paper the term waviness is used for the SF surface and roughness for the SL surface.

For scale separation, two-dimensional Gaussian filters are applied according to [7]. Filtering is performed by convolving the resampled height field $z''(x,y)$ with a 2D Gaussian kernel, where the separation scale is defined by the nesting index N_i. First, an S-filter with nesting index N_{is} is applied to suppress very short-wavelength components from measurement noise. This yields the primary surface $Z_p(x,y)$. The waviness surface $Z_W(x,y)$ is obtained by applying a low-pass filter with nesting index N_{ic} and the roughness surface $Z_R(x,y)$ is computed as the difference Z_R=Z_P-Z_W [18]. The nesting indices must be selected a priori; Table 1 provides suitable values for concrete surfaces. The resampling spacing is chosen such that the smallest relevant wavelength defined by the S-filter is resolved by multiple grid points, here at least with a ratio of 5:1, i.e. $h \leq N_{is}/5$ following the recommendation in [17].

DIN EN ISO 25178-2 [18] defines a large number of parameters for surface characterisation, of which a subset is considered here. The areal parameters S_a, S_q, S_{sk}, S_{ku} and S_{dq} are evaluated to describe the statistical characteristics of the surface. S_a and S_q represent the arithmetical mean height and the root mean square height, respectively. The skewness S_{sk} characterises the height distribution of the topography and the symmetry of the profile about the mean plane, indicating whether valleys (S_{sk}< 0) or peaks (S_{sk}> 0) dominate [19]. The kurtosis S_{ku} describes the peakedness of the height distribution. For a Gaussian height distribution, S_{ku} = 3. S_{ku} < 3 indicates flatter distributions with less pronounced peaks and valleys, whereas S_{ku} > 3 indicates more sharply pronounced peaks and valleys [19]. The root mean square gradient S_{dq} describes the mean local slope of the surface, i.e. how steep the surface is on average.

The resampled height field $z''(x,y)$ forms the basis for the calculations. The parameters are computed from Eqs. 1–5 based on the height values z_i of all points. Here, M denotes the set of all grid points with cardinality N, and M_g is the subset of M with cardinality N_g whose grid points have valid neighbours in all directions and are therefore suitable for gradient computation.

arithmetical mean height

$$S_a = \frac{1}{N} \sum_{i \in M} |z_i| \tag{1}$$

root mean square height

$$S_q = \sqrt{\frac{1}{N} \sum_{i \in M} {z_i}^2} \tag{2}$$

Skewness

$$S_{sk} = \frac{1}{N} \sum_{i \in M} \frac{{z_i}^3}{{S_q}^3} \tag{3}$$

Kurtosis

$$S_{sk} = \frac{1}{N} \sum_{i \in M} \frac{{z_i}^4}{{S_q}^4} \tag{4}$$

root mean square gradient

$$S_{dq} = \sqrt{\frac{1}{N_g} \sum_{i \in M_g} \|\nabla z_i\|^2} \tag{5}$$

In addition, volumetric parameters V_{mp}, V_{mc}, V_{vc} and V_{vv} are determined acc. to DIN EN ISO 25178-2 [18]. These parameters describe the area-related material and void volumes of the surface. V_{mp} denotes the material volume in the peak region above a defined upper threshold, whereas V_{vv} denotes the void volume in the valley region below a lower threshold. Between these thresholds, V_{mc} and V_{vc} capture the material and void contributions in the core region, respectively. The corresponding equations are omitted here for brevity and can be found in [18].

The root mean square height S_q acc. to Eq. 2 can be computed directly from the initial point cloud, independently of the resampling step and the chosen grid. For this, the distances of the points to the

reference plane are used, distinguishing between the PCA plane ($S_{q,PCA}$) and the RANSAC plane ($S_{q,RANSAC}$). The value obtained after resampling and before applying the Gaussian filters is denoted $S_{q,resampled}$. By distinguishing the three scale components — primary, waviness, and roughness — and evaluating nine parameters for each range, a total of 27 parameters are obtained. Together with three S_q values, this yields 30 parameters available for the analysis.

In addition to the global parameters, local parameters are computed for visualisation. For this purpose, the surface is evaluated using a moving square window, whose side length w is determined separately for roughness and waviness from the nesting indices N_{ic} and N_{is} and the grid spacing h, yielding w=odd$\left(\text{round}\left(\frac{N_i}{h}\right)\right)$, where odd enforces an odd window size to ensure a central grid node. Within each window, the residuals are centred about the local mean, and the local areal and volume parameters are computed.

3 EXPERIMENTAL PROGRAM AND REPRESENTATIVE TEST CASES

3.1 Experimental program

The proposed routine was applied to 18 surfaces of plain concrete and RC prisms (~ 80 × 80 × 230 mm) that were fine-processed by concrete diamond sawing, water-jet cutting, or grinding. The reinforced specimens contain a single centrally placed 16 mm diameter rebar and originate from the test series reported in [6]. The concrete strengths were: f_{cm} = 35.4 N/mm^2, $f_{cm,cube}$ = 42.7 N/mm^2 for the RC specimen, and f_{cm} = 22.8 N/mm^2 and $f_{cm,cube}$ = 29.9 N/mm^2 for the plain concrete specimen. Figure 3 illustrates exemplary cutting processes and the resulting surfaces of the processed specimens. The surfaces were subsequently captured using an ATOS Compact Scan 8M optical scanner with an accuracy of 0.01 mm, producing approximately 8 million measurement points per scan. The system for denomination the samples combines reinforcement (RC for reinforced concrete, C for plain concrete), the cutting method (s for saw, wj for water jet, g for ground), and a sequential number, for example "RC_wj_1".



Fig. 3 Cutting processes and resulting cut surfaces of the concrete prisms: (left) concrete sawing, (right) water-jet cutting.

3.2 Evaluation of the specimens

Table 1 Selected parameters for preprocessing and filtering

preprocessing		**density based cutting**				**gaussian filtering**	
Δz	threshold	h	B_{max}	m_{frac}	m_{abs}	N_{is}	N_{ic}
[mm]	[mm]	[mm]	[mm]	[-]	[-]	[mm]	[mm]
10	5	1	4	0.3	3	2	8

Table 1 summarises the initially selected parameters used to evaluate all specimens. Δz was set to 10 mm to ensure reliable separation of the surfaces of interest while retaining sufficient side-face points for the density-based cutting step. The threshold and the parameters for density-based cutting were determined by stepwise calibration based on the 18 specimens. The parameters, were selected to ensure reliable removal of side faces while minimising the loss of surface points. The nesting index N_{is} was derived from the grid spacing h and the 1:5 ratio stated in Section 2.3 (typically $h < 0.4$ mm; $N_{is} = 5 \cdot 0.4 = 2.0$ mm). N_{ic} was chosen as four times N_{is}, i.e., 8.0 mm, in line with the recommended

cut-off wavelengths in [17]. Fig. 4 illustrates the evaluation of specimen RC_wj_1, including a) the scale-limited waviness and roughness components and the local maps of the computed parameters, together with b) the corresponding real surface and c) a height profile. The global parameters computed for the entire surface are reported as numerical values underneath each image.

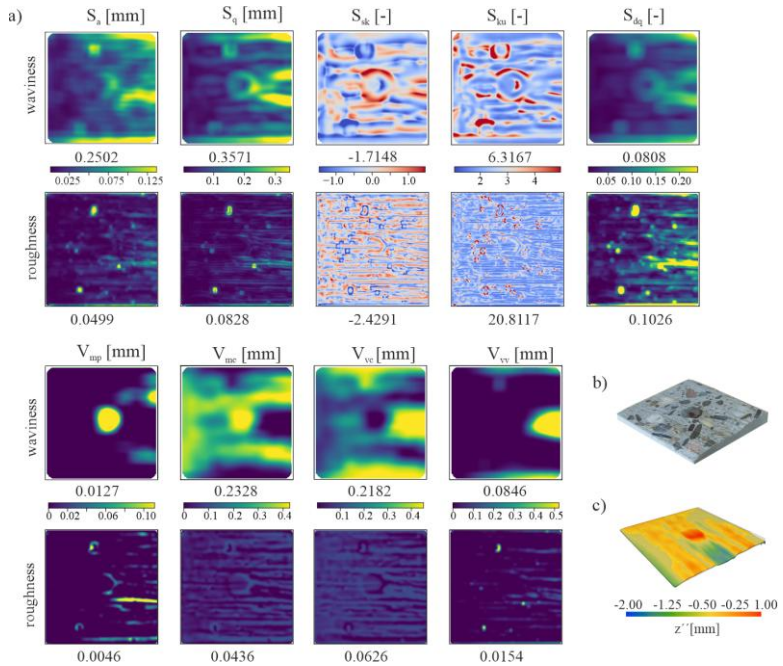


Fig. 4 Evaluation of the surface of specimen RC_wj_1: a) local and global parameters of waviness and roughness, b) original surface, c) z-coordinate heat map of $z''(x, y)$

4 DISCUSSION

The approaches for defining the reference plane are illustrated in Fig. 5, which uses a concrete surface with a pronounced breakout as an example. The RANSAC plane follows the actual geometry of the cut, whereas the PCA plane is strongly influenced by the breakout (Fig. 5b). Therefore, depending on the application — for example, when assessing the surface under compressive contact — the PCA plane is only of limited use, as it does not represent the effective contact geometry.

For surfaces without major spalls, the two planes are in close agreement. This is illustrated by the plot in Fig. 5c, which shows the relationship between the mean values obtained using both methods and the relative mean difference. For the evaluation, S_q is determined with respect to the respective reference plane. The surface with the spall shows a deviation of 52%, whereas most surfaces deviate by an average of only 3%. It is noticeable that the RC specimens tend to show greater deviation (> 3%), which is even more pronounced in the case of waterjet cutting (about 10%). In general, there is a trend whereby the percentage deviation increases as S_q, and thus the overall unevenness, increases.

Resampling of the point cloud always leads to a smoothing and thus to a systematic underestimation of the results. Fig. 5d shows the relationship between the mean value before and after resampling and the absolute difference. The value $S_{q,RANSAC}$ is consistently higher than $S_{q,resampled}$. The results also show a trend, in that the absolute difference increases with increasing S_q, indicating that the smoothing effect becomes more pronounced for uneven surfaces.

The choice of nesting indices is highly relevant, as the scale limitation determines which surface components are classified as waviness or roughness. Fig. 6 shows the effect of changing N_{ic} from 8 mm to 20 mm. Shifting the L-filter cut-off in this way assigns more long-wavelength components to the roughness surface. Consequently, the residuals and the derived parameters change. Therefore, the selection of suitable nesting indices must be linked to the specific application, identifying the scale

range that best represents the property of the cut surface under investigation. This can be achieved through sensitivity studies based on experiments or numerical simulations.

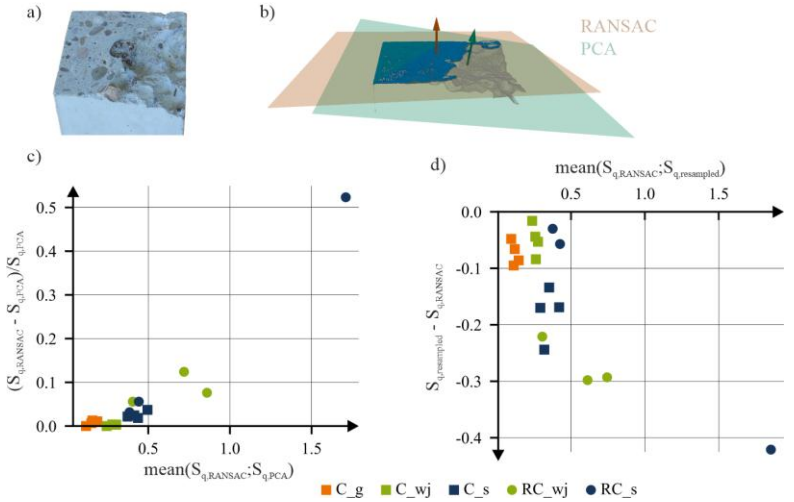


Fig. 5 Influence of the reference plane: a) concrete surface with a large spall, b) corresponding RANSAC and PCA planes, c) comparison of RANSAC and PCA based on S_q, d) influence of resampling on $S_{q,RANSAC}$

The 18 specimens, which were separated and processed using different fine processing methods, exhibit different surface qualities (see Fig. 5c). Ground surfaces show very low unevenness. Waterjet cutting leads to larger unevenness, particularly for the reinforced specimens as reflected mainly in the waviness component (see Fig. 4). Additionally, pronounced void formation is evident beneath the reinforcing bars of the RC specimens (blue spots in Fig. 6).

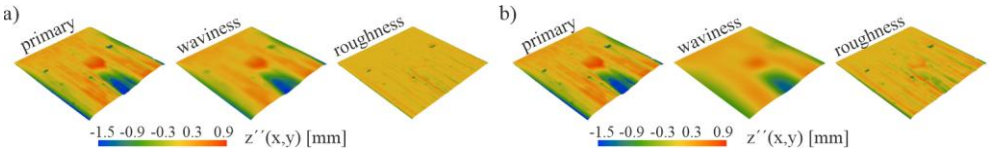


Fig. 6 Influence of scale limitation: $z''(x, y)$ coordinate heat maps of the waviness and roughness surfaces for nesting index N_{ic} of (a) 8.00 mm and (b) 20.0 mm (specimen RC_wj_1).

5 CONCLUSIONS

This paper presents a method for evaluating arbitrary surfaces from 3D scans. This provides a basis for further experiments investigating fine processing methods. The routine allows for the rapid evaluation of many rectangular specimens under consistent boundary conditions, ensuring comparability. Implementing the removal of side faces using density-based cutting reduces the manual effort required for pre-processing. The method can be extended to include additional parameters that describe surface characteristics. The following conclusions can be drawn:

(1) The initial parameter set in Table 1 is suitable for evaluating concrete surfaces with similar geometries and reliably removes the side faces to isolate the surfaces of interest. Depending on the application, the nesting indices must be defined by identifying the scale-limited range that best represents the relationship under investigation.

(2) The RANSAC plane is a more suitable reference plane for concrete surfaces than the PCA plane, because it aligns more closely with the cutting plane and is less affected by concrete spalls or voids. For surfaces with low S_q, the RANSAC plane closely resembles the PCA plane; however, the deviation increases as S_q increases.

(3) Resampling significantly influences the parameters as it smooths the measurement data. This is reflected in the lower S_q values before and after resampling, with the effect becoming more pronounced as the initial $S_{q,RANSAC}$ increases.

(4) The fine processing methods investigated result in different surface qualities. Waterjet cutting of RC specimens produces significantly greater unevenness than ground and sawn specimens, with the differences being especially pronounced in the waviness component.
(5) Distinguishing between waviness and roughness is essential when evaluating concrete surfaces. This is particularly relevant in the context of concrete dry joints, where roughness generally has a greater influence on shear transfer, whereas waviness is more important for compressive load transfer. Ongoing investigations characterise these parameters individually.

References

[1] Mark, Peter, et al. 2025. „Modular reuse of existing load-bearing structures." *Bautechnik* 102(8):424–435. doi: 10.1002/bate.70000.
[2] Zielonka, Hendrik et al. 2026. „Modular Reuse of Existing Load-Bearing Structures: from Concept to Full-Scale Demonstration.", *Beton- und Stahlbetonbau*. doi: 10.1002/best.70148
[3] Große-Kreul, Alexander et al. 2025. „Automated fine processing of reinforced concrete elements for modular reuse" *Bautechnik* 102(8):436-448. doi: 10.1002/bate.202500027
[4] Miro, Michael et al. 2025. "Reuse of Existing Reinforced Concrete Elements: Automated Fine Processing, Connection Designs, and Quality Assurance" *Beton- und Stahlbetonbau.* doi: 10.1002/best.70137
[5] Sanio, David et al. 2024. „Concrete-To-Concrete Connections for Modularly Reused RC Components – an Experimental Study on Separation Methods." In 4th fib ICCS 2024, 315–323. Cham: Springer Nature Switzerland. doi: 10.1007/978-3-031-80724-4_39.
[6] Schmidt, Boso et al. 2025. „Compressive strength of subtractively machined dry joints for connecting reused reinforced concrete components." *Beton- und Stahlbetonbau* 120(10):798–809. doi: 10.1002/best.70018.
[7] Schmidt, Boso et al. 2026. „Circular construction system with reused RC components – compressive load-bearing capacity of subtractively processed dry joints." *Journal of Building Engineering 117:114681*. doi: 10.1016/j.jobe.2025.114681.
[8] Wilkening, Marvin et al. 2025. „Investigations into roughness and load-bearing capacity of interfaces between normal-strength concrete and UHPC." *Beton- und Stahlbetonbau* 120(S1):27–39. doi:10.1002/best.202400084.
[9] Pieplow, Swantje 2026. „Automated evaluation and processing of 3D point clouds and their surface parameters".https://doi.org/10.60517/33a8802f-6e1e-48fd-aa07-73bb8a31bff2
[10] Nurunnabi, Abdul et al. 2012. „Diagnostic-Robust Statistical Analysis for Local Surface Fitting in 3D Point Cloud Data." *ISPRS Annals of the Photogrammetry, Remote Sensing and Spatial Information Sciences* I-3:269–274. doi: 10.5194/isprsannals-I-3-269-2012.
[11] Schnabel, Ruwen et al. 2007. „Efficient RANSAC for Point-Cloud Shape Detection." *Computer Graphics Forum* 26(2):214–226. doi: 10.1111/j.1467-8659.2007.01016.x.
[12] Fischler, Martin et al. 1981. „Random Sample Consensus." *Communications of the ACM* 24(6):381–395. doi: 10.1145/358669.358692.
[13] DIN EN ISO 12781-1:2011-07 „Geometrical product specifications (GPS) – Flatness – Part 1: Vocabulary and parameters of flatness. " Berlin: Beuth Verlag. doi: 10.31030/1734010.
[14] DIN EN ISO 16610-20:2015-12 „Geometrical product specifications (GPS) – Filtration– Part 20: Linear profile filters: Basic concepts". Berlin: Beuth Verlag. doi: 10.31030/2322996.
[15] Tsai, Victor J. D. 1993. „Delaunay Triangulations in TIN Creation: An Overview and a Linear-Time Algorithm." *International Journal of Geographical Information Systems* 7(6):501–524. doi: 10.1080/02693799308901979.
[16] Rippa, Samuel 1990. „Minimal Roughness Property of the Delaunay Triangulation." *Computer Aided Geometric Design* 7(6):489–497. doi: 10.1016/0167-8396(90)90011-F.
[17] DIN EN ISO 25178-3:2012-11 „Geometrical product specifications (GPS) – Surface texture: Areal – Part 3: Specification operators. Berlin: Beuth Verlag. doi: 10.31030/1876351.
[18] DIN EN ISO 25178-2:2023-09 „Geometrical product specifications (GPS) – Surface texture: Areal – Part 2: Terms, definitions and surface texture parameters". Berlin: Beuth Verlag. doi: 10.31030/3294021.
[19] Blateyron, François 2013. „The Areal Field Parameters." In Characterisation of Areal Surface Texture, 15–43. Berlin, Heidelberg: Springer. doi: 10.1007/978-3-642-36458-7_2.

Automated Industry Foundation Classes Modeling of Bridge Superstructures Via Knowledge Based Point Cloud Slicing

Marius Schellen and Christian Glock

Institute of Concrete Structures and Structural Design,
University Kaiserslautern-Landau (RPTU),
Paul-Ehrlich-Str. 14, 67663 Kaiserslautern, Germany

Summary
Ageing infrastructure and mandatory BIM requirements for German federal roads necessitate efficient digital bridge modelling. This research presents a knowledge-based method to reconstruct individual geometric objects from semantically enriched point clouds. Focusing on concrete slab and beam bridges, this approach utilises domain knowledge and standardised structural details to generate independent 3D objects. The process employs object-aligned slicing and RANSAC line-fitting for automated topology generation, implemented in a custom Python framework that exports native IFC entities. Validation using real-world datasets achieved a reconstruction coverage of 75% within a 10 cm threshold, featuring a median accuracy of -0.70 cm and an interquartile range of 4.57 cm.

1 INTRODUCTION AND MOTIVATION

Bridges are fundamental elements of infrastructure and essential for societal connectivity. In Germany the Federal Highway Research Institute alone manages over 52,500 bridge units predominantly constructed from reinforced or prestressed concrete. This inventory faces significant challenges as nearly half of the structures require repairs to prevent long term deterioration. Several thousand bridges already exhibit impaired stability necessitating immediate intervention [1]. Much of this decline is driven by age since the majority of the network was built in the 1970s and not designed for modern traffic volumes or load requirements which have nearly doubled since 1975 [2]. This maintenance demand coincides with a critical labour shortage and a shrinking working age population [3]. Simultaneously political mandates require the mandatory integration of Building Information Modeling (BIM) for construction measures on bridge structures [4]. Consequently, there is an urgent need for automated Scan to BIM solutions to create digital twins of existing bridges and ensure the long-term safety of the transport network.

1.1 Objectives

The principal objective of this research is the development of an automated processing methodology for generating BIM models from point cloud data. While the overall framework covers various bridge components this paper focuses exclusively on the reconstruction of the superstructure.

By incorporating domain specific knowledge the approach enables the precise reconstruction and separation of structural elements from point clouds. The methodology specifically targets concrete bridges with solid cross sections including roadways edge beams and load bearing structures such as slabs or girders. Key contributions include algorithms for point cloud slicing and geometric primitive fitting for longitudinal curved and sloped structures exhibiting constant or constantly varying cross-sections without abrupt changes or discontinuities. The process integrates non visible structural features through domain specific enrichment and ensures interoperability using the Industry Foundation Classes (IFC) 4.3 standard. A holistic approach is designed to combine labelled point cloud data input with final BIM output. The approach is validated using both synthetic and real world datasets to assess robustness specifically for complex superstructure geometries.

1.2 Methodology

The proposed Scan to BIM workflow requires a semantically enriched point cloud where each point is assigned a specific object class label. This research focuses on the reconstruction of the bridge superstructure which contains multiple objects following a continuous course in 3D space. The methodology begins by identifying the main alignment of the bridge. For this purpose, object-oriented

bounding boxes are iteratively applied to the segmented roadway points to determine multiple course points describing the general superstructure route. Following the course determination all points of the superstructure are processed while retaining their semantic classifications. The point cloud is segmented and projected into 2D slices perpendicular to the gradient line creating a series of cross-sections along the bridge course. Within each slice object-specific vertices are reconstructed using a Random Sample Consensus (RANSAC)-based line-fitting algorithm [5] to identify cross-sectional outlines. These geometries are subsequently extended by incorporating domain-specific knowledge such as predefined roadway thicknesses and non-visible internal outlines of edge beams or deck slabs. This domain-specific knowledge is based on standard bridge drawings for German bridge design but can also be adapted manually in the implemented framework if specific object information is available. To generate the final BIM model the reconstructed vertices and faces are integrated into an IFC-based digital twin using the Python library IfcOpenShell. The components are inserted as mesh representations to accommodate complex longitudinal curvatures and varying cross-sections. Each object is assigned its corresponding IFC class based on the semantic labels which ensures a standardised and interoperable output. This automated processing workflow transforms raw spatial data into a functional as-built model suitable for infrastructure management and maintenance planning.

1.3 Related Work and Research Gap

Current research in automated bridge reconstruction primarily follows either parametric fitting or surface-driven approaches. Projects like TwinGen and Qin et al. [6, 7] utilise parametric models which require predefined geometric templates to fit point clouds through parameter estimation. While robust against occlusions, these methods lack flexibility for irregular structures. Conversely, slicing-based methods like those of Lu and Brilakis [8] or surface reconstructions by Schatz and Domer [9] offer higher flexibility but often lack the capability to account for vertical gradients or longitudinal cross-section variations, while also suffering from noise sensitivity. A significant research gap exists between these rigid parametric models and purely discrete surface representations. This research addresses this gap by combining a highly flexible slicing-based reconstruction with domain-specific structural knowledge. By utilising a RANSAC-based algorithm, the framework achieves high robustness against noise and outliers inherent in real-world scans without requiring a fully predefined parametric model. This allows the precise reconstruction of complex longitudinal curvatures and varying cross-sections while simultaneously incorporating non-visible structural details, such as internal deck offsets, to generate valid IFC-based digital twins.

2 OPEN BIM

Building Information Modelling (BIM) serves as a collaborative technology for managing infrastructure data throughout its lifecycle. To ensure vendor neutrality and avoid proprietary lock in this research adheres to Open BIM principles using the Industry Foundation Classes (IFC) 4.3 standard. A central aspect is the spatial hierarchy defined within the IFC framework where the IfcBridge entity acts as the primary container. This structure supports a full decomposition into distinct spatial zones including the foundation, substructure and superstructure levels to reflect the functional composition of the asset. While the overall schema covers all lifecycle levels this paper focuses exclusively on the superstructure container which logically groups elements such as the roadway edge beams and load bearing deck components. The practical implementation of the reconstruction framework relies extensively on the open source library IfcOpenShell. This toolchain enables the automated generation of the general IFC model and the seamless integration of reconstructed objects. While traditional design often uses swept solid geometries or rigid parametric extrusions this research adopts a mesh based representation using IfcPolygonalFaceSet. This approach is better suited for capturing the as built condition of existing structures as it preserves geometric fidelity and structural deviations that mathematical curves might oversimplify. By combining the hierarchical IfcBridge structure with flexible mesh geometries the proposed method generates standardised digital twins that accurately reflect the physical reality of the bridge superstructure.

3 MODULAR RECONSTRUCTION FRAMEWORK AND IMPLEMENTATION

The automated transformation of semantically enriched point clouds into standardised BIM structures requires a highly integrated approach that combines spatial data processing with domain specific structural logic. The methodology developed in this research is realised within a modular Python-based framework designed to handle the geometric complexities of bridge superstructures, such as longitudinal curvatures, slopes, and continuously varying cross-sectional dimensions. This approach specifically accommodates structures without abrupt topological discontinuities, such as haunched beams or large-radius arched systems, where the cross-sectional profile evolves smoothly along the longitudinal course. By synchronising the theoretical reconstruction steps with a technical implementation using among others NumPy and Open3D, the framework ensures that the resulting digital twins are both geometrically accurate and topologically consistent. Scene specific input, including file paths to the input data and parameter values is provided by a YAML configuration file.

3.1 Automated BIM Initialisation and Spatial Hierarchy Setup

The framework begins by establishing a formal IFC environment which serves as the target structure for all reconstructed geometries. Utilising the IfcOpenShell library the system generates an empty IFC 4.3 file that incorporates the necessary project metadata and the spatial decomposition for IfcBridge projects. A critical component of this initialisation is the creation of a hierarchical container system comprising the IfcProject, IfcSite, and IfcBridge entities. Within the IfcBridge container the framework predefines spatial parts for the superstructure and substructure. This early structuring ensures that as each structural element is reconstructed it can be immediately assigned to its correct semantic class and spatial location which facilitates a continuous and automated model enrichment process.

3.2 Data Preprocessing and Global Scene Alignment

To ensure the robustness of the subsequent slicing and fitting algorithms the raw input data undergo a rigorous multi stage preprocessing sequence. The initial task involves a voxel based downsampling to homogenise the point cloud density across the entire scene. Following density homogenisation the workflow performs a global geometric alignment which is a fundamental prerequisite for the longitudinal slicing logic. The methodology assumes that the primary axis of the bridge is aligned with the global x axis. To achieve this the roadway points are isolated via their semantic labels and further refined using a Density Based Spatial Clustering of Applications with Noise (DBSCAN) algorithm [10]. This step ensures that only the points belonging to the bridge roadway are used for alignment while excluding adjacent road surfaces or terrain. A Principal Component Analysis (PCA) is then applied to the filtered roadway cluster to extract the dominant eigenvectors. Based on these vectors a three dimensional rotation matrix is calculated to align the bridge course with the x axis. The rotation matrix and the corresponding rotation centre are stored in the system memory allowing for the final reconstructed vertices to be transformed back into their original real world coordinates at the end of the process. Following the completion of the preprocessing stage the standardised point cloud data is provided as a $(n \times 7)$ NumPy array, containing xyz-coordinate information, RGB-colur information and the specific object label as defined integer values.

3.3 Superstructure Course Determination and Iterative Refinement

The core of the geometric reconstruction is the determination of the superstructure course which is defined as the three dimensional roadway centreline. This course serves as the guiding polyline for the entire slicing operation. The preprocessed and x axis aligned roadway points are partitioned into longitudinal segments using axis aligned bounding boxes with a configurable thickness in x direction (Fig. 1 (top left)). For each segment the centroid is calculated to provide an initial approximation of the bridge alignment (Fig. 1 (top mid)). This initial course represents a discrete $(m \times 3)$ coordinate array where m denotes the number of segments along the x axis.

To achieve a higher precision in structures with significant horizontal or vertical curvatures the proposed method employs an iterative refinement process. The initial segments are converted into object oriented bounding boxes which are rotated to align with the local course vectors derived from the initial centroids. The bounding box dimensions are then reduced to tightly enclose the local point clusters thereby eliminating the influence of outlying points (Fig. 1 (top right)). The centroids are recalculated from these refined boxes to reflect the true geometric centre of the curved roadway. This iterative approach ensures that the resulting superstructure course remains highly accurate even in

complex as built geometries where simple axis alignment would result in projection errors (Fig. 1 (bottom)).

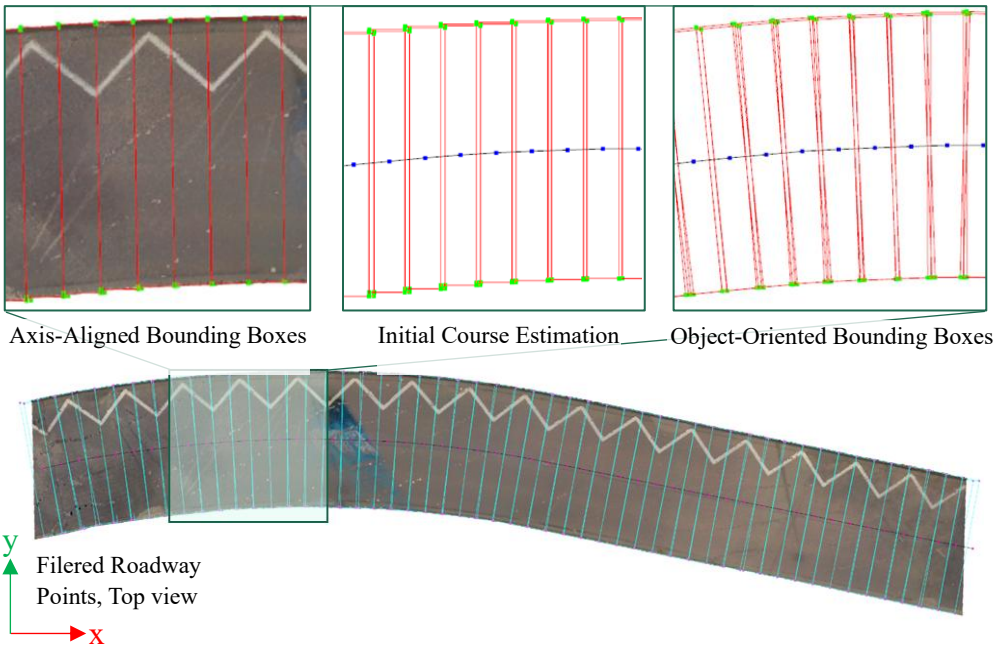


Fig. 1 Superstructure course determination using roadway segments and bounding boxes.

3.4 High Density Slice Generation and Transformation

Once the refined superstructure course is finalised the entire superstructure point cloud is reduced to a set of cross sectional slices. Each slice is generated by identifying the points within a longitudinal range of $(\pm\frac{|\vec{v}|}{2})$ relative to the local course vector $(\vec{v})$ (Fig. 1 (top right)). To maintain a consistent orientation, the points within each segment are projected onto a shared two-dimensional base plane perpendicular to the local course vector via a linear orthogonal projection This slicing approach is a critical advantage of the methodology as it allows for the reconstruction of bridges with continuous curvatures without the distortions that occur during global coordinate projections.

The resulting slices are stored as a list of independent $(n_i \times 7)$ NumPy arrays, where n_i represents the number of points in slice i (Fig. 2 (left)). To ensure the stability of the subsequent geometry fitting, the framework framework implements a point count consistency criterion. This filtering mechanism identifies and excludes slices with significant deviations in point density compared to the global average. By focusing exclusively on slices that exhibit a relatively homogeneous point distribution, the algorithm prevents the generation of faulty geometries in areas affected by severe occlusions or insufficient data coverage at the extreme longitudinal boundaries. This ensures that only slices providing a reliable foundation for RANSAC fitting are processed further.

3.5 Knowledge Based Geometry Reconstruction and Topological Merging

The geometric details of each slice are extracted through a differentiated line fitting process using the RANSAC algorithm. Each semantic object class within the $(n_i \times 7)$ array is processed independently. For components like edge beams which appear symmetrically on both sides of the bridge a DBSCAN step is integrated to separate the point clusters before fitting. The framework utilizes specific RANSAC parameters for different classes where general structural elements like the roadway and concrete deck are processed with a rigid distance threshold (ϵ_{line}), while edge beams receive a more tolerant threshold $(\epsilon_{line,312})$. This increased tolerance is essential to account for the higher levels of noise and surface

contamination found at the bridge edges which were identified during the experimental analysis of the real world datasets. Based on the default parameters or those specified in the configuration file, RANSAC line fitting is conducted to detect all linear features for the individual objects within each respective slice. The resulting inlier points are subsequently clustered using DBSCAN to isolate the specific line segment points. This step ensures that only the relevant local surface points are extracted, effectively excluding other cross-sectional points that might satisfy the line requirements but do not belong to the local geometry. Following this, the inlier points are reduced to vertices describing the endpoints of the segments by identifying the point pairs with the largest Euclidean distance. These vertices are then enriched with a line identifier to track the affiliation between detected lines and their corresponding endpoints. This process returns an $(n_i \times 8)$ array, where n_i represents the extracted vertices of the respective slice. The newly added eighth column contains the line affiliation index corresponding to the RANSAC line from which the vertices were derived

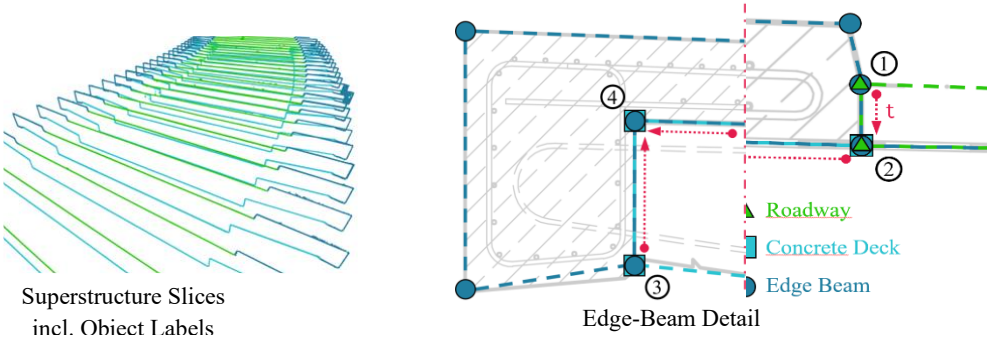


Fig. 2 Generated 2D cross-section slices and knowledge based vertex extraction and generation for adjacent roadway, concrete deck and edge beam objects.

A critical feature of the presented methodology is the integration of domain-specific knowledge to generate non-visible surfaces since laser scans only capture external boundaries. Standard German bridge design rules [11] are utilised to enrich the geometry by applying a default asphalt thickness (t) to the visible roadway line to generate a volumetric representation (Fig. 2 (right)). Following the identification of the visible roadway line by the RANSAC algorithm, the corresponding vertices with the largest Euclidean distance in 3D space, are duplicated and translated along the negative z axis by a default thickness of 0.08m to represent the asphalt layer. This thickness value is a default estimation, based on domain knowledge for typical bridge asphalt thicknesses and can be adapted in the configuration file, in case additional bridge specific information is available. Furthermore, the edge points from the roadway are duplicated to define the upper boundaries of the underlying concrete deck and adjacent edge beams (Fig. 2 (right)). Vertices for the inner corners of edge beams which are not visible in scans are generated through horizontal and vertical projections of visible points based on standardised structural details (Fig. 2 (right and mid)). All generated vertices recieve a line affiliation value of negative one. This ensures a propper distinction between detected vertices based on the input data and knowledge-based generated ones. Finally, a vertex-merging logic is applied using a distance threshold to eliminate redundant points and ensure a consistent topological connection between adjacent objects. Within this process an additional line affiliation column is added to the vertices array, resulting in a $(n_i \times 9)$ shape, storing the possible occuring two line information from two merged vertices.

3.6 Topological Sorting, IFC Mesh Generation and Model Integration

To prepare the data for the generation of the digital twin the framework performs a topological sorting of the vertices within each slice. The algorithm identifies the modal vertex count across all slices to ensure a homogeneous mesh topology. Slices that deviate from this count are excluded to prevent discontinuities in the final volume. The vertices of each object are then organised to meet the specific mesh generation requirements. Additionally, a face description logic is employed to ensure proper geometric closure. Each face is represented by a tuple which refers to the corresponding vertex indices in an enclosing order. To preserve the original spatial context all vertices are rotated back to their initial coordinate orientation using the transpose of the rotation matrix before they are passed to the final BIM

generation module. This mesh based representation was chosen to accommodate the potential variations in cross sectional geometry that occur in as built structures. A custom face reconstruction algorithm generates the three dimensional volume by first forming the front and back edge faces of each object. The lateral surfaces are then created by connecting the corresponding vertices between consecutive slices to form a sequence of quadrilateral polygons. Finally, these reconstructed objects are assigned to their respective semantic classes such as slabs or beams and correctly integrated into the spatial containers of the bridge hierarchy. This results in a structured and interoperable digital twin that accurately represents the physical reality of the bridge infrastructure.

4 RESULTS AND DISCUSSION FOR SUPERSTRUCTURE RECONSTRUCTION

The evaluation of the superstructure reconstruction is based on real-world point cloud data, utilising both the open-source dataset by Lu and Brilakis [11] and self-recorded scenes (GDS1, GDS2, and BB). It should be noted that the dataset by Kellner et al. [12] was excluded as it was published in December 2025, after the experimental phase of this research.

4.1 Evaluation Metrics and Dataset Characteristics

To assess performance, the cloud-to-mesh distance is employed as the primary metric. A reconstruction coverage metric quantifies the quality and completeness of the model by calculating the percentage of the total input points successfully represented within a defined spatial tolerance. A 10 cm threshold is applied to real-world scans to distinguish between successful reconstruction and non-covered regions affected by artifacts or noise. This pragmatic cut-off ensures that accuracy metrics exclusively reflect the geometric precision of the functional model by excluding extreme outliers. Statistical analysis is conducted exclusively for points within this threshold, using the median and interquartile range to evaluate precision. The analysis further incorporates the first and third quartiles, where the interquartile range represents the central range containing 50% of the evaluated points. This metric effectively quantifies the geometric dispersion around the median while minimizing outlier influence within the threshold. The investigated dataset exhibits high geometric variability, including curved alignments and sloped profiles. However, several scenes from the open-source dataset (Bridge 4 and 7) were excluded from the final evaluation. These scenes presented insurmountable challenges such as extreme vegetation, insufficient point coverage on complex I-girder systems, or fragmented geometries from misaligned scans that prevented stable RANSAC line fitting.

Table 1 Cloud to mesh distance evaluation of reconstructed scanned bridge objects.

Point Cloud Scenes	Total Points [n]	Coverage (10cm) [%]	Median [cm]	Q1 [cm]	Q3 [cm]	IQR [cm]
Bridge 1	5,844,576	71.18%	-1.04	-4.72	2.15	6.87
Bridge 2	2,410,611	74.24%	-1.47	-3.49	2.32	5.81
Bridge 3	3,229,090	81.78%	1.82	0.55	2.56	3.11
Bridge 5	2,743,187	93.06%	2.67	-0.92	4.57	5.49
Bridge 6	31,266,568	60.30%	-2.60	-3.84	-0.24	4.08
Bridge 8	36,818,623	89.76%	-1.76	-2.74	-0.49	3.23
Bridge 9	35,223,832	58.12%	-4.97	-5.91	1.52	7.43
Bridge 10	31,221,687	40.50%	-2.20	-4.65	0.00	4.65
GDS1	155,311,874	68.63%	3.24	0.64	3.96	4.60
GDS2	7,393,891	93.82%	-1.04	-1.55	0.28	1.83
BB	31,931,742	91.88%	-0.36	-1.92	1.25	3.17
Aggregate	343,395,681	74.84%	-0.70	-2.60	1.63	4.57

4.2 Reconstruction Performance

For the remaining eleven scenes, the framework achieved an aggregate reconstruction coverage of 74.84% across more than 343 million points. The results show significant heterogeneity depending on data quality. While Bridge 10 reached only 40.50% coverage due to sparse peripheral data, the self-recorded high-quality scans GDS2 and BB achieved values exceeding 90%.
The geometric accuracy is highlighted by an aggregate median cloud-to-mesh distance of minus 0.70cm and an IQR of 4.57cm (Table 1). The violin plot distributions, shown in Fig. 3, confirm that scenes with homogeneous point coverage and professional acquisition, such as GDS2 (Median: -1.04cm, IQR: 1.83cm) and BB (Median: -0.36cm, IQR: 3.17cm), yield superior results with a strong accumulation of points near the target geometry. In contrast, GDS1, which was captured under adverse winter conditions with surface debris, showed significantly higher deviations (Median: 3.24cm, IQR: 4.60cm), proving that acquisition quality is more decisive than point density alone.

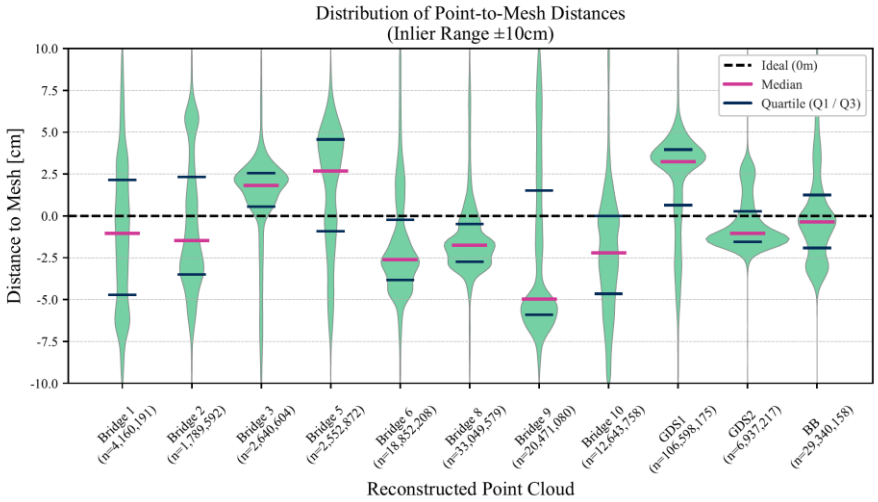


Fig. 3 Distribution of the point-to-mesh distances within a ±10 cm threshold boundary for scanned superstructure point clouds.

4.3 Discussion and Limitations

The findings demonstrate that the hierarchical coupling of structural elements ensures a coherent global geometry without gaps between adjacent objects. However, this interdependency also means that inaccuracies in the initial roadway reconstruction propagate through all subsequent stages. The reliance on RANSAC for line detection proved robust but sensitive to local noise, requiring scene-specific parameterisation. A significant limitation remains the requirement for a homogeneous vertex count across slices. Slices with inconsistent vertex numbers due to local occlusions or merging errors must be discarded, which reduces overall coverage. Furthermore, the exclusion of non-load-bearing elements like railings and occluded substructures like abutments limits the current model completeness. Future research should focus on automated parameter optimisation and the integration of the December 2025 Kellner [12] dataset to further validate the generalisability of the framework across diverse infrastructure conditions.

5 CONCLUSION AND OUTLOOK

This research presents a scalable and automated approach for the Scan to BIM reconstruction of concrete bridge superstructures. By generating independent 3D objects instead of monolithic geometries the framework provides a high level of detail that supports the complex requirements of modern infrastructure management. The consistent reliance on the IFC 4.3 standard ensures that the resulting digital twins are fully interoperable and ready for integration into federal management systems. While the developed framework offers a significant contribution to the digital transformation of the transport sector certain limitations regarding the degree of automation remain. The current methodology relies on pre segmented point clouds which necessitates a manual or semi automated preprocessing stage. Furthermore, while the approach handles standard concrete geometries with high

precision extremely irregular or heavily damaged structures may still require additional refinement. Future research should focus on the full integration of deep learning models for automated semantic segmentation to create a seamless end to end Scan to BIM solution. In conclusion this work provides a reliable and accurate foundation for the digitalisation of existing bridge infrastructure and supports the mandatory implementation of BIM in the German transport sector.

Acknowledgements

This work was part of the HumanTech project and has received funding from the European Union under Grant Agreement No. 101058236. HumanTech was a three-year project that started on the 1st June 2022 and terminated on the 31st May 2025.

References

[1] BASt. 2025. "Fokus Brücken: Brückenstatistik." Accessed February 2026. https://www.bast.de/fokusbruecken.

[2] BMVI. 2017. "Richtlinie für die Erhaltung von Ingenieurbauten (RI-EBW-PRÜF)." Accessed February 2026. https://www.bast.de/DE/Publikationen/Regelwerke/Ingenieurbau/Erhaltung/RI-EBW-PRUEF-Erhaltung.pdf.

[3] Statistik der Bundesagentur für Arbeit. 2023. "Fachkräfteengpassanalyse 2023: Blickpunkt Arbeitsmarkt." Accessed February 2026. https://statistik.arbeitsagentur.de/DE/Navigation/Statistiken/Interaktive-Statistiken/Fachkraeftebedarf/Engpassanalyse-Nav.html.

[4] Meister, Andreas, Scholz, Felix, and Banemann, Silvia. 2021. "Masterplan BIM Bundesfernstraßen." Edited by BMVI. Accessed February 2026. https://www.bundesfernstrassen-digital.de/fileadmin/user_upload/BIM_Masterplan_Bundesfernstrassen_barrierefrei.pdf.

[5] Schnabel, Ruwen, Wahl, Roland, and Klein, Reinhard. 2007. "Efficient RANSAC for Point-Cloud Shape Detection." *Computer Graphics Forum* 26:214–226. doi:10.1111/j.1467-8659.2007.01016.x.

[6] Vilgertshofer, Simon, Mafipour, Mohammad S., Borrmann, André, Martens, Jan, Blut, Timothy, Becker, Ralph, Blankenbach, Jörg, Göbels, Anne, Beetz, Jakob, Celik, Firdes, Faltin, Benedikt, and König, Markus. 2022. "TwinGen: Advanced technologies to automatically generate digital twins for operation and maintenance of existing bridges." Accessed February 2026. https://publications.cms.bgu.tum.de/2022_TwinGen_ECPPM.pdf

[7] Qin, Guocheng, Zhou, Yin, Hu, Kaixin, Han, Daguang, and Ying, Chunli. 2021. "Automated Reconstruction of Parametric BIM for Bridge Based on Terrestrial Laser Scanning Data." *Advances in Civil Engineering* 2021. doi:10.1155/2021/8899323.

[8] Lu, Ruodan, and Brilakis, Ioannis. 2019. "Digital twinning of existing reinforced concrete bridges from labelled point clusters." *Automation in Construction* 105:102837. doi:10.1016/j.autcon.2019.102837.

[9] Schatz, Yohann, and Domer, Bernd. 2024. " Semi-automated creation of IFC bridge models from point clouds for maintenance applications." *Frontiers in Built Environment* 10. doi:10.3389/fbuil.2024.1375873.

[10] Ester, Martin, Kriegel, Hans-Peter, Sander, Jörg, and Xu, Xiaowei. 1996. "A Density-Based Algorithm for Discovering Clusters in Large Spatial Databases with Noise." *Knowledge Discovery and Data Mining (KDD-96)*. https://api.semanticscholar.org/CorpusID:355163.

[11] BMDV. 2023. "Richtzeichnungen für Ingenieurbauten (RiZ-ING): Ausgabe 12/2023." Accessed February 2026. https://www.bast.de/DE/Publikationen/Regelwerke/Ingenieurbau/Entwurf/RiZ-ING-Gesamt.pdf.

[12] Lu, Ruodan, Brilakis, Ioannis, and Middleton, Campbell R. 2018. "Detection Of Structural Components In Point Clouds Of Existing RC Bridges." doi:10.5281/ZENODO.1240534.

[13] Kellner, Maximilian, Cervantes, Mariana F., Pan, Yuandong, Lu, Ruodan, Brilakis, Ioannis, and Reiterer, Alexander. 2025. "SemanticBridge: A Dataset for 3D Semantic Segmentation of Bridges and Domain Gap Analysis." https://arxiv.org/pdf/2512.15369.

Capturing Reality or Modeling It? Point Clouds vs Building Information Modeling in Bridge Monitoring

Martin Koehncke & Sylvia Kessler

Engineering Materials and Building Preservation,
Helmut-Schmidt-University / University of the Federal Armed Forces Hamburg
Holstenhofweg 85, 22043 Hamburg, Germany

Summary
Documenting Structural Health Monitoring (SHM) systems on bridges is often laborious and time-consuming, even for small projects. Digital tools like laser scanning and Building Information Modeling (BIM) offer clear advantages over paper-based methods; however, no single solution is universally applicable. This study addresses the selection of an approach that enables rapid and reliable documentation in a machine-readable format. The methodology comprises a literature review of the approaches for digital documentation and the definition of comparison criteria. The paper concludes with a discussion of future research directions. Laser scanning is efficient and rapid for sensor position documentation, whereas, BIM optimises the central allocation of alpha-numerical information within the SHM.

1 INTRODUCTION

The documentation of monitoring systems on existing bridges is often a time-consuming and complex process. Documentation of SHM systems is a key aspect of continuous bridge monitoring, since the evaluation of measurement data depends directly on knowledge of the sensors used and their positions. The most common form of documentation uses sketches and plans. Paper-based documentation is subject to the effects of ageing, and frequently constitutes a media break in processing, which results in additional costs. Different technologies offer advantages over paper-based documentation or, at least, simplify the process. The use of machine-readable documentation has been demonstrated to enhance accessibility and processing options for information, thereby facilitating further digitisation. One such technology is laser scanning, in which the surface of a structure is scanned with a laser beam and converted into a point cloud. This process is sometimes combined with colour information from images to generate a representation of the bridge's geometry and surface appearance.

The BIM method enables the central provision of building information combined with geometric information for collaboration between different stakeholders. The implementation of this approach throughout the entire life cycle is expected to minimise information loss during transitions between the different phases. [1]. In Germany, the Federal Ministry of Transport has published a standardized structure for the definition of BIM use cases and requires the use of BIM for public tenders and projects involving federal highways. Within this context, use cases refer to the tasks or processes that are intended to be supported or enabled through BIM [2].

Point clouds and BIM models can be used for the digital documentation of existing bridges and may serve as a foundation for digital twins. Digital twins are defined as the digital representation of physical systems, with the additional capability of bidirectional data exchange [3,4].

The two methods have different advantages and disadvantages, making them more or less suitable for different aspects of digital twins depending on the use case. To clarify these differences the following section examines reality capture using technologies such as laser scanning and reality modelling using approaches such as BIM in greater detail, using the documentation of an SHM system as an illustrative example. First, the research objectives of this study are introduced, followed by a description of the methodology. The results are then discussed, leading to a conclusion and an outlook on future research needs.

2 RESEARCH OBJECTIVES

The creation of digital twins can be achieved through a variety of procedures. The digital twin's function is pivotal in this regard, as it determines which aspects of the physical system are to be digitally mapped.

This publication focuses on the development of a digital twin for the documentation and subsequent evaluation of SHM systems for existing bridge structures.

First, the requirements for procedures to support the generation of digital twins are identified. Next, the procedures for capturing and modeling reality are compared and assessed against these requirements.

3 METHODOLOGY

Germany's highway network comprises almost 41,000 bridge structures, highlighting the considerable scale of the associated administrative effort [5]. Despite the relatively limited number of structures equipped with SHM systems, the effort required is nevertheless significant. Consequently, the efficiency of SHM documentation procedures should be primarily evaluated based on the time required for implementation. The costs of documentation cannot be easily determined, as the purchasing conditions for the organisations are not directly comparable. Therefore, the present evaluation focuses on technical requirements, which, in conjenction with the time demand, can be used to make a preliminary estimate of the costs. Furthermore, the associated accuracy should also be considered as a quality criterion, since rapid deployment without the necessary quality may lead to redundancy. Another important aspect is the connectivity of the documentation output to subsequent processing steps, including potential reuse for applications such as bridge inspections or structural re-analysis.

A comparison of the methods can be facilitated by examining the aspects of a physical system that are captured or modelled by each. To illustrate this, the physical system can be simplified as a cube, with each side representing a different aspect. These aspects can be differentiated into geometry, attributes, and the relations between them, as shown in Figure 1.

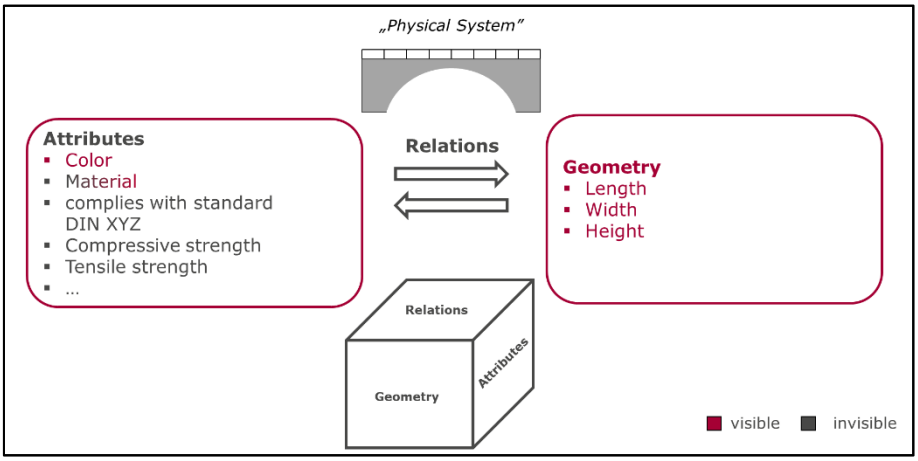


Fig. 1 Aspects of a physical system

Additionally, a distinction can be drawn between visible and invisible aspects. While the geometry of the surface is visible, certain attributes, such as compliance with a standard, remain inherently invisible. The visible sides of the cube are representative of these visible aspects, while the hidden sides are representative of the hidden geometry, attributes, and relationships. However, the invisible aspects can be supplemented by other data sources. For instance, non-destructive techniques such as ground penetrating radar (GPR) can be used to determine the exact positions of the reinforcement in the concrete.

Laser scanning is an effective method of acquiring data regarding the geometry of structures; however, it is important to note that it does not provide any information on component boundaries, semantic relationships, or alphanumeric attributes. The visual capture of the subject is limited to features that are perceptible to the human eye. Nevertheless, laser scanning enables subsequent measurements directly within the point cloud, such as determining distances between sensors mounted on the underside of a bridge deck, as demonstrated in Figure 2. The accuracy of the measurement depends directly on the selected point density during the acquisition process and post-processing.

Higher point densities increase accuracy, but also result in larger file sizes, which can reduce the efficiency of data handling and editing.



Fig. 2 Representation of a subsequent distance measurement in a laser point cloud

In contrast, BIM modelling represents knowledge about the structure, in particular the geometry and attributes of its components. In addition, the IFC data format stores basic semantic relationships between elements, enabling, for example, the identification of whether a component belongs to a larger assembly or structural system. Simplifications of the geometry, such as the generation of elements by extruding the cross-section, are frequently implemented to expedite the modelling process [6]. The level of detail of the attributes often depends on its intended use cases. In certain instances, the focus is on the basic material properties to reduce the modeling effort. Figure 3 illustrates an example IFC model.

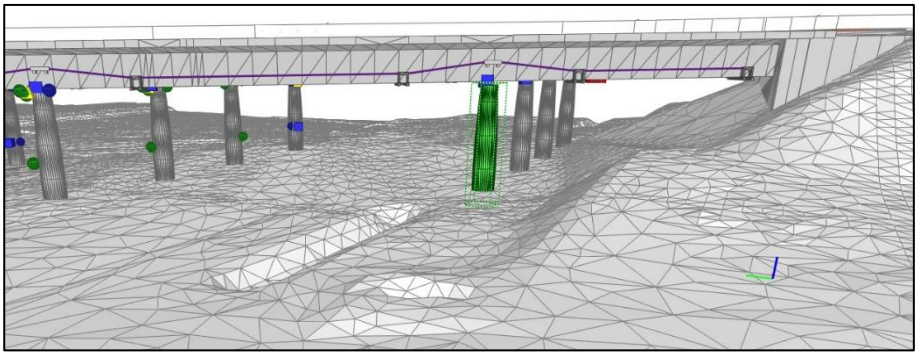


Fig. 3 Example of an BIM Modell

In addition to the use of BIM for the purpose of modelling, alternative methodologies exist for the mapping of physical systems, such as finite elements analysis (FEA). The primary objective of FEA is to predict the behaviour of complex structures through simulation and analysis, thereby supporting improved design quality. Its core principle is the mathematical formulation of relationships between discretised finite elements. However, a detailed discussion of FEA within the scope of the present comparison is beyond the focus of this publication.

The primary requirement for the evaluation process is the time required to carry out the procedure. At present, there is a lack of comprehensive overviews of the time demand for laser scanning and BIM modelling across different structures. In practice, the required effort depends strongly on factors such as the equipment used, the intended purpose and level of detail of the resulting point cloud or model, and the experience of both field surveyors and BIM modellers. Consequently, it is not possible to provide a universally applicable time value. However, several publications report time estimates for

specific structures. Nevertheless, several publications report time estimates for specific structures. Although these values are context-dependent, they provide a useful indication of the expected order of magnitude. An overview is provided in the following table.

Table 1 Overview of estimated times requirements for the generation of point clouds and BIM models

Structure	Dimension Span [m]	Dimension width [m]	Time for point cloud [h]	Time for BIM model [h]	Source
Trough bridge	5.8	3.8	1-2 capturing and 54 postprocessing	No BIM Modell created	[7]
Slab bridge	2.95	4.5			
Arch bridge	4	41.2			
Trough bridge	5.5	3.8			
Trough bridge	6.9	3.9			
Girder bridge	32.9	4.54			
Box girder bridge	66	Not specified	50	180	[8]

In the design of a trough bridge, the roadway or railroad tracks are positioned between two girders or load-bearing side walls. This configuration enables a reduction in the overall height of the bridge structure. The values given in the literature for the creation of point clouds indicate only a weak correlation between bridge size and the effort required to create them, at least for bridges up to a length of 66 m that have been examined. In contrast, the effort for BIM modelling depends strongly on the targeted level of information and the availability of input data. Consequently, a meaningful comparison is not possible without further analysis.

Another important aspect is the potential for the results to be reused in the subsequent workflows. Point clouds enable desk-based measurements, reducing the need for repeated site visits and allowing dimensions to be extracted remotely. If colour information from images is added, visible surface changes such as discolouration may also be assessed. The point clouds can also be supplemented with points of interest (PoI) to provide information on relevant points. However, it should be noted that these are not standardised, which means that the information they contain may vary. In addition to its application in surveying tasks, laser scanning is also utilised for the purposes of inspection and construction progress monitoring [4].

Conversely, BIM models are designed to store more comprehensive and structured information about a structure, which enables their use across a wide range of applications, even beyond those initially defined. The Federal Ministry of Transport in Germany has already defined 20 different use cases for federal highways. These include demand planning, visualisation for public relations, coordination of trade contractors, derivation of planning documents, approval and defect management, and project and construction documentation. A detailed description of the use cases can be found in [2]. Currently, the focus of use cases remains on the planning and realisation phase, but this is slowly shifting towards the operational phase. In the context of SHM, one example includes the maintenance of the monitoring system, which can be supported by incorporating maintenance intervals into the model or the integration of assessment and maintenance records [9]. Furthermore, the evaluation of measurement data of the SHM System can benefit from precise geometric localisation of sensors and structural components.

The data formats employed are also relevant for downstream processing, as they influence interoperability between software tools. In the context of BIM, the IFC file format is widely established as an open standard [10]. Point clouds can be stored in a variety of formats, including the E57 data format. However, it should be noted that a multitude of proprietary file formats exist, with some of these being developed by the manufacturers of the laser scanners themselves. In most cases, these formats can be readily converted into other file formats, thereby necessitating only a single additional intermediate step for further processing.

After a concise overview of the procedures, their application in the context of SHM for bridges is subsequently discussed.

4 DISCUSSION

The use of sensors for the purpose of continuous bridge monitoring is becoming increasingly prevalent in civil engineering. At present, SHM finds primary application in critical structures, characterised by their large dimensions, condition, and importance within the transport network. A notable example is the Köhlbrand Bridge in Hamburg, where monitoring is integrated into the broader framework of the main transport routes in the Port of Hamburg [11]. Such applications are often associated with complex structural systems and restricted accessibility for inspections and documentation.

Laser scanning point clouds can substantially support the documentation of SHM systems, as they enable high-precision capture of exposed surfaces without requiring direct contact with the structure. In this context, the use of unmanned aircraft systems (UAS) is becoming increasingly relevant [4]. However, point clouds are inherently limited to visible surfaces, meaning that sensors embedded within structural components cannot be identified or documented. BIM, by contrast, can represent concealed components, provided that their existence and location are known and documented. Moreover, BIM-based documentation does not necessarily require extensive on-site access if reliable design documentation is available. Nevertheless, comparing available plans with the as-built structure can be beneficial to account for modifications introduced during service life.

Both methods allow the user to define the desired level of geometric accuracy. Nevertheless, higher accuracy typically results in increased creation and processing time. This trade-off is generally less pronounced for point clouds, as geometries of varying size can often be captured with comparable effort and without substantial loss of accuracy. In addition to geometry, BIM can incorporate alphanumeric information, enabling a more comprehensive representation of physical reality. Point clouds, in contrast, capture geometric information only. Literature-based time estimates indicate clear advantages of point cloud acquisition compared to BIM model generation. For BIM, however, the required effort is highly project-specific and influenced by the targeted level of detail and the availability of input information (e.g., material properties). In the case of SHM documentation, this dependency may be less critical, as monitoring systems are often installed relatively recently and relevant information may already exist in digital form.

The connectivity of point clouds is supported through open formats such as E57; nevertheless, direct reuse is often limited because many downstream applications require alternative input types, such as meshes. Moreover, the incorporation of points of interest (PoIs) into enriched point clouds does not inherently ensure that the additional information is provided in a standardised manner, which can impede immediate evaluation and automated reuse. BIM offers more favourable conditions for subsequent use across the structure's life cycle, as the open IFC format provides information in a structured and machine-interpretable form. This also enables the later implementation of additional use cases that may not yet be defined. The IFC further supports interoperability between different software tools [12]. However, the practical benefits of the implementation are contingent upon the degree of IFC integration within the respective tools and on whether the necessary information has been modelled consistently. Since a comprehensive assessment of these aspects is beyond the scope of this study, the evaluation focuses on the available data format options. The results are summarised in Figure 4.

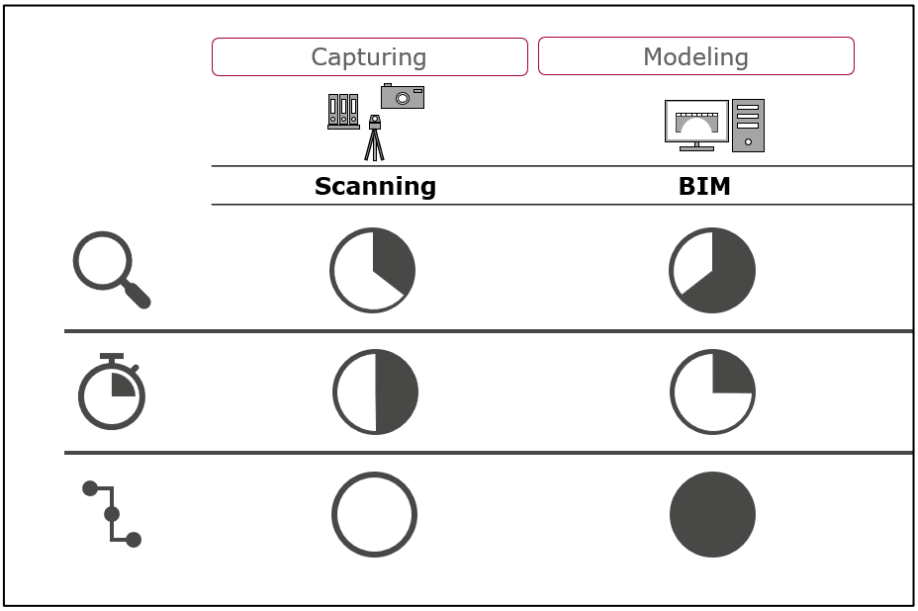


Fig. 4 Comparison of the assessment for laser scanning and BIM

5 CONCLUSION

The documentation of SHM systems represents a significant advancement in the utilisation of these systems, providing building operators with the necessary tools to operate the system and evaluate the associated measurement data. The employment of scanning technologies is advantagous for several reasons, primarily due to their ability to capture structural geometry with high precision. However, their applicability is inherently limited to visible surfaces. As acquisition times are typically manageable, laser scanning is generally well suited for documenting SHM systems. Nevertheless, the potential for reuse remains restricted, as point cloud segmentation still often requires extensive manual effort [13]. Following segmentation, the attachment of supplementary information and the transfer of data to disparate software environments is facilitated.

Despite the fact that the BIM method provides a more comprehensive representation of reality, it also involves significantly higher model creation costs and depends on the availability of input information. Its key advantage lies in the machine-readable organisation of data, which supported by standardised formats such as IFC facilitates reuse across different applications. From this perspective, modelling is better suited for SHM documentation, particularly when considering connectivity to further use cases that may not yet have been defined. Establishing standardised documentation requirements could further reduce the time effort for BIM-based approaches. Moreover, the integration BIM with digital SHM documentation can be regarded as an important contribution to advancement BIM implementation across the entire asset life cycle.

6 OUTLOOK

While the selected use case, documenting an SHM system on a bridge, enables a clear comparison of the two approaches, it represents only one element of broader bridge management. A more comprehensive evaluation, incorporating a broader range of use cases, may therefore lead to different conclusions regarding the suitability of each method. Moreover, hybrid approaches that combine scanning and modelling, as explored in several studies, should be considered in future work. This includes extending the comparison to other modelling strategies, such as FEA. Attention should be given to semi-automated workflows that integrate scanning and modelling, as these offer significant potential to combine the strengths of both procedures. This is especially relevant in view of the large number of bridge structures and the corresponding need to accelerate and simplify digital documentation processes for SHM systems. Finally, the required accuracy of models and point clouds

across different use cases should be systematically investigated, given its direct impact on the time, effort and reliability of SHM system assessment.

Acknowledgements

This research is funded by dtec.bw-Digitalization and Technology Research Center of the Bundeswehr which we gratefully acknowledge. dtec.bw is funded by the European Union – NextGenerationEU. We dedicate our very special thanks to Autobahn GmbH Nord for their guidance and commitment to the project.

References

[1] Borrmann, André, König, Markus, Koch, Christian, and Beetz Jakob. 2021. *Die BIM-Methode im Überblick*. in: Borrmann, André, König, Markus, Koch, Christian and Beetz, Jakob (Eds.), *Building Information Modeling*. Wiesbaden: Springer.

[2] Bundesministerium für Digitales und Verkehr. 2024. "Anwendungsfälle - Phase II. Rahmendokument Version 2.0."Accessed January 9, 2026. https://www.bim-bundesfernstrassen.de/fileadmin/user_upload/Rahmendokumente/bim-rd-anwendungsfaelle-phase-II.pdf.

[3] Barnes, Peter. 2019. *BIM in principle and in practice*. London: ICE Publishing.

[4] Hosamo, Haidar Hosamo and Hosamo, Mohsen Hosamo. 2022. "Digital Twin Technology for Bridge Maintenance using 3D Laser Scanning: A Review." *Advances in Civil Engineering* 2022:2194949. doi:10.1155/2022/2194949

[5] Bundesanstalt für Straßen- und Verkehrswesen. 2025. "Brückenstatistik." Accessed January 12, 2026. https://www.bast.de/DE/Publikationen/Statistik/Bruecken/Brueckenstatistik.pdf?__blob=publicationFile&v=3.

[6] Wedel, Frederik, Opitz, Daniel, Tiedemann, Christoph and Meyer-Westphal, Markus. 2022. "Das 3-D-Modell als Grundlage des digitalen Zwillings." *Bautechnik* 99:104–113. doi:10.1002/bate.202100092.

[7] Popescu, Cosmin, Täljsten, Björn, Blanksvärd, Thomas and Elfgren, Lennart. 2019. "3D reconstruction of existing concrete bridges using optical methods." *Structure and Infrastructure Engineering* 15:912–924. doi:10.1080/15732479.2019.1594315.

[8] Bednorz, Jennifer, Hindersmann, Iris, Jaeger, Klaus and Marszalik, Monika. 2020. "Methoden zur Generierung von As-Built-Modellen für Bestandsbrücken." *Bautechnik* 97:286–294. doi:10.1002/bate.202000011.

[9] Porto Oliveira, José Guilherme and Dominguez Sotelino, Elisa. 2025. "Infrastructure management via BIM model: integration of structural health monitoring and ANN-based damage assessment." *ITcon* 30:1637. doi:10.36680/j.itcon.2025.067.

[10] Borrmann, André, Beetz, Jakob, Koch, Christian, Liebich, Thomas and Muhič, Sergej. 2021 *Industry Foundation Classes – Ein herstellerunabhängiges Datenmodell für den gesamten Lebenszyklus eines Bauwerks.* in: Borrmann, André, König, Markus, Koch, Christian and Beetz, Jakob (Eds.), *Building Information Modeling*. Wiesbaden: Springer.

[11] Schwarz, Niklas and Petersen-Tulipan, Matthias. 2025. "Von smartBRIDGE Hamburg zum Digitalen Zwilling – Haupthafenroute im Hamburger Hafen." *Bautechnik* 102:186–193. doi:10.1002/bate.202500003.

[12] Isailović, Dušan, Stojanovic, Vladeta, Trapp, Matthias, Richter, Rico, Hajdin, Rade and Döllner, Jürgen. 2020. "Bridge damage: Detection, IFC-based semantic enrichment and visualization." *Automation in Construction* 112:103088. doi:10.1016/j.autcon.2020.103088.

[13] Morgenstern, Hendrik and Raupach, Michael. 2022. "Quantified point clouds and enriched BIM-Models for digitalised maintenance planning." Paper presented at the International Conference on Concrete Repair Rehabilitation and Retrofitting 2022, Cape Town, South Africa, October 3-5. doi:10.1051/matecconf/202236405001.

Data-driven assessment of urban tunnel alignment options based on resource demands for building strengthening measures

Fabian Dengg[1], Klaus Voit[2]

[1] Institute of Structural Engineering
University of Natural Resources and Life Sciences, Vienna, Austria,
Peter-Jordan-Straße 82, 1190 Vienna, Austria

[2] Institute of Applied Geology
University of Natural Resources and Life Sciences, Vienna, Austria,
Peter-Jordan-Straße 82, 1190 Vienna, Austria

Summary
Early planning decisions on urban tunnel alignment strongly influence the need for building strengthening measures. Detailed assessment is typically only possible once tunnel tracks are fixed, limiting sustainability comparisons between alternatives. This paper combines machine-learning-based prediction of strengthening measures with quantitative evaluation of material demand and CO_2 emissions. A random forest model, trained on Vienna subway project data, identifies buildings requiring strengthening, classifies intervention types, and estimates ecological impact by assigning average material quantities and global warming potential to each predicted measure. A parametric study varying tunnelling method, cross-section, and construction year shows that tracks with comparable numbers of affected buildings can differ significantly in material demand and emissions. The proposed approach supports early tunnel track decisions by providing a comparative indicator of resource and emission impact.

1 INTRODUCTION

Urban tunnelling plays an important role in developing city infrastructure. Tunnels are built for various purposes under densely populated areas, such as the extension of sewage and district heating infrastructure, public transport or road construction, as well as flood protection. As urban areas expand globally [13], the development of infrastructure frequently lags behind the pace of urban expansion, necessitating the construction of subterranean passageways beneath existing infrastructure. At the same time, for reasons of cost, accessibility and technicality, most inner-city tunnels are considered to be shallow, presenting the challenge of minimizing the impact on existing buildings and structures above ground during tunnelling works[15].

To mitigate the impacts of tunnel construction work, various preliminary measures must be implemented prior to the commencement of main construction activities. These measures include building strengthening, [16], the relocation of subsurface infrastructure such as electric cables, sewage pipes, water supply pipes, and gas pipes, as well as the reinforcement of road infrastructure in response to increased load due to construction supply traffic or altered bus lane routes. The work involves a reasonable amount of CO_2 emissions due to the large number of works involved in preliminary building strengthening measures. These can include underpinning, jet grouting and foundation slabs, as well as compensation grouting measures. A state-of-the-art identification of the affected houses is based on a detailed inspection of the existing foundation structures and ground parameters. This is combined with the calculation of the expected surface settlement due to tunnelling works. This identification process is resource- and time-consuming and can only be performed once the tunnel tracks have been finalized.

Using a machine learning-based tool to estimate the necessary building strengthening measures based on easily accessible data (e.g. construction year of building, different distances of tunnel to building, number of floors, use of building, tunneling method, cross section of tunnel, …), without the need for detailed examination, could enable the CO_2 emissions of different proposed routes to be evaluated. This approach addresses calls for a systematic sustainability assessment for tunnel infrastructure projects in an early design stage by integrating digital methods and carbon-based indicators [21].

2 IDENTIFICATION OF BUILDING STRENGTHENING

A machine learning approach was proposed based on the case study of the Vienna metro extension to identify buildings in need of strengthening measures [17].

The tool is based on a known dataset with labels (target variables) and features (property variables). For the case study, data was collected from open governance and open-source data available in Vienna. This data can be easily accessed by screening sources such as the digital city map, construction files and available construction information. This dataset is used to train the model, determine its predictive performance, and identify the features with the most influence on the prediction.

A random forest classifier (RF) was selected due to its robustness and suitability for tabular datasets [14]. This algorithm combines tree predictors generated by a set of different variables in the dataset The overall prediction result of the model is determined by analyzing the evenly weighted results of all existing tree predictors, by simple majority.

The results showed that the tool for determining the necessary strengthening measures worked best when two single RF models were combined. In the first step, the classification determines whether a measure is necessary. Positive results were then processed in the second step to determine the specific strengthening measure, which was categorized into the following classes:

- Foundation strengthening “FS” (consisting of foundation slabs, underpinning and jet grouting)
- Compensation grouting “CG”
- Combination of foundation strengthening and compensation grouting “FS + CG”

The model faces some boundary conditions due to the data it was trained with and the 'definition' that was deemed easily accessible. For this reason, no detailed data via ground characteristics, groundwater level or real foundation depth was included. Only buildings used for commercial or residential purposes were included in the model; industrial buildings or churches were excluded due to the lack of a representative number and their special characteristics (e.g. statics, long history, use, etc.).

Application of the model is covered in this paper [17] and forms the basis for comparing results by varying features of the input files. The predicted strengthening classes form the quantitative basis for the subsequent resource and emission assessment in the parametric study.

3 RESOURCES EVALUATION OF STRENGTHENING MEASURES

The dataset consists of three different classes of strengthening measures (FS, CG, FS+CG). These are analyzed in terms of the composition of each measure, the number of measures and the quantity of installed materials. These quantities are listed in Table 1 and form the basis for quantifying the CO_2 emissions caused by the installation during the preliminary works. The statistical analysis is also used to compare the tunnel track, enabling the emission impact of the predicted strengthening measures to be measured.

The processing of this data involves the estimation of the amount of installed material required for one predicted building. The average amount is weighted according to the relative quantity of each strengthening measure, except for rebar steel density, which is already related to the amount of concrete for the slab foundation.

Table 1 Summary of the installed strengthening measures of the dataset extracted for the case study [17]

	material/ dimension	min.	max.	avg.	SD	w. avg	amount
Foundation strengthening (FS)							
Underpinning	concrete [m³]	2.1	30.2	12.1	9.4	3.7	22
Foundation slap	concrete [m³]	2.0	105	30.2	19.7	18.0	43
	reinforcement [kg/m³]	30.7	209.3	115.3	36.3	-	
Jet grouting	column [m³]	120.3	2608.3	583.9	899.0	56.8	7
Compensation grouting (CG)							
Grouting/ building	[m²]	120.0	1400.0	472.1	291.2	-	33
Combination of FS and CG							
Underpinning	concrete [m³]	1.1	18.3	10.4	5.7	5.0	10
Foundation slap	concrete [m³]	17.3	95.7	46.7	22.3	24.5	11
	reinforcement [kg/m³]	13.9	212.0	82.7	57.0	-	
Grouting/ building	[m²]	100.0	1080.0	379.8	228.0	-	21

4 CO_2 EMISSIONS IN CONSTRUCTION

The construction industry contributes significantly to growing global CO_2 emissions with a material production representing a dominant share of the impacts, particularly cement and steel [1] [2]. Reinforced concrete plays a central role in emission related to construction, as it is the most used construction material [12].

Usually the concrete compression strength classes for underpinning and foundation slabs are C20/25 and C25/30. The global warming potential (GWP) of the materials is listed and calculated for the strengthening measures in Table 2. Due to limited project specific execution data, the assessment focuses on the material-based GWP (lifecycle phase A1-A3 [26]) excluding transport and on-site emissions (lifecycle phases A4-A5). Such a material-focused assessment is consistent with established life-cycle carbon accounting approaches for tunnel infrastructure, allowing for simplified evaluations in early design phases.

The following assumptions were made when estimating the GWP of the different measures:

1. For underpinning and foundation slabs, a concrete mix of 50% C20/25 and 50% C25/30 is assumed.
2. The reinforcement steel is B550 quality.
3. For jet grouting in clay, precutting with grout and the duplex method are assumed. A factor of two of the column volume towards the necessary grout volume is assumed [5][9]. The use of 760 kg/m³ of CEM I for the grout is based on a water-to-cement ratio of 1.0 [5].
4. For compensation grouting, a medium value of 78 liters of grout per m² is assumed within the given range [10]. The use of 895 kg/m³ of CEM I for the grout is assumed, based on a water-to-cement ratio of 0.8 [11].

Table 2 GWP based on [3]of installed materials and GWP per necessary piece of strengthening measure by class

	C 20/25	C 25/30	CEM I	Reinforcement steel
GWP [kg/m³]	157.0 [4]	197.0 [5]	-	-
GWP [kg/to]	-	-	665.0 [6]	560.0 [7]
	FS	CG	FS + CG	
GWP [to/pc*]	62.4 **	21,9	24,0***	

* one piece corresponds to one building with the need for strengthening measures
** 654.9 kg (underpinning) + 4,348.2 kg (foundation slap) + 57,413.4kg (jet grouting)
*** 885.0 kg (Underpinning) + 5.471,1 kg (foundation slap) + 17.631,7 kg (compensation grouting)

5 PARAMETRIC STUDY

Design-stage parameters in tunnel engineering have been shown to strongly influence lifecycle carbon performance, motivating an early comparative assessment of alternative tunnel configurations [22]. To assess the influence these parameters on predicted strengthening measures and associated CO_2 emissions. A parametric study was conducted using the trained prediction model [17] and the original case study dataset with the following variations.

Parameters were selected based on their high feature importance during model training and their practical relevance for early tunnel alignment decisions. The following variables were varied by remaining the rest of the data consistent: building construction year, tunnelling method, and corresponding tunnel cross-section. Comparative life-cycle assessments have previously been applied to evaluate method- and cross-section-dependent tunnel design choices, supporting the selected parameter variations [23]. Building age was modified in steps of 5 to 10 years and the maximum range of ±40 years (Fig. 1) to simulate tunnel tracks crossing younger or older urban quarters. The tunnelling method was changed from Tunnel boring machine (TBM) to New Austrian Tunneling Method (NATM), with the corresponding increase in cross-section from 35.68 m² to 39.5 m².

Horizontal distance and tunnel depth were kept constant to reflect realistic early design conditions, as these parameters are strongly constrained by alignment geometry, station locations and surface conditions and the resulting number of affected buildings. In total, 22 scenarios were generated, enabling a consistent comparison of predicted strengthening measures and resulting CO_2 emissions across alternative tunnel track configurations.

To ensure model validity, all parameter variations were limited to the range of the training dataset. Periods with limited building data, such as the World War intervals [18][19], were handled by mapping construction years to the nearest available construction year.

The parametric study therefore provides a controlled framework to isolate the effect of selected early-stage design parameters on predicted strengthening demand and associated emissions.

For comparison purposes, savings are defined as the relative reduction or increase in predicted material quantities and corresponding GWP between the reference case study alignment and each parametric scenario.

6 RESULTS

Fig. 1 shows the predicted number of buildings requiring strengthening measures across all scenarios. For both tunnelling methods, the number of predicted measures decreases with younger building stock, reaching an asymptotic behavior at the upper and lower bounds of the investigated age range.

For identical building-age scenarios. TBM excavation results in approximately 9-30 % fewer predicted strengthening measures than NATM excavation. This indicates that early decisions on tunnelling methods and cross-section can reduce the number of required interventions, even when the tunnel alignment remains unchanged.

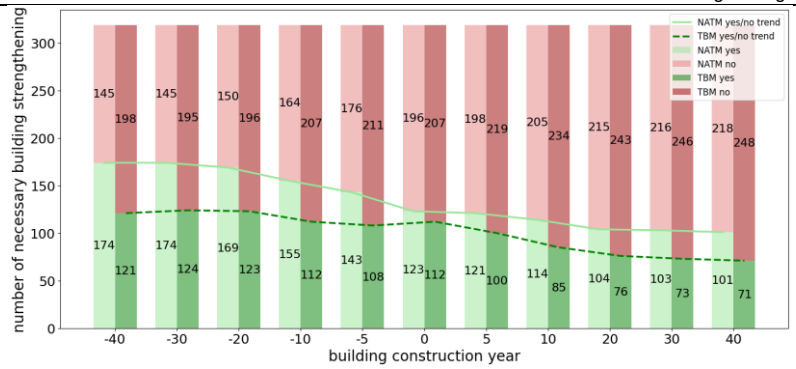


Fig. 1 Predicted number of buildings requiring strengthening measures as a function of building age variation and tunnelling method (TBM vs. NATM)

Fig. 2 illustrates the distribution of predicted strengthening classes for the scenarios requiring intervention. While the total number of measures varies with building age and tunnelling method, the relative contribution of foundation strengthening shows the strongest sensitivity.

In older building scenarios, the share of foundation strengthening measures increases substantially, whereas compensation grouting remains comparatively stable. As foundation strengthening exhibits the highest material demand and CO_2 intensity per unit, changes in class distribution have a disproportionate impact on total emissions.

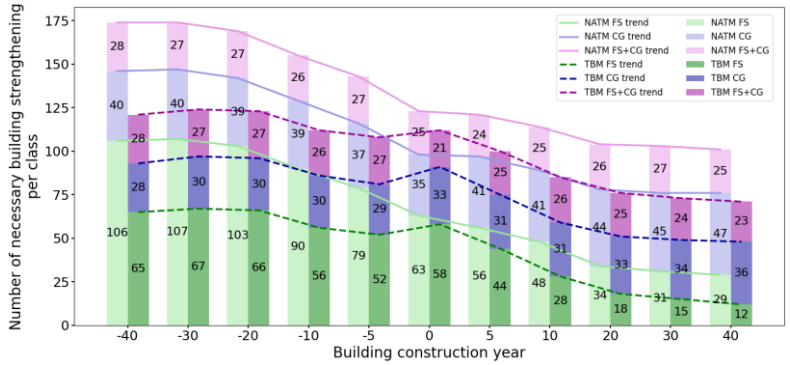


Fig. 2 Distribution of predicted strengthening classes (FS, CG, FS+CG) across building-age variations and tunnelling methods

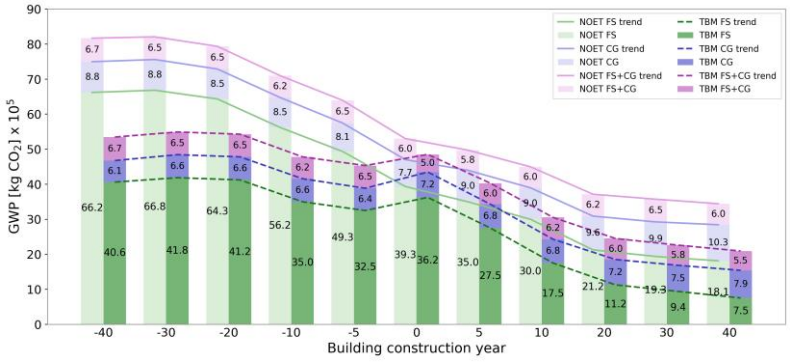


Fig. 3 Total material-based global warming potential (GWP) for all parametric scenarios illustrating relative emission savings and increases

Fig. 3 compares the summed material-based global warming potential of all scenarios. Scenarios with TBM excavation show a narrower emission range, while NATM scenarios exhibit a stronger sensitivity to building age due to changes in strengthening class distribution.

Compared to the reference case study alignment, scenarios crossing youngest building stocks result in a reduction in total GWP of up to 57 %. whereas scenarios crossing oldest building stocks lead to an increase up to 54%. These differences represent relative emission savings or increase caused solely by early design choices, prior to detailed structural or geotechnical assessment. The maximum variations occur at the extreme age modifications (±40 years) and therefore represent boundary scenarios.

7 CONCLUSIONS

The study demonstrates how a machine learning-based tool to predict the building strengthening measures prior to a tunnel project can be combined with a material-based CO_2 evaluation to support early tunnel track decisions in urban environments. The proposed workflow allows for a comparison of tunnel alignment before detailed investigation is available.

The findings demonstrate that the anticipated distribution of strengthening measures and, consequently, the related material demand and CO_2 emissions are greatly influenced by early design characteristics such as building age, tunneling technique, and tunnel cross-section. Emission savings are influenced more by the type of intervention than by the number of impacted buildings alone, as seen by the fact that foundation strengthening dominates overall emissions even though it only represents a subset of all initiatives. This is always based on, keeping the number of analyzed buildings constant.

The parametric study also shows that the emission impact of tunnel tracks with similar numbers of exposed buildings might vary significantly. Instead of depending only on geometric or risk-based criteria, it is crucial to incorporate resource-oriented indicators into early alignment discussions.

It is important to remember that the computed CO_2 values only include material-based emissions from initial building strengthening work. These represent only one part of a tunnel project's total carbon footprint. As a result, the reported findings make a focused decision-relevant contribution to a broader carbon assessment framework.

Simultaneously, alignment choices evolve in complex multi-criteria environments that are influenced by long-term urban development goals, profitability, and spatial planning methods, among other factors. Infrastructure route selection is not determined by environmental indicators alone but reflects governance and strategic steering processes in urban development [24][25]. The suggested workflow adds a sustainability-focused value without substituting current planning and decision practices.

The presented approach should not replace detailed design or safety verification. It is meant to serve as a comparative decision-support tool. Every result represents average material-based estimates and is limited by the training dataset.

When interpreting the influence of building age on predicted strengthening demand, it must be considered that inner-city tunnel projects rarely pass exclusively beneath a homogeneous “young” building stock. Urban areas typically consist of mixed construction periods, and therefore the proportion of newer buildings within the total set of affected structures is more relevant than the presence of an idealised new development area. Consequently, the emission reductions identified in the parametric study should be understood as sensitivity trends rather than as directly transferable alignment scenarios.

According to the study's findings, data-driven strengthening measure prediction can help make better informed and sustainable alignment decisions by offering early, concrete insights into the resource implications of urban tunnel projects.

Future studies will concentrate on including detailed execution-based material and process data and growing the dataset with more tunnel projects to increase predictive robustness. This would enhance the use of data-driven resource indicators in sustainable urban tunnel design and enable the shift from emission factors based on literature to project-specific carbon accounting.

References

[1] Li, Caohui, and Pradhan, Prjal, and Chen, Guoquin, et al. 2025. *Carbon footprint of the construction sector is projected to double by 2050 globally.* Commun Earth Environ 6. 83. https://doi.org/10.1038/s43247-025-02840-x

[2] United Nations Environment Programme and Global Alliance for Buildings and Construction. 2025 *Global status report for buildings and construction 2024/2025: Not just another brick in the wall.* Nairobi: United Nations Environment Programme. Available at: https://wedocs.unep.org/handle/20.500.11822/47214 (Accessed: 30 January 2026)

[3] Bundesministerium für Wohnen. Stadtentwicklung und Bauwesen (BMWSB), Bundesinstitut für Bau-. Stadt- und Raumforschung (BBSR). 2025. *ÖKOBAUDAT – Sustainable Construction Information Portal*. Available at: https://www.oekobaudat.de/ (Accessed 31.01.2026)

[4] InformationsZentrum Beton GmbH. 2023. Prozess-Datensatz: Beton der Druckfestigkeitsklasse C20/25. OEKOBAU.DAT. Available at: https://www.oekobaudat.de/OEKOBAU.DAT/datasetdetail/process.xhtml?lang=de&uuid=d5d98d4b-a9ba-4fb3-b2d2-6766f8ef5a59&version=00.02.000 (Access am 31.01.2026).

[5] InformationsZentrum Beton GmbH. 2018. Prozess-Datensatz: Beton der Druckfestigkeitsklasse C 25/30. Available at: https://www.oekobaudat.de/OEKOBAU.DAT/datasetdetail/process.xhtml?uuid=71667cf3-ede8-42d2-b0ff-6f1071ad3b86&version=00.04.000 (Access 31.01.2026).

[6] Verein Deutscher Zementwerke e. V. 2022. Portland cement CEM I. OEKOBAUDAT. Available at: https://www.oekobaudat.de/OEKOBAU.DAT/datasetdetail/process.xhtml?uuid=87371640-546c-4d9c-84cc-c13b6be94146&version=00.02.000 (Access 31.01.2026).

[7] Bauforumstahl e.V. 2023. Baustahl: Profile und Stabstahl. OEKOBAUDAT. Available at: https://oekobaudat.de/OEKOBAU.DAT/datasetdetail/process.xhtml?lang=de&uuid=20c29cbd-f9a2-4518-a1ce-c681246c29c8&version=00.03.000 (Access 31.01.2026).

[8] Guler, Erol, and Secilen, Gumus. 2021. *Jet grouting technique and strength properties of jet grout columns*. Journal of Physics: Conference Series. 1928. 012006. 10.1088/1742-6596/1928/1/012006.

[9] Croce, Paolo, and Flora, Alessandro, and Modoni, Giuseppe. 2014. *Jet Grouting: Technology. Design and Control*. CRC Press. Taylor & Francis Group.

[10] Kummerer, Clemens, and Schweiger, Helmut, and Otterbein, Rainer, and Watt, Andrew. 2002. *Numerical modelling of the effects of compensation grouting*. in Kastneg Emeriault. Dias & Guilloux (eds.) Geotechnical Aspects of Underground Construction in Soft Ground. ISSMGE. Lyon. pp. 112–118.

[11] International Society for Soil Mechanics and Geotechnical Engineering (ISSMGE). 2013. *Technical Committee 211 / Technical Committee 206. Ground improvement: lecture notes* / short course notes. ISSMGE.

[12] Massoumi, Bahman, and Enferadi, Sara, and Robbi, Andrew. 2025. *A comprehensive analysis of process-related CO_2 emissions from Iran's cement industry*. Cleaner Environmental Systems. 16. 100251. doi:10.1016/j.cesys.2024.100251

[13] United Nations. 2022. *World Urbanization Prospects: The 2022 Revision*. United Nations. Department of Economic and Social Affairs. Population Division.

[14] Breiman Leo. 2001. *Random Forests*. Machine Learning. 45. 5–32.

[15] Mair, Robert, and Burland, John., and Taylor, Neil. 1995. *Prediction of ground movements and assessment of risk of building damage due to bored tunnelling*. Geotechnical Aspects of Underhground Construction in Soft Ground. 713–718

[16] Cherney, Olga., and Smirnova, Zhanna., and Vagonova, Olga, and Razorenov, Vasiliy. 2020. *Strengthening Technologies of Different Types of Foundations in Buildings*. International Journal of Emerging Trends in Engineering Research. 8(6). 2338–2341. https://doi.org/10.30534/ijeter/2020/22862020

Physical and Mineralogical Indicators for the Water Demand of Recycled Aggregates and Concrete Performance

Amra Mešković[1*], Mohamed Abubakar Ali[1], Macielle Deiters[1], Celina Platz[2], Josipa Bosnjak[1], Angela Ullrich[3], Peter Stemmermann[3], Tobias Schack[1], Michael Haist[1]

1) *Institute of Construction Materials and Materials Testing Institute, University of Stuttgart, Pfaffenwaldring 4, 70569 Stuttgart, Germany*

2) *Leibniz Universität Hannover Institute of Building Materials Science Appelstraße 9A, 30167 Hannover, Germany*

3) *Karlsruhe Institute of Technology (KIT), Hermann-von-Helmholtz-Platz 1, 76344 Eggenstein-Leopoldshafen, Germany*

***** Correspondence: amra.meskovic@iwb.uni-stuttgart.de

Summary

Recycled fine aggregates are known to have high water absorption, but for industrial use the key challenge is estimating the variability of water demand in changing material streams. This study evaluates 26 samples from two German recycling locations, representing the first two-month excerpt of an ongoing long-term sampling campaign. Particle size, water absorption, bulk density, gas adsorption, thermogravimetric analysis, X-ray diffraction and X-ray fluorescence were used to link water demand to physical and mineralogical descriptors. Natural sand absorbed about 0.6 mass-%, whereas recycled aggregates absorbed about 5.1-5.8 mass-%. Total pore volume and thermogravimetric water loss showed strong relationships with water absorption after 10 min. The results provide initial indicator relationships for batch-to-batch scatter and support mix design, water compensation and future quality control.

1 INTRODUCTION

The construction industry is one of the largest consumers of natural resources worldwide, particularly due to the extensive use of aggregates in concrete production. At the same time, large quantities of construction and demolition waste (CDW) are generated annually. CDW represents one of the largest solid waste streams globally [1], with substantial annual quantities reported for China [2], the United States [3], the European Union [4], and Germany [5]. The recycling of these mineral materials and their reuse as recycled fine aggregates MCM streams is therefore an important route towards more resource-efficient and circular concrete production.

It is well documented that, compared with natural aggregates, recycled fine aggregates (RFA) exhibit higher water absorption, lower density, and greater variability [6]−[12]. For concrete production, however, the remaining practical challenge is not only to confirm that RFA absorb more water, but to identify measurable descriptors that allow this water demand and its variability range to be estimated for changing industrial batches. In industrial quality control, the width of the property range and its development over time are as relevant as the mean value of a single material sample. The present paper therefore reports an initial excerpt of a broader sampling programme, focusing on how the currently available batch-to-batch scatter can be interpreted and linked to physical and mineralogical indicators. This is particularly important when recycled materials are used in applications where the effective w/c ratio, fresh concrete workability, and hardened concrete performance must remain robust despite fluctuations in aggregate composition, adhered mortar content, and particle porosity.

Within the Priority Programme SPP 2436 "Net-Zero Concrete", the investigated materials are also relevant beyond their direct use as aggregates. The R-Clinker-Control research context addresses the classification and control of fluctuating MCM streams for future CO_2-minimised recycled cements (R-cements), in which milled MCM may serve as a quasi-carbon-free raw meal component. For such a control concept, physical descriptors such as particle size, density, porosity and water absorption must be linked to mineralogical descriptors such as hydrated cement paste, carbonate phases and amorphous hydration products.

The novelty of the present study is therefore the combined evaluation of water-demand indicators for industrial recycled aggregate streams. The study (i) examines an initial dataset of 26 samples from two industrial locations and several production batches to establish a first variability range for batch-to-batch and early temporal fluctuations, (ii) links $WA10_{min}$ to total pore volume and TGA-derived water loss as complementary physical and mineralogical indicators, and (iii) relates these descriptors to fresh and hardened concrete performance. This framing shifts the focus from the already known high water absorption of RFA towards practical material-stream classification and quality-control strategies based on the observed scatter of industrial recycling streams.

2 MATERIALS AND METHODS

2.1 Mixed concrete material (MCM)

2.1.1 Source and sampling

A total of twenty-six recycled aggregate samples were investigated in the present paper. The dataset represents the initial approximately two-month excerpt of an ongoing long-term sampling campaign planned over about eighteen months. In the full campaign, materials will be collected and analysed during different seasons in order to capture seasonal variability as well as differences between processing batches, material sources, and aggregate fractions. The samples presented here were obtained from two industrial locations in Germany, labelled Location A and Location B in the mineralogical data. Location A is situated in south-western Germany, whereas Location B is located in north-eastern Germany. Therefore, the results reported in this paper should be regarded as initial findings from the early stage of the broader long-term investigation. Each batch was separated into three aggregate fractions, representing different material compositions:

- CM (Concrete Material) - recycled aggregate derived predominantly from concrete, representing Type I recycled aggregate.
- V (pre-sieved MCM) - sieved mixed concrete material, representing Type II recycled aggregate.
- MCM (Mixed Concrete Material) - recycled aggregate consisting of a mixture of concrete and masonry materials, also classified as Type II recycled aggregate.

Location B provided additional CM material (Type I). The separation into Location A and Location B is used consistently in Fig. 5 to distinguish the two material origins. In addition to the recycled materials, natural siliceous sand from a Central German deposit was used as a reference aggregate for comparison with conventional natural aggregates.

2.1.2 Physical and chemical characterisation

To comprehensively assess the properties of the investigated aggregates, a series of physical and chemical characterisation methods was applied. The particle size distribution was determined by sieve analysis according to DIN EN 933-1. To obtain a higher resolution in the fine particle range, additional laser-/light-scattering measurements were carried out. The bulk density and water absorption of the aggregates were measured according to DIN EN 1097-3 and DIN EN 1097-6, respectively. The porosity of the aggregates was determined using gas adsorption measurements according to DIN ISO 9277. In addition to the physical characterisation, the chemical and mineralogical composition of the materials was analysed using thermogravimetric analysis (TGA), X-ray diffraction (XRD), and X-ray fluorescence (XRF) data where required for the mineralogical mass balance. These methods enabled the identification of major crystalline mineral phases, the quantification of carbonate- and hydration-related mass-loss ranges, and an indirect assessment of the adhered hydrated cement paste (HCP) content in the recycled aggregates. For the calculation of amorphous constituents, crystalline oxide contents derived from XRD were subtracted from bulk oxide contents determined by XRF; residual

oxides, together with TGA-derived water and carbonate contents, were assigned to amorphous carbonates, sulfates, and C-S(A)-H-like hydrated phases.

3 RESULTS

3.1 Particle size distribution

Figure 1 presents the cumulative particle size distributions of the investigated recycled sands and the natural reference sand, determined by manual sieving and laser-/light-scattering measurements; related image-based approaches for predicting aggregate grading curves have also been reported [13]. The manual sieving results (Fig. 1, left) reveal clear differences in the grading of natural and recycled aggregates. The natural sand (NA) exhibits the finest and most uniform particle size distribution, as indicated by the earlier and steeper increase in the cumulative curve. In comparison, the recycled aggregates generally show slightly coarser and broader particle size distributions. Among the RFA materials, CM (Type I) shows a particle size distribution similar to that of NA, suggesting a relatively homogeneous recycled concrete sand. In contrast, the Type II materials (V and MCM) exhibit broader and coarser distributions, reflecting the heterogeneous composition of mixed concrete and masonry particles. MCM aggregates contain the highest proportion of coarse particles, whereas V shows intermediate characteristics. The higher-resolution measurements in the fine particle range (Fig. 1, right) confirm the general trends observed in the sieving analysis: NA again shows the finest particle sizes, while the recycled materials appear slightly coarser. However, no pronounced differences between the recycled aggregates (CM, MCM, and V) were observed in this fine-particle measurement range.

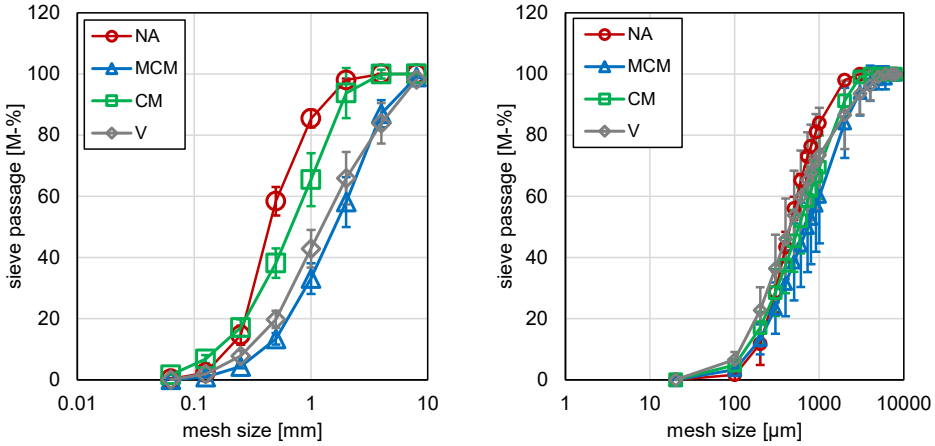


Fig. 1 Cumulative particle size distributions of natural sand (NA) and recycled sands (CM: concrete material - Type I; MCM: mixed concrete masonry - Type II; V: sieved mixed concrete material - Type II) determined by (left) manual sieving and (right) laser-/light-scattering measurement

3.2 Physical properties of aggregates

Water absorption and bulk density are key parameters for estimating the water demand and mixture robustness of concrete containing recycled aggregates. Figure 2 shows the water absorption after 10 minutes ($WA10_{min}$) for the natural sand (NA) and the recycled sands CM (Type I), MCM (Type II), and V (Type II). NA exhibits a very low WA10 of approximately 0.6 mass-%, whereas all recycled aggregates show substantially higher values, ranging from approximately 5.1 mass-% to 5.8 mass-%. Thus, the investigated RFA absorbed about eight to ten times more water than the natural sand. Among the recycled materials, CM shows the highest mean water absorption, while MCM and V are slightly lower. The individual batch values in Fig. 2 (right) also show the larger scatter of the recycled materials, confirming that water demand is not a fixed material constant but depends on the specific recycling stream and batch composition.

A complementary trend is observed for bulk density (Fig. 3, left). The natural sand exhibits the highest bulk density (approximately 2.63 kg/dm³), reflecting the dense and compact structure of the reference aggregate. In contrast, the recycled sands show lower bulk densities, ranging from approximately 2.37 to 2.44 kg/dm³. The lowest bulk density is observed for CM, which is consistent with its higher water absorption. MCM and V exhibit slightly higher densities, although they remain below the value of the natural sand. This inverse relationship between bulk density and water absorption indicates that the higher water demand of RA is strongly associated with their more porous particle structure.

To further investigate this relationship, gas adsorption measurements were conducted to quantify the total pore volume of the recycled aggregates. Measurements could not be performed for the natural sand due to technical limitations in the laboratory. Nevertheless, Fig. 3 (right) shows a strong relationship between total pore volume and WA10 for the recycled aggregates. Within the investigated material set, the coefficient of determination is approximately $R^2 = 0.95$. This value should not be interpreted as a universal predictive model, because only a limited number of material classes was available. However, it indicates that total pore volume is a useful indicator for comparing the water demand of similar recycled aggregate streams.

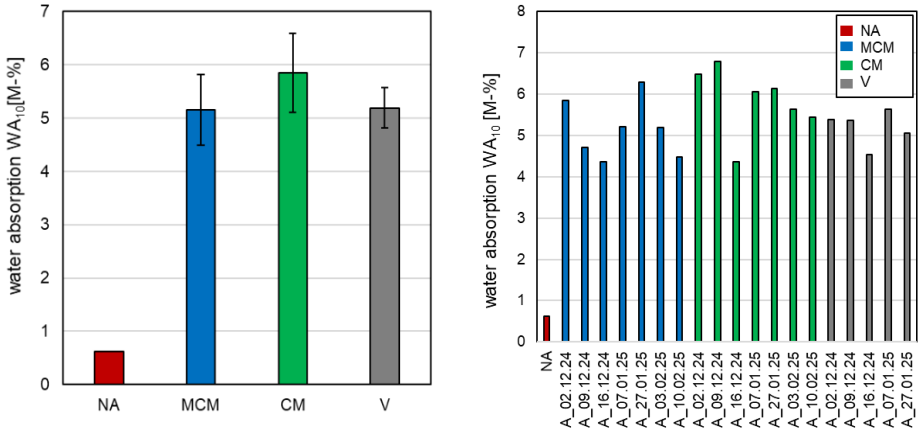


Fig. 2 Water absorption of the investigated sands after 10 minutes. (left) Mean water absorption of natural sand (NA) and recycled sands (CM: Type I; MCM: Type II; V: Type II). (right) Individual water absorption values of different batches

Thermogravimetric analysis (TGA) was used to link the physical water uptake to the composition of the aggregates. The different mass-loss steps were assigned to characteristic temperature ranges. Mass loss between 29 and 500 °C is mainly related to water release and dehydration of cementitious phases such as C-S(A)-H and ettringite. Between 500 and 900 °C, mass loss is primarily attributed to carbonate decomposition and the release of CO_2. At temperatures between 900 and 1000 °C, the mass loss is associated with decomposition of sulfate-containing phases and the release of SO_3.

The TGA results in Fig. 4 (left) show that the recycled aggregates exhibit higher mass losses than the natural sand, especially in the carbonate-related range above 500 °C. This reflects the presence of carbonate phases, cementitious residues, carbonated hydration products, and secondary mineral phases. However, the carbonate signal should not be attributed exclusively to adhered mortar, because carbonate minerals may also originate from the natural aggregate constituents. The detailed mineralogical composition of the aggregates is discussed in the following section.

To assess whether mineralogical indicators can complement porosity measurements, the TGA-derived water loss in the range 29-500 °C was compared with WA10 (Fig. 4, right). A strong relationship was observed within the investigated materials (R^2 approximately 0.95). The absorbed water measured in the water absorption test and the water released during TGA are not identical quantities; nevertheless, the relationship suggests that hydration-related phases and adhered cement paste contribute to the observed water uptake. TGA-derived water loss can therefore serve as an additional descriptor for assessing the water demand of recycled aggregates.

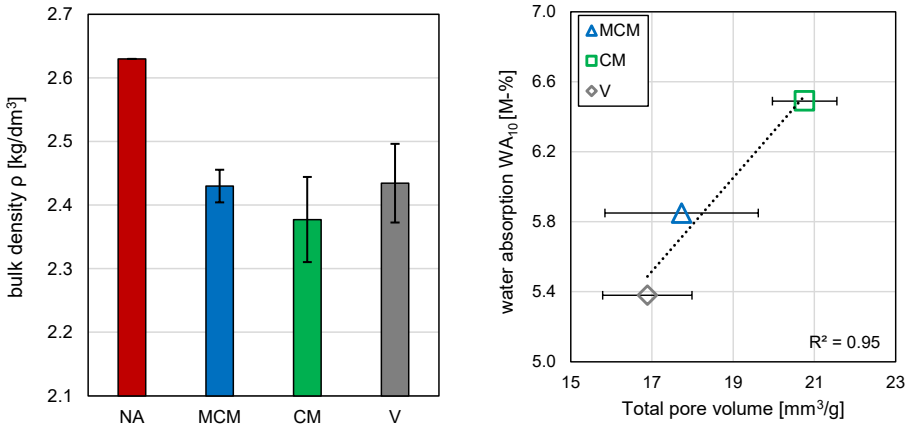


Fig. 3 Physical properties of the investigated sands. (left) Bulk density of natural sand (NA) and recycled sands (MCM, CM, and V). (right) Relationship between total pore volume and water absorption after 10 minutes for the recycled aggregates

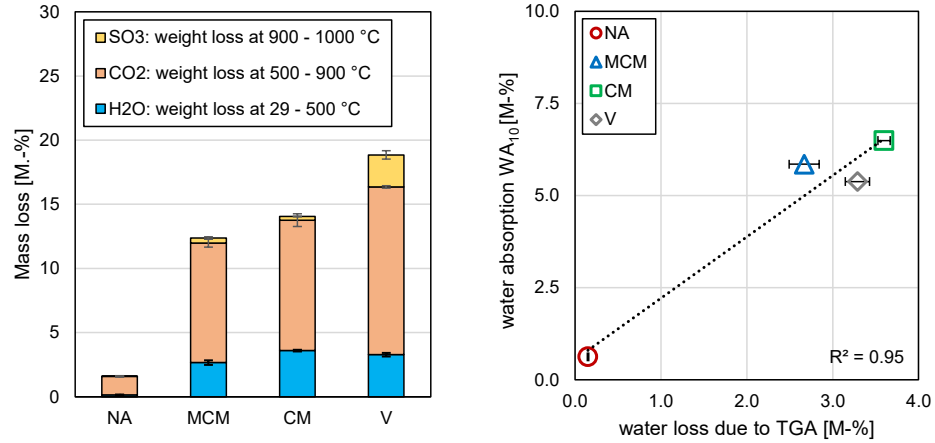


Fig. 4 Thermogravimetric analysis (TGA) results of natural sand (NA) and recycled aggregates: (left) mass loss associated with dehydration of bound water (29-500 °C), carbonate decomposition releasing CO2 (500-900 °C), and sulfate decomposition releasing SO3 (900-1000 °C); (right) relationship between TGA-derived water loss and water absorption after 10 minutes.

3.3 Mineralogical composition and inferred amorphous content

To better understand similarities and differences between natural sand (NA) and the recycled aggregates (CM, MCM, and V), crystalline mineral phases were analysed by X-ray diffraction (XRD) (Fig. 5). The figure also includes an estimate of amorphous constituents based on a TGA/XRF-supported mass-balance recalculation. Location A and Location B denote anonymised industrial sources; Location A provided V, CM, and MCM fractions, while Location B provided additional CM material. Overall, the investigated materials share several crystalline mineral phases, mainly quartz, feldspars and sheet silicates. The natural sand shows a typical mineralogical composition dominated by quartz with smaller amounts of feldspars and sheet silicates; carbonate minerals occur only in minor quantities and may originate from the natural aggregate mineralogy rather than from adhered mortar. No significant cement-related amorphous fraction is inferred for the natural sand, which is consistent with its geological origin and low water absorption.

In contrast, the recycled aggregates contain additional components related to cementitious residues from parent concrete or masonry materials. The amorphous C-S(A)-H-like fraction cannot be directly identified as a crystalline XRD phase. Instead, it was inferred by recalculating the amorphous composition: crystalline oxide contents obtained from XRD were subtracted from bulk oxide contents determined by XRF, and residual CaO, SiO_2, Al_2O_3 and water-related contributions were assigned to hydrated cementitious phases. This calculation indicates up to approximately 12 wt.% C-S(A)-H-like amorphous material in the investigated recycled aggregates. These inferred phases generally have a porous structure and high specific surface area, which increases their ability to retain and interact with water. The combined XRD/TGA/XRF-based interpretation therefore supports the conclusion that water demand is governed by both pore structure and the amount of adhered hydrated cement paste.

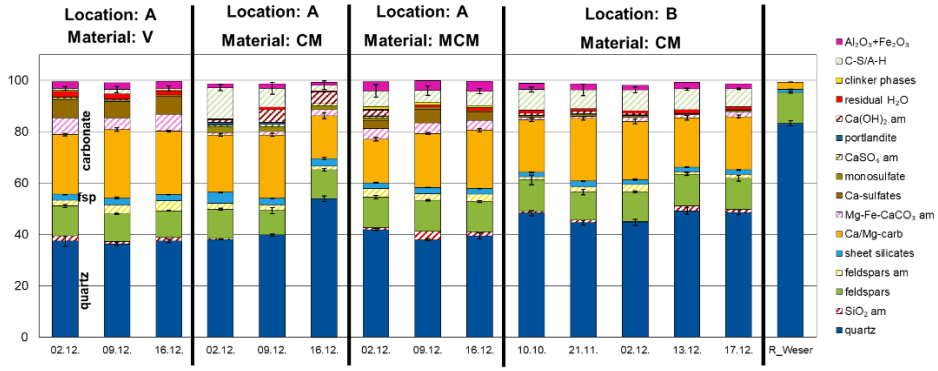


Fig. 5 Mineralogical composition of natural sand (NA) and recycled aggregates from Location A and Location B (CM: concrete material - Type I; MCM: mixed concrete masonry - Type II; V: sieved mixed concrete material - Type II). Crystalline phases were quantified by XRD; amorphous contents, including C-S(A)-H-like phases, were estimated by TGA/XRF-supported mass-balance recalculation. Locations indicate anonymised industrial sources

3.4 Influence of recycled fine aggregates on concrete properties

The incorporation of recycled fine aggregates affects both fresh and hardened concrete properties because part of the mixing water can be absorbed into the porous aggregate structure and adhered cement paste. Consequently, the nominal w/c ratio and the effective w/c ratio of the cement paste must be distinguished when RA are used.

Concrete mixtures were prepared at a constant nominal w/c ratio of 0.65 (cement: 360 kg/m³; water: 234 kg/m³). The natural aggregate mixture used natural sand (0-2 mm, 639.32 kg/m³), fine gravel (2-8 mm, 472.85 kg/m³), and coarse gravel (8-16 mm, 565.54 kg/m³). The recycled aggregate mixture used selected MCM fractions (0-2 mm, 757.08 kg/m³; 2-8 mm, 928.82 kg/m³). CEM I 42.5 R and CEM III/A 42.5 N were compared as binder systems.

Figure 6 (left) shows substantially lower flow spread for mixtures with recycled aggregates. With CEM I, the flow spread decreased from about 63 cm (NA) to 43 cm (RA); with CEM III/A, it decreased from about 62 cm to 46 cm. This reduction reflects water absorption by RA, which leaves less free water for particle lubrication unless mix water, pre-wetting, or admixture dosage is adjusted.

The compressive strength results in Fig. 6 (right) show higher strengths for the RA mixtures than for the corresponding NA mixtures. This should not be interpreted as a general beneficial effect of recycled aggregates. Rather, under the non-water-compensated conditions of this study, water absorption by RA reduced the effective w/c ratio of the cement paste and thereby increased strength. The result is therefore specific to the investigated mixtures and replacement strategy. In practice, the same mechanism may cause insufficient workability or incomplete compaction if the water demand of RA is not considered.

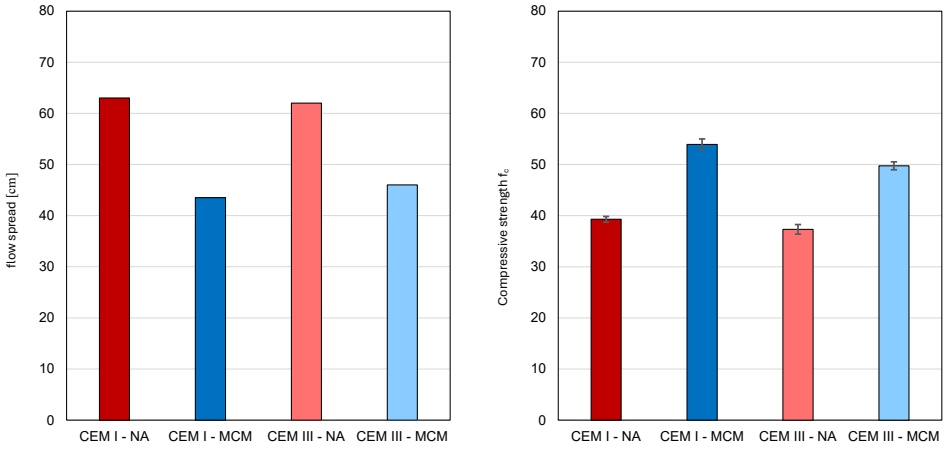


Fig. 6 Flow spread (left) and compressive strength (right) of the concrete mixtures

3.5 Practical implications for quality control

The results suggest that water absorption should not be evaluated as an isolated material property. Combining WA10 with complementary descriptors such as total pore volume, TGA-derived water loss, and XRD/TGA/XRF-derived information on hydrated and amorphous phases provides a more robust basis for estimating the water demand of fluctuating recycled aggregate streams. Because the present dataset is an initial approximately two-month excerpt, the observed scatter should be used to define preliminary variability ranges rather than final long-term control limits. In concrete production, such descriptors can support mix-water correction, pre-wetting decisions, and admixture adjustment. In the R-cement context, the same descriptors contribute to the classification of MCM streams and provide input parameters for future process-control models, which will require continued sampling over additional months and locations.

4 CONCLUSIONS

- The investigated recycled aggregates exhibited $WA10_{min}$ values of approximately 5.1-5.8 mass-%, compared with about 0.6 mass-% for natural sand. This confirms the need to account for water demand when RFA are used in concrete.
- Within the investigated material set, total pore volume showed a strong relationship with $WA10_{min}$. Although based on a limited number of material classes, this relationship identifies pore volume as a useful indicator for batch comparison.
- TGA-derived water loss combined with the XRD/TGA/XRF-based mass balance indicates that adhered hydrated cement paste and inferred C-S(A)-H-like amorphous phases contribute to water retention. Carbonate phases should be interpreted carefully because they can originate both from natural aggregate constituents and from carbonated cementitious residues. Therefore, water absorption is governed by both physical porosity and mineralogical composition.
- Concrete mixtures containing recycled aggregates showed reduced flow spread. Under the non-water-compensated conditions applied here, the reduced effective w/c ratio also led to higher compressive strength; this effect is mixture-specific and should not be generalised without considering the water-compensation strategy.
- The combined physical and mineralogical descriptors provide a basis for quality-control strategies for recycled aggregates and for the classification of MCM streams in future R-cement process control.

Overall, the main contribution of this study is not the confirmation that recycled aggregates exhibit higher water absorption than natural aggregates, but the establishment of indicator relationships that can support the assessment of variability in industrial recycled aggregate streams. The presented dataset

represents the initial approximately two-month period of an ongoing long-term sampling campaign and therefore provides a first basis for describing the expected range of variation in water demand, pore structure, and mineralogical composition.

By linking $WA10_{min}$ to physical and mineralogical descriptors, the results provide a framework for working with the inherent scatter of recycled aggregates rather than treating it only as a limitation. Such variability ranges can be used to support mix-design decisions, to plan suitable water-compensation strategies, and to estimate the potential influence of batch-to-batch and seasonal variations on fresh and hardened concrete properties. Continuing the sampling campaign over the planned long-term period and extending the dataset will allow these relationships to be validated and transformed into more robust predictive models for industrial quality control and future R-cement process control.

References

[1] Tam, Vivian W. Y., Butera, Anthony, Le, Khoa N., and Li, Wengui. 2020. ?Utilising CO2 Technologies for Recycled Aggregate Concrete: A Critical Review.? Construction and Building Materials 250:118903. doi:10.1016/j.conbuildmat.2020.118903.

[2] Zheng, Lina, Wu, Huanyu, Zhang, Hui, Duan, Huabo, Wang, Jiayuan, Jiang, Weiping, Dong, Biqin, Liu, Gang, Zuo, Jian, and Song, Qingbin. 2017. ?Characterizing the Generation and Flows of Construction and Demolition Waste in China.? Construction and Building Materials 136:405?413. doi:10.1016/j.conbuildmat.2017.01.055.

[3] U.S. Environmental Protection Agency. 2025. ?Construction and Demolition Debris: Material-Specific Data.? Accessed March 20, 2026. https://www.epa.gov/facts-and-figures-about-materials-waste-and-recycling/construction-and-demolition-debris-material.

[4] S?ez, Paola Villoria, and Osmani, Mohamed. 2019. ?A Diagnosis of Construction and Demolition Waste Generation and Recovery Practice in the European Union.? Journal of Cleaner Production 241:118400. doi:10.1016/j.jclepro.2019.118400.

[5] Kreislaufwirtschaft Bau. 2024. Mineralische Bauabf?lle ? Monitoring 2022: Bericht zum Aufkommen und zum Verbleib mineralischer Bauabf?lle im Jahr 2022. Berlin: Bundesverband Baustoffe ? Steine und Erden e.V.

[6] Berredjem, Layachi, Arabi, Nourredine, and Molez, Laurent. 2020. ?Mechanical and Durability Properties of Concrete Based on Recycled Coarse and Fine Aggregates Produced from Demolished Concrete.? Construction and Building Materials 246:118421. doi:10.1016/j.conbuildmat.2020.118421.

[7] Vintimilla Molina, Carla Teresa, and Etxeberria Larra?aga, Miren. 2023. ?Limiting the Maximum Fine and Coarse Recycled Aggregates-Type A Used in Structural Concrete.? Construction and Building Materials 380:131273. doi:10.1016/j.conbuildmat.2023.131273.

[8] Kou, Shicong, and Poon, Chi Sun. 2015. ?Effect of the Quality of Parent Concrete on the Properties of High Performance Recycled Aggregate Concrete.? Construction and Building Materials 77:501?508. doi:10.1016/j.conbuildmat.2014.12.035.

[9] Evangelista, Lu?s, and de Brito, Jorge. 2007. ?Mechanical Behaviour of Concrete Made with Fine Recycled Concrete Aggregates.? Cement and Concrete Composites 29(5):397?401. doi:10.1016/j.cemconcomp.2006.12.004.

[10] Kou, Shicong, and Poon, Chi Sun. 2009. ?Properties of Self-Compacting Concrete Prepared with Coarse and Fine Recycled Concrete Aggregates.? Cement and Concrete Composites 31(9):622?627. doi:10.1016/j.cemconcomp.2009.06.005.

[11] Khoury, Eliane, Cazacliu, Bogdan, and R?mond, S?bastien. 2019. ?Control of Effective Water in Recycled Aggregate Concrete Using Power Curves of the Mixer.? Materials Today Communications 21:100721. doi:10.1016/j.mtcomm.2019.100721.

[12] Ding, Yangfei, She, Anming, and Yao, Wu. 2023. ?Investigation of Water Absorption Behavior of Recycled Aggregates and Its Effect on Concrete Strength.? Materials 16(13):4505. doi:10.3390/ma16134505.

[13] Coenen, Max, Beyer, Dries, Heipke, Christian, and Haist, Michael. 2022. ?Learning to Sieve: Prediction of Grading Curves from Images of Concrete Aggregate.? ISPRS Annals of the Photogrammetry, Remote Sensing and Spatial Information Sciences V-2-2022:227?235. doi:10.5194/isprs-annals-V-2-2022-227-2022.

Experimental study on compressive failure of fibre reinforced polymer reinforced concrete beams with enhanced compression zones

Balint Somlai [1], Péter Schaul [2] and Sandor Solyom [1]

[1] Department of Construction Materials and Technologies, Faculty of Civil Engineering, Budapest University of Technology and Economics, Műegyetem rkp. 3, H-1111 Budapest, Hungary

[2] BarChip EMEA Ltd. Clonshaugh Business & Technology Park, Dublin, D17 FY82, Ireland

Summary

FRP rebars offer an alternative option to reinforcing steel with the potential to lower the required amount of concrete used in construction. They offer several advantages, including high strength, corrosion resistance, low density, or magnetic neutrality. Some aspects of utilizing FRP rebars, however, remain understudied. One such topic is, for example, the prevention of brittle failure. One of the proposed methods of preventing such failure is to favour compressive failure of concrete as it provides better ductility. Further improvement can be achieved if the compressed concrete is confined either by stirrups or other forms of additional reinforcement. An extensive experimental program has been designed and performed in order to assess multiple parameters influencing the effectiveness of confinement by stirrups. These parameters include concrete strength, stirrup spacing and stirrup height. Significant improvements of loadbearing capacity and ductility were observed in multiple cases.

1 INTRODUCTION

Steel bar reinforcement is one of the most commonly used construction components. An alternative solution is Fibre Reinforced Polymers (FRP) rebar, that provide better corrosion resistance, higher strength, and lower weight [1], [2]. The technology carries several drawbacks that need further improvement such as the challenges in designing for serviceability limit state [3] or the subject of this study, rigid failure of FRP rebars. This results in a failure that is undesirable in behaviour, as it does not absorb energy, does not produce large deformations and does not facilitate static redistribution. For this reason the commonly agreed upon preference for mode of failure is crushing of the compressed concrete section [2], [4], [5]. This produces more visible damage but does not always result in significantly larger deformations of more absorbed energy. A successfully tested improvement is confinement of the crushed concrete zone [6], [7].

Among the experimental results examining the effectiveness of confining the crushed concrete significant variability has been reported. Some, such as Wang et al. [5], Renic, Kisicek & Koscak [8] or Somlai & Solyom [6] have succeeded in demonstrating a potential quasi-plastic behaviour resulting from confinement. Alternatively, some research such as Michael & Hamilton or Hussain et al. [7], [9] have not produced significant improvement. The materials, confinement methods, and test setups in the cited studies are often not comparable. The number of specimens tested are usually not sufficient for more comprehensive analysis.

This paper presents the experimental setup and preliminary results of the study aimed at examining confinement under different conditions. The experiment is aimed at examining the maximum potential of confinement on GFRP reinforced beams designed to fail in compression, along with variables affecting it. This will allow for better understanding of the potentially achievable improvement and provide data on the reliability of the method. This can result in improvements in design in the future, that contributes to the adaptation of FRP technology for general reinforcement.

2 EXPERIMENTAL PROGRAMME

The experiments consisted of four-point bending tests conducted on glass FRP (GFRP) reinforced concrete beams with the constant moment zone confined with stirrups of varying configurations. Three

variables were examined on 16 unique configurations. Each configuration was tested twice to ensure accuracy and repeatability. With an additional four control specimen the total number of beams examined was 36. The variables examined were height of the stirrups, stirrup spacing and concrete strength. Measurements were taken with strain gauges, LVDTs (Linear Variable Differential Transformers) and DIC (Digital Image Correlation). Accompanying experiments were conducted to determine material properties.

2.1 VARIABLES

The configuration of the beams with the variables can be seen in Table 1. 2^k factorial design was used as the basis of the experimental configurations [10]. Factorial designs are used in a wide variety of fields as they provide robust data and have extensive existing material to draw upon. 2^k factorial design operates with variables of two levels. For each of the variables at least two observations need to be made on the two levels, and as such for all combinations to be made the minimum number of experiments is 2^k where k is the number of variables. In the case of this experimental setup the number of variables is three, with one of the variables having four levels and thus with two instances for each configuration 32 beams are needed. With control specimens the total number of beams comes to 36. Table 1 shows the properties of the configurations.

Table 1 Table summarizing the variables for each beam configuration.

Beam No.	Concrete strength	Stirrup spacing	Stirrup height
1, 2	+	+	1
3, 4	+	+	2
5, 6	+	+	3
7, 8	+	+	4
9, 10	+	-	1
11, 12	+	-	2
13, 14	+	-	3
15, 16	+	-	4
17, 18	-	+	1
19, 20	-	+	2
21, 22	-	+	3
23, 24	-	+	4
25, 26	-	-	1
27, 28	-	-	2
29, 30	-	-	3
31, 32	-	-	4
33-36	Control beams with steel rebars		

Concrete strength +	~80 MPa	
Concrete strength -	~40 MPa	
Stirrup spacing +	100 mm	
Stirrup spacing -	50 mm	
Stirrup height	1	40 mm
	2	80 mm
	3	120 mm
	4	180 mm

2.1.1 Concrete Mixture

The concrete mixtures were designed to achieve two levels of compressive strength while maintaining the same constituent materials. The amount of aggregate and the ratio of fine and coarse aggregates remained constant. The two mixtures were aimed to be approximately 40 MPa and 80 MPa in compressive strength (measured on 150 mm cubes), placing the first in the range of normal and the latter in the range of high strength concrete. While compressive strength in used to define the two levels for the variable, many other material properties, such as elastic modulus or fracture energy differ [11]. While these can highly impact beam behaviour, controlling all variables is not possible, as many of these stem from the microstructure of the material. While controlling all properties of concrete except for compressive strength would provide valuable data, the execution of such an experiment would require extensive preparation that falls outside the scope of this research. Multiple concrete properties are tested for both mixtures such as fracture energy, elastic modulus, tensile strength and complete stress-strain behaviour.

2.1.2 Stirrup Configurations

Stirrup configuration corresponds to the effectiveness of the confinement of the constant moment zone. The spacing is a linear control on the confinement while the effect of stirrup height is less well established. Previous experiments established [6] that shorter stirrups are more reliable in achieving the desired failure mode. For this reason, stirrup height is examined at four different levels. The two are treated as separate variables instead of being combined in a variable representing confinement such as confining pressure as their effects are assumed to be different. Stirrup spacings are 50 and 100 mm and stirrup heights are 40, 80, 120, and 180 mm.

2.2 Beam specifications

The beams used in the experiments were 200 × 100 × 2200 mm (height × width × length) in size manufactured with 2 pcs. of 12 mm nominal diameter longitudinal GFRP (steel for control) reinforcements on the bottom part of the cross-section. All beams were made with two 6 mm diameter longitudinal steel reinforcement on top. Stirrups were manufactured from 6 mm diameter steel rebars with heights according to the reinforcement scheme. The area between the loading points featured the confinement reinforcement while the rest had stirrups of 185 mm in height spaced at 75 mm. The span was 1950 mm with the distance between the two loading points set to 450 mm as can be seen on Fig. 1.

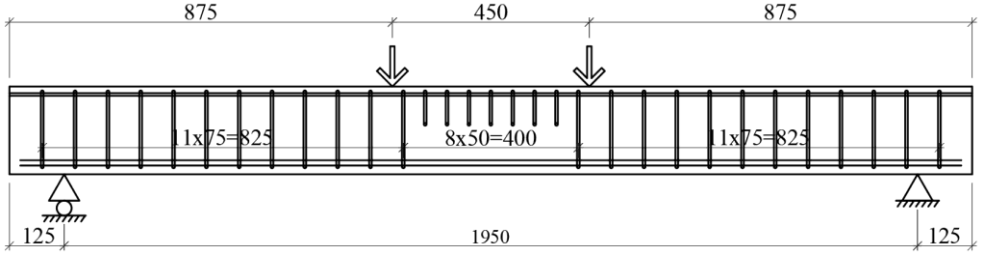


Fig. 1 Elevation schematic of the testing setup, with reinforcing scheme for 50 mm stirrup spacing

The beams were cast one by one, limited by the capacity of the available concrete mixer, along with three standard 150 mm cubes for compressive strength testing. After casting, beams were stored under cover in a wet environment for one week to ensure proper curing. Before testing the top surface was prepared for the application of strain gauges and the sides were painted with a pattern appropriate for DIC analysis as can be seen on Fig. 2.

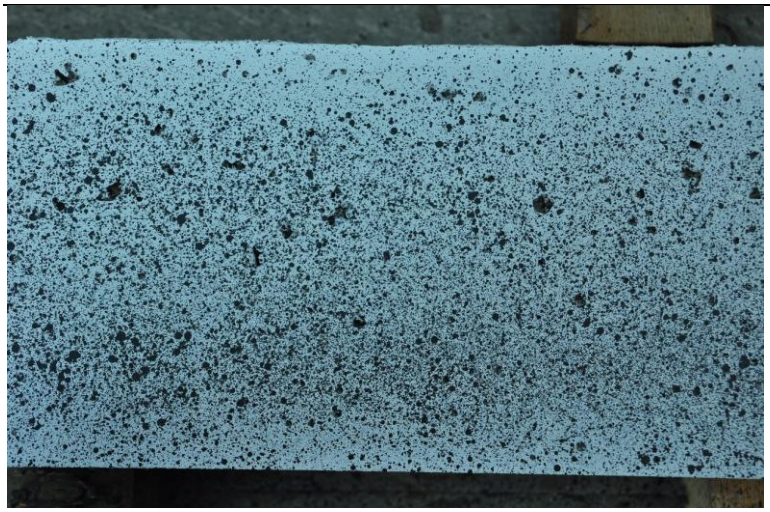


Fig. 2 Black spotted random pattern on white background used for DIC analysis.

2.3 Instrumentation

The two longitudinal tensile reinforcements received strain gauges to measure strains, and another was applied to the top of the concrete. The loading was done by an electro-mechanical universal testing system with 2 mm/min loading rate. The deflections were measured at the mid-point of the beam and at the load actuation points (Fig. 3 left). The testing system also measures the load and the displacement of the loading head. After reaching cracking load, LVDTs were applied to measure the opening of the first two visible cracks, as can be seen on Fig. 3 (right). One side of the beam was painted with a pattern consisting of a white coat with randomly applied black dots. The entire testing was recorded on the painted side to be used for DIC analysis in the future.

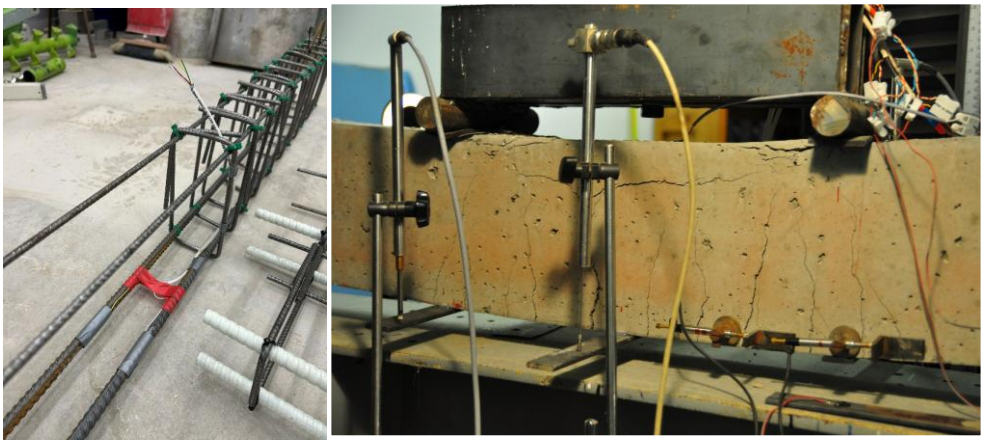


Fig. 3 The steel reinforcement with strain gauges applied to the bottom (left). The test instrumentation, with LVDTs for deflection measurements and crack openings (right).

3 RESULTS

The beams failed primarily in compression by crushing of the concrete, but after the initial cracking multiple different secondary modes of failure were observed. In many cases after failure, opening of stirrups could be observed. The use of hooked stirrups endings would be recommended to avoid this, but the scale of this experiment did not allow for this, as the radius of bending was too large. Average concrete strength of normal concrete was measured to be 39.6 MPa and high strength concrete was

measured to be average 79.4 MPa. Below, the force–deflection diagrams of all GFRP reinforced beams can be seen, split by concrete type (Fig. 4 and Fig. 5). Dashed line represents 100 mm stirrup placement while solid line represents 50 mm, and shading represents the height of the stirrups. These are also reflected in the specimen symbols, the first part of the symbol indicates the concrete type. The second part is the stirrup spacing in mm and the third is the stirrup height in mm.

Four groupings can be distinguished based on the diagrams stemming from the concrete and the stirrup spacing. In the case of both concretes, the dense stirrup configuration resulted in significantly increased maximum load compared to the sparse one. The case of normal concrete the sparse configuration did not result in any measurable excess loadbearing capacity after cracking of the compressed concrete. High strength beams with sparse stirrup spacing provided an approximately 10% additional loadbearing capacity in all stirrup heights except the smallest (40 mm) one (Fig. 6). In all four groupings no apparent pattern can be seen that would indicate that stirrup height impacts loadbearing capacity significantly. While NC-50 series shows variation in maximum load, no clear trend can be identified. Taking the 100 mm spacing, 180 mm height configuration as the baseline in both concrete cases, the average increase in loadbearing capacity for normal concrete was 27.7% while for high strength concrete it was 19.6%. This difference can be attributed to the modes of failure.

The most common mode of failure was crushing of the compressed concrete. For the normal concrete configurations most failures were of this type or concrete crushing combined with another failure (Fig. 7 right), most commonly buckling of the compressed steel, shear failure or opening of the stirrups. High strength concrete beams exhibited larger variation in mode of failure. Sparse configurations failed in a variety of modes including combined shear, compression failure around the force transfer location, opening of the stirrups and crushing of concrete. For dense configurations with high strength concrete the prevalent failure mode was fracture of the FRP rebar as can be seen on Fig. 7 (left). It is unclear whether this was due to reaching the tensile strength of the rebars or a combined action of shear and tension. In some cases, failure of the bond between FRP and concrete was observed. To better understand failure modes, further inspection of the failed specimen and study of the video documentation is needed. The latter is also important to understand cases that display steel buckling as it is not clear in some cases whether concrete failed first giving way to buckling of the steel no longer being supported of buckling occurred allowing the crushed concrete to separate from the intact sections. Opening of the stirrups was also observed in many cases but mostly because of large deformations following buckling of concrete failure, but further research could be directed at observing whether postcritical behaviour improves if hooked stirrups are used. Another question arising from the results concern the role of concrete cover. Opening of the stirrups, buckling of the compressed longitudinal steel and the initiation of the compressive failure could all be affected.

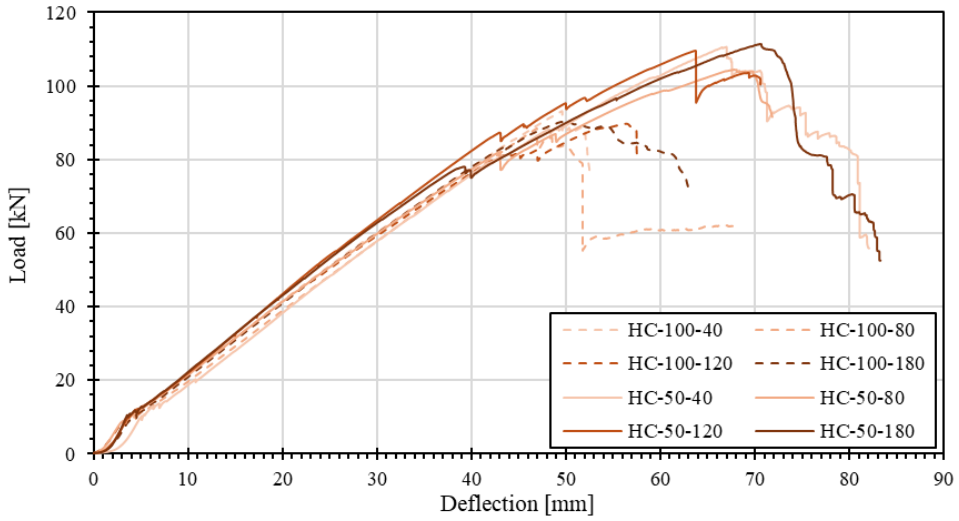


Fig.4 Load-deflection diagram of high strength concrete beams

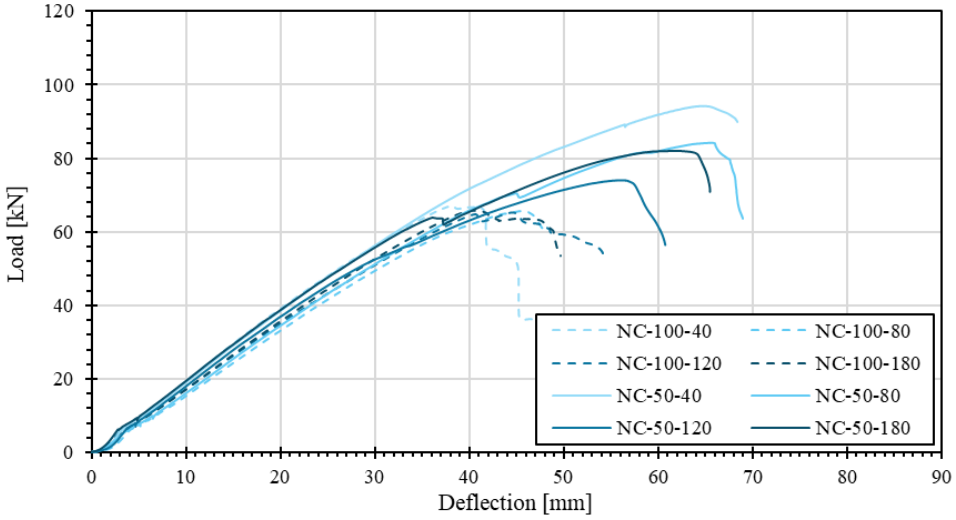


Fig.5 Load-deflection diagram of normal concrete beams

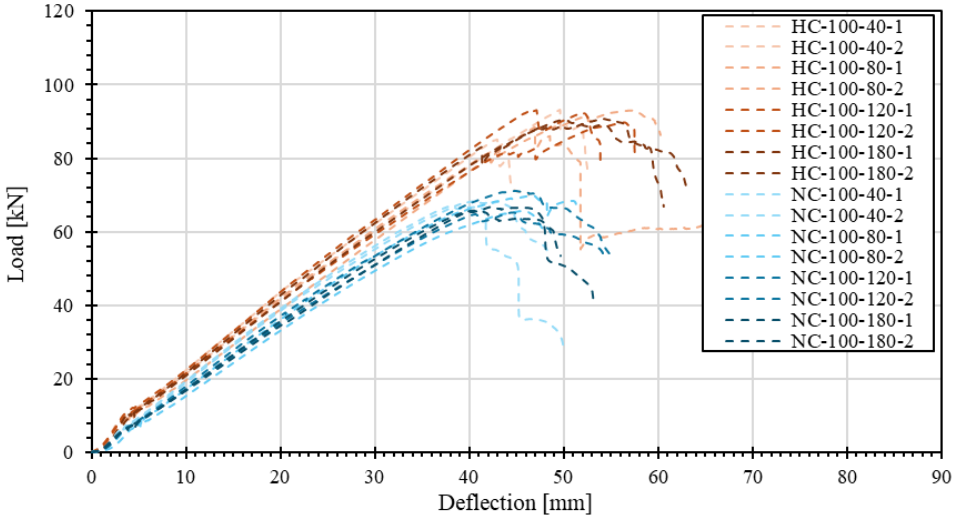


Fig. 6 Load-deflection diagram of beams with sparse stirrup configurations.



Fig. 7 Tensile failure of the FRP rebars with excessive debonding (left) and concrete crushing with buckling of the compressed longitudinal steel (right)

4 CONCLUSIONS

This paper presents the experimental findings of a comprehensive study on FRP reinforced beams focusing on compressive concrete failure. 36 beams were constructed and tested with 16 differing configurations of varying stirrup spacing, stirrup height and concrete strength. The data gathered will help deepen our understanding of confined concrete behaviour in bending, provide a better picture on the reliability of the method and can serve as the basis for improvement in the design of FRP reinforced structures. The findings based on the preliminary test results are as follows:

- Stirrup height had a smaller influence on load-bearing capacity than suggested by previous studies.
- The effect of confinement results in larger percentage increase of loadbearing capacity in high strength concrete compared to normal concrete
- An average of 19.6% increase in maximum load was observed for confined high strength concrete and a 27.7% for normal concrete.
- The effect of confinement was not observable in most cases on sparse stirrup configurations with normal concrete, while it was present in the same configurations made with high strength concrete.

Acknowledgements

The authors gratefully acknowledge Schöck Bauteile GmbH for supplying the GFRP bars used in the experimental program, Duna-Dráva Cement Ltd. for providing the cement and FUVARTRANS Ltd. for supplying the aggregates. The authors also express their sincere appreciation to Balázs Burai and Krisztián Takács for their valuable assistance in the preparation and testing of the specimens.

References

[1] Brahim Benmokrane, Omar Chaallal, Radhouane Masmoudi (1995) “Glass fibre reinforced plastic (GFRP) rebars for concrete structures” *Construction and Building Materials* 9:353–364. Accessed March 12, 2026. https://doi.org/10.1016/0950-0618(95)00048-8

[2] Task Group 9.3 (2007) *FRP reinforcement in RC structures*. International Federation for Structural Concrete, Lausanne, Switzerland

[3] Szabolcs Szinvai , Tamás Kovács (2026) “The challenges of GFRP RC beam design for limit states” Accessed June 4, 2026 https://doi.org/10.1002/suco.70668

[4] Tvrtko Renić, Tomislav Kišiček (2021) “Ductility of Concrete Beams Reinforced with FRP Rebars” *Buildings* 11:424. Accessed August 29, 2024. https://doi.org/10.3390/buildings11090424

[5] Hongwei Wang, Jinjin Xu, Xu Jiang, Xiaoyan Han, Kaiming Pan, Rena C. Yu, Zhimin Wu (2024) “Flexural behavior of GFRP-RC beams confined with CFRP in compression zone” *Engineering Structures* 302:N/A. Accessed August 30, 2024. https://doi.org/https://doi.org/10.1016/j.engstruct.2023.117348

[6] Balint Somlai, Sandor Solyom (2024) “Experimental Study of FRP Reinforced LWC Beams” Paper presented at the 14th Central European Congress on Concrete Engineering. Czech Concrete Society, Mikulov, September 22-24

[7] Antonis Michael, H.R. Hamilton (2021) “Experimental Ductility of Compression-Controlled Flexural Members Using CFRP Grid to Confine Concrete” *Materials* 14:N/A. Accessed August 27 2024 https://doi.org/https://doi.org/10.3390/ma14185163

[8] Tvrtko Renic, Tomislav Kisicek, Janko Koscak (2023) “Experimental testing of FRP reinforced concrete beams with steel compression reinforcement and a compression area confined with steel stirrups” *Materials and Structures* 56:N/A. Accessed August 29, 2024 https://doi.org/https://doi.org/10.1617/s11527-023-02269-8

[9] Qudeer Hussain, Anat Ruangrassamee , Panuwat Joyklad, Anil C. Wijeyewickrema (2022) “Shear Enhancement of RC Beams Using Low-Cost Natural Fiber Rope Reinforced Polymer Composites” *Buildings* 12:602. Accessed August 30, 2024 https://doi.org/10.3390/buildings12050602

[10] Douglas C. Montgomery (2013) *Design and Analysis of Experiments*, 8th edition. Jhon wiley & Sons, Inc., Hoboken, USA

[11] Viktor Hlavička (2021) “Comparison of the Results of Notched Three Point Bending Test with Model Code 2010 Formulas” *Concrete Structures: Journal of the Hungarian Group of fib* 22:5-12. Accessed November 12, 2025 https://doi.org/10.32970/CS.2021.1.2

Durability

From Potential to Corrosion: The Role of Chloride Thresholds in Spatial Variability of Reinforcement Corrosion in Concrete

Konstantin Fache[1], Sylvia Keßler[2], Jörg Harnisch[1]

[1] Department of Civil Engineering,
FH Münster University of Applied Sciences,
Corrensstraße 25, 48149 Münster, Germany

[2] Institute of Engineering Materials and Building Preservation,
Helmut-Schmidt-University/University of the Federal Armed Forces Hamburg,
Holstenhofweg 85, 22043 Hamburg, Germany

Summary
Current corrosion prediction models commonly assume a time- and space-invariant chloride threshold (C_T). This simplification disregards local increases in C_T caused by macrocell-induced cathodic polarisation of passive reinforcement adjacent to active corrosion sites. This study investigates the influence of a potential-dependent C_T on the initiation of additional corrosion sites in reinforced concrete, assuming that corrosion has already been initiated. Experimental data confirming the relationship between steel polarisation and C_T are used as input for a numerical study that simulates the resulting potential field and evaluates its spatial influence on the formation of additional anodes. The results demonstrate a pronounced local increase in C_T in the vicinity of the initial anode, which reduces the likelihood of subsequent corrosion initiations near existing corrosion sites. Incorporating a potential-dependent C_T into corrosion prediction models may therefore improve corrosion risk and service life prediction.

1 INTRODUCTION

1.1 Corrosion Initiation and Propagation

Reinforcement corrosion significantly affects the service life of reinforced concrete structures. Chloride-induced corrosion, resulting from exposure to de-icing salts or marine environments, represents one of the predominant durability challenges and frequently governs service life limitations. Reliable maintenance planning therefore requires robust models capable of predicting corrosion initiation and subsequent damage progression.

In sound concrete, reinforcing steel remains passive due to the high alkalinity of the pore solution, resulting in negligible corrosion rates [1]. However, chloride ions that have penetrated the concrete may locally destroy the passive layer once the chloride threshold C_T is exceeded, leading to steel depassivation and a marked increase in corrosion rate [1]. Service life models typically distinguish between two consecutive phases [2]: (1) the initiation phase, during which chlorides accumulate in the bulk concrete until reaching the chloride threshold C_T at the reinforcement level while the steel remains passive; and (2) the propagation phase, characterised by active corrosion, cross sectional loss of the rebars, and formation of expansive corrosion products that induce cracking and ultimately delamination of the concrete cover [2].

This sequential representation neglects interactions between both phases. Recent research instead promotes a holistic view of corrosion processes over the entire service life [3]. A major challenge for advanced prediction models lies in capturing the spatial variability of chloride-induced damages [4]–[6], which results from inherent systematic and stochastic variations in both exposure conditions (e.g., chloride exposure) and material resistance properties (e.g., C_T) [7]. Current modelling approaches largely ignore this variability.

A key contributor to C_T variability is macrocell formation. Once a local anode forms, actively corroding steel becomes electrochemically coupled with surrounding passive reinforcement that remains in the initiation phase [8]. Macrocell currents induce cathodic polarisation of the adjacent passive steel, thereby increasing the local C_T depending on the steel potential; an effect well-known

from the cathodic prevention technique [9]. Although C_T exhibits natural scatter, experimental studies consistently report an increase in C_T with more cathodic steel potentials [10], [11]. As a result, corrosion initiation in cathodically polarised regions may be delayed, significantly affecting damage progression and service life predictions [11], [12].

Despite the availability of probabilistic corrosion models [13], [14], C_T is commonly treated as invariant in space and time. Consequently, existing models cannot reliably predict the formation of additional corrosion sites after the first anode has developed. Addressing this limitation requires explicit consideration of potential-dependent C_T behaviour [3], [8], [15].

1.2 Potential Dependence of the Chloride Threshold

Incorporating a potential-dependent C_T into corrosion models requires a functional relationship between steel potential and C_T. To quantify the effect of cathodic polarisation on C_T, the authors conducted extensive laboratory experiments with steel rebars embedded in concrete and exposed to cyclic wetting-drying with NaCl solution while applying controlled cathodic polarisation to the steel [16].

The results confirm a potential-independent baseline chloride threshold C_{T0} for steel potentials more anodic than a threshold potential E_{T0}, and a systematic increase in C_T at more cathodic potentials. This behaviour aligns with previous findings [10], [11]. The increase in C_T is described by the cathodic prevention slope β_{CT}, defined as the cathodic potential shift required to increase C_T by one decade. Based on the author's experimental results [16], the relationship between steel potential E and C_T is expressed by Eq. (1) and (2):

$$C_T = C_{T0} = 1.30 \ \%/\text{cem wt.} \qquad \text{for } E \geq -160 \text{ mV}_{SCE} \tag{1}$$

$$C_T = C_{T0} \cdot 10^{\frac{E_{T0}-E}{\beta_{CT}}} = 1.30 \cdot 10^{\frac{-160-E}{520}} \ \%/\text{cem wt.} \qquad \text{for } E < -160 \text{ mV}_{SCE} \tag{2}$$

Potentials in this work are given in the saturated calomel electrode (SCE) scale. The parameters E_{T0}, C_{T0} and β_{CT} in Eq. (1) and (2) represent rounded values from experimental fitting for practical applicability. Although C_{T0} exceeds commonly cited design values (e.g., a mean C_T of 0.6 %/cem wt. in [13]), comparable thresholds of approximately 1 %/cem wt. have been reported in tests closely aligned with engineering practice [17]. Accordingly, Eq. (1) and (2) are adopted in this study.

1.3 Aim and Scope of this Study

This study aims to provide first insights into the influence of polarisation-induced changes in C_T on the initiation of new corrosion sites. A numerical model is developed to simulate the steel potential distribution within a reinforcement assembly following the formation of an initial corrosion site. The simulated potential field is subsequently combined with an experimentally derived potential-dependent C_T relationship. The focus lies on the modelling strategy rather than on long-term damage evolution, with the objective of supporting future corrosion prediction models that account for spatial and temporal variability in C_T.

2 NUMERICAL MODELLING

2.1 General Approach

The numerical model employs a geometry representative of reinforced concrete structures exposed to chloride-contaminated environments. A reinforced concrete slab was selected as a simple yet practice-oriented configuration, typical for structures such as bridge decks. The model was implemented using three-dimensional finite element modelling (FEM) with double axis symmetry in COMSOL Multiphysics®.

The slab has a square plan with an edge length of 3.34 m and a thickness of 0.20 m. It contains two layers of reinforcement (one rebar mat at the top and bottom, respectively), modelled as cylindrical rebars with a diameter of 8 mm, an upper concrete cover of 35 mm, and a rebar spacing of 0.15 m. The slab dimensions were chosen sufficiently large to avoid significant edge effects, which could otherwise constrain the macroelement. To utilize the double-symmetric design and save on computing capacitiy, only one quarter of the slab was modelled (Fig. 1).

The model considers the early propagation phase following the formation of a first corrosion site. The active steel area (anode) was located in the uppermost rebar layer (top part of the upper mat) at the intersection of the symmetry axes.

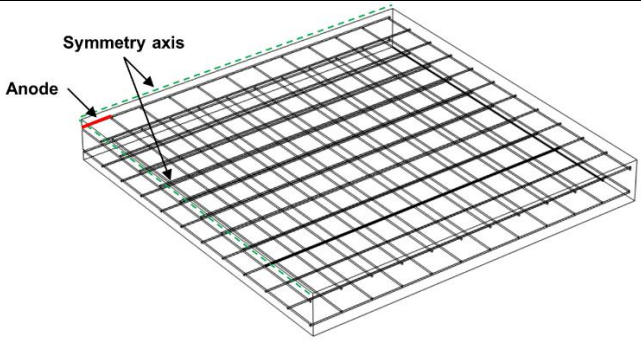


Fig. 1 Numerical model representing a quarter of the slab geometry with labelling of the symmetry axes (green) and anode (red)

The concrete was simplified as a homogeneous electrolyte with time- and space-invariant electrical resistivity ρ. Electrical behaviour within the concrete domain was governed by Ohm's law (Eq. (3)) and charge conservation (Eq. (4)):

$$i = -\frac{1}{\rho}\nabla E \tag{3}$$

$$\nabla \cdot i = 0 \tag{4}$$

where:

i: Local current density in A/m^2
E: Local value of the potential field in V
ρ: Electrical resistivity in Ωm

2.2 Boundary Conditions and Input Parameters

All rebar surfaces were defined as passive, except for the steel area designated as the anode in Fig. 1, which was considered to be fully active. Boundary conditions at the steel-concrete interface were formulated based on the electrochemical reactions occurring at the interface, while all remaining external boundaries were treated as electrically insulating.

Two reactions were considered to take place at the steel-concrete interface. The cathodic reaction was defined as oxygen reduction:

$$O_2 + 2H_2O + 4e^- \rightarrow 4OH^- \tag{5}$$

The anodic reaction was assumed to be iron oxidation:

$$Fe \rightarrow Fe^{2+} + 2e^- \tag{6}$$

Although iron oxidation predominantly occurs on active steel areas, a small dissolution current is typically also present on passive steel [18]. Accordingly, both reactions were assumed to occur on passive and active steel surfaces, albeit at different rates. Passive and active steel regions were treated as microcell corrosion systems that are electrochemically coupled to form a macrocell [19].

The current densities associated with the cathodic and anodic reactions were described using simplified Butler-Volmer kinetics. Polarisation parameters can be defined either at the reversible electrode level [20] or at the corrosion system level [19]. In this work, the reversible electrode approach was adopted. The cathodic current density i_{ca} and the anodic current density i_{an} were thus expressed as:

$$i_{ca} = -i_{0ca} \cdot 10^{\frac{-(E-E_{0ca})}{\beta_{ca}}} \tag{7}$$

$$i_{an} = i_{0an} \cdot 10^{\frac{(E-E_{0an})}{\beta_{an}}} \tag{8}$$

where:

i_{0ca}: Exchange current density of the cathodic reaction in µAcm^{-2}
E_{0ca}: Equilibrium potential of the cathodic reaction in mV$_{SCE}$
β_{ca}: Tafel slope of the cathodic reaction in mVdec^{-1}
i_{0an}: Exchange current density of the anodic reaction in µAcm^{-2}
E_{0an}: Equilibrium potential of the anodic reaction in mV$_{SCE}$
β_{an}: Tafel slope of the anodic reaction in mVdec^{-1}

The model represents an aerated concrete structure with a partially water-filled pore network. Under the selected cathodic reaction rates, sufficient oxygen availability at the steel surface was assumed, such that oxygen transport limitations could be neglected. Reverse reactions of Eq. (5) and (6) were also neglected, as the chosen polarisation parameters ensured that the mixed potential resulting from both reactions taking place on an isolated surface element remained far from the equilibrium potentials.

The total current density on a steel surface results from the superposition of the anodic and cathodic contributions. The indices 'p' and 'a' denote whether a parameter refers to passive or active steel.

$$i_{\mathrm{p}} = i_{0\mathrm{an}} \cdot 10^{\frac{(E-E_{0\mathrm{an}})}{\beta_{\mathrm{an,p}}}} - i_{0\mathrm{ca}} \cdot 10^{\frac{-(E-E_{0\mathrm{ca}})}{\beta_{\mathrm{ca,p}}}} \tag{9}$$

$$i_{\mathrm{a}} = i_{0\mathrm{an}} \cdot 10^{\frac{(E-E_{0\mathrm{an}})}{\beta_{\mathrm{an,a}}}} - i_{0\mathrm{ca}} \cdot 10^{\frac{-(E-E_{0\mathrm{ca}})}{\beta_{\mathrm{ca,a}}}} \tag{10}$$

In line with previous studies [19], [20], identical cathodic kinetics were assumed for passive and active steel ($\beta_{\mathrm{ca,p}} = \beta_{\mathrm{ca,a}}$). Consequently, passive and active steel were distinguished solely by the anodic reaction rate, expressed by the anodic Tafel slope β_{an}.

Polarisation parameters of fully active steel cannot be determined experimentally with sufficient reliability since a steel probe with a homogeneously active steel surface embedded in concrete barely can be produced [21]. Therefore, parameters for active steel were derived from experimentally obtained parameters of passive steel using a predefined macrocell driving voltage. Potentiodynamic polarisation tests were performed with passive rebars embedded in chloride-free concrete [16]. The rebars were polarised from $E_{\mathrm{corr,p}}$ by a potential shift of −600 mV and after depolarization from $E_{\mathrm{corr,p}}$ by +600 mV at a scan rate of 2 mVmin^{-1}. The corrosion potential $E_{\mathrm{corr,p}}$ and the corrosion current density $i_{\mathrm{corr,p}}$, which a passive corrosion system establishes without coupling to an active system, as well as the Tafel slopes $\beta_{\mathrm{ca,p}}$ and $\beta_{\mathrm{an,p}}$ were determined. The polarisation curve was fitted to Eq. (11):

$$i_{\mathrm{p}} = i_{\mathrm{corr,p}} \cdot \left(10^{\frac{(E-E_{\mathrm{corr,p}})}{\beta_{\mathrm{an,p}}}} - 10^{\frac{-(E-E_{\mathrm{corr,p}})}{\beta_{\mathrm{ca,p}}}} \right) \tag{11}$$

Table 1 shows the results for the passive corrosion system.

Table 1 Polarisation parameters for passive corrosion system

Parameter	Dimension	Value
$E_{\mathrm{corr,p}}$	[mV$_{\mathrm{SCE}}$]	−101.5
$i_{\mathrm{corr,p}}$	[μAcm^{-2}]	1.08E−02
$\beta_{\mathrm{ca,p}}$	[mVdec^{-1}]	160
$\beta_{\mathrm{an,p}}$	[mVdec^{-1}]	357

Reversible electrode parameters ($E_{0\mathrm{ca}}$, $E_{0\mathrm{an}}$, $i_{0\mathrm{ca}}$, $i_{0\mathrm{an}}$) were subsequently derived as points on the Tafel lines of the passive polarisation curve. Although mathematically arbitrary since an infinite number of combinations of potentials and current densities are described by the Tafel lines, these parameters were selected such that $E_{0\mathrm{ca}}$ is more positive and $E_{0\mathrm{an}}$ more negative than the corrosion potentials $E_{\mathrm{corr,p}}$ and $E_{\mathrm{corr,a}}$ of passive and active steel, respectively, and that $E_{0\mathrm{ca}}$ and $E_{0\mathrm{an}}$ approximately lie in the vicinity of the theoretical equilibrium potentials. It is emphasized that, in this work, $E_{0\mathrm{ca}}$ and $E_{0\mathrm{an}}$ are not intended to represent correct equilibrium potentials in the thermodynamic meaning.

A driving voltage ΔE, defined as the difference between $E_{\mathrm{corr,p}}$ and $E_{\mathrm{corr,a}}$, was defined to calculate $E_{\mathrm{corr,a}}$. A value of 400 mV was selected based on macrocell driving voltages ranging from 250 to 560 mV reported in the literature [1], [22]–[24], resulting in $E_{\mathrm{corr,a}} = -501.5$ mV$_{\mathrm{SCE}}$.

The anodic Tafel slope for active steel $\beta_{\mathrm{an,a}}$ was then calculated using Eq. (12), which expresses the relationship between the reversible electrode reactions and the active corrosion system [21]:

$$\beta_{\mathrm{an,a}} = \left(E_{\mathrm{corr,\,a}} - E_{0\mathrm{an}}\right) \Big/ \left(-\lg\left(\frac{i_{0\mathrm{an}}}{i_{0\mathrm{ca}}}\right) + \frac{E_{0\mathrm{ca}} - E_{\mathrm{corr,\,a}}}{\beta_{\mathrm{ca,a}}} \right) \tag{12}$$

By changing ΔE and thus $E_{\mathrm{corr,a}}$, different values for $\beta_{\mathrm{an,a}}$ and consequently different macrocell configurations can be generated. Fig. 2 shows the measured and the fitted polarisation curve for passive steel, the calculated polarisation curve for active steel and the polarisation parameters used for the

numerical simulation. Please note that Fig. 2 illustrates the polarisation behaviour of passive and active steel in uncoupled condition (i.e. before macrocell formation).

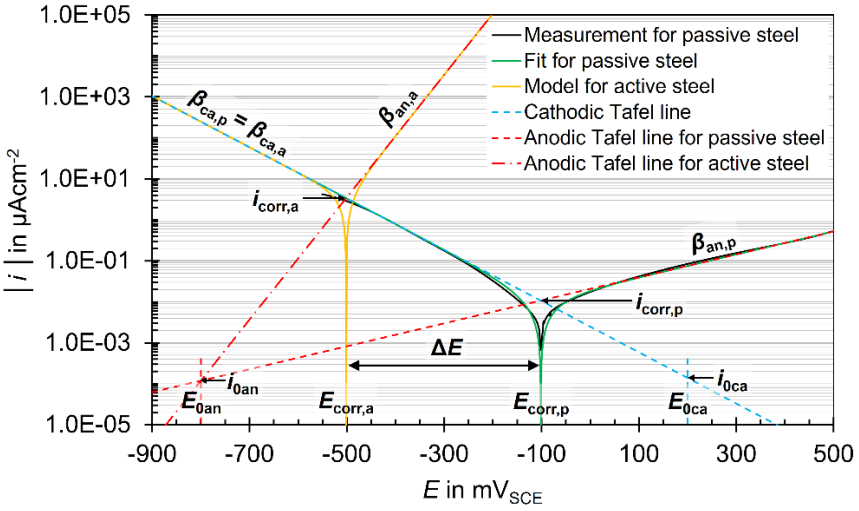


Fig. 2 Polarisation curves for passive (green) and active steel (orange) used as input parameters for the numerical model; passive curve was fitted to experimental data (black) and active curve was modelled by calculating the anodic Tafel slope of active steel $\beta_{an,a}$ using a predefined driving voltage ΔE

Concrete resistivity was set to 200 Ωm, representative of moderately moist concrete exposed to the outside [1]. The passive-to-active steel surface area ratio A_P/A_A was chosen as 1000:1, yielding an active area of 76.5 cm^2 (19.1 cm^2 for the modelled quarter). All model input parameters are summarised in Table 2.

Table 2 Input parameters for numerical simulation

Parameter	Dimension	Value
E_{0ca}	[mV$_{SCE}$]	200
E_{0an}	[mV$_{SCE}$]	−800
i_{0ca}	[µAcm^{-2}]	1.40E−04
i_{0an}	[µAcm^{-2}]	1.19E−04
ΔE[a)]	[mV]	400
$\beta_{ca,p}$[b)]	[mVdec^{-1}]	160
$\beta_{an,p}$[b)]	[mVdec^{-1}]	357
$\beta_{ca,a}$	[mVdec^{-1}]	160
$\beta_{an,a}$	[mVdec^{-1}]	67
ρ	[Ωm]	200
A_P/A_A	–	1000:1

a) ΔE is the difference between $E_{corr,p}$ and $E_{corr,a}$

b) Experimentally derived parameters

3 RESULTS AND DISCUSSION

3.1 Potential Distribution After First Corrosion Initiation

Fig. 3 presents the potential distribution on the steel surface after coupling passive and active steel areas. The results show more negative potentials in the vicinity of the active steel and progressively more positive potentials with increasing distance from the corrosion site.

Macrocell formation induces cathodic polarisation of the passive steel from $E_{corr,p}$ to a more negative potential E_p and anodic polarisation of the active steel from $E_{corr,a}$ to a more positive potential E_a. Due to spatial separation of passive and active steel areas and the electrical resistivity of the concrete, E_p remains more positive than E_a. The minimum potential of the active steel was −486 mV_{SCE}, corresponding to an anodic polarisation of approximately 16 mV relative to $E_{corr,a}$ = −501.5 mV_{SCE}. At the same time, the passive steel reached a maximum potential of −112 mV_{SCE}, resulting in a cathodic polarisation of 11 mV relative to $E_{corr,p}$ = −101.5 mV_{SCE}. Under the selected conditions, all passive rebars within in the slab experienced cathodic polarisation. At a distance of 30 cm from the symmetry axes intersection, passive steel potentials of −204 mV_{SCE} (point A in Fig. 3) and −194 mV_{SCE} (point B in Fig. 3) were obtained when measured at the crown line of the uppermost rebars.

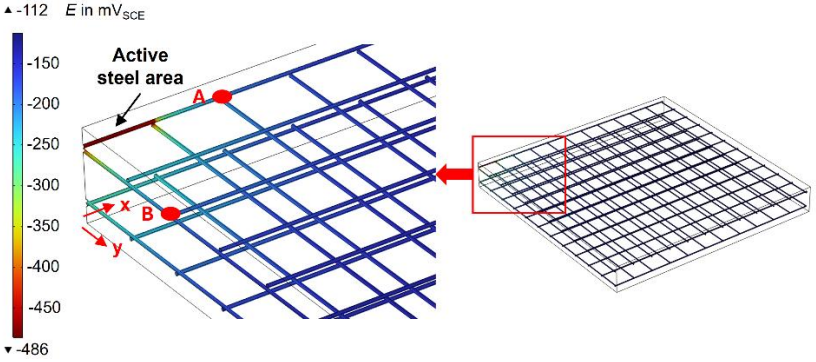


Fig. 3 Potential distribution on the steel surface after coupling of passive and active steel areas; detailed view of the left slab corner in the vicinity of the active steel area (left); points A and B are 30 cm away from the symmetry axes intersection

3.2 Influence of Potential Distribution on Chloride Threshold Distribution

Fig. 4 illustrates the C_T distribution on the steel surface obtained by combining the simulated potential field with the potential-dependent C_T relationship defined by Eq. (1) and (2). The active steel area (indicated in white in Fig. 4) was excluded, as C_T had already been exceeded there. Due to logarithmic relationship between E and C_T, a logarithmic colour scale was applied.

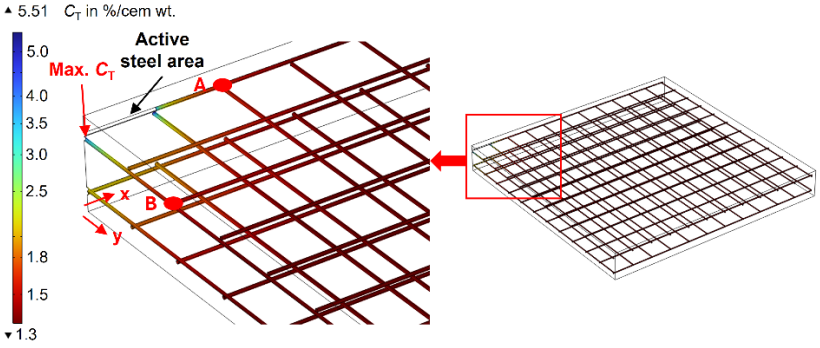


Fig. 4 Chloride threshold distribution on the steel surface according to Eq. (1) and (2) after coupling of passive and active steel areas; detailed view of the left slab corner in the vicinity of the active steel area (left); points A and B are 30 cm away from the symmetry axes intersection

A pronounced increase in C_T compared to the base value of 1.30 %/cem wt. was observed near the first corrosion site. The maximum C_T of 5.51 %/cem wt. occurred at the intersection of the first rebar aligned in y-direction with the uppermost first rebar aligned in x-direction ('Max. C_T' in Fig. 4). At point A, C_T increased to 1.58 %/cem wt., and at point B to 1.51 %/cem wt. Points A and B are identical to Points A and B in Fig. 3. These results correspond to an increase in C_T of 22 % (point A) and 16 % (point B), respectively. At the crown line in the uppermost rebar layer, the base value C_{T0} was reached at distances of approximately 53 cm (x-direction) and 60 cm (y-direction). It is emphasised that the key outcome of this work is not an absolute value for C_{T0} but the extent of its increase due to cathodic polarisation.

This local increase in C_T significantly affects the likelihood of additional corrosion initiation spots. Within a distance of approximately 50 to 60 cm from the initial anode, the probability of new corrosion sites is reduced compared to models assuming a constant C_T. Consequently, macrocell-induced polarisation contributes to spatial variability in corrosion initiation. The formation of additional anodes would further modify the spatial potential and C_T distributions.

The presented results apply to the selected modelling assumptions, including a homogeneous concrete resistivity and time- and space-invariant chloride ingress. In practice, spatial variations in resistivity and chloride transport properties may influence anode formation. Assessing the relative importance of a potential-dependent C_T under realistic exposure conditions requires coupling this approach with probabilistic chloride ingress models, for example as proposed in [13].

4 CONCLUSION

This study investigated the implications of a potential-dependent C_T for the spatial development of corrosion in reinforced concrete after the formation of a first corrosion site. A numerically simulated steel potential field was combined with an experimentally derived relationship between steel potential and C_T.

The results show that macrocell-induced polarisation locally increases C_T in the vicinity of an active corrosion site. This increase reduces the likelihood of subsequent corrosion initiations in adjacent passive steel areas compared to approaches assuming a constant C_T. Consequently, coupling between passive and active steel directly affects the spatial distribution of corrosion sites and highlights an interaction between corrosion initiation and propagation that is not represented in conventional service life models. Although the demonstrated numerical model is based on idealised assumptions, it provides a mechanistic demonstration of how changing electrochemical conditions within a reinforcement assembly can locally modify resistance parameters decisive for corrosion initiation. Incorporating potential-dependent C_T behaviour into corrosion prediction models may therefore contribute to improved assessments of corrosion risk and service life. Future research should address the interaction of this mechanism with spatial variability in concrete resistivity and probabilistic chloride ingress.

References

[1] Bertolini, Luca; Elsener, Bernhard; Pedeferri, Pietro; Redaelli, Elena, and Polder, Rob. 2013. *Corrosion of Steel in Concrete*. Weinheim: WILEY-VCH.

[2] Tuutti, Kyösti. 1982. "Corrosion of steel in concrete." PhD diss., Lund University.

[3] Angst, Ueli M.; Isgor, O. Burkan; Hansson, Carolyn M.; Sagüés, Alberto, and Geiker, Mette R. 2022. "Beyond the chloride threshold concept for predicting corrosion of steel in concrete." *Applied Physics Review* 9:011321. https://doi.org/10.1063/5.0076320

[4] Cassiani, Juan D.; Dugarte, Margareth; Arteta, Carlos A., and Kessler, Sylvia. 2022. "Durability assessment of a tunnel structure with two-sided chloride ingress – A case study located in a tropical environment." *Structural Concrcrete* 23:739–752. https://doi.org/10.1002/suco.202100550

[5] Pfändler, Patrick; Keßler, Sylvia; Huber, Maximilian, and Angst, Ueli. 2022. "Spatial variability of half-cell potential data from a reinforced concrete Structure–a geostatistical analysis." *Structure and Infrastructure Engineering* 20:1698–1713. https://doi.org/10.1080/15732479.2022.2158204

[6] Keßler, Sylvia; Fischer, Johannes; Straub, Daniel, and Gehlen, Christoph. 2014. "Updating of service-life prediction of reinforced concrete structures with potential mapping." *Cement and Concrete Composites* 47:47–52. https://doi.org/10.1016/j.cemconcomp.2013.09.018

[7] Bentz, Evan C. 2003. "Probabilistic Modeling of Service Life for Structures Subjected to Chlorides." *ACI Materials Journal* 100:391–397. https://doi.org/10.14359/12814

[8] Sagüés, Alberto A., and Alexander, Christopher L. 2023. "Exploration of Next-Generation Reinforced Concrete Corrosion Modeling with Interdependent Initiation and Propagation Stages." *Corrosion* 79:351–362. https://doi.org/10.5006/4193

[9] Pedeferri, Pietro. 1996. "Cathodic protection and cathodic prevention." *Construction and Building Materials* 10:391–402. https://doi.org/10.1016/0950-0618(95)00017-8

[10] Alonso, Cruz; Castellote, Marta, and Andrade, Carmen. 2002. "Chloride threshold dependence of pitting potential of reinforcements." *Electrochimica Acta* 47:3469–3481. https://doi.org/10.1016/S0013-4686(02)00283-9

[11] Sánchez, Andrea N. 2014. "Forecasting Corrosion of Steel in Concrete – Introducing Chloride Threshold Dependence on Steel Potential." PhD diss., University of South Florida.

[12] Sagüés, Alberto A.; Sánchez, Andrea N.; Lau, Kenny, and Kranc, Stanley C. 2014. "Service Life Forecasting for Reinforced Concrete Incorporating Potential-Dependent Chloride Threshold." *Corrosion* 70:942–957. https://doi.org/10.5006/1286

[13] International Federation of Structural Concrete. 2006. *Model Code for Service Life Design*. Lausanne: International Federation of Structural Concrete.

[14] Beck, Matthias; Burkert, Andreas; Harnisch, Jörg; Isecke, Bernd; Osterminski, Kai; Raupach, Michael; Schießl, Peter; Tian, Wei, and Warkus, Jürgen. 2012. "Deterioration Model and Input Parameters for Reinforcement Corrosion." *Structural Concrete* 13:145–155. https://doi.org/10.1002/suco.201200004

[15] Geiker, Mette; Michel, Alexander; Lepech, Michel D.; Wu, Jie, and Stang, Henrik. 2017. "Multi-scale and multi-physics deterioration modelling for design and assessment of reinforced concrete structures." *RILEM Technical Letters* 2:119–128. https://doi.org/10.21809/rilemtechlett.2017.49

[16] Fache, Konstantin; Keßler, Sylvia, and Harnisch, Jörg. 2026. "On the impact of cathodic polarization on the chloride threshold for carbon steel in concrete." *Materials and Structures* 59:144. https://doi.org/10.1617/s11527-026-03020-9

[17] Boschmann Käthler, Carolina; Ebell, Gino; Keßler, Sylvia; Schiegg, Yves; Dauberschmidt, Christoph, and Angst, Ueli M. 2021. "A comparison of methods to assess the resistance of reinforcing steel against chloride-induced corrosion in concrete – Particular consideration of 12% chromium steel." *Materials and Corrosion* 73:306–325. https://doi.org/10.1002/maco.202112826

[18] Zakroczymski, Tadeusz; Fan, Chwei J., and Szklarska-Smialowska, Zuzanna. 1985. "Kinetics and Mechanism of Passive Film Formation on Iron in 0.05M NaOH." *Journal of The Electrochemical Society* 132:2862–2867. https://doi.org/10.1149/1.2113684

[19] Sohail, Muazzam G.; Laurens, Stéphane; Deby, Fabrice, and Balayssac, Jean P. 2015. "Significance of macrocell corrosion of reinforcing steel in partially carbonated concrete: numerical and experimental investigation." *Materials and Structures* 48:217–233. https://doi.org/10.1617%2Fs11527-013-0178-2

[20] Sagüés, Alberto A., and Kranc, Stanley C. 2001 "Detailed modeling of corrosion macrocells on steel reinforcing in concrete." *Corrosion Science* 43:1355–1372. https://doi.org/10.1016/S0010-938X(00)00158-X

[21] Chalhoub, Chantal; François, Raoul; Garcia, David; Laurens, Stephane, and Carcasses, Myriam. 2020. "Macrocell corrosion of steel in concrete: Characterization of anodic behavior in relation to the chloride content." *Materials and Corrosion* 71:1424–1441. https://doi.org/10.1002%2Fmaco.201911398

[22] Gulikers, Joost J. W. 1996. "Experimental investigations on macrocell corrosion in chloride-contaminated concrete." *Heron* 41:107–123.

[23] Harnisch, Jörg. 2012. "Zum zeitabhängigen Verhalten elektrochemischer und morphologischer Kenngrößen bei der chloridinduzierten Korrosion von Stahl in Beton." PhD diss., RWTH Aachen University.

[24] Warkus, Jürgen. 2012. "Einfluss der Bauteilgeometrie auf die Korrosionsgeschwindigkeit von Stahl in Beton bei Makroelementbildung." PhD diss., RWTH Aachen University.

Probabilistic Modelling of Spatial Variability in Chloride Diffusion in the Lattice Discrete Particle Model

Jelle Billiet[1], Wouter Botte[1], Roman Wan-Wendner[1]

[1]Department of Structural Engineering and Building Materials,
Ghent University,
Technologiepark – Zwijnaarde 60, 9052 Ghent, Belgium

Summary
Corrosion of reinforcement steel is one of the major deterioration mechanisms in concrete structures. It can be induced by the penetration of chlorides to the location of the reinforcement. This process involves ionic diffusion influenced by complex hygro-thermo-chemical (HTC) and physical phenomena, the continuously evolving material structure, mechanical influences such as cracking, and environmental conditions. Understanding the intricate nature of this phenomenon and its inherent spatial variability, remains critical to the design and assessment of new and existing structures. The current contribution aims at assessing spatial variability of the diffusion process in a numerical setting with the Multiphysics-Lattice Discrete Particle Model (M-LDPM) framework. A benchmark simulation is performed to showcase the capabilities of M-LDPM in capturing meaningful variability in the chloride penetration. A probabilistic approach is adopted to account for the uncertainties involved, allowing to determine the probability of corrosion initiation, and compare to the results of traditional macro-scale diffusion models.

1 INTRODUCTION

Chloride-induced corrosion is one of the dominant deterioration mechanisms affecting reinforced concrete structures. It involves the gradual ingress of aggressive chlorides through the concrete toward the reinforcement. In general, it is assumed that when the chloride concentration at the rebar exceeds a critical threshold ($C > C_{crit}$), the protective passive layer breaks down and corrosion is initiated. Subsequently, corrosion products accumulate, leading to a reduction of the steel cross-section, loss of load-carrying capacity, and damage in the surrounding concrete, such as cracking caused by the expansive nature of the corrosion reaction. Due to their exposure to chlorides, structures in marine environments or exposed to de-icing salts are therefore particularly vulnerable and should therefore receive specific attention in service life prediction.

Numereous uncertainties are involved in the initiation of corrosion. Therefore, various reliability-based frameworks, such as the DuraCrete model [1]-[3], provide probabilistic design approaches for service life predictions and risk assessment regarding chloride-induced corrosion. Such models often relate a reliability index to the probability of exceedance of a critical concentration. In other works, numerical approaches are developed to simulate the chloride ingress with differing levels of complexity [4]-[7]. In this study, the recently proposed chloride diffusion model of Zhang et al. [4] is adopted. It is formulated within the broader Multiphysics-Lattice Discrete Particle Model (M-LDPM) framework, which consists of the existing LDPM and Hygro-Thermo-Chemical (HTC) formulations. Compared to classical macroscopic continuum models, the model allows to capture variability in the local chloride concentration, as the discretization explicitly differentiates between aggregates and matrix. This feature could make the model particularly interesting for service life predictions of small-scale problems. In this work, the framework is employed to model and investigate spatial variability of chloride diffusion. A probabilistic approach is adopted to account for the uncertainties involved, allowing the estimation of the probability of corrosion initiation, and comparison with predictions from conventional macro-scale diffusion models.

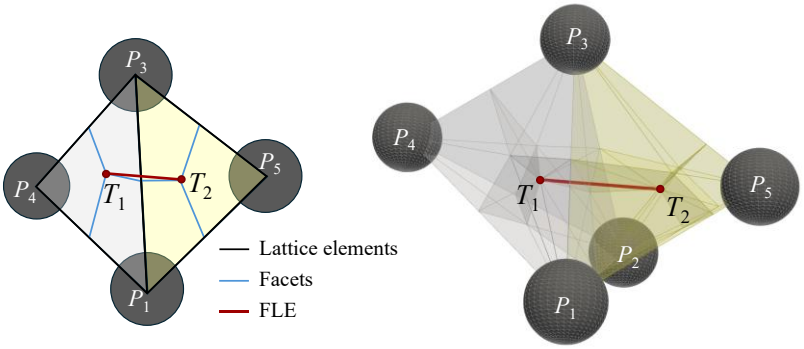
2 THE MULTIPHYSICS LATTICE DISCRETE PARTICLE MODEL (M-LDPM) FOR THE SIMULATION OF CHLORIDE TRANSPORT

In this contribution, the chloride ingress process is simulated by means of M-LDPM. It is a powerful framework that couples the well-established LDPM mechanical model with a discrete implementation of the HTC model. On the one hand, LDPM allows to reproduce the mechanical aspects of concrete

fracturing under a broad range of loading conditions, while the complementary HTC model simulates the moisture, heat and chloride transport in the hydrating concrete.

The M-LDPM coupling is achieved using a dual lattice system [4], [8]-[10]. At first, in LDPM concrete is modelled as a two-phase composite, consisting of coarse aggregate particles embedded in a mortar matrix. The model is obtained by randomly inserting spherical particles—representing the aggregates—into the model volume. Thereafter, Delaunay tetrahedralization on the particle centres is employed to construct the connecting edges between the particles. Finally, a subsequent domain tessellation is performed, thereby defining *facets*, on which failure may occur. By collecting all facets related to one aggregate piece, an LDPM *cell* is obtained. Interactions between cells are then defined on the facets. As such, the mechanical lattice system is successfully constructed.

To perform coupled simulations, a second lattice system is defined, in which the transport problems are solved. In the discrete HTC formulation, it is composed of flow channels which are embedded within the tetrahedral mesh of the LDPM model, see Fig. 1. These so-scalled Flow Lattice Elements (FLE's) collect and simulate the various fluxes between two adjacent tetrahedra, their geometry defined by the connecting edge between the respective *tet-points* T_1 and T_2. Consequently, the transport phenomena within the whole domain are simulated by the networks of FLEs connecting all tetrahedra, its tortuosity resulting in spatial variability in transport processes. As such, a coupled two-way framework is established, which has previously been used to simulate a variety of multiphysics phenomena.



(a) 2D schematic sketch (b) 3D representation

Fig. 1 Visualisation of the Flow Lattice Element (FLE); (a) 2D and (b) 3D representation

3 MODELLING OF CHLORIDE DIFFUSION ON THE MACRO-SCALE

In case of service life assessment, chloride ingress in concrete is usually modelled on the macro-scale by application of Fick's second law of diffusion [11], as given by equation (1).

$$C(x,t) = C_0 + (C_s - C_0) \cdot \mathrm{erfc}\left(\frac{x}{2 \cdot \sqrt{D_{app}(t) \cdot t}}\right) \tag{1}$$

Here, $C(x,t)$ is identified as the chloride concentration at time t and depth x from the exposed surface, and C_0 and C_s respectively denote the initial chloride content in the concrete, and the surface concentration. Finally, $D_{app}(t)$ is the apparent diffusion coefficient governing the rate of diffusion.

The *fib* bulletin 34 [3] proposes a full probabilistic design methodology based on the DuraCrete model [1], [2] for the service life design of concrete structures. To determine the probability of corrosion-induced steel depassivation at depth a, a limit state which is based on Fick's second law of diffusion is proposed:

$$C_{crit} = C(x = a, t) = C_0 + \left(C_{S,\Delta x} - C_0\right) \cdot \left[1 - \mathrm{erf}\left(\frac{a - \Delta x}{2 \cdot \sqrt{D_{app,C}(t) \cdot t}}\right)\right] \tag{2}$$

Here, C_{crit} denotes the critical chloride concentration corresponding to corrosion initiation, characterized by a Beta distribution with parameters: $\mu = 0.6$, $\sigma = 0.15$, $a = 0.2$ and $b = 2.0$. The

parameter Δx relates to the depth of the convection zone, in which the transport is significantly influenced by other transport processes. Finally, $C_{S,\Delta x}$ is the chloride content at depth Δx.

4 NUMERICAL M-LDPM SIMULATIONS OF CHLORIDE TRANSPORT

The capability of the chloride diffusion model proposed by Zhang et al. [4] in capturing the inherent variability in the chloride transport is examined by means of a simple numerical set-up (see Fig. 2). In this configuration, one of the surfaces of the specimen in YZ is exposed to a saline solution of 420 mol/m³, while the remaining surfaces are sealed, see Fig. 2. This induces a one-dimensional chloride diffusion process over a large portion of the specimen, excluding the regions near the lateral surfaces in YX where the transport process is influenced by boundary effects. The material is assumed to have a temperature of 10 °C, and saturated conditions are imposed (RH = 0.999). As such, in the absence of a spatial moisture gradient ∇h, advection effects—accounting for the transport of ionic chloride transported within a moisture flux—remain inactive. Thus, only diffusion contributes to the ingress process in these simulations, thereby providing a controlled environment for a preliminary investigation of the spatial variability that develops during the ingress process.

The model dimensions are carefully selected to balance minimizing the computational cost and retaining the quality and quantity of model output. In the direction of the chloride ingress (i.e. the X-direction), a minimum depth is required to capture the transport process up to the position of the reinforcement. In this work, a typical value of the nominal cover c_{nom} = 30 mm is assumed. In order to account for the rebar dimensions, a depth of 60 mm is adopted. Spatial variability of the diffusion process is expressed in the two directions orthogonal to the 1D-diffusion, i.e. Y and Z. As a trade-off between output richness and acceptable computational cost, dimensions of 150 mm and 500 mm are respectively chosen in the Y- and Z-direction.

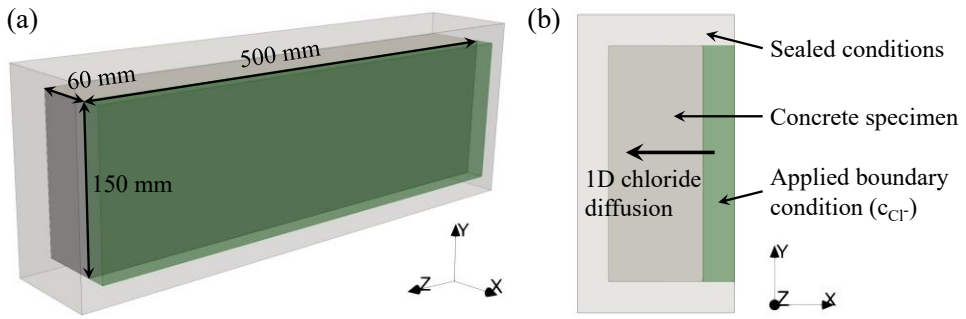


Fig. 2 Set-up of the numerical M-LDPM simulations

The model parameters and mix design follow from numerical results presented in [4], [8], which aimed at reproducing test data presented in [12] on ultra-high performance concrete (UHPC) mixtures. The mix composition is presented in Table 1, consisting of contents of water *w*, cement *c*, aggregates *a* and slag *sl*. No data was reported on the particle size distribution parameters, hence they were adjusted to d_0 = 8 mm, d_a = 25 mm and n_F = 0.5 as to limit computational cost. The relevant chloride diffusion parameters are outlined in Table 2, obtained in [4], [8] based on calibration to experimental results in [13]. These parameters are considered to be homogenous in the computational domain.

Table 1 Concrete mix design parameters of UHPC mixture used in M-LDPM simulations

Property	w [kg/m³]	c [kg/m³]	a [kg/m³]	sl [kg/m³]	d_0 [mm]	d_a [mm]	n_F [-]
Value	200	600	982	500	8	25	0.5

Table 2 Identified chloride diffusion parameters

Property	τ_a [-]	A_0 [-]	U [kJ/mol]	f_v [-]	B_0 [-]	U_b [kJ/mol]
Value	0.4	0.7	40	600	1.9	33.2

5 RESULTS AND DISCUSSION

5.1 Variability of the chloride diffusion process

Fig. 3 presents the chloride penetration profiles at different exposure durations, illustrating substantial variability resulting from the tortuosity of the meso-structure. The chloride ingress process—as captured by M-LDPM—is a continuous phenomenon, characterized by a global and decelerating increase of chloride content over the complete depth.

The variability of the chloride penetration profile at 300 days exposure is examined in more detail. Fig. 4 left presents the probability distribution of the chloride concentration C at depth x = 15 mm, whereas Fig. 4 right depicts the distribution of the depth at which the critical chloride concentration C_{crit} = 0.6 wt.-%/c (according to [3]) is reached. In both cases, the probability distribution function (PDF) appears to be Gaussian, showing a non-negligible variability. This distribution can be adopted when performing reliability analyses, i.e. deriving the probability of corrosion initiation. On the one hand, a global reliability index can be obtained by analysing the distribution of the obtained chloride data at the location of the rebar. On the other hand, also local information is obtained on the spatial characteristics of the concentration, see Fig. 5 showing C for x = 4 mm after 300 days exposure, thereby allowing to provide local reliability estimates and analyse e.g. spatial correlation, relationships with the meso-structure, material properties and features such as the wall effect. These findings highlight the potential of the M-LDPM in simulating chloride diffusion, with a particular capability of bridging the two scales i.e. macro- and meso.

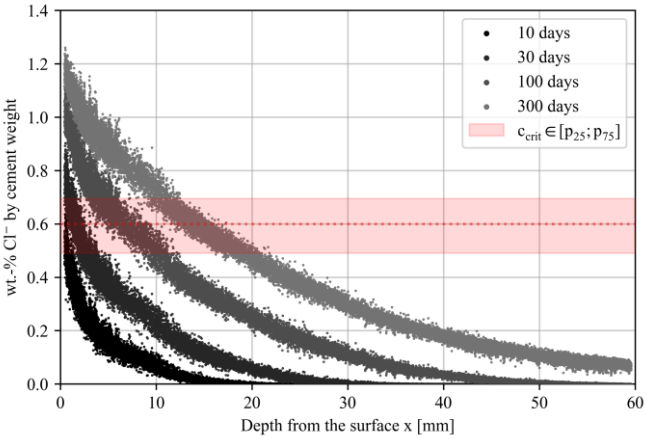


Fig. 3 Spatial variability of the time-dependent chloride ingress, for different exposure durations

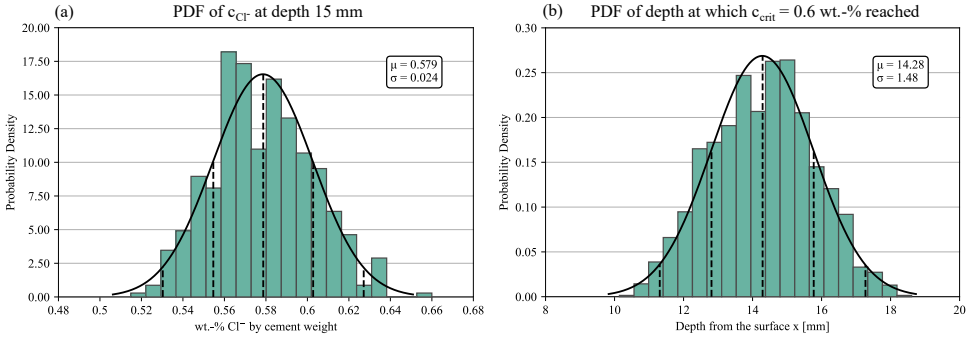


Fig. 4 Probability densities of the chloride ingress after 300 days exposure; (a) PDF of chloride concentration at 15 mm depth; (b) PDF of the depth at which a critical chloride concentration—C_{crit} = 0.6 wt.-% according to [3]—is reached

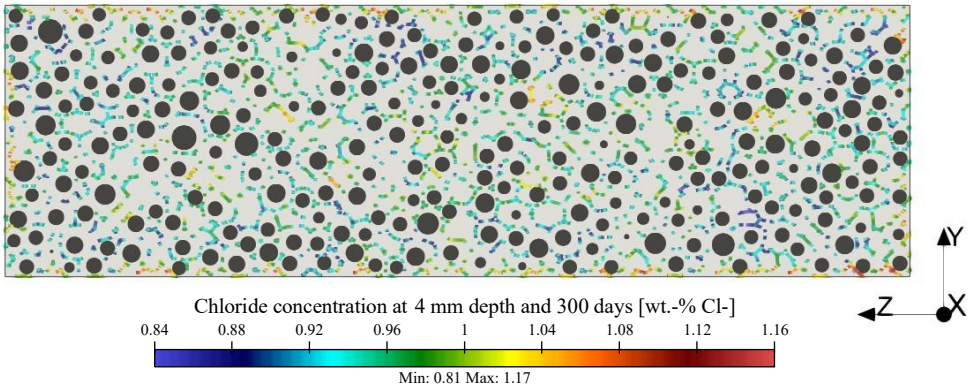


Fig. 5 Visualisation of the local chloride concentration on the FLE network, for x = 4 mm and t = 300 days (aggregate particles shown in black)

5.2 Probabilistic considerations

The obtained M-LDPM chloride ingress data allows to perform reliability analyses with respect to corrosion initiation at the rebar. Two approaches are explored. One the one hand, the probability can directly be computed from the PDF of C at the location of the rebar, using the M-LDPM data on the FLE network. As in these simulations, the rebar is not explicitly modelled, the chloride content C at $x = c_{nom}$ can be used for this purpose. Alternatively, the reliability assessment can be performed by fitting the parameters of the macro-scale model given by Eq. (1) and their subsequent application in the limit state formulation of Eq. (2). In this following, the results of both scenarios are discussed and compared.

5.2.1 Direct reliability assessment with M-LDPM chloride concentrations

At first, the reliability index β is computed directly from the M-LDPM data, where c_{nom} = 30 mm and t = 300 days are assumed. At this depth and exposure duration, the chloride field is characterized by μ = 0.296 and σ = 0.017 wt.-%/c. The probability of corrosion initiation is defined by the limit state $g(\underline{X}) = Z = R - E = C_{crit} - C(x,t) < 0$, where the critical chloride concentration C_{crit} follows a Beta distribution with μ = 0.6, σ = 0.15, a = 0.2 and b = 2.0 as outlined in [3]. Monte Carlo simulations yield a reliability index $\beta(x = 30$ mm, $t = 300$ days) = 2.556, see Fig. 6.

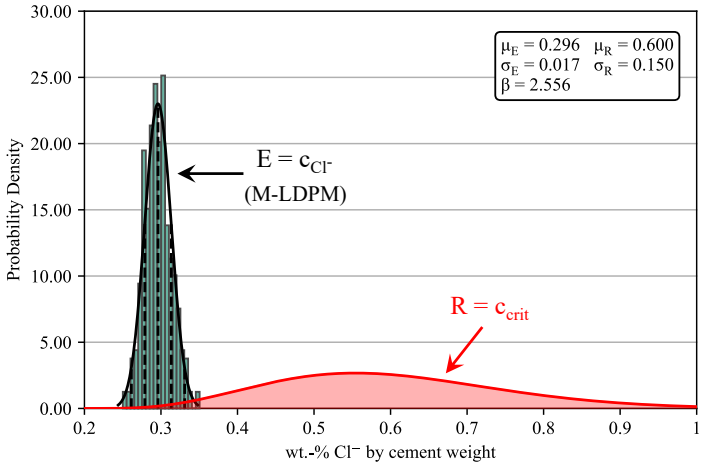


Fig. 6 Direct reliability assessment of corrosion initiation at depth 30 mm and time 300 days, with the available M-LDPM data on the chloride concentration c_{Cl^-}

One can observe that the uncertainty in this scenario is dominated by the uncertainty of the critical chloride concentration, while the chloride concentration itself is characterized by a narrow

distribution with high peak probability. It is important to indicate that, in this initial benchmark case, only the material meso-structure is contributing to the variability of the chloride content. In reality, however, also the meso-scale diffusion parameters are uncertain. Therefore, the PDF of C should ideally be derived from multiple realizations, featuring various meso-structures and a set of well-chosen probabilistic material parameters. This will be addressed in further research.

5.2.2 Indirect assessment with fitted macro-scale diffusion model

To determine the probability of failure in the second approach, first the material parameters as defined by Fick's second law of diffusion in Eq. (1) are calibrated. As outlined in Section 3, near the surface the chloride transport is significantly influenced by processes in the convection zone that are different from diffusion. To account for this, *fib* bulletin 34 introduces the parameter Δx, which defines the depth of this zone [3]. Consequently, during calibration this region near the surface can be ignored. In this contribution, the lower bound Δx = 6 mm for splash-conditions is assumed, see Fig. 7. As such, for t = 100 and 300 days respectively, C_s = 0.806 and 0.948 wt.-%/c, and $D_{app}(t)$ = 701.4 and 564.5 mm²/yr are obtained.

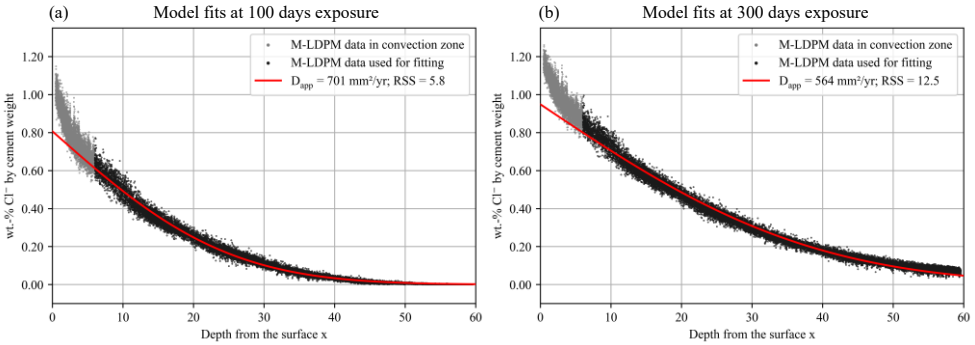


Fig. 7 Fitting of macro-scale diffusion model based on Fick's second law, for different exposure durations and assumptions; (a) 100 days exposure; (b) 300 days; (gray scatter data was not used for model fitting)

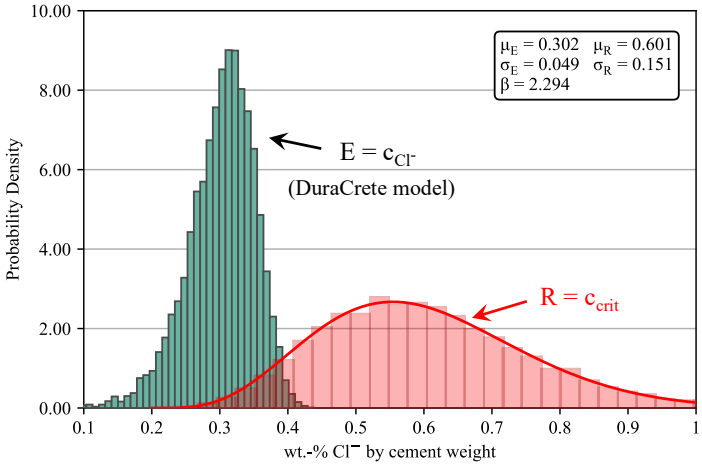


Fig. 8 Indirect reliability assessment of corrosion initiation at depth 30 mm and time 300 days by means of fitted macro-scale model

These parameters can be implemented in the DuraCrete model to obtain a reliability index. Following recommendations in [3], the diffusion coefficient is implemented as a probabilistic parameter with CoV = 0.2 and mean value as obtained during calibration. As such, for a = c_{nom} = 30 mm and t = 300 days, β = 2.294 is computed, see Fig. 8. As anticipated, the obtained variability on C(x,t) is

much larger than before, even when only accounting for uncertainty in the diffusion parameter, resulting in a higher probability of failure. The results of this approach will be extended in future works to account for the added uncertainty in the other limit state parameters, allowing for a more meaningful comparison to the M-LDPM resuls.

6 CONCLUSIONS

This paper presents a first exploration into the spatial variability of chloride diffusion captured by the Multiphysics-Lattice Discrete Particle Model (M-LDPM), where the involved uncertainties are accounting for by means of probabilistic approaches. As such, these preliminary investigations aim to assess the potential of M-LDPM as a discrete modelling framework, in which heterogeneity naturally arises from the tortuosity of diffusion paths.

To this extent, a preliminary benchmark example was simulated, in which the model dimensions were selected based on computational considerations, and the material parameters were adopted based on prior calibrations presented in [4], [8]. In the present work, these parameters were then assumed to be initially homogenous in the domain. Nonetheless, these first results clearly showed that substantial variations in the chloride concentrations were reproduced by the model due to the tortuous meso-structure and the resulting variability in transport path lengths. Both on the macro- and meso-scales, the results are shown to be highly promising, thereby they highlight the potential of M-LDPM i.e. its ability of briding both scales.

Further, the obtained M-LDPM results allow for probabilistic calculations. On the one hand, the reliability-based assessment can be performed directly from the obtained data of c_{Cl^-} at the location of the rebar. Alternatively, this assessment can be performed indirectly. Here, the parameters of a macro-scale model are calibrated based on the M-LDPM results and inserted in a probabilistic model e.g. the DuraCrete model in this work. In this second approach, the involved uncertainties can be accounted for by considering a recommended amount of variability on the calibrated parameters. In the first approach, one should simulate a broad range of numerical examples, with varying meso-structures and material parameters. In this work, the uncertainties were only (partly) considered for the second approach, thus explaining the different results, with a broader distribution being captured here. Nonetheless, both approaches have shown particularly interesting results and will be expanded upon in future work.

Finally, subject of future work will be to extend the current simulations, focussing on gaining a better understanding of the various uncertainties. Such expansions will include the following, considering for (1) uncertainty in the homogenous property in the domain; (2) uncertainty in the heterogenous material property along the domain; (3) uncertainty in the material meso-structure and (4) combinations of the previous. Finally, the explicit modelling of the reinforcement in the model will be pursued, as it allows to investigate the chloride concentrations directly on these elements. Such developments will allow to establish a more rigorous relationship between heterogeneity and chloride ingress, and ultimately enhance the possible integration of M-LDPM in durability-based frameworks.

Acknowledgements

The authors would like to acknowledge ES3inc for providing access to MARS, a specialized computational framework for structural mechanical response analysis.

References

[1] Anders, Lindvall. 2000. *DuraCrete – Probabilistic Performance Based Durability Design of Concrete Structures: Statistical Quantification of the Variables in the Limit State Functions. Report No.: BE 95-1347.*

[2] Siemens, Ton, and Edvardsen, Claus. 1999. “Duracrete: Service Life Design for Concrete Structures.” *Proceedings of the 8th International Conference on Durability of Building Materials and Components*, Vol. 2: *Durability of Building Assemblies and Methods of Service Life Prediction*:1343–1356.

[3] International Federation for Structural Concrete. 2006. *fib Bulletin No. 34: Model Code for Service Life Design.* doi:10.35789/fib.BULL.0034.

[4] Zhang, Ying, Di Luzio, Giovanni, and Alnaggar, Mohammed. 2021. “Coupled Multi-Physics Simulation of Chloride Diffusion in Saturated and Unsaturated Concrete.” *Construction and Building Materials* 292:123394. doi:10.1016/j.conbuildmat.2021.123394.

[5] Li, Yue, and Vořechovský, Miroslav. 2025. "Data-Driven Dynamic Mode Decomposition Framework for Spatio-Temporal Prediction of Concrete Chloride Ingress." *Computer-Aided Civil and Infrastructure Engineering.* doi:10.1111/mice.70161.

[6] Zhu, Yingbo, Jia, Dongge, Brigham, John C., and Fascetti, Alessandro. 2025. "Coupled Lattice Discrete Particle Model for the Simulation of Water and Chloride Transport in Cracked Concrete Members." *Computer-Aided Civil and Infrastructure Engineering* 40:982–1003. doi:10.1111/mice.13385.

[7] Ožbolt, Janko, Balabanić, Goran, Periškić, Goran, and Kušter, Mladen. 2010. "Modelling the Effect of Damage on Transport Processes in Concrete." *Construction and Building Materials* 24:1638–1648. doi:10.1016/j.conbuildmat.2010.02.028.

[8] Cibelli, Antonio, Di Luzio, Giovanni, and Ferrara, Liberato. 2023. "Numerical Simulation of the Chloride Penetration in Cracked and Healed UHPC via a Discrete Multiphysics Model." *Journal of Engineering Mechanics* 149:05023001. doi:10.1061/JENMDT.EMENG-7188.

[9] Cibelli, Antonio, Pathirage, Madura, Cusatis, Gianluca, Ferrara, Liberato, and Di Luzio, Giovanni. 2022. "A Discrete Numerical Model for the Effects of Crack Healing on the Behaviour of Ordinary Plain Concrete: Implementation, Calibration, and Validation." *Engineering Fracture Mechanics* 263:108266. doi:10.1016/j.engfracmech.2022.108266.

[10] Bousikhane, Faysal, Li, W., Di Luzio, Giovanni, and Cusatis, Gianluca. 2018. "Full Coupling between Diffusion and Mechanical Analysis in a Discrete Computational Framework." In *Book Section*, 305–310. doi:10.1201/9781315182964-38.

[11] Collepardi, Mario, Marcialis, Aldo, and Turriziani, Renato. 1972. "Penetration of Chloride Ions into Cement Pastes and Concretes." *Journal of the American Ceramic Society* 55:534–535. doi:10.1111/j.1151-2916.1972.tb13424.x.

[12] Cuenca, Estefanía, Lo Monte, Francesco, Moro, Marina, Schiona, Andrea, and Ferrara, Liberato. 2021. "Effects of Autogenous and Stimulated Self-Healing on Durability and Mechanical Performance of UHPFRC: Validation of Tailored Test Method through Multi-Performance Healing-Induced Recovery Indices." *Sustainability* 13. doi:10.3390/su132011386.

[13] Isteita, Moad, and Xi, Yunping. 2017. "The Effect of Temperature Variation on Chloride Penetration in Concrete." *Construction and Building Materials* 156:73–82. doi:10.1016/j.conbuildmat.2017.08.139.

Mechanical performance and durability of recycled concrete precast elements in infrastructure applications

Thomas Pichler[1)], **Klaus Voit**[2)], **Konrad Bergmeister**[1)]

[1)] *Institute of Structural Engineering,*
University of Natural Resources and Life Sciences, Vienna,
Peter-Jordan-Straße 82, 1190 Vienna, Austria

[2)] *Institute of Applied Geology*
University of Natural Resources and Life Sciences, Vienna,
Peter-Jordan-Straße 82, 1190 Vienna, Austria

Summary
Concrete production has a significant impact on natural resources. To reduce the dependence on primary raw materials and to establish more sustainable production processes, the recycling of demolished concrete is increasingly being encouraged. Within an *FFG*-funded research initiative, optimized mix designs using recycled concrete aggregates from demolished precast civil-engineering structures were developed. Six track base slab types, differing in replacement rates of natural and recycled aggregates and in the types of reinforcement, were manufactured and installed on site. In addition to verifying the properties of fresh and hardened concrete properties, a key objective was to demonstrate durability performance using abrasion and microscopic tests. It was found that workability was more difficult at high replacement rates of recycled aggregates, requiring increased dosages of additives. Furthermore, abrasion resistance tends to decrease when recycled aggregates are used.

1 RECYCLED AGGREGATES CONRETE – GENERAL INFORMATION

Over the last five decades, there has been a continuous increase in material demand. While worldwide material extraction in 1970 was about 30.9 billion tons, material consumption in 2020 was measured at about 95.1 billion tons [1]. Non-metallic materials accounted for 31 % of material consumption in 1970. In 2020, about half of total material consumption (45.3 billion tons) can be attributed to non-metallic materials such as sand and gravel. Therefore, sand and gravel are the second most used natural resources on earth today, after water [1], [2]. To reduce the demand for sand and gravel in the construction sector, it is essential to continue establishing the circular economy. More than a third (450 to 500 million tons) of all waste generated in the EU comes from construction and demolition waste (CDW), therefore there is a significant potential to recycle and return it to the material cycle [3].

This paper focuses on the recyclability of demolished concrete from civil-engineering structures. Recycled concrete aggregates (RCA) were used to produce new precast concrete elements. In this context, particular attention has been paid to the feasibility large-scale producibility of recycled concrete and its durability.

2 EXPERIMENTAL PROGRAM

After successful testing of fresh and hardened concrete properties of small scale specimens as part of the *ÖBV-FFG* industrial promotion project *Upcycling&CO2Storage* [4], the final step was to carry out tests on large scale specimens. The aim was to produce track base slabs for tramway infrastructure using RCA combined with steel and fibre reinforcement. The concrete slabs had to meet the following specification:

C50/60/XC4/XW2/XD3/XF4/XA1L(A)/XM2/GS11

The concrete description was adapted to the conditions for casting with RCA. Natural and recycled concrete aggregates with a maximum grain size (GS) of d_{max} = 16 mm were used. This results in the following specification for the concrete mix design:

C50/60/XC4/XW2/XD3/XF4/XA1L(A)/XM2/GS16/RAC

Six concrete mixtures were produced, a list of the concrete types is given in Table 1. The concrete types differed in terms of the replacement ratio of natural aggregates (NA) with recycled concrete aggregates and the type of reinforcement. Only the Ref_NAC mix design meets the current standards, in all other mix designs, the substitution rates for RCA exceed the maximum permitted ratio specified in the standards [5], [6]. A total number of 10 track base slabs and small test specimens for hardened concrete tests were produced and the track base slabs were installed on the premises of a public transportation company. One slab was casted for each concrete type Ref_NAC and RAC_50%_carb., while two slabs were fabricated for each of the other concrete types.

Table 1 Overview of produced concrete mixtures – substitution rates and reinforcement

Concrete type	Natural aggreates	Recycled concrete aggregates	Reinforcement
Ref_NAC	100 %		steel rebars
RAC_30%	$d < 2$ mm 100 % $d \geq 2$ mm 70 %	$d \geq 2$ mm 30 %	steel rebars
RAC_50%	$d < 2$ mm 100 % $d \geq 2$ mm 50 %	$d \geq 2$ mm 50 %	steel rebars
RAC_50%_carb.	$d < 2$ mm 100 % $d \geq 2$ mm 50 %	$d \geq 2$ mm 50 % carbonated [1)]	steel rebars
RAC_50%_fibres	$d < 2$ mm 100 % $d \geq 2$ mm 50 %	$d \geq 2$ mm 50 %	30 kg/m³ steel fibres 5 kg/m³ basalt fibres
RAC_100%		100 %	steel rebars

[1)] For carbonation procedure and further information see [7].

3 RAW MATERIAL AND FRESH CONCRETE PROPERTIES

Recycled concrete aggregates (RCA) from demolished civil-engineering structures were used as raw materials, including material from precast elements such as stairs, road slabs, and platform edges. The prefabricated elements were crushed and then washed to remove fine particles, thus recycled aggregates (natural aggregates with cement paste adhering to them) in sizes up to 16 mm were used. Natural aggregates consist of approximately 80 % siliceous and 20 % carbonate aggregates. A Portland-slag cement, CEM II A-S 42.5R [8], was used as binder for new concrete production. Conventional steel mesh reinforcement and an innovative cocktail of steel and basalt fibres were used to reinforce the track base slabs. Table 2 gives an overview of the density and water absorption rate of the raw materials. Natural aggregates have higher density and lower water absorption rate than recycled concrete aggregates. The higher water absorption of the recycled concrete aggregates has been considered in the concrete mix design.

Table 2 Material characterization of raw materials

Aggregates	Density kg/dm³	Water absorption rate	
		wa_{10min} / %	wa_{24h} / %
Natural aggregates	2.70	0.7	1.0
Recycled concrete aggregates	2.54	1.9	2.9

Concrete for slabs and test specimens was produced by *MABA Fertigteilindustrie GmbH*. During the concrete production process, the fresh concrete properties were determined. Table 3 shows the water-binder ratio (w/b), the dosage of additives, and the fresh concrete properties. The standard mixture for slab production specifies a w/b-ratio of 0.36. This value was achieved for mixtures Ref_NAC and RAC_30%. For the other mixtures, it was increased to 0.45 to ensure workability. Additive demand increased with higher replacement rates of recycled concrete aggregates. Compared with mixtures containing non-carbonated aggregates the mixtures with carbonated aggregates require fewer additives because of its denser microstructure due to carbonation [7]. The spread diameter was determined

according to ÖNORM EN 12350-5 [9]. The targeted consistency class for the concrete types was F66 (630 mm to 690 mm) in accordance with ÖNORM B 4710-1 [6]. The method according to ÖNORM EN 12350-7 [10] was used to determine the air void content. The test results ranged from 5.6 % for RAC 30% and 7.2 % for RAC_100% and were within the limits values of 4.5 % to 8.5 % according to ÖNORM B 4710-1 [6]. For the concrete in the target exposure classes, a maximum fresh concrete temperature of 32 °C is permitted according to ÖNORM B 4710-1 [6] for element thickness < 30 cm. This limit was not exceeded during concrete manufacturing, mixing types see Table 1. The fresh concrete density was determined according to ÖNORM EN 12350-6 [11]. It follows that the fresh concrete density decreases with increasing replacement rate, which is attributed to the lower density of recycled aggregates compared to natural aggregates.

Table 3 Details of the concrete mix and results of the fresh concrete properties

Fresh concrete properities	Ref_NAC	RAC_30%	RAC_50%	RAC_50%_ carb.	RAC_50%_ fibres	RAC_100%
w/*b*-ratio	0.36	0.36	0.38	0.42	0.42	0.45
Superplasticiser in % of binder	0.72	0.74	0.78	0.73	0.77	0.81
Air entraining agent in % of binder	0.20	0.26	0.26	0.24	0.26	0.23
Spreading class according to [6]	F66					
Air void content in %	5.8	5.6	7.1	6.0	6.4	7.2
Fresh concrete temperature in °C	20.4	25.8	22.5	18.9	24.5	22.9
Fresh concrete density in ($kg \cdot m^{-3}$)	2365	2328	2227	2281	2261	2113

4 HARDENED CONCRETE PROPERTIES

To examine the hardened concrete properties, test specimens were produced in form of cubes (a = 150 mm) and cylinders (d = 100 mm, h = 200 mm). In accordance with ÖNORM 12390-2 [12], the cubes were stored in a water bath until the seventh day after casting and then maintained in air until the time the tests started. The cylinders were stored in a water bath until the day of testing the hardened concrete properties. The hardened concrete properties were determined after 28 and 56 days of casting in accordance with the following standards: ÖNORM EN 12390-3 [13] (compressive strength $f_{c,cube}$), ÖNORM EN 12390-6 [14] (tensile splitting strength $f_{ct,cyl}$), ÖNORM EN 12390-13 [15] (modulus of elasticity $E_{C,S}$). Table 4 gives an overview of the hardened concrete properties, each presenting the mean value of three tests. Fig. 1shows the chart (mean value and standard deviation) of the compressive strength and tensile splitting strength tests. The results indicate that compressive strength and tensile splitting strength decrease with increasing replacement rate of recycled concrete aggregates. Compressive strength of concrete has almost reached its final value after 28 days, while tensile strengths still show increases up to 30 % between the 28th and 56th day. To achieve strength in class C50/60, a minimum compressive strength of 69 N/mm² on three individual tests is required as part of a conformity assessment in accordance with ÖNORM B 4710-1 [6]. This value is only achieved by the concrete types Ref_NAC and RAC_30%. In an individual test in accordance with ÖNORM B 4710-1 [6], a value of 61 N/mm² is required to achieve strength class C50/60. All concrete types tested achieve strength class C50/60 except for the RAC_100% mix. The modulus of elasticity also shows the same trend as compressive strength and tensile splitting strength, with a decrease from 39350 N/mm² for Ref_NAC to 25959 N/mm² for RAC_100%.

Table 4 Hardened concrete properties of analysed concrete mixtures

Hardened concrete properties	Ref_NAC	RAC_30%	RAC_50%	RAC_50%_ carb.	RAC_50%_ fibres	RAC_100%
$f_{c,cube,28}$ / (N · mm^{-2})	72.6	70.3	61.4	64.7	64.1	48.3
$f_{c,cube,56}$ / (N · mm^{-2})	81.4	67.4	60.1	68.4	65.6	49.2
$f_{ct,cyl,28}$ / (N · mm^{-2})	5.3	4.3	3.6	4.3	4.4	3.1
$f_{ct,cyl,56}$ / (N · mm^{-2})	5.5	5.1	4.7	4.6	4.8	3.7
$E_{C,S,28}$ / (N · mm^{-2})	39350	36048	33140	33683	32510	25959

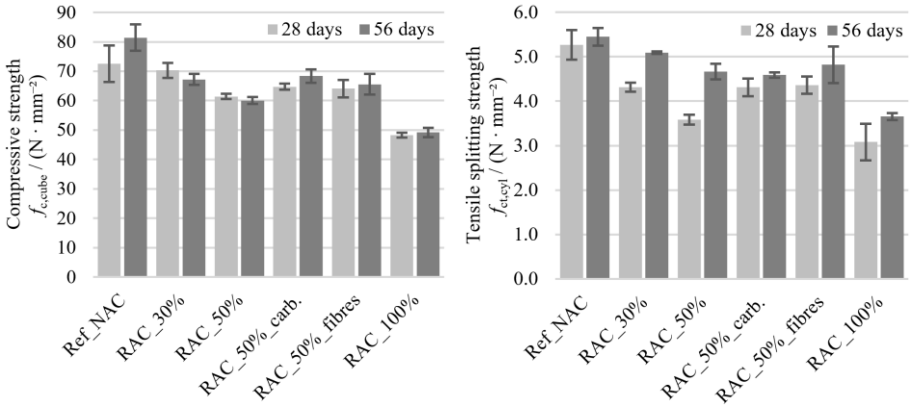


Fig. 1 Graphical representation of the results (mean value and standard deviation) for compressive strength (left) and tensile splitting strength (right) of the analysed concrete types

5 CONCRETE DURABILITY

Also, the durability properties were examined in more detail. The aim was to investigate the resistance of concrete to external influences. To this end, samples of young concrete (28 days after casting) were taken as a first step. In a further step, test cylinders will be extracted from the track base plates after approximately one year (autumn 2026), and the strength properties and changes in the concrete microstructure will be examined. During this year, the slabs are monitored at the installation site to document atmospheric conditions such as air temperature and humidity by using a data logger.

The concrete description used for track base slabs requires a concrete abrasion class of XM2. This class has to be achieved by the total amount of cement (≥ 340 kg/m³) and the *w*/*b*-ratio (0.45) [6]. The abrasion resistance of concrete depends particularly on the aggregates used. Natural aggregates are regarded as homogeneous in terms of their abrasion resistance. For recycled aggregates, variability in the source material becomes a key issue. Tests have shown that abrasion class XM2 can be achieved using high-quality material (demolished and processed C50/60 concrete) for RAC [4]. For the aggregates used here for the production of the track base slabs, the source material could not be fully classified. It was referred to as precast concrete, where the classes can range from C25/30 to C50/60. In order to verify class XM2, test cubes with an edge length of (71 ± 1.5) mm were cut out of the existing concrete matrix and subjected to the Böhme test method [16]. Fig. 2 visualises the test results for the Böhme test. In addition, it shows the mean value and standard deviation of the individual measurements as well as the limit value to achieve XM2 in accordance with ÖNORM B 4710-1 [6]. Only the reference concrete mix (Ref_NAC) complies with the limit value for XM2. RAC_50%_fibres mix achieves the limit value, and the other concrete types exceed the limit of 15 cm³ · 50 cm^{-2}. The abrasion of the installed track base slabs will be examined one year after installation (autumn 2026) by visual investigations.

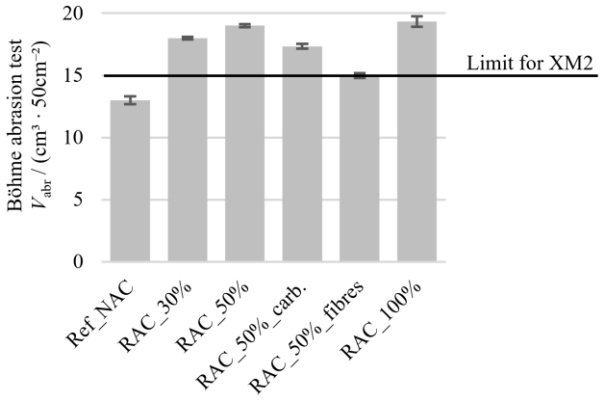


Fig. 2 Böhme abrasion test results of the different concrete types 28 days after casting

In addition to the abrasion test according to Böhme, the concrete types were investigated under a Leica DM4500 P [17] polarizing light microscope (PLM) with a Leica DMC4500 microscope camera [18] following [19], [20], [21] to evaluate concrete performance parameters such as airvoid content and to examine the concrete microstructure. Therefore, sample plates 40 · 40 · 0.02 mm³ were cut from concrete cylinders and thin sections were prepared in accordance with DS 423.40 [22]. The investigations focused on concrete microstructure, on the distribution of air voids, the development of the ITZ (interfacial transition zone), occurring microcracks and the homogeneity of capillary porosity. In addition, the *w/b*-ratio and air void content of the concrete samples were determined. The thin sections were examined for carbonation and microcracking at the concrete surface and within the concrete matrix. The examination of the quality ITZ was intended to provide information about the bonding effects between aggregates and the cement matrix. In addition, ASR (alkali-silica-reaction) analysis was carried out. Fig. 3 shows micrographs from conducted PLM and Table 5 shows a summary of the results.

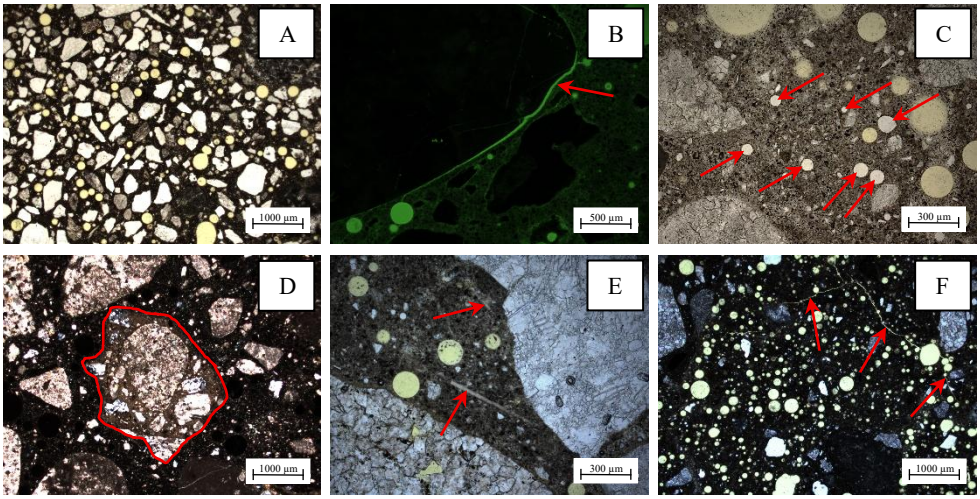


Fig. 3 Representative examples of the polarizing microscopy investigations under different illumination modes: plane-polarized light (PPL), cross-polarized light (XPL), and fluorescence illumination (FL). (A) Ref_NAC – overview of the concrete microstructure and air-void distribution, PPL; (B) RAC_30% – interfacial debonding along the ITZ, FL; (C) RAC_50% – ASR (Alkali-Silica-Reaction) gel observed in air voids, PPL; (D) RAC_50%_carb. – recycled aggregate particle with carbonated cement paste, XPL; (E) RAC_50%_fibres – basalt fiber showing good interfacial bond with the cement paste, PPL; (F) RAC_100% – overview of the air void system and occurring plastic cracks, PPL;

Table 5 Microscopic alysis (PLM) results of the different concrete types

	Ref_NAC	RAC_30%	RAC_50%	RAC_50%_ carb.	RAC_50%_ fibres	RAC_100%
Natural aggregates	clearly identifiable carbonate- and silicaterich aggregates					
Recycled aggregates		recycled concrete aggregates visible				absence of particle diameter 250 µm to 1000 µm
Cement	clinker minerals (alite and belite) as well as slag (GGBS) praticles could be identified					
Admixtures					basalt fibres visible	
w/*b*-ratio	homogen distributed *w*/*b*-ratio					
	0.40–0.45	≈ 0.45	0.40–0.45	≈ 0.45	≈ 0.45	≈ 0.50
Airvoid distribution	homogen	accumulations	accumulations	homogen	accumulations	homogen
Airvoid content in %	7.0 to 8.0	6.0 to 7.0	7.0 to 8.0	7.0 to 7.5	7.0 to 8.0	8.0 to 8.5
Carbonatization on the concrete surface	no carbonatization detectable					
Carbonatization in the concrete matrix	no carbonatization detectable			RCA caronated	no carbonatization detectable	carb. along cracks
Cracks on the concrete surface	few shrinkage cracks	elongated shrinkage cracks rarely to the grain structure		few shrinkage cracks		
Cracks in the concrete matrix	a few plastic cracks					plastic crack due to high air void content
ITZ	good bond	secondary disruptions				
ASR	no		few indicators	few indicators, less than RAC_50%		no

Under the microscope, the difference between natural and recycled aggregate is clearly visible. All concrete mixes show a homogeneous distribution of the *w*/*b*-ratio in the individual sample plates. The *w*/*b*-ratio determined in the hardened concrete differs slightly from that in the mix design. There are no areas suggesting higher water content and, consequently, poorer bonding (disruption of the ITZ). The

air voids are also well distributed both spatially and in terms of their size. No carbonation of the concrete surface is visible, this is because the concrete was already resin-coated after 28 days. A carbonation edge can be observed on the carbonated RCA used. Plastic cracks occur sporadically in the concrete matrix. The ITZ is slightly damaged in the mixtures containing recycled aggregate; furthermore, the mixtures with 50 % RCA show few signs of ASR.

6 CONCLUSIONS

This paper aims to investigate the usability of recycled concrete with different replacement rates in the infrastructure construction sector. Six concrete types were produced with aggregates ranging from 100 % natural aggregates to 100 % recycled aggregates, which were tested for their fresh and hardened concrete properties. To adjust the fresh concrete properties, the *w*/*b*-ratio was varied, and the admixture dosage was adjusted. With higher replacement rates, the amount of additives had to be increased. It should be noted that the carbonation of recycled aggregates significantly reduces the amount of admixtures required. The compressive strength, tensile splitting strength and modulus of elasticity were determined, representing hardened concrete properties. These values decreased with increasing replacement rates. The positive effect of fibres on tensile splitting strength was minimal, no improvement was observed in terms of the modulus of elasticity. In addition to the hardened concrete properties, the abrasion resistance and microstructure of the concrete types were examined. Only the reference concrete mix was able to meet the required abrasion limits. The abrasion values vary depending on the recycled aggregates used. With higher strength resistance of the RCA, it can be expected that the abrasion values will be within the limits specified for XM2. During the microscopic examinations, the same parameters were recorded for all types of concrete to ensure comparability. Similar air void contents and air void distributions were determined for all concretes produced. No carbonation was detected at the concrete surface, and only local carbonation along early shrinkage cracks was observed. In conclusion, high-quality, homogenous sorted recycled aggregates can be used in road slabs, as seen in [4]. Further findings for the procuced concrete according to Table 1 will be available after a one-year exposure period, when the microstructure of the exposed slabs and the surface damage will be examined.

Acknowledgements

The tests were carried out as part of the *ÖBV-FFG* industrial promotion project *Upcycling&CO2Storage* [4]. The aim of this research project was to employ high replacement rates of recycled aggregates in precast concrete elements to further establish the circular economy within the construction industry. The elements were cast by *MABA Fertigteilindustrie GmbH* and the track base slabs were delivered to the *Wiener Linien* factory premises. The authors would like to thank all project partners for their excellent cooperation.

References

[1] United Nations Environment Programme, ‘Global Resources Outlook 2024’, p. 181, 2024, doi: wedocs.unep.org/20.500.11822/44901.

[2] ‘Finite sand resource needs better governance’, vol. Nature Geoscience, no. Volume 17, p. 817, Sep. 2024, doi: doi.org/10.1038/s41561-024-01544-9.

[3] ‘Collection and recycling of construction and demolition waste: Key learnings’, Feb. 17, 2022. Accessed: Jan. 13, 2026. [Online]. Available: https://www.interregeurope.eu/find-policy-solutions/webinar/collection-and-recycling-of-construction-and-demolition-waste-key-learnings

[4] Österreichische Bautechnik Veranstaltungs GmbH, ‘Endbericht Upcycling&CO2storage’, Nov. 2025. Accessed: Dec. 10, 2025. [Online]. Available: https://www.bautechnik.pro/Arbeitskreise/forschung#undefined

[5] ASI, *ÖNORM B 3140, Ausgabe 2020-11-01; Rezyklierte Gesteinskörnungen für ungebundene und hydraulisch gebundene Anwendungen sowie für Beton*, Nov. 01, 2020.

[6] ASI, *ÖNORM B 4710-1, Ausgabe: 2018-01-01; Beton – Festlegung, Eigenschaften, Herstellung, Verwendung und Konformität, Teil 1: Regeln zur Umsetzung der ÖNORM EN 206 für Normal- und Schwerbeton*, Jan. 01, 2018.

[7] J. Hron, T. Pichler, O. Zeman, J. Vizi, K. Voit, and K. Bergmeister, 'Effekte einer Zwangskarbonatisierung auf rezyklierte Gesteinskörnung aus Beton und daraus hergestellte Betone', *Beton- und Stahlbetonbau*, pp. 1–11, 2025. doi: doi.org/10.1002/best.70022.

[8] Holcim (Österreich) GmbH, 'Produktdatenblatt: Der Grüne – EN 197-1 – CEM II/A-S 42,5 R WT 42'. Apr. 01, 2023. Accessed: Dec. 10, 2025. [Online]. Available: https://www.holcim.at/sites/austria/files/docs/pdb_lose_mdf_der_gruene.pdf

[9] ASI, *ÖNORM EN 12350-5, Edition: 2019-08-15; Testing fresh concrete – Part 5: Flow table test*, Aug. 15, 2019.

[10] ASI, *ÖNORM EN 12350-7, Edition: 2023-02-15, Testing fresh concrete – Part 7: Air content – Pressure methods (consolidated version)*, Nov. 15, 2019.

[11] ASI, *ÖNORM EN 12350-6, Edition: 2019-09-15; Testing fresh concrete – Part 6: Density*, Sep. 15, 2019.

[12] ASI, *ÖNORM EN 12390-2, Edition: 2019-11-15; Testing hardened concrete – Part 2: Making and curing specimens for strength tests*, Nov. 15, 2019.

[13] ASI, *ÖNORM EN 12390-3, Edition: 2019-11-15; Testing hardened concrete – Part 3: Compressive strength of test specimens*, Nov. 15, 2019.

[14] ASI, *ÖNORM EN 12390-6, Edition: 2024-05-15; Testing hardened concrete – Part 6: Tensile splitting strength of test specimens*, May 15, 2024.

[15] ASI, *ÖNORM EN 12390-13, Edition: 2021-11-01; Testing hardened concrete – Part 13: Determination of secant modulus of elasticity in compression*, Nov. 01, 2021.

[16] ASI, *ÖNORM B 4710-3, Ausgabe: 2023-01-01; Beton – Festlegung, Eigenschaften, Herstellung, Verwendung und Konformität, Teil 3: Nationale Anwendung der Prüfnormen für Beton und seiner Ausgangsstoffe*, Jan. 01, 2023.

[17] Leica Microsystems GmbH, 'DM4500 P Vielseitiges Polarisationsmikroskop für Materialanalyse, Geowissenschaften und Forschung'. Accessed: Jan. 30, 2026. [Online]. Available: https://www.leica-microsystems.com/de/produkte/lichtmikroskope/p/leica-dm4500-p/

[18] Leica Microsystems GmbH, 'DMC4500 Mikroskop-Kamera'. Accessed: Jan. 30, 2026. [Online]. Available: https://www.leica-microsystems.com/de/produkte/mikroskop-kameras/p/leica-dmc4500/

[19] DSA, *DS 423.42, Edition: 2002-04-09; Testing of concrete – Hardened concrete – Concrete composition*, Apr. 09, 2002.

[20] Nordic Council of Ministers, *NT BUILD 361 – Edition 2 (1999-11); Concrete, hardened: Water-cement ratio*, Nov. 1999.

[21] ASTM, *ASTM C856/C856M-25, Edition: 2025-04-03; Standard Practice for Petrographic Examination of Hardened Concrete*, Jan. 15, 2020.

[22] DSA, *DS 423.40, Edition: 2002-02-12; Testing of concrete – Hardened concrete – Production of fluorescence-impregnated thin sections*, Feb. 12, 2002.

Correlation Between the Splitting Crack Opening Width and the Corrosion Level in Prestressed Concrete Beams

Chifa Merabti[1], Beatrice Belletti[1], Alice Sirico[1], Olha Palii[1], Simone Ravasini[1], Javier Sánchez Montero[2]

[1]Department of Engineering and Architecture,
University of Parma,
Parco Area delle Scienze 181/A, Parma (43124), Italy

[2] *Instituto Eduardo Torroja de Ciencias de la Construcción (IETcc-CSIC)*,
Calle de Serrano Galvache 4, 28033 Madrid, Spain

Summary
Severe corrosion of prestressed concrete (PC) elements may lead to sudden failures with major safety consequences. However, the assessment of corrosion damage in prestressing strands remains challenging, as internal damage cannot be directly detected. Therefore, surface cracking might indicate corrosion severity. This study investigates the correlation between crack width and the corrosion level of prestressing strands of naturally corroded PC beams. The investigation involves an initial visual inspection of the beams, followed by three-dimensional scanning of the strands to quantify the corrosion. Based on these measurements, two analytical approaches were then adopted to correlate crack width with corrosion level: one based on experimental pit measurements from all external wires and a simplified approach using the maximum pit depth of the most corroded wire. The results show the correlation between surface crack width and corrosion severity in naturally corroded prestressed concrete beams.

1 INTRODUCTION

Concrete is the most used construction material in the world, where prestressed concrete plays a key role in major infrastructure systems, particularly bridges [1]. Despite its widespread use, recent bridges failures and collapses have drawn attention to the vulnerability of aging prestressed structures induced by corrosive phenomena. As a result, increased research efforts were devoted to try improving the efficiency of destructive and non-destructive tests in the diagnosis of the corrosion initiation and propagation [2] [3]. Due to the detrimental effects of destructive tests on prestressed concrete structures, a significant part of the ongoing research is focused on the capability of non-destructive tests to evaluate the corrosion level in prestressing reinforcement. In particular, an indirect method frequently used is based on the capability to correlate the surface damage - commonly quantified through splitting crack width and concrete spalling with the corrosion level in the ordinary reinforcement or prestressing reinforcement [2] [4]. These latter methods are suitable for reinforced concrete and pretensioned concrete members while cannot be directly applied to post-tensioned members due to the presence of the duct. In pretensioned members, even limited corrosion of prestressing strands can induce visible surface cracking, due to the relatively large diameter of the prestressing strand and the limited concrete cover commonly adopted in existing PC members [4] [5]. Even if corrosion-induced crack on concrete surface has been increasingly studied as a potential corrosion indicator [6], most of the studies available in the scientific literature were related to RC concrete elements [7] [8]. In contrast, very few studies are related to PC members [6] [9].

Recent investigations have indicated that, in prestressed concrete members subjected to chloride-induced corrosion, crack width shows a stronger correlation with corrosion pit depth rather than with average mass loss [10]. This observation is consistent with experimental evidence identifying pitting corrosion as the dominant corrosion morphology in prestressing strands, which governs crack initiation and propagation in the concrete cover. Although surface crack width represents a promising and practically accessible indicator of corrosion damage in PC beams, the current state of knowledge is constrained by the limited number of dedicated analytical models and experimental studies available in

the literature [9] [10]. Further experimental investigations, as well as refinement of existing predictive models and the development of new ones are therefore required to reliably quantify the relationship between splitting crack opening width and corrosion level in prestressing strands. In this context, an innovative aspect of this paper lies in the description of experimental measurements, and validation of analytical models applied to full-scale pretensioned PC beams subjected to natural corrosion-induced by chloride attack. By combining advances 3D scanning techniques for corrosion detection in strands with the experimental crack width measurements on PC elements and the application of existing analytical models, this paper aims to improve the current state of knowledge on the relation between corrosion in prestressing strands and visible cracking.

2 CASE STUDY

To investigate the correlation between the splitting crack opening width and the level of corrosion in prestressed concrete beams, a study was conducted on a pretensioned PC beam selected from an initial set of 11 beams obtained from a thermal power plant in Spain. The beams were decommissioned and subsequently transferred to the laboratories of the "Instituto Eduardo Torroja de Ciencias de la Construcción" in Madrid, following the occurrence of shear-related structural damage. During their service life, estimated at approximately ten years, the beams were continuously exposed to wet–dry cooling cycles with seawater, which is considered a chloride-rich environment widely recognized as a primary source of chloride ingress in concrete structures, generally leading to breakdown of the passive oxide layer, resulting a localised pitting corrosion [11]

The investigated pretensioned PC beam had a rectangular cross-section with overall dimensions of 150 × 300 mm. Longitudinal prestressing reinforcement was arranged at the bottom of the section and consists of two seven-wire strands with a nominal diameter of 12.9 mm; each composed of six outer wires with a diameter of $\emptyset_{outer}$ equal to 4.22 mm (r_{outer} =2.11mm) and one central wire with a diameter of $\emptyset_{inner}$ equal to 4.42mm (r_{inner}=2.21mm). The distance of the centroid of the strands from the outer surface was equal to 50 mm. Two non-prestressed reinforcing bars with a diameter of 5 mm were located at the upper part of the cross-section.

The mechanical properties of the concrete and steel components were based on prior research conducted on these beam [12] and are reported in Table 1 Mechanical properties of concrete and steel 1.

Table 1 Mechanical properties of concrete and steel.

Concrete	Prestressed Steel			Reinforcement Steel		
f_c[MPa]	f_{pt} [MPa]	ε_{pu}[%]	E_p[GPa]	f_y [MPa]	ε_{su}[%]	E_s[GPa]
32.2	1901.75	5	195	435	18	195

Being f_c the compressive cylinder strength, f_{pt} the ultimate tensile strength, ε_{pu} the ultimate strain and E_P the elastic modulus of prestressing steel; f_y, the yield strength, ε_{su}, the strain at maximum load and E_s the elastic modulus of reinforcing steel.

2.1 Visual Inspection and surface damage measurement

All beams extracted from the thermal plant were visually inspected to document the corrosion-induced surface damage. First, the deteriorated portions of the beams were detected, then the crack patterns were drawn to define the splitting crack location and finally the crack opening width was measured along the length of these splitting cracks by using a crack width gauge, as represented in Fig. 1.

Hence, all visible splitting cracks and areas affected by concrete spalling were identified, measured, and recorded. Crack widths were measured in millimetres along the face adjacent to strand A2 (w_{A2}) and the one adjacent to strand A1 (w_{A1}). All data about the surface deterioration were integrated into the AutoCAD model to generate the damage map reported in Fig. 1. Cracks were classified using a color-coded scheme based on measured crack opening width, ranging from moderated crack opening width values (w ≤ 0.2 mm) to severe crack opening values (w ≥ 2.0 mm), thereby enabling the visualization of crack severity and longitudinal distribution. Concrete spalling is indicated in grey. Concrete spalling is observed exclusively in the bottom region of the beam and at the extremities of the beams, while it is completely absent in the central zone. This behaviour is consistently observed on both faces of the beam (Profiles A and B). In the portion of the beams affected by cover spalling, adjacent longitudinal cracks converge and interact, leading to the detachment of the concrete cover.

Since strands were un-protected at beam's extremities, splitting longitudinal cracks run parallel to the prestressing strands with crack opening width increasing towards the edge and leading to cover spalling at beam's extremities. Moreover, visual inspection revealed a non-uniform distribution of longitudinal cracking along the beam length. All observed splitting cracks were oriented parallel to the prestressing strands, with crack widths varying across the beam width: minimum values were recorded in the central region, while crack openings progressively increased toward the side edges, eventually leading to concrete spalling. More in detail, Section I exhibited no visible cracking, except from moderate spalling at beam end; section II showed longitudinal cracks on the face adjacent to strand A2, while Section III presented more severe damage, with extensive cracking on both faces adjacent to strands A1 and A2, finally causing the concrete spalling near the beam end. It should be noted that during transportation in the laboratory, a portion of Section III was damaged. Consequently, this portion was excluded from subsequent experimental procedures and analyses, and no prestressing strands were available from this region for extraction, corrosion assessment, or mechanical evaluation. In this study, the analysis specifically focuses on the correlation between crack width and strand A2 for the portion highlighted in Fig. 1, where crack width is less than 1 mm.

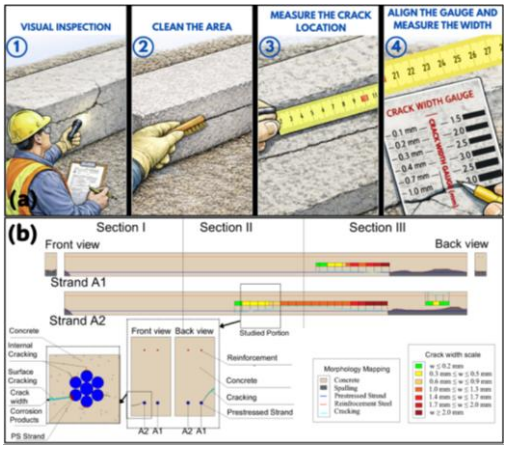


Fig. 1 (a) Crack width measurement; (b) damage mapping.

2.2 Measurement of Corrosion Morphology

The prestressing concrete (PC) strands were meticulously extracted from the beams and subsequently cleaned to eliminate rust and corrosion products. The strands were then scanned using a GOM-Scan-1-(200) optical 3D scanning system to capture the detailed surface geometry of the corroded wires. The system, equipped with two high-resolution cameras and fringe projection, uses blue LED light to reduce ambient interference and it captures up to 6 million points per scan (0.06 mm spacing) over a 200 × 125 mm² area at a 450 mm working distance. This method provides a detailed high-resolution 3D imaging of the external surface of the strand, showing the corrosion morphology for the six outer wires, as shown in Fig. 3**Fehler! Verweisquelle konnte nicht gefunden werden.**. The corrosion morphology observed in the investigated strands was predominantly characterized by localized pitting corrosion that aligns with chloride-induced corrosion. Therefore, a 3D image analysis method was employed to characterize strand corrosion through measurement of pit depth.

The resulting 3D meshes of the damaged strands were exported to ZEISS Inspect software for post-processing. In parallel, a precise three-dimensional meshes of each undamaged reference strands were generated in RHINO to serve as baseline. Using ZEISS Inspect, the meshes of the damaged and undamaged strands were superimposed to measure the corrosion morphology along the strand length. The data from transverse cross-sections taken at 1 mm intervals along the strand length were then analyzed, as shown Fig. 2**Fehler! Verweisquelle konnte nicht gefunden werden.**, by recording the maximum pit depth for each of the six external wires, $P_{\max_w,i}$. This approach enabled high-precision quantification of corrosion pit depths in each of the six outer wires of the prestressing strand, and a detailed description of the corrosion level and spatial distribution. The maximum pit depth for each wire was recorded along these transverse sections.

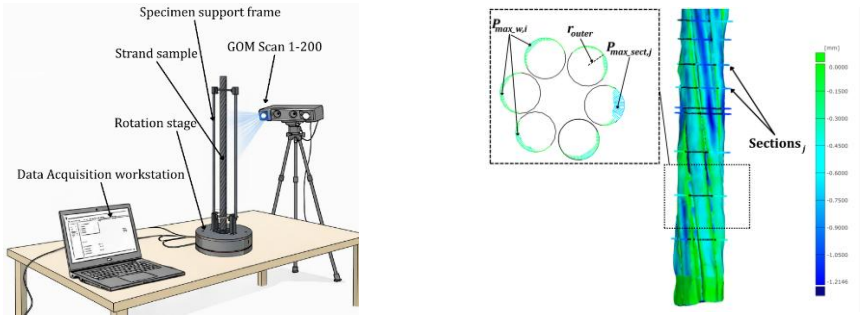


Fig. 2 (left) Schematic of the GOM-Scan-1 optical 3D scanning setup for PS strands; (right) Corrosion morphology and pit depth measurement of a strand obtained by overlapping the damaged and reference 3D meshes using ZEISS Inspect.

3 METHODOLOGY

3.1 Crack Opening Width – Corrosion Level Relationship

In the work, the crack opening width values measured on the concrete surface, w^{MEAS} were compared with the crack opening width values estimated by using the analytical formulation proposed by Ahmed et al. [10], w, as given in Eq. (1):

$$w = 0.16 \frac{e^{SL}}{R_{w/c}} (P_{\max} - P_0) \tag{1}$$

The Eq. (1) - Eq. (3) are dependent on parameters that in this paper have been properly calibrated and, in some case, modified with respect to the initial formulation proposed in previous literature [10] as follows. In Eq. (1) SL is the prestress level of the corroded strand, defined as the ratio between the residual prestressing stress of the corroded strand $\sigma_{p,\mathrm{corr}}$ and the tensile strength f_{pt} as reported in Eq. (2). In this paper the residual prestressing stress of the corroded strand $\sigma_{p,\mathrm{corr}}$ is assumed to decrease in proportion to the residual area of strands, A_{res_sect}. [9]

$$SL = \frac{\sigma_{p,corr}}{f_{pt}} \tag{2}$$

$$\sigma_{p,corr} = \left(\frac{A_{res_sect}}{A_{sect,0}}\right)\sigma_{p,0} \tag{3}$$

Being $\sigma_{p,0}$ the initial prestressing stress of the uncorroded strand and $A_{sect,0}$ the initial transversal cross section area of uncorroded strands.

The residual area of the corroded strand is obtained as given in Eq. (4).

$$\sum_{1}^{6} A_{res_wi} + A_{w,0,inn} \tag{4}$$

Being $A_{w,0,inn}$ the area of the inner wire; assumed uncorroded, and A_{res_wi} the residual area of the i-th outer corroded wire. The residual area of the corroded outer wires is calculated based on the equation derived from the SPCS model [9] as a function of the normalized pitting depth $\frac{P_{\max_w,i}}{r_{outer}}$ as shown in Eq. (5)

$$\begin{aligned} A_{res_wi} &= \left[\left(1 - 0{,}303 \cdot \frac{P_{\max_w,i}}{r_{outer}}\right) \cdot A_{w,0}\right] \quad \text{if} \quad 0 < \frac{P_{\max_w,i}}{r_{outer}} < 0.33 \\ A_{res_wi} &= \left[0.9 - 0.539 \cdot \left(\frac{P_{\max_w,i}}{r_{outer}} - 0.33\right)\right] \cdot A_{w,0} \quad \text{if} \quad 0.33 < \frac{P_{\max_w,i}}{r_{outer}} < 2.00 \end{aligned} \tag{5}$$

$R_{w/c}$ is the water-to-cement ratio, and P_0 is the corrosion pitting depth at concrete cracking (in mm) onset, which is in turn calculated by using Eq. (6):

$$P_0 = 0.036\frac{R_{w/c}}{e^{SL}}\left(\frac{c}{D}\right)^2 + 0.128 \tag{6}$$

In the original formulation, $P_{\max}$ represents the maximum summed pitting depth, defined as the sum of the corrosion penetration depths of all pits at a given cross-section. In that study, pit depths were measured using a micrometre gauge, a different technique characterized by significantly lower precision compared to high-resolution 3D scanning methods, used in this study. For this reason, a modified definition is proposed in this work to calculate P_{max} for the j-th section, as given in Eq. (7).

$$P_{\max} = P_{\max,j} = 2 \cdot \mu\left(P_{\max_w,i}\right)_j \tag{7}$$

Where $P_{max_w,i}$ represents maximum pit of the wire i for the j-th section. Then, for each section j, $P_{max,j}$ was determined using two different analytical formulations. In Model-1 $\mu\left(P_{\max_w,i}\right)_j^{AN,1}$ is computed exclusively based on the pit depth measured in each wire by 3D scanning of strand A2, while in Model-2, $\mu\left(P_{\max_w,i}\right)_j^{AN,2}$ was obtained by using the SCPS method, [9] , as illustrated in Fig. 3.

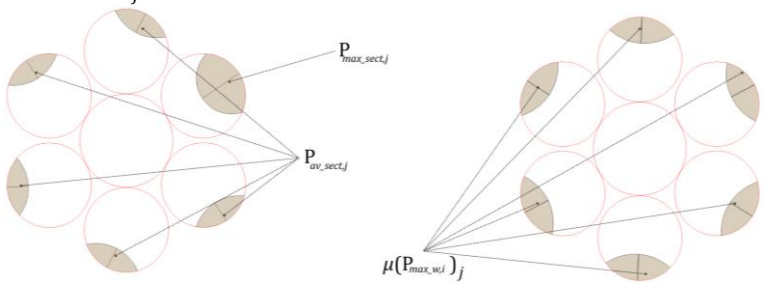


Fig. 3 Schematic Representation of Sectional Corrosion Pit Depth Parameters.

3.1.1 Model-1 based on the pit depth measurement in each wire

In the first methodology, the mean value of the maximum pitting depth in the external wires $\mu\left(P_{\max_w,i}\right)_j^{AN,1}$ is equal to the sectional average pitting depth according to Eq. (8):

$$\mu\left(P_{\max_w,i}\right)_j^{AN,1} = \mu\left(P_{\max_w,i}\right)_j = \frac{\left(\sum_{i=1}^{6} P_{\max_w,i}\right)}{6} \tag{8}$$

3.1.2 Model-2 based on SCPS method

The SCPS method depends on a single input parameter, $P_{\max_sect,j}$, that is the maximum penetration depth of the most corroded wire in each section. The average pit depth of the remaining five external wires, $P_{av_sect,j}$ is calculated with Eq. (9) [9] where r_{outer} is the outer wire radius, Fig. 1. The mean value of the maximum pitting depth in all the external wires, $\mu\left(P_{\max_w,i}\right)_j^{AN,2}$ is calculated using Eq. (10).

$$P_{av_sect,j} = r_{outer}\left(0.378\left(\frac{P_{\max_sect,j}}{r_{outer}}\right)^2 + 0.25\left(\frac{P_{\max_sect,j}}{r_{outer}}\right)\right) \tag{9}$$

$$\mu\left(P_{\max_w,i}\right)_j^{AN,2} = \frac{P_{\max_sect,j} + 5P_{av_sect,j}}{6} \tag{10}$$

3.2 Reverse Analytical Procedure from crack opening measurement to corrosion level

A reverse calculation was performed to evaluate the predictive capability of Model-1 and Model-2 with respect to the experimentally measured crack width. By rearranging Eq. (1) and Eq. (2) the corresponding average corrosion penetration depth $\mu\left(P_{\max_w,i}\right)_j^{AN}$ is obtained by inputting the measured crack width w^{MEAS} as shown in Eq. (11). By rearranging Eq. (9) and Eq. (10) the maximum pitting depth of the most corroded wire $P_{max_sect,j}^{AN,2}$ was obtained from $\mu\left(P_{\max_w,i}\right)_j^{AN}$ using Eq. (12)

$$\mu\left(P_{\max_w,i}\right)_j^{AN} = \frac{1}{2}\left(\frac{w^{MEAS} \cdot R_{w/c}}{0.16 * e^{SL}} + P_0\right) \tag{11}$$

$$P_{\max_sect,j}^{AN,2} = \left(\frac{r_{outer}}{3.78}\right)\left(-2.25 + \sqrt{5.0625 + 45.36\frac{\mu\left(P_{\max_w,i}\right)_j^{AN}}{r_{outer}}}\right) \tag{12}$$

The results of the mean pitting depth obtained from the reverse analytical procedure are compared to the experimental result obtained from Model-1, and the SCPS-based results obtained in Model-2.The results of the maximum pitting depth of the most corroded wire obtained from the reverse analytical procedure are compared to the experimental results used in Model-2.

4 RESULTS

First, the methodology is applied by inputting the corrosion level to obtain the crack opening prediction. The predicted crack widths obtained from Model-1 and Model-2 were compared with the crack widths measured in the portion of the beam highlighted in Fig. 1; the comparison between measured and analytical crack opening width values are presented in Fig. 3. Table 2 Tab Performance Assessment of Model-1 and Model-2 through Reverse Calculation Procedure reports the mean value of the ratio between analytical and measured crack opening both adopting Model-1 and Model-2.

It results a slight systematic overestimation of the crack opening when Model-1 is adopted and an underestimation when Model-2 is adopted. Nevertheless, the predicted crack widths derived from corrosion pit measurements of the prestressing strands show a clear correlation with the measured surface crack widths in both models, demonstrating their ability to capture the overall trend of corrosion-induced cracking. Quantitatively, Model-2 shows better accuracy, with an average prediction-to-measured ratio of 0.97 (3% underestimation), whereas Model-1 presents a ratio of 1.16 (16% overestimation), as reported in Table 2. Furthermore, Model-2 depends only on a single input parameter that is the pit depth of the most corroded wire, $P_{\max_sect,j}$, while Model-1 requires the knowledge of the pit depth of all the outer wires, $P_{\max_w,i}$. Finally, the methodology is applied by inputting the crack opening to predict the corrosion level. Fig. 4 (b) shows the comparison between the mean value of the maximum pitting depth in outer wires calculated with Eq. (11) according to Model-1, $\mu\left(P_{\max_w,i}\right)_j^{AN,1}$, and the mean value of the measured maximum pit depth in outer wires, $\mu\left(P_{\max_w,i}\right)_j$. The ratio $\mu\left(P_{\max_w,i}\right)_j^{AN}/\mu\left(P_{\max_w,i}\right)_j$ results equal to 1.02, as given in Table 2. Fig. 4 (c) shows the comparison between the maximum pitting depth the most corroded wire calculated with Eq. (12) according to Model-2, $P_{max_sect,j}^{AN,2}$, and the measured value, $P_{max_sect,j}$. The ratio $P_{max_sect,j}^{AN,2}/P_{max_sect,j}$ results equal to 1.19, as reported in Table 2.

Table 2 Tab Performance Assessment of Model-1 and Model-2 through Reverse Calculation Procedure.

Model-1	Model-2

$\frac{w^{AN,1}}{w}$	$\frac{\mu\left(P_{\max_w,i}\right)_j^{AN}}{\mu\left(P_{\max_w,i}\right)_j}$	$\frac{w^{AN,2}}{w}$	$\frac{P_{max_sect,j}^{AN,2}}{P_{max_sect,j}}$
1.16	1.02	0.97	1.19

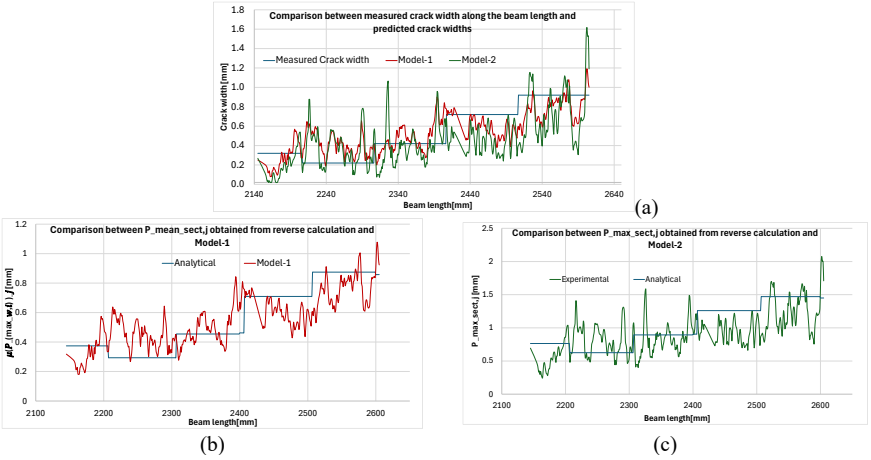


Fig. 4 Evaluation of Model-1 and Model-2 for corrosion-induced cracking: (a) measured versus predicted surface crack widths along the beam; (b) comparison between reverse-calculated and measured mean maximum pitting depth in outer wires using Model-1; (c) comparison between reverse-calculated and measured maximum pitting depth of the most corroded wire using Model-2

5 CONCLUSIONS

The present study investigates the applicability of inverse methods for predicting the corrosion level in prestressing strands from the width of splitting cracks measured on site. Experimental data were obtained from naturally corroded prestressed beams exposed to a severe chloride-rich environment, including crack mapping on the beam surface and 3D scanning of the extracted strands. Two approaches are presented to correlate crack width with the corrosion level, quantified in terms of pit depth of the outer wires. The following conclusions can be drawn:

- The corrosion pit data obtained from the 3D scans analysis showed a correlation between the corrosion of the prestressing strands and the surface crack width of the beam, where in general, beam sections exhibiting larger pit depths corresponded to wider longitudinal cracks, confirming the influence of corrosion-induced expansion on crack formation.
- Both Model-1 and Model-2 can be used to predict the crack opening when the corrosion level is inputted or inversely to predict the corrosion level when the crack opening is inputted, this provides a non-destructive tool to estimate prestressing strand corrosion severity from visible cracking, supporting inspection and maintenance decisions for aging prestressed structures. The presented methodology is in this paper investigated for crack opening values lower or equal to 1 mm.
- The proposed formulations were validated for naturally corroded beams exposed naturally chloride-induced corrosion, its direct extension to carbonation-induced corrosion should be verified by further experimental studies.
- The reliability of the presented methodology is evaluated in this paper based on few data. In future research a more extensive reliability estimation will be carried out.

Acknowledgements

The research project reported in this paper was conducted thanks to the financial support from DCP-ReLUIS (WP13 Task 2.2) 2024-2026.

References

[1] Gagg, Colin R. 2014. "Cement and Concrete as an Engineering Material: An Historic Appraisal and Case Study Analysis." Engineering Failure Analysis 40:114–140. doi:10.1016/J.ENGFAILANAL.2014.02.004.

[2] Invernizzi, Stefano, Montagnoli, Francesco, and Carpinteri, Alberto. 2022. "Very High Cycle Corrosion Fatigue Study of the Collapsed Polcevera Bridge, Italy." Journal of Bridge Engineering. doi:10.1061/(ASCE)BE.1943-5592.0001807.

[3] Morgese, Maurizio, Ansari, Farhad, Domaneschi, Marco, and Cimellaro, Gian Paolo. 2020. "Post Collapse Analysis of Morandi's Polcevera Viaduct in Genoa, Italy." Journal of Civil Structural Health Monitoring 10:69–85. doi:10.1007/s13349-019-00370-7.

[4] Mangual, Jesé, ElBatanouny, Mohamed, Ziehl, Paul, and Matta, Fabio. 2012. "Corrosion Damage Quantification of Prestressing Strands Using Acoustic Emission." Journal of Materials in Civil Engineering. doi:10.1061/(ASCE)MT.1943-5533.0000669.

[5] Dang, Canh N., Floyd, Royce W., Prinz, Gary S., and Hale, Micah W. 2016. "Determination of Bond Stress Distribution Coefficient by Maximum Likelihood Method." Journal of Structural Engineering. doi:10.1061/(ASCE)ST.1943-541X.0001460.

[6] Ma, Yafei, Yang, Jie, Su, Xiaochao, Peng, Anyin, Wang, Lei, and Huang, Ke. 2024. "Crack Propagation Characterization of Concrete under Non-Uniform Corrosion of Steel Strand Using Digital Image Correlation." Construction and Building Materials 455. doi:10.1016/j.conbuildmat.2024.139166.

[7] Chen, Hua-Peng, and Alani, Amir. 2013. "Optimized Maintenance Strategy for Concrete Structures Affected by Cracking Due to Reinforcement Corrosion." ACI Structural Journal.

[8] Benenato, Armando, Ferracuti, Barbara, Imperatore, Stefania, and Lignola, Gian Piero. 2022. "Corrosion Level Estimation by Means of the Surface Crack Width." Construction and Building Materials 342. doi:10.1016/j.conbuildmat.2022.128010.

[9] Franceschini, Lorenzo, Belletti, Beatrice, Tondolo, Francesco, and Sanchez, Javier. 2022. "Study on the Probability Distribution of Pitting for Naturally Corroded Prestressing Strands Accounting for Surface Defects." Buildings 12(10):1732. doi:10.3390/buildings12101732.

[10] Ahmed, Mshtaq, El-Sayed, Ahmed K., Alhozaimy, Abdulrahman M., Al-Negheimish, Abdulaziz I., and Alabdulkarim, Abdullah. 2024. "Prediction of Strand Corrosion Damage in Prestressed Concrete Beams through Visual Inspection of Corrosion Concrete Cracking." Construction and Building Materials. doi:10.1016/j.conbuildmat.2024.135232.

[11] Li, Fumin, Yuan, Yingshu, and Li, Chun-Qing. 2011. "Corrosion Propagation of Prestressing Steel Strands in Concrete Subject to Chloride Attack." Construction and Building Materials 25(10):3878–3885. doi:10.1016/j.conbuildmat.2011.04.011.

[12] Sirico, Alica, Palii, Olha, Ravasini, Simone, Belletti, Belleti, and Sánchez Montero, Javier. 2025. "Pitting Morphology of Prestressing Strands Subjected to Naturally Chloride Environment." Paper presented at fib CACRCS 2025, Lecco, Italy, June 30–July 3, 2025.

[13] ASTM G1-03. Standard Practice for Preparing, Cleaning, and Evaluating Corrosion Test Specimens.

[14] Belletti, Beatrice, Rodríguez, Jesus, Andrade, Carmen, Franceschini, Lorenzo, Sánchez Montero, Javier, and Vecchi, Francesca. 2020. "Experimental Tests on Shear Capacity of Naturally Corroded Prestressed Beams." Structural Concrete 21(5):1777–1793. doi:10.1002/suco.202000205.

[15] Dai, Lizhao, Bian, Hanbing, Wang, Lei, Potier-Ferry, Michel, and Zhang, Jianren. 2020. "Prestress Loss Diagnostics in Pretensioned Concrete Structures with Corrosive Cracking." Journal of Structural Engineering 146(3). doi:10.1061/(ASCE)ST.1943-541X.0002554.

Sustainability Circularity

Innovative arch-based precast ceiling-systems to enable non destructive dismantling and recycling

Aaron Dernbach, Christian Glock

Institute of Concrete Structures and Structural Design
University of Kaiserslautern-Landau (RPTU)
Paul-Ehrlich-Str. 14, 67663 Kaiserslautern, Germany

Summary
The reuse of entire reinforced concrete components is a promising strategy for reducing greenhouse gas emissions and conserving natural resources in the construction industry. Ceilings are particularly significant, accounting for over 40 % of the total concrete mass in conventional structures. In this context, the University of Kaiserslautern-Landau (RPTU), in collaboration with the German Concrete Association (DBV), is developing an alternative ceiling system. The reversible, resource-optimized design, employing low-strength concrete (C20/25) can lower concrete demand by up to 50 %. It relies on high-precision arch segments with a minimum apex thickness of 4 cm, combined with longitudinal beams suitable for serial construction. Arch-specific load-bearing and force-fit load transfer require precise dimensional tolerances and a carefully coordinated installation process, achieved through controlled cracking within the arch elements. Conventional joint grouting in precast elements is replaced by alternative connection concepts.

1 INTRODUCTION

1.1 Environmental footprint of the construction industry

The building and construction sector is at the heart of global decarbonisation efforts. Accounting for approximately 34 % of global energy-related CO_2 emissions and more than 32 % of global energy demand in 2023 [1], the construction industry represents one of the most critical sectors for achieving net-zero targets. Concrete forms the foundation of modern infrastructure is the most widely used man-made substance in the world, second only to water. The production of cement alone accounts for 8 % [2] of global greenhouse gas emissions. Considering reduced primary resources and the urgent need for climate-resilient cities, research is increasingly focusing on efficient load-bearing structures alongside the optimisation of material properties. The comparative study of structural emissions at the Siemens Campus Erlangen, illustrated in Fig. 1, confirmed the significant impact of ceilings in the context of embodied carbon [3].

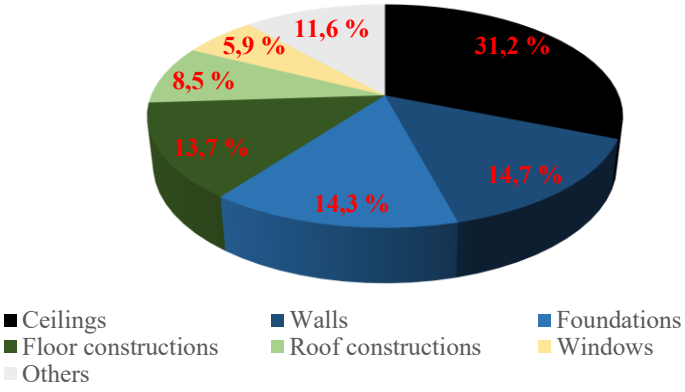


Fig. 1 Quantification of Embodied Carbon by Component Group: Life Cycle Assessment of the Siemens Campus Erlangen across Life Cycle Stages A-D

At 31,2 %, the ceilings at the Siemens Campus Erlangen in average provide the greatest potential leverage for reducing embodied carbon in the structural shell. In addition to more material-efficient

construction methods, further savings can be unlocked by prioritising “Reuse, Rebuild, Recycle” in line with the principles of Urban Mining. The reuse of entire structural components [4] —specifically ceilings -can play a decisive role in this context. However, due to complex boundary conditions, this approach must be considered as early as the design phase.

1.2 State of the art & problem description

Based on the ecological relevance quantified in Fig. 1, the following chapter analyses market-standard ceiling systems with regard to their Global Warming Potential (GWP) and their potential for circular reuse. In this context, structural barriers and conflicting objectives are critically compared. As a basis for this comparison, Heckmann [5] examined six common ceiling systems, which were evaluated in a life cycle assessment using a reference building as an example.

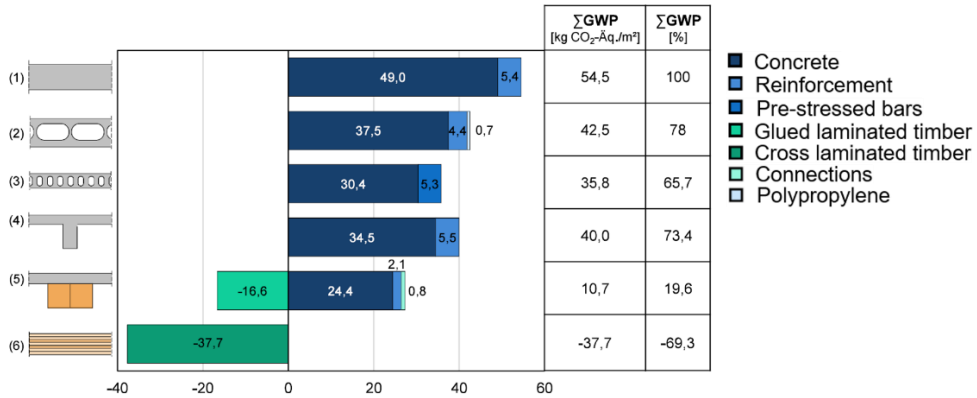


Fig. 2 GWP of common ceiling systems using a reference building as an example for life cycle stages A-D according to [5]

The reinforced concrete slab (1) performs worst with a GWP of 54,5 kg CO_2-Äq./m^2 and serves as the reference point for subsequent comparisons. Äq. stands for equivalents, used to normalize different environmental impacts into a single reference unit to ensure comparability. Due to current accounting standards for timber, the timber-concrete composite slab (5) and the cross-laminated timber slab (6) perform particularly well. The partially negative GWP values result from the end-of-life energy recovery of the timber. Steel and prestressed concrete slabs (2)–(4), with GWP values between 35,8 and 42,5 kg CO_2-Äq./m^2 produce approximately 70 % of the emissions of the reinforced concrete slab (1) [5].

The life cycle assessment, shown in Fig. 2, illustrates the theoretical potential of conventional ceiling systems, particularly through the consideration of credits in Module D. Specifically, Module D accounts for the environmental benefits gained from the potential recycling or reuse of materials after the building’s end-of-life. While normative assessments suggest a high reuse rate, the practical reality of construction reveals a profound implementation gap. The primary hurdle lies in non-destructive recovery. In monolithic or friction-locked grouted systems, such as those mentioned above, separating individual or entire components without damaging the cross-section is difficult to achieve. This is accompanied by unresolved requirements regarding residual load-bearing capacity, building law certification, and the energy expenditure required for dismantling. The transformation of precast slabs into circular systems currently fails due to a fundamental conflict of objectives between ease of assembly, reversibility and structural requirements. To ensure fire protection or building stability and to compensate for geometric imperfections, wet joining methods are standard, resulting in monolithic connections. From a circular economy perspective, such joint grouting represents an irreversible barrier that can usually only be detached through extremely laborious and destructive means.

1.3 Research approach

To close the gap between accounting principles and actual practice on the construction site described above, the disassembly capability of components, especially ceiling systems, must be considered as early as the design phase. The aim is to establish design principles that do not impose any restrictions in direct comparison to monolithic standard solutions (see Fig. 2).

To meet these requirements the RPTU is conducting research into an innovative ceiling system in collaboration with the DBV. The central research goal is to create a fully reversible structure that can be disassembled and subsequently reused. The material cycle is closed by saving up to 50 % of the primary resources used.

2 DEVELOPMENT OF A REVERSIBLE AND SUSTAINABLE PREFABRICATED SYSTEM

2.1 Generic derivation

The basic idea behind our ceiling system is based on historically proven load-bearing principles. Inspired by medieval vaulted ceilings and arches, which are already impressive due to their high material efficiency under pressure, the principle has been transfered to a modular prefabricated system. To meet the requirements of a sustainable, industrially prefabricated load-bearing system, it is divided into longitudinally tensioned beams and transversely arranged arch elements (Fig. 3 - 4).

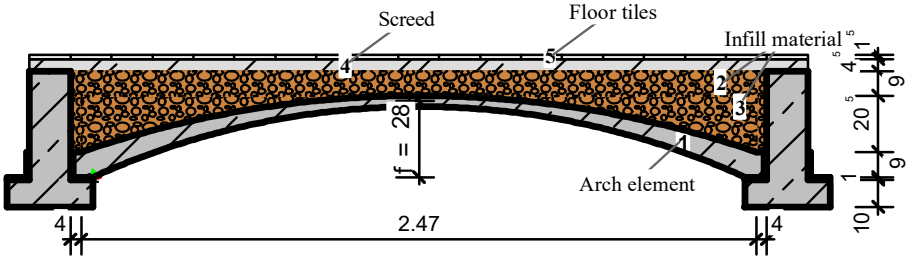


Fig. 3 Cross-section of the reversible and sustainable prefabricated system

The maximum span of the system is 8,10 m (Fig. 4). The system is designed for occupancy categories A and B, and an imposed load of 5,0 kN/m².

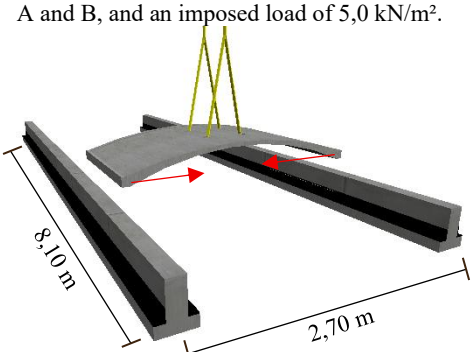


Fig. 4 Horizontal deformation capacity of the arch elements to accommodate dimensional tolerances during the assembly process

To ensure reversibility and dimensional tolerances, the system does not use conventional joint grouting. During the assembly process, tolerance requirements are to be ensured by the horizontal deformation capacity of the arch elements (indicated by the red arrows in Fig. 4). Once the arches are positioned on the beams, their self-weigth is activated, causing the arches to wedge themnselves between the beams. The force transfer is ensured by the arch thrust. As a result, joint grouting can be entirely omitted, ensuring the system remains fully reversible. The following chapters focus primarily on the arch element, while the post-tensioned beam is addressed only briefly.

2.2 Dimensional tolerances

As already described in section 1.2, the consideration of dimensional tolerances plays a decisive role in the development of a reversible prefabricated ceiling system. The external dimensions of the system directly influence the construction tolerances to be observed according to [6-8].

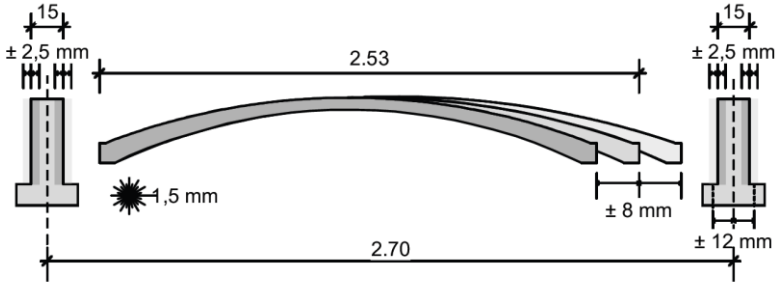


Fig. 5 Dimensional tolerances using the example of the reversible, resource-optimized prefabricated ceiling system

To account for established tolerances, the arch elements are refinded throught an iterative simulation process. This optimization ensures a high deformation capacity, allowing the system to comply with dimensional tolerances while achieving significant material savings. The tolerance requirements specified in Fig. 5 are derived from the system geometries previously defined in Fig. 3. These must be complied to ensure that the components can be assembled and disassembled, taking into account cumulative manufacturing inaccuracies. In addition to the dimensional deviations caused by manufacturing and assembly, an additional measurement uncertainty of 1,5 mm is implemented in the fit calculation using a laser measuring system. A basic distinction can be made between two refraction variants [6-8].

1. Calculation using the addition process
2. Calculation using the statistical propagation of uncertainty

The addition process is based on assumption that each individual process within a sequence is subject to the maximum permissble error and is calculated according to (1).

$$T = T_1 + T_2 + T_3 + \ldots = \sum_{i=1}^{n} T_i \tag{1}$$

This results in a maximum total error. Unlike the addition process, the calculation of the error magnitude using statistical propagation of uncertainty takes into account the probability distribution of the error magnitude. It is assumed that opposing deviations occurring simultaneously within a tolerance chain lead to partial compensation. The total tolerance is calculated according to (2).

$$T = \sum_{i=1}^{n} T_{i,inherent} + \sqrt{\sum_{i=1}^{n} \left(T_{i,production}\right)^2 + \left(T_{i,measurement}\right)^2 + \left(T_{i,assembly}\right)^2} \tag{2}$$

The German Precast Concrete Association recommends [8] the calculation of total tolerance for precast concrete structures using a combination of the two calculation methods listed above in accordance with (3).

$$T = T_{max} + \sqrt{\sum_{i=1}^{n} (T_i)^2} \tag{3}$$

The following table provides an overview of the calculated total tolerances and the resulting requirements for maximum deformation capacity per joint side. These data form the basis for the Finite Element (FE) simulations used to dimension the arch elements. The target value used for the simulations was the average parameter of 10,41 mm (Table 1) [8] as horizontal deformation capacity.

Table 1 Overall tolerances using the example of the system geometry of the prefabricated ceiling system

Calculation method [-]	Total tolerance [mm]	Total tolerance per joint [mm]
Addition process	53,0	± 13,25
Statistical propagation of uncertainty	29,8	± 7,45
Combination according to Guideline 6	41,6	± 10,41

To approach this parameter while considering additional material savings, the prefabricated arch was optimized in four gradual adjustments. The conventional grid sizes of 2.70 m were maintained during optimization and dimensioning.

2.3 Design parameters and targets

The external geometry of the prefabricated arch components is defined through a multi-stage optimization process using numerical truss models (FEM). The key objectives are to maximize material savings and ensure sufficient horizontal deformation capacity to compensate the derived dimensional tolerances. Considering the bearing joints (elastomer bearings), the effective span for the precast element is l_{eff} = 2,53 m. An essential aspect of the assembly concept is based on the activation of the arch thrust after setting. For this purpose, the horizontal deformation of the arch flanks (Fig. 4) is used to create a force connection with the webs of the joints and to ensure static force transmission without additional grouting measures. Crack formation during the assembly process at the top of the arch results in horizontal deformation, so that the elements can be assembled while maintaining dimensional tolerances.

2.4 Analysis of the rise and crack initiation

One of the most important parameters of arches is the rise. Alongside the span, it has a decisive influence on the structural and deformation behavior. The maximum rise was determinded to be f = 28 cm (Fig. 3). This value represents the optimum based on serveral boundary conditions:

- Design constraints: Compliance with the maximum desired ceiling cross-section structure and the normative requirements for sound insulation.
- Static requirements: Minimization of horizontal arch force.
- Functional cracking: In contrast to conventional concrete structures, pronounced cracking in the apex area is explicitly desired. A larger rise favors the cracking process during the installation process, while smaller spans or rise would hinder initial crack formation and thus counteract tolerance absorption.

2.5 Iterative cross-sectional optimization and zoned geometry

Taking all boundary conditions into account (structural and deformation behavior), the arch geometry was refined through four successive simulation stages to determine its final form:

1. Constant cross-sectional thicknesses: Initial investigations showed that constant cross-sectional thicknesses were insufficient to ensure the required horizontal deformations. Furthermore, they are less reccource efficient compared to cross-sectional thickness.
2. Investigation of prestressing concepts: Investigations into post-tensioned arches showed that horizontal loads applied to the flanks achieved targeted cracking and significant horizontal deformation. Ultimately, the external post-tensioning required an excessive amount of on-site effort, which proved impractical for precast construction.
3. Implementation of local cross-sectional weakening: To promote controlled cracking during formwork remocal, transport and lifting, weakening zones were specifically integrated. These act as predetermined breaking points.

These findings led to the final development of a zoned cross-section. A minimal cross-sectional thickness of 4 cm at the lifting points, combinded with a continuous increase in thickness towards the supports, ensures that the required crack formation is triggered solely by the assembly and lifting process. Minimal reinforcement ensures the load-bearing behavior within the installation process. In its final state, the zoned cross-section also offers advantages in terms of load-bearing behavior (Fig. 3).

3 EXPERIMENTAL INVESTIGATIONS

3.1 Overview

The following experimental investigations serve to verify the design logic derived in the previous chapter and the numerically determined deformation parameters. The focus lies on validating the induced crack formation in the rise and experimentally verifying the load-bearing and deformation behavior.

3.2 Fabrication of Specimens

While the prestressed beams represent standard industrial components, the arch elements were specifically produced in the laboratory in Kaiserslautern. In line with the scope defined in section 2.1, this chapter focuses solely on the arch elements.

The complex geometry of the zoned cross-section was implemented using a formwork system from Peri, which was supplemented by specific special constructions to reproduce the support flanks. The elements were concreted in a vertical orientation. The reinforcement was realized using centrally arranged mesh reinforcement (R188A). Due to the low thickness of the components, conventional installation parts (transport anchors) were not used; instead the load is absorbed during the transport and assembly process by means of structural recesses. Another focus of research was the development of a resource-efficient concrete mix. The aim was to design a low-strength concrete with good flowability. The use of a low compressive strenght class is essential for the assembly process; otherwise the required crack formation cannot be achieved. A C20/25 concrete was developed based on a CEM II/C-M from Dyckerhoff and aggregate with a maximum gravel size of 8 mm. The rheological properties were optimized by adding a melamine-based superplasticizer.

3.3 Experimental program

In a first step the deformation capacity of the arches is examined in accordance with Section 2.2 to ensure dimensional tolerances. The elements are examined immediately after formwork removal in various load bearing scenarios. A distinction was made between manual and digital measurement using a Leica scanner. The deformation capacity can be identified by superimposing the scenarios. The unloaded arch elements serve as the reference state. Based on this, three states were examined:

1. Assembly condition: The element lifted by crane to record horizontal deformations.
2. Intermediate state: The element placed on the flat top side of the formwork for examining the effects of friction.
3. Final position: The element positioned on elastomer bearings for verification of the final position.

The load-bearing and deformation behavior of the arch elements were then investigated. One primary focus of the research was on the recombinability of the components in the context of circular reuse, taking into account the limit dimensions (minimum, target, and maximum position). Based on previous numerical simulations, the eccentric single load was identified as the decisive load position. The first series of tests comprised three test specimens, which were examined in their respective tolerance positions under cyclic loading (10 load cycles). To demonstrate robustness against changing installation situations, the specimens were then disassembled, rotated by 180 degrees, and subjected to cyclic loading again. To quantify possible damage, the deformation behavior in the assembled state was recorded again after each cycle. The test series concluded with loading until the structure failed. To isolate the influence of the preload cycles on the residual load-bearing capacity and to perform a qualitative assessment of pre-damage, reference tests were carried out in parallel on unloaded elements. In addition to displacement transducer, the experimental investigations were accompanied by photogrammetric measurements. In addition to the individual tests, large-scale demonstrations on entire ceiling panels (span 8.10 m) are also planned.

4 RESULTS AND SCIENTIFIC DISCUSSION

4.1 Analysis of deformation capacity within storage and transport conditions

The following chapter exemplarily presents parts of the deformation measurements, as shown in Fig. 4 as well as the experimental test series of a target position (Fig. 7).

The first six arch elements were used to achieve the following deformation behavior (Fig. 6). As described in Section 2.2, the color markings refer to the respective tolerance levels.

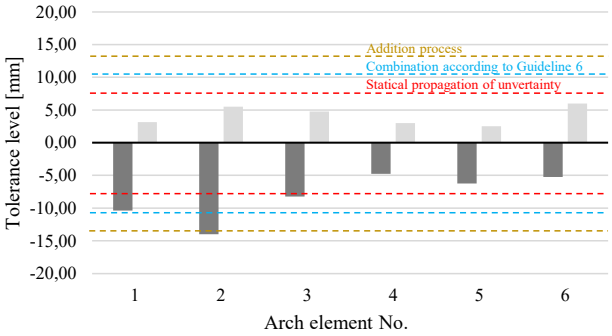


Fig. 6 Comparison of the measured total deviations of the six arch elements with the calculated limit values of various tolerance models

The negative tolerance levels describe the deformations during the assembly state (Fig. 4), while the positive tolerances describe the intermediate state.

The results indicate that the upper tolerance levels (max. position) were not attained by any of the six arch elements. Three of the six elements were able to achieve at least the lower tolerance level (min. position), considering statistical propagation of uncertainty. A correlation between formwork removal times (here after 7d) and the splitting tensile strength is clearly evident in further investigations and is part of further optimizations to comply with the tolerance levels.

4.2 Analysis of load-bearing and deformation behavior

The experimental investigation of the target position was carried out on arch elements No. 2 and 5, using different load histories. Arch element 2 served as the test object for cyclic preloading in the context of the recombination test. In contrast, arch element 5 served as a reference sample, which was tested without prior load cycles until failure was reached.

The resulting load-deformation behavior of both test series is compared in Fig. 7. Graphs 1.1 - 1.3 document the deformation characteristics of the preloaded test specimen 2, while graph 1.4 shows the primary load-deformation curve of the unloaded reference element 5.



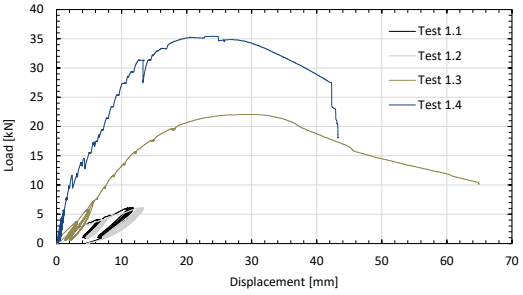


Fig. 7 Test setup (left); force-deformation behavior of the two test series using the target positon (right)

Both specimens exhibited ductile behavior with identical failure patterns. However, the reduced load-bearing capacity of the pre-loaded arch (Test 1.3) compared to the initial arch (Test 1.4) indicates pre-damage. This must be considered for potential reuse. Furthermore, aspects such as reduced strength (Test 1.3) are essential for a comprehensive evaluation of these deviations.

5 CONCLUSION AND OUTLOOK

Previous investigations demonstrate the high potential of the developed ceiling system as a recyclable, material-efficient, and ductile alternative (see Fig. 7) to conventional constructions. It has been proven that the force transfer between the vault and the joist can be reliably activated via a horizontal pressure

contact joint (arch shear). The innovative concept, which accounts for maximum deformation capacity through targeted cracking, has proven to be a functional approach. The experimental data shows that the system is capable to compensate significant construction tolerances through targeted geometric deformation.

In terms of material efficiency, the system has an excellent ecological balance: with an equivalent concrete consumption corresponding to a solid ceiling of only 6,5 cm, the arch elements achieve a significant reduction in CO_2. In combination with the complete reversibility of the components, the system also meets the requirements for circular construction.

Regarding the normative requirements of Eurocode 2, it was demonstrated that the critical single loads of $Q_k = 4kN$ were not only achieved but also exceeded many times over. The identification of the eccentric single load as the determining load case already provided reliable results in the target position, attesting to the high robustness of the structure against asymmetrical stresses. The test results obtained so far ruled out the possibility of sudden failure of the arch elements. Future research will focus on further fine-refinement of crack development and propagation. To increase the sensitivity of the tolerance analysis, the following optimization strategies will be pursued:

- Time of formwork removal: Ealier formwork removal deadlines to take advantage of lower strengths.
- Concrete technology: Development of formulations with specifically reduced splitting tensile strength while maintaining compressive strength and increasing yield strength.
- Extended test series: Conducting systematic tests at the limit tolerance levels (minimum and maximum levels) to quantitatively substantiate the statistical certainty of recombination capability.

Finally, ongoing research into recombinatorics will provide valuable insights into long-term stability and the possibilities for reusability.

Acknowledgements

The IGF project [01/F23126N] of the research association (DBV) was supported by the Federal Ministry for Economic Affairs and Climate Action through the German Federation of Industrial Reasearch Associations (AiF) under the programme for Industrial Collective Research (IGF) based on a decision by the German Bundestag.

References

[1] United Nations Environment Programme. 2025. „Not just another brick in the wall: The solutions exist – Scaling them will build on progress and cut emissions fast.” Global Status Report for Buildings and Construction 2024/2025. doi:10.59117/20.500.11822/47214.

[2] Glock, Christian, Heckmann, Michael, Dernbach, Aaron, and others. 2023. “Treibhausgas- und ressourcenreduzierter (Beton-)Bau – Herausforderungen, Lösungsansätze, Anreizsysteme — Nachhaltiges Bauen mit Beton.” *DBV-Heft 50 – Band 1*.

[3] Müller, Rebecca, Dernbach, Aaron, Jochum, Daniel, Wagner, Erik, and Glock, Chrisian. 2026. “Wissenschaftlich-ökologische Bewertung dreier Konstruktionsweisen für Bürobauten anhand Grauer Emissionen am Projektbeispiel.” *Bauingenieur*. doi:10.37544/0005-6650-2026-22

[4] Heckmann, Michael, Dernbach, Aaron, Müller, Rebecca, and Glock, Christian. 2024. “Experimentelle Untersuchungen zu Rückbau und Wiederverwendung von Spannbetonhohldielen.” *Beton- und Stahlbetonbau 119: 6 410-419.* doi:10.1002/best.202400001.

[5] Heckmann, Michael. 2024. “Entwicklung eines Benchmarksystems für die Grauen Emissionen von Deckensystemen.” PhD diss., University of Kaiserslautern.

[6] Bindseil, Peter. 2012. *Stahlbetonfertigteile nach Eurocode 2 – Konstruktion, Berechnung, Ausführung.* Köln: Werner.

[7] Ertl, Roderich. 2008. *Toleranzen im Hochbau – Kommentar zur DIN 18202, zulässige Maßabweichungen im Roh- und Ausbau*. Köln: Müller.

[8] Fachvereinigung Deutscher Betonfertigteile e.V. 2023. „Merkblatt Nr. 6 – Toleranzen und Passungsberechnung für Betonfertigteile.”

Automated Strengthening Concept for Reused Concrete Members: Stress Redistribution between Metallic and Non-Metallic Reinforcement

Ben Stöhr, Marius Hägle, Felix Hofmann, Alexander Stark

Institute of Concrete Structures and Building Materials,
Karlsruhe Institute of Technology,
Gotthard-Franz-Straße 3, 76131 Karlsruhe, Germany

Summary
The basis for a high reuse rate for concrete members, automatable strengthening methods are advantageous. Thin strengthening layers with non-metallic textile mesh can minimise new grey CO_2 emissions. Applying this method to concrete members under flexural loading, stress redistributions are to be expected. This paper combines experimental and analytical methods to characterise redistribution effects between metallic and non-metallic reinforcements with large differences in bond and axial stiffnesses. Using fibre optic sensors, continuous strain measurements were performed and stress redistributions between ribbed steel and textile mesh were identified, which decrease with increasing load. Using an analytical model approach based on the bond–slip differential equation, good agreement with the measured strains was achieved. This forms the basis for a targeted selection of strengthening materials.

1 INTRODUCTION

The reuse of dismantled, reinforced concrete members can significantly reduce resource consumption and CO_2 emissions in new structures. The intended reuse strategy envisages the standardised reuse of concrete members in a modular system with detachable connections (cf. [1], [2]). Dismantled slabs and walls are to be integrated into the concept as one-way slab systems with uniform module characteristics (cf. [3]). Environmental damage effects, such as reinforcement corrosion, can prevent the planned reuse of individual members. Targeted strengthening measures can extend the service life of the components and open up additional usage cycles. To minimise new grey emissions, thin-walled reinforcement layers with bidirectional textile mesh (cf. [4]–[7]) made of carbon fibre reinforced polymer (CFRP) should be used. In [7], the use of carbon concrete strengthening in a building construction project resulted in significant greenhouse gas reductions compared to conventional solutions. In order to ensure an economical process chain, this article aims to achieve standardised, modular reuse and automation of the necessary preparation and strengthening measures. The process flow developed for this purpose can be divided into six steps:

- Step 1: To strengthen for example the resulting composite joint of flexurally loaded members, mechanical shear teeth (including surface treatment) are to be added to the concrete surface using subtractive techniques (milling techniques). Compared to chemical processes, this can significantly reduce process times. This process has already been tested in own investigations, and systematic investigations have reduced production times and inaccuracies (cf. [1],[8]);
- Step 2: Following [5],[6] 3D printing techniques are to be used to create a thin-walled support structure that functions as formwork. This allows for easy adaptation to individual geometries and direct further processing (flow production);
- Step 3: Due to the dimensional stability of the 3D printed layer, the lightweight CFRP mesh can be placed directly on the support structure without any waiting time;
- Step 4: The upper support structure is then applied in the same way as in Step 2;
- Step 5: The cavity is to be filled with self-compacting fine concrete, which gives the strengthening layer a bond and concrete quality compared to monolithic construction;
- Step 6: Finally, specific quality controls must be carried out.

Figure 1 shows the developed process flow for automated strengthening of the flexural tension zone, which has already been successfully validated in own investigations.

In order to ensure safe dimensioning and efficient process design of the proposed strengthening concept for predominantly flexural stresses, research is needed not only into the manufacturing process, but also into the formation of the anchoring (cutting anchoring and anchoring of the CFRP mesh) and the bonded joint, as well as the mixed reinforced tension zone. This paper examines the expected stress redistribution resulting from the differences in axial stiffness and bonding between the different reinforcement types (see Figure 1). The focus is on the following research questions:

- How can small-scale tests be used to characterise redistribution effects on the one hand and record internal strain conditions on the other hand?
- How do redistribution effects occur between conventional metallic reinforcement (ribbed) and non-metallic reinforcement (CFRP mesh)?
- How can stress redistributions in hybrid cross-sections be predicted using analytical methods?

This paper aims to characterise stiffness- and bond-related redistributions using initial experimental model tests in order to validate an analytical model based on the bond–slip differential equation. This allows optimisation of the strengthening system for process standardisation with the help of suitable constitutive material models for bonding. With targeted adjustment of the stress redistribution, compatible strengthening materials can be identified for common material combinations.

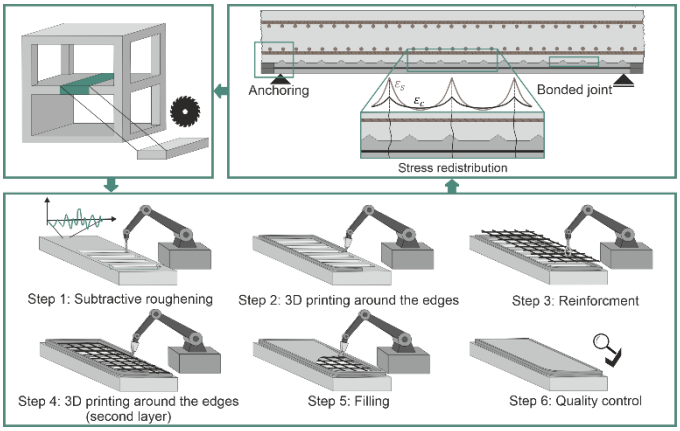


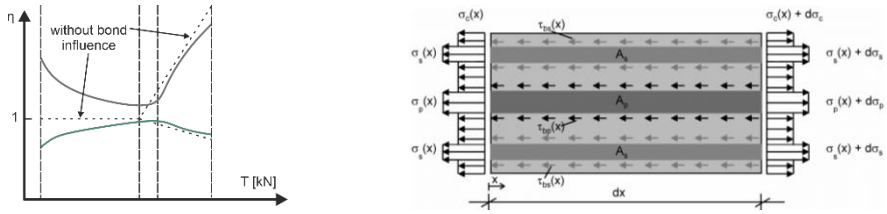
Fig. 1 Automated strengthening concept with material-minimised CFRP concrete layers, using combined subtractive and additive manufacturing techniques

2 BACKGROUND TO STRESS REDISTRIBUTION

Stress redistribution in mixed-reinforced members in a cracked state results from geometric and material differences between the reinforcement elements used. According to elasticity theory, a deviating stiffness ratio of the reinforcements in the crack leads to unequal force distributions (cf. [9]). In addition, the bond behaviour, which is determined by the three mechanisms of adhesion, friction and mechanical interlocking, can have a major influence on stress redistribution (cf. [9]–[11]). Non-metallic reinforcement, and CFRP mesh in particular, exhibit softer bond behaviour than conventional reinforcement (steel bars) due to their lower mechanical interlocking mechanism (cf. [10]). The different bond behaviour leads to different anchorage lengths in the cracked state and can result in stress redistribution.

Figure 2 shows stress redistributions η between non-metallic reinforcement and ribbed reinforcing steel according to [9]. The load distribution deviates significantly from the ideal state II (rigid bond) and is determined by the combination of stiffness and bond properties. However, with increasing load and crack formation (cf. Figure 1), it approaches the ideal state II. Due to the non-linear material behaviour of steel, a reversal point occurs as soon as the yield strain is reached. The non-metallic reinforcement must take over the further force absorption until it fails brittle (see Figure 2 a)).

An analytical description of the stress redistribution between a mixed-reinforced and a centrally stressed concrete tension member can be provided by a second-order differential equation system with two coupled equations (cf. Equations 1 and 2) [11]. Equilibrium and compatibility conditions can be used to derive relationships between stresses and displacements (slip) at the differential bar elements (see Figure 2 b)). After solving the differential equations, the stress and strain states of the reinforcement in the bond force transfer area can be derived. This takes into account the nonlinear bond behaviour and the different elastic stiffness. For further information on the derivation, cf. [11].



a) Stress redistribution [9] b) Infinitesimally small bar element [11]

Fig. 2 Model behaviour of stress redistribution in a mixed-reinforced tension bar

The model approach has already been applied in various studies (e.g. [9], [11]). BÜLTE was able to achieve good calculation results for combinations of steel reinforcement and metallic wire strands [11]. WEILAND applied the approach in a mechanical model and investigated combinations of metallic and non-metallic reinforcement (without a matrix) using flexural tests [9]. From this, fundamental considerations regarding stress redistribution were derived (see Figure 2 a)). STEINBOCK also investigated hybrid reinforced cross-sections with advanced non-metallic reinforcement elements (newer generations) using flexural tests, but without model considerations according to Figure 2. They derived a calculation model of redistribution using bond coefficients [10].

$$\frac{d^2 s_s(x)}{dx^2} = \frac{1}{E_s} \cdot \left[\tau_{bs}(s_s(x)) \cdot \frac{U_s}{A_s} \cdot \left(1 + \frac{E_s}{E_c} \cdot \frac{A_s}{A_c}\right) + \frac{E_s}{E_c} \cdot \tau_{bp}\left(s_p(x)\right) \cdot \frac{U_p}{A_c} \right] \quad (1)$$

$$\frac{d^2 s_p(x)}{dx^2} = \frac{1}{E_p} \cdot \left[\tau_{bp}\left(s_p(x)\right) \cdot \frac{U_p}{A_p} \cdot \left(1 + \frac{E_p}{E_c} \cdot \frac{A_p}{A_c}\right) + \frac{E_p}{E_c} \cdot \tau_{bs}(s_s(x)) \cdot \frac{U_s}{A_c} \right] \quad (2)$$

It should be noted that most experimental investigations were carried out using strain gauges (e.g. [11]). However, these only allow local strain measurement. Since the bond force transfer strongly depends on the location and distance of the cracks (maximum available anchorage length), comprehensive validations of the analytical calculations (e.g. internal strain curves) are not possible. In addition, there is a lack of systematic investigations (model and component tests) for newer generations of textiles in combination with conventional and historical reinforcement bars. Continuous strain measurements (e.g. using fibre optic sensors) enable comparisons between analytically calculated strain curves based on bond-slip constitutive relationships from model tests (e.g. [4]) and measured internal strain values. This would allow the influence of bond- and stiffness-related redistribution to be characterised in isolation using a combined experimental and theoretical methodology, and suitable test methods to be derived.

3 INITIAL EXPERIMENTAL INVESTIGATIONS ON STRESS REDISTRIBUTION

3.1 Materials

As part of these investigations, normal-strength concrete (NSC) was selected as a representative material for dismantled existing members (see also [2]). A self-compacting fine concrete (HSC), which

was specially developed for non-metallic reinforcement, was used for the strengthening layer. The use of superplasticisers makes it particularly suitable for automated casting processes (Step 5, cf. Figure 1). Table 1 shows the concrete composition.

Table 1 Concrete composition [kg/m³]

Concrete	Cement	Water	SP[3]	Sand H33 0.125 – 0.5 mm	Sand 0 – 2 mm	Gravel 2 – 8 mm	Gravel 8 – 16 mm
NSC	300[1]	180	-	-	567	756	567
HSC	710[2]	165	8	300	605	595[4]	-

[1]CEM I 42,5 R; [2]Nanodur Dyckerhoff; [3]Superplasticiser MC Bauchemie; [4]the maximum aggregate size is 4 mm

Table 2 contains the results of the building material tests (hardened properties).

Table 2 Concrete properties [MPa]

Concrete	Cylinder compressive strength $f_{cm,cyl.}$[1]	Cube compressive strength $f_{cm,cube}$[1]	E-modulus E_{cm}[2]	Split tensile strength $f_{ct,sp}$[3]
NSC	33	46	30.000	5
HSC	93	100	40.400	7

[1]according to [12]; [2]according to [13]; [3]according to [14]

A conventional reinforcing bar of type B500B according to [15] with a diameter of 8 mm was examined as existing reinforcement. The biaxial mesh GRID Q47-C-EP-S38-F145 from SOLIDIAN (cf. [16]) was investigated for the strengthening layer. Table 3 lists the most important material properties.

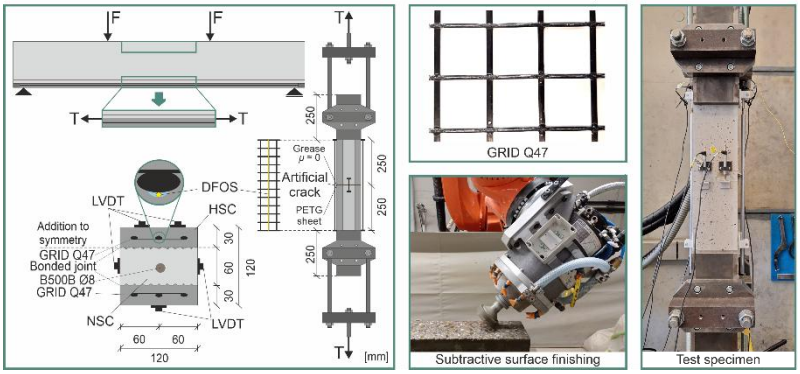
Table 3 Important properties of the used reinforcment materials

Typ	Nominal cross sectional A_{nm} [mm²]	E-modulus E_{nm} [N/mm²]	Active bond scope U_{nm} [mm]
Steel bar B500B-Ø-8	50.3[1]	200.000[2]	25.1[1]
GRID Q47-C-EP-s38-F145	4.4[3]	99.000[3]	7.4[4]

[1]Circular cross-section; [2]according to [15] ; [3]according to [16] ; [4]Circular cross-section with nominal diameter according to [16]

3.2 Methodology – Model test concept

For the isolated investigation of stress redistribution, a modified tension bar test with a length of one metre was carried out according to [4] and [11]. This idealises the reinforced tension zone by means of a centric tensile load. This is shown in Figure 3 a). The test specimen was clamped firmly with a clamping force of 90 kN over 250 mm, resulting in a free length of 500 mm.



a) Idealisation of the model test concept b) Experimental procedure

Fig. 3 Schematic representation of the model test setup

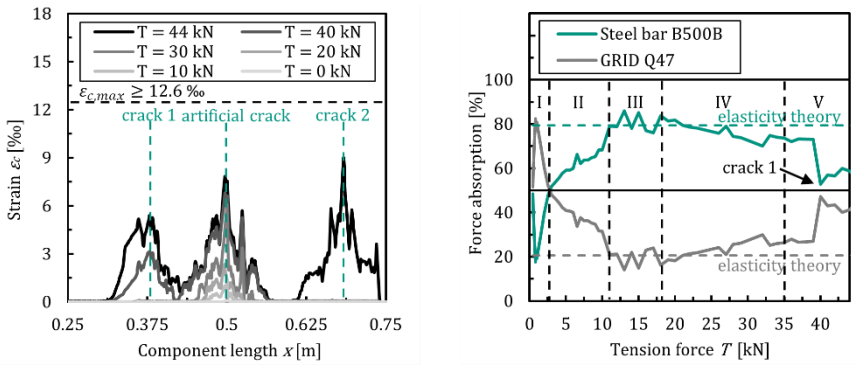
The representative tension bar for the existing structural member consists of normal concrete and a B500B-Ø-8 reinforcement bar (see chapter 3.1). To prevent inclination, two strengthening layers were arranged in the tension bar. The biaxial mesh GRID Q47 (see Figure 3 b)) was arranged with three bars in both layers. During production, the centre section (existing member) was manufactured in the first step and the strengthening layer in the second step (two days later). In order to prevent failure at the bond interface, the centre section was mechanically roughened (roughness depth approx. 3 mm) using an industrial robot (machining strategy based on [8]) in accordance with Figure 1. The cross-section has an EA_s/EA_c ratio of 3.85. The amount of reinforcement was calculated so that the specimen could fail at a maximum load of 80 kN (maximum anchoring load due to clamping).

Continuous strain measurements are performed using fibre optic sensors (DFOS) to identify stress redistributions. For this purpose, a measuring fibre (polyimide-coated single-mode sensor fibre with a core diameter of 9 µm and a cladding diameter of 125 µm) was applied to the middle of the CFRP bar over its entire free length using a cyanoacrylate adhesive (see Figure 3 a)). The strain was measured at an interval of 0.65 mm and a sampling rate of 5.21 Hz. In order to enable evaluation at a defined location over the entire load curve, an artificial crack (PETG sheet) was placed in the centre of the test specimen in accordance with [4] and a thin film of grease was applied to prevent a bond effect. To evaluate the large amount of FOS data, an evaluation tool was created in PYTHON, which was used to remove incorrect measurements. The maximum strain in the artificial crack, which is used to evaluate the redistribution, was determined by averaging three measurement points.

In addition, the test force (controlled at 1 mm/min) and the opening of the artificial crack were continuously measured with three LVDT sensors for documentation of inclinations. Two LVDT sensors arranged on the sides were also used to measure the change in length over the entire free length.

3.3 Test results and interpretation

Figure 4 a) shows the measured strains over the free length of the test specimen (artificial crack at approx. 0.5 m) for different tension forces T. The FOS measurement was able to deliver measurement results up to a force of approx. 44 kN (approx. 67.4 % of the capacity) before it failed due to progressive crack formation. The measured strains increased continuously with increasing load and remained below the limit strain of 12.6 ‰ (according to [16]).



a) Strain measurement (DFOS) on the GRID Q47 b) Force absorption

Fig. 4 Results of the test specimen

Figure 4 b) shows the force absorption between the steel reinforcement and the GRID Q47. This was determined from the measured strains (DFOS) by establishing equilibrium according to elasticity theory (equal distribution of the measured strain across all CFRP bars). Based on this, the following five phases can be observed depending on the load condition, in accordance with [9]:

- Phase I: At the start of loading, the force distribution fluctuates around 50 % up to approx. 3 kN. This can be explained by the opening of the PETG sheet;
- Phase II: In the next section, the force distribution increases to approx. 11 kN (16.8 % of the capacity) to the level of the ideal state II according to elasticity theory, considering the different stiffnesses EA (redistribution to the stiffer steel reinforcement);
- Phase III: The force distribution remains at this level and fluctuates slightly up to 18 kN;
- Phase IV: A redistribution takes place, which is attributable to differences in bond behaviour. Here, the force absorption continuously approaches each other over the loading force;
- Phase V: The progressive crack formation influences the next phase, as the maximum available anchoring length changes. The steel reinforcement reaches its yield point according to the calculated force distribution at 35 kN (53.6 % of the capacity). This leads to a redistribution to the CFRP bars until they fail brittlely at 65.3 kN (the steel bar remained intact).

The testing capacity is greater than the sum of the capacities of the individual CFRP bars (5.5 kN/bar according to [16]) and the yield force of the steel reinforcement (approx. 25.1 kN). This can be explained by the actually higher load capacities of the CFRP bars and by the additional force absorption of the steel reinforcement after yielding (hardening effects). Consequently, the redistribution effects have only a minor influence on the absolute capacity in the design situation (yield stress as design limit state). However, a significant influence can be seen over the load curve (serviceability). In addition, the redistribution determines the amount of pre-strain in the CFRP bars when the yield stress is reached and thus influences the remaining strain reserve $\Delta\varepsilon_c$ until failure.

4 ANALYTICAL MODEL FOR HYBRID REINFORCED TENSION RODS

4.1 Definition and Implementation

Figure 5 shows the schematic calculation process. The core of the model is the numerical solution of the differential equation system (equations 1 and 2), as a closed solution is generally not possible. Based on [9], [11], a calculation algorithm for successive integration was applied and implemented as the solution method. Here, strains, stresses and slip are linearised over a defined element length dx. For each section, the stress must be determined iteratively so that the equilibrium conditions are maintained at each element. For these calculations, an element size of $dx = 0.02$ provides precise results.

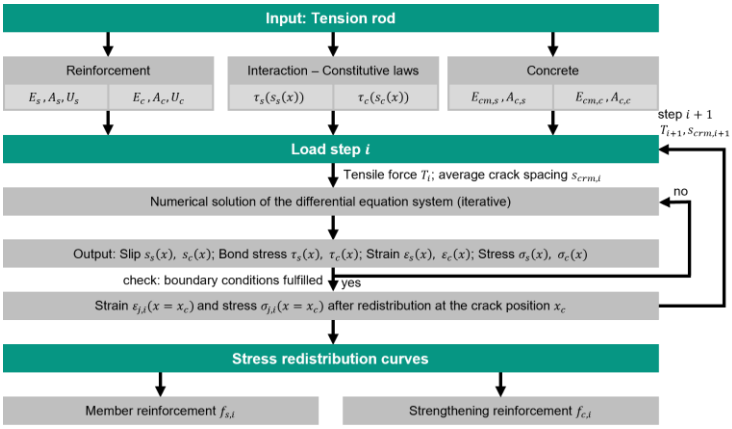


Fig. 5 Simplified schematic calculation procedure for determining stress redistribution curves

At the start of loading, state II prevails due to the artificial crack. Both types of reinforcement have a sufficiently large, uncracked length available for bond force transfer (cf. Figure 3). As the load increases and cracks form (cf. Figure 4 a)), the distance between two cracks can become less than twice the anchorage length of the bonded softer reinforcement. In this case, the bonded force anchorage areas of the bonded softer reinforcement overlap (cf. Figure 1). The anchorage lengths of the more rigid reinforcement (bonded harder), on the other hand, are shorter, so that there is initially no overlap. During the recalculation, various boundary conditions must therefore be checked depending on the load and crack state, e.g. whether overlaps as described exist. The different concrete properties in the hybrid cross-section are taken into account via a respective elastic stiffness ratio in the tension rod model, whereby the capacity in the artificial crack is zero due to the PETG sheet.

Based on the calculated stresses in the crack, stress redistribution curves can be determined for the CFRP bars and the reinforcement steel (cf. Equation 3, in accordance with [11]). By relating the redistributed stresses to the pure stress in state II without taking the elastic moduli into account, the influence of stiffness- and bond-related redistributions can be evaluated together.

$$f_{j,i} = \frac{\sigma_{j,i}(x = x_c) \cdot (A_s + A_c)}{T_i} \tag{3}$$

4.2 Validation and discussion of the results

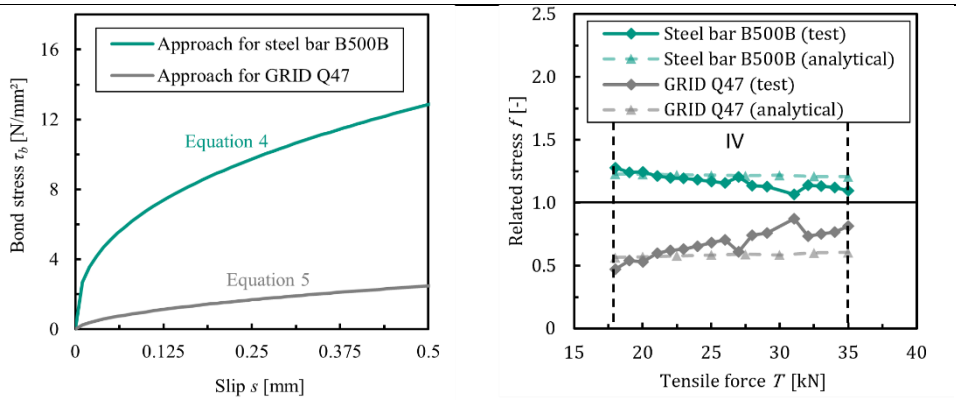
For the recalculation, all input variables must be defined in accordance with Figure 5. The properties of the concrete can be found in Table 2 and Figure 3, and the elastic and geometric properties of the reinforcement in Table 3. For the bond-stress-slip relationship, the approach according to MODEL CODE 2010 [17] is applied for the steel reinforcement bar (see Equation 4).

In [4], experimental investigations into the bonding behaviour were carried out on a comparable CFRP mesh for the same concrete mix with comparable concrete strength values. Equation 5 was calibrated based on the test results. However, a slightly softer behaviour was selected due to the smaller cross-section of the GRID Q47 mesh. Figure 6 a) shows the two constitutive laws used, which clearly demonstrate the significantly stiffer bond behaviour of the ribbed reinforcement.

$$\tau_s(s_s(x)) = 2.5 \cdot \sqrt{46} \cdot s_s(x)^{0.4} \tag{4}$$

$$\tau_c(s_c(x)) = 4 \cdot \left(1 - \frac{s_c(x)}{8}\right) \cdot s_c(x)^{0.6} \tag{5}$$

The experiment from Chapter 3 is recalculated after reaching the ideal state II (Phase III) up to the determined yield point (Phase IV) of the steel reinforcement (elastic range). The average crack spacing s_{crm} (see Figure 4 a)) was set according to the strain measurement (no overlaps of the strain curves in Phase IV). Figure 6 b) shows the stress redistribution curves calculated from the DFOS measurements using equation 3, as well as the analytical solution according to the calculation procedure in Figure 5.



a) Assumed bond stress-slip diagrams b) Stress redistribution curves

Fig. 6 Comparison of recalculations with test results in the elastic range

The analytically determined stress redistribution curves show, as in [11] (mixed-reinforced, metallic reinforcement combinations), good agreement with the experimental results in the elastic range, even with the significantly higher stiffness ratios considered. It should be noted that the calculation results are highly sensitive to input variables such as crack spacing, active bond scope or the selected constitutive laws. Due to the geometric variability of the CFRP mesh (see Figure 3 b)), statistically significant material characterisations must be carried out for more accurate analytical recalculations.

Furthermore, the measured strains and thus the stress redistribution curves were determined by averaging 3 points (see Section 3.2). Figure 4 a) shows discontinuous strain peaks with increasing crack formation, which can lead to implausible values. Therefore, the evaluation method must be validated more precisely so that reproducible internal strain states can be derived from the DFOS measurements, even if there is good agreement between the measurement and the analytical recalculation in this case.

5 CONCLUSIONS

The reuse rate of reinforced concrete members can be significantly increased in the event of damage by using automated and material-minimised strengthening methods with non-metallic reinforcement. When applying such methods, stiffness- and bond-related redistribution effects are to be expected due to the different types of reinforcement, the exact extent of which is unknown. The following findings were obtained in these investigations for the intended concept:

- To characterise redistribution effects, a model test concept based on the tension rod analogy was derived and tested. In this concept, redistributions are recorded by continuous strain measurement using fibre optic measurement systems (DFOS);
- In the initial investigations, significant redistributions were identified between ribbed reinforcing steel and a CFRP mesh. These redistribution effects decreased with increasing load and crack formation. For the steel reinforcement, a maximum redistribution of $f_{s,max} = 1.31$ was determined. Due to the yielding of the steel reinforcement, the redistributions were reversed, so that the CFRP mesh had to absorb more load and failed brittlely;
- Using an analytical calculation model based on the bond–slip differential equation, it was shown that the calculated redistributed strains corresponded well with the measured strains.

However, the calculation results are highly dependent on input variables such as the active bond scope, which are difficult to determine precisely for CFRP mesh.

Future investigations will therefore require more in-depth model verification (e.g. model consistency checks with exact material characterisations and a comparison with anchorage lengths from DFOS strain measurements) and extensions (e.g. non-linear material behaviour of steel bars). Furthermore, additional experimental investigations are required, in particular with varying stiffness ratios and different historical material combinations, which can be pre-dimensioned using the analytical calculation model. In addition, large-scale tests on beams should be carried out to verify the transferability of the results of the model analysis to real flexural tensile zones.

References

[1] Stöhr, Ben, and Stark, Alexander. 2025. "Aufbereitung von rückgebauten Stahlbetonbauteilen zu lösbaren, modularen Fertigteilen: Tragfähigkeit unter Druckbeanspruchung." *Beton- und Stahlbetonbau* 120:810–821. doi:10.1002/best.70026.

[2] Stöhr, Ben, and Stark, Alexander 2024. "Influence of Surface Characteristics on the Connection of Re-Used Concrete Members with Detachable Dry Joints." Paper presented at the 15th fib International PhD Symposium, Budapest, Hungary, August 28–30.

[3] Frank, Niklas, Renz, Robert, Hofmann, Felix, and Albers, Albert. 2025. "An Optimization Method for the Intelligent Modularization of Concrete Frame Structures." Paper presented at the fib International Symposium on Concrete Structures, Antibes, France, June 16–18.

[4] Hägle, Marius, Hofmann, Felix, and Stark, Alexander 2025. "Initial Investigations on Stress Redistributions Between Different CFRP Reinforcement Types." Paper presented at the fib International Symposium on Concrete Structures, Antibes, France, June 16–18.

[5] Engel, Sven, et al. 2025. "Multimodal Automated Fabrication with Concrete: Case Study and Structural Performance of Ribbed CFRP-Reinforced Concrete Ceilings." *Additive Manufacturing* 101:104689. doi:10.1016/j.addma.2025.104689.

[6] Tošić, Zlata, et al. 2022. "Design and Optimization of Free-Form Surfaces for Modular Concrete 3D Printing." *Automation in Construction* 141:104432. doi:10.1016/j.autcon.2022.104432.

[7] Wagner, Juliane, et al. 2026. "Sanierung und Verstärkung des ehemaligen Amtsschlachthofes Dresden mit Carbonbeton." *Beton- und Stahlbetonbau* 121:60–66. doi:10.1002/best.70063.

[8] Stöhr, Ben, Hägle, Marius, and Stark, Alexander. 2025. "Optimising Robotic Production of Interlocking Dry Joints for the Connection of Reused Concrete Members." Paper presented at the fib International Symposium on Concrete Structures, Antibes, France, June 16–18.

[9] Weiland, Silvio. 2009. "Interaktion von Betonstahl und textiler Bewehrung bei der Biegeverstärkung mit textilbewehrtem Beton". PhD diss., Technische Universität Dresden.

[10] Steinbock, Oliver. 2022. "Verstärkung von Stahl- und Spannbetonbrücken mit Carbonbeton". PhD diss., Technische Universität Dresden.

[11] Bülte, Sebastian. 2008. "Zum Verbundverhalten von Spannstahl mit sofortigem Verbund unter Betriebsbeanspruchung". PhD diss., RWTH Aachen University.

[12] Deutsches Institut für Normung e.V. 2019. Prüfung von Festbeton – Teil 3: Druckfestigkeit von Probekörpern (DIN EN 12390-3:2019-10). Berlin: Beuth Verlag GmbH.

[13] Deutsches Institut für Normung e.V. 2021. Festbeton – Teil 13: Bestimmung des Elastizitätsmoduls unter Druckbelastung (DIN EN 12390-13:2021-09). Berlin: Beuth Verlag GmbH.

[14] Deutsches Institut für Normung e.V. 2024. Festbeton – Teil 6: Spaltzugfestigkeit von Probekörpern (DIN EN 12390-6:2024-05). Berlin: Beuth Verlag GmbH.

[15] Deutsches Institut für Normung e.V. 2021. Eurocode 2: Bemessung und Konstruktion von Stahlbeton- und Spannbetontragwerken (DIN EN 1992-1-1:2021). Berlin: Beuth Verlag GmbH.

[16] Solidian GmbH. 2025. "Allgemeine bauaufsichtliche Zulassung Z-16-308." Accessed December 11. https://www.dibt.de/de/service/zulassungsdownload/detail/z-16-308.

[17] Fédération internationale du béton (fib). 2010. Model Code 2010 – Final Draft (Bulletin 65/66).

A state-of-the-art review of demountable constructions

Katharina Schachner, Alireza Fadai

Research Unit of Structural and Timber Engineering,
TU Wien,
Karlsplatz 13/E259-02, 1040 Vienna, Austria

Summary
The construction industry contributes significantly to global greenhouse gas emissions and resource consumption, positioning it as a key sector for the transition toward a circular economy. This paper systematically investigates demountable connections to assess the state of the art, identify research gaps, and compile a catalogue of existing connection systems. The study is based on a comprehensive literature review structured through categorisation and analytical evaluation methods. Results include a list of material independent connections suitable for disassembly and a summary of current research needs. The findings suggest future research directions focusing on design for disassembly strategies.

1 INTRODUCTION

The construction industry is responsible for a considerable proportion of worldwide greenhouse gas emissions, as well as significant consumption of non-renewable resources. [1]. Consequently, the construction industry is regarded as a crucial starting point for a sustainable transformation towards a circular economy. One key factor for the transformation to a circular economy in construction is dismantlability, for example in the form of demountable connections [2].

There are significant practical challenges. Case studies on the implementation of design for disassembly (DfD) are rare and difficult to adopt [3, 4]. Furthermore, designs using recycled materials often result in increased effort and material waste [4]. In Switzerland for example, despite a long tradition, only a small proportion of wooden building components are reused [5]. Other barriers include a lack of standardisation, durability issues, logistical challenges, and complex reprocessing methods that make upcycling unprofitable [2, 6]. In summary, less than 1% of buildings are fully demountable [7].

However, these gaps make the topic highly relevant. Demountable connections reduce material use, improve reusability, and lower environmental impacts [8]. They preserve the value of buildings as "material banks" and facilitate upgrades [2], for instance in earthquake regions [9]. Finally, the number of publications on the disassembly potential of buildings has increased exponentially since 2019 [6, 10].

This paper builds on these developments, and a scoping review was carried out. Therefore, relevant publications are preselected to create an overview of the current research state on demountable connections. The result is a material-independent catalogue of demountable connections. Additionally, key research gaps are identified. In conclusion the findings provide a basis for recommendations on future research needs.

1.1 Principles and key aspects of demountable connections

Demountable connections are fundamental to DfD to construct a design approach for buildings that can be dismantled and reused with minimal damage. Disassembly operates at three levels: (1) material level; it concerns the reversible separation of layers, (2) component or element level; it enables the removal, replacement, or adaptation of parts and (3) building level; it supports reconfiguration and reuse of entire structural systems. This paper focuses on the third level.

According to [11] three principles define demountable design: (1) reversible connections; allowing materials to be separated without damage, (2) independent components; enabling elements to be detached or replaced, and (3) transformability; ensuring adaptability to new requirements. Achieving reversibility depends on designing connections that can be easily replaced or reconnected [12].

Additionally, [13] defines key aspects that influence disassembly including accessibility, demountability, separability, and identifiability of connections. Furthermore, six main criteria serve as indicators for the disassembly potential of a building: (1) connection type, (2) connection accessibility,

(3) component independence, (4) geometric composition, (5) surface treatment and finishing, and (6) dismantling damage.

2 METHODS

2.1 Literature selection

The literature review was conducted following a structured multi-step approach. The primary goal of the research was to compile a comprehensive list of DfD constructions and categorise them according to predefined criteria in Table 1.

Table 1 Preselection of literature

Method	Aim	Implementation
Identification	Research question	Which demountable connections exist worldwide that are already being researched, are on the market or are being implemented using a demonstrator?
		What research is needed in the field of demountable connections?
Search strategy	Keywords	Design for disassembly, design for deconstruction, design for reuse, demountable or reversible or deconstructable or dismountable connections
Range	Language	German, english
	Research range	Architecture, civil engineering
	Year	Since 2020

The search process focused on open-access and full-text publications to ensure the availability of complete data for analysis. The literature was retrieved from the following databases and platforms: ResearchGate, ScienceDirect, and Google Scholar. The selected contributions included research reports, conference papers, theses, and peer-reviewed articles.

The initial dataset was refined through a pre-selection phase that removed duplicates and non-relevant publications. The research content of each remaining publication was verified by assessing compliance with three closed (yes/no) questions:

- Is the publication about DfD in construction?
- Is the publication about demountable connections?
- Is the state of the development beyond the theoretical stage?

Publications that did not meet all three criteria (i.e., any "no" answer) were excluded from the final dataset. After defining the framework conditions and completing the preselection of the literature, 24 articles were analysed.

2.2 Categorisation of literature and further research

The preliminary selection of demountable connections was made based on literature research according to the framework conditions in Table 1. After collecting the contributions, they were subsequently step-by-step categorised as in [14]. This system was adapted on the technology readiness levels and describes the development status of the demountable connections from the conceptual idea to practical application. The literature was classified into the following categories:

- **Land** (of the main author): 1 = Europe; 2 = Asia; 3 = Australia
- **Material** (construction material which is connected by the demountable connection): 1 = Reinforced concrete; 2 = Steel; 3 = Timber; 4 = Reinforced concrete and steel; 5 = Reinforced concrete and timber; 6 = Steel and timber
- **Connection** (description of the load transfer of the demountable connection): 1 = Force fit, 2 = Form fit; 3 = Adhesive joint; 4 = Force fit and Form fit; 5 = Form fit and adhesive joint

- **Experimental investigation**: 1 = Cites an experimental setup in the laboratory/in the operating environment; 2 = Experimental setup in the laboratory/ in the operating environment, but it is not the primary method; 3 = Experimental setup in the laboratory or in the operating environment as the primary method
- **Simulation, assessment tool**: 1 = Cites an application of an assessment tool; 2 = Application of an assessment tool, but it is not the primary method; 3 = Application of an assessment tool as a primary method
- **Applied**: 1 = Cites DfD connection with proof of functionality in the field of application (real-life case scenario, demonstrator); 2 = Prototype in laboratory or in use; 3 = Applied DfD connection with proof of successful application
- **Method**: Case study; experimental investigation (e.i.); review; report; thesis

The categories in the "Level of Application" show which application levels are mentioned particularly often and where the focus lies. Therefore, products, components and buildings regarding to disassembly were selected. The categories were ranked according to [14] as follows: 0 = does not appear; 1 = is mentioned in the text; 2 = appears, but it is not the main object; 3 = main object of study.

The 24 papers selected in the literature selection; further research needs were also analysed. Consequently, the articles were searched for the keywords "further research", "research need" and "further investigations". Based on this collection, further research needs are categorised in six categories adapted to [15]. The definition of terms was adapted to demountable connections as it follows:

- Assessment: Indicators and methods for assessing disassembability, as assessment indicator and advanced life cycle assessment for demountable constructions
- Material: Material flow analysis and standards for reused materials and material choice for demountable constructions
- Planning and design: Project guidelines for demolition, construction types and numerical and experimental investigations for demountable connections
- Technology: Data management related to deconstruction and reuse, embedded technologies
- Economics: Business models, reverse logistics, short- and long-term feasibility for reuse products and materials
- Framework: Regulatory policies that influence the circular economy by reuse through obligations or incentives

3 RESULTS

3.1 Catalogue of demountable connections

As explained in chapter 2.1, a total number of 24 papers were analysed based on the preliminary selection. Thereby, 51 connections were identified as demountable connection system and assigned to the categories described in chapter 2.2. The resulting findings are summarised in Table 2.

Table 2 Demountable connection systems and their assignment to categorisation criteria

Key dates					Level of Technology Readiness			Level of Application			Source
Reference	Description	Land	Material	Connection	Experiment	Simulation	Applied	Product	Component	Building	
[3]	Panel-to-panel connection	1	3	1	-	3	3	0	3	3	Case study
[9]	Beam-column joint	2	1	5	3	-	2	0	3	2	e.i.
[9]	Column-foundation joint	2	1	5	3	-	2	0	3	2	e.i.
[9]	Beam-floor connection	2	1	5	3	-	2	0	3	2	e.i.

[10]	bolted beam-column, slab-column connection	1	3	1	-	3	1	0	1	2	Review
[12]	Sherpa connector series XS to XXL	3	3	3	1	1	1	3	3	2	Review
[12]	Rothoblaas UV-T and UV-C connectors	3	3	3	1	1	1	3	3	2	Review
[12]	Sihga HobaFix connector	3	3	3	1	1	1	3	3	2	Review
[12]	Rothoblaas Lock-T and Lock-C connectors	3	3	3	1	1	1	3	3	2	Review
[12]	Knapp Ricon and Gigant connectors	3	3	3	1	1	1	3	3	2	Review
[12]	Knapp Megant connector	3	3	3	1	1	1	3	3	2	Review
[12]	Simpson StrongTie CBH connector	3	3	3	1	1	1	3	3	2	Review
[12]	Pitzl HPV connectors	3	3	3	1	1	1	3	3	2	Review
[12]	GH TOP UV connectors for timber-to-timber	3	3	3	1	1	1	3	3	2	Review
[12]	Eurotec Magnus XS-L connectors	3	3	3	1	1	1	3	3	2	Review
[12]	Rothoblaas X-RAD and X-Mini	3	3	3	1	1	1	3	3	2	Review
[12]	Sherpa CLT connector	3	3	3	1	1	1	3	3	2	Review
[12]	Knapp Zipbolt	3	3	3	1	1	1	3	3	2	Review
[12]	Steel-tube connector	3	3	3	1	1	1	3	3	2	Review
[12]	Timberlinx connector	3	3	3	1	1	1	3	3	2	Review
[12]	U-shaped flexural plates	3	3	3	1	1	1	3	3	2	Review
[12]	timber-concrete-composite	3	3	3	1	1	1	3	3	2	Review
[12]	Dovetail beam-column joints	3	3	3	1	1	1	3	3	2	Review
[12]	Moitoise and tenon beam-column joints	3	3	3	1	1	1	3	3	2	Review
[12]	Beam half-lap and dovetail joints	3	3	3	1	1	1	3	3	2	Review
[12]	Roof truss step joints	3	3	3	1	1	1	3	3	2	Review
[12]	GSA System	3	3	3	1	1	1	3	3	2	Review
[12]	EXPAN/ Quick connection system	3	3	3	1	1	1	3	3	2	Review
[13]	Lösbare Konusverbindung	1	3	4	1	1	3	2	2	3	Report
[13]	Buchenfurnierschichtholz Knagge	1	3	2	1	1	3	2	2	3	Report
[13]	x-fix, gefräste Nocken	1	3	2	1	1	3	2	2	3	Report
[16]	Bolted connection	1	3	2	-	2	3	0	2	3	Case study
[17]	UQ-SHERPA LTF panel connector	3	3	4	3	2	2	3	2	1	Thesis
[18]	Demountable shear connection with threaded studs	1	4	5	2	-	3	0	3	3	Case study
[18]	Demountable shear connection with embedded nuts	1	4	5	2	-	3	0	3	3	Case study
[18]	Demountable shear connection with friction-grip bolts	1	4	2	2	-	3	0	3	3	Case study
[18]	Demountable shear connection with bolts with a coupler system	1	4	5	2	-	3	0	3	3	Case study
[19]	Demountable timber-concrete composite floor	1	5	1	2	3	-	0	3	0	Case study
[20]	Self-taping screw	1	5	1	3	-	2	3	2	0	e.i.

[21]	Demountable shear connection	1	4	2	3	3	-	0	3	1	Thesis
[22]	Demountable steel-concrete composite with reduced web section	1	4	2	3	-	2	0	3	0	e.i.
[23]	Demountable timber-concrete composite floor system	1	5	4	3	3	2	0	3	0	e.i.
[24]	Demountable steel-timber composite beams	1	6	4	3	1	2	0	3	0	e.i.
[25]	Demountable steel-timber composite beams	1	6	4	3	1	2	0	3	0	e.i.
[26]	Demountable RC Beam with bolted connection	2	1	2	3	2	2	0	3	0	e.i.
[27]	Epoxy Resign-Bolted Steel-Cross laminated timber connections	2	2	5	3	-	2	0	3	0	e.i.
[28]	Steel-yielding demountable bolt	2	1	2	3	2	2	0	3	0	e.i.
[29]	Embedded node	2	2	2	3	3	2	0	3	0	e.i.
[30]	Locking bolt demountable shear connectors	2	4	5	3	2	2	0	3	0	e.i.
[31]	Clamped bolted joint	1	2	2	-	3	1	0	3	2	e.i.
[32]	Deconstructable splice joints	2	1	2	2	3	2	0	3	0	e.i.

Other demountable connections that are not included in the list due to the preselection include like lego inspired solutions like RecoBlox^{TM} [33], timber shear connections for robotic assembly [34] or Triqbriq [35]. Or a similar design to x-Fix the hilti clt panel-to-panel connector [36].

However, more of the half of the studies on demountable connections originate from Europe (59%), indicating a strong research focus in this region. Asia follows with roughly one third of the publications. At this point, it should be mentioned that due to the preselection criteria of the literature in Table 1, no papers from Africa were included in the analysis. Furthermore, contributions from America were not considered, as the found publications deal with theoretical approaches rather than practical implementations.

When comparing the construction materials, timber clearly dominates with nearly 60% of all identified demountable connections. Steel and reinforced concrete hybrid systems account for around 13%, closely followed by connections within reinforced concrete structures at 12%. In terms of load transfer, adhesive joints are the most common with 45%, while form-fitted joints follow with 21%.

Examining the level of technology readiness, about 80% of publications reference or conduct experimental studies related to demountable connections, even if testing is not always the primary research method. Simulations and assessment tools are also widely used, with close to 80% of studies employing or referencing them. Furthermore, 91% of the reviewed papers discuss successful implementations, either as laboratory prototypes or realized applications. Yet again, 59% do not exceed laboratory conditions.

Regarding the level of application, explicit products implementing demountable connections are mentioned in around 14% of the contributions. In 77% of cases, disassembability is primarily applied at the component level. Only 20% of the publications report the use of such components within buildings or demonstrators.

3.2 Research needs

According to chapter 2.2 future demands of research gaps of demountable connections were clustered in six categories. In the following sub-headings, the need for research is discussed:

3.2.1 Assessment

Many studies deal with the topic of the circular economy. Nevertheless, there is still a need to systematically identify existing gaps in research [13]. There is a fundamental lack of suitable pilot projects for studies and findings derived from them [13, 31]. The findings from the studies should be developed to material-specific guidance for the implementation of design for adaptability and reuse [3].

Furthermore, the development and evaluation of efficient and standardised criteria is of central importance for the investigation of the circular economy in construction. Data should serve as the basis for quantitative collection and analysis to be able to evaluate the recyclability of buildings. Another key objective is to systematically research and standardise the concept of design for manufacturing, assembly and deconstruction [10, 13]. It also points out that specific assessment procedures for the dismantling of individual building materials must be developed in order to ensure material-appropriate and practical analyses [10].

Another focus of research is the integration of circular approaches into existing building and product certification systems. In addition, there is a need to develop suitable teaching and training materials in order to anchor the concept of the circular economy in construction more firmly in education and practice [13].

3.2.2 Material

The identified research needs focus on wood and concrete as materials. In the field of timber construction, an in-depth investigation of the effects of moisture effects is required [12]. Similarly, alternative timber preservative treatments and potential for reuse must be investigated [3]. Additional studies are necessary systematically analyse the age effect on different timber materials [16].

Demountable connections were also investigated by reinforced concrete constructions. Therefore, further research needs are available for other mixtures like green concrete [19].

3.2.3 Planning and Design

Comprehensive experimental investigations are necessary to further develop removable and reusable structures. Tests are necessary to ensure that they are considered in the design phase [10]. This includes, the development of analytical models for predicting their mechanical properties [20].

Developing analytical models are also necessary for Calculating and designing demountable shear connection [9, 18, 23, 26, 28]. Further experimental investigations, such as push-out tests [19, 21, 23, 30] and bending tests [18, 23], is necessary to better understand the load-bearing and failure behaviour. In addition, reverse-cyclic loading must be examined [12, 22, 30]. Various authors recommend additional experimental investigations on different system types under varying load scenarios [12, 18].

To date, the re-disassembly capability of connections has only been tested in a few cases. The performance of multiple disassembly and reassembly processes has hardly been investigated and requires in-depth research [10, 12, 20, 21, 32]. In addition, a possible second use should be carried out [21].

Finally, the potential of disassembly must be calculated by displaying the structural and accessibility dependencies at connection and product levels [10]. Further examples of planning approaches and collaborations established by changing the design are needed [13, 16, 24, 25]. For that different types of connections, arrangements of connections, variations could be investigated [24, 25].

3.2.4 Technology

Further research is needed into the implementation and further development of the building information modelling method, particularly with regard to the integration of a deconstruction model [13].

In addition, the application of other digital technologies such as virtual and augmented reality could contribute to supporting planning, training and dismantling processes [13]. Similarly, more research is needed on the application of artificial intelligence order to develop a systematic methodology [17].

3.2.5 Economics

The logistics of the demountability must be developed [13].

3.2.6 Framework

The legal framework play a decisive role in supporting the decision-making processes of the circular economy in the construction industry [2]. However, there are currently no concrete recommendations for legislative changes that could promote greater implementation of the circular economy [13].

4 CONCLUSIONS

A comprehensive literature review was conducted and defined categories were evaluated. In addition, research needs were filtered from the papers and categorised. Based on the findings the following conclusions can be drawn:

- While over 90% of the reviewed works include testing or simulation, future work should focus on real-life applications and repeated disassembly processes to assess long-term performance.
- Demountable connections can be further adapted to other materials.
- There has been significant research and development into demountable connections for timber structures. Nevertheless, there is still a great need for further research. Research into green concrete also requires further investigation.
- Product data claims that connections can be dismantled. How they function in this regard in terms of connection accessibility, component independence, and dismantling damage must be questioned and further researched.
- Overall, the findings indicate a research trend focusing on component-wise approaches, while several demountable connection products have already been developed.
- In summary, experiments, simulations, and applications are each referenced in nearly half of the analysed studies, although the step beyond laboratory environments remains limited to roughly 18-29% of the cases.

References

[1] Sobek, Werner. 2021. Geschäftsbericht: 17 Thesen.

[2] Achatz, Astrid et al. 2021. Kreislaufbauwirtschaft. (Wien).

[3] Walsh, St John, and Elizabeth, Shotton. 2024. "Integrating Design for Adaptability, Disassembly, and Reuse into Architectural Design Practice." sustainability.

[4] Passarelli, Rafael Novais. 2022. Design for robustness, adaptability, disassembly and reuse, and repairability of taller timber buildings: a state of the art report.

[5] Grüter, Cäsar et al. 2023. "Design for and from disassembly with timber elements: strategies based on two case studies from Switzerland." frontiers built environment: https://doi.org/https://doi.org/10.3389/fbuil.2023.1307632.

[6] Ostapska, Katarzyna et al. 2024. "Design for Disassembly: A systematic scoping review and analysis of built structures Designed for Disassembly." Sustainable Production and Consumption: https://doi.org/10.1016/j.spc.2024.05.014.

[7] Akinade O. Olugbenga et al. 2017. "Design for Deconstruction (DfD): Critical success factors for diverting end-of-life waste from landfills." Waste Manag: https://doi.org/10.1016/j.wasman.2016.08.017.

[8] Renette, Hannes, Tomas, Gecys, and Lin, Wan-Wendner. 2025. "The impact of demountable connections on effective use of materials in timber structures." IABSE Congress.

[9] Zhang, Ruijun, Tong, Guo, and Aiqun, Li. 2024. "Experimental investigation into demountable dry connections for fully precast frame structures through shaking table tests." Thin-Walled Structures.

[10] Attia, Shady et al. 2024. "Disassembly calculation criteria and methods for circular construction." Automation in construction.

[11] Van Gulck, Lisa, and Marijke, Steeman. 2023. "Life cycle assessment of demountable building elements: Influential design and use parameters." Building and Environment. https://doi.org/10.1016/j.buildenv.2023.110876.

[12] Ottenhaus, Lisa-Mareike et al. 2023. "Design for adaptability, disassembly and reuse – A review of reversible timber connection systems." Construction and Building Materials: https://doi.org/https://doi.org/10.1016/j.conbuildmat.2023.132823.

[13] Schuster, Sandra, and Sonja, Geier. 2023. circularWOOD Paradigmenwechsel für eine Kreislaufwirtschaft im Holzbau. (Bonn: Stadt- und Raumforschung (BBSR) im Bundesamt für Bauwesen und Raumordnung (BBR) Bundesinstitut für Bau).

[14] Chiletto, T. O., E. Knapen, and R. N. Passarelli. 2024. "Design for Disassembly and Reuse A Synthesis for Timber Construction." IOP Conference Series: Earth and Environmental Science.

[15] Ahn, Namhyuck et al. 2022. "Circular economy in mass timber construction: State-of-the-art, gaps and pressing research needs." Journal of Building Engineering. https://doi.org/10.1016/j.jobe.2022.104562.

[16] Sandin, Ylva, Marlene, Cramer, and Karin, Sandberg. 2023. "How timber buildings can be designed for deconstruction and reuse in accordance with ISO 20887." World Conference on Timber Engineering, Oslo.

[17] Yan, Zidi. 2024. "Design and Performance Evaluation of reversible Connections for Modular Adaptable timber buildings." School of Civil Engineering, University of Queensland.
[18] Jakovljevic, Isidora, Milan, Spremic, and Zlatko, Markovic. 2024. "Towards circular construction: The second life cycle of steel-concrete composite structures." Savremena Gradevinska Praska.
[19] Eslami, Hooman, Laddu, Bhagya Jayasinghe, and Daniele, Waldmann. 2023. "Experimental and Numerical Investigation of a Novel Demountable Timber–Concrete Composite Floor." Buildings 13. https://doi.org/10.3390/buildings13071763.
[20] Derikvand, Mohammad, and Gerhard, Fink. 2021. "Deconstructable connector for TCC floors using self-tapping screws." Journal of Building Engineering.
[21] Jakovljević, Isidora. 2022. "DEMOUNTABLE SHEAR CONNECTIONS WITH BOLTS AND WELDED HEADED STUDS IN STEEL-CONCRETE COMPOSITE STRUCTURES."
[22] Almutairi, Fahad Falah et al. 2023. "Experimental investigation using demountable steel-concrete composite reduced web section (RWS) connections under cyclic loads." Bulletin of Earthquake Engineering: 1081-1110. https://doi.org/10.1007/s10518-023-01802-y.
[23] Eslami, Hooman. Jayasinghe, Laddu Bhagya, and Waldmann, Daniele. 2024. "Experimental and numerical study on shear behavior of a demountable CLT-concrete composite shear connection." Construction and Building Materials. https://doi.org/10.1016/j.conbuild-mat.2024.135982.
[24] Romero, Alfredo, and Odenbreit, Christoph. 2024. "Innovative demountable steel-timber composite (STC) beams: Experimental full-scale bending tests." Engineering Structures. https://doi.org/10.1016/j.engstruct.2024.118599.
[25] Romero, Alfredo, and Christoph, Odenbreit. 2024. "Experimental investigation on novel shear connections for demountable steel-timber composite (STC) beams and flooring systems." Engineering Structures. https://doi.org/10.1016/j.engstruct.2024.117620.
[26] Wu, Dongping, Yan Liang, Huachen, Liu, and Sheng, Peng. 2025. "Behavior of Demountable and Replaceable Fabricated RC Beam with Bolted Connection Under Mid-Span Compression." Buildings. https://doi.org/10.3390/buildings15152589.
[27] Lyu, Qing et al. 2025. "Experimental Study on the Shear Performance of Epoxy Resin-Bolted Steel-Cross Laminated Timber (CLT) Connections." Buildings. https://doi.org/10.3390/buildings15183400.
[28] Xiong, Liquan et al. 2025. "Sustainable steel-concrete composite beams with novel demountable shear connections under positive bending moments: experimental behavior and analytical model." Bulletin of Earthquake Engineering: 5807-5836. https://doi.org/10.1007/s10518-025-02248-0.
[29] Liu, Cong et al. 2025. "Flexural behaviour of a new modular and demountable truss beam with embedded nodes." Developments in the Built Environment. https://doi.org/10.1016/j.-dibe.2025.100636.
[30] He, Jun et al. 2024. "Cyclic inelastic performance evaluation of locking bolt demountable shear connectors in steel-concrete composite structures." Engineering Structures. https://doi.org/10.1016/j.engstruct.2024.118690.
[31] Pereiro, Xabier et al. 2023. "BIM methodology for cost analysis, sustainability, and management of steel structures with reconfigurable joints for industrial structures." Journal of Building Engineering. https://doi.org/10.1016/j.jobe.2023.107443.
[32] Fan, Junwei et al. 2022. "Research on seismic behaviour of square steel tubular columns with deconstructable splice joints." Journal of Constructional Steel Research. https://doi.org/10.1016/j.jcsr.2022.107204. https://www.sciencedirect.com/science/article/abs-/pii/S0143974X22000761?via%3Dihub.
[33] Bao, Yi, and Victor, C. Li. 2020. "Feasibility study of lego-inspired construction with bendable concrete." Automation in Construction. https://doi.org/10.1016/j.autcon.2020.103161.
[34] Hansen, Søren Gustenhoff, Anja, Kunic, and Roberto, Naboni. 2021. "A reversible connection for robotic assembly of timber structures." Engineering Structures. https://doi.org/10.1016/-j.engstruct.2021.112795.
[35] Wörner, Maximilian, and Jürgen, Reichert. 2026. "Triqbriq." Accessed 18.01.2026. https://triqbriq.de/.
[36] Hilti Aktiengesellschaft, 2025. [Online]. Available: https://productdata.hilti.com/APQ_-HC_RAW/ASSET_DOC_23268754.pdf.

Effect of Recycled Aggregates and Portland Composite Cements on the Performance of Sprayed Concrete

Zdeněk Hlavsa[1], **Barbara Kucharczyková**[2], **Jan L. Vítek**[1]

[1]*Faculty of Civil Engineering,*
Czech technical university in Prague,
Thákurova 2077/7, 166 29 Prague 6, Czechia

[2]*Faculty of Civil Engineering,*
Brno University of Technology,
Veveří 95, 602 00 Brno, Czechia

Summary
This paper examines the feasibility of using recycled aggregates and Portland composite cements in sprayed concrete to reduce environmental impact while maintaining performance. A pilot experiment evaluated setting behaviour, early-age strength development and mechanical properties of cement mortars incorporating different composite cements, alkali-free accelerators, and recycled aggregates. Solidification and early-age hardening were continuously monitored for 24 hours using the ultrasonic method. The results showed that composite cements, particularly CEM II/A-LL and CEM II/A-S, outperformed Ordinary Portland Cement when combined with suitable accelerators. Carbonated recycled cement paste accelerated setting and enhanced early-age strength, while recycled aggregates reduced long-term strength depending on their quality. Overall, the study highlights the potential of more sustainable binder–aggregate systems for sprayed concrete, however, further optimisation is needed.

1 INTRODUCTION

The concrete industry is facing increasing sustainability challenges due to high CO_2 emissions from cement production and the depletion of natural resources, such as aggregates and fresh water. Using recycled aggregates (RAs) helps to address the depletion of natural resources while reducing the demand for landfilling construction and demolition waste [1,2]. Similarly, Portland composite cements reduce clinker content by incorporating supplementary cementitious materials (SCMs), which significantly reduces embodied carbon while maintaining adequate mechanical and durability performance.

Sprayed concrete technology is widely used in underground construction, slope stabilisation, and other applications. Tunnels built using the New Austrian Tunnelling Method (NATM) are the prime example of this method's use. The conventional sprayed concrete mix usually relies on an effective combination of cement and an accelerating admixture. The performance requirements focus on pumpability, sprayability, early strength development and adhesion to the substrate.

Although incorporating RA into concrete can be environmentally beneficial, it can also affect the concrete's performance. The quality and proportion of recycled aggregate in concrete determine its performance. The higher porosity and associated water absorption of RA, together with a higher content of fine particles, can affect the hydration process of concrete in its early stages, mainly through altering internal moisture distribution and increasing water demand.

Until recent years, Ordinary Portland Cement (OPC) was the gold standard in sprayed concrete technology. Its high clinker content provided rapid hydration and early strength development, which are crucial for conventional sprayed concrete applications. However, the OPC is gradually being replaced by Portland composite cements aiming to reduce the carbon emissions of the cement industry. These cements include additional constituents, such as limestone, ground granulated blast-furnace slag (GGBS) and different types of SCMs, which can affect early hydration and strength development. This shift requires producers of chemical additives and concrete technologists to find new solutions in this important field.

Accelerators are necessary components of sprayed concrete, enabling rapid setting and early-age strength development. Previously used alkali-based accelerators are being replaced by alkali-free

accelerators, which eliminate the risk of alkali-aggregate reaction, reduce loss of long-term strength, and create a safer operating environment. Current research focuses on optimising alkali-free accelerators for use with Portland composite cements and new types of aggregates [3].

Sprayed concrete is commonly tested on-site using penetration resistance-based methods, such as penetrometer or pin penetration tests, in accordance with EN 14488-2. However, field testing of sprayed concrete is expensive and often difficult to organise. Laboratory testing of sprayed concrete without a concrete spraying machine is difficult, as the introduction of accelerating admixtures into the mix significantly reduces workability time. Standardised methods for evaluating the setting time in conventional concrete, such as the Vicat penetration resistance-based method according to EN 196-3, are insufficient for yielding meaningful results. As alternatives to penetration resistance-based methods, rheological and stiffness-based methods, such as the ultrasonic pulse velocity method, which monitors the increase in wave velocity during solidification and early-age hardening of concrete, may be adequate for laboratory testing of sprayed concrete [4].

This paper presents a pilot experimental programme that uses the ultrasonic pulse velocity method to determine the setting and early-age strength development of sprayed concrete. It provides novel insights into the performance of Portland composite cements with alkali-free accelerators, as well as the impact of RA on the performance of sprayed concrete.

2 EXPERIMENTAL PROGRAMME

This experimental programme is the next step in an ongoing research project to assess the feasibility of using RA in sprayed concrete. The broader goal of this ongoing research is to design a sprayed concrete mix with a high RA content that meets the requirements for sprayed concrete commonly used in tunnel structures. This experimental programme investigates how four commonly available accelerators perform with the most common Portland composite cements used in the Czech Republic, and compares their performance with OPC. Furthermore, the influence of three types of RA and one type of natural aggregate (NA) on the solidification process and early-age strength development is investigated.

The experimental programme is divided into two parts. The first part examines the performance of accelerating admixtures when used with different cements. All mixes in this section are made using standard CEN sand. The second part observes the influence of aggregates. One mix containing NA and three mixes containing RA are compared with the mix containing CEN 196-1 sand. In this case, the best cement and accelerator combination identified in the first part was used.

2.1 Materials

The experimental programme used four types of cement and one SCM. Ordinary Portland Cement CEM I 42.5 R (PC) from the Radotín cement plant was used as the reference cement. Three Portland composite cements widely available in the Czech Republic were used as alternatives to OPC to reduce the carbon footprint of the concrete mix. The following composite cements were used: CEM II/B-M (S-LL) 42.5 N (BM) and CEM II/A-LL 42.5 R (AL) from the cement plant Radotín, and CEM II/A-S 42.5 R (AS) from the cement plant Mokrá. All cements were produced by Heidelberg Materials CZ.

A carbonated recycled cement paste (CRCP) was used as a new type of SCM in this experiment. CRCP is produced from cement paste that is separated from sand and coarse aggregate during the recycling process of old concrete. The cement paste is then wet carbonated producing a new material that can be used as an SCM in the production of new types of cement or in concrete itself. In this case, the CRCP was used to partially replace Portland cement (20%, in this particular case), aiming to create a binder similar to the other blended cements used in the experiment. CRCP is an innovative way to reduce carbon emissions associated with cement production, as it binds CO_2 into its structure during carbonation and reduces cement consumption. Furthermore, CRCP utilises the finest fraction of recycled concrete aggregate, which is difficult to incorporate into concrete mixes due to its increased water demand and negative effect on the concrete performance. Additionally, the pozzolanic reaction of CRCP is more rapid than that of fly ash or ground granulated blast-furnace slag, which could favour its use in sprayed concrete [5].

The first part of the experimental programme involved the use of four commonly used accelerating admixtures for sprayed concrete applications in the Czech Republic. The following accelerators were used: MasterRoc SA 193 (A1), produced by MBS CZ-SK s.r.o.; Sika® Sigunit® L-93 AF (A2), produced by Sika CZ, s.r.o.; EKOSAL L (A3), produced by Stachema CZ s.r.o.;

and CHRYSO®Jet 10 AF (A4), produced by Chryso Chemie s.r.o. All of the accelerators used were in liquid form and alkali-free.

Throughout the entire experimental programme, CHRYSO®Quad 915 was used as a plasticiser to reduce the water requirement of each mix. This plasticiser is specially designed for use with concrete incorporating recycled aggregates. Its performance was previously verified by the author, who compared several commercially available plasticising admixtures in an experimental programme focused on the workability of sprayed concrete with recycled aggregates. CHRYSO®Quad 915 yielded the best results of all the tested admixtures and was therefore chosen for further experimental work [6].

Tap water was used throughout the entire experimental programme.

In the first part of the experimental programme, which focused on observing the performance of accelerating admixtures with individual cements, a standardised CEN sand (CN) was used in all mixes to eliminate the influence of aggregates on the hydration process, early-age stiffening, and hardening of the cement mortar. In the second part, four different types of aggregate were introduced. Natural aggregate (NA) consisted of a blend of two natural river sands produced in the Otradovice (OT) and Zálezlice (ZL) quarries, mixed in an OT:ZL ratio of 1:2. Recycled mixed aggregate produced by the recycling plant Kare (KR), Prague. Finally, two types of recycled concrete aggregate: one produced by a recycling plant in Dąbrowa Górnicza (GR) with an advanced recycling procedure that also produces recycled cement paste which is further used for the production of CRCP; the second was produced by a Lavaris (LV) company recycling machine that is part of a pilot production test of a high-quality RCA in Prague. Table 1 shows the basic properties of all the aggregates. The particle size distribution of the aggregates used is shown in Fig. 1. The lower and upper limits represent the recommended particle-size distribution for aggregates in sprayed concrete, as specified in the Austrian guideline [7].

Table 1 The properties of aggregates used in the experiment.

Aggregate type	CN	OT	ZL	GR	KR	LV	Method
Fineness modulus [%]	0.6	1.4	0.9	3.8	6.2	3.9	EN 933-1
Oven dried particle density [kg/m^3]	2540	2530	2520	2140	2050	2160	EN 1097-6
Loose bulk density [kg/m^3]	1690	1460	1560	1310	1250	1320	EN 1097-3
Water Absorption [%]	0.6	0.7	0.9	6.7	6.9	5.4	EN 1097-6

2.2 Mix design and specimen preparation

In the first part of the experimental programme, a plan of twenty-five cement mortar mixes was carried out. Each mortar type was prepared in five variants: one without an accelerator and four containing different types of accelerators (see section 2.1). Standardised CEN sand was used as an aggregate.

In the second part, eight mortar mixes were carried out. In this case, CEM II/A-LL 42.5 R was used exclusively as a binder, combined with the MasterRoc SA 193 accelerator and the aggregates listed in Table 1 (see section 2.1).

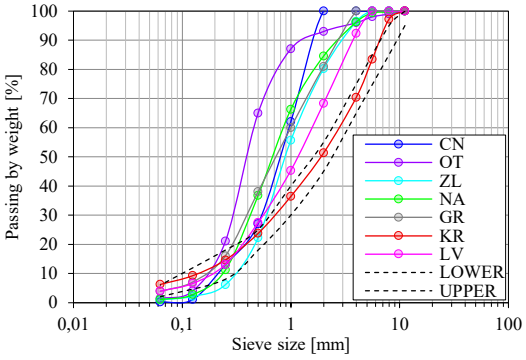


Fig. 1 Particle size distribution of aggregates.

The composition of all the mixes manufactured in the first and second parts was the same. The ratio of components followed the composition of standard cement mortar given in EN 196-1 [8], except for the water content, which was reduced according to the plasticiser addition. The final water-to-binder ratio was 0.45. The plasticiser and accelerator doses were 0.8% and 6% of the binder mass, respectively. The component dosages are listed in Table 2.

Table 2 Cement mortar mix composition.

Constituent	Binder	Aggregate	Water	Plasticiser	Accelerator
Quantity [g/batch]	450	1350	202.5	3.6	27

Four batches of cement mortar were produced for each mix variant. One batch was used to monitor the solidification and early-age hardening, while the other three were used to produce mortar prisms to determine strength characteristics. The mixing procedure followed the EN 196-1 standard [8]. After the four-minute mixing cycle, the consistency of the fresh mortar was tested in accordance with EN 1015-3. The mortar used for the consistency test was returned to the mixing container and homogenised with the remaining batch. In total, three sets of prismatic specimens (40×40×160 mm, three pieces in each) and one specimen for monitoring solidification were produced for each mortar type. For a mix without an accelerating admixture, the specimens were produced immediately. For the mix with an accelerating admixture, the bowl with the fresh mix was returned to the mixer, and a high-speed mixing cycle of approximately 20 seconds was initiated, with the accelerator applied directly into the mix by syringe during the first five seconds. The specimens were manufactured within the next five minutes. Compaction of the fresh mortar was performed on a vibration table for each mix in the same manner. The cement mortar prisms were stored and cured in the mould for the first twenty-four hours. After demoulding, the prisms were placed in a water tank until the day of testing.

The hardened cement mortar was evaluated for bulk density, compressive strength and tensile strength at 2, 7 and 28 days, in accordance with EN 1015-10 and EN 1015-11, respectively. Three specimens were used for the flexural strength test at each age. After the three-point bending test, the resulting prism halves were used to determine the compressive strength. In total, six specimens were used to determine the compressive strength at each age. The batches were produced individually, primarily due to the rapid reaction of the accelerating admixtures and the limited time available to prepare the specimens.

A total of 132 batches of fresh mortar were produced, 297 prisms were tested for tensile strength, and 594 prism halves were tested for compressive strength.

2.3 Monitoring of the solidification process by the ultrasonic method

The ultrasonic (US) device Vicasonic (Schleibinger Geräte) was used to continuously monitor the solidification process. The measuring cell consisted of a Vicat ring enclosed between the bottom and upper parts with an embedded receiver and transmitter, respectively. Both US transducers, operating at 54 kHz, were set to transmit 60 pulses per minute, with a signal level of 2000 V and a logging interval of 60 seconds. The transducer surfaces were coated with a coupling gel and a PE foil to prevent direct contact with the poured material. The apparatus was also equipped with a thermocouple wire, which was introduced through the aperture in the upper part of the cell. This setup enabled continuous, non-invasive monitoring of the hydration process by simultaneously measuring US pulse transmit time and internal temperature in materials cured under conditions that prevent moisture exchange between the specimen and the surrounding environment. The measurement cell was placed in a Q-Cell incubator to maintain a stable ambient temperature of (21±0.5)°C during the measurements. The US pulse velocity (vL) was calculated from the transmit time and the measurement path (the height of the specimen placed in the Vicat ring) to interpret the results. This measurement began just after pouring the fresh-state material, which was 10–15 minutes after the start of mixing.

3 RESULTS AND DISCUSSION

In this section, the results of the experimental programme are presented. A colour palette was designed to aid orientation among the various mixes. Mix designations consist of the cement type and the accelerating admixture (e.g., PC-A0 refers to CEM I without an accelerating admixture). Mixes

containing CEM I and CRCP (as a 20% substitute for CEM I) are denoted as RP. The CEN sand was always used as an aggregate.

The results for the consistency tests performed on fresh mortars before the application of an accelerator are shown in Fig. 2. The heights of the bars and error bars represent the average value and standard deviation of the results across the tested batches. The consistency varied depending on the type of cement tested. The type of cement and its chemical composition can significantly influence the effectiveness of the plasticiser used. In this case, mixes with A-S and B-M cements (containing GGBS), reported higher slump-flow values, whereas mixes with CEM I reported the lowest values. The consistency of the fresh mortar decreased significantly for all mixes after the accelerator was applied. Mixes containing accelerators A1, A2 and A4 showed a steep decrease in consistency, resulting in a semi-dry mix that was difficult to cast into moulds. The consistency of the A3 mix decreased the least and could still be easily compacted. However, it was not possible to measure the slump flow; therefore, no values are reported.

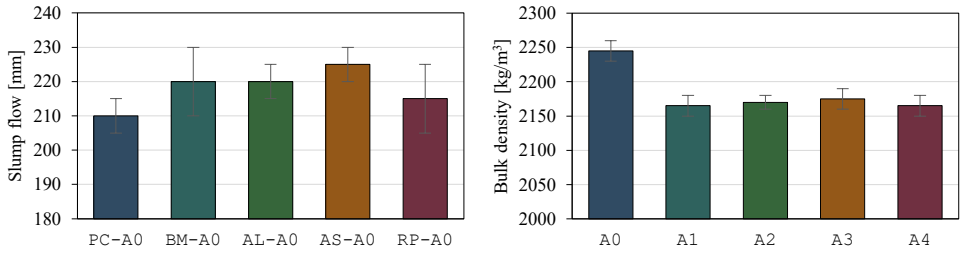


Fig. 2 Consistency of fresh mortar without accelerator (left); Bulk density of hardened cement mortar after 28 days of curing, influence of accelerating admixture (right).

The results for the bulk density of hardened cement mortars after 28 days of curing are shown in Fig. 2. Mixes with an accelerator admixture had a bulk density approximately 4% lower than those without an accelerator. This decrease was consistent across the accelerators used. There were no significant differences in the bulk density among specimens tested at 2, 7 or 28 days.

The results of the tensile strength and compressive strength tests on hardened cement mortar prisms after 2, 7 and 28 days of curing are shown in Fig. 3 and Fig. 4, respectively. Generally, the AL and AS mixes exhibited similar strength characteristics to the PC mixes at the same testing ages. However, BM and RP mixes reported tensile and compressive strength values about 20% lower after 2 and 7 days, but comparable after 28 days, with tensile strength even higher than those for PC.

Accelerating admixtures primarily influenced the 2-day, increasing tensile and compressive strength by an average of 40% and 13%, respectively, across the tested accelerators and types of cement. The highest increase, an average of 47% for tensile strength and 17% for compressive strength, reported mixes with A4. Among the tested cements, RP mixes with accelerators exhibited tensile and compressive strengths that were on average 89% and 19% higher, respectively, after two days compared to mixes without accelerators. This may indicate a positive influence of CRCP on the efficiency of accelerating admixtures and early-age strength development. However, the mixes with RP reported lower strength than those with other cement types. Therefore, a lower substitution rate of cement by CRCP, or its use alongside cement, can be considered for further testing. Among the tested accelerating admixtures, A1 showed the lowest increase in 2-day strength and a more negative effect on the strength at later ages than the other accelerators. On average, mixes with Portland composite cements had a higher tensile strength than PC mixes, whereas the compressive strength was lower in all cases.

The results of the solidification process and early-age hardening of cement mortars, measured using the ultrasonic method, are shown in the series of graphs in Fig. 5. The order of the curves for the reference mixes without accelerator along the time axis is consistent with the initial expectations based on the known properties of the cements. RP mixes containing CRCP showed an accelerated hydration process of approximately one hour compared with the mix containing only CEM I (PC). Regarding the cements with accelerators, CEM II/A-S (AS) and CEM II/A-LL (AL) reported the shortest initial setting time and the fastest early-age strength development. Whereas PC mixes reported the worst performance across all accelerators used. RP mixes reported the shortest initial setting time. However, subsequent strength development was slower than that of mixes with other cements.

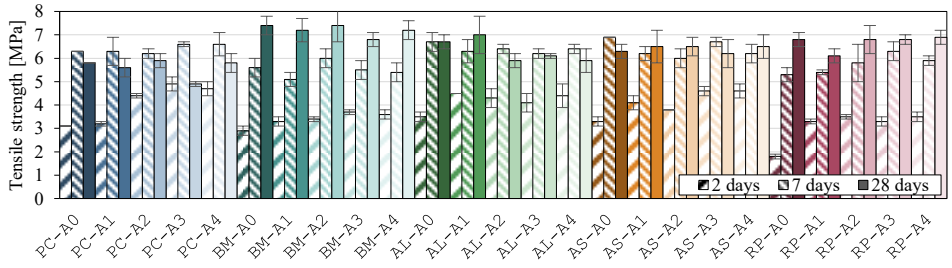


Fig. 3 Tensile strength of cement mortar prisms at the age of 2, 7, and 28 days.

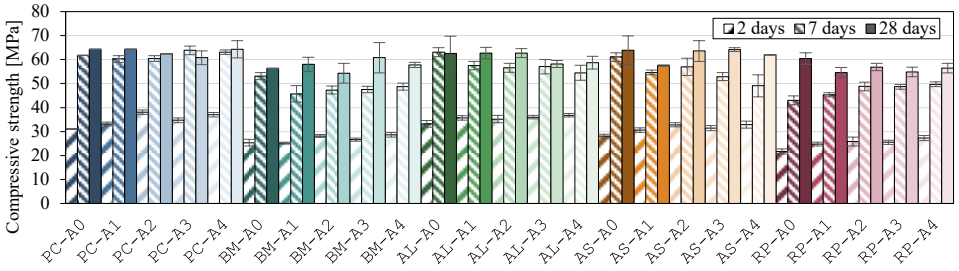


Fig. 4 Compressive strength of cement mortar prisms at the age of 2, 7, and 28 days.

The performance of accelerators varied across the tested cement types indicating the importance of finding the optimal combination of cement and accelerator. Generally, the best performance was reported equally by MasterRoc SA 193 (A1) and Sigunit® L-93 AF (A2). Chryso®Jet 10 AF (A4) had similar results but underperformed in combination with CEM I. Whereas Ekosal L (A3) showed the worst results across all mixes.

Based on the results of the first part of the experimental programme, CEM II/A-LL and Master-Roc SA 193 were selected for the second part, which aims to investigate the influence of recycled aggregate. In this case, the aggregate type and accelerator were used to distinguish the mixes (e.g. CN-A0 refers to CEN sand without an accelerating admixture).

The strength characteristics of cement mortar mixes with different types of aggregates, tested after 2, 7, and 28 days of curing, are shown in Fig. 6. Mixes with recycled aggregates KR and GR reported lower tensile and compressive strength after 28 days, by up to 40% and 54% respectively, compared to mixes with CEN sand. In contrast, mixes with natural aggregate and recycled aggregate LV showed 10% and 17% decrease in tensile and compressive strength, respectively. The influence of recycled aggregate was less pronounced at early ages.

The last graph in Fig. 5 (bottom right-hand side) shows the solidification process and early-age stiffness development for mixes with different types of aggregates. All tested aggregates were found to have a significant influence on stiffness development within the first twenty-four hours. The mix with natural aggregate (NA) exhibited a trend similar to that of the mix with CEN sand up to the first six hours, after which the rate slowed. In general, the mixes with recycled aggregates exhibited slower solidification from the outset. Furthermore, the solidification process appears to slow down in later stages. The mix with recycled aggregate KR without accelerator exhibited a significantly faster initial setting time than the other mixes. This may be due to ongoing water absorption into the aggregate's pores, which decreases free water in the cement paste and accelerates setting time.

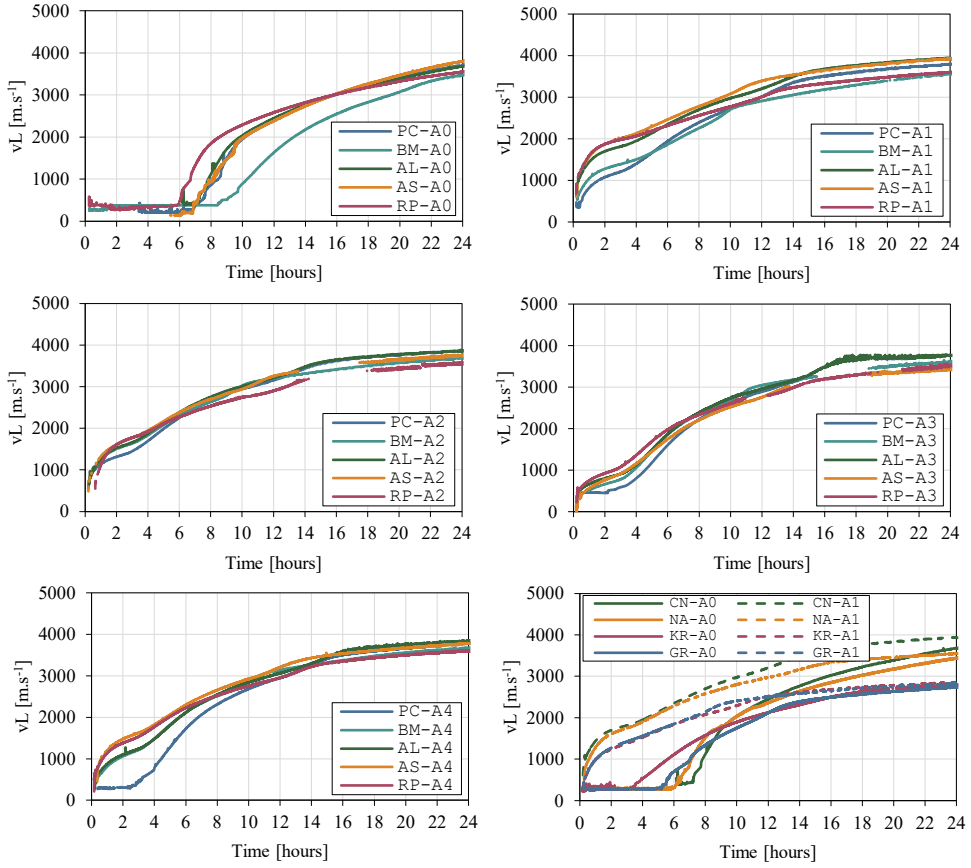


Fig. 5 Solidification process and early-age hardening of cement mortars measured by ultrasonic method.

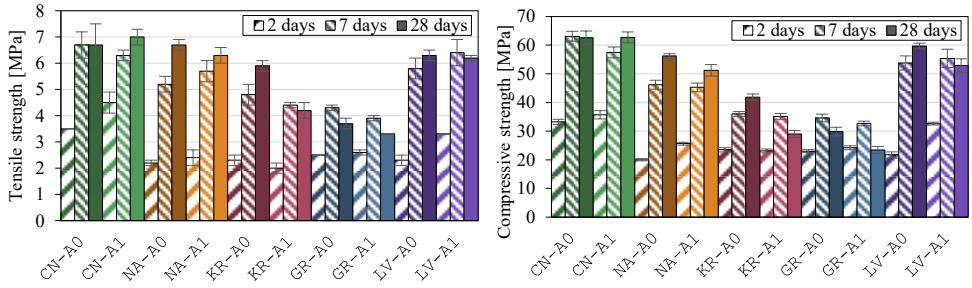


Fig. 6 Strength characteristics of cement mortar mixes with different types of aggregates tested after 2, 7, and 28 days of curing. Tensile strength (left). Compressive strength (right).

4 CONCLUSIONS

An extensive experimental programme was conducted to evaluate the performance of Portland composite cements with commercially available accelerating admixtures intended for use with sprayed concrete. An ultrasonic method was employed to monitor the solidification process and the development of early-age strength in cement mortars. Furthermore, the influence of recycled aggregate on setting and early-age strength development was evaluated. The results can be summarised as follows:

- Among the tested cements, mixes containing CEM II/A-LL or CEM II/A-S performed best in combination with an accelerating admixture. In contrast, mixes containing CEM I produced the worst results across the tested mixes, contrary to initial expectations.
- Among the tested accelerators, MasterRoc SA 193, Sigunit® L-93 AF and Chryso® Jet 10 AF performed comparably across the tested mixes. Ekosal L performed considerably worse, with a much slower start compared to the other accelerators.
- In general, mixes with accelerators had higher tensile and compressive strengths after 2 days than mixes without an accelerator. However, the strengths then equalised, with similar values reported in tests conducted after 7 and 28 days.
- Carbonated recycled cement paste (CRCP) had a positive influence on the initial setting time and the early-age strength gains in mixes with accelerators, compared to the reference mix without an accelerator. Although mixes containing CRCP exhibited lower strength at 2 and 7 days than those containing other cement types, by 28 days, the values were comparable. Based on these initial trials, the use of CRCP in sprayed concrete will be further investigated due to its promising results.
- Although many results were obtained, only one measurement of the solidification process using the ultrasonic method and one determination of the strength characteristics were conducted for each mix. Further testing is required to obtain more reliable data. Furthermore, the testing procedure should be re-evaluated and the mix design optimised to achieve more consistent results.

Acknowledgements

Experimental data were collected within a contractual research project No. SR122557206. The author would like to thank TBG Metrostav Ltd. for funding this project.

References

[1] Nedeljković, Marija, Visser, Jeanette, Šavija, Branko, Valcke, Siska, and Schlangen, Erik. 2021. “Use of fine recycled concrete aggregates in concrete: A critical review.” *Journal of Building Engineering* Volume 38. https://doi.org/10.1016/j.jobe.2021.102196.

[2] Skocek, Jan, Ouzia, Alexandre, Vargas Serrano, Encarnacion, and Pato, Nicolas. 2024. “Recycled Sand and Aggregates for Structural Concrete: Toward the Industrial Production of High-Quality Recycled Materials with Low Water Absorption.” *Sustainability* 16(2):814. https://doi.org/10.3390/su16020814.

[3] Roberto Prudêncio Jr, Luiz. 1998. “Accelerating admixtures for shotcrete.” *Cement and Concrete Composites* 20:213–219. https://doi.org/10.1016/S0958-9465(98)80007-3.

[4] De Belie, Nele D., Grosse, Christian U., Kurz, J., Reinhardt, Hans Wolf. 2005. “ Ultrasound monitoring of the influence of different accelerating admixtures and cement types for shotcrete on setting and hardening behaviour.” *Cement and Concrete Research* 35(11):2087-2094. https://doi.org/10.1016/j.cemconres.2005.03.011

[5] Zajac, Maciej, Skocek, Jan, Skibsted, Jørgen, and Ben Haha, Mohsen. 2021. “CO2 Mineralization of Demolished Concrete Wastes into a Supplementary Cementitious Material – a New CCU Approach for the Cement Industry.” *RILEM Tech Lett* 6:53–60. https://doi.org/10.21809/rilemtechlett.2021.141.

[6] Hlavsa, Zdeněk, Vítek, Jan L. “Use of fine recycled aggregate in sprayed concrete: Experimental study.” *Proceedings of the 15th fib PhD Symposium in Civil Engineering*. ISSN: 2617-4820.

[7] Richtlinie “Spritzbeton”. Wien: Österreichische Vereinigung für Beton und Bautechnik (ÖVBB), 2009.

[8] EN 196-1. *Methods of testing cement – Part 1: Determination of strength*. Brussels: European Committee for Standardization, 2016.

Workflow for evaluation of construction kits for element extraction for reuse from cast-in-place concrete structures

Marwin Dollendorf*[1], Anna-Lena Schürmann†[1], Markus Thewes†[2] and Andreas*[2] Vogel

High Performance Computing and Tunnelling, Pipeline Construction and Construction Management† at Faculty of Civil and Environmental Engineering*
Ruhr-University Bochum,
Universitätsstraße 150, 44801 Bochum, Germany

[1] equal contribution, [2] supervision and support

Summary
Despite its significant environmental impact, concrete construction remains one of the most popular methods in the building industry. The modular reuse of concrete elements is a promising strategy to reduce resource consumption. However, unlike prefabricated elements, the modular reuse of cast-in-place elements is fundamentally constrained by their non-standardised and highly individual nature. In this context, construction kits (CK) play a significant role by introducing standardised element definitions that enable the transformation of previously individual elements into reusable modules. This study develops and applies a workflow to evaluate CK quality (CKQ), focusing on maximising concrete volume that can be sourced from existing buildings. The developed workflow is applied to a CK, and the results of the corresponding indicators are discussed. Based on the values an updated version of the CK is proposed. Analysing the corresponding results shows the applicability of the proposed workflow.

1 INTRODUCTION

1.1 Motivation

Despite its high carbon footprint, concrete remains a dominant construction material. Reusing concrete elements offers a significant potential for reducing the associated emissions. The reuse of precast concrete elements benefits from their modularity and established connection techniques. In contrast, the modular reuse of cast-in-place concrete structures by cutting them into elements is technically and organisationally more demanding, as these are typically designed as individual, non-standardised elements with project-specific geometries and properties.

Existing research on the reuse of concrete elements commonly assumes a close coupling between the source building and a specific target building [1]–[3]. As a result, the reuse potential of cast-in-place concrete elements is often evaluated with respect to a predefined or anticipated target design. This dependency limits the ability to assign a general, design-independent reuse potential to existing concrete elements.

To address both the lack of standardisation and the dependency between source and target building, recent research proposes CKs that define a limited set of element types (e.g. walls, columns, slabs and beams) and their characteristics (e.g. geometries and properties). These kits provide a reference framework for assigning a general reusability potential to cast-in-place concrete elements independently of a specific target building, thereby enabling more flexible future reuse scenarios. At the same time, different strategies for defining CKs lead to different kits, for example with respect to the number and diversity of elements they contain.

While these developments highlight the potential of CKs for emphasising concrete element reuse, their impact on reuse potential of source buildings are not yet fully transparent or directly comparable. A systematic evaluation of different approaches would enable the identification of strategies that maximise reuse potential, clarify their applicable boundary conditions and assess the trade-offs involved, such as between standardisation and reusability.

1.2 Related work

This section reviews relevant literature on CKs, their underlying requirements and the quality criteria used to assess them.

1.2.1 Construction kits, modularisation and standardisation

The terms 'construction kit' and 'kit-of-parts' are frequently used in architecture, engineering and construction research, particularly in the context of industrialised and modular construction. Howe *et al.* (1999) define CKs as a set of discrete building elements that can be assembled in different ways to form complete buildings [4]. From a standardisation perspective, ISO 2848 introduces modular coordination as a principle that promotes dimensional compatibility and interchangeability, while enabling a variety of building solutions to be created from a limited number of standardised elements [5].

While CKs in modular and industrialised construction are typically used as design or production systems for new buildings, their role differs in the context of reuse. Here, the CK serves as a reference framework for identifying and extracting reusable elements from existing structures. In this specific context, Mark *et al.* (2025) describe modular reuse as the transformation of existing load-bearing structures into characterised modules that can be processed and reassembled in a construction-kit-like manner [6].

1.2.2 Requirements and quality criteria for construction kits

Established guidelines define baseline requirements for CK elements and interfaces in concrete and industrialised construction. In DIN 1045-4, geometric requirements and tolerances for precast concrete elements are specified [7], while guidance on planning, production, transportation and assembly of modular buildings, emphasising early interface coordination and continuous quality assurance are provided by the German guideline VDI/BV-BS 6208 [8]. These requirements provide an important technical basis but mainly address newly produced or prefabricated elements rather than elements extracted from existing monolithic structures.

Across the literature, CK requirements are often described as a trade-off between standardisation and adaptability. Forman *et al.* (2025) illustrate this by comparing four modularisation concepts based on different CKs (module types) and examining factors such as production type, number of module types, weight, accuracy requirements, costs, material consumption, and construction speed [9]. However, extractability from existing source buildings is not explicitly considered.

In contrast, Mark *et al.* (2025) explicitly highlight the need to estimate extractable shapes, sizes and quantities from source buildings and emphasise deconstruction, handling strategies and compliance with tolerances under uncertainty [6]. This highlights that CK quality for cast-in-place concrete element reuse cannot be assessed only through standardisation, interfaces or assembly-related criteria, but also requires criteria related to extractability from source buildings.

Another recurring requirement is digital consistency across phases [9], [10]. Cao *et al.*(2021) describe CKs as pre-engineered and pre-designed digital models that act as a 'single source of truth' and embed lifecycle-relevant information [10]. Kolbeck *et al.* (2023) further stress that modularisation is a very complex, interdisciplinary process with multicriteria goals and identify interfaces, tolerances and load-bearing capacity as crucial requirements [11].

1.2.3 Evaluation and optimisation methods used in construction kit research

Existing research applies quantitative quality measures and optimisation-based methods to assess and improve the performance of CKs. Brütting *et al.* (2021) introduce the homogenisation rate (HR) as a reuse-oriented quality measure in modular bar system optimised across multiple structures [12], while Rose *et al.* (2025) propose a geometric preselection process and agent-based models to reduce combinatorial complexity before structural evaluation [13]. Similarly, Kolbeck *et al.* (2023) apply optimisation technologies to minimise internal diversity of a CK, while maximising external diversity, highlighting the influence of component length and weight on joints, assembly and transport effort [11].

These studies show the relevance of quantitative indicators, geometric preselection and optimisation for modular systems. However, most existing approaches focus on newly designed systems or target-specific reuse scenarios, rather than on evaluating how well a CK enables the extraction of reusable elements from existing source buildings.

1.2.4 Research Gap

Overall, existing literature (i) establishes CKs as a foundation for modular design and mass customisation [10], (ii) emphasises interfaces, tolerances and interdisciplinary development processes [10], [11], and (iii) proposes optimisation and preselection methods to generate and assess modular systems [11], [13]. However, most approaches evaluate CKs with regard to manufacturability, dimensions, interface compatibility, assembly effort or structural performance.

For the reuse of cast-in-place concrete structures, the primary objective is different. CKs must be evaluated according to how well their predefined elements can be matched to existing, non-standardised source buildings and how much concrete volume can be extracted as reusable elements. Consequently, there is a lack of systematic approaches to evaluate and compare CKs specifically for the reuse of cast-in-place concrete structures by cutting them into elements, where the primary objective is not manufacturability, but the quantifiable extractability and reuse potential of elements from existing buildings.

1.3 Objective

The objective of this study is to propose and demonstrate a workflow for assessing CKs intended for the reuse of cast-in-place concrete elements. The workflow is designed to evaluate CKQ based on the outcome of geometric matching process between kit elements and existing buildings. By providing an objective basis for comparing different CK designs, the proposed approach supports systematic decision-making with respect to the overarching goal of maximising reuse potential and thereby reducing resource consumption associated with cast-in-place concrete construction.

2 METHODOLOGY

In this section the workflow used for the creation and validation of CKs is described. An overview of the workflow is shown in Fig. 1. The workflow can be applied to a CK candidate, where a decomposition is created based on this CK and a given source building. In a subsequent step this decomposition is evaluated by calculating the indicators proposed below. Finally, the CK can be altered based on the calculated values to be evaluated again with the workflow.

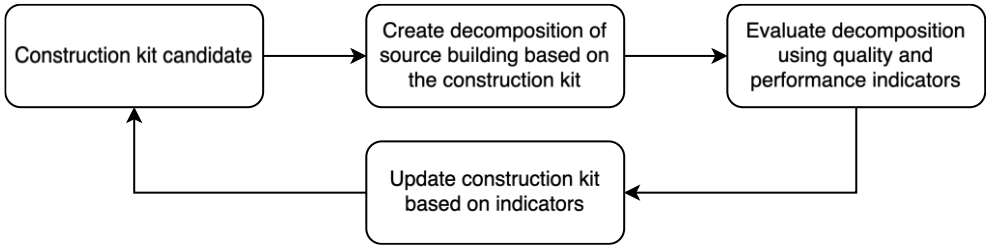


Fig. 1 Overview of the workflow

2.1 Creation of the sample construction kit

To test the evaluation workflow, a sample CK was developed based on real inventory data as described below. The data set consisted of *.ifc* models of three existing buildings as well as 2D plans of two additional buildings. A bottom-up approach was adopted, in which the properties of the elements identified in the inventory determined the definition of the CK.

In principle, the entire inventory of elements contained in the inventory could be interpreted as a CK. For the purpose of evaluation, however, a reduced CK was derived to obtain a compact and comparable test basis. To this end, inventory lists were compiled for each building, documenting all structural elements by element type (slab, wall, beam and column) together with their corresponding cross-sectional dimensions. At this stage, only simple cross-sectional geometries were considered, namely rectangular and circular sections. More complex profiles (e.g., T-shape or trapezoidal sections) were excluded to limit complexity and enable straightforward initial implementation of the workflow. Based on the compiled inventories, a statistical analysis was performed to identify the most frequently occurring cross-sectional dimensions for each element type.

For this CK, the three most frequently occurring cross-sectional dimensions per element type were selected. Accordingly, the CK contains twelve elements. The length of slab, wall and beam elements was uniformly set to 7.00 m. This value was derived from commonly used structural grids of 7.50 m in commercial buildings, allowing for tolerances related to element connections and cutting. The height of column and wall elements was set to 3.00 m, which corresponds to the lower end of typical storey heights in commercial buildings [14]. All CK elements were modelled in Autodesk Revit using existing predefined Revit families. The resulting CK was subsequently exported as *.ifc* file in the IFC4 standard and used as input for the first iteration of the evaluation workflow. The *.ifc* file, along with technical drawings of the contained elements, is made publicly available [15].

2.2 Data requirements and assumptions for source building models

The proposed workflow assumes that source buildings are represented by digital building models structured according to the IFC schema, providing sufficient geometric and semantic information at the level of the elements. Structural elements intended for reuse must be modelled as individual objects and correctly classified by element type. Cross-sectional dimensions and element extents must be explicitly defined to enable geometric matching with CK elements, which are defined using the same schema. Incomplete element specifications, missing geometric parameters or non-standard modelling practices may limit the applicability of the method.

2.3 Decomposition algorithm

To find suitable extraction patterns, an algorithm is used which is described in the following paragraphs.

In a first step, the source building and CK *.ifc* files are loaded and filtered for the included concrete elements. The algorithm then iterates through all concrete elements of the source building and tries to match the elements defined in the CK to the elements found in the building by aligning their geometries and checking for general requirements defined for the extraction process. Those requirements could limit the extractability of elements. For example, elements should only be extracted when the type of the element to extract matches the type of the element from which it is extracted or the cross section of both elements must match to keep the reinforcement layout and the rebars intact.

Employing a greedy approach such that the best-fitting solution for the current element is chosen simplifies the implementation for this initial study. In this case, the best local solution is chosen by extracting the element with the highest volume.

After the first extraction step, the remaining part of the source building element is treated as a new element and checked again against all suitable desired elements in the CK. This process continues until there is no valid extraction possible for the current element. Every element of the source building in treated in this way until a final decomposition is found. An overview of this process is shown in Fig. 2

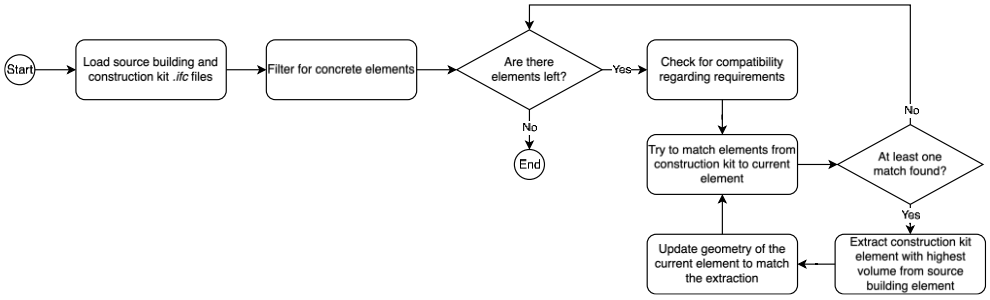


Fig. 2 Overview of the extraction algorithm

2.4 Evaluation of construction kit performance

With the decomposition that is determined by the algorithm described above the performance of the CK can be evaluated. This is done by calculating the performance or quality indicators. Three possible indicators are suggested below that can be adapted to individual use cases.

One of the indicators is the concrete volume utilisation metric $q_{utilisation}$. This metric is the volume of the extracted concrete compared to the overall concrete volume of the source building given by

$$q_{utilisation} = \frac{\sum_{i=0}^{n-1} V_i}{\sum_{j=0}^{N-1} V_j} \tag{1}$$

with the extracted element index $i = 0, 1, 2, \ldots, n\text{-}1$, the number of extracted elements n, source building element index $j = 0, 1, 2, \ldots, N\text{-}1$, the number of elements in the source building N and the individual element volumes V. This quality indicator represents the percentage of concrete extraction – when all the buildings concrete is extracted the value is 1, when no concrete is extracted at all the value is 0. This metric is intuitive as a higher concrete utilisation leads to less waste which is desirable to reduce the emissions of the construction industry.

Another metric is the number of extracted elements in relation to the theoretical maximum number of extractable elements to make this metric comparable across different buildings. This metric is calculated as

$$q_{number} = \frac{n \cdot V_{min}}{\sum_{j=0}^{N-1} V_j} \tag{2}$$

with V_{min} representing the volume of the element with the smallest volume in the CK. For the scope of this paper, this metric is used to increase the number of extracted elements, however, this might not always be applicable as a high number of elements might not be desirable in all cases. Also, this metric depends heavily on the designed CK as a single element with small volume in the CK can decrease the metric significantly.

Important for the evaluation of the CK is the amount of different extracted geometries as this defines how well the defined geometries in the CK can be matched with the elements of the source building regarding their cross sections and overall size while obeying the requirements described above. Equation (3) shows how the number of different extracted geometries m is calculated. g_k is either 0 or 1 for every element in the CK with $k = 0, 1, 2, \ldots, M\text{-}1$, where M is the number of elements in the CK. The value of g_k is 1 when the element type is extracted at least once otherwise the value is 0. Using their sum

$$m = \sum_{k=0}^{M-1} g_k \tag{3}$$

a corresponding quality metric $q_{kit\text{-}number}$ is then calculated by

$$q_{kit\text{-}number} = \frac{m}{M}\,. \tag{4}$$

This metric is suggested to limit CK complexity by penalizing overly complicated CK designs and to honour designs which cover the most common geometries without defining many elements that are not found in any building. From a commercial perspective this is desired as well because it would allow for standardisation and to offer a limited catalogue of elements to potential customers. To enhance this metric, it would be possible to apply appropriate scaling to the individual element entries to include the demand for different elements directly into the metric.

The overall quality indicator q_{total} is finally calculated by adding and scaling all previously calculated quality indicators using

$$q_{total} = \sum_i s_i q_i \tag{5}$$

where s_i represents an individual scaling factor for each quality indicator. For a normalized overall quality indicator q_{total}, these scaling factors must obey

$$\sum_i s_i = 1\,. \tag{6}$$

It is worth mentioning that with this setup it is possible to also set negative scaling factors to introduce penalties for individual metrics when scaling others accordingly to fulfil equation (6).

2.5 Update construction kit based on indicators

The next step is to use the gathered results of the quality evaluation to update the CK for the next iteration. For this, the metrics need to be analysed to find out which adjustments to the CK are necessary to improve the quality. For example, by increasing concrete utilisation. This can be achieved by increasing the desired element sizes in the CK or by adjusting or adding element cross-sections to allow for more elements to fulfil the matching requirements. For now, this update of the CK must be done manually by analysing the indicators and choosing updates that lead to a desired change of the corresponding indicators.

3 RESULTS

The evaluation results of the initial CK are shown in Table 1. To obtain those results, the algorithm described above was applied to three example source buildings to find valid decompositions. Those buildings have a concrete volume of 6985.32 m³, 5240.75 m³ and 2765.31 m³ respectively and are refered to as building 1 to 3. The scaling factors s_1 to s_3 are chosen as 1/3 for $q_{utilisation}$, q_{number} and $q_{kit\text{-}number}$ respectively to calculate q_{total}.

Table 1 Results of the extraction process for the initial construction kit

Description		Building 1	Building 2	Building 3
Extracted volume	in m³	1101.00	822.85	408.45
Number of extracted elements *n*		599	136	31
Number of different extracted geometries *m*		4	6	2
$q_{utilisation}$	in %	15.76	15.70	14.77
q_{number}	in %	1.81	0.55	0.24
$q_{kit\text{-}number}$	in %	33.33	50.00	16.67
q_{total}	in %	16.97	22.08	10.56

The results presented in Table 1 show similar values for the concrete utilisation indicator for all three investigated source buildings. However, the number of extractable elements in relation to the maximum number of extractable elements (q_{number}) as well as the number of different extracted element geometries ($q_{kit\text{-}number}$) vary for the different source buildings. While 50 % of the defined geometries of the CK can be found at least once in source building 2, only 33.33 % are found in source building 1. The results for source building 3 show an even worse value for the corresponding indicator $q_{kit\text{-}number}$, with 16.67 %. This indicates that source buildings 1 and 3 contain cross-sections that are not defined in any geometry of the matching type of the initial CK. Meanwhile, the CK seems to contain element cross-sections that can be found in source building 2. One approach to increase the value of the corresponding indicator for source building 1 and 3 can be to increase the number of different cross-sections in the CK.

Therefore, a revised version of the CK was developed, now containing six cross-sectional geometries per element type instead of three. Accordingly, the total number of elements it defines is 24. The results achieved with the updated CK are shown in Table 2.

The results for the revised CK show that more concrete volume can be extracted with the changes to the CK for all three source buildings. With the revised CK it is also possible to extract a higher absolute number of elements which increases the q_{number} indicator. Moreover, the number of individual extracted geometries is increased. However, the $q_{kit\text{-}number}$ indicator shows lower or equal values compared to the values of the initial CK. The reason for this is that the revised CK defines twice the number of elements compared to the initial CK while the number of different extracted geometries is

increased but not doubled for source buildings 1 and 2 resulting in reduced values for those two buildings. For building 3 the absolute number of different extracted geometries is exactly doubled which in turn results in no change to the $q_{kit\text{-}number}$ indicator between the two CKs.

Table 2 Results of the extraction process for the revised construction kit

Description		Building 1	Building 2	Building 3
Extracted volume	in m^3	1201.80	1152.34	450.32
Number of extracted elements n		631	189	66
Number of different extracted geometries m		5	10	4
$q_{utilisation}$	in %	17.20	21.99	16.28
q_{number}	in %	1.91	0.76	0.50
$q_{kit\text{-}number}$	in %	20.83	41.67	16.67
q_{total}	in %	13.31	21.47	11.15

Those results suggest that it is important to ensure a high variety in the elements defined in the CK while keeping complexity low. This can be concluded from the higher value for $q_{utilisation}$ while the value for $q_{kit\text{-}number}$ decreases for the revised CK compared to the initial CK. Higher values for $q_{utilisation}$ can be explained by more suitable elements being found in the example source buildings originating from the higher variety in element cross sections. As the number of elements in the revised CK is doubled while the number of different geometries found in the building is not, there are more defined elements that are not found in relation to the size of the CK. Trivially, a CK containing all imaginable element geometries would generate perfect decompositions with 100 % of concrete volume extraction as all elements of the source building are defined in the CK. However, this approach is not desirable because it significantly increases the complexity of the CK and misses the point of having a finite set of elements that can be offered to potential customers.

Overall, the results suggest that the presented workflow allows important insights into CK performance and quality as changes in the defined elements of the CK are reflected by expected changes in the resulting indicators accordingly.

4 CONCLUSION AND FUTURE WORK

This study presents a workflow for the creation and evaluation of CKs for reusable cast-in-place concrete elements that can be used to evaluate and create meaningful CKs to help in the process of establishing a cyclic reuse process for concrete buildings that were not designed to be reused.

Furthermore, quality criteria to measure the quality and performance of created CKs are proposed and an algorithm to create decompositions based on source building geometry and CK definitions is implemented. The results show that the workflow produces meaningful insights into the creation process of CKs for this specific use case and will help in the future to evaluate CKs appropriately to increase reuse capacities and thereby reduce carbon emissions and global warming potential of the construction industry.

This approach is tested with two different CKs and three example buildings showing how important the definition of the CK and its evaluation is for an efficient decomposition while maintaining low complexity and ensuring standardized elements for new constructions. However, the validation with only two CKs and three example buildings raises the need to validate this approach in the future with more different CKs and buildings to prove the usability of the approach with real world data.

To increase the impact of this approach in the future, it would be desirable to refine the presented quality indicators and include additional evaluation criteria. A key change would be to include the demand of the customers into the evaluation. This can be done by weighting the individual elements of the CK accordingly for the $q_{kit\text{-}number}$ indicator. Additionally, the set of requirements for the extraction process needs to be extended to match and depict real world applications and thereby allowing this approach to be used in applications where resource efficient deconstruction is necessary e.g. in the reuse

process of cast-in-place concrete elements described above. Furthermore, the decomposition algorithm should be improved using optimization approaches thereby increasing the fairness of the evaluation by eliminating negative impacts of element order due to the greedy behaviour. Another improvement would be to make changes to the CK automatically, eliminating the need for manual updates to the CK in every iteration of the proposed workflow.

Acknowledgements

The research for this paper is funded by the Deutsche Forschungsgemeinschaft (DFG, German Research Foundation) in the context of the collaborative research centre 1683, subproject C03 under the funding number 523205694. We thank the DFG for the financial support.

References

[1] Devènes, Julie, Bastien-Masse, Maléna, and Fivet, Corentin. 2024. "Reusability assessment of reinforced concrete components prior to deconstruction from obsolete buildings" *Journal of Building Engineering*, vol. 84. doi: 10.1016/j.jobe.2024.108584.

[2] Lambrechts, Thijs., Mudge, Fred J., Wijte, Simon N., and Teuffel, Patrick M. "Designing with recovered precast concrete elements. 2023" in *Life-Cycle of Structures and Infrastructure*, pp. 165–171. doi: 10.1201/9781003323020-17.

[3] Bastien-Masse, Malena, Küpfer, Célia, and Fivet, Corentin. 2024. "A concrete answer for circular construction: three prototypes reusing saw-cut elements" *The Structural Engineer*, vol. 102, no. 4, pp. 32–37. doi: 10.56330/ZMSY4716.

[4] Howe, A. S., Ishii, Ismau, and Yoshida, Tomohiro. "Kit-of-Parts: A Review of Object-Oriented Construction Techniques" in *Proceedings of the 16th IAARC/IFAC/IEEE International Symposium on Automation and Robotics in Construction*, pp. 165–172. doi: 10.22260/ISARC1999/0025.

[5] ISO 2848:1984-04-00. "Building construction; Modular coordination; Principles and rules"

[6] Mark, Peter *et al.* 2025. "Modulares Wiederverwenden von Bestandstragwerken" *Bautechnik*, vol. 102, no. 8, pp. 424–435. doi: 10.1002/bate.70000.

[7] DIN 1045-4:2023-08-00. "Concrete Structures - Part 4: Precast concrete products - Common Rules"

[8] VDI/BV-BS 6208:2021-08-00. "Modular construction - Planning, construction"

[9] Forman, Patrick, Sanio, David, Hoppe, Jannik, Rose, Jannis, and Mark, Peter. 2025. "Modular circularity: Build, reuse, repair, convert" *Beton- und Stahlbetonbau*, vol. 120, no. 10, pp. 771–783. doi: 10.1002/best.70021.

[10] Cao, Jianpeng, Bucher, David F., Hall, Daniel M., and Lessing, Jerker. 2021. "Cross-phase product configurator for modular buildings using kit-of-parts" *Automation in Construction*, vol. 123, p. 103437. doi: 10.1016/j.autcon.2020.103437.

[11] Kolbeck, Lothar *et al.* 2023. "Modularisation Strategies for Individualised Precast Construction—Conceptual Fundamentals and Research Directions" *Designs*, vol. 7, no. 6, p. 143. doi: 10.3390/designs7060143.

[12] Brütting, Jan, Senatore, Gennaro, and Fivet, Corentin. 2021. "Design and fabrication of a reusable kit of parts for diverse structures" *Automation in Construction*, vol. 125, p. 103614. doi: 10.1016/j.autcon.2021.103614.

[13] Rose, Jannis, Forman, Patrick, Stieler, David, Menges, Achim, and Mark, Peter. 2025. "Combinatorial optimization approach for the efficient reuse of RC components" *Structural Concrete*, vol. 26, no. 6, pp. 7180–7203. doi: 10.1002/suco.70126.

[14] Hierlein, Elisabeth and Tillmann, Mathias. "Betonfertigteile im Geschoss- und Hallenbau: Grundlagen für die Planung" FDB – Fachvereinigung Deutscher Betonfertigteilbau e. V. 2021.

[15] Schürmann, Anna-Lena, Dollendorf, Marwin, Thewes, Markus, and Vogel, Andreas. 2026. "Two sample construction kits for modular reuse of cast-in-place-concrete structures" doi: 10.60517/35572cdf-6e30-4a19-91d5-a5e4acf1e90d.

Economics of a Sustainable Design – Building Components as future Capital

Marius Valente, Alireza Fadai

Institute of Architectural Sciences,
Interdisciplinary structural design and timber engineering (ITI),
Vienna University of Technology (TU Wien),
Karlsplatz 13/E259-02, 1040 Vienna, Austria

Summary
The dissertation examines the interplay between technical, legal, and economic factors shaping the transition to a sustainable and circular construction sector. This paradigm shift is increasingly referred to by the German term "Bauwende" ("building transition"). Driven by the European Green Deal, a strategy by the European Union to achieve climate neutrality until 2050, the paper addresses key barriers to circular building practices, particularly the lack of coherent regulatory frameworks, insufficient economic incentives for reuse rather than recycling and the potential role of architects and civil engineers in advancing this transition. The results indicate that harmonized legal definitions of reuse and new design standards for regenerative materials can strengthen circular value creation in the construction sector. By integrating insights from technology, law, and economics, the paper contributes to the interdisciplinary discourse on sustainable design and the "Bauwende" in Europe.

1 INTRODUCTION

The construction sector, which is responsible for 37 % carbon dioxide equivalent emissions CO2eq per year [1], plays a decisive role in achieving the climate objectives set by the European Union (EU), particularly under the European Green Deal [2]. The overarching ambition is to achieve climate neutrality by 2050. According to the Global Status Report 2024/25 [3] there is a lack of progress and a distinctive lack of change in energy and related emissions. This finding suggests that the construction sector remains off track.

The introduction of materials and building components with low carbon footprints, in addition to the decoupling of the sector's reliance on primary resources, constitute effective mechanisms for the mitigation of environmental impact. This can be assessed in the early life-cycle stages A1-A5 [4, 5], namely the construction phases of a building (cf. Fig. 2).

In the case of existing buildings, the objectives of the Green Deal can also be further reinforced during the life cycle phases (Fig. 2) replacement (B4) and refurbishment (B5) [4] through the incorporation of circular materials and components with lower CO_{2eq} emissions. In both cases the integration of circular detachable joints and layers in accordance with the principles of Design for Disassembly and Adaptability(DfD/A) [6] necessitates effective collaboration among all the involved trades.

This study investigates the interplay between technological advances, regulatory frameworks, and market mechanisms as the key factors that can accelerate the "Bauwende", according to Stricker et al. [7]. The main objective is to explore how technical innovations, regulatory instruments, and market mechanisms can jointly accelerate the transformation towards circular value preservation and beyond fostering interdisciplinary architectonic thinking. Central questions guiding this work include: Which technical innovations are required to drive this transformation? Which regulatory instruments currently hinder progress or are being misinterpreted by stakeholders? To what extent is the reusability of building elements essential for scaling hybrid construction?

2 METHODS

Methodologically, this research follows the participatory action research design structure (Fig.1), by Creswell [8], and combines theoretical analysis with empirical research. It includes stakeholder interviews, focus group workshops, experimental setups for "Design for Disassembly and Adaptability" (DfD/A) – such as circular hybrid joints – and the critical reading of international field studies.

An in-depth review of current laws and regulations provides essential insights at different levels. By contextualising regulatory instruments of the EU with their national counterparts in the member states, it becomes possible to map the topography of the present milieu the construction sector inhibits and identify existing obstacles.

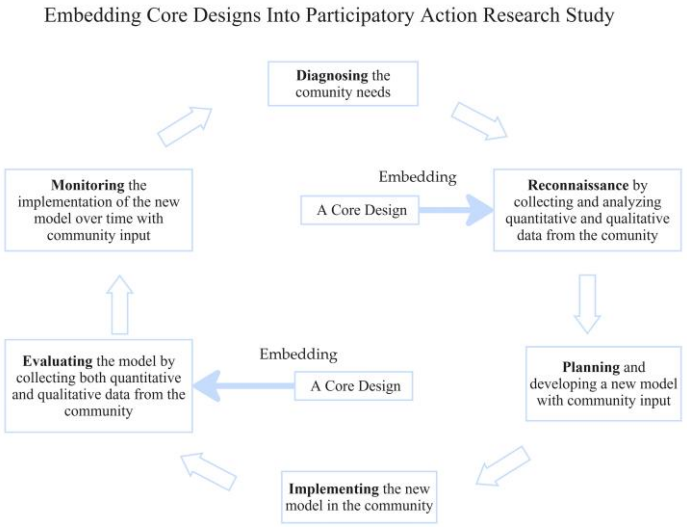


Fig.1: Core Design of the Participatory Action Research Study (Own representation, Source: Creswell 2021 [8])

Throughout all stages, both quantitative and qualitative data are collected and subsequently presented to stakeholders for participatory evaluation. Questionnaires were distributed to relevant stakeholders and, a focus group workshop was conducted to examine the correct application of relevant laws and regulations using a real-life case study from Austria.

The focus group consisted exclusively of stakeholders who held a case-specific and significant role in determining a second life of the building's components. This creates opportunities to evaluate and adapt theoretical assumptions and to implement the findings into a further developed model. These mixed methods enable a comprehensive assessment of innovation barriers and regulatory dynamics.

3 RESULTS

3.1 Terminology, Regulatory instruments, and recent developments in this field

Preliminary findings form this dissertation research indicate that the accuracy of using Circular Economy-related terminology has not significantly increased since the publication on the conceptualization of the Circular Economy (CE) by Kirchherr et al [9] in 2017. A possible explanation for these results may be the inability for stakeholders to sufficiently distance themselves from cultural and linguistic biases, which shape how they interpret and apply specific terms. Therefore, the interpretation of the correct material and building element stream at the End of Life (EoL) of a building is highly inconsistent (Fig. 2).

To establish a common conceptual basis, it is helpful to introduce an abstract terminology, that can be consistently applied across the different life cycle phases of the building industry. The Life Cycle Assessment (LCA) framework, in accordance with prEN 15978:2024 [5] (see Fig.2),is therefore adopted as the primary instrument to present and compare value and performance of the built environment. For the assessment of the individual building components, the EN 15804+A2:2022 [10] is applied.

The so-called R-Framework is a hierarchical setup to organize strategies for the increase of the CE. As identified by Potting et al. [11] all current R-Frameworks are based upon the *Ladder of Lansink*, a linear order of waste treatment methods established in 1979 by a Dutch Government resolution. Although a numbering system beginning with R0 may appear counterintuitive, this structure follows the system already established by Potting et al. [11]. To avoid further inconsistencies R0-based

numbering was adopted directly from their framework, which synthesizes two earlier publications: one by the Dutch Council for the Environment and Infrastructure(RLI) [12] from 2015 and another one by Vermeulen et al. [13] from 2014.

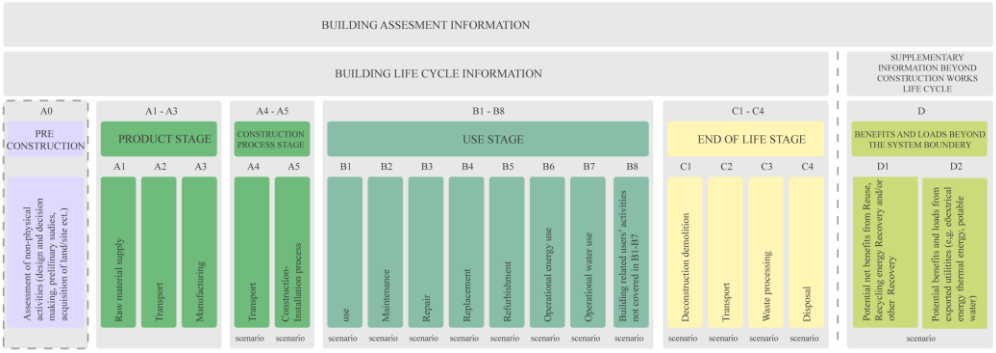


Fig. 2 Display of modular information for the different stages of the building assessment and its components (Own representation of the Phases according to EN 15804+A2:2022[10] and prEN 15978:2024[5])

Fig. 3 shows the R-Strategies [11] which are hierarchically ordered towards CE, but do not build upon each other, when cross-referenced with their definitions from current regulatory instruments. Four of them – R6-R9 – are Recovery processes defined by the Wase Framework Directive (WFD) [14].

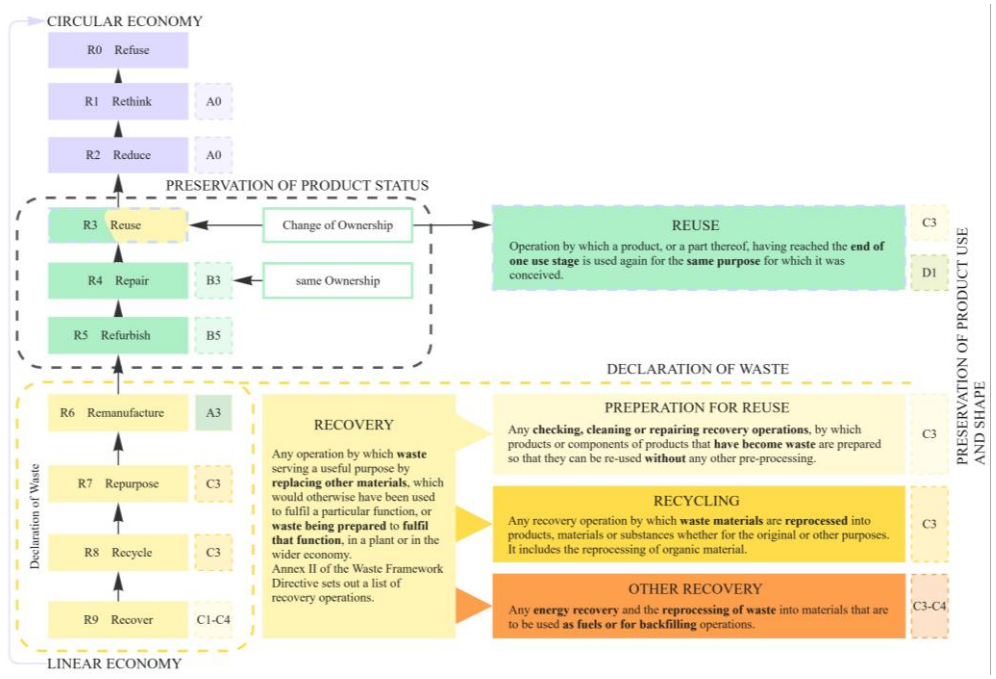


Fig. 3: This Combination and allocation of Life Cycle Stages according to the prEN15978:2024 [5] and EN15804+A2:2022 [10] with the R-Framework according to Potting et.al. [11] and the terminology of the WFD definitions provided in the EU Directive 2008/98/EC Annex II [14] on waste simplifies their relationship, highlighting their inconsistencies in their practical alignment. (Own Representation)

Three of the circular strategies outlined in the R Framework – *Refuse* (R0), *Rethink* (R1) and *Reduce* (R2*)* are later additions and have so far not been sufficiently integrated into the regulatory landscape.

At present, these three strategies can only be meaningfully allocated in the Phase A0, if at all. The interviews and the evaluated questionnaires indicate a generally positive attitude towards reusability; however, they also highlight that isolated lighthouse projects are not sufficient. It is essential to implement a fundamental economic transformation.

R0, R1 and R2 should not be understood as subsequent steps or strategies within the hierarchy, but rather as the foundational setting, which must be cultivated and taken care for, within which a sustainable construction sector can thrive or deteriorate, if neglected. The broader transition toward a sustainable construction industry depends heavily on moving away from short-term, linear economic thinking and adopting a long-term investment perspective on material and element value preservation.

By allocating the different phases of an LCA to the circularity strategies and connecting these terms with standardized definitions of the EU Waste Framework Directive (WFD) it is possible to point out a crucial interruption: a key strategy for fostering circularity R3 *Reuse* is clearly defined by the WFD as an operation in which products are used again for the same purpose, without any alteration or modification [14], and without being declared as waste (see Fig. 3). Reuse can be found in multiple Phases of the LCA, (C1, D1, and potentially A0) but its allocation happens mostly at the EoL Stage of a building, conducted mostly by experts in waste management. As established before, historically the focus of the different R strategies lies mostly within the waste management sector.

The term *Preparation for Reuse* emerged as of the key definitions that lead to misunderstandings and extensive discussion during the interviews, expert talks, and the focus group workshop. Stakeholders repeatedly relied on *common sense* interpretations rather than the formal legal definition, which contributed to inconsistent usage and confusion.

During the focus group discussions, it became evident that the *change of ownership* represents one of the major obstacles to practical reusability. When ownership changes, because of a planned building demolition, it often remains unclear whether the building itself shall be declared as *subjective waste* or only specific materials. As a result, the prevailing practice is to declare the entire building as waste, with only the categorization of contaminated and not contaminated materials. Furthermore, the decision of the categorization of the non-hazardous materials quality is highly dependent on the current market price for materials.

3.2 Material and Component Circulation as key driver of CO_{2eq} reduction

The transition toward a sustainable and circular built environment seems hindered as the EU's material circulation rate is according to European Energy Agency at a 12.2 % rate [15], showing little improvement from the 10,7 % recorded in 2010. This circularity rate includes both material recycling as well as the "reuse" of building components. However, because the available data on component reuse is insufficient, it does not allow reliable quantification.

The findings suggest that a substantial improvement in the CO_{2eq} emissions can currently not be achieved without the replacement of carbon-intense shape-giving processes with low carbon alternatives. In the construction sector the Circular Material Use Rate (CMUR) is focusing on the share of building element materials that are reintroduced into material cycles at the deconstruction site, beginning at Phase C1. At the present time, the European Union has not published any official data on the subject of Circular Component Use Rate (CCUS). The design of reusable construction elements and its implementation in future designs has the potential to reduce the need to produce them in the first place.

For existing buildings, the life-cycle phases B3, B4, and B5 (cf. Fig. 2) are of particular importance when it comes to material selection. Here as well, the use of hybrid systems, and other renewable resources offers significant potential for emissions reduction. It is also crucial that repaired, replaced, or refurbished building components are designed for disassembly and adaptability (DfD/A) as well as well documented. This becomes especially relevant in phases C1–C4. In these end-of-life phases, not only material selection but also the technical execution plays a decisive role, as it enables the legal reuse of building components.

3.3 Critical lifecycle stages for component value preservation

Phase A0, as illustrated in Fig. 2, covers all the fundamental framework conditions for the entire construction project. When the R-Strategies R1–R3, *Rethink, Reduce, Reuse,* are defined, as outlined in Fig. 3, with A0 serving as the focal point for contract award during project development, this exclusion process results in project proposals at an early stage that demonstrate a higher Disassembly

potential for reuse in accordance with the guidelines delineated in Fig. 4. It is noteworthy that this pertains not only to the architectural competition for the entire building, but also to the tender for the construction works. Consequently, it is relevant to various professional groups and service phases during the project development phase.

The LCA-Phases *Repair* (B3), *Renovation* (B4), and *Refurbishment* (B5) represent crucial intervention points throughout a building's lifecycle. Targeted actions during these stages, such as thorough documentation and the systematic replacement of dysfunctional, nonreusable elements at their EoL with alternatives that can be disassembled, can significantly improve the future reuse potential of the current built environment. By strengthening intervention quality through these phases, the overall building element value retention of the building stock can be substantially improved. Currently, no legal obligations or financial incentives exist to encourage this course of action.

From a structural engineering perspective, the findings highlight that load-bearing systems play a critical role in enabling circularity. Reversible structural connections and hybrid load-bearing systems directly influence the feasibility of reuse at the component level. However, current engineering practice still prioritizes static optimization and cost efficiency over disassembly potential.

This leads to structural designs that are difficult or impossible to dismantle without material degradation. Complex, multi-layered assemblies often make it difficult to assess whether a component has been designed with disassembly in mind. This lack of immediate recognizability hinders circular construction practices, especially during the EoL Phase (C1). The integration of DfD/A principles into structural design processes, including modular load-bearing elements and standardized connection systems, is therefore identified as a key requirement for scaling circular construction.

3.4 Technical innovations and Construction Practices in DfD/A-oriented design

Preliminary findings indicate that the market already offers a wide range of DfD/A connector products of load bearing elements. These connectors are largely material-agnostic in their application, enabling use across different construction materials without compromising functionality. Although their utilisation within the construction industry is presently minimal, there is considerable potential for their future application in this sector.

A persistent challenge arises from the layered composition of contemporary buildings and the current state of the art construction methods. Such assemblies often make it impossible to dismantle building elements without causing damage, resulting in a declaration shift from *Reuse* to *Preparation for Reuse* and consequently the legal loss of the building product status.

As illustrated in Fig. 4, guidelines and frameworks for disassembly-oriented design already exist. Their scope ranges from technical detailing and material selection to documentation requirements and EoL-strategies. These publications are applicable across all major contemporary building materials. However, the absence of visibility and documentation, regarding the integration of DfD/A elements within buildings is an additional obstacle.

3.5 Case Study from the structural engineering practice

The objective of this section is twofold: first, to illustrate the impact of pertinent factors, and second, to shed light on the obstacles that must be given consideration to in the civil engineering practice context.

As part of the ongoing dissertation research, the "Sys.Wood" project examined the environmental and circular aspects of timber hybrid construction systems. In addition, a compendium of best practices for reusable timber hybrid construction systems was collated [16]. These structures are subject to either a temporary or a permanent building permit. The following best practice case study, the building is called Building A, is presented for the purpose of exemplifying the findings and implications of successful interdisciplinary collaboration between civil engineers, architects and executing companies, as previously discussed in this paper.

3.5.1 Phase A0 as a strategic enabler of circular design and reuse

With the announcement of the competition of Building A, it was explicitly stated that the design of it must incorporate the principles of DfD/A and the structure would be dismantled after a period of five years. The building had a temporary building permit but must fulfil all normative criteria for a permanent office building.

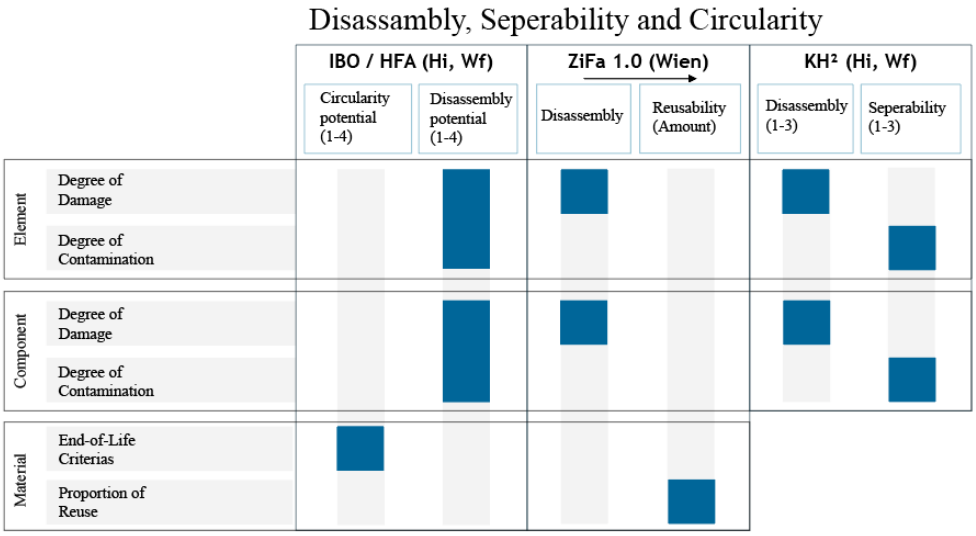


Fig. 4: Matrix of different guidelines for evaluation of disassembly and guidelines for design with separability in mind (Representation by Marius Valente and Alexander Gerger, Data sources: [17-19])

The overarching objective of the project was to enable the potential reuse of all elements, components, and materials without the necessity of declaring them as waste during and after the process of disassembly. The legal framework governing subsequent ownership had been established in advance, which was a key point for the preservation of the product status (see Fig. 3). In addition, a concept for the reuse of the building elements and components in a building with a different architectural design had to be considered.

3.5.2 Hybrid load-bearing elements and building envelope

The structural design of "Building A" was a hybrid construction, integrating elements of different construction materials. The utilization of timber, steel, and reinforced concrete was strategically employed to maximize their respective benefits. The structure's service core was composed of reinforced concrete (RC). This was also integrated into the structural concept as a bracing element, with connections to the joists and ceilings in a reversible manner. The building envelope was constructed using prefabricated elements, a method that eases subsequent disassembly of the structure while maintaining its structural integrity. Given that the core was composed of in-situ RC, it could either be reused on site as a future core or demolished, separated, being declared waste (see Fig. 3), and recycled as materials after undergoing multiple greenhouse gas (GHGs)-emitting processes.

3.5.3 Interior fit-out and Building services

The suspended ceilings, flooring systems, and all interior walls were constructed using a system that allowed for non-destructive separability, layer by layer. The design and installation of all building services, namely heating, ventilation, and air conditioning (HVAC) was undertaken with the explicit intention of facilitating their disassembly. Throughout the five-year period of "Building A"'s utilisation, its elements and components were subject to revision, repair, and replacement without substantial impact on functionality.

3.5.4 Assessment of Building A

The Real Case study results confirmed the estimated expected loss of load-bearing elements, interior fit-out and building service compounds using the previously introduced guidelines for evaluating the disassembly and separability. The wear and tear, which was attributable to both natural and unnatural causes during its use phase, did not reveal any remarkable abnormalities. The predominant loss of elements, interior fit-out components and materials was attributable to deterioration resulting from

human error during the disassembly, transport, and storage phases. It is particularly important to note that the dismantling was not carried out by the original contractor.

In-depth Interviews with the involved companies have revealed that the successful disassembly of this best-practice example was only possible since it was specified as a design requirement during the planning phase A0 (cf. Fig. 2). Furthermore, it was ensured that all the involved companies were engaged in the planning and construction process at an early stage.

4 CONCLUSIONS

The successful achievement of EU climate targets is contingent upon a substantial modification from conventional linear construction practices to more sustainable alternatives, emphasizing the preservation and reuse of materials and components. This involves meticulous planning for a range of possible scenarios, including the use of the space in various combinations of functions and activities. The investigation encompasses both the structure itself and the constituent components thereof. In order to leverage the identified potential, components must undergo a dual design process, incorporating both exchangeability and material selection that supports feasibility.

Consequently, it will be essential to ensure that all building materials are designed for disassembly and future reuse. Only through such a holistic approach can a functioning CE and genuinely sustainable construction practices be realized. DfD/A must therefore be understood as a foundational requirement for all materials entering the construction sector, regardless of their biogenic or mineral origin.

The study demonstrates that the main obstacles are not purely technical, but rather lie in inconsistent regulatory definition, missing economic incentives, and insufficient integration of circular principles in early design phases. Material selection is a powerful lever and offers significant potential for reducing CO_{2eq} emissions at the very beginning of a building's life-cycle assessment. However, insights from the interviews, the questionnaire and the focus group workshop revealed a common concern: if financial viability cannot be guaranteed, circularity in the construction sector will remain a minor practice at best.

In this context, a mixed methods research approach proved essential. Only through continuous participatory feedback loops, it is possible to identify social, ecological, and economic challenges early and respond effectively with adaptative measures.

A fundamental shift in economic thinking is imperative to enable the "Bauwende". A key conceptual contribution of this research is the redefinition of building components as capital assets, which retain value beyond their initial use phase. Although current DfD/A guidelines provide valuable direction, a critical gap remains: the mandatory integration of feasible DfD/A measures in every future construction projects.

Acknowledgements

The research projects "Circular Timber" and Sys.Wood" are funded by the Austrian Federal Ministry of Agriculture and Forestry, Climate and Environmental Protection, Regions and Water Management and implemented as part of the Austrian Wood Initiative's Think. Wood program.

REFERENCES

[1] UBM Development. 2022. in *ESG Bericht 2022*, Accessed 19.02.2026. https://www.ubm-development.com/wp-content/uploads/2023/05/ubm-esg-bericht-2022_de_sec.pdf

[2] European Comission. 2019. COM/2019/640 final, *The European Green Deal*. *Brussels* https://eur-lex.europa.eu/legal-content/EN/TXT/HTML/?uri=CELEX:52019DC0640

[3] Global Alliance for Buildings and Construction. 2025. "Global Status Report for Buildings and Construction 2024/25," United Nations Environment Programme: doi: https://doi.org/10.59117/20.500.11822/47214.

[4] Austrian Standards. 2021. ÖNORM EN 15643:2021-12-15, *Nachhaltigkeit von Bauwerken - Allgemeine Rahmenbedingungen zur Bewertung von Gebäuden und Ingenieurbauwerken*. https://www.austrian-standards.at/en/shop/onorm-en-15643-2021-12-15~p2605184

[5] Austrian Standards. 2024. ÖNORM prEN 15978:2024, *Sustainability of construction works - Assessment of environmental performance of buildings - Requirements and guidance*. https://www.austrian-standards.at/de/shop/onorm-en-15978-2024-05-15~p3537761

[6] International Organization for Standardization. 2020. ISO 20887:2020, *Sustainability in buildings and civil engineering works — Design for disassembly and adaptability —*

Principles, requirements and guidance. https://www.austrian-standards.at/de/shop/iso-20887-2020-2020-01-28~p2513393

[7] Stricker, Eva, Bayer, Dirk, Graf, Jürgen, Lenherr, Barbara, and Milla, Boris (Hg.) 2025. *Wege zur Bauwende - Klima- und ressourcenschonend konstruieren*. Zürich: Triest Verlag.

[8] Creswell, John W. 2021. *A Concise Introduction to Mixed Methods Research*, 2nd Edition ed. Thousand Oaks, California: SAGE Publications, Inc, p. 168 pages.

[9] Kirchherr, Julian, Reike, Denise, and Hekkert, Marko. "Conceptualizing the circular economy: An analysis of 114 definitions." *Resources, Conservation & Recycling,* vol. 127, pp. 221-32, 2017, doi: https://doi.org/10.1016/j.resconrec.2017.09.005.

[10] Austrian Standards. 2022. ÖNORM EN 15804, *Nachhaltigkeit von Bauwerken - Umweltproduktdeklarationen - Grundregeln für die Produktkategorie Bauprodukte (konsolidierte Fassung)*. https://www.austrian-standards.at/de/shop/onorm-en-15804-2022-02-15~p2614834

[11] Potting, José, Hekkert, Marko, Worrell, Ernst, and Hanemaaijer, Aldert 2017. in *Circular Economy: Measuring Innovation in the product chain*. The Hague: Copernicus Institute of Sustainable Development, Utrecht University https://www.pbl.nl/uploads/default/downloads/pbl-2016-circular-economy-measuring-innovation-in-product-chains-2544.pdf

[12] RLI - Council for the Environment and Infrastructure. 2015. RLI 2015/03, NUR-740, *Circular economy. From intention to implementation*. *ISBN 978-90-77323-00-7, The Hague*

[13] Vermeulen, Walter, Witjes, Sjors, and Reike, Denise. 2014. in *Advice about a framework for measuring the impact of circular procurement*. Utrecht: Faculty of Earth Sciences, Utrecht University https://dspace.library.uu.nl/server/api/core/bitstreams/8e24527c-5556-43f2-8273-f14409937852/content

[14] European Parliament and Council. 2008. Directive 2008/98/EC, *on waste and repealing certain Directives "Waste Framework Directive"*. http://data.europa.eu/eli/dir/2008/98/oj

[15] European Environment Agency. 2025. "Circular material use rate in Europe." Accessed 19.02.2026. https://www.eea.europa.eu/en/analysis/indicators/circular-material-use-rate-in-europe/circular-material-use-rate.

[16] Fadai, Alireza, Wallner Novak, Markus, Schachner, Katharina, Gerger, Alexander, Ulrych, Fabian, and Valente, Marius. 2026. "Sys.Wood: Best Practice Kreislaufwirtschaft, Hintergrunddokumentation," in *Sys.Wood: Holzbau im Lebenszyklus : Leitfaden*. Graz: Verlag der FH JOANNEUM Ges.mbH. https://www.holzcluster-steiermark.at/download/syswood_bestpracticekreislauf

[17] Koppelhuber, Jörg, Koppelhuber, Daniela, and Dold, Christian. 2024. "Grundlagen rückbauorientierte Holzbauplanung Rückbbaukatalog mit Bewertungsschema Handlungsempfehlungen Werterhaltungskonzept," in *Leitfaden „Rückbauorientiertes Planen und Bauen im Holzbau"*, https://www.koppelhuber-partner.at/leitfaden-rueckbauorientiertes-planen-und-bauen-im-holzbau/

[18] Kromoser, Benjamin, Hammerl, Mathias, and Camargo, Ingrid. 2024. in *Forschungsbericht & Erläuterung zur Studie Orientierungsleitfaden Zirkularitätsfaktor ZiFa 1.0*. Vienna: BOKU University Vienna https://www.wien.gv.at/spezial/studien/mdbd/orientierungsleitfadenzirkularitaetsfaktor2024.pdf

[19] Dolezal, Franz , Fellner, Maria, Lux, Christian , and Plößnig-Weigel, Bettina 2024. "AP2 – Nachhaltigkeit: Entwicklung und Bewertung von kreislauffähigen Holzbauteilen in Holzmassiv- und Holzrahmenbauweise, wobei für die Gebäudeklassen GK1, GK3 und GK4 Bauteile erarbeitet werden.," in *Katalog kreislauffähiger Holzbauteile*. Vienna: Holzindustrie Österreich https://www.holzindustrie.at/media/j31p1vfu/2-bericht-katalog-kreislauffaehiger-holzbauteile.pdf

Stability loss of slender columns with recycled aggregate

Anna Kováčová, Vladimír Benko

Department of Concrete Structures and Bridges,
Faculty of Civil Engineering, Slovak University of Technology in Bratislava,
Radlinského 2766/11, Bratislava 810 05, Slovak Republic

Summary
The advantages of using slenderer compressed elements are the consumption of less material and more usable space in interiors as well as exteriors. On the other hand, driven by environmental concerns, an increasing number of research studies focus on the development of more sustainable and environmentally friendly concrete alternatives. In recycled aggregate concrete (RAC), natural aggregate is partially or fully substituted with recycled concrete aggregate (RCA). Since columns represent fundamental structural elements in building construction, the authors investigate the behaviour of slender reinforced concrete columns incorporating varying proportions of coarse recycled aggregate in order to achieve a deeper understanding of the structural performance of this sustainable material, with a focus on potential failure by loss of stability.

1 INTRODUCTION

The load-bearing capacity of columns is significantly influenced by the concrete strength class as well as by the proportion of recycled aggregate used. The behavior of columns under external loading is also strongly affected by their slenderness, primarily due to second-order effects [5]. The effect of second-order theory lies in an increase in the bending moment due to column buckling, which leads to additional loading of the column. Due to the low flexural stiffness of slender columns, deformation increases until the applied axial force reaches the critical value N_{Rd}. The ultimate load-carrying capacity of the column is defined by this value. Once it is exceeded, deformation continues to increase even without any further increase in the axial force, and the column subsequently loses stability. This phenomenon leads to a significant increase in the bending moment until material failure occurs in the critical cross-section.

The mechanical properties of recycled aggregates obtained from concrete waste differ significantly from those of natural aggregates. For this reason, it is necessary to thoroughly understand their behavior when used in the design of concrete mixes applied in slender columns.

2 AGGREGATE PRODUCTION

Aggregates are the most used construction mineral resource. They are characterized by wide applicability, low cost, and high consumption volumes. Aggregates are essential for the functioning of society, particularly in the construction and maintenance of buildings and infrastructure. According to the 2022 annual report of the European Aggregate Association (UEPG) [1], aggregate consumption has tripled over the past two decades and is estimated at approximately 50 billion tons per year. Global demand is growing exponentially due to increasing urbanization, population growth, and the effects of rising sea levels. As a result, aggregates are the second most used natural resource in the world, after water.

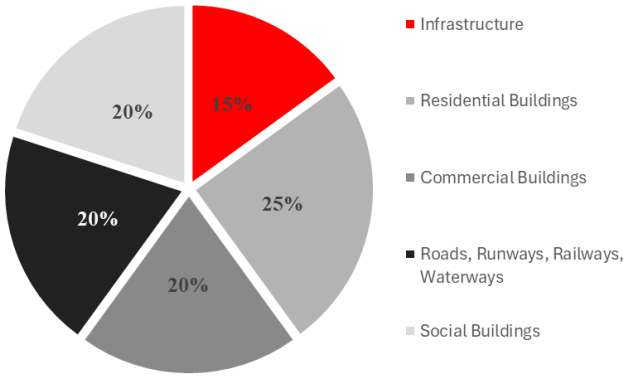


Fig. 1 End use of aggregates (Aggregates Europe UEPG 2021)

3 RECYCLED AGGREGATE

When designing concrete containing recycled aggregates, it is essential to understand the influence of their quantity and qualitative characteristics on the resulting properties of the concrete. The quality of recycled aggregates is determined by the quality and strength class of the original concrete, their water absorption capacity, and the amount of residual cement paste adhered to the surface of the particles.

All In general, the compressive strength of recycled aggregate concrete (RAC) is lower than that of conventional concrete. The strength reduction intensifies with an increasing proportion of recycled aggregates and with decreasing quality of the RCA. The quality of RCA has a more pronounced effect at lower water-to-cement ratios (w/c), since in such cases the compressive strength is influenced more by the aggregate strength than by the strength of the cement paste. It is recommended that the optimal proportion of recycled aggregates, relative to the total amount of aggregates in the concrete mix, be 30% for coarse and 20% for fine recycled aggregates. Higher proportions would reduce the concrete's strength [7].

The study by Chen H.J. [3] demonstrated that the use of washed recycled aggregates in a concrete mix increased the compressive strength of the concrete compared to unwashed recycled aggregates. This strength increase is attributed to two main factors: improved bonding and a reduced amount of water required to produce workable concrete, as waste materials adhered to the recycled aggregates were removed by washing. The use of recycled aggregates from local landfills would contribute to a reduction in the high transportation costs currently associated with the use of natural aggregates. Abbas et al. [4] found that the physical properties of recycled aggregate concrete are influenced by the quantity and characteristics of the residual mortar, as well as by additives from the original concrete mix, such as fly ash, silica fume, slag, and remnants of latex coatings.



Fig. 2 Recycled concrete aggregate (RCA)

3.1 Modulus of elasticity

Concrete with recycled aggregate (RCA) typically has a lower modulus od elasticity compared to concrete without recycled aggregate. The modulus of elasticity is closely related to the stiffness of the mortar and aggregate. According to Bairagi [11] the weakness of interface between new mortar and old mortar can lead to crack formation. This mechanism adversely affects the deformability of the concrete, which may consequently result in a reduction of compressive strength.

3.2 Shrinkage

Besides the modulus of elasticity, the long-term properties of recycled aggregate concrete (RAC), namely shrinkage, exhibit the most significant deviations compared to natural aggregate concrete (NAC). This behaviour is expected, since recycled aggregate (RA) generally has lower stiffness than natural aggregate (NA) due to adhered residual mortar and higher porosity, which reduces the internal restrain against shrinkage deformations. Furthermore, owing to the presence of residual mortar, RAC contains a higher overall mortar volume than conventional NAC, resulting in a larger fraction of the material being susceptible to time-dependent deformation.

3.3 Creep

Regarding creep, the differences observed between RAC and NAC are comparable to those reported for shrinkage. However, the experimental results generally exhibit greater variability due to the larger number of influencing parameters. In the case of RAC with coarse RA, relative to NAC, creep of RAC increases with RA substitution ration and decreases with increasing compressive strength. Similar to shrinkage behaviour, only limited number of studies distinguish between basic and drying creep. In addition, results are presented using various indicators, such as creep coefficient, creep strain, or specific creep, and experimental programmes are often characterised by relatively short observation periods. Nevertheless, on average, RAC with full (100%) replacement of coarse aggregate can be expected to exhibit approximately 30% higher creep than corresponding NAC [12].

4 STABILITY FAILURE OF SLENDER COLUMNS

Bending moments have a significant influence on the behaviour of load-bearing structures. A slender column deforms much more easily than a regular or short column. When a slender column fails due to loss of stability, deformations increase rapidly without any corresponding increase in axial force. This leads to an increase in bending moment until material failure occurs in the cross-section.

Loss of stability is influenced by the cross-section, the geometry of the element, and its boundary conditions. Slender columns can often fail due to loss of stability before the material strength is exploited; in other words, stability loss occurs within the design interaction diagrams. Loss of stability is classified as a brittle failure and is considered extremely dangerous, as the loaded element shows no visible signs of impending failure and rapid collapse.

5 EXPERIMENTAL PROGRAM

From the above considerations, it follows that the proportion of recycled aggregates significantly affects the physical and mechanical properties. In the case of stability failure of slender columns, these properties are compromised even before the design strengths of the materials are reached. However, if a certain proportion of coarse aggregates in slender columns were replaced with recycled aggregates, would the stability failure of the slender column occur even earlier than in a column with natural aggregates due to differences in the modulus of elasticity?

To confirm or refute the presented assumptions and theories, an experiment has been proposed, which will consist of short-term load tests on 10 reinforced concrete columns.

5.1 Sample design

Our goal was to meet two basic requirements, namely: failure of the column within the interaction diagram above the value $F_{cd,lim}$ (balance force for the primary compressed cross-section) and verification of the reliability of the nominal curvature method together with its comparison to a nonlinear method. As a result of pre-experimental analysis, a cross-section was selected for the experimental investigations. The reinforcement ratio could not exceed the maximum allowable percentage of reinforcement in the cross-section (4%). The concrete strength class was selected as

C40/50, and the initial eccentricity was chosen such that stability failure would occur in the upper part of the interaction diagram, it means above the value $F_{cd,lim}$.

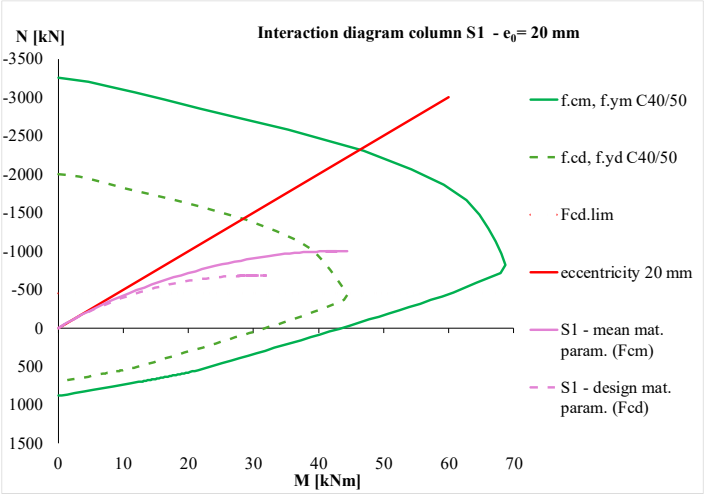


Fig. 3 Predicted behaviour of tested column by the nonlinear analysis

The columns will be produced in three series, with each series containing a different proportion of coarse recycled aggregate, namely 0%, 50%, and 100%. The columns will have a length of 3.5 m and a cross-section with dimensions of 150 × 350 mm, ensuring predominant uniaxial second-order loading, with an eccentricity e_0= 20 mm. The concrete strength class C40/50 will be used for all three series. The design intends to maintain the same concrete strength class across all the series of columns. The only difference between the series is expected to lie in the variation of the modulus of elasticity. The columns will be reinforced with eight reinforcing bars of 16 mm diameter. The stirrups will have a diameter of 6 mm and will be arranged at varying spacing along the column length. Increased stirrup density will be provided at the column head and base to prevent possible end failures.

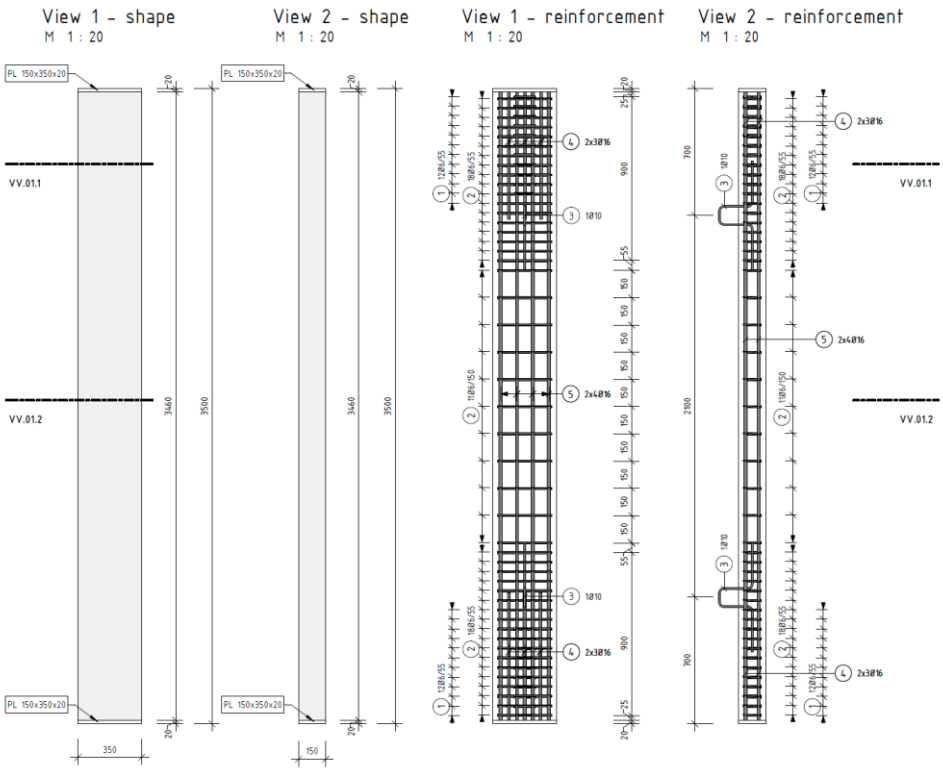


Fig. 4 Shape and reinforcement scheme of tested columns

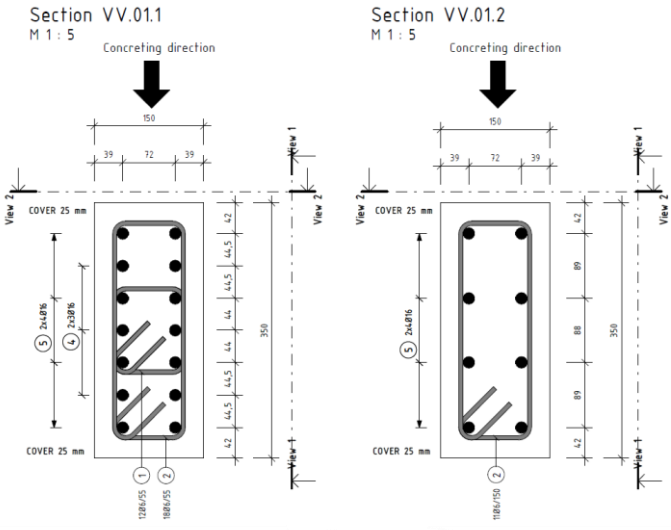


Fig. 5 Cross - sections of tested columns

6 CONCLUSIONS

From both economic and environmental perspectives, the use of recycled waste materials is essential; consequently, recycled aggregates are becoming an increasingly important resource in the construction industry. However, their application requires thorough verification of the properties of concrete

containing recycled aggregates for specific uses, as well as experimental testing of load-bearing elements made of concrete with different proportions of recycled aggregates.

The expected outcome of the experiment should highlight the risk of stability failure of a slender reinforced concrete element and the influence of coarse recycled aggregate on the resulting failure at the critical cross-section.

Acknowledgements

This work was supported by the Scientific Grant Agency VEGA under the contract No. VEGA 1/0345/26 and by the Slovak Research and Development Agency under the contract No. APVV-23-0193.

References

[1] Aggregates Europe – UEPG. 2022. "SUSTAINABLE SUPPLY OF AGGREGATES IN EUROPE." Accessed June 06, 2026. https://www.aggregates-europe.eu/wp-content/uploads/2023/03/20221205_Leoben2_Final_version.pdf

[2] Bilčík, Juraj, Fillo, Ľudovít, Benko, Vladimír, and Halvoník, Jaroslav. 2008. Betónové konštrukcie. Navrhovanie podľa STN EN 1992-1-1. Bratislava: STU Publishing House. ISBN 978-80-227-2940-6.

[3] Chen, Huei-Jeng, Yen, Tsong, and Chen, Kuan-Hung. 2003. "Use of building rubbles as recycled aggregates." Cement and Concrete Research 33:125–132.

[4] Abbas, Atef, Fathifazl, Gholamreza, Isgor, O. Burkan, Razaqpur, A. Ghani, Fournier, Benoit, and Foo, Simon. 2009. "Durability of recycled aggregate concrete designed with equivalent mortar volume method." Cement and Concrete Composites 31:555–563.

[5] STN EN 1992-1-1. 2006. Navrhovanie betónových konštrukcií. Časť 1-1: Všeobecné pravidlá a pravidlá pre pozemné stavby. Bratislava: Slovenský ústav technickej normalizácie.

[6] Farhan, Omar Shamal. 2019. "Effect of Use Recycled Coarse Aggregate on the Behavior of Axially Loaded Reinforced Concrete Columns." Journal of Engineering 25:88–107.

[7] Kwan, Wai Hoe, Ramli, Mahyuddin, Kam, Kenn Jhun, and Sulieman, Mohd Zailan. 2012. "Influence of the amount of recycled coarse aggregate in concrete design and durability properties." Construction and Building Materials 26:565–573.

[8] Benko, Vladimír, Strauss, Alfred, Taubling, Bernhard, Valašík, Anton, and Čuhák, Matej. 2017. "Reliability of slender columns." Beton- und Stahlbetonbau 112:732–741.

[9] Dobrý, Jakub. 2021. "Nonlinear analysis of slender reinforced concrete columns." PhD diss., Slovak University of Technology in Bratislava.

[10] Kendický, Peter. 2017. "Numerická a experimentálna analýza štíhlych betónových stĺpov." PhD diss., Slovak University of Technology in Bratislava.

[11] Bairagi, N. K., Ravande, Kishore, and Pareek, V. K. 1993. "Behavior of concrete with different proportions of natural and recycled aggregates." Resources, Conservation and Recycling 9:109–126.

[12] Lye, Chao Qun, Dhir, Ravindra K., Ghataora, Gurmel S., and Li, H. 2016. "Creep strain of recycled aggregate concrete." Construction and Building Materials 102:244–259.

Modular reuse of RC elements: determination of load-bearing capacities and structural design exemplified on a frame structure

Hendrik Zielonka, David Sanio, Peter Mark

Institute of Concrete Structures,
Ruhr University Bochum,
Universitätsstraße 150, 44801 Bochum, Germany

Summary

This paper examines a detachable frame corner connection made of reused reinforced concrete elements. These elements are cut off from a beam and then joined together to transfer negative bending moments. Tension is transferred via post-installed anchor rods by using injection mortar as well as a screw connection with anchor plates, while compression is transferred via contact of the concrete. Two specimens (S1 with protrusion, S2 without) were tested under quasi-static loading. Both failed due to bond failure of the end anchorage of the upper tensile reinforcement, with S2 failing prematurely because of insufficient anchorage length. The protrusion in S1 increased the load-bearing capacity by 43% compared with S2. The results demonstrate the feasibility of detachable connections for concrete reuse, while highlighting end anchorage of existing reinforcement as a decisive factor for strength and ductility.

1 INTRODUCTION

The reuse of existing load-bearing structures is a promising approach for the sustainable transformation of the construction industry. Given the construction sector's high share of CO_2 emissions, energy consumption and waste generation, the handling of existing reinforced concrete structures that have reached the end of their service life must be critically examined [1]. The demolition of these load-bearing structures currently leads predominantly to downcycling or landfill, and thus to the unnecessary destruction of structural resources that could still be used [2].

The reuse of reinforced concrete elements at the structural level preserves the structural quality of the existing building [3]. Load bearing structures are dismantled into modules, which are comprehensively characterised regarding their properties and condition. Then, they are processed if necessary, and joined to form new load bearing structures using detachable connections [4], [5]. The Collaborative Research Centre (CRC) 1683 is dedicated to researching the methods required for this. An important instrument for interdisciplinary validation is a demonstrator made of real elements (Fig. 1) as a real-world laboratory. This is constructed as a frame structure from reused concrete elements in order to investigate the load-bearing and deformation behaviour under variable loads up to failure.

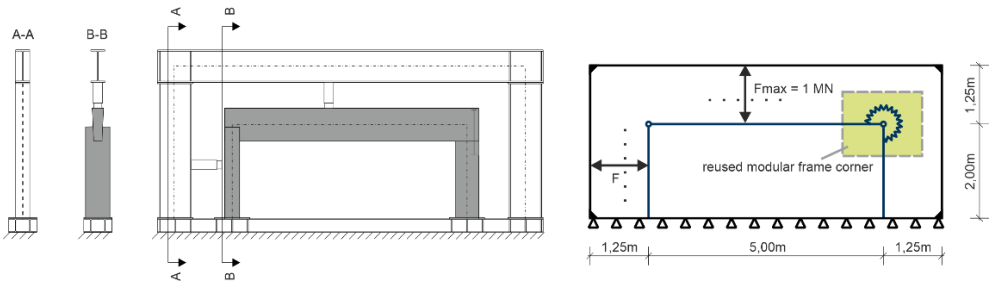


Fig. 1 Scientific demonstrator of CRC 1683, left: frame structure made of reused reinforced concrete elements with test frame and hydraulic jacks for variable application of horizontal and vertical loads, right: static system

The realisation of this frame structure requires the development and implementation of detachable and robust connections between the reused modules that can transmit axial forces, transverse forces and bending moments. An important component of the planned modular loadbearing structure is the frame

corner (highlighted in Fig. 1, right), which is to be explicitly implemented and evaluated as a connection type.

This paper presents the experimental evaluation of subsequently created detachable connections for reused RC elements using dry joints and post-installed anchor rods. For the areas of discontinuity (D areas) [6], [7] around the connection, a Strut-and-Tie model (STM) is developed to determine the load-bearing capacity, and its outcomes are compared with the results of the experimental programme. Failure mechanisms are evaluated and a connection design is derived for reused frame corners.

2 STRUT-AND-TIE MODEL FOR MONOLITHICALLY MANUFACTURED AND REUSED FRAME CORNERS

STMs are particularly suitable for analysing and dimensioning D areas, as they can rationally represent the actual, complex flow of forces via idealised compression struts, tension ties and nodes [8]. Based on Saint-Venant's principle, D areas generally extend from the source of geometrical or mechanical disturbance over a distance approximately equal to the total height of the element (h) before a linear stress state is restored [9]. In a conventional STM for monolithic frame corners with negative moment, a tension tie is routed on the outside (see Fig. 2). On the inside a compression strut is assumed, which, together with the tension tie, serves to transfer the moments. The diagonal struts and the tension ties (stirrup reinforcements) running perpendicular to the component axis carry the shear forces [10].

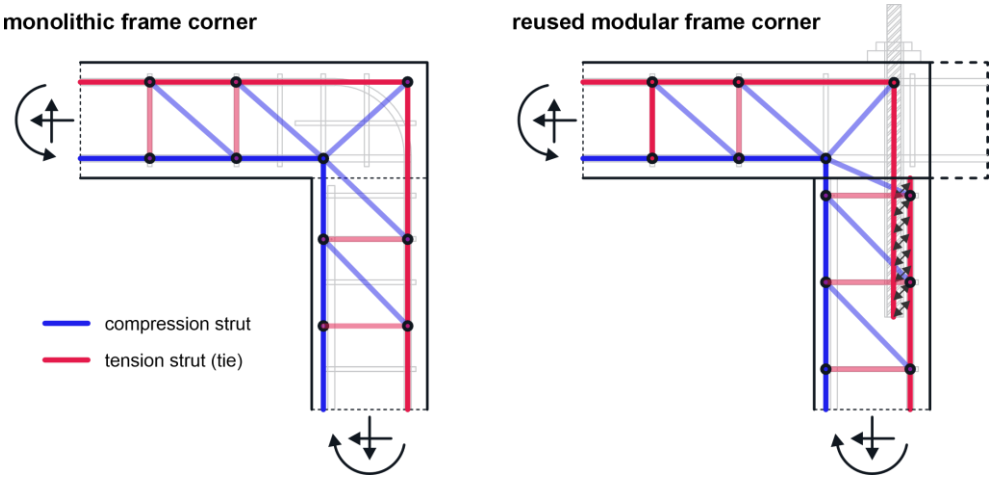


Fig. 2 STM of frame corners under negative moment, left: monolithic corner; right: corner assembled from reused elements with a post-installed anchor rod connection.

In the case of frame corners made from reused reinforced concrete elements, the tension ties in the STM are largely determined by the existing reinforcement. This results in only limited possibilities for adding new ties to the STM. The subsequent installation of these ties involves a great deal of effort. The process would require the drilling of holes and the bonding of the reinforcement bars into the element using injection mortars. Alternatively, tension straps could be installed onto the surface of the component.

The STMs for reused element connections are usually more complex than the standardised STM for frame corners found in the literature (cf. [9], [11]). This applies in particular to the introduction of concentrated loads from connecting elements, usually tension anchors, which cause transverse tensile stresses due to load distribution, as well as to the transfer of tensile forces from connecting elements to the existing longitudinal reinforcement (smaller arrows in Fig. 2, right indicating the transfer of bond forces). For a detachable connection, pressure contact between the concrete elements is necessary, which can significantly reduce the load-bearing capacity of the connection due to possible nonuniform load introduction caused by unevenness in the contact zone [12],[13]. In terms of the use of STM in modular reuse, this means that the effective strength of the applied concrete compression strut may have to be reduced.

3 EXPERIMENTAL INVESTIGATION OF FRAME CORNERS MADE FROM REUSED RC ELEMENTS

3.1 Design and manufacture of test specimens

As already stated, aim of this paper is an experimental analysis on frame corner connections for negative bending moments for the reuse of RC elements. For this purpose, new RC beam specimens with a cross-section of 15 x 20 cm and a length of 1.6 m were produced and then cut into modules acc. to Fig. 3. Two frame corners were examined, which differed only in that in specimen S1, the beam element was extended by 10 cm beyond the edge of the column element. In specimen S2, the beam element was adjusted to fit the edge of the column element by means of a saw cut.

The initial beam specimens were reinforced with two rebars Ø 12 mm with a characteristic yield strength of f_{yk} = 500 N/mm² in the upper and lower layers of the cross-section. For the shear reinforcement, stirrups Ø 8 mm (f_{yk} = 500 N/mm²) with a regular distance of 15 cm were added. Strain gauges (SG) were arranged on the longitudinal reinforcement (see Fig. 3). Accompanying tests determined the cylinder compressive strength to be f_{cm} = 41.6 N/mm² at the time of testing (concrete age 61 d). In accordance with EC2 [14], the characteristic concrete tensile strength $f_{ctk,0.05}$ = 2.52 N/mm² was derived from the compressive strength.

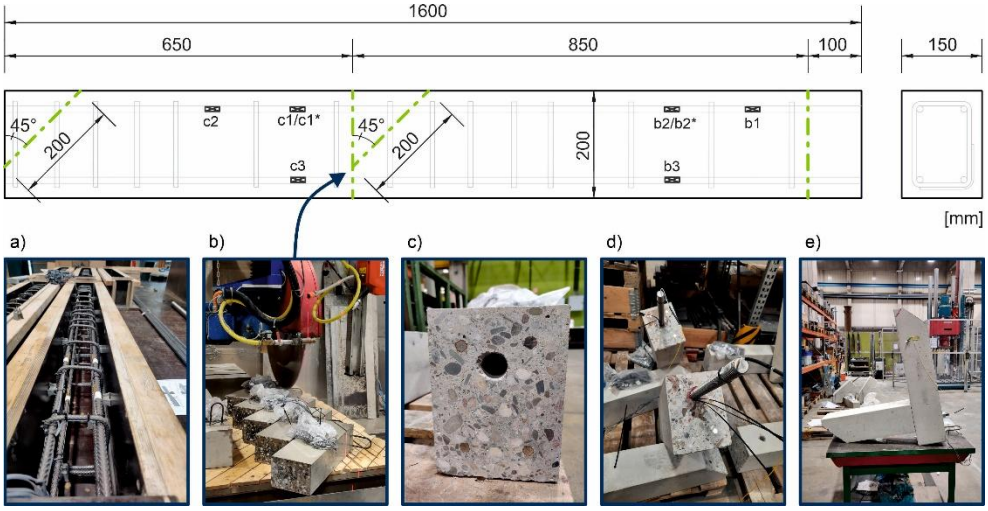


Fig. 3 Production of test specimens: a) reinforcement cage with strain gauges in the formwork, b) saw cuts, c) drill holes in test specimens, d) installation of anchor rods with injection mortar and e) assembly of the frame corner

The initial beam specimens were separated into individual modules using saw cuts 37 days after casting. The arrangement and execution of the separation cuts are shown in Fig. 3. Subsequently, holes (Ø 28 mm) were drilled using a hand-held hammer drill. The connection to the frame corner is made using an A4 stainless steel anchor rod (Ø 24 mm) with a 0.2 % characteristic yield strength of 450 N/mm² and a characteristic tensile strength of 600 N/mm². The anchor rod is bonded into the hole on one side using epoxy resin-based injection mortar HIT-RE 500 V4 [15] in the column element. The beam element is then placed on top of the column element by inserting the protruding anchor rod into a drilled hole. The dry joint connection is fixed by tightening the nut on top of an anchor plate.

3.2 Experimental setup and implementation

The specimens were tested to failure using a 1 MN universal testing machine, which applied the test load to the frame corners via the load introduction surfaces created by the saw cuts (see Fig. 4). Additional steel wedges were placed on the rigidly mounted load plate. The component tests were performed quasi-statically under displacement control at a speed of 1.0 mm/min.

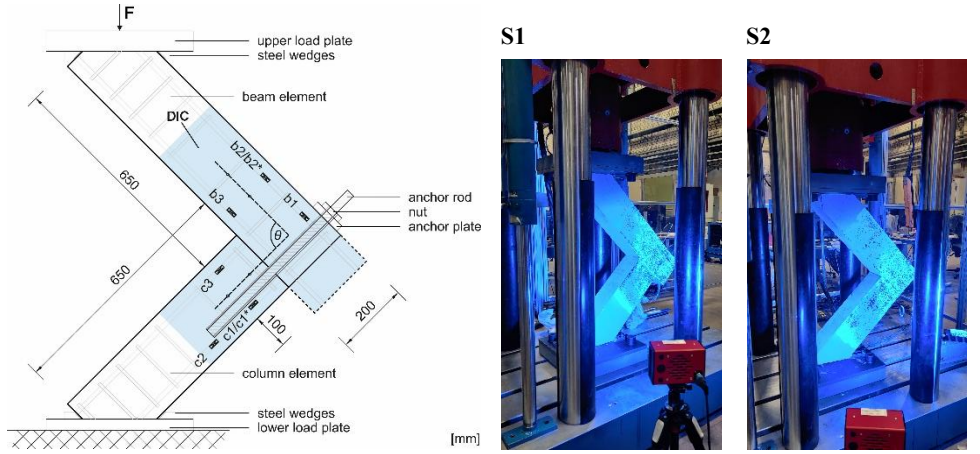


Fig. 4 Test setup for the frame corner, left: illustration of the test setup with the measurement technology used, right: practical implementation in the universal testing machine

During the experiment, data was continuously collected at a frequency of 1 Hz using various measurement techniques. The strains in the reinforcement bars embedded in concrete were measured using SG. The individual SG are attached to different positions on the reinforcement bars and labelled with a combination of letters (b = beam, c = column), sequential numbering and, if applicable, an asterisk (*) in the event of SG redundancy. The deformation behaviour of the connection and surface strains in the D area were recorded on one side using DIC.

4 RESULTS

All results shown refer to the moment at the end of the D area (20 cm from the edge of the column) on the beam element. The moment was determined based on first-order theory, neglecting element deformations, and calculated as $M = 0.35 \cdot F/\sqrt{2}$, where F denotes the test load. The factor 0.35 describes the lever arm between the load application point of the testing machine and the considered cross section.

S1 reached a maximum bending moment of $M_{k,max} = -14.04$ kNm after approximately 11 minutes of testing, whereas S2 reached $M_{k,max} = -9.82$ kNm after approximately 6 minutes. Both test specimens failed due to bond failure of the end anchorage of the longitudinal reinforcement in the beam element. For further information regarding the decisive failure mechanism, see Chapter 5.2.

4.1 Crack formation and rotational behaviour

With increasing load, the strain fields determined from the DIC showed different crack behaviour. In S1, bending cracks were initially observed outside the area of post-installed connection in the beam and in the column, which developed into shear cracks as the load increased further. In the failure state of S1, cracks were observed in the direction of the load introduction of the anchor rod, the diagonal compression strut and also burst cracks as a result of the failure of the end anchorage. In S2, bending cracks initially formed in the beam element, but these could not grow further because the test specimen failed due to insufficient end anchoring indicated by bursting cracks.

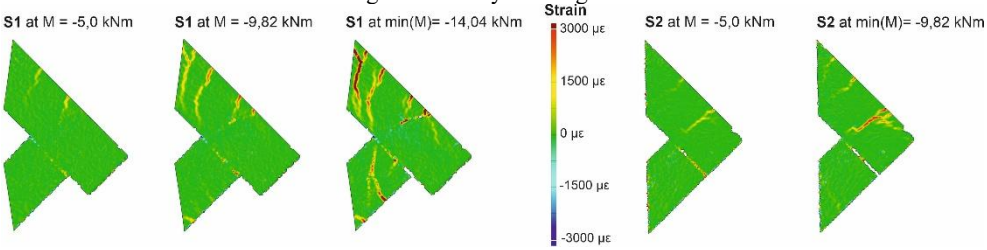


Fig. 5 Strain field of the D area on the surface from DIC measurements of both specimens at different load steps until the maximum load bearing capacity is reached

Fig. 6 shows the moment-rotation behaviour of S1 and S2 during the test, which was determined from the rotation of the connection based on DIC. In both cases, the rotation increases with increasing negative bending moment. After an initial settling behaviour (up to -2 kNm), the connection of S1 shows an approximately linear moment-rotation curve; S2 behaves analogously from the beginning. From approximately -11 kNm, the rotation of S1 increases until $\Delta\theta_{max} = -1.998°$ at $M_{k,max}$. Test specimen S2 shows an increased rotation shortly before failure (approx. -9 kNm) and reaches a rotation of $\Delta\theta_{max} = -0.936°$ at $M_{k,max}$.

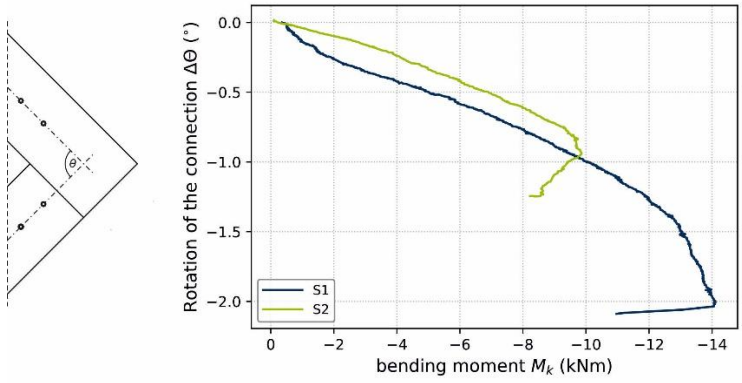


Fig. 6 Moment-rotation diagram of the reused modular frame corners

4.2 Strain development and derived forces in the reinforcment

The results of the strain measurement on the reinforcing bars of both test specimens are shown in Fig. 7 (left) in relation to the moment. In S2, the strain gauges c2, b3 and c1* failed, so these measurement data are unavailable. The strains upon reaching $M_{k,max}$ and the derived forces in the rebars, assuming a bilinear stress-strain curve with a horizontal branch in accordance with EC2 [14], are shown on the right in Fig. 7.

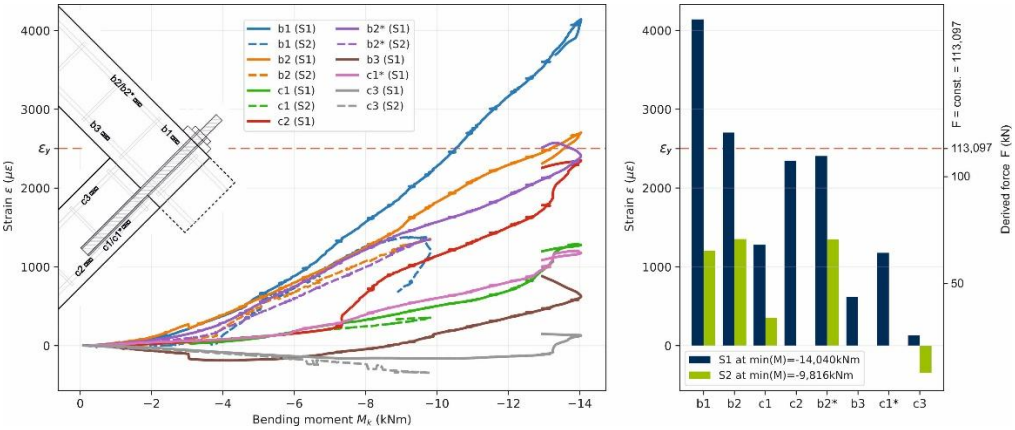


Fig. 7 Results of strain measurements using strain gauges on the reinforcements and their evaluation upon reaching $M_{k,max}$

In S1, strain gauges b1 and b2 show strains > 2.5 ‰, so the reinforcing steel yields. The strains of strain gauges c2 and b2* reached values slightly below the yielding point. The strain measurements on test specimen S2 showed that all measured data were below the yielding point of the reinforcing steel.

5 DISCUSSION

5.1 Load-bearing capacity of the connection

To estimate the theoretical maximum internal forces, the cross-sectional load-bearing capacity in the B area was determined numerically using the INCA2 program system [16]. For this purpose, the non-linear stress-strain relationships for concrete and steel according to EC2 [14] were used. On this basis, assuming an M-N interaction with evaluation for a determined moment-normal force ratio from the test geometry, the characteristic cross-section load-bearing capacities were a bending moment of M_k = - 22.8 kNm and a normal force N_k = -70.0 kN.

The STM was developed analogously to Fig. 2 based on the existing reinforcement for the D area and solved using the boundary condition of steel yielding in bar T2. The calculations yielded a load-bearing capacity of M_k = -10.4 kNm with an associated normal force of N_k = -29.6 kN. Fig. 8 compares the bar forces from the truss calculation with the bar forces derived from the strain gauges.

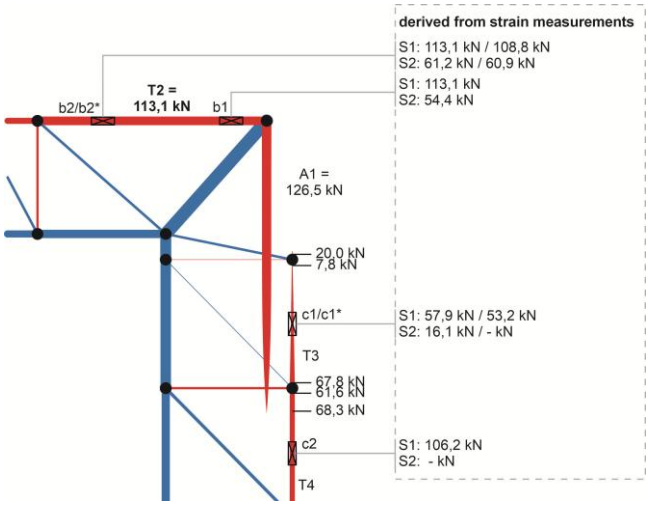


Fig. 8 Forces of the STM of the D area of the connection with representation of the forces determined by strain measurements in reinforcement bars

Compared with the results of the STM, the results for S1 show good agreement with the measurement data in the beam element with a maximum deviation of 3,8%. In particular, the measurements in the strain gauges b1, b2 and, approximately, in b2* confirmed that the reinforcement exceeds the yielding point under maximum load in this specimen. In contrast, the column element showed a maximum deviation of 55%, which can be attributed to the STMs insufficient consideration of the transfer of tensile forces from the anchor rod to the existing longitudinal reinforcement. The results for S2 are significantly below the analytically determined rebar forces. This is due to the fact that the test specimen failed in bar T2 before reaching the yield point.

At no point did the reinforcement of either specimen reach the maximum strain of 25 ‰. The potential load-bearing capacity of the connection was therefore not fully utilised in both test specimens in terms of the load-bearing capacity of the reinforcing steel, as this would require the reinforcement bars to be subjected to corresponding strains without the end anchoring of the longitudinal bars failing. The missing data from the failed SGs is not necessary to evaluate the observed failure mechanism. However, these measurements would have provided further insight into the accuracy of the STM within the column element.

5.2 Decisive failure mechanism: bond failure

The failure of both test specimens occurs locally as a bond failure between the concrete and reinforcing steel in the anchorage length of the tension-loaded longitudinal rebars of the beam element. The failure mechanism is visible on the surface due to the resulting burst cracks caused by the hoop stresses on the surface of the elements and the corresponding slip of the longitudinal reinforcement (see Fig. 9). With regard to the developed STM, the truss node associated with the failure mechanism can be classified as a compression-tension node K6 with single-layer reinforcement according to [9]. The introduction of the anchor force into the beam element does not permit the application of direct transverse pressure, as the load introduction plate is small in relation to the longitudinal reinforcement layout in the cross-

section. This results in the derived compression-tension node model for recalculating the anchorage length for this test, which is also shown in Fig. 9.

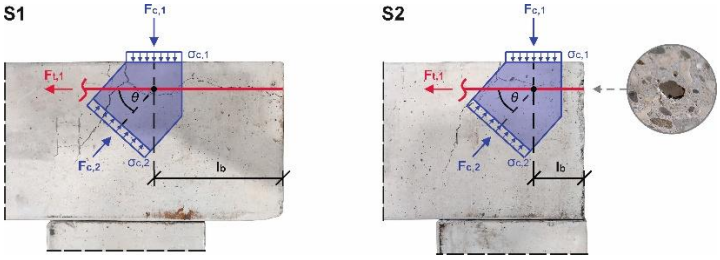


Fig. 9 Surface of the test specimens after testing superimposed with the adjusted pressure-tension node K6 based on [9]

In accordance with EC2 [14], the average bond stress f_{bm} and the resulting required anchorage length $l_{b,rq}$ of the longitudinal bars can be calculated. Here, the factors $\eta_1 = 0.7$ for unfavourable bond conditions and $\eta_2 = 2.67$ for the influence of the bar diameter are considered.

$$f_{bm} = 2{,}25 \cdot \eta_1 \cdot \eta_2 \cdot f_{ctk,0.05} = 10{,}58\ N/mm^2 \quad (1)$$

$$l_{b,rq} = \frac{d_s}{4} \cdot \frac{f_{cm}}{f_{bm}} = 141{,}72\ mm \quad (2)$$

The given geometry of the specimens limits the actual anchorage length to 162 mm for S1. Thus, based on the mean values, S1 has a sufficient anchoring length, which is also reflected in the strain data of the anchored longitudinal rebar, as these strains are above the yield strength (see Fig. 7). In addition, S1 exhibited ductile load-bearing behaviour: initial cracks first formed outside the area of influence of the load application point (see Fig. 5), the reinforcement underwent plastic deformation and the connection exhibited a significantly greater rotational capacity compared to S2. This led to a ductile load bearing behaviour (see Fig. 6) until the bond finally failed abruptly.

S2 had a significantly shorter anchorage length of 62 mm, given by the geometry, and the longitudinal reinforcement could not reach its yield point. The tensile force in the reinforcement is limited by the existing anchoring length of the two rebars Ø 12 mm and can be determined based on the calculated bond stress:

$$F_{bm,S2} = 2 \cdot f_{bm} \cdot \pi \cdot \emptyset_s \cdot l_{b,S2} = 49{,}46\ kN \quad (3)$$

The maximum anchorage force of S2 is in the same range as the tensile forces derived from the strain measurements taken by strain gauges b1, b2 and b2* during the test. A force of 54.4 kN can be calculated from the strain data for the nearest strain gauge b1 next to the anchorage length of S2, corresponding to a deviation of approximately 10%. However, the strain measurements also indicate a reduction in tensile forces towards the end anchorage of the tension strut. The tensile force decreases by 6.7 kN between strain gauges b2/b2* and b1. Consequently, the discrepancy between the maximum anchorage force and the actual force value which must be anchored is likely to be smaller. This reduction could result from bending effects or orthogonal compressive stresses on the longitudinal reinforcement due to anchor force, but cannot be represented by the STM used.

6 CONCLUSIONS

The paper presents experimental investigations of frame corners made from reused reinforced concrete elements. Two different types of frame corners were investigated for negative bending moments, with and without a protrusion at the end. For each, sawn RC beam elements were subsequently connected. The connection was made by post-installed anchor rods in the column, passing them through the beam and fixing them with anchor plates.

The investigations show that detachable connections for the transmission of negative moments in reused components can generally be achieved with the connection design presented. STMs were set up and examined to investigate load transfer in the D area. Based on the investigations, the following conclusions can be drawn:

- Both frame corners examined exhibited bond failure of the upper longitudinal reinforcement of the beam element, which was subjected to tensile stress. The lack of anchoring of the

tension strut is decisive. Compared to the monolithic reference, the load-bearing capacity is reduced by 38 % for test specimen S1 and by 57 % for test specimen S2.

- The formation of a protrusion (overhang of the beam element) increases the anchoring length and has a positive effect on the load-bearing capacity and ductility of the connection. The load-bearing capacity of S1 is increased by 43 % relative to S2. Due to the increased space requirement caused by the protrusion, alternative end anchoring concepts for longitudinal bars subjected to tensile and compressive stresses should be investigated in the future.
- The moment-rotation behavior of both connections is approximately linear, so that a constant spring stiffness could be derived for the global static system.
- As expected, the calculated load-bearing capacity of the D area from the STM is lower than in the B area. The STMs provide conservative results, as load reserves and redistributions are not taken into account. This is confirmed by the test results of S1, which showed a 35 % increase in load-bearing capacity compared to the calculated one of the D area.
- STMs are generally suitable for describing the load-bearing behavior of subsequent frame corner connections made from reused components. It should be noted that the position of the tension ties and their ultimate load-bearing capacity are determined by the actual condition of the element. The next step is to examine the extent to which the need for subsequent reinforcement (e.g., by post-installed reinforcement bars) can be derived from this.

References

[1] United Nations Environment Programme. 2021. "2021 Global Status Report for Buildings and Construction: Towards a Zero-emission, Efficient and Resilient Buildings and Construction Sector.", Nairobi

[2] Habert, Guillaume, et al., 2020. "Environmental Impacts and Decarbonization Strategies in the Cement and Concrete Industries." *Nature Reviews Earth & Environment.* doi:10.1038/s43017-020-0093-3.

[3] Große-Kreul, Alexander, et al. 2025. "Automatisierte Feinbearbeitung von Betonelementen für die modulare Wiederverwendung.", *Bautechnik* 102: 436-448. doi: 10.1002/bate.202500027

[4] Mark, Peter, et al., 2025. "Modulares Wiederverwenden von Bestandstragwerken." *Bautechnik* 102: 424–435. doi: 10.1002/bate.70000

[5] Forman, Patrick, et al. 2025. "Modulare Zirkularität – Bauen, Wiederverwenden, Reparieren, Wandeln." *Beton- und Stahlbetonbau* 120: 771–783. doi: 10.1002/best.70021

[6] Putke, Thomas, et al., 2016 "Wirtschaftliches Konstruieren Und Bewehren." *Beton-Kalender 2016*: Berlin, Wilhelm Ernst & Sohn, 695–739. doi: 10.1002/9783433603413.ch6

[7] Zilch, Konrad, et al., 2010. *Bemessung im konstruktiven Betonbau,* Berlin: Springer

[8] Fédération internationale du béton, 2013. *FIB Model Code for Concrete Structures 2010*. 1st ed. Berlin: Ernst. doi: 10.1002/9783433604090

[9] Schlaich, Jörg, and Schäfer, Kurt, 1998. "Konstruieren im Stahlbetonbau", *Beton-Kalender Beton im Hochbau, Silos und Behälter 87(2)*. Berlin: Ernst

[10] Akkermann, Jan, and Eibl, Josef, 2002. *DAfStb Heft 535: Rotationsfähigkeit von Rahmenecken*. Berlin: Beuth. doi: 10.2366/57284567

[11] Finckh, Wolfgang, 2025. *Mit Stabwerkmodellen zur Bewehrungsführung Detailnachweise im Stahlbetonbau*. Wiesbaden: Springer Fachmedien. doi: 10.1007/978-3-658-48856-7

[12] Schmidt, Boso, et al., 2025. "Drucktragfähigkeit von subtraktiv bearbeiteten Trockenfugen für das Fügen von Re-use-Stahlbetonbauteilen". *Beton- und Stahlbetonbau* 120(10): 798-809,. doi: 10.1002/best.70018

[13] Sanio, David, et al., 2024. "Concrete-To-Concrete Connections for Modularly Reused RC Components – an Experimental Study on Separation Methods", Springer. doi: 10.1007/978-3-031-80724-4_39

[14] DIN EN 1992-1-1:2025-09: *Design of concrete structures - Part 1-1: General rules and rules for buildings, bridges and civil engineering structures;* Berlin: Beuth Verlag. doi: 10.31030/3502390

[15] Hilti Entwicklungsgesellschaft mbH. 2021. *ETA-20/0541: HIT-RE 500 V4 Injection Mortar*.

[16] Pfeiffer, Uwe, 2024. *INCA2 – Program description. Version 3.0.* Last updated: March 2024.

NonMetallic Reinforcement

Textile-Reinforced Concrete Using Hemp Fibres: Flexural Behavior and Structural Implications

Malte Kaliske[(1)], Sebastian Kuhn[(2)], Jörg Schänzlin[(3)] and Marcus Ricker[(1)]

(1) Chair of Structural Concrete,
Technical University of Dortmund,
August-Schmidt-Str. 8, 44227 Dortmund, Germany

(2) Previously: Chair of Structural Concrete,
Technical University of Dortmund,
August-Schmidt-Str. 8, 44227 Dortmund, Germany
Currently: KB - Konstruktionsgruppe Bauen,
Bahnhofplatz 1, 87435 Kempten, Germany

(3) Institute of Timber Construction,
Biberach University of Applied Sciences,
Karlstraße 11, 88400 Biberach, Germany

Summary

This study examines the flexural behavior of concrete beams reinforced with hemp yarn textile meshes as a sustainable alternative to conventional reinforcement. Three-point bending tests compared beams with two and four textile layers. Two-layer beams resisted initial cracking but failed in a brittle manner with a single dominant crack. In contrast, four-layer beams showed distributed cracking and achieved an ultimate moment capacity about 70% higher, due to improved stress redistribution. Cross-sectional analysis gave tensile stresses of 587 MPa and 521 MPa for the two- and four-layer beams, exceeding the isolated yarn strength of 402.7 MPa by 46% and 29%. This confirms that composite action in the concrete enhances hemp fibre utilisation. These results support the development of design models and standards for natural fibre textile-reinforced concrete, though wider application requires further parametric studies.

1 INTRODUCTION

The utilisation of textile-reinforced concrete (TRC) in structural components has attracted considerable interest in recent years, owing to its potential for improved durability and load-bearing capacity relative to conventional reinforcement systems [1]-[3]. Alongside established synthetic textiles such as carbon and glass fibre, natural fibre alternatives — most notably hemp — have emerged as a promising option for sustainable construction, combining adequate mechanical properties with low embodied energy, renewability, and regional availability [4]. A central question concerns the flexural behaviour of textile reinforcement embedded in concrete. While the tensile strength of the textile, which is typically determined through a standardises single yarn tensile tests [5], [6] provides a fundamental parameter for assessing flexural capacity [7]-[9], the structural context of a TRC slab introduces additional complexities. Unlike the single yarn test, in which failure consistently occurs at the weakest point of the specimen under uniform tensile loading, a TRC slab contains a considerably higher number of yarns, each interacting with the surrounding concrete matrix [9]-[12].

In composite systems, the weakest yarn may be located in a region subjected to minimal bending moment. Furthermore, the failure of an individual yarn does not necessarily precipitate the failure of the entire specimen as loads are redistributed among the remaining yarns [2], [13], [14]. These mechanisms contribute to a flexural capacity of the textile within concrete that exceeds the value predicted predicted from the yarn tensile strength alone [2], [13], [15]. However, experimental data specifically characterising this effect for hemp-fibre textile reinforcement remain scarce, and the influence of reinforcement ratio on failure mode and moment capacity is not yet well understood.

This paper presents the results of a dedicated three-point bending test campaign on concrete beams reinforced with hemp yarn-based textile meshes. The aim is to quantify the relationship between the number of textile layers, the resulting flexural capacity, and the effective tensile strength mobilised

within the concrete matrix, thereby contributing to a more refined basis for the structural design of hemp TRC elements. Section 2 describes the materials and experimental programme. Section 3 presents the test results and observed failure modes. Section 4 discusses the implications for design and identifies directions for further research.

2 EXPERIMENTAL CAMPAIGN

2.1 Description of the test specimens

For the experimental investigations, a total of six concrete flexural beams were produced – three with two-layer reinforcement and three with four-layer reinforcement configurations. The two-layer reinforcement was selected to determine whether this arrangement alone would be sufficient to transfer the crack force. The four-layer configuration served as a reference for comparison with the push-out test setup, which employed an identically constructed concrete slab.

The beam dimensions were matched to those of the concrete slabs utilised in the adapted test matrix, with a cross-sectional height of 100 mm. The total specimen length of 950 mm corresponds to that of the push-out test specimens [17]. In the flexural tests, the distance from each support to the load application was set to 425 mm, yielding a span of 850 mm between supports. An additional overhang of 50 mm was provided at each end to facilitate test execution, resulting in the total length of 950 mm. The formwork configuration is illustrated in Fig. 1.

The specimens were manufactured in the testing facility of the Hochschule Biberach (Germany). The concrete mix was intended to match that used for the companion timber–concrete composite (TCC) specimens reported in [18], in order to ensure comparability across the wider experimental programme. However, as the flexural-beam specimens were produced at a different location from the precast plant where the TCC specimens were cast, a different aggregate grading curve was required. This deviation is considered to have had negligible influence on the flexural test results.

The target concrete compressive strength was set to match that of the TCC specimens. A series of companion cube samples were therefore produced to monitor compressive strength development.

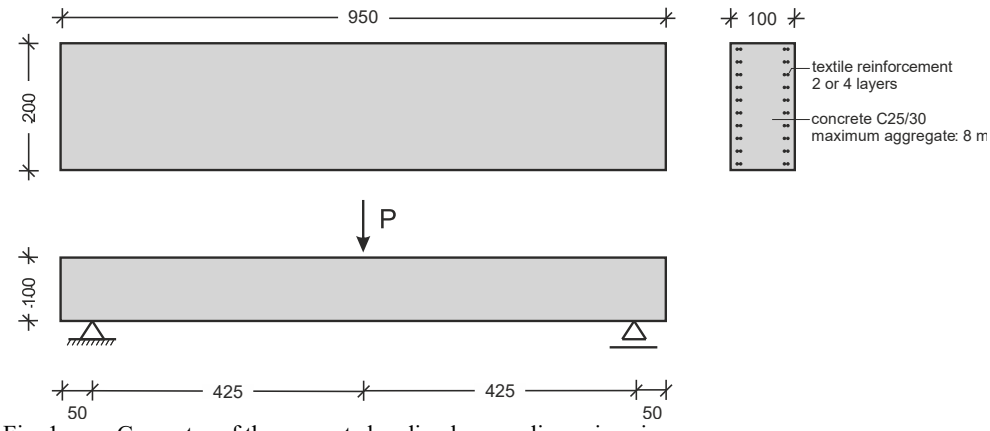


Fig. 1 Geometry of the concrete bending beams; dimensions in mm.

2.2 Description of the test campaign

The experimental investigations were conducted using a Zwick 1687 universal testing machine equipped with a bending bench on which the supports can be positioned freely. Both the supports and the load application points are fitted with rollers to ensure line contact and prevent horizontal membran forces.

Strips of non-woven fabric were placed between the specimen and the roller supports to avoid stress concentrations and ensure a non-rigid support condition. In addition to the applied force, vertical deformations were measured at the quarter points of the specimen using inductive displacement transducers (LVDTs). Supplementary LVDTs were positioned at the supports to monitor any settlement of the non-woven fabric strips. The resulting support displacements were used to correct the quarter-

point deflection measurements accordingly. Horizontal deformation at mid-span was recorded on the underside of the specimen using a further LVDT. The test setup is demonstrated in Fig. 2.

The beams were loaded under displacement control at a rate of 3 mm/min until failure. All measurement data were recorded at a sampling frequency of 10 Hz.



Fig. 2 Test set-up for the concrete bending beams.

3 RESULTS AND DISCUSSION OF THE TESTING CAMPAIGN

The primary objective of the experiments was to investigate the behaviour of a novel textile reinforcement under pure bending loads. In the two-layers speciments, the load decreased after the formation of the first crack, accompanied by a sudden increase in deformation (Fig. 3 left).

Under continued displacement-controlled loading, the load recovered, though the slope of the of the ascending branch was shallower than before cracking, reflecting the reduced stiffness of the cracked cross-section. In all specimens, the load recovered to approximately the level of the initial cracking force before failure occurred. The failure mode was brittle in all cases, although one specimen retained a degree of residual load-bearing capacity. A further common characteristic of the two-layer specimens was the formation of a single dominant crack, as illustrated in Fig. 4 (left). The mean maximum load recorded for this configuration was 6.38 kN.

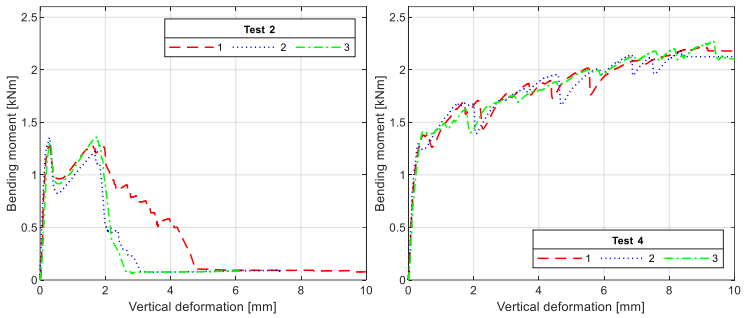


Fig. 3 Moment above the mean vertical deformation: textile reinforcement of two layers and four layers.

In contrast, the bending moment of the four-layer specimens initially mirrored that of the two-layer specimens, as shown in Fig. 3 (right). However, after the first crack formed, a significantly different behaviour was observed: the load increased beyond the initial crack level. The curve exhibited repeated drops followed by renewed load increases, each drop corresponding to the formation of a new crack. The large number of cracks observed in the four-layer specimens (refer to Fig. 4(right)) indicates that the load was successively transferred to the reinforcement through the test until its ultimate capacity was reached. As a result, the flexural capacity of the four-layer beams was approximately 70 % higher than that of the two-layer specimens. The mean maximum load for this configuration was 10.57 kN. Although failure was brittle, it was preceded by large deformations and a distributed crack pattern, both of which are indicative of a more ductile pre-peak response. The post-peak branch could not be captured reliably, as the abrupt nature of failure prevented the displacement transducers from recording a stable softening response.

These results highlight a fundamental behaviour diference between the two configurations. With two layers of reinforcement, the energy released during initial concrete cracking cannot be fully absorbed, resulting in a single dominant crack and immediate failure. With four layers, the reinforcement is sufficient to overcome the cracking phase, and the successive fluctuations in the load–deformation curve reflect a gradual transfer of forces to the textile. This progressive engagement of the reinforcement allows a distributed crack pattern to develop, which likely reached a stabilised cracking stage prior to the attainment of ultimate capacity.

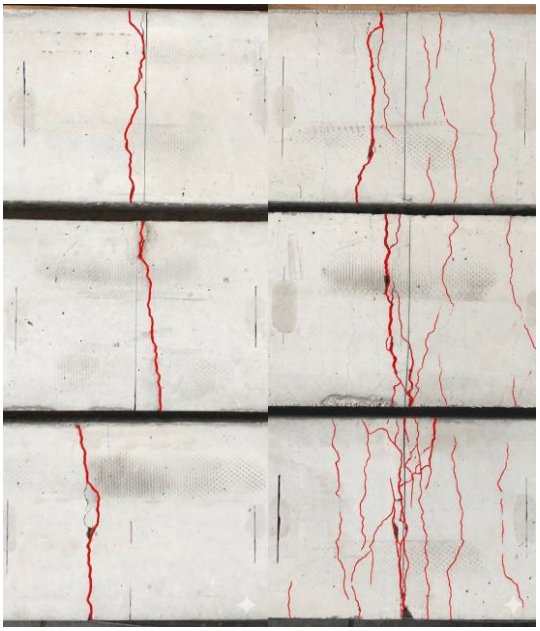


Fig. 4 Fracture patterns of the test specimens with 2 layers of reinforcement and 4 layers of reinforcement

4 IMPLICATIONS FOR ENGINEERING PRACTICE AND FUTURE RESEARCH

Translating the experimental and analytical findings of this study into engineering practice will require progress on several fronts. A rigorous design basis must be derived from the analytical model, incorporating flexural capacity into standard design calculations [19], [20] and adapting regulatory frameworks accordingly — for example, with respect to compression strut angle assumptions [21] and the application of moment–axial force interaction diagrams for combined loading scenarios. Manufacturing tolerances shall also be integrated into the design process to ensure structural reliability. At the implementation level, progress will depend on the construction of large-scale demonstration components and the execution of pilot projects supported by technical approvals, leading ultimately to general building authority certification for the widespread use of natural fibre textile-reinforced concrete.

Optimisation of manufacturing technology is equally important, particularly with regard to achieving adequate concrete compaction in notch regions, where geometric constraints impose particular challenges on consolidation. This will require the development of adapted concreting procedures [22], continued refinement of the textile reinforcement layout, and possible modification of notch geometry itself to improve composite action and facilitate consistent consolidation [23].

Complementing these practical efforts, future research should encompass the refinement of numerical simulation models to improve predictive accuracy, the application of advanced measurement techniques for high-resolution strain and displacement capture, and systematic long-term investigations into the durability and in-service behaviour of hemp-TRC elements under realistic environmental and loading conditions. Broader parametric studies covering alternative beam geometries, concrete mixes, and textile configurations will also be necessary to support generalisation of the present findings.

5 CONCLUSION

The following conclusions are drawn from this study:

- Hemp yarn-based textile reinforcement is a structurally viable and sustainable alternative to conventional concrete reinforcement.

- The reinforcement ratio exerts a decisive influence on failure mode and capacity: two-layer beams failed in a brittle manner with a single dominant crack, while four-layer beams exhibited distributed cracking and a 70% higher ultimate moment capacity.
- Effective tensile stresses of 587 MPa and 521 MPa — exceeding the isolated yarn tensile strength by 46% and 29% respectively — confirm that composite action within the concrete matrix systematically enhances hemp fibre utilisation beyond what single-yarn tests predict.
- These findings provide a quantitative foundation for the further development of design models and regulatory frameworks for natural fibre textile-reinforced concrete.
- Future work should prioritise long-term durability investigations, broader parametric studies across varying geometries and material configurations, and the refinement of numerical models to support the transition of hemp TRC towards structural design practice.

Acknowledgments

The authors would like to express their gratitude to the Bundesinstitut für Bau-, Stadt- und Raumforschung (BBSR) for funding this project (Az: 10.08.18.7-22.10) as part of the Zukunft Bau Forschungsförderung.

References

[1] Murcia, Daniel Heras, Bekir Çomak, Eslam Soliman, and Mahmoud M. Reda Taha. 2022. "Flexural Behavior of a Novel Textile-Reinforced Polymer Concrete." Polymers 14 (1): 176. https://doi.org/10.3390/polym14010176.

[2] Du, Yunxing, Xinying Zhang, Fen Zhou, Deju Zhu, Mengmeng Zhang, and Wei Pan. 2018. "Flexural behavior of basalt textile-reinforced concrete." Construction and Building Materials 183 (June): 7–21. https://doi.org/10.1016/j.conbuildmat.2018.06.165.

[3] Hutaibat, Mohammed, Bahman Ghiassi, and Walid Tizani. 2023. "Flexural behaviour of concrete thin sheets prestressed with basalt-textile reinforcement." Construction and Building Materials 404 (September): 133213. https://doi.org/10.1016/j.conbuildmat.2023.133213.

[4] Jami, Tarun, S.R. Karade, and L.P. Singh. 2019. "A review of the properties of hemp concrete for green building applications." Journal of Cleaner Production 239 (August): 117852. https://doi.org/10.1016/j.jclepro.2019.117852.

[5] Hinzen, Marcus. 2014. „Einfluss Von Kurzfasern Auf Die Frisch- Und Festbetoneigenschaften Sowie Das Tragverhalten Von Textilbeton". RWTH Aachen University's publication server. https://publications.rwth-aachen.de/record/459472/files/5218.pdf.

[6] DAfStb-Richtlinie: 2024. „Betonbauteile mit nichtmetallischer Bewehrung. Deutscher Ausschuss für Stahlbeton" (DAfStb).

[7] Lee, Minu, Jaime Mata-Falcón, and Walter Kaufmann. 2021. "Load-deformation behaviour of weft-knitted textile reinforced concrete in uniaxial tension." Materials and Structures 54 (6): 210. https://doi.org/10.1617/s11527-021-01797-5.

[8] Yao, Yiming, Yuanfeng Sun, Mengchao Zhai, Can Chen, Cong Lu, and Jingquan Wang. 2023. "Tensile behavior of textile reinforced ultra-high performance concrete." Construction and Building Materials 411 (November): 134172. https://doi.org/10.1016/j.conbuildmat.2023.134172.

[9] Zhu, Deju, Xiayang Bai, Qiyao Yao, Md Zillur Rahman, Xinliang Li, Ting Yang, and Shuaicheng Guo. 2023. "Effects of volume fraction and surface coating of textile yarns on the tensile performance of AR-glass textile reinforced concrete." Journal of Building Engineering 71 (March): 106420. https://doi.org/10.1016/j.jobe.2023.106420.

[10] Zhu, Deju, Xiayang Bai, Qiyao Yao, Md Zillur Rahman, Xinliang Li, Ting Yang, and Shuaicheng Guo. 2023. "Effects of volume fraction and surface coating of textile yarns on the tensile performance of AR-glass textile reinforced concrete." Journal of Building Engineering 71 (March): 106420. https://doi.org/10.1016/j.jobe.2023.106420.

[11] Preinstorfer, Philipp, and Johann Kollegger. 2020. "New insights into the splitting failure of textile-reinforced concrete." Composite Structures 243 (March): 112203. https://doi.org/10.1016/j.compstruct.2020.112203.

[12] Rempel, Sergej, Marcus Ricker, and Tânia Feiri. 2021. "Stochastic approach for the material properties of reinforcing textiles for the design of concrete members." Scientific Reports 11 (1): 21976. https://doi.org/10.1038/s41598-021-01032-9.

[13] Kong, Kanhchana, Zyed Mesticou, Marie Michel, Amir Si Larbi, and Angel Junes. 2017. "Comparative characterization of the durability behaviour of textile-reinforced concrete (TRC) under tension and bending." Composite Structures 179 (July): 107–23. https://doi.org/10.1016/j.compstruct.2017.07.030.

[14] Halvaei, Mana, Masoud Jamshidi, Masoud Latifi, and Mojtaba Ejtemaei. 2020. "Experimental investigation and modelling of flexural properties of carbon textile reinforced concrete." Construction and Building Materials 262 (September): 120877. https://doi.org/10.1016/j.conbuildmat.2020.120877.

[15] Kim, Hyeong-Yeol, Young-Jun You, Gum-Sung Ryu, Kyung-Taek Koh, Gi-Hong Ahn, and Se-Hoon Kang. 2020. "Flexural Strengthening of Concrete Slab-Type Elements with Textile Reinforced Concrete." Materials 13 (10): 2246. https://doi.org/10.3390/ma13102246.

[16] Zhang, Hai Yan, Hao Yu Liu, Venkatesh Kodur, Meng Yuan Li, and Yun Zhou. 2022. "Flexural behavior of concrete slabs strengthened with textile reinforced geopolymer mortar." Composite Structures 284 (January): 115220. https://doi.org/10.1016/j.compstruct.2022.115220.

[17] Kaliske, Malte, Sebastian Kuhn, Sebastian Krug, Tânia Feiri, Jörg Schänzlin, and Marcus Ricker. 2026. "Bending Behavior of Timber-Concrete Composite Structures Reinforced with Natural Fibers." In Rilem Bookseries, 404–11. https://doi.org/10.1007/978-3-032-23439-1_48.

[18] Kaliske, Malte, Sebastian Kuhn, Sebastian Krug, Tânia Feiri, Jörg Schänzlin, and Marcus Ricker. 2026. "Push-Out Tests on Timber-Concrete Composite Structures Reinforced With Natural Fibres." In Rilem Bookseries, 455–64. https://doi.org/10.1007/978-3-032-23439-1_54.

[19] Butler, Marko, Viktor Mechtcherine, and Simone Hempel. 2009. "Experimental investigations on the durability of fibre–matrix interfaces in textile-reinforced concrete." Cement and Concrete Composites 31 (4): 221–31. https://doi.org/10.1016/j.cemconcomp.2009.02.005.

[20] Alma'aitah, Mohammad, Bahman Ghiassi, and Ali Dalalbashi. 2021. "Durability of Textile Reinforced Concrete: Existing Knowledge and Current Gaps." Applied Sciences 11 (6): 2771. https://doi.org/10.3390/app11062771.

[21] Raupach, M., and C. Morales Cruz. 2016. "Textile-reinforced concrete." In Elsevier eBooks, 275–99. https://doi.org/10.1016/b978-1-78242-446-8.00013-6.

[22] Hegger, Josef, Norbert Will, and Karolin Rüberg. 2007. "Textile Reinforced Concrete — A new Composite Material." In Advances in Construction Materials, 147–56. Springer Berlin Heidelberg. https://doi.org/10.1007/978-3-540-72448-3_15

[23] Preinstorfer, Philipp, and Johann Kollegger. 2020. "New insights into the splitting failure of textile-reinforced concrete." Composite Structures 243 (March): 112203. https://doi.org/10.1016/j.compstruct.2020.112203.

Numerical analysis of lightweight textile-reinforced concrete structures

Skerdilajt Cengu, Iurii Vakaliuk, Silke Scheerer

Institute of Concrete Structures,
TUD Dresden University of Technology,
01062 Dresden, Germany

Summary
Carbon textile reinforcement (CTR), a CFRP-based reinforcement for concrete, offers high tensile strength, flexibility, low weight, and excellent corrosion resistance. These properties enable the design of thin, lightweight, and durable concrete elements with reduced material consumption while maintaining high load-bearing capacity. One approach is to resolve the compact cross-section of ceilings by shell-like substructures. However, accurate modelling of such elements remains challenging. For extensive parametric studies, a finite element (FE) program must provide reliable results with reasonable computational effort. In this study, Abaqus and ATENA were evaluated, with ATENA showing better performance. Explicit modelling options were used, and the results were compared with experimental outcomes. The numerical load-deflection response closely matched the experimental results, showing the reliability of the modelling approach and supporting the use of FEM to predict TRC behaviour.

1 Introduction

Conventional reinforced concrete structures are commonly designed as solid members with constant external and internal geometries. Such designs often result in inefficient material utilization, as large regions of concrete and steel reinforcement remain only partially loaded. In increasing demands for sustainability, resource efficiency, and CO_2 reduction in construction, new materials and structural concepts are required. Carbon textile-reinforced concrete (CRC) represents a promising solution. CRC consists of a fine-grained, high-strength cementitious matrix reinforced with carbon fibre textile grids. The non-corrosive nature, high tensile strength, and flexibility of the fibre-based reinforcement enables the design of slender, lightweight, and filigree structural elements and realization of complex geometries such as curved, folded, and shell-like structures [1].

An efficient structural concept for CRC can be based on the principle «form follows force», where the geometry is adapted to the internal force flow. Shell-like structures are suited to this approach, as loads are primarily transferred through membrane action rather than bending, resulting in high structural efficiency and reduced material demand. Within the first funding phase of the Collaborative Research Centre/Transregio (SFB/TRR) 280 [2], this design approach was investigated using a parametric, multi-objective simulation environment (MOET). Based on the numerical optimization results, selected geometries were manufactured and experimentally tested at the Otto Mohr Laboratory (OML).

Although experimental investigations are essential for validating the structural performance of newly designed elements, they are still time-consuming and expensive. As a result, experimental investigations are typically limited to a small number of geometries, loading scenarios, and support conditions. Nonlinear finite element (FE) simulations offer an efficient solution to expand the investigated design space and gain deeper insight into structural mechanisms that are difficult to access experimentally. In this study, a detailed numerical investigation of lightweight textile reinforced concrete structure is carried out using two finite element software packages, Abaqus and ATENA. The numerical models were developed and validated against the experimental results obtained during the first project phase [3]. By comparing the results obtained from both software environments, this contribution aims to evaluate their applicability for the simulation of CRC structures and to support further parametric studies and development of numerically driven, material-efficient design strategies for lightweight CRC structures.

2 Experimental Investigations

2.1 Geometry of the examined slab elements

The geometric configuration of the examined ceiling slab (Fig. 1) was developed through an iterative procedure using MOET. The usually solid interior of such an element was resolved into a shell-like membrane structure of an arbitrary curvature. The geometry was subjected to incremental loading, and an optimised configuration was generated according to the principle of form follows force, taking into account the real boundary condition in the lab and the material properties of the composite, see [3] for further details. The slab is a uniaxially spanning 211 mm high hollow-chamber structure measuring 1800 × 1800 mm. The membranes were 10 mm thick. In intersecting regions, the thickness was locally increased to mitigate stress concentrations. The supporting walls were 50 mm thick. For casting, a reduced-pressure casting process was developed to realise these filigree components with the required geometric precision [4]. CNC-cut blocks of extruded polystyrene (XPS) were used to form the internally resolved cross sections. Due to its low modulus of elasticity, its infulcene on the structural performance of the slab was neglected in this numerical study. In addition, 3D-printed spacers were used to ensure accurate positioning of the reinforcement during casting.

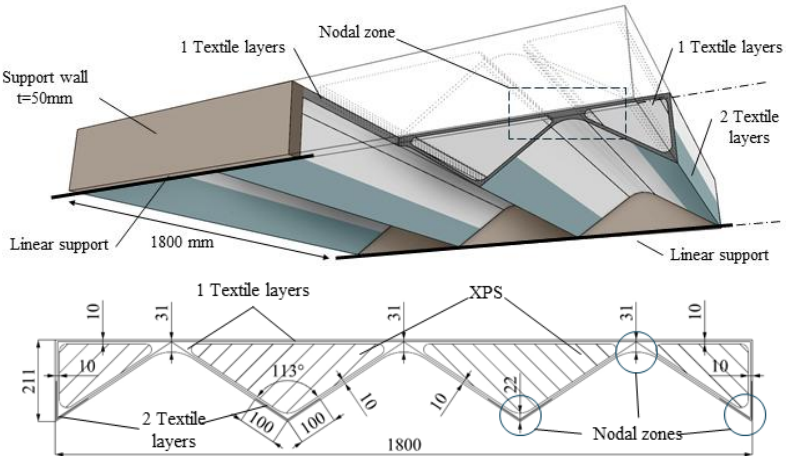


Fig. 1 Geometry of the ceiling slab (Graphic: I. Vakaliuk, S. Scheerer ([5]), edited: S. Cengu)

2.2 Materials

The test specimens were produced using C3-B2_HF-2-190-2 concrete mixture developed within the research project C^3 – Carbon Concrete Composite [6]. This concrete contains fine-grained aggregates, providing enhanced flowability and making it suitable for thin TRC elements. The mechanical properties of the plain concrete, the textile reinforcement, and the composite were determined through standardised testing procedures in accordance with [7]. The tested concrete exhibited a mean compressive strength of 118 MPa and an elastic modulus of 41 GPa, as shown in Fig. 2 (left).

Tensile strength was taken as the stress corresponding to the first cracking event, identified by a change in slope in the stress-strain response [8]. The results were obtained from uniaxial tensile testing of the TRC composite measuring 800 × 62 × 15 mm with one layer of reinforcement. The tension softening of concrete was evaluated in accordance with the Model Code 2010 [9], Fig. 2 (middle).

The textile reinforcement solidian Q85-CCE-21_E5 was used and cut to the required geometry with a tolerance of ±5 mm. The textile has a nominal tensile strength of 3950 MPa and an elastic modulus of 251 GPa. The individual yarns have a cross-sectional area of 1.81 mm² and are arranged at a uniform spacing of 21 mm, as given in the datasheet [10]. In each structural member, a textile grid was positioned

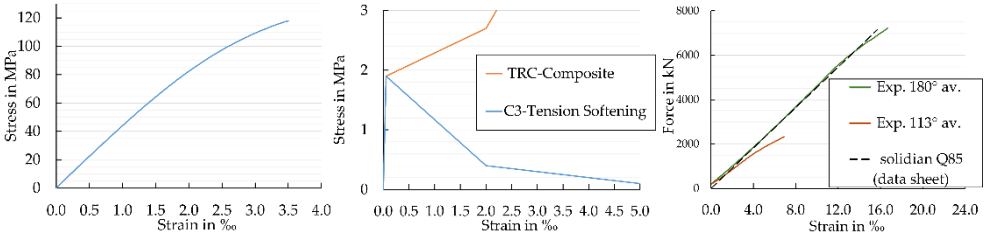


Fig. 2 Mechanical properties of the materials: a) compressive behaviour of concrete, b) tensile behaviour of composite and concrete evaluated from Model Code 2010, c) tensile behaviour of textile reinforcement (Graphic: S. Cengu, based on experimental data from Project C01 of TRR 280 [2])

along the central axis of the element. To enhance the flexural capacity of the slab, a second layer of textile was introduced in the tensile regions. The second layer of textile was manually bent to an angle of 113° using heat, corresponding to the geometric configuration of the slab. The bending process inducec local fibre damage, which was evaluated through uniaxial tensile test (exp. 113° av.) and compared with undamaged yarn (exp. 180° av.). The results indicated a reduction of approximately 70% in maximum tensile strength and 73% in elastic modulus, see Fig. 2 (right).

2.3 Test setup

Due to practical limitations associated with load introduction at nine discrete locations to replicate realistic plane loading conditions, the ceiling element was tested in an inverted configuration. As illustrated in Fig. 3 (left), the slab was supported along the bottom faces of the support walls by horizontal steel beams and restrained using four manual jacks. The load was applied from beneath the slab by means of nine synchronised hydraulic cylinders arranged in a regular 3 × 3 grid with a spacing of 600 mm. To ensure vertical load transfer, spherical joints were installed between the hydraulic cylinder and 100 mm × 100 mm distribution plates, preventing localised punching effect. The hydraulic system was operated manually under force controlled condtions. The deviation between the individual cylinders was approximately 10% at most.

Furthermore, a 3 × 4 measurement grid was established to capture the deformation behaviour of the slab. Structural vertical displacements were recorded using inductive displacement transducers (German abbreviation: IWA), over one quarter of the slab in accordance with the configuration shown in Fig. 3 (right). Further details of the experimental investigation are reported in [5**Fehler! Verweisquelle konnte nicht gefunden werden.**].

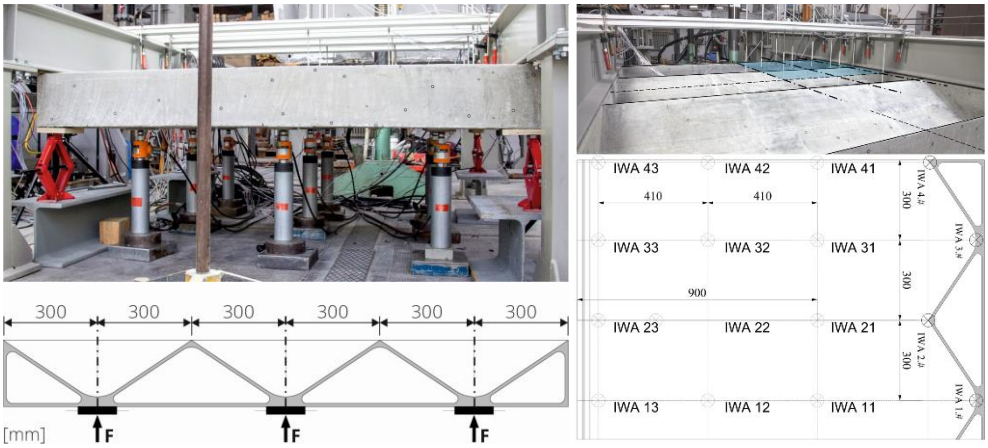


Fig. 3 Test setup: 9 point bending test (left), positioning of measuring equipment (right) (photo: Stefan Gröschel, graphic: S. Scheerer, I. Vakaliuk, edited: S. Cengu; [5])

3 Numerical Modelling

To investigate the structural behaviour of internally resolved ceiling slab, two independent finite element models were developed using different commercial software solutions. The numerical models represent the real geometry of the slab, including modelling of the carbon textile reinforcement and the boundary conditions from the experiment in the lab. The use of two different finite element modelling (FEM) softwares was intended to assess the capability of commercial tools to reproduce experimentally observed behaviour of the slab and to enable a deeper investigation of the internal stress states and the failure mechanisms which are difficult to capture experimentally. One model was developed using Abaqus (FEM 1), while the second model was implemented in ATENA (FEM 2). Despite differences in discretisation strategy, material modelling, and load introduction, both models adopted consistent mechanical properties, see Table 1, symmetry assumptions, loading magnitudes, and monitoring strategies, ensuring comparability of results across platforms. Previous research [11], [12] reported that both software solutions are able to capture the behaviour of the CRC.

The ceiling slab (see Section 2) was geometrically modelled in Rhino 8 environment [13], modelling each material of the composite explicitly. The volumetric geometry representing concrete was adjusted in the nodal areas to ease the meshing process in FEM software. The supposition was done considering the same volume of concrete in the nodal areas. Owing to the double symmetry of the slab geometry, the supports and load configuration, only one quarter of the slab was represented in the numerical model in order to improve the computational efficiency. Reinforcement was modelled as 2D line elements, creating a grid of lines with spacing of 21 mm and a length corresponding to the ones used in real specimens. The second layer of the reinforcement, placed in the tensile areas, was modelled using 2D line elements, in the 3D space, considering the same bending angle. Loading plates of 100 × 100 × 20 mm are modelled to avoid stress concentrations and ensure a more realistic loading scenario. The geometries are exported to the FEM 1 and FEM 2 software, for further processing and analysis.

Table 1 Mechanical properties of materials used in the numerical model

Parameters	Concrete	Textile 180°	Textile 113°	Loading plates
Young' modulus [MPa]	41,000	251,500	67,905	210,000
Poission's ratio [–]	0.2	0.3	0.2	0.3
Compressive strength [MPa]	118	–	–	–
Tensile strength [MPa]	2.2	3998	1200	–

3.1 FEM 1

Due to geometric irregularities, the structure was divided into two parts, the support and the resolved geometry. These parts were connected using a tie constraint with surface-to-surface discretisation, assigning the support contact face as the master surface and the intersecting surface as the slave surface. This formulation enforces a rigid kinematic connection at the interface, ensuring displacement continuity and enabling the assembly to act as a single body.

The concrete was modelled as a homogeneous three-dimensional continuum using C3D8R elements with a mesh size of 10 mm. Due to complicated geometry, the element choosen was Hex-dominated with sweep technique, but still some of the elements are disordered. The nonlinear material behaviour was represented using the concrete damage plasticity model (CDP) [14]. The adopted plasticity parameters are summarized in Table 2. The dilation angle governs the inelasticvolumetric expansion under shear loading, whereas the eccentricity parameter controls the shape of the plastic potential function and ensures numerical smoothness. The ratio f_{b0}/f_{c0} represent the relationship between biaxial and uniaxial compressive strength, while K defines the shape of the yield surface in the deviatoric plane. The viscosity parameter introduces viscoplastic regularization to enhance numerical convergence in the softening regime. A detailed description of the plasticity parameters can be found in [14]. Therefore, the tensile stress-strain relationship was generated in accordance with Model Code 2010 [9]. The resulting stress-strain curves for compression and tension were converted into cracking-strain formulation for implementation within the CDP model. This approach governs the tension stiffening behaviour, allow-ing the concrete to retain tensile capacity due to bond interaction with textile reinforcement and ensuring stress transfer within the textile.

Table 2 Plasticty parameters for CDP model

Parameters	Dilation angle	Eccentricity	f_{b0}/f_{c0}	K	Viscosity parameter
Values	50	0.1	2	0.6667	5E-05

The textile reinforcement was discretised using T3D2 truss elements with a mesh size of 21 mm and embedded into the concrete via the embedded region constraint. This approach couples the degrees of freedom of the reinforcement to those of the surrounding concrete, enforcing perfect bond and preventing relative slip. Given the strong bond characteristics of textile reinforcement in concrete, this assumption is considered appropriate. The carbon textile material was modeled as isotropic linear elastic with inactive compression strength. An elastic formulation was adopted due to the negligible plastic deformation observed during single yarn testing.

Like described before, due to symmetric properties of the ceiling slab, the numerical model was reduced to a quarter by introducing displacement constraints on the symmetry planes at the midspan of the ceiling in both directions. The support nodes, corresponding to the bottom surface of the support wall, are constrained kinematically to the reference point (RP), and the support boundary conditions are applied at this RP, allowing movement in the spanning direction, as observed during the experiment. The use of RP allows us to control and measure the behavior of a group of nodes as a single mechanical entitiy instead of constraining them individually.

The loading plates were modelled using C3D8R solid elements and assigned linear elastic material corresponding to steel. Contact between the loading plates and the ceiling slab was defined using a surface-to-surface formulation, with a tangential coefficient of 0.35 and hard contact behaviour in the normal direction, meaning that the surfaces cannot penetrate each other. Reference points were coupled to each loading plate using a continuum distributing constraint to ensure uniform and stable load transfer to the plates. A load-controlled action with a magnitude of 30 kN was applied at the corresponding reference points. Self-weight was included and applied opposite to the external load, consistent with the experimental test configuration. The analysis was performed in a single load step with a minimum increment size of $1 \cdot 10^{-7}$ and a maximum increment of 0.05.

3.2 FEM 2

Concrete was modelled using the CC3DNonLinCementitous2 material model. Due to the irregular geometry, tetrahedral elements with a mesh size of 10 mm were employed. Material parameters governing tensile and compressive behaviour were derived directly from experimental tests, see Fig. 2 and Table 1. The concrete material law considers the orthotropic smeared crack formulation for fracture in tension and the three-parameter Menetrey-Willam failure surface for hardening/softening plasticity in compression [15]. Due to lack of experimental data for the fracture energy G_f behaviour of the concrete, this value was calculated based on Model Code 2010 [9]:

$$G_f = 73 \cdot f_{cm}^{0.18} \quad (1)$$

The textile reinforcement grid was again modelled explicitly using one-dimensional truss elements. Its mechanical behaviour was represented by a bilinear stress-strain relationship calibrated from single-yarn tensile tests with compression neglected. The interaction between reinforcement and the structure was implemented using the embedded reinforcement approach available in ATENA. In regions where the textile reinforcement was manually bent during fabrication using thermal treatment, the associated material degradation was considered by locally reducing the tensile strength and elastic modulus of the reinforcement, see Table 1.

Boundary conditions were defined to replicate the experimental setup. As only one quarter of the structure was modelled, symmetry boundary conditions were applied on the corresponding faces of both the slab and the loading plates. Supports were applied directly to the bottom surface of the support region, where displacements are allowed along the spanning direction. Load introduction plates were modelled explicitly using elastic steel plates with fixed contact conditions to ensure realistic load transfer. Plates along the symmetry planes were modelled as half or quarter geometries, with the applied load scaled accordingly. A total load of 30 kN was applied incrementally over 100 steps using a linear increment. Self-weight was included and applied opposite to the loading direction to reflect the inverted testing configuration. To monitor structural response, monitoring points were defined at nodes

corresponding to displacement transducers and loading points used in the experiment, enabling direct comparison between numerical and experimental results.

4 Model comparison

Modal validation is a critical process in the development of numerical models, aiming to investigate which of the models accurately represent the structural behaviour. In this study, the validation is performed by comparing model predictions with experimental results. The deviation between the loads applied by the individual hydraulic cylinders was approximately 10%, which resulted in non-uniform deflection at those points. In FE analysis, however, the loads were applied with equal magnitude. For this reason, measuring points IWA2_1 and IWA2_2, which were not directly influenced by the load introduction, were selected for comparison between the numerical and experimental results. The sensors are located as shown in Fig. 3 (right), so there is no direct loading on this part. The forces are extracted from the reaction forces at support, scaled down with a factor of 2.25, to match the load for one hydraulic cylinder. The vertical displacements are measured in both models at the point corresponding to the same location as in the experiment.

Fehler! Verweisquelle konnte nicht gefunden werden. and Fig. 5 present the comparison between the experimental response and the two FE models at two monitoring points. Both numerical approaches capture the overall nonlinear load-displacement behaviour of the CRC slab. Textile-reinforced concrete has typically three states of stress-strain relationship. In the first state, the composite is uncracked, and the initial stiffness is governed by composite stiffness. The initial stiffness is reproduced almost identically by both models, indicating that the elastic material parameters and boundary conditions assumptions were properly defined. The second state starts with the initiation of the first crack. In this state, the load is transferred gradually to the reinfrocement's cross section.

In the post-cracking state, differences between the modelling approaches become more pronounced. The FEM 2 demonstrates excellent agreement with the experimental curve across the full loading range. The predicted stiffness degradation and subsequent hardening closely match the experimental response indicating that the calculated fracture energy provides a reasonable representation of the material behavior. The ability of the model to maintain realistic tension stiffening between cracks ensures accurate stress redistribution and progressive mobilisation of the textile reinforcement.

In contrast, FEM 1 exhibits a slightly reduced stiffness in the stabilised cracking regime. This behaviour can be attributed to differences in the constitutive framework, particularly the implementation of tensile softening within the CDP model. The CDP formulation was defined in stress-

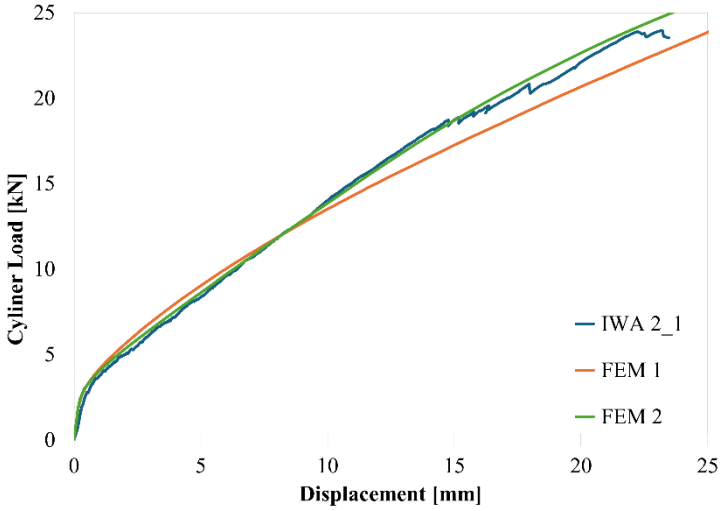


Fig. 4 Comparison of the FE models with experimental results of IWA2_1 (graphic: S. Cengu)

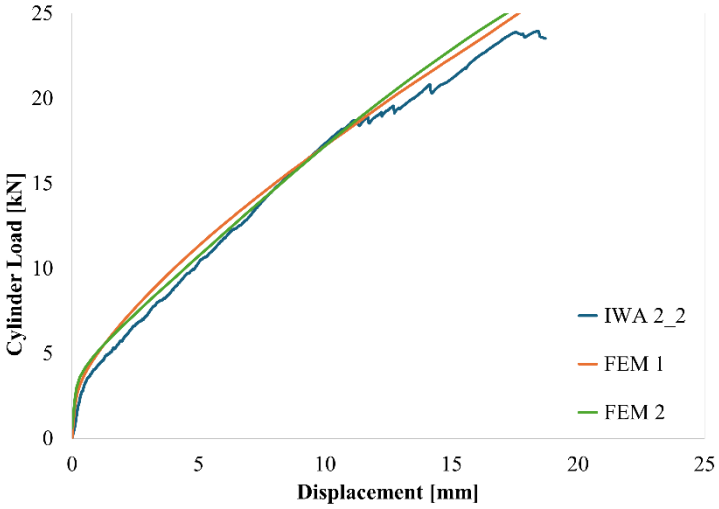


Fig. 5 Comparison of the FE models with experimental results of IWA2_2 (graphic: S. Cengu)

strain form, making it sensitive to the mesh size. Since the element size is not constant, some of the elements are disordered, the model might exhibit slightly accelerated stiffness degradation, leading to reduced effective stress transfer to the textile reinforcement. Also, variation in the cracking strain leads to different results. Near the peak load, FEM 2 slightly overestimates the experimental resistante wich may be associated with the assumption of idealised bond conditions.

5 Conclusions and Outlook

This study presented a unified modelling strategy that was implemented in two FE software packages to evaluate the structural behaviour of shell-like CRC ceiling slabs. The proposed approach enabled a consistent comparison between numerical predictions and experimental investigation.

The displacement distributions were accurately reproduced by both FE models, demonstrating that the global structural response can be captured using commercially available software. However, the comparison indicates that an accurate representation of fracture energy or tension softening is essential for predicting the nonlinear behaviour of CRC elements. FEM 2 model showed excellent agreement with experimental results, but further refinement is required to reproduce the failure point. FEM 1 model required careful calibration of the tensile softening formulation to achieve realistic post-cracking behaviour and stress transfer within the composite system. Within the serviceability limit state, both software packages provided accurate results, with FEM 1 exhibiting a slight overestimation of the structural stiffnes. The computational time in both software packages was dependent on the adopted mesh size. For a mesh size of 10 mm, the FEM 1 model required approximately 14 h of comutation, whereas FEM 2 required about 5 h. Increasing the element size to 20 mm significantly reduced the calculation time, however, a slight reduction in accuracy was observed. For general assessment of structural behavior or for parametric studies, a mesh size of 20 mm provides a good balance between computational efficiency and acceptable accuracy. FEM 2 required less calibration effort in terms of input parameters, while simultaneously providing accuracy and enhanced computational efficieny compared to FEM 1.

The findings of this study highlight the potential of FE software for simulating the behaviour of CRC structures. However, they emphasise the necessity of developing computationally efficient and robust modeling approaches. Future research will focus on further refinement of the numerical models and the execution of comprehensive parametric studies aimed at structural optimisation. Particular attention will be given to exploring different geometries, materials, and boundary conditions to enhance material efficiency while maintaining high structural performance. Furthermore, manufacturing considerations will form an integral part of future research. 3D concrete printing and innovavite casting methods will be explored to expand the design space, alongside further development of the strut-and-tie method for CRC structures.

Acknowledgements

This research was funded by the German Research Foundation (German: Deutsche Froschungsgemeinschaft, DFG) within the SFB/TRR 280 (grant number 417002380, project C01). The authors would like to thank the DFG for supporting the research project.

References

[1] Schladitz, Frank, Curbach, Manfred, Tietze, Matthias, and Lieboldt, Matthias. 2016. "Carbon and Concrete – The Future of Construction." Paper presented at the IABSE Conference, Guangzhou 2016: Bridges and Structures Sustainability – Seeking Intelligent Solutions, Guangzhou, China (People's Republic), 2016, 733–743. doi:10.2749/222137816819259167.

[2] Beckmann, Birgit, et al. 2021. "Collaborative research on carbon reinforced concrete structures in the CRC/TRR 280 project." *CEND* 3:99–109, doi:10.1002/cend.202100017.

[3] Vakaliuk, Iurii, Scheerer, Silke, and Curbach, Manfred. 2024. "Numerical Analysis of Textile Reinforced Concrete Shells: Force Interaction and Failure Types." *CivilEng* 5:224–246. doi:10.3390/civileng5010012.

[4] Vakaliuk, Iurii, Scheerer, Silke, and Curbach, Manfred. 2023. "Vacuum-Assisted Die Casting Method for the Production of Filigree Textile-Reinforced Concrete Structures." *Buildings* 13:2641. doi:10.3390/buildings13102641.

[5] Vakaliuk, Iurii, Scheerer, Silke, and Curbach, Manfred. 2024."Leichte Deckenelemente aus Carbonbeton." *Beton- und Stahlbetonbau* 119:864–872. doi: 10.1002/best.202400060.

[6] Schneider, Kai, Butler, Marko, and Mechtcherine, Viktor. 2017. "Carbon Concrete Composites C^3 – Nachhaltige Bindemittel und Betone für die Zukunft." *Beton- und Stahlbetonbau* 112:784–794. doi:10.1002/best.201700058.

[7] DIN EN 12390-1:2021-09, *Prüfung von Festbeton – Teil 1: Form, Maße und andere Anforderungen für Probekörper und Formen*; Deutsche Fassung EN 12390-1:2021. doi:10.31030/3240228.

[8] Schütze, Elisabeth, Bielak, Jan, Scheerer, Silke, Hegger, Josef, and Curbach, Manfred. 2018. "Einaxialer Zugversuch für Carbonbeton mit textiler Bewehrung." *Beton- und Stahlbetonbau* 113: 33–47. doi: 10.1002/best.201700074.

[9] Fédération internationale du béton (*fib*, ed.). 2010. *fib Model Code for Concrete Structures 2010*. Berlin: Ernst & Sohn.

[10] solidian (ed.). 2023. *Technical Data Sheet solidian Grid Q85-CCE-21-E5 2023*. Accessed November 12, 2024. https://www.solidian-kelteks.com/en/downloads.

[11] Sharei, Ehsan, Scholzen, Alexander, Hegger, Josef, and Chudoba, Rostislav. 2017 ."Structural behavior of a lightweight, textile-reinforced concrete barrel vault shell." *Composite Structures* 171:505–514. doi:10.1016/j.compstruct.2017.03.069.

[12] Spartali, Homam, Mester, Leonie, Kikis, Georgia, and Klarmann, Simon. 2024."Numerical simulations of origami-based folded carbon-reinforced concrete shells." Paper presented at 16th World Congress on Computational Mechanics and 4th Pan American Congress on Computational Mechanics – CIMNE. 2024. doi:10.23967/c.wccm.2024.093.

[13] R. M. & Associates. "Rhinoceros 3D', www.rhino3d.com." Accessed February 12, 2026. https://www.rhino3d.com/en/emea/.

Dassault Systèmes. 2016. "Simulia Abaqus 2016 – Abaqus Theory Guide." Accessed February 12, 2026. http://130.149.89.49:2080/v2016/books/stm/default.htm.

[15] Cervenka, Vladimír, Jendele, Libor, and Červenka, Jan. 2025. "ATENA Program Documentation." Accessed February 12, 2026. Available: https://www.cervenka.cz/assets/files/atena-pdf/ATENA_Theory.pdf.

Experimental and numerical investigation of the bond behaviour of fiber-reinforced polymer quadriaxial anchored fabrics

Hothaifa Abdulwahab Ali[1], Ciro Del Vecchio [2], Marco Di Ludovico[1], Andrea Prota[1]

[1] Dept. of Structures for Engineering and Architecture,
University of Napoli Federico II,
Via Claudio 21, Napoli 80125, Italy

[2] Dept. of Engineering,
University of Sannio,
Piazza Roma, 21, Benevento 82100, Italy

Summary
The use of quadriaxial FRP fabrics is increasing in seismic strengthening of reinforced concrete beam–column joints due to their multi-directional fibres that are effective in variable inclination stress fields. However, debonding from the concrete substrate limits the effective use of FRP tensile strength. To overcome this limitation and avoid interruption in the use of the structure, minimally invasive intervention relying on the use of mechanical FRP anchors that can be installed externally without partial demolition of infills is gaining popularity as an effective alternative to traditional U-wrapping. This study investigates the bond mechanisms of anchored quadriaxial CFRP fabrics using experimental and numerical approaches. Results show that fan anchors enhance the tensile strength of the system. A nonlinear finite element model is proposed and validated against experimental data with the scope of providing further insights into the interaction between fabrics and anchors.

1 introduction

Fiber-reinforced polymer (FRP)–based local strengthening techniques have proven effective in improving the seismic performance of reinforced concrete (RC) beam–column joints by increasing joint shear strength and allowing ductile response mechanisms. However, the effectiveness of externally bonded FRP systems is often limited by premature debonding at the FRP–concrete interface. Traditional solutions such as full FRP wrapping are highly invasive, requiring partial demolition of infill walls and interruption of the serviceability of existing structures. These limitations have motivated the development of minimally invasive strengthening techniques applicable mainly from the exterior of the structure [1].

In this context, FRP mechanical anchors have proven to be a promising solution to enhance the bond and tensile performance of the FRP reinforcement, enabling the effective use of large-width FRP quadriaxial fabrics for joint panel strengthening [1], [2]. Nevertheless, a robust analytical model for the anchored fabrics or sheets is still lacking, and current FRP-strengthening guidelines provide empirical and conservative approaches. An experimental investigation for unanchored and anchored CFRP quadriaxial fabrics was conducted with the purpose of proving the effectiveness of FRP fan anchors [2]. However, the bond behaviour of quadriaxial fabrics is challenging due to the complex interaction between inclined and straight fibres, concrete cracking, interface debonding, and anchor activation. Numerical modelling, therefore, represents a key tool to interpret experimental evidence and to clarify the load transfer mechanisms. To date, numerical studies on quadriaxial FRP fabrics are missing. In this context, this paper proposes a real advancement in this field, presenting the experimental results and a preliminary numerical FEM model for both bonded and anchored quadriaxial CFRP fabrics, developed using DIANA FEA.

2 the experimental study

The experimental programme was designed to investigate the effectiveness of FRP fan anchors in enhancing the tensile capacity of externally bonded quadriaxial CFRP fabrics and in preventing premature debonding from the concrete substrate. The study focused on the influence of key parameters, including the number of fabric layers, the anchor configuration, and the anchor dowel diameter. A total of 19 specimens strengthened with quadriaxial FRP fabrics, with and without mechanical anchors, were tested under monotonic displacement using a dedicated test setup specifically developed to accommodate large-width specimens. The use of wide specimens was necessary to properly activate inclined fibres and to allow the installation of multiple anchors across the specimen width, conditions that are representative of joint panel strengthening applications. More details on the experimental study can be found in [2].

2.1 Test setup

A single push-shear test was selected to investigate the bond behaviour of anchored quadriaxial CFRP fabrics. This setup (Fig. 1) provides a representative load transfer mechanism. The 250 mm wide fabric, bonded to a concrete block, allowed activation of inclined fibres and the installation of two parallel anchors. A fabric bond length of 300 mm, well above the minimum recommended length (100 mm), ensured full development of bond strength [3]. Displacement between the two blocks was measured with four LVDTs, while fibre strains were monitored using strain gauges and Digital Image Correlation (DIC) [2], providing a detailed view of the strain distribution across fibre orientations and along the fabric width.

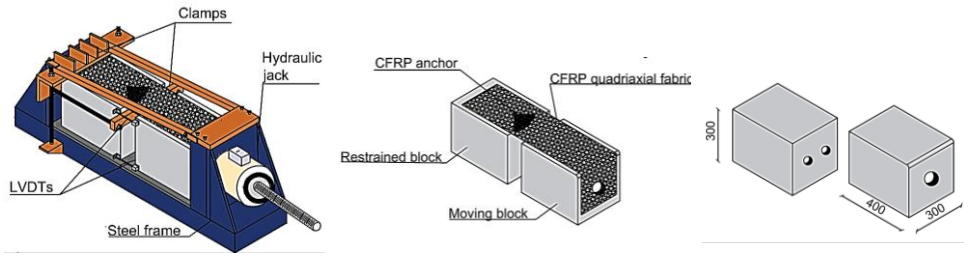


Fig. 1 View of the test setup. (dimensions in mm)

2.2 Material properties

The mean compressive strength for concrete (f_{cm}) is 24.74 MPa at 28 days, obtained using compression tests conducted on three cylindrical specimens. The quadriaxial CFRP fabric, composed of fibre layers oriented at 0°, 90°, and ±45°, had a dry fibre thickness of 0.053 mm per direction, an elastic modulus of 304 GPa, and an ultimate tensile strain of 1.2% for the longitudinal fibres, as obtained from coupon tests. A two-component epoxy resin with tensile strength exceeding 40 MPa and elastic modulus of 2500 MPa, as reported by the manufacturer, was used for fibre impregnation. The mechanical anchors were made of pultruded CFRP with diameters of 10 and 16 mm, a fibre volume fraction of 68%, and were installed using a high-strength epoxy adhesive specified for seismic applications.

2.3 Specimens' layouts

The experimental programme included specimens strengthened with quadriaxial CFRP fabrics tested without and with mechanical fan anchors. The parameters investigated in this paper include the number of fabric layers and the presence of an anchor. The unanchored specimens, Fig. 2 (left), were used as a reference, while the anchored specimens, Fig. 2 (right), were used to assess the contribution of the fan anchor. Anchors consisted of pultruded CFRP dowels with splayed fibre fans bonded to the surface fabric. All specimens were prepared using recommended surface preparation and bonding procedures to ensure consistent bond conditions. The test matrix and representative specimen layouts are summarized in Table 1. Specimens were labelled according to the format XL_Q_Y_ZWJ_N, where X denotes the number of quadriaxial FRP fabric layers (1 or 2); Q indicates the use of quadriaxial fabric; Y identifies the strengthening configuration (Bonded or Anchored, A); Z denotes the number of anchors (1 or 2); W specifies the anchor position (Front, F, or Back, B); and J indicates the anchor dowel diameter (10 or 16 mm).

Table 1 Test matrix

Specimen	Fabric thickness (mm)	No. layers	Configuration	Anchor diameter (mm)	Anchor position
1L_Q_Bond	0.053	1	Bonded	-	-
1L_Q_A_1F10	0.053	1	Anchored	10	Front
2L_Q_Bond	0.106	2	Bonded	-	-
2L_Q_A_1F10	0.106	2	Anchored	10	Front

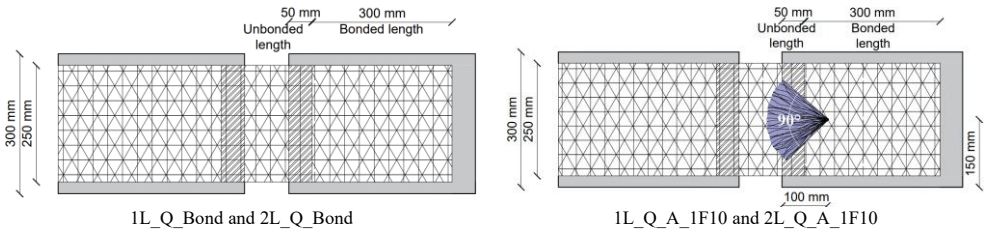


Fig. 2 Specimens' configurations: (left) unanchored specimens; (right) anchored specimens

2.4 Experimental results

Fig. 3 compares the force–displacement response of bonded and anchored quadriaxial CFRP fabrics, where three failure modes were observed: fabric debonding, fiber fracture in the fabric, and anchor failure. Unanchored specimens (1L_Q_Bond and 2L_Q_Bond), Fig. 3 (left), exhibited an initial linear response followed by debonding propagation at an approximately constant force level. In contrast, anchored specimens showed a more complex response where initial debonding was followed by anchor engagement, leading to a renewed strength increase and, in most cases, fabric or anchor fracture. The front-positioned anchored specimen (1L_Q_A_1F10), Fig. 3 (right), exhibited a fabric fracture failure mode, indicating full exploitation of the FRP tensile capacity. Specimens with anchors placed closer to the loaded edge exhibited earlier anchor engagement and higher strength enhancement, as load transfer was more effectively redirected into the concrete support. Increasing the number of fabric layers shifted the governing failure mode from fabric fracture to anchor failure (2L_Q_A_1F10), Fig. 3 (right). Overall, the results highlight a strong interaction between bond behaviour and anchor activation, governed by fibre orientation, anchor position, and load transfer mechanisms.

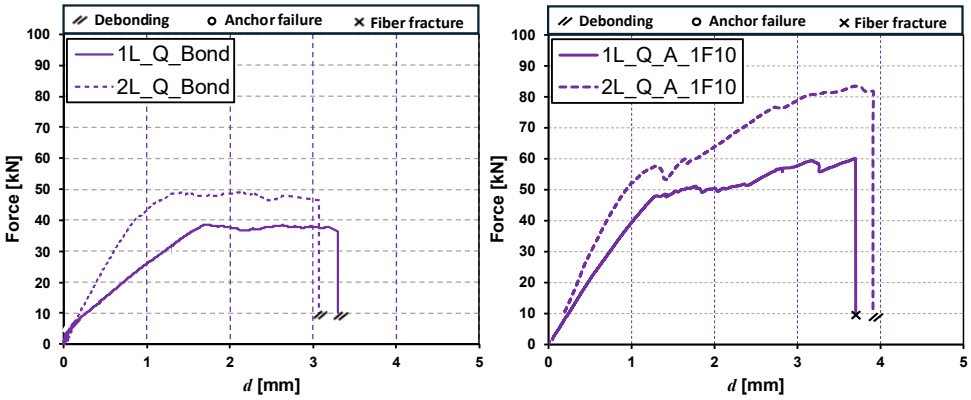


Fig. 3 Experimental force versus displacement responses grouped for: (left) unanchored one and two-layer specimens; (right) anchored one and two-layer specimens.

In bonded-only specimens (1L_Q_Bond and 2L_Q_Bond), strain propagated along the entire fabric length, indicating progressive debonding. In one-layer specimens with a single front-positioned anchor (1L_Q_A_1F10), strain propagation beyond the anchor was effectively suppressed, Fig. 4 (left). In contrast, in the two-layer specimen (2L_Q_A_1F10), a single front anchor delayed but did not fully prevent strain propagation, with strain extending up to 235 mm along the fabric; at the same distance, strain remained negligible in the one-layer anchored specimen, confirming the effectiveness of front-positioned anchors in limiting debonding.

Front-positioned anchors notably enhanced the engagement of inclined fibres, increasing ±45° fibre strain by 208% in one-layer specimens and 310% in two-layer specimens. Accordingly, front-anchored configurations developed significantly higher inclined-fibre strains than unanchored specimens, reaching 0.37% versus 0.12% in one-layer specimens and 0.45% versus 0.11% in two-layer specimens, demonstrating the effectiveness of front-positioned anchors in activating diagonal fibre families.

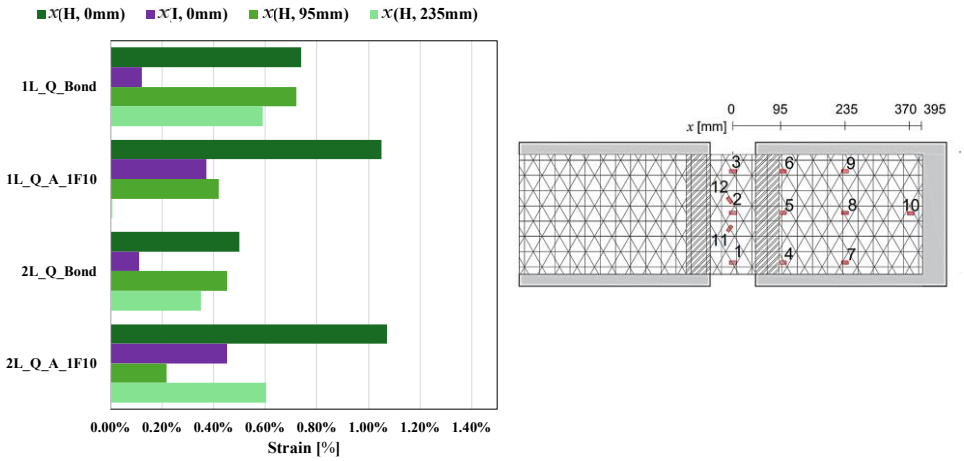


Fig. 4 (left) mean strain distribution in horizontal (H) and inclined (I) fibers at distances of 0, 95, and 235 mm; (right) the strain gauges layout.

3 finite element modelling

The objective of the finite element modelling in this study is to reproduce the experimental response and to provide a deeper interpretation of the complex load-transfer mechanisms in anchored quadriaxial CFRP fabrics, such as the activation of the inclined fibres, the engagement of the FRP fan anchors, and to quantify their contribution to the overall load-carrying capacity. Beyond experimental validation, the numerical model enables a parametric investigation of anchorage configurations not tested experimentally, thereby extending the understanding of the system behaviour, enabling the development of design recommendations. The proposed modelling also establishes the basis for future simulations of RC beam–column joints strengthened with anchored quadriaxial CFRP fabrics, consistently with previous experimental investigations [1].

3.1 Meshing and boundary conditions

A mesh with an element size of 7.5 mm was adopted based on a preliminary mesh sensitivity study, which confirmed that further refinement had a negligible effect on the global force–displacement response and predicted failure modes. Boundary conditions replicated the experimental single push-shear test setup, Fig. 5 (right). The reaction block was fully restrained, while the action block was not modeled to reduce the computational effort.

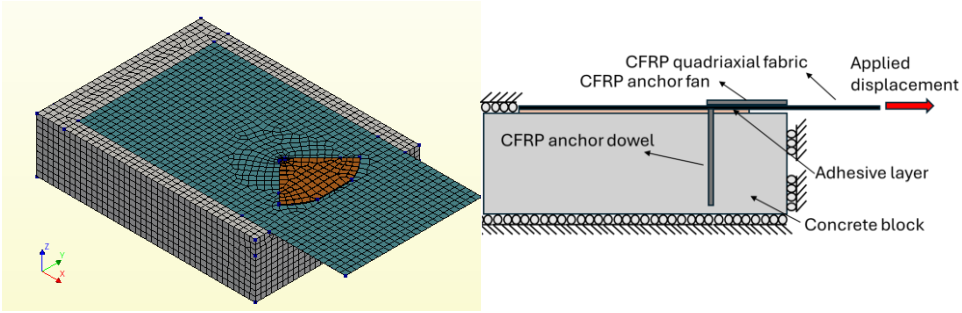


Fig. 5 (left) anchored fabric finite elements; (right) boundary conditions.

3.2 Materials and Constitutive Laws

The finite element model, Fig. 5 (left), consists of four components: the concrete block, the quadriaxial CFRP fabric, the CFRP anchor dowel and fan, and the concrete–CFRP fabric interface. A perfect bond was assumed between the CFRP anchor fan and the quadriaxial fabric, as no debonding or rupture at this interface was observed experimentally.

3.2.1 Concrete

Concrete was modelled using a total strain–based crack model (smeared crack) with a rotating crack model. The tensile response was defined using the Hordijk softening law [4]. with a mean tensile strength $f_{ctm} = 1.963$ MPa and a mode I fracture energy $G_f = 0.137$ N/mm. In compression, the nonlinear behaviour was described by the Hognestad model [5]. Three-dimensional 20-node solid elements were used to model the concrete block.

3.2.2 CFRP quadriaxial fabric

The mechanical behaviour of quadriaxial CFRP fabrics is governed by the combined contribution of multiple fibre families oriented at 0°, 90°, and ±45°, resulting in an anisotropic tensile response. In the numerical model, the fabric was represented using two-dimensional layered shell quadrilateral 8-node elements, with each layer corresponding to one fibre orientation (0°, 90°, +45°, and −45°). Each layer was assigned an elastic modulus of 304 GPa and an ultimate tensile stress corresponding to an ultimate strain of 1.2. A linear-elastic orthotropic constitutive law is used, with the material axes aligned with the fibre direction, allowing the individual stiffness contributions of the different fibre families to be explicitly captured. Brittle tensile failure was assumed to occur upon reaching the ultimate tensile strength of the fibres, in accordance with experimental observations.

3.2.3 CFRP anchor

Three-dimensional solid hexahedral elements were used to represent the FRP anchor dowel and fan. A linear elastic orthotropic constitutive law was assigned, with a tensile strength of 2512 MPa. The dowel has a nominal diameter of 10 mm, and an equivalent cross-sectional area was set to the fan–dowel transition region. In addition, material orientations were defined to adequately represent the direction of the fibres in the anchor, which changes from the embedded dowel to the anchor fan. A perfect bond was assumed between the fan and the quadriaxial FRP fabric since no bond failure was observed experimentally. A no-tension interface was assigned to the concrete-FRP anchor dowel interface.

3.2.4 Concrete-CFRP quadriaxial fabric interface

The concrete–FRP interface was modelled using face-to-face interface elements governed by a bilinear shear bond–slip law, in accordance with the CNR-DT 200 R2 2026 guidelines (Fig. 6). The maximum shear bond stress was calculated using Eq. (1), resulting in $\tau_{\max} = 3.5$ MPa. The slip corresponding to the initial stiffness, s_i, was computed using Eq. (2) based on the mechanical properties of the adhesive and concrete, namely the shear modulus of the adhesive $G_a = 1000$ MPa, the shear modulus of concrete $G_c = 12025$ MPa, the nominal adhesive thickness $t_a = 1$ mm, the effective concrete thickness contributing to interface deformability $t_c = 20$ mm, and a coefficient $c_1 = 0.6$. The ultimate slip $s_u = 0.25$ mm, which represents complete debonding and progressive loss of bond. To improve

agreement with the experimental response, the slip corresponding to the maximum bond stress was calibrated to $s_i = 0.03$ mm in the numerical model.

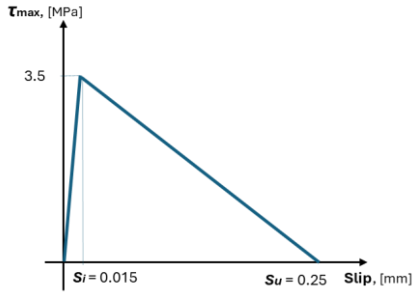


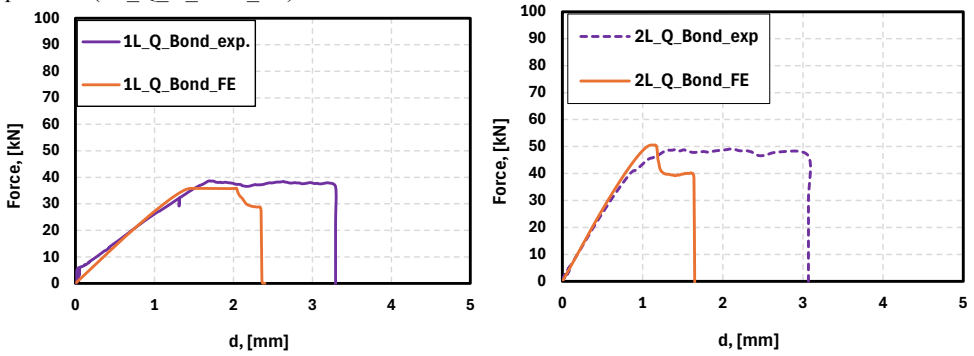
Fig. 6 Bond-slip model (CNR-DT 200 R2)

$$\tau_{max} = \frac{\sqrt{f_{cm} f_{ctm}}}{2} \quad (1)$$

$$k_1 = \frac{c_1}{t_a/G_a + t_c/G_c} \quad (2)$$

4 Model verification

The finite element model was compared with the experimental results in terms of global force–displacement response and local strain development in the quadriaxial CFRP fabric. As shown in Fig. 7, the numerical simulations accurately reproduce the initial stiffness and peak load of both bonded and anchored specimens. In bonded-only configurations (1L_Q_Bond_FE and 2L_Q_Bond_FE), the model correctly captures the onset of debonding and the subsequent force plateau associated with interface crack propagation. However, a discrepancy was noted in the numerical response, where two distinct plateaus were observed: the first corresponds to the attainment of the ultimate slip (s_u) in the bond–slip law, followed by a force drop due to significant concrete cracking, while the second plateau represents the development of stable cracking within the concrete substrate. Notably, this plateau is shorter than what was observed experimentally, attributed to the absence of the unanchored concrete block, which is in the left of each specimen, Fig. 2. For anchored specimens (1L_Q_A_1F10_FE and 2L_Q_A_1F10_FE), the numerical model successfully reproduces the characteristic two-stage response observed experimentally: initial debonding followed by anchor engagement and a renewed strength increase. The predicted peak loads are in good agreement with experimental values, but with higher stiffness in the second stage, which is related to the anchor engagement. However, the numerical response for the two-layer front-anchored specimen (2L_Q_A_1F10_FE) reproduces the initial debonding that was observed experimentally; it is less evident in the one-layer front-anchored specimen (1L_Q_A_1F10_FE). Nevertheless, the numerical model replicated the same experimental failure modes with a tensile failure in the quadriaxial fabric for one-layer front-anchored specimen (1L_Q_A_1F10_FE) and simultaneous debonding and anchor failure for two-layer front-anchored specimen (2L_Q_A_1F10_FE).



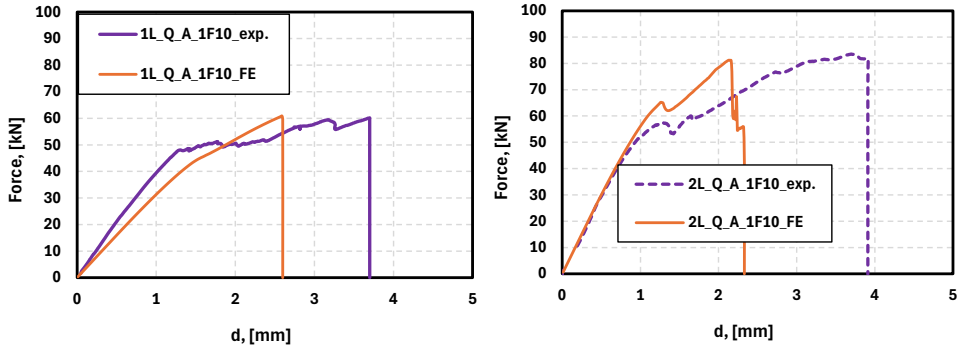


Fig. 7 Experimental–numerical comparison of force-displacement response

The comparison between experimental and numerical strain–displacement responses for the bonded-only 1-layer specimen (1L_Q_Bond, Fig. 8) demonstrates that the proposed finite element model captures the essential mechanisms governing strain development along the quadriaxial CFRP fabric. At locations close to the loaded edge for horizontal fibres (H, 0 mm), the numerical model reproduces well the initial linear strain development and the strain level at the onset of debonding, confirming an accurate representation of the interface stiffness and load transfer. The model also reproduces the limited strain development in the inclined (±45°) fibres near the loaded edge (I, 0 mm), observed experimentally. It overestimates the strain in inclined fibres; nevertheless, it correctly captures their limited engagement and the overall anisotropic strain redistribution among the different fibre orientations.

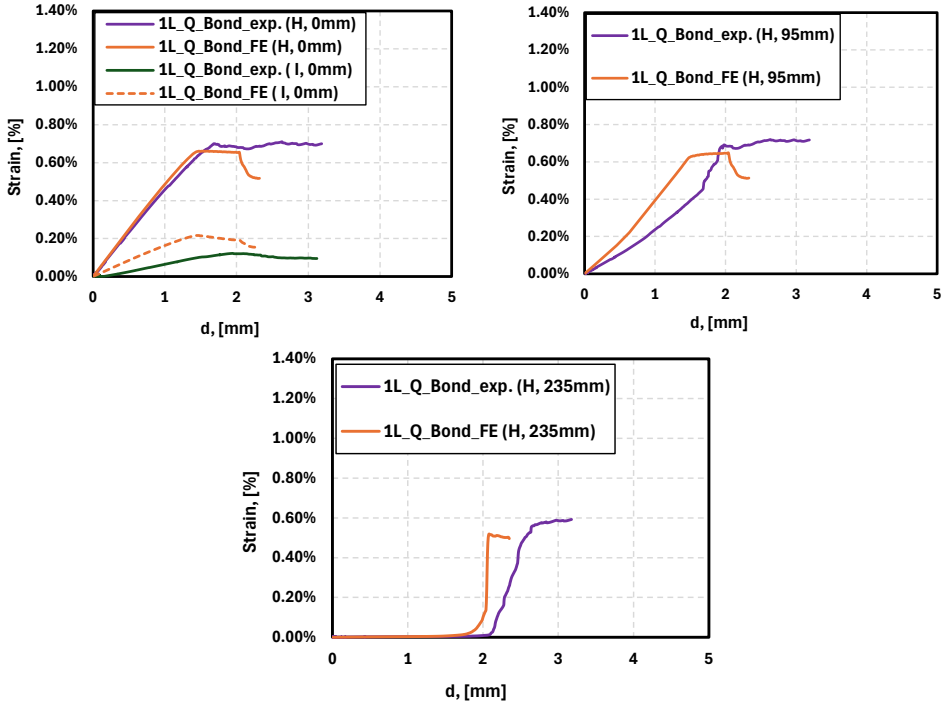


Fig. 8 Experimental–numerical comparison of strain–displacement in CFRP fabric with horizontal (H) and inclined (I) fibres at distances of 0, 95, and 235 mm (bonded-only 1-layer specimen).

At intermediate distances (H, 95 mm), the numerical and experimental curves for horizontal fibres show good agreement in terms of strain development and peak strain level, indicating that the model correctly captures the propagation of the debonding along the bonded length. At larger distances from the loaded edge (H, 235 mm), both numerical and experimental results for horizontal fibres confirm negligible strain development up to advanced displacement levels, followed by a sudden strain increase associated with debonding propagation reaching this section. This confirms its capability to simulate both the strain and the debonding propagation.

Overall, this finite element model provides a good representation of the complex interaction between concrete cracking, interface debonding, and fibre orientation for the bonded FRP quadriaxial fabrics, providing confidence in using the model for further investigations into more anchored configurations and large-scale applications.

5 CONCLUSIONS

This study presented an integrated experimental–numerical investigation on the bond behaviour of externally bonded and mechanically anchored quadriaxial CFRP fabrics commonly used for the seismic strengthening of RC beam–column joints. The main conclusions can be summarized as follows:

- Mechanical FRP fan anchors are highly effective in delaying interface debonding and in promoting a more efficient utilization of the tensile capacity of quadriaxial CFRP fabrics.
- Front-positioned anchors ensured effective activation of the inclined (±45°) fibres, resulting in higher strength enhancement and reduced strain in the fabric area beyond the anchor position.
- The proposed finite element model successfully reproduced the experimental response in terms of global force–displacement behaviour and local strain evolution for both bonded and anchored specimens.
- The modelling strategy: smeared-crack concrete, face-to-face shear bond–slip interfaces, layered orthotropic shells for the quadriaxial fabric, and solid elements for the FRP anchors, proved capable of capturing the complex interaction between concrete cracking, interface debonding, fibre orientation, and anchor engagement. However, neglecting normal stresses and mixed-mode effects in the bond-slip interface represents a modelling limitation.
- Despite certain discrepancies, the model effectively predicts peak strength and failure modes. These differences—such as the shortened debonding plateau and the overestimation of post-debonding stiffness in the anchored specimens—are anticipated to be addressed by modelling the unanchored concrete moving block, which is on the right side of each specimen, Fig. 1. This approach would enable a longer propagation of debonding and reduce the post-debonding stiffness.

Overall, this work presents new numerical insights into bonded quadriaxial FRP fabrics. The results establish a solid basis for future work on improving the response of anchored specimens, parametric studies, and extending the modelling approach to full-scale RC beam–column joints under cyclic loading conditions, supporting the development of rational, minimally invasive, and performance-based FRP strengthening solutions.

References

[1] Del Vecchio, Ciro, Di Ludovico, Marco, Balsamo, Alberto, and Prota, Andrea. 2024 “Minimally Invasive FRP Strengthening of External Beam–Column Joints.” Journal of Composites for Construction, vol. 28, no. 4. Accessed Aug. 2024. doi: 10.1061/jccof2.cceng-4525.

[2] Del Vecchio, Ciro, Ali, Hothaifa Abdulwahab, Prota, Andrea, and Di Ludovico, Marco. 2025 “Influence of FRP Fan Anchors on the Tensile Capacity of Quadriaxial Fabrics.” Journal of Composites for Construction, vol. 30, no. 1. Accessed Feb. 2026. doi: 10.1061/jccof2.cceng-5363.

[3] National Research Council. 2026 “CNR DT200 R2: Guidelines for the Design, Execution, and Control of Static Strengthening Interventions Using Fiber-Reinforced Composites.” Roma, Italy.

[4] Hordijk, Dirk Arend. 1991 “Local approach to fatigue of concrete.” PhD diss., Delft University of Technology.

[5] Hognestad, Eivind. 1951 “A Study of Combined Bending and Axial Load in Reinforced Concrete Members.” PhD diss., University of Illinois.

Investigation of Pull-Out and Beam-End Bond Behavior of CFRP Reinforcing Bars in Low-Clinker Concretes

Paul Heber[1], Oliver Sikorski[2], Alexander Schumann[3], Elisabeth Schütze[3], Paul-Martin Großkopff[4], Birgit Beckmann[1] and Steffen Marx[1]

[1] Institute of Concrete Structures, TUD Dresden University of Technology, 01062 Dresden, Germany
[2] Implenia Civil Engineering GmbH, Landsberger Straße 290a, 80687 München, Germany
[3] CARBOCON GMBH, Mohorner Straße 13, 01159 Dresden, Germany
[4] Kleihues Betonbauteile GmbH & Co. KG, Siemensstraße 21, 48488 Emsbüren, Germany

Abstract

Low-clinker eco-concretes (EC) combined with corrosion-resistant non-metallic (NM) reinforcements, such as carbon fiber-reinforced polymer (CFRP) rebars, offer a CO_2-reducing alternative for sustainable concrete construction. This study examines the bond behavior of CFRP rebars in EC through comprehensive pull-out and beam-end tests, focusing on the effects of bond length and concrete cover. Results show a reliable bond behavior characterized by a progressive zipper-like failure mode with re-anchoring along the bond length. Shorter bond lengths achieved higher bond stresses and controlled crack widths, while longer bond lengths exhibited higher bond stiffness but reduced bond stresses, exceeding permissible crack width limits. These findings underscore the potential of NM-EC systems as durable, corrosion-free and CO_2-reduced concrete structures. However, they also emphasize the need for optimized design parameters to ensure structural performance and serviceability.

1 Introduction

In response to the global imperative to reduce CO_2 emissions in the construction sector, concrete mixes with reduced cement content, so-called eco-concretes (ECs), offer a promising solution. The reduced clinker content in these mixes, however, leads to decreased alkalinity, which impairs the corrosion protection required for conventional steel reinforcement. In contrast, non-metallic (NM) reinforcements made from carbon fiber-reinforced polymer (CFRP) are inherently corrosion-resistant. This property makes them well-suited as a durable reinforcement in EC structures. Additionally, the resistance to corrosion allows for a reduction in concrete cover, enabling more slender structural elements and contributing to the conservation of primary resources. Thus, non-metallic reinforced eco-concrete (NM-EC) presents a highly promising CO_2-reducing alternative for sustainable concrete construction.

While the bond behavior of NM reinforcement has been widely studied (e.g., [1–4]), a significant portion of existing research has focused on textile-based systems such as yarns and grids (e.g., [5–10]). Therefore, for this study comprehensive pull-out (PO) and beam-end (BE) tests on CFRP rebars embedded in eco-concrete were conducted. The aim was to characterize their general bond performance and to evaluate the effects of bond length and concrete cover. Furthermore, crack propagation and crack width development in the rebar bond area were investigated.

2 Materials

2.1 Concrete

The eco-concrete (EC) mixture (see Table 1) employed in this study was formulated based on a standard concrete mix design for exposure class XF2, in accordance with DIN EN 206 and DIN 1045-2 [11, 12], utilizing Blast-furnace cement (CEM III/A). To minimize cement-related CO_2 emissions, the cement content was reduced to 280 kg/m³ and thus below the minimum threshold of 320 kg/m³ specified in the aforementioned standards [11, 12]. The CEM III/A cement used in this study comprises a clinker content ranging from 35% to 50% and is otherwise composed of blast-furnace slag [13], thereby contributing to enhanced sustainability and improved long-term durability. A water-cement ratio of 0.45 was adopted, in compliance with the requirements for durability and workability under the specified exposure conditions. Coarse aggregate with a rounded grain morphology, conforming to grading curve range A/B and with a maximum nominal grain size of 16 mm, was employed.

Additionally, limestone powder was incorporated at a dosage of 60 kg/m³ as a microfiller to enhance the packing density and refine the pore structure of the matrix. The target slump class F4 was achieved through the addition of a polycarboxylate ether (PCE)-based superplasticizer at a dosage of 0.90% by mass of cement.

Table 1 Concrete mixture composition of the developed eco-concrete

Aggregate 0/2 kg/m³	Aggregate 2/8 kg/m³	Aggregate 8/16 kg/m³	Limestone powder kg/m³	CEM III/A 52,5 N SR/NA kg/m³	Water kg/m³	Superplasticizer (PCE) kg/m³
678	486	775	60	280	126	2.52

2.2 CFRP Reinfrocing Bars

The NM rebars used in this study were REBAR D10-CCE (hereafter referred to as CFRP rebar), supplied by solidian GmbH. The rebars (see Fig. 1) have a nominal diameter of 10 mm and are composed of unidirectionally aligned carbon fibers embedded in an epoxy (EP) matrix. The surface profile is achieved by likewise EP-impregnated helical fiber strands around the rebar core. The mechanical characteristics of the CFRP rebars are documented in the manufacturer's technical datasheet [14].



Fig. 1 CFRP rebar „solidian REBAR D10-CCE" (Photo: Paul Heber)

3 Test Setup

3.1 Pull-Out Test

To investigate the general bond behavior between the CFRP rebars and EC, a series of pull-out (PO) tests was conducted in accordance with the Guideline for Non-Metallic Reinforcement (GL-NMR) [15], issued by the German Committee for Reinforced Concrete (DAfStb). The PO tests are therein based on the RILEM RC 6 test [16]. The specimens (see Fig. 2) consisted of cubic concrete blocks with an edge length of 150 mm, in which the rebars were embedded with a bond length of 5d, where d denotes the nominal rebar diameter. Following casting, the specimens were retained in the formwork for a period of two days. Subsequently, they were stored under standard conditions (20 °C, 65% relative humidity (RH)) until reaching the test age of 28 days. For load application, the loaded ends of the rebars were fitted with epoxy-filled steel sleeves. The CFRP pull-out series (CFRP-PO) comprised six specimens. The tests were performed under strain-controlled loading at a constant rate of 1.0 mm/min.

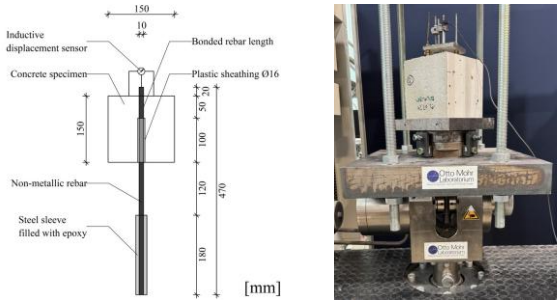


Fig. 2 Pull-out (PO) specimens and test setup (Photo: Paul Heber)

3.2 Beam-End Test

To investigate the influence of bond length and concrete cover on the bond behavior as well as on the development of concrete cracks, four series of beam-end (BE) tests – each comprising six specimens – were conducted on the CFRP rebars in accordance with GL-NMR [15]. The rebars were embedded in concrete specimens (see Fig. 3) with bond lengths corresponding to 5d (series CFRP-BE-5), 20d (series CFRP-BE-20), 40d (series CFRP-BE-40) and 45d (series CFRP-BE-45), where d denotes the nominal rebar diameter. All specimens were cast with a concrete cover of 20 mm. After two days in the formwork, the specimens were stored under standard conditions (20 °C, 65% RH) until testing at an age of 27 to 29 days. For load application, the rebar ends were fitted with heat-shrink tubing and then clamped between steel plates. All tests were performed strain-controlled at a constant rate of 1.0 mm/min. During the tests, the propagation and widths of concrete cracks on the rebar near (i.e., upper) side of the test specimens were recorded using a digital image correlation (DIC) system (see Fig. 4).

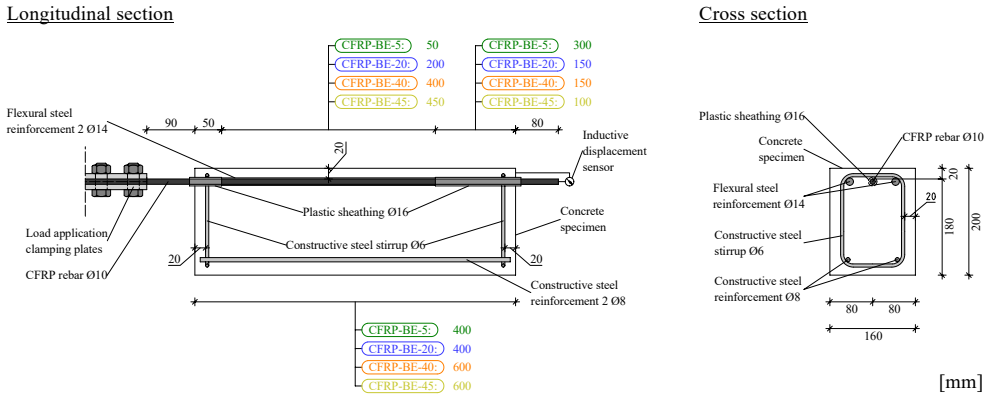


Fig. 3 Beam-end (BE) specimens (Photo: Paul Heber)

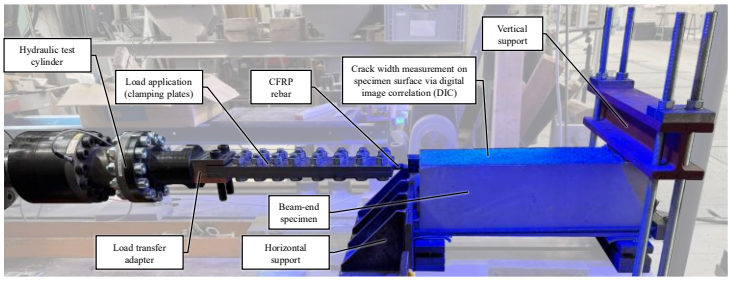


Fig. 4 Beam-end (BE) test setup (Photo: Paul Heber)

4 Experimental Results

At the time of testing the concrete of the PO specimens had an average compressive strength of 58.3 N/mm² and the concrete of the BE test series of 57.0 N/mm², respectively.

All PO and BE specimens exhibited valid failure modes characterized by the shearing and rupture of the rebar profiling, as illustrated in Fig. 5. In the BE test series, additionally cracks of the concrete surface were observed.

The evaluation of the tests necessitated the calculation of bond stress, which was determined from the applied test force (F_P), the nominal rebar diameter (d) and the bond length (l_b) using Eq. (1). The resulting bond stress-slip relationships for the PO and BE test series are presented in Fig. 6 and Fig. 7.

$$\tau_b = F_P / (d \cdot l_b \cdot \pi) \quad (1)$$

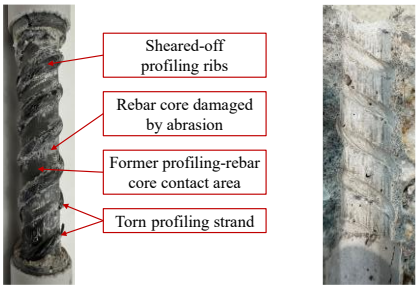


Fig. 5 (left) Damage pattern of CFRP rebars after bond testing;
(right) Intact concrete ribs after bond testing (Photos: Paul Heber)

At the onset of loading, all tests exhibited a steep initial slope in the bond stress-slip curve, which is attributed to the initial adhesive bond between the CFRP rebar and the concrete matrix [2, 17]. As loading progressed, the adhesive bond progressively degraded, leading to a transition in the dominant stress transfer mechanism toward a combination of frictional resistance and mechanical interlock (form bond). The frictional component arises from interfacial resistance at the rebar-concrete interface, while the form bond is governed by the mechanical interlocking between the rebar's profiling ribs and the surrounding concrete. Upon reaching the maximum bond stress ($\tau_{b,max}$), the adhesive bond between rebar core and profiling began to deteriorate, manifesting in the characteristic failure mode of profiling shearing and tearing, as previously observed.

Following the initial maximum and the subsequent decline in bond stress, successive increases and decreases of the bond stress-slip curve were observed. This phenomenon is consistent with a progressive, localized bond failure mechanism, described in the literature as "zipper-like" failure mode [2]. Rather than experiencing instantaneous, global debonding, the interface fails incrementally along the bond length. This progressive failure allows for re-anchoring and renewed stress transfer at adjacent segments of the bond length, resulting in secondary bond stress maxima. This behavior was consistently observed across all PO and BE test configurations.

The comparison between the PO series CFRP-PO and the BE series CFRP-BE-5, both with 50 mm bond length, showed no significant differences in bond behavior. Despite the reduced concrete cover of 20 mm in the CFRP-BE-5 specimens, these exhibited comparable bond stiffness and with maximum bond stress values ($\tau_{b,max}$) of 12.35 N/mm² on average as well as corresponding slip values (s_{max}) of 0.09 mm nearly identical values to those observed in the CFRP-PO specimens with 12.30 N/mm² and 0.08 mm, respectively. Also, the mean bond stress values at 0.15 mm slip ($\tau_{b,0.15mm}$) were nearly the same in both series with 11.43 N/mm² (CFRP-BE-5) and 11.48 N/mm² (CFRP-PO), respectively.

When analyzing the bond behavior across the four CFRP-BE series, an increase in bond length was associated with a reduction in both $\tau_{b,0.15mm}$ and $\tau_{b,max}$. The $\tau_{b,max}$ value for the CFRP-BE-5 series was 21.1%, 31.5% and 32.4% higher than those of the CFRP-BE-20, CFRP-BE-40 and CFRP-BE-45 series, respectively. Conversely, as bond length increased, bond stiffness also increased, i.e., the maximum bond stress ($\tau_{b,max}$) was achieved at lower slip values (s_{max}). Further, the specimens with longer bond lengths (CFRP-BE-40, CFRP-BE-45) demonstrated a persistent tendency toward more abrupt failure, in comparison to the shorter bond lengths (CFRP-BE-5, CFRP-BE-20). Subsequent to $\tau_{b,max}$, there was a precipitous decline in bond stress to 14% (CFRP-BE-40) and 5% (CFRP-BE-45), correspondingly, accompanied by a marked increase in slip. The $\tau_{b,max}$ values were almost identical at 8.46 N/mm² (CFRP-BE-40) and 8.35 N/mm² (CFRP-BE-45), with the corresponding s_{max} being exactly the same at 0.04 mm in both series. For the shorter bond lengths the bond stresses decreased to 85% (CFRP-BE-5) and 77% (CFRP-BE-20) and remained on a certain stress plateau. Overall, all CFRP-BE series exhibited the "zipper-like" failure mechanism characterized by re-anchoring. For bond lengths of 50 mm (CFRP-BE-5) and 200 mm (CFRP-BE-20), the subsequent average bond stress maxima exceeded $\tau_{b,max}$, with increases of 41.1% (CFRP-BE-5) and 6.7% (CFRP-BE-20), respectively. In contrast, the CFRP-BE-40 and CFRP-BE-45 series, which had longer bond lengths, demonstrated reduced subsequent bond stress maxima. This reduction can be attributed to uneven load distribution along the extended bond lengths, where the rebar sections at the loaded end experienced higher stress, while bond stress diminished towards the rear sections of the bond length.

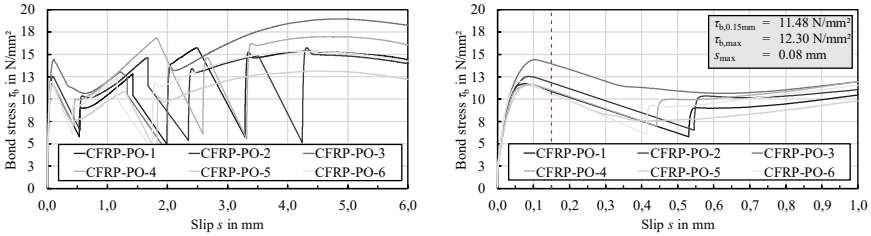


Fig. 6 Bond stress-slip relationship of the pull-out (PO) tests

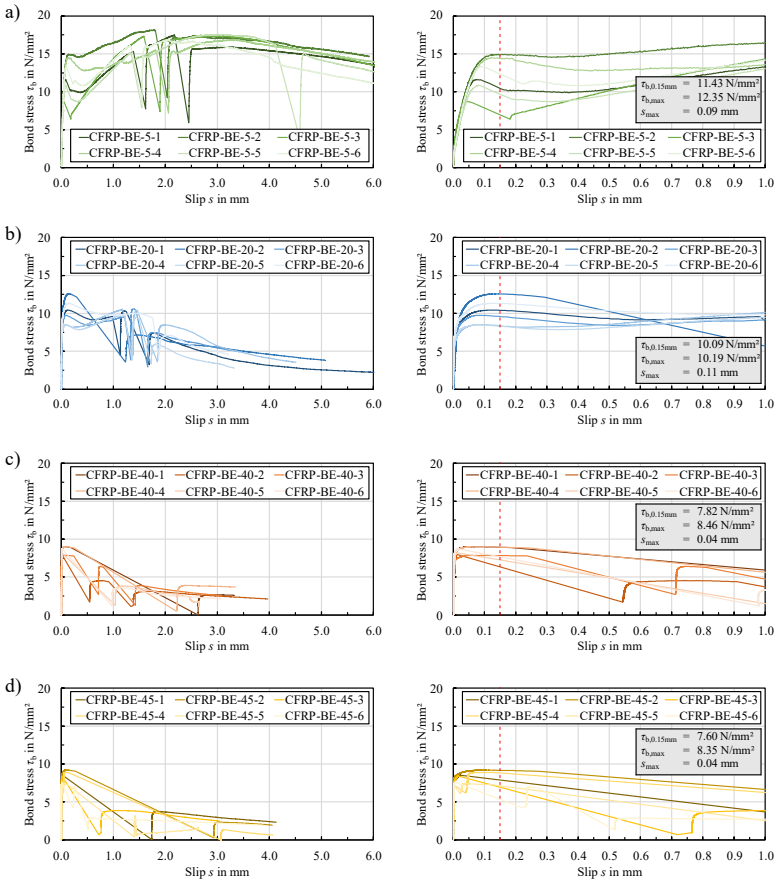


Fig. 7 Bond stress-slip relationship of the beam-end (BE) tests
(a) l_b = 50 mm, (b) l_b = 200 mm, (c) l_b = 400 mm, (d) l_b = 450 mm

During the BE tests, crack formation was observed on the upper (rebar near) side of all BE test specimens (see Fig. 4 and Fig. 8). The formation and progression of the cracks were documented by means of digital image correlation (DIC). The primary crack exhibited a parallel orientation aligned with the CFRP rebar and invariably originated at the load-facing end of the bond length. As the test progressed, the crack continued to spread toward the initially non-load-bearing end of the bond length, as the stress on those areas increased (re-anchoring). Upon exceedence of the initial bond stress maximum $\tau_{b,max}$, an abrupt and considerable increase in crack width (w), i.e., "crack opening", was observed in all test specimens, subsequently followed by the decline in bond stress.

In the DIC analysis, digital distance meters were arranged at the quarter points (measuring points (MPs)) along the respective bond lengths of the test specimens, in transverse direction to the CFRP rebar and thus to the main crack line (see Fig. 8). The mean values of the crack widths (w_{mean}) of the BE series along the respective bond length, both prior to and after crack opening at $\tau_{b,max}$, are illustrated in Fig. 8. They are furthermore given numerically in Table 2. It should be noted that the measured crack width values exhibited a high degree of scatter, as shown in Table 2. Nevertheless, for all BE test series an increase in the respective crack width toward the center of the bond length was observed.

With increasing rebar bond length, and thus increasing maximum rebar force, the crack width subsequent to the crack opening at $\tau_{b,max}$ initially increased as well, from 0.003 mm (series CFRP-BE-5) to 0.11 mm (series CFRP-BE-20) and further to 0.72 mm (series CFRP-BE-40). However, this trend did not persist in series CFRP-BE-45, which exhibited a decreased mean crack width of 0.56 mm. One potential explanation for this phenomenon is the previously mentioned wide variation in crack width values. Conversely, the bond lengths of series CFRP-BE-40 and series CFRP-BE-45 with 400 mm and 450 mm, respectively, do not differ as greatly compared to the other series. The bond stress values and stiffnesses of the two series, CFRP-BE-40 and CFRP-BE-45, were found to be nearly identical (see Fig. 7). This finding indicates that, for the CFRP rebars examined, a bond stress level is attained at a specific bond length (400 mm in this study), which remains largely unaltered by longer bond lengths. This phenomenon can be attributed to the previously mentioned successive load distribution and damage of the bond area. However, further beam-end tests with additional bond lengths are required to confirm this hypothesis, particularly concerning bond lengths exceeding the here tested maximum of 450 mm.

Overall, the mean crack widths after crack opening of the longer bond lengths, i.e., series CFRP-BE-40 and CFRP-BE-45, are above the standard crack width limit of 0.4 mm for non-metallic reinforced concrete [15]. For the investigated CFRP rebars to be used in practice, the concrete cover of 20 mm selected in the tests would therefore need to be increased. Alternatively, the applicable bond stress could be constrained to remain within the prescribed range prior to crack opening. Furthermore, transverse reinforcement could be incorporated, as is customary in such applications.

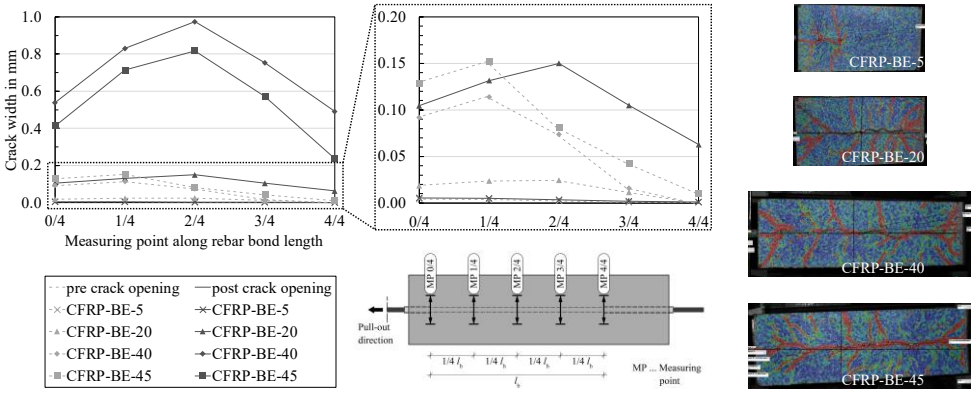


Fig. 8 (left) Crack widths at measuring points along rebar bond lengths during BE tests; (right) Crack pattern of BE tests after crack opening (post $\tau_{b,max}$); (Photos: Paul Heber)

Table 2 Average crack widths (w_{mean}) during BE tests before and after crack opening at $\tau_{b,max}$

	Pre crack opening			Post crack opening		
Series	w_{mean} mm	Standard deviation mm	Variation coefficient	w_{mean} mm	Standard deviation mm	Variation coefficient
CFRP-BE-5	0.0024	0.0017	70%	0.0034	0.0019	56%

CFRP-BE-20	0.02	0.01	65%	0.11	0.03	30%
CFRP-BE-40	0.06	0.05	83%	0.72	0.20	28%
CFRP-BE-45	0.08	0.06	71%	0.56	0.23	42%

5 CONCLUSIONS

This study investigated the bond behavior of CFRP rebars with additive profiling in low-clinker eco-concrete to support the development of sustainable, non-metallic reinforced concrete structures. The results confirm that the CFRP rebars exhibit a reliable bond with EC, underscoring the applicability of NM-EC composites for sustainable structural applications.

All tested specimens demonstrated valid failure by shearing and tearing of the rebar profiling. The observed zipper-like failure and subsequent re-anchoring phenomena confirm a bond behavior consistent with previous findings for NM rebars.

The comparison of PO and BE tests demonstrated that the reduction of concrete cover to 20 mm in the BE tests does not adversely affect the bond behavior of CFRP rebars in EC, validating one of the principal advantages of NM reinforcement. However, as the bond length increased, both mean bond stress ($\tau_{b,0.15}$) and maximum bond stress ($\tau_{b,max}$) decreased, reflecting a non-uniform stress distribution along the rebar bond length.

For the investigated concrete cover of 20 mm, cracks initiated at the loaded end and propagated along the bond length, with maximum crack widths increasing up to a bond length of 400 mm before slightly decreasing at 450 mm. Crack widths were highest at the center of the bond length and, in case of the longer bond lengths, exceeded the 0.4 mm limit, indicating insufficient crack control with the chosen concrete cover if no transverse reinforcement is applied. The consistent maximum bond stress level and bond stiffness for bond lengths longer than 400 mm, observed in the absence of tensile failure of the rebars, indicate that it is not feasible to anchor the maximum rebar tensile force under the chosen test setup. Therefore, future research should include BE tests with additional bond lengths and varying concrete covers to substantiate this observation or to determine the specific anchorage length of the CFRP rebars and the optimum concrete cover for their practical application in construction.

In summary, the results of this study validate the general technical feasibility of combining eco-concretes with CFRP reinforcement. The findings support the potential of NM-EC as a viable and durable solution for resource-efficient, corrosion-free and CO_2-reduced concrete structures.

Acknowledgements

This research is funded under grant number 03LB2085B by the Federal Ministry for Economic Affairs and Energy, based on a decision by the German Bundestag, as part of the Light-weight Construction Technology Transfer Program (Technologietransfer-Programm Leichtbau, TTP LB).

References

[1] Zhou, Jiafeng et al. 2023. “Investigations on bond performances of GFRP/stainless steel reinforcements using distributed fiber optical sensors (DFOSs).” *Journal of Building Engineering* 75:106881. doi: 10.1016/j.jobe.2023.106881.

[2] Schumann, Alexander et al. 2023. “Experimental Investigations of the Bond Behavior between Carbon Rebars and Concrete in Germany.” *Buildings* 13(12):2932. doi: 10.3390/buildings13122932.

[3] Stark, Alexander et al. 2019. “Bond behaviour of CFRP tendons in UHPFRC.” *Engineering Structures* 178:148–161. doi: 10.1016/j.engstruct.2018.10.002.

[4] Abdkader, Anwar et al. 2023. “Improved Tensile and Bond Properties through Novel Rod Constructions Based on the Braiding Technique for Non-Metallic Concrete Reinforcements.” *Materials* 16(6):2459. doi: 10.3390/ma16062459.

[5] Preinstorfer, Philipp et al. 2024. “Article of RILEM TC 292-MCC: bond behaviour of textile-reinforced concrete—a review.” *Materials and Structures* 57:97. doi: 10.1617/s11527-024-02339-5.

[6] Schmidt, Christopher and Hegger, Josef. 2025. “Experimental investigations on bond behaviour and crack development in concrete members reinforced with carbon textile grids subjected to

cyclic loading." *Construction and Building Materials* 466:140168. doi: 10.1016/j.conbuildmat.2025.140168.

[7] Bielak, Jan et al. 2018. "Characterization Procedure for Bond, Anchorage and Strain-Hardening Behavior of Textile-Reinforced Cementitious Composites." Paper presented at The 18th International Conference on Experimental Mechanics (ICEM 2018), Brussels, Belgium, July 1–5.

[8] Schmidt, Christopher. 2024. "Investigations on the bond behaviour and crack development in non-metallic textile-reinforced concrete members using fibre optic sensors." Paper presented at 20th fib Symposium, Christchurch, New Zealand, November 11–13.

[9] Sandmann, David and Marx, Steffen. 2024. "Bond behaviour of carbon textile reinforced concrete." Paper presented at the 15th fib International PhD Symposium in Civil Engineering, Budapest, Hungary, August 28–30.

[10] Rampini, Marco C. et al. 2023. "Pull-Out Tests on AR-Glass Fabrics Embedded in Plain and Fibre-Reinforced Cementitious Mortars." Paper presented at the fib Symposium 2023, Istanbul, Turkey, June 5–7.

[11] DIN Deutsches Institut für Normung e. V. 2021. "DIN EN 206:2021-06, Beton - Festlegung, Eigenschaften, Herstellung und Konformität; Deutsche Fassung EN 206:2013+A2:2021.". doi: 10.31030/3198971

[12] DIN Deutsches Institut für Normung e. V. 2023. "DIN 1045-2:2023-08, Tragwerke aus Beton, Stahlbeton und Spannbeton - Teil 2: Beton.". doi: 10.31030/3445766

[13] Institut Bauen und Umwelt e.V. 2022. "Umwelt-Produktdeklaration nach ISO 14025 und EN 15804+A1 – Holcim Duo 5 N-SR/NA, Werk Dortmund." https://epd-online.com/EmbeddedEpdList/Download?id=16785, last accessed 2025/03/22.

[14] solidian GmbH. 2023. "Technical Product Data Sheet – solidian REBAR Dxx-CCE." https://www.solidian-kelteks.com/de/downloads, last accessed 2025/03/24.

[15] Deutscher Ausschuss für Stahlbeton e. V. (DAfStb). 2024. "(2024-01) DAfStb-Richtlinie – Betonbauteile mit nichtmetallischer Bewehrung."

[16] International Union of Testing and Research Laboratories for Materials and Structures. 1994. *RILEM Technical Recommendations for the Testing and Use of Construction Materials*. London: Spon.

[17] Curbach, Manfred et al. (eds.) 2023. *Handbuch Carbonbeton – Einsatz nichtmetallischer Bewehrung*. Berlin: Ernst & Sohn.

Comparative Numerical Analysis of the Structural Performance of Steel and Basalt-Reinforced Tunnel Segments

Angeliki Kosta, Thomas Mader, Alexandros Evangelatos, Matthias Neuner, Konrad Bergmeister

Institute of Structural Engineering,
Universität für Bodenkultur Wien (BOKU),
Peter-Jordan-Straße 82,1190, Vienna, Austria

Summary
The increasing demand for durable and sustainable tunnel linings motivates the use of alternatives to conventional steel reinforcement. Basalt offers high tensile strength, low weight and excellent corrosion resistance. This study compares steel- and basalt-reinforced tunnel lining segments using finite element simulations in ABAQUS. Both models have identical geometry and reinforcement ratios and are assessed under three-point bending. The results show that steel reinforcement yields under increasing load, while basalt reinforcement remains elastic and enables greater deformation capacity, with its lower Young's modulus influencing stress redistribution after cracking. Based on the numerical stress trajectories, an innovative three-dimensional basalt reinforcement layout is proposed, in which continuous rovings are robotically placed along the principal tensile stress paths. This concept improves durability, reduces material use and highlights basalt's potential for sustainable tunnel lining segments.

1 INTRODUCTION

Recent research and the increasing frequency of natural hazards indicate potentially irreversible environmental degradation. In response, climate change mitigation has become a central objective across sectors, leading to stringent requirements for the reduction of greenhouse gas emissions. Civil infrastructure plays a major role in this context and tunnelling contributes considerably through operational energy demand and the production of construction materials. While tunnel projects worldwide have invested significant effort to reduce impacts through optimised logistics, waste management and life-cycle planning, the climate impact of precast concrete tunnel linings has so far received limited attention. In the last years, research has intensified with a clear focus on emissions from material production. Approaches include reuse of excavation material in linings and the development of environmentally optimised concretes, supported by tools for multiparametric sustainability assessment of the segmental linings. Life cycle assessment studies consistently identify concrete and steel as the dominant contributors to greenhouse emissions in conventional tunnel construction. These findings suggest that further decarbonisation requires measures that directly reduce cement and steel through substitution, minimisation and structurally efficient design.

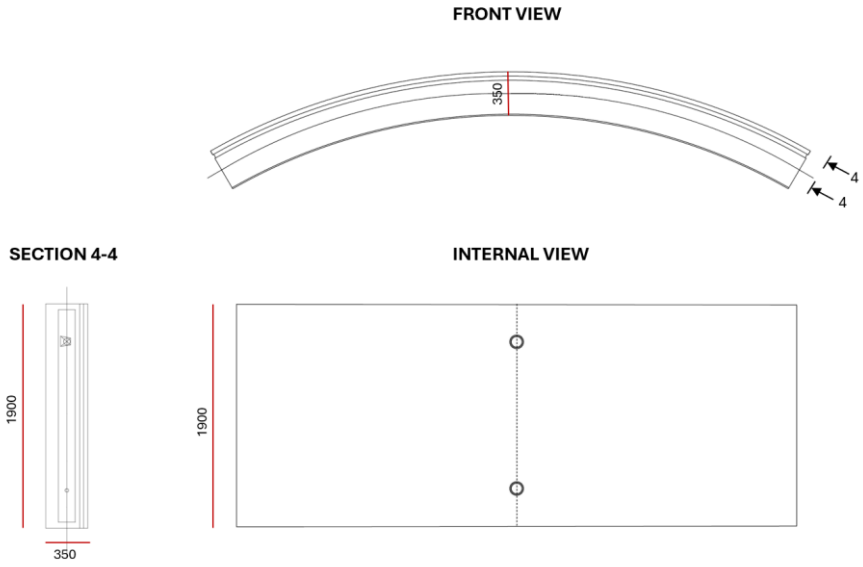
Precast concrete lining segments are frequently exposed to moisture, chlorides from de icing salts and other aggressive agents. Under such conditions, corrosion of conventional steel reinforcement can initiate cracking and spalling, reduce bond and cross section and lead to significant maintenance requirements. Reinforcement made from fiber reinforced polymers (FRPs) represents one possible alternative to steel in corrosive environments. Basalt reinforcement is particularly promising due to its high tensile strength [1], low density [2], high temperature and corrosion resistance [3] and low CO_2 emissions [4]. These properties are attractive for tunnel applications where durability governs design and where reduced reinforcement weight may also benefit segment handling and production. At the same time, basalt reinforcement differs fundamentally from steel in its mechanical response. Whereas under uniaxial tension steel yields and provides a significant plastic deformation capacity, the mechanical behavior of basalt is mainly characterized by linear elastic behavior and quasi-brittle failure. This raises important questions regarding crack development, stiffness degradation and energy dissipation in basalt reinforced tunnel lining segments.

This study investigates these aspects by means of a comparative numerical analysis conducted in ABAQUS [5]. Steel and basalt reinforced segment models are established with identical geometry and reinforcement ratios, while adopting a conventional bar reinforcement layout, in order to investigate

the influence of the reinforcement material. Both models are subjected to a three point bending test to evaluate load bearing behaviour and deformation response. The analyses indicate distinct differences in mechanical performance. The steel reinforcement reaches yielding with increasing load, whereas the basalt reinforcement remains fully elastic throughout loading. In the basalt reinforced segment, improved deformation capacity of the composite system is observed. Based on the numerical obtained stress trajectories, the work further explores resource efficient reinforcement design by proposing a three dimensional basalt reinforcement layout aligned with principal tensile stresses. Continuous basalt rovings are arranged along critical load paths with the aim of enhancing stiffness and durability while reducing reinforcement demand. The concept is developed with robotic placement in mind to ensure accurate and reproducible positioning. A full scale prototype will be tested in three point bending to validate the numerical results and assess the structural and durability related advantages of basalt reinforcement for precast tunnel lining segments.

2 materials

The analysis is performed with reference to structural elements representative of a typical precast tunnel lining segment. The precast tunnel segment considered herein is characterized by a thickness t of 35 cm, an average length l of 480 cm and a width b of 190 cm. The analysed segment is shown in



.

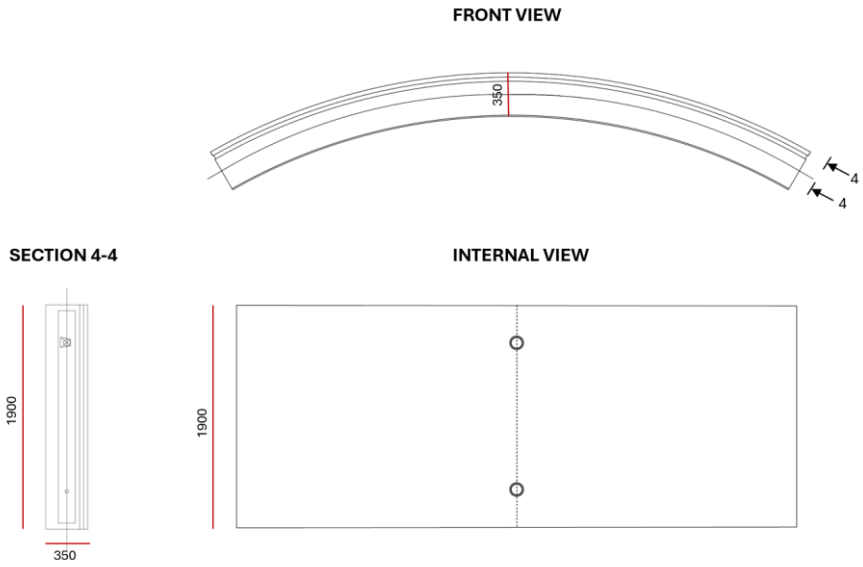


Fig. 1 Analysed tunnel lining segment geometry. Front view, internal view and Section 4–4.

2.1 Concrete

The segments are assumed to be cast from normal-weight concrete class C50/60 (Table 1). The mechanical behaviour is described by the Concrete Damage Plasticity (CDP) model by Grassl and Jirásek [6], implemented in the Marmot Library [7] and used via the UMAT User Subroutine in ABAQUS. The model is based on the combination of the theories of plasticity and damage mechanics, considering both strain hardening in the pre-peak regime and strain softening in the post-peak regime. For providing mesh-insensitive results in the softening regime, the model is regularized by a mesh-adjusted softening modulus, i.e., the crack band approach [8].

2.2 Steel

Conventional reinforcement is modelled as an isotropic linear elastic – perfectly plastic material using the von Mises failure criterion for limiting the elastic region. Reinforcing steel grade B550S is adopted, defined by a Young's modulus E_s=210 GPa, Poisson's ratio ν_s=0.25, density ρ_s = 7850 kg/m^3 and a characteristic yield strength of f_{yk} = 550 MPa (Table 1).

2.3 Basalt

The basalt reinforcement is modelled as a linear elastic material with a brittle post-peak response. The density is specified as $\rho_b = 2700$ kg/m³, corresponding to the adopted unit system. Linear elasticity is defined by a Young's modulus $E_b = 55$ GPa and Poisson's ratio $\nu_b = 0.25$. The tensile strength of the basalt reinforcement is defined by $f_{tu,b} = 1100$ MPa (Table 1).

Table 1 Material parameters in FE model

Material	Young's modulus (MPa)	Density (kg/m^3)	Poisson's ratio	*fyk* (MPa)	*fcu* (MPa)	*ftu* (MPa)	*fbu* (MPa)	G_{FI} (N/mm)
Concrete	38630	2500	0.18	15.33	58.0	4.10	66.24	0.152

Steel	210000	7850	0.25	550	-	-	-	-
Basalt	55000	2700	0.25	-	-	1100	-	-

Note: f_{yk}= characteristic yield strength, f_{cu}= compressive strength, f_{tu}= tensile strength, f_{bu}= biaxial strength, G_{FI} = fracture energy.

3 MODEL

The numerical investigation reproduces a three-point bending test on a precast tunnel lining segment conducted at the University of Leoben as shown in Fig. 2. This allows to evaluate the flexural response, crack development and load transfer mechanisms under bending-dominated loading.

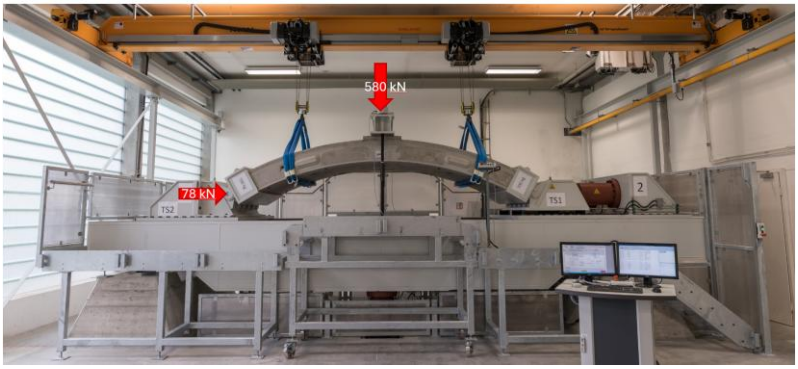


Fig. 2 Three-point bending test set-up for a precast tunnel lining segment at Montanuniversität Leoben.

3.1 Modelling approach

The segments are modelled using Abaqus/CAE [5]. For reducing the computational costs geometric symmetries are exploited. The reduced model is simply supported, i.e., the left bottom surface is coupled by a rigid body constrained to a reference point. The latter can rotate around the global 3-axis (UR3) and allows displacements in horizontal direction. All other degrees of freedom are fixed as visualized in Fig. 3. At the top surface (Fig.3) symmetry boundary conditions are applied. The concrete structure is discretized by C3D8 elements with full integration and a minimum edge length of ≈ 30 mm.

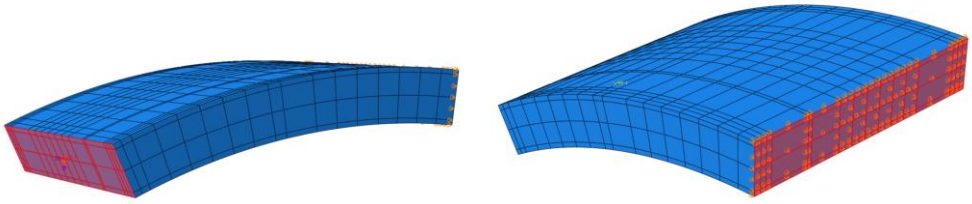
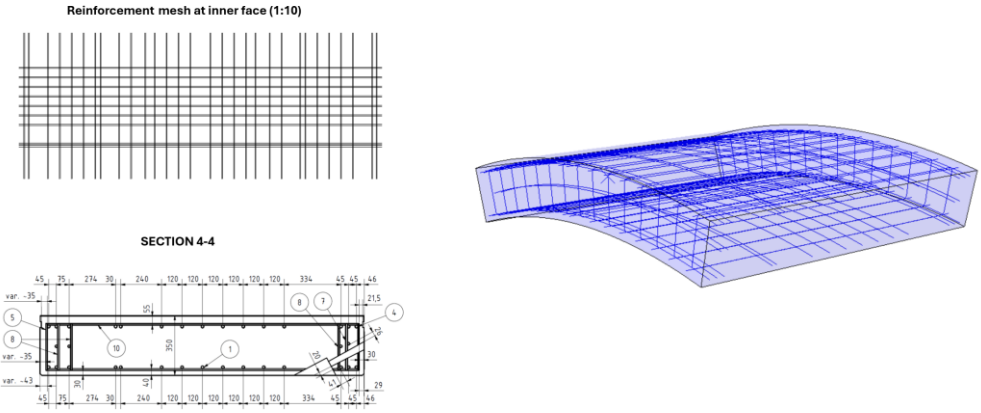


Fig. 3 Boundary Conditions.

3.1.1 Reinforcement

The reinforcement layout follows a conventional bar-reinforcement arrangement (longitudinal bars and stirrups) as shown in Fig.



4. The longitudinal reinforcement is introduced by stringer elements B31 positioned through partitioning of the concrete structure at the intended rebar locations. The stringer approach is an efficient way to include a full reinforcement cage in a three-dimensional concrete model while keeping the computational effort moderate. The stirrups were discretized using B31 elements with full integration and a minimum edge length of ≈ 15 mm. The latter were subsequently coupled to the concrete structure using the embedded region constraints, enforcing displacement compatibility by assuming perfect bond between the embedded elements and their host elements, i.e., between the stirrups and the concrete.

The different modelling workflow adopted for the stirrups results from the model development sequence. The initial model was established without the complete stirrup detailing and the transverse reinforcement was incorporated at a later stage. The influence of the additional stirrups on the structural response was investigated separately but the respective results are outside the scope of the present study.

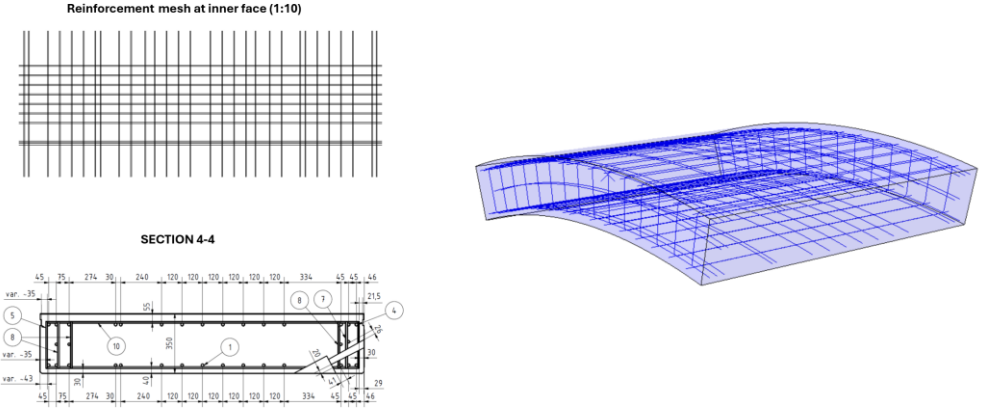


Fig. 4 Reinforcement layout adopted in the FE model.

3.1.2 Load application

In a first step the model is loaded by a horizontal load of 78 kN for the additional in-plane compressive normal force present in the test set-up and representative of ring compression in service. In difference to the experiments conducted at University of Leoben (Fig. 2) the simulation is performed displacement controlled to investigate also the post-peak behavior. Thus, a vertical displacement of 100 mm is applied in a second step at the top of the segment.

4 NUMERICAL RESULTS

Figures 5 and 6 summarise the evolution of the stress and cracking response for both the steel and basalt-reinforced segments, respectively. For each reinforcement variant, (A) shows the state directly prior to crack initiation, (B) the subsequent crack development at peak load and (C) the stress distribution and crack pattern at the end of the simulation. The top plots show the minimum principal stress trajectories, the middle the damage variable 0 $(intact) \rightarrow \omega \rightarrow 1$ $(fully\ damaged)$ and the bottom plots the maximum principal stress trajectories. The contour plots are complemented by details of the critical damaged region at the end of the simulation. In these details, the minimum principal stress S_3 is used to visualise the compressive zone at the top surface, while the maximum principal stress S_1 is used to identify the tensile zone at the bottom surface governing crack initiation and propagation.

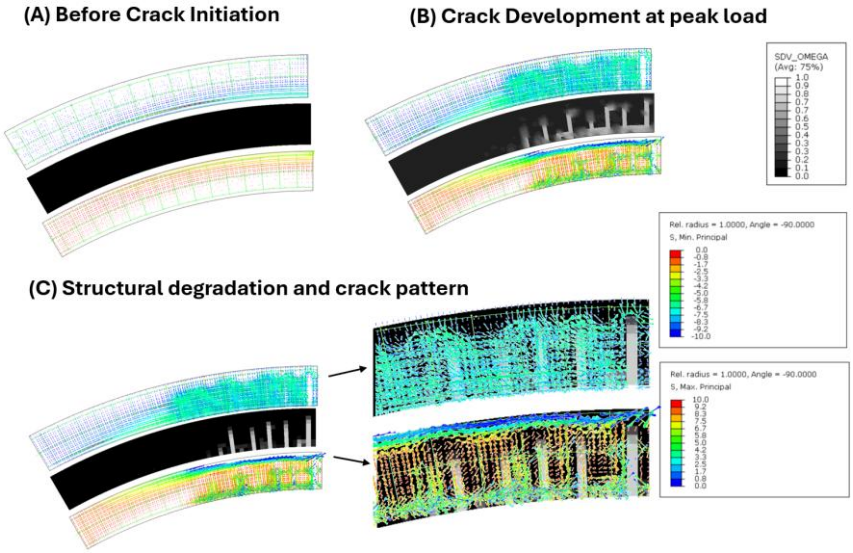


Fig. 5 Steel-reinforced tunnel lining segment.

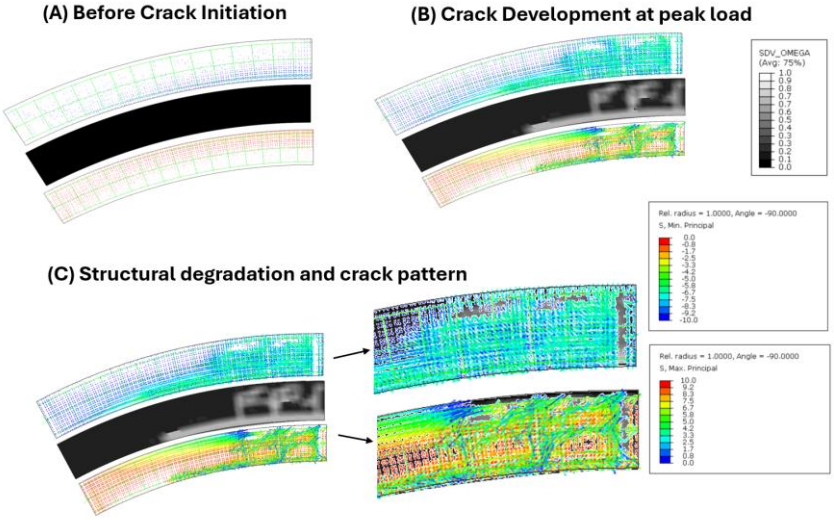


Fig. 6 Basalt-reinforced tunnel lining segment.

4.1.1 Early-stage response

Before cracking, both models exhibit an elastic bending response with its maximum bending moment at the top of the segments, resulting in a compressive zone at the upper cross-sectional area and tensile stresses concentrating at the corresponding lower area. With increasing deformation, cracking initiates at the bottom surface once S_1approaches the tensile strength of the concrete and progressively develops towards a localised crack.

4.1.2 Response at peak load

As deformation increases, a distributed cracking pattern emerges across the midspan. At this stage, the structural behavior is driven by two main factors: the stiffness degradation of the cracked concrete and the load transfer to the reinforcement. The contour plots show characteristic stress redistributions. Once a crack forms in the tensile zone, the damaged concrete loses stiffness, and tensile stresses are primarily redirected to the reinforcement. In the sections of intact concrete located between cracks, the material continues to contribute to the structural integrity, i.e., tension stiffening occurs. This stiffening effect is visually represented in the trajectories of the minimum and maximum principal stresses as arches inbetween two cracks.

4.1.3 Response at end of test and differences between steel and basalt

Differences between the steel and basalt-reinforced models become more pronounced at the advanced loading stage. In the steel-reinforced segment, reinforcement yielding (550 MPa) (Fig. 7 (left)) enables stress redistribution and promotes deformation through plastic straining of the longitudinal bars. In the basalt-reinforced segment, the reinforcement remains essentially elastic (Fig. 7 (right)) and the bar stresses remain well below the tensile strength of approximately 1100 MPa. The response is therefore governed by progressive concrete cracking and damage evolution rather than by reinforcement plasticity. Accordingly, the late-stage stress fields in the basalt case exhibit more pronounced stress gradients around the dominant crack band, reflecting the absence of a yielding mechanism and the stronger dependence of the global response on crack development. Compared to steel, stress is not that well distributed to the basalt reinforcement because its elastic modulus is closer to that of concrete. Therefore, the stiffness contrast between reinforcement and concrete is reduced, which limits stress redistribution to the reinforcement after cracking. The resulting reinforcement stresses therefore remain below the ultimate tensile strength of the basalt bars (approximately 1100 MPa in the present model).

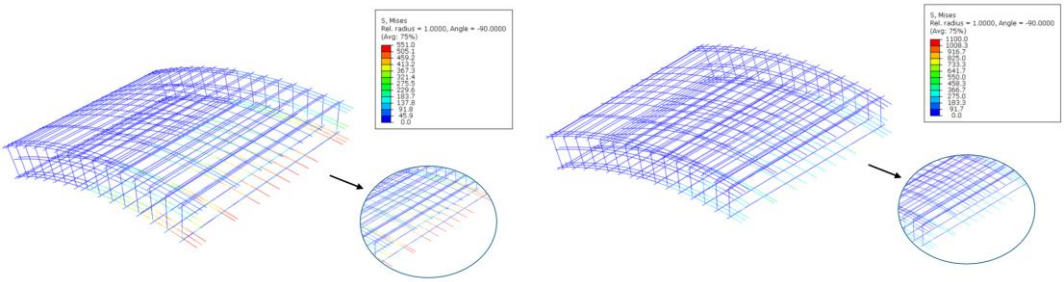


Fig. 7 (left) Steel-reinforced segment. Von Mises stress in the reinforcement at an advanced loading stage highlighting yielding in the longitudinal bars, (right) Basalt-reinforced segment. Reinforcement von Mises stress distribution at an advanced loading stage. The stress level remains below the tensile strength limit of the basalt reinforcement.

4.1.4 Load – displacement response

Figure 8 compares the computed load - displacement curves of the segment reinforced with steel and basalt. The steel-reinforced model shows a steep initial stiffness and reaches a high load of approximately 550-600 MPa already at small top displacements of 20 mm. The curve then transitions into a plateau, which is consistent with yielding in the longitudinal reinforcement and the associated redistribution of tensile stresses. In contrast, the basalt-reinforced model exhibits a lower maximum load corresponding to about 18-20 % lower load bearing capacity than the steel-reinforced model.

However, this maximum load is reached at a much larger displacement, approximately 65–75 mm. This indicates that, although the basalt-reinforced segment has a lower initial stiffness and lower peak load, it maintains load-bearing capacity over a substantially larger deformation range. The response remains governed by progressive cracking and stiffness degradation of the concrete while the basalt reinforcement remains in the elastic regime. The pronounced step-like drops visible in the basalt curve indicate discrete crack formation. Overall, the basalt response is characterised by a sustained load-bearing capacity over a larger deformation range compared to the steel-reinforced segment.

The lower load of the basalt reinforced segment is mainly a consequence of the lower Young's modulus of basalt compared to steel. For the same reinforcement ratio, this reduces the axial stiffness of the tensile reinforcement and, after cracking, a smaller share of the tensile force is transferred to the bars. This result reflects the limitations of a direct material substitution using a conventional bar layout. Higher stiffness and capacity can be obtained either by locally increasing the basalt reinforcement area or by relocating reinforcement from regions with low utilisation to the midspan tension zone. Further improvements are expected from a stress-adapted concept in which basalt is placed along the principal tensile stress trajectories. In particular, continuous basalt rovings arranged along the governing load paths and combined with bars only where required for detailing and anchorage are expected to improve post-cracking load transfer and reduce localisation.

The computed response of the steel-reinforced segment is further assessed by comparison with experimental results shown in Fig. 8. The experimental curve (black) exhibits the same characteristic features as obtained in the numerical simulation, i.e., a rapid stiffness reduction after first cracking, followed by a progressive increase towards a maximum load level and a subsequent plateau-type behaviour as cracking stabilises and reinforcement governs the response. The close qualitative agreement in stiffness evolution and overall curve shape indicates that the numerical model captures the governing mechanisms of the steel-reinforced segment, providing confidence in the calibration of the concrete model and boundary condition representation. This validation step is essential for the comparative assessment of basalt reinforcement based on the same modelling framework.

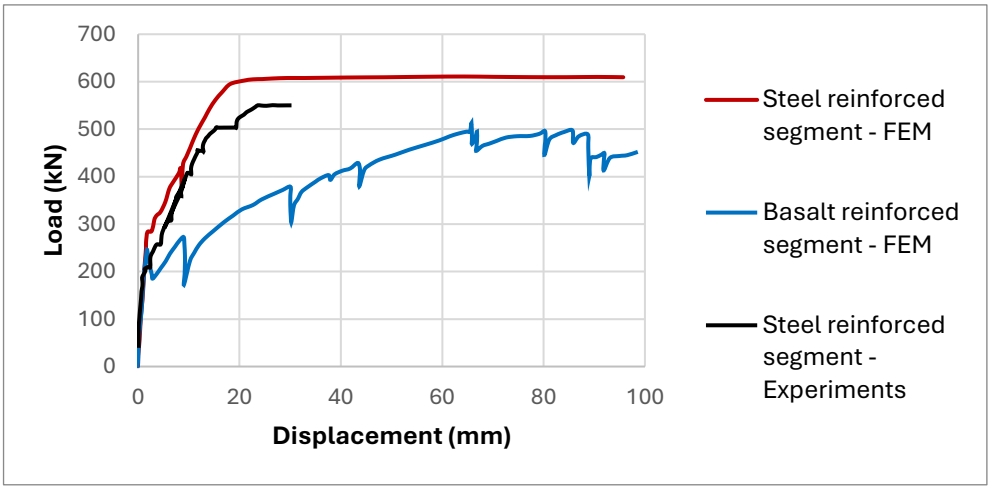


Fig. 8 Load–displacement curves.

5 Conclusions

A comparative finite element study was conducted on precast tunnel lining segments reinforced with steel and basalt, adopting identical geometry, reinforcement ratio and a conventional bar layout. The simulations indicate distinct response mechanisms. The steel-reinforced segment exhibits the expected transition to plasticity, with yielding of the longitudinal reinforcement and a subsequent redistribution of tensile forces in the cracked section. The basalt-reinforced segment remains linear-elastic at the reinforcement level over the entire loading range. Its global response is governed by progressive concrete cracking and damage evolution. Within the simulated deformation range, this results in a

sustained load-bearing capacity and a stable post-cracking behaviour despite the absence of a yielding plateau.

From the perspective of tunnel applications, the relevance of basalt reinforcement extends beyond the observed mechanical response. In aggressive underground environments, corrosion of conventional steel reinforcement is the main cause of deterioration. Basalt reinforcement offers inherent corrosion resistance and therefore addresses a key durability limitation of reinforced concrete linings. The numerical results further highlight that a direct material substitution approach is only a first step. The principal stress fields obtained from the analyses provide a rational basis for reinforcement optimisation by identifying the governing tensile load paths.

On this basis, the present work supports the development of a resource-efficient three-dimensional basalt reinforcement concept, combining continuous rovings and bars. The rovings can be aligned with principal tensile stress trajectories to reinforce the segment along critical paths, while basalt bars are retained only where required for anchorage and local force transfer. This stress-adapted strategy has the potential to reduce reinforcement demand and improve durability while maintaining structural performance and it is compatible with automated placement methods. Full-scale three-point bending tests are planned to validate the numerical findings and to quantify the structural and durability-related benefits of the 3D-stress-aligned basalt reinforcement for precast tunnel lining segments.

Acknowledgements

This work was carried out within the FFG (Austrian National Research Fund) sponsored research project *greenINFRASTRUCTURES*. The project investigates an integrated approach combining a newly developed low-emission cement (CEM II/C), recycled waste-concrete aggregates and a specifically developed ecological reinforcement concept, together with an optimised design methodology for tunnel lining segments. Moreover, this research was partially supported by the Austrian Science Fund (FWF) under Award Number 10.55776/PAT1342523. The authors gratefully acknowledge the collaboration with Montanuniversität Leoben for the experimental part of the study.

References

[1] Elgabbas, Fareed, Ahmed, Ehab A., and Benmokrane, Brahim. 2015. “Physical and Mechanical Characteristics of New Basalt-FRP Bars for Reinforcing Concrete Structures.” *Construction and Building Materials* 95:623–635. doi:10.1016/j.conbuildmat.2015.07.036.

[2] Wolf, Benjamin, Glomb, Daniel S., Kustermann, Andrea, and Dauberschmidt, Christoph. 2019. “Untersuchung des Zug- und Verbundverhaltens von Basaltfaserverstärkter Kunststoff-Stabbewehrung in Beton.” *Beton- und Stahlbetonbau* 114(7):454–464. doi:10.1002/best.201900019.

[3] Wang, Wenjie, Zhang, Yunpeng, Mo, Zonglai, et al. 2023. “A Critical Review on the Properties of Natural Fibre Reinforced Concrete Composites Subjected to Impact Loading.” *Journal of Building Engineering* 77:107497. doi:10.1016/j.jobe.2023.107497.

[4] Kromoser, Benjamin, Reichenbach, Sara, Stoiber, Nadine, Preinstorfer, Philipp, and Huber, Tobias. 2022. Potentiale von nichtmetallischer Bewehrung im Infrastruktur-Betonbau NIMETBEW. Research report. http://hdl.handle.net/20.500.12708/40501

[5] Dassault Systèmes SIMULIA Corp. 2026. *Abaqus* Version 2026. Computer software. Providence, RI, USA: Dassault Systèmes.

[6] Grassl, Peter, and Jirásek, Milan. 2006. “Damage-Plastic Model for Concrete Failure.” *International Journal of Solids and Structures* 43(22–23):7166–7196. doi:10.1016/j.ijsolstr.2006.06.032.

[7] Neuner, Matthias, Dummer, Alexander, Schreter-Fleischhacker, Magdalena, Hofer, Paul, Alkmim, Nasser, Basche, Konstantin, and Mader, Thomas. 2025. *Marmot: MAteRialMOdellingToolbox* Version v25.11. Zenodo. doi:10.5281/zenodo.17509328.

[8] Bažant, Zdeněk P., and Oh, Byung H. 1983. “Crack Band Theory for Fracture of Concrete.” *Materials and Structures* 16:155–177. doi:10.1007/BF02486267.

Numerical analysis of cracking behaviour and tension stiffening in GFRP reinforced concrete lap splices

Nicolas Sandoval, Cristina Barris and Marta Baena

Analysis and Advanced Materials for Structural Design (AMADE),
University of Girona,
Maria Aurèlia Capmany, 61, Girona (17003), Spain

Summary
Glass-Fiber-Reinforced Polymer (GFRP) bars offer a durable alternative to steel in corrosive environments. Given the distinct bond performance of GFRP compared to steel, lap splice detailing must account for the different load transfer mechanisms involved. In reinforced concrete (RC) members, the splice lengths required for adequate force transfer may induce cracking along the splice, which must be considered in the analysis. This paper presents a numerical model that simulates the behaviour of GFRP-RC tensile lap splices, including the formation of the first crack. The model incorporates any user-defined bond–slip law to describe the bar-concrete interaction, enabling detailed tracking of slip, bar stress, concrete stress, and bond stress along the splice. Results highlight the transition from uncracked to cracked states, showing how insufficient splice lengths may lead to premature debonding. The proposed approach provides a rational basis for optimizing lap splice lengths in GFRP-RC.

1 INTRODUCTION

Lap splices are an unavoidable feature of reinforced concrete (RC) structures, arising from practical constraints such as limitations on bar lengths, handling and transportation requirements, and the optimisation of reinforcement layouts. Their structural performance is therefore fundamental to ensuring adequate force transfer and serviceability of RC members. However, accurately predicting the mechanical behaviour along the lap splice length remains challenging due to the non-uniform development of bond stresses and the influence of concrete cracking, which together produce complex stress redistribution between overlapping bars and the surrounding concrete.

Several analytical [1] and empirical models [2] have been proposed to describe the behaviour of lap splices in steel-RC. Analytical formulations typically assume a linear local bond stress–slip relationship to describe the bar–concrete interaction, enabling closed-form solutions for force transfer along the splice length. In contrast, empirical models are derived from experimental data and are primarily aimed at predicting the global bond strength of lap splices, without explicitly modelling the local bond stress–slip behaviour along the splice.

In recent decades, Glass-Fiber-Reinforced Polymer (GFRP) bars have emerged as a durable alternative to steel, particularly in corrosive environments. However, GFRP differs from steel in several key aspects: it has a lower elastic modulus, it exhibits a higher Poisson's ratio that reduces the transverse bar diameter under tension [3], and it presents surface characteristics that influence bond performance [4]. Experimental studies have addressed development and lap splice lengths for GFRP-RC members, leading to empirical or semi-empirical design equations [5], [6]. Nevertheless, the force transfer mechanisms governing GFRP lap splices, and the influence of different mechanical and geometrical parameters on these mechanisms, are not yet fully understood.

This paper addresses this gap by developing a numerical model for GFRP-RC tensile lap splices, based on the finite difference method, conceived as a tool to investigate these force transfer mechanisms. The model explicitly incorporates concrete cracking and any user-defined local bond–slip law. The model enables detailed tracking of slip, bond stress, and stress redistribution along the splice during both pre-cracking and post-cracking stages.

2 THEORETICAL BACKGROUND

The structural response of RC lap splices is governed by the transfer of axial forces between overlapping reinforcement bars through bond stresses developed at the bar–concrete interface. This mechanism

depends on the relative axial stiffness of the reinforcement and the surrounding concrete and is markedly influenced by the cracking state of the concrete [7].

Fig. 1 illustrates the axial stress distribution in the concrete along a lap splice formed by two GFRP bars embedded in concrete and loaded from opposite ends before and after cracking. Both bars are subjected to the same value of axial load at their respective loaded ends, while the opposite ends remain free. In the uncracked state, the concrete contributes to force transfer along the entire lap splice. Assuming that a crack forms at mid-length, the concrete tensile stress at the crack location drops to zero, leading to a redistribution of internal forces and to a modified load transfer mechanism between the two bars.

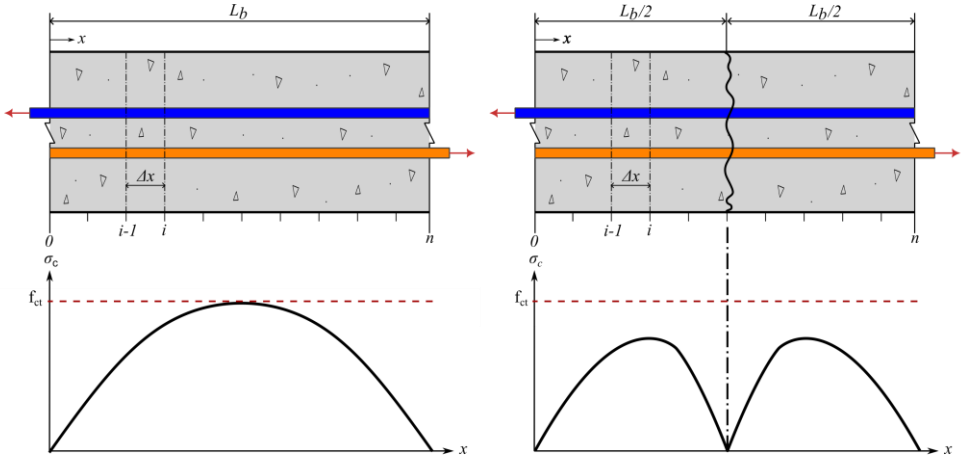


Fig. 1 Schematic representation and concrete stress distribution along the length of a RC lap splice: (left) uncracked member; (right) member cracked at the mid-length of the lap splice

This study builds on a previously established methodology, applied to FRP-RC elements subjected to single shear [8] and pure tensile loading [7] to obtain the load-slip response, and extends its application to the analysis of lap splice behaviour. The interaction between each reinforcement bar and the concrete is described by a local bond-slip relationship linking the bond stress $\tau(x)$ to the slip $s(x)$ between the bar and the surrounding concrete. Assuming linear elastic behaviour of both materials, the equilibrium of forces in a differential segment of the lap splice relates the axial stress gradient in each bar to the local bond stress acting along the interface. The slip is defined as the relative displacement between the bar and the adjacent concrete, and its variation is governed by the difference between the bar and the concrete strain. By combining the equilibrium conditions with the linear elastic constitutive laws of the reinforcement and concrete, the second derivative of the slip can be expressed in terms of the local bond stress and the axial stiffness of both materials. Applying this formulation independently to each of the two overlapping bars yields a pair of second-order differential equations that govern the evolution of slip along the splice.

$$\frac{d^2 s_1(x)}{dx^2} = -\pi\phi_f \left(\frac{\tau_1(x)}{E_f A_f} + \frac{\tau_1(x) - \tau_2(x)}{E_c A_c} \right) \tag{1}$$

$$\frac{d^2 s_2(x)}{dx^2} = \pi\phi_f \left(\frac{\tau_2(x)}{E_f A_f} - \frac{\tau_1(x) - \tau_2(x)}{E_c A_c} \right) \tag{2}$$

where $\tau_1(x)$ and $\tau_2(x)$ are the local bond stresses acting along bar 1 and bar 2, respectively, ϕ_f is the bar diameter, and $E_f A_f$ and $E_c A_c$ are the axial stiffness of the reinforcement and concrete, respectively. E_f and E_c denote the elastic moduli of the GFRP bars and the concrete, respectively, while A_f and A_c are the corresponding effective cross-sectional areas. Eqs. (1) and (2) constitute a system of differential equations with four unknown functions, $\tau_1(x)$, $\tau_2(x)$, $s_1(x)$ and $s_2(x)$. The system is fully defined by introducing the constitutive bond-slip relationship, which specifies the local interaction between the bond stress and slip.

3 NUMERICAL MODEL

The numerical model was implemented in a MATLAB code and represents a RC member containing two overlapping bars over a splice length L_b. Axial loads of equal magnitude are applied at the loaded ends in opposite directions, while the remaining ends are left unloaded (free ends). The splice region is discretised into n uniform segments of length Δx, resulting in $n+1$ nodes, with the spatial coordinate defined as $x_i = (i-1)\Delta x$.

The model is based on the following assumptions: all materials exhibit linear elastic behaviour; concrete stresses are uniformly distributed over the cross-section; and the bar–concrete interaction is governed by any user-defined local bond–slip law, assumed identical for both bars. In the uncracked state, concrete is assumed to contribute to force transfer through a continuous axial stress field. A crack is assumed to form at the mid-length of the lap splice; as a result, the concrete tensile stress at the crack location drops to zero, leading to a redistribution of internal forces and to a modified load transfer mechanism between the two bars.

A finite-difference, incremental slip procedure is employed to simulate the complete loading history. Two stages are considered in the structural response: a pre-cracking stage and a post-cracking stage, both illustrated in Fig. 1, in which a crack is present at the mid-length of the lap splice and the response is traced up to lap-splice failure.

In the first stage, starting from the initial section (x = 0) and progressing towards x = L_b, the model calculates slip and load transmission of both bars between adjacent sections for each analysed point. Variation of axial forces in each bar, N_1 and N_2, is obtained by enforcing equilibrium with the bond stresses τ_1 and τ_2 acting along the contact perimeter in a differential segment Δx (Eq. 3 applies when progressing from the loaded end towards the free end, whereas Eq. 4 applies in the opposite direction).

$$N_1(i) = N_1(i-1) - \tau_1(i-1) \cdot \pi \cdot \phi_f \cdot \Delta x \quad (3)$$

$$N_2(i) = N_2(i-1) + \tau_2(i-1) \cdot \pi \cdot \phi_f \cdot \Delta x \quad (4)$$

Analogously, the concrete axial force, N_c, is obtained from global force equilibrium considering interaction with both bars:

$$N_c(i) = N_{1_{LE}} - N_1(i) - N_2(i) \quad (5)$$

where $N_{1_{LE}}$ is the axial force applied at the loaded end of bar 1 which equals the applied load P and is identical for both bars at the loaded ends ($N_{1_{LE}} = N_{2_{LE}}$). Stresses are computed by dividing axial forces by their respective effective areas, and strains are derived from stresses using the elastic modulus of each material. Slip is updated from the strain difference between reinforcement and concrete.

$$s_1(i) = s_1(i-1) - \left[\varepsilon_{f_1}(i) - \varepsilon_c(i)\right] \cdot \Delta x \quad (6)$$

$$s_2(i) = s_2(i-1) + \left[\varepsilon_{f_2}(i) - \varepsilon_c(i)\right] \cdot \Delta x \quad (7)$$

The iterative procedure for each loading increment j, i.e. the adjustment of the tentative values $s_1(j,1)$ and $s_2(j,1)$, is based on two convergence checks: i) slip at both loaded ends must be equal (symmetry condition), and ii) strain in bar 1 at its free end must approach zero (since that end is unloaded). If these conditions are not satisfied, $s_1(j,1)$ and $s_2(j,1)$ are incremented and the process repeated until convergence is attained. Once achieved, the corresponding load is recorded, and the procedure is repeated for new initial slip values $s_1(j+1,1)$ and $s_2(j+1,1)$. The process continues until the stress in any point of the concrete $\sigma_c(j,i)$ reaches the concrete tensile strength f_{ctm}, and after which a crack forms in the middle of the splice and the post-cracking stage of the model begins.

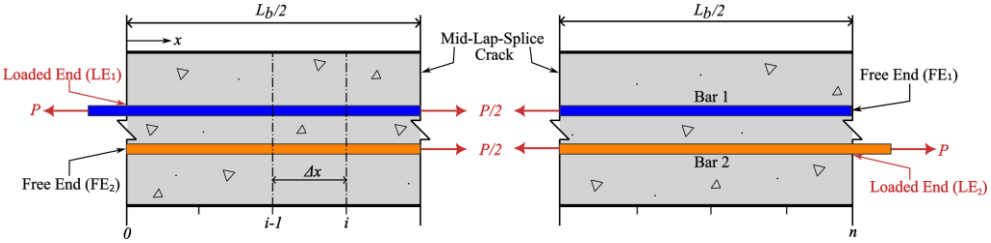


Fig. 2 Schematic representation of a RC lap splice with a mid-lap-splice crack and the applied forces at the loaded ends and at the cracked section

Once the post-cracking stage begins, the numerical procedure is based on the same principles as the pre-cracking stage, except for the convergence checks. Owing to symmetry, convergence is enforced by requiring that the axial force at the mid-length of the lap splice (at $i = (n+1)/2$) equals $P/2$ for both bars (Fig. 2). In this stage, the routine results are stored only when the average strain of the bars within the lap splice exceeds the maximum average strain attained during the pre-cracking stage. The analysis is continued while increasing the imposed slip until the applied load P reaches a maximum and subsequently starts to decrease, which is taken as the termination criterion of the analysis and interpreted as the bond failure of the lap splice.

The application of the proposed methodology is illustrated through the following example. The material and geometrical properties of the specimen considered in the calculations are reported in Table 1. The spatial discretization adopted in the numerical model is based on a uniform step size of $\Delta x = 1$ mm, resulting in a total of 360 finite elements along the bar. The bond-slip law implemented in the model is plotted in Fig. 3 for a C20/25 concrete based on the modified BEP model [3], [9], and the recommendations of CNR-DT 203/R1/2025 [4] for bars whose bond behaviour is governed by mechanical interlocking. The concrete properties were obtained from EN 1992-1-1 [10].

Table 1 Material and geometrical properties

Material	Property		Value
GFRP	Lap-splice length	L_b	360 mm
	Diameter	ϕ_f	12 mm
	Elastic Modulus	E_f	60 GPa
Concrete	Effective Area	A_c	10,000 mm^2
	Compressive Strength	f_{cm}	28 MPa
	Tensile Strength	f_{ctm}	2.2 MPa

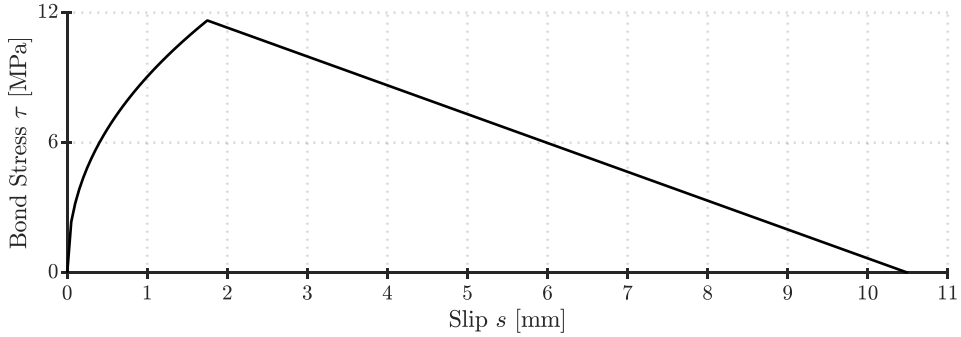


Fig. 3 Modified BEP bond–slip law for C20/25 concrete, following CNR-DT 203/R1/2025

The complete load-slip and load-mean strain curves shown in Fig. 4 highlight three key points (KPs), denoted by red circles. The first point corresponds to the pre-cracking stage, while the last two represent the post-cracking stage. In KP1, the concrete tensile stress reaches its tensile strength in the central region, resulting in concrete cracking. KP2 corresponds to the instant immediately after crack formation; consequently, the concrete stress in the middle of the lap splice drops to zero, and the load-slip response shows a decrease in both load and slip relative to KP1. KP3 marks the attainment of the maximum load-carrying capacity of the lap splice.

Fig. 5 shows the concrete stress distribution along the lap splice at the three key points (KP1-KP3). In the pre-cracking stage (KP1), the stress profile is continuous, with increasing tensile stress in the central region until the concrete strength f_{ctm} is reached. For the case analysed, this stress level is not attained again after cracking. After cracking (KP2 and KP3), the stress in the middle of the splice drops to zero, resulting in a segmented stress profile. From KP2 onward, the overall stress level in the concrete

progressively decreases as the bond stress distribution along the bars becomes increasingly uniform. At the maximum load-carrying capacity (KP3), the bond stress is nearly constant along the lap splice, leading to a reduced concrete stress field.

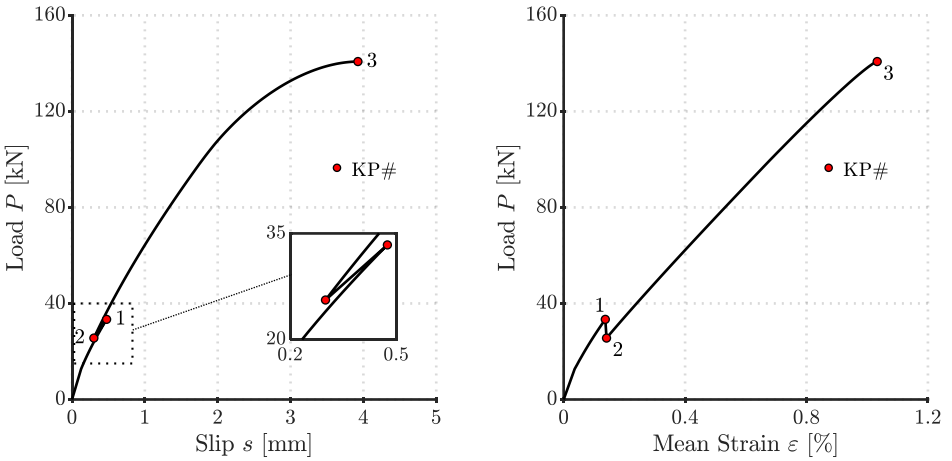


Fig. 4 Load–slip (left) and load–mean strain (right) responses of the lap splice, with key points highlighted by red circles.

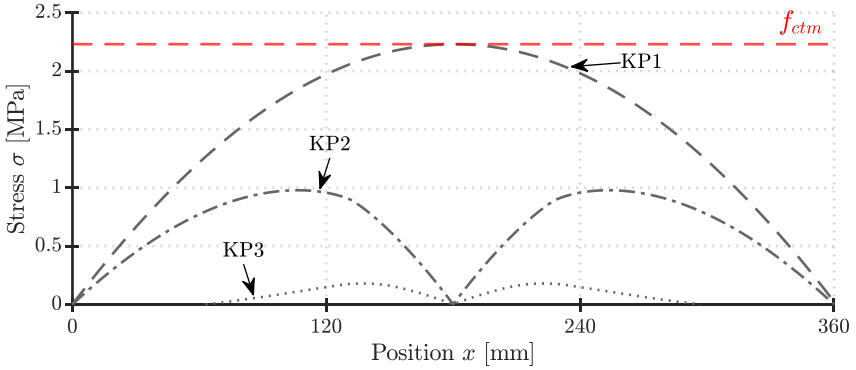


Fig. 5 Stress distribution in the concrete at three key points of the lap splice response

Figs. 6, 7 and 8 illustrate the evolution of the mechanical response of the lap splice at the three key points in terms of bar axial stress, slip, and bond stress distributions, respectively. As loading increases up to KP1, the concrete tensile stress gradually rises until it reaches its tensile strength, leading to crack formation at the mid-length of the lap splice.

At KP2, the stress state within the lap splice redistributes as the concrete can no longer sustain tensile stresses at mid-length due to cracking. As a result, two symmetric concrete tensile stress lobes develop along the lap splice, with their maxima located closer to the central crack than to the lap ends. At the crack location, the concrete tensile stress is suppressed, forcing the entire tensile force to be transferred directly between the two bars. The presence of the crack also introduces a local discontinuity in both slip and bond stress, which is manifested by a jump in their distributions at mid-length. Consequently, the axial stresses become equal at this point, giving rise to the intersection observed at mid-length, which represents force compatibility between the bars in the absence of concrete contribution. On either side of the crack, the stress gradients in the two bars reverse relative to each other: the directly loaded bar continues to increase its axial stress towards its loaded end, while the opposite bar progressively unloads towards its free end.

When the lap splice reaches its maximum load-carrying capacity (KP3), the concrete tensile stress is almost negligible and, as a consequence, the axial stresses in the bars exhibit an almost linear

variation along the lap length (Fig. 6, right). Accordingly, the bond stress along the lap splice exhibits a relatively stable profile, with reduced variation between its maximum and minimum values, as shown in Fig. 8 (right). In addition, a considerable slip develops at the unloaded ends of the bars, indicating that the bond mechanism is fully activated along the lap length.

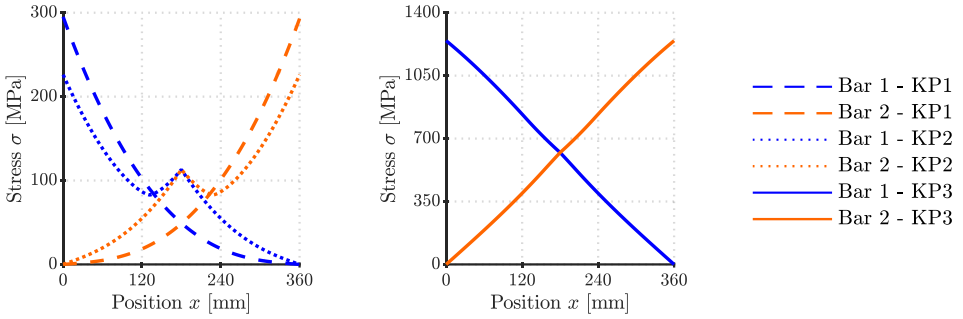


Fig. 6 Stress distribution in the bars at three key points of the lap splice response

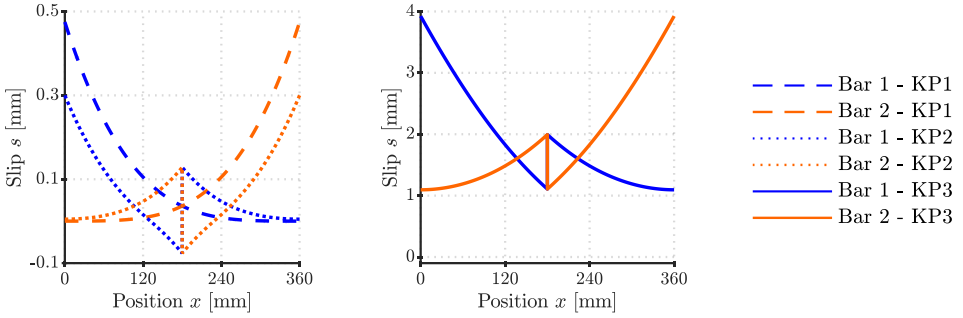


Fig. 7 Slip distribution in the bars at three key points of the lap splice response

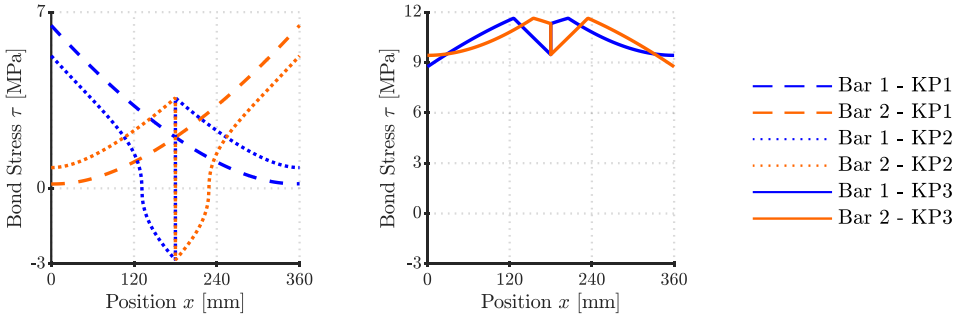


Fig. 8 Bond stress distribution in the bars at three key points of the lap splice response

4 PARAMETRIC STUDY

A parametric study was carried out to investigate the influence of the lap splice length on the load-slip and load-mean strain responses of GFRP lap splices. The analyses were conducted using the proposed finite-difference model, considering concrete strength class C20/25 and a bond slip law representative of behaviour governed by mechanical interlocking (Fig. 3). Unless stated otherwise, the parameters adopted in the analyses follow those listed in Table 1.

Four lap splice lengths were investigated. For two of them, $20\phi_f$ and $25\phi_f$, the tensile stress in the concrete never reached its tensile strength, and therefore no cracking occurred. For the remaining two cases, $30\phi_f$ and $35\phi_f$, cracking of the RC element developed at the mid-length of the lap splice. In this

study, the applied load was not limited by the tensile strength of the GFRP bars; consequently, all lap splice lengths except $20\phi_f$ were able to exceed the bar tensile capacity.

The parametric study reveals a clear influence of the lap splice length on the load–slip response of GFRP bars. Compared to longer lap splices in which concrete cracking develops, shorter lap lengths remain uncracked and exhibit a significantly lower maximum transferable load. Despite an 18% increase in load capacity for the $30\phi_f$ lap splice compared to the $25\phi_f$ lap splice case, a lower critical slip is observed (3.9 mm and 4.2 mm, respectively) (Fig. 9).

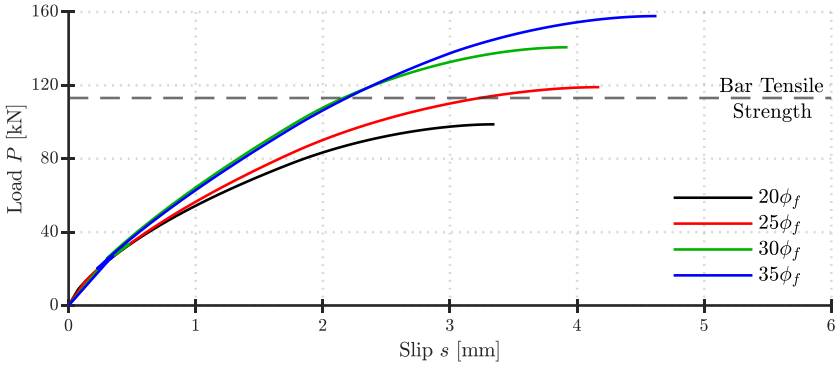


Fig. 9 Load-slip response of a 12 mm GFRP bar lap splice in a C20/25 concrete for different bonded lengths. The dashed line indicates the tensile strength of the bars.

The load–mean strain responses (Fig. 10) exhibit a markedly higher initial stiffness for all lap splice configurations compared to the bare bar, evidencing the tension stiffening effect provided by the surrounding concrete. Shorter lap lengths, $20\phi_f$ and $25\phi_f$, deviate earlier from linear behaviour, as slip contributes more significantly to the global deformation. In the responses of the $30\phi_f$ and $35\phi_f$ splices, the formation of the first concrete crack is manifested by a distinct load drop, after which the stiffness decreases and the load increases again steadily. This post-cracking branch retains a stable stiffness, enabling the splice to reach significantly higher loads than the uncracked cases.

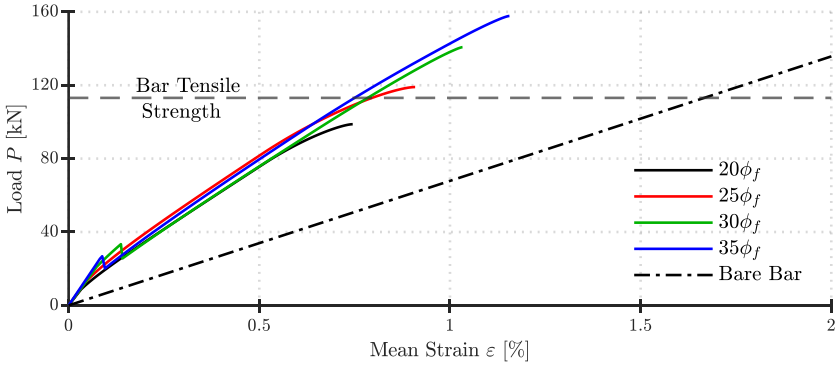


Fig. 10 Load-mean strain response of a 12 mm GFRP bar lap splice in a C20/25 concrete for different bonded lengths. The dashed line indicates the tensile strength of the bars.

5 CONCLUSIONS

This paper presents a numerical model, based on a non-linear finite difference method, intended to simulate the mechanical response of GFRP-RC lap splices under tensile loading, including the transition from uncracked to cracked behaviour. By explicitly incorporating a local bond–slip law and accounting for concrete cracking, the model enables a detailed description of the transfer of forces between overlapping bars and the surrounding concrete. Owing to the adopted numerical procedure, any desired material and geometrical properties, as well as any non-linear bond-slip law, can be introduced.

The numerical results indicate that the response of the lap splice evolves through distinct pre-cracking and post-cracking stages, characterised by markedly different stress, slip and bond stress distributions along the splice length. When the first concrete crack forms at the mid-length of the lap splice, a pronounced redistribution of internal forces is observed. After cracking, the contribution of the concrete to tensile force transfer at the crack location vanishes, and load transfer occurs directly between the two bars, giving rise to discontinuities in slip and bond stress at the cracked section. The simulations illustrate how this transition influences the global load–slip and load–mean strain responses, as well as the local stress gradients in both bars, highlighting the governing role of concrete cracking in the mechanical behaviour of GFRP lap splices.

Parametric analyses further indicate that the lap splice length significantly affects both the cracking response and the maximum transferable load. Shorter lap splices may remain uncracked but exhibit limited load-carrying capacity, whereas longer lap splices allow crack formation and sustain higher loads after cracking, emphasising the importance of explicitly accounting for cracking when assessing the effectiveness of GFRP lap splice lengths under tensile loading.

Acknowledgements

The authors acknowledge the support provided by the Spanish Ministry of Science, Innovation and Universities (MICIU/AEI) through project CPP2022-009555/MICIU/AEI/10.13039/501100011033. The first author acknowledges the support from the Generalitat de Catalunya, under the grant IFUdG2024, co-funded by Banco Santander.

References

[1] Tepfers, Ralejs. 1980. “Bond stress along lapped reinforcing bars.” Magazine of Concrete Research 32:135–42. doi: 10.1680/macr.1980.32.112.135.

[2] Canbay, Erdem, and Frosch, Robert J. 2005. “Bond strength of lap-spliced bars.” *ACI Struct. J.* 102:605–14. doi: 10.14359/14565.

[3] Pecce, Marisa, Manfredi, Gaetano, Realfonzo, Roberto, and Cosenza, Edoardo. 2001. “Experimental and Analytical Evaluation of Bond Properties of GFRP Bars.” Journal of Materials in Civil Engineering 13:282–90. doi:10.1061/(ASCE)0899-1561(2001)13:4(282).

[4] CNR (Italian National Research Council). 2025. “Guide for the Design and Construction of Concrete Structures Reinforced with Fibre-Reinforced Polymer Bars.” Rome, Italy. CNR-DT 203/R1/2025.

[5] Ortiz, Jesús D., Benmokrane, Brahim, and Nanni, Antonio. 2025. “Lap Splice Length Equation of Glass Fiber-Reinforced Polymer Bars in Flexural Reinforced Concrete Members.” ACI Structural Journal 122:175–188. doi:10.14359/51742156.

[6] Wambeke, Brad W., and Shield, Carol K. 2006. “Development Length of Glass Fiber-Reinforced Polymer Bars in Concrete.” ACI Structural Journal 103:11–17. doi:10.14359/15081.

[7] Baena, Marta, Torres, Lluís, Turon, Albert, and Miàs, Cristina. 2013. “Analysis of Cracking Behaviour and Tension Stiffening in FRP Reinforced Concrete Tensile Elements.” *Composites Part B: Engineering* 45:1360–1367. doi:10.1016/j.compositesb.2012.07.026.

[8] Gómez, Javier, Lluís Torres, and Cristina Barris. 2020. “Characterization and Simulation of the Bond Response of NSM FRP Reinforcement in Concrete.” Materials 13:1770. doi:10.3390/ma13071770.

[9] Cosenza, Edoardo, Manfredi, Gaetano, and Realfonzo, Roberto. 1996. “Bond Characteristics and Anchorage Length of FRP Rebars.” Paper presented at the *2nd International Conference on Advanced Composite Materials in Bridge Structures*, Montréal.

[10] European Committee for Standardization. 2004. *Eurocode 2: Design of Concrete Structures—Part 1-1: General Rules and Rules for Buildings*. EN 1992-1-1.

Investigation of Basalt Filaments as Mineral Reinforcement for Filigree Sustainable Lightweight Concrete Structures

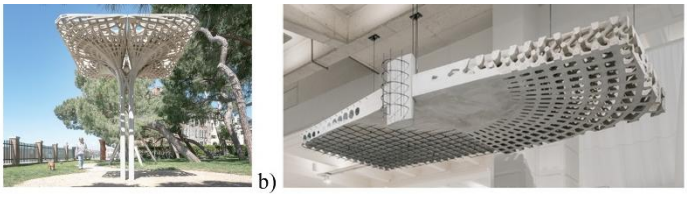
Olga Miller, Lucio Blandini

Institute for Lightweight Structures and Conceptual Design (ILEK)
University of Stuttgart,
Pfaffenwaldring 14, Stuttgart 70569, Germany

Summary
Filigree sustainable lightweight concrete structures are one of the main focuses of research at the Institute for Lightweight Structures and Conceptual Design (ILEK) of the University of Stuttgart, as they enable a significant reduction in material usage, CO_2 emission and waste production. The complex geometry of these optimised filigree structures requires new reinforcement concepts. This study investigates the suitability of basalt fibre filaments as a sustainable reinforcement for such structures, because of its low global warming potential. Basalt fibre rovings were impregnated with epoxy resin and different sand surface coatings, and experimentally tested for their tensile behaviour, bond behaviour with concrete, and durability under alkaline exposure. The results show that the manufacturing quality and the surface treatment have a significant influence on the mechanical properties, bond behaviour, and durability. Overall, basalt fibre filaments show high potential for use in lightweight concrete structures.

1 Introduction

The construction sector is one of the most resource- and emission-intensive industries. Concrete construction contributes significantly to global CO_2 emissions due to the high material consumption and the energy-intensive production of cement [1], [2]. Against this background, lightweight construction is gaining increasing importance. At the Institute for Lightweight Structures and Conceptual Design (ILEK), various sustainable lightweight construction approaches are being investigated [3]–[5]. A particular focus is placed on filigree lightweight concrete structures that can be manufactured using waste-free sand formwork techniques [6], [7]. Following a structural analysis of the component or structural element, a topology optimisation is carried out. This construction approach enables a reduction of the concrete volume by up to 50 %, resulting in a significant decrease in CO_2 emission. Examples and demonstrators of such structures are presented in [8]. The Marinaressa Coral Tree (Fig. 1 a) is still reinforced with a layer of carbon fibres, whereas the right part of the TMW Graded Slab[s] prototype (Coral slab) is already reinforced with coated basalt rebars.



a) b)

Fig. 1 Marinaressa Coral Tree (a) and TMW Graded Slab[s] (b) as examples of filigree lightweight concrete structures [8]

Filigree lightweight concrete structures impose increased demands on reinforcement material and layout. Conventional steel reinforcement is only partially suitable for thin-walled and geometrically complex components due to its limited formability, high self-weight, and susceptibility to corrosion. This results in the need for alternative reinforcement systems that allow load-oriented placement along the force paths while simultaneously providing high durability in the alkaline concrete environment.

Fibre-reinforced polymer (FRP) composites are gaining increasing importance in concrete construction, as they are corrosion-resistant and allow the use of reduced concrete cover. In this context, basalt fibre reinforced polymer (BFRP) composites represent a potential alternative to the typically used glass and carbon fibres. Basalt is a rock of mineral origin, which results in a lower global warming potential of basalt fibres compared to other fibre materials [9]. In addition, basalt fibres exhibit high tensile strength. The use of basalt fibre-reinforced reinforcement systems allows for low concrete cover and enables reinforcement elements to be arranged specifically along the load paths and contributes to the overall reduction of the ecological footprint of the structure. In [10] and [11], layout-optimised, robotically deposited fibre composite structures based on glass and carbon fibres were already produced, demonstrating the basic feasibility of this process.

In this study, the suitability of impregnated basalt fibre filaments (BFRP filaments) as reinforcement for lightweight concrete structures is investigated experimentally. The focus is placed on the manufacturing process as well as on the characterisation of the mechanical, bond-related, and durability-related behaviour.

2 Materials and Methods

2.1 Manufacturing process

For the production of BFRP filaments, basalt fibre rovings from the manufacturer C-Con with a linear density of 1800 tex were used in combination with a two-component epoxy resin system (R&G) with a viscosity of 200 mPa·s at 25 °C as the impregnation matrix. Test specimens for tensile and bond strength, as well as durability tests were produced by manual impregnation. The basalt fibre roving was passed through a syringe filled with liquid epoxy resin at an approximate pulling speed of 400 cm/min and then positioned on a plate with retaining bolts (see Fig. 2 a). Curing was carried out at room temperature over a period of 24 hours. After the curing process was complete, the samples were cut to the required length. Two variants of the manufacturing process were investigated. In the first variant (Fig. 2 b), the roving was passed only through the syringe filled with resin. In the second variant (Fig. 2 c), deflection rollers were additionally integrated, enabling deflection and slight pre-tensioning of the roving. This approach aimed to improve fibre wetting and achieve a more homogeneous impregnation. An overview of the investigated specimen series and their designations is given in Table 1. In addition, the manufacturing approach was applied at component scale to demonstrate practical feasibility.

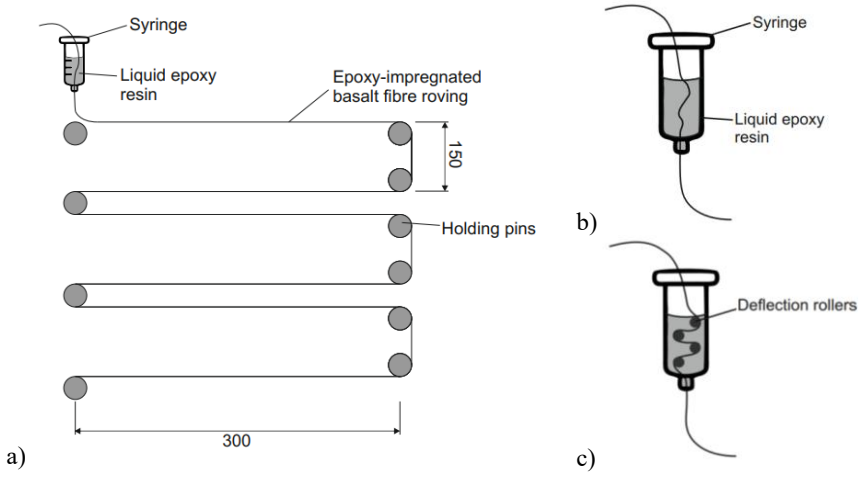


Fig. 2 Schematic illustration of the specimen impregnation process: (a) specimen layout, (b) impregnation using a syringe without deflection rollers, and (c) impregnation with deflection rollers.

Table 1 Specimen designation and manufacturing variants

Designation	Description
2-EH (1)	Double epoxy impregnation, manufactured with deflection rollers
1-EH (1)	Single epoxy impregnation, manufactured with deflection rollers
1-EH (0)	Single epoxy impregnation, manufactured without deflection rollers

2.2 Uniaxial tensile tests

To determine the tensile strength, uniaxial tensile tests were carried out on BFRP filaments. Single- and double-coated specimens manufactured with and without deflection rollers were investigated. The tests were carried out using a Zwick 1474 universal testing machine at a constant displacement rate of 2 mm/min. The filaments were anchored using internally threaded bolts, with bonding achieved using injection mortar [12].

The total length of the test specimens was 300 mm. An anchorage length of 70 mm was provided on each side, resulting in a free test length of 160 mm. The maximum breaking force, tensile strength, elastic modulus, and elongation at breakage were determined in accordance with [13]–[15]. Five test specimens were tested per test series. The test setup is shown in Fig. 3 a.

2.3 Bond tests

The bond behaviour was investigated by testing BFRP filaments embedded in concrete cubes with dimensions of 100 × 100 × 100 mm. The concrete used corresponded to strength class C50/60. Based on an average filament diameter of 3.0 mm, the effective bond length was defined as $5 \cdot d = 15$ mm. The tests were performed using a Zwick 1474 universal testing machine. Slip was recorded using a displacement transducer. The free anchorage length of the specimens outside the concrete cube was 70 mm. The bond stress was calculated according to [14], [15]. A schematic test setup is shown in Fig. 3 b.

In addition, different surface variants of the filaments were investigated, including specimens without additional sand coating and specimens with a sand coating of fine sand with a grain size of 0.06–0.3 mm and coarse sand with a grain size of 0.3–0.5 mm (see Fig. 4). Five specimens were tested per test series.

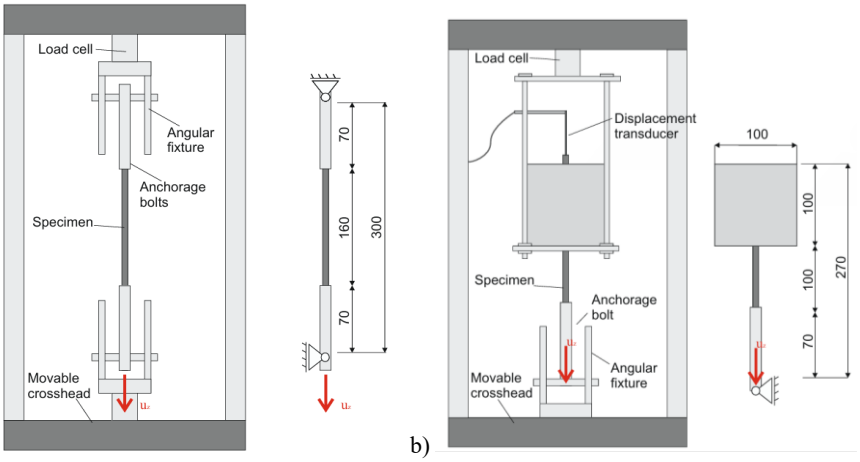


Fig. 3 Experimental setup for tensile testing (a) and bond testing (b) of BFRP filament-specimens. All dimensions in mm.

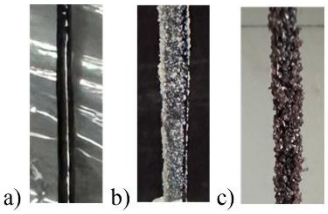


Fig. 4 Epoxy-impregnated filament specimens without sand coating (a), with fine sand coating (b), and with coarse sand coating (c)

2.4 Durability tests

To test durability, the samples were stored in a 10% NaOH solution for defined periods of time and at different temperatures (see Table 2). The pH value of the solution was at least 14. The test procedure was conducted in reference to [14], [15] using a more aggressive alkaline environment to achieve accelerated ageing conditions. After alkaline exposure, the samples were cleaned, dried, and then tested in the same way as in the tensile tests described in 2.2. In addition, a microscopic examination of the sample surfaces was carried out before and after alkaline exposure in order to qualitatively analyse possible damage mechanisms and changes in the fibre-matrix structure.

Table 2 Exposure conditions and number of specimens for durability tests

No.	Series	Exposure time [h]	Temperature [°C]	Number of specimens
#1	2-EH (1)	24	80	5
#2	2-EH (1)	72	60	5
#3	2-EH (1)	24	60	5
#4	2-EH (1)	17	40	5
#5	1-EH (1)	24	60	4

3 Results and Discussion

3.1 Tensile behaviour

The tensile behaviour of the investigated BFRP filaments is influenced by the manufacturing process. Single- and double-coated samples 1-EH (1) and 2-EH (1) manufactured with deflection rollers, exhibit a comparable load-bearing capacity. In contrast, the variant 1-EH (0), produced without deflection rollers, shows a tensile force that is approximately 12 % lower. Since single impregnated filament rovings were investigated in each test, the maximum tensile force represents the relevant measure of the load-bearing capacity of the specimens. The results of the tensile tests are summarised in Table 3.

In contrast to the tensile force, the calculated tensile stress exhibits more pronounced differences between the series. The highest stress values are observed for 1-EH (1), whereas the double-coated samples 2-EH (1) reach approximately 20 % lower stress levels. This behaviour is attributed to the increased effective cross-sectional area resulting from the additional coating, which leads to lower nominal stresses at comparable tensile forces. By considering the fibre cross-sectional area only, the coating effect can be filtered out and the resulting fibre-related stresses exhibit the same trend as the ultimate load. The elastic modulus of all investigated series lies within a similar range between approximately 15 and 18 GPa. Likewise, the elongation at breakage ranges between 3.0 % and 3.5 % and does not show significant differences between the series.

A notably higher scatter of the results is observed for the series 1-EH (0). This increased variability reflects a less stable manufacturing process in the absence of deflection rollers. By contrast, the use of deflection rollers promotes a more uniform impregnation of the filaments and results in more consistent mechanical properties. Applying a second coating further reduces the scatter, indicating that remaining inhomogeneities are increasingly compensated.

The stress–strain curves in Fig. 5 show an approximately linear-elastic behaviour up to brittle fracture. Differences between the series are primarily reflected in the achieved stress level.

Table 3 Tensile properties of BFRP specimens (mean values)

Series	Ultimate load [N]	Cross-section [mm²]	Tensile Stress [N/mm²]	Elastic modulus [GPa]	Failure strain [%]	Fibre cross-section [mm²]	Fibre-related tensile stress [N/mm²]
1-EH (0)	1304 (± 158.6)	2.7 (± 0.4)	501 (± 105)	15.6 (± 2.8)	3.48 (± 0.5)	0.7	1946 (± 264.7)
1-EH (1)	1478 (± 77.2)	2.5 (± 0.3)	604 (± 77.4)	17.9 (± 1.4)	3.37 (± 0.3)	0.7	2206 (± 128.9)
2-EH (1)	1439 (± 61)	3.0 (± 0.2)	484 (± 44.3)	16.4 (± 1.2)	2.95 (± 0.2)	0.7	2148 (± 90.3)

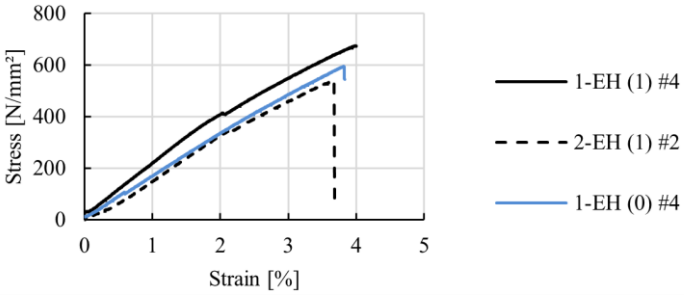


Fig. 5 Tensile stress–strain behaviour of BFRP filaments with single and double epoxy impregnation, manufactured with and without deflection rollers

3.2 Durability behaviour

The microscopic images in Fig. 6 show the specimens before and after alkaline exposure. Prior to exposure, air voids are visible within the fibre composite, which likely formed during the impregnation process. The fibres are predominantly aligned parallel to each other.

After alkaline exposure, white deposits are observed on the specimen surface. These deposits are attributed to sodium salts, potentially including sodium carbonate, that diffused through the epoxy resin matrix and precipitated at the surface. Pronounced deposits are particularly evident in regions previously containing air voids.

The evaluation of the test results in Table 4 shows that both increasing exposure time and rising temperatures lead to a reduction in the maximum load-bearing capacity of the fibre composite. Under the same exposure conditions, samples with a double epoxy resin coating (#3) exhibit a residual load-bearing capacity that is approximately 14 % higher than that of single-coated samples (#1).

In addition, double-coated samples require a significantly longer exposure time to achieve a comparable degree of degradation. Single-coated samples (#1) already exhibit a residual load-bearing capacity of approximately 67 % after 24 hours at 60 °C, whereas double-coated samples (#4) only achieve a similar residual load-bearing capacity after 72 hours at 60 °C.

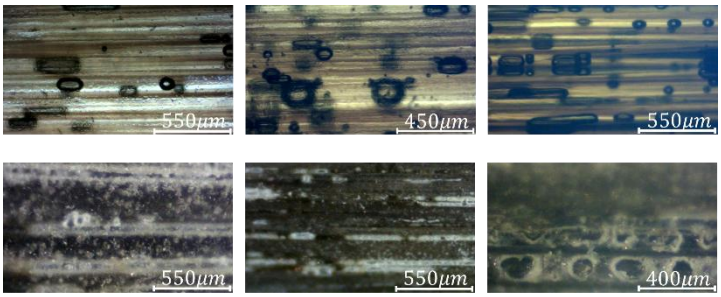


Fig. 6 Microscopic images of single epoxy-impregnated BFRP specimens before (top) and after (bottom) alkaline exposure

Overall, temperature has a greater influence on the degradation process than the duration of exposure. With the same exposure time of 24 hours, an increase in temperature from 60 °C to 80 °C (#3 vs. #5) leads to a significantly greater reduction in residual load-bearing capacity than an extension of the exposure time from 24 hours to 72 hours at 60 °C (#3 vs. #4). Despite the degradation observed under strongly alkaline conditions, sufficient residual load-bearing capacity remains, indicating potential suitability for use in concrete under less aggressive environmental conditions.

Table 4 Residual tensile strength of BFRP specimens after alkaline exposure under different temperatures and durations (mean values)

No.	Series	Exposure time [h]	Temperature [°C]	Ultimate load [N]	Residual strength [%]	Coefficient of variation [%]
#1	1-EH (1)	24	60	995 (± 309)	67	31
#2	2-EH (1)	17	40	1400 (± 87)	97	6
#3	2-EH (1)	24	60	1164 (± 201)	81	17
#4	2-EH (1)	72	60	991 (± 120)	69	12
#5	2-EH (1)	24	80	863 (± 120)	60	14

3.3 Bonding Properties

The bond behaviour of the BFRP specimens with different surface treatments is shown in Fig. 7 using representative bond stress-slip curves. The corresponding mean values of the maximum bond stress and slip are summarised in Table 5.

Coarsely sand-coated specimens achieve lower bond stresses but exhibit more uniform bonding behaviour. The increase in bond stress is moderate and the BFRP filament is pulled out progressively. This behaviour indicates a predominantly friction-dominated bond effect with lower brittleness.

In contrast, fine sand-coated specimens show a steep increase in bond stress even at very low slip, which indicates high initial stiffness. The bond failure occurs early and abruptly and is characterised by a sudden pulling out of the filament. This behaviour indicates pronounced mechanical interlocking followed by brittle bond failure and explains the increased scatter observed in the test results.

Epoxy resin-coated samples, produced using the deflection roller method, show a comparatively high bond stress and pronounced ductile bond behaviour. With increasing slip, bond stress rises continuously and reaches a pronounced plateau, before dropping abruptly due to complete filament pull-out.

Overall, the results demonstrate that not only the maximum bond stress, but also the slip behaviour and the governing failure mechanism are decisive for assessing bond performance. Surface treatments that promote ductile and progressive bond behaviour are therefore particularly suitable, as they enable a more uniform load transfer between BFRP filaments and concrete.

Table 5 Bond properties of BFRP specimens with different surface treatments (mean values)

Surface treatment	Bond stress [N/mm²]	Slip [mm]
Coarse sand	3.4 (± 2.5)	4.6 (± 2.2)
Fine sand	7.2 (± 5.1)	0.8 (± 1.2)
Epoxy matrix only	6.5 (± 2.2)	5.6 (± 4.0)

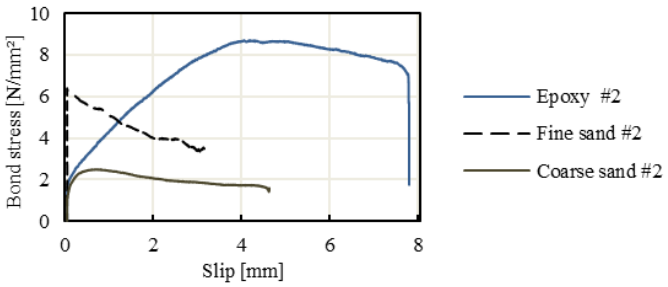


Fig. 7 Representative bond stress–slip behaviour of BFRP specimens with different surface treatments

3.4 Proof of feasibility

The practical feasibility of the proposed reinforcement concept was demonstrated at component scale. The derived fibre paths were successfully manufactured by guided placement impregnated basalt fibre rovings (Fig. 8 a) and integrated into the sand formwork (Fig. 8 b). Subsequently, the element was concreted and demoulded without defects, and the embedded fibre reinforcement remained intact and properly positioned (Fig. 8 c). This confirms that the investigated basalt fibre reinforcement system can be manufactured, integrated, and concreted in a filigree lightweight concrete component. The presented results therefore demonstrate the general applicability of the proposed reinforcement approach under realistic production conditions.



Fig. 8 Proof of feasibility of fibre winding and concreting of a filigree lightweight concrete element with BFRP filaments

4 Conclusions

The investigations show that impregnated BFRP filaments are generally suitable as reinforcement for filigree lightweight concrete structures. The mechanical properties depend largely on the manufacturing quality, with the use of deflection rollers leading to more homogeneous results. An additional epoxy resin coating improves reproducibility and resistance to alkali exposure.

The durability tests revealed the expected degradation under highly alkaline conditions, although a relevant residual load-bearing capacity is retained even under accelerated test conditions. The composite tests show that, in addition to the maximum composite stress, the slip behaviour and the composite mechanism are particularly decisive. Ductile, progressive pull-out behaviour proves to be advantageous for concrete structures.

Further experimental studies on structural components are required to assess the load-bearing behaviour, failure mechanisms, and long-term performance of BFRP-reinforced filigree concrete elements under realistic boundary conditions. In addition, the experimentally derived material, bond, and durability parameters provide a sound basis for numerical modelling and finite element analyses of such structures.

Acknowledgements

Parts of this work were conducted within the framework of a master's thesis of Daniah Khalaf. The authors gratefully acknowledge the support provided during this work. Moreover, this research was generously supported by the provision of materials by the company C-Con (Sindelfingen, Germany), and Sika (Leimen, Germany).

References

[1] Xiao, Jianzhuang, Zou, Shuai, Poon, Chi Sun, Sham, Man Lung, Li, Zongjin, and Shah, Surendra P. 2025. "We use 30 billion tonnes of concrete each year – here's how to make it sustainable." *Nature* 638, S. 888–890. https://doi.org/10.1038/d41586-025-00568-4.

[2] Springer Nature. 2021. "Concrete Needs to Lose Its Colossal Carbon Footprint." *Nature* 597:593–594. doi:10.1038/d41586-021-02612-5.

[3] Blandini, Lucio, Kovaleva, Daria, Nething, Christoph, Nigl, David, Smirnova, Maiia, Strahm, Benedikt, Eppinger, Erik, and Teichmann, Alexander. 2023. "Leicht Bauen mit Beton – Teil 1: Materialleichtbau." *Beton- und Stahlbetonbau* 118(5):310–319. doi:10.1002/best.202300025.

[4] Blandini, Lucio, Kovaleva, Daria, Haufe, Carl Niklas, Nething, Christoph, Nigl, David, Nitzlader, Markus, Smirnova, Maiia, Strahm, Benedikt, Bosch, Matthias, Funaro, Daniele, and Nistler, Maximilian. 2023. "Leicht Bauen mit Beton – Teil 2: Strukturleichtbau." *Beton- und Stahlbetonbau* 118(5):320–331. doi:10.1002/best.202300026.

[5] Blandini, Lucio. 2022. "Lightweight and Sustainable Concrete Structures: The ILEK Research Strategy." In *Proceedings of the fib International Congress 2022*, Oslo.

[6] Kovaleva, Daria. 2025. Zero-Waste Sand Formworks for Lightweight Concrete Structures. PhD diss., University of Stuttgart.

[7] Kovaleva, Daria, Nistler, Maximilian, Verl, Alexander, Blandini, Lucio, and Sobek, Werner. 2022. "Zero-Waste Production of Lightweight Concrete Structures with Water-Soluble Sand Formwork." In Proceedings of the Third RILEM International Conference on Concrete and Digital Fabrication, 3–8. doi:10.1007/978-3-031-06116-5_1.

[8] Kovaleva, Daria, Haufe, Carl Niklas, Miller, Olga, Gericke, Oliver, Strahm, Benedikt, and Blandini, Lucio. 2024. "Leicht und Nachhaltig Bauen mit Beton." *Bautechnik*. doi:10.1002/bate.70065.

[9] Kromoser, Benjamin. 2021. "Ressourceneffizientes Bauen mit Betonfertigteilen." In *Beton-Kalender 2021*. doi:10.1002/9783433610206.

[10] Oval, Robin, Orr, John, and Shepherd, Paul. 2025. "Structural design and fabrication of concrete reinforcement with layout optimisation and robotic filament winding." *Autom. Constr.,* Bd. 170, S. 105952. doi: 10.1016/j.autcon.2024.105952.

[11] Hack, Norman, Bahar, Mohammad, Hühne, Christian, Lopez, William, Gantner, Stefan, Khader, Noor, and Rothe, Tom. 2021. "Development of a Robot-Based Multi-Directional Dynamic Fibre Winding Process for Shotcrete 3D Printing." *Fibers* 9(6). doi:10.3390/fib9060039.

[12] Hilti. 2021. Injection System HIT-RE 500 V4 for Rebar Connection. ETA-20/0540.

[13] DIN EN ISO 527-4:2022-03, Kunststoffe - Bestimmung der Zugeigenschaften – Teil 4: Prüfbedingungen für isotrop und anisotrop faserverstärkte Kunststoffverbundwerkstoffe. Beuth Verlag GmbH. doi: 10.31030/3328116.

[14] DAfStb. 2024. Concrete Components with Non-Metallic Reinforcement—Commentary and Examples.

[15] ISO 10406-1. 2025. Fibre-Reinforced Polymer Reinforcement—Part 1.

Structural Assesment

Preservation state assessment of steel tendons in prestressed concrete bridges via direct and indirect inspections

Martina Giglio[1], Luca Ranedda[2], Edoardo Proverbio[1], Calogero Pio Di Vita[2]

[1] Department of Engineering, University of Messina, Contrada di Dio, 98158, Sant'Agata, Messina, Italy
[2] ANAS, DSP-Centro di Ricerca di Cesano, Via della Stazione di Cesano, 00123, Cesano, Roma, Italy

Summary
This article investigates the combined use of ultrasonic tomography (as indirect inspection) and endoscopic surveys (as direct inspection) to evaluate the preservation state of prestressing steel tendons in prestressed concrete bridges. Ultrasonic tomography is based on the propagation in concrete and subsequent reflection of mechanical shear waves by discontinuities, such as metallic elements or voids. This technique provides information also on the size and distribution of voids, even at significant depth. In parallel, direct endoscopic surveys were conducted to document the condition of the sheath, the quality of grout injection, and the surface condition of the prestressing strands. Endoscopic observations were specifically performed in correspondence with ultrasonic anomalies over at least two adjacent cross-sections. The use of both approaches enhances the reliability of indirect inspection by reducing false positive and allowing to optimize setting parameters for defect identification.

1 INTRODUCTION

The structural integrity of aging infrastructure represents a critical challenge for civil engineering worldwide. In Europe, a significant portion of the road network was built between the 1950s and 1970s, utilizing post-tensioned (PT) concrete systems [1], [2]. Recent catastrophic failures have highlighted the vulnerability of these structures, particularly those featuring complex static schemes like the Gerber system, to environmental degradation and lack of adequate maintenance [3], [4]. Among the primary causes of deterioration in PT bridges is the corrosion of prestressing tendons, often triggered by incomplete grout injection within the ducts, which leaves the steel strands exposed to moisture and aggressive agents [5], [6]. In the Italian context, the Ministry of Sustainable Infrastructure and Mobility has introduced rigorous guideline for the "special inspection" of bridges, emphasizing the need for multi-level diagnostic protocols [7], [8]. The assessment of existing PT structures is particularly complex due to the "hidden" nature of the reinforcement. Traditional visual inspections are insufficient do detect internal grout voids or localized corrosion [9]. Consequently, Non-Destructive Testing (NDT) techniques, such as Georadar and Ultrasonic Tomography (UT), have become indispensable tools for structural health monitoring [10], [11]. While Georadar is highly effective for mapping tendon trajectories (phase 1 of the diagnostic protocol), its sensitivity to metallic elements often precludes the detection of air-filled voids inside metallic ducts [12], [13]. Ultrasonic tomography, specifically utilizing the Synthetic Aperture Focusing Technique (SAFT), has emerged as a superior method for imaging the internal consistency of concrete and identifying voids within the grout matrix [14], [15]. However, the intrinsic heterogeneity of concrete and the complex geometry of structural elements, such as the multicellular box girders, introduce significant challenges in signal interpretation. This study presents the results of high-density experimental campaign conducted on Candegliano viaduct located in the SS 3 Flaminia, focusing on the phase 2 of a specialized inspection protocol. The primary objective is to evaluate the operational feasibility and accuracy of UT in identifying defects within the cables. A key contribution of this work is the systematic comparison of ultrasonic "indications" with the direct endoscopic surveys, providing a statistical basis to analyze the occurrence of false-positive signals induced by geometric attenuation and signal gain amplification [16].

2 METHODOLOGY

The diagnostic activities carried out followed a comprehensive three-phase experimental protocol designed for the special inspection of post-tensioned structures:

- Phase 1: geometric and structural survey, this involved mapping the tendon trajectories using Georadar and performing localized surveys on the anchor heads to define the reinforcement geometry.
- Phase 2: assessment of the conservation state focused on identifying internal anomalies, specifically grout voids using Ultrasonic Tomography, with subsequent direct validation via Endoscopic survey.
- Phase 3: stress state evaluation aimed to quantify the residual prestress through detensioning measurements on both the concrete and the steel strands.

This paper focuses exclusively on the results and methodological implications of Phase 2, evaluating the effectiveness of the ultrasonic-endoscopic integration for the diagnostic assessment of structure cables.

2.1 Ultrasonic testing principles

Ultrasonic Testing (UT) is an established non-destructive testing (NDT) methodology widely employed for assessing material integrity and detecting internal anomalies in engineering materials [17], [18]. Although UT applications are predominantly centered on the inspection of homogeneous materials like metals, the technique has long been adopted for structural elements made of concrete, with early attempts focusing on the transmission technique to empirically correlate pulse velocity and attenuation with material properties. However, the intrinsic heterogeneity of concrete presents significant challenges, even at a low operating frequency (typically 20-100 kHz, selected to minimize strong scattering from aggregates and pores), the resulting signal attenuation reduces the method's sensitivity for detecting discrete features such as small flaws or tendon ducts. The propagation of stress waves in solids is complex and is influenced by parameters like material composition and the location of internal defects. The wave energy is primarily carried by three modes: the fast longitudinal (compressional) waves, where particle oscillation is parallel to propagation, the shear (transverse) waves, where particle oscillation is perpendicular, and the slower surface (Rayleigh) waves.

2.1.1 Pulse-echo system

The ultrasonic inspection was performed using the pulse-echo technique, which enables internal defect detection through the analysis of reflected wave energy while requiring access from only one side of the structure [9]. To overcome the effects of structural noise and wave divergence in concrete, low-bandwidth transducers and the Synthetic Aperture Focusing Technique (SAFT) were employed to improve image resolution and enhance the localization of internal anomalies [13], [18]. The processing workflow included digital filtering, SAFT-based tomographic reconstruction, and gain normalization using the concrete backwall reflection as a reference to ensure consistent interpretation of the qualitative UT results.

2.1.2 Ultrasonic Pulse Velocity (UPV) method

In contrast, the ultrasonic pulse velocity method operates via transmission to measure wave propagation characteristics. Early attempts focused on the transmission technique to empirically correlate pulse velocity and attenuation with material properties [19], [20]. While the underlying principle of generating ultrasonic stress waves remains the same, UPV typically employs two separate transducers for transmission and reception. There are three main arrangements for UPV:

- Direct transmission, transducers on opposite faces, offering maximum energy
- Semi-direct transmission, transducers on adjacent faces
- Indirect transmission, both transducers on the same face

This method continues to be successfully employed for global structural health monitoring (SHM) as various characteristics, such as velocity, amplitude and attenuation, can be used to determine material properties, assess damage severity and feed numerical models for residual service life estimation.

2.2 Endoscopic survey

The endoscopic survey (ES) is employed as a direct and minimally invasive inspection method that serves as the ground-based control procedure for the indirect data acquired via Ultrasonic Tomography (UT) [17]. The primary function of ES is to visually confirm the presence, nature and extent of anomalies, such as grout voids, water accumulation, and the corrosion state of the prestressed steel strands, that were previously identified as ultrasonic indications. This approach is essential for enhancing the reliability of UT method and optimizing its setting parameters by minimizing the impact of false positive indications. Although the method is slightly invasive, it has minimal impact on the overall structural integrity and, since it can be performed in a higher number of locations, fully complements other more invasive evaluation techniques, such as detensioning and electrochemical measurements, enhancing the comprehensiveness of the evaluation process. The ES procedure begins with drilling small access holes, typically 2-3 cm in diameter) at target locations on the concrete surface to reach the internal components. The boreholes are deliberately positioned in direct correspondence with ultrasonic anomalies detected during the UT preliminary scan. Once drilled, the holes require thorough cleaning to ensure clear visibility inside and prevent obstruction during the subsequent inspection. The exploration is carried out through a specialized flexible endoscope.

2.2.1 Instrumentation and diagnostic

The survey utilizes a high-resolution flexible endoscope equipped with a camera and a light source (torch) at the tip for illumination. The high resolution of the camera is particularly effective in assessing the condition of the grout surrounding the tendons, allowing for the detection of the presence of voids or cavities and the identification of internal cracking or damage to the injected cementitious materials. The most critical instrumental feature for accurately documenting the complex internal geometry of the tendon duct is the use of an off-axis optical system. This lens provides a lateral view, often 90 degrees to the borehole axis, allowing for the acquisition of borehole macrographs that visually capture the circumferential surface of the grout and the lateral surface of the prestressing steel strands. This capability is vital for quantifying the extent of incomplete grouting and for accurately grading the severity of localized corrosion on the steel surface.

3 RESULTS AND DISCUSSION

In this section, the results obtained from the ultrasonic tomographic mapping are presented and compared with the direct evidence gathered through the endoscopic survey. The discussion focuses on the interpretation of high-reflectivity signals and the physical factors that led to the identification of false-positive indications.

3.1 Case study

The experimental campaign was conducted on the Candegliano viaduct located along the SS 3 Flaminia. The bridge features a structural configuration based on a Gerber system, characterized by a 60 m central span, a 30 m drop-in beam, two 15 m cantilevers and side spans of 30 m each (Fig. 1). The focus of the investigation was the drop-in beam, which consists of a multicellular box girder with four webs. This structural element is reinforced with a post-tensioning system utilizing Morandi M5 type cables. The primary objective of the experimentation was to assess the operational feasibility and the effective diagnostic accuracy of NDT techniques within the framework of “special inspections”. Specifically, the study aimed to evaluate ultrasonic tomography for detecting defects in post-tensioned cables and to validate these indirect findings through direct endoscopic survey.

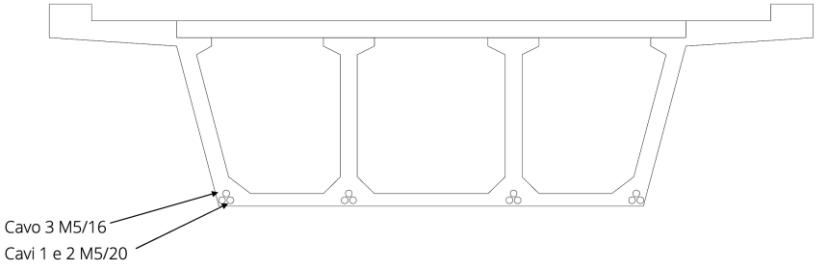




Fig. 1 General view of the Candegliano viaduct (bottom) and the section (top) of the multicellular box girder consisted of four webs.

3.2 Operational findings and mapping

The ultrasonic survey was conducted on seven macro-areas of the Candegliano viaduct deck, including the Gerber cantilevers (Pile 3 and Pile 4 sides) and the drop-in beam. Multiple tendons were inspected, with all measurement points georeferenced on a technical drawing. High-density tomographic scans were performed to reconstruct tendon trajectories within the webs, using 15 vertical scans per section for the drop-in beams and 6–7 scans for the Gerber cantilevers. Ultrasonic tomography was based on bimodal piezoelectric transducers emitting shear waves, with image reconstruction performed using the Synthetic Aperture Focusing Technique (SAFT). To assess the overall condition of the examined viaduct, a total of no.39 sections (Fig.2) were verified through direct endoscopic inspection following the ultrasonic screening. These targeted verifications were systematically performed in direct correspondence with detected ultrasonic anomalies, with the primary objective of validating the methodological reliability of the Ultrasonic Tomography (UT) results. By correlating indirect signal indications with direct visual evidence, this approach aimed to rigorously assess the diagnostic accuracy of the UT findings while simultaneously determining the actual conservation state of the cables. The results of this validation process, providing a comprehensive overview of the grout injection quality are summarized in Table 1.

Table 1 UT findings on the examined viaduct.

Injection	No. of section	%	Comment
Total	28	71.8	Completely filled with grout ensuring full protection of the strands.
Partial	6	15.4	Incomplete filling and localized grout voids.
Absent	5	12.8	Total lack of grout.

These results highlight that while approximately 28% of the sections required intervention due to grout deficiencies, the majority of high-reflectivity signals recorded by UT required careful interpretation to avoid an overestimation of the structural damage.

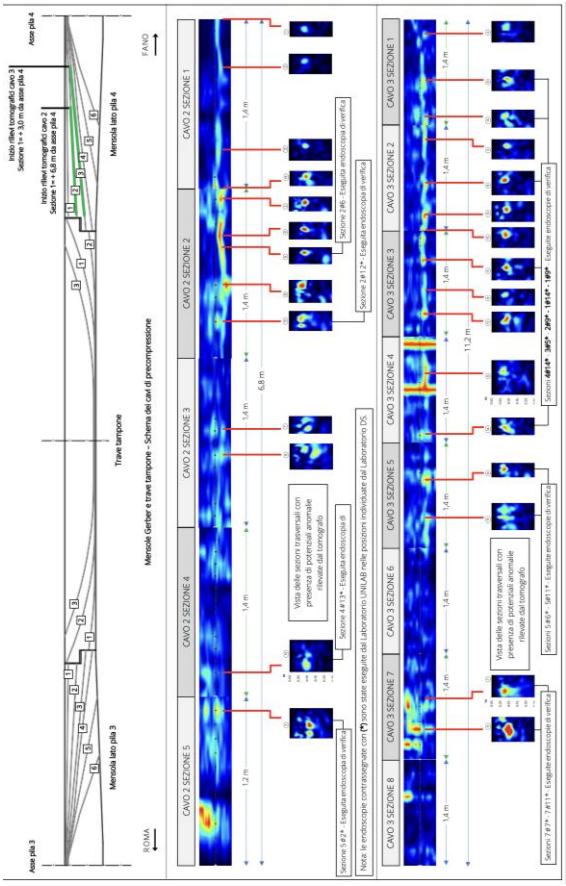


Fig. 2 Structural scheme of the Gerber cantilever illustrating the phase 2 diagnostic layout. The diagram underlines the investigated post-tensioned cables and the spatial distribution of the vertical ultrasonic scans. Highlighted sections indicate the specific scan lines where direct endoscopic validation was performed to provide ground-truth data.

3.3 Signal analysis and the false-positive mechanism

A fundamental finding of this campaign concerns the interpretive methodology required to distinguish true defects from geometric artifacts. It was observed that a reliable diagnosis cannot be achieved solely through the analysis of raw ultrasonic scans. In many instances, the raw tomographic data displayed high-reflectivity anomalies at the cable depth that appeared comparable in intensity to the backwall echo. Under standard interpretative protocols, such high-reflectivity ratio, where the cable echo is as strong as the structural boundary, typically signifies a major internal discontinuity, such as a large air-filled void. The study demonstrated that a reliable interpretation of the acquired signals requires the individual analysis of each investigated section through the systematic adjustment of the signal amplification (gain), to distinguish between actual structural defects and gain-induced artifacts, which were found to be the primary cause of false-positive indications. The distinction between these two scenarios is illustrate by comparing the results obtained in different sections of the viaducts. In Fig. 3, two vertical ultrasonic tomographic scans of the same cable section are presented, processed with different gain levels. In both instances, the amplitude of the anomaly corresponding to the prestressing duct remains consistently comparable to the intensity of the backwall echo, regardless of the amplification setting. Subsequent endoscopic surveys performed in sections exhibiting this specific signal behaviour confirmed the presence of actual grout injection defects, thereby validating the high reflectivity as a representative indicator of internal voids.

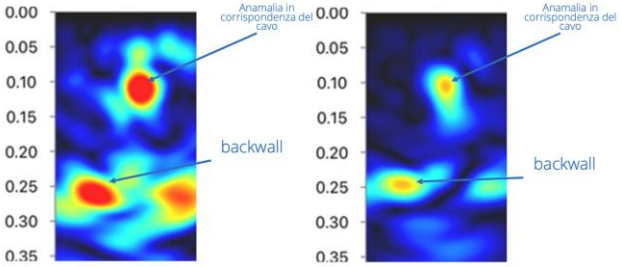


Fig. 3 Comparison between two vertical ultrasonic tomographic scans of the same investigated structural element. In the raw scan (left), anomalies associated with both the backwall, and the prestressing cable are visible with comparable apparent amplitudes. In the other scan (right), obtained by modifying the signal amplification (gain), the reduction of the gain highlights that the anomaly corresponding to the cable remains comparable to the backwall reflection, confirming that the detected ultrasonic anomaly is representative of a real physical discontinuity.

In contrast, Fig. 4 illustrates a different investigated structural section where the signal response is heavily influenced by amplification effects. In the high-gain scan (left), the cable-related anomaly appears comparable to the backwall reflection, likely due to a global oversaturation of the signal. However, when the gain is optimized and reduced (right), the amplitude of the cable anomaly significantly decreases and is no longer comparable to the known reference of the backwall echo. Endoscopic investigations in correspondence with this second type of behaviour revealed no defects in the grout injection. In these cases, the initial high-reflectivity was identified as a false-positive artifact caused by local amplification requirements, often needed to compensate for backwall signal attenuation due to complex internal geometries, such as non-parallel internal faces of the box girder. The experimental results indicate that a significant number of ultrasonic anomalies recorded during a standard screening may be false positives. However, by adopting a more rigorous analytical protocol, where individual sections are evaluated by comparing cable anomalies with known structural reflections (backwall) under optimized gain conditions, it is possible to drastically filter out non-significant anomalies.

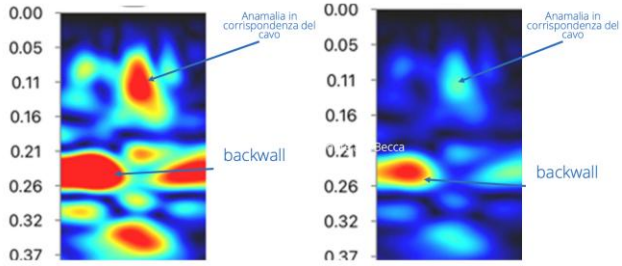


Fig. 4 Comparison between two vertical ultrasonic tomographic scans of the same investigated structural element. The raw scan (left) shows apparent anomalies associated with both the backwall and the prestressing cable. In the second scan (right), obtained by reducing the signal amplitude (gain), the backwall-related reflection remains clearly visible, whereas the anomaly previously observed at the cable location disappears. This behaviour indicates that the initial indication provided by the ultrasonic tomography corresponds to a false-positive response, which would not be identifiable without appropriate gain adjustment.

Ultrasonic testing (UT) currently provides a primarily qualitative assessment through tomographic maps showing relative variations in acoustic response rather than standardized quantitative values. As a result, data interpretation requires comparison with reference areas of known acoustic behaviour and may be affected by signal artifacts due to geometry, attenuation, or structural noise. Therefore, direct endoscopic inspection remains essential to validate ultrasonic anomalies, distinguishing actual defects from false positives and ensuring reliable diagnostic conclusions through the correlation of indirect UT results with visual evidence.

4 CONCLUSIONS

The experimental campaign represents a comprehensive and non-standard diagnostic procedure, structured through a three-phase protocol to assess the structural integrity of post-tensioned members. This study specifically focused on phase 2, which integrated high-density ultrasonic tomography with targed endoscopic surveys to investigate the conservation state of post-tensioned cables of Candegliano viaduct. Unlike common in-situ practices, which often rely on simplified or qualitative assessment, this campaign addressed the inherent difficulty of performing accurate inspections on geometries with one-sided access. The findings of this experimental framework highlight several critical points for the field of structural health monitoring. The study confirms that the application of ultrasonic tomography to post-tensioned concrete is far from routine. The high-reflectivity indications recorded across lots of scans demonstrated that raw NDT data can be highly deceptive. The intrinsic heterogeneity of the concrete matrix and the complex internal geometry of the Gerber system create an environment where signal interpretation is significantly prone of error. Through the direct verification of 39 sections, the campaign provided a statistical overview of the duct's conditions. It is crucial to clarify that the resulting statistics (reported in Table 1) do not represent a general statistical overview of the bridge's overall conservation state. Since the endoscopic inspections were conducted exclusively in correspondence with previously identified ultrasonic anomalies, these figures specifically reflect the correlation between the two investigations when considering all raw ultrasonic indications. Although the detection of partial and absent grout emphasizes the high stakes of these inspections, it also proves that without a rigorous validation phase, most of the detected "anomalies" would have been wrongly classified, as defects. A key conclusion of this work is that the "relative amplitude" of an ultrasonic signal cannot be used as a standalone indicator of decay. The emergence of false-positive was systematically linked to the attenuation of the backwall signal due to the reflector's angle of incidence. The study demonstrates that the reliability of the non-destructive investigation significantly increases if the analysis is refined by "dynamic gain-adjustment" of the signal amplification (gain) section-by-section to distinguish between structural noise artifacts and actual grout voids. In conclusion, the integration of UT and endoscopy, while operationally demanding and not yet a standard industry practice, is proven to be mandatory for special inspections of structures. This integrated approach filters out geometric artifacts that would otherwise lead to costly and unnecessary structural repairs, ensuring that interventions are target only where actual grout deficiencies and corrosion risks are visually confirmed.

References

[1] Matteini, Irene, Coccimiglio; Stefania, Scussolini; Linda, Ceravolo, Rosario: Chiorino, Mario A.; Ferro, Giuseppe A. (2024). An historical research on the development and application of prestressed concrete in Italy. Procedia Structural Integrity. 62. 738-746. 10.1016/j.prostr.2024.09.101. Concrete society.

[2] D'Amato, Michele; Ranaldo, Antonella; Rosciano, Monica; Zona, Alessandro; Morici, Michele; Gioiella, Laura; Micozzi, Fabio; Poeta, Alberto; Quaglini, Virginio; Cattaneo, Sara; et al. The Development and Statistical Analysis of a Material Strength Database of Existing Italian Prestressed Concrete Bridges. Infrastructures 2025, 10, 203. https://doi.org/10.3390/infrastructures10080203

[3] Rymsza, Janusz. Causes of the Collapse of the Polcevera Viaduct in Genoa, Italy. Appl. Sci. 2021, 11, 8098. https://doi.org/10.3390/app11178098

[4] Santarsiero, Giuseppe; Masi, Angelo; Picciano, Valentina; and Digrisolo, Andrea. The Italian Guidelines on Risk Classification and Management of Bridges: Applications and Remarks on Large Scale Risk Assessments. Infrastructures 2021, 6, 111. https://doi.org/10.3390/infrastructures6080111

[5] Kim, Tae-Hoon; Eum, Ki-Young; Sun, Chang-Ho, *et al.* Corrosion Characteristics of Prestressing Strands and Reinforcing Bars Under Accelerated Corrosion Conditions. Int J Concr Struct Mater 19, 23 (2025). https://doi.org/10.1186/s40069-024-00759-9

[6] Elsener, Bernhard. Prevention of Corrosion in Post-Tensioned Structures: Electrically Isolated Tendons. Corros. Mater. Degrad. 2022, 3, 414-421. https://doi.org/10.3390/cmd3030024

[7] Kralovanec, Jakub; Moravcik; Martin, Zahuranec; Michael and Bahleda, and Frantisek. (2024). In Situ Verification of Tendons of First Segmental Post-Tensioned Road Bridges. Civil and Environmental Engineering, 20(2), 2024. 920-932. https://doi.org/10.2478/cee-2024-0067

[8] https://www.mit.gov.it/nfsmitgov/files/media/normativa/2020-12/DM%20578%20del%2017.12.2020.pdf

[9] Tevfik Terzioglu, Madhu M. Karthik, Stefan Hurlebaus, Mary Beth D. Hueste, Stefan Maack, Jens Woestmann, Herbert Wiggenhauser, Martin Krause, Patrick K. Miller, and Larry D. Olson. Nondestructive evaluation of grout defects in internal tendons of post-tensioned girders, NDT & E International, Volume 99, 2018, Pages 23-35, ISSN 0963-8695, https://doi.org/10.1016/j.ndteint.2018.05.013

[10] Łaziński, Piotr; Jasiński, Marcin; Uściłowski, Mateusz; Piotrowski, Dawid; Ortyl, and Łukasz. GPR in Damage Identification of Concrete Elements—A Case Study of Diagnostics in a Prestressed Bridge. Remote Sens. 2025, 17, 35. https://doi.org/10.3390/rs17010035

[11] Cheilakou, Eleni; Theodorakeas, Panagiotis; Koui, Maria; Moustakidis, Serafeim; Zeris, Christos. (2013). 3D mapping of reinforcement and tendon ducts on pre-stressed concrete bridges by means of Ground Penetrating Radar (GPR). Proceedings of SPIE - The International Society for Optical Engineering. 9062. 10.1117/12.2046354.

[12] Wallace, Wai-Lok Lai; Xavier, Dérobert; Peter, Annan. A review of Ground Penetrating Radar application in civil engineering: A 30-year journey from Locating and Testing to Imaging and Diagnosis, NDT & E International, Volume 96, 2018, Pages 58-78, ISSN 0963-8695, https://doi.org/10.1016/j.ndteint.2017.04.002

[13] Krause, Martin; Mielentz, Frank; Milman, B.; Müller, Wolfgang; Schmitz, Volker, U.; Wiggenhauser, Herbert. Ultrasonic imaging of concrete members using an array system, NDT & E International, Volume 34, Issue 6, 2001, Pages 403-408, ISSN 0963-8695, https://doi.org/10.1016/S0963-8695(01)00007-X

[14] Dinh, Kien; Tran, Khiem; Gucunski, Nenad; Ferraro, Christopher, C.; Nguyen, Tu. Imaging Concrete Structures with Ultrasonic Shear Waves—Technology Development and Demonstration of Capabilities. Infrastructures 2023, 8, 53. https://doi.org/10.3390/infrastructures8030053

[15] Choi, Hajin, Bittner, James, and Popovics, John S. (2016). Comparison of Ultrasonic Imaging Techniques for Full-Scale Reinforced Concrete. *Transportation Research Record: Journal of the Transportation Research Board*, *2592*(1), 126-135. https://doi.org/10.3141/2592-14

[16] Mazzatura, Isabella; Salvatore, Walter; Caprili, Silvia; Celati Simone; Mori, Michele; and Gammino, Massimo. Damage detection, localization, and quantification for steel cables of post-tensioned bridge decks, Structures, Volume 57, 2023, 105314, ISSN 2352-0124, https://doi.org/10.1016/j.istruc.2023.105314

[17] Mazzatura, Isabella; Casas, Joan; Caprili Silvia; and Salvatore, Walter. (2024). Reliability of UT for the grouting inspection in PT bridges: A case study. 10.1201/9781003483755-308

[18] Alqurashi, Inad; Alver, Ninel; Bagci, Ulas; and Catbas, Necati. (2025). A Review of Ultrasonic Testing and Evaluation Methods with Applications in Civil NDT/E. Journal of Nondestructive Evaluation. 44. 10.1007/s10921-025-01190-0

[19] Saint-Pierre, François; Philibert, Alain; Giroux, Bernard; Rivard, Patrice. Concrete Quality Designation based on Ultrasonic Pulse Velocity, Construction and Building Materials, Volume 125, 2016, Pages 1022-1027, ISSN 0950-0618, https://doi.org/10.1016/j.conbuildmat.2016.08.158

[20] Lorenzi, Alexandre; Caetano, Luciane; Campagnolo, João; Lorenzi, Luciani; Silva, Filho; Luiz, Carlos. (2015). Application of ultrasonic pulse velocity to detect concrete flaws. The e-Journal of Nondestructive Testing (ISSN 1435-4934). 20.

Calibrating the traffic load model for assessment of existing bridges using short-term weigh-in-motion measurements

Goran Milutinovic, Rade Hajdin

Faculty of Civil Engineering,
University of Belgrade,
Bulevar kralja Aleksandra 73, Belgrade 11000, Serbia

Summary
The main bridge traffic design load used throughout the Europe is the Load Model 1 (LM1) as defined in the EN1991-2 (European standard for traffic loads on bridges). This load model is multiplied by the Nationally Determined Parameter – the α coefficient – that are customized for each country. The coefficients are to be determined based on the local traffic volume and composition. Time duration of weigh-in-motion (WIM) measurements, representating the main statistical sample for traffic load model calibration, differ from region to region, from long-term to short-term data. In this paper, a discussion is presented for calibrating the Eurocode traffic load model, i.e. determining the α coefficient, for existing bridges, when only short-term WIM data are available, which is the case in Serbia. The approach consists of a statistical study based on the results of the structural analysis of the set of bridges loaded by vehicles recorded by WIM measurements and direct comparison with LM1.

1 INTRODUCTION

The main bridge traffic design loads used throughout the Europe is the Load Model 1 (LM1) as defined in EN1991-2 (European standard for traffic loads on bridges). The LM1 consists of tandem system (TS) and uniform distributed load (UDL). The non-factored load model, i.e. the characteristic value, is set for the return period of 1000 years. This base loading is multiplied by the Nationally Determined Parameter – the α coefficient – adjusted for each country. The coefficient should be determined for each country based on the local traffic volume and composition.

Main objective of the paper is calibration of the Eurocode traffic load model, i.e. determining the α coefficient, for existing bridges, when only short-term weigh-in-motion (WIM) data are available, which is the case in Serbia. It is possible to completely reconstruct the traffic flow (axle weights and spacings, lane traveled, exact time the vehicle passed and similar) from WIM measurements. Although in some countries, long-term WIM records exist on multiple locations extending continuously more than 20 years, in many countries only short-term WIM data is available. Swiss data, as a sample of long-term data, extend continuously over 20 years on 12 locations. These long-term data represent solid basis for probabilistic study of the extreme traffic load. On the other side, as an example of short-term WIM data, measurements from Serbia has been used. To evaluate extreme traffic loads in Serbia, Swiss data are compared with Serbian data in order to calibrate the traffic load model in Serbia.

2 WIM STATISTICAL SAMPLE

Long-term WIM measurements from Switzerland and short-term bridge weigh-in-motion (B-WIM) measurements from Serbia are presented in this chapter, as well as structural analysis done with this data, creating the input for the probabilistic study performed in the paper.

2.1 Structural analysis

Structural analysis of a representative set of bridges (or more precisely structural systems), loaded by vehicles detected by WIM measurement had been already performed in [1] and [2] for Serbia. These load effects have been compared with equivalent load effects produced by the design value of Eurocode Load Model 1 (the characteristic value times the partial load factor), in order to obtain the α coefficients.

As a part of the automated process, 290,388 'loading events' from B-WIM measurements in Serbia (i.e. all vehicles detected by B-WIM, together with any other vehicle simultaneously present on the bridge) [1], [2] and 101,942,137 'loading events' from WIM measurements in Switzerland were analysed on each bridge from the same set of 26 different bridges (i.e. structural systems taking into

account the transverse stiffness) representing the entire bridge inventory, with simple and continous spans between 5m and 80m. This represents a solid sample for the probabilistic analysis, presented below. "Loading event" represent each vehicle from the WIM database, together with any other vehicle present simultaneously on the bridge. Dynamic amplification factor (DAF) is taken as 1.0, as recommended in the literature for evaluation of existing structures [3]. The dynamic factor is a matter of great debate in the bridge engineering community. While few dispute the fact that vehicles exert forces in excess of their static weights when traversing a bridge, many question the relevance at the ultimate limit state, where redistribution of forces occurs, and energy is absorbed through plastic dissipation.

Regarding the transverse load distribution, two different types of bridges have been considered:

(1) No transverse traffic load distribution – represents bridges such as concrete box girder bridge, where loads from different lanes are assumed repositioned above centroidal axis of the girder. In other words, the stresses resulting from load eccentricity are assumed to be negligibly small;

(2) With transverse traffic load distribution – represents multi girder bridges, where live load is not uniformly spread among the girders. Transverse distribution factors are computed using the so-called rigid method, (see [5] [6]), which assumes bridge cross-section deflects and rotates as a rigid body. Distribution factors for different lanes are computed, specifying the contribution of one girder, for the generic bridge cross section, shown in Fig. 1.

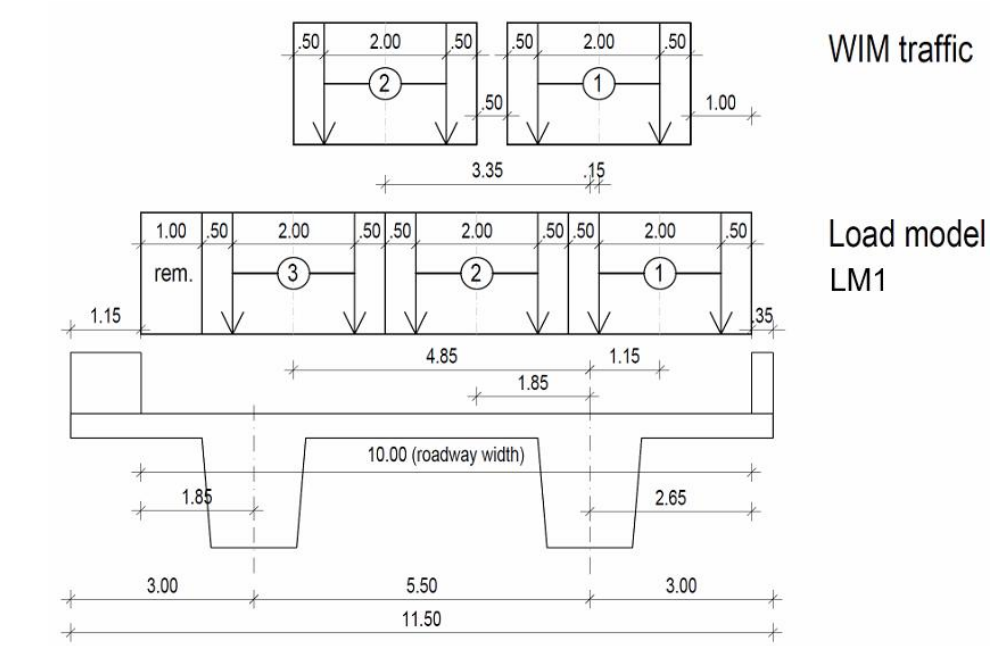


Fig. 1 Generic bridge cross section for transverse load distribution analysis

Positioning of the lanes for the actual traffic from B-WIM was done such that one line is located 1m from the barrier, with 0.5m spacing between lanes (see Fig. 1); for the LM1 (lower scheme in Fig.1) standard lane positioning for the load model was done. Then, influence lines, and moment and shear envelopes were computed for each of these 'loading events', for each bridge from the set of 26 bridges, and were compared directly with the LM1. A sample bending moment envelope from the loading event from WIM and the corresponding LM1 envelope has been shown in Fig. 2 (only for illustration, it is a fictitious bridge span configuration, not a real bridge from Serbian bridge inventory). Ratio between these two envelopes (i.e. its maximum values) represent the α coefficients.

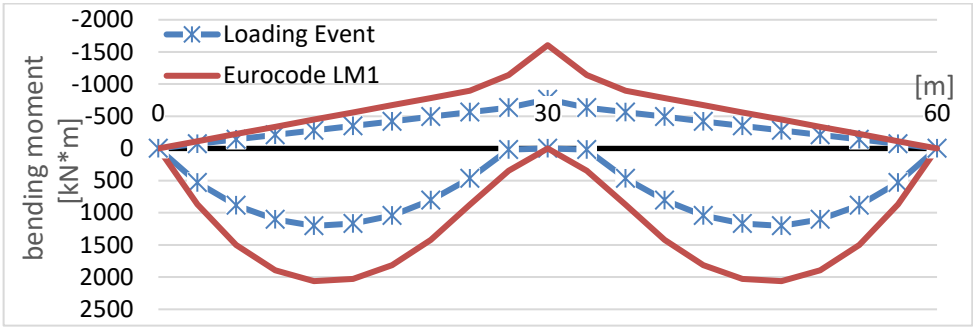


Fig. 2Sample moment envelope comparison for a 'loading event' from WIM vs LM1

2.2 Long-term Swiss WIM data

Long-term Swiss WIM data consists of measurements on 12 different locations throughout Switzerland from year 1999 to 2021. They include continuous traffic data collection – axle weights and axle spacings of each vehicle that had passed the measuring device built in the road. Only vehicles heavier than 3.5 tonnes are recorded in the database. The exact time and speed of each vehicle crossing the measuring device is given in the database, so the distance between adjacent vehicles is easily computed. Locations of the WIM stations are shown in Fig. 3 (left)[5]. Total number of trucks in these WIM data is 101,942,137. Bar chart with yearly maximums of the alpha coefficient, per WIM station, calculated by the structural analysis described in the previous chapter, is shown in Fig. 4. The value of "blended" adjustment coefficient α (i.e. one value for both, TS and UDL, and for all lanes) has been calculated equal to 0.60, to be used for evaluation of existing structures, for the case with transverse distribution using Gumbel distribution with yearly maximums, as discussed in [6], with direct WIM analysis and classical interpolation. This corresponds well in general to the value calculated in [3].



Fig. 3Left: locations of the Swiss WIM stations [5], and right: a B-WIM station in Serbia[7]

2.3 Short-term Serbian B-WIM data

B-WIM measurement were performed in Serbia on 17 locations, in duration of 14 days each, in 2020. The measurements were done by Public Enterprise "Putevi Srbije", with Cestel B-WIM system[7]. It is a portable B-WIM system, installed by mounting on the bridge superstructure, without interfering or closing the traffic during installation. It is continuously determining and recording the exact location and speed of all vehicles present on the bridge, as well as its axle weights and axle spacings. These measurements have been discussed in [7] and one B-WIM station is shown in Fig. 3 (right).

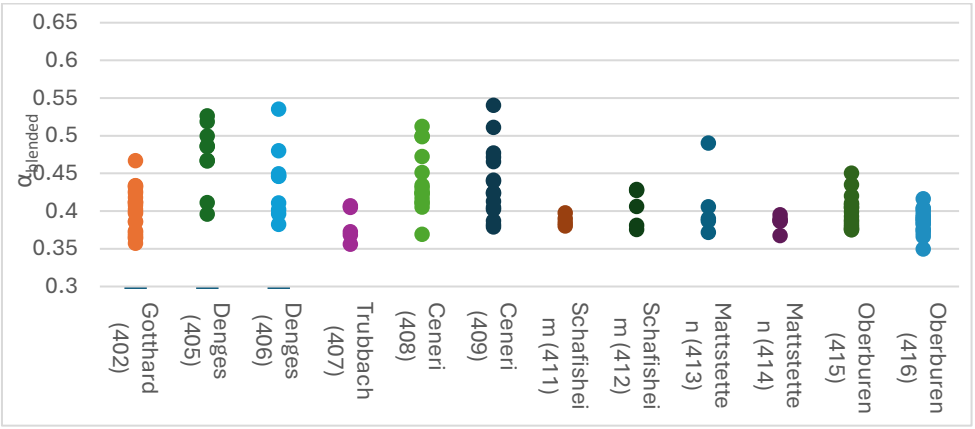


Fig. 4 Yearly maximums for α coefficients, per WIM station in Switzerland

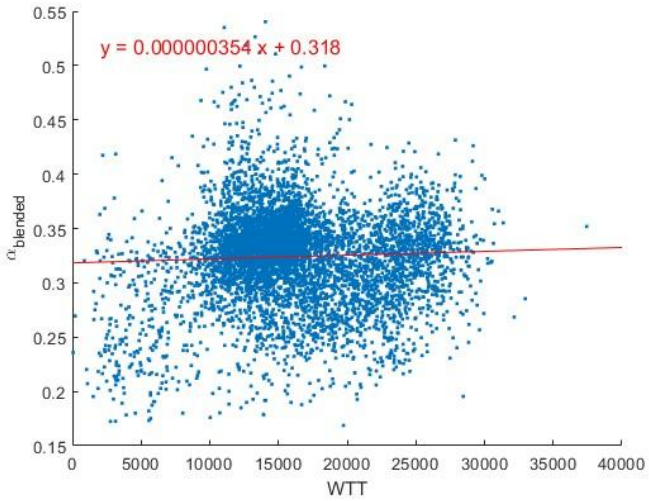


Fig. 5 Plot of weekly truck traffic (WTT) vs blended α coefficient in Switzerland

Statistical study with short-term WIM data has one questionable assumption to be verified – whether it is appropriate to extrapolate directly daily extremes from relatively short time period (though on multiple diverse locations). Theoretically speaking, if the statistical sample is not a time series, the block maxima method with any block duration can be used for extrapolation to required return period of extreme values. Nonergodic property of the process can be expressed in two ways in this case, either (a) by the traffic growth through the time, or with (b) seasonal variation through the year. Since this entire study is for existing bridges, in the present time and condition, the traffic growth will not be considered, while the seasonal variation will be explored in Chapter 4. Also, another important issue that requires attention is what is the minimum time duration of the reference period to be considered as an extreme value in order to fit the tail of extreme value distribution. It was concluded by the authors, in [6], that weekly maximums are the least time duration required to capture the extreme events.

3 CONNECTION BETWEEN ALPHA COEFFICIENT EXTREME VALUES AND AVERAGE TRUCK TRAFFIC

Since it was determined in [6] that one week is the shortest time duration required to capture the extreme event, weekly extremes from Swiss WIM data are plotted against the weekly truck traffic (WTT) in Fig. 5. Each dot represents one week of Swiss WIM data, with maximum "blended" α coefficient recorded during this week on y axis, and number of vehicles heavier than 3.5 tons (WTT) during that week on x axis. Small increase can be seen in the "blended" α coefficient, with the increase of WTT.

By plotting WTT in Switzerland and Serbia in Fig. 6 and 7, it can be concluded as expected, that larger WTT expected value is recorded in Switzerland (8492 in Serbia compared with 11871 in Switzerland), with similar standard deviations (3653 in Serbia compared with 4345 in Switzerland). For Swiss WTT better fit was obtained with normal distribution, while for Serbia WTT better fit was with lognormal distribution. From Fig. 5, it can be concluded that larger WTT does not significantly increase the level of traffic load, and although larger WTT is occurring in Switzerland, that fact alone does not influence significantly the value of the alpha coefficient.

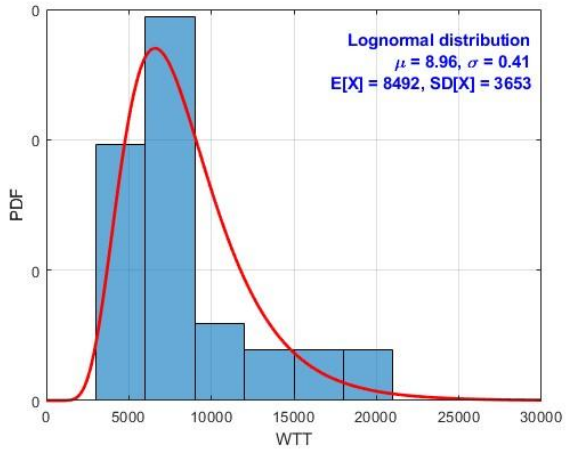


Fig. 6 Example of B-WIM stations in Serbia

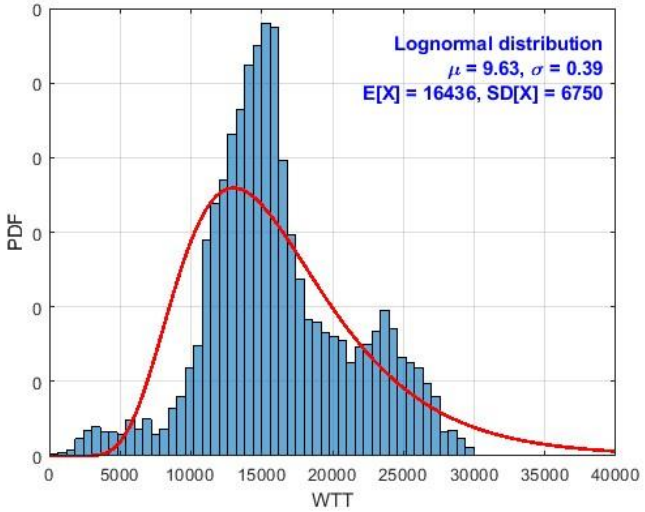


Fig. 7 Example of B-WIM stations in Switzerland

4 SEASONAL VARIATION

Seasonal variation has been explored and shown in Fig. 8 for averaged weekly maximums (multigirder bridges, i.e. with transverse load distribution) and Fig. 9 for averaged weekly truck traffic for all WIM stations in Switzerland. Averaged means that values for all location and for all years for specific week in a year has been gathered and averaged. Better uniformity is obtained for averaged weekly maximums (being the final quantitative result) than for weekly truck traffic. Probably, only for WIM station Gotthard, seasonal variation is expected due to vacation traffic – but this corresponds mostly to light cars. As WIM stations in Switzerland (representing long term data) and in Serbia (representing short

term data) are both spatially well spread across the country, entire sample including all WIM locations has been explored and plotted. It can be concluded (based on the analysis of results in Switzerland – Fig. 8 and 9) that measurements mainly from November (weeks 44 to 48) in Serbia (the only one available) represents solid statistical sample for all periods of year.

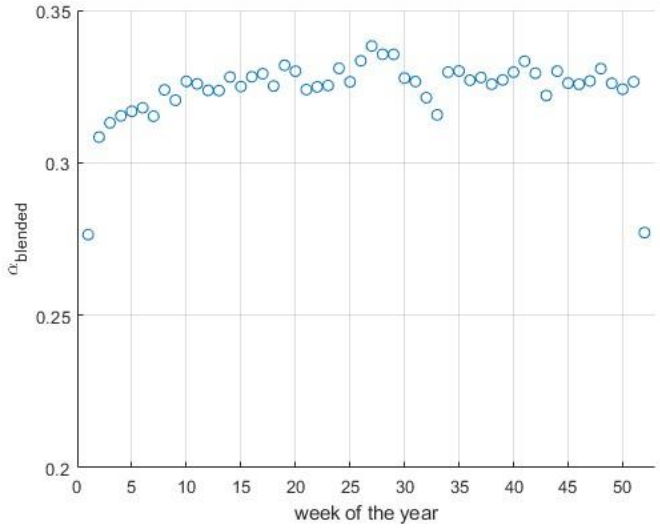


Fig. 8 Seasonal variation – averaged weekly maximums (α coefficients), with transverse distribution – Switzerland

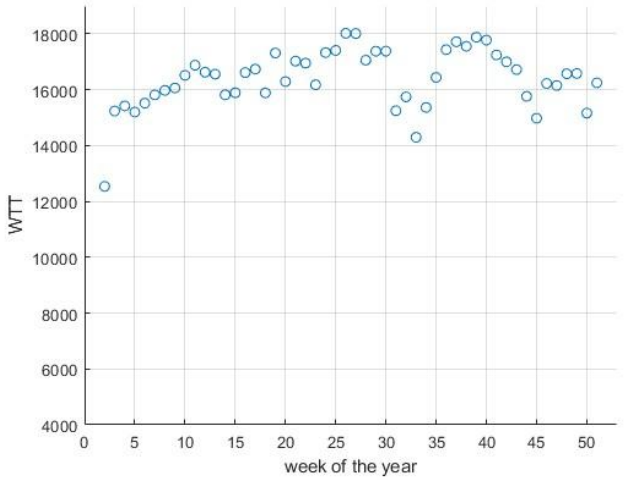


Fig. 9 Seasonal variation – averaged weekly truck traffic (WTT) – Switzerland

5 CALIBRATION OF TRAFFIC LOAD MODEL IN SERBIA FOR EXISTING BRIDGES

It has been concluded from the above for short-term WIM data, such as the one in Serbia, that (1) weekly maximums are the least time interval for the extrapolation of the traffic load [6], (2) larger WTT does not necessarily significantly increase the traffic load level (Fig. 7), and (3) there is no significant seasonal variation during the year (Fig. 8 and 9). Therefore, a classic extrapolation of the load effects has been done with Serbian data. The "blended" alpha coefficients for Serbia has been calculated using weekly maximums, by extrapolation to the 609-year-return period (histograms shown in Fig. 10 and

Fig. 11, for cases without and with transverse distributions). This return period corresponds to the following probability of failure:

$$PF = 1 - \Phi(\alpha * \beta) \quad (1)$$

where the reliability index equal to 4.2 is assumed, being the same value as used by SIA 269 [8] for existing structure, while the sensitivity factor, α, is set to 0.7, as suggested by the Eurocode, although this value is only an approximation [9].

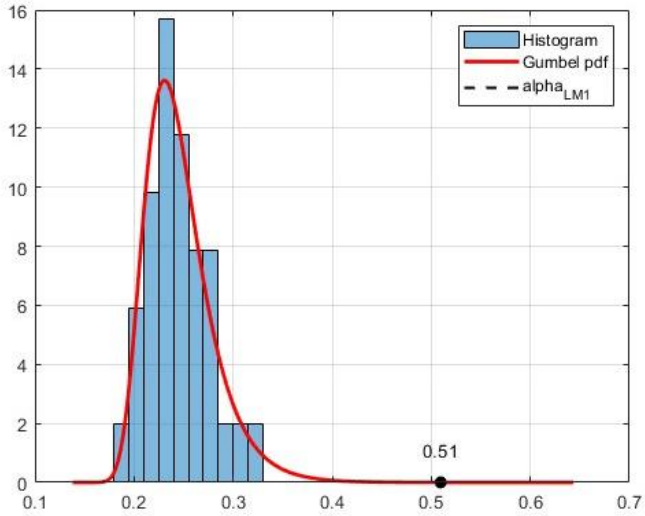


Fig. 10 Histogram and corresponding Gumbel pdf for Serbia – without transverse distribution

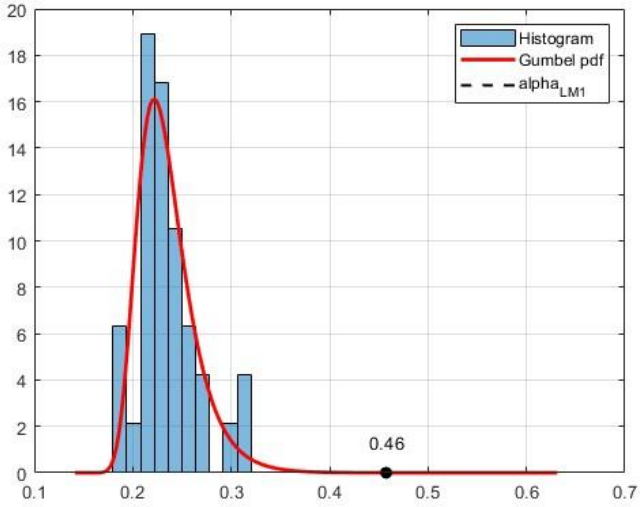


Fig. 11 Histogram and corresponding Gumbel pdf for Serbia – with transverse distribution

A key parameter in this study is the selection of the reliability index target value, which is typically determined by the bridge owners. For new structures, the reliability index is generally set at a relatively high level to ensure a low probability of failure, whereas for existing structure lower reliability index may be acceptable, leading to reduced partial safety factors. Increasing the reliabilility index for existing structures is significantly more costly than reaching the same reliability index in new construction [10],

[11], [12]. Since the present analysis concerns traffic loading on existing bridges, an appropriate reliability level must be selected in this context. The "blended" α coefficients for Serbia has been computed to 0.51 for Gumbel distribution for the case without transverse traffic load distribution and to 0.46 for the case with traffic load transverse distribution. These values are significantly lower than the current normative values in Serbia (which are only set for new bridges), being in the range between 0.8 and 1.0, depending on the type of the roads.

6 CONCLUSIONS

Probabilistic study for evaluation of the LM1 multiplier, α coefficient (i.e. appropriate traffic load model), to be used for existing bridges in Serbia is performed. It is of crucial importance, if only short-term WIM data are available to compare it with long-term WIM data results, available elsewhere, but still from a region with ties with the one in question. In this case, Serbian short WIM data are to be verified with Swiss long-term data. It has been determined earlier that weekly maximums represent the shortest time duration for the extreme event to be captured. It has been concluded in this paper that α coefficient slightly increase with WTT increase, and that Switzerland has larger WTT mean than Serbia with similar WTT standard deviation. Also, regarding seasonal variation, it has been concluded in this paper that measurements mainly from November in Serbia represents solid statistical sample for all periods of year. The blended alpha coefficients for Serbia has been computed to 0.51 using Gumbel distribution for the case without transverse traffic load distribution (e.g. box girder bridges) and to 0.46 for the case with transverse traffic load distribution (e.g. multigirder bridges).

References

[1] Milutinovic Goran and Hajdin Rade. 2024. "Preliminary estimation of adjustment factors for traffic load model LM1 for existing bridges in Serbia," in Proceedings of the DGKS Conference, Vrnjacka Banja, Serbia.

[2] Milutinovic Goran and Hajdin Rade. 2023. "Evaluation of bridge traffic load model using B-WIM measurements in Serbia," presented at the Proceedings of the SINARG Conference 2023, Nis, Serbia.

[3] Sjaarda Matthew, Mathevet Lucas, and Nussbaumer Alain. 2023. "Revision of ASTRA 82001 updating the load model for existing road bridges," EPFL, Switzerland.

[4] AASHTO LRFD Bridge Design Specification. 2024. American Association of State Highway and Transportation Officials.

[5] Sjaarda Matthew, Meystre Thierry, Nussbaumer Alain, and Hirt Manfred. 2020. "A systematic approach to estimating traffic load effects on bridges using weigh-in-motion data," Stahlbau, vol. 89, no. 7, pp. 585–598, doi: 10.1002/stab.202000048.

[6] Milutinovic Goran and Hajdin Rade. 2026. "Comparison of different extreme value reference periods of bridge traffic loads," presented at the Proceedings of the IABMAS, Orlando, USA

[7] Milutinovic Goran, Hajdin Rade, Andrijanic Ivana, Milosavljevic Milos, and Bajic Marko. 2023. "Overview of bridge traffic loads in Serbia using B-WIM," presented at the Proceedings of MASE Conference, Skopje, North Macedonia, 28–29 September 2023.

[8] SIA, SIA 269:2011 Existing structures - Bases for examination and interventions. Swiss Society of Engineers and Architects, Zurich, Switzerland.

[9] Milutinovic Goran and Hajdin Rade. 2024. "Dependence of sensitivity factors on ratio of traffic load to dead load," MDPI Appl. Sci.

[10] fib Bulletin 80, 2016. "Partial safety factor methods for existing concrete structures,"

[11] Milutinovic Goran and Hajdin Rade. 2024. "NAKNADNI PRORAČUN POSTOJEĆEG MOSTA U SKLADU SA FIB BILTENOM 80 I EVROKODOM / LOAD RATING OF A EXISTING BRIDGE ACCORDING TO FIB BULLETIN 80 AND EUROCODE," in Proceedings of the DGKS Conference 2024, *Vrnjacka Banja, Serbia*.

[12] Gino Diego, Castaldo Paolo, Bertagnoli Gabriele, Giordano Luca, and Mancini Giuseppe. 2020. "Partial factor methods for existing structures according to *fib* Bulletin 80: Assessment of an existing prestressed concrete bridge," *Struct. Concr.*, vol. 21, no. 1, pp. 15–31, doi: 10.1002/suco.201900231.

Time-Dependent Structural Safety Assessment of Corroded Prestressed Concrete Bridges: A Defect-to-Mechanics Framework

Federica Di Criscio, Livio Pedone, Stefano Pampanin

Department of Structural and Geotechnical Engineering,
Sapienza University of Rome,
via Eudossiana 18, 00184 Rome, Italy

Summary
The durability of reinforced (RC) and prestressed (PSC) concrete bridges exposed to corrosion is a critical concern for the safety, resilience and sustainability of transportation networks. While current assessment practices are mainly based on visual inspections and defect indices, the relationship between observed damage and structural capacity degradation remains poorly defined. This study proposes a simplified and mechanically based framework that translates defect-based inspection data into physically consistent corrosion damage indices using predictive corrosion models, enabling time-dependent safety assessment. The framework is applied to an archetypal PSC bridge used as a case study to demonstrate its effectiveness. Results show that both corrosion severity and the location of the corroded section strongly influence the nonlinear response of the bridge and its time-dependent safety, highlighting the framework as a mechanically consistent support for maintenance decision-making.

1 INTRODUCTION

A significant portion of existing reinforced concrete (RC) and prestressed concrete (PSC) bridges was designed before modern durability and performance-based approaches were adopted [1]-[2]. Consequently, many structures are exposed to progressive deterioration processes, with reinforcement corrosion being a critical factor affecting long-term performance and serviceability.

Corrosion is an electrochemical process that dissolves steel, reducing the effective cross-section of reinforcing bars. The resulting expansive rust generates tensile stresses in the surrounding concrete, promoting cracking, spalling, and bond degradation [3]-[4]. Two main corrosion types are distinguished: uniform, causing homogeneous steel loss, and localized (pitting), producing more severe, concentrated damage in mechanically critical regions [5].

Over the past decades, extensive research efforts have been devoted to understanding the mechanical implications of reinforcement corrosion in RC and PSC structures. Previous studies have investigated the effects of reinforcement corrosion on material properties, bond behaviour, and, more recently, on the structural and seismic performance of RC and PSC bridges, highlighting its role in increasing vulnerability under extreme loading conditions (e.g., [6]). Despite these advances, current assessment and management practices for existing bridges still rely predominantly on visual inspections, through which corrosion-related damage is identified mainly in terms of surface manifestations such as cracking, spalling, and rust staining. However, a clear and systematic link between the observed damage during in-situ inspections and mechanically meaningful indicators capable of quantifying the associated loss of structural performance is still lacking. This gap hinders the objective interpretation of inspection outcomes and limits the effectiveness of decision-making processes related to maintenance, strengthening, and risk prioritization. Moreover, the severity and precise location of corrosion are often uncertain, making it difficult to predict the residual capacity of structural elements and to plan effective maintenance strategies.

To overcome these limitations, this study introduces a simplified, mechanically-consistent framework that translates inspection-derived defect indicators into quantitative corrosion damage indices through predictive corrosion models. By updating material constitutive laws in response to localized degradation, the methodology enables time-dependent evaluation of structural safety, effectively providing a life-cycle perspective that can inform decision-making for maintenance and intervention planning. The framework is applied to an archetypal PSC bridge, demonstrating its capability to capture the combined effects of corrosion severity and location on the nonlinear response of piers and girders, and on the evolution of residual structural safety over the bridge's service life.

2 FRAMEWORK

The proposed framework establishes a systematic and quantitative pathway from inspection-based defect indicators to a mechanically grounded, time-dependent safety assessment of corroded RC and PSC bridges. A schematic overview of the methodology is provided in Fig. 1.

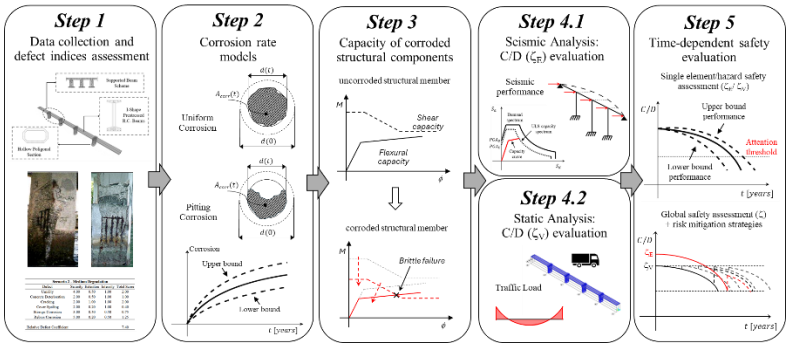


Fig. 1. Schematic illustration of the simplified procedure for evaluating the time-dependent structural safety of corroded bridges.

2.1 Data collection and defect indices assessment

The first step of the framework (Step 1) consists of collecting relevant information from bridge inventory and census data, including structural typology, static scheme, construction materials and geographical location. This information is required to define both the seismic demand and the environmental exposure conditions governing corrosion-induced degradation. In parallel, inspection records are examined to identify deterioration patterns observed during visual surveys. These observations are subsequently translated into quantitative mechanical parameters representative of the underlying corrosion mechanisms. For RC members, the adopted defect index is the percentage loss of steel cross-sectional area, μ%, for PSC elements, the maximum pitting depth, p_{max}, is considered, as it can be reliably quantified when the prestressing steel is locally accessible. These indices constitute the input parameters for both the degradation modelling and the capacity assessment performed in the subsequent steps.

2.2 Corrosion rate modelling

In Step 2, the temporal evolution of corrosion is modelled according to the scheme proposed by Tuutti [3], distinguishing initiation, propagation and structural deterioration phases. Established mechanistic models are adopted for each phase, including diffusion-based formulations for chloride ingress, electrochemical models for corrosion propagation, and statistical approaches for pitting development [7]-[8]-[9]. This step aims to (i) enable predictive assessment of future deterioration, allowing the derivation and updating of time-dependent safety curves, and (ii) allow recalibration of model parameters (e.g., corrosion rate) when in-situ observations differ from predicted conditions. Inspection observations are quantitatively associated with mechanical indices defined as percentage loss of steel cross-section for RC members (μ%) and maximum pit depth for prestressing steel (p_{max}). Experimental studies [3]-[4] indicate that visible cracking of the concrete cover typically occurs for reinforcement area losses of approximately 1–5%, whereas spalling is generally observed for corrosion levels exceeding 5–7% and becomes severe beyond 10–15% [10]. Based on these findings, ranges of corrosion damage indices are assigned according to defect type and severity, as reported in Table 1.

Within each corrosion stage, the visual assessment defines the applicable index range, while the precise mechanical defect index is calculated within this range using the following relationship:

$$\mu_{obs} = \mu_{min} + i_{obs} \cdot (\mu_{max} - \mu_{min}) \quad (1)$$

Where $i_{obs} \in [0, 1]$, and the formulation is identical to that of the prestressed case, with μ replaced by p_{max}. Once a corrosion level corresponding to an observed defect state is identified, the relevant material constitutive laws are degraded accordingly, based on experimentally and numerically calibrated models. For RC members, degradation of steel properties in terms of strength, stiffness, and ductility is evaluated following [6], while concrete strength reduction and confinement loss due to stirrup corrosion

are accounted for using the models proposed by [11] and [12], respectively. For PSC elements, additional mechanisms associated with prestressing steel are considered. In particular, the heterogeneous corrosion of individual wires within a strand may lead to progressive wire rupture and non-uniform stress redistribution (chain effect), which is captured using the model proposed by [13]. Furthermore, corrosion-induced bond deterioration is accounted for through an increase in transfer length [14] and a corresponding reduction of the effective prestressing force [15]. Through this procedure, each corrosion level is associated with a fully defined set of degraded material constitutive relationships.

Table 1 Corrosion stages, observed defects, and corresponding mechanical indices for reinforced (μ%) and prestressed (p_{max}) concrete members.

Corrosion stage	Observed defect	μ (%) – RC	p_{max} (mm) – PSC
Low	Moisture stains	0-2	0-0.5
Moderate	Visible cracking	2-5	0.5-1.5
Advanced	Initial spalling	5-10	1.5-2.5
Severe	Extensive spalling	10-20	2.5-3.5

2.3 Capacity assessment of corroded structural components

Once the degraded material constitutive laws are defined, the structural capacity is evaluated through a sectional-based procedure grounded in moment–curvature (M–ϕ) analyses performed at critical cross-sections (Step 3). The assessment is repeated for each corrosion level and provides the basis for quantifying corrosion-induced reductions in stiffness, flexural strength, and deformation capacity. To assess pier capacity, a simplified analytical procedure is adopted to convert sectional capacity into element-level nonlinear response. Each bridge pier is analysed independently and idealised as an equivalent cantilever member associated with its tributary area, with an equivalent length L_{cant} assumed equal to the pier height. The global lateral response is derived by applying a triangular force distribution consistent with the first vibration mode, allowing the derivation of an analytical pushover curve. The force–displacement response is obtained under a lumped plasticity assumption. Inelastic deformations are assumed to concentrate within an equivalent plastic hinge region, while the remaining portion of the pier responds elastically. The total displacement capacity is therefore obtained by combining the elastic contribution, evaluated along an effective length, with the plastic contribution associated with hinge development. Plastic hinging is assumed to occur at the most deteriorated section induced by corrosion, unless yielding initiates earlier at the base, in which case hinge formation develops at the pier base. This simplified analytical pushover approach provides a computationally efficient estimate of pier capacity and is adequate for expedited and parametric corrosion assessments, despite neglecting higher-order interaction effects. Shear capacity is evaluated using code-based formulations [16], accounting for corrosion-induced degradation of transverse reinforcement, and is compared with flexural capacity to assess their interaction. For prestressed concrete girders, the capacity assessment follows a consistent but simplified approach. In simply supported systems, flexural capacity is governed by the critical midspan section and can therefore be directly evaluated at the sectional level through M–ϕ analysis. For continuous girders, a global capacity assessment is performed by progressively increasing the applied load and comparing the flexural capacity of the critical sections at supports and at midspan. The sequence of plastic hinge formation is thus identified, allowing the governing collapse mechanism and the corresponding force–displacement capacity to be determined.

2.4 Structural response analysis

In Step 4, the seismic response of the bridge is evaluated using established analysis procedures available in the literature. Seismic safety is thus evaluated through a capacity vs. demand comparison performed in the Acceleration-Displacement Response Spectrum (ADRS), in line with the Capacity Spectrum Method [17]. To quantify seismic safety, a "safety index" ζ_e (i.e., capacity vs. demand ratio at the Life Safety limit state) is considered. Gravitational safety ζ_v is evaluated by comparing flexural capacity and demand under permanent and traffic loading, including the effects of prestressing, with load

combinations defined according to current design practice. Clearly, by carrying out safety evaluations at different times of the bridge's life, it is possible to estimate the decay of the safety index over time.

2.5 Time-dependent safety evaluation

The final step of the framework (Step 5) consists of constructing time-dependent safety curves that describe the progressive reduction of structural safety as corrosion advances. Each corrosion level is associated with a corresponding safety index and an exposure time predicted by the corrosion model, resulting in degradation profiles that reflect the expected evolution of structural performance. These curves can be updated as new inspection data become available, allowing the framework to support adaptive and performance-oriented management strategies for ageing bridge infrastructure.

3 CASE STUDY

The case study considers a representative prestressed concrete bridge archetype originally proposed by [18], derived from a statistical characterization of the Italian bridge stock. The bridge consists of four simply supported 30 m spans with precast prestressed concrete I-girders reinforced by seven-wire tendons, supported by 10 m-high reinforced concrete piers with hollow polygonal sections (Fig.2, left). Material properties are defined from nationwide statistical distributions, assuming mean strengths of 26.8 MPa for concrete and 370 MPa for reinforcing steel. The bridge is assumed to be located in L'Aquila; seismic demand is defined for a 100-year service life, soil class B, and strategic infrastructure classification (Fig. 2, right), resulting in PGA = 0.45 g.

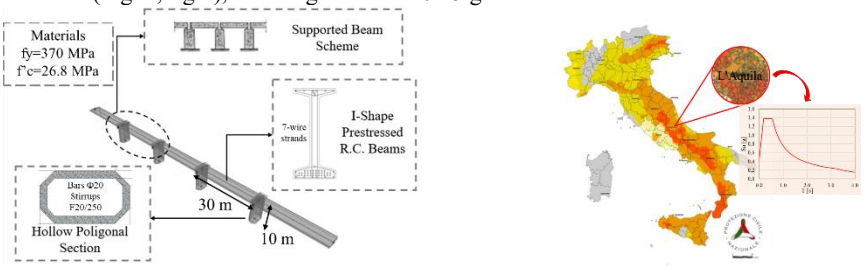


Fig. 2. Italian bridge archetype: (left) general bridge characteristics and material properties; (right) case-study site with seismic risk map and selected accelerogram.

Since the bridge is archetypal and no site-specific inspection data are available, corrosion-induced deterioration is investigated through a set of predefined hypothetical degradation scenarios. Three hypothetical corrosion damage scenarios—low, advanced, and severe—are considered (Fig. 3, left) to represent increasing levels of corrosion-induced deterioration. In addition, for the piers, different possible locations of the deteriorated cross-section along the height are examined (Fig. 3, right), allowing the influence of corrosion location on the structural response to be investigated.

For all scenarios, an intensity factor $i = 0.5$ is assumed. The low-severity scenario, characterized by superficial moisture staining and the absence of visible cracking, represents incipient corrosion conditions and is associated with a reinforcement area loss of $\mu = 1\%$. The advanced-severity scenario is characterized by initial cover spalling and corresponds to a reinforcement area loss of $\mu = 7.5\%$. The severe-severity scenario represents a further progression of corrosion damage, characterized by extensive cover spalling, and is associated with $\mu = 15\%$. For completeness, a moderate-severity scenario is hypothetically introduced for parametric purposes. This scenario represents an intermediate corrosion stage between incipient and advanced conditions, characterized by visible cracking of the concrete cover without spalling, and is associated with a reinforcement area loss of $\mu = 3.5\%$.

As the time of inspection is unknown, the temporal evolution of corrosion damage is defined based on predicted times derived from the corrosion propagation models described above. Accordingly, the following reference times are adopted: corrosion initiation time $t_{\text{initial}} = 37$ years, low corrosion stage $t_{\text{low}} = 40$ years, cracking initiation time $t_{\text{moderate}} = 55$ years, spalling initiation time $t_{\text{advanced}} = 80$ years, and severe corrosion stage $t_{\text{severe}} = 100$ years. The reference times are derived from the corrosion propagation framework described in Section 2.2 [7]-[8]-[9].

The same considerations are adopted for prestressed concrete members, for which the different damage severity stages are associated with maximum pitting depths of $p_{\max} = 0.2$, 0.85, 1.75, and 3.0 mm, corresponding to the low, moderate, advanced, and severe corrosion scenarios, respectively.

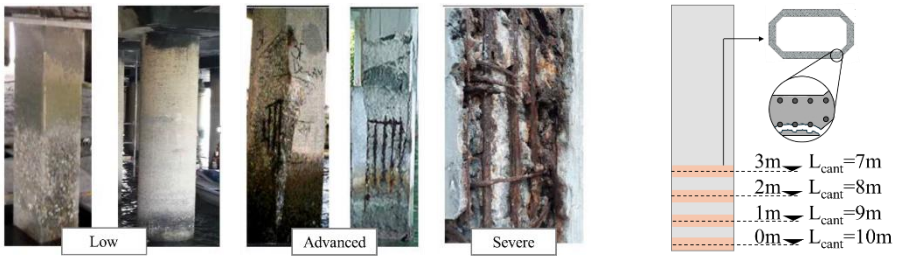


Fig. 3. Corrosion scenarios: (left) alternative levels of damage severity (after [18]); (right) assumed locations of the corroded section along the pier height.

Based on the selected values of μ% and p_{max}, the material constitutive laws are degraded accordingly. Figure 4 illustrates the resulting reduced stress–strain relationships for ordinary reinforcing steel (Fig. 4, left) and prestressing strands (Fig. 4, right). The discontinuities in Fig. 4 (right) are associated with the progressive failure of corroded prestressing wires.

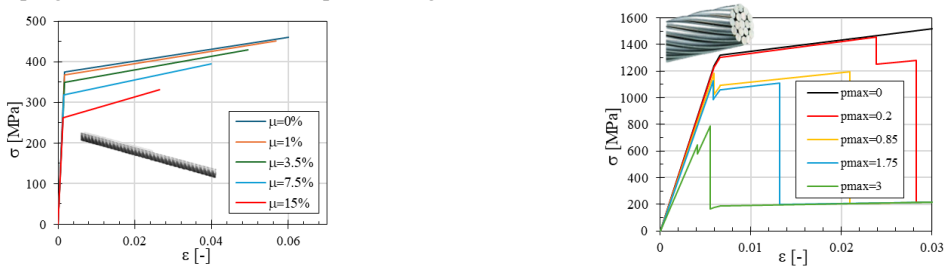


Fig.4. Degraded constitutive laws of (left) ordinary reinforcing steel and (right) prestressing steel.

3.1 Results and discussion

The structural response of the RC pier is first examined by analysing the force–displacement capacity under different corrosion conditions. Figure 5 (left) presents the global force–displacement curves obtained by assuming a fixed plastic hinge location at the pier base and increasing levels of corrosion severity. Figure 5 (right), instead, illustrates the response for a constant corrosion level (μ = 15%), while varying the height at which the degraded section is located along the pier.

An increase in corrosion severity results in a systematic degradation of the nonlinear flexural response, manifested by reductions in flexural strength and displacement capacity, together with a moderate decrease in initial stiffness (Fig. 5 left). This behaviour highlights the direct influence of corrosion-induced loss of steel cross-section on the mechanical performance of the pier. For a given corrosion level, the most adverse condition occurs when the deterioration affects the base section (Fig. 5 right). When the corroded section is located at higher elevations along the pier, the resulting capacity curve is characterized by higher flexural strength but reduced ductility. When plastic hinge formation is governed by the corroded section, the reduction in ductility is mainly associated with the shortening of the effective cantilever length. Conversely, when the corroded section is located above a critical height, it no longer governs the flexural response, as plastic hinging still develops at the pier base. In this case, however, the structural response may be controlled by the reduced shear capacity, which can prematurely intersect and truncate the flexural capacity curve.

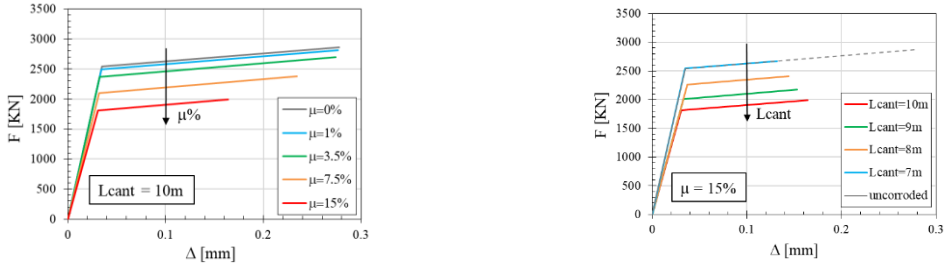


Fig.5. Force–displacement capacity curves: (left) varying corrosion level μ% with base hinge; (right) varying corroded-section location at fixed corrosion level of 15%.

Figure 6 presents the time-dependent evolution of the pier safety index under the considered corrosion scenarios. The left panel (Fig. 6, left) depicts the safety index over time: the dashed black line corresponds to the nominal defect values assigned to each corrosion stage, while the red shaded region represents the variability associated with the range of intensity indices, effectively providing upper and lower bounds of the pier safety. The right panel (Fig. 6, right) illustrates the influence of the location of the corroded section along the pier height. Corrosion concentrated at the pier base induces an earlier decrease of the safety index, though the subsequent degradation is relatively gradual. In contrast, corrosion at higher elevations results in a delayed onset of safety reduction, followed by a more rapid decline once significant deterioration occurs. These results emphasize the sensitivity of pier seismic safety to both corrosion intensity and location.

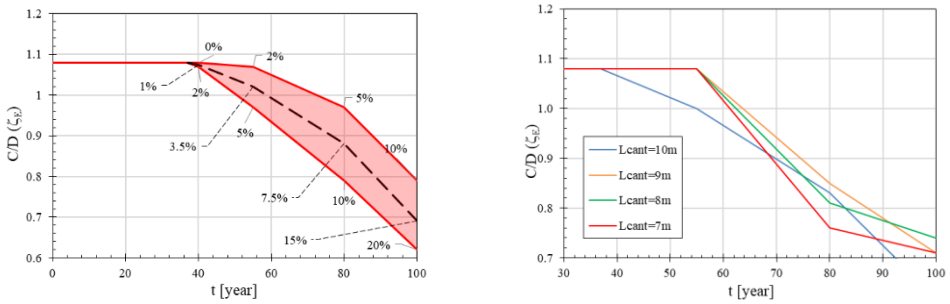


Fig.6. Time-dependent pier safety index under corrosion. Left: evolution for nominal defects and intensity bounds. Right: effect of corrosion location along the pier height.

Figure 7 shows, on the left, the comparison between the demand, expressed in terms of bending moment obtained from the envelope of distributed and concentrated traffic loads and from the effect of prestressing considered as an external action, and the structural capacity corresponding to different levels of corrosion. The capacity remains constant due to the straight profile of the prestressing tendon. On the right, the time-dependent safety assessment of the girder under gravitational loading is presented. In addition, two risk mitigation strategies based on traffic restrictions are investigated: lane closure and restriction of vehicles with a gross weight exceeding 44 t, which are found to extend the service life by 30 and 10 years, respectively, in the present case study. These results may support infrastructure managers in selecting temporary mitigation measures according to the intervention timeframe and retrofit type. For instance, limited traffic restrictions may suffice when maintenance operations can be performed without directly interfering with the deck, whereas lane closure may be necessary for interventions requiring direct access from the roadway level. In all cases, the framework provides an estimate of the time window for planning and implementing retrofit actions under operational constraints.

Figure 8 presents a comprehensive assessment of the bridge safety under the defined corrosion scenarios. The left panel (Fig. 8, left) illustrates the time-dependent evolution of the safety indices for the pier and the girder. The red shaded envelope represents the pier, accounting for the variability of corrosion intensity, while the blue shaded envelope corresponds to the girder. The overlap of the two envelopes indicates that the relative sequence of structural degradation may vary depending on the assigned defect values, implying that either the girder or the pier could reach critical conditions first.

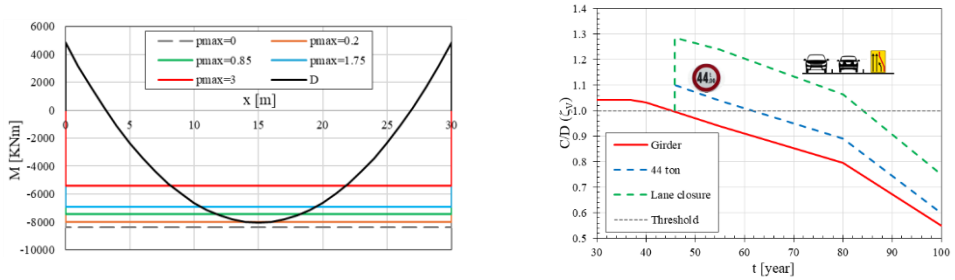


Fig.7. Comparison of bending moment demand and capacity for different corrosion levels (left), and time-dependent girder safety under gravitational loading with traffic restrictions (right).

The right panel (Fig. 8, right) provides a more detailed comparison considering safety indices computed from nominal defect values, whereas the pier envelope reflects variability associated with the spatial location of the corroded section along the pier height. In this scenario, the girder governs the onset of critical conditions despite being subjected to gravitational loading, whereas the pier, governed by seismic actions, becomes critical later. Additionally, two dashed lines illustrate the impact of two risk mitigation strategies discussed above. These results demonstrate the proposed framework, enabling the evaluation of multiple maintenance strategies under uncertainties in corrosion intensity and location.

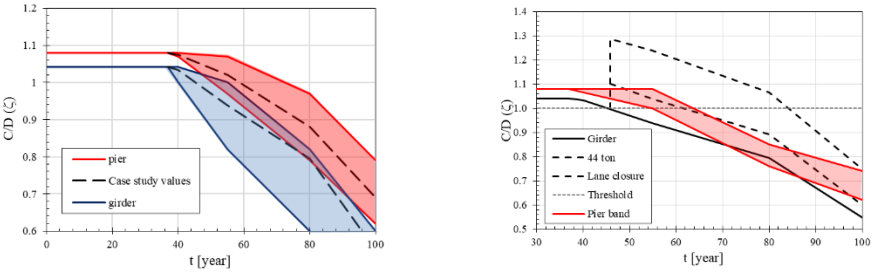


Fig.8. Global safety comparison: (Left) effects of corrosion intensity variability; (Right) effects of corrosion position variability on the pier and mitigation strategies on the girder.

4 CONCLUSIONS

This study has presented a simplified, mechanically consistent framework for the rapid assessment of RC and PSC bridges affected by corrosion. The proposed methodology translates inspection-based defect observations into quantitative corrosion damage indices, allowing the degradation of material constitutive laws to be updated and enabling time-dependent safety evaluation. Application to a representative PSC bridge case study highlighted that both corrosion severity and the location of the deteriorated section significantly affect the nonlinear response of piers and girders, as well as the temporal evolution of structural safety. The results demonstrate that the framework can support maintenance decision-making and the evaluation of mitigation strategies, such as traffic restrictions or lane closures.

However, several limitations should be noted, (i) the approach strongly relies on the association between visual observations and intensity indices, which introduces subjectivity and can significantly influence the results. (ii) The assessment remains element-based and does not fully capture the global structural behaviour, including complex interaction effects and potential collapse mechanisms. (iii) Uncertainties related to material properties, geometrical variations, loading conditions, and corrosion parameters have not been explicitly considered, limiting the robustness of the predictions. Future work will focus on probabilistic extension and validation using real bridge data.

Acknowledgements

This research is supported by the PNRR funding scheme as part of the RETURN project, Spoke 6 – TS2: Multi-Risk Resilience of Critical Infrastructures. The authors acknowledge the Italian Ministry of University and Research (MUR) for funding the Doctoral Scholarship of Federica Di Criscio. Livio

Pedone received funding (RTD-A) from the project “Centro di ricerca per l'innovazione sull'economia circolare e sulla salute” (CUP: J83C22000970001).

References

[1] fib, “Model Code for Service Life Design,” Lausanne, Switzerland, 2006.

[2] EN 1992-1-1, “Eurocode 2: Design of Concrete Structures – Part 1-1: General Rules and Rules for Buildings.,” Brussels, 2004.

[3] Tuutti, Kari. 1982. *Corrosion of Steel in Concrete.* CBI Research Report No. 4:82. Swedish Cement and Concrete Research Institute (CBI), Stockholm, Sweden.

[4] Andrade, Carmen, Alonso, Carlos, and Molina, Francisco Javier. 1993. “Cover Cracking as a Function of Bar Corrosion: Part I—Experimental Test.” *Cement and Concrete Research* 23(3):686–698.

[5] Stewart, Mark G., and Mullard, John A. 2007. “Spatial Time-Dependent Reliability Analysis of Corrosion Damage and the Timing of First Repair for Reinforced Concrete Structures.” *Engineering Structures* 29(7):1457–1464.

[6] Imperatore, Stefano, Rinaldi, Zila, and Drago, Carlo. 2017. “Degradation Relationships for the Mechanical Properties of Corroded Steel Rebars.” *Construction and Building Materials* 148:219–230.

[7] DuraCrete. 2000. *Probabilistic Performance Based Durability Design of Concrete Structures.* Final Technical Report. Document BE95-1347/R17. The European Union – Brite EuRam III Research Programme. CUR Centre for Civil Engineering Research and Codes, Gouda, The Netherlands.

[8] Vidal, Thierry, Castel, Arnaud, and François, Raoul. 2004. “Analyzing Crack Width to Predict Corrosion in Reinforced Concrete.” *Cement and Concrete Research* 34:165–174.

[9] Cui, Feng, Zhang, Hao, Ghosn, Michel, and Xu, Yu. 2018. “Seismic Fragility Analysis of Deteriorating Reinforced Concrete Bridge Substructures Subject to Marine Chloride-Induced Corrosion.” *Engineering Structures* 155:61–72.

[10] Almusallam, Abdullah A. 2001. “Effect of Degree of Corrosion on the Properties o f Reinforcing Steel Bars.” *Construction and Building Materials* 15(8):361–368.

[11] Coronelli, Davide, and Gambarova, Pietro G. 2004. “Structural Assessment of Corroded Reinforced Concrete Beams.” *Journal of Structural Engineering* 130(8):1214–1224.

[12] Mander, John B., Priestley, M. J. Nigel, and Park, Robert. 1988. “Theoretical Stress–Strain Model for Confined Concrete.” *Journal of Structural Engineering* 114(8):1804–1826.

[13] Franceschini, Lorenzo, Belletti, Bruno, Tondolo, Francesco, and Sanchez Montero, José. 2023. “A Simplified Stress–Strain Relationship for the Mechanical Behavior of Corroded Prestressing Strands: The SCPS Model.” *Structural Concrete* 24(1):189–210.

[14] Anaya, Pablo, Martin-Pérez, Bernardo, Rodriguez, José, and Andrade, Carmen. 2022. “Transfer Length of Corroded Wires in Prestressed Concrete Members.” *Structural Concrete* 23(1):147–171.

[15] Dai, Lizhao, Bian, Hanbing, Wang, Lei, Potier-Ferry, Michel, and Zhang, Jianren. 2020. “Prestress Loss Diagnostics in Pretensioned Concrete Structures with Corrosive Cracking.” Journal of Structural Engineering 146(3)

[16] Italian Ministry of Infrastructure and Transport. 2018. *Decree of 17 January 2018: Updating the Technical Standards for Construction (NTC 2018).* Rome, Italy.

[17] Applied Technology Council. 1996. *ATC-40: Seismic Evaluation and Retrofit of Concrete Buildings.* Applied Technology Council, Redwood City, California.

[18] Gentile, Michele, Molaioni, Francesco, and Pampanin, Stefano. 2021. “Simplified Analytical-Mechanical Methodology for Structural-Seismic Safety Assessment over Time of Reinforced Concrete Bridges Affected by Corrosion Phenomena.” Paper presented at the 8th International Conference on Computational Methods in Structural Dynamics and Earthquake Engineering (COMPDYN 2021), Athens, Greece.

Comparative Study of Empirical and Analytical Methods for the Determination of Masonry Compressive Strength

Mohammad Al Jabi, Steffen Marx

Institute of Concrete Structures,
TUD Dresden University of Technology,
George-Bähr-Straße 1, 01069 Dresden, Germany

Summary
Masonry structures constitute a substantial portion of existing buildings and infrastructure, many of which remain in service despite deterioration. Their preservation requires an accurate reassessment of the load-bearing capacity, which depends on a reliable determination of material properties, e.g., compressive strength. Inaccurate compressive strength estimation may lead to unsafe assessments or unnecessary interventions in structures that are, in fact, adequate. Although Eurocode 6 provides method and tables to calculate the masonry compressive strength, previous studies show that applying a single method to different masonry typologies leads to significant deviations from experimental results. This study evaluates the reliability of the adopted and developed compressive strength methods using a compiled database of experimental masonry tests. The results indicate discrepancies between the applied methods and the core sample experimental test results, highlighting the need for further research.

1 INTRODUCTION

Masonry has been used as a primary structural material for centuries and remains widely present in all construction sectors. In Germany, approximately 6,000 bridges [1] and 76% of existing buildings were predominantly constructed from masonry [2]. The mechanical behaviour of masonry is governed by the properties of its constituents and the interaction between units, mortar, and bond configuration, making the determination of realistic compressive strength values challenging [3]. Compressive strength exerts a significant influence on the structural behaviour of masonry and can be determined using standardized experimental or empirical methods; the latter is more commonly applied due to its feasibility for existing structures [4]. In addition, numerous analytical failure models have been developed based on experimental observations of specific masonry types, from which several calculation methods were derived, each requiring specific material parameters [5]. Previous comparative studies have shown that some analytical methods provide more accurate strength estimates than the commonly adopted ones, when compared against results of wall prisms [6]. This study contributes to this verification by examining the performance of selected methods using a comprehensive experimental database, aiming to clarify the applicability ranges of both standardized and analytically developed methods.
In this paper, the term "strength" refers exclusively to compressive strength.

2 MASONRY UNIT, MORTAR, AND BOND

2.1 Natural stone

Natural stone can generally be classified into three main groups according to its geological origin: igneous, sedimentary, and metamorphic rocks. Igneous rocks are formed by the solidification of magma within the Earth's crust and exhibit distinct structural and visual characteristics depending on the conditions of formation.

Stones formed through natural weathering processes, followed by deposition and compaction, are referred to as sedimentary rocks. These can be further subdivided into several subgroups based on their specific mechanisms of formation. Metamorphic rocks are created under the combined influence of elevated pressure and temperature; typical examples include marble, mica schist, quartzite, and gneiss. However, metamorphic stones play only a minor role in masonry construction [6].

The compressive strength of natural stone varies significantly depending on its geological origin. For sedimentary stones, typical strengths range from about 15–150 MN/m² for clayey or carbonate-cemented sandstone, 20–90 MN/m² for porous limestone, and 80–180 MN/m² for dense limestone. Beyond geological origin [5], the way stone is cut and shaped also plays a key role in masonry classification. Common levels of stone processing include ashlar (rectangular blocks with flat surfaces), dressed stone (rectangular blocks with partially dressed surfaces), and rubble (minimally processed stone without surface finishing). These processing types are illustrated in Fig. 1.



Fig 1. Different natural stone processing levels: Rubble stone (left), Dressed (middle), and Ashlar stone (right) [7]

2.2 Brick

The primary raw material used in brick production is loam, which consists mainly of sand, clay, and silt. Among these constituents, the clay fraction plays a decisive role in determining the mechanical and physical properties of bricks.

In the early stages of brick manufacturing, only air-dried bricks were produced. However, these exhibited low strength and reduced durability due to cracking during the drying process. To enhance their performance, various additives were introduced, most commonly additional sand, plant fibers, or other filler materials. The subsequent firing process induces significant chemical and physical transformations, altering the original material structure.

When fired at temperatures between approximately 950 °C and 1150 °C, air-dried bricks develop substantially higher strength. As early as the Middle Ages, additives such as sand, ash, or brick dust were incorporated into the clay mass to improve the quality of the final product. The color of the fired bricks depends largely on the iron and lime content of the excavated loam [7].

2.3 Mortar

2.3.1 Clay and Gypsum Mortar

The oldest binding material used as masonry mortar was clay. In addition, gypsum was also employed as a binder. To produce gypsum mortar, the quarried gypsum stone was first fired and then crushed before being processed into mortar. During the Middle Ages, the use of gypsum as a mortar binder declined significantly and was gradually replaced by other materials [5].

Historical mortars can generally be classified into mortar groups according to DIN 1053-1. Due to their relatively low strength, historical mortars typically correspond to mortar group I, for which no specific performance requirements are defined in the standard.

2.3.2 Lime Mortar

The use of lime as a binding material can be traced back to around 1000 B.C. Historically, lime mortars were generally characterized by their relatively soft consistency. The required lime was obtained from natural sources such as limestone, dolomite, or marl. These materials were first quarried, then crushed, calcined, and subsequently slaked. The resulting slaked lime was mixed with fine sand to produce the mortar [5].

Hydraulic lime differs from non-hydraulic varieties in that it contains compounds that allow it to set and harden in the presence of water, similarly to cement. To enhance both strength and resistance to moisture, hydraulically active additives, such as volcanic ash (pozzolanic earth, trass, or Santorini earth), crushed brick, or lime rich in calcium aluminates, were often incorporated [7].

2.3.3 Cement Mortar

As a result of building material advancements, Portland cement was developed at the end of the 18th century. Cement mortar is produced from a mixture of calcareous marl and clay, which is fired to the sintering temperature and subsequently ground to a fine powder [7].

2.4 Masonry Bond

2.4.1 Natural Stone Masonry Bonds

In the early stages of masonry construction, Cyclopean and polygonal masonry were predominantly employed. Masonry from this period was typically constructed as dry stone in a double-shell configuration, with the interstitial spaces filled with smaller stones and earth. Initially, construction involved simply stacking large polygonal boulders on top of one another. This type of boulder masonry is characterized by the use of unworked or minimally worked stones (Fig 1). Finally, all remaining gaps were filled with so-called spall stones. In some cases, the joints were further compacted with earth or loam [7].

Polygonal masonry represents both a technical and aesthetic advancement. In this construction method, the stone blocks were roughly shaped, with their joining faces carefully worked to fit together. Slanted joints were no longer placed arbitrarily but were arranged radially around particularly large, centrally located blocks for aesthetic purposes. This interlocking arrangement of the stones also enhanced the overall structural strength.

By the end of the earliest historical periods, Greco-Roman antiquity established a highly developed building culture, many aspects of which continue to influence masonry techniques today.

Particular technical and aesthetic importance was placed on sacred structures. For example, marble blocks intended to fit precisely without mortar were often reinforced with iron clamps and lead dowels. Greater attention was paid to accurately angled, finely dressed stones, while the stone format was reduced for economic efficiency. It was also recognized that masonry achieved a stronger bond when constructed with staggered vertical joints in each course. These developments led to the emergence of coursed and ashlar masonry.

To calculate the natural stone masonry's compressive strength using EC 6, the masonry class must be firstly identified. According to table NA.L.1 in DIN EN 1996-1-1/NA, four masonry classes are defined considering the mentioned differences in the stone cutting and shaping process, masonry bond configurations (orthogonal or polygonal bonds), and the mortar joint patterns (see Fig. 2) [7], [8].

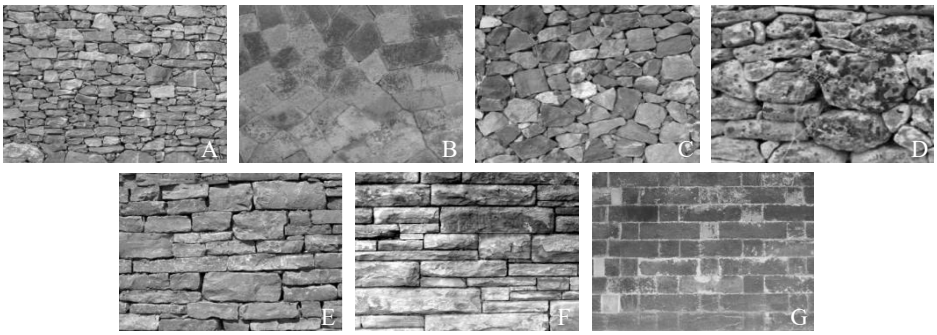


Fig 2. Bond configurations of natural stone masonry: Rubble stone masonry (A), Cyclopean masonry (B), Cyclopean rubble masonry (C), Boulder masonry (D), Layered masonry, Grade N2 (E), Irregular bond masonry, Grade N3 (F), and Regular bond masonry, Grade N3(G) [8]

2.4.2 Brick Masonry Bonds

In the Middle Ages, Gothic or Monk bond was a common masonry technique, characterized by one stretcher course followed by two or more header courses, with stretchers centered over the headers beneath. A variant, the Alternate or Wendish bond, alternated headers and stretchers in every course. Medieval bonding rules included beginning wall edges and corners with whole bricks and arranging headers to avoid vertical joints beneath them, forming vertical, zigzag, or diagonal patterns. The 13th-century Wild bond featured irregularly placed headers to connect double-shell masonry, with carefully executed corner work [7].

From the 16th century, block and cross bonds became prevalent, allowing continuous masonry walls through the full thickness. Both bonds feature alternating courses of headers and stretchers, with the block bond offset by a quarter brick and the cross bond staggered by half a brick in alternating courses. The 17th century saw the regional emergence of the Dutch or Flemish bond, alternating headers and stretchers within the stretcher course, while the American bond used only stretcher and header

courses, with at least every third course composed of headers. Decorative bonds also existed but are not relevant to this discussion (see Fig. 3) [7].

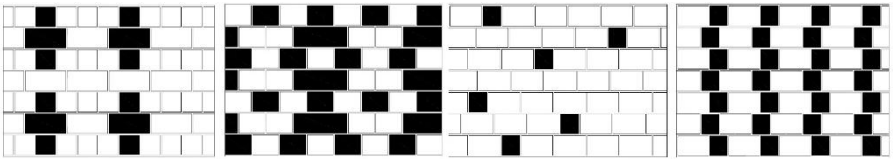


Fig 3. Brick masonry bond configurations (from the left to right): gothic, irregular, american, and cross bond, own representation based on [19]

3 DEVELOPED EMPIRICAL AND ANALYTICAL METHODS

3.1 Empirical Methods

Empirical methods are commonly used to calculate the compressive strength of masonry under centric loading. These methods incorporate test results of the stone and mortar as a function for calculating the compressive strength of different masonry types. To determine the compressive strength of brick masonry, the method in DIN EN 1996-1-1 is adopted, Eq. (1). By applying this formula, the resulting strength is considered as characteristic value in contrast to the other analytical methods which are required a transformation using local and global safety factors.

$$f_k = K \cdot f_b^{\alpha} \cdot f_m^{\beta} \tag{1}$$

Where f_k is the masonry characteristic compressive strength in N/mm^2; α and β are constants related to f_b *and* f_m respectively; $f_b$is the normalized compressive strength of the units and f_m is the mean compressive strength of mortar.

3.2 Analytical Developed Methods

3.2.1 Failure Model of Hilsdorf [9] [10] [11]

The mechanical behavior and failure of masonry under compression are governed by the differing material properties of brick and mortar. As the vertical load increases, lateral tensile stresses in the brick rise until vertical cracking initiates when the brick's failure limit is reached. Subsequent stress redistribution leads to progressive cracking with continued loading. Ultimate failure occurs when the brick can no longer restrain the lateral expansion of the mortar. The masonry compressive strength can be calculated using Eq. (2).

$$\beta_{D,MW} = \frac{\beta_{D,St} \cdot (\beta_{Z,St} + \frac{t}{m.h_{St}} \beta_{D,M\ddot{o})}}{U_u \cdot (\beta_{Z,St} + \frac{t}{m.h_{St}} \beta_{D,St})} \tag{2}$$

Where $\beta_{D,MW}$ is the masonry compressive strength; $\beta_{D,St}$ and $\beta_{Z,St}$ are the stone compressive and tensile strength; $\beta_{D,M\ddot{o}}$ is the mortar compressive strength; m is assumed to be 4.1; U_u is a factor between 1.5 and 2 for soft mortar; T is the bed joint thickness; and h_{St} is the stone height.

3.2.2 Failure Model of Stiglat [9]

This failure model was developed based on the experimental observation of just four samples of natural stone masonry consisting of sandstone under compression. Firstly, the 10 % quantile compressive strength of the sandstone $f_{c,St,10\%Fractil}$ is determined using Eq. (3).

$$f_{c,St,10\%Fractil} \cong 18{,}7\,\gamma - 355{,}2 \tag{3}$$

Based on the assigned mortar group, the masonry permissible stress (*per σ*) is determined using the following equations.

For mortar group 1: $per\ \sigma = 0{,}007.\ f_{c,St,10\%\ Fractil} \leq 0{,}7$

For mortar group 2: $per\ \sigma = 0{,}017.\ f_{c,St,10\%\ Fractil} \leq 1{,}6$

For mortar group 3: $per\ \sigma = 0{,}024.\ f_{c,St,10\%\ Fractil} \leq 2{,}4$

According to Stiglat, the failure occurs as fine cracks in the stones, not in the mortar. The cracking stress in the stones was about 50 % of the failure stress of the masonry assembly.

3.2.3 Failure Model of Ohler [12]

According to [13], a uniform lateral stress distribution in both the stone and the mortar and a multiaxial stress state within the mortar are considered. Failure of natural stone masonry is predicted to occur when the masonry stress state reaches the intersection of the failure envelopes of the stone and the mortar. This method Eq. (4) was adopted in the German norm RIL 805 for the masonry strength calculation.

$$\beta_{D,MW} = 0{,}5 \cdot \beta_{D,M\ddot{o}} + \frac{a \cdot 0{,}5 \cdot \beta_{D,St} - 0{,}5 \cdot \beta_{D,m\ddot{o}}}{1 + \frac{b \cdot h_f \cdot 0{,}5 \cdot \beta_{D,St}}{2 \cdot h_s \cdot \beta_{Z,St}}} \tag{4}$$

Where $\beta_{D,MW}$ is the masonry compressive strength; $\beta_{D,St}$ and $\beta_{Z,St}$ are the stone compressive and tensile strengths; $\beta_{D,M\ddot{o}}$ is the mortar compressive strength; a and b are factors related to the masonry type; h_f and h_s denotes the thickness of the bed joint and the stone respectively.

3.2.4 Failure Model of Pöschel and Sabha [14]

For natural stone masonry, the failure model was developed based on the experimental and numerical FE analysis results. Under the centric compressive stress, the failure occurs when the cracks initiate at the stone edges. At the early phase of loading, the mortar joint crumbles at the bed joint edges. The failure is caused by vertical cracks developed in the centre of the stones.

The mortar joints crumble at a depth equivalent to twice the height of the joint, while the remaining mortar does not fail. The masonry failure is governed by the stone; it occurs when a stress combination in the centre of the stone reaches an assumed failure limit that lies between the uniaxial compressive and tensile strength of the stone. The compressive strength can be calculated using Eq. (5).

$$\beta_{D,MW} = \frac{2\frac{t}{b}\,\beta_{D,M\ddot{o}}\left(2{,}32\frac{\beta_{Z,St}}{\beta_{D,St}} + 1{,}6\right) + \beta_{Z,St}}{\frac{t}{b}\left(2{,}32\,\frac{\beta_{Z,St}}{\beta_{D,St}} + 1{,}6\right) + \frac{\beta_{Z,St}}{\beta_{D,St}}} \tag{5}$$

Where $\beta_{D,MW}$ is the masonry compressive strength; $\beta_{D,St}$ and $\beta_{Z,St}$ are the stone compressive and tensile strengths; t is the mortar joint thickness; and b is the stone height.

3.2.5 Failure Model of Berndt [15]

Masonry failure is governed by the tensile failure of the stone under a triaxial stress state consisting of compressive and biaxial tensile stresses. Tensile stresses in the stone arise from two primary mechanisms: restrained lateral expansion caused by the head joints and splitting tension developing at the center of the stone due to crumbling at the mortar edges.

These tensile stress components are superimposed; however, due to their different spatial distributions, the maximum splitting tensile stress is considered with a reduction factor of 60%. The plastic behavior of the mortar is accounted for by incorporating the mortar's Poisson's ratio and internal friction angle into the analytical method to calculate the masonry compressive strength Eq. (6).

$$\beta_{D,MW} = \frac{\beta_{D,St}}{\left(\frac{t}{h'}\frac{\bar{\mu}_{M\ddot{o}}}{1-\bar{\mu}_{M\ddot{o}}} + k_1\frac{d'}{d}\frac{d}{h''}\right)\frac{\beta_{D,St}}{\beta_{Z,St}} + 0{,}7} \tag{6}$$

Where $\beta_{D,MW}$ is the masonry compressive strength; $\beta_{D,St}$ and $\beta_{Z,St}$ are the stone compressive and tensile strengths; h' is the stone height or 10 cm (lower value); h'' is the stone height or 20 cm (lower value); d stone width; d' is the total depth of joint flaking; k_1 is a reduction factor of 0,3; and $\bar{\mu}_{M\ddot{o}}$ is the transverse expansion in relation to the mortar joint.

4 COMPILED EXPERIMENTAL DATABASE

To investigate the accuracy of the aforementioned methods, core test results of existing masonry structures, including stone, mortar, and masonry bond as well as stone and mortar geometrical properties, are compiled. This data is provided by Baugrund Dresden GmbH, which collaborates with the Institute of Concrete Structures at TU Dresden in several research projects.

Core samples were extracted from various structural components, including arches, abutments, and wing walls, in order to capture the widest possible range of existing masonry materials. Information regarding the core diameter and tested specimen number is presented in the table below. For testing the

stone and masonry bond, the core sample testing method was used. For mortar joint, the plate compression testing method was utilized.

In this study, the dataset was classified, analyzed, and further processed by the authors to derive characteristic values for the masonry components and masonry bond. The experimental-derived characteristic compressive strengths of stone, mortar, and masonry bond were determined as the 5% fractile of a log-normal distribution fitted to the experimental results. Subsequently, both empirical and analytical methods were applied using the characteristic compressive strengths of stone and mortar, as well as geometric parameters such as joint thickness and stone height.

Table 1 summarizes the key material parameters and characteristic strength values of the stone, mortar, and masonry. The following notations are used: Class 12 and 20 refer to the brick classification according to DIN 105-1; MG indicates the mortar class according to DIN 18580, and N1 to N4 indicate the natural stone masonry class identifications according to DIN EN 1996-1-1/NA.

Table 1 Experimentally Determined Key Material Properties of Various Masonry Materials

Type	Masonry Material Properties				Chara. Compressive Strength in N/mm² and test configurations		
	Masonry Material	Masonry Unit	Mortar Group	Masonry class	Masonry unit	Mortar	Masonry
1	Rubble Masonry	Grauwacke	MG II-IIa	N1	25,96 (9,100)[1]	3,26 (19, NI[2])	5,23 (11,100)
2	Rubble Masonry	Sandstone	MG I-II	N1	40,18 (5,100)	1,85 (10, NI)	5,15 (10,100)
3	Rubble Masonry	Sandstone	MG II	N1	9,9 (6,100)	1 (8, NI)	1,3 (10,100)
4	Brick Masonry	Class 12	MG IIa	-	11,2 (5,150)	0,2 (6, NI)	6,12 (11,150)
5	Brick Masonry	Class 20	MG II	-	41,8 (5,100)	40,87 (4, NI)	30,6 (5,100)
6	Ashlar Masonry	Granite	MG IIa	N4	57,7 (10,100)	3,58 (12, NI)	56,48 (13,100)
7	Ashlar Masonry	foam lime	MG II	N4	20,2 (12,100)	0,5 (4, NI)	5,87 (4,100)

[1] (number of tested specimens, specimen core or dimension in mm)

[2] NI = no information provided

5 COMPARISON OF THE CALCULATED AND EXPERIMENTAL COMPRESSIVE STRENGTH

To ensure a consistent comparison between the compressive strengths obtained from the various analytical methods and the values derived according to Eurocode 6, the analytically determined strengths were converted into characteristic compressive strengths using appropriate safety factors as follows. For the analytical method specified in RIL 805, a partial safety factor of 2.7 was applied. For all other methods, a partial safety factor of 5 was adopted in accordance with the recommendation of Berndt [16], who proposed this value at the time these methods were developed.

The characteristic compressive strength was derived by first reducing the analytically obtained strength values by the corresponding partial safety factor and subsequently multiplying them by a factor

of 3.14. This factor is obtained by multiplying the global safety factor (2.0) with the slenderness-related reduction factor (1.33) and dividing the result by 0.85, in accordance with [17].

The following diagrams (see Figs. 4–6) present the characteristic compressive strengths obtained from all considered empirical and analytical methods together with the experimental results.

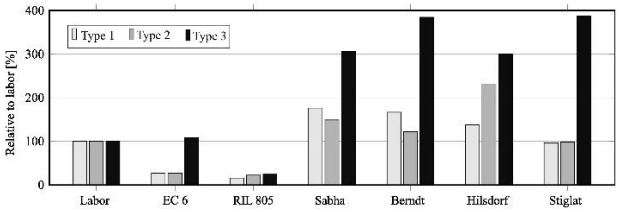


Fig 4. Comparison results of rubble masonry types

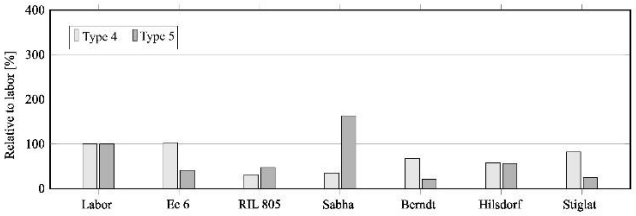


Fig 5. Comparison results of brick masonry types

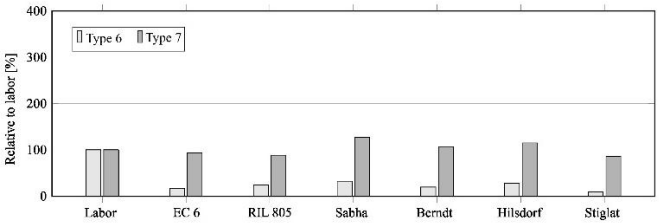


Fig 6. Comparison results of ashlar masonry

6 CONCLUSION

The comparative analysis shows that the accuracy of the investigated methods strongly depends on masonry type and material properties. For rubble masonry (Types 1 to 3), Eurocode 6 and RIL 805 generally underestimated the experimental compressive strength. Nevertheless, for masonry characterized by a relatively low stone compressive strength of approximately 9.9 MPa, the EC 6 method provided comparatively consistent predictions. In contrast, the remaining investigated methods, including Sabha, Berndt, and Hilsdorf, exhibited considerable overestimations, particularly for Type 3 masonry. Although the Stiglat method showed the closest agreement with the experimental results, of types 1 and 2, its reliability remains uncertain due to its development based on experimental observations from only four experimental specimens.

For brick masonry (Types 4–5), inconsistent results were obtained. EC 6 showed acceptable agreement only for type 4, whereas the RIL 805 method again demonstrated significant underestimation tendencies, whereas the Hilsdorf method provided comparatively more stable and consistent predictions than the other investigated methods.

For ashlar masonry (Types 6–7), the influence of the mechanical properties of the masonry constituents was clearly evident. In cases of high stone compressive strength, approximately 57 MPa, all investigated methods produced conservative predictions relative to the experimental results. Conversely, for masonry with lower stone compressive strength, approximately 20 MPa, the analytical and empirical methods showed comparatively close agreement with the experimentally determined values.

Overall, the findings highlight the limitations and uncertainties of current masonry compressive strength assessment methods. Further research should establish the applicability range and methodological limits of each prediction model; using multiple methods tailored to specific masonry types may improve result reliability. The influence of core size and joint configuration on the experimentally determined compressive strength of brick and natural stone masonry also warrants further investigation. Additionally, a unified global safety factor for both empirical and analytical predictions could help reduce discrepancies in compressive strength determination.

References

[1] Keßler, Jenny, Conrad Pelka, and Steffen Marx. 2025. "Preservation of Masonry Arch Bridges in the Network of Deutsche Bahn." In *18th International Brick and Block Masonry Conference (IB2MaC 2024)*. Lecture Notes in Civil Engineering, vol. 613. Springer.

[2] Rast, Ronald. 2019. "Mauerwerks- und Wohnungsbau in Deutschland: Status 2019 und Prognose 2021." *Mauerwerk* 23: 123–127.

[3] Nazimi, Karishma, Jose Juan Castro, Shogo Omi, and Seif Bimkubwa Ali. 2024. "Proposal of Empirical Equations for Masonry Compressive Strength: Considering the Compressive Strength Difference between Bricks and Mortar." *Buildings* 14, 1138.

[4] Graubohm, Markus, and Wolfgang Brameshuber. 2016. "Determining the Masonry Compressive Strength." *Mauerwerk* 20: 340–351.

[5] Warnecke, Peter. 1995. "Tragverhalten und Konsolidierung von historischem Natursteinmauerwerk." PhD diss., Technische Universität Braunschweig, Institut für Baustoffe, Massivbau und Brandschutz.

[6] Huster, Ulrich. 2000. "Tragverhalten von einschaligem Natursteinmauerwerk unter zentrischer Druckbeanspruchung." PhD diss., Universität Kassel.

[7] Horst, Patricia. 2014. "Festigkeitsanalyse ausgewählter Schwerpunkte von historischem Mauerwerk." Diplomarbeit., Berufsakademie Sachsen, Leipzig.

[8] DIN EN 1996-1-1. 2019. *Eurocode 6: Bemessung und Konstruktion von Mauerwerksbauten – Teil 1-1: Allgemeine Regeln für bewehrtes und unbewehrtes Mauerwerk.* Berlin: Beuth Verlag GmbH.

[9] Stiglat, K. 1984. "Zur Tragfähigkeit von Mauerwerk aus Sandstein." In: *Bautechnik* 2/1984 S.51-59 and 3/1984, S.94-100, Ernst & Sohn, Berlin.

[10] Hilsdorf, H. 1965. *Untersuchungen über die Grundlagen der Mauerwerksfestigkeit.* München: Materialprüfungsamt für das Bauwesen der Technischen Hochschule München.

[11] Hilsdorf, H. 1969. "Investigation into the Failure Mechanism of Brick Masonry Loaded in Axial Compression." In *Proceedings of International Conference on Masonry Structural Systems*, 34–41. Houston, Texas.

[12] Ohler, A. 1986. "Zur Berechnung der Druckfestigkeit von Mauerwerk unter Berücksichtigung der mehrachsigen Spannungszustände in Stein und Mörtel." *Bautechnik* 5: 163–169.

[13] Purtak, Frank. 2001. "Tragfähigkeit von schlankem Quadermauerwerk aus Naturstein." PhD diss., Technische Universität Dresden, Fakultät Architektur.

[14] Sabha, Ahmad, and Günter Pöschel. 1993. "Ein theoretisches Modell zum Tragverhalten von Elbsandstein." In *Erhalten historisch bedeutsamer Bauten: Jahrbuch 1993, SFB 315.* Berlin: Ernst & Sohn.

[15] Berndt, Eberhard. 1996. "Druck- und Schubfestigkeit von Mauerwerk - experimentell nachgewiesen an Strukturen aus Elbsandstein." *Bautechnik* 73, Heft 4, S. 222–234.

[16] Berndt, Eberhard, and Ingolf Schöne. 1994. "Ein Bemessungsvorschlag für Mauerwerk aus Elbsandstein auf der Grundlage experimentell ermittelter Tragfähigkeiten." In *Erhalten historisch bedeutsamer Bauten: Jahrbuch 1992*, SFB 315, 41–59. Berlin: Ernst & Sohn.

[17] Purtak, Frank, Gero Marzahn, and Matthias Müller. 2022. "Berechnung und Bemessung bestehender Gewölbebrücken mit der Nachrechnungsrichtlinie für Straßenbrücken." In *Mauerwerk Kalender 2022*, 397–442. Berlin: Ernst & Sohn. doi:10.1002/9783433611029.ch13.

[18] BAUGRUND Dresden Ingenieurgesellschaft mbH. 2022. *Bericht zu Materialeigenschaften und Bauteilgeometrie.* Unpublished report, Dresden.

[19] Röben. 2025. "Types of Brick Bonding." Accessed July 15, 2026. https://en.roben.pl/professionalists-zone/for-contractor/technical-informations/types-of-brick-bonding.

Comparative Assessment of Beam-to-Column Connection Modelling in Multi-Storey Precast Concrete Frame Structures

Riccardo Maurizio Ambrogio Baltrocchi, Paolo Martinelli

Department of Civil and Environmental Engineering,
Politecnico di Milano,
Piazza Leonardo da Vinci 32, Milan, 20133, Italy

Summary
Multi-storey precast concrete frame structures are increasingly used because of their high production quality and rapid on-site installation. However, their limited continuity and redundancy make them vulnerable to progressive collapse under accidental loads. Beam-to-column dry connections with steel dowels, widely adopted in these buildings, are critical for robustness assessment. Although detailed solid-element models can reproduce tests on precast frame subassemblies subjected to column removal, they are computationally impractical for buildings. This paper proposes a simplified nonlinear finite-element model using nonlinear beam elements and zero-length elements with nonlinear translational and rotational springs to idealise joints. The model is validated against experimental pushdown tests covering different precast configurations. OpenSeesPy nonlinear static analyses show the approach's capabilities and limitations, supporting its potential application to full-scale buildings.

1 INTRODUCTION

Multi-storey building structures may be exposed during their service life to extreme and accidental events, such as impact, explosions, or unforeseen local failures, which can lead to severe structural damage [1]. In this context, progressive collapse generally represents a specific failure mode characterized by a domino-type sequence of cascading collapses, whereby the initial damage propagates through the structural system [2]. The ability of a structure to withstand such type of events without suffering disproportionate damage refers to structural robustness.

Compared to common monolithic reinforced concrete (RC) structures, precast concrete (PC) buildings typically consist of discontinuous beam-to-column connections, which can result in reduced load transfer mechanisms in column removal scenarios. Experimental evidence available in the literature shows that the progressive collapse resistance of PC structures is strongly governed by the behaviour of beam-to-column joints, especially during the transition from compressive arch action (CAA) to catenary tensile action (CTA) [3]. However, research on progressive collapse of PC structures remains relatively limited (see among the others Ravasini et al. [4] and Dal Lago et al. [5]).

The literature reports numerical studies on PC specimens conducted using detailed nonlinear finite element (FE) models. These models allow the progressive collapse behaviour of the specimens to be captured with a high degree of accuracy [6]. However, the application of such models to entire buildings remains, to date, largely impractical due to the significant computational demand involved. In this regard, the development of finite element (FE) models in the OpenSeesPy environment [7], using nonlinear beam elements, combined with zero-length elements incorporating nonlinear translational and rotational springs for joint idealisation, enables acceptable results to be achieved, particularly with a view to future full-scale structural robustness assessments. However, the modelling strategies for dry beam-to-column connections found in the literature are still very limited, and their progressive collapse knowledge is not yet well known.

Therefore, this paper aims to develop an OpenSeesPy model for commonly adopted dry beam-to-column connections. The proposed model is validated through comparison of numerical results with experimental tests on PC specimens conducted by Zhou et al. [3]. Furthermore, the study assesses the influence of different dowel shear resistance formulations and of the CAA contribution on the global response of the specimens, and discusses the applicability, limitations, and potential future developments of the simplified nonlinear model for the robustness assessment of multi-storey PC dry-connected frames.

2 EXPERIMENTAL CAMPAIGN AND CASE STUDY

The experimental programme considered in this study is based on the work of Zhou et al. [3], who conducted progressive collapse tests on three half-scale moment-resisting sub-assemblages, comprising one cast-in-situ RC specimen and two PC specimens. In the present study, only the two precast specimens, hereafter referred to as PC1 and PC2, are considered. The geometry of the specimens, including the boundary conditions and loading point, is illustrated in Fig. 1. Due to symmetry about the vertical axis of load application, only half of each specimen is shown for clarity and brevity. PC1 refers to the exposed corbel type connection (Fig. 1a), while PC2 refers to the type of connection with hidden corbel (Fig. 1b). Both specimens used two 20 mm diameter steel dowels and steel angle cleats on top. An in-plane constraint frame restrained the mid-column, ensuring that vertical displacement was imposed exclusively at this location. The upper ends of the exterior columns were pin-supported, and the horizontal reaction forces were recorded using load cells, while the foundations ensured fixed boundary conditions. Vertical loading was applied at the top of the mid-column through a hydraulic jack. Linear variable differential transformers (LVDTs) were used to monitor the vertical displacement of the mid-column and the lateral displacements of the exterior columns.

Pseudo-static loading was adopted, with force-controlled loading applied during the first phase (with increments of 5 kN per step) until the peak load was reached. Subsequently, displacement-controlled loading was conducted (with increments of 25 mm per step) until failure. The measured stiffness of the pin supports at the tops of the exterior columns was 11.47 kN/mm for specimen PC1 and 11.11 kN/mm for specimen PC2. For further details on the experimental test programme, including the description of the test specimens, reinforcement details, and the test set-up, readers are referred to Zhou et al. [3].

Experimental observations indicated that damage in both PC specimens was mainly concentrated in the beam-to-column connections, resulting in a significant reduction in load capacity in the CAA phase. After reaching maximum resistance in CAA, rapid degradation of resistance was recorded. Although CTA was activated in PC2 specimen, the associated load-bearing capacity did not exceed that achieved in CAA, while CTA did not develop in sample PC1 due to insufficient structural integrity of the beam-column joints. As a result, both dry-connected PC test members exhibited limited progressive collapse resistance.

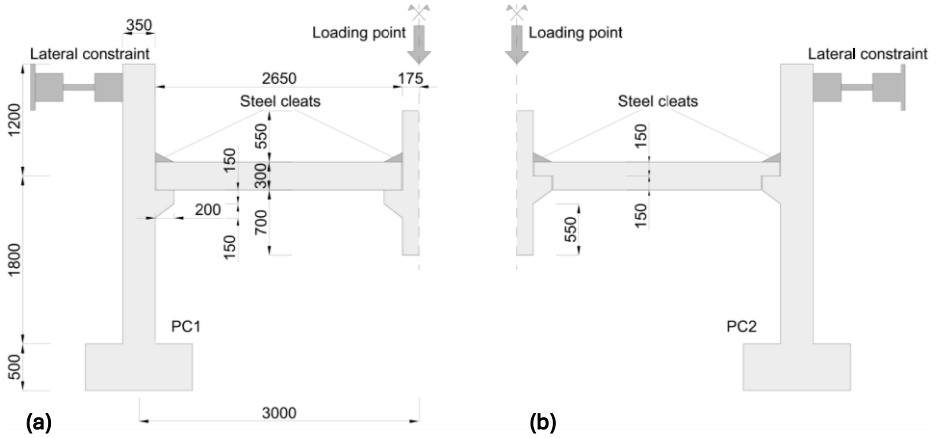


Fig. 1 Dimensions (mm) and test set-up of specimens PC1 and PC2 tested by Zhou et al. [3]: (a) PC1; (b) PC2. Only half of each specimen is depicted due to symmetry.

3 FE MODELS

3.1 Geometrical modelling

To capture both the global structural response and the local inelastic behaviour under progressive collapse in a computationally efficient manner, the numerical analyses were performed in the OpenSeesPy environment using a force-based distributed inelasticity beam–column element [8], combined with zero-length elements incorporating nonlinear translational and rotational springs for

joint idealisation. The sub-assemblages were modelled according to the geometric and mechanical details of the experimental specimens (Fig. 2a), ensuring consistency with the connection configurations governing the shear and flexural response.

Fig. 2b shows beams and columns represented by force-based beam–column elements with seven Gauss–Lobatto integration points, while geometric nonlinearity was included through the P-Δ formulation. It is noted that using a single element is sufficient to model each structural member because the equilibrium condition can be satisfied even for strong material nonlinearity [9]. Each element was characterised by a fiber-discretised cross-section composed of concrete and steel fibers (Fig. 2c), based on the Navier–Bernoulli assumption that cross-sections remain planar and normal to the reference axis during the deformation history. An individual uniaxial constitutive law was assigned to each fiber, allowing the confinement effect provided by transverse reinforcement to be explicitly accounted for in the core concrete. Columns were assumed to be fixed at the base, while two translational springs, calibrated according to the experimental results by Zhou et al. [3], were introduced at the top of the lateral columns.

The beam-to-column connections (Fig. 2d) were modelled using zero-length elements placed at the interfaces, comprising two translational springs (horizontal and vertical) and one rotational spring (Fig. 2e). A similar approach was adopted by Ravasini et al. [4] for the modelling of PC frames. Rigid links were introduced to account for the eccentricity between the column axis and the dowel insertion point at the corbel.

Finally, a pushdown analysis was performed by applying a vertical load to the central column. The Krylov–Newton algorithm was adopted as the nonlinear solution strategy, with a convergence tolerance on the displacement increment norm set to 10^{-8} and a maximum number of 200 iterations. Similarly to Zhou et al. [3], the load-vertical displacement (P–δ) values of the entire specimen were extracted from the nonlinear pushdown analysis. The displacement values read refer to the vertical settlement of the central column at node 5 (Fig. 2a).

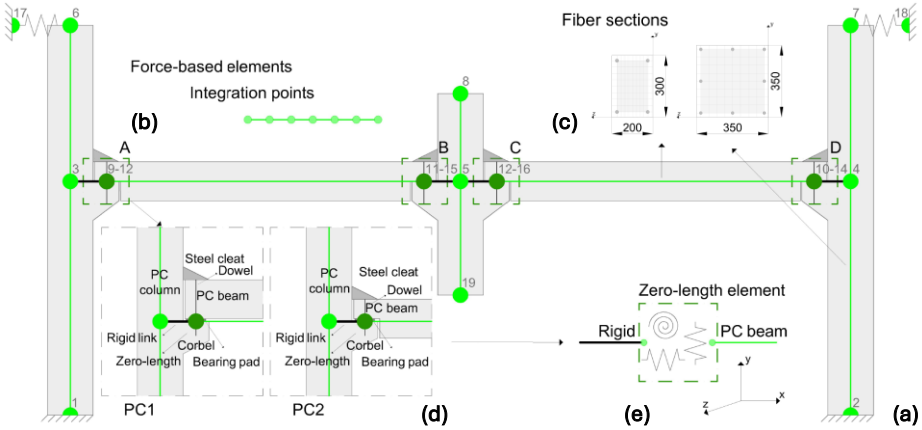


Fig. 2 Schematic FE model representation: (a) elements, nodes (in grey) and boundary conditions; (b) beam elements and integration points; (c) fiber sections of beam elements; (d) connection beam-column details; (e) zero-length element details.

3.2 Material modelling

The material models adopted in the numerical analyses are herein outlined. Unconfined concrete was assigned to the cover region, whereas confined concrete was adopted for the core to account for the confinement provided by hoop reinforcement, in accordance with the modified Kent–Park model [10] (Concrete02). The main confined and unconfined concrete parameters are reported in Table 1. The steel behaviour was described by nonlinear model of Giuffre-Menegotto-Pinto [11] (Steel02), in which yield strength f_y is taken equal to 485 MPa and 505 MPa for beam and column bars, respectively; the initial elastic modulus E_0 is assumed equal to 200 GPa and the strain-hardening ratio is as 0.003.

Table 1 Concrete properties assumed in the analyses (E_{ct} = tensile softening slope at peak tensile strength; f'_c = peak compressive strength; f_{ct} = peak tensile strength; Z_m = parameter that controls the strain softening slope in compression; ε_0 = strain at the compressive peak strength; ε_u = ultimate compressive strain; κ = confinement parameter).

	f'_c (MPa)	$\varepsilon_0 \times 10^{-3}$	$\varepsilon_u \times 10^{-3}$	κ	Z_m	f_{ct} (MPa)	E_{ct} (MPa)
Unconfined	−28.30	−2.0	−3.50	1.1	44	2.83	2500
Confined	−31.32	−2.2	−13.07	1.1	46	3.31	2500

The beam-to-column connections of the PC system were modelled by means of nonlinear translational and rotational springs, aimed at reproducing the shear and flexural response of the connection under column-removal scenarios. The vertical springs behave as rigid connections. Fig. 3a shows shear behaviour that was defined through an idealised multilinear shear–displacement relationship. Both the ultimate shear resistance of the connection, V_u, and the yielding shear force, V_y, were calculated in accordance with the recommendations of *fib* Bulletin 43 [12]. In particular, V_u was governed by the dowel contribution, while V_y was assumed equal to $0.5V_u$. Once V_u is reached, the descending branch eliminates the contribution of the spring. More than twenty-five different formulations for estimating the dowel shear resistance were considered and compared during the calibration process (the results are not reported here for the sake of brevity). The shear strength value provided by fib Bulletin 43 [12], equal to 94.49 kN, was found to be consistent with the range of predicted values and was therefore adopted for modelling purposes.

The rotational behaviour of the beam-to-column connection was represented through a moment–rotation relationship accounting for the equilibrium between the concrete compressive stress-block and the forces developed in the dowels and steel angle cleats. The positive moment–rotation branch, associated with sagging bending, was derived following the analytical approach proposed by El Debs et al. [13], while the negative branch, associated with hogging bending, was defined according to the model by Elliott et al. [14], as shown in Fig. 3b. The residual strength in both positive and negative branches was assumed to be negligible after the attainment of the ultimate rotation. Both the shear (V–Δ) and rotational (M–θ) responses were implemented in OpenSeesPy using the uniaxial 'Pinching4' material and assigned to the corresponding translational and rotational springs connecting the beam and column elements. Spring values are reported in Table 2.

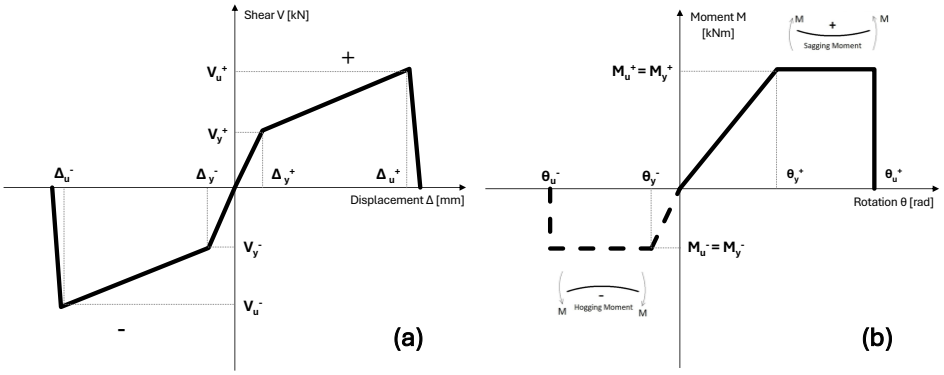


Fig. 3 Beam-to-column relationships: (a) shear-displacement; (b) moment-rotation.

Due to beam-column element inability to detect the occurrence of CAA during collapse, the contribution of arch action to the bending moment (M_{CAA}) was calculated analytically. Analytical methods for estimating the contribution for PC structures with steel dowels are scarce in the current literature, thus Abbasnia et al. [15] method, valid for RC beam systems subject to column removal scenarios, was considered. This approach is based on three fundamental assumptions: the maximum arching moment occurs after the yielding of the longitudinal bars; symmetry of cracks and failure modes with respect to the removed column; similarity between the depths of the compressed zones on both

sides of the beams connected to the removed column. Following the approach presented by [15], an M_{CAA} equal to 17.70 kNm was calculated. This contribution of arch action to the bending moment was accounted for by increasing the flexural capacity of the internal and external rotational springs during pushdown analysis, for both PC1 and PC2 specimens.

Table 2 Spring model parameters.

ID	Spring location	Translational horizontal				Rotational			
		V_y [kN]	V_u [kN]	Δ_y [mm]	Δ_u [mm]	M_y [kNm]	M_u [kNm]	θ_y [rad]	θ_u [rad]
PC1	Internal	47.25	94.49	0.25	9.74	27.95	27.95	0.0068	0.1167
	External	47.25	94.49	0.25	9.74	78.70	78.70	0.0079	0.1167
PC2	Internal	47.25	94.49	0.25	9.74	13.78	13.78	0.0137	0.1167
	External	47.25	94.49	0.25	9.74	78.70	78.70	0.0079	0.1167

4 RESULTS

In the following section, the main outcomes of the pushdown analysis for the two specimens, both with and without CAA contribution, are presented and discussed. Figures 4a and 4b show the results for specimens PC1 and PC2, respectively, while the main phases of the structural responses are summarised in Tables 3–4.

Due to the removal of the central column during the tests, the internal beam-column connections mainly work in sagging, whereas the external ones are predominantly in hogging. The comparison between the numerical and experimental P–δ curves shown in Fig. 4 indicates that the numerical models reasonably capture the overall response of both specimens, characterised by an initial quasi-linear branch followed by a nonlinear regime associated with the progressive activation and degradation of the connection springs. The comparison between numerical and experimental stiffness shows good agreement for both specimens in the initial section of the P–δ curves. The models reasonably reproduce the initial elastic stiffness, while the tests showed an early reduction in stiffness due to the first cracking, which is only partially captured by the distributed plasticity formulation and the constitutive laws adopted.

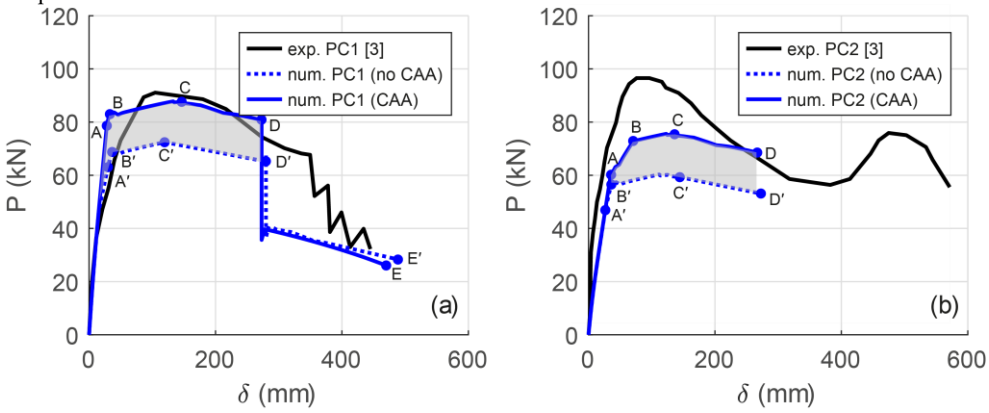


Fig. 4 Comparison of load-vertical displacement relationship between the predictions and the test results: (a) PC1 specimen; (b) PC2 specimen.

In the analyses without CAA contribution, the global response of both PC1 and PC2 is mainly governed by the rotational capacity of the internal joints in sagging. The development of nonlinearity is associated with the yielding of the internal rotational springs, which causes the transition from a predominantly flexural response of the beams to a behaviour dominated by the connections. As loading increases, the translational springs yield and the external rotational springs, representing hogging at the external joints, start contributing more significantly to the global resistance. The peak of the P–δ curves is

reached when the internal rotation springs approach their maximum rotation, beyond which a marked deterioration in resistance is observed and only limited residual capacity is expected in the event of large displacements. For PC1, neglecting CAA leads to an underestimation of the experimental peak load of about 20%, whereas including CAA reduces this error to roughly 4%. For PC2, the underestimation of the experimental peak load of about 95 kN decreases from roughly 38% without CAA to about 21% when the CAA contribution is considered.

Table 3 PC1 pushdown phases.

Specimen	Step	Limit state
PC1 – without CAA	A’	Yielding of the internal rotational springs.
	B’	Yielding of the internal and external translational springs.
	C’	Yielding of the external rotational springs.
	D’	Failure of the internal rotational springs.
	E’	Failure of the internal and external translational springs.
PC1 – with CAA	A	Yielding of the internal rotational springs.
	B	Yielding of the internal and external translational springs.
	C	Peak load of the global curve.
	D	Failure of the internal rotational springs.
	E	Failure of the internal and external translational springs.

Table 4 PC2 pushdown phases.

Specimen	Step	Limit state
PC2 – without CAA	A’	Yielding of the internal rotational springs.
	B’	Yielding of the internal and external translational springs.
	C’	Yielding of the external rotational springs.
	D’	Failure of the internal rotational springs.
PC2 – with CAA	A	Yielding of the internal and external translational springs.
	B	Yielding of the internal rotational springs.
	C	Peak load of the global curve.
	D	Failure of the internal rotational springs.

When the CAA contribution is included (the CAA effect is depicted as a grey area in Fig. 4), the numerical response of both specimens exhibits two main changes. First, the peak load increases significantly, approaching the maximum resistance observed in the tests conducted by Zhou et al. [3]. For PC1, the inclusion of CAA leads to a good match with the experimental peak load, while for PC2 the estimate is significantly improved, but still with an underestimation from the experimental value. At higher load levels, the inclusion of CAA allows the numerical curves to better match the experimental response in the CAA phase, particularly for PC1, while the subsequent CTA branch of PC2 is not captured due to a lack of convergence of the numerical analyses. Despite these improvements, the post-peak response in numerical models remains more fragile than that observed experimentally, especially for large vertical displacements. In PC1, the tests showed a peak mainly dominated by CAA followed by a degradation phase influenced by shear failure of the dowels, yielding of the reinforcements and concrete failure at the outer ends of the beams [3]. The CAA model reproduces the maximum strength and general trend of the CAA phase but predicts a more pronounced drop in strength upon reaching the maximum rotation of the internal springs, without fully capturing the more gradual decay observed experimentally. In PC2, the experimental curve was characterised by

a pronounced CTA, which provides considerable residual load capacity; behaviour that is be reproduced by the simplified numerical model.

The analysis of stress and strain distributions in the fibers of the sections confirms that the damage is mainly localized in the external connections between beams and columns, in agreement with experimental observations. For PC1, with and without CAA, the fibers of the columns remain basically elastic along their entire height, while the damage is concentrated in the external beams in the hogging zone, where concrete crushing and reinforcement yielding occur. The internal sagging connection between beam and column remains largely elastic during collapse, highlighting the critical area of the external connections in determining the onset of failure. This is consistent with the failure of the dowels and local damage to the concrete in the external joints.

A similar pattern is observed for PC2, where the most severe damage again develops at the external beam–column connection. The numerical results show extensive yielding of the beam reinforcement and significant degradation of the surrounding concrete in the hogging region, while the internal joint and the column fibres preserve a mainly elastic behaviour. When CAA is considered, the demand at the external joint increases, as higher axial forces and bending moments are transferred through the arching mechanism, but the internal connection in sagging remains less critical than the external one. Under the examined column-removal scenario, this confirms that the external joints, where hogging bending combines with the shear demand on the dry connections, are the key regions for progressive collapse resistance.

5 CONCLUSIONS

This paper aims to validate the models developed in OpenSeesPy for the progressive collapse and robustness assessment of multi-storey precast concrete frames with dry beam-to-column connections. Beams and columns are represented by nonlinear beam, elements, while joints are idealised through zero-length elements with non-linear translational and rotational springs. The numerical pushdown curves reproduce reasonably well the experimental envelopes and the sequence of governing failure mechanisms in both specimens, with the exposed and hidden corbels. In particular, the inclusion of an analytically derived compressive arch contribution led to peak loads in good agreement with the CAA stage of the experimental tests, although the simplified model could not fully capture the sharp strength degradation and the CTA response observed experimentally at large deformations due to lack of convergence of the numerical analyses.

The use of such simplified model represents a clear advantage for robustness assessment, as the set-up and computational cost are lower compared with more detailed finite element approaches, leaving feasible scenarios for future full-scale simulations. On the other hand, the simplified springs cannot fully capture the complex interaction among the dowel bars, corbels, steel angle cleats, and the surrounding concrete, nor the development of CAA in fully dry connections, which must therefore be accounted for separately. Future work will aim to maintain a simplified modelling approach while evaluating the effects of different beam-to-column connection models, in order to better capture their local behaviour and provide insight into still poorly understood aspects of robustness design.

References

[1] Starossek, Uwe, and Haberland, Marco. 2012. “Robustness of Structures.” International Journal of Lifecycle Performance Engineering 1(1):3–21. doi:10.1504/IJLCPE.2012.051279.

[2] André, João, Anghileri, Mattia, Belletti, Beatrice, Biondini, Fabio, Caspeele, Robby, Demonceau, Jean-François, Izzuddin, Bassam, Martinelli, Paolo, Molkens, Tom, O’Connor, Alan, Parisi, Fulvio, Sio, João, Sousa, Maria Luisa, and Thienpont, Thomas. 2024. Guidance on the Design for Structural Robustness. JRC Science for Policy Report JRC138689. Luxembourg: Publications Office of the European Union. doi:10.2760/525706.

[3] Zhou, Yun, Chen, Taiping, Pei, Yilin, Hwang, Hyeon-Jong, Hu, Xiang, Yi, Weijian, and Deng, Lu. 2019. “Static Load Test on Progressive Collapse Resistance of Fully Assembled Precast Concrete Frame Structure.” Engineering Structures 200:109719. doi:10.1016/j.engstruct.2019.109719.

[4] Ravasini, Simone, Belletti, Beatrice, Brunesi, Emanuele, Nascimbene, Roberto, and Parisi, Fulvio. 2021. “Nonlinear Dynamic Response of a Precast Concrete Building to Sudden Column Removal.” Applied Sciences 11(2):599. doi:10.3390/app11020599.

[5] Dal Lago, Bruno, Gajera, Krunal, and Martinelli, Paolo. 2025. "Robustness of Dry-Assembled Precast Wall and Coupled Wall-Frame High-Rise Structures with Voided Prestressed Slabs." Structural Design of Tall and Special Buildings 34:e2189. doi:10.1002/tal.2189.

[6] Elsanadedy, Hussein, Almusallam, Tarek, Al-Salloum, Yousef, and Abbas, Husain. 2017. "Investigation of Precast RC Beam-Column Assemblies under Column-Loss Scenario." Construction and Building Materials 142:552–71. doi:10.1016/j.conbuildmat.2017.03.120.

[7] Zhu, Minjie, McKenna, Frank, and Scott, Michael. 2018. "OpenSeesPy: Python Library for the OpenSees Finite Element Framework." SoftwareX 7:6–11. doi:10.1016/j.softx.2017.10.009.

[8] Spacone, Enrico, Filippou, Filip, and Taucer, Fabio. 1996. "Fibre Beam–Column Model for Non-Linear Analysis of R/C Frames: Part I. Formulation." Earthquake Engineering & Structural Dynamics 25(7):711–25. doi:10.1002/(SICI)1096-9845(199607)25:7<711::AID-EQE576>3.0.CO;2-9.

[9] Feng, De-Cheng, Wang, Zhun, and Wu, Gang. 2019. "Progressive Collapse Performance Analysis of Precast Reinforced Concrete Structures." Structural Design of Tall and Special Buildings 28(5):e1588. doi:10.1002/tal.1588.

[10] Kent, Dudley Charles, and Park, Robert. 1971. "Flexural Members with Confined Concrete." Journal of the Structural Division 97(7):1969–90. doi:10.1061/JSDEAG.0002957.

[11] Menegotto, Marco, and Pinto, Paolo Emilio. 1973. "Method of Analysis for Cyclically Loaded R.C. Plane Frames Including Changes in Geometry and Non-Elastic Behavior of Elements under Combined Normal Force and Bending." In Proceedings of the IABSE Symposium on Resistance and Ultimate Deformability of Structures Acted on by Well Defined Repeated Loads, Lisbon, Portugal, 15–22.

[12] International Federation for Structural Concrete (fib). 2008. Structural Connections for Precast Concrete Buildings: Guide to Good Practice. fib Bulletin 43. Lausanne: International Federation for Structural Concrete. doi:10.35789/fib.BULL.0043.

[13] El Debs, Mounir Khalil, Miotto, Anamaria, and El Debs, Ana Lúcia de Cresce. 2010. "Analysis of a Semi-Rigid Connection for Precast Concrete." Proceedings of the Institution of Civil Engineers – Structures and Buildings 163(1):41–51. doi:10.1680/stbu.2009.163.1.41.

[14] Elliott, Kim, Davies, Gwynne, Ferreira, Marcelo, Gorgun, Halil, and Mahdi, A. 2003. "Can Precast Concrete Structures Be Designed as Semi-Rigid Frames? Part 2 – Analytical Equations & Column Effective Length Factors." The Structural Engineer 81(16):28–37.

[15] Abbasnia, Reza, and Mohajeri Nav, Foad. 2016. "A Theoretical Method for Calculating the Compressive Arch Capacity of RC Beams against Progressive Collapse." Structural Concrete 17(1):21–31. doi:10.1002/suco.201400119.

Comparative Assessment of Residual Prestress in Prestressed Concrete Bridges through Long-Term Deflection

Giuseppe Zarrella[1], Daniele Losanno[1], Alfred Strauss[2]

[1]Department of Structures for Engineering and Architecture,
University of Naples Federico II,
via Claudio 21, 80125 Naples, Italy

[2]Institute of Structural Engineering, Department of Civil Engineering and Natural Hazards,
University of Natural Resources and Life Sciences,
Gregor-Mendel-Straße 33, 1180 Vienna, Austria

giuseppe.zarrella@unina.it
daniele.losanno@unina.it
alfred.strauss@boku.ac.at

Summary
This paper presents a displacement-based methodology for assessing the residual prestress in existing prestressed concrete (PC) bridges by means of deflection measurements in the unloaded configuration. The novel approach addresses the increasing demand for safety assessment of ageing road infrastructures, for which the direct evaluation of residual prestress can be challenging. To this end, the long-term behaviour of PC structures is investigated through a multilevel framework, including analytical assessment based on *fib* Model Code formulations for time-dependent phenomena, a fully probabilistic numerical approach using finite element (FE) modelling, and a comparison with on-site investigation results obtained from an existing roadway bridge. The results show that the proposed approach is able to provide a reliable estimate of the residual prestress from deflection measurements, both in cases of full knowledge and in scenarios affected by uncertainty in the initial prestress level.

1 INTRODUCTION

The demand for safety assessments and extraordinary maintenance interventions has increased significantly in recent years, as a large portion of the road infrastructure network—constructed mainly after the Second World War—has reached or is approaching to the end of its nominal service life. In this context, extending the service life and ensuring the continued operation of these structures require the execution of targeted on-site investigations and monitoring systems [1].

For prestressed concrete (PC) structures, the level of residual prestress plays a crucial role both in serviceability conditions, such as crack control, and in the safety checks against ultimate limit state, notably shear capacity. Conversely, the flexural capacity is only marginally affected by variations in the residual prestress level [2]. The state of the art of on-site techniques for estimating existing prestress levels mainly relies on semi- or fully destructive methods [3], such as saw-cut [4] or strand-cut tests [5], as well as dynamic [6] or high precision displacement-based techniques [7].

The aim of this paper is to develop a displacement-based technique for assessing the residual prestress level in existing PC bridges by exploiting deflection measurements in the unloaded configuration. To this end, the long-term behaviour of an existing PC bridge is first investigated by adopting a simplified analytical method in accordance with *fib* Model Code (MC) formulations [8]. A fully probabilistic numerical approach based on finite element (FE) modelling is then proposed to account for time dependency and mechanical variability of the input variables. On-site investigations of the roadway bridge provided reference values of both residual prestress and deflection, which permitted a proper FE model validation. The results are compared through a multilevel framework, encompassing analytical, numerical and experimental outcomes, in order to provide a qualitative assessment of the residual prestress under both conditions of full knowledge and uncertainty in the initial prestress level of the case study bridge.

2 BRIDGE CASE STUDY

The PC bridge case study refers to an operating roadway bridge designed in the 1970s. The structure consists of two independent simply supported spans of 33.50 m, with an overall deck width of 9.55 m. Each span is composed of four post-tensioned I-girders with a top slab and a total length of 32.50 m (32.00 m clear span between supports), connected by two transverse diaphragms at the end zones and two intermediate diaphragms Fig. 1 (a), Fig. 1 (b). The prestressing system comprises four tendons arranged in a parabolic profile: two tendons made of 32 wires of Φ7 (Type A), and two tendons made of 42 wires of Φ7 (Type B) (Fig. 2).

The construction stages of the bridge deck included the tensioning of the Type B tendons 7 days after concrete pouring (Stage 1), the tensioning of the Type A tendons at 28 days (Stage 2), and the casting of the longitudinal joints and transverse diaphragms, grouting of the ducts, and laying of the road pavement at 60 days (Stage 3). The design initial jacking stress $\sigma_{p,0}$ was specified at 1050 MPa.

In 2022, approximately 50 years after construction, rehabilitation and upgrading works were carried out, including a 10 cm increase in slab thickness, which modified the cross-sectional properties and slightly affected the applied loads. The measurement of the existing deflection was performed in the unloaded configuration, after the completion of the retrofit interventions during acceptance tests, on a structural configuration different from the original one Fig. 1 (c).

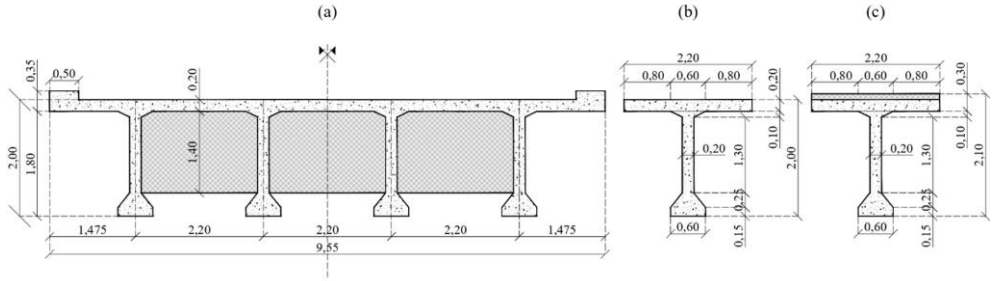


Fig. 1 Geometry of the bridge deck: (a) deck original cross-section, (b) original girder cross-section and (c) strengthened girder cross-section.

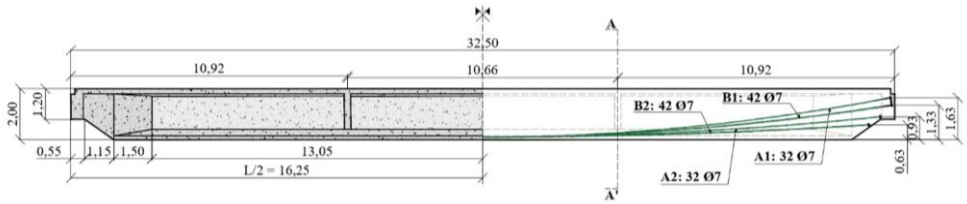


Fig. 2 Longitudinal section of the girder with tendon layout.

The compressive strength of the concrete was evaluated by means of destructive tests on sampling cores, while the elastic modulus E_c and the reduced mechanical properties at curing times lower than 28 days (dd), i.e. $f_c(t_1)$ and $E_c(t_1)$, were obtained in accordance with MC formulations (Table 1).

Table 1 Mechanical properties of the concrete.

f_{cm} [MPa]	E_{cm} [MPa]	$f_{cm}(t_1)$ [MPa]	$E_{cm}(t_1)$ [MPa]
30.7	31234	25.1	28262

The existing deflection of the edge girder was assessed through a topographic survey performed using a LiDAR (Light Detection and Ranging) system, which provided an upward camber $\bar{v}$ = 31.5 mm. The residual prestress was evaluated by means of saw-cut tests carried out on the four external girders of the bridge prior to retrofit interventions, yielding a compressive stress state $\bar{\sigma}_c$ in the lower flange ranging from 4.12 MPa to 6.66 MPa, with a mean value of 5.35 MPa. In terms of residual prestress in

the tendons, these values correspond to a range from 699 MPa to 810 MPa, with a mean value of 753 MPa.

3 ANALYTICAL MODEL

The assessment of the long-term behaviour of PC elements can rely on well-known formulations derived from elastic beam theory and linear viscoelastic theorems. Assuming that the concrete is subjected to a stress state limited to 45% of f_{cm}, the long-term deformations depend on the creep coefficient $\varphi(t,t_0)$, where t denotes the time of observation and t_0 the time of loading.

For the bridge case study, only the original construction stages were considered in the evaluation of $\varphi(t,t_0)$. Instantaneous losses, such as friction, were evaluated in accordance with the MC 2010, while anchorage seating losses were accounted for by assuming an elastic shortening of 5 mm.

Time-dependent phenomena were evaluated following the MC 2010 formulations, with environmental parameters derived from data recorded at the nearest meteorological station. For calibration of the numerical model, the relative humidity RH was directly introduced into the analysis and set equal to 73%, while temperature T effects were neglected. Considering the material properties reported in Table 1, the values of $\varphi(t,t_0)$ are summarised in Table 2.

Table 2 Creep coefficients considered in the analytical approach.

Stage	t [y]	t_0 [dd]	$\varphi(t,t_0)$
1	50	7	2.62
2	50	21	2.18
3	50	60	1.90

Finally, prestress losses due to time-dependent phenomena were evaluated according to Eurocode 2 (i.e., 100% of creep and shrinkage and 80% of prestressing steel relaxation), while deflections were computed using the Age-Adjusted Effective Modulus (AAEM) method, assuming $\chi = 0.8$ [9].

4 FINITE ELEMENT MODEL

4.1 Geometrical model

The finite element model (FEM) of the PC girder was developed using ATENA Science [10], with the geometric and mechanical properties defined in the GiD preprocessor and the analysis performed in ATENA Studio.

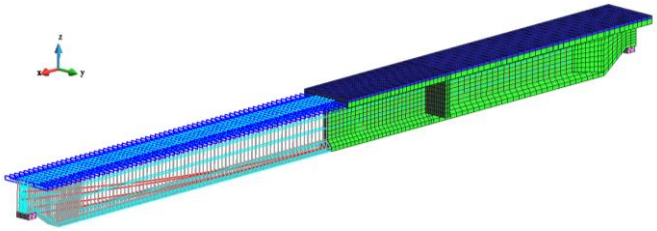


Fig. 3 3D geometry and mesh of the numerical 3D FEM.

The concrete matrix and the supports were modelled using three-dimensional solid elements, while both mild steel and prestressing steel reinforcements were represented by one-dimensional embedded elements. The mesh consists of 24,535 nodes and 5,273 linear elements, including 70 tetrahedral and 12,784 hexahedral elements. The hexahedral elements have a regular uniform size of 30 × 10 × 20 mm along the X, Y, and Z axes, respectively, with an aspect ratio not exceeding 3:1 [11]. Mild steel reinforcements were discretised using a subdivision factor equal to 1, whereas prestressing tendons were discretised with a subdivision length of 0.10 m (Fig. 3).

To reproduce the construction stages up to the measurement of the camber, 11 intervals were defined in GiD and subdivided into load steps (Table 3).

Table 3 Intervals and load steps of the load history.

Interval	Time Span	Load Steps	Description
1	7 dd - 7.1 dd	10	1st Tensioning (tendon type B)
2	7.1 dd – 28 dd	1	Creep
3	28 dd - 28.1 dd	10	2nd Tensioning (tendon type A)
4	28.1 dd – 60 dd	1	Creep
5	60 dd - 60.1 dd	5	Cast of long. joints and transverse beams
6	60.1 dd - 60.2 dd	5	Grouting and asphalt layer
7	60.2 dd -50 y	10	Creep
8	50 y – 50 y 0.1 dd	5	Unloading permanent loads
9	50 y 0.1dd – 50 y 0.2 dd	5	Casting new reinforcing slab
10	50 y 0.2 dd – 50 y 0.3 dd	5	New permanent loads
11	50 y 0.3 dd – 50 y 0.4 dd	5	Shrinkage of the new slab

4.2 Materials

Creep and shrinkage effects were implemented by defining a *Solid Creep Concrete* material based on the MC 2010 formulations, coupled with a three-dimensional elastic material (*CC3DElastIsotropic*), characterised by the elastic modulus E_{cm} and compressive strength f_{cm}, reported in Table 1. The adoption of a perfectly elastic constitutive law for concrete was motivated by two considerations: first, to avoid the occurrence of local damage during tendon stressing at supports; second, to ensure consistency with the assumed linear viscoelastic behaviour of concrete.

For the prestressing tendons, two distinct material definitions were introduced to differentiate between the ungrouted condition at the time of jacking (unbonded tendons) and the grouted condition under service conditions (bonded tendons). For prestressing steel, a bilinear elastoplastic stress–strain constitutive model with hardening was assumed, characterised by a conventional yield stress $f_{p1,k}$ = 1420 MPa, an ultimate stress $f_{p,uk}$ = 1620 MPa, a Young's modulus E_s = 201.1 GPa, and an ultimate strain $\varepsilon_{p,uk}$ = 7.00%. Friction losses were evaluated by adopting a friction coefficient f = 0.19 and a wobble coefficient β = 0.005 rad/m. Mild steel reinforcements were modelled using a one-dimensional bilinear elastoplastic constitutive law with hardening, with mechanical properties derived from a database of laboratory tests performed on rebars with similar properties [12].

4.3 Random variables

Different random variables (RVs) affecting the long-term behaviour of PC girders can be grouped into three categories. The first group includes the mechanical properties of concrete, namely f_c and E_c. The second group comprises the environmental parameters, i.e. T and RH, while the third group includes the design-related parameters, i.e. t_0 and $\sigma_{p,0}$.

Due to the implementation within the SARA framework [13] and the automatic generation of the input files, T is not directly introduced into the numerical model, but it is indirectly accounted for with an equivalent value of the relative humidity $\overline{RH}$ [14]. The adopted approach assumes an inverse relationship between T and RH, with higher T generally associated with lower RH. Based on this assumption, equivalent T–RH pairs are defined to evaluate $\varphi(t,t_0)$ and to identify an $\overline{RH}$ providing the same value of $\varphi(t,t_0)$ according to the MC 2010 formulations. From a probabilistic standpoint, this approximation results in an increased coefficient of variation (CoV) for $\overline{RH}$.

Regarding the $\sigma_{p,0}$, it is not always possible to rely on original design value, either due to incomplete documentation or inaccuracies during jacking operations for post-tensioned tendons. To model this parameter as a RV, a range of realistic design values available in the literature [15][16] was therefore considered and subsequently compared with the effective initial stress $\sigma_{p,0}$.

Concerning the construction stage timing, it is reasonable to assume that the largest variability is associated with the initial prestressing of the tendons, as this stage is characterized by relatively short t_0 values that significantly influence the creep coefficient $\varphi(t,t_0)$. In the present approach, t_0 is not explicitly treated as a RV, but its impact will be addressed in future studies. Based on the above

considerations, a set of four RVs is defined in Table 4, and their mutual dependence is accounted for through a statistical correlation matrix (Table 5) [17].

Table 4 Random variables in FEM.

RVs	Mean	CoV	PDF
f_c	30.7 MPa	14.6%	Lognormal
E_c	31234 MPa	4.9%	Lognormal
$\bar{R}\bar{H}$	72%	26.0%	Normal
$\sigma_{p,0}$	1109 MPa	6.7%	Lognormal

Table 5 Correlation matrix of RVs.

RVs	f_c	E_c	$\bar{R}\bar{H}$	$\sigma_{p,0}$
f_c	1	1	0	0
E_c	1	1	0	0
$\bar{R}\bar{H}$	0	0	1	0
$\sigma_{p,0}$	0	0	0	1

5 INTERPRETATION OF RESULTS

The first simulation was aimed at the validation of the FEM through a deterministic analysis defined by considering the mean values of the RVs in Table 3 together with the prescribed initial prestress $\sigma_{p,0}$ = 1050 MPa from original reports (hereafter referred to as the "DESIGN" configuration). The numerical results were then compared with those obtained from the analytical approach and with the available experimental deflection. The comparison focused on the long-term deflection Fig. 4 (left) and on the residual prestress in the equivalent tendon Fig. 4 (right).

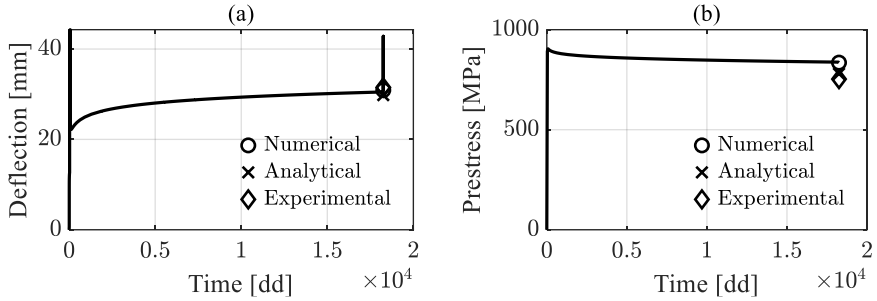


Fig. 4 Deterministic numerical model vs analytical approach: (left) deflection and (right) residual prestress.

Table 6 Multilevel comparison in final configuration of the case-study bridge (Interval 11).

Method	Deflection [mm]	ε [%]	Prestress [MPa]	ε [%]
Experimental	31.5		753	
Analytical	29.8	-5.4%	780	+3.6%
Numerical	30.5	-3.2%	837	+11.1%

The multilevel comparison reported in Table 6 highlights a good agreement among the different methods at the time of measurement, thus validating the numerical model for subsequent probabilistic analyses. In addition, only limited differences in deflection and residual prestress were observed at the end of Interval 11 compared to Interval 7 (Table 3), due to comparable permanent load variations resulting in a deflection increase of around 0.4 mm (+1.3%). Based on this evidence, and considering

that these construction stages (#8 to #11) are characterised by purely elastic behaviour, Intervals 8 to 11 were excluded from subsequent analyses in order to reduce the computational effort.

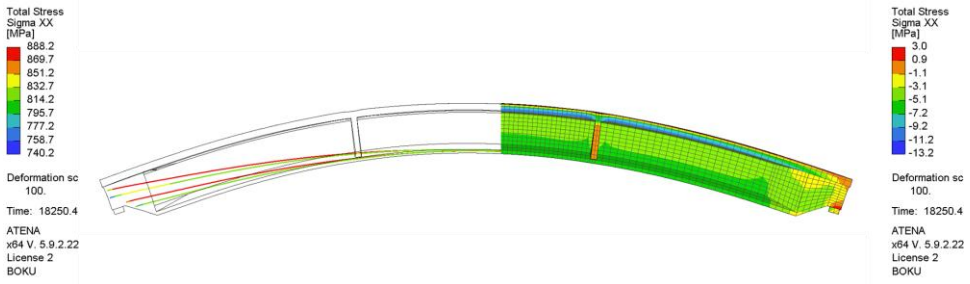


Fig. 5 Numerical results in the final FEM configuration (Interval 11).

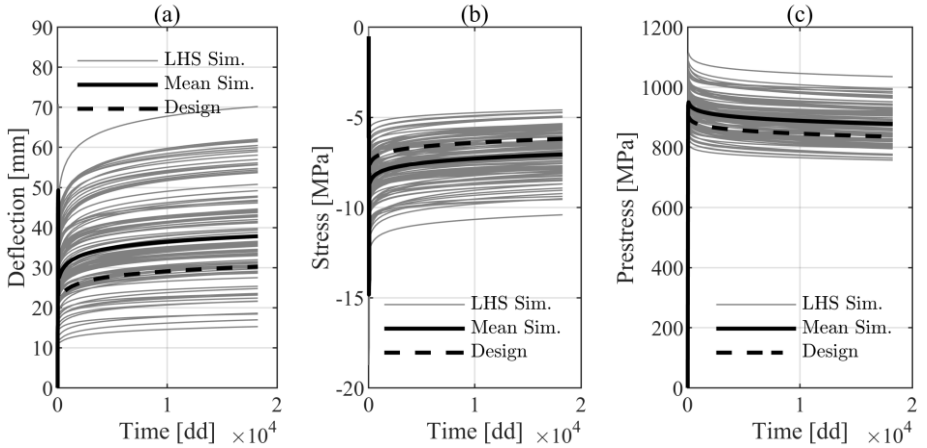


Fig. 6 Output from 100 FEA simulations: (a) deflection, (b) stress-state in the saw-cut test section and (c) residual prestress in the equivalent tendon.

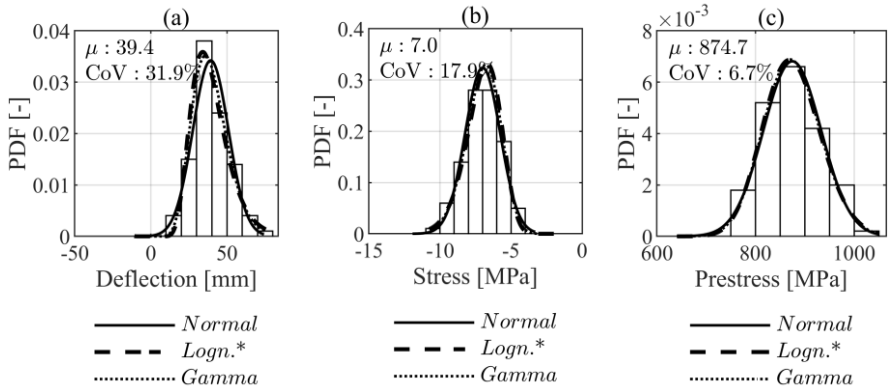


Fig. 7 Scatter plots and fitted PDFs at time of observation: (a) deflection, (b) stress-state in the saw-cut test section and (c) residual prestress in the equivalent tendon.

The probabilistic analysis was carried out generating 100 simulations using the Latin Hypercube Sampling (LHS) technique. The results of the simulations, together with the comparison with the mean-value analysis (MEAN) and with the calibrated numerical model (DESIGN), are presented in Fig. 6 in terms of deflection, concrete compressive stress at the flange level, and average residual prestress along the tendon. The corresponding scatter distributions of the control variables are shown in Fig 7. The

probability density functions (PDFs) that best fit the monitored data were identified using the Kolmogorov–Smirnov test implemented in MATLAB [18] (through a KS parameter), and the corresponding results are reported in Table 7.

The best fitting PDFs are obtained with lognormal distributions, as indicated by the highest KS statistic. Based on these results, while the long-term deflection is associated with a relatively high CoV (≈ 32%), the residual prestress exhibits a CoV of approximately 7%. This indicates a reduced sensitivity of the residual prestress to time-dependent phenomena, with its value being mainly affected by the initial prestress level. It is also worth noting that, whether using the actual design value or a dataset of realistic values, both measured deflection and residual prestress can be accurately estimated.

Table 7 Kolmogorov–Smirnov test.

Data	PDF	Mean [μ]	Std. deviation [σ]	CoV	KS
Deflection [mm]	Lognormal	39.4	12.6	31.9%	0.80
Stress [MPa]	Lognormal	7.00	1.25	17.9%	0.97
Prestress [MPa]	Lognormal	874.7	58.4	6.7%	0.99

For the assessment of residual prestress, once the residual deflection is measured, it is possible to determine the percentile x corresponding to the measured deflection $\bar{v}$ and infer the corresponding residual prestress σ_p. Adopting the PDFs defined in Table 7, Table 8 reports the corresponding results together with the computed errors relative to the mean values obtained from on-site measurements.

Table 8 Residual prestress via deflection measurement.

	Deflection [mm]	Stress [MPa]	Prestress [MPa]
Percentile	28.7%	28.7%	28.7%
Assessed	31.5	6.24	841
Measured	31.5	5.25	753
Error		18.8%	11.7%

It is important to note that the PDFs were obtained by assuming the initial prestress value as a RV, rather than adopting the design value, thus simulating the case of limited knowledge of the bridge. If this information is known, the accuracy of the results can be further improved, as shown in Table 6.

6 CONCLUSIONS

This study focused on the long-term behaviour of prestressed concrete (PC) bridges through a multilevel analysis combining residual prestress levels and deflection in the unloaded configuration. The methodology integrates analytical formulations based on the *fib* Model Code, fully probabilistic finite element (FE) simulations, and on-site experimental investigations.

The application of the methodology to a 50-year-old roadway bridge demonstrated the influence of different random variables including environmental and mechanical parameters, on the calculation of residual prestress and deflection, even under limited knowledge of the initial prestress of the tendons. Probabilistic results showed that long-term deflection is highly sensitive to time-dependent phenomena (CoV ≈ 32%), whereas residual prestress exhibits lower variability (CoV ≈ 7%), being mainly controlled by the initial prestress level. The comparison between analytical, numerical and experimental outcomes confirmed the accuracy and robustness of the proposed framework.

Overall, the study highlights the potential of combining deflection-based measurements with probabilistic modelling as a non-destructive and practical tool for evaluating residual service life of ageing infrastructures. Furthermore, the methodology will be explored for PC bridges with different levels of knowledge, including scenarios with limited information on the construction stages and spatial variability of material properties at the deck level, providing a flexible approach for real-world applications in operation and safety management.

References

[1] Strauss, A., Zimmermann, T., and Bergmeister, K. 2023. "Data based reliability and risk based assessment for service life extension of structures." *Civil Engineering Practice and Application* 11(1): e1993. https://doi.org/10.1002/cepa.1993.

[2] Losanno, D., Galano, S., Parisi, F., Pecce, M. R., and Cosenza, E. 2024. "Experimental investigation on nonlinear flexural behavior of post-tensioned concrete bridge girders with different grouting conditions and prestress levels." *Journal of Bridge Engineering* 29(3). https://doi.org/10.1061/JBENF2.BEENG-6466.

[3] fib – International Federation for Structural Concrete. 2022. *Management of Post-Tensioned Bridges.* fib Bulletin No. 110. Lausanne, Switzerland: fib.

[4] Chávez, A. A., Gonzalez-Libreros, J., Wang, C., Capacci, L., Biondini, F., Elfgren, L., and Sas, G. 2024. "Assessment of residual prestress in existing concrete bridges: The Kalix Bridge." *Engineering Structures* 311: 118194. https://doi.org/10.1016/j.engstruct.2024.118194.

[5] Losanno, D., Galano, S., and Parisi, F. 2024. "Influence of strand rupture on flexural behavior of reduced-scale prestressed concrete bridge girders with different prestressing levels." *Engineering Structures* 301: 117358. https://doi.org/10.1016/j.engstruct.2023.117358.

[6] De Angelis, A., Losanno, D., Parisi, F., and Pecce, M. R. 2024. "Identification of modal parameters of scaled bridge PC beams by OMA dynamic tests." *Journal of Bridge Engineering* 29(8): 04024051. https://doi.org/10.1061/JBENF2.BEENG-6763.

[7] Bonopera, M., and Chang, K.-C. 2021. "Novel method for identifying residual prestress force in simply supported concrete girder bridges." *Advances in Structural Engineering* 24(2): 13694332211022067. https://doi.org/10.1177/13694332211022067

[8] Fédération Internationale du Béton (fib). 2010. *fib Model Code for Concrete Structures 2010.* Berlin, Germany: Ernst & Sohn.

[9] European Committee for Standardization (CEN). 2004. *Eurocode 2: Design of Concrete Structures – Part 1-1: General Rules and Rules for Buildings (EN 1992-1-1).* Brussels, Belgium: CEN.

[10] Červenka, V., Jendele, L., and Červenka, J. 2016. *ATENA Program Documentation – Part 1: Theory.* Prague, Czech Republic: Červenka Consulting.

[11] Strauss, A., Krug, B., Slowik, O., and Novák, D. 2018. "Combined shear and flexure performance of prestressed concrete T-shaped beams: Experiment and deterministic modeling." *Structural Concrete* 19(1): 16–35.

[12] Verderame, G. M., Ricci, P., Esposito, M., and Sansiviero, F. C. 2011. *Le caratteristiche meccaniche degli acciai impiegati nelle strutture in c.a. realizzate dal 1950 al 1980.* Paper presented at the XXVI Convegno Nazionale AICAP, Padua, Italy, May 19–21. (in Italian).

[13] Havlásek, P., and Pukl, R. 2015. *SARA Studio – User's Manual.* Prague, Czech Republic: Červenka Consulting s.r.o.

[14] Rahimi-Aghdam, S., Bažant, Z. P., and Cusatis, G. 2019. "Extended microprestress–solidification theory (XMPS) for long-term creep and diffusion size effect in concrete at variable environment." *Journal of Engineering Mechanics* 145(2): 04018125. https://doi.org/10.1061/(ASCE)EM.1943-7889.0001559.

[15] Associazione Nazionale Italiana Cemento Armato Precompresso (ANICAP). 1966. *Realizzazioni italiane in cemento armato precompresso 1962–1966.* Paper presented at the V Congresso Internazionale del Precompresso (FIP), Paris, France, 1966. (in Italian)

[16] Associazione Nazionale Italiana Cemento Armato Precompresso (ANICAP). 1970. *Realizzazioni italiane in cemento armato precompresso 1966–1970.* Paper presented at the 6th Congresso Internazionale del Precompresso (FIP), Prague, Czechoslovakia, 1970. (in Italian).

[17] Slowik, O., Novák, D., Novák, L., Strauss, A., et al. 2021. "Stochastic modelling and assessment of long-span precast prestressed concrete elements failing in shear." *Engineering Structures* 228: 111500. https://doi.org/10.1016/j.engstruct.2020.111500.

[18] The MathWorks, Inc. 2024. *MATLAB (Release R2024b)* [Software]. Natick, MA: The MathWorks, Inc.

Repair strategies for marine reinforced concrete structures: Mechanisms, materials and nature-based solutions

Amruthamol Nellinilkunnathil Ashokkumar[a,b], Emilio Bastidas-Arteaga[a] and Panagiotis Spyridis[b]

[a]*Laboratoire des Sciences de l'Ingénieur pour l'Environnement (LaSIE),*
La Rochelle Université,
23 Avenue Albert Einstein, 17031 La Rochelle, France

[b]*Faculty of Agriculture, Construction and Environment,*
University of Rostock,
Justus-von-Liebig-Weg 6, 18059 Rostock, Germany

Abstract

Marine reinforced concrete (RC) structures are highly vulnerable to chloride ingress, carbonation, and other deterioration mechanisms that accelerate corrosion and reduce service life. This review synthesizes current repair and protection strategies by relating deterioration mechanisms to appropriate repair approaches. Conventional methods, including surface protection, electrochemical techniques, and composite strengthening, are critically compared with emerging sustainable solutions such as microbially induced calcium carbonate precipitation, enzyme-induced calcium carbonate precipitation, and bio-based coatings. The reviewed strategies are assessed in terms of repair mechanism, applicability to marine exposure conditions, durability, and implementation constraints. The review identifies key research gaps in coupled deterioration, repair compatibility, and long-term validation, highlighting hybrid and sustainable strategies for resilient, minimally disruptive rehabilitation of marine RC structures.

1 INTRODUCTION

RC structures in marine environments, such as port infrastructures, seawalls, jetties, breakwaters, quay walls, offshore platforms, and coastal bridges, are exposed to aggressive environmental actions that accelerate deterioration compared to inland structures. Chloride-rich seawater, cyclic wetting-drying, wave-induced abrasion, biogenic activity, and climate-driven factors lead to complex deterioration mechanisms. These mechanisms include chloride penetration, reinforcement corrosion, sulfate attack, carbonation, abrasion, freeze-thaw, fatigue, and microbial-induced corrosion[1], [2]. These effects manifest as cracking, spalling, delamination, cover loss, reinforcement section loss, and reduction in stiffness and load-carrying capacity [1]-[3].

Conventional repairs, such as patching, epoxy injection and protective coatings, often show limited long-term performance in splash and tidal zones, motivating durability-focused solutions. Recent developments have expanded toward performance-driven repair technologies, including composite-based strengthening (e.g., FRP wraps/laminates and jacketing), electrochemical approaches (cathodic protection and chloride extraction), and low-permeability overlays to mitigate corrosion and restore structural capacity [1].

Nature-based and bio-inspired strategies are emerging as sustainable alternatives, enhancing crack sealing, reducing aggressive ion transport, and improving long-term durability. These include microbial- and enzyme-induced calcite precipitation (MICP/EICP) and natural fiber-reinforced overlays. While promising, field implementation remains limited due to variability in performance, exposure validation, and practical deployment challenges [1], [2].

This review synthesizes repair strategies for marine RC structures by examining deterioration mechanisms, damage patterns, and corresponding repair materials and methods, with special emphasis on nature-based and sustainable technologies. Comparative discussions highlight advantages, constraints, and future directions for resilient and durable marine concrete repairs.

2 DAMAGE AND DETERIORATION MECHANISMS OF REINFORCED CONCRETE IN MARINE ENVIRONMENTS

The marine environment is particularly aggressive due to the presence of chloride-rich seawater, cyclic wetting–drying conditions, high humidity, dissolved oxygen, sulphates, and, in certain climates, freeze–thaw cycles. These factors act individually and synergistically, leading to deterioration of both the concrete matrix and embedded steel reinforcement [1]-[3]. Table 1 summarizes the principal deterioration mechanisms affecting reinforced concrete structures in marine environments, together with their influencing factors and resulting consequences.

Table 1 Comparative summary of the deterioration mechanisms affecting RC in marine environments

Mechanism	Description	Influencing Factors	Effects / Consequences	Refs.
Chloride-induced corrosion	Penetration of chloride ions disrupts passive film on steel, initiating electrochemical corrosion	Chloride concentration, permeability, cover depth, cracking, moisture, oxygen availability	Pitting corrosion, cracking, spalling, bond loss, reduction of steel cross-section	[1], [2], [3]
Carbonation-induced corrosion	CO_2 reacts with hydration products, reducing pH and causing steel depassivation	Relative humidity (50–80%), CO_2 concentration, permeability, temperature	Uniform corrosion, cracking, reduced durability	[2], [4]
Cracking (physical)	Cracks from mechanical/thermal/shrinkage effects	Load level, thermal gradients, shrinkage, restraint	Increased permeability, accelerated chloride ingress	[3], [4]
Corrosion–fatigue interaction	Combined cyclic loading and corrosion damage	Stress range, chloride level, cover thickness, load frequency	Reduced fatigue life, microcrack growth	[5]
Sulphate attack	Sulphates react to form gypsum and ettringite causing expansion	Sulphate concentration, permeability, cement composition	Expansion, cracking, strength loss	[1]
Magnesium attack	Mg^{2+} reacts causing decalcification	Magnesium concentration, exposure zone	Matrix softening, cohesion loss	[1]
Freeze–thaw damage	Ice formation causes internal stresses	Saturation degree, temperature cycles, salt presence	Scaling, cracking, spalling	[4]
Alkali–silica reaction	Alkalis react with reactive silica forming expansive gel	Moisture, reactive aggregates, alkali content	Internal cracking, permeability increase	[1], [4]
Leaching / decalcification	Dissolution of calcium compounds	Long-term exposure, water flow	Increased porosity, alkalinity loss	[1], [3]
Biogenic deterioration	Microbial activity alters surface chemistry	Biological growth, oxygen, sulphates	Surface degradation, acidification	[2], [3]

2.1 Chloride-Induced Corrosion of Reinforcement

Chloride ingress is the most critical deterioration mechanism in marine RC structures [1], [2], occurring via diffusion, capillary absorption, permeation, and convection, which are intensified in splash and tidal zones by cyclic wetting and drying [1]. When chloride concentration at the steel surface exceeds a

critical threshold, the passive film is disrupted, initiating localized pitting corrosion even in non-carbonated concrete [2], [3]. Resulting corrosion products generate expansive stresses, causing cracking, delamination, spalling, bond loss, and reduction of steel cross-section [1], [2]. Corrosion initiation also depends on permeability, cover depth, cracking, and moisture availability, emphasizing the role of material quality and structural detailing [3].

2.2 Carbonation-Induced Corrosion

Carbonation occurs when atmospheric CO_2 diffuses into concrete, reacts with hydration products, and lowers pore solution alkalinity [2], [4]. As pH drops from highly alkaline to ~8–9, the passive layer destabilizes, enabling corrosion in the presence of moisture and oxygen. Carbonation rates depend on relative humidity, temperature, CO_2 concentration, and concrete permeability, with optimal progression at 50–80% RH typical of coastal zones [4]. Although slower than chloride ingress, carbonation can severely accelerate corrosion when combined with chlorides [2].

2.3 Cracking and Physical Damage

Cracking in marine RC structures may arise from mechanical loading, thermal effects, shrinkage, autogenous deformation, or corrosion expansion [4]. While cracking may initially be structural or service-related, it becomes a critical durability concern because it increases permeability and provides preferential pathways for aggressive agents.

Crack depth is often more influential than crack width, as cracks reaching reinforcement significantly accelerate localized corrosion and deterioration [3].

2.4 Fatigue and corrosion–fatigue interaction

Marine structures such as piles, decks, and quay elements are often subjected to repeated cyclic actions from waves, currents, and operational activities. Mechanical fatigue induces microcracking and stiffness degradation over time.

In marine exposure, fatigue interacts strongly with chloride-induced corrosion. Corrosion reduces reinforcement cross-sectional area and bond performance, while cyclic stresses accelerate crack propagation from corrosion pits. Corrosion–fatigue models indicate that fatigue life decreases with increasing chloride concentration, diffusion coefficient, stress range, and load frequency, and increases with greater cover thickness and higher critical chloride thresholds[5].

2.5 Chemical and Physical Matrix Deterioration

Sulphate ions react with calcium hydroxide and aluminate phases to form gypsum and ettringite, causing expansion, cracking, and strength loss [1]. Magnesium ions aggravate deterioration by forming brucite and magnesium silicate hydrate, leading to decalcification and loss of cohesion, mainly affecting submerged and tidal elements [1]. In cold coastal regions, freeze–thaw cycles generate internal stresses from water expansion, resulting in microcracking, scaling, and spalling, with salts intensifying damage in splash and tidal zones through crystallization pressures and osmotic effects [4].

2.6 Influence of Marine Exposure Zones

Marine RC structures are typically classified into atmospheric, splash/tidal, and submerged exposure zones [1]. The splash and tidal zones are generally the most aggressive due to alternating wetting–drying cycles, high oxygen availability, and chloride accumulation. Atmospheric zones are more susceptible to carbonation and airborne chlorides, while submerged zones are dominated by diffusion-controlled chemical attack with relatively lower corrosion rates [1], [3].

2.7 Secondary and Long-Term Chemical Deterioration

In marine environments, alkali–silica reaction between pore-solution alkalis and reactive aggregates can form expansive gels, causing internal stresses, cracking, increased permeability, and accelerated chloride ingress, often acting synergistically with carbonation and corrosion [1], [4]. Long-term seawater exposure may also leach calcium hydroxide, decalcifying hydration products, increasing porosity, reducing alkalinity, and weakening the cement matrix [1], [3]. Additionally, biological activity from algae, bacteria, and sulphate-reducing microorganisms can locally modify surface chemistry, promote acidification, and contribute to material degradation, interacting with other deterioration mechanisms over time [2], [3].

3 CATEGORIES OF REPAIR STRATEGIES

Chloride ingress to the reinforcement is a dominant driver of corrosion, followed by cracking, spalling and progressive loss of cross-section and serviceability. A recurring challenge in practice is the "repair of repairs", where repaired zones fail prematurely due to incompatibility, inadequate surface preparation, and insufficient durability performance under marine exposure [6], [7]. Therefore, repair strategy selection must focus not only on strength restoration, but also on durability, compatibility with substrate concrete, and long-term performance in harsh marine conditions.

3.1 Surface protection and coating-based repair strategies

Surface coating are widely applied in marine RC structures to limit seawater-driven deterioration mechanisms such as chloride ingress, sulfate attack, and physical erosion [8], [9]. They primarily protect external concrete surfaces, rather than embedded reinforcement [8]. The key performance targets for coatings in marine RC include low permeability, high adhesion, abrasion resistance, and durability under wet–dry cycling and seawater exposure [8], [9].

Polymer coatings, including epoxy and acrylic coatings are reported to form highly impermeable barriers, and polyurethane coatings can reduce the chloride diffusion coefficient by up to 86%, indicating strong resistance against chloride ingress through pores and cracks [8]. However, polymer systems may require rigorous surface preparation and may have durability limitations depending on exposure and aging [8]. Recent multifunctional waterborne polyurethane–carbon fiber coatings (WPU/CF) provide additional acid, salt, and UV resistance, as well as self-cleaning properties, and represent a lower-cost alternative for harsh offshore conditions [10].

Alkali-activated / geopolymer-based coatings are explored as sustainable alternatives due to chemical resistance and durability. [9] noted that geopolymer coatings can provide marine corrosion protection, but their wider coating use is restricted by drying shrinkage, especially in metakaolin-based systems, which can induce microcracks and accelerate ion ingress. To address this, [9] synthesized organic-modified metakaolin geopolymer (MG) composites using waterborne epoxy resin (WR: 10–30%) and silane coupling agents (SCA: 1%), which significantly reduced drying shrinkage and improved adhesion and abrasion resistance, and enhanced chloride protection, though carbonation resistance still requires improvement [9].

Bio-based and natural sustainable marine coatings offer sustainability-aligned alternatives to conventional antifouling/anticorrosion systems that rely on toxic biocides and persistent additives. [11] reviewed bio-based polymers, plant-derived oils, marine biopolymers (e.g., chitosan and alginate), and eco-friendly additives developed for marine exposure, highlighting both antifouling and corrosion-protection mechanisms, but challenges remain regarding long-term durability, mechanical stability, scalability, and certification [11].

3.2 Electrochemical Repair Strategies

Electrochemical repair methods are widely applied in chloride-contaminated reinforced concrete, particularly when deterioration is extensive and complete concrete removal is impractical. In marine structures, conventional patch repair frequently leads to recurring deterioration due to residual chloride contamination and the formation of galvanic cells at patch interfaces (incipient anode effect) [7], [12]. Electrochemical strategies address reinforcement corrosion by modifying the steel's electrochemical condition through polarization or by altering the surrounding concrete chemistry, thereby extending service life with minimal removal of sound material [12].

Cathodic protection (CP) suppresses anodic dissolution by supplying protective current to the reinforcement and is considered the only technique capable of halting corrosion without full concrete replacement [13], [14]. Systems include impressed current (ICCP), galvanic/sacrificial (GCP/SACP), and hybrid configurations. ICCP employs an external power source and is suitable for widespread deterioration but requires continuous monitoring and durable anode systems. Galvanic systems rely on sacrificial metals such as zinc, offering simpler installation with limited maintenance but reduced lifespan control. Hybrid systems (HCP) combine short-term impressed current with long-term galvanic protection, balancing durability and monitoring demands, and have demonstrated effective service-life extension in marine bridge applications [15].

Electrochemical Chloride Extraction (ECE) and realkalization drive chlorides away from steel and restore alkalinity in carbonated concrete. ECE can remove 50–90% of chlorides but requires higher current densities, which may risk hydrogen evolution or microstructural changes [12]. Hybrid field

applications combining ECE with sacrificial anodes provide both temporary and long-term corrosion mitigation [15].

3.3 Composite-based repairs

Fiber reinforced polymer (FRP) systems are widely used in marine RC structures because they provide corrosion resistance and allow strengthening without major section replacement [16]. They enhance bending and shear capacity, confine structural elements, and act as a barrier against water, oxygen, and chloride ingress. Corrosion-induced deterioration is especially severe in splash zones, making FRP a practical choice for rehabilitation. Installation can be challenging in submerged or partially submerged conditions, with prepreg systems suitable for mostly dry surfaces and wet layup systems often preferred underwater. Surface preparation like removing debris, marine organisms, and corrosion products, is critical for proper bonding and long-term performance. Techniques like vacuum bagging or pressure bagging can improve resin compaction and adhesion, ensuring durability [16].

3.4 Nature-based repair strategies

Nature-based repair strategies aim to improve sustainability and compatibility by leveraging biologically driven mineral formation or renewable materials to enhance crack sealing, durability, and corrosion resistance. Their value for marine RC lies in their potential to provide minimally disruptive repair functions, especially for crack sealing and surface protection, although their long-term performance under realistic marine cycling is still less established than conventional engineered systems.

3.4.1 Biomineralization-based self-repair of concrete cracks

Biomineralization-based self-healing concrete involves microorganisms or enzymes inducing calcium carbonate ($CaCO_3$) precipitation within cracks during service, enabling autonomous or semi-autonomous crack sealing. Unlike polymeric sealants and grouts, these systems rely on mineral formation that is chemically compatible with cementitious matrices. According to [17], biomineralized self-healing systems can repair cracks up to ~2.0 mm, and may lead to substantial mechanical enhancement of strength increases up to 135% under optimized laboratory conditions [17].

3.4.2 MICP

Among biomineralization routes, ureolysis-based microbial-induced calcite precipitation (MICP) remains the most widely investigated due to its relatively high efficiency and controllability. In bacterial MICP, negatively charged bacterial cell walls and extracellular polymeric substances act as nucleation sites, attracting Ca^{2+} and promoting $CaCO_3$ deposition that bridges and seals crack faces. [17] states that microbial action can provide repeated healing potential when moisture and oxygen become available, supporting long-term durability improvement beyond single-event sealing [17].

Fungal biomineralization is also discussed as an emerging route, benefiting from filamentous growth and high environmental tolerance. Fungi can generate organic acids that dissolve Ca-bearing phases (releasing Ca^{2+}), followed by pH rise and $CaCO_3$ precipitation when supersaturation is reached. Several fungal strains have demonstrated healing of cracks on the order of ~1.3 mm, with reported improvements in strength and durability-related indicators (e.g., water absorption reduction and improved chemical resistance). However, fungal repair is still considered exploratory compared with bacterial MICP because of slower growth kinetics and uncertainties related to long-term stability and compatibility with cementitious substrates [17].

3.4.3 EICP

Enzyme-induced calcium carbonate precipitation (EICP**)** is positioned as a practical alternative to microbial systems, where urease is supplied directly (often from plant sources) to catalyze urea hydrolysis and carbonate generation, followed by $CaCO_3$ precipitation in the presence of calcium ions. Because EICP does not rely on living organisms, it avoids biosafety concerns and can reduce sensitivity to oxygen availability. [17] note that EICP can offer fast repair kinetics (sometimes within 24 h–7 days depending on system design), with reported crack closure and significant recovery of compressive strength using plant-derived urease sources [17]. At the same time, the review appropriately cautions that EICP should not be treated as "fully green" by default, because urea hydrolysis generates NH_4^+/NH_3 and can contribute to nitrogen pollution if not managed properly [17]. This is particularly important

when positioning EICP for marine/coastal infrastructure, where nutrient release could raise environmental compliance concerns [17].

4 DISCUSSION

Across the reviewed strategies, marine RC repair performance is controlled not only by strength restoration but by transport resistance, compatibility with the substrate concrete, and stability under cyclic splash/tidal exposure. Barrier-type surface systems (polymer/cementitious/bituminous and geopolymer-based coatings) can delay chloride ingress but remain vulnerable to mechanical damage, ageing, and application-quality issues, and they cannot address pre-existing internal chloride contamination. Electrochemical approaches (ICCP, galvanic and hybrid CP, and temporary ECE treatments) directly target reinforcement corrosion and are therefore effective for chloride-contaminated structures, although their performance depends on exposure-zone moisture/resistivity, monitoring requirements, and special constraints for prestressed members. Composite strengthening methods such as FRP provide rapid strengthening and protection but are strongly limited by bond durability and underwater installation reliability. Nature-based concepts including biomineralization (MICP/EICP), seaweed-derived biopolymers and natural-fibre overlays offer sustainability advantages and crack-control potential, yet most evidence remains laboratory-scale or non-marine, and robust field demonstrations and standardized durability assessment protocols are still limited. Table 2 compares the principal repair and protection strategies for marine reinforced concrete structures, highlighting their mechanisms, suitable marine exposure zones, advantages, and limitations.

Table 2 Comparison of repair and protection strategies for marine RC structures

Repair strategy	Mechanism	Marine exposure zone	Advantages	Limitations
Polymer-based surface coatings	External barrier to reduce chloride/water ingress	Atmospheric, splash (also tidal if abrasion not extreme)	Strong permeability reduction, rapid protection, can significantly reduce chloride transport	Requires excellent surface preparation, aging/UV degradation, abrasion damage in splash zone
Geopolymer /alkali-activated coatings	Low-carbon barrier layer + chemical resistance	Atmospheric/splash	Potentially lower CO_2, chemical resistance, can be designed dense	Drying shrinkage/microcracking risk (esp. metakaolin systems), needs optimisation for carbonation resistance
Bio-based/natural marine coatings	Eco-friendly antifouling + corrosion protection	Mainly atmospheric/splash (emerging)	Lower toxicity vs biocide systems, aligns with environmental regulations	Limited long-term field data, durability under UV/abrasion, scaling/certification barriers
ICCP	Arrest corrosion by polarizing steel	All zones	Most effective long-term corrosion control, works even with residual chlorides	Needs power supply + monitoring, installation complexity, anode durability issues
GCP/SACP	Local corrosion control without external power	Patch zones, localized repairs	Simple, good for preventing incipient anode at patch edges	Limited current output, uncertain life, sensitive to moisture/resistivity, possible passivation
HCP	Short impressed phase + long-	Splash/tidal	Practical compromise: early "boost" + reduced	Design complexity, performance depends on

	term galvanic phase		long-term maintenance	exposure zoning and monitoring
ECE	Temporary chloride removal + repassivation	Chloride-contaminated zones	Can reduce chlorides without full concrete removal	High current risks (microstructural damage, debonding), careful control needed
FRP composite wraps/jackets	Strengthening + barrier effect, confinement and crack control	Splash/tidal/submerged (with suitable installation method)	High strength-to-weight, corrosion resistant, adaptable for urgent repairs	Bond quality critical, underwater installation challenges, surface preparation essential
MICP	Crack sealing by biomineralization	Mainly crack sealing in service (emerging for marine)	Autonomous/semi-autonomous healing, compatibility with cementitious matrix	Environmental sensitivity, nutrient/ammonia concerns (ureolysis route), scaling challenges
EICP	Rapid $CaCO_3$ precipitation without living bacteria	Crack filling/surface sealing	Faster kinetics, avoids live bacteria handling	Urea hydrolysis byproducts (NH_4^+/NH_3), limited data on performance under cyclic chloride exposure and tidal wet–dry conditions

5 CONCLUSIONS

This review synthesized deterioration mechanisms in marine reinforced concrete (RC) infrastructure and examined repair and retrofit strategies with emphasis on minimally disruptive and sustainable solutions suitable for aggressive exposure zones.

Marine deterioration is governed by coupled actions rather than a single mechanism. Chloride-induced corrosion remains the dominant driver of damage, but its progression is strongly accelerated by cracking, wetting–drying cycles, oxygen availability, and secondary chemical/physical processes such as carbonation, sulphate–magnesium attack, freeze–thaw/salt crystallization, and biogenic effects. The splash and tidal zones consistently emerge as the most severe environments due to simultaneous chloride accumulation, cyclic moisture exchange, and mechanical actions, which together increase transport and destabilize repair interfaces.

Across all categories, durability depends not only on material strength but on interface performance and exposure compatibility. Effective strategy selection therefore requires alignment with (i) damage state, (ii) exposure severity, and (iii) practical constraints such as access, downtime, and monitoring capacity. Hybrid approaches combining ingress control, corrosion mitigation, and crack management appear most promising for long-term service life in splash and tidal conditions.

Key research gaps include: (1) evaluation under coupled marine deterioration rather than single-factor testing; (2) improved bond and dimensional compatibility metrics for overlays and coatings; (3) long-term cracked-state transport and corrosion assessment; and (4) development of standardized durability and service-life frameworks applicable to both conventional and low-carbon repair systems. Addressing these gaps is essential for transitioning from short-term restoration toward resilient and sustainable marine repair design.

Acknowledgements

This work has benefited from State aid managed by the Agence Nationale de la Recherche under the Plan France 2030, bearing the reference ANR-19-GURE-0007 EU-CONEXUS Plus, and is co-funded by the European Union as part of the Horizon Europe programme, Marie Sklodowska-Curie Actions call COFUND 2023 and under the Grant Agreement N°101179124.

References

[1] Qu, Fulin, Li, Wengui, Dong, Wenkui, Tam, Vivian W. Y., and Yu, Tao. 2021. "Durability deterioration of concrete under marine environment from material to structure: A critical review." *Journal of Building Engineering* 35:102074. doi:10.1016/j.jobe.2020.102074.

[2] James, Amala, Bazarchi, Ehsan, Chiniforush, Alireza A., Panjebashi Aghdam, Parinaz, Hosseini, M. Reza, Akbarnezhad, Ali, Martek, Igor, and Ghodoosi, Farzad. 2019. "Rebar corrosion detection, protection, and rehabilitation of reinforced concrete structures in coastal environments: A review." *Construction and Building Materials* 224:1026–1039. doi:10.1016/j.conbuildmat.2019.07.250.

[3] Melchers, Robert E. 2020. "Long-Term Durability of Marine Reinforced Concrete Structures." *Journal of Marine Science and Engineering* 8(4):290. doi:10.3390/jmse8040290.

[4] Ma, Jiwei, Yang, Qiuwei, Peng, Xi, and Xia, Kangshuo. 2025. "Review on Durability Deterioration and Mitigation of Concrete Structures." *Coatings* 15(9):982. doi:10.3390/coatings15090982.

[5] Shao, Wei, Wang, Yongxin, and Shi, Danda. 2022. "Corrosion-fatigue life prediction of reinforced concrete square piles in marine environments." *Engineering Failure Analysis* 138:106324. doi:10.1016/j.engfailanal.2022.106324.

[6] Ghasemzadeh, Farnam, Sajedi, Siavash, Shekarchi, Mohammad, Layssi, Hamed, and Hallaji, Milad. 2014. "Performance Evaluation of Different Repair Concretes Proposed for an Existing Deteriorated Jetty Structure." *Journal of Performance of Constructed Facilities* 28(4):04014013. doi:10.1061/(ASCE)CF.1943-5509.0000496.

[7] Robbins, Daniel B., and Lebel, Linn B. 2016. "Developing State-of-the-Art Marine Concrete Repair." *Ports 2016*. New Orleans, LA: American Society of Civil Engineers, pp. 441–450. doi:10.1061/9780784479919.045.

[8] Lee, Taehwi, Kim, Dongchan, Cho, Sanghwan, and Kim, Min Ook. 2025. "Advancements in Surface Coatings and Inspection Technologies for Extending the Service Life of Concrete Structures in Marine Environments: A Critical Review." *Buildings* 15(3):304. doi:10.3390/buildings15030304.

[9] Zhang, Mo, Xu, Hongyan, Phalé Zeze, Armande Loraine, Liu, Xiongfei, and Tao, Mingjiang. 2022. "Coating performance, durability and anti-corrosion mechanism of organic modified geopolymer composite for marine concrete protection." *Cement and Concrete Composites* 129:104495. doi:10.1016/j.cemconcomp.2022.104495.

[10] Liu, Yuanjun, and Liu, Yi. 2025. "Multifunctional polyurethane-based foam carbon fiber coating film: an innovative study on a material with high corrosion resistance, aging resistance, excellent self-cleaning performance, superior sound and wave absorption properties." *Applied Materials Today* 43:102647. doi:10.1016/j.apmt.2025.102647.

[11] Putra, Nicky Rahmana, Sahlan, Sahlan, Nugroho, Wibowo Harso, Widodo, Widodo, Mujahid, Ahmad Syafi'ul, Kasharjanto, Afian, Saiful, Mochamad, Qomariyah, Lailatul, and Irianto, Irianto. 2025. "Natural sustainable coatings for marine applications: advances, challenges, and future perspectives." *Green Processing and Synthesis* 14(1):20250035. doi:10.1515/gps-2025-0035.

[12] Barkai, Benjamin. 2024. *A General Overview of Cathodic Protection in Reinforced Concrete*. Report No. SRNL--STI-2024-00435, 2439252. doi:10.2172/2439252.

[13] Wilson, Keir, Jawed, Mohammed, and Ngala, Vitalis. 2013. "The selection and use of cathodic protection systems for the repair of reinforced concrete structures." *Construction and Building Materials* 39:19–25. doi:10.1016/j.conbuildmat.2012.05.037.

[14] Brueckner, Rene, Cobbs, Ryan, and Atkins, Chris. 2022. "A review of developments in cathodic protection systems for reinforced concrete structures." *MATEC Web of Conferences* 361:02001. doi:10.1051/matecconf/202236102001.

[15] Becerra Mosquera, José Antonio, Pardo Landrove, José Enrique, Millán Pérez, José Manuel, and Carro-Lopez, Diego. 2017. "Structures with chloride attack. Application of cathodic protection in the bridge to Illa de Arousa." *Hormigón y Acero* 68(283):201–207. doi:10.1016/j.hya.2017.05.006.

[16] Rubino, Felice, Nisticò, Antonio, Tucci, Fausto, and Carlone, Pierpaolo. 2020. "Marine Application of Fiber Reinforced Composites: A Review." *Journal of Marine Science and Engineering* 8(1):26. doi:10.3390/jmse8010026.

[17] Zong, Meirong, Wang, Wenhao, Ma, Haozhe, Cedrick, Nshuti, Sun, Yuting, Yan, Xiancui, Liu, Hui, Zhu, Pinghua, and Hua, Minqi. 2025. "Progress in Self-Repair Technology for Concrete Cracks via Biomineralization." *Materials* 18(21):5004. doi:10.3390/ma18215004.

Post-installed basalt fibre reinforced polymer bars

Marco Kendlbacher, Konrad Bergmeister

Institute of Structural Engineering,
BOKU University,
Peter-Jordan-Straße 82, 1190 Vienna, Austria

Summary
The non-corrosive, non-magnetic properties, high tensile strength and chemical resistance of basalt fibre reinforced polymer (BFRP) bars makes it a durable and innovative alternative to steel reinforcement for concrete structures especially with high environmental exposure. As part of a FFG-funded project, the necessity for investigating in the post-installation of BFRP bars was identified. Therefore, this research aims to explore the bond behaviour of post-installed BFRP bars. For this, an appropriate test setup was developed particularly for measuring the free-end slip, in order to eliminate the influence of bar elongation on the measurement. Experimental tests on Ø8, Ø12 and Ø22 BFRP bars were carried out with an intended embedment depth of 56 mm ($7 \cdot Ø_{nm}$), 84 mm ($7 \cdot Ø_{nm}$) and 110 mm ($5 \cdot Ø_{nm}$) respectively. A tendency of decreasing ultimate bond stress with increasing bar diameter and different bond failure modes for post-installed BFRP bars could be assessed. Finally, the various failure modes and possible mechanical models are described.

1 INTRODUCTION

Post-installed reinforcement bars for connecting different structural concrete members have a broad field of application along the construction industry [1]. Currently the main material used for post-installation is reinforcing steel. As the importance of sustainability and durability of concrete structures steadily increases, the use of non-metallic reinforcement as an alternative to steel reinforcement is a widely investigated topic in research. Thanks to their favourable properties, fibre reinforced polymers (FRPs) represent a promising construction material. Thus, the application of non-metallic reinforcement aims for an improvement of sustainability in concrete constructions and prolonged durability.

Investigations on post-installed steel reinforcement are carried out since over 30 years ([2], [3]) but due to the lack of research for FRP bars in this area, this paper focuses on the determination of bond characteristics and influence parameters on the behaviour of post-installed BFRP bars.

2 EXPERIMENTAL INVESTIGATION

The study serves for the determination of the pull-out resistance of post-installed BFRP bars. For this there was measured the load, the slip (relative displacement referred to the concrete surface) of the unloaded end of the bar and the actual embedment depth. This allows the determination of bond stress-slip curves in order to get the maximum pull-out resistance.

2.1 Materials

The materials used in the tests were BFRP bars with different diameters, a normal concrete slab and injection mortar.

Table 1 Characteristics of the used basalt fibre reinforced polymer bars

Characteristic	Ø8	Ø12	Ø22
Manufacturer	Deutsche Basalt Faser GmbH		
Surface treatment	sand coated and wrapped		
Mean tensile strength $f_{nm,m}$ in MPa	677[1)]	661[1)]	–[2)]
Mean Young's modulus $E_{nm,m}$ in MPa	39377[1)]	39616[1)]	–[2)]

[1)] own investigations
[2)] no value available

The BFRP bars as non-metallic reinforcement were manufactured in a pultrusion process, where basalt rovings get covered by a matrix. The fibres themselves as well as the bars have a brittle material behaviour and under tension stress the material keeps linear elastic until failure. The main characteristics of the BFRP bars are listed in Table 1.

As ground plate for the installations served a reinforced concrete slab with a concrete strength class of C20/25 and outer dimension of $90 \times 50 \times 15\ \mathrm{cm}^3$, which had been produced with the production date 2021-09-01.

The injection mortar epoxy mortar FIS EM Plus from fischerwerke GmbH & Co. KG [4] was used for the post-installation of the BFRP bars as well as for further parts of the test setup.

2.2 Test setup

To manage a successful testing procedure there needs a particular attention to be paid on the mechanical properties of the BFRP bars, which needs the load application mechanism to be adapted. Due to the anisotropic material properties and the unidirectional alignment of the fibres along the bars, the main load-bearing direction is obtained in the longitudinal direction of the bar. Since basalt fibres are very brittle, they have a significant sensitivity to transverse pressure. That is why a clamping directly onto the bar would lead to a premature failure at the clamping point. Tapping a thread, as it would be usually done on reinforcing bars, is also not leading to success.

To ensure that the test load could be applied to the bar, aluminium sleeves (from Fix Metall GmbH) with the dimensions listed in Table 2, were glued to one end of the bar using epoxy mortar FIS EM Plus. The length of the bars was chosen in accordance with the test setup shown in Fig. 1 so that after the installation of the bar the end that is covered by the aluminium sleeve protrudes sufficiently far from the test setup.

For the drilling of the boreholes the recommended borehole diameters for the respective bar diameters (see Table 2) were applied in accordance with the specifications of ETA-22/0001 [5]. The drilling was carried out using a hammer drilling method with a standard drill bit under the utilisation of a drilling guide and the depth of the borehole was chosen in accordance with the intended embedment depth (see Table 2).

Looking closer to the test setup, as shown in Fig. 1, it can be seen, that it is not possible to measure the slip at the loaded end of the bar near the concrete surface, as the entire bar is completely covered by the test apparatus. This makes it necessary to create a counter borehole on the bottom side of the concrete slab so that the slip at the unloaded end can be measured, as it is the case, for example, in typical pull-out tests. It is helpful to select the nominal diameter for the counter borehole as large as possible – subject to the availability of the drill bit in the laboratory – to ensure sufficient space for the installation of a displacement transducer. This counter borehole was then temporarily sealed with XPS to prevent the injection mortar from flowing out during the installation of the grouted bars.

The installation of the BFRP bars was followed in accordance with ETA-22/0001 [5]. To this, after drilling the boreholes must be cleaned ($2 \times$ blowing out with oil-free compressed air, $2 \times$ brushing with an appropriate stainless-steel brush and again $2 \times$ blowing out with oil-free compressed air). The cartridge of injection mortar must then be fitted with a static mixer and inserted into a suitable dispenser. The BFRP bars are then installed. The boreholes were filled with mortar to approximately 2/3 of their depth and the bars were inserted into the filled borehole with a rotational motion with the necessity of a completely filled annular clearance (overflow of the mortar out of the borehole opening). It is important to consider the working time t_{work} which depends on the temperature of the concrete body. The experimental procedure may only be carried out once the curing time t_{cure} has elapsed.

After curing of the injection mortar, the XPS was accurately removed from the counter borehole, allowing the installation of the displacement transducer (WA20 from Hottinger Brüel & Kjaer GmbH) for the slip measurement. As shown in Table 2 and Fig. 1, the force was measured using a compression force sensor, the application of the force was done via a hollow piston cylinder, and the load was introduced using a suitable anchorage system (housing and wedges). The tests were carried out as confined tests, for that, a steel plate with a hole of appropriate diameter ($1.5 \cdot \varnothing_{nm}$ to $2.0 \cdot \varnothing_{nm}$) was placed between the concrete surface and the hollow piston cylinder.

Table 2 Specifications for the test setup according to each diameter of the bars

Specification	Ø8	Ø12	Ø22

Embedment depth l_b	$7 \cdot Ø_{nm} = 56$ mm	$7 \cdot Ø_{nm} = 84$ mm	$5 \cdot Ø_{nm} = 110$ mm
Borehole diameter d_0	12 mm	16 mm	30 mm
Concrete slab	Concrete strength class: C20/25 Dimensions: $90 \times 50 \times 15$ cm^3		
Aluminium sleeve (EN AW-6060) (Fix Metall GmbH)	Ø12 × 1.0 mm^2, $L_g = 120$ mm	Ø16 × 1.0 mm^2, $L_g = 140$ mm	Ø28 × 1.5 mm^2, $L_g = 240$ mm
Anchorage (Paul Maschinenfabrik GmbH & Co. KG)	A50-38 wedges: R10.0	A50-38 wedges: 0.62	A80-50/10 wedges: R28
Compressive force sensor	K-18 100 kN (Lorenz Messtechnik GmbH)		CT-B-KN2C (Gefran S.p.A.)
Hollow piston cylinder (LUKAS Hydraulik GmbH)	LHOZ 10/50-20,5	LHOZ 10/50-20,5	LZMH 25/100-33
Displacement transducer (Hottinger Brüel & Kjaer GmbH)	WA20 (20 mm)		
Injection mortar system	Fischer FIS EM Plus (according to ETA-22/0001 [5])		

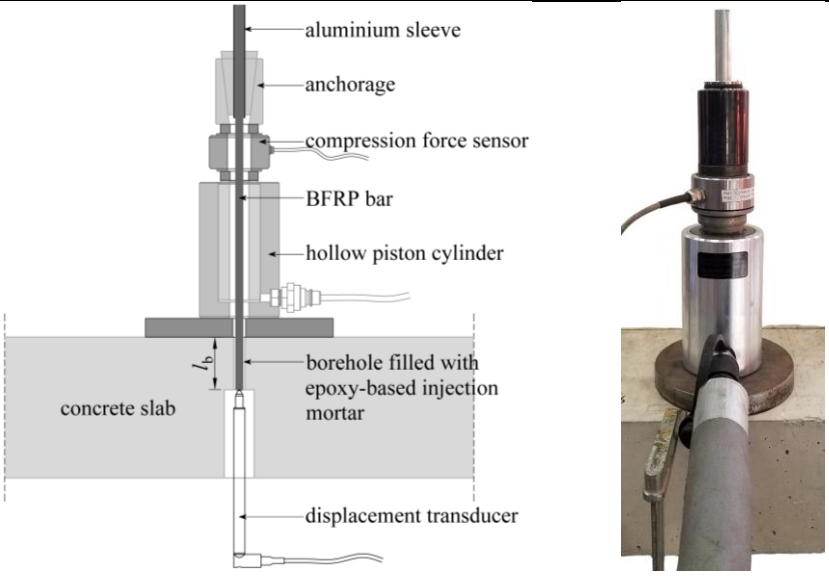


Fig. 1 Test setup for confined pull-out test for post-installed basalt-fibre reinforced polymer bars and large concrete cover. The intended embedment depth is labelled with l_b.

2.3 Experimental procedure

The tests have been performed in uncracked concrete. After installing and setting up the test as described, the compression force sensor and the displacement transducer were connected to appropriate measurement amplifiers to record the data. The hollow piston cylinder was connected to a hydraulic hand pump with which the cylinder was activated. The load was applied by manually pumping the hydraulic hand pump so that the peak force occurred at around 2 min and the test duration was around 5 min. To determine the real bond stresses the actual embedment depths were measured after the tests have been executed.

3 EVALUATION OF THE TEST RESULTS

3.1 Description of the failure modes and mechanical models

The evolution of the bond stress is in general composed of 3 bond mechanisms:

- adhesive bond,

- mechanical interlocking and
- friction

These different bond mechanisms result in a non-linear bond stress behaviour $\tau(x)$ along the embedded length as illustrated in Fig. 2 (left). For practical use it is sufficient to assume a constant distributed bond strength along the embedment depth, also labelled as "uniform bond model", since it is also difficult to measure the bond stress distribution depending to the embedment depth [3], [6]–[10].

For a confined test setup, as performed within this paper, the following failure modes can occur, as shown in Fig. 2 (right):

a) pull-out failure: failure between injection mortar and borehole surface
b) bond failure between injection mortar and bar:
   - b_1) shear failure at the interface bar-mortar
   - b_2) interlaminar shear failure of the bar
c) tensile failure of the bar

The evaluation of the test results by assuming a constant bond stress distribution can be calculated with the following equation:

$$\tau_b = \frac{F}{u_{nm} \cdot l_b} = \frac{F}{\varnothing_{nm} \cdot \pi \cdot l_b} \tag{1}$$

with

- F as measured force,
- l_b as embedment depth,
- u_{nm} as circumference of the non-metallic bar

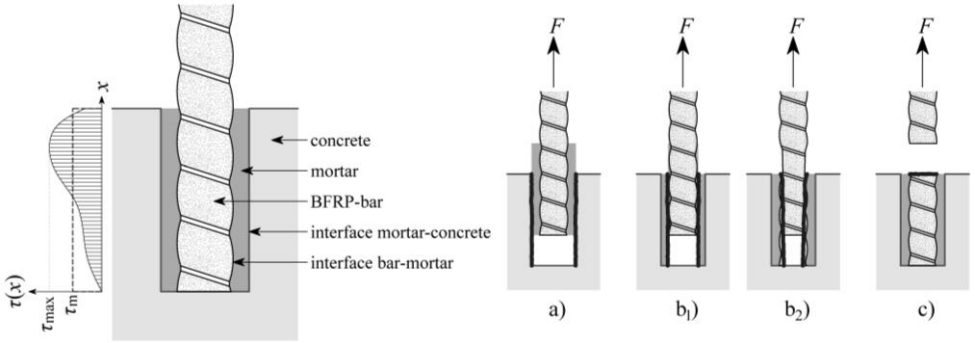


Fig. 2 Mechanical model for confined test setup with the failure modes a) pull-out failure at the interface mortar-concrete, b_1) shear failure at the interface bar-mortar, b_2) interlaminar shear failure inside of the bar and c) tensile failure of the bar.

Having tensile failure, the governing equation is:

$$F_{max} = f_{nm,t} \cdot A_{nm} = f_{nm,t} \cdot \frac{\varnothing_{nm}^2 \cdot \pi}{4} \tag{2}$$

with

- $f_{nm,t}$ as tensile strength of the non-metallic bar,
- A_{nm} as cross section of the non-metallic bar

To calculate the necessary embedment length equation (1) and equation (2) are set equal what leads to:

$$l_b = \frac{\varnothing_{nm}}{4} \cdot \frac{f_{nm,t}}{\tau_b} \tag{3}$$

3.2 Test results

In this section the results of the performed tests are provided. In the evaluation of the results, the measured forces were converted into bond stress τ_b using equation (1).

The results of the experimental investigations are shown as bond stress-slip curves in Fig. 3 for Ø8 bars, Fig. 4 for Ø12 bars and Fig. 5 for Ø22 bars. These figures show the valid tests, the mean curve calculated from the valid tests, the ultimate bond stress $\tau_{b,mean}$ and the 95 % confidence interval based on the number of valid tests. In addition to the confidence interval, the normal distribution at specified sections is shown for a better feeling of the scattering. Further the area of interest up to a free-end slip s of 1 mm is separately shown, since the workable area as stated in [11] is $s \ll 1\,\text{mm}$.

The bond stress-slip curves can in general be divided into the ascending branch until the maximum bond stress occurs and the descending branch afterwards. These branches can be described by analytical models referred to as bond laws as outlined in [3], [9]–[11].

Compared to post-installed steel reinforcement from [3] the ultimate bond stress for Ø8 and Ø12 rebars with an embedment depth of $10 \cdot Ø$ using a similar type of injection mortar was at a same level as for the BFRP bars.

3.3 Result of the Ø8 BFRP bars with embedment depth of 56 mm

In this section the results of the tests of BFRP bars with a diameter of 8 mm post-installed in concrete C20/25 are provided. A total number of 6 tests were conducted. Due to the small diameter of the bars, there occurred difficulties in the measurement of the slip at the unloaded end since there was limited space for the measuring point of the displacement transducer which at a certain slip was blocked by remaining injection mortar and smaller concrete chunks. This resulted in only 3 valid tests for the Ø8 BFRP bars.

The mean value of the ultimate bond stress ($n = 3$) is $\tau_{b,mean,Ø8} = 21.54\,\text{MPa}$ with a coefficient of variation $v = 7.81\,\%$. The 95 % confidence interval in Fig. 3 shows a wide scattering due to the low number of tests.

All BFRP bars failed with a complete shear off at the outer surface (interlaminar shear failure) what leads to the assumption that the interlaminar shear capacity of the bar is the limiting factor. The bond stress-slip curve in Fig. 3 shows an exponential ascending branch until the maximum bond stress and a steeper but not rapidly reducing descending branch governed by internal friction.

3.4 Result of the Ø12 BFRP bars with embedment depth of 84 mm

The same difficulties in measuring the slip as stated for the Ø8 bars also occurred for the Ø12 bars what lead to 3 valid tests out of a total of 6 tests.

Compared to the Ø8 BFRP bars the Ø12 bars resisted lower testing forces resulting in lower bond stresses. The mean value of the maximum bond stress at these tests is $\tau_{b,mean,Ø12} = 13.33\,\text{MPa}$ with $v = 4.96\,\%$. Up to a slip of 1 mm all the Ø12 bars had a similar behaviour as it can be seen in Fig. 4 by the small scattering of the confidence interval. The slip corresponding to the maximum bond stress was lower than for the Ø8 bars and it seems that the failure mode is a combination of pull-out and interlaminar shear failure. A potential reason for that could be a difference in the production process and therefore a better interlaminar behaviour which results in a stiffer ascending branch and a lower slope on the descending branch, since it seems that the internal friction is higher.

As denoted in [3], [12] there is a general tendency for the decrease of the maximum bond stress with the increase of bar diameter. This can also be observed within this testing campaign for the comparable tests on Ø8 and Ø12 bars with an embedment depth of $7 \cdot Ø_{nm}$.

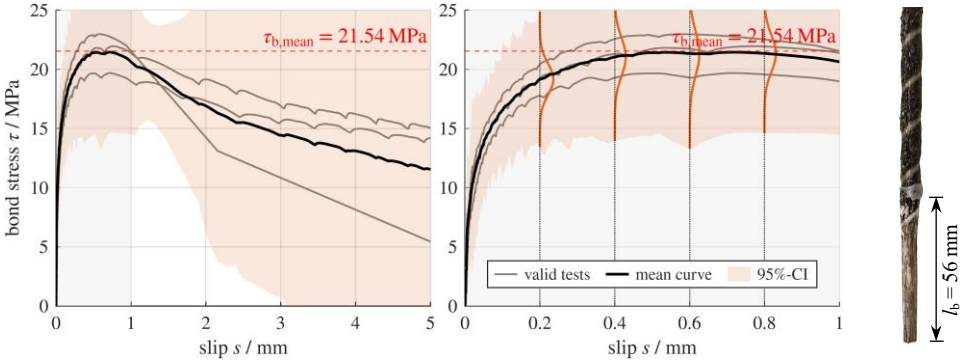


Fig. 3 *left and middle*: Experimental bond stress-slip curves for BFRP bars with a diameter of $Ø_{nm} = 8\,mm$ and an intended embedment depth of $7 \cdot Ø_{nm} = 56\,mm$. The grey area denotes a region of interest up to a free-end slip of 1 mm and the orange band shows the 95 % confidence interval. The number of valid tests was $n = 3$; *right*: Embedded surface of a representative Ø8 bar after interlaminar shear failure.

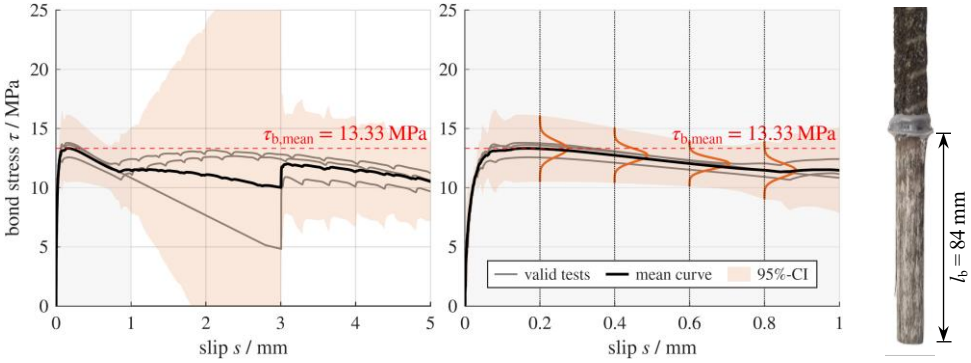


Fig. 4 *left and middle*: Experimental bond stress-slip curves for BFRP bars with a diameter of $Ø_{nm} = 12\,mm$ and an intended embedment depth of $7 \cdot Ø_{nm} = 84\,mm$. The grey area denotes a region of interest up to a free-end slip of 1 mm and the orange band shows the 95 % confidence interval. The number of valid tests was $n = 3$; *right*: Embedded surface of a representative Ø12 bar after combined pull-out and interlaminar shear failure.

3.5 Result of the Ø22 BFRP bars with embedment depth of 110 mm

For these tests the previously mentioned difficulties did not occur since the bar diameter was big enough to have a completely free measuring environment. A total of 6 tests were carried out, all of which were valid.

The resulting bond stress-slip curves of the Ø22 bars in Fig. 5 show a similar behaviour to the tests with Ø12 bars in Fig. 4. For the Ø22 BFRP bars the ultimate bond stress is $\tau_{b,mean,Ø22} = 16.42\,MPa$ with $v = 5.44\,\%$. The small scatter of the 95 % confidence interval ($n = 6$), as it can be seen in Fig. 5, allows a more precise statement on the reliability of the results.

All bars failed in the typical manner of a pull-out failure, since the surface of the bars was mostly intact over the embedment depth which means that the interface between bar and injection mortar failed. As the bars were manufactured after an optimisation in the production process the bars were of a better quality what can be seen in the results. Although the bar diameter was greater than for the other tests and the embedment depth was reduced to $5 \cdot Ø_{nm}$ a higher maximum bond stress could be reached compared to the Ø12 BFRP bars. This eventuates in the assumption of a better interlaminar shear behaviour for the Ø22 bars, since the failure mode was not restricted by the internal friction as for the other tests.

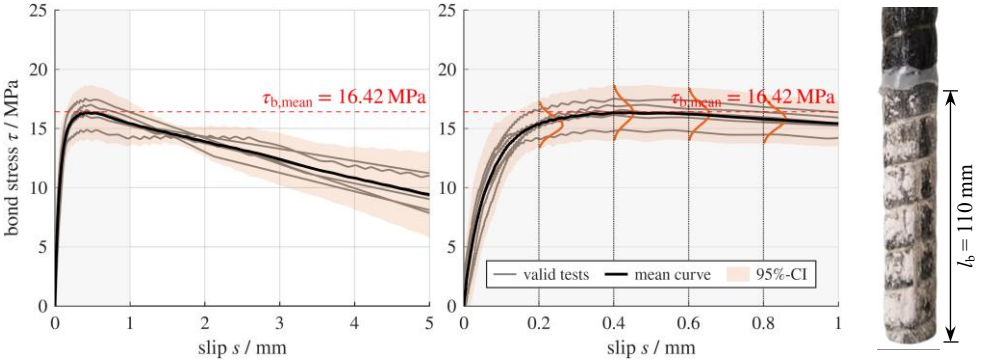


Fig. 5 *left and middle*: Experimental bond stress-slip curves for BFRP bars of diameter $Ø_{nm}$ = 22 mm with an intended embedment depth of $5 \cdot Ø_{nm}$ = 110 mm. The grey area denotes a region of interest up to a free-end slip of 1 mm and the orange band shows the 95% confidence interval. The number of valid tests was n = 6; *right*: Embedded surface of a representative Ø22 bar after pull-out failure.

4 CONCLUSIONS

Within the scope of this paper the bond behaviour of post-installed basalt fibre reinforced polymer bars in normal uncracked concrete C20/25 was experimentally investigated. The test method was partially in accordance with EAD 330499 [13], ISO 10406-1:2015 [14], the test setup for confined testing shown in [3] and considerations on the measuring of the free-end slip.

With the preliminary tests it can be observed that the interlaminar shear strength of BFRP bars, which complies with the internal friction near the bar surface, can be the dominant mechanical property depending on the embedment depth. As a lower range of embedment depth leads to pull-out failure (interface between injection mortar and BFRP bar) because the interlaminar shear strength is not reached, an embedment depth in the mid-range can lead to an interlaminar shear failure of the bar (failure of the bar itself, as also observed in [11] for bars from the same manufacturer) or a combination of both.

To make a more precise assertion on the bond behaviour it needs further investigations in the interlaminar shear behaviour of the BFRP bars, variation of the embedment depth, better quality control in the production process of the bars to get a better comparability over the range of the different bar diameters and there needs to be done an optimisation on the experimental setup to ensure a valid configuration for smaller bar diameters. Varying the embedment depth until tensile failure becomes the decisive failure mode will give a better understanding of the actual bond resistance.

References

[1] Spieth, Hannes A. 2005. “Bemessung und Anwendung von nachträglich eingemörtelten Bewehrungsanschlüssen.“ *Beton- und Stahlbetonbau*, vol. 100, S1, pp. 74–77, 2005, doi: 10.1002/best.200590173.

[2] Darwin, David and Salamizavaregh, Shahin. 1993. *Bond strength of grouted reinforcing bars*. University of Kansas Center for Research, Lawrence, Kansas/USA, SM Report No. 32.

[3] Spieth, Hannes A. 2002. “Tragverhalten und Bemessung von eingemörtelten Bewehrungsstäben.“ Dissertation, Institute of Construction Materials, University of Stuttgart, Stuttgart.

[4] fischerwerke GmbH & Co. KG. “Epoxy mortar FIS EM Plus: The powerful injection mortar for rebar connections and cracked concrete.” [Online]. Available: https://www.fischer-international.com/en/products/chemical-fixings/injection-mortar/epoxy-mortar-fis-em-plus (accessed: Apr. 6 2026).

[5] ETA-22/0001. 2024. *fischer Injektionssystem FIS EM Plus: Nachträglich eingemörtelte Bewehrungsanschlüsse mit verbessertem Verbund- und Spaltverhalten*. European Organisation for Technical Assessment (EOTA). Berlin.

[6] Ritter, Laura. 2013. “Der Einfluss von Querzug auf den Verbund zwischen Beton und Betonstahl.” Dissertation, Institut für Massivbau, Technische Universität Dresden, Dresden.

[7] Caspari, Christian. 2022. “Zur Verbundverankerung von Glasfaserkunststoffbewehrungsstäben in Betonbauteilen unter Kurzzeit- und Langzeitbeanspruchung.” Dissertation, Fachgebiet für Massivbau und Baukonstruktion, RPTU Kaiserslautern-Landau, Kaiserslautern.

[8] Mihala, Ronald. and Bergmeister, Konrad. 2011. “Befestigungstechnik – einbetonierte und eingemörtelte Bewehrungsstäbe sowie Gewindestangen.” *Beton-Kalender 2012*, K. Bergmeister, F. Fingerloos, and J.-D. Wörner, Eds.: Wiley, pp. 175–208.

[9] Niewels, Jörg. 2008. “Zum Tragverhalten von Betonbauteilen mit Faserverbundkunststoff-Bewehrung.“ Dissertation, Institut für Massivbau, Rheinisch-Westfälische Technische Hochschule (RWTH) Aachen, Aachen.

[10] Pritschow, Andreas. 2016. “Zum Verbundverhalten von CFK-Bewehrungsstäben in Bauteilen aus ultrahochfestem Beton.“ Dissertation, Institut für Leichtbau Entwerfen und Konstruieren, Universität Stuttgart, Stuttgart.

[11] Hofmann, Sebastian; Proske, Tilo and Graubner Carl-Alexander. 2020. “Verbundverhalten besandeter basaltfaserverstärkter Kunststoffbewehrung.“ *Beton und Stahlbetonbau*, vol. 115, no. 7, pp. 514–522, 2020, doi: 10.1002/best.201900076.

[12] Eligehausen, Rolf. 1979. “Übergreifungsstöße zugbeanspruchter Rippenstäbe mit geraden Stabenden.“ Lehrstuhl für Werkstoffe im Bauwesen, Universität Stuttgart, Stuttgart.

[13] EAD 330499-02-0601. 2022. *Bonded fasteners and bonded expansion fasteners for use in concrete*. European Organisation for Technical Assessment (EOTA). Brussels.

[14] ISO 10406-1:2025. 2025. *Fibre-reinforced polymer (FRP) reinforcement of concrete - Test methods - Part 1: FRP bars*. International standard, 3rd ed., 2025. [Online]. Available: https://www.iso.org/standard/84321.html.

Sustainable Concrete

Comparison of Two Different Activation Methods for Concrete Fines: Thermal and Carbonation Activation

Maureen Denu, Jan P. Höffgen, Ravi A. Patel, Frank Dehn

Institute of Concrete Structures and Building Materials,
Karlsruher Institute of Technology (KIT),
Gotthard-Franz-Str. 3, 76131 Karlsruhe, Germany

Summary
Concrete is the most widely used building material. However, cement clinker production generates large CO_2 emissions. Reducing these requires lower clinker use, e. g., by incorporating recycled concrete fines (RCF) as a binder. RCF can be activated thermally or via carbonation, yet direct comparisons under identical conditions are lacking. This study evaluates both methods using thermogravimetric analysis (TGA) and mortar strength tests on binary mortar systems. Activated RCF was blended with Ordinary Portland cement (OPC) to reduce the clinker content to 50 wt.-%. Results show that thermally activated RCF and carbonation activated RCF both lead to only about~25 % compressive strength reduction, respectively, demonstrating effective reactivity recovery and significant clinker substitution.

1 INTRODUCTION

The ever-increasing amount of construction and demolition waste (C&DW), coupled with the steadily rising demand for concrete, presents a significant global challenge. So far, it has not been possible to fully recycle concrete in a closed loop, meaning that recycling, rather than downcycling, has not yet been achieved. While coarse aggregates can be reused in new concrete up to 50 vol.-% per exposure class according to EN 206:2013+A2:2021, the application of fine recycled aggregates is possible only to a limited extent. These fine fractions, commonly referred to as recycled concrete fines (RCF), account for 20-40 wt.-% of concrete waste [1, 2]. Due to their high hardened cement paste content, they can be used as Supplementary Cementitious Material (SCM). An additional activation of the hardened cement paste increases the recycling potential. In this way, resource efficiency can be effectively combined with a reduction in CO_2 emissions by lowering the demand for Ordinary Portland Cement (OPC). In this context, thermal [3-5] and carbonation activation [6-8] represent two promising approaches for activation of RCF.

Thermal activation reverses the hydration reaction of the cement, thereby causing its dehydration. Initially, at temperatures above 110 °C, chemically bound water is evaporated and the aluminate phases (AFt, AFm) start to dehydrate [3, 9]. Subsequently, at approximately 400–550 °C, portlandite decomposes [3, 9], producing reactive CaO, which is a reactive hydraulic compound. In addition, the C–S–H phase begins to decompose from around 100 °C, and at higher temperatures, a slightly modified form of belite (α-C_2S or β-C_2S) is formed [10, 11]. However, CO_2 is released above 600–900 °C [12].

Carbonation activation is based on the targeted use of CO_2, which may be captured from clinker production exhaust gases. At low CO_2 concentrations, such as ambient atmospheric exposure, carbonation predominantly affects the calcium hydroxide formed during cement hydration. This reaction leads to the formation of calcium carbonate and is associated with a densification of the cement paste microstructure. Such slow, environmentally driven reactions are referred to as *natural carbonation*. In contrast, *enforced carbonation* involves deliberately intensifying the process by increasing CO_2 availability or enhancing material reactivity, for example, through particle size reduction. Such elevated CO_2 concentrations, which can be present in flue gas or CO_2-saturated aqueous media, induce the breakdown of the primary cement hydration phases. Calcium silicate hydrate (C-S-H), portlandite, ettringite, and AFm phases are transformed into calcium carbonate and amorphous silica or alumina–silica gels (Al-Si), fundamentally altering the mineralogical composition of the material. These amorphous gels are pozzolanic and react with $Ca(OH)_2$ and water to form secondary C-(A)-S-H-phases. [6, 13]

Enforced carbonation can be classified into three distinct activation modes: dry, semi-dry, and wet carbonation [6]. In this study, the wet carbonation activation method was selected to achieve the highest

possible degree of carbonation (DOC) without the strict necessity of applying elevated pressure or higher temperature. This approach relies solely on the efficient transport of CO_2 through water, enabling its penetration into nearly all pore spaces of the material.

Although some literature [1-13, 15] addresses these methods, different starting materials and mix designs are used, making direct comparisons difficult. Therefore, in this study, both activation methods are applied to the same laboratory-produced starting material, and mechanical as well as characterization tests are conducted in parallel.

2 MATERIALS

Since the activation predominantly occurs in the cement matrix rather than in the inert fraction, sand or coarse aggregates, laboratory material was prepared without aggregates. For the production of the recycled cement paste (RCP), a CEM I 42.5 R cement paste with a water-to-binder ratio (w/b) of 0.5. A total of 75 kg was produced and intermittently stirred to prevent bleeding. Shortly before setting, the material was transferred into 10 l buckets, sealed, and stored for four months at an average laboratory temperature of 20 °C.

After storage, the RCP was crushed inside the buckets into pieces of approximately 100 mm. The particle size was subsequently reduced to 2 mm using a jaw crusher and then further ground in a rotary mill equipped with a classifier to achieve a maximum particle size of 100 µm (see Figure 1). Table 1 shows the chemical composition of RCP.



Fig. 1 Production and stepwise size reduction of the RCP material (left: ≤ 100 mm, center: ≤ 2 mm, right: ≤ 100 µm)

Table 1 Chemical composition RCP1 (RFA-WDX) [wt.-%]. LOI: Loss on ignition at 950 °C

	Na_2O	MgO	Al_2O_3	SiO_2	P_2O_5	K_2O	CaO	TiO_2	MnO	Fe_2O_{3tot}	LOI
RCP	0.1	1.8	4.7	19.3	0.1	0.6	46.2	0.3	0.1	1.3	21.3

3 METHODS

3.1 Thermal Activation

After mechanical grinding, during which the particle size was reduced to below 100 µm, thermal activation was carried out. This first involved drying the material at 105 °C for 24 h, followed by activation at 600 °C for 6 h in a muffle furnace. The heating rate was 5 K/min. In each batch, 1.5 kg of material was processed in a crucible. The material before and after thermal activation is shown in Figure 2. After activation, the material was cooled in the muffle furnace to temperatures below 200 °C and subsequently allowed to reach room temperature in a container containing silica gel beads.

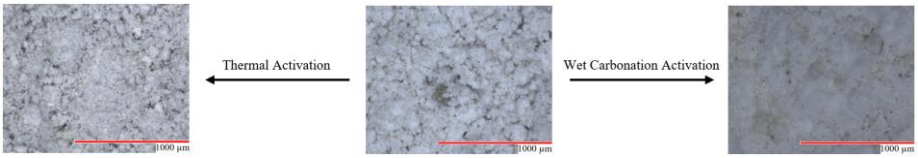


Fig. 2 Light microscopy images: Central: RCP material before activation, Left: tRCP material after thermal activation, Right: cRCP after wet carbonation activation

3.2 Wet Carbonation Activation

The RCP was mixed with a saturated aqueous solution of highly concentrated CO_2 gas, while continuous stirring was applied to keep the particles suspended throughout the experiment. The water-to-solid ratio was 3:1, and 3 kg of cRCP material could be produced per batch. In addition, an average temperature of 40 °C was maintained to accelerate the reaction. This enabled a higher degree of carbonation of the C-S-H phases, resulting in a higher amount of pozzolanic reaction products [6]. To achieve a high degree of carbonation (DOC), the carbonation duration was set to 24 h. Subsequently, the RCP slurry was dried in an oven at 30 °C for two weeks. The material before and after wet carbonation activation is shown in Figure 2.

3.3 Thermogravimetric analysis (TGA)

The thermogravimetric analysis (TGA) was used to assess the success of the RCF activation. For this purpose, 100 mg of material was weighed into a crucibleand heated to 1200 °C at a heating rate of 10 K/min. During this process, the mass change was recorded as a function of temperature.

3.4 Mechanical properties

The mechanical performance of the activated RCPs was evaluated by means of mortar strength tests. Both binary systems were investigated at varying substitution levels. The test specimens were prepared based on with EN 196-1:2016-04. However, the water-to-binder (w/b) ratio was set to 0.5, and the paste content was increased to 0.5 to ensure workability even when using the activated materials and to limit the addition of superplasticizer. Furthermore, rhine river sand was used instead of the CEN-sand. After demolding, the prisms were stored under water at 20 °C until testing. At the individual testing ages, a three-point flexural strength test was first carried out on a prism with dimensions of 40 × 40 × 160 mm^3, in order to subsequently determine the compressive strength on prism halves, each with a pressure surface of 40 × 40 mm^2 and a height of 40 mm. Flexural strength tests were conducted at 2 d and 28 d. Compressive strength tests used six prism halves at 28 d, and three halves at 2 d. The remaining three halves reentered storage until the age of 91 d in order to determine another compressive strength.

4 RESULTS AND DISCUSSION

4.1 Validation of the Activation

When the unactivated recycled cement paste (RCP) is analyzed, a pronounced mass loss is observed between 450-500 °C, which can be attributed to the decomposition of portlandite. In addition, a further mass loss occurs in the range of approximately 600-900 °C, indicating the decomposition of $CaCO_3$ (Figure 3).

For the thermally activated RCP (tRCP), TGA results show that almost no decomposition, and thus no additional mass loss, occurs up to 600 °C. This indicates that the activation process was effective, as all decomposable phases had already been transformed during activation.

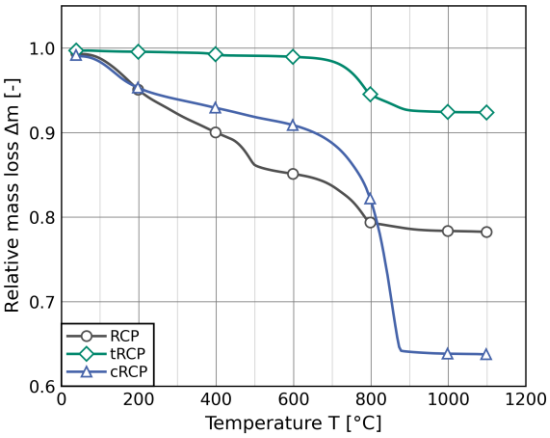


Fig. 3 Relative mass loss of RCP, tRCP, and cRCP

In the case of wet carbonation activation, a pronounced mass loss is observed in the temperature range of 600–900 °C (Figure 3). This indicates the decomposition of $CaCO_3$ formed during the carbonation process. Based on the measured mass loss, the amount of CO_2 stored in the material can be quantified. By comparing this value with the theoretically storable CO_2 content, calculated from the chemical composition of the starting material using the Steinour equation (Eq. 1), the DOC can be determined (Eq. 2) [6].

$$CO_2^{max.} = 0.785 \times (CaO - 0.7 \times SO_3) + 1.091 \times MgO + 1.420 \times Na_2O + 0.935 \times K_2O \quad (1)$$

$$DOC\ [\%] = 100 \times \frac{CO_2^{measured}}{CO_2^{max}} \quad (2)$$

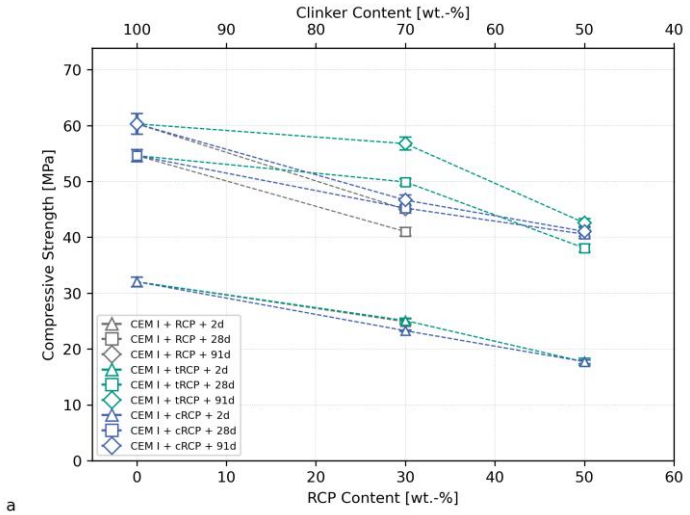
Accordingly, a DOC of approximately 80% was achieved in this study by calculating CO_2^{max} based on the chemical composition (Table 1) and investigating the $CO_2^{measured}$ with the help of the TGA.

4.2 Mechanical Properties

For the binary systems, a mortar based on CEM I 42.5 R was used as the reference and was subsequently replaced stepwise with non-activated RCP, thermally activated RCP (tRCP), or wet-carbonated RCP (cRCP), up to a clinker substitution level of 50 wt.-% (Figure 4a). It can be observed that increasing the replacement level leads to a pronounced reduction in compressive strength.

After 2 days, both activation methods result in similar compressive strength (Figure 5a), with a reduction of approximately 20–40 % at replacement levels of 30–50 wt.-% compared to the CEM I reference. However, a different trend emerges at later ages. After 28 and 91 days, at a 30 wt.-% replacement, the wet-carbonated material (cRCP) exhibits a decrease of around 20 %, whereas the thermally activated material (tRCP) shows only a 5 % reduction. At a 50 wt.-% replacement, the strength loss for both activation methods converges to approximately 25 %. If the compressive strength of the mortar is compared with the compressive strength of the reference mortar (100 wt.-% OPC), the strength activation index (SAI) is obtained [10].

$$SAI\ [\%] = \frac{f_{measured,x\ days}}{f_{refernce,x\ days}} \times 100 \quad (3)$$



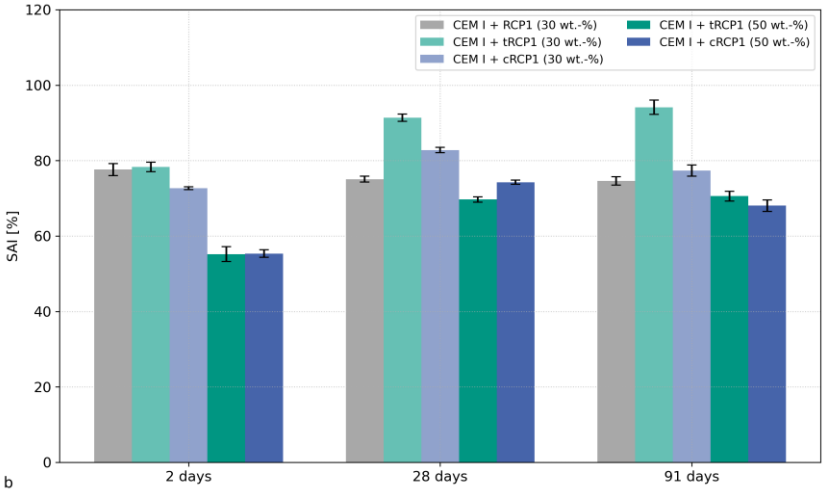


Fig. 4 a: Compressive strength of binary mortar systems containing OPC and RCP, tRCP, or cRCP (including standard deviations)
b: SAI of a binary mortar systems containing OPC and RCP, tRCP, or cRCP over time (including standard deviations)

It can be seen that at a replacement rate of 30 wt.-% with the thermally activated material, about 94 % is achieved after 91 days, whereas the carbonated material reaches 77 % (see Figure 4b). So a higher amount of reactive phases can be indicated in the thermally activated material and/or an insufficient CaO content for the pozzolanic reaction of cRCP.

Another important aspect, in addition to the comparison of strength values, is the temporal strength development of the materials. Using the equation from *fib* Model Code 2020 [14] (Eq. 4), the strength development can be calculated.

$$f_{cm}(t) = f_{cm,ref} \times \exp\left(s_c \times \left[1 - \left(\frac{t_{ref}}{t}\right)^{0.5}\right]\right) \times \left(\frac{28}{t_{ref}}\right)^{0.5} \quad (4)$$

In this context, it is important to adjust the strength development coefficient (s_c), which accounts for the cement type, as well as the 28 days reference strength ($f_{c,\,ref,\,28d}$) [15]. In this procedure, s_c and $f_{cm,}$

$_{ref,\ 28d}$ were adjusted to minimize the squared error (X^2) between the measured values after 2, 28, and 91 days, and the corresponding calculated values (Eq. 5). Table 2 presents the results for $f_{cm,\ ref,\ 28d,}$ s_c, $f_{cm,\ ref,\ 28d}$, the measured 28 day compressive strength ($f_{cm,\ measured,\ 28d}$) as well as X^2.

$$X^2 = \sum_{i=1}^{n} (f_{cm,modelled} - f_{cm,measured})^2 \quad (5)$$

If the fitted parameter s_c (Table 2) is compared with the cement classes specified in the *fib* Model Code 2020 [14] for the strength range of 35–60 MPa, it becomes apparent that a CEM I 42.5 R, which was used here, corresponds to a s_c value of 0.2. A cement consisting of OPC with blast-furnace slag (S) in an amount greater than 35 wt.-% and less than 65 wt.-%, or with fly ash (V) in the range of 20–35 wt.-%, has a s_c value of 0.4. Consequently, the activated variants are located between these classes.

Table 2 Fitted parameters and measured 28 day compressive strength

Tests series	s_c	$f_{cm,\ ref,\ 28d}$	$f_{cm,\ measured,\ 28d}$	X^2 (squared error)
	[-]	MPa	MPa	[-]
100 wt.-% CEM I	0.20	55.0	54.6	0.2
70 wt.-% CEM I + 30 wt.-% RCP1	0.19	41.3	41.0	0.1
70 wt.-% CEM I + 30 wt.-% tRCP1	0.26	50.4	49.9	0.3
70 wt.-% CEM I + 30 wt.-% cRCP1	0.22	43.5	45.2	5.0
50 wt.-% CEM I + 50 wt.-% tRCP1	0.28	37.8	38.1	0.1
50 wt.-% CEM I + 50 wt.-% cRCP1	0.27	38.1	40.6	9.8

Figures 5 and Table 2 show that the strength development can be modelled in this way and has a similar X^2 for the unactivated material as well as the activated material as an OPC mortar, indicating that this approach is suitable for predicting strength development. In contrast, X^2 for the wet carbonated material is relatively high, so the model does not predict well the strength development. One possible explanation is that the amorphous al-silica gel initially reacts with the available water and portlandite, forming a C-(A)-S-H phase [6]. However, the reaction requires that all pores, including the inner ones, are wetted with water. Therefore, the initial rate of the strength-enhancing phase is moderate, comparable to other SCMs. For example, blended cements such as CEM III or CEM II/B typically exhibit a s_c of around 0.5 with a substitution levels of more than 65 wt.-% blast furnance slag (S) or approximately 35 wt.-% fly ash (V) [14].. Once the portlandite required for the pozzolanic reaction is depleted, the increase in strength levels off. Therefore, the existing *fib* model [14], which assumes a sufficient number of reactants, does not fit the reaction of the wet carbonated material (cRCP). This assumption needs to be confirmed by further, more in-depth investigations.

The increase in strength after 28 days (of around 80 % of the final 91 days strength) is very similar when comparing the two activation methods in a binary system. However, it also becomes evident that at a replacement level of 30 wt.-%, the strength development from 2 days onwards is significantly higher for the thermally activated variant compared to the wet-carbonated variant. This is consistent with the previous hypothesis of the higher amount of reactive phases.

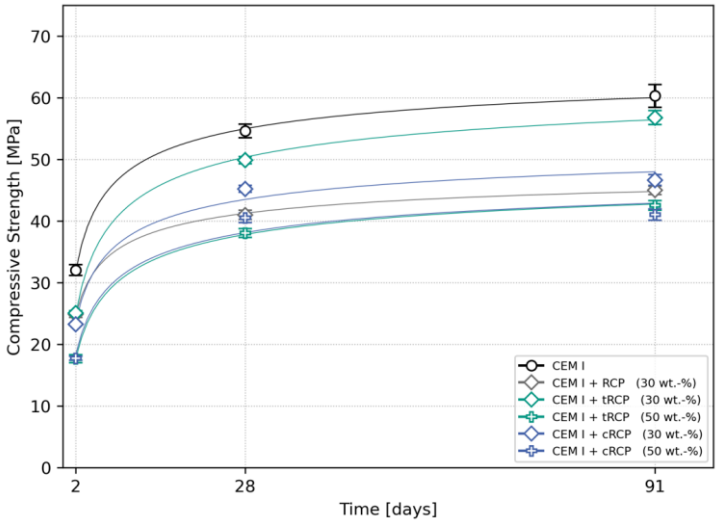


Fig. 5 Compressive strength binary system mortar containing OPC and RCP, tRCP, or cRCP, depending on the time (regression curves follow *fib* Model Code 2020 [14] (Eq. 4))

5 CONCLUSIONS

This study investigates the activation of recycled concrete fines (RCF) through thermal and wet carbonation activation to enhance their performance as supplementary cementitious materials (SCMs). The work focuses on comparing both activation methods under consistent conditions and evaluating their influence on material reactivity, mechanical performance, and strength development behavior in binary mortar systems. The main findings and their innovative scientific and practical contributions can be summarized as follows:

- Both activation methods effectively enhance the reactivity of recycled cement paste (RCP) and can be validated with TGA measurements
- Thermally as well as wet carbonated activated RCPs exhibit only moderate strength reductions (app. 25 %) at high substitution (up to 50 wt.-%) in binary mortar systems, indicating strong potential for high clinker reduction
- At a substitution rate of 30 wt.-%, thermally activated RCP achieves significantly higher performance retention (SAI app. 94 %) compared to wet carbonated RCP (SAI app. 77 %). This difference suggests an influence of the CaO content, but this requires further and deeper investigation, especially on the influence of the activation method on the microstructure
- Conventional strength prediction models (*fib* Model Code 2020) are suitable for non.-activated and thermally activated RCP, but coefficients and reference strength at 28 d need to be recalibrated for activated RCP, especially for the wet carbonated activated RCP

Acknowledgements

The authors declare that there are no financial interests or personal relationships that could have influenced the content or materials discussed in this manuscript.

This paper includes content generated with the assistance of OpenAI's ChatGPT, a large language model. ChatGPT was used for purposes such as language refinement and grammar correction. All final edits and content decisions were made by the authors, who take full responsibility for the accuracy and integrity of the work.

The authors would like to thank the Deutsche Forschungsgemeinschaft (DFG, German Research Foundation) for its financial support.

References

[1] Höffgen, Jan Pascal, Bauer, Manuel, Dehn, Frank. 2022. "THINKTANK Industrielle Ressourcenstrategien Entwicklung einer Strategie zum Umgang mit Betonbrechsanden in Baden-Württemberg" ThinkTank, Karlsruher Institut für Technologie.

[2] Ouyang, Xiaowei, Li, Xiaofeng, Li, Jiaming, Ma, Yuwei, Zhang, Mingzhong, Li, Zongjin, Fu, Jiyang. 2025. "Multiscale microstructure and reactivity evolution of recycled concrete fines under gas-solid carbonation" Cement and Concrete Composites 157. doi:10.1016/105903.

[3] Höffgen, Jan Pascal, Vogel, Michael, Blask, Oliver, Dehn, Frank. 2023. "Entwicklung thermisch-mechanisch aktivierter Betonbrechsande als Betonzusatzstoff – Projektvorstellung und erste Ergebnisse" Beton- und Stahlbetonbau 118:239-246. doi:10.1002/best.202200127.

[4] Zhang, Dongsheng, Zhang, Shuxiang, Huang, Bowen, Yang, Qiuning, Li, Jiabin. 2022. "Comparison of mechanical, chemical, and thermal activation methods on the utilisation of recycled concrete powder from construction and demolition waste" Journal of Building Engineering 61. doi:10.1016/105295.

[5] Wu, Huixia, Yang, Dingyi, Ma, Zhiming. 2021. "Micro-structure, mechanical and transport properties of cementitious materials with high-volume waste concrete powder and thermal modification" Construction and Building Materials 313. doi:10.1016/125477.

[6] Zajac, Maciej, Maruyama, Ippei, Iizuka, Atsushi, Skibsted, Jørgen. 2023. "Enforced carbonation of cementitious materials" Cement and Concrete Research 174. doi:10.1016/107285.

[7] Ma, Zihan, Jiang, Yi, He, Jionghuang, Shen, Peiliang, Qin, Qinglong, Gu, Zhenjiang, Li, Jiangshan, Poon, Chi Sun. 2024. "Revealing the connection between carbonation regimes and early pozzolanic reactivity of recycled concrete powder: Impact of composition and microstructure" Cement and Concrete Research 186. doi:10.1016/107697.

[8] Jiang, Yi, Li, Long, Lu, Jian-xin, Shen, Peiliang, Ling, Tung-Chai, Poon, Chi Sun. 2022. "Mechanism of carbonating recycled concrete fines in aqueous environment: The particle size effect" Cement and Concrete Composites 133. doi:10.1016/104655.

[9] Aquino Rocha, Joaquin Humberto, Toledo Filho, Romildo Dias. 2023. "The utilization of recycled concrete powder as supplementary cementitious material in cement-based materials: A systematic literature review" Journal of Building Engineering 76. doi:10.1016/107319.

[10] Sui, Yuwun, Ou, Chuping, Liu, Shu, Zhang, Jinshuai, Tian, Qingbo. 2020. "Study on Properties of Waste Concrete Powder by Thermal Treatment and Application in Mortar" Applied Sciences 10. doi:10.3390/app10030998.

[11] Bogas, José Alexandre, Real, Sofia, Carrico, Ana, Abrantes, João Carlos De Castro, Guedes, Mafalda. 2022. "Hydration and phase development of recycled cement" Cement and Concrete Composites 127. doi:10.1016/104405.

[12] Alonso, Cruz, Fernández, Lorenzo. 2004. "Dehydration and rehydration processes of cement paste exposed to high temperature environments" Journal of Materials Science 39:3015–3024. doi:10.1023/B:JMSC.0000025827.65956.18.

[13] Poon, Chi Sun, Shen, Peiliang, Jiang, Yi, Ma, Zihan, Xuan, Dongxing. 2023. "Total recycling of concrete waste using accelerated carbonation: A review" Cement and Concrete Research 173. doi:10.1016/j.cemconcre.2023.107284.

[14] International Federation for Structural Concrete (fib). 2020. fib Model Code for Concrete Structures 2020 (Version 1). Lausanne: International Federation for Structural Concrete (fib). ISBN: 978-2-88394-175-5.

[15] Höffgen, Jan Pascal, Dehn, Frank. 2025 "Influence of thermally activated artificial concrete fines composition on mortar strength development" Developments in the Built Environment 24. doi:10.1016/j.dibe.2025.100775.

Direct shear behaviour of concrete incorporating electric arc furnace slag aggregates

Lara Clerici, Alan Piemonti, Giovanni Plizzari, Antonio Conforti

Università degli Studi di Brescia,
Via Branze 43, Brescia (25123), Italy

Summary
The reuse of Electric Arc Furnace (EAF) slag, employed as a partial replacement for natural aggregates in concrete, represents a key strategy not only to reduce landfill disposal but also to preserve natural resources, promoting the principles of the circular economy. In this research, EAF slag was employed as a partial replacement for natural aggregates in concrete, with the aim of enhancing both its mechanical performance, such as compressive strength and modulus of elasticity, and its behaviour under load. To this end, direct shear tests were carried out on concrete mixtures containing different replacement levels for natural aggregates with EAF slag (10%, 25% and 50%). The results showed that the incorporation of EAF slag increased the shear stress transferred across cracks, with the most significant improvements observed in concretes with higher replacement percentages. The enhancement was mainly attributed to the higher resistance to fragmentation and the rougher surface texture of EAF slag compared to natural aggregates.

1 INTRODUCTION

In structural concrete, shear resistance in members lacking specific reinforcement is primarily governed by the transfer of internal forces across the cracked interface. This capacity is traditionally attributed to the contribution of the uncracked concrete in the compression zone, the dowel action exerted by longitudinal rebars, and most significantly, the mechanical interlocking of aggregates across the crack faces [1]. This aggregate interlock represents the most important component of stress transmission, resulting from the surface roughness created as cracks propagate around the aggregates. As shear slip develops, the interaction between these aggregates provides substantial resistance. This mechanism is further enhanced when longitudinal reinforcement limits the crack width by providing a restraining force orthogonal to the plane [1]. Several variables influence the efficiency of this interlocking mechanism, including the concrete type [2]-[3], potential pre-cracking [4], the presence of normal stresses [5]-[6]-[7], and the reinforcement passing through the crack [5]-[6]. Furthermore, the specific interface type [3]-[8], the width of the crack opening [9], and the type and grain size of the aggregates used [9].

Despite these known factors, the literature remains sparse regarding the shear performance of full-scale beams utilizing Electric Arc Furnace (EAF) slag as substitute for natural aggregates. Specifically, the lack of detailed data on the aggregate interlock of EAF slag concrete represents a significant knowledge gap that hinders the wider industrial reuse of this material.

Notable progress was made by Faleschini and Pellegrino [10], who studied reinforced concrete beams where EAF slag replaced 65% of the coarse natural aggregates by weight. Their results indicated that beams without stirrups achieved higher shear strength when containing EAF slag, likely due to superior bond and cohesion between the slag and the cement matrix. However, in beams with stirrups, isolating the specific slag interlock contribution proved difficult since the steel reinforcement dominates the shear capacity.

Subsequent research by Faleschini et al. [11] focused on isolating this mechanism through push-off tests on Z-shaped specimens. While these tests resulted in brittle failure due to the absence of transverse reinforcement, the EAF slag specimens consistently demonstrated higher peak strengths than conventional concrete. Although the overall failure modes were similar, the slag concrete exhibited distinct crack path morphologies at the interface.

Over time, various experimental setups have been proposed to model real-world structural behaviour, with the Z-specimen, the FIP specimen [12], and the JSCE SF6 specimen [13] being the most prevalent. Each configuration offers specific advantages and disadvantages. Considering the technical challenges of this assessment and the increasing industrial interest in EAF slag, the present study aims to provide new insights into the interlocking behaviour of concrete featuring three different

substitution percentages: 10, 25, and 50%. These specific levels were chosen to demonstrate how the concrete industry could potentially absorb the entire national production of EAF slag, thereby promote circular economy practices and reduce landfill disposal.

2 MATERIALS AND MIX DESIGN

2.1 Materials

The experimental program utilized CEM II/B-LL 42.5 R cement along with a combination of natural aggregates including fine sand (0/1 mm), medium sand (0/4 mm), and gravel (6/20 mm). The physical properties of these natural components are summarized in the following table:

Table 1 Physical properties of natural aggregates used in mix design.

Material	Grain Size [mm]	Specific Gravity [kg/m^3]	Water Absorption [%]
Fine sand	0/1	2700	1.00
Medium sand	0/4	2730	1.16
Gravel	6/20	2784	0.99

The EAF slag, implemented as a partial substitute for both fine and coarse natural aggregates, characterized by a grain size of 0/16 mm, possesses a higher specific gravity of 3750 kg/m³ and a water absorption of 1.00%. Chemically, the slag is primarily composed of CaO, SiO_2, Fe_XO_Y, and MgO, which together represent approximately 90% of its total weight. Notably, the slag used in this study contains negligible amounts of free-CaO and free-MgO, which is critical for avoiding the short-term and long-term volumetric instability typically associated with these compounds [14]. To ensure adequate workability across all mixtures, a superplasticizer was incorporated in small dosages relative to the cement mass.

2.2 Mix design

The experimental campaign involved the development of four distinct concrete mixtures. The control batch, labeled PC, was composed entirely of natural aggregates, while the remaining three compositions, S10%, S25%, and S50%, integrated EAF slag as a partial replacement for natural aggregates at percentages of 10%, 25%, and 50%, respectively. To ensure a consistent water-to-cement ratio of 0.5 across all samples, the moisture content of the aggregates was determined prior to the mixing process, allowing for precise adjustments to the mix design. Additionally, the EAF slag underwent a 24-hour pre-saturation period, during which it was submerged in three-quarters of the required mixing water. This step was critical to stabilize the absorption behaviour of the slag [14].

Table 2 Mix design.

	PC	S10%	S25%	S50%
Cement [kg/m^3]	320	320	320	320
Water [l/m^3]	160	160	160	160
Fine sand 0/1 mm [kg/m^3]	95	95	95	95
Medium sand 0/4 mm [kg/m^3]	829	752	674	462
Gravel 6/20 mm [kg/m^3]	1023	904	688	412
EAF slag 0/16 mm [kg/m^3]	0	265	662	1322

Superplasticizer [l/m^3]	0.30	0.60	0.91	1.51
Water/cement ratio [-]	0.5	0.5	0.5	0.5

The physical and mechanical performance of each mixture was characterized through several evaluations. In the fresh state, these included slump (UNI EN 12350-2), air content (UNI EN 12350-7), and density (UNI EN 12350-6). In the hardened state, compressive strength tests were performed on 150x150x150 mm cubic specimens (UNI EN 12390-3) after a 28-day curing period in a controlled environment at 20±2°C with a relative humidity exceeding 95%. These formulated mixtures were subsequently employed to manufacture the specimens dedicated to the direct analysis of the aggregate interlock mechanism.

3 SPECIMENS GEOMETRY AND TEST SETUP

3.1 Specimens geometry

The experimental campaign focuses on investigating the aggregate interlock mechanism within concrete incorporating EAF slag. To achieve this, a modified version of the JSCE SF-6 methodology, originally intended for direct shear testing, was selected. This approach was preferred over traditional Z-shaped push-off specimens due to its documented effectiveness as a more stable and refined alternative in existing literature.

For each concrete mixture, five prismatic specimens with dimensions of 150x150x450 mm were made, integrating both reinforcement cages and longitudinal rebars. The inclusion of reinforcing cages made of Ø6 rebars (f_y = 596 MPa, f_u = 621 MPa) was necessary to provide structural stability during testing and to prevent premature splitting failures. Furthermore, two Ø8 longitudinal rebars (f_y = 564 MPa, f_u = 660 MPa) were positioned to cross the crack planes. These rebars served a dual purpose: they ensured the specimen remained stable by preventing unintended out-of-plane rotations and allowed for more precise monitoring of post-cracking behaviour. While the presence of these longitudinal rebars introduces a dowel effect alongside the aggregate interlock mechanism, prior research indicates that the dowel action contributes a relatively minor portion of the total shear strength. Consequently, this contribution can be isolated and accounted for during the analytical processing of the experimental data.

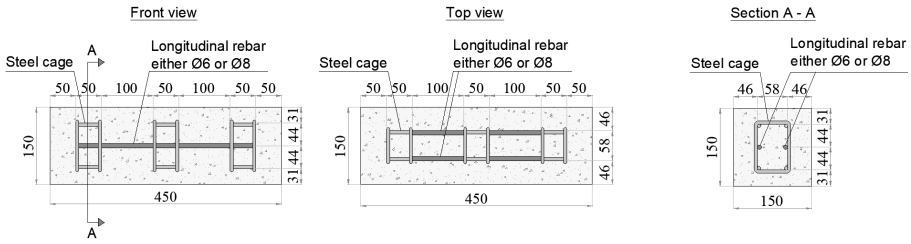


Figure 1 Geometry and reinforcement details.

3.2 Test setup

Following the 28-day curing period, notches measuring 5 mm in width and 20 mm in depth were cut around the entire perimeter of the specimens to establish a reduced cross-section of 110x110 mm. This modification was designed to pre-define the failure plane, ensuring that cracking and subsequent relative displacement would occur specifically between the central loaded block (B) and the two external supporting blocks (A and C). The experimental setup and the distribution of the monitoring system were arranged to capture the mechanical response during testing. Linear Variable Differential Transformers (LVDTs) were positioned on the front face of the specimen to continuously monitor both shear slip and crack opening increments. To ensure accuracy and symmetry in the data, two additional horizontal LVDTs were mounted on the back face of the specimen specifically to record crack width variations.

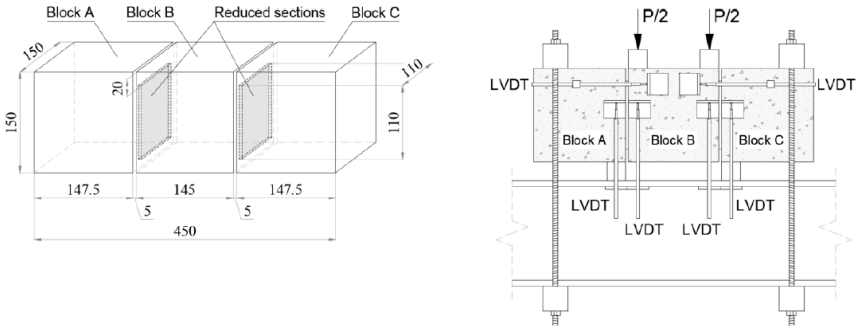


Figure 2 Specimen configuration after notches and subdivision into 3 blocks (A, B and C) (left) and load scheme and instrumentation applied (right).

4 RESULT AND DISCUSSIONS

4.1 Material characterization

The results obtained from the characterization of the four concrete mixtures, including their respective coefficients of variation (CV), are detailed in Table 3.

Table 3 Fresh and hardened properties of concretes.

	PC	S10%	S25%	S50%
Slump [mm]	170	185	185	150
Air content [%]	2.9	2.1	3.0	2.7
Density [kg/m^3]	2441	2533	2634	2836
Compressive strength [MPa]	46.17	46.20	47.85	58.79
CV	1.2%	4.5%	1.9%	5.1%

The slump remained consistent across the PC, S10%, and S25% mixtures, whereas the S50% mix exhibited a reduction in workability despite a higher dosage of superplasticizer. Regarding the air content, values were similar for the PC, S25%, and S50% batches, with the S10% mixture showing a marginally lower volume. A clear upward trend in density was observed as the substitution level of natural aggregates with EAF slag increased, a direct consequence of the slag's significantly higher specific gravity. The compressive strength for the S10% and S25% mixtures was either comparable to or slightly higher than the reference PC mix. Notably, the S50% mixture demonstrated a substantial increase in compressive performance, yielding a strength gain of approximately 27% relative to PC.

4.2 Aggregate interlock assessment

The correlation between shear stress (τ) and the average relative slip (δ) observed between blocks A, B, and C at the reduced sections is illustrated in Fig. 3. To quantify these parameters, the shear stress and the mean slip values were derived using Eq. 1 and Eq. 2, as follows:

$$\tau = \frac{P}{2 \cdot A} \tag{1}$$

$$\delta = \frac{\delta_A + \delta_{B,left} + \delta_{B,right} + \delta_C}{2} \tag{2}$$

where τ is the shear stress, P is the overall applied load (assumed equally distributed over the two slip surfaces), A is the area of the slip surface (reduced cross section 110x110mm), δ is the relative mean slip, δ_A is the slip of block A, $\delta_{B,left}$ is the slip of block B (evaluated with LVDT placed on the left side

of the block), $\delta_{B,right}$ is the slip of block B (evaluated with LVDT placed on the right side of the block), and δ_C is the slip of block C.

As illustrated in Fig. 3, all specimens demonstrated a similar pre-cracking response until reaching a slip of approximately 0.2 mm. Following the attainment of the peak load, the specimens transitioned into a softening phase. Apart from the S50% mixture, which exhibited notably higher peak load values, the capacities of the other three mixtures were relatively consistent with one another. The post-cracking stage also displayed minimal variation across the different series. Generally, the experimental data reflected low variability among the mixtures, with the primary outlier being the peak strength of the S50% batch. Despite this overall consistency, a marginal improvement in stress transfer was detectable in the mixtures incorporating EAF slag compared to PC.

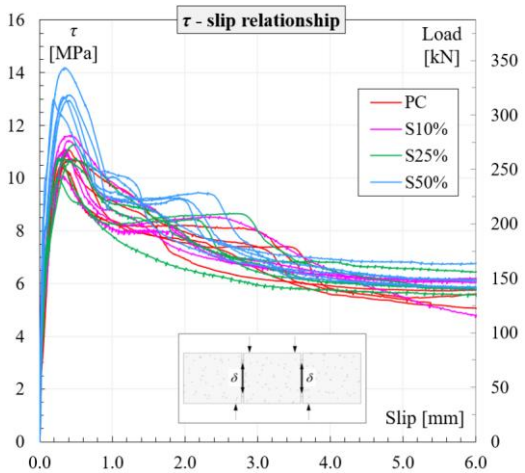


Figure 3 Shear stress (τ) vs. relative mean slip (δ).

The shear stress $\tau_{0.2}$ transferred at a crack opening equal to w_{peak} + 0.2mm is presented for each mixture in Fig. 4. The selection of a 0.2 mm increment beyond the peak crack width is based on established literature indicating that this value typically represents the critical threshold for shear collapse in structural members [15]-[16]. The graph distinguishes between two shear stress values for each mixture: the total transferred stress and the stress calculated by isolating and excluding the dowel action provided by the Ø8 longitudinal rebars. To quantify the specific contribution of this dowel effect, the analytical model proposed by Millard and Johnson [17] was employed, using Eq. 3-4-5-6:

$$F_d = F_{du} \cdot \left[1 - e^{\left(\frac{-k_i \cdot \delta}{F_{du}}\right)}\right] \tag{3}$$

$$F_{du} = 1.30 \cdot D_b^2 \cdot \sqrt{f_c' \cdot f_y \cdot (1 - A'^2)} \tag{4}$$

$$k_i = 0.166 \cdot k_f^{0.75} \cdot D_b^{1.75} \cdot E_s^{0.25} \tag{5}$$

$$k_f = 127 \cdot \beta \cdot \sqrt{f_c'} \cdot \left(\frac{1}{D_b}\right)^{\frac{2}{3}} \tag{6}$$

where β is a coefficient varying between 0.6 (longitudinal rebars placed within 25.4 mm from each other) to 1 (distance between longitudinal rebars greater than 25.4 mm, as in the present experimental campaign), D_b is the diameter of the longitudinal bar (Ø8), f'_c is the concrete compressive strength, f_y is the steel yield strength, E_s is the steel elastic modulus, A' is the ratio between the applied axial force and the yield strength of the longitudinal rebar (A' is 0 in this case, since no external axial force was applied), δ is the slip along the shear surface obtained experimentally, F_{du} is the ultimate force related to the dowel effect, and F_d is the force related to the dowel effect given by the longitudinal rebar.

The data presented in the graph indicates that at the specific crack opening of w_{peak} + 0.2mm, the shear strength contribution attributed to the dowel effect remains relatively minor, accounting for approximately 8-10% of the total capacity. This observation reinforces the conclusion that aggregate interlock serves as the primary mechanism for shear transfer in these elements. Furthermore, the results

demonstrate that the interlocking mechanism is marginally more efficient in the EAF slag mixtures compared to the conventional PC concrete, with the most pronounced improvement observed in the S50% specimens characterized by the highest slag content.

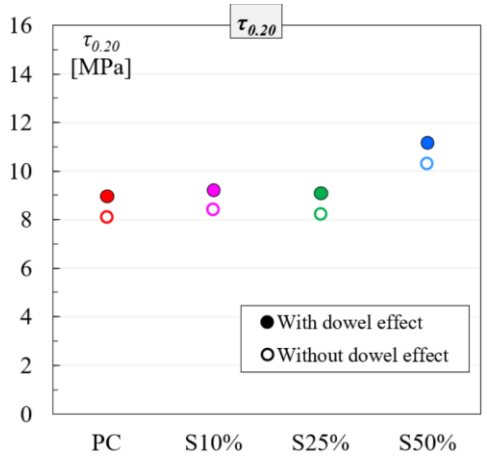


Figure 4 Comparison between shear stress in presence or absence of the dowel effect, for a crack width equal to w_{peak} + 0.2 mm.

5 CONCLUSIONS

The objective of this research was to examine the contribution of the aggregate interlock mechanism, specifically the capacity of aggregates to transmit shear stresses following crack formation in concrete specimens made with various replacement levels of EAF slag. All specimens, including those produced with conventional natural aggregates and those incorporating partial substitutions with EAF slag, showed a comparable shear behavior characterized by an initial elastic response, subsequent crack formation, and a progressive softening phase. Moreover, the correlation between crack opening and slip was similar in both types of mixtures, suggesting that the deformation mechanisms developing along the crack surface were essentially alike. For crack widths typically associated with shear failure in reinforced concrete structures (0.10-0.20 mm), the incorporation of EAF slag improved shear transfer mechanisms governed by aggregate interlock, with greater benefits observed as the replacement level increased. This enhancement can be linked to the intrinsic characteristics of the slag particles, namely their pronounced angularity, rough surface morphology, and elevated stiffness. These features promote local crack deviation, generate additional contact areas between crack faces, and reduce the likelihood of particle crushing. The effect was especially evident for mixtures containing 50% slag replacement, which showed shear stress increases of approximately 20-25% relative to the reference concrete. In conclusion, based on the findings from both the material characterization and the aggregate interlock analysis, the integration of EAF slag as a partial substitute for natural aggregates in concrete production is shown to be a viable strategy. This approach aligns with the fundamental principles of environmental sustainability and the circular economy by facilitating the high-value reuse of industrial products.

Acknowledgements

The authors are grateful to Arvedi Spa, in particulary Roberto Muselli, for providing the EAF slag. We also would like to thank the technicians of the Material Testing Laboratory “Pietro Pisa” of the University of Brescia, Augusto Botturi, Andrea Delbarba and Luca Martinelli, for their fundamental support during the experimental activities presented in this paper.

References

[1] Park, Robert, and Thomas, Paulay. 1975. *Reinforced Concrete Structures*, John Wiley & Sons.

[2] Mattock, Alan H., Li, Wing-Kwong , and Wang, Te-Chao. 1976. "Shear transfer in lightweight reinforced concrete." *PCI J* 21(1), 20–39. doi:10.15554/pcij.01011976.20.39

[3] Presvyri, Stella. 2019. "Aggregate interlock - Extending the aggregate interlock model to high strength cooncrete." MSc thesis, Delft University of Technology.

[4] Hofbeck, John A., Ibrahim, Ibrahim O., and Mattock, Alan H.1969. "Shear transfer in reinforced concrete." *J. Am. Concr. Inst.* 66(2), 119–128. doi:10.14359/7349

[5] Walraven, Joost C., Vos, Evert, and Reinhardt, Hans-Wolf. 1979a. "Experiments on shear transfer in cracks in concreet - Part I: Description of results." *Technical report* 5-79-3, Delft University of Technology. https://repository.tudelft.nl/file/File_084fb08f-d622-43b1-8edd-0664d66bbd68?preview=1

[6] Walraven, Joost C. 1979b. "Experiments on shear transfer in cracks in concreet - Part II: Analysis of results." *Technical report* 5-79-10, Delft University of Technology. https://repository.tudelft.nl/file/File_d55d4724-365a-4988-918c-a1e67de9601a?preview=1

[7] Walraven, Joost C., and Reinhardt, Hans-Wolf. 1981a. "Theory and experiments on the mechanical behaviour of cracks in plain and reinforced concrete subjected to shear loading." *HERON J.* 26(1A).

[8] Tassios, Theodossius P., and Vintzeleou, Elizabeth N. 1987. "Concrete-to-concrete friction." *J. Struct. Eng.* 113(4), 832–849. doi:10.1061/(ASCE)0733-9445(1987)113:4(83)2

[9] Walraven, Joost C. 1981b. "Fundamental analysis of aggregate interlock." *J. Struct. Div.* 107(11), 2245–2270. doi:10.1061/JSDEAG.0005820

[10] Faleschini, Flora, and Pellegrino, Carlo. 2013. "Experimental behavior of reinforced concrete beams with electric arc furnace slag as recycled aggregate." *ACI Mater. J.* 110(2), 197–205. doi:10.14359/51685534

[11] Faleschini, Flora, Trento, Daniel, Ortega-López, Vanesa, and Zanini, Mariano Angelo. 2023. "Shear transfer in fly ash concrete with electric arc furnace aggregates." *Mag. Concr. Res.* 75(17), 906–918. doi:10.1680/jmacr.22.00280

[12] FIP (Federation Internationale de La Precontrainte), 1978. "Shear at the interface of precast and in situ concrete." *FIP Technical Report*. https://www.fib-international.org/publications/fip-reports/shear-at-the-interface-of-precast-and-in-situ-concrete-pdf-detail.html

[13] JSCE (Japanese Society of Civil Engineers) 1990. *JSCE-SF6 - Method of test for shear strength of steel fiber reinforced concrete.* http://library.jsce.or.jp/Image_DB/spec/con_lib/no03/CLIno03_0067.pdf

[14] Piemonti, Alan. 2023. "Electric arc furnace slag (EAF): use in concrete for structural applications." PhD diss., University of Brescia.

[15] Xiao, Jianzhuang, Xie, Hui, and Yang, Zhenhua. 2012. "Shear transfer across a crack in recycled aggregate concrete." *Cem. Concr. Res.* 42(5), 700–709. doi: 10.1016/j.cemconres.2012.02.006

[16] Conforti, Antonio, Minelli, Fausto, and Plizzari, Giovanni Antonio. 2017. "Influence of width-to-effective depth ratio on shear strength of reinforced concrete elements without web reinforcement." *ACI Struct. J.* 114(4), 995–1006. doi:10.14359/51689681

[17] Millard, Steven G., and Johnson, Roger P. 1984. "Shear transfer across cracks in reinforced concrete due to aggregate interlock and to dowel action." *Mag. Concre. Res.* 36(126), 9–21. doi:10.1680/macr.1984.36.126.9

The effect of waste building materials as cement replacement on the properties of sustainable mortars

Mario Filipović, Goran Baloević

Faculty of civil engineering, architecture and geodesy,
University of Split,
Matice hrvatske 15, 21000 Split, Croatia

Summary
Cement production has a large impact on the environment due to significant emissions of carbon dioxide and use of natural resources. Current scientific research and environmental strategies are focused on using alternative materials that could replace cement partially or fully in the construction industry. This research explores the potential of using recycled waste building materials as supplementary cementitious materials and mineral fillers in mortars. The study aims to evaluate how fine powders obtained from crushed concrete (RCP), clay brick (RCBP) and limestone (LF) influence the performance of mortars. Laboratory mixes with replacement up to 20% were examined. The samples were compared with a reference mixture. This paper presents and discusses the fresh properties, mechanical performance and durability (capillary water absorption, shrinkage, expansion), drawing the main conclusions.

1 INTRODUCTION

The use of recycled materials as a replacement for a portion of the primary binder (SCM), i.e., cement, is motivated by a number of environmental, technical and economic factors. The primary motivation for replacing ordinary Portland cement (OPC) with recycled powder lies in the drastic reduction of greenhouse gas emissions [1], [2]. It is estimated that the production of one ton of clinker emits approximately 850 kg to 1 ton of CO_2. The production of cement (OPC) requires very high temperatures (1450–1550 °C), which makes it one of the most demanding industrial processes [1], [3], [4]. Cement-based materials are the second most used products after water, with production increasing by 2.5% annually [1]. Regarding the amount of waste generated globally, construction waste accounts for approximately 30% to 40% of total solid waste [5], [6], [7]. The integration of such waste into construction materials is essential for achieving circular economy goals by transforming waste into reusable raw materials.

Scientific studies show that recycled construction waste powders serve not only as inert fillers but also can act as active components contributing to the cement matrix. Clay brick powder contains amorphous aluminosilicates that react with calcium hydroxide forming additional C-S-H and C-A-S-H phases [3], [7], [8], [9]. As a highly porous material, brick enables water absorption, which is gradually released within the matrix, supporting continuous cement hydration and reducing autogenous shrinkage, which is particularly important in high-performance concretes [7], [8], [9], [10], [11]. The most common replacement levels of cement with RCBP are from 10% to 20% [3], [7]. Concrete, as a widely studied material, is highly suitable for reuse. Recycled concrete is unique because it may contain particles of old, unhydrated cement clinker that can be reactivated upon contact with water [10], [12]. Furthermore, studies indicate that heating concrete powder to temperatures of 450–600 °C (TARC–thermoactivated recycled concrete) dehydrates old hydration products, resulting in a material with favourable hydraulic and pozzolanic properties similar to OPC [1]. One of the well-known fillers is limestone powder. In addition to filling the voids between particles (filler effect), limestone particles can act as nucleation sites that accelerate cement hydration, primarily of tricalcium silicate (C_3S) [13]. Instead of being used as cement replacement only, recycled materials can also be used as aggregate replacement in coarser fractions (0–4 mm for sand and >4 mm for coarse aggregate) [2], [8], [14]. Regarding mechanical properties, many studies have reported an initial decrease (early strength) due to reduced clinker content [7], [3]. However, at later ages, strength recovery occurs due to the pozzolanic reaction. Mortars with 10% and 20% replacement often achieve similar or even higher strengths than reference mortars after 28 or 90 days [3] .

This study is focused on the investigation of the fresh, mechanical and durability properties of mortars produced with recycled clay brick powder (RCBP), recycled concrete powder (RCP) and

limestone powder (LF). The objective of this research is to evaluate how these materials influence individual properties when used both as a partial replacement of cement (SCM) and as an addition to cement (mineral filler) in the context of sand replacement. Based on the conducted literature review, it has been concluded that cement replacement is most effective at the levels of 10% and 20%, therefore the same approach was applied in this study. In addition to test and analysis of the mechanical properties, fresh and hardened durability properties were also evaluated, and the results were compared and discussed in detail.

2 EXPERIMENTAL DETAILS

2.1 Materials

For the purpose of laboratory mixtures, recycled powders were prepared prior to testing. Portland cement CEM II/A-LL 42.5R with density of 3.15 kg/dm^3 was used. Cement has a standardised compressive strength of 27 MPa at 7 days and 52 MPa at 28 days. Brick powder (RCBP) was collected from a manufacturer of brick elements as a by-product of processing and grinding of hollow clay bricks. Concrete powder (RCP) was collected from a local contractor during the grinding of reinforced concrete base slabs. Limestone filler (LF) was obtained from an aggregate producer and is certified for use in concrete and mortar. Specific densities were determined according to EN 1097-7 as 2.62 kg/dm^3, 2.57 kg/dm^3 and 2.63 kg/dm^3 for RCBP, RCP and LF, respectively.

Since RCBP and RCP contained coarser particles (>100 µm), additional grinding and sieving were required. RCBP was sieved through a 100 µm sieve. RCP was dried and ground in a ball mill (1 kg material : 3 kg steel balls) for 2.5 hours, then sieved (<100 µm, 95% passing). Sand (0–4 mm) of limestone origin was used and tested according to EN 933-1 and EN 1097-6. The sand was pre-saturated to prevent water absorption during mixing. Fine particles content in the sand (<0.063 mm) was 9.95%. Tap water was used for all laboratory mixtures.



Fig. 1 Powder materials (a-recycled concrete powder RCP, b-limestone powder LF, c-recycled clay brick powder RCBP)

2.2 Mix design and specimen preparation

To understand the influence of RCBP, RCP and limestone filler (LF), a total of 10 recipes shown in Table 1 were prepared. The initial 7 recipes (the first recipe represents the reference mix) were defined based on cement replacement by mass in amounts of 10% and 20%. The remaining 3 recipes were made using volumetric replacement of sand while the amount of cement was equal as in the reference mix. Volumetric replacement of sand is expressed via mass using the previously obtained densities of each powder. For the first seven mixtures, the mixing process was carried out by first homogenising the binder and recycled powder in a dry state, after which water and sand were added in accordance with the EN 196-1 standard. In contrast, for the BP, CP and OP mixtures, the recycled powder was previously mixed with the sand and introduced into the mixture simultaneously with the sand, also in accordance with EN 196-1. The water-binder ratio for all mixtures was kept constant at 0.5 to observe the influence of additives on workability and mechanical properties compared to the reference mortar. Mixture labels were formed as follows: B-limestone powder (LF), C-recycled concrete powder (RCP) and O-recycled brick powder (RCBP). Suffix “P” denotes mixtures where the powder replaces sand by volume (e.g., BP10, CP10, OP10).

Table 1 Mortar mix proportions (kg per 1 m³ of mortar)

Mix ID	Binder (cement)	Replacement type	RCBP	RCP	LF	Water	Sand	w/b
REF	450	Cement (mass)				225	1350	0.5
O10	450	Cement (mass)	45			225	1350	0.5
O20	360	Cement (mass)	90			225	1350	0.5
B10	405	Cement (mass)			45	225	1350	0.5
B20	360	Cement (mass)			90	225	1350	0.5
C10	405	Cement (mass)		45		225	1350	0.5
C20	306	Cement (mass)		90		225	1350	0.5
BP10	450	Sand (volume)			135	225	1215	0.5
OP10	450	Sand (volume)	110			225	1215	0.5
CP10	450	Sand (volume)		120		225	1215	0.5

Note MixID10 – stands for 10% replacement, MixID20 – stands for 20% replacement, O – recycled clay brick powder (RCBP), B-limestone filler and C - recycled concrete powder (RCP).

2.3 Methods

Test methods include the determination of setting time, consistency, mechanical properties, dimensional stability and water absorption. Setting time and standard consistency are determined using a Vicat apparatus in accordance with EN 196-3, by monitoring needle penetration in samples prepared with varying water contents. The consistency of fresh mortar is evaluated using a flow table in accordance with EN 1015-3, by measuring the spread diameter in two perpendicular directions. Mechanical properties are determined in accordance with EN 1015-11, including compressive strength tests performed on 40 × 40 mm specimens after 7 and 28 days. Dimensional stability, including shrinkage and swelling, is assessed according to EN 12617-4 by monitoring length changes of mortar specimens over time under controlled conditions. Capillary water absorption is determined in accordance with EN 13057 on pre-dried specimens by measuring the increase in mass at specified time intervals.

2.4 Results and discussion

2.4.1 Setting time (Vicat apparatus)

The initial setting time is shown in

Fig. 2. Cement replacement resulted in a shortening of the initial setting time, most pronounced with RCP due to unhydrated clinker particles reactivating in water [10], followed by LF acting as nucleation sites for C_3S hydration [13], while RCBP showed negligible influence, indicating its pozzolanic reaction occurs at later ages.

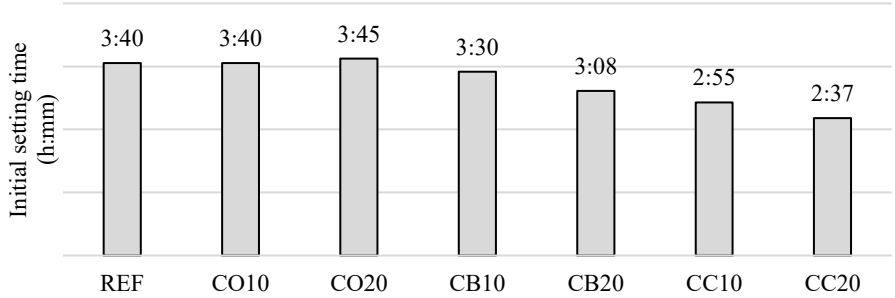


Fig. 2 Initial setting time
Note: CO–cement/RCBP, CB-cement/LF, CC–cement/RCP

2.4.2 Workability (flow test per EN 1015-3)



Fig. 3 Workability of mortars

By analysing the workability results of the mortars on the flow table (Fig. **4**), it can be seen that the reference mixture (REF) gives the highest spread value of 167.5 mm. The incorporation of any powder as a replacement of cement or sand results in a reduction of workability compared to the REF. By partial replacement of the cement with RCBP from 10% to 20%, the workability was reduced from 165 mm to 155 mm, respectively, confirming the high water absorption capacity of this material. RCP causes significant reduction in workability to 150 mm, suggesting that its particle morphology creates greater internal friction within the mixture compared to RCBP. The highest negative impact on workability was recorded in mixture OP10 replacing sand with clay brick powder. Unlike other materials the mixture with a high proportion of limestone filler (LF) B20 shows a slight increase in workability.

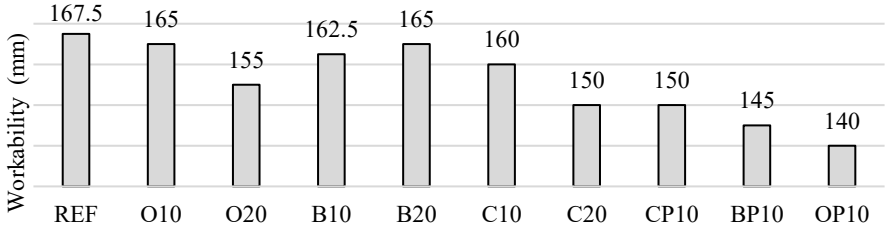


Fig. 4 Flow table test results

2.4.3 Compressive strength

Fig. 5 presents the results of compressive strength after 7 and 28 days. According to the obtained results, significant deviations in mechanical behaviour can be observed depending on whether recycled powders are used as a cement replacement (SCM) or as a partial replacement of the sand. Samples O10 and O20 show relatively similar values compared to the reference mixture. Although sample O20 has a larger reduction in strength, these values suggest a subsequent contribution to the pozzolanic reaction of the brick, which compensates for the loss of cement. Mixtures B10 and B20 show a similar trend as samples with RCBP, but with slightly greater reduction. Mixtures C10 and C20 show the largest drop in strength, indicating that RCP in these conditions acts primarily as an inert filler without a significant pozzolanic or hydraulic contribution that would compensate for the reduction of cement. The best values are visible in mixtures where the cement remains at the same level as in the reference mixture and recycled powders are used as substitutes of sand. RCBP reaches extraordinary results (OP10) of 73.95 MPa after 28 days, a 19.3% higher value compared to REF. Already after 7 days, this mortar had higher compressive strength compared to REF after 28 days. This increase results from synergistic effects: RCBP densifies the interfacial transition zone (ITZ) as a fine filler, while its amorphous aluminosilicates react with $Ca(OH)_2$ from cement hydration, forming additional C-S-H and C-A-S-H phases [3], [9].

2.4.4 Pozzolanic activity index

The pozzolanic index PAI is defined as the relative ratio of the compressive strength of mortar with a proportion of replacement material and the compressive strength of the reference mortar (REF). For the analysis of the pozzolanic index, mixtures with partial cement replacement (B, C and O series) are relevant, since PAI is standardly calculated based on clinker replacement. RCBP shows the most pronounced pozzolanic character among the tested materials. PAI for sample O10 increases from 88.9% (7 days) to 95.7% (28 days). Even at 20% cement replacement for O20, the mortar retains 88.3% of the strength of the reference mortar. This suggests that brick powder is not just an inert filler. For limestone filler and RCP, it can be said that they influence more as inert fillers or weakly reactive materials since PAI for the B series decreases from 90.1% to 89%. Mixture C20 with RCP addition showed the lowest PAI after 7 days (76.5%). Although a slight recovery occurs after 28 days, RCP remains the least effective cement replacement. By comparing the results, RCBP is the only material where PAI consistently grows in the later phase at all clinker replacement levels. According to criteria often used in literature (minimum 75% and 90% PAI after 28 days), the PAI value of 95.7% for O10 at 28 days is consistent with values reported in literatures [3], [7], confirming RCBP as a viable SCM comparable to fly ash or natural pozzolan.

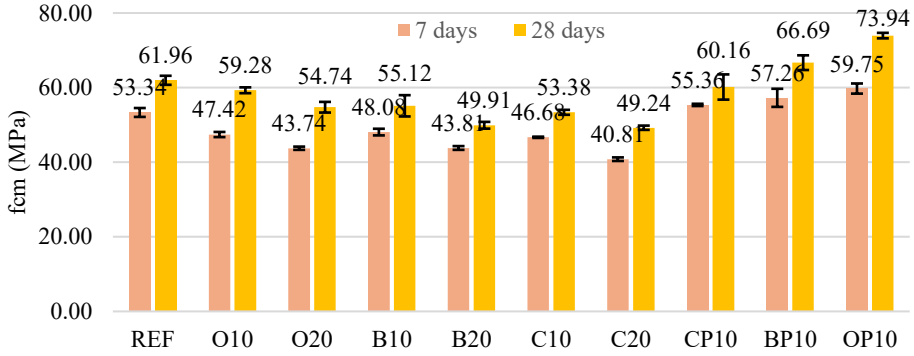


Fig. 5 Compressive strength at 7 and 28 days (Note: Error bars represent standard deviation n=3)

2.4.5 Shrinkage and expansion

Mortar drying shrinkage is a critical factor for crack formation and the obtained results show large deviations between cement replacement and sand replacement. It can be observed that replacing 10% and 20% of cement with RCBP and limestone filler results in lower shrinkage compared to the reference mortar (0.47 mm/m). Samples B10 (0.37 mm/m), O20 (0.39 mm/m), and O10 (0.44 mm/m) show better dimensional stability. On the other hand, a highly negative impact of sand replacement can be observed (OP10, BP10, CP10). These mixtures show the largest shrinkage for all samples. Replacing rigid sand grains with fine powders increases paste volume (the only shrinking phase) and total specific surface area, intensifying capillary tension during drying.

It is important to note that although the OP10 mixture achieves relatively high compressive strength values, it does not necessarily guarantee dimensional stability, since OP10 showed almost twice greater shrinkage (1.07 mm/m) than the reference mortar (0.47 mm/m). These results suggest that using these powders may not necessarily be favourable in mixtures when used as a sand replacement, as they can cause critical volume instability despite excellent mechanical properties.

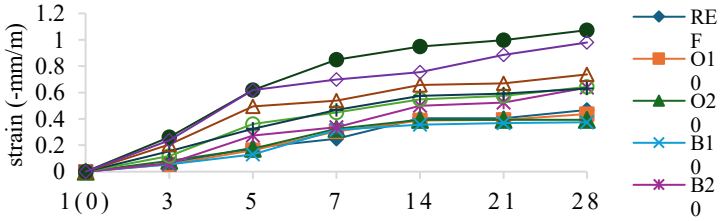


Fig. 6 Drying shrinkage of specimens

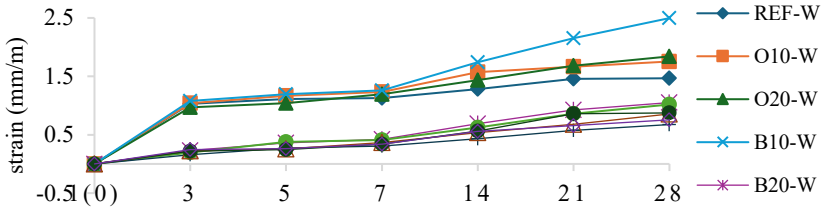


Fig. 7 Expansion of specimens

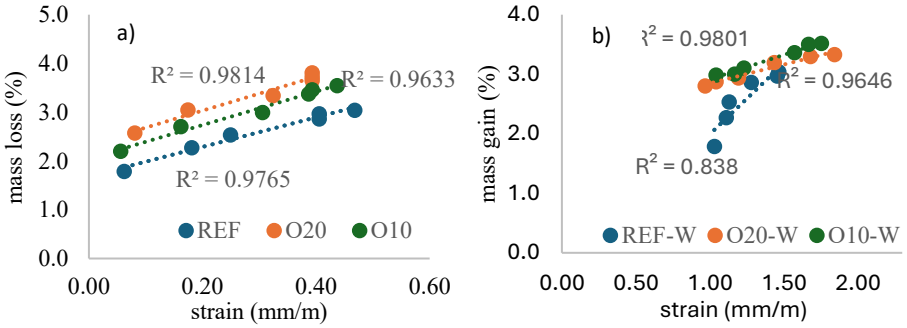


Fig. 8 a) Shrinkage-mass loss correlation, b) Expansion-mass gain correlation. Note: Specimens designated with the suffix "W" were immersed in water throughout the testing period to evaluate their swelling behaviour.

Specimens immersed in water (Fig. 7) show a different dimensional response than drying specimens. LF mixtures exhibit the largest swelling, which may be attributed to the higher residual $Ca(OH)_2$ content, as LF does not consume it through pozzolanic reaction. RCBP and RCP mixtures show reduced swelling, likely because part of the $Ca(OH)_2$ is consumed by pozzolanic reaction or clinker reactivation. The correlation between mass gain and expansion strain in Fig. 8 (R^2 from 0.84 to 0.98) indicates that water uptake is the primary driver of dimensional change.

2.4.6 Water absorption test

The absorption analysis follows the process from the first 12 minutes to 24 hours, providing insight into how different proportions of the mentioned materials redefine the diffusion properties of the material. All samples show the most intense absorption in the first interval, which is characteristic of filling surface and coarse capillary pores.

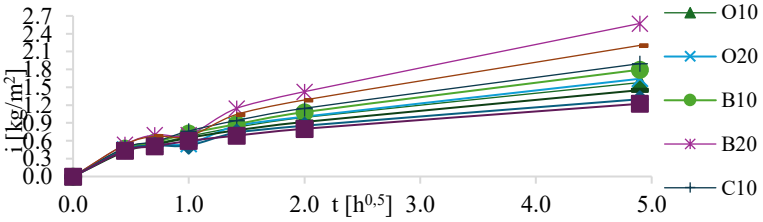


Fig. 9 Water absorption of specimens

The reference mortar (REF) has the lowest initial absorption (0.35%), indicating that the pure cement matrix has the most closed initial structure. Samples made with RCBP show moderate initial values (around 0.40%), suggesting that although brick has high porosity, its fine granulation partially limits the instantaneous penetration of water. After 24 h, the differences between samples become more pronounced, revealing the long-term absorption capacity of the matrix. Sample B20 achieves the

highest cumulative absorption of 2.33%, followed by C20 with 2.03%. Samples O10 and O20 have significantly lower total absorption, suggesting that the pozzolanic reaction of the brick refines the pores over time and slows further absorption. Regarding sand replacement with these materials, sample OP10 has a cumulative absorption of only 1.13%, which is less even than the reference mortar (1.25%). Although OP10 has the largest shrinkage and the highest compressive strength, it absorbs the least water. This proves that an extremely dense matrix with very fine capillaries was created in this mixture. CP10 and BP10 also show relatively low absorption, suggesting that these powders act as micro-fillers when added alongside a full cement dose. The extreme values – lowest absorption in OP10 (which also reaches the highest strength) and highest in B20 – may reflect differences in capillary pore connectivity, with potential implications for durability.

3 CONCLUSION

This paper summarises the influence of recycled clay brick powder (RCBP), recycled concrete powder (RCP), and limestone powder (LF) on fresh, mechanical and durability properties when applied as SCM at 10% and 20% levels and as a partial sand replacement as well. All replacement additives reduce the workability of the mortar compared to the reference sample (REF = 167.5 mm). The largest reduction in properties was observed in OP10 and RCP mixtures (150 mm). Limestone filler (LF) at 20% replacement slightly improves workability, which can be attributed to the particle shape. All replacement materials shortened the initial setting time, an effect most pronounced with RCP, which can be attributed to nucleation by fine particles and reactivation of unhydrated clinker.

Compressive strength results show a clear difference depending on whether the powders are used as SCM or as a sand replacement. When used as SCM, all additives reduce compressive strength compared to REF, with samples containing RCP exhibiting the largest reduction; thus, RCP acts primarily as an inert filler with the lowest pozzolanic index. RCBP demonstrates the best properties, with a pozzolanic index of 88.9% increasing to 95.7% from 7 to 28 days at 10% cement replacement. All additions at 10% replacement fulfil the minimum PAI value conditions, qualifying them as suitable SCM materials. In volumetric sand replacement without reducing the cement dose, an increase in compressive strength compared to REF is observed (OP10 has 19.3% higher strength), which is attributed to the synergistic influence of matrix filling with fine particles and pozzolanic activity.

Regarding dimensional stability, replacing cement with RCBP and LF improves stability compared to REF (0.47 mm/m), with B10 achieving the lowest shrinkage values (0.37 mm/m). Conversely, samples with sand replacement experience the highest shrinkage, where OP10 reaches 1.07 mm/m, nearly double that of REF. Increased paste volume consequently leads to increased shrinkage. For samples immersed in water, RCP mixtures show the greatest resistance to swelling, while samples with LF exhibit exceptionally large swelling (B10-W – 2.5 mm/m), potentially leading to degradation in moist environments.

Capillary water absorption reflects permeability trends. In cement-replacement samples, B20 and C20 recorded the highest cumulative absorption (2.33% and 2.03%, respectively), reflecting a lack of materials to fill the pores. It is important to note that the OP10 sample had the lowest cumulative absorption (1.13%), even lower than REF, which progressively decreases during curing.

Overall, RCBP proved to be the most promising material. At 10% replacement, it functions as an effective SCM, showing good pozzolanic properties and a positive impact on dimensional stability. Its application as a sand replacement yields exceptionally high mechanical properties and low permeability. These findings support the wider use of construction waste as a sustainable cement replacement. Future testing should include long-term property analysis (e.g., at 90 days) and microstructural analysis (SEM, XRD, TGA) to fully understand the long-term effects of these materials.

References

[1] Getachew, Ephrem Melaku, Yifru, Begashaw Worku, Taffese, Woubishet Zewdu, and Yehualaw, Mitiku Damtie. 2023. "Enhancing Mortar Properties through Thermoactivated Recycled Concrete Cement", *Buildings* 13:2209, Accessed March 25, 2025. doi:10.3390/buildings13092209.

[2] Kalinowska-Wichrowska, Katarzyna, Pawluczuk, Edyta, Bołtryk, Michał, Jimenez, Jose Ramón, Fernandez-Rodriguez, Jose Maria, and Suescum Morales, David. 2022. "The Performance of Concrete Made with Secondary Products—Recycled Coarse Aggregates,

Recycled Cement Mortar, and Fly Ash–Slag Mix", *Materials* 15:1438, Accessed February 15, 2025. doi:10.3390/ma15041438.

[3] Sallı Bideci, Özlem, Bideci, Alper, and Ashour, Ashraf. 2024. "Utilization of Recycled Brick Powder as Supplementary Cementitious Materials—A Comprehensive Review", *Materials* 17:637, Accessed December 16, 2025. doi:10.3390/ma17030637.

[4] Zhao, Yasong, Gao, Jianming, Liu, Chuanbei, Chen, Xuemei, and Xu, Zhenhai. 2020. "The particle-size effect of waste clay brick powder on its pozzolanic activity and properties of blended cement", *Journal of Cleaner Production* 242:118521, Accessed June 13, 2025. doi:10.1016/j.jclepro.2019.118521.

[5] Chen, Xue-Fei, Zhang, Xiu-Cheng, and Peng, Ying. 2025. "Recycled Clay Brick Powder as a Dual-Function Additive: Mitigating the Alkali–Silica Reaction (ASR) and Enhancing Strength in Eco-Friendly Mortar with Hybrid Waste Glass and Clay Brick Aggregates", *Materials* 18:2838, Accessed January 25, 2026. doi:10.3390/ma18122838.

[6] Martínez-García, Rebeca, Sánchez de Rojas, María Isabel, Morán-del Pozo, Julia María, Fraile-Fernández, Fernando J., and Juan-Valdés, Andrés. 2021. "Evaluation of Mechanical Characteristics of Cement Mortar with Fine Recycled Concrete Aggregates (FRCA)", *Sustainability* 13:414, Accessed March 25, 2025. doi:10.3390/su13010414.

[7] Wu, Jian-Dong, Guo, Li-Ping, and Qin, Yao-Yi. 2021. "Preparation and characterization of ultra-high-strength and ultra-high-ductility cementitious composites incorporating waste clay brick powder", *Journal of Cleaner Production* 312:127813, Accessed March 21, 2025. doi:10.1016/j.jclepro.2021.127813.

[8] Huang, Qian, Zhu, Xiaohong, Xiong, Guangqi, Wang, Chaoqiang, Liu, Dongsheng, and Zhao, Liang. 2021. "Recycling of crushed waste clay brick as aggregates in cement mortars: An approach from macro- and micro-scale investigation", *Construction and Building Materials* 274:122068, Accessed June 25, 2025. doi:10.1016/j.conbuildmat.2020.122068.

[9] Mansoor, Saif Saad, Hama, Sheelan Mahmoud, and Hamdullah, Dhifaf Natiq. 2024. "Effectiveness of replacing cement partially with waste brick powder in mortar", *Journal of King Saud University - Engineering Sciences* 36:524–32, Accessed March 21, 2025. doi:10.1016/j.jksues.2022.01.004.

[10] Chen, Xi, Li, Ying, Bai, Hualei, and Ma, Liyuan. 2021. "Utilization of Recycled Concrete Powder in Cement Composite: Strength, Microstructure and Hydration Characteristics", *Journal of Renewable Materials* 9:2189–2208, Accessed June 12, 2025. doi:10.32604/jrm.2021.015394.

[11] Mohammed, Tarek Uddin, Joy, Jamil Ahmed, Zahid, Chowdhury Zubayer Bin, and Islam, Redwan Ul. 2024. "Investigating the synergistic effects of internal curing and pozzolanic activity in mortar utilizing clay-burnt brick fines", *Heliyon* 10:e38739, Accessed March 16, 2025. doi:10.1016/j.heliyon.2024.e38739.

[12] Sun, Chang, Chen, Qiuyi, Xiao, Jianzhuang, and Liu, Weidong. 2020. "Utilization of waste concrete recycling materials in self-compacting concrete", *Resources, Conservation and Recycling* 161:104930, Accessed June 12, 2025. doi:10.1016/j.resconrec.2020.104930.

[13] Gudissa, Wendimu, and Dinku, Abebe. 2010. "The Use of Limestone Powder as an Alternative Cement Replacement Material: An Experimental Study." *Journal of EEA* 27: 33–43.

[14] Debieb, Farid, and Kenai, Said. 2008. "The use of coarse and fine crushed bricks as aggregate in concrete", *Construction and Building Materials* 22:886–93, Accessed March 25, 2025. doi:10.1016/j.conbuildmat.2006.12.013.

Water absorption of crushed sand: Measurement and impact on mortars performances

Manel BOUDIAF[1,2], Ouali AMIRI[1], Emmanuel ROZIERE[1], Jerome CLAVERIE[1], Vincent RELLIER[2], François CUSSIGH[2] and Romain LAFON[2]

[1] Civil Engineering and Mechanics Research Institute (GeM), UMR CNRS 6183
Nantes University
58 Rue Michel Ange, BP 420, 44600, Saint-Nazaire, Cedex, France.

[2] VINCI Construction, France

Summary

Crushed sand (CS) is increasingly used as a sustainable alternative to natural river sand in mortar and concrete production, making the accurate characterization of its physical properties of pivotal importance, particularly water absorption which has a direct impact on the effective water content of the mix. This study evaluates manufactured sands from various petrographic origins to investigate how water absorption measurement method influences mortar performance. The European standard EN 1097-6 and an evaporative method were employed to determine the water absorption capacities of each sand type, the results revealed significant discrepancies in water absorption values between the two methods. Mixes were then proportioned based on absorption values obtained from each method to assess the impact on fresh and hardened properties. Additionally, water porosity measurements of the samples were conducted to estimate the actual effective water content and to identify which measurement approach more accurately represents the true material behavior.

1 INTRODUCTION

The extensive use of concrete in modern construction has resulted in the overexploitation of natural sand resources from rivers and coastal areas, raising environmental concerns. Consequently, manufactured sand has increasingly been considered as a sustainable alternative aggregate for concrete production However, these materials often exhibit different physical characteristics compared to river sands according to their mother rock and crushing processes. Among these characteristics, water absorption behavior plays a particularly critical role, as it strongly influences both the fresh and hardened properties of concrete through its effect on the availability of effective water in the mix which is directly impacted by the amount of water absorbed by aggregates influencing workability and strength development. The water absorption is measured commonly using standard EN 1097-6 [4], the test was de-signed mainly for rounded natural aggregates since the use of other types of such as the manufactured ones was not very common, the particles are saturated then dried to attend a saturated surface dry (SSD) condition (Fig. 1) in which the intragranular porosity is completely filled with water, without any excess water on the surface of the grains. To verify that this state is achieved, the standard specifies the use of a slump test for fine aggregates. For natural rounded sand, a dry sample typically forms a stable conical pile with a slope angle between 15° and 30°. When additional water is introduced, the capillary menisci develop between particles, reducing the slump and increasing the cone angle, this clear change in behavior enables the operator to accurately identify the SSD [3]. In contrast, crushed sands display inherently low slumps even in dry conditions due to their angular shape, rough surface (Fig. 3) and higher powder content [1]. These characteristics enhance interparticle friction and enable the sand to maintain its conical shape, making it less sensitive to moisture variation. Moreover, the tamping process (15 strokes per layer) further stabilizes the cone, making identification of the SSD state more difficult and less reliable. To overcome these limitations, an evaporative method [2] based on controlled drying of pre-saturated particles has been proposed. As drying progresses, the inter-particle water gradually evaporates until only the intra-particle water remains within the sample. At this point, a marked decrease in the drying rate is observed. The authors suggested that this transition can be used to determine the water absorption capacity of fine particles. The results of [3] suggest that this method is not suitable for all porous particles but should be suitable for crushed and recycled sand. In this paper,

the two methods for measuring water absorption are compared through an experimental study on mortars prepared with four different manufactured sands.

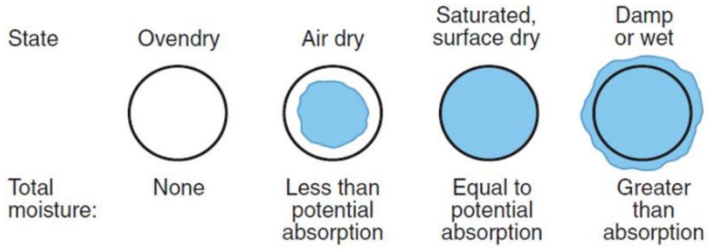


Fig. 1. Different states of moisture content in aggregates (from [6])

2 MATERIALS AND METHODS

2.1 Materials

The Portland limestone cement CEM II/A-LL 42 with a specific surface area of 4600 cm2/g and a density of 3.03g/m3 was used in this study. Four crushed sands were provided from different quarries in France. These materials exhibited distinct petrographic characteristics: CSA was derived from amphibolitic rock, CSB from granitic rock, CSC from hornfels, and CSD from gneissic rock. The particle size distribution of the sands is presented in Fig. 2 and Table 1 compiles their physical properties (fines content, fineness modulus, sand equivalent test, and specific density).

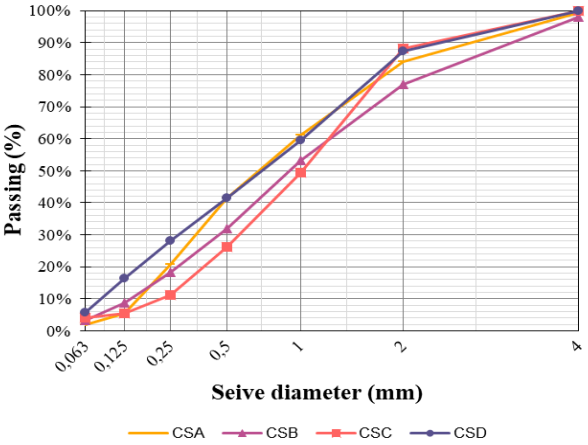


Fig. 2 Grading curves of tested sands

Table 1 Physical characteristics of the crushed sands

Sands	CSA	CSB	CSC	CSD
Specific density (kg/m^3)	2841	2630	2753	2733
Fineness modulus	2.88	3.13	3.20	2.67
Sand Equivalent (%)	82	80	77	73
Methylene blue value (g/kg)	0.5	0.4	0.6	0.4
Powder content <63µm (%)	1.9%	3.9%	4.2%	6%

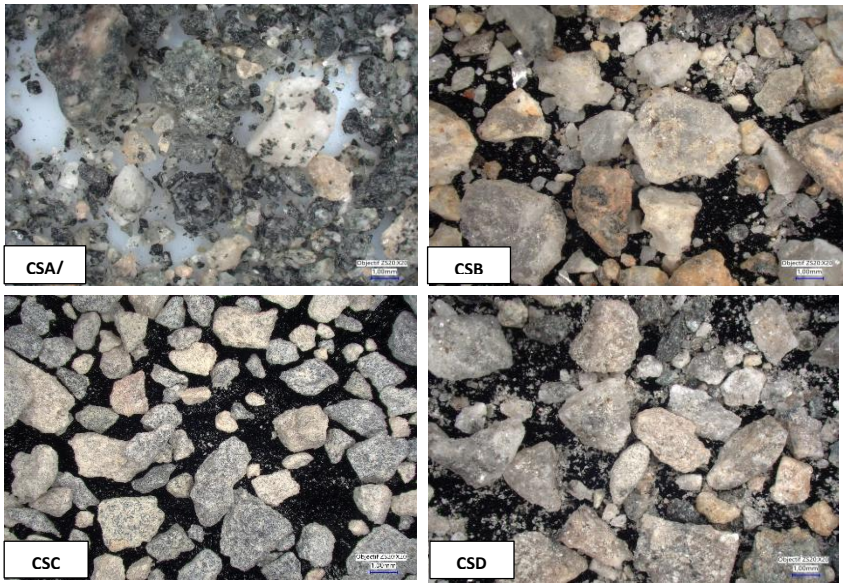


Fig. 3 Optical microscope images of the crushed sands (x20)

2.2 Water absorption measurements

2.2.1 EN 1097-6 method.

The standard outlines the procedure for determining the particle density and water absorption of fine aggregates, the samples were initially immersed in water at 20 °C for 24 h to ensure full saturation of the particles. Following immersion, the samples were drained and gently dried using a low-heat air stream, the saturated surface dry (SSD) state is achieved, for coarse aggregates (> 4 mm) this state is indicated by the color change that indicates the change of moisture, this visual indicator cannot be reliably applied to finer particles, such as sand, where the color change is too subtle to observe. Therefore, for fine aggregates, the standard specifies the use of a slump test. The SSD mass was then recorded. Subsequently, the samples were oven-dried at 105 °C to a constant mass to determine the dry mass. The water absorption of the sand was calculated according to (Eq. 1)

$$\boldsymbol{WA}\ (\%) = \frac{\mathbf{100} \times (\boldsymbol{M_{SSD}} - \boldsymbol{M_{dry}})}{\boldsymbol{M_{dry}}} \quad (1)$$

However, this procedure presents several practical limitations. The drying of aggregates by means of a flow of warm air is effective for removing excess moisture from very wet sand, but its efficiency decreases significantly as the SSD condition is approached. Moreover, the drying process often leads to material loss, which can compromise the accuracy and repeatability of the measurements.

2.2.2 Evaporative method.

The sand samples were spread on a flat circular plate to form a thin and homogeneous layer of particles 4–5 mm, then saturated for 24 h, during the drying experiment, the sample mass was recorded every 4 minutes. The experimental setup was refined using a plexiglass enclosure limiting the effects of ambient air circulation. To ensure measurement reliability, three samples were tested for each sand type, and the mean value of the three measurements was considered representative. The water content corresponding to the end of the constant-rate evaporation phase was taken as the water absorption of the sand, as illustrated in Fig. 4.

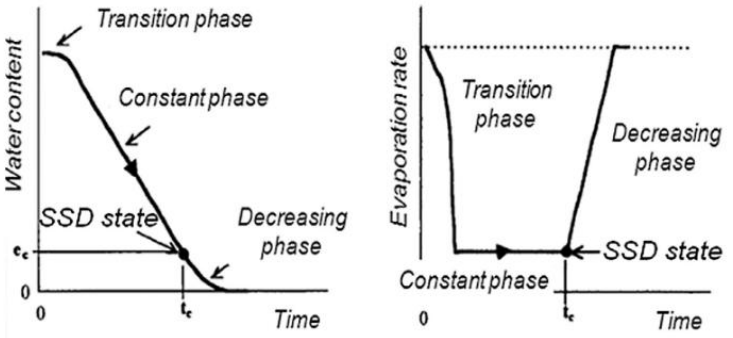


Fig. 4 Water content (left) and evaporation rate (right) in a porous material [2]

2.3 Mix design

To compare the two methods used for measuring water absorption, mixtures with equivalent consistencies and a constant target effective water-to-cement ratio were prepared. With each crushed sand, two distinct mixes were produced: one based on the absorption coefficient determined according to the standardized method (I), and the other based on the coefficient obtained from the evaporative method (II). The plasticizer was added incrementally until the mix achieved the desired consistency with a slump flow of 180 ±5 mm, measured with a mini cone whose dimensions are proportional to those of the standard Abrams cone according to a homothetic ratio of two. The mix design of the mortars is presented in Table 2.

Table 2 Mix proportions of mortars (kg/m3)

Mortar	Cement	Limestone filler	Sand	Target Effective Water	Added water	Admixture
CSA I	477.17	136.34	1489.80	276.46	280.89	2.91
CSA II	477.17	136.34	1489.80	276.46	310.21	1.19
CSB I	477.17	136.34	1341.84	276.46	279.88	2.86
CSB II	477.17	136.34	1341.84	276.46	309.44	1.81
CSC I	477.17	136.34	1404.59	276.46	284.58	4.53
CSC II	477.17	136.34	1404.59	276.46	304.98	3.05
CSD I	477.17	136.34	1392.86	276.46	279.51	3.91
CSD II	477.17	136.34	1392.86	276.46	307.12	4.58

3 RESULTS AND DISCUSSION

3.1 Water absorption coefficient

The water absorption coefficients obtained using the two methods are presented in Fig. 3. Accurately determining the saturated surface-dry (SSD) state of crushed sands using the slump test proved to be challenging, as the materials generally retained the cone shape without exhibiting significant collapse. This behavior leads to relatively low absorption values. For the evaporative method, the transition between the evaporation of intragranular water and intergranular water is identified graphically from the drying rate curve. The corresponding time is then projected onto the moisture content curve to determine the associated water content, which is taken as the water absorption coefficient of the aggregates. A Python-based data processing routine was developed to ensure consistent analysis of the experimental data. The values obtained using the evaporative approach are approximately 2.7 to 5 times higher than those measured using the standard method. Previous work by [2] suggests that adsorbed

water may be included in the absorption measured by the evaporative method, whereas it may be partially or entirely excluded in the standard method depending on drying conditions.

Table 3 Water absorption of the sands measured with EN 1097-6 and the evaporative method

WA (%)	CSA	CSB	CSC	CSD
EN 1097-6	0.46 ±0.03	0.40 ±0.03	0.8 ±0.02	0.44 ±0.04
Evaporative method	2.32 ±0.02	2.55 ±0.06	2.22 ±0.04	2.35 ±0.08

3.2 Water porosity and compressive strength

Water porosity was measured in accordance with NF P18-459 [5]. Mortars from series II exhibited porosity values approximately 2–3% higher than those of series I (Fig. 5). The results of the compressive strength tests are presented in Fig. 6. Overall, the strengths measured for all mortars in series II were higher than those of series I, which is consistent with the observed porosity results. These findings suggest the presence of excess mixing water in Series II. In this series, the water absorption coefficients used to estimate the amount of water absorbed by the aggregates were determined using the evaporative method. This may indicate a systematic overestimation of the absorption coefficient associated with the adopted protocol, leading to an increased effective water content in the mixtures.

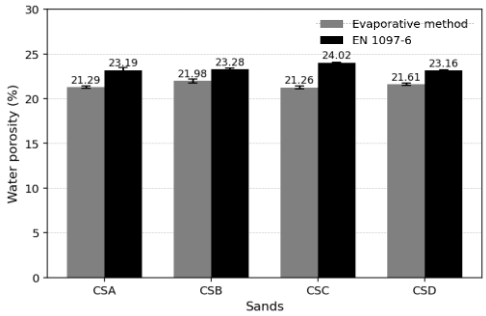


Fig. 5 Water porosity of mortars at the age of 28 days

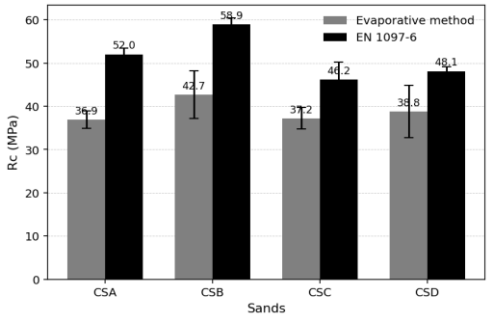


Fig. 6 Compressive strength of mortars at the age of 28 days

4 CONCLUSION AND PERSPECTIVES

A comparative assessment of the standard EN 1097-6 method and the evaporative approach for determining the water absorption coefficient of crushed sands highlights several limitations associated with the conventional procedure. In particular, the determination of the saturated surface-dry (SSD) condition using the cone test proves to be challenging when applied to crushed sands.

The evaporative method, which is based on monitoring the drying behavior of aggregates, appears to be a promising alternative, as it reduces operator-dependent variability. However, the experimental results obtained in this study indicate that the current protocol tends to overestimate the water

absorption coefficient. This overestimation is reflected in the reduced mechanical performance observed for mortars in series II using the water absorption determined by the evaporative method. These findings underline the need for further refinement of the experimental procedure. Specifically, the current data acquisition frequency, set at one measurement every four minutes, may not be sufficient to accurately capture the transition between different drying regimes. A shorter recording interval is therefore recommended. In addition, a more robust and automated analysis of drying curves is required to reliably identify the transition between intergranular and intragranular water evaporation.

The development of a standardized evaporative protocol, including clear guidelines for sample preparation, drying conditions, data acquisition frequency, and automated curve analysis, could provide a reliable alternative method for assessing the water absorption of crushed and recycled sands. Such an approach would contribute to improved mortar and concrete mix design by enabling more accurate control of effective water content, while reducing variability associated with operator influence and experimental conditions.

References

[1] S.K. Kirthika, S.K. Singh, and Ajay Chourasia. 2020. Alternative fine aggregates in production of sustainable concrete- A review. *Journal of Cleaner Production* 268, (September 2020), 122089. https://doi.org/10.1016/j.jclepro.2020.122089

[2] Jean-Michel Mechling, André Lecomte, and K Merriaux. 2003. Mesure de l'absorption d'eau des additions minérales des bétons par évaporométrie. *Materials and Structures*.

[3] Jennifer Naël-Redolfi, Emmanuel Keita, and Nicolas Roussel. 2018. Water absorption measurement of fine porous aggregates using an evaporative method: Experimental results and physical analysis. *Cement and Concrete Research* 104, (February 2018), 61–67. https://doi.org/10.1016/j.cemconres.2017.11.003

[4] NF EN 1097-6. Norme NF EN 1097-6 Essais pour déterminer les caractéristiques mécaniques et physiques des granulats. Partie 6 : Détermination de la masse volumique réelle et du coefficient d'absorption d'eau.

[5] NF P18-459. 2022. NF P18-459 Béton - Essai pour béton durci - Essai de porosité et de masse volumique. Retrieved February 8, 2026

[6] Suvash Paul. 2011. MECHANICAL BEHAVIOUR AND DURABILITY PERFORMANCE OF CONCRETE CONTAINING RECYCLED CONCRETE AGGREGATE. https://doi.org/10.13140/RG.2.1.1471.6882

Drying Shrinkage of Blast-Furnace Slag Cement Systems under Heat-Curing: Sulfate Optimization and Cement Type Effects

[1,3]Asiya Nurhasanah Habirun, [1]Shingo Asamoto, [1]Yao Luan, [2]Keisuke Takahashi

[1)]Graduate School of Science and Engineering
Saitama University,
255 Shimo-Okubo, Sakura-ku, Saitama-shi, Saitama 338-8570, Japan

[2)]Innovation Design Institute
Kagawa University,
2217-20 Hayashi-cho, Takamatsu-shi, Kagawa 761-0396, Japan

[3)]Department of Civil Engineering, Faculty of Engineering
Universitas Muhammadiyah Sumatera Barat,
Jl. Bypass No. 43, Aur Kuning, Bukittinggi, West Sumatra 26181, Indonesia

Summary
This study investigated the drying shrinkage behavior of blast-furnace slag (BFS)-blended cement systems subjected to heat curing. The effect of sulfate optimization through controlled gypsum addition was examined using high-early-strength Portland cement (HPC) mortar specimens with a water-to-binder ratio of 0.55 and 40% BFS replacement, cured at 20°C and 60°C. Increasing SO_3 content significantly influenced drying shrinkage behavior depending on curing temperature. Furthermore, the influence of cement type on shrinkage behavior and aluminate hydrate phase formation was examined using HPC, ordinary Portland cement (OPC), and Type B slag cement cured at 20°C and 65°C. Curing temperature and cement type significantly affected shrinkage, with $CaCO_3$ impurities in OPC-based systems promoting carbonate AFm phase formation that may instead increase drying shrinkage depending on curing temperature.

1 INTRODUCTION

The use of BFS as a supplementary cementitious material enhances concrete durability and significantly reduces the carbon footprint of cement production. Although BFS has often been utilized to reduce hydration heat in massive concrete, BFS concrete has been reported to exhibit a higher possibility of thermal cracking compared with ordinary Portland cement (OPC) concrete [1]. With the continued growth of precast concrete applications, the use of BFS-blended binders is expected to rise. In precast production, high-temperature curing is often applied to accelerate early-age strength development. The curing conditions for precast concrete intensify early-age hydration heat due to elevated internal temperature. Such a high-temperature history at early ages in both massive and precast concrete is therefore associated with an increased risk of initial cracking.

It was reported that the use of BFS appears to increase autogenous shrinkage, accompanied by greater variability [2]. Asamoto et al. (2023) reported that BFS-based concretes cured at elevated temperatures exhibit increased drying shrinkage and differences in the coefficients of thermal expansion between mortar and coarse aggregate can cause damage around the interfacial transition zone. These coupled effects, namely large autogenous shrinkage, increased drying shrinkage driven by early-age high-temperature exposure, and thermally induced interfacial damage may increase the risk of initial cracking under hot conditions. Despite these findings, the mechanism behind shrinkage development in BFS cement under high-temperature conditions remains inadequately understood [3], particularly with respect to the role of sulfate optimization across different cement types under heat-curing conditions.

BFS, which has a higher Al_2O_3 content than that in cement and increased fineness, exhibits elevated reactivity in cement–BFS systems, accelerating early-age aluminate hydration. Partial cement

replacement reduces available SO_3, which may lead to uncontrolled aluminate reactions and reduced sulfate resistance particularly at low BFS replacement levels [4]. Optimization of SO_3 content increases total hydration heat and early-age compressive strength, whereas excessive SO_3 results in their reduction [5], [6]. Similar sulfate-balance-dependent behavior has been shown to influence sulfate ingress, durability, and hydration kinetics in BFS concretes [4]. Apart from this, the transformation of aluminate phases during hydration has been reported to contribute to shrinkage, particularly through the conversion of ettringite to monosulfate [7]. Our recent study under high-temperature curing conditions demonstrated that shrinkage in BFS-blended systems can be effectively mitigated through the addition of gypsum and limestone [8]. This improvement is related to the optimization of aluminate-related hydrate phases, as conceptually described in previous studies on gypsum-induced ettringite stabilization [5] and limestone-assisted monocarbonate stabilization [6]. Accordingly, regulating aluminate reactions through optimization of SO_3 content represents a crucial initial step before the application of further shrinkage mitigation strategies.

To further clarify the mechanism of aluminate hydrate phase stabilization governing drying shrinkage mitigation, the present study investigates the drying shrinkage behavior of BFS-blended cement pastes subjected to heat-curing, with particular emphasis on shrinkage mitigation through sulfate ion optimization achieved by controlled gypsum addition. Additionally, the drying shrinkage behavior of BFS-containing cement pastes was systematically examined using different base cement types to clarify the coupled effects of cement type and curing temperature. Particular attention is given to the finding that the effect of gypsum addition on drying shrinkage is not straightforward, as its effectiveness varies depending on both the curing temperature and the base cement type.

2 EXPERIMENTAL PROGRAM

2.1 Materials and Mix Proportions

High-early-strength Portland cement (HPC) and BFS used in this study had physical properties and chemical compositions similar to those employed in the previous investigation [8]. The mix proportions for the mortar specimens are summarized in Table 1. The specimens were mixed and cast in prismatic molds with dimensions of 40 × 40 × 160 mm. All mixtures had a BFS replacement ratio of 40% and water-to-binder ratio of 55%. Except for the pure BFS-cement system (MIX-CS), gypsum was added to adjust the SO_3 content in blended cement to two target levels: 2.15wt%, corresponding to the SO_3 content of Portland blast-furnace slag cement type B specified in JIS R 5211: 2009 (MIX-1), and 3.43%, which satisfies the maximum allowable SO_3 limit specified in JIS R 5211:2009 (less than 4wt%). Natural river sand with a surface-dry density of 2.59 g/cm3 and a fineness modulus of 2.63 was used as fine aggregate. The aggregate volume fraction was 50% for all mix proportions.

Table 1 Mix Proportion of Mortar Specimens.

Group	Unit weight (kg/m3)				
	Water	Binder			Sand
		HPC	BFS	Gypsum	
MIX-CS	301	328	219	0	1295
MIX-1	301	328	217	3.28	1295
MIX-2	300	319	212	15.52	1295

Table 2 Mix Proportion of Cement Paste Specimens.

Group	Unit weight (kg/m3)			
	Water	Binder		
		Cement	BFS	Gypsum
BB	304	553	0	0
HPC-S	301	328	219	0
OPC-S	301	328	219	0
HPC-SG	300	319	212	15.52
OPC-SG	300	319	212	15.52

In addition to studying sulfate optimization by changing gypsum amount, the influence of different base cements incorporating BFS, as well as its influence to curing temperature, were examined. Three different BFS cement paste mixtures were used : ordinary Portland cement (OPC) with 40% BFS replacement, HPC with 40% BFS replacement, and one commercially available Portland blast-furnace slag cement type B (BB). To confirm the influence of sulfate optimization on HPC-BFS and OPC- BFS systems, gypsum was added to adjust the SO_3 content to 2.61 wt%. Paste specimens were prepared with a 55% water to binder ratio. The specimens were mixed and cast into truncated cube molds with bottom dimensions of 30 × 30 mm, top dimensions of 20 × 20 mm, and a height of 20 mm. The mix proportions of the cement paste specimens are summarized in Table 2.

2.2 Specimen Preparation and Curing Conditions

The mortar was prepared using a Hobart mixer. For the drying shrinkage test, specimens were initially cast under controlled conditions of 20±1°C and 60±10% RH. After casting, they were sealed and kept at this temperature for the first 2 hours. Subsequently, a high-temperature curing regime was applied: the temperature was raised linearly to 60°C over 3 hours, held at 60°C for 10 hours, and then reduced back to 20°C over the following 3 hours. This heat-curing profile (hereafter referred to as "60°C") complies with the JSCE recommendations [9]. For comparison, a set of specimens was also cured under a constant temperature of 20°C ("20°C"). To examine the effect of higher curing temperature of cement paste, specimens were cured under a constant temperature of 20°C and maximum curing temperature 65°C, like a curing temperature that was used in a previous study [3]. The curing profile is shown in Fig. 1.

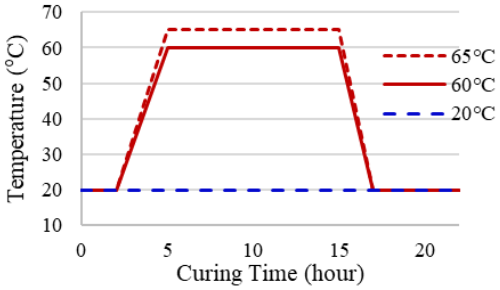


Fig. 1 The curing temperature history

2.3 Drying Shrinkage Test

2.3.1 Mortar Specimens

All specimens were demolded after the initial curing period and subsequently water-cured at 20°C until the age of 7 days. Water curing was adopted to allow sufficient hydration before drying, so that the measured deformation represents only drying shrinkage rather than early-age effects. Immidiately after water curing, drying-shrinkage measurements were initiated by removing the sealing and placing the specimens in an environmental chamber controlled at 20 ± 1°C and 60 ± 5% RH. Two metal pins were fixed along the longitudinal surface of each specimen following the procedure specified in JIS A 1129. The distance between the pins was monitored using a portable length comparator at predetermined intervals: immediately before exposure (day 0), and subsequently on days 1, 3, 7, 14, 28, and 56. The mass of each specimen was measured to quantify moisture loss during drying. For each mixture and curing condition, three specimens were tested to ensure reproducibility.

2.3.2 Cement Paste Specimens

Following the initial curing period, the specimens were demolded and subsequently water-cured at 20°C until the age of 7 days. After completion of water curing, one strain gauge (gauge length: 10 mm) was glued on each specimen surface, and the shrinkage strain was continuously monitored for a duration of 7 days. Shrinkage measurements were recorded at 30-minute intervals to capture the time-dependent deformation behavior. In addition, the mass loss associated with moisture evaporation was measured every day throughout the drying shrinkage testing period.

2.4 XRD

X-ray diffraction (XRD) analysis was conducted to investigate the formation of calcium aluminate hydration products in cement paste prepared with different cement types and curing temperatures of 20°C and 65°C. The specimens were prepared using the same mix proportions, specimen geometry, temperature history, and curing treatments as those employed in the drying shrinkage tests for cement paste, as described in Section 2.3.2. The specimens were tested at 1 and 7 days after the start of drying. On the day of testing, the cement paste specimens were crushed and ground into fine powder prior to analysis. XRD measurements were performed using a Rigaku MiniFlex 600 diffractometer operated at an X-ray tube voltage of 40 kV and a current of 15 mA. The diffraction patterns were collected over a 2θ range of 3 to 30° at a scanning speed of 10.0°/min, using Cu-Kα radiation (λ = 1.54 Å).

3 RESULTS AND DISCUSSION

3.1 Results of Shrinkage and Mass Loss

In general, mixtures subjected to a high curing temperature exhibited approximately 20% lower drying shrinkage and mass loss than those cured at normal temperature (Fig. 1). For all mixtures, approximately half of the mass loss and shrinkage occurred within the first six days of drying. At 20°C, MIX-CS showed the highest mass loss and drying shrinkage among all mixtures. The addition of gypsum in MIX-1 and MIX-2 resulted in a progressive and notable reduction in drying shrinkage. In contrast, at 60°C, the addition of gypsum resulted in a noticeable increased in drying shrinkage, with the highest SO_3 content (MIX-2) showing approximately 8% greater shrinkage than the mixture without gypsum at the same curing temperature.

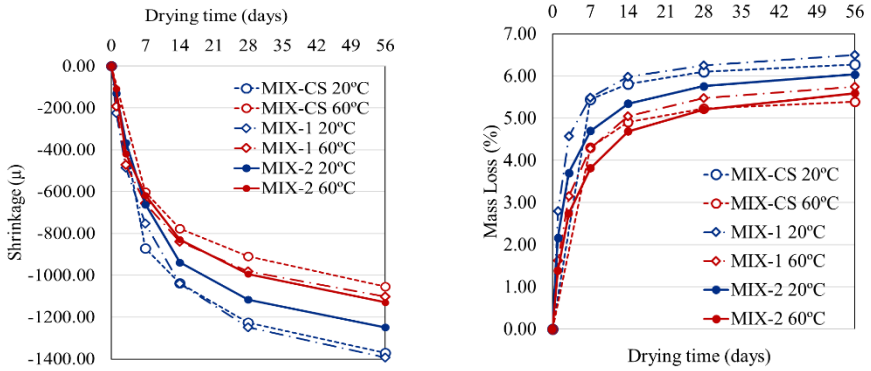


Fig. 2 Drying shrinkage and mass loss of various mixtures cured at 20°C and 60°C

The present results indicate that the reduced drying shrinkage under high-temperature curing in the HPC–BFS system shows a similar tendency to the behavior reported by Thomas and Jennings (2004) for OPC [10]. In contrast, certain experimental observations have reported that higher curing temperatures lead to increased shrinkage in BFS cement systems [3, 4]. However, previous experimental investigations on steam-cured OPC and BFS concretes have demonstrated that the influence of steam or high-temperature curing on shrinkage depends on the curing regime and material composition [11]. Despite these findings, additional experiments were conducted to clarify whether the curing temperature and mix proportion govern the relatively low shrinkage observed in the HPC-BFS system.

3.2 Influence of Mixture Proportions and Curing Temperature

Fig. 3 indicates that curing at a high temperature of 65°C generally increases drying shrinkage compared to curing at 20°C. For the HPC-S specimens cured at 65°C, higher drying shrinkage is observed during the early stage of drying, particularly within the first few days, after which the shrinkage development tends to slow down toward 7 days. It is expected that the shrinkage of paste cured at 65°C would eventually become smaller than that of paste cured at 20°C after 7 days, showing a tendency similar to that of the HPC-BFS mortar system shown in Fig. 2. On the other hand, OPC-S and BB specimens cured at 65°C exhibited approximately 25% and 47% greater shrinkage, respectively, than those cured at 20°C, maintaining a clear difference between the curing conditions.

This is consistent with the tendency reported in the previous study [3]. In terms of mass loss, the HPC-S specimens cured at 20°C exhibit the highest mass loss among all mixtures. Based on these results, curing temperature influences the shrinkage behavior of HPC–BFS systems, and the shrinkage response differs depending on the base cement type.

Fig. 4 shows the influence of gypsum addition on each mixture system. For both the HPC-S and OPC-S systems cured at 65°C, the addition of gypsum (HPC-SG and OPC-SG) reduced the drying shrinkage strain. Meanwhile, the mass loss increased with gypsum addition during the first seven days of drying. Gypsum addition contributes to mitigating the initial shrinkage increase of BFS-containing pastes cured at elevated temperatures, with a more pronounced effect observed in OPC-based systems.

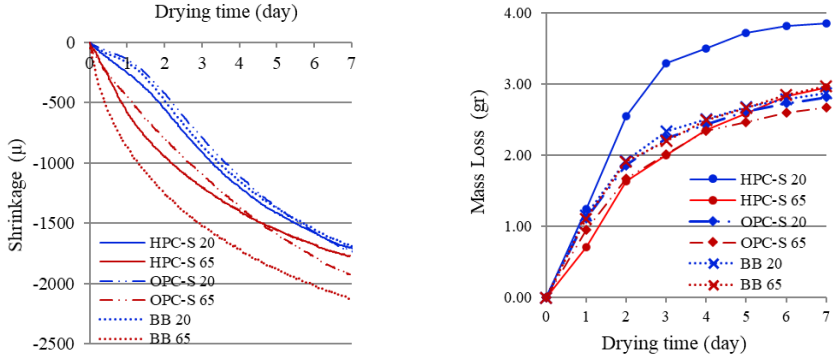


Fig. 3 Drying shrinkage and mass loss of various BFS cement paste mixtures cured at 20°C and 65 °C

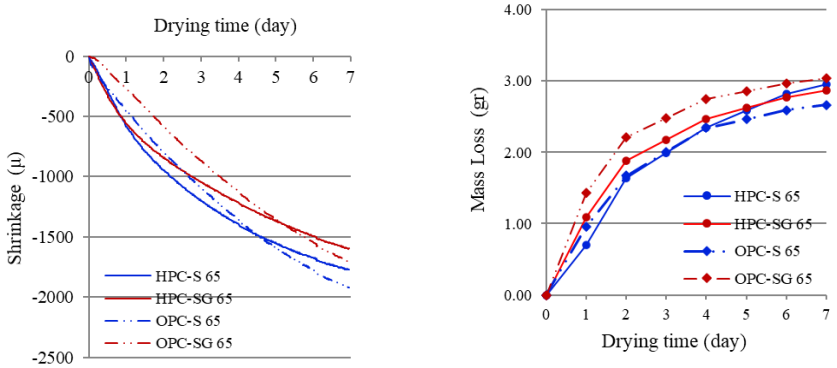


Fig. 4 Drying shrinkage and mass loss of HPC and OPC incorporating BFS and gypsum cured at 65 °C

The XRD results provide further insight into the shrinkage behavior observed in the different cement systems. As shown in Fig. 5, clear differences between HPC- and OPC-based systems are observed in terms of AFm-related phase assemblages. In the HPC-based cement, monosulfate (Ms) is the dominant AFm phase after curing, while ettringite (Ett) is scarcely detected, particularly under high-temperature curing conditions. This phase stability may contribute to the lower drying shrinkage observed in specimens subjected to high-temperature curing, as no significant transformation from ettringite to monosulfate occurs during drying. In contrast, the OPC-S and BB systems exhibit the formation of AFm carbonate phases, including hemicarbonate (hc) and monocarbonate (mc), indicating a more complex phase evolution during hydration and drying. This difference may be related to cement impurities, as OPC contains minor impurities, mainly $CaCO_3$ (below 5 wt.%), and BB cement is produced based on OPC, whereas HPC is a specially manufactured cement with reduced impurities. The relatively low shrinkage of HPC-based mixtures is associated with a more stable sulfate–aluminate phase assemblage. The higher shrinkage observed in OPC–BFS and BB systems is primarily governed by early-age aluminate hydration processes. Although carbonate AFm phases are identified at later

ages, the minimal changes in their phase assemblage between 1 and 7 days suggest that these phases reflect the hydration pathway and curing history established at early ages, rather than acting as the direct driving factor for the observed shrinkage. However, further investigation is required to clarify the mechanisms responsible for shrinkage increase under high-temperature curing, including the effects of the main hydration products, C–S–H and C–A–S–H [12, 13].

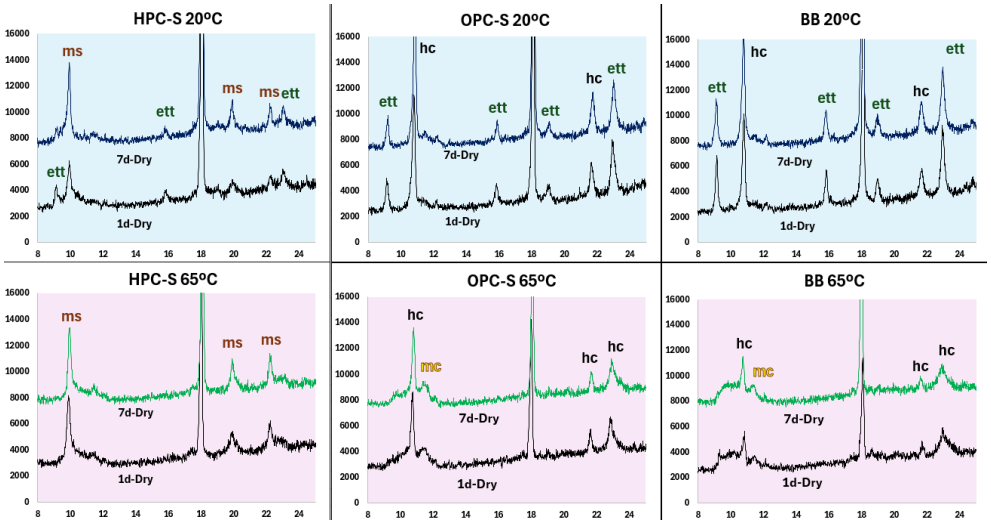


Fig. 5 XRD results of various mixtures cured at 20°C and 65 °C

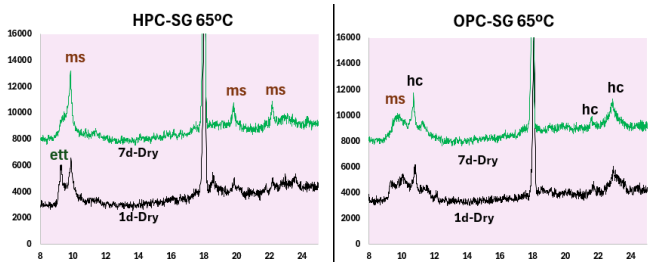


Fig. 6 XRD results of HPC and OPC incorporating BFS and gypsum cured at 65 °C

With gypsum addition, different phase evolution is observed between the HPC-SG and OPC-SG systems under high-temperature curing (Fig. 6). In the HPC-SG system, ettringite is clearly detected at 1 day of drying and subsequently transforms into monosulfate after 7 days. Meanwhile, the OPC-SG system shows the presence of AFm-sulfate phases throughout the drying period. Although gypsum addition leads to a reduction in drying shrinkage at high temperature, the direct correlation between shrinkage mitigation and the formation of AFm-sulfate or AFm-carbonate phases remains unclear.

The contrasting shrinkage behavior between cement systems can be interpreted in terms of AFm phase stability during drying. In the HPC–BFS system, monosulfate (Ms) was the dominant AFm phase, and ettringite (Ett) was not detected after high-temperature curing, suggesting that the Ett-to-Ms transformation may have been already complete before the start of drying. This is noteworthy because previous studies have suggested that Ett-to-Ms transformation during drying can contribute to shrinkage development in BFS-blended systems [7]. By completing this transformation prior to drying, the HPC–BFS system under high-temperature curing appears to avoid this shrinkage-inducing mechanism, which may explain its relatively lower shrinkage compared to normal-temperature curing. In contrast, in the OPC–BFS and BB systems, carbonate-bearing AFm phases (hemicarbonate and monocarbonate) were formed due to $CaCO_3$ impurities present in OPC and BB at levels below 5 wt%. Although the presence of carbonate AFm phases was initially expected to stabilize Ett and suppress shrinkage by maintaining sufficient sulfate ions, Ett was not detected in these systems under high-temperature curing. This suggests that the formation of carbonate AFm phases may not necessarily contribute to shrinkage

reduction and may instead be associated with increased drying shrinkage depending on the curing temperature. This is contrary to the initial expectation based on the limestone-assisted monocarbonate stabilization mechanism reported in previous studies [5, 6] and suggests that the effectiveness of $CaCO_3$ in suppressing shrinkage appears to be highly dependent on the curing temperature and base cement type. These findings suggest that $CaCO_3$ addition to BFS-blended systems, including limestone-containing low-carbon cements, warrants careful consideration of curing temperature, as it does not always lead to shrinkage mitigation. The role of C–(A)–S–H microstructural changes in governing shrinkage behavior also warrants further investigation.

4 CONCLUSIONS

This study investigated the drying shrinkage behavior of BFS-blended cement systems under normal and elevated curing temperatures, with particular emphasis on sulfate optimization through gypsum addition and the influence of cement type. Based on the experimental results obtained in this study, the following conclusions can be drawn:

- Mortar mixtures based on the HPC–BFS system subjected to high-temperature curing exhibited approximately 20% lower drying shrinkage and mass loss than those cured at normal temperature. However, among the high-temperature cured specimens, gypsum addition resulted in a noticeable increase in drying shrinkage, with the highest SO_3 content (MIX-2) showing approximately 8% greater shrinkage than the mixture without gypsum at the same curing temperature.
- Elevated curing temperature significantly increased drying shrinkage during the early stage of drying in the HPC–BFS paste system, although the difference diminished by 7 days of drying. In contrast, OPC–BFS and BB paste systems exhibited approximately 25% and 47% greater shrinkage, respectively, under high-temperature curing compared to normal temperature.
- The cement type governed the AFm phase assemblage and its associated shrinkage behavior. In the HPC–BFS system, the Ett-to-Ms transformation was complete before drying, which is associated with lower shrinkage under high-temperature curing. In contrast, carbonate AFm phases formed in OPC–BFS and BB systems due to $CaCO_3$ impurities did not contribute to shrinkage reduction, highlighting that $CaCO_3$ addition to BFS-blended systems may increase drying shrinkage depending on the curing temperature.

Acknowledgements

This research was supported by JSPS Grants for Scientific Research 23K26173.

References

[1] [1] Usui, Tatsuya, Miyahara, Shigeyoshi, Maruya, Tsyusoshi, Otomo, Takeshi. 2014. “Drying Shrinkage Characteristics of Concrete with Slag Cement Subjected to Different Curing Temperature Conditions“ *Proceedings JSCE annual conference V* 665–666. (in Japanese)

[2] [2] Ekaputri, Januarti Jaya. Tetsuya Ishida, Koichi Maekawa. 2010. “Autogenous Shrinkage of Mortars Made with Different Types of Slag Cement” *JCI Annual Conference*, Vol.32, No.1.

[3] [3] Asamoto, Shingo, Kurashige, Isao, and Chun, Pang-Jo. 2023. “Effect of high temperature at early ages on drying shrinkage and creep of concrete focusing on microcracking damage,” *Materials and Structures* vol. 56, no. 4, pp. 1–15, doi: 10.1617/s11527-023-02156-2.

[4] [4] Scully, Kevin and Drewniok, Michal. 2025. “Sulfate Addition to Ground Granulated Blast-furnace Slag for use as a Supplementary Cementitious Material in Concrete” *International Conference on Durability of Concrete Structures*. doi: 10.5703/1288284318162.

[5] [5] Fincan, Mustafa. 2021. “Sulfate Optimization in the Cement-Slag Blended System Based on Calorimetry and Strength Studies” PhD diss., University of South Florida.

[6] [6] Harada, Katsuki. Matsushita, Hiromochi. 2003. “Effect of Gypsum Content in Cement on the Autogenous Shrinkage of Low-Heat Portland Blast-Furnace Slag Cement Concrete” Kyushu University Collections.

[7] [7] Takahashi, Toshiyuki, Nakata, Hideki, Yoshida, Kozaburo, and Goto, Seishi. 1996. "Influence of Hydration on Autogenous Shrinkage of Cement Pastes" *Concrete Research and Technology* vol. 7, no. 2, pp. 137‐142 doi: 10.3151/CRT1990.7.2_137. (in Japanese)

[8] [8] Habirun, Asiya Nurhasanah, Asamoto, Shingo, Luan, Yao, and Takahashi, Keisuke. 2025. "Study on Drying Shrinkage of Slag Cement Mortar with Heat Curing: Influence of Limestone, Gypsum, and Shrinkage-Reducing Agent," *Proceedings of JCI Annual Convention*.

[9] [9] Japan Society of Civil Engineers. 2007. "Standard specifications for concrete structures −2007 (construction)" Materials and Construction, pp.484-485

[10] [10] Thomas, Jeffrey J, and Jennings, Hamlin M. 2004. "Effect of heat treatment on the pore structure and drying shrinkage behavior of hydrated cement paste," *Journal of the American Ceramic Society* Vol. 85, Issue 9 pp. 2293-2298 doi: 10.1111/j.1151-2916.2002.tb00450.x.

[11] [11] Boukendakdji M., Brooks. JJ., and Wainwright PJ. 1996. "Influences of Steam Curing on Strength, Shrinkage and Creep of OPC and Slag Concretes" *Radical Concrete Technology* pp. 366–372. ISBN 0 419 21480 1

[12] [12] Taylor, Harry F. W. 1997. "Cement chemistry (2nd edition)," *Thomas Telford Publishing.* London.

[13] [13] Scrivener, Karen L., John, Vanderley M., and Gartner, Ellis M. 2018. "Eco-efficient cements: Potential economically viable solutions for a low-CO2 cement-based materials industry," *Cement Concrete Research.* vol. 114, pp. 2–26, doi: 10.1016/J.CEMCONRES.2018.03.015.

[14]

Influence of the Strand Spacing on the Material Strength of 3D-Printed Concrete

Elisabeth Radl[1,2], Marc-Patrick Pfleger[1,2], Patrick Huber[2] and Tobias Huber[2]

[1]Research Center for Building and Design, Hochschule Campus Wien, Favoritenstraße 226, 1100 Vienna, Austria

[2]Institute for Structural Engineering Research Unit of Structural Concrete, TU Wien, Karlsplatz 13, 1040 Vienna, Austria

Summary

In 3D concrete printing (3DCP), strand spacing is an important process parameter. A small spacing can reduce the inter-filament voids but compromise geometric accuracy, and vice versa. This study investigates the influence of strand spacing on the mechanical properties and internal structure. Two specimen series with different strand spacings were tested for compressive and splitting tensile strength in different directions to capture anisotropy. CT-scans were conducted to evaluate pore distribution and void formation. The results confirm the directional dependency of 3D-printed concrete and show that increased spacing significantly amplifies this. Reduced strength was observed in directions where the contact surfaces were directly stressed. CT analyses showed that larger spacing resulted in more noticeable and continuous voids, which explained the reduced performance. These results demonstrate the relationship between printing parameters, internal structure and direction-dependent properties.

1 INTRODUCTION

3D concrete printing is establishing itself increasingly as a forward-looking construction method, attracting widespread scientific and practical interest [1]. While constructive issues are gradually being addressed, the importance of the digital process chain is also becoming apparent. This process often requires several software solutions, which can lead to interface problems and increased complexity. Additionally, new questions arise during programming, particularly regarding the relationship between printing speed, strand width and strand spacing. Especially in multi-strand printing, it is crucial how well lateral layer bonding is formed and whether cavities occur between the individual strands [2], [3]. These cavities create weak points within the concrete structure, which in turn lead to reduced mechanical strength. Due to the layer-wise and strand-based extrusion process, the resulting material differs from conventionally cast concrete. Strand-based production and the formation of contact surfaces between adjacent filaments introduce pronounced structural anisotropy. Consequently, the mechanical properties must be evaluated with consideration of the principal material directions. To enable comparison between studies, many research groups use the same directional notation system (u, v, w), where the u-direction corresponds to the printing direction, the v-direction is horizontal and perpendicular to the printing path, and the w-direction represents the build direction. This directional classification has become common in experimental investigations of 3D-printed concrete to capture the material's anisotropic behaviour [4].

Despite increasing research activity across various institutions, there are currently no standardized specimen geometries or testing procedures for 3D-printed concrete. As a result, the dimensions of test specimens vary considerably depending on the institution [4], [5]. Consequently, the internal structure represented within a specimen may differ substantially. Depending on the size of the specimen and the width of the printing strand, a test specimen may contain either a single strand or multiple strands, including their contact surfaces.

The internal structure of 3D-printed concrete typically comprises two types of voids. Intra-filament voids, which are found within individual extruded strands, and inter-filament voids, which are located at the contact surfaces between adjacent strands. Inter-filament voids mainly originate from the elliptical geometry of the extruded strand and are influenced by strand spacing, extrusion rate and printing speed. Over-extrusion can result in increased compaction and improved bonding, whereas under-extrusion or increased strand spacing can lead to the formation of continuous voids between strands. Previous studies have shown that these voids affect strength development and failure mechanisms, particularly depending on the loading direction [6]. Although the fundamental directional dependence of the material has been discussed comprehensively at an international level, few

systematic studies have examined the relationship between strand spacing, internal structure and strength values to date [6]. In particular, the link between void formation between printing strands and directional dependence on compressive and splitting tensile strength requires further clarification.

Therefore, this study investigates how strand spacing influences the mechanical behaviour of 3D-printed concrete.

2 EXPERIMENTAL PROGRAM

2.1 Printing Setup and materials

The used printing system consists of an ABB 6-axis articulated robot mounted on a 7 m traverse axis. The material is supplied by a MAI Pictor screw pump. The mixture consists of standard binder (CEM II) 910 kg/m³, aggregate with a maximum grain size of 2 mm 818 kg/m³, silica fume 45 kg/m³, water 376 kg/m³, superplasticizer 2.6 kg/m³, viscosity-modifying admixture 0.9 kg/m³, and glass fibers 2.3 kg/m³. First, the dry components are mixed, then water and superplasticizer are added. Finally, the viscosity-modifying admixture and glass fibers are mixed in.

2.2 Test specimens

Concrete beams are produced using an extrusion-based 3D concrete printing process. These beams are then used to extract test specimens for mechanical strength tests and CT investigations. Two specimen series (A1 and A2) with different strand spacings are manufactured. While all other printing parameters remained constant, the strand spacing is set to 12 mm for series A1 and 15 mm for series A2, respectively. An overview of the printing parameters is given in Table 1.

Table 1 Overview of the printing parameters selected for the A1 and A2 series

Series	Nozzle diameter D [mm]	Layer height L [mm]	L/D [-]	Strand spacing A [mm]	A/D [-]	Flow rate [kg/min]	Printing speed [mm/s]	Layer time [s]
A1	12	8	0.67	12	1.0	3.2-3.6	200	66
A2	12	8	0.67	15	1.25	2.2-3.6	200	66

Fig. 1 shows a schematic illustration of the printed beams and the orientation and location of the extracted core specimens. Approximately one hour after printing, the beams are cut using a saw to facilitate further handling and processing. Subsequently, the specimens are covered with a thin plastic foil to minimize water evaporation.

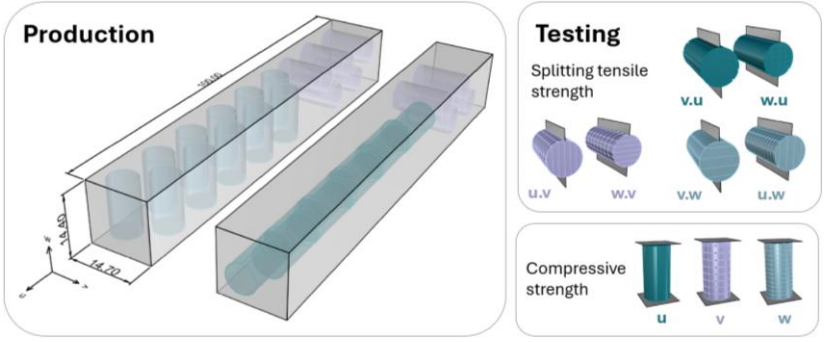


Fig. 1 Schematic illustration of the beams from which the cylinders were taken and the test specimens, including test configurations for the strength tests

After a 21-day curing period, core specimens with a diameter of 60 mm and a length of 120 mm are extracted from the 3D-printed concrete beams. Core extraction is performed in all three directions (u, v and w) for compressive and splitting tensile strength tests. The specimens are subjected to surface preparation before compression tests. The surfaces are ground flat using a grinding device. For the

splitting tensile strength tests, 4 mm thick, 6 mm wide hardwood strips are attached to the top and bottom of the specimens according to the respective testing directions.

2.3 CT-Scans

Computed tomography (CT) scans are used to analyze the internal structure of the 3D-printed specimens and investigate their pore content. The focus was on identifying both the inter-filament voids formed between adjected printing strands and the intra-filament voids located within individual strands. Compared to other studies, which frequently employ micro-CT systems due to their high spatial resolution, this study used CT scans [7],[8]. One study employing micro-CT scans shows scans of specimens measuring 40 mm in diameter and 100 mm in height, requiring scan times over 200 minutes and the use of microfocus X-ray tubes with voltages of up to 240 kV [7].

However, such long scan times, limited scanning volumes and the requirement to scan specimens individually significantly restrict the feasibility of investigating large numbers of samples. In the present study, therefore, a CT system designed for medical applications is used. A SOMATOM go.All scanner, manufactured by Siemens Healthineers, is employed. This system operated within a tube voltage range of 70-140 kV and enables flexible placement of multiple specimens within a single scan. The cylindrical specimens are arranged side by side on the scanning surface, enabling the simultaneous scanning of 10-15 specimens. Consequently, the total scan time for 10-15 specimens is reduced to approximately 2 to 5 min. The CT-scan is performed at a voltage ranging from 100 to 140 kV, with a voxel size of 0.3307 x 0.3307 x 0.4999 mm³.

2.4 Testing

Mechanical testing is carried out 36 days after printing, based on Austrian Standards [9], [10]. Both testing procedures are performed under force-controlled conditions. For the compressive strength tests, a constant loading rate of 2.0 kN/s is applied. The splitting tensile strength tests are conducted at a rate of 0.56 kN/s. These tests evaluate the direction-dependent mechanical behaviour of the 3D printed specimens in relation to the selected strand spacing.

3 RESULTS

3.1 Manufacturing and testing

Clear visual differences are observed between specimen series A1 and A2 during the printing process. In series A1, the adjacent filaments are pressed visibly against each other at the vertical contact surfaced after the extrusion. This resulted in no visible inter-filament voids during printing. However, a slight deviation from the intended rectangular cross-section is seen. Due to the increased lateral confinement of the strands and the limited available space for material flow, the cross-section gradually changes towards a trapezoidal shape with increasing height. In contrast, the beams of series A2 exhibit partially visible voids between adjacent strands during printing, while the overall cross-section retained its rectangular shape. These differences can be seen in Figs. 2a and 2b.



(a) (b) (c) (d)

Fig. 2 Printing process of series (a) A1 and (b) A2 with visible voids between the printing strands; Inter-filament voids in the core drilled test specimens in *w*-direction from (c) A1 and (d) A2

After core drilling, inter-filament voids become visible in specimens from both series. While such voids were present in both series, they were significantly more apparent in the A2 specimens. Figs. 2c and 2d shows representative core specimens extracted in the *w*-direction. In both cases, inter-filament voids can be seen; however, in A1, they are irregularly distributed, whereas in A2, they are more uniformly distributed across the entire cross-section.

Splitting tensile strength tests are carried out in six different directions, as shown in Fig. 1. Core drilled specimens are extracted in the directions *u, v, w* and are then tested in the respective orthogonal directions. For example, a core extracted in the *u*-directions is tested in both the *u*- and *v*-directions. A characteristic failure mode is observed in all splitting tensile tests. A single crack starts at the center of the specimen and grows perpendicular to the hardwood strips, resulting in a splitting of the cross-section. The fracture patterns show varying degrees of homogeneity. While the layered structure of the printing process is clearly visible in some specimens, others show an almost homogeneous internal structure.

Figs. 3b and 3c show the fracture pattern of specimens drilled in the *w*-direction and tested in the *u*-direction. In series A2, the vertical layer orientation is more apparent than in A1. Figs. 3c and 3d show a specimens drilled in the *u*-direction and tested in *v*-direction, in which the vertical printing layers are visible in A1 but barely recognizable in A2. This suggests that failure occurs both between two strands and within a strand. It should be noted that the specimens' labels shown in Figs. 2, 3 and 4 indicate the orientation during the core extraction and are later adapted for the subsequent testing and evaluation.

The results of the splitting tensile strength teste are summarized in Fig. 3a. The measured loads were calculated to give splitting tensile strength values $f_{ct,sp,60/120}$ in N/mm² according to Austrian Standards [9], taking into account the specimen diameter and the length of the load application area.

For each testing direction, three specimens are tested and the mean value is calculated. Lower splitting tensile strength values were seen for series A2 in the *u.w* and *u.v* direction. These reductions occurred in all cases where the specimens were loaded in the *u*-direction. In the remaining testing directions comparable splitting tensile strength values were obtained for both series.

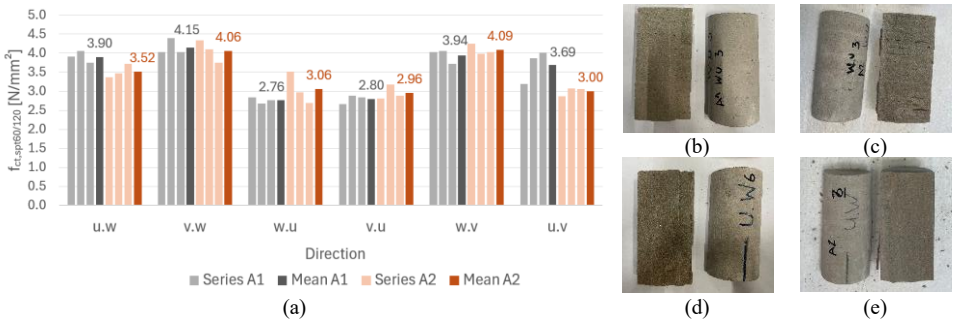
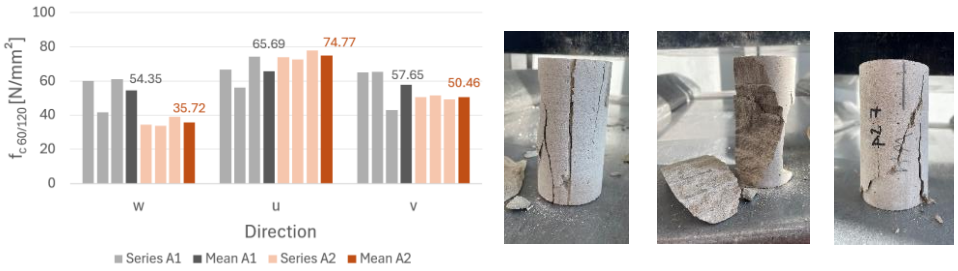


Fig. 3 (a) Overview of the splitting tensile strength depending on the loading direction; fracture pattern of a *w*-specimen loaded in *u*-direction from series (b) A1 and (c) A2; fracture pattern of a u-specimen loaded in *w*-direction from series (d) A1 and (e) A2

During the compressive strength tests, different failure modes are observed, including cone and shear (Fig. 4d), cone (Fig. 4c) and columnar failure types (Fig. 4b). No clear correlation can be identified between a specific failure mode and a particular loading direction. However, it is seen that specimens loaded in the *u*-direction predominantly exhibited columnar failure. The compressive strength results are presented in Fig. 4a in N/mm². The difference between the two series is mainly observed in the *w*-direction, where the compressive strength values of the series A2 are significantly lower than those of series A1.



(a) (b) (c) (d)

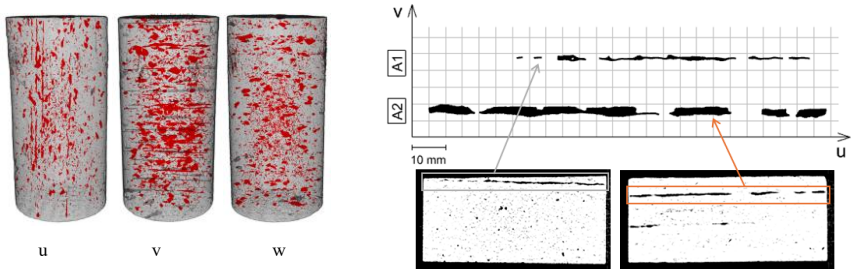
Fig. 4 (a) Overview of the compressive strength depending on the loading direction; fracture pattern of a specimen loaded in (b) *u*-direction (columnar failure); (c) *v*-direction (cone failure) and (d) *w*-direction (cone and shear failure)

3.2 CT-Scanning

CT-scans were used to analyse the pore content of the specimens. The DICOM datasets were analysed using 3D-Slicer software. A threshold-based approach was applied to segment voids and solid material. In this context, the threshold defines the grey scale intensity value that separates low-density regions (air/voids) from high-density regions (solid concrete) within the CT dataset. A comparable threshold range was selected for both specimen series to ensure consistency of the evaluation. The results shown in Tabel 2, point out that the pore content increases from approximately 4.5 % in series A1 to around 6.3-6.5 % in series A2 for all directions. It should be noted that the porosity percentages reported in Table 2 refer to the total pore volume of each specimen. At the current stage of evaluation, a detailed size distribution analysis and a quantitative distinction between inter-filament and intra-filament voids have not yet been performed.

Table 2 Overview of the pore content in volume percent in relation to the specimen direction for series A1 and A2

	A1	A2	A2 / A1
u	4.55 %	6.37 %	+40.0 %
v	4.54 %	6.33 %	+ 39.4 %
w	4.54 %	6.51 %	+ 43.3 %



(a) (b)

Fig. 5 (a) Illustration of the pore distribution on specimens in the *u*, *v* and *w*-direction of the series A1; (b) comparison of an inter-filament void of a test specimen in the *u*-direction of series A1 and A2

Depending on the extraction direction of the core specimens, different pore distribution patterns can be seen. Fig. 5a shows a visualization of specimens in each direction from series A1. Both, intra-filament voids within the extruded strands and inter-filament voids at the interface between adjacent printing strands can clearly be identified. Intra-filament voids are generally very fine and uniformly distributed over the entire cross-section, whereas inter-filament voids appear as larger, connected cavities that are oriented along the printing direction. The presence of inter-filament voids is particularly visible in the

u- and *w*-directions. Fig. 5b shows a direct comparison of the inter-filament voids between series A1 and A2.

4 DISCUSSION

The results of the compressive strength tests generally show the highest strength values for loading in *u*-direction and the lowest values in *w*-direction (Fig. 4a, Table 3). Additionally, reduced compressive strength values were observed for specimen series A2 in both directions. Each printed strand exhibits a vertical contact surface (Fig. 6, shown in blue) and a horizontal contact surface (shown in orange) with adjacent filaments. Regardless of the specimen series, the horizontal contact surface is typically larger, and the filaments are more compressed in this direction compared to the vertical contact surface. Consequently, when loaded in the *w*-direction, the shorter contact surface is oriented parallel to the direction of loading, whereas when loaded in the *v*-direction, it is the longer contact surface that is activated. This results in the inter-filament surface opening earlier and premature failure when loaded in the *w*-direction.

The increased strand spacing in series A2 further increases these effects due to reduced contact interface formation between adjacent strands. In contrast, when loaded in the *u*-direction, each strand is aligned with the loading direction. The strands therefore act as adjacent load-bearing "columns" in compression and inter-filament voids have only a minor influence on the load bearing capacity.

Based on the strength in *u*-direction, A1 shows reductions of 12.2 % in the *v*-direction and 17.2 % in the *w*-direction. By contrast, the values of series A2 decrease by 32.5 % in the *v*-direction and by 52.2 % in the *w*-direction, clearly demonstrating the poorer connection of the contact surfaces.

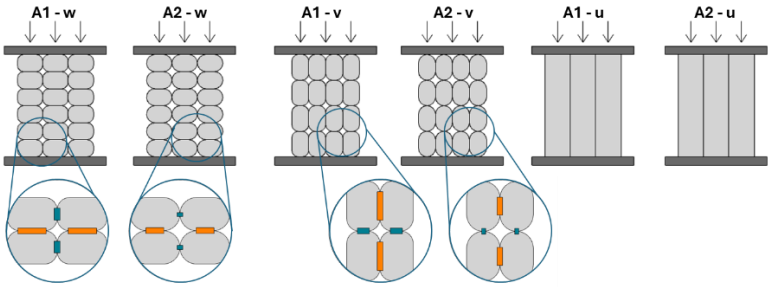


Fig. 6 Orientation of the printing strands depending on the test direction in connection with the contact surfaces between to strand

Table 3 Overview of the mean values of the compressive strength and comparisons between the testing directions and between the series A1 and A2

		u	v	w
A1	$f_{cm,i}$ [N/mm²]	65.69	57.65	54.35
	$f_{cm,i}$ / $f_{cm,u}$ [%]	100%	-12.23 %	-17.26 %
A2	$f_{cm,i}$ [N/mm²]	74.77	50.46	35.72
	$f_{cm,i}$ / $f_{cm,u}$ [%]	100%	-32.51 %	-52.22 %
	A2 / A1 [%]	+13.82 %	-12.47 %	-34.27 %

For the splitting tensile strength tests, two loading directions are investigated for each core extraction direction. In the testing configurations *u.w* and *w.v*, the load was applied parallel to the printing strand or along continuous contact surface. In these configurations, the inter-filament surfaces were directly stressed, which led to crack initiation along the contact joints and earlier splitting of the cross-section. Consequently, both series exhibited a reduction in splitting tensile strength compared to the respective configuration rotated by 90°.

A clear difference between the two series can be observed (Fig. 3a, Table 4). In series A1, the reduction in tensile strength between the orthogonal configurations is approximately 6 %, whereas

reductions of approximately 12–26 % occur in series A2. The greater reduction in series A2 indicates that less developed contact surface, resulting from increased strand spacing, significantly affects splitting tensile performance when the surfaces are directly stressed. The highest splitting tensile strength values are observed in the *v.w* and *w.v* configurations (see Table 4). In these cases, the printing strands and embedded glass fibers are predominantly orientated perpendicular to the loading direction. This contributes to strengthening the cross-section. Regardless of the loading direction, the lowest splitting tensile strengths are obtained for cores extracted in the *u*-direction. This beavior can be attributed to the alignment of the printing strands with the loading direction, whereby the tensile stress acts in the strand orientation and promotes separation along the contact surfaces.

Table 4 Overview of the mean values of the splitting tensile strengths and comparisons between the testing directions and between the series A1 and A2

		 v.w	 u.w	 w.v	 u.v	 w.u	 v.u
A1	$f_{ct,sp,i}$ [N/mm²]	4.15	3.90	3.94	3.69	2.76	2.80
	$f_{ct,sp,i}$ / $f_{ct,sp,u}$ [%]	-6.02 %		-6.34 %		+1.45 %	
A2	$f_{ct,sp,i}$ [N/mm²]	4.06	3.55	4.09	3.00	3.06	2.96
	$f_{ct,sp,i}$ / $f_{ct,sp,u}$ [%]	-12.56 %		-26.65 %		3.26 %	
	A2 / A1 [%]	-2.17 %	- 8.90 %	+3.81 %	-18.70 %	+10.80%	+5.71 %

Literature indicates that the porosity values reported for 3D printed concrete vary over a very wide range. Although printed concrete is often said to have increased porosity in the interlayer regions compared to cast concrete, the extent of this difference depends heavily on the mixture composition and the testing methodology used. Total porosity values reported in the literature range from below 1 % to over 40 %, highlighting substantial variability between studies [11].

In addition to these influencing factors, the evaluation procedure itself introduces further uncertainty. In CT-based analyses, for example, the calculated porosity depends heavily on the correct selection of the segmentation threshold. However, the optimal threshold can differ between scan sessions due to variations in conditions or parameters during scanning or reconstruction. This can lead to inconsistencies in the quantified porosity values. Therefore, it may be advisable for future investigations to include a reference specimen made of a very dense material within each scan series to enable improved calibration and comparability of the threshold-based evaluation.

5 CONCLUSION

Inter-filament voids, caused by wide strand spacing and flow discontinuities (under-extrusion), have a significant impact on the mechanical performance of 3D-printed concrete objects. The vertical contact surfaces between adjacent strands are crucial, as reduced bonding in these areas results in pronounced direction-dependent differences in compressive strength, particularly in the w-direction. Similarly, the lowest splitting tensile strength is found in the *w* and *v* directions for cores extracted in the *u*-direction. Although interfilament voids are observed in both material series, they are more apparent in series A2, which may indicate greater variance in the results. Pore analysis confirms the presence of these inter-filament voids and highlight their contribution to anisotropic mechanical behaviour.

Acknowledgements

The authors acknowledge the funding (FFG grant number 5138043) provided by the Federal Ministry for Innovation, Mobility and Infrastructure (BMIMI), Republic of Austria; Federal Ministry for Economy, Energy and Tourism (BMWET), Republic of Austria and Austrian Research Promotion Agency (FFG) and sponsors from industry.

Further, the authors acknowledge the fruitful cooperation between the involved partners in the project "C3PRO": TU Wien; Hochschule Campus Wien and Austrian Association for Construction Technology (ÖBV).

References

[1] Garcés, Gonzalo, García Alvarado, Rodrigo, Bunster, Victor, and Muñoz Sanguinetti, Claudia. 2025."Additive Construction 4.0: A Systematic Review of 3D Concrete Printing for Construction 4.0." *Engineering, Construction and Architectural Management.* doi:10.1108/ECAM-07-2024-0875.

[2] Luo, Xiaoyu, Zhao, Yuqi, Yang, Min, Yao, Xiaofei, Hu, Jiawei, Shi, Hao, Li, Mingyang, Zhao, Yuan, Qin, Jinhui, and Tian, Ziyang. 2025. "Introducing Cement Composite Agents during Printing Process to Enhance the 3D-Printed Concrete Interfaces between Layers and Filaments." *Construction and Building Materials* 505:144707. doi:10.1016/j.conbuildmat.2025.144707.

[3] Cuevas, Karla, Weinhold, Joachim, Stephan, Dietmar, and Kim, Ji-Su. 2023. "Effect of Printing Patterns on Pore-Related Microstructural Characteristics and Properties of Materials for 3D Concrete Printing Using In Situ and Ex Situ Imaging Techniques." *Construction and Building Materials* 405:133220. doi:10.1016/j.conbuildmat.2023.133220.

[4] Bos, Freek, Robens-Radermacher, Annika, Muthukrishnan, Shravan, Versteegen, Jelle, Wolfs, Rob, Santhanam, Manu, Menna, Costantino, and Mechtcherine, Viktor. 2024. "Database of the RILEM TC 304-ADC Interlaboratory Study on Mechanical Properties of 3D Printed Concrete (ILS-mech)*." Dataset. Zenodo*. doi:10.5281/zenodo.12200570.

[5] Joergensen, Henrik Broener, Hansen, Steen Nedergaard Lillebro, Jespersen, Esra, and Naboni, Roberto. 2024. "Experimental Investigation of Key Structural Parameters for Structural Design of 3D-Printed Concrete." Paper presented at the *fib Symposium* 2024 ReConStruct, Christchurch, New Zealand, November.

[6] Liu, Xingzi, Buswell, Richard, Cavalaro, Sergio Henrique Pialarissi, and Kolawole, John Temitope. 2026. "Influence of Inter-Filament Voids on the Failure Mechanism and Compressive Strength of 3D Printed Concrete." *Construction and Building Materials* 510:145266. doi:10.1016/j.conbuildmat.2026.145266.

[7] Chen, Yanjuan, Kuva, Jukka, Mohite, Ashish, Li, Zhongsen, Rahier, Hubert, Al-Neshawy, Fahim, and Shu, Jiangpeng. 2023. "Investigation of the Internal Structure of Hardened 3D-Printed Concrete by X-CT Scanning and Its Influence on the Mechanical Performance." *Materials* 16(6):2534. doi:10.3390/ma16062534.

[8] Sikora, Pawel, Techman, Mateusz, Federowicz, Karol, El-Khayatt, Ahmed M., Saudi, H. A., Abd Elrahman, Mohamed, Hoffmann, Marcin, Stephan, Dietmar, and Chung, Sang-Yeop. 2022. "Insight into the Microstructural and Durability Characteristics of 3D Printed Concrete: Cast versus Printed Specimens." *Case Studies in Construction Materials* 17:e01320. doi:10.1016/j.cscm.2022.e01320.

[9] Austrian Standards Institute. 2024. "ÖNORM EN 12390-6: Testing hardened concrete - Part 6: Tensile splitting strength of test specimens. " Vienna: *Austrian Standards Institute*. Issued May 15, 2024.

[10] Austrian Standards Institute. 2019. "ÖNORM EN 12390-3: Testing hardened concrete - Part 3: Compressive strength of test specimens." Vienna: *Austrian Standards Institute*. Issued November 15, 2019.

[11] Bradshaw, James, Wen, Si, Khan, Mehran, and McNally, Ciaran. 2025. "Emerging Insights into the Durability of 3D-Printed Concrete: Recent Advances in Mix Design Parameters and Testing." *Designs* 9(4):85. doi:10.3390/designs9040085.

Mitigating shrinkage effects in thin layers of high performance fiber reinforced concrete for jacketing bridges piers

Ivan Beltracchi[1], Adriano Reggia[1], Davide Sirtoli[2], Pietro Lura[2], Giovanni Metelli[1], Giovanni A. Plizzari[1]

[1] University of Brescia,
Via Branze 43, 25123 Brescia, Italy
[2] EMPA - Swiss federal laboratories for Materials Science and Technology
Ueberlandstrasse 129, 8600 Dübendorf, Switzerland (Canton of Zurich)

ivan.beltracchi@unibs.it

Summary

HPFRCs are increasingly being investigated for the strengthening of existing bridges, because of their superior mechanical properties and crack-control capacity. This research, conducted at the University of Brescia and EMPA, investigates the use of HPFRC for jacketing bridge piers to improve axial and seismic performance. Particular attention is devoted to shrinkage mitigation, in a mix with low w/c ratio, which may compromise long-term performance and durability. The study evaluates superabsorbent polymers (SAP) as internal curing agents through hydration-based models and laboratory testing, building on investigations carried out at EMPA to define SAP dosages and additional water. On this basis, an experimental campaign was conducted at the University of Brescia to assess the use of SAP-modified HPFRC in jacketing. The campaign evaluated restrained shrinkage effects, thereby providing insight into the interaction between material properties and structural performance. Results highlight the importance of controlling early-age cracking, to ensure reliability of long-term bridge applications.

1 INTRODUCTION

Shrinkage is one of the most significant deformation mechanisms affecting the early-age and long-term performance of cementitious materials, particularly HPFRCs. Owing to its dense microstructure and low w/c ratio, HPFRC is especially susceptible to early-age autogenous shrinkage, and to environmental exposure. These phaenomena may induce excessive desiccation (for the low amount of available water within mix) and microcracking, thereby compromising durability and mechanical performance. Shrinkage originates from several mechanisms. Chemical shrinkage, described by Powers [1], results from the lower volume of hydration products compared with the initial constituents, generating internal voids and promoting self-desiccation. Jensen and Hansen [2]-[3] demonstrated that this process begins after hydration starts and becomes severe for w/c ratios below 0.35. The capillary stresses generated during hydration lead to autogenous shrinkage even under sealed conditions, often reaching several hundred microstrain during the first days after setting. Drying shrinkage, driven by moisture exchange of water with the environment, governs long-term deformation, while thermal and carbonation shrinkage further contribute to the overall dimensional changes of concrete [4].

Under restrained conditions, happening for example when an overlay of new material is applied along an existing structure to strengthen in, shrinkage generate early-age self-induced tensile stresses. These stresses may exceed the tensile strength of the matrix, causing microcracks which affect permeability and the exposure to aggressive agents, reducing therefore durability. The evaluation of cracking can be derived through standardized ring test, according to ASTM procedures [5]-[3]. In HPFRC, fibers effectively bridge cracks under mechanical loading but may also restrain early-age volumetric contractions, promoting stress accumulation before sufficient matrix strength is achieved and reducing the strain-hardening and multiple-cracking capacity of the composite. Several approaches have been studied to mitigate shrinkage. Conventional external curing methods are effective in limiting drying shrinkage but have less influence on autogenous shrinkage because self-desiccation occurs internally. Similarly, modifications of the mix design or the use of shrinkage-reducing admixtures may

decrease it but often compromise mechanical performance or show limited effectiveness in low w/c ratio systems. Internal curing has therefore emerged as an effective strategy. When implemented by means of pre-wetted lightweight aggregates (LWA), internal curing is less suitable for dense matrices because of limitations related to particle distribution and water-release kinetics [6].

Among internal curing techniques, superabsorbent polymers (SAP) have attracted considerable attention. These cross-linked polymers absorb large amounts of water during mixing and progressively release it as internal relative humidity decreases, directly mitigating self-desiccation and promoting continued hydration [4]-[7]. Their absorption and desorption are affected by the ionic composition of pore solution (particularly by calcium and aluminium ions) and the interaction with solid phases (matrix and aggregates), while particle morphology affects both absorption kinetics and the geometry of residual macropores. Although SAP create isolated macropores within the matrix [8], they can reduce autogenous shrinkage by up to 70–100% in HPFRC and UHPFRC [4]-[9]-[10], while improving hydration, limiting internal stresses, enhancing crack distribution through more effective fiber bridging, and increasing durability. Despite a possible reduction in early-age mechanical strength values due to additional porosity, the higher degree of hydration often compensates at later ages. Furthermore, the stable pore system generated by collapsed SAP improves freeze–thaw resistance and reduces the penetration of aggressive agents, contributing to the long-term durability of cementitious composites [4].

2 EXPERIMENTAL CAMPAIGN

The research presented in this paper investigates the shrinkage-related behaviour of HPFRC used for structural strengthening applications. The study is based on the retrofit of an existing deteriorated bridge (Fig. 1 a), where HPFRC jacketing was applied to the columns and cap beam, as described in [11]-[12]. To experimentally evaluate the effectiveness of this strengthening technique, the intervention was reproduced on 1:2 scaled bridge columns (Fig. 1 b). The experimental campaign focused on assessing the structural improvements provided by thin HPFRC layers (3–5 cm) applied along short and long sides of rectangular cross-sections under both vertical and seismic loads [11].



Fig. 1 Case study (left) and experimental campaign (right) carried out for HPFRC jacketing [11].

To reproduce the jacketing system adopted in the actual retrofit intervention, four RC blocks (35 × 50 × 90 cm), cast more than 10 years ago, were selected to represent portions of existing bridge columns requiring strengthening. An overlay of 5 cm was adopted, consistent with the retrofit application. Owing to the age of the RC blocks, shrinkage and creep effects were assumed to have fully developed and settled, thereby allowing the substrate to be regarded as a rigid restraint for external HPFRC layers. Prior to casting, the blocks external surfaces were sandblasted to achieve a uniform surface roughness of approximately 3 mm, ensuring adequate bond between existing RC core and jacketing layers.
Under these restrained conditions, the evolution of material deformations, together with the influence of environmental exposure, was monitored to evaluate the onset of cracking and the overall behaviour of the jacketing layer along short and long sides of the rectangular cross-section, characterized by different degrees of restraint. The experimental program consisted of two main sets of specimens:

- Reference series: material without fibers (HPC) and the same with fibers (HPFRC).
- SAP-modified series: HPC and HPFRC incorporating SAP according to the selected mix design, hereafter referred to as HPC+SAP and HPFRC+SAP, respectively.

2.1 Test setup

Restrained deformations of jacketing were monitored using eight strain gauges (Fig. 2 left). Specifically, one strain gauge was installed horizontally on each short side, and two along each long side. In addition, one strain gauge was placed vertically in the centre of each long side. To complement strain gauge measurements, manual readings were performed using steel pins glued to specimen surfaces. These measurements were used to determine relative surface deformations up to 28 days.

To compare restrained and free shrinkage, six prismatic specimens (40 × 40 × 160 mm) were cast. Free drying shrinkage was measured on three prisms exposed to laboratory environment, whereas autogenous shrinkage was evaluated on three prisms sealed with aluminium tape to prevent moisture exchange [13]. Measurements started after demoulding and were recorded automatically using a rigid steel frame equipped with micrometres acting on one of the square end faces of each prism (Fig. 2 right). In parallel with the rheological characterization, the mechanical properties of the four mixtures were evaluated through the following testing program:

- Flexural and compressive strength: 12 prismatic specimens (40 × 40 × 160 mm), tested at 1, 3, 7, and 28 days in accordance with EN 12390-1 [14].
- Compressive strength: 12 cubic specimens (100 × 100 × 100 mm), tested at 1, 3, 7, and 28 days according to and EN 12390-3 [15].
- Secant modulus of elasticity: three cylindrical specimens (100 mm diameter × 200 mm height), tested at 28 days in accordance with EN 12390-13 [16].



Fig. 2 Strain gauges layout (left) and rigid steel frame (right) to measure restrained deformations within jacketing layers and free shrinkage within material.

2.2 Materials

The estimation of the required SAP dosage was based on an experimental program conducted on the reference mixtures HPC- HPFRC. Both mixtures are designed with a w/b ratio of 0.23 and, in the case of HPFRC, included 1.5% by volume of short straight steel fibers (13 mm length, with aspect ratio of 62). The mixtures were prepared using commercially available bags of pre-mixed dry material with the following composition:

- Cement CEM I 52.5-R: 565 kg/m^3;
- GGBSFS (Ground Granulated blast furnace slag) as cement replacement: 272 kg/m^3;
- Mellflux Powder and other Superplasticizers: 3+30 kg/m^3;
- Aggregates: 1342 kg/m^3 (maximum size equal to 4 mm).

2.2.1 SAP amount

To ensure internal curing in the blended cement system, the SAP absorption capacity (grams of water/grams of SAP) was determined using the Teabag test, following the Guidelines proposed by Viktor Mechtcherine in RILEM [17]. The testing procedure is therefore illustrated in Fig. 3.

The test results confirmed previous findings reported in the literature [8], showing that the standard Teabag method overestimates the actual absorption capacity of SAP. This issue is mainly attributed to the presence of excess interparticle water retained within the system and to the unrestricted swelling of polymers, which occurs in the absence of the inner confinement caused by solid matrix (aggregates)

and by cement hardening paste. Consequently, the initial average absorption capacity of 50 g/g was reduced to 15 g/g. This corrected value was obtained by removing the excess interparticle water and subjecting the swollen SAP particles to centrifugation, thereby applying a higher pressure to better reproduce the physical interaction between the polymers and pore solution. This approach provides a more realistic estimate of SAP absorption within cementitious materials.

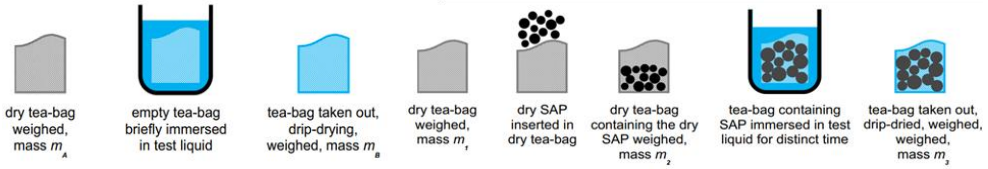


Fig. 3 Teabag test to extract SAP grade of absorption within pore solution of cement matrix [17].

2.2.2 Extra water for internal curing (IC)

Extra water required for IC was estimated on the basis of a semi-empirical hydration model for blended cements, described in [18]. By assuming the maximum expected degree of hydration for the mixture, the required extra water was determined by solving the internal equilibrium equations between chemical shrinkage, capillary water, gel water, gel solid, cement and silica fume, with this last parameter substituted by GGBSF within this mix.

By solving these equations, the relative volume of initially entrained water should be equal to the volume of chemical shrinkage to avoid self-desiccation. Since degree of hydration (called G_{hydr}) was assumed maximum, extra water needed for internal curing (w_{IC}) should be estimated with:

$$w_{IC}\ \left[\frac{kg}{m^3}\right] = \frac{G_{hydr} * \rho_c \rho_s \left(\frac{w}{c}\right)_{INITIAL} * \left(7\left(\frac{s}{c}\right) + 2\right)}{3\rho_w \left(3\left(\frac{s}{c}\right) + 4\right)\left(\rho_s \rho_w + \rho_c \rho_w \left(\frac{s}{c}\right) + \rho_c \rho_s * \left(\frac{w}{c}\right)_{INITIAL}\right)} \quad (1)$$

With ρ_c, ρ_s, ρ_w, the average density of cement, slag and water, while s, c and w are the amount of cement, slag and water within mix design (in kg/m^3).

By following, 86 kg/m^3 of extra water (added to 188.3 kg/m^3 for mix design) were derived, thus giving a final w/b ratio of 0.33. According to the estimated SAP absorption capacity (15), 5.73 kg/m^3 of polymers (0.68% as volumetric percentage) have been added to absorb this extra water for the IC.

2.3 Environmental conditions

All specimens were placed in a climatic chamber, maintained at 20°C and 50% relative humidity (RH) to simulate typical environmental conditions for RC/HPFRC structures. Cubes, cylinders and prisms casted for mechanical characterization were cured under controlled conditions (according to EN 12390-2 standard [19]), in a climatic chamber at 20±2°C with RH ≥95% up to 24 hours before testing.

3 RESULTS

This section summarizes the main strain-gauges results obtained for the four investigated mixtures. In contrast to the reference HPC (black curves within Fig. 5 left-right) and HPFRC specimens (red curves within Fig. 5 left-right), the use of SAP (Fig. 6 left-right) resulted in negligible restrained deformations after a common initial plastic expansion (before setting and demoulding), common for all samples. Under local uncracked conditions, reference mixtures progressively developed restrained deformations up to -300 microstrain, except in areas where local cracking caused abrupt changes in the measured response. This scatter and cracking behaviour, observed between the 2nd and 4th day, are reflected in the recorded data, as the curves show greater variability due to concentrated local effects and to the degree of internal restraint, which is higher along the short sides because of the lateral edges, thereby inducing higher stress concentrations.

By contrast, the SAP-modified specimens remained close to zero after the initial early-age expansion. The similarity between the responses of the HPC+SAP (grey curves) and HPFRC+SAP (yellow curves) specimens further indicates that internal curing has a greater influence on restrained shrinkage mitigation than fiber addition alone, leading to improved deformation compatibility within the thin jacketing layer and reducing the development of self-induced tensile stresses.

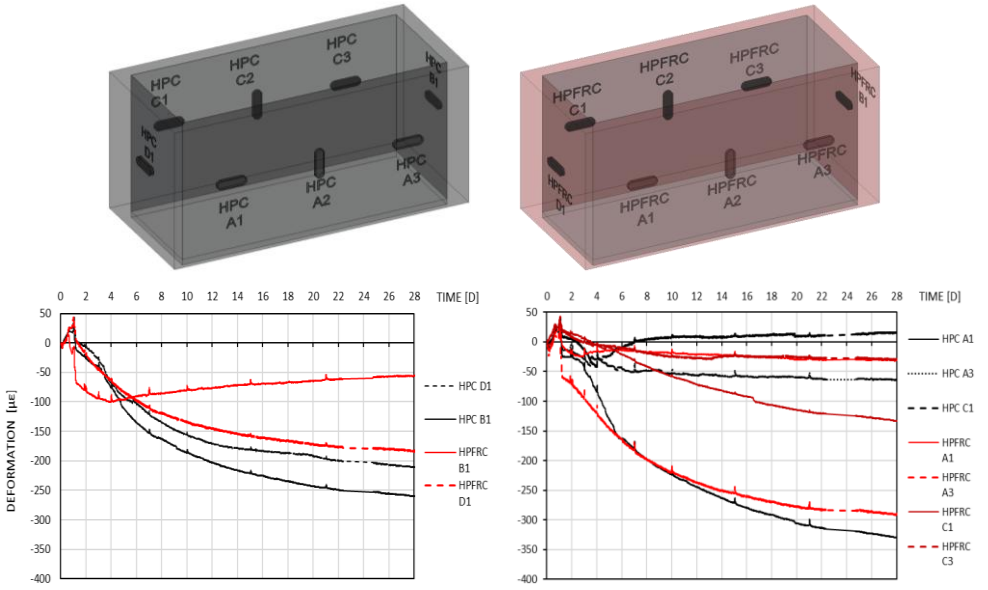


Fig. 5 Inner horizontal deformations acquired by strain gauges along time for short sides (left) and long sides (right) of reference mixtures HPC (black curves) and HPFRC (red curves).

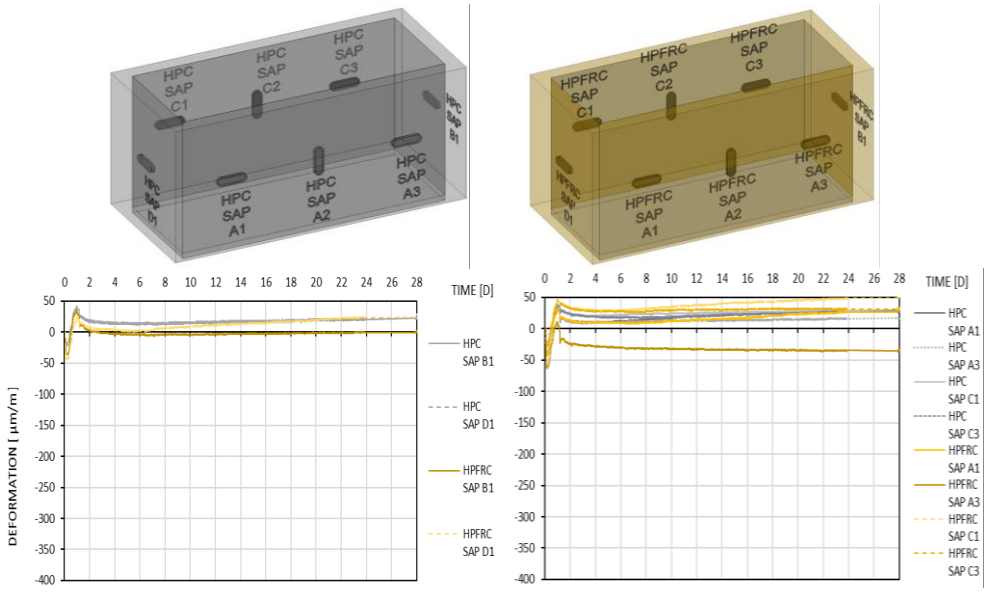


Fig. 6 Inner horizontal deformations acquired by strain gauges along time for short sides (left) and long sides (right) of HPC+SAP (grey curves) and HPFRC +SAP (yellow curves).

3.1 Crack pattern

The analysis of restrained shrinkage-induced deformations highlights a higher cracking tendency in HPC specimens (Fig. 7 left) compared with HPFRC-jacketed elements (Fig. 7 right), characterized by a larger number of cracks and greater crack widths (0.3-0.5 mm). Conversely, fibers within HPFRC promotes a more distributed cracking pattern with reduced crack openings (0.1-0.2 mm). The equivalent total crack width approach confirms comparable deformation levels along different specimen faces, with average values of 0.6 mm for HPFRC and 0.7 mm for HPC, measured along three directions on the long sides. The limited differences observed among the measurements can reasonably be attributed

to material heterogeneity and measurement uncertainty. In SAP-modified mixtures (Fig. 8 left and right), no visible macrocracking was observed, indicating that internal expansion mechanisms effectively reduced self-induced stresses below the evolving tensile capacity of the materials.

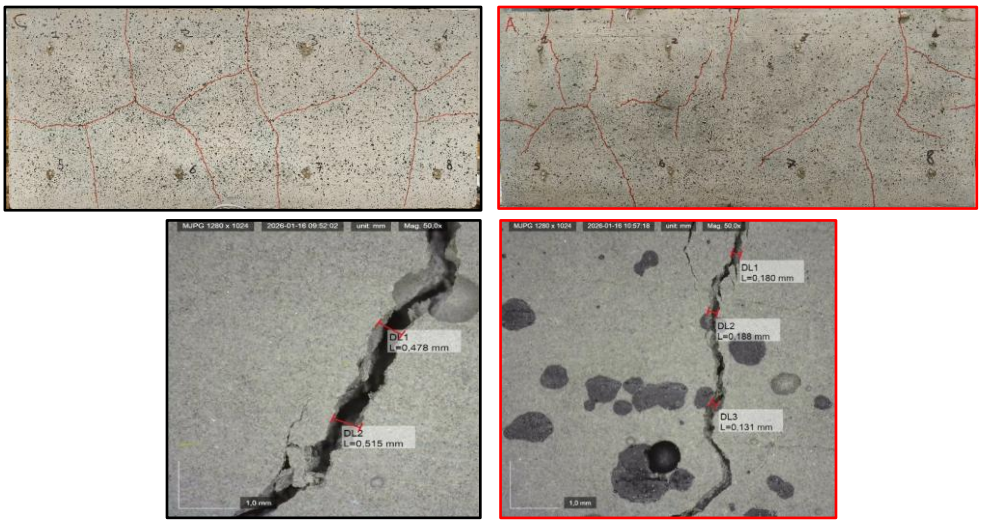


Fig. 7 Crack pattern and estimated cracks opening of HPC (left), and HPFRC (right) specimen.



Fig. 8 External long sides of uncracked HPC+SAP (left) and HPFRC+SAP specimen (right).

3.2 Mechanical properties

The mechanical properties of the four investigated high-performance mixtures, as determined through the experimental campaign carried out at the University of Brescia, are compared in the following graphs. As shown in Fig. 9 (left), the development of compressive strength indicates that HPFRC achieves the highest mechanical performance compared with HPC. However, the incorporation of SAP leads to a clear reduction in compressive strength in both matrices, as a consequence of the macropores left in the cementitious matrix after internal curing, due to the release of the extra water previously absorbed by the polymers.

A similar trend can be observed in the flexural strength results presented in Fig. 9 (right). HPFRC consistently outperforms the unreinforced mixtures, reaching a 28-day flexural strength of approximately 21 MPa. Notably, despite the incorporation of SAP, the HPFRC+SAP mixture still achieves a flexural strength of 15 MPa, slightly higher than that of the HPC mixture. This suggests that the crack-bridging effect provided by the fibers is able to compensate, at least in part, for the mechanical drawbacks associated with the SAP-induced voids.

Finally, the secant Elastic Moduli at 28 days are summarized in Fig. 10 (left). The addition of steel fibers increases the Elastic Modulus from 33.0 GPa for HPC to 36.1 GPa for HPFRC. Conversely, the introduction of SAP leads to a marked reduction in stiffness, lowering it down to 27.0 GPa for HPC+SAP and 29.9 GPa for HPFRC+SAP. This reduction in stiffness is consistent with the observed decrease in compressive strength and highlights the dominant influence of SAP-induced porosity, reflected in density reduction shown in Fig. 10 (right), on the overall elastic properties of the HPFRC.

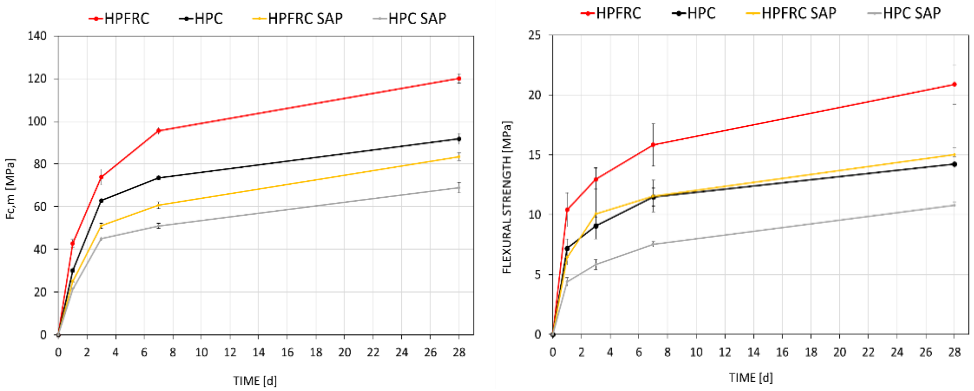
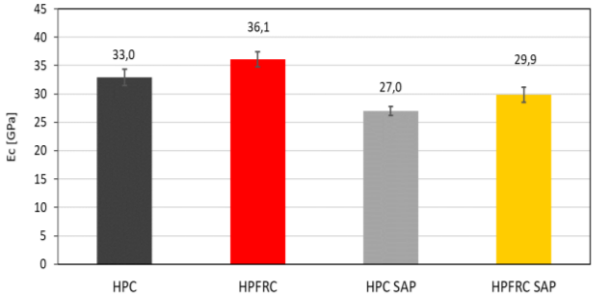


Fig. 9 Compressive (left) and flexural strength (right) of reference mixtures HPC (black), HPFRC (red) and the SAP-added ones, HPC+SAP (grey) and HPFRC+SAP (yellow).



Mixture	28th day Density (ρ)
HPC	2350 kg/m^3
HPFRC	2450 kg/m^3
HPC+SAP	2200 kg/m^3
HPFRC+SAP	2300 kg/m^3

Fig. 10 Secant Elastic Moduli (left) and densities measured at the 28th day hardened state (right) of reference mixtures HPC, HPFRC and the SAP-added ones HPC+SAP, HPFRC+SAP.

4 FINAL REMARKS

The results of this experimental campaign provide a representative assessment of the structural behaviour of the investigated concrete jacketing systems, as the test setup reproduces the combined effects of material shrinkage, environmental exposure, and restraint imposed by the existing RC substrate. The reference mixtures (HPC and HPFRC) exhibited progressive tensile strain development, with crack initiation occurring between 3 and 5 days. HPC showed the highest susceptibility to cracking, with crack widths of up to 0.5 mm, whereas the presence of fibers in the mix promoted a more distributed cracking pattern and reduced the equivalent crack opening by approximately 13%. However, fibers had only a limited influence on the overall evolution of restrained shrinkage, which remained primarily governed by the cementitious matrix and its chemical composition, both under free and restrained shrinkage conditions.

The incorporation of SAP significantly modified the mixture design, mainly through the increase in the effective water content required for internal curing, and consequently affected the evolution of free shrinkage and the mechanical performance of the material. Both HPC+SAP and HPFRC+SAP maintained nearly stable strains (within approximately +/-50 microstrain), corresponding to an 85-90% reduction in restrained shrinkage compared with the reference mixtures, while no visible cracking was observed throughout the testing period. These results indicate that SAP effectively mitigates self-desiccation through internal curing, thereby preserving volumetric stability and preventing the development of shrinkage-induced tensile stresses. Under these conditions, the influence of steel fibers on the global deformation response became negligible.

Mechanical characterization showed that SAP reduced Elastic modulus by 20-22% and decreased both compressive and flexural strengths by approximately 40% at 1 day and 25-30% at 28 days. Nevertheless, partial strength recovery was observed at later ages, likely due to the continued hydration promoted by internal curing. Despite the reduction in mechanical performance, SAP improved material behaviour by preventing the transition from restrained deformation to cracking. These findings

demonstrate the effectiveness of SAP as an internal curing strategy for thin concrete jacketing applications, in which improved crack resistance may outweigh moderate reductions in mechanical properties.

Acknowledgements

The authors gratefully acknowledge HEIDELBERG Materials for supporting this research. They also wish to express their sincere appreciation to Dr. Eng. Bruno Leporace, Eng. Michele Rossini, Mr. Augusto Botturi, Mr. Andrea Del Barba, and Mr. Luca Martinelli for their valuable support throughout the experimental project. The authors further extend their gratitude to the entire EMPA Concrete and Asphalt Group for their assistance in many tests performed within this material-detailed study.

References

[1] Powers, Treval Clifford. 1968. "The properties of fresh concrete." *Wiley*.

[2] Ole Mejlhede, Jensen; Per Freiesleben, Hansen. 2001. "Water-entrained cement-based materials: I. Principles and theoretical background." *Cement and Concrete Research 31(4)*, 647–654.

[3] Ole Mejlhede, Jensen; Per Freiesleben, Hansen. 2002. "Water-entrained cement-based materials: II. Experimental observations." *Cement and concrete research*, 32(6), 973-978.

[4] Mechtcherine, Viktor; Wyrzykowski, Mateusz; Schröfl, Christof. et al. 2021. "Application of super absorbent polymers (SAP) in concrete construction." *update of RILEM state-of-the-art report*. *Materials and Structures* 54, 80. https://doi.org/10.1617/s11527-021-01668-z

[5] ASTM C1581-C1581M. "Standard Test Method for Determining Age at Cracking and Induced Tensile Stress Characteristics of Mortar and Concrete under Restrained Shrinkage."

[6] Bentz, P. Dale, Weiss, W. Jason. 2011. "Internal curing: a 2010 state-of-the-art review". Gaithersburg: US Department of Commerce, National Institute of Standards and Technology.

[7] Mechtcherine Viktor; Dudziak, L., Schröfl, C., & Hempel, S. 2006. "Mitigation of autogenous shrinkage of UHPC using SAP." *RILEM Proceedings PRO52*.

[8] Justs, Janis; Wyrzykowski, Mateusz; Bajare, Diana; Lura, Pietro. 2015. "Internal curing by superabsorbent polymers in ultra-high-performance concrete". *Cement and concrete research* 76, 82-90.

[9] Wyrzykowski, Mateusz; Igarashi, Shin-Ichi; Lura, Pietro; Mechtcherine, Viktor. 2018. "Recommendation of RILEM TC 260-RSC: using superabsorbent polymers (SAP) to mitigate autogenous shrinkage." *Materials and Structures, 51(5)*, 135.

[10] Lura, Pietro, et al. 2006. "Compressive strength of cement pastes and mortars with superabsorbent polymers." *Int. RILEM Conf. Volume Changes of Hardening Concrete*, 20-23 August, (Lyngby, Denmark), PRO 52, eds. Jensen, Lura and Kovler, 117–126

[11] Beltracchi, Ivan, et al. 2024. "Experimental tests of bridge columns reinforced with high performance fiber reinforced concrete (HPFRC)." *15th Fib Symposium in Civil Engineering Proceedings* p.p. 907-914, Budapest.

[12] Reggia, Adriano, et al. 2022. "Actual achievements and future challenges of HPFRC for structural rehabilitation of bridges." *ICCRRR 2022 MATEC Web of Conferences* 364, 04018.

[13] ASTM International. 2009. "ASTM C157-09: Standard Test Method for Length Change of Hardened Hydraulic-Cement Mortar and Concrete".

[14] CEN European Committee for Standardization. 2021. "EN12390-1: Testing hardened concrete-Part 1: Shape, dimensions and other requirements for specimens and moulds." *Ed. by CEN* Brussels, Belgium.

[15] CEN European Committee for Standardization. 2019. "EN12390-3: Testing hardened concrete - Part 3: Compressive strength of test specimens." *Ed. by CEN* Brussels, Belgium.

[16] CEN European Committee for Standardization. EN12390-13: Testing hardened concrete - Part 13: Determination of secant modulus of elasticity in compression. Brussels, Belgium, 2021

[17] Mechtcherine, Viktor. 2023. "Guidelines for using superabsorbent polymers (SAP) in concrete construction." *RILEM Technical Letters* 8: 59-65.

[18] Lura, Pietro, et al. 2003. "Autogenous shrinkage in high-performance cement paste: An evaluation of basic mechanisms." *Cement and concrete research* 33.2: 223-232.

[19] CEN European Committee for Standardization. 2019. "EN12390-2: Testing hardened concrete - Part 2: Making and curing specimens for strength tests." *Ed. by CEN*. Brussels, Belgium.

Experimental investigation of novel precast tunnel segments with hybrid steel–basalt fiber reinforcement

Makrini Macha, Alexandros Evangelatos, Konrad Bergmeister, Robert Galler

Institute of Structural Engineering,
BOKU University,
Peter Jordan Straße 82, Vienna 1180, Austria

Summary
In this study, the mechanical performance of precast tunnel lining segments reinforced with a hybrid fiber system combining basalt and steel fibers is investigated. Basalt fibers are used to control microcrack development, while steel fibers provide crack bridging and load transfer after cracking. In addition, basalt fibers offer inherent fire-resistant properties, making them suitable for applications that require enhanced thermal stability. The main scope of the experimental research arises from the need of enhanced durability and crack resistance in fiber-reinforced tunnel elements while reducing the steel fiber content. Material characterization was conducted through small-scale tests, followed by full-scale bending tests on tunnel segments. The results indicate that hybrid fiber reinforcement provides structural behavior comparable to that of conventional steel fiber reinforcement. This suggests that basalt fibers could potentially replace a portion of steel fibers without reducing the load-bearing capacity.

1 INTRODUCTION

In recent years, considerable efforts have been devoted to the development of innovative reinforcement solutions for tunnel lining segments, particularly based on fiber reinforced concrete (FRC), with the aim to enhance the load-bearing capacity, improve the crack control, and increase the production efficiency [1-3]. In conventional applications, reinforcement is typically provided by a single fiber type, most commonly macro steel fibers. These fibers are particularly effective in enhancing the residual tensile strength and toughness of concrete at larger crack openings through their crack-bridging action. As noted by [4], the reinforcing mechanisms of FRC are primarily activated after cracking of the concrete matrix, which results in an enhanced post-cracking residual tensile strength while the influence on the tensile behavior of the uncracked material is constrained.

In contrast, short fibers are activated during the early stages of crack development and contribute to the control of microcracking. As shown by [5], microfibers improve stress transfer within the cementitious matrix, reduce crack localization, and provide a smoother transition from the elastic to the post-cracking response. This observation led to the development of hybrid fiber reinforced concrete (HFRC), where fibers with different geometrical and mechanical characteristics are combined to act at different stages of crack evolution.

The concept of hybrid reinforcement is based on a multi-scale crack-control mechanism, since cracking occurs through a multi-level process, starting from microscopic to macroscopic scales. According to [6-7] the cracking process in concrete evolves from distributed microcracking to localized macrocracks, and therefore a single fiber type cannot effectively address all relevant crack scales. Furthermore, experimental studies by [5], [8], and [9] demonstrated that the combination of different fiber sizes can improve the tensile strength and toughness compared with single-fiber systems.

This concept can be extended to the combination of basalt fibers (BF) and steel fibers (SF). BF is a natural material produced from volcanic rock, exhibit high tensile strength, corrosion resistance, and a low environmental footprint [10]. Due to their fine dispersion within the concrete matrix, BF primarily contribute to the microcracking regime by the stress transfer across microcracks. Also, during plastic shrinkage and hardening, BF help to reduce the formation of fine cracks. Several studies have reported significant improvements in first-crack behavior and flexural performance [11-13]. According to the reported literature, the complementary action of basalt and steel fibers is theoretically illustrated in Fig. 1. BF are mainly active during the early stages of cracking, where they control microcrack development, while SF become effective at larger crack openings by bridging macrocracks and maintaining load transfer.

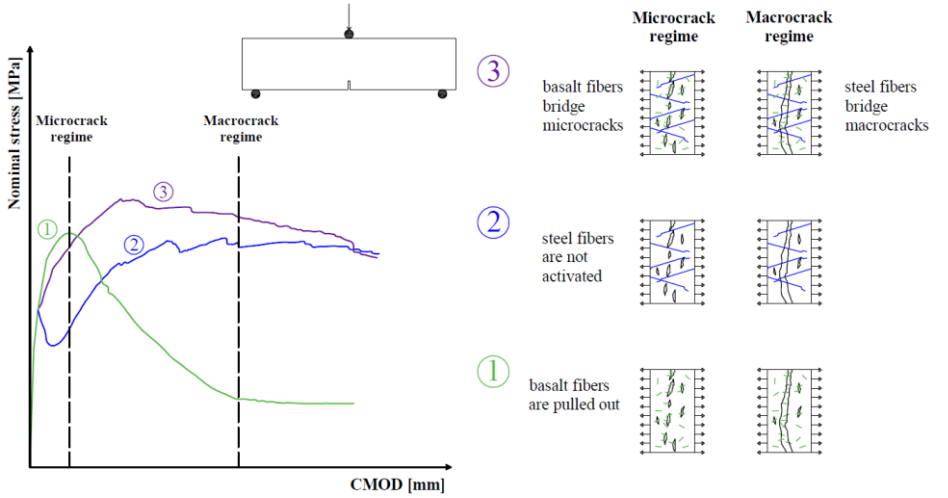


Fig. 1 Theoretical stress–CMOD response of concrete reinforced with basalt fibers, steel fibers, and a hybrid basalt–steel fiber system under three-point bending (adapted from [14]).

Although promising results have been reported for hybrid fiber systems, studies on full-scale tunnel lining segments reinforced with basalt–steel fiber combinations are limited. Furthermore, their structural response and numerical representation have not yet been sufficiently investigated. Therefore, in this study the behavior of precast tunnel lining segments reinforced with a hybrid steel–basalt fiber system through experimental testing is examined.

2 EXPERIMENTAL INVESTIGATION

2.1 Segment geometry

The investigated tunnel lining segment corresponds to the geometry used in the Koralm Tunnel, which is one of the largest railway tunnel projects in Europe and forms part of the Baltic–Adriatic corridor. The lining ring consists of six segments and has an outer diameter of 9.5 m. The selected segment spans a central angle of 60° and has a length of 4745 mm. The segment width is 1913 mm and the thickness is 350 mm. The dimensions and cross-sectional details of the tested segment are depicted in Fig. 2.

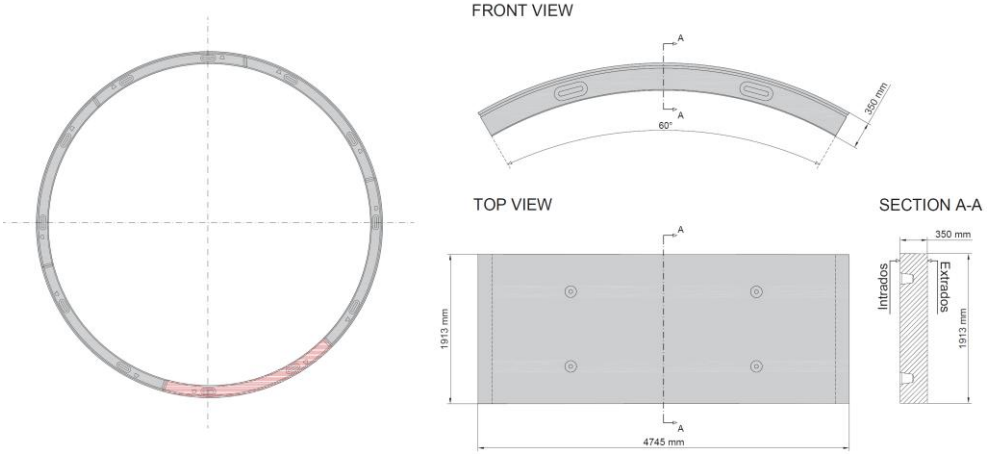


Fig. 2 Geometry of the tunnel lining segment: ring configuration (left), front view and top view (center), and cross-section A–A (right).

2.2 Materials and testing procedure

Two concrete mixtures were investigated in this study - a conventional steel fiber reinforced concrete (SFRC) and a hybrid fiber reinforced concrete (HFRC) consisting of both steel and basalt fibers. The selected fiber combination was intended in order to investigate different crack-control mechanisms provided by each fiber type. The fibers used in the experimental program are shown in Fig. 3, while their main mechanical and geometrical properties are summarized in Table 1.

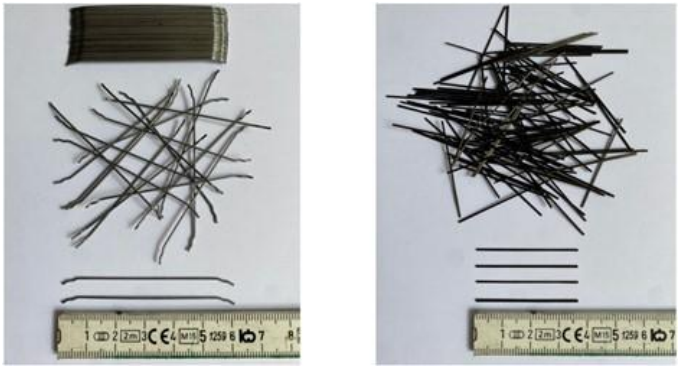


Fig. 3 Steel fibers (left) and basalt fibers (right) used in the experimental program.

The SF were double-hooked-end fibers with a length of 60 mm and a diameter of 0.75 mm, corresponding to an aspect ratio of 80. BF were straight fibers with a length of 36 mm and a diameter of 0.5 mm, resulting in an aspect ratio of 72. During mixing, the fiber bundles disperse into individual filaments with a minimum diameter of approximately 0.013 mm, and this increases the number of fibers per unit volume. The selected BF exhibit a higher nominal tensile strength of 2670 MPa compared with 2200 MPa for the SF. The thermal limit of application for this type of fiber is from -260 °C to +700 °C. In tunnel structures, the high thermal stability of BF is particularly relevant under fire exposure, where elevated temperatures may lead to cracking, spalling, and loss of mechanical performance of the concrete.

Table 1 Mechanical and geometrical properties of the steel and basalt fibers.

Property	Dimension	Steel fibers	Basalt fibers
Length	[mm]	60	36
Diameter	[mm]	0.75	0.5
L/D ratio	[-]	80	72
Density	[g/cm^3]	7.7	2.2
Tensile strength	[N/mm^2]	2200	2670
Geometry	[-]	Double-hooked end	Straight

The compositions of the investigated concrete mixtures are presented in Table 2. Three tunnel segments were produced for each mixture. The SFRC-TS mixtures contained 45 kg/m³ of SF, while the HFRC-TS mixtures contained 30 kg/m³ of SF and 7.5 kg/m³ of BF. Despite the minor variations in the constituent quantities resulting from industrial production processes, the mixtures exhibited comparable compositions. The hybrid mixture was designed to partially replace SF with BF. The material characterization was conducted by testing small-scale specimens, under compression, splitting tension and three-point bending according to the European Standard for testing FRC, EN 14651 [15], on notched prisms. Full-scale bending tests on tunnel segments were performed in the Testing Facilities of Montan University in Leoben, as shown in Fig. 4.

Table 2 Concrete mixture compositions of the SFRC and HFRC tunnel lining segments (kg/m³).

Segment code	Cement	Water	w/b	Aggregates	SF	BF
SFRC-TS1	326	158	0.49	1998	45	-
SFRC-TS2	331	158	0.48	1998	45	-
SFRC-TS3	329	152	0.46	2014	45	-
HFRC-TS1	329	128	0.40	2077	30	7.5
HFRC-TS2	329	150	0.46	2056	30	7.5
HFRC-TS3	330	151	0.46	2034	30	7.5

The testing procedure of the HFRC-TS was adopted from a previous experimental campaign to ensure comparability of results. The SFRC-TS tested in an earlier study were selected as reference specimens. In accordance with the previous investigations, the tests were performed without external lateral confinement. A horizontal force of 80 kN was applied to maintain stable machine control and to prevent sudden load redistribution caused by crack formation in the tensile zone of the segment crown. After reaching the prescribed horizontal force, the vertical load was increased in increments of 25 kN. Each load increment was applied over a period of 180 s, followed by a 30 s holding phase. During these intervals, photogrammetric measurements were performed along one side of the segment to enable detailed crack monitoring and evaluation. The test continued until the displacement capacity of either the vertical or horizontal hydraulic actuator was reached, corresponding to large deformations in the segment and the inability of the testing system to impose additional displacement.

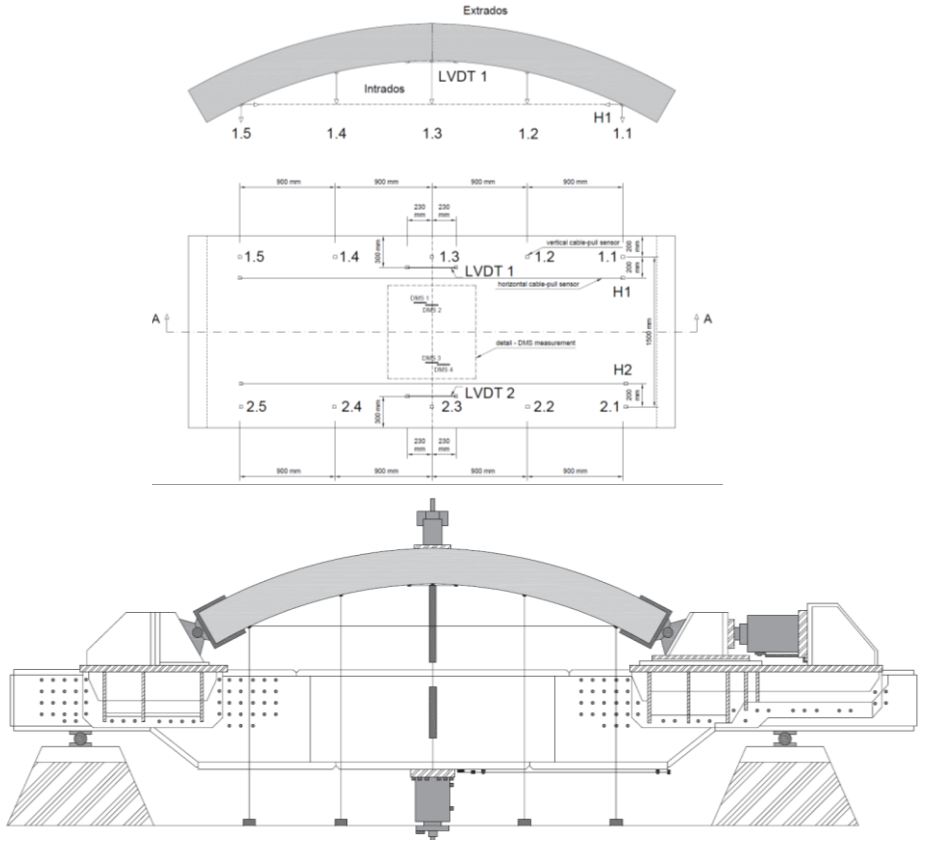


Fig. 4 Experimental set-up and instrumentation of tunnel lining segments.

2.3 Results

2.3.1 Small-scale specimens

The mechanical properties of the HFRC-TS mixtures were characterized for this study. The compressive strength and splitting tensile strength were determined at 28 days to verify the conformity of the concrete mixtures with the specified strength class and to assess the influence of the hybrid fiber reinforcement. The obtained results indicated the compressive strength class of C70/85, while the splitting tensile strength was found to be between 5.9 and 6.6 MPa.

The flexural behavior of the HFRC was evaluated by means of three-point bending tests on notched prisms in accordance with EN 14651 [15]. Six specimens with dimensions of 150 × 150 × 550 mm were tested for each concrete mixture. The nominal flexural stress–CMOD relationships are presented in Fig. 5. All three HFRC mixtures exhibited a similar response, characterized by an initial linear elastic branch, followed by a stable post-cracking behavior with gradual softening as the crack mouth opening displacement increased. The HFRC-TS1 mixture exhibited comparatively lower flexural strength values than HFRC-TS2 and HFRC-TS3. This behavior is attributed to its lower water-to-binder ratio, which resulted in a stiffer concrete matrix and influenced the post-cracking response.

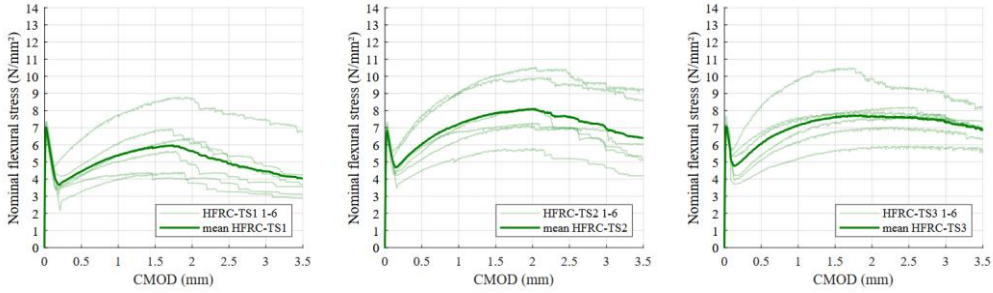


Fig. 5 Flexural strength of hybrid fiber (30 kg/m³ SF + 7.5 kg/m³ BF) concrete mixtures.

The average flexural parameters obtained from the bending tests are summarized in Table 3 and compared with the SFRC reference mixtures reported by Kühbacher [16]. In that study, the same concrete mixtures intended for precast tunnel lining segments were reinforced exclusively with SF at dosages of 30, 45, and 60 kg/m³ (SFRC30, SFRC45, and SFRC60). The hybrid mixtures achieved average limit of proportionality (LOP) values between 6.9 and 7.4 MPa, exceeding those of the SFRC30 and SFRC60 reference mixtures despite the reduced SF dosage. The residual flexural tensile strengths ranged from 4.5–6.3 MPa for f_{R1}, 5.8–7.9 MPa for f_{R2}, 4.9–7.9 MPa for f_{R3}, and 4.1–7.2 MPa for f_{R4}. As expected, the residual strengths at larger crack openings remained lower than those of the SFRC45 and SFRC60 mixtures, indicating that the post-cracking response continues to be governed primarily by the SF.

Table 3 Mean values of the limit of proportionality (f_L) and residual flexural tensile strengths (f_{R1}–f_{R4}) obtained from the three-point bending tests according to EN 14651 [15].

Mixture	f_L	f_{R1}	f_{R2}	f_{R3}	f_{R4}
SFRC30	5.6	5.2	6.1	5.9	5.3
SFRC45	7.0	7.3	8.9	8.9	8.2
SFRC60	6.1	8.8	10.5	9.7	9.1
HFRC-TS1	7.4	4.5	5.8	4.9	4.1
HFRC-TS2	6.9	6.1	7.9	7.7	6.4
HFRC-TS3	7.2	6.3	7.9	7.9	7.2

According to the fib Model Code 2010 [17], the structural classification of FRC is based on the characteristic values of the LOP and the residual flexural tensile strengths f_{R1k} and f_{R3k}. The characteristic values were determined as the 5% fractile of the test results using the mean value f_m and the standard deviation (s), as in (1):

$$f_k = f_m - k_n \cdot s \tag{1}$$

where k_n is a statistical coefficient depending on the number of tested specimens. For the present investigation, six specimens were tested for each mixture and a value of k_n equal to 2.18 was adopted. The obtained characteristic values satisfy the fib Model Code requirements, (2) and (3), for structural application of FRC.

$$\frac{f_{R1k}}{f_{Lk}} = 0.52 > 0.4 \tag{2}$$

$$\frac{f_{R3k}}{f_{R1k}} = 1.09 > 0.5 \tag{3}$$

2.3.2 Tunnel lining segments

Fig. 6 presents the load–deflection response and the relationship between the applied vertical force and the measured maximum crack width. The load–deflection curves show a comparable structural response for both reinforcement concepts. As illustrated in Fig. 6 (left), the HFRC-TS reached maximum vertical loads of 267.6, 279.2, and 256.7 kN, resulting in an average peak load of 267.8 kN. This value is in close agreement with the approximately 270 kN obtained for the reference SFRC segments, despite the reduction of the SF dosage from 45 kg/m³ to 30 kg/m³. After the maximum load, all segments exhibited a gradual reduction in load-carrying capacity. The slightly steeper post-peak softening observed for the hybrid segments can be attributed to the lower SF dosage, as SF primarily govern the residual load-carrying capacity.

The crack width evaluation further confirms the comparable performance of the hybrid solution. As shown in Fig. 6 (right), the relationship between crack width and applied load follows a similar behaviour for both HFRC and SFRC segments. The HFRC segments achieved comparable crack control and maintained a stable load transfer mechanism throughout the loading process. Despite the reduction of the SF content by approximately 33%, the HFRC segments exhibited an ultimate load and deformation capacity comparable to those of the reference SFRC segments. This means that the addition of BF contributes to the structural response by improving crack control during the early stages of loading.

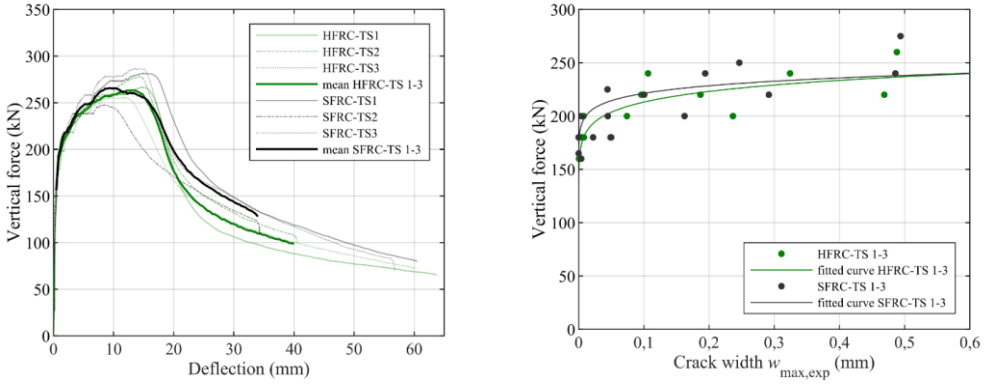


Fig. 6 Vertical deformation (left) and crack width behavior (right) of HFRC compared to SFRC segments.

3 CONCLUSIONS

The experimental investigation demonstrated that precast tunnel lining segments reinforced with a hybrid combination of steel and basalt fibers exhibit structural performance comparable to conventional SF reinforced segments. Although the SF dosage was reduced from 45 kg/m³ to 30 kg/m³, the hybrid segments reached an average maximum load of approximately 268 kN, which is in close agreement with the reference SFRC segments. The hybrid mixtures also showed enhanced flexural performance before crack localization, while maintaining comparable crack-width development and post-cracking behavior under full-scale loading. These findings show that BF can effectively compensate for part of the SF content and offer a promising reinforcement concept for precast tunnel lining segments with potential benefits in terms of material efficiency, durability, and sustainability. Current research focuses on the numerical modelling of the experimentally observed behaviour to support the design of the proposed hybrid reinforcement concept.

Acknowledgements

The authors gratefully acknowledge the financial support provided by the Austrian Research Promotion Agency (FFG) within the framework of the research project "Green Infrastructures – CO_2-optimized and resource-efficient waterproof concrete tanks (white tanks), tunnel linings, and structural components for civil engineering". The authors also express their sincere appreciation to Katzenberger Beton-Fertigteile Produktions GmbH & Co. KG for producing the test specimens and for their valuable technical support throughout the project. The authors further acknowledge N.V. Bekaert S.A. for supplying the steel fibers as a project partner.

References

[1] Trabucchi, Ivan, Smarslik, Mario, Tiberti, Giuseppe, Petraroia, Diego N., Plizzari, Giovanni A., and Mark, Peter. 2021. “A Hybrid Solution Proposal for Precast Tunnel Segments.” *Structural Concrete* 22(5): 3168–3182. doi: 10.1002/suco.202000629.

[2] Caratelli, Andrea, Meda, Alberto, Rinaldi, Zila, and Romualdi, Paolo. 2011. “Structural Behaviour of Precast Tunnel Segments in Fiber Reinforced Concrete.” *Tunnelling and Underground Space Technology* 26(2):284–91. doi: 10.1016/j.tust.2010.10.003.

[3] Conforti, Andrea, Trabucchi, Ivan, Tiberti, Giuseppe, Plizzari, Giovanni A., Caratelli, Andrea, and Meda, Alberto. 2019. “Precast Tunnel Segments for Metro Tunnel Lining: A Hybrid Reinforcement Solution Using Macro-Synthetic Fibers.” *Engineering Structures* 199:1–11. doi: 10.1016/j.engstruct.2019.109628.

[4] Di Prisco, Marco, Plizzari, Giovanni, and Vandewalle, Lucie. 2009. “Fibre Reinforced Concrete: New Design Perspectives.” Materials and Structures 42(9):1261–1281. doi:10.1617/s11527-009-9529-4.

[5] Markovic, I. 2006. *High Performance Hybrid-Fibre Concrete – Development and Utilisation*. PhD diss., Delft University of Technology, Delft, The Netherlands

[6] König, G., and Kützing, L. 1998. “Mit einem Fasercocktail zur Duktilität von Druckgliedern aus Hochleistungsbeton.” *Bautechnik* 75(2):62–66. doi:10.1002/bate.199800730.

[7] Kützing, L., and König, G. 2001. “Duktiler Hochleistungsbeton mit Fasercocktail – Technologie, Bemessung, Anwendungen.” *Bautechnik* 78(2):105–114. doi:10.1002/bate.200100550.

[8] Vandewalle, Lucie. 2007. “Postcracking Behaviour of Hybrid Steel Fiber Reinforced Concrete.” In *Proceedings of the 6th International Conference on Fracture Mechanics of Concrete and Concrete Structures (FraMCoS-6)*, Catania, Italy, 17–22 June 2007.

[9] Lawler, John S., Zampini, Davide, and Shah, Surendra P. 2005. “Microfiber and Macrofiber Hybrid Fiber-Reinforced Concrete.” *Journal of Materials in Civil Engineering*.

[10] Fiore, Scalici, Tommaso, Di Bella, and Valenza. 2015. “A Review on Basalt Fibre and Its Composites.” *Composites Part B: Engineering* 74:74–94. doi:10.1016/j.compositesb.2014.12.034.

[11] Zhou, Hao, Jia, Bin, Huang, Hui, and Mou, Yanling. 2020. “Experimental Study on Basic Mechanical Properties of Basalt Fiber Reinforced Concrete.” *Materials* 13(6):1362. doi:10.3390/ma13061362.

[12] Arslan, Mehmet Emin. 2016. "Effects of Basalt and Glass Chopped Fibers Addition on Fracture Energy and Mechanical Properties of Ordinary Concrete: CMOD Measurement." *Construction and Building Materials* 114:383–391. doi:10.1016/j.conbuildmat.2016.03.176.

[13] Kizilkanat, Ahmet B., Kabay, Nihat, Akyüncü, Veysel, Chowdhury, Swaptik, and Akça, Abdullah H. 2015. "Mechanical Properties and Fracture Behavior of Basalt and Glass Fiber Reinforced Concrete: An Experimental Study." *Construction and Building Materials* 100:218–224. doi:10.1016/j.conbuildmat.2015.10.006.

[14] Medeghini, Filippo. 2025. *Steered Fiber Orientation and Targeted Material Placement: Optimizing the Mechanical Response of Steel Fiber Reinforced Concrete*. PhD dissertation, Ruhr University Bochum and Università degli Studi di Brescia, Bochum.

[15] CEN. 2007. *EN 14651:2005+A1:2007. Test Method for Metallic Fibre Concrete – Measuring the Flexural Tensile Strength (Limit of Proportionality (LOP), Residual).* Brussels: European Committee for Standardization (CEN).

[16] Kühbacher, Manuel Thomas. 2023. *Faserbeton im Tunnelbau*. PhD dissertation, Montanuniversität Leoben, Lehrstuhl für Subsurface Engineering, Leoben, Austria.

[17] fib. 2013. *fib Model Code for Concrete Structures 2010*. Berlin: Ernst & Sohn. doi:10.1002/9783433604090.

Soil Structure Interactions

Workflow for consistent soil-structure interaction regarding structural and geotechnical design

Christian Wallner [a], Franz Tschuchnigg [b], Dirk Schlicke [a]

a Institut for Structural Concrete, Graz University of Technology, Lessingstraße 25, 8010 Graz, Austria

b Institut for Soil Mechanics, Foundation Engineering and Computational Geotechnics, Graz University of Technology, Rechbauerstraße 12, 8010 Graz, Austria

Summary

This paper proposes a decision-oriented workflow for consistent regard of soil–structure interaction within the Eurocode framework. Although settlements, stiffness, load combinations, and construction stages are individually regulated, a unified procedure linking these interdependent aspects is lacking. The workflow systematically couples settlement mechanism, structural stiffness, load level, soil behaviour, and time dependency. It clarifies which load combination governs settlements, how global and local stiffness control redistribution of stresses, and how construction stages influence both settlements and internal forces. Compared to classical system stiffness concepts, the approach improves transparency by explicitly defining modelling boundary conditions instead of condensing them into global assumptions. It does not introduce new mechanical models, but structures existing concepts into a consistent, code-compatible strategy. The result is a more reliable and transparent soil–structure interaction assessment without increasing geotechnical investigation effort.

1 SOIL-STRUCTURE INTERACTION

Soil–structure interaction (SSI) influences structures primarily through differential settlements. These settlements act as imposed deformations on the structure and generate additional internal forces due to compatibility requirements in statically indeterminate systems. Typical systems with monolithically connected foundations and superstructures experience therefore load redistributions in both the foundation system and in the structure above. A consistent representation of SSI is therefore essential for structural design, particularly for serviceability limit state verification and, in specific cases, also for ultimate limit state assessment.

As illustrated in

Fig. 1, a realistic description of SSI requires that three boundary conditions are defined and considered simultaneously at any stage of the analysis :

- the mechanical properties of the soil,
- the distribution of structural loads, and
- the effective stiffness of the structure.

These aspects are strongly interrelated. Structural loads effect soil stiffness in a stress- and strain-dependent manner, leading to settlements and differential ground movements. These movements act as imposed deformations on the structure and affect the internal force distribution. At the same time, the structural stiffness may change due to cracking, plasticity, and time-dependent effects such as creep. This stiffness modification influences the distribution of founding forces on the soil and thus the further development of settlements. Soil–structure interaction must therefore be understood as a coupled and potentially cyclic process rather than a one-directional dependency.

In summary, a consistent assessment of SSI requires clarification of which structural stiffness interacts with which load distribution, which soil properties are affected, and over which relevant time period this interaction takes place.

In the current European design framework, differential settlements and ground movements are classified as imposed deformations and are primarily addressed within the serviceability limit state (SLS). According to EN 1992 [1], their effects shall be considered in serviceability verifications, particularly with respect to deformation limits, crack widths, and stress control.

If settlements are explicitly included in structural analysis, EN 1990 [2] defines them as indirect actions. While load effects from permanent and variable actions are multiplied by corresponding partial

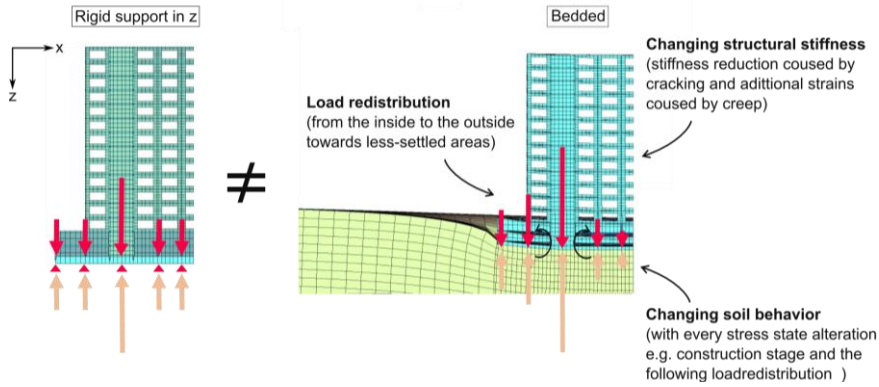


Fig. 1 Soil–structure interaction and its governing boundary conditions at any given state: soil properties, structural stiffness, and load distribution.

safety factors, imposed deformations due to settlements are assigned a factor of $\gamma_{Settlement} = 1.0$ in both SLS and ultimate limit state (ULS) verifications.

In embedded 3D soil–structure models, however, load-induced stresses and restraint stresses from settlements are inherently superimposed. This prevents a clear separation of action effects and makes the code-compliant application of different partial safety factors non-transparent. As emphasized in [3], settlement-induced restraint effects should therefore be treated separately in ULS verifications. A consistent approach is to introduce the settlement profile as an independent load case in the structural model. By applying prescribed nodal displacements, restraint effects can be evaluated separately from external load effects, enabling a transparent and code-consistent verification.

Moreover, imposed settlement profiles allow the consideration of verification-specific settlement scenarios. Distinct settlement troughs may be defined for deformation and crack control in SLS, and for critical ULS checks such as punching of foundation slabs [4], reflecting different load levels and structural stiffness states. This differentiation provides a rational basis for both safe and resource-efficient design.

According to EN 1997, appropriate predicted settlements shall be considered where soil–structure interaction significantly influences structural action effects, as also required in EN 1992-1-1:2023 [5]. Consequently, fundamental aspects of soil mechanics such as stress-dependent stiffness [6], strain-level effects [7], and stress history [8] must be taken into account.

Eurocode 7 further requires that the assessment of differential settlements and foundation design consider :

- the occurrence and rate of settlements (immediate or delayed),
- the structural stiffness during and after construction,
- the load distribution and construction sequence, and
- random and systematic variations in ground properties.

Despite this guidance, a consistent and practically applicable procedure for integrating these interdependent aspects into structural analysis is not provided within classic SSI [9]. In particular, the required coupling of structural stiffness, load distribution, changing soil properties, and time-dependent effects is not defined within a unified framework. The following sections therefore discuss these aspects separately and subsequently combine them into a coherent workflow for soil–structure interaction, aligned with current and forthcoming Eurocode provisions.

In this study, the soil profile and material parameters are assumed to be known. The influence of parameter uncertainty on settlement prediction and structural response is beyond the present scope and requires separate investigation.

2 DISCUSSION ON THE INTERACTION RELEVANT BEHAVIORS

2.1 Time dependend settlement behavior

According to EN 1997, it must be assessed whether expected settlements occur predominantly immediately or in a delayed manner. Initially, soil response may be governed by undrained behaviour, followed by consolidation processes. Soil permeability is decisive in this context: coarse-grained soils typically exhibit immediate settlements, whereas fine-grained soils tend to show time-dependent behaviour due to consolidation.

A key question is which load level is relevant for settlement prediction and over which time period it should be considered. The literature consistently indicates that permanent actions, particularly self-weight, must be fully included, while variable actions should be considered only to the extent that they persist over time. EN 1990 provides a suitable framework through its rare, frequent, and quasi-permanent load combinations with the associated factors ψ_0, ψ_1, and ψ_2, reflecting the probability and duration of variable actions.

Based on the investigations presented in [10], settlement-relevant load levels can be differentiated according to the governing soil behavior, as summarised in Table 1. For drained, coarse-grained soils, a reduced characteristic combination (including α_n) provides a realistic representation of immediate settlements. For low-permeability cohesive soils, the quasi-permanent combination is more appropriate, as long-term consolidation significantly affects both settlements and internal force redistribution.

If soil behaviour cannot be clearly classified, sensitivity analyses are recommended. Where neither mechanism clearly dominates, a sequenced loading approach may be applied: quasi-permanent loading is considered until a defined consolidation degree is reached, followed by a reduced characteristic level to capture short-term effects. Short-term deformation increments after consolidation may become relevant if they increase total settlements by approximately 5%.

Table 1 Settlement relevant load combinations and corresponding govering behavior.

Load combination	Formula	Behavior	Soil type	Duration
characterisitc (α_n)	$q_\alpha = q \cdot \alpha_n$	immediate	coarse grained	$t_\alpha \ll t_{\text{consol}}$
quasi-permanent	$q_{\text{Q-p}} = q \cdot \psi_2$	delayed	fine gained	$t_{\text{Q-p}} \approx t_{\text{consol}}$
sequenced	$q_{\text{Q-p}} \rightarrow q_\alpha$	intermediate	layerd/mixed	staged

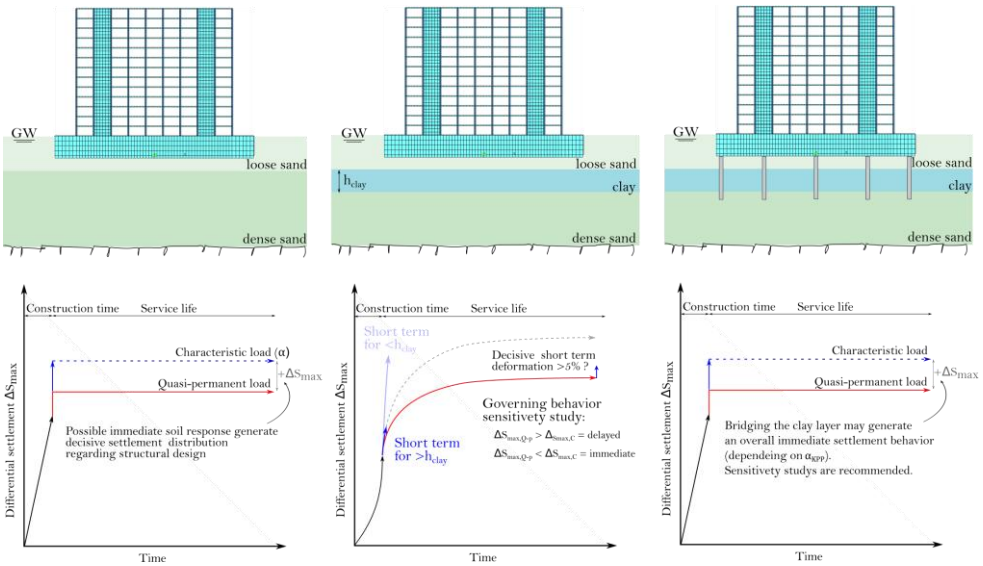


Fig. 2 Influence of soil type and foundation system on the governing settlement behaviour and corresponding load combination

Fig. 2 applies the proposed framework to three representative case studiesin oreer to provide qui-guidance for practical decision-making.

In Case Fig. 2 (left), a building founded on sand exhibits a predominantly immediate settlement response with negligible time dependency. For structural design, the settlement distribution derived from the reduced characteristic load combination is therefore decisive.

Case Fig. 2 (middle) introduces a clay layer beneath the building, leading to delayed settlement behaviour governed by consolidation. A sensitivity study considering permeability and time-dependent effects is required to determine the governing load combination and relevant duration. The dominant mechanism depends primarily on the thickness and permeability of the fine-grained layer.

Case Fig. 2 (right) demonstrates that the foundation system itself may alter the soil response behavor. Using the same stratigraphy as in Case Fig. 2 (middle) but introducing end-bearing piles that bridge the clay layer, shifts the governing behaviour back to predominantly immediate settlements. In this configuration, the load is mainly transferred to the underlying sand, resulting in a response comparable to Case 2 (left).

2.2 Effective structural stiffness

In many geotechnical models, only the foundation is represented explicitly, while structural loads from a separate structural analysis are applied externally. However, a realistic prediction of differential settlements requires consideration of the bending, shear, and torsional stiffness of the entire structural system, including both foundation and superstructure.

Studies in [11] show that considering the explicitly modelled structural stiffness leads to a reduction of differential settlements. As illustrated in Fig. 3 (left), this influence depends on the global structural behaviour. Foundation slabs and stiff basement walls contribute significantly to overall system stiffness. In flexible buildings, only a limited portion of the upper floors effectively participates in settlement redistribution, whereas stiff wall-type systems remain engaged over several storeys.

Practical guidline for global effective structural stiffness :

- **Flexible structures:** foundation and basement + approx. $1/3$ of the structure (≥ 2 floors)
- **Stiff structures:** foundation and basement + approx. $2/3$ of the structure (≥ 4 floors)

For reliable settlement prediction, structural stiffness must be consistent with the governing load level, and construction state. In this context, the bending stiffness of horizontal elements, particularly slabs and foundation plates, as well as stiff vertical elements such as basement walls, is decisive.

Experimental and numerical studies [12] indicate that the effective bending stiffness EI of flexural members may reduce to 20–70 % of the uncracked value in ULS, depending on reinforcement and cracking behaviour. Practical recommendations suggest stiffness reductions to approximately 60 % in SLS and 40 % in ULS [3]. This simplified assumption, however, should always be double-checked with the moment-curvature behavior of the cross section under decisive load level.

In addition to cracking, time-dependent effects such as creep further reduce effective stiffness. These effects are most pronounced during early construction stages but also influence long-term settlement development. Traditional approaches often apply global stiffness reductions, for example by reducing slab or structural stiffness by up to 50 % [13], [14]. Such simplifications, however, neglect the staged interaction between load application and increase of global stiffness in the the course of the construction progress.

Practical guidline for **local effective structural stiffness** reduction (Fig. 3 (right)) :

- **Cracking:** Approx. slab stiffenss by $EI \approx 0.6 \times EI_{\mathrm{uncracked}}$ once $M_{\mathrm{Ed}} > M_{\mathrm{cr}}$:
- **Cracking & creep:** staged stiffness adaptation using an equivalent foundation stiffness approach according to [15].

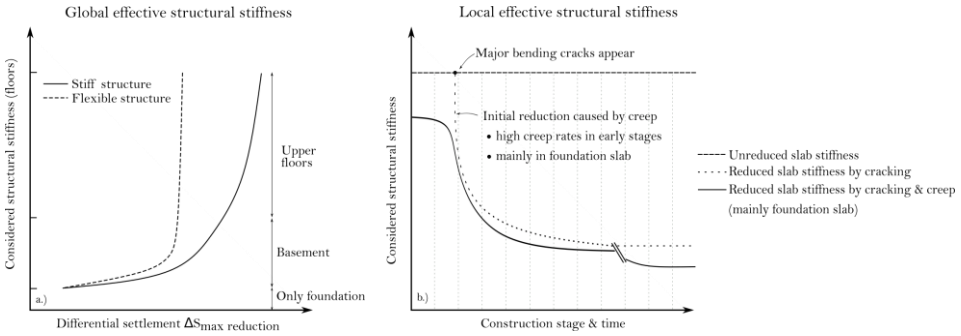


Fig. 3 Effect of structural stiffness representation on settlement behaviour: global participation and local stiffness reduction.

2.3 Application of loads

In most geotechnical settlement analyses, only the foundation is modelled explicitly, while structural loads are introduced as external actions derived from structural analysis. The chosen load representation directly affects the settlement pattern and should be assessed with respect to two criteria:

1. **Representative foundation load pattern**, ensuring realistic stresses at the SSI interface.
2. **Possibility of load redistribution**, allowing structural adaptation to settlements through internal force redistribution.

Fig. 4 compares three common modelling strategies :

- **Holistic approach:** Loads are applied at their actual positions within the structural system, ensuring realistic load transfer and inherent redistribution.
- **Smeared loads:** Total building loads are averaged and applied as uniform pressures at foundation level, reducing local stress concentration.
- **Explicit point and line loads:** Building loads at foundation level. Local stress concentrations are captured, but redistribution requires iterative evaluation to ensure compatibility.

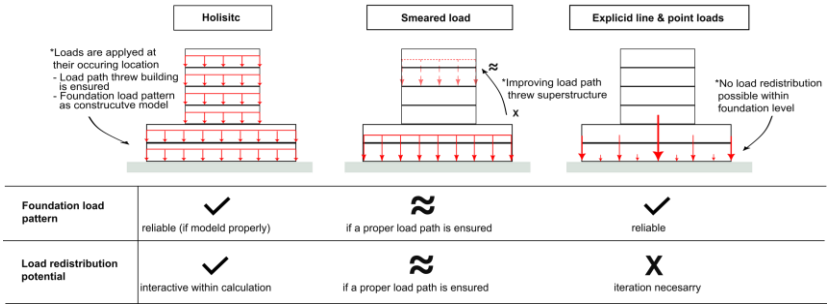


Fig. 4 Load modelling strategies and their ability to represent realistic load distribution and the ability for structural stress redistribution.

2.4 Interaction of load & stiffness (sequenced construction)

The representation of construction sequences is critical for capturing the interaction between evolving loads and structural stiffness. From a geotechnical perspective, this is essential because soils exhibit nonlinear behaviour, and settlement prediction depends on the loading path as well as the stress and stiffness history [16].

The construction process also influences internal force distribution within the structure [17]. In three-dimensional models, staged construction initially shifts internal forces towards stiffer components, such as cores or central walls, thereby modifying the load distribution relevant for

settlement analysis. As settlements develop, forces are further redistributed towards less-settled regions, which in turn alters foundation reactions.

A further key aspect is the gradual increase in structural stiffness during construction. Successive load application combined with increasing stiffness must be represented consistently to capture soil–structure interaction [18]. Activating the full superstructure with its final stiffness and total loading from the outset, the so-called wished-in-place approach, leads to unrealistically high stiffness and thus underestimates settlements, particularly in early stages when bending stiffness is still reduced (Fig. 5 (left)).

A more detailed stage-wise representation mitigates this effect and allows realistic redistribution in both soil and structure. The influence of construction staging is particularly significant for immediate settlement behaviour, whereas its impact is generally smaller in predominantly delayed consolidation scenarios (Fig. 5 (right)).

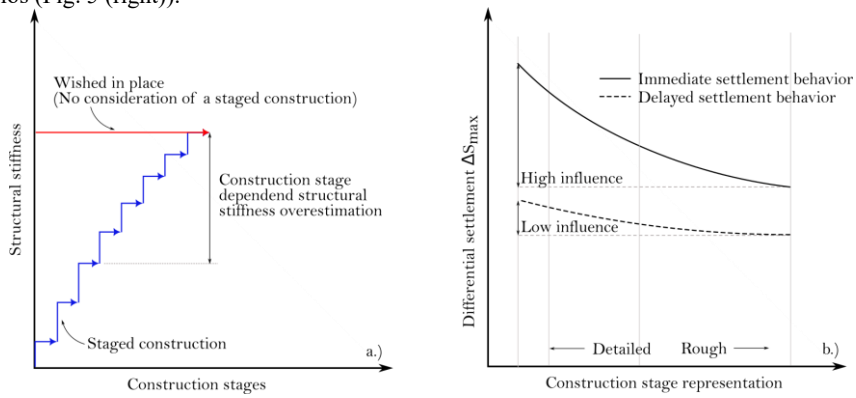


Fig. 5 Influence of construction staging on settlement prediction: (a) wished-in-place modelling leading to underestimated early settlements; (b) staged construction allowing realistic load–stiffness interaction.

3 PROPOSED WORKFLOW FOR CONSISTENT SOIL-STRUCURE INTERACTION

As outlined in the introduction, reliable soil–structure interaction assessment requires a consistent definition of which structural stiffness interacts with which load distribution, effecting which soil properties, and over which time period.

Fig. 6 synthesizes the previously discussed aspects from Eurocode 7 and related literature into a structured decision-oriented workflow. The objective is not to introduce new mechanical models, but to provide a consistent framework for selecting and combining modelling assumptions. The workflow guides the definition of the governing boundary conditions with respect to :

- Time-dependent settlement behaviour (immediate or delayed response),
- Structural stiffness (flexible or stiff system, including staged stiffness evolution),
- Soil conditions (permeability and consolidation characteristics),
- Settlement-relevant load level, and
- Construction sequence effects.

4 CONCLUSION

Compared to classical system stiffness approaches, the proposed workflow does not aim to increase modelling complexity, but to ensure consistency between load level, structural stiffness, soil behavior, and time dependency. Traditional concepts based on system stiffness often condense these interacting parameters into global assumptions, which may obscure construction-stage effects, stiffness evolution, and settlement-relevant load combinations. By structuring these boundary conditions within a decision-oriented framework, the proposed approach enhances transparency, Eurocode compatibility, and the reliability of modern 3D-based soil–structure interaction assessments.

The central finding is that reliable SSI assessment depends on the consistent coupling of settlement mechanism, structural stiffness, load level, and construction sequence. Time-dependent soil behaviour governs the settlement-relevant load combination, while structural stiffness, both global and local,

controls the redistribution capacity of the system. The selected load modelling strategy determines whether realistic stress transfer and internal force redistribution can occur. Construction staging further influences both settlement magnitude and internal force development, particularly in systems dominated by immediate settlement behaviour.

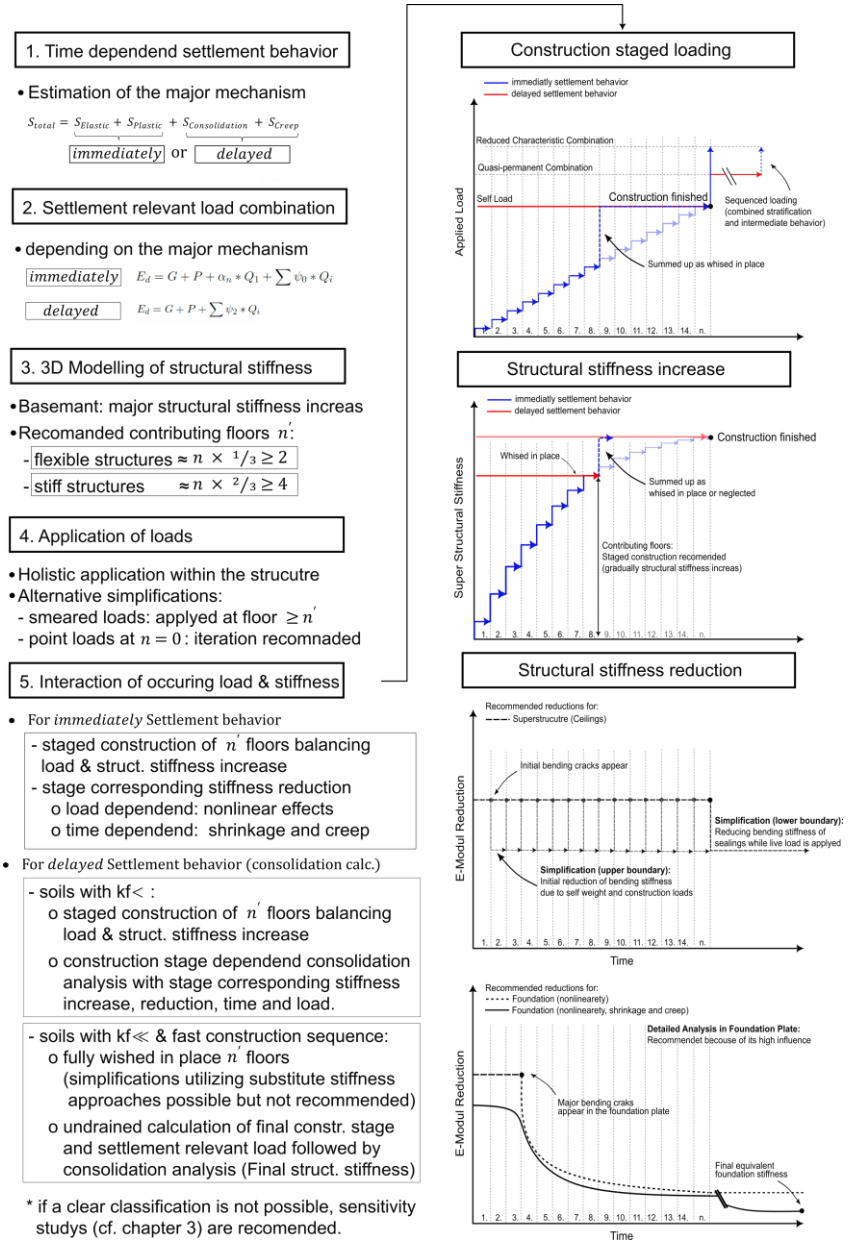


Fig. 6 Decision-oriented workflow for consistent soil–structure interaction, linking settlement mechanism, structural stiffness, load level, and construction sequence to enable transparent modelling and verification.By systematically linking these parameters, the workflow reduces ambiguity in modelling assumptions and supports a transparent and code-consistent design process. It does not introduce new mechanical models but clarifies how established geotechnical and structural concepts should interact in practice.

Future work should validate the workflow through additional case studies, extend it to other foundation systems, and further investigate time-dependent structural effects.

Acknowledgements

This study was conducted within the framework of the collective research project Agile Structural Design for Resource-Responsible Construction, funded by the Austrian Research Promotion Agency (FFG) under project number FO999913808, and supported by the TU Graz.

References

[1] ÖNORM EN 1992-1-1 (2015-02-15) *Eurocode 2: Design of concrete structures – Part 1-1: General rules and rules for buildings*. Vienna: Austrian Standards Institute.

[2] ÖNORM EN 1990 (2013-03-15) *Eurocode – Basis of structural design – consolidated version*. Vienna: Austrian Standards Institute.

[3] Schlicke, Dirk. (2023) *Ressourcenverantwortungsvolles Bauen mit Beton durch agile Tragwerksplanung* in: *Agile Digitalisierung im Baubetrieb*. Springer Vieweg, Wiesbaden, S. 683–699.

[4] Sever, Yolcu; Griniov, Efim; Schlicke, Dirk (2025) *Fracture-Mechanical Finite Element Simulation of Concrete Structures Using Smeared Crack Models* in: Beton- und Stahlbetonbau 120, H. 12, S. 1005–1017. https://doi.org/10.1002/best.70044

[5] Draft ÖNORM EN 1992-1-1 (prEN 1992-1-1) (2021-10-01) *Eurocode 2: Design of concrete structures – Part 1-1: General rules — Rules for buildings, bridges and civil engineering structures*. Vienna: Austrian Standards International.

[6] Schanz, Tom; Vermeer, Pieter A.; Bonnier, P. G. (2019) *The hardening soil model: Formulation and verification* in: Brinkgreve, R. B. J. [Hrsg.] *Beyond 2000 in Computational Geotechnics*. Routledge, S. 281–296.

[7] Benz, Thomas.; Schwab, Radu.; Vermeer, Pieter. (2009) *Small-strain stiffness in geotechnical analyses* in: Bautechnik 86, S1, S. 16–27. https://doi.org/10.1002/bate.200910038

[8] Melnikov, Roman et al. (2016) *OCR and POP Parameters in Plaxis-based Numerical Analysis of Loaded over Consolidated Soils* in: Procedia Engineering 165, S. 845–852. https://doi.org/10.1016/j.proeng.2016.11.783

[9] DIN Fachbericht 130 (1990) *Baugrund – Berechnungsgrundlagen*. Berlin.

[10] Wallner, Christian; Resch, Jakob; Schlicke, Dirk (2025) *Settlement Relevant Load Combinations and Force Redistribution in Structural Design* in: Buildings 15, H. 19, S. 3596. https://doi.org/10.3390/buildings15193596

[11] Wallner, Christian; Stummer, Sabrina; Schlicke, Dirk (2025) *Influence of Structural Stiffness Representation in Settlement Calculations and Practical Advice* in: Buildings 15, H. 18, S. 3270. https://doi.org/10.3390/buildings15183270

[12] Fastabend, Martin (2002) *Zur ingenieurmäßigen Bestimmung des Steifigkeitsabfalls von Stahlbeton im Zustand II* in: Beton- und Stahlbetonbau 97, H. 8, S. 415–420. https://doi.org/10.1002/best.200201870

[13] Fischer Daniel (2009) *Interaktion zwischen Baugrund und Bauwerk*. Universität Kassel.

[14] 4018 (1980) *DIN 4018 – Baugrund – Setzungsberechnung*. Berlin.

[15] Christian Wallner; Thomas Stegmüller; Dirk Schlicke *Time and load dependent structural stiffness representation for settlement calculations – Numerical investigations and practical recommendations* in: 21th fib Symposium Proceedings in Lissabon 2026.

[16] Pinheiro dos Santos, Yago Ryan et al. (2021) *Soil-structure interaction analysis in reinforced concrete structures on footing foundation* in: Soils and Rocks 44, H. 2, S. 1–12. https://doi.org/10.28927/sr.2021.058020

[17] Laggner, Thomas M. et al. (2021) *Statische Analyse mit linear elastischen 3D-Gebäudemodellen* in: Beton- und Stahlbetonbau 116, H. 5, S. 360–369. https://doi.org/10.1002/best.202000055

[18] Sert, S.; Kılıç, A. N. (2016) *Numerical Investigation of Different Superstructure Loading Type Effects in Mat Foundations* in: International Journal of Civil Engineering 14, H. 3, S. 171–180. https://doi.org/10.1007/s40999-016-0013-6

Concrete edge failure of bonded anchors under shear in recycled aggregate concrete

Zdravka Mikulić, Prof. Konrad Bergmeister

Institute of Structural Engineering,
BOKU University,
Peter-Jordan-Strasse 82, 1190 Vienna, Austria

Summary

The study investigates the shear edge failure behaviour of bonded anchors installed in recycled aggregate concrete (RAC) with 50% and 100% replacement levels, compared with conventional natural aggregate concrete (NAC). Experimental tests were conducted for two embedment depths and two edge distances to evaluate the influence of geometric parameters and concrete composition on shear resistance and load–displacement response. The results show that increasing edge distance and embedment depth significantly enhances shear capacity, while the influence of recycled concrete aggregate (RCA) content on the measured resistance remains limited within the investigated parameter range. Comparison with the EN 1992-4 design model for shear-induced concrete edge failure indicates that the calculated concrete edge failure resistances are of appropriate magnitude for the tested configurations. The conclusions are limited to the investigated materials, geometric configurations and sample size.

1 INTRODUCTION

The increasing demand for sustainable construction has led to a growing interest in the use of recycled concrete aggregate (RCA) as a partial or full replacement for natural aggregate in structural concrete. The reuse of concrete waste contributes to the reduction of landfill disposal and the conservation of natural resources, aligning with current environmental and circular economy objectives. As a result, recycled aggregate concrete (RAC) is increasingly considered for structural applications, provided that its mechanical performance and structural reliability can be adequately assessed. This development is also reflected in recent revisions of concrete design standards, including EN 1992-1-1:2023 [1], where the structural use of recycled aggregate concrete is increasingly addressed.

Compared to normal aggregate concrete (NAC), RAC is characterised by a more complex and heterogeneous microstructure due to residual cementitious phases and other mineral constituents associated with the recycled aggregate particles, increased porosity and pre-existing microcracks [2]. These features influence not only the global mechanical properties of concrete, such as stiffness and tensile strength, but also the local stress transfer mechanisms governing the behaviour of fastenings. Consequently, the applicability of existing design approaches for anchorage systems, which are largely calibrated for NAC, remains an open question when RAC is used as base material.

Post-installed bonded anchors are widely employed in structural engineering applications due to their versatility, high load-carrying capacity and adaptability to various geometric and loading conditions. They rely on the bond between the steel element, the adhesive mortar and the surrounding concrete for load transfer, making their performance sensitive to the mechanical and microstructural properties of the concrete. While extensive experimental and analytical research exists on the behaviour of bonded anchors in NAC, only a few studies have addressed their performance in RAC, especially with respect to failure modes governed by concrete fracture. Therefore, additional experimental evidence is required to assess whether the governing mechanisms and design assumptions established for conventional concrete remain valid for RAC.

Concrete edge failure under shear represents one of the most critical and brittle failure mechanisms for anchors installed close to a free edge [2][3]. This failure mode is governed by the tensile fracture behaviour of concrete and is therefore expected to be influenced by the altered microstructural characteristics of RAC. Design models for shear edge resistance, such as those adopted in Eurocode-based approaches, are primarily derived from experimental databases obtained for NAC. The extent to which these models remain applicable to RAC, particularly at high replacement ratios of natural aggregate, is still insufficiently documented.

The present study investigates concrete edge failure of bonded anchors under shear installed in RAC with different replacement levels of natural coarse aggregate. An experimental programme was carried out on three concrete types, including a reference NAC and two RAC mixtures with 50% and 100% recycled coarse aggregate replacement. The influence of effective embedment depth (h_ef) and edge distance (c_1) on the concrete edge failure resistance under shear was systematically examined. The results are analysed in terms of load-bearing capacity, failure characteristics and scatter, and are compared with predictions based on existing design concepts.

By providing experimental data on shear-induced concrete edge failure of bonded anchors in RAC, this study contributes to the assessment of existing design approaches for fastening applications in recycled aggregate concrete.

2 EXPERIMENTAL PROGRAMME AND METHODOLOGY

2.1 Concrete materials and production

Three types of concrete were used as base material for anchor installation: a reference NAC and two RAC mixtures with 50% and 100% replacement of the natural coarse aggregate by RCA, denoted as RAC50 and RAC100, respectively.

All mixtures were produced using CEM II/A-LL cement with a maximum aggregate size of 16 mm. A constant water-to-cement ratio (w/c) of 0.68 was adopted for all mixtures to isolate the influence of aggregate replacement on the mechanical properties of the concrete and, consequently, on the anchorage behaviour. Although this w/c ratio is higher than values typically used for high-performance structural concretes, it is representative of concretes commonly employed in cast-in-place and precast construction, thereby enabling a consistent and practice-oriented comparison between NAC and RAC mixtures.

For RAC50 and RAC100, only the aggregate fraction above 4 mm was replaced by RCA, while the fraction below 4 mm remained natural. The 4 mm limit corresponds to the producer's grading concept and defines the boundary between replaced and non-replaced aggregate fractions. The RCA was classified as Type 1 (RC-1) according to the German provisions given in DIN 1045-2 [5] in conjunction with the DAfStb Guideline [6], indicating a recycled aggregate primarily consisting of concrete fragments with restricted contents of brick and other mineral components. RCA originated from mixed concrete rubble from various, non-documented sources. This resulted in an inherently heterogeneous material considered representative of typical recycling streams in construction practice. The use of such aggregate was therefore intended to reflect realistic boundary conditions rather than idealised laboratory conditions. To approximate practical production conditions, all concretes were supplied by a precast concrete manufacturer. The mix compositions, as provided by the producer, are summarised in Table 1. Each batch was delivered in the form of a concrete slab measuring 190 × 190 × 30 cm. The slabs were cured under standard conditions and tested at comparable concrete ages to ensure consistency across all mixtures.

Table 1 Concrete mix compositions adopted in the experimental programme

Mix design parameter	Unit	NAC	RAC50	RAC100
fine NA: 0- 2 mm	[kg/m^3]	724	671	663
fine NA: 2-8 mm	[kg/m^3]	471	341	0
coarse NA: 8-16 mm	[kg/m^3]	701	267	0
coarse RCA: 4-16 mm	[kg/m^3]	0	548	1067
cement	[kg/m^3]	265	270	280
water	[kg/m^3]	185	185	190
w/c	[-]	0.68	0.68	0.68

2.2 Anchor system and installation

The anchor system investigated in this study consisted of a two-component, epoxy-based injection mortar used in combination with M12 threaded steel rods of strength class 12.9.
Bonded anchors were selected to investigate the influence of concrete material properties on shear-induced anchorage behaviour, as they allow controlled embedment depths and a well-defined load transfer mechanism without additional expansion forces that could affect the edge region.

By keeping the anchor type, diameter, steel grade and installation procedure constant across all tests, the experimental programme was designed to isolate the influence of concrete composition on shear-induced concrete edge breakout behaviour.

Installation was carried out in accordance with the manufacturer's product installation instructions, including the prescribed borehole cleaning procedure, given its influence on bonded anchor performance.

2.3 Mechanical characterisation of concrete

Compressive strength was determined on 35-day-old concrete cubes in accordance with ÖNORM EN 12390-3 [7], while splitting tensile strength and the secant modulus of elasticity were obtained from tests on 35-day-old cylinders following ÖNORM EN 12390-6 [8] and ÖNORM EN 12390-13 [9], respectively. All tests were carried out using a 5000 kN testing machine. These tests were used to characterise the base concrete at the age relevant for the anchor tests and to support the interpretation of the shear edge failure results.

2.4 Test series and anchor configurations

For the shear edge tests, four geometric anchor configurations were defined by combining two effective embedment depths, h_{ef} = 50 mm and 100 mm, with two edge distances, c_1 = 45 mm and 75 mm. The smaller edge distance corresponds to the minimum recommended value for the selected anchor diameter, while the larger edge distance was used to assess the influence of increased edge distance on concrete edge breakout resistance. The configurations are shown in Fig. 1. For each parameter combination and concrete mixture, three specimens were tested (n = 3).

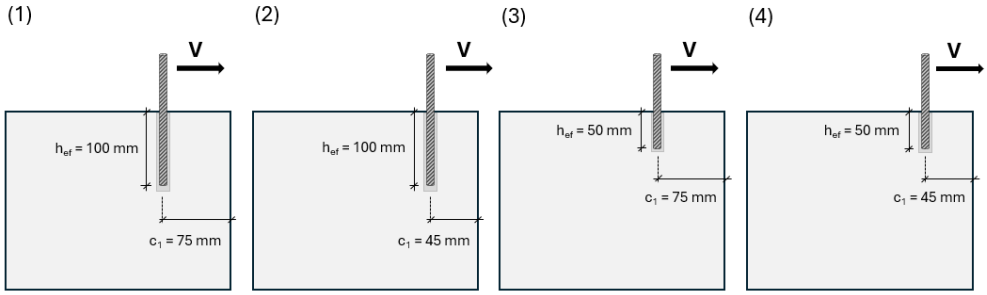


Fig. 1 Anchor configurations for shear edge tests

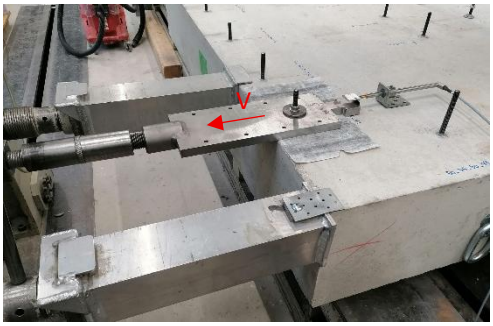


Fig. 2 Experimental test setup for shear tests on bonded anchors near a concrete edge

Shear tests were performed on single anchors installed close to a free concrete edge, with the load applied perpendicular to the edge to promote concrete edge breakout.

Loading was applied under displacement control. Identical installation procedures and boundary conditions were maintained for all specimens to ensure comparability of the results. An overview of the experimental test setup is shown in Fig. 2.

2.5 Evaluation procedure

The shear tests were evaluated using the maximum recorded load, defined as the ultimate shear resistance V_u. For each configuration, mean values and coefficients of variation were calculated. The mean resistance $V_{u,m}$ was additionally normalised to a reference compressive strength of 20 MPa, denoted as $V_{u,m,20}$, using the square-root strength dependence for concrete edge breakout in EN 1992-4 [10]. Due to the limited number of specimens per configuration (n=3), the evaluation was restricted to descriptive statistics, and no characteristic resistance was derived directly from the test series.

3 TEST RESULTS

3.1 Mechanical properties of concrete

The mechanical properties of NAC, RAC50 and RAC100 are summarised in Table 2. RAC50 showed a moderate increase in compressive strength compared with NAC, whereas RAC100 exhibited a slight reduction. The scatter of the compressive strength results remained low for all concretes, indicating consistent material quality across the investigated mixtures.

The splitting tensile strength showed only minor variation between the three concretes, suggesting that the tensile resistance was not significantly affected by the replacement of natural coarse aggregate within the investigated range. In contrast, the modulus of elasticity decreased noticeably with increasing RCA content, from 25.6 GPa for NAC to 19.5 GPa for RAC100. This reduction reflects the lower stiffness of recycled aggregates and their associated adhered old mortar.

Overall, the results indicate that while the strength-related properties remained broadly comparable, the deformational properties were clearly affected using RCA. This difference is relevant for the interpretation of the load–displacement behaviour and fracture response of the bonded anchors.

Table 2 Mechanical properties of concrete

Properties	f_c [MPa] (CoV [%])	$f_{ct,sp}$ [MPa] (CoV [%])	E_c [GPa] (CoV [%])
NAC	30.2 (1.4)	2.6 (4.5)	25.6 (3.3)
RAC50	33.6 (1.2)	2.9 (9.0)	22.9 (3.2)
RAC100	29.0 (3.0)	2.8 (1.4)	19.5 (0.1)

3.2 Shear test results

The ultimate shear resistance of bonded anchors installed near a concrete edge is summarised in Tables 3 and 4. For all investigated concretes, increasing the edge distance resulted in a clear increase in shear resistance. Concrete edge breakout is the governing failure mode for all tests under shear loading. For h_{ef} = 50 mm, increasing the edge distance from 45 mm to 75 mm resulted in a mean shear resistance increase of approximately 60-90%, depending on the concrete type. For h_{ef} = 100 mm, the corresponding increase ranged between approximately 95% and 110%.

For both embedment depths, NAC and RAC exhibited consistent trends with respect to edge distance. At the smaller edge distance, lower shear capacities were observed due to the stronger edge influence, whereas increasing the edge distance led to higher resistances, reflecting the enlargement of the concrete breakout body.

Comparing the concrete types at equal geometric configurations, the mean shear resistances of RAC50 were close to those of NAC. For RAC100, the measured values were of similar magnitude to NAC and RAC50. This trend remained consistent after normalisation, particularly for h_ef = 100 mm, where both mean and normalised values exhibited a very close agreement. Coefficients of variation ranged between 1.9% and 13.6%, with the highest scatter observed for RAC100 at h_{ef} = 100 mm and c_1 = 75 mm.

Table 3 Mean shear resistance of bonded anchors (h_{ef} = 50 mm)

Concrete	c_1 [mm]	c_1/h_{ef}	$V_{u,m}$ [kN]	CoV [%]	$V_{u,m,20}$ [kN]
NAC	45	0.90	8.15	5.2	7.42
	75	1.50	15.24	5.3	13.87
RAC50	45	0.90	9.70	2.5	8.37
	75	1.50	15.79	9.3	13.62
RAC100	45	0.90	9.26	1.9	8.60
	75	1.50	15.88	5.7	14.75

Table 4 Mean shear resistance of bonded anchors (h_{ef} = 100 mm)

Concrete	c_1 [mm]	c_1/h_{ef}	$V_{u,m}$ [kN]	CoV [%]	$V_{u,m,20}$ [kN]
NAC	45	0.45	9.97	8.6	9.07
	75	0.75	20.63	4.2	18.77
RAC50	45	0.45	9.78	5.1	8.43
	75	0.75	20.11	6.3	17.34
RAC100	45	0.45	10.61	3.6	9.85
	75	0.75	20.48	13.6	19.02

Increasing the embedment depth from 50 mm to 100 mm resulted in higher shear resistances for all concrete types and edge distances. Within the investigated parameter range, the results indicate that shear resistance is primarily influenced by geometric parameters, while the effect of RCA content appears limited compared with the influence of edge distance and embedment depth.

The load–displacement responses for c_1 = 45 mm are shown in Fig. 4. NAC, RAC50 and RAC100 exhibited comparable overall curve shapes, indicating that the governing shear transfer and concrete edge breakout mechanisms were not fundamentally altered using recycled aggregate. RAC showed slightly increased scatter and, in some configurations, a more pronounced post-peak deformability, particularly for RAC100. This behaviour is consistent with the reduced modulus of elasticity of RAC mixtures and their increased deformability. Overall, within the investigated parameter range, the load–displacement response was governed primarily by the geometric configuration, while no clear systematic influence of RCA content was observed.

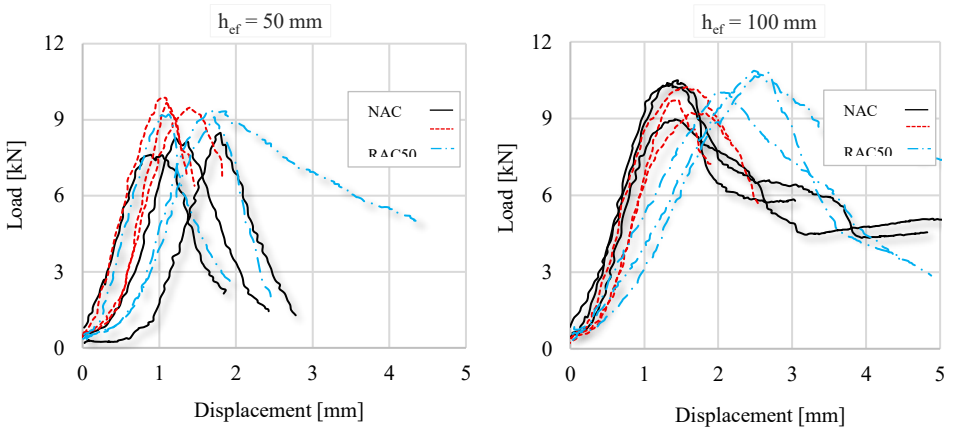


Fig. 4 Load–displacement behaviour for c_1=45 mm: comparison of NAC, RAC50 and RAC100

Representative failure patterns are shown in Fig. 5. While all specimens failed by concrete edge breakout, distinct differences in fracture morphology were observed between the investigated concrete types. NAC exhibited relatively smooth and coherent fracture surfaces, with crack propagation predominantly occurring through the cement matrix and partly along the aggregate-matrix interface. In contrast, RAC specimens showed progressively rougher and more irregular fracture textures with increasing RCA content, most pronounced for RAC100. The fracture surfaces of RAC mixtures appeared more fragmented, with crack paths frequently following the interface between old mortar and RCA particles rather than penetrating through the aggregate itself.

Local bond-related features were observed in isolated RAC50 specimens, where hardened adhesive mortar remained attached to the concrete and clear imprints of the threaded steel bar ribs were visible in the mortar after pull-out. However, these did not influence the global failure mechanism. The interpretation of fracture morphology is based on macroscopic visual inspection of the breakout surfaces.

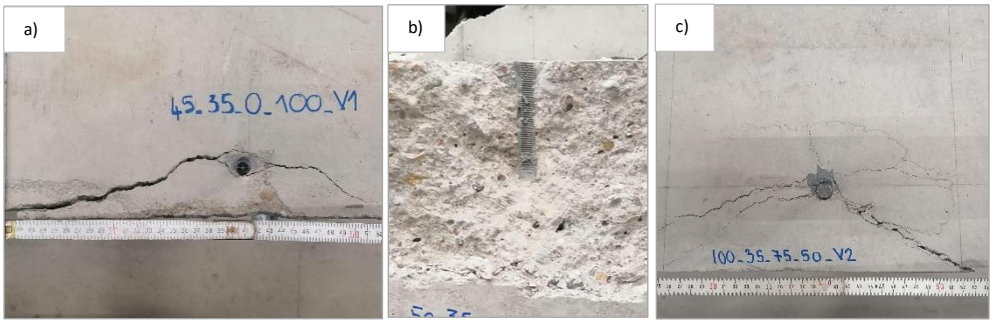


Fig. 5 Representative concrete edge breakout failure patterns: (a) NAC (smooth fracture surface); (b) RAC50 (rougher fracture surface with local anomalies near the anchor); (c) RAC100 (irregular fracture surface)

4 TEST-TO-CODE COMPARISON WITH EN 1992-4

4.1 Design model according to EN 1992-4

Design provisions for concrete edge breakout under shear given in ÖNORM EN 1992-4:2019 [10], the currently implemented Austrian standard for the design of fastenings in concrete, are primarily calibrated on conventional concrete. Since RAC differs in microstructure and stiffness, the comparison aims to assess whether the model provides resistance estimates of appropriate magnitude for the investigated RAC mixtures.

EN 1992-4 describes concrete edge breakout under shear by an idealised concrete failure body. The initial characteristic resistance is calculated as a function of concrete compressive strength, nominal anchor diameter, effective load-bearing length and edge distance, see Eq. (1).

$$V_{Rk,c}^{0} = k_9 \cdot d_{nom}^{\alpha} \cdot l_f^{\beta} \cdot \sqrt{f_{ck}} \cdot c_1^{1.5} \tag{1}$$

In Eq. (1), $V_{Rk,c}^{0}$ is the initial characteristic resistance, d_{nom} the nominal anchor diameter, l_f the effective load-bearing length, f_{ck} the characteristic compressive strength and c_1 the edge distance. The factor k_9 accounts for the concrete condition; since all tests were performed in uncracked concrete, k_9=2.4 was used. The exponents α and β were determined according to EN 1992-4.

The modification factors for spacing, additional edge effects, load eccentricity and load inclination were taken as 1.0, since single anchors were tested under shear perpendicular to one free edge and without eccentricity. The measured shear capacities were compared with the corresponding code-based resistances calculated for each configuration using the respective embedment depth, edge distance and concrete compressive strength.

4.2 Test-to-code comparison

Due to the limited number of tests per configuration (n=3), the evaluation was performed primarily using mean resistances. To relate the code-based characteristic resistance to the experimental mean values, a mean resistance was derived assuming an infinite sample size (n→∞) and a conservative maximum coefficient of variation of 15%, in accordance with the statistical definition of the 5% fractile. Mean-based ratios were therefore used as a global indicator of model performance while limiting the influence of statistical scatter associated with the small sample size.

The mean test-to-code ratios are presented in Fig. 6 as a function of the edge distance ratio c_1/h_{ef}. For illustrative purposes, a deviation band of ±20% around unity is indicated to support the visual assessment of the agreement between experimental and calculated resistances. Most values lie close to unity and remain within the evaluation band, indicating good overall agreement between experimentally measured and code-based resistances.

For NAC, the ratios are generally close to 1.0 across all configurations. RAC50 and RAC100 exhibit comparable levels, with several configurations showing slightly higher ratios, yet without any systematic trend towards unconservative predictions. No consistent influence of increasing RCA content on the test-to-code ratio can be observed.

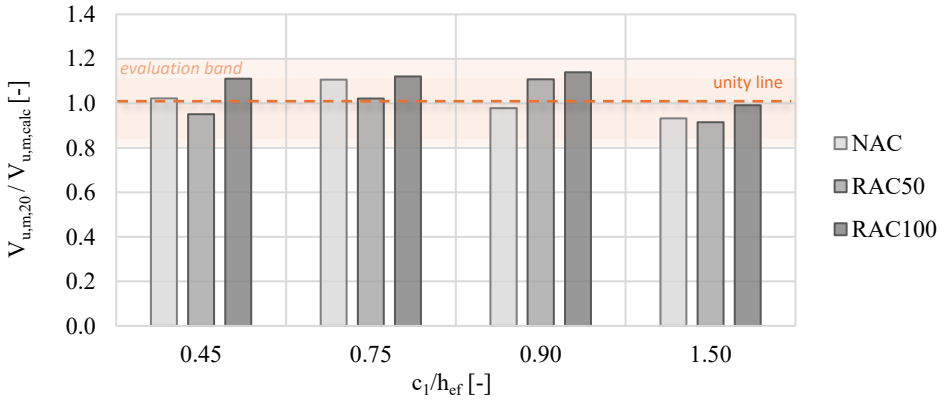


Fig. 6 Mean test-to-code ratios according to EN 1992-4 for concrete edge breakout under shear load as a function of edge distance ratio c_1/h_{ef}

Overall, the results indicate that the EN 1992-4 model provides resistance estimates of appropriate magnitude for both NAC and RAC within the investigated parameter range. The observed deviations remain moderate and no systematic influence of RCA content on the test-to-code ratio can be identified. From a preliminary design-oriented perspective, this suggests that the formulation provides appropriate resistance estimates for the tested bonded anchor system and investigated RAC mixtures. However, due to the limited number of tests and restricted parameter range, the results do not allow a general validation of the model for RAC.

5 CONCLUSIONS

The increasing use of RCA in structural applications requires a critical assessment of its influence on material properties and structural performance. Based on the experimental investigations conducted in this initial phase of the ongoing PhD research, the following conclusions can be drawn for the investigated bonded anchor system, concrete mixtures and geometric configurations:

- The replacement of natural coarse aggregate by RCA did not lead to a systematic reduction in compressive or splitting tensile strength within the investigated mixtures. In contrast, the modulus of elasticity decreased noticeably with increasing RCA content, indicating a clear influence of RCA on the deformational properties of concrete.
- At identical geometric configurations, the mean shear resistances of RAC50 and RAC100 were of similar magnitude to those of NAC. The shear resistance was governed primarily by

the geometric configuration, particularly edge distance and embedment depth, while no clear systematic reduction related to RCA content was observed.

- The load–displacement responses of NAC and RAC specimens showed comparable overall curve shapes. RAC mixtures exhibited a tendency towards slightly increased post-peak deformability, consistent with their reduced stiffness. All specimens failed by concrete edge breakout. Differences in fracture morphology were observed, with RAC specimens showing rougher and more irregular fracture surfaces; however, the governing failure mode remained unchanged.
- The comparison between experimentally measured resistances and the EN 1992-4 predictions yielded mean test-to-code ratios predominantly close to unity and fully within a ± 20% deviation band. No monotonic trend with increasing RCA content was identified. The observed deviations remained moderate and did not indicate systematic unconservative behaviour for RAC within the investigated parameter range. Accordingly, within the investigated parameter range, the EN 1992-4 formulation provided resistance estimates of appropriate magnitude for the tested bonded anchor system and RAC mixtures up to 100% replacement of the coarse aggregate. This finding should be interpreted as preliminary due to the limited number of specimens and the restricted range of anchor configurations.

The conclusions of this study are limited to the tested bonded anchor system, concrete compositions and geometric configurations. Further investigations covering a broader parameter range and larger sample sizes are required to support a more comprehensive statistical assessment and broader design conclusions.

Acknowledgements

The authors thank laboratory technician Đuro Petričević for his support during the experimental work and Dr.-Ing. Elisabeth Zeman and Dr.-Ing. Oliver Zeman for their assistance and valuable discussions.

References

[1] EN 1992-1-1:2023. Eurocode 2 – Design of concrete structures – Part 1-1: General rules and rules for buildings, bridges and civil engineering structures. European Committee for Standardization, Brussels.

[2] Xiao, Jianzhuang, Li, Wengui, Fan, Yuhui, Huang, Xiao. 2012. “An overview of study on recycled aggregate concrete in China (1996–2011).” *Construction and Building Materials.* Accessed December 15, 2025. doi: 10.1016/j.conbuildmat.2011.12.074.

[3] Sharma, Akanshu, Eligehausen, Rolf, Asmus, Jörg 2015. “Experimental investigations on concrete edge failure of headed stud groups in reinforced concrete.” *Transactions, SMiRT-23*, Manchester, United Kingdom, August 10–14, 2015, Division V, Paper ID 781.

[4] Eligehausen, Rolf, Mallée, Rainer, Silva, John F. 2006. *Anchorage in Concrete Construction*. Wiley-VCH.

[5] DIN 1045-2:2023-08 Concrete, reinforced and prestressed concrete structures – Part 2: Concrete - Deutsches Institut für Normung, Berlin.

[6] DAfStb Richtlinie „Beton nach DIN EN206-1 und DIN 1045-2 mit rezyklierter Gesteinskörnung nach DIN EN 12620“. 2019. Beuth, Berlin

[7] ÖNORM EN 12390-3:2019-06 “Testing hardened concrete Part 3: Compressive strength of test specimens” Austrian Standards International Standardization and Innovation.

[8] ÖNORM EN 12390-6:2010 “Testing hardened concrete Part 6: Splitting tensile strength of test specimens” Austrian Standards International Standardization and Innovation.

[9] ÖNORM EN 12390-13:2013 “Testing hardened concrete Part 13: Determination of secant modulus of elasticity in compression” Austrian Standards International Standardization and Innovation.

[10] ÖNORM EN 1992-4:2019 “Eurocode 2 – Design of concrete structures Part 4: Design of fastenings for use in concrete” Austrian Standards International Standardization and Innovation.

Kinematic measurements of concrete-to-concrete interfaces in full-scale continuous precast girders

Emilia Andrade Borges[1], Max Hendriks[1,2], Yuguang Yang[1]

[1]Faculty of Civil Engineering and Geosciences,
Delft University of Technology,
Stevinweg 1 2628CN, Delft, the Netherlands

[2]Department of Structural Engineering,
Norwegian University of Science and Technology,
Richard Birkelands vei 1A 7491, Trondheim, Norway

E.A.AndradeBorges@tudelft.nl

Summary
This study investigates the concrete-to-concrete interface behaviour of a 15 m continuous precast girder with a cast-in-situ top layer that exhibited interface failure. Detailed measurements of the evolution of slip *s* and crack opening *w* were obtained along the interface using Digital Image Correlation (DIC) up to ultimate load. The results show (i) spatial variation of kinematics linked to the interaction between the critical shear crack in the web and the interface plane, and (ii) two distinct crack opening paths. The measured *s* and *w* were used as input to constitutive models for aggregate interlock, friction, and dowel action to explore the corresponding stress distribution. Two main challenges remain: the unknown real stress evolution at interface, and the interaction between mechanisms. The findings motivate a dedicated small-scale experimental campaign to bridge the gap between measured kinematics and stresses, to better understand the mechanisms contributing to shear capacity at concrete-to-concrete interfaces.

1 INTRODUCTION

Continuous precast girder bridges have been widely used in the Netherlands since the 1960s. A significant number of these structures do not comply with current design standards, and the uncertainties regarding their actual shear capacity have motivated a research programme with large-scale testing at Delft University of Technology [1].

Among the parameters governing shear resistance, the concrete-to-concrete interface between the precast girder and the cast-in-situ top layer plays a key role in ensuring shear transfer. Although such interfaces have been extensively studied in small-scale tests, their behaviour in full-scale continuous members remains insufficiently understood. Consequently, the applicability of existing models for interface capacity assessment is uncertain.

This study takes the first step towards improving this understanding by: (i) measuring the kinematics, slip *s* and crack opening *w*, in large-scale specimens; (ii) using the measured kinematics as input to selected constitutive models from literature to explore the associated stress distribution and provide a mechanical interpretation; and, (iii) identifying the remaining challenges and defining the next steps required to bridge the gap between kinematics and stresses.

2 EXPERIMENTAL CAMPAIGN

2.1 Specimen, loading protocol, and global response

The experimental campaign consists of eight large-scale continuous specimens. The specimen considered in the present study, N02TL, is illustrated in Fig. 1 (a) and (b). This 15m-long specimen consists of two precast prestressed girders, a shorter cantilever and a longer main span, connected by a 160 mm-thick cast-in-situ top layer and a crossbeam. Prestressing of the main precast girder is provided by twenty-two 12.9 mm diameter FeP 1860 strands, each initially prestressed to a force of 79 kN per strand. The concrete compressive strength of 150 mm cubes for the precast girder is 106.2 MPa, and for the top layer 55.7 MPa.

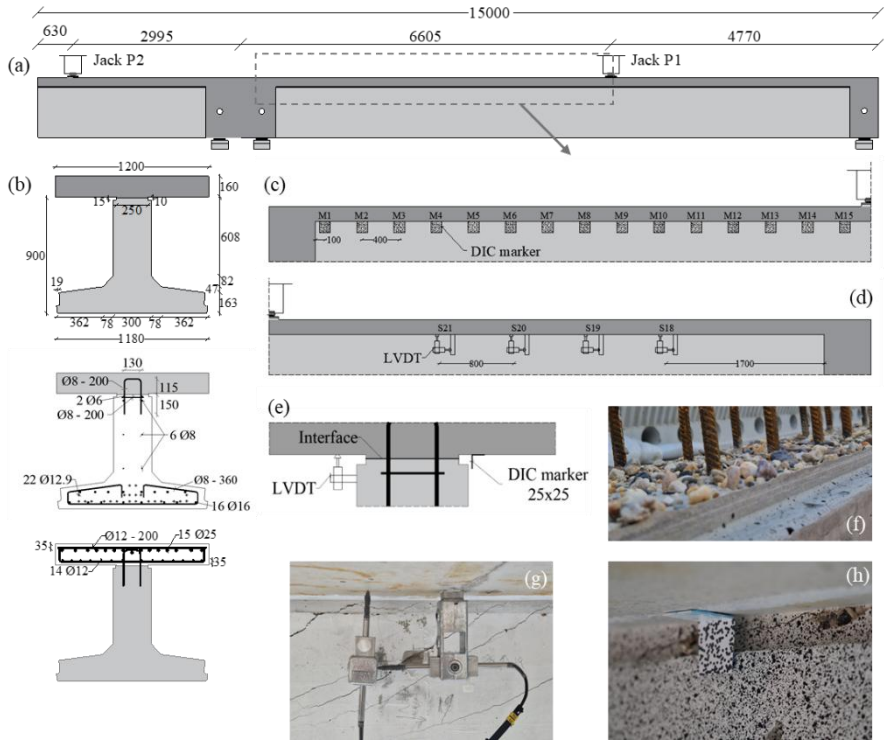


Fig. 1 Overview of specimen N02TL: (a) longitudinal view with dimensions, boundary, and loading conditions; (b) cross-section and reinforcement layout; (c) DIC marker locations; (d) LVDT locations; (e) zoomed-in cross-sectional view of interface instrumentation; (f) roughened interface surface; (g) LVDT installation; (h) DIC marker installation.

The interface between the precast girder and the cast-in-situ top layer consists of a construction joint intentionally roughened by spraying large aggregates (31.5mm) during casting of the precast girder (see Fig. 1 (f)). The reinforcement consists of 8 mm diameter bars spaced at 200 mm. The embedded length of the reinforcement in the precast girder is 150 mm, which was verified as sufficient by pull-out tests. The specimen is supported by elastomeric bearings at two locations, and loads are applied via hydraulic jacks P1 and P2. Jack P1 is operated under displacement control at a constant rate of 0.02 mm/s, while jack P2 follows in force control maintaining a fixed P1:P2 load ratio of 1:0.63. Loading is applied in increments of 50 kN for jack P1, and each target load level is held to allow for data acquisition. This loading protocol continues until failure of the specimen.

Relative displacements at the interface between the girder and the top layer, namely opening and sliding, were monitored using four Linear Variable Differential Transformers (LVDTs), labelled S18 to S21, and 15 Digital Image Correlation (DIC) markers, labelled M1 to M15, as shown in Fig. 1 (c) - (h). LVDTs readings were recorded every 1 s. The DIC setup consisted of two Canon EOS 5DS R cameras (50.6 MP, 8688 x 5792 pixels) with 24 mm lenses, providing an overlapping field of view of approximately 800 mm. Calibration resulted in a measurement accuracy of 0.03 mm. During the first 15 load stages, five pictures were captured at each target load level; from load stage 16 onward, additional images were taken every 8 s during loading.

The load-displacement response of specimen N02TL at jack P1 is shown in Fig. 2 (a). The behaviour is initially linear, followed by a reduction in stiffness at approximately $0.7P_u$ which corresponds to cracking at the mid-span region. As the load increases, damage concentrates at the intermediate support, where the critical shear crack develops in the web and propagates towards the interface with the cast-in-situ top layer (Fig. 2 (b)). The subsequent horizontal propagation of this crack along the interface governs the failure of the specimen, which occurs at a load P_u of 1980 kN.

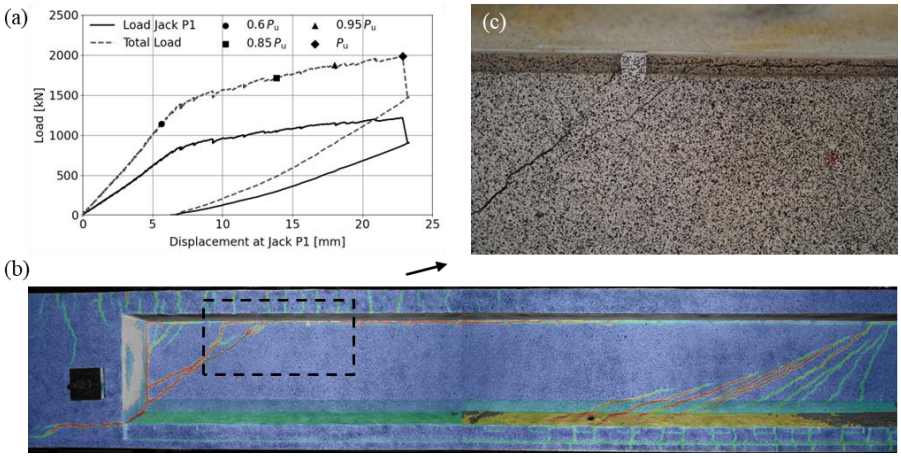


Fig. 2 Global behaviour and failure of specimen N02TL: (a) load-displacement response, where total load represents the combined contribution of both jacks; (b) crack pattern at ultimate load P_u; (c) zoomed-in view of the critical shear crack propagating from the web and reaching the interface.

The observed failure is classified as an interface failure initiated and controlled by shear cracking in the web (see Fig. 2 (c)). This highlights the coupled nature of shear behaviour and interface capacity in the specimen. Such interaction suggests a localized change in interface kinematics that could ultimately govern failure. This observation motivates a more detailed investigation of the evolution of slip and crack opening at the interface.

2.2 Interface kinematics

The instrumentation presented in Section 2.1 was designed to allow a detailed measurement of the evolution of interface slip *s* and crack opening *w* throughout the full loading history up to the ultimate load P_u. Selected load stages are used to illustrate this evolution; all marked in the global load-displacement response shown in Fig. 2 (a). The spatial evolution of *s* and *w*, measured with DIC and validated against LVDT measurements, are presented in Fig. 3 (a) and (b). Each symbol represents the measurement at a specific DIC marker (M1-M15), with the horizontal axis indicating the marker positions along the interface as shown in Fig. 1 (c).

At the load level $0.6P_u$, neither significant *s* nor *w* is detected, with measured values remaining below the DIC accuracy threshold of 0.03 mm. A closer examination of the kinematic evolution shows that significant *s* and *w* begin to develop when the applied load exceeds approximately $0.65P_u$. This load level corresponds to the formation of the crack that later develops into the critical shear crack and intersects the interface at the location of marker M3. At this stage, both *s* and *w* increase rapidly from values below the measurement accuracy to approximately 0.2 mm. Consequently, at $0.85P_u$, a mobilized region becomes apparent for both s and w, primarily involving markers M3 to M5. This region continues to expand in a similar manner for both kinematic components at $0.95P_u$. Reaching P_u, corresponding to the specimen failure, is associated with a rapid and pronounced extension of the mobilized area, covering approximately 60% of the span of interest.

For all load stages, slip magnitudes generally exceed crack opening values, although both remain of the same order of magnitude. An exception is observed at marker M3, where, due to its proximity to the intersection between the critical shear crack and the interface, *w* exceeds *s* from $0.95P_u$ onward. The maximum values of both *s* and *w* are consistently found in this location, indicating a strong localization of deformation.

Additional insight into the interface behaviour can be obtained by examining the crack opening path, defined as the relationship between *w* and *s* for individual markers, as shown in Fig. 3 (c). In the region close to the critical shear crack (markers M1-M4), the *w*-*s* relationship is approximately linear, indicating comparable crack opening and sliding behaviour.

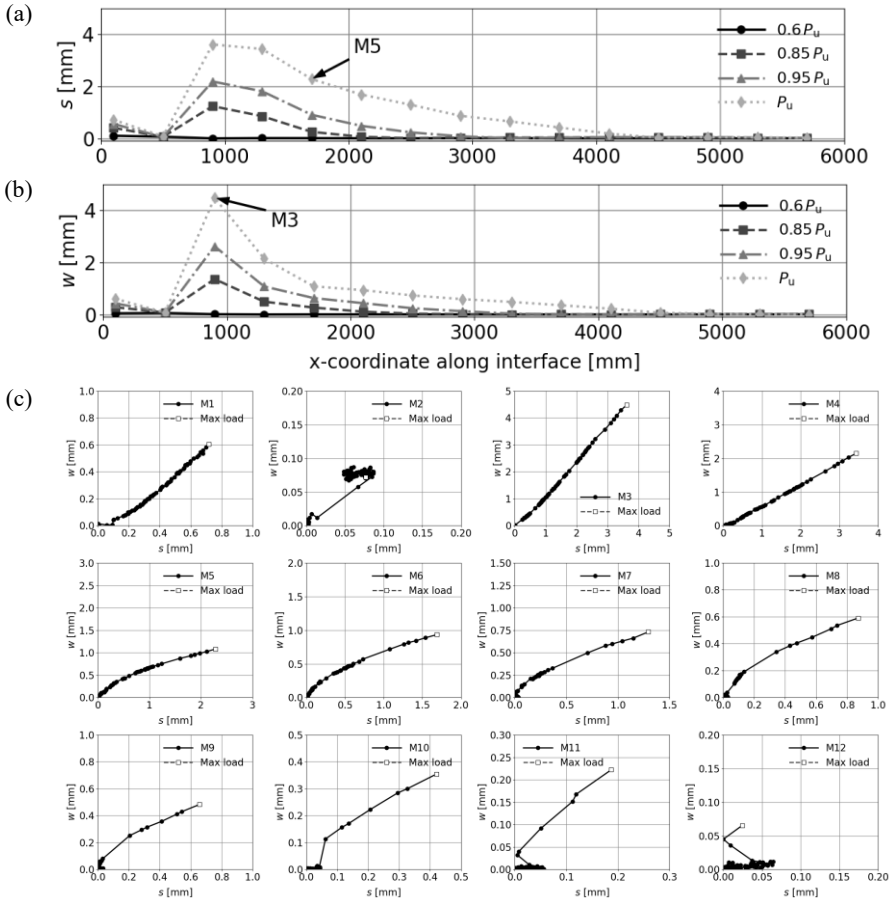


Fig. 3 Interface kinematics obtained from DIC at load stages $0.6P_u$, $0.85P_u$, $0.95P_u$, and P_u: (a) evolution of slip s along span; (b) evolution of crack opening w along span; (c) crack opening path w-s for markers M1 to M12 up to P_u, axis limits are adjusted for each marker to allow full visualization of the kinematic paths.

Marker M3 exhibits a more opening-dominated response, consistent with its location at the shear crack-interface intersection. For markers M5 onward, the response becomes predominantly slip-dominated, with similar w-s paths. These relationships are consistent with experimentally observed crack opening paths reported in literature [2]-[5]. These detailed kinematic measurements provide an opportunity to explore the associated stress distribution at the interface. To this end, a brief review of available constitutive models is first presented, followed by the selection of models adopted for the present study.

3 ESTIMATION OF STRESS DISTRIBUTION AT THE INTERFACE

3.1 Review of Constitutive Models

The study of shear capacity in concrete-to-concrete interfaces spans several decades, with research dating back to the 1960s. The need to estimate shear resistance at ultimate limit state has historically driven the development of capacity-based models, resulting in several relevant contributions [2], [6]-[11]. With the development of numerical calculation programmes capable of analysing the structural response throughout the entire loading history, increasing attention has been given to constitutive relations [12]. These models primarily aim to describe the shear stress – slip relationship and, in certain

cases, also incorporate the role of normal stress and crack opening. Compared to approaches focused solely on ultimate capacity, constitutive models can provide a mechanical interpretation of interface behaviour and capture the complex interaction between the contributing mechanisms.

In reinforced concrete-to-concrete interfaces, the contributing mechanisms can be classified according to the role of the reinforcement crossing the interface. Its axial contribution can be modelled following two main approaches. In smeared shear-friction models, reinforcement provides a global clamping force, and the resulting normal stresses is related to shear resistance through a friction coefficient μ [2], [13]. Alternatively, local approaches explicitly model aggregate interlock, where shear and normal stresses arise from contact mechanics between opposing crack faces [14]-[17]. Although aggregate interlock and friction are often treated as separate mechanisms at the modelling level, they are physically linked through equilibrium of normal forces acting at the interface.

Reinforcement also contributes to shear transfer by transmitting forces perpendicular to its axis, a mechanism known as dowel action. The linear component is commonly presented as a beam on an elastic foundation [18], while the non-linear contributions range from empirical [13], [19] to plasticity-based models [20], [21]. Adhesion represents an additional contribution, resulting from the chemical bond between concrete layers. Since it does not rely on the presence of reinforcement, the rebars are not activated by this mechanism. Due to its brittle nature and the very small relative slip required for its degradation, adhesion is generally of limited relevance for constitutive modelling.

3.2 Model selection and application

To study the stress distribution at the interface for the specimen presented in Section 2, three stress transfer mechanisms are considered. For each mechanism, a representative formulation from literature was selected to illustrate its possible contribution based on the measured kinematics obtained during the test.

Aggregate interlock

The first mechanism considered is aggregate interlock. For this mechanism, the two-phased model by Walraven [14] is selected to evaluate the stresses transferred across the interface. The model represents the interface as a combination of (i) a rigid-plastic matrix and (ii) stiff spherical aggregate particles. Shear displacement induces contact on the surface of the particles, generating coupled normal and tangential stresses. With increasing sliding, the effective contact area is reduced due to local yielding of the matrix until equilibrium is achieved. In this model, the stresses require both crack opening w and slip s as input, together with the maximum aggregate size d_a and concrete compressive strength f_c. In the present study, the full constitutive expression was adopted.

Interface friction

The second mechanism considered is interface friction. A simple friction-based approach is used, in which the shear resistance τ is proportional to the normal stress σ_N at the interface via a friction coefficient μ, (Eq. 1). σ_N is obtained through the reinforcement stress σ_s acting over the reinforcement area A_s, and distributed over an interface area of reinforcement spacing a_s and width b (Eq. 2). σ_s is derived from the crack opening w and the effective reinforcement length l_{eff} (Eq. 3).

$$\tau = \mu \cdot \sigma_N \tag{1}$$

$$\sigma_N = \frac{\sigma_s \cdot A_s}{a_s \cdot b} \tag{2}$$

$$\sigma_s = E_s \cdot \varepsilon_s \text{ where } \varepsilon_s = \frac{w}{l_{eff}} \tag{3}$$

Dowel action

The third mechanism considered is dowel action. A second-order plasticity model proposed by Sørensen et al. [21] is used, in which concrete and reinforcement are considered rigid-plastic materials, and the interface is assumed smooth and frictionless. The model uses the slip s as the input to determine the shear capacity τ. For the linear elastic branch, the analogy of a beam on an elastic foundation is applied [18]. The dowel action contribution F_D is distributed over an interface of width b and reinforcement spacing a_s (Eq. 4).

$$\tau = \frac{F_D}{a_s \cdot b} \tag{4}$$

For all cases, the slip s and crack opening w values from DIC are used as direct input. For values below the DIC accuracy threshold of 0.03 mm, no stress calculation is performed. The corresponding

input parameters for all models are shown in Table 1. The models are evaluated independently and are not intended to be superimposed, as equilibrium requirements link aggregate interlock and friction, and dowel action reduces the available reinforcement capacity that could otherwise contribute to axial clamping.

Table 1 Input parameters for the calculation of interface stresses in the constitutive models.

Parameter	Value	Dimension
Maximum aggregate size d_a	32	[mm]
Cube compressive strength f_c	55.7	[MPa]
Interface reinforcement diameter d	8	[mm]
Cylinder compressive strength f_{c1} and f_{c2}	44.6 and 84.9	[MPa]
Reinforcement yielding strength f_y	508	[MPa]
Reinforcement modulus E_s	172	[GPa]
Effective bond length $l_{eff} = 5d$ [22]	40	[mm]
Interface reinforcement spacing a_s	200	[mm]
Interface width b	250	[mm]
Friction coefficient μ [23]	0.9	[-]

The calculated stress distributions along the interface are presented in Fig. 4 for $0.95P_u$ and P_u. The results show clear differences in magnitude and sensitivity to the measured kinematics. The aggregate interlock model, which uses both *s* and *w* as input, predicts the highest shear stresses. This allows it to capture the significant reduction at marker M3, where the large *w* locally decreases the contact area.

The friction-based model produces lower stresses, remaining below 0.8 MPa. Its response rapidly reaches reinforcement yielding once *w* exceeds approximately 0.25 mm, reflecting its high dependence on the assumed effective bond length. Consequently, the stress distribution shows little spatial variability along the interface.

As previously mentioned, aggregate interlock and friction are mechanically linked through the normal stress equilibrium at the interface. Aggregate interlock generates coupled normal and shear stresses, which must be balanced by the reinforcement-induced clamping action. If this equilibrium cannot be sustained, the corresponding shear stresses cannot be mobilised.

The dowel action contribution follows the spatial distribution of *s* (see Fig. 3 (a)), with values below 0.6 MPa. This model assumes a smooth surface, where experimental campaigns have shown the relevant contribution of dowel action to shear capacity. Nevertheless, in rough surfaces, the contribution of this in comparison to axial forces remains uncertain. For reference, the interface capacity according to the final preliminary release of Eurocode 2 (FprEC2) [24] is included in Fig. 4 (b). As this formulation does not incorporate interface kinematics, it provides a uniform capacity value and cannot capture the impact of spatial variability observed experimentally.

3.3 Outlook

The kinematic measurements of specimen N02TL show that interface behaviour is not governed solely by the global shear demand, but also by the interaction between the critical shear in the web and the concrete-to-concrete interface. This interaction produces a non-uniform distribution of slip *s* and crack opening *w*, whose effect on the stress distribution cannot be determined from these large-scale experiments due to complex boundary conditions and competing failure mechanisms. Understanding the stress distribution is, however, essential to give physical meaning to the kinematics and to identify the mechanisms contributing to the shear resistance.

Constitutive models from the literature provide a natural first step in linking realistic kinematics to potential stress transfer mechanisms. As shown in Section 3.2, the models respond to the spatial variation in *s* and *w*, but questions remain regarding (i) the influence of different crack opening paths on the predicted stresses, (ii) the interaction between mechanisms (e.g. reinforcement contribution to

dowel action and friction), and (iii) how all mechanisms could be combined to represent the full interface behaviour.

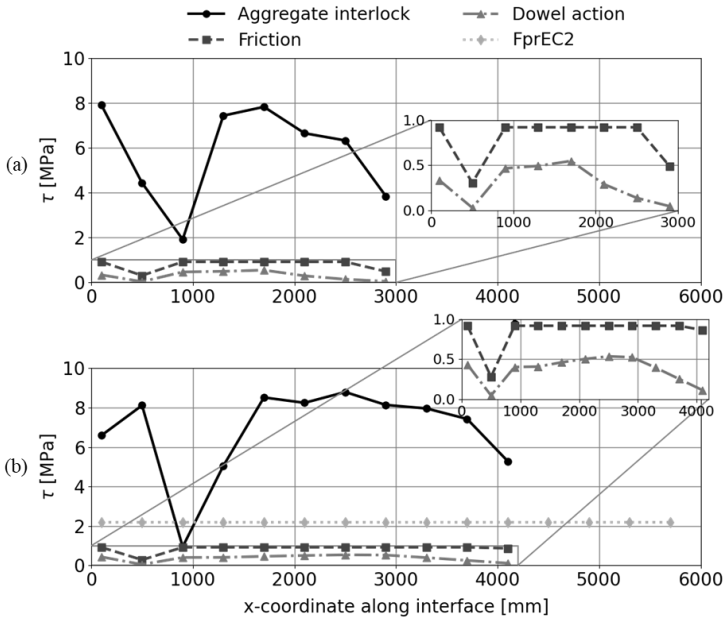


Fig. 4 Shear stress distribution along the interface calculated using the selected constitutive models: (a) at $0.95P_u$; (b) at P_u, including the ultimate capacity according to FprEC2.

Overall, these results demonstrate that the measured *s* and *w* can lead to different mechanical interpretations depending on the adopted constitutive model. Given that the actual stress state at the interface cannot be verified in this large-scale test, the absolute stress magnitudes remain uncertain. This uncertainty motivates dedicated small-scale experiments to investigate the impact of (i) crack opening paths, (ii) interface properties, and (iii) the independent and interactive role of each mechanism, using relevant input from the large-scale campaign and existing bridges in the Netherlands. These studies aim to provide constitutive relations that allow a physical understanding of the interface kinematics observed in this and other tests.

4 CONCLUSIONS

The detailed kinematic study of specimen N02TL shows that interface behaviour is governed by the interaction between the critical shear crack in the web and the concrete-to-concrete interface. This interaction leads to (i) a pronounced spatial variation of slip *s* and crack opening *w*, and (ii) two distinct crack opening paths along the interface. An effort was made to interpret the kinematics mechanically by using *s* and *w* as input to selected constitutive models from literature. The various results are currently irrefutable, and two key limitations remain: (i) the interaction between mechanisms, and (ii) the actual stress state is unknown, preventing direct comparison of the calculated stresses. These findings motivate a dedicated small-scale experimental campaign aimed at bridging the gap between the measured kinematics and stress. This approach will support the development of constitutive relations capable of providing a clearer physical meaning of the observed behaviour.

Acknowledgements

The authors wish to express their gratitude to the Dutch Ministry of Infrastructure and the Environment (Rijkswaterstaat) for financing this research project.

References

[1] Ibrahim, Mohammed, Yang, Yuguang, Roosen, Marco, and Hendriks, Max. 2022. “Challenges on the shear behavior of existing continuous precast girder bridges”. 14th International PhD Symposium in Civil Engineering, Rome, September 5-7.
[2] Tassios, Theodossios, and Vintzileou, Elizabeth. 1987. “Concrete-to-Concrete Friction.” Journal of Structural Engineering 113:832–849.
[3] Fédération internationale du béton. 2008. Bulleting 43: Structural connections for precast concrete buildings. International Federation for Structural Concrete.
[4] Figueira, Diogo, Sousa, Carlos, Calçada, Rui, and Neves, Afonso. 2016. “Push-Off Tests in the Study of Cyclic Behavior of Interfaces between Concretes Cast at Different Times.” Journal of Structural Engineering 142. doi: 10.1061/(asce)st.1943-541x.0001364.
[5] Palieraki, Vasiliki, Vintzileou, Elizabeth, and Trezos, Constantinos. 2023. “Experimental Behavior of RC Interfaces between Concretes Cast at Different Times Subjected to Cyclic Actions.” Journal Structural Engineering 149. doi: 10.1061/JSENDH.STENG-11735.
[6] Birkeland, Peter, and Birkeland, Halvard. 1966. “Connections in Precast Concrete Construction.” Journal Proceedings 63:345–368.
[7] Mattock, Alan, and Hawkins, Neil. 1972. “Shear Transfer in Reinforced Concrete - Recent Research.” PCI Journal.
[8] Tsoukantas, Spyros, and Tassios, Theodossios, 1989. “Shear Resistance of Connections between Reinforced Concrete Linear Precast Elements.” Structural Journal, 86:242–249.
[9] Loov, Robert, and Patnaik, Anil. 1994. “Horizontal Shear Strength of Composite Concrete Beams with a Rough Interface”. PCI Journal 39:48-69.
[10] Randl, Norbert, and Wicke, Manfred. 2000. “Schubübertragung zwischen alt- und neubet-on. Experimentelle untersuchungen, theoretischer hintergrund und bemessungsansatz.” Bet-on- und Stahlbetonbau, 95: 461–473. doi: 10.1002/best.200000870.
[11] Randl, Norbert. 2010 “Design recommendations for interface shear transfer in fib Model Code 2010.” Structural Concrete 14:230–241. doi: 10.1002/suco.201300003.
[12] Walraven, Joost. 1981. “Fundamental Analysis of Aggregate Interlock,” Journal of the Structural Division 107.
[13] Palieraki, Vasiliki, Vintzileou, Elizabeth, and Silva, John. 2022. “Modeling Reinforced Interfaces Cold Joints Subjected to Cyclic Shear.” Structural Journal 119:225-238.
[14] Walraven, Joost. 1980. “Aggregate Interlock: A theoretical and experimental analysis.” Delft University of Technology, Delft.
[15] Bazant, Zdenek, and Gambarova, Pietro. 1980. “Rough Cracks in Reinforced Concrete.” Journal of the Structural Division, 106: 819–842.
[16] Walraven, Joost and Reinhardt, Hans. 1981. “Theory and Experiments on the Mechanical Behaviour of Cracks in Plain and Reinforced Concrete Subjected to Shear Loading.” Heron 26.
[17] Li, B, and Maekawa, Koichi, and Okamura, Hajime. 1989. “Contact density model for stress transfer across cracks in concrete.” Journal of Faculty of Engineering, 40.
[18] Dei Poli, Sandro, Di Prisco, Marco, and Gambarova, Pietro. 1992. “Shear Response, Deformations, and Subgrade Stiffness of a Dowel Bar Embedded in Concrete”. Structural Journal 89:665-675.
[19] Vintzeleou, Elizabeth and Tassios, Theodossios. 1987. “Behavior of Dowels under Cyclic Deformations.” Structural Journal 84:18-30.
[20] Sørensen, Jesper. 2018. “Design and modeling of structural joints in precast concrete structures.” Technical University of Denmark, Department of Civil Engineering.
[21] Sørensen, Jesper, Hoang, Linh, Olesen, John, and Fischer, Gregor. 2017. “Testing and modeling dowel and catenary action in rebars crossing shear joints in RC,” Eng. Struct. 145: 234–245. doi: 10.1016/j.engstruct.2017.05.020.
[22] Fédération internationale du béton. 2014. “Bond and anchorage of embedded reinforcement: background to the fib Model Code for Concrete Structures 2010: technical report.”
[23] Fédération internationale du béton. 2010. Model code 2010 Volume 1.
[24] European Standard. 2023. “Eurocode 2 - Design of concrete structures-Part 1-1: General rules and rules for buildings, bridges and civil engineering structures.”

Reliability Concepts

Reliability quantification of degrading concrete discontinuity regions via strut-and-tie modelling

Kito Luyten, Wouter Botte, Robby Caspeele

Department of Structural Engineering and Building Materials,
Ghent University,
Tech Lane Ghent Science Park, Ghent (9052), Belgium

Summary
Reinforced concrete discontinuity regions, such as half-joints, experience time-dependent deterioration that reduces their capacity and can shift the governing failure mechanism. This paper investigates how different corrosion mechanisms and exposure scenarios influence the residual strength and failure modes of half-joint girders when assessed using multiple strut-and-tie models (STMs). A probabilistic framework is adopted, incorporating uncertainties in material properties, loads, and corrosion initiation and propagation through Monte Carlo simulations. The results show that the dominant STM and its critical elements can shift significantly over time, depending on the nature of the degradation mechanism and its spatial distribution. The study highlights the importance of integrating uncertainties into the assessment to obtain an accurate and in-depth understanding of the structure's behaviour and to identify when degradation may trigger changes in the governing failure mechanism.

1 INTRODUCTION

Reinforced concrete structures can experience progressive degradation throughout their service life, primarily due to corrosion. When structures approach the end of their intended lifetime, accurately assessing their residual load-carrying capacity becomes essential for ensuring safety, planning maintenance, and avoiding unnecessary strengthening interventions. This challenge is particularly pronounced in discontinuity regions, such as half-joint connections, which exhibit nonlinear stress fields.

Strut-and-tie models (STMs) offer an efficient method for analysing these regions, providing lower-bound estimates of structural capacity with limited computational effort. While STMs are well established for the design of new structures, their applicability to existing members remains less explored.

To date, reliability-based limit analysis has been adopted in only a limited number of research investigations [1-2]. Especially in relation to discontinuity regions, there is a significant research gap regarding the integration of uncertainties. A probabilistic extension of limit analysis for the assessment of existing concrete structures is hence essential to improve our understanding of the built patrimony and its remaining service life, which is often governed by the capacity of critical components such as discontinuity regions.

Therefore, in this contribution, the influence of different corrosion mechanisms and exposure scenarios on the residual capacity of a concrete half-joint girder is investigated using multiple STM configurations within a probabilistic framework. Chloride-induced corrosion is considered, with emphasis on global versus local ingress and uniform versus pitting behaviour. By analysing the evolution of governing failure modes, residual capacities, and reliability indices, the study demonstrates how the corrosion process can shift the critical ties within an STM and alter which model, in theory, provides a more accurate lower-bound estimate.

2 STRUT-AND-TIE MODELS

The structural capacity and safety of concrete half-joints (HJs) can be evaluated using strut-and-tie models (STMs). Since STMs are based on the static method of limit analysis, they provide a lower-bound estimate of the load-carrying capacity.

Various STM configurations are reported in the literature, including models with orthogonal reinforcement (Fig. 1a), diagonal reinforcement (Fig. 1b), or a combination of both (Fig. 1c). In this contribution, all three models are considered. Detailed procedures for stress evaluation, resistance verification, and modelling assumptions in STMs are provided in [3-6].

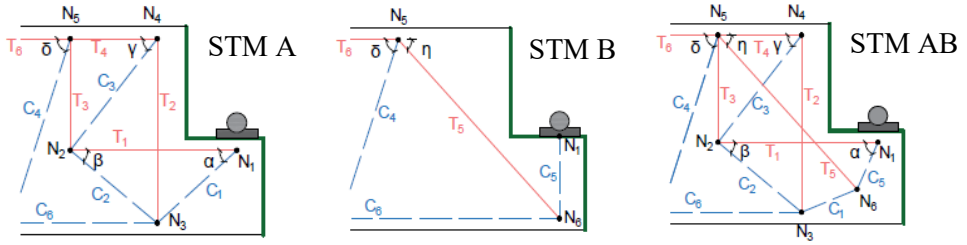


Fig. 1 Different considered STMs (a) Model A, (b) Model B, and (c) Model AB

3 MODELLING TIME-DEPENDENT DEGRADATION

A time-dependent degradation mechanism is imposed on the concrete half-joint to investigate the evolution of its load-carrying capacity over time. In the present study, one-dimensional diffusion of chlorides is incorporated, with and without considering pitting. Further, two different corrosion scenarios are considered. In the first scenario, there is ingress of harmful substances from all faces of the concrete specimen, whereas in the second scenario, it is assumed that an asphalt layer protects the top side of the half-joint girder, but contaminated water (e.g. with de-icing salts) is leaking in between the half-joint connection. The latter leads to a corrosion front originating from the re-entrant corner and vertical nib surface, indicated by the green lines in Fig. 1.

3.1 Chloride-induced corrosion

For chloride-induced corrosion, the chloride ingress into concrete is modelled by solving Fick's second law of diffusion, assuming a constant chloride concentration at the exposed concrete surface and an initially chloride-free concrete matrix [7-8]. Under these conditions, the initiation period for corrosion can be expressed according to Eq. (1) with c [mm] denoting the concrete cover, $C_{s,Cl}$ [wt-%/cem] the surface chloride concentration, and $C_{cr,Cl}$ [wt-%/cem] the critical chloride content at which corrosion initiates. The ageing exponent is given by a_{Cl} [-], while D_0 [mm²/year] is the initial diffusion coefficient at t_0 = 28 days, which can be determined using Eq. (2). The term D_{RCM} [mm²/year] represents the chloride migration coefficient, k_t [-] is a transfer parameter which is equal to 1, and k_e [-] is the environmental transfer parameter. The latter depends on the regression variable b_e [K], the real temperature of the structural element T_{real} [K], and the reference temperature T_{ref} = 293 K.

$$T_i = \left[\frac{c}{2\sqrt{D_0 t_0^{a_{Cl}}}} \cdot \frac{1}{erf^{-1}\left(1 - \frac{C_{cr,Cl}}{C_{s,Cl}}\right)} \right]^{\frac{2}{1-a_{Cl}}} \tag{1}$$

$$D_0 = k_e D_{RCM} k_t \quad \text{with} \quad k_e = exp\left(b_e \left(\frac{1}{T_{ref}} - \frac{1}{T_{real}}\right)\right) \tag{2}$$

3.2 Corrosion propagation

3.2.1 Uniform corrosion

Once the initiation time is reached, the rebars start to corrode. For uniform corrosion, a linear reduction in rebar radius x(t) [mm] over time can be assumed according to Eq. (3) [8-9], where V_{corr} [mm/year] represents the corrosion rate. The corresponding corrosion degree α(t) is determined by Eq. (4). Here, A_0 [mm²] denotes the initial cross-sectional rebar area and ϕ_0 [mm] the initial rebar diameter.

$$x(t) = \begin{cases} 0 & t \le T_i \\ V_{corr} \cdot (t - T_i) & t > T_i \end{cases} \tag{3}$$

$$\alpha(t) = \frac{A_0 - A(t)}{A_0} \quad with \quad A(t) = \left(\frac{\phi_0}{2} - x(t)\right)^2 \cdot \pi \tag{4}$$

3.2.2

Pitting corrosion

Chloride-induced corrosion typically does not result in a uniform reduction of the bar diameter. Instead, it leads to a localised cross-section loss, often producing deep pits [10]. The reduced cross-sectional area due to pitting can be determined using Eqs. (5) to (7). The corresponding pit depth p(t) [mm] is calculated as: $p(t) = T_{prop} \cdot V_{corr} \cdot R$, where R [-] is the pitting factor. This pitting factor has been investigated probabilistically in [11]. Assuming independence between adjacent segments of the reinforcement, it was shown that the time-independent pitting factor R follows a Gumbel distribution with parameters $\mu = \mu_0 + \frac{1}{\alpha_0}\ln\left(\frac{A}{A_0}\right)$ and $\alpha = \alpha_0$. In this formulation, A is the circumferential area of the rebar segment. The reference values A_0, μ_0 and α_0 have been experimentally determined for a rebar of length 125 mm and diameter 8 mm, yielding $\mu_0 = 5.08$ and $\alpha_0 = 1.02$ based on the measurements reported in [12].

$$A(t) = \begin{cases} \frac{\pi D_0^2}{4} - A_1 - A_2 & p(t) < \frac{\sqrt{2}}{2} D_0 \\ A_1 - A_2 & \frac{\sqrt{2}}{2} D_0 < p(t) < D_0 \\ 0 & D_0 < p(t) \end{cases} \tag{5}$$

$$A_1 = arcsin\left(\frac{2p(t)}{D_0}\sqrt{1-\left(\frac{p(t)}{D_0}\right)^2}\right)\left(\frac{D_0}{2}\right)^2 - p(t)\sqrt{1-\left(\frac{p(t)}{D_0}\right)^2} \cdot \left|\frac{D_0}{2} - \frac{p(t)^2}{D_0}\right| \tag{6}$$

$$A_2 = arcsin\left(\sqrt{1-\left(\frac{p(t)}{D_0}\right)^2}\right)p(t)^2 - p(t)\sqrt{1-\left(\frac{p(t)}{D_0}\right)^2} \cdot \frac{p(t)^2}{D_0} \tag{7}$$

4 PROBABILISTIC CAPACITY CALCULATIONS FOR A HALF-JOINT CASE STUDY

4.1 Reinforcement layout of the case study

In this contribution, a case study is considered to compare the effect of different exposure scenarios on the probabilistic capacity assessment of multiple STMs. The investigated structural element is a concrete half-joint girder that is clamped at the left-hand side and loaded with a point load at the nib. This simulates how the lower half of a HJ connection would be loaded in a real bridge. This configuration is the inverse of the specimens reported by [4] [13].

The beam has a width b of 400 mm, a height h of 700 mm, and a span length l of 1570 mm measured between the load point and the clamped end. The concrete cover c is 40 mm, while the nib has a height h_n of 325 mm and a length l_n of 260 mm. The reinforcement layout, illustrated in Fig. 2, consists of: 5 ϕ25 top bars, 5 ϕ20 bottom bars, 3 ϕ12 U-bars, 4 ϕ10 double-legged stirrups near the nib, 5 ϕ10 triple-legged stirrups near mid-span, and 4 ϕ12 diagonal bars [4-5]. This configuration aligns closely with the STMs presented in Section 2. For structural members featuring different reinforcement arrangements, alternative STM configurations may be required.

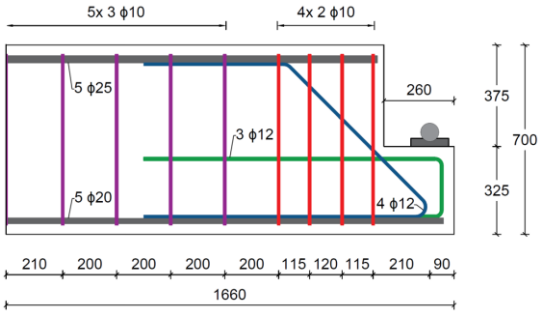


Fig. 2 Reinforcement arrangement – Case study [dimensions in mm]

4.2 Probabilistic models of the stochastic variables

The input parameters for the probabilistic calculations and their stochastic distributions are listed in the tables below. The dimensions and initial reinforcement areas are treated as deterministic. The distributions for the material properties are based on [3]. The reference period for the variable load is 50 years for its design and 1 year for the probabilistic assessment of the degrading structure. The corresponding target reliability index for assessment β_{ass} is 3.3.

Table 1 Stochastic load and material properties, and model uncertainties

Parameters	Distribution	Mean (μ)	COV (δ)
Permanent load, G [kN]	Normal	109	0.10
Variable load (t_{ref} = 50 years), Q_{50} [kN]	Gumbel	44	0.35
Variable load (t_{ref} = 1 years), Q_1 [kN]	Gumbel	15	1.10
Concrete strength, f_c [MPa]	Lognormal	38	0.15
Steel yield strength, f_y [MPa]	Lognormal	560	0.054
Resistance model uncertainty, K_R [-]	Lognormal	1.2	0.15
Load model uncertainty, K_E [-]	Lognormal	1.0	0.10

Some parameters for the time-dependent behaviour depend on the acting exposure class or cement type. In this contribution, a concrete made from CEM I/B with a w/c ratio of 0.55 is considered, exposed to exposure classes XD1 (moderate humidity) and XD3 (cyclic wet and dry).

Table 2 Stochastic properties for chloride-induced corrosion

Parameters	Distribution	Mean (μ)	COV (δ)	Reference
Regression variable, b_e [K]	Normal	4800	0.15	[7]
Diffusion coefficient, D_{RCM} [mm²/year]	Normal[a] (truncated)	621.3	0.20	
Ageing exponent, a_{Cl} [-]	Beta[b]	0.30	0.40	
Temperature of structure, T_{real} [K]	Normal	284	0.025	Local weather data
Critical chloride concentration, $C_{cr,Cl}$ [wt-%/cem]	Lognormal	0.6	0.25	[15]
Pitting factor, R [-]	Gumbel[c] (truncated)	5.65	0.22	[11]

[a] lower bound = 0 [b] lower bound = 0 & upper bound = 1 [c] lower bound = 1

Table 3 Stochastic properties for chloride-induced corrosion based on exposure class [14]

Parameters	Exposure class	Distribution	Mean (μ)	COV (δ)
Surface chloride concentration, $C_{s,Cl}$ [wt-%/cem]	XD1	Lognormal	1.0	0.75
	XD3	Lognormal	3.0	0.75
Rebar radius corrosion rate, $V_{corr,Cl}$ [mm/year]	XD1	Weibull	0.004	1.50
	XD3	Weibull	0.03	1.35

4.3 Reliability calculations based on Monte Carlo simulations

Monte Carlo (MC) simulations were performed in a fully vectorised manner to account for the probabilistic nature of the variables. In this study, 10^5 simulations are executed for each structural resistance calculation. Within the STM, degraded mechanical properties are assigned to every tension tie based on the concrete cover of the individual reinforcement bars composing that tie. Since a STM behaves as a series system, the capacity of the entire system is governed by its weakest element, and the failure of any element in the system can be verified based on the limit state Eq. (8), where R is the element's resistance and ξ represents the factor translating the load to the load effect at the element

considered. In the assessment over time, an annual reference period is used for the variable load, as the resistance decreases over time due to corrosion.

$$g(X) = K_R\, R \;-\; K_E\, \xi\, (G \;+\; Q_1) \tag{8}$$

The failure probability and the density distribution of the structural capacity can be calculated for every moment in time. Failure occurs when $g(X) < 0$. Using the failure probability P_f, the corresponding reliability index β is derived from $P_f = \Phi(-\beta)$.

5 CORROSION EFFECT ON THE STRUCTURAL CAPACITY AND FAILURE MODE

This section evaluates how different exposure scenarios affect the residual capacity, failure modes, model dominance, and reliability index (β) of the concrete half-joint girder. Global ingress (from all faces) and local ingress (primarily along the joint) are considered for both uniform chloride-induced corrosion and chloride-induced pitting corrosion.

The dominant model refers to the STM that provides the highest residual capacity for a given sample and time, which will consequently, in theory, be the best approximation of the actual capacity considering the lower-bound theorem.

5.1 Global corrosion scenario

5.1.1 Uniform chloride-induced corrosion

In the first corrosion scenario, chlorides can diffuse from all exposed faces. Because the stirrups have the smallest concrete cover, they start to corrode first. In exposure class XD1, chloride-induced corrosion progresses relatively slowly. The mean capacities obtained from the three STMs decrease over 100 years from 181 kN to 172 kN (model A), 223 kN to 219 kN (model B), and 400 kN to 381 kN (model AB) (Fig. 3a). The governing failure mode in model A is yielding of the stirrups (T_2), while model B fails due to yielding of the diagonal (T_5). In model AB, the failure mode gradually shifts from a 74%/26% division between T_2 and T_5 to a 82%/18% division (Fig. 3b), due to the lower concrete cover on the stirrups compared to the diagonal rebars. Failure due to crushing of node N_1 remains marginal (≈ 0.6%). Further, STM AB is the sole dominant model up to approximately 30 years, after which model B becomes dominant in a negligibly small subset of samples (< 1%). Lastly, the reliability indices corresponding to the models gradually reduce over the 100-year service life from 1.53 to 1.18 for model A, from 2.35 to 2.09 for model B, and from 4.61 to 2.56 for model AB (Fig. 3c).

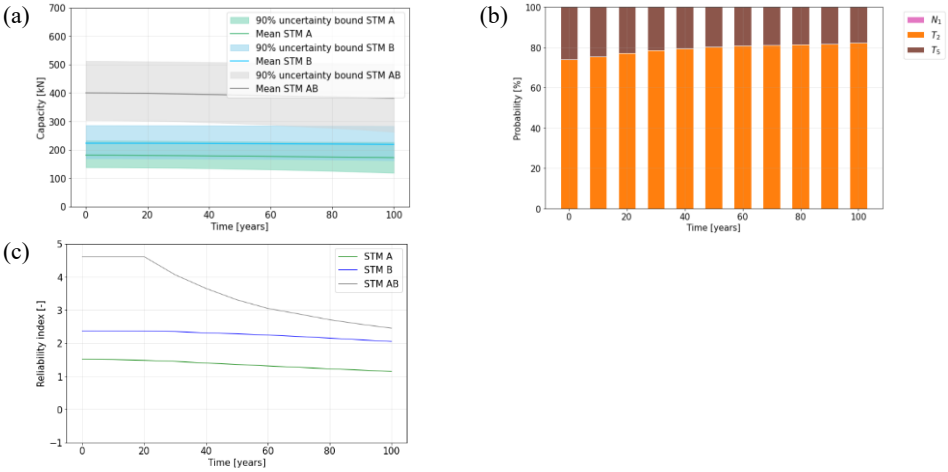


Fig. 3 Uniform chloride corrosion XD1 (a) Capacity, (b) Failure mechanisms STM AB, and (c) Reliability index

Exposure class XD3, on the other hand, is much more severe, resulting in a faster decay of the residual capacity of the considered half-joint. The failure modes for the different models are the same as when exposed to XD1. But the capacity loss occurs more rapidly due to the more severe corrosion process. Hence, in model AB, the probability that failure, if it occurs, is caused by yielding of T_2 increases

considerably faster over time than in exposure class XD1, reaching approximately 90% by year 20 (Fig. 4b).

Because T_2, the critical element of model AB, has a small concrete cover, its initiation time is shorter, and corrosion starts earlier than in model B, where T_5, with a larger cover, is the critical element. Consequently, in combination with the fast corrosion rate in XD3, the mean residual capacity of model AB begins to decrease earlier than that of model B (Fig. 4a). Hence, from about year 20, model B emerges as the second dominant model alongside model AB (Fig. 4c), reflecting the greater corrosion resistance of its critical tie (T_5) owing to its larger concrete cover. Additionally, the reliability index of the latter drops below that of STM B after approximately 30 years (Fig. 4d). Note that the capacity of STM AB is not required to be at least equal to that of model A or model B, as all three strut-and-tie models are independent, statically determinate systems. Although STM AB uses the same reinforcement that is present in the other models, it represents a different load-transfer mechanism and therefore does not encompass the other models or their capacities.

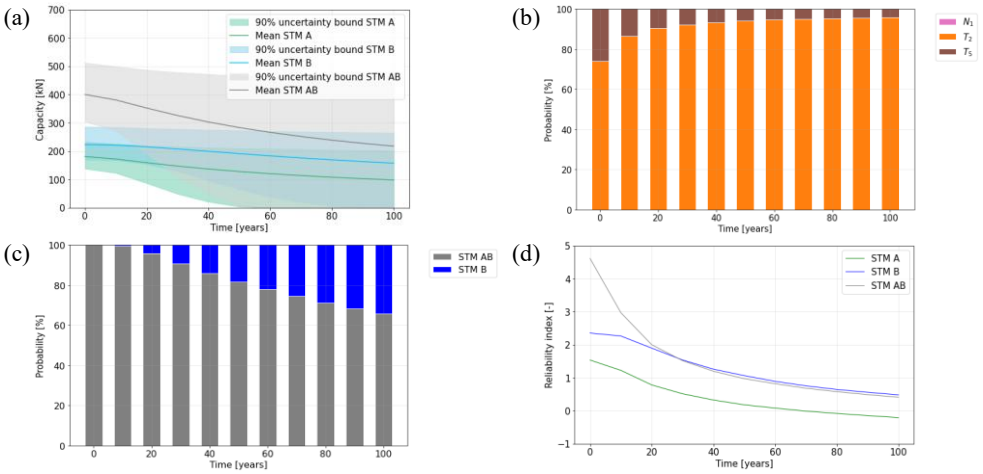


Fig. 4 Uniform chloride corrosion XD3 (a) Capacity, (b) Failure mechanisms STM AB, (c) Dominant STM, and (d) Reliability index

5.1.2 Chloride-induced pitting corrosion

When pitting is taken into account, the shift in model dominance becomes more pronounced. Localised pit formation in corroding stirrups of models A and AB leads to a significant capacity reduction compared to uniform corrosion under XD1 (Fig. 5a) and the reliability index β of model AB falls below that of model B after about 55 years (Fig. 5b).

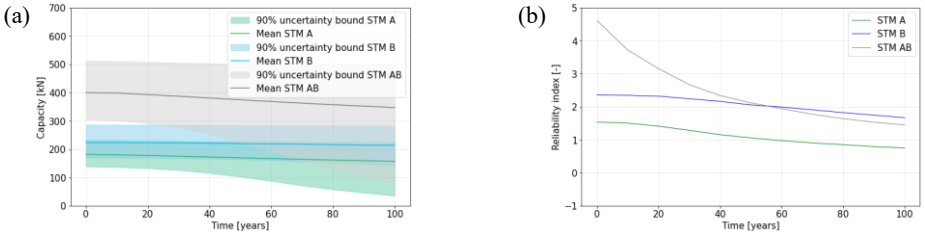


Fig. 5 Chloride pitting corrosion XD1 (a) Capacity, and (b) Reliability index

Due to the stochastic nature of pitting, some bars can experience a larger cross-sectional loss than bars that started corroding earlier. As a result, over time, a small fraction of the samples fails in a different mode than with uniform chloride-induced corrosion (i.e. T_1 in STM A, T_6 in STM B, and T_1 in STM AB). The appearance/emergence of these additional failure modes is present for both investigated exposure classes (XD1 and XD3). Their probability of occurrence at XD1 is negligible (< 0.3%), but for XD3 it becomes more noticeable (Figs. 6b to 6d). This phenomenon illustrates the need to perform on-site measurements to determine the current corrosion degree and the location of the corrosion front

to be able to update the residual capacity calculations and reduce the uncertainty on the failure mechanism, as new failure modes can emerge over time.

The probability that model B is the dominant STM increases over time, even more pronounced than for class XD1, due to the faster corrosion process (Fig. 6e). Furthermore, model A is dominant in only 0.21% of the samples at year 100 (Fig. 6e), i.e. when severe pitting in the diagonal reinforcement significantly reduces the residual capacities of models B and AB. Model B provides the highest reliability from year 10 onwards (Fig. 6f). Since, in theory, STMs provide lower-bound estimates for the actual capacity, model B can be assumed to approximate the actual failure probability the best from that moment in time onwards, since the stirrups in STM A and AB are significantly affected by the corrosion process.

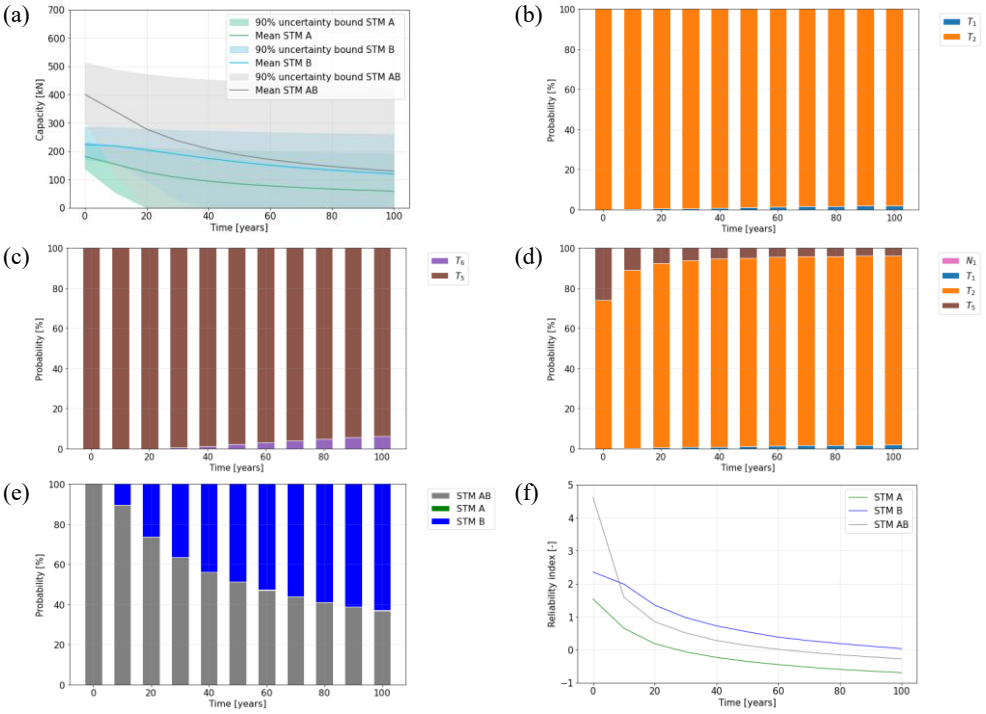


Fig. 6 Chloride pitting corrosion XD3 (a) Capacity, (b) Failure mechanisms STM A, (c) Failure mechanisms STM B, (d) Failure mechanisms STM AB, (e) Dominant STM, and (f) Reliability index

5.2 Local corrosion scenario

In the second corrosion scenario considered, chloride ingress is limited to the joint region.

Consequently, the stirrups are less affected compared to the case of global chloride exposure. This shift increases the likelihood that ties T_1 and T_5 govern the structural response of the STMs.

5.2.1 Uniform chloride-induced corrosion

Overall, the structural behaviour of the half-joint under local XD1 corrosion is comparable to that observed under global XD1 exposure. The main difference lies in a less pronounced reduction of the residual capacity for models A and AB, since their critical tie T_2 is less severely corroded. After 100 years, the mean residual capacities amount to 177 kN and 390 kN for models A and AB, respectively. Accordingly, their reliability indices are higher and the associated failure probabilities lower than in the global corrosion scenario. In contrast, the capacity reduction of model B remains unchanged.

A more interesting difference that is observed between global and local chloride exposure is the emergence of different failure modes. Similarly to Section 5.1.2 under pitting corrosion, the failure modes at the design of the structure, i.e. at year 0, are not necessarily representative for the entire lifespan. Especially when the structure is exposed to class XD3, the shift in the governing failure

mechanism is significant. In models A and AB, the probability of failure governed by tie T_1 increases substantially over time (Figs. 7b and 7c). Furthermore, for STM AB, the probability of failure associated with tie T_5 decreases over time under global chloride ingress. In contrast, under the local corrosion scenario, this probability initially decreases when the first stirrup starts to corrode and failure of T_2 increases, but it subsequently increases due to the limited corrosion of the other stirrups. This occurs because the first stirrup has a smaller concrete cover than tie T_5 and therefore begins to corrode earlier, while the remaining stirrups remain unaffected for much longer as they have a higher concrete cover. Model B remains fully governed by the failure of tie T_5 throughout its service life. Since the capacity reduction of STM B is identical for XD3 in both global and local scenarios, while the residual capacities of models A and AB are higher under local corrosion, the relative probability that model B governs the structural behaviour is lower in the local corrosion scenario than in the global case (Figs. 4c and 7d).

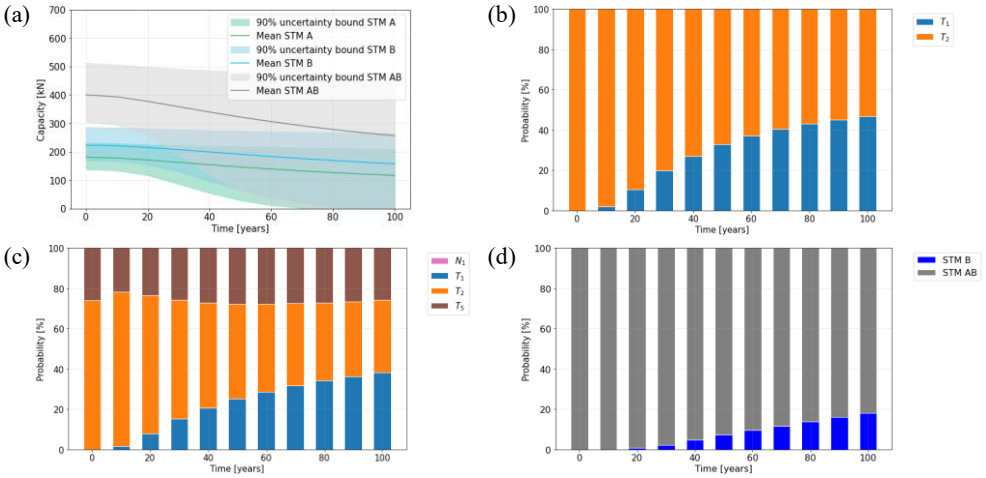


Fig. 7 Uniform chloride corrosion XD3 (a) Capacity, (b) Failure mechanisms STM A, (c) Failure mechanisms STM AB, and (d) Dominant STM

5.2.2 Chloride-induced pitting corrosion

Similar trends are observed when comparing the global and local pitting corrosion scenarios to those identified for uniform corrosion. For both exposure classes XD1 and XD3, the residual capacities and reliability indices of models A and AB are higher in the local corrosion scenario (Figs. 8a and 8e), as the stirrups experience less deterioration. As a result, the probability of failure governed by the yielding of the horizontal U-bar (T_1) increases in models A and AB (Figs. 8b and 8c). Additionally, in STM AB, the probability of diagonal tie (T_5) failure increases under local corrosion, whereas it decreases under global corrosion. These shifts in governing failure mechanisms are more pronounced for exposure class XD3 than for XD1 due to the more severe corrosion process in XD3.

Finally, the probability that model B governs the structural response is lower under local chloride ingress than under global chloride ingress when pitting corrosion is considered. Conversely, there is a noticeable increase (up to 4%) in the probability that STM A becomes the dominant model (Fig. 8d). This behaviour can be attributed to the localised corrosion scenario of the diagonal reinforcement and horizontal U-bar. Since the diagonal reinforcement is structurally more critical, the combined effect of localised corrosion and the pitting factor may cause a substantial reduction of its cross-sectional area. This reduction decreases the capacity of models B and AB relative to model A, thereby increasing the likelihood that STM A governs the structural response.

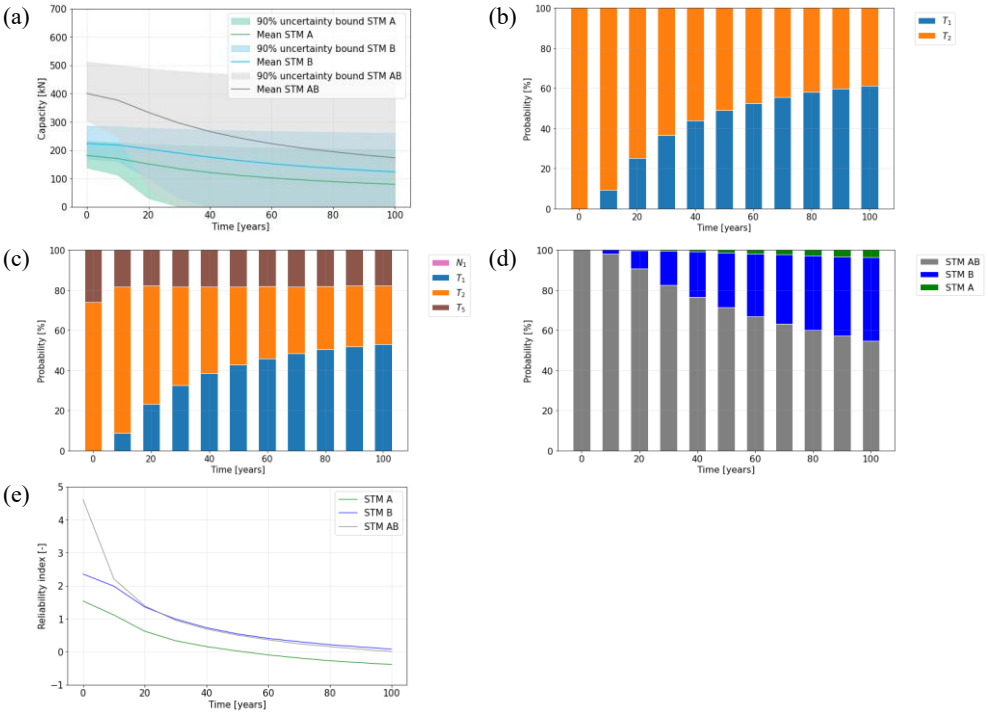


Fig. 8 Chloride pitting corrosion XD3 (a) Capacity, (b) Failure mechanisms STM A, (c) Failure mechanisms STM AB, (d) Dominant STM, and (e) Reliability index

6 CONCLUSIONS AND FURTHER RESEARCH

In this study, the residual capacity of a degrading concrete half-joint girder was quantified using strut-and-tie modelling, considering uncertainties. The results demonstrate that the structural behaviour and governing failure modes are strongly dependent on both the corrosion mechanism and the exposure scenario. Different scenarios lead to distinct shifts in the critical failure mechanism and to different probabilities of occurrence for each potential failure mode, as the corrosion process is determined by the exposure class, both in terms of initiation time and corrosion propagation. Additionally, the interplay of the concrete cover, rebar diameter, and whether there is pitting corrosion determines the residual capacity of the discontinuity region. The importance of the rebar diameter is evident as a 1 mm reduction in rebar radius or increase in pit depth affects the residual steel cross-section differently depending on the original bar diameter.

The pitting factor embodies an inherent spatially random characteristic, i.e. in some Monte Carlo samples, the pitting factor on the diagonal will be larger than that of the other ties, while in other samples it will be the other way around. This behaviour increases the spread on the residual capacities and can alter which reinforcement elements become governing for the failure mode. This variability influences not only the residual strength but also the time-dependent reliability level of the structure. In addition, the degradation mechanism determines which STM provides the highest lower-bound estimate.

The model that is suitable for design is not necessarily the most accurate throughout the entire service life. The dominant STM may change as corrosion progresses. Predicting these transition points in time is crucial to assess the residual capacity of the structure with the most appropriate STM and hence to ensure safety, appropriate maintenance planning, and avoiding unnecessary strengthening interventions.

For this specific case study, global corrosion primarily led to the failure of the stirrups due to their small concrete cover. In contrast, localised ingress at the re-entrant corner shifted the governing mechanism to the U-bar or diagonal reinforcement, illustrating the strong influence of spatial corrosion development.

Overall, the findings highlight the necessity of time-dependent probabilistic assessment to distinguish between evolving failure mechanisms and to obtain reliable estimates of the structural safety.

Acknowledgements

This research was supported by FWO-Flanders (FWO Fellowship Fundamental Research - 11I8625N).

References

[1] Biondini, Fabio, and Frangopol, Dan M. 2008. "Probabilistic limit analysis and lifetime prediction of concrete structures.", *Structure and Infrastructure Engineering* 4(5):399–412. doi:10.1080/15732470701270157.

[2] Wu, Di, Gao, Wei, Tin-Loi, Francis, and Pi, Yong-Lin. 2016. "Probabilistic interval limit analysis for structures with hybrid uncertainty." *Engineering Structures* 114:195–208. doi:10.1016/j.engstruct.2016.02.015.

[3] European Committee for Standardization (CEN). 2004. "Eurocode 2: Design of Concrete Structures – Part 1-1: General Rules and Rules for Buildings." (EN 1992-1-1). Brussels, Belgium.

[4] Desnerck, Pieter, Lees, Janet M., and Morley, Chris T. 2018. "Strut-and-Tie Models for Deteriorated Reinforced Concrete Half-Joints." *Engineering Structures* 161:41–54. doi:10.1016/j.engstruct.2018.01.013.

[5] Passos Sério Lourenço, Maria F., et al. 2021. "Design and Assessment with Strut-and-Tie Models and Stress Fields: From Simple Calculations to Detailed Numerical Analysis." fib Bulletin 100. Lausanne: Fédération Internationale du Béton (fib). doi:10.35789/fib.BULL.0100.

[6] Luyten, Kito, Botte, Wouter, and Caspeele, Robby. 2024. "Probabilistic Quantification of the Structural Capacity in Concrete Discontinuity Regions Using Strut-and-Tie Models." In *Proceedings of the 20th International Probabilistic Workshop*, edited by J. C. Matos et al., 429–439. Cham: Springer Nature Switzerland. doi:10.1007/978-3-031-60271-9_40.

[7] Schießl, Peter, et al. 2006. "Model Code for Service Life Design." fib Bulletin 34. Lausanne: Fédération Internationale du Béton (fib). doi:10.35789/fib.BULL.0034.

[8] Vereecken, Eline. 2022. "Applied Bayesian Pre-Posterior and Life-Cycle Cost Analysis for Determining and Optimizing the Value of Structural Health Monitoring for Concrete Structures." PhD diss., Ghent University.

[9] Lay, Sascha, Schießl, Peter, and Cairns, John. 2003. "Instructions on Methodology and Application of Models for the Prediction of the Residual Service Life for Classified Environmental Loads and Types of Structures in Europe." LIFE-CON Deliverable D3.2. European Community.

[10] Val, Dimitry V., and Melchers, Robert E. 1997. "Reliability of Deteriorating Reinforced Concrete Slab Bridges." *Journal of Structural Engineering* 123(12):1638–1644. doi:10.1061/(ASCE)0733-9445(1997)123:12(1638).

[11] Stewart, Mark G. 2004. "Spatial Variability of Pitting Corrosion and Its Influence on Structural Fragility and Reliability of Reinforced Concrete Beams in Flexure." *Structural Safety* 26(4):453–470. doi:10.1016/j.strusafe.2004.03.002.

[12] González, Juan A., et al. 1995. "Comparison of Rates of General Corrosion and Maximum Pitting Penetration on Concrete Embedded Steel Reinforcement." *Cement and Concrete Research* 25(2):257–264. doi:10.1016/0008-8846(95)00006-2.

[13] Desnerck, Pieter, Lees, Janet M., and Morley, Chris T. 2016. "Impact of the Reinforcement Layout on the Load Capacity of Reinforced Concrete Half-Joints." *Engineering Structures* 127:227–239. doi:10.1016/j.engstruct.2016.08.061.

[14] Gehlen, Christoph, et al. 2015. "Benchmarking of Deemed-to-Satisfy Provisions in Standards: Durability of Reinforced Concrete Structures Exposed to Chlorides." fib Bulletin 76. Lausanne: Fédération Internationale du Béton (fib). doi:10.35789/fib.BULL.0076.

Comparison between Deterministic and Probabilistic Ground Motion Estimation Methods for Performance-Based Seismic Design

Hanse Moon, Ju-Hyung Kim, and Hong-Gun Park

Department of Architecture and Architectural Engineering,
Seoul National University,
Gwanak-ro 1, Seoul (08826), Republic of Korea

Summary
This study investigated the influence of soil variability on seismic response based on the probabilistic framework of design codes for nuclear structures. A performance-based seismic assessment was conducted on a 25-story RC building using deterministic and probabilistic ground motion estimation methods, applying multiple simulations of 3D linear/nonlinear time history analyses. Linear analysis showed that the dispersion of the seismic responses was consistent with that of the input spectra in the probabilistic method, while the median responses were similar between the different methods. In nonlinear analysis, the discrepanciy in response dispersion between the methods was amplified, especially in beam deformations. The probabilistic method produced greater median responses than the deterministic method due to the interaction between soil variability and system nonlinearity.

1 INTRODUCTION

While design codes for nuclear power plants [1], [2] provide rigorous probabilistic frameworks, current design codes for ordinary buildings [3]–[6] do not prescribe probabilistic approaches, and the effects of uncertainty in soil properties on structural behavior remain underexplored. Thus, current deterministic seismic design approaches for buildings need to be compared with probabilistic approaches. Unlike nuclear structures, ordinary buildings are permitted to undergo large ductility and deformation, and therefore, the effects of probabilistic analysis on inelastic behavior should be investigated.

In the present study, multiple three-dimensional linear-elastic and nonlinear time history analyses were conducted on a typical reinforced-concrete residential building. To investigate the effects of soil variability on structural behavior, three ground motion estimation methods were compared: (a) deterministic site response analysis using fixed values of investigated soil properties; (b) probabilistic site response analysis explicitly incorporating soil variability; and (c) spectrum matching to a wide-banded soft soil design spectrum, using soil factors without performing site response analysis.

2 METHODOLOGY

2.1 Input ground motion estimation methods

AIK-KCI Guidelines [3] specify that ground motions should be generated by performing site response analyses on recorded rock outcrop motions. The rock motions were selected from NUREG/CR-6728 [7], which is recommended for spectrum matching to a rock spectrum. Each ground motion consists of a pair of orthogonal horizontal components. The earthquake magnitudes range from 5.91 to 6.93. The hypocentral distances range from 0.0 km to 129.1 km, covering from near to far-field records. The average shear wave velocity of the top 30 m ranges from 257 m/s to 2016 m/s. These records are sourced from the PEER ground motion database [8].

Figure 1 shows the flowchart of the three ground motion estimation methods used in the present study. 30 pairs of ground motion records were used for each method, including the two deterministic approaches, to ensure consistency with the probabilistic approach. The seed ground motion records were spectrum-matched to the S_1 (hard rock) design spectrum according to KDS 41 17 00: 2022 [4] and AIK-KCI Guidelines [5] using the open-source software *RspMatch 2009* [9].

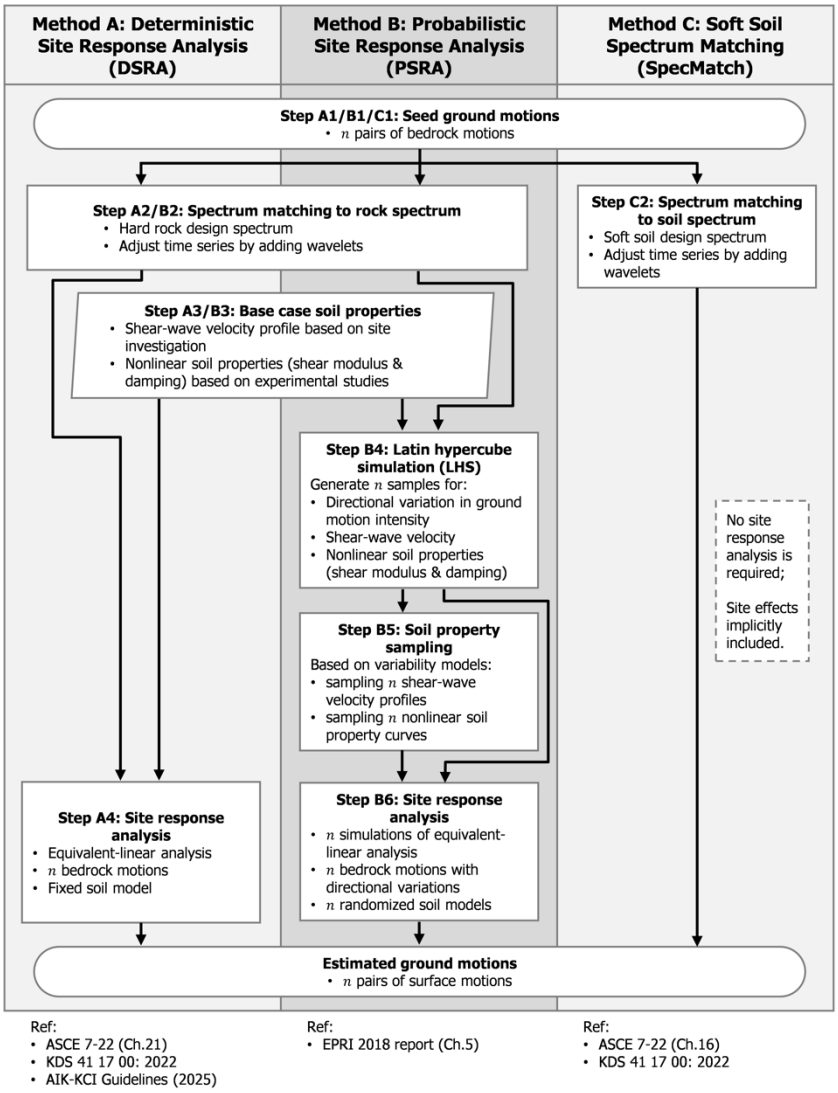


Fig. 1 Flowchart of ground motion estimation methods

2.1.1 Deterministic site response analysis (DSRA)

The first method, deterministic site response analysis (DSRA), uses fixed values of the investigated soil properties, which is specified in performance-based seismic design codes in South Korea [4], [5]. Site response analysis was conducted using the open-source software *Strata v.0.8.0* [10], which performs equivalent-linear site response analysis in the frequency domain.

2.1.2 Probabilistic site response analysis (PSRA)

The second method, probabilistic site response analysis (PSRA), explicitly considers the variability in soil properties, which is specified in the EPRI 2018 report [1] for seismic assessment of nuclear structures. hypercube sampling (LHS) is used, which stratifies the probability distribution of the input variable into non-overlapping intervals with equal probability, thereby allowing for fewer simulations ($n = 30$) [2].

Based on the EPRI 2018 Report [1], the directional variation was modeled using a lognormal distribution with a median of 1.10 and a logarithmic standard deviation of 0.11. For each pair of ground motions, H_1 component was scaled by the factor, while the H_2 component was divided by it. The

statistical distribution of shear wave velocity at the site was modeled using the empirical model proposed by Toro [11]. According to Toro's model [11], shear wave velocity follows a multivariate lognormal distribution with a correlation coefficient between adjacent soil layers. The site investigation data were used for the median ($V_{median}(d_i)$). The statistical distributions of shear modulus and damping ratio were modeled using the empirical model proposed by Darendeli [12]. According to Darendeli's model [12], the shear modulus and damping ratio of soil at arbitrary shear strain follow a multivariate normal distribution with a negative correlation coefficient of –0.5. The base case nonlinear soil properties, including shear modulus and damping ratio, were derived from existing studies on soil types in South Korea [13], [14].

2.1.3 Soft soil spectrum matching (SpecMatch)

The third method, spectrum matching directly to a soft soil design spectrum (SpecMatch), corresponds to one of the approaches specified in ASCE 7-22 [3]. The seed ground motion records were spectrum-matched to the S_3 (shallow soft soil) design spectrum corresponding to the building site [4].

2.2 Prototype building, site condition, nonlinear analysis modeling, and time history analysis

2.2.1 Prototype building

Figure 2 shows the 25-story prototype building used in the present study. The structural system consists of a reinforced concrete moment-resisting frame with core walls, and the building was designed in accordance with the Korean Building Code [15].

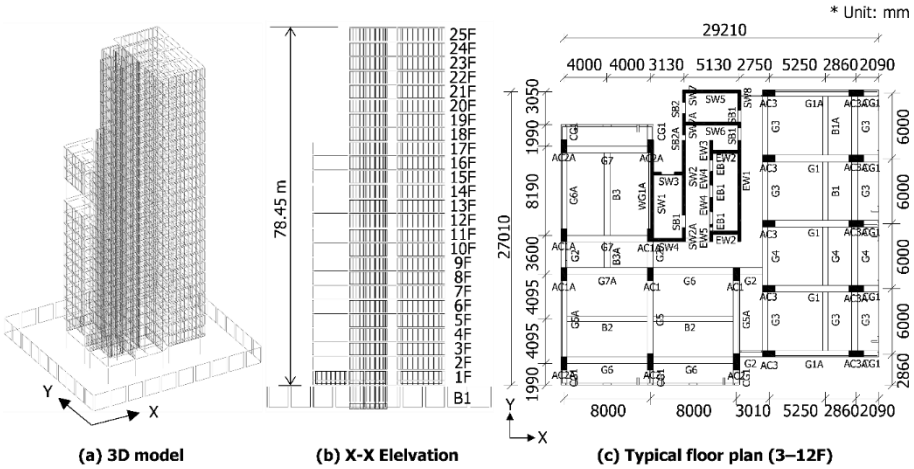


Fig. 2 Prototype building

2.2.2 Site condition

The design effective ground acceleration of the building was 0.2 g. The site condition was S_3 (shallow soft soil) according to KDS 17 10 00: 2024 [16], where the depth to bedrock was 18.5 m, the average shear wave velocity was 214 m/s [16] and the elastic site period was estimated as 0.345 s [17].

2.2.3 Nonlinear analysis modeling

Nonlinear analysis modeling followed the AIK–KCI Guidelines [5], [6]. Beams and columns were modeled as concentrated plastic hinge models. In the concentrated plastic hinge models, flexural behavior was modeled as deformation-controlled behavior with nonlinear force-deformation relationships for the plastic hinges. Walls were modeled as fiber model. The shear behavior was defined as force-controlled behavior using linear-elastic shear stiffness. Slabs were modeled as rigid diaphragms.

2.2.4 Time history analysis

Time history analysis was conducted in accordance with the AIK-KCI Guidelines [5]. The three-dimensional model of the target building was prepared using the commercial software *Perform 3D*

v5.0.1 [18] as shown in Fig. 2. A series of analyses were conducted twice for each pair of ground motions with two incident angles: (a) H_1 and H_2 loading applied in the +X and +Y directions, respectively (i.e., 0°); and (b) in the +Y and –X directions, respectively (i.e., 90°). As a result, a total of 60 analyses (2 incident angles × 30 ground motion pairs) were conducted for each ground motion estimation method.

3 RESULTS

3.1 Comparison based on response spectra

Figure 3 compares the response spectra and amplification factors resulting from the three ground motion estimation methods. At the fundamental period of the target building, the mean SRSS spectral accelerations for DSRA and PSRA were relatively similar: 0.110 g and 0.124 g in the X-direction, and 0.124 g and 0.155 g in the Y-direction, respectively. However, the variability in the response spectra differed significantly between the two methods: the coefficients of variation at the fundamental period were 0.035 for DSRA and 0.251 for PSRA in the X-direction, and 0.038 and 0.368 in the Y-direction, respectively.

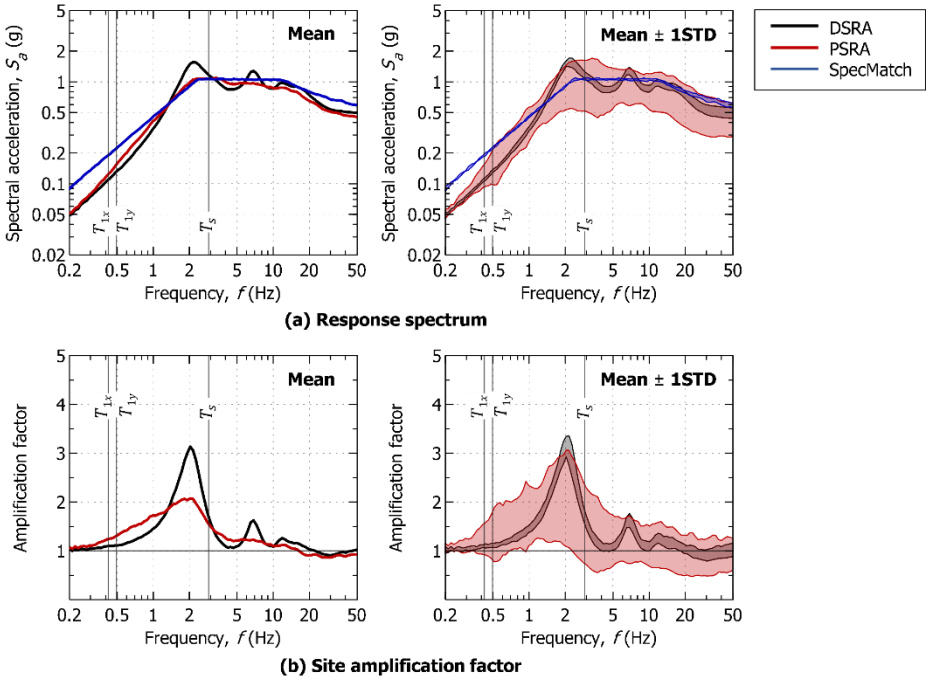


Fig. 3 Surface SRSS response spectra and site amplification factors of three ground motion estimation methods (T_{1x} is the fundamental period in the X-direction (= 2.371 s); T_{1y} is the fundamental period in the Y-direction (= 2.022 s); and T_s is the site period (= 0.345 s))

3.2 Comparison based on linear/nonlinear time history analysis

Figure 4 shows the medians and logarithmic standard deviations of elastic responses for all structural elements. Each plotted point corresponds to one structural element: the element index on the x-axis indicates an individual member (or story), and the y-axis shows the median or logarithmic standard deviation of its end rotation responses (or interstory drifts) across the 60 analyses. In the figure, the element indices for member rotations are arranged in ascending order based on the medians of DSRA.

Medians of elastic structural responses were similar between the three ground motion estimation methods. However, the logarithmic standard deviations of PSRA were greater than those of DSRA and SpecMatch due to the introduction of soil variability. The logarithmic standard deviations of PSRA were widely scattered, but remained within a consistent range across different types of response. The

magnitude of the dispersion was comparable to the coefficient of variation of SRSS response spectra at the fundamental period (0.251 in the X-direction and 0.368 in the Y-direction).

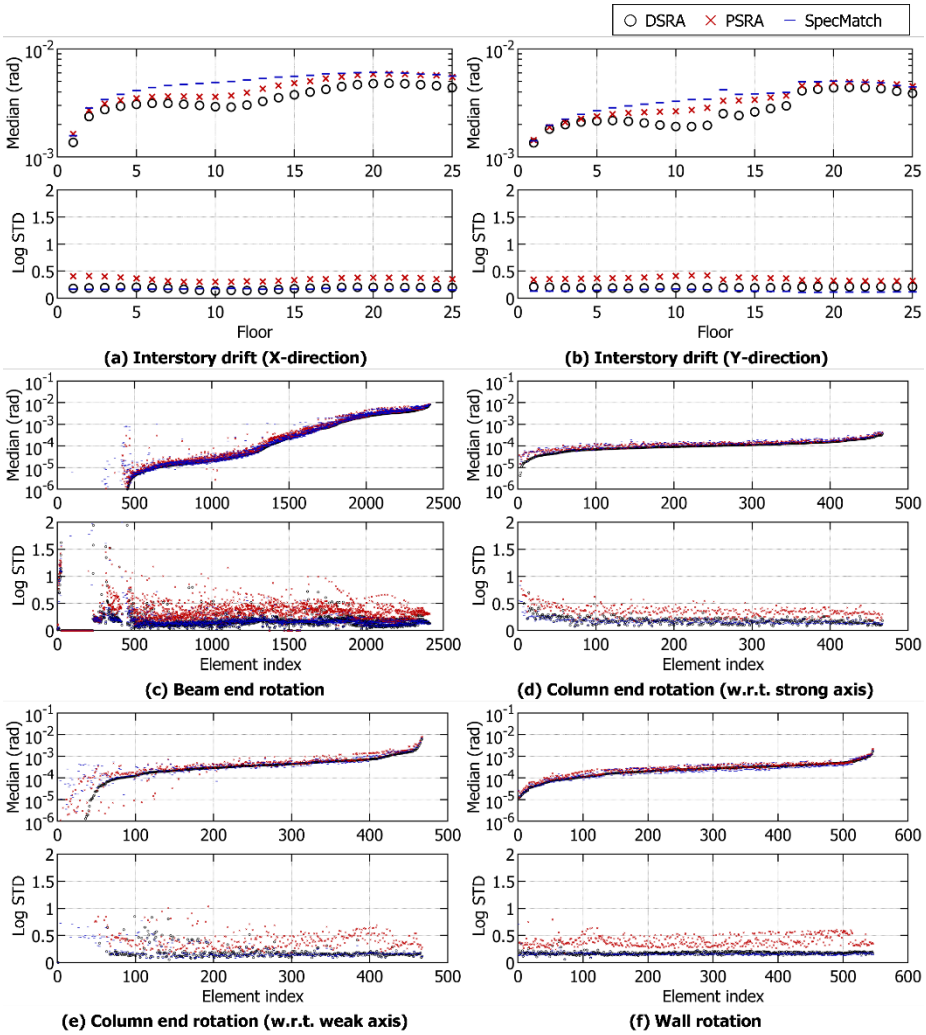


Fig. 4 Results of linear time history analysis of the building model

Figure 5 shows the medians and logarithmic standard deviations of structural responses for all structural elements. Unlike the linear-elastic analysis, the medians of PSRA and SpecMatch were greater than those of DSRA, across all response types. This amplification can be attributed to the onset of nonlinear behavior, particularly the formation of plastic hinges. Minor variations in ground motion characteristics introduced by PSRA may have triggered earlier yielding in structural components, leading to a greater spread in plastic deformation. The gap between logarithmic standard deviations of PSRA and the other methods were amplified compared to the linear-elastic case. Although the variability remained within a bounded range across different response types, beam end rotations showed significantly larger and more scattered variation. This may be attributed to the fact that beams generally yielded earlier and showed larger inelastic deformations compared to vertical members in high-rise buildings. As shown in the figure, the median end rotations of vertical members remained below 0.001 rad, indicating limited inelastic behavior, whereas beam end rotations reached as high as 0.01 rad. Given that nonlinear mechanisms in the structure are predominantly driven by plastic hinge formation in beams, the larger variability in beam responses likely affected the variation in interstory drift ratios; logarithmic standard

deviations of interstory drift ratios in PSRA were greater in the nonlinear analysis compared to those in the linear-elastic analysis.

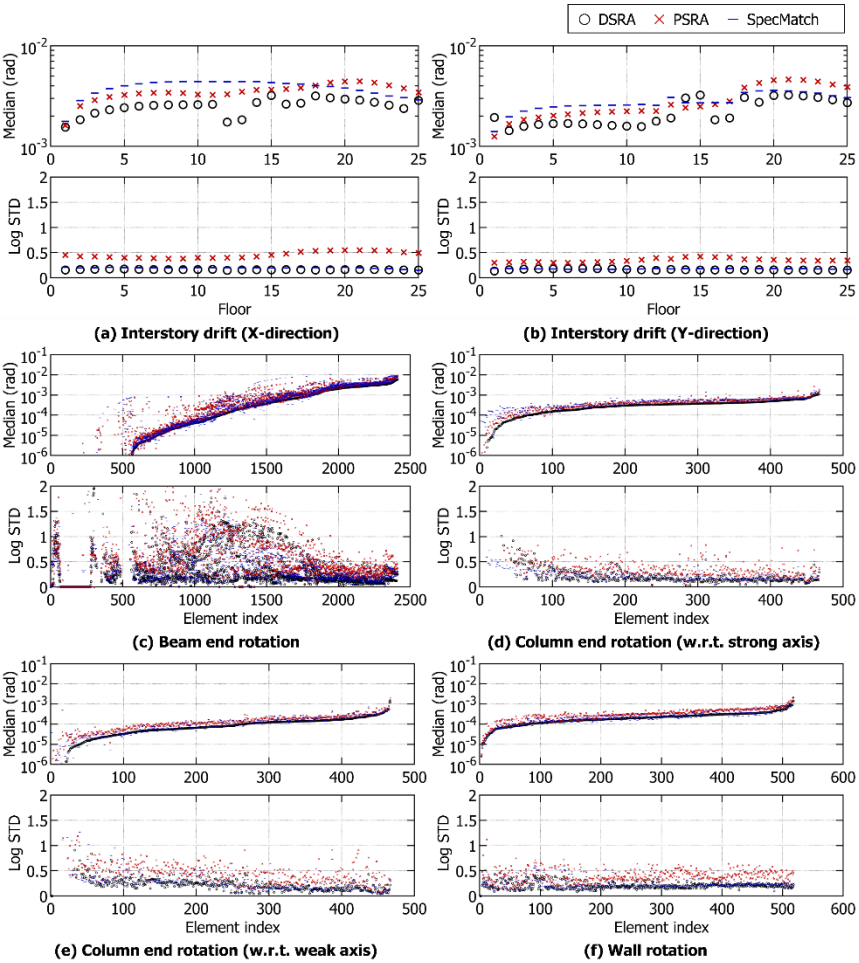


Fig. 5 Results of nonlinear time history analysis of the building model

4 CONCLUSIONS

In order to investigate the influence of soil variability on the seismic response of building structures, multiple simulations of three-dimensional linear and nonlinear time history analyses were conducted on a 25-story reinforced concrete moment-resisting frame building. Three ground motion estimation methods were compared: (a) deterministic site response analysis (DSRA) using site-specific soil properties; (b) probabilistic site response analysis (PSRA) considering soil variability; and (c) spectrum matching to a soft soil design response spectrum (SpecMatch) without performing site response analysis. The major findings are summarized as follows:

- 1.Regarding response spectra, PSRA showed greater dispersion due to the incorporation of soil variability. The mean spectral accelerations of PSRA and DSRA were similar at the fundamental period of the building.
- 2.In the linear analysis results, the dispersion of the seismic responses was greater in PSRA than that in DSRA and SpecMatch. The magnitude of the dispersion was consistent with that of the SRSS spectral accelerations at the fundamental period of the input response spectra.
- 3.In the nonlinear analysis results, the discrepancy in the response dispersion between PSRA and the other methods was amplified compared to the linear case, particularly in beam end

rotations that experienced larger inelastic deformations than vertical members. Unlike in the linear case, the median responses in PSRA were greater than those in DSRA, attributed to the interaction between soil variability and system nonlinearity.

-

While the seismic design and analysis procedures in the present study followed Korean guidelines, the key findings reflect the fundamental behaviors of building structures regardless of the specific code type.

Acknowledgements

This research was supported by a grant (RS-2022-00143493) from Digital-Based Building Construction and Safety Supervision Technology Research Program funded by Ministry of Land, Infrastructure and Transport of Korean Government.

References

[1] Electric Power Research Institute. 2018. *Seismic Fragility and Seismic Margin Guidance for Seismic Probabilistic Risk Assessments*. Palo Alto, CA: Electric Power Research Institute.

[2] American Society of Civil Engineers. 2022. *Seismic Analysis of Safety-Related Nuclear Structures (ASCE 4-16)*. Reston, VA: American Society of Civil Engineers. doi:10.1061/9780784414255.

[3] American Society of Civil Engineers. 2022. *Minimum Design Loads and Associated Criteria for Buildings and Other Structures (ASCE 7-22)*. Reston, VA: American Society of Civil Engineers. doi:10.1061/9780784415788.

[4] Korea Construction Standards Center. 2022. *Building Seismic Design Code (KDS 41 17 00: 2022; in Korean)*. Gyonggi-Do, Republic of Korea: Korea Construction Standards Center.

[5] Architectural Institute of Korea. 2025. *Guidelines for Performance-Based Seismic Design of Reinforced Concrete Buildings (AIK-KCI Guidelines; in Korean)*. Seoul, Republic of Korea: Architectural Institute of Korea.

[6] Architectural Institute of Korea, and Korea Concrete Institute. 2025. *Guidelines for Nonlinear Analysis and Performance-Based Design (AIK–KCI Guidelines; in Korean)*. Seoul, Republic of Korea: Architectural Institute of Korea and Korea Concrete Institute.

[7] Risk Engineering, Inc. 2001. *Technical Basis for Revision of Regulatory Guidance on Design Ground Motions: Hazard- and Risk-Consistent Ground Motion Spectra Guidelines. NUREG/CR-6728*. Washington, DC: U.S. Nuclear Regulatory Commission, Office of Nuclear Regulatory Research.

[8] Ancheta, Timothy D., Darragh, Robert B., Stewart, Jonathan P., Seyhan, Emel, Silva, Walter J., Chiou, Brian S. J., Wooddell, Katie E., Graves, Robert W., Kottke, Albert R., Boore, David M., Kishida, Tadahiro, and Donahue, Jennifer L. 2014. "NGA-West2 Database." *Earthquake Spectra* 30:989–1005. doi:10.1193/070913EQS197M.

[9] Al Atik, Linda., and Abrahamson, Norman. 2010. "An Improved Method for Nonstationary Spectral Matching." *Earthquake Spectra* 26:601–17. doi:10.1193/1.3459159.

[10] Kottke, Albert R., and Rathje, Ellen M. 2009. *Technical Manual for Strata*. Report No. 2008/10. Berkeley, CA: Pacific Earthquake Engineering Research Center, University of California.

[11] Toro, Gabriel R. 1995. *Probabilistic Models of Site Velocity Profiles for Generic and Site-Specific Ground-Motion Amplification Studies*. Technical Report No. 779574. Upton, NY: Brookhaven National Laboratory.

[12] Darendeli, Mehmet B. 2001. "Development of a New Family of Normalized Modulus Reduction and Material Damping Curves." PhD diss., The University of Texas at Austin.

[13] Kim, Dong-Soo, and Choo, Yun-Wook. 2001. "Dynamic Deformation Characteristics of Cohesionless Soils in Korea Using Resonant Column Tests." *Journal of Korean Geotechnical Society* 17:115–28.

[14] Yoon, Jun-Ung. 2002. "Deformational Characteristics of Weathered Granite Using RC/TS and Small-Strain Triaxial Tests (in Korean)." MS diss., Korea Advanced Institute of Science and Technology.

[15] Architectural Institute of Korea. 2016. *Korean Building Code (KBC 2016)*. Seoul, Republic of Korea: Architectural Institute of Korea.

[16] Korea Construction Standards Center. 2024. *Seismic Design: General (KDS 17 10 00: 2024; in Korean)*. Gyonggi-Do, Republic of Korea: Korea Construction Standards Center.

[17] Dobry, Ricardo., Oweis, Issa., and Urzua, Alfredo. 1976. "Simplified Procedures for Estimating the Fundamental Period of a Soil Profile." *Bulletin of the Seismological Society of America* 66:1293–321.

[18] Computers and Structures, Inc. 2011. *User Guide Perform-3D: Nonlinear Analysis and Performance Assessment for 3D Structures*. Version 5. Berkeley, CA: Computers and Structures, Inc.

Reliability of GFRP embedded reinforcement at extreme temperatures

Jakub Ježek, František Girgle, David Vašátko, Đorđe Čairović, Martin Zlámal, Petr Štěpánek

Institute of Concrete and Masonry Structures,
Brno University of Technology, Faculty of Civil Engineering
Veveří 95, 602 00 Brno, Czech Republic

Summary
The article addresses the design of reinforced concrete structures using composite materials in extreme conditions. The new generation of Eurocodes will allow for the use of internal FRP reinforcement, however, EN 1992-1-2, which deals with the design of concrete structures for the accidental situation of fire exposure, does not recognize FRP, but to design a safe structure according to EN standards, reliable material properties of FRP reinforcement at elevated temperatures are required. The article presented GFRP tensile strength as a function of temperature in accordance with standard approaches, based on all available experimental data. Building on these results, the reliability index was calculated using two different standards methods. The results show that a safety factor of 1.1 for the design strength of FRP reinforcement generally provides adequate reliability in accidental design situations. However, one calculation approach indicates insufficient reliability at temperatures around 400 °C.

1 INTRODUCTION

In recent decades, the use of FRP (fibre reinforced polymer) composite materials to reinforce concrete structures in construction practice has grown significantly. As a result, the new generation of European standards allows for the design of internal FRP reinforcement in selected load-bearing structural elements, as defined in Annex R of EN 1992-1-1[1], which also specifies the basic requirements and design procedures for the ultimate limit state and serviceability limit state. The Annex also includes the definition of fundamental material properties and safety factors.

In contrast, the new generation standard EN 1992-1-2 [2] for the design of concrete structures under fire conditions does not recognise the concept of FRP reinforcement. The most available approach applicable to FRP reinforcement mentioned in EN 1992-1-2 is the zone method; however, modification of the material parameters used in the calculation models is required, as the standard specifies only the temperature-dependent reduction factors for the strength and modulus of elasticity of steel. Therefore, when designing for fire resistance of FRP reinforced structures, it is necessary to obtain the relevant material parameters experimentally, from manufacturers' documentation, or technical literature.

Due to the lack of sufficiently standardised guidelines for the design of FRP reinforced concrete structures at high temperatures, a study was conducted to determine the relationship between tensile strength and temperature of GFRP (glass fibre reinforced polymer) reinforcement in accordance with the standard [3]. The article builds on this study and investigates the partial material factor for accidental design situations, specified in the second generation of EN 1992-1-1, and whether the partial factor can also be applied to the design of concrete structures exposed to extreme temperatures.

2 DESIGN ASSUMPTION FOR FRP

The new generation of EN 1992-1-1 in Annex R [1] specifies the design value of the tensile strength of embedded FRP reinforcement using the following relationship

$$f_{ftd} = \frac{f_{ftk,100a}}{\gamma_{FRP}} \tag{1}$$

where γ_{FRP} stands for partial factors for FRP reinforcement (see Chapter 2.1),
$f_{ftk,100a}$ is design long-term strength. When not directly determined from production data, it can be obtained with the formula

$$f_{ftk,100a} = C_t \cdot C_c \cdot C_e \cdot f_{ftk0}, \tag{2}$$

where C_t is the factor considering temperature effects. It can gain a value of 1.0 for indoor and underground environments or 0.8 for outdoor members if heating through solar radiation cannot be excluded,

C_c is the coefficient of creep effect. If this value is not determined based on tests for a specific type of GFRP reinforcement, it is recommended to consider a value of 0.35,

C_e is the coefficient between the strength after ageing and before ageing. The coefficient can be determined by test according to ISO 10406-1, or the value should be considered as 0.7,

f_{ftk0} is the 5% quantile of short-term tensile strength determined according to ISO 10406-1.

2.1 Partial factors for FRP reinforcement

The new generation of EN 1992-1-1 [1] also specifies partial material factors for FRP reinforcement for individual design situations, whose values are summarised in Table 1. The standard defines a partial material factor for accidental design situations as $\gamma_{FRP} = 1.1$, and as fire design situations are classified as accidental design situations [4], this factor should also be applied in the design of concrete structures with internal FRP reinforcement exposed to fire.

The partial material factor for steel reinforcement is determined based on a probabilistic analysis with a defined target probability of failure. The calculation takes into consideration the coefficients of variation of all parameters influencing the resulting load-bearing capacity of the reinforcement. The purpose of this factor is to ensure the required level of structural reliability corresponds to the design situation under consideration. The verification process of the factor's value in the situation of fire is presented in Chapter 3.

For FRP reinforcement, a partial material factor was determined on the basis of a similar probabilistic analysis for the design situation corresponding to a reliability index of $\beta_{tgt} = 3.8$, resulting in $\gamma_{FRP} = 1.3$. However, due to the FRP reinforcement not exhibiting a plastic zone in the stress-strain diagram, which leads to material failure occurring suddenly without warning (unlike steel reinforced structures, which prior to failure exhibit significant deflections and develop wide cracks), and due to the high variability of product properties, limited availability of experimental data and validated numerical models, the γ_{FRP} value was subsequently increased to the final value of $\gamma_{FRP} = 1.5$ as reported in Table 1 to account for all the negative effects of the FRP reinforcement [5].

Table 1 Partial factors for FRP reinforcement and reliability index [1]

Design situation	γ_{FRP}	β_{tgt}
Persistent and transient design situation (γ_{FRPU})	1.50	3.8
Accidental design situation (γ_{FRPA})	1.10	2.0
Serviceability limit state (γ_{FRPS})	1.00	1.5

2.2 GFRP Reinforcement at high temperature

Standard EN 1992-1-2 [2], Design of concrete structures – General rules – Structural fire design, specifies the relationship for determining the design values of material properties as

$$X_{d,\theta} = k_\theta \cdot \frac{X_k}{\gamma_{M,fi}}, \tag{3}$$

where X_k is the characteristic value of a strength or stiffness property for normal temperature,

k_θ is the temperature-dependent reduction factor ($X_{k,\theta}/X_k$) for a strength or stiffness property,

$\gamma_{M,fi}$ is the partial factor for the relevant mechanical material property for the fire situation. The standard specifies a value of 1.0 unless a different value is given in the National Annex. For the purpose of this study, this value was also verified.

Considering equation (3) and substituting the relationships given in equations (1) and (2), we obtain the following relationship, which expresses the calculation of the design tensile strength of FRP reinforcement as a function of temperature

$$f_{ftd,\theta} = k_{\theta FRP} \cdot \frac{C_t \cdot C_c \cdot C_e \cdot f_{ftk0}}{\gamma_{FRPA}}, \tag{4}$$

where $k_{\theta FRP}$ is the temperature-dependent reduction factor for FRP reinforcement.

Several scientific studies [6], [7], [8], [9] have investigated the reduction factors for the tensile strength of FRP reinforcement as a function of temperature. A key finding of the previously mentioned

studies is that the value of said reduction factor depends on the type of load-bearing fibres, as the thermosetting matrix begins to degrade at approximately 100 °C, after which the load transfer is primarily provided by the fibres themselves [6]. Thus, it is necessary to differentiate between reduction factors of the different types of load-bearing fibres, such as GFRP (glass fibre reinforced polymer), CFRP (carbon fibre reinforced polymer), AFRP (aramid fibre reinforced polymer), etc., as each behaves differently under the effects of fire. The research presented in this article focuses primarily on GFRP reinforcement, as this type of FRP reinforcement is currently the most widely used for internal reinforcement of concrete structures.

One of the first authors to publish reduction factors for the tensile strength and modulus of elasticity of FRP reinforcement as a function of temperature was Saafi [10], who derived reduction factors for different types of fibres. As Saafi's curves were designed conservatively, they remain the most widely used. Another contribution was the dissertation by Bisby (2003) [11], who compiled a database of previously published experimental results and proposed average reduction functions for tensile strength and modulus of elasticity for different fibre types. Nigro et.al. [12] also developed a similar database and published average reduction functions. The functions of Nigro and Bisby are very similar, as both authors drew on comparable sources [12]. The most recent database, updated with new experimental results and original measurements, was published by Rosa et al. [6] (2022). It provided updated average functions of tensile strength and modulus of elasticity of GFRP reinforcement as a function of temperature. However, it should be noted that none of the published functions has been derived in accordance with the requirements of the Eurocodes, which define material characteristics as the 5% quantile [4]. Therefore, these functions cannot be directly applied to the design of structures in accordance with standard procedures.

Due to the absence of a standard-based reduction factor, an updated database including all available results of tensile tests of GFRP reinforcement at elevated temperatures was compiled in a previous study [3]. This database was subsequently expanded with the results of our own experimental data and was evaluated in accordance with the requirements of EN 1990 [4]. The 5% quantile was determined by using two methods: the interval method, in which the data were divided into intervals and each interval was statistically evaluated separately, and the quantile regression method, in which the required quantile regression function was found. Based on the analysis, the characteristic function of the tensile strength of GFRP reinforcement as a function of temperature was proposed. The compiled database, analysis results, and the proposed curve, compared with Saafi's curve, are presented in Figure 1.

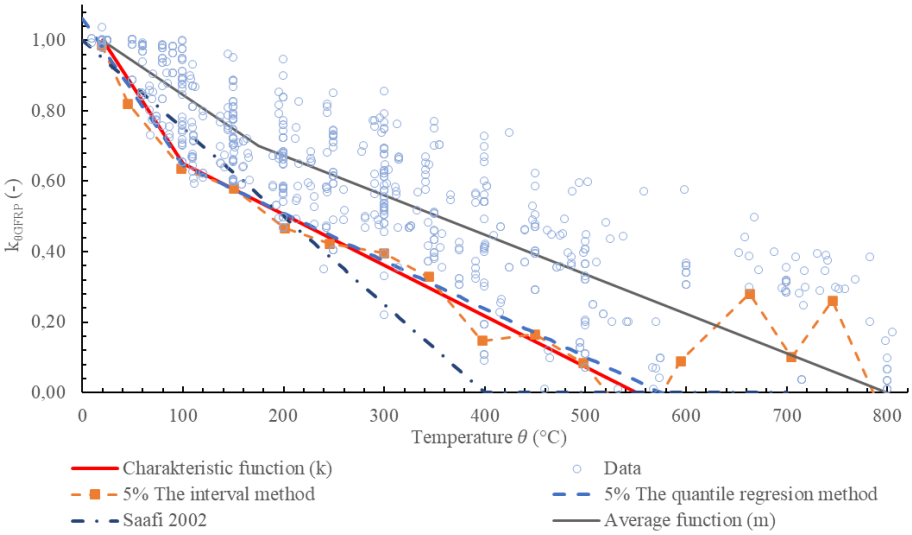


Fig 1. Database of tensile tests on GFRP reinforcement as a function of temperature and determination of reduction factors in accordance with standard requirements [3], [10].

3 CALCULATION OF THE RELIABILITY INDEX FOR PARTIAL FACTOR

The new generation of standards allows the determination of partial material factors based on available data for material properties and required reliability. Annex A of EN 1992-1-1 [1] provides the following relationship for reinforcement

$$\gamma_s = \frac{\exp(\alpha_R \cdot \beta_{tgt} \cdot V_{Rs})}{\mu_{Rs}}, \quad (5)$$

where α_R is the sensitivity factor for resistance. The study considers the recommended standard value of 0.8,

β_{tgt} is the reliability index,

V_{RS} is the coefficient of variation of the resistance, which for steel reinforcement can be calculated from

$$V_{Rs} = \sqrt{V_{fy}^2 + V_d^2 + V_{\theta s}^2}\,. \quad (6)$$

The individual terms in the relationship represent the coefficients of variation associated with the individual sources of material and model uncertainty. For steel reinforcement, the calculation includes:

V_{fy} is the coefficient of variation of tensile strength,

V_d is the coefficient of variation of the effective depth,

$V_{\theta S}$ is the coefficient of variation of model uncertainty.

Last term of the equation (5) is $\mu_{RS,}$ which represents the bias factor of the resistance, and for steel reinforcement is calculated from

$$\mu_{Rs} = \frac{f_{ftm0}}{f_{ftk0}} \cdot \mu_d \cdot \mu_{\theta S}, \quad (7)$$

where $\frac{f_{ftm0}}{f_{ftk0}}$ is the bias factor of tensile strength,

μ_d is the bias factor of the effective depth,

$\mu_{\theta S}$ is the bias factor of model uncertainty.

3.1 Calculation of the reliability index for FRP

Equations (6) and (7) clearly indicate that they were derived exclusively for steel reinforcement. Furthermore, Equation (4) shows that, compared to steel, the tensile strength of FRP reinforcement is affected by a greater number of material uncertainty sources. Therefore, it is necessary to extend Equations (6) and (7) to include additional components representing these material uncertainties before they can be used in the calculation of the partial factor. For tensile strength, the calculation of the variation coefficient will have the following form

$$V_{RFRP} = \sqrt{V_{f_{ftk0}}^2 + V_d^2 + V_{\theta s}^2 + V_{Ct}^2 + V_{Cc}^2 + V_{Ce}^2}, \quad (8)$$

and the calculation of the bias factor will have following form

$$\mu_{RFRP} = \frac{f_{ftm0}}{f_{ftk0}} \cdot \mu_d \cdot \mu_{\theta S} \cdot \mu_{Ct} \cdot \mu_{Cc} \cdot \mu_{Ce}, \quad (9)$$

where the added variation coefficients and bias factors represent the uncertainties of the coefficients Ct, Cc, and Ce, which affect the resulting strength of the FRP reinforcement. However, if the characteristic long-term tensile strength $f_{ftk,100a}$ is determined directly from combined long-term experimental testing, the number of variables is reduced, and Equations (8) and (9) would have to be modified.

To determine the material factor for the design situation for fire, it is necessary to consider an additional significant source of uncertainty – the strength reduction factor as a function of temperature. Figure 1 illustrates a considerable variation of experimental results at elevated temperature; therefore, this effect cannot be neglected. Consequently, the Equations used to calculate the coefficient of variation and the bias factor take the following form

$$V_{\theta RFRP} = \sqrt{V_{RFRP}^2 + V_{k\theta FRP}^2}, \quad (10)$$

$$\mu_{\theta RFRP} = \mu_{RFRP} \cdot \mu_{k\theta FRP}, \quad (11)$$

where the added variation coefficients and bias factors represent the uncertainties of the temperature's influence on tensile strength.

To verify the material factor for an accidental design situation, it is necessary to know all the coefficients of variation corresponding to the individual influences on the tensile strength of FRP reinforcement, while also accounting for the increase in the factor value due to brittle failure, as discussed in Section 2.1. The required coefficients of variation can be estimated by rearranging Equation (5). The following values are substituted into the equation

for the ultimate limit state design situation, the material factor is taken as $\gamma_{FRPU} = 1.5$ with a reliability index of $\beta_{tgt} = 3.8$,

for the serviceability limit state design situation, the material factor is taken as $\gamma_{FRPS} = 1$ with a reliability index of $\beta_{tgt} = 1.5$.

The material factors and the target reliability were determined according to Table 1. By substituting these values into the rearranged Equation (5), we obtain two equations with two unknowns. The coefficient of variation and the bias factor can now be calculated without the influence of temperature. Solving the equations gives us $V_{RFRP} = 0.22$ and $\mu_{FRP} = 1.3$.

These values are of purely mathematical significance and are consistent with the previously determined material factors, including the effect of the increase described in Section 2.1. They are not experimentally verified but serve solely to verify the material factor for an accidental design situation, and their calculation is based on the other coefficients specified in the standard. For example, if the value of $\gamma_{FRPU} = 1.3$ mentioned in Section 2.1 is used, the resulting values are $V_{RFRP} = 0.14$ and $\mu_{FRP} = 1.18$.

Based on the database compiled and described in Section 2.2 and its statistical evaluation, the coefficients of variation and bias factors of the GFRP tensile strength reduction factor as a function of temperature $V_{k\theta FRP}$ and $\mu_{k\theta FRP}$ were determined in intervals of 50 °C. Thanks to the mathematical simplifications described in the previous sections, all parameters required for the calculation of the material factor are now known. By substituting Equations (10) and (11) into Equation (5), the reliability index of FRP for the accidental fire design situation can be determined as

$$\beta_{tgt} = \frac{\ln(\mu_{RFRP} \cdot \mu_{k\theta FRP} \cdot \gamma_{FRPA})}{\propto_R \cdot \sqrt{V_{RFRP}^2 + V_{k\theta FRP}^2}}. \tag{12}$$

The reliability index for FRP reinforcement was determined in two variants using the procedure presented in this chapter. In the first variant, the influence of all material uncertainties was considered in accordance with Equation (12). In the second variant, only the uncertainty associated with the temperature-dependent reduction factor of the tensile strength of GFRP reinforcement was considered. Using the second variant, Equation (12) was simplified to the following form

$$\beta_{tgt} = \frac{\ln(\mu_{k\theta FRP} \cdot \gamma_{FRPA})}{\propto_R \cdot V_{k\theta FRP}}. \tag{13}$$

The results of the calculations are presented in a separate Section 3.3, where they are also compared with an alternative calculation variant.

3.2 Alternative approach calculation of the reliability index for FRP

Annex C of EN 1990 [4] allows the determination of design values for material properties based on measured experimental data. The standard specifies procedures and relationships depending on the assumed probability distribution of the data. In accordance with these requirements, an analysis of the probability distribution of the data within individual temperature intervals was performed. It was found that, in most cases, the analysed data are best approximated by a normal distribution.

Based on this analysis, it is possible to use the relationship specified in the standard for calculating the design strength, assuming a normal distribution of data. Considering the influence of the strength reduction factor depending on temperature, the equation is adjusted for FRP reinforcement in the following manner

$$f_{ftd,\theta} = m_{\theta FRP} \cdot \left(1 - \propto_R \beta_{tgt} \cdot \sqrt{V_{RFRP}^2 + V_{k\theta FRP}^2}\right), \tag{14}$$

where $m_{\theta FRP}$ is the average value tensile strength calculated from

$$m_{\theta FRP} = f_{ftm0} \cdot m_{Ct} \cdot m_{Cc} \cdot m_{Ce} \cdot m_{k\theta FRP}, \tag{15}$$

where f_{ftm0} is the average short-term tensile strength, which, in this study, was assumed to have a normalised value of 1.0, and, based on our investigation of GFRP of short-term tensile strength, the characteristic value f_{ftk0} was assumed to be 0.95.

m_{cc}, m_{ce} and m_{ct} represent the average value of the coefficients Ct, Cc, and Ce affecting the resulting strength of the FRP reinforcement. The value of these coefficients is assumed same as with the present standard value, except for m_{cc}, which is based on the study by Benmokrane et al. [13], who focused on the influence of creep on GFRP reinforcement, and determined the average value of the creep behaviour coefficient at a 100-year mark as 0.51.

$m_{k\theta FRP}$ is the mean value of the coefficient for the temperature-dependent reduction factor of GFRP tensile strength. In the study described in Chapter 2.2, the temperature-dependent coefficient $m_{k\theta FRP}$ was also determined.

By substituting Equations (15) and (14) into Equation (4), the reliability index for FRP reinforcement can be expressed, and its values can be determined as a function of temperature. The resulting expression takes the following form

$$\beta_{tgt} = \frac{1 - \frac{k_{\theta FRP} \cdot C_t \cdot C_c \cdot C_e \cdot f_{ftk0}}{\gamma_{FRP} \cdot f_{ftm0} \cdot m_{Ct} \cdot m_{Cc} \cdot m_{Ce} \cdot m_{k\theta FRP}}}{\alpha_R \cdot \sqrt{V_{RFRP}^2 + V_{k\theta FRP}^2}}. \quad (16)$$

As in the previous chapter, the calculation was performed in two variants. Considering all influencing factors and considering only the effects of temperature. The results of both variants and their comparison are presented in Section 3.3. When only the temperature effect is considered, Equation (16) is simplified in the following manner

$$\beta_{tgt} = \frac{1 - \frac{k_{\theta FRP}}{\gamma_{FRP} \cdot m_{k\theta FRP}}}{\alpha_R \cdot V_{k\theta FRP}^2}. \quad (17)$$

3.3 Results and comparison

Based on the relationships derived in Sections 3.3 and 3.4, a total of eight temperature-dependent reliability index trends for the tensile strength of GFRP reinforcement were determined and are presented in Figures 2 and 3, with each figure illustrating the influence of different partial material factors. Figure 2 corresponds to EN 1992-1-1[1], which specifies γ_{FRPA} = 1.1, while Figure 3 corresponds to EN 1992-1-2 [2], which specifies $\gamma_{M,fi}$ = 1.0. Each figure includes two different calculation methods for two variants of input material uncertainties, considering all influencing factors and considering only the effects of temperature. The obtained results show very good agreement; therefore, it can be concluded that the calculation methods used, including the applied simplifications, can be regarded as reliable. Both figures also include the required safety limit for accidental design situations according to EN 1990 [4], which is β_{tgt} = 2.0.

The results obtained in this study and presented in Figure 2 indicate that the coefficient value γ_{FRP} = 1.1, specified in EN 1992-1-1, provides the required level of safety, except at temperatures of approximately 400 °C. At this temperature, the reliability index, which was determined in accordance with EN 1990 Annex C [4], reaches a value of 1.99 when all sources of uncertainty are included and 1.79 when only the influence of temperature is considered. The second calculation method also indicates a decrease around this temperature; however, this value still exceeds the required reliability index of 2.0. This behaviour is associated with the increased deviation of GFRP tensile strength values as a function of temperature, which can be observed at approximately 400 °C in the database presented in Figure 1.

However, in contrast, the results presented in Figure 3 indicate that the use of the coefficient value specified in EN 1992-1-2 [2] as $\gamma_{M,fi}$ = 1.0 may lead to an unsafe structural design under the effects of fire, particularly at temperatures around 20–100 °C, around 200–250 °C, and at approximately 400 °C.

Based on the study, it can be concluded that the material factor for GFRP reinforcement in an accidental design situation, as specified in Annex R of EN 1992-1-1 [1], generally provides a sufficient level of safety and can be applied to the tensile strength calculation of GFRP reinforcement for structures subjected to fire load, while ensuring the required level of reliability. However, it should be noted that, in one of the applied calculation procedures, the required level of safety at temperatures around 400 °C was not satisfied. This occurrence is attributed to the higher deviation of experimental data. If future experimental investigations of GFRP reinforcement reveal an even greater variability of material properties at elevated temperatures, the use of γ_{FRP} = 1.1 may no longer be adequate.

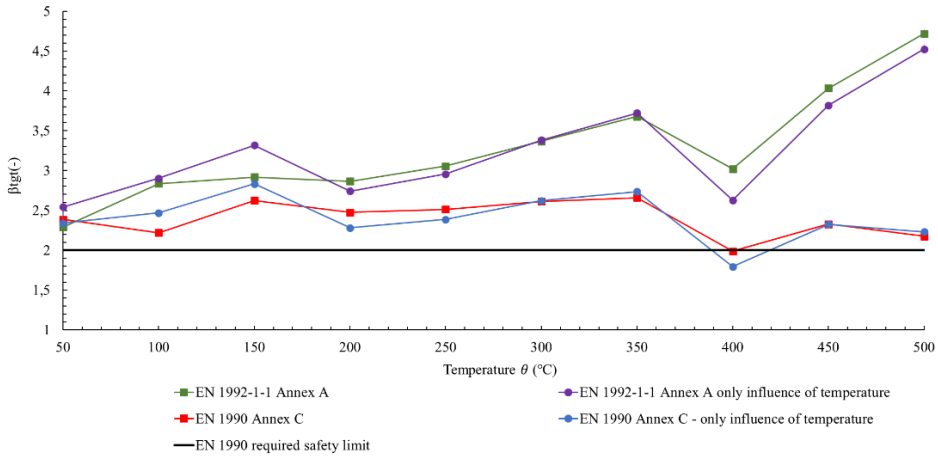


Fig 2. Calculation of the reliability index for GFRP reinforcement at elevated temperatures with $\gamma_{FRPA} = 1.1$ [1],[4].

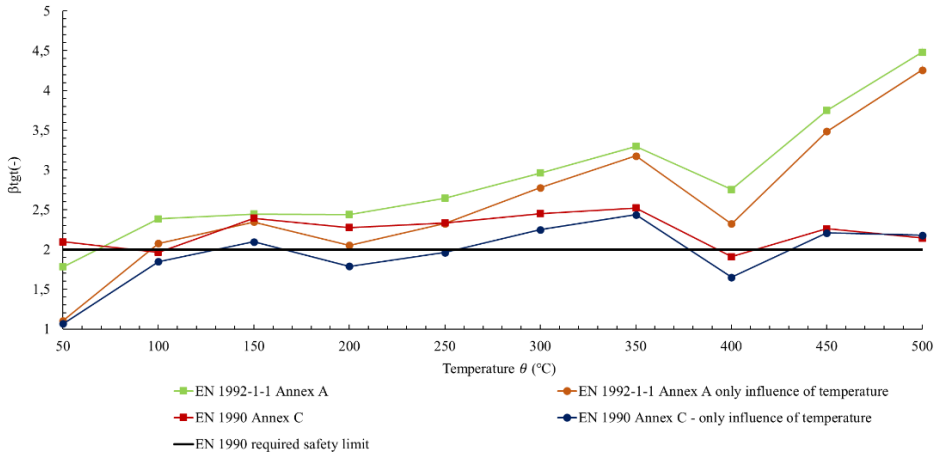


Fig 3 Calculation of the reliability index for GFRP reinforcement at elevated temperatures with $\gamma_{M,fi} = 1.0$ [1],[2],[4].

4 CONCLUSIONS

This study focused on determining the design tensile strength of GFRP reinforcement in accordance with the new generation of Eurocodes, with a focus on fire design situations.

A design approach for the tensile strength of GFRP reinforcement under elevated temperatures was presented in accordance with Eurocode principles, addressing the fact that the current fire design standard EN 1992-1-2 [2] does not consider FRP reinforcement.

In accordance with the two standards, two procedures of determining the reliability index for GFRP reinforcement were used, and both were consistent with the probabilistic concepts defined in standards [1], [2], [4]. Based on the compiled tensile tests database of GFRP reinforcement at elevated temperatures, each reliability index was calculated with two different sets of input material uncertainties.

The obtained results were compared with the required reliability presented in the standards for accidental design situations. It was demonstrated that the value $\gamma_{M,fi} = 1.0$ given in EN 1992-1-2 [2] may lead to an unsafe structural design under the effects of fire. The partial safety factor for accidental design situation $\gamma_{FRP} = 1.1$ specified in EN 1992-1-1 [1] (Annex R) generally provides an adequate level of safety for the GFRP reinforcement tensile strength at elevated temperatures.

However, at temperatures around 400 °C, one of the applied calculation methods using $\gamma_{FRP} = 1.1$ resulted in the reliability index falling below the target value, which is attributed to the higher deviation of experimental tensile strength data at approximately 400 °C.

These findings indicate that the adequacy of the partial safety factor $\gamma_{FRP} = 1.1$ is strongly dependent on the variability of available experimental data. If future test results exhibit a higher deviation of GFRP tensile strength at elevated temperatures, the current value may become inadequate.

Acknowledgements

This paper was written with the support of the BUT project no. *"FAST-S-25-8769 – Advanced analyses of existing concrete and masonry structures",* BUT project no. *"FAST-S-26-8945 – Advanced analyses of existing concrete and masonry structures"* and TA ČR, project no. *"TH82020005 – Novel bendable thermoplastic rebars for improved durability and sustainability of concrete structures."*

References

[1] EN 1992-1-1 Eurocode 2-Design of Concrete Structures-Part 1-1: General Rules and Rules for Buildings, Bridges and Civil Engineering Structures. 2023. Brussel: European committee for standardization.

[2] EN 1992-1-2 Eurocode 2: Design of Concrete Structures - Part 1-2: General Rules - Structural Fire Design. 2023. Brussel: European committee for standardization.

[3] Ježek, Jakub, František Girgle, David Vašátko, Đorđe Čairović, Martin Zlámal, and Petr Štěpánek. 2025. "Design Characteristics of GFRP Reinforcements at Extreme Temperatures." Advances in Science and Technology, The 30th Concrete Structures and Technology (Switzerland), 2025. doi:10.4028/p-6JoZ4C.

[4] EN 1990 Eurocode - Basis of Structural and Geotechnical Design. 2023. Brussel: European Committee for Standardizaton.

[5] Craig Giaccio, Andre Weber, Anett Ignatiadis, and Martin Kurth. 2023. Validation of Expressions for Embedded FRP Reinforcement Background Document for FprEN 1992-1-1, CEN/TC 250/SC 2 N2087,

[6] Rosa, Inês C., João P. Firmo, and João R. Correia. 2022. "Experimental Study of the Tensile Behaviour of GFRP Reinforcing Bars at Elevated Temperatures." Construction and Building Materials 324 (March 2022). doi: 10.1016/j.conbuildmat.2022.126676

[7] Mcintyre, Emma, Antonio Bilotta, Luke Bisby, and Emidio Nigro. 2014. "Mechanical Propertie of Fibre Reinforced Polymer Reinforcment for Concrete at High Temperature." Edinburgh Research Explorer 2 (2014).

[8] Wang, Lu Xiao, and Zha, Xiao Xiong. 2011. "Experimental Research on Mechanical Behavior of GFRP Bars under High Temperature." Applied Mechanics and Materials 71–78: 3591–3594. doi: 10.4028/www.scientific.net/AMM.71-78.3591.

[9] Rozsypalova, Iva, Jan Prokes, Đorde Cairović, Frantisek Girgle, Petr Daňek, and Petr Štěpánek. 2021. "Research on the Residual Tensile Strength of Composite Reinforcing Bars Exposed to Elevated Temperatures." IOP Conference Series: Materials Science and Engineering 1205 (1): doi:10.1088/1757-899x/1205/1/012011.

[10] Saafi, Mohamed. 2002. "Effect of Fire on FRP Reinforced Concrete Members." Composite Structures 58 (1): 11–20. doi:10.1016/S0263-8223(02)00045-4.

[11] Bisby, Luke Alexander. 2003. Fire Behaviour of Fibre-Reinforced Polymer (FRP) Reinforced or Confined Concrete. PhD diss., Queen's University, Kingston, Ontario, Canada.

[12] Nigro, Emidio, Giuseppe Cefarelli, Antonio Bilotta, Gaetano Manfredi, and Edoardo Cosenza. 2014. "Guidelines for Flexural Resistance of FRP Reinforced Concrete Slabs and Beams in Fire." Composites Part B: Engineering 58: 103–112. doi: 10.1016/j.compositesb.2013.10.007.

[13] Benmokrane, Brahim, Vicki L. Brown, Khaled Mohamed, Antonio Nanni, Marco Rossini, and Carol Shield. 2019. "Creep-Rupture Limit for GFRP Bars Subjected to Sustained Loads." Journal of Composites for Construction 23 (6). doi:10.1061/(ASCE)CC.1943-5614.0000971.

Reliability Assessment of Conventional versus Eco-Concrete under Overstrength Condition

Saeideh Faghfouri, Alfred Strauss

Institute of Structural Engineering,
University of Natural Resources and Life Sciences,
Peter-Jordan-Straße 82, Vienna 1190, Austria

Summary

The construction sector faces growing pressure to reduce its environmental footprint, motivating the adoption of sustainable materials such as eco-concrete incorporating recycled aggregates or alternative binders. While these materials provide substantial environmental benefits, their mechanical variability and long-term structural reliability remain key concerns for designers and engineers. This study presents a comparative assessment of conventional and eco-concretes, employing a statistical evaluation of compressive strength to examine their long-term performance and providing a rigorous framework to evaluate structural reliability and service life. Results indicate that, despite slightly lower mean strengths, eco-concretes exhibit lower CoV values, reflecting stable and predictable behavior. These findings suggest that eco-concrete can achieve reliability levels comparable to conventional concrete, supporting their use in sustainable infrastructure with a target design life of 150 years.

1 INTRODUCTION

Conventional concrete remains the most widely used building material worldwide, offering high compressive strength, and decades of proven structural performance. However, its high cement content contributes significantly to CO_2 emissions, motivating the development and adoption of eco-materials. Eco-concretes represent a promising solution to reduce the environmental footprint of construction. Despite their ecological advantages, eco-concretes often exhibit greater mechanical variability, raising concerns regarding structural reliability.

Several studies have investigated the mechanical performance of eco-concretes. Mohammed et al. demonstrated that machine learning models can predict compressive strength variability in green concretes, enabling more accurate reliability assessments [1]. Miano et al. evaluated destructive and non-destructive tests to estimate compressive strength distribution in sustainable concretes, highlighting the importance of statistical characterization [2]. Kashem analyzed the effect of rice husk ash on compressive strength, noting increased variability compared to conventional concrete [3]. Kim assessed high-strength concrete variability, providing insights relevant for reliability-based design [4]. Further studies emphasize the need to incorporate statistical variability in design codes and life-cycle assessment of concrete structures [5].

The primary objective of this study is to provide a comprehensive comparative analysis of conventional and eco-concretes, focusing on their compressive strength variability and the implications for structural reliability over extended service life. The study systematically quantifies both the mean performance and the variability of these materials by calculating key statistical parameters such as mean compressive strength, standard deviation, and coefficient of variation (CoV). In addition, confidence intervals (CI) are constructed to estimate the range within which the true population mean lies. By combining these statistical metrics with reliability assessment, the study evaluates whether eco-concretes can achieve performance levels and safety margins comparable to conventional concrete. A particular focus is placed on the 5% fractile of compressive strength, which serves as a decisive parameter in structural design, to determine whether current design codes and safety concepts adequately account for the variability inherent in eco-materials. Furthermore, the study aims to assess the implications of these findings for long-term service life (SL), highlighting potential adjustments to design standards and providing insights for the adoption of eco-concretes in sustainable infrastructure projects.

2 THEORETICAL CONCEPTS

This section presents theoretical concepts related to the limit values of the coefficient of variation of compressive strength for the service life 100- and 150-years considering consequence classes, which serve as reference values. The methodology underlying these concepts, as described in section 2.1 and 2.3, is fully explained in [6] – [10]. In addition, section 2.3 introduces the fundamental mathematical concepts relevant to this context, including confidence intervals for estimating the population mean. [5], [11] – [13]

2.1 Reliability-Based Limit Values of CoV

A central concept in structural engineering is the reliability index β, which quantifies the probability of failure. According to EN 1990 [14], target reliability indices defined for long service lives can be converted into annual reliability indices, enabling consistent safety evaluation over time:

$$\beta_{1,n} = -\Phi^{-1}(p_{f1,\mathrm{n}}) \tag{1}$$

Where $p_{f1,\mathrm{n}}$: Failure probability for service life n at the first year [7]; n: Number of years (intended service life); $\beta_{1,n}$: Reliability index for the intended time period n at the first year of service life n; Φ^{-1} is inverse standard normal distribution function. The coefficient of variation (CoV) plays a critical role in this context. It describes the variability of concrete compressive strength relative to its mean value. By applying partial safety factors and assuming a normal distribution of material properties, the limit values of this variability considering target reliability indices $\beta_{1,n}$ can be calculated and linked to reliability requirements:

$$V_{x(\mathrm{N})} = \frac{\gamma_{\mathrm{m}} - 1}{\alpha_{\mathrm{R}} \cdot \beta_{1,n} \cdot \gamma_{\mathrm{m}} - \mathrm{k_n}} \tag{2}$$

where $\mathrm{k_n}$ is 5% fractil coefficient and is an unfavourable value for characteristic value with unknown $V_{x(\mathrm{N})}$, α_{R} is sensitivity factor of resistance defined in Table 1 according EN 1990 [14]. γ_{m} is partial safety factor. These calculated limit values of the coefficient of variation $V_{\mathrm{x(N)}}$ shown in Table 1 serve as benchmark values for evaluation whether concrete- both conventional and eco-concrete-meets safety and durability requirements.

Table 1 Threshold values $V_{\mathrm{x(N)}}$ considering target reliability indices $\beta_{1,\,\mathrm{n}}$ related to CC.

CC-classes	SL* / years	$\beta_{1,n}$	γ_m	α_{R}	$\mathrm{k_n}$	$V_{x(\mathrm{N^*})}$
CC3	100	5.3	1.5	0.8	1.645	0.11
CC3	150	5.4	1.5	0.8	1.645	0.10

SL: Service Life; N: normal distribution;

2.2 Classical solution to define failure probability

According to the classical approach, the probability of failure $\boldsymbol{P_f}$ can be calculated using Eq. (3) with probability density functions of resistance "R" and actions "S" illustrated in Fig. 1 [17]:

$$P_f = \int_{-\infty}^{+\infty} f_s\,(x) \cdot F_R(x)dx \tag{3}$$

where f_S is Probability density function of actions and $F_R(x)$ is the distribution function of resistance. The definition of failure probability according to Eq. (3) is combined with the coefficient of variation (CoV) to facilitate the interpretation of the conformity test results obtained from the case studies presented in section 4.

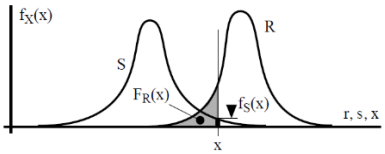


Fig. 1 Figure captions Probability density functions of resistance "R" and actions "S" [17].

2.3 Conformity Testing and Estimation of Coefficient of Variation

Concrete quality is assessed through conformity testing, following ONORM B4710-1[15]. This study focuses on continuous production, where a sufficient number of samples allows statistical evaluation:

$$f_{cm} \geq (f_{ck} / 0.92) + (1.48 \cdot \sigma) \quad ; \qquad \text{for} \qquad n \geq 3 \tag{4}$$

where f_{cm} is mean cylinder compressive strength of concrete, $f_{ck,cube}$ is characteristic cylinder compressive strength and σ is standard deviation. This conformity criterion is a crucial component of quality assurance in continuous production. The conformity criteria are used to determine whether test results satisfy required strength levels. A key aspect is the 5% fractile value which represents the lower bound of strength distribution and ensures that most of the material meets the required performance. According to Eq. (3), in this research the analysis considered two conditions for cube concrete:

Dry storage conditions :

$$f^{*}_{ck,cube} = f_{ck,cube}/0.92 \tag{5}$$

$$f^{*}_{cm,cube} = f^{*}_{ck,cube} + (1.48 \cdot \sigma) \tag{6}$$

And in-situ conditions, a conversion factor of 0.84 applies:

$$f^{**}_{\mathrm{ck,cube}} = f^{*}_{\mathrm{ck,cube}} * 0.84 \tag{7}$$

$$f^{**}_{\mathrm{cm,cube}} = f^{**}_{\mathrm{ck,cube}} + (1.48 \cdot \sigma) \tag{8}$$

By considering these criterion of conformity, to estimate admissible CoV* and CoV** values for dry storage and in-situ conditions respectively, in the first step the mean-value was calculated according to Eq. (5) and (7) with assuming a conservative standard deviation of 3 as start value, continuously with the fixed characteristic strengths $\boldsymbol{f^{*}_{ck,cube}}$, $\boldsymbol{f^{**}_{ck,cube}}$, an iterative loop was performed, while the mean compressive strength was systematically varied using scaling factors between q = 0.9 and q = 1.3. The flowchart presented in Fig. 2 illustrates the calculation procedure.

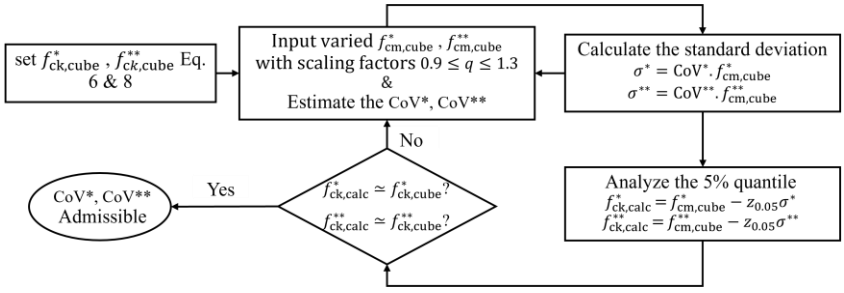


Fig. 2 Calculation procedure of admissible CoV values based on ÖNORM B 4710-1 [15]. ($z_{0.05}$ is the %5 quantile of the standard normal distribution [11], [14].

2.4 Overstrength

Table 2 shows the CoV* and CoV** derived from the requirements of the conformity assessment discussed in section 2.3 considering Eqs. (5) and (7) according to illustrated procedure in Fig. 2.

Table 2 Calculated CoV* and CoV** values for dry storage and in-situ conditions respectively from statistical analysis of mean values of concrete classes according to ONORMB4710-1 based on normal distribution.

q	0.90	0.95	1.00	1.05	1.10	1.15	1.20	1.25	1.30
C20/25, $f^{*}_{ck,cube}$ = 27.2 [N/mm²], $f^{**}_{ck,cube}$ = 22.8 N/mm²									
q. $f^{*}_{cm,cube}$	28.5	30.0	31.6	33.2	34.8	36.4	37.9	39.5	41.1
COV*	0.03	0.06	0.09	0.11	0.13	0.15	0.17	0.19	0.21
q. $f^{**}_{cm,cube}$	24.5	25.9	27.3	28.6	30	31.4	32.7	34.1	35.4
COV**	0.04	0.07	0.10	0.12	0.15	0.17	0.18	0.20	0.22

Fig. 3 illustrates CoV*-$f^{*}_{cm,cube}$and CoV**-$f^{**}_{cm,cube}$diagram of these calculations for dry storage and in-situ conditions for concrete strength classes C25/30 respectively.

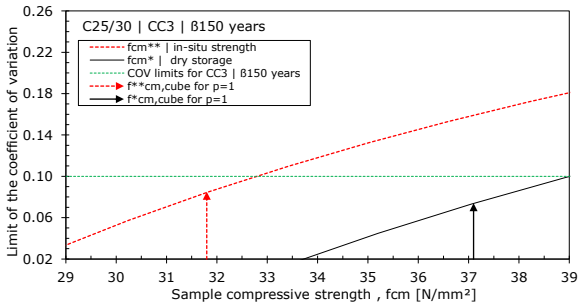


Fig. 3 CoV*-$f^{*}_{cm,cube}$and CoV**-$f^{**}_{cm,cube}$diagram of dry storage and in-situ conditions respectively for concrete strength classes C25/30 basis on normal distribution.

A key finding is the interaction between mean compressive strength and variability (CoV). When the mean strength is higher than required (Overstrength), a higher CoV is acceptable, because the lower tail of the distribution still meets safety limits. When the mean strength decreases, the allowable CoV must also decrease to maintain reliability. In the case of q = 1.0, i.e., without overstrength in the mean values of the samples, the determined CoV values are below the limit specified in the design standards of CoV ≤ 0.10 for a service-life of 150 years in consequence class CC3 discussed in section 2.1 and illustrated in Table 1. It follows that compliance with the conformity criteria [15] explored in section 2.2 allows an extension of the service-life to 150 years while maintaining unchanged partial safety factors in accordance with the design standards illustrated in Table 1.

In general, a sample from the conformity assessment does not exactly exhibit the theoretical mean value. In most cases, overstrength is present, that is, q ≥ 1.0, see Table 2. As overstrength increases, the scatter typically also increases, since the distance between the mean value and the theoretically smallest sample value becomes larger. As can be seen in Table 2 and Fig. 3, a higher CoV can be accepted when the sample mean value is higher. This coefficient can be reduced back to the case q = 1.0 and compared with the specified limit value of CoV = 0.10 discussed in section 2.1 and illustrated in Table.1. Even if the compressive strength is below a theoretical target, a very low CoV (indicating hight production quality) can ensure that the 5% fractile remains above the required threshold. However, final verification must always be performed through a comprehensive reliability assessment. The standards and design procedures originally developed for conventional concrete and calibrated for a target service life of 50 years [14] and 100 years [16] are generally applied to the design and assessment of eco-concrete structures. However, these standards are based on assumptions regarding the variability of decisive material parameters, such as concrete compressive strength, where the scatter values prescribed in current design codes may be significantly larger and therefore more conservative than those observed for conventional and eco-concretes. The results and provided diagrams for concrete classes C20/25 and C25/30 illustrated in Table 2 and Fig. 3 serve as practical tools for evaluating real data from conformity test results for both conventional and eco-concretes. The diagrams illustrate how different combinations of mean strength and CoV relate to reliability requirements. They can be used by engineers to assess whether measured test results meet the criteria for extended service life, including 150 years.

2.5 Statistical Estimation and Confidence Intervals

In practice, concrete properties are determined from limited samples, while the true population parameters remain unknown. This introduces sampling uncertainty, especially when the number of specimens is small. To address this, confidence intervals (CI) are used to estimate the range in which the true mean compressive strength is likely to lie. For small sample sizes, the t-distribution is applied instead of the normal distribution. For a two-sided 90% CI, the bounds are given as:

$$P(LC < \mu_X < UC) = 1 - \alpha \quad (9)$$

$$LC = \bar{x} - t_{\alpha/2,n-1}\frac{s_X}{\sqrt{n}} \tag{10}$$

$$UC = \bar{x} + t_{\alpha/2,n-1}\frac{s_X}{\sqrt{n}} \tag{11}$$

where $t_{\alpha/2,n-1}$ is the critical value of the t-distribution with f = n-1 degrees of freedom, LC and UC represent the lower and upper bounds of the population mean $f^*_{cm,cube}$ in [N/mm²] with α = 10% corresponds to a confidence level 90%. In structural engineering, the lower bound of the confidence interval is particularly important and provides a conservative estimate for safety verification.

3 METHODOLOGY TO ASSESS COEFFICIENT OF VARIATION

To evaluate the performance and reliability of both conventional and eco-concretes, the following methodology to assess CoV from Conformity Tests proposed as flowchart in Fig. 4 is developed as a multi-step procedure that integrates statistical analysis with probabilistic reliability assessment. Building upon previously established approaches, the method is adapted to address the particular characteristics of new eco-materials and to accommodate normal distributions.

The process begins with the collection of data from representative samples. Specimens were taken from different application areas, including tunnel sections for conventional concrete and road sections for eco-concrete of strength class C25/30. The sampling strategy was designed to consider both the number of specimens and prior knowledge from earlier tests, ensuring that the dataset provides a reliable basis for subsequent statistical evaluation. Next, a statistical characterization of the material is performed. For each sample set, the mean compressive strength, standard deviation, and coefficient of variation (CoV) are calculated to quantify material variability according to equations of the first and second statistical moments of the sample [17]. In order to define acceptable performance thresholds, boundary functions for the CoV should be established, particularly for overstrength conditions, reflecting the expected 150-year design service life. Both confidence intervals (CI) i.e. lower and upper bounds were calculated according to Eqs. (9) to (11) for the samples to capture the range in which a defined proportion of the population is expected to fall. Here, the normal assumptions are used to interpret the results from standard compressive strength tests as well as non-destructive evaluations. This step ensures that the uncertainty and variability of the measured indicators are properly incorporated, enabling an accurate probabilistic assessment of material performance. By applying normal distributions, the method allows a realistic representation of the statistical properties of both conventional and eco-concretes, supporting robust assessment of the quality indicators. Finally, a multi-stage reliability evaluation is conducted. As presented in Fig. 4, the first stage involves the analysis of dry-storage samples. The Samples stored under dry conditions are evaluated based on the criteria in Table 2 and Fig. 3. To assess whether the CoV of compressive strength from conformity test meets the requirements for a 150-year service life, the confidence interval of the mean compressive strength from conformity test must be determined. The width of this interval depends on the sample size n, and for long term service life verification, the lower bound of the confidence interval is the decisive parameter.

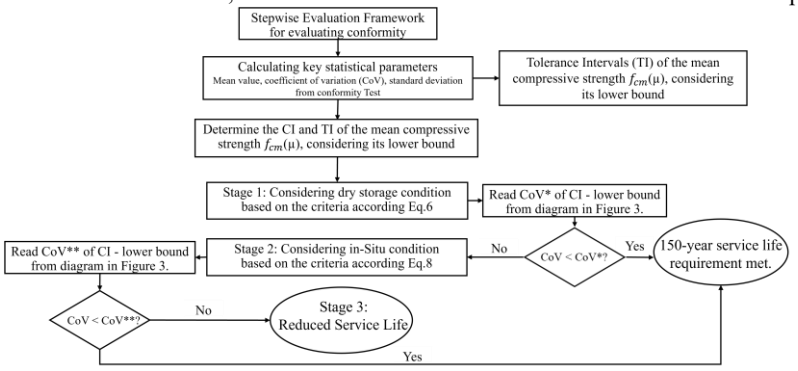


Fig. 4 Stepwise Evaluation Framework for evaluating conformity test.

The calculation procedure for this interval was described in section 2. The coefficient of variation of sample in dry condition for the lower bound (CoV*) should be taken from diagram in Fig. 3. If CoV from conformity test is smaller than CoV*, this means that the requirement for a service life 150 years

is met. If the acceptance criteria are not met, the procedure proceeds with in-situ sampling taken directly from the structure itself as second stage. These Samples are then evaluated with respect to compressive strength and coefficient of variation (CoV**) of in-situ condition illustrated in Fig. 3 developed from values presented in Table 2. And finally, if neither Stage 1 nor stage 2 demonstrates compliance with the criteria, an agreement can be reached with the client to adopt a reduced design service life. This adjustment should follow the principles outlined in chapter 2.

Alternatively, suitable compensatory measures to maintain the required level of structural reliability over the intended service period. At each stage, the statistical metrics and distributional assumptions are combined with conservative design parameters, including the 5% fractile of compressive strength, to evaluate whether existing codes and safety concepts adequately capture the variability of conventional and eco-materials.

4 CASE STUDIES

In this study, two datasets of compressive strength were analysed: eco-concretes and conventional concretes, both belonging to strength class C25/30. In this section, we extend this analysis by determining the lower and upper bounds of the population mean and the corresponding CoV using the confidence interval method for both eco-concretes and conventional concretes in concrete class C25/30.

The resulting estimates for the investigated case studies including coefficient of variation (CoV) of samples, standard deviations s_x, the lower and upper bound of the 90% CI calculated according to Eqs. (9) to (14) in section 2, CoV* and CoV** taken from the diagram in Fig. 3 for the lower bound of the mean values $\bar{x}$, are presented in Table 3. The results show that, in all tested locations, the 90% confidence interval for the population mean at all specified locations exceeds the characteristic compressive strength of 32.6 MPa required for concrete class C25/30 according to EN 1990:2013 [14] defined by the 5% fractile value of 37.1 MPa (Table 2).

Table 3 Statistical Values of samples of two case studies from conformity test

Location	Statistical Values from Conformity Test						Confidence Intervals (CI)			
	CoV	S_x	x^1_{min}	x^1_{max}	$\bar{x}^1$	n	LC[1]	UC[1]	COV*	COV**
Conventional concrete (tunnel samples)										
Tunnel Concrete O.1 ~ O.4	0.06	2.5	37.7	45.3	41.7	13	40.4	42.9	0.12	0.23
	0.11	5.1	36.0	51.7	45.8	14	43.3	48.2	0.16	0.27
	0.06	2.8	43.4	51.6	49.1	7	47.0	51.1	0.21	0.31
	0.09	3.9	40.5	52.4	46.4	12	44.3	48.4	0.17	0.28
ECO concrete (street samples)										
Block 44	0.01	0.7	48.3	49.6	49.0	3	47.8	50.1	0.22	0.32
Block 16	0.02	0.7	43.7	45.1	44.5	3	43.2	45.7	0.16	0.26
R3-6	0.01	0.5	34.0	34.9	34.5	3	33.7	35.2	0.02	0.12

1: Unit: [N/mm²]; x_{min} and x_{max}: minimum and maximum values of compressive strength obtained from the conformity testing of the samples; $\bar{x}$: mean values of compressive strength obtained from the conformity testing; n: sample size;

Furthermore, the measured CoV values from conformity test are consistently lower than the derived CoV limits discussed in section 2.1 and 2.4 illustrated in Tables 1 and 2, demonstrating that the actual variability is smaller than conservative design assumptions. In cases where the sample mean falls slightly below the theoretical 37.1 MPa reference, such as Eco concrete presented in Table 3 location R3-6, the substantially lower coefficient of variation (CoV) compensates for this difference. This means, the verification procedure should be based on two key statistical measures: (i) the mean value and (ii) the standard deviation. From a probabilistic perspective referred in section 2.2 as shown in Fig. 1, a lower mean combined with significantly reduced variability as shown in Fig. 5a and 6a can yield the same or even higher 5% fractile value, which is the decisive design parameter.

The results in Table 3 show, that as with conventional concrete, measured CoV values remain below conservative design assumptions, confirming that both conventional and eco-concrete, also operates in an overstrength regime while exhibiting stable and predictable behaviour. From a probabilistic standpoint, the 90% CI implies that if the sampling and analysis were repeated many times, the true population mean would fall within the calculated interval in 90% of cases. This interpretation enhances

the statistical reliability of the compressive strength estimates and supports their integration into semi-probabilistic design frameworks.

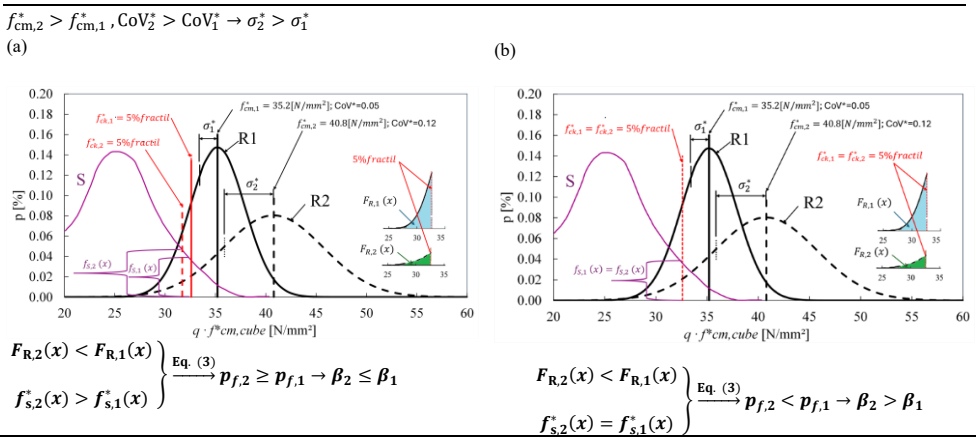


Fig. 5 Probability density function of hypothetical action "S" and of two different compressive Strength of Concrete as resistance of material "R" (a): with different fractile value. (b): with equal fractile value.

From a reliability-based design perspective according to Eq. (3), as shown in Fig. 5b theoretical a material with higher mean strength, such as conventional concrete, may occasionally perform above expectations, however the larger variability more than threshold values illustrated in Table 1 according to Eq. (2) also carries a higher risk of local weakness or premature failure, because the larger variability results in a wider distribution of strength values, consequently, some regions may perform better than expected due to exceptionally high local strength. At the same time, the increased variability raises the likelihood of weaker regions, which can act as local weak points and initiate cracking of failure. Therefore, both the mean strength and the consistency of the material properties are important for reliable structure performance. Conversely, as illustrated in Fig. 5a a material with slightly lower mean strength but smaller variability, such as eco-concrete, provides more predictable and stable performance, which translates into higher structural reliability over time.

5 CONCLUSIONS

The results of this study demonstrate that eco-concretes can achieve structural reliability levels comparable to those of conventional concretes when evaluated within a probabilistic and reliability-based framework. As discussed in previous section and illustrate in Fig. 5a, although the investigated eco-concretes exhibited slightly lower mean compressive strengths, they showed significantly reduced coefficients of variation, indicating more homogeneous and predictable material behaviour. This reduced variability proved to be a decisive factor in maintaining adequate 5% fractile values, which govern structural design according to Eurocode principles. The analysis confirmed that structural safety cannot be assessed solely on the basis of mean strength; rather, the interaction between mean value and scatter must be considered. A lower coefficient of variation (indicating hight production quality) can effectively compensate for moderate reductions in average strength, ensuring that the characteristic strength remains above the required limit. Consequently, eco-concretes should not be judged as inferior solely due to lower mean values, as their statistical stability offers clear advantages from a reliability perspective. From a design and code perspective, the findings suggest that current Eurocode safety concepts are generally applicable to eco-concretes, but conformity criteria may need refinement to explicitly reflect their favourable variability characteristics. Integrating confidence interval approaches into real data driven conformity assessment would provide a more transparent and objective basis for decision-making.

Overall, eco-concrete represents a technically viable and environmentally beneficial alternative for long-life infrastructure. When assessed using reliability-based methods, it is capable of fulfilling the performance requirements for a design service life of 150 years, thereby supporting the transition toward sustainable construction without compromising structural safety.

References

[1] Mohammed, Ahmad Khalil, Hassan, A.M.T., and Mohammed, Ahmed Salih. 2023. "Predicting the compressive strength of green concrete at various temperature ranges using different soft computing techniques." *Sustainability*, 15(15), 11907. https://doi.org/10.3390/su151511907.

[2] Miano, Andrea, Ebrahimian, Hossein, Jalayer, Fatemeh and Prota, Andrea. 2023. "Reliability estimation of the compressive concrete strength based on destructive and non-destructive tests." *Sustainability*, 15(19), 14644. https://doi.org/10.3390/su151914644.

[3] Kashem, Abul, Karim, Rezaul, Das, Pobithra, Dip Datta, Shuvo, and Alharthai, Mohammad. 2024. "Compressive strength prediction of sustainable concrete incorporating rice husk ash (RHA) using hybrid machine learning algorithms and parametric analyses." *Case Studies in Construction Materials* Volume 20, e03030, ISSN 2214-5095, https://doi.org/10.1016/j.cscm.2024.e03030.

[4] Kim, Wonchang, and Lee, Taegyu. 2023. "A Study to Improve the Reliability of High-Strength Concrete Strength Evaluation Using an Ultrasonic Velocity Method." *Materials* 16(20), 6800. https://doi.org/10.3390/ma16206800.

[5] Hartnack, Sonja, and Roos, Malgorzata. 2021. "Teaching: confidence, prediction and tolerance intervals in scientific practice: a tutorial on binary variables." *Springer Nature Emerg Themes Epidemiol* 18, 17. https://doi.org/10.1186/s12982-021-00108-1.

[6] Faghfouri, Saeideh, Strauss, Alfred, Seywald, Christian, Pichler, Walter, and Frangopol, Dan M. 2025." Conformity testing methods ensuring longevity of engineering structures." Paper presented at ninth international symposium on life-cycle civil engineering. IALCCE, Melbourne, Australia, July 15-19.

[7] Strauss, Alfred, and Faghfouri, Saeideh. 2025." Towards Sustainable Infrastructure: A Reliability-Based Approach to Service Life Assessment." Paper presented at the 3rd Conference of the European Association on Quality Control of Bridges and Structures - EUROSTRUCT, Dublin, Ireland, September 2-5. https://doi.org/10.1002/cepa.3395.

[8] Strauss, Alfred, Faghfouri, Saeideh, Bergmeister, Konrad, Pichler, Walter, and Seywald, Christian. 2025. "Nutzungsdauer von Tragwerken unter Berücksichtigung der CC-Versagensfolgeklassen. " *Tunnelbau. Beton- und Stahlbetonbau*. https://doi.org/10.1002/best.202500027

[9] Strauss, Alfred, and Faghfouri, Saeideh. 2025. "A reliability-oriented approach to ensuring longevity of critical infrastructure." Paper presented at 21. Internationalen Probabilistic Workshop (IPW 2025). Rostock, Deutschland, September 10-12. https://doi.org/10.1002/cepa.3361

[10] Strauss, Alfred, Bergmeister, Konrad, and Seywald, Christian. 2023. "Verlängerung der technischen Nutzungsdauer von Infrastrukturbauwerken auf Basis semiprobabilistischer Betrachtungen. " *Beton- und Stahlbetonbau.* 118(8): 575-588.

[11] Hartung, Joachim, Elpelt, Bärbel, and Klösener, Karl-Heinz. 2005. *Statistik*. Munich: Oldenbourg Wissenschaftsverlag.

[12] International Organization for Standardization (ISO), 2014. ISO 16269-6: Statistical Interpretation of Data — Part 6. ISO, Geneva.

[13] Ang, Alfredo H.S., and Tang, Wilson H.2007. *Probability Concepts in Engineering*. New York, NY: John Wiley & Sons.

[14] Austrian Standards International. ONORM 1990:2013: Basis of structural design. Austrian Standards International, Vienna.

[15] Austrian Standards Institute, 2001. ONORM B 4710: Concrete – Production and Conformity. Austrian Standards, Vienna.

[16] ONORM B 4008-2:2029. Assessment of load capacity of existing structures- Part 2: Bridge construction.

[17] Schneider J. Introduction to safety and reliability of structures. vol. 5. IABSE; 2006.

Probabilistic shear strength modelling based on nonlinear fracture mechanics

Jakub Večeře[1], Drahomír Novák[1], David Lehký[1], Damian Szczech[2]

[1]Institue of Structural Mechanics
Brno University of Technology
Veveří 331/95 602 00 Brno, Czech Republic

[2]Department of Concrete Structures
Lodz University of Technology
Al. Politechniki 6, 90-924 Lodz, Poland

Summary
The paper presents computational modelling of the shear strength of T-shaped beams with steel and/or GFRP longitudinal reinforcement. A finite-element model with a nonlinear fracture-plastic material law is developed and validated against experiments using load–deflection curves, beam deflections, and crack patterns. After calibration, a stochastic extension incorporates material variability, modelling key fracture-mechanical parameters as correlated random variables. Monte Carlo simulations estimate statistical characteristics of shear strength, and sensitivity analysis identifies the most influential random variables. Finally, statistical properties of shear strength are derived and compared with those implied by selected model codes.

1 INTRODUCTION

Shear failure of reinforced concrete beams without shear reinforcement (stirrups) is one of the most critical and least predictable failures. In contrast to bending failure, shear failure is characterized by sudden course with minimal warning signs, which places increased demands on the accuracy of design calculation models and their reliability. Therefore, the issue of shear strength has been the subject of intensive experimental and theoretical research [1]–[5]. One of those experiments was performed at Lodz University of Technology by a team led by Prof. Renata Kotynia [3]. Main topic of the research was to investigate the differences between steel and composite GFRP reinforcement of 33 concrete beams in terms of ultimate shear strength and crack pattern, as well as identifying the most influential parameters which can influence ultimate shear strength. Examined parameters were concrete compressive strength (C25/30 for Series I and C30/37 for Series II), longitudinal reinforcement ratio, concrete cover (15 and 30 mm) etc. However, these research programmes are very demanding in the terms of time and cost and are further limited by the relatively small number of individual tests that can usually be performed. Therefore, nonlinear stochastic computational modelling becomes an effective tool, which nowadays can accurately describe crack patterns and can also be used to obtain the influence of individual parameters on the ultimate shear strength.

This study is focused on nonlinear stochastic computational modelling of selected twelve concrete beams using the software package SARA [6], which combines software ATENA [7] and probabilistic software FReET [8], [9]. This package enables a realistic simulation of shear failure of concrete beams while considering the variability of material and geometrical parameters. Stochastic representations of the material and geometrical parameters were developed, followed by uncertainty propagation analysis. To compare data from nonlinear finite element analysis (NLFEA) and experimental measurements, a concept of model uncertainty was used. Furthermore, results based on selected shear strength design formulas were compared with NLFEA model. Sensitivity analysis in the form of coefficient of variations was performed and discussed.

2 NONLINEAR STOCHASTIC COMPUTATIONAL MODELLING

ATENA offers an effective tool for realistic modelling of structural response including post-peak behaviour and shear failure mechanism [7]. Reinforcement modelling considers the bond behaviour between reinforcement and concrete, which is important for realistic simulation of reinforced concrete structures. The Rankine failure criterion combined with the smeared crack approach and fracture energy

enables modelling of tensile cracking within the NLFEA framework by using rotational and fixed crack models. Concrete compression, which is based on the Menétrey-Willam model, simulates concrete crushing and crack closure under compression [10].

FReET (Feasible Reliability Engineering Tool) [8], [9] is probabilistic software for statistical, sensitivity and reliability engineering analysis. Simulation of uncertainties is performed at the level of random variables (RV) for example material properties or geometrical parameters. FReET can be linked with MS Excel which makes it easier to define responses/limit states equations [11].

The deterministic NLFEA 2D model was calibrated using reference beams S-512-30-15 and G-512-30-15, for which detailed experimental measurements were available. Calibration focused mainly on parameters influencing crack development and shear failure mechanisms. In particular, the crack model was adjusted from a fixed crack approach (rotation factor 1.0) to a partially rotating crack model (rotation factor 0.7), which improved the representation of crack propagation and stress redistribution. Furthermore, the reduction factor of concrete compressive strength was modified from 0.8 to 0.5 to better capture crushing behaviour in the compression zone. For beams reinforced with GFRP bars, reduced bond properties between reinforcement and concrete were adopted. The bond parameters were approximately reduced to 50% of those typically used for steel reinforcement, reflecting the lower bond efficiency and different surface characteristics of GFRP reinforcement. Other material parameters were adopted according to ATENA recommendations and available experimental measurements. Calibration was performed by comparing numerical and experimental load–deflection curves, ultimate shear strength and observed crack patterns.

A 2D model was divided to four different macroelements – web, flange, load pad and supports. The middle of the beam (marked in red in Fig. 1) used quadratical mesh size 0.02 m. Other parts of the beam were divided to quadratical mesh size 0.1 m. Number of nodes is 5 772 and number of DOF (Degrees of Freedom) is 11 544.

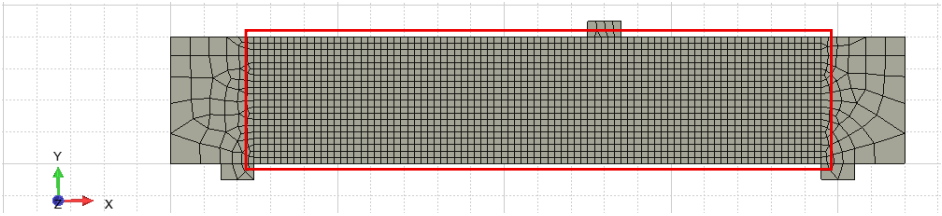


Fig. 1 2D model of the beam and mesh size.

2.1 Stochastic model

To capture influence of material and geometrical uncertainties, input parameters for NLFEA model are considered as random variables, described with their mean values, coefficients of variations (COVs) and probability density functions (PDF). Overview of the parameters which are used in ATENA are provided in Table 1. Mean values are not listed in the Table 1, because they differ for each simulated experiment (e. g. different reinforcement, concrete strength, concrete cover). Statistical correlation has been considered between concrete parameters (according to Table 2) [14].

Table 1 Random variables.

Variable	PDF	COV	References
Concrete compressive strength, f_c	Log-normal	0.15	[12], [13]
Concrete tensile strength, f_t	Log-normal	0.25	[14]
Young's modulus of concrete, E_c	Log-normal	0.12	[15]
Fracture energy, G_f	Weibull	0.2	[14]
Young's modulus of steel, E_s	Normal	0.02	[16], [17]
Young's modulus of GFRP, E_{GFRP}	Normal	0.1	[18]

Table 2 Statistical correlation for concrete parameters.

Variable	f_c	f_t	E_c	G_f
f_c	1	0.6	0.3	0
f_t	0.6	1	0	0.8
E_c	0.3	0	1	0
G_f	0	0.8	0	1

2.2 Results of stochastic NLFEA modelling

Twelve beam models were developed – 6 with GFRP reinforcement and 6 with steel reinforcement, which differs in longitudinal reinforcement (diameter, number of bars), concrete compressive strength and concrete cover. For each beam, ten stochastic simulations were performed using Latin Hypercube Sampling. Although this number is relatively limited for probabilistic studies, each nonlinear simulation was computationally demanding due to the detailed fracture-plastic constitutive model and nonlinear solution procedure. Therefore, ten simulations were considered a reasonable compromise between computational cost, statistical robustness and accuracy.

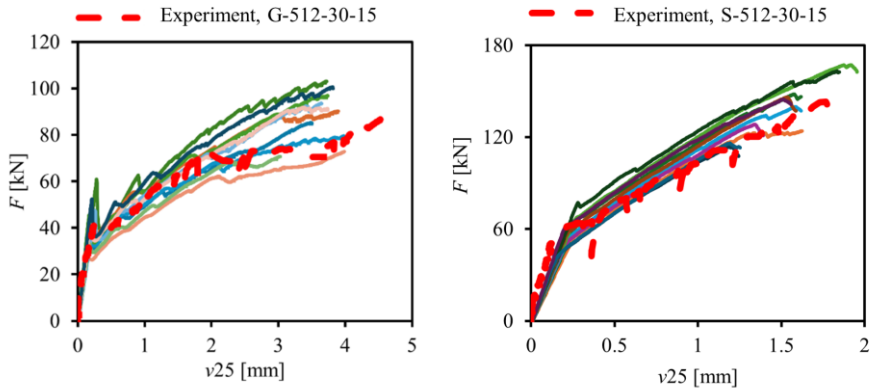


Fig. 2 *L-D* curves for each task of the NLFEA model, G-512-30-15 (left), S-512-30-15 (right).

Stochastic results in the form of load vs. deflection (*L-D*) curves in monitoring point *v*25 are shown on Fig. 2, for the beam S-512-30-15 (right) and for the beam G-512-30-15 (left). Majority of the *L-D* curves are in plastic part (beyond the yield strength) stiffer than experimental curve. This phenomenon usually occurs in 2D computational models of reinforced beams.

3 UNCERTAINTIES PROPAGATION

3.1 Methodology

Stochastic modelling with fully probabilistic approach considers the influence of the material and geometrical uncertainties as random variables. Model uncertainty θ reflects the ability of the prediction model to reproduce experimental data. In deterministic way, model uncertainty θ is defined as ratio of experimental results V_{exp} and prediction result V_m. This ratio implies the prediction model quality, when model uncertainty $\theta < 1.0$ model predicts higher shear strength, thus is unconservative. Otherwise, when model uncertainty $\theta > 1.0$, prediction model underestimates experimental results, thus is conservative.

For stochastic modelling, where random variables enter calculations including statistical correlation, model uncertainty should be random variable as well, see Equation (1). Experimental study is designed to cover different parameters and their influence on shear strength (different concrete cover etc.), thus cannot be considered from statistical point of view as samples from the fundamental set. That is the reason, why the assessment is performed deterministically for $i = 1, 2, \ldots, n$ (n is number of experiments) and then the mean value and COV_θ is calculated from all experiments.

$$\theta_i = \frac{V_{\text{exp}}}{V_{\text{m},i}} \tag{1}$$

The resulting value of $\text{COV}_{V\text{m}}$, was determined as the average of the individual $\text{COV}_{V\text{m},i}$ values obtained from stochastic simulations. Deterministic calculations of model uncertainty are made for n experimental results. From these calculations mean values of all θ_i, where $i = 1, 2, \ldots, n$ and COV_θ can be determined.

The shear strength which considers uncertainties is obtained as:

$$V_\text{s} = \theta \cdot V_\text{m} \tag{2}$$

V_s is random variable and is described by mean value and coefficient of variation $\text{COV}_{V\text{s}}$, which can be approximately described according to Equation (3) fulfilling these conditions. The PDF of each calculation must be normal or log-normal, each calculation must be independent of others and COVs should be lower than 0.3 or 0.4, (higher values causes significant error). Such calculations have been applied already for shear strength model assessment in e.g. [2], [20]–[23].

$$\text{COV}_{V\text{s}} \sim \sqrt{\text{COV}_{V\text{m}}{}^2 + \text{COV}_\theta{}^2} \tag{3}$$

3.2 Results of model uncertainty

Results for beams reinforced with steel are summarized in Table 3. In Table 4, mean value of model uncertainty and COV_θ are listed in first two rows. $\text{COV}_{V\text{m}}$ is determined and $\text{COV}_{V\text{s}}$ is calculated according to Equation (3). Model uncertainty θ for beam S-512-30-15 is 1.017 which is near 1.0, reflecting the fact, that NLFEA model was tuned on this beam. Other data (model uncertainty) differ slightly; the biggest difference is noticeable in beams with higher concrete compressive strength (Series II).

Fig. 3 shows that ATENA tends to overestimate shear strength, thus is unconservative, all PDFs are on the left side. Two different types of lines imply two different types of concrete – Series I (C25/30) is depicted by solid lines and Series II (C30/37) by dashed lines. A smaller variability of model uncertainty is seen for beams with higher concrete compressive strength (for Series I the variability is 0.800 to 1.017 and for Series II 0.730 to 0.779).

Table 3 Model uncertainty for beams with steel reinforcement.

	N.	Beam	Mean value θ_i [-]	$\text{COV}_{V\text{m},i}$ [-]
Series I	1	S-512-30-15	1.017	0.128
	2	S-316-30-15	0.927	0.097
	3	S-418-30-35	0.800	0.110
Series II	4	S-512-35-15	0.779	0.126
	5	S-316-35-15	0.730	0.126
	6	S-318-35-35	0.746	0.123

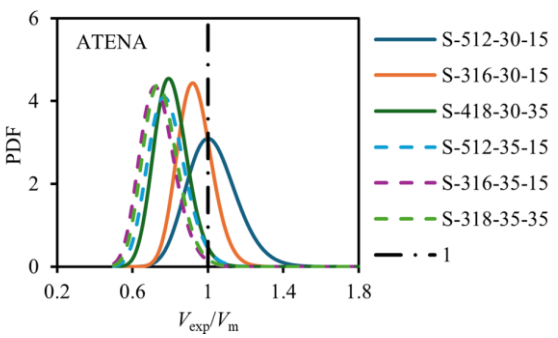


Fig. 3 PDF of $V_{\text{exp}}/V_\text{m}$ (modelled as log-normal) for beams with steel reinforcement.

Table 4 Statistical model uncertainty and COVs for beams with steel reinforcement.

Variable	Value [-]
Mean value of model uncertainty θ	0.833
COV_θ from each deterministic value of θ	0.137
COV_{Vm}	0.118
COV_{Vs} with model, material and geometrical uncertainties	0.181

Similar trends can be observed for beams reinforced with GFRP (Tables 5 and 6, Fig. 4). The calibrated beam G-512-30-15 again shows model uncertainty close to 1.0, while Series II beams exhibit a more pronounced overestimation of shear resistance and lower variability compared to Series I beams (Series I 0.888 to 1.042 and Series II 0.744 to 0.831).

Table 5 Model uncertainty for beams with GFRP reinforcement.

	N.	Beam	Mean value θ_i [-]	$COV_{Vm,i}$ [-]
Series I	1	G-512-30-15	0.994	0.128
	2	G-316-30-15	0.888	0.106
	3	G-418-30-35	1.042	0.096
Series II	4	G-512-35-15	0.744	0.110
	5	G-316-35-15	0.801	0.096
	6	G-418-35-35	0.831	0.109

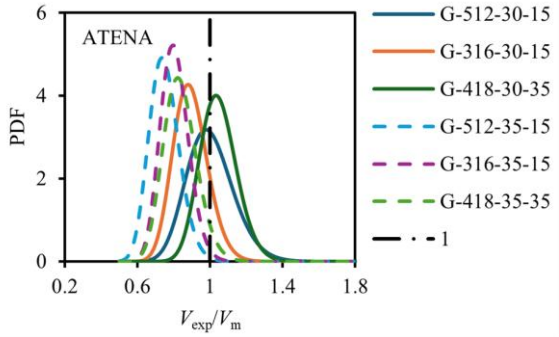


Fig. 4 PDF of V_{exp}/V_m (modelled as log-normal) for beams with GFRP reinforcement.

Table 6 Statistical model uncertainty and COVs for beams with GFRP reinforcement.

Variable	Value [-]
Mean value of model uncertainty θ	0.883
COV_θ from each deterministic value of θ	0.130
COV_{Vm}	0.107
COV_{Vs} with model, material and geometrical uncertainties	0.168

4 SENSITIVITY ANALYSIS

Sensitivity analysis based on Monte Carlo type LHS simulations is performed in the form of COVs, which reflects direct influence of variability of each input parameter. All input variables are fixed at their deterministic (mean) values, while stochastic variability is considered only for a single variable

$X_{,i}$. The result of this procedure is a partial coefficient of variation $COV_{X,i}$ which can be used to calculate the resulting COV_X of the shear strength, according to Equation (4) [19]. For graphical representation it is useful to consider $COV^2_X = 100$ % and then to calculate percentage of each of the COV^2_{Xi} on the response variability.

$$COV_X \sim \sqrt{\sum_i^n (COV_{X,i})^2} \tag{4}$$

Fig. 5 and Fig. 6 show the results for beams reinforced with steel and GFRP. Without considering model uncertainty, fracture energy and tensile strength of concrete represent the most influential parameters governing shear resistance. In contrast, the stiffness of longitudinal reinforcement (steel or GFRP) has negligible influence, as failure is governed primarily by concrete fracture mechanisms. Young's modulus of concrete and concrete compressive strength is shown as sum, because of smaller influence. After including model uncertainty, it becomes the dominant contributor to the total variability of shear strength for both reinforcement types.

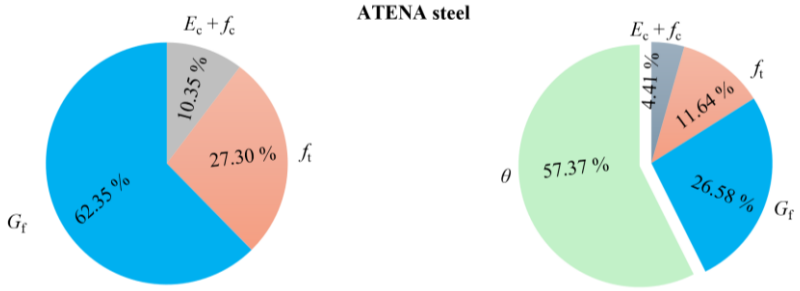


Fig. 5 Sensitivity analysis in the form of COV^2s for beams reinforced with steel.

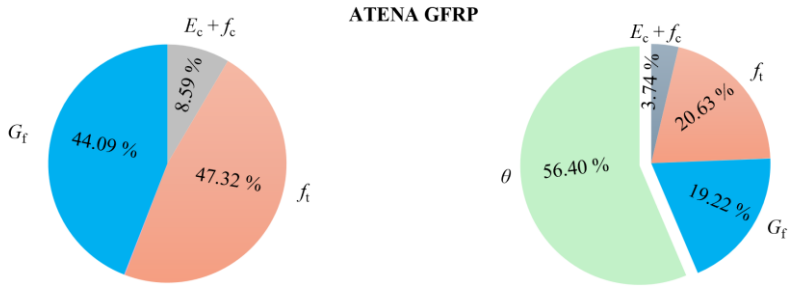


Fig. 6 Sensitivity analysis in the form of COV^2s for beams reinforced with GFRP.

5 CONCLUSION

The aim of this study was to evaluate the shear strength of reinforced (steel or GFRP) concrete T-beams without stirrups using NLFEA enhanced by stochastic modelling and comparison of experimental results with numerical predictions for these beams. NLFEA models captured the global structural response, crack development and governing shear failure mechanisms with satisfactory agreement to experiments. Stochastic description of material and geometrical properties proved essential for quantifying the variability of shear strength. The study shows that model uncertainty represents a major influential parameter of total variability and should be considered in reliability assessments.

The numerical model slightly overestimated shear strength, particularly for beams with higher concrete strength (Series II). This may indicate that the adopted constitutive relationships and fracture parameters calibrated primarily on lower-strength concrete (Series I) do not fully capture the reduction of aggregate interlock and size-dependent fracture mechanisms occurring in stronger concretes. Furthermore, the 2D modelling approach may contribute to increased structural stiffness and shear resistance compared to the experimental response.

From previous studies [22], [23] model uncertainty and COV_{Vs} can be derived for comparison between code models with NLFEA results, see Table 7. In the terms of model uncertainty, ATENA is

closer to Eurocode model. However, regarding COV_{Vs}, fib Model Code demonstrates better agreement, as fib Model Code considers higher number of parameters – random variables, and therefore resulting in higher variability.

From a practical reliability perspective, the lower model uncertainty of ATENA and Eurocode models indicates a closer agreement with experimental mean shear resistance, whereas the higher variability predicted by the fib Model Code reflects a more conservative treatment of uncertainty. Consequently, fib Model Code may provide safer reliability estimates for probabilistic design applications, especially when material variability plays a dominant role.

Table 7 Comparison of the model uncertainty and COV_{Vs}.

	Beams with steel reinforcement		Beams with GFRP reinforcement	
Variable	θ	COV_{Vs}	Θ	COV_{Vs}
ATENA	0.833	0.181	0.883	0.168
EN 1992-1-1	0.836	0.126	0.890	0.103
fib Model Code	0.750	0.178	0.805	0.163

Sensitivity analysis identified fracture energy and concrete tensile strength as the most influential parameters, while the stiffness of longitudinal reinforcement had negligible effect on shear strength. This confirms that shear failure in beams without transverse reinforcement is dominated primarily by concrete fracture properties. The proposed deterministic-stochastic modelling framework provides an efficient alternative to extensive experimental tests and offers a rational basis for probabilistic design. The obtained statistical characteristics of shear strength can contribute to improving safety formats and reliability-based calibration of design models, especially for GFRP beams, as this area has not yet been sufficiently researched.

Acknowledgements

This research work was funded by the National Science Centre, Poland under the OPUS call in the Weave programme project no. 2023/51/I/ST11/00069 and by the Czech Science Foundation project no. 25-14337L for the bilateral project, titled “Multi-fidelity modelling of shear concrete strength based on experiments, simulation and probabilistic approaches (MMOSS)”. Authors would also like to acknowledge the support from the European Union within the framework of the Interreg Austria-Czechia 2021-2027 program, project No. ATCZ00068 IREC.

The authors gratefully acknowledge Prof. Kotynia and Dr. Kaszubska for providing the experimental data.

References

[1] Kani, Gaspar N. J. 1964. “The Riddle of Shear Failure and Its Solution.” *ACI Journal Proceedings* 61(4):441–468. doi:10.14359/7791.

[2] Kaszubska, Monika, and Kotynia, Renata. 2022. “Selected Shear Models Based on the Analysis of the Critical Shear Crack for Slender Concrete Beams without Shear Reinforcement.” *Materials* 15(22):8259. doi:10.3390/ma15228259.

[3] Kotynia, Renata, and Kaszubska, Monika. 2020. *Research of the Flexural Reinforcement Effect on the Shear Strength of Concrete Beams without Transverse Reinforcement.* Lodz: Department of Concrete Structures, Lodz University of Technology. ISBN 978-83-7283-901-5.

[4] Zhang, Tao, Visintin, Phillip, and Oehlers, Deric J. 2016. “Shear Strength of RC Beams without Web Reinforcement.” *Australian Journal of Structural Engineering* 17(1):1–10. doi:10.1080/13287982.2015.1122502.

[5] Yang, Yuguang. 2014. *Shear Behaviour of Reinforced Concrete Members without Shear Reinforcement.* PhD diss., Delft University of Technology, Delft, The Netherlands. doi:10.4233/uuid:ac776cf0-4412-4079-968f-9eacb67e8846.

[6] Červenka Consulting s.r.o. 2026. *SARA (Structural Analysis and Reliability Assessment) – User’s Manual.* Accessed February 2, 2026. Available at: https://www.cervenka.cz/products/sara/.

[7] Pukl, Radomír. 2009. "Software ATENA für Entwurf und Untersuchung von Beton- und Stahlbetonbauten." *Beton und Stahlbeton* 104(4).

[8] Novák, Drahomír, Vořechovský, Miroslav, and Rusina, Radoslav. 2026. *FReET.* Accessed February 2, 2026. Available at: http://www.freet.cz.

[9] Novák, Drahomír, Rusina, Radoslav, and Vořechovský, Miroslav. 2026. *FReET – Feasible Reliability Engineering Tool: User's Manual.* Prague: Červenka Consulting Ltd. Accessed February 2, 2026. Available at: http://www.freet.cz/download/FReET_user.pdf.

[10] Červenka, Jan, and Papanikolaou, Vassilis K. 2008. "Three Dimensional Combined Fracture-Plastic Material Model for Concrete." *International Journal of Plasticity* 24(12):2192–2220. doi:10.1016/j.ijplas.2008.01.004.

[11] Novák, Drahomír, Vořechovský, Miroslav, and Rusina, Radoslav. 2025. "Making Reliability Analysis Easy Using MS Excel and FReET Software." *Procedia Structural Integrity* 73:119–124. doi:10.1016/j.prostr.2025.10.019.

[12] Shimizu, Yasushi, Hirosawa, Masaya, and Zhou, Jiandong. 2000. "Statistical Analysis of Concrete Strength in Existing Reinforced Concrete Buildings in Japan." In *Proceedings of the 12th World Conference on Earthquake Engineering (12WCEE)*, Auckland, New Zealand, January 30–February 4, 2000, Paper No. 1499.

[13] Nowak, Andrzej S., Rakoczy, Anna Maria, and Szeliga, Elżbieta K. 2011. "Revised Statistical Resistance Models for R/C Structural Components." *ACI Special Publication* 284:61–76.

[14] Doležel, Jiří, Šomodíková, Martina, Lehký, David, and Novák, Drahomír. 2015. "Probabilistic Analysis of Load Bearing Capacity of Reinforced Concrete Beam Bridge in Relation to Its Residual Lifetime." *Beton – Technology, Structures, Rehabilitation* 15(5):42–48. ISSN 1213-3116. (In Czech).

[15] Anghileri, Mattia, Rosati, Gianpaolo, Biondini, Fabio, Savino, Pierclaudio, and Tondolo, Francesco. 2023. "Experimental Tests for Mechanical Characterization of Prestressed Concrete Bridge Deck Beams." In *Life-Cycle of Structures and Infrastructure Systems*. Boca Raton, FL: CRC Press. doi:10.1201/9781003323020-253.

[16] Arrayago, Itsaso, Rasmussen, Kim J. R., and Real, Esther. 2020. "Statistical Analysis of the Material, Geometrical and Imperfection Characteristics of Structural Stainless Steels and Members." *Journal of Constructional Steel Research* 175:106378. doi:10.1016/j.jcsr.2020.106378.

[17] Allen, David E. 1972. *Statistical Study of the Mechanical Properties of Reinforcing Bars.* Building Research Note No. BRN-85. Ottawa, ON: National Research Council Canada. doi:10.4224/40000624.

[18] Boateng, George Oti, Kankam, Charles K., Mansal, Edward C., Afrifa, Russell Owusu, Kwarteng, Felix, Ohene-Coffie, Francis, and Kpo, Selase A. K. 2024. "Evaluating the Mechanical Properties of Fiberglass-Reinforced Polymer Bar." *Journal of Engineering Research and Reports* 26(7):150–160. doi:10.9734/JERR/2024/v26i71200.

[19] Yu, Qianhui, Fernández Ruiz, Miguel, and Muttoni, Aurelio. 2022. "Considerations on the Partial Safety Factor Format for Reinforced Concrete Structures Accounting for Multiple Failure Modes." *Engineering Structures* 264:114442. doi:10.1016/j.engstruct.2022.114442.

[20] Baghi, Hadi, Barros, Joaquim A. O., Kaszubska, Monika, and Kotynia, Renata. 2018. "Shear Behavior of Concrete Beams Reinforced Exclusively with Longitudinal Glass Fiber Reinforced Polymer Bars: Analytical Model." *Structural Concrete* 19:162–173. doi:10.1002/suco.201700175.

[21] Sýkora, Michal, Krejsa, Jan, Mlčoch, Jan, Prieto, Miguel, and Tanner, Peter. 2018. "Uncertainty in Shear Resistance Models of Reinforced Concrete Beams According to fib MC2010." *Structural Concrete* 19:284–295. doi:10.1002/suco.201700169.

[22] Novák, Drahomír, Večeře, Jakub, Šomodíková, Martina, and Kotynia, Renata. 2025. "Shear Strength Code Models Uncertainties Assessment Based on Probabilistic Simulation." In *Proceedings of the International Probability Workshop 2025 (IPW 2025).* Rostock, Germany.

[23] Večeře, Jakub, Novák, Drahomír, Šomodíková, Martina, and Kotynia, Renata. 2025. "Reliability Assessment of Design Formulas for Shear Capacity of Glass Fibre Reinforced Polymer Concrete Elements." In *30th Betonářské dny 2025 – Proceedings,* 411–423. ISBN 978-80-908943-2-7. (In Czech).

Quantification of Spatial Variability of Concrete Parameters for the Reliability Assessment of Reused Concrete Elements

Oleksandr Al-Shboul[(1)], Razhan Ahmed[(2)], Stefanie Schoen[(2)], Luigi Schiano[(3)], David Ringeloth[(4)], Marc Fina[(3)], Jelena Bijeljic[(4,5)], Gerrit E. Neu[(2)], Ernst Niederleithinger[(4)], Steffen Freitag[(3)], Iurie Curoșu[(1)]

(1) Chair of Construction Materials,
Ruhr University Bochum,
Universitätsstraße 150, 44801 Bochum, Germany

(2) Institute for Structural Mechanics,
Ruhr University Bochum,
Universitätsstraße 150, 44801 Bochum, Germany

(3) Institute for Structural Analysis,
Karlsruhe Institute of Technology,
Kaiserstraße 12, 76131 Karlsruhe, Germany

(4) Division 8.2 "NDT Methods for Civil Engineering",
Bundesanstalt für Materialforschung und -prüfung,
Unter den Eichen 87, 12205 Berlin, Germany

(5) Faculty of Civil Engineering and Architecture,
University of Niš,
Aleksandra Medvedeva 14, 18000 Niš, Serbia

Summary
The reuse of reinforced concrete (RC) elements represents an important prerequisite for a sustainable and environmentally friendly construction sector. Reliable assessment and characterisation of the element properties and overall condition is essential. The uncertain material and structural properties, previous service conditions, and experimental data impose significant challenges for structural reliability assessment and design for reuse. This study presents results from a measurement campaign on an old RC beam, extracted from a demolished building with the purpose of reuse. The element investigations combine destructive tests (compressive strength, tensile strength) and non-destructive tests (rebound hammer, radar, ultrasound) to derive the mechanical properties and reinforcement detailing. Different sets of measurements are integrated into a nonlinear computational model to investigate the influence of uncertain parameters on the load-bearing behaviour of the RC element.

1 INTRODUCTION

Reinforced concrete structures are still typically demolished after reaching the end of their service life, which results in downcycling or disposal of the concrete [1]. However, the old structural elements possess enough load-bearing capacity and durability reserves for being reused in new constructions. Their reuse requires a controlled demolishing process and suitable assessment strategies for a quick but reliable characterisation while explicitly considering uncertainties affecting load-bearing and durability predictions [2].

A central question in reuse assessment is how the spatial variability and dispersion of measured material and structural parameters should be quantified and how this uncertainty propagates into load-bearing capacity and reliability predictions. The destructive specimen extraction for subsequent laboratory based tests is uneconomical and they imply statistical gaps [3]. Spatially denser information is typically obtained from non-destructive testing (NDT); however, strength estimation from NDT depends on calibration and is affected by measurement scatter and test conditions [4]. For this reason,

reuse-oriented assessment concepts must rely on combined strategies that integrate multiple NDT methods, enabling a comprehensive yet efficient documentation procedure to support reliable and scalable reuse while minimising destructive interventions [5].

Against this background, this study evaluates the influence of different measurement strategies on the predicted bending resistance of a reused reinforced concrete beam using nonlinear finite element simulations. The investigations are based on a beam extracted in a controlled manner from a campus building of Ruhr University Bochum (Germany) within the DFG-funded Collaborative Research Centre CRC 1683. The workflow comprises (i) identification of geometry and reinforcement detailing using radar and ultrasonic measurements and (ii) determination of mechanical properties from core compression, pull-off tensile and rebound hammer tests. The rebound dataset is evaluated to quantify measurement noise and location-dependent variation. Based on these data, input scenarios are defined and compared in the numerical simulations.

2 EXPERIMENTAL CAMPAIGN

2.1 Tested Structural Element

The focus of this investigation is a prefabricated RC beam manufactured in the early 1970s during the erection of the RUB campus in Bochum. The beam was extracted during the demolishing process of an office building and stored for the purpose of the research carried out in CRC 1683 [1], see Fig. 1. The beam has a trapezoidal cross-section with a height of 69 cm and edge thicknesses of 18 cm and 24 cm, respectively. The length of the beam is 6.93 m.



Fig. 1 Investigated beam element.

2.2 Methods

Different methods were applied to determine the reinforcement layout (radar), element geometry and major defects (ultrasound), and the mechanical properties of the concrete (rebound hammer, core compressive strength, and pull-off tests). For this purpose the beam was divided into multiple testing regions, in which various non-destructive and subsequently destructive investigations were performed. The resulting measurements provide datasets that are first subjected to statistical evaluation, after which the processed concrete parameters are used as input for the numerical modelling.

Radar (GPR): The radar method [6] employs high-frequency electromagnetic pulses transmitted into the material by using a transmitter antenna, while a receiver antenna records the reflected signals. GPR is highly sensitive to reinforcement, moisture, and larger voids. The measurements were performed by scanning the surface along parallel lines in two perpendicular directions to detect the reinforcement in both orientations. The datasets were subsequently merged during data processing. The rebar depth and position were obtained using images produced with the InterSAFT software [8] from the collected data. In this study, a SIR-20 system (GSSI) equipped with a 2 GHz antenna was used for the investigations. The survey area covered 500 cm × 69 cm with a grid line spacing of 5 cm in both scanning directions.

Ultrasonic pulse-echo (UPE): The ultrasound measurements were conducted using the UPE method [7], in which the transmitter and receiver were on the same side of the object. Ultrasonic waves are sent into concrete using dry point contact transducers. The waves are reflected at interfaces with a significant change of acoustic impedance (product of velocity and density), such as the back surface, cavities, major structural defects, and thicker reinforcement bars. Using an estimated or measured wave velocity, the location and approximate geometry of these reflectors can be reconstructed. For measuring, the A1040 Mira 3D Pro system was deployed on a survey area of 500 × 69 cm, comprising two measurement sets: one with polarization parallel to the beam length (20 × 10 cm grid) and another orthogonal to it (20 × 5 cm grid). The datasets were merged and processed using InterSAFT software [8].

Rebound hammer yields an indirect measure of concrete compressive strength by assessing near-surface hardness through a rebound index [9]. Strength estimation requires a correlation between rebound index and compressive strength, typically established via calibration against core test results or validated conversion relationships [9]. In this study, two devices were used: Type R (rebound distance) and Type Q (plunger velocity). Measurements were performed on the top face of the beam at multiple marked 20 cm × 20 cm regions (Fig. 2b).

Pull-off test determines the near-surface tensile strength by applying a uniaxial tensile load to a bonded steel dolly until failure [10]. Circular steel dollies (Ø 50 mm ± 0.5 mm) were bonded using a fast-curing adhesive, and a shallow circumferential groove (≈ 5 mm) was introduced to define the test area [10]. Loading was applied normal to the surface at 0.05 ± 0.01 MPa/s until fracture, while the peak force was recorded. Six positions were tested to capture spatial variability.

Compression tests: Core extraction and testing were performed as reference and calibration basis for the in-situ NDT [11]. Five cores were extracted and tested under uniaxial compression (Fig. 2c) following the standard procedure for compressive strength of hardened-concrete specimens [12]. The cores had nominal dimensions of 50 mm × 50 mm, i.e. a slenderness ratio of 1.0.

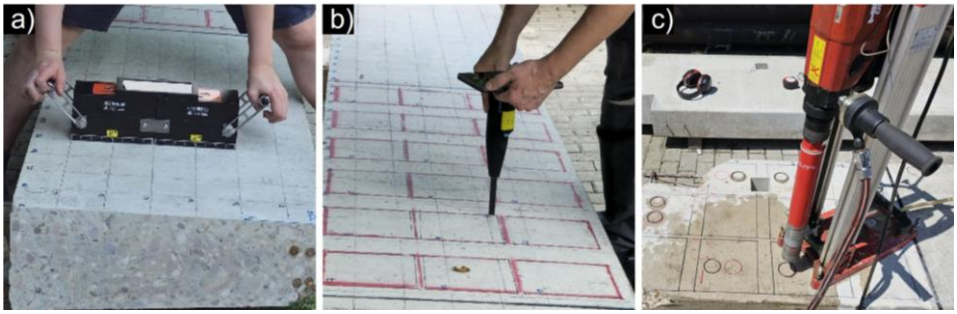


Fig. 2 Test methods: a) ultrasonic test, b) rebound hammer test, c) core extraction.

3 RESULTS AND DISCUSSION

3.1 Geometry and reinforcement layout

Radar and UPE provide insights into the geometry and material quality of structural elements. Fig. 3a illustrates a GPR C-scan (depth slice of 1-5 cm, SAFT reconstruction) identifying the upper reinforcement layer with rebar spaced 17 cm vertically at the edges and 25 cm in the centre, and 15 cm horizontally. High amplitude reflections indicate a double longitudinal rebar at a depth of 5 cm (confirmed by Fig. 3c). Fig. 3b presents a SAFT-reconstructed UPE image at x = 4.13 m, showing an inclined backwall reflection (depth 18 to 24 cm) along with visible longitudinal rebars at 5-6 cm depth. The shear-wave velocity was quantified at 2850 m/s, indicating good to very good concrete quality, with no anomalous reflections, indicating on a crack and void free concrete element.

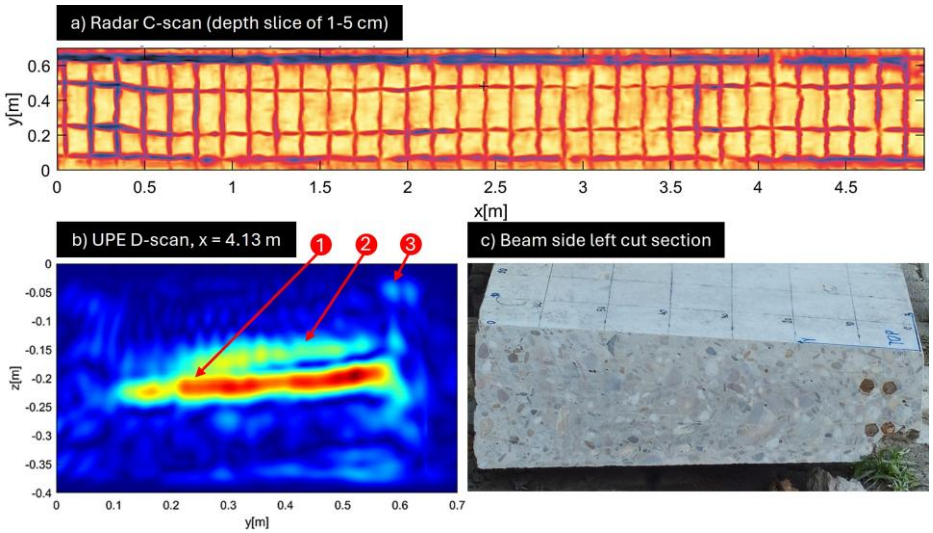


Fig. 3 Radar and UPE test results: a) Radar C-Scan, b) UPE D-scan at x = 4.13 m: 1- backwall, 2- horizontal rebar of second layer, 3- longitudinal rebars, c) cross-section of the beam.

3.2 Mechanical properties:

Figure 4 presents the mechanical properties of the beam obtained from core compression tests as well as rebound hammer and pull-off experiments. The compressive strength is described by both destructive core results and non-destructive rebound numbers (R- and Q-type), which show a relatively high strength with low scatter. Note that the Q-type rebound values are slightly higher and the R-type slightly lower than the core reference values. The near-surface tensile strength yielded moderate variability.

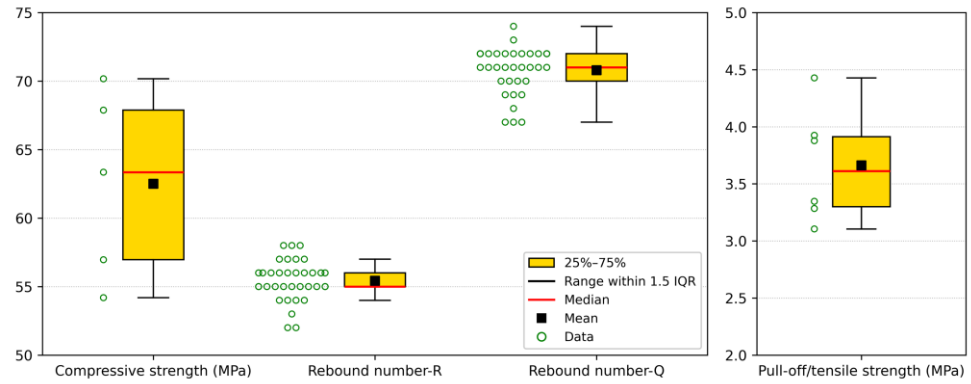


Fig. 4 Boxplots of the mechanical properties with the data points.

3.3 Statistical analysis of the measurement data

Since rebound hammer testing provides a dense set of readings along the element, it enables a meaningful probabilistic description of dispersion in the measured data, including effects related to the measuring instruments, surface conditions, operator influence, and true material heterogeneity. In contrast, core tests are limited in number due to their destructive nature. Therefore, statistical evaluation was applied to the rebound hammer measurements (Types Q) to quantify measurement noise and spatial variability in the test data. 11 samples at 35 positions, which means in total 385 samples have been used for the statistical analysis.

3.3.1 Measurement noise and spatial variability

Figure 5 presents the residual statistics of rebound hammer readings (Type Q) computed as deviations of the 11 samples from the corresponding local spot mean, considering all 35 positions. The empirical probability density functions (PDFs) and cumulative density functions (CDFs) show a narrow distribution and good agreement with the fitted normal distribution models. The relative-error curves indicate small deviations between the fitted and empirical distributions. The mean absolute error (MAE) and root mean squared error (RMSE) values confirm that the within-spot repeatability of the rebound measurements is moderate and statistically stable.

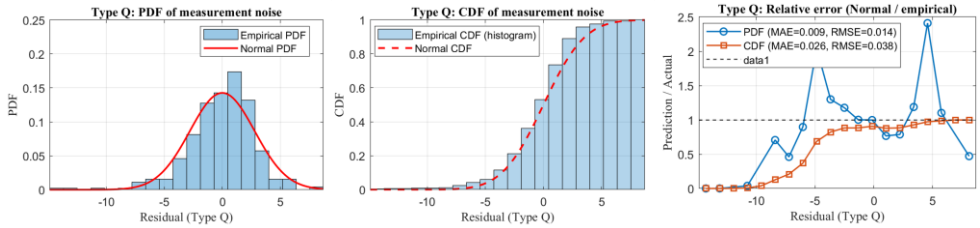


Fig. 5 Distribution of rebound hammer residuals (measurement noise) for Type Q.

Figure 6 shows the distribution of rebound hammer spot means along the beam (Type Q). The spot means exhibit a wider spread than the residuals, indicating differences between locations. The normal fits capture the central trend, while tail deviations reflect non-uniform surface behaviour and the limited number of measurements. This variation may be caused by the inherent concrete variability or testing artefacts. The MAE and RMSE values quantify the magnitude of the spatial dispersion.

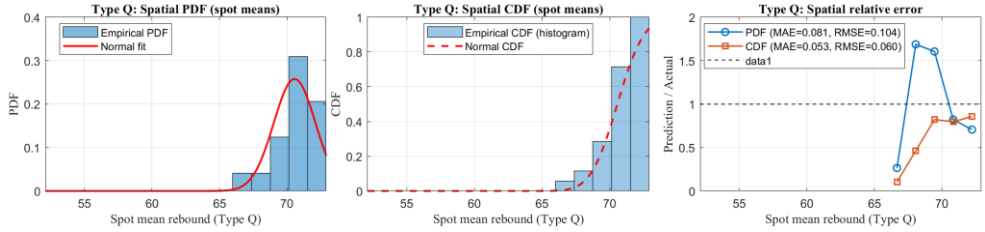


Fig. 6 Distribution of rebound hammer spot means (spatial variability) for Type Q.

To further characterise the spatial variation of the measurements, kriging interpolation was applied to the spot means of the rebound hammer Type Q measurements at 18 locations in the middle area of the beam (see red zones in Figure 1). The kriging fit in Figure 7 provides a continuous spatial representation of the rebound measurements, which motivates further numerical analyses of spatial variability.

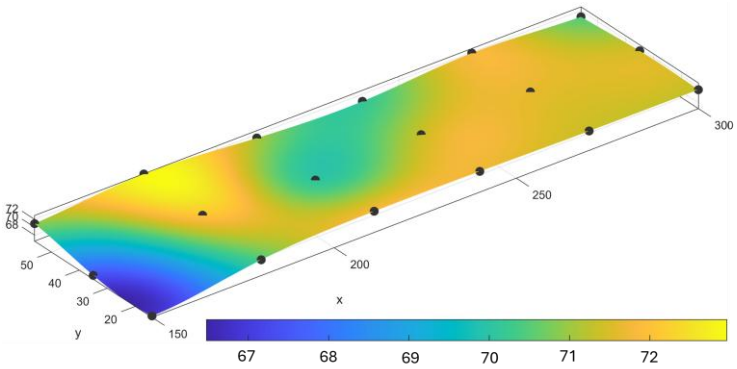


Fig. 7 Spatial data fit using a kriging model for mean spot values of rebound hammer Type Q.

3.4 Effect of the measurement strategy on the load-bearing prediction

In order to investigate the effect of different measurement strategies on the load-bearing capacity prediction, the extracted beam is modelled in a material-nonlinear simulation framework to assess the bending resistance under consideration of the tension stiffening effect. To make reliable predictions regarding the load-bearing capacity and the fracture response, a modelling approach based on discrete representation of cracks using zero-thickness cohesive Interface Elements is adopted. All material nonlinearities due to cracking under tension are modelled by the cohesive-frictional traction-separation relationship of the interface elements, which are inserted between the solid finite elements. In order to account for reinforcement bars, rebars are explicitly modelled as beam elements with an elastic-plastic material law to represent the yielding and linear hardening of the rebars. The bond-slip mechanism is accounted for by a constraint condition coupling the beam elements with the surrounding concrete. For more information regarding the modelling approach and numerous validations see [13], [14].

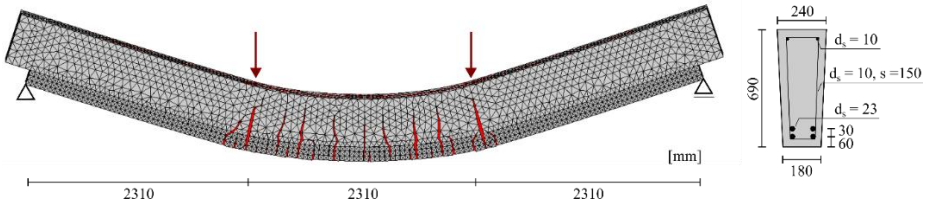


Fig. 8 Numerical model of the extracted beam to predict its load-bearing capacity.

The finite element representation of the beam (element size between 50 and 75 mm) is subjected to a 4-point bending load (see Fig. 8), where the load is applied in a displacement-controlled manner ($\Delta u \approx$ 0.01 mm). As no documentation regarding the reinforcement layout was available, the rebar arrangement was assumed based on the cut-out inspection. The resulting assumed cross-section is shown in Figure 8 (right). Based on the presented measurement types in Section 2, the following measurement strategies (MS) (ranked in order of decreasing measurement effort) with the corresponding concrete properties are analysed:

1. MS 1: As a reference, the tensile strength explicitly measured by pull-off tests (f_t = 3.66 (mean) / 3.11 (min) / 4.43 (max) [MPa]) and the compressive strength obtained by uniaxial compression tests (f_c = 62.51 (mean) / 54.19 (min) / 70.17 (max) [MPa]) are used as model input. The elasticity modulus E_c and the mode I fracture energy $G_{f,I}$ are then derived based on the measured compressive strength using empirical formulas given in [15] and [16], respectively.
2. MS 2: In the second measurement scenario, only the compressive strength determined from uniaxial compression tests is considered as available input. The characteristic tensile strength f_{ctk} is then derived using the measured compressive strength in the empirical formula provided in [15].
3. MS 3: As the third measurement strategy with the least effort involved, only the strength obtained from the non-destructive rebound hammer tests are considered as model input. As in the second measurement strategy, all other concrete properties are derived using the same empirical formulas, with the strength measured by the rebound hammer tests. The compressive strength of type Q (f_c = 70.8 (mean) / 54 (min) / 74 (max) [MPa]) and type R (f_c = 55.4 (mean) / 50 (min) / 58 (max) [MPa]) tests are analysed.

For the rebar behaviour, an elasticity modulus of 200 GPa, a yield strength of 315 MPa and a hardening modulus of 1488 Mpa is employed. The bond-slip behaviour given in [16] is assumed, where the bond strength is derived by the compressive concrete strength.

Figure 9 shows the load-deflection responses (a) and the predicted bending resistances (b) obtained by the nonlinear FE-simulations of the extracted beam. Coloured lines represent responses corresponding to the mean values of the respective measurement strategy, while black lines include predictions using best and worst-case values. It can be observed that all measurement strategies result in similar load-bearing predictions, demonstrating that less accurate concrete property measurements may be sufficient for assessing the resistance of beams subjected to a bending failure. However, the presented simulation results are just based on mean, min and max values of the statistical measurement data. A comprehensive uncertainty quantification and probabilistic safety assessment of reused reinforced concrete elements would require more sampling-based simulations, e.g., to compute failure probabilities. In addition, simulations using mean concrete property values from pull-off and uniaxial

compression tests were conducted, where two further scenarios are investigated (reduction of the diameter of the bottom longitudinal rebar from 23 to 20 mm (indicated in Fig. 9 as "Rebar corrosion") and reduction of the distance of the bottom longitudinal rebar centre to the cross-section bottom from 60 to 40 mm (indicated in Fig. 9 as "Concrete cover"). The results indicate that the concrete cover has a minor effect on the load-bearing capacity, while the rebar diameter significantly impacts the bending resistance prediction (353 vs. 289 kNm). Therefore, an accurate detection of the rebar diameter, the position of the rebars and the rebar strength is crucial for realistic performance assessments of reused structural members.

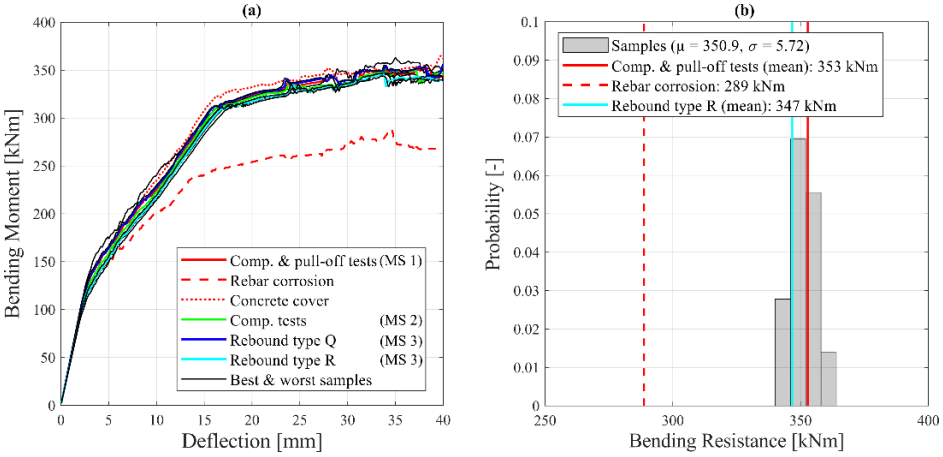


Fig. 9 The load-deflection responses (a) and the predicted bending resistances (b) obtained by the nonlinear FE-simulations of the extracted beam.

4 CONCLUSIONS

This study investigated how spatial dispersion in measured concrete parameters and different practical measurement strategies affect the predicted bending resistance of a reused reinforced concrete element. The combined radar and ultrasonic investigations enabled a consistent reconstruction of the beam geometry and reinforcement layout, while the measured shear-wave velocity and the absence of anomalous reflections indicated high concrete quality without significant internal damage or defects.

Destructive and non-destructive measurements yielded a high and consistent compressive strength and pull-off tests provided a relatively high tensile strength with moderate scatter (Fig. 4). The statistical evaluation of the dense rebound dataset demonstrated that within-spot measurement noise is limited and well described by a normal distribution (Fig. 5), whereas spot-mean values exhibit larger location-dependent variation along the beam (Fig. 6), which motivates to investigate random field approaches in the future.

Nonlinear FE simulations under 4-point bending showed that the different concrete property input strategies (reference: cores + pull-off; reduced: cores only; minimal: rebound only) lead to similar load–deflection and resistance predictions for bending-dominated failure, indicating that reduced concrete testing effort can still be sufficient for reliable capacity assessment in this case. A sensitivity study revealed that reinforcement assumptions govern the capacity prediction more strongly than concrete-property variations: reducing the bottom rebar diameter markedly decreased the bending resistance (353 vs. 289 kNm), while the concrete cover variation had only a minor effect. Overall, the results highlight that robust reuse assessment should prioritise accurate reinforcement characterisation (diameter, position, strength) while using statistically supported concrete parameters from combined DT/NDT as model input.

Ultimately, the experimental results and numerical analyses confirm high material quality and robust bending resistance, supporting the element reusability from the load bearing perspective. The combined DT and NDT measurements deliver a consistent, quantifiable set of parameters that can be used in further evaluations, such as durability analysis and predicting the remaining service life.

Acknowledgements

The authors gratefully acknowledge the German Research Foundation (DFG) for funding the Collaborative Research Centre CRC 1683 “Interaction Methods for the Modular Reuse of Existing Structures” (project no. 523205694) and thank all colleagues from the participating institutes for their support.

References

[1] Mark, Peter, Sanio, David, Balzani, Daniel, Curoşu, Iurie, Hafner, Annette, König, Markus, Kuhlenkötter, Bernd, Thewes, Markus, Baille, Wiebke, Hackl, Klaus, Hagedorn, Philipp, Meschke, Günther, Nestorović, Tamara, Neu, Gerrit, Sauer, Roger A., Tafili, Merita, Vogel, Andreas, Weber, Sebastian, Wichern, Marc, Wichtmann, Torsten, Niederleithinger, Ernst, Freitag, Steffen, Menges, Achim, and Simon, Sven. 2025. “Modulares Wiederverwenden von Bestandstragwerken.” Bautechnik 102(8):424–435. doi:10.1002/bate.70000.

[2] Curoşu, Iurie, Balzani, Daniel, Freitag, Steffen, Neu, Gerrit, Niederleithinger, Ernst, Simon, Sven, and Weber, Sebastian. 2025. “Methoden zur Bewertung abgebauter Stahlbetonelemente für deren Wiederverwendung.” Bautechnik 102(8):483–492. doi:10.1002/bate.70002.

[3] Ottosen, Lisbeth M., Kunther, Wolfgang, Ingeman-Nielsen, Thomas, and Karatosun, Serkan. 2024. “Non-Destructive Testing for Documenting Properties of Structural Concrete for Reuse in New Buildings: A Review.” *Materials* 17(15):3814. doi:10.3390/ma17153814.

[4] Ali-Benyahia, Khoudja, Kenai, Said, Ghrici, Mohamed, Sbartaï, Zoubir-Mehdi, and Elachachi, Sidi-Mohammed. 2023. “Analysis of the Accuracy of In-situ Concrete Characteristic Compressive Strength Assessment in Real Structures Using Destructive and Non-destructive Testing Methods.” Construction and Building Materials 366:130161. doi:10.1016/j.conbuildmat.2022.130161.

[5] Karatosun, Serkan, Thygesen, Katja Irene Møller, Gustafsson, Karoline Fogh, Christiansen, Alexander Mollan Bohn, and Ottosen, Lisbeth M. 2025. “Development and Validation of an NDT-Based Reusability Assessment Guideline for Structural Concrete Elements.” Paper presented at the International Symposium on Non-Destructive Testing in Civil Engineering, Izmir, Türkiye, September 24–26. doi:10.58286/31670.

[6] Deutsche Gesellschaft für Zerstörungsfreie Prüfung e.V. (2024) Merkblatt B10: Merkblatt über das Radarverfahren zur Zerstörungsfreien Prüfung im Bauwesen. DGZfP, Berlin.

[7] Deutsche Gesellschaft für Zerstörungsfreie Prüfung e.V. (2018) Merkblatt B4: Merkblatt über Ultraschallverfahren zur zerstörungsfreien Prüfung im Bauwesen. DGZfP, Berlin.

[8] Mayer, Klaus, Krause, Martin, Wiggenhauser, Herbert, and Milmann, Boris. 2015. “Investigations for the Improvement of the SAFT Imaging Quality of a Large Aperture Ultrasonic System.” Paper presented at the International Symposium on Non-Destructive Testing in Civil Engineering, Berlin, Germany, September 15–17.

[9] DIN EN 12504-2 (2021) Prüfung von Beton in Bauwerken – Teil 2: Zerstörungsfreie Prüfung – Bestimmung der Rückprallzahl. Deutsche Fassung der EN 12504-2:2021. Beuth, Berlin.

[10] DIN EN 1542 (1999) Produkte und Systeme für den Schutz und die Instandsetzung von Betontragwerken – Prüfverfahren – Messung der Haftfestigkeit im Abreißversuch. Deutsche Fassung der EN 1542:1999. Beuth, Berlin.

[11] DIN EN 12504-1 (2019) Prüfung von Beton in Bauwerken – Teil 1: Bohrkerne – Entnahme, Untersuchung und Prüfung auf Druckfestigkeit. Deutsche Fassung der EN 12504-1:2019. Beuth, Berlin.

[12] DIN EN 12390-3 (2019) Prüfung von Festbeton – Teil 3: Druckfestigkeit von Probekörpern. Deutsche Fassung der EN 12390-3:2019. Beuth, Berlin.

[13] Gudžulić, Vladislav. 2024. “Virtual Lab for Mechanical Testing of Steel and Steel-Fiber Reinforced Concrete.” PhD diss., Ruhr University Bochum, Institute for Structural Mechanics.

[14] Neu, Gerrit. 2023. “Computational Approaches to a Robust Segmental Lining Design in Mechanized Tunneling.” PhD diss., Ruhr University Bochum, Institute for Structural Mechanics, Bochum, Germany.

[15] European Committee for Standardization (CEN). 2005. EN 1992 (Eurocode 2): Design of Concrete Structures. Brussels: CEN.

[16] Federation internationale du béton (fib). 2013. Model Code for Concrete Structures 2010. Ernst & Sohn

Safety formats for nonlinear finite element analysis of holistic 3D models

Julia Ober, Dirk Schlicke

Institute of Structural Concrete,
Graz University of Technology,
Lessingstraße 25, 8010 Graz, Austria

Summary
The holistic analysis of 3D structural models is becoming increasingly important, as it provides an integrated view of the structural system and facilitates interdisciplinary collaboration. To ensure reliable results in analysis and design, these models must comply with the safety format of Eurocode 2. In this context, it must be examined whether linear elastic stiffness assumptions lead to unrealistic design forces in holistic 3D models. Highly redundant systems exhibit force redistribution in the ULS due to cracking and yielding, and in the SLS due to cracking, shrinkage, and creep. To investigate this issue, a reinforced concrete building is analysed using linear and nonlinear holistic 3D models based on different verification approaches according to Model Code 2010 and 2020. The results show that linear elastic ULS analysis of holistic 3D models overestimates safety demands, whereas nonlinear analysis enables a more realistic assessment of structural safety by identifying global and local failure mechanisms.

1 INTRODUCTION

The design of reinforced concrete structures is typically based on a linear elastic static analysis for determining the internal forces, followed by a nonlinear cross-section design. While this approach is computationally efficient, it does not accurately reflect the typical load-bearing behaviour of reinforced concrete members. [1] In contrast, determining the internal forces nonlinearly allows for a much more realistic regard of the load-bearing behaviour and possible redistribution of forces in the structure, as it takes into account changes in stiffness due to cracking and plastic deformations. [2–6]

Within the framework of Eurocode 2 [6], the design of reinforced concrete structures in the ultimate limit state generally involves complying with the following condition:

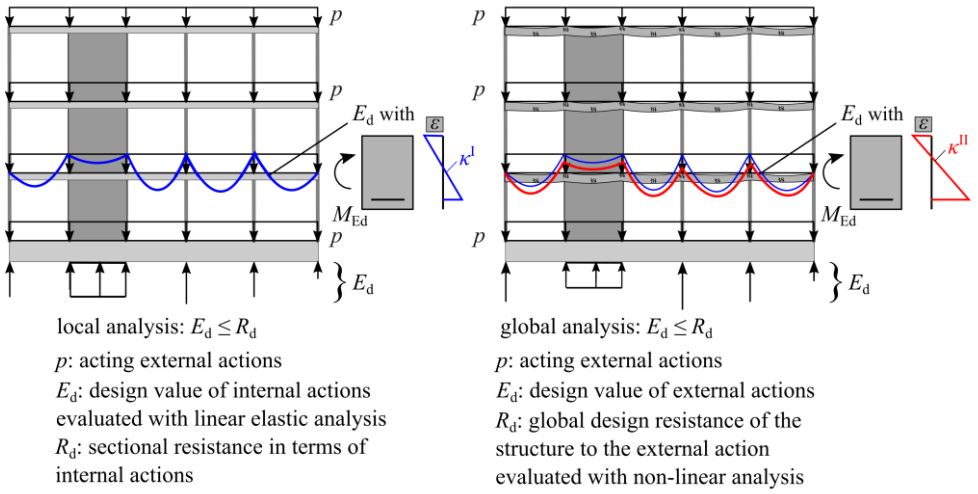
$$E_{\mathrm{d}} \leq R_{\mathrm{d}} \tag{1}$$

Whereas E_{d} denotes the design value of the internal forces resulting from external actions, R_{d} denotes the design value of the cross-sectional resistance. Eurocode 2 strictly separates the internal forces resulting from external actions from the corresponding resistances of the member cross-sections. This procedure for evaluating structural safety can be classified as a local approach, as it focuses on cross-sectional verifications of individual structural members and neglects the global structural response to the hereby accepted cross-sectional deformations as well as the redistribution of internal forces within the system. In contrast, the use of nonlinear analyses follows a global approach, in which the structural performance is assessed by comparing the global action effects for a given load combination with the overall structural resistance in accordance with Eq. (1). The nonlinear structural response and the associated redistribution of internal forces are directly captured within the analysis. The differences between the approaches are schematically illustrated in Fig. 1.

However, if the relevant forces are determined using nonlinear calculation models a conceptual problem arises: The superposition of individual load cases is fundamentally inadmissible under nonlinear material behaviour. To realistically represent a member's load-bearing and deformation behaviour, it is necessary to iteratively adjust the stiffness changes with regard to cracking and nonlinear material behaviour. However, this approach conflicts with the design philosophy of Eurocode 2 [7], which is based on using fixed design values for material parameters. [8–10]

Another key aspect of nonlinear calculations for holistic 3D models is the interactive deformation and stiffness development of slabs, walls, and columns. In slab-type elements, crack formation and plastic deformation lead to pronounced reductions in bending, torsional and axial stiffness, significantly influencing the overall load-bearing and deformation behaviour. In conventional columns without distinct second order effects, however, cracking can usually be excluded and the stiffness remains significantly higher than that of slabs, leading to relative stiffness increases or lower stiffness

degradation. [11; 12] Moreover, another problem with non-linear designs is that the actual design result (i.e. concrete strength class and required reinforcement) must be known as an input variable and, depending on the assumption, can also lead to different overall solutions.



local analysis: $E_d \leq R_d$

p: acting external actions

E_d: design value of internal actions evaluated with linear elastic analysis

R_d: sectional resistance in terms of internal actions

global analysis: $E_d \leq R_d$

p: acting external actions

E_d: design value of external actions

R_d: global design resistance of the structure to the external action evaluated with non-linear analysis

Fig. 1 Comparison between local structural analysis and global structural analysis

In order to overcome the conceptual limitations associated with nonlinear analysis, the fib Model Code 2010 [13] and 2020 [14] defines three safety concepts for the determination of the design resistance R_d:

In the partial safety factor method (PSF), the design is based on design values for material properties corresponding to the low quantile of the respective probability distribution. This ensures a uniform level of safety, although the application of partial safety factors can lead to deviations from the desired level of reliability. The partial safety factor method is the standard procedure for taking material and model uncertainties into account, as set out in the Eurocode. It is based on the separate application of partial safety factors for materials and actions, thereby enabling deterministic design at a defined level of reliability.

In the global safety factor method (GSF), the reference value for load-bearing capacity is defined as the mean resistance value. The underlying material parameters correspond to representative mean values of the material properties, reflecting the expected in-situ properties of the building material. This value is then reduced by a global safety factor to capture all uncertainties arising from material, geometry, and modelling. This can be based on a nonlinear finite element analysis using representative mean values of the material properties. This method ensures a uniform level of safety independent of the type of failure. The global factor γ_R explicitly considers the model uncertainty determined by benchmark analyses. Without validation, the conservative value of $\gamma_R = 1.3$ is applied. [15]

The sampling-based method (also known as the probabilistic method according to Model Code 2010 [13]) calculates the design load-bearing capacity using a probability density function determined by a probabilistic analysis. This process involves defining the model based on a nonlinear finite element analysis to enable a deterministic investigation of the load-bearing capacity as a function of the material properties. The material parameters are described by random distributions characterised by their mean value and standard deviation and are then randomised. A probabilistic load-bearing capacity analysis is then performed using Monte Carlo simulations or Latin Hypercube Sampling (LHS). This provides the probability distribution of the load-bearing capacity and its parameters. The design load-bearing capacity is then determined based on the probability of failure.

The outlined design concepts differ in terms of their methodological complexity and the significance of the results obtained. While the partial safety factor method is closest to the established method of linear elastic static analysis and nonlinear design and allows for comparatively simple application, the global safety factor method requires more detailed consideration of material and model

uncertainties. Finally, the sampling-based method is the most computationally complex, but also the most theoretically sound, due to its comprehensive probabilistic approach.
To evaluate nonlinear analysis methods in the present study, a reference model is used to compare linear elastic and nonlinear approaches. Linear elastic analyses are performed with constant and modified stiffness properties, whereas nonlinear analyses are based on the PSF and GSF. A fully probabilistic assessment has not yet been considered at this stage of the research.

2 REFERENCE MODEL

The reference model is defined as a highly simplified skeletal structure with a single core, selected to allow a transparent assessment of load redistribution and stiffness-related effects. The example structure is composed of eight above-ground storeys and is founded on a shallow foundation, shown in Fig. 2. The column grid is 6.0 × 5.0 m. The slab thickness is 0.28 m, and the thickness of the foundation slab is 0.9 m. For the foundation slab, floor slabs, and core walls, a concrete strength class of C30/37 is assumed. The columns are modelled with a concrete strength class of C35/45 and a constant cross-section of 0.4 × 0.4 m over all storeys. The subsoil is idealised as dense sand with a stiffness modulus of 30000 kN/m², modelled as a linear elastic half-space. To keep the numerical model as simple as possible, only self-weight, permanent loads, and a uniformly distributed live load of 5 kN/m² are applied.

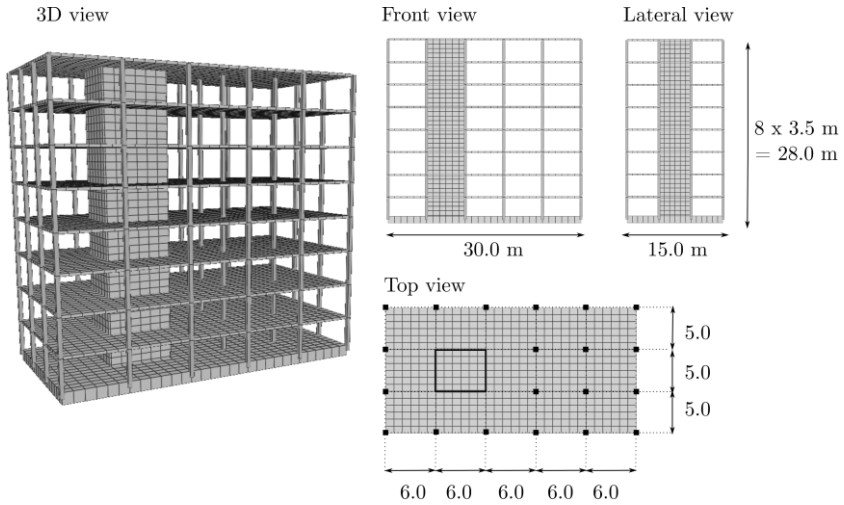


Fig. 2 Overview of the structural model used for the analysis

The soil–structure interaction was regarded according to the considerations in [16] and [17]. In detail, the settlement trough was firstly derived from a linear elastic half-space solution and afterwards directly implemented into the structural model with an individual load case of prescribed displacements. The safety factor for this settlement load case was applied according to [18]. In the next analysis step, all additional actions corresponding to the governing load combination are applied to the pre-deformed and subsequently fixed structural system.

The columns are modelled in a simplified manner using linear elastic concrete sections without explicit consideration of reinforcement. This simplification is adopted because the influence of the reinforcement ratio on load redistribution would be compensated for in the SLS assessment. In addition, creep and shrinkage effects are not yet considered within the nonlinear analyses.

For the nonlinear analyses, a prior definition of the provided reinforcement is necessary. For ease of use, the reinforcement layout was initially defined based on a linear elastic analysis and design under serviceability limit state (SLS) conditions. For the foundation slab, the reinforcement arrangement was specified as follows: The upper reinforcement layer consists of 16 mm bars at 150 mm spacing (13.40 cm²/m), while the lower layer consists of 16 mm bars at 200 mm spacing (10.05 cm²/m). For the floor slabs, the reinforcement layout was assumed to be identical for all eight storeys above ground. In this case the assumption was based on the SLS analyses as well as the punching shear verifications in the

ultimate limit state (ULS). The upper reinforcement layer consists of a base mesh of 10 mm bars at 150 mm spacing, providing a reinforcement area of 5.24 cm²/m. Additional reinforcement is provided in the edge zones and core region using 12 mm bars at 100 mm spacing (11.31 cm²/m), while 10 mm bars at 100 mm spacing (7.85 cm²/m) are used in the column zones. In the lower reinforcement layer of the floor slabs, a uniform reinforcement mesh consisting of 10 mm diameter bars a spacing of 150 mm was provided, corresponding to a reinforcement area of 5.24 cm²/m.

3 METHOD

Based on the reference model, four analysis cases are defined for subsequent analysis. Case 1 includes a linear elastic analysis (LE) of the 3D model with full member stiffnesses for the horizontal elements and hinged columns. Case 2 (LE ms) uses a linear elastic 3D model with modified stiffness properties. In the slab-type elements the bending stiffness is reduced to 80 % (depending on the moment–curvature behavior), the torsional stiffness to 30 %, and the axial stiffness to 10 %, in accordance with [16]. In addition, the column connection stiffness is reduced to 40 %. In case 3 (PSF), the design is carried out using the partial safety factor method. Safety factors are applied to both actions and resistances, starting from characteristic material properties, in accordance with the semi-probabilistic safety concept of Eurocode 2. The structural response is evaluated using a nonlinear analysis. In case 4 (GSF), the global safety factor method is applied. Material properties are defined on a mean-value basis, and structural safety is ensured by applying a global resistance factor $\gamma_R = 1.3$ within a nonlinear analysis framework. Fig. 3 provides an overview of the applied modelling cases in the structural analysis.

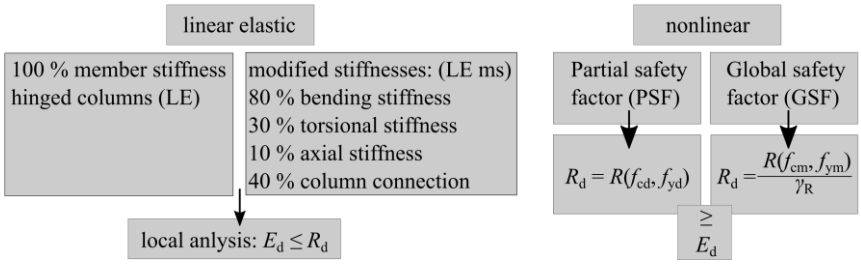


Fig. 3 Overview of the different modelling cases considered in the structural analysis

4 RESULTS

The evaluation of the results is carried out for linear elastic analyses with and without stiffness modification within the semi-probabilistic safety concept, as well as for nonlinear analyses considering the PSF and GSF design approaches.

To evaluate force redistribution within the structural system, the normal forces transferred to the foundation slab under ULS loading are determined by separately summing the contributions from the core and from the columns. Fig. 4 presents the summed normal forces from the core (red curve) and from the columns (blue curve), together with their respective percentage shares of the total vertical load. For the considered model, the linear elastic analysis shows a relatively balanced distribution of vertical forces between the core and the columns. In contrast, the linear elastic analysis with modified member stiffnesses and the nonlinear analysis using the PSF or GSF approach results in a higher proportion of the vertical load being redistributed to the columns.

Another important design aspect is the punching shear verification of the slabs under ULS conditions. The floor slabs show in this regard only minor variations between the different modelling cases. On the contrary, the punching forces in the foundation slab are strongly dependent on the modelling approach. The main reason for this behavior is that the soil structure interaction is regarded by prescribed displacements. In the linear elastic approach, the resulting punching shear forces are a direct result of the shear stressing due to the imposed settlement trough and the required slab thickness can be determined from the least required slab thickness for punching shear verification. In the linear elastic approach with modified stiffness as well as in the nonlinear approaches, however, the resulting stiffness reductions in the foundation slab due to cracking and yielding cause an immediate reduction of bending stressing as well as shear stressing. As a consequence, the thickness of the foundation slab

can be optimized according to the least required slab thickness for punching shear verification. The optimization, however, requires an iterative solution which has been performed in the preparation of the paper. The results are presented in Fig. 5. These results indicate a pronounced influence of the modelling approach on the expected punching shear forces in the foundation slab as well as on the required thickness of the foundation slab.

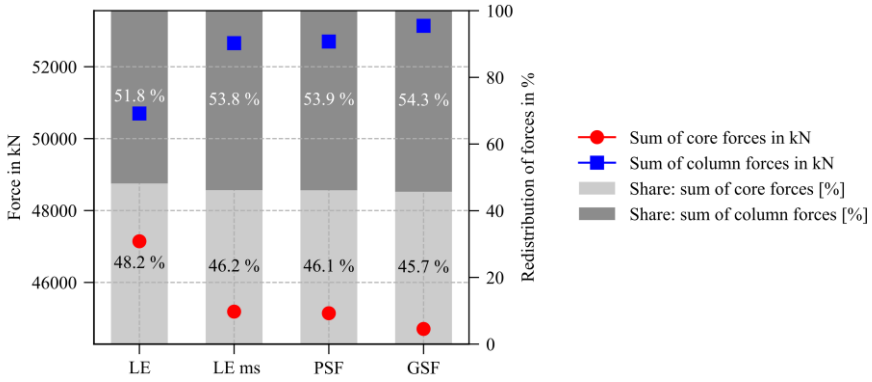


Fig. 4 Distribution of founding forces on the foundation slab between columns and core for different modelling cases

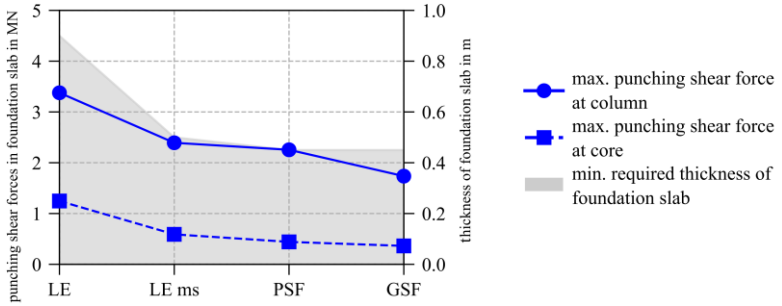


Fig. 5 Maximum punching shear forces in foundation slab

To further investigate the structural behavior of the foundation slab and the floor slab, as well as the influence of the respective calculation approaches, the bending moments along a representative section were additionally evaluated and are presented in Fig. 6. For better comparability, the thickness of the foundation slab was hereby kept with a constant thickness of 0.9 m in all modelling approaches. The linear elastic analysis overestimates the bending moments in the foundation slab compared to the nonlinear structural analyses (PSF and GSF). In the floor slab, the two nonlinear structural analyses result in very similar bending moment distributions. The linear elastic approaches result in slightly higher bending moments.

For the SLS assessment, the maximum concrete and steel stresses are evaluated for the quasi-permanent and characteristic load combinations. The corresponding SLS stress limits are adopted as upper bounds and illustrated in Fig. 7. For the investigated cases, the application of the GSF approach allows for a moderate reduction of the resulting stress levels. However, it is observed that the maximum steel stresses for all four cases remain close to the respective upper limit values, as the reinforcement used in the analyses was selected to the minimum required level.

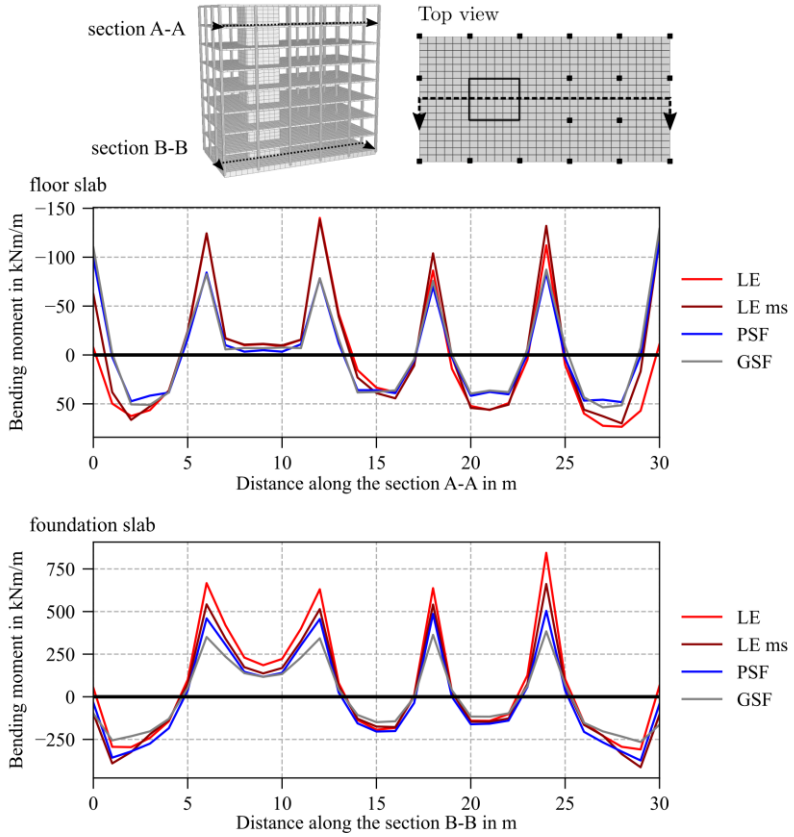


Fig. 6 Bending moment in sections A-A and B-B

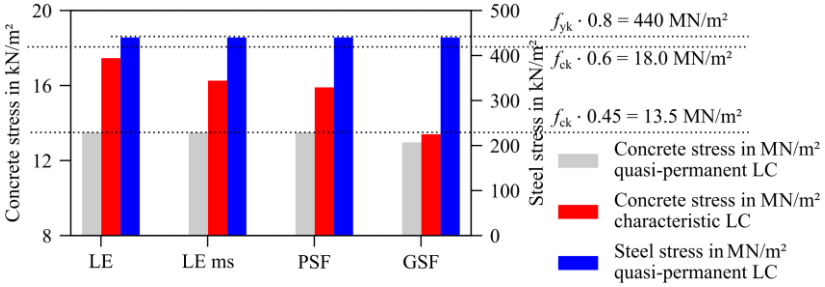


Fig. 7 Maximum concrete and steel stresses for different load case combinations (SLS)

5 DISCUSSION

The results demonstrate that accounting for the nonlinear behaviour of reinforced concrete in the static analysis and design with holistic 3D models leads to noticeable differences compared to linear elastic analyses. From the obtained internal forces, it can be concluded that the nonlinear approaches indicate a potential for reduced required reinforcement and, consequently, a possible reduction in foundation slab thicknesses. This highlights the influence of the selected analysis and design approach on the resulting structural demand and design outcome. It should be noted that construction stages were not considered in the present analyses but will be considered in future studies with particular focus on frame action developing during the construction process.

To further investigate the effect of stiffness reduction in the holistic 3D model, Fig. 8 presents the ratio between bending moments obtained from the GSF approach and those derived from the linear

elastic (LE) analysis. For the foundation slab, load redistribution is primarily connected to the form of the global settlement trough and lesser to local interactions between span and load application points. In addition, local redistributions are identified near the core and in selected column regions. For the floor slab, the results show that the ratio of bending moments obtained from nonlinear to linear elastic analysis decreases markedly in the span regions and lesser in the column regions. This is in contrast to the expectation that moments over the supports are typically redistributed into the field area. However, in the present case with pronounced reinforcement amounts at the upper surface over the columns due to punching shear verifications and a rather moderate reinforcement layout at the bottom surface the opposite can be observed.

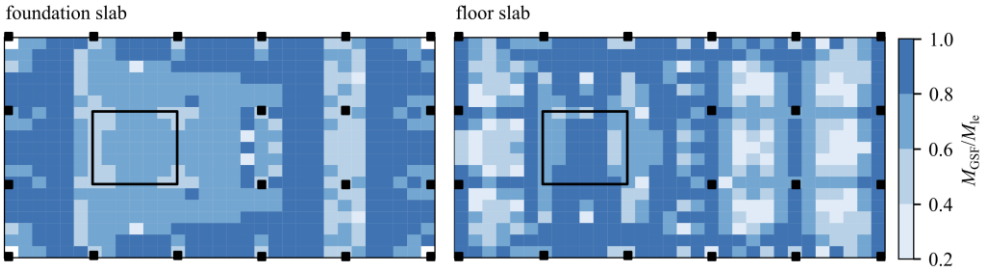


Fig. 8 Bending moment ratio between GSF method and the linear elastic method (LE) at ULS

6 CONCLUSIONS

The results clearly demonstrate that the consideration of the member-specific nonlinear behaviour of reinforced concrete is highly relevant when analysing holistic 3D structural models. The comparison between linear elastic analyses and the GSF-based nonlinear approach shows that, on the one hand, reductions in design loads are achievable and, on the other hand, that the structural response of the members is represented in a more realistic manner.

As a pragmatic alternative for engineering practice, linear elastic analyses with modified stiffness properties were investigated. This approach provides results that are closer to those obtained from the GSF method and therefore represents a viable compromise between modelling effort and accuracy when fully nonlinear analyses are not feasible. However, it must also be emphasized that an unreflected general reduction of member stiffness, e.g. slabs are always reduced by $EI^{II} = 0.8 \cdot EI^{I}$, entails the risk of underestimating the structural response when the reduction rate is not representative for the actual behaviour. Therefore, a simple check on basis of moment-curvature-behaviour should always be performed.

It is also important to note that soil–structure interaction was considered by means of prescribed displacements in accordance with the approach proposed in [16] and further discussed in [17]. and by applying a partial safety factor of 1.0 according to [18]. This procedure enables a more realistic representation of the structural behaviour, as it allows a clear distinction between load-induced internal forces and those resulting from soil settlements.

From a global perspective, the investigation was limited to a highly simplified and regular skeletal structure modelled without regard to construction stages. Consequently, further studies are required to assess the applicability of the observed effects to more complex structural configurations. In particular, the consideration of construction stages appears to be essential, as the development of frame action during construction may significantly influence stress distributions and governing design locations. Furthermore, the present study focuses primarily on vertical loading scenarios. To achieve a comprehensive assessment of structural behaviour and failure mechanisms, future investigations should also address horizontal loading conditions and the associated global failure modes of the structure. Furthermore, a more detailed investigation using a probabilistic approach is planned.

Acknowledgements

This work was carried out as part of the research project “Agile Structural Design”, funded by the Austrian Research Promotion Agency (FFG). The authors acknowledge the Austrian Association for Construction Technology (ÖBV) and the consortium partners for their technical support.

References

[1] Ober, Julia, Lienbacher, Lukas Clemens, and Schlicke, Dirk. 2026. "Tragwerksplanung mit 3D-Gesamtmodellen in der Praxis." *Beton- und Stahlbetonbau* 121, no. 4: 292–302. doi:10.1002/best.70066.

[2] Engen, Morten, Hendriks, Max A. N., Øverli, Jan Arve, and Åldstedt, Erik. 2015. "Solution Strategy for Non-linear Finite Element Analyses of Large Reinforced Concrete Structures." *Structural Concrete* 16, no. 3: 389–397. doi:10.1002/suco.201400088.

[3] Červenka, Vladimír, and Červenka, Jan. 2006. "Probabilistic Estimate of Global Safety Factor – Comparison of Safety Formats for Design Based on Non-linear Analysis." Prague: Červenka Consulting. Version October 31, 2006.

[4] Červenka, Vladimír, Červenka, Jan, and Pukl, Radomír. 2014. "Design Resistance of Concrete Structures by Numerical Simulation." Paper presented at the 8th International Conference AMCM 2014, Wrocław, Poland, June 16–18.

[5] Schlune, Hendrik, Plos, Mario, and Gylltoft, Kent. 2011. "Safety Formats for Nonlinear Analysis Tested on Concrete Beams Subjected to Shear Forces and Bending Moments." *Engineering Structures* 33, no. 8: 2350–2356. doi:10.1016/j.engstruct.2011.04.008.

[6] Blomfors, Mattias, Engen, Morten, and Plos, Mario. 2016. "Evaluation of Safety Formats for Non-linear Finite Element Analyses of Statically Indeterminate Concrete Structures Subjected to Different Load Paths." *Structural Concrete* 17, no. 1: 44–51. doi:10.1002/suco.201500059.

[7] Austrian Standards International. 2015. ÖNORM EN 1992-1-1: Eurocode 2 - Bemessung und Konstruktion von Stahlbeton- und Spannbetontragwerken – Teil 1-1: Allgemeine Bemessungsregeln und Regeln für den Hochbau. Vienna: Austrian Standards International.

[8] König, G., Tue, Nguyen Viet, and Ahner, C. 1997. "Consistent Safety Format." In Non-linear Analysis: Discussion Papers from the Working Party in Commission 1, *CEB Bulletin d'Information* No. 239, 1–16. Lausanne: Comité Euro-International du Béton.

[9] Castaldo, Paolo, Gino, Diego, and Mancini, Giuseppe. 2019. "Safety Formats for Non-linear Finite Element Analysis of Reinforced Concrete Structures: Discussion, Comparison and Proposals." *Engineering Structures* 193: 136–153. doi:10.1016/j.engstruct.2019.05.029.

[10] Tecusan, Remus, and Zilch, Konrad. 2017. "Sicherheitsaspekte bei nicht-linearen FEM Berechnungen / Safety Aspects in Non-linear FEM Calculations." *Bauingenieur* 92, no. 12: 518–527. doi:10.37544/0005-6650-2017-12-34.

[11] Fastabend, Michael. 2002. "Zur ingenieurmäßigen Bestimmung des Steifigkeitsabfalls von Stahlbeton im Zustand II." *Beton- und Stahlbetonbau* 97, no. 8: 415–420. doi:10.1002/best.200201870.

[12] Glaßner, Johannes, Vojvodic, Goran, and Tue, Nguyen Viet. 2024. "Stumpfstöße von Stahlbetonstützen mit hochfestem Betonstahl und großen Bewehrungsgraden." *Beton- und Stahlbetonbau* 119, no. 9: 687–695. doi:10.1002/best.202400032.

[13] Fédération Internationale du Béton. 2013. fib Model Code for Concrete Structures 2010. Lausanne: International Federation for Structural Concrete (fib).

[14] Fédération Internationale du Béton. 2023. fib Model Code for Concrete Structures (2020). Lausanne: International Federation for Structural Concrete (fib).

[15] Engen, Morten, Hendriks, Max A. N., Monti, Giorgio, and Allaix, Diego L. 2021. "Treatment of Modelling Uncertainty of NLFEA in fib Model Code 2020." *Structural Concrete* 22, no. 6: 3202–3212. doi:10.1002/suco.202100420.

[16] Schlicke, Dirk, Tschuchnigg, Franz, Fischnaller, Hannes, and Pfaff, Klaus. 2023. "Statische Analyse und Bemessung von Gebäuden mittels 3D-Gesamtmodellen." In *2024 Beton-Kalender*: Hochbau; Digitales Planen und Baurobotik, edited by Bergmeister, Konrad, Fingerloos, Frank, and Wörner, Johann-Dietrich, 505–571. Berlin: Ernst & Sohn. doi:10.1002/9783433611494.ch8.

[17] Sever, Yolcu, and Schlicke, Dirk. 2024. "Design Forces for Punching Shear Verification in Thick Raft Foundations with Special Regard to Partial Safety Factors." Paper presented at the 15th fib International PhD Symposium in Civil Engineering, Budapest, Hungary, August 28–30.

[18] Austrian Standards International. 2013. ÖNORM EN 1990: Eurocode – Grundlagen der Tragwerksplanung. Vienna: Austrian Standards International.

Numerical modelling and experimental validation of fibre orientation in Ultra-High Performance concrete flow

Lucas Poitevin, Lucas Bauer, Bruno Massicotte

Groupe for Research in Structural Engineering (GRS),
Polytechnique Montréal,
2500 chemin de Polytechnique, Montréal QC H3T 0A3, Canada

Summary
UHPFRC is an orthotropic material whose mechanical properties depend on the orientation and density of the fibres. The main objective is thus to develop a numerical model that predicts the fibre orientation as a function of the flow. For this purpose, a Coupled Eulerian-Lagrangian (CEL) model is developed to determine the velocity field of the UHPFRC flow. From the obtained velocity field, a post-processor using Jeffery's equations determines the fibre orientation.

The numerical results were subsequently validated experimentally on specimens representative of a lap splice joint and compared with results from the literature. It was found that the CEL model accurately reproduces the flow behaviour. Moreover, the results obtained from the post-processor were consistent with the observed fibre orientations. An average discrepancy of approximately 7% is observed between experimental and numerical orientation coefficients.

1 INTRODUCTION

1.1 Context

Since the second half of the 20th century, numerous transportation infrastructures have been constructed in Canada and more broadly around the world. Today, a significant portion of this network exhibits structural deficiencies and requires repair or replacement interventions [1].

In this context, Accelerated Bridge Construction (ABC), based on the prefabrication of elements in a plant followed by on-site assembly, makes it possible to significantly reduce construction time and the impact on traffic. Several studies have demonstrated the relevance of using Ultra-High-Performance Fibre-Reinforced Concrete (UHPFRC). Owing to its mechanical properties, particularly in tension, it allows the assembly of prefabricated elements while meeting regulatory requirements, notably seismic ones [2]-[3].

However, this material exhibits orthotropic behaviour, and its mechanical properties strongly depend on the orientation and dispersion of the steel fibres contained within the cementitious matrix [4].

1.2 Influence of fibre orientation on mechanical properties

Several experimental campaigns have highlighted the influence of fibre orientation on the mechanical properties of UHPFRC, particularly in tension [4]-[5]. A favourable orientation of the fibres with respect to the loading direction makes it possible to significantly increase the tensile strength and ductility and consequently, the post-cracking load-bearing capacity.

An unfavourable orientation, however, leads to a strong reduction in mechanical performance when compared to the favourable one. This reduction is observed in the pre-peak phase, with a decrease in the maximum stress and the absence of a strain-hardening phase for an unfavourable orientation. A change in behaviour is also observed in the post-peak phase as illustrated in Fig. 1.

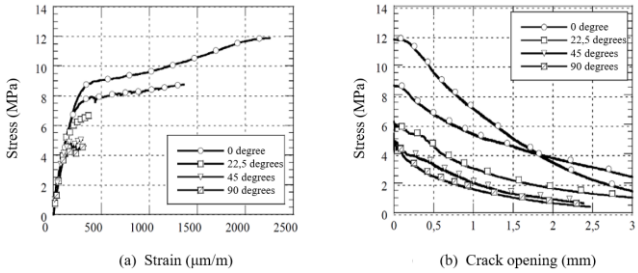


Fig. 1 Tensile behaviour of 4% UHPFRC under direct tension for different fibre orientations [4]

1.3 Parameters influencing fibre orientation

Since fibre orientation plays a determining role in mechanical properties, it is therefore essential to identify and understand the parameters influencing this orientation.

Beyond the way UHPFRC is placed, the boundary effect has been identified as one of the first factors impacting fibre orientation [6]. Due to the contact between the fibres and the formwork, the fibres tend to preferentially align in the same plane as the formwork surfaces.

However, the influence of the boundary effect remains essentially localized, not extending beyond a distance in the order of the fibre length. At the scale of the entire casting, the predominant parameter impacting fibre within the matrix flow is the shear rate. This originates from a velocity gradient at the fibre extremities, generating hydrodynamic moments that can modify their orientation during casting. [6]

It is important to note that the impact of the boundary effect and the shear rate are closely linked to the rheological properties of UHPFRC. Higher viscosity generally leads to higher shear rates, promoting a preferential fibre orientation [7]. Modelling fibre orientation therefore proves to be complex, since the shear rate depends both on the geometry of the cast element and on the rheological behaviour of the material, which also influence the magnitude of the boundary effect.

1.4 Research objectives

The variety of parameters influencing fibre flow prohibits to properly control fibre orientation during casting operations and, consequently, the associated mechanical properties of UHPFRC. This greatly affects the confidence on the actual tensile properties which leads in limiting the design strength by adopting conservative material properties.

In this context, this work consists in developing a numerical flow model as well as a post-processor allowing the prediction of fibre orientation in UHPFRC as a function of flow and placement conditions. The proposed model is then validated through a dedicated experimental campaign and complemented by previous experimental results from the literature.

2 NUMERICAL MODELLING OF FLOW

2.1 Selection of the modelling approach

A reliable modelling of UHPFRC flow must consider the main parameters influencing fibre orientation. Based on the flow velocity information, it is possible to derive the shear rate and, more generally, the different hydrodynamic stresses likely to act on the fibres.

Several flow modelling approaches for UHPFRC or FRC have already been proposed in the literature. SPH (Smoothed-Particle hydrodynamics), SPH-DEM (SPH-Discrete Element Method) or Lattice-Boltzmann models provide a particle-based description of the flow, offering a local view of the potential fibre positions. These methods are particularly suited for a microscopic description of the casting process. However, they are very computationally expensive, which limits their use to restricted geometries or short simulation times [8].

Another modelling strategy consists in adopting a macroscopic approach to the flow. The fluid is generally assumed to be homogeneous. This approach does not allow access to information on fluid-particle interactions. Nevertheless, it remains a good compromise between accuracy and computational cost. CFD (Computational Fluid Dynamics), PFEM (Particle Finite Element Method), or CEL (Coupled

Eulerian–Lagrangian) models are commonly used in this framework. CFD models have been shown to provide initial satisfactory results regarding fibre orientation [9].

Among the models mentioned, CEL offers good portability. Indeed, it makes it possible to combine the advantages of Eulerian and Lagrangian modelling approaches. The fluid evolves within an Eulerian volume allowing a uniform mesh, in which velocity gradients can be easily computed. It is also possible to easily introduce obstacles into the model. These are assumed to be Lagrangian elements, and fluid-solid interactions are defined by the user through contact laws. Finally, this type of model is readily accessible, as it is already implemented in commercial software such as Abaqus. For these reasons, it is adopted in this article.

2.2 Modelling assumptions

As the present article focuses in particular on the connection joint between prefabricated elements, a geometry representative of an lap splice joint is modelled. The specimens consist of UHPFRC elements incorporating three coplanar reinforcing bars. This choice of three bars makes it possible to represent the effect of a succession of reinforcements on the flow, while limiting the size of the computational domain. Since the model is macroscopic, the ribs of the reinforcing bars are not represented. The dimensions of the modelled joints are detailed later in the section on the experimental campaign.

Despite its non-Newtonian behaviour, UHPFRC is modelled here as a Newtonian fluid. This assumption aims to facilitate the development and validation of the fibre orientation post-processor, while keeping computational times limited. Indeed, in Abaqus, the modelling of non-Newtonian fluids relies on the use of an apparent viscosity inversely proportional to the shear rate. Thus, for low shear rates, the apparent viscosity diverges, leading to a significant increase in computational time. Tables 1 and 2 summarize all the parameters used for the modelling. The rheological parameters were selected based on literature data from [10] and on the typical properties of the UHPFRC mixtures used in the laboratory.

Table 1 Rheological characteristics of the simulated UHPFRC based on literature data [10].

Parameters	Unit	Value
Dynamic viscosity η	Pa.s	75
Density ρ	kg/m^3	2400

Table 2 Fluid-reinforced contact laws in Abaqus

Loading direction	Interaction laws	Description
Normal	Hard contact	No penetration allowed
Tangential	Rough	Infinite friction coefficient

Reinforcing bars are modelled as rigid Lagrangian elements, as the action of the fluid on the bars is negligible compared to their stiffness. Boundary conditions are defined based on velocity criteria. For all formwork surfaces, the velocity along the x, y, and z axes is set to zero. Finally, the inlet velocity of the UHPFRC is assumed to be equal to 70 mm/s, which represent a flow rate of 1 dm^3/s, a value representative of the experimentally studied placement conditions. The CEL analysis is carried out within an explicit solution scheme. The effects of gravity are also considered in the modelling, with a gravitational acceleration of 9,81 m/s^2. Fig. 2 illustrates the boundary conditions and the mesh.

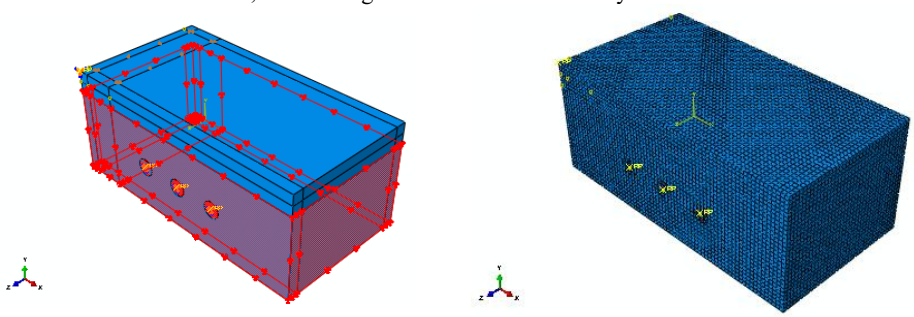


Fig. 2 Boundary conditions (left) and mesh (right) adopted for CEL modelling

3 DEVELOPMENT OF A POST-PROCESSOR FOR FIBER ORIENTATION

3.1 Modelling of the fibre behaviour

In the literature, particularly in the field of composites, analytical equations have been developed to model the behaviour of ellipsoids immersed in a fluid, namely Jeffery's equations [11]. Beyond the field of composites, they have already provided encouraging results in the context of high-performance concretes [12]. For this reason, they are adopted in the development of the proposed post-processor, in order to remain consistent with existing work.

By defining $\vec{p}$, the unit vector oriented along the major axis of an ellipsoid is assumed to be rigid and non-deformable, its time evolution is given by :

$$\frac{d\vec{p}}{dt} = \boldsymbol{W}.\vec{p} + \lambda.[\boldsymbol{D}.\vec{p} - (\vec{p}^T.\boldsymbol{D}.\vec{p}).\vec{p}] \quad (1)$$

With $\boldsymbol{W} = \frac{1}{2}.(\boldsymbol{L} - \boldsymbol{L}^T)$, $D = \frac{1}{2}.(\boldsymbol{L} + \boldsymbol{L}^T)$, $\boldsymbol{L} = \nabla\vec{u}$, $\lambda = \frac{r^2-1}{r^2+1}$ and $r = length_{fibre}/diameter_{fibre}$

In this study, the fibres are modelled as slender ellipsoids, which makes it possible to assume the parameter $\lambda \approx 1$. Jeffery's model is also based on the assumption of a Stokes flow and on the absence of interactions between fibres.

In the case of UHPFRC, these assumptions can be considered acceptable given the relatively low flow velocities and the high viscosity of the material in its fresh state. Moreover, the absence of aggregates and the low fibre content make it possible to neglect fibre to fibre interactions.

It should nevertheless be noted that an extension of Jeffery's model exists, known as the Tucker-Folgar model, which makes it possible to account for fibre to fibre interactions through the introduction of a diffusion term, and which has also shown relevance for FRC [12].

3.2 Implementation in a Python post-processor

3.2.1 Selection of a Monte-Carlo approach

Adopting a macroscopic perspective, this study aims to evaluate second-order orientation tensors associated with each element of the Eulerian mesh modelled. In the literature, orientation tensors are often determined directly using tensor-based models such as the Tucker-Folgar formulation. However, these approaches lead to a closure problem, requiring additional assumption regarding higher-order tensors [13].

In the present study, fibre orientations are determined at the individual fibre scale using Jeffery's equations. Consequently, no closure model is required. The orientation tensors are reconstructed a posteriori from the explicit simulation of a bundle of fibres using a stochastic approach. The number of fibres is selected as a compromise between statistical accuracy and computational cost. In the present study, a set of 60 fibres is considered.

3.2.2 Resolution method

To compute orientation tensors for each mesh element, an initial implicit calculation is performed to determine the trajectory of the fibre bundle, from the casting point to the final mesh element. Once the position of the entry point is identified, the displacement of the fibre bundle is computed using an explicit Euler scheme expressed as follows.

$$X^i_{t+\Delta} = X^i_t + \Delta t.v^i(X^i, t) \quad (2)$$

In parallel, the orientation of a fibre i at time $t + \Delta t$, defined by a unit vector $\vec{p}^i_{t+\Delta t}$, is given by the following equation:

$$\overrightarrow{p_{t+\Delta t}}^i = \vec{p}^i_t + \Delta t.\left[\nabla u_t.\vec{p}^i_t - \left(\vec{p}^{i\,T}_t.(\nabla u_t + \nabla u_t^T).\vec{p}^i_t\right).\vec{p}^i_t\right] \quad (3)$$

Using an explicit analysis based on an Euler resolution scheme, the choice of the time step is critical to obtain consistent results. To ensure the stability of the method, the Courant number, also referred to as CFL (Courant-Friedrichs-Lewy), is used. Based on numerical tests, a conservative threshold of $CFL \leq 0{,}2$ is retained.

4 VALIDATION OF THE FLOW MODEL AND THE POST-PROCESSOR

4.1 Experimental campaign

4.1.1 Specimen geometry

Once the numerical modelling was completed, an experimental phase was carried out. As presented in the modelling section, the specimens studied are representative elements of connection joints. For this campaign, the reinforcing bars are made of PVC rather than steel, to allow post-casting sectioning for the analysis of fibre orientation.



Fig. 3 Specimen geometry (left) and formwork of a manufactured specimen (right)

Table 3 Dimensions of the specimens expressed in bar diameters $d_b = 32mm$

Specimens	Anchor length (l_d)	Spacing between bar (c_{si})	Spacing between bar and surface (c_{so})
$c_{si} = 3; c_{so} = 2$	8	3	2
$c_{si} = 2; c_{so} = 2$	8	2	2
$c_{si} = 1{,}5; c_{so} = 2$	8	1,5	2

For this experimental campaign, the UHPFRC used is Ductal© UHPFRC containing 2% fibres by volume, a value representative of the structural applications studied. The entry point of the UHPFRC is located at one end of the formwork, along its length.

4.1.2 Flow analysis method

To carry out an initial qualitative experimental validation of the numerical flow modelling, an image analysis of the casting was performed. This relies on image processing in Matlab using the PIVLab post-processor (Particle Image Velocimetry), applied here in a qualitative manner.

The image processing consists of enhancing the contrast of the images to allow apparent particle tracking at the free surface. Although this method is not intended to provide accurate local velocity measurements nor a full-field PIV characterization, it provides estimation of the order of magnitude of the flow velocity and allowing the characterization of the flow behaviour. The camera was placed above the specimen, facing the free surface.

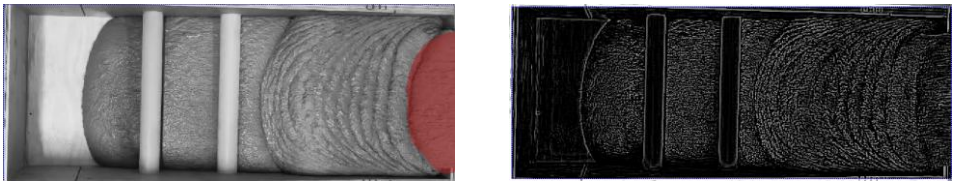


Fig. 4 Video capture of the casting (left) and post-processing in PIVLab (right)

4.1.3 Fibre orientation analysis method

To determine fibre orientation within a cementitious matrix, two main families of methods are commonly uses: non-destructive methods, such as X-ray tomography, and destructive methods with the scan of sections to obtain an orientation factor. Due to limited experimental facilities, a destructive approach based on sectioning and image analysis was adopted.

To obtain a global view of fibre orientation within the specimens, several sections spaced at 10mm were cut, polished, scanned, and then binarized. To ensure reliable results, each ellipse is assigned a score corresponding to the number of points identified to trace it. The higher the score, the greater the reliability. According to Delsol's work, a score of at least 6 is required to obtain satisfactory reliability [4].

As illustrated in Fig. 5, this approach allows determining fibre orientation up to a sign ambiguity on θ. For this reason, fibre orientation is quantified using the factor η_θ (Eq. (4)) commonly used in the literature [4]-[5], and based on the cosine of θ, which resolves the uncertainty related to the sign.

$$\eta_{\theta,exp} = \frac{1}{N}\sum_i \cos^2(\theta_i) \quad (4)$$

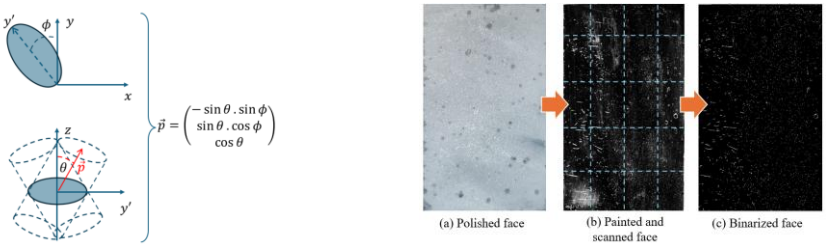


Fig. 5 Processing steps required to determine fibre orientation

5 RESULTS AND DISCUSSION

5.1 Flow

The first experimental and numerical results show a marked influence of the formwork geometry on UHPFRC flow patterns. Two distinct behaviours can be identified depending on the spacing between the reinforcing bars, as show Fig. 6.

For values of $c_{si} \leq 2.d_b$, the bottom of the formwork fills rapidly, leading to an upward filling of the inter-bar regions.

Conversely, for $c_{si} > 2.d_b$, bottom filling is delayed and inter-bar regions are primarily filled from the top. These regimes are consistently observed in both experiments and simulations, indicating that the numerical model correctly captures the dominant geometry-driven flow mechanisms.

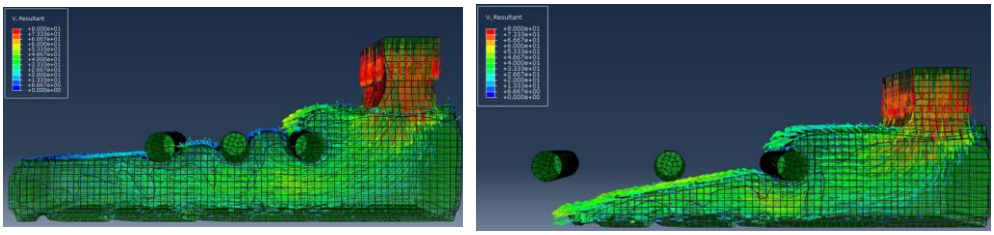


Fig. 6 Speed vectors from CEL: $c_{si} = 1{,}5.d_b$ (left), $c_{si} = 3.d_b$ (right)

Quantitative velocity comparisons are mainly feasible during free-flow phases. In these configurations, tracking the flow front at four successive instants over one second indicates discrepancies on the order of 15% between experimental and numerical results. When the flow becomes constrained by the reinforcing bars, direct velocity measurements are no longer reliable, as velocity vectors are essentially vertical. Nevertheless, the numerical model accurately reproduces the observed filling patterns, suggesting a satisfactory representation of the dominant flow mechanisms

5.2 Fibre orientation

As indicated previously, fibre orientation is quantified using the orientation factor η_θ defined by Eq. (4), obtained from image analysis of the scanned sections. For the results from the post-processor, the orientation factor is calculated by projecting the orientation tensor along the same analysis axis (along x) using the following relation :

$$\eta_{\theta,num} = n^T.A.n = \langle \cos^2(\theta_{num}) \rangle \quad (5)$$

The comparison is carried out on several sections at different positions within the same joint. Sections corresponding to the inter-bar zones are here prioritized to understand fibre orientation in this critical area. The results obtained are presented in the Table 4.

Table 4 Comparison of $\eta_{\theta,num}$ and $\eta_{\theta,exp}$ for different sections in different joints

Specimens	Position x (mm)	$\eta_{\theta,exp}$	$\eta_{\theta,num}$	Relative error (%)
	160	0,630	0,630	0

$c_{si} = 1{,}5$; $c_{so} = 2$	189	0,535	0,628	17,4
	204	0,635	0,625	1,57
	224	0,635	0,649	2,20
	239	0,624	0,672	7,69
	$\overline{\eta_\theta} \pm s_{\eta_\theta}$	**0,612±0,043**	**0,640±0,020**	**5,77±7,11**
$c_{si} = 2$; $c_{so} = 2$	133	0,557	0,501	10,1
	204	0,665	0,660	0,752
	271	0,700	0,598	14,6
	284	0,689	0,601	12,8
	357	0,632	0,649	2,69
	$\overline{\eta_\theta} \pm s_{\eta_\theta}$	**0,649±0,057**	**0,602±0,063**	**8,18±2,87**

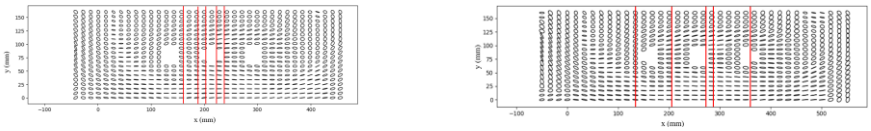


Fig. 7 Post-processor results with positions of the experimental scan highlighted in red. Joint $c_{si} = 1{,}5$; $c_{so} = 2$ (left), Joint $c_{si} = 2$; $c_{so} = 2$ (right)

On average, the relative difference between the numerical and experimental orientation factors are 5,8% and 8,2% for the two specimen, respectively. In detail, the inter-bar regions show lower relative error, on the order of 2%. Higher discrepancies are observed near the reinforcing bars, where relative differences reach approximately 15%. This shows that the post-processor is able to consistently reproduce fibre orientation in the sections located between the reinforcing bars. Additional tests on joints of different sizes are planned to confirm or refute these initial results.

For more open geometries such as slabs, the post-processor exhibits a reduced ability to highlight strong preferential orientations. Comparisons with experimental data from Svec et al. [14] show consistent global trends but increased diffusion in numerical orientation tensors, as shown in Fig. 8. These discrepancies may be attributed to differences in material behaviour, as fibre-reinforced concrete was studied instead of UHPFRC, as well as to modelling assumptions, particularly the Newtonian flow hypothesis and imposed inlet flow rate. In addition, experimentation is made with FRC and not BFUP.

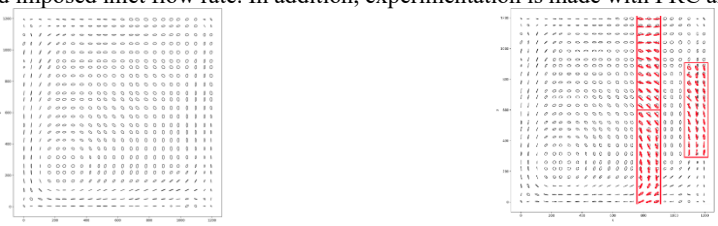


Fig. 8 Comparison of post-processor results with experimental data from Svec et al. [14]. Numerical results from post-processor (left), In red, experimental results from Svec et al. (right)

6 CONCLUSIONS

In this study, UHPFRC flow was modelled using the CEL method. Based on the obtained velocity fields, a post-processor based on Jeffery's equations was implemented to predict fibre orientation and reconstruct orientation tensors at the macroscopic scale.

An experimental campaign carried out on specimens representative of lap splice connections cast with 2% UHPFRC allowed the validation of the proposed approach. The results show that the numerical model correctly reproduces the flow regimes observed experimentally for different geometries, as well as the order of magnitude of velocities, except during free-surface flow phases where the Newtonian fluid assumption leads to an overestimation.

The post-processor shows good predictive capability, with an average 7% difference between numerical and experimental orientation factors. The difference is about 2,5% in the inter-bar regions but reaches approximately 17% near the reinforcing bars due to complex flow. Qualitative comparison

with results from literature also confirm the model's ability to reproduce general fibre orientation, though with a more dispersed predicted alignment.

These results constitute an initial validation of the coupling between flow modelling and fibre orientation prediction in UHPFRC. Future work will focus on improving the flow model by introducing non-Newtonian behaviour and on coupling the orientation tensors with mechanical models to predict the orthotropic behaviour of the material.

References

[1] Ministère des transports et de la mobilité durable du Québec. 2022. "Bilan de l'état des structures." Accessed January 23. http://www.bv.transports.gouv.qc.ca/per/0994120/15_2022.pdf

[2] Russell, Henry, and Graybeal, Benjamin. 2013. *Ultra-High Performance Concrete: A State-of-the-Art Report for the Bridge Community*. Washington, DC: U.S. Department of Transportation, Federal Highway Administration.

[3] Darveau, Philippe. 2018. "Développement de piles de ponts préfabriquées résistant aux séismes." M. Sc. A. diss., Polytechnique Montréal.

[4] Delsol, Sébastien. 2012. "Evaluation du coefficient d'orientation dans les betons renforces de fibres metalliques." M. Sc. A. diss., Polytechnique Montréal.

[5] Maya Duque, Luis Felipe, and Graybeal, Benjamin. 2017. "Fiber Orientation Distribution and Tensile Mechanical Response in UHPFRC." *Materials and Structures* 50:55. Accessed January 6, 2026. doi:10.1617/s11527-016-0914-5

[6] Martinie, Laetitia, Lataste, Jean-François, and Roussel, Nicolas. 2015. "Fiber Orientation during Casting of UHPFRC: Electrical Resistivity Measurements, Image Analysis and Numerical Simulations." *Materials and Structures* 48:947-957. Accessed January 14, 2026. doi:10.1617/s11527-013-0205-3.

[7] Wang, Rui, Gao, Xiaojian, Huang, Huanghuang, and Han, Guangshuai. 2017. "Influence of Rheological Properties of Cement Mortar on Steel Fiber Distribution in UHPC." *Construction and Building Materials* 144:65-73. doi:10.1016/ j.conbuildmat.2017.03.173.

[8] Osalu, Sahar Mohammadzadeh, Ben Ftima, Mahdi, and Massicotte, Bruno. 2025. "A Coupled Eulerian-Lagrangian Method for Predicting Fibre Orientation in Fibre Reinforced Concrete Elements." Paper presented at 5th International RILEM Conference on Numerical Modeling Strategies for Sustainable Concrete Structures, Rotterdam, The Netherlands, July 7-9.

[9] Ferrara, Liberato, Cremonesi, Massimiliano, Faifer, Marco, Toscani, Sergio, Sorelli, Luca, Baril, Marc-Antoine, Réthoré, Julien, Baby, Florent, Toutlemonde, François, and Bernardi, Sébastien. 2017. "Structural Elements Made with Highly Flowable UHPFRC: Correlating Computational Fluid Dynamics (CFD) Predictions and Non-Destructive Survey of Fiber Dispersion with Failure Modes." *Engineering Structures* 133:151-171. Accessed January 28, 2026. doi:10.1016/j.engstruct.2016.12.026.

[10] Khayat, Kamal Henri, Meng, Weina, Vallurupalli, Kavya, and Teng, Le. 2019. "Rheological Properties of Ultra-High-Performance Concrete - An Overview." *Cement and Concrete Research* 124:105828. Accessed February 3, 2026. doi:10.1016/j.cemconres.2019.105828.

[11] Jeffery, George Barker. 1922. "The Motion of Ellipsoidal Particles Immersed in a Viscous Fluid." *Proceedings of the Royal Society of London. Series A* 102:161-179. Accessed February 9, 2026. doi:10.1098/rspa.1922.0078.

[12] Kolařík, Filip, Patzák, Bořek, and Thrane, Lars Nyholm. 2015. "Modeling of Fiber Orientation in Viscous Fluid Flow with Application to Self-Compacting Concrete." *Computers & Structures* 154:91-100. Accessed February 17, 2026. doi:10.1016/j.compstruc.2015.03.007.

[13] Tucker, Charles L. 2022. "Planar Fiber Orientation: Jeffery, Non-Orthotropic Closures, and Reconstructing Distribution Functions." *Journal of Non-Newtonian Fluid Mechanics* 310:104939. Accessed February 24, 2026. doi:10.1016/j.jnnfm.2022.104939.

[14] Švec, Oldřich, Žirgulis, Giedrius, Bolander, John E., and Stang, Henrik. 2014. "Influence of Formwork Surface on the Orientation of Steel Fibres within Self-Compacting Concrete and on the Mechanical Properties of Cast Structural Elements." *Cement and Concrete Composites* 50:60-72. Accessed January 12, 2026. doi:10.1016/j.cemconcomp.2013.12.002.

Author Index

Abbas, A. **356**
Adam, V. **397**
Ahmad, M. **543**
Ahmed, R. **971**
Akula, P.K. **301**
Al Jabi, M. **801**
Al-Askary, A.S.J. **130**
Al-Dali, A. **241**
Al-Shboul, O. **971**
Ali, H.A. **735**
Ali, M.A. **606**
Alnsour, R. **332**
Amin, A. **10**
Amin, N. **519**
Amiri, O. **865**
Amiri, S.S. **267**
Asamoto, S. **90, 871**
Ashokkumar, A.N. **825**
Autrup, F. **259**
Baena, M. **760**
Baloević, G. **857**
Baltrocchi, R.M.A. **809**
Baral, S. **468**
Barris, C. **760**
Bastidas-Arteaga, E. **825**
Bauer, L. **987**
Beckmann, B. **217, 397, 743**
Becks, H. **527**
Belletti, B. **648**
Beltracchi, I. **887**
Benko, V. **705**
Bergmeister, K. **639, 751, 833, 895, 912**
Bijeljic, J. **971**
Billiet, J. **631**
Blandini, L. **768**
Blay, K. **267**
Borges, E.A. **920**
Bosnjak, J. **606**
Botte, W. **631, 929**
Boudiaf, M. **865**
Brentana, G. **502**
Burczyk, M. **420**
Burdziński, M. **348**
Čairović, Đ. **947**
Carleschi, E. **209**
Casali, L. **48**
Caspeele, R. **929**
Cengu, S. **727**
Claßen, M. **106, 194, 527**
Claverie, J. **865**
Clerici, L. **850**
Coffetti, D. **48**
Colombo, M. **34, 284**
Conforti, A. **850**
Coppola, L. **48**
Curbach, M. **40**
Curoșu, I. **971**
Cussigh, F. **865**
De Domenico, D. **26, 559**
de Sousa, C. **397**
Degée, H. **519**
Dehn, F. **842**

Deiters, M. **606**
del Vecchio, C. **735**
Della Vecchia, G. **82**
Dengg, F. **599**
Denu, M. **842**
Derkowski, W. **186**
Dernbach, A. **656**
Di Criscio, F. **793**
di Ludovico, M. **735**
di Prisco, M. **34, 155, 284**
Di Vita, C.P. **777**
Dohnalová, L. **122**
Dollendorf, M. **689**
Eliáš, J. **568**
Ergin, T. **34**
Evangelatos, A. **751, 895**
Fache, K. **623**
Fadai, A. **444, 673, 697**
Faghfouri, S. **955**
Faleschini, F. **146**
Feix, J. **233, 251**
Fekete, K. **293**
Ferrara, L. **82**
Filipović, M. **857**
Fina, M. **971**
Freitag, S. **971**
Fritz, F. **485**
Fröschl, L. **233**
Gaddi, C. **284**
Galatà, C. **26**
Galler, R. **895**
Gamage, T. **356**
Gerger, A. **444**
Giglio, M. **777**
Girgle, F. **947**
Giulivo, G. **477**
Glock, C. **381, 584, 656**
Goodier, C.I. **267**
Gorse, C. **267**
Görtz, S. **164**
Grashorn, J. **551**
Grba, D. **511**
Griniov, E. **364**
Großkopff, P. **743**
Grzesiak, S. **397**
Gundala, V. **66**
Gündogdu, B. **217**
Habirun, A.N. **871**
Hägle, M. **664**
Haist, M. **606**
Hajdin, R. **785**
Harnisch, J. **623**
Harsányi, P. **225**
Havlásek, P. **122**
Heber, P. **743**
Hendricks, J. **106, 194**
Hendriks, M. **920**
Hlavsa, Z. **681**
Hoang, L.C. **56**
Höffgen, J.P. **842**
Hofmann, F. **664**
Hofmann, J. **412, 420, 428, 436**
Holder, J. **428**
Holý, M. **138, 309**
Huber, P. **485, 493, 879**
Huber, T. **485, 493, 879**

Hung, N.D. **452**
Hwang, H. **201**
Issa, M. **241**
Jaelani, Y. **551**
Jeong, H. **317**
Jespersen, E. **259**
Ježek, J. **947**
Jeziorski, M. **186**
Jørgensen, H.B. **259**
Kaliske, M. **720**
Kang, J. **317**
Kaufmann, W. **372**
Kendlbacher, M. **833**
Keßler, S. **551, 592, 623**
Kian, N. **74**
Kim, J.-H. **939**
Kim, J.M. **317**
Kim, K.S. **317**
Kněž, P. **138, 309**
Koehncke, M. **592**
Kolísko, J. **309**
Konzilia, J. **251**
Kopecskó, K. **130**
Kosta, A. **751**
Kováčová, A. **705**
Kovács, T. **2**
Kucharczyková, B. **681**
Kuhn, S. **720**
Kumar, M.V.N.S. **66**
Kummer, Y. **372**
La Mazza, D. **559**
Labò, S. **405**
Lafon, R. **865**
Lakhani, H. **428**
Lande, I. **172, 468**
Larsen, J. **56**
Lee, J. **201**
Lehký, D. **511, 963**
Lengert, K. **164**
Leutbecher, T. **98**
Liebold, F. **397**
Linden, C. **106, 194**
Long, J. **178**
Longo, M. **559**
Longo, O. **405**
Longo, P. **559**
Losanno, D. **817**
Luan, Y. **871**
Lühr, S. **389**
Lura, P. **887**
Luyten, K. **929**
Macha, M. **895**
Macorini, L. **178**
Mader, T. **751**
Madsen, G. **468**
Mahadik, V. **412, 420, 436**
Mancini, G. **559**
Marini, A. **405**
Mariolopoulou, E. **155**
Mark, P. **576, 711**
Marsili, F. **551**
Martinelli, P. **809**
Marx, S. **40, 217, 743, 801**
Marzec, I. **340**
Massicotte, B. **987**
Maugeri, N. **559**

Mellios, N. **543**
Mendoza, C.R. **535**
Menna, C. **477**
Merabti, C. **648**
Mešković, A. **606**
Messina, D. **26**
Metelli, G. **887**
Mezera, A. **138**
Mihaylov, B. **519**
Mikulić, Z. **912**
Miller, O. **768**
Milutinovic, G. **785**
Montero, J.S. **648**
Moon, H. **201, 939**
Muciaccia, G. **82, 332**
Mudadu, A. **477**
Müller, R. **381**
Murcia-Delso, J. **535**
Nemessányi, C. **114**
Neu, G.E. **971**
Neuner, M. **751**
Niederleithinger, E. **971**
Niedostatkiewicz, M. **348**
Novák, D. **963**
Noxpanco, G.G. **340**
Ober, J. **979**
Oller, E. **535**
Ortiz, G. **535**
Özdemir, A. **412**
Pahn, M. **389, 397**
Palii, O. **648**
Pampanin, S. **793**
Park, H. **201**
Park, H.-G. **939**
Patel, R.A. **842**
Pedone, L. **793**
Pellegrino, C. **146**
Pfleger, M. **493, 879**
Pichler, T. **639**
Piemonti, A. **850**
Pieplow, S. **576**
Platz, C. **606**
Plizzari, G.A. **209, 405, 502, 850, 887**
Pluzsik, A. **114**
Poitevin, L. **987**
Pornsiri, N. **90**
Potůčková, S. **309**
Poulsen, P.N. **56**
Preinstorfer, P. **251**
Prota, A. **735**
Proverbio, E. **26, 777**
Radl, E. **493, 879**
Rafique, M.A. **146**
Ragab, A. **397**
Raisinger, J. **568**
Rampini, M.C. **34, 155, 324**
Randl, N. **225**
Ranedda, L. **777**
Rapelli, S. **48**
Ravasini, S. **648**
Recupero, A. **26, 559**
Reggia, A. **209, 887**
Rellier, V. **865**
Rezaie Oshtolagh, M. **559**
Ricker, M. **720**
Ringeloth, D. **971**

Romeo, F. **324**
Rousakis, T. **543**
Roziere, E. **865**
Ruppert, F. **381**
Saccomanno, C. **324**
Saengsoy, W. **90**
Salvi, S. **48**
Sandoval, N. **760**
Sanio, D. **576, 711**
Schachner, K. **673**
Schack, T. **606**
Schänzlin, J. **720**
Schaul, P. **614**
Scheerer, S. **727**
Schellen, M. **584**
Schiano, L. **971**
Schlicke, D. **364, 904, 979**
Schmidt, J. **40**
Schmied, J. **389**
Schoen, S. **971**
Schulz, J.M. **56**
Schumann, A. **743**
Schürmann, A. **689**
Schütze, E. **743**
Sengupta, A.K. **19, 301**
Shamsaddinlou, A. **559**
Sidhu, A.S. **146**
Sikorski, O. **743**
Sirico, A. **648**
Sirtoli, D. **887**
Šmilauer, V. **122**
Solyom, S. **614**
Somlai, B. **614**
Sorg, C. **381**
Šplíchal, B. **511**
Spyridis, P. **460, 543, 825**
Stark, A. **664**
Stemmermann, P. **606**
Štěpánek, P. **947**
Stephan, C. **389**
Stöhr, B. **664**
Strauss, A. **511, 817, 955**
Szczech, D. **963**
Szép, J. **293**
Szinvai, S. **2**
Takahashi, K. **90, 871**
Tang, P. **10**
Tangtermsirikul, S. **90**
Tezeswi, T.P. **66**
Thewes, M. **689**
Thoma, K. **372**
Thomassen, M. **172**
Tiberti, G. **502**
Toosi, A.S. **82**
Trabucchi, I. **502**
Tschuchnigg, F. **904**
Tung, N.D. **74, 452**
Ullrich, A. **606**
Upcin, B.D. **436**
V G, J.G. **19**
Vakaliuk, I. **727**
Valente, M. **697**
van Ratingen, L. **519**
Vanquaille, A. **519**
Vašátko, D. **947**
Vazzoler, A. **405**

Večeře, J. **963**
Vereecken, E. **519**
Verstrynge, E. **519**
Viet Tue, N. **225**
Vítek, J.L. **275, 681**
Vízner, T. **275**
Vogel, A. **689**
Voit, K. **599, 639**
Vollum, R. **178**
Vysochinskiy, D. **468**
Wachter, J. **251**
Walkner, R. **233**
Wallner, C. **904**
Wan-Wendner, R. **631**
Waters, K. **267**
Wellmann, T. **527**
Yang, Y. **920**
Yolcu Sever, R. **364**
Yoon, Y. **317**
Yousef, A. **460**
Yüksel, S. **98**
Zani, G. **324**
Zarrella, G. **817**
Zhang, J. **2**
Zielonka, H. **711**
Zierul, L. **397**
Zlámal, M. **947**

From Research to Structural Reality

Book of Abstracts for the 16th *fib* International PhD Symposium

held in Vienna, Austria
September 9-11, 2026

Editors: A. Strauss and K. Bergmeister

The *fib*, Fédération internationale du béton, is an international non-profit association bringing together 45 national member groups and approximately 1,000 corporate and individual members. The fib promotes the development and dissemination of scientific and practical knowledge aimed at advancing the technical, economic, aesthetic, and environmental performance of concrete construction.
The 16th *fib* International PhD Symposium provides an international platform for doctoral researchers working in the field of concrete structures and related areas of structural engineering. The symposium brings together young researchers, established academics, and practitioners to exchange research findings, discuss emerging scientific developments, and foster international collaboration.
The symposium covers a broad range of topics related to concrete and prestressed concrete structures, structural analysis and design, materials and durability, structural assessment and monitoring, reliability and sustainability, and innovative approaches to the future of concrete construction.

The Book of Abstracts presents the diverse research contributions of the participating PhD researchers and reflects the breadth and dynamism of current doctoral research in concrete and structural engineering.

International Federation for Structural Concrete
Fédération Internationale du Béton
https://www.fib-international.org/

ISSN 2617-4820
ISBN 978-2-940643-32-5